UNIVERSITY OF THE WITWATERSRAND, JOHANNESBURG

69th Annual Conference of the South African Institute of Physics

SOUTH AFRICAN INSTITUTE OF PHYSICS

7-11 July 2025



Conference Proceedings



PROCEEDINGS EDITOR-IN-CHIEF:
W.A. Horowitz, University of Cape Town

PUBLISHER:
The South African Institute of Physics (SAIP)

COPYRIGHT NOTICE:
© 2025 by the South African Institute of Physics
All rights reserved.

The conference was hosted by the University of the Witwatersrand, on 7—11 July 2025. The Proceedings of SAIP 2025, the 69th Annual Conference of the South African Institute of Physics, will be available electronically only on the SAIP website: `www.saip.org.za`.

Permission to make digital or hard copies of part or all of this work for personal or classroom use is granted without fee provided that copies are not made or distributed for profit or commercial advantage and that copies bear this notice and the full citation on the first page. Abstracting with credit is permitted.

To copy otherwise, to republish, to post on servers, or to distribute to lists, requires specific permissions and/or a fee. Request permission from the SAIP Office:

phone: +27 (0)12 756 4900 / 4903
email: `info@saip.org.za`

ISBN: 978-1-0492-1907-3

South African Institute of Physics
CSIR Main Campus, Building 4W
Meiring Naude Rd, Pretoria.

version compiled on 2025-12-17 12:44:15+02:00

TABLE OF CONTENTS

Copyright **ii**

Table of Contents **iii**

Editorial **xi**

The Local Organisers **xiii**
- Message from the Organisers xiii
- Local Organising Committee xiv

Divisions, Editorial Team, and Reviewers **xv**
- Divisions and Division Chairs xv
- Editorial Team xvi
- List of Reviewers xviii

Student Prizes **xxix**
- Physics of Condensed Matter and Materials xxix
- Nuclear, Particle, and Radiation Physics xxx
- Photonics xxxi
- Astrophysics and Space Science xxxi
- Physics for Development, Education, and Outreach xxxii
- Applied Physics xxxii
- Theoretical and Computational Physics xxxii

Group Photo of Delegates **xxxiii**

A Physics of Condensed Matter and Materials **1**

A.1 An anomaly in a formula to calculate the refractive index in $Al_xGa_{1-x}As$ 2

A.2 Structural and electrical transformations in Ag-implanted polyethylene terephthalate (PET) induced by swift heavy ion irradiation 6

A.3 Up-conversion and thermometric performance of CaF_2:Tb^{3+},Yb material 12

A.4 Physiochemical, optical and magnetic properties of nickel-magnesium ferrite nanoparticles for various applications 18
A.5 Design and Characterization of Polymer-Coated Mg-Zn Ferrite Nanoparticles: A Glycol-Thermal Approach for Biomedical Application 24
A.6 Synthesis, structural, magnetic, and gas sensing properties of rare earth-substituted cobalt and zinc ferrites: A comparative study 30
A.7 Effect of Ce and Gd on the magnetic and mechanical properties of $Nd_2Fe_{14}B$ permanent magnets 36
A.8 Investigation of Poly(2,5)-benzimidazole (ABPBI)-Carbon Nanotube Composites for Low Earth Orbit Applications: An Integrated Computational and Experimental Study 42
A.9 First principles study of the structural, mechanical and electronic properties of Mooihoekite ($Cu_9Fe_9S_{16}$) 48
A.10 Optimisation-Deposition and Conversion of Lead Halide Thin Films to 2D Metal Halide Perovskite Thin Films via Low-Pressure CVD 54
A.11 Investigating the effect of metal ions of different oxidation states (M^{x+}, x = 1, 2, 3 & 4) on the PL emission of $Zn_4B_6O_{13}$:Eu^{3+}. 60
A.12 Study on the impact of Pr^{3+}, Ce^{3+}, and Pb^{2+} ions on luminescence properties of BaB_8O_{13}:Gd^{3+} for potential applications in phototherapy. 66
A.13 Luminescence Study on the Impact of Alkaline Earth Metal Ions on Na_3PO_4:Ce^{3+} Phosphors for Potential Colour Display Applications. 72
A.14 Understanding the influence of lithium polysulfides on boron oxide for an efficient lithium sulfur battery: A DFT study 78
A.15 $ZnMn_2O_4$-Based Anode Materials for Advanced Supercapacitor Batteries: A Study on the Impact of Co, Ni, and Cu Partial Substitution on Electrochemical Performance 84
A.16 Structural and Optical properties of rare-earth doped Magnesium ferrites 90
A.17 Thermodynamic Properties of (Gd,Pr)$OsGa_4$ Intermetallic Compounds 96
A.18 Rare-Earth Perovskites in the Quantum Age: Bridging Materials Science and Technologies 102
A.19 Investigating the Photoluminescent Properties of Fe^{3+} doped $ZnAl_2O_4$: A Multifunctional Material for Emerging Applications. 108
A.20 Structural and optical properties of rare earth (Sm^{3+})-doped hematite nanostructures 114
A.21 Characterization of defects in neutron-irradiated SnO_2 using positron annihilation technique 120
A.22 Structural and Morphological properties of a Novel Double Perovskite Sm_2MgRuO_6 126
A.23 Ab initio studies of Pt-Cr alloys for jewellery applications: energetic stabilities and structural properties 132
A.24 The effect of Ir on the mechanical, thermodynamic, electronic and magnetic properties of FePt alloy: A DFT study 138
A.25 The effects of annealing temperature on physical properties of $Ce_2Zr_2O_7$ materials 144
A.26 Predicting the magnetocaloric effect on perovskite oxides using Machine Learning 150
A.27 Synthesis and characterization of TiO_2: Evaluation for possible application as light trapping layer in thin film solar cells. 156
A.28 Effect of Temperature on Structural and Optical Properties of Sm_2O_3 162

A.29 Density functional theory study on the effect of pressure on structural, mechanical and electronic properties of A15 Mn_3Ru alloy . . . 168
A.30 A First-Principles Study of the Structural, Mechanical, Dynamical and Electronic properties of HfSnPt: Half-Heusler Structure . . . 176
A.31 Mechanical and electronic properties of $LiTi_2(PO_4)_3$ solid-state electrolyte material. . . . 182
A.32 Cooperative Energy Transfer and Upconversion Luminescence of $Sr_5(PO_4)_3OH:Eu^{3+}$, Yb^{3+} phosphor powders . . . 190
A.33 The influence of Ultraviolet-Ozone irradiation time on structural and optical properties of SnO_2 thin films deposited using the slot-die method . . . 198
A.34 Development of cellulose nanocrystal sheet embedded with carbon nanotubes for sensor application . . . 206
A.35 DFT-based evaluation of Li_2MnO_3 as a promising cathode coating material for lithium-ion batteries . . . 214
A.36 Assessing the Freysoldt, Neugebauer & van de Walle (FNV) and Kumagai-Oba (KO) finite-size corrections for Ce-vacancy complexes in diamond 220

B Nuclear, Particle, and Radiation Physics 227
B.1 Probabilistic Risk Assessment for Calculating Health Effects Associated with a Potential Nuclear Accident in the Vicinity of a Nuclear Facility . . . 228
B.2 Alpha and beta radiation effects on Re_2MnCoO_6 (Re = La, Sm, Nd) . . . 236
B.3 Fuzzy-based Groundwater Quality Index Model: A Case of Rural Areas in North-West Province, South Africa . . . 244
B.4 Statistical discrimination of uranium ore concentrate using trace element signature: Developing nuclear forensic fingerprint . . . 252
B.5 Enhancing Gamma-Ray Spectrometry Through Convolutional Neural Networks and Kolmogorov-Arnold Networks . . . 258
B.6 Linear polarization measurement on gamma rays from non-oriented nuclear states 264
B.7 Analysis of Long-Term Stability Uncertainty in Luminosity Measurements Using the Tile Calorimeter of the ATLAS Detector for Run 3 Proton-Proton Collisions at $\sqrt{s} = 13.6$ TeV in 2023 . . . 272
B.8 Progress on test of the generalized Brink-Axel hypothesis in ^{63}Ni . . . 278
B.9 Characterization of instrumental background in (p,γ) reaction studies . . . 284
B.10 Analysis of ^{61}Cu from the ^{60}Ni(p,γ) Reaction at iThemba LABS . . . 292
B.11 Burn-in Testing for Transformer-Coupled Buck Converters in the ATLAS Tile Calorimeter's Low Voltage Power Supplies . . . 298
B.12 Triboson Excesses in light of a Real Higgs Triplet Model . . . 304
B.13 The PANDORA Project: Investigating Photonuclear Reactions in Light Nuclei 310
B.14 Investigation of X-rays and Gamma-ray Shielding Properties of Heavy Metal Oxide Glass Materials . . . 316
B.15 Ongoing validation of the High Granularity Timing Detector (HGTD) demonstrator for the ATLAS phase II upgrades . . . 322
B.16 Particle Flow Algorithm (PFA) for forward region jet reconstruction with the ATLAS Inner Tracker (ITk) detector setup at the High Luminosity Large Hadron Collider (HL-LHC) . . . 328
B.17 Detecting Anomalies in Measured Thermal Neutron Flux Profiles of SAFARI-1 Research Reactor . . . 336
B.18 Investigating the Photon Shielding Properties of Silicate Glass Samples from 1–15 MeV Using Phys-X/PSD, X-COM, and GEANT4 Simulations . . . 342

B.19 Parton Production Spectra and Energy Loss in High-Energy O+O-Collisions . . 350
B.20 Using Machine Learning in the search for dark photons in the $H \to Z + \gamma_D$ with the ATLAS detector at the LHC . . . 354
B.21 Probing the pygmy states of ^{154}Sm with a quasi-monochromatic linearly-polarised photon beam . . . 362
B.22 Quality Assurance for LVPS Boards in the Phase-II Tile Calorimeter Upgrade . 368
B.23 The nuclear level density of ^{192}Os(α, $d\gamma$)^{194}Ir . . . 374
B.24 Exploring toponium formation at the LHC . . . 380
B.25 Progress on the Experimental test of the generalized Brink-Axel Hypothesis in ^{139}La nucleus . . . 386
B.26 A search for tWZ production in the Tetralepton channel using ATLAS Run 2 data . . . 392
B.27 Effect of Strontium Oxide on Radiation Attenuation Properties of Boro-tellurate Glass Systems at High Radiation Energies . . . 398
B.28 Real-Time Anomaly Detection in High Energy Physics . . . 406
B.29 Search for a new spin-0 scalar and a spin-1 boson using Run2 ATLAS detector data . . . 412
B.30 Measurement of the top quark Yukawa coupling from tt kinematic distributions in the dilepton final state with the ATLAS experiment . . . 418
B.31 Searches for scalar resonances with di-photon in association with leptons and taus using the easyjet analysis framework in ATLAS detector at the LHC . 424
B.32 The use of Machine Learning techniques to analyse the $gg \to h \to Z\gamma$ process within the SMEFT framework at the Large Hadron Collider (LHC) . . . 430
B.33 Monte Carlo Generation Involving Searches for Diphoton Resonances in Association with $\tau^+\tau^-$ or b-jets at the Electroweak Scale in the ATLAS Detector at the LHC . . . 436
B.34 Analysing $gg \to h \to Z\gamma$ decay at the LHC using SMEFT . . . 442
B.35 Preparing for Diphoton Resonance Searches in the Leptonic, 0-τ Final States: Event Selection and Background Characterization Using ATLAS Run 3 . 448
B.36 Study of Low-Medium Spin States in ^{156}Er . . . 454
B.37 Orthogonality study for the $S \to Z_d Z_d \to 2\ell 2\nu/2\ell 2j$ with the ATLAS detector at the LHC . . . 460
B.38 Simulation of X-ray and gamma radiation shielding properties of lithium-antimony-Lead-germanate glasses modified with chromium oxide using Phy-X/PSD software . . . 466
B.39 Radiation contamination in gold mine tailings soil samples using HPGe spectrometry . . . 472
B.40 Exciting the Hoyle state in ^{12}C selectively populated using the ^{10}B(^{6}Li, ^{4}He)^{12}C reaction . . . 480

C Photonics **487**
C.1 Comparative Theoretical Analysis of Entangled Quantum States for Enhanced Sensing Applications . . . 488
C.2 Nanoformulation of Pheophorbide-a for Photodynamic Therapy in a Human Lung Cancer Spheroid Model . . . 496
C.3 Photonic-biosensing towards drug-resistant Tuberculosis diagnosis . . . 504
C.4 A comparison of two biosensing recognition elements using SPR for the detection of drug-resistant genes . . . 510

C.5 Enhancing the Efficacy of Photodynamic Therapy: The Role of Hypocrellin B, Quercetin, and their combinations in a Human Breast Cancer Cell Line . . . 516
C.6 Evaluation of Pheophorbide *a* Phototoxicity on Melanoma Cells Grown as Three-Dimensional Multicellular Tumour Spheroids . . . 522
C.7 Evaluation of the Phototoxic effect of Chemically Synthesized Silver Nanoparticles on Breast Cancer Cells . . . 528
C.8 Rate equations for the control of Yb-171 ions . . . 534
C.9 *In vitro* effects of blue laser light as an antimicrobial agent on microbial-infected fibroblast cells . . . 538
C.10 Photothermal Effects of Green-Synthesized Gold Nanoparticles using *Kniphofia porphyrantha* on MCF-7 Human Breast Cancer Cells . . . 544
C.11 Riboflavin-mediated Photodynamic Therapy Induces Cytotoxic Effects in A549 Lung Cancer Cells . . . 552
C.12 Numerical Modeling and Simulation of a Fabry–Perot Sensor for Refractive Index Measurement . . . 560
C.13 Voltage-Based Wavelength Tuning of a DFB Laser using a Frequency-to-Voltage Converter for OPLL Applications . . . 568
C.14 Synthesis and characterization of Cerium III ion doped zinc selenide thin films . 574
C.15 Label-free optical biosensing as an alternative for HIV-1 drug-resistant mutation detection . . . 582

D Astrophysics and Space Science 589
D.1 Developing a critical component of a fiber cable for the Affordable Multiple Aperture Spectroscopy Explorer Prototype (AMASE-P) . . . 590
D.2 Characterisation and Calibration of the Kepler KL4040 sCMOS camera for Optical Observations at the UFS/Boyden Observatory . . . 598
D.3 Multi-Wavelength Observations of AGN Activity in the Fornax Cluster . . . 604
D.4 Exploring the properties of pulsars and their nebulae through observations and modelling . . . 610
D.5 Searching for persistent radio emission towards selected Fast Radio Burst positions616
D.6 Solar wind temperature anisotropy during Ulysses' first fast latitude scan . . . 624
D.7 Understanding Interacting Dark Energy from a Dynamical Systems Analysis Approach . . . 630
D.8 Constraining the Teleparallel Universe . . . 636
D.9 Cosmic-Ray Neutron Detectors for Soil Moisture Monitoring . . . 642
D.10 Identification of Cosmic Filaments using the Simba-C simulation and DisPerSE Filament Finder . . . 650
D.11 Investigating the latitudinal-dependent solar differential rotation rate using SDO/HMI Dopplergrams . . . 660
D.12 Tracing the origin of radio emission in galaxies with MIGHTEE . . . 666
D.13 Wits Astronomical Plate Archive - preservation of a century of Southern Hemisphere astronomy at the Johannesburg Observatory . . . 674
D.14 Trends of Thermal Structure in the MLT Region Using SABER Observations Over Sutherland, South Africa . . . 680

E Physics for Development, Education, and Outreach 687
E.1 Integrating modern technology into a selection of first-year physics experiments . 688
E.2 Transforming Physical Sciences teaching through targeted professional development . . . 696
E.3 Reimagining Curriculum Renewal: A case study of Physics and Astronomy . . . 702

E.4 Physics Students' Epistemological Beliefs about Science . . . 710
E.5 Pre-service student teachers' misconceptions about a simple electric circuit . . . 718
E.6 Quantum computing education availability in South Africa . . . 724
E.7 An Introduction to Quantum Computing - Teaching the Basics . . . 732
E.8 Some roles of physics in climate science with examples in Southern Africa . . . 738

F Applied Physics **745**
F.1 Energy Balance Closure Analysis Based on Eddy Covariance Flux Tower Observations . . . 746
F.2 What are the most suitable basic solar irradiance models for Southern Africa? . . . 752
F.3 Monitoring of the performance of a small-scale PV system based on Power Law (PLM) approach . . . 758
F.4 First-Principles Investigation of the Structural, Mechanical, and Optical Properties of $CsPbI_3$ Perovskite for Solar Cell Applications . . . 764
F.5 Listening with Light: Acoustic sensing over live fibre networks using Coherent Optical Transceivers . . . 770
F.6 First-principles study of various sodium-oxide molecules on nitrogen-doped graphene for high-performance sodium-oxygen battery . . . 776
F.7 A novel approach to quantifying electron densities of HiP-CT imaging . . . 782
F.8 TGF-β Pathway Modulation: A Key Mechanism of Photobiomodulation Induced Tenogenesis . . . 788
F.9 First-Principle Study of $NaMnNbPO_4$ as a Cathode Material for Sodium-Ion Battery . . . 794
F.10 TileCoM Firmware Developments for ATLAS Tile Calorimeter Phase-II Upgrades 800
F.11 DFT Study of the TiO_2 Anatase (100) Surface Doped with Be for Application in DSSCs . . . 806
F.12 Deep Learning for High Throughput Decision Making on Diamond Content of PET Activated Kimberlite Rocks . . . 812
F.13 IoT-Based Environmental Conditions Monitoring of a Sawtooth Greenhouse: A Foundation for Anomaly Detection and Computational Fluid Dynamics . . . 818
F.14 Extraction of Natural Dye from Bidens pilosa: Solvent Effects and Dye Adsorption on TiO_2 Nanoparticles for Dye-sensitized Solar Cell Applications . . . 824
F.15 The South African contribution based on the TileCoM and Tile GbE Switch to the Tile Pre-Processor Modules for the ATLAS Tile Calorimeter: Progress and Current Status. . . . 832
F.16 Simulation and Image Reconstruction for a Low-Cost PET Detector Concept . 838
F.17 Thermal analysis of Ampreg-21 Epoxy and Bi composite material using the Cone Calorimeter . . . 844
F.18 Integration of grid-scale battery energy storage in solar microgrids for rural communities in Limpopo province . . . 850
F.19 Preliminary Investigation of the Mechanical Properties of Tissue Biopsies . . . 856
F.20 Synthesis and characterization of biomass-based graphitic carbon for sustainable energy storage . . . 862
F.21 The detection of HIV using plasmonically active colloidal gold nanoparticles . . . 868
F.22 Wind Energy Potential in Local Areas . . . 874
F.23 A Python-Flask Application for Modelling Surface Plasmon Resonance in Biosensors for Educational and Research use . . . 880
F.24 Development and Qualification of a Fiber Optic Sensor Package for ITk Environmental Monitoring . . . 886

F.25 The development of the atmospheric monitoring system for a balloon-borne system . . . 892
F.26 Automated photovoltaic module imaging for high throughput data capture and analysis . . . 898
F.27 DFT studies of the photocatalytic properties of $BaTiO_3$ doped with V and W for hydrogen production . . . 904
F.28 Reconfigurable Payload Power Management System for Rockets . . . 910
F.29 Design of a slotted Invelox-based wind delivery system for domestic low wind speed operation . . . 916
F.30 Optimizing the Geometry of an Empty Concentrator-Diffuser Augmented Wind Turbine Using Genetic Algorithm . . . 922
F.31 Enhancing Rural Electrification: An In-depth Analysis and Optimization of PV/Hydrogen Fuel Cell/Battery-Powered Microgrids . . . 928

G Theoretical and Computational Physics 935
G.1 Computational Fluid Dynamics Study of Turbulence Effects in Heat Pipe Heat Exchangers for Power-Cell Micro-Reactors . . . 936
G.2 Adiabatic elimination approach to the completely positive master equation for open quantum Brownian motion . . . 942
G.3 Fluorinated Graphdiyne under Strain: A First-Principles Study of Electronic and Optical Properties . . . 948
G.4 Laplacian eigenmodes in twisted periodic topologies for new physics models . . . 954
G.5 Equilibrium and elastic properties of hexagonal molybdenum disulphide . . . 960
G.6 Eigenvalue Determination for a Toy and Woods–Saxon Potentials using an Unsupervised PINN . . . 968
G.7 Coherent State Path Integrals and Vacuum Structure in Thermal ϕ^4 Theory on a Finite Volume . . . 974
G.8 Numeric exploration of Non-trivial emergent phenomena in Quark-Gluon Plasma 980
G.9 Parameterizing the Geometry of the QGP on an Event-by-Event Basis . . . 986
G.10 Classical and Quantum Mechanics of Non-holonomic Constraints . . . 992
G.11 Energy Loss as a Probe of Quark-Gluon Plasma Formation Across Collision System Size . . . 998
G.12 Solving the one-dimensional Schrodinger equation using a set of Daubechies wavelet scaling functions. 1004
G.13 Discriminating Multiprong Jet Substructure with right handed charged gauge boson and heavy right handed neutrino 1008
G.14 Probing the Dead Cone using the Lund Jet Plane 1014
G.15 Piston-Driven Shock Wave Test Problem for Validating Magnetohydrodynamic Models in Astrophysics 1020
G.16 Reservoir Computing for Predicting Chaotic Dynamical Systems 1026
G.17 Testing $f(Q)$ gravity as a solution for the H_0 and S_8 tensions 1032

This page intentionally left blank.

EDITORIAL

The University of the Witwatersrand (Wits University) hosted the annual South African Institute of Physics (SAIP) Conference during July 2025. The conference took place in the vibrant heart of Johannesburg, a city known for its energy, innovation, and spirit of transformation – qualities that resonated strongly with this year's themes recognising the International Year of Quantum Science and Technology 2025 and the International Decade of Sciences for Sustainable Development 2024-2033. In parallel with the main conference, a Teacher Development Workshop for 110 Physical Sciences educators from the Gauteng region was held, strengthening links between the research and education communities and extending the reach of the conference's impact. Certain papers from this meeting are collected in this peer-reviewed volume. Submissions for the proceedings of SAIP 2025 were handled by an Editorial Board headed by an Editor-in-Chief and Associate Editors responsible for submissions in the various divisions.

The Editorial Board of the SAIP 2025 Proceedings received 180 manuscripts for consideration by the advertised deadline. All of these manuscripts met the relevant criteria and were submitted to a full peer-review process involving many individual reviewers, resulting in a total of 161 papers accepted for publication. The list of reviewer names appears elsewhere in this volume, and it is noted that several reviewers took responsibility for more than one manuscript. The style of these proceedings is inspired from the (British) Institute of Physics Conference Series and the Institute of Electrical and Electronics Engineers transactions, journals and conferences (IEEEtran), similar to previous SAIP Proceedings. Authors were requested to ensure that the defined layout was adhered to in their submitted PDF documents. The Associate Editors conducted the layout review for each manuscript in parallel with the content review in order to expedite the review process. Manuscripts that deviated considerably from the specified layout requirements, while still broadly appropriate in their composition, were referred back to the authors for correction. This was done alongside the content reviews prepared by knowledgeable experts in each field, as well as consideration of Turnitin reports to ensure that all submissions were original and free of plagiarism. The Editorial Board again aimed to reduce the time between submission and publication, with authors informed of the outcome of their submissions before the December holiday closure and the final proceedings published online shortly thereafter.

In accordance with the South African Department of Higher Education and Training (DHET) Research Outputs Policy, the SAIP 2025 Proceedings meet all criteria required for recognition and subsidy. All published contributions are full papers presenting original research and new scholarly findings; no abstracts, extended abstracts, summaries, or poster-type submissions were accepted. Each manuscript underwent a rigorous peer-review process involving a minimum of two independent reviewers. The Proceedings carry a valid ISBN identifier and publication year, and the Editorial Board comprises subject matter experts drawn from multiple South African institutions, with full details listed in this volume. These Proceedings are intended for a specialist scholarly audience, consistent with DHET requirements for academic research dissemination, and include the complete set of published papers, author affiliations, reviewer acknowledgements, and the required publication metadata. All accepted submissions include author affiliations and contact information and the full text of the papers. The Editorial Board affirms that the published output meets all DHET criteria for accredited conference proceedings.

The publication of the SAIP Proceedings depends heavily on the efficiency of the Associate Editors and the goodwill of reviewers from the South African scientific community. The Editor-in-Chief wishes to acknowledge the hard work of the Associate Editors, who devoted significant time and care to evaluating papers and reviewer reports to ensure that acceptable academic standards were met and that the proceedings remain credible. The majority of the content reviews were completed with great diligence and professionalism. The Editorial Board expresses its sincere thanks to all participating Reviewers for their pro bono work, particularly those who reviewed more than one paper. The rigorous peer-review process described above has ensured that these proceedings contain thoroughly reviewed manuscripts of high professional quality, reporting on novel work that has not been published elsewhere.

This year, the Editorial Board once again benefited from the expertise of the Technical Associate Editor, Dr Bruno Letarte from North-West University (NWU). He took responsibility for finalising the complete document and ensuring that it met the highest technical standards. The Editor-in-Chief wishes to recognise Dr Letarte's significant contribution in preparing the final document. The Editorial Board deeply appreciates the many hours he dedicated to producing this exceptional publication.

The SAIP2025 Editorial Team
W. A. Horowitz, Editor-in-Chief

THE LOCAL ORGANISERS

It was a great pleasure for the School of Physics, Faculty of Science, University of the Witwatersrand to host the 69th Annual Conference of the South African Institute of Physics.

The conference recognized the "International Year of Quantum Science and Technology", 2025 and the International Decade of Sciences for Sustainable Development, 2024–2033". The conference scientific programme comprised of 300 and 204 oral and poster presentations, respectively, 7 invited plenary speakers, an Industry Day, Physics for Development and Industry Day, the Southern Africa Physics Network (SAPhysNet) Forum meeting, Women in Physics in South Africa (WiPiSA) 20th Anniversary Celebration Panel Discussion and 5 Winter Schools.

The conference served as an enriching experience for 600 delegates that included local and international experts, invited guests, academics, researchers, industry partners, postdoctoral fellows, and postgraduate students across all branches of physics. The conference was a platform that resulted in excellent scientific discussions, exchange of ideas, fostering of collaborations and was a forum to inspire our students and young researchers to continue with a career in Physics. The support of business and government are acknowledged including all the conference exhibitors and sponsors for their involvement in enhancing the success of the conference.

In terms of social events, our students organised an exciting PHYSICS QUIZZ CUP and further all delegates were invited to participate in immersive shows at the Wits Anglo American Digital Dome.

A special thanks to the Minister of DSTI, Professor Blade Nzimande who delivered the official Opening and Keynote Address at the Welcome Reception, the University of the Witwatersrand Vice-Chancellor and Principal, Professor Zeblon Vilakazi and the Dean of Faculty of Science, Professor Nithaya Chetty for their support in ensuring a successful conference. We also wish to congratulate Professor Philemon Mjwara who was elected as a Fellow of the South African Institute of Physics (FSAIP) in recognition of his outstanding contributions to physics education, research, and development in South Africa. The formal presentation of the award was bestowed to Professor Mjwara at the Conference Banquet.

Finally, I would like to express my sincere appreciation to all members of the local organising committee, in particular to Dr Robert Warmbier (Co-Chair), Professor Phil Ferrer (Chair: Scientific Programme), Ms Michelle Gallant (Wits Functions & Events / Advancement Division), Professor Rudolph Erasmus (ex-officio), Dr Angela Dudley, Dr Brian Masara and Mr Tebogo Mokhine (SAIP Office) for their tremendous efforts and time devoted in organising the conference.

LOC 2025

Local Organising Committee

- **Prof Deena Naidoo**, Co-Chair: Local Organising Committee
- **Dr Robert Warmbier**, Co-Chair: Local Organising Committee
- **Associate Professor Philippe Ferrer**, Chair: Scientific Programme
- **Associate Professor Rudolph Erasmus**, Ex-Officio
- **Dr Angela Dudley**, LOC Member
- **Professor Andrew Forbes**, LOC Member
- **Professor Matt Hilton**, LOC Member
- **Dr Isobel Kolbe**, LOC Member
- **Dr Mukesh Kumar**, LOC Member
- **Associate Professor Mervin Naidoo**, LOC Member
- **Ms Farah-Naaz Samuels**, LOC Member
- **Dr Brian Masara**, SAIP Office
- **Mr Tebogo Mokhine**, SAIP Office
- **Ms Michelle Gallant**, Wits Functions and Events/Advancement



DIVISIONS, EDITORIAL TEAM, AND REVIEWERS

Divisions and Division Chairs

- **Physics of Condensed Matter and Materials**
  – Prof Koos Terblans, University of the Free State
- **Nuclear, Particle, and Radiation Physics**
  – Prof Sifiso Ntshangase, University of Zululand
  – Dr Mukesh Kumar, University of the Witwatersrand
- **Photonics**
  – Dr Angela Dudley, University of the Witwatersrand
- **Astrophysics and Space Science**
  – Dr Geoff Beck, University of the Witwatersrand
  – Dr Katlego Moloto, North-West University
- **Physics for Development, Education, and Outreach**
  – Prof Sam Ramaila, University of Johannesburg
- **Applied Physics**
  – Prof Alan Matthews, University of KwaZulu-Natal
- **Theoretical and Computational Physics**
  – Prof Alan Cornell, University of Johannesburg
- **Women in Physics**
  – Dr Katekani Shingange, MINTEK

Editorial Team

Editor-in-chief:

– **W. A. Horowitz** is an Associate Professor of Physics at the University of Cape Town. Among other honours, Prof Horowitz has received the Claude Leon Merit Award for Early-Career Researchers and the Meiring Naudé Medal for Outstanding Early Career Contributions to Science from the Royal Society of South Africa. Prof Horowitz' research explores the non-trivial emergent many-body properties of the strong force using the methods of perturbative quantum field theory and the AdS/CFT correspondence.

Associate Editors:

- **Physics of Condensed Matter and Materials**
  – **Wendy Bonakele Mdlalose** is a physics lecturer at the University of KwaZulu-Natal, specializing in nanostructured magnetic materials for biomedical, agricultural, and electromagnetic applications. Her research focuses on polymer-coated ferrites for drug delivery, cancer therapy, nano-fertilizers, and microwave absorption. She is an active contributor to multidisciplinary research, supervises postgraduate students, and collaborates across sectors to advance nanotechnology solutions in health, food security, and energy.

  – **Pankaj Mohanty** is a Lecturer in the Department of Physics at the University of Johannesburg, South Africa, specializing in experimental condensed matter physics and materials science. His work explores nanoparticles, thin films, magnetism, and ion irradiation. He has received multiple awards, including the University of Johannesburg Excellence Award for Research (2019) and several international best presentation awards. Dr. Mohanty has supervised numerous postgraduate students to distinction and collaborates with institutions such as NECSA (South Africa), Elettra (Italy), and IUAC (India).

- **Nuclear, Particle, and Radiation Physics**
  – **Mukesh Kumar** Mukesh Kumar is the Deputy Director of the Institute for Collider Particle Physics, the National Coordinator of the SA–CERN Technology Transfer Pillar, and a Senior Lecturer in the School of Physics at the University of the Witwatersrand. He is an NRF Y-rated research physicist in the field of high-energy particle physics. His research focuses on Higgs boson, top quark, and dark matter physics at the Large Hadron Collider (CERN), as well as at future $e^{-}p$ and $e^{+}e^{-}$ colliders. He is a member of the TileCal Speakers Committee for the ATLAS detector at CERN and is involved in diphoton+lepton and dark-photon physics analyses within the ATLAS Collaboration.

  – **Obed Shirinda** is a Senior Lecturer of Physics in the department of Physical and Earth Sciences at the Sol Plaatje University. He is an NRF C-rated research physicist in the field of nuclear physics. His research is focused on nuclear structure physics describing features of rotating nuclei by using nuclear physics models (such as Particle rotor models (PRM), Cranked shell model (CSM), Total Routhian surface (TRS), etc.) and experimental equipment.

- **Photonics**
  – **Pieter Neethling** Pieter Neethling is an Associate Professor in the Physics Department at Stellenbosch University. He is currently the Director of the Stellenbosch Photonics Institute at Stellenbosch University and the Chairman of the Photonics Division of the SAIP. His research focus is applied laser spectroscopy with applications in chemical and biological systems.

- **Astrophysics and Space Science**
  – **Eugene Engelbrecht** is a Professor of Physics at North-West University, whose research covers topics relevant to the transport of charged particles in turbulent astrophysical plasmas, including both theoretical and observational aspects pertaining to cosmic ray modulation, non-linear diffusion theories, and plasma turbulence.

- **Physics for Development, Education, and Outreach**
  – **Dale Taylor** is an Associate Professor in the Physics Department at the University of Cape Town. Her current focus is co-curricular support towards science student success and early alert systems for targeted support. She supervises doctoral students in Physics Education Research and Astronomy Education Research. She has extensive reviewing experience, including 15 international education journals.

- **Applied Physics**
  – **Raesibe Sylvia Ledwaba** is an Associate Professor of Physics and Acting Deputy Director at the Materials Modelling Centre, University of Limpopo. Her current research focus is on All-Solid-State Battery Technology (ASSB), utilizing multiscale modelling and machine-learning approaches to identify suitable solid electrolyte materials to replace flammable liquid electrolytes in lithium-ion batteries. She is involved in several projects cathode and anode materials prediction and development for next-generation battery systems.

  – **Deon Marais** is a Chief Scientist at the South African Nuclear Energy Corporation (Necsa), where he is involved with the development of neutron beamline instrumentation, data acquisition and analysis tools. His work focuses on neutron diffraction and he is actively involved in national initiatives to expand South Africa's neutron-scattering capabilities and user community.

- **Theoretical and Computational Physics**
  – **Aniekan Magnus Ukpong** is a Senior Lecturer in Physics at the University of KwaZulu-Natal and Principal Investigator for the Centre for High-Performance Computing Research Programme No. MATS0941. Dr. Ukpong is a 2019 recipient of the IOP's Outstanding Reviewer Award from the *Journal of Physics: Condensed Matter*. Dr. Ukpong's research leverages scientific computing to understand many-body physics in condensed matter systems using realistic materials as a modelling platform.

- **Technical**
  – **Bruno Letarte** is a Senior Lecturer at the Centre for Space Research of the North-West University. He specialises in observational astronomy, photometry as well as spectroscopy, with his main interest in stellar astrophysics. He manages the optical telescope at the Nooitgedacht observatory, used to train undergraduate and postgraduate students.

Proceedings Online Administration:

– **Tebogo Mokhine**, South African Institute of Physics

List of Reviewers

- **Dr Jalal Abdallah** – The University of Texas at Arlington, United States of America
- **Dr Ibrahim Abdallah Ali** – Sudan University of Science and Technology, Sudan
- **Dr Paul Adedeji** – University of Johannesburg, South Africa
- **Dr Alnadhief Alfedeel** – North-West University, South Africa
- **Dr Fernando Carrio Argos** – CERN, Switzerland
- **Dr Bako Audu** – University of the Western Cape, South Africa
- **Dr Nadir Azhari** – University of the Free State, South Africa
- **Dr Joseph Bahder** – New Mexico State University, United States of America
- **Dr Avula Balakrishna** – Amity University, India
- **Dr Lunga Bam** – NECSA, South Africa
- **Dr Bharati Bamana** – University of Johannesburg, South Africa
- **Dr Kevin Barends** – University of Cape Town, South Africa
- **Dr Monica Barnard** – North-West University, South Africa
- **Dr Geoff Beck** – University of the Witwatersrand, South Africa
- **Prof Aroon Beesham** – University of Zululand, South Africa
- **Dr Mohamed Belfkir** – CERN, Switzerland
- **Dr Evans Benecha** – UNISA, South Africa
- **Prof Muaaz Bhamjee** – University of Pretoria, South Africa
- **Dr Srimoy Bhattacharya** – University of the Witwatersrand, South Africa
- **Dr Puleng Nontobeko Biyela** – University of Zululand, South Africa
- **Dr Marguerite Blignaut** – Stellenbosch University, South Africa
- **Prof Mark Blumenthal** – University of Cape Town, South Africa
- **Dr Christopher Bongani** – iThemba LABS, South Africa
- **Prof Moritz Braun** – University of South Africa, South Africa
- **Dr Felix Brutus Masok** – Plateau State University, Nigeria
- **Dr Daphney Bucher** – University of Cape Town, South Africa
- **Dr Calib Buckton** – Stellenbosch University, South Africa
- **Prof Andy Buffler** – University of Cape Town, South Africa

- **Prof Zinhle Buthelezi** – University of the Witwatersrand, South Africa
- **Prof Roland Cristoper Caballar** – University of Santo Tomas, Philippines
- **Dr Philippe Calfayan** – CERN, Switzerland
- **Prof Turgay Celik** – University of the Witwatersrand, South Africa
- **Prof Nhamo Chaukura** – Sol Plaatje University, South Africa
- **Prof Simon Connell** – University of Johannesburg, South Africa
- **Prof Lesley Cornish** – University of the Witwatersrand, South Africa
- **Prof Mitchell Cox** – University of the Witwatersrand, South Africa
- **Prof Romeel Dave** – University of Edinburgh, United Kingdom
- **Prof Marelie Davel** – North-West University, South Africa
- **Prof Trevor Derry** – University of the Witwatersrand, South Africa
- **Dr U.M. Dhanalekshmi** – National University of Science and Technology, Oman
- **Prof Sathish Dhilip Kumar** – University of Johannesburg, South Africa
- **Prof Mantsae Diale** – University of Pretoria, South Africa
- **Dr Redrisse Djoumessi** – University of Johannesburg, South Africa
- **Dr Mpilo Dlamini** – North-West University, South Africa
- **Dr Sanele Dlamini** – University of Mpumalanga, South Africa
- **Dr Anton Dmytriiev** – North-West University, South Africa
- **Dr Kwadwo Dompreh** – University of Cape Coast, Ghana
- **Dr Lindsay Donaldson** – iThemba LABS, South Africa
- **Dr Cathryn Driver** – NECSA, South Africa
- **Mr Jean du Plessis** – MIT, United States of America
- **Dr Angela Dudley** – University of the Witwatersrand, South Africa
- **Dr Adams Duniya** – Botswana University of Science and Technology, Botswana
- **Prof Rocco Duvenhage** – University of Pretoria, South Africa
- **Prof Thomas Ebenhan** – North-West University, South Africa
- **Dr Abdualazem Ebrahim** – Nanjing University, China
- **Dr Raymond Ehlers** – University of California Berkeley; Lawrence Berkeley National Laboratory; CERN, United States of America; Switzerland
- **Dr Ernest Ejeh** – iThemba LABS, South Africa

- **Dr Huzifa Elnour** – Stellenbosch University, South Africa
- **Prof N. Eugene Engelbrecht** – North-West University, South Africa
- **Dr Nicolas Erasmus** – SAAO; Stellenbosch University, South Africa
- **Prof Rudolph Erasmus** – University of the Witwatersrand, South Africa
- **Prof Fabian Ezema** – University of Nigeria, Nigeria
- **Mr Coleridge Faraday** – University of Cape Town, South Africa
- **Dr Jeff Fearon** – Seabridge School, South Africa
- **Prof Stefan Ferreira** – North-West University, South Africa
- **Prof Phil Ferrer** – University of the Witwatersrand, South Africa
- **Dr Luca Fiorini** – CERN, Switzerland
- **Dr Siege Fortsch** – iThemba LABS, South Africa
- **Mr Eugene Fouche** – Stellenbosch University, South Africa
- **Prof Thomas Franz** – University of Cape Town, South Africa
- **Prof Manjunath Gandhi** – University of Pretoria, South Africa
- **Dr Animik Ghosh** – Huzhou University, China
- **Dr Mpho Gift Doctor Gololo** – University of Johannesburg, South Africa
- **Prof Irvy (Igle) Gledhill** – University of the Witwatersrand, South Africa
- **Dr Julia Lynn Gonski** – CERN, Switzerland
- **Dr Mmusi Gopane** – Sol Plaatje University, South Africa
- **Prof Anthony Hechanova** – Abu Dhabi Polytechnic University, United Arab Emirates
- **Prof Albert Helberg** – North-West University, South Africa
- **Dr Mark Herbert** – University of the Western Cape, South Africa
- **Prof Thulani Hlatshwayo** – University of Pretoria, South Africa
- **Dr Mark Hodgkinson** – University of Sheffield, United Kingdom
- **Prof W. A. Horowitz** – University of Cape Town, South Africa
- **Prof Nicolette Houreld** – University of Johannesburg, South Africa
- **Dr Ammar Ibraheem** – University of Hafr Al Batin, Saudi Arabia
- **Mr Gregory Ireland** – University of Cape Town, South Africa
- **Dr Yaseera Ismail** – Stellenbosch University, South Africa
- **Prof Moshawe Jack Madito** – UNISA, South Africa

- **Dr Greg Jackson** – Subatech (Subatomic Physics and Associated Technologies), France
- **Dr Susan Jacobs** – Univerity of Johanneburg, South Africa
- **Dr Hassnae El Jarrari** – CERN, Switzerland
- **Dr Thulani Jili** – University of Zululand, South Africa
- **Dr Danzil Joseph** – Stellenbosch University, South Africa
- **Dr Jitcy Joseph** – National Institute of Health, South Africa
- **Dr Abraham Dimitri Kapimkenfack** – Tshwane University of Technology, South Africa
- **Dr James Keaveney** – University of Cape Town, South Africa
- **Dr Garreth Kemp** – University of Johannesburg, South Africa
- **Dr Thuthukile Khumalo** – iThemba LABS, South Africa
- **Mr Mphiriseni Khwanda** – University of Johannesburg, South Africa
- **Dr Duncan Kiboi Boiyo** – Moi University, Kenya
- **Mr Amos Kiyumbi** – Stellenbosch University, South Africa
- **Dr Lehlohonolo Koao** – University of Free State, South Africa
- **Dr Isobel Kolbé** – University of the Witwatersrand, South Africa
- **Dr Győző Kovács** – University of Wroclaw, Hungary
- **Dr Hannes Kriel** – Stellenbosch University, South Africa
- **Prof Ted Kroon** – University of the Free State, South Africa
- **Dr Tjaart Krüger** – University of Pretoria, South Africa
- **Dr Martin Kudinha** – Cape Peninsula University of Technology, South Africa
- **Dr Satendra Kuma** – Indian Institute of Information Technology, India
- **Dr Mukesh Kumar** – University of the Witwatersrand, South Africa
- **Dr Elena Lawrie** – iThemba LABS, South Africa
- **Prof Derik Le Roux** – University of Pretoria, South Africa
- **Dr Katlego Lentswe** – North-West University, South Africa
- **Dr Bruno Letarte** – North-West University, South Africa
- **Dr Ndanduleni Lethole** – University of Fort Hare, South Africa
- **Dr Juandre Light** – North-West University, South Africa
- **Dr Bo Liu** – CERN, Switzerland

- **Prof Ilani Loubser** – North-West University, South Africa
- **Dr George Lowani Zimba** – Facility for Rare Isotope Beams Michigan State University, United States of America
- **Dr Daniela Macina** – CERN, Switzerland
- **Dr Molepo Mahlanga** – University of the Witwatersrand, South Africa
- **Dr Lucky Makhathini** – University of Western Cape, South Africa
- **Dr Kemeridge Malatji** – University of Limpopo, South Africa
- **Dr Fairouz Malek** – French National Centre for Scientific Research (CNRS), France
- **Dr Peane Maleka** – iThemba LABS, South Africa
- **Prof Thembinkosi Malevu** – North-West University, South Africa
- **Dr Vernon Maluba Chisapi** – University of Zambia, Zambia
- **Prof Eric Maluta** – University of Venda, South Africa
- **Dr Grant Manuel** – NECSA, South Africa
- **Dr Refilwe (Edwin) Mapasha** – University of Pretoria, South Africa
- **Dr Bongani Maqabula** – University of Johannesburg, South Africa
- **Prof Delia Marshall** – University of the Western Cape, South Africa
- **Dr Filipe Martins** – Laboratório de Instrumentação e Física Experimental de Partículas - LIP, Portugal
- **Dr Mamogo Masenya** – iThemba LABS, South Africa
- **Dr Mpho Maswanganye** – University of Limpopo, South Africa
- **Prof Manny Mathuthu** – North-West University, South Africa
- **Mr Marome Bester Matseba** – Central University of Technology, South Africa
- **Prof Alan Matthews** – University of KwaZulu-Natal, South Africa
- **Dr Rachid Mazini** – University of the Witwatersrand, South Africa
- **Dr Jean Jules Mboukam** – Tshwane University of Technology/iThemba LABS, South Africa
- **Prof Pontsho Mbule** – University of South Africa, South Africa
- **Dr Kim McAlpine** – South African Radio Astronomy Observatory, South Africa
- **Dr Jacqueline McCleland** – Nelson Mandela University, South Africa
- **Dr Wendy Mdlalose** – University of KwaZulu-Natal, South Africa
- **Prof Pieter Meintjies** – University of the Free State, South Africa

- **Dr Motlalepula Rebecca Mhlongo** – Sefako Makgatho Health Sciences University, South Africa
- **Prof Gugu Mhlongo** – University of South Africa, South Africa
- **Mr Prince S Mkwae** – University of Zululand, South Africa
- **Ms Loesa Mntuyedwa** – Central University of Technology, South Africa
- **Dr Kwena Modibane** – University of Limpopo, South Africa
- **Dr Pankaj Mohanty** – University of Johannesburg, South Africa
- **Dr Paul Molefe** – University of Johannesburg, South Africa
- **Prof Sabata Moloi** – UNISA, South Africa
- **Dr Katlego Moloto** – North-West University, South Africa
- **Dr Mervlyn Moodley** – University of KwaZulu-Natal, South Africa
- **Prof Mathew Moodley** – University of KwaZulu-Natal, South Africa
- **Dr Leotlela Mosebetsi** – University of the Witwatersrand, South Africa
- **Dr Thuto Mosuang** – University of Limpopo, South Africa
- **Dr Vinny Motjoadi** – University of Johannesburg, South Africa
- **Dr Rapelang Motsoeneng** – University of the Free State, South Africa
- **Dr Lumkile Msebi** – University of Western Cape, South Africa
- **Prof Mandla Msimanga** – Tshwane University of Technology, South Africa
- **Prof Justice Msomi** – Walter Sisulu University of Technology, South Africa
- **Dr. Busiso Mtunzi** – NUST Zimbabwe, Zimbabwe
- **Dr Yagoub Mubarak** – University of Johannesburg, South Africa
- **Prof Sophy Mulaudzi** – University of Venda, South Africa
- **Prof Kiristian Müller-Nedebock** – Stellenbosch University, South Africa
- **Dr Bharati Naik** – University of the Witwatersrand, South Africa
- **Dr Isaac Nape** – University of the Witwatersrand, South Africa
- **Dr Frank Ndjomatchoua** – University of Cambridge, United Kingdom
- **Prof Ceboliyozakha Ndlangamandla** – University of Zululand, South Africa
- **Prof Pieter Neethling** – Stellenbosch University, South Africa
- **Dr Amore Nel** – SANSA, South Africa
- **Dr Fhulufhelo Nemangwele** – University of Venda, South Africa

- **Dr Stanislav Nemecek** – Institute of Physics of the Czech Academy of Sciences, Czech Republic
- **Dr Henri Neser** – North-West University, South Africa
- **Dr Retief Neveling** – iThemba LABS, South Africa
- **Dr Mkhuseli Ngxande** – Stellenbosch University, South Africa
- **Dr Amos Nhlapo** – Sefako Makgatho Health Sciences University, South Africa
- **Dr Eric Njoroge** – University of Pretoria, South Africa
- **Dr Edward Nkadimeng** – CERN, Switzerland
- **Dr Solethu Nkosi** – University of Limpopo, South Africa
- **Dr Sibusiso Nqayi** – University of Johannesburg, South Africa
- **Dr Robert Nshimirimana** – NECSA, South Africa
- **Prof Petros Ntoahae** – University of Limpopo, South Africa
- **Dr NN Nyangiwe** – Tshwane University of Technology, South Africa
- **Dr Hlanganani Nyembe** – Nelson Mandela University, South Africa
- **Dr David Obada** – Ahmadu Bello University - Zaria, Nigeria
- **Prof Kingsley Obodo** – University of KwaZulu-Natal, South Africa
- **Dr Samuel Ogana** – North-West University, South Africa
- **Dr Ituen Okon** – University of Uyo, Nigeria
- **Dr Saturnin Ombinda-Lemboumba** – CSIR, South Africa
- **Prof Nico Orce** – University of the Western Cape, South Africa
- **Dr Nadir Osman** – Sudan University of Science and Technology, Sudan
- **Dr Suzan P Bvumbi** – University of Venda, South Africa
- **Dr Aviv Padawer-Blatt** – University of Victoria, Canada
- **Dr Andronikos Paliathanasis** – Durban University of Technology, South Africa
- **Prof Luna Pellegri** – University of the Witwatersrand, South Africa
- **Dr. Rory Pentz** – Cape Peninsula University of Technology, South Africa
- **Dr Itumeleng Phage** – Central University of Technology, South Africa
- **Dr Jennifer Pienaar** – De Montfort University, United Kingdom
- **Dr Graeme Pleasance** – Stellenbosch University, South Africa
- **Dr Nakka Praveenkumar** – University of KwaZulu-Natal, South Africa

- **Dr Mkwae Prince** – University of Zululand, South Africa
- **Dr Jan-Louis Raath** – SANSA, South Africa
- **Prof Krishna Rajagopal** – MIT, United States of America
- **Prof Sergei Rakitianski** – University of Pretoria, South Africa
- **Prof Sam Ramaila** – University of Johannesburg, South Africa
- **Prof Gaotsiwe Rampho** – University of South Africa, South Africa
- **Dr Ntsoko Phuti Rapheeha** – University of the Witwatersrand; CERN, South Africa; Switzerland
- **Prof Vaibhav Rawoot** – Jaypee Institute of Information Technology, India
- **Dr Nawahl Razak** – University of Cape Town, South Africa
- **Prof Leelakrishna Reddy** – University of Johannesburg, South Africa
- **Prof Quinn Reynolds** – MINTEK, South Africa
- **Dr Ramachandran Samivel** – King Saud University, Kingdom of Saudi Arabia
- **Dr Bruno Scheihing** – Kavli Institute for Theoretical Physics; University of California - Santa Barbara, United States of America
- **Dr Chandreyee Sengupta** – North-West University, South Africa
- **Prof Sifiso Senzo Ntshangase** – University of Zululand, South Africa
- **Prof Dawid Serfontein** – North-West University, South Africa
- **Dr Haifa Rejeb Sfar** – CERN, Switzerland
- **Dr Rajan Sheeja** – University of South Africa, South Africa
- **Prof Charles Sheppard** – University of Johannesburg, South Africa
- **Dr Obed Shirinda** – Sol Plaatje University, South Africa
- **Dr Chipo Shonhiwa** – University of Science Education Bindura, Zimbabwe
- **Prof Elias Sideras-Hadad** – University of the Witwatersrand, South Africa
- **Prof Ilya Sinayskiy** – University of KwaZulu-Natal, South Africa
- **Prof Buyisiwe Sondezi** – University of Johannesburg, South Africa
- **Mr Chrey Sookha** – SALT, South Africa
- **Dr Matthew Spangler-Bickell** – GE HealthCare, United States of America
- **Prof Lynndle Square** – North-West University, South Africa
- **Dr Christine Steenkamp** – Stellenbosch University, South Africa

- **Dr Ruhann Steyn** – North-West University, South Africa
- **Dr Rasidi Sule** – Covenant University, Nigeria
- **Dr Taariq GH Surtee** – University of the Witwatersrand, South Africa
- **Prof Hendrik Swart** – University of Free the State, South Africa
- **Dr Adam Takacs** – Heidelberg University, Germany
- **Prof Mark Tame** – Stellenbosch University, South Africa
- **Prof Dale Taylor** – University of Cape Town, South Africa
- **Dr. Henerica Tazvinga** – South African Weather Service, South Africa
- **Dr Nicolas Thantsha** – Tshwane University of Technology, South Africa
- **Dr Charles T Thethwayo** – University of Zululand, South Africa
- **Dr Wasitha Thilakanatne** – Dalhousie University, Canada
- **Dr David Tinarwo** – University of Venda, South Africa
- **Dr Kamohelo Tshabalala** – University of Free State, South Africa
- **Dr David Tshwane** – CSIR/NiTheCS, South Africa
- **Dr Luke Ugwuoke** – Stellenbosch University, South Africa
- **Dr Aniekan Ukpong** – University of KwaZulu-Natal, South Africa
- **Dr Theresa Urban** – University College London, South Africa
- **Prof Kenny Uren** – North-West University, South Africa
- **Dr Zelalem Urgessa** – Nelson Mandela University, South Africa
- **Prof Iyabo Usman** – University of the Witwatersrand, South Africa
- **Dr Paul Vaandrager** – University of Pretoria, South Africa
- **Dr Fanie van den Heever** – North-West University, South Africa
- **Prof Ernest Van Dyk** – Nelson Mandela Universty, South Africa
- **Dr Hendrik Jacobus Van Heerden** – University of the Free State, South Africa
- **Dr Sam van Leuven** – University of the Witwatersrand, South Africa
- **Dr J.J. van Zyl** – Stellenbosch University, South Africa
- **Prof Christo Venter** – North-West University, South Africa
- **Dr Robert Warmbier** – University of the Witwatersrand, South Africa
- **Dr David Waswa** – Nelson Mandela Universty, South Africa
- **Dr Ingrid Webster** – Stellenbosch University, South Africa

- **Dr Jennifer Williams** – Rhodes University, South Africa
- **Prof Hartmut Winkler** – University of Johannesburg, South Africa
- **Dr Dawit Worku** – Cape Peninsula University of Technology, South Africa
- **Prof Shaun Wyngaardt** – Stellenbosch University, South Africa
- **Dr Tawanda Zininga** – Stellenbosch University, South Africa
- **Prof Konstantinos Zoubos** – University of Pretoria, South Africa

This page intentionally left blank.

STUDENT PRIZES

The Annual Conference of the South African Institute of Physics provides an important platform for emerging researchers to share their work with the broader physics community. The student prizes awarded at the conference recognise outstanding student contributions and celebrate excellence in research and presentation. This section is dedicated to and celebrates our students, whose achievements point to the vitality and future of physics in South Africa. We are extremely proud of the following prizewinners.

Note that there are several instances of two equal runners up among the prizewinners, both labelled as #2.

A Physics of Condensed Matter and Materials

Honours Poster:

Nicholas Snyman (North-West University)

Wirsam MSc Poster Award (Condensed Matter Physics):

M.S.L. Mthimkulu (University of Johannesburg)

Wirsam MSc Poster Award (Materials Physics):

M.C. Matlala (University of Limpopo)

Busch Vacuum MSc Oral Award (Condensed Matter Physics):

Arthur van der Spuy (University of the Witwatersrand)

Busch Vacuum MSc Oral Award (Materials Physics):

Dineo Motjope (University of Zululand)

Busch Vacuum PhD Poster Award (Condensed Matter Physics):

Irénée Mouadje (University of Johannesburg)

Busch Vacuum PhD Poster Award (Materials Physics):

Arnold Mutubuki (Nelson Mandela University)

Frank Nabarro PhD Oral Award (Condensed Matter Physics & Material Physics):

Murei Mulibana (University of Johannesburg)

Frank Nabarro PhD Oral Award (Semiconductor Physics):

Andi Isni Pujirana (Nelson Mandela University)

Wirsam MSc Publication Award (Condensed Matter Physics & Material Physics):

Arthur van der Spuy (University of the Witwatersrand)

Wirsam MSc Publication Award (Semiconductor Physics):

Katlego L. Morulane (University of the Free State)

PhD Publication Award (Semiconductor Physics):

Vhahangwele Makumbane (University of the Free State)

B Nuclear, Particle, and Radiation Physics

NPRP-1 MSc Poster Award

1. Nosihle Msabala (University of Zululand)
2. Tshegofatso Bokhutlo (Botswana International University of Science and Technology)

NPRP-2 MSc Poster Award

Joshua Browne (University of Cape Town)

NPRP-1 MSc Oral Award

1. Lilian Moremi (Tshwane University of Technology)
2. N.N. Khanyeza (University of Pretoria)

NPRP-2 MSc Oral Award

1. Kutlwano Makgetha (University of the Witwatersrand)
2. Njokweni Mbuyiswa (University of the Witwatersrand)
2. Stephan Potgieter (University of Cape Town)

NPRP-1 PhD Poster Award

Mbulelo Dondolo (University of the Witwatersrand)

NPRP-2 PhD Poster Award

1. Nidhi Tripathi (University of the Witwatersrand)
2. Vongani Chabalala (University of the Witwatersrand)

NPRP-1 PhD Oral Award

1. Sebenzile Magagula (University of the Witwatersrand)
2. Refilwe Emil Molaeng (University of the Witwatersrand)
2. Ayabulela Tsewu (University of Johannesburg)

NPRP-2 PhD Oral Award

1. Cameron Garvey (University of Cape Town)
2. Thabo James Lepota (University of the Witwatersrand)
2. Xola Mapekula (University of Johannesburg)

C Photonics

MSc Poster Award

Jacques Buys (University of Stellenbosch)

MSc Oral Award

Christopher Rawlings (University of the Witwatersrand)
Calvin Groenewald (University of the Witwatersrand)

MSc (Quantum Tech) Oral Award

Fazilah Nothlawala (University of the Witwatersrand)

PhD Poster Award

Cade Peters (University of the Witwatersrand)

PhD Oral Award

Cade Peters (University of the Witwatersrand)
Eugene Fouche (University of Stellenbosch)

PhD (Quantum Tech) Oral Award

Pedro Dinis Ornelas (University of the Witwatersrand)

D Astrophysics and Space Science

Honours (Astrophysics) Poster Award

Christo Pretorius (North-West University)

Honours (Space Science) Encouragement Prize

Thembalethu Zulu (North-West University)

MSc (Astrophysics) Poster Award

Lobone Dire (North-West University)

MSc (Astrophysics) Oral Award

Trevor Nyambe (North-West University)

MSc (Space Science) Oral Award

1. Fanelesibonge Khoza (University of KwaZulu-Natal)
2. Kenny Monontsi (North-West University)

PhD (Astrophysics) Poster Award

Thando Kekana (University of Johannesburg)

PhD (Astrophysics) Oral Award

Tamador Aldowma (University of Johannesburg)

PhD (Space Science) Oral Award

1. Jonathan Stephanus Troskie (North-West University)
2. Sanele Lionel Khanyile (Rhodes University)

E Physics for Development, Education, and Outreach

Honours Oral Award

Nthangeni Rofhiwa (University of Venda)

MSc Oral Award

Cathy Maako (University of the Witwatersrand)
Elizabeth Hagemann (Nelson Mandela University)

F Applied Physics

Honours Poster or Oral Award

Avhatakali Ramalata (University of Venda)

MSc Poster Award

Shandukani Kharavho (University of Venda)

G Theoretical and Computational Physics

Poster Award

Gaopallwe Katlego Pule (University of Johannesburg)

MSc Oral Award

1. Nia O'Callaghan (University of Cape Town)
2. Ofentse Matlhakola (University of the Witwatersrand)
2. Rens Roosenstein (University of Cape Town)

PhD Oral Award

1. Coleridge Faraday (University of Cape Town)
2. Hannah Van Der Schyf (University of the Witwatersrand)


SOUTH AFRICAN INSTITUTE OF PHYSICS
69th Annual Conference of the South African Institute of Physics
UNIVERSITY OF THE WITWATERSRAND, JOHANNESBURG
7-11 July 2025

This page intentionally left blank.

DIVISION

A

PHYSICS OF CONDENSED MATTER AND MATERIALS

An anomaly in a formula to calculate the refractive index of $Al_xGa_{1-x}As$

Japie Engelbrecht

Facility for High Resolution Electron Microscopy, Nelson Mandela University, Gqberha 6071, South Africa

E-mail: japie.engelbrecht@mandela.ac.za

Abstract. A formula to calculate the refractive index n of $Al_xGa_{1-x}As$ was proposed by Adachi in 1985. There are two equations for the calculation of the band gap, namely for the mole fraction $x \leq 0.45$ and for $0.45 \leq x \leq 1$. This article reports on an anomaly that occurs when the mole fraction x is used to calculate the refractive index of $Al_xGa_{1-x}As$, and the subsequent use of the obtained refractive indices to calculate the epilayer thickness of $Al_xGa_{1-x}As$ is compared.

1 Introduction

The ternary alloy $Al_xGa_{1-x}As$ is a useful material for both electronic and optical applications. Consequently, $Al_xGa_{1-x}As$ has been used in high-speed, high-frequency microwave devices [1,2], high electron mobility transistors (HEMT) [3], quantum well infrared photo detectors [4], and other electro-optic devices. In order to design and manufacture opto-electronic devices with the required optical properties, the refractive index of the applicable material must be known. The refractive index n is a function not only of the wavelength λ, but also of the mole fraction x of the alloy in the case of ternary semiconductor alloys [5]. A relationship exists between the band gap E_g of a semiconductor and the mole fraction x [6], as well as the refractive index n and the band gap [7]. This leads to the advantage of the experimental determination of the band from the point of inflection of an infrared reflectance spectrum [8] from which the mole fraction x and thus the refractive index can then also be calculated. It is to be noted that the band gap E_g of $Al_xGa_{1-x}As$ changes from direct to indirect at a mole fraction of $x \leq 0.45$ [1,9] (Figure 1).

A formula to calculate the refractive index of $Al_xGa_{1-x}As$ was proposed by Adachi in 1985 [1]:

$$n(\lambda) = \sqrt{A_0\left[f(x) + \frac{f(x_{so})}{2}\left(\frac{E_0}{E_0+\Delta_0}\right)^{\frac{3}{2}}\right] + B_0} \quad (1)$$

$$(x) = \frac{2 - \sqrt{1+x} - \sqrt{1-x}}{x^2}$$

$$x = \frac{hc}{\lambda E_0}$$

$$x_{so} = \frac{hc}{\lambda(E_0 + \Delta_0)}$$

The parameters $A_0 = 6.3 + 19.0x$ and $B_0 = 9.4 - 10.2x$ are fitting parameters in terms of the Al mole fraction x (see Reference [1]). $E_0(x) = 1.425 + 1.155\,x + 0.37\,x^2$ eV is the fundamental band gap.

$E_0(x) + \Delta_0(x) = 1.765 + 1.115\,x + 0.37\,x^2$ eV includes the spin-orbit splitting energy $\Delta_0(x)$, h is Planck's constant, c is the speed of light, λ is the wavelength and hc/λ the photon energy.

The band gap energies presented in Figure 1 can readily be obtained from the two expressions proposed to provide for the direct and indirect band gap energies [9]:
For the mole fraction $0 \leq x \leq 0.45$, the direct band gap $E_g(x) = 1.424 + 1.247x$ (2)

In the indirect band gap where $0.45 < x < 1$, the band gap $E_g(x) = 1.9 + 0.125x + 0.143x^2$ (3)

The refractive index n for $Al_xGa_{1-x}As$ can hence be calculated using formula (1), taking into account the restrictions of equations (2) and (3).

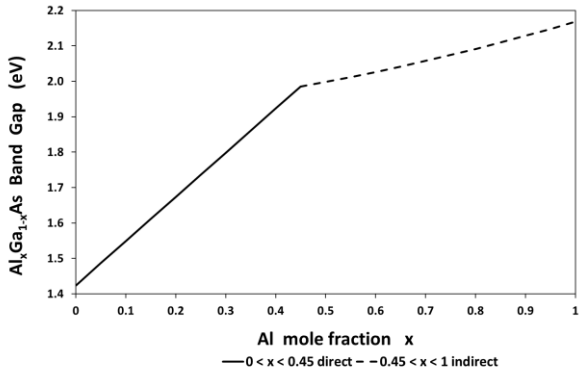

Figure 1: Band gap of $Al_xGa_{1-x}As$ as a function of Al mole fraction x

2 Experimental Procedure and Data Analysis

$Al_xGa_{1-x}As$ samples with different thickness and Al mole fraction x were grown using organo-metallic vapor phase epitaxial (OMVPE). A Bruker 80V FTIR spectrometer was used to measure infrared reflectance spectra, with a Pike 10Spec specular reflectance attachment, which allowed for near-normal incidence onto the samples. Fifty scans were acquired at a resolution of 4 cm^{-1} in the wavelength range 4,000 – 20,000 cm^{-1} (0.5 – 2.5 eV). The infrared (IR) reflectance spectra were then analyzed using the method proposed by Holtz et al. [8] to find the bandgap Eg. The bandgap was then used to calculate the Al mole fraction x for each sample from the appropriate equation (2) or (3), whereafter the refractive index was calculated from (1). Finally, the epilayer thickness for each sample is then calculated from the IR reflectance spectra and the parallel plate interference equation of Reizman [9]:

$$1/d = (2/p)[n_2/\lambda_2 - n_1/\lambda_1] \quad (4)$$

where n_1 and n_2 are refractive indices calculated at the specific wavelengths λ_1 and λ_2 where the interference minima occur on the reflectance spectrum under consideration (Figure 2).

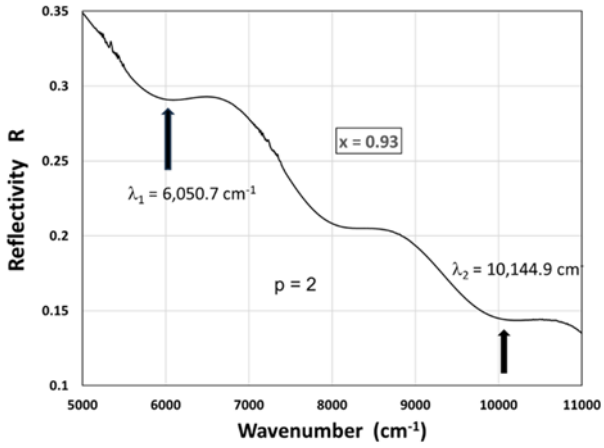

Figure 2: The infrared reflectance spectrum from an $Al_xGa_{1-x}As$ sample with Al mole fraction x = 0.93 and two minima (p =2) at wavenumber values as indicated. The negative slope of the spectrum is due to surface roughness.

The mole fraction x = 0.93 equates a band gap E_g = 2.14. An anomaly arises when equations (2) and (3) are used to calculate the refractive indexes for the same bandgap E_g (= 2.14 in this example). While different values for the refractive indices from equations (2) and (3) are obtained, calculated thicknesses of the epilayer only differ in the 3rd decimal (Table 1), even though the "wrong" equation (2) was used in the calculations.

	n_1	n_2	Film Thickness (μm)
$x \leq 0.45$ (equation 2)	2.962	3.022	0.785
$0.45 \leq x \leq 1$ (equation 3)	2.950	3.012	0.787

Table 1 Results from equations (1) and (2).

3. Conclusion

An interesting anomaly arises when use is made of the incorrect expression for the Al mole fraction *x* for a specific band gap E_g of an $Al_xGa_{1-x}As$ ternary alloy. An incorrect refractive index n as a function of wavenumber (or wavelength) is obtained, yet when the refractive indices are used to calculate epilayer thicknesses, the thicknesses only differ in the 3rd decimal place.

References

[1] S. Adachi "GaAs, AlAs and $Al_xGa_{1-x}As$: "Material parameters for use in research and device applications" *Journal of Applied. Physics.* Vol. 58, R1, 1985.

[2] S. Adachi *Physical properties of III-V semiconductor compounds, InP, InAs, GaAs, GaP, InGaAs and InGaAsP* John Wiley and Sons (NY) Chapter 4, 1992.

[3] T.R. Lenka and A.K.Panda AlGaN/GaN-based HEMT on SiC substrate for microwave characteristics using different passivation layers, *International Journal of Recent Trends in Engineering* Vol. 1, 186, 2009.

[4] A. Billha and M.K. Das, Influence of doping on the performance of GaAs/AlGaAs QWIP for long wavelength applications, *Opto-Electronic Review* Vol. 24, 25, 2017.

[5] B. Jensen and A. Torabi, Quantum theory of the dispersion of the refractive index near the fundamental absorption edge in compound semiconductors *IEEE Journal of Quantum Electronics* Vol. QE-19 448, 1983.

[6] R.E. Nahory. M.A. Pollack, W.D. Johnston Jr and R.L Barns, Band gap composition and demonstration of Vegard's law for $In_{1-x}Ga_xAs_yP_{1-y}$ lattice matched to InP, *Applied Physics Letters* Vol. 33, 659, 1978.

[7] P. Hervé and L.K.J. Vandamme, General relation between refractive index and energy gap in semiconductors, *Infrared Physics and. Technology* Vol. 35, 609, 1994.

[8] M. Holtz, T. Prokofyeva, M. Seon, K. Copeland, J. Vanbuskirk, S. Williams, S.A. Nikishin, V. Tretyakov and H.J. Temkin. Composition dependence of the optical phonon energies in hexagonal $Al_xG_{1-x}N$, *Applied Physics* Vol. 89, 7977, 2001.

[9] H.C. Casey Jr and M.B. Panish, *Heterostructure Lasers,* Academic Press (NY) Parts A and B, 1978.

[10] F. Reizman, Optical thickness measurement of thin transparent films on silicon, *Journal of Applied Physics* Vol. 36, 3804, 1965.

Structural and electrical transformations in Ag-implanted polyethylene terephthalate (PET) induced by swift heavy ion irradiation

J.J. Mboukam[1], D.C. Chilukusha[1,3], M. Madhuku[2] and M. Msimanga[1,2]

[1]Photovoltaic NanoComposites R and D Platform Physics Department, Tshwane University of Technology P Bag X680, Pretoria 0001, South Africa
[2]iThemba LABS, Tandem and Accelerator Mass Spectrometry Department, P. Bag 11, Johannesburg, Wits 2050, South Africa
[3]Department of Physics, Mulungushi University, Kabwe, 10101, Zambia

E-mail: mboukamjj@tut.ac.za

Abstract. The present study investigates the combined effects of ion implantation and swift heavy ion irradiation on the structural and electrical properties of polyethylene terephthalate (PET). Samples were prior implanted with 150 keV Ag^{+}-ions at fluence of 1×10^{17} ions/cm^2 then irradiated with 30 MeV Au^{7+}-ions. Atomic force microscopy (AFM) images and optical micrographs reveal blistering induced by swift heavy ions, especially for the implanted sample. Raman studies show the characteristic D and G bands, with the G band being more intense, indicating the presence of amorphous and graphite-like structures in the samples. The band intensities decrease depending on the processing conditions, signifying optical and structural transformations in the implanted and/or irradiated PET. Current-voltage (I-V) measurements indicate an increase in the conductivity of the implanted samples, which is further enhanced upon irradiation, highlighting a transition from insulating to semiconducting behavior.

1 Introduction

The exceptional mechanical, chemical, and thermal properties of polyethylene terephthalate (PET) make it a popular polymer in various industrial and scientific applications [1]. However, its application in advanced electronics and optoelectronics is hampered by its electrically insulating characteristics. A successful method for altering these characteristics is ion implantation followed by swift heavy ion (SHI) irradiation [2, 3]. While additional SHI irradiation causes structural changes such as carbonisation, defect formation, and the production of nanoclusters, the addition of silver (Ag) ions into PET can generate conductive pathways [2, 3]. Silver is one of the noble metals that has been widely employed for generating nanoparticles within polymer matrices due to its propensity to nucleate and aggregate at high fluence [2]. A number of variables, including ion fluence, energy, and the characteristics of the polymer, affect the size and dispersion of these nanoparticles and make them conductive [2]. The electrical conductivity of the polymer can be considerably changed through the disruption from electronic excitations and sputtering processes due to high energy deposition during irradiation [4, 5], which makes it appropriate for use in sensors and flexible electronic devices, such as optical waveguides, picosecond optical switches, and other nano- and optoelectronic devices [3, 6].

This work, therefore, examines the synergistic effects of 150 keV Ag^{+}-ions implantation and 30 MeV Au^{7+}-ions swift heavy ion irradiation on the structural and the electrical characteristics of PET.

2 Experimental Details

Commercial foil of PET ($C_{10}H_8O_4$) with a thickness of 130 μm was purchased from Sigma-Aldrich and cut into pieces of 12 mm $\times$ 12 mm. This was followed by the cleaning steps in chemical solutions of ethanol and acetone, respectively, using an ultrasonic bath as in Ref [3]. Following preparation, the samples were implanted at 1×10^{17} ions/cm^2 with 150 keV Ag^+-ions using a Varian-Extrion implanter (model 200-20A2F). A low current of 0.40 µA was used during the process at liquid nitrogen temperature in order to limit sample damage from beam-induced heating [7]. The range of the silver particles into the PET matrix was determined to be about 102 nm using the Stopping and Range of Ions in Matter (SRIM/TRIM) simulation code [8, 9]. Pristine and Ag^+-ions implanted PET samples were irradiated with 30 Mev, Au^{7+}-ions at a fluence of 2×10^{13} ions/cm^2 with an irradiation current of about 11.52 nA, using a 6 MV Tandem Accelerator under high vacuum (10^{-6} mbar). Raman spectroscopy was performed using a WITec alpha 300 RAS$^+$ confocal micro-Raman microscope with a 532 nm laser source. The system's integrated platform was also employed to perform atomic force microscopy (AFM) and optical imaging of the samples. Current-voltage measurements were conducted using a Keithley 2450 source-meter unit (SMU) in four-wire configuration, as shown in Figure 1. Ohmic contacts to the PET film were made with copper tape of (1 mm^2) separated by 5 mm. The SMU was operated in PC-controlled remote mode via "SweepMe" software (version 1.5.5). Measurements were performed under ambient conditions by sweeping the voltage from -3 to 3 V in steps of 0.05 V, with the compliance current set to 5 mA.

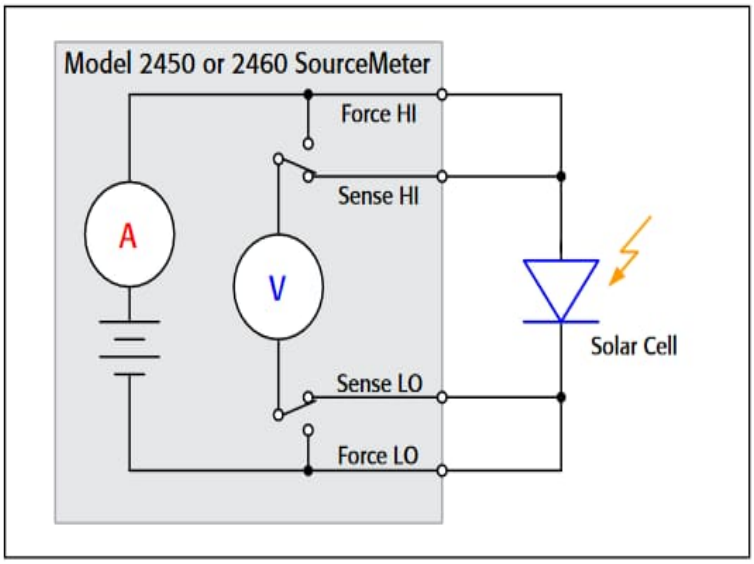

Figure 1: Schematic diagram of the electrical characterisation device.

3 Results and discussion

3.1 Structural Analyses:AFM

Atomic Force Microscopy (AFM) and optical micrographs provide valuable information about the surface morphology and topographical features of the implanted/irradiated PET. Figure 2 (top images) depicts the 3D-surface topography of the samples: Ag^+-implanted (left), pristine irradiated with 30 MeV Au^{7+}-ions (middle), and Ag^+-implanted followed by Au ion irradiation (right). The surface morphology of the implanted PET at 1×10^{17} ions/cm^2 initially shows a smooth texture. However, it drastically increases in surface roughness upon implantation and subsequent irradiation, leading to the formation of conductive carbon clusters at the near surface of the thin film, supported by UV-Vis studies [6]. The images also provide evidence of blistering induced by swift heavy ion irradiation, which is more pronounced for the subsequentially implanted and irradiated sample. The roughness parameters, i.e., the arithmetic mean roughness, (R_a), the root mean square roughness, (R_q), the Peak-to-peak height (R_z) along with the surface Kurtosis (Rku) were computed and gathered in Table 1. Concerning the micrographs (bottom images), one can observe changes in surface contrast and texture, particularly in the implanted and irradiated samples, suggesting structural or compositional alterations near the surface, implying the formation of conductive carbon clusters at the near surface of the samples.

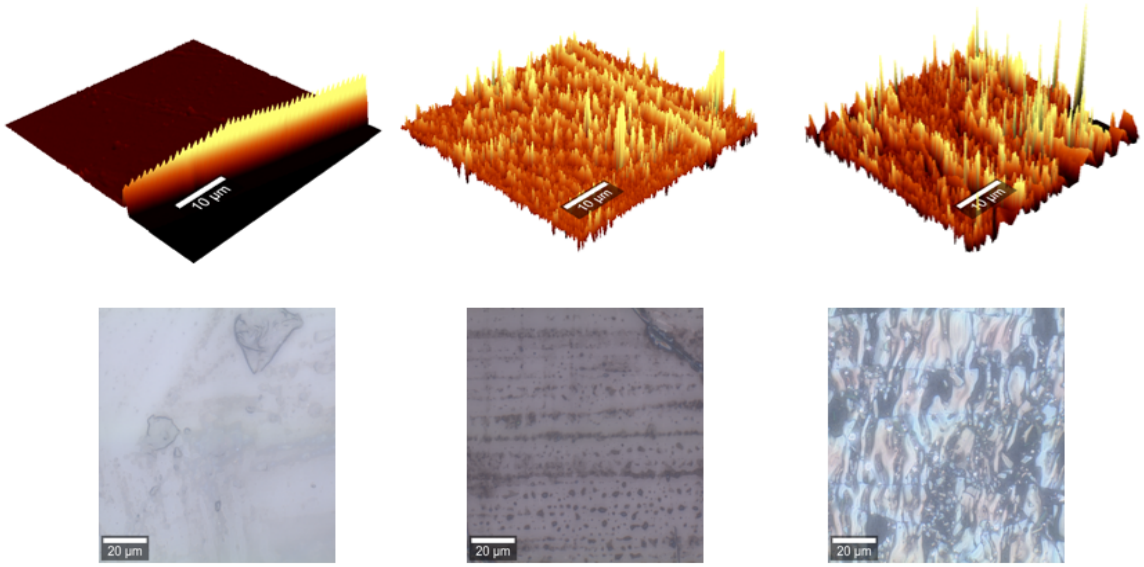

Figure 2: The top panel shows AFM images of PET films: implanted with 150 KeV Ag^{+} ions (left), irradiated with 30 MeV Au ions (middle), and implanted-irradiated (right). The bottom panel presents corresponding optical micrographs.

Table 1: Surface roughness parameters of PET films under different treatments.

Parameter	Implanted only	Irradiated only	Sequentially implanted and irradiated
R_a[nm]	28.06	50.25	236.42
R_q[nm]	46.51	121.39	353.51
R_z[nm]	961.54	1399	3981.5
Rku	40.81	14.37	11.77

3.2 Structural Analyses:Raman Spectroscopy

The Raman spectra of implanted and irradiated PET show progressive structural changes, as illustrated in figure 3. The peaks observed on the pristine spectrum at 857, 1286, 1613, and 1723 cm^{-1} are ascribed to the C–C breathing (ring and complex O-C stretching mode), ring C = C stretching, and C=O stretching modes [3], respectively. The energy deposition from implantation and irradiation causes these peaks to reduce and even disappear, as observed in the implanted and/or irradiated spectra (see red, blue and pink spectra), suggesting the structural modification of the polymers. Figure 3 shows the structural modification of the polymers through implantation and irradiation processes with D and G bands at at 1345 and 1583 cm^{-1}. Due to nuclear stopping and electronics processes, which are both frequently in charge of the intense degassing of the irradiated PET and the subsequent carbonisation of the near-surface layer of polymers, these bands are indicative of graphite-like structures originating from sp^2 hybridised C atoms [3]. While the D band identifies breathing modes specific to rings, the G band denotes stretched modes shared by both rings and chains [3]. It has been noted that the centroid of the G band (1582 cm^{-1}) precisely corresponds to the one of pure graphite/graphene. The ratio of D and G peaks (I_D/I_G) can be used to determine the well-organised carbon structures or damage that have typically been produced from rings as a result of implantation and radiation-induced by heavy ions. The calculated ratios were obtained to be 0.25, 0.87 and 0.95 for the irradiated PET (red spectrum), Ag-implanted PET at fluence of 1×10^{17} ions/cm^2 (blue spectrum) and Ag-implanted at fluence of 1×10^{17} ions/cm^2 and then irradiated at fluence of 2×10^{13} ions/cm^2 with Au^{7+} ions (pink spectrum), respectively. The obtained ratio values are higher than those reported for Si-ion irradiation [3], confirming that the the degree of damage depends on the ion type and ion fluence. The increase of this factor confirms the gradual modification of the polymer matrix. On the other hand, the enhanced contrast, manifested as increased variation in light and dark regions on the optical micrograph images confirm the structural changes in the samples during implantation and/or irradiation and corroborate with the AFM results.

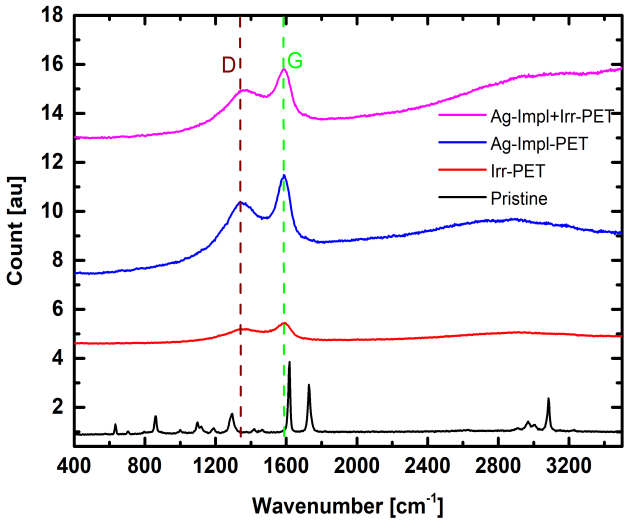

Figure 3: Raman spectra for pristine PET (black spectrum), for the irradiated PET (red spectrum), for Ag-implanted PET at fluence of 1×10^{17} ions/cm^2 (blue spectrum) and Ag-implanted at fluence of 1×10^{17} ions/cm^2 and then irradiated at fluence of 2×10^{13} ions/cm^2 with Au^{7+} ions (pink spectrum), respectively.

3.3 Electrical characterisation

Figure 4 presents the I-V characteristics of pristine irradiated PET, Ag-implanted PET, and Ag-implanted PET further irradiated with 30 MeV Au^{7+}-ions. The pristine irradiated sample (blue curve) exhibits negligible current response across the entire ±3 V range, consistent with its insulating nature. In contrast, the Ag-implanted sample (orange curve) shows a moderate increase in conductivity, attributed to the formation of defect sites and partial clustering of silver within the PET matrix [3, 6]. The highest conductivity is observed in the Ag-implanted and Au-irradiated sample (green curve), which exhibits a nearly linear and symmetric IV profile, indicating enhanced charge transport pathways. This improvement is likely due to the formation of conductive Ag nanoclusters and carbonaceous structures induced by the combined effects of implantation and swift heavy ion irradiation [6].

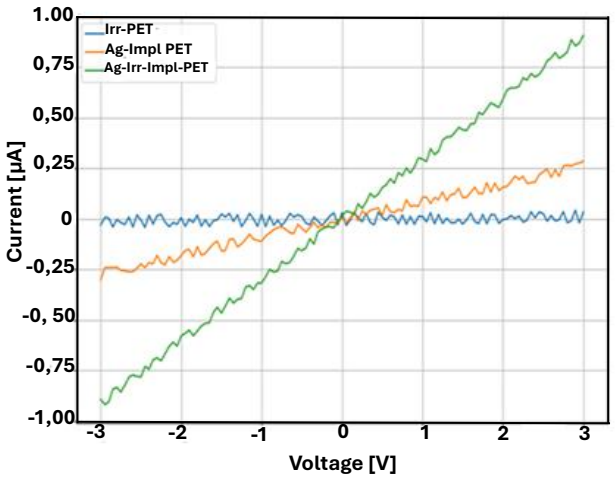

Figure 4: Voltage dependencies of electric current for samples implanted with 150 keV and further irradiated with 30 MeV Au^{7+}-ions.

4 Summary

Pristine and Ag-implanted PET at fluence of 1×10^{17} ions/cm^2 with 150 keV and further irradiated with 30 MeV Au^{7+}-ions have been investigated. These successive treatments of polyethylene terephthalate (PET) produce synergistic effects that significantly affect the structural and electrical properties of the samples. AFM and optical microscopy indicated significant surface morphological modifications such as blistering and increased roughness, which were particularly noticeable in the joint-processed sample. Raman spectroscopy results revealed gradual carbonisation, as demonstrated by the appearance of D and G bands and increasing I_D/I_G ratio from 0.25 to 0.95, suggesting the development of a disordered graphitic network. Current-voltage studies revealed an evolution from insulator to semiconductor characteristics, with implanted and irradiated PET exhibiting the maximum conductivity. The increase in conductivity is due to the concurrent growth of conductive Ag nanoclusters and carbonaceous pathways. These findings demonstrate that combined ion beam processing is an effective way for tailoring polymer characteristics for advanced applications in flexible electronic and optoelectronic technologies.

Acknowledgments

JJ Mboukam thanks TUT and the National Research Foundation (Grant Number PSTD23042697816) for financial support.

References

[1] R. Nisticò, "Polyethylene terephthalate in the packaging industry," *Polymer testing*, vol. 90, p. 106707, Oct. 2020.

[2] V. Popok, "Ion implantation of polymers: formation of nanoparticulate materials," *Reviews on advanced materials science*, vol. 30, no. 1, pp. 1–26, Feb. 2012.

[3] J. J. Mboukam, D. C. Chilukusha, M. Madhuku, and M. Msimanga, "Annealing of ag-implanted polyethylene terephthalate films by low-temperature swift $^{28}si^{4+}$-ion irradiation: Effects on structural and optical properties," *Radiation Physics and Chemistry*, vol. 223, p. 111991, Oct. 2024.

[4] T. Sharma, S. Aggarwal, S. Kumar, V. Mittal, P. Kalsi, and V. Manchanda, "Effect of gamma irradiation on the optical properties of cr-39 polymer," *Journal of materials science*, vol. 42, no. 4, pp. 1127–1130, Feb. 2007.

[5] R. C. Ramola, S. Chandra, A. Negi, J. M. S. Rana, S. Annapoorni, R. G. Sonkawade, P. K. Kulriya, and A. Srivastava, "Study of optical band gap, carbonaceous clusters and structuring in cr-39 and pet polymers irradiated by 100 mev o^{7+}-ions," *Physica B: Condensed Matter*, vol. 404, no. 1, pp. 26–30, Jan. 2009.

[6] J. J. Mboukam, D. C. Chilukusha, M. Madhuku, and M. Msimanga, "Optical and structural transformations in polyethylene terephthalate films subjected to ag^{+}-ion implantation and subsequent au^{7+}-ion irradiation," *Physica B: Condensed Matter*, vol. 695, p. 416518, Dec. 2024.

[7] J. J. Mboukam, M. A. Masenya, M. Madhuku, and M. Msimanga, "Cryogenic heavy ion rbs-erda depth profiling of ion implanted pet films," *Nuclear Instruments and Methods in Physics Research Section B: Beam Interactions with Materials and Atoms*, vol. 546, p. 165151, Jan. 2024.

[8] J. F. Ziegler, M. D. Ziegler, and J. P. Biersack, "The stopping and range of ions in matter," *Nuclear Instruments and Methods in Physics Research Section B: Beam Interactions with Materials and Atoms*, vol. 268, no. 11-12, pp. 1818–1823, Sep. 2010.

[9] J. J. Mboukam, D. C. Chilukusha, M. Madhuku, and M. Msimanga, "Characterisation of ag-implanted pet using time-of-flightelastic recoil detection technique," in *PROCEEDINGS of the 68th Annual Conference of the South African Institute of Physics, July 1–5, 2024*. South African Institute of Physics, (SAIP), 2024, pp. 103–108.

This page intentionally left blank.

Up-conversion and thermometric performance of CaF_2:Tb^{3+}, Yb^{3+} material

Mubarak Yagoub and Buyisiwe Sondezi

Department of Physics, University of Johannesburg, Cnr Kingsway Avenue and University Road, Auckland Park, 2006, South Africa.

E-mail: mubaraky@uj.ac.za

Abstract. We report on up-conversion and thermometric properties of CaF_2: Tb^{3+}, Yb^{3+} material. The CaF_2: Tb^{3+}, Yb^{3+} material exhibited ultraviolet-visible, sharp peaks, and broadband near-infrared emission upon 980 nm laser excitation due to the up-conversion energy transfer from Yb^{3+} to Tb^{3+} ions. The sharp emission peaks originated from the Tb^{3+}:4f-4f transition, while the broadband emission was attributed to the anomalous emission of the Yb^{2+} ion. The presence of the Yb^{2+} in the studied material was investigated by X-ray photoelectron spectroscopy. The existence of the Yb^{2+} anomalous emission in the material was found to be a potential luminescence thermometer using the luminescence intensity ratio method. The temperature-dependent Tb^{3+}:$^5D_4$ and Yb^{2+} dual-band demonstrated a high-temperature sensitivity of ~1.0%/K at 415 K. This result suggested that the material has potential for sensitive thermometry applications.

1 Introduction

The application of luminescent materials in thermometry has recently intensified due to their ability to provide a robust solution for remote temperature measurements [1, 2]. A temperature-sensitive material usually contains a host doped with foreign activator ions, such as transition metal and/or rare-earth ions [1]. The mechanism of temperature measurement using luminescent thermometry relies on the change of the luminescence intensity or the lifetime with temperature. The change in the luminescence intensity ratio (LIR) normally utilizes the ratio between two different emission bands to calculate the temperature [2]. There are two LIR temperature measurement principles, namely non-thermally coupled energy levels (NTCL) and thermally coupled energy levels (TCL). The choice of using one of the principles over the other depends on certain requirements about the energy difference between the levels [3]. For example, the magnitude of the energy difference in TCL must be in the range of 200-2000 cm^{-1} [4]. If the TCL condition is not met, the NTCL has been adapted to improve the LIR sensitivity [4]. The type of luminescence material can significantly influence temperature sensitivity and precision [1].

Up-conversion luminescence has recently been investigated in thermometry applications [5, 6]. Many contributions on up-conversion-based thermometry materials have been reported, such as $La_2Ti_2O_7$:Er^{3+}, Yb^{3+}, $Ba_3Lu_2Zn_5O_{11}$:Yb^{3+}, Er^{3+} [7], Y_2O_3: Ho^{3+}, Yb^{3+} [6], $Ca_{14}Al_{10}Zn_6O_{35}$: Er^{3+}, Yb^{3+} [8], and $Ca_2Gd_8(SiO_4)_6$: Yb^{3+}, Tb^{3+} [9]. The most used host materials for up-conversion temperature measurement are oxide materials doped with rare-earth activator ions. Thus, it is of great significance to explore the fluoride up-conversion materials in temperature measurement applications. Fluoride compounds such as CaF_2 material have, however, been widely utilized as a host material due to their high stability and transparent behaviour [10]. CaF_2:Tb^{3+}, Yb^{3+} material has

exhibited intense green and anomalous near-infrared up-conversion emission originating from the Tb^{3+} and Yb^{2+} ions, respectively [11]. The existence of the anomalous emission of Yb^{2+} in CaF_2:Tb^{3+}-Yb^{3+} might affect the thermometry properties of the system. Therefore, the thermometry performance of Tb^{3+}, Yb^{3+} ions doped CaF_2 up-conversion material was explored in this study. The temperature measurement based on LIR technology and the influence of the Yb^{2+} anomalous emission on the material's thermometry performance will be presented.

2 Experimental

CaF_2: Tb^{3+} (5 mol%), Yb^{3+} (5 mol%) up-conversion material was synthesised using the coprecipitation route. $TbCl_3$ (99.99%), $YbCl_3$ (99.99%), $CaCl_2$ (99%), and NH_4F (99%) were purchased from Sigma Aldrich and used without further purification. All the chloride precursors were dissolved in 30 mL of distilled water. 5 mL of NH_4F aqueous solution was added dropwise to the chloride solution while stirring over a period of 30 minutes. The mixture was left to stir thoroughly until a white suspension was obtained. The solution was allowed to precipitate and washed with distilled water and ethanol three times. The collected product was then dried in an oven at 80 ^oC for 12 hours. Finally, the powder was ground and annealed in (Ar 96%/H_2 4%) atmosphere at 600 ^oC for 2 h. A Bruker Advance D8 diffractometer equipped with Cu K_α X-rays (λ = 0.154 nm) and Lynx Eye detector was utilized to characterize the structure of the CaF_2: Tb^{3+}, Yb^{3+} material. The voltage and current of the system were maintained at 40 kV, 40 mA for the measurements. X-ray photoelectron spectroscopy (XPS) spectra were collected using A PHI 5000 Versaprobe system equipped with an Al K_α x-ray beam (hν = 1486.6 eV), produced with a 25 W and 15 kV electron beam and an Ar+ ion gun, which was used to minimize charging that could occur on the surface. A Multipack version 8.2 software was used to perform the peak fitting. A 980 nm laser excitation equipped with a PMT detector was used to collect the up-conversion emission. The temperature-dependent up-conversion measurements were done in the range of 290-600 k.

3 Results and Discussions

The X-ray Powder Diffraction (XRPD) patterns of the CaF_2: Tb^{3+}, Yb^{3+} material are shown in Fig. 1 (a). The studied material exhibited diffraction peaks that were associated with the cubic phase of CaF_2 (ICSD: 35–0816). The incorporation of the dopant ions, Tb^{3+} and Yb^{3+}, caused a slight shift towards the lower diffraction angles, which is consistent with our previous studies [11, 12]. The shift of XRPD patterns is normally associated with the successful substitution of the dopants into the CaF_2 lattice. To further confirm the incorporation of the dopants, XPS was conducted on the studied up-conversion material. Fig. 1(b) shows the general XPS survey of the CaF_2: Tb^{3+}, Yb^{3+} material, where peaks from Ca 2p, F 1s, Tb 3d, and Yb 4d were all detected. To further identify the Yb ion's oxidation states, the high-resolution XPS peak of the Yb 4d XPS peak is presented in Fig.1(c). The fit confirmed a mixed oxidation state of Yb ion, Yb^{3+} and Yb^{2+}. Due to the strong exchange interaction that occurs in Yb^{3+} ions, the Yb^{3+} 4d XPS peak does not exhibit the predicted 2/3 intensity ratio, but shows several fitting peaks, see Fig. 1(c), [11, 13]. However, the Yb^{2+} ion consists of a filled 4f level. Therefore, the exchange interaction with the core levels is negligible, and the two spin-orbit splitting peaks of $4d_{3/2}$ and $4d_{5/2}$, (Fig. 1(c)), were expected. The XPS, therefore, confirmed that the material indeed consists of two oxidation states of the Yb ion, that is, Yb^{2+} and Yb^{3+}. The presence of the Yb^{2+} ion within the material might influence the up-conversion emission characteristics of the material.

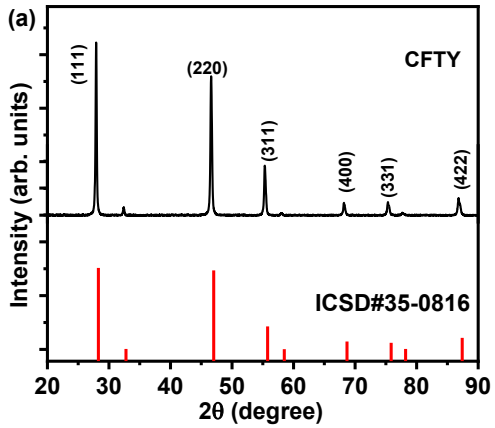

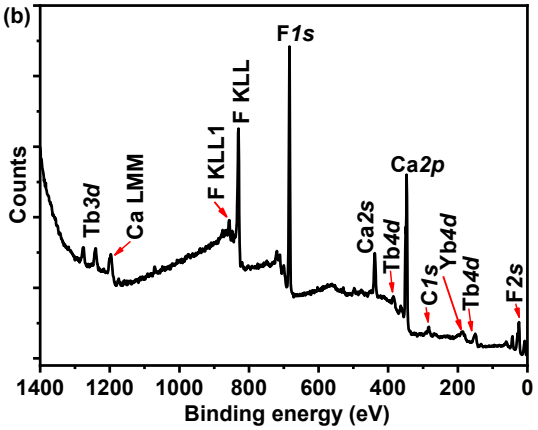

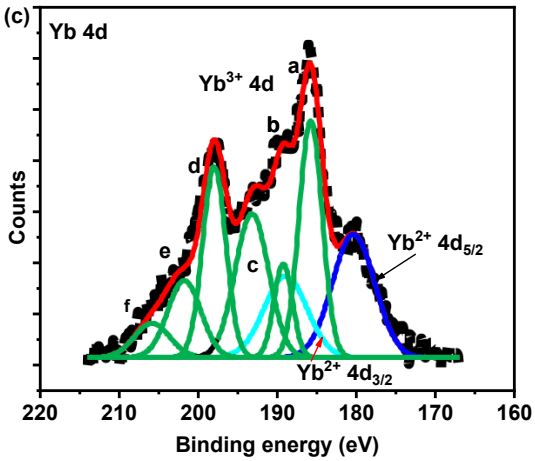

Figure 1: (a) XRPD patterns of the CaF_2:Tb^{3+}, Yb^{3+} (CFTY) up-conversion material. (b) XPS survey of the corresponding studied material, and (c) High-resolution XPS of the Yb 4d peak showing the Yb^{3+} and Yb^{2+} oxidation states.

Figure 2(a) shows the up-conversion emission of the CaF_2: Tb^{3+}, Yb^{3+} material excited using 980 nm, where sharp peaks and broadband emissions were observed. The sharp emission peaks are attributed to the $^5D_3$-^7F_j (j = 6, 5, and 4) and $^5D_4$-^7Fj (j = 6, 5, 4, and 3) within the 4f-4f transitions of Tb^{3+} ions due to a cooperative energy transfer between Yb^{3+} and Tb^{3+} ions. The up-conversion emission from the $^5D_4$ level has been demonstrated to occur through two-photon cooperative energy transfer [12]. Firstly, the 980 nm photon excites an electron from the $^2F_{7/2}$ ground state to the $^2F_{5/2}$ excited state of the Yb^{3+} ion. The second incoming photon would cooperatively transfer the electron from the Yb^{3+}:$^2F_{5/2}$ excited state to the $^5D_4$ level of the Tb^{3+} ion, from where the $^5D_4$-^7F_j (j = 6, 5, 4, and 3) transitions could occur, Figure 2(b). The up-conversion emission observed from the Tb^{3+}:$^5D_3$ excited state requires a three-photon process to occur. There are different ways to populate the $^5D_3$ excited state, which have been thoroughly discussed in detail somewhere [11, 12, 14].

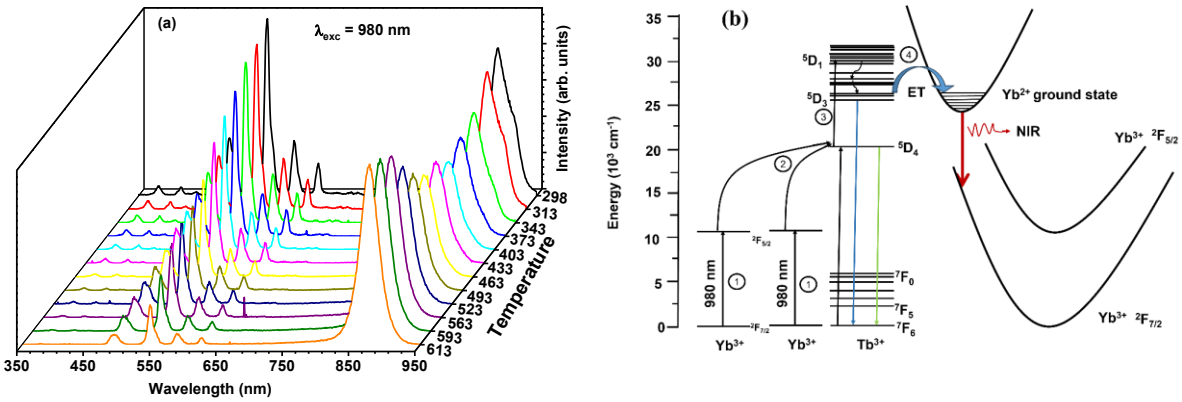

Figure 2: (a) Up-conversion emission of Yb^{3+}-Tb^{3+} doped CaF_2 material excited by 980 nm, (b) A schematic diagram of the proposed up-conversion energy transfer processes and NIR emission involving Yb^{3+}, Tb^{3+}, and Yb^{2+} ions.

The NIR emission in Figure 2(b) is associated with the Yb^{2+} ion's anomalous emission, which has previously been observed in various fluoride hosts upon down-conversion and up-conversion processes [11]. Furthermore, such emissions of the Yb^{2+} ion were found to strongly depend on charge compensation ions, such as Li^+ [11]. Figure 2(b), however, shows the schematic diagram of the up-conversion mechanism that is responsible for the NIR emission. The energy transfer up-conversion process was clearly explained in our previous study [11]. After

the population of the Tb^{3+}:$^5D_1$ excited state, the electrons probably transfer to the Yb^{2+} ground state, which gives rise to the NIR emission, process 4 in Figure 2(b).

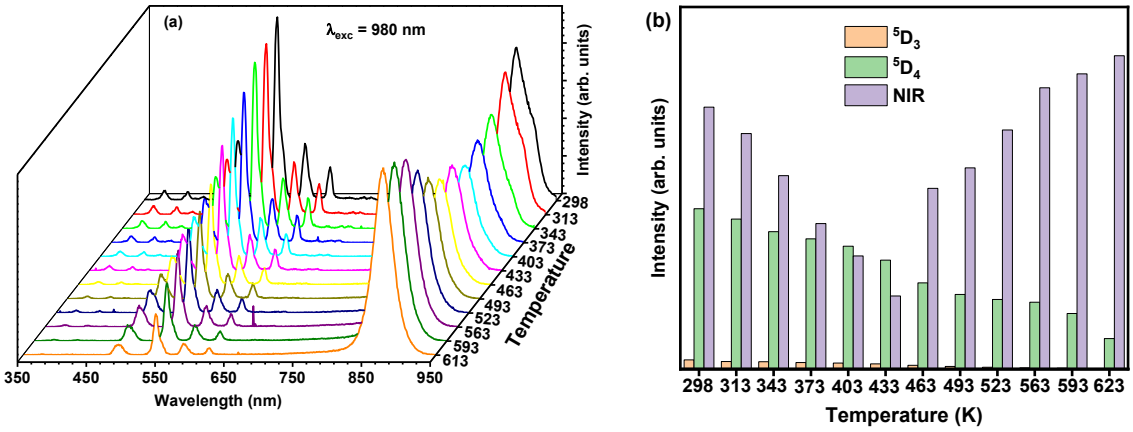

Figure 3: (a) Temperature-dependent emission spectra of CaF_2:Tb^{3+}, Yb^{3+} up-conversion material, and (b) Contrast histogram of integrated intensities at different temperatures.

The temperature-dependent up-conversion spectra of the CaF_2:Tb^{3+}, Yb^{3+} were recorded to explore the application of the material in temperature sensing. From Figure 3 (a), the temperature has a significant impact on the emission of the material. As the temperature increased, the intensity of the $^5D_3$ and $^5D_4$ transitions of the Tb^{3+} ion gradually decreased. The intensity of the NIR emission was, however, first decreased and then increased with temperature. The changing trend of the emission intensity can clearly be seen through the integral intensity histogram shown in Figure 3(b). The quenching rate of the $^5D_4$ emission intensity is more pronounced than the $^5D_3$ emission intensity of the Tb^{3+} ion. The $^5D_3$ emission intensity gradually decreased until it vanished at high measurement temperatures. The NIR emission was quenched at a faster rate at low temperatures before it increased at high measurement temperatures. The increase in the NIR emission at high temperatures can be attributed to the increase in lattice vibration, which might increase the energy transfer from host defects and the Tb^{3+}:$^5D_3$ level to the Yb^{2+} ions [1, 15].

The temperature-sensitive nature of the up-conversion emission suggests that the material could have a potential application in thermometry. Therefore, the thermometric parameters using the LIR technique were determined. The $^5D_4$ and $^5D_3$ transitions of the Tb^{3+} ion can be considered as thermally coupled levels, see Figure 2(b). According to the Boltzmann distribution, the temperature sensing sensitivity of the thermally coupled levels is restricted to the energy separation between the levels of 200-2000 cm^{-1} [1, 4]. Therefore, the theoretical relationship of LIR of Tb^{3+}:$^5D_4$/$^5D_3$ can be fitted using the thermally coupled level, Eq. (1) [2].

$$LIR = \frac{I_{5D4}}{I_{5D3}} = A + B \times exp\left(-\frac{\Delta E}{k_B T}\right) \qquad (1)$$

A, B, and ΔE are constants related the $^5D_3$ and $^5D_4$ levels. The LIR fitting curve of the $\frac{I_{5D4}}{I_{5D3}}$ is shown in Figure 4(a). The model was in good agreement with the fitted values of the LIR $\left(\frac{I_{5D4}}{I_{5D3}}\right)$. However, the LIR $\left(\frac{I_{NIR}}{I_{5D4}}\right)$ as a function of measurement temperatures is shown in Figure 4(b), where the non-thermally coupled model was utilized [6], Eq. (2).

$$LIR = \frac{I_{NIR}}{I_{5D4}} = C_0 + C_1 T + C_2 T^2 + C_3 T^3 \qquad (2),$$

where T is the absolute temperature and C_0, C_1, C_2, and C_3 are the polynomial's fitting parameters. The test values of the LIR $\left(\frac{I_{NIR}}{I_{5D4}}\right)$ is fitted well with the proposed model.

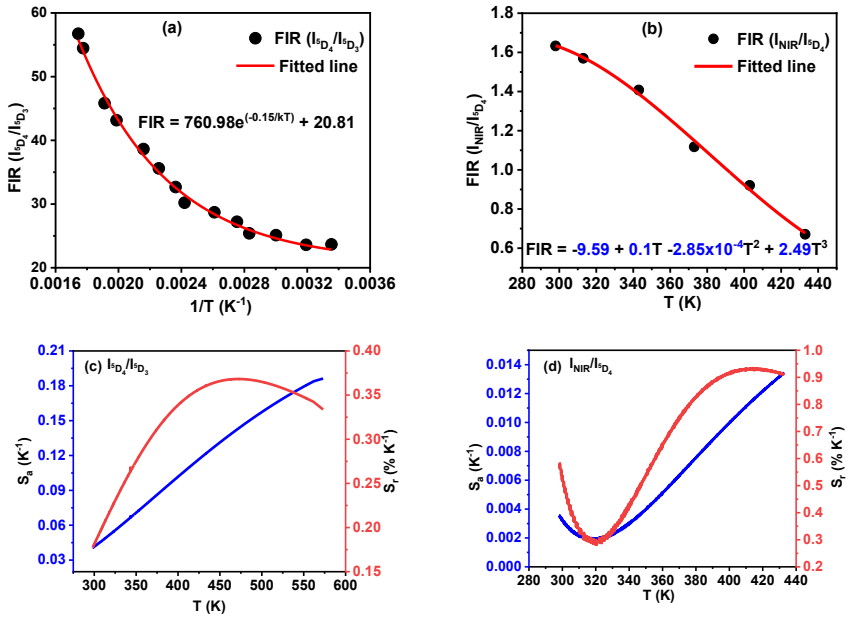

Figure 4: (a) and (b) fitting curve of FIR value as a function of temperature. Absolute sensitivity (S_a) and relative sensitivity (S_r) versus temperature for (c) I_{5D4}/I_{5D3} and (d) I_{NIR}/I_{5D4}.

For temperature sensing applications, the absolute sensitivity S_a and the relative sensitivity S_r are prominent indices to determine the performance of the material's temperature sensing. These two parameters can be calculated using equations (3) and (4).

$$S_a = \left|\frac{\mathrm{d(LIR)}}{\mathrm{d(T)}}\right| \qquad (3)$$

$$S_r = \left|\frac{1}{\mathrm{LIR}}\frac{\mathrm{d(LIR)}}{\mathrm{d(T)}}\right| \times 100\% \qquad (4)$$

Where d(LIR) is the change in the LIR relative to the change in the absolute temperature, d(T). It is worth mentioning that the absolute sensitivity and relative sensitivity were calculated from the fitted LIR data. Figure 4(c) and (d) show a double Y-axis of the calculated S_a and S_r as a function of temperature for both LIR $\left(\frac{I_{5D4}}{I_{5D3}}\right)$ and LIR $\left(\frac{I_{NIR}}{I_{5D4}}\right)$, respectively. For LIR $\left(\frac{I_{5D4}}{I_{5D3}}\right)$, as the temperature increases, S_a increased as a whole, whereas the S_r value increased with temperature and attained a maximum value of 0.39 %K^{-1} at 466 K, then started to decrease. The situation was changed for LIR $\left(\frac{I_{NIR}}{I_{5D4}}\right)$, where S_a decreases and then increases with temperature. The S_r reached a maximum value of 0.93 %K^{-1} at 415 k, then it decreased. Although the Tb^{3+}:4f-4f transition offers good sensitivity overall thermal response, the Tb^{3+}:$^5D_4$ and NIR ratio has better sensitivity, which is closer to unity. In Summary, CaF_2:Tb^{3+}, Yb^{3+} showed excellent temperature sensitivity, which could be a suitable candidate material for thermometry applications.

4 Conclusion

The CaF_2:Tb^{3+}, Yb^{3+} up-conversion material was prepared and demonstrated to be sensitive to temperature. The material exhibited sharp emission peaks in the UV-Vis region and a broadband emission in the NIR region. The sharp emission peaks originated from the $^5D_3$-^7F_j and $^5D_4$-^7F_j transitions of the Tb^{3+} ion due to the cooperative energy transfer from the Yb^{3+} ion. The broadband emission in the NIR region was attributed to the anomalous emission of the Yb^{2+} ion. The presence of the Yb^{2+} ion was confirmed using XPS analysis. The LIR technique was used to calculate relative and absolute sensitivities. The CaF_2:Tb^{3+}, Yb^{3+} offers good performance as a luminescence thermometer, especially the ratio of the $^5D_4$ to NIR band, which has a temperature sensitivity close to 1%K^{-1} at 415 K. The results showed that this CaF_2:Tb^{3+}, Yb^{3+} up-conversion material has potential application in the field of optical temperature sensing.

Acknowledgment

The Authors acknowledge financial assistance from the University Research Council (URC). The use of the characterization facilities at the University of the Free State, Department of Physics, obtained with financial support from the South African Research Chairs Initiative of the Department of Science and Technology and the National Research Foundation of South Africa (grant 84415) is hereby acknowledged.

References

[1] S. N. Ogugua, C. Abram, B. Fond, R. E. Kroon, F. Beyrau, and H. C. Swart, "Effect of annealing conditions on the luminescence properties and thermometric performance of $Sr_3Al_2O_5Cl_2:Eu^{2+}$ and $SrAl_2O_4:Eu^{2+}$ phosphors," *Dalton Transactions*, vol. 53, no. 10, pp. 4551–4563, Feb. 2024, doi: 10.1039/d3dt03836j.

[2] Y. Chen, Y. Shen, L. Zhou, J. Lin, J. Fu, Q Fang, R. Ye, Y. Shen. S, Xu, L. Liei, and D. Deng, "Temperature-dependent luminescence of Bi^{3+}, Eu^{3+} co-activated La_2MgGeO_6 phosphor for dual-mode optical thermometry," *J Lumin*, vol. 249, p. 118995, Sep. 2022, doi: 10.1016/J.JLUMIN.2022.118995.

[3] W. Dai, J. Hu, G. Liu, S. Xu, K. Huang, J. Zhou, and M. Xu, "Thermometer of stable $SrAl_2Si_2O_8$: Ce^{3+}, Tb^{3+} based on synergistic luminescence," *J Lumin*, vol. 217, p. 116807, Jan. 2020, doi: 10.1016/J.JLUMIN.2019.116807.

[4] G. Gao, D. Busko, S. Kauffmann-Weiss, A. Turshatov, I. A. Howard, and B. S. Richards, "Wide-range non-contact fluorescence intensity ratio thermometer based on Yb^{3+}/Nd^{3+} co-doped La2O3 microcrystals operating from 290 to 1230 K," *J Mater Chem C Mater*, vol. 6, no. 15, pp. 4163–4170, Apr. 2018, doi: 10.1039/C8TC00782A.

[5] S. Wang, "Sensitive Ho^{3+},Yb^{3+} co-doped mixed sesquioxide single crystal fibers thermometry based on upconversion luminescence," *J Alloys Compd*, vol. 891, p. 162062, Jan. 2022, doi: 10.1016/J.JALLCOM.2021.162062.

[6] V. Makumbane, M. Y. A. Yagoub, Z. Xia, R. E. Kroon, and H. C. Swart, "Up-Conversion Luminescence and Optical Temperature Sensing Behaviour of Y_2O_3:Ho^{3+}, Yb^{3+} Phosphors," *Crystals 2023, Vol. 13, Page 1288*, vol. 13, no. 8, p. 1288, Aug. 2023, doi: 10.3390/CRYST13081288.

[7] J. Chen, J. J. Guo, Y. H. Chen, X. S. Peng, G. A. Ashraf, and H. Guo, "Up-conversion properties of $Ba_3Lu_2Zn_5O_{11}$:$Yb3^{+}$,Er^{3+} phosphors for optical thermometer based on FIR technique," *J Lumin*, vol. 238, p. 118294, Oct. 2021, doi: 10.1016/J.JLUMIN.2021.118294.

[8] L. Zhou, Y. Chen, Y. Shen, J. Lin, J. Fu, L. Lei, R. Ye. D. Deng, and S. Xu, "Designing Optical Thermometers Using Down/Upconversion $Ca_{14}Al_{10}Zn_6O_{35}$: Ti^{4+}, Eu^{3+}/Yb^{3+}, Er^{3+} Thermosensitive Phosphors," *Inorg Chem*, vol. 61, no. 28, pp. 10667–10677, Jul. 2022, doi: 10.1021/ACS.INORGCHEM.2C00769/SUPPL_FILE/IC2C00769_SI_001.PDF.

[9] J. Wei., "Temperature sensing behavior in Yb^{3+}–Tb^{3+} and Eu^{3+} doped $Ca_2Gd_8(SiO_4)_6O_2$ phosphors based on upconversion and downshifting luminescence," *Journal of Materials Science: Materials in Electronics*, vol. 29, no. 14, pp. 12061–12066, Jul. 2018, doi: 10.1007/S10854-018-9312-9/TABLES/2.

[10] M. Y. A. Yagoub, H. C. Swart, and E. Coetsee, "Energy transfer study between Ce^{3+} and Tb^{3+} ions in a calcium fluoride crystal for solar cell applications," *J Lumin*, vol. 187, pp. 96–101, Jul. 2017, doi: 10.1016/J.JLUMIN.2017.02.066.

[11] M. Y. A. Yagoub, H. C. Swart, and E. Coetsee, "Anomalous emission of Yb^{2+} in CaF_2:Tb^{3+}, Yb^{3+} up-conversion phosphor," *Physica B Condens Matter*, vol. 669, Nov. 2023, doi: 10.1016/j.physb.2023.415298.

[12] M. Y. A. Yagoub, H. C. Swart, and E. Coetsee, "The role of Li^{+} interstitial ions in up-conversion intensity of CaF_2:Yb^{3+}, Tb^{3+} phosphors," *Mater Res Bull*, vol. 156, p. 111986, Dec. 2022, doi: 10.1016/J.MATERRESBULL.2022.111986.

[13] Y. Ohno, "XPS studies of the intermediate valence state of Yb in $(YbS)_{1.25}CrS_2$," *J Electron Spectros Relat Phenomena*, vol. 165, no. 1–3, pp. 1–4, Sep. 2008, doi: 10.1016/J.ELSPEC.2008.05.009.

[14] T. Grzyb, R. J. Wiglusz, A. Gruszeczka, and S. Lis, "Down- and up-converting dual-mode YPO_4:Yb^{3+},Tb^{3+} nanocrystals: synthesis and spectroscopic properties," *Dalton Transactions*, vol. 43, no. 46, pp. 17255–17264, Nov. 2014, doi: 10.1039/C4DT02234C.

[15] E. H. H. Hasabeldaim, H. C. Swart, and R. E. Kroon, "Luminescence and stability of Tb doped CaF_2 nanoparticles," *RSC Adv*, vol. 13, no. 8, pp. 5353–5366, Feb. 2023, doi: 10.1039/d2ra07897j.

Physiochemical, optical, and magnetic properties of nickel -magnesium ferrite nanoparticles for various applications

STM Nxumalo, WB Mdlalose, and PB Khoza

School of Chemistry and Physics, University of KwaZulu-Natal, P/Bag X54001, Durban 4000, South Africa

E-mail: 223153020@.stu.ukzn.ac.za

Abstract. This study explores the structural, morphological, optical, and magnetic properties of $MgFe_2O_4$, $Ni_{0.5}Mg_{0.5}Fe_2O_4$, and $NiFe_2O_4$ nanoparticles synthesized via the glycol-thermal method. Characterization techniques including X-ray diffraction (XRD), Fourier transform infrared (FTIR) spectroscopy, high-resolution transmission electron microscopy (HRTEM), ultraviolet-visible (UV-Vis) spectroscopy, Mössbauer spectroscopy, and vibrating sample magnetometry (VSM) were employed. The XRD confirmed single-phase spinel structures with decreasing crystallite sizes (11.40–8.60 nm) and lattice parameters (8.38–8.33 Å) as Ni content increased. FTIR supported the spinel structure findings. TEM revealed semi-spherical particles with varying degrees of agglomeration. Optical band gaps decreased from 2.25 to 1.67 eV with increasing Ni content. Magnetic analysis showed a mix of ferrimagnetic and paramagnetic behavior, with saturation magnetization increasing from 45.74 to 70.39 emu/g. These findings highlight the potential of these materials for biomedical and electronic applications.

1 Introduction

Spinel ferrites with the general formula of MFe_2O_4 (where M could be Mg^{2+}, Ni^{2+}, etc.) are attracting significant research interest due to their versatile physical properties, making them suitable for applications; this includes sensors, supercapacitors, and magnetic devices [1]. At the nanoscale, these properties can be tuned by altering crystallite size and cation distribution within the spinel structure.

Nickel and magnesium ferrites are soft magnetic materials with high electrical resistance and low coercivity[2]. Magnesium (Mg^{2+}) is a non-magnetic ion without an unpaired electron and could prefer any of the tetrahedral (A) and octahedral (B) sites of the ferrite structure. $NiFe_2O_4$ nanostructures offer excellent stability and electrochemical performance, making them ideal for energy storage, data recording, and biomedical applications [3]. In most new studies, substitution leads to an improvement in the properties of spinel ferrites due to their adjustable properties [4]. Incorporating Ni ions into the $MgFe_2O_4$ lattice can significantly influence the structural, morphological, optical, and magnetic properties of magnesium ferrite [1]. The main focus of this work is to investigate the effect of nickel-substituted magnesium in concentrations x = 0.0, 0.5, 1.0 synthesized using the glycol thermal method. The structural, morphological, optical, and magnetic analyses were carried out in detail.

This study demonstrates how Ni substitution in $Ni_xMg_{1-x}Fe_2O_4$ nanoparticles affects their structure, magnetism, and optical properties, revealing tunable cation distribution, superparamagnetic behaviour, and band gap narrowing—highlighting their potential for biomedical and optoelectronic applications.

2 Methodology

2.1 Synthesis of nickel-magnesium ferrite nanoparticles

Nickel-substituted magnesium ferrite nanoparticles (NPs) with the general formula of $Ni_xMg_{1-x}Fe_2O_4$ (at x = 0.0, 0.5, and 1.0) were synthesized using the glycothermal method in a Watlow series stirred pressure reactor, model PARR 4843. Magnesium (II) chloride hexahydrate ($MgCl_26H_2O$), nickel (II) chloride hexahydrate ($NiCl_26H_2O$), and iron (III) chloride hexahydrate ($FeCl_36H_2O$) from Sigma Aldrich were used as high-purity starting materials. Stoichiometric calculations were conducted to ensure the synthesis of the target compound. The weighed combination of precursor materials was individually transferred to a beaker containing 40 ml of deionized water and stirred with a magnetic stirrer for about 20 minutes. A 5 M sodium hydroxide (NaOH) solution was added dropwise to the mixture under continuous stirring to induce co-precipitation, while the pH was monitored to approximately 9–10. The precipitate was then washed several times with deionized water to remove the chlorine ions in the solution. The cleaned precipitate was mixed with 200 mL of ethylene glycol and transferred to the pressure reactor, heated at 200 °C for 6 hours, then cooled to room temperature. The resulting product was washed with deionized water and 200 mL of ethanol. The final precipitate was dried overnight under 250 W infrared light and ground homogeneously, using a mortar and an agate pestle as the end product.

2.2 Characterization techniques

The synthesized ferrite NPs were characterized using a range of analytical techniques. The X-ray diffraction (XRD)
patterns were obtained using Cu Kα radiation (λ = 1.5406 Å) by XRD Diffractometer MiniFlex 600. Fourier transmission infrared (FTIR): Recorded using a PerkinElmer Spectrum IR (version 10.7.2). High-resolution transmission electron microscope (HRTEM): Conducted with a JOEL 1400 microscope. Ultraviolet-visible (UV-vis): Cary-60 absorption instrument. Mössbauer spectroscopy (MS) source containing cobalt-57 sealed within a rhodium matrix. Vibrating sample magnetometer (VSM): Cryogenic Model 3505 Ltd., UK.

3 Results and discussions

3.1 Structural Information

3.1.1 XRD analysis

XRD patterns for $MgFe_2O_4$, $Ni_{0.5}Mg_{0.5}Fe_2O_4$, and $NiFe_2O_4$ are shown in Figure 1(a). Diffraction patterns are consistent with the Fd3m spatial group forming a cubic spinel structure that corresponds to ICDD reference numbers 9003597, 9005842, and 9003776 for $MgFe_2O_4$, $Ni_{0.5}Mg_{0.5}Fe_2O_4$, and $NiFe_2O_4$, respectively. No impurity peaks were observed. The average crystallite size was calculated using the Debye-Scherrer formula, estimated from the highest intensity peak (311). $D = \frac{K\lambda}{\beta \cos\theta}$, where K is the Scherer constant ($K = 0.94$), λ is the X-ray wavelength, β is the peak width at half maximum, and θ is the Bragg's diffraction angle. The other key crystallographic parameters were also calculated; these include the lattice parameter (a), microstrain, x-ray density, and volume of the unit cell. The results are presented in Table 1.

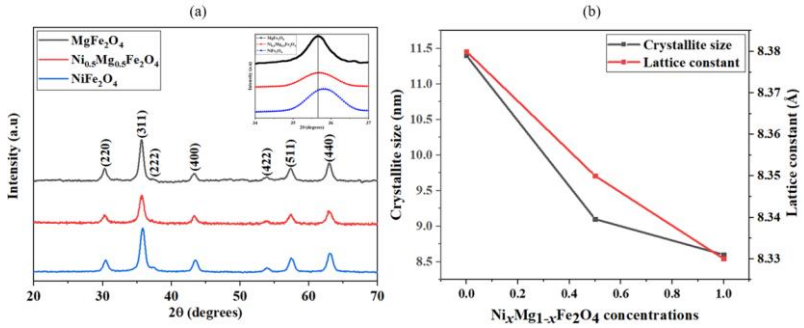

Figure 1: (a) X-ray diffraction pattern of the NPs, the inset is the magnified view of the (311) peak alignment, and (b) behaviour change in crystallite size along with lattice constant.

The results reveal the significant change of Ni^{2+} substitution on the structural characteristics of the ferrite materials. Figure 1(b), the crystallite size decreases with increasing nickel content from 11.40 to 8.600 nm, which corresponds to decreasing Mg^{2+} concentration. This also affected the change in the lattice parameter to decrease from 8.38 Å to 8.33 Å. This trend is attributed to the larger ionic radius of Mg^{2+} (0.072 nm) compared to Ni^{2+} (0.069 nm), which also leads to a reduction in lattice parameters as Ni content increases [5]. Additionally, $Ni_{0.5}Mg_{0.5}Fe_2O_4$ and $NiFe_2O_4$ exhibit higher stacking faults and dislocation densities than $MgFe_2O_4$; this could be due to the increase in lattice strain.

x	x_c (311) peak ±0.01	D_{XRD}(nm) ± 0.20	a (Å)	Unit cell Volume/ $(Å)^3$	Dislocation density x 10^{-3} (nm^{-3})	Micro strain x 10^{-3}	ρ_{XRD} $(g.cm^{-3})$	K_o (N/m)	K_t (N/m)
(a)	35.66	11.40	8.38	588.5	0.200	9.90	4.52	118.4	211.0
(b)	35.69	9.100	8.35	582.2	0.400	12.3	4.96	123.7	194.1
(c)	35.82	8.600	8.33	578.0	0.400	14.4	5.39	130.4	204.0

Table 1: The centroid (x_c), crystallite size (D_{XRD}), lattice parameter (a), unit cell volume, dislocation density, microstrain (ϵ), XRD density, force constants (K_o and K_t), for (a) $MgFe_2O_4$, (b) $Ni_{0.5}Mg_{0.5}Fe_2O_4$, and (c) $NiFe_2O_4$.

3.1.2 FTIR analysis

FTIR spectra for $MgFe_2O_4$, $Ni_{0.5}Mg_{0.5}Fe_2O_4$, and $NiFe_2O_4$ NPs in the range of 4000-600 cm^{-1} are shown in Figure 2. It displays many vibratory patterns, which provide information on the structure and chemical composition of the ferrite NPs. Safaei, *et al.* [6] reported that the absorption band at around 1400 cm^{-1} corresponds to the stretching vibrations of the C-O bond. According to Ramnandan *et al.* [7], the band near 1600 cm^{-1} corresponds to H_2O molecules. This may be due to the deionized water used during the synthesis method. A prominent band between 3100-3400 cm^{-1} corresponds to O–H stretching vibrations, which indicate the presence of residues of hydroxyl groups [8].

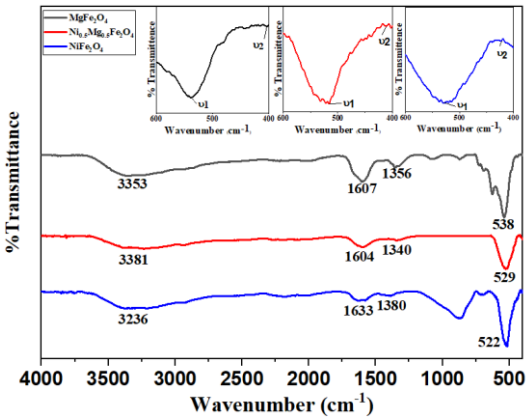

Figure 2: FTIR spectra for prepared ferrite NPs in the range of 400-4000 cm^{-1}, and the inset shows the magnified view in the range of 400-600 cm^{-1}.

In the 400-600 cm^{-1} range of the FTIR spectra, two distinct absorption bands, ν_1 (516-538 cm^{-1}) and ν_2 (403-423 cm^{-1}), were observed. These correspond to M-O stretching vibrations at the tetrahedral (A) and octahedral (B) sites [9]. Their presence confirms the structure of spinel ferrite. In addition, the force constants (K) of both sites, K_t (tetrahedral) and K_o (octahedral), have been calculated by the Waldron method to determine the strength of the bonding [5]. Calculations of K for both sites are shown in Table 1. The results show how the substitution of Ni affects the bonding dynamics in the spinel structure.

3.1.3 TEM analysis

In Figure 3, TEM images reveal that the NPs are almost spherical and show significant agglomeration. This could be caused by the magnetic interactions between particles. However, substitution with Ni has been found to reduce clustering, indicating that Ni^{2+} ions with a smaller ionic radius than Mg^{2+} inhibit grain growth and promote better particle dispersion. The particle size distribution analysis obtained using ImageJ software showed a decreasing trend in the average particle size as the Ni content increased. These values are consistent with the crystallite sizes obtained from XRD, reinforcing the correlation between structural and morphological characteristics.

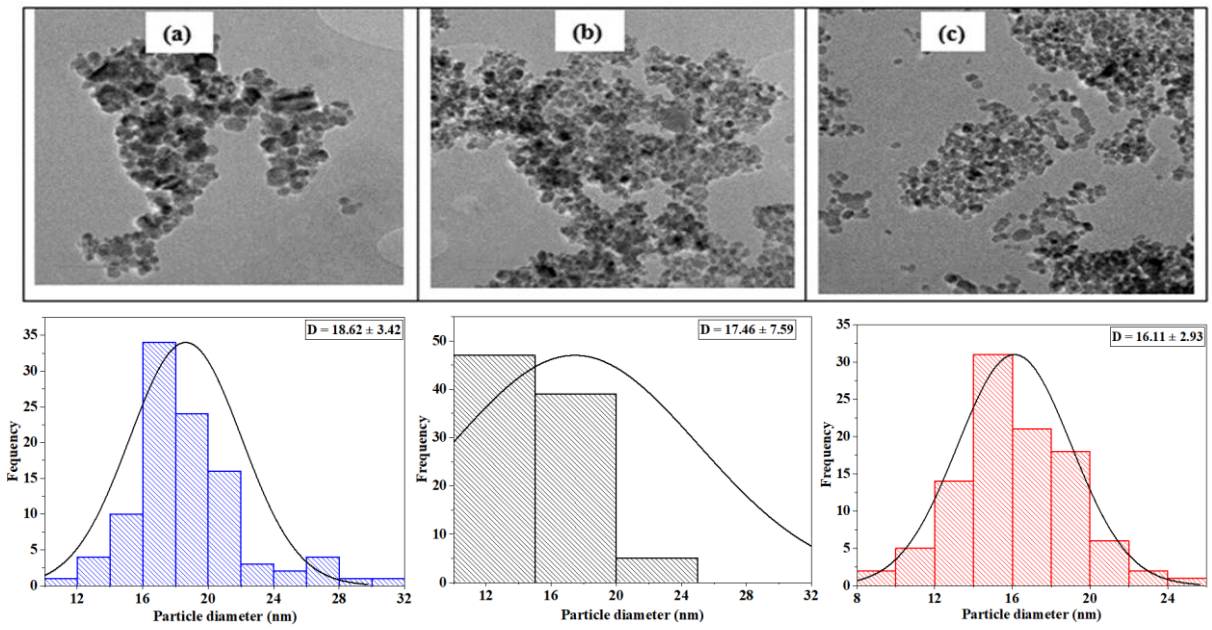

Figure 3: TEM micrographs and ImageJ particle diameter (D) size distribution of (a) $MgFe_2O_4$, (b) $Ni_{0.5}Mg_{0.5}Fe_2O_4$, and (c) $NiFe_2O_4$.

3.2 Optical Measurements

Optical characterisation of samples was recorded using a UV-visible absorption spectrophotometer. Absorption as a function of wavelength spectra for $MgFe_2O_4$, $Ni_{0.5}Mg_{0.5}Fe_2O_4$, and $NiFe_2O_4$ NPs were obtained at room temperature at a wavelength of 200-800 nm and are shown in Figure 4. Absorption intensity is increased from 3.84-4.70 a.u. This suggests that the substitution of Ni increases optical absorption. According to Ateia *et al.* [10] Substitution with smaller crystallites may increase surface area, leading to better absorption and scattering of light. Figure 4 shows the energy bandgap estimated using Tauc plots, which were found to be decreasing from 2.25 eV to 1.67 eV as the concentration of Ni increased.

3.3 Magnetic measurement

To analyze the distribution of Fe ions, ^{57}Fe MS spectroscopy was conducted at room temperature. As shown in Figure 5(a), the spectra were fitted with two sextets and one doublet. The sextets indicate a ferromagnetic phase with iron at sites A and B, while the doublet suggests smaller particles with superparamagnetic behavior, indicating a paramagnetic phase. The MS spectra reveal two distinct sites (A and B) with different isomeric shifts (δ) and hyperfine fields (H), reflecting different Fe environments. In $MgFe_2O_4$, the A-site has a higher isomer shift (0.95 mm/s) than the B-site (0.18 mm/s). This is likely due to a partial reduction of Fe^{3+} to Fe^{2+}, which increases electron density and broadens the spectral band (0.82 mm/s) [11]. It also has a higher A-site fraction (fA = 81%) compared to $Ni_{0.5}Mg_{0.5}Fe_2O_4$ (fA = 51%) and NiFe2O4 (fA = 39%) NPs, indicating a more ordered spinel structure.

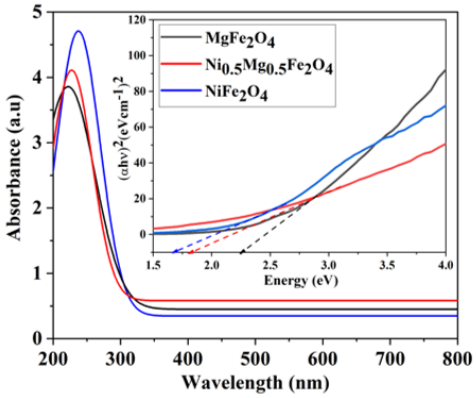

Figure 4: UV-Vis optical spectra of $MgFe_2O_4$, $Ni_{0.5}Mg_{0.5}Fe_2O_4$, and $NiFe_2O_4$ NPs. The inset in Figure 4 shows the corresponding Tauc plots used for energy bandgap estimation.

Content	Peak Wavelength (nm)	Absorption Intensity (a.u)	Band Gap (eV)	Wavelength Range (nm)
$MgFe_2O_4$	222	4.06	2.25	200-300
$Ni_{0.5}Mg_{0.5}Fe_2O_4$	228	4.11	1.82	200-300
$NiFe_2O_4$	237	4.70	1.67	200-300

Table 2: UV-Vis absorption data and bandgap results for $MgFe_2O_4$, $Ni_{0.5}Mg_{0.5}Fe_2O_4$, and $NiFe_2O_4$ NPs.

These changes reflect the effect of cation distribution on the optical properties of the spinel ferrites. Table 2 shows the variation in peak wavelength, absorption intensity, energy bandgap, and the absorption wavelength range of ferrite samples.

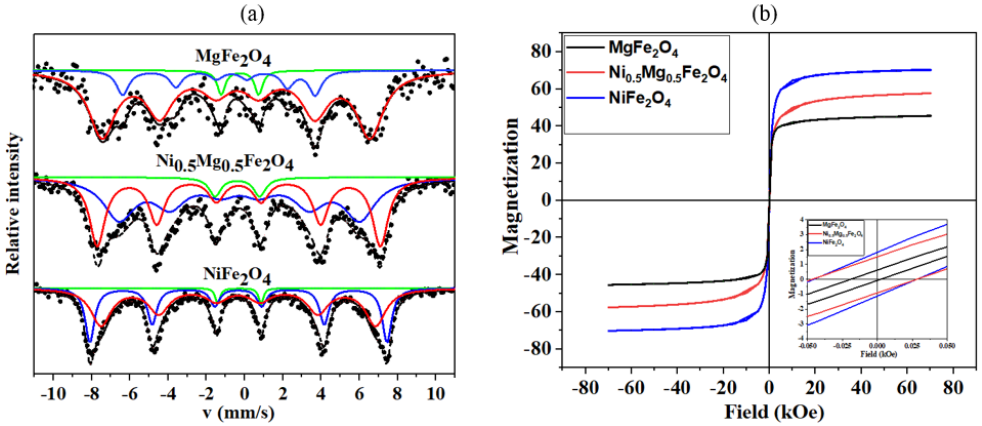

Figure 5: (a) Room temperature ^{57}Fe Mössbauer spectra and (b) vibrating sample magnetometer results for $MgFe_2O_4$, $Ni_{0.5}Mg_{0.5}Fe_2O_4$, and $NiFe_2O_4$.

In $Ni_{0.5}Mg_{0.5}Fe_2O_4$ (A-site) and $NiFe_2O_4$ (B-site), the line broadening was observed to be 0.98 mm/s and 0.64 mm/s, respectively. This is probably due to cation disorder affecting the local electronic and magnetic environments [11]. This disorder causes Fe^{2+} and Fe^{3+} ions to occupy different lattice sites, which increases hyperfine interactions. Hyperfine fields range from 212-325 kOe, which is consistent with ferrimagnetic ordering. Iron ions were predominantly concentrated in the A-site of $MgFe_2O_4$ and $Ni_{0.5}Mg_{0.5}Fe_2O_4$, while the B-site was more concentrated for $NiFe_2O_4$.

Figure 5(b) shows the M–H curves of $MgFe_2O_4$, $Ni_{0.5}Mg_{0.5}Fe_2O_4$, and $NiFe_2O_4$ NPs measured at room temperature using VSM at a range up to 70 kOe. The S-shaped curves confirm their superparamagnetic nature. These NPs exhibit magnetism under an external field, which makes them ideal for drug delivery and controlled therapy [12]. Magnetic measurements show an increase with increasing Ni content. Saturation magnetization (M_S) from 45.74-70.39 emu/g, indicating enhanced magnetic ordering or crystallinity. Coercivity (H_C) also increases from 11-37 Oe, indicating a stronger magnetic anisotropy. The magnetic moment (μ) and remanence ratio (M_r/M_s) also increase from 1.36-2.51 Oe and 0.0136-0.0257, respectively, reflecting the improved magnetic efficiencies. Similar observations were reported by Jabeen *et al*. [13], which indicates that this type of behaviour is essential for energy storage applications.

3 Conclusion

In summary, we have successfully synthesized $Ni_xMg_{1-x}Fe_2O_4$ NPs with a Ni concentration of x = 0.0, 0.5, and 1.0 using the glycol thermal method. Ni substitution in $MgFe_2O_4$ NPs significantly alters their structural, optical, and magnetic properties, as evidenced by reduced crystallite size and lattice parameters. A narrowed optical band gap from 2.25-1.67 eV and enhanced saturation magnetisation from 45.74-70.39 emu/g. These changes were confirmed through XRD, FTIR, TEM, UV-Vis, Mössbauer spectroscopy, and VSM. The findings suggest that Ni incorporation enhances light absorption and magnetic response, which makes the materials promising for applications in medical diagnostics, magnetic devices, and optoelectronics.

Acknowledgments

The National Research Foundation (NRF), Pretoria, South Africa, for the funding through the Thuthuka Grant.

References

[1] S. V. Rathod, V. U. Magar, S. V. Rajmane, D. R. Sapate, and K. M. Jadhav, "Structural and optical characterization of Mg-doped nickel ferrite thin films," *Journal of Materials Science: Materials in Electronics*, vol. 36, no. 3, p. 191, Jan. 2025, doi: 10.1007/s10854-025-14227-x.

[2] T. Ajeesha, R. Ramesh, S. V. Raj, and M. K. Kumar, "Nickel substituted $MgFe_2O_4$ nanoparticles via co-precipitation method for photocatalytic applications," *Physica B: Condensed Matter*, vol. 606, Apr. 2021, doi: 10.1016/j.physb.2020.412660.

[3] Z. Jabeen, M. A. Khan, S. R. Ansari, and A. Ahmad**,** "Hydrothermal synthesis of nickel-substituted magnesium ferrites ($NixMg_{1-x}Fe_2O_4$) and insight into the detailed structural, magnetic, and electrochemi cal properties," *Surfaces and Interfaces*, vol. 40, Aug. 2023, doi: 10.1016/j.surfin.2023.103130.

[4] R. M. Meshram, P. N. Ukey, D. S. Choudhary, and Y. S. Bopche, "A Review on Nanoscale Su-bstitutional Nickel Spinel Ferrite," vol. 20, 2022, doi: 10.48047/NQ.2022.20.1. NQ22437.

[5] S. Z. H. Hashmi, A. A. Khan, M. S. Qureshi, and R. N. Malik, "Synthesis of Nickel-doped Magnesium spinel ferrites ($NixMg_{1-x}Fe_2O_4$) nanomaterials and study of their structural, electrical, and magnetic properties," *Materials Chemistry and Physics*, vol. 305, Sep. 2023, doi: 10.1016/j.matche mphys.2023.127912.

[6] M. Safaei, A. R. Zamanian, S. H. Hashemi, and F. Ghorbani, "Antibacterial effect of polylactic-co-glycolic acid/selenium nanocomposite against dental biofilm," *Polimery/Polymers*, vol. 70, no. 3, pp. 186–193, 2025, doi: 10.14314/polimery. 2025.3.4.

[7] D. Ramnandan, S. Mokhosi, A. Daniels, and M. Singh, "Chitosan, polyethylene glycol and polyvinyl alc ohol modified $MgFe_2O_4$ ferrite magnetic nanoparticles in doxorubicin delivery: A comparative study in *vitro*," *Molecules*, vol. 26, no. 13, Jul. 2021, doi: 10.3390/molecules26133893.

[8] M. De, G. Bera, and H. S. Tewari, "Characterization of Magnesium Substituted Nickel Ferrites Nano Particles Synthesized Using Combustion Technique," 2015. [Online]. Available: www.researchpu blish.com

[9] M. P. Dojcinovic, N. V. Stankovic, D. M. Petrovic, and B. M. Todorovic, "Humidity and temperature sensing of mixed nickel–magnesium spinel ferrites," *Chemosensors*, vol. 11, no. 1, Jan. 2023, doi: 10.3390/chemosensors11010034.

[10] E. E. Ateia, A. A. H. El- Bassuony, G. Abdellatif, and A. T. Mohamed, "The Impact of Ni Substitution on the Structural and Magnetic Properties of Mg Nano-Ferrite," *Silicon*, vol. 10, no. 4, pp. 1687–1696, Jul. 2018, doi: 10.1007/s12633-017-9653-7.

[11] B. Wareppam, E. Kuzmann, V. K. Garg, and L. H. Singh, "Mössbauer spectroscopic investigations on iron oxides and modified nanostructures: A review," Feb. 28, 2023, *Springer Nature*. doi: 10.1557/s43578-022-00665-4.

[12] A. Ali, M. A. Shah, S. Khan, and R. Ahmad, "Review on recent progress in magnetic nanoparticles: synthesis, characterization, and diverse applications," Frontiers in Chemistry, Jul. 13, 2021, *Frontiers Media S.A*., doi: 10.3389/fchem. 2021.629054.

[13] Z. Jabeen, M. A. Khan, S. R. Ansari, and A. Ahmad, "Hydrothermal synthesis of nickel-substituted magnesium ferrites ($NixMg_{1-x}Fe_2O_4$) and insight into the detailed structural, magnetic, and electrochemical properties," *Surfaces and Interfaces*, vol. 40, Aug. 2023, doi: 10.1016/j.surfin.2023.103 130

Design and Characterization of Polymer-Coated Mg-Zn Ferrite Nanoparticles: A Glycol-Thermal Approach for Biomedical Application

SS Mthimkhulu and WB Mdlalose

Discipline of Physics, University of KwaZulu-Natal, Private Bag X54001, Durban 4000, South Africa

E-mail: 224193376@stu.ukzn.ac.za

Abstract. This study presents the synthesis and comprehensive evaluation of $MgFe_2O_4$, $Mg_{0.5}Zn_{0.5}Fe_2O_4$, and $ZnFe_2O_4$ nanoparticles for potential use in anticancer therapy. Nanoparticles were synthesized via a glycol-thermal method and coated with chitosan (CHI) to enhance biocompatibility and stability. Structural and magnetic properties were characterized using XRD, FTIR, TEM, Mössbauer spectroscopy, and VSM. XRD confirms the formation of a single-phase cubic spinel structure, with chitosan coating increasing crystallite size and lattice parameters. FTIR confirmed chitosan coating. TEM analysis revealed spherical morphology with reduced agglomeration post-coating. Mössbauer spectroscopy showed that $MgFe_2O_4$ and $Mg_{0.5}Zn_{0.5}Fe_2O_4$ led to ferrimagnetic behaviour, while $ZnFe_2O_4$ resulted in paramagnetism. Magnetic measurements via VSM indicated superparamagnetic behaviour in all samples, with $Mg_{0.5}Zn_{0.5}Fe_2O_4$ exhibiting the highest saturation magnetization (68.49 emu/g). Cytotoxicity assays on CaCo-2 cells demonstrated that chitosan coating significantly improved biocompatibility, particularly for $ZnFe_2O_4$, raising cell viability above 100%. These findings highlight the potential of chitosan-coated Mg-Zn ferrite nanoparticles as promising candidates for targeted drug delivery and anticancer applications.

1 Introduction

Nanoferrites have gained significant attention in biomedical applications, including drug delivery, magnetic hyperthermia, targeted therapy, and imaging resonance, due to their distinctive magnetic properties [1]. These nanoferrites, such as zinc and magnesium, have promising structural and magnetic properties in biomedical applications due to their biocompatibility, degradability, and low toxicity at concentrations less than 125µg/mL [2]. However, they have shown drawbacks. One of the major drawbacks is the cytotoxicity brought by different factors such as synthesis methods, types of materials, reaction time, and temperature. However, their potential cytotoxicity, which varies based on synthesis conditions, poses a challenge for medical use. To mitigate or eliminate these toxic effects, natural polymers such as chitosan, polyvinyl alcohol (PVA), and polyethylene glycol (PEG) are commonly employed to coat nanoferrites [3]. The polymer-coated nanoferrites are promising for targeting drug delivery and other treatments for cancer cells due to their safer delivery and reducing the side effects on healthy tissues. The incorporation of nanoferrites with polymers brought enhancement in the visibility of growing tumours and other abnormalities [4]. This surface modification enhances biocompatibility, making them safer and more effective for clinical applications. In this study, $MgFe_2O_4$, $Mg_{0.5}Zn_{0.5}Fe_2O_4$, and $ZnFe_2O_4$ nanoparticles (NPs) were synthesized and coated with chitosan (CHI) for potential applications in cancer

treatment, using the glycol-thermal method. The nanoparticles were synthesized and subsequently coated with chitosan via the glycol-thermal and wet coating methods, respectively. Comprehensive characterization of the structural, morphological, and magnetic properties of the NPs was conducted using various techniques, including X-ray diffraction (XRD, MinFlex 300/600 with Cu X-ray tube), transmission electron microscopy (TEM, JEOL 1400 operated at 200 kV), Fourier-transform infrared spectroscopy (FTIR, PerkinElmer Spectrum IR Version 10.7.2), Mössbauer spectroscopy, and vibrating sample magnetometer (VSM, cryogenic Ltd., UK).

2 Experimental

2.1 Synthesis method

All three samples were synthesized using the same procedure. For the synthesis of $MgFe_2O_4$, magnesium chloride ($MgCl_2$) and iron(III) chloride hexahydrate ($FeCl_3 \cdot 6H_2O$) were dissolved in deionized water under continuous stirring. Sodium hydroxide was added dropwise to the solution to induce precipitation, maintaining the pH between 9 and 10. The resulting precipitate was transferred into a Büchner funnel and filtered under vacuum. Multiple washes with deionized water were performed to remove residual chlorides. The solvent was then replaced with 200 mL of ethylene glycol, chosen for its high boiling point (197 °C). The mixture was transferred to a stainless-steel pressure reactor (Watlow Series, PARR 4843) and heated at 200 °C for 6 hours. After the reaction, the product was washed again to remove ethylene glycol, followed by a final wash with ethanol. The resulting powder was dried under an infrared lamp for 24 hours, then ground and weighed using an agate mortar and pestle. $Mg_{0.5}Zn_{0.5}Fe_2O_4$, and $ZnFe_2O_4$ NPs were also synthesized following the same method described.

2.2 Coating method

The obtained $MgFe_2O_4$, $Mg_{0.5}Zn_{0.5}Fe_2O_4$, and $ZnFe_2O_4$ NPs were coated with chitosan using a modified version of the wet chemistry method described by Mngadi *et al.* [5]. To prepare the chitosan solution, 1 g of chitosan was dissolved in 200 mL of acetic acid, and the pH was adjusted to 4.8 by adding sodium hydroxide. The synthesized nanoparticles 0.4 g were then dispersed in the chitosan solution and stirred for 30 minutes. The mixture was further stirred at room temperature for 18 hours using an IKA RW 20 Digital Dual-Range Mixer System. The resulting homogenous mixture was centrifuged with deionized water five times at 300 rpm for 30 minutes. After centrifugation, the sample was dried under infrared radiation for 24 hours, ground, and labeled as CHI-$MgFe_2O_4$, CHI-$Mg_{0.5}Zn_{0.5}Fe_2O_4$, and CHI-$ZnFe_2O_4$.

3 Results

X-ray Diffraction exhibits all the synthesized and coated NPs patterns as shown in Figure 3.1. All diffraction planes (*hkl*) (111), (220), (311), (222), (400), (422), and (440) were confirmed by the original magnetite pattern that was for a single cubic spinel structure [5]. No impurities were detected after chitosan coating. The crystallite sizes were calculated using Scherrer's equation. It was found to be decreasing after chitosan coating, except for the doped sample, which was increasing. The increase of crystallite size in the $Mg_{0.5}Zn_{0.5}Fe_2O_4$ sample was due to the substitution of the ionic radii of magnesium (0.65 Å) with zinc (0.83 Å), since zinc has a greater ionic radius than magnesium, which leads to lattice expansion [6]. FTIR spectra are seen in Figure 3.2. A broad peak around 3000-3500 cm^{-1} is associated with hydrogen bonding. Around 2800-3000 cm^{-1} and 1650-1660 cm^{-1}, there are two stretching bands that represent the amid groups. The N-H stretching bonding peaks at 1500-1800 cm^{-1} are associated with chitosan, which appears on the coated samples, confirming chitosan coating. The strongest peak at 500-550 cm-1 is due to Fe-O bonding.

TEM exhibited spherical-shaped particles with an average particle distribution of 15.67 nm and 13.66 nm for as-prepared and chitosan-coated NPs, respectively. The Gaussian fit was utilized to estimate particle distribution using ImageJ software. All NPs exhibited spherical shapes, as seen in Figure 3.3. The chitosan-coated NPs are less agglomerated. On the doped $Mg_{0.5}Zn_{0.5}Fe_2O_4$, the bigger particles were associated with Mg^{2+}, whereas the small NPs were for Zn^{2+}. Magnesium has bigger particles due to the high synthesis temperature of 200°C, which caused them to be bigger in shape and size [7]. The decrease in particle sizes of $MgFe_2O_4$ and $ZnFe_2O_4$ after chitosan and an increase in $Mg_{0.5}Zn_{0.5}Fe_2O_4$ were observed, which affects the magnetic properties.

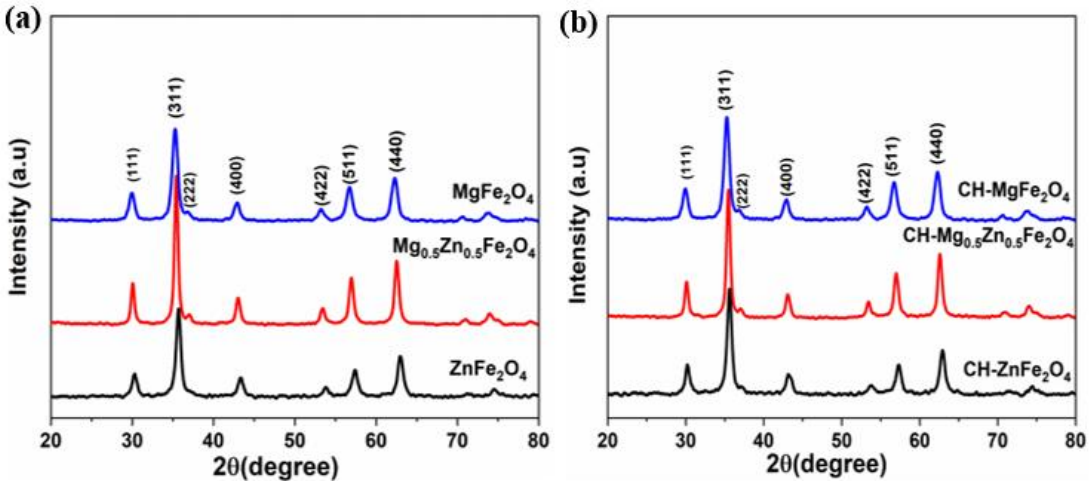

Figure 3.1: X-ray diffraction pattern of (a) as-prepared and (b) chitosan-coated nanoparticles.

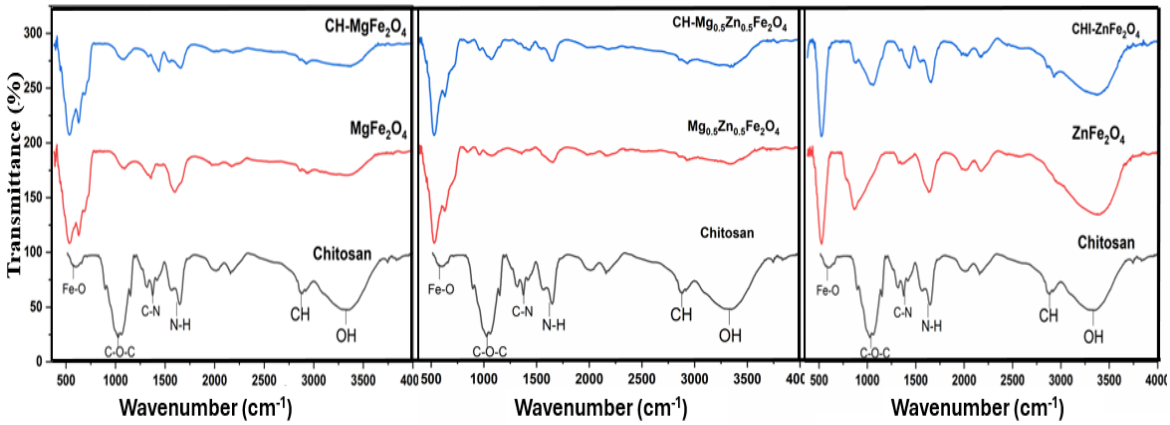

Figure 3.2: Fourier Transform Infrared images of as-prepared and chitosan-coated NPs.

Samples	D_{XRD} (nm)±1.3	D_{TEM} (nm)±3.1	a (Å)±0.04	M_S(emu/g) ±2.46	H_C(Oe)± 0.002
$MgFe_2O_4$	13.78	15.01	8.348	62.95	10.00
CHI-$MgFe_2O_4$	12.95	13.02	8.358	64.47	13.00
$Mg_{0.5}Zn_{0.5}Fe_2O_4$	16.24	21.00	8.404	68.49	33.00
CHI-$Mg_{0.5}Zn_{0.5}Fe_2O_4$	16.76	17.02	8.399	58.81	26.00
$ZnFe_2O_4$	11.68	11.02	8.426	25.19	66.00
CHI-$ZnFe_2O_4$	11.17	10.96	8.431	27.16	69.00

Table 1: Crystallite size (D_{XRD}), particle size (D_{TEM}), lattice parameter (a), saturation magnetization (M_S), coercivity field (H_C) parameters.

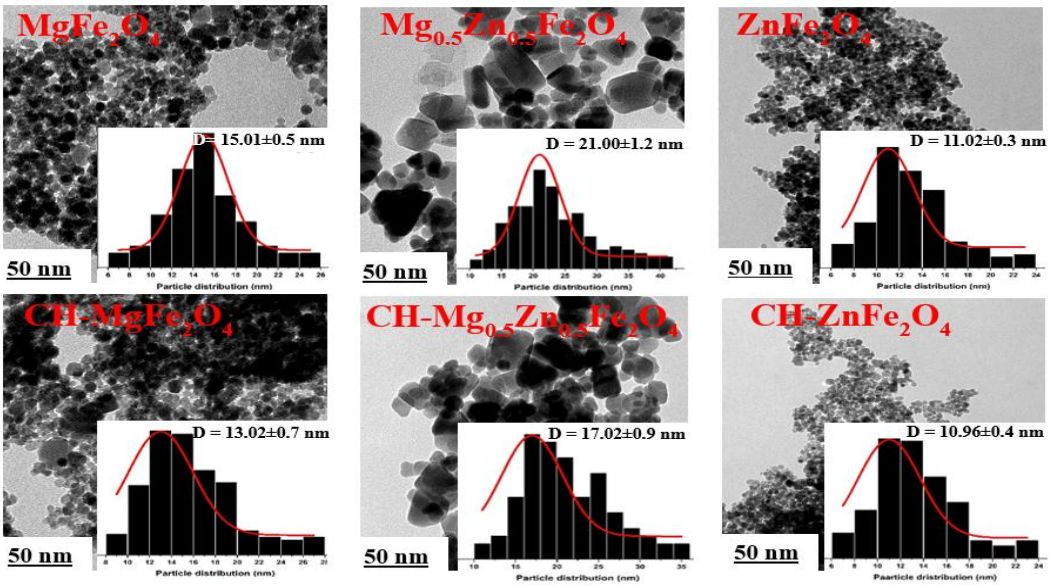

Figure 3.3: TEM images of as-prepared and chitosan-coated NPs

Magnetic properties are revealed by Mössbauer spectroscopy and the vibrating sample magnetometer. Mössbauer spectroscopy investigates the dominance of Fe-ions in a sample and the type of magnetization behavior [8]. The Mössbauer spectra obtained for the $MgFe_2O_4$ and $Mg_{0.5}Zn_{0.5}Fe_2O_4$ samples were successfully fitted with two sextets, indicating ferromagnetic behaviour. Based on the average of isomer shifts (*IS*) and hyperfine fields (H_f) for the $MgFe_2O_4$ sample, Sextet A (*IS* = 0.31 mm/s, H_f = 296 kOe) was attributed to Fe^{2+} ions occupying tetrahedral sites, while Sextet B (*IS* = 0.32 mm/s, H_f = 325 kOe) corresponded to Fe^{2+} ions located on the octahedral sites [9]. A similar analysis was conducted for the $Mg_{0.5}Zn_{0.5}Fe_2O_4$ sample, where Sextet A (*IS* = 0.37 mm/s, H_f = 337 kOe) was attributed to Fe ions occupying the tetrahedral sites, while Sextet B (*IS* = 0.36 mm/s, H_f = 306 kOe) was assigned to Fe ions located at the octahedral sites. Notably, the $MgFe_2O_4$ sample exhibited a predominance of Fe ions in tetrahedral sites, whereas Fe ions were more concentrated in octahedral sites in the $Mg_{0.5}Zn_{0.5}Fe_2O_4$ sample. In contrast, the $ZnFe_2O_4$ sample displayed a spectrum fitted with two doublets, suggesting that all Fe ions were present in paramagnetic states across two distinct sites. Moreover, the magnetic properties of the nanoparticles were validated through VSM measurements, with the results presented in Table 1.

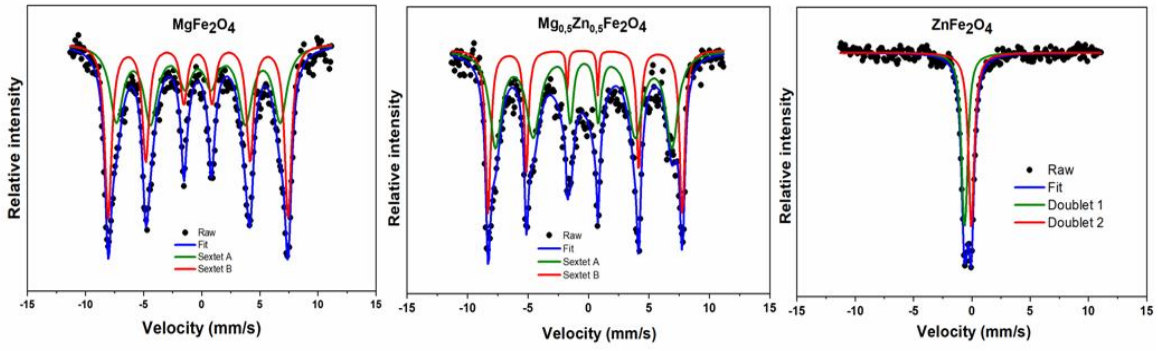

Figure 3.4: Mössbauer spectroscopy of nanoparticles at room temperature.

From the small average values, saturation (M_s = 52.21 emu/g) and remanent (M_r = 0.81 emu/g) magnetizations exhibited superparamagnetic behaviour in all samples, as seen in Figure 3.4. However, an increase in the values of M_s was observed, which is attributed to the action of chitosan as a stabilizing agent [10]. Moreover, the decrease in saturation of the $Mg_{0.5}Zn_{0.5}Fe_2O_4$ sample was due to the new non-magnetic layer added, which caused disturbance in the magnetization interaction, leading to a decrease in magnetization [10]. $MgFe_2O_4$ and $Mg_{0.5}Zn_{0.5}Fe_2O_4$ NPs have higher saturation magnetization than zinc, which was revealed by Mössbauer

spectroscopy with ferromagnetic behaviour. $ZnFe_2O_4$ has a hysteresis loop of the lowest saturation magnetization (26.17 emu/g), revealing pure superparamagnetic Fe-ions, as confirmed by Mössbauer results. All synthesized and chitosan-coated nanoparticles exhibited superparamagnetic behaviour, as indicated by saturation (M_s) and remanent (M_r) magnetization values [10]. Chitosan coating stabilizes the particles, reduces agglomeration, which leads to an increase in M_s, and improves domain alignment [11]. However, $Mg_{0.5}Zn_{0.5}Fe_2O_4$ showed reduced M_s due to the presence of a non-magnetic layer disrupting magnetic interactions. $MgFe_2O_4$ and $Mg_{0.5}Zn_{0.5}Fe_2O_4$ have higher M_s than $ZnFe_2O_4$, which showed the lowest M_s and purely superparamagnetic behaviour, consistent with Mössbauer results. The superparamagnetic properties of ferrite nanoparticles make them promising for cancer treatment, though they have the potential to induce cytotoxic effects. However, additional research is needed to evaluate their toxicity on various cell lines [5]. One of the features of suitable magnetic materials for medical applications is that the particles are superparamagnetic [3]. Hence, VSM results suggest that these materials could be used in cancer treatment applications. However, they exhibit toxicity to healthy cells; as a result, the evaluation in different cell lines was performed.

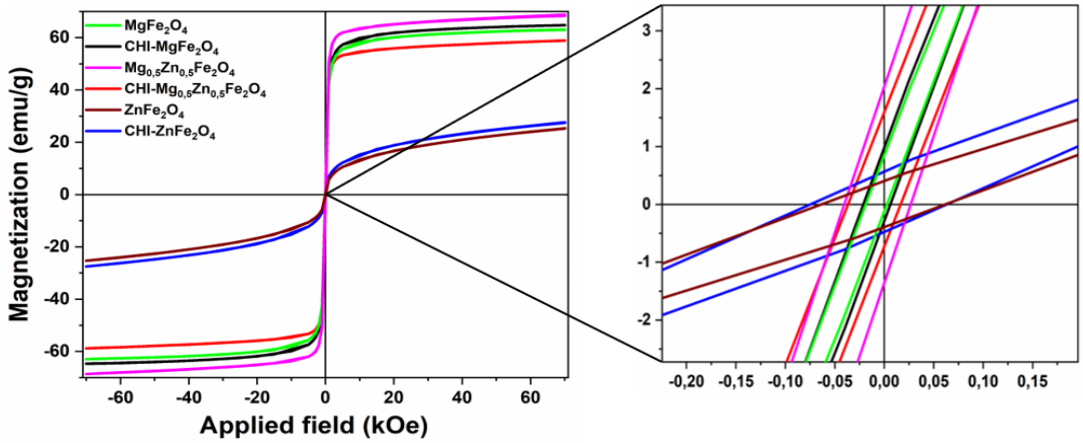

Figure 3.5: Hysteresis loop of as-prepared and chitosan-coated (CHI) nanoparticles measured at room temperature.

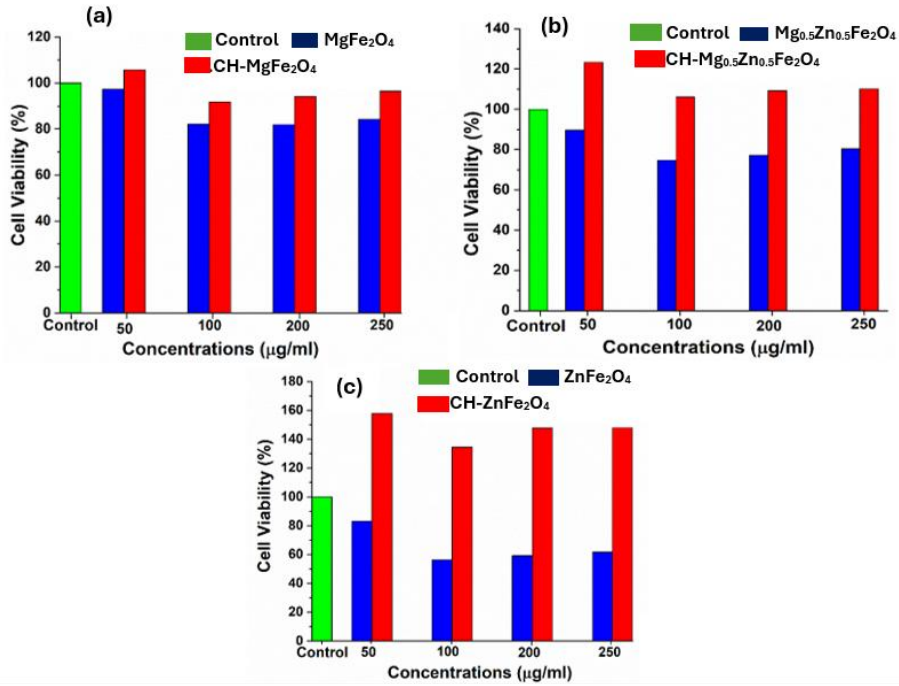

Figure 3.6: MTT Cell viability assay in the Human Colorectal Adenocarcinoma (CaCo-2) cell line.

A cytotoxicity study using the MTT assay on CaCo-2 cells showed that $MgFe_2O_4$ and $Mg_{0.5}Zn_{0.5}Fe_2O_4$ nanoparticles had low toxicity, maintaining over 75% cell viability, while $ZnFe_2O_4$ showed higher toxicity with viability below 60%. Chitosan-coated nanoparticles significantly improved biocompatibility, with CHI-$MgFe_2O_4$ showing over 90% viability and both CHI-$Mg_{0.5}Zn_{0.5}Fe_2O_4$ and CHI-$ZnFe_2O_4$ exceeding 100%. The chitosan coating effectively reduced nanoparticle-induced toxicity, making these nanocomposites promising for drug delivery and gene therapy applications.

4 Conclusion

All synthesized and chitosan-coated $MgFe_2O_4$, $Mg_{0.5}Zn_{0.5}Fe_2O_4$, and $ZnFe_2O_4$ nanoparticles exhibited a cubic spinel structure and spherical morphology, with reduced agglomeration after chitosan coating. Magnetic characterization showed ferromagnetic behaviour for $MgFe_2O_4$ and $Mg_{0.5}Zn_{0.5}Fe_2O_4$, and paramagnetic behaviour for $ZnFe_2O_4$. All samples displayed superparamagnetic properties. Cytotoxicity studies on CaCo-2 cells revealed that uncoated nanoparticles were more toxic at higher concentrations, while chitosan-coated nanoparticles significantly improved cell viability [12]. These results highlight the potential of chitosan-coated nanoparticles for safe and effective use in gene delivery and drug nanocarrier applications.

References

[1] S. Bucak, B. Yavuztürk, A. D. Sezer, S. Bucak, B. Yavuztürk, and A. D. Sezer, "Magnetic Nanoparticles: Synthesis, Surface Modifications and Application in Drug Delivery," *Recent Advances in Novel Drug Carrier Systems*, Oct. 2012, doi: 10.5772/52115.

[2] S. R. Mokhosi, W. Mdlalose, A. Nhlapo, and M. Singh, "Advances in the Synthesis and Application of Magnetic Ferrite Nanoparticles for Cancer Therapy," *Pharmaceutics 2022, Vol. 14, Page 937*, vol. 14, no. 5, p. 937, Apr. 2022, doi: 10.3390/PHARMACEUTICS14050937.

[3] N. L. Ndlovu, W. B. Mdlalose, B. Ntsendwana, and T. Moyo, "Evaluation of Advanced Nanomaterials for Cancer Diagnosis and Treatment," Apr. 01, 2024, *Multidisciplinary Digital Publishing Institute (MDPI)*. doi: 10.3390/pharmaceutics16040473.

[4] R. Verma, A. Chauhan, R. Kalia, K. M. Batoo, and R. Kumar, "Magnetic nanoferrites as an alternative for magnetic resonance imaging application," *Magnetic Nanoferrites and their Composites: Environmental and Biomedical Applications*, pp. 237–256, Jan. 2023, doi: 10.1016/B978-0-323-96115-8.00013-1.

[5] S. Mngadi, S. Mokhosi, M. Singh, and W. Mdlalose, "Chitosan-functionalized $Mg_{0.5}Co_{0.5}Fe_2O_4$ magnetic nanoparticles enhance delivery of 5-fluorouracil in vitro," *Coatings*, vol. 10, no. 5, May 2020, doi: 10.3390/COATINGS10050446.

[6] K. O. Abdulwahab, M. M. Khan, and J. R. Jennings, "Ferrites and ferrite-based composites for energy conversion and storage applications," *Taylor and Francis Ltd.* 2023, doi: 10.1080/10408436.2023.2272963.

[7] M. A. Durand, "The Coefficient of Thermal Expansion of Magnesium Oxide," *Physics (College Park Md)*, vol. 7, no. 8, pp. 297–298, Aug. 1936, doi: 10.1063/1.1745396.

[8] E. J. Choi, Y. Ahn, and K. C. Song, "Mössbauer study in zinc ferrite nanoparticles," *J Magn Magn Mater*, vol. 301, no. 1, pp. 171–174, Jun. 2006, doi: 10.1016/J.JMMM.2005.06.016.

[9] E. Tunable, A. lacovo, J. Frigerio, S. Meille, and S. Nakajo, "Mössbauer effect study of a polycrystalline $Fe_{1+x}Cr_{2-x}O_4$ spinel grown by solid-state synthesis," *J Phys Conf Ser*, vol. 2164, p. 12067, 2022, doi: 10.1088/1742-6596/2164/1/012067.

[10] T. M. Freire, L. Dutra, D. Queiroz, N. Ricardo, K. Barreto, and J. Denardin, F. Wurm, C. Sousa, A. Correia, P. De lima-Neto, P. Fechine, "Fast ultrasound assisted synthesis of chitosan-based magnetite nanocomposites as a modified electrode sensor," *Carbohydr Polym*, vol. 151, pp. 760–769, Oct. 2016, doi: 10.1016/J.CARBPOL.2016.05.095.

[11] S. Fiddaroini, K. Indu, L. Madaniyah, S. Amalia, M. Rahman, and A. Sabarudin, "Chitosan-Coated silver nanoparticles with various floral honey bioreductors: A promising nonalcoholic hand gel sanitizer formulation," *OpenNano*, vol. 21, p. 100228, Jan. 2025, doi: 10.1016/J.ONANO.2024.100228.

[12] F. Salehi, H. Behboudi, G. Kavoosi, and S. K. Ardestani, "Chitosan promotes ROS-mediated apoptosis and S phase cell cycle arrest in triple-negative breast cancer cells: evidence for intercalative interaction with genomic DNA," *RSC Adv*, vol. 7, no. 68, pp. 43141–43150, Sep. 2017, doi: 10.1039/C7RA06793C.

Synthesis, structural, magnetic, and gas sensing properties of rare earth-substituted cobalt and zinc ferrites: A comparative study

NL Ndlovu[1], PS Mkwae[2], and WB Mdlalose[1]

[1]Discipline of Physics, University of KwaZulu-Natal, Durban, South Africa
[2]Discipline of Physics, University of Zululand, Dlangezwe, South Africa

E-mail: 216006188@stu.ukzn.ac.za

Abstract. The as-prepared ferrites ($CoFe_2O_4$ and $ZnFe_2O_4$) are commonly well known for their ease of tuning of structural, morphological, and magnetic properties. They were synthesized to evaluate the rare earth (RE) element substitution effect on the properties of cobalt and zinc ferrites for the investigation of gas sensing properties using the glycol-thermal method. Results demonstrated favourable properties for ammonia (NH_3) and liquid petroleum gas (LPG) sensing, response, and sensitivity. Characterization techniques such as XRD, FTIR, HRTEM, and VSM confirmed the presence of single cubic spinel structure nanoparticles, with average crystallite sizes of 10.2 ± 0.5 nm for $CoRE_xFe_{2-x}O_4$ and 9.26 ± 1.0 nm for $ZnRE_xFe_{2-x}O_4$ (RE = gadolinium (Gd), neodymium (Nd), and x = 0, 0.1). The Gd cobalt and Nd zinc ferrites substitutions exhibited competitively optimal results for NH_3 and LPG gases, respectively. These results were promising for further investigation of the relationship between gas exposure and sensor material behaviour.

1 Introduction

Detection of hazardous and flammable gases, such as liquid petroleum gas (LPG), is important for safety in residential, commercial, and industrial settings [1]. Metal oxide semiconductors, especially spinel ferrites, have lately attracted considerable attention due to their chemical stability, low cost, and tunable properties [1, 2]. Among them, $CoFe_2O_4$ (CF) and $ZnFe_2O_4$ (ZF) stand out because of their combined magnetic and semiconducting characteristics, which enhance surface reactivity essential for gas sensing [1]. Ferrites crystallize in the spinel structure with a general formula AB_2O_4, where divalent cations occupy the tetrahedral (A) sites and trivalent cations are distributed over the octahedral (B) sites. This cation distribution plays a crucial role in defining the magnetic, electrical, and surface properties of ferrites, and modifications through rare-earth substitution can alter lattice dynamics and, consequently, functional performance. CF is a hard magnetic ferrite with a cubic spinel structure that combines high chemical stability, moderate electrical conductivity, and catalytic activity [3]. These properties make it a versatile material for gas sensors, data storage, catalysis, and biomedical applications. In gas sensing, detection arises from the interaction of target gas molecules with the active surface: oxygen species adsorbed on CF nanoparticles readily interact with reducing or oxidizing gases, producing measurable changes in resistance [1-3]. ZF, another member of the spinel ferrite family, also exhibits excellent chemical stability and semiconducting behaviour, with lower magnetic coercivity compared to CF [1, 2, 4, 5]. It has been widely investigated for sensing gases such as ethanol, ammonia, and LPG. Nevertheless, the superior

magnetic properties and catalytic activity of CF often provide an advantage in applications requiring rapid response and recovery [4, 5].

Recent studies have revealed that nanoparticle-based sensors exhibit higher sensitivity and faster response times than their bulk counterparts [6]. This is largely due to the increased surface-to-volume ratio, which enhances the interaction between the sensor surface and gas molecules. Additionally, the tunability of cobalt ferrite through synthesis parameters or substitution strategies further widens the gap for improving sensor selectivity and performance [6]. In this work, cobalt and zinc ferrite nanoparticles were synthesized via a simple and cost-effective glycol-thermal method [7]. The structural, magnetic, and gas sensing properties were thoroughly examined using X-ray Diffraction (XRD), Fourier-transform infrared spectroscopy (FTIR), high-resolution transmission electron microscopy (HRTEM), vibrating sample magnetometer (VSM), and gas sensor measurements. The core aim was to evaluate the potential of these nanoparticles in detecting NH_3, H_2, CO_2, and LPG at 1000 ppm and operating at temperatures of 225 ^oC, contributing to the advancement of affordable and reliable gas sensing technologies.

2 Experimental

The synthesis precursors used to synthesize $CoRE_xFe_{2-x}O_4$ and $ZnRE_xFe_{2-x}O_4$ were cobalt nitrate hexahydrate ($Co(NO_3)_2 \cdot 6H_2O$, 98%), zinc nitrate hexahydrate ($Zn(NO_3)_2 \cdot 6H_2O$, 98%), ferric iron (III) chloride ($FeCl_3$, 98%), gadolinium (III) chloride hexahydrate ($GdCl_3 \cdot 6H_2O$, 99.0%), neodymium (III) chloride hexahydrate ($NdCl_3 \cdot 6H_2O$, 99.9%), sodium hydroxide (NaOH) as a precipitating reagent. The deionized water, ethanol (C_2H_5OH, 99 %), and ethylene glycol ($(CH_2OH)_2$, 99 %) were used as solvents. All were bought from Sigma-Aldrich and were used without any further purification.

2.1 Synthesis Process

The synthesis followed the conventional co-precipitation and glycol thermal method mentioned by [7], with the stoichiometric ratio of 1:2 not being changed by the RE element substitution. The total trivalent cations remained the same, maintaining the overall charge balance.

2.2 Characterization Techniques

The characterization of the ferrite samples involved several techniques. XRD measurements were conducted with a Mini Flex 300/600 Cu X-ray tube at 40 kV, with phase identification verified using the ICDD: PDF database and analyzed with EVA software and the average crystallite size was estimated through the Debye-Scherrer equation. FTIR confirmed the presence of reactive surface sites by identifying characteristic functional group peaks. The JEOL 1400 at 200 kV, HRTEM provided insights into particle size distribution, morphology, and crystallinity. The magnetic properties were confirmed via VSM (cryogenic Ltd., UK 300 k to 4 K), and gas exposure behaviour was conducted. These combined techniques gave a comprehensive understanding of the structural, surface, magnetic, and gas sensing properties were evaluated using a controlled test chamber, where the gas sensing mechanisms of ferrite-based materials are primarily studied through the modulation of electrical conductivity in response to gas exposure, monitored upon exposure to different gases at constant 1000 ppm concentrations of gases at 225 ^oC operating temperature.

3 Results and Discussion

XRD patterns in Figure 1(a, b) confirmed the formation of a single-phase cubic spinel structure across all samples. The diffraction peaks at specific 2θ values matched well with magnetite ferrite's standard ICDD card number (ICDD No. 1534941). The analysis indicated a slight increase in crystallite size upon RE substitution, as evidenced by the subtle narrowing of diffraction peaks. A slight shift of diffraction peaks to lower 2θ values with Gd- and Nd- substitution indicated lattice expansion due to the incorporation of larger rare-earth ions [8]. This structural distortion is consistent with the reported lattice parameter (Table 1), especially in $CoNd_{0.1}Fe_{1.9}O_4$ (CFNd) and $ZnNd_{0.1}Fe_{1.9}O_4$ (ZFNd). The Debye–Scherrer equation exhibited crystallite sizes ranged from 8.98 nm to 11.1 nm, showing slight refinement due to RE-substitution. FTIR spectra (Figure 1(c, d)) displayed characteristic metal oxygen (Fe–O) vibrations at tetrahedral (~580 cm^{-1}) and octahedral (~430 cm^{-1}) sites [9]. Additional bands related to O–H and H–O–H confirmed surface hydroxyl groups, which are important for gas sensing via surface adsorption [9].

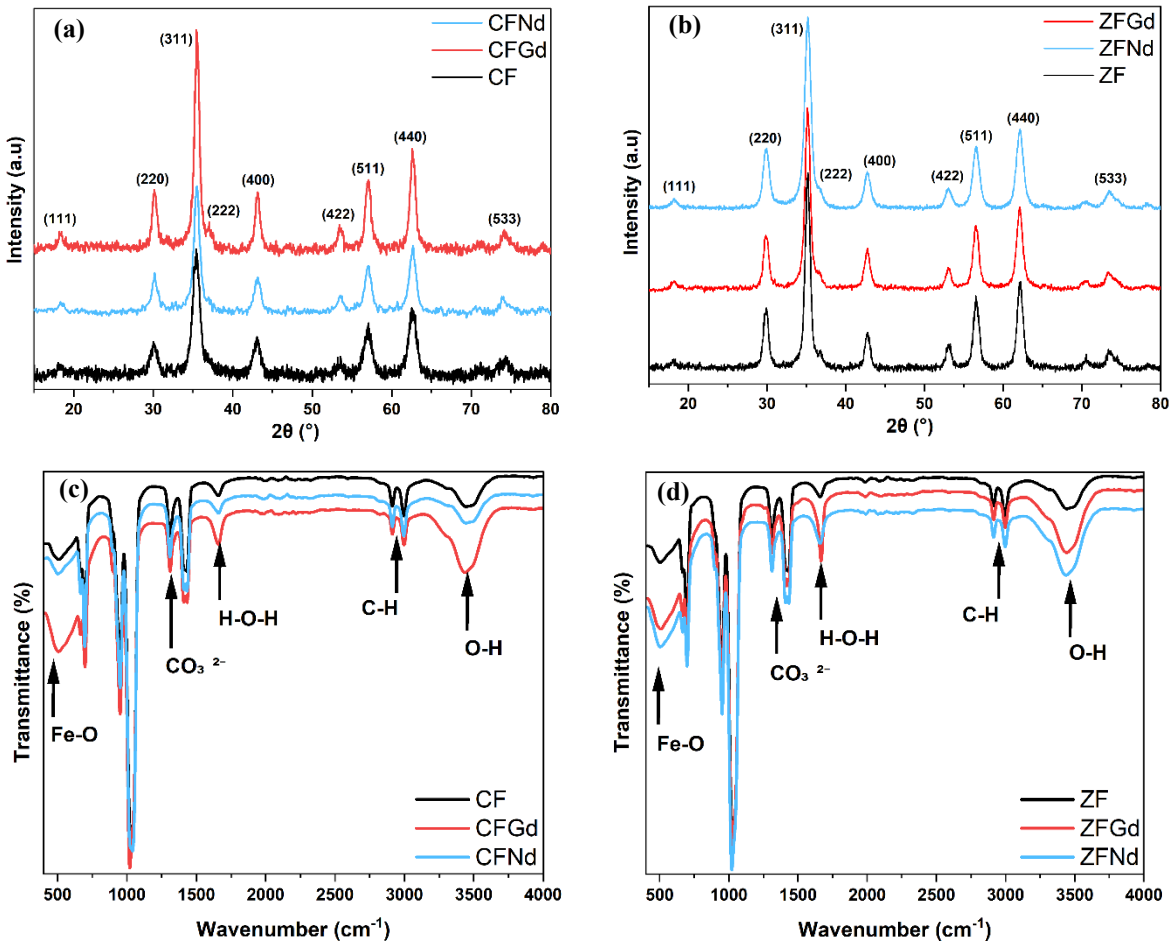

Figure 1: (a) and (b) XRD patterns of synthesized ferrite samples showing phase purity and crystallinity. (c) and (d) FTIR spectra identifying characteristic Fe–O and RE–O vibrational modes.

Sample	a (Å)	D_{XRD} (nm)	ε (%)	D_{TEM} (nm)
CF	8.40	9.10 ± 0.5	1.50	9.50 ± 0.2
CFGd	8.39	10.3 ± 0.5	1.20	10.8 ± 0.3
CFNd	8.40	11.1 ± 0.5	1.00	12.2 ± 0.2
ZF	8.46	8.98 ± 1.3	1.10	7.01 ± 0.2
ZFGd	8.45	9.50 ± 0.7	1.17	9.72 ± 0.1
ZFNd	8.47	9.30 ± 1.1	1.30	9.87 ± 0.2

Table 1: Crystallographic a (cubic lattice parameter), D_{XRD} (crystallite size), ε (micro strain), and D_{TEM} (particle diameter size) for RE-substituted zinc and cobalt ferrites.

XRD and FTIR analyses confirmed the cubic spinel ferrite structure, while the presence of residual CO_3^{2-} species was attributed to incomplete removal of synthesis byproducts. Detailed assignments of vibrational and stretching wavenumbers for the functional groups are summarized in Table 2. Shifts observed upon Gd- and Nd-substitution indicate altered lattice dynamics and enhanced surface functionality, which are beneficial for gas sensing performance [10]. HRTEM analysis further confirmed the nanoscale nature of the ferrites and supported the XRD observations, showing that the Gd- and Nd-substituted samples exhibited slightly larger and more uniform particle size distributions compared to the unsubstituted samples, as illustrated in Figure 2. The insets display Gaussian-fitted size distributions, with average particle sizes reported in Table 1. These results are consistent with the XRD data, suggesting that rare-earth substitution not only distorts the lattice parameters but

also slows grain growth, confirming the structural impact of RE-substitution observed across both XRD and TEM data.

Site	Fe-O Stretching (cm^{-1})	C-H Stretching (cm^{-1})	CO_3^{2-} Symmetric bend (cm^{-1})	O-H Bending (cm^{-1})	H-O-H Bending (cm^{-1})
Octahedral	~400- 450	~2800- 3000	~1380- 1450	~3400- 3500	~1600- 1630
Tetrahedral	~580- 600				

Table 2: FTIR absorption bands and functional group assignments.

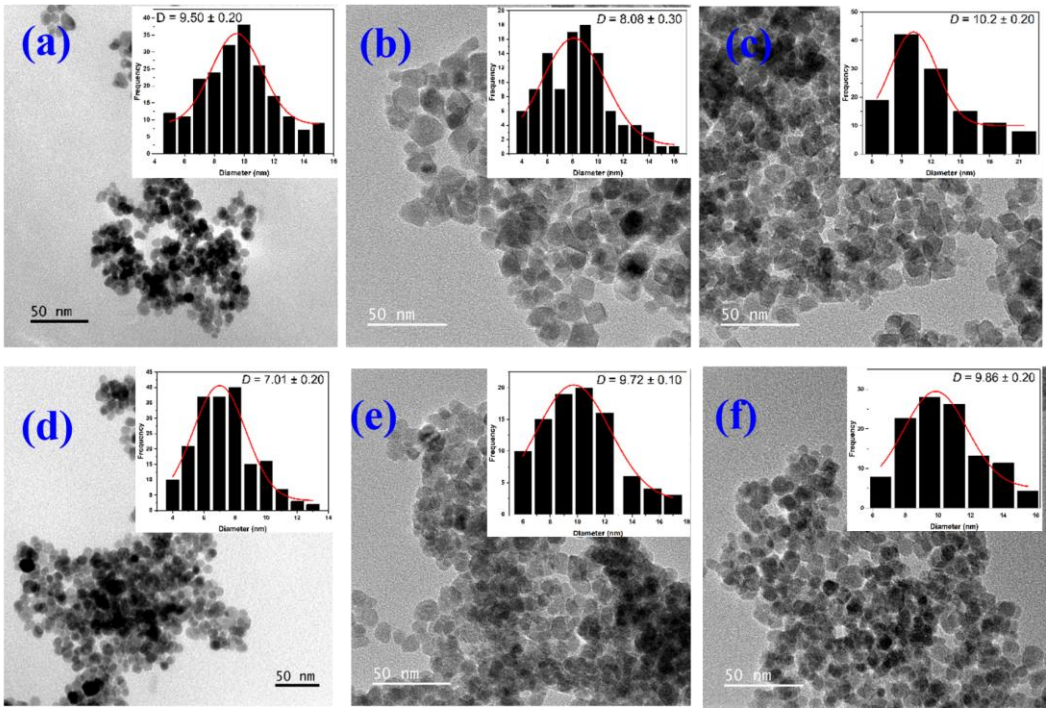

Figure 2: Comparative TEM and particle diameter distributions (inserts) patterns of (a) CF, (b) CFGd, (c) CFNd, (d) ZF, (e) ZFGd, and (f) ZFNd ferrites substituted nanoparticles.

The magnetization hysteresis (M–H) loops for the ferrite samples in Figure 3 revealed both ferromagnetic and paramagnetic behaviour with distinct hysteresis. RE substitution led to a decrease in saturation magnetization (*Ms*), which can be attributed to the influence of RE ions on the superexchange interactions between Fe^{3+} ions. In contrast, an increase in coercivity (*Hc*) was observed for the cobalt RE-substituted ferrite, resulting from lattice distortions caused by the larger ionic radii of the RE ions. This increase in *Hc* is noteworthy, as slightly higher values are advantageous for gas sensing at elevated temperatures and for enhancing surface reactivity. Interestingly, the ZF ferrites displayed the opposite trend compared to CF, which is likely due to the inconclusive measurements of the as-prepared compound.

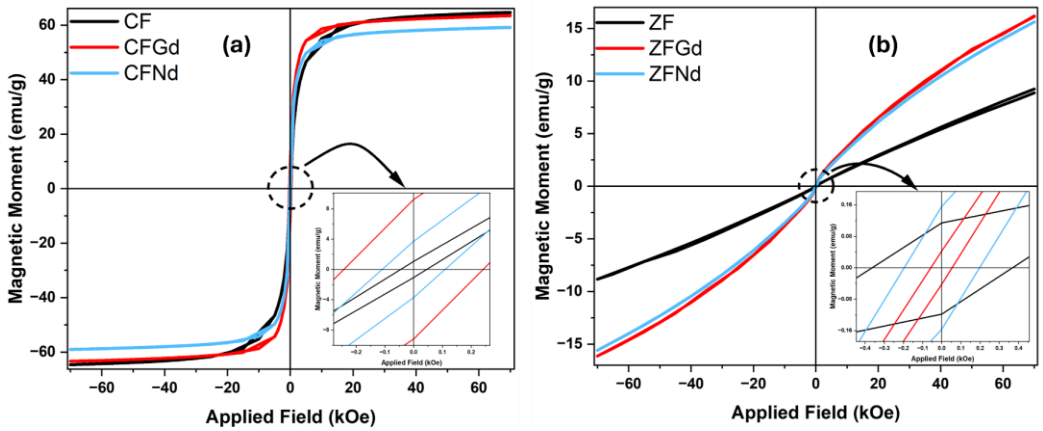

Figure 3: M–H curves from VSM measurements showing magnetic hysteresis behaviour.

Table 3 compares the gas response, response time, and recovery time for selected ferrite sensors against ammonia (NH_3), hydrogen (H_2), carbon dioxide (CO_2), and liquid petroleum gas (LPG) gases at a concentration of 10 k ppm at 225 °C. CFGd exhibited a significantly high response to LPG (975) and moderate sensitivity to NH_3, with fast response and recovery times. ZFNd, on the other hand, demonstrated a rapid and strong response to NH_3 (11.0), H_2 (5.2), and LPG (42.1), suggesting efficient surface interaction due to enhanced surface area and defect density. These observations correlate with the increased oxygen adsorption inferred from FTIR and particle size behaviour from HRTEM.

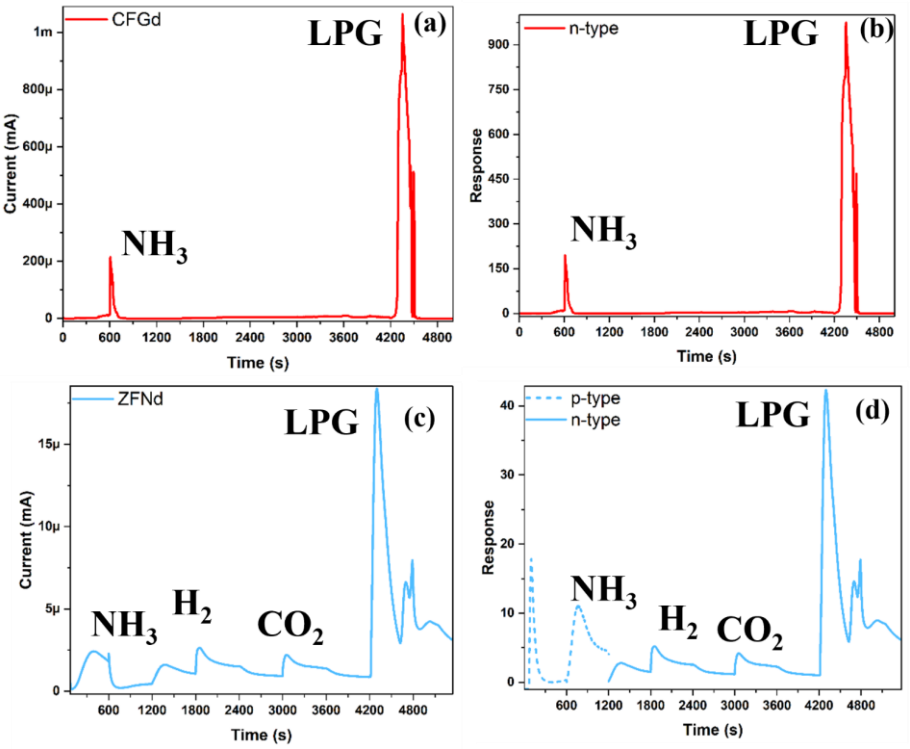

Figure 4: (*top*) CFGd and (*bottom*) ZFNd ferrites (a) and (c) exposure, (b) and (d) response to different gas concentrations of 10 k ppm at 225 °C.

Sample	Gases response				Response time (s)				Recovery time (s)			
	NH_3	H_2	CO_2	LPG	NH_3	H_2	CO_2	LPG	NH_3	H_2	CO_2	LPG
CFGd	195	--	--	975	9.60	--	--	160	3.90	--	--	--
ZFNd	11.0	5.20	4.15	42.1	0.00	10.9	31.7	119	387	268	10.9	574

Table 3: Response and recovery times of ferrite-based sensors to different target gases concentration of 10 k ppm at 225 °C.

4 Conclusion

In this study, rare-earth-substituted cobalt and zinc ferrites were successfully synthesized using a glycol-thermal method and thoroughly characterized to evaluate their structural, morphological, magnetic, and gas-sensing properties. XRD confirmed the formation of a single-phase cubic spinel structure with slight lattice distortion upon Gd- and Nd-substitution. HRTEM analysis validated nanoscale particle formation and revealed particle size refinement in substituted samples, which was consistent with XRD results. FTIR results confirmed enhanced surface functionality and adsorption attributed to the potential in enhanced gas exposure interaction. Magnetic measurements demonstrated substitution-dependent magnetization variations, indicated changes in magnetic anisotropy and superexchange interactions. Gas sensing experiments revealed that CFGd exhibited excellent LPG response and fast dynamics, while ZFNd showed high and rapid sensitivity to NH_3 and other gases, highlighting the role of rare-earth elements in enhancing gas-sensing behaviour. Overall, the results suggested that rare-earth doping offered a viable strategy to tailor ferrite properties for targeted gas sensing applications. The study provided a strong foundation for further optimization of doped ferrite nanoparticles in smart sensor systems.

Acknowledgements

The National Research Foundation (NRF), University of KwaZulu-Natal, University of Zululand and iThemba Labs are responsible for the financial support and data acquisition.

References

[1] P. S. Mkwae, "Comparative study of rare-earth-based ferrites for flammable and volatile organic compound gas sensors," 2023. Accessed: Jul. 29, 2025. [Online]. Available: https://uzspace.unizulu.ac.za/handle/10530/2540

[2] S. J. Salih and W. M. Mahmood, "Review on magnetic spinel ferrite (MFe_2O_4) nanoparticles: From synthesis to application," Heliyon, vol. 9, no. 6, p. e16601, Jun. 2023, doi: 10.1016/J.HELIYON.2023.E16601.

[3] F. Azam, H. Ali, and M. Anis-Ur-Rehman, "Investigation of structural, electrical, and resistive switching effect of Co-Gd ferrites by substituting Nd^{+3} for RRAM applications", Accessed: Jul. 28, 2025. [Online]. Available: https://ssrn.com/abstract=5129776

[4] R. Kumar, O. Al-Dossary, G. Kumar, and A. Umar, "Zinc oxide nanostructures for NO_2 gas–sensor applications: A review," Nanomicro Lett, vol. 7, no. 2, pp. 97–120, Apr. 2015, doi: 10.1007/S40820-014-0023-3.

[5] M. W. A. Khan, N. M. Shaalan, F. Ahmed, S. Sherwani, A. Aljaafari, A. K. Alsukaibi, K. M. Alenezi, and K. Al-Montair, "Gas Sensing Performance of Zinc Oxide Nanoparticles Fabricated via Ochradenus baccatus Leaf," Chemosensors 2024, Vol. 12, Page 28, vol. 12, no. 2, p. 28, Feb. 2024, doi: 10.3390/CHEMOSENSORS12020028.

[6] A. R. Jalalvand and M. M. Karami, "Roles of nanotechnology in electrochemical sensors for medical diagnostic purposes: A review," Sens Biosensing Res, vol. 47, p. 100733, Feb. 2025, doi: 10.1016/J.SBSR.2024.100733.

[7] S. J. C. Masuku, J. Z. Msomi, T. A. Nhlapo, and T. Moyo, "The effect of particle size on structural and magnetic properties of $Zn_{0.5}Co_{0.5}Fe_2O_4$ prepared by glycol-thermal technique," Solid State Sci, vol. 148, p. 107424, Feb. 2024, doi: 10.1016/J.SOLIDSTATESCIENCES.2023.107424.

[8] L. Reddy, "The Role of Anions in Rare-earth Activated Inorganic Host Materials for its Luminescence Characteristics," J Fluoresc, vol. 35, no. 3, pp. 1205–1240, Mar. 2025, doi: 10.1007/S10895-023-03561-0/FIGURES/36.

[9] M. Hussain, A. Mehmood, F. Ali, Z. A. Sandhu, M. A. Raza, S. Sajid, M, T. Khan, A. H. Bhali, A. Hussain, and M. S. Arshid, "Tuning the Magnetic Behaviour of Zinc Ferrite via Cobalt Substitution: A Structural Analysis," ACS Omega, vol. 9, no. 2, pp. 2536–2546, Jan. 2024, doi: 10.1021/ACSOMEGA.3C07251/ASSET/IMAGES/LARGE/AO3C07251_0009.JPEG.

[10] Z. Zhang, D. Zhang, L. Yang, M. Hou, J. Gao, Y. Xia, and S. Guo, "Gd-modified In2O3 for the enhanced xylene sensing," Journal of Porous Materials, vol. 31, no. 3, pp. 1043–1051, Jun. 2024, doi: 10.1007/S10934-024-01582-Z/FIGURES/9.

Effect of Ce and Gd on the magnetic and mechanical properties of $Nd_2Fe_{14}B$ permanent magnets

Mphamela Baloyi[1], Ramogohlo Diale[1,2] and Hasani Chauke[1]

[1]Materials Modelling Centre, University of Limpopo, Polokwane, South Africa
[2]MINTEK, Advanced Materials Division, Randburg, South Africa

E-mail: mphamela.baloyi@gmail.com

Abstract. Neodymium-based permanent magnets ($Nd_2Fe_{14}B$) can be used in various applications such as electric vehicle motors and wind power generators due to their high magnetic field strength and demagnetisation resistance. However, they suffer from low operating temperatures below 585 K and poor ductility. In this study, we investigate the effect of rare earth elements such as Gd and Ce on the $Nd_2Fe_{14}B$ magnets. Their structural, electronic, mechanical properties and magnetic moment were calculated using the ab initio density functional theory approach. The partial substitution of Nd with Gd improves the ductility and mechanical stability of $Nd_2Fe_{14}B$ permanent magnets. The Pugh, Poisson ratio and Cauchy pressure increase by Gd substitution, which reduces the brittleness of the material. These discoveries shed light on the future production of permanent magnetic alloys with desirable mechanical characteristics.

1 Introduction

A material that sustains its magnetic properties due to its intrinsic structure is referred to as a permanent magnet (PM) [1]. Alnico, ferrite, ceramic, and rare-earth magnets are among the several types of magnets that are included in PM. Motors, generators, sensors, transducers, mechanical devices, latches, and imaging systems are only a few of the many uses for these magnets [1]. Due to their severe brittleness and susceptibility to corrosion, rare earth magnets are typically coated or plated to stop corrosion [2]. Samarium cobalt ($SmCo_5$) and neodymium ($Nd_2Fe_{14}B$) are prominent rare-earth magnets owing to their outstanding magnetic characteristics. $SmCo_5$ magnets possess a high Curie temperature of 993 K and are resistant to oxidation. However, they are less frequently used since they are more expensive and have a weaker magnetic field strength [3].

Sintered NdFeB magnets are the most extensively employed commercial PM materials because they provide the highest energy product [4]. Furthermore, because of their great remanence, these magnets may maintain a strong magnetic field after being magnetized. The demand for sintered $Nd_2Fe_{14}B$ magnets has been rising annually due to the development of clean energy technology, such as wind turbines and hybrid electric vehicles [5]. However, previous studies indicated that $Nd_2Fe_{14}B$ magnets possess poor mechanical properties, displaying brittle behaviour [6] and low Curie temperature (Tc) (585 K) [7]. As temperatures rise, $Nd_2Fe_{14}B$ experiences a decline in magnetic properties, as its magnetic order diminishes approaching the Curie temperature. In addition, these magnets display poor magnetocrystalline anisotropy at high temperatures, which suggests that a specific magnetic orientation of the magnet weakens as the temperature rises [8]. Neodymium is one of the key components in $Nd_2Fe_{14}B$ magnets, contributing significantly to their magnetic strength. However, due to the scarcity of neodymium and the limitations of $Nd_2Fe_{14}B$ permanent magnets, the partial replacement of Nd with other accessible rare earth elements is being studied.

Previous research on the impact of terbium on the magnetic characteristics of $Nd_2Fe_{14}B$ magnets has shown that terbium raises *Tc* while decreasing magnetic moments to 19.20 μB [9]. By substituting Gd, Zheng et al. [10] examined the enhanced thermal stability of nanocrystalline melt-spun Nd-Pr-Fe-B alloys. In addition to being substantially less expensive than Dy and Tb and even less expensive than Nd and Pr, Gd raises the Curie temperature of the $RE_2Fe_{14}B$ phase to 643 K [10]. It was also reported that the $Ce_2Fe_{14}B$ magnet has a high magnetic strength of 22.70 μ_B and a high saturation magnetisation of 1.16 T, which indicates that the material can be very strongly magnetised [3].

The thermodynamic, mechanical, and magnetic characteristics of ternary $Nd_2Fe_{14}B$, quaternary $NdGdFe_{14}B$, and $NdCeFe_{14}B$ permanent magnetic alloys are investigated using first-principles density functional theory (DFT) calculations. It was found that the Gd replacement improved the ductility of $Nd_2Fe_{14}B$ magnets. The crystal structures of $Nd_2Fe_{14}B$ doped magnetic alloys with a space group of P4_2/mnm are shown in Figure 1. Ce and Gd are rare earth elements (RE) that substitute for Nd.

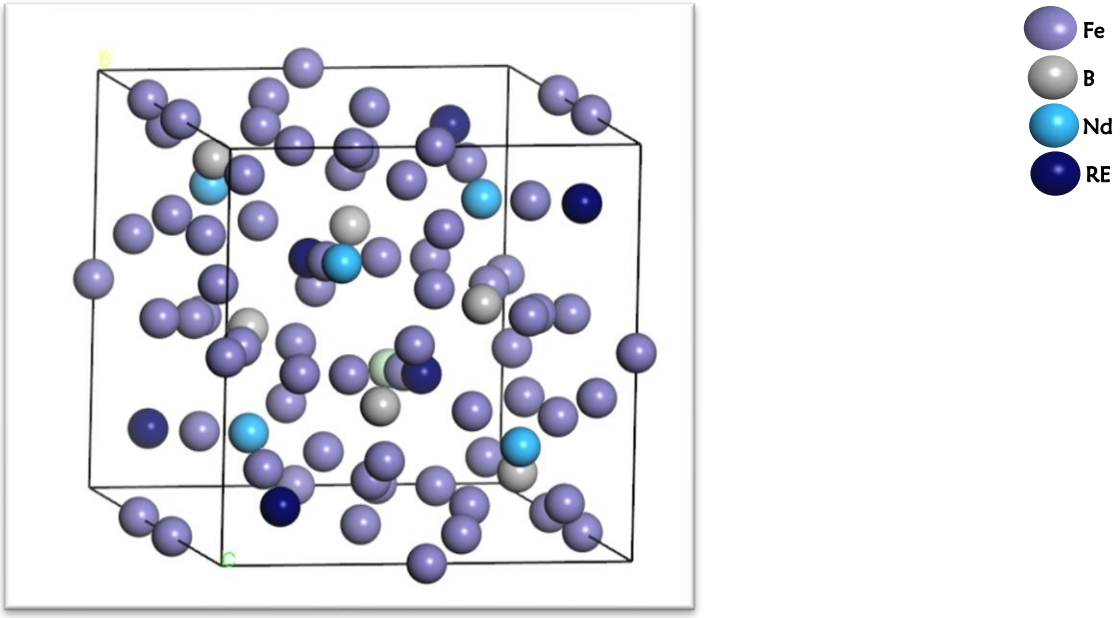

Figure 1: Crystal structure of $Nd_2Fe_{14}B$ doped permanent magnets.

2 Computational Method

The ab initio Density Functional Theory (DFT) [12] is employed as incorporated in the Vienna ab initio simulation package (VASP) [11], which was used to perform calculations of structural, magnetic, and elastic properties. The Projector Augmented Wave (PAW) was used to characterise electron-ion interactions [13]. For the exchange-correlation functional, the spin-polarised generalised gradient approximation parameterised by Perdew, Burke and Ernzerhof (GGA-PBE) [14] was chosen. A total energy cut-off of 400 eV was adopted, as it was sufficient to converge the total energy of the tetragonal $NdREFe_{14}B$ permanent magnets (RE = Gd, Ce). As per Monkhorst and Pack [15], an appropriate k-point mesh of 6x6x3 was used, considering that the energy at that point showed a constant trend, resulting in variances in energy of less than 1 meV/atom. The spin-polarisation was included, which is significant for Nd-based magnets. Before calculating any properties, geometry optimisation was done to fully relax each structure. With a strain of 0.005, the calculated elastic constants for every structure were obtained. Following that, the Poisson ratio, bulk modulus, shear modulus, and elastic modulus were computed.

3 Results and Discussions

3.1 Structural and Thermodynamic Properties

Table 1 shows the calculated lattice parameters for $Nd_2Fe_{14}B$, $NdGdFe_{14}B$ and $NdCeFe_{14}B$ permanent magnets. The calculated *a* parameter for $Nd_2Fe_{14}B$ is 8.25 Å, which is comparable with the experimental value of 8.82 Å

within 5% [7]. Moreover, the *c* parameter was found to be 12.12 Å, and this is 1% comparable with the experimental value (12.25 Å Ref). Nd was substituted with both Gd and Ce rare earth elements. $NdCeFe_{14}B$ magnets have lattice parameters of *a* = 8.63 Å and *c* = 12.95 Å. We note that for Nd substitution with Gd, the *a* parameter increased from 8.25 Å to 8.29 Å, whereas the *c* parameter decreased from 12.12 Å to 11.47 Å.

Table 1: Lattice parameters of $Nd_2Fe_{14}B$, $NdGdFe_{14}B$ and $NdCeFe_{14}B$ permanent magnets.

Structures	**Parameters**	**Calculated (Å)**	**Experimental (Å)**
$Nd_2Fe_{14}B$	*a*	8.25	8.82
	c	12.12	12.25
$NdGdFe_{14}B$	*a*	8.29	
	c	11.47	
$NdCeFe_{14}B$	*a*	8.63	
	c	11.95	

The heats of formation (ΔH_f) for $Nd_2Fe_{14}B$, $NdGdFe_{14}B$ and $NdCeFe_{14}B$ permanent magnets are calculated as shown in Table 2. ΔH_f values are calculated to evaluate the thermodynamic stability of alloys, where negative ΔH_f values display a stable material, whereas positive ΔH_f values allude to the instability of the material. The following equation estimates the ΔH_f [16];

$$\Delta H_f = E_c - \sum_i x_i E_i, \quad (1)$$

where E_c is the calculated total energy of the compound, E_i is the calculated total energy of element *i* in the compound, and x_i is the composition of each element. The computed heats of formation for $Nd_2Fe_{14}B$ were found to be -6.49 eV/atom. This indicates that the magnet is thermodynamically stable. Substitution of Nd with Gd and Ce displays a slight increase in the calculated ΔH_f. $NdGdFe_{14}B$ has a calculated ΔH_f of -6.26 eV/atom, which is less thermodynamically stable than that of $Nd_2Fe_{14}B$ magnets. Furthermore, $NdCeFe_{14}B$ permanent magnets have the ΔH_f with the value of -6.35 eV/atom. These results suggest that both $NdGdFe_{14}B$ and $NdCeFe_{14}B$ permanent magnets are thermodynamically stable since ΔH_f was found to be negative. Reduced thermodynamic stability of $NdGdFe_{14}B$ and $NdCeFe_{14}B$ is indicated by an increase in the computed ΔH_f.

Table 2: Heats of formation of $Nd_2Fe_{14}B$, $NdGdFe_{14}B$ and $NdCeFe_{14}B$ permanent magnets.

Structures	**ΔH_f (eV/atom)**
$Nd_2Fe_{14}B$	-6.49
$NdGdFe_{14}B$	-6.26
$NdCeFe_{14}B$	-6.35

3.2 Elastic properties

Table 3 shows the elastic constants for $Nd_2Fe_{14}B$, $NdGdFe_{14}B$ and $NdCeFe_{14}B$ permanent magnets. Elastic constants are computed to ascertain the magnets' mechanical stability, resistance to stress from external forces, and interatomic bonding circumstances. When a material meets the stability requirements for that particular crystal structure, it is deemed mechanically stable. The following is the condition of tetragonal crystal stability [17]:

$$C_{44} > 0, C_{66} > 0, C_{11} > |C_{12}| \; and \; C_{11} + C_{12} - \frac{2C_{13}^2}{C_{33}} > 0. \quad (2)$$

Calculated elastic constants for $Nd_2Fe_{14}B$ satisfy the Born stability criterion, suggesting mechanical stability. Moreover, $NdGdFe_{14}B$ and $NdCeFe_{14}B$ permanent magnets are mechanically stable with the computed elastic constants satisfying the Born stability criterion. Substitution of Nd with both Gd and Ce enhances the mechanical

stability of $Nd_2Fe_{14}B$. The fact that C_{11} is greater than C_{13} suggests that the structures are more rigid along the *a*-axis than the *c*-axis. This explains why the computed c parameter decreased.

Table 3: Elastic constants of $Nd_2Fe_{14}B$, $NdGdFe_{14}B$ and $NdCeFe_{14}B$ permanent magnets.

Structures	**$Nd_2Fe_{14}B$** (GPa)	**$NdGdFe_{14}B$** (GPa)	**$NdCeFe_{14}B$** (GPa)
C_{11}	298	382	215
C_{12}	159	143	51
C_{13}	66	141	23
C_{33}	94	333	160
C_{44}	66	113	24
C_{66}	120	117	117
C'	69	120	83

Pugh's ratio, Poisson's ratio and Cauchy pressure are calculated to determine the ductility of $Nd_2Fe_{14}B$, $NdGdFe_{14}B$ and $NdCeFe_{14}B$ permanent magnets as shown in Table 4. Pugh's ratio (k = B/G) is used to assess the ductility of these magnets. The material is considered ductile when k is greater than 1.75; otherwise, the material is brittle, as proposed by Pugh [18]. $Nd_2Fe_{14}B$ magnets were found to be brittle since the calculated k, with a value of 1.13, is less than the critical value of 1.75. Substitution of Nd with other REs such as Ce and Gd is considered to enhance the ductility of $Nd_2Fe_{14}B$ magnets. Gd substitution displays an increase in the value of k to 1.91, which alludes to the ductility of $NdGdFe_{14}B$ magnets. Moreover, the substitution of Nd with Ce shows an increase in the value of k to 1.58. $NdCeFe_{14}B$ permanent magnets are brittle since k is less than 1.75. Gd substitution enhances the ductility of $Nd_2Fe_{14}B$ permanent magnets.

Material is considered to be ductile when the Poisson ratio (v) is greater than 0.26; otherwise, it is brittle. $Nd_2Fe_{14}B$ is observed to be brittle since the calculated v is less than 0.26, with a value of 0.20. The calculated v is in good accordance with the experimental value (0.22) within 5% [19]. From our results, we notice that v is greater than 0.26 for $NdGdFe_{14}B$, indicating ductility. Ce substitution has enhanced the Poisson's ratio of $Nd_2Fe_{14}B$ to 0.24, and $NdCeFe_{14}B$ is brittle. For the Cauchy pressure, a positive value indicates ductility; otherwise, it is brittle [20]. Similar to Pugh's and Poisson's ratios, both $Nd_2Fe_{14}B$ and $NdCeFe_{14}B$ are brittle, while $NdGdFe_{14}B$ is ductile. Ductility of $Nd_2Fe_{14}B$ is enhanced by substituting Nd with Gd.

Table 4: Pugh's ratio, Poisson's ratio and Cauchy pressure for $Nd_2Fe_{14}B$, $NdGdFe_{14}B$ and $NdCeFe_{14}B$ permanent magnets.

Structures	**$Nd_2Fe_{14}B$**	**$NdGdFe_{14}B$**	**$NdCeFe_{14}B$**
B/G	1.13	1.91	1.58
v	0.20	0.28	0.24
Cauchy Pressure (GPa)	-0.18	29.52	-1.28

3.3 Magnetic properties

Figure 2 presents the calculated total spin magnetic moments for $Nd_2Fe_{14}B$, $NdGdFe_{14}B$ and $NdCeFe_{14}B$ permanent magnets. We note that our findings on the magnetic moments are in good agreement with previous calculations [21]. The total spin magnetic moment for $Nd_2Fe_{14}B$ is 35.63 μB. Substitution of Nd with Ce and Gd compromises the total spin magnetic moments of $Nd_2Fe_{14}B$. The calculated magnetic moments of the $NdCeFe_{14}B$ and $NdGdFe_{14}B$ magnets were found to be 26.05 μ_B and 27.95 μ_B, respectively, which is less than that of the $Nd_2Fe_{14}B$ magnets. This suggests that the magnetic moments of the $Nd_2Fe_{14}B$ magnet were reduced due to Ce and Gd having less number of unpaired electrons. Gd was reported to be beneficial in enhancing the Curie

temperature of $Nd_2Fe_{14}B$ and other magnetic properties [10]; however, it reduces the magnetic moments of the alloys. Decreasing magnetic moments indicate a decline in performance and strength of magnets.

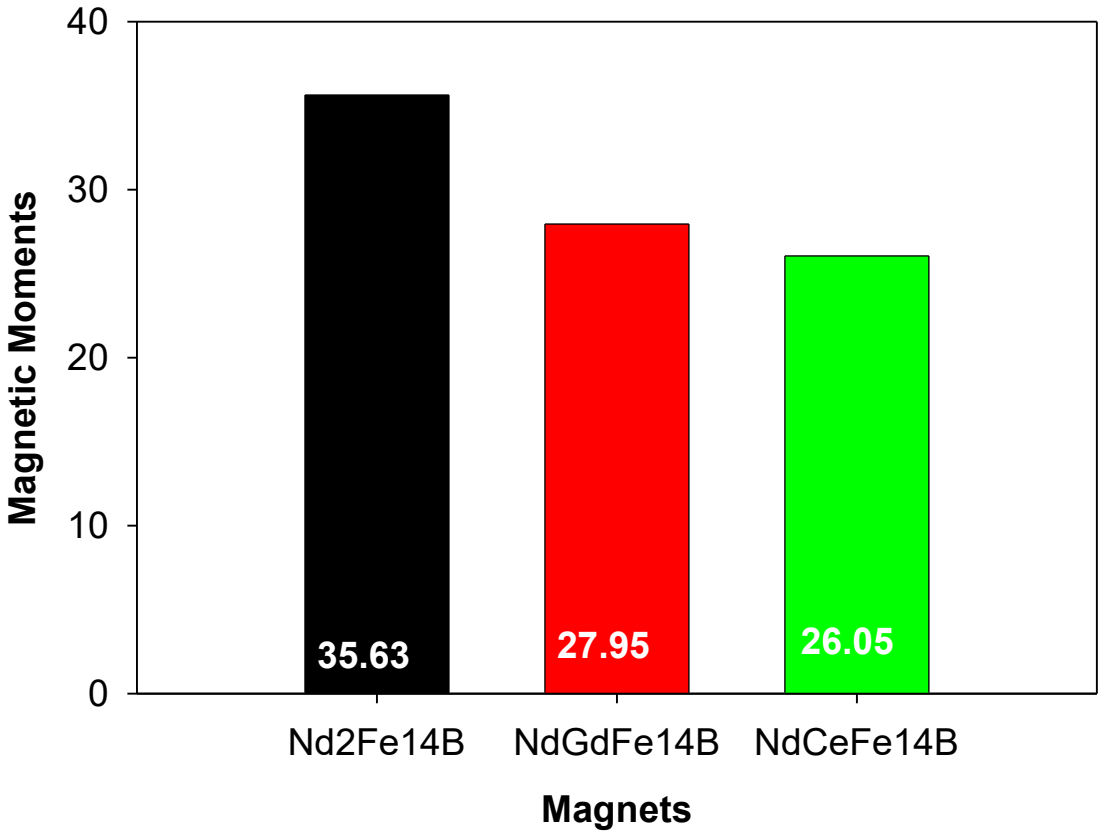

Figure 2: Magnetic moments (μ_B) of $Nd_2Fe_{14}B$, $NdGdFe_{14}B$ and $NdCeFe_{14}B$ permanent magnets.

4 Conclusions

The first-principle approach was employed to investigate the structural, thermodynamic, mechanical and magnetic properties of $Nd_2Fe_{14}B$, $NdGdFe_{14}B$ and $NdCeFe_{14}B$ permanent magnets. The calculated structural properties are in good accordance with experimental data within 5%. Energy of formation predicts the thermodynamic stability of $Nd_2Fe_{14}B$, c and $NdCeFe_{14}B$ permanent magnets. Mechanical properties suggest that Gd substitution enhanced the ductility of $Nd_2Fe_{14}B$ magnets. Gd substitution improved the Pugh's ratio from 1.13 to 1.91. This alludes to the ductility of the $NdGdFe_{14}B$ permanent magnet. We found that $Nd_2Fe_{14}B$ exhibits a high magnetic spin value of 35.63 µB, followed by $NdGdFe_{14}B$ (27.95 µB). Furthermore, the $NdCeFe_{14}B$ magnet possesses a low magnetic moment as compared to the pristine structure and $NdGdFe_{14}B$. Gd and Ce substitutions improve ductility but reduce the magnetic moments of pure $Nd_2Fe_{14}B$ magnets. Analysis of magnetic and mechanical properties predicted $NdGdFe_{14}B$ alloys to be promising candidates for magnetic applications such as electric vehicles and wind turbines. The next stage will be to investigate how temperature affects the NdGdFe14B and NdCeFe14B permanent magnets.

References

[1] Q. Gong, M. Yi, R. F. L. Evans, O. Gutfleisch, and B. X. Xu, "Anisotropic exchange in Nd–Fe–B permanent magnets," *Mater Res Lett*, vol. 8, no. 3, pp. 89–96, 2020, doi: 10.1080/21663831.2019.1702116.

[2] M. Sagawa, S. Fujimura, N. Togawa, H. Yamamoto, and Y. Matsuura, "New material for permanent magnets on a base of Nd and Fe (invited)," *J Appl Phys*, vol. 55, no. 6, pp. 2083–2087, 1984, doi: 10.1063/1.333572.

[3] X. Yin *et al.*, "An Efficient Process for Recycling Nd–Fe–B Sludge as High-Performance Sintered Magnets," *Engineering*, vol. 6, no. 2, pp. 165–172, Feb. 2020, doi: 10.1016/j.eng.2019.11.007.

[4] J. Zheng *et al.*, "Magnetic Properties and Microstructure of Ce-Cu-Al Low Melting Alloy Bonding Sm2Fe17N3 Magnet Fabricated by the Hot-Pressing Method," *Magnetochemistry*, vol. 8, no. 11, pp. 1–16, 2022, doi: 10.3390/magnetochemistry8110149.

[5] L. Li *et al.*, "Micromagnetic simulations on demagnetization processes in anisotropic Nd 2 Fe 14 B magnets," *Journal of Rare Earths*, vol. 37, no. 6, pp. 628–632, Jun. 2019, doi: 10.1016/j.jre.2018.10.018.

[6] J. Yu, S. Jiang, D. Sun, P. Lin, and Y. Zhang, "Correlation of mechanical properties and electronic structures for NdFeB permanent magnet under hydrostatic pressure based on first-principle calculation," *Journal of Materials Research and Technology*, vol. 18, pp. 3410–3427, May 2022, doi: 10.1016/j.jmrt.2022.03.189.

[7] M. Sagawa, K. Hiraga, H. Yamamoto, and Y. Matsuura, "Permanent magnet materials based on the rare earth-iron-boron tetragonal compounds (invited)," *IEEE Trans Magn*, vol. 20, no. 5, pp. 1584–1589, 1984, doi: 10.1109/TMAG.1984.1063214.

[8] M. Sagawa, S. Fujimura, H. Yamamoto, Y. Matsuura, and S. Hirosawa, "Magnetic properties of rare-earth-iron-boron permanent magnet materials," *J Appl Phys*, vol. 57, no. 8, pp. 4094–4096, Apr. 1985, doi: 10.1063/1.334629.

[9] M. E. Baloyi, R. G. Diale, P. E. Ngoepe, and H. R. Chauke, "Effect of Terbium on the magnetic properties of Nd2Fe14B permanent magnets," *MRS Adv*, vol. 10, pp. 1123–1126, 2025, doi: 10.1557/s43580-025-01295-8.

[10] J. Zheng *et al.*, "Enhanced thermal stability of nanocrystalline melt-spun Nd-Pr-Fe-B alloys by Gd substitution," *J Magn Magn Mater.*, vol. 604, p. 172316, 2024, doi: https://doi.org/10.1016/j.jmmm.2024.172316.

[11] G. Kresse and J. Hafner, "Ab. initio molecular dynamics for liquid metals," *Phys Rev B*, vol. 47, p. 222, 1994.

[12] W. Kohn and L. J. Sham, "Self-Consistent Equations Including Exchange and Correlation Effects," *Phys Rev B*, vol. 140, pp. 1133–1138, 1965.

[13] G. Kresse and D. Joubert, "From ultrasoft pseudopotentials to the projector augmented-wave method," *Phys Rev B*, vol. 59, pp. 1758–1175, 1999.

[14] J. P. Perdew, K. Burke, and M. Ernzerhof, "Generalized Gradient Approximation Made Simple," *Phys Rev Lett*, vol. 77, pp. 3865–3868, 1996.

[15] H. J. Monkhorst and J. D. Pack, "Special points for Brillonin-zone integrations," *Phys Rev B*, vol. 13, pp. 5188–5192, 1976.

[16] R. E. Watson and L. H. Bennett, "Heats of Formation of Transition-Metal Alloys," *Phys Rev Lett*, vol. 43, pp. 1130–1132, 1979.

[17] M. J. Phasha, P. E. Ngoepe, H. R. Chauke, D. G. Pettifor, and D. Nguyen-Mann, "Link between structural and mechanical stability of fee- And bcc-based ordered Mg-Li alloys," *Intermetallics (Barking)*, vol. 18, no. 11, pp. 2083–2089, 2010, doi: 10.1016/j.intermet.2010.06.015.

[18] J. W. Glen and S. F. Pugh, "The effect of phase transformations on the orientation of zirconium crystals," *Acta Metallurgica*, vol. 2, no. 3, pp. 520–529, 1954, doi: https://doi.org/10.1016/0001-6160(54)90073-5.

[19] G. Tian *et al.*, "Ab initio calculation of electronic structure and magnetic properties of R2Fe14BNx (R = Pr,Nd)," *AIP Adv*, vol. 8, no. 5, p. 1, 2018, doi: 10.1063/1.5007022.

[20] D. G. Pettifor, "Theoretical predictions of structure and related properties of intermetallics," *Materials Science and Technology*, vol. 8, no. 4, pp. 345–349, 1992, doi: 10.1179/mst.1992.8.4.345.

[21] A. E. Aly, "Density of States of Rare-earth Permanent Magnet Nd_2Fe_{14} B Using Spin-orbit Coupling," *International Journal of Pure and Applied Physics*, vol. 5, no. 3, pp. 215–229, 2009, [Online]. Available: http://www.ripublication.com/ijpap.htm

Investigation of Poly(2,5)-benzimidazole (ABPBI)–Carbon Nanotube Composites for Low Earth Orbit Applications: An Integrated Computational and Experimental Study

Luwy Swanepoel[1], Lynndle Square[1,2], Kingsley Obodo[1,2,3], Lionel Fourie[4] and Christopher Arendse[4]

[1]Centre for Space Research, North-West University, Potchefstroom, 2531, South Africa
[2]National Institute for Theoretical and Computational Sciences, NITheCS, South Africa
[3]School of Agriculture & Science, University of KwaZulu-Natal, Scottsville, Pietermaritzburg, 3209, South Africa
[4]Department of Physics and Astronomy, University of the Western Cape, Bellville, Cape Town, 7535, South Africa

E-mail: 34200894@mynwu.ac.za

Abstract. Spacecraft materials for Low Earth Orbit (LEO) must be lightweight, durable, and radiation-resistant. This study examines poly(2,5)-benzimidazole (ABPBI) reinforced with carbon nanotubes (CNTs) using experimental and computational approaches. ABPBI films with 1–3 wt% multi-walled carbon nanotubes (MWCNTs) were prepared and characterised with powder X-ray diffraction (p-XRD), ultraviolet–visible (UV–Vis) absorption, and photoluminescence (PL) spectroscopy. Increasing the CNT content led to stronger electronic interactions, shown by blue-shifted absorption peaks, larger Stokes shifts, and reduced emission intensity. Complementary simulations modelled ABPBI monomers interacting with single-walled CNTs (SWCNTs) using density functional theory (DFT). The simulated absorption spectra, density of states (DOS), and band structures (BS) showed stronger UV absorption and a reduced band gap. Together, these results show that CNTs transform ABPBI from an insulator to a semiconductor, highlighting ABPBI–CNT composites as promising materials for long-term space applications.

1 Introduction

ABPBI is a high-performance polymer valued for its exceptional thermal and chemical stability, low density, and high tensile strength, key traits for space materials that must be both lightweight and durable to reduce launch costs and withstand LEO conditions [1, 2]. Its hydrogen-rich structure naturally shields against harmful secondary radiation [1], while its wide band gap prevents unwanted electrical conduction. To enhance ABPBI's performance, CNTs are added as nanofillers. They reinforce mechanical strength, improve conductivity, reduce thermal expansion, and aid charge dissipation, critical for polymer stability in harsh environments [3, 4]. CNTs also enhance UV absorption through π–π interactions and offer protection against atomic oxygen erosion [2]. MWCNTs are preferred experimentally, as their multiple layers provide superior strength, bonding, and dispersion in ABPBI films, making them more practical for hot-casting fabrication [2]. SWCNTs, by contrast, have simpler one-layer structures and a defined chirality, making them computationally efficient. Their (3,3) armchair symmetry enables accurate modelling of nanoscale effects such as orbital hybridisation and charge transfer with minimal computational cost [5]. Despite structural differences, SWCNTs, DWCNTs, and MWCNTs show similar thermal and structural trends, allowing computational SWCNT data to validate experimental MWCNT results [6].

Despite these advantages, how CNTs specifically influence ABPBI's electronic and optical behaviour remains unclear. Most research isolates either experiments or simulations, rarely bridging both. This study closes that gap by synthesising ABPBI–MWCNT composites and modelling ABPBI–SWCNT systems, aiming to reveal how CNTs enhance optical absorption, charge transfer, and electronic properties for space applications.

2 Methodology

2.1 Experimental Synthesis and Characterisation

The ABPBI/MWCNT composites were synthesised using in-situ polymerisation, previously done by [1, 7, 8] and then characterised using p-XRD, UV-Vis absorption, and PL spectroscopy.

2.2 Computational Modelling

ABPBI–SWCNT interactions were studied using DFT in BIOVIA Materials Studio (MS) 2020, with CASTEP (Cambridge Serial Total Energy Package) for periodic supercell simulations and DMol^3 for isolated-molecule optimisations [5]. DFT offers a good trade-off between accuracy and cost in many-electron systems [9], although it tends to underestimate band gaps, weak interactions, and excitations. All calculations were run on the NICIS CHPC (National Integrated Cyber Infrastructure System and Centre for High Performance Computing) server for faster convergence [10]. A (3,3) armchair SWCNT was built and extended into a supercell to mimic bulk behaviour and then geometry-optimised in CASTEP using a 500 eV cut-off energy, a $2\times2\times1$ k-point mesh, and lattice dimensions of $7.415\times7.415\times19.676$ Å. The ABPBI monomer was optimised in DMol^3 using the GGA-PBE (Generalised Gradient Approximation—Perdew–Burke–Ernzerhof) functional, chosen for efficiency and accuracy in predicting polymer structure, although it underestimates excitations and weak interactions [5]. Monomer adsorption on the SWCNT was modelled with the Adsorption Locator to find the most stable positions, then fully relaxed in CASTEP [5]. DOS, BS, and optical spectra were computed for the monomer, SWCNT, and composite, with the final energies used to calculate the adsorption energy. In short, CASTEP handled periodic systems, DMol^3 molecular optimisation, and Adsorption Locator interaction studies. While DFT/GGA-PBE limits accuracy for band gaps and adsorption energies, the workflow provides reliable insights into ABPBI–SWCNT interactions.

3 Results and Discussion

3.1 Experimental Results

The p-XRD pattern of the ABPBI/MWCNT composite (Figure 1), measured with a with a PANalytical X'Pert Pro diffractometer using a cobalt X-ray tube, shows two broad peaks near $2\theta = 12°$ and $32°$, suggesting a semi-crystalline structure with both ordered and disordered regions [1]. The $2\theta = 12°$ peak corresponds to the ABPBI chain spacing, while the $32°$ peak arises from π–π stacking between ABPBI aromatic rings and MWCNT graphitic walls, as well as nanotube-induced structural effects [1, 11]. These features suggest partial alignment and good integration of MWCNTs within the polymer matrix. Compared to studies on pristine ABPBI, peak broadening and slight shifts indicate that MWCNTs disrupt chain packing and introduce internal strain [1]. Minor additional peaks may result from residual MSA or cobalt X-ray artefacts. Overall, p-XRD confirms the formation of a well-integrated, compact nanocomposite.

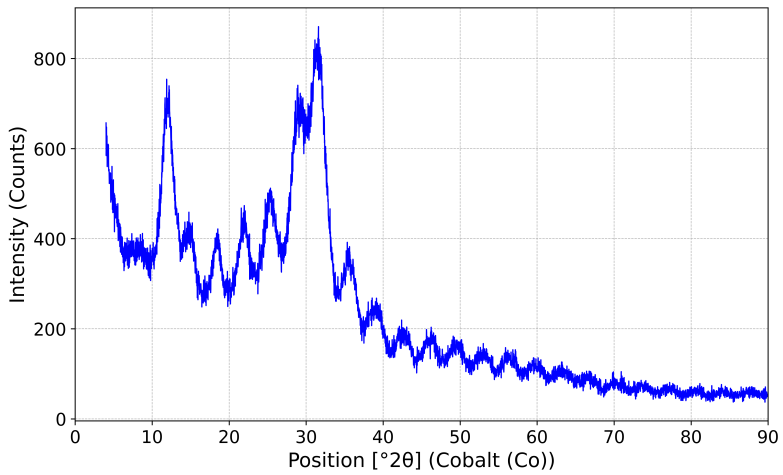

Figure 1: Experimental p-XRD analysis of the ABPBI/MWCNT composite.

The UV-Vis and PL results (Figure 2) show that pristine ABPBI strongly absorbs UV light via π-π^* transitions along its conjugated backbone. Adding 1–3 wt% MWCNTs increases absorbance in the 230–450 nm range, indicating stronger π-π stacking and polymer-nanotube interactions. The absorption peak (λ_{max}) in Table 1 blue shifts from 466 nm (pristine) to 413 nm (1 wt%) and 336–339 nm at higher loadings, reflecting improved charge transfer and tighter electronic coupling [12, 13]. Despite this, the absorption edge remains near 466 nm, suggesting that the core electronic structure is preserved. The emission peak shifts from 586 nm (pristine) to 517 nm (1 wt%) and slightly red-shifts to 565–566 nm at 2–3 wt%, while the PL intensity decreases with more CNTs, indicating non-radiative traps and increased energy loss [14]. Wider Stokes shifts (gap between absorption and emission peaks) with CNT loading suggest greater internal energy dissipation. Overall, MWCNTs enhance UV absorption and charge transfer while suppressing emission.

Composite	**Absorption**		**Emission**	
	λ_{max} (nm)	λ_{onset} (nm)	λ_{Em} (nm)	$\Delta\lambda_{St}$ (nm)
Pristine ABPBI	466	483	586	103
ABPBI/MWCNT 1 wt%	413	466	517	104
ABPBI/MWCNT 2 wt%	339	467	565	226
ABPBI/MWCNT 3 wt%	336	466	566	230

Table 1: Optical properties of the ABPBI/MWCNT composites. λ_{onset} = absorption peak edge; $\Delta\lambda_{St}$ = Stokes shift.

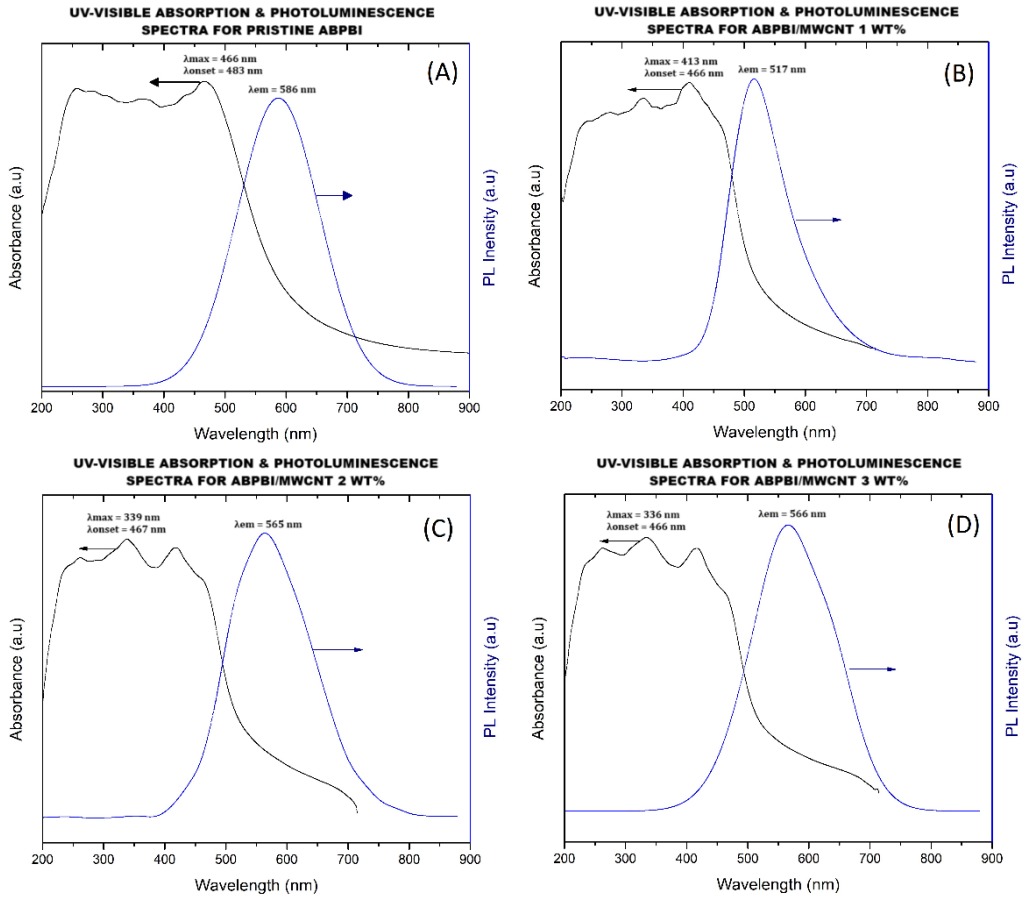

Figure 2: Experimental UV–Vis and PL spectra for (A) pristine ABPBI, (B) ABPBI/MWCNT 1 wt%, (C) ABPBI/MWCNT 2 wt% and (D) ABPBI/MWCNT 3 wt%.

3.2 Computational Results

The BS and DOS of the SWCNT (Figure 4) show several bands crossing the Fermi level, confirming no band gap and easy electron excitation. This metallic behaviour explains its excellent conductivity. Sharp DOS peaks are van

Hove singularities, typical of 1D systems where electrons are confined along the tube axis. These discrete energy levels enhance electronic excitations, accounting for the strong UV absorption below 100 nm (Figure 3) arising from pronounced π–π^* transitions in the carbon–carbon double bonds.

The ABPBI monomer shows insulating behaviour, with a wide band gap of 4.12 eV (Figure 5), which separates valence and conduction bands and limits electron excitation, confirming poor electrical conductivity. The DOS shows no electronic states at the Fermi level, indicating the absence of free charge carriers. Such a wide gap is typical of conjugated aromatic polymers, where electrons are highly localised. Despite this, the absorption spectrum (Figure 3) shows a strong UV peak around 100 nm, revealing that the aromatic rings still support localised electronic excitations.

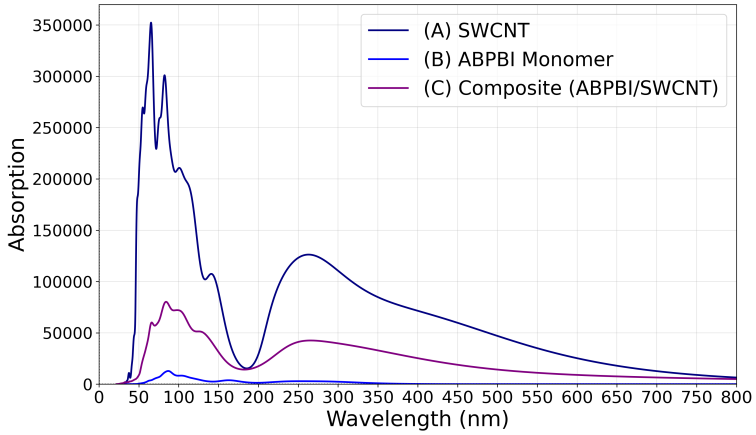

Figure 3: Simulated UV-Vis spectra: (A) SWCNT, (B) ABPBI Monomer and (C) Composite.

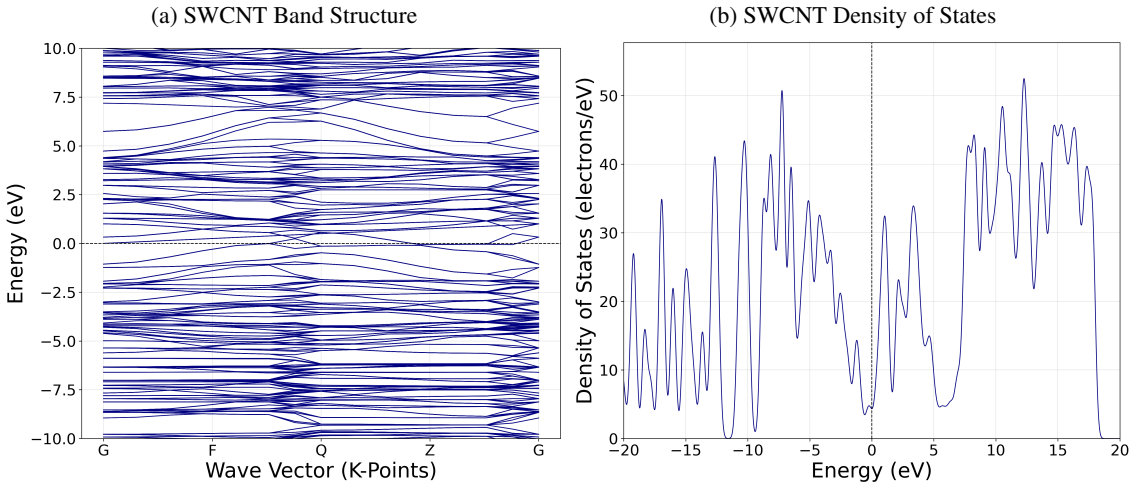

Figure 4: SWCNT Simulated: (a) Band Structure and (b) Density of States. The Fermi level (black dotted line) is set to 0 eV in MS as a reference for all energies.

When ABPBI adsorbs on the SWCNT, the BS (Figure 6) becomes denser near the Fermi level, and the band gap narrows to 0.005 eV, allowing easier electron excitation. This arises from π–π stacking and orbital hybridisation between the monomer and nanotube, introducing new states at the Fermi level. The DOS shows pronounced peaks near 0 eV, confirming charge transfer and strong electronic interactions. The calculated adsorption energy of -3.18 eV confirms stable binding to the SWCNT. In the UV–vis spectra (Figure 3), the composite shows broader, stronger peaks, reflecting enhanced absorption and coupling. Overall, MWCNTs transforms ABPBI from an insulator to a semiconductor, boosting conductivity and optical performance.

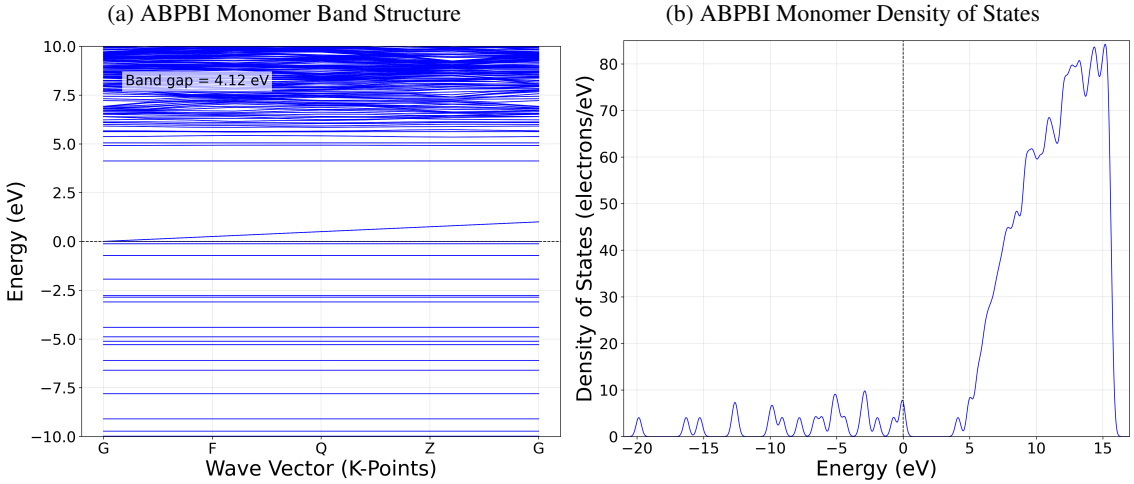

Figure 5: ABPBI Monomer Simulated: (a) Band Structure and (b) Density of States.

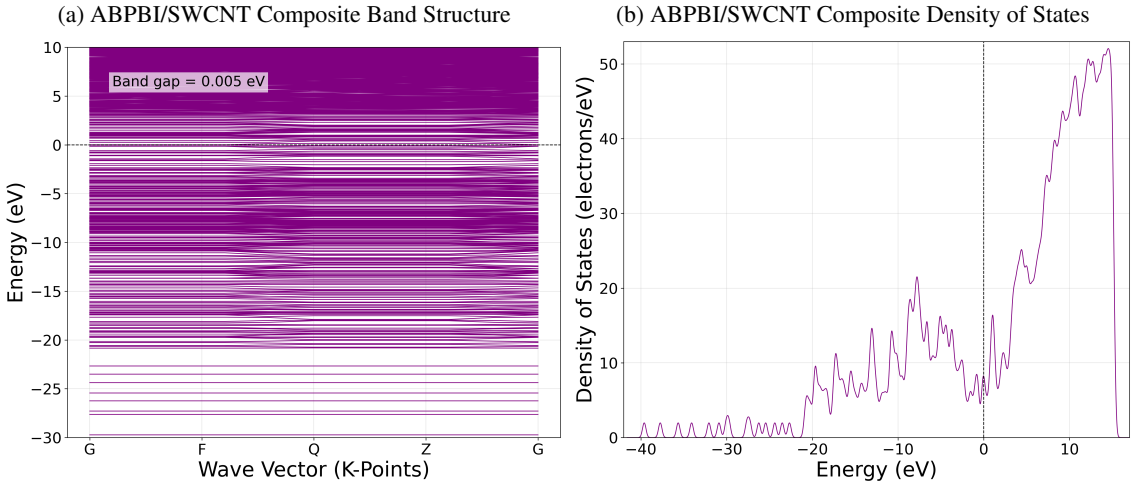

Figure 6: ABPBI/SWCNT Composite Simulated: (a) Band Structure and (b) Density of States.

4 Conclusion

This study demonstrated that incorporating CNTs into ABPBI significantly enhances its optical and electronic behaviour. p-XRD shows that CNTs disrupt polymer chain packing, add strain, and improve integration, while UV–Vis spectra shows stronger and blue-shifted absorption peaks and PL spectra shows reduced emission due to internal energy trapping. Computational simulations align with the experimental UV absorption trends and showed a band gap reduction from 4.12 eV to 0.005 eV, confirming a transition from insulating to semiconducting behaviour via π–π stacking and charge delocalisation. While the strong UV absorption is not a favourable characteristic for a protective LEO coating, the composite still shows promising potential for other space-related applications. Future work should use hybrid or time-dependent DFT methods and model the polymer for more realistic predictions. Overall, this highlights the strong potential of CNT–ABPBI composites for advanced space applications.

Acknowledgements

The authors acknowledge NRF, Thuthuka instrument (UID No. 138417) and NICIS CHPC.

References

[1] L. F. Fourie, L. Square, C. Arendse, and M. Msimanga, "Abpbi/mwcnt for proton radiation shielding in low earth orbit," *APL Materials*, vol. 11, no. 68, p. 071103, 2023.

[2] E. H. Ellis and L. C. Square, "Reactive molecular dynamics simulations of the surface interactions between atomic oxygen and poly(2,5)-benzimidazole carbon nanotube composite," Master's thesis, North-West University, 2023.

[3] B. I. Yakobson and P. Avouris, "Mechanical properties of carbon nanotubes," *Topics in Applied Physics*, vol. 80, pp. 287–327, 2001.

[4] E. W. Fenta and B. A. Mebratie, "Advancements in carbon nanotube-polymer composites: Enhancing properties and applications through advanced manufacturing techniques," *Heliyon*, vol. 10, p. e36490, 2024.

[5] BIOVIA, Dassault Systèmes, "Biovia materials studio overview," https://www.3ds.com/assets/invest/2023-10/biovia-materials-studio-overview.pdf, 2023, accessed: 2024-11-11.

[6] L. Square, B. Oryema, P. Mafoko, E. Ellis, and H. Vorster, "Comparative analysis of single-walled, double-walled, and multi-walled carbon nanotube-reinforced poly(2,5-benzimidazole) composites: Enhanced structural and thermal stability for radiation shielding in low earth orbit," *Radiation Physics and Chemistry*, vol. 232, p. 112658, 2025.

[7] L. Square, L. F. Fourie, E. Ellis, and M. Msimanga, "Effects of atomic oxygen irradiation on the structural and thermal properties of abpbi/mwcnt composites," *2023 IEEE 23rd International Conference on Nanotechnology (NANO)*, pp. 963–966, 2023.

[8] L. Swanepoel, L. Square, and O. Kingsley, "The effect of microgravity on the abpbi carbon nanotube composite for leo applications – an experimental and computational approach," 2024, unpublished Honours Report, North-West University.

[9] L. S. Pedroza, A. J. da Silva, and K. Capelle, "Gradient-dependent density functionals of the perdew–burke–ernzerhof type for atoms, molecules and solids," *Physical Review B - Condensed Matter and Materials Physics*, vol. 79, no. 20, p. 201106, 2009.

[10] CHPC, "About the CHPC. National Integrated Cyber Infrastructure System (NICIS) and Centre for High Performance Computing (CHPC)," https://www.chpc.ac.za/about-the-chpc/, 2024, accessed: 11 Nov. 2024.

[11] J.-Y. Kang, S.-M. Eo, I.-Y. Jeon, Y. S. Choi, L.-S. Tan, and J.-B. Baek, "Multifunctional poly (2, 5-benzimidazole)/carbon nanotube composite films," *Journal of Polymer Science Part A: Polymer Chemistry*, vol. 48, no. 5, pp. 1067–1078, 2010.

[12] C. S. Allen, G. Liu, Y. Chen, A. W. Robertson, K. He, K. Porfyrakis, J. Zhang, G. A. D. Briggs, and J. H. Warner, "Optically enhanced charge transfer between c 60 and single-wall carbon nanotubes in hybrid electronic devices," *Nanoscale*, vol. 6, no. 1, pp. 572–580, 2014.

[13] A. Davoody, F. Karimi, M. Arnold, and I. Knezevic, "Theory of exciton energy transfer in carbon nanotube composites," *The Journal of Physical Chemistry C*, vol. 120, no. 30, pp. 16 354–16 366, 2016.

[14] B. F. Habenicht and O. V. Prezhdo, "Nonradiative quenching of fluorescence in a semiconducting carbon nanotube:<? format?> a time-domain ab initio study," *Physical review letters*, vol. 100, no. 19, p. 197402, 2008.

First principles study of the structural, mechanical and electronic properties of Mooihoekite ($Cu_9Fe_9S_{16}$)

Mashishi Kagiso, Ngoepe Phuti, Mkhonto Peace and Mehlape Mofuti

Materials Modelling Centre, University of Limpopo, Polokwane, South Africa

E-mail: 201914374@myturf-ul.ac.za

Abstract. Mooihoekite ($Cu_9Fe_9S_{16}$) is a copper–iron sulfide with a metal-rich tetragonal structure derived from chalcopyrite. It commonly occurs as intergrowths with other sulfides in complex ore deposits. Despite its relevance in flotation environments and its coexistence with minerals such as Chalcopyrite and Haycockite, the flotation behaviour of Mooihoekite itself remains poorly understood. This limits the optimization of separation processes, where mineral-specific surface and electronic properties are crucial. To address this gap, this study applies dispersion-corrected density functional theory (DFT-D3+U) to examine the structural, electronic, and mechanical properties of Mooihoekite. The results show semiconducting behaviour with a band gap of about 0.5 eV and antiferromagnetic ordering, reflected in the symmetry of spin-up and spin-down DOS. Elastic constant analysis confirms mechanical stability, while the Pugh ratio and Poisson's ratio point to ductile behaviour. The calculated Debye temperature (318 K) agrees reasonably with experimental values (292 K). These findings provide a theoretical framework for future surface and interface studies aimed at clarifying Mooihoekite's role in flotation and improving the selective recovery of copper and iron sulphides.

.

1 Introduction

Transition-metal sulfides represent a geologically significant class of materials distinguished by their structural versatility and functional diversity [1]. These compounds exhibit tunable electronic structures, varied magnetic behaviors, and significant catalytic activity, rendering them essential for a range of applications including energy storage, electrocatalysis, and thermoelectric conversion [2]. Among them, Mooihoekite ($Cu_9Fe_9S_{16}$) stands out as a notable copper-rich iron sulfide, commonly associated with chalcopyrite ($CuFeS_2$) and pentlandite ($(Fe,Ni)_9S_8$) within magmatic sulfide assemblages. Mooihoekite ($Cu_9Fe_9S_{16}$) is a structurally complex and partially disordered transition-metal sulfide, distinguished by its intricate Cu–Fe–S bonding network. Beyond its fundamental mineralogical interest, Mooihoekite is relevant for potential technological applications, including thermoelectric, catalytic, and electrochemical processes. Mineralogical investigations have shown that Mooihoekite frequently forms intergrowths with haycockite, particularly within hortonolite dunite pegmatites at the Mooihoek Farm locality in Lydenburg, South Africa [3]. Mooihoekite belongs to the chalcopyrite-derived series of sulfides, which

are characterized by the incorporation of additional transition-metal atoms into interstitial lattice sites. These modifications give rise to non-stoichiometric compositions that deviate from the ideal $CuFeS_2$ structure, resulting in altered physicochemical properties. The structure of Mooihoekite is derived from a cubic close-packed arrangement of sulfide anions, with metal cations occupying tetrahedral sites, consistent with a structural lineage related to the Li_2O-type framework. Excess Cu and Fe atoms occupy interstitial voids, contributing to increased metallic content and structural complexity [4]. These modifications are of particular interest in the context of ore processing, as they influence both the thermodynamic stability and reactivity of the mineral under reducing and oxidizing conditions.

Electrochemical investigations have shown that Mooihoekite exhibits moderate oxidative reactivity, performing more efficiently than chalcopyrite but less than haycockite [5]. This behavior is attributed to its partially open structure, which facilitates electron mobility and the release of constituent metal ions. Thermoelectric studies on nanostructured Mooihoekite have revealed semiconducting transport behavior, low lattice thermal conductivity, and tunable electrical properties through Fe doping. A maximum dimensionless figure of merit (zT) of 0.21 at 800 K has been reported for Mooihoekite, highlighting its potential as a functional thermoelectric material [6]. Magnetic characterization using Mössbauer spectroscopy, magnetic susceptibility, and X-ray diffraction techniques has revealed weak ferromagnetic behavior, with a net magnetic moment of approximately 0.2 μB per formula unit, persisting over a wide temperature range. Furthermore, Mössbauer spectra displayed two distinct hyperfine patterns, indicating that Fe atoms occupy multiple local environments due to structural disorder [7].

Despite the availability of experimental data, a critical gap remains in linking its structurally complex and partially disordered atomic arrangement to its macroscopic properties. Although experimental methods are effective at quantifying macroscopic properties such as reactivity and thermoelectric performance, they often fall short in elucidating the underlying electronic structure, bonding interactions, and mechanical stability that govern these behaviours. First-principles methods are especially powerful in this context, as they are able to clearly outline the electronic structure, bonding interactions and mechanical stability. These govern the surface chemistry, which directly impacts interactions with flotation reagents and ultimately flotation recoveries of metal sulfides. In this study, first-principles calculations based on dispersion-corrected density functional theory (DFT-D) were employed to examine the structural, electronic, and mechanical properties of Mooihoekite ($Cu_9Fe_9S_{16}$).

2 Methodology

The optimized structure of Mooihoekite ($Cu_9Fe_9S_{16}$) was calculated using first-principles density functional theory (DFT) within the Vienna Ab initio Simulation Package (VASP) [8, 9]. Structural relaxation employed the conjugate-gradient algorithm, converging ionic forces to 0.02 eV $Å^{-1}$ while maintaining self-consistency in the electron density. Valence electron–ionic core interactions were modelled using the projected augmented wave (PAW) method [10] with the electronic exchange–correlation described by the Perdew–Burke–Ernzerhof (PBE) generalized gradient approximation (GGA) functional [11] with the incorporation of the Hubbard U correction (GGA+U) [12]. The choice of U_{Eff} can influence the predicted electronic band gap, magnetic ordering, and bonding characteristics, which in turn affect the reliability of calculated bulk properties. An effective U_{Eff} of 4 eV was able to accurately capture electron correlation in localized Fe d-orbitals which is essential for describing Mooihoekite's structural and electronic properties. Van der Waals forces were accounted for via the Grimme DFT-D3 method [13] by adding a semi-empirical dispersion function to the conventional Kohn-Sham DFT energy which is not accounted for by the conventional DFT method. A plane-wave basis set with a 500 eV kinetic energy cut-off ensured total energy convergence to 10^{-6} eV, with residual Hellman–Feynman forces below 10^{-2} eV $Å^{-1}$. The Brillouin zone was sampled with a 4×4×7 Monkhorst–Pack k-point mesh [14] which was sufficient to converge the total energy of the system, while a denser 9×9×9 mesh with 0.2 eV width Gaussian smearing was used for electronic structure calculations.

3 Results and discussions

3.1 Structural properties

Mooihoekite crystallizes in the tetragonal system, with reported lattice parameters of a = 10.58 Å and c = 5.37 Å, forming a highly ordered and anisotropic crystal structure (Figure 1) [3]. Cu and Fe atoms occupy distinct crystallographic sites within a framework derived from a sphalerite-like arrangement. Structural stability is maintained through the incorporation of additional metal atoms at interstitial positions, rather than by cation

substitution or sulfur vacancy formation. These interstitial atoms display tetrahedral coordination with sulfur (~2.3 Å) and octahedral coordination with surrounding metals (~2.7 Å), giving rise to Fe–Cu–Fe and Fe-Fe-Fe metallic clusters. The relaxed bond lengths and lattice parameters show excellent agreement with experimental results [3, 4], as summarized in Table 1, underscoring the reliability of the computational model. Moreover, the heats of formation (ΔH_F) calculated using equation (1) indicate that the material is thermodynamically stable, as evidenced by the negative (ΔH_F) value.

The heat of formation was calculated using the following equation:

$$\Delta H_f\ (Cu_9Fe_9S_{16}) = \frac{1}{N}\left[(\mathrm{E}_{\mathrm{Cu_9Fe_9S_{16}}} - (9\mathrm{E}_{\mathrm{Cu}} + 9\mathrm{E}_{\mathrm{Fe}} + 16\mathrm{E}_{\mathrm{S}})\right] \quad (1)$$

Where N is the number of atoms, $\mathrm{E}_{\mathrm{Cu_9Fe_9S_{16}}}$ is the total energy of the system and E_{Cu}, E_{Fe}, and E_{S} are the individual energies of the constituent elements.

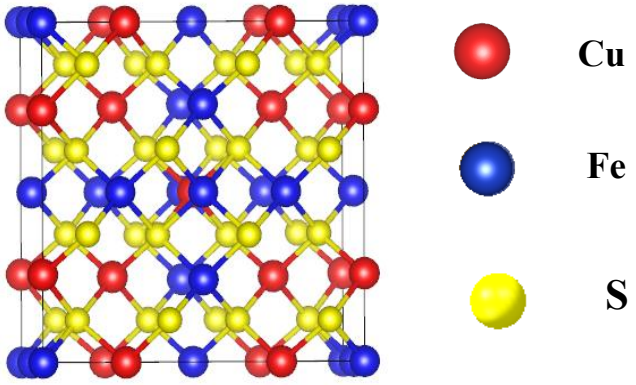

Figure 1: Crystal structure of Moohoekite ($Cu_9Fe_9S_{16}$) with space group $P\bar{4}2$-m.

Structure	Lattice parameters (Å)	Unit cell volume (Å)^3	Heats of formation (ΔH_F) (eV/Atom)
$Cu_9Fe_9S_{16}$	a=10.45814[10.5800] c=5.40684 [5.3700]	591.360 [603.023]	-0.76

Interatomic distances (Å)		
Bonds	Calculated	Experimental [4]
Fe-S	2.279	2.280
Cu-S	2.240	2.330
Fe-Fe	2.749	2.731

Table 1: Structural properties of Moohoekite ($Cu_9Fe_9S_{16}$).

3.2 Mechanical properties

The elastic stiffness tensor relates the stress tensor to the strain tensor through Hooke's law, defining a material's mechanical response. Due to the symmetry of the stress and strain tensors, the elastic stiffness tensor, in its most general form, contains only 21 independent nonzero components [15]. For the tetragonal $Cu_9Fe_9S_{16}$ crystal, the number of independent elastic stiffness components is reduced to six i.e. C_{11}, C_{12}, C_{13}, C_{33}, C_{44} and C_{66}. Here we present the calculated elastic constants, bulk modulus (B), shear modulus (G), Young's modulus (E), Poisson ratio (σ), and the Pugh ratio (B/G) in table 2 together with available experimental data.

For a tetragonal crystal, the requirement for mechanical stability leads to the following restrictions on its elastic constants [16].

$$\mathbf{C_{11} > 0,\ C_{33} > 0,\ C_{44} > 0,\ C_{66} > 0;\ (C_{11}-C_{12}) > 0,\ (C_{11} + C_{33} - 2C_{13}) > 0;\ 2(C_{11} + C_{12}) + C_{33} + 4C_{13} > 0}$$

The calculated elastic constants of mooihoekite satisfy all the mechanical stability criteria for a tetragonal crystal, confirming that $Cu_9Fe_9S_{16}$ is mechanically stable. As presented in Table 2, the elastic constants indicate that C_{33} is slightly larger than C_{11}, suggesting that the material exhibits marginally higher stiffness along the crystallographic *c*-axis compared to the *a*- and *b*-directions. Furthermore, C_{33} is significantly greater than the shear components C_{44} and C_{66}, which indicates that the material is mechanically anisotropic [17]. The relatively high bulk modulus (87.83 GPa) indicates moderate resistance to volume compression, while the low shear modulus (27.47 GPa) reflects a greater susceptibility to shear deformation. The Pugh's ratio (B/G) and Poisson ratio (σ) are calculated to determine the ductility or brittleness of materials where B/G > 1.75 and σ >0.26 imply ductility, otherwise brittleness [18, 19]. The Pugh ratio (B/G = 3.20) and Poisson's ratio v (0.35) both point to ductile behaviour, suggesting an intrinsic ability to withstand strain without fracturing which is crucial for both its stability in natural ore deposits and its potential use in devices.. The calculated Young's modulus (74.84 GPa) indicates the material's stiffness and resistance to uniaxial deformation. A higher Young's modulus corresponds to greater rigidity [20], reflecting strong bonding interactions within the crystal lattice, particularly between the Cu–S and Fe–S polyhedra. The Debye temperature is a key parameter related to various physical properties of solids, such as specific heat, thermal conductivity, and melting point. Notably, quantum effects become negligible above this temperature. For Mooihoekite the calculated Debye temperature is 318.7 K which shows reasonable agreement with the experimental value [6] (given in parentheses in Table 2).

GPa	**C_{11}**	**C_{12}**	**C_{13}**	**C_{33}**	**C_{44}**	**C_{66}**
$Cu_9Fe_9S_{16}$	118.53	69.10	72.84	124.44	27.94	32.5
Elastic moduli (GPa)	**Bulk (B)**	**Shear (G)**	**Young's (E)**	**B/G**	***v***	**Θ_D (K)**
	87.83	27.47	74.62	3.20	0.35	318.6(292)

Table 2: The calculated elastic constants (C_{ij}), Bulk modulus (B), Shear modulus (G), Young's modulus (E), Poisson ratio (*v*), Pugh ratio (B/G), and Debye temperature (Θ_D) of $Cu_9Fe_9S_{16}$ crystal structure

3.3 Electronic properties

The density of states (DOS) is a fundamental tool for analyzing the electronic structure of materials, as it describes the number of electronic states at each energy level (E) that are available. In this study, the total and partial density of states (DOS) for $Cu_9Fe_9S_{16}$ were computed using the GGA+U approach; the findings are illustrated in Figure 2. The total DOS (TDOS) reveals an overall spin symmetry between the spin-up and spin-down DOS, featuring significant contributions from both the valence and conduction bands, though the valence band had more density of states. The–visible dominance of spin-up and spin-down symmetry in the DOS, suggest that the material exhibits a predominantly antiferromagnetic consistent with experimental findings [7]. Importantly, the application of the Hubbard U correction leads to the emergence of a narrow band gap of approximately 0.5 eV near the Fermi level, suggesting semiconducting behavior as reported in literature [21], hence addressing the well-known tendency of standard GGA, which tends to underestimate band gaps

The site-resolved partial density of states (PDOS) of $Cu_9Fe_9S_{16}$ reveals a complex and highly diverse magnetic and electronic structure across its five distinct iron sites. In contrast, Fe2 and Fe3 exhibit display moderate spin polarization, characterized by sharp peaks near the Fermi level, indicating finite magnetic moments and potential contribution to charge transport. Fe4 stands out due to pronounced spin asymmetry characterized by deep valleys and sharp peaks in its density of states, identifying it as a primary magnetic site with influence on low-energy electronic behaviour. Fe5, owing to its unique bonding environment, exhibits intense spin-polarized states at the Fermi level, indicative of strong magnetic behaviour. Meanwhile, the copper sites exhibit minimal magnetic activity, with Cu1 and Cu2 presenting fully occupied 3d states located deep in the valence band, characteristic of a Cu^{1+} oxidation state and contributing marginally to the magnetic and conduction properties. Cu3, however, displays a more active electronic profile near the Fermi level, suggesting a potential role in conduction and magnetic coupling. The sulfur atoms, characterized by deep 3s states and valence 3p states from approximately –7 eV to 0 eV, form strong bonds with neighbouring Cu and Fe atoms. They remain nearly spin-symmetric, acting primarily as ligands that mediate magnetic interactions rather than carriers of magnetic moments.

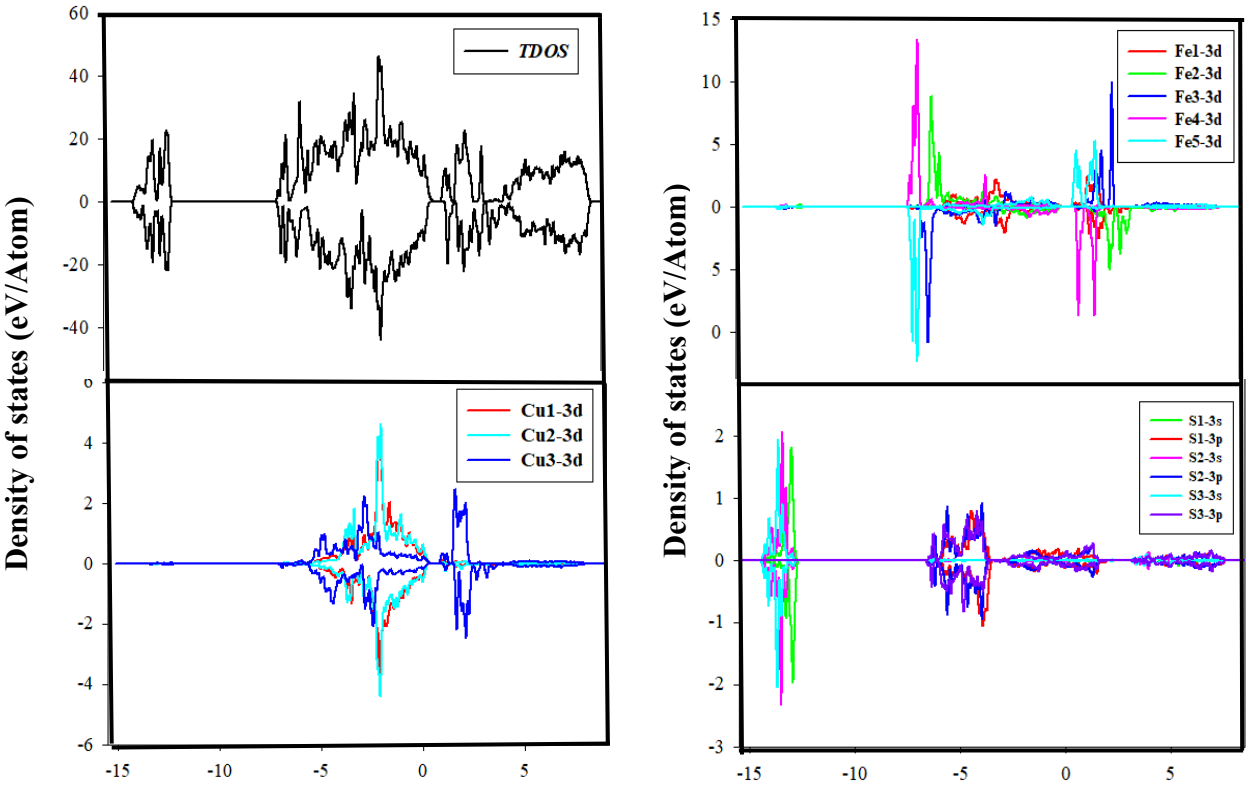

Figure 2: The total and partial density of states of $Cu_9Fe_9S_{16}$ (the zero energy is taken as the fermi level (E_F)

4 Conclusion

In this study, first-principles density functional theory (DFT) calculations incorporating van der Waals dispersion corrections (DFT-D3) and Hubbard U correction were employed to systematically investigate the bulk properties of Mooihoekite ($Cu_9Fe_9S_{16}$). The optimized structural parameters exhibit excellent agreement with experimental crystallographic data, thereby validating the reliability of the computational approach. Electronic structure analysis reveals that Mooihoekite is a narrow-gap semiconductor, with an estimated band gap of approximately 0.5 eV and displays antiferromagnetic ordering, as evidenced by the spin symmetry in both the total and projected density of states. A detailed site-resolved analysis highlights the varying magnetic behaviour of the five distinct Fe atoms, with Fe4 and Fe5 demonstrating strong spin polarization and contributing significantly to the overall magnetic character. In contrast, the Cu atoms predominantly remain in a nonmagnetic Cu^{1+} state. The mechanical properties derived from the calculated elastic constants confirm that the material is mechanically stable, anisotropic, and ductile, with a Pugh ratio (B/G) of 3.20 and a Poisson's ratio of 0.35. Furthermore, the calculated Debye temperature of 318 K aligns well-with experimental data, reinforcing the material's thermal stability under moderate conditions. Collectively, these findings establish a benchmark for understanding Mooihoekite's electronic, magnetic, and mechanical behaviour, while also providing practical guidance for experimentalists seeking to synthesize and characterize the material in real-world applications. The insights gained can further inform strategies to explore its surface chemistry, optimize thermoelectric performance, and integrate this semiconducting, magnetically active sulfide into functional devices.

Acknowledgements

This research was conducted at the Materials Modelling Centre (MMC), University of Limpopo. We acknowledge the computational resources provided by the Centre for High Performance Computing (CHPC) and the financial support from the National Research Foundation (NRF).

References

[1] F. Hulliger, Crystal chemistry of the chalcogenides and pnictides of the transition elements., Berlin: Springer, 1968, pp. 83-229.

[2] M. Schlesinger, K. King, C. Sole and W. Davenport, Extractive Metallurgy of Copper, Oxford: Elesevier, 2011, pp. 13-30.

[3] L. Cabri and S. Hall, "Mooihoekite and haycockite, two new copper-iron sulfides and their relationship to chalcopyrite and talnakhite," *American mineralogist,* vol. 57, pp. 689-708, 1972.

[4] S. Hall, " Crystal structures of the chalcopyrite series," *Canadian mineralogist,* vol. 13, pp. 168-172, 1975.

[5] D. Vaughan, K. England, G. Kelsall and Q. Yin, "Electrochemical oxidation of chalcopyrite ($CuFeS_2$) and the related metal-enriched derivatives $Cu_5Fe_4Fe_8$, $Cu_{18}Fe_{16}Fe_{32}$,and $Cu_9Fe_9Fe_{16}$," *American Mineralogist,* vol. 80, p. 725–731, 1995.

[6] Q. Xianxiu, Q. Pengfei, D. Tingting, H. Hui, D. Xiaolong, S. Xun and C. Lidong, "Thermoelectric Properties of Nano-grained Mooihoekite $Cu_9Fe_9Fe_{16}$," *Zeitschrift für anorganische und allgemeine Chemie,* vol. 646, pp. 1116-1121, 2020.

[7] M. Townsend, J. Horwood, R. Hall and L. Cabri, "Mössbauer, Magnetic Susceptibility and Crystallographic Investigations of $Cu_5Fe_4Fe_8$, $Cu_{18}Fe_{16}Fe_{32}$ and $Cu_9Fe_9Fe_{16}$," *American mineralogist,* p. 10, 1972.

[8] G. Kresse and J. Furthmuller, "Efficient Iterative Schemes for ab Initio Total-Energy Calculations Using a Plane-Wave Basis Set," *Computational Materials Science,* vol. 54, p. 11169, 1996.

[9] G. Kresse and G. Joubert, "From Ultrasoft Pseudopotentials to the Projector Augmented-Wave Method," *Physical Review B :Condensed Matter,* vol. 59, pp. 1758-1775, 1999.

[10] P. Blochl, "Projector augmented-wave method," *Phys. Rev B:Condensed Matter Phys,* vol. 50, p. 17953, 1994.

[11] P. Perdew, K. Burke and M. Ernzerhof, " Generalized Gradient Approximation Made Simple," *Phys. Rev. Lett.,* p. 1396, 1997.

[12] B. Himmetoglu, A. Floris, S. de Gironcoli and M. Cococcioni, "Hubbard-corrected DFT energy functionals: The LDA+U description of correlated systems," *International Journal of Quantum Chemistry,* vol. 114, pp. 14-49, 2014.

[13] S. Grimme, " Density Functional Theory with London Dispersion Corrections," *WIREs Computational Molecular Science,* vol. 1, pp. 211-228, 2011.

[14] H. Monkhorst and J. Pack, "Special Points for Brillouin-Zone Integrations," *Physical Review B : Solid State,* p. 5188, 1976.

[15] W. Zou, C. Tang and W. Lee, "Identification of symmetry type of linear elastic stiffness tensor in an arbitrarily orientated coordinate system," *International Journal of Solids and Structures,* vol. 50, pp. 2457-2467, 2013.

[16] Z. Wu, E. Zhao, H. Xiang, X. Hao, X. Liu and J. Meng, "Crystal structures and elastic properties of superhard IrN_2 and IrN_3 from first principles," *Physical review B,* vol. 76, p. 054115, 2007.

[17] M. Zhou, X. Gao and Y. Cheng, "Structural, electronic, and elastic properties of ($CuFeS_2$," *Applied physics. A,* vol. 118, pp. 1145-1152, 2015.

[18] S. Pugh, "Relations between the elastic moduli and the plastic properties of polycrystalline pure metals," *The London, Edinburgh, and Dublin Philosophical Magazine and Journal of Science,* vol. 45, pp. 823-843, 1954.

[19] N. Frantsevich, F. Voronov and S. Bakuta, Handbook on Elastic Constants and Moduli of Elasticity for Metals and Nonmetals, Kiev: Naukova Dumka, 1982.

[20] K. Molala, P. Mkhonto, M. Mehlape and P. Ngoepe, "A DFT and cluster expansion study of $(Fe,Ni)_9S_8$ pentlandite and unravelling doping with Mn, Co, Cu and precious metals," *Materials Chemistry and Physics,* vol. 331, p. 130146, 2025.

[21] Y. Li, Y. Liu, J. Chen, C. Zhao and C. Weiyong, "Comparison study of crystal and electronic structures for chalcopyrite (($CuFeS_2$) and pyrite (FeS_2)," *Physiochemical problems of mineral processing,* vol. 57, pp. 100-111, 2021.

Optimisation-Deposition and Conversion of Lead Halide Thin Films to 2D Metal Halide Perovskite Thin Films via Low-Pressure CVD

MSL Mthimkulu[1,2], S Ngqoloda[2,3], CJ Arendse[2], MLA Letswalo[1] and BM Sondezi[1]

[1]Department of Physics, University of Johannesburg, Johannesburg 2006, South Africa
[2]Department of Physics and Astronomy, University of the Western Cape, Bellville 7535, South Africa
[3]Advanced Materials Division, Mintek, Randburg 2169, South Africa

E-mail: bmsondezi@uj.ac.za and letswalom@uj.ac.za

Abstract. Three-dimensional (3D) metal halide perovskites (MHPs) are recognised as a prime candidate for optoelectronic devices, thanks to their excellent optical and electrical properties, as well as the ease of synthesis techniques. However, the 3D MHPs are prone to degradation, two-dimensional (2D) MHPs have proven to be more stable. Herein, 2D MHP thin films were synthesised by converting lead bromide ($PbBr_2$) thin films into 2D MHP thin films using a sequential two-step low-pressure chemical vapour deposition (LPCVD) method. The first step involved depositing PbBr2 thin films on glass/FTO/TiO_2 substrates. The second step exposed the as-prepared PbBr2 thin films to phenyl-ammonium iodide (PEAI) vapour at two different temperatures of 170 °C and 190 °C during the conversion process. The structural and optical properties of the converted thin films were characterised using X-ray diffraction (XRD), ultraviolet-visible (UV-Vis), and photoluminescence (PL) spectroscopy. The results showed that the converted thin films did not fully convert to 2D MHPs, as evidenced by the presence of lead iodide (PbI2) diffraction peaks in the XRD patterns. The optical properties indicate the partial formation of 2D MHPs with a stoichiometry of $(PEA)_2PbBr_xI_{4-x}$ ($0 \leq x < 1$). The results suggest that the conversion temperature of 170 °C is more suitable for obtaining high-quality 2D MHP thin films due to the lower defect density.

1 Introduction

Three-dimensional (3D) metal halide perovskite (MHP) has been known as an emerging semiconductor since Kojima and colleagues used it as a photosensitiser in dye-sensitised solar cells in 2009, reporting a power conversion efficiency (PCE) of 3.1% [1]. The exceptional optical and electrical properties of the 3D MHP, including tunable direct band gap, ambipolar charge transport, low nonradiative recombination rates, and high absorption coefficient, have led to a significant increase in PCE over the past two decades, reaching over 25.5% [2, 3]. Silicon (Si) remains the predominant choice in optoelectronic devices due to its abundance and well-known semiconductor properties, having a PCE of 26.6% for single-junction Si-based solar cells. 3D MHP thin films have proven to be simpler to synthesise compared to Si, lowering production costs. Together with the flexibility of the 3D MHP, intense research has been conducted into the perovskite material [4, 5].

The general stoichiometry of 3D MHPs is ABX3, where A is an organic monovalent cation like methylammonium (MA+, CH3NH +), B is a divalent metal cation, like lead (Pb2+), or tin (Sn2+), and X is a monovalent halogen anion, like bromine (Br-), iodine (I-), or chlorine (Cl-) [6, 7]. The B cation is coordinated with six X anions to form a [BX6]-4 octahedron. Each octahedron at the unit cell's corners shares an X anion to form a continuous 3D lattice. The A cation is enclosed between four octahedra and has 12 X anions forming a cuboctahedron [8]. Despite perovskite-based solar cells reaching a validated PCE of over 25% [9], 3D MHPs degrade in the presence of heat, light, and moisture due to their inherent chemical and structural instabilities, making it challenging to incorporate them into commercial devices. These difficulties highlight the pressing need for more reliable and affordable substitutes, which is fueling the intense study of 2D MHP [9, 10].

2D MHP has a general stoichiometry of (A')2An-1BnX3n+1 (n ϵ $\mathbb{Z}$+) where A' represents a large organic cation such as phenethyl-ammonium (PEA+, C8H9NH +), A, B and X represent the same ions as in the 3D MHP and n refers to the number of the metal halide octahedral units, where the limit n = ∞ relates to 3D MHP. The A' cation is large and cannot fit in the gap between the metal halide octahedra, unlike the smaller A cation, which occupies these gaps. The A' cation behaves as an insulating layer separating the octahedral units, which are connected by halide anions that share corners. One way to conceptualise the geometry of the 2D MHP is as a slice of the 3D MHP structure across the <100> crystallographic directions [10, 12]. The nearly constant conductivity of the [BX6]-4 octahedra layer and the insulation of the organic spacer layer give rise to the natural multiple quantum well (MQW) structure of 2D MHPs, where the perovskite inorganic layer functions as a "well" and the organic spacer layer as a "wall" [13]. Excitons, rather than electrons and holes, are formed when a 2D MHP is excited because of the quantum confinement effect, which raises the binding energy [13, 14]. The performance of optoelectronic devices can be enhanced by utilising these 2D MHP properties.

This study uses a sequential two-step low-pressure chemical vapour deposition (LPCVD) method to synthesise (PEA)2PbBryI4-y ($0 \leq y \leq 4$) 2D MHP thin films. The first step is the deposition of lead bromide (PbBr2) thin film on glass/FTO/TiO2 substrates, followed by the second step, which is to expose the as-deposited PbBr2 thin film to phenethyl-ammonium iodide (PEAI) vapour for conversion of the PbBr2 thin film into a 2D MHP thin film. The furnace was set to two distinct temperatures, 170 °C and 190 °C, to investigate the conversion temperature.

The application, such as perovskite-based solar cells, the perovskite thin film is usually deposited on a hole-transport layer such as tin dioxide (SnO2), or titanium dioxide (TiO2) on fluorine-doped tin oxide (FTO) coated glass (glass/FTO), or indium tin oxide (ITO) coated glass (glass/ITO). It is important to study the properties of the perovskite material deposited on these hole-transport layers because the underlying layer may affect the crystallisation of the perovskite thin films, which in turn influences the properties. Hence, the precursor lead halide thin films were deposited on glass/FTO coated with a TiO2 film (glass/FTO/TiO2) substrates.

2 Experimental

2.1 Substrate preparation

Glass substrates coated with fluorine-doped tin oxide (FTO) (purchased from Techinstro with resistivity < 10 Ω/sq) were cut into dimensions of 1.5 cm × 1.0 cm. Subsequent 15-minute ultrasonication with a Helmanex detergent solution and isopropyl alcohol was used to clean the substrates, followed by rinsing with de-ionised (DI) water. They were then blow-dried with nitrogen (N2) gas and subsequently treated with UV-ozone for 20 minutes to remove any further organic contaminants. A method published by Ngqoloda et al. [16] was used to spin-coat titanium dioxide (TiO2) onto the FTO to form a glass/FTO/TiO2 substrate. Lead bromide (PbBr2) thin film was then deposited onto the glass/FTO/TiO2 substrate via the LPCVD method, similar to that followed by Klue [17].

2.2 Lead halide thin film conversion into a two-dimensional perovskite thin film

A quartz crucible containing 40 mg of PEAI (CAS-No: 151059-43-7, <= 98% purity, Sigma-Aldrich) salt was placed at the centre of the first zone of a LPCVD tube furnace. The as-prepared PbBr2 thin film was placed horizontally on a silicon wafer in the centre of the second zone. The quartz tube was securely closed on both ends with metal flanges, and the reaction tube was pumped to an initial pressure of 0.01 mbar. The furnace was set to increase the substrate temperature (zone 2), reaching a nominal temperature of 100 °C. Zone 1 was set to heat up to two distinct nominal temperatures of 170 °C and 190 °C. For each conversion, the temperature was set to dwell at the respective nominal temperatures for 60 minutes. During the conversion process, N2 gas was set to flow downstream at 100 standard cubic centimetres (SCCM). The conversion pressure was maintained at 1 mbar.

Once the 60-minute dwelling time was reached, the substrates were allowed to cool to room temperature under a N2 flow.

2.3 Characterisation

The film thicknesses were determined using a Dektak 6M stylus thickness profiler; the structural properties of the converted thin film were determined using Empyrean XRD equipment from PANalytical. A copper K-alpha 1 (CuKα1) X-ray radiation source with a wavelength of 1.5406 Å was utilised to produce a continuous scan over the range 2θ = 5° - 100° with a step size of 0.02°, a voltage of 45 kV, and a tube current of 40mA, employing a 0.76 mm fixed divergence slit. An Ocean Optics UV spectrophotometer was utilised to measure optical transmission with a spectral resolution of 0.5 nm between 250 and 1000 nm. The room-temperature photoluminescence (PL) spectra of the converted films were measured in a reflection geometry using an excitation light-emitting diode (LED) source set to 365 nm.

3 Results and discussion

3.1 Film thickness

It was found that after converting $PbBr_2$ thin film into a 2D MHP thin film, approximately 10 mg and 30 mg of the initial 40 mg of PEAI had evaporated at conversion temperatures of 170 °C and 190 °C, respectively. The higher PEAI consumption at a 190 °C conversion temperature was due to the increased sublimation rate at higher temperatures, resulting in a higher PEAI vapour concentration during the conversion process. The thickness of the $PbBr_2$ precursor film was determined to be 145 nm. It was observed that exposing the precursor $PbBr_2$ thin film to PEAI vapour increased the film thickness to 478 nm and 853 nm for conversion temperatures of 170 °C and 190 °C, respectively. The thickness increase is due to the diffusion and intercalation of PEAI molecules within the precursor thin films. During the intercalation reaction, the PEA^+ embed themselves between the $[BX_6]^{-4}$ octahedra to form a 2D MHP. Additionally, the thickness increased at 190 °C, which is attributed to the excess supply of PEAI.

3.2 Structural properties

XRD analysis was done on the converted $PbBr_2$ thin films, and the XRD patterns are provided in Figure 1(a). Diffraction peaks belonging to a 2D perovskite triclinic structure with a P-1 space group were identified. The diffraction peaks start at low angles of 2θ ~ 5.4°, 10.8°, 16.2°, 21.6°, 27.0°, 32.4°and 37.8° are indexed to the (002), (004), (006), (008), (00$\underline{1}$0), (00$\underline{1}$2), and (00$\underline{1}$4) planes, respectively, for both conversion temperatures, which agrees to previous reports [10, 19]. The periodic nature of the (00l) family diffraction peaks at intervals of 2θ ~5.4° is evidence that the PEAI diffused into the $PbBr_2$ thin film to intercalate within the $[BX_6]^{-4}$ octahedra, forming a 2D layered perovskite structure (n = 1) [10, 18-20].

The XRD patterns of the converted thin films exhibit additional peaks at 2θ ~ 12.9°, 25.6°, and 38.7°, which were indexed to the (001), (002), and (003) planes, respectively, corresponding to a 2H hexagonal crystal system of lead iodide (PbI_2) with a P-3m1 space group [24]. These PbI_2 diffraction peaks indicate that the iodine (I) ions from the PEAI vapour replace the bromine (Br) ions in the $PbBr_2$ thin film throughout the conversion process. The ability of 2D MHPs to withstand the intrusion of foreign molecules into the structure is one of their special qualities. This capability may prevent additional diffusion of PEAI molecules into the thin film after the diffusion of PEA^+ ions has reached its capacity, also referred to as the conversion thickness threshold, thereby interrupting the intercalation (conversion) reaction and resulting in the presence of the underlying PbI_2 layer within the converted thin film [10].

At the elevated conversion temperature, a decrease in the 2D MHP and PbI_2 diffraction peak intensity, along with peak broadening, was observed. Peak broadening in XRD is primarily caused by microstrain or internal stress in the crystal lattice, and defects or disorder such as stacking faults and dislocations. In addition, higher-intensity diffraction peaks that belong to PEAI were observed in these XRD patterns. This is due to the excess PEAI vapour that condenses on the thin film, as they cannot defuse further due to the conversion thickness threshold. The schematic diagram showing the possible layers of the thin films are provided in Figure 1(b).

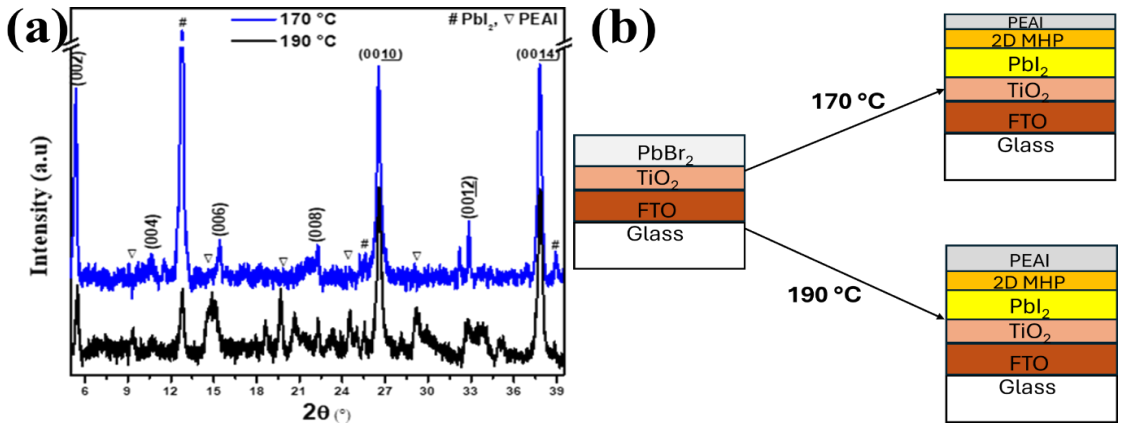

Figure 1. (a) The converted PbBr2 thin-film XRD patterns and (b) shows a schematic diagram of the different layers of the thin film before and after the conversion.

3.3 Optical properties

Excitons, which are bound electron-hole pairs, can dissociate into free carriers that later recombine to emit light. In (00l) 2D metal halide perovskites, a small Stokes shift and sharp emission arise from the recombination of free excitons. When exposed to incident radiation, electrons are excited from the ground state to the excited state, creating holes in the ground state. The free excitons then recombine, releasing energy as fluorescence [22]. As per the absorption spectra shown in Figure 2(a), the absorption peaks of the converted thin films have been determined to be 2.43 eV and 2.49 eV for the thin films converted at 170 °C and 190 °C, respectively. The fundamental band-edge exciton absorption is responsible for these absorption peaks [23].

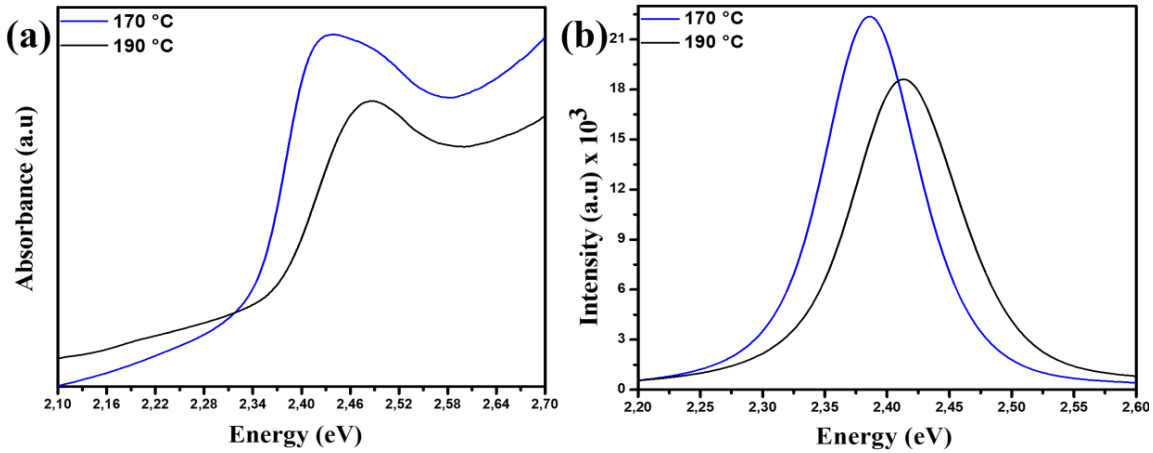

Figure 2. (a) Absorbance spectra of the converted PbBr2 thin films and (b) PL spectra of the converted PbBr2 thin films.

According to the PL spectra shown in Figure 2(b), the PL peaks of the thin films that were converted were calculated to be 2.39 eV and 2.41 eV for the thin films that were converted at 170 °C and 190 °C, respectively. A quenching effect is noticeable at elevated conversion temperature. This may be due to the excess PEAI on the surface, which acts as a quencher by interacting with excited states and dissipating energy non-radiatively, resulting in a decrease in PL intensity.

Yang et al. [20] reported (PEA)2PbI4 and (PEA)2PbBrI3 2D MHP with absorption energies of ~ 2.38 eV and 2.50 eV, respectively. Additionally, they observed PL peaks at ~ 2.37 eV and 2.49 eV, respectively. From this study, it was observed that the absorption and PL peaks are higher than those of the (PEA)2PbI4 2D MHP and lower than those of the (PEA)2PbBrI3 2D MHP. This suggests that a (PEA)2PbBrI3 perovskite thin film

was not formed; however, the 2D MHP thin films that formed have a stoichiometry of (PEA)2PbBrxI4-x ($0 \leq x < 1$).

The Stokes shift is the difference between the positions of the band maxima of the absorption and that of PL emission at the same electronic transition. The slight Stokes shifts of 53.0 meV and 75.4 meV were determined for the thin films converted at 170 °C and 190 °C, respectively, suggesting that the emission originates almost entirely from the recombination of intrinsic excitons, which indicates a low defect density. However, a slight increase of 22.41 meV in the thin film converted at the elevated temperature indicates that the excess PEAI increases the defect density.

According to the Tauc plot shown in Figure 3(a), the band gap (Eg) of the converted thin film was determined to be 2.38 eV for thin films converted at 170 °C and 2.36 eV for thin films converted at 190 °C. The higher Eu, which denotes within the band edge, is the cause of the thin film's lower Eg when converted at a higher conversion temperature.

The Urbach energy (Eu) was calculated from the linear region shown in bold in Figure 3(b). Eu was estimated to be 84.89 meV and 135.96 meV for the thin film converted at 170 °C and 190 °C, respectively. The optical band edge is defined by the Eu, which may be the broadening of the PL peak, suggesting that the elevated conversion temperature increases the defect density as a result of the excess PEAI, introducing alternating vibronic structures [25], and is complemented by the Stokes shift.

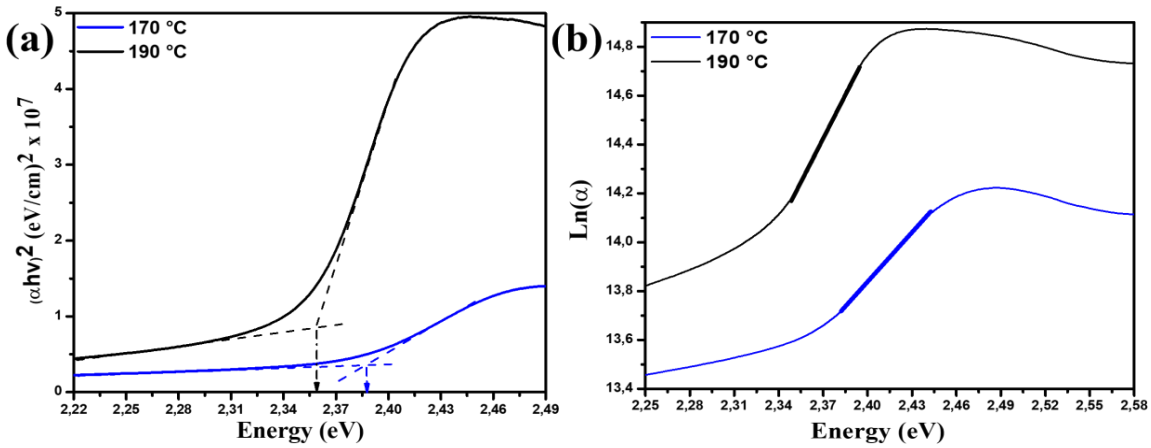

Figure 3. (a) Tauc plot of the converted thin films and (b) Urbach energy plot of the converted thin films.

4 Conclusion

The XRD analysis revealed 2D MHP peaks, which were more intense for the thin films converted at 170 °C. These peaks indicated that the thin films had undergone partial conversion, as evidenced by the presence of PbI_2 peaks. The absence of $PbBr_2$ peaks in the XRD patterns shows that most $PbBr_2$ transforms into PbI_2 before the conversion starts. Afterward, PEA^+ initiates the intercalation reaction. Since both temperatures use the same starting film, the conversion thickness threshold remains similar. The reaction proceeds layer by layer from the top downward. At higher temperatures, increased PEAI vapor leads to greater condensation on the film surface, causing PbI_2 intensity to decrease while PEAI intensity increases. It was observed that the thin films converted at 170 °C had a smaller E_u than the thin films converted at 190 °C. The ideal conversion temperature was determined to be 170 °C. Two-dimensional metal halide perovskites are utilized in heterojunction solar cells due to their enhanced stability and superior control over electronic properties, hence improving device performance and efficiency relative to conventional materials.

References

[1] A. Kojima, et al., Journal of the American Chemical Society., 6;131(17):6050-1, May. 2009.

[2] (NREL), N.R.E.L. "Solar Cell Efficiency Chart," Sep. 2023. [online]. Available: https://www.nrel.gov/pv/cell-efficiency.html.

[3] N. G. Park, The Journal of Physical Chemistry Letters, 1;4(15):2423-9, Aug. 2013.

[4] L. Cheng, et al, Advanced Materials, 32(15):1904163, Apr. 2020.

[5] Q. Zhang., et al, "Advances in small perovskite-based lasers," Small Methods., 1(9):1700163, Sep. 2017.

[6] R. Wang., et al, Advanced Functional Materials., 29(47):1808843, Nov. 2019.

[7] N. S. Kumar, and K. C. Naidu, Journal of Materiomics., 1;7(5):940-56, Sep. 2021.

[8] P. Roy, et al, Solar Energy., 198:665-88, Mar. 2020.

[9] W. Fu., et al, Materials Today., 1;58:275-96, Sep. 2022.

[10] S. S. Magubane, R. Burns, S. Ngqoloda, C. J. Oliphant, P. F. Miceli, and C. J. Arendse, ACS Applied Electronic Materials., 5;5(10):5352-61, Jul. 2023.

[11] X. Zhang., et al, Advanced Energy Materials., 8(14):1702498, May. 2018, doi: 10.1002/aenm.201702498.

[12] L. Zhang., et al, Light: Science & Applications., 19;10(1):61, Mar 2021.

[13] X. Chen, H. Zhou, and H. Wang, Frontiers in Chemistry., 19;9:715157, Aug. 2021.

[14] M. Ren, S. Cao, J. Zhao, B. Zou, and R. Zeng, Nano-Micro Letters., 13(1):163, Dec. 2021.

[15] K. Wang, J. Y. Park, Akriti, and L. Dou, EcoMat., 3(3):e12104, Jun. 2021.

[16] S. Ngqoloda, C. J. Arendse, T. F. Muller, F. R. Cummings, and C. Oliphant, Materials Today: Proceedings., 1;36:303-8, Jan. 2021.

[17] S. C. Klue, "Optimisation of lead halide perovskite thin films by chemical vapour deposition," M.S. thesis, Dept. Phy., UWC., CPT, 2021.

[18] Y.A. Chen. et al, The Journal of Physical Chemistry C., 28;125(48):26601-12, Nov. 2021.

[19] S. Yang., et al, Angewandte Chemie., 3;129(15):4316-9, Apr. 2017.

[20] A. Zanetta., et al, Advanced Materials., 34(1):2105942, Jan. 2022.

[21] H. Sun., et al, Journal of crystal growth., 1;405:29-34, Nov. 2014.

[22] X. Gao., et al, Advanced Science., 6(22):1900941.

[23] T. Zhang., et al, Nature communications, 2022 10;13(1):60, Jan. 2022.

[24] M. G. La-Placa., et al, Journal of Materials Chemistry C., 8(6):1902-8, 2022

[25] T. B. Ren., et al, Journal of the American Chemical Society, 24;140(24):7716-22, May. 2018.

Investigating the effect of metal ions of different oxidation states (M^{x+}, x = 1, 2, 3, & 4) on the PL emission of $Zn_4B_6O_{13}:Eu^{3+}$

ET Maleho, MLA Letswalo and BM Sondezi

Department of Physics, University of Johannesburg, 55 Beit St, Doornfontein, Johannesburg, 2028, South Africa.

E-mail: letswalom@uj.ac.za

Abstract. In this study, Eu^{3+} (fixed at 2 mol%) activated $Zn_4B_6O_{13}$ phosphors incorporated with metal ions of different oxidation states M^{x+} (x = 1 - 4) were successfully prepared by combustion synthesis method. The luminescence characteristics of $Zn_4B_6O_{13}:Eu^{3+}$ were improved by partially substituting metal ions with various oxidation states (Na^{+}, Ca^{2+}, Bi^{3+}, Mn^{4+}). The crystal structure properties of the prepared materials were studied by X-ray diffraction (XRD), which revealed the formation of a zinc metaborate cubic crystal structure for all the samples. Surface features and the elemental analysis of the phosphor materials were studied by SEM and EDS, respectively. Excitation and emission scans were recorded for the different samples. Upon excitation at 395 nm, the emission spectrum exhibited five distinct peaks at 580 nm, 592 nm, 614 nm, 653 nm, and 706 nm, corresponding to the $^5D_0 \rightarrow {}^7F_J$ (J = 0 - 4) transitions, confirming the presence of the Eu^{3+} ion. The optimal emission of the Eu^{3+} dopant in the $Zn_4B_6O_{13}$ host was for the Bi^{3+} co-doped sample, which resulted in the phosphor achieving an excellent PL intensity and a color purity of 92.33%. Tunable luminescence from the reddish-orange area (0.637, 0.356) of Commission Internationale de l'éclairage (CIE) towards the red area (0.646, 0.351) was achieved by substituting different oxidation states M^{x+} (x = 1 - 4). Therefore, different oxidation states M^{x+} (x = 1 - 4) and Eu^{3+} doped $Zn_4B_6O_{13}$ phosphor may be suitable candidates for the development of display devices and white light-emitting diodes.

1 Introduction

At present, scientists' attention has been attracted by the rare earth ions activated luminescent materials due to their applications in various aspects [1, 2, 3]. One of the most important requirements for high-performing materials is the selection of the host material in which the rare earth ions can be incorporated. One of the interesting applications of such materials is solid-state lighting, which is considered the next generation of lighting due to its attractive qualities such as low energy costs, long lifespan, and environmental friendliness [1, 4]. Many researchers have been exploring different borate materials as host lattices mainly because of their convenient properties, such as large band gap, high thermal stability, low cost, and effective luminescence efficiency [5, 6, 7]. Amongst other borates, zinc metaborate with the chemical equation $Zn_4B_6O_{13}$, displays excellent crystallinity and high mechanical hardness [2, 5]. Moreover, it also exhibits high optical transmission capacity, which makes it relevant for luminescence applications [5, 7]. For instance, Liang Pan et al. [3] synthesized $Zn_4B_6O_{13}$ and Eu^{3+}/Tb^{3+} single-doped $Zn_4B_6O_{13}$ phosphors for w-LED applications. Zhao et al. [5]

prepared multimodal emission in Tb^{3+}/Yb^{3+} doped $Zn_4B_6O_{13}$ for application in information encryption and anti-counterfeiting.

It is well known that rare earth ions show stable emissions resulting from the f-f electron transitions, which make them suitable to be used as luminescent activators [5, 8, 9]. Eu^{3+} is one of the most investigated RE ions and is considered the main RE ion that achieves red light emission, which is important for improving the red-light component [10]. Eu^{3+} ions are essential for light-emitting phosphors and versatile display applications when excited with a wavelength in the UV region [11]. The most prominent emission peak is normally observed at 611 nm, which is due to the electric dipole transition $^5D_0 \rightarrow {}^7F_2$ transition of Eu^{3+} ions [11, 12]. In this work, we aim to improve the luminescence properties of this important material by incorporating Na^+, Ca^{2+}, Bi^{3+}, and Mn^{4+} ions.

2 Experimental procedure

2.1 Synthesis

All the investigated phosphors were prepared by combustion synthesis using urea as a fuel. Firstly, the raw materials $Zn(NO_3)_26H_2O$(99%), H_3BO_3(99.5%), $Eu(NO_3)_36H_2O$(99.99%), $NaNO_3$(99.5%), $Ca(NO_3)_24H_2O$(99%), $Bi(NO_3)_35H_2O$(98%), and $MnCl_24H_2O$(98%) were accurately weighed according to the stoichiometric calculations for $Zn_4B_6O_{13}$, $Zn_4B_6O_{13}$:(2%)Eu^{3+}, and $Zn_4B_6O_{13}$: (2%)M^{x+}/(2%)Eu^{3+} samples. The weighed materials were transferred to the beaker and dissolved in 60 mL of deionized water. Then the mixture was stirred for about 10 min until a clear solution was formed. Then urea was added as a fuel and continued to stir for 20 min. The resulting mixture was then transferred into a crucible and placed in a furnace at 600 °C. The furnace was left to cool at room temperature. The powder samples were then ground and annealed at 900 °C for 1 hour. Finally, the annealed mass was thoroughly ground using a mortar and pestle and was taken for characterization.

2.2 Characterization

The XRD patterns of the prepared materials were obtained using by Bruker D8 Advanced X-ray diffractometer with Cu-Kα radiation (λ = 1.54 Å). The morphology and the elemental analysis were tested by JOEL JSM-7401 SEM coupled with EDS for elemental composition. PL excitation and emission scans were carried out using Cary Eclipse spectrometer with a 150W xenon lamp as an excitation source. For chromaticity co-ordinates, the 1931 CIE software was employed.

3 Results and discussion

3.1 X-Ray diffraction analysis

Figure 1 (a) depicts the XRD pattern comparison of $Zn_4B_6O_{13}$: Eu^{3+}, $Zn_4B_6O_{13}$: Eu^{3+} doped with metal ion of different oxidation states M^{x+} (x = 1 to 4), and the undoped $Zn_4B_6O_{13}$. The concentration of Eu^{3+} and M^{x+} were both kept at 2 mol%. The XRD patterns of the undoped $Zn_4B_6O_{13}$ host material reveal the formation of a cubic crystallographic system of space group I-43m, which is completely consistent with standard card PDF# 01-080-7675 ($Zn_4B_6O_{13}$ structure) and previous studies [1, 5]. Doping with Eu^{3+} shows the presence of superlattices diffraction peaks at angle 2θ of 29.1°, 38°, 46°, 48°, and 52° corresponding to (211), (310), (321), (400), and (330) planes of $Zn_4B_6O_{13}$ structure, respectively. This shows complete incorporation of Eu^{3+} into $Zn_4B_6O_{13}$ matrix, replacing the Zn atoms [1]. Further incorporating metal ions of different oxidation states (M^{x+}, x = 1 to 3) did not alter the crystal structure of the $Zn_4B_6O_{13}$ material. No peaks of impurity phases of Na^+, Ca^{2+}, or Bi^{3+} were detected. This shows that the materials also adopt the cubic ordered zinc metaborate lattice structure. All samples show sharp, intense XRD peaks, which reveal that the prepared materials are of high well-ordered crystallinity [1]. From all prepared materials, no characteristic peaks from other forms of borate such as ZnB_4O_7, ZnB_2O_4, or $Zn_3(BO_3)_2$ were observed [4, 13]. The XRD results confirm that the crystalline $Z_4B_6O_{13}$ with Eu^{3+} and M^{x+} (x = 1 to 3) doping could be achieved by the mentioned combustion synthesis sample preparation conditions. In contrast, incorporating the Mn^{4+} ion resulted in an extra peak appearing in the $Z_4B_6O_{13}$. XRD patterns. **Figure 2.** Shows the XRD patten of $Zn_4B_6O_{13}$:Mn, $Zn_4B_6O_{13}$:Mn/Eu^{3+}, and $Zn_4B_6O_{13}$:Eu^{3+} on the magnified region of 2θ angles (20° – 36°). From the enlarged XRD (**Figure 2 (b)**), there is a clear observation of the secondary structure. This can be identified by the extra peaks marked with an asterisk (*) that do not belong to the $Zn_4B_6O_{13}$ cubic crystal structure profile. As observed from the Eu^{3+} and Mn^{4+} singly doped $Zn_4B_6O_{13}$ materials, it is evident that the incorporation of the Mn^{4+} ions into $Zn_4B_6O_{13}$ is the one that causes the impurity

phase into the structure and not the incorporation of Eu^{3+}. This observed impurity phase might result from the Mn^{2+} rather than Mn^{4+} due to Mn^{2+} being the more stable ion than Mn^{4+}.

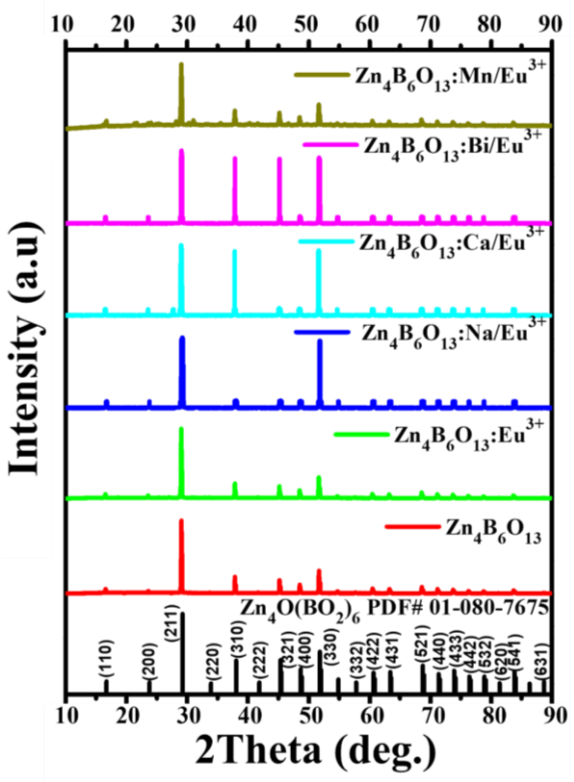

Figure 1: **(a)** XRD profile of $Zn_4B_6O_{13}$: Eu^{3+} doped with metal ions of different oxidation states M^{x+} (x = 1 to 4).

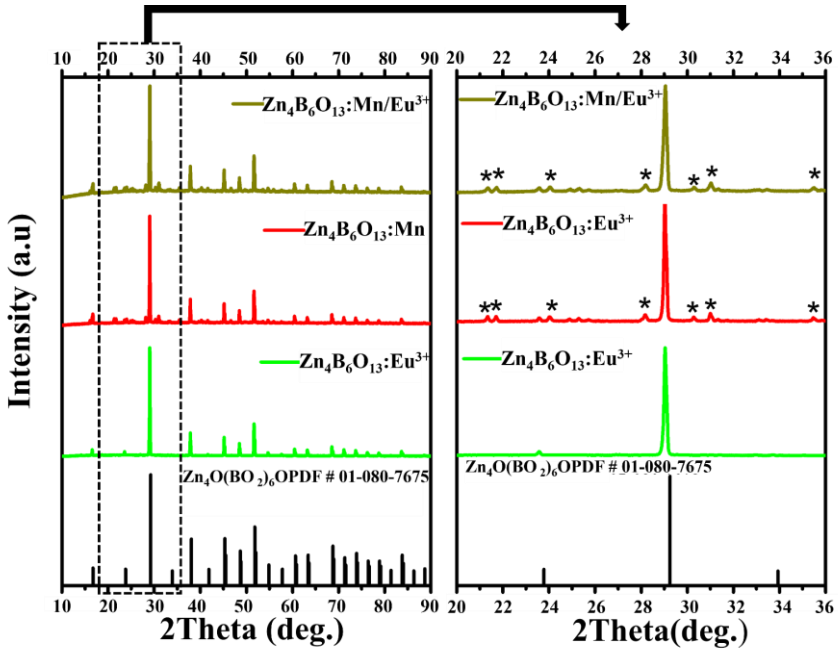

Figure 2**:** XRD patterns of **(a)** $Zn_4B_6O_{13}$:Eu^{3+}, $Zn_4B_6O_{13}$:Mn, and $Zn_4B_6O_{13}$:$Mn/Eu^{3+}$and **(b)** Enlarged XRD pattern (2θ: 20°-36°).

3.2 Morphological studies and elemental composition

The SEM images and corresponding EDS spectra of undoped $Zn_4B_6O_{13}$, Eu^{3+} doped $Zn_4B_6O_{13}$, monovalent (Na^+), and divalent (Ca^{2+}) doped $Zn_4B_6O_{13}$:Eu^{3+} phosphors are displayed in **Figure 3**. From the insert, SEM images in **Figure 3 (a)** and **(b)** for undoped $Zn_4B_6O_{13}$ and $Zn_4B_6O_{13}$:Eu^{3+} materials, respectively, the observed surface structures are of similar nature, however, more agglomeration is seen from the undoped $Zn_4B_6O_{13}$ sample. Both materials are characterized by irregular polyhedron morphology with smooth surfaces and sharp edges. The observed surface structures are characteristic of the $Zn_4B_6O_{13}$ cubic structure and agree with previous studies [3, 15]. The Na^+ doped $Zn_4B_6O_{13}$:Eu^{3+} (**Figure 3 (c)**) sample shows more agglomeration with deposits of irregular shapes on the surfaces, and the Ca^{2+} doped $Zn_4B_6O_{13}$:Eu^{3+} sample (**Figure 3 (d)** insert) shows voids with different particle sizes across the surface. However, the characteristic polyhedron morphology of $Zn_4B_6O_{13}$ is maintained in both materials [3]. The EDS spectra of **Figure 3 (a)** and **(b)** correspond to undoped $Zn_4B_6O_{13}$ and $Zn_4B_6O_{13}$:Eu^{3+} materials, respectively. The Eu element peaks are only observed from the Eu^{3+} doped $Zn_4B_6O_{13}$ sample, and all other expected elements are present in both samples with no extra impurity element peaks. This confirms that Eu^{3+} ion was successfully doped into $Zn_4B_6O_{13}$ and occupies the Zn^{2+} sites. The existence of elements Zn, B, O, Na, and Eu in $Zn_4B_6O_{13}$:Na/Eu^{3+} and Zn, B, O, Ca, and Eu in $Zn_4B_6O_{13}$:Ca/Eu^{3+} is confirmed by the EDS, **Figure 3 (c)** and **(d)**, respectively. The presence of C and Ir is due to carbon tape coating during measurements.

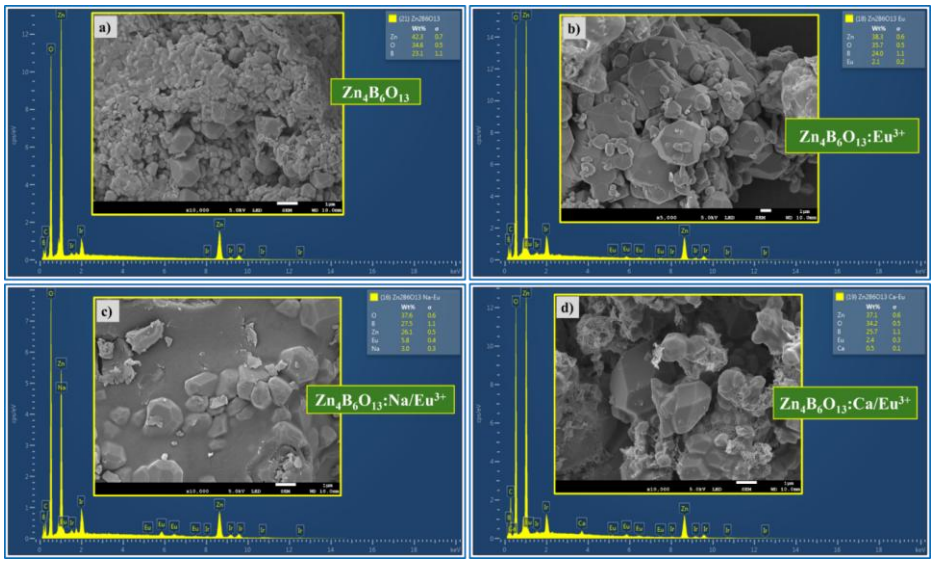

Figure 3: EDS spectra and inserts SEM images of **a)** $Zn_4B_6O_{13}$ host, **b)** $Zn_4B_6O_{13}$:Eu^{3+}, **c)** $Zn_4B_6O_{13}$:Na/Eu^{3+} host, and **d)** $Zn_4B_6O_{13}$:Ca/Eu^{3+}.

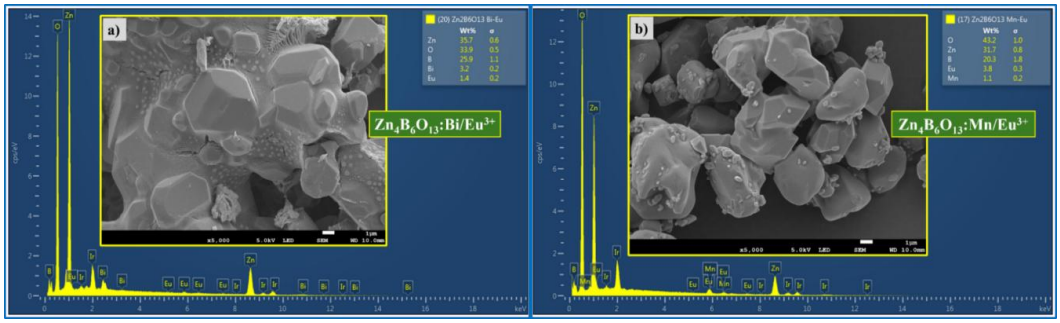

Figure 4: EDS spectra and inserts SEM images of **a)** $Zn_4B_6O_{13}$:Bi/Eu^{3+}, **b)** $Zn_4B_6O_{13}$:Mn/Eu^{3+}

Figure 4**:** presents the EDS spectra and SEM images (inserts) of **(a)** $Zn_4B_6O_{13}$:Bi/Eu^{3+} and **(b)** $Zn_4B_6O_{13}$:Mn/Eu^{3+}. The $Zn_4B_6O_{13}$:Bi/Eu^{3+} sample shows a distribution of polyhedral surfaces of different sizes on the material's surface. The $Zn_4B_6O_{13}$:Mn/Eu^{3+} material is characterized by a combination of both solid polyhedron and round morphology with some particle deposits on the surfaces. This may be due to the formation

of secondary phase structure as discussed earlier in the XRD analysis. The microstructural characteristics of materials may influence the PL properties of phosphor materials [16]. Respective EDS diagrams confirm the presence of all elements with no impurities.

3.3 Photoluminescence study of $Zn_4B_6O_{13}:Eu^{3+}/M^{x+}$

Figure 5 depicts the **(a)** Excitation scan, **(b)** PL emission spectra and **(c)** CIE coordinates for $Zn_4B_6O_{13}:M^{x+}/Eu^{3+}$ materials. From the excitation scan (**Figure 5 (a)**) under 614 nm emission wavelength, the Eu^{3+} excitation peak profile is observed from all the prepared materials [3]. These excitation bands are observed at wavelengths of 362, 381, 395, and 465 nm corresponding to $^7F_0 \rightarrow {}^5D_4$, $^7F_0 \rightarrow {}^5L_7$, $^7F_0 \rightarrow {}^5L_6$, and $^7F_0 \rightarrow {}^5D_2$ transitions of Eu^{3+} ions, respectively [3, 11]. Amongst these excitation wavelengths of Eu^{3+}, the highest excitation peak is at 395 nm. A broad absorption band between 200 – 300 nm is ascribed to the charge transfer band (CTB) due to ligand to metal transition (O^{2-} - Eu^{3+}) [12, 17]. The PL emission scan was carried out under the prominent excitation wavelength of 395 nm of Eu^{3+} (**Figure 5 (b)**). All samples show the Eu^{3+} PL spectral bands at wavelengths 580 nm, 592 nm, 614 nm, 654 nm, and 704 nm due to $^5D_0 \rightarrow {}^7F_0$, $^5D_0 \rightarrow {}^7F_1$, $^5D_0 \rightarrow {}^7F_2$, $^5D_0 \rightarrow {}^7F_3$, and $^5D_0 \rightarrow {}^7F_4$, transitions, respectively [12, 11, 18]. The hypersensitive electric dipole transition ($^5D_0 \rightarrow {}^7F_2$) is mostly favored compared to the magnetic dipole transition, which indicates that the Eu^{3+} occupies the low-symmetric sites in the crystal lattice [3, 19]. The effect of the metal ions of different oxidation states on the peak intensity is greater, and the order of the emission intensity from strong to weak is $Zn_4B_6O_{13}:Bi/Eu^{3+}$ > $Zn_4B_6O_{13}:Ca/Eu^{3+}$ > $Zn_4B_6O_{13}:Na/Eu^{3+}$ > $Zn_4B_6O_{13}:Eu^{3+}$ > $Zn_4B_6O_{13}:Mn/Eu^{3+}$. All the M^{x+} samples show high intensity compared to Eu^{3+} singly doped $Zn_4B_6O_{13}$ material, except for the Mn^{4+} doped sample, which has the lowest intensity and this may be due to the secondary structure introduced by incorporating Mn^{4+} ions. The doped Na^+, Ca^{2+}, Bi^{3+} and Mn^{4+} metal ions in the $Zn_4B_6O_{13}$ structure substitute the Zn atoms. Studies show that by doping with metal ions, the photoluminescence intensities of phosphors may be enhanced by creating asymmetry in the crystal fields and also introducing charge compensations [14, 18]. This assists in enhancing energy transfer between the metal ions and the co-doped activator ion ($M^{x+} \rightarrow Eu^{3+}$) [18]. Compared to the $Zn_4B_6O_{13}:Eu^{3+}$ material, the luminescence intensity increase is 4.9, 4.2, and 3.5 times for $Zn_4B_6O_{13}:Bi/Eu^{3+}$, $Zn_4B_6O_{13}:Ca/Eu^{3+}$, and $Zn_4B_6O_{13}:Na/Eu^{3+}$ phosphor, respectively, which significantly enhances the luminescence performance. **Figure 5 (c)** represents the CIE diagram for the prepared materials. The $Zn_4B_6O_{13}:Eu^{3+}$ shows adjustable color light from reddish-orange to red emission with the incorporation of metal ions of different oxidation states M^{x+} (x =1 to 3). The CIE coordinates for $Zn_4B_6O_{13}:Eu^{3+}$, $Zn_4B_6O_{13}:Na/Eu^{3+}$, $Zn_4B_6O_{13}:Ca/Eu^{3+}$, $Zn_4B_6O_{13}:Bi/Eu^{3+}$, and $Zn_4B_6O_{13}:Mn/Eu^{3+}$ are situated at (0.637, 0.356), (0.641, 0.354), (0.646, 0.352), (0.646, 0.351), and (0.578, 0.388), respectively. The corresponding color purities are 89.75%, 91.32%, 92.33%, and 75.59% respectively.

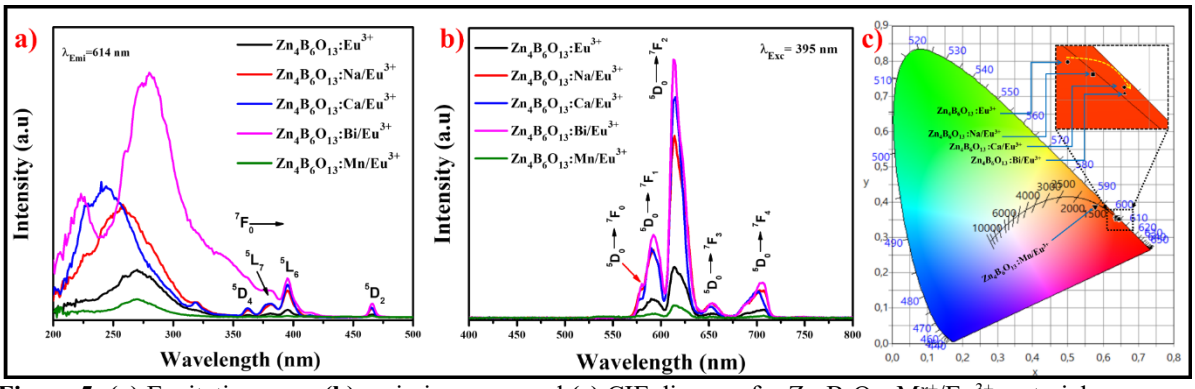

Figure 5: (a) Excitation scan, **(b)** emission scan, and **(c)** CIE diagram for $Zn_4B_6O_{13}:M^{x+}/Eu^{3+}$ materials.

4 Conclusion

XRD results confirm the successful synthesis of $Zn_4B_6O_{13}:M^{x+}/Eu^{3+}$ and the material compositions are further confirmed by EDS results. The SEM images confirm the characteristic polyhedron morphology of the $Zn_4B_6O_{13}$ cubic crystal structure. PL comparative study of the influence of metal ions of different oxidation states M^{x+} (x =1 to 4) on the emission properties of Eu^{3+} doped $Zn_4B_6O_{13}$ shows that the order of PL intensity from strong to weak is $Zn_4B_6O_{13}:Bi/Eu^{3+}$ > $Zn_4B_6O_{13}:Ca/Eu^{3+}$ > $Zn_4B_6O_{13}:Na/Eu^{3+}$ > $Zn_4B_6O_{13}:Eu^{3+}$ > $Zn_4B_6O_{13}:Mn/Eu^{3+}$. This suggests that Bi^{3+} can improve the absorption bands and limit the nonradiative transitions, which further enhance the luminescence properties of the prepared phosphors. The results suggest that these materials may be a viable option for UV and LED chips and a key element in the fabrication of wLEDs.

References

[1] Liu, Y., Li, C., Din, M.A.U., Tang, L., Lin, Y. and Cheng, N., 2022. Optical properties of Eu^{3+}/Pr^{3+} doped $Zn_4O(BO_2)_6$ synthesized by solid-state reaction. *Ceramics International*, *48*(11), pp.15737-15747.

[2] Yang, Y., Jiang, X., Gong, P., Molokeev, M.S., Li, X., Li, Y., Wu, X., Wu, Y. and Lin, Z., 2017. High mechanical strength in $Zn_4B_6O_{13}$ with an unique sodalite-cage structure. *RSC Advances*, *7*(4), pp.2038-2043.

[3] Liang, P., Mingzhen, W.A.N.G. and Zhihong, L.I.U., 2017. Synthesis and spectroscopic studies of $Zn_4B_6O_{13}$ and Eu/Tb single-doped $Zn_4B_6O_{13}$ phosphors. *Journal of Rare Earths*, *35*(5), pp.441-445.

[4] Lian, W.L., Liang, P. and Liu, Z.H., 2020. Controllable hydrothermal synthesis and morphology evolution of $Zn_4B_6O_{13}$:Tb/Eu phosphors with tunable luminescent properties. *Advanced Powder Technology*, *31*(4), pp.1633-1642.

[5] Zhao, S., Wang, Z., Ma, Z., Fan, F. and Liu, W., 2020. Achieving multimodal emission in $Zn_4B_6O_{13}$:Tb^{3+}, Yb^{3+} for information encryption and anti-counterfeiting. *Inorganic Chemistry*, *59*(21), pp.15681-15689.

[6] Wang, P.D., Jia, Z.Y., Zhong, Y.H., Mei, H.Y., Li, C.M. and Cheng, N.P., 2018. Effect of pressure on the elastic properties and optoelectronic behavior of $Zn_4B_6O_{13}$:First-principles investigation. *Chinese Physics B*, *27*(5), p.057101.

[7] Alemi, A., Mohseni, N., Dolatyari, M. and Bakhtiari, A., 2012. New Method for Synthesis of Zinc Metaborate $Zn_4B_6O_{13}$ Crystals via Sol-Gel Process and Investigation of DFT Calculations. *Int. J. Bio-Inorg. Hybd. Nanomat*, *1*(2), pp.79-86.

[8] Chen, W., Ouyang, Y., Mo, M., Zhang, H. and Su, Q., 2021. Observation of energy transfer from Eu^{2+} to Eu^{3+} and tunable luminescence in phosphors YF_3:Eu prepared by hydrothermal method. *Journal of Luminescence*, *229*, p.117672.

[9] Dereń, P.J., Stefanska, D., Ptak, M. and Wisniewski, P., 2021. Method to measure the degree of reduction of Eu^{3+} to Eu^{2+}: how anion and cation vacancies influence the degree of reduction. *The Journal of Physical Chemistry C*, *125*(44), pp.24505-24514.

[10] Li, X., Yang, C., Liu, Q., Wang, X. and Mi, X., 2020. Enhancement of luminescence properties of SrAl2Si2O8: Eu^{3+} red phosphor. *Ceramics International*, *46*(11), pp.17376-17382.

[11] Verma, N., Michalska-Domańska, M., Ram, T., Kaur, J., Misra, A.K., Dubey, V., Dubey, N., Tiwari, K. and Rao, M.C., 2023. Optimizing the luminescence efficiency of an europium (Eu^{3+}) doped SrY_2O_4 phosphor for flexible display and lighting applications. *RSC advances*, *13*(29), pp.20217-20228.

[12] Cao, R., Huang, Z., Lan, B., Li, L., Yi, X., Luo, Z., Liao, C. and Wang, J., 2022. Adjustable luminescence properties of Eu^{3+} and Bi^{3+} codoped $Ca_3Zn_3Te_2O_{12}$ phosphor. *Materials Research Bulletin*, *152*, p.111851.

[13] Kucuk, N., Kaynar, Ü.H., Akca, S., Alajlani, Y., Yin, L., Wang, Y., Guinea, J.G., Bulcar, K., Dogan, T., Karabulut, Y.Ü.K.S.E.L. and Ayvacikli, M.E.H.M.E.T., 2020. Enhancing the blue luminescence behaviour of the Li co-doped novel phosphor ZnB_2O_4: Tm^{3+}. *Journal of Alloys and Compounds*, *838*, p.155587.

[14] Cao, R., Huang, T., Nie, J., Zhang, L., Chen, Y., Li, L., Lan, B. and Wang, J., 2024. Energy transfer and tunable-color luminescence properties of a single-phase $CaSrNb_2O_7$: Sm^{3+}, Bi^{3+}. *Journal of Molecular Structure*, *1297*, p.136962.

[15] Maleho, E.T., 2022. *Investigation of the photoluminescence studies of ZnO: RE^{3+} (where RE= Dy, Sm and Sm/Dy) nanophosphors via different anionic group (BO_3^{3-}, PO_4^{2-} and SO_4^{2-}) substitutions* (Doctoral dissertation, University of Johannesburg).

[16] Jasira, S.V., Veena, V.P., Shilpa, C.K., Ancy, S.S. and Nissamudeen, K.M., 2025. Innovative white light emission from europium-doped barium cerate: A comprehensive study from structural analysis to emission spectroscopy. *Journal of Molecular Structure*, p.142547.

[17] Li, Y., Zhang, J., Zhang, X., Luo, Y., Lu, S., Ren, X., Wang, X., Sun, L. and Yan, C., 2009. Luminescent properties in relation to controllable phase and morphology of $LuBO_3$: Eu^{3+} nano/microcrystals synthesized by hydrothermal approach. *Chemistry of Materials*, *21*(3), pp.468-475.

[18] Klement, R., Drdlíková, K., Kachlík, M., Drdlík, D., Galusek, D. and Maca, K., 2021. Photoluminescence and optical properties of Eu^{3+}/Eu^{2+}-doped transparent Al_2O_3 ceramics. *Journal of the european ceramic society*, *41*(9), pp.4896-4906.

[19] Bispo-Jr, A.G., Saraiva, L.F., Lima, S.A., Pires, A.M. and Davolos, M.R., 2021. Recent prospects on phosphor-converted LEDs for lighting, displays, phototherapy, and indoor farming. *Journal of Luminescence*, *237*, p.118167.

Study on the impact of Pr^{3+}, Ce^{3+}, and Pb^{2+} ions on luminescence properties of $BaB_8O_{13}:Gd^{3+}$ for potential applications in phototherapy

MLA Letswalo, SB Sebopa, and BM Sondezi

Department of Physics, University of Johannesburg, 55 Beit St, Doornfontein, Johannesburg 2028, South Africa.

E-mail: letswalom@uj.ac.za

Abstract. A series of BaB_8O_{13} phosphors doped with different concentrations of 2 mol.% Gd^{3+} ions and 1.0 mol.% co-doped with Pr^{3+}, Pb^{2+} and Ce^{3+} ions were synthesized by the combustion synthesis method. The X-ray powder diffraction (XRD) analysis confirmed the pristine crystalline structure and uniformity of the compounds, with an average crystalline size of approximately 33–45 nm. Scanning Electron Microscopy (SEM) was performed to study the surface morphology of the compound, and the bandgap was influenced by the incorporation of 2 mol.% Gd^{3+} ions and 1.0 mol.% co-doped with Pr^{3+}, Pb^{2+} and Ce^{3+} as confirmed from the diffuse reflectance data. The photoluminescence (PL) excitation spectra of $BaB_8O_{13}:Gd^{3+}$ phosphor showed excitation peaks at 274 nm. The crucial role of gadolinium (Gd^{3+}) ions in barium-based hosts lies in their narrow-band emission spectrum, specifically at 311 – 315 nm, which is in the narrow band ultraviolet B (NB-UVB) range and is attributed to the $^6P_{7/2}$ to $^8S_{7/2}$ transition and a prominent emission peak at around 347 nm that could result from oxygen vacancy in the BaB_8O_{13} compound. The effects of co-doping sensitizers to Gd^{3+} ions on PL emission at 311 nm were as follows: $Ce^{3+} > Pr^{3+}, > Pb^{2+}$. Through effective energy transfers from the sensitizers, the broad emission at 387 nm was suppressed while the PL emission of the Gd^{3+} ion at 311 nm was increased. Through phototherapy, such material with enhanced NB-UVB emission could serve as a viable treatment option for various skin conditions, including vitiligo, eczema, and psoriasis.

1 Introduction

Natural sunlight, also known as heliotherapy, was used in ancient times to treat a variety of skin diseases successfully [1]. Nowadays, artificial light, known as phototherapy, is used effectively to treat a whole array of skin diseases with heightened success. Phototherapy is the interaction of light of specific wavelengths on tissues of the skin to induce a change in its immune response system with reduced erythemal side effects [2]. Phosphor compounds can be used for coating purposes on phosphor-based lamps; they could also be considered in the treatment of a myriad of skin diseases, in addition to the conventional psoriasis skin treatment.[3]. Phosphor materials that absorb strongly in the UVC region [200 -280 nm] and for emissions in the narrow-band NB-UVB region [311 – 315 nm] are good for the treatment of skin diseases such as psoriasis, as they align with the action spectrum of the disease. Minimal literature points towards light emissions in the UVA region [320 - 400 nm], which is useful for a broader treatment of other skin diseases [1-4]. A typical phosphor material is host-dependent, and, in this regard, barium octa-borate BaB_8O_{13} has been chosen as a host because it has high thermal and chemical stability, it has superior optical properties, and it has strong absorption in the UVC region [4]. Additionally, an ideal dopant such as gadolinium ion (Gd^{3+}), a rare earth ion whose emission was found to be aligned to an NB-UVB region that is attributed to $^6P7_{/2}$ to $^8S_{7/2}$ transition for a wavelength excitation of 274 nm.

In general, these 4*f* -4*f* transitions in Gd^{3+} ions are weak; sensitizers such as Bi^{3+}, Ce^{3+}, Pr^{3+}, and Pb^{2+} are incorporated to enhance their emission in the NB-UVB region by effectively absorbing the excitation energy and transferring it non-radiatively to the Gd^{3+} activator ion. In this work, BaB_8O_{13} is synthesized using the combustion method; thereafter, it is doped with Gd^{3+} and co-doped with Pr^{3+}, Ce^{3+}, and Pb^{2+} ions. The structural, morphological, and optical properties are determined by X-ray diffraction (XRD), scanning electron microscopy (SEM), and UV-visible techniques, respectively. The luminescence properties of these phosphor materials are studied using the photoluminescence (PL) techniques.

2 Experimental details

2.1 Sample preparation

Barium octa-borate BaB_8O_{13} doped with Gd^{3+} ions was synthesized by the combustion synthesis method. In preparation of this compound, barium nitrate (Ba $(NO_3)_2$, boric acid H_3BO_3 and urea (CH_4N_2O) were used as raw materials. Stoichiometric proportions of the precursor materials were weighed and mixed in distilled water, then ground with a mortar and pestle until a homogeneous solution was produced. To ensure better homogeneity of the solution, the mixture was then transferred to a crucible and thereafter transferred to the furnace for annealing at a constant temperature of 800 ^oC for approximately 4 hours. Once the furnace was cooled down to room temperature, the mixture was again ground to make it ready for characterization.

2.2 Material characterization technique

X-ray diffraction measurements were performed using a PAN analytical X-pert powder diffractometer with CuKa line radiation, a wavelength of 1.5406 Å. SEM measurements were also done to determine the surface morphology and particle sizes of the prepared samples. A JSM-2100 SEM microscope operating at 20 kV was used. Energy dispersive spectroscopy (EDS) at specific points on the sample was done to obtain the elemental composition of the prepared materials. Ultraviolet - visible (UV-vis) spectroscopy was performed to measure the sample's absorbance and/or transmittance. This was done within a spectral range of 200 - 800 nm. Optical measurements were done using a photoluminescent spectrometer, employing a Horiba QN8000 instrument, encased with a xenon lamp as a light source, and a PPD-850 detector with a fluorescence spectrophotometer with a spectral measuring range of 200 – 600 nm.

3 Results and Discussion

3.1 Structural investigation

Figure 1 shows the X-ray diffraction patterns of pure and Ce^{3+}/ Pr^{3+}/ Pb^{2+} ions doped BaB_8O_{13}:Gd^{3+} (2 mol%) nanoparticles, in the range of 10° to 50°. XRD patterns show an orthorhombic crystal structure formation with lattice parameters a = 13.2Å, b = 17.38Å, and c = 8.56Å [5] of space group $P4_122$. These patterns are well compatible with the reference patterns from the JCPDS file #00-006-0277, as indicated in Figure 1. This pristine orthorhombic structure exhibits no impurity peaks, confirming the successful incorporation of Gd and Gd co-doped Pr, Ce, and Pb ions. When a small Gd^{3+} ion (r = 1.05 Å) substitutes for a larger Ba^{2+} ion (r = 1.35 Å) in the host lattice, it causes a decrease in the Gd^{3+}– O^{2-} bond distance, which leads to an increase in the crystal field splitting and a shift in the peak positions [3].

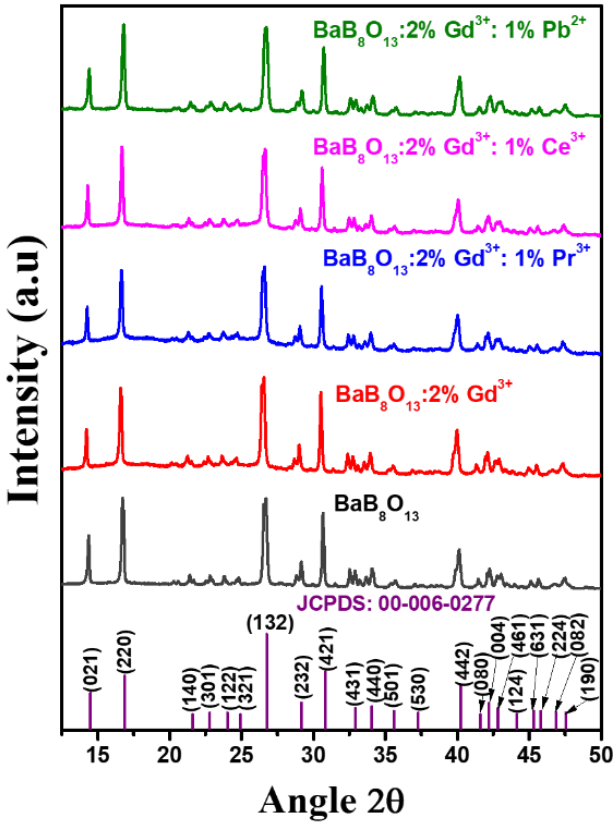

Figure 1: X-ray diffraction patterns of pure and Ce^{3+}/ Pr^{3+}/ Pb^{2+} ions doped BaB_8O_{13}:Gd^{3+} (2 mol %) nanoparticles.

3.2 Morphological investigation

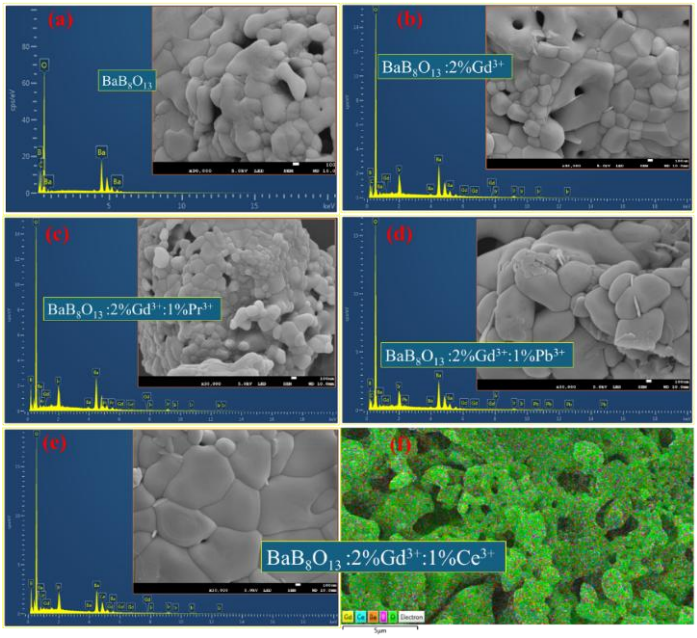

Figure 2: SEM and EDS images of (a) BaB_8O_{13} (host), (b) BaB_8O_{13}:Gd^{3+} (2 mol%), co-doped 1 mol% (c) Pr^{3+}, (d) Pb^{2+}, (e) Ce^{3+}, and (f) EDS mapping of Ce^{3+} (1 mol%) doped BaB_8O_{13}:Gd^{3+} (2 mol%).

Figure 2 (a-e) shows the SEM images of pure and Ce^{3+}/ Pr^{3+}/ Pb^{2+} ions doped BaB_8O_{13}:Gd^{3+} (2 mol %) nanoparticles. SEM images reveal the formation of a pristine crystalline material with a uniform crystal structure. The average crystalline size, determined using the Scherrer equation, was 36.69 nm for the host material. It increased slightly to 37.05 nm with Gd^{3+} doping, but decreased to 35.75 nm with Pr^{3+}, 35.97 nm with Ce^{3+}, and 35.82 nm with Pb^{2+} co-doped Gd^{3+} ions. Furthermore, it is revealed that the synthesized particles are inhomogeneous, clustered closely and evolve in size and shape when doped with 2 mol% Gd^{3+} or Gd^{3+} co-doped with either Pr^{3+}, Ce^{3+}, or Pb^{2+} ions, as shown in Figure 2 (a-e). In general, the topology and morphology of the prepared samples change with doping and co-doping. EDS spectra of the sample compounds verify the existence of the elements such as Barium, Boron and Oxygen. Extra elements, such as carbon and iridium, noted in the spectra, probably originated from carbon tape mountings and layer coatings (used to prevent charging). Moreover, the selected chemical image mapping scans describe the uniform distribution of these elements throughout the materials, as depicted in Figure 2(f).

3.3 Optical investigation

UV-Vis diffuse reflectance spectra of the doped and co-doped materials in the wavelength range from 200 to 800 nm were measured, as shown in Figure 3 (a). In the case of the host material, high absorption makes it an ideal candidate for luminescence. Remarkable absorptions were also observed for the doped and co-doped samples at their respective absorption edges: specifically, around 250 nm for the Gd^{3+} co-doped with 1 mol% of either Pr^{3+} or Pb^{2+} of BaB_8O_{13}. A redshift exhibiting absorption edges at 450 and 750 nm was observed with 2 mol% Gd^{3+} doped and Gd^{3+} co-doped with 1 mol% Ce^{3+} BaB_8O_{13}, respectively. The band gap of these samples was estimated using the Kubelka-Munk absorption coefficient (K/S), given by: $F(R) = K/S = \frac{(1-R)^2}{2R}$, where R is the reflectivity, K the absorption coefficient and S the scattering coefficient [6,7]. The band gap of the samples is obtained by extrapolating the linear section of the Tauc plots, as shown in Figure 3(b). The optical band gap of these samples ranges from 3.13 eV to 5.39 eV.

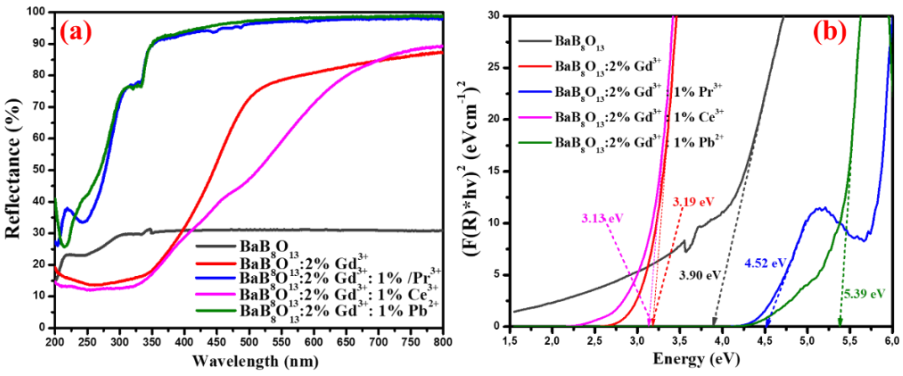

Figure 3: (a) Reflectance spectra and (b) Tauc plots of pure and Ce^{3+}/ Pr^{3+}/ Pb^{2+} ions doped BaB_8O_{13}:Gd^{3+} (2 mol %) nanoparticles

The PL excitation spectra of the BaB_8O_{13} host material, measured at an emission wavelength of 311 nm, is shown in the insert of Figure 4 (a), while its PL spectra is shown in Figure 4(a) The PLE spectra of host shows a broad spectrum in the UVC region with a maximum at 274 nm, attributed to $^8S_{7/2}$ to ^6I_J transition, corresponding to 4*f* to 5*d* orbital transition and a charge transfer from O^{2-} (2p orbital) to Gd^{3+} (4*f* orbital) [3]. Figure 4(b) shows the PL emission spectra of Gd^{3+}-doped BaB_8O_{13} and Gd^{3+} co-doped with 1 mol% of either Pr^{3+}, Ce^{3+}, or Pb^{2+} BaB_8O_{13} recorded under an excitation wavelength of 274 nm. The PL spectrum shows a sharp NB-UVB emission at 311 nm due to the $^6P_{7/2}$ to $^8S_{7/2}$ transition, followed by a broadband emission centred around 387 nm for all samples except for co-doped 1 mol% Ce^{3+}, which has a maximum around 350 nm. In addition, the broad emission of the host at 347 nm is red-shifted to around 350–387 nm as the sensitizers are incorporated. It is observed that after doping BaB_8O_{13} with 2 mol% Gd^{3+} and Gd^{3+} co-doping with either 1 mol% of Pr^{3+} or Ce^{3+}, the broadband emissions appear to be suppressed, allowing for the Gd^{3+} emission at 311 nm to be enhanced, suggesting that whilst the broadband emissions are reduced, the PL emission of Gd^{3+} is enhanced. Further on, it is noticed that 516, 599, and 645 nm emissions are attributed to Pb^{2+} s-p charge-related transitions [8]. Additionally, emissions

in the visible regions are also observed for these samples, which makes these samples also applicable for light-emitting diodes (LEDs). The broadband emissions are attributed to oxygen vacancies (or oxygen interstitials) and surface defects [9]. When Ce^{3+} is co-doped with 2 mol% Gd^{3+}, it has a lower band gap energy, which accounts for its enhanced emissions at 311 nm compared to the other co-dopants. In this respect, the 2 mol% Gd^{3+} doped BaB_8O_{13} and Gd^{3+} co-doped with 1 mol% Ce^{3+} has the strongest emission in the NB-UVB region at 311 nm, while the compound Gd^{3+} co-doped with Pb^{2+} and single doped 2% mol% Gd^{3+} ions has the strongest emission in the broadband region.

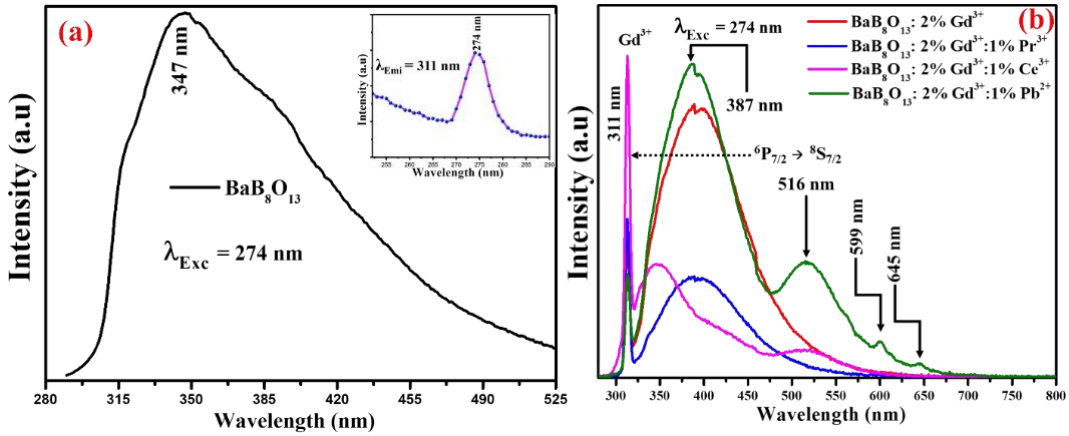

Figure 4**:** (a) PL emission spectra at 274 nm excitation of BaB_8O_{13} (host) [Insert figure shows the PL excitation around 274 nm], (b) PL emission spectra of doped and co-doped ions of Gd^{3+}/Pr^{3+}/Ce^{3+}/Pb^{2+} samples.

3.4 Energy transfer mechanism

Figure 5 shows the schematic model of the possible energy transfers from the sensitizers (Ce^{3+}, Pr^{3+} and Pb^{2+}) ions to the activator Gd^{3+} ion in the doped BaB_8O_{13} phosphor material. An observation of the PL spectra in Figure 4 informs that enhanced emissions at 311 nm are obtained for the 1 mol% Ce^{3+} co-doped BaB_8O_{13}:2%Gd^{3+} phosphor, implying efficient energy transfers occur mainly from Ce^{3+} to Gd^{3+} when equilibrium is established between their excited states. Additionally, some energy transfers of moderate intensity occur from Pr^{3+} to Gd^{3+} ions at 311 nm. Furthermore, low-intensity energy transfer does occur from Pb^{2+} to Gd^{3+} ions at 311 nm.

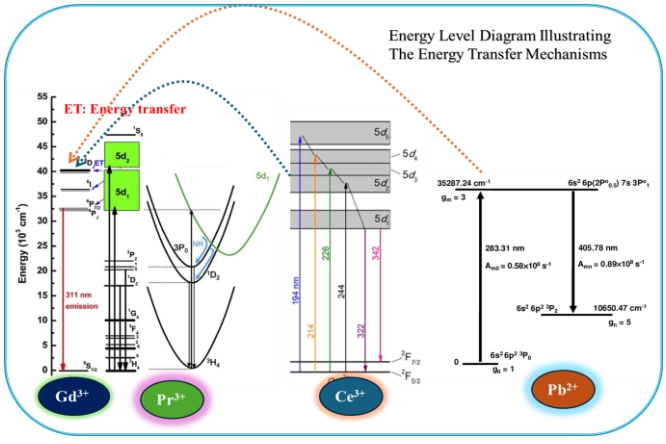

Figure 5: Schematic model energy transfer diagram of co-doped ions of Pr^{3+}/Pb^{2+}/Ce^{3+} to Gd^{3+} ions in the BaB_8O_{13} host [10, 11].

4 Conclusion

In summary, pure and 1 mol% of Ce^{3+}/ Pr^{3+}/Pb^{2+} doped BaB_8O_{13}: Gd^{3+} (2 mol%) samples with sensitizers exhibit NB-UVB, UVA, and visible emissions when synthesized by the combustion method at 800 °C. The PL spectra show that the UV-B emissions fall in the 311 nm region when excited by a wavelength of 274 nm. The sharp UV-B emissions at 311 nm correspond to the $^6P_{7/2}$ to $^8S_{7/2}$ transition from its metastable state to its ground state, and a broad band emission at around 375 nm due to oxygen defect-related sources. The XRD data for the BaB_8O_{13} material conforms with JCPDS data, having an orthorhombic structure. The SEM results confirm the presence of elements existing in the Gd^{3+} doped BaB_8O_{13} materials. UV-vis measurements indicate that these materials are good for luminescence studies due to their strong absorptions in the UV region. The energy transfer $Ce^{3+} \rightarrow Gd^{3+}$ ions make this compound BaB_8O_{13}:Ce^{3+}/Gd^{3+} an ideal candidate for applications in phototherapy lamps, followed by BaB_8O_{13}:Pr^{3+}/Gd^{3+} and BaB_8O_{13}:Pb^{2+}/Gd^{3+} encapsulated lamps in that order. The broadband emissions of the BaB_8O_{13}:Pb^{2+}/Gd^{3+} and BaB_8O_{13}:Gd^{3+} compounds, together with the strong NB-UVB emission of BaB_8O_{13}:Ce^{3+}/Gd^{3+} make them ideal for treating a multitude of skin diseases. Furthermore, emission is also observed in the visible region, thus allowing them to operate in LED lights.

References

[1] B. P. Bawanthade, A. A. Mistry, N. Ugemuge, I. S. Chaudari, and S. J. Dhoble, "Synthesis and study of optical properties of a Gd^{3+}-doped $NaYF_4$ phosphor for phototherapy lamp application," *Luminescence*, vol. 39, no. 4, Apr. 2024, doi: 10.1002/bio.4736.

[2] J. Krutmann, and A. Morita, "Mechanisms of ultraviolet (UV) B and UVA phototherapy," *Journal of Investigative Dermatology Symposium Proceedings*, vol. 4, no. 1, pp. 70–72, Sep. 1999, doi: 10.1038/sj.jidsp.5640185.

[3] A. Sharma, M. Rakshita, P. P. Pradhan, K. A. K. Durga Prasad, S. Mishra, K. Jayanthi, and D. Haranath, "Efficacy of photodynamic therapy using UVB radiation-emitting novel phosphor material for non-surgical treatment of psoriasis," *Journal of Materials Research/Pratt's Guide to Venture Capital Sources*, vol. 38, no. 10, pp. 2812–2822, Apr. 2023, doi: 10.1557/s43578-023-01008-7

[4] M. M. Lanje, M. M. Yawalkar, J. S. Dahegaonkar, and S. J. Dhoble, "Enhancement of photoluminescence emission of Gd^{3+} activated borate phosphors for phototherapy lamps: A review," *Journal of Physics Conference Series*, vol. 1913, no. 1, p. 012031, May 2021, doi: 10.1088/1742-6596/1913/1/012031.

[5] E. Erdoğmuş, E. Korkmaz, and V. E. Kafadar, "Luminescence of a novel Near-UV emitting phosphor BaB_8O_{13}:Pb^{2+}," *Journal of Applied Spectroscopy*, vol. 80, no. 6, pp. 945–949, Jan. 2014, doi: 10.1007/s10812-014-9870-4.

[6] H. Yu, D. Deng, Y. Hua, C. Li, and S. Xu, "Orange- to green-emitting $Li(Sr,Ca)_4(BO_3)_3$:Eu^{2+} phosphor: emission-tunable properties and white light emitting diode application," *RSC Advances*, vol. 6, no. 86, pp. 82824–82831, Jan. 2016, doi: 10.1039/c6ra13029a.

[7] P. Gupta, A. K. Bedyal, V. Kumar, Y. Khajuria, V. Sharma, O. M. Ntwaeaborwa, and H. C. Swart "Energy transfer mechanism from Gd^{3+} to Sm^{3+} in $K_3Gd(PO_4)_2$:Sm^{3+} phosphor," *Materials Research Express*, vol. 2, no. 7, p. 076202, Jul. 2015, doi: 10.1088/2053-1591/2/7/076202.

[8] J. Kuang and Y. Liu, "Luminescence Properties of a Pb^{2+} Activated Long-Afterglow Phosphor," *Journal of the Electrochemical Society*, vol. 153, no. 3, p. G245, Jan. 2006, doi: 10.1149/1.2163780.

[9] M. A. Lephoto, K. G. Tshabalala, S. J. Motloung, G. H. Mhlongo, and O. M. Ntwaeaborwa, "Photoluminescence studies of green emitting BaB_8O_{13}:Bi^{3+} phosphors prepared by solution combustion method," *Journal of Luminescence*, vol. 200, pp. 94–102, Apr. 2018, doi: 10.1016/j.jlumin.2018.04.014.

[10] Y. Wu and G. Ren, "Energy transfer and radiative recombination processes in $(Gd,Lu)_3Ga_3Al_2O_{12}$:Pr^{3+} scintillators," *Optical Materials*, vol. 35, no. 12, pp. 2146–2154, Jun. 2013, doi: 10.1016/j.optmat.2013.05.039.

[11] F. Vidal, M. Chaker, C. Goueguel, S. Laville, H. Loudyi, K. Rifai, and M. Sabsabi, "Enhanced Laser-Induced Breakdown Spectroscopy by Second-Pulse selective wavelength excitation," *AIP Conference Proceedings*, Jan. 2008, doi: 10.1063/1.2999951.

Luminescence Study on the Impact of Alkaline Earth Metal Ions on $Na_3PO_4:Ce^{3+}$ Phosphors for Potential Colour Display Applications

Amanda Sefage, Machaba Letswalo and Buyi Sondezi

Department of Physics, University of Johannesburg, Auckland Park, 2005, Johannesburg, South Africa

E-mail: asefage@uj.ac.za

Abstract. This study of the addition explores the impact of metal ions calcium (Ca), strontium (Sr), and barium (Ba) on the optical properties of sodium tri-phosphate (Na_3PO_4). The resulting nanophosphors, sodium calcium phosphate ($NaCaPO_4$), sodium strontium phosphate ($NaSrPO_4$), and sodium barium phosphate ($NaBaPO_4$), were synthesized via solid-state reaction techniques and doped with cerium (III) ions (1 mol% Ce^{3+}). The synthesized nanophosphors were annealed at 900°C for 4 hours. A combination of characterization techniques, including X-ray powder diffraction (XRD), field emission scanning electron microscopy (FE-SEM), and photoluminescence (PL) spectroscopy, was employed to comprehensively characterize the phosphor materials. Additionally, Commission Internationale de l'Eclairage (CIE) plots were generated from the PL data to evaluate and compare the color-tuning properties of each phosphor material. XRD analysis revealed that $NaSrPO_4$ phosphors adopted a monoclinic phase structure, whereas Na_3PO_4 adopted a tetragonal $NaCaPO_4$ and $NaBaPO_4$ phosphors crystallized into an orthorhombic phase structure. Notably, doping with 1 mol% Ce^{3+} did not alter the crystal structure phases of these phosphor materials. According to the CIE diagram, it is observed from the PL emission spectra that the introduction of Ce^{3+} ions and the metal ions on the Na_3PO_4 host phosphors had an impact on the luminescent properties of these materials, which suggests it is good for light-emitting diodes (LEDs) with emissions from the blue to violet region.

1 Introduction

This study explores the impact of the addition of metal ions (M = Ca, Sr, and Ba) on the luminescent properties of Na_3PO_4 (tetragonal, $P\bar{4}21c$) [1]. The focus is on the application of these nanophosphors for colour display devices, results from the variation of the M atoms and additionally replacing these atoms with the rare-earth Ce^{3+} ions for optimum violet-colour emissions using the solid-state reaction method. Rare earth-doped alkaline metal phosphates phosphors have been showing interest in the development and investigation of new efficient luminescent materials due to their remarkable luminescent behaviours based on their structural properties (orthophosphate) [2]. Luminescence properties of rare earth ions in various host materials are affected by the crystal structure, phase transition and chemical surroundings [3]. Ce^{3+} is also sensitive to the crystal field environment. This study will demonstrate the application of the solid-state reaction method to synthesize and incorporate alkaline metal ions into the host lattice matrix, followed by the single doping of the resultant compound with Ce^{3+} ions, yielding final mixtures of $NaBaPO_4:xCe^{3+}$, $NaCaPO_4:xCe^{3+}$, and $NaSrPO_4:xCe^{3+}$ (x = 0 and 1 mol%), as phosphors for the investigation of high-intensity blue to violet color emissions. Photoluminescence results indicate

improved violet color emissions generated by the $NaMPO_4$:xCe^{3+} phosphor materials. These findings suggest that the synthesized materials may serve as attractive options for color display systems.

2 Experimental

2.1 Synthesis technique

The solid-state synthesis method was used to create a series of Ce^{3+} doped sodium phosphates (Na_3PO_4) together with the introduction of alkaline metal ions into the host lattice of Na_3PO_4 to form an orthophosphate, mixture ($NaMPO_4$). To create a uniform powder, the stoichiometric amounts of Na_3PO_4, $NaBaPO_4$, $NaCaPO_4$, and $NaSrPO_4$ for each series were weighed and ground for 30 minutes with an agate mortar and pestle with the use of acetone as a wetting agent to form a homogeneous powder. Different amounts of $CeCO_3$ powder were added to each host phosphate to introduce Ce^{3+} ions into each mixture. All homogeneous powders were annealed at 900 °C for 4 hours. After annealing, each series was further ground to create a fine, uniform powder.

The above-mentioned compounds were combined in accordance with the specified stoichiometric ratios for each series.

$$3\ Na_2CO_3 + 2\ NH_4H_2PO_4 = 2\ Na_3PO_4 + 2\ NH_3 + 3\ CO_2 + 3\ H_2O \quad (1)$$

$$Na_2CO_3 + 2\ BaCO_3 + 2\ NH_4H_2PO_4 = 2\ NaBaPO_4 + 2\ NH_3 + 3\ CO_2 + 3\ H_2O \quad (2)$$

$$Na_2CO_3 + 2\ CaCO_3 + 2\ NH_4H_2PO_4 = 2\ NaCaPO_4 + 2\ NH_3 + 3\ CO_2 + 3\ H_2O \quad (3)$$

$$Na_2CO_3 + 2\ SrCO_3 + 2\ NH_4H_2PO_4 = 2\ NaSrPO_4 + 2\ NH_3 + 3\ CO_2 + 3\ H_2O \quad (4)$$

2.2 Characterisation

X-ray powder diffraction was used to characterise the produced nanophosphors (Bruker AXS D8 Advance X-ray diffractometer, Cu Kα, λ= 0.15406 nm, 40 kV, 40 mA, $10° \leq 2\theta \geq 80°$). A xenon flash lamp was used as an excitation source in a Cary eclipse fluorescence Varian spectrophotometer to perform the PL spectra measurements. A JEOL JSM-7800F high field emission scanning electron microscope with an EDS was used in this investigation to obtain SEM micrographs of the prepared samples. The PL emission data was used to determine the colour chromaticity behaviour of the prepared sample.

3 Results and Discussions

3.1 Powder X-ray diffraction (XRD) analysis

Figure 1 illustrates the XRD spectra of Na_3PO_4: xCe^{3+} and $NaMPO_4$ nanophosphors (x = 0.0 and 1.0 mol %, M = Ca, Sr, and Ba), each material indicates a singular crystalline phase in the host and doped Ce^{3+} materials. The figure also demonstrates that Na_3PO_4 aligns well with the tetragonal $P\bar{4}21c$ powder diffraction patterns from the PDF#31-1323 [4], but a decrease in intensity is observed when doped with Ce^{3+}. Nevertheless, the intense diffraction peaks appear to shift to lower 2θ angles, indicating an expansion of both crystalline structures resulting from the interstitial substitution of Ce^{3+} ions within the crystal lattice [5]. As the spectra are analysed, the inclusion of Ba^{2+}, Ca^{2+}, and Sr^{2+} ions into the Na_3PO_4 lattice results in the formation of well-defined crystalline phases corresponding to $NaBaPO_4$ (PDF# 33-1210), $NaCaPO_4$ (PDF# 29-1193), and $NaSrPO_4$ (PDF# 33-1282) [6, 7]. However, a significant shift of the prominent peaks towards lower 2θ angles is observed, even for the Ce^{3+} doped samples. The diffraction patterns of the novel host lattices correspond well to the monoclinic ($NaSrPO_4$) and orthorhombic ($NaBaPO_4$, and $NaCaPO_4$) phase structures, respectively.

The inclusion of Ce^{3+} ions in the $NaCaPO_4$ combination results in a reduction in peak intensity. The spectra demonstrate that doping with Ce^{3+} (1.14 Å) ions results in decreased crystallinity without modifying its crystal structure; nevertheless, the reduction in crystallinity may be attributed to the reduced ionic radius of Ca^{2+} ions (1.00 Å). A portion of this work has been previously documented utilizing both solid-state and combustion reaction methods [8,9]. The present study investigates the influence of alkaline ions on sodium triphosphate as a medium for these metal ions

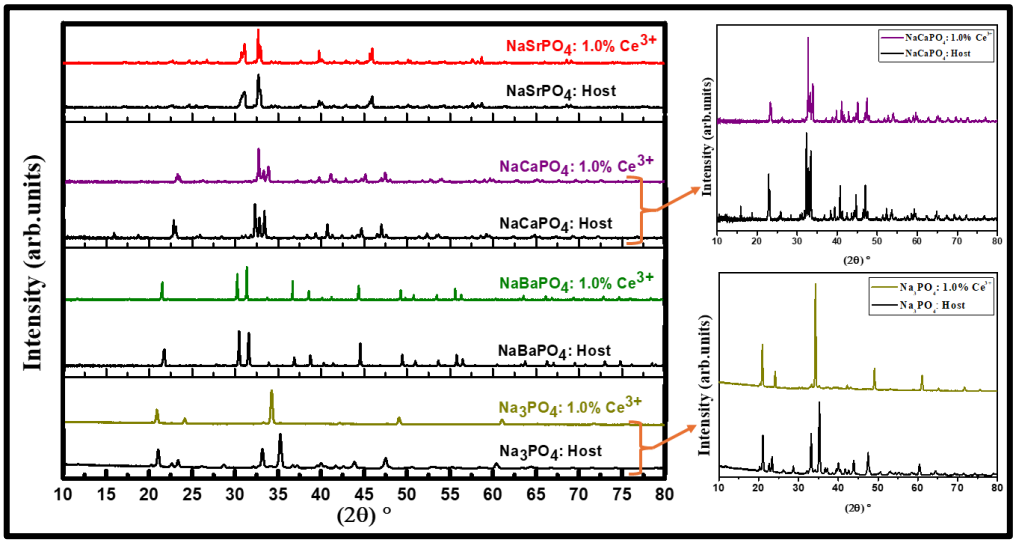

Figure 1: XRD spectra of Na_3PO_4: xCe^{3+} and $NaMPO_4$:xCe^{3+} nanophosphors (x = 0.0 and 1.0 mol% %, M= Ca, Sr, and Ba), indicating a single crystalline phase on the host material (Na_3PO_4).

According to the Scherrer equation, the crystalline sizes of the prepared samples were determined and observed to be in the range of 50.5 to 133 nm, as presented in Table 1 below. It is observed that $NaBaPO_4$: xCe^{3+} exhibits the most significant particle growth resulting from the Ce^{3+} ions doping. In addition, it is also observed that the Ba^{2+} alkaline ions play a significant role in the Na_3PO_4 host lattice itself. One can also observe that Na_3PO_4 and $NaCaPO_4$ exhibit considerable size stability, indicating effective structural accommodation of the Ce^{3+} ions. $NaSrPO_4$ displays a moderate rise, indicating a degree of sensitivity to the incorporation of the dopant.

x mol%	Na_3PO_4:xCe^{3+} size (nm)	$NaBaPO_4$:xCe^{3+} size (nm)	$NaCaPO_4$:xCe^{3+} size (nm)	$NaSrPO_4$:xCe^{3+} size (nm)
0.00	51.2	74.4	50.7	50.7
1.00	50.5	133	50.4	67.0

Table 1: Estimated crystalline sizes of Na_3PO_4:xCe^{3+} and $NaMPO_4$:xCe^{3+} nanophosphors (x = 0.0 and 1.0 mol%, M = Ca, Sr, and Ba).

3.2 Powder Surface morphology and chemical composition analysis

Figures 2 (a), (d), and (g) present the FE-SEM images of $NaBaPO_4$:xCe^{3+}, $NaCaPO_4$:xCe^{3+}, and $NaSrPO_4$:xCe^{3+} phosphors at x = 0.0 mol%, while Figures 2 (c), (f), and (i) depict the FE-SEM micrographs of $NaBaPO_4$:xCe^{3+}, $NaCaPO_4$:xCe^{3+}, and $NaSrPO_4$:xCe^{3+} phosphors at x = 1.0 mol%. The SEM images reveal that the particles in the host materials exhibit various sizes and shapes, and the irregularity of the particles becomes more pronounced following doping with Ce^{3+} ions, suggesting an increase in agglomeration due to Ce^{3+} ion incorporation. The SEM host micrographs indicate that $NaBaPO_4$ particles are larger and more irregular than those of $NaCaPO_4$ and $NaSrPO_4$ materials and this is also evidenced in Table 1 above. The morphology of these materials tends to cluster and resembles a dried paste following Ce^{3+} ion doping, as illustrated in Fig. 2 (c), (f), and (g). This is due to the distortion of particle morphology caused by Ce^{3+} ion impurities under identical temperature conditions maintained for the host materials [10].

The analyzed materials were subjected to EDS spectroscopy to ascertain the presence of various elements in the synthesized phosphors. The EDS spectra of $NaBaPO_4$:xCe^{3+}, $NaCaPO_4$:xCe^{3+}, and $NaSrPO_4$:xCe^{3+} phosphors, with x = 0.0 and 1.0 mol%, are presented in Fig. 2, (b), (e), and (h), respectively. The EDS spectra of these

phosphors validated the existence of distinct elements, including Na, O, P, Ba, Ca, Sr, and Ce atoms. This is further confirmed by the clearly defined intensity peaks of the individual elements.

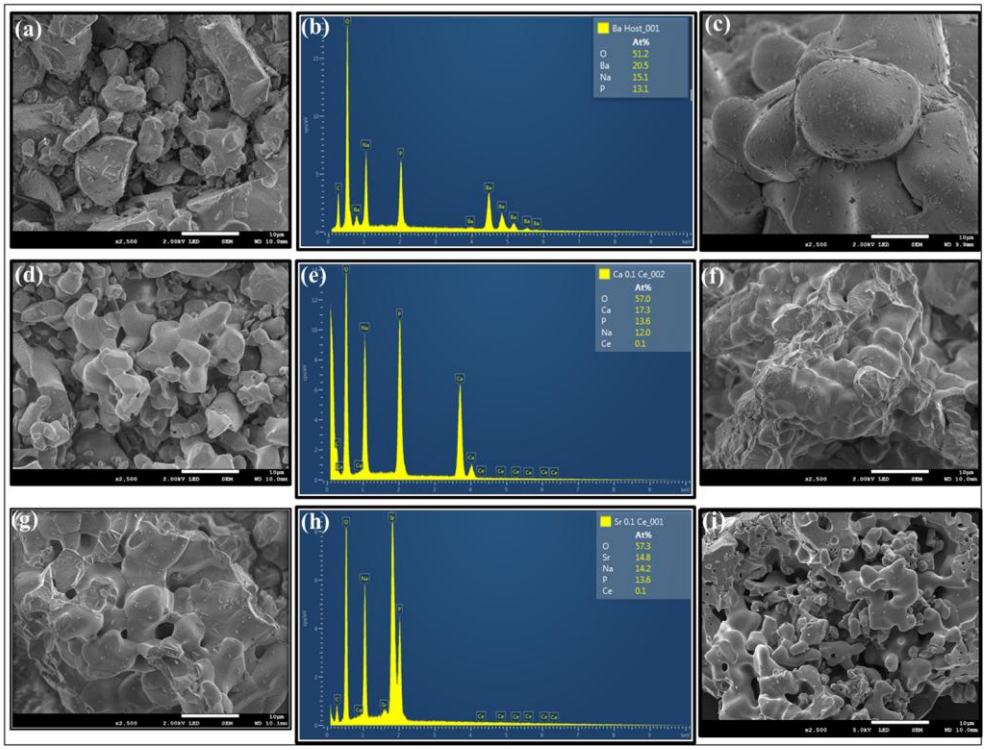

Figure 2: SEM micrographs of: (a) $NaBaPO_4$, (c) $NaBaPO_4$:1.0%Ce^{3+}, (d) $NaCaPO_4$, (f) $NaCaPO_4$:1.0%Ce^{3+}, (g) $NaSrPO_4$, and (i) $NaSrPO_4$:1.0%Ce^{3+} demonstrating high agglomerate, fine, and irregularly shaped particles. Figure 2 (b), (e), and (h): EDS spectra confirming the relevant elements: Ba, Ca, and Sr, respectively, with Na, O, P, and Ce.

3.3 Photoluminescence studies

The excitation spectra (PLE) of Na_3PO_4:$x$$Ce^{3+}$ and $NaMPO_4$:$x$$Ce^{3+}$ phosphors (where x = 0.0 and 1.0 mol %, M = Ba, Ca, and Sr) were recorded throughout the range of 225-360 nm, while observing the prominent emission peak at 385 nm, as illustrated in Figure 3 (a). This spectrum reveals three wide PLE intensity peaks within the wavelength region of 230-300 nm. The three excitation bands mostly result from the 4f → 5d transition between the energy levels of the Ce^{3+} ion [10]. The insert in Figure 3 (a) indicates that Na_3PO_4:$x$$Ce^{3+}$ does not react to the excitation wavelength of Ce^{3+}, likely due to the absence of alkaline metal ions that may promote energy transfer to or from the dopant. The excitation intensity bands of the Ce^{3+} ion are markedly enhanced in the 1.0 mol% Ce^{3+}-doped $NaBaPO_4$ material, likely due to the ionic radius relationship between Ce^{3+} and Ba^{2+} ions [11].

The intense band at 281 nm was deemed suitable for recording the emission spectra of the $NaMPO_4$:$x$$Ce^{3+}$ samples, where x = 0.0 and 1.0 mol%. The photoluminescence spectra of Na_3PO_4:$x$$Ce^{3+}$ and $NaMPO_4$:$x$$Ce^{3+}$ were recorded in the 300-500 nm range using a 281 nm UV excitation wavelength, as illustrated in Figure 3(b). A broad emission band was seen at a wavelength of 360 -385 nm, which can be attributed to the 5d→4f transition between the energy levels of the Ce^{3+} ion. The emission bands (360 nm) of 1.0 mol% Ce^{3+} ions in $NaBaPO_4$ are marked higher than those of the other samples, with 1 mol% for $NaBaPO_4$ followed by 1 mol% Ce^{3+} doped in $NaCaPO_4$, attributable to the differing ionic radii. The insert in Figure 3b indicates no emission from the Na_3PO_4:$x$$Ce^{3+}$ material, and this is likely attributed to the lack of alkaline metal ions [12]. Maleka et al have noted that various alkaline earth ions slightly alter the Ce^{3+} emission maxima and that the hosts displayed excellent crystallinity along with broad UV–blue emission bands [9]. The findings by [8] indicated that luminescence intensity reaches a peak at an optimal dopant level before concentration quenching becomes predominant, aligning with the trends observed by [9].

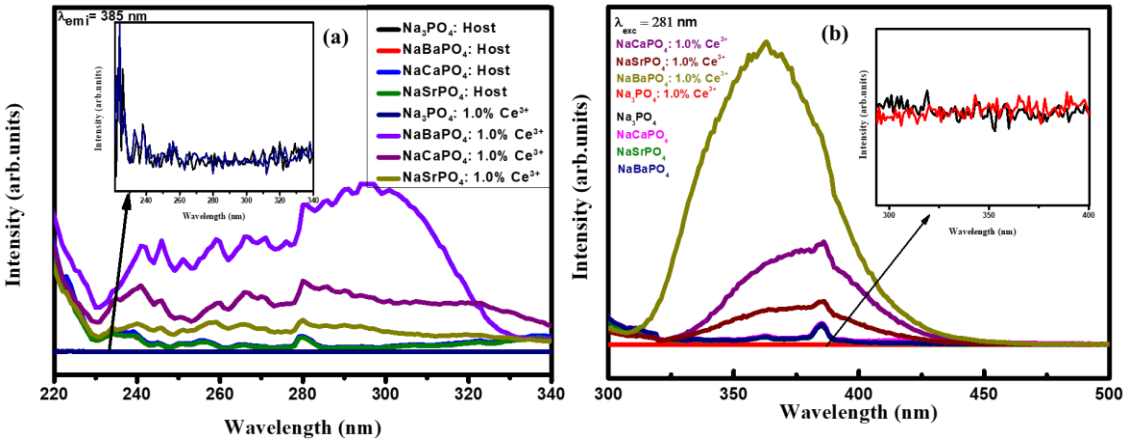

Figure 3: (a) PL excitation spectra of Na_3PO_4: xCe^{3+} and $NaMPO_4$: xCe^{3+} nanophosphors (x = 0.0, and 1.0 mol %, monitored at λ_{emi} = 385 nm. (b) PL emission spectra of Na_3PO_4: xCe^{3+} and $NaMPO_4$: xCe^{3+} nanophosphors (x = 0.0, 1.0 mol % and M = Ca, Sr, and Ba) monitored at λ_{exc} = 281 nm.

3.4 Commission International de l'Eclairage (CIE)- colour coordinates

Figure 4 presents the CIE plots of $NaMPO_4$:xCe^{3+} phosphors, with x values of 0.0 and 1.0 mol%, and M representing Ca, Sr, and Ba. According to the CIE chromaticity diagram, all color coordinates for orthophosphate materials are situated within the blue-to-violet spectrum of the color range. The color coordinates of $NaMPO_4$ host materials emit light in the pure blue area; however, a shift towards the violet region occurs upon doping with Ce^{3+} ions [13]. The Na_3PO_4:xCe^{3+} material is absent from the figure, which aligns well with the PL emission spectra shown in Figure 3 (b). The results suggest that the synthesized phosphor materials are viable options for bluish-violet color-emitting applications in colour display systems.

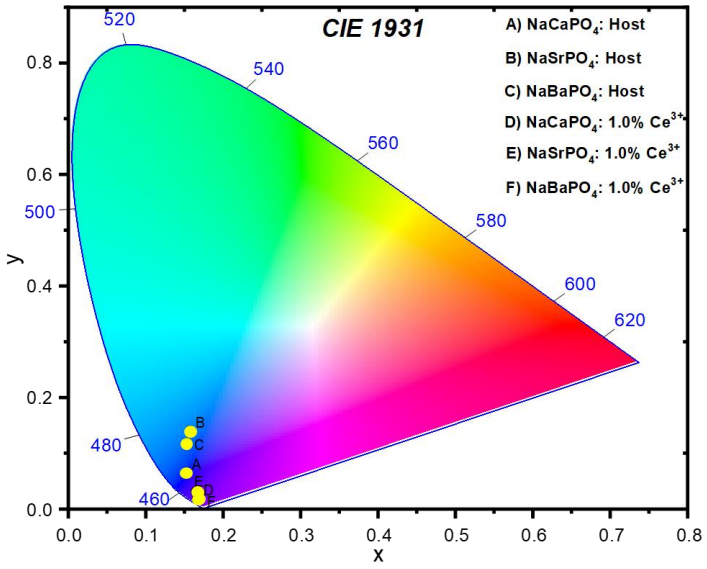

Figure 4: CIE chromatic-diagram of $NaMPO_4$: xCe^{3+} nanophosphors (x = 0.0, and 1.0 mol %, M= Ca, Sr, and Ba)

4 Conclusion

This study explored the Na_3PO_4:xCe^{3+} and $NaMPO_4$:xCe^{3+} samples with concentrations x = 0.0 and 1.0 mol %, where M represents alkaline Ba, Ca, and Sr, synthesized via the solid-state reaction technique. This study examined the structural and optical properties of the synthesized samples. XRD examinations revealed that the

synthesized Na_3PO_4 materials crystallized into a tetragonal structure, which subsequently transformed into monoclinic and orthorhombic phase structures upon addition of the alkaline. This is detailed in the preceding XRD analysis section. SEM investigations confirmed that particle agglomeration was observed with Ce^{3+} ion doping. The photoluminescence spectra were obtained using a 281 nm excitation wavelength, revealing a broad emission band at 360-385 nm. The PL data and CIE color diagram results confirm that the current materials may serve as viable choices for violet color-emitting devices.

References

[1] M.B. Bechir, M.H Dhaou, Synthesis, optical and dielectric properties of orthophosphate M_3PO_4 (M = Li, Na) compounds, *SSRN*, 2018.[Online]. Electronic copy available at: https://ssrn.com/abstract=4086983.

[2] A. Balakrishna, L. Reddy, O. M. Ntwaeaborwa, H. C. Swart, Remarkable influence of alkaline earth ions on the enhancement of fluorescence from Eu^{3+} ion doped in sodium ortho-phosphate phosphors, *Journal of Molecular Structure,*vol. 1203, 2020. DOI.org/10.1016/j.molstruc.2019.127375.

[3] K.N. Shinde, S.J. Dhoble, H.C Swart and K. Park, Phosphate phosphors for solid-state lighting, *Springer series in materials science*, vol.174, 2012. DOI: 10.1007/978-3-642-34312-4_2.

[4] J. Zhou, S Lin, L. Deng, Jun Li, T Zeng, Z. Huang, H. Huang, Performance study of Na_3PO_4-expanded graphite composites for lowtemperature thermochemical heat storage, *Energy Proceedings*, Vol. 55, 2025. DOI.org/10.46855/energy-proceedings-11583.

[5] J.G.O. Netoa , O.C.S. Netoa , F. Pedrochi, A. Steimacher, J.S. Filhoa , F.F. de Sousa, L.M. Silva, A.O. Santos, Structural, vibrational, thermal, and optical properties of L-threonine crystals containing Ce^{3+} ions, *Journal of Molecular Structure*.vol. 1254, 2022. DOI:10.1016/j.molstruc.2021.132316.

[6] Chen, K.H., Weng, M.H., Pan, C.T., Yang, R.Y., Effect of different sintering method on the microstructure and photoluminescent properties of $NaSrPO_4$:Tb^{3+} phosphors, *Powder Technology*, vol. 288, pp.117-122. 2016. DOI:10.1016/j.powtec.2015.10.037.

[7] Chen, K. H., Weng, M. H., Pan, C. T., and Yang R. Y., Crystal structure and luminescent properties of Tb^{3+}, Ce^{3+}, and codoped NaSrPO4 phosphors prepared by microwave sintering, *Sensors and Materials*, vol. 29, pp. 1607–1614, 2017.

[8] A.P. Sefage, The Effect of Ce^{3+} on the Luminescence Properties of the $ABPO_4$ (A= Na, B = Mg, Ca, Sr, and Ba) Using the Solid-State Reaction Method, Johannesburg: University of Johannesburg, Available from https://hdl.handle.net/10210/499121. MSc dessertation, University of Johhansburg, South Africa, 2021.

[9] P.M. Maleka, L. Reddy, T.J. Nkosi, A. Balakrishna, R.E. Kroon, H.C. Swart, O.M. Ntwaeaborwa, Structural and morphological characterization of photoluminescent cerium-doped near UV-blue sodium ortho-phosphate phosphors, *Journal of Luminescence*,vol. 226, 2020. DOI.org/10.1016/j.jlumin.2020.117409

[10] I. A.M Ibrahim, Z. Lenčéš, P. Šajgalík, L. Benco, and M.Marsman, Electronic structure and energy level schemes of RE^{3+}:$LaSi_3N_5$ and RE^{2+}:$LaSi_3N_{5-x}O_x$ phosphors (RE= Ce, Pr, Nd, Pm, Sm, Eu) from first principles, *Journal of Luminescence*, 164, pp.131-137. 2015.

[11] H.Wu, C.Yang, X.Zhang, B. Lei, M. Zheng, H. Zhang, Luminescence properties and energy transfer of Ce^{3+}, Tb^{3+} codoped $Ba_2GaB_4O_9Cl$ Phosphor, *Materials Research Bulletin*,vol. 176,2024. DOI.org/10.1016/j.materresbull.2024.112797.

[12] A. Balakrishna, L. Reddy, O.M. Ntwaeaborwa , H.C. Swart, Remarkable influence of alkaline earth ions on the enhancement of fluorescence from Eu^{3+} ion doped in sodium ortho-phosphate phosphors, *Journal of Molecular Structure,* vol. 1203. 2020. DOI.org/10.1016/j.molstruc.2019.127375.

[13] B. Yuan, J. Gou, C. Qi, L. Kong, M. Qu, G. Luana, and X. Zhang Energy transfer for Ce^{3+} / Tb^{3+} / Sm^{3+} induced bright white emission in single-phase $CaLa_4(SiO_4)_3O$:Ce^{3+}, Tb^{3+}, Sm^{3+} phosphors and their application in white-light-emitting diodes, *Royal Society of Chemistry*. vol. 14.pp.7061-7072. 2024.

Understanding the influence of lithium polysulfides on boron oxide for an efficient lithium sulfur battery: A DFT study

C Fwalo[1,2], BD Mahapane[1] and RE Mapasha[1,3]

[1]Department of Physics, University of Pretoria, Pretoria, South Africa
[2] Department of Physics, Copperbelt University, Kitwe, Zambia
[3]National Institute for Theoretical and Computational Sciences, Matieland, South Africa

Email:fwalochewe99@gmail.com

Abstract. Ongoing research on lithium-sulfur battery (LiSB) aims to overcome setbacks caused by shuttle effects by exploring various cathode materials, with a particular focus on 2D materials such as boron oxide (BO) monolayer. The BO is gaining popularity due to its unique properties, such as ballistic electronic transport, mechanical strength, and large surface areas, making it a promising candidate as a cathode additive in LiSB. In this study, density functional theory (DFT) was used to investigate the interaction of lithium polysulfide (Li_2S_x, where x = 1, 2, 4, 6, and 8) and S_8 with BO. The focus was on calculating the adsorption energy, charge density distribution, and metallic characteristics. The results showed Li_2S_x and S_8 strongly adsorbed on BO, with adsorption energy values between -0.34 and -1.64 eV, strong enough to prevent them from decomposing during the electrochemical processes. The charge density distributions support that there are strong electronic interactions in the systems, significant for the enhancement of battery cycle life. Furthermore, it was found that post-adsorption of non-conductive Li_2S and S_8 on BO, the metallic properties remained stable. Overall, results support BO as the best candidate for the cathode electrode in the next-generation LiSB.

1 Introduction

Enhancing energy storage systems to meet the growing demand has led to extensive investigations into battery technologies, particularly metal chalcogenide-based batteries like lithium-sulfur (LiSB) and sodium-sulfur batteries (NaSB) [1, 2], as well as lithium-selenium (LiSeB) and sodium-selenium batteries (NaSeB) [3]. Additionally, lithium and sodium-oxygen batteries have been explored [4, 5]. These systems exhibit significant potential due to their high specific capacities and high-power output [1, 6]. In recent years, LiSB has emerged as a promising candidate due to its low operational costs and environmentally friendly attributes [3]. During the charging process, the sulfur cathode reacts with lithium ions from the anode, yielding products such as Li_2S_x and S_8 [7].

Regardless the advantages over lithium-ion batteries (LIB), LiSB faces numerous issues such as poor adsorption of the formed Li_2S_x and S_8, limited diffusion and poor electronic conduction [7]. These challenges are strongly linked to the materials used for the cathode. To address these challenges, significant research has focused on modifying cathode materials by tailoring their electronic properties and employing diverse fabrication techniques. Due to their unique and novel properties, like structural and electronic properties, Two-dimensional (2D) materials like graphene [8] and silicene [9] are being explored for applications in metal-ion and air batteries [5]. Additionally, metal borides such as the BO monolayer [10, 11] have attracted considerable attention in recent years due to their ballistic

electronic transport, lighter weight, and large surface areas, demonstrating their potential for use as cathode materials. Despite the extensive research on modifying the electronic properties of BO and its synthesis for numerous electronic applications, there is scarce information about its use as a cathode in LiSB. In this study, DFT was used to investigate the effects of Li_2S_x and S_8 on the electronic properties of BO and determined its use as a cathode additive in LiSB. The study focused on the electronic characteristics of BO before and after the adsorption of the species of Li_2S_x and S_8. Systematically, we optimized the pristine BO and subsequently fully optimized the configurations of Li_2S_x and S_8 on it. Further, we calculated the adsorption energies and associated charge density distributions for both the most and least stable discharge products of Li_2S and S_8, respectively. Finally, we assessed the electronic conductivity of pristine BO and after adsorption of the Li_2S_x and S_8.

2 Computational Methods

In this work, for performing all the calculations, the DFT implemented in the quantum ESPRESSO code [12] was used. To treat the exchange and correlation energies, we used the generalized gradient approximation (GGA) [13] implemented in the functional of Perdew-Burke-Ernzerhof (PBE) [14]. The description of the core electrons was achieved using the projector augmented wave (PAW) [15]. Furthermore, a kinetic energy cut-off of 748 eV was used, with Monkhorst- Pack scheme [16], and K-points sampling of 6 × 6 × 1 within the Brillouin zone [17]. To fully optimize the BO structure, all its atomic positions were converged within an energy convergence of 10^{-5} eV and with a force convergence of 10^{-6} eV/Angstrom calculate the adsorption energy $\boldsymbol{E_{(ads)}}$ of Li_2S_x and S_8, on BO, we used the following equation:

$$E_{ads} = E_{(complex)} - E_{(BO)} - E_{(adsorbate)} \quad (1)$$

Here, $E_{(complex)}$ represents the total energy of the BO is adsorbed with the adsorbate, $E_{(BO)}$ is the total energy of the pristine BO, where $E_{(adsorbate)}$ denotes the total energy of the adsorbate. Additionally, for the calculation of the charge density distributions, we used the following equations:

$$\rho = \rho_{(adsorbate+BO)} - \rho_{(BO)} - \rho_{(adsorbate)} \quad (2)$$

Here $\rho_{(adsorbate+BO)}$ represents the total charge density for the complex system (BO adsorbed with Li_2S_x and S_8), $\rho_{(BO)}$ charge is the charge density for the isolated substrate from the complex system, $\rho_{(adsorbate)}$ charge density for the isolated Li_2S_x and S_8 from the complex system.

3 Results and Discussions

3.1 Adsorption of the Li_2S_x and S_8 on the BO

Comprehending materials' ability to adsorb species is very significant in the operation of the battery. This is because during the electrochemical process, discharge products are adsorbed by the electrode and are the ones that determine the specific capacity and energy density of the system.



Figure 1: Optimized molecules of Li_2S_x and S_8 in free space: where the black and green balls denote Li and S atoms, respectively.

The stronger (higher) the adsorption energy, the lower the diffusion, the more efficient the battery becomes. Therefore, we introduced the molecules as discharge products on the BO. The

discharge products considered on the BO included the optimized molecules of Li_2S_x and S_8 as shown in Figure 1.

System	Adsorption energy (eV)
Li_2S@BO	-1.64
Li_2S_2@BO	-1.02
Li_2S_4@BO	-1.03
Li_2S_6@BO	-0.77
Li_2S_8@BO	-0.58
S_8@BO	-0.34

Table 1: Calculated adsorption energies (eV) or the configurations of the Li_2S_x and S_8 on BO.

The molecules were tested at different adsorption sites on the BO based on its symmetry (Figure 2a), where it was determined that site H was the most stable; all the molecules diffused towards it. This approach has also been used in the previous study, and a similar trend was observed where the H site was observed to be the most energetic and stable site for the Li_2S_x and S_8 as the adsorbates [18]. Subsequently, we optimized all the configurations at the identified site and calculated their corresponding adsorption energies as presented in Table 1. Notably, with an increase in the S atoms added to the adsorbates, depicting what happens during the electrochemical process, a decrease in the adsorption energy was observed, attributed to an increase in the repulsion between the S atoms. However, the adsorption energy did not decrease drastically to zero.

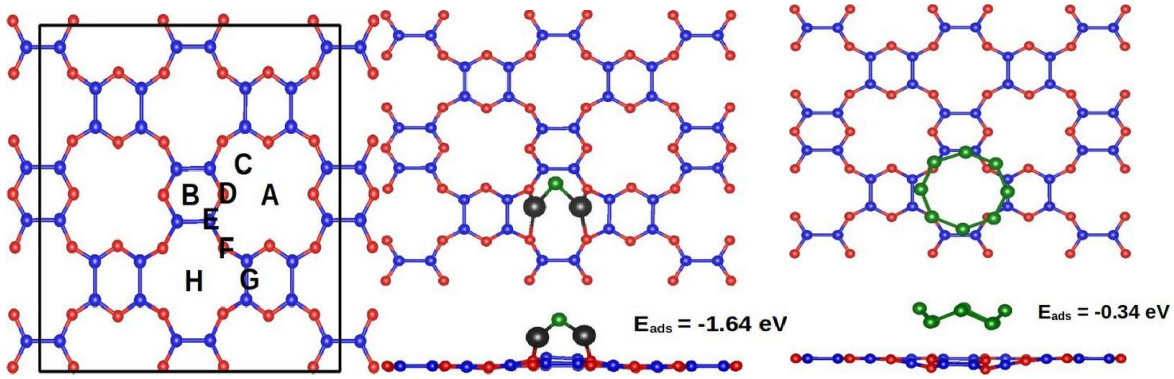

Figure 2: Optimized Configurations of the Li_2S_x and S_8 on BO: (a) Possible adsorption sites and (b) Li_2S on BO, and (c) S_8 on BO. Where the black, blue, red, and green balls denote lithium (Li), carbon (C), oxygen (O), and sulfur (S) atoms, respectively.

Ultimately, the calculated adsorption energies for Li_2S_x and S_8 indicate that these species are strongly adsorbed on the BO surface. This strong adsorption suggests that they can effectively prevent dissociation into the electrolyte during the discharging process. Consequently, this finding highlights the potential of BO to mitigate the ongoing shuttle effects in LiSB. As the discharge products are adsorbed on the surface of BO, electronic interactions within the systems are expected to occur. To investigate this phenomenon, we calculated the charge density distributions, as illustrated in Figure 3. Firstly, we investigated the Li2S on BO (Figure 3a and observed that charge accumulated (yellow) towards the BO surface from the Li atoms, suggesting electronic interactions. And for the system of

S8 on BO (Figure 3b), a different trend was observed with charge density accumulating towards the adsorbate, supported by the low adsorption energy obtained for S_8.

3.2 Charge density distributions of the Li_2S and S_8 on BO

As the discharge products are adsorbed onto the surfaces of BO, electronic interactions within the systems are expected to occur. To investigate this, we calculated the charge density distributions, as illustrated in Figure 3. Firstly, we probed for the Li_2S on BO (Figure 3a), where it was observed that charge accumulated (yellow) towards the BO from the Li atoms, suggesting electronic interactions. And for the S_8 on BO (Figure 3b), a different trend was observed with charge accumulation towards the adsorbate, supported by the low adsorption energy obtained for S_8.

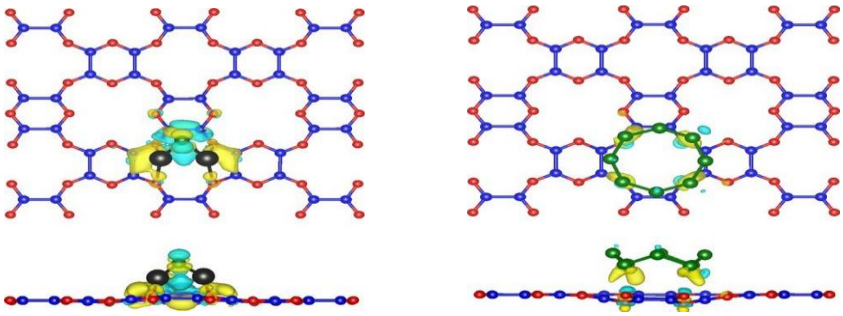

Figure 3: Charge density distributions of the most stable Li_2S on BO, and (b) least stable S_8 on BO. Where charge accumulation and depletion are denoted by yellow and cyan colors, respectively.

Despite the charge being transferred towards the adsorbate, the BO is able to anchor the molecule; this is very significant as it is being prevented from dissociating into the electrolyte during the discharging process.

3.3 Conductivity properties of the BO adsorbed with Li_2S *and* S_8

Understanding materials' electronic conductivity is very significant for their use as cathode additives, as it reveals their capabilities to enhance the charging and discharging process in the batteries. Therefore, to investigate BO's electronic conductivity, we systematically calculated and analyzed the band structures before and after adsorption of the most and least stable adsorbates, as illustrated in Figure 4a.

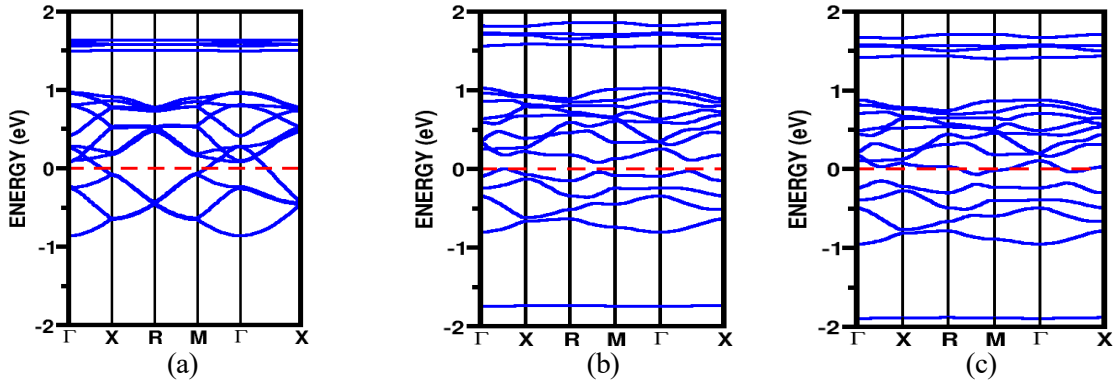

Figure 4: Electronic band structures of the pristine BO and after it's adsorbed with the most and least stable adsorbates: (a) Pristine BO, (b) most stable Li_2S on BO, and (c) least stable S_8 on BO.

The findings indicated that pristine BO is metallic, characterized by the overlap of the valence and conduction bands, which facilitates the free flow of electrons, an essential feature for a viable electrode. Furthermore, we examined the alterations in the electronic structure following the adsorption of non-conductive Li_2S and S_8, as depicted in Figures 4b and 4c, respectively. The results revealed that the adsorption of Li_2S impacted the electronic band structure of BO, leading to the formation of a band gap of 0.061 eV. Despite this gap, it was evident that the molecule was strongly adsorbed, as indicated in Table 1. The small gap created suggests that electrons can easily transition between the valence and conduction bands with minimal energy input.

In the case of S_8, it was observed that the valence and conduction bands still overlap despite the low adsorption energy value reported in Table 1. This observation is significant as it highlights the influence of BO on the adsorbate and promotes enhanced ion transport within the system. Consequently, the use of BO as a cathode could lead to an improved cycle life for LiSB applications.

4 Conclusion

In conclusion, we used DFT to investigate the influence of BO on the adsorbed Li_2S_x and S_8, assessing its potential application in LiSB. The findings revealed that Li_2S_x and S_8 are strongly adsorbed on BO, with adsorption energy values from -0.34 to -1.64 eV, which is sufficient to prevent their decomposition during electrochemical processes. The charge density distributions indicate strong electronic interactions within the systems, which are crucial for enhancing battery cycle life. Additionally, it was determined that BO exhibits metallic properties, characterized by overlapping bands, making it a significant candidate for use as an electrode. Interestingly, even after the adsorption of Li_2S and S_8, which are non-conductive, the electronic conductivity remained stable. Overall, results support BO as an electrode material for next-generation LiSB. This study focused entirely on the theoretical findings. Therefore, we recommend future studies to consider an experimental approach and validate with our theoretically calculated values, for the practical applications of the BO as a cathode additive in the LiSB.

Acknowledgements

The University of Pretoria, Department of Innovation and Research, is gratefully acknowledged for its financial support. Additionally, the Center for High-Performance Computing (CHPC) in Cape Town is recognized for providing exceptional computational resources. R.E.M. acknowledges the National Institute for Theoretical and Computational Sciences for its funding.

References

[1] L. Zhang, P. Liang, H.-b. Shu, X.-l. Man, F. Li, J. Huang, Q.-m. Dong, and D.-l. Chao, "Borophene as efficient sulfur hosts for lithium–sulfur batteries: suppressing shuttle effect and improving conductivity," *The Journal of Physical Chemistry C*, vol. 121, no. 29, pp. 15549–15555, 2017.

[2] S. Grixti, S. Mukherjee, and C. V. Singh, "Two-dimensional boron as an impressive lithium-sulphur battery cathode material," *Energy Storage Materials*, vol. 13, pp. 80–87, 2018.

[3] S. S. Deshpande, M. D. Deshpande, K. Alhameedi, R. Ahuja, and T. Hussain, "Carbon nitride monolayers as efficient immobilizers toward lithium selenides: potential applications in lithium–selenium batteries," *ACS Applied Energy Materials*, vol. 4, no. 4, pp. 3891–3904, 2021.

[4] C. Fwalo, A. Kochaev, and R. Mapasha, "Investigating electrocatalytic properties of β12-borophene as a cathode material for an efficient lithium-oxygen battery: a first-principles study," *Applied Nanoscience*, pp. 1–16, 2024.

[5] C. Xia, C. Kwok, and L. Nazar, "A high-energy-density lithium-oxygen battery based on a reversible four-electron conversion to lithium oxide," *Science*, vol. 361, no. 6404, pp. 777–781, 2018.

[6] Q. Li, H. Liu, Z. Yao, J. Cheng, T. Li, Y. Li, C. Wolverton, J. Wu, and V. P. Dravid, "Electrochemistry of selenium with sodium and lithium: kinetics and reaction mechanism," *ACS Nano*, vol. 10, no. 9, pp. 8788–8795, 2016.
[7] F. Chen, C. Gao, H. Li, J. Hou, and D. Jiang, "FeS monolayer as a potential anchoring material for lithium-sulfur batteries: A theoretical study," *Surface Science*, vol. 707, p. 121818, 2021.
[8] A. H. Castro Neto, F. Guinea, N. M. Peres, K. S. Novoselov, and A. K. Geim, "The electronic properties of graphene," *Reviews of Modern Physics*, vol. 81, no. 1, pp. 109–162, 2009.
[9] D. Jose and A. Datta, "Structures and chemical properties of silicene: unlike graphene," *Accounts of Chemical Research*, vol. 47, no. 2, pp. 593–602, 2014.
[10] F. Claeyssens, N. L. Allan, N. C. Norman, C. A. Russell, "Design of three-dimensional solid-state boron oxide networks: Ab initio calculations using density functional theory," *Physical Review B*, vol. 82, no. 9, p. 094119, 2010.
[11] J. Zhang, X. Yan, Z. Cheng, Y. Han, Y. Zhang, Y. Dong, "Applications, prospects and challenges of metal borides in lithium sulfur batteries," *Journal of Colloid and Interface Science*, vol. 657, pp. 511–528, 2024.
[12] P. Giannozzi, O. Andreussi, T. Brumme, O. Bunau, M. B. Nardelli, M. Calandra, R. Car, C. Cavazzoni, D. Ceresoli, M. Cococcioni, et al., "Advanced capabilities for materials modelling with quantum espresso," *Journal of Physics: Condensed Matter*, vol. 29, no. 46, p. 465901, 2017.
[13] S. Grimme, "Semiempirical GGA-type density functional constructed with a long-range dispersion correction," *Journal of Computational Chemistry*, vol. 27, no. 15, pp. 1787–1799, 2006.
[14] J. P. Perdew, K. Burke, and M. Ernzerhof, "Perdew, Burke, and Ernzerhof reply," *Physical Review Letters*, vol. 80, no. 4, p. 891, 1998.
[15] P. E. Blöchl, "Projector augmented-wave method," *Physical Review B*, vol. 50, no. 24, p. 17953, 1994.
[16] H. J. Monkhorst and J. D. Pack, "Special points for Brillouin-zone integrations," *Physical Review B*, vol. 13, no. 12, p. 5188, 1976.
[17] D. J. Chadi, "Special points for Brillouin-zone integrations," *Physical Review B*, vol. 16, no. 4, p. 1746, 1977.
[18] R. Mapasha, C. Fwalo, E. Igumbor, S. Hasan, T. Hussain, "First-principles study on the role of Ti, V, and Sc catalysts in enhancing the catalytic effects of boron oxide monolayer for efficient lithium-selenium batteries," *FlatChem*, p. 100918, 2025.

$ZnMn_2O_4$-Based Anode Materials for Advanced Supercapacitor Batteries: A Study on the Impact of Co, Ni, and Cu Partial Substitution on Electrochemical Performance

S Bixa, MLA Letswalo, and B Sondezi

Department of Physics, University of Johannesburg, 55 Beit St, Doornfontein, Johannesburg, 2028, South Africa.

E-mail: letswalom@uj.ac.za and bmsondezi@uj.ac.za

Abstract.

A series of $ZnMn_2O_4$ samples partially doped with Co, Ni, and Cu 1 wt% were synthesized via the combustion method and evaluated for improved electrochemical performance. The synthesized powders were thoroughly characterized using X-ray Diffraction (XRD), Field–Emission Scanning Electron Spectroscopy (FE-SEM), Energy Dispersive X-ray Spectroscopy (EDS), and electrochemical techniques to evaluate their performance as anode materials for supercapacitor batteries. The XRD results revealed a tetragonal structure and the incorporation of Co, Ni, and Cu metals did not alter the crystal structure of $ZnMn_2O_4$. From FE-SEM data, the pure sample showed a diamond-crystal-like shape in morphology and the doped samples' morphology modified the particle shapes and sizes. The optimum particle size of the doped $ZnMn_2O_4$ was found to be in the range of 36.33 - 41.29 nm. EDS showing all the element compounds of the material. Notably, the Co-doped $ZnMn_2O_4$ exhibited superior performance in battery cycling stability test (GCD), demonstrating exceptional discharge capacity, cycling stability, and rate capability compared to other metal oxides with 686.88 Fg^{-1} specific capacitance. Furthermore, the Co-doped $ZnMn_2O_4$ showed great performance in (CV) at a low scan rate of $5mVs^{-1}$ with 48.85 Fg^{-1} specific capacitance, and it also displayed a pseudocapacitance behavior. From EIS, Cu-doped $ZnMn_2O_4$ exhibits the lowest resistance due to a smaller semicircular arc. Furthermore, its steeper vertical line indicates that it has good potential for use as an anode material in supercapacitor applications.

1 Introduction

The burning of fossil fuels releases gas emissions, which have serious consequences and lead to ecological concerns and global warming. A carbon-free society built on sustainable and renewable energy resources could solve these problems. The need to meet environmental and energy demands has prompted humanity to re-evaluate its efforts in energy revitalization. The development of larger and better-capacity energy storage systems (ESSs) has made this need possible. The energy storage sources, like supercapacitors and lithium-ion batteries, might be considered beneficial in such endeavours [1]

$ZnMn_2O_4$ (ZMO), a spinel-structured material with a general formula of AB_2O_4, exhibits unique properties that work well in energy storage batteries. ZMO, a spinel-structured metal oxide, has been highly researched for its applications in supercapacitor batteries due to its environmental friendliness, effectiveness, and high electrical conductivity. The structural stability during charge and discharge for these materials processes is vital for sustaining the lifespan of these energy storage device systems and performance [2]. Xueling Zhu et al. [3] synthesized Co-doped $ZnMn_2O_4$ hollow nanospheres, using the hydrothermal method at

lower concentrations. They observed that incorporating Co into $ZnMn_2O_4$ material could enhance its electrochemical behavior, thereby revealing the great value of specific capacitance, around 296 Fg^{-1} at 0.25 Ag^{-1} [3]. Hasan M et al. [4] used the sol-gel method to study Ni-doped $ZnMn_2O_4$ for its porous architectural structure at varied concentrations. They found the material to possess exceptional capacitive behavior, with a value of 8.49 Fg^{-1}, thereby proving the material to be a supercapacitor. Salma Aman et al. [5] used the hydrothermal method to study Cu-substituted $ZnMn_2O_4$/rGO spinel nanosized composite as an electrode for the Oxygen evaluation reaction (OER). Their results confirmed enhanced electrocatalytic efficiency for a material of a hybrid nature [5].

The study investigates the ZMO and doped with 1 wt% concentrations of Cu, Co & Ni samples synthesized by using the combustion method, cycle life, and power density characteristics. The reason for choosing 1 wt% is to compare the performance of the dopants while maintaining the structural integrity. Electrochemical properties such as cyclic voltammetry (CV), galvanostatic charge and discharge (GCD), and electrochemical impedance spectroscopy (EIS) will be discussed after characterizing the samples using X-ray diffraction (XRD), scanning electron microscopy (SEM), and energy dispersive X-ray spectroscopy (EDS).

2 Experimental details

2.1 Synthesis of $ZnMn_2O_4$

ZMO doped Co, Ni, and Cu (x = 0 and 1 wt%) were synthesized through the combustion method. The starting materials in this study are $Zn(NO_3)_2.6H_2O$ 99%, $MnCl_2.4H_2O$ 99%, (CH_4N_2O) 99%, $Cu(No_3)_2.3H_2O$ 99% which were obtained from India SRL laboratory. A volume of 40 ml of de-ionized (DI) water was poured into a 250 ml beaker and stirred for about 10 minutes, and then 3.868 g of zinc nitrate was added to the beaker until it was dissolved. A 5.148 g mass of manganese chloride was then added to the solution and stirred for about 10 minutes until it was dissolved and the color of the solution changed to pink (solution-A). Further 15.626 g of urea was dissolved in 40 ml of DI water the solution and stirred until it dissolved (solution-B). Then, slowly add drop by drop solution-B to solution-A and after that, a few drops of ammonia solution were added to the solution until a pH of 9 was reached. The solution was further stirred for 4 hours and finally formed a brownish color. The solution was taken to the furnace and heated at 500 ˚C for 1 hour. After cooling, it was ground, then annealed at 550 ˚C for 2 hours and 30 minutes. The doped samples were prepared by partially substituting $Zn(NO_3)_2.6H_2O$ with calculated amounts of Co, Ni and Cu dopants, corresponding to 0.0376, 0.1134, and 0.190g, respectively.

The electrochemical performance of the supercapacitors was investigated by using a Biologic EC-lab V11.50 SP 300 potentiostat with 3 electrodes, working (active material), Counter (Platinum), and reference (Ag/Agcl) electrode in 2 M KOH electrolytes for CV, GCD, and EIS. The three-electrode system was constructed with the ratio of 80 wt%:10 wt%: 10 wt%. First, the synthesized powder ZMO sample (80 wt%), with carbon black (10 wt%), and a binder, polyvinylidene fluoride binder (PVDF, 10 wt%) where solvent N-methyl-2-pyrrolidone (NMP) was used to form a solution. The resulting solution was coated onto a nickel foam substrate using a brush. After that, the sample was dried in a vacuum oven at 80 ˚C for half a day, and the composite-coated substrate was cut into pieces of ~10 mm diameter. The mass of active material that was loaded was about 2 mg. The X-ray diffraction was studied using a Bruker D8 Advanced diffractometer. The apparatus was set with a copper X-ray tube (0.154 nm wavelength) that ran at 40 mA filament current and 40 KV supply voltage. Additionally, the K Cu and Bremsstrahlung radiation were absorbed by a monochromatic X-ray using a nickel filter. The XRD was prepared by first cleaning the sample holder with ethanol, and then a small amount of powder was placed in the sample holder and placed in the X-ray diffraction in opposite directions. The 2θ scans were performed in the range of 5º-80º with a step size of 0.012 per step. SEM and EDS were performed using a JEOL JSM-7800F field and Oxford Aztec software for all the micrographs. A magnification of 10.000, an accelerating voltage of 5kV, and a WD of 10 mm were used to obtain all the results. The sample holder specimen stub was cleaned with ethanol, and carbon tape was placed on top of the specimen stub. A small amount of ~ 1 mg powder was spread on top of the carbon tape, then it went to the spin coating with a carbon rod for about 4 spins to prevent charging.

3. Results and Discussion

3.1 X-ray diffraction analysis

Figure 1(a) presents all the XRD characterized samples in the2θ range of 10-80º. In particular, pure ZMO spinel, and Cu, Ni, & Co with concentration 1 wt% doped ZMO samples are shown in that order. The XRD pattern reveal major peaks corresponding with the planes (101), (112), (200), (103), (211), (202), (004), (220), (204), (105), (312), (303), (321), (224) along with several minor diffraction peaks [6]. The XRD pattern

corresponds to that of a tetragonal spinel structure of ZMO, with unit cell lattice parameters of $a = b$ 5.71937Å, c = 9.28138Å, and V = 303.621Å^3 and a space group of 141/amd. This is consistent with the standard references JCPDS file no:01-077-0470 [6].

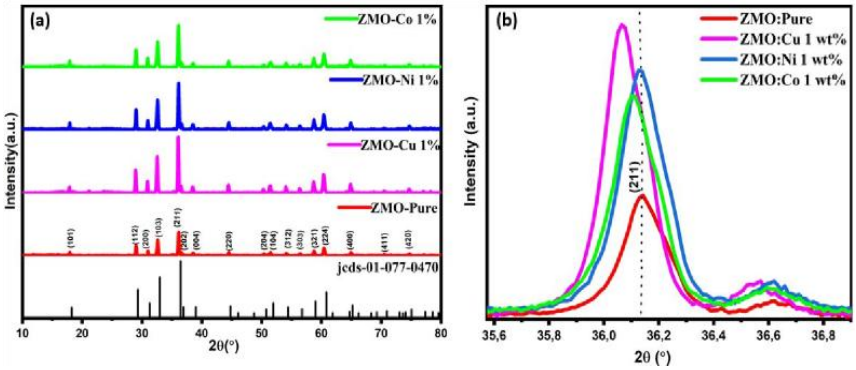

Figure 1: (a) XRD patterns of pure $ZnMn_2O_4$ and Co, Ni, and Cu 1 wt% doped $ZnMn_2O_4$, (b) enlarged diffraction pattern peaks of (211) at various concentrations.

Figure 1(b) shows an enlarged diffraction pattern of XRD in the selected 2θ range of 35.6˚ to 37.02˚ corresponding to the (211) plane. As the concentration of Cu 1 wt% is being introduced to the material (ZMO), the crystal lattice contracts, resulting in an increase in the intensity of the diffraction peaks. Differences in the ionic radii of the dopants Co, Ni and Cu, having (0.0745 nm), (0.069 nm) and (0.074 nm) respectively, cause a shift. while Ni increased in intensity. The improved intensity may be attributed to enhanced crystallinity in the particle arrangements, a shift to the left would suggest less clustering and lower strain, while a change to the right might suggest more clustering and higher strain [7].

3.2 Surface morphology and elemental composition

The morphology of Co, Ni, and Cu doped ZMO material was investigated using scanning electron microscopy (SEM), and Energy-dispersive X-ray spectroscopy (EDS) was used for the element composition. Figure 2(a-d) illustrates the SEM micrographs and EDS characterization of the material [8]. Figure 2(a) shows the diamond crystal-like shape with irregular nanoparticles exhibiting aggregation with a size of 39. 78 nm. The addition of 1 wt% onto host ZMO revealed nanoparticle catalytic behavior as illustrated in Figure 2 (b). Such nucleated ZMO: Cu 1 wt% with 40.78 nm possesses larger nanoparticle sizes, which could be attributed to the Cu ionic radius of 0.074 nm. Figure 2(c) illustrates ZMO-Ni; the number of catalyst-type nanoparticles increases, suggesting a potential enhancement in the material's electrochemical properties. The nanoparticles exhibit a smaller size of 41.29 nm, which can be attributed to the lower ionic radius of Ni, 0.069 nm. When Co is incorporated into the host structure with a size of 36.33 nm, as illustrated in Figure 2(d), the number of catalyst-like nanoparticles further increases, and they adopt a distinct diamond-like morphology.

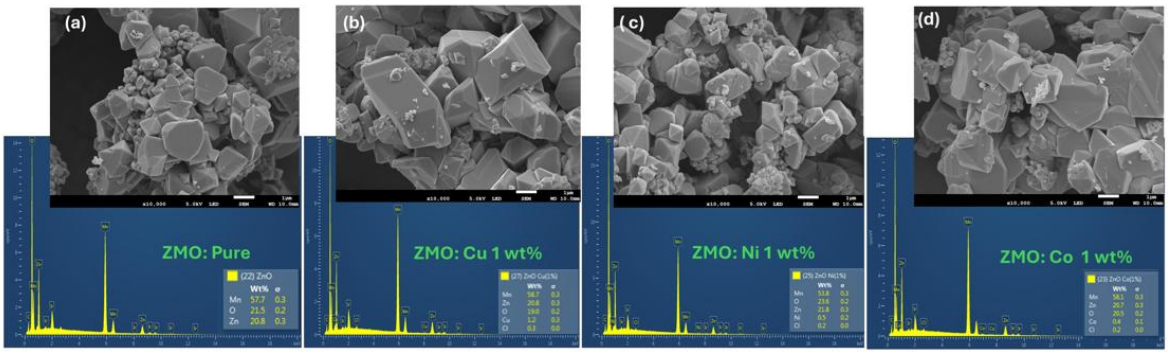

Figure 2: SEM with EDS image of Co, Ni, and Cu-doped $ZnMn_2O_4$ nanoparticles (a) ZMO, (b) ZMO: Cu 1 wt%, (c) ZMO: Ni 1 wt%, and (d) ZMO: Co 1 wt%

Additional element Cl can be detected in Figure 2(b), (c) and (d) EDS spectra of $ZnMn_2O_4$: Cu, Ni, and Co, such that Cl ions originate from the manganese chloride synthesis reagent. The Ir element was used as a

coating on the non-conducting material to ensure the accuracy of the obtained results [8-9].

3.3 Electrochemical performance

3.3.1 Cyclic voltammetry (CV)

The electrochemical performance of the prepared materials was measured in CV under a potential window range of 0-0.6 V at a scan rate of 5 to 100 mVs^{-1} in the presence of 2 M potassium hydroxide (KOH) electrolyte solution in a three-electrode system [4]. All the CV curves of pure ZMO, 1 wt% Cu, Ni, and Co doped ZMO exhibit pseudo-capacitive behavior, observed with both anodic and cathodic peaks presented in Figure 3(a-d), respectively. The recognition of faradic current signifies electric transport in metallic oxide materials [2-10]. Figure 3(a) shows the pure ZMO sample with an anodic (oxidation) peak at 0.45V, which is due to the Mn^{2+} to Mn^{3+} transition at a low scan rate of 5 mVs^{-1}. The cathodic reduction peaks present at 0.41and 0.35V are due to the Mn^{3+} to Mn^{2+} and Zn^{2+} to Zn^{0} transitions, respectively. Figure 3(b) illustrates Cu-doped ZMO with 1 wt%, showing an oxidation peak around 0.45V due to Mn^{2+} to Mn^{3+} transition and enhanced by the presence of Cu^{2+} to Cu^{+} transitions. The two peaks in the reduction peak, the first peak being 0.40V, are attributed to the reduction of Mn^{2+} to Mn^{3+}. The second peak, which is 0.33V, is influenced by the presence of the Cu^{2+} to Cu^{+} transition [11]. Figure 3(c) shows the Ni-doped ZMO with 1 wt%, illustrating an oxidation peak at 0.42V, which is due to the Mn^{3+} to Mn^{4+} transition in the presence of Ni^{2+} to Ni^{+} transitions [4]. A reduction peak is noticed at 0.50V as a result of Mn^{4+} to Mn^{3+} transition at 5 mVs^{-1} scan rate and with a slight move to higher potentials as the scan rate rises to 100 mVs^{-1} in all CV curves. Figure 3(d) shows the Co-doped ZMO with a concentration of 1 wt%, which exhibits an anodic peak at 0.42V due to the Mn^{2+} to Mn^{3+} transition. Furthermore, the presence of Co^{2+} to Co^{+} increases the potential to 0.46V. The cathodic peak observed at 0.34V is due to the Mn^{3+} to Mn^{2+} transition at a lower scan rate of 5 mVs^{-1} with a shift to higher potentials as the scan rate increases to 100 mVs^{-1} at 0.28V in all CV [7].

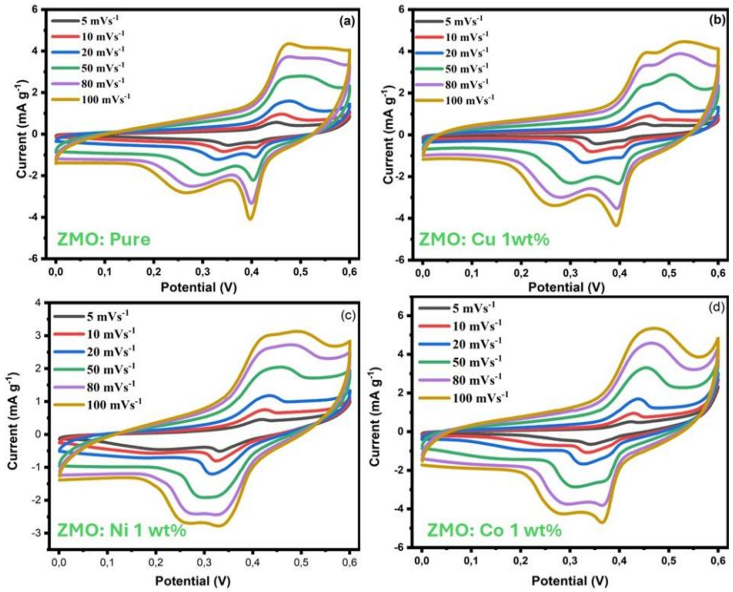

Figure 3: Shows CV curves of Co, Ni, and Cu $ZnMn_2O_4$ concentrations of (x = 0, 1 wt%) at varying scan rates.

The calculations for specific capacitance for the CV curves were computed using the following formula [11]

$$\text{Specific capacitance}(C_s) = \frac{\int I\,dv}{s \times m \times \Delta V} \qquad (1)$$

where *I, S, V*, and *m* represent the current rate in (mAs^{-1}), scan rate (mVs^{-1}), potential window (V), and the active mass (mg), respectively.

The specific capacitance was calculated at varying scan rates of 5, 10, 20, 50, 80, and 100 mVs^{-1} for all samples. The calculated values are for Figure 3(a): 25.45, 18.97, 15.02, 10.80, 9.16, and 8.53 Fg^{-1}, respectively; In Figure 3(b), the specific capacitance calculations are 24.65, 17.78, 14.44, 11.37, 10.03, and 9.49 Fg^{-1}, respectively Figure 3(c): 31.37, 20.99, 14.70, 9.59, 7.89, and 7.26 Fg^{-1}, respectively. Additionally, Figure 3(d) shows the specific capacitance of ZMO: Co 1 wt% to be: 45.85, 29.47, 20.57, 14.03, 12.01, and 11.29 Fg^{-1}.

3.3.2 *Galvanostatic charge-discharge (GCD)*

The electrochemical performance for (GCD) is performed under a potential window of 0-0.6 V at various current densities of 3 to 5 Ag^{-1}. The three-electrode system was conducted in 2 M of potassium hydroxide (KOH) electrolyte, as shown in Figure 4(a-d). GCD curves show a symmetrical pattern for all current densities, indicating high coulombic efficiency. Moreover, the nonlinear charge/discharge profile further confirms a pseudocapacitive behavior of Co, Ni, and Cu-doped ZMO materials [7]. Figure 4(a) shows the GCD behavior of ZMO at various current densities, revealing that the charge and discharge processes take longer at lower current densities, which indicates that more charge is stored, suggesting that the material has a higher capacity at a lower current density. The discharge time also took longer, indicating that the material can release charge more slowly, which is favorable for battery-type applications requiring steady energy [10]. Figure 4(b) shows Cu-doped ZMO material with 1 wt% concentration, which exhibits an increase in charge and discharge time when compared to the ZMO material. Figure 4(c) shows the Ni-doped material with a decrease in charge-discharge due to the potential window, which reduces conductivity. Figure 4(d) shows greater potential than pure ZMO and other doped ZMO materials [12].

The charge /discharge specific capacitance was computed using the following formula [9].

$$\text{Specific capacitance}(C_s) = \frac{\int I dt}{m\Delta V} \qquad (2)$$

where I, dt, m, ΔV represents the current rate, change in discharge time, material mass, and potential window for the current densities of 3, 4, and 5 Ag^{-1}.

The calculated specific capacitances for the ZMO sample are in Figure 5(a) 60.78, 48.03, 35.93 Fg^{-1}, (b)75.81, 63,89, 52.90 Fg^{-1}, (c)41.87, (Ni)31.58, 23.55 Fg^{-1}, and (d)686.88, 83.40, 75.15 Fg^{-1}

3.3.3 *Electrochemical impedance spectroscopy (EIS)*

Figure 4(e) shows the (EIS) spectrum, which was done to assess the electrochemical behavior of pure ZMO (x = 0, 1 wt%) and doped ZMO materials, measured within a frequency range of 10MHz – 100KHz in a potential window of 0-0.6V with an amplitude of 10 mV[12]. The Nyquist plots for the Cu, Ni, and Co concentrations were fitted using the equivalent electronic circuit as displayed in the Figure. The circuit is made up of R_1, which is an internal resistance (Rs), including the contact resistance of the current collector interfaces as well as the intrinsic resistance of the electrode and electrolyte. R_2 represents the charge transfer resistance (R_{ct}) observed in the low-frequency region, W_2 represents the Warburg resistance (Z_w), which is observed in the low-frequency zone, which is associated with electrode diffusion [11-12]. Cu-doped ZMO shows a steeper vertical line at low frequency, which exhibits better capacitive behaviour. The lowest resistance when compared to others is due to the smallest semicircle.

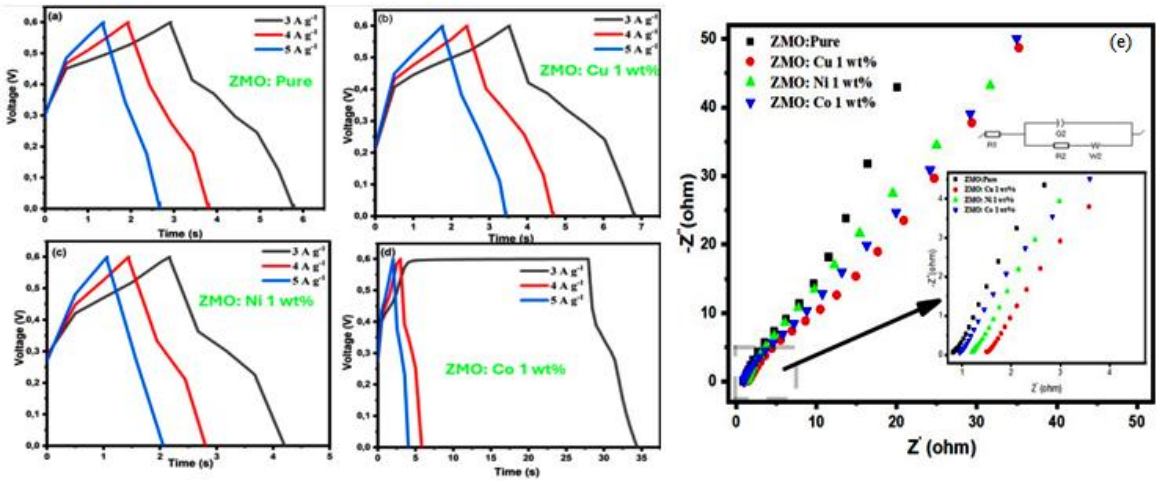

Figure 4: (a-d) Galvanostatic charge-discharge and (e) Nyquist plots of Co, Ni, and Cu-doped $ZnMn_2O_4$ at varying current densities.

4. Conclusion

The Co, Ni, and Cu-doped ZMO at concentrations of 1 wt% were successfully synthesized. XRD analysis shows a well-indexed single phase, with no impurities. Scanning Electron Microscopy (SEM) shows a similar morphology with nanoparticles that might enhance the conductivity of the material as concentrations are added. The electrochemical performance revealed that incorporating Co, Ni, and Cu into ZMO shows good stability, making it a great material for battery applications. C-V showing a common pseudo-capacitor behavior with Co 1 wt% having a greater value of 45.85 Fg^{-1} specific capacitance at a low scan rate of 5 mVs^{-1}. The highest specific capacitance obtained for the ZMO: Co 1 wt% material was of the value, of 686.88 Fg^{-1} in GCD at 3 Ag^{-1} current density. This suggests that Co-doped ZMO materials hold great potential for supercapacitor battery applications.

References

[1]. P. Deva, S. Ravi, and C. Manoharan, "Synthesis of mesoporous structured $ZnMn_2O_4$ nanoparticles as electrode for supercapacitor application," Emergent Materials, Jun. 2024, doi: 10.1007/s42247-024-00759-1.

[2]. P. Kommu, G. P. Singh, Ch. S. Chakra, S. Jana, V. Kumar, and A. S. Bhattacharyya, "Preparation of $ZnMn_2O_4$ and $ZnMn_2O_4$/graphene nano composites by combustion synthesis for their electrochemical properties," Materials Science and Engineering B, vol. 261, p. 114647, Aug. 2020, doi: 10.1016/j.mseb.2020.114647.

[3]. X. Zhu, Z. Wei, L. Ma, J. Liang, and X. Zhang, "Synthesis and electrochemical properties of Co-doped $ZnMn_2O_4$ hollow nanospheres," Bulletin of Materials Science, vol. 43, no. 1, Dec. 2019, doi: 10.1007/s12034-019-1970-6.

[4]. M. Hasan, S. Zawar, G. M. Mustafa, A. Ghaffar, A. Razaq, and S. Atiq, "Porous Architecture of Ni substituted $ZnMn_2O_4$ nanospheres as an electrode material for supercapacitor applications," Physica B Condensed Matter, vol. 633, p. 413767, Feb. 2022, doi: 10.1016/j.physb.2022.413767.

[5]. S. Aman, N. Ahmad, S. Manzoor, M.M. Alanazi, S.A. Abdelmohsen, R.Y. Khosa, A.G. Al-Sehemi, R. Hua, H.A. Alzahrani, and A.H. Chughtai, "Effect of Copper substitution on the electrocatalytic activity of $ZnMn_2O_4$ spinel embedded on reduced graphene oxide nanosheet for the oxygen evolution process," Catalysis Surveys From Asia, vol. 27, no. 2, pp. 165–179, Feb. 2023, doi: 10.1007/s10563-023-09389-9.

[6]. A. Sobhani and S. Alinavaz, "$ZnMn_2O_4$ nanostructures: Synthesis via two different chemical methods, characterization, and photocatalytic applications for the degradation of new dyes," Heliyon, vol. 9, no. 11, p. e21979, Nov. 2023, doi: 10.1016/j.heliyon.2023.e21979.

[7]. Y. Tao, Z. Li, L. Tang, X. Pu, T. Cao, D. Cheng, Q. Xu, H. Liu, Y. Wang, and Y. Xia, "Nickel and cobalt Co-substituted spinel $ZnMn_2O_4$@N-rGO for increased capacity and stability as a cathode material for rechargeable aqueous zinc-ion battery," Electrochimica Acta, vol. 331, p. 135296, Nov. 2019, doi: 10.1016/j.electacta.2019.135296.

[8]. Y. Zhao, K. S. Kumar, M. A. Ghanem, N. Roy, J. S. Kim, and S. W. Joo, "In-Situ synthesis of synergistic $ZnMn_2O_4$/MnOOH nanocomposite as a cutting-edge pseudocapacitive electrode material for All-Solid-State asymmetric supercapacitors," Ceramics International, Sep. 2024, doi: 10.1016/j.ceramint.2024.09.326.

[9]. A. Samage, P. Kuppe, M. Halakarni, B.K. Ganesan, S.V. Kamath, H. Yoon, and N.S. Kotrappanavar, "Room temperature and rapid synthesis of $ZnMn_2O_4$ nanostructured spinel using deep eutectic solvent for high energy asymmetric supercapacitors," Journal of Energy Storage, vol. 97, p. 112934, Jul. 2024, doi: 10.1016/j.est.2024.112934.

[10]. J. K. Ramesh, S. Rostami, J. Rajesh, R.M.B. Princess, R. Govindaraju, J. Kim, R. Adelung, P. Rajkumar, and M. Abdollahifar, "$ZnMn_2O_4$ Applications in Batteries and Supercapacitors: A Comprehensive Review," Journal of Materials Chemistry A, Jan. 2025, doi: 10.1039/d5ta00815h.

[11]. J. Wang, L. Shi, X. Wang, and L. Yang, "Controllable preparation of flowered Cu-doped $Zn_{1-x}Cu_xMn2O4$ spinel and its application in electrode materials for supercapacitors," Journal of Materials Science Materials in Electronics, vol. 36, no. 15, May 2025, doi: 10.1007/s10854-025-14885-x.

[12]. S. Saadi-Motaallegh, M. Javanbakht, H. Omidvar, and S. Habibzadeh, "A Novel Ni-doped $ZnMn_2O_4$/Mn_2O_3 nanocomposite synthesized by pulsed potential as superior zinc ion battery cathode material," Journal of Alloys and Compounds, vol. 963, p. 171119, Jun. 2023, doi: 10.1016/j.jallcom.2023.171119.

Structural and optical properties of rare-earth doped magnesium ferrite

NO Ngubelanga[1], SA Ogundipe[1], D Hile[1], S Masikane[2], CL Ndlangamandla[1] and PS Mkwae[1]

[1]Department of Physics, University of Zululand, Private Bag X1001, KwaDlangezwa 3886, South Africa.
[2]Department of Chemistry, University of Zululand, Private Bag X1001, KwaDlangezwa 3886, South Africa.

E-mail: 201815897@stu.unizulu.ac.za

Abstract. Nanoparticles of magnesium ferrite ($MgFe_2O_4$) and rare earth-doped variants ($Mg(RE)_{0.2}Fe_{1.8}O_4$, RE = La and Sm) were synthesized via a hydrothermal method and annealed at 500℃, 700℃ and 900℃. Structural and optical characterization were performed using XRD, UV-Vis, HRTEM, and PL spectroscopy. XRD confirmed the formation of a cubic spinel structure, with sharp preferred diffraction peaks at 900℃ indicating improved crystallinity. Doping with La and Sm reduced crystallinity, crystallite size and bandgap energy, suggesting enhanced structural refinement and electronic properties. HRTEM images supported these improvements, showing clearer lattice fringes at higher annealing temperatures. Photoluminescence results revealed a shift from dual-wavelength emission (495 and 503) in pure $MgFe_2O_4$ to a single suppressed peak at 500 nm (2.48 eV) upon doping. These modifications position RE-doped $MgFe_2O_4$ as a strong candidate for advanced gas sensing applications, where tunable optical and structural features are crucial.

1 Introduction

Spinel ferrites, especially at the nanoscale, are widely used in sensors, catalysis, medicine, and many other applications[1]. They have caught the eye of researchers due to their high resistivity, moderate permeability, and structural versatility[1, 2]. Among the various forms of spinel ferrites, magnesium ferrite ($MgFe_2O_4$), a cubic spinel oxide, has gained attention for its promising structural, optical, and gas-sensing properties[1, 2]. Its performance depends heavily on factors such as grain size, porosity, and synthesis method. Doping $MgFe_2O_4$ with elements like rare-earth metals (e.g., La^{3+}, Sm^{3+}) is a common strategy used to enhance properties such as sensitivity, selectivity, and operating temperature by modifying the microstructure and electrical conductivity. Among various synthesis techniques, the hydrothermal method offers a cost-effective and environmentally friendly route to produce doped $MgFe_2O_4$ with improved characteristics[1-4]. This study adopted the hydrothermal method to synthesize La^{3+} and Sm^3-doped $MgFe_2O_4$, aiming to enhance its structural and optical properties for advanced functional applications.

2 Experimental

2.1 Material Synthesis

Mg $(Re)_{0.2}Fe_{1.8}O_4$, where Re is $La^{3+,}$ Sm^{3+} rare earth elements, was synthesized via the hydrothermal technique using high-purity metal chlorides as starting materials. The desired stoichiometric ratios of $MgCl_2.6H_2O$ (99%),

$LaCl_3.6H_2O$ (99%), $SmCl_3.6H_2O$ (99%), and $FeCl_3.6H_2O$ (99%) were dissolved in 400ml of distilled water under constant magnetic stirring. When the solutes had completely dissolved, Ammonia solution (25%) was added dropwise until a stable PH of approximately 8.39 was reached to form a precipitate. The precipitate was then filtered and washed thoroughly with deionized water using a Whatman glass microfiber filter (GF/F) with the aid of a suction flask operated on a vacuum pump. The absence/presence of chloride ions was tested using $AgNO_3$. The mixture was then transferred to an 80 ml Autoclave bottle, closed, and incubated at 100°C for 4 hours. The samples were allowed to cool down and washed with deionized water and ethanol and were left to dry under 80°C ultraviolet light for 24 hours. The samples were then ready for characterization.

3 Results and Discussion

3.1.1 Structural properties

To study the structural properties of Mg $(Re)_{0.2}Fe_{1.8}O_4$, where Re is La or Sm, X-ray diffraction and HR-TEM were used. The XRD spectra showed notable diffraction peaks of pure magnesium ferrite, which appeared at approximately 35.6° , corresponding to the diffraction plane of (311), which indicates the formation of $MgFe_2O_4$. However, a trace of another phase, denoted with an asterisk (*), can be observed at around 33°. This phase, belonging to hematite (Fe_2O_3)[5] in Figure 1(a), is brought about by the increase in annealing temperature. It is very sharp and narrow, suggesting a small amount of that phase with a large crystallite size. This means that the higher temperature may help new phases to form, likely starting from small amounts of hematite already in the sample, because the material wasn't perfectly mixed[5]. In contrast, the secondary phase peaks at 33˚, observed

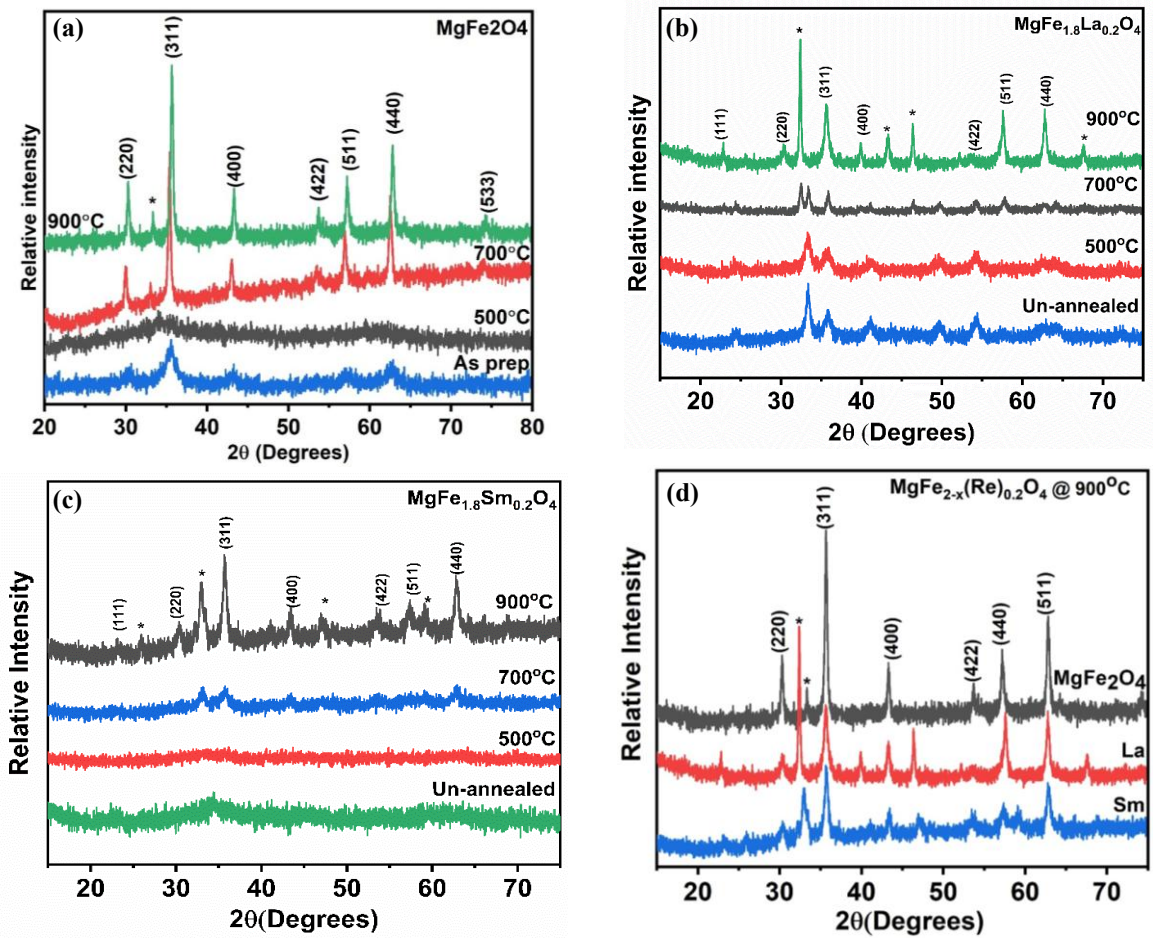

Figure 1: XRD patterns of (a)$MgFe_2O_4$ (b) $MgFe_{1.8}La_{0.2}O_4$, (c) $MgFe_{1.8}Sm_{0.2}O_4$, as prepared and annealed at temperatures 500˚, 700˚ and 900˚, and (d) $MgFe_{1.8}(Re)_{0.2}O_4$ annealed at 900°C

in Figure 1(b) is much stronger and more intense and is observed in the unannealed samples also. This phase belongs to the ortho-ferrites, which is brought about by the high doping concentration. A similar observation was noted by Kumbhar et al.[4] who concluded that as the doping concentration increased so did the intensity of the

orthoferrite phase. Interestingly, Figure 1(c) showed broadened diffraction peaks at low temperature as compared to Figure 1(b). This means that Sm doping brought greater micro strains to the material than La doping, which led to a decrease in crystallite size. Again, Kumbhar et al [4] attests to similar findings when they did an Sm^{3+} and Dy^{3+} substitution on $MgFe_2O_4$. Figure 1(d) compares doping effects at an annealing temperature of 900℃, where the intensity of diffraction peaks was easier to compare. From these spectra, it can be observed that upon La and Sm doping, the crystallite planes (311), (400), (422), (440), (511) belonging to $MgFe_2O_4$ are maintained. However, the intensity decreases with increasing molar mass, implying reduced crystallite size. XRD parameters were calculated and recorded in Table 1. Analysis of results showed the crystallite size to range from ~24.44 nm (undoped) to as low as ~3.97nm (Sm-doped), confirming nanoparticle formation. Crystallite size and X-ray density results were observed at an annealing temperature of 900℃ and were plotted in Figure 2. The trend was consistent with literature findings[2].

Table 1: calculated XRD parameters for $MgFe_2O_4$ and $MgFe_{2-x}(RE)_xO_4$ where RE = La, Sm at different annealing temperatures

Composition	***Annealing temperature(˚C)***	**Crystallite size(nm)**	**Lattice parameter(Å)**	**Xrd density(g/cm^3)** ***($\times 10^{-11}$)***
$MgFe_2O_4$	-	*5.46±0.002*	*8.750±0.006*	*4.10*
$MgFe_2O_4$	*500*	*8.98±0.002*	*8.745±0.011*	*4.11*
$MgFe_2O_4$	*700*	*15.10±0.002*	*8.778±0.009*	*4.06*
$MgFe_2O_4$	*900*	*24.44±0.0004*	*8.433±0.0008*	*4.58*
$MgFe_{1.8}La_{0.2}O_4$	-	*11.0710±0.002*	*8.450±0.017*	*5.10*
$MgFe_{1.8}La_{0.2}O_4$	*500*	*8.239±0.002*	*8.461±0.025*	*5.08*
$MgFe_{1.8}La_{0.2}O_4$	*700*	*23.99±0.002*	*8.444±0.013*	*5.11*
$MgFe_{1.8}La_{0.2}O_4$	*900*	*21.536±0.002*	*8.573±0.015*	*4.87*
$MgFe_{1.8}Sm_{0.2}O_4$	-	*3.969±0.003*	*8.626±0.016*	*4.42*
$MgFe_{1.8}Sm_{0.2}O_4$	*500*	-	-	-
$MgFe_{1.8}Sm_{0.2}O$	*700*	*11.527±0.008*	*8.344±0.002*	*4.91*
$MgFe_{1.8}Sm_{0.2}O_4$	*900*	*18.144±0.003*	*8.339±0.0006*	*4.92*

The HRTEM images in Figure 3 revealed clear lattice fringes suggestive of the high crystallinity of the samples. In the undoped $MgFe_2O_4$ (Figure 3a), well-defined lattice fringes were observed with an interplanar spacing (d-spacing) of 0.138 nm. The corresponding SAED pattern shows common center diffraction rings with distinct bright spots, an indication of polycrystalline nature, correlating with the XRD results discussed above. La doping (Figure 6b) slightly increased the lattice spacing (d = 0.284 nm), which can be attributed to the introduction and presence of the larger La^{3+} ion (1.032 Å) compared to Fe^{3+} (0.645 Å) into the crystal lattice. The Sm-doped sample (Figure 3c) showed lattice fringes with a d-spacing of 0.254 nm. The slightly smaller d-spacing compared to the La-doped sample can be related to the smaller ionic radius of Sm^{3+} (0.958 Å) compared to La^{3+}, but still larger than Fe^{3+}, causing a fair lattice expansion. The SAED patterns for both doped samples confirm the polycrystalline nature with preserved spinel symmetry, yet with broadened and slightly scattered diffraction rings in the Sm-doped case, which confirms increased lattice disorder and reduced crystallite size, consistent with the XRD analysis above and with the finding of Kumbhar et al.[4].

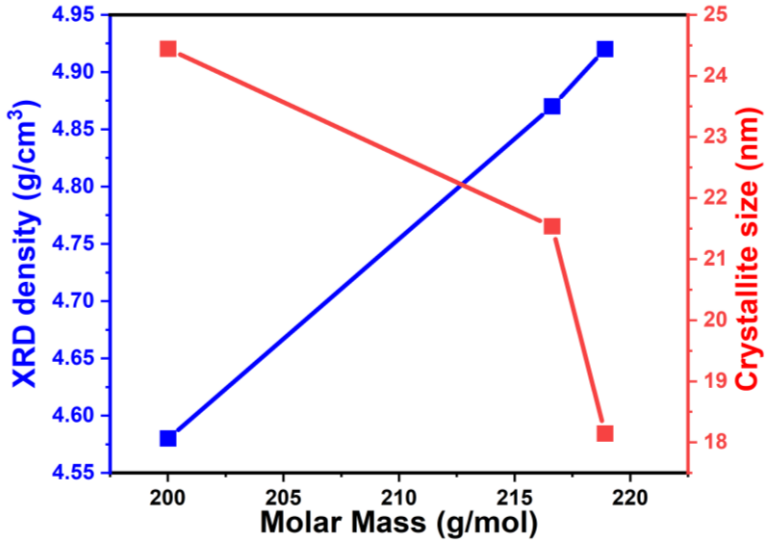

Figure 2: Shows the trend in crystallite size and XRD density with increasing dopant molar mass at 900 °C annealing temperature.

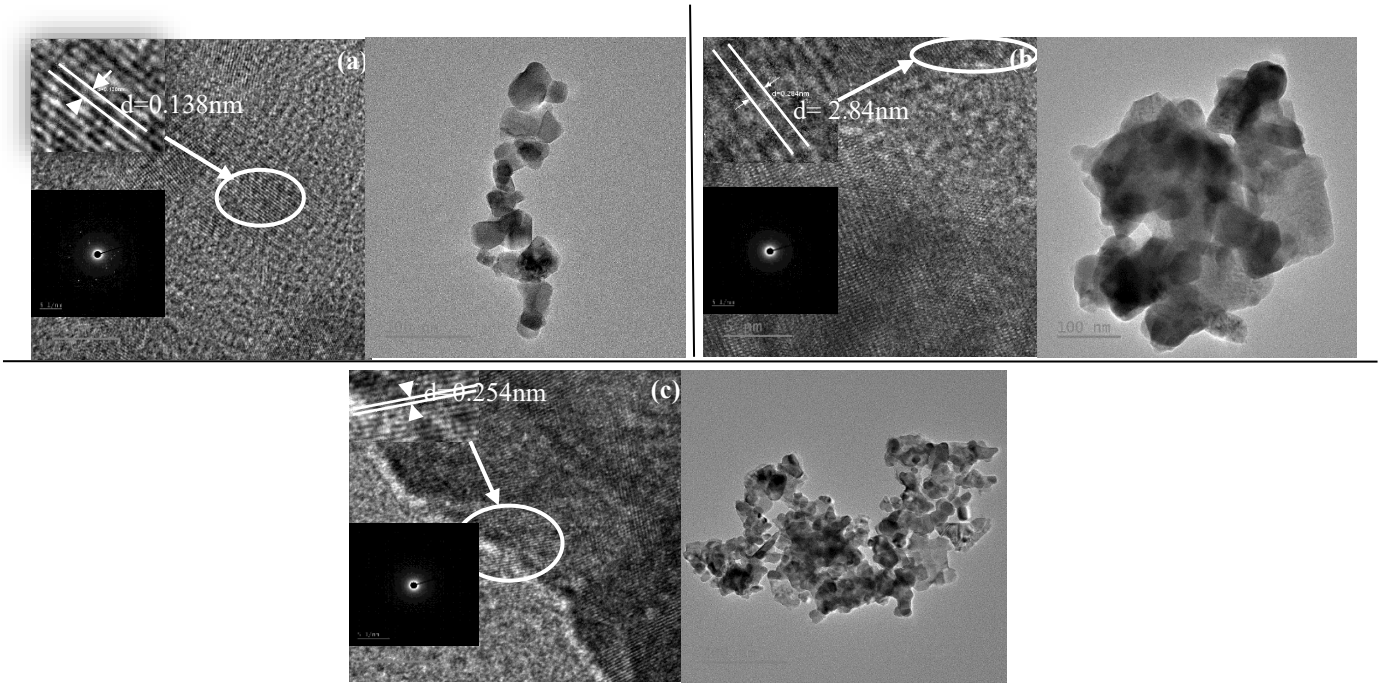

Figure 1: HRTEM micrograph of (a)$MgFe_2O_4$ (b)$MgFe_{1.8}La_{0.2}O_4$ (c) $MgFe_{1.8}Sm_{0.2}O_4$ annealed at 900˚C

3.1.2 Optical analysis

The optical properties of the samples were studied using UV-Vis and Photoluminescence spectroscopy. The bandgap from UV-visible spectroscopy was estimated using Tauc's plot. The estimated values of the band gap were observed to decrease with increasing molar mass(g/mol) of the dopant, i.e., doping with rare earth elements from left to right in the periodic table, the band gap tends to decrease. Additionally, it can be observed that annealing temperatures greatly affect the band gap. From Figure 4 (a-d), the bandgap of $MgFe_2O_4$ is observed to be widening with increasing annealing temperature, which can be attributed to increasing crystallinity and ordered lattice arrangement. On the other hand, the La, Sm-Variants of MgFe2O4. fluctuate between a widened and reduced bandgap. Of interest are the results found at an annealing temperature of 900℃, where a difference in bandgap energy of undoped and doped samples can easily be observed. At this temperature, the band gap for undoped magnesium ferrite was found to be 2.60eV and rare earth substitution was shown to reduce the band

gap. As the atomic weight of the rare earth increased so did the band gap, this was evident by the band gap of Magnesium doped with lanthanum and samarium being 2.11 and 2.35 respectively.

The PL spectra, shown in Figure 5(a–d), show notable emission peaks in the visible region (~ 490 – 510 nm), with peak intensities centered at 495 nm and 505 nm. Figure 5(a) shows the undoped sample to have dual light emission, while doping seems to suppress the duality into a single peak emission. Additionally, doping with La^{3+} lowered the PL intensity, while doping with Sm^{3+} made no impact. As the annealing temperature increased (Figures 5b–d), the PL intensity of undoped $MgFe_2O_4$ first increased at 500 °C and 700 °C, then slightly reduced at 900 °C. This trend indicates improved crystallinity and reduction of surface defects at intermediate temperatures, followed by potential dopant diffusion or grain growth-induced quenching at higher temperatures [1]. In contrast, both La- and Sm-doped samples consistently exhibited suppressed PL intensity across all annealing stages, which implies lower electron-hole recombination[1]. These findings are consistent with those of Tony et al [1]who concluded that higher doping concentrations suppress PL intensity, and this reveals efficient charge carrier separation, an excellent photocatalytic ability.

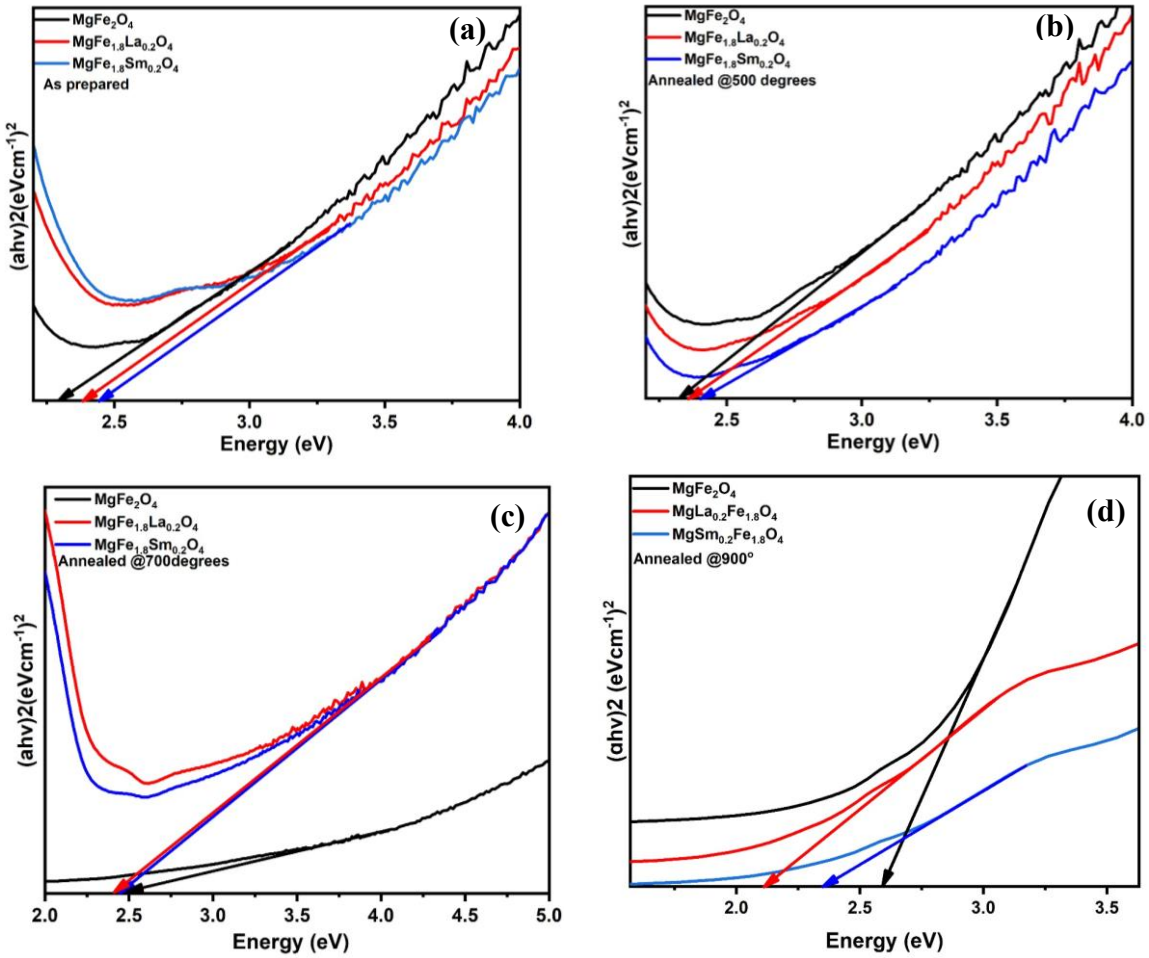

Figure 3: Tauc's plots of $MgFe_2O_4$, $MgLa_{0.2}Fe_{1.8}O_4$, and $MgSm_{0.2}Fe_{1.8}O_4$ at different annealing temperatures: (a) As-prepared, (b) 500 °C, (c) 700 °C, and (d) 900 °C

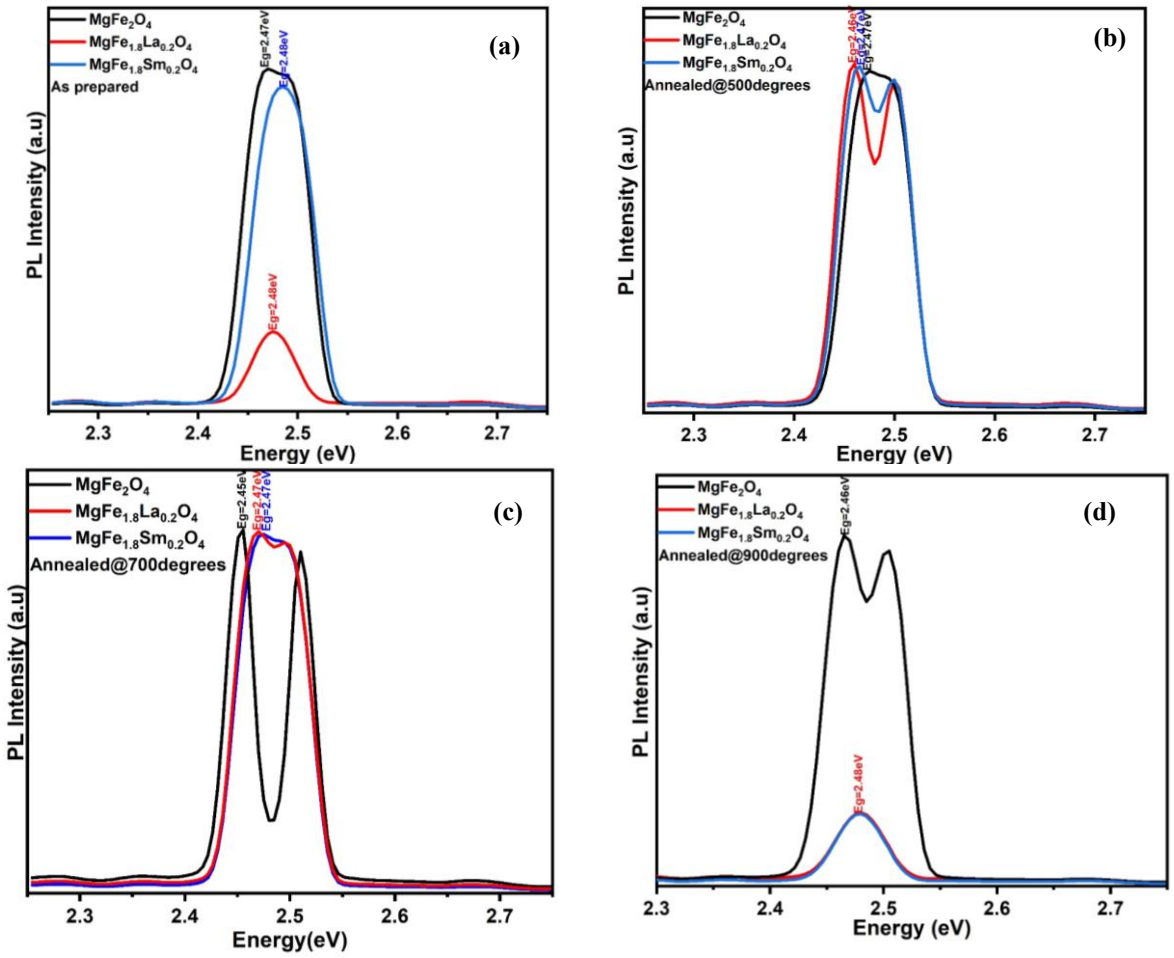

Figure 4: Deconvoluted emission spectra of the samples (a) as prepared and (b) 500℃ ,(c) 700℃, (d) 900℃

4 Conclusion

Rare-earth (Re = La and Sm) doped magnesium nano ferrites were effectually synthesized following a hydrothermal approach. XRD authenticated the formation of spinel ferrite with varying crystallite sizes ranging from 3 nm to 24 nm. Doping with La^{3+} and $Sm^{3+,}$ the crystallite size decreased from 24 nm to 21,5 nm and 18,1 nm, respectively and increased XRD density. The band gap was reduced from 2.60 eV to 2.11 eV ($La^{3+)}$ and 2.35 eV (Sm^{3+}). The PL spectra showed an increased electron-hole pair separation with rare-earth doping. Therefore, $MgFe_2O_4$ can be proposed as a good candidate for advanced applications in sensors.

References

[1] A. R. Tony and A. J. Verjhula, "Yttrium doped magnesium ferrite nanoparticles: a potential solar light driven photocatalyst for deterioration of hazardous dyes," *Journal of Materials Science: Materials in Electronics,* vol. 35, no. 7, p. 481, 2024.

[2] P. S. Mkwae *et al.*, "Insightful acetone gas sensing behaviour of Ce substituted $MgFe_2O_4$ spinel nano-ferrites," *Journal of Materials Research and Technology,* vol. 9, no. 6, pp. 16252-16269, 2020.

[3] R. Kumbhar, T. Shinde, S. Kamble, V. Mathe, and J. Ghodake, "Influence of rare earth ions (Sm^{3+}, Dy^{3+}) substitution on magnetic and microwave performance of magnesium ferrite," *Physica B: Condensed Matter,* vol. 619, p. 413161, 2021.

[4] R. Kumbhar *et al.*, "Structural, magnetic and dielectric properties of rare earths (Sm^{3+}, Dy^{3+}) substituted $MgFe_2O_4$," *Indian Journal of Physics,* vol. 98, no. 9, pp. 3251-3258, 2024.

[5] E. Fantozzi, E. Rama, C. Calvio, B. Albini, P. Galinetto, and M. Bini, "Silver doped magnesium ferrite nanoparticles: physico-chemical characterization and antibacterial activity," *Materials,* vol. 14, no. 11, p. 2859, 2021

Thermodynamic properties of (Gd,Pr)$OsGa_4$ Intermetallic Compounds

B. Sondezi[1], **and R Djoumessi Fobasso**[1]

[1]Rare Earth-Based oxides and Nano Group, Department of Physics, University of Johannesburg, Johannesburg, Auckland Park 2006, South Africa

E-mail: redrissed@uj.ac.za

Abstract. Intermetallic compounds containing rare-earth and transition metals exhibit rich magnetic and electronic properties, making them crucial for understanding correlated electron systems. Among these, the layered compounds $PrOsGa_4$ and $GdOsGa_4$ are particularly intriguing due to their interplay of localized 4f moments and conduction electrons, prompting a detailed investigation of their physical behavior. For this purpose, polycrystalline samples of $PrOsGa_4$ and $GdOsGa_4$ were prepared by arc-melting technique using high-purity elemental constituent elements. The Rietveld crystal structure refinement of powder X-ray diffraction patterns with a full-profile refinement confirms that both samples crystallize in the orthorhombic $CeOsGa_4$-structure type with space group Pmma (number 51). The structure exhibits two types of two dimensionally alternating layers that are slightly puckered, having $OsGa_3$ layer sandwiched between Pr(Gd)Ga layers. Here, we present the physical properties of these compounds through temperature (T) dependent magnetic susceptibility $\chi(T)$ and magnetization $M(B)$, heat capacity $C_{\rm p}(T)$, and electrical resistivity $\rho(T)$. They consistently reveal that the compounds undergo an antiferromagnetic/ferromagnetic type orderings below 14 K and 16 K for $GdOsGa_4$ and $PrOsGa_4$, respectively. These transition temperatures are notably higher than those observed in related $RMgGa_4$ and $RTGa_4$ systems, highlighting the role of Os in enhancing magnetic interactions and potential for applications in low-temperature magnetism. The $\chi(T)$ data obey the Curie-Weiss law above 50 K. The layered structure and tunable electronic properties of these materials could inspire further exploration where control of 4f-electron interactions with conduction electrons is critical. The study may therefore contribute towards a better understanding of the physics of this class of materials.

1 Introduction

Gallium (Ga)-rich intermetallic compounds have recently drawn significant attention due to their structural complexity and tunable electronic/magnetic properties, which are relevant for advanced technologies such as cryogenic cooling [1]. Amongst the first reported Ga-rich compounds, there are $RE_2Co_3Ga_9$ (RE: Y, Ho) [2, 3], and $RE_2T_3Ge_9$ (RE: Y, Sm, Gd-Yb; T: Rh, Ir) [4]. In these series, there is a layered arrangement of the T-Ga atoms and the RE ions reside in interstitial sites. Moreover, the rare-earth ions dominate the magnetism in these materials with paramagnetism at high temperatures and either antiferromagnetic (AFM) or ferromagnetic (FM) orderings at low temperatures depending on the rare-earth of interest. It also depends on the transition element. For instance, in Co-based compounds in this series, the rare-earth ions dominate the magnetic behavior since the Co atoms are non magnetic or exhibit a weak magnetism. However, others such as Fe- or Ru- based may exhibit stronger magnetic interactions. Gd^{3+} ions often leads to strong magnetic ordering while Pr^{3+} ions usually exhibits crystalline electric field effects. This can lead to interesting properties. Despite their potential, Gd- and Pr-based variants in this family remain understudied. We therefore report on the physical properties of $PrOsGa_4$ and $GdOsGa_4$ compounds. This will give us an insight into the low-temperature magnetic transitions in these materials and serves as model systems for studying 4f-electron correlations in layered materials.

2 Synthesis and experimental details

The compounds were synthesized via arc-melting method. For this purpose, stoichiometric quantities of the elements Pr, Gd, Os, Ga were accurately weighed and arc-melted under ultra high purity argon atmosphere, on a water cooled copper hearth. The samples were remelted three times, to promote homogeneity. The resulting as-cast ingot was encapsulated in tantalum foil, sealed under vacuum within a quartz ampoule, and subjected to a 14-day annealing process at 1200° C to enhance its homogeneity, after which it was quenched in cold water. The phase purity of the annealed product was verified via powder X-ray diffraction (XRD) at ambient temperature on a Rigaku diffractometer employing Cu-Kα radiation ($\lambda = 1.54$ Å). The resulting diffraction patterns were refined using the Rietveld method as implemented in the FULLPROF software suite. Magnetic characterization was conducted with a commercial Quantum Design Dynacool system, measuring over a temperature interval of 2 K to 380 K and in applied fields up to 9 T. Specific heat capacity, $C_{\mathrm{P}}(T)$, was determined on the same apparatus from 2 K to 300 K using the thermal relaxation technique. Electrical resistivity, $\rho(T)$, was acquired from 2 K to 300 K via the standard four-probe alternating current (AC) method using the Dynacool system.

3 Results and Discussion

3.1 Structural properties

The Rietveld crystal structure refinement of the room-temperature powder XRD patterns of both samples are displayed in Figure 1. The samples form in the orthorhombic $CeOsGa_4$ structure type (space group Pmma, number 51). The obtained lattice parameters are reported in the table 1 below. The crystal structure, illustrated in Fig. 2, consists of slightly puckered, two-dimensional layers that alternate along one axis. These layers form a characteristic sequence where a slab of $OsGa_3$ is sandwiched between layers of PrGa or GdGa.

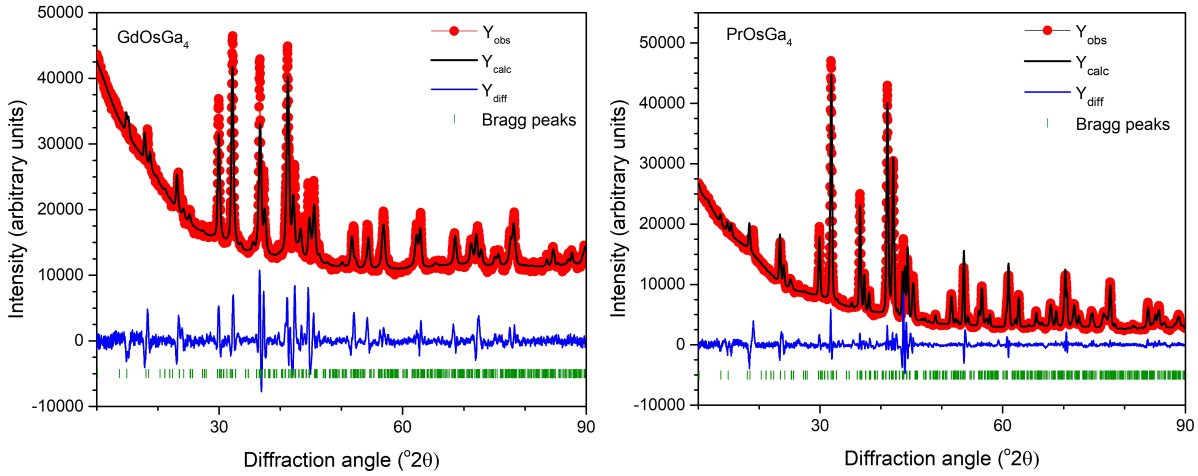

Figure 1: Powder X-ray diffraction of both compounds. The experimentally measured data points are plotted in red, while the theoretical profile generated from the Rietveld refinement is represented as a black line. The residual difference between the observed and calculated patterns is illustrated by the blue curve. The expected positions of the Bragg reflections for the $CeOsGa_4$ crystal structure are marked by the vertical green tick marks.

Table 1: The lattice parameters of $PrOsGa_4$ and $GdOsGa_4$.

Compound	a (Å)	b (Å)	c (Å)	V (Å)^3
$PrOsGa_4$	9.59720 (5)	8.90463 (5)	7.744332 (5)	661.83(2)
$GdOsGa_4$	9.487082 (5)	8.954183 (5)	7.699494 (5)	654.065(4)

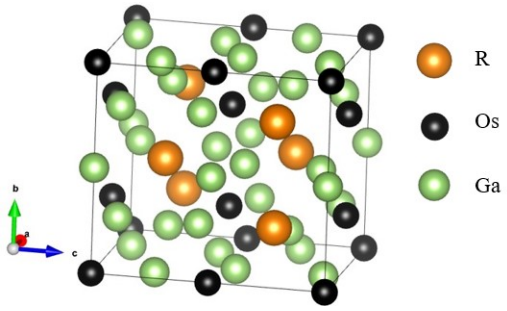

Figure 2: Crystal structure of $ROsGa_4 (R = Pr, Gd)$

3.2 Magnetic properties

The temperature dependences of magnetic susceptibility $\chi(T)$ of $GdOsGa_4$ and $PrOsGa_4$ measured in an applied magnetic field B = 0.1 T and in field cooled mode are shown in Figure 3. The high temperature regions of both compounds (T $\geq$ 50 K) both follow the Curie-Weiss law given by expression 1.

$$\chi(T) = \chi_0 + C/(T - \theta_P), \tag{1}$$

where χ_0 is the temperature independent susceptibility, C is the Curie-Weiss constant, and θ_P is the paramagnetic Weiss temperature. From the least-squares fit of equation (1) to the $GdOsGa_4$ data, we obtained an effective magnetic moment μ_{eff} = 8.191 (3) μ_B/Gd^{3+} ion and a Weiss temperature θ_P = -21.791 (3) K. In this expression, χ_0 represents a temperature-independent term, C is the Curie constant, and θ_P denotes the paramagnetic Weiss temperature. A least-squares fit of equation (1) to the data for $GdOsGa_4$ yielded an effective magnetic moment of μ_{eff} = 8.191 (3) μ_B/Gd^{3+} ion and a Weiss temperature of $\theta_P = -21.791(3)$ K. The negative value of the paramagnetic Weiss temperature indicates the dominance of antiferromagnetic interactions in the high temperature region of $GdOsGa_4$. The μ_{eff} value informs that Gd ions are fully responsible for the magnetism in this material as the obtained value is very close and in agreement with the theoretical value of Gd^{3+} ions, which is 7.94 μ_B. Similarly, the least-squares fit of equation (1) to the $PrOsGa_4$ data leads to a calculated effective magnetic moment μ_{eff} of 3.67 (2) μ_B/Pr^{3+} ion and a negative paramagnetic Weiss temperature θ_P = -1.19 (1) K. The obtained negative θ_P value confirms the antiferromagnetic coupling of the Pr^{3+} ions in this system, whilst the effective magnetic moment value is close to the theoretical value of 3.58 μ_B/Pr^{3+} ions.

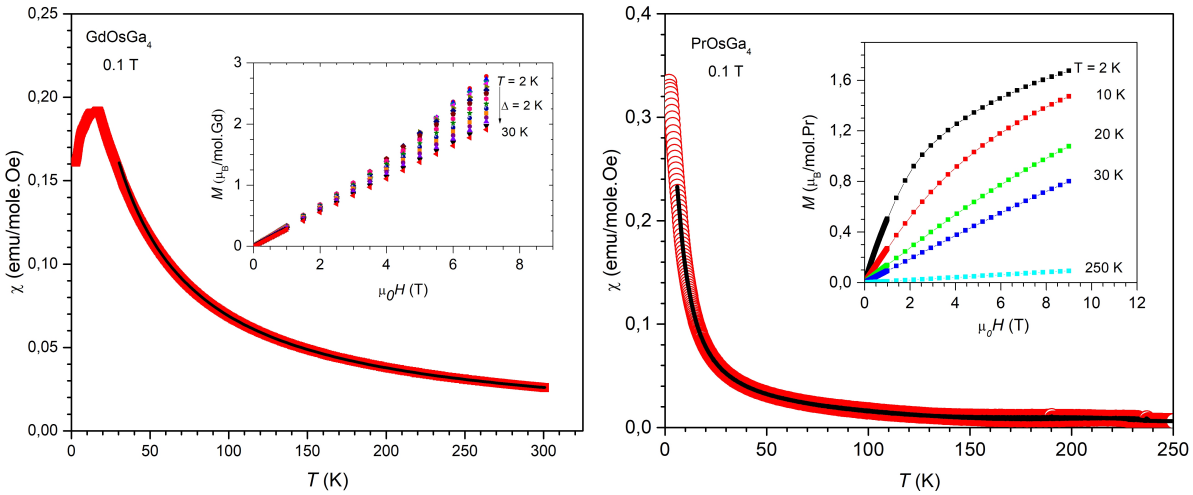

Figure 3: Main panels: Temperature dependence of the dc magnetic susceptibility $\chi(T)$ for both compounds, measured in an applied field of 0.1 T. The experimental data is plotted as red circles, while the solid black line corresponds to the Curie-Weiss fit described in the text. Insets: Magnetization isotherms $M(B)$ collected at temperatures both above and below the magnetic transition.

A kink deviation from linearity is observed at T_N = 14 K for $GdOsGa_4$ and marks an onset of an antiferromagnetic ground state ordering. This is due to an emergence of an antiparallel ordering which reduces the magnetic response of the system compared to the paramagnetic phase. Similary, at T_C = 16 K, a deviation from linearity is observed in $PrOsGa_4$ and it is associated this time to a ferromagnetic ordering which arises from spontaneous magnetization. The magnetic ordering temperatures observed here, T_N = 14 K for $GdOsGa_4$ and T_C = 16 K for $PrOsGa_4$, are among the highest reported for the $ROsGa_4$ family [5]. This becomes particularly evident when compared to the isostructural compound $CeOsGa_4$, which orders antiferromagnetically at a significantly lower temperature of T_N =3.8 K [5]. Furthermore, the related compounds $CeRhGa_4$ and $CeIrGa_4$ do not exhibit any magnetic ordering down to the lowest measured temperatures [6].
The inset of the left panel of Figure 3 shows the magnetization data of $GdOsGa_4$ measured from 2 K to 30 K with intervals of 2 K. These includes temperatures below and above the transition temperature. All measured isotherms show linear behaviour over the entire applied magnetic field range, confirming long range antiferromagnetic ordering even for data measured well below the ordering temperature. This observation is consistent with the antiferromagnetic ordering observed in the $\chi(T)$ data and can be the sign of weakly interacting local moments when the exchange coupling is negligible compared to the Zeeman energy. Similarly, the magnetization data of $PrOsGa_4$ were measured but in 2, 10, 20 and 30 K. The data at 2 K and 10 K shows a slight curvature at low applied magnetic fields but does not fully saturate up to 9.0 T. This confirms the presence of short-range correlation in the paramagnetic region.

3.3 Specific heat

The temperature dependences of specific heat of $GdOsGa_4$ and $PrOsGa_4$ are shown in figure 4. The data were measured from room temperature down to 1.8 K in zero applied magnetic field. The high temperature data upto T= 280 K reaches the Dulong Petit approximation (green line in figure 4), giving a value of 142 J/mol.K, which is in close agreement with the theoretical value of 149 J/mol.K, as calculated from 3NR (where N is the number of atoms per formula unit and R is the universal gas constant). A similar behavior has been observed in $PrOsGa_4$ and is commonly observed in normal metals. The kink observed around the transition temperatures, T_c= 14 K for $GdOsGa_4$ and T_c= 16 K for $PrOsGa_4$ is a sign of a short-range order-like transition. This corroborates with the results obtained with $\chi(T)$.

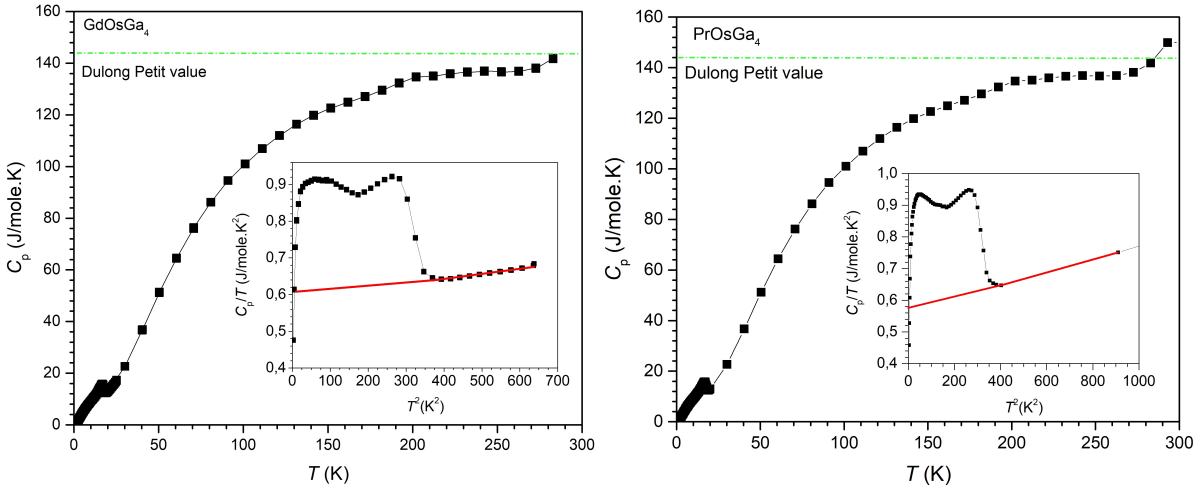

Figure 4: Temperature variations of specific heat capacity of $GdOsGa_4$ (left panel) and $PrOsGa_4$ (right panel), measured in zero field from 300 K to 1.8 K. The insets in both graphs represent the plot of $C_P(T)/T$ vs T^2 for both compounds. The red line represents the linear fit used to estimate the Sommerfeld coefficient as explained in the text.

The insets of figure 4 shows the C_P/T vs T^2 curves, with the Debye fit of the data just above the ordering temperature in both cases, represented by a red line. The red line is the fit according to the expression:

$$\frac{C_P}{T} = \gamma + \beta T^2, \tag{2}$$

where γ is the Sommerfeld coefficient and β is the constant associated with the Debye temperature θ_D. The first term is the electronic contribution and the second term is the lattice (phononic) contribution.

It is important to note that this linear fit in the C_P/T vs. T^2 plot is applicable in the temperature range just above the magnetic ordering transition, where the contributions are primarily electronic and phononic. The clear upward deviation from linearity observed at lower temperatures ($T \ll T_C/T_N$) is a common feature in magnetically ordered systems. This deviation is attributed to the emergence of additional contributions, primarily from magnetic excitations (spin waves or magnons). In the magnetically ordered state, these magnon contributions, which are not accounted for in equation 2, become significant and cause the specific heat to exceed the values predicted by the simple metallic model. This behavior confirms the dominant role of magnetic interactions at low temperatures in both compounds. The Sommerfeld coefficient is found to be $\gamma = 0.5876(2)$ J/mol.K^2, and $\gamma = 0.5645(1)$ J/mol.K^2 for $GdOsGa_4$, and $PrOsGa_4$, respectively. These value suggests that the compounds belong to the heavy-fermion family.

4 Electrical resistivity

The electrical resistivity, $\rho(T)$, of $GdOsGa_4$ and $PrOsGa_4$, measured in zero applied magnetic field and from 300 K to 2 K are displayed in figure 5. The resistivity drops as the temperature is lowered, confirming the metallic char-

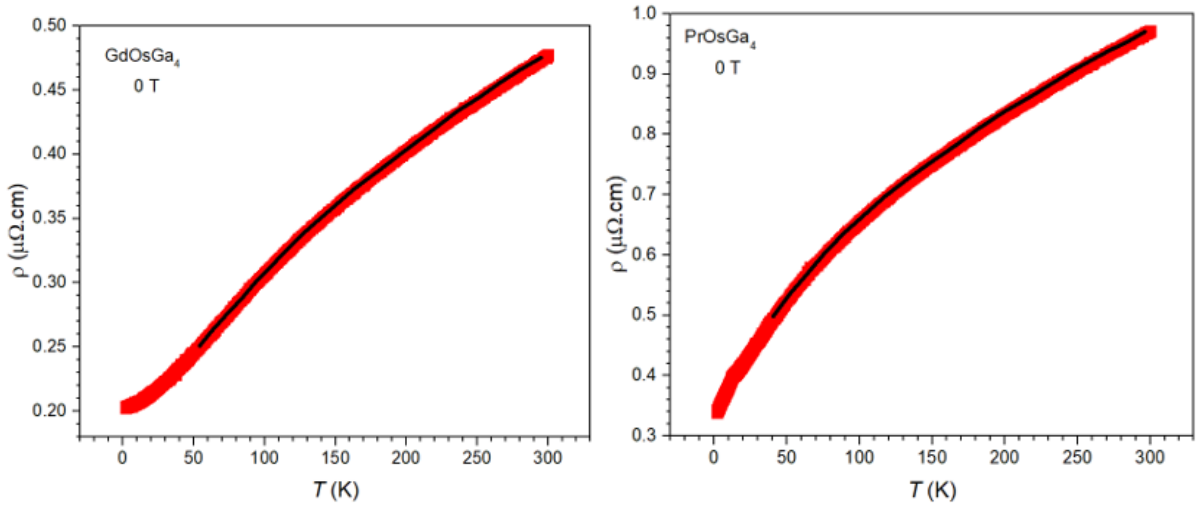

Figure 5: Temperature dependence of electrical resistivity of $GdOsGa_4$ and $PrOsGa_4$ measured in zero applield magnetic field. The black lines represent the Bloch-Grüneisen fit as explained in the text.

acter of $GdOsGa_4$. The compound $PrOsGa_4$ exhibits a comparable metallic character. At elevated temperatures, the Bloch-Grüneisen anticipates a linear dependence of resistivity on temperature ($\rho \propto T$) for both materials. The observed curvature in the $\rho(T)$ data can be explained by intraband scattering processes, such as those involving a partially filled d-electron band. To quantitatively analyze the electron-phonon interaction, the resistivity data for both $GdOsGa_4$ and $PrOsGa_4$ were modeled using the Bloch-Grüneisen relation presented in equation (3) below.

$$\rho(T) = \rho_0 + \frac{4A_0}{\theta_{\mathrm{R}}}\left(\frac{T}{\theta_{\mathrm{R}}}\right)^5 \int_0^{\theta_{\mathrm{R}}/T} \frac{x^5 dx}{(e^x - 1)(1 - e^x)} \tag{3}$$

In equation (3), the parameter ρ_0 corresponds to the residual resistivity originating from crystal defects and impurities. A_0 represents the strength of the electron-phonon coupling, while θ_R denotes a characteristic phonon energy scale, also known as the Debye temperature derived from resistivity measurements. The parameters listed in the following table were obtained by fitting the experimental $\rho(T)$ data for both compounds to this model using a least-squares optimization.

5 Conclusion

The study provided a comprehensive study of the structural, magnetic and physical properties of the two intermetallic compounds $GdOsGa_4$ and $PrOsGa_4$. Both compounds, $GdOsGa_4$ and $PrOsGa_4$ crystallize in the same

Table 2: Parameters derived from the Bloch-Grüneisen fit of $PrOsGa_4$ and $GdOsGa_4$.

Compound	ρ_0 ($\mu\Omega$.cm)	A_0 ($\mu\Omega$.cm.K^{-8})	θ_R (K)
$GdOsGa_4$	0.217(2)	5.90(2)	259.4(2)
$PrOsGa_4$	0.521(2)	9.92(1)	200.5(2)

orthorhombic $CeOsGa_4$-type structure belonging to the Pmma space group. A magnetic behavior is observed in both materials. $GdOsGa_4$ data exhibit clear antiferromagnetic ordering at T_N = 14 K while $PrOsGa_4$ is ferromagnetic at T_C = 16 K. The obtained ordering temperatures are significantly higher than those of other members in the $RTGa_4$ (T = Rh, Ir, Os) series. This contrast, along with the lack of order in Ce(T=Rh,Ir)Ga_4, highlight the fact that the combination of a localized 4f moment (Gd^{3+}, Pr^{3+}) with the Os conduction electron system is the key recipe for achieving enhanced magnetic interactions in this structural family. These results are corroborated by magnetic susceptibility, magnetization, and specific heat measurements, which also confirm the dominance of localized 4f moments in both systems. Electrical resistivity measurements further affirm the metallic nature of both compounds, with electron-phonon interactions well-described by the Bloch-Grüneisen model. In summary, this work elucidates the interplay between localized 4f moments and conduction electrons in layered intermetallics, providing a foundation for future studies on tunable magnetic and electronic properties in rare-earth-based materials.

References

[1] N. Shohata, "Magnetic properties of rare earth gallium intermetallic compounds," *Journal of the Physical Society of Japan*, vol. 42, no. 6, pp. 1873–1880, Jan 1977.

[2] J. Niermann, B. Fehrmann, M. W. Wolff, and W. Jeitschko, "Preparation and crystal structure of ternary rare-earth platinum metal aluminides $R_2T_3Al_9$ (T= Rh, Ir, Pd) with $Y_2Co_3Ga_9$-type structure and magnetic properties of the iridium compounds," *Journal of Solid State Chemistry*, vol. 177, no. 7, pp. 2600–2609, Mar 2004.

[3] C. Routsi and J. Yakinthos, "Crystal structure and magnetic properties of $R_2Co_3Al_9$ compounds (R= Y, Pr, Gd, Tb, Dy, Ho, Er, Tm)," *Journal of alloys and compounds*, vol. 323, pp. 427–430, Jul 2001.

[4] O. Sichevych, W. Schnelle, Y. Prots, U. Burkhardt, and Y. Grin, "Crystal structure and physical properties of new ternary gallides $Eu_2Rh_3Ga_9$ and $Eu_2Ir_3Ga_9$," *Zeitschrift für Naturforschung B*, vol. 61, no. 7, pp. 904–911, Jun 2006.

[5] B. Sondezi and A. Strydom, "Physical properties study of the $CeOsGa_4$ compound," *Acta Physica Polonica A*, vol. 133, no. 3, pp. 398–400, 2018.

[6] P. M. Mabidi, "Physical properties of the intermetallic $CeTGa_4(T = Rh, Ir, Os)$ compounds," *MSc thesis, University of Johannesburg (South Africa)*, 2020.

Rare-Earth Perovskites in the Quantum Age: Bridging Materials Science and Technologies

R Djoumessi Fobasso[1], **B. Sondezi** [1]

[1]Rare Earth-Based oxides and Nano Group, Department of Physics, University of Johannesburg, Auckland Park 2006, South Africa

E-mail: redrissed@uj.ac.za

Abstract. Perovskite materials are known to have unique optoelectronic and quantum properties. These make them good candidates for the next generation of quantum technologies. This article reviews the properties of perovskites that make them good candidates for bridging materials science with cutting-edge quantum applications. These applications include but are not limited to quantum computing, quantum dots, spin qubits, communication, superconducting systems, and sensing. The first part focuses on the structural properties of perovskites and the second part focuses on fundamental properties such as quantum spin liquid and photoluminescence that make them ideal candidates for quantum-enabled devices. Next, the work highlights the challenges and future prospects for the development of perovskite materials from a quantum perspective. Finally, a preliminary investigation of the new perovskite $YbInO_3$ is made based on Monte-carlo simulation method. Monte Carlo simulations of the novel perovskite $YbInO_3$ reveal a magnetic phase transition at 65 K. The findings, include sharp energy fluctuations as well as peaks in susceptibility and specific heat which point to the onset of magnetic ordering. The results revealed that $YbInO_3$ is an attractive choice for studying its quantum magnetic characteristics due to its ability to stabilise the ordered phase with increasing lattice size and its potential for geometric frustration.

1 Introduction

Getting affordable and clean energy is the 7th UN Sustainable Development Goal. One way of achieving this goal is to ensure that renewable energy sources like solar, wind, and thermal energy are accessible at reasonable prices to everyone. Solar energy is recognized as an effective way to deal with environmental pollution and global warming and, most importantly, make electricity accessible to everyone. Most of the photovoltaic cells were silicium based. Discovered in the 1830's, the existence of perovskites revolutionized the world of science 180 years later. Indeed, it was only in 2010 that Tsutomu Miyasaka highlighted its potential in the photovoltaic industry [1]. They serve as a good example for bridging quantum technologies and materials science. Due to their characteristics, perovskite materials have significant technical significance across various real-world applications such as solar cells with their exceptional optoelectronic properties, photocatalysts, light-emitting devices, energy conversion and storage, sprintronic devices, gas sensing, etc... [2, 3, 4, 5].

There are several quantum phenomena in perovkistes due to several factors such as electron structure and correlations, spin-orbit entanglement, lattice dynamics, and spin-orbit coupling (SOC). The latter leads to several quantum mechanical phenomena which plays a key role in condensed matter physics by influencing the electronic, magnetic and optical properties of materials. For instance, quantum spin liquids can arise in rare-earth perovskites because of the SOC which hybridize the spin and orbital degrees of freedom and sometimes prevent a magnetic order to happen at even lower temperatures. That is the case in $YbAlO_3$ which is a quasi-1D quantum magnet [6] exhibiting a quantum spin liquid state due to the SOC splitting the Yb^{3+} Kramers doublet, leading to

fractionalized spinon excitations. This material has potential in quantum information science, optoelectronics and spintronics [7, 8]. A disorder-induced spin liquid state has also been found in $TbInO_3$ [9, 10]. Topological quantum states were also found to occur in rare-earth perovskites due to SOC. That is the case of $NdNiO_3$, a perovskite quantum material which under strain shows SOC-induced Dirac crossings in its electronic structure [11]. This is an example of SOC-Driven Band Inversions. SOC introduces the Dzyaloshinskii-Moriya Interaction (DMI), stabilizing quantum skyrmions as it is the case in $GdFeO_3$ which hosts nanometer-scale skyrmions under magnetic fields [12]. In the field of quantum coherence and qubits, long coherence quantum bits can be formed from the SOC-split energy levels of rare-earth ions such as Er^{3+} and Nd^{3+}. In materials such as $YAlO_3$, the single-photon emission for quantum communication is enabled when doped with rare-earth ions such as Eu^{3+} and Yb^{3+} [13]. These rare-earth perovskites demonstrate how quantum effects can be used to create quantum networks and non-volatile memory, among other next generation technologies. The unique mix of spin, optical, and electrical features of rare earth perovskites has made them a viable platform for quantum technologies. Long coherence periods and strong SOC are made possible by these materials' use of rare earth ion shielded 4f electrons, which is an essential combination for quantum applications.

Rare-earth perovskites with the form AB_3, where A is a rare-earth ion, have emerged as a particularly rich sub-class due to the peculiar characteristics provided by the localised 4f electrons. This series reveals a remarkable diversity of physical phenomena that are directly related to the choice of A- and B-site cations [9, 11, 12, 14]. For instance, $GdFeO_3$ serves as a classic antiferromagnet [12], while having metal-insulator transitions, $NdNiO_3$ is a member of the rare-earth nickelate family and can host topologically non-trivial electronic bands upon strain [11].

This article aims to illuminate the path toward perovskite-driven quantum technologies, which are potentially important materials for technological applications, especially in solar cells, offering insights for researchers across materials science, physics, and engineering. This work provides a computational analysis of a promising material namely $YbInO_3$, to demonstrate how theoretical predictions might lead to potential applications. Specifically, we will explore how perovskites materials serve as a bridge in material science and subdomains such as quantum light sources, spin-based quantum technologies.

2 Crystal structure and phase formation

The perovskites of interest here are materials with general chemical formula ABO_3 where A is a rare-earth, B is a transition metal, and form within the Pm-3m space group (n°. 221). In this group, the A cation is assigned the coordinates (0, 0, 0), the B cation is positioned at (1/2, 1/2, 1/2), and the O anions are situated at (1/2, 1/2, 0), (1/2, 0, 1/2), and (0, 1/2, 1/2) locations. Figure 1 gives a schematic representation of the perovskite crystal structure. The rare-earth atoms occupy the center of the cube. The B atoms occupy the corners of the cube and the O atoms occupy the sides of the cube. The corner-sharing BX_6 octahedra form a 3D network as seen on the picture. It is possible to customize the properties of perovskites by substituting atoms in different sites (A, B, and O). For instance, toxic chemical like Pb^{2+} ions is substituted by Sn^{2+} on the B site in halide perovskites [15] to reduce the toxicity of the material while affecting the band structure.

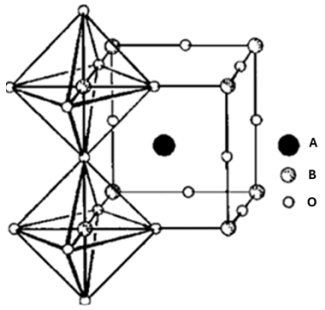

Figure 1: General crystal structure representation of perovskites with general chemical formula ABO_3.

One of the earliest report on the series is in 1950's with the crystal structure study of $GdFeO_3$ by Geller [16] and its magnetic property studies by Gilleo [17]. The first and most comprehensive study on the series ABO_3 was synthesized by V.M. Goldschmidt wherein they identified their overall structural characteristics. Furthermore, they examined the components that determine the kind of structure and provided clear evidence of the significant effect of ionic radius and ionic polarizability as variables. He derived the so-called "tolerance factor t" given by

equation (1), which determine the type of structure expected depending on the ionic radii [18].

$$t = \frac{R_A + R_O}{\sqrt{2}(R_B + R_O)}, \tag{1}$$

where R_A and R_B are the ionic radius of the A and B cations respectively, R_O is the ionic radius of oxygen. For $t = [0.77 - 1.00]$, a perovskite structure is obtained. Specifically, a cubic perovskite structure is obtained for $t = [0.80-1.00]$. It also indicates that the material possesses ferroelectric properties or not. In 2014, TIDROW [19] developed a new model based on some physical constraints and compared it with the Goldschmidt formalism. First, he found that for low-symmetry crystals, the obtained tolerance lies with Goldschmidt's tolerance in the interval $0.77 < \mathbf{t} < 1.00$. Second, he found that, that structural instability increases in the region close to the upper limit tolerance interval t = 1.00. Third, the cubic phase can be formed in perovskite even for tolerance factor value less than 1.00 and outside the tolerance factor range $0.77 < t < 1.05$.

3 Case study: Monte Carlo simulation of the new material $YbInO_3$

The preliminary investigation of the new perovskite material $YbInO_3$ was carried out. The Yb^{3+} ion possesses a strongly correlated $4f^{13}$ electron configuration, which is a Kramers ion. This makes it a prime candidate for hosting complex magnetic phenomena, such as geometric frustration and quantum spin liquid states. Its magnetic moment is well-suited for investigation using the Ising model in our Monte Carlo simulations. Indium was chosen primarily for its non-magnetic nature (In^{3+} has a closed-shell electronic configuration, d^{10}). This choice allows us to isolate the magnetic interactions originating solely from the Yb^{3+} ions on the A-site. This simplifies the magnetic Hamiltonian and helps us attribute the observed magnetic phase transition at 65 K to the Yb-sublattice, without complications from magnetic interactions on the B-site. Therefore, the $YbInO_3$ combination was selected to create a model system where the magnetic properties are likely dominated by a frustrated rare-earth sublattice, making it an ideal candidate for our study of quantum magnetic phenomena." The Goldschmidt parameter introduced earlier was calculated to determine the crystal structure of the compound. A tolerance factor of 0.8 suggests an orthorhombic structure, according to Philipp et al. [20]. The database of quantum materials (OQMD) [21], which is a database of DFT-calculated thermodynamic and structural properties of materials, was used to estimate the lattice constants in the absence of experimental data in the $YbInO_3$ system. These are a = 5.973 Å, b = 7.488 Å, and c = 5.696 Å. The starting point for our analysis is the hamiltonian H where only the first nearest neighbor was considered:

$$H = -\sum_{\langle ij \rangle} J_{ij} S_i S_j \tag{2}$$

where J_{ij} is the exchange coupling parameter; $\langle ij \rangle$ denotes the first nearest neighbors; and S_i and S_j are spins at site ***i*** and ***j***, respectively. The energy of the system E = -5.74 eV used was obtained from the OQMD. Monte Carlo simulation combined with Metropolis algorithm has been performed in the frame of Ising model to simulate the energy of the system; magnetization; magnetic susceptibility (χ); and specific heat (C_v) using the following formula:

$$E = \frac{< H >}{N}, \tag{3}$$

$$M = \frac{|\sum_{\mathrm{i}}^{\mathrm{Yb}} - \sum_{\mathrm{i}}^{\mathrm{In}}|}{N}, \tag{4}$$

$$\chi = \frac{(\langle M^2 \rangle - \langle M \rangle^2)}{k_{\mathrm{B}} T}, \tag{5}$$

$$C = \frac{(\langle E^2 \rangle - \langle E \rangle^2)}{k_{\mathrm{B}} T^2}, \tag{6}$$

where k_{B} is the Boltzmann constant, T the temperature, and N the number of spins in the system. The quantities listed above have been simulated as function of the lattice size ranging from L = 8 to L = 24. The transition

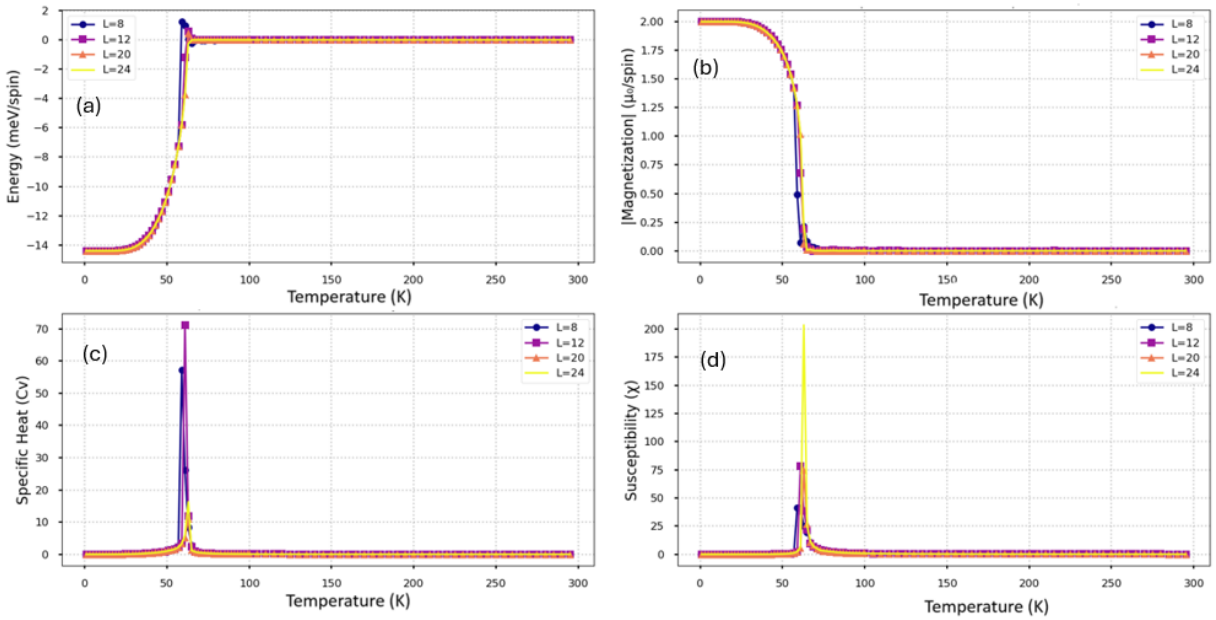

Figure 2: (a): Internal energy as a function of temperature for different lattice sizes. (b): Total magnetization as a function of temperature for different lattice sizes. (c): Specific heat as a function of temperature for different lattice sizes. (d): Magnetic susceptibility as a function of temperature for different lattice sizes.

temperature T_C has been found by this simulation around 65 K for small lattice sizes. The sharp drop in the energy curve at 65 K depicts the presence of a magnetic phase transition in the material. This phase transition lies with the peak observed in the magnetic susceptibility and specific heat curve. The gradual increase in the energy curve is a sign of thermal population of excited states leading by a plateau which is a sign of energy saturation. The sample therefore becomes paramagnetic. The increase in lattice size stabilizes the ordered phase as observed in all four graphs. Our findings show long range order at 65 K in contrast to other reported perovskites like $YbAlO_3$ and $TbInO_3$ which exhibit Quantum Spin Liquids behaviour [6, 9]. The fact that $YbInO_3$ does order magnetically suggests that while it may be frustrated (as indicated by its lattice geometry), the balance of exchange interactions (J_{ij}) in $YbInO_3$ ultimately leads to long-range order, unlike in the true Quantum Spin Liquids systems. The signature of the phase transition in $YbInO_3$ is qualitatively similar to that observed in classic antiferromagnets like $GdFeO_3$. However, the transition temperature (65 K for $YbInO_3$) is significantly lower than that of $GdFeO_3$ (660 K). This large difference can be attributed to two factors. First, the 4f orbitals of Yb^{3+} are more localized and shielded than the 4f orbitals of Gd^{3+}, leading to weaker superexchange interactions between magnetic ions. Second, The magnetic lattice in $YbInO_3$ is likely frustrated, which suppresses the transition temperature compared to an unfrustrated antiferromagnet like $GdFeO_3$. The gradual broadening of the specific heat peak with increasing lattice size in our simulations can be a signature of this underlying frustration.

4 Conclusion

Rare-earth perovskites offer a unique interplay of electron correlations, strong spin-orbit coupling, and structural versatility. These make them stand at the forefront of the quantum materials revolution. They offer a platform to discover and study materials such as quantum spin liquids and qubit hosts. By combining theory, computational and experimental work, rare-earth perovskites will open up new possibilities in fields such as spintronics and quantum computing. Preliminary structural and DFT results of $YbInO_3$ suggest a magnetic ordering in the material. Knowing that this material is prone to frustration due to the geometry of the lattice, it is worth investigating the experimental physical properties to get an insight into the features of the material.

References

[1] A. Kojima, K. Teshima, Y. Shirai, and T. Miyasaka, "Organometal halide perovskites as visible-light sensitizers for photovoltaic cells," *Journal of the american chemical society*, vol. 131, no. 17, pp. 6050–6051, Apr.

2009.

[2] L. Zhu, R. Ran, M. Tade, W. Wang, and Z. Shao, "Perovskite materials in energy storage and conversion," *Asia-Pacific Journal of Chemical Engineering*, vol. 11, no. 3, pp. 338–369, May 2016.

[3] H. Khan, S. E. Lofland, J. Ahmed, K. V. Ramanujachary, and T. Ahmad, "Emerging rare earth perovskite nanostructures for efficient electrochemical energy conversion and storage," *International Journal of Hydrogen Energy*, vol. 58, pp. 954–963, Mar. 2024.

[4] L. Zhang, L. Mei, K. Wang, Y. Lv, S. Zhang, Y. Lian, X. Liu, Z. Ma, G. Xiao, Q. Liu *et al.*, "Advances in the application of perovskite materials," *Nano-Micro Letters*, vol. 15, no. 1, p. 177, Jul. 2023.

[5] H. Yamamoto, S. Okamoto, and H. Kobayashi, "Luminescence of rare-earth ions in perovskite-type oxides: from basic research to applications," *Journal of Luminescence*, vol. 100, no. 1-4, pp. 325–332, Dec. 2002.

[6] L. Wu, S. Nikitin, Z. Wang, W. Zhu, C. D. Batista, A. Tsvelik, A. M. Samarakoon, D. A. Tennant, M. Brando, L. Vasylechko *et al.*, "Tomonaga–luttinger liquid behavior and spinon confinement in $YbAlO_3$," *Nature communications*, vol. 10, no. 1, p. 698, Feb. 2019.

[7] S. Nikitin, T. Xie, A. Podlesnyak, and I. A. Zaliznyak, "Experimental observation of magnetic dimers in diluted Yb: $YbAlO_3$," *Physical Review B*, vol. 101, no. 24, p. 245150, Jun. 2020.

[8] L. Wu, S. E. Nikitin, M. Brando, L. Vasylechko, G. Ehlers, M. Frontzek, A. T. Savici, G. Sala, A. D. Christianson, M. D. Lumsden *et al.*, "Antiferromagnetic ordering and dipolar interactions of $YbAlO_3$," *Physical Review B*, vol. 99, no. 19, p. 195117, May 2019.

[9] L. Clark, G. Sala, D. D. Maharaj, M. B. Stone, K. S. Knight, M. T. Telling, X. Wang, X. Xu, J. Kim, Y. Li *et al.*, "Two-dimensional spin liquid behaviour in the triangular-honeycomb antiferromagnet $TbInO_3$," *Nature Physics*, vol. 15, no. 3, pp. 262–268, Mar. 2019.

[10] J. Kim, X. Wang, F.-T. Huang, Y. Wang, X. Fang, X. Luo, Y. Li, M. Wu, S. Mori, D. Kwok *et al.*, "Spin liquid state and topological structural defects in hexagonal $TbInO_3$," *Physical Review X*, vol. 9, no. 3, p. 031005, Jul. 2019.

[11] A. Arab, X. Liu, O. Köksal, W. Yang, R. U. Chandrasena, S. Middey, M. Kareev, S. Kumar, M.-A. Husanu, Z. Yang *et al.*, "Electronic structure of a graphene-like artificial crystal of $NdNiO_3$," *Nano letters*, vol. 19, no. 11, pp. 8311–8317, May 2019.

[12] A. Moskvin, "Dzyaloshinskii interaction and exchange-relativistic effects in orthoferrites," *Journal of Experimental and Theoretical Physics*, vol. 132, pp. 517–547, Apr. 2021.

[13] M. Persson, "Stark shifts and ion-ion interaction in europium doped $YAlO_3$-on the road to quantum computing," *Lund Reports in Atomic Physics*, Mar. 2002.

[14] T. Katsufuji and H. Takagi, "Coupling between magnetism and dielectric properties in quantum paraelectric $EuTiO_3$," *Physical Review B*, vol. 64, no. 5, p. 054415, Jul. 2001.

[15] G. Volonakis, M. R. Filip, A. A. Haghighirad, N. Sakai, B. Wenger, H. J. Snaith, and F. Giustino, "Lead-free halide double perovskites via heterovalent substitution of noble metals," *The Journal of Physical Chemistry Letters*, vol. 7, no. 7, pp. 1254–1259, Mar. 2016.

[16] S. Geller, "Crystal structure of gadolinium orthoferrite, $GdFeO_3$," *The Journal of Chemical Physics*, vol. 24, no. 6, pp. 1236–1239, Jun. 1956.

[17] M. Gilleo, "Magnetic properties of a gadolinium orthoferrite, $GdFeO_3$, crystal," *The Journal of Chemical Physics*, vol. 24, no. 6, pp. 1239–1243, Jun. 1956.

[18] V. M. Goldschmidt and D. Holmsen, *Geochemische Verteilungsgesetze Der Elemente*. In Kommission bei J. Dybwad, 1927, no. 1.

[19] S. C. Tidrow, "Mapping comparison of goldschmidt's tolerance factor with perovskite structural conditions," *Ferroelectrics*, vol. 470, no. 1, pp. 13–27, Jul. 2014.

[20] J. Philipp, P. Majewski, L. Alff, A. Erb, R. Gross, T. Graf, M. Brandt, J. Simon, T. Walther, W. Mader *et al.*, "Structural and doping effects in the half-metallic double perovskite A_2CrWO_6 (A= Sr, Ba, and Ca)," *Physical Review B*, vol. 68, no. 14, p. 144431, Oct. 2003.

[21] J. E. Saal, S. Kirklin, M. Aykol, B. Meredig, and C. Wolverton, "Materials design and discovery with high-throughput density functional theory: the open quantum materials database (oqmd)," *Jom*, vol. 65, no. 11, pp. 1501–1509, Sep. 2013.

Investigating the Photoluminescent Properties of Fe^{3+} doped $ZnAl_2O_4$: A Multifunctional Material for Emerging Applications

ED Magasi[1], OM Ntwaeaborwa[2], MLA Letswalo[1] and BM Sondezi[1]

[1]Physics Department, University of Johannesburg, Auckland Park, Johannesburg 2006, South Africa.
[2]Department of Physical and Earth Science, Sol Plaatjie University, Kimberley 8301, South Africa.

E-mail: bmsondezi@uj.ac.za and letswalom@uj.ac.za

Abstract. Zinc aluminate ($ZnAl_2O_4$) is a member of the spinel family, which has attracted great research interest due to its diverse properties such as hydrophobicity, chemical stability, impressive fluorescence efficiency, and thermal stability. These properties make it a suitable candidate for application in displays, magnetic refrigerators, catalysis, and light-emitting diodes (LEDs). In this study, a well-separated $ZnAl_2O_4$ doped with Fe^{3+} ions was synthesised via the Pechini synthesis method. X-ray diffractometer (XRD) spectra confirmed the formation of a pure $ZnAl_2O_4$ material that crystallized in single-phase cubic symmetry, belonging to the Fd3m space group of $ZnAl_2O_4$. This crystal structure was influenced by the incorporation of Fe^{3+} ions, as seen by the changes in the lattice parameters, indicating a successful substitution of Fe^{3+} ions into the $ZnAl_2O_4$ lattice sites. Energy dispersive X-ray spectroscopy was used for elemental composition investigations, which validated Zn, Al, and O's presence in the pristine sample and confirmed the presence of Zn, Al, O, and Fe in doped $ZnAl_2O_4$ samples. Photoluminescence (PL) spectroscopy, excited using a xenon lamp, revealed two broad emission bands at approximately 440 nm and 745 nm. These emissions are attributed to the $^4T_1 \rightarrow {}^6A_1$ and $^4T_2 \rightarrow {}^6A_1$ transitions of Fe^{3+} ions, which occupy the tetrahedral (Tet) and the octahedral (Oct) coordination sites, respectively, within the $ZnAl_2O_4$ lattice. The CIE (Commission Internationale de I'Eclairage) confirmed that pure $ZnAl_2O_4$ color emission lay in the blue region and upon doping with varying concentrations of Fe^{3+}, the coordinates were tuned towards the white colour region, indicating a potential for tunable white emission.

1 Introduction

Zinc aluminate ($ZnAl_2O_4$) is a significant member of the spinel-aluminate group, which has gained enormous scientific attention in the last three decades due to its outstanding physical and chemical properties [1,2]. These unique sets of properties facilitate their extensive use in applications such as ceramics [3], displays [4], and light-emitting diodes [5]. Additionally, its wide direct band gap of 3.8 eV enables its utilization as a dielectric material, sensor, and optical material [6]. This wide bandgap can be tuned by introducing rare earth or transition metals as dopants to serve as luminescent centers. The emergence of several reports on $ZnAl_2O_4$ doped with transition metals and rare earth ions shows that there is a clear consensus in the scientific community that $ZnAl_2O_4$ is a promising host material for several activator ions [7, 8]. The intended application informs the researcher about

the appropriate dopant and dopant concentration required. For economic reasons, doping with transition metals is explored by researchers in addition to doping with rare earth ions. Additionally, $ZnAl_2O_4$ doped with transition metals has gained attention because of the interesting luminescent properties which are induced by the unique electron configuration of these transition metals. Moreover, transition metals are suitable for tunable radiation sources in optical devices because of their unique emission observed in both the visible and infrared regions [9]. Fe^{3+} in particular has broadband emissions in the higher energy region when doped in a tetrahedral site and in the lower energy region when doped in an octahedral site [9].

Literature shows that several researchers do not consider the effects of charge imbalance when doping and this can lead to poor luminescence efficiency via the formation of charge defects [10-12]. Therefore, this study investigates how Fe^{3+} incorporation into the substitutional Al^{3+} site of $ZnAl_2O_4$ affects the crystal structure and photoluminescence characteristics while maintaining charge balance, with a view toward optimizing white-light emission for LED applications. Charge balance was maintained by substituting a trivalent ion (Al^{3+}) with another trivalent ion (Fe^{3+}), ensuring a direct charge-balanced system.

2 Experimental details

2.1 Sample preparation

Pechini synthesis was used to prepare $ZnAl_2O_4$ phosphors doped with varying mol% of Fe^{3+}. The starting materials included zinc nitrate hexahydrate ($Zn(NO_3)_2{\cdot}6H_2O$) (99.98%), aluminum nitrate nonahydrate ($Al(NO_3)_3{\cdot}9H_2O$) (99.98%), iron nitrate nonahydrate ($Fe(NO_3)_3{\cdot}9H_2O$) (>98%), tartaric acid ($C_4H_6O_6$) and nitric acid (HNO_3). The pristine sample was prepared by dissolving stoichiometric amounts of $Zn(NO_3)_2{\cdot}6H_2O$ and $Al(NO_3)_3{\cdot}9H_2O$ in 10 millilitres of nitric acid in a glass beaker, and $C_4H_6O_6$ in 40 millilitres of distilled water in a separate glass beaker. Separately, the two solutions were stirred for 20 minutes at 150 ℃ on a hot plate. The two solutions were then mixed, and the mixture was stirred at 150 ℃ for about 2 hours, forming a polymerized resin. After 10 hours of drying at 80 ℃, the sample was crushed into a fine powder and calcined for 3 hours at 600 ℃. The same procedure was repeated with stoichiometric amount of $Fe(NO_3)_3{\cdot}9H_2O$ added to substitute $Al(NO_3)_3{\cdot}9H_2O$ for the synthesis of $ZnAl_{(2-x)}Fe_xO_4$ (x = 0.01, 0.025, 0.05, 0.08 mol%) samples.

2.2 Instrumentation

Powder X-ray diffraction (XRD) investigation using CuK_α ($\lambda = 1.5405$Å) radiation on a MiniFlex600 diffractometer at 40 kV and 15 mA was conducted to characterize the crystal structures. Scanning electron microscopy (SEM) analyses were conducted at 20 kV (using TESCAN VEGA 3 XMU, LMH instrument, Brno, Czech Republic) equipped with an energy dispersive X-ray spectroscopy (EDS) system. To minimize sample charging during SEM characterization, carbon coating was used on the samples. The morphological and chemical composition characterization of the particles in all samples was performed using secondary electron (SE) imaging and spot EDS, respectively. A Horiba QM8000 spectrofluorometer equipped with double excitation and emission monochromators was used to measure photoluminescence spectra. The signal from the sample was detected using a PPD-850 Si photodiode detector, and the excitation source was an Xe lamp.

3 Results and Discussion

3.1 Powder X-ray diffraction analysis

The X-ray diffraction (XRD) patterns of $ZnAl_{(2-x)}Fe_xO_4$ (x=0, 0.01, 0.025, 0.05, 0.08 mol%) are shown in fig. 1(a). The peaks of all the synthesized samples are consistent with the standard phase data of $ZnAl_2O_4$ referenced from the JCPDS file no. 82-1043. The absence of impurity or additional peaks from these samples indicates a single-phase formation, suggesting that the materials crystallized in a single-phase cubic spinel compound belonging to $Fd3m$ space group of $ZnAl_2O_4$. The phase structure of $ZnAl_2O_4$ phosphors was not altered when different Fe^{3+} ion concentrations were introduced into the pristine $ZnAl_2O_4$. This shows that $ZnAl_{(2-x)}Fe_xO_4$ powder samples were successfully synthesized.

It is apparent from Fig. 1(a) that peak (311) is the most intense and was subsequently used to analyze the effects of doping on the peak position, as shown in Fig. 1(b). A noticeable shift towards smaller angles was observed, and this reveals that the dimensions of unit cells (cell parameters) are affected by doping with Fe^{3+} ions

as depicted in Fig. 1(b). This change of lattice parameters observed in Table 1 may be attributed to the substitution of an ion with a smaller ionic radius (Al^{3+} =0.054 nm) by an ion with a larger ionic radius (Fe^{3+}=0.065 nm). Similar results have been reported by several researchers when substituting ions of different ionic radii [13, 14].

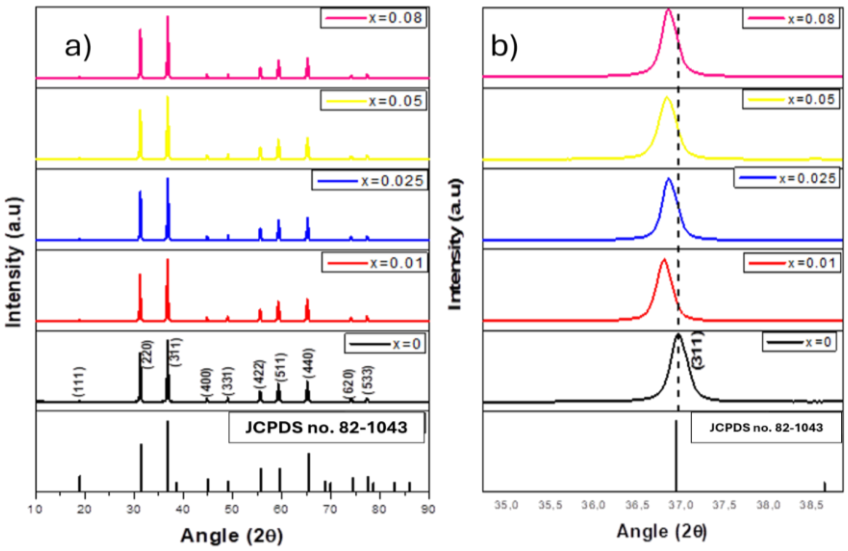

Figure 1: (a) XRD pattern of $ZnAl_{(2-x)}Fe_xO_4$(x =0, 0.01, 0.025, 0.05, and 0.08 mol%) and (b) enlarged XRD pattern of high intensity (311).

Samples	Lattice parameters
	a (Å)
x = 0	8.089
x = 0.01	8.081
x = 0.025	8.087
x = 0.05	8.082
x = 0.08	8.091

Table 1: Depicts estimated lattice parameters of $ZnAl_{(2-x)}Fe_xO_4$ (x=0, 0.01, 0.025, 0.05, 0.08 mol%).

3.2 Morphological and chemical composition analysis

The morphology and the chemical composition of the $ZnAl_{(2-X)}Fe_xO_4$ phosphor materials were examined from the SEM-SE images and EDS, as shown in Fig. 2. Fig. 2(a-d) depicts the EDS spectra of all the phosphors in this work. The presence of Zn, Al, and O in the pristine sample and Fe in the 0.08 mol% doped sample is confirmed by the EDS spectra displayed in Fig. 2(a) and Fig. 2(d), respectively. Fig. 2(e) depicts the morphology of the pristine $ZnAl_2O_4$, which is characterized by irregularly shaped particles with small particles encrusted on the surface of larger particles. These irregularly shaped particles are reduced in size upon doping with 0.01 mol% of Fe^{3+} as shown in Fig. 2(f). Further increment of the dopant concentration to 0.05 and 0.08 mol% resulted in the morphology of the samples showing soft agglomerates that display plate-like irregular morphology with observable grain boundaries and small particles encrusted on the surface of larger particles, as seen in Fig. 2(g and h).

The PL excitation spectra of $ZnAl_2O_4$ phosphors were obtained while maintaining the emission wavelength at 415 nm and scanning the spectrum in the wavelength range of 250-400 nm, as displayed in Fig. 3(a). In the excitation spectra, two prominent broad bands with peaks at 283 and 375 nm were observed and are attributable to the band-to-band transition of $ZnAl_2O_4$ [7,15]. The deconvoluted PL spectra of the undoped $ZnAl_2O_4$ shown in Fig. 3(b), exhibit a broad band between 3 and 4.8 eV. The most prominent broad peak, which has a maximum at 3.49 eV, is assigned to the band-to-band transition of the AlO_6 anion grouping of $ZnAl_2O_4$, while the 3.28 eV

peak is due to the intrinsic intra-bandgap defects such as oxygen vacancies (V_o) of $ZnAl_2O_4$ [9,16]. There is limited literature reporting the 3.10 and 3.91 eV peaks.

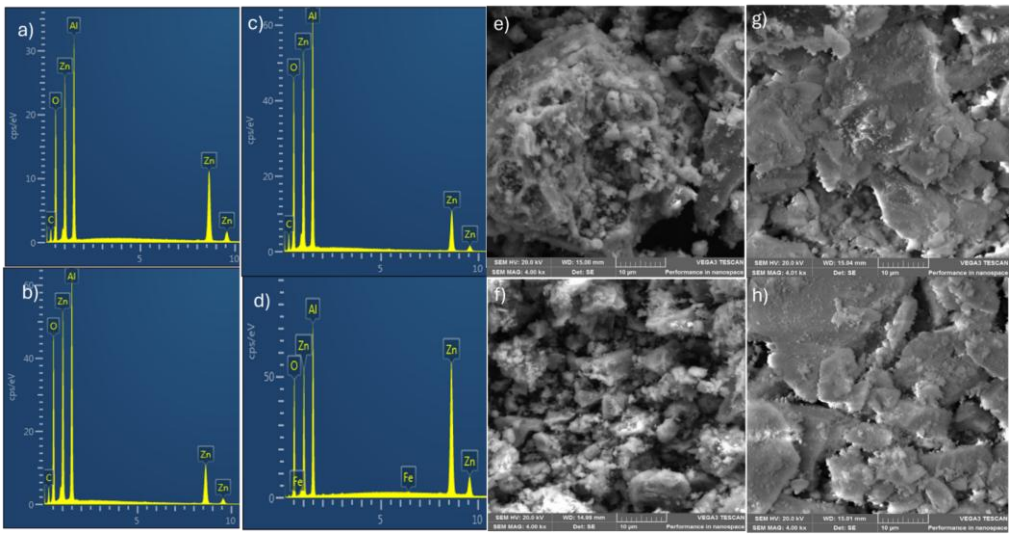

Figure 2: EDS spectra of $ZnAl_{(2-x)}Fe_xO_4$ (a) x = 0, (b) x = 0.01, (c) x = 0.05 and (d) x = 0.08 and corresponding and SEM-SE images (e-h).

3.3 Photoluminescence studies

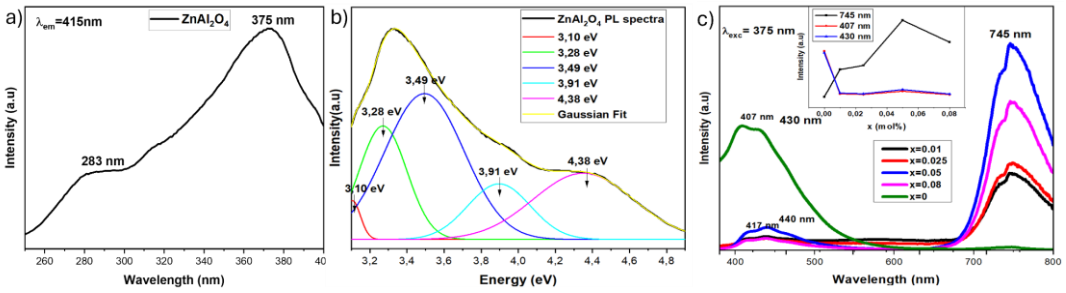

Figure 3: The PL (a) excitation (under λ_{em}= 415 nm) spectra of $ZnAl_2O_4$, (b) the deconvoluted PL excitation spectra of $ZnAl_2O_4$ and (c) emission spectra (under λ_{ex}=375 nm) of $ZnAl_{(2-x)}Fe_xO_4$(x=0, 0.01, 0.025, 0.05, and 0.08 mol%) phosphors. The variation of 407, 430, and 745 nm peaks as a function of Fe^{3+} concentration is shown in the inset of (c).

The PL emission spectra of the $ZnAl_{(2-x)}Fe_xO_4$ (x = 0, 0.01, 0.025, 0.05, and 0.08 mol%) are shown in Fig. 3(c). 407, 430 and 745 nm peaks are observed in this emission spectra with the 407 and 430 nm peaks red shifted to 417 and 440 nm, respectively, upon the introduction of Fe^{3+} dopant into the host material. Doping with Fe^{3+} ions clearly quenches the emission intensities of the 407 and 430 nm peaks and improves the intensity of the 745 nm peak, as can be seen in the emission spectra. The maximum intensities of the 407 and 430 nm peaks are observed in pristine $ZnAl_2O_4$ and their quenching upon doping with Fe^{3+} suggests that these peaks can be attributed to the defect-related intra-band transitions such as oxygen vacancies (V_o) and Zn^{2+} interstitials in the spinel lattice, which are reduced by the introduction of Fe^{3+} ions [5,17]. Several researchers have observed similar cationic redistribution effects and the quenching of the defect-related emissions when introducing Fe^{3+} ions into the crystal structures of different host materials such as ZnO and ZnS with Fe^{3+} [18,19]. This further suggests that the radiative transitions changed and $ZnAl_2O_4$ no longer emits but rather captures primary excited energy and transfers it to Fe^{3+} dopants. The relation between emission intensities and Fe^{3+} concentration is depicted in the insert of Fig. 3(c). This inset shows a sharp drop of the 407 and 430 nm peaks and an enhancement of the 745 nm peak upon the introduction of Fe^{3+} dopant.

The intensity of the 745 nm peak, on the other hand, increased remarkably upon doping with Fe^{3+} ions, with the maximum intensity observed when x = 0.05 mol% Fe^{3+} doping concentration, beyond which the emission intensity decreases. This quenching of the emission intensity at higher concentration can be attributed to concentration quenching effects. The 417 and 440 nm emission peaks can be attributed to tetrahedral coordinated Fe^{3+} ions while the 745 nm peak can be attributed to the octahedral coordinated Fe^{3+} ions because $ZnAl_2O_4$ has two different substitutional sites namely, tetrahedral, and octahedral site and Fe^{3+} dopants emit at shorter wavelength (blue region) when occupying tetrahedral sites and emit at longer wavelength (red region) when occupying octahedral site [7]. Pathak et al. [8] observed similar peaks at 440 and 740 nm, which were attributed to the tetrahedral-coordinated and octahedral-coordinated Fe^{3+} ions, respectively. Furthermore, the emission from the tetrahedral coordinated Fe^{3+} ions in this study is ascribed to the $^4E + {}^4A_1(^4G) \rightarrow {}^6A_1(^6S)$ transition, while the emission related to the octahedral coordinated Fe^{3+} ions belongs to the $^4T_2(^4G) \rightarrow {}^6A_1(^6S)$ transition [20, 21].

3.4 Commission Internationale de I'Eclairage (CIE) chromaticity studies

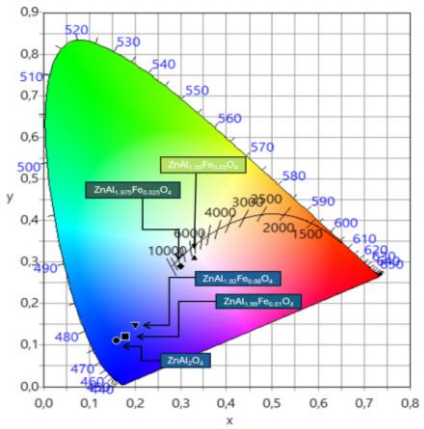

Figure 4: CIE chromaticity diagram of $ZnAl_{(2-x)}Fe_xO_4$ (x=0, 0.01, 0.025, 0.05, and 0.08 mol%).

From the emission spectra, the CIE coordinates of $ZnAl_{(2-x)}Fe_xO_4$ phosphors were calculated to determine the possible color emission points lying on the horse-shoe curve of the visible spectrum as shown in Fig. 8. The calculated color coordinates (x, y) of pure $ZnAl_2O_4$ were found to be (0.16; 0.11) which shifted towards the white region upon doping with Fe^{3+}. Doping with x = 0.05 mol% Fe^{3+} ions influenced these coordinates and shifted them to (0.33; 0.31), which are closer to those of white color coordinates. The standard coordinates of white color are (0.33; 0.33) [5]. Increasing the Fe^{3+} dopants concentration to x = 0.08 shifted the coordinates to (0.30; 0.29), which is a shift towards the blue region. This indicates that $ZnAl_{(2-x)}Fe_xO_4$ is a promising phosphor for use as a source of blue and white light in LED lighting systems.

4 Conclusion

In this work, the effects of Fe^{3+} concentrations on the photoluminescent properties of $ZnAl_2O_4$ were investigated. The XRD patterns demonstrated a successful crystallization of a single-phase cubic spinel $ZnAl_2O_4$ that was not affected by the Fe^{3+} doping. PL emission peaks attributable to defect-related intra-band transitions were observed for undoped $ZnAl_2O_4$ and were quenched upon doping with Fe^{3+}. Significant enhancement of the 745 nm peak attributed to octahedrally coordinated Fe^{3+} was observed, with the maximum emission peak observed for the 0.05 mol% doped sample, above which the intensity dropped. Pristine $ZnAl_2O_4$ emitted in the blue region, which shifted towards white color upon doping. These findings not only contribute to understanding transition metal-doped spinel phosphors but also pave the way for designing efficient, tunable phosphor materials for LED technology.

References

[1] Z. Xu, Y. Li, Z. Liu, and Z. Xiong, "Low-temperature synthesis of nanocrystalline $ZnGa_2O_4$: Tb^{3+}phosphors via the Pechini method," Materials Science and Engineering, B, 110(3), pp.302-306, 2004.

[2] M.A. Lahmer, "The effect of Fe^{3+}-doping on the electronic, optical and magnetic properties of $ZnAl_2O_4$; a first-principles study," Computational Condensed Matter, 20(14), pp.387-392, 2019.
[3] X. Duan, D. Yuan, X. Wang, and H. Xu, "Synthesis and characterization of nanocrystalline zinc aluminium spinel by a new sol-gel method," Journal of Sol-Gel Science and Technology, 35(3), pp.221-224, 2005..
[4] B. Huang, Y.S. Chang, H.L. Chen, C.C. Hwang, C.J. Jian, Y.S. Chen, and M.T. Tsai, "Preparation and luminescence of green-emitting $ZnAl_2O_4$:Mn^{2+} phosphor thin films," Thin Solid Films, 570(9), pp.451-456, 2014.
[5] D. Zhang, B. Zhu, S. Ren, Q. Wang, Q. Wang, S. Li, B. Zhang, and W. Wang, "The white light caused by defects and complex cation distribution in $ZnAl_{(2-x)}Fe_xO_4$ magnetic nanocrystals," Materials Research Express, 8(12), pp.2590-2601, 2021.
[6] S. Sameera, V. Vidyadharan, S. Sasidharan, and K.G. Gopchandran, "Nanostructured zinc aluminates: A promising material for cool roof coating," Journal of Science: Advanced Materials and Devices, 4(4), pp.524-530, 2019.
[7] S.N. Ogugua, O.M. Ntwaeaborwa, and H.C. Swart, "Luminescence, structure, and insight on the inversion degree from normal to inverse spinel in a $ZnAl_{(2-x)}Fe^{3+}XO_4$ system," Boletín de la Sociedad Española de Cerámica y Vidrio, 60(3), pp.147-162, 2021.
[8] N. Pathak, S.K. Gupta, K. Sanyal, M. Kumar, R.M. Kadam, and V. Natarajan, "Photoluminescence and EPR studies on Fe^{3+} doped $ZnAl_2O_4$: an evidence for local site swapping of Fe^{3+} and formation of inverse and normal phase," Dalton Transactions, 43(24), pp.9313-9323, 2014.
[9] B.S. Ravikumar, H. Nagabhushana, S.C. Sharma, and B.M. Nagabhushana, "Low temperature synthesis, structural and dosimetric characterization of $ZnAl_2O_4$: Ce^{3+}nanophosphor," Spectrochimica Acta Part A: Molecular and Biomolecular Spectroscopy, 122(6), pp.489-498, 2014.
[10] P. Kumari, and Y. Dwivedi, "Structural and photophysical investigations of bright yellow emitting Dy:$ZnAl_2O_4$ nanophosphor," Journal of Luminescence, 178(3), pp.407-413, 2016.
[11] M. Bouguerra, M. Samah, M.A. Belkhir, A. Chergui, L. Gerbous, G. Nouet, D. Chateigner, and R. Madelon, "Intense photoluminescence of slightly doped ZnO–SiO_2 matrix," Chemical physics letters, 425(1-3), pp.77-81, 2006.
[12] M. Jain, Manju, M. Kumar, H.H. Lee, S.O. Won, K.H. Chae, G. Gupta, A. Vij, and A. Thakur, "Role of Fe^{3+} in altering the degrees of freedom in $ZnAl_2O_4$ spinel," Journal of Applied Physics, 130(5), p.055103, 2021.
[13] Y. Zhang, R. Huang, H. Li, D. Hou, Z. Lin, J. Song, Y. Guo, H. Lin, C. Song, Z. Lin, and J. Robertson, "Germanium substitution Cr^{3+} doped zinc aluminate phosphors with bright and super-long near-infrared persistent luminescence," Acta Materialia, 155, pp.214-221, 2018.
[14] S. Siragam, R.S. Dubey, L. Pappula, and G.S. Babu, "Zinc Aluminate-Based Composite Nanoparticles for Microwave Applications," ACS Omega, 7(27), pp.23393-23400, 2022.
[15] M.C. Neves, T. Trindade, M. Peres, J. Wang, M.J. Soares, A. Neves, and T. Monteiro, "Photoluminescence of zinc oxide supported on submicron silica particles," Materials Science and Engineering: C, 25(5-8), pp.654-657, 2005.
[16] S.V. Motloung, F.B. Dejene, H.C. Swart, and O.M. Ntwaeaborwa, "Effects of Pb^{2+} ions concentration on the structure and PL intensity of Pb-doped $ZnAl_2O_4$ nanocrystals synthesized using sol–gel process," Journal of Sol-Gel Science and Technology, 70(3), pp.422-427, 2014.
[17] M. Jain, M. Kumar, H.H. Lee, S.O. Won, K.H. Chae, G. Gupta, A. Vij, and A. Thakur, "Thermally induced cation ordering in $ZnAl_2O_4$:Mg^{2+}, Fe^{3+} for sensing thermal history through photoluminescence," Journal of Materials Science, 56(21), pp.12111-12120, 2021.
[18] N. Eryong, L. Donglai, Z. Yunsen, B. Xue, Y. Liang, J. Yong, J. Zhifeng, and S. Xiaosong, "Photoluminescence and magnetic properties of Fe-doped ZnS nanoparticles synthesized by chemical co-precipitation," Applied Surface Science, 257(21), pp.8762-8766, 2011.
[19] K. Kumar, M. Chitkara, I.S. Sandhu, D. Mehta, and S. Kumar, "Photocatalytic, optical and magnetic properties of Fe-doped ZnO nanoparticles prepared by chemical route," Journal of Alloys and Compounds, 588, pp.681-689, 2014.
[20] Z. Wen-Chen, W. Xiao-Xuan, H. Lv, and M. Yang, "An alternative interpretation of the optical spectra for Fe^{3+}-doped $KTaO_3$ crystals," Journal of luminescence, 126(1), pp.91-93, 2007.
[21] G.T. Pott, and B.D. McNicol, "The luminescence of Fe^{3+} and Cr^{3+} in α-gallia," Journal of Luminescence, 6(3), pp.225-228, 1973.

Structural and optical properties of rare earth (Sm^{3+})-doped hematite nanostructures

Ntokozo G Cebekhulu[1], Ceboliyazakha L Ndlangamadla[1], Prince S Mkwae[1], Donald D Hile [1], Sipho E Mavudla[2], and Siphamandla Masekane [2]

[1]Department of Physics, University of Zululand, KwaDlangezwa Campus, KwaZulu-Natal, South Africa.

[2] Department of Chemistry, University of Zululand, KwaDlangezwa Campus, KwaZulu-Natal, South Africa.

E-mail: ntokozongc200@gmail.com

Abstract. Samarium (Sm^{3+})(0-6%) doped hematite (α-Fe_2O_3) nanostructure were synthesized using the hydrothermal method and characterized to evaluate structural and optical modifications. X-ray diffraction confirmed the rhombohedral of α-Fe_2O_3 structure in the 3RC spacing group with reduced crystallite size upon the (Sm^{3+}) doping. Transmission electron microscopy revealed morphology changes from spherical particles to nanorods with increasing dopant concentration. Fourier transform infrared spectroscopy verified Fe-O bonding and indicated a shift in the transmittance due to Sm^{3+} incorporation. Ultraviolet-visible spectroscopy analysis shows a progressive band gap narrowing from 2.23 eV to 1.81 eV as Sm^{3+} content increased, enhancing light absorption. The observed structural and optical transformations suggest the potential of Sm^{3+}-doped α-Fe_2O_3 for improved performance in optoelectronic and sensing applications.

1 Introduction

Hematite (α-Fe_2O_3) has been viewed as one of the promising materials in different applications such as gas sensing, water purification, and solar cells[1]. This material shows the crystalline structure, which is rhombohedral in the 3Rc space group, with the band gap energy typically ranging from 1.9 - 2.2 eV. α-Fe_2O_3 is a non-toxic material, low cost, and it is more stable at temperatures below 657 K[2][3]. However, based on a previous reported study on hematite, it is clear that there is a noticeable gap in the performance of this material. High operating temperature conditions, low response, and long stability tend to cause problems for hematite material. This study aims to fulfil the gap on the α-Fe_2O_3 material, which has lower response and recovery time, especially in gas sensing applications[4]. Based on the existing reported works, there are many methods of improving the properties of the materials, which include decorating the material with other elements such as palladium, forming the hetero junction structure (n-n),(p-p), and (n-p). Another effective method is through doping with other elements. This work reports an investigation of the effect of doping with the rare earth element on the α-Fe_2O_3 material [4]. This is mainly because most rare earth elements have been viewed as one of the promising metals in enhancing the properties of the materials [5].

2 Experimental method

Hydrothermal synthesis was used as the main method for preparing the undoped and Sm^{3+} doped α-Fe_2O_3 materials. The starting materials are as follows: Iron chloride purity 99%, distilled water, ammonia solution, samarium with the purity of 99%, and ethanol. The calculated mass of the iron source was mixed with distilled water using a magnetic stirrer to form the solution, and the pH was kept at a value of 8 for all prepared samples. The ammonia solution was added dropwise to the prepared solution to form the precipitate. As-prepared solution was transferred into the autoclave system, and it was heated at the operating temperature of $160\,^{\circ}\mathrm{C}$ for 4hr. After the reaction was completed, the autoclave was allowed to cool naturally at room temperature. The as-prepared solution was then washed in a centrifuge using distilled water and ethanol. A silver nitrate standard solution was used to test for the presence of chlorides to confirm the completion of the washing process. The final product was dried in an oven for 4hr and it was also calcined in open air with a temperature of $500\,^{\circ}\mathrm{C}$ on the Furnace system to obtain the α-Fe_2O_3 materials. For the Sm^{3+}-doped samples, the same procedure was repeated but with the addition of different percentages (2, 4, and 6%) of Sm^{3+} ions.

3 Characterization Techniques

The structural properties of α-Fe_2O_3, and Sm^{3+}-α-Fe_2O_3 doped were characterized using X-ray diffraction (XRD), which used $\mathrm{Cu}/K\alpha$ radiation as the source with the wavelength of $\lambda = 1.5418$ [6]. The morphology was analysed using transmission electron microscopy (TEM). The chemical bonding of the undoped and doped material was investigated using the Fourier transform infrared (FT-IR) spectroscopy instrument. The optical properties were carried out using Ultraviolet-visible (UV-Vis) spectroscopy with a wavelength range from 200 - 800 nm to study the properties of the undoped and Sm-doped nanostructures materials.

4 Result and Discussion

4.1 XRD analysis

The (XRD) pattern displayed in Figure 1 (a) shows the diffraction peaks corresponding to nanoparticles of α-Fe_2O_3 NPs with the peaks allocated to the (012), (104),(110),(113),(024),(116),(214) and (300) planes, confirming the Rhombohedral structure in R3c space group. Figure 1 (b) represents the enlarged pattern of the XRD for the most intense peaks to further study the influence of doping with Sm^{3+} on α-Fe_2O_3 Np. The crystallite size (D) of the undoped and Sm^{3+}-doped materials was determined using Scherrer's equation [7][8].

$$D = \frac{K\lambda}{\beta \cos\theta} \tag{1}$$

where D is crystallite size in nanometers (nm), K is the shape constant with an approximate value of 0.9, λ is the wavelength of the XRD, β is the full width at half maximum (FWHM), and θ represents the braggs angles in (radians). Other important parameters, such as micros train and dislocation density, were calculated to investigate the effect of Sm^{3+} doping using the following equations:

$$\varepsilon = \frac{\beta_{\text{strain}}}{4 \tan\theta} \tag{2}$$

$$\delta = \frac{1}{D^2} \tag{3}$$

Micro strain ε in equation 2 provides information about the crystal plane of the material, whether it is stretched or compressed.While δ on equation 3 represent the dislocation density which helps to find the defect in the materials. The crystallite size (D) calculated from the Scherrer equation, micros train, and dislocation density is presented in the Table 1 for further analysis.

Samples	2θ (deg)	FWHM	$D\,(nm)$	Strain	Dislocation density (m^{-2})
Pure	33.36	0.205	43	0.033	5.40×10^{-4}
2% Sm	33.34	0.365	33	0.060	9.18×10^{-4}
4% Sm	33.36	0.247	35	0.041	8.16×10^{-4}
6% Sm	33.36	0.315	28	0.052	1.27×10^{-3}

Table 1: Crystallographic parameters for undoped and Sm-doped samples.

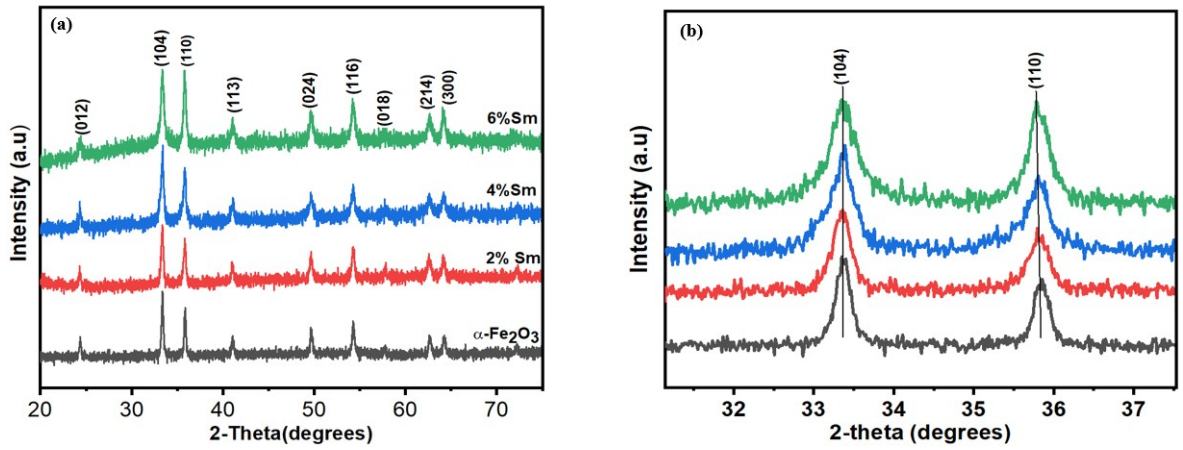

Figure 1: XRD patterns of (a) α-Fe_2O_3 and Sm-α-Fe_2O_3, and (b) Zoomed XRD for peaks (104) and (110).

Based on Figure 1 (b), it is clear that doping with Sm^{3+} influences the peaks position, the broadening, and the intensity. Pure α-Fe_2O_3 has narrower peaks compared to the Sm^{3+} doped α-Fe_2O_3 NPs.Doping with various Sm^{3+} influences the nano size of the materials. The calculated crystallite size (nm) shows a decrease with increasing Sm^{3+} percentages. However, in most cases, the materials with the smallest have the potential to be used in different applications. Hence, in work, the smallest crystallite size was found in the samples doped with 6% of Sm^{3+}. This suggests that 6% Sm^{3+} can show good results in the application of these materials. The morphology of the undoped and Sm-doped is presented in Figure 2.

4.2 TEM analysis

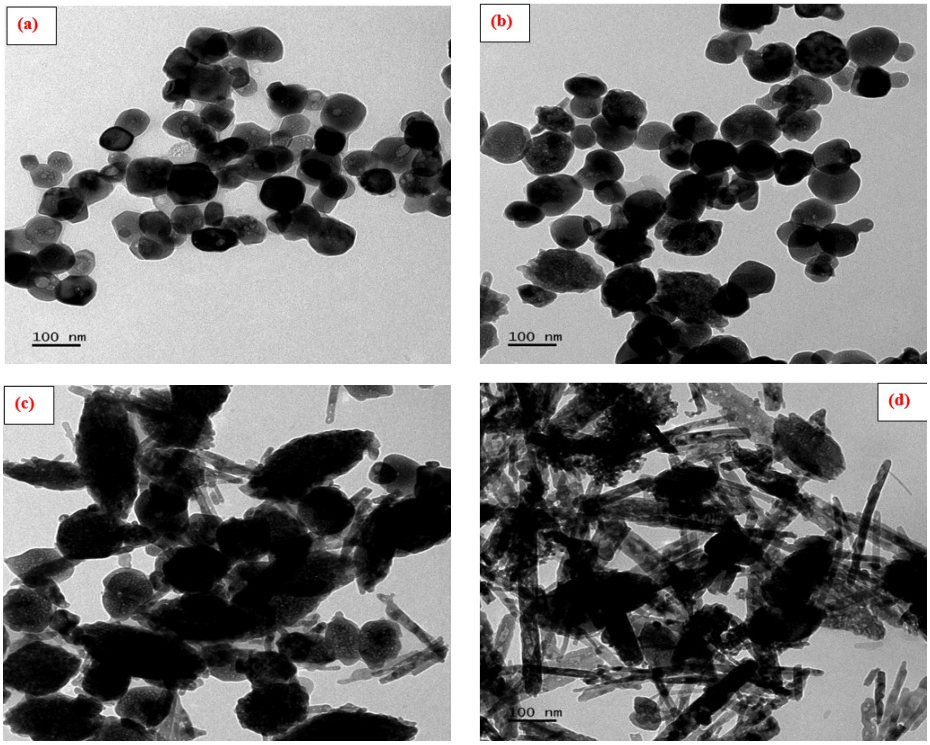

Figure 2: The (TEM) images of the (a) undoped (b) 2% Sm^{3+} (c) 4% Sm^{3+} and 6% Sm^{3+} doped α-Fe_2O_3.

The Morphology of α-Fe_2O_3 and Sm^{3+}-α-Fe_2O_3 was determined using (TEM). Figure 2 represents the TEM images with the particle size of 77, 90, 119, and 115 nm for α-Fe_2O_3, 2, 4, and 6 % Sm^{3+} doped samples, respectively. The increase in the particle size for all doped samples suggest that Sm^{3+} ion incorporation promote the particle growth. Doping with various percentages of Sm^{3+} does influence the morphology as well as the particle size of the material. The α-Fe_2O_3 and 2% Sm^{3+} doped show spherical nanoparticles. However, from 4% Sm^{3+} doped, the morphology start to change from spherical nanoparticles to the nanorods, which increases in the number and size with 6% Sm^{3+} doped. Figure 3 (a-d) represent the calculate particle size of the materials. It is clearer that doping with Sm influence both crystalline and particles size.

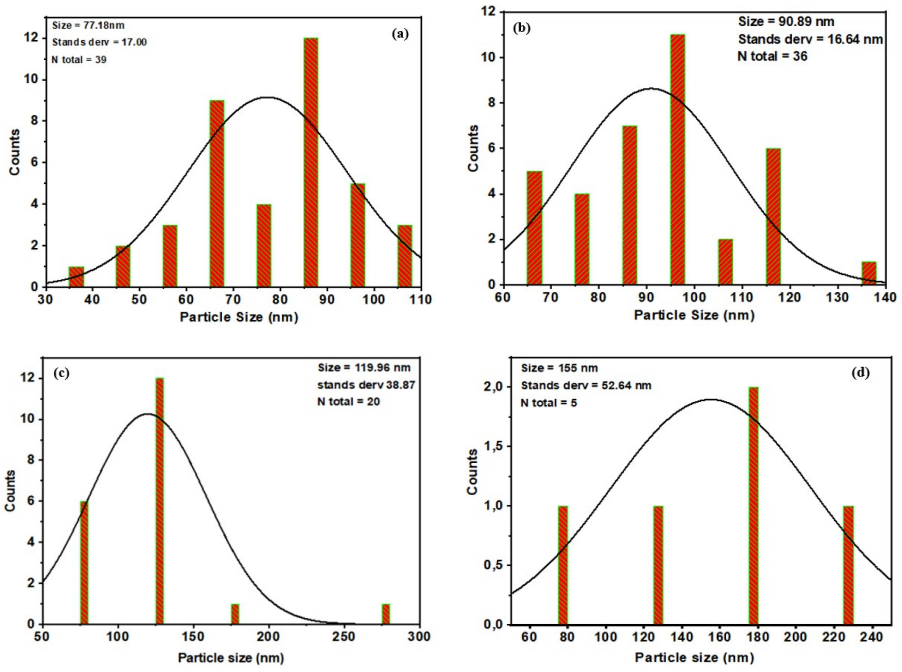

Figure 3: Particle size with fit histograms for the (a) undoped (b) 2% Sm^{3+} (c) 4% Sm^{3+} and 6% Sm^{3+} doped α-Fe_2O_3 NPs with the black line showing a lognormal fit to the data to determine average particle size.

4.3 FT-IR spectrum analysis

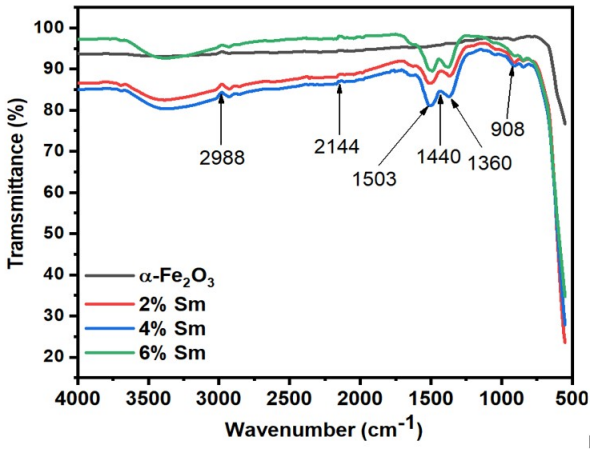

Figure 4: FT-IR analysis of the undoped and Sm-doped materials.

The functional groups of α-Fe_2O_3 and Sm^{3+}-α-Fe_2O_3 were determined using FT-IR spectroscopy in the wavenumber range of 500–4000 cm^{-1} as shown in Figure 4. All doped samples with Sm^{3+} show almost similar trends at different transmittances. Base FT-IR spectroscopy results of materials show bonding at the following wave numbers: 2988 cm^{-1}, 2144 cm^{-1}, 1503 cm^{-1}, and 908 cm^{-1}. The wave number of 2988 cm^{-1} represents the bonding between the C-H atoms, 2144 cm^{-1}, represents the triple bond between the carbon atom, 1503 cm^{-1}, represents the single bond between carbon, and the smallest wave number in this work confirms the formation of the vibration bond, which is between the atom Fe-O. The shifting in the transmittance is due to the effect of doping with Sm^{3+} ions. The optical properties of undoped and Sm-doped were investigated using the UV-Vis spectroscopy to further study the properties of the materials.

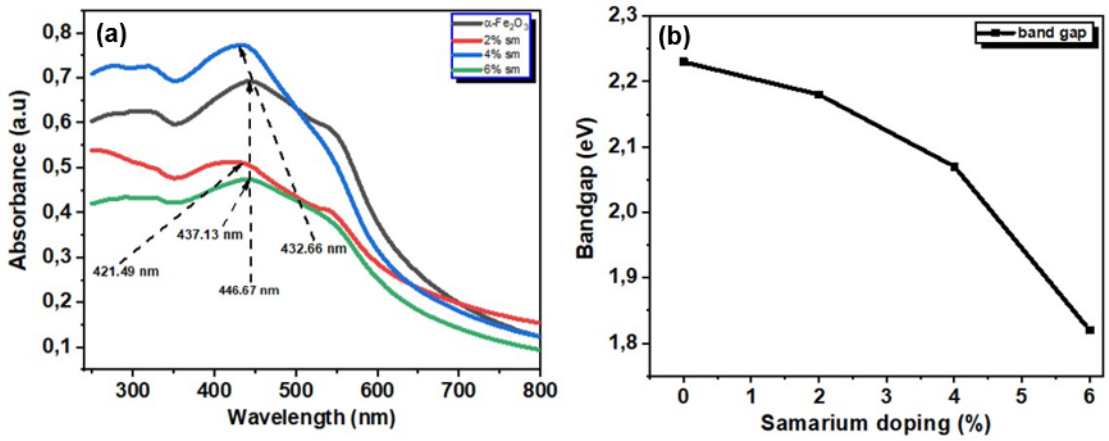

Figure 5: Showing the (a) UV-Vis spectrum analysis, (b) Variation in the band gap of undoped and Sm-doped.

The optical properties of undoped and doped materials with various percentages of Sm^{3+} ions were analysed using the UV-Vis spectroscopy with the wavelength range from 200 to 800 nm. Figure 5 (a) represents UV-vis absorbance spectrum for the α-Fe_2O_3 NPs and Sm^{3+} doped-α-Fe_2O_3 NPs materials. While Figure 5 (b) shows the variation of the band gap energy (eV) of the individual materials calculated using the Tauc plot method. The α-Fe_2O_3 sample shows the high band gap energy of 2.23 eV, which is in line with previous reported work on α-Fe_2O_3 NPs[10]. However, doping with various Sm^{3+} ions leads to decrease in the band gap values. Increasing the percentage of Sm^{3+} doping reduces the band gaps of the material from the undoped value of 2.23 to 1.81 eV at 6% Sm^{3+}. The decrease in the band of the material suggests that those materials can be useful in different applications, such as gas sensing[11].

5 Conclusion

The hydrothermal method was successfully used to synthesis the α-Fe_2O_3 NPs and Sm- α-Fe_2O_3 NPs with 0-6% Sm^{3+} ions. XRD was used to further confirm the formation of α-Fe_2O_3 structure.From the XRD result, it was observed that doping with Sm^{3+} results in an increase in the microstrain of the materials. These results suggest that more defects were created on the materials, and this has a huge role in increasing the gas sensing performance of the materials. While TEM was used to study the surface morphology of the undoped and doped materials. This study demonstrates that Sm^{3+} doping significantly influences the structural, morphological, and optical properties of hematite nanostructures. The reduction in the crystallite size, morphological transition to nanorods, and narrowed band gap highlight the enhanced potential of Sm^{3+}-doped α-Fe_2O_3 for the use in advanced applications such as in gas sensors,photocatalysis, and solar energy conversion systems.

Acknowledgments

The authors acknowledge financial support from the Department of Physics and the National Research Foundation (NRF). I would also like to thank the Department of Chemistry and the UKZN team for characterization techniques (XRD, TEM, UV-Vis, FT-IR).

References

[1] Mirzaei, A., Hashemi, B., and Janghorban, K. *α-Fe_2O_3 based nanomaterials as gas sensors*. *Journal of Materials Science: Materials in Electronics*, **27**, 3109–3144 (2016).

[2] Mathevula, L. E. *Optical and Magnetic Properties of Rare Earth Doped α-Fe_2O_3 for Future Bio-Imaging Applications*, MSc Dissertation, (2018).

[3] Yousef. *Construction of Fe_2O_3/Transition Metal Dichalcogenides Heterostructures for Dyes Photodegradation*. (2023).

[4] Goel, N., Kunal, K., Kushwaha, A., and Kumar, M. *Metal oxide nanostructures-based gas sensors*. *Authorea Preprints*, (2022).

[5] Zhou, R., Lin, X., Xue, D., Zong, F., Zhang, J., Duan, X., Li, Q., and Wang, T. *Enhanced H_2 gas sensing properties by Pd-loaded urchin-like $W_{18}O_{49}$ hierarchical nanostructures*. *Sensors and Actuators B: Chemical*, 900–907 (2018).

[6] Zhang, X., Li, H., Wang, S., Fan, F.-R. F., and Bard, A. J. *Improvement of hematite as photocatalyst by doping with tantalum*. *The Journal of Physical Chemistry C*, 16842–16850 (2014).

[7] Ramadhan, S. F., Muheb, A. S., and Ramadhan, R. A. *Characterization study of synthetic iron oxide nanoparticles at different temperature*. *International Journal of Current Engineering and Technology*, 1686 (2013).

[8] Nasiri, S., Rabiei, M., Palevicius, A., Janusas, G., Vilkauskas, A., Nutalapati, V., and Monshi, A. *Modified Scherrer equation to calculate crystal size by XRD with high accuracy, examples Fe_2O_3, TiO_2 and V_2O_5*. *Materials Chemistry and Physics*, 100015 (2023).

[9] Mushtaq, Muzammil and Sathyakam, P Uma and Vijayaraghavan, R *Performance, comprehension and applications of hematite-based photoanodes in PEC water splitting Next Materials*

[10] Alrobei, Hussein *Synthesis and Characterization of Alpha-Hematite Nanomaterials for Water-Splitting Applicationsalrobei2018synthesis*

[11] Nikolic, Maria Vesna and Milovanovic, Vladimir and Vasiljevic, Zorka Z and Stamenkovic, Zoran Semiconductor gas sensors: Materials, technology, design, and application

Characterization of defects in neutron-irradiated SnO_2 using the positron annihilation technique

DP Motjope[1], L Ngwazi[1], TP Jili[1], PZ Ngcobo[1], M Madhuku[2], A Kwelilanga[2] and PN Biyela[1]
[1]Physics Department, University of Zululand, P/B X1001, Kwadlangezwa, 3886, South Africa
[2]iThemba LABS, 92 Empire Rd, Johannesburg, 2017, South Africa

E-mail: dineopatience02@gmail.com

Abstract. In this work, the two-component density functional theory is employed in the modelling of defects in neutron-irradiated SnO_2. Since defects are localized, the local density approximation (LDA) is utilized. Although LDA gives a good approximation of electron-positron annihilation momentum density at high momentum electron states, it does not consider the variational nature of the electron density. This has an unintended consequence of having overestimated annihilation rates or lower positron lifetimes compared to experimental values. This deficiency in LDA is corrected by using the generalized gradient approximation (GGA), which considers the variation nature of electron density. The accumulation of annihilation spectrum using a coincidence setup is utilized to allow for the determination of annihilation parameters, S and W. The experimentally obtained S-parameter values 0.370812 for unirradiated and 0.374281 for neutron-irradiated SnO_2 suggest an increase in the defect density. Two positron lifetimes, 240 ps and 263 ps for bulk and defect respectively, were obtained in the framework of the generalized gradient approximation (GGA). The average positron lifetime of 252 ps suggests that neutron-irradiation caused displacement damage or open volume vacancies in the material.

1. Introduction

Tin oxide (SnO_2) of space group $P4_2/mnm$ has drawn much attention due to its application in transparent electrodes [1], electron magnetic shielding [2], as well as n-type thin film transistors [3] and in gas sensing [4,5]. Recently, tin oxide has being reviewed as a component in advanced nuclear fuel designs [6]. Therefore, the radiation impact on such a material has, to a lesser extent, been exploited using other techniques and, to even a lesser extent, using positron annihilation technique (PAT). Radiation, especially moderate to fast neutrons, is bound to cause spatial damage in the target material. PAT is a sensitive and non-destructive tool [7-10] for studying the density of defects as well as their nature following the damage caused by the radiation. Irradiation of materials with neutrons introduces several defects, such as vacancies, vacancy clusters, voids, and other types of defects.

In this work, we investigate the defects in pelletized SnO_2 caused by the bombardment of neutrons from Americium-beryllium (AmBe) of activity 300 Gbq. The experimentally obtained Doppler broadening of the annihilation line, which is characterized by the S-parameter, shall serve as a measure of a positron-electron annihilation momentum density at annihilation sites as well as in the bulk. We further extend our study to the annihilation rates due to positrons annihilating with core and valence electrons of tin and oxygen atoms using the local density approximation (LDA) as well as the generalized gradient approximation (GGA).

2. Experiment

Powder SnO_2 was pelletized to a diameter of 0.8 cm and a thickness of 0.4 cm using a pelletizer at the University of Witwatersrand. X-ray diffraction (XRD) was used to ascertain if there was no structural deformation during the powder compression into pellets. The XRD used is a Bruker D8 equipped with a Goebel Mirror. The diffractometer utilized Cu-Kα radiation. Rietveld refinements were carried out using TOPAS 4.2. Figure 1shows the arrangement used during the irradiation of the sample. XRD was also used to check if any structural damage occurred after irradiation.

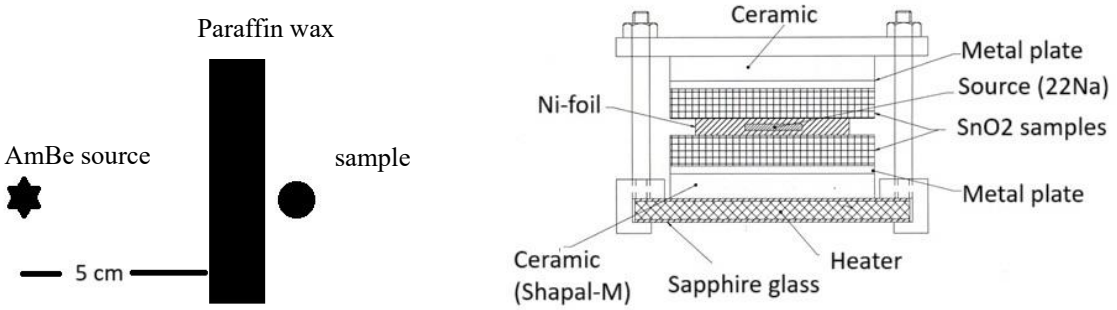

Figure 1: *(left)* The AmBe neutron source – paraffin wax – sample arrangement. This arrangement was employed for irradiation purposes. *(right)* Sandwich arrangement in which ^{22}Na is placed between two equal irradiated samples. This is the source-sample arrangement for the Doppler broadening experiment.

The sample was irradiated for 24 hours with neutrons in the energy range from 0.223 MeV to 2,3 MeV as shown figure 1(left). The irradiated samples and the positron source were organized in a standard sandwich arrangement as shown in Figure 1(right). The activity of the ^{22}Na source, whose decay scheme is shown in Figure 2(a), was 15 μCi. This arrangement was maintained at an average pressure of about 2×10^{-6} Torr. The circuit diagram used for the annihilation measurement is shown in Figure 2(b). A positron emitted from ^{22}Na rapidly thermalizes and diffuses until it finds a vacancy where it annihilates with low momentum electron, producing a pair of gammas (511 keV) in opposite directions. These two photons were detected by a high-purity germanium (HPGe) detector with a resolution of 1.27 keV (FWHM) at the photopeak of 511 keV.

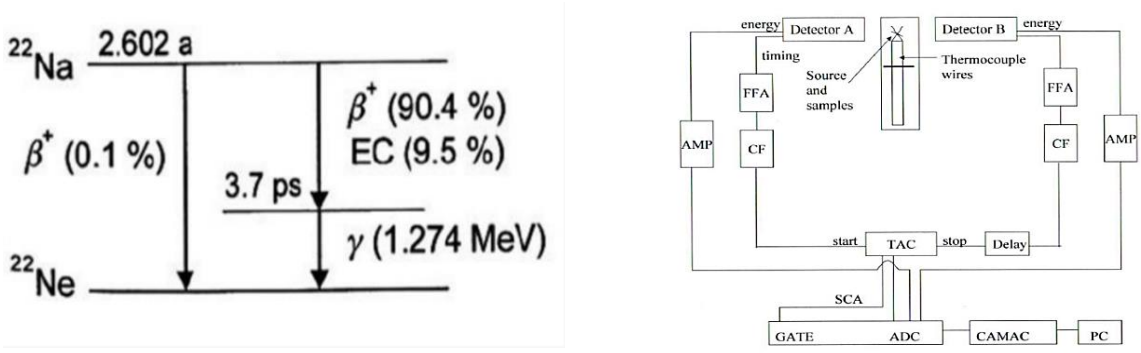

Figure 2: *(left)* The decay scheme of ^{22}Na to ^{22}Ne. The decay is accompanied by the emission of 1275 keV gamma, which is a start signal in positron lifetime measurements. *(right)* Circuit diagram for both Doppler broadening and lifetime measurements.

3. Results and discussion

X-ray diffraction confirmed the absence of structural damage after pressing tin oxide powder into pellets. The XRD pattern is shown in Figure 3 (*right*)

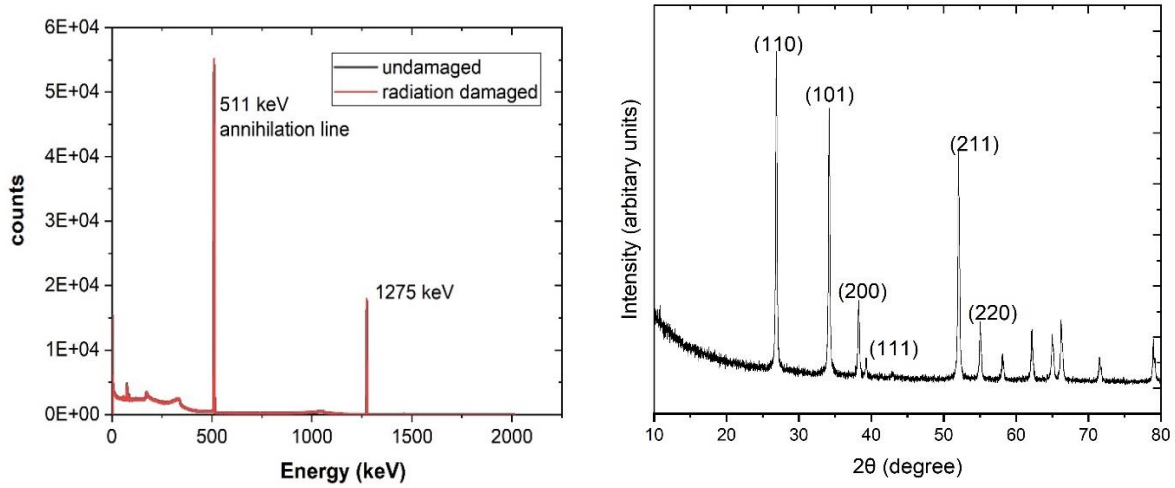

Figure 3: *(left)* Annihilation spectra for unirradiated and irradiated SnO_2 samples. *(right)* XRD confirmation of the structure of SnO_2 after irradiation.

The positron-electron annihilation spectra for unirradiated and irradiated samples are shown in Figure 3 (*left)*. The measure of the density of defects is the S-parameter, which is defined as the ratio of the total counts in the centroid (around 511 keV) to the total counts under the annihilation curve. Expanded view for both annihilation curves is shown in Figure 4. Table 1 shows the calculated S-parameters. The calculated annihilation rates using the generalized gradient approximation show two lifetime components. The bulk positron lifetime τ_b component for positrons annihilating in a defect-free region. The second component τ_d refers to the positron lifetime for positrons annihilating with electrons at defect sites. Table 2 shows both lifetime components as well as the average positron lifetime.

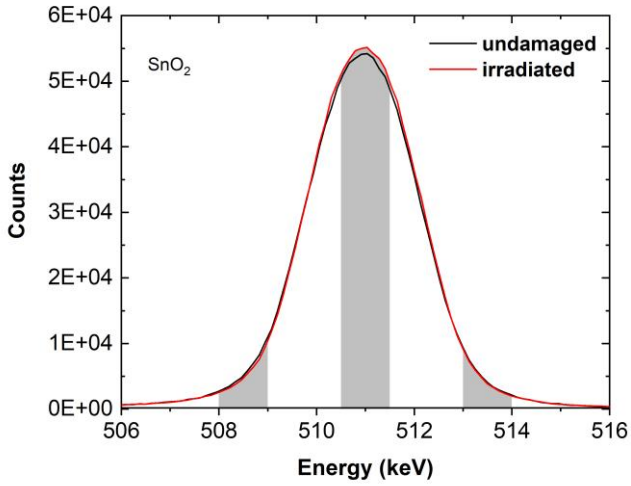

Figure 4. The peak of the neutron-irradiated annihilation peak is more pronounced than that of the unirradiated annihilation peak.

	Unirradiated SnO_2	Irradiated SnO_2
Centroid	469999	478720
Total area	1267485	1279038
S-param	0.370612	0.374281
W-param	0.036882	0.033784

Table 1. The calculated S- and W- parameters from the annihilation curve with its centroid around 511 keV.

	LDA	GGA
Bulk	220 ps	241 ps
Defect	246 ps	263 ps
Average	233 ps	252 ps

Table 2. The calculated positron lifetime components using local density approximation (LDA) as well as the generalized gradient approximation (GGA).

The positron lifetime components are derived from the electron-positron annihilation rate given by equation 1 [11-16],

$$\lambda = \pi r_o^2 c \int n_+(r) n_-(r) \gamma\big(n_-(r)\big) dr \quad (1)$$

where r_o is the classical electron radius, n_+ and n_- are the positron and electron densities respectively. γ is the enhancement factor.

Using local density approximation (LDA), the annihilation rates are overestimated, especially for low momentum electron-positron annihilations. Figure 5 shows the comparison between LDA and the generalized gradient approximation (GGA), which considers the variational nature of charge density. Table 2 is derived from these values of annihilation rates from core states to defect sites as well as in the bulk.

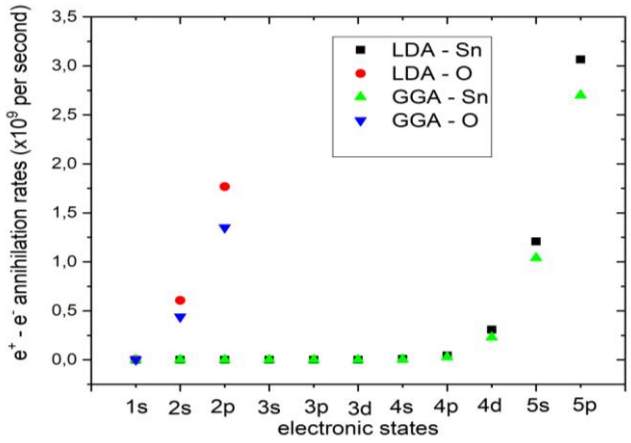

Figure 5. Comparison of positron-electron annihilation rates in individual atoms (Sn and O). The annihilation rates are small in core states but increase with low momentum electrons.

The average positron lifetime of 252 ps suggests a vacancy-type defect, which is a displacement damage due to the collisions of neutrons with lattice atoms. The cross-section of neutrons with tin is about 124 mb, which is not large enough for any transmutation doping to take place. The concentration of defects, C_v, due to neutron irradiation is given by equation 2 [17],

$$C_v = \frac{N_{at}}{\mu_v \tau_b} \frac{\tau_{av} - \tau_b}{\tau_v - \tau_{av}} \quad (2)$$

where N_{at} is the atomic density of SnO_2, and μ_v is the specific trapping coefficient. τ_{av}, τ_b and τ_v are the average, bulk, and vacancy positron lifetimes, respectively.

4. Conclusion

The positron annihilation technique, which characterizes defects in neutron-irradiated tin oxide in the energy range from 0.223 MeV to 2.23 MeV, shows that the positrons annihilate at open volume vacancies as well as in the bulk. The change in the S-parameter from 0.370812 (unirradiated SnO_2) to 0.374281 for the neutron-irradiated sample clearly shows that the neutrons, in the suitable energy range, can cause displacement damage or vacancies in the sample. The average positron lifetime of 252 ps in the framework of the generalized gradient approximation clearly indicates the presence of open volume vacancy or point defects.

Acknowledgement

We gratefully acknowledge financial support from the National Research Foundation and the Research Committee of the University of Zululand. The authors would like to thank iThemba LABS and the School of Physics at the University of the Witwatersrand for making facilities available to the researchers.

References

[1] F. Mei, R. Li and T. Yuan, *Tin oxide materials – synthesis, properties and applications,* Elsevier, Chapter 20, pp 579-597, 2020.

[2] J. Huang, B.S. Yan, C.Y. Chen and W.T. Lo, "Ceramic materials for electronic applications," *Ceramic International,* vol 27, no. 3, pp 363-365, 2001

[3] K.J. Saji and A.P. Reena Mary, *ECS Journal of Solid State Science and Technology*, vol 4, no. 9, pp Q101-Q104, 2023

[4] N.A. Pandit and T. Ahmad, "Tin-oxide based hybrid nanostructures for efficient gas sensing," *Molecules,* vol. 27, no. 20, p.7038, 2022

[5] J.F. Mcleer, P.T. Mosely, J.O.W. Norris, D.E. Williams, P. Taylor and B.C. Tofield, *Materials Chemistry and Physics,* vol. 17, no. 6, pp 577-583, 1987

[6] I. Kim, F. Khatkhatay, L. Jiao, G. Swadeney, J. Cole, J. Gan and H. Wang, *Journal of Nuclear Materials, vol.* A20, no 1-3, pp. 143-148, 2012

[7] D.T. Peterson and J.G. Byrne, *Material Science Engineering,* vol. A, no. 110, pp.L27-L29, 1989

[8] M. Yamawaki et. al, *Japan Journal of Applied Physics,* vol. 59, pp 066502-1 – 066502-4, 2020

[9] C. Tobi, Z. Homonnay and K. Suvegh, *Radioanalytical and Nuclear Chemistry,* vol. 332, pp. 2741-2747, 2023

[10] I. Prochazka, *Material Structure,* vol. 8, no. 2, pp. 55-60, 2001

[11] K. Itawa, R. Greaves, T.J. Murphy, M.D. Tinkle and C.M. Surko, *Physical Review A,* vol. A, no. 51, pp. 473, 1995

[12] F. Tuomisto and I. Makkonen, *Rev. Mod. Phys.,* vol. 85, pp. 1583, 2013

[13] J. Slotte et. al., "Direct observations of the vacancy and its annealing in germanium," *Physical Review B,* vol. 83, no. 23, pp. 235212-1 – 235212-5, 2011

[14] C.S. Sundar, *Bulletin of Material Science,* vol. 17, no. 7, pp. 1215-1232, 1994

[15] Y. Dong et. al., *Physical Review B,* vol. 109, pp 104104, 2024

[16] F. Selim, *Material Characterization,* Elsevier, vol. 174, pp. 110952, 2024.

[17] X. Hu et.al., *Physical Review B,* vol. 95, pp. 104103, 2017

Structural and Magnetic Properties of a Novel Double Perovskite Sm_2MgRuO_6

I. B. M. Mouadje, R. Djoumessi Fobasso, B. Sondezi

Physics Department, University of Johannesburg, Auckland Park 2006, South Africa

E-mail: 224221523@student.uj.ac.za

Abstract. This study highlights Sm_2MgRuO_6's promise as a room-temperature ferromagnetic material for spintronic applications and offers important new insights into the structure-property correlations of the material. Computational modeling and experimental characterization work together to create a strong foundation for creating functional perovskites of the future. Double perovskite oxides ($A_2B'B''O_6$) have garnered a lot of interest because of their special set of functional characteristics. These materials hold great promise for energy and spintronic applications, where exact control over magnetic interactions and cation ordering is essential. In order to comprehend its potential for cutting-edge technologies, we synthesized the unique double perovskite Sm_2MgRuO_6 by solid-state reaction and examined its structural and magnetic properties. The crystal structure of Sm_2MgRuO_6 was found by X-ray diffraction (XRD) at room temperature and Rietveld refinement confirm that it crystallizes in the monoclinic $P2_1/n$ space group with lattice parameters a = 5.41194 Å, b = 5.66563 Å, and c = 7.71585 Å. Similar to Nd_2MgRuO_6, but with partial disorder, the structure displays a cationic ordering of Mg^{2+} and Ru^{4+} on the octahedral sites that resembles rock salt. We used Monte Carlo (MC) simulations, a robust computational method that simulates thermodynamic characteristics and phase transitions in intricate systems using random sampling, to clarify the magnetic behavior. Based on a Heisenberg spin Hamiltonian, the MC results show that Sm^{3+} and Ru^{4+} interactions induce ferromagnetic ordering.

***Keywords*:** Double Perovskites, DFT, Monte Carlos, Ferromagnetism

1 Introduction

Considering their potential for magnetoresistive and spintronic applications, double perovskites of the form $A_2B'B''O_6$ containing magnetic B′ and B″ ions at the octahedral sites have attracted a lot of attention. Notable examples include multiferroic $Ba_2FeMnCoO_6$ [2] and Dy_2NiMnO_6 [3], Sr_2FeMoO_6 displaying room-temperature colossal magnetoresistance [1], and Sr_2CrIrO_6, a ferrimagnetic insulator with a record-high Curie temperature (~90 K) that can undergo doping to transition to half-metallicity [4,5].

Systems featuring magnetic interactions between A- and B-site cations, on the other hand, are still not as well studied. Compared to their 3d counterparts, ruthenium-based double perovskites have distinct magnetic characteristics because of the interaction between high spin-orbit coupling and 4d electron itinerancy [6].

While their Ru^{5+} ions are magnetically attenuated by non-magnetic Na^+/Li^+ [8–10], Nd_2MgRuO_6 exhibits coupled A- and B-site spin ordering with antiferromagnetic configurations [7]. Rare-earth ordering (Er, Ho) has been reported for Ru^{4+}-based counterparts (e.g., Ln_2NiRuO_6), but no long-range Nd magnetism has been seen [11].

The structural and magnetic characteristics of Sm_2MgRuO_6, a new Ru^{4+} ($4d^4$) double perovskite stabilized by Mg^{2+}, are presented in this work. The rock-salt ordering of B-site cations is driven by the substantial ionic radius difference (Ru^{4+}: 0.62 Å, Mg^{2+}: 0.72 Å), which isolates Ru^{4+} and permits weak magnetic interactions.

2 Experimental and Simulation details

2.1 Experimental Method

The usual high-temperature solid-state reaction approach was used to create the Sm_2MgRuO_6 polycrystalline compound under carefully regulated temperature and time parameters. High purity (99.99%) stoichiometric quantities of Magnesium (IV) oxide (MgO), Ruthenium (IV) oxide (RuO_2), and Samarium (III) oxide (Sm_2O_3) were combined and heated to 800 °C for 12 hours in oxygen. Before any characterisation procedures could be used, the pre-heated powders were sintered once again for 36 hours at 1250 °C with intermediate grinding. The appearance of a relatively strong superlattice reflection at $2\theta \sim 19^{O}$ in the XRD pattern with Cu-Kα radiation (λ=1.5418 Å) at ambient temperature suggests that the Mg and Ru cations at the perovskite B-site may be crystallographically ordered. The Scherre's formula was used to investigate the average crystallite size and it was found to be ~ 15 nm. Using an accelerating voltage of 20 kV, the microstructure, element distribution, and chemical compositions of Sm2MgRuO6 were examined using a scanning electron microscope (SEM) equipped with Energy Dispersive X-Ray Spectroscopy (EDS) capabilities.

2.2 Simulation details

Using Monte Carlo (MC) techniques, which randomly sample spin configurations to reveal equilibrium parameters and transition temperatures, we examined the magnetic behavior.

The following is the Hamiltonian that describes the system:

$$H = -J_{Sm-Ru}\sum_{\langle i,j\rangle} S_i^{Sm} S_j^{Ru} \tag{1}$$

where $J_{Sm\text{-}Ru}$ is the exchange interaction between Sm-Ru, $S^{Sm} = \pm\frac{5}{2}, \pm\frac{3}{2}$ and $\pm\frac{1}{2}$ is the spin moment of Sm^{3+}, and $S^{Ru} = \pm 1$ the spin moment of Ru^{4+}.

The energy for various configurations AFM and FM are obtained by substituting them in equation (1).

$$E_{AFM} = 6(\frac{5}{2})J_{Sm-Ru} \tag{2}$$

$$E_{FM} = -6(\frac{5}{2})J_{Sm-Ru} \tag{3}$$

With $E_{FM} = -3578.15960891\ \ Ry$ and $E_{AFM} = -3578.15174973\ \ Ry$

The value of the coupling interaction between Sm and Ru is obtained by combining Eqs. (2) and (3):

$J_{Sm-Ru} = \frac{E_{AFM} - E_{FM}}{12(\frac{5}{2})}$, the exchange coupling value that the GGA+U technique yielded is

$J_{Sm-Ru} = 5.345meV$.

3 Results and Discussion

3.1 Structural Characterization

Fig. 1 plots the XRD pattern of Sm2MgRuO6 that was produced using the Rietveld refinement by the FULLPROF program [11]. The Sm_2MgRuO_6 crystallizes with monoclinic DP-type P $2_1/n$ symmetry as a result of a better fitting result with the $P2_1/n$ space group. Without any indication of impurity phases, the refinement pattern displays the oxide's phase-purity and crystallographic data. The reliability factors that were derived from the refinement are $\chi^2 = 2.89$, Rp = 5.0538%, and Rwp = 6.4635%. a = 5.66563(9) Å, b = 5.66563(2) Å, c = 7.71585(6) Å, and

V = 236.584(9)Å^3 are the lattice parameters.
The tolerance factor t is given by:

$$t = \frac{r_{Sm} + r_O}{\sqrt{2}\left(\frac{r_{Mg} + r_{Ru}}{2} + r_O\right)} \quad (4)$$

where r is ionic radius, can be used to evaluate the structural stability of perovskite-type oxides [12]. A phase stability is confirmed with t ranging from 0.78 to 1.05 [13]. The stability of the DP-type crystal structure is further confirmed by the value of t for Sm_2MgRuO_6, which is 0.81.

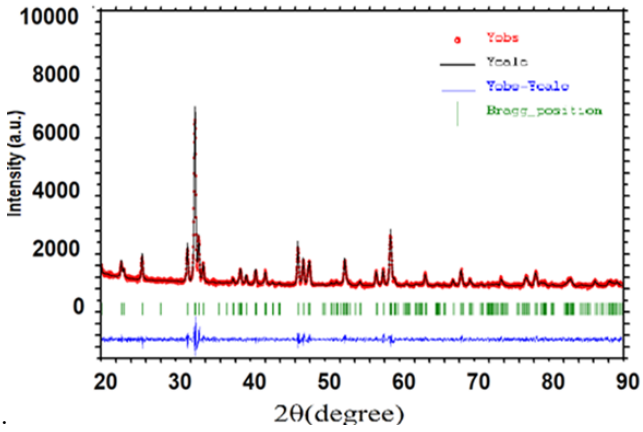

Fig. 1: Powder x-ray diffraction pattern of Sm_2MgRuO_6

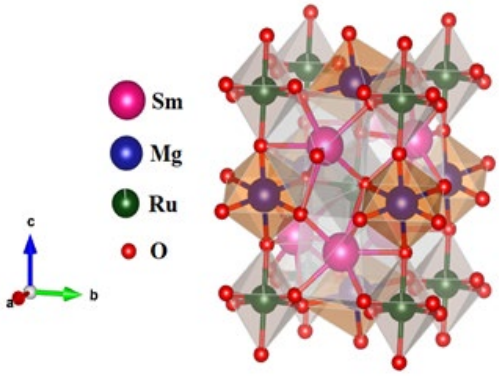

Fig. 2: $P2_1/n$ Structure

The nearest neighbor environments of each element and the precise crystal structure of Sm_2MgRuO_6 DP oxide are shown in **Fig. 2**. Twenty independent atoms, including four Sm, two Mg, two Ru, and twelve O atoms, make up a single ordered unit. The MgO_6 and RuO_6 octahedrons are formed by the coordination of six O atoms by the Mg and Ru atoms, respectively. For MgO_6, the bond distance ranges and average are 1.827–2.300 Å and 1.953 Å, respectively**.** The values for MgO_6 and RuO_6 are 2.089 Å and 1.850–2.164 Å, respectively. For MgO_6 and RuO_6 units, the O-Mg-O and O-Ru-O bond angles fall between 86.193°, 92.087°, 88.431° and 92.230° respectively. With bond lengths ranging from 2.275 Å to 2.733 Å, the Sm atom forms the 8-coordination polyhedron in the gap of the MgO_6/RuO_6 octahedron. There are three distinct O ions (O_1, O_2, and O_3), which are presumed to be three distinct 4e sites, whereas the Sm atom occupies the 4e Wyckoff location. Mg and Ru ions are independent of 2d and 2c.
The atomic positions of Sm, Mg Ru and O are summarized in Table 1 for Sm_2MgRuO_6 DP oxide.

Table 1. The atomic positions of Sm_2MgRuO_6 DP oxide.

Wyckoff site	Atom	x	y	z
4e	Sm	0.5152(4)	0.5605(5)	0.2462(6)
2d	Mg	1/2	0	0
2c	Ru	0	1/2	0
4e	O_1	0.0988(8)	0.4713(3)	1/4
4e	O_2	0.3207(7)	0.7281(4)	-0.0477(8)
4e	O_3	0.4048(1)	0.9698(0)	0.2641(9)

Fig. 3 shows the element EDS mapping results of Sm_2MgRuO_6 DP oxide along with the secondary electron SEM image of the typical microstructure. The existence of spherical particles with agglomerations in certain places

confirms that Sm_2MgRuO_6 is polycrystalline. Fractions verified the stoichiometric compositions of 68.0%, 15.3%, 12.4%, and 4.4% for Sm, Ru, O, and Mg atoms, respectively, based on several EDS mapping analyses (Fig. 4). These numbers are in close proximity to the synthetic Sm_2MgRuO_6 oxide's nominal atomic ratio of 2:1:1:6.

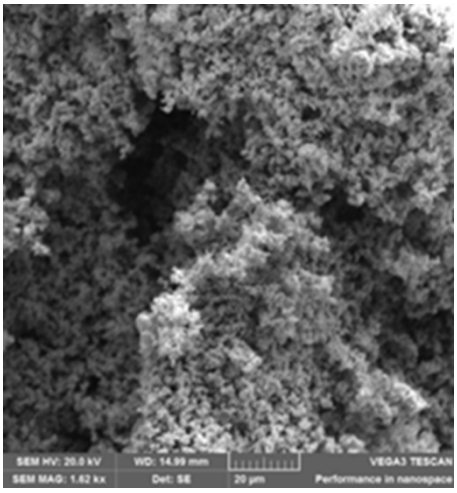

Fig. 3: SEM image of Sm_2MgRuO_6

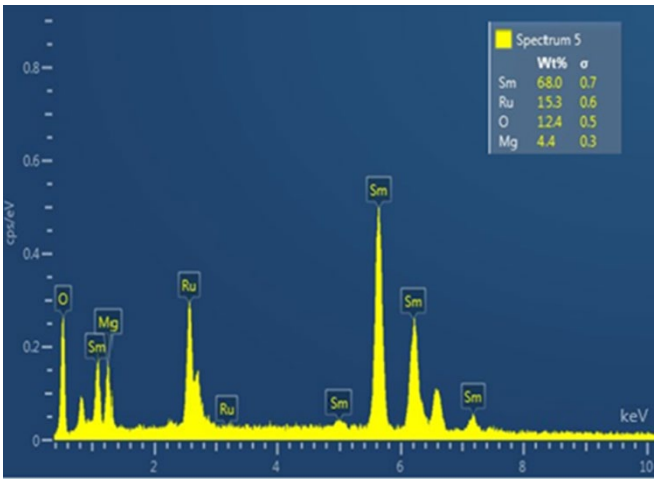

Fig. 4: EDS image Sm_2MgRuO_6

3.2 Magnetic Properties: Monte Carlo Simulation

This complex system's magnetic behavior was simulated using a Metropolis algorithm in conjunction with an MCS. The simulation program envisioned the system as a cubic bulk with $L_B = 20$, which is still below the thermodynamic limit for this class of materials, which was established at $L_{ThL} = 32$ [14], [15]. The initial configuration was generated at random so that Ru-spins are randomly located in the sites of Ru-sublattice and Sm-spins are randomly located in the sites of Sm-sublattice. Every MCS step involves a sequential traversal of every site in the system and an attempt at a single-spin flip. The program incorporates a Metropolis algorithm to assist in determining whether single spin flips should be accepted or rejected. After using the first 3000 steps to attain equilibrium, the simulation recovered the data from 5000 MCS steps. The energy-calculating equations for magnetization, magnetic susceptibility (χ), and specific heat (C_V) are provided by:

$$E = \frac{\langle H \rangle}{N} \tag{5}$$

$$M = \frac{1}{N}\left|\sum_i S_i^{Sm} - \sum_i S_i^{Ru}\right| \tag{6}$$

$$C_V = \frac{\beta}{k_B}\left(\langle E^2 \rangle - \langle E \rangle^2\right) \tag{7}$$

with $\beta = \frac{1}{k_B T}$ where N is the number of spins in the system, T is the absolute temperature, and k_B is the Boltzmann constant.

Figs. 5, **6** and **7** show the fluctuation of these variables with lattice sizes ranging from L = 12 to L = 20 in order to investigate the impact of the lattice size of the unit cell. **Fig. 5** displays internal energy as a function of temperature.

For tiny lattice sizes, the simulated transition temperature has been determined to be 275 K. The transition temperature reaches a high at T_C = 276.76 K as the systems get bigger.

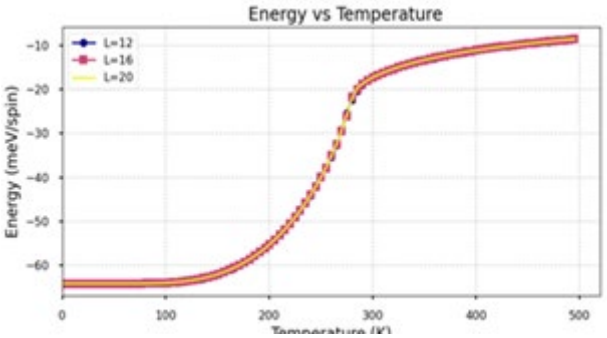

Fig.5: Temperature-dependent internal energy for various lattice sizes

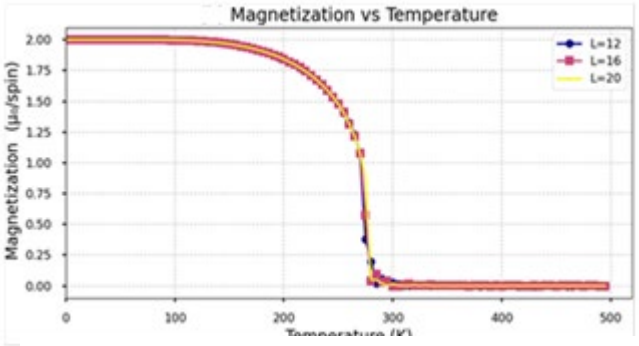

Fig.6: Temperature-dependent magnetization for various lattice sizes

The relationship between temperature and total magnetization is displayed in **Fig. 6**. A magnetic saturation value of M_T = 2μB is reached by the curve. This magnetization curve tends to attain the minimal value M_T = 0,15μB by steadily decreasing after T_C. Various lattice sizes showed comparable effects. There was a minor rise in the critical temperature of around T_C = 276.76 K. **Fig. 7** displays the simulated specific heat as a function of temperature (C_V). At 275 K, the transition temperature is reliably determined. The transition temperature bifurcates to 276.76 K for large system sizes. A second order phase transition is indicated by the curve's Gaussian structure. The findings indicate that a little difference in the critical temperature (T_C) is caused by a change in the system's size.

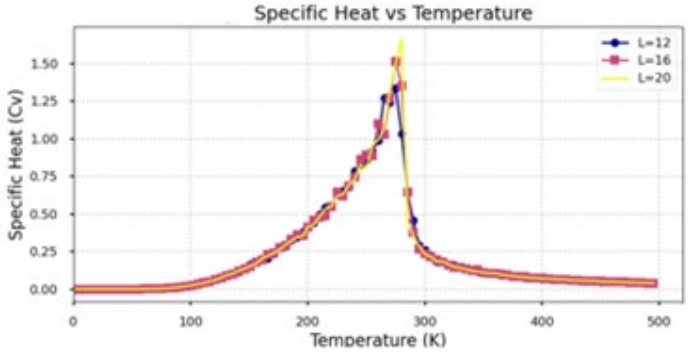

Fig.7: Specific Heat as a function of temperature for different lattice sizes

To date, the critical temperature T_C found in this present work has the lowest value compared to the majority of results reported in the literature by other authors in similar studies such as $La_{0.67}Sr_{0.33}MnO_3$ (T_C = 358 K [16]), Mn_2FeReO_6 (T_C =520 K [17]), Sr_2CrReO_6 (T_C = 610 K [18]), Sr_2CrOsO_6 (T_C = 725 K [19]), Sr_2CrMoO_6 (T_C = 458 K [20]), Sr_2CrWO_6 (T_C = 500 K [21]), Ca_2CrMoO_6 (T_C = 125 K [22]).

4 Conclusion

In our findings, a high-quality single-phased polycrystalline Sm_2MgRuO_6 oxide has been successfully generated with a B-site ordered monoclinic $P2_1/n$ (No. 14) DP type crystal structure. A mixed experimental and theoretical study has been conducted. The oxide Sm_2MgRuO_6 is a monoclinic double perovskite (DP) of the B-site ordered type. The Curie temperature of Sm_2MgRuO_6 is confirmed by Monte Carlo simulations to be 276.76 K for L=20.

Sm^{3+} and Ru^{4+} exhibit ferromagnetic interactions, indicating that structural deformation controls its distinct magnetic characteristics.

References

[1] K.I. Kobayashi, T. Kimura, H. Sawada, K. Terakura, Y. Tokura, Nature 395 (1998) 677–680.
[2] S. Yáñez-Vilar, E.D. Mun, V.S. Zapf, B.G. Ueland, S. Gardner, J.D. Thompson,J. Singleton, M. Sánchez-Andújar, J. Mira, N. Biskup, M.A. Señarís-Rodríguez, C.D. Batista, Phys. Rev. B 84 (2011) 134427.
[3] M.Azuma,K.Takata, T. Saito, S. Ishiwata, Y. Shimakawa, M. Takano, J. Am. Chem.Soc. 127 (2005) 8889–8892.
[4] Y. Krockenberger, K. Mogare, M. Reehuis, M. Tovar, M. Jansen, G. Vaitheeswaran, V. Kanchana, F. Bultmark, A. Delin, F. Wilhelm, A. Rogalev, A. Winkler, L. Alff, Phys. Rev. B 75 (2007) 020404.
[5] K. Samanta, P. Sanyal, T.S. Dasgupta, Sci. Rep. 5 (2015) 15010.
[6] G. Cao, A. Subedi, S. Calder, J.-Q. Yan, J. Yi, Z. Gai, L. Poudel, D.J. Singh, M.D. Lumsden, A.D. Christianson, B.C. Sales, David Mandrus, Phys. Rev. B 87 (2013) 155136.
[7] R.P. Singh, C.V. Tomy, Phys. Rev. B 78 (2008) 024432.
[8] W.R. Gemmill, M.D. Smith, H.-C. zur Loye, J. Solid State Chem. 177 (2004) 3560–3567.
[9] A.A. Aczel, D.E. Bugaris, J. Yeon, C. de la Cruz, H.-C. zur Loye, S.E. Nagler, Phys. Rev. B 88 (2013) 014413.
[10] S.J. Makowski, J.A. Rodgers, P.F. Henry, J.P. Attfield, J.W.G. Bos, Chem. Mater. 21 (2009) 264–272.
[11] J. Rodriguez-Carvajal, Laboratoire Leon Brillouin CEA-CNRS, France, 2007.
[12] C. Bartel , C. Suton , B. Goldsmith , R. Oyang , C. Musgrave , M. Schefler , Sci. Adv.
5 (2019) eaav0693.
[13] O. El Rhazouani, Z. Zarhri, A. Benyoussef, A. El Kenz, J. Mag. Mag. Mat. 401 (2016) 897.
[14] O. El Rhazouani, A. Benyoussef, A. El Kenz, J. Magn. Magn. Mat. 377 (2015) 319.
[15] A. Loudaini, M. Aggour, O. Mounkachi, L. Bahmad, Solid State Com. 295 (2019) 5–11.
[16] M. Kibbou, Y. Benhouria, M. Boujnah, I. Essaoudi, A. Ainane, R. Ahuja, J. Magn. Magn. Mater. 495 (2020) 165833.
[17] O. El Rhazouani, A. Benyoussef, Z. Zarhri, A. El Kenz, J. Magn. Magn. Mater. 401 (2016) 897–901.
[18] O. El Rhazouani, Z. Zarhri, A. Benyoussef, A. El Kenz, Phys. Lett. Sect. A: Gen. At. Solid State Phys. 380 (13) (2016) 1241–1246.
[19] O. El Rhazouani, A. Slassi, Comput. Condens. Matter 11 (2017) 55–59.
[20] O. El Rhazouani, A. Slassi, Y. Ziat, A. Benyoussef, Phys. A, Stat. Mech. Appl. 476 (2017) 38–42.
[21] O. El Rhazouani, Y. Ziat, A. Benyoussef, , Mod. Electron. Mater. 3(3) (2017) 99–103.
[22] A.S. Erchidi Elyacoubi, R. Masrour, A. Jabar, M. Ellouze, E.K. Hlil, Mater. Res. Bull. 99 (2018) 132–135.

Ab initio studies of Pt-Cr alloys for jewellery applications: energetic stabilities and structural properties

Mawisha Mafifi[1], Donald Mkhonto[2], Chewe Fwalo[1], Maje Phasha[2] and Edwin Mapasha[1]

[1]Department of Physics, University of Pretoria, Private bag X20, Hatfield, 0028, South Africa, [2]Advanced Materials Division, MINTEK, Private bag X3015, Randburg, 2125, South Africa

E-mail: mawisham@gmail.com

Abstract. The platinum (Pt)-based materials are widely used in various industries applications; Including metallurgy, medicine, jewellery, fuel cells, and hydrogen evolution reactions due to their excellent electrochemical properties. However, in its pristine form, Pt is relatively soft, thus prone to surface scratching, a concern in jewellery applications. Hence, alloying to enhance its mechanical integrity is key to improving scratch resistance. This study employs density functional theory (DFT) within Quantum Expresso package calculations to investigate the effect of alloying Pt with high corrosion resistant chromium, Cr ($Pt_{100-x}Cr_x$) on phase stability, structural and mechanical properties. Our results revealed a decrease in lattice parameters of $Pt_{100-x}Cr_x$ as the Cr concentration increases. This observation also extends to cohesive energies and cell volumes. Phonon dispersion analysis indicates the material's dynamical stability, with positive frequencies despite an increase in Cr alloy composition. Additionally, strong electronic interactions between Pt and Cr were observed, supported by the complex charge distributions witnessed in the systems. With an increase in metalicity of $Pt_{100-x}Cr_x$ as the Cr concentration increases, suggests possibility of an improved mechanical hardness of the system, making the material suitable for jewellery applications.

1 Introduction

Since the resurgence of platinum (Pt)-based jewellery before the 1990s, Pt has become one of the key precious metals in jewellery manufacturing. It is often regarded as a cornerstone of the jewellery industry, particularly in the global market for marriage and engagement rings [1] [2]. This is due to its unique lustrous white colour [3], purity and consistency [2], as well as its resistance to wear and alteration over time [1]. In its pure form 1000 parts per thousand (ppt), Pt is relatively soft. The hardness of pure Pt is relatively low, reaching only around 40 on the Vickers hardness scale [3]. Forth is reason, pure Pt is not commercially viable for jewellery applications, especially items like engagement and wedding rings, are precious objects often passed down through generations [1]. To address this issue, Pt is alloyed with other metals to increase its hardness and overall durability, making it more suitable for long-lasting.

Due to its natural softness, it is prone to surface scratching which poses a concern to jewellery application. To solve this setback, recently, the jewellery industry has classified Pt-based alloys into three main categories based on their Pt content: Pt at 950, Pt at 900, and Pt at 850 ppt [4]. These alloys typically range in Pt content from 95% to 85% [4] [5], in the jewellery product. Although, this is a narrow range alloy percentage, it is necessary for physical modification of Pt, as even small changes in composition can significantly alter the physical and mechanical

properties required for jewellery applications [6]. Therefore, elements that can enhance its mechanical properties, are essential, particularly to improve scratch resistance [1], [2], [3].

Despite significant research on Pt-based alloys [7], [8], there remains a gap in understanding the atomic-scale interactions between Pt and chromium ($Pt_{100-x}Cr_x$), and how these interactions affect the alloy's mechanical performance. Additionally, the long-term stability and phase behavior of $Pt_{100-x}Cr_x$ alloys under operational conditions are not fully understood. Using the density-functional theory (DFT) approach, the study aims to address this gap in knowledge by providing a comprehensive study of Pt-Cr alloy formation, electronic structure and their influence on mechanical properties.

2 Methodology

All the calculations reported in this work have been performed using the Quantum ESPRESSO (QE) code which implements DFT using the planewave pseudopotential approach [9]. The general gradient approximation (GGA) as parameterized by Perdew-Burke-Ernzerhof (PBE) [10]was used as the exchange-correlation functional. Interaction between the nuclei and electrons was described by pseudopotential (PP) which valence electron configurations of [Xe] $4f^{14}$ $5d^9$ $6s^1$ and [Ar] $3d^5$ $4s^1$ for Pt and Cr respectively. The PPs have been taken from QE pseudopotential repository. To achieve convergence in the structural relaxation calculations, we have used plane wave kinetic energy cut-off of 400 eV and Methfessel-Paxton (MP) smearing width of 0.05 eV [11] as well as Monkhorst-Pack special k-point grid of a (7×7×7), where a is the calculated lattice parameter of face-centred cubic (FCC) Pt. These parameters along with force and energy convergence thresholds of 10^{-4} N and 10^{-6} eV, respectively were sufficient to converge the structures to their respective ground state configurations. To produce the $Pt_{100-x}Cr_x$ an alloy compositions (x is the concentration of Cr), we have used the 2×2×2 supercell of FCC Pt containing 32 atoms. Specifically, we produced alloy corresponding to x = 3.13, 9.37, and 15.63. Alloy composition of $Pt_{100-x}Cr_x$ with x = 3.13 is produced by introducing 1Cr alloy to the system thus becomes $Pt_{96.88}Cr_{3.12}$. In the case of x = 9.38, we introduced 3Cr to the system giving $Pt_{90.63}Cr_{9.37}$. Lastly for x = 15.63, we introduced 5Cr to yield $Pt_{84.37}Cr_{15.63}$. These compositions were then investigated using the aforementioned calculation parameters to explore the structural properties and relative energetic stability of the $Pt_{100-x}Cr_x$ alloys. The corresponding crystal structures of various alloys compositions are shown in Figure 1

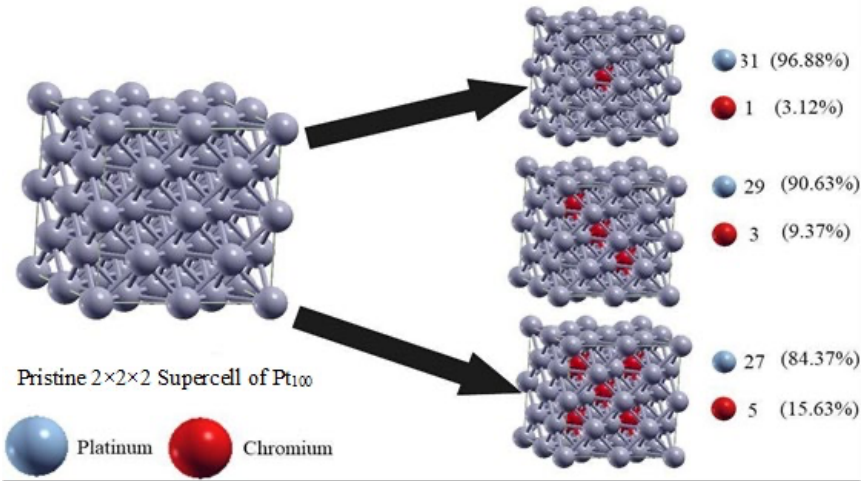

Figure 1. The ball and stick geometry models of pristine 2×2×2 Supercell of Pt (100% Pt composition) as well as $Pt_{100-x}Cr_x$, where X = 3.13, 9.38, and 15.63.

3 Results and Discussion

In this study, a 2×2×2 face-centered cubic supercell containing 32 Pt atoms was used, as shown in Figure 1. Before introducing any Cr alloying, full structural optimization was performed on the 1×1×1 (unit cell) pristine FCC structure to obtain its ground state properties, ensuring that they are comparable to experimental values. Table 1 presents the calculated equilibrium lattice parameter and cohesive energy of the pristine Pt FCC structure. The predicted lattice constant is 3.99 Å, which is in good agreement with previously reported experimental values of 3.93 Å [10] and DFT results of 3.98 Å [11]. At the equilibrium lattice constant, the cohesive energy is 5.42 eV, corresponding well with previous DFT work, were the cohesive energy of 5.67 eV was obtained [12]. These two

values are in agreement with the experimental value of 5.84 eV [13], although slightly lower due to the different techniques utilized. These results, obtained using full geometry optimization criteria, are further supported by the manual variation of cohesive energy with respect to changes in lattice constants, as shown in Figure 2, where the red horizontal line indicates the equilibrium structure.

Pt composition	Lattice Constant (Å)	Cell volume (Å^3)	Cohesive energy (eV)	$\Delta_{\text{Cohesive energy}}$ (eV)
100% (Pristine)	7.98	508.17	5.42	0.00
96.88%	7.93	498.68	4.88	0.54
90.63%	7.84	481.89	4.73	0.15
84.38%	7.75	465.48	4.71	0.02

Table 1. The calculate equilibrium lattice constants (Å), volume cells (Å^3) and cohesive energies (eV) of the pristine Pt and various Pt-Cr alloy compositions in a 2×2×2 FCC supercell. $\Delta_{\text{Cohesive energy}}$ (eV) is the change in energy relative to subsequence Cr% concentration.

Furthermore, the equilibrium lattice constants and energetic stability of $Pt_{100-x}Cr_x$ alloys as shown in Table 1 and Figure 2, substituting Pt atoms with Cr atoms leads to a slight, approximately linear decrease in the lattice constant, with the extent of reduction depending on the alloy composition. This trend is consistent with the findings of Murakami *et al.*, [14]which studied $Pt_{100-x}Ir_x$ and $Pt_{100-x}Ru_x$ compositions. Consequently, the cohesive energy also decreases slightly with increasing Cr concentration. For example, the $Pt_{84.38}Cr_{15.62}$ alloy exhibits an equilibrium lattice constant of 7.75 Å and a cell volume of 465.48 Å^3, resulting in a cohesive energy of 4.71 eV. The $Pt_{90.63}Cr_{9.37}$ alloy yields a cohesive energy of 4.73 eV from the lattice constant of 7.84 Å and cell volume of 481.89 Å^3, while the $Pt_{96.88}Cr_{3.13}$ alloy yields a cohesive energy of 4.88 eV from the lattice constant of 7.93 Å and cell volume of 498.68 Å^3. It was confirmed that the slight decrease in lattice parameter is influenced by increasing Cr concentration due to its smaller atomic radius compared to Pt, which consequently reduces the cell volume. This leads to variations in the bonding network between Pt-Pt, Pt-Cr, and Cr-Cr interactions in the $Pt_{100-x}Cr_x$ alloy system. Within the Cr concentration range of 0% to 15.62%, the $Pt_{100-x}Cr_x$ alloy system still maintains structural integrity as indicated by the negligible change in cohesive energy ($\Delta_{\text{cohesive energy}}$). This suggests that at higher Cr concentrations in the Pt system, the alloy may not lose phase stability, hence encouraging this study to continue examine other properties such as mechanical, energetic, and elastic properties.

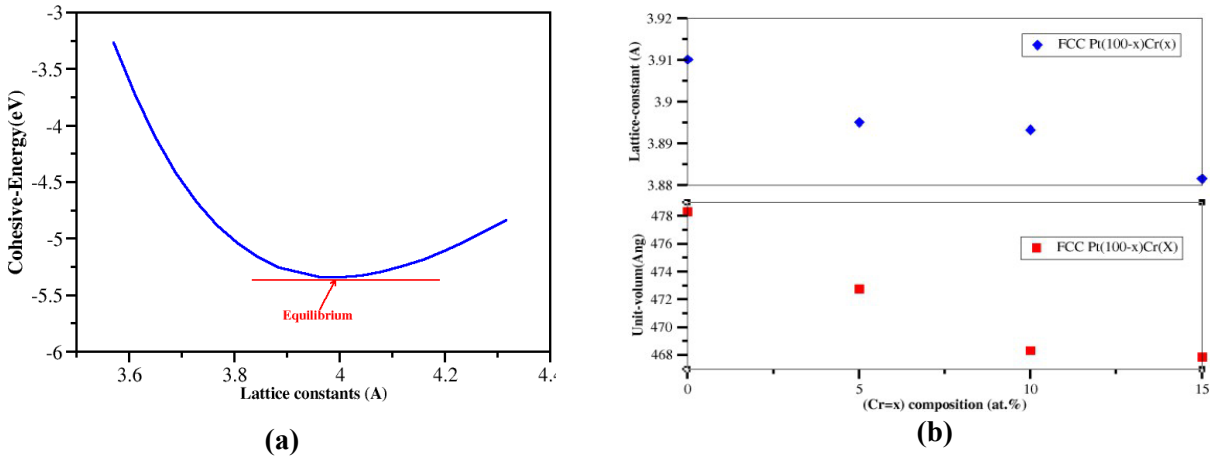

Figure 2. (a) Variation in cohesive energies (eV) as a function of lattice constants (Å) for 100% pristine Pt. The red horizontal line (tangent) touches the equilibrium lattice parameter corresponding to ground state cohesive energy. (b) Lattice constants (diamond symbol) and cell volume (square symbol) as a function of Pt-Cr compositions.

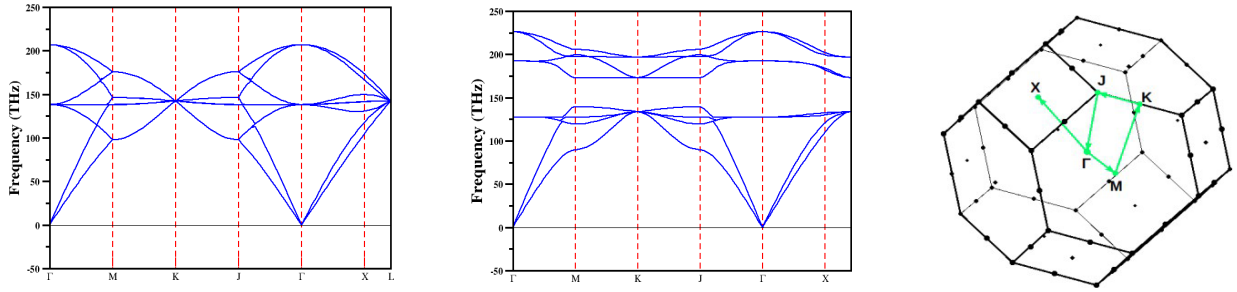

(a) Pt_{100}composition **(b) $Pt_{84.38}Cr_{15.62}$ alloy** **(c) Brillion zone of FCC Pt**

Figure 3. The calculated phonon dispersion relations. (a) Pristine Pt material system, (b) Pt $_{84.38}$ $Cr_{15.62}$ alloy system and (c) The Brillion zone of FCC of Pt indicating the k-points path follows.

Figure 3 presents the phonon dispersion curves for both the Pt 100% composition and the $Pt_{84.38}Cr_{15.62}$ alloy composition (the structure with the highest Cr content considered in this study), used to evaluate the dynamical stability of the materials. It is noted in Figure 3(a) that Pt 100% composition phase possess positive modes through the entire spectrum of wave vectors, in agreement with the previous studies. The $Pt_{84.38}Cr_{15.62}$ alloy composition (Figure 3(b)) retains the positive modes dispersions which confirms dynamical stability ambient conditions. The phonon dispersion of Pt_{100} depict no gap, there is however an increase in gap as Cr alloy increases and evident at $Pt_{84.38}Cr_{15.62}$ alloy. The mass difference between Pt and Cr play a significant role when they share a lattice, their vibrational frequencies split into acoustic and optical branches hence the mismatch happen and small gap occur [15].

(a) Pt_{100} **(b) $Pt_{96.88}Cr_{3.13}$** **(c) $Pt_{90.63}Cr_{9.3}$** **(d) $Pt_{84.38}Cr_{15.62}$**

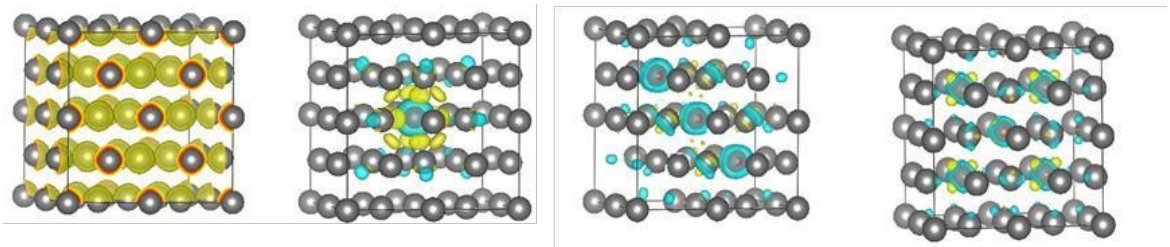

Figure 4. The charge density distribution of (a) Pristine Pt material system, (b) Alloyed Pt system (Pt_{100}) ($Pt_{96.88}Cr_{3.13}$), (c) Alloyed Pt system ($Pt_{90.63}Cr_{9.37}$) and (d) Alloyed Pt system (Pt $_{84.38}Cr_{15.62}$)

Figure 4(a) presents the charge density distribution for the Pt 100% composition. It can be observed that the charge is uniformly distributed across all Pt atoms within the unit cell. This suggests that the bonding in the Pt 100% composition structure is likely covalent in nature. To investigate the charge interaction between Cr dopants and the Pt host atom in Pt-Cr alloy compositions, the charge density differences were calculated, as shown in Figure 4(b-d). In this figure 4(b-d), the yellow clouds represent charge depletion, while cyan clouds indicate charge accumulation. These calculations were performed at an iso-value of 0.002 e/Å^3. It is evident that the majority of the charge is transferred from the Cr atoms to their nearest neighbor Pt atoms. As the Cr percentage increases (9.37% and 15.62%), the accumulated charge extends over a larger region of the cell.

The charge interactions between Pt and Cr alloys were quantified using Bader charge analysis [16] to better understand the electron transfer between the overlapping d-orbitals and s-orbitals of Pt and Cr. For the $Pt_{31}Cr_1$ alloy composition, a charge transfer of 1.38 e^- was observed from the Cr atom to the Pt atom. This charge transfer slightly decreased as the Cr content increased; for instance, the $Pt_{96.88}Cr_{3.13}$ alloy showed a transfer of 1.16 e^-, while the $Pt_{84.38}Cr_{15.62}$ alloy showed a transfer of 1.15 e^-. These results are not particularly surprising, given that Pt (2.28) is more electronegative than Cr (1.66) on the Pauling scale.

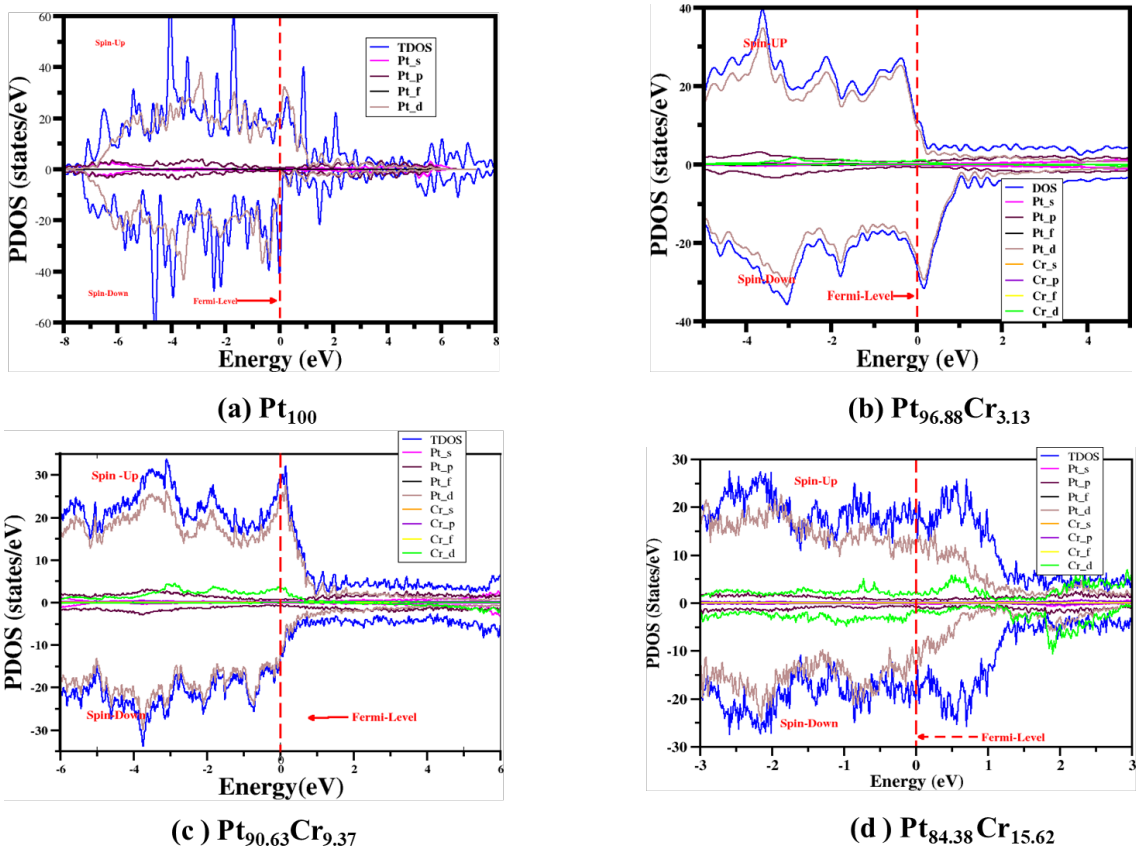

Figure 5. The calculated total and partial density of states for (a) Pt_{100} composition, (b) $Pt_{96.88}Cr_{3.13}$ composition, (c) $Pt_{90.63}Cr_{9.37}$ composition, and (d) $Pt_{84.38}Cr_{15.62}$ composition.

The electronic properties are crucial in jewellery applications, where conductivity plays a key role. To explore this, we investigated the enhancement of electrical conductivity in pristine Pt material due Cr alloy compositions. This was achieved by calculating the Density of States (DOS) and Partial Density of States (PDOS), as shown in Figure 5.

The results revealed that for the Pt_{100} composition (Figure 5a), high peaks of electronic states were observed along the Fermi level, with the valence and conduction bands overlapping. This suggest that, Pt material upon alloying with Cr exhibits an increase in mechanical hardness through the analysis of metallic behavior, confirmed by an increase in electronic states along the Fermi level [17](Figure 5b). Despite this reduction, the electronic conductivity of the system remained intact. For the $Pt_{96.88}Cr_{3.13}$ system (Figure 5c), a slight increase in electronic states along the Fermi level was observed. This could be attributed to the hybridization of Cr d-orbitals with Pt d-orbitals, further suggesting that doping with Cr increases the ductility of the Pt material [18]. Finally, for the $Pt_{84.38}Cr_{15.62}$ system (Figure 5d), no substantial change in electronic states was observed. This can be attributed to the saturation of the system with Cr. Nonetheless, the metallic nature of the system was preserved, as indicated by the overlapping bands. Ultimately, these findings suggest that alloying Pt with Cr atoms stabilizes its electronic conductivity, even at higher concentrations, which is significant for jewellery applications.

4 Conclusion

This study aims to enhance the mechanical strength of Pt FCC alloys using Cr as an alloying element, with a focus on jewellery applications, employing first-principles methods. We investigate the structural properties, cohesive energies, and electronic characteristics through DFT calculations. The results reveal a decreasing trend in lattice parameters as the Cr content increases, due to the smaller atomic radius of Cr. This observation also extends to cohesive energies and cell volumes. Phonon dispersion analysis indicates the material's dynamical stability, with positive frequencies despite an increase in Cr alloy composition. Additionally, strong electronic interactions between Pt and Cr were observed, particularly with charge accumulation around the Pt atoms. An increase in Cr-d orbital density of states at the Fermi level as Cr concentration rises suggests the potential for improved ductility, making the material suitable for jewellery applications.

Acknowledgement

Authors would like to acknowledge the University of Pretoria for financial support and availability of resources. MINTEK is also acknowledged for financial support. We are grateful to CHPC Cape Town for the availability of their world class Lengau computational cluster.

References

[1] V. Stamenkovic *et al.*, "Changing the Activity of Electrocatalysts for Oxygen Reduction by Tuning the Surface Electronic Structure," *Angew. Chemie*, vol. 118, pp. 2963–2967, Apr. 2006, doi: 10.1002/ange.200504386.

[2] V. Climent, N. M. Marković, and P. N. Ross, "Kinetics of oxygen reduction on an epitaxial film of palladium on Pt(111)," *J. Phys. Chem. B*, vol. 104, no. 14, pp. 3116–3120, 2000, doi: 10.1021/jp993480t.

[3] N. M. Marković, C. A. Lucas, V. Climent, V. Stamenković, and P. N. Ross, "Surface electrochemistry on an epitaxial palladium film on Pt(111): Surface microstructure and hydrogen electrode kinetics," *Surf. Sci.*, vol. 465, no. 1–2, pp. 103–114, 2000, doi: 10.1016/S0039-6028(00)00674-9.

[4] C. W. Corti, "The 22nd Santa Fe symposium on jewelry manufacturing technology," *Platin. Met. Rev.*, vol. 53, no. 1, pp. 21–26, 2009, doi: 10.1595/147106709X395503.

[5] T. Trosch, F. Lalire, S. Pommier, R. Völkl, and U. Glatzel, "Optimisation of a jewellery platinum alloy for precision casting: Evaluation of mechanical, microstructural and optical properties," *Johnson Matthey Technol. Rev.*, vol. 62, no. 4, pp. 364–382, 2018, doi: 10.1595/205651318X696837.

[6] T. Biggs, S. S. Taylor, and E. Van Der Lingen, "The hardening of platinum alloys for potential jewellery application," *Platin. Met. Rev.*, vol. 49, no. 1, pp. 2–15, 2005, doi: 10.1595/147106705X24409.

[7] C. Zhang *et al.*, "Thermodynamic modeling of the Cr-Pt binary system using the cluster/site approximation coupling with first-principles energetics calculation," *Acta Mater.*, vol. 56, no. 19, pp. 5796–5803, 2008, doi: 10.1016/j.actamat.2008.07.057.

[8] K. Lekganyane, M. Khodja-Moller, D. Mkhonto, R. Mostert, and M. Phasha, "The development of platinum alloys for jewellery applications by considering both the conventional and the advanced manufacturing techniques-review paper," *MATEC Web Conf.*, vol. 406, p. 01005, 2024, doi: 10.1051/matecconf/202440601005.

[9] P. Giannozzi *et al.*, "QUANTUM ESPRESSO: A modular and open-source software project for quantum simulations of materials," *J. Phys. Condens. Matter*, vol. 21, no. 39, 2009, doi: 10.1088/0953-8984/21/39/395502.

[10] J. P. Perdew, K. Burke, and M. Ernzerhof, "Generalized gradient approximation made simple," *Phys. Rev. Lett.*, vol. 77, no. 18, pp. 3865–3868, 1996, doi: 10.1103/PhysRevLett.77.3865.

[11] J. Feng, B. Xiao, J. Chen, Y. Du, J. Yu, and R. Zhou, "Stability, thermal and mechanical properties of PtxAly compounds," *Mater. Des.*, vol. 32, no. 6, pp. 3231–3239, 2011, doi: 10.1016/j.matdes.2011.02.043.

[12] T. Murakami, R. Sahara, D. Harako, M. Akiba, T. Narushima, and C. Ouchi, "The effect of solute elements on hardness and grain size in platinum based binary alloys," *Mater. Trans.*, vol. 49, no. 3, pp. 538–547, 2008, doi: 10.2320/matertrans.MRA2007265.

[13] A. Kokalj and M. Causà, "Periodic density functional theory study of Pt (111): Surface features of slabs of different thicknesses," *J. Phys. Condens. Matter*, vol. 11, no. 39, pp. 7463–7480, 1999, doi: 10.1088/0953-8984/11/39/304.

[14] P. J. Hill, L. A. Cornish, P. Ellis, and M. J. Witcomb, "The effects of Ti and Cr additions on the phase equilibria and properties of (Pt)/Pt3Al alloys," *J. Alloys Compd.*, vol. 322, no. 1–2, pp. 166–175, 2001, doi: 10.1016/S0925-8388(01)01018-0.

[15] P. Bosi, F. Duprè, F. Menzinger, F. Sacchetti, and M. C. Spinelli, "Phonon modes in Pd-Pt and other substitutional alloys with large mass disorder," *Nuovo Cim. B Ser. 11*, vol. 46, no. 2, pp. 337–362, 1978, doi: 10.1007/BF02728625.

[16] W. Tang, E. Sanville, and G. Henkelman, "A grid-based Bader analysis algorithm without lattice bias," *J. Phys. Condens. Matter*, vol. 21, no. 8, 2009, doi: 10.1088/0953-8984/21/8/084204.

[17] T. Zhang, H. Q. Yin, C. Zhang, X. H. Qu, and Q. J. Zheng, "Effect of Mn doping on mechanical properties and electronic structure of WCoB ternary boride by first-principles calculations," *Chinese Phys. B*, vol. 27, no. 10, 2018, doi: 10.1088/1674-1056/27/10/107101.

[18] N. O. Monama, "Electronic Structure Studies of Palladium Sulphide (PdS) and Platinum (Pt) Ternaries," 2008.

The effect of Ir on the mechanical, thermodynamic, electronic and magnetic properties of FePt alloy: A DFT study

M C Matlala[1], M G Matshaba[2], R G Diale[3] and H R Chauke[1]

[1]Materials Modelling Centre, University of Limpopo, Private Bag X 1106, Sovenga, 0727, South Africa
[2]Department of Physics, University of Limpopo, Private Bag X 1106, Sovenga 0727, South Africa
[3]Advanced Materials Discipline, Mintek, Private Bag X 3015, Randburg 2125, South Africa

E-mail : 202002565@myturf.ul.ac.za

Abstract. $L1_0$-ordered FePt alloy is a perfect candidate for high-density magnetic recording media due to its high coercivity and magnetic anisotropy energy. However, it was reported that this alloy faces challenges including issues with thermal stability and media noise. Hence, ternary alloying with Ir was conducted to enhance mechanical stability in response to the change in direction of the magnetic spin moment of the binary FePt system. Structural, thermodynamic, mechanical, magnetic, and electronic properties of $L1_0$-ordered $Fe_{50}Pt_{50-x}Ir_x$ alloys ($0 \leq x \leq 25$) were studied using the density functional theory. The determined magnetic moments and lattice parameters of the binary $Fe_{50}Pt_{50}$ were in well agreement with previous experimental and theoretical results to within 5 %. In all $Fe_{50}Pt_{50-x}Ir_x$ alloys, the calculated heats of formation were negative, demonstrating their thermodynamic stability. The magnetic moments and density of states were determined to evaluate the magnetic behaviour of $Fe_{50}Pt_{50-x}Ir_x$ alloys. These results contribute to understanding the role of Ir in tailoring FePt-based alloys for magnetic recording applications.

1 Introduction

The growing demand for higher storage density in magnetic devices drives to the need for materials with high coercivity, strong thermal stability, and optimized magnetic anisotropy [1]. FePt alloys, meet these criteria, particularly in their chemically ordered $L1_0$ phase, exhibiting outstanding magnetic properties such as high coercivity and high magneto-crystalline anisotropy energy (MAE), making them best candidates for high-density magnetic recording devices [2]. However, it was reported that this alloy faces challenges, including issues with thermal instability and media noise [3]. Among these problems, high ordering temperature problem is well addressed in previous studies, but the problem associated with thermal stability and reduction of media noise remain unsolved [4]. Hence, ternary alloying is proposed to enhance the mechanical stability in response to the orientation of the magnetic spin moment of the binary FePt system, which can solve the problem associated with

thermal stability and media noise. Previous studies indicated that alloying FePt with elements like Cu, Mn, and Ni can effectively modify structural, mechanical, energetic and magnetic properties. For instance, Singh et al. [5] performed annealing on $Fe_{50}Pt_{50}$/Cu multilayer and shown that addition of Cu reduces the Fe-Pt ordering temperature. Chiang et al. [6] also achieved lower ordering temperature on Fe-Pt by addition of Cu which introduces dynamic stress while Wen et al. [7] showed that doping Ni on Fe-Pt alloy decreases the thermodynamic stability. Furthermore, Gruner et al. [8] indicated that Mn enhances phase stability on Fe-Pt alloy using first principle study. According to the literature, addition of Ir to $L1_0$ ordered FePt can influence its magnetic and structural properties, including coercivity and MAE. In this study, ternary alloying of $L1_0$ ordered FePt with iridium (Ir) was performed using density functional theory to investigate the structural, magnetic, mechanical, thermodynamic and electronic properties.

2 Methodology

All the results from this work were performed using density functional theory (DFT) within the Vienna ab initio Simulation Package (VASP) [9, 10]. Electron-ion interactions in the system were modelled using Projector Augmented Wave (PAW) pseudopotential [11], and the exchange–correlation potential was described using the Perdew–Burke–Ernzerhof (PBE) form of the generalized gradient approximation (GGA) [13].

A plane wave cutoff energy of 400 eV and k- spacing of 0.07 /Å were used in all the calculations. A 2x2x2 supercell with 32 atoms was constructed on $L1_0$ FePt system. Ir substitution was constructed using MedeA substitutional search tool, where platinum atoms where systematically substituted with iridium atoms. All $Fe_{50}Pt_{50-x}Ir_x$ alloys ($0 \leq x \leq 25$) structures were optimized, where internal atom positions were allowed to relax and elastic properties were calculated using strain of 0.005.

3 Results and discussion

3.1 Structural and thermodynamic properties

The equilibrium lattice parameters as shown in Figure 1 were obtained by performing geometry optimization on $Fe_{50}Pt_{50-x}Ir_x$ alloys ($0 \leq x \leq 25$). Lattice parameters of binary structure ($Fe_{50}Pt_{50}$) were determined as a = b = 3.86 Å and c = 3.76 Å which are in well agreement with the experimental results where a = b = 3.86 Å and c = 3.71 Å [14]. The equilibrium lattice parameters of the $L1_0$ $Fe_{50}Pt_{50}$ alloy reduces as the Ir composition was increased, this is because the atomic radius of Ir (1.36 Å) is less than that of Pt (1.39 Å).

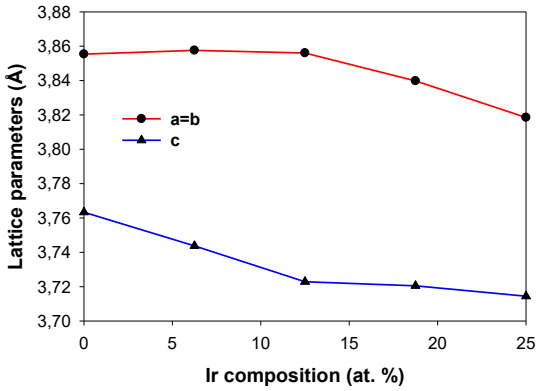

Figure 1: The equilibrium lattice parameters for $Fe_{50}Pt_{50-x}Ir_x$ alloys ($0 \leq x \leq 25$).

The thermodynamic stability of material can be predicted using heats of formation, which give important information about energy change due to the formation of a material/crystal [15]. The most stable structures are those with lower (more negative) heats of formation because they require less energy to form. The heats of formation were calculated using equation 1:

$$\Delta H_f = E_C - \sum_i x_i E_i \qquad (1)$$

The calculated heats of formation as shown in Figure 2 were negative, showing thermodynamic stability. The binary structure ($Fe_{50}Pt_{50}$) is observed as the most stable structure with heat of formation of -0.47 eV/atom. It also observed that the heats of formation increase linearly with the increase in iridium (Ir) composition, suggesting that Ir reduces thermodynamic stability.

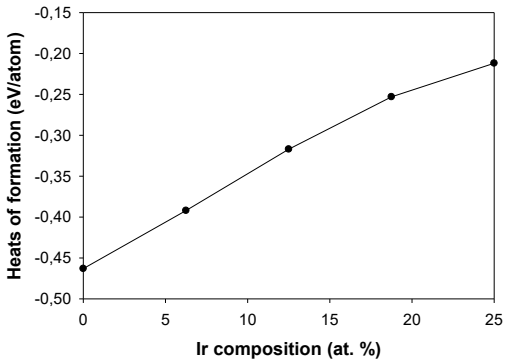

Figure 2: Heats of formation against Ir composition for $Fe_{50}Pt_{50-x}Ir_x$ alloys ($0 \leq x \leq 25$).

3.2 Magnetic properties

Magnetic moment is one of the magnetic properties that is used to predict the magnetic strength of a material, which is an important fixture for magnetic recording devices application. Figure 3 shows the calculated magnetic moments for $Fe_{50}Pt_{50-x}Ir_x$ alloys with Ir composition of 6.25%, 12.50%, 18.75% and 25%. The calculated magnetic moment of binary structure ($Fe_{50}Pt_{50}$) is 3.31 μB, which in well agreement with the experimental value of 3.24 μB [16]. From Figure 3, it is showed that magnetic moment of $Fe_{50}Pt_{50}$ alloy reduces as the Ir composition was increased, this suggests that Ir does not enhance magnetic strength of FePt alloy. According to Schmidt et al. [17], this behaviour is because of antiferromagnetic interaction between the FePt and Ir moments, resulting in partial reduction of magnetic moment.

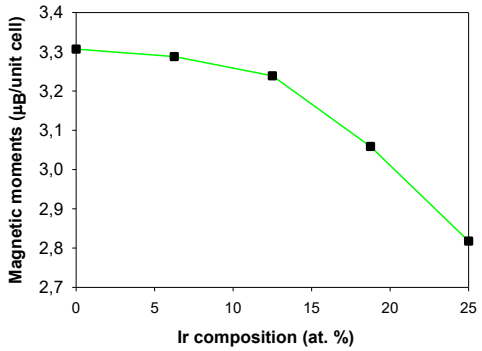

Figure 3: Magnetic moments against Ir composition for $Fe_{50}Pt_{50-x}Ir_x$ alloys.

3.3 Elastic properties

The elastic properties provide important information about mechanical behaviour of materials as they respond to applied stress or strain. Elastic constants are important parameters for predicting the mechanical stability of a material. $Fe_{50}Pt_{50-x}Ir_x$ alloys exhibits tetragonal shape possessing six elastic constants namely C_{11}, C_{12}, C_{13}, C_{33}, C_{44}, and C_{66}. Tetragonal systems mechanical stability is given the following conditions [18]:

$$c_{44} > 0,\ c_{66} > 0,\ c_{11} > |c_{12}| \text{ and } c_{11}+c_{12} - \frac{2C_{13}^2}{C_{33}} > 0 \qquad (2)$$

Figure 4 represent the calculated elastic constants of the $Fe_{50}Pt_{50-x}Ir_x$ alloys ($0 \leq x \leq 25$). The stability conditions should be met for a material or structure to be stable [19]. All the calculated elastic constants as shown in Figure 4 are positive, indicating that $Fe_{50}Pt_{50-x}Ir_x$ alloys are stable, does they satisfy the tetragonal stability criterion as indicated by equation 2. From Figure 4, it is observed that addition of iridium enhances rigidity since C_{44}, C_{66} and C_{11} increases as the iridium composition was increased, this is desirable for high temperature reliability.

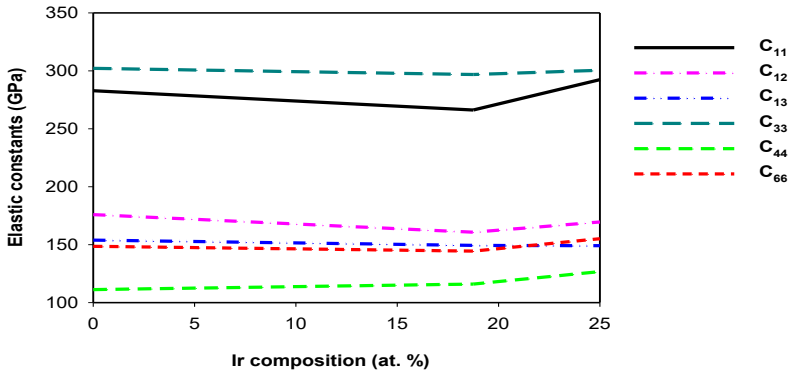

Figure 4: Elastic constants (GPa) against Ir composition for $Fe_{50}Pt_{50-x}Ir_x$ alloys ($0 \leq x \leq 25$).

3.4 Electronic properties

To analyse the electronic structures of $Fe_{50}Pt_{50-x}Ir_x$ alloys, density of states (DOS) where computed as shown in figure 5. A significant asymmetry in spin ups and spin downs is observed in the total DOS suggesting ferromagnetic behavior, which was also indicated by the calculated positive magnetic moments. Since the is no energy gap around the fermi level, this implies that the systems are metallic. From the partial DOS it is observed that iron (Fe) is the one that contribute more to the magnetism in $Fe_{50}Pt_{50-x}Ir_x$ alloys. Furthermore, it observed that Ir increases the DOS at the Fermi level. $Fe_{50}Pt_{50}$ system have less states near fermi level indicating that is more thermodynamically stable, which is in well agreement with the calculated heats of formation. Lastly it observed that the material retains its magnetism, this makes these materials best candidates for application in magnetic recording devices.

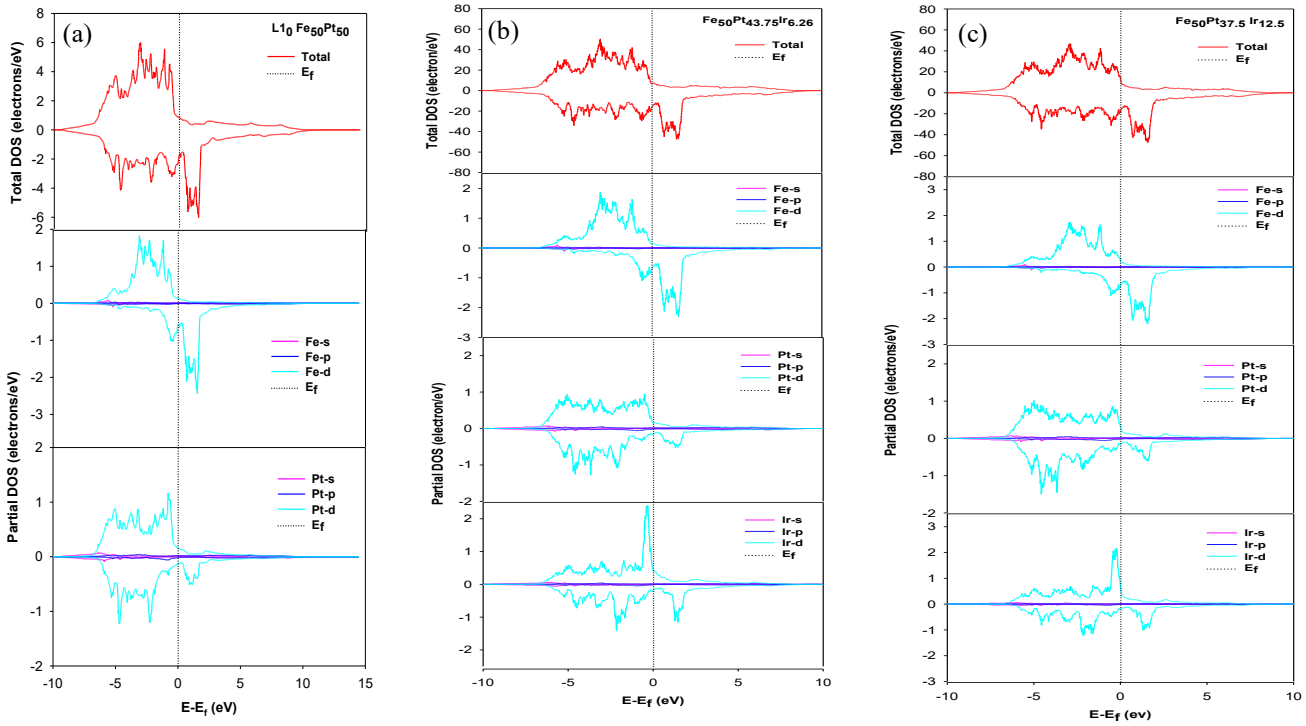

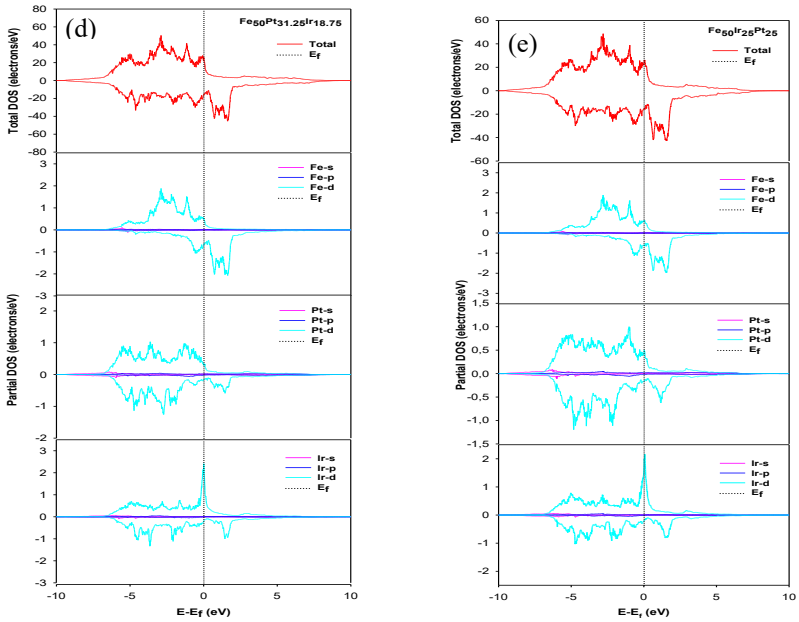

Figure 5 (a-e): The spin-polarized total and partial density of states for $Fe_{50}Pt_{50-x}Ir_x$ alloys.

4 Conclusion

The density functional theory was effectively employed to study the effect of iridium (Ir) substitution on the properties of the $L1_0$ ordered $Fe_{50}Pt_{50-x}Ir_x$ ($0 \leq x \leq 25$) alloys. The results of lattice parameters are in good agreement with the experimental values within 5%. In all $Fe_{50}Pt_{50-x}Ir_x$ alloys, heats of formation were negative, demonstrating thermodynamic stability. It was found that substitution of Ir slightly reduced magnetic strength of FePt alloy, however it improved elastic rigidity. The total DOS showed that $Fe_{50}Pt_{50-x}Ir_x$ alloys are ferromagnetic and partial DOS indicated that iron (Fe) contribute more to the magnetism in $Fe_{50}Pt_{50-x}Ir_x$ alloys. Future work will focus on studying the temperature dependence of the structural, magnetic, mechanical and electronic properties of FePt–Ir alloy to further understand thermal behaviour.

References

[1] G. W. Qin, Y. P. Ren, N. Xiao, B. Yang, L. Zuo, and K. Oikawa, "Development of high density magnetic recording media for hard disk drives: Materials science issues and challenges," *Int. Mater. Rev.*, vol. 54, pp. 157–179, 2009.

[2] N. Lethole, P. Ngoepe, and H. Chauke, "Compositional dependence of magnetocrystalline anisotropy, magnetic moments, and energetic and electronic properties on Fe-Pt alloys," *Materials*, vol. 15, p. 5679, 2022.

[3] K. Shibata, "FePt magnetic recording media: Problems and possibilities for practical use," *Jpn. Inst. Met.*, vol. 44, pp. 1542–1545, 2003.

[4] A. Alsaad, A. A. Ahmad, and T. S. Obeidat, "Structural, electronic and magnetic properties of the ordered binary FePt, MnPt, and $CrPt_3$ alloys," *Heliyon*, vol. 6, p. 3596, 2020.

[5] S. Singh, C. L. Prajapat, M. Gupta, and S. Basu, "Room temperature superparamagnetism in ternary $(Fe_{50}Pt_{50})_{0.42}Cu_{0.58}$ phase at interfaces on annealing of $Fe_{50}Pt_{50}$/Cu multilayer," *J. Magn. Magn. Mater.*, vol. 462, pp. 58–69, 2018.

[6] C.-H. Lai, C. C. Chiang, and C. H. Yang, “Low-temperature ordering of FePt by formation of silicides in underlayers,” *J. Appl. Phys*., vol. 97, 2005.

[7] Z. Wen, Y. Wang, W. Zhao, M. Jiang, Y. Ren, & G. Qin, “Effects of Ni addition on the order–disorder transitions of Fe–Pt intermetallic compounds: An experimental study on Fe–Ni–Pt phase diagrams,” *J. Mater. Sci. & Tech.*, vol. 182, pp. 54–66, 2024.

[8] M. E. Gruner and P. Entel, “Structural and magnetic properties of ternary $Fe_{1-x}Mn_xPt$ nanoalloys from first principles,” *Beilstein J. Nanotechnol*., vol. 2, pp. 162–172, 2011.

[9] W. Kohn and L. J. Sham, “Self-consistent equations including exchange and correlation effects,” *Phys. Rev.*, vol. 140, pp. 1133–1138, 1965.

[10] J. Hafner and G. Kresse, “The Vienna ab-initio simulation program VASP: An efficient and versatile tool for studying the structural, dynamic, and electronic properties of materials,” *Appl. Sci.*, vol. 351, pp. 351–358, 1997.

[11] P. E. Blöchl, “Projector augmented-wave method,” *Phys. Rev. B*, vol. 50, pp. 17953–17979, 1994.

[12] J. P. Perdew, K. Burke, and M. Ernzerhof, “Generalized gradient approximation made simple,” *Phys. Rev. Lett.*, vol. 77, pp. 3865–3868, 1996.

[13] J. P. Perdew and A. Zunger, “Self-interaction correction to density-functional approximations for many-electron systems,” *Phys. Rev. B*, vol. 23, pp. 5048–5079, 1981.

[14] A. Alsaad, A. A. Ahmad, and T. S. Obeidat, “Structural, electronic and magnetic properties of the ordered binary FePt, MnPt, and $CrPt_3$ alloys,” *Heliyon*, vol. 6, p. 3596, 2020.

[15] N. Lethole and T. Sibila, "Effect of Mn on the structural, energetic, electronic and elastic properties of ordered L10 FePt Alloy,"*MATEC Web of Conferences*, vol. 406, p. 03017, 2024.

[16] J. Lyubina, I. Opahle, M. Richter, O. Gutfleisch, K. Müller, and L. Schultz, “Influence of composition and order on the magnetism of Fe–Pt alloys: Neutron powder diffraction and theory,” *Appl. Phys. Lett.*, vol. 89, no. 032506, 2006.

[17] N. Y. Schmidt, S. Laureti, F. Radu, H. Ryll, C. Luo, F. d’Acapito, S. Tripathi, E. Goering, D. Weller, and M. Albrecht, “Structural and magnetic properties of FePt-Tb alloy thin films,” *Phys. Rev. B*, vol. 100, pp. 1–8, 2019.

[18] F. Mouhat and F.-X. Coudert, "Necessary and sufficient elastic stability conditions in various crystal systems," *Phys. Rev. B*, vol. 90, p. 224104, 2014.

[19] R. Diale, P. Ngoepe, J. Moema, M. Phasha and H. Chauke, " Thermodynamic and magnetic properties of Pt50Mn50-xMx (M= Cr, Fe) alloys: A first-principles study,"*MATEC Web of Conferences*, vol. 370, p. 02006, 2022.

The effects of annealing temperature on physical properties of $Ce_2Zr_2O_7$ material

Yissah Saheed O.[1], Moise B Tchoula Tchokonte[2], Sibusiso Nqayi[1] and Buyisiwe Sondezi [1]

[1] Rare-Earth Based Oxides and Nano Materials Group, Department of Physics, University of Johannesburg Cnr. Kingsway Avenue and University Road, Ackland Park 2006, South Africa.
[2] Department of Physics and Astronomy, University of Western Cape, Private Bag X17, Bellville 7535, South Africa

E-mail: 224099692@student.uj.ac.za

Abstract. Pyrochlore oxides are a fascinating class of materials known for their remarkable thermal stability and adaptability, making them excellent candidates for energy-related applications. This study explored the effects of thermal treatment on structural, morphological, optical, thermodynamic and magnetic properties of $Ce_2Zr_2O_7$ nanoparticles (CZONPs) prepared using sol-gel method. Followed by thermal annealing treatment. The micro-structure, size, optical, and magnetic properties of prepared materials were analyzed using X-ray diffraction (XRD), transmission electron microscopy (TEM), scanning electron microscopy (SEM), and energy-dispersive X-ray spectroscopy (EDS) respectively. The results showed mixed phases of $CeZrO_4$ and $Ce_2Zr_2O_7$ at various annealing temperature ranges. The ratio between these phases was changing as a function of annealing temperature. The pure phase of CZONPs was obtained at high temperature. These findings point to a strong correlation between pyrochlore's stability, making the material highly relevant for high-temperature applications.

1 Introduction

Pyrochlores are complex metal oxides with a general formula of $A_2B_2O_7$. Where A site represents an 8-fold coordinated metal, usually rare earth, and B site represents 6-fold coordinated metals such as transitional metals. The *A* site cation generally has an oxidation state of +2 or +3, and the *B* site cation has a corresponding oxidation state of +5 or +4 [1]. A study by (Fuentes et al., 2024) shows that the stable crystalline phase structure of an $A_2B_2O_7$ compound is determined ratio of the radius rA/rB [2]. When the radius ratio is greater than 1.78, a monoclinic layered perovskite phase will be observed. i.e. $P2_1$. When the radius ratio is the range of 1.46 -1.78 and ordered pyrochlore phase will be formed which belong to the space group (SG) of *Fd-3m*. This can also be referred to an ordered defective fluorite in which 1/8 of the oxygen are unoccupied [5-6]. If the radius ratio is within the range of 1.17 - 1.45 a disordered defective fluorite will be formed, which belong to the SG of Fm-3m. [3]. And if the radius ratio is close to 1.17 – 1.0 rare earth C-type phase will be formed. The structure is similar to Y_2O_3 whose A and B cation distribute even more randomly in the sublattices [3-4]. Previous studies have showed that X-ray diffraction (XRD) and transmission electron microscopy (TEM) spectroscopy are very effective in distinguishing $A_2B_2O_7$ compounds containing different phase structures [4].

Pyrochlore-type Cerium–zirconium oxide $Ce_2Zr_2O_7$ are attractive materials used as structural ceramic which have gained significant attention in recent years, due to its defect-tolerant structure, high oxygen mobility, and their

ability to reversibly store and release oxygen, making them indispensable in automotive catalysts (AC), solid oxide fuel cells (SOFCs), and thermal barrier coatings (TBC) [2,3,4].

Synthesis methods greatly influence the final properties of Cerium–zirconium oxide with annealing temperature playing a pivotal role in defining phase composition and structural integrity [5]. Lower temperatures favours high surface areas and defect-rich structures, beneficial for catalysis, while higher temperatures improve crystallinity and thermal robustness [6]. Despite its importance, systematic studies on the effects of annealing on Cerium–zirconium oxide remain scarce. This research work aims to synthesis CZONPs and provides a detailed investigation of how annealing temperature modulates its structural, morphology, optical, thermodynamic, and magnetic, physical properties [7].

2 Experimental Procedure

2.1 Chemicals used

Cerium (II) nitrate hexahydrate, $Ce(NO_3)_3.6H_2O$ (with the assay of 99%, Sigma Aldrich) which has mass of 434.22g, and Zirconium (IV) sulphate hydrate, $Zr(SO_4)_2.4H_2O$ (with the assay of 99%, Sigma Aldrich) which has mass of 283.34g, and Citric Acid Anhydrous $C_6H_6O_7$ which has mass of 192.13g, ammonia (NH3) and Distilled water were used for the preparation of the materials.

2.2 Preparation procedure and synthesis of $Ce_2Zr_2O_7$ nanocomposite.

Nanocrystalline $Ce_2Zr_2O_7$ (CZONP) powder was produced using sol-gel method. To produce the powder the following compounds were used as precursors: 4.34g of Ce $(NO_3)_3.6H_2O$, 2.83g of Zr $(SO_4)_2.4H_2O$ and 16.01g of $C_6H_6O_7$ were poured into a beaker with a magnetic stirrer, and 150ml of distilled water. The beaker was placed on a magnetic stirrer, and it was allowed to stir for 30 minutes before adding 3 drops of Ammonia (NH3) and it was allowed to stir for 1 hour 30 minutes, then allowed to age for 24 hours at room temperature. After aging, the sample forms gel and the beaker was placed on hot plate with temperate of 60^0C for 4hours 20mins for the gel to turn dry. The dried gel was allowed to cool; it was crushed into fine powered using mortar and pestle and was divided into five (5) portions. The materials were then annealed at 500^0C, 800^0C, 1000^0C, 1200^0C and 1500^0C respectively at 4^0C/minute for four (4) hours in the air furnace. The material was crushed again after the annealing process.

2.3 Materials characterization

The X-ray diffraction (PXRD) of the materials was performed using EMPYREAN X-RAY Diffractometer, Paralytical, Germany, with Ni-filtered Cu Kα radiation wavelength of 1.5406Å, working at 40 kV and 40 mA with the radiation with 2.5 step, (θ/2θ Bragg Brentano geometry). The PXRD measurements were performed in the 2θ range from 10° to 80°. Identification of present phases was conducted using MAUD v. 2.99 software [9]. The Rietveld structural refinement calculations were conducted using the obtained XRD data and the MAUD software to determine relevant structural parameters of the powders annealed at different temperatures.
Morphology and elemental distribution of the obtained annealed powders materials were analysed using a transmission electron microscopy (TEM), and scanning electron microscope (SEM) VEGA3, TESCAN, Czech Republic, operated at 20keV and coupled with X-max energy dispersive spectrometer (EDS).

3 Results and discussions

3.1 Structural analysis

The XRD patterns presented in Figure 1 indicate that the powder annealed at 500°C shows typical amorphous behaviour without a long range of atom ordering. The pattern of the materials annealed at 800°C, 1000°C, 1200°C, and 1400°C shows a clear reflection peak with double phases of $Ce_2Zr_2O_8$ and ZrO_2, a diffraction peak at scattering angle (2θ) of 29°, 33°, 48°, 57°, and 60°, correspond to the reflections from (222), (400), (440), (622), and (444), crystal planes respectively as demonstrated in Figure 1(a). These reflections correspond to the Cubic $Ce_2Zr_2O_7$ structure as confirmed by the International Centre for Diffraction Data (ICDD) card number No. 04-002-0615 [11] which was detected at 1500°C suggesting the sample exhibits pure Pyrochlore phase in space group 227 (*Fd-3m*) [3] as shown in Figure 1 (b) as there was a peak shifted towards higher 2θ angle in Figure 1(b) as very narrow diffraction lines in its XRD pattern. This can further suggest its highly crystallinity state. The result of the structural Rietveld refinement of the XRD Pattern of $Ce_2Zr_2O_7$ annealed at 1500C is presented in Figure 2 below.

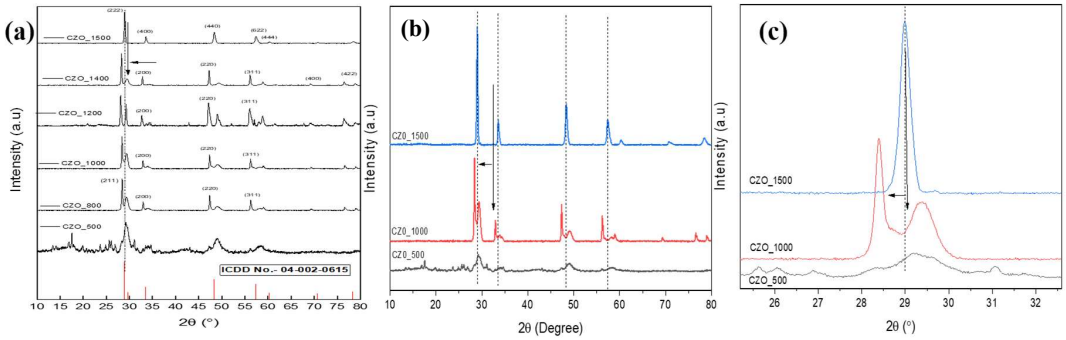

Figure 1: (a) XRD patterns for CZONPs at different annealing temperature of 500^0C, 800^0C,1000^0C, 1200^0C,1400^0C and 1500^0C for 4 hours. (b) and (c) Comparison of selected XRD patterns for CZONPs annealed at 500, 1000, and 1500 °C.

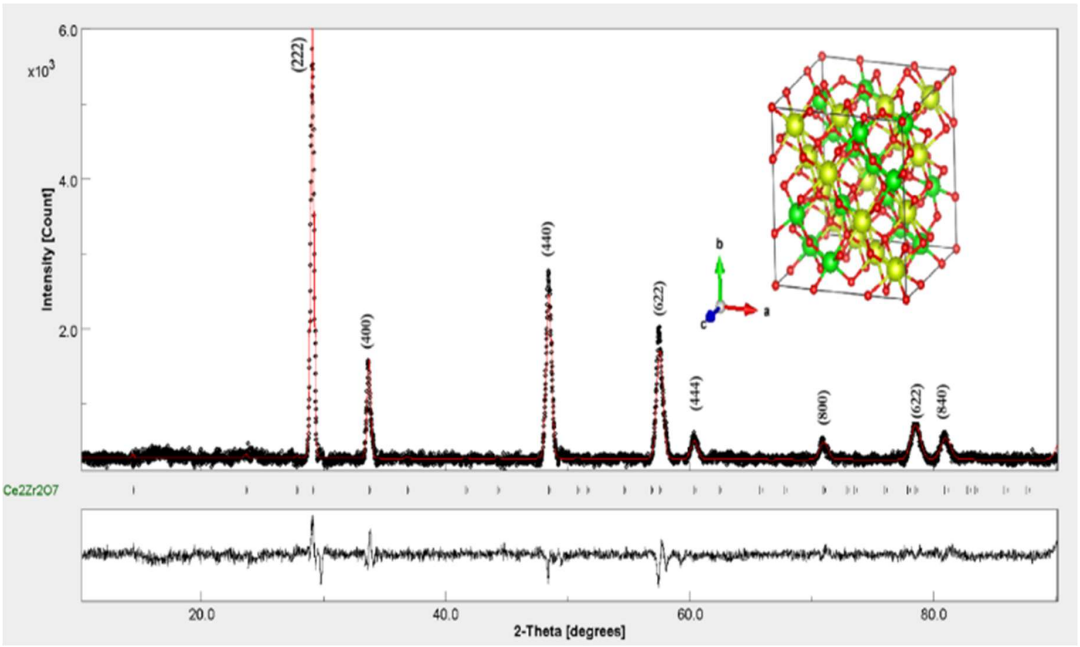

Figure 2: Rietveld refinement of $Ce_2Zr_2O_7$ annealed at 1500 °C. Dots: experimental data; solid line: calculated profile; tick marks: Bragg reflections; bottom line: difference curve.

The average crystallite size of the materials was obtained using Debye-Scherrer equation and Williamson-Hall method fitting was used to determine the strain in the materials.

$$D = \frac{K*\lambda}{\beta cos\theta} \quad (2)$$

Where β= Full width at half maximum of the selected peaks FWHM, K=0.94 and λ=0.1540nm

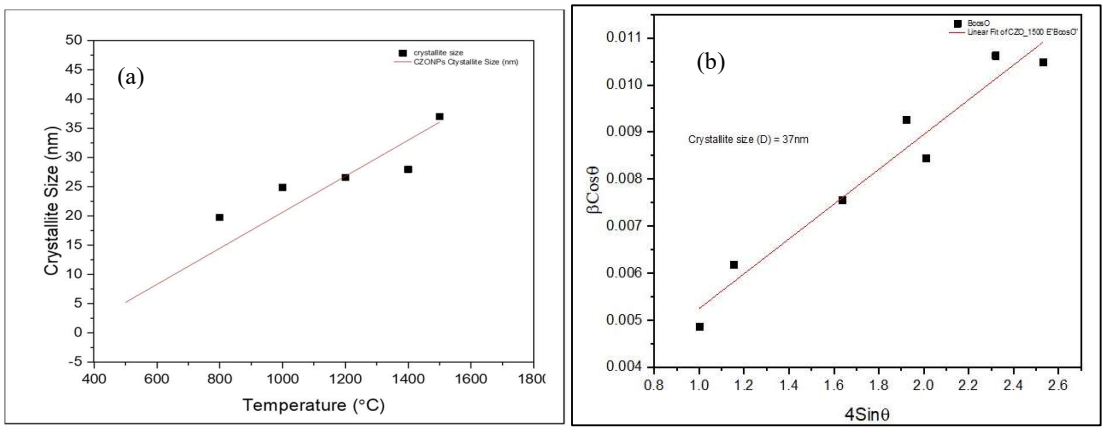

Figure 3: (a)Variation of crystallite sizes with annealing temperature, (b) Williamson–Hall plot for $Ce_2Zr_2O_7$ annealed at 1500°C.

The calculated values of Crystallite size D(nm), Strain and lattice parameters are shown in Table1 for the respective materials, it can be observed that as the temperature increases, the lattice size also increase from 800°C to 1400°C and finally decrease at 1500°C which change of phase as recrystallization occur, the result obtained is in line with other previous study [6]. The average crystallite size increases with an increase in the annealing temperature which ranges from 19nm to 40nm, this was shown in Figure 3(a).
The lattice strain of the materials was obtained using Williamson-Hall fitting Figure 3b).

$$\beta_T Cos\,\theta = \varepsilon(4Sin\theta) + 4\frac{K\lambda}{D} \quad (1)$$

β_T = Full width at half maximum of the selected peaks (FWHM), ε = strain, K=0.94, λ =0.1540 nm

3.2 Morphology analysis

Figure 4 represents the TEM images and SAED patterns of CZONPs annealed at (a) 500°C, (b) 1000 °C, and (c) 1500°C materials showing particle morphology. The powder annealed at 500°C depicted very small isometric particles which are heavily agglomerated as shown in Figure 4(a) and as annealing temperature was increased to 1000°C the results show cubic and hexagonal like shapes in Figure 4(b), showing improved crystallinity and a mixed phase. When the annealing temperature increased to 1500°C the material shows cubic like shapes with highly crystalline as shown in Figure 4(c).

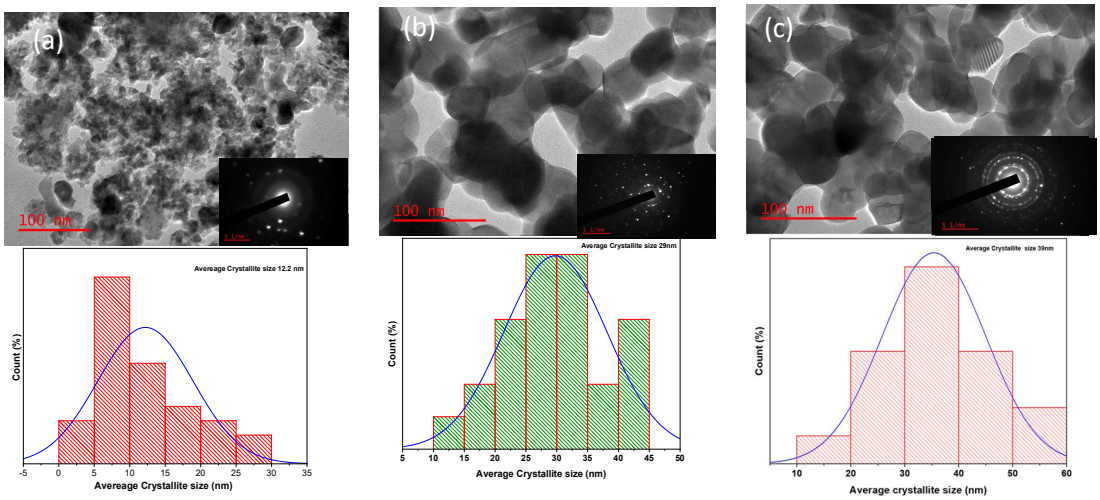

Figure 4: TEM images (insert SAED) with their corresponding normal distribution patterns of $Ce_2Zr_2O_7$ nanoparticles (a) 500 °C, (b) 1000 °C, and (c) 1500 °C materials showing particle morphology.

3.3 Elemental composition

The elemental formation of was analyzed using EDS. Figure 5 represents SEM micrograph and EDS elemental mapping of $Ce_2Zr_2O_7$ annealed at 1500 °C shows the presence of Ce, Zr and O and $Ce_2Zr_2O_7$ materials contain expected elements and corresponding peaks.

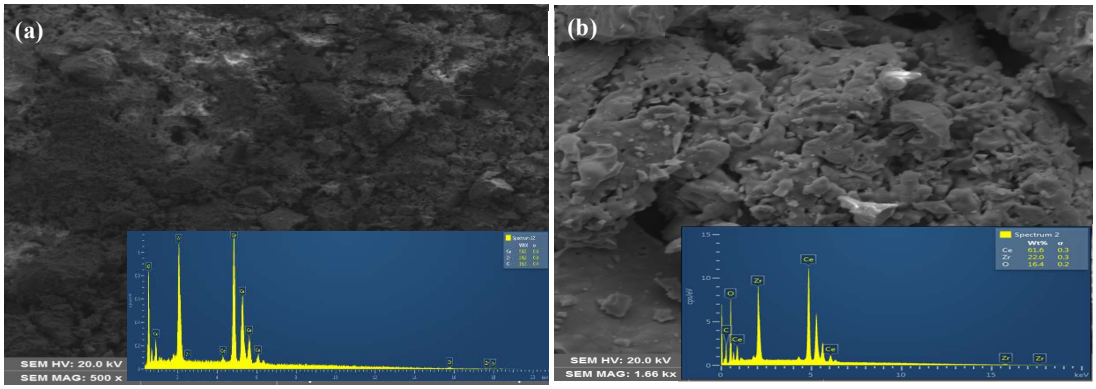

Figure 5: SEM micrograph and EDS elemental of $Ce_2Zr_2O_7$ annealed at (a) 500^0C and (b)1500^0C °C.

The corresponding EDS mapping demonstrates that all cations were present in the analysed powder sample according to its nominal composition. Moreover, the observed elemental distribution showed that elements were randomly and homogeneously distributed throughout the analysed powder sample indicating that the powder chemical homogeneity was achieved due to the selected synthesis procedure. The typical morphology of the obtained compositionally complex oxide powder is shown in Figure 5 (a) and (b), it can be observed that the sample prepared by sol-gel method and annealed at 1500^0C for (4) hours.

Temperature (^{0}C)	**1500^{0}C**	**1400^{0}C**		**1200^{0}C**		**1000^{0}C**		**800^{0}C**	
Rwp	11.2	14.9		13.4		12.8		13.9	
Rexp	5.5	4.5		4.4		4.7		4.6	
GOF	2.0	3.2		3.05		2.73		3.02	
Phase	C- $e_2Zr_2O_7$	C- $Ce_2Zr_2O_8$	t-ZrO_2	C- $Ce_2Zr_2O_8$	t-ZrO_2	C- $Ce_2Zr_2O_8$	t-ZrO_2	C- $Ce_2Zr_2O_8$	t-ZrO_2
Space Group	*Fd-3m*	*P213*	*P21/nmc*	*P213*	*P21/nmc*	*P213*	*P21/nmc*	*P213*	*P21/nmc*
Weight (%)	100	24	76	42	58	55	35	40	60
a (Å)	10.61	10.81	3.67	10.78	3.64	10.75	3.65	10.71	3.69
b ((Å)	10.61	10.81	5.19	10.78	5.53	10.75	5.80	10.71	5.25
c ((Å)	10.61	10.81		10.78		10.75		10.71	
α, β, ϒ	90^0	90^0	90^0	90^0	90^0	90^0	90^0	90^0	90^0
Crystallite Size (nm)	37	27.97		26.85		24.87		19.7	
Strain (x10^{-4})	3.0	3.3		8.6		10.7		23.9	

Table 1: Rietveld refinements of the X-Ray powder diffraction patterns for CZONPs at different annealing temperature of 500^0C, 800^0C,1000^0C, 1200^0C,1400^0C and 1500^0C for 4 hours

4 Conclusion

The $Ce_2Zr_2O_7$ materials were successfully synthesized using the sol-gel method. The study investigated the structure, and morphology of the materials, and found that annealing temperature significantly affects CZONPs. TEM studies reveal the particles morphology which is cubic. The SAED pattern helps confirm the crystallinity and crystallite sizes. The research discovered higher annealing temperatures improve crystallinity, phase purity, reduce strain ($23E^{-4}$ to $3E^{-4}$). Depending on the target application, annealing parameters can be tuned to optimize the material performance. Further research will focus on the optical, thermodynamic, and magnetics properties of the materials.

Acknowledgement

Special thanks to University of Johannesburg, URC for the bursary support. Dr. Mubarak Yagoub for his support and the use of Spectrum facilities in the FoS in UJ is acknowledged.

References

[1] Giampaoli, G., 2018 *Tuning Functional Properties of Pyrochlore and Related Oxides via Cation and Anion Substitutions.*

[2] Muhammad Ashan, Gaber A.M. Mersal, Ahmed Fallatah, M, Ibrahim, Mohamed M, Ahmad, Khurshed, El-Bahy, Zeinhom M. 2005 *Achieving superior supercapacitive performance with rGO-integrated pyrochlore type $Ce_2Zr_2O_7$* Materials Science in Semiconductor *Processing, vol: 185, pg. 108912*

[3] Fuentes, A.F., E.C. O'Quinn, S.M. Montemayor, H. Zhou, M. Lang and R.C. Ewing, 2024 *Pyrochlore-type lanthanide titanates and zirconates: Synthesis, structural peculiarities, and properties.* Applied Physics Reviews. 11(2).

[4] Preuss, A. and R. Gruehn, 1994 *Preparation and structure of cerium titanates Ce2TiO5, Ce_2TiO_7, and $Ce_4Ti_9O_{24}$.* Journal of Solid State Chemistry. 110(2): p. 363-369.

[5] Sardar, S., 2020 *Manufacturing of pyrochlore ($A_2B_2O_7$) nanoparticles using sol gel method*, University of Leeds.

[6] Ashan, M., G.A. Mersal, A.M. Fallatah, M.M. Ibrahim, K. Ahmad and Z.M. El-Bahy, 2025 *Achieving superior supercapacitive performance with rGO-integrated pyrochlore type $Ce_2Zr_2O_7$.* Materials Science in Semiconductor Processing. 185: p. 108912.

[7] Muhammad, P., A. Zada, J. Rashid, S. Hanif, Y. Gao, C. Li, Y. Li, K. Fan and Y. Wang, 2024 *Defect engineering in nanocatalysts: From design and synthesis to applications.* Advanced Functional Materials. 34(29): p. 2314686.

[8] Subramanian, M., G. Aravamudan and G.S. Rao, 1983 *Oxide pyrochlores—a review.* Progress in Solid State Chemistry. 15(2): p. 55-143.

[9] http://maud.radiographema.com

[10] Ahmad Umar, Rajesh Kumar, Girish Kumar, H. Algarni, S.H. Kim**,** 2015 *Effect of annealing temperature on the properties and photocatalytic efficiencies of ZnO nanoparticles,* Journal of Alloys and Compounds, Vol. 648, Pg. 46-52,

[11] Kabekkodu, S. N., Dosen, A. & Blanton, T. N. 2024. *PDF-5+: a comprehensive Powder Diffraction File for materials characterization*, Powder Diffr. 39, 47–59.

Predicting the magnetocaloric effect on perovskite oxides using Machine Learning

E.T. Sibanda[1], **C. Harley**[2], **O.M. Ntwaeaborwa**[3] **and B. Sondezi**[1]

[1]Department of Physics, University of Johannesburg, P.O. Box 524, Auckland Park, Johannesburg, Gauteng, South Africa
[2]2Department of Electrical and Electronic Engineering, University of Johannesburg, P.O Box 524, Auckland Park, Johannesburg, Gauteng, South Africa
[3]Department of Physical and Earth Sciences, Sol Plaatje University, Private Bag X 5008, Kimberley, Northern Cape, South Africa

E-mail: bmsondezi@uj.ac.za

Abstract. This study aims to utilize machine learning methodology to model and predict the magnetocaloric effects in perovskite oxides, with a particular focus on both single and double perovskite structures. A semi-automated data collection process was employed, where ChatGPT systematically extracted and curated experimental data from published studies. As a result, a comprehensive database containing 1204 entries was assembled, with each entry capturing properties such as composition, synthesis method, crystal structure, space group, particle morphology, lattice parameters (a, b, c), magnetic phase transition, and transition temperature (K). The target property is the negative magnetic entropy change (ΔS_{max}). Machine learning models were trained using both compositional and experimental features, including linear and non-linear algorithms, to predict the negative magnetic entropy change of the materials. Among the evaluated models, the Extra Trees algorithm demonstrated the best performance, achieving a training R^2 of 0.998, and a test R^2 of 0.815. These results provide valuable guidelines for future research on magnetocaloric materials and demonstrate the potential of combining advanced data extraction techniques with machine learning methodologies for accelerated materials discovery. Furthermore, the proposed approach is transferable and can be extended to other perovskite-related material domains, such as catalysts and solar cell materials.

1 Introduction

Energy efficiency and sustainability are priority topics in modern society, as evidenced by the widespread adoption of electric vehicles [1], the push for green building initiatives [2], and increased investment in renewable energy [3], among other developments [4, 5]. Refrigeration and air conditioning account for a significant portion of power consumption among various energy end uses in both commercial and residential areas [6, 7]. Conventional gas compression systems, which dominate the market, are increasingly criticized for their inefficiency and use of harmful refrigerants. Magnetic refrigeration (MR), which leverages the magnetocaloric effect (MCE) in magnetic materials near room temperature, has emerged as a promising alternative [6, 7]. MR systems offer significantly higher efficiency, smaller footprints, solid-state operation, and environmental safety [6, 7].

MCE has been extensively studied over the years, and a large body of experimental data has been published [8–10]. The MCE itself is a thermodynamic process in which the temperature of a magnetic material changes in response to an external magnetic field. When an adiabatic magnetic field is applied, Spins in the material align with the field, reducing the magnetic entropy. The lattice entropy compensates for this reduction, leading to a temperature increase. Conversely, removal of the field results in spin randomization, increased magnetic entropy,

and cooling of the material [8, 9]. The performance of magnetocaloric materials is commonly evaluated using the maximum magnetic entropy change (ΔS_{max}) and the relative cooling power (RCP), which together reflect the strength and practical effectiveness of the MCE.

Perovskites have attracted significant interest in the search for novel magnetocaloric materials due to their flexible crystal structures, broad compositional tunability, and versatile magnetic properties [11, 12]. Perovskites come in a range of crystal shapes, including single perovskites, double perovskites, spinel, pyrochlore, tungsten-bronze, and bismuth-layered structures, each with distinct features for technological applications [12–14]. Single and double perovskites are especially important due to their flexible structures and potential uses, while being among of the least understood materials in condensed matter physics [12, 13]. Single perovskites with an ABO_3 structure allow substitutions at both *A*- and *B*-sites with ions of various oxidation states and ionic radii, and the option to substitute oxygen with halides [12]. This structural flexibility allows for the formulation of a variety of compounds with properties such as high-temperature superconductivity, magnetoresistance, ferroelectricity and a giant magnetocaloric effect [14]. Double perovskites expand upon the single perovskite structure by adding another layer of *B*-site ordering, allowing for mixed valencies and complex charge balancing. These materials are distinguished by ordered arrangements at both the *A*- and *B*-sites, leading to specialized phenomena such as tunable magnetic properties and tailored electrical behaviours [12, 13]. Double perovskites enable precise control over magnetic and electronic properties due to their unique capacity for *B*-site ordering and site-specific charge distribution, making them highly valuable in advanced materials research. The perovskite structure can incorporate a diverse range of elements from the periodic table in the *A*- and *B*-sites, despite the significant ionic size difference.

Traditionally, the exploration of this class of materials has relied on experimental trial-and-error methods, where researchers systematically vary compositions and conditions to observe outcomes [15–20]. In recent years, computational techniques such as Monte Carlo simulations and first-principles calculations have provided valuable insights into magnetic behavior at the atomic scale. However, experimental approaches remain slow and resource-intensive, while computational methods are often limited by their high computational cost and dependence on accurately defined physical models. As a promising alternative, data-driven methodologies using machine learning (ML) allow researchers to analyze datasets, identify patterns, and predict material properties more efficiently, thereby accelerating the discovery [15–20]. Recent years have seen significant progress in the application of machine learning to perovskite and related materials, leading to advances in property prediction, materials discovery, and design [16–20]. Notable in this field is the work of Castro-Anaya *et al*, who compiled the largest magnetocaloric perovskite dataset to date by manually extracting over 1,200 property measurements and generating 517 compositional and structural features, including crystallite size [21]. By systematically benchmarking models such as Kernel Ridge Regression, Artificial Neural Networks, Random Forests, and Extreme Gradient Boosting, they achieved test R^2 scores up to 0.89 for magnetocaloric properties and used these models for the virtual screening of more than 1.2 million hypothetical perovskites, revealing chemical trends and optimal compositions for both room-temperature and cryogenic applications [21]. Pedro B. Castro *et al* assembled a dataset of 1,644 compounds, primarily alloys and rare-earth borides, and applied Extreme Gradient Boosting to guide experimental synthesis, leading to the identification and validation of HoB_2, a compound exhibiting a record magnetocaloric effect near the hydrogen liquefaction point [22]. In structural prediction, Alfares *et al*, applied Gaussian Process Regression and other algorithms to a set of 122 ABX_3 perovskites, using 12 carefully selected descriptors to achieve test R^2 values as high as 0.99 for lattice constant prediction, supporting high-throughput computational design for electronics and optoelectronics [23]. PV Balachandran Alfares *et al* developed a hierarchical classification strategy based on Random Forest and Gradient Tree Boosting, combined with density functional theory validation, to identify dozens of new stable ABO_3 perovskites from 390 experimentally reported compounds and 625 hypothetical candidates, achieving cross-validation accuracies up to 94% [24]. These are only a few instances from a fast-growing body of literature that demonstrate the effectiveness of data-driven approaches in materials research. These works demonstrate how extensive and diverse datasets, sophisticated model selection, and rigorous feature engineering speed up the discovery of materials.

Data-driven approaches are changing the landscape of material discovery and optimization, especially for functional oxides and perovskite materials. Despite recent improvements, there are still limitations in the availability and curation of high-quality, comprehensive data, as well as the use of machine learning to explore both single and double perovskite systems. This study addresses these challenges through a unique, semi-automated data collection strategy utilizing ChatGPT-4o, a large language model developed by OpenAI based on the GPT-4 architecture [25]. As a large language model, ChatGPT-4o is capable of understanding and generating human-like text by leveraging extensive training on diverse scientific literature and datasets, enabling it to aggregate and extract relevant experimental details for perovskite oxides from unstructured sources efficiently. Using this approach, a curated dataset of 1204 entries with rich experimental detail and comprehensive units was compiled. By focusing on single and double perovskite oxides and applying a suite of machine learning models to predict the negative magnetic entropy change (ΔS_{max}), this work provides new insights and practical tools for accelerating the design of magnetocaloric materials. The methodology presented is broadly transferable, offering a blueprint for similar

advances in other perovskite-based domains such as catalysis and photovoltaics.

2 Methodology

This study uses a structured machine learning approach to accelerate the discovery of magnetocaloric materials. A dataset of 1727 perovskite oxides was collected from peer-reviewed journal articles, focusing on single and double perovskite oxides with reported magnetocaloric properties. A semi-automated data extraction workflow was adopted, utilizing ChatGPT-4o to assist in retrieving key values such as composition, crystal structure, lattice parameters, synthesis method, magnetic phase transition type, transition temperature, and maximum magnetic entropy change. This method builds on recent developments in materials informatics and offers advantages over traditional manual curation and rule-based text mining tools [21, 24, 26–28]. However, several challenges were experienced with ChatGPT, including hallucination where it fabricated values, forgetting instructions during extraction, and occasional inconsistencies in interpreting scientific data. To mitigate these issues and ensure the reliability of the dataset, all extracted data were manually validated and standardized to guarantee accuracy and consistency.

The dataset was thoroughly preprocessed, involving cleaning, standardizing, and organizing all features to prepare them for machine learning. This process included converting numerical values to consistent types, standardizing categorical variables, and removing incomplete entries. After preprocessing, 1204 data entries remained. Feature engineering was performed to add domain-informed and data-driven descriptors, such as average ionic radii, octahedral factor, unit cell volume, lattice ratios, and interaction terms. Spearman correlation [29] and multicollinearity filtering were applied to select the most relevant features. The final dataset was split into training and testing sets, with all features standardized. A range of regression models was benchmarked, and the Extra Trees Regressor was selected based on cross-validated performance [30]. The machine learning models and all preprocessing steps were implemented using Scikit-Learn, a widely used Python library for machine learning [31]. Hyperparameter tuning was conducted using both grid search and Bayesian optimization.

3 Results

To evaluate the predictive capability of various machine learning algorithms for magnetocaloric property prediction, a comprehensive benchmarking analysis was conducted using the curated and engineered dataset. Eleven regression models were tested, including linear, robust, ensemble, and neural network methods. Each model was trained on the same training set and evaluated on the same test set to ensure comparability. Figure 1 summarizes the test set root mean squared error (RMSE) and coefficient of determination (R^2) for each algorithm. Linear models such as Ridge, Lasso, and ElasticNet, along with Support Vector Regression (SVR) and robust estimators like Huber and Bayesian Ridge, demonstrated only modest predictive power, with R^2 values ranging from 0.36 to 0.40 and RMSEs above 4.0. Ensemble tree models consistently outperformed their linear and robust counterparts. Random Forest and Gradient Boosting achieved test R^2 values of 0.617 and 0.509, respectively. The Extra Trees Regressor provided the best initial performance, achieving an R^2 of 0.791 and an RMSE of 2.40, reflecting its strength in modeling non-linear, high-dimensional relationships inherent to magnetocaloric data. These results highlight the critical importance of model selection and the superior capacity of randomized ensemble algorithms to capture the complex relationships between features and target properties in magnetocaloric systems. Compared to linear, robust, and even other tree-based models, the Extra Trees Regressor showed a clear reduction in prediction error and a substantial gain in explained variance, confirming its suitability for this type of high-dimensional and non-linear data.

Building on this initial benchmark, further hyperparameter optimization of the Extra Trees Regressor was performed using both grid search and Bayesian optimization. The optimized configurations and corresponding model performance are summarized in Table 1. The slight gap between training and test performance highlights the ongoing challenge of overfitting in materials informatics, a limitation also observed in other recent studies. Continued improvements in dataset diversity, feature engineering, and model regularization will be important for further advances. The results obtained in this work are highly competitive with the best published studies, and in several cases surpass previously reported metrics for similar materials property prediction tasks. Notably, Castro-Anaya *et al.* [21] achieved a test R^2 of 0.78–0.89 for magnetocaloric property prediction using kernel ridge regression and XGBoost on curated perovskite datasets, with RMSEs in the range of 0.8–30.0 for various properties. Ucar *et al.* [32] reported a Random Forest R^2 of 0.815 for magnetic entropy change across a large compositional space. This marks a significant improvement over the baseline ensemble models. The gains in out-of-sample accuracy after tuning demonstrate not only the flexibility of the Extra Trees approach, but also the effectiveness of feature engineering and comprehensive search strategies in harnessing the predictive potential of complex materials data. These improvements highlight the strength of ensemble learning for materials informatics tasks where data heterogeneity, feature interactions, and non-linearities are prevalent. The increase in R^2 and reduction in RMSE following model optimization indicate that the model is able to capture more of the underlying

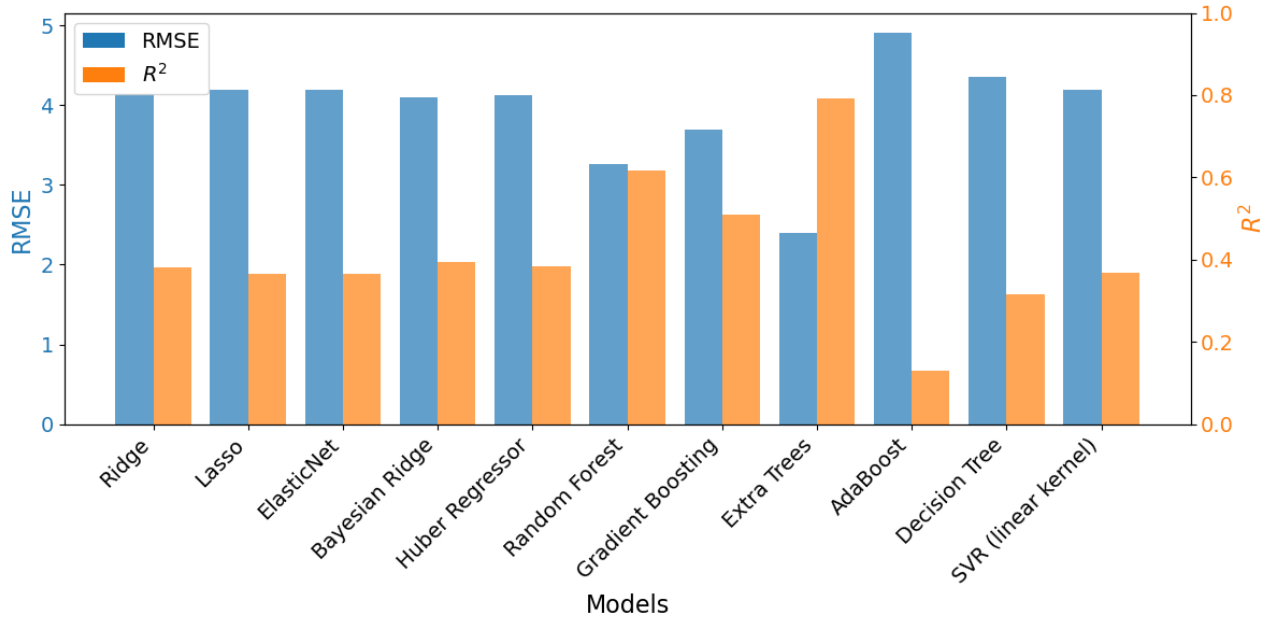

Figure 1: Benchmarking results for regression models predicting the magnetocaloric property, showing test set RMSE and R^2 values for each model. A higher R^2 value indicates better goodness-of-fit and more variance in the target property explained by the model, while a lower RMSE reflects smaller prediction errors and higher accuracy.

physical relationships and provide more reliable predictions for new, unseen compositions. Such generalization is particularly valuable for guiding experimental design and accelerating discovery in magnetocaloric materials. These results demonstrate that a data-driven workflow, combined with domain knowledge and careful feature engineering can deliver highly accurate and generalizable predictions for complex functional materials, enabling high-throughput screening and supporting innovation in materials research.

Method	**max_depth**	**max_features**	**min_samples_leaf**	**min_samples_split**	**n_estimators**
GridSearchCV	25	0.75	1	2	350
Bayesian Optimization	19	≈ 0.71	1	2	707
Training R^2	**Training MAE**	**Training RMSE**	**Test R^2**	**Test MAE**	**Test RMSE**
0.998	0.155	0.303	0.815	1.221	2.263

Table 1: Optimized hyperparameters found by GridSearchCV and refined by Bayesian optimization, alongside corresponding training and test performance metrics for the Extra Trees model.

4 Conclusion

In this work, we developed a robust and scalable machine learning framework for predicting the magnetocaloric effect in single and double perovskite oxides, combining a semi-automated data extraction pipeline powered by ChatGPT with comprehensive feature engineering and systematic model benchmarking. Our workflow enabled the creation of one of the largest and most standardized experimental datasets for this class of materials, capturing detailed compositional, structural, and processing attributes across more than 1204 samples. Benchmarking of the regression algorithms demonstrated that the Extra Trees Regressor delivered strong initial performance with a test R^2 of 0.791 and an RMSE of 2.404. After hyperparameter optimization using grid search and Bayesian optimization, the model achieved an improved predictive accuracy with a test R^2 of 0.815 and RMSE of 2.263 metrics that compare favorably with or exceed those reported in recent literature. While the data-driven approach greatly accelerates dataset assembly and property prediction, it also underscores persistent challenges in materials

informatics, such as inconsistent reporting and incomplete data. Nonetheless, our results establish that combining domain knowledge, advanced language models for data mining, and ensemble learning offers a powerful path forward for high-throughput materials discovery. The methods and insights developed here are broadly transferable and can accelerate the rational design of functional perovskites in fields ranging from magnetocalorics to catalysis and photovoltaics, ultimately supporting innovation and sustainability in materials science.

Acknowledgments
Financial aid from the South African National Research Foundation (SANRF), as well as the University of Johannesburg, is acknowledged.

Author Declarations
The authors have no conflicts to disclose.

Data Availability
The data that support the findings of this study are available from the corresponding authors upon reasonable request.

References

[1] M. Pan, S. Cao, Z. Zhang, N. Ye, H. Qin, L. Li, and W. Guan, "Recent progress on energy management strategies for hybrid electric vehicles," *Journal of Energy Storage*, vol. 116, p. 115936, 2025.

[2] A. A. Baeroom, M. F. Hossen, M. A. Abid, and F. Shahzad, "Green buildings and sustainability: A review of economic and environmental impacts," *International Journal of Multidisciplinary Research and Growth Evaluation*, vol. 6, pp. 1089–1094, 2025.

[3] B. I. Oladapo, M. A. Olawumi, T. O. Olugbade, and S. O. Ismail, "Data analytics driving net zero tracker for renewable energy," *Renewable and Sustainable Energy Reviews*, vol. 208, p. 115061, 2025.

[4] A. A. Firoozi, D. Oyejobi, and A. A. Firoozi, "Innovations in energy-efficient construction: Pioneering sustainable building practices," *Cleaner Engineering and Technology*, p. 100957, 2025.

[5] O. Zaghdoud, "Technological progress as a catalyst for energy efficiency: A sustainable technology perspective," *Sustainable Technology and Entrepreneurship*, vol. 4, no. 1, p. 100084, 2025.

[6] N. Mezaal, K. Osintsev, and T. Zhirgalova, "Review of magnetic refrigeration system as alternative to conventional refrigeration system," in *IOP Conference Series: Earth and Environmental Science*, vol. 87, no. 3. IOP Publishing, 2017, p. 032024.

[7] B. Monfared, R. Furberg, and B. Palm, "Magnetic vs. vapor-compression household refrigerators: A preliminary comparative life cycle assessment," *International journal of refrigeration*, vol. 42, pp. 69–76, 2014.

[8] N. R. Ram, M. Prakash, U. Naresh, N. S. Kumar, T. S. Sarmash, T. Subbarao, R. J. Kumar, G. R. Kumar, and K. C. B. Naidu, "Review on magnetocaloric effect and materials," *Journal of Superconductivity and Novel Magnetism*, vol. 31, no. 7, pp. 1971–1979, 2018.

[9] M.-H. Phan and S.-C. Yu, "Review of the magnetocaloric effect in manganite materials," *Journal of Magnetism and Magnetic Materials*, vol. 308, no. 2, pp. 325–340, 2007.

[10] J. Liu, T. Gottschall, K. P. Skokov, J. D. Moore, and O. Gutfleisch, "Giant magnetocaloric effect driven by structural transitions," *Nature materials*, vol. 11, no. 7, pp. 620–626, 2012.

[11] W. Zhong, C.-T. Au, and Y.-W. Du, "Review of magnetocaloric effect in perovskite-type oxides," *Chinese Physics B*, vol. 22, no. 5, p. 057501, 2013.

[12] G. George, S. Ede, and Z. Luo, *Fundamentals of Perovskite Oxides: Synthesis, Structure, Properties and Applications*. CRC Press, 2020.

[13] N. Arul and V. Nithya, *Revolution of Perovskite*. Singapore: Springer Singapore, 2020.

[14] M. Vijatović Petrović and J. Bobić, "Perovskite and aurivillius: Types of ferroelectric metal oxides," *Magnetic, ferroelectric, and multiferroic metal oxides*, pp. 35–49, 2018.

[15] A. Zunger, "Inverse design in search of materials with target functionalities," *Nature Reviews Chemistry*, vol. 2, no. 4, p. 0121, 2018.

[16] Y. Liu, T. Zhao, W. Ju, and S. Shi, "Materials discovery and design using machine learning," *Journal of Materiomics*, vol. 3, no. 3, pp. 159–177, 2017.

[17] P. Raccuglia, K. Elbert, P. Adler, C. Falk, M. Wenny, A. Mollo, M. Zeller, S. Friedler, J. Schrier, and A. Norquist, "Machine-learning-assisted materials discovery using failed experiments," *Nature*, vol. 533, no. 7601, pp. 73–76, 2016.

[18] A. Merchant, S. Batzner, S. Schoenholz, M. Aykol, G. Cheon, and E. Cubuk, "Scaling deep learning for materials discovery," *Nature*, vol. 624, no. 7990, pp. 80–85, 2023.

[19] S. Steinmann, Q. Wang, and Z. Seh, "How machine learning can accelerate electrocatalysis discovery and optimization," *Materials Horizons*, vol. 10, no. 2, pp. 393–406, 2023.

[20] A. Cheetham and R. Seshadri, "Artificial intelligence driving materials discovery? perspective on the article: Scaling deep learning for materials discovery," *Chemistry of Materials*, vol. 36, no. 8, pp. 3490–3495, 2024.

[21] L. E. Castro-Anaya, E. Marese, J. A. Lozano, G. F. Peixer, J. R. Barbosa Jr, and S. Y. Gomez Gonzalez, "Machine learning methodologies applied to magnetocaloric perovskites discovery," *Journal of Chemical Information and Modeling*, vol. 65, no. 4, pp. 1812–1825, 2025.

[22] P. B. d. Castro, K. Terashima, T. D. Yamamoto, Z. Hou, S. Iwasaki, R. Matsumoto, S. Adachi, Y. Saito, P. Song, H. Takeya *et al.*, "Machine-learning-guided discovery of the gigantic magnetocaloric effect in hob2 near the hydrogen liquefaction temperature," *NPG Asia Materials*, vol. 12, no. 1, p. 35, 2020.

[23] A. Alfares, Y. A. Sha'aban, and A. Alhumoud, "Machine learning-driven predictions of lattice constants in abx3 perovskite materials," *Engineering Applications of Artificial Intelligence*, vol. 141, p. 109747, 2025.

[24] P. V. Balachandran, A. A. Emery, J. E. Gubernatis, T. Lookman, C. Wolverton, and A. Zunger, "Predictions of new ab o 3 perovskite compounds by combining machine learning and density functional theory," *Physical Review Materials*, vol. 2, no. 4, p. 043802, 2018.

[25] J. Achiam, S. Adler, S. Agarwal, L. Ahmad, I. Akkaya, F. L. Aleman, D. Almeida, J. Altenschmidt, S. Altman, S. Anadkat *et al.*, "Gpt-4 technical report," *arXiv preprint arXiv:2303.08774*, 2023.

[26] M. Polak and D. Morgan, "Extracting accurate materials data from research papers with conversational language models and prompt engineering–example of chatgpt, arxiv, 2023," *arXiv preprint arXiv:2303.05352*, 2023.

[27] S. Huang and J. M. Cole, "A database of battery materials auto-generated using chemdataextractor," *Scientific Data*, vol. 7, no. 1, p. 260, 2020.

[28] J. Zhao and J. M. Cole, "A database of refractive indices and dielectric constants auto-generated using chemdataextractor," *Scientific data*, vol. 9, no. 1, p. 192, 2022.

[29] L. Myers and M. J. Sirois, "Spearman correlation coefficients, differences between," *Encyclopedia of statistical sciences*, vol. 12, 2004.

[30] P. Geurts, D. Ernst, and L. Wehenkel, "Extremely randomized trees," *Machine learning*, vol. 63, no. 1, pp. 3–42, 2006.

[31] F. Pedregosa, G. Varoquaux, A. Gramfort, V. Michel, B. Thirion, O. Grisel, M. Blondel, P. Prettenhofer, R. Weiss, V. Dubourg *et al.*, "Scikit-learn: Machine learning in python," *Journal of machine learning research*, vol. 12, no. Oct, pp. 2825–2830, 2011.

[32] H. Ucar, S. Aksoy, H. E. Karaca, and M. Acet, "Machine learning models for prediction of magnetocaloric effect in various classes of materials," *Computational Materials Science*, vol. 208, p. 111389, 2022.

Synthesis and characterization of TiO_2: Evaluation for possible application as light trapping layer in thin film solar cells.

R. Jaffar*, C. Donga, L.E. Mathevula and P.S. Mbule

Department of Physics, University of South Africa, Johannesburg, 1710, South Africa

E-mail : rjaffar6424397@gmail.com

Abstract. In this work, titanium dioxide (TiO_2) nanoparticles (NPs) were prepared through the sol–gel method with 2 hours reaction time. The synthesized NPs were then annealed at 500°C for 3 hours. Structural, morphological, compositional, and optical characterization was carried out using X-ray diffraction (XRD), Raman spectroscopy, scanning electron microscopy (SEM) and UV-Vis diffuse reflectance spectroscopy. The XRD results verified the crystallinity, tetragonal structure and the anatase phase of the TiO_2 NPs while the dislocation line density and average crystallite size were estimated using the Debye–Scherrer relation. The average crystallite size was found to be ~4.8 before annealing and ~3.7 nm after annealing while the dislocation density increased from 1.0×10^{13} to 2.45×10^{14} lines.m^{-2}. Raman spectroscopy further validated the presence of the anatase phase through peak analysis. The presence of sharp and intense Raman peaks showed crystallinity and reduced structural disorder after annealing. SEM analysis revealed the presence of both small and large particles suggesting heterogeneous size distribution. UV–Vis analysis showed absorption in the range of 390–450 nm. After annealing, the band gap values decreased from ~2.85 to 2.73 eV. The SCAPS-1D software was used to simulate the possible power conversion efficiency (PCE) of the proposed perovskite solar cells (PSC) device. The simulated device achieved higher PCE values of ~25.71% and ~24.42% from unannealed and annealed TiO_2 NPs, respectively. This study links the structural and optical modifications of TiO_2 NPs with their simulated photovoltaic performance and provides new insight into how the overall device efficiency can be influenced by these modifications.

1 Introduction

Perovskite solar cells (PSCs) have attracted significant attention due to their superior optoelectronic characteristics, which include low recombination losses, high absorption coefficients and effective charge transport. The most promising of these are organic–inorganic lead halide perovskites, which have excellent charge carrier mobility, strong light absorption and efficient exciton mobility [1]. All of these parameters contribute significantly to the high power conversion efficiencies (PCEs) achieved by PSCs. Since their introduction by Kojima et al. in 2009, PSCs have rapidly advanced, with methyl ammonium lead iodide ($CH_3NH_3PbI_3$)-based devices now achieving PCEs exceeding 25%, making them competitive with conventional silicon-based solar cells [2]. Ongoing investigation has focused on improving the performance, stability, and scalability of PSCs by modifying the perovskite layer and other device components**.** The electron transport layer (ETL) is one of the layers that is most important for charge extraction and overall device efficiency. The superior optical and electrical properties, good energy level alignment, and chemical stability of titanium dioxide (TiO_2) make it one of the most used ETL materials in PSCs. Particularly TiO_2

nanoparticles (NPs) have a large surface area, which makes them perfect for solar applications [3]. In this work the characteristics of TiO_2 NPs have been evaluated experimentally. Additionally, a modified planar n–i–p architecture (ITO/TiO_2/$CH_3NH_3PbI_3$/Spiro-OMeTAD/Au) is investigated using SCAPS-1D simulation to determine the impact of TiO_2 NPs optimization on device performance**.** The novelty of this study lies in correlating the annealing-induced structural and optical changes in sol–gel synthesized TiO_2 NPs with their effect on the simulated performance of PSCs. This work demonstrates how slight variations in crystallite size and defect density directly influence the optical band gap and device efficiency.

2 Experimental

2.1 Sol-gel synthesis of TiO_2 NPs

Titanium tetraisopropoxide (TTIP, 97%), isopropanol (70% in aqueous solution), nitric acid (70%) and deionized water were utilized to synthesize (TiO_2 NPs) by the sol-gel method. 5 ml of TTIP was slowly added to 6 ml of isopropanol under continuous stirring at room temperature, and the mixture was stirred for 15 minutes. Then, 75 ml of deionized water was gradually added, forming a white precipitate which rapidly dissolved into a white solution. The mixture was heated and stirred at 85°C for 1 hour. Subsequently, 2.5 ml of nitric acid was added dropwise with constant stirring, followed by continued heating for 2 more hours to induce peptization. After cooling to room temperature, the solution was oven-dried at 65°C for 6 hours and 30 minutes. The dried NPs were ground into a fine powder and annealed at 500°C for 3 hours under atmospheric conditions. Figure 1 illustrates the proposed PSC device configuration for SCAPS-1D simulation.

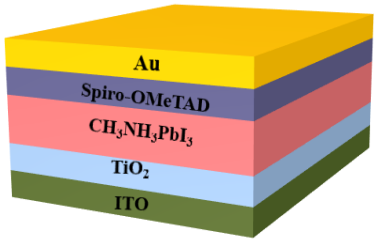

Figure 1. The proposed device configuration under AM1.5G illumination at 1000 W.m^{-2}.

2.2 PSC Device Simulation Using SCAPS-1D

The continuity and Poisson's equations were used to simulate the PSC device using SCAPS-1D software. Poisson's equation explains the electric potential caused by the distribution of charges while the continuity equations explain how electrons and holes behave in the device. These are shown by equations 1 to 3 [4].

$$\nabla^2\psi = \frac{q}{\varepsilon}(n - p + N_A - N_D) \quad (1)$$

$$\nabla . J_n - q\frac{\partial n}{\partial t} = +qR \quad (2)$$

$$\nabla . J_p + q\frac{\partial p}{\partial t} = -qR \quad (3)$$

where ψ represents the electric potential, n and p denote the densities of electrons and holes, respectively, while N_A and N_D correspond to the concentrations of acceptors and donors. The symbol q signifies the charge of an electron, and ε indicates the dielectric constant of the materials involved. Jn and Jp represent the current densities of electrons and holes, and R denotes the rate of recombination. Figure 1 shows the proposed architecture of the PSC, which has been simulated using SCAPS-1D with a lead-based perovskite absorber, specifically ($CH_3NH_3PbI_3$), recognized for its advantageous properties and enhanced efficiency, with Spiro-OMeTAD serving as the hole transport layer. The device configuration is as follows: ITO/TiO_2/$CH_3NH_3PbI_3$/Spiro-OMeTAD/Au. Incident light is transmitted through the indium tin oxide (ITO) front contact, with TiO_2 NPs serving as the light trapping and electron transport layer (ETL), $CH_3NH_3PbI_3$ functioning as the light absorber, Spiro-OMeTAD designated as the hole transport layer (HTL), and gold (Au) designated as the rear contact. Simulations were conducted at 300 K under AM 1.5 G illumination (1000 W. m^{-2}) [5]. TiO_2 with band gap values of 2.85 eV before and 2.73 eV after annealing at 500 °C were compared.

3 Results and Discussion

3.1 X-ray diffraction (XRD) analysis

The XRD patterns of TiO_2 NPs in the 2θ range of 20–70° (Figure 2(a)) show sharp and well-defined diffraction peaks corresponding to the characteristic anatase planes, indicating good crystallinity and phase purity. The average crystallite size and dislocation density calculated using the Debye–Scherrer equation, further support the structural analysis. XRD peaks match well with the diffraction peaks of the anatase phase of TiO_2 NPs. The peak positions at 25.21°, 37.80°, 48.04°, 53.89°, 55.05°, 62.69°, and 68.77° match with the lattice planes (101), (004), (200), (105), (211), (204), and (116), respectly, consistent with JCPDS card no. 21-1272. A tetragonal structure was observed, belonging to the space group $I4_1/amd$ (#141). Diffraction peaks for TiO_2 NPs before annealing (black line) are more intense, especially at the (101) plane, indicating better crystallinity. After annealing (red line), the peak intensity decreases slightly and becomes broader, indicating particle agglomeration during annealing as the heat treatment may sometimes allow nanoparticles to merge or agglomerate, and reduce diffraction intensity. No rutile or impurity peaks were detected in the XRD patterns before or after annealing, confirming the stability of the anatase phase, in agreement with previous studies reporting anatase phase stability up to 600 °C [6]. Using the Debye-Scherrer equation, the average crystallite size and dislocation line density were also calculated [7].

$$D = \frac{K\lambda}{\beta COS\theta} \qquad (4)$$

where D is the typical crystallite size, k is the shape factor (usually 0.9), λ is the X-ray wavelength (1.5406 Å) β is the full width at half maximum (FWHM) of the main diffraction peak, and θ is the Bragg angle. The dislocation line density (**δ**) of TiO_2 NPs was calculated as

$$\delta = \frac{1}{D^2} \qquad (5)$$

The average crystallite size decreased from 4.8 nm before annealing to 3.7 nm after annealing, while the dislocation density increased from 1.0×10^{13} to 2.45×10^{14} lines.m^{-2}. The increase in dislocation density suggests that defects were generated during annealing, which could impact their optoelectronic properties [8].

3.2 Raman analysis

Raman spectra were recorded to analyze structural changes, as shown in Figure 2(b). Raman analysis revealed a prominent $E_g(1)$ mode at 144 cm^{-1}, indicative of the anatase phase and similar to the symmetric stretching vibrations of oxygen atoms in the O–Ti–O bonds [9]. Additionally, the A_1g mode, arising from anti-symmetric bending, is also present. An additional Raman peak, corresponding to overlapping (A_{1g} + B_{1g}) modes around 515 cm^{-1} and an $E_g(3)$ mode near 640 cm^{-1}, was observed, further confirming the presence of anatase phase [9]. These vibrational features are consistent with the tetragonal crystal structure (space group $I4_1/amd$ (#141) and align well with the XRD results. Before annealing, the Raman peaks, most notably $E_g(1)$ at around 144 cm^{-1}, are sharp and intense, indicating a well-developed anatase phase. After annealing, these peaks become weaker and slightly broader, suggesting grain growth and reduced phonon confinement, which can lead to decreased vibrational intensity and band broadening.

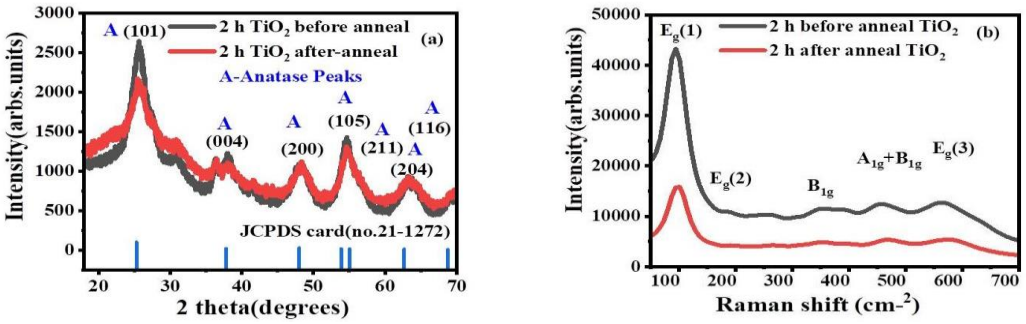

Figure 2: (a) XRD patterns and (b) Raman spectra of TiO_2 NPs.

3.3 Scanning Electron Microscopy (SEM) Analysis

SEM images of TiO_2 NPs before and after annealing are shown in Figure 3 (a) and (b). The SEM images show the presence of both small and large particles suggesting a heterogeneous size distribution. This is likely resulting from incomplete particle growth during the sol–gel synthesis. After annealing, the large particles become more pronounced, indicating slight grain growth resulting from the thermal treatment.The limited stirring time caused moderate uniformity, while annealing increased particle structure and atomic rearrangement [10].

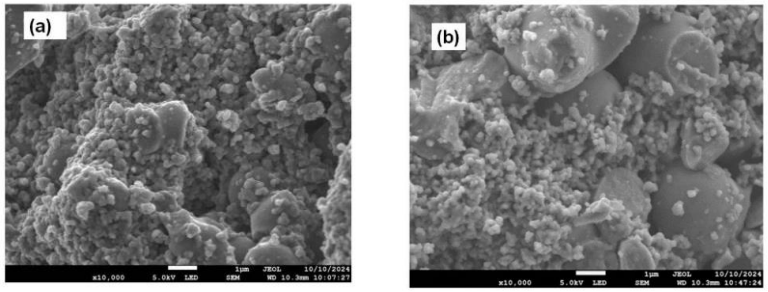

Figure 3: SEM images of TiO_2 NPs (a) unannealed and (b) annealed for 2 hours.

3.4 Diffuse Reflectance Spectroscopy (DRS) UV–Vis Analysis

Figure 4(a) and (b) shows UV–Vis DRS results and band gap energy of TiO_2 before and after annealing. The optical characteristics of TiO_2 NPs were analyzed using DRS UV–Vis in the 200–700 nm range, as shown in Figure 4(a). The spectra exhibited a slight absorption edge shift around 390 nm and 450 nm after annealing, and the photon absorption of TiO_2 NPs in the UV range. The band gap values were estimated from Tauc plots using the Kubelka–Munk function F(R), revealing a slight narrowing of the band gap after annealing as shown in Figure 4(b) [11].

$$F(R) = \frac{(1-R)^{\frac{1}{2}}}{2(R)} \qquad (6)$$

where Kubelka-Munk function is denoted by F(R). Tauc plots were used to measure the optical band gap of TiO_2 NPs $(F(R)\,h\nu)^{1/2}$ as a function of $h\nu$, which showed an indirect transition. The band gap decreased from 2.85 eV before annealing to 2.73 eV after annealing. The observed band gap reduction after annealing is likely due to rearrangement of surface atoms, and the formation of oxygen vacancies, which introduce localized states within the band gap [12].

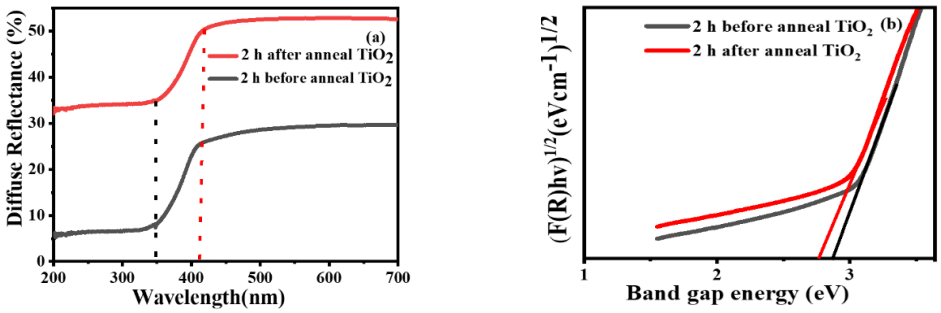

Figure 4: (a): UV–Vis spectra and (b) estimated band gap energy of TiO_2 NPs, unannealed and annealed at 2 hours.

3.5 SCAPS-1D Simulation

The photovoltaic performance of the $CH_3NH_3PbI_3$-based PSC was assessed using SCAPS-1D simulation, with the electron transport layer (ETL) being experimentally set as TiO_2 NPs. The simulated device structure (ITO/TiO_2/$CH_3NH_3PbI_3$/SpiroOMeTAD/Au) showed PCE of 25.71% for TiO_2 NPs before annealing 24.42% after annealing. This slight decreases for TiO_2 NPs after annealing correlates with the experimental

data, which show that annealing has a direct impact on the efficiency of the device. Agglomeration and heterogeneous particle size distribution affects charge transport. The current–voltage (J–V) curves further support this trend by showing a reduced current density after annealing, indicating changes in charge collection, as shown in Figure 5 [13]. Overall, the simulation confirms that TiO_2 NPs in the anatase phase offer a highly effective ETL, balancing structural and optical properties for efficient solar cell operation[14].

Device Parameters	ITO (Indium Tin Oxide) [14]	Before annealing TiO_2 (ETL) [Own work]	After annealing TiO_2 (HTL) (ETL) [Own work]	$CH_3NH_3PbI_3$ (Perovskite) [14]	Spiro-OMeTAD [14]
T(nm)	5	30	30	700	200
Eg (eV)	3.5	2.85	2.73	1.6	3.0
χ (eV)	4	4	4	4	2.45
εr	9	9	9	9	3
Nc (cm^{-3})	2.2 x10^{18}	2 x10^{18}	2.2 x10^{18}	2.2 x10^{18}	2.2 x10^{18}
Nv (cm^{-3})	1.8 x10^{18}	1.8 x10^{19}	1.8 x10^{19}	2.2x10^{19}	1.9 x10^{19}
μn ($cm^{-2}V^{-1}S^{-1}$)	30	20	20	2.0	2 x10^{-4}
μp ($cm^{-2}V^{-1}S^{-1}$)	5	10	10	2.0	2 x10^{-4}
Ev (cm/s)	1 x10^{7}	1 x10^{7}	1 x10^{7}	1 x10^{7}	1 x10^{7}
hv (cm/s)	1 x10^{7}	1 x10^{7}	1 x10^{7}	1 x10^{7}	1 x10^{7}
NA (cm^{-3})	0	0	0	1 x10^{13}	1 x10^{18}
ND (cm^{-3})	2 x10^{20}	1 x10^{16}	1 x10^{16}	0	0

Table 1: Shows the input Simulation parameters for the proposed perovskite device configuration.

Sample	V_0(V)	(Jsc) mA/cm^2	(FF)%	(PCE) %
TiO_2 Unannealed	1.3400	23.606397	81.28	25.71
TiO_2 Annealed	1.3348	23.582969	77.58	24.42

Table 2: SCAPS-1D simulated results of the proposed perovskite device configuration.

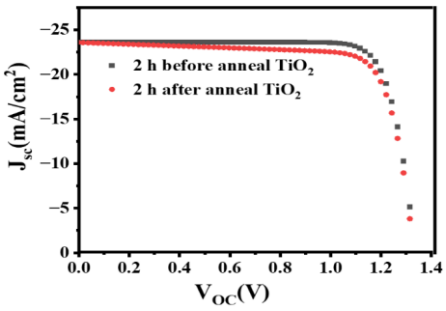

Figure 5: Simulated current density (J) as a function of voltage (V) for the proposed perovskite device configuration.

4 Conclusion

In this work, TiO_2 nanoparticles made using the sol–gel method and heated at 500 °C for three hours showed clear structural and optical improvements. XRD and Raman tests confirmed the presence of the anatase phase with improved crystallinity after heating. SEM images revealed more uniform particles, and UV–Vis results indicated a slight decrease in the band gap as the particle size increased. SCAPS-1D simulations suggest these changes could improve the performance of $CH_3NH_3PbI_3$-based perovskite solar cells. Overall, these findings suggest that TiO_2 nanoparticles are effective for light trapping and serve as a suitable electron transport layer (ETL), potentially enhancing the efficiency and stability of $CH_3NH_3PbI_3$-based perovskite solar cells.

5 Acknowledgements
We gratefully acknowledge the use of SCAPS-1D for our simulations and thank the University of South Africa for providing financial support for this study.

References

[1] B. P. Kore, M. Jamshidi, and J. M. Gardner, "The impact of moisture on the stability and degradation of perovskites in solar cells," *Materials Advances*, vol. 5, no. 6, pp. 2200–2217, 2024.

[2] M. Baro and P. Borgohain, "SCAPS-1D device simulation of highly efficient perovskite solar cells using diverse charge transport layers," *Journal of Electronic Materials*, vol. 52, no. 11, pp. 7623–7644, 2023.

[3] K. Santhi, M. Navaneethan, S. Harish, S. Ponnusamy, and C. Muthamizhchelvan, "Synthesis and characterization of TiO_2 nanorods by hydrothermal method with different pH conditions and their photocatalytic activity," *Applied Surface Science*, vol. 500, p. 144058, 2020.

[4] M. K. Hossain *et al.*, "Numerical analysis in DFT and SCAPS-1D on the influence of different charge transport layers of $CsPbBr_3$ perovskite solar cells," *Energy & Fuels*, vol. 37, no. 8, pp. 6078–6098, 2023.

[5] G. Shukla and S. Angappane, "Dimensional constraints favour high-temperature anatase phase stability in TiO_2 nanorods," *Applied Surface Science*, vol. 577, p. 151874, 2022.

[6] R. Jaffar *et al.*, "Structural, optical, dielectric and photovoltaic properties of Sn-doped CdS films prepared with green synthesis route," *Optical Materials*, vol. 133, p. 112964, 2022.

[7] Y. Alaya *et al.*, "Annealing effect on the physical properties of TiO_2 thin films deposited by spray pyrolysis," *RSC Advances*, vol. 13, no. 32, pp. 21852–21860, 2023.

[8] A. Bhatia *et al.*, "Electrochemical lithium insertion into TiO_2 anatase ALD thin films for Li-ion microbatteries: an atomic-scale picture provided by Raman spectroscopy," *Advanced Materials Interfaces*, vol. 10, no. 10, p. 2202141, 2023.

[9] A. C. Sparavigna, "Fitting q-Gaussians onto anatase TiO_2 Raman bands," 2023.

[10] D. K. Muthee and B. F. Dejene, "Effect of annealing temperature on structural, optical, and photocatalytic properties of titanium dioxide nanoparticles," *Heliyon*, vol. 7, no. 6, 2021.

[11] K. Manickam, V. Muthusamy, S. Manickam, T. Senthil, G. Periyasamy, and S. Shanmugam, "Effect of annealing temperature on structural, morphological and optical properties of nanocrystalline TiO_2 thin films synthesized by sol-gel dip-coating method," *Materials Today: Proceedings*, vol. 23, pp. 68–72, 2020.

[12] S. Mohamed and A. A. Alhazime, "Suppressing photoluminescence and enhancing light absorption of TiO_2 via TiO_2/TiN/TiO_2 plasmonic multilayers for better solar harvesting," *Journal of Materials Research and Technology*, vol. 18, pp. 4470–4478, 2022.

[13] H. Abnavi, D. K. Maram, and A. Abnavi, "Performance analysis of several electron/hole transport layers in thin-film $MAPbI_3$-based perovskite solar cells: A simulation study," *Optical Materials*, vol. 118, p. 111258, 2021.

[14] C. Son, H. Son, and B.-S. Jeong, "Enhanced conversion efficiency in $MAPbI_3$ perovskite solar cells through parameters optimization via SCAPS-1D simulation," *Applied Sciences*, vol. 14, no. 6, p. 2390, 2024.

Effect of temperature on structural and optical properties of Sm_2O_3

B Bharati[1,2], P Mohanty[2], B Sondezi[2] and S Sitha[1]

[1]Department of Chemical Sciences, University of Johannesburg, P.O. Box 524, Auckland Park, Johannesburg 2006, South Africa
[2]Department of Physics, University of Johannesburg, P.O. Box 524, Auckland Park, Johannesburg 2006, South Africa

E-mail: bharatib@uj.ac.za,bharatib47@gmail.com

Abstract. In this work, the Sm_2O_3 sample was synthesized and the focus has then been on how the calcination temperature affects the structural and photocatalytic properties of the material. Therefore, the synthesized powder sample was calcined at two different temperatures: 500 and 700 ˚C. The structural and optical properties, as well as photocatalytic properties, have been studied. The structural analysis through X-ray diffraction (XRD) confirmed that the compounds crystallize in a cubic structure with a lattice parameter, *a*, of 10.94 Å. The crystallite size calculated from the XRD data is 16 nm for the 500 ˚C calcined sample and 23 nm for the 700 ˚C calcined sample. Fourier transform infrared (FTIR) spectra have demonstrated the presence of Sm-O stretching vibrations in both of the synthesized samples. Band gap, 4.50±0.01 eV and 3.50±0.01 eV, for 500 and 700 ˚C calcined samples, obtained from the UV-Visible (UV-Vis) measurement, respectively. The photocatalytic performance of both samples was examined by degrading the Methylene Blue (MB) dye with irradiation of UV light, and it was found that the sample calcined at 700 ˚C is more efficient compared to the 500 ˚C calcined sample.

1 Introduction

In recent times, metal oxides are used in several areas, and particularly a number of research events have been commenced to explore rare-earth metal oxides. Metal oxides are widespread because of their irreplaceable properties. A variety of rare-earth-metal-based compounds are widely used in numerous fields of existing science and technology due to the outcome of their infrequent optical, chemical, magnetic, electrical and catalytic properties arising from their distinctive 4*f* electrons [1, 2]. The rare-earth metal oxides are extensively useful in the arenas of biochemical probes, optical transmission, luminescence devices, medical diagnostics, etc [3]. These rare-earth metal oxide compounds are the most stable rare-earth compounds with the rare-earth ions left behind in the trivalent state [3]. It is known that R_2O_3 nano-compounds display better catalytic and luminescence properties [3]. Lanthanides' rare-earth metal compounds are extensively used in numerous fields of current science and technology [2]. It has been widely used in nano sensors, photoelectronics and micro-circuit batteries, which have provoked considerable interest over the past several years [1]. The usage of a metal oxide as a photocatalyst is very common for the removal of organic contaminants [2, 4-13]. Rare earth metals are used in a wide range of applications, such as ultraviolet (UV) detectors, high-resolution x-ray imaging, catalysts and fluorescent materials, owing to their high chemical stability and UV absorption capability [2].

Lanthanide rare-earth metal compounds are nowadays being used in photocatalysis, owing to their exceptional *f*-electronic arrangement [2]. The nanoparticles are very small units that exist in the range of 1-100 nm, in which substantial quantities of atoms are situated in the interfacial region in a disorderly fashion, resulting in unusual physical and chemical properties [3, 12-14]. Therefore, rare earth metal oxide nanoparticles are the most attractive materials for photocatalysis [2, 4-11]. Recently, a few reports have studied the photocatalytic properties of rare-earth metal oxide nanoparticles [2, 4-11]. Sm_2O_3 is a species of encouraging rare earth oxide functional materials in recent times because of its better chemical and thermal stability [15-18]. Photocatalytic properties of Sm_2O_3 have not been much explored in the reported literature. Hence, in this report, Sm_2O_3 nanoparticles have been synthesized. Further, the sample was calcined at two different temperatures and then the effect of calcination temperature on the structural and photocatalytic properties of the Sm_2O_3 sample was studied.

2 Experimental details

The sol-gel method was used to synthesize the Sm_2O_3 sample, [12, 13]. For the synthesis of 1 g of Sm_2O_3, at first a stoichiometric amount of $Sm(NO_3)_3.6H_2O$ (Sigma-Aldrich) and 50 ml of absolute ethanol were mixed to make the solution. With the help of a magnetic stirrer, the prepared solution of the precursors was stirred for 3 h. Then the solution was kept for 24 h for aging. After aging, the liquid was heated at 80 ˚C to get the solid sample. After drying, the solid sample was crushed into powder. The powdered sample was then calcined with the heating and cooling rate of 5 ˚C per minute at two different temperatures, 500 ºC and 700 ºC, for three hours in a box furnace. The prepared samples were used for characterization, using the Rigaku X-ray diffraction (XRD) technique with Cu-*K*α radiation (λ = 1.5406 Å), Shimadzu IRSpirit-X Fourier transform infrared (FTIR) spectrometer, and Shimadzu UV-1800, UV-Visible (UV-Vis) spectrometer. Then, the photocatalysis measurements of the samples were carried out by degrading the dye methylene blue (MB) with irradiation of UV light. Further, in this report, the samples calcined at 500 and 700 ˚C are referred to as Sm_2O_3-500 and Sm_2O_3-700, respectively.

3 Results and discussion

The powder X-ray diffraction (PXRD) patterns of Sm_2O_3 calcined at two different temperatures are presented in Figure 1. The PXRD pattern of Sm_2O_3-500 shows sharp peaks at 28.29 (222), 32.70 (044), 42.22 (431), 47.04 (440) and 55.74 (622), which demonstrates the pure cubic phase of the sample (JCPDS 15-0813) shown in Figure 1(a) [14]. Figure 1(b) displays the PXRD peaks for Sm_2O_3-700 and the most intense peaks are at 28.55 (222), 33.02 (044), 42.35 (431), 47.10 (440) and 56.04 (622), which signify the cubic crystal structure of the material (JCPDS 15-0813) [3]. The XRD patterns of the samples are fitted in accordance with the cubic crystal structure of Sm_2O_3 [14, 16]. From the Le-Bail refinement of XRD data, both samples exhibit a lattice parameter of 10.9 Å. Unlike Sm_2O_3-500, peaks of XRD data for Sm_2O_3-700 are sharper and more intense, indicating higher crystallinity of the Sm_2O_3-700 sample [14]. XRD results show an increase in crystallinity with increasing calcination temperature. The sharpness of the peaks is due to the larger size of the crystallites. Hence, the crystallite size of the samples has been calculated using Scherrer's equation given below,

$$\text{Crystallite size (D)} = \frac{K\lambda}{\beta\cos\theta}$$

where D is known as the crystallite size, K is the Scherrer constant, λ is the X-ray wavelength, β is the full width at half maximum, and θ is the Bragg angle [14, 17, 18]. The obtained crystallite size for Sm_2O_3-500 is 16 nm, whereas for Sm_2O_3-700 it is 23 nm. As the temperature increases, the growth of the particle increases; this has been observed in this case.

FTIR spectra of both the Sm_2O_3 samples are presented in Figure 2. The FTIR absorption spectrum for Sm_2O_3-500 and Sm_2O_3-700 is nearly the same, as shown in Figure 2 (a) and Figure 2 (b), respectively. Both samples show the characteristic absorption bands of pure Sm_2O_3 crystals at around 456, 548 and 740 cm^{-1}, corresponding to Sm-O stretching vibrations [14, 15]. The results obtained corroborate the reported FTIR results in Refs. [14, 15]. Additionally, UV-Visible absorbance measurements for the samples were carried out and the band gap for both samples was calculated using the Tauc plot [2, 13]. The band gap found for Sm_2O_3-500 and Sm_2O_3-700 is 4.50±0.01 eV and 3.50±0.01 eV, respectively.

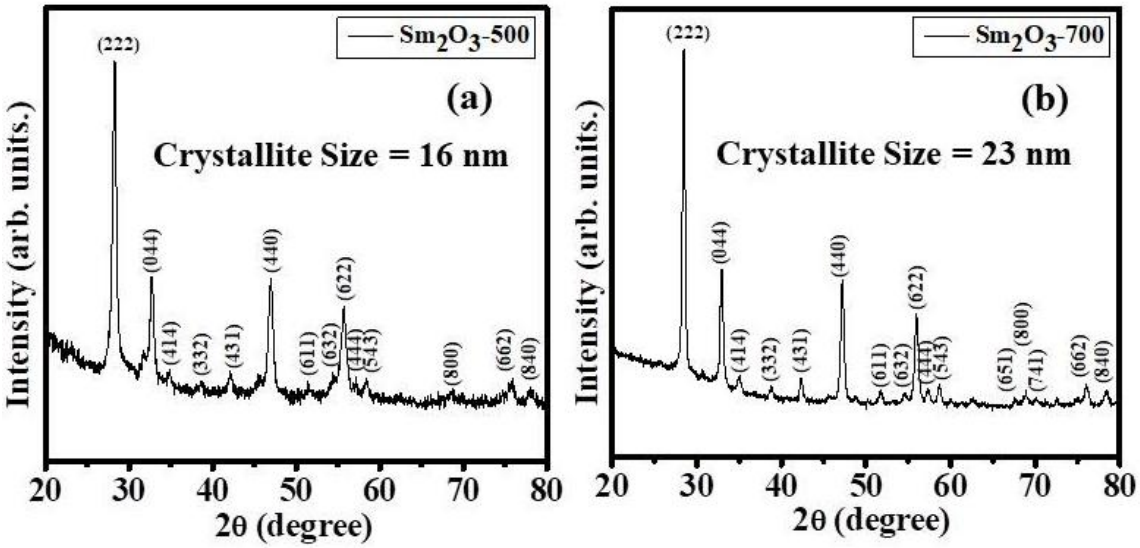

Figure 1: XRD pattern of samples (*a*) Sm_2O_3-500 and (*b*) Sm_2O_3-700.

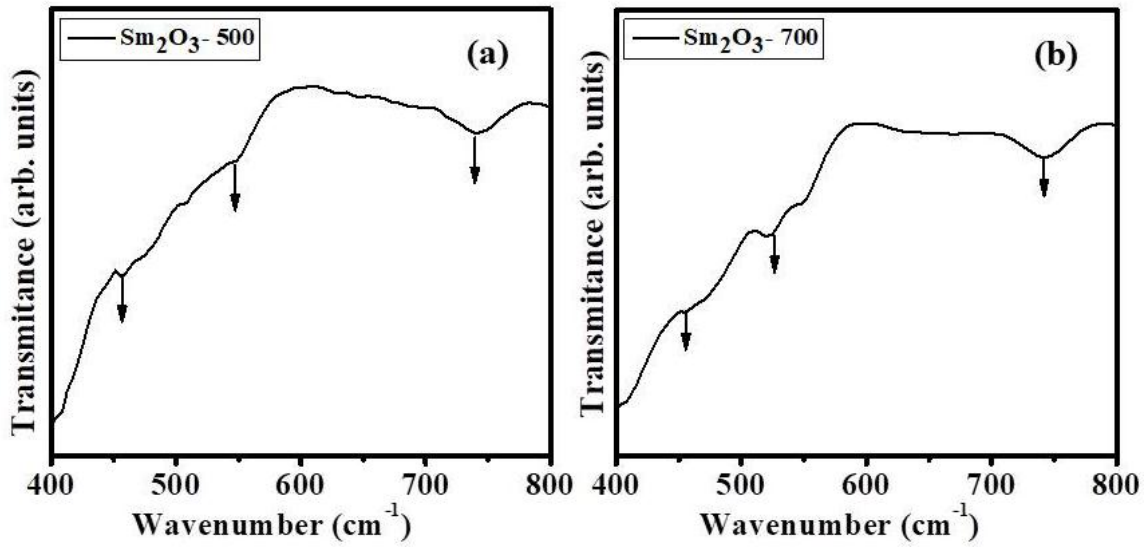

Figure 2: FTIR spectra of samples (*a*) Sm_2O_3-500 and (*b*) Sm_2O_3-700.

Figure 3(a) and 3(b) present the photocatalytic measurements of the synthesized samples, Sm_2O_3-500 and Sm_2O_3-700, respectively. For the photocatalytic analysis, two containers, each containing 50 ml of an aqueous methylene blue (MB) solution, were prepared with 20 mg of different Sm_2O_3 samples: Sm_2O_3-500 and Sm_2O_3-700. Initially, without irradiation of UV radiation, UV-Visible measurements were performed, and an absorbance peak at 310.65 nm was observed, which is the characteristic peak of MB. Then, for up to 20 minutes, the UV irradiation on both containers with the MB solution was carried out. In every 5 minutes, interval MB sample was collected and UV-Visible measurements were carried out. Gradually, the MB peak intensity decreases with increasing irradiation time, indicating that the dye gets degraded with irradiation. During irradiation with UV radiation, excitation of an electron from the valence band to the conduction band takes place. Therefore, a hole is created in the valence band. Then, the electron hole pair generates the highly

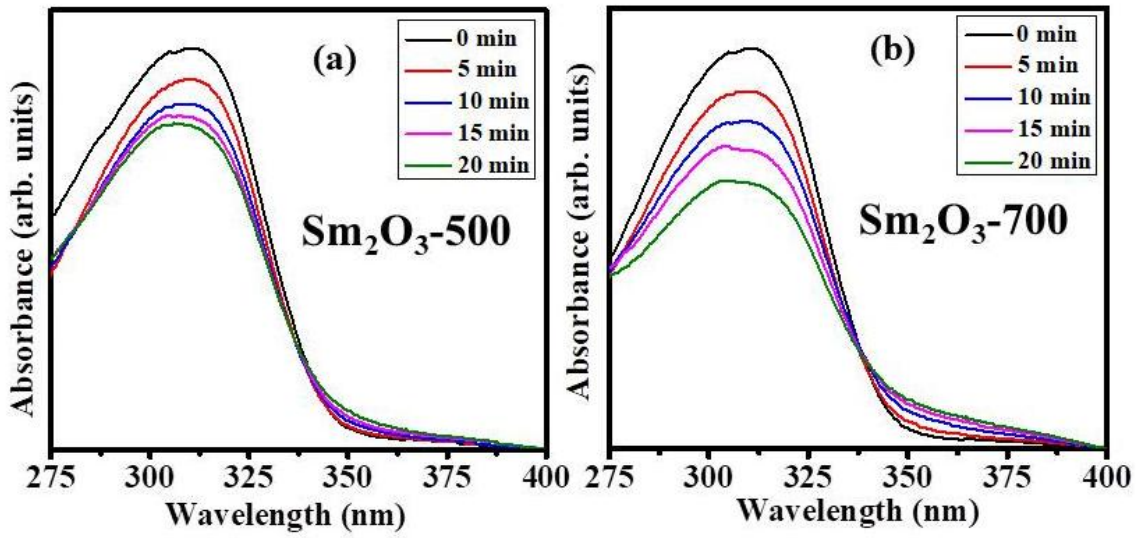

Figure 3: UV-Visible spectra of the MB dye with irradiation time (*a*) sample Sm_2O_3-500 and (*b*) sample Sm_2O_3-700.

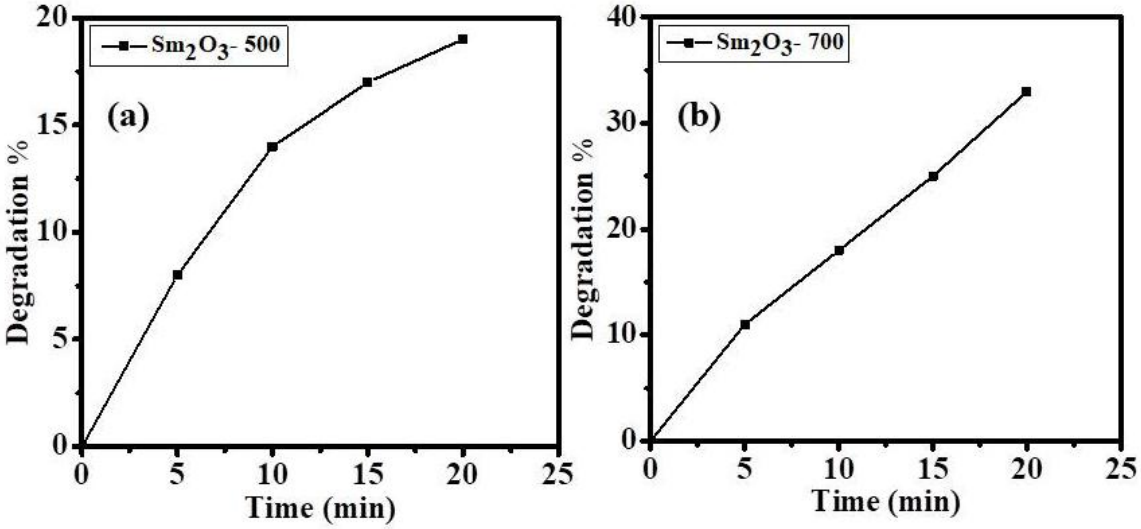

Figure 4: Dye degradation percentage (%) with irradiation time for the sample (a) Sm_2O_3-500 and (b) Sm_2O_3-700.

reactive $OH^{\cdot}$ radicals from the aqueous solution of dye. Further, the $OH^{\cdot}$ radical reacts with the dye and degradation of the dye takes place [2]. The degradation efficiency was calculated using the following equation:

$$\text{Degradation Efficiency (in percentage)} = \frac{(C_0 - C_t)}{C_0} \times 100$$

where C_0 is the initial concentration of the dye and C_t is the concentration of dye at the time, t [2, 4]. Finally, it has been found that after 20 minutes of irradiation with UV light, Sm_2O_3-500 degrades only 19% of the dye shown in Figure 4(a). However, Figure 4(b) demonstrates that Sm_2O_3-700 degrades 33% of the MB dye in 20 minutes. It has been observed from the XRD and UV-Visible analysis that with increasing calcination temperature, crystallite size increases and band gap decreases. The decrease in band gap is the consequence of increasing dye degradation [13]. Recently, Jeon et al. [2] have shown the photocatalytic studies with pure Gd_2O_3 nanoparticles. Rahul et al. [4] and Luo et al. [5] studied the photocatalytic properties of La_2O_3.

Similarly, some reports show the photocatalytic properties of the rare earth metal oxide composite materials [6-11]. All these reports are performed on the photocatalytic studies with rare-earth oxides to degrade the organic pollutants. Therefore, in this report, the effect of calcination temperature on the photocatalytic characteristics of one of the rare earth metal oxides, that is, Sm_2O_3 nanoparticles, has been evaluated. It was found that compared to the 500 ˚C calcined sample, the 700 ˚C calcined sample is more efficient for photocatalysis.

4 Conclusions

In this report, syntheses of Sm_2O_3 nanoparticles were carried out by the sol-gel technique. The synthesized sample was calcined at two different temperatures, which are 500 and 700 ˚C. Thereafter, the cubic crystal structure of the samples was confirmed by XRD. From the XRD data, the crystallite size of the samples was calculated. The crystallite size of the Sm_2O_3-500 sample was calculated to be 16 nm, while the Sm_2O_3-700 sample had a crystallite size of 23 nm. Both samples exhibited Sm-O stretching vibrations, which were confirmed by FTIR spectra. The band gap evaluated from UV-Visible data is 4.50±0.01 eV and 3.50±0.01 eV for Sm_2O_3-500 and Sm_2O_3-700, respectively. The photocatalytic analysis revealed that Sm_2O_3-700 was more efficient than Sm_2O_3-500 in degrading the dye methylene blue (MB) under UV irradiation.

Acknowledgments:

Financial support from the University of Johannesburg (UJ) GES is acknowledged. Prof Mallick and their research group are acknowledged for all the support for photocatalytic measurements.

Reference

[1] L. Yin, D. Wang, J. Huang, G. Tan, " Controllable synthesis of Sm_2O_3 crystallites with the assistance of templates by a hydrothermal calcination process," Materials Science in Semiconductor Processing, Vol. 30, pp. 9-13, 2015.

[2] S. Jeon, J-W. Ko, W-B. Ko, "Synthesis of Gd_2O_3 nanoparticles and their photocatalytic activity for degradation of azo dyes," Catalyst, Vol 11, pp. 742, 2021.

[3] M.M. Khan, S.N. Matussin, "Sm_2O_3 and Sm_2O_3-based nanostructures for photocatalysis, sensor, CO conversion, and biological applications," Catalysis Science and Technology, Vol. 13, pp. 2274, 2023.

[4] S. Rahul, G. Amal, R.S. Babu, A.D. Raj, G. Jayakumar, S.A. Rag, "Unraveling the photocatalytic performance of La_2O_3 nanoparticles for the degradation of six organic dyes," Langmuir, Vol. 41, pp. 16378-16390, 2025.

[5] X. Luo, L. Xu, L. Yang, J. Zhao, T. Asefa, R. Qiu, Z. Huang, "Ball milling of La_2O_3 tailors the crystal structure, reactive oxygen species, and free radical and non-free radical photocatalytic pathway," ACS Applied Materials and Interfaces, Vol.16, pp. 18671-18685, 2024.

[6] B. Subramanian, K.J. Jothi, M.M. Mohideen, R. Karthikeyan, A.S.K. Kumar, G.A. Sundaram, K. Thirumalai, M.D. Albaqami, S. Mohammad, M. Swaminathan, "Synthesis and characterization of Dy_2O_3@TiO_2 nanocomposites for enhanced photocatalytic and electrocatalytic applications," ACS Engineering Au, Vol 4, pp. 474-490, 2024.

[7] K. Jayaprakash, A. Sivasamy, "Superior photocatalytic performances of Dy_2O_3/graphitic cabon nitride nanohybrid for the oxidation of Rhodamine B dye under visible light irradiation: A superoxide free radicals approach," Colloids and Surfaces A: Physicochemical and Engineering Aspects, Vol. 676, pp. 132260, 2023.

[8] Y. Xie, J. Wu, C. Sun, Y. Ling, S. Li, X. Li, J. Zhao, K. Yang, "La_2O_3-modified graphite carbon nitride achieving the enhanced photocatalytic degradation of different organic pollutants under visible light irradiation," Materials Chemistry and Physics, Vol. 246, pp. 122846, 2020.

[9] Z. Zhu, H. Xia, R. Wu, Y. Cao, H. Li, "Fabrication of La_2O_3/g-C_3N_4 heterojunction with enhanced photocatalytic performance of tetracycline hydrochloride," Crystals, Vol. 11, pp. 1349, 2021.

[10] A. Marizcal-Barba, I. Limon-Rocha, A. Barrera, J.E. Casillas, O.A. Gonzalez-Vargas, J.L. Rico, C. Martinez-Gomez, A. Perez-Larios, "TiO_2-La_2O_3 as photocatalysts in the degradation of naproxen," Inorganics, Vol. 10, pp. 67, 2022.

[11] A. Barrera, F. Tzompantzi, J. Campa-Molina, J.E. Casillas, R. Perez-Hernandez, S. Ulloa-Godinez, C. Velasquez, J. Arenas-Alatorre, "Photocatalytic activity of Ag/Al_2O_3-Gd_2O_3 photocatalysts prepared by the sol-gel method in the degradation of 4-chlorophenol," RSC Advances, Vol. 8, pp. 3108, 2018.

[12] B. Bharati, N.C. Mishra, A.S.K. Sinha, C. Rath, "Unusual structural transformation and photocatalytic activity of Mndoped TiO_2 nanoparticles under sunlight," Materials Research Bulletin, Vol. 123, pp. 110710, 2020.

[13] B. Bharati, A.K. Sonkar, N. Singh, D. Dash, C. Rath, "Enhanced photocatalytic degradation of dyes under sunlight using biocompatible TiO_2 nanoparticle," Materials Research Express, Vol. 4, pp. 085503, 2017.

[14] S. Biswas, H, Naskar, S. Pradhan, Y. Chen, Y. Wang, Rajib Bandyopadhyay, Panchanan Pramanik, "Sm_2O_3 nanorod-modified graphite paste electrode for trace level voltammetric determination of acetaminophen and ciprofloxacin," New J. Chemistry Vol. 44, pp. 1921, 2020.

[15] B.T. Sone, E. Manikandan, A. Gurib-Fakim, M. Maaza, "Sm_2O_3 nanoparticles green synthesis via callistemon viminalis' extract," Journal of Alloys and Compounds, Vol. 650, pp. 357-362, 2015.

[16] H.M. Shiri, A. Ehsani, M.J. Khales, "Electrochemical synthesis of Sm_2O_3 nanoparticles: application in conductive polymer composite films for supercapacitor," Journal of Colloid and Interface Science, Vol. 505, pp. 940-946, 2017.

[17] K.H. Goh, A.S.M.A. Haseeb, Y.H. Wong, "Physical and electrical properties of thermal oxidized Sm_2O_3 gate oxide thin film on Si Substrate: influence of oxidation durations," Thin Solid Films, Vol. 606, pp. 80-86, 2016.

[18] S.R. Jamnani, H.M. Moghaddam, S.G. Leonardi, G. Neri, "A novel conductometric sensor based on hierarchical self-assembly nanoparticles Sm_2O_3 for VOCs monitoring," Ceramic International, Vol. 44, pp. 16953-16959, 2018.

Density functional theory study on the effect of pressure on structural, mechanical and phonon properties of A15 Mn_3Ru compound

B.O Mnisi[1], E.M. Benecha[2] and M.M. Tibane[1]

[1]Physics department, University of South Africa, Roodepoort, South Africa
[2]College of Science Engineering and Technology, University of South Africa, Roodepoort, South Africa

E-mail: mnisibo@unisa.ac.za

Abstract. Ruthenium alloys hold strong potential for aerospace applications. This study uses first-principles DFT calculations to examine the effects of pressure on the structural, mechanical and phonon properties of Mn_3Ru in the A15 phase. At zero pressure, Mn_3Ru has a negative formation energy of -0.64 eV, indicating thermodynamic stability. However, at 50–200 GPa, the heat of formation becomes positive, suggesting instability. The alloy is mechanically unstable at 0 and 50 GPa due to negative C_{44} values but stabilizes between 100–200 GPa. Phonon dispersion confirms dynamic stability across all pressures. Overall, pressure significantly enhances the mechanical and dynamic properties of Mn_3Ru, supporting its use in high-temperature structural applications.

1. Introduction

High-temperature structural materials characterized by elevated melting points have garnered significant interest for engineering applications [1], particularly in the aerospace and gas turbine engine industries. Nickel-based superalloys (NBSAs) have been the conventional choice owing to their remarkable mechanical, chemical, and physical properties. However, NBSAs typically operate at approximately 85% of their melting temperature [2], which imposes limitations on their performance in advanced high-temperature structural applications. Consequently, there is a growing need to explore alternative materials that can withstand higher temperature capabilities. For a material to be considered suitable for such demanding applications, it must possess a density of 5–9 g/cm^3, a melting temperature above 1000 °C, and demonstrate good ductility, conductivity, and phase stability [3]. The quest for advanced materials with these characteristics has led to the investigation of several intermetallic compounds including the platinum group metals (PGMs), refractory metals (RMs) (containing magnesium, platinum, and ruthenium) and chromium-based alloys. While these materials offer promising attributes, they also present several limitations in high-temperature performance. For instance, RMs are prone to severe oxidation at elevated temperatures (500 °C) [4], magnesium alloys lack sufficient strength and fatigue resistance [5], and titanium alloys possess a significant loss of strength with increasing temperature. While PGMs [6] exhibit properties that can rival those of nickel-based superalloys, they also possess inherent drawbacks, such as brittleness, high cost, and weight limitations due to the high-densities of Pt (21.45 g/cm^3), Ir (22.56 g/cm^3), Pd (12.02 g/cm^3), Ru (12.37 g/cm^3), Os (22.59 g/cm^3) and Rh (12.42 g/cm^3). Chromium-based intermetallics, particularly Cr_3X and X_3Cr (with X = Pt or Ru) across various phases, have attracted attention due to their notable structural and mechanical characteristics [7].

The successful synthesis of A15 Cr_3Ru alloy via the arc-melting technique, followed by annealing at 1073.15 K [8], has spurred substantial research in Ru-based alloys. A recent study [9] using first-principles density functional theory (DFT) investigated the effect of transition metal (Mn, Mo, Pt, Pd, Fe, Co, Re, and Zr) alloying on the structural, electronic, and mechanical properties of cubic A15 Cr–Ru intermetallics, specifically Ru_3Cr and Cr_3Ru. The results showed that incorporating Mn at different concentrations significantly enhances the stability of A15 Ru_3Cr and Cr_3Ru intermetallics. In our recent study, we examined the properties of 3d-transtition metal Ru alloys in different phases, including *A15, $D0_c$, B2, tP16* and $L1_2$ using first-principles DFT calculations at zero pressure [10–13]. It was found that many of these compounds demonstrate favorable heats of formation, making experimental synthesis feasible.

To date, the effect of pressure on this specific class of materials has not been explored, either theoretically or experimentally. External factors such as temperature, pressure, strain, and electric or magnetic fields can significantly modify the properties of materials. Specifically, pressure is a key thermodynamic variable that impacts material properties by altering the microscopic structures, interatomic electrostatic interactions, electronic orbitals, and chemical bonding [14,15]. For decades, pressure has served as an invaluable tool for identifying materials that would be inaccessible under standard conditions [16]. Previous studies have examined the phase stability of $D0_c$ Mn_3Ru and tP16 Cr_3Ru phases under pressure [17,18]. The $D0_c$ Mn_3Ru phase maintained a negative heat of formation across a wide range of pressures, indicating robust stability. In contrast, tP16 Cr_3Ru showed stability only at pressures of 1 and 20 GPa, suggesting potential for experimental studies. However, the effect of pressure on A15 Mn_3Ru remains unexplored, despite its known impact on material properties through phase transitions and deformation [15]. This study investigates the phase stability of A15 Mn_3Ru at pressures of 0 GPa, 50 GPa, 100 GPa, 150 GPa and 200 GPa using density functional theory.

2. Computational details

All the first principles-DFT [19] calculations reported in this study were carried out using the CASTEP code [20] within Materials Studio suite (Version 2020). The properties of Mn_3Ru in the A15 phase were modeled based on its unit cell, as shown in Figure 1. The Ultrasoft pseudopotentials [21] were used to treat the ion–electron interactions. The exchange–correlation energy was described using the generalized gradient approximation (GGA) method with the Perdew–Burke–Ernzerhof (PBE) functional [22,23], incorporating an on-site Coulomb interaction (Hubbard U) of 2.5 eV for both Mn and Ru atoms [24]. Structural optimization was carried using the Broyden–Fletcher–Goldfarb–Shanno (BFGS) algorithm [26] with a 15×15×15 Monkhorst–Pack k-point grid [25] for Brillouin zone sampling and a plane wave cutoff energy of 800 eV. Geometry optimization was considered complete when the force on each atom was 0.01 eV/Å, the internal stress was 0.02 GPa, and atomic displacements did not exceed 0.0005 Å. The x, y, and z directions were subjected to evenly distributed hydrostatic pressure.

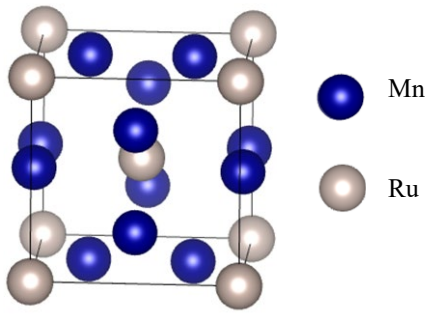

Figure 1: Crystal structure of A15 Mn_3Ru alloy. Blue spheres represent Mn atoms and brown indicates the Ru atoms.

3. Results and discussion

3.1 Structural and thermodynamical properties

Ruthenium-transition metal phases belong to the A15-type X_3Z structural family, where X atoms occupy six equivalent positions at the c-site (0.25, 0, 0.5), and Z atoms are located at the body-centered cubic (bcc) position (0, 0, 0), as illustrated in Figure 1. Table 1 presents the calculated lattice constants, heats of formation, magnetic moments, and densities of the A15 Mn_3Ru phase under varying pressure conditions. The results show that the lattice constants of Mn_3Ru decrease with increasing pressure. The thermodynamic stability of the Mn_3Ru alloy under pressure was assessed using Equation 1.

$$\Delta H_f = \frac{1}{x+y}(E(Mn_3Ru) - xE^g_{Ru} - yE^g_{Mn}), \quad (1)$$

Pressure Mn_3Ru (GPa)	Lattice constants (Å)	ΔH_f (eV/atom)	Magnetic moments (μ_B/atom)	Density ρ = g/cm^3
0	5.37	-0.64	3.88	5.72
50	4.71	0.92	2.40	8.23
100	4.43	0.89	0.49	10.19
150	4.23	1.24	0.49	11.63
200	4.12	1.62	1.03	12.58

Table 1: Calculated lattice constants, volume, heat of formation, magnetic moment and density of Mn_3Ru alloys in A15 phase under pressure.

where $x+y$ = total number of atoms of Mn and Ru atoms, ΔH_f = heat of formation, $E(Mn_3Ru)$ = total energy of the system, E^g_{Ru} and E^g_{Mn} = total energies of each element. A negative heat of formation suggests stability whilst positive formation energy indicates instability. At zero pressure, Mn_3Ru exhibits a negative heat of formation, indicating thermodynamic stability. In contrast, under applied pressure, it shows a positive heat of formation, suggesting thermodynamic instability. However, previous studies [7,9] have suggested that doping can reduce the heat of formation in certain materials, offering an additional approach for achieving experimental synthesis under elevated pressure conditions.

The structural stability of a material is closely linked to its magnetic moments due to the mixing of atomic orbitals. To support this, we examined the magnetic properties of the Mn_3Ru alloy, as presented in Table 1. As anticipated, applying pressure leads to a reduction in the alloy's magnetic moments, which can be attributed to diminished orbital hybridization. This trend is consistent with our recent findings on D0c Mn_3Ru and tP16 Cr_3Ru phases under pressure [17,18].

A key principle in understanding lightweight materials is density, which refers to the mass per unit volume of a material. Within the DFT framework, the density of a material is calculated as

$$\rho^{cal} = \left(\frac{M_W * N}{Vol * A_0}\right) \quad (2)$$

where ρ^{cal} = the density, M_W = average molecular weight of the individual elements in a unit cell, N = Total number of atoms, A_0 = Avogadro's number (6.022×10^{23}) and Vol = volume of the unit cell. The calculated densities of Mn_3Ru exhibit a significant increase under pressure, ranging from 5.72 g·cm^{-3} at 0 GPa to 12.58 g·cm^{-3} at 200 GPa, as detailed in Table 1. At zero pressure, the density of Mn_3Ru (5.72 g·cm^{-3}) is lower than that of NBSAs (6.14 g·cm^{-3} [27]), which are commonly used in aerospace applications due to their strength-to-weight ratio and thermal stability. The lower density of Mn_3Ru at ambient pressure suggests that it may be advantageous for applications where weight reduction is critical, although its density increases significantly under high-pressure conditions. Further investigation into the mechanical properties and performance of Mn_3Ru under varying pressures is thus necessary to assess its potential for aerospace applications.

3.2 Mechanical properties

The elastic constants of crystals play an important role in predicting the mechanical behavior of materials. Therefore, the elastic and mechanical properties of the cubic Mn_3Ru alloy were evaluated under pressure. For

cubic Mn_3Ru alloy, three independent elastic constants C_{11}, C_{12} and C_{44} were considered, as summarized in Table 2. Mechanical stability was assessed using the criteria [28] given in equation (3).

$$C_{44} > 0; C_{11} - C_{12} > 0; C_{11} + 2C_{12} > 0 \quad (3)$$

Pressure Mn_3Ru (GPa)	C_{11} (GPa)	C_{12} (GPa)	C_{44} (GPa)	B_H (GPa)	G_H (GPa)	E_H (GPa)	B_H/G_H	T_m (K)
0	145	48	-4	80	5	14	16.0	1410
50	261	49	-706	120	-19	-62	-6.3	2096
100	1241	1146	48	1178	48	142	25	7887
150	1231	432	76	698	159	444	4.4	7828
200	1494	500	72	865	178	480	5.01	9383

Table 2: Calculated elastic constants, bulk modulus (B_H), shear modulus (G_H), Young modulus (E_H), bulk to shear ratio and melting temperature T_m for A15 Mn_3Ru alloy.

The calculated results show that the Mn_3Ru alloy meets the conditions in Equation 3 at 100 GPa and 200 GPa, confirming its mechanical stability. However, at 0 GPa and 50 GPa, the results indicate mechanical instability due to negative C_{44} which quantifies the material's resistance to shear deformation when a tangential stress is applied along the [010] direction on the (100) crystallographic plane. Therefore, a negative value of C_{44} indicates that the crystal structure cannot withstand shear forces and may spontaneously distort, signalling mechanical instability.

The elastic modulus was calculated using the Voigt–Reuss–Hill (VRH) approach [29–31] while, the bulk modulus, shear modulus, and Young's modulus were calculated using the Hill's approximation [31], as given as

$$B_H = \left(B_V + B_R\right)/2 \quad (4)$$

$$G_H = \left(G_V + G_R\right)/2 \quad (5)$$

$$E_H = \left(9B_H G_R\right)/\left(3B_H + G_H\right) \quad (6)$$

The bulk modulus (B) represents a material's resistance to volume change, with a higher B value indicating lower compressibility [32]. Likewise, the shear modulus (G) reflects a material's capacity to resist shear deformation; a higher G value indicates greater resistance to shape distortion [33]. Young's modulus (E) measures the stiffness of solid materials, with larger E values representing stiffer materials [34]. We find that these moduli increase significantly from 100 GPa to 200 GPa, suggesting not only an enhancement in resistance to volume change but also improved plastic deformation characteristics and greater overall stiffness at high pressure conditions. According to Pugh's criterion [32], a bulk to shear (B/G) ratio exceeding 1.75 indicates ductility. The Mn_3Ru alloy at zero and varying pressures exhibit B/G values above this ductility threshold, except at 50 GPa. Notably, the bulk-to-shear ratio exhibits a significant increase at 100 GPa, indicating enhanced ductile behavior under these conditions. However, it should be noted that the ultra-high B/G ratios of 16 and 25 obtained in this study are unusual for common materials, indicating that Pugh's criterion may have limitation at high pressures.

The melting point of a material is a critical parameter for high-temperature structural applications, particularly in aerospace and gas turbine engines, where thermal resistance is vital. In this study we calculated the melting temperatures of cubic Mn_3Ru under varying pressure conditions using Equation 7. In general, it is observed that the melting temperature of the Mn_3Ru increases with pressure compared to ambient conditions. Specifically, the melting points increase rapidly with pressure, reaching 9383 K at 200 GPa. While these findings make Mn_3Ru

highly suitable for high-temperature structural applications, future studies should explore the underlying mechanisms governing melting temperature changes with pressure.

$$T_m = 553K + \left(591K / Mbar\right) * C_{11}(Mbar) \pm 300K \tag{7}$$

3.3 Phonon stability

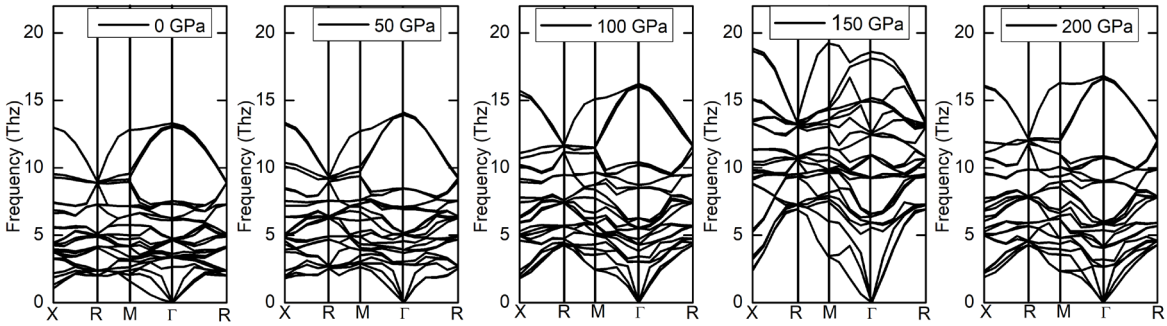

Figure 2: Calculated phonon dispersion curves of Mn_3Ru alloy in the A15 phase at 0 GPa, 50 GPa, 100 GPa, 150 GPa and 200 GPa.

In DFT studies, the absence of imaginary phonon modes is a common criterion for assessing the stability of different materials. Imaginary frequencies suggest that the system's energy can be reduced through certain atomic displacements, indicating that the structure is not experimentally feasible [35]. This information is obtained by analyzing the phonon spectra of the material. To investigate the phonon stability of Mn_3Ru under pressure, we plotted its phonon dispersion curves, as shown in Figure 2. The phonon spectra of Mn_3Ru at zero and varying pressures show no imaginary phonon modes, indicating its dynamic stability.

4. Conclusion

DFT calculations were employed to investigate the effect of pressure on the structural, mechanical, and phonon properties of Mn_3Ru in the A15 phase. At zero pressure, Mn_3Ru exhibits a negative formation energy of –0.64 eV, indicating thermodynamic stability. However, as the pressure increases from 50 to 200 GPa, the formation energy becomes positive, suggesting thermodynamic instability. The alloy is mechanically unstable at 0 and 50 GPa but becomes mechanically stable between 100 and 200 GPa. Phonon dispersion analysis confirms dynamic stability at all the pressure ranges studied. These results highlight the crucial role of pressure in enhancing the mechanical and dynamic stability of Mn_3Ru, underscoring its potential high-temperature structural applications.

References

[1] M. Yamaguchi, H. Inui, and K. Ito, “High-temperature structural intermetallics,” *Acta Mater*, vol. 48, no. 1, pp. 307–322, 2000.

[2] L. A. Cornish, B. Fischer, and R. Völkl, “Development of platinum-group-metal superalloys for high-temperature use,” *MRS Bull*, vol. 28, no. 9, pp. 632–638, 2003.

[3] S. Floreen and R. H. Kane, “Effects of environment on high-temperature fatigue crack growth in a superalloy,” *Metallurgical Transactions A*, vol. 10, no. 11, pp. 1745–1751, 1979.

[4] I. S. Kim, B. G. Choi, H. U. Hong, J. Do, and C. Y. Jo, “Influence of thermal exposure on the microstructural evolution and mechanical properties of a wrought Ni-base superalloy,” *Materials Science and Engineering: A*, vol. 593, pp. 55–63, 2014.

[5] A. Luo and M. O. Pekguleryuz, "Review Cast magnesium alloys for elevated temperature applications," *J Mater Sci*, vol. 29, pp. 5259–5271, 1994.

[6] J. K. Odusote, L. A. Cornish, and J. M. Papo, "High Temperature Oxidation of Pt-Al-Cr-Ru Alloy: Scale Morphology and Adherence," *Metallography, Microstructure, and Analysis*, vol. 1, no. 3–4, pp. 142–149, 2012, doi: 10.1007/s13632-012-0024-x.

[7] M. M. Tibane, "Phase stability study of Pt-Cr and Ru-Cr binary alloys," PhD thesis, University of Limpopo, Mankweng (Sovenga), 2011.

[8] Y. Nishihara, Y. Yamaguchi, M. Tokumoto, K. Takeda, and K. Fukamichi, "Superconductivity and magnetism of bcc Cr-Ru alloys," *Phys Rev B*, vol. 34, p. 3446, 2021.

[9] B. O. Mnisi, E. M. Benecha, H. R. Chauke, P. E. Ngoepe, and M. M. Tibane, "Effect of transition metal doping on Cr–Ru alloys using first principles approach," *Bulletin of Materials Science*, vol. 43, pp. 1–9, 2020.

[10] B. O. Mnisi, E. Benecha, and M. Tibane, "Investigation of the thermodynamic, structural, electronic,mechanical and phonon properties of D0c Ru-based intermetallic alloys: An ab-initio Study," *Mater Res Express*, vol 11, no 4, p.046506, Apr. 2024, doi: 10.1088/2053-1591/ad3a40.

[11] B. O. Mnisi, E. M. Benecha, and M. M. Tibane, "First-principles study of stability and electronic properties of B2 X-Ru alloys for high-temperature structural applications," *Mater Adv*, vol. 5, no. 13, pp. 5632–5643, May 2024, doi: 10.1039/d4ma00478g.

[12] B. O. Mnisi, M. Evans Benecha, and M. Meriam Tibane, "First-Principles Study on Thermodynamic, Structural, Mechanical, Electronic, and Phonon Properties of tP16 Ru-Based Alloys," *Alloys, vol. 3, no 2,* pp.126-139, 2024, doi: 10.3390/alloys3020007.

[13] B. O. Mnisi, E. M. Benecha, and M. M. Tibane, "Density functional theory study of phase stability and electronic properties for L12 X3Ru and XRu3 alloys," *European Physical Journal B*, vol. 98, no. 5, p. 106, May 2025, doi: 10.1140/epjb/s10051-025-00956-9.

[14] D. Chen, Z. Chen, Y. Wu, M. Wang, N. Ma, and H. Wang, "First-principles study of mechanical and electronic properties of TiB compound under pressure," *Intermetallics*, vol. 52, pp. 64–71, 2014.

[15] D. Xie, H. Guo, X. Yang, and T. Ma, "First-principles study of structural, mechanical, and electronic properties of typical iron-containing phases in Al-Cu alloys under different pressures," *Physica B Condens Matter*, vol. 555, pp. 112–117, Feb. 2019, doi: 10.1016/j.physb.2018.11.055.

[16] R. J. Hemley, "Effects of high pressure on molecules," *Annu. Rev. Phys. Chem*, vol. 51, pp. 763–800, 2000.

[17] B. O. Mnisi, E. M. Benecha, and M. M., "Stability of Novel D0c Mn3Ru Alloy Under Variable Pressure Conditions: A First-Principles DFT Study," *JOM*, vol 77, no 11, pp. 1-8, 2025, doi: 10.1007/s11837-025-07450-8.

[18] Mnisi BO, Benecha ME, and Tibane MM, "Effect of pressure on structural, electronic, and mechanical properties of tP16 Cr3Ru intermetallic alloy: A first principles density functional theory study," in *Effect of pressure on structural, electronic, and mechanical properties of tP16 Cr3Ru intermetallic alloy: A first principles density functional theory study in The Proceedings of SAIP2024*, Prof. Aletta Prinsloo, Ed., Johannesburg: The 68th Annual Conference of the South African Institute of Physics, Dec. 2024, pp. 129–134.

[19] P. Hohenberg and W. Kohn, "Inhomogeneous electron gas," *Physical review*, vol. 136, no. 3B, p. B864, 1964.

[20] M. D. Segall *et al.*, "First-principles simulation: ideas, illustrations and the CASTEP code," *Journal of Physics: Condensed Matter*, vol. 14, no. 11, p. 2717, 2002.

[21] D. Vanderbilt, "Soft self-consistent pseudopotentials in a generalized eigenvalue formalism," *Physical review B*, vol. 41, no. 11, pp. 7892–7895, 1990.

[22] J. P. Perdew, K. Burke, and M. Ernzerhof, "Perdew, burke, and ernzerhof reply," *Phys Rev Lett*, vol. 80, no. 4, p. 891, 1998.

[23] J. Perdew, K. Burke, and M. Ernzerhof, "PBE and PBE0," *Phys Rev Lett*, vol. 77, no. 18, pp. 3865–3868, 1996, doi: 10.1103/PhysRevLett.77.3865.

[24] A. I. Liechtenstein, V. I. Anisimov, and J. Zaanen, "Density-functional theory and strong interactions: Orbital ordering in Mott-Hubbard insulators," *Phys Rev B*, vol. 52, no. 8, p. R5467, 1995.

[25] H. J. Monkhorst and J. D. Pack, "Special points for Brillouin-zone integrations," *Phys Rev B*, vol. 13, no. 12, p. 5188, 1976.

[26] Thomas H, Fisher, and Jan Almlóf, "General Methods for Geometry and Wave Function Optimization,"*Phys.chem*, vol. 96, pp. 9768–9774, 1992.

[27] A. I. Popoola and J. E. Lowther, "Computational Study of Platinum Group Superalloys," *Int J Mod Phys B*, vol. 28, no. 09, p. 1450066, 2014.

[28] F. Mouhat and F. X. Coudert, "Necessary and sufficient elastic stability conditions in various crystal systems," *Phys Rev B Condens Matter Mater Phys*, vol. 90, no. 22, Dec. 2014, doi: 10.1103/PhysRevB.90.224104.

[29] W. Voigt, *Lehrbuch der kristallphysik*, vol. 962. Teubner Leipzig, 1928.

[30] A. Reuss, "Calculation of the flow limits of mixed crystals on the basis of the plasticity of monocrystals," *Z. Angew. Math. Mech*, vol. 9, pp. 49–58, 1929.

[31] R. Hill, "The elastic behaviour of a crystalline aggregate," *Proceedings of the Physical Society. Section A*, vol. 65, no. 5, p. 349, 1952.

[32] S. F. Pugh, "XCII. Relations between the elastic moduli and the plastic properties of polycrystalline pure metals," *The London, Edinburgh, and Dublin Philosophical Magazine and Journal of Science*, vol. 45, no. 367, pp. 823–843, 1954.

[33] W.-C. Hu, Y. Liu, D.-J. Li, X.-Q. Zeng, and C.-S. Xu, "First-principles study of structural and electronic properties of C14-type Laves phase Al2Zr and Al2Hf," *Comput Mater Sci*, vol. 83, pp. 27–34, 2014.

[34] A. D. McNaught and A. D. McNaught, *Compendium of chemical terminology*, vol. 1669. Blackwell Science Oxford, 1997.

[35] A. Yadav, C. M. Acosta, G. M. Dalpian, and O. I. Malyi, "First-principles investigations of 2D materials: Challenges and best practices," *Cell Press*, vol 6, no 9, pp 2711-2734, Sep. 06, 2023. doi: 10.1016/j.matt.2023.05.019.

This page intentionally left blank.

First-principles study of the Structural, Mechanical, Dynamical, Electronic and Lattice Thermal Conductivity properties of HfSnPt: A half-Heusler alloy

Ibrahim O A Ali[1], B O Mnisi[1], E M Benecha[2] and M M Tibane[1]

[1] Department of Physics, University of South Africa, Johannesburg, South Africa, 1709.
[2] College of Science, Engineering and Technology, University of South Africa, Johannesburg, South Africa, 1709.

E-mail: ibraphysics@gmail.com

Abstract. Density functional theory (DFT) is employed to investigate the structural, electronic, and stability related properties of half-Heusler HfSnPt in its cubic phase. Phase stability is assessed using formation and cohesive energies, both of which indicate thermodynamic stability. Mechanical behavior is analyzed through independent elastic constants, bulk, shear, and Young's moduli, supported by descriptors such as Pugh's and Poisson's ratios, the Kleinman parameter, Zener anisotropy factor, and melting temperature. The calculated elastic constants satisfy all mechanical stability criteria for cubic crystals. Electronic band structure analysis reveals that HfSnPt is a semiconductor with an indirect band gap of 0.889 eV. Phonon dispersion curve indicates dynamically stability due to the absence of soft modes. Overall, HfSnPt exhibits thermodynamic, mechanical, and dynamical stability, coupled with a high melting point, suggesting its strong potential for high-temperature structural applications.

1 Introduction

Thermoelectric (TE) materials can directly convert waste heat into electrical energy, offering compact and reliable solid-state power generation for applications in microelectronics, automotive systems, and industrial processes [1]. The efficiency of a TE material is determined by the dimensionless figure of merit, $ZT = \alpha^2\sigma T/k$, where α is the Seebeck coefficient, σ is the electrical conductivity, T is the absolute temperature, and k is the thermal conductivity [2]. While many compounds with $ZT \approx 1$ show promise, they often suffer from drawbacks such as thermal instability, toxicity, or complex synthesis [3]. Half-Heusler (HH) alloys have emerged as promising TE candidates because they consist of cost-effective and environmentally friendly elements, exhibit thermal stability, and possess high power factors [3, 4]. However, their performance is limited by high lattice thermal conductivity. Representative HH alloys such as TiNiSn, ZrNiSn, and NbFeSb have been widely studied, showing semiconducting behavior and good thermoelectric efficiency [5, 6]. These examples highlight the potential of HH systems but also emphasize the need to explore novel compositions. Among the various candidates, Half-Heusler (HH) alloys composed of cost-effective, lightweight, and environmentally friendly elements exhibit high power factors but are typically limited by their high lattice thermal conductivity [3, 4, 7]. HH compounds adopt the MgAgAs-type structure (space group F-43m) with a partially filled face-centered cubic (fcc) lattice [8], and their semiconducting behavior depends on the valence electron count [9]. Previous studies on HfSnPt and related HH alloys confirm their semiconducting nature and thermodynamic stability [10, 11, 12], but detailed insights into the structural, elastic, vibrational, and thermal transport properties of HfSnPt remain underexplored. To address this gap, we present a first-principles investigation of HfSnPt, focusing on its structural, electronic, mechanical, dynamical, and lattice thermal conductivity properties. The novelty of this work lies in providing a comprehensive assessment of

the stability and transport properties of HfSnPt, with comparisons to well-established HH alloys such as TiNiSn, ZrNiSn, and NbFeSb. This study clarifies its potential as a robust high-temperature thermoelectric material and candidate for structural applications.

2 Computational details

All calculations for the HfSnPt compound were performed using the Vienna Ab initio Simulation Package (VASP) within the framework of density functional theory (DFT). The generalized gradient approximation (GGA) with the Perdew–Burke–Ernzerhof (PBE) functional [13] was used to treat exchange-correlation effects. The projector augmented wave (PAW) method [14] was employed to describe the interactions between valence electrons and ionic cores. To obtain a more accurate description of the electronic structure, especially near the Fermi level, the Heyd-Scuseria-Ernzerhof (HSE06) hybrid functional [15] was applied. This functional incorporates a portion of exact exchange and uses a screening parameter (μ) of 0.1 Å^{-1}. Furthermore, spin–orbit coupling (SOC) effects were included due to the presence of heavy atoms like Hf and Pt, which introduce significant relativistic interactions. a 10×10×10 k-point meshes was used in sampling the Brillouin zone (BZ), with an energy cut-off of 600 eV, which was found to be sufficient for energy convergence. The convergence threshold for self-consistent field iteration was set at 10^{-8} eV. The structural, mechanical, and electronic properties were derived from fully relaxed unit cells of HfSnPt. Phonon and thermodynamic properties were calculated using the finite displacement method implemented in the PHONOPY package [16], with a 2×2×2 supercell and a 4×4×4 Monkhorst-Pack k-point grid. The third-order force constants were computed via PHONO3PY [17], considering all symmetry-inequivalent atomic displacements (255 in total) without imposing cutoff limits. A 24×24×24 q-point mesh was adopted to evaluate the lattice thermal conductivity accurately.

3 Results and discussion

3.1 Structural Properties

The HfSnPt compound adopts the face-centered cubic C1$_b$ structure, belonging to the F43m space group. In this configuration, Hf atoms occupy the 4a Wyckoff position (0, 0, 0), Sn atoms are located at 4b (0.5, 0.5, 0.5), and Pt atoms reside at 4c (0.25, 0.25, 0.25). The atomic arrangement within the unit cell is depicted in Figure 1. The experimental lattice constant for HfSnPt is reported as 6.31 Å [18]. To determine its equilibrium geometry, the total energy was minimized with respect to volume using the PBE exchange-correlation functional. The optimization, performed at the ground state, yielded a lattice constant in close agreement with the experimental value.

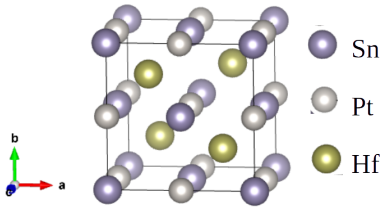

Figure 1: The crystal structure of HfSnPt half-Heusler compound

Table 1: The lattice parameter (a), density (ρ), formation energy (ΔH), cohesive energy (E_{coh}), equilibrium volume (V_0), bulk modulus (B), and its pressure derivative ($B_0^{'}$) of cubic HfSnPt calculated in this study, compared with available experimental values

X	Method	a (Å)	ρ (g/cm^3)	ΔH (eV/atom)	E_{coh} (eV/atom)	V_0 (Å^3)	B (GPa)	$B_0^{'}$
HfSnPt	VASP	6.38	12.59	-0.45	-5.99	259.69	139.25	4.65
HfSnPt	Exp. [18]	6.31	...	...	...	...	...	...

The calculated structural properties for HfSnPt are summarized in Table 1, including lattice constant, density, formation energy, cohesive energy, equilibrium volume (V_0), and bulk modulus. We note that the formation energy of HfSnPt alloy is negative (-0.45 eV), indicating thermodynamic stability. Additionally, its cohesive energy is -5.99 eV/atom, suggesting good structural integrity. The density of HfSnPt is predicted to be approximately 12.59 g/cm^3, which is relatively high compared to several engineering materials. For instance, it surpasses that of Ni_3Al (6.14 g/cm^3) [19], a known lightweight alloy, and is comparable to dense materials such as HfB_2 (11.20 g/cm^3) [20]. This high density might limit its applicability in weight-sensitive applications despite its promising stability.

3.2 Electronic Properties

The electronic band structure and density of states (DOS) calculations reveal that HfSnPt is a semiconductor with an indirect band gap. The valence band maximum (VBM) occurs at the Γ-point, while the conduction band minimum (CBM) is located at the X-point as shown in Figure 2, confirming its indirect band gap nature. Using the GGA functional, the band gap is approximately 0.889 eV, which narrows to 0.664 eV when spin-orbit coupling (SOC) is included. In contrast, the HSE06 hybrid functional predicts a wider gap of about 1.22 eV as shown in Table 2, consistent with the known tendency of GGA to underestimate band gaps [21].

Table 2: Comparison of calculated energy band gaps (in eV) for HfSnPt using various first-principles functionals.

X	Method	GGA	GGA+SOC	HSE06
HfSnPt	VASP	0.889	0.664	1.22

Despite all constituent elements being metallic in their elemental form. The observed semiconducting behavior is attributed to the 18-electron rule and the ordered cubic $C1_b$ structure, which promote a filled valence band and an empty conduction band. While indirect semiconductors like HfSnPt have lower optical absorption than direct-gap materials, they offer longer carrier lifetimes and better thermal stability, making them promising candidates for thermoelectric devices, power electronics, and LEDs.

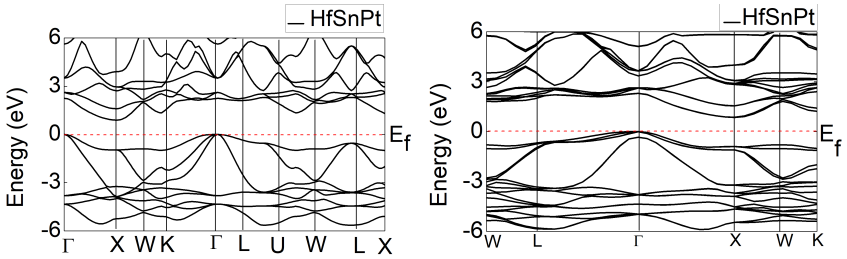

Figure 2: Calculated band structure of the HfSnPt alloy (*left*) using the GGA functional with the VASP code, and band structure (*right*) using GGA+SOC with the CASTEP code.

3.3 Mechanical Properties

The mechanical properties of HfSnPt were assessed using elastic constants derived from first-principles calculations. The elastic constants values (C_{11}, C_{12}, and C_{44}) for HfSnPt shown in Table 3, satisfy the Born criteria [22] as shown in equation 1, confirming the mechanical stability of the cubic phase. Its elastic constants are comparable to those of other robust intermetallics like TiNiSn and ZrNiSn [23].

$$C_{11} - C_{12} > 0; C_{11} + 2C_{12} > 0; C_{44} > 0. \tag{1}$$

Using the Voigt-Reuss-Hill approximation, the bulk modulus (B), shear modulus (G), and Young's modulus (E) for HfSnPt in Table 4 indicate high rigidity and low compressibility. These values are consistent with trends observed in solid solutions like $(Ti_{1-x}M_x)_2AlC$ [24], where heavier atoms increase bond strength and stiffness.

Table 3: Mechanical parameters of cubic HfSnPt, where C_{ij} (GPa) are the independent elastic coefficients, ζ is the Kleinman parameter, and T_m (K) is the melting temperature.

X	Method	C_{11}	C_{12}	C_{44}	$C_{12} - C_{44}$	ζ	T_m (K)
HfSnPt	VASP	214.99	104.05	75.18	28.85	0.81	1918

The Pugh's ratio (B_H/G_H) exceeds the critical value of 1.75, and Poisson's ratio is above 0.26, indicating a ductile behavior in HfSnPt alloy. Additionally, the Cauchy pressure is positive, indicating metallic bonding and supporting the material's ductile behavior similar to trends in other ternary borides like M_2GaB (M = Sc, V, Nb, Ta) [25]. The Kleinman parameter (ζ) for HfSnPt is calculated to be 0.81, suggesting that bond-stretching dominates its

Table 4: Calculated bulk modulus (B_H), shear modulus (G_H), Young's modulus (E_H), B_H/G_H ratio, Poisson's ratio (ν), Zener anisotropy factor (A_μ), and Vickers hardness (H_V, Chen and Tian models) of HfSnPt. All moduli are in GPa.

X	Method	B_H (GPa)	G_H (GPa)	E_H (GPa)	E_H/G_H	ν	A_μ	H_V (GPa)
HfSnPt	VASP	141.03	66.57	172.55	2.11	0.29	1.36	6.73 (7.04)

deformation mechanism, consistent with behavior seen in high-valent borides [26]. Hardness estimates using both the Chen-Niu [27] and Tian [28] models place HfSnPt in the moderately hard category, with Vickers hardness values between 6.73 and 7.04 GPa depending on the model used. These results are consistent with comparable intermetallics such as ZnN and NiN [29]. The melting temperature, derived from the magnitude of C_{11} as shown in equation 2 [30], is predicted to be higher than that of Ni_3Al (1691 K) [19], implying strong thermal resistance and stability suitable for extreme environments, including turbine engines.

$$Tm = [553K + (5.9\text{K/GPa})C_{11}] + 300\text{K}. \tag{2}$$

Finally, the Zener anisotropy factor (A_μ) of approximately 1.36 indicates slight elastic anisotropy significantly lower than layered materials like MAX phases [31], pointing to a more uniform mechanical response, which is favorable for structural applications.

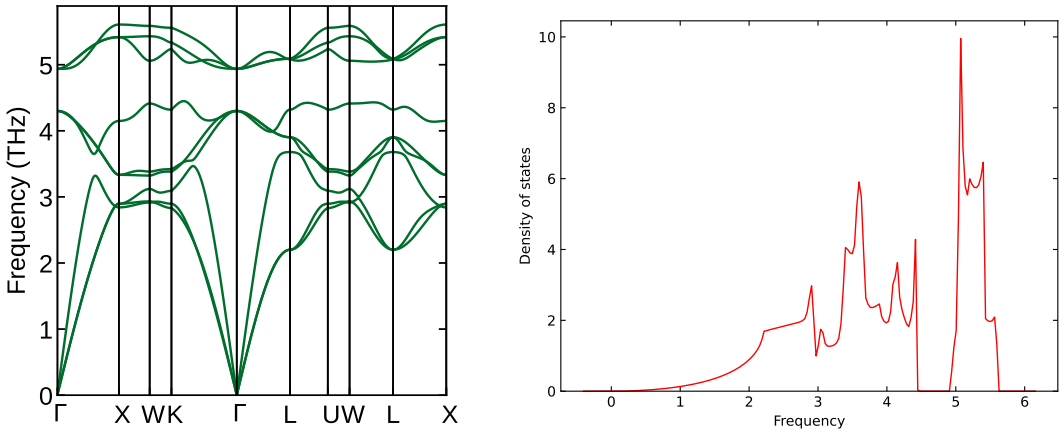

Figure 3: (*left*) Phonon dispersion curves of the HfSnPt. (*right*) phonon total density of states of the HfSnPt.

3.4 Phonon Properties

Phonon calculations were carried out for HfSnPt half-Heusler alloy, using the finite displacement method [32], which is essential for evaluating its vibrational and thermodynamic behavior. The resulting phonon dispersion curves (PDC) and phonon density of states (PDOS) offer insight into the dynamic stability and thermal characteristics of the compound [16]. As shown in Figure 3, the phonon spectrum of HfSnPt displays no imaginary frequencies along high-symmetry paths of the Brillouin zone, confirming its dynamical stability at 0 K [16]. The absence of soft modes suggests that the structure is resistant to spontaneous lattice distortions or phase transitions. Moreover, the lowest vibrational modes originate from the acoustic branches near the Γ-point, a typical signature of dynamically stable intermetallics. The stable phonon profile supports the compound's predicted mechanical robustness and thermal reliability, indicating its potential for high-temperature structural applications.

3.5 Lattice thermal conductivity

The lattice thermal conductivity (k_l) plays a vital role in determining a material's performance in both heat management and thermoelectric applications [33]. For HfSnPt, our first-principles calculations reveal a room-temperature value of approximately 16.4 W/m·K as shown in Figure 4, which is higher than that of traditional half-Heusler thermoelectrics like HfNiSn (14.6 W/m·K) [34]. This suggests that the presence of Pt strengthens the lattice, enhancing phonon transport. As temperature increases, k_l for HfSnPt decreases due to phonon-phonon Umklapp

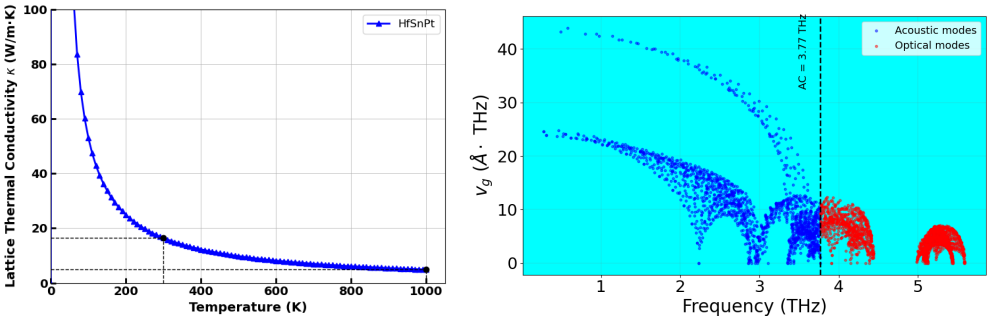

Figure 4: Calculated lattice thermal conductivity (*left*) and phonon group velocity (*right*) of HfSnPt.

scattering, dropping to about 4.9 W/m·K at 1000 K. The close values of k_l along the $x-$, $y-$, and z-directions confirm isotropic thermal transport, consistent with the symmetry of the cubic structure. These findings indicate that HfSnPt, with its high thermal conductivity and isotropic behavior, could be well-suited for thermal dissipation in high-power or microelectronic devices, although its high k_l may limit its effectiveness in thermoelectric energy conversion.

4 Conclusion

In this study, the structural, electronic, mechanical, phonon, and thermal properties of HfSnPt were investigated using first-principles calculations within the GGA framework implemented in the VASP code. The negative formation and cohesive energies confirm that HfSnPt is thermodynamically and structurally stable, indicating feasibility for experimental synthesis. Electronic band structure analysis revealed that HfSnPt is an indirect semiconductor. The SOC effect was found to slightly reduce the band gap, while calculations using the HSE06 hybrid functional predicted a broader gap, aligning with previous findings that hybrid functionals offer improved accuracy. Phonon dispersion results showed no imaginary frequencies, confirming the dynamical stability of HfSnPt. The compound also demonstrated mechanical stability and ductility, supported by a B_H/G_H ratio greater than 1.75 and a melting point exceeding 1900 K. At room temperature, the lattice thermal conductivity was calculated to be 16.4 W/m·K, decreasing with temperature due to enhanced Umklapp scattering, reaching approximately 4.9 W/m·K at 1000 K. This thermal behavior, along with its structural resilience, positions HfSnPt as a promising candidate for high-temperature structural and thermoelectric applications, particularly in environments requiring thermal stability and long service life, such as aerospace systems.

References

[1] G. J. Snyder and E. S. Toberer, "Complex thermoelectric materials," *Nature materials*, vol. 7, no. 2, pp. 105–114, 2008.

[2] A. A. Khan, I. Khan, I. Ahmad, and Z. Ali, "Thermoelectric studies of IV–VI semiconductors for renewable energy resources," *Materials Science in Semiconductor Processing*, vol. 48, pp. 85–94, 2016.

[3] Q. Ren, C. Fu, Q. Qiu, S. Dai, Z. Liu, T. Masuda, S. Asai, M. Hagihala, S. Lee, S. Torri *et al.*, "Establishing the carrier scattering phase diagram for ZrNiSn-based half-Heusler thermoelectric materials," *Nature communications*, vol. 11, no. 1, p. 3142, 2020.

[4] S. Sakurada and N. Shutoh, "Effect of Ti substitution on the thermoelectric properties of (Zr, Hf) NiSn half-Heusler compounds," *Applied Physics Letters*, vol. 86, no. 8, 2005.

[5] C. Uher, J. Yang, S. Hu, D. Morelli, and G. Meisner, "Transport properties of pure and doped MNiSn (M= Zr, Hf)," *Physical Review B*, vol. 59, no. 13, p. 8615, 1999.

[6] H. Joshi, D. Rai, A. Laref, and R. Thapa, "Electronic, and thermoelectric properties of half-Heusler compounds MCoSb (M= Ti, Zr, Hf): a first principles study," *Materials Research Express*, vol. 6, no. 6, p. 066307, 2019.

[7] F. Aliev, V. Kozyrkov, V. Moshchalkov, R. Scolozdra, and K. Durczewski, "Narrow band in the intermetallic compounds MNiSn (M= Ti, Zr, Hf)," *Zeitschrift für Physik B Condensed Matter*, vol. 80, pp. 353–357, 1990.

[8] W. Jeitschko, "Transition metal stannides with MgAgAs and $MnCu_2Al$ type structure," *Metallurgical Transactions*, vol. 1, pp. 3159–3162, 1970.

[9] Y. Kimura and Y.-W. Chai, "Ordered structures and thermoelectric properties of MNiSn (M= Ti, Zr, Hf)-based half-Heusler compounds affected by close relationship with heusler compounds," *Jom*, vol. 67, pp. 233–245, 2015.

[10] Y. G. Yu, X. Zhang, and A. Zunger, "Natural off-stoichiometry causes carrier doping in half-Heusler filled tetrahedral structures," *Physical Review B*, vol. 95, no. 8, p. 085201, 2017.
[11] S. E. Gulebaglan and E. K. Dogan, "A comparison study of the structural electronic, elastic and lattice dynamic properties of ZrInAu and ZrSnPt," *Zeitschrift für Naturforschung A*, vol. 76, no. 6, pp. 559–567, 2021.
[12] A. El Yousfi, H. Bouda, A. El Hachimi, M. Arshad, A. El Kenz, and A. Benyoussef, "First-principles calculations to investigate optical and electrical properties of the half-Heusler materials TiXSn (X= Ni, Pt)," *Molecular Simulation*, vol. 49, no. 8, pp. 778–791, 2023.
[13] J. P. Perdew, K. Burke, and M. Ernzerhof, "Generalized gradient approximation made simple," *Physical review letters*, vol. 77, no. 18, p. 3865, 1996.
[14] G. Kresse and D. Joubert, "From ultrasoft pseudopotentials to the projector augmented-wave method," *Physical Review B*, vol. 59, no. 3, p. 1758, 1999.
[15] L. Schimka, J. Harl, and G. Kresse, "Improved hybrid functional for solids: The HSEsol functional," *The Journal of Chemical Physics*, vol. 134, no. 2, 2011.
[16] A. Togo and I. Tanaka, "First principles phonon calculations in materials science," *Scr. Mater.*, vol. 108, pp. 1–5, Nov 2015.
[17] A. Togo, "First-principles phonon calculations with phonopy and phono3py," *Journal of the Physical Society of Japan*, vol. 92, no. 1, p. 012001, 2023.
[18] A. Dwight, "Alloying behavior of zirconium, hafnium and the actinides in several series of isostructural compounds," *Journal of the Less Common Metals*, vol. 34, no. 2, pp. 279–284, 1974.
[19] A. Popoola and J. Lowther, "Computational study of platinum group superalloys," *International Journal of Modern Physics B*, vol. 28, no. 09, p. 1450066, 2014.
[20] W. G. Fahrenholtz, G. E. Hilmas, I. G. Talmy, and J. A. Zaykoski, "Refractory diborides of zirconium and hafnium," *Journal of the American Ceramic Society*, vol. 90, no. 5, pp. 1347–1364, 2007.
[21] J. P. Perdew and M. Levy, "Physical content of the exact kohn-sham orbital energies: band gaps and derivative discontinuities," *Physical Review Letters*, vol. 51, no. 20, p. 1884, 1983.
[22] F. Mouhat and F.-X. Coudert, "Necessary and sufficient elastic stability conditions in various crystal systems," *Physical Review B*, vol. 90, no. 22, p. 224104, 2014.
[23] A. Musari, B. Adetunji, P. Adebambo, and G. Adebayo, "Lattice dynamics and thermodynamic investigation of MNiSn (M= Hf, Ti and Zr) half-Heusler compounds: Density functional theory approach," *Materials Today Communications*, vol. 22, p. 100671, 2020.
[24] M. Ali and S. Naqib, "Recently synthesized $(Ti_{1-x}Mo_x)_2AlC$ solid solutions: deciphering the structural, electronic, mechanical and thermodynamic properties via ab initio simulations," *RSC advances*, vol. 10, no. 52, pp. 31 535–31 546, 2020.
[25] M. Rana, S. Islam, K. Hoque, G. Biswas, M. Hossain, S. Naqib, and M. A. Ali, "DFT prediction of the stability and physical properties of M_2GaB (M= Sc, V, Nb, Ta)," *Journal of Materials Research and Technology*, vol. 24, pp. 7795–7815, 2023.
[26] M. Ali, M. Hossain, M. Uddin, M. Hossain, A. Islam, and S. Naqib, "Physical properties of new max phase borides M_2SB (M= Zr, Hf and Nb) in comparison with conventional MAX phase carbides M_2SC (M= Zr, Hf and Nb): Comprehensive insights," *Journal of Materials Research and Technology*, vol. 11, pp. 1000–1018, 2021.
[27] X.-Q. Chen, H. Niu, D. Li, and Y. Li, "Modeling hardness of polycrystalline materials and bulk metallic glasses," *Intermetallics*, vol. 19, no. 9, pp. 1275–1281, 2011.
[28] Y. Tian, B. Xu, and Z. Zhao, "Microscopic theory of hardness and design of novel superhard crystals," *International Journal of Refractory Metals and Hard Materials*, vol. 33, pp. 93–106, 2012.
[29] B. Mnisi, E. Benecha, and M. Tibane, "Density functional theory studies of structural, electronic and optical properties of cubic 3d-transition metal nitrides," *Intermetallics*, vol. 137, p. 107272, 2021.
[30] M. Fine, L. Brown, and H. Marcus, "Elastic constants versus melting temperature in metals," *Scripta metallurgica*, vol. 18, no. 9, pp. 951–956, 1984.
[31] M. W. Qureshi, M. Ali, and X. Ma, "Screen the thermomechanical and optical properties of the new ductile 314 MAX phase boride Zr_3CdB_4: A DFT insight," *Journal of Alloys and Compounds*, vol. 877, p. 160248, 2021.
[32] D. Alfè, "Phon: A program to calculate phonons using the small displacement method," *Computer Physics Communications*, vol. 180, no. 12, pp. 2622–2633, 2009.
[33] D. M. Rowe, *CRC handbook of thermoelectrics*. CRC press, 1995.
[34] S. N. Eliassen, A. Katre, G. K. Madsen, C. Persson, O. M. Løvvik, and K. Berland, "Lattice thermal conductivity of $Ti_xZr_yHf_{1-x-y}NiSn$ half-Heusler alloys calculated from first principles: Key role of nature of phonon modes," *Physical Review B*, vol. 95, no. 4, p. 045202, 2017.

Mechanical and electronic properties of $LiTi_2(PO_4)_3$ solid state electrolyte material

Gift Matleke, Donald Hlungwani, Cliffton Masedi, Phuti Ngoepe and Raesibe Sylvia Ledwaba

Materials Modelling Centre, University of Limpopo, Private Bag x1106 Sovenga, 0727, Polokwane, South Africa

E-mail: molatelomatleke22@gmail.com

Abstract. $LiTi_2(PO_4)_3$ (LTP) is economically viable, and it is receiving significant research attention as a potential solid-state electrolyte for lithium-ion batteries (LIBs). This is due to its NASICON-type structure built from corner-sharing octahedral (LiO_6, TiO_6) and tetrahedral (PO_4) to form a chemically stable structural framework that facilitates Li^+ transport. Unfortunately, the ionic conductivity ($< 10^{-6}$ S/cm) of lithium ions was found to be insufficient for practical use in LIBs. In this study, the electronic, structural and mechanical properties of LTP are studied for model validation, modelling parameter accuracy and to form a foundation for the partial substitution of oxygen with sulphur. The Vienna Ab Initio Simulation Package (VASP) was used to investigate the ground-state structure of LTP. The electronic inactivity of the material was confirmed by band structure and density of states (DOS) calculations through a band gap of ~2.49 eV comparable to the literature value of 2.38 eV. The Bulk, Young's and shear modulus were found to be 101.01 GPa, 151.78 GPa and 60.74 GPa, respectively. The higher shear moduli (> 8 GPa) indicates that the material can resist the formation of the dendrites against Li metal during operation. This lays a solid foundation for future analysis of the impact of sulphur-doping on the mechanical and electronic properties of LTP to yield insights on improvement of its performance and safety.

1 Introduction

The rapidly growing demand of energy storage systems has led to the eruption of studies focusing on the development of the most productive and safe secondary batteries (lithium-ion batteries) [1]. In 1990, Sony engaged in the commercialisation of lithium-ion batteries for the evolution of the energy storage industry [2]. These secondary batteries used conventional organic liquid electrolytes (LEs), which exhibits low thermal stability and high flammability, leading to thermal runaway and fatal explosions during operation [1, 3]. Consequently, solid electrolytes (SEs) are currently potential substitutes for LEs owing to alleviated hazardous gas production, safety concerns, and their high energy density [3]. The SEs exhibit high mechanical strength, which prevents formation of dendrites' and consequently limiting cyclic performance [4]. The predicted shear modulus for an effective solid electrolyte to prevent dendrite formation, as reported by Monroe and Newman, must be twice as high as that of lithium metal. The standard shear modulus of lithium metal is 3.4 GPa, so the shear modulus of the solid electrolyte must be more than 6.8 GPa [5]. Solid electrolytes can be classified into three categories, namely inorganic solid electrolytes (ISE), polymer solid electrolytes (PSE) and composite solid electrolytes (CSE), with ISEs in the forefront due their high the ionic conductivities of $< 10^{-2}$ S•cm^{-1} [4, 1]. The sodium superionic conductor (NASICON)-type solid electrolytes $LiTi_2(PO_4)_3$ (LTP) have been mostly explored and are regarded as the potential future generation of solid electrolytes due to their compatibility with lithium metal electrodes and structural stability [6]. NASICON-type solid electrolytes adhere to a chemical formula $AM_2(PO_4)_3$ (A = Li, Na; M = Ti, Ge, Zr) and possess a 3D framework comprised of a corner-sharing PO_4 tetrahedral and TiO_6 octahedral, creating channels on the c-axis to facilitate the Li-ion mobility [7]. Its 3D framework portrays a high stability with the Ti^{4+} /Ti^{3+} redox couple to accommodate Li^+ extraction and insertion,

which contributes to high ion mobility, and long cycle life [8]. Goodenough and Park have reported that rechargeable batteries with the 30 000 charge/discharge cycle with a decent rate which is equivalent to a 10-year operation life have been obtained. This has mitigated the life cycle issue in the high-performance batteries production industry. Although ISEs demonstrate a very reasonable high ionic conductivity (~10^{-4} S/cm), the performance of LTP remain inferior to that of ISEs and LEs. This lower ionic conductivity hampers its adoption in commercial battery industry. LTP exhibits the total conductivity between 10^{-7} and 10^{-10} units and an activation energy of 0.36 eV [9, 6]. An ideal solid electrolyte must exhibit a wide band gap to inhibit the electronic conduction, to reduce hazardous concerns, and promotes lithium-ion conduction. In addition, the brittle nature of oxides makes it susceptible to mechanical degradation, such as cracking, during electrochemical cycling. These fractures increase interfacial resistance and disrupt lithium-ion pathways thus low ionic conductivity, accelerating the fade over time. Ahmed et al have investigated the effect of sulphur in LATP and concluded that partial substitution of oxygen with sulphur can enhance the ionic conductivity in the material in prospects of less electronegativity and the larger ionic radii of sulphur compared to the oxygen and this will consequently reduce the electrostatic interactions between Li and S and shortened Li Pathways [11]. In this study, the Vienna Ab initio simulation package (VASP) [10] has been utilized to study structural and electronic properties of LTP are investigated to validate the viable application of LTP as a solid electrolyte.

2 Computational method

Spin-polarized DFT calculations were executed using VASP code [10] with the projected augmented wave (PAW) [12] pseudopotentials and the generalised gradient - Perdew, Burke, and Ernzerhof for solid system (GGEPBEsol) exchange correction functional. A Hubbard U correction of 4 eV was applied to Ti. A plane-wave cutoff energy of 650 eV, and 5 X 5 X 5 γ- centred K-point mesh were used, with an electronic convergence criterion of 10^{-6} eV.

3 Results and Discussion

3.1 Thermodynamic and structural properties

The optimized lattice parameters have been meticulously computed in the VASP code using the GGA-PBEsol. Table 1 below outlines the calculated and experimental values of LTP. The crystal structure of the LTP as reported by Lou et al. [12], is rhombohedral with the space group of R-3c. The calculated lattice parameters are a = b = 8.550 Å and c = 20.770 Å which are comparable with the theoretical values. This validates that our results are accurate. Furthermore, the predicted value of energy of formation was found to be less than zero (exothermic reaction), indicating that LTP is thermodynamically stable. This signifies that the LTP will not chemically react with the electrodes during the charge/discharges process.

		Calculated	Experimental [13]	|Δ|(%)
Lattice Parameters (Å)	a=b	8.550	8.480	0.82
	c	20.770	20.684	0.41
Angles (°)	α = β	90.0	90.0	0.00
	γ	120.0	120.0	0.00
Volume	V (Å^3)	1321.6	1288.0	0.00
Heats of formation	ΔH_f (kJ/mol)	-4646.3	-	-

Table 1: Structural properties and energy of formation of $LiTi_2(PO_4)_3$

The LTP crystal structure has two different lithium positions, named NI and NII, where the TiO_6 octahedral are aligned along the C-axis with NI sites between two octahedral (sandwich shape). The Li^+ ions preferably occupy the NI which lower energy bah4rsssssrriers than the NII [13].

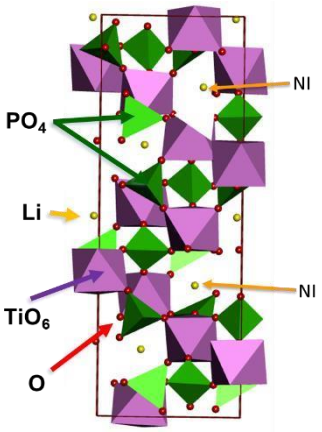

Figure 1: Structural representation of $LiTi_2(PO_4)_3$.

3.2 Electronic properties

In this section, observation will be focused on the density of states (DOS) and band structures. This study uses the DOS to validate the electronic properties and the band gap of the LTP. The Partial Density of State (PDOS) shows that titanium has the highest contribution to the overall DOS. Furthermore, Ti exhibits the antiferromagnetic property in Figure 2 (b), signifying that the material's low electronic conductivity is due to the Ti element [14]. Antiferromagnetic property arise from the $3d^1$ electron which is self-trapped in the Ti^{3+} ions forming a small polaron which results in a very low electronic conductivity due to its restricted mobility. In consideration of the transference number $t+=\frac{\sigma_i}{\sigma_i+\sigma_e}$ a very low σ_e will consequently reduce the t+ to unity. The $t_+\sim1$ concludes that the only current passing through the electrolyte is carried by Li+ ions [15]. DOS shows that the Fermi energy (E_f) lies in the low DOS region, and the broad peak in the valence band shows the vigorous orbital hybridization. As such, this suggest that the LTP exhibits a good stability. The total density of states (TDOS) displayed in Figure 2 (b), shows that the band gap of LTP is ~2.49 eV with a percentage difference of < 5% compared to the experimental value reported by Chen et al [1]. The band structure describes the energy levels the electrons can occupy in LTP, which is efficient for giving a good account of its electronic structure. The energy level is divided and depicted by bands as denoted in Figure 2 (c). The valence band is represented by all the states below the fermi level shown in Figure 2 (c) and the conduction band is given by all the states above the fermi level. The DOS and band structure in Figure 2 indicates that LTP is a semiconductor with an indirect band gap of ~2.49 eV, which is essential for preventing short-circuiting during operation.

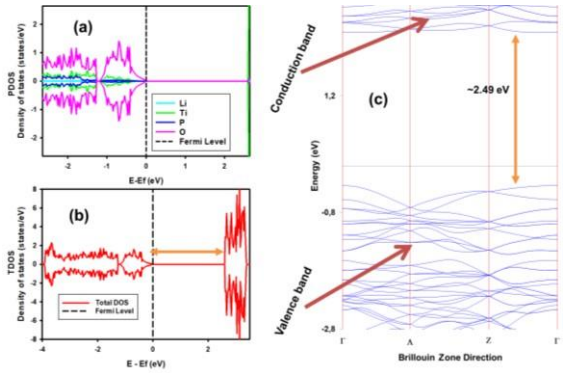

Figure 2: The analysis of a) PDOS, b) TDOS c) band structure $LiTi_2(PO_4)_3$.

3.3 Mechanical properties

An understanding of elastic constants gives a full overview of the mechanical stability and the elastic properties of solids. Mechanical stability of the material is usually given by the elastic matrix (commonly called the stiffness matrix) with size of 6X6. This comprises of 21 independent components which consist of several demarcations. The rhombohedral crystal has seven independent elastic constants C_{11}, C_{12}, C_{13}, C_{14}, C_{33}, C_{44}, and C_{66} which follow the Born mechanical stability conditions. This method was discovered by Born, and for a rhombohedral crystal structure to be considered mechanical stable, the following conditions should be met: (1) the matrix C is defined as positive, (2) all eigen-values of C are positive, (3) all the leading principal minors of C, (4) an arbitrary set of minors of C are all positive:

$$C_{11} > |C_{12}|;\ C_{44} > 0 \quad (1)$$

$$C13^2 < \frac{1}{2} C\,33(C11 + C12) \quad (2)$$

$$C14^2 < \frac{1}{2} C44(C11 - C12) = C44C66 \quad (3)$$

The voigt notation matrix is:

$$\begin{matrix} C11 & C12 & C13 & C14 & 0 & 0 \\ 0 & C11 & C13 & -14 & 0 & 0 \\ 0 & 0 & C33 & 0 & 0 & 0 \\ 0 & 0 & 0 & C44 & 0 & 0 \\ 0 & 0 & 0 & 0 & C44 & C14 \\ 0 & 0 & 0 & 0 & 0 & C66 \end{matrix} \quad (4)$$

The Moduli of the rhombohedral LTP can be obtained from the elastic constants in the following:

$$E = \frac{(C11-C12)(C11C33-C13^2)-C14^2C33}{C11C33-C13^2} \quad (5)$$

$$G = C_{44} \quad (6)$$

$$K = \frac{(C11+C12)C33-2C13^2}{C11+C12+2C33-4C13} \quad (7)$$

$$v = \frac{3B-E}{6B} \quad (8)$$

The shear (G), Young`s (E) and bulk (B) moduli were calculated based on the elastic constants using VoigtReuss-Hill approximation method. The Young's modulus determines the stiffness of the material. Shear modulus describes the materials ability to deform under shear stress, whilst the bulk modulus displays the resistance of the material to a volume change under pressure [15]. The shear modulus of an ideal solid electrolyte must be greater than 6.8 GPa for dendrite suppression [5], Young's modulus should be ranging from 10 to 50 GPa to have a well balance interface contact and mechanical strength [16], whilst bulk modulus has to be as high as possible to prevent porosity-induced degradation [5]. The large Young's modulus, signifies that the LTP can break due to the volume expansion during the charge/discharge process hence the compatibility of interface contact is compromised. The calculated Bulk, Young's and shear moduli were found to be 101.01 GPa, 151.78 GPa and 60.74 GPa, respectively. These are in good agreement with the experimental values with < 6%. Moreover, the higher shear moduli (> 8 GPa) indicate that the material can resist the formation of the detrimental dendrites against Li metal during operation.

Cij	C_{11}	C_{12}	C_{13}	C_{14}	C_{33}	C_{44}	C_{66}	v	K	C'	A
LTP	221.64	75.64	46.3	-10.2	192.2	67.38	69.29	0.22	1.49	73	0.923

Table 2: Elastic properties (GPa), Poisson's ratio (v) and Pugh's ratio (K) of $LiTi_2(PO_4)$.

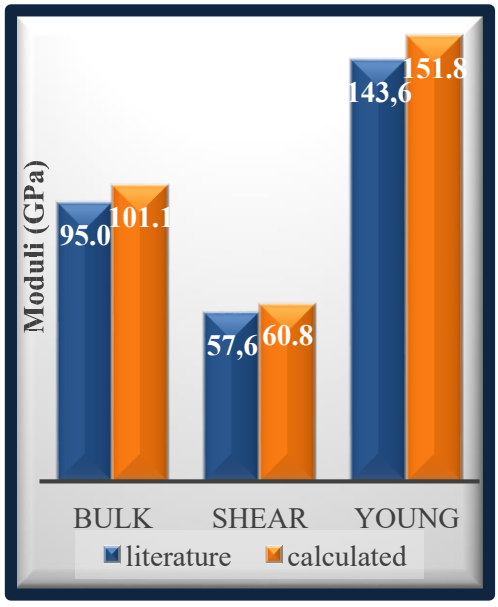

Figure 3: The moduli value of $LiTi_2(PO_4)_3$ [17].

4. Conclusion

This study used the computational approach to investigate the electronic, mechanical, structural and thermodynamic properties of $LiTi_2(PO_4)_3$, regarding its potential for a successful implementation in battery storage industry as a solid electrolyte. The electrical properties display a band gap of ~ 2.49 eV, which is imperative for application as SSE in LIBs. This will resist electronic conduction between electrodes through the electrolyte. Then, only focus on the ion transportation as per transference number. Its antiferromagnetic nature can be improved by cation doping. Even though the Born elastic stability condition is satisfied, the LTP is brittle, which justifies its fragmentation and cracking during the charge/discharge process due to the volume change. This can be mitigated by the partial oxygen substitution by the sulphur. This is motivated by the contribution of sulphur in the lithium sulphur batteries. The shear modulus justifies the ability of the material to prevent the dendrite formation. The structural and the thermodynamic properties reported justify the stability of LTP. The study shows the good attributes of LTP as the SE.

5. Acknowledgment

The authors would like to acknowledge the Material Modelling Centre (MMC) at the University of Limpopo and the Centre for High-Performance Computing (CHPC) under the National Integrated Cyber Infrastructure System (NICIS) for high-performance computing facilities.

References

[1] D. Karabelli, K.P. Birke, and M. Weeber, "A performance and cost overview of selected solid-state electrolytes: race between polymer electrolytes and inorganic sulfide electrolytes," *MDPI,* vol. 7, pp. 1818, 2021. https://doi.org/10.3390/batteries7010018

[2] G.E. Blomgren, "The development and future of lithium-ion batteries," *J. Electrochem. Soc.,* vol. 164, pp. A5019-A5025, 2017. https:// 10.1149/2.0251701jes

[3] J. Huang, K. Wu, G. Xu, M. Wu, S. Dou, and C. Wu, "Rprogress and strategic perspectives of inorganic solid electrolytes: fundamentals, modifications, and applications in sodium metal batteries," *Chem. Soc. Rev.,* vol. 52, pp. 4933-4995, 2023. https://doi.org/10.1039/D2CS01029A

[4] T. Ye, L. Li, and Y. Zhang, "Recent progress in solid electrolytes for energy storage devices," *Adv. Funct. Mater.,* vol. 30, pp. 2000077-2000077, 2020. https://doi.org/10.1002/adfm.202000077

[5] Y. Ren, C. Sun, J. Liu, G. Cai, X. Tan, and C. Zhang, "Effect of the mechanical strength on the ion transport in a transition metal lithium halide electrolyte: first-principle calculations," *Mater. Today Commun.,* vol. 33, pp. 104570-104570, 2022. https://doi.org/10.1016/j.mtcomm.2022.104570

[6] J. Janek & W.G. Zeier, "Challenges in speeding up solid-state battery development," Nature Energy, vol. 8, pp. 230-230, 2023. https://doi.org/10.1038/s41560-023-01208-9

[7] L. Maake, B. Shibiri, P. Ngoepe, and R. Ledwaba, "Analysing phase change of LiTi2(PO4)3 solid electrolyte material due to temperature variation," *MATEC Web of Conferences,* vol. 406, pp. 0600606006, 2024. https://doi.org/10.1051/matecconf/202440606006

[8] O. Zoubir, A. Lallaoui, M. Oubla, A.Y. Tesio, A. Caballero, and Z. Edfouf, "In-situ one-step hydrothermal synthesis of liti2(po4)3@rgo anode for high performance lithium-ion batteries," *Multi. Dig. Pub. Inst.,* vol. 18, pp. 1329-1329, 2025. https://doi.org/10.3390/ma18061329

[9] S. Yu, H. Tempel, R. Schierholz, O. Aslanbas, X. Gao, J. Mertens, G.J.L de Haart, H. Kungl, and R.A. Eichel, "LiTi2(PO4)3/C Anode material with a spindle-like morphology for batteries with high-rate capability and improved cycle life," *Chemistry A Europe Journal,* vol. 3, pp. 1157-1169, 2016. https://doi.org/10.1002/celc.201600125

[10] R. Sukumar, P. Iyngaran, and N. Kuganathan, "Structural and defect properties of LiTi2(PO4)3," *Biointerface Research in Applied Chemistry,* vol. 11, pp. 13268-13275, 2021.

[11] D.A. Ahmed, A. Kızılaslan, M. Çelik, G.B. Vonbun-Feldbauer, and T. Cetinkaya, "Sulfur-doped Li1.3Al0.3Ti1.7(PO4)3 as a solid electrolyte for all-solid-state batteries: First-principles calculations," *Electrochimica Acta,* vol. 46, pp. 142872-142872, 2023. https://doi.org/10.1016/j.electacta.2023.142872

[12] J. Hafner and G. Kresse, "The Vienna ab-initio Simulation Program (VASP): an efficient and versatile tool for studying the structural, dynamic, and electronic properties of materials," *Prop. Com. Inorg. Sol.,* Vols. 8-10, pp. A1040-A1040, 1997. https://10.1007/978-1-4615-5943-6_10

[13] V. Heine, "The pseudopotential concept," *solid state sciences,* vol. 24, pp. 1-36, 1970. https://doi.org/10.1016/S0081-1947(08)60069-7

[14] Y. Lou, X. Jiang,Y. Lu, L. Liu, X. Li, Z. Wang, L. Han, Z. Lou, and A. Lu, "Enhancement of electrical properties of LiTi2(PO4)3 ceramics via trivalent cation doping and microstructure regulation strategies," *Solid State ionics,* vol. 390, pp. 4450-4450, 2023. https://doi.org/10.1016/j.ssi.2022.116111

[15] T. Luo, X. Liu, C. Wen, T. Ning, X. Jiang, and A. Lu, "Solid state ion doping and crystal structure engineering for enhanced ionic conductivity in LiTi2(PO4)3 electrolytes," *Applied Physics A,* vol. 129, pp. 518-518, 2023. https://doi.org/10.1007/s00339-023-06796-7

[16] K. Arbi, M. Tabellout, and J. Sanz, "NMR and electric impedance study of lithium mobility in fast ion conductors LiTi2 − xZrx(PO4)3 ($0 \leq x \leq 2$)," *Solid State Ionics,* vol. 180, pp. 1613-1619, 2010. https://doi.org/10.1016/j.ssi.2009.11.010

[17] I.G. Austin and N.F Mott, "Polarons in crystalline and non-crystalline materials," Advances in physics, vol. 18, pp. 41-102, 1969. https://doi.org.10.1080/00018736900101267

[18] M. Mphahlele, M. Masedi, K. Malatji, P. Ngoepe, and R. Ledwaba., "The role of Ru doping on the electronic, mechanical and vibrational properties of Li2MnO3 cathode material," *in the proceedings of the MATEC Web of Conferences*, pp. 06015-06015, 2024. https://doi.org/10.1051/matecconf/202440606015

[19] L. Porz, T. Swamy, B.W. Sheldon, D. Rettenwander, T. Fromling, H.L. Thaman, S. Berendts, R. Uecker, W.C. Carter, and Y.M. Chiang, "Mechanism of lithium metal penetration through inorganic solid electrolytes," *Advanced Energy Materials,* vol. 7, pp. 1701003-1701003, 2017. https://doi.org/10.1002/aenm.201701003

[20] Z. Deng, Z. Wang, I.H. Chu, J. Lou, and S.P. Ong, "Elastic properties of alkali superionic conductor electrolytes from first principles calculations," *Journal of the Electrochemical. Society.,* vol. 163, pp. A67A74, 2016. 10.1149/2.0061602jes

[21] J.B. Goodenough, & K.S. Park, "The li-ion rechargeable battery: a perspective.," *Journal of the American Chemical Society,* vol. 135, pp. 1167-1176, 2013. https://doi.org/10.1021/ja3091438

[22] G. Sun, J. Kurti, P. Rajczy, M. Kertesz, J. Hafner, & G. Kresse, "Performance of the vienna ab initio simulation package (VASP) in chemical applications," *Journal of Molecular Structure,* vol. 624, pp. 3745, 2003. https://doi.org/10.1016/S0166-1280(02)00733-9

[23] J. Wolfenstine, J.L Allen, J. Sakamoto, D.J. Siegel, & H. Choe, "Mechanical behavior of Li-ionconducting crystalline oxide-based solid electrolytes: a brief review," *Nature,* vol. 24, p. 1271–1276, 2018. onics (2018) 24:1271–1276 https://doi.org/10.1007/s11581-017-2314-4

This page intentionally left blank.

Cooperative Energy Transfer and Upconversion Luminescence of $Sr_5(PO_4)_3OH:Eu^{3+}$, Yb^{3+} phosphor powders

P.P. Mokoena[1*], B. M. Jaffar[2], H.C. Swart[3], O.M. Ntwaeaborwa[1]

[1]Department of Physics and Earth Sciences, Sol Plaatje University, Kimberley, South Africa
[2]School of Physics, University of the Witwatersrand, Private Bag 3, Johannesburg, South Africa
[3]Department of Physics, Box 339, University of the Free State, Bloemfontein 9300, South Africa

E-mail address: puseletso.mokoena@spu.ac.za

Abstract. In this study, strontium hydroxyapatite ($Sr_5(PO_4)_3OH$) doped with europium (Eu^{3+}) and ytterbium (Yb^{3+}) were successfully synthesized by combustion method. The phosphors' structural, morphological, and optical features were investigated using X-ray diffraction (XRD), high resolution scanning electron microscopy (HRSEM), energy dispersive X-ray spectroscopy (EDS), and photoluminescence (PL) spectroscopy. XRD results verified crystallisation of the pure hexagonal phase of strontium hydroxyapatite ($Sr_5(PO_4)_3OH$), while HRSEM revealed a network of particles with irregular morphologies, with little brilliant particles on the surfaces of bigger particles. The EDS analysis confirms that bright particles were dominated by rare earth elements, while darker particles are primarily composed of the host material. Upon UV excitation, prominent orange emission and minor red emission peaks corresponding to Eu^{3+} transitions were observed. The red emission was enhanced significantly upon co-doping with Yb^{3+}, which facilitated non-radiative energy transmission from Ytterbium (Yb^{3+}) to Europium (Eu^{3+}). The enhanced red upconversion luminescence of $Sr_5(PO_4)_3OH:Eu^{3+},Yb^{3+}$ phosphors show a promising potential for applications in photodynamic therapy (PDT).

1. Introduction

The multifunctional inorganic materials have attracted considerable attention due to their wide-ranging prospective uses in the biomedical field, such as drug delivery, sensing, and bioimaging [1]. Inorganic host lattices such as phosphates materials have drawn a significant attention as a host over the years due to their diverse properties, including electric, magnetic, ferroelectric, catalytic, and optical characteristics, along with their strong resistance to heat and moisture. [2]. They have exceptional qualities like crystal structural flexibility, the capacity to incorporate a wide variety of dopant ions, biocompatibility, bioactivity, biodegradability, the lack of immunological responses, low cytotoxicity and inflammatory reactions [3]. Strontium phosphate ($Sr_5(PO_4)_3OH$) are the ideal nanomaterials due to their inexpensive nature, availability, safety, and environmental benefits [4]. $Sr_5(PO_4)_3OH$ doped with rare earth ions such as Eu^{3+}, Ho^{3+}, Er^{3+}, Tm^{3+}, and Yb^{3+} may generate luminescence that covers from the visible to near-infrared spectrum through an up-conversion process [5]. Rare earth ions upconversion luminescence (UCL) processes depends on the numerous f-electron configurations of rare earth ions at the fundamental intermediate excitation states. They can convert two or more sub-bandgap NIR photons into a single usable above-bandgap photon. Through the decades of research, researchers have discovered that most efficient UCL are from the following rare earth ions: $Er^{3+}/Ho^{3+}/Tm^{3+}$ and Yb^{3+} in which energy transfer upconversion mechanism plays a prominent role [6]. Europium (Eu^{3+}) is commonly known as a red light emitter, but it has never been used an UCL ion in the near infrared (NIR) excitation regime because it cannot be directly

excited by NIR. It has been found that co-doping with an infrared sensitiser (energy donor) such as Yb^{3+} ion results in the red UC emission of Eu^{3+} ion under NIR excitation. The red UCL of Eu^{3+} is due to the cooperative energy transfer (CET) mechanism from the pairs of Yb^{3+} ions to single Eu^{3+} [7]. This study reports on the UCL and CET of $Sr_5(PO_4)_3OH:Eu^{3+},Yb^{3+}$ phosphor powders. The enhanced red upconversion luminescence of $Sr_5(PO_4)_3OH:Eu^{3+},Yb^{3+}$ phosphors show a promising potential for applications in photodynamic therapy (PDT).

2. Materials and methodology

$Sr_5(PO_4)_3OH$ co-doped Eu^{3+}/Yb^{3+} phosphor powders were synthesized by combustion process using urea as a fuel. $Sr(NO_3)_2{\cdot}4H_2O$, $NH_4)_2HPO_4$, $Eu(NO_3)_3{\cdot}5H_2O$, $Yb(NO_3)_3{\cdot}6H_2O$ and $CO(NH_2)_2$ were used as precursors. Under complete reaction conditions, the theoretical equation for the formation of $Sr_5(PO_4)_3OH$ is given by:

$$15Sr(NO_3)_2{\cdot}4H_2O + 9(NH_4)_2HPO_4 + 16CH_4N_2O = 3Sr_5(PO_4)_3OH + 16CO_2 + 131H_2O + 40N_2 \quad (1)$$

All starting materials, in stoichiometric quantities, were dissolved in 2 ml of distilled water and rapidly agitated until a thick pasty solution was formed. The solution was kept in a furnace at 600 °C. The solution boiled, dehydrated and decomposed producing combustible gases such as CO_2, NH_3 and H_2O by forming the host material. The combustion ashes were cooled to room temperature and gently ground using a pestle and mortar yielding a fine powder. The materials synthesized were $Sr_5(PO_4)_3OH$, $Sr_5(PO_4)_3OH:Eu^{3+}$, $Sr_5(PO_4)_3OH:Yb^{3+}$ and $Sr_5(PO_4)_3OH:Eu^{3+},Yb^{3+}$ with different concentrations of Eu^{3+} (1, 2, 3, 5, and 7 mol %), Yb^{3+} (7 mol %), and Eu^{3+}:Yb^{3+} (3:7 mol %). All the powders were annealed at 800 °C in air for 2 hours.

3. Characterization

The phase of $Sr_5(PO_4)_3OH$ powder was identified by using a Bruker AXS D8 X-ray Diffraction (XRD) in the 20 - 50° (2θ) range [8]. Particle morphology and corresponding elemental compositions of the phosphors were investigated using a JEOL JSM-7800F thermal field emission scanning electron microscope (FE-SEM) equipped with Oxford Aztec 350 X-Max80 Energy x-ray Dispersive Spectroscopy (EDS). The UV-Visible spectra were evaluated using a Perkin Elmer Lambda 950 UV-Vis spectrometer. The spectrometer was operated in the diffuse reflectance mode in the range 200 -1000 nm. The photoluminescence properties were investigated using Cary eclipse fluorescence coupled with monochromatized xenon lamp, and the upconversion measurements by photoluminescence (PL) system consisting of a fibre-coupled 980 nm NIR (near infrared) laser as the excitation source, iHR320 Horiba Yvon imaging spectrometer, R943 -02 Hamamatsu Photonics photomultiplier (PMT) detector and a SR830 Standford Research System lock-in amplifier.

4. Results and discussion

4.1 Powder X-ray diffraction analysis

The XRD patterns of $Sr_5(PO_4)_3OH$ and $Sr_5(PO_4)_3OH:Eu^{3+},Yb^{3+}$ nanoparticles are shown in Figure 1(a). The main diffraction peaks of both nanoparticles are comparable to standard data referenced by ICDD (International Centre for Diffraction Data) Card No. 00-033-1348, with no trace or impurities or additional phases [8]. The ionic radii of Eu^{3+} (0.95 Å) and Yb^{3+} (0.868 Å) are slightly smaller than that of Sr2+ (1.13 Å). Therefore Eu^{3+}/Yb^{3+} can be easily substituted into Sr^{2+} sites. The nanoparticles crystallizes in a hexagonal structure in the $P6_3/m$ space group [9].

The average crystallite size was 43 ± 2 nm. Sharp and narrow peaks confirm the powder's crystallinity. Figure 1(b) shows the crystal structure of $Sr_5(PO_4)_3OH$ drawn by VESTA 3D visualization program referenced by ICSD (Inorganic Crystal Structure Database) Code 9011131. The Sr^{2+} ions are present in two non-equivalent cationic sites Sr(1) and Sr(2). The Sr1 and Sr2 atoms are connected to 8 and 9 oxygen atoms to constitute the distorted $Sr(1)O_8$ and $Sr(2)O_9$ polyhedra, respectively [2]. The Sr(1) and Sr(2) atoms crystallographic site with trigonal symmetry (C_3) is coordinated by nine oxygen atoms from the PO_4^{3-} groups, creating $[Sr(1)O_9]$ clusters. The second Sr(2) site is seven coordinated by six oxygen atoms from the PO_4^{3-} groups and one hydrogen ion inside the hexagonal channels of the structure [8].

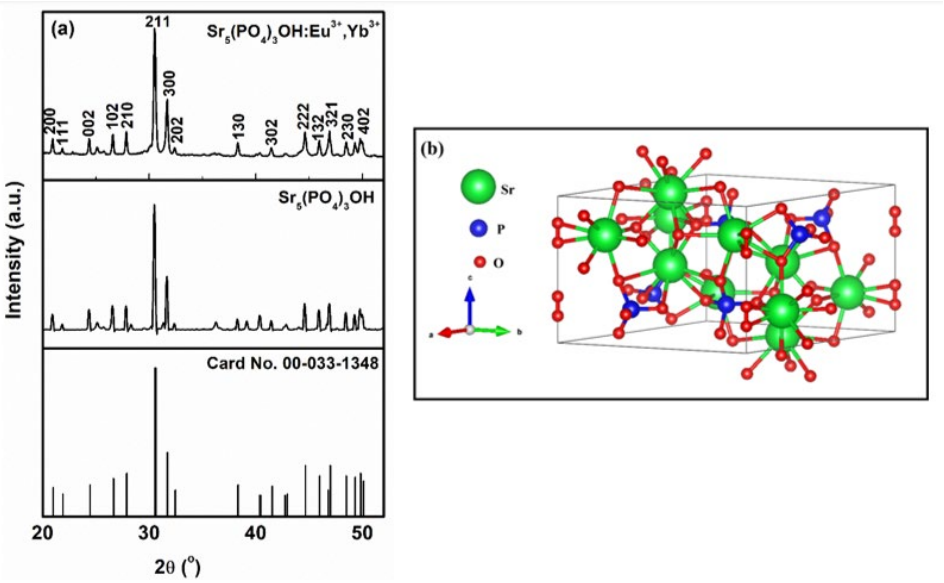

Figure 1. (a) XRD patterns compared with the ICDD Card No. 00-033-1348; (b) Crystal structure of the $Sr_5(PO_4)_3OH$ unit cell.

4.2 Particle morphology and chemical composition analysis

SEM micrographs and EDS spectra of $Sr_5(PO_4)_3OH$ co-doped Eu^{3+}/Yb^{3+} phosphor powder are shown in Figure 2 (a-d). The phosphor powders consist of a network of irregular shaped particles, with little brilliant particles coated on the surface of the bigger particles as shown by figure 2 (a). The little brilliant particles are suspected to be Eu^{3+} and Yb^{3+} ions. The particle morphology was taken with backscattered electron detector. The particles with heavy atoms with backscattered electron detector appear brighter, because they are stronger than light particles [10]. Figure 2 (b) shows the elemental composition of each element in phosphor powders ($Sr_5(PO_4)_3OH:Eu^{3+},Yb^{3+}$) confirming the presence of all the elements in the material. The inset shows where the EDS analysis was taken as indicated by S3 and S4. The corresponding weight % for each element is represented by the bar graph next to it. The weight % of Eu^{3+} and Yb^{3+} in S3 were 3 and 9%, and in S4 were 8 and 16% respectively [88]. This confirms that small bright particles are dominated by rare earth ions, while darker particles are dominated by the host. The elemental mapping in figure 2 (c-d) shows that the elements are uniformly distributed on the surface of the $Sr_5(PO_4)_3OH:Eu^{3+},Yb^{3+}$ phosphor.

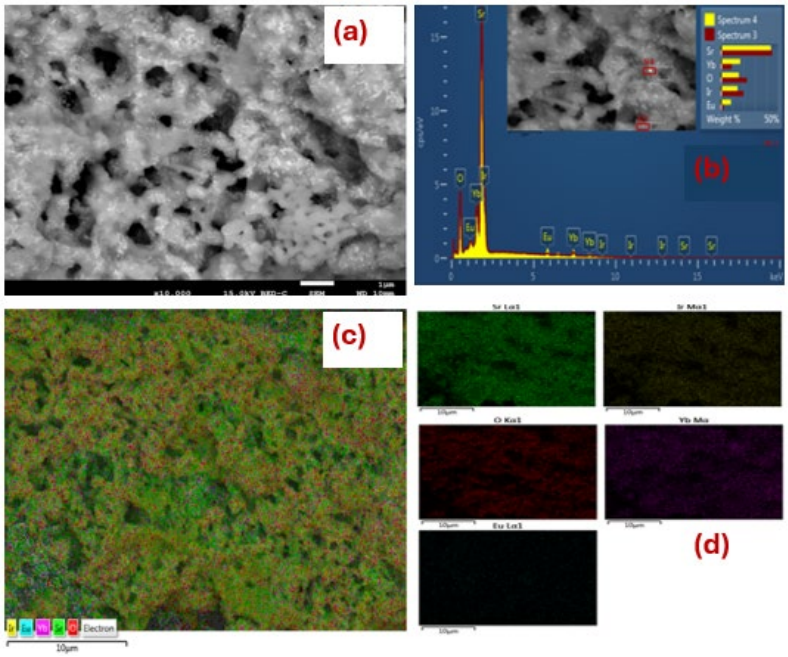

Figure 2. (a) morphology, (b) elemental analysis spectrum and (c-d) EDS mapping of $Sr_5(PO_4)_3OH$ co-doped Eu^{3+}/Yb^{3+} phosphor powder.

4.3. UV-Vis spectra: optical and bandgap analysis

The UV-Vis diffuse reflectance spectra and bandgap energy (i) $Sr_5(PO_4)_3OH$, (ii) $Sr_5(PO_4)_3OH:Yb^{3+}$, (iii) $Sr_5(PO_4)_3OH:Eu^{3+}$ and (iv) $Sr_5(PO_4)_3OH:Eu^{3+},Yb^{3+}$ phosphor powders are shown in Figure 3 (a-b). The $Sr_5(PO_4)_3OH$ spectrum exhibit three prominent bands at 221, 273 and 378 nm nm attributed to interband transition of host and intrinsic defects, respectively [11]. The additional band at 978 nm in $Sr_5(PO_4)_3OH:Yb^{3+}$ spectrum is assigned to $^2F_{7/2}\rightarrow{}^2F_{5/2}$ transition of Yb^{3+} ion [11]. Furthermore, the other bands observed in the visible region of $Sr_5(PO_4)_3OH:Eu^{3+}$ and $Sr_5(PO_4)_3OH:Eu^{3+},Yb^{3+}$ spectra at 391 and 458 nm are attributed to ($^7F_0\rightarrow{}^5L_6,{}^5D_2$) transitions of Eu^{3+} ion, respectively [13]. To estimate the optical energy band gap of the phosphor powders, a plot between F(R) and energy was drawn using Kubelka-Munk (KM) method [14]. By extrapolating the value of the function F(R) =0, the optical energy band gap value of the $Sr_5(PO_4)_3OH$, $Sr_5(PO_4)_3OH:Eu^{3+}$, $Sr_5(PO_4)_3OH:Yb^{3+}$ and $Sr_5(PO_4)_3OH:Eu^{3+},Yb^{3+}$ were estimated to be 5.1, 5.1, 4.7 and 5.2 eV, respectively. The increase in bandgap (blue shift) is due to Burstein-Moss effect, which correspond to degenerate doping. The excess electrons populate the states, pushing the Fermi levels and absorption edges to higher energy state resulting in an increased bandgap energy [12].

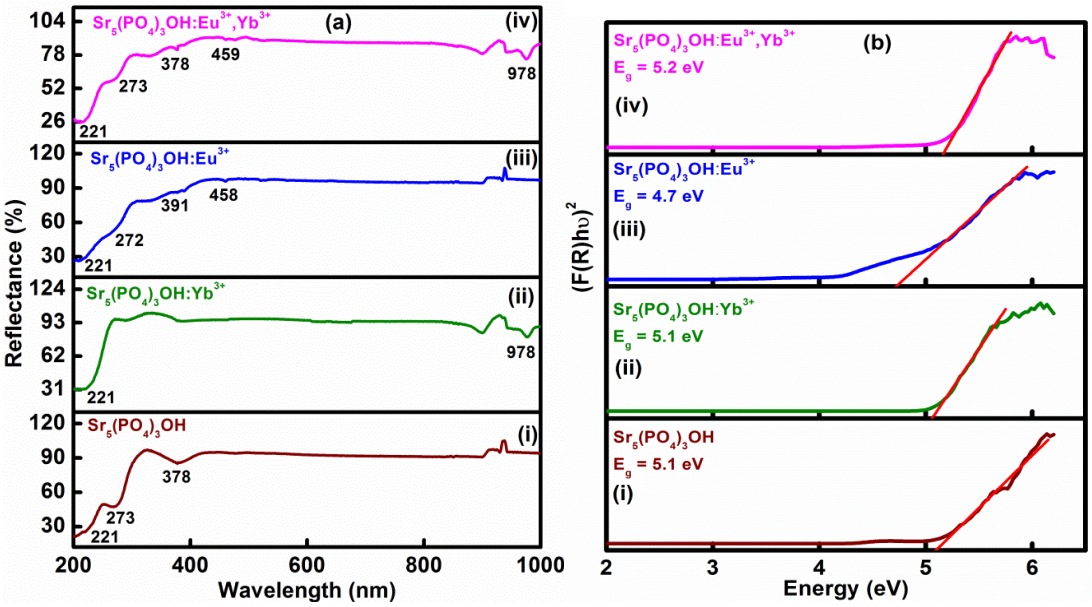

Figure 3. (a) diffuse reflectance spectra and (b) optical energy bandgap of (i) $Sr_5(PO_4)_3OH$, (ii) $Sr_5(PO_4)_3OH:Eu^{3+}$, (iii) $Sr_5(PO_4)_3OH:Yb^{3+}$ and (iv) $Sr_5(PO_4)_3OH:Eu^{3+},Yb^{3+}$ phosphor powders.

4.4. Photoluminescence spectral analysis.

Figure 4 (a) presents the excitation and emission spectra $Sr_5(PO_4)_3OH$ with different concentrations of Eu^{3+} (1-7 mol%). The broad band at 245 nm is associated with the charge-transfer band (CTB), arising from the transition of a ligand O^{2-} 2p orbital to the empty states at about $4f^6$ configuration of Eu^{3+} (Eu^{3+}-O^{2-} transition) [15]. The other peaks at 361, 380, 395, 412, 464 and 529 nm are due to direct excitation of the *f-f* transitions of Eu^{3+} ions [16]. The emission peak at 591 nm of the magnetic dipole transition $^5D_0\rightarrow{}^7F_1$ is generated from Eu^{3+} ions, indicating an inversion center site environment for Eu^{3+} ions which correspond to the orange light. The peaks at 613, 652, and 699 nm are corresponding to electric dipole transition ($^5D_0\rightarrow{}^7F_{2,3,4}$) transitions of Eu^{3+}, respectively [17].

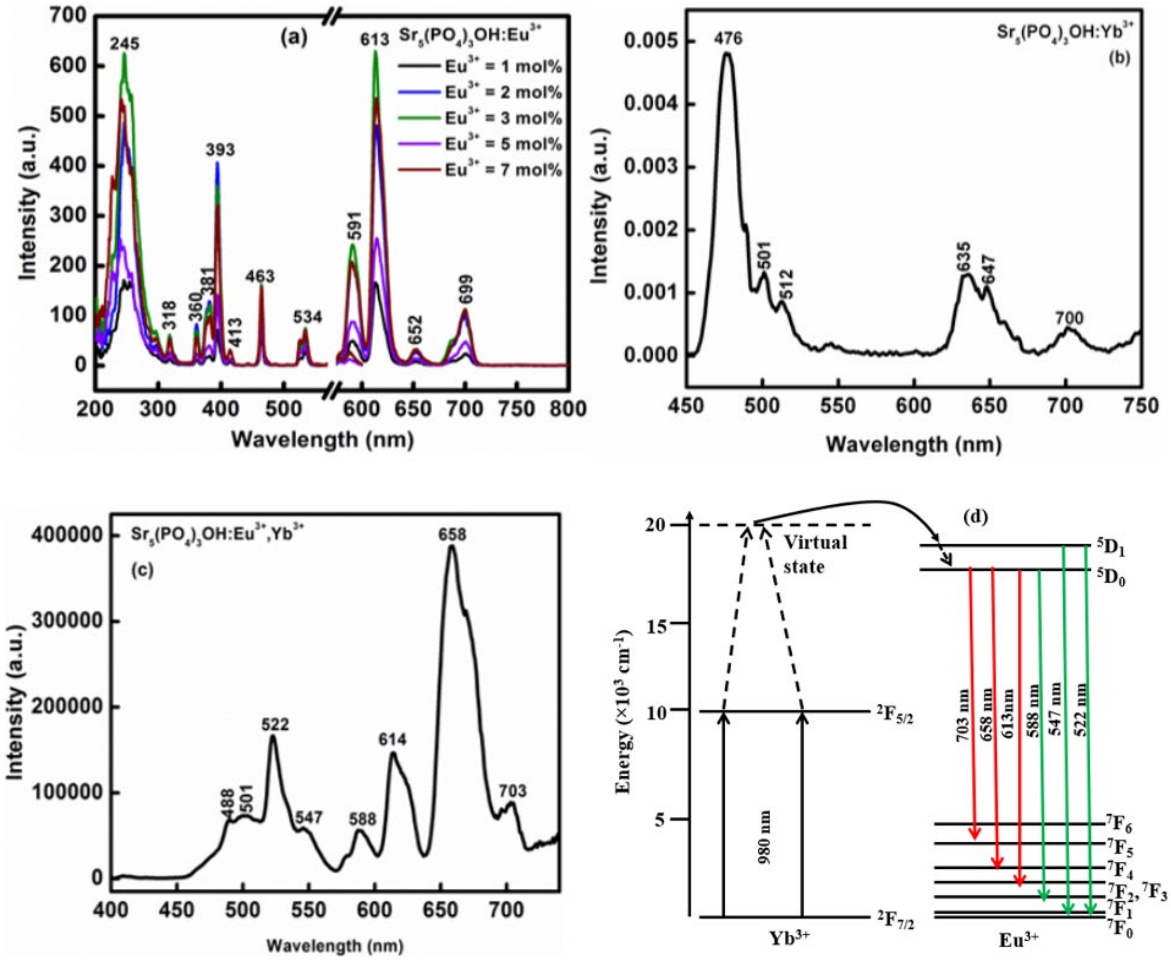

Figure 4. PL spectral of (a) $Sr_5(PO_4)_3OH:Eu^{3+}$, (b) $Sr_5(PO_4)_3OH:Yb^{3+}$, (c) $Sr_5(PO_4)_3OH:Eu^{3+},Yb^{3+}$ and (d) Energy transfer mechanism.

The luminescence intensity increased from 1 to 3 mol % and decreased at a higher concentration due to concentration quenching effects. Upon the infrared excitation of 980 nm for $Sr_5(PO_4)_3OH:Yb^{3+}$ phosphor as shown in Figure 4(b), the intense luminescence was observed at 476 nm and 522-700 nm attributed to *f-f* transitions of Yb^{3+} ion. Under the similar excitation, the upconversion luminescence in the red region of Eu^{3+} ion from $^5D_0 \rightarrow {}^7F_{j\ (j=1,2,3,4)}$ were detected in $Sr_5(PO_4)_3OH:Eu^{3+},Yb^{3+}$ phosphors, as shown in Figure 4(c). The strongest emission peak is observed at 658 nm attributed to $^5D_0 \rightarrow {}^7F_3$ transition of Eu^{3+} ion, and this is due to energy transfer from Yb^{3+} to Eu^{3+} [18]. Figure 4(d) shows the energy transfer between Eu^{3+} and Yb^{3+}. Through cooperative energy transfer process, Yb^{3+} act as a sensitizer for Eu^{3+}. This suggest that the Eu^{3+} ions are excited due to the presence of Yb^{3+} ions. Consequently, rapid non-radiative relaxation to the metastable $^5D_0$ state can result in a cooperative energy transfer from a pair of Yb^{3+} ions to a single Eu^{3+} ion, and the red Eu^{3+} emission is observed [19]. Dipole-dipole interaction between pairs of Yb^{3+} and the state of Eu^{3+} ions facilitates the energy transfer. After being stimulated from $^2F_{7/2}$ to $^2F_{5/2}$, two Yb^{3+} ions transfer all their energy to the Eu^{3+} ion's $^5D_1$ state. The Eu^{3+} ion at the $^5D_1$ level undergoes a radiative transition from the various energy states $^5D_0$ to the ground state after relaxing non-radiatively to the luminous level $^5D_0$.

5. Conclusion

$Sr_5(PO_4)_3OH:Eu^{3+},Yb^{3+}$ phosphors were successfully prepared using urea combustion process. The diffraction pattern verified the formation of a single phase of $Sr_5(PO_4)_3OH$ when compared to standard data. All of the elements contained in the samples were also confirmed by the EDS spectra. The emission peaks in the 591-699 nm region for the $Sr_5(PO_4)_3OH:Eu^{3+}$ system were attributed to Eu^{3+} transitions. Energy transfer from Yb^{3+} to Eu^{3+} during co-doping with Yb^{3+} increased the red emission peak at 658 nm. Through the use of enhanced red emission, photosensitisers can be activated to treat malignant cells via photodynamic therapy.

References

[1] I. Yıldırım , D. Ç. Altındal , A. en Yılmaz, "Eu^{3+} doped MB_4O_7 (M= Ca and Sr) nanoparticles for cancer treatment, Journal of Drug Delivery Science and Technology, vol. 105, pp 106611, 2025, doi: https://doi.org/10.1016/j.jddst.2025.106611

[2] Y.J. Liu, L. Liang, R.R. Wang, J.N. Wu, J.B. Huang, G.M. Cai, J.Y. Si, "Crystal structure, electronic structure and thermal stability of new phosphate $Sr_2In(PO_4)(P_2O_7)$", *Materials Research Bulletin*, vol. 177, pp 112844, 2024, doi https://doi.org/10.1016/j.materresbull.2024.112844

[3] P. Ivanchenko, G. Escolano-Casado, L. Mino, L. Dassi, J. F. Fernandez-Sanchez, G. Martra , J. Gomez-Morales, "Structural and surface studies of luminescent Ca/Eu phosphate nanomaterials: From the bulk to surface features", *Colloids and Surfaces B: Biointerfaces*, vol. 217, pp 112620, 2022, doi https://doi.org/10.1016/j.colsurfb.2022.112620

[4] M. Eagambaram, K. S. Mani, S. Sahoo, "Cobalt intercalated strontium phosphate for cost-effective high-performance supercapacitors", *Journal of Energy Storage*, vol. 119, pp 116312, 2025, doi https://doi.org/10.1016/j.est.2025.116312

[5] Y.Chen, S.W. Xi, C.Tong, H. hu Tan, L. Xu, N. Li, J.X. Xu, "Preparation of $NaYF_4$:Yb^{3+},Tm^{3+}@$NaGdF_4$:Ce^{3+},Eu^{3+} double-jacket microtubes for dual-mode fluorescent anti-counterfeiting", *Transactions of Nonferrous Metals Society of China*, vol. 30, pp 3333-3346, 2020 DOI: 10.1016/S1003-6326(20)65465-6

[6] Hsiu-Wen Chiena, Chien-Hsin Yang, Min-Ting Tsai, Tzong-Liu Wang, "Photoswitchable spiropyran-capped hybrid nanoparticles based on UV emissive and dual-emissive upconverting nanocrystals for bioimaging", *Journal of Photochemistry & Photobiology A: Chemistry*, vol. 392, pp 112303, 2020, doi: https://doi.org/10.1016/j.jphotochem.2019.112303

[7] P.A. Loiko, G.E. Rachkovskaya,G.B. Zakharevich, A.A. Kornienko, E.B. Dunina, A.S. Yasukevich, K.V. Yumashev, "Cooperative up-conversion in Eu^{3+},Yb^{3+}-doped SiO_2–PbO–PbF_2–CdF_2 oxyfluoride glass", *Journal of Non-Crystalline Solids*, vol. 392-393, pp 39, 2014, doi; https://doi.org/10.1016/j.jnoncrysol.2014.04.004

[8] Katarzyna Szyszka, Marta Kardach, Damian Szymanski, Rafal J. Wiglusz, "Synthesis, characterization, and temperature-dependent luminescence of Tb^{3+}-activated and self-activated $Sr_{10}(PO_4)_6Cl_2$ phosphors", *Journal of Luminescence*, vol. 275, pp 120788, doi: https://doi.org/10.1016/j.jlumin.2024.120788

[9] Mokoena, Puseletso Pricilla. *Upconversion of infrared to visible light in rare-earths doped phosphate phosphors for photodynamic therapy application*. Diss. University of the Free State, 2017.

[10] P.P. Mokoena, M. Gohain, B.C.B Bezuidenhoudt, H.C. Swart, O.M. Ntwaeaborwa, "Luminescent properties and particle morphology of $Ca_3(PO_4)_2$:Gd^{3+}, Pr^{3+} phosphor powder prepared by microwave assisted synthesis", *Journal of Luminescence*, vol. 155, pp 288-292, 2014, doi: https://doi.org/10.1016/j.jlumin.2014.06.058

[11] P.P. Mokoena, I.M. Nagpure, V. Kumar, R.E. Kroon, E.J. Olivier, J.H. Neethling, H.C.Swart, O.M. Ntwaeaborwa, "Enhanced UVB emission and analysis of chemical states of $Ca_5(PO_4)_3OH$:Gd^{3+},Pr^{3+} phosphor prepared by co-precipitation", *Journal of Physics and Chemistry of Solids*, vol. 75, pp 998-1003, 2014, doi: https://doi.org/10.1016/j.jpcs.2014.04.015

[12] Z. Huang, M. Yi, H. Gao, Z. Zhang, Y.Mao, "Enhancing single red band upconversion luminescence of $KMnF_3$:Yb^{3+}/Er^{3+} nanocrystals by Mg^{2+} doping", *Journal of Alloys and Compounds*, vol. 694, pp. 241-245, 2017, doi: https://doi.org/10.1016/j.jallcom.2016.09.322

[13] J. Chen, W. Zhao, J. Wang, N. Wang, Y. Meng, J. He, X. Zhang, "Energy transfer and thermal stability of $K_2Ba(WO_4)_2$: Eu^{3+}, Sm^{3+} phosphors", *Ceramics International*, vol. 41, pp 11945-11952, 2015, doi: https://doi.org/10.1016/j.ceramint.2015.06.006

[14] Anindya Pala, Purnendu Naskera, Sudeep Paula, Amit Roy Chowdhury, Arijit Sinhaa, Mitun Das, "Strontium doped hydroxyapatite from Mercenaria clam shells: Synthesis, mechanical and bioactivity study", *Journal of the Mechanical Behavior of Biomedical Materials*, vol. 90, pp 328, 2019, https://doi.org/10.1016/j.jmbbm.2018.10.027

[15] C. Shivakumara, R. Saraf, S. Behera, N. Dhananjaya, H. Nagabhushana, "Synthesis of Eu^{3+}-activated $BaMoO_4$ phosphors and their Judd–Ofelt analysis: Applications in lasers and white LEDs", *Spectrochimica Acta Part A: Molecular and Biomolecular Spectroscopy*, vol. 151, pp 141, 2015, doi: https://doi.org/10.1016/j.saa.2015.06.045

[16] V. Naresh, K. Gupta, C.P. Reddy, B.S. Ham, "Energy transfer and colour tunability in UV light induced $Tm^{3+}/Tb^{3+}/Eu^{3+}$: ZnB glasses generating white light emission", *Spectrochimica Acta Part A: Molecular and Biomolecular Spectroscopy*, vol. 175, pp 43, 2017, doi: https://doi.org/10.1016/j.saa.2016.12.023

[17] El Mahdi Bouabdalli, Mohamed El Jouad, Samira Touhtouh, Nathalie Gaumer, El Kebir Hlil, Abdelowahed Hajjaji, "The effect of europium on structural properties, photoluminescence behavior, and Judd-Ofelt analysis in strontium phosphate glasses for photonic applications", *Radiation Physics and Chemistry*, vol. 226, pp 112238, 2025, doi: https://doi.org/10.1016/j.radphyschem.2024.112238

[18] H. Rahimian, H. Mokhtari, S.P. Shirmardi, "Improvement of Eu^{3+} emissions in oxyfluoride glass and nano glass-ceramic by electron beam irradiation", *Journal of Luminescence*, vol. 187, pp 535, 2017, doi: https://doi.org/10.1016/j.jlumin.2017.03.025

[19] H. Xia, J. Feng, Y. Ji, Y. Sun, Y. Wang, Z. Jia, C. Tu, "2.7 μm emission properties of $Er^{3+}/Yb^{3+}/Eu^{3+}$: $SrGdGa_3O_7$ and $Er^{3+}/Yb^{3+}/Ho^{3+}$: $SrGdGa_3O_7$ crystals", *Journal of Quantitative Spectroscopy & Radiative Transfer*, vol. 173, pp 7, 2016, doi: https://doi.org/10.1016/j.jqsrt.2015.12.018

This page intentionally left blank.

The influence of Ultraviolet-Ozone irradiation time on structural and optical properties of SnO_2 thin films deposited using the slot-die method

F.V. Molefe[1,2], T.E. Seimela[2], N.N. Nyangiwe[1], M. Msimanga[1], M. Diale[2]

[1]Department of Physics, Tshwane University of Technology, Pretoria, South Africa
[2]Department of Physics, University of Pretoria, Pretoria, South Africa

E-mail: Mmantsae.diale@up.ac.za

Abstract. Tin (IV) oxide (SnO_2) is a promising metal oxide (MO) semiconductor with potential in perovskite solar cells (PSCs) as an electron transport layer (ETL). The development of an additive-free SnO_2 thin film with enriched optical properties using a cost-effective method remains a challenge. Herein, we report the influence of Ultraviolet-ozone (UVO) at different irradiation times, ranging from 2.5 min to 5 min, on SnO_2 thin films. The additive-free hydrothermally synthesized SnO_2 thin films were deposited on a fluorine-doped tin oxide (FTO) substrate using the slot-die method. The thin films were characterised using a range of analytical techniques to evaluate their structural and optical properties. X-ray diffraction (XRD) confirmed SnO_2 crystallization into the tetragonal cassiterite phase. The surface irradiation of SnO_2 thin films with UVO led to an increase in average crystallite size. Variation in the bandgap energy was observed following distinct changes in optical absorption upon UVO-irradiation. The photoluminescence (PL) studies revealed the enhancement in defect emission intensity following an increase in UVO-irradiation time. These findings emphasize the significance of UVO-irradiation in tuning the optical properties of SnO_2 thin films for application as an ETL in PSCs.

1 Introduction

For several decades, photovoltaic (PV) devices have been considered viable methods of producing renewable energy and trusted to replace fossil fuels. Several renewable technologies have been explored, such as geothermal, solar, and wind [1]. PV devices such as perovskite solar cells (PSCs) and organic solar cells (OSCs) have encountered challenges associated with the transition from laboratory to industrial scale [2]. Thin film devices for these technologies rely solely on the solution-processed materials.

PV devices use the bulk heterojunction (BHJ) configuration to separate excitons at the donor/acceptor interface [3]. This configuration is highly favoured due to the reported impressive power conversion efficiency (PCE) of 25.5 % in PSCs [4]. The efficiency, cost-effectiveness, flexibility, and lightweight construction make PSCs a viable alternative to silicon-based SCs [5]. In traditional n-i-p architecture, PV devices use inorganic metal oxides (MOs) such as CuO, SnO_2, TiO_2, and ZnO etc. as indispensable electron transport layers (ETLs) to achieve high performance [6]. The ETL in PSCs plays a vital role in functioning, stability, scalability and efficiency as it allows the extraction of electrons from the perovskite layer while blocking holes. Organic ETL materials such as carbazole-based PACs have been explored due to their excellent charge transportation, through which over 25% efficiency has been achieved [7]. However, they lack long-term stability at high temperatures and under ultraviolet illumination, which can hinder their application in PV devices; hence, inorganic MOs are highly favoured.

It should be noted that MOs demonstrate the greatest potential due to their high transparency, conductivity and user-friendly preparation approaches. A significant shift from TiO_2 to SnO_2 as the preferred ETL has been reported [8]. This is due to misalignment of TiO_2 with perovskite materials, leading to enhanced exciton recombination, which has a negative effect on device performance. Among MOs, SnO_2 has extraordinary electron mobility ($240 cm^2V^{-1}s^{-1}$) and compatible band alignment with perovskite materials that alleviate charge transportation at a reduced recombination rate [9]. However, the presence of metal-vacancy defects on the surface causes deterioration of device stability and efficiency. Such defects tend to trap photogenerated carriers and hinder the charge transfer process. Other researchers pretreated SnO_2 precursors with water-soluble polymers to modify their interface in PSCs [10]. Moreover, various process parameters during deposition, such as annealing, thickness, and time, were explored, leaving out post-treatment of the films. Thus, it is desirable to expose thin films to radiation as a way of passivation and reducing surface defects.

The performance of an ETL within the SC device relies on several factors, such as the specific surface area (SSA) and the operation environment [11]. The preparation and design of ETL with large SSA and extraordinary charge transfer are of high significance. SnO_2 can be prepared using various synthesis methods i.e. chemical precipitation, hydrothermal, and solvothermal reaction to produce different structures and shapes (nanoflower, nanoneedle etc.). For over a decade, research has mainly focused on using the spin coater to deposit MOs for SC applications. However, other solution-based deposition methods have been developed such as blade coating, dip coating, slot-die coating and spray coating [12]. Some deposition techniques have numerous issues associated with cost, stability, and reproducibility. Bu et al. demonstrated the feasibility of using the slot-die coating as the most successful method for large area mass production of solution-processed films [13]. Slot-die is a prevalent wet chemical deposition method that is operated at ambient environment to deposit a variety of materials desirable for optoelectronic applications [14]. It has the potential for scaling up the deposition of different essential layers for PSCs.

The primary goal of this study is to undertake the preliminary endeavour in growing SnO_2 thin films using the slot-die coater. The effect of UVO-irradiation time is investigated to gain insights into the structural and optical properties. The SnO_2 thin films were treated with UVO for 2.5 and 5 min after annealing. A significant change in structural and optical properties was observed. UVO-irradiation considerably improved the crystallite size and structural disorder, thereby minimizing the oxygen vacancies and enhancing the optical transmittance. UVO treatment has proven to be technologically efficient in producing SnO_2 with reduced defect density, desirable for PSCs as an effective ETL.

2 Experimental

2.1 Materials

The precursors were procured from Sigma-Aldrich Pty. Ltd., South Africa and used in their analytical grade state without further purification. The reagents used for the preparation of SnO_2 nanoparticles were tin tetrachloride (IV) pentahydrate ($SnCl_4 \cdot 5H_2O$ 98%) and ammonium hydroxide (NH_4OH, 28-30%).

2.2 Materials synthesis

The SnO_2 nanoparticles were synthesized as presented in Figure 1 through the following procedure: 4g $SnCl_2 \cdot 5H_2O$ was dissolved in 60 ml of ethanol and 20 ml of deionised (DI) water. An NH_4OH solution was added dropwise while stirring continuously using a magnetic hotplate until the pH was adjusted to 14. The obtained solution mixture was transferred into a Teflon autoclave (60 ml) and heated at 200°C for 24 hrs. After cooling, the product was thoroughly washed with ethanol and DI water using a centrifuge to remove residues.

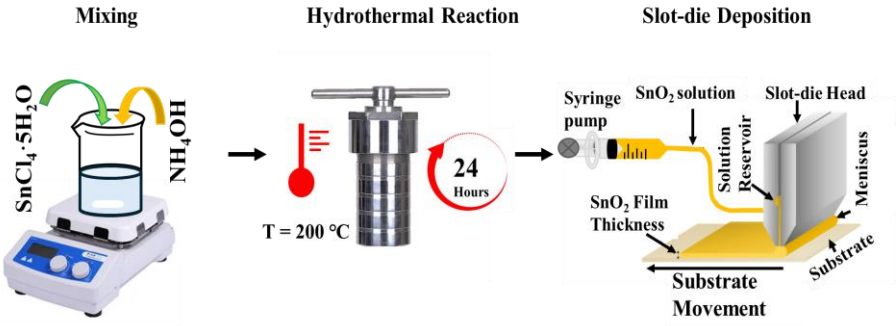

Figure 1: Schematic representation of the SnO_2 synthesis and slot-die thin film deposition.

2.3 Thin film deposition

The 12 mm × 12 mm FTO substrates were cleaned sequentially for 10 min in a Sonic-Clean Labotec ultrasonic bath using Sunlight detergent solution, ethanol, and deionized (DI) water. The substrates were blow-dried using nitrogen (N_2) gas, followed by UVO cleaning for 10 min and fixed on a slot die hot plate prior to deposition. The slot-die coating was performed as presented in Figure 1 using the Ossilla (L2005A1) coater at the speed of 0.5 mm/s, dispense rate 5 uL/s with the substrate preheated to 80℃. The downstream coating gap was retained at ~0.1 mm. The as-deposited SnO_2 thin films were annealed at 550℃ for 2 hrs and exposed to UVO-irradiation for different times (2.5 and 5 min) at room temperature.

2.4 Thin film characterization

The phase identification and purity were probed using Bruker D2 phaser XRD (Cu-K_α radiation, λ=1.5418 Å, 40 kV, 30 mA at a scanning speed of 0.05°/min. The absorption characteristics were measured using an Agilent Cary 60 BIO ultraviolet-visible (UV-Vis) spectrophotometer. A fluorescence spectrophotometer (Hitachi F-7000) equipped with a 150 W xenon arc lamp was used to acquire luminescence measurements.

3 Results and discussion

3.1 Structural analysis

Figure 2(a) shows the XRD diffractograms of as-deposited and UVO-irradiated SnO_2 thin films acquired in the 2θ range 20 - 60°. The as-deposited thin film exhibited a poor crystalline phase of SnO_2 with characteristic peaks at 26.6°, 33.6°, 37.9°, 51.7°, 54.4° and 56.8°. The observed diffraction peaks align well with the tetragonal rutile phase (cassiterite) from reference JCPDS#41-1445 [15], without impurities from precursors. The diffractions marked with asterisks (✯) are associated with the fluorine-doped tin oxide (FTO) substrate used. Moreover, the diffractions marked with the sun (☼) at 37.7°, ~54.6°, and ~56.7° become more apparent with an increase in UVO-irradiation time. The crystallite size of the thin films was estimated using the Debye-Scherrer equation, adopting the (110) and (101) dominant and resolved peaks [16]. The obtained values for the as-deposited, 2.5 and 5 min irradiated thin films were 5.93, 6.68, and 6.84 nm, respectively. These values indicate that UVO-irradiation led to an increase in crystallite size.

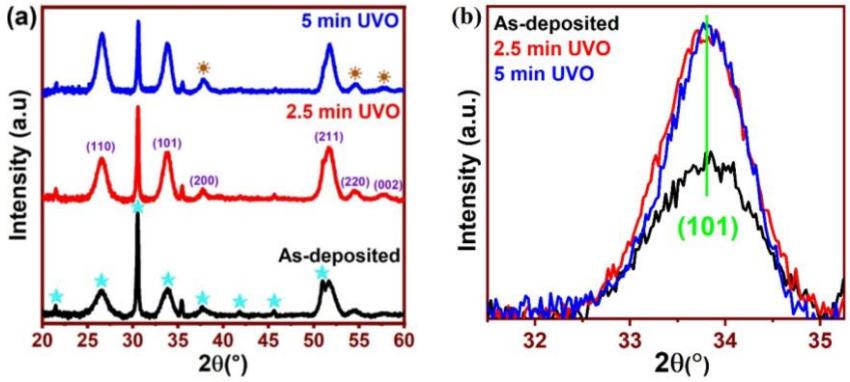

Figure 2: (a) XRD spectra of as-deposited and UVO-irradiated SnO_2 thin films, (b) close inspection of the (101) XRD peak.

An enlarged view of the (101) reflection for the as-deposited and UVO-irradiated thin films is presented in Figure 2(b). Upon UVO-irradiation, there is no appreciable peak shifting, indicating that oxygen ions were well incorporated into the SnO_2 crystal lattice and did not cause the structural distortions. Liu et al. reported similar findings on UVO-treated NiO thin films, which showed no change in 2θ diffraction angle values [17]. Notably, there is an increase in diffraction intensity for the UVO-irradiated thin films, indicative of improved crystallinity.

3.2 Optical analysis

The UV-Vis absorption spectra of as-deposited and UVO-irradiated SnO_2 thin films are presented in Figure 3(a). The as-deposited thin film exhibited significant absorption at ~305 nm in the ultraviolet region, distinctive of an electron transfer from the valence band (VB) to the conduction band (CB) in SnO_2 [18]. A decline in absorbance is observed throughout the entire spectral region, concurrent with the shift to the lower wavelengths. The reduction in absorbance is associated with an increase in transmittance. This is caused by improved crystallinity,

which minimizes grain boundaries that scatter light, thereby allowing the photons to be transmitted through the lattice [19]. The observed blueshift represents the modification of the electronic states of SnO_2 by UVO-irradiation.

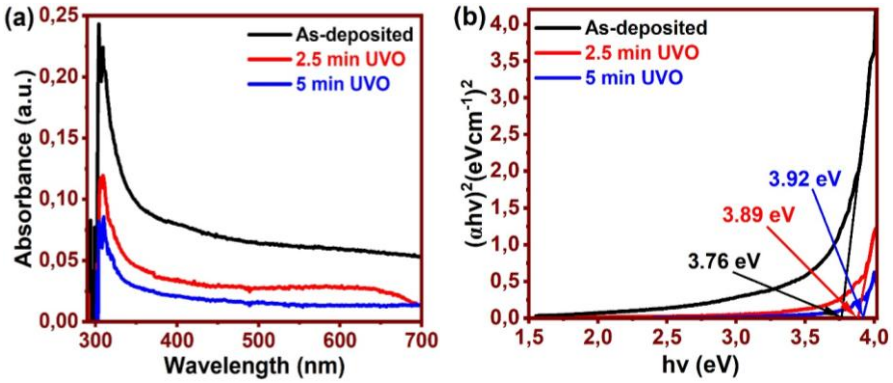

Figure 3: (a) Absorption spectra and (b) $(\alpha hv)^2$ vs (hv) for the as-deposited and UVO-irradiated SnO_2 thin films.

Figure 3(b) shows the optical energy bandgap (E_g) estimated using the Tauc's plot based on the relation $(\alpha hv)^n$ vs hv due to the direct transition n = 2, by extrapolating $(\alpha hv)^2$ to 0 [20]. The values of optical E_g increase with an increase in UVO-irradiation time. An E_g increase indicates the enhancement of transparency in the visible region while maintaining strong electrical conductivity, which is beneficial for ETL in PSCs [21]. This is attributed to the Burstein–Moss effect, due to an increase in free carrier concentration occupying the lower energy states in the CB [22]. This behaviour suggests that UVO-irradiation strengthens the interatomic bonding. Further analysis of absorption characteristics is conducted by determining the Urbach energy (E_U), thereby probing the localized defect levels in the E_g using equation (1) [23]:

$$\alpha = \alpha_0 \exp\left(\frac{hv}{E_U}\right), \quad (1)$$

where α is the absorption coefficient, α_0 represents the pre-exponential factor, and E_U denotes the band tail energies. The E_U values are estimated by applying the natural logarithm to equation (1) and taking the reciprocal of the slope of the linear fit below the E_g from the plot of $ln(\alpha)$ vs hv presented in Figure 4(a). The values of E_U decrease with an increase in UVO-irradiation time. Thus, UVO-irradiation reduces the structural disorder, which represents a better atomic arrangement and less internal stress [24].

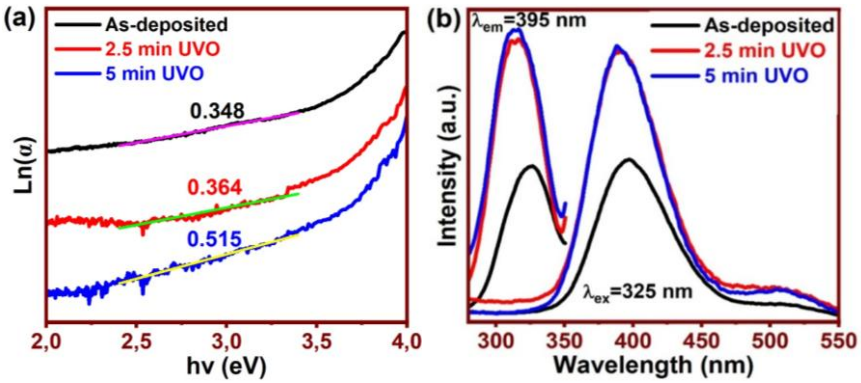

Figure 4: (a) Ln(α) vs hv (b) PL characteristic spectra of as-deposited and UVO-irradiated SnO_2 thin films.

Figure 4(b) illustrates the excitation and emission characteristics of the as-deposited and UVO-irradiated SnO_2 thin films. The optimal excitation was achieved at λ_{ex}=325 nm and used to monitor the emission obtained at λ_{em}=395 nm. The excitation spectra show a strong absorption, which should be ascribed to the transition of electrons from the VB to the CB in SnO_2. The as-deposited and UVO-irradiated thin films exhibit well-defined emissions peaking in the ultraviolet region (340 – 470 nm) and green region (470 – 550 nm). Generally, PL emission of SnO_2 thin films emanates from various intrinsic defects such as tin interstitials (Sn_i), oxygen vacancies (V_O) and dangling bonds [25]. Upon UVO-irradiation for 2.5 min, the emission intensity at 395 nm progressively increased, and at 5 min of irradiation, there was an insignificant change. This emission is ascribed to an electron transition from the lower edge of the CB to the doubly ionized V_O^{2+} situated above the VB [26].

Similarly, the 509 nm peak resembled an enhancement in the intensity with UVO-irradiation. This emission represents the creation of singly ionized (V_O^+) [27]. According to Ahmed *et al.* [28], the negatively charged oxygen develops a repulsive force and produce an acceptor state (holes) by shifting the VB levels upper into the forbidden gap. Owing to a weak repulsive force, an acceptor energy level is introduced by V_O^+, which causes the recombination of electrons trapped at V_O^+ with holes produced in the VB. This leads to an increase in 509 nm emission mediated by V_O^+. It can be concluded that 5 min UVO-irradiation time is optimal for achieving high intensity, with the likelihood of reduced intensity for longer irradiation times. It is well noted that excitation and emission spectra are slightly blueshifted, and this agrees well with the E_g widening observed in the absorption results. Thus, V_O defects were minimised, symbolising the enhancement of thin film quality through the increase in oxygen density. The increase in emission intensity indicates a delay in the recombination rate, which is vital for an ETL towards more photogenerated electron-hole pair generation and charge transfer.

4 Conclusion

The influence of UVO-irradiation time on SnO_2 thin films grown using the slot-die method was successfully investigated. The thin film properties were studied using XRD, UV-Vis, and PL techniques. The UVO-irradiated thin films revealed an increase in crystallite size with an increase in UVO-irradiation time. There was a substantial variation in E_g upon increasing UVO-irradiation time, which signified the changes in defect states and light transmission. An estimated E_U was reduced with the increase in UVO-irradiation time, suggesting lessened crystal disorder and defect density. The PL emission revealed a reduction in O defects upon increasing the UVO-irradiation time. Thus, the improved structural and optical properties are attributed to enhanced transmittance and reduced recombination losses. These discoveries underscore the importance of UVO-irradiation and provide guidelines for developing effective ETL for PSCs.

Acknowledgements

The authors are thankful for the financial support of the project provided by the University of Pretoria (UP) Physics Department through the National Research Foundation (NRF) - South African Research Chairs Initiative (SARChI), UID: 115463. Additionally, the support from Tshwane University of Technology (TUT) for conference attendance is highly appreciated.

References

[1] L. Wang and J. Pang, "Assessing the impact of climate mitigation technology and environmental tax on renewable energy development: A dynamic threshold approach," *Renew Energy*, vol. 244, p. 122683, May 2025, doi: 10.1016/j.renene.2025.122683.

[2] R. Keshavarzi *et al.*, "Organic and perovskite solar cells based on scalable slot-die coating technique: Progress and challenges," Apr. 01, 2025, *Elsevier B.V.* doi: 10.1016/j.nantod.2024.102600.

[3] P. Bi *et al.*, "Donor-acceptor bulk-heterojunction sensitizer for efficient solid-state infrared-to-visible photon up-conversion," *Nature Communications* , vol. 15, no. 1, Dec. 2024, doi: 10.1038/s41467-024-50177-4.

[4] L. Chen *et al.*, "Non-ionic polymeric polyacrylamide (PAM) modified SnO2 electron transport layer for high-efficiency perovskite solar cells," Aug. 01, 2024, *Elsevier B.V.* doi: 10.1016/j.solmat.2024.112907.

[5] A. Chandrakar and A. Khare, "A comprehensive review of flexible perovskite solar cells: Materials, mechanisms, properties, applications, and commercialization status," Sep. 15, 2025, *Elsevier Ltd*. doi: 10.1016/j.solener.2025.113649.

[6] Q. Zhang *et al.*, "Multifunctional organic molecule with synergistic modified SnO2 for efficient perovskite solar cells," *J Alloys Compd*, vol. 1010, Jan. 2025, doi: 10.1016/j.jallcom.2024.177653.

[7] X. Cui *et al.*, "Promising Cobalt Oxide Hole Transport Layer for Efficient and Stable Inverted Perovskite Solar Cells," *Adv Funct Mater*, Feb. 2025, doi: 10.1002/adfm.202425119.

[8] C. Yan *et al.*, "Influence of surface groups on SnO2 nanoparticles in enhancing perovskite photodetector performance," *Org Electron*, vol. 138, Mar. 2025, doi: 10.1016/j.orgel.2024.107194.

[9] R. Panyathip *et al.*, "Surface modification of SnO2 electron transporting layer by graphene quantum dots for performance and stability improvement of perovskite solar cells," *Ceram Int*, vol. 50, no. 19, pp. 34840–34848, Oct. 2024, doi: 10.1016/j.ceramint.2024.06.293.

[10] Y. Wang *et al.*, "Poly(acrylic acid)-modified SnO2/CdS double electron transport layers for efficient and stable Sb2(S,Se)3 solar cells," *Solar Energy Materials and Solar Cells*, vol. 281, Mar. 2025, doi: 10.1016/j.solmat.2024.113322.

[11] C. Luo *et al.*, "SnO2 mesoporous nanostructures serve as battery-type cathode for hybrid supercapacitor with superior electrochemical performance," *Colloids Surf A Physicochem Eng Asp*, vol. 712, May 2025, doi: 10.1016/j.colsurfa.2025.136440.

[12] R. Patidar, D. Burkitt, K. Hooper, D. Richards, and T. Watson, "Slot-Die Coating of Perovskite Solar Cells: An Overview."

[13] T. Bu *et al.*, "Universal passivation strategy to slot-die printed SnO 2 for hysteresis-free efficient flexible perovskite solar module," *Nat Commun*, vol. 9, no. 1, Dec. 2018, doi: 10.1038/s41467-018-07099-9.

[14] Y. Bouachiba *et al.*, "An investigation into the effect of Gd on the optoelectronic properties of ZnO waveguide thin films by prism coupler," *J Lumin*, vol. 275, Nov. 2024, doi: 10.1016/j.jlumin.2024.120740.

[15] P. Kamakshi, C. Joshitha, S. Chella, and G. Kumar K, "Enhancing photocatalytic applications with SnO2/Ti3C2 Mxene nanocomposite: Synthesis and characterization," *Chem Phys Lett*, vol. 833, Dec. 2023, doi: 10.1016/j.cplett.2023.140945.

[16] F. V Molefe, L. F. Koao, B. F. Dejene, and H. C. Swart, *Influence of zinc acetate concentration in the preparation of ZnO nanoparticles via chemical bath deposition*.

[17] Z. Liu, "Efficient polymer solar cells with low-temperature thermal annealing and ultraviolet-ozone treatment solution-processible NiO films as ITO-modified films," *Synth Met*, vol. 314, Sep. 2025, doi: 10.1016/j.synthmet.2025.117945.

[18] H. A. Alali, F. Tiss, K. Omri, K. Alamer, and Z. H. Alhashem, "Effect of Mn doping on microstructure and photocatalytic properties of ZnO nanoparticles synthesized via a hydrothermal method," *Mater Res Express*, vol. 11, no. 12, Dec. 2024, doi: 10.1088/2053-1591/ad9fd8.

[19] M. A. Sayeed and H. K. Rouf, "Al-doped SnO2 thin films: impacts of high temperature annealing on the structural, optical and electrical properties," *Journal of Materials Research and Technology*, vol. 15, pp. 3409–3425, Nov. 2021, doi: 10.1016/j.jmrt.2021.09.145.

[20] A. Alsulami and A. Alsalme, "Enhancement of the structural, optical, and optoelectrical properties of nebulizer spray pyrolyzed SnO2 thin films by strontium doping," *Physica B Condens Matter*, vol. 699, Feb. 2025, doi: 10.1016/j.physb.2024.416783.

[21] D. Bouras *et al.*, "Enhanced CO2 sensing properties of Fe/Al-doped SnO2 thin films: A comprehensive study of structural, optical, and electrical characteristics," *J Alloys Compd*, vol. 1034, Jun. 2025, doi: 10.1016/j.jallcom.2025.181387.

[22] M. A. Bezzerrouk *et al.*, "Effect of Sr doping on microstructure, morphology, photoluminescence, optical properties and photocatalytic performance of SnO2 thin films," *Opt Mater (Amst)*, vol. 167, Oct. 2025, doi: 10.1016/j.optmat.2025.117292.

[23] S. R. Al-Mhyawi *et al.*, "Preparation and modulating of the thermal, optical, dielectric, and electrical properties of PCL/PMMA-NiO/SnO2 nanocomposites for energy storage devices," *Ceram Int*, vol. 51, no. 21, pp. 32623–32636, Sep. 2025, doi: 10.1016/j.ceramint.2025.04.440.

[24] C. Muiva, D. P. Sebuso, and E. Muchuweni, "Microstructural and optical properties of nanostructured Al/Ag co-doped ZnO thin films (AgxAl0.03ZnO0.97-x) by spray pyrolysis for optoelectronic applications," *Physica B Condens Matter*, vol. 690, Oct. 2024, doi: 10.1016/j.physb.2024.416206.

[25] P. Asha Hind, P. Kumar, U. K. Goutam, and B. V. Rajendra, "Tuning of electrical properties and persistent photoconductivity of SnO2 thin films via La doping for optical memory applications," *Mater Sci Semicond Process*, vol. 186, Feb. 2025, doi: 10.1016/j.mssp.2024.109073.

[26] B. Teldja, B. Noureddine, B. Azzeddine, and T. Meriem, "Effect of indium doping on the UV photoluminescence emission, structural, electrical and optical properties of spin-coating deposited SnO2 thin films," *Optik (Stuttg)*, vol. 209, May 2020, doi: 10.1016/j.ijleo.2020.164586.

[27] A. Ahmed, T. Ali, M. Naseem Siddique, A. Ahmad, and P. Tripathi, "Enhanced room temperature ferromagnetism in Ni doped SnO2 nanoparticles: A comprehensive study," *J Appl Phys*, vol. 122, no. 8, Aug. 2017, doi: 10.1063/1.4999830.

[28] A. Ahmed, M. Naseem Siddique, U. Alam, T. Ali, and P. Tripathi, "Improved photocatalytic activity of Sr doped SnO 2 nanoparticles: A role of oxygen vacancy," *Appl Surf Sci*, vol. 463, pp. 976–985, Jan. 2019, doi: 10.1016/j.apsusc.2018.08.182.

This page intentionally left blank.

Development of cellulose nanocrystal sheet embedded with carbon nanotubes for sensor application

Aime Diakanwa Diantantu, Somnath Bhattacharyya, Daniel Wamwangi and Ibrahim Usman

School of Physics, University of Witwatersrand, Johannesburg, South Africa.

E-mail: aime.diantantu@students.wits.ac.za

Abstract. Cellulose is an important natural material, which is biocompatible and hydrophobic, and can form strong and stable stiff-chain monomolecular structures with film and hydrogel-forming properties. The focus of this investigation was to develop a mixed nano-materials sheet, which can be used as a gas sensor system. The Micro-cellulose sheet was treated with TEMPO (2,2,6,6-tetramethylpiperidine-1-oxyl) oxidation to prepare TEMPO-Oxidized Nanocellulose (TONC). However, nanocellulose is not electrically conductive which is necessary for energy device applications. Therefore, the TONC was blended with various concentration of Multi-Walled Carbon nanotubes (MWCNTs) to get conductive nanocomposites, which are oven dried at various temperatures to determine the effect on the conductivity. The optimum drying temperature was determined to be 60℃, with conductivity increasing with MWCNTS loading. The extent of the oxidised cellulose (TONC) was characterised by field emission scanning electron microscopy (FE-SEM) to determine the morphology and the Fourier-transform infrared spectroscopy (FT-IR) to identify the functional groups in the neat TONC paper. The SEM showed an increasing porosity with increasing oxidation time. The carboxyl groups also increase with increasing oxidation time.

1 Introduction

Petrochemicals like plastics and semiconductors are essential for energy production. To reduce environmental impact, "green" carbon-based compounds like cellulose must be found for affordable, sustainable, and energy-efficient alternatives [1]. Cellulose, the largest polymer on Earth, is constantly renewed through photosynthesis, similar to the world's reserves of minerals and fossil fuels [2]. Cellulose's diverse nature allows for easy extraction from various materials like bacteria, paper, wood, and cotton [3]. Paper has recently been investigated for use in energy storage and electronics applications [4]. Paper, made of cellulose fibers with diameters of around 20μm, has inherent disadvantages in emerging applications due to peak-to-peak roughness, non-transparent fiber diameter, and limited mechanical qualities due to packing density [4]. Paper's energy storage applications are limited by drawbacks. Mechanical treatment, acid hydrolysis, and enzymatic hydrolysis are methods used to isolate cellulose nanofibrils in micro cellulose paper [1]. Mechanical treatment is commonly used for nanocellulose fibrillation, involving high-pressure homogenization, cryo-crushing, ultrasonic treatment, grinding, and/or micro-fluidization [5]. The process typically results in fiber shredding rather than cellulose fibril separation, leading to micro-fibrillated cellulose with low aspect ratio, polymerization, and crystallinity, resulting in poor mechanical qualities [3]. The method of cellulose fiber pre-treatment, which involves interfibrillar hydrogen bonds, is associated with excessive energy consumption, prompting the development of alternative

methods [6]. TEMPO-mediated oxidation is a widely used chemical pre-treatment technique for chemically altering native cellulose by adding negatively charged groups to improve nanofibril delamination [7]. TEMPO-oxidation treatment can reduce energy usage to less than 7MJ/kg, compared to mechanical treatment which consumes energy up to 700-1400 MJ/kg for nanofibrils [8]. TONC paper, a type of TEMPO-oxidized Nanocellulose, is known for its excellent flexibility, high tensile strength, and high Young's modulus. Its porous structure allows it to bend in various angles without deformation, making it ideal for electronic devices and wearable electronics [9]. Nanocellulose paper offers ultrahigh transparency due to its smaller diameter and interstices than visible light wavelength, reducing scattering. Its minimal thermal expansion is advantageous for heat-generating electronic components, with a thermal coefficient as low as 0.1ppm/K [10]. This study aims to create conductive TONC/MWCNTs paper by oxidizing the hydroxyl group on micro-cellulose fibre's surface with the carboxyl group using TEMPO reagent, thereby enhancing its electrical and thermal conductivity and tensile strength. The study will analyze the nanocomposite paper's structure and morphology using FE-SEM, TEMPO oxidation's effectiveness, and the relationship between composition, drying temperature, and electrical conductivity. Recently, [11] published a study on blending the additive (MWCNTs) with the substrate (TONC) using surfactants to uniformly distribute MWCNTs in the TONC fibre network. [12] Also published a study based on blending TONC with Single-Walled Carbon nanotubes (SWCNTs). This study looks at blending unmodified MWCNTs on the TONC fibre network and observing its behaviour.

2 Experimental Methods

2.1 Materials

Micro-cellulose paper (Provided by SAPPI Saiccor Ltd, RSA) was used as the cellulose fibre source. TEMPO (2,2,6,6-tetramethylpiperidine-1-oxyl, free radical, 98% Sigma-Aldrich), Sodium bromide (Pure, Riedel-De Haen), Sodium Hypochlorite (NaOCl, 13-15%, Rochelle Chemicals), Sodium Hydroxide (NaOH, 98 %, Merck), Methanol (HPLC, 99.9%, Sigma-Aldrich),Hydrochloric Acid (HCl, 32%, ACE), Multi-Walled Carbon Nanotubes (MWCNTs, 95% Sigma Aldrich) and Distilled water were used without further purification.

2.2 Preparation of TEMPO-oxidized Nanocellulose fibres (TONCs)

The TONC was prepared by shredded Micro cellulose paper [6] and [13], dissolved in distilled water, and oxidized using TEMPO and Sodium Bromide. The reaction was terminated with Methanol and pH adjusted to 7. The TONC was then washed with distilled water, dissolved in distilled water, and disintegrated using ultra-sonication. The insoluble fraction was stored at 4℃ before further use. The procedure was modified from previous reports. The whole process is as shown in the flow diagram highlighted in Figure 1.

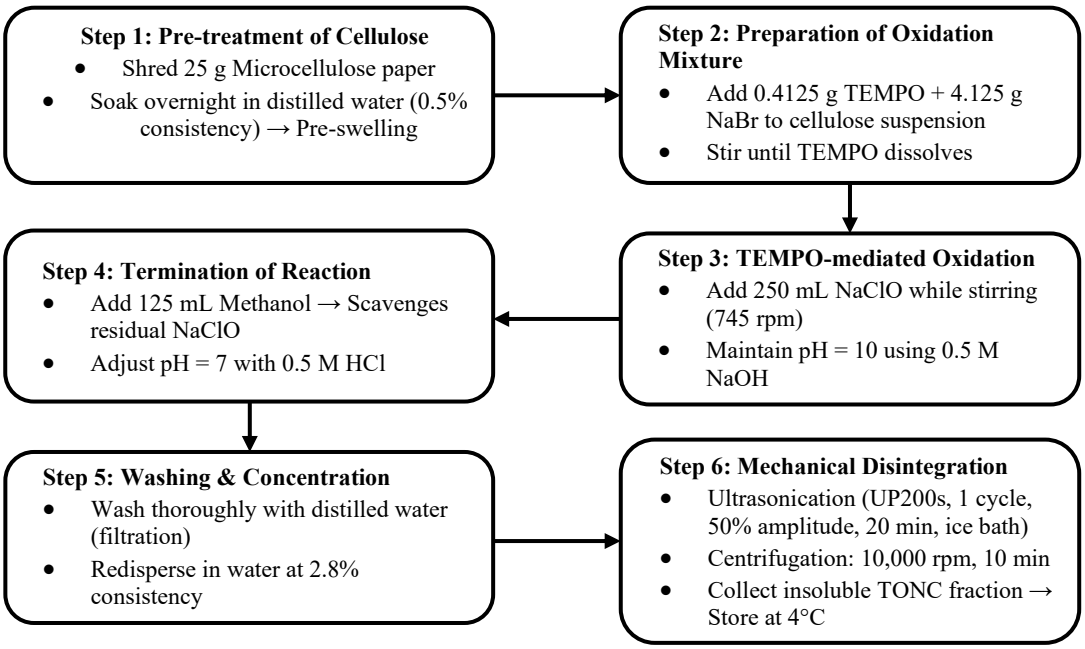

Figure 1: Flow diagram of the stepwise preparation of TONC.

2.3 Preparation of the Conductive paper

TONC was diluted in distilled water, then MWCNTs were added, sonicated, centrifuged, and dried. The resulting mixture was cut into paper sheets and analyzed for properties.

3 Characterization

The study utilized FE-SEM and FT-IR for characterizing nanocomposite paper and neat TONC paper. FE-SEM observed morphology, while FT-IR identified functional groups in neat TONC paper using PerkinElmer Spectrum. Samples were coated with gold-palladium and fixed to a metalized linter.

3.1 Morphology of TONC paper

The SEM of TONC paper shows an increase in porosity with increasing oxidation time due to carboxyl groups causing uniform fiber dispersion. Similar observations with regards to the increased porosity of TONC have been reported in [18] where such extended oxidation times led to wider pores that resulted in increased dispersion in water. The maximum oxidation time of 96 hours resulted in the most individualized fibres (Figure 2).

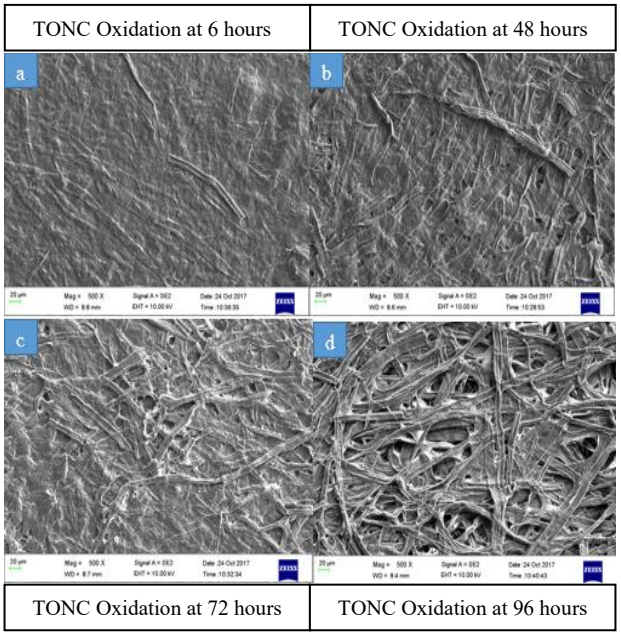

Figure 2: FE- SEM of TONC paper at different oxidation times. (a) 6 hours (b) 48 hours (c) 72 hours (d) 96 hours.

The FE-SEM images compare TONC/MWCNTs composite paper with varying amounts of MWCNTs (0,2- 1 wt%) in figure 2. The MWCNTs are dispersed in the TONC fibre network, with most contact in the composite's pore structure. At 1 wt%, MWCNTs are easily visible at the surface, but agglomerates are observed. Functionalization is needed to increase dispersion. Consider Figure 3 below.

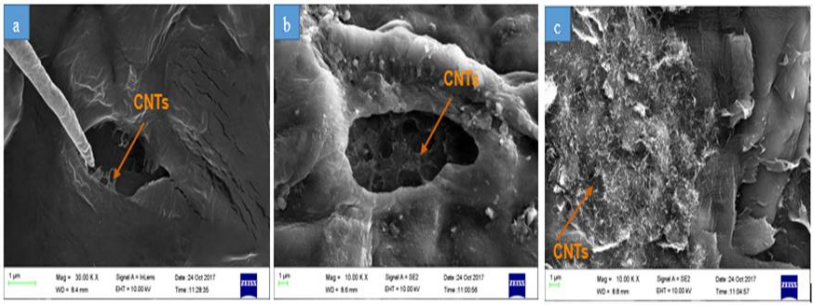

Figure 3: FE-SEM images of the TONC/MWCNTs composite paper containing different amounts of MWCNTs (a) 0.2 wt% (b) 0.6wt% (c) 1 wt%.

3.2 FTIR

FTIR Spectroscopy has been extensively used to identify distinct functional groups in cellulose, resulting from chemical changes during various chemical treatments [14]. FTIR spectra of micro-cellulose and treated TONC show a dominant increase in peaks at 3300 cm^{-1} and 2900 cm^{-1}, corresponding to O-H stretch and C-H stretch, respectively. The oxidation time increases the peaks mentioned above, indicating an increase in carboxyl group concentration. Other peaks at 1730 cm^{-1} is assigned to the C=O stretch vibration of carboxylate in its sodium form [15]. Figure 4 below shows FTIR results of micro cellulose paper and oxidized nanocellulose, and Table 1 summarises the FTIR peak ranges (cm^{-1}) for O-H, -C=O and -C-H groups.

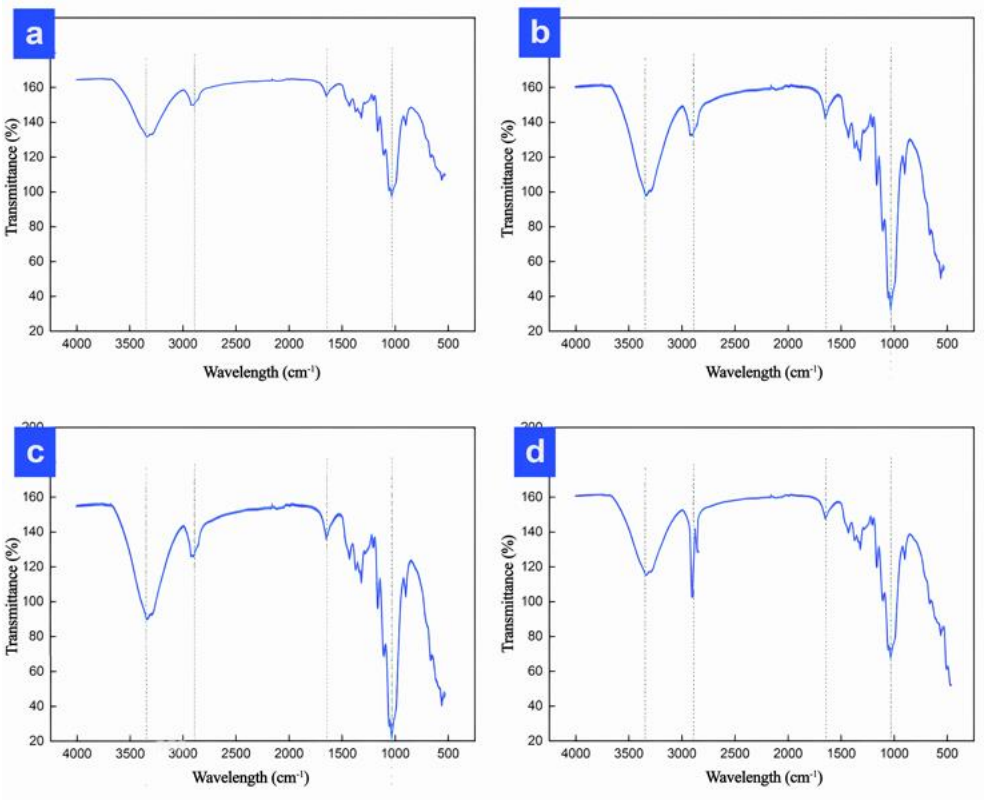

Figure 4: FTIR of micro cellulose paper and oxidized nanocellulose. (a) micro cellulose (b) 6 hours (d) 24 hours (c) 48 hours and (d) 72 hours.

Table-1: Summary of FTIR range (cm^{-1}) for O-H, -C=O and -C-H groups.

Functional Group	FTIR Peak Range (cm^{-1})
$\boldsymbol{O-H}$	3200–3600
$\boldsymbol{-C=O}$	1720–1740
$\boldsymbol{-C-H}$	2800–3000

3.3 Conductivity

Figure 5a shows the conductivity of the nanocomposite paper having varying concentrations of MWCNTs (0,2 – 1wt%). The conductivity is calculated by using equation 1 below.

$$\sigma = \frac{L}{A \times R} \tag{1}$$

Where $\sigma = conductivity(\text{k}\Omega.\text{cm})^{-1}$, $R = Resistance(Ohm)$, $L = Electorode\ legth(cm)$, $A = cross-sectional\ area\ (cm^2)$

The nanocomposite's resistance is measured using a resistance meter, and its conductivity increases with concentration of MWCNTs. The highest attainable conductivity is 0.16 kΩ. cm^{-1}, making it highly resistant to electrical flow. The nanocomposite's conductivity is studied by drying it at various temperatures (22, 40, 60, and 80°C), as illustrated in Figure 5b. The conductivity of nanocomposite paper increases with temperature, peaking

at 60℃. Temperatures above 60℃ cause a decrease in conductivity and molecular contact, potentially causing agglomeration. This causes the nanocomposite paper to not be uniform [16]. The optimal drying temperature is 60 degrees Celsius, resulting in the highest obtained conductivity of 0.16 kΩ. cm^{-1} from figure 5.

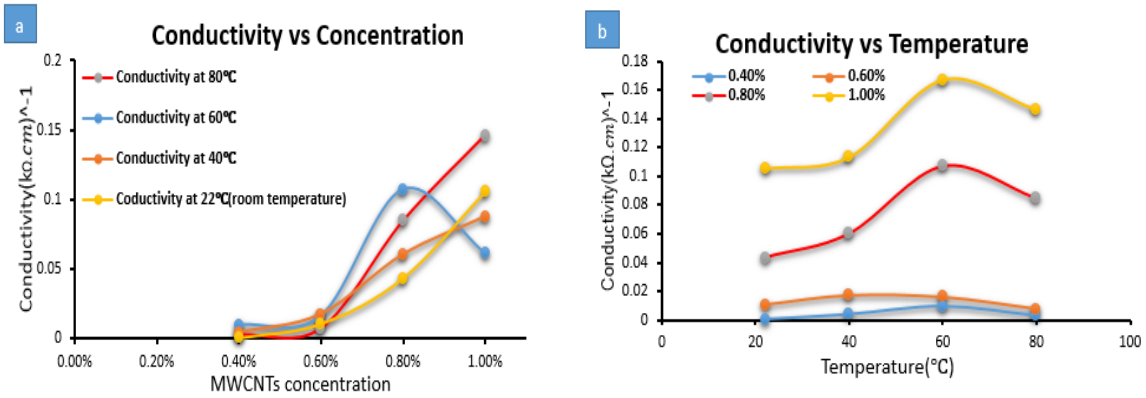

Figure 5: Conductivity of the TONC/MWCNTs nanocomposite paper at various concentration and dying temperature. (a) Effect of concentration on conductivity, and (b) effect of temperature on conductivity.

3.4 TONC Paper

The transparency of TONC paper increases with oxidation time, with 96 being the most transparent. This is due to mechanical treatment, thinning of nanofibrils, and minimal light diffraction [17], as shown in Figure 6.



Figure 6: TONC paper at 6, 24, 48 and 96 hours of oxidation time.

4 Conclusion

The MWCNT/TONC composite paper was fabricated via TEMPO oxidation of micro cellulose and mixing with MWCNTS at different concentrations. A variety of characterization and conductivity analyses were conducted in order to determine their properties. FE-SEM images show increasing porosity with increasing oxidation time. In addition, the images show individually dispersed MWCNTs in low concentrations with contact between the MWCNTs increasing with increasing concentration However, agglomerates appear with higher MWCNTs loading. FTIR confirmed the successful conversion of the hydroxyl groups to carboxyl groups which was shown by an increase in peaks for C-H stretch, O-H stretch and C=O stretch, which are all associated with the presence of carboxyl groups in the nanocellulose. Carbon nanotubes are hydrophobic in nature and tend to agglomerate in aqueous solutions due to their van der Waal forces. To overcome the forces, it is necessary to functionalize the carbon nanotube and introduce COO^- charged groups (i.e. carboxylate anions) to insure inform dispersal in the TONC/MWCNTs nanocomposite paper. Comparison between other nanocomposites containing other conductive materials such as graphene and/or graphene oxide. The use of other drying techniques that minimize the damage in the structure of the nanocomposite during drying.

References

[1] Du, X., Zhang, Z., Liu, W. & Deng, Y., 2017. Nanocellulose-based conductive materials and their emerging applications in energy devices-A Review. Nano Energy, Volume 35, pp. 299-320.

[2] Krässig, H. A., 1993. Cellulose: Structure Accessiblity and reactivity. Amsterdam: Gordon and Breach Science Publishers.

[3] Nechyporchuk, O., Belgacem, M. N. & Bras, J., 2016. Production of cellulose nanofibrils: A review of recent advances. Industrial Crops and Products, Volume 93, pp. 2-25.

[4] Hu, L. & Cui, Y., 2012. Energy and environment nanotechnology in conductive paper and textiles. Energy Environmental Science, 5(4), pp. 6423-6435.

[5] Dufresne, A., 2012. Nanocellulose: From Nature to High Performance Tailored Materials. s.l.:De Gruyter.

[6] Isogai, A., Saito, T. & Fukuzumi, H., 2011. TEMPO-oxidized cellulose nanofibres. *Nanoscale,* 3(1), pp. 71-85..

[7] Haniffa, C. et al., 2017. Effect of TEMPO-oxidization and rapid cooling on thermo-structuralproperties of nanocellulose. *Carbohydrates Polymers,* 173(2017), pp. 91-99.

[8] Missoum, K., Belgacem, M. N. & Bras, J., 2013. Nanofibrillated cellulose surface modification: A review.. *Materials,* 6(5), pp. 1745-1766.

[9] Luo, Y., Zhang, L. X., Liao, C. & Li, X., 2014. The cellulose Nanofibres for oteelctronic Conversion and Energy Storage. *Journal of Nanomaterials,* Volume 14, pp. 1-13.

[10] Sabo, R., Yermakov, A., Law, C. T. & Elhajjar, R., 2016. Nanocellulose-Enabled Electronics, Energy Harvesting. *Journal of Renewable Materials,* 4(5), pp. 297-132.

[11] Salajkova, M., Valentini, L., Zhou, Q. & Berglung, L., 2013. Tough nanopaper structure based on cellulose nanofibres and carbon nanotubes. *Composites Science and Technology,* Volume 87, pp. 103-110.

[12] Koga, H., 2013. Transparent, conductive, and printable composites consisting of TEMPO-oxidised nanocellulose and carbon nanotubes. *Biomacromolecules.*

[13] Habibi, Y., Chanzy, H. & Vignon, M. R., 2006. TEMPO-mediated surface oxidation of cellulose whiskers. *Cellulose,* pp. 679-687.

[14] Ristolainen, M., Alén, R., Malkavaara, P. and Pere, J., 2002. *Reflectance FTIR microspectroscopy for studying effect of xylan removal on unbleached and bleached birch kraft pulps.*

[15] Poletto, M., Ornaghi, H. L. & Zattera, A. J., 2014. Native cellulose structure: structure, characterisation and thermal properties. *Materials,* 7(9), pp. 6105.

[16] Peng, Y.K., Lai, C.W., Liu, C.L., Chen, H.C., Hsiao, Y.H., Liu, W.L., Tang, K.C., Chi, Y., Hsiao, J.K., Lim, K.E. and Liao, H.E., 2011. A new and facile method to prepare uniform hollow MnO/functionalized mSiO2 core/shell nanocomposites. *ACS nano*, *5*(5), pp.4177-4187.

[17] Hu, L., Zheng, G., Yao, J. & Liu, N., 2012. Transparent and conductive paper from nanocellulose fibres. *Energy and environmental science,* Volume 6, pp. 1-6.

[18] Wu, Y., *et al.,* (2025). TEMPO oxidized cellulose nanofibers from electrospun regenerated cellulose: Processing feasibility and application potentials. *International Journal of Biological Macromolecules*, (148063), 148063. https://doi.org/10.1016/j.ijbiomac.2025.148063

This page intentionally left blank.

DFT-based evaluation of Li_2MnO_3 as a promising cathode coating material for lithium-ion batteries

Mogau Kgasago[1], Katlego Phoshoko[2], Phuti Ngoepe[1], and Raesibe Ledwaba[1]

[1]Materials Modelling Centre, University of Limpopo, Private Bag x1106 Sovenga, 0727, South Africa

[2]Data Intensive Research Initiative of South Africa, Council for Scientific and Industrial Research, P.O. Box 395, Pretoria, 0001, South Africa

E-mail: 201818190@myturf.ul.ac.za

Abstract: An ideal coating material should combine chemical stability, mechanical strength, and suitable conductivity to enhance cathode durability. Li_2MnO_3 has previously been used as a coating material due to its stabilizing effect on the core, but other beneficial properties it may offer as a coating material are still underexplored. In this study, these ideal coating properties of Li_2MnO_3 were investigated using Density Functional Theory (DFT). To enhance accuracy, spin configurations were also considered, and calculations were performed using the GGA+U functional. The findings show that Li_2MnO_3 is thermodynamically stable, mechanically robust, and a semiconductor with a band gap of 2.17 eV. These results affirm Li_2MnO_3 as a promising cathode coating material, possessing the key attributes which are thermodynamic, electronic, and mechanical stability needed to enable durable, high-performance lithium-ion battery systems.

1 Introduction

$LiMn_2O_4$ is a sustainable, affordable, and thermally stable alternative to cobalt-rich cathodes [1]. Its ability to accommodate extra lithium in octahedral sites makes it particularly attractive as a pre-lithiation agent. Prelithiation, which involves indirectly adding extra active lithium to the anode via the cathode, has emerged as a key solution to mitigate initial capacity losses in lithium-ion batteries [2]. Pre-lithiating pristine spinel $LiMn_2O_4$ (with an initial theoretical capacity of 147 mAh/g) can raise its capacity to 284 mAh/g [3]. However, this is still lower than that of layered oxides. The main limitations of $LiMn_2O_4$ arises from capacity loss caused by manganese (Mn) dissolution, the Jahn–Teller effect, and other degradation mechanisms [4]. Addressing these issues is essential before $LiMn_2O_4$ can be fully utilized as an effective pre-lithiation agent. Various strategies have been proposed to enhance the stability and performance of $LiMn_2O_4$. These include doping, surface coatings, and other surface modification techniques aimed at improving its structural integrity and electrochemical properties [5-7]. Among these, core–shell designs have shown particular promise. These designs retain the high-rate capability and capacity of the core while introducing a protective shell to improve structural stability [8]. For example, Tomon et al. developed a $LiMn_2O_4$@C core–shell structure that significantly improved battery performance [9]. The carbon shell helped minimize Mn loss, stabilized phase transitions, and maintained structural integrity during cycling, leading to enhanced cycling stability and longer lifespan compared to pristine $LiMn_2O_4$ [9]. However, despite these improvements, the incompatibility between the carbon shell and the oxide core causes interfacial phase separation over extended cycling, which eventually degrades the electrode's performance.

To overcome such compatibility issues, a more chemically and structurally compatible shell material is needed. Layered Li_2MnO_3 is a promising candidate due to its high lithium content, good thermal stability, and its ability to co-exist with $LiMn_2O_4$ [10]. These features make Li_2MnO_3 a suitable shell material for enhancing both the

stability and capacity of spinel-based core–shell cathodes. Unlike previous DFT studies that primarily evaluated Li_2MnO_3 as a coating material in isolation, this work uniquely examines its interaction with the $LiMn_2O_4$ spinel, giving insights into their structural and electronic compatibility. In this study, we use density functional theory (DFT) to systematically evaluate the structural and electronic compatibility of Li_2MnO_3 as a shell for $LiMn_2O_4$. By analyzing oxidation states, electronic density of states, and lithium-ion pathways, we aim to determine whether Li_2MnO_3 can effectively stabilize $LiMn_2O_4$ and support its application as a high-capacity cathode material.

2 Method

First-principles calculations based on Density Functional Theory (DFT**)** were performed using the Vienna Ab Initio Simulation Package (VASP 6.0) [11, 12]. The Generalized Gradient Approximation (GGA) with the Perdew-Burke-Ernzerhof (PBE) exchange-correlation functional [13] was used, along with the DFT+U approach [14] to correct for strong on-site Coulomb interactions in the Mn 3*d* orbitals. The Hubbard U parameter was set to 4 eV for $LiMn_2O_4$ and 5 eV for Li_2MnO_3, values benchmarked by testing several U inputs and selecting those that produced the lowest ground-state energies [14]. Total energy convergence tests were performed prior to all property calculations to ensure numerical accuracy. The Brillouin zone was sampled with a 5×5×5 k-point grid for $LiMn_2O_4$ and 4×4×4 for Li_2MnO_3, and a plane-wave energy cut-off of 500 eV was used for all simulations. Convergence criteria were set to 1×10^{-6} eV for electronic self-consistent calculations and 0.01 eV/Å for ionic relaxation forces to ensure accuracy. An antiferromagnetic (AFM) spin configuration was applied, with the magnetic moments of Mn atoms initialized in alternating spin orientations. Structural optimization was performed for all materials, allowing full relaxation of lattice parameters and atomic positions. Single-point energy calculations were conducted to obtain structural and electronic properties. The computed results were validated against available experimental data to ensure reliability. Additionally, Li^+ diffusion pathways were explored using the bond valence method implemented in the pyAbstantia program.

3 Results and discussion

3.1 Optimized ground-state structures

The calculated lattice parameters using the GGA+U method show strong agreement with experimental values, demonstrating the reliability of the approach. For $LiMn_2O_4$, the calculated lattice constant of 8.33 Å slightly overestimates the experimental value of 8.24 Å, resulting in a difference of approximately 1.09%, which falls within the expected range for GGA-based methods. In the case of Li_2MnO_3, the computed parameters (a = 4.95 Å, b = 8.54 Å, c = 5.03 Å) closely match the experimental values (a = 4.94 Å, b = 8.53 Å, c = 5.05 Å), with percentage deviations of 0.20%**,** 0.12%, and 0.40%, respectively. The agreement of the lattice parameters of both spinel and layered structures confirms that GGA+U is well-suited for modeling lithium manganese oxides and provides a solid foundation for further property analysis.

System	Lattice parameters (Å)	
	GGA+U	Experimental
$LiMn_2O_4$ Fd-3m	8.33	8.24 [15]
Li_2MnO_3 C/2m	a=4.95	a=4.94 [16]
	b=8.54	b=8.53
	c=5.03	c=5.05

Table 1: Calculated lattice parameters for $LiMn_2O_4$ and Li_2MnO_3 using GGA+U.

3.2 Mn–O bond lengths

Figure 2 shows the Mn–O bond environments in $LiMn_2O_4$ and Li_2MnO_3. In $LiMn_2O_4$, two types of Mn were identified: Mn^{3+} with longer, distorted Mn–O bonds (up to 2.18 Å), and Mn^{4+} with shorter, more uniform bonds. The distortion around Mn^{3+} is a result of the Jahn–Teller effect, which contributes to structural instability during cycling. In contrast, Li_2MnO_3 displays uniform Mn–O bond lengths (~1.91–1.93 Å) consistent with literature values (1.932-1.939 Å) [7], indicating the presence of Mn^{4+} and the absence of distortion. This structural stability suggests that Li_2MnO_3 can act as a stabilizing shell, helping to suppress distortion driven degradation in the $LiMn_2O_4$ core.

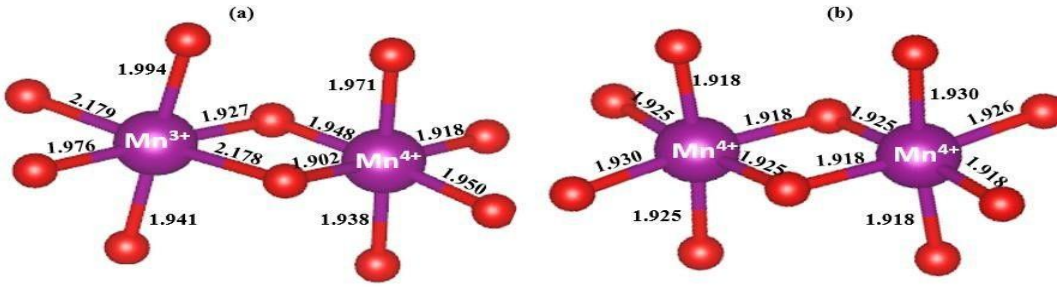

Figure 1: Optimized Mn–O bond environments showing (a) distorted Mn^{3+} and Mn^{4+} octahedra in $LiMn_2O_4$ due to Jahn–Teller effects, and (b) uniform Mn^{4+} coordination in Li_2MnO_3.

3.3 Magnetic moments

Table 2 presents the magnetic moments of Mn in both materials to confirm the oxidation states present in $LiMn_2O_4$ and Li_2MnO_3. In $LiMn_2O_4$, Mn^{3+} exhibits a higher magnetic moment (~3.8 μB) than Mn^{4+} (~3.0 μB), confirming the presence of mixed-valent states. This mixture contributes to structural issues, as Mn^{3+} is known to cause Jahn–Teller distortion and dissolve into the electrolyte, leading to capacity fading. In contrast, Li_2MnO_3 shows consistent magnetic moments around 3.1 μB for all Mn atoms, indicating a uniform Mn^{4+} state. This stable electronic environment enhances Li_2MnO_3's role as an ideal shell material, as it can help suppress the instabilities of $LiMn_2O_4$ and improve the structural and electrochemical performance of the core.

Material	Valence State	Magnetic Moments (μB)
$LiMn_2O_4$	Mn_{3+}	3.8
	Mn^{4+}	3.0
Li_2MnO_3	Mn^{4+}	3.1

Table 2: The calculated magnetic moments of Mn in $LiMn_2O_4$ and Li_2MnO_3.

3.4 Density of states

The Mn partial density of states (PDOS) for $LiMn_2O_4$ and Li_2MnO_3 are shown in Figure 2. In $LiMn_2O_4$, the Mn *d* states approach the Fermi level, resulting in a narrow band gap of approximately 0.5 eV, displaying a semiconducting behaviour. Li_2MnO_3 shows a band gap of around 2.1 eV, with no Mn *d* states at the Fermi level. This indicates semiconducting behavior and a Mn^{4+} state. Although its conductivity is low compared to $LiMn_2O_4$, this electronic stability demonstrated by a wider band gap is beneficial in a core–shell configuration. As a shell material, Li_2MnO_3 will still allow for conductivity under certain conditions. These band gap values are consistent with experimental reports, validating the accuracy of the electronic structure calculations [17, 18]. These PDOS results support the complementary nature of the two materials: $LiMn_2O_4$ offers electrochemical activity, while Li_2MnO_3 provides structural and electronic stability. The wider band gap of Li_2MnO_3 further indicates good coating stability but limited electronic conductivity, emphasizing the importance of optimizing its layer thickness. Together, this balance justifies combining the two in a core–shell architecture to enhance overall battery performance.

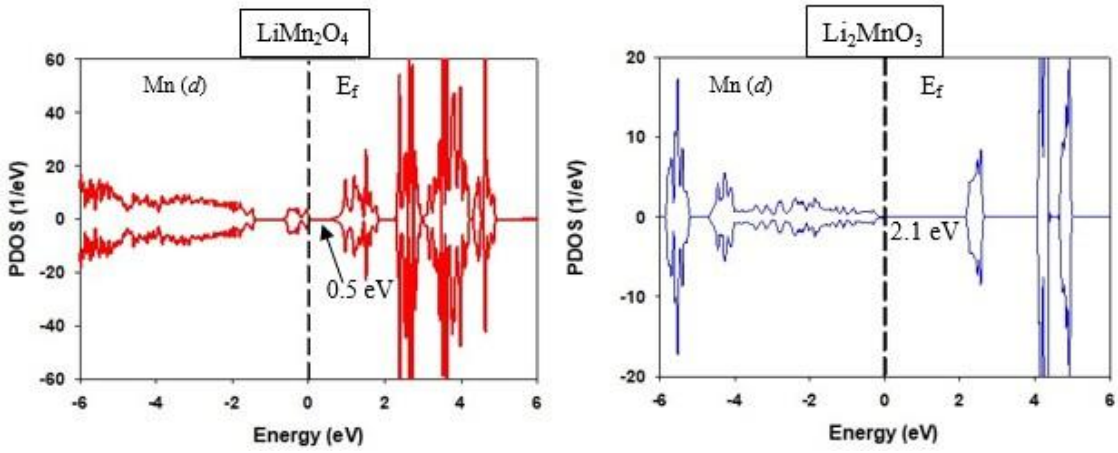

Figure 2: Partial density of states (PDOS) of Mn *d*-orbitals in $LiMn_2O_4$ and Li_2MnO_3, showing electronic structure and band gap differences.

3.5 Lithium-ion diffusion pathways

Figure 3 displays the Li^+ diffusion pathways in $LiMn_2O_4$ and Li_2MnO_3. In $LiMn_2O_4$, lithium ions migrate through a 3D network of channels, enabling fast diffusion and high-rate performance. Li_2MnO_3, however, supports lithium transport through a 2D layered pathway. While less open than the 3D framework, this more confined structure offers better control over lithium movement, helping to maintain structural integrity over time. The diffusion pathway analysis helps guide the choice of shell thickness, since the 2D transport in Li_2MnO_3 may work better with a thinner shell that matches the faster 3D diffusion in the $LiMn_2O_4$ core, allowing smoother lithium exchange at the interface. The well-ordered layers and uniform Mn^{4+} oxidation state contribute to a more stable and predictable diffusion environment, which is less susceptible to collapse or stress-induced degradation. In the context of a core–shell structure, this makes Li_2MnO_3 a valuable shell material. Its 2D diffusion pathway acts as a stabilizing barrier, regulating lithium flow and protecting the high-capacity $LiMn_2O_4$ core from surface degradation.

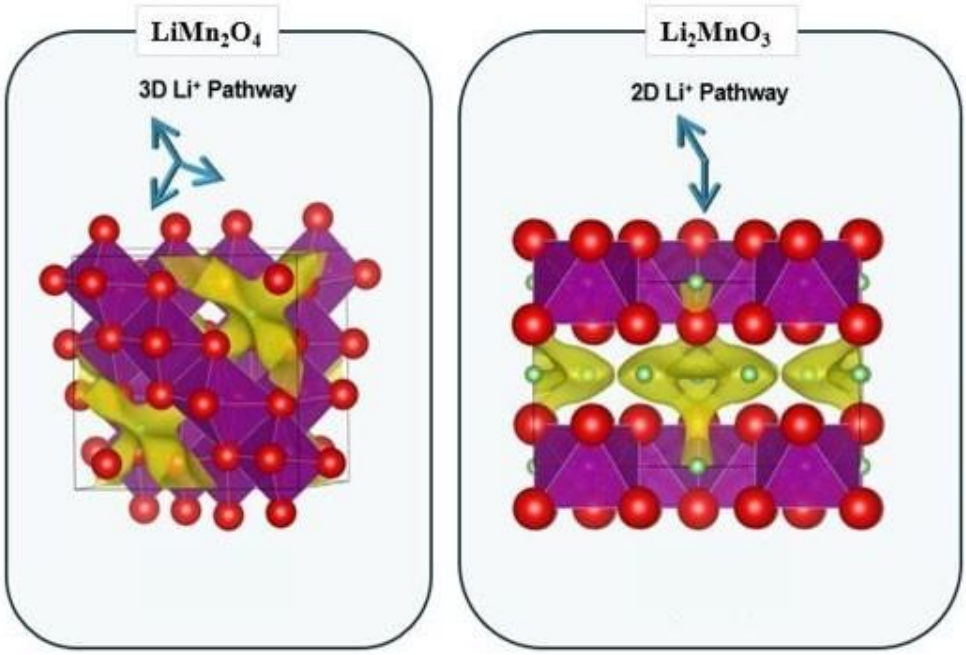

Figure 3: The lithium-ion diffusion pathways: 3D network in spinel $LiMn_2O_4$ vs 2D layered pathways in Li_2MnO_3.

4 Conclusion

The structural and electronic properties confirm that $LiMn_2O_4$ and Li_2MnO_3 have complementary properties that support their use in a core–shell configuration. $LiMn_2O_4$ shows a mixed-valent Mn^{3+}/ Mn^{4+} state, a narrow band gap, and a 3D lithium diffusion network, features that contribute to good conductivity and capacity but also cause structural instability due to Jahn–Teller distortion and Mn dissolution. In contrast, Li_2MnO_3 is characterized by a stable Mn^{4+} state, a wider semiconducting band gap, and a layered 2D lithium-ion pathway. While its own electronic conductivity and lithium mobility are limited, its structural uniformity and electronic stability make it ideal for surface protection. Together, the results demonstrate that Li_2MnO_3 can serve as a stabilizing shell for the $LiMn_2O_4$ core, suppressing surface degradation, enhancing structural durability, and enabling long-term performance. This core–shell combination might offer a strategic balance between electrochemical activity and stability, showing the benefit of $LiMn_2O_4$@Li_2MnO_3 as a promising architecture for advanced lithium-ion battery cathodes.

Acknowledgements

The authors acknowledge the financial support of the National Research Fund (NRF) and Materials Modelling Centre at the University of Limpopo, as well as the computational resources provided by the National Integrated Cyberinfrastructure System (NICIS).

References

[1] J. Ma, T. Liu, J. Ma, C. Zhang, J. Yang, "Progress, Challenge, and Prospect of $LiMnO_2$: An Adventure toward High-Energy and Low-Cost Li-Ion Batteries," *Advanced Science,* vol. 11, pp. 1-20, 2024.

[2] F. Holtstiege, P. Bärmann, R. Nölle, M. Winter, T. Placke, "Pre-Lithiation Strategies for Rechargeable Energy Storage Technologies: Concepts, Promises and Challenges," *Batteries,* vol. 4, no. 4, pp. 1-39, 2018.

[3] N. M. Jobst, G. Gabrielli, P. Axmann, M. Hölzle, M. Wohlfahrt-Mehrens, "Compensation of the Irreversible Loss of Si-Anodes via Prelithiated NMC/LMO Blend Cathode," *Journal of The Electrochemical Society,* vol. 168, pp. 1-8, 2021.

[4] R. S. Ledwaba, J. C. Womack, C. Skylaris, P. E. Ngoepe, "Intercalation voltages for spinel $Li_xMn_2O_4$ ($0 \leq x \leq 2$) cathode materials: Calibration of calculations with the ONETEP linear-scaling DFT code," *Materials Today Communications,* vol. 27, pp. 1-5, 2021.

[5] G. Tan, S. Wan, J. Chen, H. Yu, Y. Yu, "Reduced Lattice Constant in Al-Doped $LiMn_2O_4$ Nanoparticles for Boosted Electrochemical Lithium Extraction," *Advanced Materials,* vol. 36, pp. 1-10, 2024.

[6] J. Li, B. Zhang, S. Yuan, J. Hou, H. Wu, Y. Huang, W. Han, Z. Feng, Y. Liu, P. Dong, Y. Zhang, Y. Zhang, "Research progress on surface modifcation of spinel $LiMn_2O_4$ cathode materials for lithium-ion batteries," *Ionics,* pp. 1-16, 2025.

[7] M. Michalska, D. A. Buchberger, J. B. Jasinsk, A. K. Thapa, A. Jain, "Surface Modification of Nanocrystalline $LiMn_2O_4$ Using Graphene Oxide Flakes," *Materials,* vol. 12, pp. 1-12, 2021.

[8] S. Tubtimkuna, D. L. Danilov, M. Sawangphruk, P. H. Notten, "Review of the Scalable Core–Shell Synthesis Methods: The Improvements of Li-Ion Battery Electrochemistry and Cycling Stability," *Small Methods,* vol. 7, no. 2300345, 2023.

[9] C. Tomon, S. Sarawutanuku, N. Phattharasupakun, S. Duangdangchote, P. Chomkhuntod, N. Joraleechanchai, P. Bunyanidhi, M. Sawangphruk, "Core-shell structure of $LiMn_2O_4$ cathode material reduces phase transition and Mn dissolution in Li-ion batteries," *Communications Chemistry,* vol. 552, pp. 1-12, 2022.

[10] J. Xu, S. Zhu, Z. Xu, H. Zhu, "The basic physical properties of Li_2MnO_3 and $LiMn_2O_4$ cathode materials," *Computational Materials Science,* vol. 229, pp. 1-7, 2023.

[11] W. Kohn, L. J. Sham, "Self-consistent equations including exchangeand correlation effects," *Physical Review,* vol. 140, pp. A1133-A1138, 1965.

[12] G. Kresse, J. Hafner, "Ab initio molecular-dynamics simulation of the liquid-metal–amorphous semiconductor transition in germanium," *Physical Review B,* vol. 49, pp. 14251 - 14269, 1994.

[13] J. P. Perdew, K. Burke, M. Ernzerhof, "Generalized gradient approximation made simple," *Physics Review Letter,* vol. 77, pp. 3865-3868, 1996.

[14] S. L. Dudarev, G. A. Botton, S. Y. Savrasov, C.J. Humphreys, A. P. Sutton, "Electron-energy-loss spectra and the structural stability of nickel oxide: An LSDA+ U study," *Physical Review B,* vol. 57, pp. 1505 - 1509, 1998.

[15] Y. Idemoto, K. Horiko, K. Ui, N. Koura, "Thermodynamic stability and crystal structure dependence of Li content for $Li_xMn_{2-y}M_yO_4$ (M = Mg, A1, Cr, Mn) as a cathode active material for Li secondary battery," *Electrochemistry,* vol. 72, no. 10, pp. 680-687, 2004.

[16] P. Strobel, B. Lambert-Andron, "Crystallographic and magnetic structure of Li_2MnO_3," *Journal of solid state chemistry,* vol. 75, pp. 90-98, 1988.

[17] X. Li, J. Wang, S. Zhang, L. Sun, W. Zhang, F. Dang, H. J. Seifert, "Intrinsic Defects in $LiMn_2O_4$: First Principles Calculations," *ACS Omega,* vol. 6, p. 21255−21264, 2021.

[18] R. Xiao, H. Li, L. Chen, "Density Functional Investigation on Li_2MnO_3," *Chemical Material,* vol. 24, p. 4242−4251, 2012.

This page intentionally left blank.

Assessing the Freysoldt, Neugebauer & van de Walle (FNV) and Kumagai–Oba (KO) finite-size corrections for Ce-vacancy complexes in diamond

W. Dednam[1] **and E. B. Lombardi**[1]

[1] Research and Academic Computing: High-Performance Computing (HPC), College of Science, Engineering and Technology, University of South Africa, Tshwane, 0001, South Africa

E-mail: dednaw@unisa.ac.za

Abstract. Lanthanide-doped diamond couples the ultra wide band gap, high thermal conductivity and radiation hardness of the host with the rich electron physics of the dopant, promising solid-state qubits, single-photon emitters and spin-memory elements. Supercell density functional theory treatments of the charged Ce-vacancy complexes that underlie these functionalities suffer from spurious image–image interactions and an ill defined electrostatic zero energy; post processing finite-size corrections are therefore mandatory for quantitative defect thermodynamics.

We benchmark the two principal correction schemes – the reciprocal space potential alignment monopole method of Freysoldt, Neugebauer, van de Walle (FNV) and the real space multipole expansion of Kumagai Oba (KO) – for Ce_{V2}, Ce_{V3} and Ce_{V4} in a 216-atom diamond supercell. Uncorrected neutral formation energies agree with literature to within 0.5eV for all three and confirm Ce_{V3} as the most stable neutral complex. Introducing positive charge exposes limitations of FNV: once the anisotropic Ce $4f$ charge density departs from the isotropic monopole assumed in that formalism, FNV corrections fail to converge. In contrast, KO, which accounts for higher multipoles, remains numerically stable and delivers consistent corrections.

Our results show that KO is indispensable for heavy-atom defects with non-spherical charge distributions, while FNV is reliable only for nearly isotropic cases. This enables accurate assessment of rare-earth dopants in diamond and other wide-gap semiconductors.

1 Introduction

Doped diamond complexes are promising for spintronic [1, 2, 3, 4] and quantum optics applications [5, 6, 7, 8]. Diamond is an attractive host for these defects because it is a radiation-hard, ultra wide band gap semiconductor capable of hosting deep defect states. For example, nitrogen-doped diamond already exhibited promise towards spintronic applications in theoretical density-funtional theory (DFT) calculations in Ref. [1], and the negative nitrogen vacancy cluster has been shown to exhibit spin conherence times at room temperature up to the order of milliseconds and spin-relaxation times beyond that, which is very promising for quantum memory applications [2]. Subsequent works have continued to explore such advantageous aspects of this defect centre (see Ref. [4] and references therein).

Lanthanide-doped diamond has also recently been explored for its potential, particularly in quantum optics applications. Several studies have explored Cerium [9, 10], Erbium [11, 12], Europium [5, 13, 14], Praseodymium [15, 16] and Ytterbium [11, 17] as dopants in diamond complexes of various forms.

Density-functional theory (DFT) has served as the workhorse for modelling a broad range of diamond complexes [1, 3, 15, 13, 9, 14, 18, 16, 19, 20]. However, the periodic-boundary condition (PBC) supercell model used in DFT creates spurious electrostatic interactions between a charged defect and its periodic images, so explicit correction terms are required [21, 22, 23, 24, 25, 26]. Conventional potential alignment schemes give only a partial correction [22], whereas advanced image charge schemes such as FNV [23, 25] and KO [26] are required to remove this systematic bias and ensure reliable formation energies for charged defects in supercell DFT. In this work we assess these two principal correction schemes, the *scalar* Freysoldt, Neugebauer, van de Walle (FNV) and the *tensor* Kumagai–Oba (KO), and apply them to the Ce_{V2}, Ce_{V3} and Ce_{V4} complexes in diamond studied in Ref. [9].

2 Methods

The FNV and KO finite-size corrections outlined below follow their implementation in the `SPINNEY` post-processing code, with conventions as defined by Ref. [27]. The formation energy of a charged defect supercell in DFT is conventionally defined as [27]:

$$E_f\big[D^q\big] = \big\{E\big[D^q\big] + E_{\mathrm{corr}}\big[D^q\big]\big\} - E_P - \sum_i n_i\mu_i + q(\varepsilon_{\mathrm{VBM}} + \Delta\varepsilon_F)\,. \tag{1}$$

where $E_f\big[D^q\big]$ is the ground-state DFT total energy of the defect supercell in charge state q and E_P is the neutral pristine diamond supercell. n_i is the number of removed (<0) or added (>0) atoms and μ_i is the chemical potential of atom type i. E_{VBM} is the valence-band maximum (VBM) of the pristine supercell. $\Delta\varepsilon_F$ is the Fermi level relative to the VBM. Finally, $E_{\mathrm{corr}}\big[D^q\big]$ consists of two terms: the image-charge correction and potential alignment.

Under PBC, a charged defect interacts with its own periodic images and the neutralising background ($\frac{-q}{\Omega}$, with Ω the supercell volume). Image-charge corrections remove this artificial long-range interaction, so that $E_f\big[D^q\big]$ converges toward the dilute-defect limit in the ideal case [26]. A potential alignment correction is also needed since the DFT Poisson solver sets the cell-average potential $V_{\mathrm{avg},\Omega}$ to zero arbitrarily [26]. The charged cells inherit this potential shift, which, in turn, alters Kohn-Sham eigenvalues and total energies.

The FNV method defines the correction terms as [27]:

$$E_{\mathrm{corr}}\big[D^q\big] = -\,E_{\mathrm{model}} - q\,\Delta V_{\mathrm{model},\,q/b}\big|_{\mathrm{far}} \tag{2}$$

where E_{model} is the electrostatic (Madelung) energy of a model charge density, which can be a point charge (PC) or a charge density fitted to a suitable (radially isotropic) function. $\Delta V_{\mathrm{model},\,q/b}\big|_{\mathrm{far}}$ is the value of $\Delta V_{\mathrm{model},\,q/b}$, the difference between the defect-induced potential $V_{q/b}$ and the and the charge-density model potential $V_{\mathrm{model},q}$ far away from the defect inside Ω. For convenience, the overall correction term in Eq. (1) has traditionally been analyzed in Ewald summation form divided into real and reciprocal space parts [21, 26]. The electrostatic component of this correction can thus be defined as [26, 27]:

$$E_{\mathrm{model}} = \frac{1}{2\,\varepsilon\,\Omega}\sum_{\mathbf{G}\neq\mathbf{0}}\frac{4\pi}{|\mathbf{G}|^2}\left|\tilde{\rho}_{\mathrm{model,d}}(\mathbf{G})\right|^2 \;-\; \frac{1}{\pi\,\varepsilon}\int_0^\infty \kappa\left|\tilde{\rho}_{\mathrm{model,d}}(\kappa)\right|^2 d\kappa, \tag{3}$$

where $\tilde{\rho}_{\mathrm{model,d}}(\mathbf{G}) = \int_\Omega \rho_{\mathrm{model,d}}(\mathbf{r})\,e^{-i\mathbf{G}\cdot\mathbf{r}}\,d^3r$, $\kappa = |\mathbf{G}|$, and ε is the dielectric constant of the relaxed defect supercell calculated within the linear response regime in our DFT calculations. The first term of Eq. (3) is just the Fourier transform of the electrostatic energy of $\rho_{\mathrm{model,d}}$ and the second term corrects for the self-energy of an isolated charge density [26]. The model charge density is defined as [23, 27]:

$$\rho_{\mathrm{model,d}}(\mathbf{r}) = qx\,\frac{e^{-|\mathbf{r}-\mathbf{r}_0|/\gamma}}{N_\gamma} + q(1-x)\,\frac{e^{-|\mathbf{r}-\mathbf{r}_0|^2/\beta^2}}{N_\beta}, \tag{4}$$

where $N_\gamma = 8\pi\,\gamma^3$, $N_\beta = \pi^{3/2}\,\beta^3$, and x, β and γ are fitting parameters with $\mathbf{r}_0$ is centred on the defect [23, 24, 26]. Equation (4) represents a weighted sum of an exponentially decaying radial charge distribution and a localised Gaussian charge distribution. If the weighting factor $x = 1$, then the model charge density is completely delocalised, with the opposite case occurring when $x = 0$: the charge density is fully localised.

Importantly, the potential alignment $\Delta V_{\mathrm{model},\,q/b}\big|_{\mathrm{far}}$ in the FNV correction varies strongly around the defect as the extent of relaxation of atoms around it increases [24, 26]. A planar average of this potential is used in the FNV correction [23, 27]. Hence, relaxation of atoms at the defect gives rise to an anisotropic charge distribution which the scalar FNV correction may not be able to accurately capture [24, 26].

To remedy this inherit deficiency, the *tensor* KO extension of the *scalar* FNV correction was introduced [26]:

$$E_{\mathrm{corr}}\big[D^q\big] = -\,E_{\mathrm{PC}} - q\,\Delta V_{\mathrm{PC,q/b}} \tag{5}$$

$$E_{\mathrm{PC}} = \frac{1}{2\Omega}\sum_{\mathbf{G}\neq\mathbf{0}} \frac{4\pi}{\mathbf{G}^{\mathrm{T}}\varepsilon\,\mathbf{G}}\left|\tilde{\rho}_{\mathrm{model,d}}(\mathbf{G})\right|^2 = \frac{2\pi q^2}{\Omega}\sum_{\mathbf{G}\neq\mathbf{0}} \frac{1}{\mathbf{G}^{\mathrm{T}}\varepsilon\,\mathbf{G}} \tag{6}$$

$$\tilde{\rho}_{\mathrm{model,d}}(\mathbf{G}) = \int_\Omega \rho_{\mathrm{model,d}}(\mathbf{r})\,e^{-i\mathbf{G}\mathbf{r}}\,d^3r = \int_\Omega q\,\delta(\mathbf{r}-\mathbf{r}_0)\,e^{-i\mathbf{G}\mathbf{r}}\,d^3r = q, \tag{7}$$

where now ε is the dielectric *tensor* also obtained from a DFT linear response calculation on the relaxed defect supercell. In practice, ε is diagonalized and both ε and $\mathbf{G}$ are rotated into the principal-axis frame (where ε is diagonal), so that $\mathbf{G}^{\mathrm{T}}\varepsilon\,\mathbf{G} = \sum_i \varepsilon_i\,G_i^2$ [26]. Note that here the constant (and divergent) electrostatic self-interaction term cancels exactly in Eq. (5) because it appears with the same magnitude but opposite sign in the electrostatic energy E_{PC} and the reference potential V_{PC} used to define the alignment term $\Delta V^{\mathrm{far}}_{\mathrm{PC,q/b}}$ in the KO scheme [26]. Hence, no explicit self-energy contribution is needed when Eq. (5) is used in Eq. (1).

Figure 1 shows the Ce-vacancy complexes considered in this work: Ce inserted into a divacancy, a trivacancy or at the site of 4 C atoms removed. They have been created from a relaxed 216-atom diamond supercell with lattice constant 3.574 Å, in close analogy with the structures employed in Ref. [9]. [1]

We performed DFT calculations in `CASTEP` [28] on the input structures, which were randomly distorted from ideal symmetry to ensure energetically favourable final geometries, using on-the-fly-generated (OTFG) ultra-soft pseudopotentials [29]. An energy cutoff of 540 eV and a $3 \times 3 \times 3$ k-mesh were employed. To account for localisation of the $4f$ orbitals on Ce, we used PBE+U [30, 31] with $U = 6.0$ eV. We considered initial charge states $q = -1, 0, +1, +2, +3, +4$. The chosen range ($-1 \leq q \leq +4$) spans the relevant Ce oxidation states ($\mathrm{Ce}^{2+} - \mathrm{Ce}^{6+}$), where adding or removing electrons corresponds to negative or positive q, respectively [9, 10]. Different initial spin states for each charge state were also considered ($S = 0 \ldots 7$). The structures were relaxed to a tolerance of 0.01 eV/Å.[2]

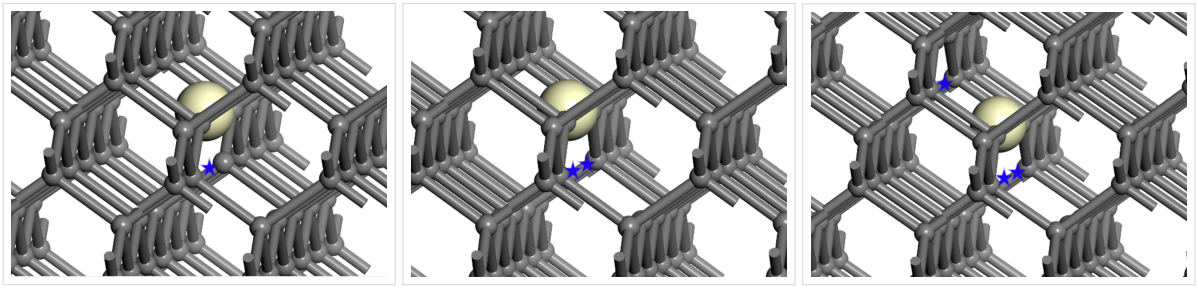

Figure 1: The initial (*left*) $\mathrm{Ce_{V2}}$, (*middle*) $\mathrm{Ce_{V3}}$ and (*right*) $\mathrm{Ce_{V4}}$ complexes used in this work. Blue stars indicate the nearest-neighbour atoms of Ce that have been removed by analogy with Ref. [9].

3 Results

The relaxed vacancy complexes are shown in Fig. 2. The dopant and nearest neighbour carbon atoms within the second-nearest neighbour shell of pristine diamond (2.53 Å) are highlighted. The extent of coordination and the increasing disparity between neighbouring bond lengths indicate the growing disorder about the relaxed point defects.

It should not come as a surprise that the FNV corrections become increasingly unreliable as the disorder around the dopant grows [25, 26]. In a 216-atom cell, FNV performs well for deep, localised states, consistent with its formal applicability [24, 25]. Its breakdown for more delocalised or anisotropic cases reflects the monopole-model assumption rather than a finite-size artefact. As summarised in tables 1–3, the enclosed charge derived from the fitted parameters x, β and γ in Eq. (4) assesses localisation *within the supercell*. The FNV and KO potential-alignment terms are also listed to enable comparison with the conventional approach, which systematically overestimates the required shift by $\approx$ 30–40% for non-neutral charge states [22]. For $q = 0$ all methods coincide, confirming that the discrepancy is a systematic bias rather than numerical noise.

[1] We use a different naming convention for our Ce-vacancy complexes because the Ce atoms do not remain at substitutional sites after relaxation, as implied by the naming convention of Ref. [9]: CeV, CeV2 and CeV3.

[2] The `CASTEP` utility `c2x` was employed to convert output binary files to Gaussian `cube` format read by `SPINNEY`.

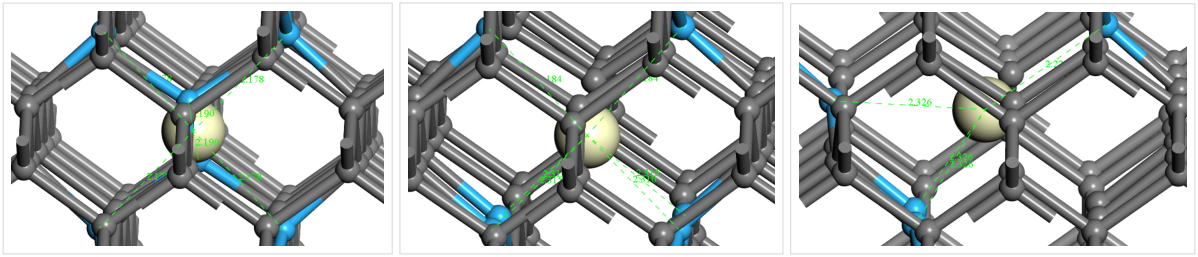

Figure 2: The optimised (*left*) Ce_{V2}, (*middle*) Ce_{V3} and (*right*) Ce_{V4} complexes. The dopant and nearest-neighbour (nn) carbon atoms within the second nn shell of pristine diamond are shown. The bond distances are also shown. In Ce_{V2}, all six nearest neighbours are ≈ 2.2 Å from the Ce atom. In Ce_{V3}, two nearest neighbours are ≈ 2.2 Å, and the other four ≈ 2.3 Å, from the Ce atom. In Ce_{V4}, one nearest neighbour is ≈ 2.2 Å, and the other three ≈ 2.3 Å, from the Ce atom. All other carbon atoms are further than the second nn shell of pristine diamond (2.53 Å) from the Ce atom.

q	$S_{\min}$	FNV total	FNV ΔV_{far}	KO total (eV)	KO ΔV_{far}	Conventional ΔV	q_{enc}
-1	0.98754	0.226	0.118	0.217	0.126	0.163	-0.99999996
0	0.0000022	0.0	-0.003	0.0	0.001	0.0	0.0
$+1$	1.0007	0.205	-0.119	0.210	-0.114	-0.157	0.99999994
$+2$	2.00004	0.774	-0.222	0.771	-0.222	-0.303	1.9999998
$+3$	2.08479	1.893	-0.346	1.796	-0.345	-0.3134	2.9999994
$+4$	2.17017	27.245	-0.098	0.865	-0.087	-0.3365	3.9998

Table 1: FNV and KO total correction and potential alignment values (eV) for vacancy complex Ce_{V2}. $S_{\min}$ corresponds to the spin state of lowest total energy. The conventional potential alignment is included for comparison. The enclosed charge within each supercell is calculated as $q_{\text{enc}}(r) = 4\pi \int_0^r \rho_{\text{model,d}}(r')\, r'^2\, dr'$ with $\rho_{\text{model,d}}$ as defined in Eq. (4) and the integration performed on interval $0 < r \leq \frac{1}{2} L_{\min}$ with $L_{\min} = \min_i \|\mathbf{a}_i\|$ and $\mathbf{a}_i$ the supercell side lengths.

q	$S_{\min}$	FNV total	FNV ΔV_{far}	KO total (eV)	KO ΔV_{far}	Conventional ΔV	q_{enc}
-1	1.0	0.317	0.113	0.202	0.116	0.121	-0.9999995
0	0.0019	0.0	-0.003	0.0	0.003	0.0	0.0
$+1$	0.99811	297.953	297.953	0.201	-0.102	-0.134	7.3×10^{-6}
$+2$	0.00062	1498.712	749.356	0.725	-0.197	-0.227	9.2×10^{-6}
$+3$	0.787866	2967.798	989.266	1.415	-0.268	-0.288	1.4×10^{-5}
$+4$	0.188895	3526.123	881.531	1.712	-0.234	-0.345	1.8×10^{-5}

Table 2: FNV and KO total correction and potential alignment values (eV) for vacancy complex Ce_{V3}. The meanings of the remaining columns carry over from table 1.

With the exception of charge state $q = +4$, Ce_{V2} in table 1 shows consistent FNV and KO corrections, and their potential alignments agree well with the conventional scheme. Where the defect remains localised (e.g. CeV_2 and $q = -1$ of CeV_3), the two methods agree to within $\approx 5\%$. Quantitatively, across these deep, localised cases (CeV_2 excluding $q = +4$), the FNV and KO corrections differ by only $3.1 \pm 2.0\%$ (mean $\pm$ sd, $N = 5$), confirming that both schemes reliably capture the electrostatics in this regime. For $q = +3$, possible metastable spin states have been found; only the most stable spin state is reported: $S_{\min}$ corresponds to the lowest total energy, with excited spin states differing by at most 6×10^{-5} eV. The enclosed charge calculated from Eq. (4) also matches the specified charge state. The discrepancy between FNV and KO for $q = +4$ suggests a highly anisotropic charge distribution, highlighting a known deficiency of the FNV scheme [25].

We immediately observe in table 2 how the situation changes when we consider the next vacancy complex with increased disorder: Ce_{V3}. FNV only yields reasonable total correction and potential alignment values for the

q	$S_{\min}$	FNV total	FNV ΔV_{far}	KO total (eV)	KO ΔV_{far}	Conventional ΔV	q_{enc}
-1	1.0	292.236	-292.236	0.147	0.079	0.119	-4.6×10^{-6}
0	0.0	0.0	-0.001	0.0	0.001	0.0	0.0
$+1$	0.990084	285.872	285.872	0.186	-0.104	-0.122	7.3×10^{-6}
$+2$	0.00087	1113.150	556.575	0.727	-0.202	-0.237	1.4×10^{-5}
$+3$	0.961946	2218.033	739.344	1.450	-0.268	-0.322	2.2×10^{-5}
$+4$	0.337866	2843.334	710.833	1.886	-0.252	-0.392	2.9×10^{-5}

Table 3: FNV and KO total correction and potential alignment values (eV) for vacancy complex Ce_{V4}. The meanings of the remaining columns carry over from table 1.

$q = -1$ charge state. The FNV model charge enclosed in the supercell also tallies with this charge. The FNV correction and potential alignment values blow up for all positive charge states, and the fact that the essentially zero fitted charge densities do not agree with them suggests that the charge is delocalised, and that these defects are shallow, unlike the localised deep states in Ce_{V2}. For $q = 0$, all non-zero initial spin states turn out to be metastable, with total energies that differ by up to ≈ 0.01 eV from $S_{\min}$. These energetically less favourable spin states have $S \approx 2.0$ compared to $S_{\min} \approx 0.002$.

For the largest and most disordered vacancy cluster, Ce_{V4}, the FNV correction fails across the board in table 3, and all non-zero charge states yield shallow defects with the FNV model charge delocalised beyond the confines of a single defect supercell. The total energy difference between metastable spin states (for a given charge state) is up to ≈ 0.05 eV for $q = +2$. The less energetically favourable spin states all end up as $S \approx 2.0$ whilst $S_{\min} \approx 1 \times 10^{-5}$. In constrast to $q = +4$ of Ce_{V2}, the FNV correction ultimately fails here not because the defect is anisotropic but rather because it is shallow, as is evident from the delocalised model charge in the last columns of tables 2 and 3.

The KO correction, on the other hand, delivers consistent values across all charge states, as expected from its point-charge electrostatics and atomic-site potential alignment model. Where KO agrees with FNV in this *relatively large* supercell, we infer that the defect state remains deep and localised. When defects are shallow or anisotropic, the FNV correction becomes numerically unstable, whereas KO remains stable and continues to capture the electrostatics reliably across all regimes, consistent with its tensor formulation and point-charge reference [26]. It does not assume spherical charge symmetry, making it the preferred scheme for rare-earth dopants with anisotropic $4f$ charge densities in diamond.

Finally, the stability of the neutral vacancy complexes follows the same trend as in Refs. [9, 16]: $E_f[D^0]_{\text{Ce}_{\text{V2}}} = 15.5259$ eV, $E_f[D^0]_{\text{Ce}_{\text{V3}}} = 14.3588$ eV and $E_f[D^0]_{\text{Ce}_{\text{V4}}} = 14.5393$ eV, confirming Ce_{V3} as the most stable neutral configuration.

In conclusion, the FNV and KO schemes have been evaluated for the three Ce-vacancy complexes across multiple charge and spin states. FNV fails for shallow or anisotropic defects, whereas KO remains reliable throughout. FNV's breakdown also identifies shallow levels, while accurate formation energies may ultimately require hybrid functionals, as intended in future work.

References

[1] E. B. Lombardi, A. Mainwood, K. Osuch, and E. C. Reynhardt, "Computational models of the single substitutional nitrogen atom in diamond," *J. Phys. Condens. Matter*, vol. 15, no. 19, pp. 3135–3149, 2003.

[2] N. Zhao, J.-L. Hu, S.-W. Ho, J. T. K. Wan, and R. B. Liu, "Atomic-scale magnetometry of distant nuclear spin clusters via nitrogen-vacancy spin in diamond," *Nat. Nanotechnol*, vol. 6, no. 4, pp. 242–246, April 2011.

[3] E. M. Benecha and E. B. Lombardi, "Cu doped diamond: Effect of charge state and defect aggregation on spin interactions in a 3 d transition metal doped wide band-gap semiconductor," *J. Appl. Phys.*, vol. 123, no. 18, p. 185706, 2018.

[4] M. Gulka, D. Wirtitsch, V. Ivády, J. Vodnik, J. Hruby, G. Magchiels, E. Bourgeois, A. Gali, M. Trupke, and M. Nesladek, "Room-temperature control and electrical readout of individual nitrogen-vacancy nuclear spins," *Nat. Commun.*, vol. 12, no. 1, pp. 1–8, 2021.

[5] A. Magyar, W. Hu, T. Shanley, M. E. Flatté, E. Hu, and I. Aharonovich, "Synthesis of luminescent europium defects in diamond," *Nat. Commun.*, vol. 5, pp. 1–6, 2014.

[6] V. S. Sedov and E. al., "Diamond-EuF3 nanocomposites with bright orange photoluminescence," *Diam. Relat. Mater.*, vol. 72, pp. 47–52, 2017.

[7] P. Rembold, N. Oshnik, M. M. Müller, S. Montangero, T. Calarco, and E. Neu, "Introduction to quantum optimal control for quantum sensing with nitrogen-vacancy centers in diamond," *AVS Quantum Science*, vol. 2, no. 2, 2020.

[8] V. Sedov, S. Kuznetsov, A. Martyanov, and V. Ralchenko, "Luminescent diamond composites," *Funct. diam.*, vol. 2, no. 1, pp. 53–63, 2022. [Online]. Available: https://doi.org/10.1080/26941112.2022.2071112

[9] X. Tan, X. Wei, L. Chen, and Z. Liu, "Study of the structural stability and electronic structure of Ce-related defects in diamonds," *Opt. Mater. Express*, vol. 10, no. 5, p. 1286, 2020.

[10] X. Tan, J. Wang, X. Wei, C. Pan, Y. Ren, S. Sun, and H. Jia, "First-principle study on the influence of common impurities in diamond on the electronic structure of Ce-related defects," *Opt. Mater. Express*, vol. 11, no. 10, p. 3421, 2021.

[11] J. Cajzl, B. Akhetova, P. Nekvindová, A. Macková, P. Malinský, J. Oswald, Z. Remeš, M. Varga, and A. Kromka, "Co-implantation of Er and Yb ions into single-crystalline and nano-crystalline diamond," *SIA*, vol. 50, no. 11, pp. 1218–1223, 2018.

[12] D. Propst, J. Kotakoski, and E. H. Åhlgren, "Impurity atom configurations in diamond and their visibility via scanning transmission electron microscopy imaging," *EST*, vol. 5, no. 3, 2023.

[13] D. E. Vanpoucke, S. S. Nicley, J. Raymakers, W. Maes, and K. Haenen, "Can europium atoms form luminescent centres in diamond: A combined theoretical–experimental study," *Diam. Relat. Mater.*, vol. 94, no. February, pp. 233–241, 2019.

[14] X. Tan, Z. Liu, Z. Liu, Y. Ren, S. Sun, and H. JIa, "Principle study of the europium vacancy color center in a diamond," *Opt. Mater. Express*, vol. 10, no. 12, p. 3277, 2020.

[15] X. Tan, T. Liu, X. Liu, Y. Ren, S. Sun, H. Jia, Z. Liu, L. Chen, and X. Wei, "Structural stability of Pr-related defects in diamond and electronic structure single photon source: A first-principles study," *AIP Advances*, vol. 8, no. 10, p. 105202, 2018.

[16] I. M. Morris, K. Klink, J. T. Singh, J. L. Mendoza-Cortes, S. S. Nicley, and J. N. Becker, "Rare isotope-containing diamond colour centres for fundamental symmetry tests," *Phil. Trans. R. Soc. A*, vol. 382, no. 2265, 2024.

[17] D. G. Babar, J. Nuwad, S. K. Agarwalla, D. Jain, G. Sridhar, and V. Sudarsan, "Enhancing Luminescence Properties of Lab-Grown Diamond Films with Upconversion Nanoparticles for High-Performance Surface Temperature Sensing in Advanced Applications," *ACS Appl. Opt. Mater.*, vol. 2, no. 8, pp. 1546–1558, 2024.

[18] J. Cajzl, P. Nekvindová, A. Macková, M. Varga, and A. Kromka, "Erbium ion implantation into LiNbO3, Al2O3, ZnO and diamond - measurement and modelling - an overview," *Phys. Chem. Chem. Phys.*, vol. 24, no. 32, pp. 19 052–19 072, 2022.

[19] N. Ghafari Cherati, A. Pershin, and Á. Gali, "Sulfur in diamond and its effect on the creation of nitrogen-vacancy defect from ab initio simulations," *Phys. Rev. Research*, vol. 7, no. 1, p. 13278, 2025.

[20] Z. Wang, P. Jin, P. Qu, F. Cao, X. Han, and Z. Wang, "Progress in first-principles studies on doped semiconductor diamond," *EPJ ST*, vol. 123, 2025.

[21] G. Makov and M. C. Payne, "Periodic boundary conditions in ab initio calculations," *Phys. Rev. B*, vol. 51, no. 7, pp. 4014–4022, 1995.

[22] S. Lany and A. Zunger, "Assessment of correction methods for the band-gap problem and for finite-size effects in supercell defect calculations: Case studies for ZnO and GaAs," *Phys. Rev. B*, vol. 78, no. 23, pp. 17–20, 2008.

[23] C. Freysoldt, J. Neugebauer, and C. G. Van De Walle, "Fully Ab initio finite-size corrections for charged-defect supercell calculations," *Phys. Rev. Lett.*, vol. 102, no. 1, pp. 1–4, 2009.

[24] H. P. Komsa, T. T. Rantala, and A. Pasquarello, "Finite-size supercell correction schemes for charged defect calculations," *Phys. Rev. B*, vol. 86, no. 4, pp. 1–16, 2012.

[25] C. Freysoldt, B. Grabowski, T. Hickel, J. Neugebauer, G. Kresse, A. Janotti, and C. G. Van De Walle, "First-principles calculations for point defects in solids," *Rev. Mod. Phys.*, vol. 86, no. 1, pp. 253–305, 2014.

[26] Y. Kumagai and F. Oba, "Electrostatics-based finite-size corrections for first-principles point defect calculations," *Phys. Rev. B*, vol. 89, no. 19, 2014.

[27] M. Arrigoni and G. K. Madsen, "Spinney: Post-processing of first-principles calculations of point defects in semiconductors with Python," *Comput. Phys. Commun.*, vol. 264, p. 107946, 2021.

[28] S. J. Clark, M. D. Segall, C. J. Pickard, P. J. Hasnip, M. I. J. Probert, K. Refson, and M. C. Payne, "First principles methods using CASTEP," *Z. Kristallogr. Cryst. Mater*, vol. 220, no. 5/6, pp. 567–570, 2005.

[29] D. Vanderbilt, "Soft self-consistent pseudopotentials in a generalized eigenvalue formalism," *Phys. Rev. B*, no. 11, pp. 7892–7895, apr 1990.

[30] J. P. Perdew, K. Burke, and M. Ernzerhof, "Generalized gradient approximation made simple," *Phys. Rev. Lett.*, vol. 77, no. 18, pp. 3865–3868, oct 1996.

[31] S. L. Dudarev, G. A. Botton, S. Y. Savrasov, C. J. Humphreys, and A. P. Sutton, "Electron-energy-loss spectra and the structural stability of nickel oxide: An lsda+u study," *Phys. Rev. B*, vol. 57, pp. 1505–1509, Jan 1998.

DIVISION

B

NUCLEAR, PARTICLE, AND RADIATION PHYSICS

Probabilistic Risk Assessment for Calculating Health Effects Associated with a Potential Nuclear Accident in the Vicinity of a Nuclear Facility

M.P Dondolo[1,2], I.T. Usman[1], I Korir[2], A Joubert [2], and H van Graan[2]

[1]School of Physics, University of the Witwatersrand, Johannesburg, South Africa
[2]National Nuclear Regulator, Centurion, South Africa

E-mail: 394962@students.wits.ac.za

Abstract. This study aims to present the preliminary results of a probabilistic risk assessment that was conducted to benchmark the MACCS code model and data analysis typical of the South African Nuclear Power Plant (NPP) environment. This was done to determine potential atmospheric release and consequences of radioactive material for postulated severe accident case based on current South African NPP configuration. This work was done in support of the South African nuclear regulator independent analysis verification of similar code that is currently employed by the nuclear operator. The MACCS code was successfully customised to perform probabilistic risk assessment of the South African NPP. Some of the discerning data used to perform the assessment included source term, meteorological dataset, site dataset, and other important plant specific datasets required to complete the full scope of a Level 3 probabilistic risk assessment. The analysis of implementing protective measures to counteracts the anticipated health effects was also taken into consideration. Therefore, this study outlines a full risk assessment that is done in anticipation and to counter the risk associated with the release of radioactive material by the aforementioned NPP during postulated severe accident scenario resulting in radiological releases to the site and environment.

1 Introduction

By putting in place safety guidelines and rules, the South African National Nuclear Regulator (NNR) aims to protect people, property, and the environment from nuclear damage. It also exercises regulatory control over safety and other activities covered by the NNR Act by granting and amending nuclear authorization. In this study, probabilistic risk assessment (PRA) research was conducted to benchmark the MELCOR Accident Consequence Code System (MACCS) code model and data analysis typical of the South African Nuclear Power Plant (NPP) environment. This was done to determine potential atmospheric release and consequences of radioactive material for postulated severe accident case based on current South African NPP configuration. Radiation exposures and health issues following a nuclear accident and emergency procedures are of great concern to the public and to the local authorities tasked with emergency preparedness and response tasked with ensuring public health, safety, and well-being.

The analysis of implementing protective measures to counteracts the anticipated health effects was also taken into consideration. The goal of the current study was to develop a MACCS model with Koeberg Nuclear Power Station (KNPS) data, by replicating part of the State-of-the-Art Reactor Consequence Analyses (SOARCA) approach that is followed by the USNRC. This model will be used to estimate the off-site radiological consequences of potential accident releases of radioactive materials in the vicinity of the KNPS. The model will also enable the reviewers of NNR to verify the off-site radiological consequences of KNPS against the regulatory standards/requirements. The scope of this work covers the following important aspects of Level 3 PRA analysis:

- Atmospheric transport, dispersion and deposition, and
- Dosimetry and health issues associated with radiation.

The traditional scenario-based approach to PRA, which involves the methodical use of procedures, simulations, data, and analytical tools, addresses the three basic questions (figure 1) that serve as the foundation for a generally recognized mathematical definition of risk. These are as follows [1]:

"What can possibly go wrong?"

"How probable/likely is it to happen?" and

"If it does occur, what would be the consequences?".

Technical understanding of the elements that could lead to an activity or action's unfavourable outcomes is necessary to respond to the questions in Figure 1 below. Accident scenarios—sequences of events linking the cause to the adverse outcomes—are created and measured in order to identify the solutions.

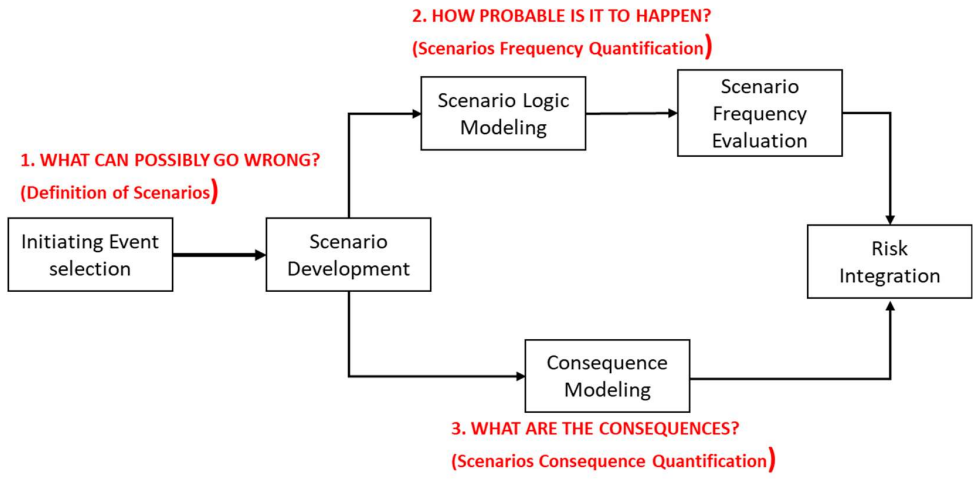

Figure 1: Fundamental Questions to PRA [2].

For NPPs, PRA analysis is often conducted at three levels, each of which expands the PRA model's breadth and complexity [3]. The results of these levels include the following:

- Level 1: Reactor core damage frequency as determined by plant damage states.
- Level 2: Radiation leakage into the environment and loss of confinement.

- Level 3: Off-site environmental consequences, including harm to human health and monetary losses.

Nuclear licensees and licence applicants for a nuclear facility are under the obligation to perform a risk analysis. MACCS and most of the dispersion codes model the following seven exposure pathways [3, 4, 5], some of which are depicted in Figure 2 below:

- External exposure to radiation in the plume (cloudshine),
- External exposure to radiation deposited on the ground (groundshine),
- Internal exposure from the inhalation of radionuclides directly from the plume (direct inhalation),
- Internal exposure from the inhalation of resuspended material (resuspension inhalation),
- External exposure to material deposited onto the skin (skin deposition),
- Internal exposure from the ingestion of food from farmland (food ingestion), and
- Internal exposure from drinking water ingestion.

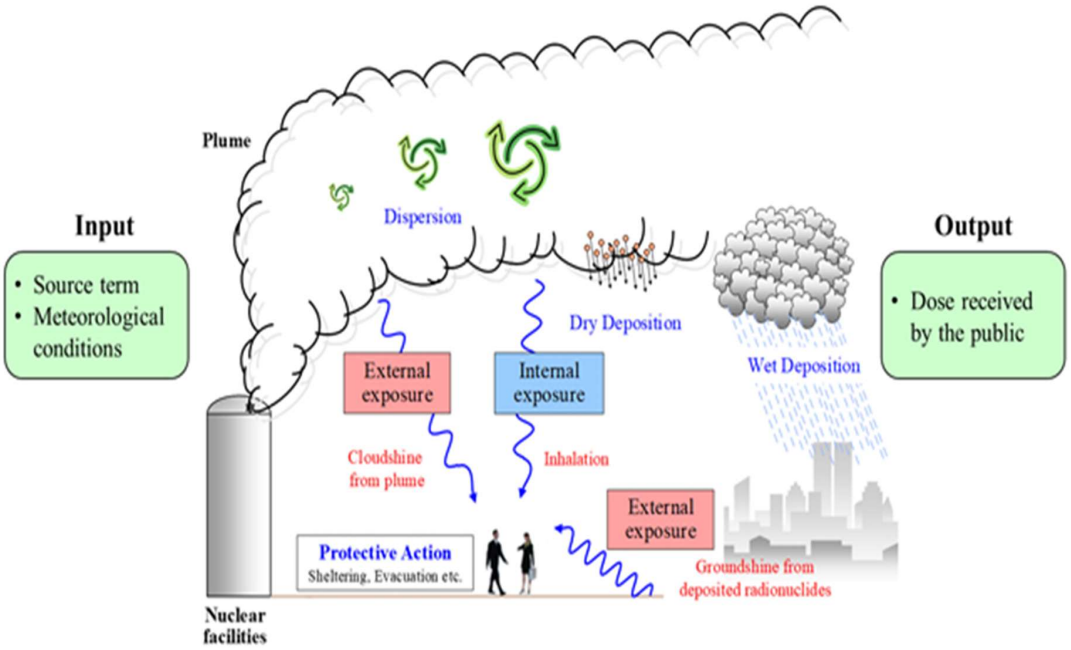

Figure 2: Radiation dose from nuclear facility [4].

2 Method

The method followed in this work was mainly quantitative in nature, i.e., a computer simulation using the Windows-based interface of MELCOR Accident Consequence Code System (WinMACCS) software, with license obtained from the USNRC in collaboration with Sandia National Laboratories

through the Cooperative Severe Accident Research Programme (CSARP) agreement. The WinMACCS code was chosen because it simulates the impact of severe accidents at nuclear power plants (NPPs) and other nuclear facilities on the surrounding environment. It is considered robust, reliable, and reproducible due to its integrated approach, which includes a user-friendly interface with input validation, extensive modeling capabilities, and features for handling uncertainty. The software's design minimizes user errors, facilitates consistent analysis by organizing inputs, and provides tools for exploring the effects of parameter uncertainties, ensuring the results are more dependable than with other codes. The main modules in the WinMACCS code consists of the ATMOS, EARLY and the CHRONC modules [5] as shown in Figure 3 below. ATMOS -Atmospheric transport and diffusion, EARLY – Early phase of the Emergency, CHRONC – Late phase of the emergency. The focus of this document is limited to the ATMOS and EARLY modules only.

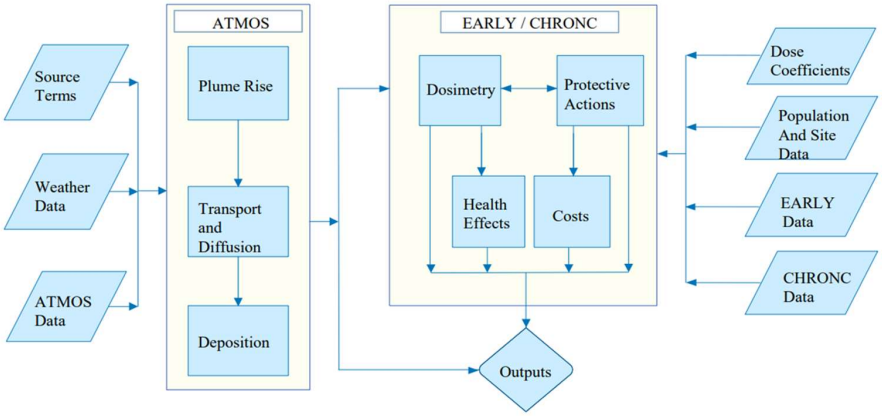

Figure 3: Overview of WinMACCS Code Scope [3].

3 Results and Discussion

Centerline ground-level χ/Q is the ratio of air concentration (χ) to source strength (Q), averaged across the duration of the interval [4]. This parameter is shown in Figures 4 and 5 during the early and the late phases of the emergency as it was observed in the simulations. MACCS produced a number of radionuclides during the release of the plume into the environment. However, only Iodine (I-131) and Caesium isotopes (Cs-134, Cs-137) were selected as they are the main radionuclides of concern [8] during the early weeks of a radiological/nuclear emergency. This is because they are released in large quantities and pose both short- and long-term health risks. I-131 is an immediate threat due to its short half-life of about 8 days and tendency to accumulate in the thyroid, while caesium isotopes have longer half-lives (Cs-137 is 30 years), causing long-term contamination and health risks from exposure to soft tissues and organs.

Figures 4 and 5 obtained in the simulations shows a similar exponential decrease to that of figure 6 below, which was obtained from the verification of MACCS against AERMOD and Analytical expression, for nearfield test cases. Which implies that the code was well replicated and can be used by the NNR to perform independent verification of the currently employed codes by the nuclear facilities.

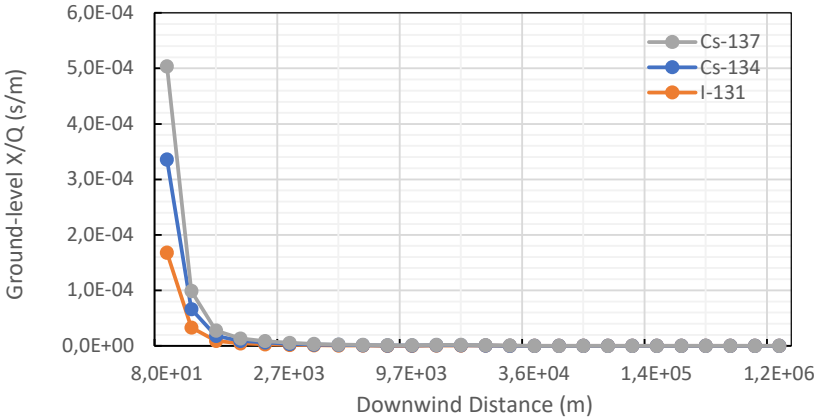

Figure 4: Ground-level X/Q in the Early Phase (hours to days) of the Emergency.

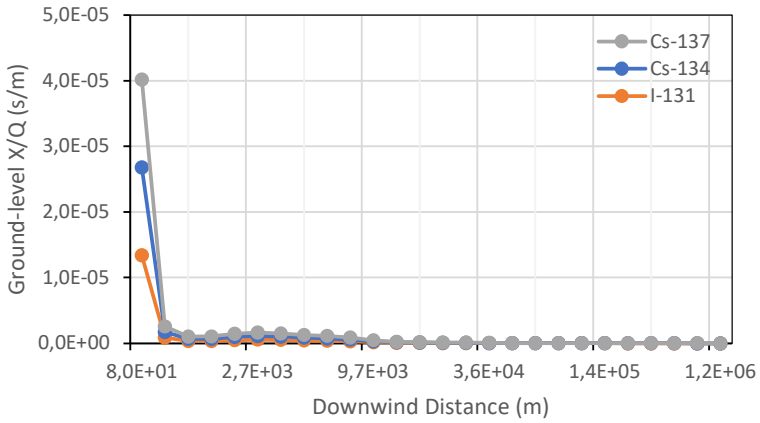

Figure 5: Ground-level X/Q in the Late Phase (months to years) of the Emergency.

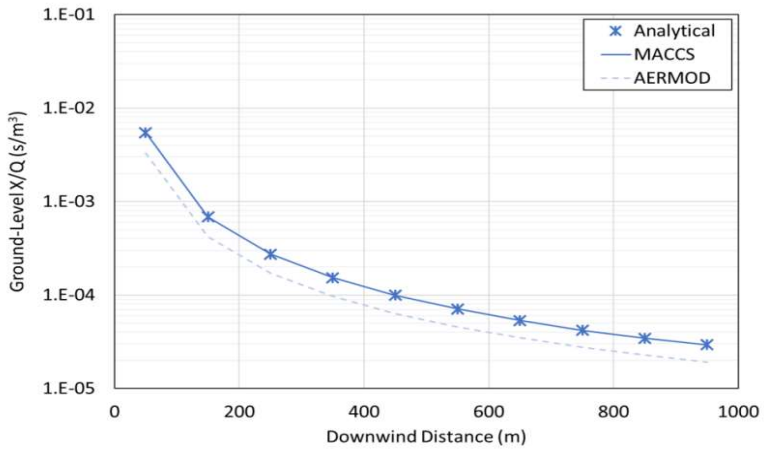

Figure 6: Ground level X/Q versus downwind distance with AEMOD, MACCS and analytical expression [9].

The population in the vicinity of the plant were divided into three Cohorts in MACCS in the simulations. The three cohorts were the following: Cohort 1: General Population (89.5%), Cohort 2: Evacuating Population (0.5%), Cohort 3: Evacuation Tailing (10%). Figure 6 depicts the results of Cohort 1 which was similar in results to cohorts 2 and 3. The legends in the graph in figure 7 below represents: PID -Plume Inhalation Dose, CD – Cloudshine, GD -Groundshine, RESID -Resuspension Inhalation Dose, SDD – Skin Deposition Dose.

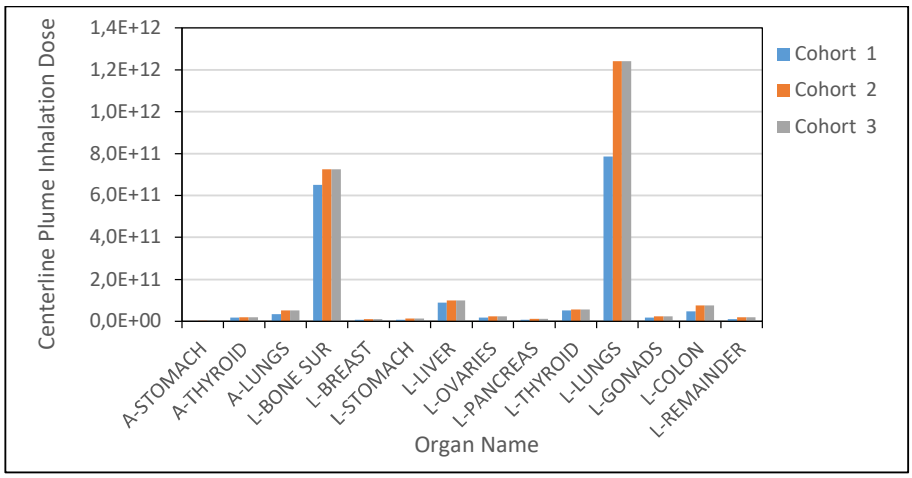

Figure 7: Total Dose to all Cohorts.

During the early phase of the nuclear/radiological emergency, the most significant radionuclide of interests would be I-131 due to the uptake by the thyroid glands through inhalation [6]. In figures 4 and 5, the results depict I-131 and other important radionuclides that can be produced with the plume during the release of radiation to the environment. As illustrated, the graph is decreasing exponentially, indicating that the normalized concentration of radionuclides present in the plume is highly concentrated at the source/stack and continues to decrease as it is diluted in the atmosphere away from the source (NPP) of the plume. The source of the plume (NPP) as located at distance zero in the graph in figures 4 and 5. In figure 6, the total centerline plume inhalation dose for cohort 1 was observed to be much less than that of cohorts 2 and 3. This was due to the fact that cohort 1 constitute the population that is most likely to be exposed over long durations and they were the focus of the assessments. Therefore, the protective measures focused on cohort 1 as it consisted of most of the population, and the dose received by them was much less.

4 Conclusion

The behavior of the centerline ground-level χ/Q can be expected since the radiation tends to diffuse exponentially from a region of high concentration to a region of low concentration. It conforms to the corresponding Gaussian Plume Dispersion equation as they are exponential functions, and they continue to decay with time. This result implies that the MACCS code was successfully replicated and can be used to perform off-site consequence analysis, with meaningful results. In the current simulated scenario, the general population was protected through following the protective measures of evacuation and also used to provide recommendations to mitigate the dose to the public and the environment. Therefore, the MACCS code forms a valuable tool in providing the recommendations to implement protective actions in protecting the public from the radiation release from a nuclear accident.

Although there may be a great deal of research in implementing the MACCS code elsewhere it has not been done locally in South Africa, hence this work builds onto the currently existing knowledge of Level 3 PRA based in MACCS. Therefore, this study will take existing research further by applying the same technique in a local South African NPP i.e. KNPS using the MACCS code. This report makes a unique contribution by implementing the MACCS code by South African NPP, and it can serve as a building block towards performing a level 3 PRA assessment using a different code than that of the licensee for verification.

References

[1] D. Hudson, Risk analysis of multi-unit accident effects on public health and safety using state-of-the-art models: U.S. Nuclear Regulatory Commission safety goal policy implications,, Maryland: Johns Hopkins University, Baltimore, 2017.

[2] Safety assessment: purpose and scope. Introduction of relevant IAEA Safety Standards in ANSN Workshop on Safety Revies and Assessment for Licensing NPPs, Daejeon, Republic of Korea: Daejeon , 2019.

[3] A. Nosek and N. Bixler, "SANDIA REPORT: "MACCS Theory Manual"," Sandia National Laboratories, Washington, DC 20555, 2021.

[4] Authority-for-Nuclear-Safety-and-Radiation, "ANVS Guide on Level 3 PSA," Authority-for-Nuclear-Safety-and-Radiation, Netherlands, 2020.

[5] A. Caldwell, "Addressing Off-site Consequence Criteria Using Level 3 Probabilistic Safety Assessment," Department of Nuclear Power Safety KTH Royal Institute of Technology, Stockholm, Sweden, 2012.

[6] Japan-Atomic-Energy-Agency, "Evaluation of radiation dose due to radioactive materials released into the environment in a nuclear emergency," Japan-Atomic-Energy-Agency, Japan, 2020.

[7] J. Leute, F. Walton and R. Mitchell, "MACCS (MELCOR Accident Consequence Code System) User Guide – Version 4.0," Sandia National Laboratories, Albuquerque, New Mexico 87185, 2021.

[8] A. N. Laboratory, Radiological and Chemical Fact Sheets to Support Health Risk Analyses for Contaminated Areas, Chicago Opreations Office: U.S Department of Energy, 2007.

[9] D. .. Clayton, "Implementation of Additional Models into the MACCS Code for Nearfield Consequence Analysis," Sandia National Laboratories, Albuquerques, Nex Mwxico, 2021.

[10] D. M. Osborn, "Seamless Level 2/Level 3 Probabilistic Risk Assessment Using Dynamic Event Tree Analysis," Graduate Program in Nuclear Engineering The Ohio State University, Ohio, 2013.

[11] N. Bixler, J. Jones, D. Osborn and S. Weber, " NUREG/CR-7009: MACCS Best Practices as Applied in the State-of-the-Art Reactor Consequence Analyses (SOARCA) Project," U.S. Nuclear Regulatory Commission, United States, 2014.

This page intentionally left blank.

Alpha and beta radiation effects on Re_2MnCoO_6 (Re = La, Sm, Nd)

Tinashe Dhliwayo[1,2], Odireleng M Ntwaeaborwa[3] and Buyisiwe M Sondezi[1]

[1]Rare Earth-Based Oxides and Nano Group, Department of Physics, University of Johannesburg, Cnr
Kingsway Avenue and University Road, Auckland Park 2006, South Africa.
[2]Advanced Energy, Abu Dhabi Polytechnic, MBZ, Abu Dhabi, UAE.
[3] Department of Physical and Earth Sciences Sol-Plaatjie University, Kimberly, South Africa.

E-mail: Tinashe.dhliwayo@actvet.gov.ae

Abstract. The rise in global demand for nuclear technology has led to an increase in radioactive waste and radioactive materials. Some of these radioactive materials and nuclear waste undergo radioactive decay, emitting alpha and beta particles. Both alpha and beta particles can cause significant damage along their path of travel. Consequently, there is a need to identify/develop materials suitable for use in radiation shielding. This study, therefore, aimed at investigating the effects of alpha and beta radiation on Re_2MnCoO_6 (Re = La, Sm, Nd) prepared by the solid-state method. The continuous slowing-down approximation (CSDA) range of beta particles in the samples and the stopping power of the samples have been calculated using the ESTAR method. At 0.5 MeV, the CSDA range of beta particles is 0.273 g/cm^2 for Sm_2MnCoO_6, 0.270 g/cm^2 for Nd_2MnCoO_6, and 0.269 g/cm^2 for La_2MnCoO_6. The mass stopping power of all three samples decreases with energy up to 1 MeV, beyond which it starts to increase again. The ion ranges, energy deposition, and displacement damage caused by alpha particles have been estimated using the ion transport Monte Carlo simulations using the Stopping and Range of Ions in Matter (SRIM) code with the Full Damage Cascades Mode. A 4 MeV alpha particle has a range of about 23.3 µm in Sm_2MnCoO_6, 22.7 µm in Nd_2MnCoO_6, and 22.3 µm in La_2MnCoO_6. The mass stopping power for all three samples ranged between 0.320 MeV.cm^2/g and 0.414 MeV.cm^2/g for a 0.1 MeV alpha particle. The results show that double perovskites are possible candidates as matrices for radioactive waste immobilization.

1 Introduction and Background

The rise in global demand for energy has generated interest in the use of nuclear energy across the globe, and especially in Africa and the Middle East. This, therefore, means large amounts of spent nuclear fuel and other nuclear-related waste will be produced.

Nuclear waste can be classified as high-level waste (HLW), intermediate-level waste (ILW), and low-level waste (LLW) based on its radioactivity level. Even though HLW has the lowest volume [1, 2] but it is considered the most hazardous because it is highly radioactive, generates large amounts of heat, and contains long-lived radionuclides [3]. The main sources of radiation in nuclear waste are beta decay from fission products and alpha decay of the actinide elements [3]. The recoil nuclei and gamma rays also contribute to the radiation damage of the material. Polonium-212 ($E_\alpha \approx 8.78\ MeV$) and polonium-213 ($E_\alpha \approx 8.38\ MeV$) are some of the actinides with the most energetic alpha emissions. Fission products like yttrium-90 ($E_\beta \approx 2.28\ MeV$) and rhodium-106 ($E_\beta \approx 3.54\ MeV$) are amongst the highest beta emitters.

Disposal of waste depends on the category of the radioactive waste and ranges from landfill to deep geological repositories [4]. High-level waste is proposed to be disposed of using a multi-barrier system, with the first barrier being the waste form [5]. High-level waste needs to be immobilized in a suitable waste form before it can be stored in a multi-barrier system. Immobilization is a process where the waste is made immovable in the form of wasteforms [6]. There are various methods for creating wasteforms, including vitrification, solidification, and containment [7], and the effectiveness of the wasteform is determined by the chemical durability and radiation durability of the matrix. The wasteforms can be classified into three main types, namely glass, ceramic, and glass–ceramic wasteforms.

This study investigates the effects of alpha and beta radiation on selected double perovskite ceramics, possible candidates for ceramic wasteform. Double perovskites are represented by a general formula $A_2BB'O_6$, where A is a lanthanide cation, B and B′ are transition cations. These materials are of interest because of their structural and compositional flexibility [8].

2 Materials and Methods

2.1 Synthesis of materials

Samples were synthesized using the solid-state method [9]. The stoichiometric ratios of the starting powder materials were measured and ground into fine powders, which were then calcined at 900°C for 12 hours before being annealed at 1200 °C for an additional 48 hours. The annealed samples were finely ground and characterized by powder X-ray diffraction (XRD) to ascertain that the right structures were crystallized. These were achieved through continuous scanning using Cu-Kα radiation (40 kV, 30 mA) at a range of 10° to 90° with a step size of 0.02° and a scanning speed of 0.145 s/step.

2.2 Radiation damage measurements

The continuous slowing-down approximation (CSDA) range of beta particles in the samples and the stopping power of the samples were calculated using the ESTAR software, a radiation simulation software developed by the National Institute of Standards and Technology (NIST). The ranges, energy deposition, and displacement damage caused by alpha particles were calculated by the ion transport Monte Carlo simulations using the Stopping and Range of Ions in Matter (SRIM) code with the Full Damage Cascades mode. The energy range of the alpha particles varied from 0 MeV to 10 MeV, and from 0 MeV to 6 MeV for beta particles.

3 Results

3.1 XRD and Rietveld analysis

Table 1 shows the refinement parameters of the three samples, and they are consistent with the data published in the literature [9]. The volume of the oxides decreases with the increase in the lanthanide ion radius. However, the density increases as the volume decreases due to the increase in mass of the lanthanide ion. Figures 1a, 1b, and 1c represent powder X-ray diffraction curves of La_2MnCoO_6

(LMCO), Sm_2MnCoO_6 (SMCO), and Nd_2MnCoO_6 (NMCO), respectively. The black lines are the experimental data, the red lines represent the least squares Rietveld refinement fits, and the purple curves at the bottom represent the difference between the experimental and the theoretical data. All reflections were indexed as a monoclinic structure according to the Bragg law [9].

Cell parameters	LMCO	NMCO	SMCO
a (Å)	5.525	5.447	5.360
b (Å)	5.486	5.619	5.564
c (Å)	7.774	7.713	7.607
β (°)	89.880	89.443	90.004
V ($Å^3$)	235.6	228.3	226.9
ρ (gcm^{-3})	3.437	3.512	3.598

Table 1: Sample parameters after refinement.

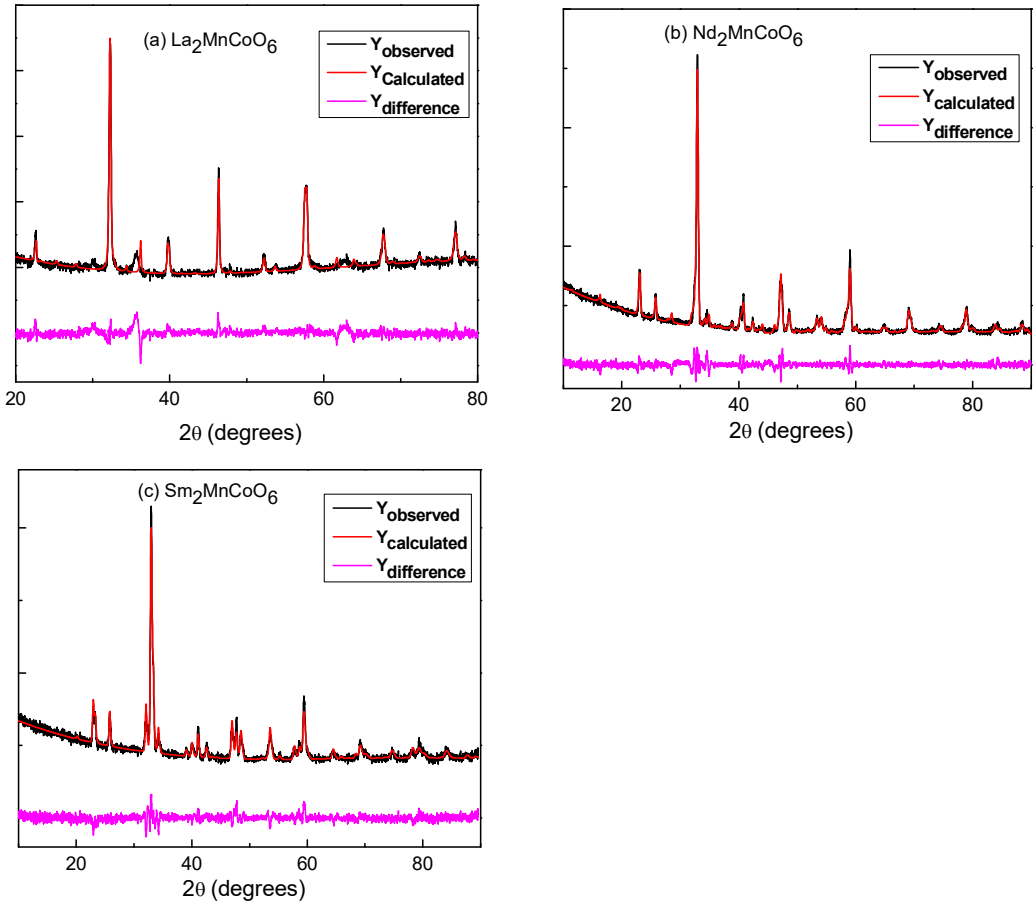

Figure 1: Rietveld refinement of XRD data for (a) La_2MnCoO_6, (b) Nd_2MnCoO_6, and (c) Sm_2MnCoO_6.

3.2 Stopping power

Stopping power is the average energy lost by ionizing radiation per unit distance travelled in a medium. The energy is lost through ionization, excitation, and Bremsstrahlung radiation. It is affected by the type of charged particle, energy of the charged particle, and material density and atomic number of the material. The Bethe formula shown in equation 1 is used to calculate the stopping power of materials [10].

$$-\frac{dE}{dx} = 4\pi \frac{z^2 e^4}{m_e v^2} NB \quad (1)$$

where m_e is the electron mass, v is the particle speed, N is the atomic density of the medium, and B is a variable that is proportional to the atomic number of the medium, Z. The ratio of stopping power and density of the material gives the specific energy loss (mass stopping power).

Figure 2a shows the variation of mass stopping power of different materials with alpha particle energy. All three samples show that the alpha particle starts picking up electrons at the energy (E_{max}) of between 0.70 MeV and 0.8 MeV, and the slowing down process starts. The stopping powers at maximum energy are 0.917 MeV.cm^2/mg for LMCO, 0.842 MeV.cm^2/mg for NMCO, and 0.824 MeV.cm^2/mg for SMCO. LMCO has the highest stopping power across the energy range under investigation, compared to the other two samples, as illustrated in Figure 2a. This shows that LMCO is more effective in stopping alpha particles with the energy of between 0.01 MeV and 10 MeV.

Figure 2b shows that all materials exhibit a non-linear decrease in stopping power with increasing energy up to around 1 MeV, followed by a gradual increase at higher energies. This behaviour is typical due to the Bethe-Bloch equation, where the stopping power initially decreases with energy and then increases due to radiative losses at higher energies [11]. This is because at high energies, the beta particle begins to behave like a relativistic particle, and the Bethe formula is no longer applicable. All three materials exhibit similar stopping powers across the investigated energy range.

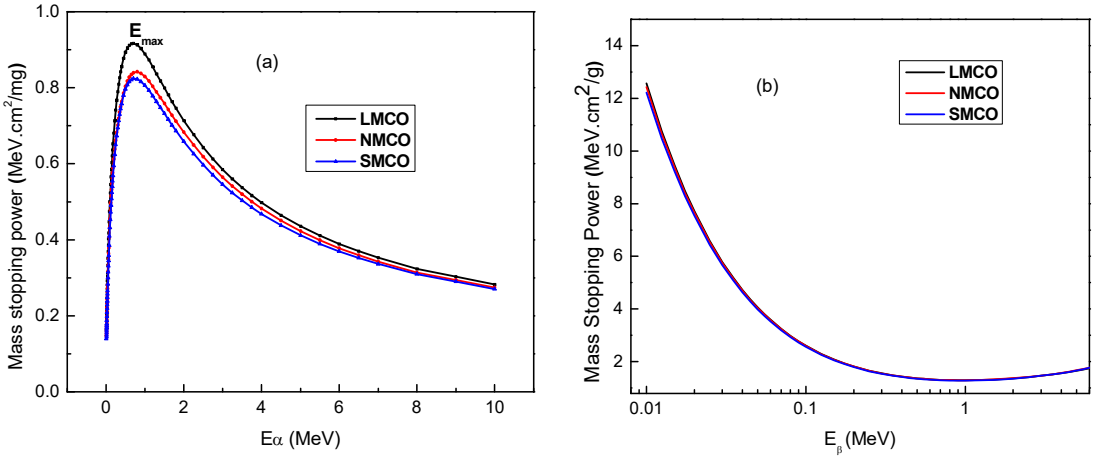

Figure 2: Specific energy loss as a function of (a) alpha particle energy, (b) beta particle energy.

3.3 The range and CSDA range

Range is the average depth of penetration of a particle in a material before losing all its energy. The Continuous Slowing Down Approximation (CSDA) concept assumes that the particle loses energy

continuously and gradually, without any abrupt changes due to scattering or other interactions [11, 12]. It is calculated using equation 2 [12].

$$R_{CSDA} = \int_0^{E_0} \frac{1}{S(E)} dE \quad (2)$$

where *S(E)* is the stopping power, and E_0 is the incident energy of the radiation particle.

Figure 3 shows the variation of range (μm) as a function of alpha particle energy. The range of alpha particles in all materials increases with the energy of the alpha particles. Alpha particles have a shorter range in LMCO compared to the other two samples. Again, this shows that LMCO stops alpha particles faster compared to the other two materials.

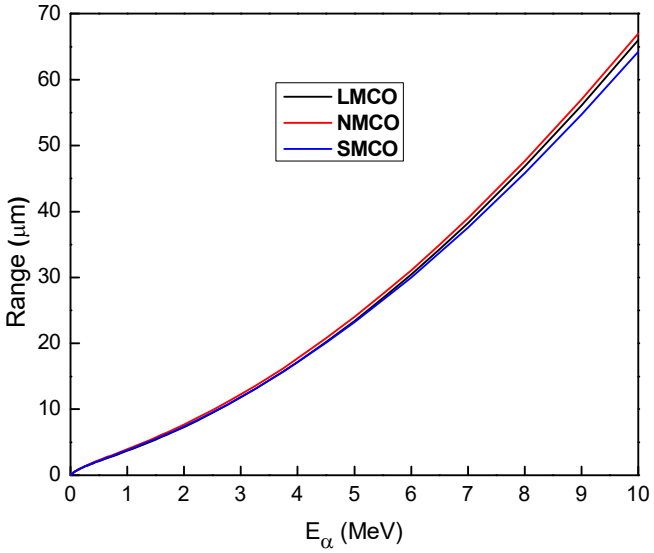

Figure 3: Variation of range as a function of alpha particle energy.

Figure 4 shows that the CSDA range of beta particles increases with energy for all materials, as higher-energy beta particles penetrate deeper into the material. The relationship is non-linear, with a steeper increase at lower energies and a more gradual rise at higher energies. LMCO consistently shows the highest average CSDA range across the energy spectrum.

3.4 Alpha particle collision events

SRIM uses the Norgett-Robinson-Torrens (NRT) model, shown in equation 3, to calculate the number of vacancies created and displacements caused [13].

$$\nu_{NRT} = \frac{\kappa T_d}{2E_d} \quad (3)$$

where κ (~0.8) is the displacement efficiency, T_d (MeV) is the average damage energy, and E_d (MeV) is the displacement energy. The model defines a vacancy as the number of times an atom is displaced from its lattice position [13].

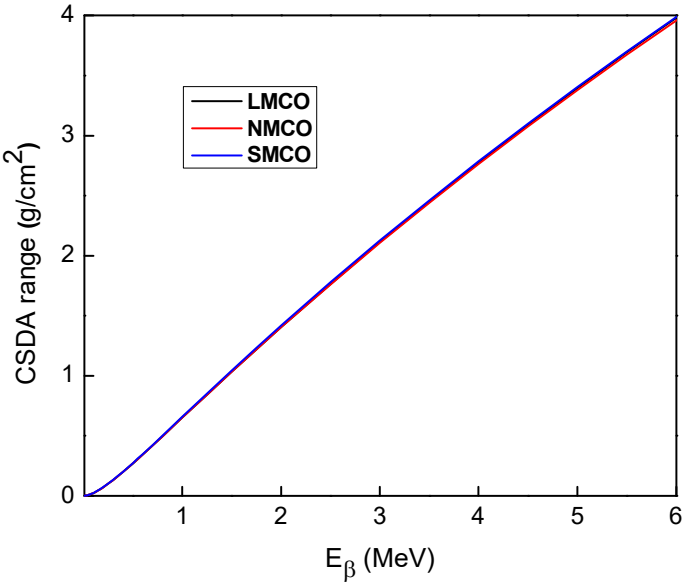

Figure 4: Variation of range as a function of beta particle energy.

Figure 5 illustrates the full cascade collision events of a single 8.78 MeV alpha particle in the three materials. The particle created 192 vacancies in LMCO, 256 vacancies in NMCO, and 304 vacancies in SMCO. There is a 33% and 58% increase in the number of vacancies created in NMCO and SMCO, respectively, as compared to LMCO. This indicates that the alpha particle causes little damage in LMCO compared to the other two materials. The displacement density of the collision cascade increases with an increase in the atomic density of the material.

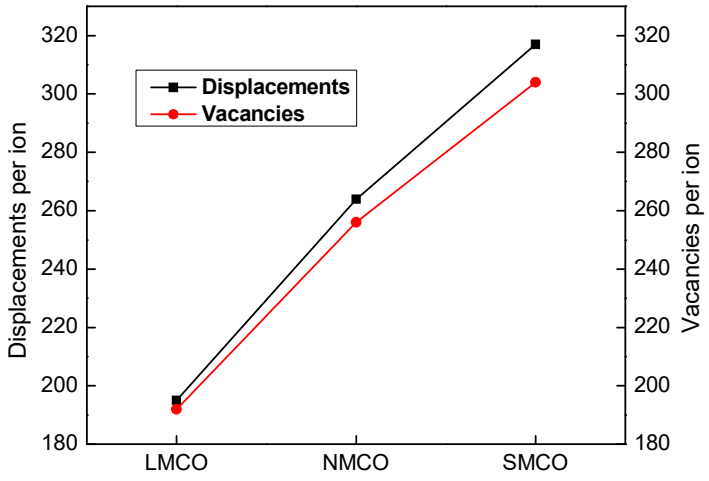

Figure 5: Collision events of an 8.78 MeV alpha particle in LMCO, NMCO, and SMCO.

4 Conclusion

We synthesized LMCO, NMCO, and SMCO using the solid-state reaction method. All samples were indexed to a monoclinic structure that belongs to a space group $P2_1/n$ (14) using XRD analysis. The mass stopping power and particle ranges were measured using SRIM for alpha particles and ESTAR for beta particles. LMCO performed better than the other two materials when irradiated with alpha particles, but all three performed the same when irradiated with beta particles. For a 1 MeV beta particle, the stopping powers of the materials are 1.234 MeV/(g/cm^2), 1.231 MeV/(g/cm^2), and 1.217 MeV/(g/cm^2) for LMCO, NMCO, and SMCO, respectively. An 8 MeV alpha particle has a range of 57.6 μm in LMCO, 60.0 μm in NMCO, and 61.0 μm in SMCO. The analysis of the obtained results suggests that double perovskites are radiation tolerant, but further analysis needs to be done on the chemical durability, loading capacity, and durability under aqueous conditions.

References

[1] J. S. McCloy, A.G., *Glass-ceramics for nuclear-waste immobilization.* MRS Bulletin, 2017. **42**. doi:10.1557/MRS.2017.8

[2] R. K. Pilania, L.C.D., *Matrices for radioactive waste immobilization: a review.* Frontiers in Materials, 2023. **10**. 10.3389/fmats.2023.1236470

[3] D. J. Gregg, J.S.M., J. D. Vienna, A. M. Macfarlane, W. J. Weber, G. R. Lumpkin, *Glass and ceramic nuclear waste forms: The scientific battle.* Bulletin of the Atomic Scientists, 2025. **81**. https://doi.org/10.1080/00963402.2024.2441044

[4] S. A. Darda, H.A.G., V. Damideh, M. Aboughaly, I. Hassen, *A comprehensive review on radioactive waste cycle from generation to disposal.* Radioanal. Nucl. Chem, 2021. **329**. doi:10.1007/S10967-021-07764-2

[5] C. M. Jantzen, M.I.O., *On selection of matrix (wasteform) material for higher activity nuclear waste immobilization (review).* Russ. J. Inorg. Chem, 2019. **64**. doi:10.1134/S0036023619130047

[6] Y. Jo, K.G., N. Çevirim-Papaioannou, O. D. Blanco, B. de Blochouse, M. Altmaier, et al., *Solubility of niobium(V) in cementitious systems relevant for nuclear waste disposal: characterization of the solubility-controlling solid phases.* J. Hazard. Mater, 2022. **440**. doi:10.1016/J.JHAZMAT.2022.129810

[7] J. Li, D.X., X. Wang, K. Liu, Y. Mao, M. Wang, et al, *Encapsulation of cesium with a solid waste-derived sulfoaluminate matrix: A circular economy approach of treating nuclear wastes with solid wastes.* J. Hazard. Mater, 2021. **146**. doi:10.1016/J.JHAZMAT.2021.126156

[8] K. Ji, Y.Y., G.T. Moyo, C. Ritter, J. P. Attfield,, *Double and double double perovskites in the RMnMnTaO6 series.* Journal of Solid State Chemistry, 2022. **313**. https://doi.org/10.1016/j.jssc.2022.123329

[9] R.C. Sahoo, S.D., T.K. Nath, *Effect of rare earth site substitution on magnetic and transport properties of Ln2CoMnO6 (Ln = La, Sm and Gd) double perovskites.* Journal of Magnetism and Magnetic Materials, 2018. **460**: p. 409–417. https://doi.org/10.1016/j.jmmm.2018.04.039

[10] NIST. *https://www.nist.gov/pml/stopping-power-range-tables-electrons-protons-and-helium-ions*. 2024 [cited 2025 June].

[11] S.I. Eidelman, B.A.S., *Interactions of Particles and Radiation with Matter*, in *Handbook of Particle Detection and Imaging.*, M.T. I. Fleck, C. Grupen, I. Buvat, Editor. 2021, Springer, Cham. https://doi.org/10.1007/978-3-319-93785-4_1

[12] Y. Katsumura, H.K., *Interactions Between Radiation and Matter.* , in *An Advanced Course in Nuclear Engineering, Radiation Applications*, H. Kudo, Editor. 2018, Springer,: Singapore. https://doi.org/10.1007/978-981-10-7350-2_2

[13] S. Agarwal, Y.L., C. Li, R.E. Stoller, S.J. Zinkle,, *On the use of SRIM for calculating vacancy production: Quick calculation and full-cascade options.* Beam Interactions with Materials and Atoms, 2021. **503**. https://doi.org/10.1016/j.nimb.2021.06.018

This page intentionally left blank.

Fuzzy-based Groundwater Quality Index Model: A Case of Rural Areas in North-West Province, South Africa

Oluwakayode Samuel Oyedokun[1] and Olanrewaju Bola Wojuola[1]

[1]Department of Physics, North-West University, Mahikeng, South Africa

E-mail: olu.oyedokun@nwu.ac.za

Abstract: Groundwater is a major source of freshwater in rural and peri-urban communities in the developing world. In this study, a fuzzy logic model based on the concept of fuzzy set theory was investigated for assessing the quality of groundwater for drinking purposes. The Takagi-Sugeno fuzzy inference system was used to model the groundwater quality index using electrical conductivity and the concentration of calcium in groundwater. These two input parameters explained much of the variance in the groundwater quality variable with R-squared values of 0.81 and 0.73, respectively. The inputs were classified into "*Low*", "*Moderate*" and "*High*" using the trapezoidal membership functions, while the output was described using linear function. The rule base was created and optimized using the grid partition algorithm and the learning capacity of the adaptive neuro-fuzzy inference system (ANFIS). Groundwater data was split into 70:30 for training and testing the rule base. In the testing phase, the predicted output was close to the actual groundwater quality with a testing error (root mean square error) of 2.2489. The fuzzy groundwater quality model predicted a quality level of 82.2 when electrical conductivity and calcium concentration were classified as "*Moderate*" 146 (mS/m) and 85.5 (mg/l) respectively, based on South African National Standards (SANS) guidelines. This result shows that a fuzzy inference system can be deployed in evaluating groundwater quality and groundwater data can be used in tuning the fuzzy rules where expert knowledge is lacking.

1 Introduction

The issue of water quality cannot be overemphasized, as consumption of poor water quality has been linked to transmission of diseases such as cholera, dysentery, diarrhoea, typhoid, hepatitis A and polio [1]. According to World Health Organization's assessment of the burden of disease due to water sources, more than 1 million deaths each year can be attributed to drinking from unclean water sources [1]. Clean water is important for public health. It is a major theme of the Sustainable Development Goal (SDG-6) to provide access to clean and potable water for everyone by 2030 [2]. While the quality of water cannot be based on human senses, biological, physicochemical and hydro-chemical parameters like major anions and cations are important for water quality assessment. Field measurements of these parameters require considerable time and resources. In contrast, water quality models could significantly reduce the required time and cost by utilizing specific water quality indicators. Many countries have also developed regulations and standards on safe limits for water and

mathematical-based approaches to present these data in a clear and easy-to-understand manner. The quality of water can be modelled using soft computing techniques such as the artificial neural network, adaptive neuro-fuzzy inference systems, and fuzzy logic systems.

In many rural communities, groundwater is the sole source of water supply. Although groundwater is perceived to be contaminant-free, natural processes and anthropogenic activities are reportedly polluting these natural resources [3]. The complexity of the hydrogeological system further reinforces the need to develop a more effective technique for groundwater quality modelling. Fuzzy logic system is one of the approaches that has been used as a non-conventional tool in solving and overcoming complex water-related problems [4, 5]. The use of Fuzzy logic has an advantage, it can simulate human ability to make effective decisions and give fuzzy output from a set of rules. Many works exist on fuzzy logic applications, and in particular, different types of fuzzy model architectures were developed for groundwater quality indices [4-6]. However, most authors developed systems by imposing some configurations without sufficient scientific justification. While some attempts were made to evaluate different configurations, sets of input parameters and numbers of rules based on expert knowledge. The use of data to formulate the rule base of the fuzzy inference system in cases where expert knowledge is lacking has not been carefully investigated. In previous works, fuzzy systems were developed mainly to compare their accuracy with conventional methods.The authors constructed fuzzy inference systems by proposing some variations regarding the design of the model architecture, particularly devoted to selecting a set of input variables critical to groundwater quality [4, 5]. Dahiya, et al. [7] developed a fuzzy logic model for estimating groundwater quality using 10 input parameters grouped into four classes and 55 fuzzy rules. Vadiati, et al. [5] also developed a fuzzy logic model approach for groundwater classification using critical water quality parameters and 65 fuzzy rules based on expert knowledge of the significance of each parameter to groundwater quality. This study aims to tune the fuzzy rule base with empirical data and develop a predictive fuzzy logic model for groundwater quality assessment.

2 Materials and methods

2.1 Data and sample analysis

Data used in building the fuzzy model were obtained from a preliminary study conducted by Masindi and Foteinis [3]. The published data represent the water quality condition of the rural settlements and peri-urban areas of the North-West Province, South Africa. Water samples from 42 boreholes were accessed and analyzed in terms of drinking water quality. These boreholes are the primary source of water for the local communities. Some of the boreholes are owned and managed by private users; some are shared or communal, while others are owned by local municipalities, operated and managed by the water board. The groundwater quality index (GQI) was then calculated from the concentration of water quality parameters, as explained by Jha, et al. [4]

2.2 Fuzzy logic system

The fuzzy logic theory uses the principles of possibility theory to define solutions to problems that are complex, uncertain and nonlinear in nature. A fuzzy system is composed of four primary sections: fuzzification, fuzzy rules, fuzzy inference and defuzzification (Fig. 1).

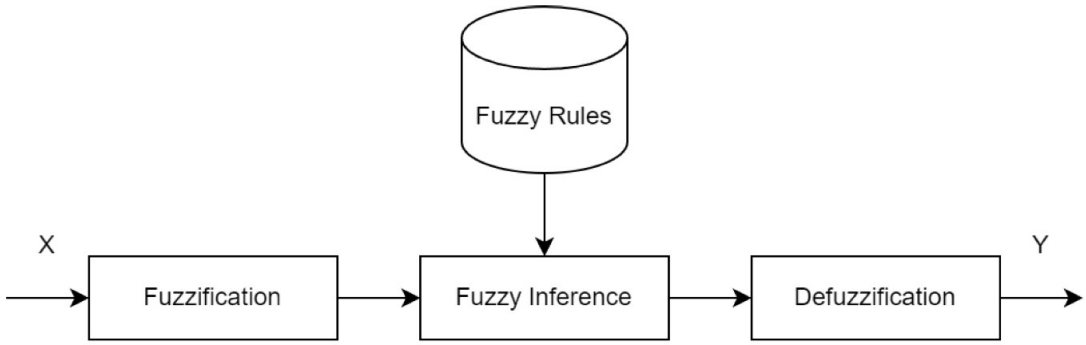

Figure 1: Basic steps of a fuzzy inference system.

Fuzzification is the transformation of a crisp set into a fuzzy set. The process generally creates fuzzy sets defined by a membership function. The fuzzy set is an ordered pair of a domain of interest and the membership value in the interval [0,1]. The fuzzy set A ⊂ X is given by Equation (1):

$$A = \{(x_1, \mu_A(x) | \, x \in X\}, \, 0 \leq \mu_A(x) = 1 \tag{1}$$

where x_1 are the elements of the universe of discourse X, and $\mu_A(x)$ is the membership function of x in A.

The fuzzy rule-base is a set of rules that represent all possible fuzzy relations between the input parameters and the output variables. These rules are expressed in logical IF-THEN statements as shown in the expression below.

If x_1 is $A_{i,1}$ and x_2 is $A_{i,2}$ and x_3 is $A_{i,3}$ ..., x_m is $A_{i,m}$ then y is $B_{i,1}$ =1,……,k

where y is the variable to be determined, and x_1, x_2, x_3, …, x_m are the input parameters. $A_{i,j}$ are the linguistic terms that the fuzzy variables represent, and i is the index of the rule k. $B_{I,1}$ is the linguistic term assumed by the fuzzy output.

The fuzzy inference is an important part of the fuzzy model. It considers all the possible fuzzy rules in the fuzzy rule-base and learns how to transform a set of inputs into corresponding outputs. The fuzzy inference is the approximate reasoning phase for all possible rule combinations.

The defuzzification step transforms the fuzzified output into a crisp value. The frequently used defuzzification methods are centroid of area, mean of maximums, minimum of the maximums, and center of gravity.

2.3 Building the fuzzy model

The fuzzy model was developed using the Sugeno Type-1 inference engine of MATLAB fuzzy logic toolbox. Two input features i.e. electrical conductivity (mS/m), calcium (mg/l) were selected for the fuzzy groundwater quality model (Table 1). The numerical inputs were transformed into linguistic variables such as "*Low*", "*Moderate*" and "*High*" using the trapezoidal membership function. The grid partition algorithm was used to generate the initial rule base by constructing a fuzzy rule matrix. By mapping the input features data space onto the fuzzy output space, the rule base was constructed from all possible combinations of the inputs and membership functions. The rules were tuned using adaptive neuro-fuzzy algorithms trained on 70% of the available data and 10 possible iterations.

Parameters	pH	Ca^{2+} (mg/l)	EC (mS/m)	Hardness	Mg^{2+} (mg/l)	SO_4^{2-} (mg/l)	Cl^- (mg/l)	F^- (mg/l)	NO_3^- (mg/l)
R^2	0.11	0.73	0.81	0.70	0.53	0.24	0.59	0.03	0.47

Table 1: Correlation analysis of input parameters with estimated groundwater quality index.

3 Results and discussion

In this study, a fuzzy model for groundwater quality prediction was developed. Pearson's correlation of the water quality indicators showed that the two most important input features for the developed model are electrical conductivity and calcium concentration, referred to as "input 1" and "input 2", respectively (Figure 2). These input features explained the highest proportion of variance in the groundwater quality variable. The reduction in feature dimension ensured that less important features were removed. The grid partition and adaptive neuro-fuzzy algorithms generated and optimized the required rule matrix after 10 iterations. In the study of Vadiati, et al. [5] seven critical parameters with three membership functions were used in developing the fuzzy logic groundwater quality index, which resulted in 65 baseline rules with associated computational complexities. The Sugeno fuzzy inference system developed in this work had nine sets of tuned fuzzy rules for mapping the input and output parameters. Although the number of rules can be further reduced using rule reduction methods, this is beyond the scope of this work [8]. The output of the fuzzy inference system is a linear function that relates to the 3^n combinations of the input features and the membership functions, enabling the fuzzy model to generalize well on test data.

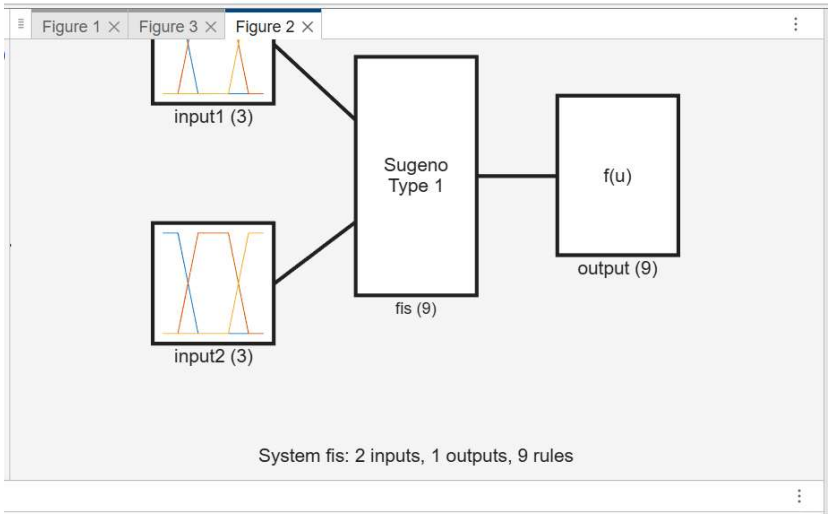

Figure 2: Input-Output structure of fuzzy inference system.

The predicted groundwater quality score of 82.2 resulted from the positioning of the two input parameters in the steady state peaks, which represents a complete membership of the input parameters in the class "*Moderate*". Previous studies on fuzzy models for water quality classification used trapezoidal membership functions (MFs), describing the input and the output classes with linguistic terms such as "*Excellent*", "*Good*", "*Poor*", "*Very Poor*" and "*Unfit for Drinking*" [4, 5]. The trapezoidal MFs were selected for this model, which allowed for the smooth representation of a steady state peak before the membership value starts to fall, as shown in Figure 3. The selection of the number of MFs and types depends on the characteristics of the problem and the size [9]. As seen in the rule viewer, the Fuzzy-based model predicted groundwater quality as good when electrical conductivity and calcium concentration are within permissible limits referred to in this work as "*Moderate*". Based on recommended guidelines for desirable groundwater quality, the physicochemical parameters are

expected to be low in concentration, and if any of the parameters exceed the permissible limit, the water may require treatment before consumption [3].

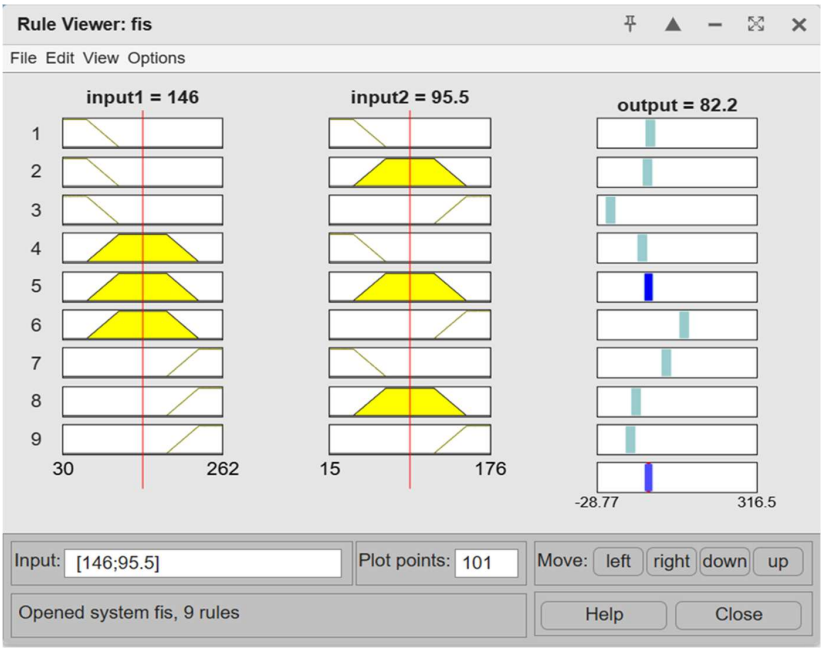

Figure 3: Fuzzy inference system rule viewer for a two-input one-output system.

Table 2 provides the process of approximate reasoning based on the fuzzy IF-THEN rules to map the input descriptors onto the output as desired by water quality experts. It indicates IF electrical conductivity is "*Low*" and calcium is "*Low*" THEN the groundwater quality is "*High Quality*".

Fuzzy rule matrix	**Low**	**Moderate**	**High**
Low	*High Quality*	*Low Quality*	*Low Quality*
Moderate	*Low Quality*	*Moderate Quality*	*Moderate Quality*
High	*Low Quality*	*Moderate Quality*	*Low Quality*

Table 2: Fuzzy rules matrix for 2-input and 3-membership functions.

In Figure 4, a regular pattern is observed in the actual and predicted groundwater quality trend, indicating no overfitting or underfitting problem. The predictive errors in the model's training and testing phase were 1.0086 and 2.2489, respectively.

4 Conclusion

The development of Takagi-Sugeno fuzzy inference system for fuzzy-based groundwater quality model was implemented for a case study of North-West Province of South Africa. A two-input one-output system was built to serve as a preliminary investigation of the applicability of using the grid partition and adaptive neuro-fuzzy algorithm for tuning the rule base of a fuzzy inference system. The grid partition search algorithm generated the rule matrix, and the adaptive neuro-fuzzy inference system (ANFIS) was used to learn the input and the output relationship based on groundwater quality data without the expert knowledge or manually tuning the rules. The results show that the ANFIS tuning method successfully created an efficient fuzzy rule-based system. Future studies will explore rule reduction techniques to develop a scalable multiple-input and single-output fuzzy-based groundwater model.

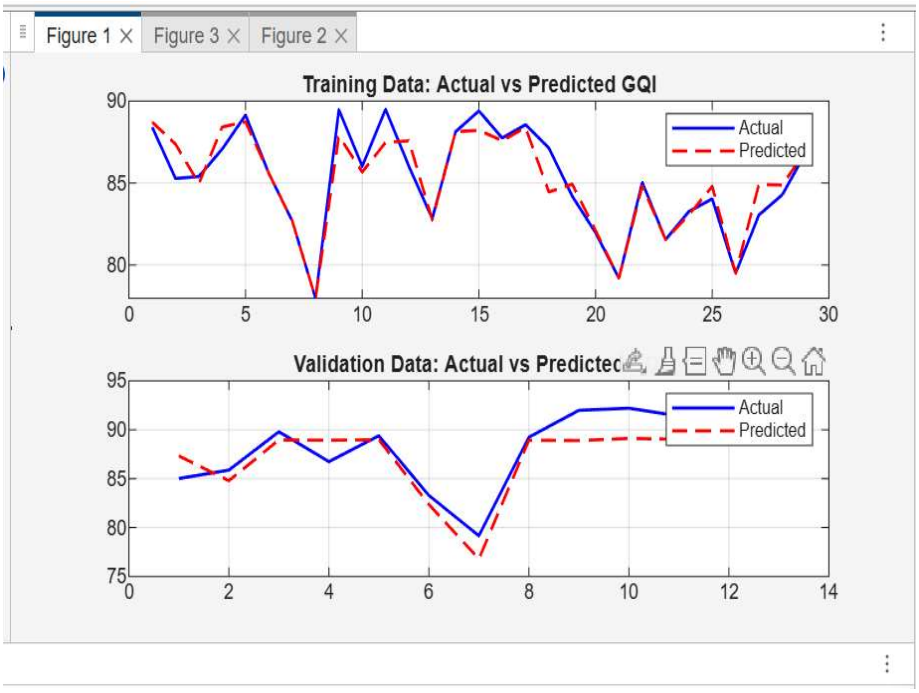

Figure 4: The training and the testing phases after iterations (max = 10).

References

[1] WHO, "Water, sanitation and hygiene: burden of disease." [Online]. Available:https://www.who.int/data/gho/data/themes/topics/water-sanitation-and-hygiene-burden-of-disease

[2] U. Nations, Transforming Our World: The 2030 Agenda for Sustainable Development A/RES/70/1: United Nations, 2015. [Online]. Available: https://sustainabledevelopment.un.org/content/documents/2125203020Agenda20for20Sustainable%20Development%20web.pdf.

[3] V. Masindi and S. Foteinis, "Groundwater contamination in sub-Saharan Africa: Implications for groundwater protection in developing countries," Cleaner Engineering and Technology, vol. 2, p. 100038, 2021.

[4] M. K. Jha, A. Shekhar, and M. A. Jenifer, "Assessing groundwater quality for drinking water supply using hybrid fuzzy-GIS-based water quality index," Water research, vol. 179, p. 115867, 2020.

[5] M. Vadiati, A. Asghari-Moghaddam, M. Nakhaei, J. Adamowski, and A. Akbarzadeh, "A fuzzy-logic based decision-making approach for identification of groundwater quality based on groundwater quality indices," Journal of Environmental Management, vol. 184, pp. 255-270, 2016.

[6] C. K. Kgatwe, O. O. Olatunji, P. A. Adedeji, and N. Madushele, "Fuzzy Inference Engine in Condition Monitoring of Industrial Equipment: An Overview," in 2023 14th International Conference on Mechanical and Intelligent Manufacturing Technologies (ICMIMT), 2023: IEEE, pp. 262-267.

[7] S. Dahiya, B. Singh, S. Gaur, V. Garg, and H. Kushwaha, "Analysis of groundwater quality using fuzzy synthetic evaluation," Journal of Hazardous Materials, vol. 147, no. 3, pp. 938-946, 2007.

[8] J. Kerr-Wilson and W. Pedrycz, "Generating a hierarchical fuzzy rule-based model," Fuzzy Sets and Systems, vol. 381, pp. 124-139, 2020.

[9] S. Thaker and V. Nagori, "Analysis of fuzzification process in fuzzy expert system," Procedia computer science, vol. 132, pp. 1308-1316, 2018.

This page intentionally left blank.

Statistical discrimination of uranium ore concentrate using trace element signature: Developing nuclear forensic fingerprint

Liteboho Ntsohi[1], Iyabo Usman[1], Risimati Mavunda[1,2], Oscar Kureba[3] and Mistura Ajani[4]

[1]School of Physics, University of the Witwatersrand, Johannesburg 2050, South Africa
[2]Department of Mechanical Engineering, University of Johannesburg, , Johannesburg, South Africa.
[3]Department of Physics and Astronomy, Botswana International University of Science and Technology, Private Bag 16, Palapye, Botswana
[4]Department of Physics with Electronics, University of Ilesa, Ilesa Osun State, Nigeria.

E-mail: liteboho.ntsohi@students.wits.ac.za

Abstract. Effective attribution of nuclear materials intercepted outside regulatory control requires the identification of unique, source inherent characteristics. To date, a limited number of characteristics have been validated as signatures for uranium ore and uranium ore concentrate (UOC), including rare earth element (REE) patterns and trace elements, which serve as geological and geographical indicators. In this study, the concentrations of 11 trace elements, including Ti, V, Ni, Cu, Zn, Ga, Rb, Sr, Y, Zr, Pb, as well as REEs, Th and U in 38 samples from three African regions: Botswana (Southern Africa), Kenya (East Africa), and Nigeria (West Africa) were measured using Inductively Coupled Plasma Mass Spectrometry (ICP-MS). The resulting compositional data were transformed and analyzed using statistical techniques, such as Multivariate Analysis of Variance (MANOVA), Linear Discriminant Analysis (LDA), Principal Component Analysis (PCA), and Hierarchical Cluster Analysis (HCA) to test for regional differences, determine the statistical significance of the differences observed, and test the potential discriminative power of individual trace elements. MANOVA revealed statistically significant regional differences in trace element compositions ($p < 0.0001$). LDA identified the elements most responsible for group separation, achieving a high classification accuracy of 91.67% through cross-validation. The first two components in PCA explained 79.15% of the total variance, while HCA further supported the separation of samples into regionally distinct clusters. These results demonstrate the potential of trace element signatures, in combination with multivariate statistical methods, to effectively discriminate uranium samples by region of origin.

1 Introduction

Much like conventional forensics, nuclear forensic science relies on characteristic data and modelling to infer historical information such as origin and production processes [1]. Effective attribution of nuclear materials intercepted outside regulatory control (MORC) is central to nuclear forensic investigations [2]. Uranium Ore Concentrate (UOC) and its precursor, mined ore, are common intermediate front-end products of the nuclear fuel cycle that are commonly traded between countries and are frequently encountered in illicit trafficking incidents [3]. Characteristic parameters in UOC, such as isotopic and, most importantly, trace impurities, depend heavily on the nature of the ore and can function as geographical and geological signatures [4]. Consequently, forensic

attribution of UOC can be based on signatures that persist from uranium ore to UOC. The rare earth element (REE) pattern, in particular, chondrite normalised pattern, serves as a powerful geological and geographical indicator and has become the subject of many studies on the attribution of uranium ores and UOC [2, 4]. Lin et al. demonstrated that with the help of iterative OPLS-DA, the signature implied in REE pattern can be used to attribute UOCs to their origins [3]. Xuepeng et al. on the other hand, combined REE concentration with Nd-Ce isotopic ratio and successfully compare and distinguish UOC from different countries using multivariate statistical techniques [1]. These studies and similar ones validated REE signatures as forensically significant, however, a single signature is sometimes not enough to ascertain the source of MORC; instead, to increase precision, a conglomerate of signatures that complement each other is required to determine the source, and to create a robust nuclear fingerprint [2, 5]. To date, a limited number of characteristic parameters have been validated as forensically significant signatures for mined uranium ore/UOC. The aim of this study was to demonstrate that a combination of trace element concentration signature, REE concentration signature and Th and U signature can be used effectively to compare and discriminate mined ore/UOC for geographical source attribution. Comparing the concentrations of multiple elements in samples from different countries to determine the origin is a complex task [3]. The complexity is brought on by the multidimensional nature of the data, which makes it difficult to visualize the data and recognize patterns. To overcome this multidimensionality, statistical techniques such as DA, PCA and HCA are applied [6, 7]. In this study, Inductively Coupled Plasma Mass Spectroscopy(ICPMS) measurements of trace elements were subjected to a combination of supervised and unsupervised multivariate statistical algorithms such as MANOVA, DA , PCA and HCA; to reduce dimensionality and visualize the data, enabling the analyst to test whether there are statistically significant differences between samples from different countries, respectively. The methodology described in this study provides a promising approach to nuclear forensic interpretation and source attribution.

2 Materials and Methods

For the purpose of this study, the mined uranium ore samples served as UOC surrogate. Five samples were collected from Botswana, 29 from Kenya, and 4 from Nigeria [8, 9]. The samples were crushed, milled and acid digested using deionized water, aquarigia (a 1:3 mixture of HNO_3 and HCl, respectively) and H_2O_2 in preparation for ICPMS analysis [8, 10]. Trace element concentration measurements were then performed using Agilent Technology, 7700 Series ICP-MS. To validate the trace element parameter as a forensically relevant signature, the concentration of 29 trace elements/variables: Be, B, Sc, Ti, V, Ni, Cu, Zn, Ga, Ge, As, Se, Rb, Sr, Y, Zr, Mo, Cd, In, Sn, Te, Cs, Ba, W, Re, Hg, Tl, Pb, Bi, REEs, Th, and U in the 38 samples were measured. The resulting concentrations in ppb were extracted and prepared for subsequent analysis. Of the 27 trace elements measured, only 11 elements (Ti, V, Ni, Cu, Zn, Ga, Rb, Sr, Y, Zr, Pb) were detected in all samples. These elements were used as input data for subsequent analysis. The data were subjected to MANOVA, to test whether there are statistically significant differences between samples from different countries, while DA , PCA and HCA were used for classification, dimensionality reduction, visualization and clustering, respectively. Data preparation is integral to successful multivariate statistical analysis [11]. Due to the nature of compositional data, Centered log ratio (CLR) transformation was applied to the dataset in CoDAPack software, a software designed to implement suitable methods for compositional data based on Aitchisons' log-ratio methodology [12]. XLSTAT 2025 was used to perform statistical analysis on the transformed data matrix.

3 Results and discussion

3.1 Multivariate Analysis of variance (MANOVA)

Wilks test and Pillai test were performed in MANOVA (significance level $\alpha = 0.05$) to test if the trace element signature varies significantly between countries. For this, two hypothesis were synthesized; null hypothesis (H_0), and an alternative hypothesis (H_A). H_0 assumes that the variables or the interaction of the corresponding column has no significant effect on the dependent variables (i.e Botswana=Kenya=Nigeria), while H_A assumes that the variable or the interaction of the corresponding column has a significant effect on the dependent variable (atleast one country is different). From the results shown in Table 1, the computed p-value is less than the significance level $\alpha = 0.05$ and $F_{statistic} > F_{critical}$, therefore the H_0 was rejected and H_A was accepted. The risk of rejecting H_0 while it is true was found to be less than 0.01%. It was therefore concluded that atleast one of the countries shows statistically significant differences when comparing the trace element signature. The next section illustrates how the specific elements were identified and determined in driving the variance.

3.2 Unidimensional test for equality of means

Unidimensional test for equality of means is a preliminary statistical test used in DA that is based on Analysis of variance(ANOVA). The test uses a hypothesis similar to that described in MANOVA for each variable separately, helping to identify individual elements that contribute significantly to group differences [13]. In addition to the p-value and the f-value, the test also evaluates the value of lambda for each element. Lambda is a measure of

	Samples	
	Wilks' test	Pillai's Test
F Observed values	63.609	43.178
DF1	54	54
DF2	48	50
F Critical value	1.599	1.589
p-value	<0.0001	<0.0001

Table 1: One-way MANOVA statistics for uranium ore samples using trace element signature

the proportion of variance in dependent variables unaccounted for by differences in the levels of the independent variable (grouping variable) [14]. A lambda value of zero indicates that there exists no variance not explained by the independent variable (which is ideal). The closer the lambda is to zero, the more the variable/element in question contributes to the model. In combination with p-value < α and $F_{value} > F_{sig}$ a null hypothesis can be rejected. Figure 1 is a graphical representation of lambda result of the test. Elements with lambda > 0.5 do not contribute significantly to variance and were not selected for subsequent PCA and HCA.

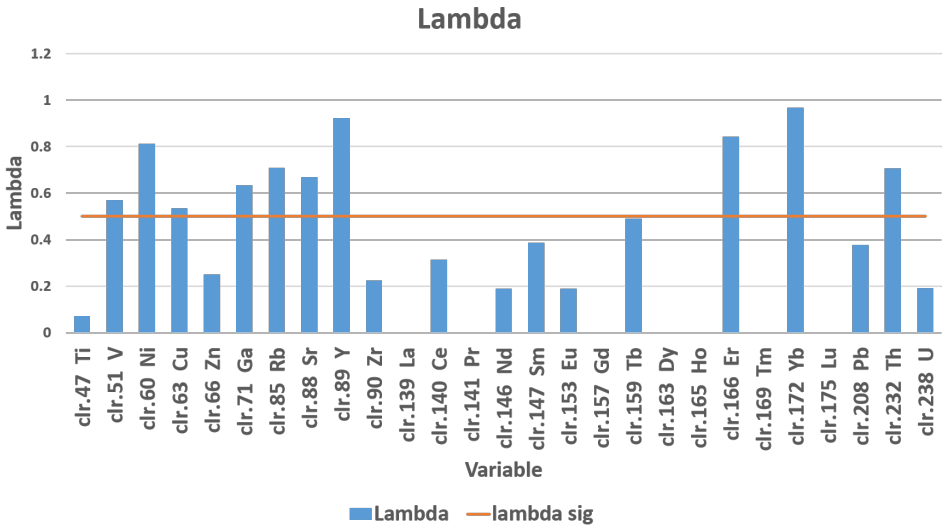

Figure 1: Bar graph showing calculated lambda for the individual elements

3.3 Discriminant Analysis (DA)

DA was used for its pattern recognition capability, which was used to build a classification model from trace element data. DA generated discriminant functions by maximizing the between-class variance to within class variance ratio to ensure high efficiency of the classification model [1]. The prediction/classification ability of the model was evaluated using cross-validation [1]. One random sample was removed per country from the dataset to form the test set, while the remaining n-3 samples were used to train the model. Once training was complete, the model was used to predict the origin of the test set. Due to the relatively small data size and the unequal distribution of the samples from each country, the process was repeated so that 30% of the largest group(Kenya) is used to test the accuracy of the model. The procedure was therefore repeated nine times. The performance of the model can be seen in Table 2. The results show that samples from Botswana and Kenya were correctly classified all the time; however, on two occasions a sample from Nigeria was misclassified as Botswana. The developed model had a prediction ability of 91%, which is acceptable.

	from/to	Botswana	Kenya	Nigeria	% correct
Training Sample	Botswana	9	0	0	100%
	Kenya	0	9	0	100%
	Nigeria	0	0	9	100%
	Recognition ability				100%
Cross-validation	Botswana	9	0	0	100%
	Kenya	0	9	0	100%
	Nigeria	2	0	7	75%
	Prediction ability				91.67%

Table 2: Confusion matrix for training and cross-validation results based on trace element concentrations

3.4 Principal Component Analysis (PCA)

To reveal whether the samples form natural clusters based on their trace element parameters, unsupervised methods; PCA and HCA were applied. PCA is a dimensionality reduction tool which transforms data from a multidimensional space and enables visualization in fewer dimensions (PCs) while preserving the most important variations. PCs are linear combinations of the original data. To determine the number of significant PCs, eigenvalues were examined. Applying the Kaiser-Guttmann rule, only principal components/factors with eigenvalue greater than 1 were considered significant dimensions. The first two PCs, F1 and F2, met the criteria and accounted for 79.15% of the total variance. These were used to construct the PC biplot shown in Figure 2. The Left hand side of Figure 2 shows the results of the Kaisers varimax orthogonal rotation. The rotation moves the component axis so that the projections of each variable (trace element) onto the factor axes are either near 1 or the origin. The position of the variable is indicative of significance. However, due to the removal of insignificant variables prior to running PCA, all elements are closer to 1 than to the origin. This further corroborates the findings of unidimensional tests in DA. The Right hand side of Figure 2 shows the clustering that is formed. Three samples from Nigeria create a group high on the F2 axis; however, one sample, Nig1, is detached from the group. Samples from Botswana also form a distinct group, and the same is observed for samples from Kenya with the exception of three samples (MS14, MS15, MS8) that are detached from the group. These results are in agreement with those obtained during DA.

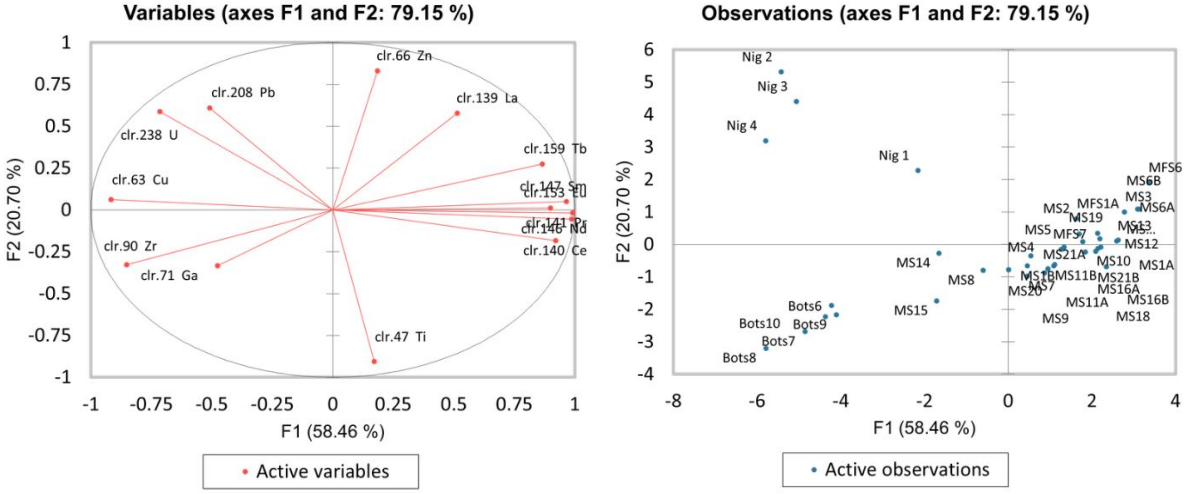

Figure 2: (LHS: PC loading biplot of trace elements in ore samples. RHS: PC score plot illustrating the differentiation between ore samples according to their origin

3.5 Hierarchical Cluster Analysis (HCA)

Unlike DA, HCA does not assign a sample to a class (country), rather it separates the samples into clusters so that the level of association is strong between samples in the same cluster and weak between samples in different clusters [1]. This was achieved using Wards' method with Euclidean distance to calculate the sample interpoint

distance. HCA was performed on uranium ore samples with trace element parameters as input variables. The generated dendogram is shown in Figure 3 with a dissimilarity threshold of 52. The results indicate 5 distinct clusters and one subgroup. C1 contained 5 samples labeled Bots6, Bots7, Bots8, Bots9 and Bots10 which are all from Botswana. C2 is a cluster of 1 sample labeled Nig 1 while C3 contains samples labeled Nig 2, Nig 3, Nig 4. Both clusters contain samples from Nigeria. The same can be observed with C4 and C5 which contain samples from Kenya only. The separation of samples from similar countries into distinct clusters is evidence of the discriminative ability of the trace element signature. This shows that the signature has the ability not only to separate ores on the basis of country of origin but also to distinguish between samples for different regions within the country, while still recognizing that the samples are related. The results obtained support the findings of PCA and DA, showing regionally consistent clusters.

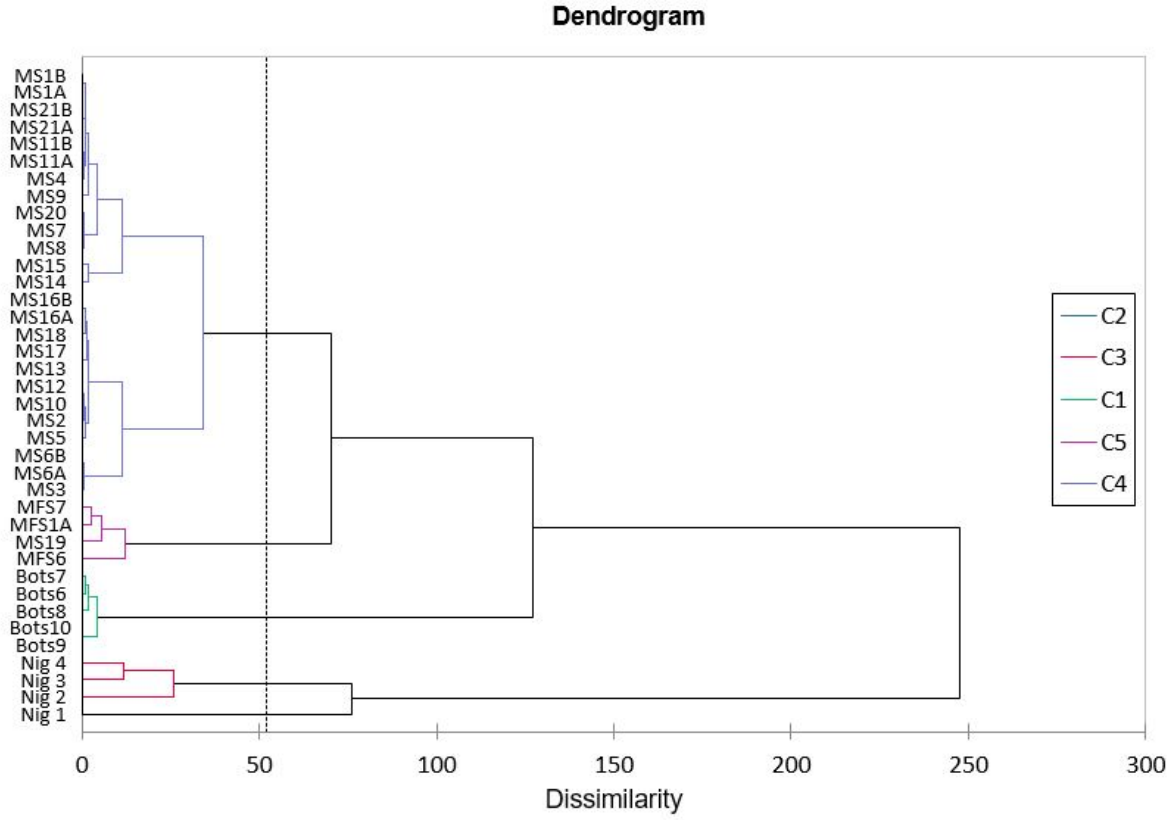

Figure 3: HCA dendrogram of uranium ore samples from three regions based on trace element concentrations

4 Conclusion

This study demonstrated that the trace element signature is forensically significant and could be applied in combination with REE signature to discriminate uranium ore/UOC samples from various countries and regions throughout Africa for source attribution purposes. By using multiple multivariate statistical techniques (MANOVA, DA, PCA, and HCA), the study showed how these techniques were effective tools for signature validation and interpretation for source attribution. MANOVA revealed statistically significant differences among countries/regions ($F_{statistic} > F_{critical}$, $p < 0.05$), indicating that trace element signature varies by source. Unidimensional test used in DA identified Ti, Zn, Zr, Ce, Pr, Nd, Eu and Pd as key elements driving the differences between samples of different origins. The classification model developed using trace element parameters was found to have predictive accuracy of 91.76%, further demonstrating the strength of the trace element signature for classification. Results from PCA and HCA also demonstrated that trace element signature could be used to distinguish samples of unknown origin. The application of both tools resulted in clusters that were consistent with the sampling locations. Although the results revealed that the trace element signature is a good geographical signature, the sample size was small and the sample sizes were not balanced between the countries. To strengthen these findings, extensive

research is required on a larger set of uranium ore samples from sources across the continent. In addition, incorporating machine learning techniques would improve classification and prediction accuracy and assist in developing a comprehensive continental reference database for nuclear forensic applications.

5 Acknowledgement
This work was supported by the AFRETEC Network by Carnegie Mellon Africa Funds.

References

[1] X. Shao, W. Bu, Y. Ni, H. Wang, X. Liu, C. Yang, and F. Hao, "Origin assessment of uranium ores using multivariate statistical method based on their rare-earth elemental parameters," *Nuclear Analysis*, vol. 1, no. 3, p. 100027, 2022.

[2] L. Ghimire and E. Waller, "The role of nuclear forensics for determining the origin of nuclear materials out of regulatory control and nuclear security," *International Journal of Nuclear Security*, vol. 7, no. 1, p. 10, 2022.

[3] M. Lin, Y. Zhao, L. Zhao, L. Li, F. Wang, L. Zhu, X. Hu, and W. Ning, "Tracing origins of uranium ore concentrates (uocs) by multidimensional statistical analysis of rare-earth impurities," *Journal of Analytical Atomic Spectrometry*, vol. 30, no. 2, pp. 396–402, 2015.

[4] V. Badaut, M. Wallenius, and K. Mayer, "Anion analysis in uranium ore concentrates by ion chromatography," *Journal of radioanalytical and nuclear chemistry*, vol. 280, no. 1, pp. 57–61, 2009.

[5] E. Keegan, M. Wallenius, K. Mayer, Z. Varga, and G. Rasmussen, "Attribution of uranium ore concentrates using elemental and anionic data," *Applied Geochemistry*, vol. 27, no. 8, pp. 1600–1609, 2012. [Online]. Available: https://www.sciencedirect.com/science/article/pii/S0883292712001321

[6] Q. T. Nguyen, T. T. Nguyen, V. N. Le, N. T. Nguyen, N. M. Truong, M. T. Hoang, T. P. T. Pham, and Q. M. Bui, "Towards a standardized approach for the geographical traceability of plant foods using inductively coupled plasma mass spectrometry (icp-ms) and principal component analysis (pca)," *Foods*, vol. 12, no. 9, 2023. [Online]. Available: https://www.mdpi.com/2304-8158/12/9/1848

[7] D. Granato, J. S. Santos, G. B. Escher, B. L. Ferreira, and R. M. Maggio, "Use of principal component analysis (pca) and hierarchical cluster analysis (hca) for multivariate association between bioactive compounds and functional properties in foods: A critical perspective," *Trends in Food Science Technology*, vol. 72, pp. 83–90, 2018. [Online]. Available: https://www.sciencedirect.com/science/article/pii/S0924224417306362

[8] L. Ntsohi, I. Usman, R. Mavunda, and O. Kureba, "Characterization of uranium in soil samples from a prospective uranium mining in serule, botswana for nuclear forensic application," *Journal of Radiation Research and Applied Sciences*, vol. 14, no. 1, pp. 23–33, 2021.

[9] P. Kilavi, M. Kaniu, J. Patel, and I. Usman, "Assessment of heavy metal pollution in soil and associated risks in the environs adjacent to a heavy mineral sand mine on the south coast of kenya," *Water, Air, & Soil Pollution*, vol. 234, no. 12, p. 748, 2023.

[10] S. O. John and I. T. Usman, "Isotopic profiling of natural uranium mined from northern nigeria for nuclear forensic application." *South African Journal of Science*, vol. 118, no. 3-4, 2022.

[11] S.-L. J, "Development and validation of a method for origin determination of uranium-bearing material - jrc-itu-tn-2008/25," Ph.D. dissertation, Vilnius University, Vilnius (Lithuania), Karlsruhe (Germany), 2008.

[12] S. Thió-Henestrosa and J. A. Martín-Fernández, "Detailed guide to codapack: a freeware compositional software," in *Compositional Data Analysis in the Geosciences: From Theory to Practice*. Geological Society of London, 01 2006. [Online]. Available: https://doi.org/10.1144/GSL.SP.2006.264.01.08

[13] B. G. Tabachnick and L. S. Fidell, *Multivariate Analysis of Variance (MANOVA)*. Springer Berlin Heidelberg, 2025, p. 1616–1619. [Online]. Available: http://dx.doi.org/10.1007/978-3-662-69359-9_398

[14] P. Lovie, "Book reviews : Everitt BS, dunn G 1991: Applied multivariate data analysis," *Statistical Methods in Medical Research*, vol. 0, pp. 114–115, 2016.

Enhancing Gamma-Ray Spectrometry Through Convolutional Neural Networks and Kolmogorov–Arnold Networks

V. Maluleke[1,2], F. Nemangwele[1], E.K. Nkadimeng[2], N.B. Ndabeni [2], and P. Maleka [2]

[1]Department of Physics, University of Venda, Thohoyandou,South Africa
[2]Separated Sector Cyclotron Department, NRF-iThemba LABS, Cape Town, South Africa

E-mail: vuako.maluleke@univen.ac.za

Abstract. Gamma (γ)-ray spectrometry remains a cornerstone technique in nuclear science and environmental radioactivity assessment, offering precise identification and quantification of radionuclides. Despite its efficacy, conventional analytical methods often rely on manual processing, which can introduce subjectivity, reduce throughput, and hinder real-time analysis. In this study, an automated framework is proposed for γ-ray spectrometry by employing two advanced deep learning architectures: Convolutional Neural Networks (CNN) and Kolmogorov–Arnold Networks (KAN). The models are trained and evaluated using high-resolution spectral datasets acquired from the ERL hyper-pure germanium (HPGe) detector at iThemba LABS. Input features include energy, channel, peak area, and centroid, extracted through digital signal processing techniques. Model performance is assessed based on standard classification metrics such as accuracy, precision, recall, and F1-score, and is directly compared to conventional machine learning (ML) classifiers, including Artificial Neural Networks (ANN), K-Nearest Neighbors (KNN), and Support Vector Machine (SVM). Results demonstrate that CNN and KAN outperform these traditional models in classification robustness and generalization capability. This work highlights the potential of deep learning for automating γ-ray spectrum interpretation, thereby enhancing the efficiency, reproducibility, and scalability of nuclear measurement systems. Detailed performance comparisons and implications for real-world deployment will be discussed during the presentation.

1 Introduction

Gamma (γ)-ray spectrometry is a fundamental tool in nuclear science, environmental monitoring, and radiological protection[1]. It allows for the precise identification and quantification of radionuclides by analyzing the energies and intensities of emitted γ rays. This technique has been extensively used in applications such as radioactive waste characterization, nuclear forensics, medical imaging, and environmental radiation assessments. Despite its accuracy and utility, conventional γ-ray spectrum analysis remains heavily dependent on manual procedures or basic rule based algorithms, both of which can be limited in speed, scalability, and consistency[2]. The typical γ-ray spectrum consists of a continuous background superimposed with discrete peaks corresponding to specific energy transitions in radioactive isotopes. Accurate interpretation requires precise peak identification, energy calibration, and nuclide classification, all of which are vulnerable to human error or measurement uncertainties[3]. Variations in detector resolution, noise, or overlapping peaks often introduce additional complexity, necessitating advanced computational techniques that can robustly handle such challenges.

In recent years, machine learning (ML), particularly deep learning, has emerged as a transformative solution for pattern recognition and automated data processing. Convolutional Neural Networks (CNN), a class of deep learning models, have proven highly effective in image and signal classification tasks due to their ability to automatically extract hierarchical features from input data[4]. When applied to γ-ray spectra, CNN can learn to detect and distinguish subtle spectral features, even in noisy or distorted data, without the need for handcrafted preprocessing pipelines[4, 5].

Kolmogorov–Arnold Networks (KAN), a newer addition to the ML landscape, offer a powerful and theoretically grounded approach for modeling complex nonlinear functions[6]. Based on the Kolmogorov–Arnold representation theorem, KAN use piecewise polynomial operations instead of traditional neural network activations, providing greater interpretability and control over model behavior. In γ-ray spectrometry, KAN show potential for precise energy calibration, spectral denoising, and function approximation tasks that require smooth, high fidelity mappings[7]. The integration of CNN and KAN offers a compelling opportunity to revolutionize γ-ray spectrometry. CNN excel at learning discriminative features from the spectral data, enabling robust peak detection and classification, while KAN complement this with accurate modeling of energy relationships and other continuous properties[8, 9, 10]. Together, these models can form a synergistic framework that automates the entire spectrometric analysis process, from raw data input to final radionuclide identification, with minimal human intervention. This paper presents a novel methodology that combines CNN and KAN architectures to enhance the efficiency and accuracy of γ-ray spectrum analysis. We demonstrate how this dual model approach can outperform traditional techniques in terms of sensitivity, speed, and adaptability across various operational scenarios. By applying this integrated deep learning framework, we aim to contribute toward the development of intelligent, scalable, and real time radiation monitoring systems that meet the demands of modern nuclear science and environmental safety.

2 Methodology

2.1 Data

Spectral data were collected from five commonly studied radionuclides: ^{40}K, ^{137}Cs, ^{152}Eu, ^{22}Na, and ^{60}Co. Each γ-ray spectrum consisted of 8192 channels, representing uncalibrated count values. These channels capture the photon interaction frequencies recorded by the ERL Hyper Pure Germanium (HPGe) detector AT iThemba LABS, with each channel corresponding to a discrete signal intensity proportional to the incident γ-ray energy. The dataset was constructed to ensure a diverse representation of peak structures and energy ranges, allowing for effective model training and validation.

2.2 Calibration and Key Equations

To convert raw channel values into corresponding energy values (in keV), linear energy calibration was performed using the following equation:

$$E = a + b \cdot Channel \tag{1}$$

where:

- E is the energy in keV, a and b are the calibration constants determined from known reference peaks[11].

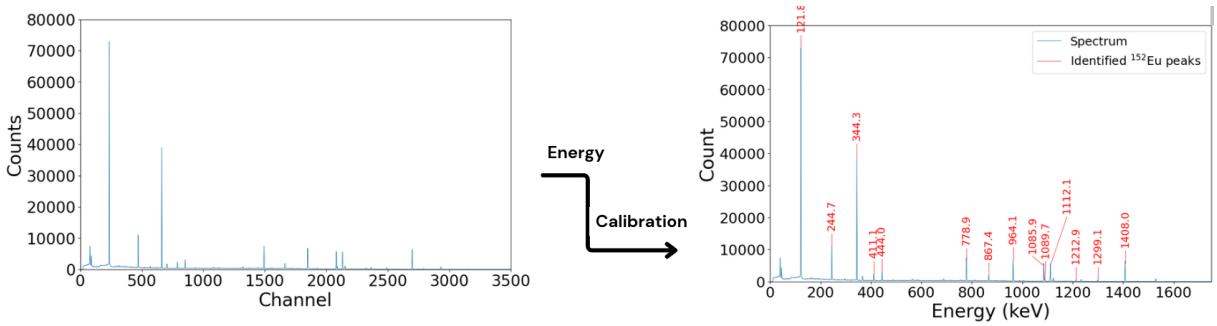

Figure 1: γ-ray spectra of ^{152}Eu before (left) and after (right) energy calibration. The calibration process maps channel numbers to their corresponding energy values (keV), enabling accurate peak identification.

The centroid of a photopeak is used to accurately identify the peak position in the energy spectrum. It is calculated using a weighted average of energy values as:

$$\text{Centroid} = \frac{\sum_i E_i N_i}{\sum_i N_i} \tag{2}$$

where E_i is the energy at channel i, and N_i is the corresponding count at that channel. This equation ensures the most probable energy associated with the peak is used for identification[12].

Model performance was quantitatively assessed using classification accuracy, calculated as:

$$\text{Accuracy} = \frac{TP + TN}{TP + TN + FP + FN} \tag{3}$$

where:

- TP = True Positives, TN = True Negatives, FP = False Positives, FN = False Negatives[13].

2.3 Peak Fitting

After calibration, prominent photopeaks in the energy spectrum were analyzed through curve fitting to extract precise peak characteristics. Each peak was modeled using a Gaussian function of the form:

$$f(E) = A \cdot \exp\left(-\frac{(E-\mu)^2}{2\sigma^2}\right) \tag{4}$$

where:

- A is the amplitude (peak height), μ is the mean (centroid of the peak), σ is the standard deviation [14].

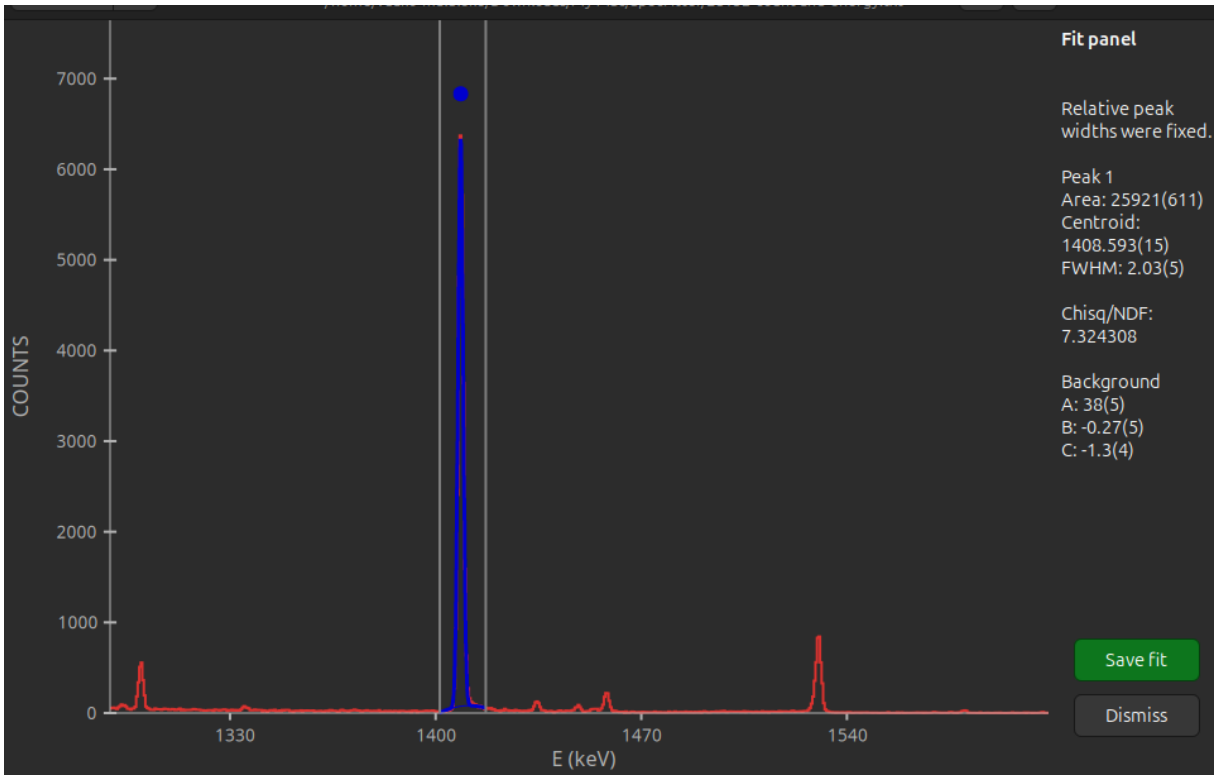

Figure 2: Gaussian peak fitting applied to the calibrated γ-ray spectrum of ^{152}Eu.

This fitting process allows for improved resolution in identifying overlapping peaks and provides accurate estimates of energy and intensity, which are critical for nuclide classification and quantitative analysis.

2.4 Model Training and Deployment

Following preprocessing and peak fitting, the characteristics for each detected peak ware extracted and standardized including channel, count, energy, peak area, and centroid. The data set was divided into training subsets (75%), validation subsets (15%), and test subsets (10%).

Both CNN and KAN models were trained using supervised learning. The input features consisted of count, energy, peak width, peak centroid, and channel values extracted from the gamma spectra. The CNN processed these features as a 1D tensor through five convolutional layers followed by fully connected layers to classify isotopes, while the KAN used the same normalized features as a flat vector with multiple fully connected layers and kernel activations to capture non-linear relationships, also applied for isotope classification. The labels were one-hot encoded, and class weights were applied in the KAN to address data imbalance. Both models were optimized using the Adam optimizer with categorical cross-entropy loss and validated to prevent overfitting. After training, the models were integrated into an analysis pipeline that accepts raw spectral input, performs automated preprocessing and calibration, detects peaks, and outputs real-time predictions of radionuclide identity.

3 Results and Discussion

3.1 Evaluated results

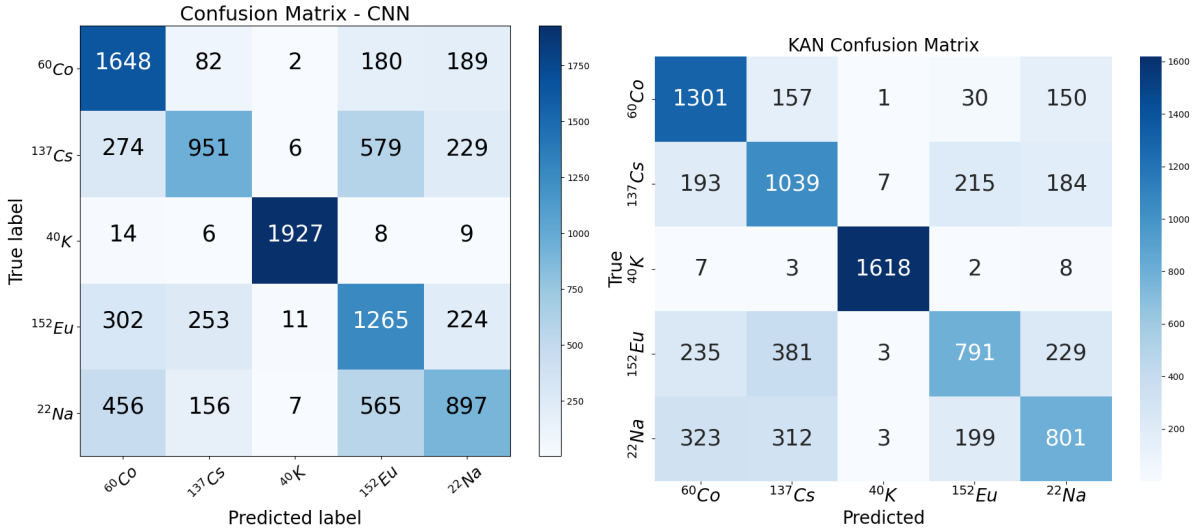

Figure 3: Confusion matrices illustrating the classification performance of the CNN model (left) and the KAN model (right) on γ-ray spectra of five radionuclides: ^{60}Co, ^{137}Cs, ^{152}Eu, ^{22}Na, and ^{40}K. Each matrix shows the predicted labels along the horizontal axis and the true labels along the vertical axis. Diagonal elements represent correct classifications (true positives), while off-diagonal elements indicate misclassifications, including false positives and false negatives. False negatives appear when a true radionuclide is incorrectly predicted as another class, impacting recall, while false positives occur when a model incorrectly assigns a radionuclide label to a non-matching input. The CNN and KAN models both demonstrate strong classification ability, with KAN showing slightly better separation for isotopes with overlapping spectral features.

Table 1: Comparison of Classification Performance Metrics for CNN, KAN, and Traditional ML Models

Perfomance (%)	CNN	KAN	ANN	KNN	SVM
Accuracy	68	**70**	62	66	53
Area Under Curve (AUC)	**91**	89	89	90	80
Precision	**69**	68	63	67	57
Recall	67	**69**	62	66	53
F1-Score	67	**68**	62	66	51

3.2 Deploying the results

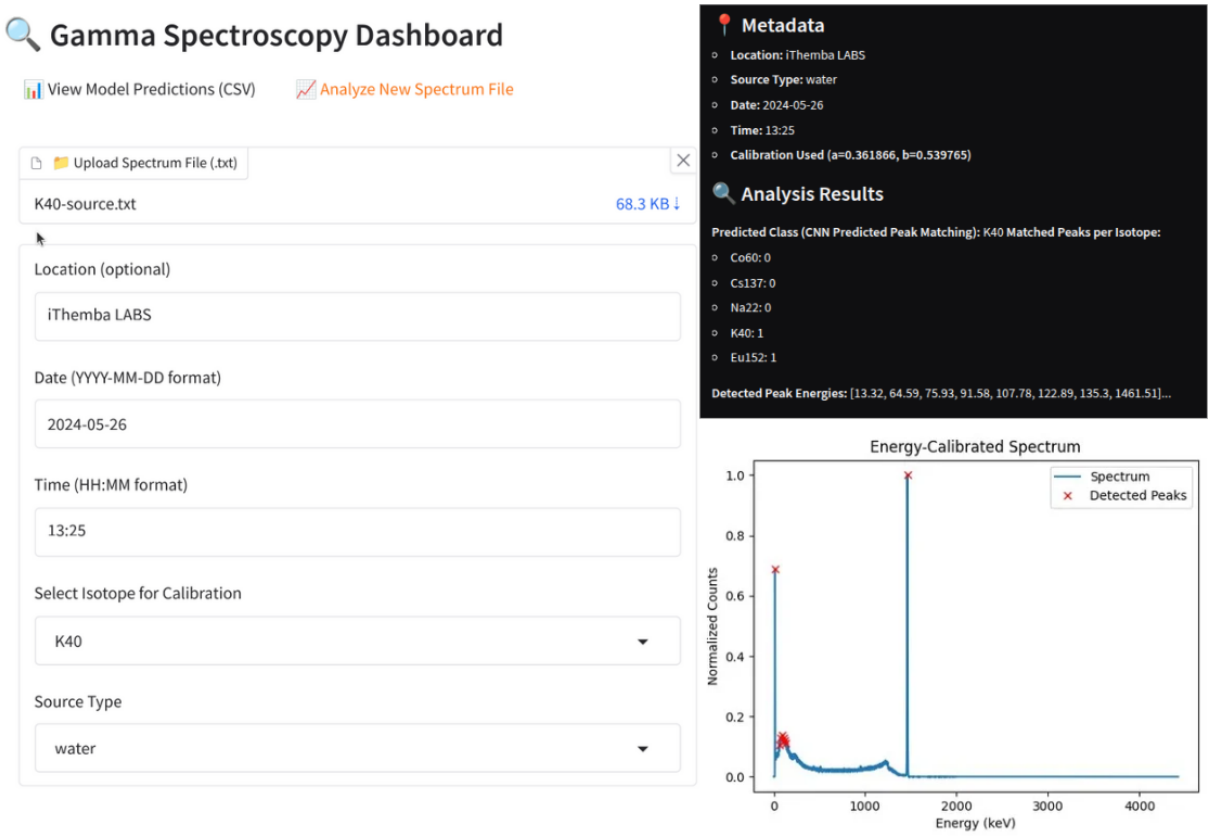

Figure 4: Screenshot of the deployed Gradio dashboard for automated gamma-ray spectrum analysis. The interface allows users to upload raw spectral data, perform energy calibration, and receive isotope identification results.

The results of this study demonstrate that integrating CNN and KAN enables robust, automated analysis of γ-ray spectra. The models were able to accurately classify isotopes and calibrate energy spectra, showing superior performance compared to conventional ML classifiers such as ANN, KNN, and SVM. Specifically, CNN and KAN achieved higher accuracy, precision, recall, F1-score, and AUC compared to these traditional models (see Table 1), highlighting their enhanced ability to capture nonlinear spectral features and generalize across different spectrum patterns, even in the presence of overlapping peaks or noise.

For deployment, the trained models were integrated into an interactive Gradio-based dashboard. This interface allows users to upload raw spectral data consisting of only channel numbers and count values. Upon uploading, the dashboard performs energy calibration using the trained model. In one test case using an uploaded spectrum sample, the system correctly detected a single peak corresponding to ^{40}K at 1460 keV and another peak initially matching ^{152}Eu. However, due to the presence of only one peak attributed to ^{152}Eu, the model did not conclusively identify it as the source, in agreement with the known characteristic that ^{152}Eu emits multiple distinct peaks. This example highlights the model's sensitivity and interpretative accuracy, as it recognized that a single peak is insufficient for confirming ^{152}Eu, while confidently detecting ^{40}K, which is characterized by a dominant single peak at 1460 keV.

4 Conclusion

In this study, we demonstrated that the combined use of CNN and KAN offers a powerful and automated approach for γ-ray spectrum analysis. The models significantly outperformed conventional ML classifiers, including ANN, KNN, and SVM, in accurately classifying radionuclides such as ^{60}Co, ^{137}Cs, ^{22}Na, ^{152}Eu, and ^{40}K. Both CNN and KAN architectures proved capable of detecting and classifying photopeaks with high precision and performing energy calibration, aligning closely with expected values for known isotopes. Quantitative evaluation using metrics such as accuracy, confusion matrix, precision, recall, F1-score, and AUC confirmed the robustness and reliability of

the proposed framework. The dashboard's ability to both calibrate unprocessed spectra and classify radionuclides enhances accessibility and application in real-world scenarios, such as environmental monitoring and on-site nuclear analysis. By transforming raw input data into calibrated, labeled spectra with minimal user interaction, this system presents a practical and scalable solution for gamma spectrometry tasks. These results underscore the potential of deep learning techniques to enhance the efficiency, accuracy, and automation of γ-ray spectrometry, offering scalable solutions for real-time nuclear monitoring and environmental radiological assessment.

5 Acknowledgement

The authors gratefully acknowledges the financial and institutional support provided by the National Research Foundation (NRF), the South African Isotope and Nuclear Technology Society (SAINTS), and the Department of Science and Innovation (DSI). Special thanks are extended to the University of Venda for academic support and to iThemba LABS for providing the research infrastructure and technical resources necessary to complete this study.

References

[1] A. Aschersleben *et al.*, "Signal–background separation and energy reconstruction of gamma rays using pattern spectra and convolutional neural networks for the small-sized telescopes of the cherenkov telescope array," *arXiv preprint arXiv:2307.05301*, 2023.

[2] B. Paleti, "Identification of gamma emitting natural isotopes in environmental sample spectra: convolutional neural network approach," *Journal of Radioanalytical and Nuclear Chemistry*, vol. 332, pp. 5273–5281, 2023.

[3] H. Chen-Mayer *et al.*, "Encoding pgaa spectra as images for material classification with convolutional neural networks," *Journal of Radioanalytical and Nuclear Chemistry*, 2025, in Press.

[4] A. Nicholson *et al.*, "Neural network approaches for mobile spectroscopic gamma-ray source detection," *Radiation*, vol. 2, no. 2, pp. 242–259, 2020.

[5] H. Shahabinejad *et al.*, "Processing scintillation gamma-ray spectra by artificial neural network," *Journal of Radioanalytical and Nuclear Chemistry*, vol. 324, pp. 1003–1011, 2020.

[6] I. Lobanov *et al.*, "Hyperkan: Kolmogorov-arnold networks make hyperspectral image classifiers smarter," *arXiv preprint arXiv:2407.05278*, 2024.

[7] L. Cherednichenko and M. Poptsova, "Kolmogorov-arnold networks for genomic tasks," *Briefings in Bioinformatics*, vol. 26, no. 2, 2025.

[8] A. Abasov *et al.*, "Application of kolmogorov-arnold networks in high energy physics," *arXiv preprint arXiv:2409.01724*, 2024.

[9] Unknown, "Stft-kan—short time fourier transform based kolmogorov-arnold network," https://www.reddit.com/r/MachineLearning/comments/1jnqe2p, 2025, machine Learning forum discussion.

[10] Z. Zhao, Y. Zhang, S. Liu, and et al., "Deep learning-based gamma-ray spectrum analysis," *Applied Radiation and Isotopes*, vol. 168, p. 109412, 2021.

[11] G. F. Knoll, *Radiation Detection and Measurement*, 4th ed. John Wiley & Sons, 2010.

[12] N. Tsoulfanidis and S. Landsberger, *Measurement and Detection of Radiation*, 4th ed. CRC Press, 2015.

[13] C. Sammut and G. I. Webb, "Evaluation measures," in *Encyclopedia of Machine Learning and Data Mining*. Springer, 2017, pp. 403–408.

[14] G. Gilmore, *Practical Gamma-Ray Spectrometry*, 2nd ed. John Wiley & Sons, 2008.

Linear polarization measurement on gamma rays from non-oriented nuclear states

B. Similindi[1,2], E.A. Lawrie[1,3], S.N.T. Majola[2] J.J. Lawrie[3], S.H Mthembu[1,3], N.Xulu[1,4], S.L. Shabane[1,2]

[1]iThemba LABS, National Research Foundation, PO Box 722, Somerset West 7129, South Africa
[2]Physics Department, University of Johannesburg, PO Box 524, Auckland Park, 2006, South Africa
[3]Physics Department, University of the Western Cape, Bellville 7535, South Africa
[4]Physics Department, University of Zululand, KwaDlangezwa 3886, South Africa

E-mail: beatricesimilindi5@gmail.com

Abstract. Gamma-ray spectroscopy is a powerful tool in nuclear structure, but the interpretation of the intrinsic properties of the nucleus becomes complex if the parity of the emitted radiation is not known. This study aimed at developing a technique to measure linear polarization of γ rays emitted from non-oriented nuclear states for the clover detectors of the iThemba LABS AFRODITE array. Orientation was created by gating on a γ ray detected in one clover detector while measuring the polarization of another γ ray detected in coincidence in another detector. The clover detectors used in this study comprise four Ge crystals which were used as Compton polarimeters. It allowed us to measure linear polarization by studying the horizontal and vertical Compton scattering of γ rays in the four Ge crystals and measuring the polarization anisotropy, $A_p(E_\gamma)$. Theoretical values for all observed γ rays emitted by an ^{152}Eu source were derived and compared with the measured polarization anisotropy to deduce the polarization sensitivity, $Q(E_\gamma)$. Furthermore, the degree of linear polarization was determined experimentally for the γ rays observed in ^{194}Hg populated in the β decay of ^{194}Tl using the deduced polarization sensitivity, $Q(E_\gamma)$, to demonstrate how the technique works for non-oriented nuclear states. The measured polarization sensitivity can be used in experiments (where oriented and/or non-oriented nuclear states are populated) that intend to measure γ rays whose parities as well as mixing ratios are unknown.

1 Introduction

Gamma rays are usually emitted for each nuclear transition from an initial excited state to a state with lower excitation energy. There is a relationship between the properties of the nuclear states and the properties of the emitted γ rays which ensures that the conservation laws are properly obeyed. For instance, the energy of the emitted γ ray is equal to the difference between the energies of the initial and final nuclear states and so is the angular momentum and its projection along the axis of quantization [1]. Therefore, information on the properties of the nuclear states and even the structure of the nucleus of interest can be obtained by measuring the properties of the emitted γ ray such as its angular momentum and parity.

For nuclei produced in fusion-evaporation reactions, the angular momentum carried away by the emitted γ ray is often determined by carrying out angular distribution measurements. Such measurements give information on how the intensity of the emitted γ ray is distributed in space. But to determine the nature of the emitted γ ray as to whether it is electric or magnetic in nature, additional measurements such as linear polarization are needed [1]. Angular distribution and linear polarization measurements are necessary for the assignment of spins and parities

and also for determining the mixing ratios of γ rays with mixed multipole nature. However, unlike in nuclear reactions where the nuclei are oriented or aligned (their angular momenta are aligned perpendicular to the beam direction), in β decays the daughter nuclei are produced with nuclear states which are not oriented at all. This lack of orientation makes the angular distribution of the γ rays isotropic, thus it is impossible to measure the angular momenta carried away by the emitted γ rays. This also makes it impossible to distinguish whether the emitted γ ray is of electric or magnetic nature. In this work, we aimed to develop a technique to measure the linear polarization of γ rays emitted from non-oriented nuclear states using the clover detectors of the iThemba LABS AFRODITE array [2, 3]. This includes measuring the polarization sensitivity factor $Q(E_\gamma)$ for these clover detectors using a ^{152}Eu radioactive source and also applying the technique with in-beam data where non-oriented nuclear states were produced in β decay. The polarization sensitivity for a few other arrays made of clover detectors have been measured previously [4], [5], [6], [7] and [8].

2 Theoretical Background

2.1 Angular Correlation

Among the various methods used to determine the multipolarities of the γ rays emitted by non-oriented states, the most often used method is the angular correlation. Angular correlation involves observing a sequential γ-ray emission. Orientation is created by choosing the emission of the first γ ray in a fixed direction while the second γ ray is detected in a direction different from that of the first. In practice, this corresponds to an event where two detectors positioned at an angle θ with respect to each other fire in coincidence. Thus, we select data where the first γ ray is detected in detector one, the second γ ray is observed in detector two, within a specified coincidence window. The angular correlation function $\mathrm{W}(\theta)$ describes the probability of finding the second γ ray (γ_2) at an angle θ with respect to the direction of emission of the first γ ray (γ_1). The angular correlation function is given as:

$$W(\theta) = \sum_{n=0,2,4} a_n P_n(\cos\theta), \tag{1}$$

where a_n are the corresponding angular correlation coefficients, $a_n = A_n(\gamma_1)A_n(\gamma_2)$, with $A_n(\gamma_1)$ and $A_n(\gamma_2)$ being the angular distribution coefficient for the first and second emitted γ ray, respectively, while the $P_n(\cos\theta)$ are Legendre polynomials.

2.2 Linear Polarization

The direction of emission of the two coincidence γ rays form a coincidence plane, see figure 1. The polarization of the γ ray refers to the orientation of its electric field vector with respect to the coincidence plane determined by the angle ψ in figure 1. Measuring the linear polarization of the first γ ray requires setting a coincidence gate on the second γ ray. Depending on the orientation of the electric field of the γ ray with respect to the coincidence plane the probability for the emitted γ ray to undergo Compton scattering in a vertical or horizontal direction differs. For instance, when the electric field vector is perpendicular to the coincidence plane horizontal Compton scattering, (in detectors $\mathrm{D_1}$-$\mathrm{D_3}$), is more probable, while vertical, (in detectors $\mathrm{D_1}$-$\mathrm{D_4}$) Compton scattering is more likely when the electric field is parallel to the coincidence plane.

The directional polarization correlation describes the intensity of γ_1 depending on the angle θ with respect to γ_2 and the orientation of the electric field vector $\vec{E}$ with respect to the coincidence plane and is given as:

$$\mathrm{W}(\theta,\psi) = \sum_{\mathrm{n}=2,4} \mathrm{a_n}' \mathrm{P_n}^{(2)}(\cos\theta)\cos(2\psi), \tag{2}$$

where $\mathrm{P}_\nu^{(2)}(\cos\theta)$ are the associated Legendre polynomials [9]. The coefficients $a_n{}'$ for pure transitions are calculated as :

$$a_n{}' = A_n(\gamma_1)(-1)^\sigma f_n(LL')A_n(\gamma_2), \tag{3}$$

where σ and $f_n(LL')$ refer to the transition for which we measure polarization, γ_1 in figure 1, and, $\sigma = 0$ for electric and $\sigma = 1$ for magnetic radiation. The values of L and L' refer to the multipole order, and for a pure transition $L' = L$ and for a mixed one, $L' = L + 1$. The value of the angular momentum L is obtained from the angular momentum and parity selection rules [1] while the $f_n(LL')$ are given in [9].

Linear polarization of the emitted γ ray is defined in terms of the probabilities for the electric field vector to be parallel to the coincidence plane, W (θ, ψ = 0°), and to be perpendicular to the coincidence plane, W (θ, ψ = 90°), as:

$$\mathrm{P}(\theta) = \frac{\mathrm{W}(\theta,\psi=0^\circ) - \mathrm{W}(\theta,\psi=90^\circ)}{\mathrm{W}(\theta,\psi=0^\circ) + \mathrm{W}(\theta,\psi=90^\circ)}. \tag{4}$$

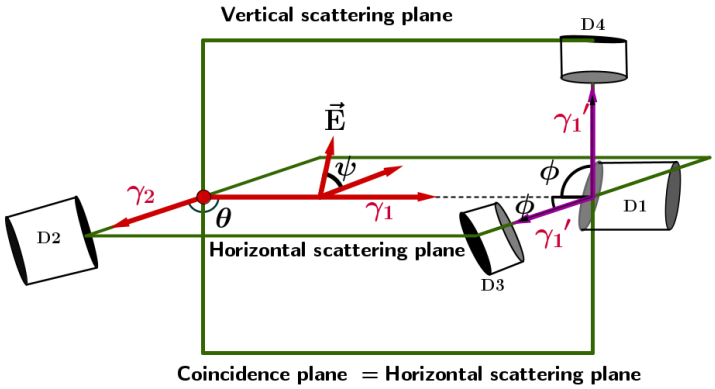

Figure 1: Illustration of a typical linear polarization set up, where the polarization of γ_1 is measured in coincidence with γ_2. The polarization (determining the orientation of the electric field vector $\vec{E}$) is deduced by measuring the number of Compton scattered, (in detectors D_1-D_3 and in detectors D_1-D_4) events. Compton scattering planes are defined by the direction of γ_1 and the direction of the scattered γ ray, γ_1'.

2.3 Polarization anisotropy

The expression for the number of vertically and horizontally Compton scattered events is proportional to the differential cross section as given by the Klein-Nishina formula [10]:

$$\frac{\mathrm{d}\sigma}{\mathrm{d}\Omega} = \frac{\mathrm{r}_0^2}{2}\left(\frac{\mathrm{E}'_\gamma}{\mathrm{E}_\gamma}\right)^2\left(\frac{\mathrm{E}'_\gamma}{\mathrm{E}_\gamma} + \frac{\mathrm{E}_\gamma}{\mathrm{E}'_\gamma} - 2\sin^2\phi\cos^2\varepsilon\right), \tag{5}$$

where r_0 is the classical electron radius given as $r_0 = \frac{e}{m_e c^2}$ with $m_e c^2 = 511$ keV the rest energy of the electron, ε is the angle between the electric field vector of the emitted γ ray and the Compton scattering plane, whereas ϕ is the Compton scattering angle between γ_1 and γ_1', see figure 1. For horizontal and vertical Compton scattering, we have $\psi = \varepsilon$ and $\varepsilon = 90 - \psi$, respectively. The experimentally measured horizontally, N_h, and vertically, N_v, scattered events are,

$$\mathrm{N_h} = \mathrm{W}(\theta, \psi = 0^\circ)\frac{\mathrm{d}\sigma(\phi, \varepsilon = 0^\circ)}{\mathrm{d}\Omega} + \mathrm{W}(\theta, \psi = 90^\circ)\frac{\mathrm{d}\sigma(\phi, \varepsilon = 90^\circ)}{\mathrm{d}\Omega}, \tag{6}$$

$$\mathrm{N_v} = \mathrm{W}(\theta, \psi = 0^\circ)\frac{\mathrm{d}\sigma(\phi, \varepsilon = 90^\circ)}{\mathrm{d}\Omega} + \mathrm{W}(\theta, \psi = 90^\circ)\frac{\mathrm{d}\sigma(\phi, \varepsilon = 0^\circ)}{\mathrm{d}\Omega}. \tag{7}$$

Experimentally we measure the polarization anisotropy, $A_p(E_\gamma)$ which is:

$$A_p(E_\gamma) = \frac{aN_v - N_h}{aN_v + N_h}, \tag{8}$$

where $a = N_h/N_v$ is the relative efficiency and is obtained from direct spectra of horizontally and vertically scattered γ rays emitted by non-oriented nuclear states. The polarization sensitivity $Q(E_\gamma)_{\mathrm{exp}}$ reflects the efficiency of the set-up for linear polarization and is obtained by comparing the polarization anisotropy, $A_p(E_\gamma)$, and the theoretical linear polarization, P(θ), for a cascade of transitions linking three states with known spins and parities. It is expressed as:

$$\mathrm{Q(E_\gamma)_{exp}} = \frac{\mathrm{A_p(E_\gamma)}}{\mathrm{P}(\theta)}. \tag{9}$$

3 Experimental Setup and Data Analysis

The data analysed in this study was collected using the iThemba LABS AFRODITE array [2, 3]. This setup consisted of 8 clover detectors positioned at 90° and 135° with respect to the beam direction. Linear polarization depends on the angle θ defined by the directions of the γ rays emitted in coincidence which in our case was the angle between two clover detectors in the same plane. Thus, pairs of clover detectors were formed defining

angles θ = 45°, 90°, and 135°. Since polarization is symmetric around 90°, the statistics in the corresponding symmetric detectors angles were summed resulting in $\theta = 45°$ and 90° for linear polarization measurements. It is also important to mention that the data collected was a run with a ^{152}Eu radioactive source for 12 hours which was meant for efficiency calibration purpose. In-beam experimental data were also collected following a fusion-evaporation reaction involving an ^{18}O beam and ^{181}Ta target from which depending on the number of neutrons evaporated, thallium nuclei with mass numbers 194, 195, and 196 were formed. However, within these data some γ-ray transitions belonging to ^{194}Hg produced following the β decay of ^{194}Tl were observed. The data showed good statistics for linear polarization measurements, see the spectra gated on the 428- and 748-keV transitions in figure 2. The observed 428-, 636-, 735- and 748-keV transitions link low-spin states in ^{194}Hg populated below $I = 6^+$ state with excitation energy of 1799.5 keV [11].

To measure the polarization anisotropy, data were sorted into vertical and horizontal polarization matrices comprising events where two coincident gamma rays were detected, one of which had Compton-scattered in horizontal or vertical direction with respect to the coincidence plane. The sorted matrices were then converted into RADWARE [12] format. Gated spectra were created to reveal coincidence counts in the corresponding Compton-scattered γ rays. The gated spectra consist of all γ rays emitted in coincidence with the γ ray on which the gate is set, see gated spectra in figure 2. For each gated spectrum corresponding background was created by gating on a background region next to the peak of interest.

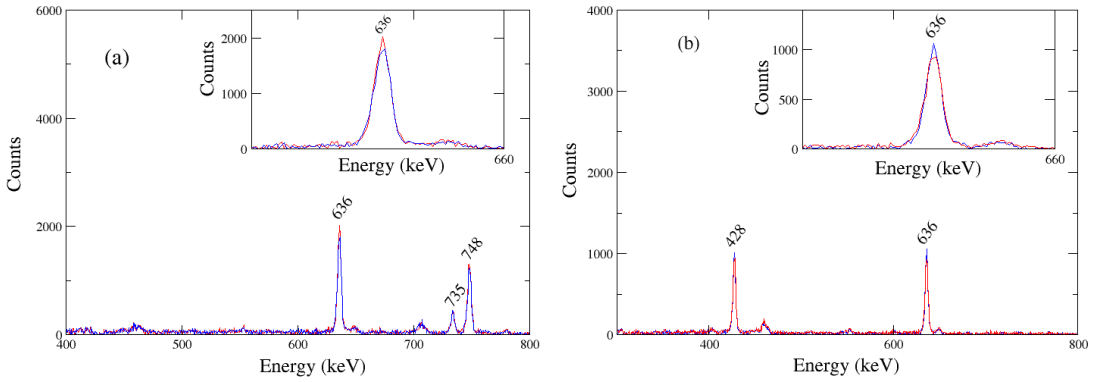

Figure 2: Spectra of vertically (red) and horizontally (blue) Compton scattered events for the gamma rays in ^{194}Hg, gated on the γ-ray transitions with energies of (a) 428 keV and (b) 748 keV.

Linear polarization depends on the Compton scattering of the emitted γ ray between the adjacent detectors, and the features of the gating transition. Figure 2 illustrates the difference in the intensities of the vertically and horizontally scattered intensities of the same 636-keV ($4^+ \rightarrow 2^+$) γ ray depending on the relevant gating transition, which is E2 and E1 for panels (a) and (b) , respectively, while the corresponding cascades are $4^+ \rightarrow 2^+ \rightarrow 0^+$ and $5^- \rightarrow 4^+ \rightarrow 2^+$, respectively.

4 Results and Discussion

4.1 Polarization Sensitivity $Q(E_\gamma)$

The measured values of $A_p(E_\gamma)$ and $Q(E_\gamma)_{\text{exp}}$ are listed in table 1 for $\theta = 45°$ and $\theta = 90°$. They are also plotted in figure 3. For the 344-keV transition these values were measured by gating on the 411- and 778-keV γ rays. The deduced polarization sensitivity, $Q(E_\gamma)_{\text{exp}}$ was fitted with the expression:

$$Q(E_\gamma) = Q_{pt}\big(E_\gamma \cdot b_1 + b_0\big), \tag{10}$$

where b_0 and b_1 are the fitting parameters [4]. Values of $b_1 = 0.00009(9)$ and b_0 = 0.23(6), see figure 3 were deduced.

Table 1: The γ-ray transition used as a gate, the energy of the γ ray for which polarization anisotropy was measured, the known multipolarity ML and the known mixing ratio δ for the transitions with M1+E2 multipolarity taken from [11], the relative efficiency a, the measured polarization anisotropy, $A_p(E_\gamma)$, and the derived polarization sensitivity, $Q(E_\gamma)_{\text{exp}}$ at $\theta = 45°$ and $\theta = 90°$ for the γ rays emitted by the ^{152}Eu source.

					$\theta = 90°$		$\theta = 45°$	
Gate	E_γ(keV)	ML	δ	a	$A_p(E_\gamma)$	$Q(E_\gamma)_{\text{exp}}$	$A_p(E_\gamma)$	$Q(E_\gamma)_{\text{exp}}$
g122	245	E2	–	0.962(4)	0.042(19)	0.25(11)	0.003(12)	0.04(18)
g778	344	E2	–	0.964(2)	-0.009(11)	0.08(11)	-0.007(8)	0.13(14)
g411	344	E2	–	0.964(2)	0.037(23)	0.22(14)	0.016(15)	0.23(22)
g344	411	E2	–	0.977(6)	0.037(21)	0.22(13)	0.005(14)	0.08(21)
g344	778	E1	–	0.975(2)	0.022(8)	0.21(8)	0.006(6)	0.11(11)
g245	867	M1+E2	$-6.5(3)$	0.979(4)	-0.029(16)	0.17(9)	0.002(10)	0.01(9)
g122	964	M1+E2	$-9.3(6)$	0.985(2)	0.007(10)	0.14(20)	-0.021(7)	0.06(2)
g122	1112	M1+E2	$-8.7(3)$	0.981(3)	-0.008(10)	0.03(4)	-0.002(7)	0.03(11)
g122	1408	E1	–	0.986(2)	-0.019(9)	0.04(2)	-0.007(6)	0.04(3)

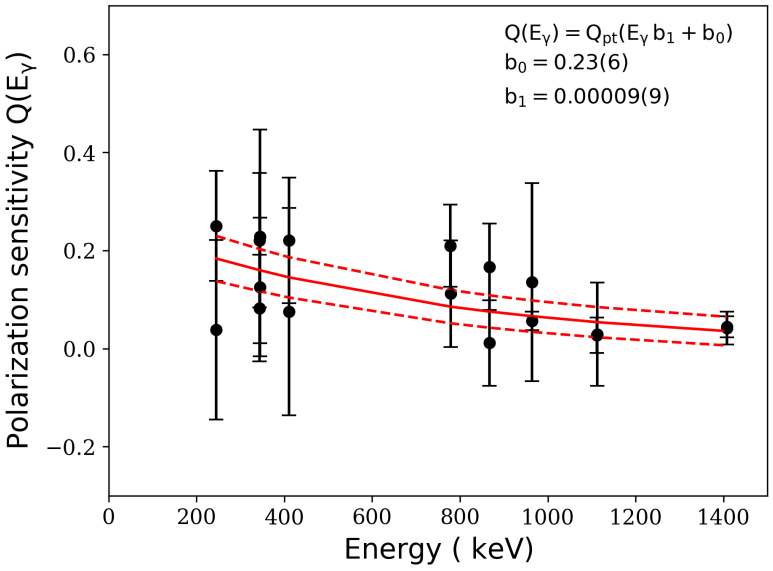

Figure 3: Polarization sensitivity results obtained for the clover detectors of the AFRODITE array with ^{152}Eu data (see table 1). The solid line is the fit of our data with its corresponding uncertainties in dotted lines.

4.2 Testing the technique with ^{194}Hg

We demonstrate linear polarization measurements for non-oriented states using data from an in-beam experiment where some nuclear states were produced after β decay. The degree of linear polarization for the transitions in ^{194}Hg was established experimentally by using the determined AFRODITE polarization sensitivity $Q(E_\gamma)$, see figure 3, and by measuring the polarization anisotropies, $A_p(E_\gamma)$, and using eq 9. The results are given in table 2.

The results for the 636-keV γ ray were obtained from three different coincident gates, two of which form a quadrupole-quadrupole (E2-E2) cascades with the 636-keV transition and hence they have the same theoretical value for the corresponding linear polarization and the third forms a dipole-quadrupole (E1-E2) cascade. The values for the experimental and theoretical polarizations are in good agreement for all measured transitions in ^{194}Hg as is evident in figure 4. Therefore, the technique works well for γ rays emitted from non-oriented nuclear states and it can be applied to transitions with unknown parities.

Table 2: The cascade of γ rays, γ-ray transition used as a gate, the known multipolarity ML, the energy of the γ ray for which polarization was measured , the measured polarization anisotropy, $A_p(E_\gamma)$, and linear polarization $P(\theta)_{\text{exp}}$ for the γ rays of ^{194}Hg using the clover detector pairs at $\theta = 45°$ and $\theta = 90°$. The theoretical values of $P(\theta)$ are also listed for comparison.

				$\theta = 45°$			$\theta = 90°$		
Cascade	Gate	E_γ(keV)	ML	$A_p(E_\gamma)$	$P(\theta)_{\text{exp}}$	$P(\theta)$	$A_p(E_\gamma)$	$P(\theta)_{\text{exp}}$	$P(\theta)$
$4^+ \rightarrow 2^+ \rightarrow 0^+$	g636	428	E2	0.020(21)	0.14(15)	0.068	0.037(21)	0.25(16)	0.167
$5^- \rightarrow 4^+ \rightarrow 2^+$	g748	636	E2	-0.004(13)	-0.04(12)	-0.055	-0.017(31)	-0.16(29)	-0.103
$6^+ \rightarrow 4^+ \rightarrow 2^+$	g735	636	E2	0.007(29)	0.06(26)	0.068	0.025(36)	0.23(34)	0.167
$4^+ \rightarrow 2^+ \rightarrow 0^+$	g428	636	E2	0.009(13)	0.08(12)	0.068	0.017(24)	0.16(23)	0.167
$6^+ \rightarrow 4^+ \rightarrow 2^+$	g636	735	E2	0.028(26)	0.29(29)	0.068	0.004(21)	0.05(22)	0.167
$5^- \rightarrow 4^+ \rightarrow 2^+$	g636	748	E1	0.001(16)	0.01(18)	0.055	0.005(23)	0.06(25)	0.103

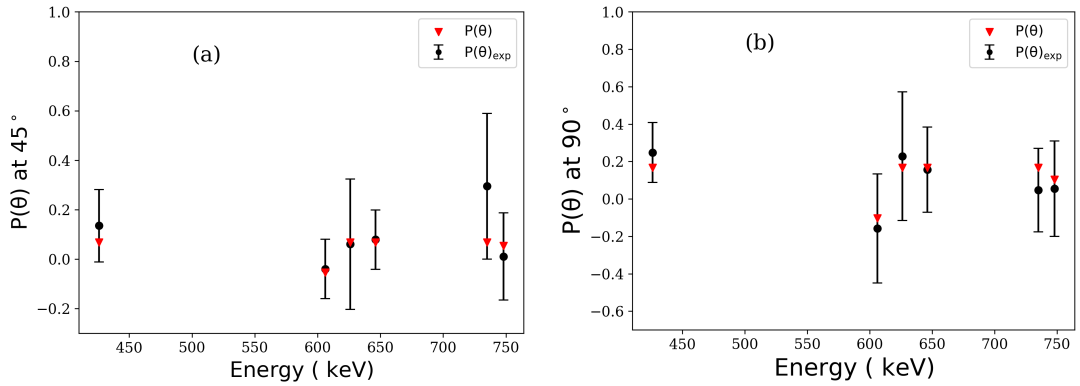

Figure 4: A comparison between the measured linear polarization $P(\theta)_{\text{exp}}$ (in circles) and the corresponding theoretical value (in triangles) for the clover detector pairs at $\theta = 45°$ (a) and $\theta = 90°$ (b) for the 428-, 636-, 735- and 748-keV transitions of ^{194}Hg, see also table 2. The three data points for the 636-keV γ ray are shifted a bit in energy, for better visibility.

5 Summary

This study describes a technique to measure the linear polarization of γ rays emitted from non-oriented nuclear states. The technique has been developed for the clover detectors of the iThemba LABS AFRODITE array and the AFRODITE polarization sensitivity, $Q(E_\gamma)$, has been deduced. In addition, the technique has been applied to measure the degree of linear polarization for the γ rays of ^{194}Hg observed in the β decay of ^{194}Tl produced in an in-beam experiment. The degree of linear polarization obtained experimentally for the transitions in ^{194}Hg are found in very good agreement with the corresponding theoretical values, which shows that the technique works well for non-oriented nuclear states. This is the first time that the polarization sensitivity of AFRODITE is been measured. Thus, the measured polarization sensitivity can be used in any other experiment (where oriented or non-oriented nuclear states are populated) that intends to measure γ rays with unknown multipolarities and also to determine the mixing ratios of transitions with mixed multipole nature.

Acknowledgement

This work was partially supported by the National Research Foundation, South Africa and the International Atomic Energy Agency (IAEA) Marie Sklodowska-Curie Fellowship Programme (MSCFP).

References

[1] K. S. Krane, *Introductory Nuclear Physics* (John Wiley & Sons, 1991).

[2] R. T. Newman and others., *Balkan Physics Letters* **Special Issue**, 182 (1998).

[3] J. F. Sharpey-Schafer., *Nuclear Physics News* **14**, 5 (2004).

[4] G. Duchêne et al., *Nucl. Instrum. Methods Phys. Res. A* **432**, 90–110 (1999).

[5] P.M. Jones et al., *Nucl. Instrum. Methods Phys. Res. A* **362**, 556–560 (1995).

[6] Y. Kojima et al., *Nucl. Instrum. Methods Phys. Res. A* **990**, 164984 (2021).

[7] K. Starosta et al., *Nucl. Instrum. Methods Phys. Res. A* **423**, 16 - 26 (1999).

[8] A. Herzan, et al., *Phys. Rev. C* **92**, 044310 (2015).

[9] L. W. Fagg and S. S. Hanna, *Rev. Mod. Phys.* **31**, 711 (1959).

[10] O. Klein and Y. Nishina., *Z. Phys.* **52**, 853–868 (1929).

[11] "National Nuclear Data Center", `https://www.nndc.bnl.gov/`, accessed June 2025.

[12] D. Radford., *Nucl. Instrum. Methods Phys. Res. A* **361**, 305 (1995).

This page intentionally left blank.

Analysis of Long-Term Stability Uncertainty in Luminosity Measurements Using the Tile Calorimeter of the ATLAS Detector for Run 3 Proton-Proton Collisions at $\sqrt{s} = 13.6$ TeV in 2023

Phuti Rapheeha[1,2,3], **Bruce Mellado**[1,2], **and Karim Djouani**[3]

[1]School of Physics and Institute for Collider Particle Physics, University of the Witwatersrand, Johannesburg, Wits 2050, South Africa
[2]iThemba LABS, National Research Foundation, Somerset West 7129, South Africa
[3]School of Electrical Engineering, Tshwane University of Technology, Staatsartillerie Road, Pretoria West 0001, South Africa

E-mail: ntsoko.phuti.rapheeha@cern.ch

Abstract. Precision luminosity measurements are crucial for determining the fundamental properties of physics processes at the Large Hadron Collider. In the ATLAS experiment, luminosity uncertainties often represent one of the leading sources of systematic uncertainty in cross-section measurements, directly impacting sensitivity to new physics searches and background estimations.

The ATLAS primary luminometer, LUCID, is calibrated only once per data-taking year. Studying its long-term stability is therefore essential, as it significantly contributes to the total luminosity uncertainty. In this study, the Tile Calorimeter is used to evaluate and monitor the long-term stability of the luminosity measurements. TileCal is particularly well-suited for this task because its D-layer cells, located in the outermost radial layers, exhibit minimal radiation-induced degradation over time.

The study presents results from the ATLAS detector based on 2023 proton-proton collisions at a centre-of-mass energy of $\sqrt{s} = 13.6$ TeV. A long-term stability uncertainty of $\delta\mathcal{L}/\mathcal{L} = 0.1\%$ is achieved for the 27.58 fb^{-1} of data recorded by ATLAS.

1 Introduction

The instantaneous luminosity ($\mathcal{L}$) quantifies the rate at which proton-proton (pp) collisions take place in the collider per unit time. It is a fundamental quantity, as it determines the expected event yield for a given physics process. The connection between instantaneous luminosity and the observed event rate can be expressed as

$$\frac{dN_{pp\to X}}{dt} = \sigma_{pp\to X} \times \mathcal{L}, \tag{1}$$

where $dN_{pp\to X}/dt$ is the rate of events for the process $pp \to X$, and $\sigma_{pp\to X}$ is the corresponding production cross-section.

As it can be seen in Equation 1, uncertainties in the luminosity measurement directly propagate to uncertainties in cross-section measurements. For many precision measurements within the Standard Model, luminosity uncertainties are among the leading systematic uncertainties [1, 2]. Precise luminosity estimates are crucial for new

physics searches, directly affecting both the determination of background levels and the overall sensitivity of the analyses.

Beyond precise physics measurements, accurate and stable luminosity measurements are critical for determining trigger pre-scales and for the efficient functioning of the Large Hadron Collider (LHC). As a result, the ATLAS experiment maintains a dedicated program for luminosity calibration and monitoring.

For inelastic pp collisions at the LHC, the instantaneous luminosity per bunch crossing can be written in terms of the average number of interactions, μ, as:

$$\mathcal{L}_b = f_{\text{LHC}} \frac{\mu}{\sigma_{\text{inel}}}, \tag{2}$$

where f_{LHC} denotes the LHC bunch revolution frequency and σ_{inel} denotes the total inelastic pp cross-section. Alternatively, the bunch luminosity can equivalently be formulated in terms of the beam parameters at the interaction point(IP):

$$\mathcal{L}_b = f_{\text{LHC}} \frac{n_1 n_2}{\Sigma_x \Sigma_y}, \tag{3}$$

where n_1 and n_2 are the bunch intensities, and Σ_x and Σ_y are the widths of the beam overlap in the x and y planes, respectively.

Detectors sensitive to inelastic pp interactions can serve as luminometers by measuring the visible interaction rate, μ_{vis}. This rate is connected to the true average number of interactions through $\mu_{\text{vis}} = \epsilon, \mu$, where ϵ denotes the detector efficiency for recording inelastic events. The corresponding visible cross-section is expressed as $\sigma_{\text{vis}} = \epsilon, \sigma_{\text{inel}}$.

The instantaneous bunch luminosity can equivalently be expressed using the visible interaction rate as:

$$\mathcal{L}_b = f_{\text{LHC}} \frac{\mu_{\text{vis}}}{\sigma_{\text{vis}}}, \tag{4}$$

where σ_{vis} denotes the visible cross-section. This form is particularly useful for detector-based luminosity measurements, where μ_{vis} is obtained from detector signals, and σ_{vis} is obtained from dedicated beam-separation scans, commonly called Van der Meer (VdM) scans [3, 4]. These scans are performed under special low-pileup conditions using low-intensity bunches that are widely spaced in time, thereby reducing the probability of overlapping events between consecutive bunch crossings. Since returning the LHC from these special conditions to standard high-luminosity physics running requires many hours, VdM scans are typically limited to once per year, which in turn motivates the need for continuous long-term stability monitoring with independent detectors.

The ATLAS experiment employs several detectors for luminosity measurements, illustrated in Figure 1. The primary luminometer is the Luminosity Cherenkov Integrating Detector (LUCID) [5], located in the forward region. Additional subsystems—including the inner tracking detectors, the Tile Calorimeter (TileCal), the endcap electromagnetic calorimeter (EMEC), and the forward calorimeter (FCal)—provide independent cross-checks of the LUCID measurement in offline analyses. Further details on the operating principles of these luminosity detectors are available in Reference [6].

LUCID is absolutely calibrated once per data-taking year during the VdM scans. Because this calibration is infrequent, it is crucial to monitor the detector's response over time to ensure the stability of the luminosity measurements. The efficiency of the luminometer may degrade due to irradiation, ageing, or other detector-specific effects, necessitating appropriate corrections. After all known corrections are applied, any residual variations are treated as systematic uncertainties related to long-term stability and linearity. In this study, the TileCal is employed as a reference luminometer to assess the time-dependent stability of LUCID throughout the 2023 pp collision data-taking period at $\sqrt{s} = 13.6$ TeV. These results contribute to the determination of the long-term stability uncertainty of the total luminosity uncertainty in ATLAS.

2 The ATLAS Tile Calorimeter

The TileCal forms the central part of the hadronic calorimeter system in the ATLAS detector. It plays a pivotal role in the reconstruction of hadrons, τ-leptons, and jets, and contributes to the measurement of missing transverse momentum associated with non-interacting particles. The TileCal also provides essential information to the ATLAS trigger system.

It covers the barrel region of the ATLAS detector up to pseudorapidity $(|\eta|) < 1.7$ and is segmented into three sections along the beam axis. It consists of a central Long Barrel (LB), which spans the region $|\eta| < 1.0$, and two Extended Barrels (EB), located in the forward and backward regions covering $0.8 < |\eta| < 1.7$. The detector is symmetric about the interaction point, with regions of $\eta > 0$ corresponding to the A-side and regions of $\eta < 0$ corresponding to the C-side.

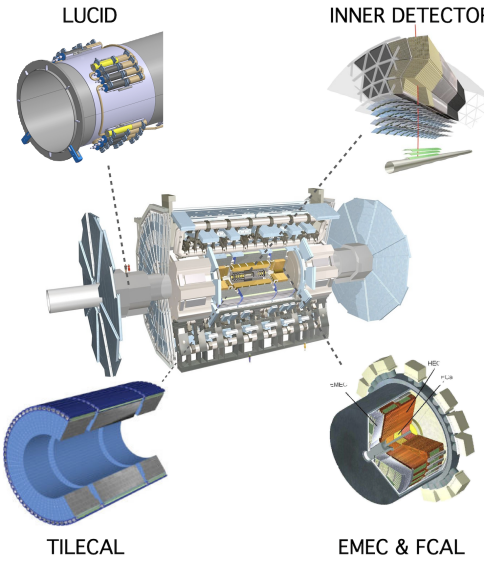

Figure 1: ATLAS sub-detectors used for luminosity measurements: LUCID (forward), TileCal (central hadronic), Inner Detector (tracking), and EMEC & FCal (electromagnetic and forward calorimeters), shown at their approximate positions within the detector.

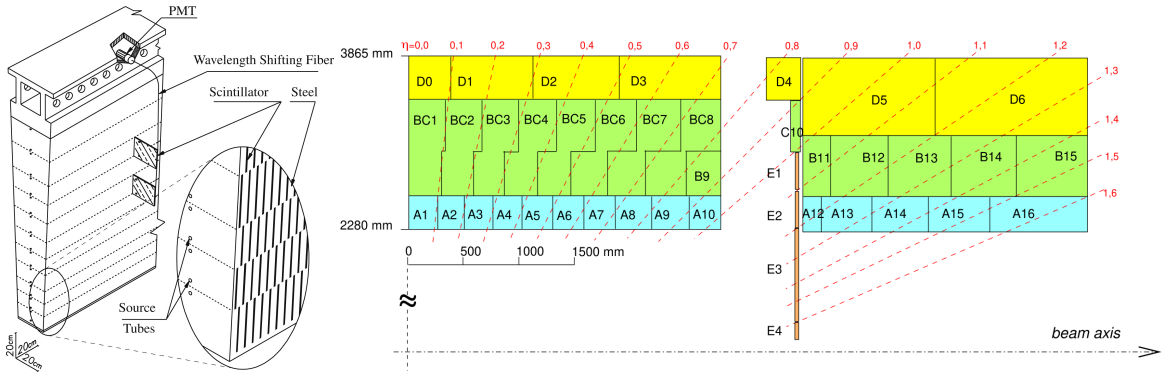

Figure 2: (*left:*) Schematic of a TileCal module [7], illustrating its mechanical structure and optical readout components. (*right:*) Map of TileCal cells in the ϕ–η plane on the A-side of the detector. Cell boundaries are indicated by solid lines, corresponding to groups of fibres from scintillating tiles that are routed to PMTs for readout.

It is a sampling calorimeter made of low-carbon steel absorbers interleaved with plastic scintillating tiles that act as the active medium. Charged particles crossing the scintillators produce light, which is collected along the tile edges and guided via wavelength-shifting fibres to a pair of photomultiplier tubes (PMTs) mounted in a steel girder at the outer radius of each module.Using two PMTs per cell enhances redundancy and improves the signal-to-noise ratio. The PMT signals are shaped into current pulses and digitised at two amplification levels: high and low gain. With a gain ratio of 64, this scheme provides a broad dynamic range for signal measurements. The dual readout is particularly advantageous for luminosity monitoring, as it ensures sensitivity to small signals at low luminosity while preventing saturation at high luminosity, thereby enabling stable performance across the full range of LHC operating conditions.

The readout of TileCal is divided along the beam axis into four partitions: two long barrels (LBA and LBC) and two extended barrels (EBA and EBC). Each TileCal partition consists of 64 modules with equal azimuthal width $\Delta\phi = 0.1$, which are positioned radially and oriented perpendicular to the beam line. A schematic view of a single module is presented on the left of Figure 2. Within each module, the three-dimensional cell structure is defined by the ϕ, η, and radial segmentation. The longitudinal layers A, BC, and D, are segmented with a granularity of $\Delta\eta \times \Delta\phi = 0.1 \times 0.1$ for the first two layers increasing to $\Delta\eta \times \Delta\phi = 0.2 \times 0.1$ in the outermost layer. The

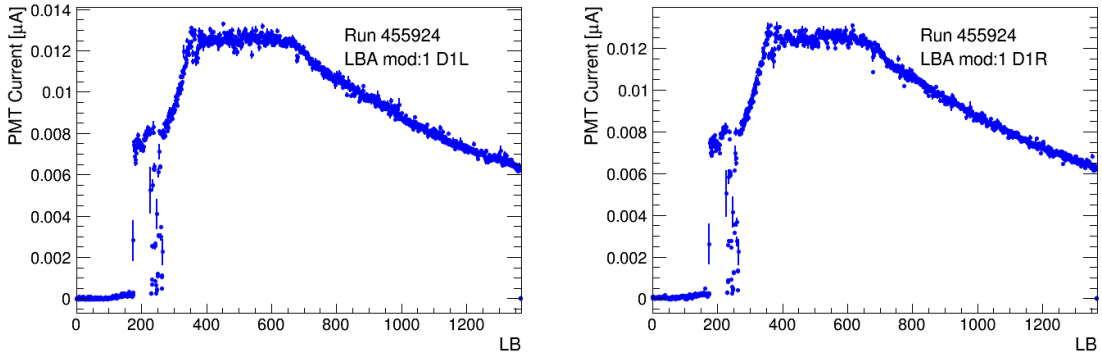

Figure 3: Distributions of raw PMT currents versus LB for the left (D1L, *left*) and right (D1R, *right*) PMTs in module 1 of the LBA partition during Run 455924.

corresponding cell arrangement for half of a LB and EB module is illustrated on the right of Figure 2.

A comprehensive overview of the TileCal design is given in the Technical Design Report [8], with further details on its construction, optical readout system, and installation in ATLAS provided in References [9, 10].

3 Methodology

Although TileCal was not initially intended for luminosity measurements, the anode current I_{PMT} drawn by each photomultiplier tube scales with the particle flux through a TileCal cell, and therefore correlates with the bunch-integrated luminosity. This current is obtained from the raw PMT signal, recorded in ADC counts, and is computed as:

$$\langle I_{\mathrm{PMT}} \rangle = \frac{\langle \mathrm{ADC} \rangle - p}{\text{Int. gain}}, \tag{5}$$

where $\langle \mathrm{ADC} \rangle$ denotes the average ADC counts per LB, Int. gain is the integrator gain constant and p is the pedestal. The pedestal, which represents the baseline ADC measurement dominated by electronic noise, is calculated from periods at the start of physics runs when the detector is active but no collisions are occurring.

The anode currents as a function of luminosity block (LB) drawn by the PMTs of cell D1 located in module 1 of the LBA partition are shown in Figure 3. An LB is a time interval, typically lasting a few seconds, during which the data-taking conditions in ATLAS are assumed to be stable. The ATLAS central trigger processor [11] defines and numbers these intervals, which provide the basic unit for recording and reporting luminosity measurements.

The PMT currents are converted into luminosity estimates through calibration constants. The relation between the average anode current and the corresponding luminosity is expressed as:

$$\mathcal{L}_{\mathrm{PMT}} = \alpha \langle I\mathrm{PMT} \rangle, \tag{6}$$

where α denotes the calibration constant, and $\langle I_{\mathrm{PMT}} \rangle$ is the average PMT current within a LB. The constants α are derived for each PMT and subsequently used to compute luminosities from PMT currents via Equation 6.

The anchoring constants used in this study are obtained from physics Run 455924, selected as the reference run for the 2023 data-taking campaign. This run features a wide luminosity range and smooth changes in instantaneous luminosity, making it ideal for deriving the calibration constants. Typically, only one run is chosen per year to determine the calibration constants, ensuring consistency across the dataset.

For each TileCal cell, the luminosity is computed as the average of the luminosities from the left and right PMTs. The luminosity of a given cell type is then determined by averaging over the corresponding cells across all modules.

In principle, every TileCal cell is capable of contributing to luminosity measurements. Cells located in the D-layer, the outermost radial layer of TileCal, exhibit the most stable response over time, with minimal variation due to radiation damage. This stability makes them particularly well suited for long-term luminosity monitoring. For this study, the D6 cells are used to determine the long-term stability uncertainty, consistent with their use in Run 2. The D5 cells are included as an additional handle for systematic cross-checks.

Figure 4 presents a comparison between the TileCal luminosities derived from the D5 and D6 cells (on both the A and C sides) and the reference track-counting luminosity. The good agreement observed across all cases

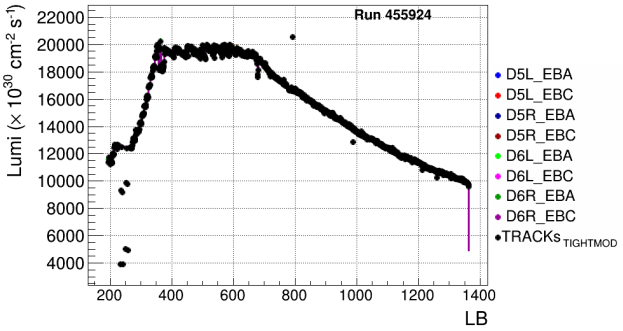

Figure 4: Comparison of TileCal luminosities derived from D5 and D6 cells with the reference track-counting luminosity. The results are shown for both the A and C sides of the detector.

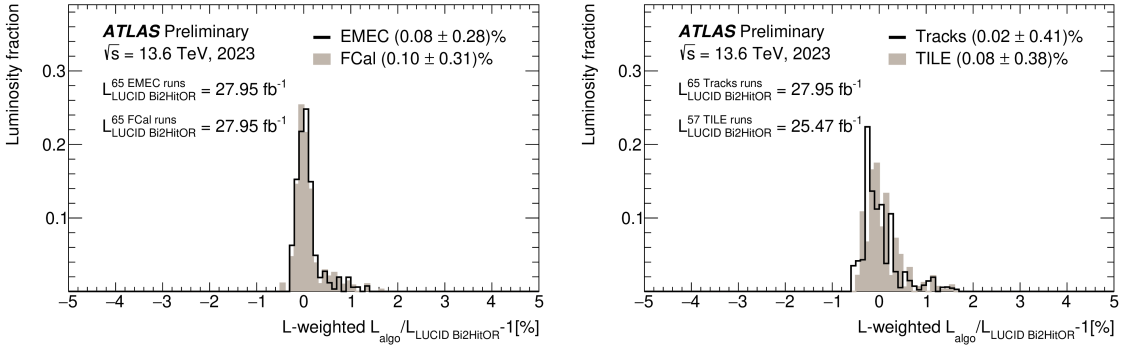

Figure 5: Relative differences in run-integrated luminosity between the baseline LUCID measurement and (*left*) EMEC and FCal, and (*right*) TileCal and track-counting luminosity measurements, using A-side and C-side averages [12]

demonstrates the effectiveness of the cross-calibration procedure in converting anode PMT currents into reliable TileCal luminosity measurements.

This study uses physics runs included in the standard good run list (GRL), which specifies runs and LBs deemed suitable for physics analyses. The GRL is compiled based on stringent data quality criteria, including detector performance, operational stability, and data-taking conditions. Only runs with at least 100 LBs in the GRL are considered for the long-term stability studies.

4 Results

Physics analyses primarily care about integrated deviation rather than per-run fluctuations. The long-term stability of LUCID luminosity measurements is evaluated by benchmarking run-integrated luminosities obtained by calorimeter-based algorithms to the baseline LUCID measurement. For a given data-taking year, the long-term stability uncertainty is defined as the maximum mean offset observed between LUCID and any of the calorimeter-derived estimates.

Figure 5 shows the distributions of the relative differences in run-integrated luminosity between the LUCID baseline and the calorimeter and track-counting measurements. Each fill is weighted by its integrated luminosity, giving greater emphasis to longer fills with higher statistical weight. The mean and RMS values shown in the legend correspond to the average fractional deviation over the full 2023 data-taking period and its spread, respectively. The largest observed mean deviation, 0.1% from FCal, sets the preliminary long-term stability uncertainty.

5 Conclusions

Precise luminosity measurements are essential for both precision physics analyses and optimal LHC operation. This study evaluated the long-term stability of the LUCID luminosity measurement in ATLAS by comparing

run-integrated luminosities to those derived from calorimeter-based and track-counting methods, with a focus on TileCal D-layer cells as a reference.

The analysis used data from the 2023 pp collision period at $\sqrt{s} = 13.6$ TeV. Calibration constants were derived from a dedicated reference run and applied consistently to convert TileCal PMT currents into luminosity estimates. Run-integrated luminosities from TileCal D6 cells and other calorimeter-based measurements were compared to the LUCID baseline measurement. The largest observed mean deviation, 0.1% from the FCal, was used to define the preliminary long-term stability uncertainty for the 2023 LUCID luminosity measurement. This level of stability corresponds to a sub-percent contribution to the total luminosity uncertainty, directly impacting cross-section measurements where luminosity is a dominant systematic.

References

[1] Aad, Georges and others, "Measurement of the associated production of a top-antitop-quark pair and a Higgs boson decaying into a $b\bar{b}$ pair in pp collisions at $\sqrt{s} = 13$ TeV using the ATLAS detector at the LHC," *Eur. Phys. J. C*, vol. 85, no. 2, p. 210, 2025.

[2] G. Aad *et al.*, "Snowmass White Paper Contribution: Physics with the Phase-2 ATLAS and CMS Detectors," Geneva, 2022, all figures including auxiliary figures are available at https://atlas.web.cern.ch/Atlas/GROUPS/PHYSICS/PUBNOTES/ATL-PHYS-PUB-2022-018. [Online]. Available: https://cds.cern.ch/record/2805993

[3] S. van der Meer, "Calibration of the effective beam height in the ISR," CERN, Geneva, Tech. Rep., 1968. [Online]. Available: https://cds.cern.ch/record/296752

[4] C. Rubbia, "Measurement of the luminosity of pp collider with a (generalised) Van der Meer Method," CERN, Geneva, Tech. Rep., 1977. [Online]. Available: https://cds.cern.ch/record/1025746

[5] F. Lasagni Manghi, "The LUCID detector ATLAS luminosity monitor and its electronic system," *Nuclear Instruments and Methods in Physics Research Section A: Accelerators, Spectrometers, Detectors and Associated Equipment*, vol. 824, pp. 311–312, 2016, frontier Detectors for Frontier Physics: Proceedings of the 13th Pisa Meeting on Advanced Detectors. [Online]. Available: https://www.sciencedirect.com/science/article/pii/S0168900215015272

[6] Aad, Georges and others, "Luminosity determination in pp collisions at $\sqrt{s} = 13$ TeV using the ATLAS detector at the LHC," *Eur. Phys. J. C*, vol. 83, no. 10, p. 982, 2023.

[7] Aad, G. and others, "Readiness of the ATLAS Tile Calorimeter for LHC collisions," *Eur. Phys. J. C*, vol. 70, pp. 1193–1236, 2010.

[8] Abdallah, J. and others, *ATLAS tile calorimeter*, ser. Technical design report. ATLAS. Geneva: CERN, 1996. [Online]. Available: https://cds.cern.ch/record/331062

[9] J. Abdallah *et al.*, "The optical instrumentation of the ATLAS tile calorimeter," *JINST*, vol. 8, p. P01005, 2013.

[10] Abdallah, J. and others, "Mechanical construction and installation of the ATLAS tile calorimeter," *JINST*, vol. 8, p. T11001, 2013.

[11] Aad, Georges and others, "Operation of the ATLAS trigger system in Run 2," *JINST*, vol. 15, no. 10, p. P10004, 2020.

[12] "Preliminary analysis of the luminosity calibration for the ATLAS $\sqrt{s} = 13.6$ TeV data recorded in 2023," CERN, Geneva, Tech. Rep., 2024, all figures including auxiliary figures are available at https://atlas.web.cern.ch/Atlas/GROUPS/PHYSICS/PUBNOTES/ATL-DAPR-PUB-2024-001. [Online]. Available: https://cds.cern.ch/record/2900949

Progress on test of the generalized Brink-Axel hypothesis in ^{63}Ni

M.F. Nkalanga[1], B.V. Kheswa[1], M. Wiedeking[2], S.N.T. Majola[1], A. Tsewu[1], V. W. Ingeberg[3], P.L. Masiteng[1], P. Jones[4].

[1] Department of Physics, University of Johannesburg 55 Beit Street, Doornfontein, Johannesburg, 2028, South Africa.

[2] Lawrence Berkeley National Laboratory, 1 Cyclotron Rd, Berkeley, CA 94720, United States.

[3] Department of Physics, University of Oslo, N-0316 Oslo, Norway.

[4] SSC Laboratory, iThemba LABS, P.O. Box 722, 7129 Somerset West, South Africa.

E-mail: mhlanganon@uj.ac.za.

Abstract. The validity of the generalized Brink-Axel hypothesis was tested for the first time on ^{63}Ni. This hypothesis is assumed in various experimental methods and nuclear reactions models. It's experimental test across the nuclear chart is crucial. The results show the γ-ray strength function of ^{63}Ni does not depend on the initial excitation energy; supporting the validity of the generalized Brink-Axel hypothesis. However, it still remains important to test the dependence of the γ-ray strength function of ^{63}Ni on its final excitation energy as well. This will be done in future to draw the final conclusion about the generalized Brink-Axel hypothesis on ^{63}Ni.

1 Introduction

With the nuclear excitation energy increasing to the quasi-continuum region, the quantum state's width and spacing become wider and decreases, respectively, this allows for statistical γ-decay description of the nuclei. The statistical quantities, nuclear level density (NLD) and γ-ray strength function (gSF), are fundamental key into describing nuclei excited up to the quasi-continuum region. The NLD is the number of nuclear states at a fixed excitation energy bin, and it can be estimated with a variety of theoretical models including the constant temperature model [1, 2]:

$$\rho(E_x) = \frac{1}{T} e^{(Ex-E_0)/T} \tag{1}$$

where T is the nuclear temperature, E_x is the excitation energy, and E_0 is a energy shift constant. The gSF is the probability of a nucleus to excite by absorbing or de-excite by releasing a γ-ray. The gSF is correlated to the nuclear level density, average radiative width of the states and γ-ray energy through [3]:

$$f_{J^\pi}(E_\gamma) = \frac{\bar{\Gamma}_{J^\pi}(E_i, E_\gamma)\rho_{j^\pi}(E_i)}{E_\gamma^{2\lambda+1}} \tag{2}$$

where $f_{J^\pi}(E_\gamma)$ is the gSF, E_γ is the γ-ray energy, $\bar{\Gamma}_{J^\pi}$is the average radiative width, ρ_{J^π} is the NLD, λ is the multipolarity of the γ-ray, and E_i is the initial excitation energy. The gSF between the initial excitation and final excitation energy states is often assumed, based on the generalized Brink-Axel (gBA) hypothesis [4–6], to be independent of the properties of the states, and it solely depends on the γ-ray energy. This hypothesis is a fundamental assumption in various experimental methods, such as the Oslo Method which has gained global recognition and used in many studies in the literature to extract the gSF and NLD [7–10]. It is also used as the

fundamental assumption in large network nucleosynthesis calculations [11]. Therefore, experimental test of the gBA hypothesis is important for the reliability of the gSF data from the Oslo Method and elemental abundances calculated under the assumption that the gBA hypothesis is valid. Some theoretical and experimental studies have been found to support the Brink-Axel hypothesis [12–22], while others show results disputing it [23–25]. However, the gBA hypothesis has not been tested within ^{63}Ni mass region. This work presents the first test of the generalized Brink-Axel hypothesis in ^{63}Ni. In particular, we tested the variation of the γ-ray strength function on the initial excitation energies.

2 Methods

The nucleus ^{63}Ni was populated through the ^{64}Ni(p,d)^{63}Ni* nuclear reaction. The ^{64}Ni target had a thickness of 4.56 mg/cm^2 and it was irradiated with proton beam of 27.4 MeV produced and supplied by the SSC at iThemba LABS. AFRODITE array together with double sided silicon detectors were employed for the particle–γ coincidences measurements [26, 27]. The AFRODITE array was equipped with eight high-purity germanium detectors and two large lanthanum bromide doped with cerium detectors, for the detection of γ-rays. Charged particles were detected using the silicon detectors, segmented into 16 rings and 48 sectors, with a ΔE–E configuration, placed behind the target inside the target chamber. The front detector (ΔE) had a thickness of 309 μm, and the back detector (E) had a thickness of 1041 μm. For δ-electron shielding, an aluminium foil 10 μm thick, was placed in front of the ΔE detector.

Particle–γ coincidences data were sorted out by setting a time-gate on the time-difference spectrum between the detected prompt particles and γ-rays. The large lanthanum bromide detectors data were used in this analysis due to their superior γ-ray detection efficiency. The corresponding (p,d) reaction channel for ^{63}Ni was selected using a graphical cut on the particle identification (PID) matrix. The deuteron energy detected on the silicon detectors is used to compute the excitation energy of ^{63}Ni using two-body reaction kinematics, and a particle-γ matrix (excitation energy vs γ-ray energy) was constructed. Using the $LaBr_3$(Ce) response function simulated for the AFRODITE array with GEANT4 [28], the γ spectrum of ^{63}Ni was unfolded with the unfolding method explained in Ref. [29]. The unfolded γ spectrum was used to get the primary matrix shown in Fig 1 containing primary γ-rays obtained with the first generation method discussed in Ref. [30].

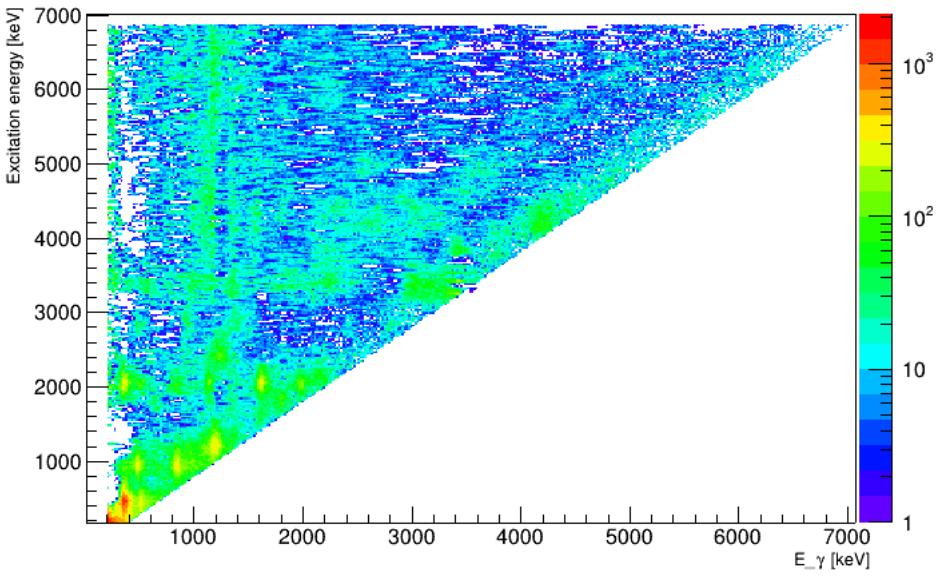

Figure 1: Primary matrix containing primary γ-rays for ^{63}Ni.

The gBA hypothesis in ^{63}Ni was tested using the method of Ref. [12]. The primary matrix in Fig 1 contains primary-γ spectra, $g(E_i, E_\gamma)$, at each excitation energies (E_i). The $g(E_i, E_\gamma)$ are normalized to $P(E_\gamma, Ei)$ through:

$$P(E_\gamma, E_i) = \frac{g(Ei, E_\gamma)}{\Sigma g(E_i, E_\gamma)} \tag{3}$$

where $U(E_\gamma, E_i)$ is the decay probability matrix of the nucleus to de-excite by releasing a γ-ray from a state with initial excitation energy (E_i). If the NLD is known, particularly extracted from the Oslo method techniques [26], the transmission coefficients ($\mathcal{T}$) at different initial excitation energies are derived as follows [12]:

$$\mathcal{T}(E_i, E_\gamma) = N(E_i)\frac{U(E_\gamma, E_i)}{\rho(E_i - E_\gamma)}] \tag{4}$$

where $\rho(E_i - E_\gamma)$ is the NLD as function of final excitation energy, and $N(E_i)$ is the normalization factor to correct for scaling given by [12]:

$$N(E_i) = \frac{\int_0^{E_i} N(E_\gamma, E_i)\, dE_\gamma}{\int_0^{E_i} \mathcal{T}(E_\gamma)\, \rho(E_f)\, dE_\gamma} \tag{5}$$

For different initial excitation energies, the shape of the γ-ray strength function ($f(E_\gamma)$) is obtained from Eq 4 through the following equation:

$$f(E_\gamma) = \frac{\mathcal{T}(E_\gamma)}{2\pi E_\gamma^3} \tag{6}$$

3 Results and discussion

Figure 2 shows the extracted gSF for ^{63}Ni (black data) at different initial excitation energies, compared with the gSF (blue line) of ^{63}Ni extracted from the entire 3200 keV to 6700 keV excitation energy region using the standard Oslo Method [26]. The results show that the gSF remain the same in both magnitude and shape at all different initial excitation energies, within the experimental error bars. Therefore, the initial excitation energy data from ^{63}Ni supports the gBA hypothesis in the quasi-continuum region. These observations are consistent with other previous studies that tested the gBA hypothesis's validity [12, 31, 32]. The gBA hypothesis is fundamental in the Oslo method analysis [7–10], therefore, these initial excitation energy results support the reliability of the Oslo method analysis.

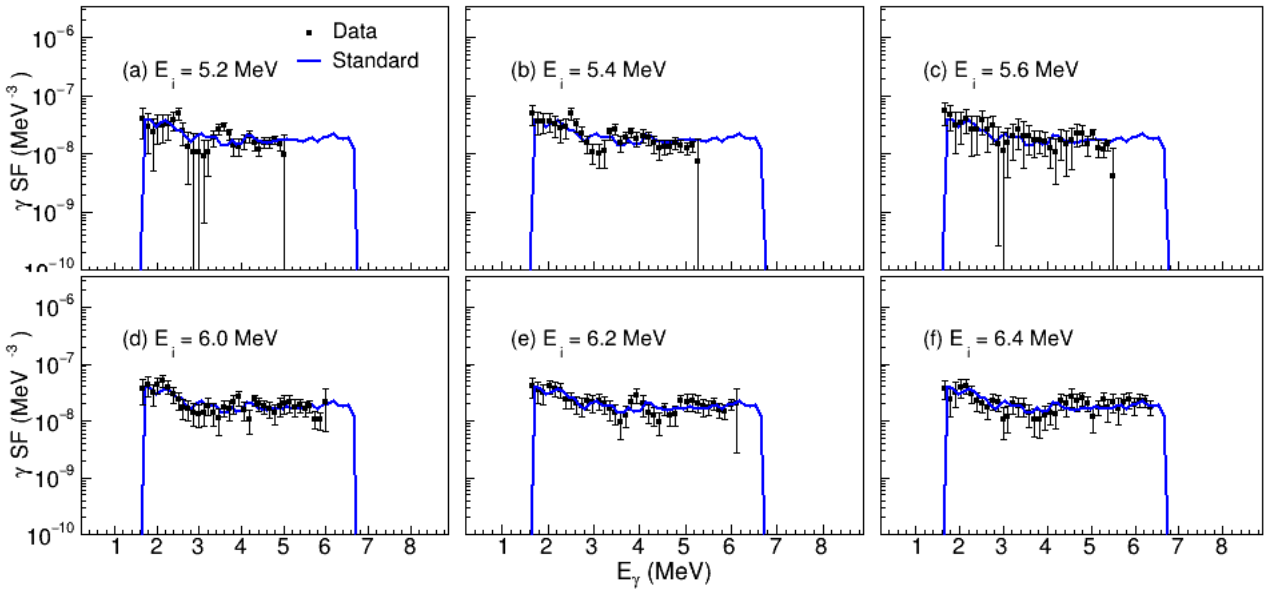

Figure 2: gSF for ^{63}Ni extracted and compared at initial excitation energies.

4 Conclusion

The gSF for ^{63}Ni is obtained and compared at different initial excitation energies. The results show no significant variations except with minor statistical fluctuations. These fluctuations, due to low statistics in the extracted excitation energy region, do not disprove the validity of gBA hypothesis. In future we shall conclude the analysis by investigating the variation of the gSF of ^{63}Ni at different final excitation energies.

5 Acknowledgements
The authors extend their gratitude appreciate and thank iThemba LABS for beam time for the experiment, and the University of Johannesburg. This work supported by the U.S. Department of Energy, Office of Science, Office of Nuclear Physics under Contract No. DE-AC02-05CH11231.

References

[1] T. Ericson, "The statistical model and nuclear level densities," *Advances in Physics*, vol. 9, no. 36, pp. 425–511, 1960. [Online]. Available: https://doi.org/10.1080/00018736000101239

[2] A. Gilbert and A. G. W. Cameron, "A composite nuclear-level density formula with shell corrections," *Can. J. Phys.*, vol. 43, no. 8, pp. 1446–1496, 1965. [Online]. Available: https://doi.org/10.1139/p65-139

[3] G. A. Bartholomew, E. D. Earle, A. J. Ferguson, J. W. Knowles, and M. A. Lone, "Photon strength functions from (p,γ) reactions," vol. 7, pp. 229–285, 1973.

[4] D. Brink, "Some aspects of the interaction of light with matter," 1955.

[5] P. Axel, "Electric dipole ground-state transition width strength function and 7-mev photon interactions," *Phys. Rev.*, vol. 126, no. 2, pp. 671–683, apr 1962.

[6] G. Bartholomew, E. Earle, A. Ferguson, J. Knowles, and M. Lone, "Gamma-ray strength functions," *Advances in Nuclear Physics: Volume 7*, pp. 229–324, 1973.

[7] F. Giacoppo, F. L. B. Garrote, L. A. Bernstein, D. L. Bleuel, T. K. Eriksen, R. B. Firestone, A. Görgen, M. Guttormsen, T. W. Hagen, B. V. Kheswa, M. Klintefjord, P. E. Koehler, A. C. Larsen, H. T. Nyhus, T. Renstrøm, E. Sahin, S. Siem, and T. Tornyi, "Level densities and thermodynamical properties of pt and au isotopes," *Phys. Rev. C*, vol. 90, no. 5, p. 054330, Nov. 2014.

[8] M. Guttormsen, Y. Alhassid, W. Ryssens, K. O. Ay, M. Ozgur, E. Algin, A. C. Larsen, F. L. B. Garrote, L. C. Campo, T. Dahl-Jacobsen, A. Görgen, T. W. Hagen, V. W. Ingeberg, B. V. Kheswa, M. Klintefjord, J. E. Midtbø, V. Modamio, T. Renstrøm, E. Sahin, S. Siem, G. M. Tveten, and F. Zeiser, "Strong enhancement of level densities in the crossover from spherical to deformed neodymium isotopes," *Phys. Lett. B*, vol. 816, p. 136206, 2021.

[9] K. L. Malatji, M. Wiedeking, S. Goriely, C. P. Brits, B. V. Kheswa, F. L. B. Garrote, D. L. Bleuel, F. Giacoppo, A. Görgen, M. Guttormsen, K. Hadynska-Klek, T. W. Hagen, V. W. Ingeberg, M. Klintefjord, A. C. Larsen, P. Papka, T. Renstrøm, E. Sahin, S. Siem, L. Siess, G. M. Tveten, and F. Zeiser, "Re-estimation of ^{180}ta nucleosynthesis in light of newly constrained reaction rates," *Physics Letters B*, vol. 791, pp. 403–408, 2019. [Online]. Available: https://www.sciencedirect.com/science/article/pii/S0370269319301674

[10] B. Kheswa, M. Wiedeking, F. Giacoppo, S. Goriely, M. Guttormsen, A. Larsen, F. Bello Garrote, T. Eriksen, A. Görgen, T. Hagen, P. Koehler, M. Klintefjord, H. Nyhus, P. Papka, T. Renstrøm, S. Rose, E. Sahin, S. Siem, and T. Tornyi, "Galactic production of 138la: Impact of 138,139la statistical properties," *Physics Letters B*, vol. 744, pp. 268–272, 2015. [Online]. Available: https://www.sciencedirect.com/science/article/pii/S0370269315002403

[11] W. Hauser and H. Feshbach, "The inelastic scattering of neutrons," *Phys. Rev.*, vol. 87, pp. 366–373, Jul 1952. [Online]. Available: https://link.aps.org/doi/10.1103/PhysRev.87.366

[12] M. Guttormsen, A. C. Larsen, A. Görgen, T. Renstrøm, S. Siem, T. G. Tornyi, and G. M. Tveten, "Validity of the generalized brink-axel hypothesis in ^{238}Np," *Phys. Rev. Lett.*, vol. 116, p. 012502, 2016. [Online]. Available: https://link.aps.org/doi/10.1103/PhysRevLett.116.012502

[13] M. Stefanon and F. Corvi, "Resonance neutron capture gamma rays in 177hf," *Nuclear Physics A*, vol. 281, pp. 240–260, 1977. [Online]. Available: https://www.sciencedirect.com/science/article/pii/0375947477900239

[14] S. Raman, O. Shahal, and G. G. Slaughter, "Test of axel-brink predictions by a discrete approach to resonance-averaged (n, γ) spectroscopy," *Phys. Rev. C*, vol. 23, pp. 2794–2797, 1981. [Online]. Available: https://link.aps.org/doi/10.1103/PhysRevC.23.2794

[15] S. Kahane, S. Raman, G. G. Slaughter, C. Coceva, and M. Stefanon, "Electric dipole transitions from neutron capture in ^{167}Er resonances," *Phys. Rev. C*, vol. 30, pp. 807–819, 1984. [Online]. Available: https://link.aps.org/doi/10.1103/PhysRevC.30.807

[16] M. A. Islam, T. J. Kennett, and W. V. Prestwich, "Radiative strength functions of germanium from thermal neutron capture," *Phys. Rev. C*, vol. 43, pp. 1086–1098, 1991. [Online]. Available: https://link.aps.org/doi/10.1103/PhysRevC.43.1086

[17] J. Kopecky and M. Uhl, "Test of gamma-ray strength functions in nuclear reaction model calculations," *Phys. Rev. C*, vol. 41, pp. 1941–1955, 1990. [Online]. Available: https://link.aps.org/doi/10.1103/PhysRevC.41.1941

[18] T. Koeling, "A calculation of neutron capture γ-ray spectra," *Nuclear Physics A*, vol. 307, pp. 139–162, 1978. [Online]. Available: https://www.sciencedirect.com/science/article/pii/0375947478904323

[19] A. Höring and H. A. Weidenmüller, "Gamma emission in precompound reactions. i. statistical model and collective gamma decay," *Phys. Rev. C*, vol. 46, pp. 2476–2492, 1992. [Online]. Available: https://link.aps.org/doi/10.1103/PhysRevC.46.2476

[20] J. Z. Gu and H. A. Weidenmüller, "Coulomb excitation of double giant dipole resonances," *Nuclear Physics A*, vol. 690, pp. 382–408, 2001. [Online]. Available: https://www.sciencedirect.com/science/article/pii/S0375947401003566

[21] E. Běták, F. Cvelbar, A. Likar, and T. Vidmar, "Model calculations of the radiative capture process and the brink–axel hypothesis," *Nuclear Physics A*, vol. 686, pp. 204–216, 2001. [Online]. Available: https://www.sciencedirect.com/science/article/pii/S0375947400005625

[22] M. S. Hussein, B. V. Carlson, and L. F. Canto, "Multiple giant resonances in nuclei: their excitation and decay," *Nuclear Physics A*, vol. 731, pp. 163–174, 2004. [Online]. Available: https://www.sciencedirect.com/science/article/pii/S0375947403018669

[23] L. Netterdon, A. Endres, S. Goriely, J. Mayer, P. Scholz, M. Spieker, and A. Zilges, "Experimental constraints on the γ-ray strength function in ^{90}Zr using partial cross sections of the $^{89}\mathrm{Y}(p,\gamma)^{90}\mathrm{Zr}$ reaction," *Physics Letters B*, vol. 744, pp. 358–362, 2015. [Online]. Available: https://www.sciencedirect.com/science/article/pii/S0370269315002610

[24] C. W. Johnson, "Systematics of strength function sum rules," *Physics Letters B*, vol. 750, pp. 72–75, 2015. [Online]. Available: https://www.sciencedirect.com/science/article/pii/S0370269315006553

[25] J. Isaak, D. Savran, B. Löher, T. Beck, M. Bhike, U. Gayer, Krishichayan, N. Pietralla, M. Scheck, W. Tornow, V. Werner, A. Zilges, and M. Zweidinger, "The concept of nuclear photon strength functions: A model-independent approach via ($\gamma \rightarrow$,γ' γ'') reactions."

[26] V. W. Ingeberg, P. Jones, L. Msebi, S. Siem, M. Wiedeking, A. A. Avaa, M. V. Chisapi, E. A. Lawrie, K. L. Malatji, L. Makhathini, S. P. Noncolela, and O. Shirinda, "Nuclear level density and γ-ray strength function of ^{63}Ni," *Phys. Rev. C*, vol. 106, p. 054315, Nov 2022. [Online]. Available: https://link.aps.org/doi/10.1103/PhysRevC.106.054315

[27] J. F. Sharpey-Schafer, "Nucl. phys. news," *Nucl. Phys. News*, vol. 14, p. 5, 2004.

[28] V. W. Ingeberg, S. Siem, M. Wiedeking, K. Sieja, D. L. Bleuel, C. P. Brits, T. D. Bucher, T. S. Dinoko, J. L. Easton, A. Görgen, M. Guttormsen, P. Jones, B. V. Kheswa, N. A. Khumalo, A. C. Larsen, E. A. Lawrie, J. J. Lawrie, S. N. T. Majola, K. L. Malatji, L. Makhathini, B. Maqabuka, D. Negi, S. P. Noncolela, P. Papka, E. Sahin, R. Schwengner, G. M. Tveten, F. Zeiser, and B. R. Zikhali, "First application of the oslo method in inverse kinematics," *The European Physical Journal A*, vol. 56, no. 2, p. 68, 2020. [Online]. Available: https://doi.org/10.1140/epja/s10050-020-00070-7

[29] M. Guttormsen, T. S. Tveter, L. Bergholt, F. Ingebretsen, and J. Rekstad, "The unfolding of continuum γ-ray spectra," *Nucl. Instrum. Methods Phys. Res., Sect. A: Accel. Spectrom. Detect. Assoc. Equip.*, vol. 374, pp. 371–376, 1996. [Online]. Available: https://www.sciencedirect.com/science/article/pii/0168900296001970

[30] M. Guttormsen, T. Ramsøy, and J. Rekstad, "The first generation of γ-rays from hot nuclei," *Nucl. Instrum. Methods Phys. Res., Sect. A: Accel. Spectrom. Detect. Assoc. Equip.*, vol. 255, pp. 518–523, 1987. [Online]. Available: https://www.sciencedirect.com/science/article/pii/0168900287912216

[31] B. V. Kheswa, "The rigorous test of the generalized brink–axel hypothesis in the a = 138 nuclear mass region," *Acta Physica Polonica B*, vol. 54, p. A1, 2023. [Online]. Available: https://doi.org/10.5506/APhysPolB.54.8-A1

[32] M. Markova, P. von Neumann-Cosel, A. C. Larsen, S. Bassauer, A. Görgen, M. Guttormsen, F. L. Bello Garrote, H. C. Berg, M. M. Bjørøen, T. Dahl-Jacobsen, T. K. Eriksen, D. Gjestvang, J. Isaak, M. Mbabane, W. Paulsen, L. G. Pedersen, N. I. J. Pettersen, A. Richter, E. Sahin, P. Scholz, S. Siem, G. M. Tveten, V. M. Valsdottir, M. Wiedeking, and F. Zeiser, "Comprehensive test of the brink-axel hypothesis in the energy region of the pygmy dipole resonance," *Phys. Rev. Lett.*, vol. 127, p. 182501, Oct 2021. [Online]. Available: https://link.aps.org/doi/10.1103/PhysRevLett.127.182501

Characterization of instrumental background in (p,γ) reaction studies

T Bokhutlo[1,2], R Neveling[2], CO Kureba[1], KL Malatji[2,3], P Adsley[4], A Bahini[2], JAC Bekker[2,5], SD Binda[2,4], LM Donaldson[2], L Jafta[2,6], P Jones[2], S Jongile[2], TC Khumalo[2], SPE Magagula[2,5], TG Modise[2,7], RE Molaeng[2,5], AA Netshiya[2,5,8], L Pellegri[2,5] and M Wiedeking[2,4,9]

[1]Department of Physics and Astronomy, Botswana International University of Science and Technology, Palapye, Botswana
[2]iThemba LABS, Cape Town, South Africa
[3] Department of Nuclear Engineering, University of California, Berkeley, California, USA
[4]Cyclotron Institute, Texas A&M University, College Station, Texas, USA
[5]School of Physics, University of the Witwatersrand, Johannesburg, South Africa
[6]Department of Physics and Astronomy, University of the Western Cape, Cape Town, South Africa
[7]Department of Physics, University of Botswana, Gaborone, Botswana
[8]Department of Chemical and Physical Science, Walter Sisulu University, Mthatha, South Africa.
[9]Lawrence Berkeley National Laboratory, Berkeley, California, USA

E-mail: bt23019064@biust.ac.bw

Abstract. Understanding and mitigating background radiation is essential for high-precision experiments. This work investigates background contributions in radiative proton capture measurements at the low energy nuclear astrophysics beamline of the iThemba LABS Tandetron facility. These experiments aim to study the statistical properties of proton rich nuclei, particularly the Photon Strength Function (PSF), via charged particle capture reactions. However, accurate extraction of physical observables can be challenging due to the presence of instrumental background arising from beam interactions with materials other than the target. This study presents a systematic characterization of such background, identifying key sources and evaluating their impact on the measured spectra.

1 Introduction

Radiative capture reactions are essential for probing how excited nuclei undergo electromagnetic decay. Of particular interest is the Photon Strength Function (PSF), which characterizes the average reduced transition probability for gamma-ray emission or absorption within a nucleus [1]. PSFs play a vital role in modeling nuclear reaction rates in astrophysical environments and nuclear reactors. In a typical radiative capture reaction, such as the (p,γ) reaction, the proton is captured by a nucleus to form an excited compound system that de-excites via gamma emission [1]. The energies and intensities of these emitted gamma rays provide insights into the nuclear level structure and electromagnetic transition probabilities associated with the compound nucleus. For precision nuclear measurements, isolating events produced by the reaction of interest from background-induced artifacts can be crucial to ensure accurate results. This study reports on results obtained at the H-line of the iThemba LABS 3 MV Tandetron facility, where a proton beam was used for PSF investigations. Initial experiments revealed anomalous structures that did not originate from the target material. This work aims to identify potential sources of background, a necessary prerequisite for implementing appropriate mitigation measures.

2 Experimental Setup

The 3 MV Tandetron accelerator was installed in 2017 at iThemba LABS after the 6 MV Van de Graaff accelerator was decommissioned. The accelerator is capable of producing a terminal voltage of up to 3 MV, delivering particle beams with intensities of up to 150 μA [2]. The facility supports rapid switching between light and heavy ion beams of protons, alphas and ^{3}He, providing enhanced flexibility for multidisciplinary research. Currently the following beamlines are connected to the accelerator: low energy nuclear astrophysics array (H-line), particle induced x-ray emission array (K-line), and Rutherford Backscattering spectrometry (M-line) [2].

The H-line, which is illustrated in Fig. 1 is used to study radiative capture reactions. Relevant beamline elements directly upstream from the scattering chamber include three quadrupole magnets and a set of vertical and horizontal steerer magnets. In addition, a removable Faraday cup and a beam profiler positioned in front of the cup are used to measure the beam's intensity and shape before it enters the quadrupole triplet section. The aluminum scattering chamber has a spherical shape with a 12 cm diameter to allow for a small distance between the target and the gamma detectors placed around the scattering chamber. Inside the scattering chamber is an aluminum target ladder with 4 holders, which can be changed manually without breaking vacuum. At approximately 850 mm downstream from the scattering chamber is a fixed faraday cup used as a beam dump and has a lead shielding which is 5 cm thick. This Faraday cup consists of a 55.5 mm diameter high-conductivity copper cup. The assembly includes multiple copper components (e.g. core block, outer casing, inlet and outlet pipes) and is supported by Shapal-M ceramic insulating bushings for electrical isolation. Magnetic suppression is achieved via permanent $SmCo_5$ magnets (Vacomax 145) mounted with magnet steel, which helps to deflect secondary electrons. The entire unit is soldered under vacuum conditions, ensuring high vacuum integrity. The cup is mounted using a stainless steel (304) frame and fasteners to provide mechanical stability within the beamline environment.

The detector support structure surrounding the scattering chamber consists of an angular distribution table on the beam right side, and a subset of the original AFRODITE [3] detector frame on the beam left side. For the first few experiments on the H-line, the high purity Germanium (HPGe) Clover detectors [4] as well as large volume 3.5"x8" $LaBr_3$:Ce detectors [5] available at iThemba LABS were used to populate the detector support structure. The angular distribution table can accommodate 3 HPGe Clover detectors over a wide range of angles (26° - 141°). The old AFRODITE frame has 15 available positions, of which 4 are meant for small detectors such as the 2"x2" $LaBr_3$:Ce detectors. Of the remaining 11 positions, space limitations imposed by the beamline infrastructure result in only 8 being accessible for the available HPGe Clover detectors. Alternatively, 9 positions are accessible for large volume 3.5"x8" $LaBr_3$:Ce detectors. These positions are at the polar angles (i.e. relative to the beam direction which defines the polar axis) of 45°, 90° and 135°.

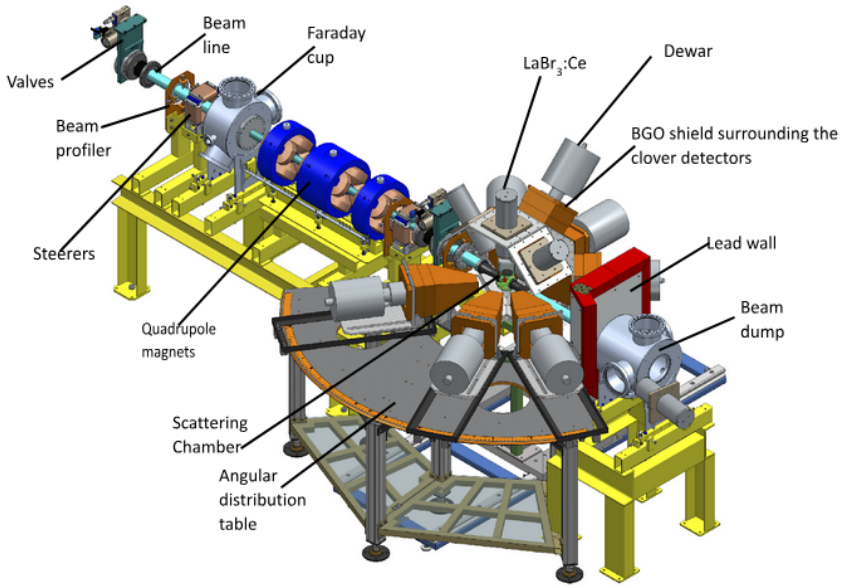

Figure 1: A schematic overview of the H-line at the iThemba LABS Tandetron facility.

3 Results and Analysis

This is a newly established facility and, so far only three datasets have been acquired. In this work, the focus is placed on the first experiment performed in 2023, which investigated the ^{60}Ni(p,γ)^{61}Cu reaction over a proton energy range of 2240 to 4320 keV, with measurements taken at 31 beam energies spaced at intervals of 60–80 keV apart [6]. The ^{60}Ni target had an areal density of 1 mg/cm^2. The experimental setup employed a total of four HPGe detectors and three $LaBr_3$:Ce detectors for gamma-ray detection. Among the four HPGe detectors, two were mounted on the Half-AFRODITE frame, one at 90° and one at 135°, while the remaining two detectors were positioned on the table at 90° and 45° respectively. The three $Labr_3$:Ce detectors were also mounted on the half-AFRODITE frame, with two placed at 90° and the third positioned at 45°. By combining high resolution HPGe detectors and fast response $LaBr_3$:Ce detectors, the setup allowed for both precise energy determination and time coincidence measurements, enhancing the overall efficiency and time resolution of the experiment.

The Q-value of the ^{60}Ni(p,γ)^{61}Cu reaction is 4799.8 keV; consequently, for a beam energy of e.g. E_p = 2480 keV, the direct gamma transition to the ground state from the highest excited populated energy level is expected at 7279.8 keV, excluding energy loss through the target and recoil energy of the residual nuclei. The expectation is that this should be the highest prompt gamma-ray energy observed in the detectors and Compton background, considering the ideal conditions where the beam only interacts with the nuclei in the target foil. Furthermore, since the proton beam will lose some energy ΔE_{tgt} as it passes through the target, one can expect a group of high energy gamma rays to appear from (E_p + Q) to (E_p + Q - ΔE_{tgt}), depending on the availability of states in ^{61}Cu to be populated. Other than the first and second escape peaks in the HPGe detectors, one also expects to see peaks in the gamma-ray energy spectrum representing the decay from the highly excited ^{61}Cu nucleus to its low-lying excited states, such as any of the following: 475 keV 1/2$^-$, 870 keV 5/2$^-$, 1.310 keV 7/2$^-$, 1394 keV 5/2$^-$ etc. However, what is observed as shown in Fig. 2, are strong and very broad structures between 5000 and 7000 keV (especially at the lower beam energies) as well as clear peak structures at energies higher than expected from the ^{60}Ni(p,γ)^{61}Cu reaction.

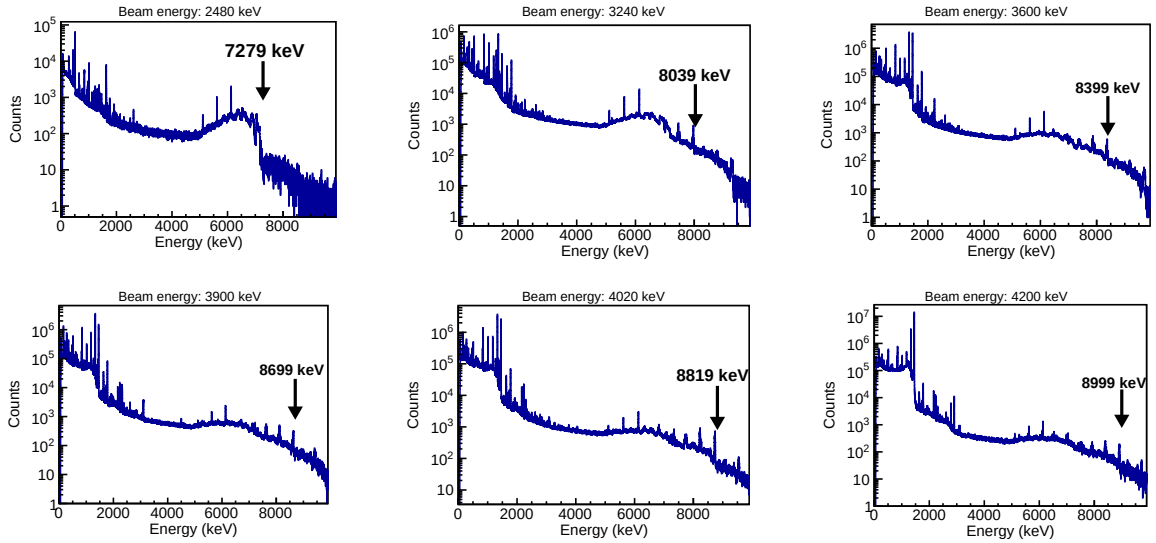

Figure 2: Gamma ray energy spectra with x-axis (Counts) and y-axis (gamma-energy (keV) obtained with a single HPGe detector placed at 135° for the ^{60}Ni(p,γ)^{61}Cu radiative capture reaction for different beam energies. The arrows indicate the position of the highest expected gamma-ray transitions from ^{61}Cu compound nuclei.

The impact of environmental background can be assessed through data acquired ideally without beam. Unfortunately, the only data available are for an empty target run, i.e. without a target but with beam only. Well-known low-energy gamma rays such as those appearing at 1460 keV (^{40}K) and 2614 keV (^{232}Th decay chain) are shown in Fig. 3(a). Since there were three $LaBr_3$:Ce detectors placed close to the HPGe detectors, intrinsic $LaBr_3$:Ce activity can be observed at 788 keV and 1436 keV. Contributions from these sources to the observed spectra were minimal during the experiment. Next, one can ascertain whether the background comes from a badly tuned beam interacting with beamline elements upstream of the target, as well as the target frame itself, by looking at data from the empty target beam run. Ion-optical calculations show [7] that a properly tuned beam has a sufficiently

small cross section and remains well within the 60.5 mm diameter of the beampipe, posing no risk of contact with the walls. Observations using a scintillating beamviewer at the target position confirm that the beam can achieve a diameter of less than 2 mm at the target location. Given that the target frame has an opening of 8 mm (height) by 14 mm (width), a well-tuned beam should easily pass through without striking the frame. Furthermore, ion-optical calculations indicate that the nominal beam diameter at the beamstop is approximately 7 mm. For a well-tuned beam, the most likely cause of background from upstream of the target must be from slit scattering at the beamline slits closer to the Tandetron, or the curved beampipe from the switching magnet.

The empty target spectrum shown in Fig. 3(b) reveals a similar structure between 5000 and 7000 keV as seen with target (see Fig. 2 top left), but much reduced in intensity. While it is not impossible for stray beam particles to interact with beamline elements to cause some background, clearly the bulk of the background did not originate from sources upstream of the target, or from beam "halo" created upstream from the target that interacted with beamline elements at the target and downstream of the target. Since the majority of the background only becomes apparent when the beam interacts with the ^{60}Ni target, one has to consider either some level of target contamination, or that the interaction with the target influences the beam to interact with the beampipe or other hardware downstream from the target.

Indeed, in the presence of the target, the observed gamma-ray spectra contain a number of background peaks. These peaks were consistently observed for all beam energies. Gamma rays at low energies are observed for the nuclei ^{27}Al, ^{28}Si, ^{56}Fe, ^{57}Co, ^{60}Ni and ^{61}Cu, which result from (p,p') and (p,γ) reactions from ^{27}Al, ^{56}Fe and ^{60}Ni. This is shown in Fig. 3(c). While one would expect the gammas from interaction with ^{60}Ni, the contributions from ^{27}Al and ^{56}Fe are concerning, since it implies that a significant number of protons interact with nuclei that are not in the target foil. The question is thus: how do the protons, supposedly well focused onto the target, end up hitting significant amounts of ^{27}Al and ^{56}Fe? In addition, the structures between 5000 and 7000 keV are known to originate from the ^{19}F(p,$\alpha\gamma$)^{16}O reaction [8]. The gamma rays at 6128.89(4), 6917.1(6), and 7116.85(14) keV from ^{16}O decay are highlighted in Fig.3(d). The states at 6917 and 7116 keV exhibit pronounced Doppler broadening as a consequence of their very short (few femtosecond) half-life. These broad structures makes it more difficult to identify and resolve the gamma rays originating from the particle capture reactions, and complicates spectral analysis. Finally, the fact that there are high-energy gamma rays beyond those expected from the ^{60}Ni(p,γ)^{61}Cu reaction implies that proton capture reactions on nuclei with higher *Q*-values are also being observed. The arrow in Fig.3(e) indicates a structure of observed high-energy gamma rays consistent with the ^{56}Fe(p,γ)^{57}Co reaction, which has a *Q*-value of 6027 keV.

4 Background Characterization

It is evident that the majority of the background arises from proton interactions with ^{19}F, ^{27}Al, and ^{56}Fe. A key piece of evidence in identifying the location of these interactions is the beam intensity measured at the fixed Faraday cup located at the end of the beamline. When an empty target frame is used, the beam current measured by the removable Faraday cup upstream of the target agrees with the reading on the fixed Faraday cup, indicating minimal loss. In contrast, when a ^{60}Ni target is inserted, the fixed Faraday cup registers only about 60% of the beam current delivered. It is, therefore, clear that introduction of the target causes both beam intensity loss as well as a dramatic background increase. To investigate how the introduction of the 1 mg/cm^2 thick ^{60}Ni target can lead to beam intensity loss on the Faraday cup, a SRIM simulation was performed where 10,000 protons at an energy of 4020 keV were directed perpendicular onto a 1 mg/cm^2 thick ^{60}Ni foil. The results of the simulation revealed that a significant percentage of these protons undergo angular deviation from their original trajectory after traversing the target. These redirected protons intersect with parts of the scattering chamber and the beampipe, as shown in Fig. 4.

The scattering chamber is mostly made of aluminum (which only has one stable isotope, namely ^{27}Al), but also has some Vesconite components. The conical section between the scattering chamber and the beamline connecting the chamber is made of Vesconite, while the main beampipe downstream of the scattering chamber all the way to the beamstop is made of stainless steel. Vesconite is a self-lubricating polymer commonly used in vacuum and beamline assemblies due to its mechanical strength, thermal stability, and low out-gassing properties. However, as highlighted [8], Vesconite contains a significant amount of fluorine, originating from its polytetrafluoroethylene (PTFE) based composition. In [8] they studied beamline-induced backgrounds observing the intense gamma-ray emission resulting from proton interactions with Vesconite, specifically from the ^{19}F(p,$\alpha\gamma$)^{16}O reaction, which produces high-energy gamma lines at 6128(4), 6917(6), and 7116(14) keV. Stainless steel, which contains iron, nickel, and chromium, is known to contribute to gamma-ray background through reactions like ^{56}Fe(p,γ)^{57}Co and ^{60}Ni(p,γ)^{61}Cu.

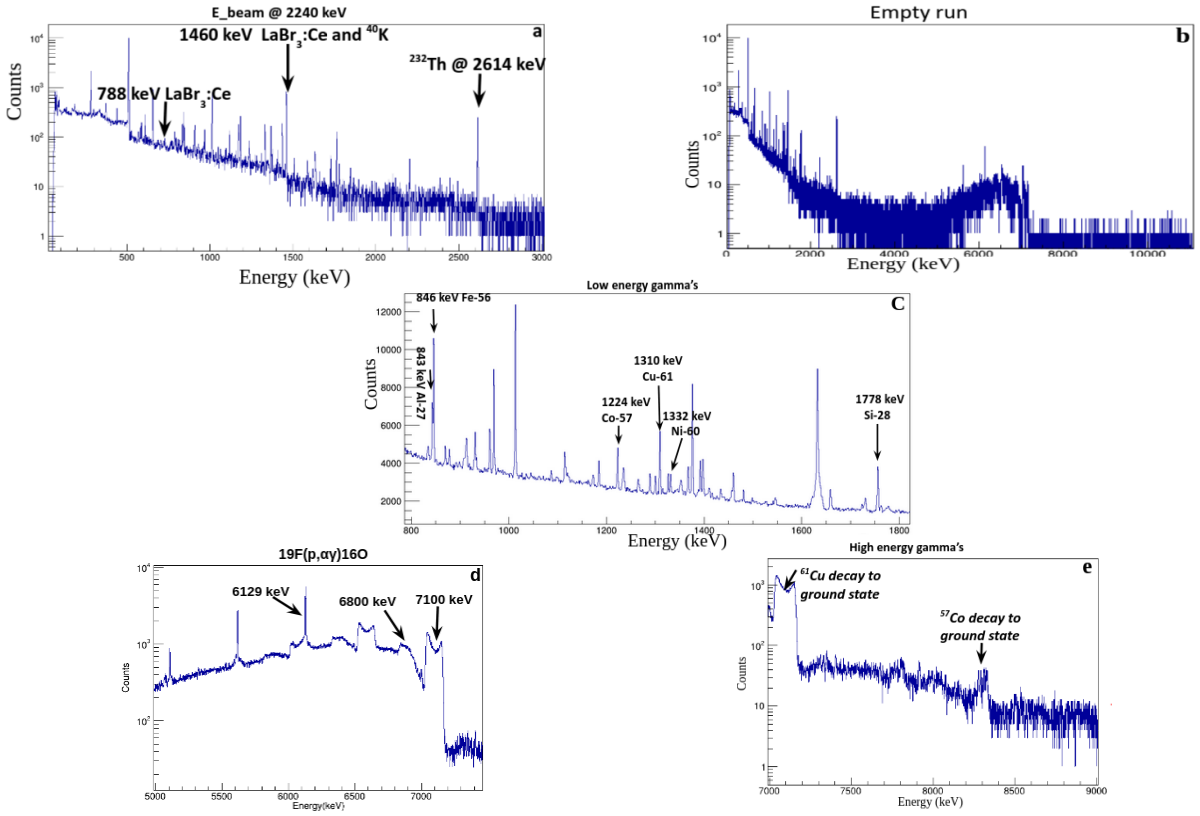

Figure 3: Identification of different backgrounds from ^{60}Ni(p,γ)^{61}Cu at E_{beam}= 2240 keV: a) environmental background and radiation from the LaBr$_3$:Ce detector, b) empty target run showing the full gamma-ray energy range, c) low-energy gamma rays from a target-in run, d) oxygen related structures originating from the ^{19}F(p,$\alpha\gamma$)^{16}O reaction and e) high-energy gamma rays corresponding to direct transitions to the ground state.

A distinction is made below between three distinct downstream beamline components. Firstly, protons deflected at large angles between 63.4° and 90° strike the interior walls of the scattering chamber. As it is made of both aluminum and Vesconite, it is a potential source of background gamma rays through reactions such as ^{27}Al(p,γ)^{28}Si and ^{19}F(p,$\alpha\gamma$)^{16}O. Although these high-angle deviations represent a small fraction of the beam (estimated at less than 5%), they are important due to the amount of material with which the protons can interact. Secondly, a substantial fraction of the beam, estimated around 6%, was found to exit the target at intermediate angles between 26.6° and 63.4°, leading to interactions with the Vesconite cone located between the scattering chamber and the main beamline, and thus contributes to fluorine-induced background features. Lastly, proton deviation between 3.03° and 26.6°, representing the most dominant post-target trajectories at an estimated 20% of the incident protons, will hit the inner walls of the stainless steel beampipe.

5 Summary and Conclusion

This study investigated the sources of instrumental background in radiative proton capture (p,γ) experiments at the iThemba LABS Tandetron facility, with a focus on improving the extraction of gamma-ray strength functions (PSFs). Through gamma-ray spectroscopy, SRIM simulations, and beam diagnostics, it was shown that post-target beam divergence leads to unintended interactions with surrounding beamline components, including the scattering chamber, the Vesconite beamline tube, and the stainless steel beampipe. These interactions give rise to background gamma rays, particularly from reactions on ^{27}Al, ^{56}Fe, and ^{19}F. A major contributor to high-energy background was the ^{19}F(p,$\alpha\gamma$)^{16}O reaction, producing Doppler-broadened gamma rays from PTFE-based Vesconite components. To mitigate these effects, several recommendations are proposed.

Firstly, to reduce the impact of the strong oxygen peaks from the ^{19}F(p,$\alpha\gamma$)^{16}O reaction, efforts should focus

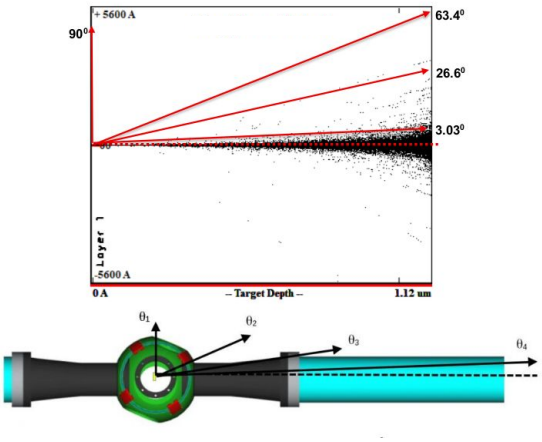

Figure 4: (Top) SRIM simulation showing the angular distribution of protons transmitted through a 1 mg/cm^2 ^{60}Ni target. The plot highlights four distinct angular ranges corresponding to interactions with different beamline components (bottom).

on minimizing the amount of Vesconite in the setup. A key step is replacing the conical beamline components made of Vesconite with aluminum. Although this substitution may increase aluminum-induced background, such background is relatively minor in the 5000–7000 keV energy range, which is currently dominated by gamma-ray background from oxygen. Secondly, the possibility to have a high-Z collimator downstream from the target should be investigated. The high proton number will imply a high Coulomb barrier, which means that the material is not likely to undergo nuclear reactions and contribute to the gamma ray spectrum. Such a collimator should be connected to the beam current measurement, and should be positioned close enough to the target so that it can intercept most of the angular beam spread before the beam can interact with any of the beamline elements. Implementing these improvements is expected to significantly enhance the signal-to-noise ratio, enabling more accurate and reliable measurement of weak gamma transitions. The findings serve as an essential step toward establishing a low-background, high-precision experimental platform for nuclear astrophysics research at iThemba LABS Tandetron facility.

6 Acknowledgments

The authors would like to thank the accelerator team at the Tandetron facility of iThemba LABS for providing high quality experimental conditions, as well as the Research and Development Technical Support (RDTS) team for their assistance with the design, software, and detector maintenance. This research was supported in part by the National Research Foundation (NRF) of South Africa (Grant No's. 118846, 92600, 90741, 92789, and REP_SARC180529336567). Additional support was provided by the U.S. Department of Energy, Office of Science, Office of Nuclear Physics under Contract No. DE-AC02-05CH11231 The financial assistance of the NRF and iThemba LABS is gratefully acknowledged. Any opinions, findings, and conclusions expressed in this material are those of the authors and do not necessarily reflect the views of the NRF.

References

[1] S. Goriely, A. Bauswein, and H.-T. Janka, "R-process nucleosynthesis in dynamically ejected matter of neutron star mergers," *The European Physical Journal A*, vol. 55, no. 10, p. 172, 2019. [Online]. Available: https://doi.org/10.1140/epja/i2019-12801-2

[2] Z. Khumalo, C. Mtshali, M. Msimanga, N. Mongwaketsi, and F. Mashele, "A new 3 MV Tandetron™ accelerator at iThemba Laboratory for Accelerator-Based Sciences," *Journal of Instrumentation*, vol. 20, no. 06, p. T06001, jun 2025. [Online]. Available: https://dx.doi.org/10.1088/1748-0221/20/06/T06001

[3] M. Lipoglavšek, N. Soić, A. Palacz, T. O. Tuček, S. Širca, P. Vidmar, M. Korolija, M. Lozar, J. Mrazek, N. H. Medina, D. G. Jenkins, R. L. Gill, and D. S. Haslip, "High-resolution γ-ray spectroscopy with an array of clover detectors at the beam line of a tandem accelerator," *Nuclear Instruments and Methods in Physics*

Research Section A: Accelerators, Spectrometers, Detectors and Associated Equipment, vol. 557, pp. 523–527, 2006.

[4] G. Duchêne, F. Beck, P. Twin, G. de France, D. Curien, L. Han, C. Beausang, M. Bentley, P. Nolan, and J. Simpson, "The clover: A new generation of composite Ge detectors," *Nuclear Instruments and Methods in Physics Research Section A: Accelerators, Spectrometers, Detectors and Associated Equipment*, vol. 432, pp. 90–110, 1999.

[5] E. V. D. V. Loef, P. Dorenbos, C. W. E. V. Eijk, K. Krämer, and H. U. Güdel, "High-energy-resolution scintillator: Ce^{3+} activated $LaBr_3$:Ce," *Applied Physics Letters*, vol. 79, no. 10, pp. 1573–1575, 2001.

[6] M. Wiedeking, "Testing the validity of the Brink-Axel hypothesis," Feb. 2020, iThemba LABS research proposal.

[7] H. Barnard, Private communication, 2024, iThemba LABS.

[8] D. Dell'Aquila and M. Vigilante, "An overview of the $^{19}\mathrm{F}(p,\alpha_0)^{16}\mathrm{O}$ reaction with direct methods," in *Journal of Physics: Conference Series*, vol. 703, no. 1, 2016, p. 012015. [Online]. Available: https://doi.org/10.1088/1742-6596/703/1/012015

This page intentionally left blank.

Analysis of ^{61}Cu from the ^{60}Ni(p,γ) Reaction at iThemba LABS

T.G. Modise[1], K.L. Malatji[2,3], N. Palalani[1], M. Wiedeking[2,4,5], L.M. Donaldson[2], F.O. Ogundare[1], P. Adsley[6,7], A. Bahini[2], J.A.C. Bekker[2,5], S.D. Binda[2,5],T.K.J. Bokhutlo[8], S. Hart[2,9], L. Jafta[2,10], P. Jones[2], S. Jongile[2], B.V. Kheswa[2,12], T.C. Khumalo[2,5], S.P.E. Magagula[2,5], R.E. Molaeng[2,5], A.A. Netshiya[2,5,11], R. Neveling[2], L. Pellegri[2,5]

[1] Department of Physics, University of Botswana, Gaborone, Botswana
[2] SSC Laboratory, iThemba LABS, Faure, South Africa
[3] Department of Nuclear Engineering, University of California, Berkeley, USA
[4] Lawrence Berkeley National Laboratory, Berkeley, California, USA
[5] School of Physics, University of the Witwatersrand, Johannesburg, South Africa
[6] Cyclotron Institute, Texas A & M University, College Station, Texas, USA
[7] Department of Physics and Astronomy, Texas A & M University, College Station, Texas, USA
[8] Department of Physics and Astronomy, Botswana International University of Science and Technology, Palapye, Botswana
[9] Department of Physics, University of Cape Town, Cape Town, South Africa
[10] Department of Physics and Astronomy, University of the Western Cape, Bellville, South Africa
[11] Department of Chemical and Physical Sciences, Walter Sisulu University, Mthatha, South Africa
[12] Department of Applied Physics and Engineering Mathematics, University of Johannesburg, South Africa

E-mail: 201402237@ub.ac.bw

Abstract. The radiative proton-capture reaction ^{60}Ni(p,γ)^{61}Cu was performed using the H-line of the 3 MV Tandetron facility at iThemba LABS. The γ rays decaying from the quasi-continuum to low-lying states are used to study statistical properties such as the photon strength function of ^{61}Cu. Preliminary spectra following calibration, addback and Compton suppression are presented.

1 Introduction

For the longest time in nuclear physics, efforts have been ongoing to determine with certainty the available quantum levels and their decay properties for nuclei from the ground state up to any possible excitable level. In the excitation-energy region of the quasi-continuum, nuclear level density (NLD) and the photon strength function (PSF) are statistical properties that aide in the study of nuclear structure. The PSF is an average electromagnetic quantity of nuclei. In particular, it quantifies the probability of a nucleus to emit or absorb a γ ray of a given energy, E_γ [1]. PSFs are used as input for reactor designs, nuclear waste transmutation and in modeling astrophysical nuclear reactions [1]. PSFs and NLDs are also vital in capture cross-section calculations as they are used as inputs in the Hauser-Feshbach models. [2].

The generalized Brink-Axel hypothesis suggests that the photon strength function of a nucleus only depends on the emitted γ-ray energy, E_γ and not the detailed structure of the initial and final states (energy, spin and parity) involved in the transition [3]. While the hypothesis is widely used for PSF energy regions such as the giant dipole resonance (GDR), it remains under investigation for the low-energy region.

The ^{61}Cu nucleus is a system with well-known discrete levels with definite spin and parity assignments. These states seem to be sufficiently populated in (p,γ) reactions up to about 3 MeV with very few close-lying states in the first 2-3 MeV excitation-energy region [4]. The level spacing of the discrete levels is favorable for (p,γ) measurements and for the test of the validity of the Brink-Axel hypothesis. For the purposes of this work, only the experimental setup, analysis and preliminary results will be discussed.

2 Experimental Details

The experiment was performed using the H-line of the 3 MV Tandetron facility at the iThemba Laboratory for Accelerator Based Sciences (iThemba LABS). Proton beams of energies ranging from 2.24- 4.32 MeV, at 60-80 keV intervals, were directed onto a ^{60}Ni target in order to study the ^{60}Ni(p, γ)^{61}Cu reaction. The highest possible state for the reaction ($Ex_{\max}$) will have an energy equal to the sum of Q_value energy for the reaction and the proton energy, minus the recoil energy (E_{recoil}) and energy lost (E_{loss}) in the target as described by Eq 1. The formation of the compound nucleus is demonstrated in Figure 1. For ^{60}Ni(p,γ)^{61}Cu, the highest populated state is approximately 9.1 MeV for a maximum beam energy of 4.32 MeV.

$$Ex_{\max} = E_{\text{beam}} + Q_value - E_{\text{loss}} - E_{\text{recoil}} \tag{1}$$

This will confine the excitation levels of interest in this study to energies below the neutron separation energy, which is 11.7 MeV and above proton separation energy of 4.80 MeV.

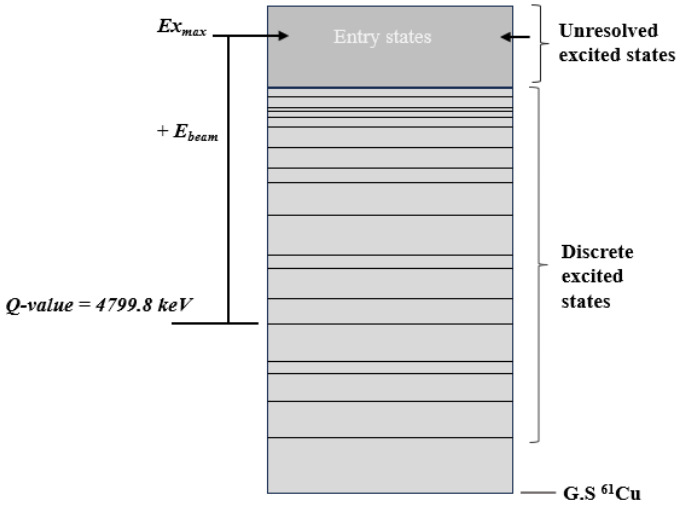

Figure 1: Compound nucleus formation and variation of level density with Ex.

The ^{60}Ni target had an areal density of 1 mg/cm^2 and was enriched to levels greater than 99%. Emitted γ rays were detected by 4 Clover detectors, where each detector is made up of four segmented coaxial high purity Germanium (HPGe) crystals enclosed by a Bismuth Germanite (BGO) Compton suppression shield. The set up also consisted of 3 large-volume Lanthanum Bromide dopped with Cerium ($LaBr_3$:Ce) detectors. A sample configuration of the H-line at the Tandetron facility is shown in Figure 2.
A total of 32 beam energies were measured in 60-80 keV intervals resulting in 32 γ-ray spectra that cover different excitation-energy regions. These spectra contain well-resolved primary γ-ray transitions that decay to low-lying states.

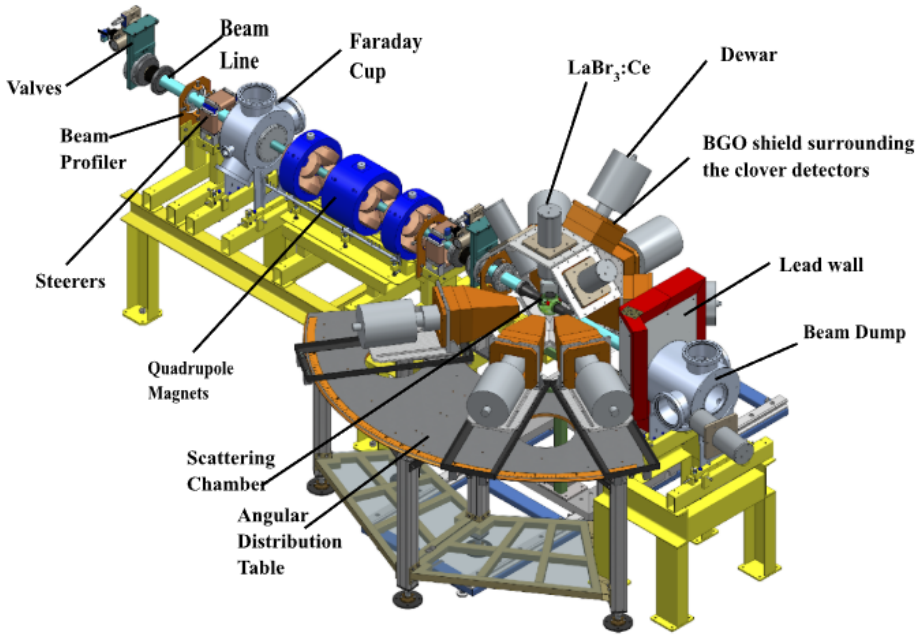

Figure 2: An illustration of the H-Line (K.L.Malatji manuscript in preperation)

3 Analysis and Preliminary Results

The spectra for crystals are characterized by channel number and counts. Energy calibration was performed on the spectrum of each crystal to transform the channel number to energy. The change to energy is performed using a linear equation, which is extracted by matching a channel number to a known energy in the spectrum from the in-beam data. This results in a graph as shown in Figure 3. The constants obtained are then used to generate a linear equation as provided in Equation 2.

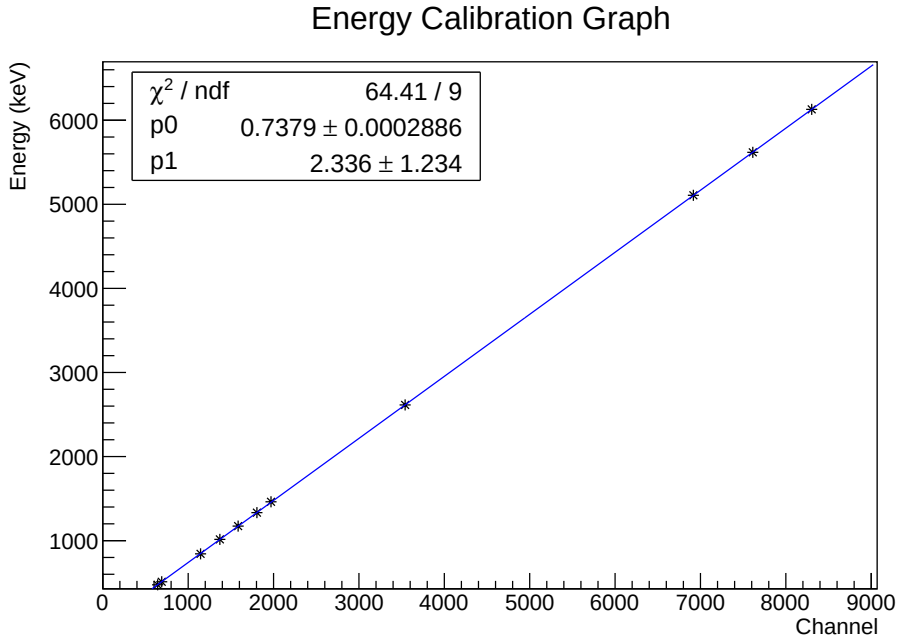

Figure 3: The calibration graph used to extract the constants required for energy calibration.

$$E(\text{keV}) = 0.7379 * Ch + 2.336 \quad (2)$$

From the energy calibrated spectra, addback and BGO suppression techniques were performed. The spectrum of each Clover detector was constructed by summing the energies deposited on its four segmented crystals. A typical Clover detector spectrum following the energy calibration is shown in Figures 4 and 5 as a black line. The full energy peaks of some γ rays were recreated using the addback technique. The technique reconstructs full energy peaks by "adding back" events from the Compton continuum, also from the first and second escape peaks. After the implementation of the addback technique, the resulting spectrum is shown in Figures 4 and 5 as a red line. The implementation of this technique results in the increase of intensity of the full energy peaks for the entire energy range as shown in Table 1 for the 5618 and 6129 keV γ- peaks.

The spectrum obtained when both addback and Compton suppression were implemented is shown in Figures 4 and 5 as a blue line. It is seen that the Compton suppression reduced the Compton continuum of the spectrum. This is achieved by veto of events that escape the Clover detector after Compton scattering within the crystals. These escape events are registered in the BGO shield. After application of time gates, the events that are in coincidence on both the BGO shield and Clover detectors are then vetoed out.

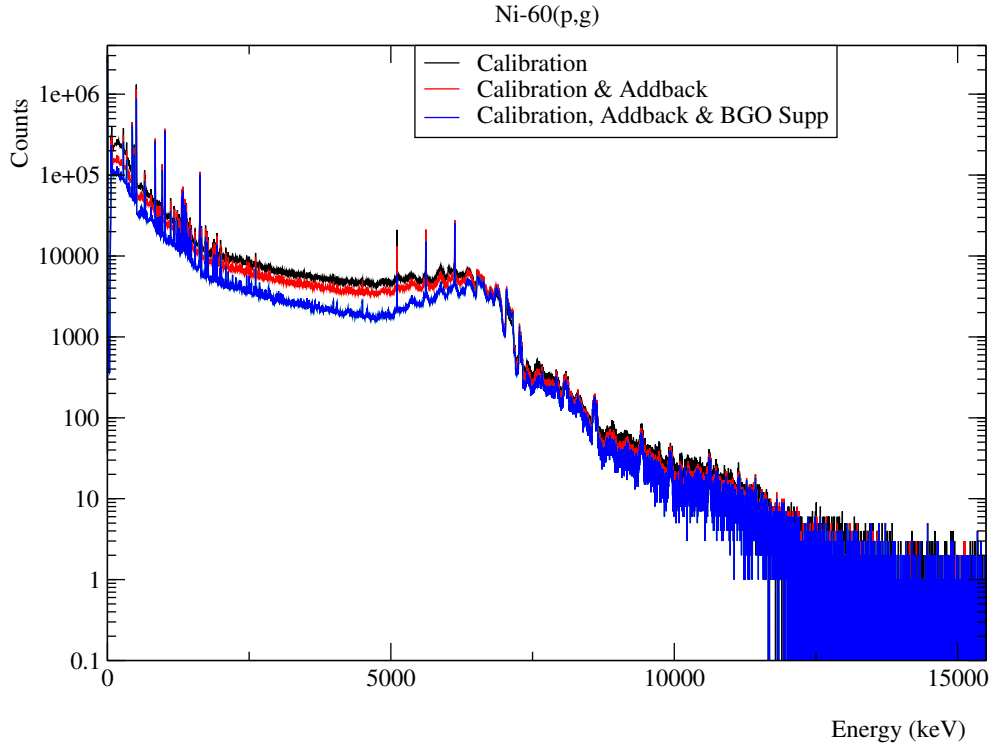

Figure 4: The ^{61}Cu spectrum illustrating the effect of addback and BGO suppression techniques.

From Figure 5, the 5618 keV peak is the first escape of the 6129 keV peak (511 keV difference). Similarly, the 5107 keV peak is the second escape of the 6129 keV peak (1022 keV difference). The second escape peak in the blue spectrum shows a considerable reduction in counts from the initial black spectrum. In Table 1, the counts for the 5107 keV peak reduce by 43%. After addback and BGO suppression techniques, the counts for the 5618 and 6129 keV peaks increased by 17% and 54% respectively as a result of addback and BGO suppression.

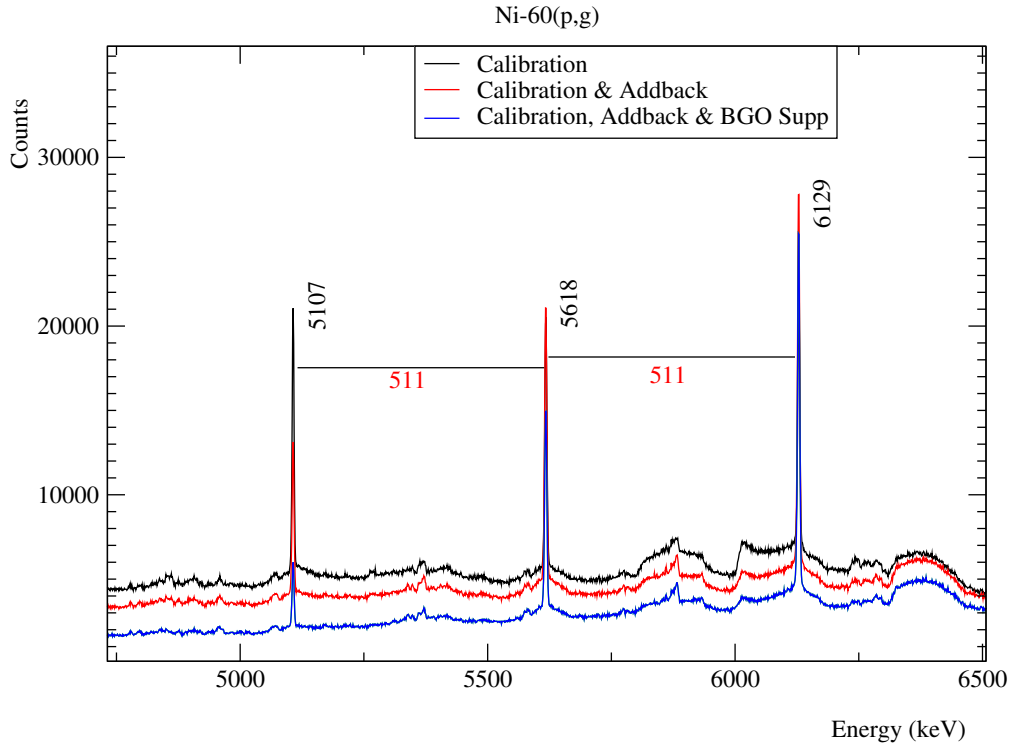

Figure 5: ^{19}F(p,$\alpha\gamma$)^{16}O contaminant peaks used to illustrate the variation of counts after energy calibration (black), addback technique (red) and BGO suppression (blue) are applied on the spectrum.

	6129 keV	**5618 keV**	**5107 keV**
Calibration	81965	84694	77881
Calibration + Addback	125949	98883	44567
Calibration + Addback + BGO	119248	67420	19312

Table 1: Variation of counts under the full-energy peak, first escape and second escape peaks as addback and BGO suppression techniques are applied on the spectra.

4 Conclusion and Outlook

Energy level schemes are to be constructed for the 32 spectra obtained from the experiment. This will identify the decays from the quasi-continuum to the low-lying known states, which provide critical information about the PSF. This will be followed by the utilization of the model-independent ratio method [5] and the shape method [6] to investigate the statistical γ-ray decay to individual well-established discrete states. So far the data appears to be of high quality after all the analysis and we are hoping for a better outcome on the objectives of the study.

Acknowledgments

The authers thank the accelerator team at the Tandetron facility of iThemba LABS for providing high-quality experimental conditions, as well as the Research and Development Technical Support (RDTS) team for the overall support with design, maintenance of the software and detectors. This research work is supported in part by the National Research Foundation (Grant No:118846, 92600, 90741, 92789 and REPSARC 180529336567). It is also based upon work supported by the U.S. Department of Energy, Office of Science, Office of Nuclear Physics under Contract No. DE-AC02-05CH11231.

References

[1] Neumann-Cosel, Peter von, "Gamma strength functions and the Brink-Axel hypothesis," in *Compound-Nuclear Reactions: Proceedings of the 6th International Workshop on Compound-Nuclear Reactions and Related Topics CNR* 18*. Springer, 2021, pp. 155–163.

[2] S. Harissopulos, E. Vagena, M. Axiotis, A. Spyrou, G. Provatas, A. Lagoyannis, P. Dimitriou, and H. W. Becker, "Capture reaction cross-section measurements relevant to p process: the case of (α, γ) reactions on ^{63}Cu, ^{72}Ge, ^{118}Sn and the ^{107}Ag (ρ, γ) ^{108}Cd reaction," in *EPJ Web of Conferences*, vol. 227. EDP Sciences, 2020, p. 01008.

[3] Kheswa, BV, "THE RIGOROUS TEST OF THE GENERALIZED BRINK–AXEL HYPOTHESIS IN THE A= 138 NUCLEAR MASS REGION," *Acta Physica Polonica B*, vol. 54, no. 8, pp. 8–A1, 2023.

[4] K. Nilson, B. Erlandsson, and A. Marcinkowski, "Gamma-ray strength function measurements for ^{59}Co, ^{61}Cu and ^{62}Cu," *Nuclear Physics A*, vol. 391, no. 1, pp. 61–71, 1982.

[5] M. Wiedeking, L. Bernstein, M. Krtička, D. Bleuel, J. Allmond, M. Basunia, J. Harke, P. Fallon, R. Firestone, B. Goldblum *et al.*, "Low-energy enhancement in the photon strength of ^{95}Mo," *Physical Review Letters*, vol. 108, no. 16, p. 162503, 2012.

[6] M. Wiedeking, M. Guttormsen, A.-C. Larsen, F. Zeiser, A. Görgen, S. N. Liddick, D. Mücher, S. Siem, and A. Spyrou, "Independent normalization for γ-ray strength functions: The shape method," *Physical Review C*, vol. 104, no. 1, p. 014311, 2021.

Burn-in Testing for Transformer-Coupled Buck Converters in the ATLAS Tile Calorimeter's Low Voltage Power Supplies

Thabo Pilusa[1,2], Ryan Mckenzie[1,2], Roger Van Rensburg[1], Vongani Chabalala[1,2], Chuene Mosomane[2], and Bruce Mellado[1,2]

[1] School of Physics and Institute for Collider Particle Physics, University of the Witwatersrand, Johannesburg, Wits 2050, South Africa

[2]iThemba LABS, National Research Foundation, PO Box 722, Somerset West 7129, South Africa

E-mail: thabo.pilusa@cern.ch

Abstract. The High Luminosity Large Hadron Collider (HL-LHC) is scheduled to commence operations in 2030, targeting a luminosity five times than that of the current LHC run. This substantial increase in luminosity necessitates significant upgrades to the LHC detector systems. The Phase-II upgrades of the ATLAS detector involve a complete upgrade to the low voltage power supply (LVPS) system of its Tile Calorimeter (TileCal). The TileCal includes 256 LVPS boxes, each composed of eight transformer-coupled buck converter boards alongside auxiliary components. The Phase-II upgrade buck-converter boards are designed to step down the input voltage from 200 V DC to 10 V DC, which is required to power the front-end electronics of the ATLAS detector. Half of the required buck-converter boards are slated for production in South Africa in 2025, with 104 units already produced during the preparatory pre-production phase. The LVPS boxes are located on-detector, limiting access to the buck-converter boards during the operation of the ATLAS detector. If a failure occurs in the boards, the front-end electronics that they supply power to will remain inoperative until the year-end technical stop. To ensure long-term reliability of the boards within the TileCal and identify potential early life failures, all boards undergo a rigorous burn-in testing process. This process subjects the boards to extreme operational conditions beyond their standard operating parameters within TileCal. Such testing is essential to ensure that there are no failures in the boards, guaranteeing uninterrupted data taking during operation of the ATLAS detector.

1 Introduction

The Large Hadron Collider (LHC) [1], located in Switzerland at the European Organization for Nuclear Research (CERN), forms the largest particle accelerator in the world. The LHC is a 27 km underground ring straddling the border between Switzerland and France, built to accelerate and collide beams of particles, primarily protons or heavy ions, at near light speeds. The primary collision of interest for this study is proton-proton (pp) collision events of a significant size, as they will be the cornerstone of new physics discovery and applicable to the main mission of the ATLAS detector. The LHC has two particle beams travelling in opposite directions in separate beam pipes, with the two tubes kept at ultra high vacuum, crossing at four predetermined points, which are the 4 major detectors. The 4 primary detectors consist of ATLAS [2], CMS [3], LHCb [4], and ALICE [5].

The ATLAS detector is a large multi-purpose instrument at the LHC for observing high energy collisions. The detector consists of several subsystems, each responsible for capturing detectors' signatures from particle collisions.

As particles go through the detector, they have unique properties (type, energy, and trajectory), which produce unique signatures that can be accurately reconstructed.

The TileCal is a sampling calorimeter and a central component of the ATLAS experiment's hadronic calorimetry, designed to measure hadrons, jets, and hadronic τ-lepton decays, as well as missing transverse energy. It also aids in muon identification and provides critical input to the Level-1 calorimeter trigger system. The High-Luminosity Large Hadron Collider (HL-LHC) is set to commence operations in 2029 with the goal of drastically increasing the LHC's luminosity. The high rate particle collision environment requires new electronics developments inside and outside the detector to maintain performance levels due to unavoidable increases in pile-up and radiation which consequently provides a justification for the ATLAS TileCal Phase-II Upgrades [6].

2 The Low Voltage Power Supply System

The upgrade of the TileCal's LVPS forms a key component of the TileCal Phase-II upgrade project. The LVPS forms the second phase in a three-stage low voltage (LV) distribution system that provides power to the front-end electronics of TileCal.

The first stage of this LV system is located away from the detector and comprises Auxiliary Boards responsible for switching individual buck converter boards on or off within each LVPS box, as well as supplying +200 V DC power. Each TileCal module is equipped with one LVPS box, resulting in a total of 256 LVPS boxes across the system.

An LVPS box can contain up to eight buck converter boards along with an Embedded Local Monitoring Board (ELMB), a fuse board, and a cooling plate that supports and cools the buck converter boards [7]. Each buck converter board contains a single-output, DC/DC dual-transistor synchronous forward converter designed to be resilient against radiation and magnetic fields, by using the LT1681 chip (Figure 1). Key features of the board include active circuitry for overcurrent and overvoltage protection, ensuring safe operation within specified limits. The board steps down the +200 V DC input from external supplies, delivering a lower voltage to point-of-load regulators on the front-end electronics for further regulation which forms the third part of the LV system.

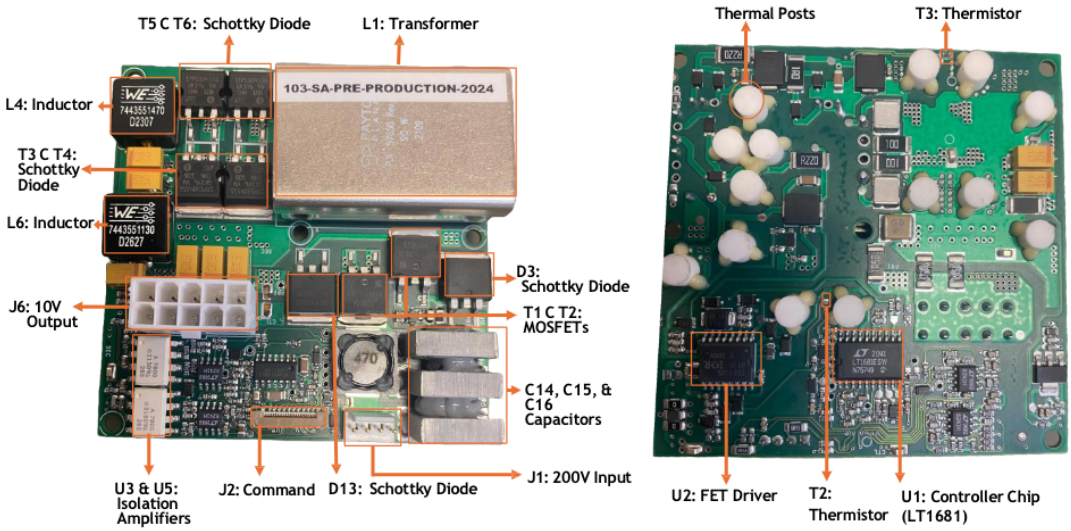

Figure 1: The South African V8.6.0 pre-production buck converter board with the top (left) and bottom (right) perspectives.

3 Quality Assurance Testing of Buck Converter Boards

In order to mitigate the risk of the buck converter boards failing during the operation of the ATLAS detector, a Burn-in test station has been implemented to identify and remove faulty units. Figure 2 outlines the procedure undertaken to ensure the boards are in optimal operating conditions before being integrated within the TileCal.

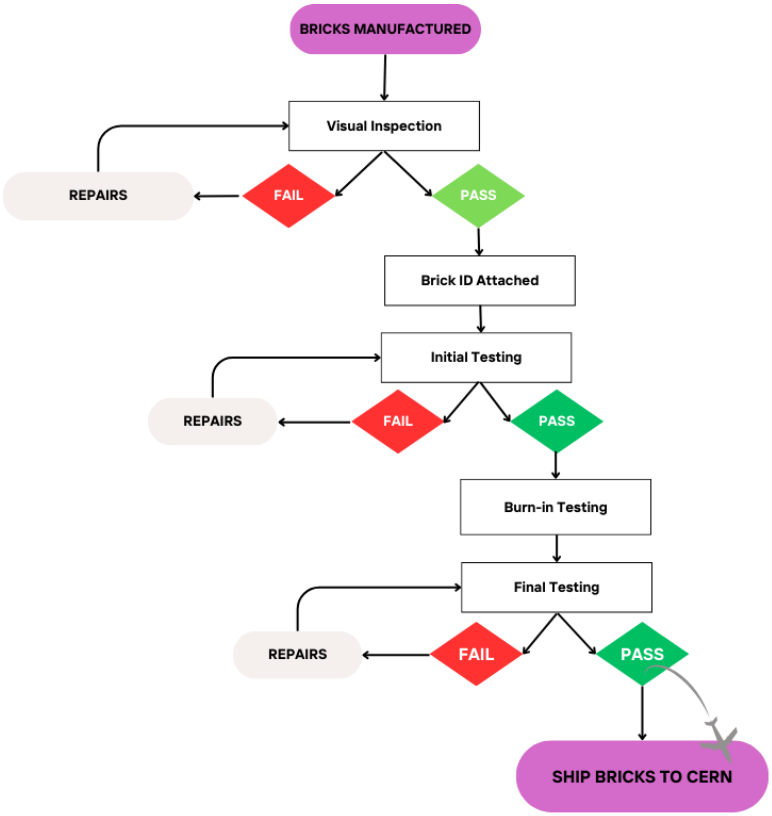

Figure 2: The LVPS buck converter boards quality assurance testing procedure.

3.1 Burn-in Testing

Latent defects within the boards, which would normally only show up later during use, can be forced to show up early if the boards are deliberately stressed. The boards are subjected to operating temperatures of 60°C, with a constant load of 6 A, for 8 hours. The test temperature is beyond the typical TileCal operating temperature of 30 - 40°C and will unveil thermal stresses early in the test, including factors such as solder fatigue and component drift. The load of 6 A is the maximum operating current, stressing the power regulation circuitry and associated protection features. The duration of the burn-in test of 8 hours, while clearly short when compared to the multi-year running of TileCal, corresponds to an accelerated aging factor. Using thermal acceleration models (Arrhenius law) we can estimate that running at 60°C for 8 hours is equivalent to several weeks of normal running at 35°C. .



Figure 3: Fully operational Wits Burn-in test station system. a) The Burn-in station test bed. b) Water chiller for regulating water to and from the cooling plates. c) BK Precision PVS60085M HV power supply which powers the fLVPS boards. d) User interface with the LabVIEW software.

3.2 Temperature Monitoring During Burn-in

The pre-production buck converter boards underwent an 8-hour burn-in test, during which two relevant temperatures T_2 and T_3 were monitored. These temperatures, measured on thermistors as shown in Figure 1, provide the temperature of the board undergoing evaluation. While they were comparable to one another, T_2 and T_3 are slightly different locations on the fLVPS board; T_2 is connected to the circuit over temperature protection (OTP) protection set at 70°C to avoid damaging components of the board, and T_3, located at the PCB edge between the thermal posts of the T_5 and T_6 Schottky diodes, is used simply for observing temperature data.

The Burn-in station is designed to accommodate up to eight buck converter boards; however, in some burn-in testing cases, as shown in Figure 4, testing only used six of the possible eight boards due to maintenance of some of the testing channels on the Burn-in station. In Figure 4, the burn-in test records did show the temperature at T_2 and T_3 starting around 40°C, and rising subsequently, stabilizing around the 20-minute mark at which they reach their burn-in temperature. This thermal profile was maintained through the duration of the test. The burn-in test was closely monitored to observe any unusual tripping or issues that could push the testing temperature outside of the OTP thresholds.

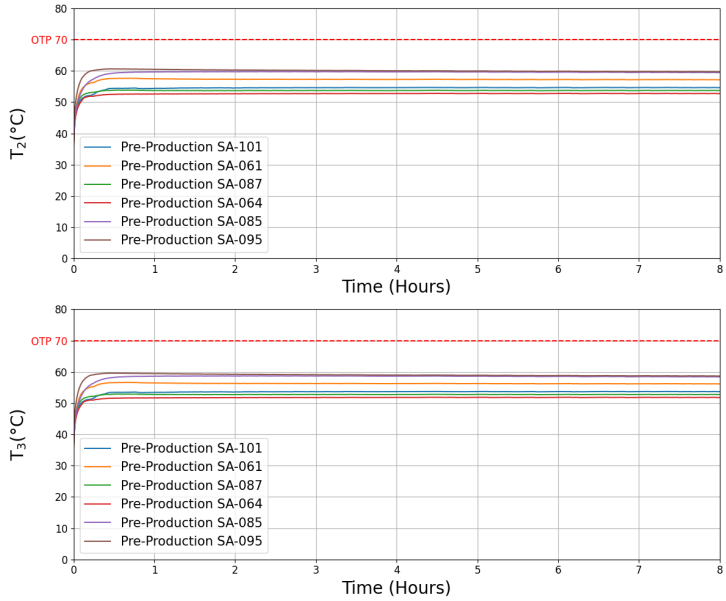

Figure 4: The T_2 (top) and T_3 (bottom) temperature monitoring of 6 pre-production LVPS boards undergoing burn-in simultaneously.

4 Conclusions and Outlook

We have made substantial progress in testing and assessing the buck converter boards. The purpose of the burn-in test was carefully outlined, showing how essential it is to test the reliability of the buck converter boards. During this step, 104 units were subjected to near maximum load in long-based burn-in tests, which gave us the opportunity to monitor how they behaved under significant stress.

There are currently two Burn-in stations at the University of the Witwatersrand, with one in full operation and the other one being commissioned and prepared for the main production of the buck converter boards towards the end of 2025.

References

[1] 0. Brüning et al, *"LHC Design Report"*, ser. CERN Yellow Reports: Monographs. Geneva: CERN, 2004. [Online]. Available: https://cds.cern.ch/record/782076

[2] The ATLAS Collaboration, "The ATLAS Experiment at the CERN Large Hadron Collider," *Journal of Instrumentation*, vol. 3, no. 08, p. S08003, aug 2008. [Online]. Available: https://dx.doi.org/10.1088/1748-0221/3/08/S08003

[3] The CMS Collaboration, "The CMS experiment at the CERN LHC," *Journal of Instrumentation*, vol. 3, no. 08, p. S08004, aug 2008. [Online]. Available: https://dx.doi.org/10.1088/1748-0221/3/08/S08004

[4] The LHCb Collaboration, "The LHCb Detector at the LHC," *Journal of Instrumentation*, vol. 3, no. 08, p. S08005, aug 2008. [Online]. Available: https://dx.doi.org/10.1088/1748-0221/3/08/S08005

[5] The ALICE Collaboration, "The ALICE experiment at the CERN LHC," *Journal of Instrumentation*, vol. 3, no. 08, p. S08002, aug 2008. [Online]. Available: https://dx.doi.org/10.1088/1748-0221/3/08/S08002

[6] The ATLAS Collaboration, "Technical Design Report for the Phase-II Upgrade of the ATLAS Tile Calorimeter," CERN, Geneva, Tech. Rep., 2017.

[7] R. McKenzie on behalf of the ATLAS Hadronic Tile-Calorimeter, "A Burn-in Apparatus for the ATLAS Hadronic Tile-Calorimeter Phase-II Upgrade Transformer-Coupled Buck-Converters," in *Technology and Instrumentation in Particle Physics (TIPP2023)*, 2023. [Online]. Available: https://indico.tlabs.ac.za/event/112/contributions/3321/attachments/1244/1688/ATLAS_TileCal_LVPS_Brick_Burn_in_Apparatus_TIPP2023.pdf

This page intentionally left blank.

Triboson Excesses in light of a Real Higgs Triplet Model

Srimoy Bhattacharya[1,2], **Siddharth P. Maharathy**[1,2,3], **Mukesh Kumar** [1], **Andreas Crivellin**[4], **Yaquan Fang** [5], **Rachid Mazini** [1], **and Bruce Mellado**[1,2]

[1]School of Physics and Institute for Collider Particle Physics, University of the Witwatersrand, Johannesburg, South Africa
[2]iThemba LABS, National Research Foundation, PO Box 722, Somerset West 7129, South Africa
[3]Indian Institute of Science Education and Research Pune, Dr. Homi Bhabha Road, Pune 411008, India
[4]Physik-Institut, Universität Zürich, Winterthurerstrasse 190, CH–8057 Zürich, Switzerland
[5]Institute of High Energy Physics ,19B, Yuquan Road, Shijing District, 100049, Beijing,China

E-mail: srimoy.bhattacharya@wits.ac.za

Abstract. Recent multilepton anomalies, which are defined as persistent excesses in final states with multiple leptons, missing energy, and (b-)jets, suggest the presence of a new scalar beyond the Standard Model (SM). Excesses in the diphoton, $Z\gamma$, and WW channels suggest a Higgs-like scalar S with mass $m_S \approx 152 \pm 1$ GeV, while the ZZ channel agrees with the Standard Model.This signature can be explained with a Real Higgs Triplet (RHT) model with hypercharge $Y = 0$, where S does not couple to ZZ at tree level. The Triplet scalars with mass m_s can be produced via Drell–Yan process and decay to electroweak bosons, enhancing triboson final states such as WWZ, WZZ, and WWW. Intriguingly, both ATLAS and CMS have reported significant excesses in triboson channels, with observed (expected) significances reaching 6.4σ (4.7σ) for VVZ production, where VVZ denotes the combined contribution of WWZ and ZZZ, and 4.4σ (3.6σ) specifically for the WWZ channel. These results raise the possibility that the signals may be manifestations of an extended Higgs sector. We explore the potential of the RHT model to generate triboson-like signatures via the electroweak production and decay of triplet scalars.

1 Introduction

The discovery of the Higgs boson in 2012 confirmed that the Standard Model (SM) provides a complete description of known particle physics phenomena. Nevertheless, measurements from various LHC experiments have shown hints of potential physics beyond the SM (BSM). In particular, the so-called "multilepton anomalies" have attracted attention, representing deviations from SM expectations in events that contain multiple leptons, missing energy, and occasionally (b-)jets. These anomalies may indicate the production of new BSM scalar particles, produced at the electroweak scale, sometimes in association with Standard Model particles.

A particularly compelling scenario involves the production of a heavier scalar resonance, which primarily decays into a pair of lighter scalars, S, with mass $\approx 150 \pm 5$ GeV. This cascade decay naturally gives rise to final states rich in electroweak bosons and leptons, offering a coherent explanation for the multilepton excesses observed in LHC data. In Refs. [1, 2], the sidebands of SM Higgs searches by ATLAS and CMS [3–10] have been analyzed, concluding that the observed data favor a narrow scalar resonance with a mass of approximately 152 GeV in the diphoton and $Z\gamma$ invariant mass spectra, with a global significance exceeding 5σ. However, no

Center of Mass Energy	Process	Observed Cross section (fb)	Expected Cross section (fb)
$\sqrt{s} = 13$ TeV	WWZ	$442 \pm 94(\text{stat.})^{+60}_{-52}(\text{syst.})$ [11]	329.0 [11]
		$300^{+120}_{-100}(\text{stat.})^{+50}_{-40}(\text{syst.})$ [12]	354.0 [12]
		$280^{+120}_{-110}(\text{stat.})^{+40}_{-30}(\text{syst.})$ [13]	373.0 [13]
	WZZ	$200^{+111}_{-91}(\text{stat.})^{+65}_{-37}(\text{syst.})$ [11]	93.1 [11]
		$200^{+160}_{-110}(\text{stat.})^{+70}_{-20}(\text{syst.})$ [12]	91.6 [12]
	WWW	$820 \pm 100(\text{stat.}) \pm 80(\text{syst.})$ [14]	511.0 ± 18 [14]
	tWZ	$248 \pm 38(\text{stat.}) \pm 35(\text{syst.})$ [15]	136.0^{+9}_{-8} [15]
$\sqrt{s} = 13.6$ TeV	WWZ	$700^{+270}_{-230}(\text{stat})^{+90}_{-60}(\text{syst})$ [13]	402 [13]
	tWZ	$242 \pm 62(\text{stat.}) \pm 46(\text{syst.})$ [15]	147.8^{+10}_{-9} [15]

Table 1: Observed and expected inclusive cross sections for WWZ, tWZ, WZZ and WWW study.

excess is seen in the ZZ channel. This pattern disfavors simple Higgs doublet extensions but aligns naturally with a Real Higgs Triplet (RHT) model with hypercharge $Y = 0$, where the new scalar S does not couple to ZZ at tree level. The RHT model also predicts triboson signatures - WWW, WZZ, WWZ, - from pair-produced triplet scalars decaying into electroweak bosons. Hints of excesses in these channels have been also observed by the CMS and ATLAS collaborations.

Table 1 provides a concise overview of recent ATLAS and CMS measurements of inclusive cross sections for WWZ, WZZ, WWW, and tWZ production at $\sqrt{s} = 13$ and 13.6 TeV, in comparison with SM predictions at Next to Leading Order (NLO) in QCD. These channels are of particular interest since several measurements show excesses relative to the SM. In the WWW channel, for instance, ATLAS measures 820 fb versus the SM expectation of 511 fb. The corresponding CMS result [12] is omitted due to a stringent selection cut on the azimuthal separation $\Delta\phi\left(\vec{p}_T^{\,3\ell}, \vec{p}_T^{\,\text{miss}}\right) > 2.5$, which suppresses new physics–sensitive topologies. Except for the last two WWZ measurements listed in Table 1, which fall below the SM expectation, all other measurements exhibit a clear excess. These deviations are particularly intriguing, since in the RHT model, additional scalars can enhance triboson and top-associated production. The observed excesses thus provide an opportunity to probe and constrain such extensions of the SM.

In this proceeding, we test whether the RHT model with a 152 GeV scalar can explain these triboson anomalies. We simulate Drell–Yan production and decays of the triplet components, compute triboson cross-sections, and compare the results with LHC data to evaluate the model's viability and its implications for extended Higgs sectors.

2 Model Description: The Real Higgs Triplet Model (RHT)

This work explores an extension of the Standard Model scalar sector that includes a real $\text{SU}(2)_L$ Higgs triplet with hypercharge zero ($Y = 0$), known as the RHT [16–23]. In this setup, one obtains a CP-even neutral scalar (Δ^0) together with a pair of charged Higgs bosons ($\Delta^\pm$), which remain nearly mass-degenerate as a consequence of electroweak precision constraints.

After electroweak symmetry breaking, the physical scalar spectrum consists of the SM- Higgs h, identified with the 125 GeV scalar, the neutral triplet-like scalar Δ^0, and the charged scalars $\Delta^\pm$. Here, masses of the triplet scalars are approximately

$$m^2_{\Delta^0} \approx \frac{1}{2}\lambda_\Delta v^2_\Delta + \frac{A v^2_\phi}{4 v_\Delta}, \quad m^2_{\Delta^\pm} = \frac{A(v^2_\phi + 4v^2_\Delta)}{4 v_\Delta}. \tag{1}$$

where

$$\lambda_\Delta = \frac{2}{v^2_\Delta}\left(m^2_{\Delta^0} - m^2_{\Delta^\pm}\right) \tag{2}$$

and v_ϕ and v_Δ are the respective vacuum expectation values (VEVs) of the SM Higgs $\text{SU}(2)_\text{L}$ doublet (Φ) with hypercharge $Y = \frac{1}{2}$ and the Higgs triplet (Δ) with $Y = 0$ respectively. The mixing angle α between the neutral scalars governs the deviation of Higgs couplings from their SM expectations and is constrained by precision Higgs measurements. The triplet vacuum expectation value v_Δ contributes at tree level only to the W boson mass.

Selection Type	ATLAS	CMS
Event Selection Criteria		
Electron	$p_T > 7$ GeV, $\|\eta\| < 2.47$	$p_T > 10$ GeV and $\|\eta\| < 2.5$
Muon	$p_T > 5$ GeV (> 15 GeV for calo-tag)and $\|\eta\| < 2.7$	$p_T > 10$ GeV and $\|\eta\| < 2.4$
Jet	$p_T > 20$ GeV, $\|\eta\| < 4.5$	$p_T > 25$ GeV and$\|\eta\| < 2.4$, anti-k_T ($R = 0.4$)
b-jets	= 0	= 0
Event Preselection Criteria		
Lepton Multiplicity	≥ 3 charged leptons	≥ 2 leptons (channel-dependent)
Z boson mass window (if applicable)	Z- mass band < 40 GeV	-
Inclusive 3ℓ Event Selection		
Preselection	✓	✓
No. of Leptons	≥ 3	≥ 3
Lepton p_T	> 15 GeV, at least one > 27 GeV	one > 25 GeV, others > 20 GeV (or all > 25 GeV if 0 SFOS)
SFOS dilepton mass	> 12 GeV; Z- mass band < 20 GeV	> 20 GeV; Z- mass band > 20 GeV for SFOS
Jet and b-jet	No b-jets; SRs based on 1 or 2 jets	No jets (1 allowed if 0 SFOS); no b-jets
Kinematic variables	—	$m_T^{\text{3rd}} > 90$ GeV, $\|\vec{p}_T^{3\ell}\| > 50$ GeV, $\Delta\phi > 2.5$, $\|m_{3\ell} - m_Z\| > 10$ GeV
3ℓ Signal Regions		
Region definitions	**SR1 :3**ℓ-1j : 1 jet	**3**ℓ-0SFOS
	SR2 :3ℓ-2j-inV : ≥ 2 jets, $60 < m_{jj} < 110$ GeV	**3**ℓ-1SFOS
	SR3 :3ℓ-2j-outV : ≥ 2 jets, $m_{jj} < 60$ or > 110 GeV	**3**ℓ-2SFOS
Inclusive 4ℓ Event Selection		
Preselection	✓	✓
No. of Leptons	Exactly four	Exactly four
Lepton p_T	30, 15, 8, 6 GeV	Z pair > 25, 10 GeV; others > 25, 10 GeV
SFOS dilepton mass	> 12 GeV,Z- mass band < 20 GeV	Z1: Z- mass band < 10 GeV, Z2: Z- mass band > 10 GeV
$\Delta R_{\ell\ell}$	> 0.1	—
E_T^{miss}	> 10 GeV	—
b-jets	= 0	= 0
4ℓ Signal Regions		
Common categories	**4**ℓ**-DF**: different-flavour W leptons ($e\mu$)	
	4ℓ**-SF-inZ**: same-flavour W leptons, Z- mass band < 20 GeV	
	4ℓ**-SF-outZ**: same-flavour W leptons, Z- mass band > 20 GeV	
Inclusive 5ℓ Event Selection		
Preselection	✓	✓
Leptons	≥ 5 leptons	≥ 5 leptons; leading two > 25 GeV, others > 10 GeV
Z boson candidates	≥ 2 SFOS pairs with Z- mass band < 20 GeV	≥ 2 SFOS pairs with Z- mass band < 15 GeV
Other cuts	—	$m_T > 50$ GeV
b-jets	= 0	= 0

Table 2: Combined summary of the object selection, event preselection, and inclusive/signal region selection criteria in ATLAS and CMS analyses [11, 12]. In this table the Z- mass band is defined as $|m_{\ell\ell} - m_Z|$.

Regarding collider phenomenology, the triplet-like scalars are primarily produced via Drell-Yan processes,

$$q\bar{q} \to Z^*/\gamma^* \to \Delta^+\Delta^-, \qquad q\bar{q}' \to W^{\pm *} \to \Delta^0\Delta^\pm. \tag{3}$$

The neutral scalar Δ^0 predominantly decays into WW, with loop-induced channels such as $\gamma\gamma$ and $Z\gamma$ becoming relevant when the scalar is nearly degenerate with $\Delta^\pm$. The charged scalars $\Delta^\pm$ typically decay to WZ, $\tau\nu$, or tb, depending on their masses. The phenomenological implications include multilepton and diphoton final states, and the model can accommodate LHC anomalies such as excesses near 152 GeV in the diphoton spectrum. The parameter space consistent with theoretical and experimental constraints generally prefers small mixing angle α and triplet vacuum expectation values v_Δ of order 1 to 3 GeV.

3 Event Generation and Simulation

Event generation in this work is carried out with `MadGraph5_aMC@NLO` [24, 25], with parton showering via `Pythia 8.3` [26] and detector simulation using `Delphes 3.5.0` [27], configured with CMS detector parameters. Final-state objects are reconstructed from the `Delphes` output, with jets clustered using the anti-k_T algorithm (radius $R = 0.4$) via `FastJet 3.3.4` [28].

The selection criteria summarized in Table 2 follow a tiered strategy involving lepton multiplicity, SFOS (same-flavor opposite-sign) pair counting, jet requirements, and Z-vetoes. CMS enforces tighter object-level cuts (e.g., $p_T > 10$ GeV for leptons), while ATLAS allows softer leptons to enhance sensitivity. Signal regions are defined separately in 3ℓ, 4ℓ, and 5ℓ categories, with additional kinematic requirements such as m_T, $\Delta\phi$, and E_T^{miss} cuts enhancing signal-to-background separation. Our analysis follows this structure closely, particularly employing the 3ℓ and 4ℓ categories with zero b-jet and Z-veto conditions, ensuring a consistent comparison with the reported excesses in multilepton channels.

4 Analysis and Results

This section covers the phenomenology related to the RHT model that was presented in earlier sections. This model provides a framework that can reproduce features of recent experimental results and guide future collider searches, such as at the LHC.

As a validation step for the analysis framework and examine the kinematic features of the signal, we present various distributions of key observables. In particular, we examine the invariant mass distributions of same-flavour opposite-sign (SFOS) di-leptons that are compatible with the decay of an on-shell Z boson. According to the selection criteria, each event must contain at least one SFOS di-leptons with an invariant mass within a 40 GeV window around the Z boson pole mass ($m_Z = 91.188$ GeV). Figure 1 shows the reconstructed Z boson mass from such SFOS pairs in the three signal regions (SR1, SR2, and SR3). These plots help confirm the presence of Z-boson candidates in the selected events and demonstrate the consistency of the reconstruction with the expected Z mass peak. This validation is particularly important in triboson final states such as WWZ, WZZ, tWZ, and WWW, where Z bosons are expected in the decay chain.

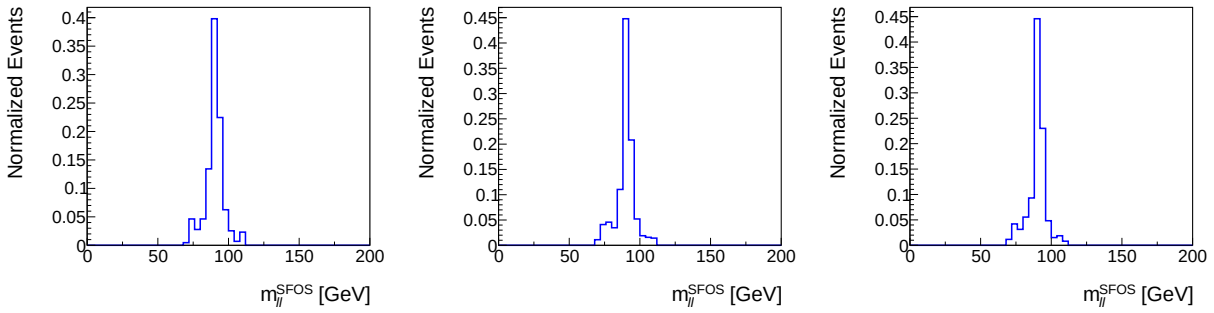

(a) SR1 (b) SR2 (c) SR3

Figure 1: Reconstructed invariant mass distributions of SFOS lepton pairs in each signal region (SR1, SR2, and SR3).

Future Work

Future work will focus on comparisons with ATLAS and CMS data, relying on their background estimations rather than re-modeling them. Following the ATLAS methodology, the signal regions will be further subdivided and optimized to enhance the separation between signal and background events. These discriminants can then be combined in a binned maximum-likelihood fit to extract a global signal strength parameter μ, defined as the ratio of the observed triboson production cross section to the SM expectation. Ultimately, this strategy aims to determine whether the RHT model can quantitatively account for the observed excesses in triboson final states. Future extensions will include a global combination across channels and sensitivity projections for the upcoming Run 3 data.

References

[1] A. Crivellin, Y. Fang, O. Fischer, S. Bhattacharya, M. Kumar, E. Malwa, B. Mellado, N. Rapheeha, X. Ruan, and Q. Sha, "Accumulating evidence for the associated production of a new Higgs boson at the LHC," *Phys. Rev. D*, vol. 108, no. 11, p. 115031, 2023.

[2] S. Bhattacharya, G. Coloretti, A. Crivellin, S.-E. Dahbi, Y. Fang, M. Kumar, and B. Mellado, "Growing Excesses of New Scalars at the Electroweak Scale," 6 2023.

[3] CMS Collaboration, "Measurements of Higgs boson production cross sections and couplings in the diphoton decay channel at $\sqrt{s}$ = 13 TeV," *JHEP*, vol. 07, p. 027, 2021.

[4] ATLAS Collaboration, "Measurement of the properties of Higgs boson production at $\sqrt{s}$=13 TeV in the $H \to \gamma\gamma$ channel using 139 fb^{-1} of pp collision data with the ATLAS experiment," 8 2020.

[5] ATLAS Collaboration, "CP Properties of Higgs Boson Interactions with Top Quarks in the $t\bar{t}H$ and tH Processes Using $H \to \gamma\gamma$ with the ATLAS Detector," *Phys. Rev. Lett.*, vol. 125, no. 6, p. 061802, 2020.

[6] CMS Collaboration, "Measurements of $\mathrm{t\bar{t}}H$ Production and the CP Structure of the Yukawa Interaction between the Higgs Boson and Top Quark in the Diphoton Decay Channel," *Phys. Rev. Lett.*, vol. 125, no. 6, p. 061801, 2020.

[7] ATLAS Collaboration, "Search for dark matter in events with missing transverse momentum and a Higgs boson decaying into two photons in pp collisions at $\sqrt{s}$ = 13 TeV with the ATLAS detector," *JHEP*, vol. 10, p. 013, 2021.

[8] CMS Collaboration, "Search for dark matter produced in association with a Higgs boson decaying to $\gamma\gamma$ or $\tau^+\tau^-$ at $\sqrt{s} = 13$ TeV," *JHEP*, vol. 09, p. 046, 2018.

[9] CMS Collaboration, "Search for the decay of a Higgs boson in the $\ell\ell\gamma$ channel in proton-proton collisions at $\sqrt{s} = 13$ TeV," *JHEP*, vol. 11, p. 152, 2018.

[10] ATLAS Collaboration, "Measurements of WH and ZH production in the $H \to b\bar{b}$ decay channel in pp collisions at 13 TeV with the ATLAS detector," *Eur. Phys. J. C*, vol. 81, no. 2, p. 178, 2021.

[11] ATLAS Collaboration, "Observation of VVZ production at $\sqrt{s} = 13$ TeV with the ATLAS detector," Dec 2024, arXiv:2412.15123 [hep-ex], CERN-EP-2024-321.

[12] CMS Collaboration, "Observation of the Production of Three Massive Gauge Bosons at $\sqrt{s}$ =13 TeV," *Phys. Rev. Lett.*, vol. 125, no. 15, p. 151802, 2020.

[13] CMS Collaboration, "Measurement of WWZ and ZH production cross sections at $\sqrt{s} = 13$ and 13.6 TeV," May 2025, arXiv:2505.20483 [hep-ex].

[14] ATLAS Collaboration, "Observation of WWW Production in pp Collisions at $\sqrt{s}$ =13 TeV with the ATLAS Detector," *Phys. Rev. Lett.*, vol. 129, no. 6, p. 061803, 2022.

[15] CMS Collaboration, "Observation of tWZ production at the CMS experiment," CMS-PAS-TOP-24-009, CMS Physics Analysis Summary, 2025.

[16] D. A. Ross and M. J. G. Veltman, "Neutral Currents in Neutrino Experiments," *Nucl. Phys. B*, vol. 95, pp. 135–147, 1975.

[17] J. F. Gunion, R. Vega, and J. Wudka, "Higgs triplets in the standard model," *Phys. Rev. D*, vol. 42, pp. 1673–1691, 1990.

[18] P. H. Chankowski, S. Pokorski, and J. Wagner, "(Non)decoupling of the Higgs triplet effects," *Eur. Phys. J. C*, vol. 50, pp. 919–933, 2007.

[19] T. Blank and W. Hollik, "Precision observables in $SU(2) \times U(1)$ models with an additional Higgs triplet," *Nucl. Phys. B*, vol. 514, pp. 113–134, 1998.

[20] J. R. Forshaw, A. Sabio Vera, and B. E. White, "Mass bounds in a model with a triplet Higgs," *JHEP*, vol. 06, p. 059, 2003.

[21] M.-C. Chen, S. Dawson, and T. Krupovnickas, "Higgs triplets and limits from precision measurements," *Phys. Rev. D*, vol. 74, p. 035001, 2006.

[22] R. S. Chivukula, N. D. Christensen, and E. H. Simmons, "Low-energy effective theory, unitarity, and non-decoupling behavior in a model with heavy Higgs-triplet fields," *Phys. Rev. D*, vol. 77, p. 035001, 2008.

[23] P. Bandyopadhyay and A. Costantini, "Obscure Higgs boson at Colliders," *Phys. Rev. D*, vol. 103, no. 1, p. 015025, 2021.

[24] J. Alwall, M. Herquet, F. Maltoni, O. Mattelaer, and T. Stelzer, "MadGraph 5 : Going Beyond," *JHEP*, vol. 06, p. 128, 2011.

[25] J. Alwall, R. Frederix, S. Frixione, V. Hirschi, F. Maltoni, O. Mattelaer, H. S. Shao, T. Stelzer, P. Torrielli, and M. Zaro, "The automated computation of tree-level and next-to-leading order differential cross sections, and their matching to parton shower simulations," *JHEP*, vol. 07, p. 079, 2014.

[26] T. Sjöstrand, S. Ask, J. R. Christiansen, R. Corke, N. Desai, P. Ilten, S. Mrenna, S. Prestel, C. O. Rasmussen, and P. Z. Skands, "An introduction to PYTHIA 8.2," *Comput. Phys. Commun.*, vol. 191, pp. 159–177, 2015.

[27] J. de Favereau, C. Delaere, P. Demin, A. Giammanco, V. Lemaître, A. Mertens, and M. Selvaggi, "DELPHES 3, A modular framework for fast simulation of a generic collider experiment," *JHEP*, vol. 02, p. 057, 2014.

[28] M. Cacciari, G. P. Salam, and G. Soyez, "FastJet User Manual," *Eur. Phys. J. C*, vol. 72, p. 1896, 2012.

The PANDORA Project: Investigating Photonuclear Reactions in Light Nuclei

J A C Bekker[1,2], L Pellegri[1,2], A Tamii [3], P-A Söderström[4] , D Allard [5], A Bahini [1], B Baret [5], D Balabanski [4], SD Binda [1,2], JW Brummer[1] JK Dahl[6], JWM Finsrud [6], Y Fujikawa [7], F Furukawa[3], T Furuno [8], A Gavrilescu [4], A Giaz[9], A Görgen [6], Y Honda [8], VW Ingeberg[6], R Iwasaki[3], P Jones[1], I Jurosevic[10], T Kawabata[8], T Khumalo[1,2], N Kobayashi [3], A Kusoglu [4], KCW Li [6], EM Martinsen [6], RE Molaeng[1,2], R Neveling[1], P von Neumann-Cosel[10], S Okamoto[7], T Okamura[8], S Ota [3], W Paulsen [6], K Sakanashi [8], Y Sasagawa[3], H Shibakita[3], H Shimojo [8], S Siem [6], M Spall [10], J Tanaka[3], C Wang [11], O Wieland[9], Z Yang [11], K Zhou [11]

[1]SSC Laboratory, iThemba LABS, P.O. Box 722, Somerset West 7129, South Africa.
[2]School of Physics, University of the Witwatersrand, Johannesburg 2050, South Africa.
[3]Research Center for Nuclear Physics (RCNP), Osaka University, Ibaraki 567-0047, Japan
[4]Extreme Light Infrastructure-Nuclear Physics (ELI-NP)/Horia Hulubei National Institute for Physics and Nuclear Engineering (IFIN-HH), Str. Reactorului 30, Bucharest-Măgurele 077125, Romania
[5]Laboratoire Astroparticule et Cosmologie, Université Paris Cité, CNRS, F-75013 Paris, France
[6]Department of Physics, University of Oslo, P.O. Box 1048, Blindern, N-0316 Oslo, Norway
[7]Department of Physics, Kyoto University, Kitashirakawa Oiwake-Cho, 606-8502 Kyoto, Japan
[8]Department of Physics, Osaka University, Toyonaka, Osaka 560-0043, Japan
[9]Dipartimento di Fisica dell'Università degli Studi di Milano, I-20133 Milano, Italy
[10]Institut für Kernphysik, Technische Universität Darmstadt, 64289 Darmstadt, Germany
[11]School of Physics and State Key Laboratory of Nuclear Physics and Technology, Peking University, Beijing 100871, China

E-mail: jacob.bekker@wits.ac.za

Abstract. The PANDORA (Photo-Absorption of Nuclei and Decay Observation for Reactions in Astrophysics) project focuses on both experimental and theoretical studies of photo-nuclear reactions involving light nuclei with mass numbers below $A = 60$. This research plays a crucial role in understanding ultra-high-energy cosmic rays (UHECRs), where energy loss mechanisms are primarily driven by electromagnetic interactions between nuclei and the cosmic microwave background, particularly through the isovector giant dipole resonance (IVGDR). However, current propagation models and reaction calculations are hindered by the limited availability of reliable experimental data for several key nuclei. In this context, the project presents new results on ^{12}C , obtained through inelastic (p,p') scattering at 392 MeV using the virtual photon method, conducted at the Research Center for Nuclear Physics (RCNP) in Japan.

1 Introduction

Nuclear astrophysics relies heavily on accurate experimental data to model and interpret physical phenomena [1]. A prime example is the simulation of ultra-high-energy cosmic ray (UHECR) propagation, where nuclei undergo photodisintegration via absorption of Lorentz-boosted cosmic microwave background photons. These simulations require input from a wide range of nuclei with mass numbers below 56 [2]. While it is impractical to obtain detailed data for every relevant nucleus, a subset of nuclei plays a significant role in driving these interactions and validating propagation models.

This experimental campaign aims to determine the total photoabsorption cross section in the excitation energy region of the isovector giant dipole resonance (IVGDR) for light nuclei, approximately 16–30 MeV. In addition to the total photoabsorption, the partial branching ratios for charged-particle decay channels were also determined. This can be achieved using relativistic Coulomb excitation in combination with the virtual photon absorption method [3], a method in which the electric interaction between the target and projectile nuclei is expressed as a spectrum of virtual photons absorbed by the target. The IVGDR region is dominated by a dense spectrum of E1 gamma transitions, making it a vital channel for understanding the photodisintegration processes that shape the energy and mass evolution of UHECRs during their journey through space.

The PANDORA project was established to address this specific need for total photoabsorption cross sections and decay branching ratios required for UHECR propagation models, and also for diverse applications in nuclear structure and astrophysics [4]. In this paper, we present preliminary results from measurements performed on ^{12}C.

2 Experimental Method

The experiment utilized a 392 MeV proton beam produced by the Ring cyclotron at RCNP, Japan, and analyzed using the Grand Raiden (GR) spectrometer. The parameters of the GR are shown in Table 1. The momentum dispersion allows a spatial resolution of 0.1-0.2 mm and with the multi-wire drift chambers (MWDC) used as focal plane detectors, one can achieve energy resolutions of up to 40 keV at 392 MeV beam energy. The GR's

Parameter	**Value**
Mean orbit radius	3 m
Total deflection angle	162°
Angular range	0° – 90°
Focal plane length	150 cm
Tilting angle of focal line	45.0°
Vertical magnification (M_Y)	5.98
Horizontal magnification (M_X)	-0.417
Momentum dispersion (D)	15.451 mm
Momentum range	5%
Momentum resolution	37076
Acceptance angle (horizontal)	$\pm$ 20 mr
Acceptance angle (vertical)	$\pm$ 70 mr
Solid angle	$\sim$ 5.6 msr
Maximum magnetic field strength	18 kG
Maximum particle rigidity	54 kG·m

Table 1: Technical specifications of the GR magnetic spectrometer.

ability to operate at 0°, combined with the semi-relativistic proton energies provided by the cyclotron, are critical for suppressing contributions from reaction channels other than E1 Coulomb excitation [5]. The GR was also operated in the GRAF mode which allows data to be taken at 4.5° and 6.6° central angle settings, which will be used to isolate the E1 component of the cross sections. The GR and GRAF [6] are shown together in a schematic in Figure 2.

The detection system at the focal plane employs two MWDCs to determine particle trajectories and two plastic scintillators for timing and identification. Secondary decay particles from the target were detected using SAKRA, a backward-angle double-sided silicon strip detector (DSSSD) array. The experimental setup also included a $LaBr_3$:Ce array, named SCYLLA, for potential detection of secondary gamma rays resulting from IVGDR decay. Photographs of the focal plane and SAKRA detector systems are shown in Figure 2.

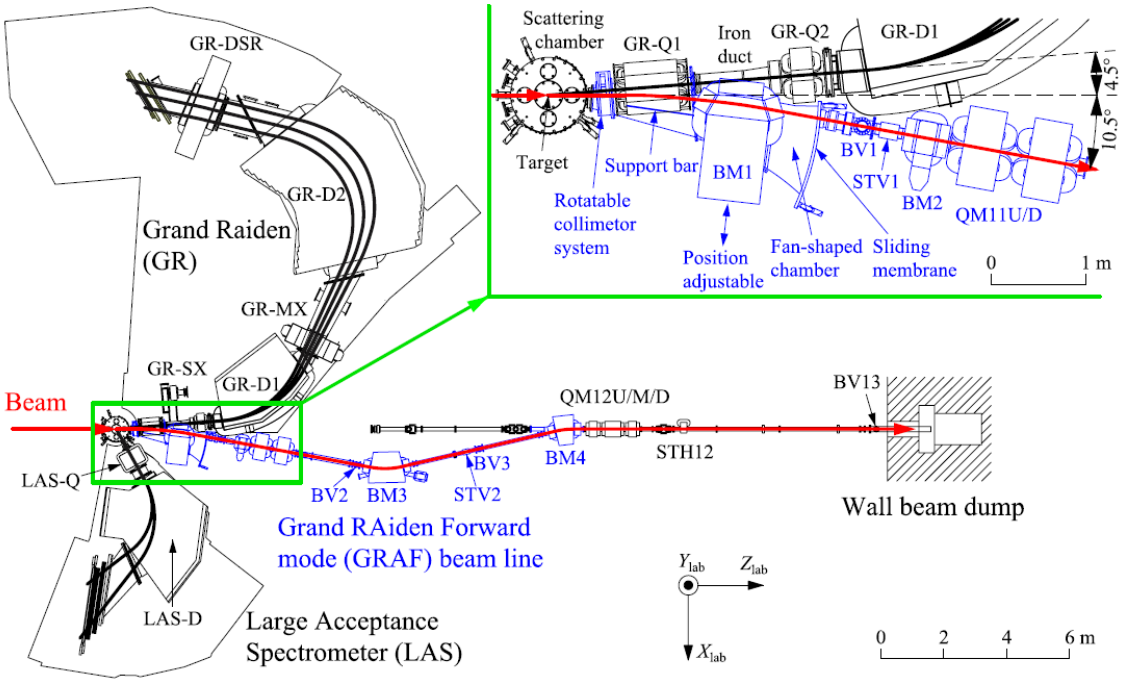

Figure 1: A diagram of the GRAF beamline showing how it aligns with the GR spectrometer. [6]

3 Focal Plane Results

In studies of photo-induced nuclear reactions, the double-differential cross section (DDCS) is a fundamental observable that provides the probability of nuclear excitation as a function of both emission angle and energy of the scattered particle [7]. It is experimentally determined using:

$$\frac{d^2\sigma}{d\Omega\, dE} = \frac{10^{27} \cdot N_c}{N_0 \cdot \rho \cdot D \cdot \Delta\Omega \cdot \Delta E \cdot \epsilon_{tot}}, \tag{1}$$

with the parameters defined as:

- N_c: Amount of events in an energy bin,
- N_0: Number of incident protons on the target,
- ρ: Areal density of the target in mg/cm^{2}in this case 1 mg/cm^2,
- $\Delta\Omega$: Detector solid angle (3.36 msr),
- ΔE: Width of the energy bin (0.05 MeV),
- ϵ_{tot}: Total detection efficiency of the GR spectrometer, usually around 0.85-0.90,
- D: Fraction of recorded events, corrected for live-time usually 0.98,
- 10^{27}: Unit conversion factor to yield $\mathrm{mb}/(\mathrm{sr} \cdot \mathrm{MeV})$.

The total number of incident protons, N_0, is determined from the current integrator using:

$$N_0 = \frac{CI \cdot R \cdot 10^{-12}}{e}, \tag{2}$$

where CI is the integrator readout, R the range setting (nA), and e the elementary charge.
To assess MWDC performance, the efficiency of each wire plane (e.g., X_1 or X_2) is calculated as:



Figure 2: *(Left)*: The focal plane detection system, with plastic scintillators positioned behind the vertical drift chambers. The zero-degree beam line is visible, passing within centimeters of the detectors. *(Right)*: The cherry blossom-shaped SAKRA DSSSD array prior to installation in the scattering chamber. It covers approximately 25% of the downstream solid angle.

$$\epsilon(X_{1,2}) = \frac{N_{\text{events}}(X_1 X_2, U_1, U_2)}{N_{\text{events}}, (X_{2,1}, U_1, U_2)}, \tag{3}$$

where the numerator represents full 4-plane coincidences and the denominator omits the plane under test. This efficiency quantifies each plane's contribution to reliable track reconstruction and each plane's efficiency is usually between 0.88-0.95. The results of the calculation and its comparison to a previous experiment is shown in Figure 3, where the agreement is well realised although the previous experiment used dispersion matching to obtain a resolution of 100 keV, in this case we did not require such a high resolution and only used an achromatic tune, thus leading to our resolution being 300 keV.

The virtual photon method allows conversion of the DDCS into the total photoabsorption cross section [3], which recasts Coulomb excitation as the absorption of a spectrum of virtual photons. For the present kinematics, the Eikonal approximation was necessary to ensure the method remains valid at 0° scattering angles.

4 Coincidence Results

Additional information on the decay modes of excited ^{12}C was obtained by analyzing coincidence events between the GR focal plane and the SAKRA array (Figure 4). A simple kinematics Monte Carlo simulation by J.J. Van Zyl of the IVGDR decay kinematics were used to guide identification of physical loci.

True coincidences were isolated using timing information from plastic scintillators and the RF clock signal. Clear decay branches to the ground and excited states of ^{11}B were identified in both simulation and experiment. The proton punch-through threshold at 8 MeV is visible in the data, indicating the energy beyond which protons exit the first layer of silicon detectors without full energy deposition.

Graphical cuts, combined with SAKRA time-of-flight information, are being applied to distinguish between protons and α-particles. This separation allows for construction of particle-specific histograms, enabling calculation of branching ratios for each decay channel — a crucial input for constraining IVGDR decay models in light nuclei. The energy resolution of the SAKRA array was 100 keV which is far smaller than the 300 keV of the focal plane.

5 Conclusion and Outlook

For the double differential cross sections we obtained in this experiment the agreement was well in line with a previous experiment and the coincidence data that we were able to obtain using the SAKRA detection system shows promising PID capabilities. This is the first setup where secondary charged decay particles and γ -decay coincidences have been measured in conjunction with 0° focal plane scattering data.

The next phase of analysis involves isolating the pure E1 contribution from other multipolarities present in the excitation spectrum. This is achieved using either Multipole Decomposition Analysis (MDA) or the Difference of Spectra (DoS) method. This is necessary, since even though the experimental setup was chosen to minimize

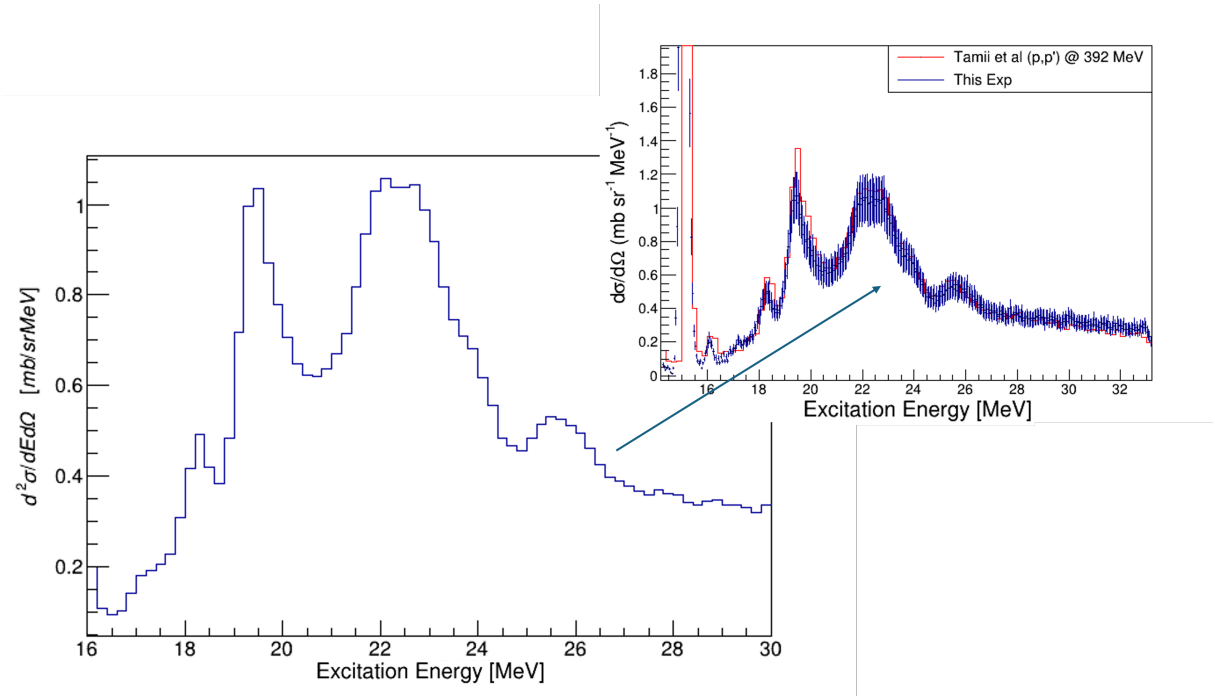

Figure 3: Comparison of the DDCS for 392 MeV protons on ^{12}C from this work with a previous experiment that used dispersion matching. The current setup did not employ dispersion matching due to the less stringent resolution requirements for GDR studies.

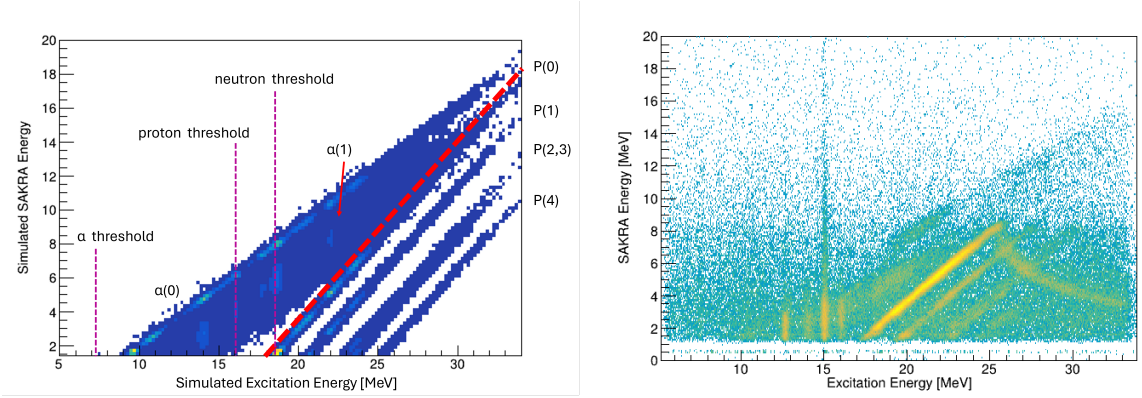

Figure 4: *(Left)*: Kinematic simulation of ^{12}C decay showing the loci of decay products with the P(x) indicating the proton decay states. The red separation line differentiates α-particles and protons based on threshold energies. *(Right)*: Experimental coincidence data between the focal plane and SAKRA for ^{12}C. Proton punch-through is clearly visible.

the contributions from other multipolarities, they cannot be completely eliminated and still contribute towards the measured spectra. Both require Distorted Wave Born Approximation (DWBA) calculations to generate theoretical angular distributions.

In MDA, angular distributions for various multipolarities, along with a quasifree background component, are simultaneously fitted to the data. The dominant contribution from the MDA that will require subtracting will be the quasifree scattering background that can become a large component of the scattering cross section for lighter nuclei based on previous experiments [8]. The resulting E1 component is extracted bin-by-bin [9]. Alternatively, the DoS method identifies the first minimum in the E1 angular distribution and subtracts the spectrum at that finite

angle from the 0° data, isolating the E1 response after correcting for geometric and instrumental effects [10].

Once the pure E1 contributions are extracted, the corresponding branching ratios and total photoabsorption cross sections can be finalized.

Acknowledgments

This work is based on research supported in part by the National Research Foundation (NRF) of South Africa through grants JSPS230914149307, JSPS200819554019, and SARC180529336567. Additional support from the SAINTS Prestigious Doctoral Scholarship and NRF Postdoctoral Grant (reference number PSTD240423215494) is gratefully acknowledged. The financial assistance of the NRF (iThemba LABS) and the University of the Witwatersrand towards this research is also acknowledged. The opinions expressed and conclusions drawn are those of the author and should not be regarded as reflecting the views of the NRF (iThemba LABS) or the University of the Witwatersrand.

References

[1] L. A. Bernstein, D. A. Brown, D. A. Koning, B. T. Rearden, C. E. Romano, A. A. Sonzogni, A. S. Voyles, and W. Younes, "Our future nuclear data needs," *Annual Review of Nuclear and Particle Science*, vol. 69, pp. 109–136, 2019.

[2] D. Boncioli, A. Fedynitch, and W. Winter, "Nuclear physics meets the sources of the ultra-high energy cosmic rays," *Scientific Reports*, vol. 7, p. 4882, 2017.

[3] C. A. Bertulani, "Theory and applications of coulomb excitation," 2009.

[4] A. Tamii, L. Pellegri, P.-A. Söderström, D. Allard, S. Goriely, T. Inakura, E. Khan, E. Kido, M. Kimura, E. Litvinova *et al.*, "Pandora project for the study of photonuclear reactions below a= 60," *The European Physical Journal A*, vol. 59, no. 9, p. 208, 2023.

[5] M. Fujiwara, H. Akimune, I. Daito, H. Fujimura, Y. Fujita, K. Hatanaka, H. Ikegami, I. Katayama, K. Nagayama, N. Matsuoka *et al.*, "Magnetic spectrometer grand raiden," *Nucl. Instrum. Methods in Physics Research Section A: Accelerators, Spectrometers, Detectors and Associated Equipment*, vol. 422, no. 1-3, pp. 484–488, 1999.

[6] N. Kobayashi, K. Miki, T. Hashimoto, C. Iwamoto, A. Tamii, N. Aoi, M. Carpenter, K. Hatanaka, J. Isaak, E. Ideguchi *et al.*, "Excitation and γ-decay coincidence measurements at the GRAF beamline for studies of pygmy and giant dipole resonances," *Eur. Phys. J. A*, vol. 55, no. 12, p. 231, 2019.

[7] K. S. Krane, D. Halliday *et al.*, *Introductory Nuclear Physics*. Wiley New York, 1988, vol. 465.

[8] M. Jingo *et al.*, *Eur. Phys. J. A*, vol. 54, p. 234, 2018.

[9] S. Freed and S. Weissman, "Multiple nature of elementary sources of radiation—wide-angle interference," *Physical Review*, vol. 60, no. 6, p. 440, 1941.

[10] A. Bahini, V. O. Nesterenko, I. T. Usman, P. von Neumann-Cosel, R. Neveling, J. Carter, J. Kvasil, A. Repko, P. Adsley, N. Botha, J. W. Brümmer, L. M. Donaldson, S. Jongile, T. C. Khumalo, M. B. Latif, K. C. W. Li, P. Z. Mabika, P. T. Molema, C. S. Moodley, S. D. Olorunfunmi, P. Papka, L. Pellegri, B. Rebeiro, E. Sideras-Haddad, F. D. Smit, S. Triambak, and J. J. van Zyl, "Isoscalar giant monopole resonance in ^{24}Mg and ^{28}Si: Effect of coupling between the isoscalar monopole and quadrupole strength," *Phys. Rev. C*, vol. 105, p. 024311, Feb 2022. [Online]. Available: https://link.aps.org/doi/10.1103/PhysRevC.105.024311

Investigation of X-rays and Gamma-ray Shielding Properties of Heavy Metal Oxide Glass Materials

N. Msabala[1], S.S. Ntshangase[1], B.V. Kheswa[2], L. Mdletshe[1], A. Sefage[2], B.R. Zikhali[1], M. N. Zuma[1] and S. Mthalane[1]

[1]Department of Physics, University of Zululand, Private Bag X1001, KwaDlangezwa 3886, South Africa
[2]Department of Physics, University of Johannesburg, 55 Beit Street, Doornfontein, South Africa

E-mail: nosihlen686@gmail.com

Abstract. Exposure to high levels of ionizing radiation poses serious health risks, especially for workers in medical, industrial, and nuclear environments. Traditional shielding materials like lead have significant drawbacks, including toxicity and environmental concerns. This study focuses on developing lead-free heavy metal oxide glass materials that offer effective X-ray and gamma-ray attenuation while maintaining transparency, structural durability, and cost efficiency. In this work, the radiation shielding parameters of the glass system, with the chemical composition $x\mathrm{Bi_2O_3} - (55 - x)\mathrm{B_2O_3} - 15\mathrm{BaO} - 10\mathrm{ZnO} - 18\mathrm{SiO_2} - 2\mathrm{Nd_2O_3}$ (where x =15, 20, 25, 30, and 35 mol%). was investigated. The radiation shielding properties were investigated through simulations using XCOM software over a photon energy range of 0.03 to 0.3 MeV. The results show that increasing $\mathrm{Bi_2O_3}$ content significantly increases the mass attenuation coefficient (MAC), indicating better shielding performance compared to similar glass compositions reported in the literature.

1 Introduction

As technology advances, ionizing radiation has become an essential tool across numerous industries, including medical diagnostics, nuclear research, and mining. However, exposure to high levels of ionizing radiation can severely affect biological systems, leading to long-term illnesses such as cancer and other health complications [1, 2]. Traditionally, materials like lead (Pb) and concrete have been widely used to shield against X-rays and gamma rays due to their high density and attenuation properties [3]. Lead, in particular, has long been favored for its effective X-ray and gamma-ray radiation absorption capabilities. However, it poses several significant drawbacks, including low material strength, handling difficulties, lack of transparency, and high costs [4]. Moreover, lead is toxic and non-biodegradable, raising environmental and health concerns due to its persistence in nature and the risk of inhalation, skin absorption, or ingestion [4]. Concrete is another commonly used shielding material, valued for its affordability, ease of manufacture, and structural durability [5]. Yet, its effectiveness can be compromised by structural cracking, variations in water content, and long-term degradation, which may allow ionizing radiation to penetrate through the damaged sections [6]. Therefore, the proper design, composition, and maintenance of concrete structures are vital to ensure their long-term shielding performance. Due to the environmental and safety drawbacks of conventional materials like lead and concrete, there is a growing need to develop alternative shielding materials that are safer, more effective, cost-efficient, and environmentally friendly. Among the promising alternatives are heavy metal oxide glass systems, which combine high density and excellent attenuation properties with desirable mechanical, thermal, and optical characteristics.

In this study, a new lead-free heavy metal oxide glass system composed of $Bi_2O_3 - B_2O_3 - BaO - ZnO - SiO_2 - Nd_2O_3$ is investigated for its potential as an effective radiation shielding material. Bismuth oxide (Bi_2O_3) is a key component due to its high atomic number (Z = 83) and density, which increases the probability of photoelectric absorption and enhances X-ray attenuation [7, 8]. Boron trioxide (B_2O_3) acts as a network former, providing structural stability, chemical durability, and thermal resistance, while also contributing to neutron shielding [9, 10]. Barium oxide (BaO), with a high atomic number (Z = 56), further increases the glass density and shielding effectiveness while lowering the melting temperature and improving workability [11, 12, 13]. Zinc oxide (ZnO) improves the optical properties, mechanical strength, and chemical durability of the glass, making it suitable for medical and industrial applications requiring transparency [14, 15]. Silicon dioxide (SiO_2) serves as the primary glass former, contributing to a strong, thermally stable, and mechanically robust glass network [16]. Additionally, neodymium oxide (Nd_2O_3), a rare earth oxide, enhances the optical performance by absorbing specific wavelengths and improves resistance to radiation-induced damage, which is particularly valuable in medical imaging environments [17, 18].

The aim of this research is to develop and assess this Bi_2O_3-based glass system to achieve a high mass attenuation coefficient (MAC) and robust structural performance, providing an effective, transparent, and environmentally sustainable alternative for shielding against X-rays and gamma rays.

2 Simulation Methods

In this work, different MAC were extracted using the XCOM software program, developed by the National Institute of Standards and Technology (NIST) [19]. It provides detailed information on photoabsorption, coherent scattering, and Compton (incoherent) scattering, and it offers reliable attenuation and absorption coefficients for elements, compounds, and mixtures across a broad energy range from 1 keV to 100 GeV [20]. In this study, XCOM was used to evaluate the X-ray shielding performance of the glass system with the composition $xBi_2O_3 - (55 - x)B_2O_3 - 15BaO - 10ZnO - 18SiO_2 - 2Nd_2O_3$ (where x =15, 20, 25, 30, and 35 mol%). The MAC was determined by inputting the weight fractions of each compound (see Table1) in the glass and calculating their interaction with photons in the energy range of 0,03 to 0,3 MeV.

Compounds	Weight fractions (%)				
	S1	S2	S3	S4	S5
Bi_2O_3	0.477	0.561	0.626	0.679	0.723
B_2O_3	0.190	0.147	0.112	0.085	0.062
BaO	0.157	0.138	0.124	0.112	0.102
ZnO	0.056	0.049	0.044	0.040	0.036
SiO_2	0.074	0.065	0.058	0.053	0.048
Nd_2O_3	0.046	0.040	0.036	0.033	0.030

Table 1: Weight fractions (%) of different compounds in the prepared glass samples (S1–S5).

The mass attenuation coefficient (MAC) describes how effectively a material reduces the intensity of a radiation beam as it passes through it. It is calculated by dividing the linear attenuation coefficient (LAC) by the material's density and represents the rate of attenuation per unit mass [19, 21]. Mathematically, it is defined as

$$\mu_m = \frac{\mu}{\rho}, \tag{1}$$

where μ is the linear attenuation coefficient (in cm^{-1}), which measures the likelihood of photon interactions within the material depending on its thickness, and ρ is the material's density. The MAC is a key parameter for comparing the shielding performance of different materials.

3 Results and Discussion

The performance of the glass samples was evaluated in terms of their MAC across the selected photon energy range. Figure 1 illustrates how the MAC varies for the glass compositions S1–S5 within 0.03–0.3 MeV. The results show that all samples maintain high attenuation at lower photon energies, with MAC values ranging from 16.072 to 22.094 cm^2/g at 0.03 MeV. As the photon energy increases, an exponential reduction in MAC is observed, which

aligns with the decreased probability of interaction between radiation and atomic electrons. At higher energies, radiation is less effectively attenuated because interactions shift from the electron shells to the atomic nucleus, which generally results in lower attenuation overall. A slight peak near 0.038 MeV is linked to the K-absorption edges of Neodymium (Nd) and Barium (Ba), where incoming photons have sufficient energy to eject K-shell electrons. The K-edge energies for Nd and Ba are approximately 0.044 MeV and 0.037 MeV, respectively, which supports the observed increase in attenuation. Similarly, the sharp feature around 0.091 MeV corresponds to the K-edge of Bismuth (Bi), which occurs at 0.091 MeV, further enhancing photon absorption due to increased interaction probability at this energy. Figure 1 clearly demonstrates that increasing the Bi_2O_3 concentration leads to consistently higher MAC values, confirming that a higher bismuth content improves shielding efficiency in these lead-free glasses.

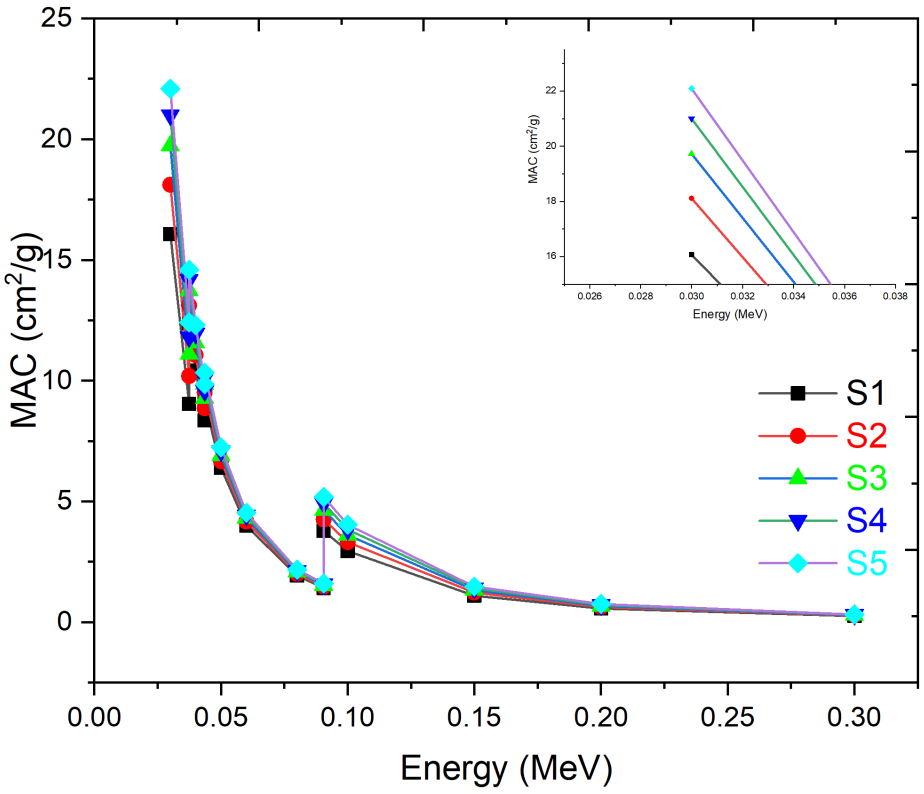

Figure 1: MAC of $Bi_2O_3 - B_2O_3 - BaO - ZnO - SiO_2 - Nd_2O_3$ glass system as a function of energy. The inset shows the zoomed-in part from 0.030 to 0.035 MeV.

To further evaluate the performance of the prepared glasses, Figure 2 compares the MAC values of the samples S1–S5 with those reported for similar glass systems in previous studies [4, 22, 23] at 0.1 MeV and 0.3 MeV. At both energies, the new glasses display noticeably higher MAC values than the reference glasses (BiTeEu-3,BiTeEu-4, BSABa25, BSABa28, LiBPTe0 and LiBPTe10 compositions), demonstrating the enhanced shielding capability of the developed materials. For example, at 0.1 MeV, the S-series samples achieve MAC values between 2.946 and 4.033 cm^2/g, whereas the literature samples remain below 2.600 cm^2/g. A similar trend is observed at 0.3 MeV, where the S1–S5 glasses consistently outperform the reference systems. This improvement is directly linked to the optimized Bi_2O_3 content, which increases the glass density and the probability of photon interaction [24]. Overall, these results highlight that the proposed glass system offers superior attenuation characteristics and is a promising lead-free alternative for effective radiation shielding applications.

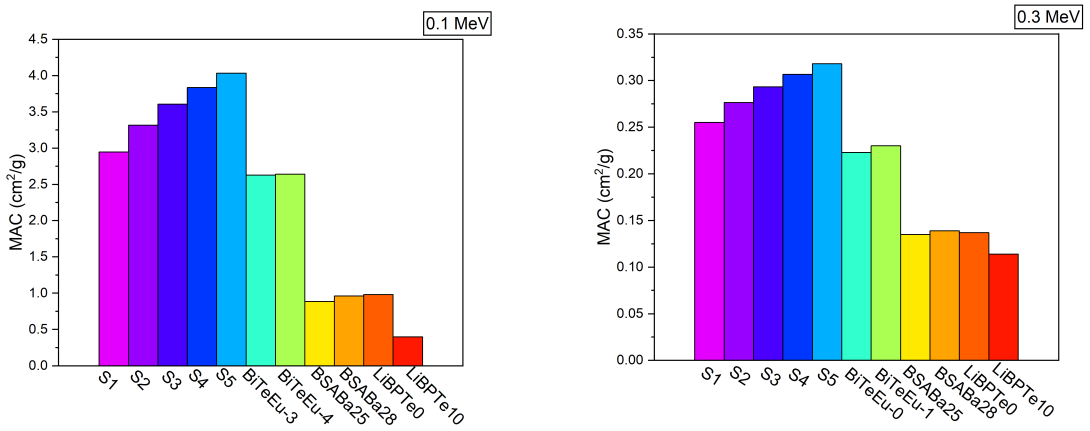

Figure 2: Comparison of the MAC of the prepared glass samples with six reference radiation shielding glasses from the literature at photon energies of 0.1 MeV and 0.3 MeV.

4 Conclusion

The MAC results confirm that the developed heavy metal oxide glasses demonstrate excellent X-ray attenuation performance across the investigated energy range. The continuous MAC curves indicate that increasing Bi_2O_3 content significantly improves the shielding effectiveness, especially at lower photon energies where photoelectric absorption dominates. The comparative analysis with previously reported glass systems further validates the improved performance of the new compositions, which consistently achieve higher MAC values at both 0.1 MeV and 0.3 MeV. These findings highlight that the proposed lead-free glasses are strong candidates for replacing conventional shielding materials, offering a safer, transparent, and effective solution for radiation protection in medical, industrial, and nuclear applications.

References

[1] E. M. Rosen, R. Day, and V. K. Singh, "New approaches to radiation protection," *Frontiers in oncology*, vol. 4, p. 381, 2015.

[2] M. De Santis, E. Cesari, E. Nobili, G. Straface, A. F. Cavaliere, and A. Caruso, "Radiation effects on development," *Birth Defects Research Part C: Embryo Today: Reviews*, vol. 81, no. 3, pp. 177–182, 2007.

[3] R. N. Ihsani, H. Heryanto, P. L. Gareso, and D. Tahir, "Innovative radiation shielding: a review natural polymer-based aprons with metal nanoparticle fillers," *Polymer-Plastics Technology and Materials*, vol. 63, no. 6, pp. 738–755, 2024.

[4] D. Ş. Baykal, H. O. Tekin, and R. B. Ç. Mutlu, "An investigation on radiation shielding properties of borosilicate glass systems," *International Journal of Computational and Experimental Science and Engineering*, vol. 7, no. 2, pp. 99–108, 2021.

[5] H. Alrebdi, A. Almuqrin, M. Hanfi, M. Sayyed, and K. Mahmoud, "Influence of the sro insertion to a binary $PbO - B_2O_3$ glass system: Mechanical properties and radiation shielding study," *Transactions of the Indian Ceramic Society*, vol. 81, no. 2, pp. 76–83, 2022.

[6] M. Elsafi, M. El-Nahal, M. Sayyed, I. Saleh, and M. Abbas, "Effect of bulk and nanoparticle Bi_2O_3 on attenuation capability of radiation shielding glass," *Ceramics International*, vol. 47, no. 14, pp. 19 651–19 658, 2021.

[7] V. Fruth, A. Ianculescu, D. Berger, S. Preda, G. Voicu, E. Tenea, and M. Popa, "Synthesis, structure and properties of doped Bi_2O_3," *Journal of the European Ceramic Society*, vol. 26, no. 14, pp. 3011–3016, 2006.

[8] W. Dong and C. Zhu, "Optical properties of surface-modified Bi_2O_3 nanoparticles," *Journal of Physics and Chemistry of Solids*, vol. 64, no. 2, pp. 265–271, 2003.

[9] K. Alsafi, Y. A. Ismail, D. A. Aloraini, H. M. Almutairi, W. M. Al-Saleh, and K. S. Shaaban, "Exploring the radiation shielding properties of $B_2O_3 - SiO_2 - ZnO - Na_2O - WO_3$ glasses: a comprehensive study on mechanical, gamma, and neutron attenuation characteristics," *Progress in Nuclear Energy*, vol. 170, p. 105151, 2024.

[10] M. Sayyed, M. Mhareb, B. C. Şakar, K. Mahmoud, E. Şakar, H. A. Thabit, K. M. Kaky, and S. Baki, "Experimental investigation of structural and radiation shielding features of $Li_2O - BaO - ZnO - B_2O_3 - Bi_2O_3$ glass systems," *Radiation Physics and Chemistry*, vol. 218, p. 111640, 2024.

[11] S. Biradar, A. Dinkar, A. Manjunatha, G. Bennal, B. Devidas, M. Hareesh, K. Siri, M. Nandan, and H. Sayyed, "Es-soufi, mn chandrashekara." comprehensive investigation of borate-based glasses doped with BaO: An assessment of physical, structural, thermal, optical, and radiation shielding properties."," *Optical Materials*, vol. 150, p. 115176, 2024.

[12] K. S. Shaaban, D. A. Aloraini, K. Alsafi, H. M. Almutairi, W. M. Al-Saleh, and A. S. Alzahrani, "Role of CeO2 in the enhancement of the properties of the $SiO_2 - B_2O_3 - BaO - Li_2O$ glass system: structural, mechanical and radiation shielding study," *Materials Today Communications*, vol. 38, p. 108309, 2024.

[13] M. Sayyed, "BaO-doped $B_2O_3 - Na_2O - PbO - SiO_2$ glasses: improved radiation shielding properties for protection applications," *Silicon*, vol. 16, no. 6, pp. 2473–2479, 2024.

[14] A. B. Djurišić and Y. H. Leung, "Optical properties of ZnO nanostructures," *Small*, vol. 2, no. 8-9, pp. 944–961, 2006.

[15] D. K. Sharma, S. Shukla, K. K. Sharma, and V. Kumar, "A review on ZnO: Fundamental properties and applications," *Materials Today: Proceedings*, vol. 49, pp. 3028–3035, 2022.

[16] K. Alsafi, D. A. Aloraini, W. M. Al-Saleh, and K. S. Shaaban, "Impact of La_2O_3 on structural, optical, gamma rays, and neutron properties of $B_2O_3 - SiO_2 - ZnO$ glasses: K. alsafi et al." *Journal of Electronic Materials*, vol. 53, no. 7, pp. 3980–3993, 2024.

[17] A. Ali and M. Shaaban, "Electrical properties of libbate glass doped with Nd_2O_3," *Solid state sciences*, vol. 12, no. 12, pp. 2148–2154, 2010.

[18] R. Lok, E. Budak, and E. Yilmaz, "Structural characterization and electrical properties of Nd_2O_3 by sol–gel method," *Journal of Materials Science: Materials in Electronics*, vol. 31, no. 4, pp. 3111–3118, 2020.

[19] H. O. Tekin, V. P. Singh, and T. Manici, "Effects of micro-sized and nano-sized WO_3 on mass attenauation coefficients of concrete by using MCNPX code," *Applied Radiation and Isotopes*, vol. 121, pp. 122–125, 2017.

[20] A. Arectout, H. Boukhal, M. Jarmouni, K. Laazouzi, M. Assalmi, A. Nouayti, M. Hadouachi, H. El Yaakoubi, and E. Chakir, "Investigation of photon interaction parameters in human body tissues using GAMOS, FLUKA, and XCOM studies," *Nuclear Analysis*, vol. 4, no. 1, p. 100141, 2025.

[21] M. Hosamani and N. Badiger, "Determination of effective atomic number of composite materials using backscattered gamma photons–a novel method," *Chemical Physics Letters*, vol. 695, pp. 94–98, 2018.

[22] A. N. D'Souza, M. Murari, M. Sayyed, H. Al-Ghamdi, A. H. Almuqrin, and S. D. Kamath, "Comprehensive study on structural, optical, mechanical and radiation blocking nature of Eu^{3+}-doped bismuth tellurite glasses," *Chemical Papers*, vol. 78, no. 10, pp. 5773–5791, 2024.

[23] A. Aşkın, M. Sayyed, A. Sharma, M. Dal, R. El-Mallawany, and M. Kaçal, "Investigation ofthe gamma ray shielding parameters of $(100 - x)[0.5\,Li_2O - 0.1\,B_2O_3 - 0.4\,P_2O_5] - x\,TeO_2$ glasses using Geant4 and FLUKA codes," *Journal of Non-Crystalline Solids*, vol. 521, p. 119489, 2019.

[24] H. M. Zakaly, S. A. Issa, H. Saudi, and T. Soliman, "Decoding the role of bismuth oxide in advancing structural, thermal, and nuclear properties of $[B_2O_3 - Li_2O - SiO_2] - Nb_2O_5$ glass systems," *Radiation Physics and Chemistry*, vol. 223, p. 111984, 2024.

This page intentionally left blank.

Ongoing validation of the High Granularity Timing Detector (HGTD) demonstrator for the ATLAS phase II upgrades

Thabo James Lepota[1], **Rachid Mazini**[1] **and Mukesh Kumar**[1]

[1]School of Physics and Institute for Collider Particle Physics, University of the Witwatersrand, Johannesburg, 2050, South Africa

E-mail: 568571@students.wits.ac.za

Abstract. The High Granularity Timing Detector (HGTD) demonstrator was developed to validate the design and performance of its components. The setup included a printed circuit board (PEB), 54 modules, flex tails, a cooling system, and a data acquisition (DAQ) server. Tasks performed involved connecting flex tails, conducting alignment and Inter-Integrated Circuit (I2C) tests, and performing scanning tests to check bump connections. Threshold voltage (Vth) scans were conducted with High Voltage (HV) off at different injected charge values to verify electrical contact between readout electronics and the sensor. Module tuning and charge scans were performed by analysing the Time-Over-Threshold (TOT). A comparison of Vth scans with HV both off and on was done to validate module performance. I2C test failures and high voltage issues, such as large leakage current causing modules to turn off, were identified. Furthermore, clock jitter measurements and calibration methods, mitigating pileup effects in the forward region, were intended to ensure that the detector's timing capabilities meet specifications and to identify potential issues with clock distribution or signal integrity. In parallel, work progressed on the second-generation demonstrator, incorporating a slice of the prototype vessel with final design features and an increased number of active components to further refine and validate the HGTD design and its integration aspects, such as the Faraday cage.

1 Introduction

With the ATLAS experiment undergoing phase II upgrades, a new detector called High Granularity Timing Detector (HGTD) shown in Figure 1 will be installed in the endcaps to cope with the challenge of mitigating pileup effects experienced on the High Luminosity Large Hadron Collider (HL-LHC) [1], which are the product of proton-proton collisions, they create overlapping signals that distort the reconstruction of precise event vertices. With the quick timing capabilities of the HGTD to differentiate tracks coming from closely spaced vertices by utilising their time separation.

The HGTD covers a radial range from 12 cm to 64 cm and geometrically, it occupies a psuedorapidity range of $(2.4 < \eta < 4.0)$. Low Gain Avalanche Detectors (LGADs) with small pixel size of 1.3×1.3 mm^2 to reach good time resolution of approximately 30 ps per track. The design makes sure there is high radiation tolerance up to fluences of 3.7×10^{15} neq/cm^2, doses of 4.1 MGy, depending on the radial distance, an average hit count of 2 to 3 per track and low occupancy below 10%, which is suitable for the harsh environment of the HL-LHC [2].

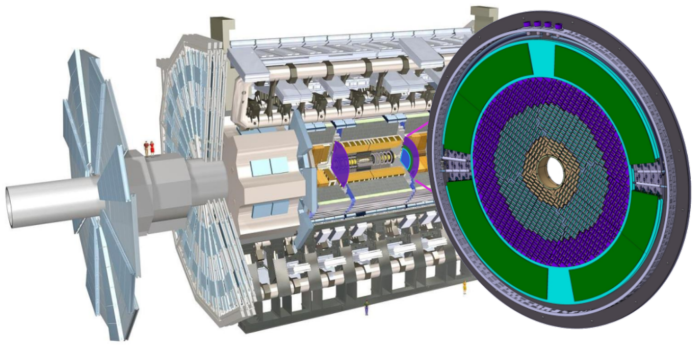

Figure 1: Schematic of the major upgrades to the ATLAS detector for the HL-LHC era, with HGTD location shown [3].

1.1 Physics motivation

There is more role played by the HGTD which extends beyond pileup suppression. It significantly enhances the identification of Higgs boson signal and improves measurements sensitive to the weak mixing angle, particularly in forward and cental-forward electron channels. The timing information enables precise luminosity measurements. This measurements which have a linear relation between pileup density and the number of HGTD hits shown in Figure 2, are important for accurate Higgs boson studies.

1.1.1 Pileup challenge at HL-LHC: At the HL-LHC, pileup from simultaneous proton-proton interactions causes a huge challenge for event reconstrution and particle identification. Regardless of the collisions occurring in close proximity, there is a separation in time leading to noisy conditions. The HGTD aims to use precise timing to classify signals belonging to the primary collision vertex from pileup background, thereby completely limiting pileup contamination.

1.1.2 Impact of HGTD: The HGTD's timing information, with resolution of $\sim$30 ps, allows separating electrons from pileup jets associated with timing differences, forward electron identification is enhanced. In forward regions with high pileup, theres an improved precision in measurements of the weak mixing angle, a important electroweak parameter. Sensitivity gains in Drell–Yan processes of approximately 13% in Central–Forward and 25% in Forward–Forward lepton pair production channels. Increased electron purity enables higher precision electroweak physics [2].

1.1.3 Luminosity measurement: For Higgs boson physics, a precision luminosity measurements ($\sim$1%) is important. The HL-LHC campaign demands HGTD's high granularity results in low occupancy and linear hit rate response, facilitating bunch-by-bunch luminosity estimation using fast readout [2].

2 Overview of the HGTD demonstrator

The HGTD demonstrator serves as a testbed to validate the design, performance, and integration of HGTD components before final installation. The demonstrator aims to evaluate key parameters including whether the required sensor timing resolution of ($\sim$30 ps) can be achieved, along with radiation hardness, thermal performance, and mechanical and electrical integration.

2.1 Demonstrator components and setup

An overview of the demonstrator setup is shown in Figure 3. The role of key components is described below:

1. LGAD sensor modules: 54 modules assembled with readout Application Specific Integrated Circuit (ASIC)s.
2. Power Supply: High Voltage (HV) applied to fully deplete sensors; Low Voltage (LV) powers front-end electronics.
3. Peripheral Electronic Board (PEB): Distributes power, monitors environmental conditions (temperature and humidity), and interfaces with the data acquisition (DAQ) system [5].

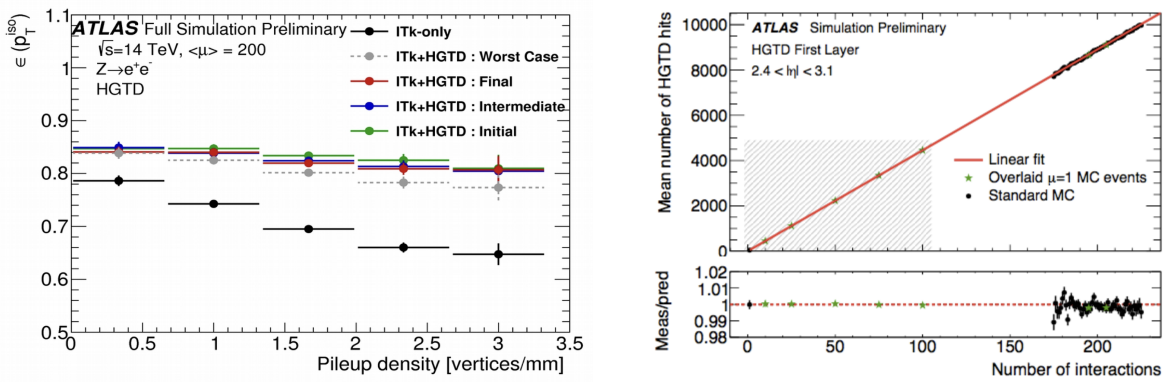

Figure 2: (*left*) Electron isolation efficiency as a function of pileup density (μ). Without timing, the Inner Trackers (ITk)s efficiency deteriorate significantly at high μ. Whereas the ITk and HGTD system maintains performance, especially with sharper timing resolution. The increasing distance between curves points out the HGTD's important role in suppressing pileup-induced fake hits. (*right*) Linearity between number of hits as a function of average number of interactions per bunch crossing (pileup) [4].

4. Flex tails: For signal and power routing to and from the detector modules.
5. CO_2 cooling system: Maintains thermal stability under realistic power loads.
6. DAQ server: Controls synchronised data acquisition through the Front-End Link eXchange(FELIX) readout system operating at 1.28 Gbps to handle the high data rates expected during physics runs.[6].

These components form the integrated test setup representing key aspects of the final HGTD system design.

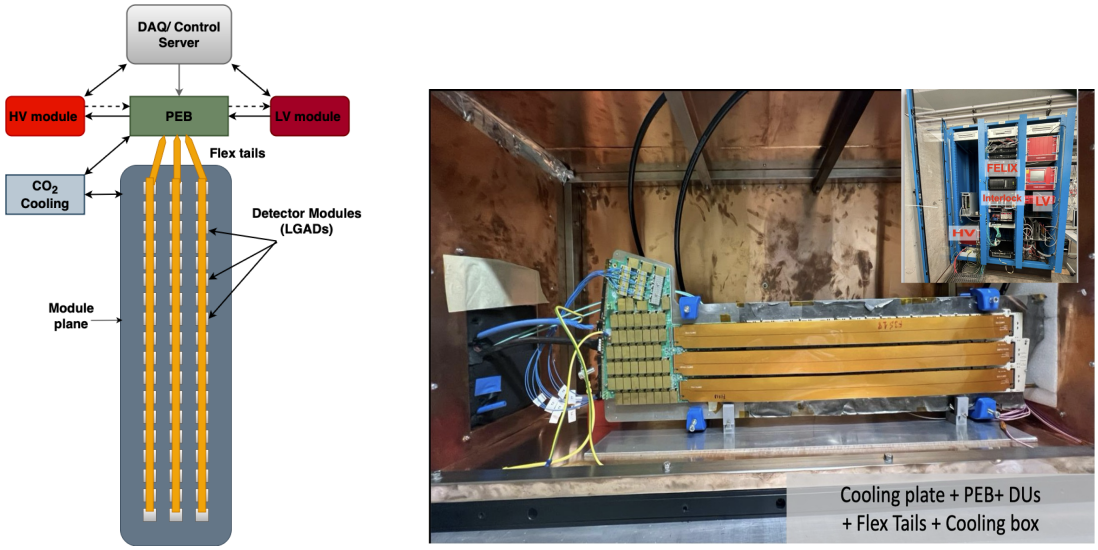

Figure 3: (*left*) Schematic of the HGTD demonstrator. (*right*) The actual demonstrator and its components located at CERN [7].

3 Validation and test results

3.1 Initial tests and alignment

Alignment tests: All IpGBT (Low-Power Gigabit Transceiver) links were required to be correctly aligned before data taking [8]. This was achieved by disabling equalisation and enabling pre-emphasis on the transceivers using

a preparatory Python script. Most channels aligned successfully, though a few required power cycling and re-initialisation. Inter-Integrated Circuit (I2C) communication: The I2C test phase verified communication between the PEB and the detector modules by writing and reading back register values. While most modules responded correctly, a small subset ($\sim$8%) failed these checks. Failure analysis identified the root causes as broken wire bonds on the readout ASICs and, in a few cases, physical damage to the flexible printed circuits. As a result, the faulty modules were replaced from a qualified spare batch. For future production, we have implemented enhanced electrical screening and visual inspection steps prior to module integration to intercept these failure modes earlier.

3.2 Threshold scan analysis

Threshold scans are a critical diagnostic and quality assurance tool used during the assembly and validation of the HGTD modules. These scans help verify electrical connectivity, bump-bond integrity which refers to the reliability and quality of the electrical connections between a silicon sensor and its ASIC, and sensor performance at an early stage. Sigmoid (S)-curves are used to ensure all pixels respond uniformly to injected charges, identify faulty bump bonds or sensor defects and calibrate thresholds for optimal detector performance.

Threshold scans were performed with the sensor bias both ON and OFF to evaluate bump bonding and charge collection efficiency. With HV off, electronic response was measured for charges of 12 and 36 Digital-to-Analogue Charge (DAC) units to establish baseline noise and threshold behaviour. This was done to verify good electrical connectivity between the HGTD module's readout electronics and the LGAD sensor. With HV applied, full sensor depletion enabled improved charge collection, as evident from shifts in discriminator thresholds. The difference between on and off scans highlighted disconnected or weak bumps that degrade detector efficiency. The charge collection efficiency when HV is OFF diffuses slowly with lower signal-to-noise, this behaviour is deduced from S-curves and when HV is ON, charge collection is accelerated by electric field, S-curves have a sharper transition, confirming good operation. Representative examples of the type of data acquired from single-module tests are shown in Figure 4. The S-curve response (Figure 4 *Top left*) and threshold distribution (Figure 4 *Top right*) illustrate the characteristic behaviour and uniformity expected from a well-performing module. The accompanying threshold map (Figure 4 *Bottom*) is included for illustrative purposes, demonstrating the type of analysis used to identify bump-bonding defects. It is important to emphasise that the results in Figure 4 originate from earlier single-module tests and are presented here as qualitative examples of the methodology; they are not the quantitative findings from the integrated demonstrator.

3.3 System cooling and temperature monitoring

The CO_2 cooling system is designed to maintain the HGTD modules at their nominal operational temperature of approximately -30°C, ensuring stable performance and minimising thermal noise in the LGAD sensors. Preliminary temperature measurements on both the PEB and the mounted modules indicate that the system is effectively achieving the required cooling targets, confirming good thermal coupling between the cooling loops and the detector assembly. During initial tests, temperature gradients across the PEB and modules were within acceptable limits, suggesting uniform heat extraction and no significant localised hot spots. However, further validation is ongoing under full operational load conditions to characterise the steady-state temperature profile, assess thermal stability over extended operation periods, and verify the correlation between the thermal sensors and the detector readout. These measurements are critical for confirming that the demonstrator cooling performance scales appropriately with the expected power dissipation in the final HGTD configuration and to ensure reliable operation in the high-radiation, high-rate environment of the HL-LHC.

4 Test beam activities

A preliminary test beam study was conducted to evaluate the performance of the HGTD demonstrator using the full readout chain. Three modules were connected through long flex tails to the PEB and operated at 1280 Mbps positions, interfacing with FELIX readout. Alignment and lpGBT configuration were successful; however, communication with the ATLAS LGAD Timing Integrated Read-Out Chip (ALTIROC) readout chip proved unstable, leading to frequent errors. These tests highlighted key integration challenges in the full DAQ chain and emphasised the need for further debugging and optimisation of the control firmware and interface configuration for future beam campaigns.

5 Summary and outlook

The HGTD demonstrator has reached a major integration milestone, enabling remote operation of all systems through the DCS and an automated DAQ. Key validation steps, such as lpGBT alignment, I2C communication, threshold scans, and thermal cooling to -30°C, have been successfully completed. These tests confirm the setup's electrical and thermal integrity. Initial test beams revealed ALTIROC communication instabilities, but provided critical data for firmware optimisation.

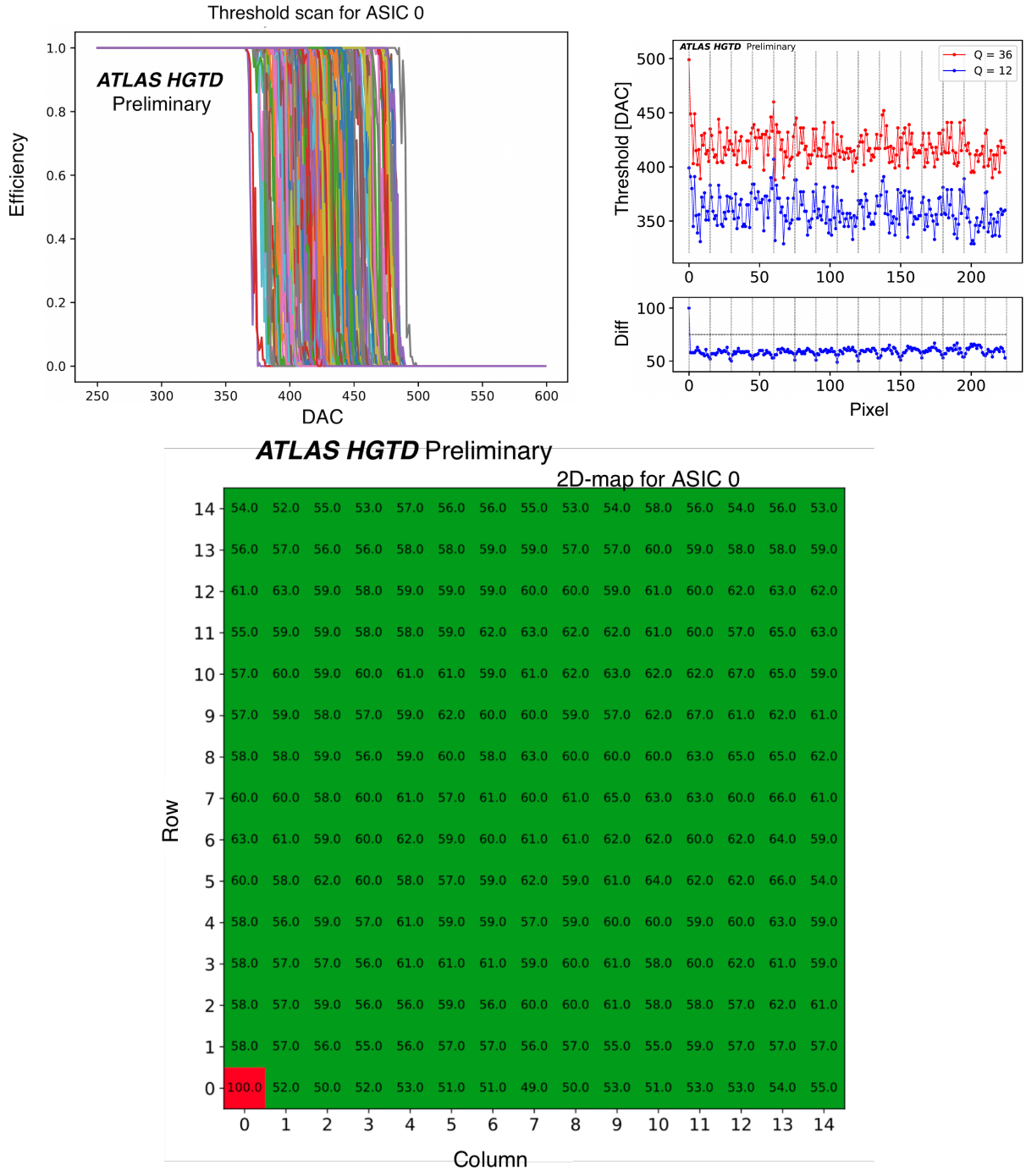

Figure 4: Illustrative plots from single-module tests: (*Top left*)) Pixel response (S-curve) for injected charges of Q=12 and Q=36, showing the characteristic sigmoidal shape. (*Top right*)) Distribution of pixel threshold values, indicating uniform performance across the module. (*Bottom*) Threshold two dimensional (2D) maps for ASIC 0 showing consistent bump-bond connectivity with few isolated outliers. The (0,0) pixel is left by design to allow other studies [9].

Looking forward, the system is prepared for upcoming beam tests to measure timing resolution and charge collection efficiency. Development of a second-generation demonstrator, featuring a Faraday cage and more active components, is already underway. These steps ensure continuous progress toward the final HGTD qualification for

the ATLAS Phase-II upgrade.

References

[1] ATLAS Collaboration, "Technical Design Report for the ATLAS Phase-II Upgrade," CERN, Tech. Rep. LHCC-P-012, 2017. [Online]. Available: https://cds.cern.ch/record/2285584

[2] ATLAS Collaboration, "Technical design report: A high-granularity timing detector for the atlas phase-ii upgrade," CERN, Tech. Rep. ATL-PHYS-PUB-2018-037, 2018. [Online]. Available: https://cds.cern.ch/record/2623663

[3] R. M. Bianchi and A. Collaboration, "ATLAS experiment schematic or layout illustration," 2022, general Photo. [Online]. Available: https://cds.cern.ch/record/2837191

[4] ATLAS Collaboration, "Technical design report: A high-granularity timing detector for the atlas phase-ii upgrade," CERN, Tech. Rep. CERN-LHCC-2020-007, ATLAS-TDR-031, 2020. [Online]. Available: https://cds.cern.ch/record/2719855

[5] L. Han, L. Zhang, J. Zhang, S. Chen, M. Qi, and Z. Liang, "Demonstration system of the hgtd peripheral electronics boards for atlas phase ii upgrade," *Nuclear Instruments and Methods in Physics Research Section A: Accelerators, Spectrometers, Detectors and Associated Equipment*, vol. 1045, p. 167651, 2023. [Online]. Available: https://www.sciencedirect.com/science/article/pii/S0168900222009433

[6] Y. Bimgdi, "DAQ Activities of HGTD," 2023. [Online]. Available: https://cds.cern.ch/record/2879970

[7] A. Hoecker, "ATLAS Phase II Upgrades: HGTD, LAr electronics, TDAQ," 2025, general Photo. [Online]. Available: https://cds.cern.ch/record/2929118

[8] D. Hernandez Montesinos, S. Baron, S. Biereigel, P. Hazell, S. Kulis, P. Vicente Leitao, P. Moreira, D. Porret, and K. Wyllie, "Overview of the production and qualification tests of the lpgbt," vol. 19, no. 04, p. C04048, apr 2024. [Online]. Available: https://dx.doi.org/10.1088/1748-0221/19/04/C04048

[9] "HGTD Public Plots on ATLAS TWiki," https://twiki.cern.ch/twiki/bin/view/AtlasPublic/HGTDPublicPlots, ATLAS Collaboration, 2025, [Online; accessed 19-August-2025]. [Online]. Available: https://twiki.cern.ch/twiki/bin/view/AtlasPublic/HGTDPublicPlots

Particle Flow Algorithm (PFA) for forward region jet reconstruction with the ATLAS Inner Tracker (ITk) detector setup at the High Luminosity Large Hadron Collider (HL-LHC)

Thabo James Lepota[1], **Rachid Mazini**[1] **and Mukesh Kumar**[1]

[1]School of Physics and Institute for Collider Particle Physics, University of the Witwatersrand, Johannesburg, 2050, South Africa

E-mail: 568571@students.wits.ac.za

Abstract. The ATLAS experiment at the High Luminosity Large Hadron Collider (HL-LHC) will require advanced reconstruction techniques, particularly in the forward region, to cope with increased pileup. This work presents a Particle Flow Algorithm (PFA) development for the ITk detector, focusing on tower clusters rather than traditional topological clusters in the ($0 \leqslant \eta < 2$) region. The forward region indicates ($\eta > 2.5$). The strategy integrates tracker momentum measurements with calorimeter energy deposits through cell-based subtraction, prioritising energy density layers to resolve overlaps between tracking and calorimetric data. By employing TopoTowers, which aggregate calorimeter cells into fixed $\eta - \phi$ grids, we aim to improve spatial granularity critical for forward jet reconstruction. The framework processes Event Summary Data (ESD), containing raw detector level information (tracker hits, calorimeter clusters), and is processed into Analysis Object Data (AOD), a condensed format storing high level physics objects (jets, leptons) optimised for analysis. The study refines energy subtraction and calibration by implementing Gaussian fitting of $\langle E/p \rangle$ distributions across calorimeter layers. This approach addresses the high pileup HL-LHC environment, balancing precision in jet energy resolution with computational scalability for the ITk detector's upgraded granularity.

1 Introduction

The High Luminosity Large Hadron Collider (HL-LHC) will operate at an unprecedented instantaneous luminosity, leading to an average of $\mu = 200$ simultaneous proton-proton collisions per bunch crossing (pileup) [3]. This extreme environment poses significant challenges for particle reconstruction, particularly in the forward region ($\mid \eta \mid > 2.5$, where η represents pseudorapidity, a dimensionless quantity related to the polar angle θ relative to the beam axis, defined as $\eta = -ln[tan(\theta/2)]$, and where the calorimeter granularity is coarser and tracking information is traditionally limited. The ATLAS Phase II upgrades aim to address these challenges by introducing the Inner Tracker (ITk) detector shown in Figure 1, which extends tracking coverage up to ($\mid \eta \mid \approx 4$), and the High Granularity Timing Detector (HGTD), which provides $\sim$30 ps timing resolution to help distinguish between primary and pileup vertices [4]. The Particle Flow Algorithm (PFA) has demonstrated significant improvements in jet and missing transverse energy (MET) reconstruction in the central detector region by combining tracking and calorimeter information [5]. However, its application in the forward region has been limited. With the improved capabilities of the ITk and HGTD, we propose an adapted PFA strategy that uses a mixed input of TopoClusters ($\mid \eta \mid < 2$) with TopoTowers fixed size $\eta - \phi$ calorimeter towers in the to better match the forward detector geometry.

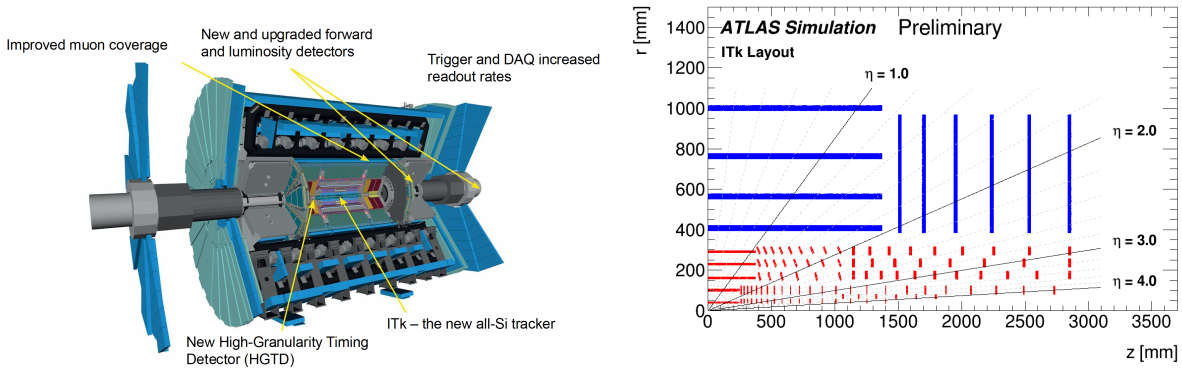

Figure 1: (*left*) Schematic of the important upgrades to the ATLAS detector for the HL-LHC era, showing the location of ITk detector [1]. (*right*) Schematic showing of the ITk layout for the HL-LHC phase of ATLAS. A zoomed view of pixel detector showing only one quadrant which is an active detector. Shown in blue are active elements of the strip detector and red shows the pixel detector. The horizontal axis lies along beam line with zero being the interaction point. The vertical axis is the radius measured from the interaction region [2].

TopoTowers do not replace calorimeter cells but subdivide the real granularity into smaller elements to work with. This modification is expected to improve energy resolution and reduce algorithmic complexity in high pileup environments, ultimately improving physics performance in forward jet dominated processes such as vector Boson Fusion (VBF) and high energy Quantum Chromodynamics (QCD) studies [2]. Figure 2 shows how the PFA works, the key features includes data integration whereby it uses both calorimeter systems and tracking to optimise object reconstruction. Track–cluster matching is performed to link charged particle tracks with calorimeter deposits. The energy-over-momentum ratio (E/p) is then computed to ensure that the calorimeter energy linked to charged tracks is accurately subtracted, thereby avoiding double counting. In addition, a split-shower correction is applied, which allows more than one cluster to be matched to a single track, accounting for hadronic showers that extend across multiple clusters and preventing E/p underestimation or misreconstruction [6].

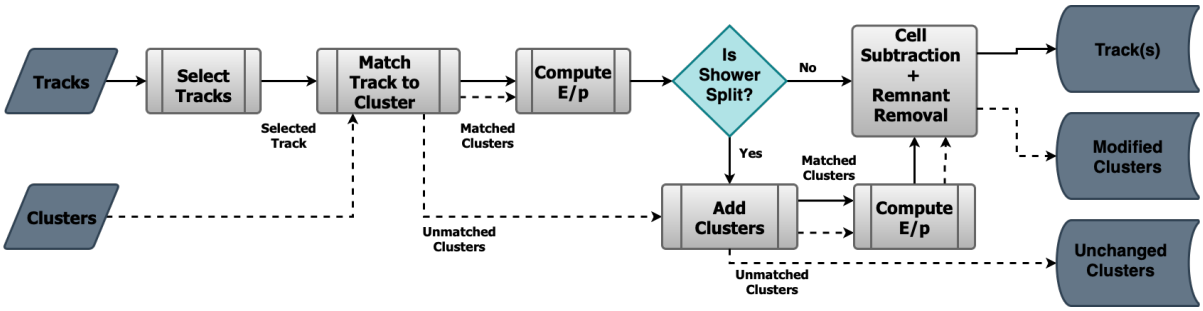

Figure 2: Flowchart of the track–cluster matching procedure in the PFA. Beginning with track selection and proceeding until the energy linked with the selected tracks has been removed from the calorimeter. At the end, charged particles, charged particles, unmodified TopoClusters/TopoTowers, and remnants of which have not been modified by the algorithm, and remnants of TopoClusters/TopoTowers with partial energy removal remain.

2 Methodology

Detector and data samples: TopoClusters and TopoTowers are two calorimeter clustering techniques used in this study to optimise jet reconstruction across different detector regions [7]. TopoClusters are dynamic, fine-grained 3D clusters formed from calorimeter cells based on signal significance and spatial connectivity, optimised for isolated particle reconstruction in central regions ($\mid \eta \mid < 2.5$). In contrast, TopoTowers subdivide calorimeter cells into fixed size (0.1×0.1 in $\eta - \phi$) designed for computational efficiency and noise suppression in the coarser, high pileup forward calorimeter regions ($\mid \eta \mid > 2.5$). These clusters form a mixed list used in the particle flow algorithm with no cell overlap between central TopoClusters and forward TopoTowers. Since roughly two-thirds

of visible jet energy is carried by charged pions, the algorithm assumes charged pions for track candidates and calibrates energy subtraction by measuring the ratio of calorimeter energy to track momentum E/p.
Reconstruction data flow from Event Summary Data (ESD), containing full detector-level details, to Analysis Object Data (AOD), where physics optimised objects are stored. TopoTowers are incorporated explicitly in the forward η regions as shown in Figure 3, which shows the PFA logic used in this study. It is important to note that Figure 3 represents the same PFA code but with charged calorimeter shower subtraction disabled to study energy deposits and facilitate calibration.

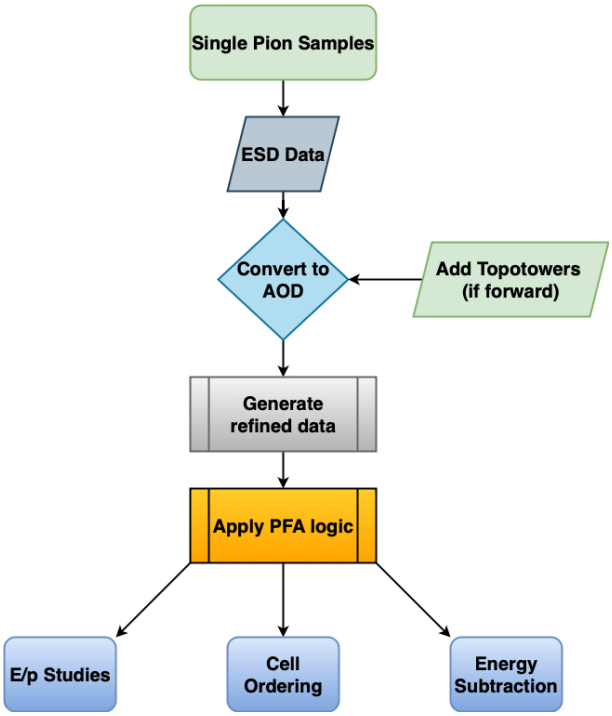

Figure 3: Framework workflow for the PFA analysis in the ATLAS forward region. The process begins with single pion samples which are processed as ESD data. This data is then converted to AOD format, where TopoTowers are added for forward region reconstruction. Refined data are generated and the PFA logic is applied, building up to in three key analysis outputs: E/p Studies, Cell Ordering, and Energy Subtraction.

PFA adaptation for forward region: The PFA code is run with its standard charged shower subtraction disabled. Instead, the algorithm uses the measured E/p and energy density profiles to perform a more granular, cell-based subtraction.

E/p Measurement approach: The E/p ratio, defined as calorimeter energy (E) within a $\Delta R < 0.2$ cone around a charged track normalised by track momentum (p), is used to measure the response for energy subtraction. Binning depends on: Track pseudorapidity, η in fine bins up to 4.0, p in bins from 0 to 100 GeV, and the calorimeter layer (the first electromagnetic barrel layer, EME1). Gaussian fits and histogram mode analyses of E/p distributions provide mean and resolution estimates for calibration. To calibrate the E_{track}/p distributions, a fitting strategy is used, which involves using Gaussian fits within the predefined bin, where the fit range is set to surround the data between the mean plus or minus the root mean square (RMS) of the distribution. This provides a mean relevant for most pions, excluding skewed outliers. To ensure reliability, the fit results undergo validation: if the absolute difference between the histogram mean and the Gaussian fit mean exceeds 0.1, an alternative metric is used for the calibration constant specifically, the histogram mode is selected if it is greater than 0.1; otherwise, the histogram mean is adopted. Fit quality is assessed using the chi squared per degree of freedom (χ^2/NDF), with acceptable thresholds set at less than 2.0 for central detector regions and less than 3.0 for the forward region, reflecting the different detector resolutions and granularities. Complementing this, energy density profiling is performed to guide shower subtraction by calculating the average energy density per concentric ring around the track axis, where each ring corresponds to a fixed $\Delta\eta \times \Delta\phi$ area of 0.05×0.05. We fit these profiles and store the fit parameters such that the particle flow algorithm can reproduce the energy density cell ordering at runtime. The subtraction algorithm

prioritises cells with the highest energy density first, ensuring that the core energy deposits belonging to charged particles are removed before peripheral and potentially pileup contaminated cells.

Cell ordering and energy subtraction strategy: Energy subtraction is implemented cell by cell with priority given to cells of highest energy density within coaxial rings defined in $\eta - \phi$ space around the track. This ensures correct subtraction of core shower energy before peripheral deposits, particularly important in coarse forward calorimeters.

3 Results

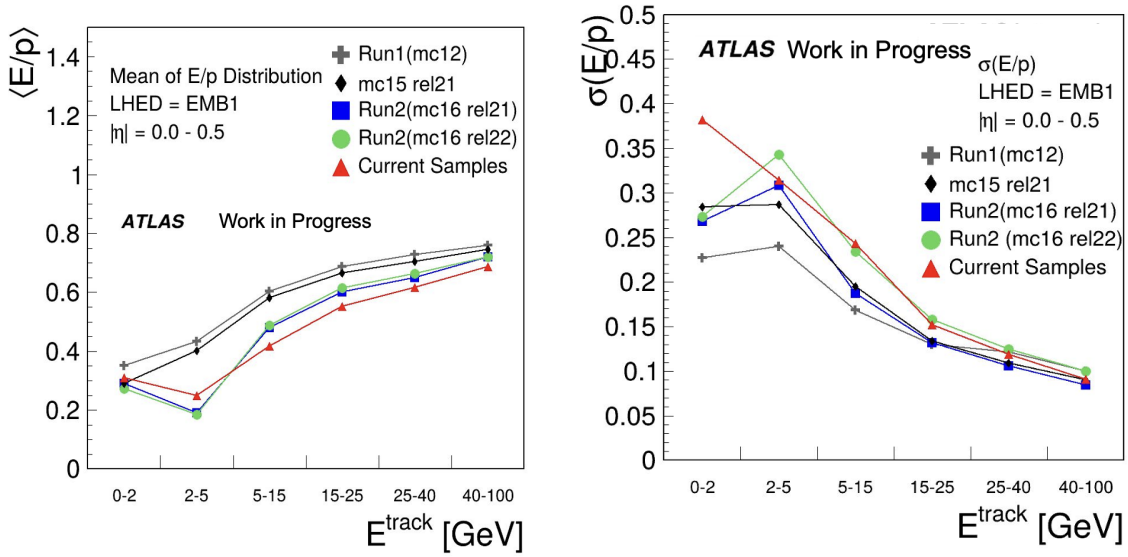

Figure 4: Central region results (LHED = EMB1) for $0 \leqslant |\ \eta\ | < 0.5$, showing (*left*) the mean E/p ratio rising and plateauing with increasing E_{track}. (*right*) the resolution $\sigma(E/p)$ improving with E_{track}. Data from Run 1, Run 2, and current MC samples are overlaid for comparison and validation of the particle flow calibration.

Central region validation: Figure 4 presents key central region results for the first electromagnetic barrel calorimeter layer (EMB1) within the pseudorapidity interval $0 \leqslant |\ \eta\ | < 0.5$. The left panel displays the mean E/p ratio, defined as the calorimeter energy measured in a cone of $\Delta R < 0.2$ around a charged particle track normalised by the track momentum (E_{track}). As observed, the mean E/p increases with rising track transverse momentum, reaching a plateau between roughly 0.6 and 0.7 at higher momenta (above $\sim$15 GeV). This behaviour reflects the calorimeter's intrinsic response to charged hadrons and accounts for energy losses in upstream material, validating the PFA's calibration approach in the central detector region. The right panel shows the resolution $\sigma(E/p)$, characterised by the standard deviation of the E/p distribution, which improves significantly with increasing E_{track}. At low transverse momenta (below 5 GeV), the resolution is comparatively poor (around 0.4–0.5), due to larger fluctuations in shower development and threshold effects. As E_{track} increases, the resolution stabilises to values between approximately 0.15 and 0.3, indicative of better shower containment and detector response consistency. Overlaid data from Run 1, Run 2, and current MC samples exhibit close agreement, demonstrating robust detector performance and effective calibration of the PFA across multiple data taking periods. Figure 5 shows histograms of E/p distributions for charged tracks in different transverse momentum bins, with Gaussian fits applied over mean $\pm$ RMS. Fit parameters (mean, standard deviation, error) and quality (χ^2/NDF) are indicated. At low momenta (0–2 GeV), the Gaussian mean is around 0.3–0.4, reflecting energy loss and partial shower containment, increasing to about 0.6–0.7 at higher momenta, consistent with calorimeter response. Fit quality is generally good ($\chi^2/\text{NDF} < 2$), supporting the fit's robustness. In some low-momentum bins, discrepancies between Gaussian and histogram statistics trigger a validation step employing alternative metrics to ensure reliable calibration.

Cell ordering: The cell ordering plots shown in Figure 6 analyse the average energy density distribution in the ATLAS EMB1 (the first electromagnetic barrel layer) calorimeter around charged particle tracks with $0 < |\eta_{\text{track}}| < 0.5$ and $5\,\text{GeV} < E_{\text{track}} < 15\,\text{GeV}$. By grouping calorimeter cells into concentric rings in η-ϕ space, the dependence of energy deposition on radial distance from the track axis is investigated. For a

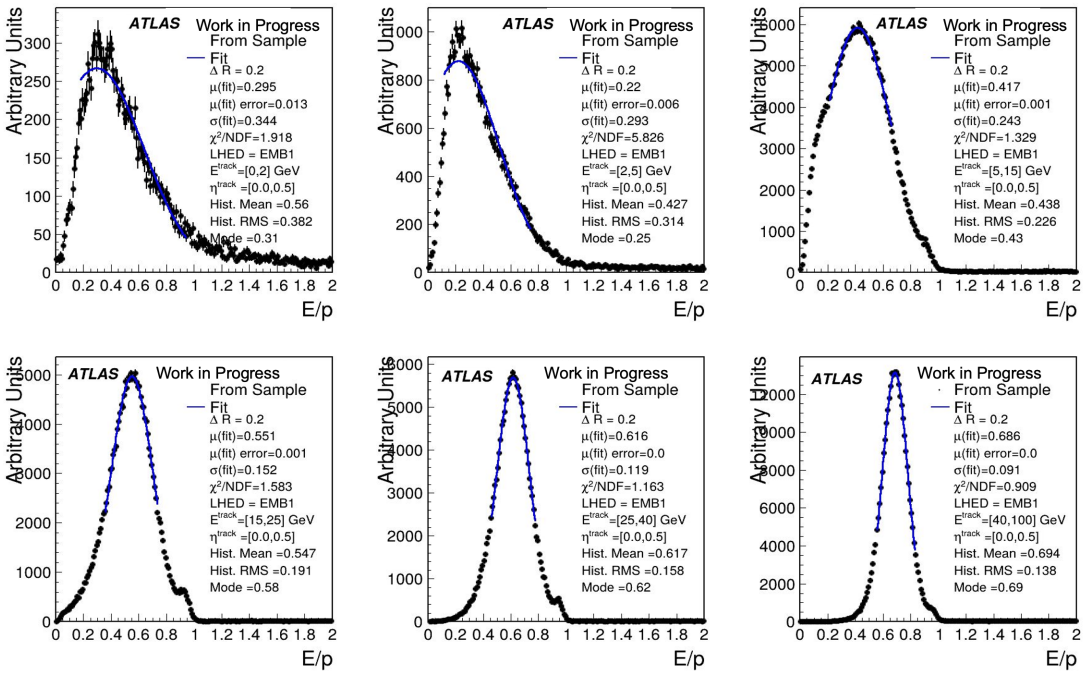

Figure 5: shows fits of Gaussian functions to the E/p distributions in several momentum bins for the EMB1 layer in the central region ($0 <| \eta_{track} |< 0.5$).

fixed ring number of 1, the energy density distribution shows a broad spread (RMS = 0.635) with a mean of $\log_{10}(\langle E_{\text{density}} \rangle) = -1.44$, while at a larger ring number of 10, the distribution narrows (RMS = 0.45) with a lower mean of -1.72, consistent with the expected shower profile. As you vary the ring number there is a steep decline in energy density from $\sim 10^{-0.2}$ to $10^{-1.6}$ as the ring number increases, well described by a two component fit.

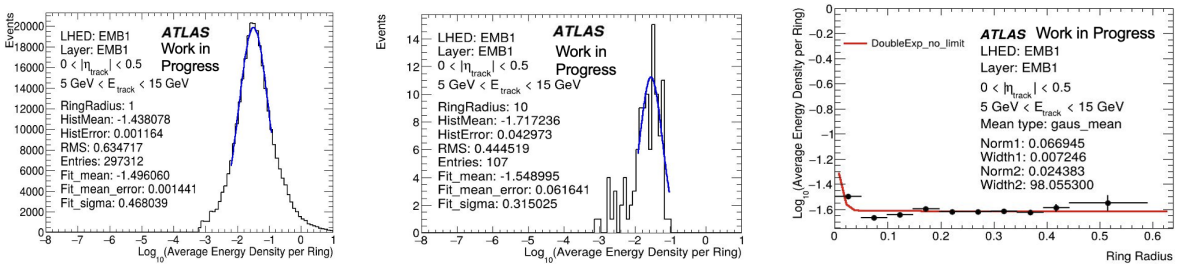

Figure 6: Distribution of average energy density per ring in the ATLAS EMB1 calorimeter for charged particle tracks with $0 <| \eta_{track} |< 0.5$ and 5 GeV$| \eta_{track} |<$15 GeV. (*left*) Energy density profile for a fixed ring radius of 1, showing a broad distribution with fit results overlaid. (*middle*) Distribution for a larger ring radius of 10, exhibiting a narrower spread. (*right*) Dependence of energy density on ring radius, fitted with a two component model. Larger radii sample the sparse, homogeneous lateral shower distribution, while smaller radii capture the dense shower core.

Forward region: The performance of the forward region is characterised using distributions shown in Figure 7. Figure 7 (*left*) shows a consistent response with mean $E/p = 0.54$) across η regions with 7790 forward entries, and a slight η–dependence with mean $\eta = -0.015$ The energy density profiles with 114223 simulated events showing an asymmetric distribution with mean of 0.196 ± 0.41 GeV/mm^2, where most deposits cluster at low energy while maintaining a significant high density tail (see Figure 7 (*middle*)). Figure 7 (*right*) maps the Layer with Highest Energy Deposits (LHED) across the forward calorimeter layers.

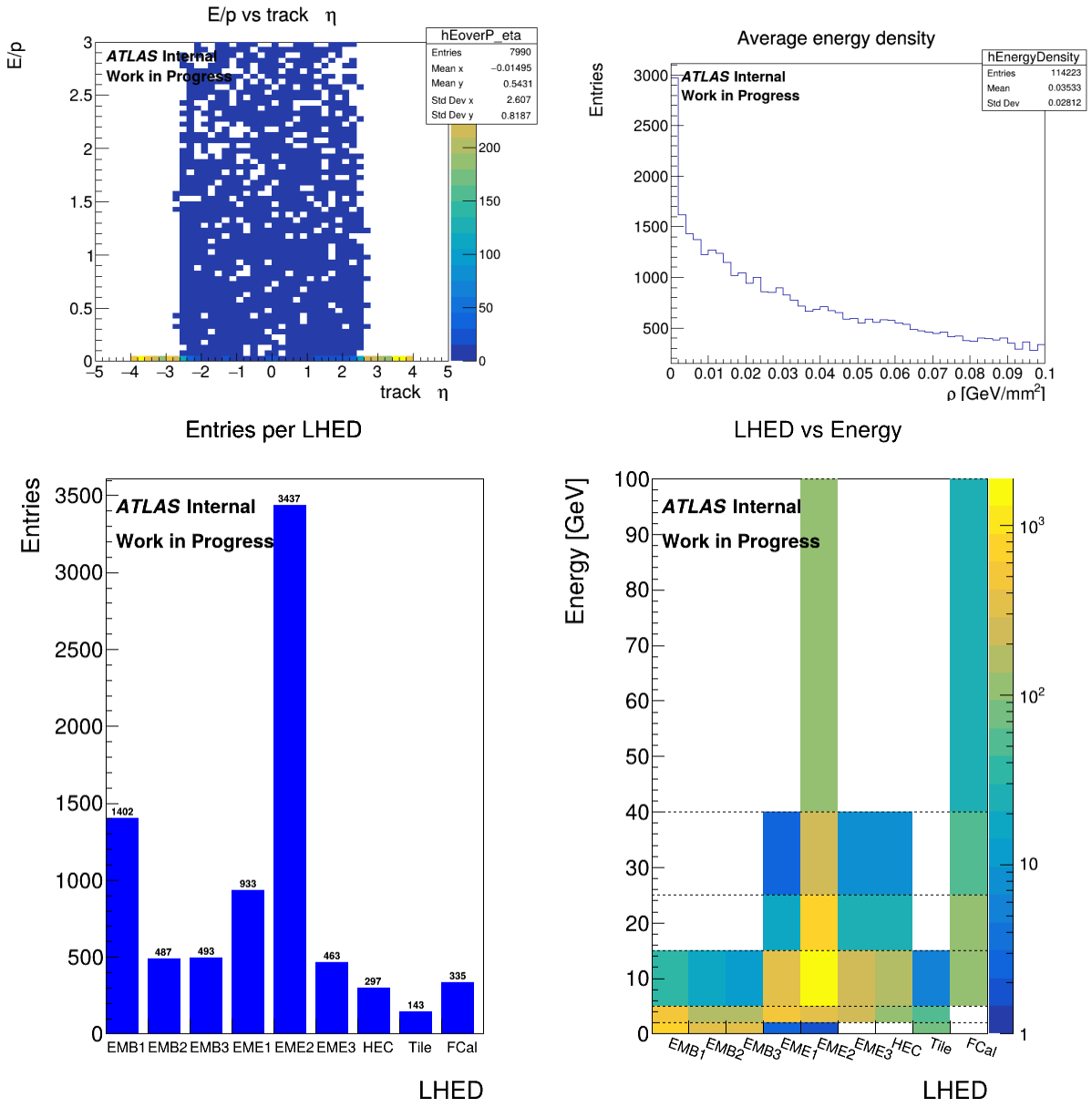

Figure 7: E/p distributions for the forward region ($|\ \eta\ | > 2$). (*top left*) E/p as function η, with entries extended to 4, shows an average E/p of 0.54 with η-dependence across detector regions. (*top right*) Energy density distribution in forward calorimeter cells shows the asymmetric profile shows mainly low energy deposits with mean 0.19 GeV/mm^2) with a high energy tail. (*bottom left*) Distribution of Layer of Highest Energy Deposits (LHED) across forward calorimeter cells with entries showing that there is a presence of entries in the forward region. (*bottom right*) The mapping shows energy deposit patterns throughout the barrel electromagnetic calorimeter.

4 Summary and Outlook

Figures and references demonstrate the impact of coarse granularity: TopoTowers replacing spatial resolution for pileup robustness and computational simplicity, but calibration must compensate for the loss of detail. Detector layout and timing diagrams illustrate how ITk and HGTD create the first opportunity for forward region PFA by extending high precision tracking and timing into areas previously uninstrumented for such analyses. The PFA workflow in the forward region is now at an advanced stage: TopoTower clustering and PFA adaptation (cell/tower energy subtraction and E/p binning) are complete, and preliminary E/p distributions and energy density profiles show stable, expected behaviour in the absence of pileup. Validation of the implemented methods using realis-

tic physics samples (with jets and $Z \rightarrow ee$ samples), as well as ongoing tuning of E/p calibration and tower subtraction, are in progress. The remaining steps focus on refining subtraction parameters, broadening validation to complex event topologies, and exploring the use of machine learning for further improvement. This progress enables robust jet and MET reconstruction in the forward detector, a critical advancement for ATLAS operation at the HL-LHC.

References

[1] R. M. Bianchi and ATLAS Collaboration, "ATLAS experiment schematic or layout illustration," 2022. [Online]. Available: https://cds.cern.ch/record/2837191

[2] ATLAS Collaboration, "Expected Tracking Performance of the ATLAS Inner Tracker at the HL-LHC," CERN, Tech. Rep., 2019. [Online]. Available: https://cds.cern.ch/record/2669540

[3] ATLAS Collaboration, "Technical design report for the atlas phase-ii upgrade," CERN, Tech. Rep., 2017. [Online]. Available: https://cds.cern.ch/record/2285584

[4] ATLAS Collaboration, "Technical Design Report: A High-Granularity Timing Detector for the ATLAS Phase-II Upgrade," CERN, Tech. Rep., 2020. [Online]. Available: https://cds.cern.ch/record/2719855

[5] ATLAS Collaboration, "R=0.4 jets input comparison and monte carlo calibration with the atlas detector," CERN, Tech. Rep., 2022. [Online]. Available: https://cds.cern.ch/record/2824558

[6] ATLAS Collaboration, "Topological cell clustering in the ATLAS calorimeters and its performance in LHC Run 1," *Eur. Phys. J. C*, vol. 77, p. 490, 2017. [Online]. Available: https://cds.cern.ch/record/2138166

[7] ATLAS Collaboration, "Jet reconstruction and performance using particle flow with the atlas detector," *Eur. Phys. J. C*, vol. 77, no. 7, p. 466, 2017.

This page intentionally left blank.

Detecting Anomalies in Measured Thermal Neutron Flux Profiles of SAFARI-1 Research Reactor

Rethabile Kgolobe[1], Pavel M. Bokov[3], Simon H. Connell[2], Charis Harley[1], Bongani G. Maqabuka[2,3], Lesego E. Moloko[3], and Rian H. Prinsloo[3]

[1]Electrical and Electronic Engineering Science, University of Johannesburg, Johannesburg, South Africa

[2] Mechanical Engineering Science, University of Johannesburg, Johannesburg, South Africa

[3] The South African Nuclear Energy Corporation (Necsa), Pretoria, South Africa

E-mail: rethabilethuto3@gmail.com

Abstract. Accurate measurement, analysis, and correct interpretation of the neutron flux distribution within the reactor core are essential for safety, performance, and operational information. In SAFARI-1, the axial thermal neutron flux profiles are measured at the beginning of each operational cycle using copper wires. This study investigates changes in these profiles caused by the control rod movement, focusing on key features of the flux profile: bottom minimum, peak maximum, and top minimum, to estimate anomalies. The approach involves data preprocessing, visualization, and statistical analysis. Polynomial fits were applied to smooth the data and extract key feature points, standard deviation, mean absolute deviation, Pearson's Correlation Coefficient, and other correlation metrics to assess flux profiles' sensitivity to control bank positions. A statistical method based on the likelihood of the data compared to specific models was also used to estimate errors and determine correlations. Results demonstrated that the top minimum points remained consistent and less correlated to bank positions, confirming its suitability for estimating anomalies. This approach improves the accuracy of detecting axial shifts from incorrect wire insertion and neutron flux measurements. Hypothesis testing at a 95% confidence level validates the trend behavior tracking control rod bank positions.

1 Introduction

In nuclear reactors, such as the SAFARI-1 (South African Fundamental Atomic Research Installation-1) research reactor, accurate measurements of neutron flux distributions are crucial as they contribute to monitoring the reactor core parameters, ensuring safety, and optimum performance during reactor operations [1]. The SAFARI-1 reactor is a 20 MW pool-type Material Testing Reactor (MTR), located at Pelindaba, South Africa, and is operated by the South African Nuclear Energy Corporation SOC Ltd (Necsa). It is designed in an 8×9 core grid structure that accommodates 26 fuel, 6 follower-type control rod assemblies, and other components, which are explained in detail in [2]. The SAFARI-1 core top view, fuel and control assemblies top view with fuel plates and the copper wire insertions in the assemblies are shown in Figure 1.

In SAFARI-1, axial neutron flux profiles are measured at the beginning of each operational cycle [1]. The measurements are conducted by inserting natural copper wires along the length of each of the 32 assemblies, containing fissile material, of which 26 are fuel and 6 are control assemblies. The radioactive β decay of the ^{64}Cu with a half-life of 12.7 h, is measured at 180 points along the wire for the 32 assemblies and stored in the datasets [3]. The resulting data are used to analyze the distribution of neutron flux and power, estimate core parameters such as peak-clad temperatures, and support detection of anomalies such as fuel element misloads [1]. However, the

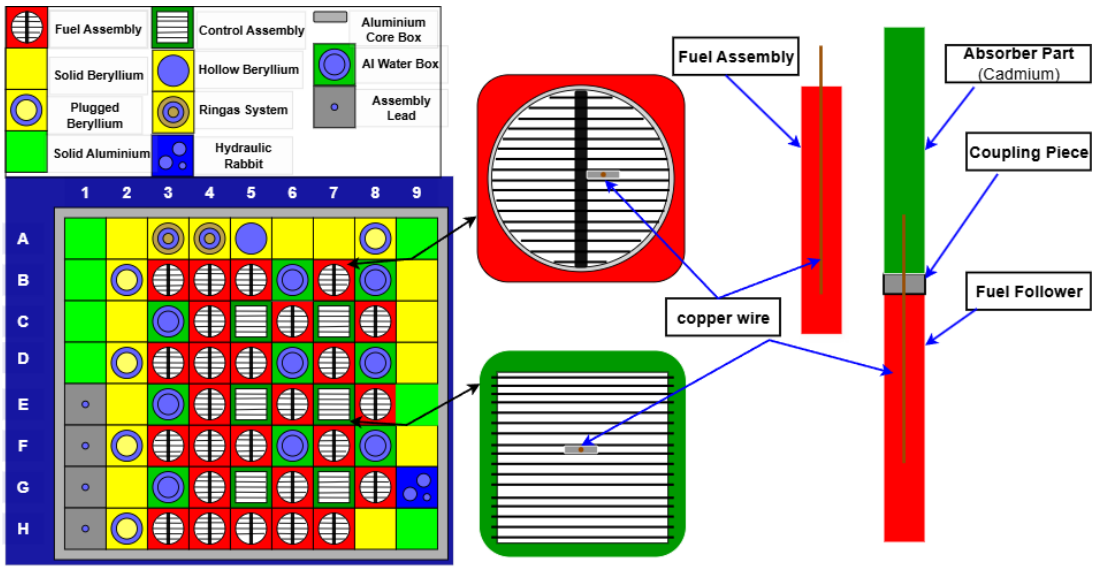

Figure 1: The SAFARI-1 core top view and fuel and control assemblies with fuel plates (left and middle) and side view (right).

accuracy and reliability of these measured neutron flux distributions depend on the accuracy of the copper wire measurement process, such as the correct insertion of the copper wire in the assemblies.

The manual insertion of the wires may result in inaccurate measurements, such as an axial shift in neutron flux, which can potentially lead to misinterpretations and wrong operational decisions. Note that in these experiments, relative activity shapes across the core are of primary concern (reactor power is quite uncertain at the low power levels during the experiment). Although techniques exist to analyze and detect axially shifted measurements of the neutron flux, mathematically-backed methods for detecting anomalies due to copper wire incorrect insertions in the SAFARI-1 research reactor would be of great value. In this study, statistical techniques are used to detect anomalies in the neutron flux measurements caused by the incorrect insertion of copper wires, focusing only on fuel assemblies. By analyzing the key features of the neutron flux profiles specifically, the bottom minimum, maximum, and top minimum (as indicated in Figure 2), the research aims to develop techniques that will detect anomalies in the neutron flux profiles caused by incorrect copper insertion in the SAFARI-1 research reactor. The

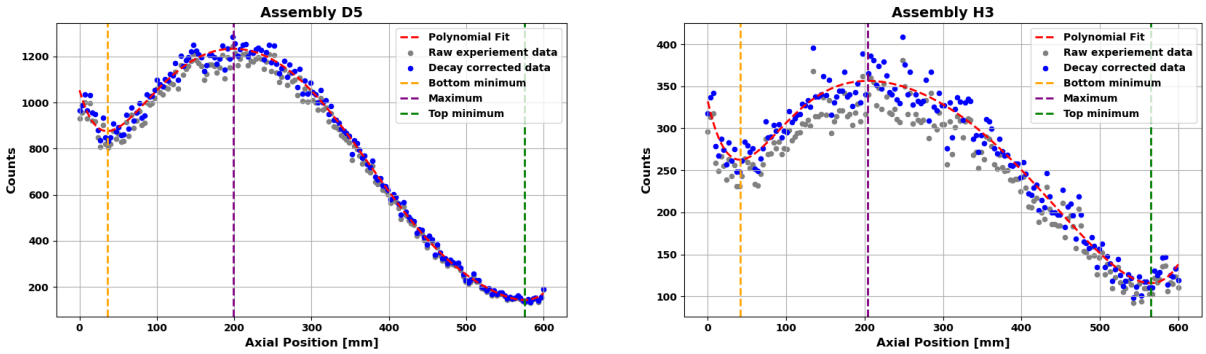

Figure 2: Experimental data, key features and decay corrected counts for assembly D5 (left) and H3 (right)

motivation of this study comes from the need to maintain accurate and reliable neutron flux measurements in the SAFARI-1 research reactor. The study's approaches are to (1) assess the stability of neutron flux key features and their relationship to the control bank positions, (2) detect anomalies of neutron flux measurements, and (3) validate the techniques used through statistical methods. To achieve these goals, the research uses polynomial fitting, statistical methods and likelihood function evaluation to obtain the errors of the key features. Hypothesis testing is

performed to evaluate trends of the observed changes and assess this in the context of the expected behavior.

2 Related Work

Statistical methods have been used to analyze and detect anomalies in the neutron flux profiles. For example, [4] employed a Bayesian statistical method found in Markov Chain Monte Carlo (MCMC) simulations to evaluate the neutron flux groups from activation data of different resulting isotopes at the Pavia University (Italy) TRIGA Mark II reactor. Their study showed promising results compared with Monte Carlo simulations of the reactor fluxes performed with the Monte Carlo N-Particle Transport (MCNP) code. Recent work has been done using statistical methods to detect anomalies in the neutron flux distribution. A recent study [5] used a combined method of anomaly detection and quantification for neutron flux data that considered delayed neutron monitoring data, significantly affecting reactor performance. Their proposed methods showed promising results and outperformed other anomaly detection methods regarding rates of false alarm, anomaly detection, and precision. Another recent study [1] focused on improving the accuracy of the neutron flux prediction in the SAFARI-1 research reactor using the statistical variance test and shift-correction procedure. The study used the t'Lam G statistical test to detect variance outliers and mean squared error (MSE) was minimized to correct flux shifts. The results demonstrated an improved magnitude and reduced the normalized root mean squared error (NRSME) for all the core positions, enhancing the accuracy of the flux prediction.

In this work, we proposed an approach to analyze key features of the neutron flux measurements (bottom minimum, maximum, and top minimum) and detect anomalies in the neutron flux profiles of the SAFARI-1 reactor. Specifically, use statistical metrics such as the standard deviation and mean absolute deviation (MAD) to assess the stability of the key feature points and their sensitivity to control bank positions using the Pearson's correlation coefficient, Spearman's rank correlation, Kendall tau correlation, and Xi correlation method.

3 Statistical Analysis

3.1 Decay Correction

In this study, to ensure accurate neutron flux measurements, a decay correction was applied to decay back the accumulated radioactive ^{64}Cu isotope during copper wire measurements. The activity of the ^{64}Cu isotope was corrected to the time at which the first data point of the first assembly was measured [6]:

$$\tilde{N} = Ne^{\lambda \Delta t}, \tag{1}$$

where N is the count measured at time t, $\tilde{N}$ is its decay-corrected value, $\lambda = 1.5160 \times 10^{-5}\ \mathrm{s}^{-1}$ is the decay constant for ^{64}Cu. In addition, the decay correction was applied for each of 180 data points along the wires to account for the radioactive decay during the measurement. Hence, for a point j of assembly i, the total time Δt was adjusted as follows:

$$\Delta t = (t_i - t_0) + j\delta t, \quad j = 1, \ldots, 180, \tag{2}$$

where j is the index of a measurement point along the wire, $\delta t = 1$ s represents the time taken to measure each data point, t_0 and t_i are the beginning of measurement times for the first assembly (wire) and assembly (wire) i, respectively.

3.2 Polynomial Fit

Decay-corrected neutron flux measurements from equation (1) were fitted using a polynomial of degree p:

$$P(x) = a_0 + a_1 x + a_2 x^2 + \ldots + a_p x^p, \tag{3}$$

where a_k are the polynomial coefficients generated by minimizing the squared error between $P(x)$ and measurements $\{(x_j, \tilde{N}_j)\}_{j=1}^{180}$ along the wire. The first derivative of the fitted polynomial, $P'(x)$, was used to determine the location of the flux profile extrema: maximum, as well as top- and bottom minima, used as key features in this study.

3.3 Variability Assessment

To assess the variability of key features found in (Eq. 3), the following equations are used:

$$\text{stdev} = \sqrt{\frac{1}{S}\sum_{s=1}^{S}(x_s - \bar{x})^2}, \quad \text{and} \quad \text{MAD} = \frac{1}{S}\sum_{s=1}^{S}|x_s - \bar{x}|, \tag{4}$$

where S represents the total number of key feature points, x_s represents the s-th key feature point at each cycle and $\bar{x}$ represents the sample mean of the key feature points [7].

3.4 Correlation Methods

The relationship between key features and control bank positions is calculated using equations in Table 1. The calculations of these correlation coefficients is to investigate which key feature is less sensitive to the movement of control rods.

Coefficient	Formula	Description
Pearson's r	$r = \frac{\sum_{i=1}^{n}(x_i - \bar{x})(y_i - \bar{y})}{\sqrt{\sum_{i=1}^{n}(x_i - \bar{x})^2 \sum_{i=1}^{n}(y_i - \bar{y})^2}}$	Measures the linear relationship between two variables [8].
Spearman's ρ	$\rho = 1 - \frac{6\sum_{i=1}^{n} d_i^2}{n(n^2-1)}$	Non-parametric test that measures the dependence between variables [8].
Kendall's τ	$\tau = 1 - \frac{\text{number of discordant pairs}}{\binom{n}{2}}$	Non-parametric test that measures the degree of association between variables [8].
Xi Correlation ξ	$\xi(X,Y) = 1 - \frac{n\sum_{i=1}^{n-1}\lvert r_{i+1} - r_i\rvert}{2\sum_{i=1}^{n} l_i(n - l_i)}$	Measure how much one variable is a function of the other [9].

Table 1: Correlation coefficients used in this study

3.5 Hypothesis Testing

To test whether the relationship between the three previously described key features and the bank positions is described by a linear function, the three key features, α, extracted from Eq. (3) and denoted as y_s^α, are fitted by the line $y^\alpha = m^\alpha x + c^\alpha$, at the bank positions x_s for cycle s and the errors σ_s^α. The key feature errors were evaluated by profiling the likelihood function of the data (using the MINOS algorithm of the Minuit package [10]). In this process, the data close to the extremum for each key feature was assumed to follow a quadratic shape (as the null hypothesis, H_0) and the chi-squared function was taken as an approximation to the negative twice log of the likelihood function. The errors for each bin of the flux profiles was scaled from its propagated Poisson value to achieve a reduced chi-squared value of one for this exercise. When evaluating the linear relationship for the three key features y_s^α as a function of bank position, the straight line was regarded as the null hypothesis and the likelihood function of the data was again taken as the chi-squared function. The errors σ_s^α had again to be scaled to achieve a reduced chi-squared value of one. The critical chi-square value χ^2_{crit} is used to reject or accept the H_0 at a 95% confidence level:

$$\chi^2_{\text{crit}} = \chi_{1-\alpha,\text{dof}}, \tag{5}$$

with $\alpha = 0.05$, H_0 is rejected if $\chi^2 > \chi^2_{\text{crit}}$ and H_0 is accepted if $\chi^2 < \chi^2_{\text{crit}}$, dof is $N - \nu$ where N is the number of cycles and ν is the number of fit parameters.

4 Results

The results of this study demonstrate a significant variation in neutron flux profiles within the SAFARI-1 research reactor, mainly due to control rod movement. However, a general trend in terms of the sensitivity of the flux shape to control the bank position and the signal-to-noise ratio may be observed when moving from assemblies in the radially central region to the periphery of the active core. The findings presented in this paper are therefore restricted to core positions D5 and H3, which can be regarded as two limiting cases, based on the arguments provided in [3]. Figure 3 shows the key features of the neutron flux profile measured at core position D5 (center of the reactor core). Table 2 provides the statistical information on these key features across cycles.

A polynomial of order eight was successfully fitted to smooth the neutron flux measurements. This approach captures the distribution of these neutron flux measurements very well, enabling the calculation of key features shown by orange, purple, and green vertical lines in Figure 2. The analysis focuses on three key features of the neutron flux profiles: bottom minimum, maximum, and top minimum. The results indicate that the maximum points have the highest variability compared to the other key features and are strongly positively correlated to control rod positions with Spearman's values of 0.5417 (including shifted measurements) and 0.5252 (excluding shifted

measurements) for D5, 0.3582 (Including shifted measurements) and 0.3894 (excluding shifted measurements) for H3. In contrast, the bottom minimum showed lower variability and weaker correlations with Spearman's values of 0.3289 (including shifted measurements) and 0.3307 (excluding shifted measurements) for D5, 0.3331 (including shifted measurements) and 0.3560 (excluding shifted measurements) for H3. However, this key feature has missing values for some historical cycles, introducing bias and inconsistencies in the analysis. The top minimum points demonstrated consistent results with standard deviation and MAD, and a moderate positive correlation with Spearman's values of 0.2432 (including shifted measurements) and 0.2358 (excluding shifted measurements) for D5, 0.3843 (including shifted measurements) and 0.4711 (excluding shifted measurements) for H3, this rise in correlation is due to the removal of axially shifted measurements, leading to cleaner and more correlated measurements to the bank positions. The second part of this work was focused on estimating the errors (uncertainties) of the key

Position	Key Feature	Outliers	Std	MAD	Pearson	Spearman	Kendall	Xi
C-D5	Bottom Minimum	Including	9.32	7.52	0.282	0.329	0.222	0.069
		Excluding	9.06	7.51	0.291	0.331	0.224	0.120
	Maximum	Including	18.87	11.43	0.423	0.542	0.385	0.258
		Excluding	18.54	11.22	0.390	0.525	0.377	0.158
	Top Minimum	Including	16.72	7.47	0.201	0.243	0.167	0.080
		Excluding	9.64	6.70	0.196	0.236	0.163	0.049
C-H3	Bottom Minimum	Including	10.15	6.79	0.297	0.333	0.225	0.008
		Excluding	9.96	6.72	0.320	0.356	0.241	0.049
	Maximum	Including	21.91	13.46	0.331	0.358	0.238	0.116
		Excluding	22.43	14.18	0.350	0.389	0.256	0.131
	Top Minimum	Including	14.47	6.78	0.267	0.384	0.278	0.007
		Excluding	9.89	6.88	0.427	0.471	0.333	0.037

Table 2: Correlation analysis for D5 and H3

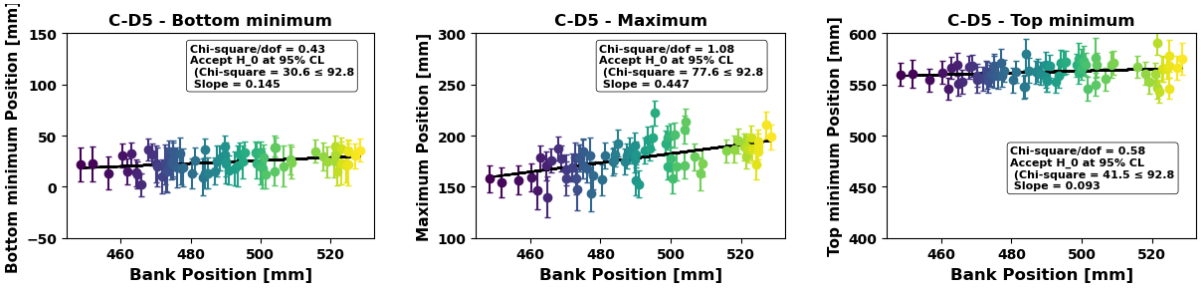

Figure 3: Bottom minimum, maximum, and top minimum along bank positions.

features, y_s^α, as described in the section on hypothesis testing. The error values of the neutron flux measurements were scaled by 1.5 to achieve a reduced chi-square of ≈ 1. This indicates an additional systematic error source for the flux measurements. The profiled errors of the key features, σ_s^α, were then used in the linear trend hypothesis testing. Figure 3 indicates the linear trends and the chi-square values. Once again, the systematic errors, σ_s^α, had to be fractionally increased by $8\,\text{mm}/\sigma_s^\alpha$ to attain a reduced chi-square of unity. The hypothesis testing is then applied on the chi-squared value described above. For the three key features, y_s^α, the linear hypothesis is accepted at the 95% confidence limit value. Additionally, the linear trends in Figure 3 have slopes of 0.145, 0.447, and 0.093 for the bottom minimum, maximum, and top minimum key features, respectively.

Assembly H3 indicates higher variability and lower correlation, while D5 indicates low variability with high correlation. These findings are expected, as H3 is located at the periphery of the active core and distant from the control bank positions. In contrast, D5 is located near the center of the reactor core, where it experiences more of the effect of the control rods. The linear trend was accepted for all three cases. The slopes of the linear trends validated the different roles of the key features. Anomalies resulting from the incorrect insertion of copper wires were detected

by monitoring the positions of the top minimum points determined using a polynomial fit, as shown in Figure 2. These positions of the top minimum points allowed the detection of points that are outliers within the 500 mm to 600 mm range. Points deviating from the average within this range were identified as anomalies due to incorrect insertion of coppers wires. The study's findings provide insights into the relationship between key features and control rod movements and their reliability in estimating axially shifted neutron flux measurements.

5 Conclusion & Future Work

This study provides insight into the distributions of the neutron flux measurements in the SAFARI-1 research reactor, indicating the effect of control rod movement and copper wire insertions on neutron flux profiles. The research methodology involved data preprocessing, statistical analysis, and hypothesis testing. The study assessed the variability of key features and their sensitivity to control rod movement, indicating that the top minimum points of the neutron flux profiles are a stable and reliable means of estimating when these profiles are anomalous due to incorrect insertion of copper wires. Additionally, the anomalies due to incorrect insertion of copper wires were detected by tracking the positions of top minimum points, detecting outliers within the 500 mm to 600 mm range of the top minimum positions. These results demonstrated the importance of considering the features of neutron flux profiles when assessing reactor performance. Future research will include the development of data-driven techniques such as machine learning (ML) and artificial intelligence (AI) to detect axially shifted neutron flux measurements.

Acknowledgments

This study, as part of a master's project, is financially supported by Lesedi Nuclear Services. Lesedi Nuclear Services is hereby acknowledged with gratitude, and Necsa is acknowledged for the provision of additional neutron flux data.

References

[1] L. E. Moloko, P. M. Bokov, and K. N. Ivanov, "Estimation of the axial neutron flux profiles in the SAFARI-1 core using artificial neural networks," in *Proceedings of the International Conference on Mathematics and Computational Methods Applied to Nuclear Science and Engineering (M&C 2021), Virtual Meeting*, 2021, pp. 1644–1653.

[2] R. H. Prinsloo, O. Zamonsky, L. E. Moloko, B. Erasmus, and S. A. Groenewald, "SAFARI-1 benchmark description: IAEA CRP T12029," 2022.

[3] L. E. Moloko, P. M. Bokov, X. Wu, and K. N. Ivanov, "Prediction and uncertainty quantification of SAFARI-1 axial neutron flux profiles with neural networks," *Annals of Nuclear Energy*, vol. 188, p. 109813, 2023.

[4] D. Chiesa, E. Previtali, and M. Sisti, "Bayesian statistics applied to neutron activation data for reactor flux spectrum analysis," *Annals of Nuclear Energy*, vol. 70, pp. 157–168, 2014.

[5] D. Toshniwal, P. K. Gupta, V. Khurana, P. Upadhyay *et al.*, "ADQ—anomaly detection and quantification from delayed neutron monitoring data of nuclear power plants," *IEEE Sensors Journal*, vol. 23, no. 7, pp. 7207–7216, 2023.

[6] M. Dawood, X. Jiang, and K. Schäfers, *Correction techniques in emission tomography*. CRC Press Boca Raton, 2012, vol. 69.

[7] S. Lee, "Comparing standard deviation and median absolute deviation (mad) metrics," https://www.numberanalytics.com/blog/comparing-standard-deviation-and-mad-metrics, 2025, retrieved July 18, 2025.

[8] M. Shaqiri, T. Iljazi, L. Kamberi, and R. Ramani-Halili, "Differences between the correlation coefficients pearson, kendall and spearman," *Journal of Natural Sciences and Mathematics of UT*, vol. 8, no. 15-16, pp. 392–397, 2023.

[9] S. Chatterjee, "A new coefficient of correlation," *Journal of the American Statistical Association*, vol. 116, no. 536, pp. 2009–2022, 2021.

[10] F. James and M. Roos, "Minuit," *CERN program library long writeup D*, vol. 506, p. 1993, 1994.

Investigating the Photon Shielding Properties of Silicate Glass Samples from 1–15 MeV Using Phys-X/PSD, X-COM, and GEANT4 Simulations

M. N. Zuma, S. Mthalane, B. Bhengu, S.S Ntshangase, L. Mdletshe, N. Msabala

Department of Physics, University of Zululand, Private Bag X1001, KwaDlangezwa, 3886, South Africa

E-mail: mf04ndo@gmail.com

Abstract. This study investigates the photon shielding properties of calcium aluminosilicate glass samples in the energy range of 1–15 MeV using Phys-X/PSD simulation. Four glass samples (S1–S4), differing in CaO and Al_2O_3 concentrations, were analyzed based on key radiation shielding parameters: linear attenuation coefficient (LAC), half-value layer (HVL), and mean free path (MFP). Results show a clear inverse relationship between photon energy and LAC, with S1 exhibiting the highest attenuation due to its higher CaO content and density. Similarly, HVL and MFP values increase with photon energy but remain lower in CaO-rich samples, indicating better shielding performance. These findings are consistent with previous studies conducted in the lower energy range (0.284–1.33 MeV), confirming the reliability of the simulation. Overall, calcium aluminosilicate glass demonstrates excellent potential as a non-toxic, transparent, and effective shielding material for for high-energy photon applications.

1 Introduction

Ionizing radiation plays a crucial role across diverse areas such as space exploration, industrial processes, and nuclear medicine [1]. It is extensively applied in medical imaging, cancer therapy, sterilizing medical tools, in nuclear engineering for non-destructive testing [2] as well as in research institutions to produce radioactive isotopes for multiple purposes [3].

Despite their wide applications, ionizing radiation poses serious health risks such as cellular damage, genetic mutations, cancer, acute radiation syndrome, and long-term complications [4, 5]. Therefore, effective radiation shielding is essential to protect practitioners, patients, and the environment. While traditional shielding materials are effective, materials such as lead, concrete, and water, they present limitations for instance lead is toxic, concrete develops cracks that reduce its credibility, and water must be used in large volumes, which is unsuitable for compact or specialized shielding needs. [6, 7, 8]. These limitations have prompted many scientists across the world to explore alternative radiation shielding materials that are non-toxic, transparent, lightweight, and more versatile in certain environments.

One of the most widely explored alternatives is glass, primarily due to its unique optical properties, such as transparency, refractive control, and structural tunability. These characteristics make glass materials particularly attractive for applications that require both effective radiation shielding and visual monitoring. Hence, this work investigates the photon shielding properties of the calcium aluminosilicate glass system in the higher energy region from 1 to 15 MeV. This glass system has previously been investigated in the energy range of 0.284 to 1.33 MeV by M.I. Sayyed [9].

Sample	**CaO (mol%)**	**Al_2O_3 (mol%)**	**SiO_2 (mol%)**	**Density, ρ (g/cm^3)**
S1	50.3	16.7	33	2.90
S2	41.9	27.6	33	2.82
S3	35.3	31.7	33	2.80
S4	29.0	38.0	33	2.76

Table 1: Chemical composition and density of the calcium aluminosilicate glass samples.

2 Method and Data Analysis

The calcium aluminosilicate glass samples analyzed in this study were prepared by Takashi *et al.* [10]. Their chemical compositions and densities are summarized in Table 1. The samples, labeled S1 through S4, differ primarily in the concentration of CaO and Al_2O_3.

A previous study examined the photon shielding properties of these glass samples in the low-energy range (0.284–1.33 MeV) using the Phys-X/PSD simulation toolkit [9], showing that glasses with higher CaO content provided superior shielding compared to those richer in Al_2O_3. Therefore, this study extends the analysis to the 1–15 MeV range, where photon interactions are dominated by Compton scattering and pair production, which are relevant for medical, industrial, and nuclear applications. This study focuses on the following shielding parameters:

- Linear Attenuation Coefficient (LAC)
- Half-Value Layer (HVL)
- Mean Free Path (MFP)

To explore this energy region, this study used the GEANT4 simulation toolkit [11, 12], the web-based Phy-X/PSD software [13], and the NIST X-COM photon cross-sections database [14] to perform Monte Carlo simulations and verify photon interaction parameters. Each parameter and its relevance to radiation shielding is discussed in the following subsections.

2.1 Linear Attenuation Coefficient

The linear attenuation coefficient or LAC is the most fundamental radiation shielding parameter that is used to measure the amount of radiation that passes through a material. It is the measure of the amount of radiation intensity that passes through the radiation shielding material. This parameter is derived from the Beer-Lambert law as shown in equation 1 [15].

$$I = I_0 e^{-\mu x}, \tag{1}$$

where I_0, and I are respectively the intensities of radiation before and after it passes through material, x is the thickness of the material measured in centimeters (cm), and μ is the linear attenuation coefficient (LAC) measured in per centimeter (cm^{-1}) and can be mathematically expressed by equation 2 [16].

$$\mu = \frac{1}{x} ln \left(\frac{I_0}{I} \right), \tag{2}$$

2.2 Half-Value Layer

The half-value layer or (HVL) is a radiation shielding parameter that describes the thickness of a material needed to attenuate the radiation intensity by half of its initial value. In simple words, it is the thickness of a material required to shield radiation intensity by 50% of the initial radiation intensity and can be calculated using the equation 2. Generally lower values of the HVL profile indicate effective shielding capability.

$$HVL = \frac{ln(2)}{\mu}, \tag{3}$$

2.3 Mean Free Path

The final parameter assessed for radiation shielding is the mean free path or (MFP), which represents the average distance a photon travels before interacting with the material. In practical applications, shorter MFP values indicate more effective shielding. MFP depends on the density of the material, and atomic composition, as well as the energy of the incoming radiation. Materials with higher atomic numbers and densities generally exhibit shorter

Energy (MeV)	S1 (2.90 g/cm^3)			S2 (2.82 g/cm^3)			S3 (2.80 g/cm^3)			S4 (2.76 g/cm^3)		
	GEANT4	Phys-X	X-COM	GEANT4	Phys-X	X-COM	GEANT4	Phys-X	X-COM	GEANT4	Phys-X	X-COM
1	0.1931	0.1839	0.1839	0.1822	0.1785	0.1785	0.1795	0.1770	0.1770	0.1744	0.1742	0.1742
2	0.1357	0.1296	0.1296	0.1280	0.1258	0.1258	0.1260	0.1246	0.1246	0.1223	0.1225	0.1225
3	0.1119	0.1061	0.1061	0.1055	0.1026	0.1026	0.1039	0.1016	0.1016	0.1005	0.0999	0.0999
4	0.0986	0.0931	0.0931	0.0928	0.0900	0.0900	0.0913	0.0890	0.0890	0.0883	0.0872	0.0872
5	0.0905	0.0850	0.0850	0.0849	0.0821	0.0821	0.0834	0.0809	0.0809	0.0806	0.0795	0.0795
6	0.0841	0.0798	0.0798	0.0790	0.0767	0.0767	0.0773	0.0756	0.0756	0.0745	0.0742	0.0742
7	0.0803	0.0760	0.0760	0.0753	0.0728	0.0728	0.0736	0.0720	0.0720	0.0712	0.0704	0.0704
8	0.0780	0.0734	0.0734	0.0728	0.0702	0.0702	0.0711	0.0692	0.0692	0.0684	0.0676	0.0676
9	0.0754	0.0713	0.0713	0.0702	0.0682	0.0682	0.0686	0.0672	0.0672	0.0659	0.0654	0.0654
10	0.0742	0.0696	0.0699	0.0694	0.0666	0.0666	0.0682	0.0655	0.0655	0.0651	0.0638	0.0638
11	0.0728	0.0687	0.0687	0.0677	0.0654	0.0654	0.0661	0.0644	0.0644	0.0635	0.0627	0.0627
12	0.0722	0.0679	0.0679	0.0671	0.0646	0.0646	0.0655	0.0633	0.0633	0.0629	0.0615	0.0615
13	0.0719	0.0670	0.0670	0.0666	0.0637	0.0637	0.0650	0.0624	0.0624	0.0624	0.0610	0.0610
14	0.0716	0.0667	0.0667	0.0666	0.0632	0.0632	0.0647	0.0621	0.0621	0.0621	0.0602	0.0602
15	0.0711	0.0661	0.0661	0.0657	0.0629	0.0629	0.0628	0.0620	0.0620	0.0613	0.0599	0.0599

Table 2: Comparison of the linear attenuation coefficients (LAC, in cm^{-1}) for calcium aluminosilicate glass samples (S1–S4) across photon energies from 1 to 15 MeV obtained from GEANT4, Phys-X and X-COM simulations.

MFPs, enhancing their attenuation capability. Mathematically the MFP can be determined using the following equation.

$$\lambda = \frac{1}{\mu}, \tag{4}$$

where λ denote the mean free path (MFP) expressed in centimeters (cm).

3 Results and Discussion

3.1 Linear Attenuation Coefficient

Table 2 presents the LAC values obtained using GEANT4, Phys-X/PSD, and X-COM. The results show that LAC decreases with increasing photon energy, reflecting reduced attenuation at higher energies. S1, with the highest density and CaO content, has the largest LAC, while S4 shows the smallest. The three toolkits display strong overall agreement, with only minor discrepancies. This inverse relationship arises because, at higher energies, photon interactions shift from photoelectric absorption to Compton scattering and pair production, which are less effective at fully absorbing photons per unit thickness. Among the samples, S1 shows the highest LAC values, followed by S2, S3, and S4, as shown in Figure 1.

This ordering corresponds directly to the decreasing concentration of CaO and increasing Al_2O_3 content from S1 to S4, as denser and more absorptive components like CaO contribute to greater attenuation. The small but consistent differences in LAC values highlight the role of composition and density in enhancing photon shielding. Overall, these results indicate that S1 offers the most effective shielding performance in the energy range, making it a promising candidate for applications requiring enhanced radiation protection.

3.2 Half-value layer

From the table of chemical composition and densities, Table 1, it can be seen that the density of the glass systems (S1–S4) decreases with decreasing CaO concentration (ranging from 50.3 to 29.0 mol%). This proportionality indicates that increasing the amount of CaO has a direct impact on the density of the calcium aluminosilicate glass samples. In conjunction with this, we have also investigated how these glass samples can effectively attenuate ionizing radiation by 50% of the initial value across the energy range of 1 to 15 MeV. Figure 2 illustrates the half-value layer of the glass systems (S1–S4).

The HVL plot indicates that glasses with increased CaO content exhibit lower HVL values than those with elevated Al_2O_3 content throughout the energy spectrum. From the glass samples with the highest amount of CaO to the lowest (S1-S4), The present work recorded HVL values at 1 MeV as 3.77 cm, 3.88 cm, 3.92 cm, and 3.98 cm. While at maximum energy (15 MeV), the HVL for all the glass systems (S1-S4) was recorded as 10.47 cm, 11.04 cm, 11.26 cm, and 11.59 cm, indicating that the glass samples can strongly attenuate the intensity of ionized radiation by half of its initial value at lower energies and require a thinner layer to attenuate, but as the energy increases,

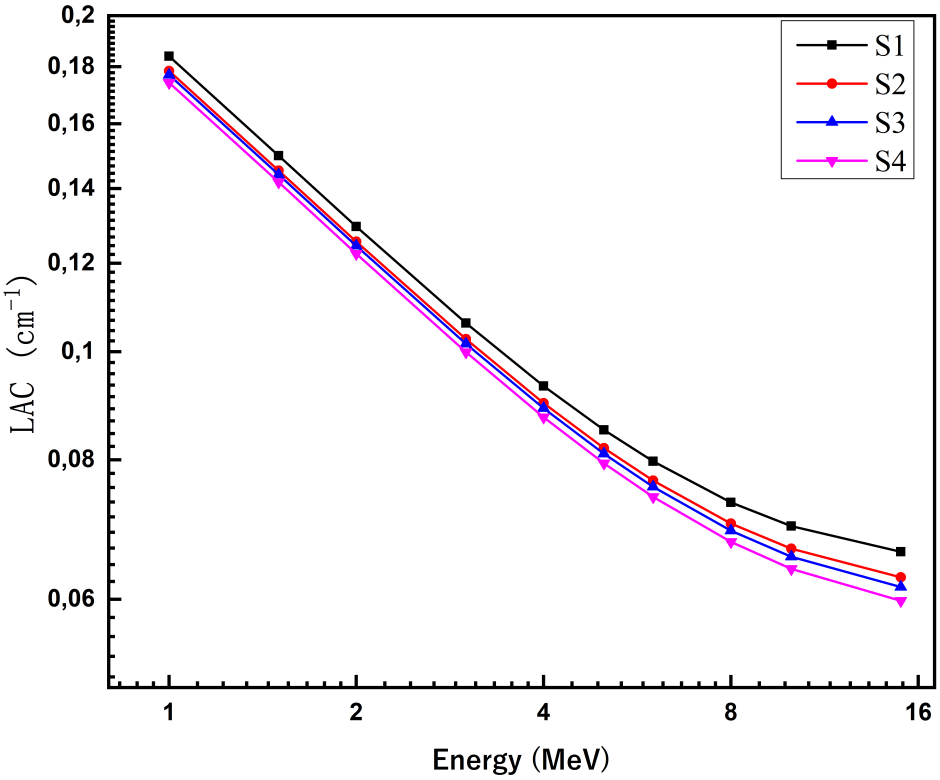

Figure 1: Variation of the linear attenuation coefficient (LAC) with photon energy (1–15 MeV) for calcium aluminosilicate glass samples S1–S4, simulated using Phys-X/PSD.

there is a need to thicken the layer to effectively reduce the intensity by 50%. At 15 MeV, the required glass thickness is nearly three times greater than at lower energies. Furthermore, reducing the concentration of Al_2O_3 and adding more CaO content could improve the shielding properties of (S2-S4), as this will have a significant impact on the density of glass systems.

3.3 Mean Free Path

This section presents the mean free path results for the calcium aluminosilicate glasses. As discussed in section 2.3, MFP is influenced by several factors, including material density. In the selected glasses, density decreases as the CaO content drops from 50 mol% to 29.0 mol% (S1 to S4), directly affecting the MFP, as shown in Table 1. Glasses with higher CaO content (S1) exhibit lower and more favorable MFPs compared to those richer in Al2O3 (S4), indicating that increasing Al2O3 while reducing CaO lowers the glass density and diminishes shielding effectiveness. For optimal MFP performance, CaO content should remain higher than Al2O3. Figure 3 shows the MFP as a function of photon energy from 1 to 15 MeV, where the minimum MFP at 1 MeV is 5.44 cm for S1 and increases to 5.60 cm for S4, demonstrating the influence of composition on photon attenuation. The performance of these glass samples at energies above 2 MeV is consistent with results obtained at lower energies [9], further confirming that samples with higher CaO content, such as S1, provide superior shielding capabilities.

4 Conclusion

The investigated calcium aluminosilicate glass samples demonstrate excellent photon shielding performance across the 1–15 MeV range. The LAC results confirm that samples with higher CaO content and density, particularly S1,

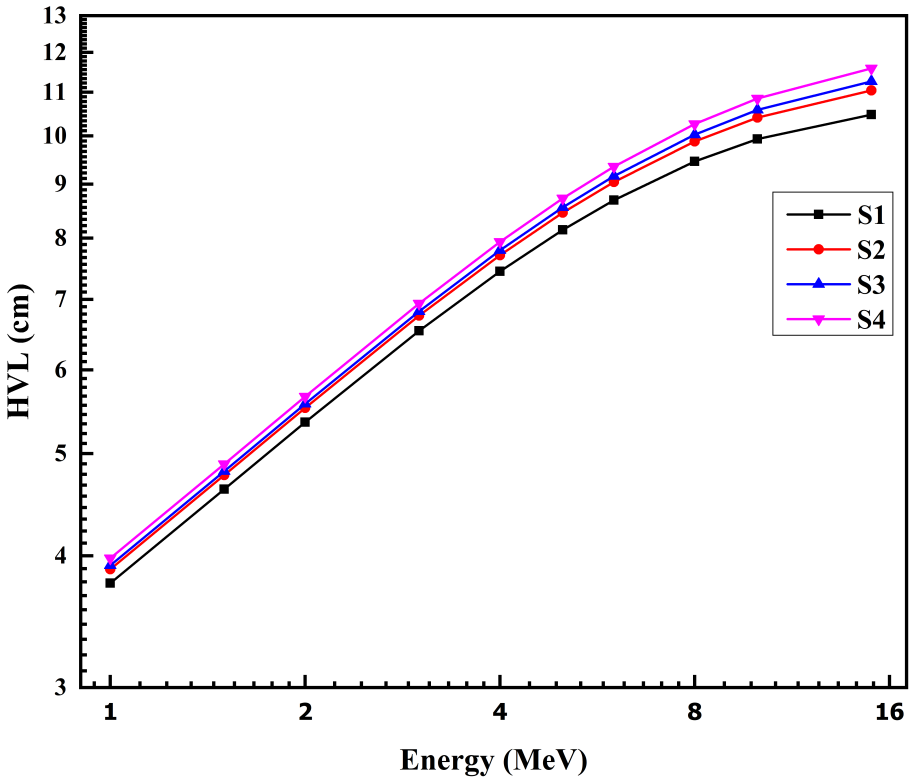

Figure 2: Variation of the half-value layer (HVL) of the calcium aluminosilicate glass system across photon energies ranging from 1 to 15 MeV.

consistently provide superior attenuation. Comparisons between GEANT4, Phys-X/PSD, and X-COM show strong agreement, with only minor discrepancies, thereby reinforcing the robustness of the simulations. Moreover, our findings align well with the results reported by M.I. Sayyed [9] in the lower energy region (0.284–1.33 MeV), further validating the reliability of this study. Thus, calcium aluminosilicate glass emerges as a promising and reliable candidate for radiation shielding applications across a wide photon energy range.

Acknowledgments
I would like to extend my heartfelt appreciation to my colleagues involved in this project, the Department of Physics at the University of Zululand, and the developers of the simulation platforms Phys-X/PSD, X-COM, and GEANT4 for their invaluable tools and support.

References

[1] F. A. Cucinotta, F. K. Manuel, J. Jones, G. Iszard, J. Murrey, B. Djojonegro, and M. L. Wear, "Space radiation and cataracts in astronauts," *Radiation Research*, vol. 156, no. 5, pp. 460–466, 2006.

[2] E. B. Podgorsak, *Radiation Oncology Physics: A Handbook for Teachers and Students*. Vienna: International Atomic Energy Agency, 2006. [Online]. Available: https://www.iaea.org/publications/7006/radiation-oncology-physics-a-handbook-for-teachers-and-students

[3] R. W. Weeks, "The production and use of radioisotopes in nuclear medicine," *Journal of Nuclear Medicine*, vol. 36, no. 12, pp. 44N–51N, 1995. [Online]. Available: https://jnm.snmjournals.org/content/36/12/44N

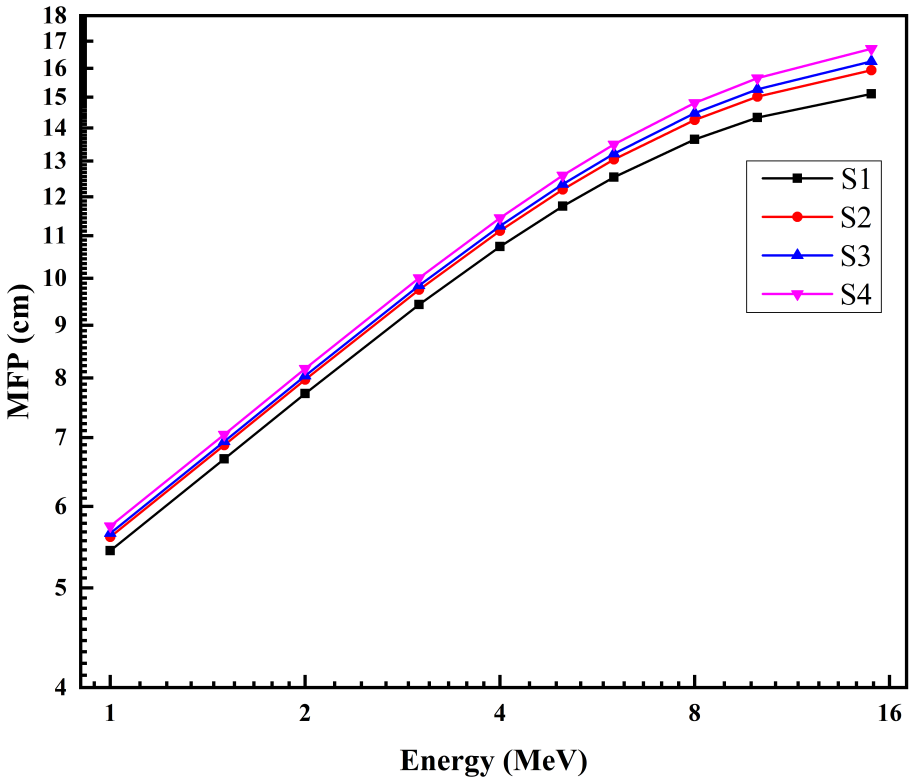

Figure 3: Mean free path (MFP) of the calcium aluminosilicate glass systems as a function of photon energy in the 1–15 MeV range.

[4] A. Kronenberg and F. A. Cucinotta, "Space radiation protection issues," *Health physics*, vol. 103, no. 5, pp. 556–567, 2012.

[5] N. Frane and A. Bitterman, "Radiation safety and protection," Northwell Health at Hofstra School of Medicine, 2023, last updated May 22, 2023.

[6] Mo-Sci, "Radiation shielding and the utilization of glass," News-Medical.net Whitepaper, 2021.

[7] K. I. Hussein, M. S. Alqahtani, I. Grelowska, M. Reben, H. Afifi, H. Zahran, I. S. Yaha, and E. S. Yousef, "Optically transparent glass modified with metal oxides for x-rays and gamma rays shielding material," *X-Ray Spectrometry*, 2021, sAGE Journals.

[8] R. Kurtulus, "Recent developments in radiation shielding glass studies: A mini-review on various glass types," *Radiation Physics and Chemistry*, 2024.

[9] M. Sayyed, "The impact of chemical composition, density and thickness on the radiation shielding properties of cao–al2o3–sio2 glasses," *Silicon*, vol. 15, no. 18, pp. 7917–7926, 2023.

[10] S. Takahashi, D. R. Neuville, and H. Takebe, "Thermal properties, density and structure of percalcic and peraluminus cao–al2o3–sio2 glasses," *Journal of Non-Crystalline Solids*, vol. 411, pp. 5–12, 2015. [Online]. Available: https://www.sciencedirect.com/science/article/pii/S0022309314006590

[11] S. Agostinelli, J. Allison, K. Amako *et al.*, "Geant4—a simulation toolkit," *Nuclear Instruments and Methods in Physics Research Section A: Accelerators, Spectrometers, Detectors and Associated Equipment*, vol. 506, no. 3, pp. 250–303, 2003.

[12] J. Allison, K. Amako, J. Apostolakis *et al.*, "Recent developments in geant4," *Nuclear Instruments and Methods in Physics Research Section A: Accelerators, Spectrometers, Detectors and Associated Equipment*, vol. 835, pp. 186–225, 2016.

[13] E. Şakar, F. Özpolat, B. Alım, M. I. Sayyed, and M. Kurudirek, "Phy-X / PSD: Development of a user friendly online software for calculation of parameters relevant to radiation shielding and dosimetry," *Radiation Physics and Chemistry*, vol. 166, p. 108496, 2020.

[14] M. J. Berger and J. H. Hubbell, "Xcom: Photon cross sections database, web version," National Institute of Standards and Technology (NIST), Gaithersburg, 1987/1999, originally published as NBSIR 87-3597.

[15] G. F. Knoll, *Radiation Detection and Measurement*, 4th ed. John Wiley & Sons, 2010, a standard reference on the physics and detection of radiation.

[16] M. S. Al-Buriahi, M. I. Sayyed, M. U. Khandaker, and D. A. Bradley, "Investigation of gamma-ray shielding competence of silicate-based glasses using theoretical, experimental and simulation approaches," *Applied Radiation and Isotopes*, vol. 160, p. 109150, 2020.

This page intentionally left blank.

Parton Production Spectra and Energy Loss in High-Energy O+O-Collisions

Mohammad Faaris Alam[1], **W. A. Horowitz**[1,2]

[1]Department of Physics, University of Cape Town, Private Bag X3, Rondebosch 7701, South Africa
[2]Department of Physics, New Mexico State University, Las Cruces, New Mexico, 88003, USA

E-mail: almmoh008@myuct.ac.za

Abstract. We outline a framework for computing parton production spectra for high-momentum light quarks and gluons in high-energy oxygen–oxygen (O+O) collisions at LHC Run-3 energies. These spectra are a crucial input for modelling parton energy loss in small collision systems, which in turn enables phenomenological investigations into the possible formation of a quark-gluon plasma (QGP) under such conditions. We describe the theoretical ingredients involved and motivate the need for updated spectra at previously uncalculated collision energies. This work lays the groundwork for future quantitative studies of energy loss in O+O collisions and contributes to the broader effort to probe QGP formation in small systems.

1 Introduction

The goal to understand the most fundamental constituents of all the observed matter in the universe has been one of the central goals of modern physics. Quantum field theories have proven remarkably successful in this endeavour, culminating in the Standard Model of Particle Physics [1], which is the best description of our understanding of elementary particles and their interactions. Within this framework, the strong nuclear force—responsible for binding quarks into hadrons—is described by the theory of quantum chromodynamics (QCD).

Despite its success, the high-energy behaviour of QCD remains incompletely understood. At high energies and densities, such as those achieved in heavy-ion collisions, QCD predicts the formation of exotic states of matter like the quark-gluon plasma (QGP), where quarks and gluons become de-confined within hadrons. Studying such regimes is crucial for probing the non-linear and collective dynamics of QCD.

Experimental investigations of QCD in these extreme conditions are carried out at large-scale facilities such as the Large Hadron Collider (LHC) at CERN [2] and the Relativistic Heavy Ion Collider (RHIC) at Brookhaven National Laboratory [3]. Broadly speaking, these experiments can be categorized into two types, analogous to different ways of examining a watermelon[1]: one can either smash it open to see what it's made of, or slice it carefully to inspect its internal structure. The former corresponds to high-energy hadronic or nuclear collisions—such as those performed at the LHC and RHIC—where the goal is to study the emergent properties of QCD matter under extreme conditions. The latter corresponds to deep-inelastic scattering (DIS), where an electron scatters off a nucleon or nucleus, probing its internal partonic structure. Such DIS experiments were performed at the Hadron-Elektron Ring Anlage (HERA) at DESY in Hamburg, Germany [4] and at the Stanford Linear Accelerator Center (SLAC) in the USA [5].

This work focuses on the first of these approaches, particularly on parton production and energy loss in high-energy heavy-ion collisions. In light of the recent Run-3 data at the LHC [6, 7], we investigate parton production spectra and energy loss mechanisms in high-energy oxygen–oxygen (O+O) collisions—a novel collision system

[1]Analogy adapted from Asmita Mukherjee's seminar available at: https://www.youtube.com/watch?v=r8zRBCigWTw.

providing new opportunities to explore QCD dynamics in small systems at high energy. At high energies, the term *small systems* refers to collision systems involving at least one light projectile, such as proton–proton (pp), proton–nucleus (pA), or light-ion collisions (e.g. oxygen–oxygen) [8]. In contrast, *heavy-ion collisions* involve the interaction of large nuclei such as gold ($Au + Au$) at RHIC or lead ($Pb + Pb$) at the LHC. And underlying both small- and large-system collisions are the fundamental degrees of freedom of quantum chromodynamics (QCD): *partons*, namely quarks and gluons.

2 Quark Gluon Plasma

The quark-gluon plasma (QGP) is believed to be formed in relativistic heavy-ion (A+A) collisions at sufficiently high energy densities [9, 10, 3]. Experimental signatures from RHIC and the LHC have confirmed the existence of the QGP in such systems, where the medium behaves like a nearly perfect fluid with low shear viscosity.

In recent years, attention has turned to the possibility that a QGP may also be formed in smaller collision systems, such as proton–nucleus (p+A) and even proton–proton (p+p) interactions. While the smaller size and shorter lifetime of these systems complicate the interpretation of experimental results, collective behaviour and QGP-like signatures have been observed, motivating further investigation into the dynamics of energy loss in such environments [2, 8, 11].

One of the key tools in probing the QGP is the energy loss experienced by high-momentum partons as they traverse the medium. These energetic quarks and gluons, produced early in the collision, act as microscopic probes—functioning as a type of *femtoscope*—that can reveal properties of the medium through the modification of their spectra. By studying how these partonic probes lose energy via interactions with the QGP, one can gain insights into its density, temperature, and transport coefficients.

This work contributes to that effort by computing the parton production spectra and estimating the energy loss of high-momentum quarks in high-energy oxygen–oxygen (O+O) collisions at $\sqrt{s_{NN}} = 5.36$ TeV [6, 7]. Such small collision systems, studied during Run-3 at the LHC, provide a unique environment to investigate the onset of QGP formation in small systems and to test the limits of energy-loss models typically applied to larger systems.

3 Parton Production Spectra

A key ingredient in modeling energy loss in high-energy collisions is the initial production spectra of partons. These spectra quantify the number of high-momentum partons—primarily light quarks and gluons—produced in the early stages of the collision. Since energy loss calculations require knowledge of the initial parton population, accurate predictions of these spectra are crucial.

The production spectra can be obtained from the inclusive cross-section for the process $AB \to f + X$, where A and B are the incoming hadrons or nuclei (in our case, oxygen nuclei), and f denotes a final-state parton of a specific flavour. For a parton of flavour f, the differential cross-section with respect to transverse momentum p_T and rapidity y_f is given by [12, 13]:

$$\begin{aligned}\frac{d\sigma^{AB\to f+X}}{dp_T^2 dy_f} = \int dy_2 \sum_{\langle ij\rangle\langle kl\rangle} \frac{1}{1+\delta_{kl}}\frac{1}{1+\delta_{ij}} \Bigg\{ & x_1 f_{i/A}(x_1,Q^2)\, x_2 f_{j/B}(x_2,Q^2) \\ & \times \left[\frac{d\hat{\sigma}}{d\hat{t}}^{ij\to kl}(\hat{s},\hat{t},\hat{u})\delta_{fk} + \frac{d\hat{\sigma}}{d\hat{t}}^{ij\to kl}(\hat{s},\hat{u},\hat{t})\delta_{fl}\right] \\ & + x_1 f_{j/A}(x_1,Q^2)\, x_2 f_{i/B}(x_2,Q^2) \left[\frac{d\hat{\sigma}}{d\hat{t}}^{ij\to kl}(\hat{s},\hat{u},\hat{t})\delta_{fk} + \frac{d\hat{\sigma}}{d\hat{t}}^{ij\to kl}(\hat{s},\hat{t},\hat{u})\delta_{fl}\right] \Bigg\} \end{aligned} \tag{1}$$

The sum runs over parton channels $\langle ij\rangle, \langle kl\rangle \in \{gg, gq, g\bar{q}, qq, q\bar{q}, \bar{q}\bar{q}\}$, where $q \in \{u, d, s, \dots\}$. Here, q denotes a quark, $\bar{q}$ denotes an anti-quark and g denotes a gluon. The up, down, top, bottom, charm and strange flavours of quarks are denoted by u, d, b, c and s respectively with the anti-quark flavour represented by a bar over the flavour (so for example, an anti-up quark would be $\bar{u}$. The parton distribution functions (PDFs) $f_{i/A}(x, Q^2)$ describe the probability of finding parton i inside hadron A carrying momentum fraction x at scale Q. The variables x_1 and x_2 are given by [13],

$$x_1 = \frac{p_T}{\sqrt{s}}\left(e^{y_f} + e^{y_2}\right), \quad x_2 = \frac{p_T}{\sqrt{s}}\left(e^{-y_f} + e^{-y_2}\right), \tag{2}$$

and the rapidity integration range is constrained as in [12] to

$$-\log\left(\frac{\sqrt{s}}{p_T} - e^{-y_f}\right) \leq y_2 \leq \log\left(\frac{\sqrt{s}}{p_T} - e^{y_f}\right). \tag{3}$$

The partonic differential cross-sections $d\hat{\sigma}/d\hat{t}^{ij\to kl}$ are computed from perturbative QCD and depend on the Mandelstam variables $\hat{s}, \hat{t}, \hat{u}$. These matrix elements scale as $\alpha_s^2(\mu^2)$, where α_s is the strong coupling evaluated at the renormalisation scale μ, which is typically set to $\mu \sim Q \sim p_T$ [12].

While reference plots of production spectra for various collision systems and energies exist in the literature—such as those provided by Eskola and Honkanen [12]—these are often limited to earlier LHC energies and heavier systems like Pb+Pb. We aim to extend such computations to include oxygen–oxygen (O+O) collisions at LHC Run-3 energies, which remain relatively unexplored, in further studies. These small systems offer a unique opportunity to probe QCD phenomena such as the possible formation of a QGP in minimal-volume environments.

4 Conclusion and Outlook

In this work, we outlined a framework for computing parton production spectra in high-energy oxygen–oxygen (O+O) collisions at the LHC. These spectra are a necessary input for studying parton energy loss in small systems, and ultimately, for investigating the formation and characteristics of the quark-gluon plasma (QGP) under such conditions.

To validate our methodology and numerical implementation, we first aim to reproduce the established theoretical results in [12] for well-studied collision systems. This serves both as a consistency check and a foundation for reliable extrapolation to previously uncalculated regimes.

Our next step is to compare the computed production spectra with recent experimental data from the O+O Run-3 at the LHC, which concluded just a few weeks ago at the time of this writing. These comparisons will not only test the accuracy of our approach but also enable us to refine theoretical models of parton dynamics in small systems.

Ultimately, the calculated spectra will serve as input to quantify the energy loss of high-momentum light quarks traversing the QGP created in O+O collisions. This will allow us to make the first quantitative predictions for parton energy loss in this specific system, potentially offering new insights into the properties of QCD matter in the small-system regime. Through such studies, we hope to better characterize the transport properties and collective behaviour of the QGP, and to contribute toward understanding its emergence in systems beyond traditional heavy-ion collisions.

Acknowledgments

FA and WAH gratefully acknowledge support from the South African National Research Foundation and the SA-CERN Collaboration.

References

[1] David Griffiths. *Introduction to elementary particles*. 2008.

[2] Vardan Khachatryan et al. Evidence for collectivity in pp collisions at the LHC. *Phys. Lett. B*, 765:193–220, 2017.

[3] Miklos Gyulassy and Larry McLerran. New forms of QCD matter discovered at RHIC. *Nucl. Phys. A*, 750:30–63, 2005.

[4] M. Breidenbach, J. I. Friedman, H. W. Kendall, E. D. Bloom, D. H. Coward, H. DeStaebler, J. Drees, R. E. Taylor, and J. D. Bjorken. Observed behavior of highly inelastic electron-proton scattering. *Phys. Rev. Lett.*, 23:935–939, 1969.

[5] H. Abramowicz et al. Combination of measurements of inclusive deep inelastic $e^{\pm}p$ scattering cross sections and QCD analysis of HERA data. *Eur. Phys. J. C*, 75(12):580, 2015.

[6] Ibrahim Jaser Abualrob et al. Evidence of nuclear geometry-driven anisotropic flow in OO and Ne−Ne collisions at $\sqrt{s_{\rm NN}}$ = 5.36 TeV. 9 2025.

[7] Georges Aad et al. Measurement of the azimuthal anisotropy of charged particles in $\sqrt{s_{\rm NN}} = 5.36$ TeV ^{16}O+^{16}O and ^{20}Ne+^{20}Ne collisions with the ATLAS detector. 9 2025.

[8] James L. Nagle and William A. Zajc. Small System Collectivity in Relativistic Hadronic and Nuclear Collisions. *Ann. Rev. Nucl. Part. Sci.*, 68:211–235, 2018.

[9] John Adams et al. Experimental and theoretical challenges in the search for the quark gluon plasma: The STAR Collaboration's critical assessment of the evidence from RHIC collisions. *Nucl. Phys. A*, 757:102–183, 2005.

[10] K Aamodt et al. Elliptic flow of charged particles in Pb-Pb collisions at 2.76 TeV. *Phys. Rev. Lett.*, 105:252302, 2010.

[11] Rajendra Nath Patra. Collective phenomena study in small systems using the bulk of particle production in high-multiplicity pp collisions at $\sqrt{s}$ =13 TeV with ALICE. *PoS*, EPS-HEP2023:214, 2024.

[12] K. J. Eskola and H. Honkanen. A Perturbative QCD analysis of charged particle distributions in hadronic and nuclear collisions. *Nucl. Phys. A*, 713:167–187, 2003.

[13] Alexander Huss, Aleksi Kurkela, Aleksas Mazeliauskas, Risto Paatelainen, Wilke van der Schee, and Urs Achim Wiedemann. Predicting parton energy loss in small collision systems. *Phys. Rev. C*, 103(5):054903, 2021.

Using Machine Learning Algorithms in the search for dark photons in the $H \to Z + \gamma_D$ with the ATLAS detector at the LHC

Karabo Tau[1], **Rachid Mazini**[1] **and Mukesh Kumar**[1]

[1]School of Physics, University of the Witwatersrand, Johannesburg 2050, South Africa

E-mail: 2341256@students.wits.ac.za

Abstract. The search for new physics is one of the key goals of the ATLAS Collaboration. With the discovery of the Higgs boson in 2012, the Standard Model (SM) gained an essential ingredient towards the understanding of fundamental particles and their interactions — but it cannot yet be considered complete. The nature of dark matter (DM), which constitutes about 27% of the universe, remains a major open question. DM may belong to a complex "dark sector" of particles beyond the SM, with its own internal symmetries and interactions. Among these hypothetical particles, the "dark photon" (γ_D) is a predicted mediator for interactions within this sector. If dark photons couple to SM particles, they could be produced in high-energy proton-proton collisions at the Large Hadron Collider (LHC) and detected by the ATLAS experiment. This study investigates the production of γ_D via Higgs boson decay $H \to Z + \gamma_D$, where the Z boson decays into two leptons of the same flavor and opposite sign (e^+e^- or $\mu^+\mu^-$), and the undetected γ_D results in missing transverse energy (MET). The resulting final state, $e^+e^-/\mu^+\mu^-$+ MET, provides a distinct signature for the presence of γ_D. However, the SM presents several physics processes with similar final states that are produced with a higher probability in pp collisions. To distinguish the γ_D signal from these backgrounds, Machine Learning (ML) algorithms are employed. Algorithms such as Boosted Decision Trees (BDT), Deep Neural Networks (DNN), and Graph Neural Networks (GNN) are trained on ATLAS Monte Carlo simulation data to identify the most effective method for signal-background discrimination. The selected model is then applied to ATLAS data to enhance sensitivity in the search for dark photons.

1 Introduction

The presence of DM is well supported by a wide range of astrophysical and cosmological evidence, with its density measured to be approximately five times that of ordinary baryonic matter, yet its particle nature remains unknown [1]. A compelling possibility is that DM resides in a hidden or "dark" sector, a theoretical collection of fields and particles beyond the SM that interact only very weakly with ordinary matter. These interactions may occur through mediator particles known as dark photons, which act as "portals" connecting the dark and visible sectors. One of the most promising such portals is the vector portal, which involves a spin-1 particle; the dark photon arising in models with an additional dark $U(1)$ gauge symmetry. The portal is realised through kinetic mixing between the dark photon and the familiar photon (or Z boson) of the SM [2]. This mixing endows the dark photon with a tiny but measurable coupling to ordinary matter, making it accessible in collider experiments like ATLAS.

Beyond its role as a DM mediator, the dark photon framework may also help address other outstanding puzzles in physics, such as the origin of the Yukawa hierarchy (the large spread in fermion masses) or discrepancies between simulations and observations in small-scale cosmic structure formation [2].

1.1 THEORETICAL FRAMEWORK ($H \to Z + \gamma_D$)

We use a minimal model to generate at 1-loop where $H \to \gamma\gamma_D$, $Z\gamma_D$ decays as shown in Figure 1. The model introduces two scalar messengers: $SU(2)_L$ doublet S_L and $SU(2)_L$ scalar singlet S_R. The scalar messengers mix with the Higgs field via a generic interaction Lagrangian:

$$\mathcal{L} \sim \mu \left(H^\dagger S_L S_R + \text{h.c.} \right)$$

which is manifestly $SU(2)_L$ invariant, and μ is a mass parameter.

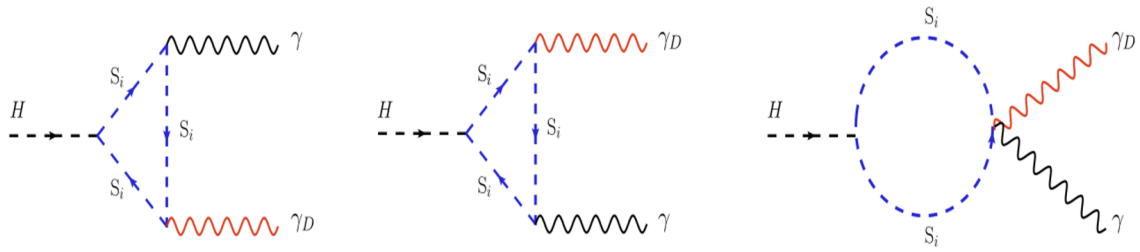

Figure 1: Feynman diagrams of the $H \to \gamma\gamma_D$, $Z\gamma_D$ decay amplitude, where γ and γ_D are the photon, and dark photon respectively.

The Branching Ratios of $H \to \gamma\gamma_D$, $Z\gamma_D$, $\gamma_D\gamma_D$, $\gamma\gamma$ have the following model-independent parameterization:

$$\begin{aligned}
\text{BR}_{\gamma\gamma_D} &= \frac{\text{BR}^{\text{SM}}_{\gamma\gamma}\, r_{\gamma\gamma_D}}{1 + r_{\gamma_D\gamma_D}\, \text{BR}^{\text{SM}}_{\gamma\gamma}}, \\
\text{BR}_{Z\gamma_D} &= \frac{\text{BR}^{\text{SM}}_{\gamma\gamma}\, r_{Z\gamma_D}}{1 + r_{\gamma_D\gamma_D}\, \text{BR}^{\text{SM}}_{\gamma\gamma}}, \\
\text{BR}_{\gamma_D\gamma_D} &= \frac{\text{BR}^{\text{SM}}_{\gamma\gamma}\, r_{\gamma_D\gamma_D}}{1 + r_{\gamma_D\gamma_D}\, \text{BR}^{\text{SM}}_{\gamma\gamma}}, \\
\text{BR}_{\gamma\gamma} &= \frac{\text{BR}^{\text{SM}}_{\gamma\gamma} \left(1 + \chi\sqrt{r_{\gamma\gamma}}\right)^2}{1 + r_{\gamma_D\gamma_D}\, \text{BR}^{\text{SM}}_{\gamma\gamma}}.
\end{aligned} \tag{1}$$

The r_i parameters are given by:

$$\begin{aligned}
r_{\gamma\gamma_D} &= 2X^2 \left(\frac{\alpha_D}{\alpha}\right), \\
r_{Z\gamma_D} &= 2X^2 R_Z^2 \left(\frac{\alpha_D}{\alpha}\right), \\
r_{\gamma_D\gamma_D} &= X^2 \left(\frac{\alpha_D}{\alpha}\right)^2, \\
r_{\gamma\gamma} &= X^2,
\end{aligned} \tag{2}$$

$$X \equiv \frac{\xi^2}{3F(1-\xi^2)}, \quad \xi \equiv \frac{\Delta}{\tilde{m}^2} \tag{3}$$

where $F \sim 6.5$ comes from the SM $H \to \gamma\gamma$ form factor, and Δ depends on the mass difference of the two scalars.

1.2 The ATLAS detector

The ATLAS [3] experiment, located at the LHC [4], is a general-purpose particle detector built to capture a wide range of physics processes. Its design is symmetric along the beam axis, ensuring uniform coverage for particles produced in proton-proton collisions. At its core is the Inner Detector (ID), which tracks the paths of charged

particles as they pass through. This system is encased by a thin superconducting solenoid magnet that generates a 2 Tesla magnetic field, essential for measuring particle momenta. Surrounding the ID are layers of calorimeters, electromagnetic and hadronic, that measure the energy deposited by particles. Outside the detector is the Muon Spectrometer (MS), which uses three large air-core toroidal magnets (one central barrel and two end-cap sections) to precisely track and identify muons. These magnets are arranged with eight-fold symmetry around the calorimeter system [3].
The electromagnetic calorimeter (EMCAL) surrounds the ID and absorbs energy from particles that interact electromagnetically as they move through the detector. The EMCAL covers $|\eta| < 3.2$. The Hadronic calorimeter (HCAL) surrounds the EMCAL and is made up of steel plates and plastic scintillator plates which absorb energy from hadrons. These HCAL components provide hadronic coverage of $|\eta| < 1.7$, and LAr technology is also used for the HCAL end-cap region. The entire HCAL covers a pseudorapidity range of $|\eta| < 4.9$ [5, 6]. The muon spectrometer defines the overall dimensions of the ATLAS detector; the three large superconducting toroid systems of high-precision tracking chambers provide exceptional muon momentum measurement [6].

1.3 Search for $H \to Z + \gamma_D$

The search for dark photons in the $H \to Z + \gamma_D$ is a compelling probe of hidden sectors, however it presents a challenging experimental signature: a pair of same-flavour, oppositely charged leptons from the Z boson decay, accompanied by MET from the undetected γ_D. While clean in principle, this final state ($e^+e^-/\mu^+\mu^-$ + MET) is affected by various backgrounds. Both irreducible backgrounds such as ($VV\gamma$) final states where V is any of the W/Z bosons with both bosons decaying leptonically and $ZH \to \ell\ell$ + $\nu\nu$, and reducible backgrounds such as $t\bar{t}$, single-top and $Z + jets$, where MET arises from neutrinos or detector effects.
The discriminating power of any single kinematic variable is limited so traditional cut-based selections struggle to separate the small signal from these diverse backgrounds without sacrificing efficiency. To overcome this we plan to employ machine learning techniques that can exploit correlations across many observables, such as the Z boson kinematics, event topology, and MET characteristics, to achieve significantly better signal-to-background discrimination. This study focuses on the associated ZH production mode, including both gluon-gluon fusion and vector contributions. Table 1 summarises the baseline kinematic selections applied so far to the signal ($gg \to HZ\gamma_D$, VBF$HZ\gamma_D$) and background samples ($\ell\ell\nu\nu$, $t\bar{t}$, $Z + jets$) as part of this ongoing analysis.

Two leptons (e^+e^- / $\mu^+\mu^-$)
Leading transverse momentum (p_T) > 27 GeV and sub-leading (p_T) > 15 GeV
Electron eta (η) cut: $\|\eta\|$ < 2.47, exclude 1.37 < $\|\eta\|$ < 1.52
Muon η cut: $\|\eta\|$ < 2.7
Dilepton invariant mass: 65 GeV $< m_{\ell\ell} <$ 110 GeV
MET > 15 GeV
$N_{\text{jet}} \leq 2$, with $p_T^{\text{jet}} > 30$ GeV, $\|\eta\| < 4.5$

Table 1: Kinematic selection criteria for the $\ell^+\ell^- + E_T^{\text{miss}}$ signal region.

1.4 Machine Learning

Machine Learning (ML) is a way for computers to learn how to perform tasks by finding patterns in data, rather than following explicit step-by-step instructions. In our case, we train an algorithm using simulated collision events that resemble what we expect to see in real ATLAS data. The algorithm learns from these examples to distinguish between signal and background [7]. Machine Learning is either supervised or unsupervised, whereby supervised learning is a case where the target variables are labeled and the model uses the input features (such as p_T or MET) to learn the mapping to the target. These methods are typically used for either classification (assigning to discrete categories) or regression (predicting continous values).
In contrast, unsupervised learning works with unlabeled data and tries to uncover hidden structures on its own. Common unsupervised tasks include clustering (grouping similar events together), association (finding correlations

between variables), and dimensionality reduction (simplifying complex data while keeping the most important information) [7]. For this analysis, we use supervised classification, since we have well-defined simulated samples for both the signal process ($H \rightarrow Z + \gamma_D$) and the main SM backgrounds. The goal is to train a model that can reliably tell them apart based on kinematic features, ultimately improving our sensitivity to a potential dark photon signal.

1.5 TMVA BDT study

The Toolkit for Multivariate Data Analysis (TMVA) provides a structured environment for developing, evaluating and deploying multivariate classifiers in parallel [8]. A standard TMVA workflow typically involves two stages. First, a training phase where classifiers are developed and validated using datasets with predefined signal and background content. Second, an application phase, where the best performing trained models are applied to classify events whose origin (signal or background) is unknown [8].
In this analysis, we employed the ROOT implementation of TMVA, specifically leveraging its `TMVA::Factory` and `TMVA::DataLoader` classes to manage the classification pipeline. To enhance our ability to detect the dark photon signal (γ_D), we implemented a Boosted Decision Tree (BDT) classifier using the Adaptive Boost (AdaBoost) method. Signal events were labeled as positive instances ($x = 1$), while background events were assigned the negative label ($x = 0$). For model development, the full dataset was partitioned according to the TMVA default settings where 75% is allocated for training and 25% is reserved for independent testing. The model was trained using the set of input variables listed in Table 2.

DeltaR lepton (ΔR ($\ell^+\ell^-$))
Missing Transverse Energy significance (met_sig)
$\Delta\phi$ (Z, MET)
$\Delta\phi$ (jet, MET)
Longitudinal momentum component of γ_D (p_z_γ_D)
Leading jet eta (jet_1 η)
Leading lepton transverse momentum ($lep_{1_}\ p_T$)
Sub-leading lepton transverse momentum ($lep_{2_}\ p_T$)
Number of jets (N_ jets)
Number of central jets ($\|\eta\|$ < 2.5)
Number of forward jets ($\|\eta\|$ > 2.5)
p_T_imbalance
Invariant mass of the dilepton system (m$\ell\ell$)

Table 2: Input variables for the BDT

2 Results

This section will cover the preliminary results that were achieved from the TMVA BDT study, the input variables selected are shown in Table 2. The study includes the two signal events and the three background events mentioned above. The results show the correlation matrix distributions, the BDT response and cut efficiencies, and the background rejection versus signal efficiency.

2.1 Correlation Matrix distributions

The linear correlation coefficients for the kinematic input variables used in the BDT training are illustrated in Figure 2. For the signal samples, several strong correlations are observed. Notably, lep1_pt and lep2_pt show a positive correlation (approximately +77%), while number of jets (Njets_f) exhibits strong correlations with both

centralJets_f (+81%) and forwardJets_f (+65%). Conversely, pt_imbalance shows strong negative correlations with lep1_pt (-77%) and lep2_pt (-77%), indicating that higher lepton transverse momenta are typically associated with smaller momentum imbalance in the event. In contrast, the background correlation matrix shows overall weaker correlations, with most coefficients lying below $\pm 30\%$.

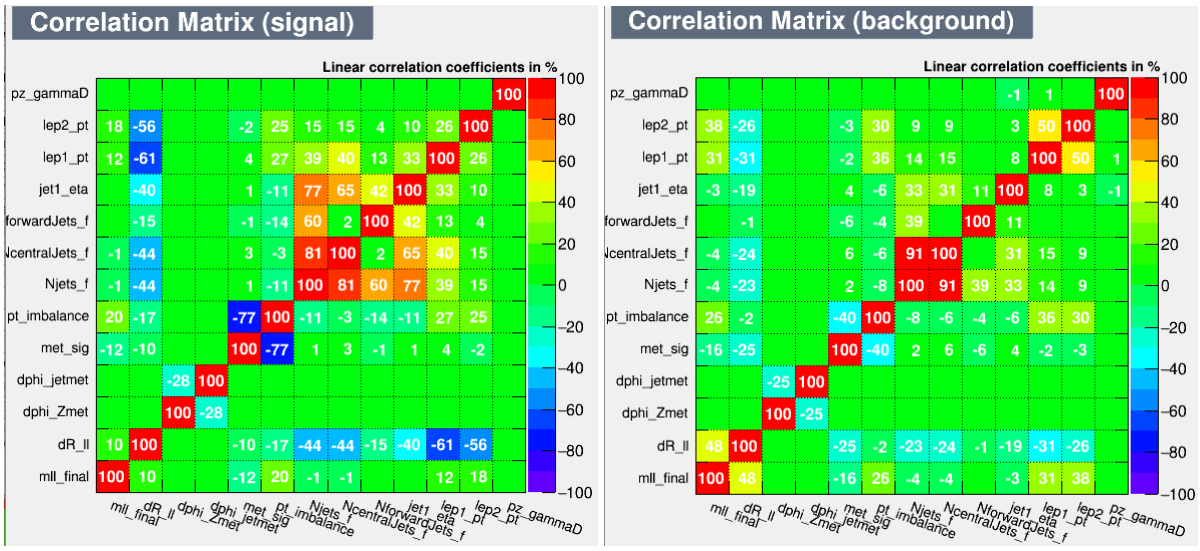

Figure 2: The correlation matrices for the signal (*left*) and background (*right*) samples, illustrating the linear correlation coefficients for the 13 kinematic input variables used in the BDT training.

2.2 *BDT response and performance*

The BDT response and the corresponding cut efficiencies are shown in Figure 3 . In the response plot, the signal (blue) and background (red) distributions are clearly separated, with good agreement between training and test samples. The Kolmogorov-Smirnov (K-S) test: signal (background) probabilities are 0.723 (0.241), respectively, indicating that there is no overtraining. The optimal cut value of -0.03 yields a maximum significance of 27.42, representing a good balance between signal efficiency and background rejection.

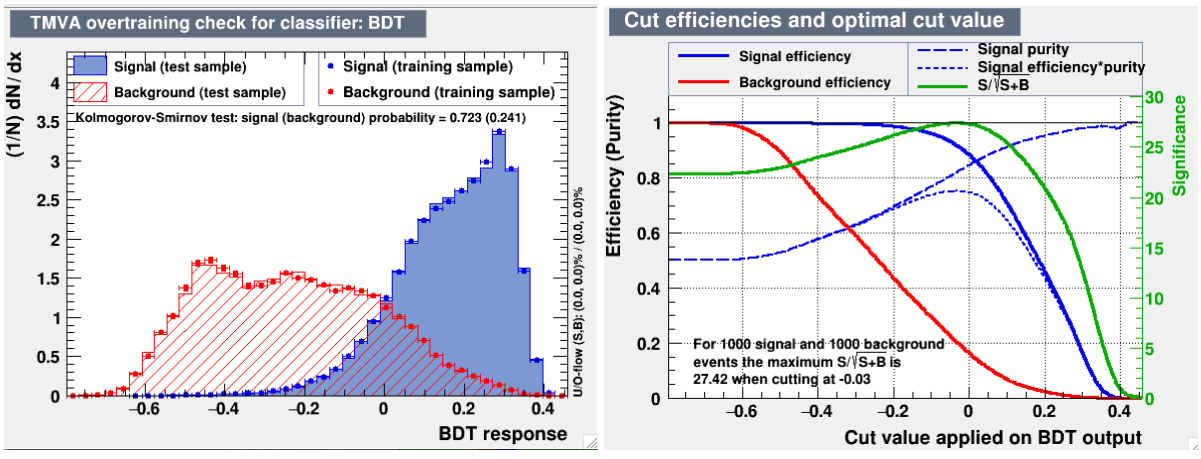

Figure 3: The BDT response distribution (*left*) with K-S test. Signal (background) probability = 0.723 (0.241) and the corresponding cut efficiencies (*right*) with optimal cut at BDT -0.03.

2.3 *Background rejection vs. Signal efficiency (ROC Curve)*

The Receiver Operating Characteristic (ROC) curves are shown in Figure 4. The left plot presents background rejection vs. signal efficiency, while the right plot presents the inverse background efficiency vs. signal effi-

ciency. The curve demonstrates excellent classifier performance, achieving a large area under the ROC curve (AUC $= 0.934$).

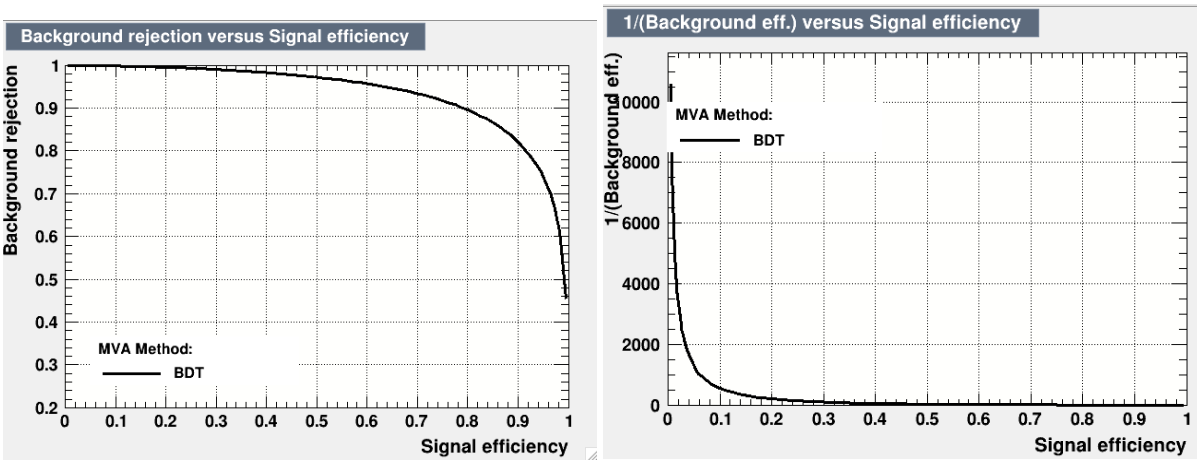

Figure 4: ROC curves showing background rejection versus signal efficiency (*left*) and inverse background efficiency versus signal efficiency (*right*) for the BDT classifier with an integrated AUC of 0.934.

3 Conclusion

This study presents a ML based approach to the search for dark photons in the Higgs boson decay channel ($H \to Z + \gamma_D$) using stimulated ATLAS data. By employing a BDT classifier through the ROOT TMVA framework, we demonstrated that multivariate techniques significantly enhance the separation power between signal and background samples. The very preliminary results presented are the first tentative attempt at the LHC to search for such a signal. An extensive study of SM background processes is under way, as well as an optimisation of ML algorithms for new physics signal extraction using the ATLAS detector data collected in *pp* collisions at 13 TeV and 13.6 TeV. Future work will involve extending the study to include additional ML algorithms such as DNN and GNN to further exploit event topology information. Ultimately, this approach aims to increase the sensitivity of searches for exotic Higgs decays and shed light on possible connections between the SM and a hidden dark sector.

References

[1] G. Aad, B. Abbott, D. C. Abbott, K. Abeling, S. H. Abidi, and et al., "Search for dark photons from higgs boson decays via zh production with a photon plus missing transverse momentum signature from pp collisions at $\sqrt{s} = 13$ tev with the atlas detector," *Journal of High Energy Physics*, vol. 2023, no. 7, jul 2023. [Online]. Available: http://dx.doi.org/10.1007/JHEP07(2023)133

[2] M. Fabbrichesi, E. Gabrielli, and G. Lanfranchi, *The Physics of the Dark Photon: A Primer*. Springer International Publishing, 2021. [Online]. Available: http://dx.doi.org/10.1007/978-3-030-62519-1

[3] TheATLASCollaboration, "The atlas experiment at the cern large hadron collider," *Journal of Instrumentation*, vol. 3, no. 08, p. S08003, aug 2008. [Online]. Available: https://doi.org/10.1088/1748-0221/3/08/S08003

[4] L. Evans and P. Bryant, "Lhc machine," *Journal of Instrumentation*, vol. 3, no. 08, p. S08001, aug 2008. [Online]. Available: https://doi.org/10.1088/1748-0221/3/08/S08001

[5] J. Long, "The atlas inner detector tracking trigger at 13 tev in lhc run-2 and new developments on standard and unconventional tracking signatures for the upcoming lhc run-3," 2022. [Online]. Available: https://cds.cern.ch/record/2835232

[6] S. Liao, B. Mellado, and X. Ruan, "Performance of missing transverse energy reconstruction in pp collisions at 13 tev in the diphoton channel with atlas," 2022. [Online]. Available: https://events.saip.org.za/event/100/papers/42/files/27-Shell-may_Revised_09_Sept_2019.pdf

[7] J. Davies, "The Search for Dark Matter at the ATLAS Detector using Machine Learning," Ph.D. dissertation, Queen Mary, U. of London (main), Queen Mary, U. of London (main), 2025.

[8] A. Höcker, P. Speckmayer, J. Stelzer, F. Tegenfeldt, H. Voss, and K. Voss, *TMVA: Toolkit for Multivariate Data Analysis with ROOT*, CERN, 2007, arXiv:physics/0703039. [Online]. Available: http://tmva.sourceforge.net/

This page intentionally left blank.

Probing the pygmy states of ^{154}Sm with a quasi-monochromatic linearly-polarised photon beam

R E Molaeng[1,2], L Pellegri[1,2], L M Donaldson[2], I T Usman[1], P Adsley[3], A D Ayangeakaa[4,5], J J Carroll[6], C J Chiara[6], S W Finch[5,6], D Gribble[4,5], A Gupta[7], J Isaak[7], X K James[4,5], R V F Janssens[4,5], S R Johnson[4,5], J Kleemann[7], T Kowalewski[4,5], B Löher[8], O Papst[7], N Pietralla[7], K Prifti[7], J Santucci[3], A Saracino[4,5], D Savran[8], B Wellons[3], V Werner[7]

[1]School of Physics, University of the Witwatersrand, Johannesburg, South Africa
[2]SSC Laboratory, iThemba LABS, Faure, South Africa
[3]Department of Physics & Astronomy and Cyclotron Institute, Texas A&M University, College Station, Texas, USA
[4]Department of Physics and Astronomy, University of North Carolina, Chapel Hill, North Carolina, USA
[5]Triangle Universities Nuclear Laboratory, Durham, North Carolina, USA
[6]U.S. Army Combat Capabilities Development Command Army Research Laboratory, Adelphi, Maryland, USA
[6]Department of Physics, Duke University, Durham, North Carolina, USA
[7]Technische Universität Darmstadt, Department of Physics, Institute for Nuclear Physics, Darmstadt, Germany
[8]GSI Helmholtzzentrum für Schwerionenforschung GmbH, Darmstadt, Germany

E-mail: 1511527@students.wits.ac.za

Abstract. The quasi-monochromatic linearly-polarised photon beam produced at the HIγS facility of the Triangle Universities Nuclear Laboratory (TUNL) with an energy spread below 2% is highly selective to a narrow excitation energy region, allowing for the isolation of weakly excited states. This polarised beam in conjuction with the Clover Array configuration enables spin-parity assignments through angular distributions and azimuthal γ-intensity asymmetries. In this work the low-lying dipole strength, commonly referred to as the Pygmy Dipole Resonance (PDR), is investigated from 3.8 MeV up to 7.1 MeV. The electric dipole nature of these states was preliminarily verified from the experimental data for excitations ranging from 3.8 to 6.4 MeV with state by state analysis in ^{154}Sm.

1 Introduction

The Pygmy Dipole Resonance (PDR) is described within the three-fluid hydrodynamical model as an out-of-phase oscillation of a core that has $N = Z$ against a neutron skin [1]. It is located below the well known Giant Dipole Resonance (GDR) and manifests in even-even nuclei as a concentration of 1^- states below the neutron threshold. Nonetheless, this simplistic collective picture of the PDR and its connection to neutron excess has been questioned. This is because some studies show low-lying $E1$ strength in nuclei with little or no neutron skin [2, 3]. Also, when advanced microscopic self-consistent mean-field models are used, transition densities reveal that the PDR is isospin mixed [4]. An alternative interpretation of the origin of this low-lying $E1$ strength suggests a toroidal excitation mode [5, 6, 7].

An attempt to test for collectivity of the PDR can be done in the case of an axially deformed nucleus. If the PDR is associated with a collective picture as described by the three-fluid hydrodynamical model, a splitting of the strength with respect to the K quantum number can be expected as is the case for the GDR in deformed nuclei. A potential interpretation would be that a deformed $N = Z$ core oscillates against a neutron skin along the two asymmetry axes. Recently two studies on ^{154}Sm, one using $(\alpha, \alpha'\gamma)$ and the other (p, p$'\gamma$) reactions, have showed no proof of K-splitting [8]. Another study on the axially deformed ^{150}Nd through a (γ, γ') reaction also showed no splitting with respect to the K quantum number [9]. The current study can provide complementary information on the investigation of the K quantum number and the role of deformation in the PDR region, and extend the use of the (γ, γ') reaction to the case of ^{154}Sm.

In this current study a Laser Compton Backscattering (LCB) technique which generates a quasi-monochromatic photon beam with a narrow energy range is used to investigate the PDR in ^{154}Sm. At energies lower than the particle emission threshold, reactions with photons are purely electromagnetic, allowing for the nuclear response information to be extracted in a model-independent way. Currently, two facilities are using this type of photon source for nuclear physics research: the LCB facility at the Tsukuba Electron Ring for Accelerating and Storage (TERAS) at the National Institute of Advanced Industrial Science and Technology (AIST), as well as the High Intensity γ-ray Source (HIγS) facility at Triangle Universities Nuclear Laboratory (TUNL). Due to the conservation of polarisation in the scattering process, the photon beam produced by LCB benefits from being nearly 100% linearly polarised when a corresponding linearly polarised laser is utilised. This characteristic is useful for determining spin-parity quantum numbers of nuclei during experiments. This advantage of LCB has been exploited to determine the $E1$ character in the PDR region in several isotopes [10].

In this type of experiments, low-spin transfer is preferred and therefore $E1$ transitions can be disentangled from $M1$ transitions through their angular distributions (adapted from angular correlation formalism described in [11]) and more specifically by using the asymmetry method. The asymmetry (ϵ) of a γ-ray transition is deduced by

$$\epsilon = \frac{A_{\parallel} - A_{\perp}}{A_{\parallel} + A_{\perp}} = p\Sigma \tag{1}$$

where $A_{\parallel}$ is the intensity, corrected for the full-energy peak efficiency, of the ground-state transitions in detectors placed parallel to the polarisation plane, while $A_{\perp}$ refers to those that are perpendicular to the polarisation plane. The polarisation plane refers to the geometric plane defined by the propagation direction of the γ-ray beam and the oscillation direction of its electric field vector. The analysing power

$$\Sigma = \frac{W_{\parallel} - W_{\perp}}{W_{\parallel} + W_{\perp}} \tag{2}$$

measures the sensitivity to the parity quantum number of a γ-ray transition, where $W_{\parallel}$ and $W_{\perp}$ are the angular distributions of a specific γ-ray emitted in the parallel and perpendicular direction to the polarisation plane, respectively. Since detectors are not point-like objects, the factor p accounts for the solid-angle effects and intrinsically incorporates both the polarisation sensitivity and the degree of polarisation. This factor is inherently accounted for in Geant4 simulations, with angular distributions weighted by the detector acceptance. Figure 1 shows a three-dimensional visualisations of how the radiation of different multipolarities is emitted with respect to the polarisation plane and direction (visualisation created with the mpl_toolkits.mplot3d module of the Matplotlib library). By placing detectors in a certain direction, the detection of the γ-rays with the multipolarity of interest can be optimised and be easily disentangled from others.

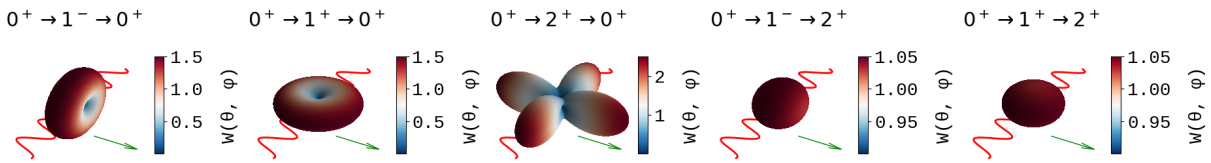

Figure 1: Angular distributions for different Nuclear Resonance Fluorescence (NRF) transitions excited with linearly polarised photon beams. Sinusoidal line shows the γ-beam in the polarisation plane while the green arrow shows the polarisation direction.

2 Experiment details

The experiment took place at the HIγS facility. This facility, which is operated by TUNL, is a new-generation Compton γ-ray source with an increased γ-ray flux and a wide range of beam energy from 1-100 MeV [12]. The facility provides a quasi-monocromatic linearly or circularly polarised photon beam with an energy spread of 3-5% for (γ, γ') experiments. However, with special beam tuning and selection of collimator, and by compromising on photon flux, it is possible to achieve an energy spread below 2%. This photon beam is generated using intracavity Compton backscattering of laser light from electron beam bunches.

In the current experiment a linearly polarised photon beam ranging from 3.8-7.1 MeV as shown in Figure 2 was impinged on 2.5 g of ^{154}Sm in oxide form, enriched to >90% for the isotope of interest. The target was mounted at the target position of the Upstream Target Room (UTR) and the Clover array consisting of five High-Purity Germanium (HPGe) clover detectors, four large-volume cerium-doped Lanthanum Bromide ($LaBr_3$:Ce) and three Cerium Bromide ($CeBr_3$) detectors in a tight geometry around the target measured the subsequent γ-decay [13]. The HPGe detectors provided high energy resolution, whereas $LaBr_3$:Ce detectors offered both high efficiency and high counting rates, and $CeBr_3$ detectors provided high counting rates. A coaxial HPGe detector can be moved in-beam at 0° to measure the spectral distribution of the photon beam.

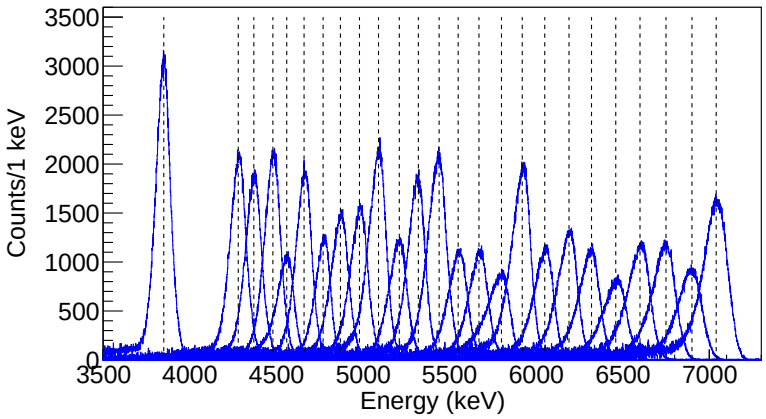

Figure 2: Beam-profile measurements, ranging from 3.8 to 7.1 MeV, with a spread of $< 2\%$ of the beam energy.

3 Data analysis and discussions

As mentioned earlier, the asymmetry method depicted in Eq. 1 requires theoretical asymmetry values to be deduced from Geant4 simulations. This is done by simulating the γ-rays of a given transition with a defined angular distribution W. For this purpose a compact *utr* Geant4 simulation code was used [14]. To verify that the simulations setup matches the experimental setup, an efficiency curve comparison of an isotropic source was done for both setups. In the simulations, the efficiency is determined from a monoenergetic γ-ray source placed at the target position while in the experiment a ^{56}Co source was used. Due to the tight detector geometry, measuring distances from the detectors to the target was challenging. Callipers were used to measure distances from the detector face to the outer radius of the beam pipe, with uncertainties of at least 3 mm or larger in some cases. To account for this uncertainties, detector distances in the simulation were adjusted and in some cases a scaling factor was applied to match simulated efficiencies with experimental efficiencies. In all cases, the general shape of energy dependency of the efficiency was well reproduced by the Geant4 simulations. A comparison of such efficiencies

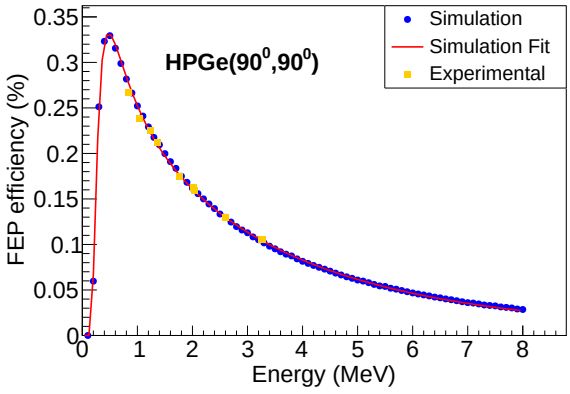

Figure 3: Comparison of the absolute Full-Energy Peak (FEP) efficiency of the experimental setup and the Geant4 simulation setup for an HPGe clover detector with an isotropic source.

for an HPGe clover detector at ($\theta = 90°, \phi = 90°$), where θ and ϕ are the polar and azimuthal angles, respectively, with respect to the polarisation plane is shown in Figure 3.

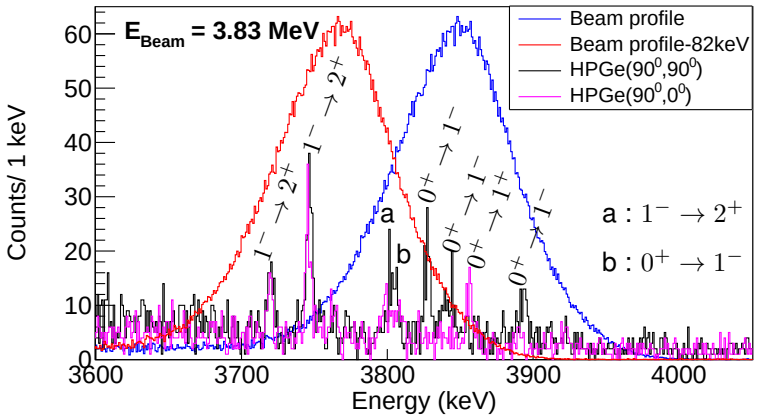

Figure 4: Energy spectrum of the beam profile (blue), beam profile shifted by 82 keV to the left (red), and γ decay measured with HPGe Clover detectors at $(90°, 0°)$ and $(90°, 90°)$ (magenta and black, respectively). The shifted beam profile highlights the position of the energy of the transition to the 2_1^+ state.

Typical spectra obtained in these NRF experiments are shown in Figure 4. In addition to the beam profile, the shifted profile is also shown. It has been shifted by 82-keV to the left to show where the decay to the 2_1^+ of ^{154}Sm would be located on the γ-decay spectrum. Variations in the peak intensities observed in the two detectors reflect the angular distributions associated with the respective transitions indicated on the peaks. By applying the asymmetry calculations defined in Eq. 1, the spins and parities of the transitions can be assigned. In this work more than 30 states between 3.8-6.4 MeV have been preliminarily characterised as $J^\pi = 1^-$. One state at 3.856 MeV was characterised as of $J^\pi = 1^+$ nature.

4 Summary and outlook

In summary, the high-selectivity with high-resolution capabilities at the HIγS facility has allowed for the measurements of the low-lying dipole transitions in ^{154}Sm. These states have been preliminarily verified to be predominantly of $E1$ nature. While the analysis is on-going, we expect to extract the branching ratios, cross-sections and investigate the K quantum number of the PDR states in ^{154}Sm. Average properties will also be extracted from the $LaBr_3$ spectra through an adapted fitting procedure used in [9, 15].

Acknowledgements

This work is based on the research supported in part by the National Research Foundation of South Africa (Grants No. MND210503598725, No. REP_SARC180529336567) and the US Department of Energy (Grants No. DE-FG02-97ER41041 (UNC), No. DE-FG02-97ER41033 (TUNL)).

References

[1] R. Mohan, M. Danos, L.C. Biedenharn, Phys. Rev. C 3 (1971) 1740.

[2] T.D. Poelhekken et al., Phys. Lett. B 278 (1992) 423.

[3] F. Bauwens et al., Phys. Rev. C 62 (2000) 024302.

[4] E.G. Lanza et al., Prog. Part. Nucl. Phys. 129 (2023) 104006.

[5] J. Endres et al., Phys. Rev. Lett. 105 (2010) 212503.

[6] J. Kvasil et al., Phys. Rev. C 84 (2011) 034303.

[7] A. Repko et al., Eur. Phys. J. A 55 (2019) 242.

[8] L. Pellegri et al., First Observation of the Pygmy Dipole Resonance in a Heavy Deformed Nucleus [Manuscript submitted for publication] (2025).

[9] O. Papst et al., Phys. Rev. Lett. 135 (2025) 052501.

[10] A. Zilges et al., Prog. Part. Nucl. Phys. 122 (2022) 103903.

[11] L.W. Fagg and S.S. Hanna, Rev. Mod. Phys. 31 (1959) 711.

[12] H.R. Weller et al., Prog. Part. Nucl. Phys. 62 (2009) 257–303.

[13] A. D. Ayangeakaa, U. Friman-Gayer, and R. V. F. Janssens, Innovation News Network (2021), https://innovationnewsnetwork.com/nuclear-structure/10491/https://innovationnewsnetwork.com/nuclear-structure/10491/, (last accessed July 2025).

[14] U. Friman-Gayer et al., https://github.com/u-eff-gee/utr u-eff-gee/utr:GEANT 4 simulation of the Upper Target Room (UTR) at the HIGS facility (last accessed 2025) https://github.com/u-eff-gee/utrhttps://github.com/u-eff-gee/utr.

[15] J. Kleemann et al., Phys. Rev. Lett. 134 (2025) 022503.

This page intentionally left blank.

Quality Assurance for LVPS Boards in the Phase-II Tile Calorimeter Upgrade

Vongani Chabalala[1,2], Thabo Pilusa[1,2], Ryan Mckenzie[1,2], Chuene Mosomane[2], and Bruce Mellado[1,2]

[1] School of Physics and Institute for Collider Particle Physics, University of the Witwatersrand, Johannesburg Wits 2050, South Africa

[2]iThemba LABS, National Research Foundation, PO Box 722, Somerset West 7129, South Africa

E-mail: vongani.cyril.chabalala@cern.ch

Abstract. The Phase-II upgrades of the Tile Calorimeter (TileCal) in the ATLAS detector are crucial for advancing high-energy physics research and preparing CERN for the High Luminosity Large Hadron Collider (HL-LHC) era. This upgrade includes major improvements to the detector systems, notably the integration of radiation-resistant transformer-coupled buck converters, known as Low-Voltage Power Supply (LVPS) boards. These boards are crucial for converting 200V direct current (DC) power into the 10V DC power required for detector operation. In collaboration with the University of Wits and iThemba LABS, over a thousand LVPS boards will be developed. A comprehensive quality assurance (QA) process is being implemented to improve the reliability of the LVPS boards used in the ATLAS Hadronic TileCal. These boards must operate reliably under the challenging conditions expected during the High-Luminosity LHC (HL-LHC) era, which include higher radiation levels, increased trigger rates, and significant event pile-up. Rigorous initial testing is a critical part of this QA process, ensuring that each board meets the performance and durability standards required for long-term operation in this demanding environment. The next phase will involve compiling the data from these tests and analyzing it further using advanced machine learning techniques. This data-driven approach provides deeper insights into the boards' behavior under extreme conditions, enabling optimization of their design and performance to meet the rigorous requirements of the HL-LHC upgrade.

1 Introduction

The Tile Hadronic Calorimeter (TilCal) shown in Figure 1 is located around the LAr calorimeter and measures the energy of hadronic particles that don't leave all their energy in the LAr calorimeter. It collects about 30% of the energy from particle jets and is important for measuring jets, missing energy, jet structure, separating electrons from other particles, and helping with triggering, including detecting muons. It consists of central long barrels (LB) and end-cap barrels (EBA and EBC), forming four logical sub-detectors with an inner radius of 2.28 m and an outer radius of 4.23 m. The two LB sections are each 2.82 m long, while the end-cap barrels are 2.91 m long, providing coverage up to a rapidity of 1.6. As shown in Figure 1, the calorimeter is constructed from alternating layers of steel and plastic scintillator plates. When particles interact with the steel layers, they produce secondary particle showers. These secondary particles then pass through the plastic scintillators, generating photons, which are subsequently converted into an electrical signal. The signal intensity is proportional to the energy deposited by the original particle. The Low-Voltage Power Supply (LVPS) system is located in each wedge-shaped section of

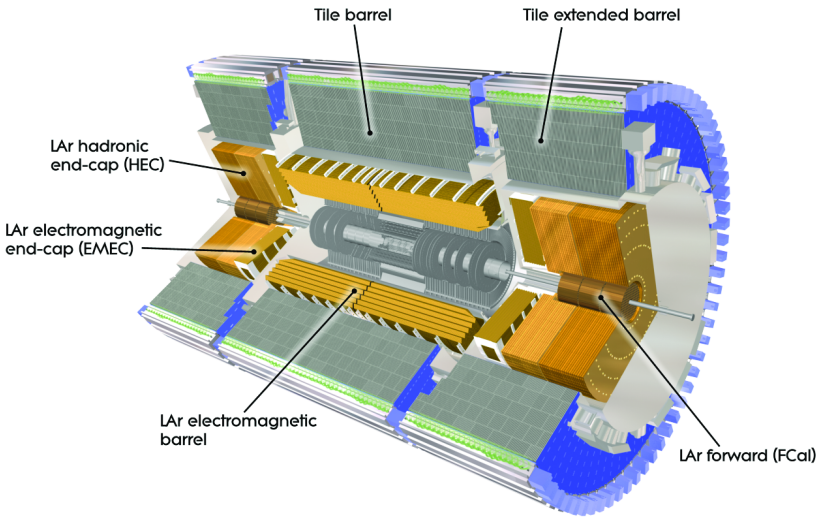

Figure 1: The ATLAS Inner Detector and Tile Calorimeter at CERN's Large Hadron Collider (LHC) [1, 4].

the TileCal. It sits inside an electronics drawer, where it provides power to all the front-end detector electronics, which are also placed in the same drawer [1, 2, 3]. The upgrades in TileCal for Phase II (part of the HL-LHC project) aim to handle more than ten times the current amount of data (integrated luminosity). To achieve this, several components of the calorimeter will be upgraded, including the Low-Voltage Power Supply (LVPS) boards, which are located on the detector [3].

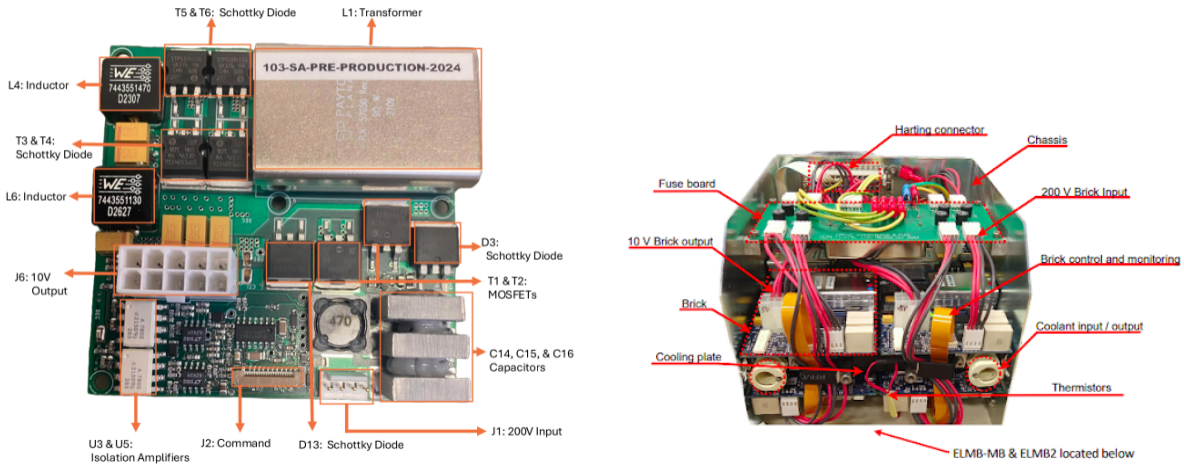

Figure 2: *(left)* Top view of the WITS LVPS board. *(right)* The LVPS box is installed within the TileCal.

2 TileCal Low Voltage Power Supply

As part of the ATLAS Phase-II upgrade, the Low Voltage Power Supply (LVPS) board shown in Figure 2 is a critical component responsible for delivering power to the detector electronics. Each board functions as an isolated DC-DC converter, stepping down a 200 V input to a regulated 10 V output, and delivering up to 100 W of power. It operates using a two-switch Forward converter topology at 300 kHz and includes a step-down transformer for electrical isolation, along with auxiliary windings for internal control and monitoring. The board measures key electrical parameters such as input/output voltage and current, and temperatures on both primary and secondary

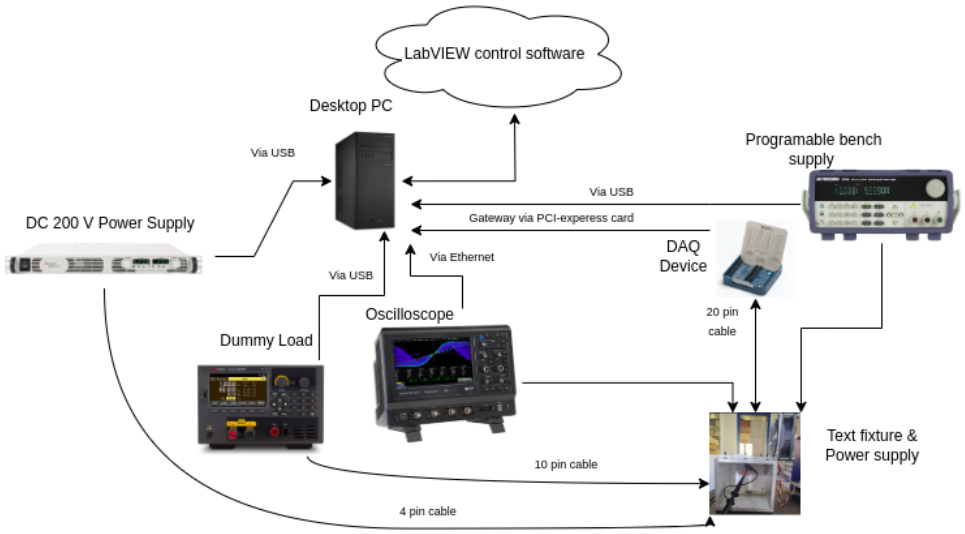

Figure 3: Block diagram of the test station used for QA of the LVPS boards [3].

sides and transmits this data to the ELMB motherboard. The ELMB also provides start-up and control signals to the board. The LVPS supports a nominal current of 3 A, with peak capability up to 6 A, and features built-in protection mechanisms for overcurrent (10.5 A), overvoltage (12 V), and overtemperature (70°C). Designed for operation in the harsh environment inside the ATLAS detector, the LVPS is custom-built for radiation hardness and high reliability. It is resilient to single-event upsets, tolerant of neutron-induced displacement damage, and can withstand a total ionizing dose of up to 40 krad, while also operating reliably in magnetic fields above 0.02 T. Half of the LVPS boards are produced and tested by the University of the Witwatersrand in collaboration with iThemba LABS. Each LVPS box contains eight identical boards, installed within the TileCal structure. Each LVPS box contains eight identical boards, all of which are installed within the Tile Calorimeter (TileCal), as illustrated in Figure 2 [2, 3, 5]. This paper focuses solely on the development of the test station used for the initial and final assessment of the pre-production LVPS boards and their output performance.

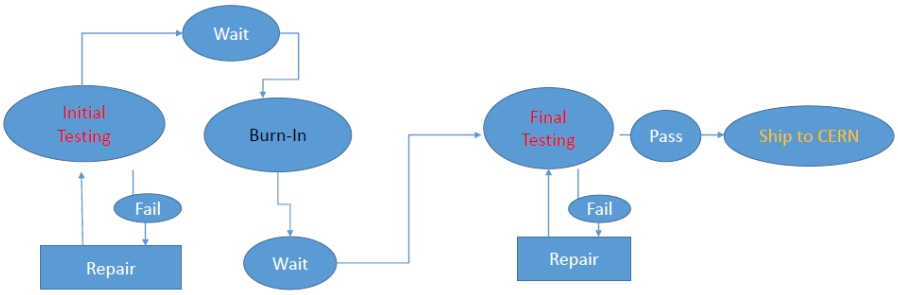

Figure 4: Diagram of the final quality assurance process used for the LVPS Boards.

3 Development of the Test Station

The University of the Witwatersrand and iThemba LABS developed an upgraded version of the test station to ensure the reliability and quality of the new TileCal Low Voltage Power Supply (LVPS) boards. The test station quickly quantifies a multitude of performance metrics for an LVPS board. It includes a 200 V DC power supply, which provides precise and controlled power delivery to the LVPS board. An oscilloscope is employed to visualize and analyze electrical signals generated by the board. A data acquisition (DAQ) system is used to collect, measure, record, and analyze both physical and electrical signals associated with the board's operation. The LVPS board is mounted on a metal case that provides structural support. An interface board connects the DAQ system to external

Parameter	Minimum	Maximum
Frequency Standard Deviation	0	1000
Duty Cycle Standard Deviation	0	0.1
Frequency Maximum (Hz)	290000	350000
Frequency Minimum (Hz)	250000	310000
Minimum Stable Load (A)	2	2.3
Minimum Output Voltage (V)	9.8	10.2
Over Voltage Protection (V)	11.5	12
Over Current Protection (A)	6.25	6.75
Output Root Mean Square Voltage	0	0.5
Clock Duty Cycle Average	0	40
Clock Duty Cycle Average Standard Deviation	0	0.15
Start-Up Delay (Max)	0.08	0.2

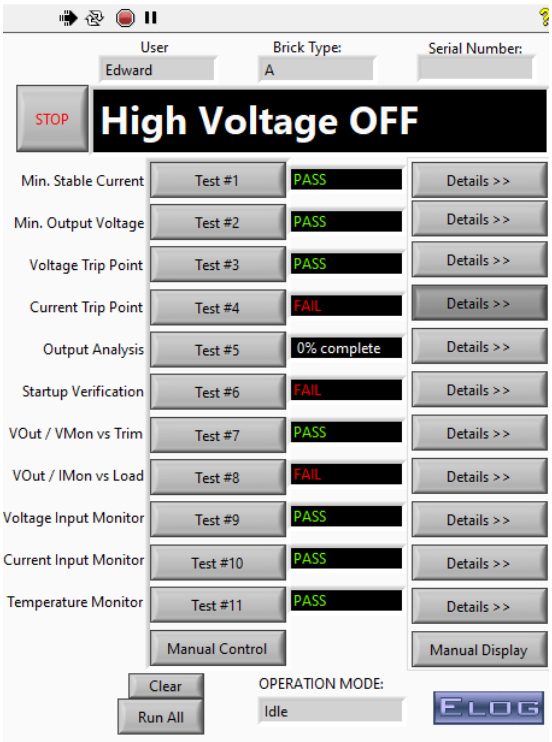

Figure 5: Overview of LVPS board testing: *(left)* validated electrical parameters and their acceptable ranges; *(right)* test hardware configuration.

measurement instruments and control hardware, while a dummy load receives power from this interface board to simulate real operating conditions. LabVIEW software is used to control the entire test setup and to read out specific parameters necessary for the evaluation, as illustrated in Figure 3 [3].

4 LVPS Board Production and Quality Assurance Procedure

To ensure the reliability of the LVPS boards used in TileCal, a robust quality assurance (QA) process has been established. Over a thousand units are planned for production, with each one undergoing rigorous testing according to the criteria outlined in Figure 5. The QA workflow, illustrated in Figure 4, is structured into three main phases: initial testing at the board assembly site, followed by a burn-in process, and final testing at Wits. The initial and final testing phases use the same equipment and procedures, differing only in their timing: initial testing is conducted before the Burn-in process, while final testing takes place afterward. These tests assess multiple performance parameters to ensure that each Brick operates according to its design specifications. Testing both before and after Burn-in helps identify any performance degradation caused by the process and allows for the detection and removal of LVPS boards that suffer permanent damage, ensuring that only fully qualified boards are delivered to CERN for integration into the detector system. Key parameters evaluated during testing include the output voltage (10 V) and the Over Current Protection (OCP) feature. The OCP acts as a safety mechanism designed to protect both the power supply and the connected electronics from potential damage due to excessive current. Figure 5 (right) shows the LabVIEW test panel running on the PC, listing all required tests for the LVPS board. Each board is tested individually for a duration of 10 minutes. A failure in any single test results in the board being marked as failed. Only fully passing boards are approved for shipment to CERN.

5 Pre-production Test Station Results

Each LVPS board underwent both initial and final testing, with each test lasting approximately 10 minutes. The data collected throughout the process was recorded and subsequently analyzed. Figures 6 present the output voltage and Over Current Protection (OCP) results for all LVPS boards that successfully passed each stage of testing, including the initial evaluation, Burn-In phase, and final assessment. The results show that all boards tested successfully stepped down the input voltage from 200 V to 10 V as expected. Output voltage and OCP

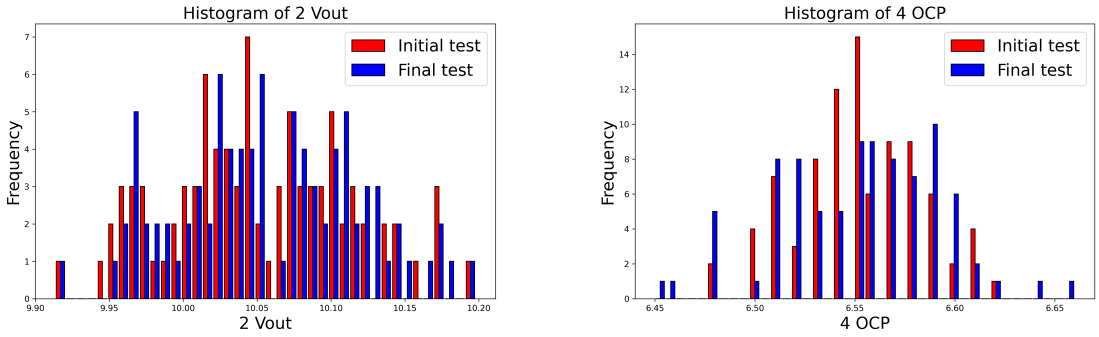

Figure 6: *(left)* Comparison of output voltage and *(right)* OCP characteristics as a function of the number of LVPS boards (frequency).

characteristics were evaluated across all LVPS boards. The output voltage remained within the expected range, while the OCP threshold scaled appropriately with the number of boards, confirming correct functionality and effective protection behavior. All boards that met the required performance criteria were shipped to CERN for installation into the LVPS boxes.

6 Conclusions and Outlook

The upgraded Low Voltage Power Supply (LVPS) system for the Tile Calorimeter is a critical component of the ATLAS Phase-II upgrade, designed to deliver stable 10V power from a 200V input with built-in protections and monitoring, ensuring reliable operation under the harsh conditions of the High-Luminosity LHC. To guarantee the quality and performance of these boards, a dedicated test station was developed by the University of the Witwatersrand and iThemba LABS. This automated system enables efficient and repeatable evaluation of all critical performance metrics during both the initial and final testing stages. The testing procedure includes a burn-in phase to detect early failures and ensure reliability under realistic conditions. The pre-production testing campaign demonstrated that the LVPS boards consistently met design specifications, particularly in maintaining output voltage and effective overcurrent protection. All passing boards were qualified for integration into the ATLAS detector. The successful development of both the LVPS boards and the associated test infrastructure represents a significant milestone in ensuring the readiness of TileCal for future high-luminosity operations at the LHC.

References

[1] J. Abdallah, P. Adragna, C. Alexa, R. Alves, P. Amaral, A. Ananiev, K. Anderson, X. Andresen, A. Antonaki, V. Batusov *et al.*, "Mechanical construction and installation of the atlas tile calorimeter," *Journal of Instrumentation*, vol. 8, no. 11, p. T11001, 2013.

[2] E. Nkadimeng, R. Mckenzie, S. Moayedi, S. Nemecek, H. Hadavand, B. Mellado, and R. Van Rensburg, "A monitoring and control test bench for assessing the upgraded low voltage power supplies for the atlas tile calorimeter phase-ii upgrade front-end electronics," *Journal of Instrumentation*, vol. 17, no. 07, p. P07025, 2022.

[3] E. Nkadimeng, "Reliability testing and upgrade of a low voltage power supply for the front-end electronics of the atlas tile calorimeter phase-ii upgrade," Ph.D. dissertation, University of the Witwatersrand, Johannesburg (South Africa), 2022.

[4] V. C. Chabalala, "An overview of the test station involved in the production of the lvps bricks for the phase ii upgrade of the tile calorimeter." *Presentation Slides of DIS2025, Cape Town, South Africa*, 2025.

[5] R. Mckenzie, "Quality assurance testing of the atlas tile-calorimeter phase-ii upgrade low-voltage power supplies," *Proceedings of the SAIP2021, Johannesburg, South Africa*, pp. 22–30, 2021.

This page intentionally left blank.

The nuclear level density of ^{192}Os($\alpha, d\gamma$)^{194}Ir

S. P. E. Magagula[1,2], M. Wiedeking [1,2,3], L. Pellegri [1,2], B. V. Kheswa [4], A. C. Larsen [5], K. S. Beckmann [5], F. L. Bello Garrote [5], L. Crespo Campo [5], A. Görgen [5], M. Guttormsen [5], I. Kullmann [5], K. L. Malatji [1], V. Modamio [5], T. Renstrøm [5], E. Sahin [5], S. Siem [5], G. M. Tveten [5], F. Zeiser [5], J.E. Midtbø [5]

[1]SSC Laboratory, iThemba LABS, Somerset West 7129, South Africa.
[2]School of Physics, University of the Witwatersrand, Johannesburg 2050, South Africa.
[3]Lawrence Berkeley National Laboratory, Berkeley, California, USA.
[4]Department of Physics, University of Johannesburg, Doornfontein 2028, South Africa.
[5]Department of Physics, University of Oslo, N-0316 Oslo, Norway.

E-mail: spemagagula@gmail.com

Abstract. The nuclear level density (NLD) refers to the number of energy levels per unit of excitation energy. In this study, the NLD of the ^{194}Ir isotope was extracted from coincidence measurements of the ^{192}Os(α,dγ) reaction through the Oslo Method. The data were obtained from an experiment conducted at the Oslo Cyclotron Laboratory, where a 30 MeV α beam was directed onto the ^{192}Os target. Particular emphasis is placed on the normalization procedure employed in the extraction of the NLD. Additionally, the pairing energy, which manifests in the structure of the NLD, was determined to be 1.43 MeV.

1 Introduction

In nuclear physics and nuclear astrophysics, the nuclear level density (NLD) plays a pivotal role as an input parameter while calculating reaction cross sections with the Hauser Feshbach model [1], which are essential for understanding elemental abundances, neutron densities, and nucleosynthesis in general. NLD data are an essential component in the design of nuclear power plants [2, 3] and are also used in calculations related to the transmutation of nuclear waste [4]. Because the NLD is a fundamental parameter necessary for understanding many complex nuclear phenomena, it must be extracted accurately and normalized as precisely as possible.

In this study, a new experimental NLD of the ^{194}Ir nucleus is obtained using the ^{192}Os($\alpha, d\gamma$)^{194}Ir reaction and is presented along with a detailed explanation of its step-by-step normalization process. The following sections will give details of the experimental setup, data analysis, normalization technique, and conclusions drawn from the shape of the measured NLD. The ^{194}Ir NLD data will give important information on calculating neutron capture cross sections, which will in turn be useful in determining neutron density in a giant branch star and around the Ir mass region. Since these data are intended for the calculation of neutron capture cross sections, and these for ^{194}Ir are well studied, the ^{194}Ir findings will be used to benchmark other Ir isotopes.

2 Experimental details

The experiment was conducted in 2017 at the Oslo Cyclotron Laboratory over a 5-day period. The accelerator MC-35 Scanditronix cyclotron was used, which was coupled to two detector systems: the Silicon Ring (SiRi) [5] particle telescope used for detecting charged particles, and the CACTUS array, which is a sodium iodide (NaI(Tl)) [6] detector system used for γ-ray detection.

SiRi is an array of eight silicon detectors, individually comprising a thin front detector (130 μm) and a thick back detector (1550 μm). Each front detector is segmented into eight silicon strips, yielding a total of 64 $\Delta E - E$ silicon detector configurations. At the time of the experiment, the CACTUS detector array consisted of 26 NaI(Tl) detectors. The experiment used a 30 MeV α beam for the ^{192}Os$(\alpha, d\gamma)^{194}$Ir reaction. The ^{192}Os target that was used in the experiment had a thickness of 0.33 mg/cm^2 and was on ^{12}C backing [7]. While the isotopic enrichment of the target was very good approximately 99%, it was slightly oxidized. In addition, a self-supporting ^{60} Ni target was positioned within the target chamber under similar experimental conditions for 2 hours for calibration purposes. On the basis of the slight oxidation the ^{16}O$(\alpha, p\gamma)$ reaction also took place. From the ^{16}O$(\alpha, p\gamma)^{19}$F, the ^{19}F known peaks were also used for the γ-calibration.

3 Data analysis

Data were analyzed with the Oslo method [8, 9], which is internationally recognized in nuclear physics and has been used in various studies [10, 11, 12]. The Oslo method [8] is a combination of techniques that allows users to simultaneously extract the NLD and γ-ray strength function (γ-ray SF) from particle - γ coincidence data. There are four fundamental steps to the Oslo method, namely: Unfolding of the coincidence matrix [13], the extraction of the primary γ matrix [14], extraction and normalization of the NLD and γ-ray SF. We assume that the generalized Brink-Axel hypothesis [15, 16, 17] is true, and hence the γ-ray transmission coefficient ($\mathcal{T}$) is independent of the excitation energy, spins and parities of the initial and final states. Therefore, from the first generation matrix $P(E_x, E_\gamma)$ it can be deduced that:

$$P(E_x, E_\gamma) \sim \mathcal{T}(E_\gamma)\, \rho(E_x - E_\gamma). \tag{1}$$

Here $\rho(E_x - E_\gamma)$ is the NLD at the final excitation energy $E_f = E_x - E_\gamma$ following the release of the first γ-ray. Furthermore, we fit a theoretical first-generation matrix, which is written as a function of the NLD and the transmission coefficient ($\mathcal{T}$), to the experimental one using χ^2 minimization in which the NLD and $\mathcal{T}$ are taken as free parameters. Thus, the NLD and $\mathcal{T}$ are simultaneously extracted from the experimental first-generation matrix [8].

4 Results and discussion

The Oslo method gives the shape of the NLD or the functional form of ρ and $\mathcal{T}$, this means that it is possible to obtain infinite fits for one possible solution of the NLD. Hence, to acquire the correct slope and absolute value, the data must be normalized.

The following equation gives an operational form of the NLD [8, 9],

$$\tilde{\rho}(E_x - E_\gamma) = \rho(E_x - E_\gamma) A exp[\alpha(E_x - E_\gamma)]. \tag{2}$$

To normalize the NLD we need to determine the absolute value of A. Hence, ρ is modified to fit the known discrete states at low energies and resonance spacing measurements at the neutron separation energy S_n, see figure 1 and Table 2. The NLD at a given E_x is defined as follows, see Table 1 [18],

$$\rho(E_x) = \frac{\sqrt{\pi}}{12} \frac{exp(2\sqrt{aU})}{a^{1/4} E_x^{5/4}} \frac{1}{\sqrt{2\pi}\sigma}, \tag{3}$$

where σ is the spin cut-off parameter and a is the level density parameter [19, 20]. The s-wave resonance spacing D_0 is given by

$$\frac{1}{D_0} = \frac{1}{2}[\rho(S_n, J = I + 1/2) + \rho(S_n, J = I - 1/2)]. \tag{4}$$

I is the spin of the ^{192}Os ground state in neutron capture reactions. Under the Ansatz that the +$\frac{1}{2}$ and -$\frac{1}{2}$ states contribute equally to the NLD at S$_n$, the NLD at S$_n$ is given by [9]

$$\rho(S_n) = \frac{2\sigma^2}{D_0} \frac{1}{(I+1)exp[-(I+1)^2/2\sigma^2] + exp[-I^2/2\sigma^2]}, \tag{5}$$

and σ is given at S$_n$ as:

$$\sigma^2 = 0.0146 A^{5/3} \frac{1 + \sqrt{1 + 4a(E_x - E_1)}}{2a}. \tag{6}$$

Here E_1 is the free parameter for the energy shift, see Table 2 [19, 20].

Excitation energy E (MeV)	**Level density $\rho(E)$ (MeV^{-1})**
-0.2365	15.1002
-0.1125	25.6821
0.0114999	45.1112
0.1355	56.3542
0.2595	93.4311
0.3835	150.574
0.5075	251.802
0.6315	327.927
0.7555	421.614
0.8795	540.419
1.0035	749.203
1.1275	968.746
1.2515	1276.23
1.3755	1737.85
1.4995	1915.95
1.6235	2324.34
1.7475	3143.24
1.8715	3974.98
1.9955	5548.38
2.1195	6593.5
2.2435	7739.18
2.3675	9802.55
2.4915	13326
2.6155	16560.3
2.7395	18296.7
2.8635	25132.5
2.9875	32840.7
3.1115	40358.3
3.2355	46991.3
3.3595	62620
3.4835	83999.8
3.6075	89275.3
3.7315	101597
3.8555	143846
3.9795	161770
4.1035	230256
4.2275	267099
4.3515	328708
4.4755	341566
4.5995	449712
4.7235	413983

Table 1: The extracted values of the nuclear level density $\rho(E)$ as a function of excitation energy E, after normalization this data is also drawn in figure 1. with the NLD denoted by green squares

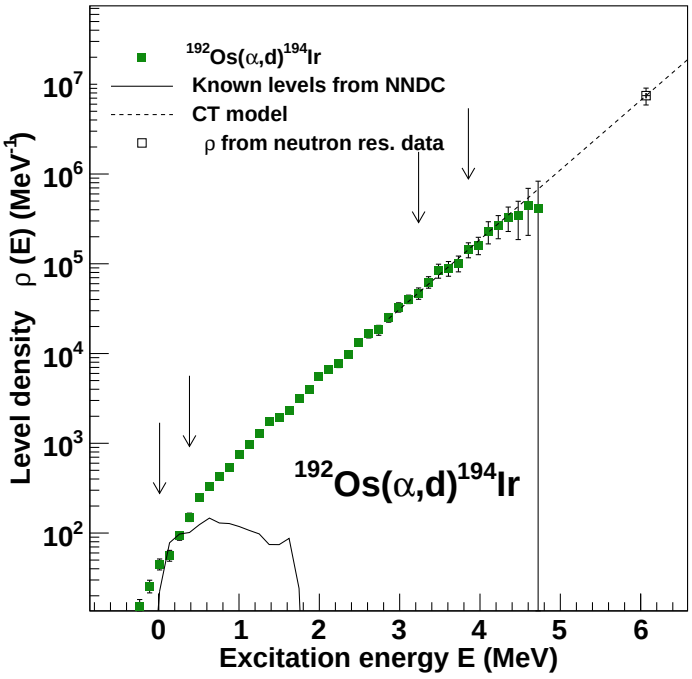

Figure 1: The nuclear level density of ^{192}Os(α,dγ)^{194}Ir, the green data points are the data from the Oslo experiment and the unfilled square is the NLD at neutron separation energy S_n which is calculated using resonance data [21]. The black solid line is the known discrete levels [22]. The dotted black line represents the constant temperature interpolation between the experimental NLD and the NLD at S_n. The 4 black arrows indicate the anchor points that were used to normalize the experimental data 2 at low energies and 2 at high energies.

The main results in figure 1 show the NLD (green squares) of the ^{194}Ir that was successfully extracted in this study. The open square, which is the NLD at S_n, was calculated as shown by equation 5, with the resonance spacing value taken from Mughabghab [21]. The true E_x in figure 1 has been shifted by approximately 1 MeV to the left due to the energy resolution, note that E_x in equations is the same as E in figures. The solid black line shows the known discrete levels and were sourced from NNDC [22]. The two anchor points at low energies normalize the experimental ρ to these discrete levels. Figure 2 shows the cumulative levels test used to determine the position of the anchor points. The blue line in figure 2 represents the cumulative levels of the experimental ρ, and the red data represent the cumulative level density for discrete levels. Where these two lines diverge is the highest energy that can be used for low-level normalization, which is where the level scheme is taken as complete. The black dotted line in figure 1 between experimental ρ and $\rho(S_n)$ is the constant temperature (CT) [23] interpolation at $E_x < 2\triangle$, where $\triangle$ is the pairing gap energy.

Isotope	S_n (MeV)	D_0 (eV)	E_1 (MeV)	a (MeV^{-1})	$\rho(S_n)$ (MeV^{-1})
^{194}Ir	6.067 $\pm$ 0.001 MeV	3.98 $\pm$ 0.36	-1.227	17.869	7.467$\times$10^6 $\pm$ 1.591$\times$10^6

Table 2: Normalization parameters that were used for the extraction and normalization of the nuclear level density, S_n is the neutron separation energy [22], D_0 is the resonance spacing from Ref. [21], a is the level density parameter, E_1 is the Fermi-gas shift parameter and $\rho(S_n)$ is the nuclear level density at the neutron separation energy.

The anchor points indicated by arrows at high energies normalize the experimental data to the CT model and were placed at E_x = 3.22 and 3.87 MeV above $E_x = 2\triangle$. A slope change is observed around 1.4 MeV in figure 1, which is believed to be the first pairing gap; the first pairing gap energy was calculated and found to be 1.43 MeV. The

reason for the change in slope is that most thermal energy is used for pair breaking; hence, there is not enough energy for level excitation. After pair breaking, the free nucleons become excited to the accessible single-particle states near the Fermi surface, resulting in the exponential rise of the NLD [24]. While there is more pair breaking at higher energies, the feature seems to be stronger at the first pair breaking [25].

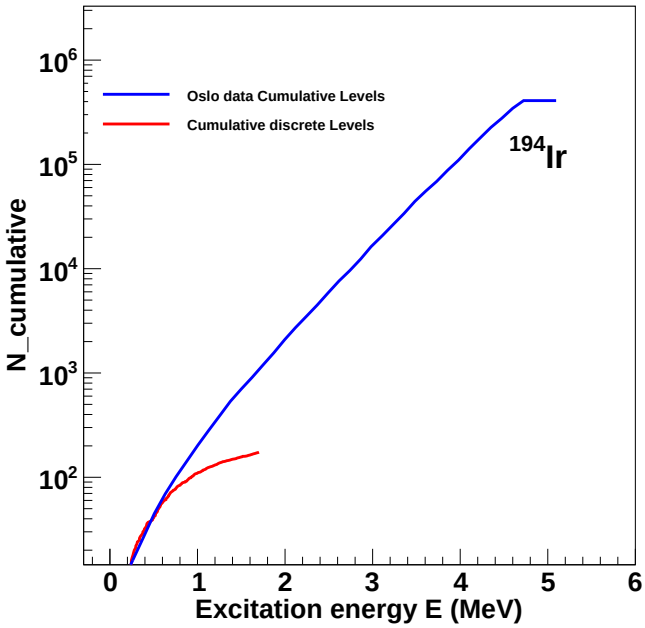

Figure 2: The cumulative levels test to determine low levels normalization points. Here, the level scheme is considered complete up to an excitation energy of 0.68 MeV.

5 Summary and Conclusion

The NLD of ^{194}Ir was successfully measured see Table 1. A comprehensive normalization was carried out using the constant temperature model, known discrete levels, and the level density at the neutron separation energy, $\rho(S_n)$. Furthermore, the first pairing gap energy was observed and determined to be 1.43 MeV. These results contribute to a broader research effort, with related findings presented at the conference which seek to answer questions about the s-process. In the future, the normalization method applied in this work will be compared with alternative normalization techniques and resonance data from various sources.

6 Acknowledgments

This work is based on research supported in part by the National Research Foundation of South Africa (Grant Number: PMDS22070734847), SAINTS Prestigious Doctoral Scholarship, U.S. Department of Energy, Office of Science, Office of Nuclear Physics under Contract No. DE-AC02-05CH11231, the SARChI under grant No REP-SARC180529336567 and the experiment was financed through ERC-STG-2014 under Grant Agreement No. 637686.

References

[1] A. J. Koning et al. *see also http://www. talys. eu*, 60:211, 2008.

[2] M. Ho et al. *Energy Procedia*, 160:459–466, 2019.

[3] Yoshiaki Oka et al. Springer, 2014.

[4] C. Rodriguez et al. *Nuclear Engineering and Design*, 222(2-3):299–317, 2003.

[5] M. Guttormsen et al. *Nuclear Instruments and Methods in Physics Research Section A: Accelerators, Spectrometers, Detectors and Associated Equipment*, 648(1):168–173, 2011.

[6] M. Guttormsen et al. *Physica Scripta*, 1990(T32):54, 1990.

[7] N. Nenoff et al. *Nuclear Physics A*, 629(3-4):621–634, 1998.

[8] A. Schiller et al. *Nuclear Instruments and Methods in Physics Research Section A: Accelerators, Spectrometers, Detectors and Associated Equipment*, 447(3):498–511, 2000.

[9] A. C. Larsen et al. *Physical Review C—Nuclear Physics*, 83(3):034315, 2011.

[10] F. Giacoppo et al. *Physical Review C*, 91(5):054327, 2015.

[11] M. Guttormsen et al. *Physics Letters B*, 816:136206, 2021.

[12] C. P. Brits et al. *Physical Review C*, 99(5):054330, 2019.

[13] M. Guttormsen et al. *Nuclear Instruments and Methods in Physics Research Section A: Accelerators, Spectrometers, Detectors and Associated Equipment*, 374(3):371–376, 1996.

[14] M. Guttormsen et al. *Nuclear Instruments and Methods in Physics Research Section A: Accelerators, Spectrometers, Detectors and Associated Equipment*, 255(3):518–523, 1987.

[15] D. M. Brink. *Nuclear Physics*, 4:215–220, 1957.

[16] P. Axel. *Physical Review*, 126(2):671–683, 1962.

[17] L. Crespo Campo et al. *Physical Review C*, 98(5), 2018.

[18] H. A. Bethe. *Physical Review*, 50(4):332, 1936.

[19] T. von Egidy and D Bucurescu. *Physical Review C—Nuclear Physics*, 72(4):044311, 2005.

[20] J. Zhang et al. *arXiv preprint arXiv:2506.02322*, 2025.

[21] S. Mughabghab. In *Atlas of Neutron Resonances*, pages 89–822. Elsevier, Nov 2018.

[22] National Nuclear Data Center. Nudat 3.0 database. `https://www.nndc.bnl.gov/nudat3/`, 2025. Brookhaven National Laboratory, U.S. Department of Energy.

[23] A. Gilbert et al. *Canadian Journal of Physics*, 43(8):1446–1496, 1965.

[24] K. Kaneko et al. *Physical Review C—Nuclear Physics*, 74(2):024325, 2006.

[25] J. Wang et al. *Phys. Rev. C*, 111:034324, Mar 2025.

Exploring toponium formation at the LHC

Aminul Hossain[1], **James Keaveney**[1]

[1]Department of Physics, University of Cape Town, Cape Town, South Africa

E-mail: hssami005@myuct.ac.za

Abstract. The top quark, the heaviest known elementary particle ($m_t \approx 172.52\,\text{GeV}$), plays a crucial role in probing the Standard Model (SM) at high energies. At the Large Hadron Collider (LHC), top quark pair production ($t\bar{t}$) is the dominant mechanism for top production. The top quark predominantly decays into a b-quark and a W^+ boson, with the W^+ boson subsequently decaying either hadronically or leptonically. The dileptonic decay channel ($pp \to t\bar{t} \to b\bar{b}W^+W^- \to b\bar{b}l^+\nu_l l^-\bar{\nu}_l\,(l = e, \mu)$) provides a clean and sensitive probe of the near-threshold region of $t\bar{t}$ production, where there is just sufficient energy to produce the top quark pair. This threshold region is especially sensitive to key SM parameters, namely the top mass, width, and Yukawa coupling. It also offers a unique opportunity to explore the formation of a previously unexplored quasi-bound state of a top and anti-top quark, eponymously referred to as toponium. Earlier studies indicated discrepancies between theoretical predictions and experimental data in this region, partly due to the absence of toponium effects in standard perturbative calculations. We present an updated and comprehensive study of toponium-induced corrections to various kinematic distributions, including $m_{t\bar{t}}$, $m^{e\mu}$ and $\Delta\phi(l\bar{l})$ at next-to-next-to-leading order (NNLO) in QCD. Additionally, we incorporate toponium corrections into 2-D differential observables such as $\Delta\phi^{e\mu}\, m^{e\mu}$, at NNLO. This analysis compares the improved predictions, now incorporating toponium effects, to LHC data and includes a systematic assessment of theoretical uncertainties.

1 Introduction

The CDF and DØ experiments discovered the Standard Model (SM) top quark at the Tevatron at Fermilab in 1995 [1, 2]. The most precise measurement of the top quark mass, determined through a collaborative effort by the CMS and ATLAS Collaboration, is 172.52 ± 0.33 GeV [3]. Because of its large mass, the top quark decays extremely rapidly, with a characteristic lifetime on the order of 10^{-25} s. It couples strongly to the Higgs field, and possesses the largest Yukawa coupling in the SM ($y_t \sim 1$). These properties make it a sensitive probe for testing physics beyond the Standard Model (BSM). Near production threshold ($\sqrt{s} \sim 2m_t$), slowly moving top quarks allow for the study of non-perturbative QCD effects, including the formation of toponium (a quasi-bound $t\bar{t}$ state with mass $2m_t \approx 346$ GeV) that unlike other quarkonia, cannot form stable bound states due to the top quark's short lifetime [4]. The anticipated mass of toponium is $2m_t \approx 346$ GeV, which is within the threshold region. At the Large Hadron Collider (LHC), a spin-0 toponium state is predicted to form in the gluon-fusion channel, where the primary contribution arises from the colour-singlet $t\bar{t}$ states [5, 6]. Recent analyses by ATLAS and CMS [7, 8] have revealed discrepancies between experimental measurements and SM predictions in the threshold region, motivating this comprehensive study combining next-to-next-to-leading order (NNLO) QCD calculation with toponium corrections modelled via non-relativistic QCD (NRQCD) and Green's function re-weighting [9]. In this work, we investigate these threshold discrepancies by systematically comparing theoretical predictions to data across a range of observables. These observables include the single-differential distributions of the top-antitop mass system $m(t\bar{t})$, dilepton mass system $m^{e\mu}$, angular difference between leptons $\Delta\phi(\ell\bar{\ell})$, as well as the double-differential distribution $\Delta\phi^{e\mu}\, m^{e\mu}$. These observables are chosen for their sensitivity to near-threshold QCD dynamics and spin correlations in dileptonic $t\bar{t}$ decays. The dileptonic decay channel provides particularly clean signatures with low backgrounds, enabling precise measurements of kinematic distributions. Our approach, implemented through MADGRAPH5_aMC@NLO [10], PYTHIA8 [11] and Rivet [12], provides a comprehensive and systematic treatment of these effects across multiple differential observables at NNLO precision.

2 Modelling and Motivation

2.1 *Threshold discrepancies*

Figure 1 (*left*) represents the normalised differential cross section of the dilepton mass system as a function of dilepton mass, measured by the ATLAS experiment at $\sqrt{s} = 13$ TeV with $36.1\,\text{fb}^{-1}$ of data collected in 2015-2016 [8]. The normalised differential cross sections of $m^{e\mu}$ for data is represented by points, which is compared to MC predictions represented by lines. The ratio plot compares the SM predictions to data. The $m^{e\mu}$ distribution reveals discrepancies between theory and data within the first few bins, as highlighted in the ratio plot of figure 1 (*left*), which serves as a proxy for the threshold region.

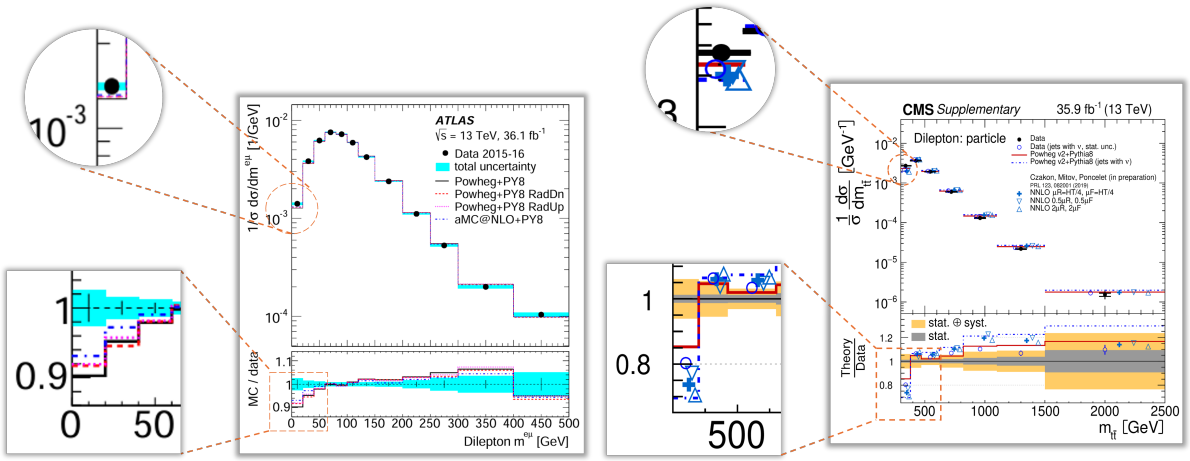

Figure 1: (*left*) Normalised differential cross section of the dilepton mass system ($m^{e\mu}$) where the measured values are shown by the black points and Monte Carlo (MC) predictions are indicated by lines [8]. (*right*) Normalised differential $t\bar{t}$ production cross section as a function of $m(t\bar{t})$, with black points representing data excluding neutrinos in jets, and blue circles representing data including neutrinos in jets, and theoretical predictions shown as lines (NLO) and crosses (NNLO) [7].

In a 2016 analysis, CMS conducted measurements of the differential cross section of the top quark pair at $\sqrt{s} = 13$ TeV at the LHC, with an integrated luminosity of $35.9\,\text{fb}^{-1}$ [7]. Figure 1 (right) illustrates the normalised differential cross section of the $t\bar{t}$ production as a function of the $m(t\bar{t})$. The data points are represented by solid dots (jets excluding neutrinos) and blue circles (jets including neutrinos), NLO predictions in lines while NNLO predictions are shown in blue crosses. The inclusion of neutrinos in the jet definition has a noticeable impact on the data, resulting in an improved agreement with the NNLO predictions. This improvement is particularly evident, when zooming in on the threshold region of the ratio plot, where the discrepancy between data and NNLO is reduced when neutrinos are included.

2.2 *Toponium modelling*

The study by Fuks et al. [9] investigates toponium formation near $t\bar{t}$ production threshold at the LHC, employing non-relativistic QCD (NRQCD) and Green's function re-weighting to capture non-perturbative QCD effects. Hard scattering events for colour-singlet $t\bar{t} \to bW^+\bar{b}W^- \to l^+\nu l^-\bar{\nu}$ production are generated in MadGraph5_aMC@NLO [10]. Matrix elements are re-weighted using the ratio of interacting $(\tilde{G}(E, p^*))$ and free $(\tilde{G}_0(E, p^*))$ Green's functions, where E is the binding energy and p^* is the top quark momentum in the toponium rest frame. The Green's functions are obtained by solving the Lippmann-Schwinger equation using a Coulomb-like QCD potential, and the results are tabulated for interpolation [9]. Re-weighted events are showered in Pythia8 [11], with fictitious Z' resonance injected to preserve the toponium system's invariant mass during showering. This ensures colour-singlet consistency and avoids radiation from intermediate top quarks. The showered events are processed using Rivet [12], where kinematic cuts are applied to precisely emphasise the phase space of the observables measured by ATLAS and CMS. The analysis highlights enhancements in di-lepton angular distributions and invariant mass spectra, consistent with ATLAS and CMS observations of threshold anomalies.

2.3 *Theoretical predictions*

This paper presents next-to-next-to-leading-order (NNLO) QCD predictions for key observables in $t\bar{t}$ pair production with decay into dilepton final states, significantly improving upon lower-order calculations [13]. Figure 2 (right) shows the normalised differential distribution for the azimuthal angle difference for leptons, $\Delta\phi(\ell\bar{\ell})$, comparing NNLO, NLO, and LO predictions to particle-level ATLAS data [8]. Figure 2 (left) displays the dilepton

invariant mass $m^{e\mu}$, where NNLO corrections resolve discrepancies near thresholds (e.g., $m^{e\mu} < 100\,\text{GeV}$) that persist at NLO. The NNLO results (red shaded band) exhibit narrower uncertainty bands (scale variations reduced to 1–5%) compared to NLO (blue, 10–20%) and LO (green), with improved agreement to data [13].

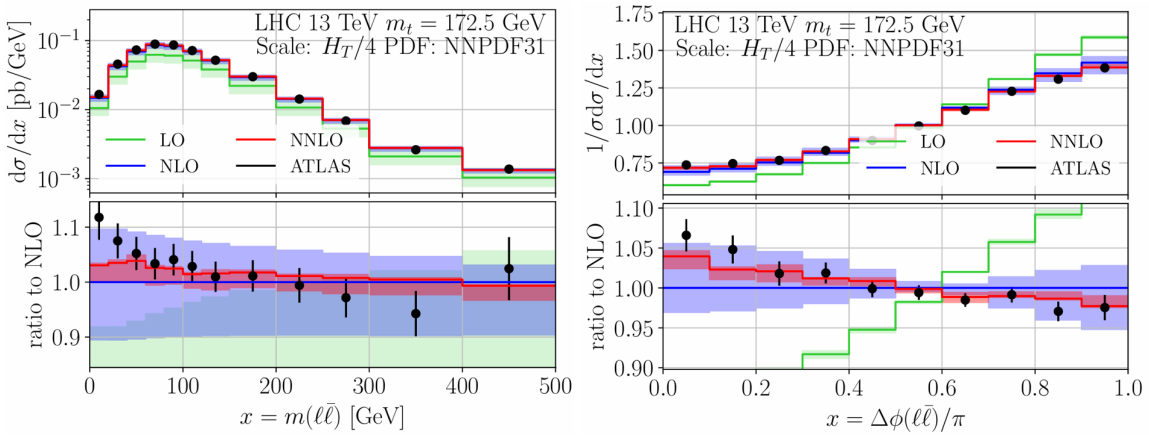

Figure 2: (*left*) Absolute differential cross section of $m(l\bar{l})$. (*right*) Normalised differential cross section of $\Delta\phi(l\bar{l})$. In both plots, ATLAS data are shown as solid points, and theory predictions at LO (green), NLO (blue) and NNLO (red) are represented by lines. The ratio to the NLO predictions is shown on the lower panel, with shaded bands indicating scale uncertainties [13].

This work also presents a comparison between NNLO predictions with particle-level measurement for the top-antitop mass system, $m(t\bar{t})$. This observable is particularly sensitive near the production threshold, around $m(t\bar{t}) \sim 346$ GeV, where higher-order QCD corrections become increasingly significant [13]. A critical advancement is the NNLO calculation of the double-differential cross section as a function of $\Delta\phi^{e\mu}$ and $m^{e\mu}$, which probes correlated behaviour of spin-sensitive angular variables and invariant mass. While single-differential $\Delta\phi(l\bar{l})$ observable require top-quark reconstruction, subject to large experimental uncertainties, the double distribution $\Delta\phi^{e\mu}\, m^{e\mu}$, can be measured with high precision making it a proxy for studying spin-correlation effects in dilepton final states [13]. Building on the NNLO QCD predictions for $m(t\bar{t})$, $m^{e\mu}$, $\Delta\phi(\ell\bar{\ell})$, and $\Delta\phi^{e\mu}\, m^{e\mu}$ distributions [13], this work systematically enhances the theoretical predictions by incorporating toponium effects across all observables. Here, the NNLO predictions are taken as the SM baseline without toponium contributions. The complete predictions (NNLO+Toponium) enables a systematic comparison with ATLAS and CMS data, particularly in the threshold region.

3 Results

3.1 Toponium correction to NNLO observables

To systematically incorporate toponium effects into the NNLO predictions, we define a correction term η_t,

$$\eta_t = \text{Toponium} - \text{Singlet Overlap}, \tag{1}$$

which isolates the toponium contribution by subtracting the singlet component. The singlet overlap represents contributions already contained in the NNLO predictions. This correction terms η_t, is added to the absolute NNLO differential cross sections,

$$\left.\frac{d\sigma}{dX}\right|_{\text{NNLO}+\eta_t} = \left.\frac{d\sigma}{dX}\right|_{\text{NNLO}} + \left.\frac{d\sigma}{dX}\right|_{\eta_t}, \tag{2}$$

where $X \equiv m(t\bar{t}), m^{e\mu}, \Delta\phi(l\bar{l}), \Delta\phi^{e\mu}\, m^{e\mu}$. The combined prediction (NNLO+Toponium) is normalised to analyse shape modifications arising from toponium effects.

3.2 Toponium-Enhanced NNLO Predictions for Kinematic Observables

Figure 3 and 4 presents three particle level single-differential cross-section measurements for dilepton events originating from top-antitop production. In the plots, the measured distributions are shown with total uncertainties (orange band combining the uncertainties from data and theoretical predictions), and are compared to NNLO and NNLO+Toponium predictions. The ratio of data to each prediction is presented in the bottom panel. Figure 3 *(*left) presents the normalised differential cross section of $m^{e\mu}$. The horizontal axis shows the invariant mass [GeV], the vertical axis shows the normalised cross section. The NNLO+Toponium corrections exhibits better agreement with data, particularly in the low-mass region ($m^{e\mu} < 100\,\text{GeV}$), which is a proxy for the threshold region. Figure 3 *(*right) presents the normalised differential cross section of $\Delta\phi(l\bar{l})$. The horizontal axis shows the

azimuthal separation, divided by π, ranging from 0 to 1 and the vertical axis shows the normalised cross section. The NNLO+Toponium correction exhibits a visibly improved agreement with data.

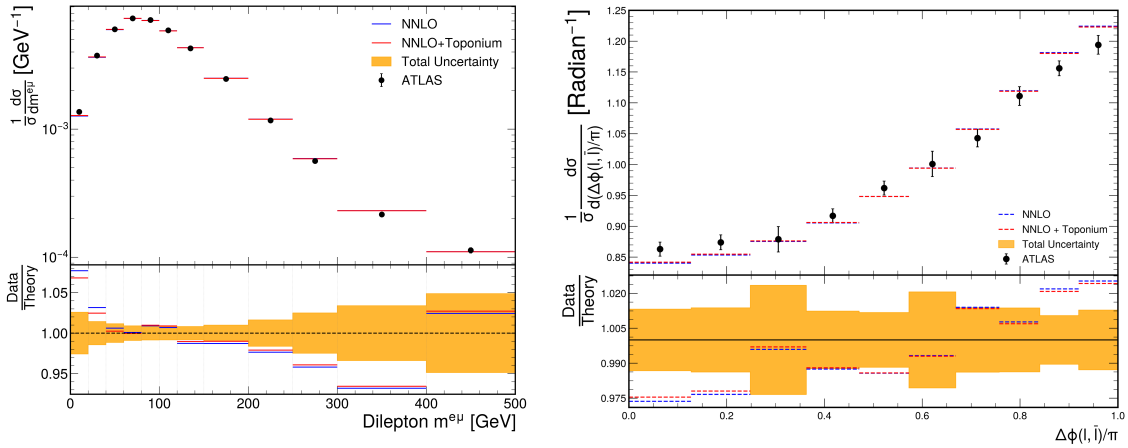

Figure 3: (*left*) Normalised differential cross section for the dilepton mass system $m^{e\mu}$. (*right*) Normalised differential cross section for the azimuthal angle difference between leptons, $\Delta\phi(l\bar{l})$. In both plots, ATLAS particle-level measurements are indicated by black points with vertical bars showing combined statistical and systematic uncertainties (stat. $\oplus$ sys.). The theoretical predictions at NNLO (QCD) are shown as blue lines, while the NNLO predictions including toponium corrections are shown as red lines. The bottom panel, in each plot, presents the ratio of measured value to each theoretical prediction. The total uncertainty (data $\oplus$ theory) is presented using shaded orange band.

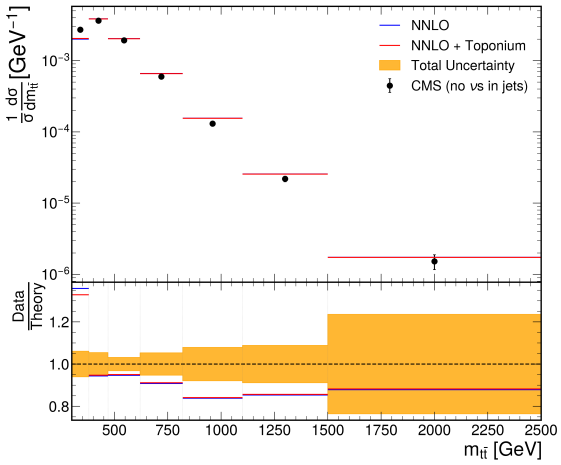

Figure 4: Normalised differential cross section for $m(t\bar{t})$ at particle level using CMS data (black) with jets excluding neutrinos, compared to NNLO (blue) and NNLO+Toponium (red) predictions. The ratio of the measured value to each theoretical prediction in presented in the bottom panel, and the shaded uncertainty bands (orange) represents the total uncertainty. It is clear from the ratio plot that the red curve is closer to data, despite the neutrino exclusion.

The normalised differential cross section of the top-antitop invariant mass distribution at particle level in figure 4, compares CMS data (black points, jets excluding neutrino 4-momenta) to NNLO predictions (blue) and NNLO+Toponium corrections (red). The x-axis represents $m_{t\bar{t}}$ in GeV, while the y-axis shows the unit-normalised cross section. The ratio panel reveals a 5–8% enhancement in the threshold region ($m_{t\bar{t}} \sim 346$ GeV) due to toponium effects. CMS internal studies with data (including neutrino 4-momenta) shows better NNLO agreement, suggesting that the threshold discrepancy is partly artificial [14, 13]. The NNLO+Toponium correction, nevertheless, enhances the threshold region.

Figure 5 presents the normalised double-differential cross section for the dilepton mass system $m^{e\mu}$ (0–500 GeV) and azimuthal angle difference $\Delta\phi^{e\mu}$ (0–π), at particle level for dilepton events. The comparison is made between ATLAS data and NNLO QCD predictions, with and without toponium correction. The most pronounced improvement from the inclusion of toponium effects is observed in the low-mass region ($m^{e\mu} < 80\,\text{GeV}$), where

the NNLO+Toponium prediction enhances the cross section and provides better agreement with the data, particularly at small azimuthal separations ($\Delta\phi^{e\mu} < \pi/2$). This region is especially sensitive to threshold dynamics in $t\bar{t}$ production.

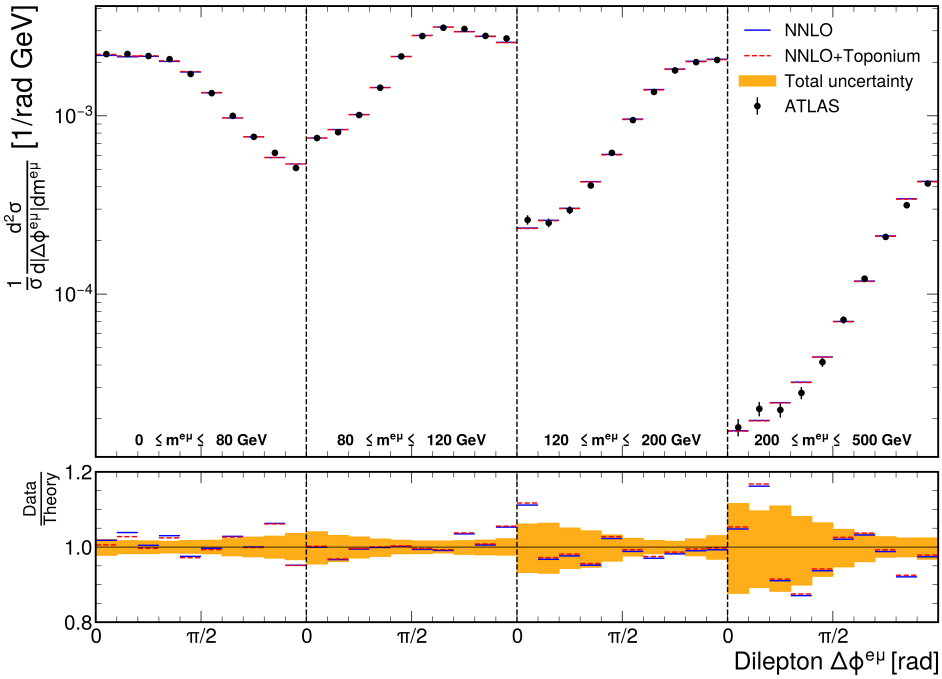

Figure 5: Normalised double-differential cross section for the dilepton mass system $m^{e\mu}$ and azimuthal angle difference $\Delta\phi^{e\mu}$, at particle level. The ATLAS data are represented by black points, with vertical error bars representing data uncertainty (stat. $\oplus$ sys.). The data are compared to NNLO (blue) and NNLO predictions including toponium corrections (red). The ratios of data to each prediction are shown in the lower panel, and the orange bands in the ratio panels represent the combined theoretical and experimental uncertainties.

In the mass range ($120 < m^{e\mu} < 500\,\text{GeV}$), toponium corrections gradually decrease in magnitude. For $m^{e\mu} > 200\,\text{GeV}$, the influence of toponium becomes negligible, where any remaining differences between theory and measurements are consistent with normalisation uncertainties. The ratios of data to each prediction is presented, separately, in the lower panel of the figure, with vertical bars representing data uncertainties and orange bands showing the combined experimental and theoretical uncertainties. These ratio plots confirm that the improved agreement at low $m^{e\mu}$ and small $\Delta\phi^{e\mu}$ arises from physical effects associated with toponium.

4 Conclusions

This study investigates the role of threshold dynamics in $t\bar{t}$ pair production in the dileptonic final states and the potential impact of toponium, which is a quasi-bound state of top-antitop pair. Using particle-level single-differential distribution such as $m(t\bar{t})$, $m^{e\mu}$, $\Delta\phi(l\bar{l})$, and the double-differential distribution $\Delta\phi^{e\mu}\,m^{e\mu}$, we compare ATLAS and CMS measurements with NNLO QCD predictions. Significant discrepancies are observed in the threshold region (e.g., $m^{e\mu} < 100\,\text{GeV}$ and $m(t\bar{t}) \sim 346\,\text{GeV}$), particularly in observables sensitive to invariant mass and angular correlations. To address this, we incorporate toponium corrections modelled using Green's function re-weighting in the colour-singlet channel. The corrections are applied additively to NNLO predictions which improves agreement with data, especially at low dilepton masses and small opening angles ($\Delta\phi^{e\mu} < \pi/2$). The improvement is pronounced in the double-differential observable ($\Delta\phi^{e\mu}\,m^{e\mu}$), highlighting a localised region where toponium correction improves data-to-theory agreement. In contrast, the corrections diminish above $m^{e\mu} > 200\,\text{GeV}$. These results demonstrate that bound-state dynamics near threshold, such as toponium, is non-negligible in top quark pair production. The systematic inclusion of these effects in theoretical predictions at NNLO QCD is crucial for enhancing the precision of Standard Model predictions.

References

[1] F. Abe *et al.*, "Observation of top quark production in $\bar{p}p$ collisions," *Phys. Rev. Lett.*, vol. 74, pp. 2626–2631, 1995.

[2] S. Abachi *et al.*, "Observation of the top quark," *Phys. Rev. Lett.*, vol. 74, pp. 2632–2637, Apr 1995. [Online]. Available: https://link.aps.org/doi/10.1103/PhysRevLett.74.2632

[3] CMS and ATLAS Collaborations, "Combination of measurements of the top quark mass from data collected by the atlas and cms experiments at $\sqrt{s} = 7$ and 8 tev," *Phys. Rev. Lett.*, vol. 132, p. 261902, Jun 2024. [Online]. Available: https://link.aps.org/doi/10.1103/PhysRevLett.132.261902

[4] B. Fuks, K. Hagiwara, K. Ma, and Y.-J. Zheng, "Signatures of toponium formation in lhc run 2 data," *Phys. Rev. D*, vol. 104, p. 034023, Aug 2021. [Online]. Available: https://link.aps.org/doi/10.1103/PhysRevD.104.034023

[5] V. S. Fadin, V. A. Khoze, and T. Sjostrand, "On the Threshold Behavior of Heavy Top Production," *Z. Phys. C*, vol. 48, pp. 613–622, 1990.

[6] K. Hagiwara, Y. Sumino, and H. Yokoya, "Bound-state effects on top quark production at hadron colliders," *Physics Letters B*, vol. 666, no. 1, p. 71–76, Aug. 2008. [Online]. Available: http://dx.doi.org/10.1016/j.physletb.2008.07.006

[7] CMS Collaboration, "Measurements of $\mathrm{t\bar{t}}$ differential cross sections in proton-proton collisions at $\sqrt{s} = 13$ tev using events containing two leptons," *JHEP*, vol. 02, p. 149, 2019.

[8] ATLAS Collaboration, "Measurement of the $t\bar{t}$ production cross-section and lepton differential distributions in $e\mu$ dilepton events from pp collisions at $\sqrt{s} = 13\,\mathrm{TeV}$ with the atlas detector," *Eur. Phys. J. C*, vol. 80, no. 6, p. 528, 2020.

[9] B. Fuks, K. Hagiwara, K. Ma, and Y.-J. Zheng, "Simulating toponium formation signals at the LHC," *Eur. Phys. J. C*, vol. 85, no. 2, p. 157, 2025.

[10] J. Alwall, R. Frederix, S. Frixione, V. Hirschi, F. Maltoni, O. Mattelaer, H. S. Shao, T. Stelzer, P. Torrielli, and M. Zaro, "The automated computation of tree-level and next-to-leading order differential cross sections, and their matching to parton shower simulations," *JHEP*, vol. 07, p. 079, 2014.

[11] C. Bierlich *et al.*, "A comprehensive guide to the physics and usage of pythia 8.3," 2022. [Online]. Available: https://arxiv.org/abs/2203.11601

[12] C. Bierlich, A. Buckley, J. Butterworth, C. H. Christensen, L. Corpe, D. Grellscheid, J. F. Grosse-Oetringhaus, C. Gutschow, P. Karczmarczyk, J. Klein, L. Lönnblad, C. S. Pollard, P. Richardson, H. Schulz, and F. Siegert, "Robust independent validation of experiment and theory: Rivet version 3," *SciPost Physics*, vol. 8, no. 2, Feb. 2020. [Online]. Available: http://dx.doi.org/10.21468/SciPostPhys.8.2.026

[13] M. Czakon, A. Mitov, and R. Poncelet, "Nnlo qcd corrections to leptonic observables in top-quark pair production and decay," *Journal of High Energy Physics*, vol. 2021, no. 5, May 2021. [Online]. Available: http://dx.doi.org/10.1007/JHEP05(2021)212

[14] CMS Collaboration, "Additional results for Ref. [72]; see additional figures on pp. 189–222," https://cms-results.web.cern.ch/cms-results/public-results/publications/TOP-17-014/index.html, accessed: September 9, 2025.

Progress on the Experimental test of the generalized Brink-Axel Hypothesis in ^{139}La nucleus

Ayabulela Tsewu[1], Bonginkosi Vincent Kheswa[1], Mathis Wiekeding[2], Mhlangano Nkalanga[1], Paulus Masiteng[1], Siyabonga Majola[1]

[1]Department of Physics, University of Johannesburg, 55 Beit Street, Doornfontein, 2028, SA
[2]Nuclear Science Division, Lawrence Berkeley National Laboratory, Berkeley, CA94720, USA

E-mail: ayabulelat@uj.ac.za

Abstract. The Brink-Axel (BA) hypothesis is a foundational assumption in nuclear structure and astrophysics, postulating that the γ-ray strength function (GSF) for photo-absorption depends solely on the gamma ray energy and not on the excitation energy of the nucleus. However, experimental studies across various mass regions have produced conflicting results regarding its validity. This report reflects an experimental investigation of the Brink-Axel hypothesis in the ^{139}La nucleus using particle-γ coincidence data obtained from the ^{139}La(^{3}He,^{3}He'γ)^{139}La reaction at the Oslo Cyclotron Laboratory. The primary γ-ray spectra were extracted for a range of excitation energies below the neutron binding energy. In particular, the GSF were studied at various initial excitation energies over the γ-ray energy interval $1.5 \leq \mathrm{E}_\gamma \leq 8.5$ MeV. The extracted GSF shows a consistent slope and magnitude across all initial excitation energy bins, indicating no dependence on the populated nuclear states. These results provide experimental support for the Brink–Axel hypothesis in ^{139}La and contribute to the broader effort to determine the conditions under which the GSF exhibits excitation-energy dependence. However, it remains vital to test the dependence of GSF on the final excitation energy of ^{139}La to draw a stronger conclusion about the validity of the gBA hypothesis in this nucleus. This is the future plan of the present study.

1 Introduction

The GSF characterizes the average probability that a nucleus undergoes γ decay or photoabsorption. It is very useful in the quasi-continuum region, where the density of quantum states is very high and their wave functions are very close to each other and are impossible to resolve experimentally. The $downward$ (γ decay) γ-ray strength $f(E_\gamma)\downarrow$ is linked to the average partial γ decay width $\overline{\Gamma}$ and the nuclear level density $\rho(E_i, J^\pi)$ at the initial excitation energy E_i according to

$$f(E_\gamma)\downarrow = \frac{\overline{\Gamma}(E_i, E_\gamma)\,\rho(E_i, J^\pi)}{E_\gamma^{2\lambda+1}}, \tag{1}$$

where λ denotes the multipolarity of the transition. Conversely, the upward (γ absorption) strength $f(E_\gamma)\uparrow$ is linked to the photon absorption cross section $\langle\sigma(E_\gamma)\rangle$ via

$$f(E_\gamma)\uparrow = \frac{\langle\sigma(E_\gamma)\rangle}{3(\pi\hbar c)^2 E_\gamma}, \tag{2}$$

where the quantities $\hbar$ and c are the reduced Planck's constant and the speed of light, respectively. The $f(E_\gamma)\downarrow$ and $f(E_\gamma)\uparrow$ are identical according to the considerations of detailed balance, given that the same nuclear configurations are populated [1].

Furthermore, the generalized Brink-Axel (gBA) hypothesis, which is a modified version of the original Brink hypothesis, suggests that the $upward$ and $downward$ strengths are functions of the gamma ray energy and are independent of the nuclear properties of the initial and final states, including excitation energies, spins, and parities [2, 3]. The gBA hypothesis is very critical in nuclear physics and nuclear astrophysics because some experimental methods, including the Oslo method [4] and ratio method [5], used to measure GSF are based on the assumption that the gBA hypothesis is true across the nuclear chart. However, various studies have reported controversial results on the validity of the gBA. For instance, the work of Refs. [6, 7, 8] contradicted the gBA hypothesis, while the results of Refs. [9, 10, 11] agree with it. Thus, the gBA hypothesis needs to be thoroughly tested across the nuclear chart, as stated by Ref. [9].

In this paper, we report on the first experimental assessment of the gBA hypothesis in ^{139}La nucleus. In particular, we investigated how the $downward$ GSF varies as a function of the initial excitation energy E_i. This nucleus is of interest in this study because it is in the p-process path, which was used by Ref. [12] to the origin of ^{138}La, which had been an open question for many decades. Their work assumed that the gBA hypothesis is true, without experimental proof.

2 Experimental methods

This work utilizes experimental data acquired at the cyclotron facility in Oslo, as documented in Refs. [12]. A self-supporting natural ^{139}La target, 2.5 mg/cm^2 thick, was irradiated with a ^{3}He beam of 38 MeV to excite states in ^{139}La through the inelastic scattering reaction ^{139}La(^{3}He,^{3}He$'\gamma$)^{139}La. Reaction ejectiles were detected using the SiRi array [13], which consists of 8 trapezoidal-shaped ΔE–E silicon detector telescopes, with active depths of 130 μm and 1550 μm for the front and back detectors, respectively. Each ΔE telescope is segmented into 8 strips, providing 64 ΔE–E sub-telescopes. The array was placed 50 mm from the target at a laboratory angle of $\theta_{\rm lab} = 47^\circ$ relative to the beam axis, covering about 6% of the total solid angle. Coincident gamma rays were measured using the CACTUS array [14], which is composed of 26 collimated NaI(Tl) detectors ($5'' \times 5''$) surrounding the target in spherical geometry. The total γ-ray detection efficiency of the array was 14.1% at $E_\gamma = 1.3$ MeV.

Particle–γ coincidence events were recorded within a 3 μs acquisition window, and a refined offline time gate of 50 ns was applied during analysis to suppress random coincidences for ^{139}La data. Using kinematics and the Q-value of the reaction, the measured ^{3}He energies were changed into excitation energies E_i of the residual ^{139}La nucleus. Figure 1 depicts the first-generation matrix of ^{139}La obtained from the measured particle-γ coincidence events using the first generation method of Ref. [15]. This matrix displays the intensity of primary γ rays as a function of excitation energy E_x and E_γ. The first generation matrix comprises first generation γ spectra $g(E_i, E_\gamma)$ which result from primary γ rays emitted at initial excitation energy E_i. These are normalized in a manner that the likelihood of the nucleus to release a gamma ray of energy E_γ is expressed as

$$P(E_i, E_\gamma) = \frac{g(E_i, E_\gamma)}{\sum_{E_\gamma} g(E_i, E_\gamma)}, \tag{3}$$

In this work, we focus on studying the dependence of GSF on the initial excitation energy using the formalism derived by Ref. [9]. In particular, we began by extracting the transmission coefficient $\mathcal{T}(E_i, E_\gamma)$ of the gamma ray from the first generation matrix shown in Fig. 1, as a function of initial excitation energy and γ ray energy using the equation

$$\mathcal{T}(E_i, E_\gamma) = \frac{N(E_i) P(E_i, E_\gamma)}{\rho(E_i - E_\gamma)}, \tag{4}$$

where $\rho(E_i - E_\gamma)$ is the nuclear level density of initial excitation energy obtained using the Oslo Method, while $N(E_i)$ is a normalization parameter given by

$$N(E_i) = \frac{\int_0^{E_i} \mathcal{T}(E_\gamma)\rho(E_i - E_\gamma)\, dE_\gamma}{\int_0^{E_i} P(E_\gamma, E_i)\, dE_\gamma}. \tag{5}$$

Thus, the dependence of GSF on the initial excitation energy is obtained using

$$f(E_\gamma) = \frac{\mathcal{T}(E_\gamma)}{2\pi E_\gamma^3}. \tag{6}$$

This method allowed for the extraction of GSF at narrow initial excitation energy bins of 105 keV width. Thus, allowing a detailed investigation of the dependence of GSF ^{139}La on initial excitation energy.

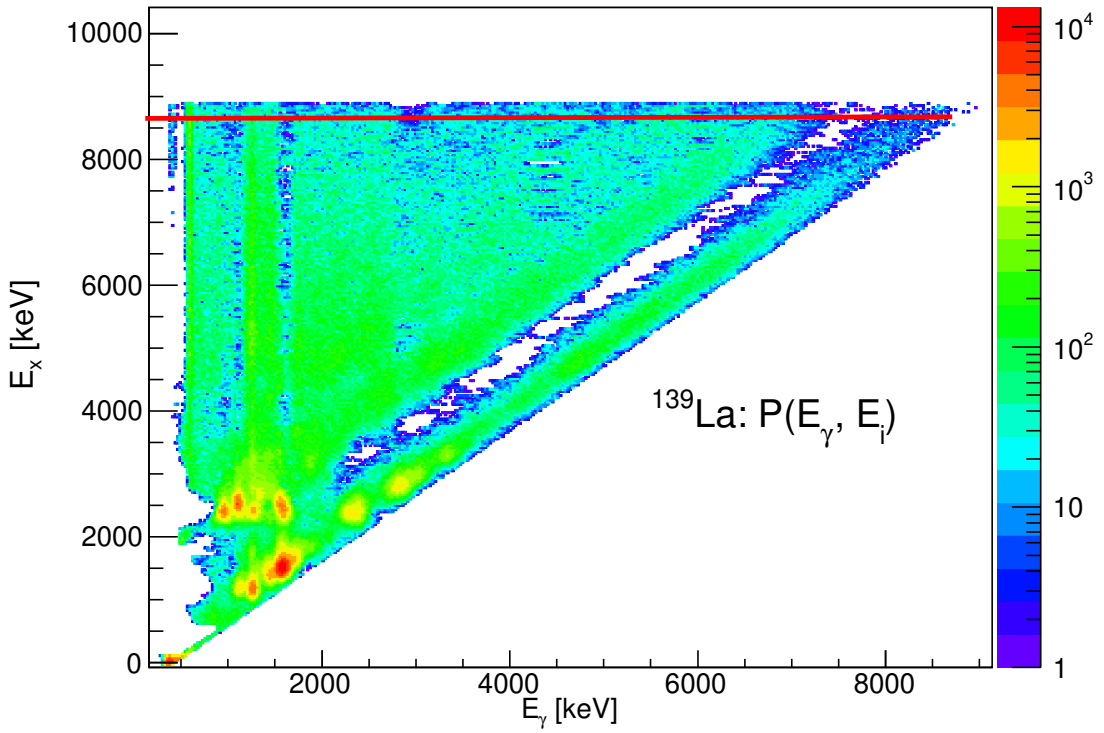

Figure 1: The distribution of primary γ rays from ^{139}La, organized in a matrix of gamma energy (E_γ) versus excitation energy (E_x). Red horizontal line marks the ^{139}La neutron separation energy (Sn).

3 Results and Discussion

The experimental results on the dependence of the GSF of ^{139}La on the initial excitation energy E_i, as obtained through the high-resolution analysis of the primary γ-ray matrix, are presented. GSF were extracted following Eqs. (3)–(5), starting from the normalized first-generation probability matrix $P(E_\gamma, E_i)$, which was constructed from the unfolded primary γ-ray matrix $g(E_i, E_\gamma)$ is portrayed in Figure 1.

Figure 2 shows the GSF extracted for six initial excitation energy bins: (a) 3.85 MeV, (b) 4.12 MeV, (c) 4.40 MeV, (d) 4.67 MeV, (e) 4.94 MeV, and (f) 5.22 MeV. The black experimental data points are compared to the standard Oslo Method result (blue curve), representing an average strength function of ^{139}La over a wide excitation range. The standard Oslo Method data sharply go to zero around $E_\gamma \approx 1.8$ MeV and $E_\gamma \approx 8.4$ MeV, as these represent the minimum and maximum of γ-ray energies where the standard Oslo Method was applied. Across all E_i bins, the shape and magnitude of the GSF agree closely with the standard result. This agreement implies that the GSF remains unaffected by the initial excitation energy, consistent with the gBA hypothesis.

The results for ^{139}La are in line with previous findings for ^{138}La [11], confirming the applicability of the gBA hypothesis in nuclei with $A \sim 138$–139. They also confirm the reliability of the Oslo Method for investigating statistical γ emission in odd-mass rare-earth isotopes.

4 Conclusion

This study offers experimental evidence that confirms the Brink-Axel hypothesis. Using particle–γ coincidence data from the ^{139}La(^{3}He,^{3}He'γ)^{139}La reaction, we extracted primary γ-ray spectra over a range of excitation energies below the binding energy. The GSF was evaluated as a function of the initial excitation energy within the interval $1.5 \leq E_\gamma \leq 8.5$ MeV. The extracted GSF exhibits a consistent slope and magnitude across all excitation energy bins, showing no dependence on the populated nuclear states. These findings provide experimental support confirming the Brink Axel hypothesis in ^{139}La and contribute to a global effort to understand the conditions under which the GSF remains independent of excitation energy. However, it is still important to further confirm the gBA hypothesis on the final excitation energy of ^{139}La to draw a stronger conclusion about the credibility of the

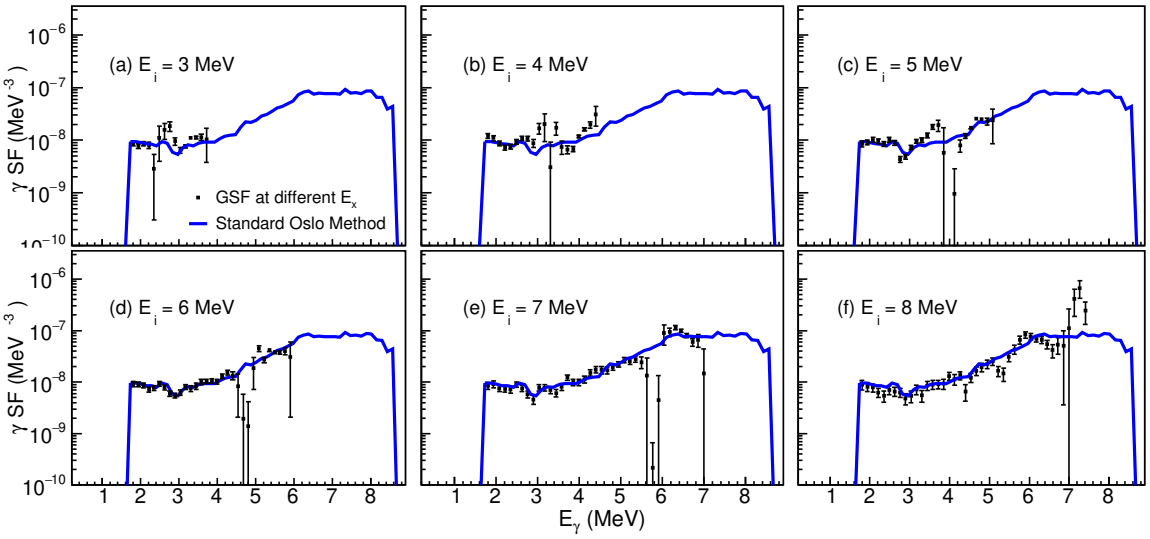

Figure 2: The GSF of ^{139}La at various initial excitation energies.

generalized Brink-Axel hypothesis on this nucleus. This is the future plan of this investigation.

Acknowledgments
This material is based upon work supported by the U.S. Department of Energy, Office of Science, Office of Nuclear Physics, under Contract No. DE-AC02-05CH11231.

References

[1] R. Capote, M. Herman, P. Obložinskỳ, P. G. Young, S. Goriely, T. Belgya, A. V. Ignatyuk, A. J. Koning, S. Hilaire, V. A. Plujko, M. Avrigeanu, O. Bersillon, M. B. Chadwick, T. Fukahori, Z. Ge, Y. Han, S. Kailas, J. Kopecky, V. M. Maslov, G. Reffo, M. Sin, E. S. Soukhovitskii, and P. Talou, "Ripl–reference input parameter library for calculation of nuclear reactions and nuclear data evaluations," *Nuclear Data Sheets*, vol. 110, no. 12, pp. 3107–3214, 2009.

[2] D. M. Brink, "Doctoral Thesis," Ph.D. dissertation, Oxford University, 1955.

[3] P. Axel, "Electric Dipole Ground-State Transition Width Strength Function and 7-MeV Photon Interactions," , vol. 126, no. 2, pp. 671–683, 1962.

[4] A. Schiller, L. Bergholt, M. Guttormsen, E. Melby, J. Rekstad, and S. Siem, "Extraction of level density and γ strength function from primary γ spectra," *Nuclear Instruments and Methods in Physics Research Section A: Accelerators, Spectrometers, Detectors and Associated Equipment*, vol. 447, no. 3, pp. 498–511, 2000.

[5] M. Wiedeking, L. Bernstein, M. Krtička, D. Bleuel, J. Allmond, M. Basunia, J. Harke, P. Fallon, R. Firestone, B. Goldblum *et al.*, "Low-energy enhancement in the photon strength of mo 95," *Physical Review Letters*, vol. 108, no. 16, p. 162503, 2012.

[6] J. Isaak, D. Savran, M. Krtička, M. Ahmed, J. Beller, E. Fiori, J. Glorius, J. Kelley, B. Löher, N. Pietralla *et al.*, "Constraining nuclear photon strength functions by the decay properties of photo-excited states," *Physics Letters B*, vol. 727, no. 4-5, pp. 361–365, 2013.

[7] L. Netterdon, A. Endres, S. Goriely, J. Mayer, P. Scholz, M. Spieker, and A. Zilges, "Experimental constraints on the γ-ray strength function in 90zr using partial cross sections of the y89 (p, γ) zr90 reaction," *Physics Letters B*, vol. 744, pp. 358–362, 2015.

[8] J. Isaak, D. Savran, B. Löher, T. Beck, M. Bhike, U. Gayer, N. Pietralla, M. Scheck, W. Tornow, V. Werner *et al.*, "The concept of nuclear photon strength functions: A model-independent approach via ($\gamma\rightarrow$, γ γ) reactions," *Physics Letters B*, vol. 788, pp. 225–230, 2019.

[9] M. Guttormsen, A.-C. Larsen, A. Görgen, T. Renstrøm, S. Siem, T. G. Tornyi, and G. M. Tveten, "Validity of the generalized brink-axel hypothesis in np 238," *Physical Review Letters*, vol. 116, no. 1, p. 012502, 2016.

[10] L. C. Campo, M. Guttormsen, F. B. Garrote, T. K. Eriksen, F. Giacoppo, A. Görgen, K. Hadynska-Klek, M. Klintefjord, A.-C. Larsen, T. Renstrøm *et al.*, "Test of the generalized brink-axel hypothesis in ni 64, 65," *Physical Review C*, vol. 98, no. 5, p. 054303, 2018.

[11] B. Kheswa, "The rigorous test of the generalized brink–axel hypothesis in the a= 138 nuclear mass region," *Acta Physica Polonica B*, vol. 54, no. 8, pp. 8–A1, 2023.

[12] B. V. Kheswa, M. Wiedeking, F. Giacoppo, S. Goriely, M. Guttormsen, A.-C. Larsen, F. B. Garrote, T. K. Eriksen, A. Görgen, T. W. Hagen *et al.*, "Galactic production of 138la: Impact of 138,139 la statistical properties," *Physics Letters B*, vol. 744, pp. 268–272, 2015.

[13] M. Guttormsen, T. Ramsøy, and S. Siem, "The silicon particle-telescope system at ocl," *Physica Scripta*, vol. T107, pp. 179–182, 2004.

[14] M. Guttormsen, L. Bergholt, J. Rekstad, and T. Tveter, "The cactus multidetector system at ocl," *Physica Scripta*, vol. T32, pp. 54–60, 1990.

[15] M. Guttormsen, T. Ramsøy, and J. Rekstad, "The first generation of γ-rays from hot nuclei," *Nuclear Instruments and Methods in Physics Research Section A: Accelerators, Spectrometers, Detectors and Associated Equipment*, vol. 255, no. 3, pp. 518–523, 1987.

This page intentionally left blank.

A search for tWZ production in the Tetralepton channel using ATLAS Run 2 data

Thobani Sangweni[1], **James Keaveney**[1] **and Kevin Barends**[1]

[1]Physics Department, University of Cape Town, Cape Town, South Africa

E-mail: sngnko003@myuct.ac.za

Abstract. The tWZ process is a rare and unobserved Standard Model process which refers to the production of a single top quark with an associated Z and a W boson. The tWZ process is sensitive to top-electroweak couplings, and thus it will be an important input into global Standard Model Effective Field Theory (SMEFT) fits. Additionally, this process can be used as a background in other top processes, such as *ttZ* cross-section measurements. A search for tWZ production was performed using proton-proton collision data with an integrated luminosity of 140 fb^{-1} at a centre-of-mass energy of $\sqrt{s} = 13$ TeV measured using the ATLAS detector at CERN. This search will focus on 4-lepton final states (electrons and muons). The analysis has been re-implemented on Release 25 and on the latest ATLAS-recommended analysis frameworks, TopCPToolKit and FastFrames. The signal regions (SRs) and control regions (CRs) were defined based on multiplicities of physics objects, such as the number of jets, Z boson candidates, b-tagged jets, etc. A deep neural network was trained to discriminate between signal and background events. The signal parton shower systematic uncertainty will be evaluated for the first time. The expected signal strength of tWZ production μ_{tWZ} and expected signal significance Z_0^{exp} are extracted using a blinded profile-likelihood fit to multiple SRs and CRs with full systematic uncertainties.

1 Introduction

The tWZ process comprises uncommon electroweak interactions that include a single resonant top quark, along with a Z boson and a W boson. The likelihood of this process occurring is extremely low and is estimated to be around 136 fb at next-to-leading (NLO) order in Quantum Chromodynamics (QCD) corrections under Standard Model (SM) calculations at $\sqrt{s} = 13$ TeV [1]. This sensitivity to the top quark electroweak couplings makes the process a potentially important input in global effective field theory (EFT) fits, which aim to look for signs of so-called new 'higher energy physics' in lower energy [2]. The production of a top quark pair in association with a Z boson ($t\bar{t}Z$) is the major background process to tWZ. Interference between the $t\bar{t}Z$ process and the signal process at NLO must be taken into consideration while modelling the two. The only difference between these two processes is the number of the resonant top quarks, which results in an additional b-jet in the $t\bar{t}Z$ final state. This and the fact that the $t\bar{t}Z$ cross-section is roughly five times more than that of our signal makes it an overwhelming background. In this document, the analysis procedure for the search for tWZ production in the tetralepton channel is highlighted, based on an integrated luminosity of 140 fb^{-1} [3]. The ATLAS detector collected the proton-proton collision data used in this analysis at the Large Hadron Collider at a centre-of-mass energy of $\sqrt{s}$ =13 TeV. The data collection spanned the years 2015 to 2018, which is known as the ATLAS Run 2 dataset. The integrated luminosity of the Full Run 2 dataset was 140 fb^{-1}, which only contained events included in the official ATLAS Good Runs List. The CMS collaboration recently noted some strong evidence for this process [4].

The analysis is performed using events with multiple lepton final states (electrons and muons). There is a higher expected signal purity in final states where the initial W and Z bosons both decay leptonically compared to final states with hadronically decaying W or Z bosons. Depending on the decay mode of the W boson from the top quark, the final state has either three or four leptons. The trilepton final state occurs when the W boson from the top quark decays hadronically, which happens $\sim 67\%$ of the time, as shown in Figure 1 (left). This analysis focuses on the tetralepton final state, which occurs when the W boson from the top quark decays leptonically, which happens $\sim 33\%$ of the time for all lepton flavours combined, as shown in Figure 1 (right). We focus on the tetralepton channel because there is a lot less background contribution compared to the trilepton channel, despite its statistical limitations.

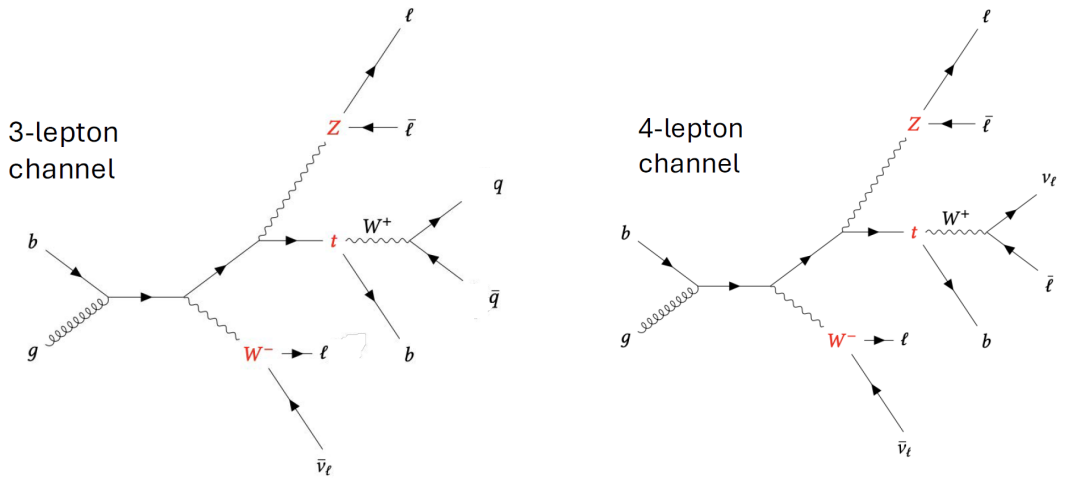

Figure 1: tWZ decay modes with the highest signal purity, resulting in the trilepton (left) and tetralepton (right) final states.

2 Monte Carlo samples and data

In order to evaluate the data against the Standard Model (SM) predictions, Monte Carlo (MC) samples were created for the tWZ signal process as well as background processes like $t\bar{t}Z$ and ZZ+jets utilising the SM. The MC samples for the tWZ production process were generated using the MadGraph5_aMC@NLO [1, 5] event generator at next-to-leading order (NLO) in QCD. The generated events were then interfaced with Pythia8 [6] to simulate the parton showering and hadronisation. The generator tune used was A14 [7] with the NNPDF2.3lo Parton distribution Function (PDF) set [8]. The nominal samples for a significant background, $t\bar{t}Z$, were generated using the Sherpa (v.2.2.11p3) event generator [9] with next-to-leading order accuracy, with the parton showering calculations handled by the default Sherpa MC tune and utilising the set of NNPDF3.0nnlo PDFs. The process tWZ and the background process $t\bar{t}Z$ share identical initial and final state particles, resulting in overlapping diagrams at next-to-leading order (NLO) accuracy in Quantum Chromodynamics (QCD). A diagram removal scheme is used to mitigate the overlap and double-counting. There are two different diagram removal schemes that modify which diagrams contribute to the final state, DR1 and DR2 [10]. The DR1 method is employed to eliminate the overlap between the nominal tWZ process and $t\bar{t}Z$. A different sample for tWZ utilises the DR2 scheme, which is used in comparison with the nominal tWZ sample to estimate the modelling of the tWZ signal's theoretical systematic.

The samples for diboson process with four charged leptons final state (ZZ+jets), which is one of the major background processes and samples for the diboson process with three charged leptons and a neutrino final state (WZ+jets), both are modelled with the Sherpa (v2.2.2) event generator, employing the NNPDF3.0nnlo PDF set. The diboson events that include one extra parton are modelled with NLO precision, while those containing two or more additional partons are modelled with LO precision. In this analysis, the ZZ+jets events are split and categorised into $ZZ + b$, $ZZ + c$ and $ZZ + l$ derived from the most massive jet flavour generated in the event. If an event of ZZ+jets has a b-jet, then it is classified as a $ZZ + b$ event. If there is a c-jet present and there is no b-jet in the event, it is classified as a $ZZ + c$ event. Otherwise, the event is classified as a $ZZ + l$ event. Samples from other non-major backgrounds are also included in the analysis.

3 Object Definitions and Event Preselections

A collection of experimental signatures in the different subdetectors that seek to represent true particles created in the proton-proton collision is known as a physics object. The missing transverse momentum ($E_{\mathrm{T}}^{\mathrm{miss}}$), jets, and leptons, of which only electrons and muons are taken into consideration, are the physical objects defined in this analysis. Various components of the ATLAS detector are utilised to detect electrons and muons. The electromagnetic (EM) calorimeter is used to reconstruct electrons, while the muon spectrometer (MS) is used to reconstruct muons. There are two categories of lepton objects: loose leptons (which meet less stringent isolation and identification requirements) and leptons that are both tight and loose (which satisfy more rigorous ID and isolation standards). Both tight and loose leptons meet all the requirements for being a loose lepton, in addition to a few more. We will refer to leptons that are both tight and loose as simply tight leptons [11]. Through adjustments established in a separate investigation, the electron energy scale and resolution are calibrated in simulated samples [12]. Similar motivations drive the calibrations of the muon momentum scale and resolution [13].

To suppress backgrounds from low-energy misidentified objects and ensure good reconstruction performance, loose electrons are required to have $p_{\mathrm{T}} > 10$GeV and $|\eta| < 2.47$, where η is the pseudorapidity. Furthermore, given that $1.37 < |\eta| < 1.52$ marks the edge separating the end-cap of the barrel and the electromagnetic calorimeter, the object cannot be located within this interval. The Tight Likelihood Identification Criteria, which aim to identify electrons based on the multivariate likelihood discriminant, must be met by candidates. The candidate electron must pass a strict cut on the likelihood discriminant, which is calibrated to minimise the false positive rate while ensuring an adequate level of signal efficiency. The track that passes through the inner detector linked to the loose electron must have a longitudinal impact parameter z_0 and a transverse impact parameter d_0, where $z_0 \sin(\theta) < 0.5$mm and $\frac{|d_0|}{\sigma(d_0)} < 5$, where θ is the angle between the track and the $+\hat{z}$ axis and $\sigma(d_0)$ is the measurement uncertainty for d_0. This condition mitigates pileup signals from secondary vertices that are distant from the principal interaction point. An overlap removal process that ignores all but one of these objects is used to prevent situations in which a single detector signal can produce many distinct reconstructed objects.

Using the anti-k_T technique [14] and a distance parameter $R = 0.4$, particle flow candidates are clustered to form jets, which defines a radius in which soft particles (particles that originate from hadronisation of quarks and gluons) can be considered as part of the jet around the hard particles (particles originating from the hard scattering process). The jets are recreated utilising the four-momenta of both hard and soft particles. Selected jets are required to have transverse momentum $p_{\mathrm{T}} > 20$GeV and pseudorapidity $|\eta| < 4.5$. In addition, jets must be separated from specific leptons by a distance $\Delta R = \sqrt{(\Delta\eta)^2 + (\Delta\phi)^2} > 0.4$, where $\Delta\eta$ denotes the difference in pseudorapidity and $\Delta\phi$ represents the difference in the azimuthal angle between the jet and the lepton. Jets that are found to contain hadrons that originate from the hadronisation of b-quarks are found to contain b-hadrons, which is known as flavour-tagging. Flavour-tagging is conducted using an algorithm that utilises a graph neural network, known as GNv02 [15].

4 Region Definitions

Events from data and simulations are grouped into categories based on the quantity and type of physics objects present in the event.These are divided into two groups: control regions (CRs) and signal regions (SRs). Signal areas are designed in a way that increases the proportion of tWZ signal events to background events, allowing for the fit procedure to be most sensitive to the SRs. On the other hand, control regions focus on particular background processes to refine and verify their modelling and to yield more precise background estimates, which are subsequently applied to the signal regions. In this analysis, specific control regions are established for each significant background ($t\bar{t}Z$ and ZZ+jets) in the tetralepton channel. Every event must include four leptons, with the lepton with the highest energy having a transverse momentum $p_{\mathrm{T}} > 28$GeV, the second-highest energy lepton with $p_{\mathrm{T}} > 18$GeV, and the third and fourth-highest energy leptons requiring $p_{\mathrm{T}} > 10$GeV. Additionally, the total charge of the leptons must be neutral, and all lepton pairs that have opposite signs and have the same flavour (OSSF) in the event should have a mass exceeding 10GeV. The OSSF lepton pairs are considered a Z candidate if their invariant mass lies inside the Z boson mass window $m_Z \pm 10$GeV, where $m_Z = 91.18$GeV.

Five distinct regions were established in the tetralepton channel. This channel features two signal regions that require events to include 4 tight leptons, one Z candidate, a minimum of one jet, and precisely one b-tagged jet. The tWZ opposite-flavoured (OF) signal region and the tWZ same-flavoured (SF) signal region vary based on the flavours of the leptons that do not come from the Z candidate. The tWZ OF SR encompasses events where the two non-Z leptons possess different flavours, whereas the tWZ SF signal region includes events where the two non-Z leptons share the same flavour. One other SR with looser requirements to increase the overall number of the tWZ events where 3 of the leptons were tight and 1 was loose and not tight (3T1L). The $t\bar{t}Z$ CR required 4 tight

leptons, 1 Z candidate, at least 2 jets and exactly 2 b-tagged jets. Finally, the ZZ+jets CR required 4 tight leptons, 2 Z candidates, a minimum of one jet and precisely one b-tagged jet. The event preselections and region definitions were done using ATLAS-recommended frameworks called TopCPToolkit [16], and FastFrames [17], respectively. A bulk of my contribution to the analysis was reimplementing the entire analysis pipeline in the recommended software. The criteria applied to the two non-Z leptons in the definitions of the signal regions result in the tWZ SF SR having a significant contribution from ZZ+jets events, while the tWZ OF SR has minimal contributions from ZZ+jets events. This selection allows $t\bar{t}Z$ production to be the predominant background contribution in the tWZ OF SR. Because of the more relaxed lepton requirement in the tWZ 3T1L SR region, this region also includes background contributions from processes that involve an extra non-prompt or fake lepton. The simulated samples indicate that there are very few events with fake or non-prompt leptons outside of the tWZ 3T1L SR, as shown in Figure 2. Fakes are currently included in $t\bar{t}Z$ for now, and ZZ+jets is separated by flavour. There is a discrepancy between the data and Monte Carlo in the $t\bar{t}Z$ control region. Nevertheless, this is not a matter for worry since all ATLAS analyses report this discrepancy.

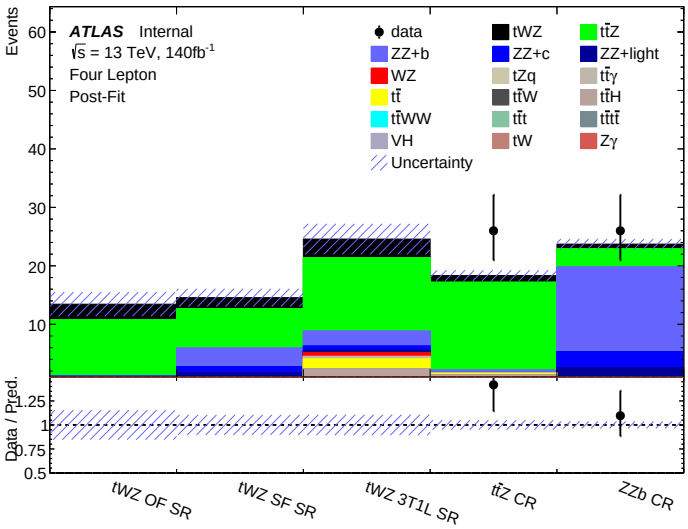

Figure 2: Region Postfit summary plot showing a histogram indicating the number of simulated events and data for all regions in the tetralepton channel. The number of signal and background Monte Carlo events is shown in different colours and stacked on the upper panel. The bottom section illustrates the ratio of actual data events to simulated events in every region. The observed ATLAS data is only shown in the control regions, as all signal regions are blinded.

5 Fit Procedure and Results

All SRs are dominated by events from background, which are predominantly from $t\bar{t}Z$ and ZZ+jets. A specific deep neural network (DNN), which is a machine learning model, was developed to differentiate between signal and background events. The DNN is a binary classifier and was trained and tested on all 5 regions using simulated tWZ, $t\bar{t}Z$ and ZZ+jets events. The DNN produced scores between 0 and 1 for each event, where a label of 1 indicated a signal event and a label of 0 indicated a background event. The DNN output score distribution for both the CRs is shown in Figure 3 with a comparison to the data. These control plots illustrate how well the simulation models the data. We observe reasonable agreement between simulation and data in both regions, suggesting that the score distribution is well described by the simulation. This score distribution was designed to be maximally sensitive to the signal, thus allowing for the extraction of an improved signal strength $\mu_{tWZ} = \sigma_{obs}/\sigma_{SM}$ and statistical significance Z_0, where σ_{obs} is the observed cross-section and σ_{SM} is the expected cross-section according to the SM. In this analysis, only an *Asimov* dataset [18] was used for the extraction. This dataset is designed in such a way that the optimal parameter values of the model align with the anticipated outcomes of the simulation. The measured signal strength μ_{tWZ} was extracted through *stat-only* (only statistical fluctuations are evaluated) profile likelihood fits using the tetralepton dataset.

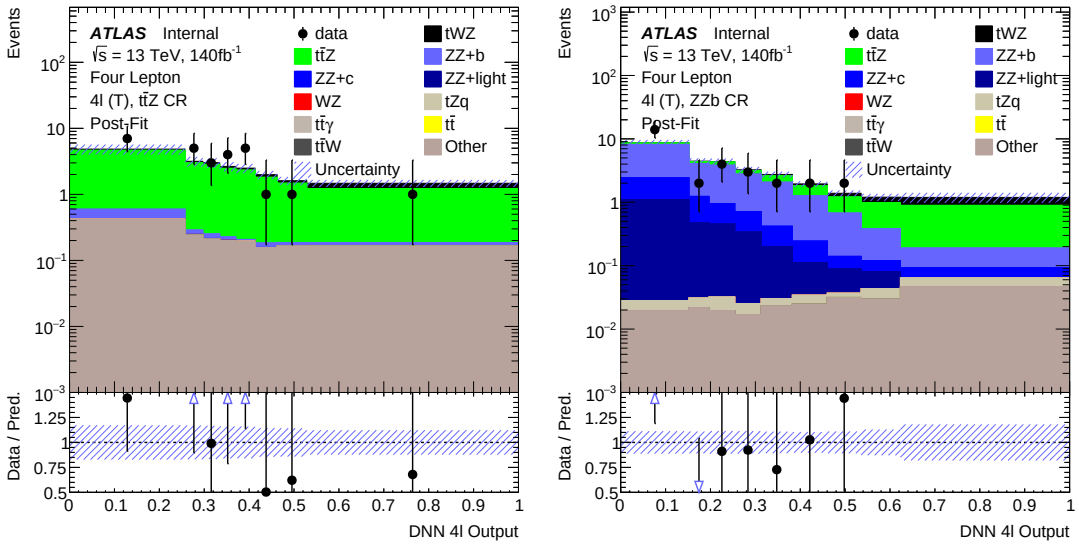

Figure 3: Postfit distributions of the DNN output scores for the control regions $t\bar{t}Z$ (left) and ZZ+jets (right). The dashed band shows the postfit statistical uncertainty. The ratio of data to the predictions from MC simulations is shown below the distributions.

The signal strength was found to be one, which was expected for fits performed using an Asimov dataset. The expected signal significance that is associated with the μ_{tWZ} measurement extracted from the Asimov fit was $Z_0^{exp} = 1.44\,\sigma$. The expected significance shows that, if the observed ATLAS data agree with the simulated signal and background predictions, the analysis does not have sufficient sensitivity to achieve a discovery of tWZ production. This expected significance represents the median strength with which the background-only hypothesis would be rejected if the Standard Model signal were truly present

6 Conclusion

The production of one resonant top quark with an associated Z boson and a W boson, which is known as tWZ production, is a rare SM process that has not yet been observed in ATLAS. With 140 fb^{-1} of proton-proton data gathered using the ATLAS detector at $\sqrt{s} = 13$ TeV, the generation of tWZ in tetralepton final states was examined. The analysis strategy's experimental sensitivity was demonstrated through the use of Asimov datasets. When analysing the tetralepton Asimov dataset, a signal strength value $\mu_{tWZ} = 1^{+0.82}_{-0.72}$ was extracted. The expected significance of this measurement was found to be $Z_0^{exp} = 1.44\,\sigma$. It was concluded that the measurement was statistically limited.

References

[1] J. Alwall, R. Frederix, S. Frixione, V. Hirschi, F. Maltoni, O. Mattelaer, H.-S. Shao, T. Stelzer, P. Torrielli, and M. Zaro, "The automated computation of tree-level and next-to-leading order differential cross sections, and their matching to parton shower simulations," *Journal of High Energy Physics*, vol. 2014, no. 7, Jul. 2014. [Online]. Available: http://dx.doi.org/10.1007/JHEP07(2014)079

[2] J. Keaveney, "Constraining the smeft with a differential cross section measurement of twz production at the hl-lhc," *Physical Review D*, vol. 107, 2023. [Online]. Available: https://journals.aps.org/prd/pdf/10.1103/PhysRevD.107.036021

[3] G. Aad, B. Abbott, and et al, "Luminosity determination in pp collisions at $\sqrt{s} = 13$ tev using the atlas detector at the lhc," *The European Physical Journal C*, vol. 83, no. 10, Oct. 2023. [Online]. Available: http://dx.doi.org/10.1140/epjc/s10052-023-11747-w

[4] "Observation of tWZ production at the CMS experiment," CERN, Geneva, Tech. Rep., 2025. [Online]. Available: https://cds.cern.ch/record/2932252

[5] R. Frederix, S. Frixione, V. Hirschi, D. Pagani, H.-S. Shao, and M. Zaro, "The automation of next-to-leading order electroweak calculations," *Journal of High Energy Physics*, vol. 2018, no. 7, Jul. 2018. [Online]. Available: http://dx.doi.org/10.1007/JHEP07(2018)185

[6] T. Sjöstrand, S. Ask, J. R. Christiansen, R. Corke, N. Desai, P. Ilten, S. Mrenna, S. Prestel, C. O. Rasmussen, and P. Z. Skands, "An introduction to pythia 8.2," *Computer Physics Communications*, vol. 191, pp. 159–177, 2015. [Online]. Available: https://www.sciencedirect.com/science/article/pii/S0010465515000442

[7] "ATLAS Pythia 8 tunes to 7 TeV data," CERN, Geneva, Tech. Rep., 2014, all figures including auxiliary figures are available at https://atlas.web.cern.ch/Atlas/GROUPS/PHYSICS/PUBNOTES/ATL-PHYS-PUB-2014-021. [Online]. Available: https://cds.cern.ch/record/1966419

[8] R. D. Ball, V. Bertone, S. Carrazza, C. S. Deans, L. Del Debbio, S. Forte, A. Guffanti, N. P. Hartland, J. I. Latorre, J. Rojo, and M. Ubiali, "Parton distributions with lhc data," *Nuclear Physics B*, vol. 867, no. 2, pp. 244–289, 2013. [Online]. Available: https://www.sciencedirect.com/science/article/pii/S0550321312005500

[9] E. Bothmann, G. S. Chahal, S. Höche, J. Krause, F. Krauss, S. Kuttimalai, S. Liebschner, D. Napoletano, M. Schönherr, H. Schulz, S. Schumann, and F. Siegert, "Event generation with Sherpa 2.2," *SciPost Phys.*, vol. 7, p. 034, 2019. [Online]. Available: https://scipost.org/10.21468/SciPostPhys.7.3.034

[10] S. Frixione, E. Laenen, P. Motylinski, C. White, and B. R. Webber, "Single-top hadroproduction in association with a w boson," *Journal of High Energy Physics*, vol. 2008, no. 07, p. 029, jul 2008. [Online]. Available: https://dx.doi.org/10.1088/1126-6708/2008/07/029

[11] G. Aad, B. Abbott, D. Abbott, and et al, "Electron and photon performance measurements with the atlas detector using the 2015–2017 lhc proton-proton collision data," *Journal of Instrumentation*, vol. 14, no. 12, p. P12006–P12006, Dec. 2019. [Online]. Available: http://dx.doi.org/10.1088/1748-0221/14/12/P12006

[12] G. Aad, B. Abbott, and et al, "Electron and photon performance measurements with the atlas detector using the 2015–2017 lhc proton-proton collision data," *Journal of Instrumentation*, vol. 14, no. 12, p. P12006, dec 2019. [Online]. Available: https://dx.doi.org/10.1088/1748-0221/14/12/P12006

[13] Aad, G. and Abbott, B. and et al, "Muon reconstruction and identification efficiency in ATLAS using the full Run 2 pp collision data set at $\sqrt{s} = 13$ TeV," *The European Physical Journal C*, vol. 81, no. 7, jul 2021. [Online]. Available: http://dx.doi.org/10.1140/epjc/s10052-021-09233-2

[14] M. Cacciari, G. P. Salam, and G. Soyez, "The anti-ktjet clustering algorithm," *Journal of High Energy Physics*, vol. 2008, no. 04, p. 063–063, Apr. 2008. [Online]. Available: http://dx.doi.org/10.1088/1126-6708/2008/04/063

[15] "Explaining the ATLAS GN2 Flavour Tagging Algorithm with Integrated Gradients," CERN, Geneva, Tech. Rep., 2025, all figures including auxiliary figures are available at https://atlas.web.cern.ch/Atlas/GROUPS/PHYSICS/PUBNOTES/ATL-PHYS-PUB-2025-029. [Online]. Available: https://cds.cern.ch/record/2936634

[16] CERN, "Topcptoolkit documentation," accessed: 2025-09-09. [Online]. Available: https://topcptoolkit.docs.cern.ch/latest/

[17] T. Dado, M. Dubovsky, D. A. Baron Moreno, R. Quinn, K. Benkdendorfer, K. Voss, and D. Biswas, "Fastframes," Apr. 2024. [Online]. Available: https://doi.org/10.5281/zenodo.16418658

[18] G. Cowan, K. Cranmer, E. Gross, and O. Vitells, "Asymptotic formulae for likelihood-based tests of new physics," *The European Physical Journal C*, vol. 71, 2011. [Online]. Available: https://doi.org/10.1140/epjc/s10052-011-1554-0

Effect of Strontium Oxide on Radiation Attenuation Properties of Boro-tellurate Glass Systems at High Radiation Energies

S. Mthalane[1], B. Bhengu[1], M.N Zuma[1], N. Msabala[1], L. Mdletshe[1], C.B Mtshali[2], H.A.A Abdelbagi[1], T.T Hlatshwayo[3], S. S. Ntshangase [1]

[1]Physics Department, University of Zululand, KwaDlangezwa 3886, South Africa
[2]Materials Research Department, iThemba LABS, P.O. Box 722, Somerset West, 7129, South Africa
[3]Physics Department, University of Pretoria, Pretoria 0002, South Africa

E-mail: msifiso999@gmail.com

Abstract. In the present study, the radiation shielding properties of five glass compositions $40SrO–30B_2O_3–10TeO_2–20Bi_2O_3$, $35SrO–30B_2O_3–10TeO_2–25Bi_2O_3$, $30SrO–30B_2O_3–10TeO_2–30Bi_2O_3$, $25SrO–30B_2O_3–10TeO_2–35Bi_2O_3$, and $20SrO–30B_2O_3–10TeO_2–40Bi_2O_3$, were investigated using Phy-X/PSD software, and validated through GEANT4 simulations. The mass attenuation coefficients (MAC), linear attenuation coefficients (LAC), and effective atomic numbers of the glasses were determined across the energy range of 1–15 MeV. Results showed that increasing the Bi_2O_3 while decreasing SrO content enhances the radiation shielding capability of the glasses. Additionally, the half-value layer (HVL), and tenth-value layer (TVL), were evaluated, revealing that glasses with higher Bi_2O_3 concentrations attenuate a greater amount of photons with smaller thicknesses. $20SrO–30B_2O_3–10TeO_2–40Bi_2O_3$ glass demonstrated superior radiation shielding performance and can be used in both nuclear and medical applications.

1 Introduction

The increasing usage of ionizing radiation across the industrial, medical, food, and research sectors has become significantly vital to modern economic, social, and technological advancements. However, despite its significance, ionizing radiation raises serious safety concerns due to its risks to human health and environment (i.e soil, plants, water, etc.) [1, 2, 3]. Therefore, it is crucial to develop effective preventative measures to minimize radiation exposure and safeguard individuals from its harmful effects. In the past few decades, various shielding materials have been developed and implemented to reduce ionizing radiation exposure, with lead (Pb) and concrete being among the most employed materials. These materials have been favoured due to their high density and high linear attenuation coefficients (LAC), which enable them to effectively attenuate ionizing radiation [4,5]. Nevertheless, lead is a highly toxic metal known to negatively impact human health. In addition, lead can be inhaled, allowing it to accumulate in the body, which may result in memory loss, cognitive decline, and an increased risk of heart disease. On the other hand, concrete can offer effective radiation shielding under certain conditions, but it also has notable limitations [4,6,7]. For example, if the water content in concrete exceeds optimal levels, its structural strength decreases, and its overall density is reduced. Additionally, in high-temperature environments, the absorbed radiation energy can cause the water to evaporate [6,8,9]. This not only

compromises the structural integrity of the concrete, but also leads to cracking, which can allow ionizing radiation to penetrate, thereby posing significant health risks to humans. Considering these limitations of concrete, along with the toxic nature of lead (Pb), researchers have increasingly turned their focuses to developing an alternative material to replace both concrete and lead in radiation shielding applications.

In recent years, researchers have increasingly focused on glass materials due to their excellent physical properties, optical properties, resistance to corrosion, light weight, non-toxicity and radiation shielding properties [5,7-9]. One of the main reasons for glass materials to be preferred for specialized applications such as in environments like nuclear laboratories is their inherent transparency. This property allows glass to serve as effective radiation shielding while allowing observers to monitor activities inside areas containing ionizing radiation sources.

There are several types of glass formers, such as tellurium dioxide (TeO_2), boron oxide (B_2O_3), germanium dioxide (GeO_2), and silica (SiO_2) which are the glass network backbones. Various modifier oxides, including heavy metal oxides (HMOs) and light metal oxides (LMOs), can be mixed with glass formers, resulting in glass with enhanced radiation shielding properties [6,9]. Added HMOs or (LMO) to glass formers can particularly increase the density of the glass and its atomic number, thereby enhancing its ability to attenuate radiation, which is an essential characteristic for applications requiring effective shielding [6,10]. Thabet *et al.* [7] studied the gamma-ray shielding capability of xBi_2O_3+(75-x) B_2O_3+15 TeO_2 +5MgO+5PbO; x = 0, 10, 20, 25, 30, 40, 50, 60], where the shielding properties of these glasses were improved by increasing bismuth oxide (Bi_2O_3) content. Moreover, Kaky *et al.* [8] investigated the influence of Bi_2O_3 on gamma-ray attenuation properties of the following glass system: (50-x) B_2O_3+ $5SiO_2$ + 40MgO + xBi_2O_3, where x = 5, 10, 15, and 20. As a result of these results, it is evident that adding more Bi_2O_3 further improves radiation attenuation in the glass system.

Recently, the mechanical, structural, and radiation shielding properties of boro-tellurite glasses modified by varying concentrations of strontium and bismuth oxides have been investigated for photon energies below 0.81 MeV [7]. Therefore, it is critical to observe the behaviour of this glass system in energy regions above 0.81 MeV, which is the main purpose of this work. This study investigates the gamma-ray attenuation properties of boro-tellurite glasses modified with varying concentrations of strontium and bismuth oxides, using Geant4 simulations. The results were also analysed using Phy-x\PSD software to evaluate key shielding parameters, including the linear attenuation coefficient (LAC), mass attenuation coefficient (MAC), half-value layer (HVL), tenth-value layer (TVL), mean free path (MFP), and effective atomic number (Z_{eff}) of the glass system used in this study.

2 Experimental Methods

The radiation shielding properties of glass systems with compositions 40SrO + $30B_2O_3$ + $10TeO_2$ + $20Bi_2O_3$, 35SrO + $30B_2O_3$ + $10TeO_2$ + $25Bi_2O_3$, 30SrO + $30B_2O_3$ + $10TeO_2$ + $30Bi_2O_3$, 25SrO + $30B_2O_3$ + $10TeO_2$ + $35Bi_2O_3$, and 20SrO + $30B_2O_3$ + $10TeO_2$ + $40Bi_2O_3$ were evaluated using Phy-X/PSD software. In addition, Phy-X/PSD results were compared with Geant4 Monte Carlo Simulations (MCS) results. The Geant4 (MCS) framework offers several advantages, most notably its flexibility in designing and simulating complex experimental setups, such as the gamma radiation source, glass samples, detectors, and collimators within a computational environment. The glass codes, glass compositions and density of the investigated glasses are shown below in Table 1, taken from [7].

Glass code	Glass compositions	Density (g/cm^3)
TBSB1	40SrO+$30B_2O_3$+10TeO+$20Bi_2O_3$	4.32
TBSB2	35SrO+$30B_2O_3$+10TeO+25Bi2O_3	4.65
TBSB3	30SrO+30B2O_3+10TeO+30Bi2O_3	5.07
TBSB4	25SrO+30B2O_3+10TeO+35Bi2O_3	5.40
TBSB5	20SrO+30B2O_3+10TeO+40Bi2O_3	5.69

Table 1: The investigated glass samples and their densities.

Radiation shielding parameters such as the mass attenuation coefficient (MAC), linear attenuation coefficient (LAC), half-value layer (HVL), tenth-value layer (TVL), and effective atomic number (Z_{eff}) are crucial for ensuring shielding materials efficiency. Therefore, the accurate determination of these factors is essential for the development of efficient shielding materials aimed at reducing gamma radiation exposure.

A fundamental parameter in assessing shielding effectiveness is the mass-attenuation coefficient (MAC). The MAC quantifies the material's capacity to attenuate or reduce the intensity of incident gamma radiation as it traverses the substance. It is energy-dependent and closely related to material density, however a material with a higher atomic number typically exhibits greater MAC values. A higher MAC indicates that a material is more effectively shielded from radiation per unit mass, showing superior attenuation performance. The MAC is also closely related to the LAC and serves as its density-independent counterpart. The MAC can be calculated using the following formula [5,6]:

$$\text{MAC} = \frac{\mu}{\rho}, \tag{1}$$

where μ is the LAC and ρ is the density of the material. The LAC represents the fraction of gamma radiation attenuated per unit thickness of a material. A higher LAC value indicates that the material is more effective at reducing the intensity of incoming photons. In other words, materials with high LAC values are better at shielding radiation. The LAC can be calculated using the following formula [5,6]:

$$I = I_o e^{-\mu t}, \tag{2}$$

where t represents the thickness of the material, I_o denotes the initial radiation intensity before entering the material, and I is the intensity of the radiation after transmission through the material.

Another important radiation shielding parameters are the half-value layer (HVL) and tenth-value layer (TVL), which are defined as the thickness of a material required to reduce the intensity of incoming radiation by 50% and 90%, respectively. Lowest HVL and TVL values indicate better shielding efficiency. The HVL and TVL can be calculated using the following formula [5,6]:

$$\text{HVL} = \frac{In(2)}{\mu}, \tag{3}$$

and

$$\text{TVL} = \frac{In(10)}{\mu}, \tag{4}$$

The last parameter considered in the study is the effective atomic number Z_{eff} which plays an important role in evaluating the radiation shielding properties of a material. The Z_{eff} represents the average atomic number taking into account the contribution of all constituent elements to its composition. The Z_{eff} depends on the type of radiation and the interactions between the particles and the material. A higher Z_{eff} value indicates a greater ability to attenuate radiation, making the material more effective as a shielding material. The effective atomic number can be calculated using the following formula [5,6]:

$$Z_{eff} = \frac{\sum f_i A_i \left(\frac{\mu}{\rho}\right)_i}{\sum f_i \left(\frac{A_i}{Z_i}\right) \left(\frac{\mu}{\rho}\right)_i}, \tag{5}$$

where f_i, A_i, and Z_i represent the mole fraction, atomic weight, and atomic number of each element, respectively, in the absorber material.

3 Results and discussion

The selected $SrO + B_2O_3 + TeO_2 + Bi_2O_3$ glass systems were evaluated for their radiation attenuation performance by calculating several shielding parameters in the energy range of 1 to 15 MeV. In this study, the linear attenuation coefficient (LAC) was the first radiation-shielding parameter assessed as a function of photon energy. Figure 1 illustrates the LAC profile for the $SrO–B_2O_3–TeO_2–Bi_2O_3$ glass system across a photon energy from 1 to 15 MeV. As shown in Figure 1, the LAC of the glass system decreases exponentially as the photon energy

increases from 1 to 6 MeV and slowly increases as the photon energy goes from 6 MeV to 15 MeV. The decrease in the LAC as the function of energy is primarily due to the Compton effect, which dominates as photon energy increases, while pair production becomes more dominant interaction at energies above approximately 6 MeV and continues up to 15 MeV. This behaviour of LAC values as a function of photon energy has also been observed in the literature [5]. Furthermore, it can be noticed that TBSB1 exhibits the lowest LAC while TBSB5 exhibits the highest LAC value. In particular, within the energy range of 1 to 15 MeV, LAC value falls within the range of 0.2724 to 0.173 cm^{-1}, 0.297 to 0.194 cm^{-1}, 0.329 to 0.209 cm^{-1}, 0.354 to 0.228 cm^{-1}, 0.377 to 0.237 cm^{-1}, for TBSB1, TBSB2, TBSB3, TBSB4 and TBSB5, respectively. The trend of decreasing LAC from TBSB5 to TBSB1 highlights that increasing the Bi_2O_3 content while reducing the SrO content leads to a lower LAC. Same behaviour was observed in a previous study where increasing Bi_2O content resulted in a higher LAC value [9].

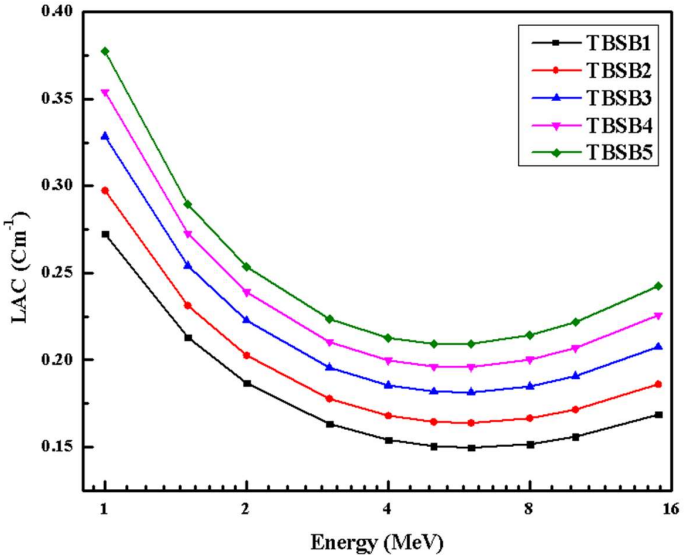

Figure 1: Linear attenuation coefficients (LAC) for the TBSB1-TBSB5 glass samples.

The MAC values calculated using Phy-X/PSD align closely with those from Geant4 Monta Carlo (MC) simulations, as shown in Table 2. These theoretical results demonstrate consistent agreement across all glass samples (TBSB1–TBSB5). Comprehensive validation studies confirm the reliability of Phy-X/PSD and Geant4 simulations, supported by experimental data in [5,7]. Therefore, the MAC values and related parameters derived from Phy-X/PSD are deemed accurate when compared with the experimental results, reinforcing their utility for analysis. Notably, the MAC value decreases as the photon energy increases, indicating more photon interactions at lower energies (e.g., 1 MeV) and fewer interactions at higher energies, allowing more gamma-ray photons to pass through the material. It can also be observed that glass samples TBSB1 have low MAC values and TBSB5 have higher MAC values. This may be due to decreasing the content of SrO while increasing Bi_2O_3.

Figures 2(a) and 2(b) present the HVL and TVL, respectively, plotted against photon energy for the five glass samples (TBSB1-TBSB5) studied. From Figure 2, it can be observed that the glass TBSB5 has the lowest TVL and HVL, whereas TBSB1 has the highest TVL and HVL. For instance, within the energy range of 1 to 15 MeV, the TVL is within the interval 8.453 to 13.66 cm, 7.743 to 12.376 cm, 7.006 to 11.093 cm, 6.504 to 10.202 cm, 6.1 to 9.495 cm, for TBSB1, TBSB2, TBSB3, TBSB4, TBSB5, respectively. Conversely, Figure 2(a) illustrates that within the photon energy range of 1–15 MeV, the HVL values for glass samples TBSB1, TBSB2, TBSB3, TBSB4, and TBSB5 vary between 2.544–4.112 cm, 3.331–3.737 cm, 2.113–3.343 cm, 1.962–3.071 cm, and 1.843–2.857 cm, respectively. These results show that the TVL and HVL of these five glass systems decrease as the content of SrO decreases while Bi_2O_3 increases. It can be observed that the TVL and HVL when the photon energy is around 5 MeV the trend starts to change and slowly decreases. This was also observed in the literature in [9].

Energy (MeV)	MAC (cm²/g), TBSB1		MAC (cm²/g), TBSB2		MAC (cm²/g), TBSB3		MAC (cm²/g), TBSB4		MAC (cm²/g), TBSB5	
(MeV)	Geant4	Phy-X/PSD	Geant4	Phy-X/PSD	Geant4	Phy-X/PSD	Geant4	Phy-X/PSD	Geant4	Phy-X/PSD
1	0.061	0.063	0.061	0.064	0.061	0.064	0.066	0.063	0.066	0.063
1.5	0.048	0.049	0.048	0.050	0.049	0.050	0.051	0.049	0.051	0.050
2	0.042	0.043	0.042	0.043	0.043	0.044	0.044	0.043	0.044	0.043
3	0.037	0.038	0.036	0.038	0.037	0.039	0.039	0.038	0.044	0.038
4	0.034	0.036	0.034	0.036	0.034	0.036	0.037	0.035	0.039	0.036
5	0.033	0.036	0.033	0.035	0.033	0.036	0.036	0.034	0.038	0.035
6	0.033	0.034	0.033	0.035	0.033	0.036	0.036	0.034	0.037	0.034
8	0.033	0.035	0.033	0.035	0.033	0.035	0.036	0.034	0.037	0.034
10	0.034	0.036	0.034	0.037	0.034	0.038	0.038	0.034	0.039	0.035
15	0.036	0.039	0.037	0.040	0.037	0.040	0.042	0.037	0.042	0.038

Table 2: Comparison between MAC values obtained from Geant4 simulations and Phy-X/PSD calculations for TBSB1-TBSB5 glass samples.

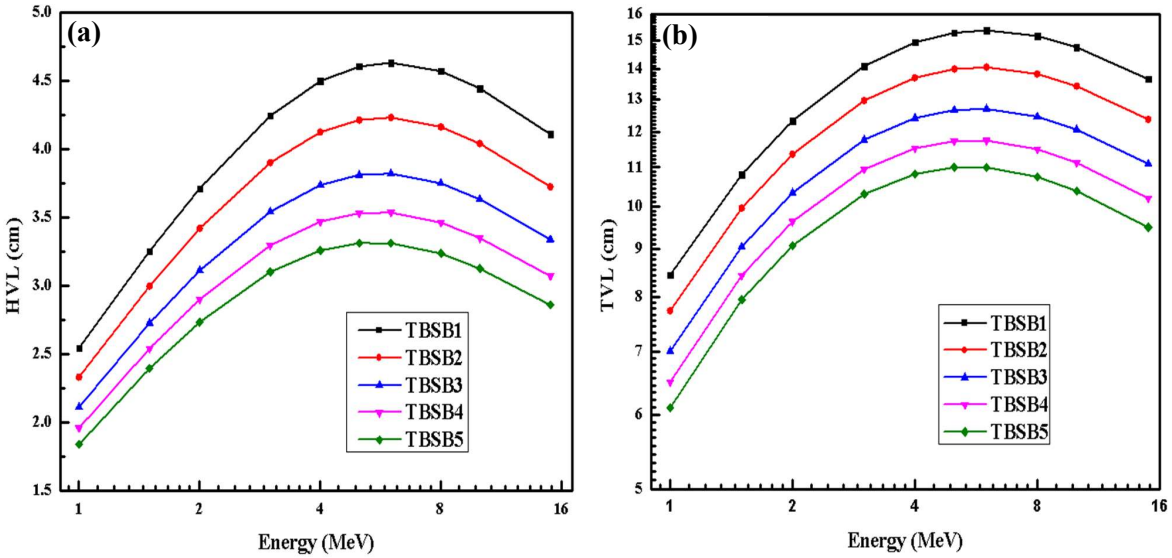

Figure 2: (a) Half value layer (HVL) and (b) tenth value layer (HVL) for the TBSB1-TBSB5 glass samples.

Figure 3 shows the variation of the effective atomic number ($Z_e$ff) as a function of photon energy for glass samples from TBSB1 to TBSB5. From Figure 3 it can be seen that from 1 to 1.5 MeV the Z_{eff} decrease for all glass samples. This is due to the predominant Compton effect in this energy region. Similar behaviour was observed in the literature in [5,6]. As depicted in Figure 3, from 1.5 MeV the $Z_e$ff increases with an increase in photon energy. Throughout the energy range of 1.5 to 15 MeV, a steady increase in Z_{eff} is observed across all glass systems. This gradual increase of Z_{eff} show that there are more electrons available for photon interaction, which shows that there is possibility for photons to interact with the material in the energy range from 1.5 to 15 MeV. The same behaviour has been observed in the literature in [10,11].

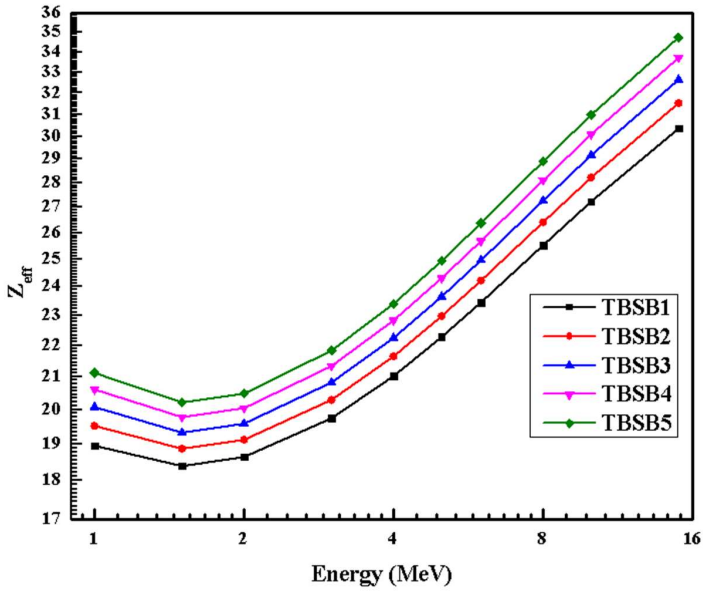

Figure 3: Effective atomic number for the TBSB1-TBSB5 glass samples.

4 Conclusion

The gamma-ray shielding properties of glass systems $40SrO–30B_2O_3–10TeO_2–20Bi_2O_3$, $35SrO–30B_2O_3–10TeO_2–25Bi_2O_3$, $30SrO–30B_2O_3–10TeO_2–30Bi_2O_3$, $25SrO–30B_2O_3–10TeO_2–35Bi_2O_3$, and $20SrO–30B_2O_3–10TeO_2–40Bi_2O_3$ were investigated using Phy-X/PSD software and validated with Geant4 MC simulations. The mass attenuation coefficient (MAC) results obtained from Phy-X/PSD showed good agreement with those obtained from Geant4 MC simulations. The linear attenuation coefficient (LAC), half-value layer (HVL), tenth-value layer (TVL), and effective atomic number (Z_{eff}) were calculated using Phy-X/PSD. Among the compositions studied, glass with $20SrO–30B_2O_3–10TeO_2–40Bi_2O_3$ exhibited the highest MAC, LAC, and Z_{eff} values, along with the lowest HVL and TVL values compared to the other glass samples, indicating superior radiation shielding performance over the other glass samples. The results indicate that decreasing the SrO content and increasing the Bi_2O_3 content enhance the gamma-ray shielding performance of the $20SrO–B_2O_3–TeO_2–Bi_2O_3$ glass system within the energy range between 1 and 15 MeV. Therefore, boro-tellurite glass systems containing high Bi_2O_3 and low SrO concentrations demonstrate strong potential for gamma-ray shielding applications, particularly in linear accelerators, research particle accelerators, and radiation processing industries operating within the 1–15 MeV energy range.

Acknowledgements

The authors thank the National research foundation, iThemba LABS and the University of Zululand for supporting this work.

References

[1] D. A. Alorain, A. H. Almuqrin, M. Sayyed, and M. Elsafi, Impact of wo3 and bao nanoparticles on the radiation shielding characteristics of polydimethylsiloxane composites, e-Polymers 23, 20230037 (2023).

[2] Sharma, G. Reddy, L. Varshney, H. Bharathkumar, K. Vaze, A. Ghosh, H. Kushwaha, and T. Krishnamoorthy, Experimental investigations on mechanical and radiation shielding properties of hybrid lead–steel Fiber reinforced concrete, Nuclear Engineering and Design 239,1180 (2009).

[3] F. Br´echignac, D. Oughton, C. Mays, L. Barnthouse, J. C. Beasley, A. Bonisoli Alquati, C. Bradshaw, J. Brown, S. Dray, S. Geras' kin, et al., Addressing eco-logical effects of radiation on populations and ecosystems to improve protection of the environment against radiation: Agreed statements from a consensus symposium, Journal of environmental radioactivity 158, 21 (2016).

[4] H. Alrebdi, A. Almuqrin, M. Hanfi, M. Sayyed, and K. Mahmoud, Influence of the SrO insertion to a binary PbO-B_2O_3 glass system: Mechanical properties and radiation shielding study, Transactions of the Indian Ceramic Society 81, 76 (2022).

[5] M. Al-Buriahi, E. M. Bakhsh, B. Tonguc, and S. B. Khan, Mechanical and radiation shielding properties of tellurite glasses doped with ZnO and NiO, Ceramics International 46, 19078 (2020).

[6] S. A. Issa, A. Ene, H. M. Zakaly, et al., Evaluating the effectiveness of tellurium-molybdenum oxide glass systems for radiation shielding protection, Multidisciplinary Materials Chronicles 1, 19 (2024).

[7] N. Alonizan, M. Mhareb, K. Mahmoud, M. Sayyed, N. Dwaikat, Q. Drmosh, M. Y. Alqahtani, and N. A. Saleh, Mechanical, structural, and radiation shielding characteristics for transparent boro-tellurite glasses modified with strontium and bismuth oxide ratios, Optical Materials 146, 114524 (2023).

[8] H. A. Thabit, M. Sayyed, F. O. Okoh, S. Yasmin, M. Kamislioglu, et al., Impact of bi2o3 on the glass system B_2O_3-TeO_2–MgO–PbO on the purpose of radiation shielding efficacy, Progress in Nuclear Energy 173, 105240 (2024).

[9] K. M. Kak, M. Sayyed, M. K. Hamad, S. Biradar, M. Mhareb, U. Altimari, and M. M. Taki, Bismuth oxide effects on optical, structural, mechanical, and radiation shielding features of borosilicate glasses, Optical Materials 155, 115853 (2024).

[10] M. Ouis and H. ElBatal, Comparative studies of ir spectra, optical and thermal properties of binary CdO-B_2O_3, SrO-B_2O_3, and BaO-B_2O_3, Silicon 9, 703 (2017).

[11] R. El-Mallawany, M. Sayyed, M. Dong, and Y. Rammah, Simulation of radiation shielding properties of glasses contain Pbo, Radiation Physics and chemistry 151, 239 (2018).

This page intentionally left blank.

Real-Time Anomaly Detection in High Energy Physics

Ryan Justin Atkin[1,2], **James Michael Keaveney**[1] **and Claire David**[2]

[1]Department of Physics, University of Cape Town, Cape Town, South Africa
[2]African Institute for Mathematical Sciences, Cape Town, South Africa

E-mail: ryan.atkin@uct.ac.za

Abstract. While searches for physics beyond the Standard Model (BSM) have yet to yield conclusive discoveries, they continue to motivate the development of more flexible, data-driven strategies. At the ATLAS experiment at the Large Hadron Collider (LHC), trigger systems are used to rapidly select potentially interesting proton-proton collisions for further analysis. Traditional triggers rely on pre-defined criteria, such as high-momentum particles, which may miss more subtle or unconventional signs of new physics. To overcome this limitation, machine learning algorithms are being developed to identify anomalous events in real time based on their overall detector signature, rather than specific features. Using unsupervised learning techniques, these algorithms learn to characterise typical collision patterns directly from the data, without input from Standard Model or BSM theory. Events that diverge significantly from these patterns are flagged as anomalous for further study. These events are stored for detailed offline analysis. This approach enables a broad and largely model-independent search for unexpected phenomena in the vast datasets of Run-3 and beyond. It could potentially reveal signals that targeted BSM searches might overlook.

1 Introduction

The Standard Model (SM) of particle physics describes all the known elementary particles and their interactions via three of the four fundamental forces of nature. The SM is a very successful theory whose predictions have been backed up by many experimental results. However, there are some phenomena the SM does not explain, alluding to the SM being an incomplete theory. These unexplained phenomena include, but are not limited to, the origin of dark matter [1], the dominance of matter over anti-matter in the universe [2], and the lack of a description of gravity. So far, direct searches for theories beyond the SM (BSM) have yet to provide any conclusive evidence for these new theories. As such, there is an increasing focus on other methods to find new physics. One of these methods is using Anomaly Detection (AD), which involves studying data that significantly deviates from the typical dataset. For example, consider a dataset that is completely dominated by hadronic objects. An event that has no hadronic objects and only electrons or muons would then clearly deviate from what all the other events contain. Using AD avoids any model assumptions, allowing the data to speak for itself, and provides the potential to find signals that the current searches cannot.

2 ATLAS trigger system

In order to study anomalous events, they first need to be found. In the ATLAS experiment [3] at CERN, triggers are used to select collisions that are likely to contain interesting physics. Given that there are around 40 million proton-proton collisions that occur within the ATLAS experiment every second, and that most of these are low-energy inelastic-scattering collisions, not all of the collisions can be saved to disk. Instead, two levels of trigger systems are used to reduce the data rate to a manageable amount, as well as select the most interesting collisions.

The first level trigger, or L1 trigger, is a hardware-based trigger with the trigger logic implemented on Field-Programmable Gate Array (FPGA) boards. The L1 trigger has to look at every collision to determine if there is anything interesting, and needs to make this decision within 2.5 μs. To keep within this short latency, only coarse information from the calorimeters and muon spectrometer are used to reduce the data rate from $\sim$40 MHz to $\sim$100 kHz.

The data that passes the L1 decision is sent to the High-Level Trigger (HLT). The HLT is a software-based trigger that performs a basic reconstruction of the objects, using all parts of the detector within a region where the L1 trigger fired, also known as the Region-of-Interest (RoI). The HLT triggers are seeded by corresponding L1 triggers, forming what are known as “trigger chains". For example, the muon HLT triggers will only look at data that fired one of the muon L1 triggers. Each collision can fire multiple different triggers though. So while the L1 trigger processes every collision, the HLT trigger only looks at a subset of the data. The HLT trigger then needs to make its decision within tens of milliseconds, reducing the data rate further from $\sim$100 kHz to $\sim$1 kHz. All data that pass at least one of the HLT triggers is sent off detector for permanent storage.

The current set of triggers all use standard physics signals to trigger on. Therefore, to trigger on anomalous collisions, new triggers are needed. In order to learn from the data itself and try to exploit unknown features in the data, machine learning techniques are used to create these new AD triggers.

3 Generic Event-Level Anomalous Trigger Option (GELATO)

The triggers used for anomaly detection in the ATLAS experiment are the Generic Event-Level Anomalous Trigger Option (GELATO) triggers, designed by the ATLAS AD trigger group. To classify a collision as anomalous, an algorithm needs to be able to distinguish between a typical collision and one that looks different from this. To this end, both the L1 and HLT GELATO use a form of deep neural network known as Auto-Encoders (AEs). These networks aim to reconstruct the input data as best as possible. If the typical dataset makes up 99.9% of all the data, the AE will learn to reconstruct this well. When it is given the 0.1% that is anomalous to this typical dataset, the AE will struggle to reconstruct it and thus have a large reconstruction error. The GELATO L1 trigger uses a more complex version of the AE, known as a Variational Auto-Encoder General Adversarial Network (VAE-GAN) [4]. A diagram illustrating the structure of a VAE-GAN is given in Figure 1. There are three components to a VAE-GAN, the generic AE, the variational part and the adversarial part.

A generic AE (the top section of Figure 1) has two main components, the encoder and decoder. The encoder reduces the number of dimensions at each layer down into the latent space. This reduction tries to find an efficient and compressed representation of the data, while learning the important features and removing noise. The decoder expands the dimensions back out from the latent space to the same number of dimensions as the input. The AE is an unsupervised model trying to reconstruct the inputs, and is trained by minimising the loss function $\mathcal{L}_{MSE}$, defined by the Mean Square Error (MSE), between the outputs of the decoder and the inputs to the encoder. This differs from supervised learning where the loss function is the difference between what the events are labelled as, and what the algorithm predicts the label to be. The MSE loss function is shown in Equation 1, where x_i and $\hat{x_i}$ are the inputs and outputs respectively, and n is the number of inputs/outputs. In a generic AE, collisions with a large MSE would be considered anomalous.

For the variational part of the VAE-GAN (middle section of Figure 1), an addition is made to the latent space of the generic AE. Instead of the final layer of the encoder mapping directly onto the latent space, it maps onto mean (μ_z) and standard deviation (σ_z) vectors that have the same dimensions as the latent space (n_z). The μ_z and σ_z are used to create an n_z-dim standard normal distribution, from which the latent space variables are sampled. With the inclusion of the variational part comes the addition of the Kullback-Leibler (KL) divergence loss, $\mathcal{L}_{KL}$, to the total loss function. The definition of $\mathcal{L}_{KL}$ is given in Equation 2. Here, μ_k and σ_k are the components of the μ_z and σ_z vectors, and β is a parameter that is varied to control how much of an impact the KL divergence has on the total loss function. The KL divergence encourages the latent space to follow a standard normal distribution, ensuring a well-behaved latent space.

The adversarial part of the VAE-GAN (bottom section of Figure 1) includes an additional discriminator D. This discriminator is a simple Deep Neural Network (DNN) that learns to differentiate between the “real" and “fake" signals, or inputs (x_i) and outputs ($\hat{x_i}$) respectively. The discriminator is trained using the loss function $\mathcal{L}_D$, as defined in the lower section of Figure 1. The total loss function of the VAE-GAN is altered by including the adversarial loss $\mathcal{L}_{Adv}$, shown in Equation 3. Here the λ is a parameter that is varied to control how much of an impact the GAN has on the total loss function, and $D(\hat{\boldsymbol{x}})$ is the output of the discriminator when given the output

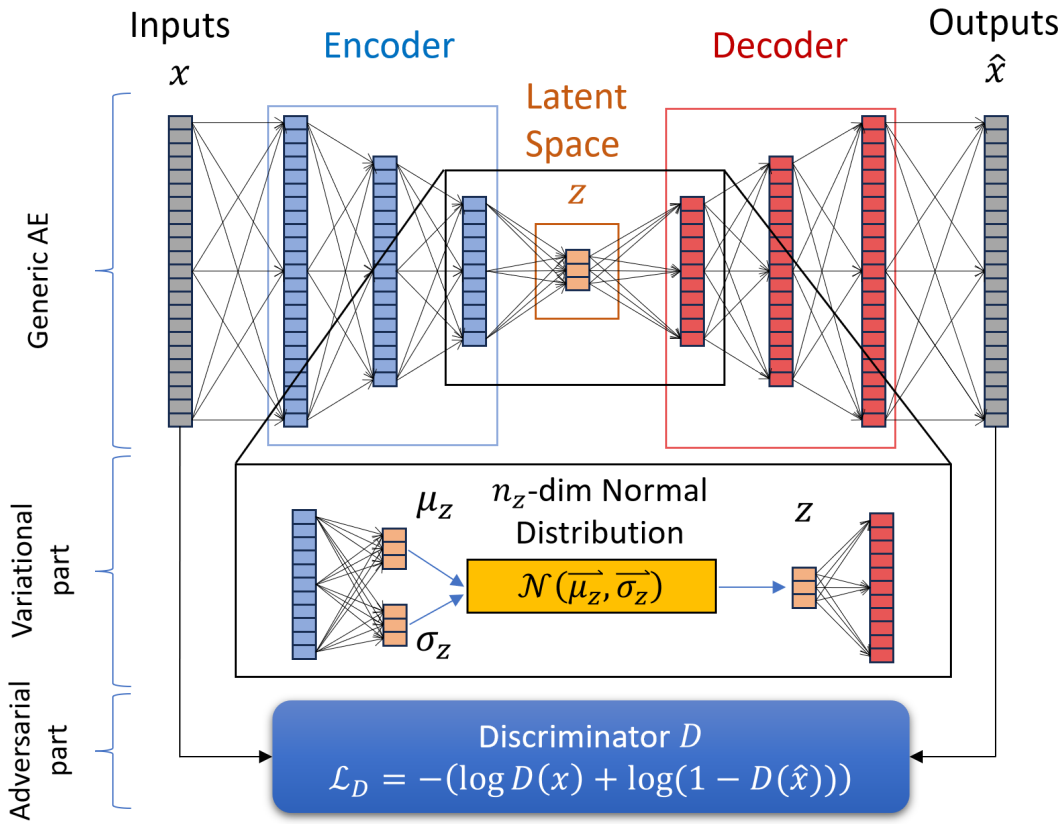

Figure 1: Illustration of the structure of a Variational Auto-Encoder General Adversarial Network (VAE-GAN). The upper section shows the generic Auto-Encoder (AE). The middle section shows the variational latent space, which includes a sampling from a standard normal. The lower section represents the GAN, or discriminator, showing the loss function used to train the discriminator.

of the VAE-GAN as input. The decoder tries to fool the discriminator into classifying the output $\hat{x}_i$ as real, with the discriminator acting as an adversary to the decoder. This helps to regularise the output, creating more realistic data-like reconstructions. The combination of these three loss functions are used to define the total loss function of the VAE-GAN, as in Equation 4.

$$\mathcal{L}_{MSE} = \frac{1}{n}\sum_{i=1}^{n}(\hat{x}_i - x_i)^2 \tag{1}$$

$$\mathcal{L}_{KL} = \beta\frac{1}{2}\sum_{k=1}^{n_z}\left(\mu_k^2 + \sigma_k^2 - \ln\sigma_k^2 - 1\right) \tag{2}$$

$$\mathcal{L}_{Adv} = \lambda \log D(\hat{\boldsymbol{x}}) \tag{3}$$

$$\mathcal{L}_{Reco} = \mathcal{L}_{MSE} + \mathcal{L}_{KL} - \mathcal{L}_{Adv} \tag{4}$$

3.1 GELATO L1

Given the required latency of the L1 triggers, and the hardware constraints, the L1 GELATO can't use the full structure of the VAE-GAN when it is implemented on the FPGA boards. Instead, the full VAE-GAN structure is used when training the L1 GELATO, but only the encoder and the μ_z vector are implemented onto the FPGA boards for use in the ATLAS experiment. Due to this simplification of the algorithm, the metric used to determine whether a collision was anomalous or not (also known as the AD score) is the clipped KL divergence $\mathcal{L}_{KL}^{clipped} = \beta\frac{1}{2}\sum\mu_k^2$.

This is why the use of a VAE-GAN was necessary as it ensured that the clipped KL score would be good enough to find the anomalous collisions. This allows for a quick and efficient algorithm to be implemented on the FPGAs.

The inputs to the GELATO L1 consist of 44 variables. These cover the transverse momentum p_T, pseudorapidity η, and angular direction ϕ of 15 objects: six jets, four taus, 4 muons and the missing transverse energy E_T^{miss}. The encoder has 2 hidden layers, with the first having 32 dimensions and the second 16 dimensions, which is then reversed in the decoder. The latent space has only three dimensions. The threshold on the clipped KL divergence score used to separate anomalous from typical data is determined by requiring a unique rate of 1 kHz. The unique rate is the amount of data passing the GELATO L1 per second that do not pass any other L1 triggers.

3.2 GELATO HLT

Given that the HLT has a longer latency than the L1 triggers, the algorithm has more time to perform inference, allowing a more computationally intensive algorithm to be implemented in the ATLAS experiment. The GELATO HLT therefore uses a full generic AE (top section of Figure 1) for both the training and implementation of the trigger. Since the output of the decoder is used to calculate the score, there is no need for the use of the variational and GAN parts to ensure a well behaved latent space.

The inputs to the GELATO HLT are also slightly different, using 47 inputs covering the p_T, η and ϕ 16 objects: six jets, three electrons, three muons, three photons, and E_T^{miss}. The encoder is larger as well, with four layers of dimension 100, 100, 64 and 32 nodes, which are reversed for the decoder. The latent space has a dimension of four. In order to reduce the noise, a minimum p_T selection is applied to the objects. All jets need to have $p_T > 50$ GeV, while the electrons, muons and photons need $p_T > 30$ GeV. If an object fails these requirements, they are set to zero. Both the loss function and the AD score for the GELATO HLT are the masked MSE. This is just Equation 1, but only using the non-zero x_i and $\hat{x_i}$. The GELATO HLT threshold is determined such that the unique data rate is 10 Hz.

3.3 Training and testing data

The data used to train both the GELATO L1 and HLT was the Enhanced Bias (EB) [5] dataset. This is real data collected by the ATLAS experiment during the 2024 data taking period. A minimal set of L1 triggers, spanning a wide range of energies and objects, was used to select this data. Each event in the dataset has a dedicated weight mostly based on the prescales of the triggers that are used to "unbias" the data. This provides a dataset that contains rare events while maintaining an unbiased spectrum of events. The EB dataset is also used to determine the thresholds on the AD scores based on the unique rate of EB data with AD scores above the threshold.

A broad selection of Monte Carlo (MC) samples are used as signal models to demonstrate the model independent nature of the GELATO triggers. They represent both Standard Model (SM) and Beyond the Standard Model (BSM) processes, and are also known to struggle with the standard ATLAS triggers. The MC samples are summarised in Table 1 [6].

Data	
Enhanced Bias	Data collected in 2024 by the ATLAS experiment using a minimal set of L1 triggers
SM MC processes	
$Z \to \nu\nu$ (b filter)	Z decaying to $\nu\nu$ with a b filter
VBF $hh \to bbbb$	VBF hh decaying to $b\bar{b}b\bar{b}$
BSM MC processes	
HAHM ggF: $h \to Z_d Z_d \to 2l2\nu$	Hidden Abelian Higgs Model (HAHM) with $m_Z d$ = 28 GeV produced via ggF h
HNL$\to e\mu\nu$	Heavy Neutral Lepton (HNL) with m = 7.5 GeV, $c\tau$ = 1 mm
ggF $h \to$SUEP$\to$full-had	Soft Unclustered Energy Pattern (SUEP) produced via ggF h
VBF $h \to aa \to 4b$	aa produced via VBF h with m_a = 55 GeV, τa = 1 ns
ggF $h \to aa \to 4b$	aa produced via ggF h with m_a = 16 GeV, τa = 10 ns

Table 1: Summary of the data used for training the GELATO triggers, and the MC samples used for testing the GELATO triggers [6]. The MC samples are split by whether they are SM or BSM processes.

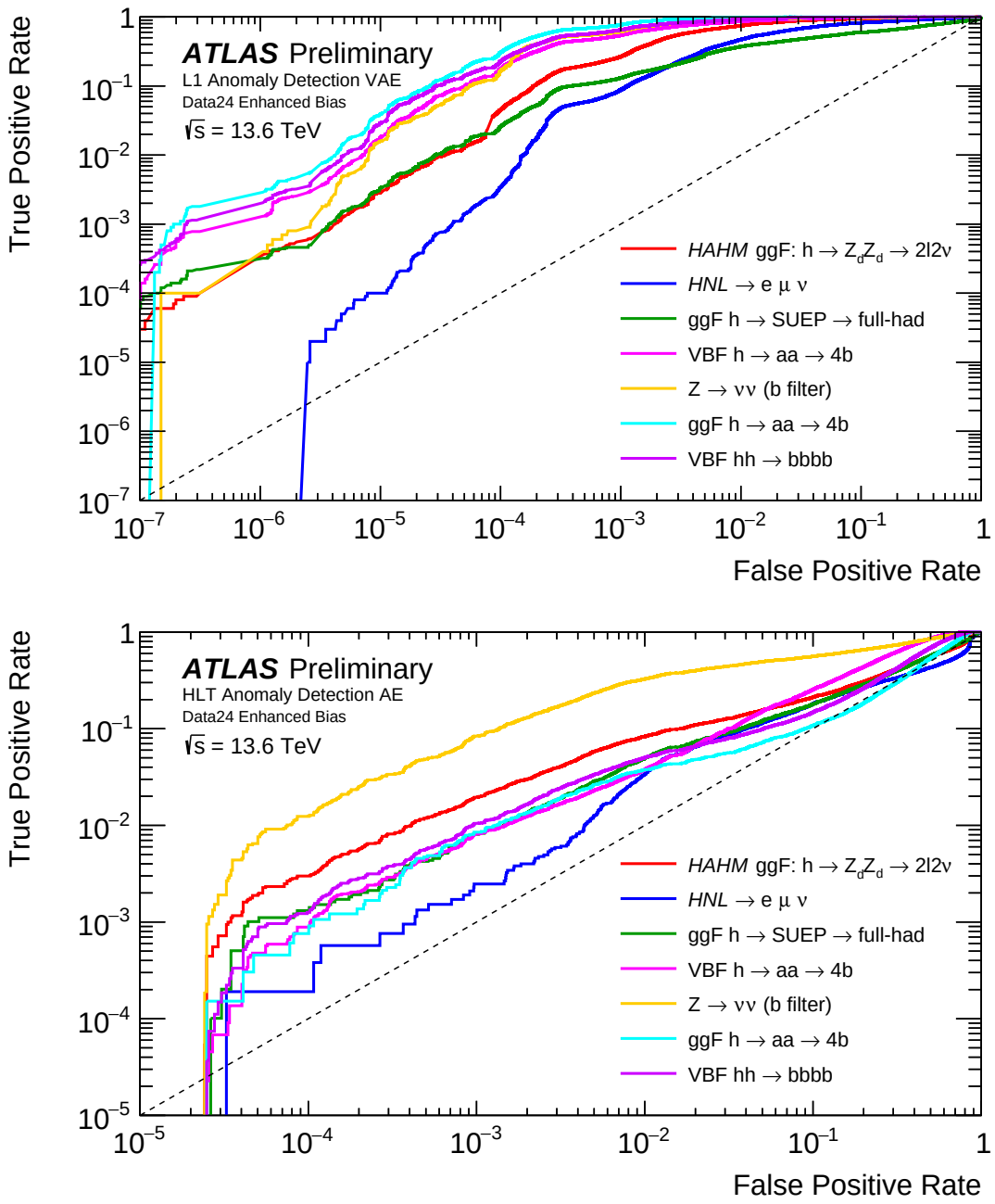

Figure 2: The ROC curves for the GELATO L1 (top) and GELATO HLT (bottom) [6]. The y-axes show the TPR defined as the weighted yield of MC signal events passing the GELATO triggers at various AD score thresholds. The x-axes shows the FPR defined as the weighted yield of EB background events passing the GELATO triggers at various AD score thresholds. The diagonal dashed lines represent using a 50% probability to classify the event as either anomalous or typical. The coloured lines are the different MC samples used as signal proxies, covering both SM and BSM processes. All events used in the calculations for the lower plot passed the GELATO L1. The descriptions of the different MC samples are given in Table 1.

4 Discussion

The Receiver Operating Characteristic (ROC) curves for both the GELATO L1 and HLT are shown in Figure 2. For these ROC curves, the MC processes are considered the different signal processes, while the EB dataset is considered the background. For every AD score obtained in the signal datasets, the weighted fraction of those samples above that AD score determines the True Positive Rate (TPR). The same is done for the EB dataset, which gives the False Positive Rate (FPR). For the given AD scores, the TPR is plotted against the FPR to evaluate the signal-background discrimination of the GELATO triggers. If the GELATO triggers classified purely randomly, the diagonal dashed lines in Figure 2 would be obtained. So, if the ROC curve of a MC process is above this dashed line, it means the GELATO trigger can distinguish between the signal and background. Given that all the MC processes are above the dashed line for both the GELATO L1 and HLT, these new triggers show strong discriminating power between signal and background across a wide variety of possible processes.

A study of the correlations of the input variables at the HLT stage, with the GELATO L1 and HLT scores, was performed for the events that passed the GELATO L1. It was found that the GELATO L1 and HLT AD scores were not strongly correlated to any single variable, showing that the algorithms are learning more information about the data. The correlation of the AD scores with the η and ϕ of all the objects was negligible, all being around 1 or 2 % correlation. However, the correlation between the GELATO AD scores with the ϕ of E_T^{miss} was found to be around 10%. The highest correlations of the AD scores were with the highest p_T objects of each object class. Interestingly though, when looking at the correlations of the events that passed the GELATO HLT only and no other HLT triggers, there were higher correlations for the sub-leading objects compared to the leading objects. This suggests that while very high p_T objects are considered more anomalous, they are likely to be triggered by some of the other triggers. The uniquely anomalous events thus likely have lower p_T objects with higher multiplicities.

5 Conclusion

In order to find new and interesting physics at the LHC in a model agnostic way, the first anomaly detection triggers have been developed for the ATLAS experiment, called the GELATO triggers. These are machine learning based algorithms, using a generic auto-encoder or a VAE-GAN depending on the level of trigger. The GELATO L1 has already been implemented in the ATLAS experiment, while the GELATO HLT has been added to the trigger lists but is still under resource cost and data rate studies. For future plans, a way to calibrate the GELATO triggers needs to be determined. The common triggers use well-defined trigger-object correspondences for calibration, but with anomalous data, there are no obvious corresponding objects. In conjunction with determining a calibration method, an offline analysis is ongoing to examine these anomalous events in greater detail and assess their potential to reveal novel physics. The GELATO triggers represent a shift towards more model-agnostic physics searches and will only improve in future.

References

[1] Planck Collaboration, "Planck2015 results: I. overview of products and scientific results," *Astronomy and Astrophysics*, vol. 594, p. A1, Sep. 2016. [Online]. Available: http://dx.doi.org/10.1051/0004-6361/201527101

[2] M. B. Gavela, P. Hernandez, J. Orloff, and O. Pene, "Standard model cp-violation and baryon asymmetry," *Modern Physics Letters A*, vol. 09, no. 09, pp. 795–809, Mar. 1994. [Online]. Available: http://dx.doi.org/10.1142/S0217732394000629

[3] ATLAS Collaboration, "The ATLAS Experiment at the CERN Large Hadron Collider," *Journal of Instrumentation*, vol. **3**, no. 08, p. S08003, 2008. [Online]. Available: http://stacks.iop.org/1748-0221/3/i=08/a=S08003

[4] E. Govorkova et. al., "Autoencoders on field-programmable gate arrays for real-time, unsupervised new physics detection at 40 mhz at the large hadron collider," *Nature Machine Intelligence*, vol. 4, no. 2, pp. 154–161, Feb. 2022. [Online]. Available: http://dx.doi.org/10.1038/s42256-022-00441-3

[5] ATLAS Collaboration, "Trigger monitoring and rate predictions using Enhanced Bias data from the ATLAS Detector at the LHC," CERN, Geneva, Tech. Rep., 2016, all figures including auxiliary figures are available at https://atlas.web.cern.ch/Atlas/GROUPS/PHYSICS/PUBNOTES/ATL-DAQ-PUB-2016-002. [Online]. Available: https://cds.cern.ch/record/2223498

[6] ATLAS Collaboration., "Public combined trigger plots for collision data," https://twiki.cern.ch/twiki/bin/view/AtlasPublic/CombinedTriggerPublicResults, 2025.

Search for a new spin-0 scalar and a spin-1 boson using Run2 ATLAS detector data

Xola Mapekula[1,2], **Simon Connell**[1], **Loan Truong**[1], **Matthew Connell**[1], **Carlos Solans Sanchez**[2]

[1]Department of Mechanical Engineering Science, University of Johannesburg, Johannesburg, South Africa
[2]CERN, Geneva, Switzerland

E-mail: xola.mapekula@cern.ch

Abstract. We present a search for a new spin-0 scalar particle, S, produced in association with a spin-1 boson. The scalar S is studied in the decay channel $S \to Z_d Z_d \to 4\ell$, where each dark vector boson (Z_d) promptly decays into an oppositely charged lepton pair ($\ell = e, \mu$). The analysis focuses on the scalar mass interval from 20 GeV to 1 TeV, excluding the region corresponding to the Higgs boson, defined as 115 GeV $< m_S <$ 130 GeV. while the Z_d mass is considered between 15 and 300 GeV. The Z_d bosons are assumed to be produced on-shell, requiring $m_{Z_d} < \frac{1}{2} m_S$. The analysis employs proton-proton collision data from ATLAS at $\sqrt{s} = 13$ TeV, with an integrated luminosity of 139 fb^{-1}. No significant excess is observed, and a 95% confidence level upper limit is set on the production cross section times branching ratio as a function of m_S and m_{Z_d}.

1 Introduction

Extensions of the Standard Model (SM) that introduce a $U(1)_d$ gauge symmetry naturally give rise to dark matter candidates. A prominent example is the "Hidden Abelian Higgs Model (HAHM)", which predicts a dark sector linked to the SM through this additional symmetry [1, 2]. In the HAHM framework, the dark sector gauge field is associated with a "$U(1)_d$ symmetry", which kinetically mixes with the SM $U(1)_Y$ through a coupling parameter ϵ [3, 4, 5]. This mechanism introduces an extra scalar particle, S, which can act as either a lighter or heavier SM Higgs boson partner.

In this framework, the "$U(1)_d$ gauge symmetry" is realized through the exchange of a light Z_d boson which couples to the dark charge that is part of hidden sector states, thereby connecting the dark sector to SM [2].

In the HAHM model, Higgs boson production also generates the scalar S via mixing with coupling κ [3] (see Figure 1). The S particle and the Higgs boson could mix via the Higgs coupling parameter κ. Any production mode of the Higgs would also be a production mode of the new scaler. The dominant production mode would therefore be via gluon-gluon fusion as proton-proton collisions occur. The value ϵ, which denotes the kinetic mixing parameter, governs lifetime of the Z_d boson with SM particles, under the assumption of negligible states other than SM. By contrast, the gauge couplings determine the decay modes of Z_d. The branching ratios do not depend on precise value of ϵ for $\epsilon \ll 1$. For 1 GeV $< m_{Z_d} <$ 60 GeV, the branching ratio of Z_d decays to e^+e^- or $\mu^+\mu^-$ is typically 10%–15% [6]. In the same parmeter space region, the decays are prompt provided $\epsilon 10^{-5}$ [6]. This process is shown by the Feynman diagram in Figure 1.

This study is an extension of previous work where a search for a resonantly-produced Higgs decaying to $Z_d Z_d$ or $Z_d Z$ pairs [7, 8, 9] was performed, where each Z_d decays into either an muon or electron pair with opposite electric charge. In this iteration of the search, we include a new scalar S with $m_S < 800$ GeV and $m_{Z_d} < 300$ GeV, using $\sqrt{s} = 8$ and 13 TeV ATLAS data.

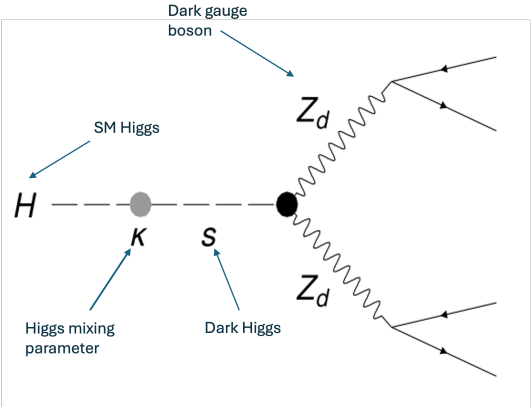

Figure 1: Feymann diagram of an Higgs decaying into a pair of dark gauge bosons, via the mixing parameter (κ).

2 ATLAS detector

The ATLAS detector, situate along the circumference of the large Hadron Collider, was developed and constructed find evidence of the existence of the the Higgs boson while also exploring physics beyond SM. The detector captures snapshots of proton-proton collisions occurring at its interaction point located along the LHC's circular path, around which the detector is positioned. The subdetectors of the ATLAS detector include: an Inner Detector, an Electro-magnetic Calorimeter, a Hadronic Calorimeter and a Muon Spectrometer.

Charged particle trajectories, momenta, and charges are measured by the inner detector ($|\eta| < 2.5$), while the electromagnetic ($|\eta| < 3.2$) and hadronic ($|\eta| < 1.7$) calorimeters measure energy deposits. The region $|\eta| < 2.7$ is covered by the muon spectrometer for muon momentum measurements.

3 Main Backgrounds

Monte Carlo simulations estimate the expected shapes and yields of background and signal events. Simulations include detector and pileup effects. To correct for minor variations in isolation and reconstruction impact parameter efficiencies, event weights are used to correct simulated events. Pile-up uncertainties account for about 1% due to differences between predicted and measured cross sections that are inelastic. The selection efficiency depends on lepton trigger, reconstruction, identification, isolation, and momentum scale. Tag-and-probe studies of dilepton resonances (Z, J/ψ, Υ) provide corrections for differences between simulation and data while also defining the associated residual uncertainties [10, 11].

Backgrounds involving four-lepton final states are estimated using simulated data. The $ZZ^\star \to 4\ell$ process, which is the dominant contribution, accounts for about 90–95% of the total background. Backgrounds related to Higgs production are removed by applying the requirement $m_{4\ell}$ < 115 GeV and $m_{4\ell} > 130$ GeV. A complete summary of the samples together with the event generators used is presented in Table 1.

3.1 Signal Simulation

Signal samples with different mass values for S and Z_d were produced in ggH production mode using MadGraph5_aM@NLO v2.2.3 [12]. The couplings ϵ (dark vector–SM) and κ (Higgs–dark sector) were set to 10^{-4} to ensure prompt Z_d decays. The S mass (m_S) was chosen to be at least twice dark gauge boson mass m_{Z_d} while m_S varies from below the Higgs mass (m_H) to above the m_H. Two signal regions are used for this search. Each signal region (SR1 and SR2) is defined according to the m_S, which differs from that of them_H. SR1 is defined by $m_{4\ell} < 115$ GeV, where either $m_{ab,cd} < 50$ GeV or $m_{ab} > 106$ GeV. SR2 requires $m_{4\ell} > 130$ GeV, and $|m_{ab,cd} - m_Z| > 4$ GeV, and $|m_{ad,bc} - m_Z| > 8$ GeV, where the m_{ab} and m_{cd} are the masses of the leading and sub-leading dilepton pairs in the S quadruplet. The expected signal distributions for SR1 (30 GeV $< m_{4\ell} <$ 115 GeV) and SR2 (130 GeV $< m_{4\ell} <$ 800 GeV) are shown in Figure 2.

3.2 Event Selection

Table 2 summarizes the event selection cuts, which are mostly derived from the $H \to ZZ^* \to 4\ell$ analysis [13]. The analysis considers muons and electrons as the final-state objects. To identify electrons, the electromagnetic calorimeter energy deposits are associated with charged particle tracks in the inner detector. Events may contain at most one calorimeter-tagged or standalone muon; all other muons must be combined muons. The selection targets a quadruplet comprising pairs of leptons that have the same flavor with opposite charge (SFOS). The quadruplet

Process	ME generator	ME PDF	PS/UE/HF model	UE tune
$S \to Z_d Z_d \to 4\ell$	MADGRAPH5 aMC@NLO	NNPDF2.3lo	PYTHIA/EVTGEN	A14
ggF	POWHEG BOX	PDF4LHC15 NNLO	PYTHIA/EVTGEN	AZZNLO
VBF	POWHEG BOX	CT10 NLO	PYTHIA/EVTGEN	AZZNLO
VH	Pythia	NNPDF2.3lo	PYTHIA/EVTGEN	A14
$ggZH$	POWHEG BoX	NNPDF3.0nlo	PYTHIA/EVTGEN	AZZNLO
$b\bar{b}H$	MADGRAPH5 aMC@NLO	NNPDF2.3lo	PYTHIA/EVTGEN	A14
$t\bar{t}H$	POWHEG BOX	NNPDF2.3lo	PYTHIA/EVTGEN	A14
ZZ	SHERPA	NNPDF3.0nnlo	SHERPA	SHERPA
VVV	SHERPA	NNPDF3.0nnlo	SHERPA	SHERPA
$t\bar{t}Z$	SHERPA	NNPDF3.0nnlo	SHERPA	SHERPA
$Z + jets$	SHERPA	NNPDF3.0nnlo	SHERPA	SHERPA
$t\bar{t}$	POWHEG BOX	NNPDF3.0nlo	PYTHIA/EVTGEN	A14
WZ	POWHEG BOX	CT10 NLO	PYTHIA/EVTGEN	A14

Table 1: A list of processes simulated with MC for this analysis which include reducible and irreducible background together with the generators used to mordel the events, parton showers and parton distribution functions.

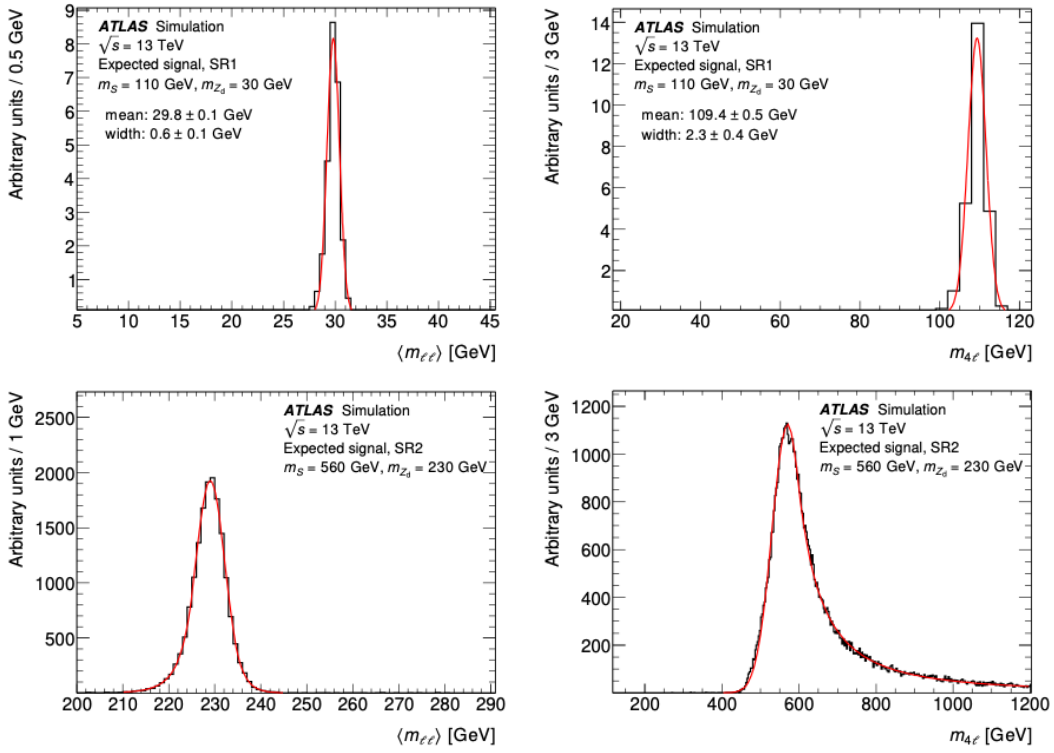

Figure 2: Expected signal distributions for $m_{4\ell}$ and $m_{\ell\ell}$ in the two signal regions SR1 and SR2.

with the smallest lepton pair mass difference is chosen. Leptons belonging to a particular quadruplet must be isolated from other tracks observed in the inner detector and from electromagnetic calorimeter energy deposits. Dilepton pairs formed with either electron or muon pairs must not be consistent with the SM Z-boson mass.

4 Results

The $m_{\ell\ell}$ distribution in the $(m_S, m_{\ell\ell})$ plane was obtained using 2D interpolation. The expected SM backgrounds, which are listed in Table 3, are statistically consistent the observed event count. Figure 3 shows the observed data in SR1 and SR2. SR2 contains a horizontal band showing the effect of the Z-veto cut listed in Table 3.

Group	**Cut**	**Criteria**
Electrons	η	$\lvert\eta\rvert < 2.47$
	ID	LooseLH working point
	OQ	Not from bad cluster
	$z_0 \sin\theta$	< 0.5 mm
Muons	p_T	> 6 GeV (15 GeV if calo-tagged)
	η	$\lvert\eta\rvert < 2.47$
	ID	Loose
	$z_0 \sin\theta$	< 0.5 mm
	$\lvert d_0\rvert$	< 1 mm (if not stand-alone)
Quadruplets	Composition	≥ 1 quadruplet with 2 SFOS dilepton pairs
	Overlap	No overlap removed e or μ
	p_T	$p_T^1 > 20$, $p_T^2 > 15$, $p_T^3 > 10$ GeV
	Trigger	≥ 1 lepton matches trigger
	ΔR	> 0.1 (same-flavor), > 0.2 (different-flavor)
	Muon Quality	$N_{\text{stand-alone/calo-tagged } \mu} < 2$
Ranking	Selection	Minimal Δm quadruplet
Event selection	Isolation	All leptons pass Fixed-CutLoose
	Impact Parameter	$\lvert d_0^{BL}\rvert < 5(3)$ for $e(\mu)$
	Quarkonia Veto	Exclude J/ψ, $\psi(2S)$, $\Upsilon(1S, 3S)$ mass windows
	Low mass veto	All dilepton masses > 5 GeV
	Z veto SR1	$m_{ab} \notin [50, 106]$ GeV
	Z veto SR2	$m_{ab}, m_{cd} \notin [83.2, 99.2]$ GeV
	Loose SR	All dilepton masses > 10 GeV
	H veto SR1	$m_{4\ell} < 115$ GeV
	H veto SR2	$m_{4\ell} > 130$ GeV
	Medium SR	New SR definition
	Tight SR	$\lvert E'_{ab}/m_{4\ell} - 0.5\rvert < 0.008$

Table 2: A list of the event selection criteria used in the analysis. Quarkonia veto uses $m_{\psi(2S)} = 3.686$ GeV, $m_{J/\psi} = 3.096$ GeV, $m_{\Upsilon(3S)} = 10.355$ GeV, $m_{\Upsilon(1S)} = 9.461$ GeV with $\sim 3\times$ mass resolution windows.

Region	Mass range	Expected yield	Background yield
SR1	($m_{4\ell} < 115$ GeV)	36	32 ± 3.3
SR2	($m_{4\ell} > 130$ GeV)	55	68 ± 8

Table 3: Expected and observed signal and background yields

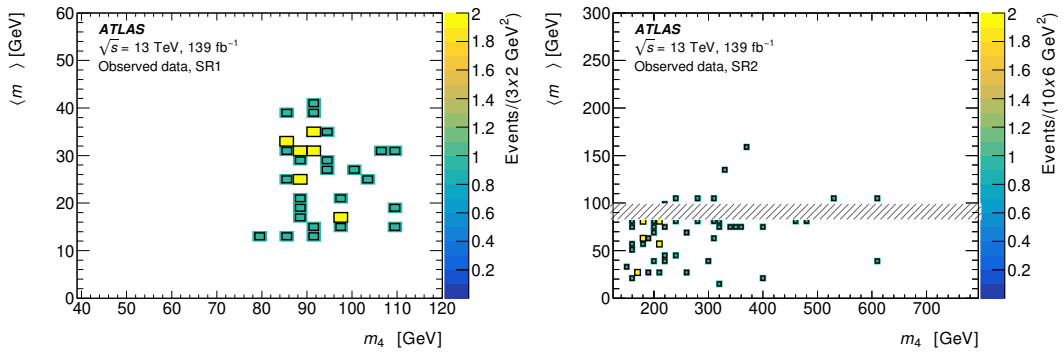

Figure 3: Histogram showing the observed data in both SR1 and SR2 signal regions. The Z Veto exclusion requirement is shown by the horizontal band.

4.1 Limit Setting

CLs limits are computed by making use of profile likelihood test statistic on $\sigma(gg \to S) \times BR(S \to Z_d Z_d \to 4\ell)$ which depends on m_{Z_d} and $m_{4\ell}$. The expected and observed limits for SR1 and SR2 are shown in Figure 4. In addition, a 2.7σ local significance was observed where the smallest p_0-value in SR1 is at (m_S, m_{Z_d}) = (110 GeV, 30 GeV) while in SR2 , a 2.8σ local significance was observed where the smallest p_0-value was found at (m_S, m_{Z_d}) = (350 GeV, 75 GeV). The look-elsewhere effect was used to convert the local significances for SR1 and SR2 into global significances, giving rise to a global significance of 1.6σ in SR1 and 0.5σ in SR2.

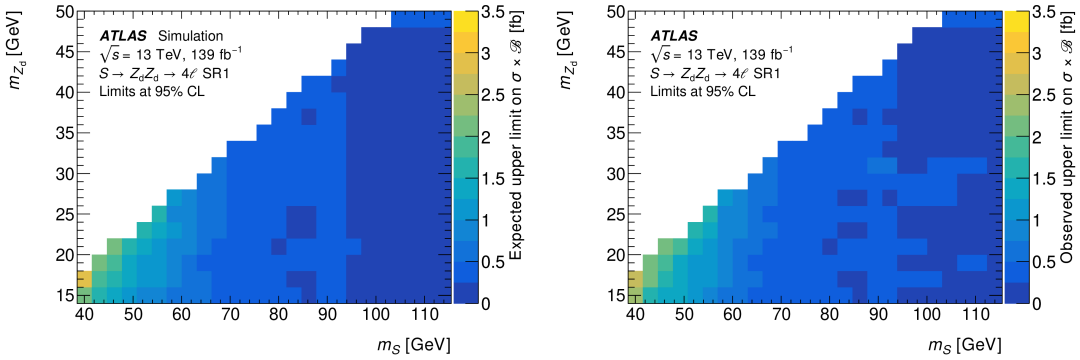

(a) Expected limit in SR1 as a function of $m_{4\ell}$ and m_{Z_d}.

(b) Observed limit in SR1 as a function of $m_{4\ell}$ and m_{Z_d}.

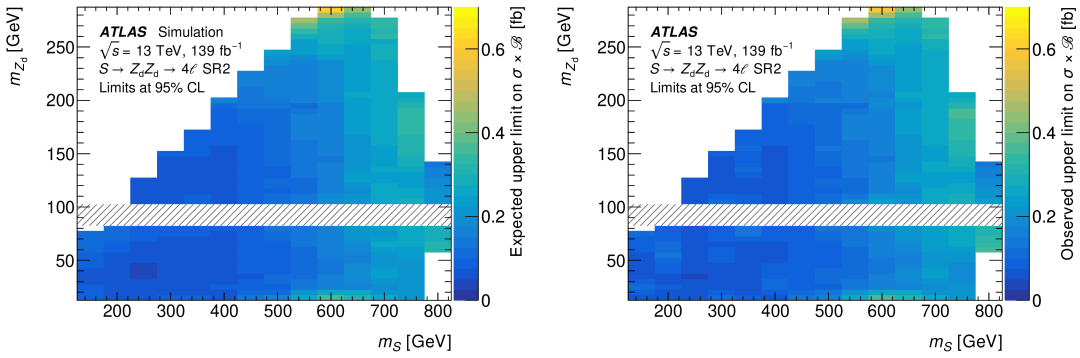

(c) Expected limit in SR2 as a function of $m_{4\ell}$ and m_{Z_d}.

(d) Observed limit in SR1 as a function of $m_{4\ell}$ and m_{Z_d}.

Figure 4: Upper limits on $\sigma(gg \to S) \times BR(S \to Z_d Z_d \to 4\ell)$ for $m_{4\ell}$ and m_{Z_d} in SR1 and SR2.

5 Conclusions

A search for a new spin-0 scalar particle, S, decaying into a four-lepton final state via two promptly decaying spin-1 bosons $S \to Z_d Z_d$ was conducted. The the search was conducted using two distinct signal regions: one with 30 GeV $< m_{4\ell} <$ 115 GeV and another with 130 GeV $< m_{4\ell} <$ 800 GeV. The data are consistent with SM backgrounds. 95% CL upper limits are set on $\sigma(gg \to S) \times$ BR$(S \to Z_d Z_d \to 4\ell)$ as a function of $m_{\ell\ell}$ and $m_{4\ell}$, constraining the dark sector predicted by HAHM.

References

[1] S. Gopalakrishna, S. Jung, and J. D. Wells, "Higgs boson decays to four fermions through an abelian hidden sector," *Phys. Rev. D*, vol. 78, p. 055002, 2008.

[2] J. D. Wells, "How to Find a Hidden World at the Large Hadron Collider," 2008.

[3] H. Davoudiasl, H.-S. Lee, I. Lewis, and W. J. Marciano, "Higgs decays as a window into the dark sector," *Physical Review D*, vol. 88, no. 1, p. 015022, 2013.

[4] D. Curtin, R. Essig, and Y.-M. Zhong, "Uncovering light scalars with exotic higgs decays to $b\bar{b}\mu^+\mu^-$," *Journal of High Energy Physics*, vol. 2015, no. 6, p. 25, 2015.

[5] H. Davoudiasl, H.-S. Lee, and W. J. Marciano, ""dark" z implications for parity violation, rare meson decays, and higgs physics," *Physical Review D*, vol. 85, no. 11, p. 115019, 2012.

[6] D. Curtin, R. Essig, S. Gori, and J. Shelton, "Illuminating dark photons with high-energy colliders," *Journal of High Energy Physics*, vol. 2015, no. 2, p. 157, 2015. [Online]. Available: http://dx.doi.org/10.1007/JHEP02(2015)157

[7] ATLAS Collaboration, "Search for Higgs bosons decaying into new spin-0 or spin-1 particles in four-lepton final states with the ATLAS detector with $139\,\text{fb}^{-1}$ of pp collision data at $\sqrt{s} = 13\,\text{TeV}$," *JHEP*, vol. 03, p. 041, 2022.

[8] ATLAS collaboration, "Search for Higgs boson decays to beyond the Standard Model light bosons in four-lepton events with the ATLAS detector at $\sqrt{s} = 13\,\text{TeV}$," *JHEP*, vol. 06, p. 166, 2018.

[9] ATLAS Collaboration, "Search for new light gauge bosons in Higgs boson decays to four-lepton final states in pp collisions at $\sqrt{s} = 8\,\text{TeV}$ with the ATLAS detector at the LHC," *Phys. Rev. D*, vol. 92, p. 092001, 2015.

[10] ATLAS Collaboration, "Electron and photon performance measurements with the atlas detector using the 2015–2017 lhc proton–proton collision data," *JINST*, vol. 14, p. P12006, 2019.

[11] ATLAS Collaboration, "Muon reconstruction and identification efficiency in ATLAS using the full Run 2 pp collision data set at $\sqrt{s} = 13\,\text{TeV}$," *Eur. Phys. J. C*, vol. 81, p. 578, 2021.

[12] J. Alwall, R. Frederix, S. Frixione, V. Hirschi, F. Maltoni, O. Mattelaer, H. S. Shao, T. Stelzer, P. Torrielli, and M. Zaro, "The automated computation of tree-level and next-to-leading order differential cross sections, and their matching to parton shower simulations," *JHEP*, vol. 07, p. 079, 2014.

[13] ATLAS Collaboration, "Measurements of the properties of the Higgs-like boson in the four lepton decay channel with the ATLAS detector using $25\,\text{fb}^{-1}$ of proton–proton collision data," ATLAS-CONF-2013-013, 2013. [Online]. Available: https://cds.cern.ch/record/1523699

Measurement of the top quark Yukawa coupling from tt kinematic distributions in the dilepton final state with the ATLAS experiment

Cameron Garvey[1], **James Keaveney**[1]

[1]Physics, University of Cape Town, Cape Town, Rondebosch, Cape Town, 7700, South Africa

E-mail: GRVCAM001@myuct.ac.za

Abstract. An extraction of the top quark Yukawa coupling (Y_t) from top quark pair production is presented using proton-proton collisions at 13 TeV, corresponding to an integrated luminosity of 140 fb^{-1}, recorded by the ATLAS experiment. Corrections from a Higgs boson exchange between the top quark and top anti-quark can produce non-negligible modifications to differential distributions near the energy threshold of production. The kinematic distributions sensitive to these modifications, are the invariant mass of the system ($m_{t\bar{t}}$) and the azimuthal angle of the top quark with respect to the beamline in the rest frame of the system. This analysis aims to constrain Y_t indirectly using the kinematic distributions of $t\bar{t}$ pair events using the eμ dilepton final state. Machine learning was used to reconstruct the mass of the top quark system as this provides the greatest sensitivity to variations in Y_t. A binned profile likelihood fit was then implemented to extract a blinded estimation of Y_t using Asimov data including a complete set of statistical and systematic uncertainties. The extracted Y_t^2 = 1.00$\pm$1.73 and is systematically limited

1 Preliminaries

Since the experimental verification of the Higgs boson by ATLAS [1] and CMS [2], an essential objective of the Large Hadron Collider (LHC) physics program has been the precise characterization of the Higgs' properties, including its mass and coupling strengths with Standard Model (SM) particles. Of these couplings, coupling of the Higgs to the top quark, known as the top quark Yukawa coupling (Y_t), is of notable significance. As the most massive SM particle, the top quark has the largest Yukawa coupling, around unity. This large coupling means that top quark loops contribute significantly to radiative corrections of the Higgs potential, which affect theoretical predictions such as the stability of the electroweak vacuum [3]. There are two approaches used to measure the Y_t, which are direct and indirect. The direct method aims to measure processes where top quarks are generated alongside a Higgs boson, such as $t\bar{t}H$. The indirect approach measures processes where a virtual Higgs is exchanged between top quarks, such as in $t\bar{t}$. The research presented addresses the indirect extraction of Y_t from the kinematic distributions of $t\bar{t}$ in the dilepton channel. In Figure 1 the $t\bar{t}$ Feynman diagrams are presented with leading order (LO) electroweak (EW) corrections where a top quark pair exchanges a virtual Higgs boson. The virtual exchange of a Higgs enhances $t\bar{t}$ production near the threshold energy thus affecting the kinematics of the $t\bar{t}$ system. These affects allow one to infer the strength of Y_t. This inference utilises the impact that varying Y_t has on the kinematic distributions of $t\bar{t}$. It will thus prove important to access observables that are sensitive to these variations. The analysis focuses on dilepton $t\bar{t}$. Specifically we are targetting the case where there is exactly one electron and one muon. It is required to also have two jets initiated by bottom quarks.

The paper will be presented as follows. Firstly, I will introduce the data and simulation that are used, followed by the selection criteria put in place to preferentially select for eμ $t\bar{t}$ production. I will then outline the EW corrections that were implemented to the $t\bar{t}$ simulation to allow for the variation of Y_t. A discussion of the methods used to construct observables that are sensitive to variations in Y_t is then provided. Finally, the results of the extraction are presented.

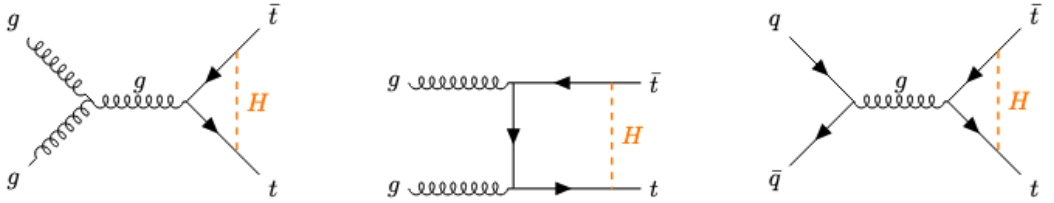

Figure 1: A set of Feynman diagrams for the electroweak corrections for top quark pair production where a virtual Higgs is exchanged, are shown. The left and middle diagrams show $t\bar{t}$ as initiated by gluon-gluon while the right shows qq initiated.

2 Simulation and event selection

The data used was recorded from proton-proton collisions at the LHC with $\sqrt{s}$ = 13 TeV, using the ATLAS experiment. The dataset corresponds to Run 2 and covers the 2015 to 2018 data-taking period. The total integrated luminosity corresponds to 140 fb^{-1} [4].

To accurately model the data recorded in the dilepton channel, we need to include simulation of all physics processes that can pass our selection criteria. The signal simulation is a dilepton $t\bar{t}$ simulation produced using ATLAS full simulation with POWHEG[5]. and PYTHIAV8.230[6], at NLO in QCD. Apart from the signal process, $t\bar{t}$, several background processes are expected to pass the event requirements. The dominant background contribution is due to tW followed by a much smaller contribution from Z+jets. The tW process is simulated using POWHEG v.2 and PYTHIA v8.309 at NLO in QCD. The process including a Z with extra jets, is produced using SHERPA 2.2.11[7]. The $t\bar{t}$, tW and Z+jets processes cover the dominant and sub-dominant processes that pass our selection criteria, but this does not cover all processes that could pass our selections. Examples of such processes are ttW, ttH, ttZ, etc, and it is expected that these processes should minimally impact the analysis.

The selections put in place for the dilepton eμ channel are as follows. For an event to be included in this analysis it needs to have passed a single lepton trigger where the lepton is muon or electron. It is then required that there are charged leptons with opposite charges, one electron and one muon, each with a transverse momentum (p_{T}) larger than 28 GeV. Two jets with a $p_{\mathrm{T}} > 20$ GeV are required. Of the required jets within the event it is required that at least two of the jets are tagged as originating from a b quark using the `DL1d` $b-$tagger[8]. Finally, it is required that the dilepton mass ($m_{\ell\ell}$ is greater than 10 GeV to minimise the contributions from low mass resonances.

3 Electroweak corrections

The simulation of $t\bar{t}$ is implemented at NLO in QCD and as such, does not include the necessary EW corrections such as those shown in Figure 1. The calculations of the EW corrections to $t\bar{t}$ production is described in [9] and have been implemented using `HATHOR` [10]. The corrections are implemented by first calculating the differential $t\bar{t}$ cross section including the LO QCD contributions as well as the mixed contributions of order $\alpha_S^2\alpha_{weak}$. The calculations are computed in terms of variables sensitive to variations in Y_t. These variables are the mass of the combined top quarks (m_{tt}) and the azimuthal angle of the top quark in relation to the beam line in the rest frame of $t\bar{t}$, known as $\cos\theta^*$. The ratio of the calculated cross section including the EW contributions to the LO QCD cross section is then computed and binned in terms of a double differential distribution of m_{tt} and $\cos\theta^*$. To apply the correction a multiplicative weight $\omega(m_{tt},\cos\theta^*)$ is defined from the differential distribution and requires access to the kinematics of the top quarks. At this point it is important to define truth and detector level within simulation. Truth level refers to the stage immediately after the matrix element calculation, involving quarks and gluons before hadronisation, whereas detector level includes the simulation of final-state particles after hadronisation, decay, and their interaction with the ATLAS detector. To apply the weight $\omega(m_{tt},\cos\theta^*)$ it is necessary to accesses the truth information for each event to compute the m_{tt} and $\cos\theta^*$. This is done for each of the gg, $u\bar{u}$, $d\bar{d}$ initial states. Figure 2 shows the effects of varying Y_t on the distributions where the values of Y_t used, correspond to 0, 1, 2, and 3. The horizontal axis shows the truth level m_{tt} and the vertical axis of the top frame presents the expected event count. The vertical axis on the bottom frame shows the ratio of each of the Y_t varied histograms to the histogram with Y_t =1. Larger deviations from a ratio of one indicate a greater sensitivity to variations in Y_t. From Figure 2 it should be noted that the majority of the sensitivity to variations in Y_t arises when the energy of the top quarks is approximately twice m_{top} and is known as the threshold region.

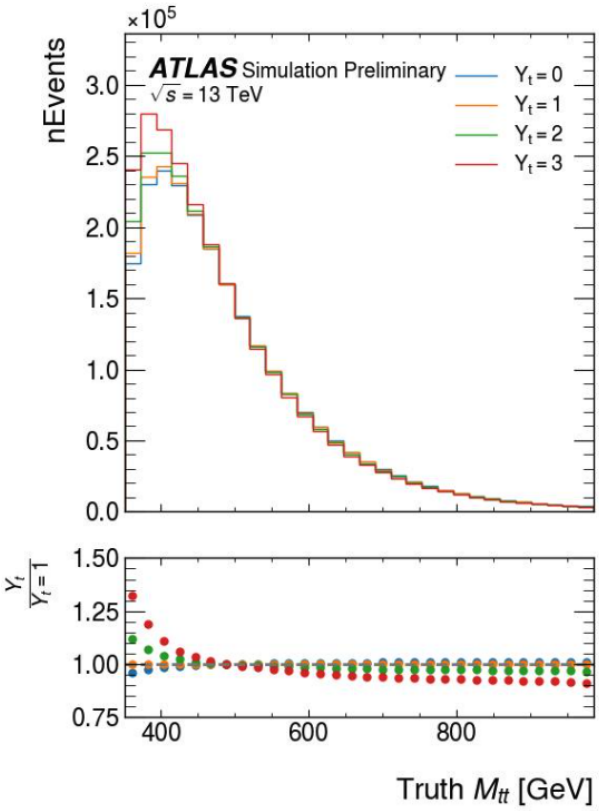

Figure 2: A histogram showing the variations of Y_t as a function of truth level m_{tt} for the top quark pair simulation in the eμ region. The bottom frame shows the ratio of each of the Y_t varied histograms to the histogram with Y_t =1.

4 Construction of kinematic observables sensitive to variations in Y_t

The variables that were found to be most sensitive to variations in Y_t at truth level were the m_{tt} and $\cos\theta^*$. These variables are not directly accessible at detector level due to the inability to detect neutrinos. As such, several observables were tested, which aimed to work as proxy variables for the m_{tt}. The first and simplest attempt involved using the measurable particles produced in the decay of the $t\bar{t}$, namely the electron, muon and two $b-$jets, and calculating the combined mass ($m_{\ell\ell bb}$). Using the $m_{\ell\ell bb}$ observable provided a severely degraded sensitivity when compared to the truth level m_{tt}. To this end, a deep neural network (DNN) was used to regress and reconstruct the truth m_{tt} using information available at detector level. The DNN was implemented using `Keras` [11] and was trained on $t\bar{t}$ simulation. A set of eighteen physics inspired variables were defined for training the DNN. These variables were the mass and δR of the different lepton-$b-$jet combinations as well as the missing transverse momentum. Figure 3a shows a normalised histogram of the difference between the reconstructed m_{tt} and the truth level m_{tt} in the eμ channel. The y-axis shows the fraction of events and the mean and σ of the distribution are 14.75 and 111.01. From Figure 3a it can be inferred that the reconstructed m_{tt} is on average slightly larger than the truth level m_{tt}. Overall the bias of the reconstruction is minimal.

Figure 3b shows the Y_t variations as a function of the m_{tt} reconstructed using the DNN. The description of the horixontal axis and the bottom panel is the same as found in Figure 2. From the bottom panel in Figure 3b the sensitivity to variations in Y_t can be seen. The reconstructed m_{tt} was found to be more sensitive than the $m_{\ell\ell bb}$ but less sensitive than the truth m_{tt}.

5 Fit methodology and results

A binned profile likelihood fit was used to extract the Y_t. To extract the best fit value for Y_t, the fit must include a parametric dependency where varying the value of Y_t directly controls the shape of the chosen kinematic distribution. This is implemented using a method known as template morphing. The template morphing method uses a set of histograms where each histogram corresponds to a specific values of Y_t and linearly interpolates between the

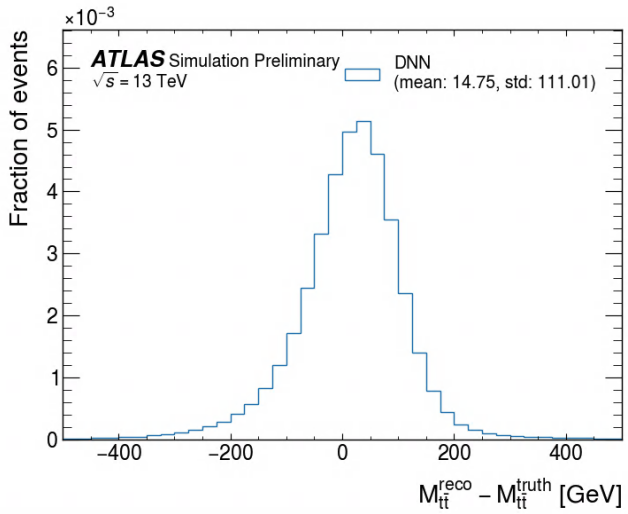

(a) A normalised histogram of the difference between the reconstructed m_{tt} and the truth level m_{tt} is shown.

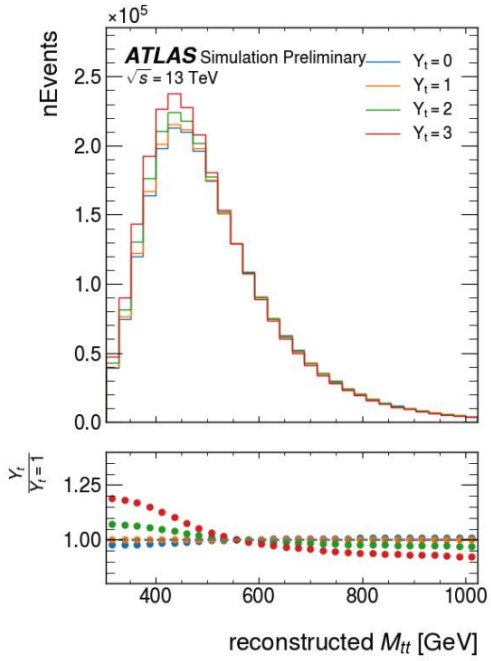

(b) A set of histograms showing the variations of Y_t for the reconstructed m_{tt}. The bottom frame in each figure shows the ratio of each of the Y_t varied histograms to the histogram with Y_t =1.

bins of each the histograms to allow Y_t to continuously vary within the fit. The templates used in the fit correspond to the histograms given in Figure 3b each for the different values of Y_t =0,1,2,3. It should be noted that due to technical considerations the Y_t^2 is extracted instead of Y_t. A complete set of systematic uncertainties are considered including detector and theoretical systematics. The results shown are fully blinded and the fit is performed using Asimov data [12]. Table 1 shows the extracted values for Y_t^2 when using the $m_{\ell\ell bb}$ and the reconstructed m_{tt} distributions. The uncertainties quoted cover both statistical and systematic uncertainties

Variable	**Extracted Y_t^2**
$m_{\ell\ell bb}$	1.00±1.73
Reconstructed m_{tt}	1.00±1.56

Table 1: A table summarising the extracted values for Y_t^2 when using different variables. The uncertainties quoted cover both statistical and systematic uncertainties

The extracted values of Y_t^2 =1 is expected as we are using Asimov data. Comparing the fits results of the fits using the $m_{\ell\ell bb}$ and the reconstructed m_{tt} distribution it can clearly be seen that there is a reduction in the uncertainty when using the reconstructed m_{tt}. This reduction provides a strong indication that reconstructing the truth m_{tt} using a DNN provides an increase in sensitivity to the variations in Y_t. The systematic uncertainty reduces from ± 1.45 using $m_{\ell\ell bb}$ to ± 1.18 using m_{tt}. This analysis is systematically limited where the most impactful systematic uncertainties are due to the $t\bar{t}$ modelling and the $b-$tagging.

6 Conclusion

The top quark Yukawa coupling was measured from $t\bar{t}$ production using pp collisions at $\sqrt{s}$ = 13 TeV, corresponding to a total integrated luminosity of 140 fb^{-1}, recorded by the ATLAS experiment. The analysis focused on the dilepton channel and specifically the case where there is one electron and one muon. A set of criteria was put in place to enhance the contribution of dileptonic $t\bar{t}$ events while minimising background contributions. The $t\bar{t}$ simulation is implemented at NLO in QCD and as such does not contain the necessary EW corrections. These EW corrections were implemented using `Hathor` allowing for the variation of Y_t in $t\bar{t}$ simulation through the

use of a multiplicative event weight. Varying the value of Y_t affects the shape of the kinematic distributions of $\mathrm{t\bar{t}}$ production and decay. To effectively measure Y_t one needs to construct observables that are maximally sensitive to variations in Y_t. Such an observable was constructed using a DNN which allowed for the reconstruction of $\mathrm{m_{tt}}$. A blinded fit was then implemented using template morphing and the extracted result was $Y_t^2 = 1.00^{+1.56}_{-1.50}$. The analysis is systematically limited by the $\mathrm{t\bar{t}}$ modelling and $b-$tagging systematics. The results shown provide an independent measurement of Y_t. Moving forward the result could be improved by also reconstructing $\cos\theta^*$ and extracting Y_t from a two dimensional distribution of the two variables.

References

[1] ATLAS, "Observation of a new particle in the search for the standard model higgs boson with the atlas detector at the lhc," *Physics Letters B*, vol. 716, no. 1, p. 1–29, Sep. 2012. [Online]. Available: http://dx.doi.org/10.1016/j.physletb.2012.08.020

[2] CMS, "Observation of a new boson at a mass of 125 gev with the cms experiment at the lhc," *Physics Letters B*, vol. 716, no. 1, p. 30–61, Sep. 2012. [Online]. Available: http://dx.doi.org/10.1016/j.physletb.2012.08.021

[3] D. Buttazzo *et al.*, "Investigating the near-criticality of the higgs boson," *Journal of High Energy Physics*, vol. 2013, no. 12, dec 2013. [Online]. Available: https://doi.org/10.1007%2Fjhep12%282013%29089

[4] G. e. a. Aad, "Luminosity determination in pp collisions at $\sqrt{s} = 13$ tev using the atlas detector at the lhc," *The European Physical Journal C*, vol. 83, no. 10, Oct. 2023. [Online]. Available: http://dx.doi.org/10.1140/epjc/s10052-023-11747-w

[5] C. Oleari, "The powheg box," *Nuclear Physics B - Proceedings Supplements*, vol. 205-206, pp. 36–41, 2010, loops and Legs in Quantum Field Theory. [Online]. Available: https://www.sciencedirect.com/science/article/pii/S0920563210001994

[6] T. Sjöstrand *et al.*, "An introduction to pythia 8.2," *Computer Physics Communications*, vol. 191. [Online]. Available: http://dx.doi.org/10.1016/j.cpc.2015.01.024

[7] E. Bothmann *et al.*, "Event generation with sherpa 2.2," *SciPost Physics*, vol. 7, no. 3, Sep. 2019. [Online]. Available: http://dx.doi.org/10.21468/SciPostPhys.7.3.034

[8] "Neural Network Jet Flavour Tagging with the Upgraded ATLAS Inner Tracker Detector at the High-Luminosity LHC," CERN, Geneva, Tech. Rep., 2022. [Online]. Available: https://cds.cern.ch/record/2839913

[9] J. H. Kühn *et al.*, "Weak Interactions in Top-Quark Pair Production at Hadron Colliders: An Update," *Phys. Rev. D*, vol. 91, no. 1, p. 014020, 2015.

[10] M. Aliev *et al.* Hathor version 2.1-b3. [Online]. Available: https://www.physik.hu-berlin.de/de/pep/tools/hathor.html

[11] F. Chollet *et al.*, "Keras," https://keras.io, 2015.

[12] G. Cowan *et al.*, "Asymptotic formulae for likelihood-based tests of new physics," *The European Physical Journal C*, vol. 71, no. 2, Feb. 2011. [Online]. Available: http://dx.doi.org/10.1140/epjc/s10052-011-1554-0

This page intentionally left blank.

Searches for scalar resonances with di-photon in association with leptons and taus using the easyjet analysis framework in ATLAS detector at the LHC

Kutlwano Makgetha[1,2], Vuyolwethu Kakancu[1,2], Njokweni Mbuyiswa[1,2], Kgothatso Ntumbe[1,2], Paballo Ndhlovu[1,2], Phuti Rapheeha[2,3], Reda Mekouar[4], Mukesh Kumar[1], Rachid Mazini[1] and Bruce Mellado[1,2]

[1]School of Physics and Institute for Collider Particle Physics, University of the Witwatersrand, Johannesburg, Wits 2050, South Africa
[2]iThemba LABS, National Research Foundation, PO Box 722, Somerset West 7129, South Africa
[3]School of Electrical Engineering, Tshwane University of Technology, Staatsartillerie Road, Pretoria West 0001, South Africa
[4]Institute of High Energy Physics, Beijing, University of Chinese Academy of Sciences, 19B Yuquan Road, Shijingshan District, Beijing, China

E-mail: 2134657@students.wits.ac.za

Abstract. Recent studies have identified growing excesses in scalar resonances with di-photon at the Large Hadron Collider (LHC), suggesting the presence of scalar particles beyond the Standard Model. These scalar resonances are motivated by the multi-lepton anomalies at the LHC which indicate a potential new scalar particle S with a mass of approximately 152 GeV, originating from a heavier scalar H, with a global significance of $\sim 5\sigma$. Motivated by these findings, the HBSM group within the HMBS physics group at ATLAS has launched a new analysis using the easyjet analysis framework. This analysis focuses on searching for scalar resonances through di-photon production in the process $gg \to H \to SS'$, where $S \to \gamma\gamma$ and $S' \to \tau_h\tau_\ell$. We are preparing to use the analysis tools to analyse the 2022-2024 Run 3 data with an integrated luminosity of 35.7 fb^{-1} at $\sqrt{s} = 13.6$ TeV.

1 Introduction

The Standard Model (SM) of particle physics is the foundational theoretical framework that describes elementary particles and three of the four fundamental forces: electromagnetic, strong, and weak interactions [1–3]. It categorises particles into two main groups: fermions, which have a spin of $\frac{1}{2}$, and bosons, which have integer spins. Fermions, including quarks and leptons, are the fundamental constituents of matter, while bosons act as force carriers that mediate interaction between fermions. Key examples of bosons include photons (which mediate the electromagnetic force), gluons (which mediate the strong force), and the $W^{\pm}$ and Z bosons (which mediate the weak force). Despite its successes, the SM has limitations, including multi-lepton anomalies observed at the LHC. These anomalies, which include excesses in dilepton and trilepton events (with and without b-jets), align with multiple ATLAS and CMS observations where SM backgrounds are expected to dominate. A potential explanation for these excesses involves a heavier scalar resonance H decaying into lighter scalars S and S' (mass $m_S \approx 150 \pm 5$ GeV) [4–9]. The Two-Higgs Doublet Model with a scalar singlet (S) [10] is a minimal extension of the SM that addresses experimental phenomena, such as the excess of diphoton events at the LHC. In this model,

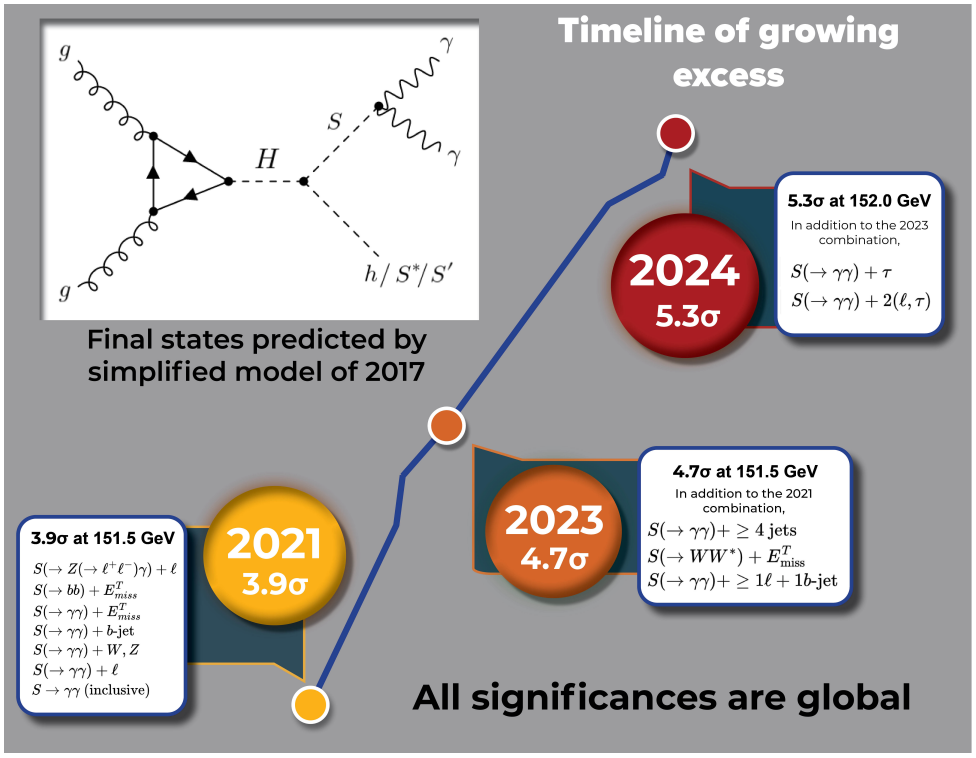

Figure 1: Timeline of multi-lepton anomalies leading to the prediction of a narrow resonance with $m_S \approx 150 \pm 5$ GeV, including a table summarising final states, characteristics, SM background, and significances [6]

DSID	H Mass (GeV)	S Mass (GeV)	S' Mass (GeV)	Cross-sections (fb)	Events
562134	250	150	95	1.154	120000
562135	260	160	100	0.412	120000
562136	300	175	125	0.053	120000
562137	350	225	125	0.010	120000
562138	400	275	125	0.004	120000

Table 1: Simulation Parameters for $X \to H \to SS' \to \gamma\gamma\tau^+\tau^-$ signal.

the Higgs-like scalar S decays to electroweak bosons ($\gamma\gamma$, WW^*, ZZ^*), yielding final states rich in leptons, photons, and missing transverse energy (see Figure 1). Using the LHC data has revealed a narrow resonance at $m_S = 152$ GeV in diphoton and $Z\gamma$ invariant mass spectra, with $\sim 5\sigma$ global significance [11], corroborating previous findings [12, 13]. While the S' production mechanism remains unclear, data suggest its association with $H \to SS'$, and the decay chain $H \to SS'$ followed by $S \to WW^*$ further explains the observed lepton-rich anomalies.

2 Data Analysis

As outlined in the introduction, these are the proposed final states for the entire analysis $S' \to \tau_h\tau_\ell$, $S' \to \ell + b$ (where $\ell = e, \mu, \tau$), $S' \to 2(\ell, \tau, b)$. We are conducting this analysis using the easyjet analysis framework [16] using the 2022-2024 ATLAS run 3 data with an integrated luminosity of 35.7 fb^{-1} at $\sqrt{s} = 13.6$ TeV. This preliminary work uses Monte Carlo (MC) simulations with pile-up profiles matching 2022 data; however, the completed analysis will look at the full Run 3 data.

2.1 Simulation Details and Filters

We use an analysis package in the easyjet analysis framework that has two photons and multiple leptons, as this package already has our desired final states and is well-defined. We study the diphoton production with top quark

Selection Criterion	Photons	Taus	Electrons	Muons
Minimum Transverse Momentum (p_T)	25 GeV	25 GeV	10 GeV	10 GeV
Maximum Pseudorapidity (η)	2.37	2.5	2.5	2.5
Identification	Loose	RNN	MediumDNN	MediumPFlow
Isolation Requirement	Non-Isolated	Loose	LooseVarRad	LooseVarRad

Table 2: The baseline preselection to the relevant candidates (photons, the hadronic τ, and leptons). These cuts reduce the backgrounds and keep events most consistent with the targeted $\gamma\gamma{+}1\ell\,1\tau$ and $\gamma\gamma{+}0\ell\,1\tau$ final states [14].

Year	Trigger Chains
2022	HLT_2g50_loose_L12EM20VH HLT_g35_medium_g25_medium_L12EM20VH HLT_2g22_tight_L12EM15VHI
2023	HLT_2g50_loose_L12eEM24L HLT_g35_medium_g25_medium_L12eEM24L HLT_g45_medium_g20_medium_L1eEM40L_2eEM18L HLT_2g22_tight_L12eEM18M

Table 3: The primary diphoton trigger chains listed by year [15].

pairs ($\gamma\gamma t\bar{t}$) as one of our dominant backgrounds because top quarks decay into W bosons and b quarks, with W bosons further decaying into a charged lepton and missing transverse energy. We have requested full MC production for the $\gamma\gamma\tau^+\tau^-$ signal and its mass scans, and are preparing a similar request for the dilepton and one lepton final states at $\sqrt{s} = 13.6$ TeV. Object selections for the dominant $\gamma\gamma t\bar{t}$ background are complete. We are currently studying the $V\gamma\gamma$ background, applying the object selection methods described in this paper. Upon receiving the $\gamma\gamma\tau^+\tau^-$ signal samples, we will incorporate them into our analysis. For signal, we used Madgraph5@NLO for matrix element calculations and Pythia8 for parton showering and hadronisation. Events were generated using AthGeneration release 23.6.23 to produce an EVNT file. Truth-level information was obtained using Athena release 25.0.9. The gluon-gluon fusion (ggF) is the production mode, and systematic uncertainties are included in the ggF process. We have requested 120000 events. Table 1 summarises the simulation setup for different scalar masses and cross-sections:

2.2 Object Selections

Tau leptons decay via 1-prong and 3-prong topological modes. A 1-prong τ decays into one charged hadron (such as a pion) along with neutrinos, resulting in a single track in the detector and missing energy. A 3-prong τ, on the other hand, decays into three charged hadrons (typically pions) and a neutrino, producing a more complex but distinct signature with three visible tracks. In this work, we are only interested in the visible hadronic tau (τ_h) candidates. To identify τ_h candidates, we used different levels of selection criteria, known as working points (WP), which can be classified as loose, medium, and tight (see Table 2). We used the Recurrent Neural Network (RNN) loose identification because we want to include more τ_h candidates, aiming to maximise signal efficiency, even if it means accepting more background [17, 18]. Specifically, RNN was used because taus decay into multiple particles (prongs), and their decay products form a sequence of tracks that can be modeled sequentially. RNNs are good at capturing dependencies in sequences. We selected the Medium Deep Neural Network (DNN) LooseVarRad electron WP to ensure detector stability and balance efficiency with background rejection. Electron classification is performed using DNN. For the muon, we used the MediumPflowLooseVarRad WP to improve muon identification by combining information from the muon spectrometer to reconstruct particles more precisely and keep a relatively high efficiency for the muons. All photon selections use the loose WP, except where explicitly stated otherwise in the trigger name (e.g., medium or tight) [19].

The hadronic taus, electrons, and photon candidates are excluded from the transition region ($1.37 < |\eta| < 1.52$) due to the overlapping geometric coverage and changing detector characteristics between the barrel and endcap subdetectors. This region presents reconstruction challenges as particles may traverse gaps or boundaries between detector components, such as the electromagnetic calorimeters, leading to reduced precision in tracking and energy measurements. Muon reconstruction relies on the muon spectrometer, which extends to higher pseudorapidity and doesn't exhibit the same transition effects. The pseudorapidity ($|\eta| < 2.5$) cut ensures reliable particle reconstruc-

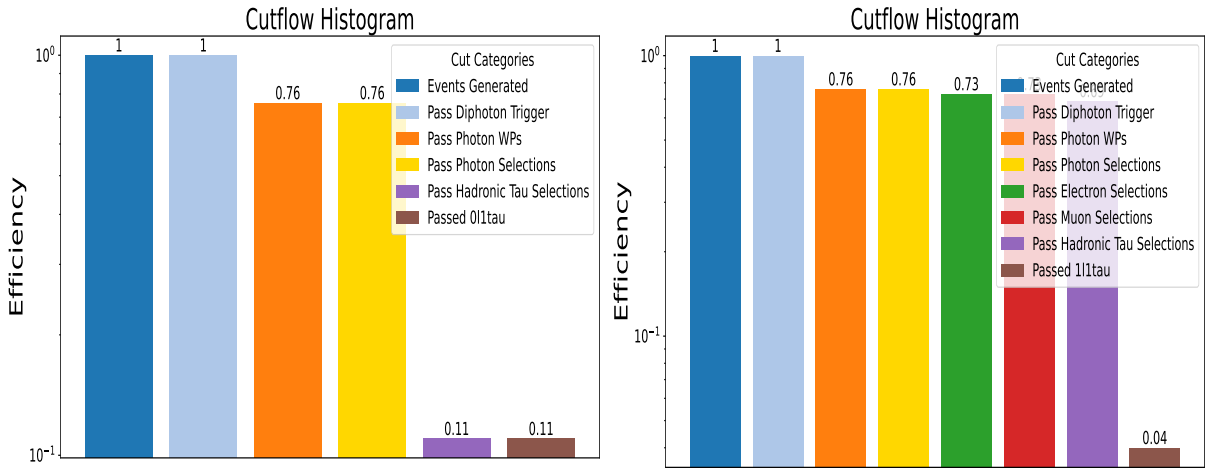

Figure 2: Cutflow histogram for the $0\ell1\tau$ (left) and $1\ell1\tau$ (right) final states.

tion within the detector's well-instrumented region, beyond which tracking, calorimeter, and trigger performance degrade due to reduced silicon tracker coverage and detector acceptance. The diphoton triggers listed in Table 3 are carefully designed to balance signal efficiency and background rejection, taking into account pile-up effects and optimising for different experimental conditions. The use of varying energy thresholds, identification criteria, and Level-1 requirements ensures that the triggers are versatile and robust, capable of capturing a wide range of diphoton events while minimising noise.

3 Preliminary Results

Before plotting the kinematic distributions, a preselection is performed where events coming from $0\ell1\tau$ and $1\ell1\tau$ final states are selected; in both of these channels, high diphoton trigger efficiency is observed; the cutflow for each of these final states can be seen in Figure 2. Photon identification and isolation reduce the event count by approximately 24%, as anticipated. In the $0\ell1\tau$ channel, tau selection results in the largest reduction (11% passing) due to tau purity requirements. In the $1\ell1\tau$ channel, tau rejection reduces the efficiency to 4%, demonstrating effective jet fake tau suppression. The $0\ell1\tau$ and $1\ell1\tau$ selections yield 60732 and 19246 events, respectively, indicating effective selection from the initial 534144 generated events.

To evaluate the effectiveness of our selection criteria, kinematic distributions are normalised before and after the application of the event selection; results are presented in Figures 3 and 4. In particular, the leading and subleading photon transverse momentum (p_T) distributions show a clear suppression of low-p_T events after selection, indicating efficient rejection of soft photons and consistent application of isolation requirements. The leading photon pseudorapidity (η) distribution is concentrated within $|\eta| < 2.5$, in agreement with the detector's geometric acceptance. For the hadronic tau, the leading τ_{had} p_T distribution is enriched at high momentum after selection with the tau multiplicity, confirming that the majority of selected events contain exactly one reconstructed hadronic tau, as required by the analysis strategy.

In the $1\ell1\tau$ channel, lepton multiplicity is dominated by single-lepton events, with higher multiplicities effectively suppressed, and this is due to the object selections working well. The leading electron and muon p_T distributions exhibit a marked shift toward higher momenta after selection, demonstrating that our tight identification, isolation, and p_T thresholds efficiently reject soft leptons from pile-up and misidentification, while preserving high-quality, prompt leptons.

For both final states, we look at the object multiplicities to check whether or not the selections worked well. For the $1\ell1\tau$ final state after the selections, we are left with events with only 1 lepton and 1 tau, as the multiplicity distributions show only events with 1 lepton and 1 tau. For the $0\ell1\tau$ final state after the selections, we are left with events with only 0 lepton and 1 tau, as the multiplicity distributions show only events with 0 lepton and 1 tau.

4 Conclusion and Future Plans

We will use the kinematic variables related to each channel and create new input variables using feature engineering, then use the Toolkit for Multivariate Data Analysis (TMVA) method. After ranking the features, we will select the most important and least correlated ones for machine learning. To characterise the background, we will compare the 2D sideband and TMVA methods for estimating background events in the signal region. We plan

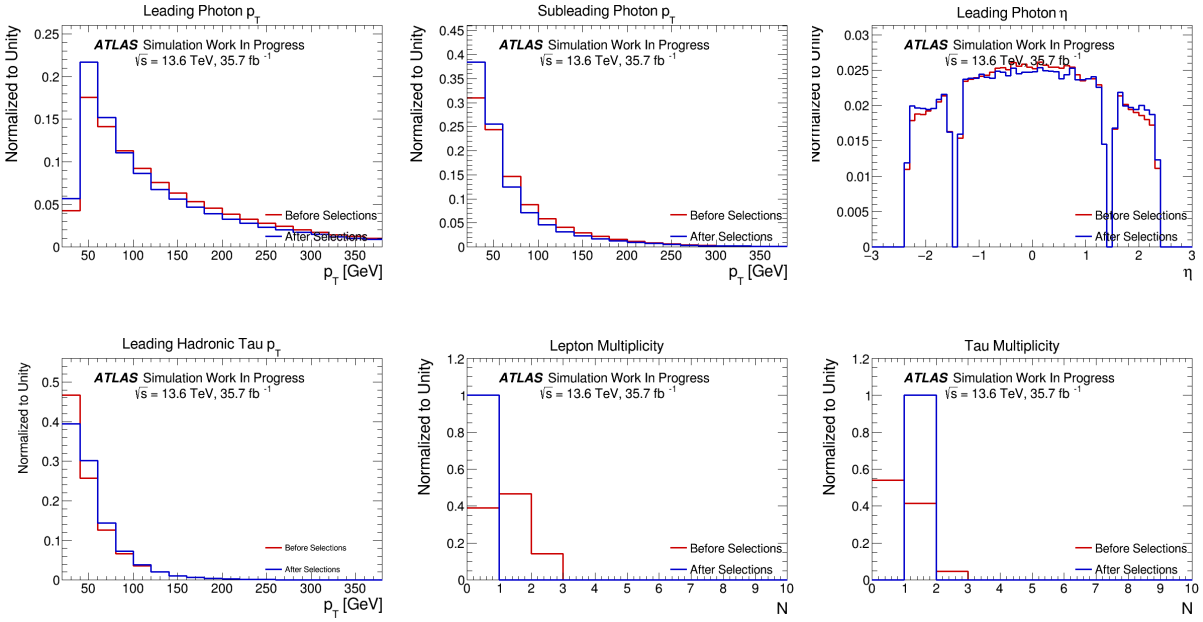

Figure 3: Selected kinematics for the $0\ell 1\tau$ final state.

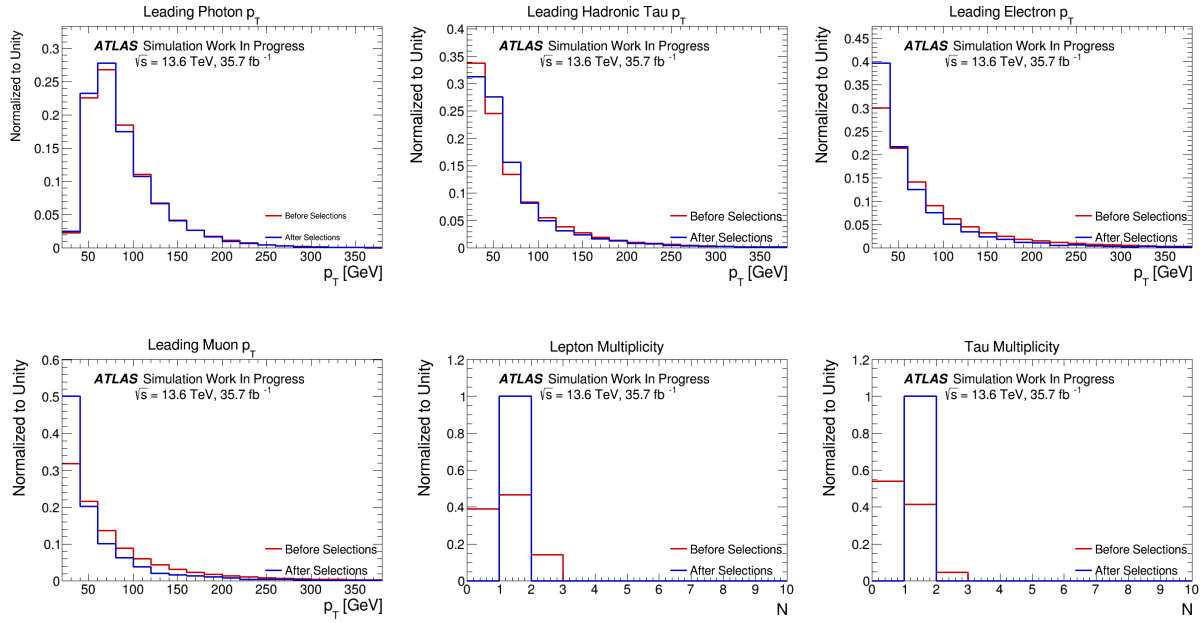

Figure 4: Selected kinematics for $1\ell 1\tau$ final state.

to use the Deep Neural Networks and get an output that will be plotted to define the signal region where we will compare our significance to the one obtained using a cut-based approach.

Acknowledgments
KM would like to express gratitude to the SA-CERN Excellence bursary for funding this research.

References

[1] G. Altarelli, "The standard model of particle physics," *arXiv preprint hep-ph/0510281*, 2005.

[2] G. Kane, *Modern elementary particle physics: explaining and extending the standard model*. Cambridge University Press, 2017.

[3] R. L. Workman *et al.*, "Review of Particle Physics," *PTEP*, vol. 2022, p. 083C01, 2022.

[4] S. von Buddenbrock, A. S. Cornell, A. Fadol, M. Kumar, B. Mellado, and X. Ruan, "Multi-lepton signatures of additional scalar bosons beyond the Standard Model at the LHC," *J. Phys. G*, vol. 45, no. 11, p. 115003, 2018.

[5] S. Buddenbrock, A. S. Cornell, Y. Fang, A. Fadol Mohammed, M. Kumar, B. Mellado, and K. G. Tomiwa, "The emergence of multi-lepton anomalies at the LHC and their compatibility with new physics at the EW scale," *JHEP*, vol. 10, p. 157, 2019.

[6] A. Crivellin and B. Mellado, "Anomalies in particle physics and their implications for physics beyond the standard model," *Nature Rev. Phys.*, vol. 6, no. 5, pp. 294–309, 2024.

[7] A. Crivellin, Y. Fang, O. Fischer, S. Bhattacharya, M. Kumar, E. Malwa, B. Mellado, N. Rapheeha, X. Ruan, and Q. Sha, "Accumulating evidence for the associated production of a new Higgs boson at the LHC," *Phys. Rev. D*, vol. 108, no. 11, p. 115031, 2023.

[8] S. Bhattacharya, B. Lieberman, M. Kumar, A. Crivellin, Y. Fang, R. Mazini, and B. Mellado, "Emerging Excess Consistent with a Narrow Resonance at 152 GeV in High-Energy Proton-Proton Collisions," 3 2025.

[9] G. Coloretti, A. Crivellin, S. Bhattacharya, and B. Mellado, "Searching for low-mass resonances decaying into W bosons," *Phys. Rev. D*, vol. 108, no. 3, p. 035026, 2023.

[10] S. von Buddenbrock, N. Chakrabarty, A. S. Cornell, D. Kar, M. Kumar, T. Mandal, B. Mellado, B. Mukhopadhyaya, R. G. Reed, and X. Ruan, "Phenomenological signatures of additional scalar bosons at the LHC," *Eur. Phys. J. C*, vol. 76, no. 10, p. 580, 2016.

[11] S. Von Buddenbrock, A. S. Cornell, E. D. Iarilala, M. Kumar, B. Mellado, X. Ruan, and E. M. Shrif, "Constraints on a 2hdm with a singlet scalar and implications in the search for heavy bosons at the lhc," *Journal of Physics G: Nuclear and Particle Physics*, vol. 46, no. 11, p. 115001, 2019.

[12] A.-T. Mulaudzi, M. Kumar, A. Goyal, and B. Mellado, "Constraining 2hdm+ s model through w-boson mass measurements," *arXiv preprint arXiv:2312.08807*, 2023.

[13] A. Crivellin and B. Mellado, "Anomalies in particle physics and their implications for physics beyond the standard model," *Nature Reviews Physics*, vol. 6, no. 5, pp. 294–309, 2024.

[14] David Richard Shope et al, "RunConfig-yyml-base.yaml," https://gitlab.cern.ch/easyjet/easyjet/-/blob/main/yyMLAnalysis/share/RunConfig-yyml-base.yaml, 2025.

[15] ATLAS Collaboration, "Trigegamma recommendations run 3," https://twiki.cern.ch/twiki/bin/view/Atlas/TrigEgammaRecommendationsRun3, 2023.

[16] EASYjet Team, "easyjet: an athanalysis physics-analysis framework (runs 2 3)," https://gitlab.cern.ch/easyjet/easyjet, Jan. 2022, cERN GitLab repository; created January 19, 2022; Apache License 2.0; 1 668 commits, 6 branches, 46 tags, 7 releases.

[17] A. Collaboration *et al.*, "Identification of hadronic tau lepton decays using neural networks in the atlas experiment," ATL-PHYS-PUB-2019-033, Tech. Rep., 2019.

[18] G. Aad, B. Abbott, J. Abdallah, S. Abdel Khalek, O. Abdinov, R. Aben, B. Abi, M. Abolins, O. S. AbouZeid, H. Abramowicz *et al.*, "Identification and energy calibration of hadronically decaying tau leptons with the atlas experiment in pp collisions at s= 8 tev," *The European Physical Journal C*, vol. 75, no. 7, p. 303, 2015.

[19] A. Collaboration *et al.*, "Electron and photon performance measurements with the atlas detector using the 2015-2017 lhc proton-proton collision data," *arXiv preprint arXiv:1908.00005*, 2019.

The use of Machine Learning techniques to analyse the $gg \to h \to Z\gamma$ process within the SMEFT framework at the Large Hadron Collider (LHC)

Kutlwano Makgetha[1,2], Njokweni Mbuyiswa[1,2], Srimoy Bhattacharya[1,2], Abduluazem Fadol[1], Mukesh Kumar[1] and Bruce Mellado[1,2]

[1]School of Physics and Institute for Collider Particle Physics, University of the Witwatersrand, Johannesburg, Wits 2050, South Africa
[2]iThemba LABS, National Research Foundation, PO Box 722, Somerset West 7129, South Africa

E-mail: 2134657@students.wits.ac.za

Abstract. Building on the ATLAS and CMS evidence of the Higgs boson (h) decaying into a Z-boson and a photon (with a 3.4σ significance), the current Standard Model (SM) predictions for the $h \to Z\gamma$ signal rate exceed the measured value by $(2.4 \pm 0.9)\sigma$, indicating possible new physics effects or systematic uncertainties that warrant further investigation. This analysis investigates this rare process using machine learning (ML) techniques, where we use classifiers such as the Extreme Gradient Boost (XGBoost) and the kernel density estimation to analyse the production modes of $h \to Z\gamma$, including gluon-gluon fusion (ggF), within the framework of the Standard Model Effective Field Theory. This machine learning approach aims to constrain the six-dimensional Wilson coefficients and shed light on potential deviations from the SM prediction.

1 Introduction

Recent measurements by ATLAS and CMS have reported evidence on the decay of the $h \to Z\gamma$ process, which cannot be fully explained within the Standard Model (SM). We look for potential answers beyond the SM (BSM), and that is where Standard Model Effective Field Theory (SMEFT) comes into play. The SMEFT [1] provides a systematic approach for BSM physics by introducing higher-dimensional operators. These operators are suppressed by powers of a high-energy scale Λ, allowing for the parameterisation of new physics effects. We build upon the findings presented in [2], where the initial step is to identify the specific operators within the SMEFT framework that play a role in our decay process. These operators are essentially mathematical expressions that represent potential deviations from the SM predictions [3, 4], and once we have identified the relevant operators, we will calculate their corresponding Wilson coefficients. These coefficients are numerical values that determine the strength of the operator's contribution to the decay process. The SMEFT@NLO package is a computer program designed to automate this calculation as it uses models created with `FeynRules` [5], which is another software tool that helps define the interactions between particles in the SM and any potential extensions.

2 Data Analysis

2.1 Object Selections

To optimise the signal events over background noise, we applied minimal cuts, including object and channel-specific selections, based on transverse momentum (p_T), invariant masses, pseudorapidity ($|\eta$), missing transverse energy (E_T^{miss}), and jet reconstruction.

Selection	**Criteria**
Photon requirement	(γ) At least one photon candidate
Lepton requirement (ℓ)	At least two same-flavour, opposite-charge leptons ($\ell = e, \mu$)
Muon(μ) selections	$\lvert\eta^{\mu^\pm}\rvert < 2.7$, $p_T^{\mu^\pm} > 25$ GeV
Electron (e) selections	$\lvert\eta^{e^\pm}\rvert < 2.47$ excluding $1.37 < \lvert\eta^{e^\pm}\rvert < 1.52$, $p_T^{e^\pm} > 25$ GeV
Photon selections	$\lvert\eta^{\gamma}\rvert < 2.47$ excluding $1.37 < \lvert\eta^{\gamma}\rvert < 1.52$, $p_T^{\gamma} > 10$ GeV
Jet reconstruction	anti-k_t algorithm, $R = 0.4$
Jet-photon separation	Jets within $\Delta R < 0.4$ of any photon are rejected
Dilepton ($\ell\ell$) mass window	$81 < m^{\ell^+\ell^-} < 101$ GeV
$Z\gamma$ system	$p_T(Z\gamma) > 50$ GeV
Photon-lepton separation	$\Delta R(\gamma, \ell) > 0.4$
Missing transverse energy	$E_T^{\text{miss}} < 40$ GeV
Channel-specific cuts	
Leptonic ($\ell^+\ell^-\gamma$) channel	$100 < m^{Z\ell^+\ell^-\gamma} < 140$ GeV, $m^{\ell\ell} + m^{Z\ell\ell\gamma} > 182$ GeV
Jet ($jj\gamma$) channel	$50 < m^{Zjj\gamma} < 200$ GeV
Neutrino ($\nu\bar{\nu}\gamma$) channel	$30 < E_T^{\text{miss}} < 100$ GeV

Table 1: The summary of object selections for the three channels.

The next subsection discusses the Machine learning (ML) techniques that contribute to optimising the significance estimation derived from the applied cuts.

2.2 Signal and background discrimination using Machine Learning

We use the XGBoost classifier, which is the implementation of the Boosted Decision Trees (BDT) model that uses second-order optimisation. Unlike traditional BDTs that only use first-order gradients, XGBoost takes advantage of both gradients and Hessians for better convergence. For our work, it is trained for 3500 boosting rounds (`n_estimators`) to improve its learning capability. The learning rate is set at 0.05, striking a balance between the speed of convergence and the stability of the model. This method includes Lasso and Ridge regularisation set to 0.0001 to prevent overfitting. We have also added a `gamma` parameter to control the minimum reduction in loss required for making additional splits in the trees. Our objective function, `binary:logistic`, is aimed at optimising binary classification using the logistic loss function (`logloss`). The trees have a maximum depth of 5 (`max_depth`), which helps balance model complexity and performance. We enable early stopping after 50 rounds (`early_stopping_rounds`), ensuring that training stops when no improvement is observed.

This method promotes stable learning while reducing the risk of overfitting. The next step was to select all the generated signal and background MC samples and ensured that we used the same number of signal and background events such that the signal-to-background ratio was 1. The ggF production is categorised into three distinct categories: $jj\gamma$, $\ell^+\ell^-\gamma$, and $\nu\bar{\nu}\gamma$. For the ggF production categories, we exclusively used the XGBoost classifier. We later trained our classifier on the same MC-simulated samples for performance comparison. Then the performance of both classifiers was assessed using the Kernel Density Estimation (KDE) [6, 7] to estimate the probability density functions of predicted values.

3 Preliminary Results

After generating the MC samples, we used a random forest classifier to evaluate feature importance and used the features with the highest importance to optimise our model. Below, we present the selected features for each channel, their respective channels, their corresponding optimised Receiver Operating Curve (ROC) and associated Area Under the Curve (AUC) scores. We describe the methods used to calculate Z-scores, which are used to quantify the statistical significance of the observed signals using the Machine-Learned Likelihood (MLL) approach [8, 9] and KDE. We also compare different binning values for the classifier's outputs. We used a python script to evaluate the classifier's sensitivity by calculating the binned significance for $N_{\text{bins}} = 10, 25, 50, 100$. The background and

signal histograms produced were normalised to account for the expected event counts, and the binned significance Z, which is calculated as:

$$Z(i) = \sqrt{2 \sum_i \left[(S_i + B_i) \cdot \ln\left(1 + \frac{S_i}{B_i}\right) - S_i \right]}$$

where S_i and B_i represent the normalised bin values for signal and background events in the i-th bin, respectively. Finally, the KDE method offers a continuous analysis, avoiding the limitations of discrete binning.

Channel	**Jet**	**Neutrino**	**Lepton**
Z (10 bins)	5.22	6.27	24.08
Z (25 bins)	5.31	6.48	24.00
Z (50 bins)	5.33	6.59	23.92
Z (100 bins)	5.44	6.69	23.82
Z (KDE)	10.66	11.34	27.78

Table 2: The ggF production Z-scores for jet, neutrino, and lepton channels.

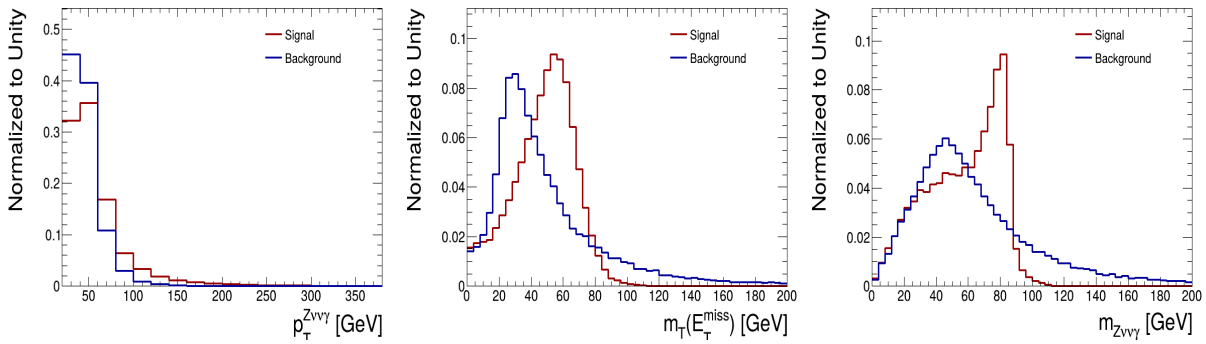

Figure 1: The three most important kinematics, i.e, the transverse momentum (left), missing transverse energy (center), and the invariant mass of the entire system (right) normalised to unity of the ggF production ($\nu\bar{\nu}\gamma$ category).

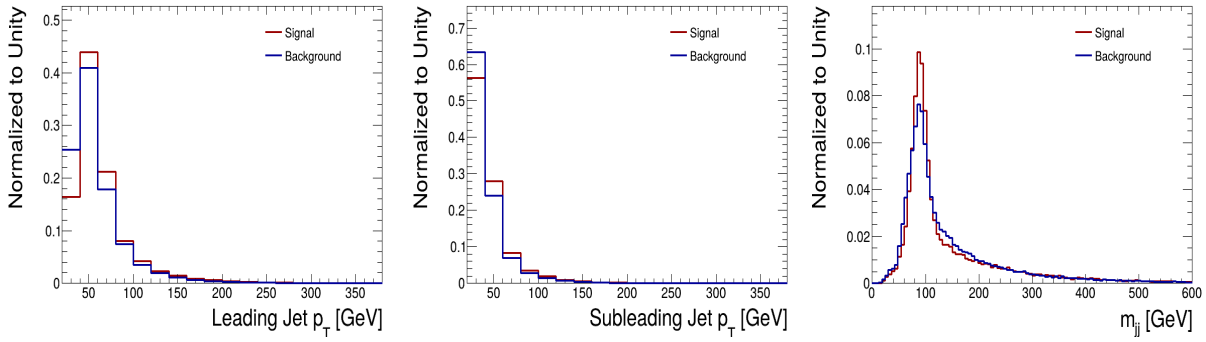

Figure 2: The three most important kinematics, i.e, the leading jet transverse momentum (left), subleading jet transverse momentum (center), and dijet mass system (right), normalised to unity of the ggF production ($jj\gamma$ category).

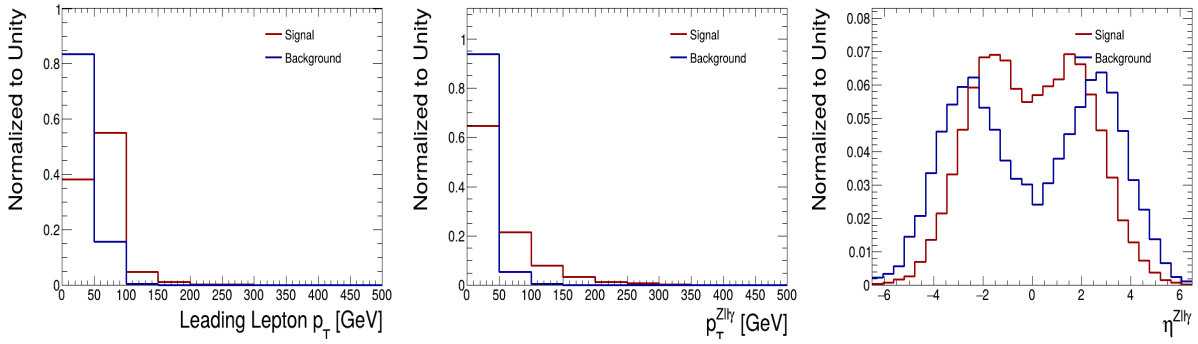

Figure 3: The three most important kinematics, i.e, the leading lepton transverse momentum (left), transverse momentum of the system (center), and pseudorapidity of the system (right) normalised to unity of the ggF production ($\ell^+\ell^-\gamma$ category).

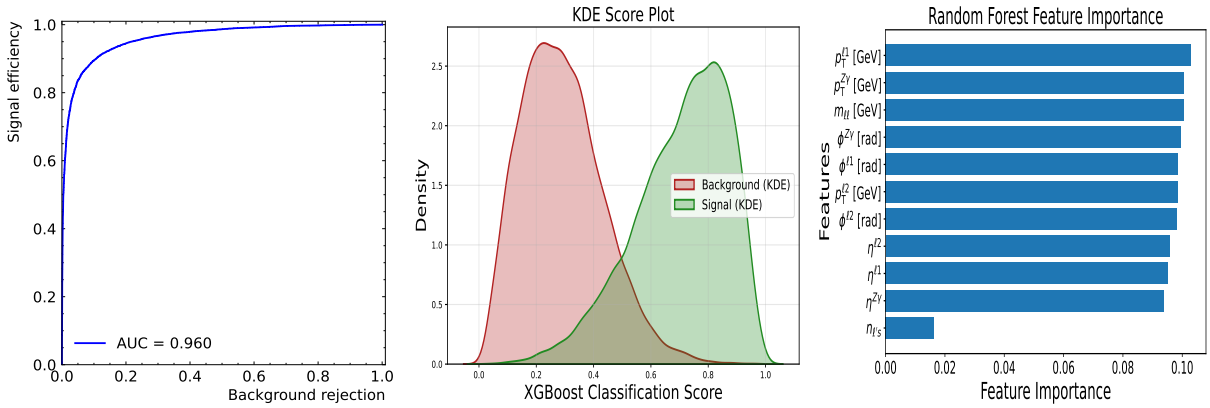

Figure 4: Comparison of the ROC Curve with its associated AUC score (left), XGBoost performance with KDE (center), and feature importance (right) for the ggF production ($\ell^+\ell^-\gamma$ category) without the invariant mass.

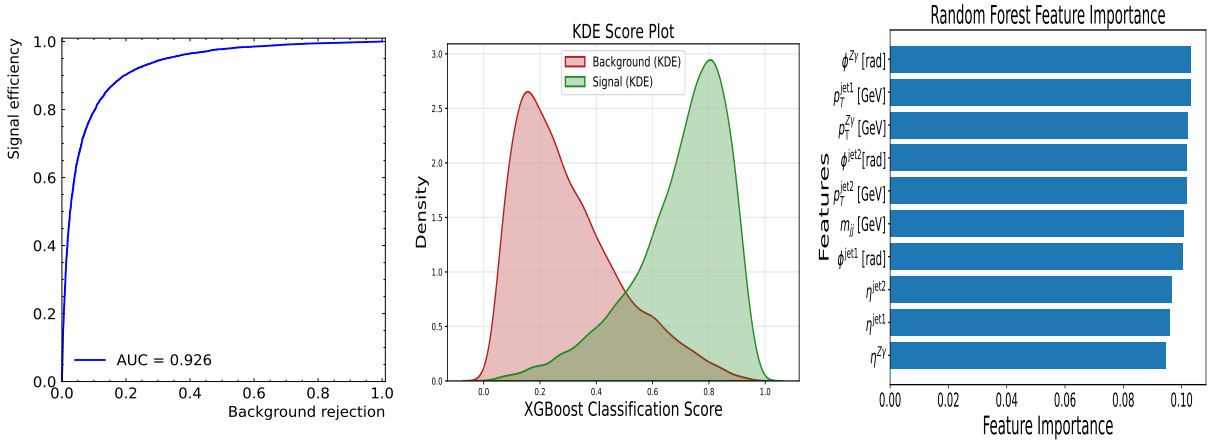

Figure 5: Comparison of the ROC Curve with its associated AUC score (left), XGBoost performance with KDE (center), and feature importance (right) for the ggF production ($jj\gamma$ category) with the invariant mass.

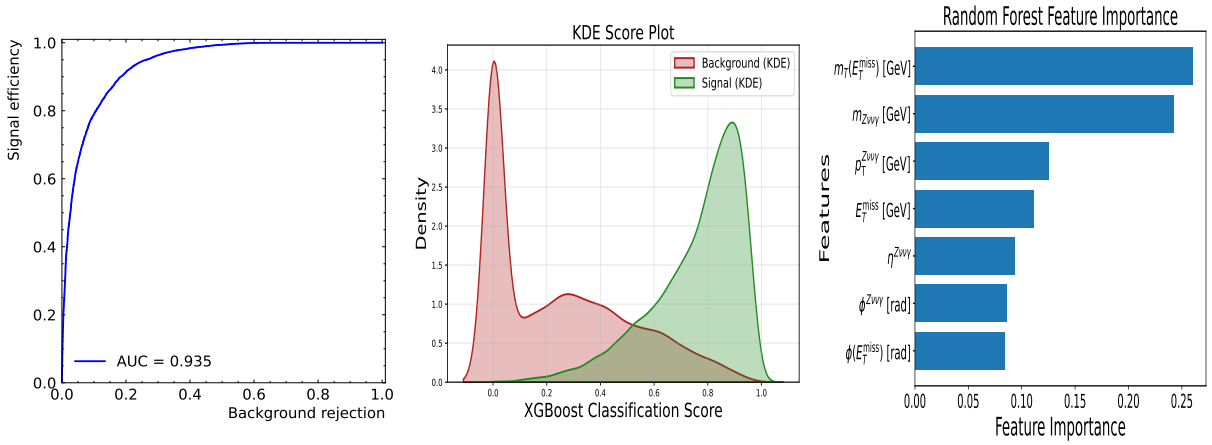

Figure 6: Comparison of the ROC Curve with its associated AUC score (left), XGBoost performance with KDE (center), and feature importance (right) for the ggF production ($\nu\bar{\nu}\gamma$ category) with the invariant mass.

4 Conclusion and Future Plans

We evaluated the XGBoost classifier's performance in the ggF channel using ROC scores, demonstrating its signal-background separation capability. Next month, we will extend this analysis to the VBF, $t\bar{t}H$, and VH production channels, assessing performance both before and after optimization using each channel's key features. We also plan to compare the performance of a BDT classifier against XGBoost. Our results indicate that Kernel Density Estimation (KDE) improves with larger ensemble sizes because it avoids output binning, while the binning method benefits from increased bin counts; KDE consistently outperforms binning.

Acknowledgments

KM would like to express gratitude to the SA-CERN Excellence bursary for funding this research.

References

[1] I. Brivio and M. Trott, "The standard model as an effective field theory," *Physics Reports*, vol. 793, pp. 1–98, 2019.

[2] S. Dawson and P. P. Giardino, "Higgs decays to zz and z γ in the standard model effective field theory: An nlo analysis," *Physical Review D*, vol. 97, no. 9, p. 093003, 2018.

[3] J. Elias-Miro, J. Espinosa, E. Masso, and A. Pomarol, "Higgs windows to new physics through d= 6 operators: constraints and one-loop anomalous dimensions," *Journal of High Energy Physics*, vol. 2013, no. 11, pp. 1–42, 2013.

[4] R. Alonso, E. E. Jenkins, A. V. Manohar, and M. Trott, "Renormalization group evolution of the standard model dimension six operators iii: gauge coupling dependence and phenomenology," *Journal of High Energy Physics*, vol. 2014, no. 4, pp. 1–47, 2014.

[5] A. Alloul, N. D. Christensen, C. Degrande, C. Duhr, and B. Fuks, "Feynrules 2.0—a complete toolbox for tree-level phenomenology," *Computer Physics Communications*, vol. 185, no. 8, pp. 2250–2300, 2014.

[6] M. Rosenblat, "Remarks on some nonparametric estimates of a density function," *Ann. Math. Stat*, vol. 27, pp. 832–837, 1956.

[7] E. Parzen, "On estimation of a probability density function and mode," *The annals of mathematical statistics*, vol. 33, no. 3, pp. 1065–1076, 1962.

[8] E. Arganda, X. Marcano, V. M. Lozano, A. D. Medina, A. D. Perez, M. Szewc, and A. Szynkman, "A method for approximating optimal statistical significances with machine-learned likelihoods," *The European Physical Journal C*, vol. 82, no. 11, p. 993, 2022.

[9] E. Arganda, M. de los Rios, A. D. Pérez, and R. S. Seoane, "Imposing exclusion limits on new physics with machine-learned likelihoods," *PoS ICHEP2022*, vol. 1226, 2022.

This page intentionally left blank.

Monte Carlo Generation Involving Searches for Diphoton Resonances in Association with $\tau^+\tau^-$ or b-jets at the Electroweak Scale in the ATLAS Detector at the LHC

Njokweni Mbuyiswa[1,2], Kutlwano Makgetha[1,2], Vuyolwethu Kakancu[1,2], Paballo Ndhlovu[1,2], Kgothatso Ntumbe[1,2], Reda Mekouar[3], Phuti Rapheeha[1,2,4], Mukesh Kumar[1], Rachid Mazini[1], Bruce Mellado[1,2]

[1]School of Physics and Institute for Collider Particle Physics, University of the Witwatersrand, Johannesburg, Wits 2050, South Africa.
[2]iThemba LABS, National Research Foundation, PO Box 722, Somerset West 7129, South Africa.
[3]Institute of High Energy Physics, Chinese Academy of Sciences, 19B Yuquan Road, Shijingshan District, Beijing, China
[4]School of Electrical Engineering, Tshwane University of Technology, Staatsartillerie Road, Pretoria West 0001, South Africa

E-mail: 2314612@students.wits.ac.za

Abstract. A Monte Carlo generation campaign has been submitted under the ATLAS HBSM subgroup to study a simplified model featuring the resonant production of scalar particles at the electroweak scale. The process under consideration is $gg \to H \to SS'$, where the scalar S (with a mass of approximately 150 GeV) decays to a diphoton final state ($\gamma\gamma$), and the accompanying scalar S' (with a mass of approximately 95 GeV) decays to either $b\bar{b}$ or $\tau^+\tau^-$. The motivation for these studies is rooted in the persistent multi-lepton anomalies observed in various channels at the LHC, as highlighted in combined searches for scalar resonances by ATLAS and CMS and further explored in the context of electroweak-scale scalar states decaying into photons, leptons, or b-jets [1, 2, 3]. The MC production is designed for Run 3 conditions at a center-of-mass energy of $\sqrt{s} = 13.6$ TeV and will facilitate detailed kinematic studies and optimization of selection strategies in these channels.

1 Introduction

Recent anomalies observed in multilepton and diphoton final states at the LHC have sparked interest in extended Higgs sectors, such as the Two-Higgs-Doublet Model with a singlet scalar (2HDM+S) [4]. These anomalies, including excesses observed around 152 GeV in the diphoton channel [3, 5, 6], and in multi-lepton events, [7, 8, 9, 10, 1] suggest the possible existence of new scalar particles. In this context, a search is conducted for a heavy scalar H produced by gluon-gluon fusion ($gg \to H$) that decays to two lighter scalars: $H \to SS'$, where $S \to \gamma\gamma$ and S' decays to other Standard Model (SM) particles, as illustrated in Figure 1. The decay process that are currently being requested are for $S' \to \tau^+\tau^-$ or $b\bar{b}$. This signature provides a clean experimental handle due to the presence of two isolated photons and either a pair of taus or b-jets. This paper focuses on the Monte Carlo (MC) request and generation of simulated signal events for this Beyond Standard Model (BSM) process. Generating accurate MC samples is a critical prerequisite for any physics analysis at the Large Hadron Collider (LHC). These

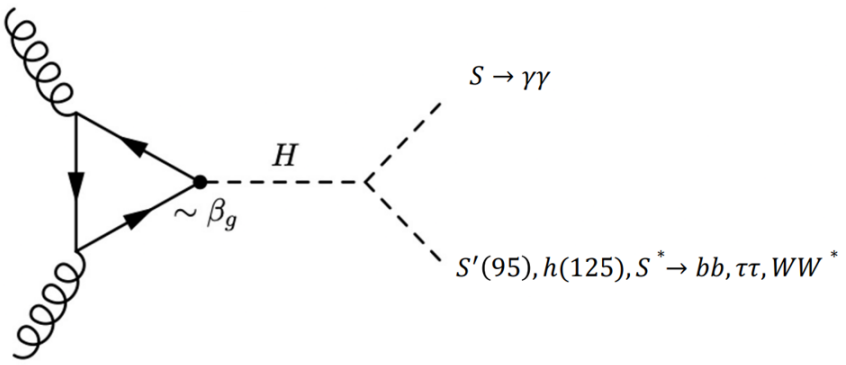

Figure 1: Feynman diagram illustrating a hypothetical heavy scalar boson H produced via gluon-gluon fusion (ggF), with subsequent decays into lighter scalar states. One branch decays into a diphoton final state ($S \to \gamma\gamma$), while the other decays into a lighter scalar or Higgs-like particle ($S'(95), h(125), S^*$) which further decays into fermions or vector bosons ($bb, \tau\tau, WW^*$), providing signatures such as b-jets, taus, leptons, and jets. This process is sensitive to new physics via the gluonic coupling $\sim \beta_g$.

samples allow us to model the expected signal, optimize event selection criteria, estimate detection efficiencies, and compare with observed data. The workflow follows the official ATLAS MC production pipeline, which includes event generation, detector simulation, digitization, reconstruction, and derivation of analysis-ready datasets. A key part of this process is the formal MC request submission based on the recommended ATLAS procedure. Before submission, small-scale signal samples are generated and validated to ensure the physics model is correctly implemented. A detailed request including benchmark points, cross sections, and truth-level filters is then prepared. This request was reviewed by the ATLAS MC production team, who assigned official dataset identifiers (DSIDs). Once approved, large-scale production was initiated across different pile-up conditions (mc23a/d/e) and simulation types (FullSim and AF3). The final datasets are distributed on the World-wide LHC Computing Grid (WLCG) for use in physics analyses.

1.1 The ATLAS Detector

The ATLAS detector [11] is a multipurpose particle detector located at the LHC at CERN. It is designed to detect and measure the particles produced in high-energy beams of protons colliding at center-of-mass energies of up to 13.6 TeV. The detector has a cylindrical geometry with forward–backward symmetry and consists of several layered subdetectors that surround the interaction point. Starting from the innermost layer, the Inner Detector tracks charged particles using silicon pixel and strip detectors, as well as a transition radiation tracker. Surrounding the Inner Detector are the calorimeters, which measure the energy of particles. The electromagnetic calorimeter is made using liquid argon as a sampling medium, which is required for precise measurements of electron or photon energy. The hadronic calorimeter, on the other hand, uses scintillator tiles in some sections and liquid argon in other sections, and has the ability to measure the energy of jets produced by quarks and gluons. Outside the calorimeters is the muon spectrometer, which will identify and track all muons, since according to the electromagnetic spectrum muons are the only charged particles likely to penetrate into all of the inner detector layers. It uses large toroidal magnetic fields and multiple layers of precision tracking chambers. The entire detector is supported by a sophisticated trigger and data acquisition system that selects interesting events in real time.

1.2 Monte Carlo Simulation Procedure

The MC simulation process follows a well-defined series of steps that mimic the production, propagation, and detection of particles at the LHC. The first step is event generation, where the hard-scattering process is modeled using MadGraph5 [12], which calculates the matrix element for $gg \to H \to SS'$. Next, parton showering and hadronization are handled by Pythia8 [13], which simulates the radiation of quarks and gluons and the transformation of partons into hadrons. For b-hadrons, decays are further refined using EvtGen. Following generation, the simulation enters the detector simulation stage. Two types are utilized, which are FullSim and ATLFAST3

(AF3). GEANT4-based FullSim [14] provides a detailed, step-by-step simulation of particle interactions with detector materials, including electromagnetic and hadronic shower modeling, multiple scattering, and energy loss. AF3, by contrast, uses a parameterized detector response, approximating calorimeter and tracking responses using templates and smearing functions derived from GEANT4. This drastically reduces computational time while maintaining reasonable accuracy for many analyses. The next stage is digitization, where the energy deposits from detector simulation are converted into electronic signals, mimicking the readout of the real detector. This includes modeling noise, pile-up effects, and readout thresholds. Subsequently, reconstruction algorithms process these digitized signals to identify physics objects such as missing transverse momentum (MET), jets, muons, photons and electrons. The same software stack used for real data is applied, ensuring consistency between simulation and experiment. Finally, the data is saved in ROOT format during the derivation step, producing xAOD files that can be used for physics analysis. This full pipeline ensures a comprehensive and realistic simulation of events in the ATLAS detector.

2 Monte Carlo Simulation, Validation and Request Setup

Signal samples were generated for benchmark mass points motivated by observed anomalies. The heavy scalar H is to be produced through gluon fusion with masses ranging from 250 to 400 GeV. The decay chain $H \to SS'$ involves S (decaying to $\gamma\gamma$) with mass 150–325 GeV and S' (decaying to $\tau^+\tau^-$ or $b\bar{b}$) with mass 95–125 GeV. A total of 240,000 events were requested, distributed across both channels. Three pile-up conditions are considered which is 2022 (20k), 2023 (20k), and 2024 (80k) to match LHC Run 3 conditions (mc23a/d/e). We consider both simulation types, FullSim and AF3. The branching-ratios used in the cross-section calculation were taken from the CERN Yellow Report benchmarks [15], ensuring compatibility with other ATLAS reinterpretation studies. The complete cross-section for the final state is calculated as:

$$\sigma_{\text{total}} = \sigma(gg \to H) \times \text{Br}(H \to SS') \times \text{Br}(S \to \gamma\gamma) \times \text{Br}(S' \to \tau\tau \text{ or } b\bar{b}) \tag{1}$$

In collider physics, kinematic variables are used to describe the motion and spatial distribution of particles produced in high-energy proton-proton collisions. The transverse momentum, denoted p_{T}, is the component of a particle's momentum perpendicular to the beam axis. Pseudo-rapidity, η, describes the angular position of a particle relative to the beam axis and is defined as $\eta = -\ln[\tan(\theta/2)]$, where θ is the polar angle. It is preferred over the polar angle because it is approximately invariant under Lorentz boosts along the beam direction. The angular separation between two particles in the ϕ–η plane is quantified by $\Delta R = \sqrt{(\Delta\phi)^2 + (\Delta\eta)^2}$, which is used to associate decay products with reconstructed jets or to isolate objects from one another. Jets, which are collimated sprays of hadrons resulting from quarks or gluons, are reconstructed using the anti-k_T algorithm [16] with a distance parameter $R = 0.4$. At the truth level, jets are clustered from stable generator-level particles and stored in the `AntiKt4TruthJets` container. A jet is considered a truth b-jet if it contains a b-hadron within a cone of $\Delta R < 0.4$ and the b-hadron has $p_{\text{T}} > 5$ GeV. These definitions ensure consistent and physically meaningful object identification before detector effects are applied. The following truth-level selection criteria were applied during event generation to retain only events with the desired signal topology while reducing sample size for computational efficiency. These selections are summarized in Table 2.

Selection	**Requirement**
Photons	≥ 2 photons, $p_{\text{T}} > 20$ GeV, $\lvert\eta\rvert < 2.5$
b-jets	$\geq$ 2 jets matched to b-hadrons ($\Delta R < 0.4$, $p_{\text{T}} > 5$ GeV)
Jet kinematics	$p_{\text{T}} > 20$ GeV, $\lvert\eta\rvert < 2.5$ for all jets
Taus	≥ 2 visible taus from S', $\lvert\eta\rvert < 2.5$, $p_{\text{T}}^{\tau had} >$ 25GeV
Jet algorithm	anti-k_T, R=0.4
Jet container	`AntiKt4TruthJets`

Table 1: Truth-level selection criteria.

3 Results

The generated signal samples were validated using kinematic distributions at the truth level. These distributions confirm that the event generation and decay chains are correctly implemented and that the samples reflect the

expected physical behavior. The p_{T} distributions for the subleading and leading photon shown in Figure 2 further validate the simulation by showing the expected transverse momentum spectra for the two photons. The sum of these will show a clear peak at 150 GeV, corresponding clearly to the input mass of the scalar resonance S. This confirms that the $S \to \gamma\gamma$ decay is properly modelled in the simulation. The distributions shown in Figure 3 show the correct implementation of the truth level selections. These plots collectively demonstrate that the MC generation accurately reproduces the physics processes of interest, making the samples suitable for further analysis. The derived information, as shown in Table 3, was a key part of our MC request and has been reviewed and approved by the ATLAS production team.

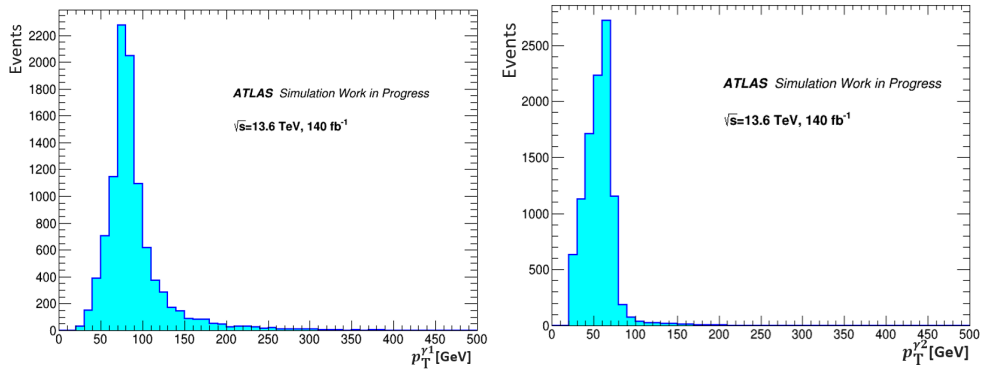

Figure 2: Distribution of the leading photon (left) and the subleading photon (right) p_{T} for the same benchmark point. The distributions begin after 20 GeV, reflecting the correct implementation of the truth level selections.

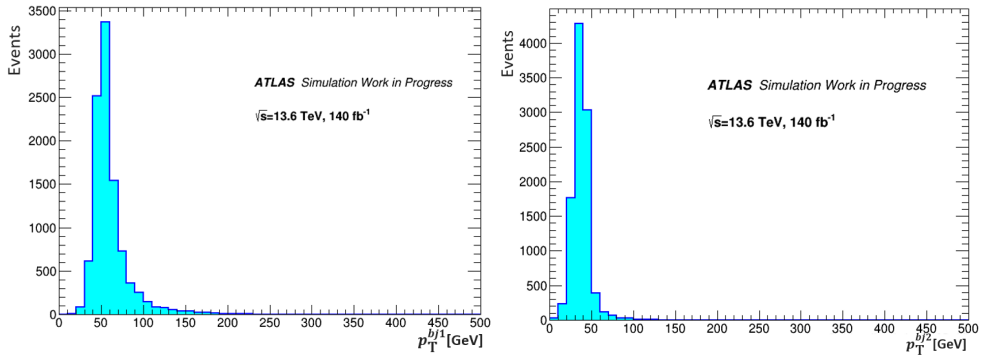

Figure 3: Distribution of the leading b-jet (left) and the subleading b-jet (right) p_{T} for the same benchmark mass. The distributions begin after 20 GeV, reflecting the correct implementation of the truth level selections.

4 Conclusion

We have successfully completed the Monte Carlo request and validation for a new physics signal involving a heavy scalar H decaying to SS', with $S \to \gamma\gamma$ and $S' \to \tau^+\tau^-$ or $b\bar{b}$. Small-scale samples were generated, validated using truth-level kinematic distributions, and used to submit a formal request for large-scale production under LHC Run 3 conditions. The request included detailed specifications for mass benchmarks, pile-up scenarios, and simulation types (FullSim and AF3). The datasets are now being produced and will soon be available on the WLCG. These MC samples will enable the search for diphoton resonances associated with τ's or b-jets, probing anomalies at the electroweak scale. Future work includes the integration of these signals into the full analysis framework, estimation of background processes, and sensitivity studies for exclusion or discovery.

Channel	m_H [GeV]	m_S [GeV]	$m_{S'}$ [GeV]	Efficiency (%)	σ [fb]
$\gamma\gamma + \tau^+\tau^-$	250	150	95	18.6	1.154
	260	160	100	22.6	0.412
	300	175	125	33.6	0.053
	350	225	125	34.2	0.010
	400	275	125	35.1	0.004
$\gamma\gamma + b\bar{b}$	250	150	95	44.7	11.1
	260	160	100	47.7	3.904
	300	175	125	56.2	0.483
	350	225	125	57.9	0.092
	400	275	125	60.1	0.003

Table 2: Summary of simulation details for benchmark mass points, including total selection efficiency and cross section after truth-level filtering. These values are used in the ATLAS MC request and will inform sensitivity studies.

References

[1] A. Crivellin, Y. Fang, O. Fischer, S. Bhattacharya, M. Kumar, E. Malwa, B. Mellado, N. Rapheeha, X. Ruan, and Q. Sha, "Accumulating evidence for the associated production of a new higgs boson at the large hadron collider," 2023.

[2] S. Bhattacharya, G. Coloretti, A. Crivellin, S.-E. Dahbi, Y. Fang, M. Kumar, and B. Mellado, "Growing Excesses of New Scalars at the Electroweak Scale," 6 2023.

[3] S. Bhattacharya, B. Lieberman, M. Kumar, A. Crivellin, Y. Fang, R. Mazini, and B. Mellado, "Emerging Excess Consistent with a Narrow Resonance at 152 GeV in High-Energy Proton-Proton Collisions," 3 2025.

[4] A. Drozd, B. Grzadkowski, J. F. Gunion, and Y. Jiang, "Extending two-higgs-doublet models by a singlet scalar field—the case for dark matter," *Journal of High Energy Physics*, vol. 2014, no. 11, pp. 1–40, 2014.

[5] G. Coloretti, A. Crivellin, S. Bhattacharya, and B. Mellado, "Searching for low-mass resonances decaying into W bosons," *Phys. Rev. D*, vol. 108, no. 3, p. 035026, 2023.

[6] A. Crivellin, Y. Fang, O. Fischer, S. Bhattacharya, M. Kumar, E. Malwa, B. Mellado, N. Rapheeha, X. Ruan, and Q. Sha, "Accumulating evidence for the associated production of a new Higgs boson at the LHC," *Phys. Rev. D*, vol. 108, no. 11, p. 115031, 2023.

[7] S. Buddenbrock, A. S. Cornell, Y. Fang, A. Fadol Mohammed, M. Kumar, B. Mellado, and K. G. Tomiwa, "The emergence of multi-lepton anomalies at the LHC and their compatibility with new physics at the EW scale," *JHEP*, vol. 10, p. 157, 2019.

[8] S. von Buddenbrock, R. Ruiz, and B. Mellado, "Anatomy of inclusive tt w production at hadron colliders," *Physics Letters B*, vol. 811, p. 135964, 2020.

[9] Y. Hernandez, M. Kumar, A. S. Cornell, S.-E. Dahbi, Y. Fang, B. Lieberman, B. Mellado, K. Monnakgotla, X. Ruan, and S. Xin, "The anomalous production of multi-lepton and its impact on the measurement of Wh production at the LHC," *Eur. Phys. J. C*, vol. 81, no. 4, p. 365, 2021.

[10] S. von Buddenbrock, A. S. Cornell, A. Fadol, M. Kumar, B. Mellado, and X. Ruan, "Multi-lepton signatures of additional scalar bosons beyond the Standard Model at the LHC," *J. Phys. G*, vol. 45, no. 11, p. 115003, 2018.

[11] G. Aad *et al.*, "The ATLAS experiment at the CERN Large Hadron Collider: a description of the detector configuration for Run 3," *JINST*, vol. 19, no. 05, p. P05063, 2024.

[12] J. Alwall, R. Frederix, S. Frixione, V. Hirschi, F. Maltoni, O. Mattelaer, H.-S. Shao, T. Stelzer, P. Torrielli, and M. Zaro, "The automated computation of tree-level and next-to-leading order differential cross sections, and their matching to parton shower simulations," *Journal of High Energy Physics*, vol. 2014, no. 7, pp. 1–157, 2014.

[13] T. Sjöstrand, S. Ask, J. R. Christiansen, R. Corke, N. Desai, P. Ilten, S. Mrenna, S. Prestel, C. O. Rasmussen, and P. Z. Skands, "An introduction to pythia 8.2," *Computer physics communications*, vol. 191, pp. 159–177, 2015.

[14] S. Bein, P. Connor, K. Pedro, P. Schleper, and M. Wolf, "Refining fast simulation using machine learning," *EPJ Web Conf.*, vol. 295, p. 09032, 2024.

[15] LHC Physics (CERN Yellow Report), "Cern yellow report working group on bsm at 13tev — gluon-gluon fusion process (twiki)," https://twiki.cern.ch/twiki/bin/view/LHCPhysics/CERNYellowReportPageBSMAt13TeV#gluon_gluon_Fusion_Process, 2025, accessed July 30, 2025.

[16] A. Behring *et al.*, "Flavoured jet algorithms: a comparative study," 6 2025.

Analysing $gg \to h \to Z\gamma$ decay at the LHC using SMEFT

Njokweni Mbuyiswa[1,2], Kutlwano Makgetha[1,2], Srimoy Bhattacharya[1], Abdualazem Fadol[1,3], Katlego Machete[1,2], Mukesh Kumar[1], and Bruce Mellado[1,2]

[1] School of Physics and Institute for Collider Particle Physics, University of the Witwatersrand, Johannesburg, Wits 2050, South Africa.
[2] iThemba LABS, National Research Foundation, PO Box 722, Somerset West 7129, South Africa.
[3]Institute of High Energy Physics, Chinese Academy of Sciences, 19B Yuquan Road, Shijingshan District, Beijing, China

E-mail: 2314612@students.wits.ac.za

Abstract. The ATLAS and CMS collaborative effort resulted in the first evidence of the Higgs boson (h) decay into a Z-boson and a photon, with a statistical significance of 3.4σ. The measured signal rate relative to the SM prediction was found to be 2.2 ± 0.7 times the leading order Standard Model (SM) prediction. Recent study shows that even with next-to-leading order QCD corrections and the signal-background interference, this excess in $h \to Z\gamma$ cannot be explained within the SM. With this motivation we perform our analysis of the above-mentioned process through gluon-fusion and constraint the corresponding six-dimension Wilson coefficients in SMEFT through the cross section measurement and different sensitive kinematic observables. For this study we consider $Z \to \ell^+\ell^-$ ($\ell^\pm = e^\pm, \mu^\pm$).

1 Introduction

The earliest indication for the very rare case of the "Higgs boson decaying to a photon and a Z boson has been reported, with a statistical significance of about 3.4σ" [1]. The result emerges from a combined analysis of data accumulated by the CMS and ATLAS collaborations when studying the colliding of beams of protons at the Large Hadron Collider (LHC) operated in CERN. Both collaborations utilized datasets corresponding to a center of mass energy of 13 TeV and an integrated luminosity of approximately 140 fb^{-1}. The observed signal yield is 2.2 ± 0.7 times the rate predicted by the Standard Model (SM) [1]. In the SM, the decay that we are investigating is expected to have a very small branching fraction of roughly $(1.51 \pm 0.1) \times 10^{-3}$, assuming a Higgs boson mass that is about 125 GeV ($m_h \approx 125$ GeV) [2, 3]. Since this process proceeds via loop-induced diagrams (see Figure 1), it is particularly sensitive to potential contributions from physics beyond the Standard Model (BSM), which could enhance the branching ratio relative to the SM prediction. Among current theoretical frameworks, "the Standard Model Effective Field Theory" (SMEFT) provides the most compelling approach to interpreting such deviations. SMEFT extends the SM by incorporating higher-dimensional operators—"constructed from SM fields and respecting the SM gauge symmetries—that are suppressed by a new physics scale Λ" [4]. The SMEFT Lagrangian is given by:

$$\mathcal{L}_{\text{SMEFT}} = \mathcal{L}_{\text{SM}} + \sum_{n>4} \sum_{i} \frac{c_i^{(n)}}{\Lambda^{n-4}} \mathcal{O}_i^{(n)}, \tag{1}$$

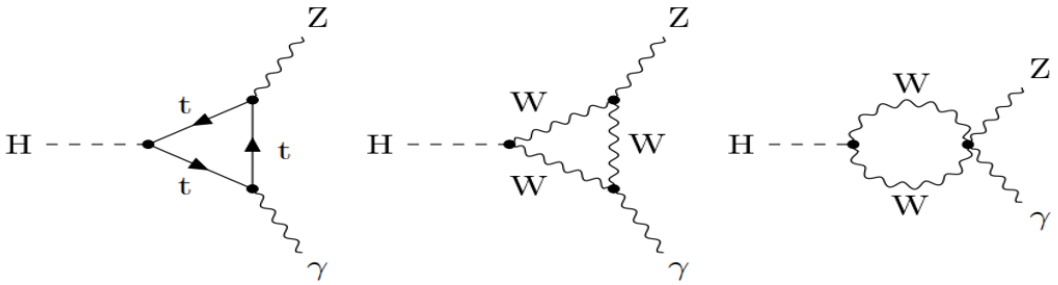

Figure 1: The first diagram (a) include contributions from a top quark loop shows the vertex for this decay. Diagrams (b) and (c) depict loop-induced contributions mediated by W bosons.

where n denotes the mass dimension of the operators, $\mathcal{L}_{\text{SM}}$ is the Standard Model Lagrangian, $\mathcal{O}_i^{(n)}$ are the higher-dimensional operators, and $c_i^{(n)}$ represent their associated Wilson coefficients. The Wilson coefficients and the relevant operators that correspond to each of them, determined for this analysis that contribute the $h \to Z\gamma$ decay vertex, are:

$$\texttt{cpBB}(C_B) \to O_{\varphi B} = (\varphi^+\varphi - \frac{v^2}{2})B^{\mu\nu}B_{\mu\nu}, \tag{2}$$

$$\texttt{cpWB}(C_{WB}) \to O_{\varphi WB} = (\varphi^+\tau_I\varphi)B^{\mu\nu}W^I_{\mu\nu}, \tag{3}$$

$$\texttt{cpW}(C_W) \to O_{\varphi W} = (\varphi^+\varphi - \frac{v^2}{2})W^{\mu\nu}_I W^I_{\mu\nu}, \tag{4}$$

Here, the symbol v refers to the vacuum expectation value (vev) of the Higgs, which has a value of approximately 246 GeV, and τ_I ($I = 1, 2, 3$) are the Pauli matrices acting on the SU(2)$_L$ indices of the Higgs doublet field φ [5, 6].
The SMEFT offers a robust and model-independent framework for probing the phenomenological consequences of novel physics beyond the Standard Model. By methodically incorporating higher-dimensional in a structured expansion operators up to a specified mass dimension, it enables the exploration of new physics signatures across a range of energy scales. In this preliminary analysis, we adopt a simplified scenario in which all relevant Wilson coefficients are set to one.

2 Monte Carlo Event Generation

Simulated proton-proton collision events were generated with MADGRAPH5 [7] for both signal and major significant background contributions. The underlying event modelling, hadronization and parton showering were handled using PYTHIA8 [8], ensuring the final state particles resulting from the hard scattering processes were realistically simulated. These events were processed through the DELPHES3.4.2 [9] to model detector responses and effects accurately. Jets were "reconstructed using the anti-k_T algorithm [10] as implemented in FASTJET [11], with a jet radius parameter of $R = 0.4$". The factorization and renormalization scales were dynamically chosen for both background and signal processes. The centre of this analysis is on the rare Higgs-mediated transition $h \to Z\gamma$, producing a photon and a Z boson in the final state.

The initial stage involves determining the higher-dimensional operators that contribute to this decay mode within the framework of the SMEFT [12]. The relevant operators were derived following the formulation outlined in [13], in which the electroweak corrections at one-loop order for this decay process are evaluated. The Wilson coefficients for these operators were obtained using the `SMEFT@NLO` package [14], which leverages models developed in `FeynRules` [15]. MC event generation was performed for both signal and background processes using a combination of tools.

Using the `SMEFT@NLO` model, the signal process $gg \to h \to Z\gamma$ was simulated and subsequently interfaced for further analysis. This channel represents the decay of the Higgs boson into a photon and a Z boson, as predicted by the SMEFT framework. The analysis also includes several Standard Model background processes that can produce signatures mimicking the signal. These background processes considered are $pp \to \ell^+\ell^-\gamma$, representing the background from dilepton pair production accompanied by a photon for the dilepton final state of the signal; $pp \to jj\gamma$, representing the background arising from the production of two light-flavor jets in association with a photon for the dijet final state of the signal; $pp \to b\bar{b}\gamma$, representing the background arising from the production of two b-tagged jets in association with a photon for di-$b$jet final state of the signal; and $pp \to \text{MET} + \gamma$, representing

the background from the production of missing transverse energy (MET) due to neutrinos, also accompanied by a photon for the di-neutrino final state for the signal.

Jets within $\Delta R = 0.2$ of leptons or photons were excluded. Electrons were also removed if they were within $\Delta R = 0.02$ of muons or other electrons. These object definitions defined in Table 1 were essential for ensuring accurate and efficient simulation of the background and signal processes, serving as a foundation for the analysis of the SMEFT framework being used to study the Higgs boson transition, yielding a photon and a Z boson in the final state. The selection criteria for the case whereby the Z breaks down into two oppositely charged leptons of the same flavour are described in Table 2.

Object	**Pseudorapidity ($\lvert\eta\rvert$)**	**Transverse Momentum (p_T)**
Muons	$\lvert\eta_\mu\rvert < 2.7$	$p_{\mathrm{T}}^{\mu} > 10$ GeV
Electrons	$\lvert\eta_e\rvert < 2.47$ (excluding $1.37 < \lvert\eta_e\rvert < 1.52$)	$p_{\mathrm{T}}^{e} > 10$ GeV
Photons	$\lvert\eta_\gamma\rvert < 2.47$ (excluding $1.37 < \lvert\eta_\gamma\rvert < 1.52$)	$p_{\mathrm{T}}^{\gamma} > 10$ GeV
Jets	Anti-k_t with $\Delta R = 0.4$, $\lvert\eta_j\rvert < 4.4$	$p_{\mathrm{T}}^{j} > 25$ GeV

Table 1: Object definitions at the generator level.

Selection Category	**Criteria**
Photon Selection	At least one photon must satisfy the object definition criteria.
Lepton Selection	Two same-flavor, opposite-sign leptons (electrons or muons) must satisfy the object definition criteria.
Z Boson Reconstruction	Invariant mass of the lepton pair within 81 GeV $< m_{\ell\ell} <$ 101 GeV.
Transverse Momentum of $Z\gamma$ System	p_{T} of the $Z\gamma$ system > 50 GeV to reduce background.
ΔR Cuts	Angular separation cuts such as $\Delta R(\gamma, \ell) > 0.4$ to ensure well-separated objects.
Missing Transverse Energy	If applicable, require MET < 40 GeV to reduce background from processes involving neutrinos.

Table 2: Selection Criteria for $Z\gamma$ analysis whereby the Z decays into two oppositely charged leptons of the same flavour.

3 Preliminary results

As described in the object definitions and selection criteria, we pick events that have exactly two leptons and one photon. The distributions in Figure 2 show that a bulk of our generated samples for both the background and signal fit that criteria. In putting the events through the other cuts we plot the distributions scaled to unity in order to make a distinction in where the background and signal peaks. For the kinematic distributions of the $m_{\ell\ell}$ and $m_{Z\gamma}$ in Figure 3, we plan to perform a Gaussian fit at least two standard deviation from their peak in order to find their resolution.

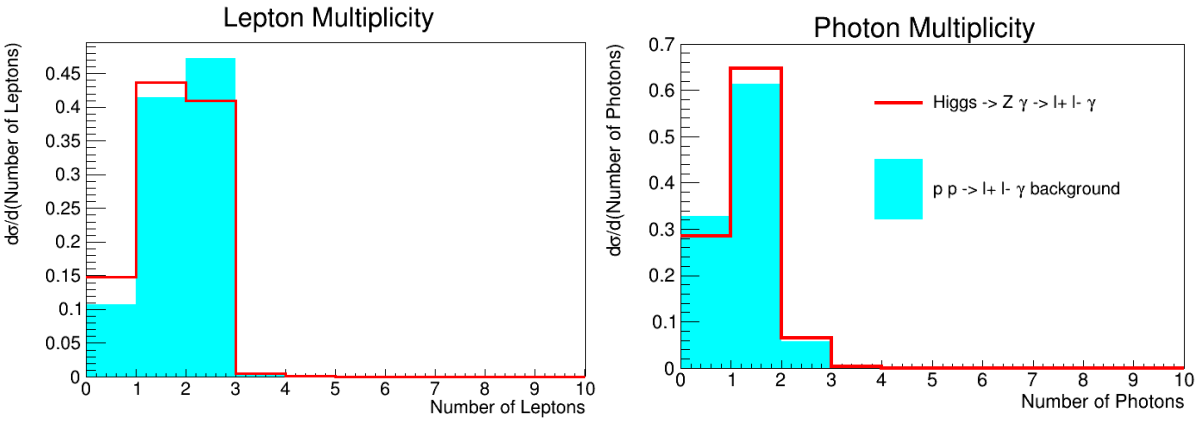

Figure 2: These are the distributions of the photon and lepton multiplicity after the object definition criteria. As expected from the MC generated samples, there are more events that have two leptons and one photon.

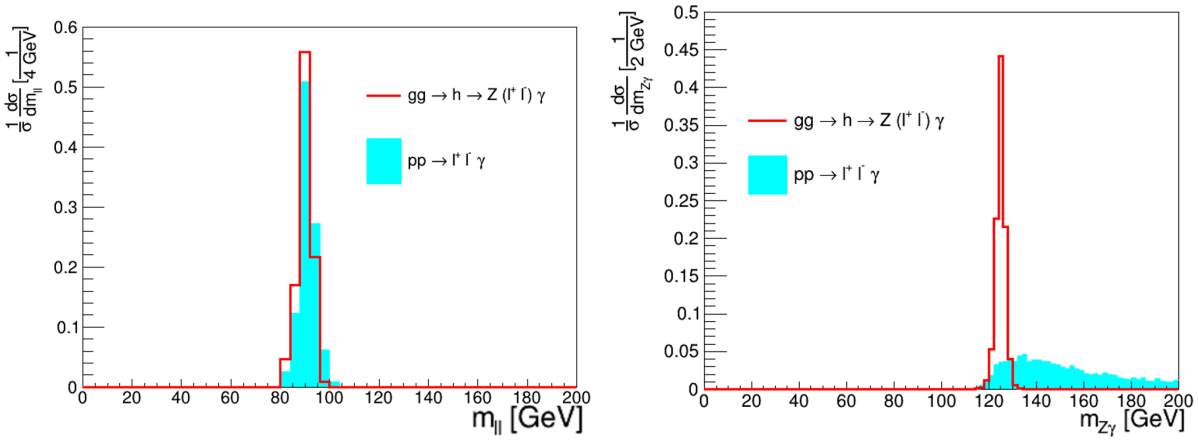

Figure 3: The distribution of $m_{\ell\ell}$ system (*left*) peaks around the Z mass of 90 GeV after the minimal selection criteria as expected. The distribution of the $m_{Z\gamma}$ system (*right*) after the selection criteria peaks at about the higgs boson mass as expected.

4 Conclusion and Future Plans

This work represents an ongoing effort to extract meaningful constraints on dimension-six operators in the SMEFT through the study of the rare decay process $h \to Z\gamma$. Based on the preliminary results shown in Figure 3, our aim is to refine the resolution of the differential distributions by optimizing the invariant mass window, thus improving the signal-to-background ratio. Our future analysis will employ both inclusive and bin-by-bin differential approaches to constrain the SMEFT Wilson coefficients. In the inclusive method, we will integrate over all kinematic regions of interest, whereas in the bin-by-bin method, we will analyze individual bins of the differential distribution, allowing for improved sensitivity to deviations from SM predictions in specific kinematic regions. Subsequent steps involve reweighting the differential distributions using corrected cross sections derived from constrained values of the SMEFT Wilson coefficients. These constraints will be determined by computing the decay amplitude for the $h \to Z\gamma$ process within the SMEFT framework, incorporating contributions from relevant Feynman diagrams. Comparison with experimental measurements will allow us to fit the Wilson coefficients using a χ^2 minimization procedure, defined as:

$$\chi^2 = \sum_{k=1}^{n} \left(\frac{\sigma_k^{\text{BSM}} - \sigma_k^{\text{SM}}}{\Delta\sigma_k} \right)^2 \text{ with } \Delta\sigma_k = \sqrt{\frac{\sigma_k^{\text{SM}}}{\mathcal{L}} + \left(\delta_s\, \sigma_k^{\text{SM}}\right)^2}, \tag{5}$$

where $\mathcal{L}$ is the integrated luminosity, σ_k is the cross section in the k-th bin of a distribution of n-bins and δ_s is the systematic uncertainty. The cross section in the presence of new physics contributions can be expressed in quadratic form as [16, 17, 18, 19]:

$$\sigma^{\text{BSM}} = \sigma^{\text{SM}} + \sum_i C_i A_i + \sum_{i,j} C_i C_j B_{ij},$$

where C_i are the Wilson coefficients, and the parameters A_i, B_{ij} capture the interference and pure BSM contributions respectively. To obtain robust and realistic constraints on the BSM couplings, we plan to perform a multi-parameter analysis by simultaneously varying all relevant SMEFT Wilson coefficients within a benchmark range of $[-1, 1]$, extracting the posterior distributions after marginalization using a Markov Chain Monte-Carlo (MCMC) technique. The analyses will utilize a binned sensitive distribution which we will find determine using Random Forest classification [20] algorithm. We will be applying the `GetDist` package [21] to extract credible intervals and plot posterior projection while accounting for any correlations and degeneracies found among the parameters in the multidimensional space. We will also set exclusion limits at the 95 percent confidence level on the Wilson coefficients. In parallel, we plan to extend this analysis to other final states where the Z boson decays into hadronic jets ($Z \to jj$), b-tagged jets ($Z \to b\bar{b}$), and neutrinos ($Z \to \nu\bar{\nu}$), each with their own dominant background processes and associated systematics. These additional channels are expected to increase overall sensitivity to SMEFT effects. We will also investigate other Higgs production modes beyond gluon fusion, including associated production with top quarks ($t\bar{t}H$), associated production with a vector boson (VH) and Vector Boson Fusion (VBF) to explore operator structures not fully accessible in a single production mechanism. These steps will collectively provide a more comprehensive probe of electroweak interactions and possible new physics effects within the SMEFT framework using the rare $h \to Z\gamma$ decay channel.

References

[1] G. Aad *et al.*, "Evidence for the Higgs Boson Decay to a Z Boson and a Photon at the LHC," *Phys. Rev. Lett.*, vol. 132, no. 2, p. 021803, 2024.

[2] A. Djouadi, J. Kalinowski, and M. Spira, "Hdecay: A program for higgs boson decays in the standard model and its supersymmetric extension," *Computer Physics Communications*, vol. 108, no. 1, pp. 56–74, 1998.

[3] D. de Florian, D. Fontes, J. Quevillon, M. Schumacher, F. Llanes-Estrada, A. Gritsan, E. Vryonidou, A. Signer, P. de Castro Manzano, D. Pagani *et al.*, *arXiv: Handbook of LHC Higgs Cross Sections: 4. Deciphering the Nature of the Higgs Sector*. Cern, 2016, no. arXiv: 1610.07922.

[4] G. Passarino and M. Trott, "The standard model effective field theory and next to leading order," *arXiv preprint arXiv:1610.08356*, 2016.

[5] B. Grzadkowski, M. Iskrzynski, M. Misiak, and J. Rosiek, "Dimension-Six Terms in the Standard Model Lagrangian," *JHEP*, vol. 10, p. 085, 2010.

[6] D. Barducci *et al.*, "Interpreting top-quark LHC measurements in the standard-model effective field theory," 2 2018.

[7] J. Alwall, R. Frederix, S. Frixione, V. Hirschi, F. Maltoni, O. Mattelaer, H.-S. Shao, T. Stelzer, P. Torrielli, and M. Zaro, "The automated computation of tree-level and next-to-leading order differential cross sections, and their matching to parton shower simulations," *Journal of High Energy Physics*, vol. 2014, no. 7, pp. 1–157, 2014.

[8] T. Sjöstrand, S. Ask, J. R. Christiansen, R. Corke, N. Desai, P. Ilten, S. Mrenna, S. Prestel, C. O. Rasmussen, and P. Z. Skands, "An introduction to pythia 8.2," *Computer physics communications*, vol. 191, pp. 159–177, 2015.

[9] J. De Favereau, C. Delaere, P. Demin, A. Giammanco, V. Lemaitre, A. Mertens, and M. Selvaggi, "Delphes 3: a modular framework for fast simulation of a generic collider experiment," *Journal of High Energy Physics*, vol. 2014, no. 2, pp. 1–26, 2014.

[10] M. Cacciari, G. P. Salam, and Soyez, "The anti-k_t jet clustering algorithm," *JHEP*, vol. 04, p. 063, 2008.

[11] M. Cacciari, G. P. Salam, and G. Soyez, "FastJet User Manual," *Eur. Phys. J. C*, vol. 72, p. 1896, 2012.

[12] Z.-Q. Chen, L.-B. Chen, C.-F. Qiao, and R. Zhu, "Two-loop electroweak corrections to the higgs boson rare decay process $h \to z\gamma$," 2024.

[13] S. Dawson and P. P. Giardino, "Higgs decays to z z and z γ in the standard model effective field theory: An nlo analysis," *Physical Review D*, vol. 97, no. 9, p. 093003, 2018.

[14] C. Degrande, G. Durieux, F. Maltoni, K. Mimasu, E. Vryonidou, and C. Zhang, "Automated one-loop computations in the standard model effective field theory," *Physical Review D*, vol. 103, no. 9, p. 096024, 2021.

[15] A. Alloul, N. D. Christensen, C. Degrande, C. Duhr, and B. Fuks, "Feynrules 2.0—a complete toolbox for tree-level phenomenology," *Computer Physics Communications*, vol. 185, no. 8, pp. 2250–2300, 2014.

[16] R. Rahaman, "On two-body and three-body spin correlations in leptonic $t\bar{t}Z$ production and anomalous couplings at the LHC," *JHEP*, vol. 02, p. 077, 2023.

[17] K. Mosala, P. Sharma, M. Kumar, and A. Goyal, "Axion-like particles at future $e^{-}p$ collider," *Eur. Phys. J. C*, vol. 84, no. 1, p. 44, 2024.

[18] R. Rahaman and R. K. Singh, "Unravelling the anomalous gauge boson couplings in $ZW^{\pm}$ production at the LHC and the role of spin-1 polarizations," *JHEP*, vol. 04, p. 075, 2020.

[19] B. Ravina, E. Simpson, and J. Howarth, "Observing $t\bar{t}Z$ spin correlations at the LHC," *Eur. Phys. J. C*, vol. 81, no. 9, p. 809, 2021.

[20] A. Iqbal, J. Verboncoeur, and P. Zhang, "A Supervised Machine Learning Framework for Multipactor Breakdown Prediction in High-Power Radio Frequency Devices and Accelerator Components: A Case Study in Planar Geometry," 7 2025.

[21] A. Lewis, "GetDist: a Python package for analysing Monte Carlo samples," 10 2019.

Preparing for Diphoton Resonance Searches in the Leptonic, 0-τ Final States: Event Selection and Background Characterization Using ATLAS Run 3

Kgothatso Ntumbe[1,2], Baballo-Victor Ndhlovu[1,2], Kutlwano Makgetha[1,2], Njokweni Mbuyiswa[1,2], Phuti Rapheeha[1,2,4], Reda Mekouar[3], Thabo Pilusa[1,2], Vuyolwethu Kakancu [1,2], Bruce Mellado[1,2], Mukesh Kumar[1,2], Rachid Mazini[1]

[1] School of Physics and Institute for Collider Particle Physics, University of the Witwatersrand, Johannesburg, Wits 2050, South Africa
[2]iThemba LABS, National Research Foundation, PO Box 722, Somerset West 7129, South Africa
[3]Institute of High Energy Physics, Beijing, University of Chinese Academy of Sciences, 19B Yuquan Road, Shijingshan District, Beijing, China
[4]School of Electrical Engineering, Tshwane University of Technology, Staatsartillerie Road, Pretoria West 0001, South Africa

E-mail: 2445026@students.wits.ac.za

Abstract. This work presents a preparatory study for scalar resonance searches in final states containing two photons and leptons, with events including taus explicitly vetoed, under ATLAS Run 3 conditions. The analysis targets BSM frameworks such as 2HDM+S and the Real Higgs Triplet Model, making use of background Monte Carlo samples (e.g $tt\gamma\gamma$, $\gamma\gamma jj$) and employing the EasyJet framework for event selection and kinematic investigations.The 2HDM+S and Triplet model BSM frameworks are being used to study new scalar particles that may decay into final states involving photons and leptons. In particular, these models motivate searches for di-photon signatures accompanied by leptons. This study focuses on scalar resonance production via the process $gg \to H \to SS'$, where $S \to \gamma\gamma$, and S' decays into one or more leptons and/or hadrons. Relevant decay modes of S' include τ, $\ell + b$ ($\ell = e, \mu$), and multi-body final states such as 2ℓ, 2τ, or combinations thereof. Among the various final states, particular attention is given to the channels $\gamma\gamma + \ell, 0\tau$ and $\gamma\gamma + 2\ell, 0\tau$, given their sensitivity to scalar resonances and experimental accessibility. We are currently developing analysis strategies and selection tools in preparation for the analysis of ATLAS Run 3, corresponding to $\sqrt{s} = 13.6$ TeV. The goal is to identify signal-like events while mitigating dominant SM backgrounds.

1 Introduction

The Standard Model (SM) provides a precise description of known interactions but leaves open questions such as dark matter, neutrino masses, and the matter–antimatter asymmetry, motivating searches for physics beyond the SM. Extensions of the scalar sector, including the Two-Higgs-Doublet Model with a singlet (2HDM+S) [1] and the Real Higgs Triplet Model [2], predict heavy resonances decaying to diphoton and multilepton final states accessible at the LHC. In benchmark 2HDM+S scenarios with $m_H \simeq 270$ GeV, gluon-fusion production reaches cross-sections of $\mathcal{O}(5\text{–}10)$ pb, with $H \to Sh$ and $A \to ZH$ dominating and leading to $\gamma\gamma + \ell$ and $\gamma\gamma + 2\ell$ final states [1]; representative branching ratios are shown in Fig. **??**. These signatures exploit the excellent photon resolution and clean prompt-lepton reconstruction in ATLAS, while the main backgrounds arise from $\gamma\gamma jj$, $t\bar{t}\gamma\gamma$, and $V\gamma\gamma$ production. This work develops a preparatory analysis for ATLAS Run 3 using the EasyJet framework, employing background Monte Carlo samples to define selections, calibrations, and cutflows. At this stage, signal samples are still in production, but the background-driven studies presented here provide the basis for future sensitivity analyses once signal is incorporated.

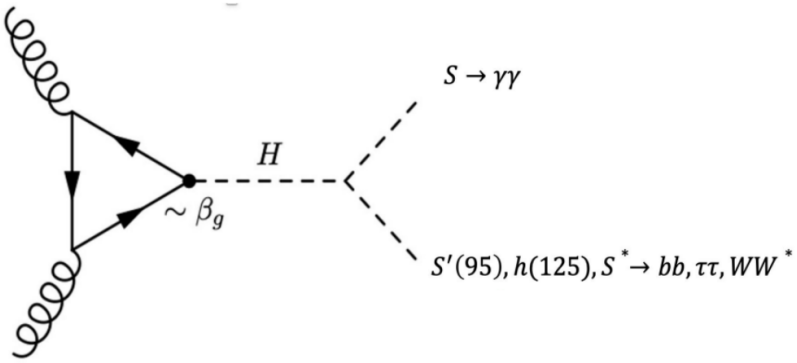

Figure 1: Feynman diagram illustrating the production of a heavy scalar resonance H via gluon-gluon fusion, mediated by a top loop with coupling $\sim \beta_g$. The resonance decays into two lighter scalars: $S \to \gamma\gamma$ and S', where S' can be either a new scalar ($S'(95)$), the SM-like Higgs boson ($h(125)$), or another scalar state. The S' decays into final states such as $b\bar{b}$, $\tau^+\tau^-$, or off-shell W^+W^-, leading to rich experimental signatures[1].

State	Dominant Decays	BR [%]
$H(270)$	$H \to Sh$	~ 70
	$H \to VV, f\bar{f}$	10 each
$S(150)$	$S \to \gamma\gamma$	~ 10
	$S \to b\bar{b}$	~ 60
	$S \to VV$	~ 20
$A(400)$	$A \to ZH$	~ 80
	$A \to t\bar{t}$	10

Table 1: Illustrative branching ratios (BRs) for benchmark 2HDM+S scenarios with $m_H \simeq 270$ GeV [1]. Values are approximate and shown for representative channels relevant to $\gamma\gamma + \ell$ final states.

2 Background Characterization

In the absence of signal samples, our current analysis strategy is driven by a detailed study of relevant Standard Model (SM) background processes. These backgrounds serve as a testbed for developing and validating object reconstruction, event selection, and calibration procedures within the `Easyjet` framework[3]. We focus on three main background categories: diphoton plus jets ($\gamma\gamma$+jets), top quark pair production with associated diphotons ($t\bar{t}\gamma\gamma$), and electroweak diboson plus diphoton production ($V\gamma\gamma$, where $V = W, Z$)[4]. The production of photons in these processes arises through several mechanisms, as illustrated by their leading-order Feynman diagrams. In the $\gamma\gamma$+jets background, photons are predominantly produced via initial-state radiation (ISR) from incoming quarks or gluons, as well as from final-state radiation (FSR) off outgoing partons. In $t\bar{t}\gamma\gamma$, genuine prompt photons can

originate from top quark decay chains, particularly from radiation off top decay products, and from radiation associated with $W \to \ell\nu$ decays[5]. These diagrams also allow for diagrams with photons emitted from virtual or real intermediate bosons, enhancing their similarity to BSM diphoton signatures.

The $V\gamma\gamma$ processes, such as $W\gamma\gamma \to \ell\nu\gamma\gamma$ and $Z\gamma\gamma \to \ell\ell\gamma\gamma$, feature photons produced directly from gauge boson radiation or from radiation off the fermionic legs. These processes are especially relevant due to their final-state configurations involving genuine leptons and photons, which directly overlap with our signal region of interest. Collectively, these SM backgrounds provide a realistic environment to evaluate the performance of lepton and photon isolation criteria, test tau vetoes, and optimize event selection strategies. By using these samples to construct cutflows and kinematic distributions, we aim to ensure that the analysis is robust and scalable when simulated signal samples become available. The event selections applied to the $\gamma\gamma+1\ell,0\tau$ and $\gamma\gamma+2\ell,0\tau$final states incor-

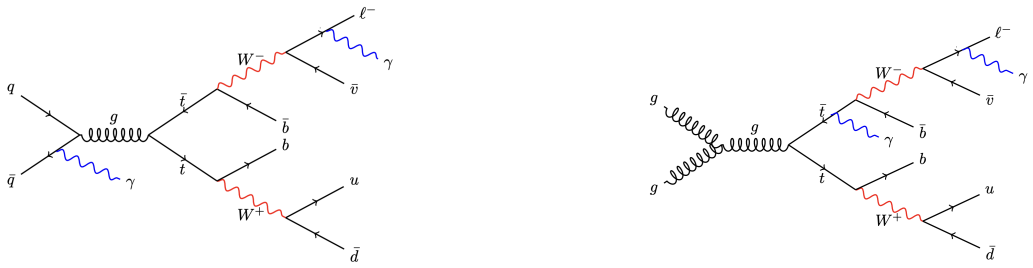

(a) ISR + FSR photon emission in $q\bar{q} \to t\bar{t}$.

(b) FSR photon emission in $gg \to t\bar{t}$.

Figure 2: Representative Feynman diagrams contributing to the $\gamma\gamma+2\ell$ final state in $t\bar{t}\gamma\gamma$ production. (a) Initial-state radiation (ISR) from the quark leg and final-state radiation (FSR) from the $W^- \to \ell\bar{\nu}$ decay. (b) Gluon-gluon fusion with one photon radiated from the $\bar{t}$ line and another from the leptonically decaying W^- boson. These configurations are important irreducible backgrounds in resonance searches involving photons and leptons[5].

porates strict requirements on photon and lepton reconstructions to ensure signal-like quality while suppressing background contributions. Photon candidates must pass Loose identification and FixedCutLoose isolation working points, both of which have been extensively validated in ATLAS Run 2 using 2015-2017 data [6, 7]. The identification criteria rely on shower shape variables and calorimeter cluster information, while isolation selections suppress contributions from nearby hadronic activity. As reflected in Table 2, approximately 76% of the events in the $t\bar{t}\gamma\gamma$ sample pass the photon ID and isolation criteria, in line with reported efficiencies for photon transverse momenta above 25-35 GeV and $|\eta| < 2.37$.

The feasibility of the $\gamma\gamma+\ell$ and $\gamma\gamma+2\ell$ channels relies on efficient online selection. For ntuple production, the following Run 3 trigger chains were used:

- **2022:** `HLT_g35_medium_g25_medium_L12EM20VH`, `HLT_2g50_loose_L12EM20VH`, `HLT_2g22_tight_L12EM15VHI`.
- **2023:** `HLT_g35_medium_g25_medium_L12eEM24L`, `HLT_2g50_loose_L12eEM24L`, `HLT_g45_medium_g20_medium_L1eEM40L_2eEM18L`, `HLT_2g22_tight_L12eEM18M`.
- **2024:** `HLT_g35_medium_g25_medium_L12eEM24L`.

The trigger menus combine diphoton thresholds of $\mathcal{O}(25\text{–}50)$ GeV with medium/tight identification and photon+lepton seeds, ensuring high efficiency for $S \to \gamma\gamma$ decays with isolated leptons. Trigger-level isolation reduces fake backgrounds, and the logical OR of chains secures nearly full acceptance. Photons are required to have $p_T > 25$ GeV and $|\eta| < 2.37$ (excluding $1.37 < |\eta| < 1.52$), with tight ID and isolation. Electrons ($p_T > 25$ GeV, $|\eta| < 2.47$) and muons ($p_T > 25$ GeV, $|\eta| < 2.5$) must satisfy MediumLH/Medium ID and Loose isolation [6, 8], selections that balance efficiency and fake rejection. After lepton selection, about 73% of events remain, consistent with $t\bar{t}\gamma\gamma$ leptons from W decays passing kinematic and isolation cuts. The final 0-τ requirement enforces one or two high-quality leptons, yielding cumulative efficiencies of 38% ($\gamma\gamma+1\ell$) and 3.6% ($\gamma\gamma+2\ell$), reflecting both top branching fractions and stringent object-level criteria.

Cut Description	$\gamma\gamma+1\ell$		$\gamma\gamma+2\ell$	
	Events Passed	**Efficiency**	**Events Passed**	**Efficiency**
Total events	534144	1.0	534144	1.0
Pass Photon ID and Isolation	405764	0.76	405764	0.76
Pass Photon Selections	405558	0.74	405558	0.74
Pass Lepton Selections	392068	0.73	392068	0.73
Final Selection (1ℓ or $2\ell+0\tau$)	201682	0.38	19028	0.036

Table 2: Cutflow comparison for the $\gamma\gamma+1\ell$ and $\gamma\gamma+2\ell$ final states using simulated $t\bar{t}\gamma\gamma$ events. The table shows the number of events passing each selection step and the corresponding relative efficiency, normalized to the total number of events.

3 Results

The results presented in this section are entirely based on Standard-Model background simulations, as signal Monte Carlo samples are currently in production and not yet available. We focus on the kinematic properties of photons and leptons in the $\gamma\gamma+1\ell$, 0-τ and $\gamma\gamma+2\ell$, 0-τ final states, currently using the $t\bar{t}\gamma\gamma$ sample as representative background. This sample allows us to study the characteristic distributions of key observables such as photon transverse momenta, diphoton invariant mass, lepton kinematics, angular separations, and missing transverse energy. While these distributions do not yet include contributions from potential BSM signals, they form the baseline for selection tuning and shape analysis. The insights gained here will inform future signal-region optimization and cut-based or multivariate strategies once signal samples are available. Object kinematics: $\gamma\gamma+1\ell,0\tau$ using the $t\bar{t}\gamma\gamma$ sample

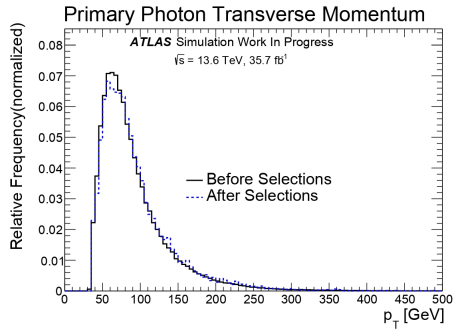

(a) Lead photon p_T

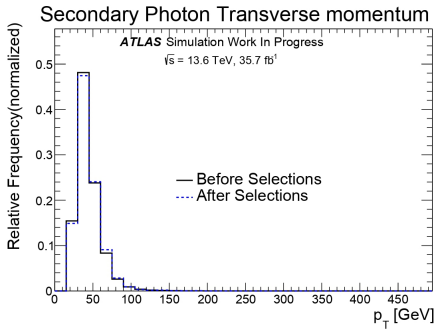

(b) Sublead photon p_T

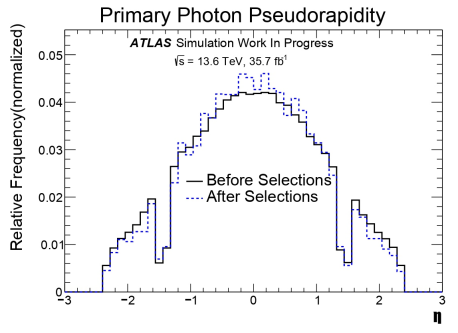

(c) Lead photon η

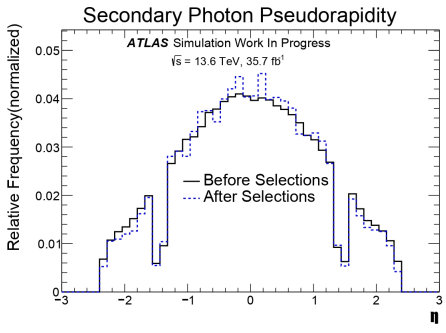

(d) Sublead photon η

Figure 3: Photon kinematic distributions for the above-mentioned $\gamma\gamma+leptons$, 0-τ final state. Top row: transverse momentum distributions show thresholds at $p_T = 35$ GeV (leading) and 25 GeV (subleading) due to event selection. Middle row: pseudorapidity distributions reveal dips around $|\eta| \approx 1.5$, corresponding to the calorimeter transition region[5] excluded by selection. These distributions are derived from the $tt\bar{\gamma}\gamma$ Ntuple sample used.

We begin by looking at object-level selection, by exploring our photon-object kinematics from the $t\bar{t}\gamma\gamma$ Ntuple, looking at the transverse momentum and pseudorapidity.

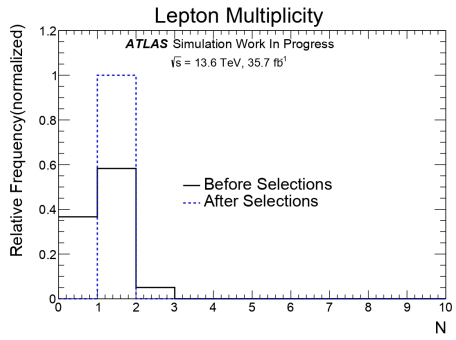

(a) Total lepton count per event.

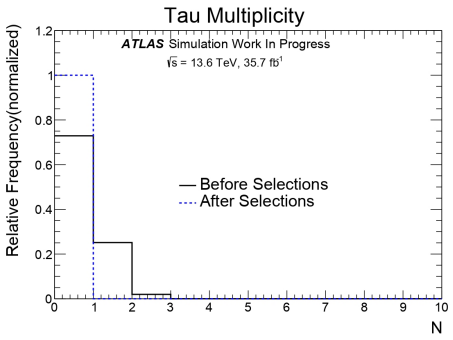

(b) Tau multiplicity per event.

Figure 4: Total lepton and tau multiplicity distributions before and after selection. The lepton count plot confirms the selection's focus on $\gamma\gamma + 1\ell, 0\tau$ final state. The tau distribution shows a sharp suppression after selection, indicating that the 0-τ veto is functioning effectively to exclude events containing hadronically decaying tau candidates.

3.1 Object kinematics: $\gamma\gamma + 2\ell, 0\tau$ using the $t\bar{t}\gamma\gamma$ sample

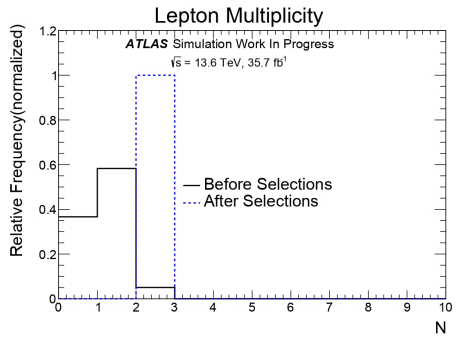

(a) Total lepton multiplicity per event.

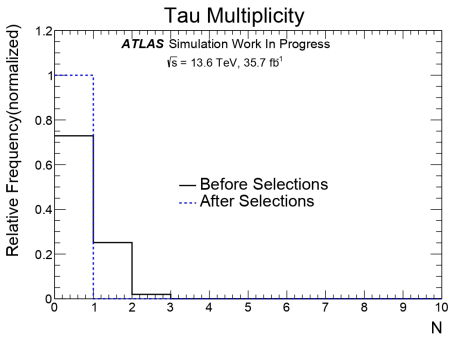

(b) Tau multiplicity per event.

Figure 5: Lepton and tau multiplicity distributions before and after event selection for the $\gamma\gamma + 2\ell, 0\tau$ final state. Panel (a) shows a sharp concentration at two leptons after selection, matching the signal topology. Panel (b) confirms effective suppression of events containing tau candidates, validating the 0-τ requirement. The small residual tau contamination before selection is removed by applying hadronic tau vetoes.

4 Conclusion

This study presents the development and validation of an event selection strategy for diphoton final states in the $\gamma\gamma + 1\ell, 0\tau$ and $\gamma\gamma + 2\ell, 0\tau$ channels, targeting scalar resonance decays predicted by models such as 2HDM+S. Using the $t\bar{t}\gamma\gamma$ background sample, we established baseline distributions and evaluated kinematic properties of photons and leptons under ATLAS Run 3-like conditions. Our analysis applied strict selection criteria based on established ATLAS identification and isolation recommendations for photons, electrons, and muons, achieving efficient suppression of hadronic tau contamination as confirmed by tau multiplicity distributions.

The object-level studies demonstrated the effectiveness of the implemented selections in shaping signal-like topologies from background-rich samples. Lepton and tau multiplicities, as well as photon kinematic distributions, all reflect the designed event categories, validating our initial strategy. These distributions serve as reference benchmarks for later inclusion of signal Monte Carlo, which is currently in production.

Furthermore, the EasyJet framework provided a modular and reproducible infrastructure for this preparatory study, allowing rapid testing and refinement of cuts. The insights gained here are essential for optimizing future analyses targeting new physics in diphoton and multilepton final states. Once signal samples are incorporated, we will extend this work toward sensitivity studies and potential resonance reconstruction, contributing to the broader ATLAS BSM search program during Run 3.

References

[1] S. von Buddenbrock, A. S. Cornell, E. D. R. Iarilala, M. Kumar, B. Mellado, X. Ruan, and E. M. Shrif, "Constraints on a 2hdm with a singlet scalar and implications in the search for heavy bosons at the lhc," *Journal of Physics G: Nuclear and Particle Physics*, vol. 46, no. 11, p. 115001, Sep. 2019. [Online]. Available: http://dx.doi.org/10.1088/1361-6471/ab3cf6

[2] S. Ashanujjaman, S. Banik, G. Coloretti, A. Crivellin, S. P. Maharathy, and B. Mellado, "Anatomy of the real Higgs triplet model," *JHEP*, vol. 04, p. 003, 2025.

[3] Easyjet Collaboration, "Easyjet framework," https://gitlab.cern.ch/easyjet/easyjet, 2024, accessed: July 2025.

[4] ATLAS Collaboration, "Measurement of $Z\gamma\gamma$ production in pp collisions at $\sqrt{s} = 13$TeV with the ATLAS detector," *Eur. Phys. J. C*, 2023, arXiv:2211.14171.

[5] ATLAS Collaboration, "Observation of $t\bar{t}\gamma\gamma$ production at $\sqrt{s} = 13$ tev with the atlas detector," *arXiv e-Print*, vol. arXiv:2506.05018, 2025. [Online]. Available: https://arxiv.org/abs/2506.05018

[6] ATLAS Collaboration, "Electron reconstruction and identification in the ATLAS experiment using the 2015 and 2016 LHC proton–proton collision data at $\sqrt{s} = 13$ tev," *The European Physical Journal C*, vol. 79, no. 8, 2019. [Online]. Available: http://dx.doi.org/10.1140/epjc/s10052-019-7140-6

[7] ATLAS COLLABORATION, "Electron and photon efficiencies in lhc run 2 with the atlas experiment," *JHEP*, vol. 2024, no. 5, 2024. [Online]. Available: https://doi.org/10.1007/JHEP05(2024)162

[8] ATLAS Collaboration, "Muon reconstruction and identification efficiency in atlas using the full run 2 pp collision data set at $\sqrt{s} = 13$ tev," *The European Physical Journal C*, vol. 81, no. 7, 2021. [Online]. Available: http://dx.doi.org/10.1140/epjc/s10052-021-09233-2

Study of Low-Medium Spin States in ^{156}Er

N.N Khanyeza[1,3], S.N.T Majola[2], T.T Hlatshwayo[1], B.V Kheswa[2] and P.L Masiteng[2]

[1]Department of Physics, University of Pretoria, Hatfield 0028, South Africa
[2]Department of Physics, University of Johannesburg, Auckland Park 2006, South Africa
[3]Council of Scientific and Industrial Research, Pretoria 0001, South Africa

E-mail: nqobi.khanyeza1@gmail.com

Abstract. This study investigates the low to medium spin states of the nucleus ^{156}Er through the analysis of the gamma-gamma coincidence relationships following the ^{147}Sm(^{12}C, 3n)^{156}Er reaction at 65 MeV. The experiment was performed using the African Omni-purpose Detector for Innovative Techniques and Experiments (AFRODITE) array at iThemba LABS. From the collected data, a detailed nuclear level scheme was constructed, leading to the identification of nine rotational bands. The present study confirms nearly all previously reported bands while also proposing modifications to certain band assignments. These results provide new insights into the nuclear structure of ^{156}Er and contribute to a deeper understanding of shape evolution in the $A \sim 160$ mass region.

1 Introduction

Nuclei with neutron numbers $N = 88$–92 are well-known examples for studying normal deformed states at high angular momentum [1]. These studies have helped us better understand how nuclear shapes change as angular momentum increases and how different particles align inside the nucleus.

This work focuses on the rare-earth nucleus ^{156}Er, which contains 68 protons and 88 neutrons. It lies in the middle of the rare-earth region, where nuclei transition from nearly spherical shapes to well deformed quadrupole structures. Over the last 20 to 30 years, ^{156}Er has been studied extensively [2, 3, 4], both experimentally and theoretically, particularly at high spin states due to its abundant physics. However, its structure at low to medium spin is still not fully understood, which is why there is growing interest in studying it further.

For example, Rees *et al.* [5] found that ^{156}Er might be soft in the gamma direction, meaning it can easily change between different non-axial shapes. They also suggested that $(\nu h_{9/2}, f_{7/2})$ rotationally aligned structures exist alongside the usual $\nu(i_{13/2})^2$ particle alignments seen in nuclei around mass 150-160. Before this, such a phenomenon was only seen in ^{163}W [6] and ^{161}Ta [7].

A review of the existing data indicates that an incorrect assignment may have led to the mischaracterisation of the above mentioned phenomenon in ^{156}Er. Therefore, accurate parity assignment is important for determining the underlying configuration and for interpreting the alignment behaviour.

In effect, this study aims to investigate the spectroscopy of ^{156}Er, particularly the band associated with the aligned $(\nu h_{9/2}, f_{7/2})^2$ configuration with the aim to best the validity of the above mentioned, which suggests that competing alignment exists in the A $\sim$ 150-160 region.

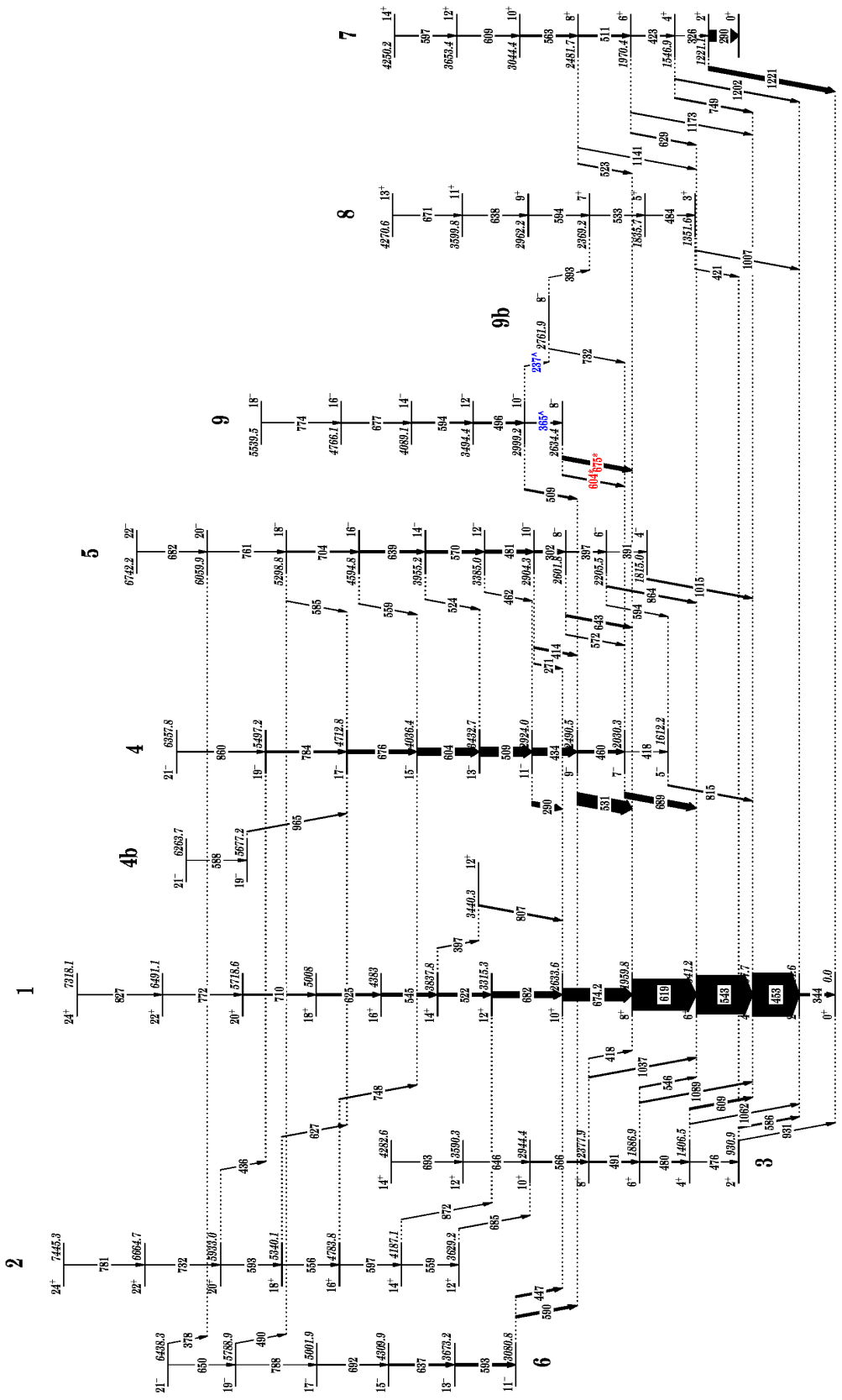

Figure 1: Level scheme deduced for ^{156}Er, populated via the $^{147}\mathrm{Sm}(^{12}\mathrm{C}, 3n)^{156}\mathrm{Er}$ reaction at 65 MeV. Transition energies are in keV, with arrow widths proportional to the measured relative intensities. Newly observed transitions are shown in red with an asterisks(*) and updated transitions from previous work in blue with a caret (^).

2 Experimental Method and Data Analysis

The nucleus ^{156}Er was produced using the fusion-evaporation reaction $^{147}\mathrm{Sm}(^{12}\mathrm{C}, 3n)^{156}\mathrm{Er}$. This reaction was carried out at a beam energy of 65 MeV, chosen to maximise the cross section for the 3 neutron evaporation channel while minimising competing channels such as 2 neutron and 4 neutron reactions, thereby favouring the population of low to medium spin states in ^{156}Er. The experiment was conducted at the iThemba Laboratory for Accelerator Based Sciences (iThemba LABS) in Cape Town, South Africa. A ^{12}C ion beam was accelerated by the Separated-Sector Cyclotron (SSC) and delivered to a self-supporting enriched ^{147}Sm target with a thickness of 6 mg/cm^2.

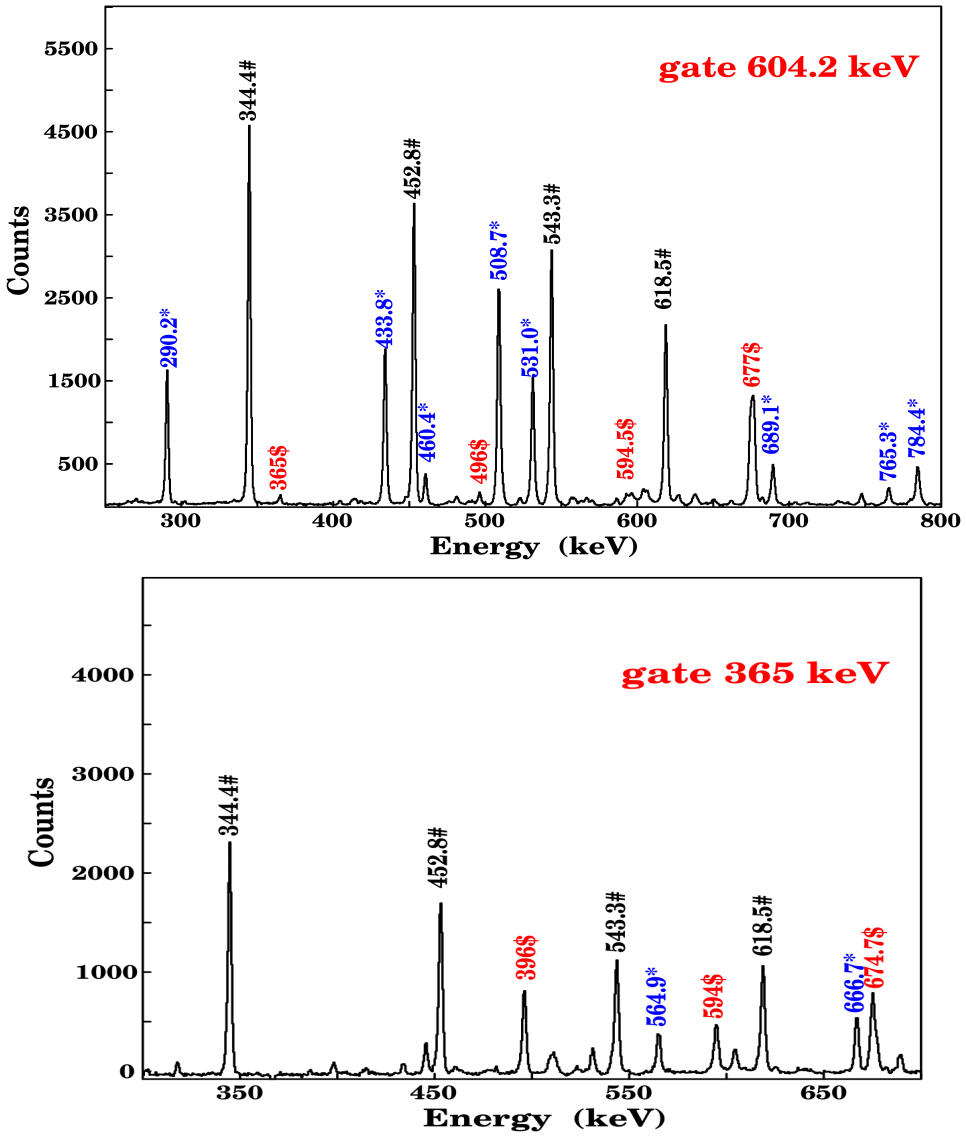

Figure 2: (*Top*) Spectrum showing the gamma rays in coincidence with the 604.2 keV transition. (*Bottom*) Spectrum showing the gamma rays in coincidence with the 365 keV transition. In both spectra, the transitions belonging to Band 9 are coloured in red and marked with a dollar sign ($). Other transitions belonging to ^{156}Er are shown in blue and marked with an asterisk (*), while transitions belonging to the ground state band are shown in black and marked with a hash symbol (#).

Gamma rays emitted from the excited nucleus were detected using the AFRODITE gamma ray spectrometer. AFRODITE is an acronym for the African Omnipurpose Detector for Innovative Techniques and Experiments [8]. It is an array capable of detecting both high and low energy photons with high efficiency. This is achieved by

combining large volume escape-suppressed High Purity Germanium CLOVER detectors, suited for high resolution spectroscopy, with Low Energy Photon Spectrometer detectors for enhanced sensitivity to low energy transitions. At the time of the experiment, the AFRODITE array consisted of eight Compton suppressed CLOVER-type HPGe detectors arranged to optimise angular coverage and coincidence detection efficiency. Each CLOVER detector was fitted with absorbers composed of 0.15 mm of tin followed by 0.07 mm of brass. This configuration was used to suppress low energy X-rays and Compton background, thereby enhancing the clarity of the gamma ray.

Data collection was carried out using a gamma gamma coincidence trigger and spanned five continuous days, during which approximately 1.4×10^9 gamma gamma coincidence events were recorded [3]. The raw data were then calibrated, gain matched and sorted into a symmetric gamma gamma coincidence matrix using the MIDAS[1] data acquisition system and the MTSort offline sorting package. MIDAS handled real time digitisation and event building, while MTSort converted time stamped raw events into a matrix format compatible with RADWARE[2] analysis software.

The sorted matrix formed the basis for both the initial and present analyses. The RADWARE software suite was used for further offline processing: `GF3` was used for peak fitting of the gamma ray spectra, while `ESCL8R` was used to construct and update the level scheme of ^{156}Er. While the initial analysis produced a preliminary level scheme, the present secondary analysis focused on a more detailed investigation of Band 9, whose structure and spin parity assignments remained partially unresolved in previous work [5]. Gated coincidence spectra were used to verify known transitions and to explore possible new or extended placements within the band structure. The outcomes of this analysis will guide future Directional Correlation of Oriented States ratio measurements, which are expected to confirm multipolarities and refine spin parity assignments in ^{156}Er.

3 Results

Nine rotational bands were identified in ^{156}Er, with observed states extending up to a maximum spin-parity of 24^+.

A new configuration of Band 9 was established. The 365 keV gamma ray, previously believed to connect the 2999.2 keV level in Band 9 to the yrast 10^+ state in Band 1, was observed to feed a newly identified band head.

Coincidence relationships observed in the gated spectra provide additional evidence regarding the structure of Band 9. The 495.8 keV transition is observed in coincidence with the 604.2 keV transition, but not with the 603.7 keV transition. The 365 keV transition appears in coincidence with both the 495.8 keV and 604.2 keV transitions. Additionally, the 674.7 keV transition is observed in coincidence with the 365 keV transition, whereas the 674.2 keV transition is not.

Alignment analysis as a function of rotational frequency was plotted for Bands 1, 2, 4, 5, and 9. Band 9 exhibited an alignment of approximately 7.5 $\hbar$. Alignments are shown in Figure 3a.

4 Discussion

The observed spin-parity of 24^+ in this experiment is lower than the 46^+ states reported by Rees *et al.* [5], who used a heavier ^{48}Ca beam at 215 MeV, compared to the ^{12}C beam at 65 MeV used in this work. The lower energy and lighter ion in our experiment favour the population of low to medium spin states, while the higher energy, heavier ion used by Rees *et al.* contributes more angular momentum, allowing access to higher-spin levels.

Further support for this revised assignment comes from the alignment data. Band 9 shows an alignment of approximately 7.5 $\hbar$, which is lower than that observed in Band 1 and is typical of negative-parity two-quasiparticle bands. In contrast, Band 1 displays higher alignment values consistent with the alignment of $i_{13/2}$ neutrons.

This alignment behaviour is also seen in other negative-parity bands within ^{156}Er, as illustrated in Figure 3b. These bands exhibit similar rotational properties and alignment values in the range of 6–7.5 $\hbar$, indicating that they likely share a comparable two-quasiparticle configuration. The consistency across bands strengthens the interpretation that Band 9 follows the same structural trends typical of negative-parity configurations in the $A \sim 160$ mass region.

Similar alignment trends have also been reported in neighbouring nuclei such as ^{156}Dy, where negative-parity bands typically align between 6 and 7 $\hbar$ [9]. This reinforces the argument that Band 9 in ^{156}Er likely has negative parity.

These coincidence relationships support a revised configuration of Band 9. The 365 keV gamma ray, previously believed to connect the 2999.2 keV level in Band 9 to the yrast 10^+ state in Band 1, is now interpreted to feed a newly identified band head. The presence of strong coincidence between the 365 keV, 495.8 keV, and 604.2 keV transitions, and the absence of coincidence with the 603.7 keV and 674.2 keV transitions, suggests that the 365 keV transition feeds Band 9 via the 674.7 keV transition, not Band 1. This is supported by the gated spectra shown in Figure 2, where the 365 keV transition appears in both the 604.2 keV- and 674.7 keV-gated spectra.

[1] `http://nnst.dl.ac.uk/MIDAS/manual/MTsort/edoc033`

[2] `http://radware.phy.ornl.gov/rw/esclev/esclev.html`

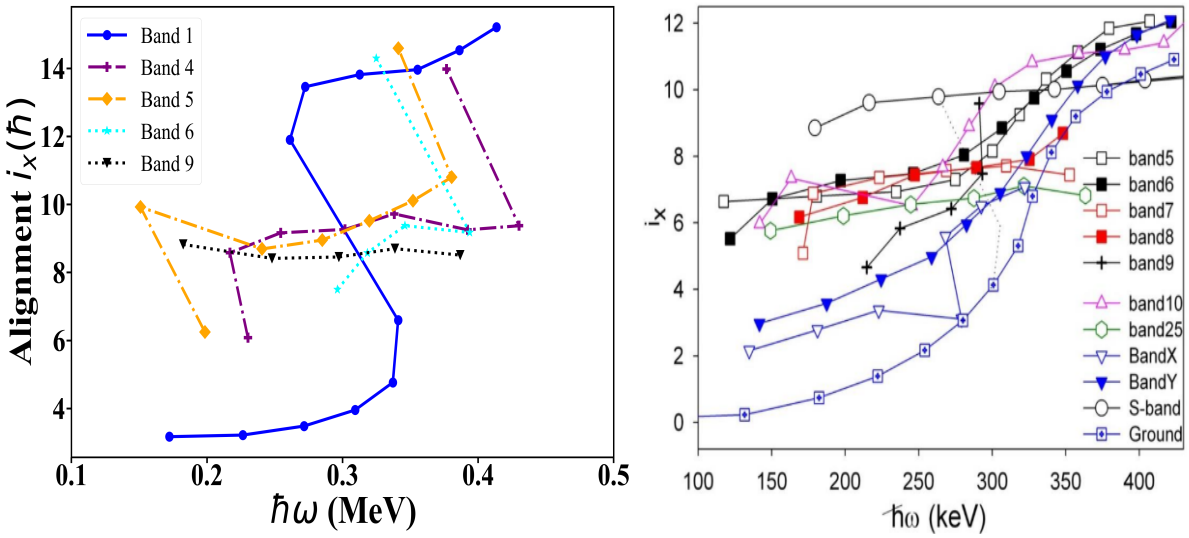

(a) Measured alignments, i_x, as a function of rotational frequency, ω, for the negative parity bands in ^{156}Er.

(b) Measured alignments, i_x, as a function of rotational frequency, $\hbar\omega = 0.2$, for different bands observed in ^{156}Dy [9].

Figure 3: Measured alignments, i_x, as a function of rotational frequency, ω. (*a*) Band 9 in ^{156}Er, originally assigned positive parity based on the $(\nu h_{9/2}, f_{7/2})$ configuration, showing lower alignment ($\sim 7.5\ \hbar$) than typical $i_{13/2}$ alignments. (*b*) Multiple negative-parity bands in neighbouring nuclei, also around 7.5 $\hbar$, supporting that Band 9's parity was likely misassigned.

The reassignment of the 365 keV gamma ray transition in andand 9 significantly impacts the interpretation of its structure. This, together with strong stretched $E2$ cross-band transitions at 591 keV and 386 keV between bands 5 and 9, suggests strong mixing between the 2999.2 keV level in Band 9 and the 2904.3 keV level in band 5.

Such mixing is only allowed between states with the same spin and parity, which implies that the 2999.2 keV level must have spin parity 10^-, supporting a negative-parity assignment for Band 9. This contrasts with the earlier interpretation by Rees *et al.* [5], who assigned positive parity based on a proposed $(f_{7/2}, h_{9/2})$ configuration.

To confirm the revised spin-parity assignments, further work is needed. Planned steps include Directional Correlation from Oriented states (DCO) ratio and polarization measurements and theoretical modelling using approaches such as configuration-constrained or cranked shell model calculations. These studies will help clarify the nature of the rotational bands in ^{156}Er and may contribute to broader applications in gamma ray detection.

5 Conclusion

This study investigated low- to medium-spin states in ^{156}Er using a γ-γ coincidence analysis of data from the ^{147}Sm(^{12}C,3n)^{156}Er reaction at 65 MeV. The experiment, conducted at iThemba LABS using the AFRODITE spectrometer, yielded approximately 1.4×10^9 coincidence events. A key outcome of this secondary analysis was the reassignment of the 365 keV transition in Band 9. Rather than linking to the 10^+ state in Band 1 as previously proposed, this transition appears to feed a newly identified band head.

These findings challenge the earlier positive-parity interpretation by Rees *et al.* [5] and align well with observed trends in negative-parity bands across the rare-earth region, including neighbouring nuclei such as ^{156}Dy.

In order to confirm the validity of our interpretation, future work should focus on performing DCO ratio and polarization measurements to confirm multipolarities and refine spin-parity assignments. Theoretical modelling will also be essential to validate the proposed band structures and further elucidate the role of quasiparticle configurations of band in question (band 9) in ^{156}Er. If confirmed to be true these findings contribute to a deeper understanding of quasiparticle alignments and structural evolution in even-even nuclei within the $A \sim 160$ mass range.

References

[1] J. Simpson *et al.*, "High-spin gamma -ray spectroscopy of ^{165}W and ^{166}W," *Journal of Physics G: Nuclear and Particle Physics*, vol. 18, no. 7, p. 1207, 1992.

[2] M. Shayestefar and A. Kardan, "Structures of terminating bands in er isotopes," *Nuclear Physics A*, vol. 1046, p. 122871, 2024.

[3] M. Stankiewicz, "Physics of low and intermediate spin states of atomic nuclei in the mass a∼160 region," Ph.D. dissertation, University of Cape Town, 2012.

[4] F. Stephens, *High-spin properties of some nuclei around A=160*. North-Holland., 1985.

[5] J. Rees *et al.*, "Non-yrast positive-parity structures in the γ-soft nucleus ^{156}Er," *Phys. Rev. C*, vol. 83, p. 044314, 2011.

[6] J. Thomson *et al.*, "Competing quasiparticle configurations in ^{163}W," *Phys. Rev. C*, vol. 81, p. 014307, Jan 2010.

[7] K. Lagergren *et al.*, "γ-soft shapes and quasiparticle excitations in $^{161}_{73}\mathrm{ta}_{88}$," *Phys. Rev. C*, vol. 83, p. 014313, 2011.

[8] E. Gueorguieva, R. Bark, T. Hlatshwayo *et al.*, *Nuclear spectroscopy with the AFRODITE -ray array at iThemba labs*. Prime Time Education, Jan. 2005.

[9] S. Majola, "Exploring the spectroscopy of vibrational levels in the 160 mass region," Ph.D. dissertation, University of Cape Town and iThemba LABS, 2015.

Orthogonality study for the $S \to Z_d Z_d \to 2\ell 2\nu/2\ell 2j$ with the ATLAS detector at the LHC

Doomnull Unwuchola[1], Lerothodi Leeuw[1], Michiel Veen[2], Loan Truong[3], Simon Connell[3], Rafael Coelho Lopes De Sa[2], Ketevi Assamagan[4]

[1]Department of Physics and Astronomy, University of the Western Cape, Cape-Town, South Africa.

[2]Department of Physics, University of Massachusetts, Massachusetts, U.S.A.

[3]Department of Mechanical Engineering Sciences, University of Johannesburg, Johannesburg, South Africa.

[4]Brookhaven National Laboratory, New York, USA.

E-mail: doomnull@gmail.com

Abstract. The Hidden Abelian Higgs Model is used for a search for an additional scalar decaying to two Z-dark bosons (Z_d) to two leptons ($\ell = e, \mu$) and two neutrinos ($2\ell 2\nu$). The search uses pp collision data collected with the ATLAS detector at the LHC with an integrated luminosity of 140 fb^{-1} at a centre-of-mass energy of $\sqrt{s} = 13$ TeV. This is a complementary follow-up to the study of the 4ℓ final states. In the $2\ell 2\nu$ channel analysis, the same data of Run-2 with the ATLAS detector is used to search for an additional scalar with a distinct mass from the Higgs boson. A technique is introduced to separate signal events of the $2\ell 2j$ channel from that of the $2\ell 2\nu$ channel using Monte-Carlo simulated data. This work presents the technique and result of the orthogonality study done to achieve this.

1 Introduction

The Standard Model (SM) explains a wide range of phenomena but leaves unanswered questions such as the origin of dark matter [1–5]. The Hidden Abelian Higgs model (HAHM) [1] is a Beyond Standard Model (BSM) theory that can provide a viable dark matter (DM) candidate. This asserts a 'hidden' or 'dark' sector of particles and fields, including a field having a $U(1)_{\text{d}}$ symmetry that mixes kinetically with the SM $U(1)_{\text{Y}}$ hypercharge gauge field by some coupling strength ϵ, and a dark Higgs symmetry breaking mechanism that mixes with the SM Higgs boson by some coupling strength κ. All that results in an additional scalar boson S along with a new gauge boson Z_d or 'dark photon' [6–8]. Motivated by the HAHM model, the search of $S \to Z_d Z_d \to 2\ell 2\nu$, along with the search for $S \to Z_d Z_d \to 2\ell 2j$ with the respective signal Feynman diagrams shown in Figure 1, is a complementary follow-up to the study of the 4ℓ final states [9] where $\ell = e, \mu$.

Assuming a SM-like universality for the decay of Z_d to leptons, the $2\ell 2\nu$ channel is expected to have more events and higher sensitivity because the Branching Ratio in the Standard Model is: $BR(ZZ \to 2\ell 2\nu) = 6 \times BR(ZZ \to 4\ell)$. The background composition is largely driven by Z + jets events, with subleading contributions from non-resonant dilepton, diboson, and fake-lepton processes. To suppress the background our chosen mass range is $m_S \leq 183$ GeV and $m_{Z_d} < 70$ GeV. Considering the potential overlapping signatures due to misreconstructed jets and missing transverse momentum ($E_{\text{T}}^{\text{miss}}$) involved in the $2\ell 2j$, a clear identification of events for $2\ell 2j$ channel is essential for the separation (orthogonality) from that of the $2\ell 2\nu$ channel.

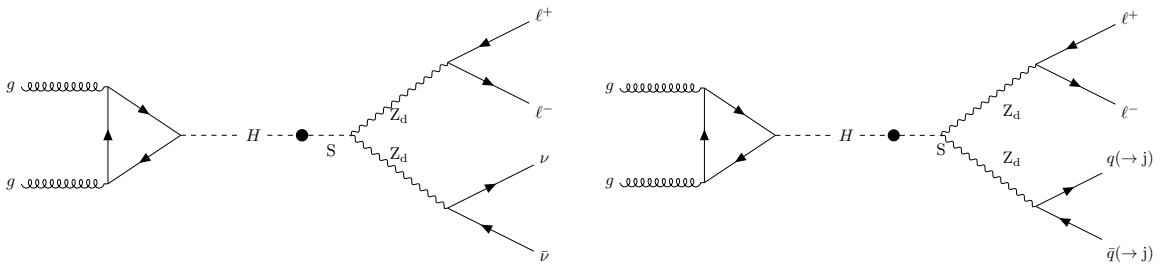

Figure 1: (*left*) The Feynman diagram for the $2l2\nu$ channel. (*right*) The Feynman diagram for the $2\ell2j$ channel.

2 Object and Event Selection

The ATLAS experiment [10] uses a right-handed coordinate system with its origin at the nominal interaction point (IP) in the centre of the detector and the z-axis along the beam pipe. The x-axis points from the IP to the centre of the LHC ring, and the y-axis points upwards. Polar coordinates (r, ϕ) are used in the transverse plane, ϕ being the azimuthal angle around the z-axis[1]. The object and event selection is crucial for isolating events consistent with the $2\ell2\nu$/$2\ell2j$ final states. Event selection begins with the basic quality preselection and the identification of leptons.

Preselection begins with the definition of the target signal region and base object requirements. In the description below, selections are applied for both analyses unless stated otherwise. For the electrons, baseline selection requires a minimum transverse momentum p_{T} of 7 GeV, pseudorapidity in $|\eta| < 2.47$, and fulfillment of the medium ID criteria [9, 11, 12]. For the $2\ell2j$ channel where mis-reconstructed jets contribute to the $E_{\mathrm{T}}^{\mathrm{miss}}$, the electrons must not come from the wrong calorimeter groups, and for both analyses the electrons must have a longitudinal impact parameter $|z_0 \sin\theta| < 0.5\,\mathrm{mm}$ which ensures that they are associated with the primary vertex. Similar quality requirements apply to muons, with a minimum p_{T} of 5 GeV for standard muons or 15 GeV for calorimeter-labeled muons, and a pseudorapidity $|\eta| < 2.47$. The muons must meet medium ID and impact parameter requirements, with exemptions granted for stand-alone muons [9, 11, 12]. The endcap and forward regions are instrumented with LAr calorimeters for EM and hadronic energy measurements up to $|\eta| = 4.9$, so jets are required to have p_{T} > 30 [GeV] and $|\eta| < 4.5$. The b-jets are vetoed and selections on the various $E_{\mathrm{T}}^{\mathrm{miss}}$ related variables [13] in the event selection criteria in this study are replaced by a Neural Network score. For the event selection, the kinematic selections on leptons are p_{T} > 20, 10 [GeV] and $\Delta R_{\ell\ell} > 0.2$.

For the $2\ell2j$ final state, a likelihood function that will select events where the di-lepton mass matches the di-jet mass is proposed. The orthogonality study was done on the final states with $S \to Z_d Z_d \to 2\ell2j$ production where its appropriate Z_d can be reconstructed. For events where one of the jets is not reconstructed, they cannot be used for $2\ell2j$, so they are classified as $2\ell2\nu$. For events with 2 or more jets, we use the likelihood function.

To have both low and high scalar bosons' masses m_S, and to have both constrained ($m_S = 2\,m_{Z_d}$) and unconstrained ($m_S > 2\,m_{Z_d}$) points, the mass points used in this study are [m_S , m_{Z_d}] : [70, 20], [70, 35], [84, 31], [110, 30], [110, 55] and [183, 50] GeV.

3 The likelihood definition

The likelihood function, L, is defined to evaluate the compatibility between the dijet and dilepton systems [14–16]:

$$L = \max_{j_1,j_2} \max_{E_1,E_2} \mathrm{G}(m_{jj}(E_1,E_2) - m_{\ell\ell} \mid 0,5) \times \mathrm{G}(E_1 \mid E_{j_1}, \sqrt{E_{j_1}}) \times \mathrm{G}(E_2 \mid E_{j_2}, \sqrt{E_{j_2}}), \tag{1}$$

where G is a Gaussian distribution $\mathrm{G}(x \mid \mu, \sigma)$; E_{j_1}, E_{j_2} represent the measured jet energies; E_1, E_2 represent the hypothetical jet energies tested in the maximisation; and $m_{\ell\ell}$ is the measured dilepton invariant mass given as:

$$m_{\ell\ell} = \sqrt{(E_1 + E_2)^2 - (\vec{p}_1 + \vec{p}_2)^2}. \tag{2}$$

Here, E_1, E_2 are the measured lepton energies, and $\vec{p}_1, \vec{p}_2$ are the three-momenta of the leptons. Then, $m_{j_1 j_2}$ is the measured or initial dijet mass, computed from the four-momenta of jet 1 and jet 2 before any energy rescaling.

[1]The pseudorapidity η is defined in terms of the polar angle θ as $\eta = -\ln\tan(\theta/2)$ and is equal to the rapidity $y = \frac{1}{2}\ln\left(\frac{E+p_z}{E-p_z}\right)$ in the relativistic limit. Angular distance is measured in units of $\Delta R = \sqrt{(\Delta y)^2 + (\Delta\phi)^2}$ [9, 10].

It is a fixed value, given by the invariant mass formula:

$$m_{j_1 j_2} = \sqrt{(E_{j_1} + E_{j_2})^2 - (\vec{p}_{j_1} + \vec{p}_{j_2})^2}. \tag{3}$$

Here, E_{j_1}, E_{j_2} are the measured jet energies, and $\vec{p}_{j_1}, \vec{p}_{j_2}$ are the three-momenta of the jets; $m_{j_1 j_2}$ is the fixed, measured dijet mass, based on detector-reconstructed jet momenta and energies. From $m_{j_1 j_2}$, the modified jet mass $m_{jj}(E_1, E_2)$ is defined to vary with the chosen values E_1 and E_2, and rescales $m_{j_1 j_2}$ when performing the likelihood maximisation. Its explicit formula is as below:

$$m_{jj}(E_1, E_2) = m_{j_1 j_2} \sqrt{\frac{E_1}{E_{j_1}}} \sqrt{\frac{E_2}{E_{j_2}}}. \tag{4}$$

Figure 2 shows the negative log-likelihood distributions for the two analyses at a given mass point before applying any specific selection. The demarcated lines mark the selections which result in the percentage of events for the $2\ell 2j$, $2\ell 2\nu$ channels and the events with less than 2 jets. This means from the total events from a masspoint of $2l2j$ simulated data: $100\%_{2\ell 2j}$ events = $[\%_{2\ell 2j} + \%_{2\ell 2\nu} + \%_{<2j}]$ events. As required by the $2\ell 2j$ sample of event selection, when not considering the less than 2-jet events, the percentages inside the parentheses as in Figure 2 are: $(100\%)_{2\ell 2j}$ of $\geq$ 2-jet events = $[(\%)_{2\ell 2j} + (\%)_{2\ell 2\nu}]$. Considering the jet energy scale and resolution measurements with their associated uncertainties in ATLAS [17], the conservative value of 5 GeV was used for the standard deviation of the modified dijet and dilepton invariant mass term [17].

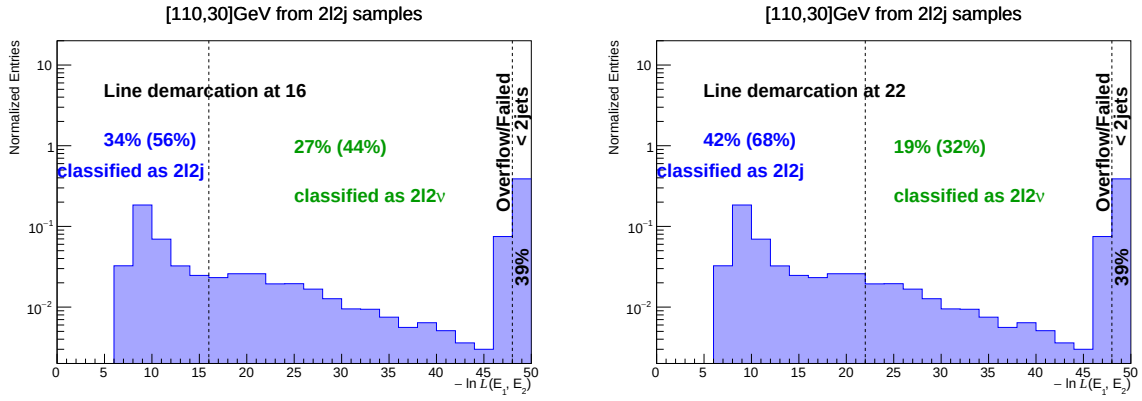

Figure 2: (*left*) The distributions of the negative log-likelihood function for mass point $[m_S, m_{Z_d}] = [110, 30]$ GeV after selecting events that have at least 2 jets. The demarcated line at value $-\ln L(\mathrm{E}_1, \mathrm{E}_2)$ = 16 separates the selected $2\ell 2j$ and $2\ell 2\nu$ events respectively. (*right*) The similar distribution as in the left plot, with the only difference is the demarcated line for the separation being at the value of $-\ln L(\mathrm{E}_1, \mathrm{E}_2)$ = 22 showing what percentage of the sample selected for $2l2j$ analysis channel and what percentage are then selected for the $2l2\nu$ analysis channel.

4 Orthogonality Strategy

The main goal is to loop over all jet pairs (j_1, j_2) of energies (E_1, E_2) in order to maximise the likelihood function L by adjusting the hypothetical jet energies E_1, E_2 to best match the dijet system to the dilepton system (to ensure that they come from Z_d particles of the same mass point). This involves penalising any mismatch between the adjusted dijet mass and the observed dilepton mass in the considered Gaussian distribution for the correspondence between the reconstructed mass from the jets and the leptons. This distribution is centred at 0 with the width of $\sigma = 5\,\mathrm{GeV}$, written as $\mathrm{G}(m_{jj}(E_1, E_2) - m_{\ell\ell} \mid 0, 5)$. This Gaussian term ensures that the dijet mass m_{jj} is consistent with the dilepton mass $m_{\ell\ell}$ with width $\sigma = 5\,\mathrm{GeV}$ following the approach used in kinematic likelihood fits in Ref. [18]. Concurrently, the probabilistic model of the "true" jet energy E_i given the measured energy E_{j_i} is also expressed by a Gaussian distribution centred at E_{j_i} with the width of $\sigma = \sqrt{E_{j_i}}$ (reflects calorimeter resolution), shortly written by the term $\mathrm{G}(E_i \mid E_{j_i}, \sqrt{E_{j_i}})$ for $i = 1, 2$.

So the key components are to iterate over the event data and find the combination that maximises the likelihood L, to match the modified dijet mass to the dilepton mass ($m_{jj} \approx m_{\ell\ell}$), and to compare the hypothesised jet energies E_1, E_2 with the measured E_{j_1}, E_{j_2}. The interpretation is that a higher L implies more likely that the event matches the $2\ell 2j$ topology and thus, implies a lower $-\ln L$ results to the event being chosen as $2\ell 2\nu$. Subsequently, the selection value on the likelihood L is chosen to separate (orthogonalise) event types of $2\ell 2j$ and $2\ell 2\nu$ respectively.

4.1 Algorithm

The mathematical equation of the fit applied in the code is based on a Gaussian likelihood minimisation. The full likelihood function in terms of the probability density function, P, of the leptons and jets is then:

$$L(E_1, E_2) = P_{\text{lep}}(M_{\text{combined}}) \cdot P_{\text{jet1}}(E_1) \cdot P_{\text{jet2}}(E_2). \tag{5}$$

Each term is modeled as a Gaussian distribution. E_1 and E_2 are the energies of jet 1 and jet 2, $P_{\text{lep}}(M_{\text{combined}})$ is the probability density function of the combination of the invariant mass of the jets and leptons.

$$M_{\text{combined}} = m_{j_1 j_2} \sqrt{\frac{E_1}{E_{j_1}}} \sqrt{\frac{E_2}{E_{j_2}}},$$

$$L(E_1, E_2) = \exp\left(-\frac{(M_{\text{combined}} - M_{\text{lep}})^2}{2 \cdot \sigma_{\text{lep}}^2}\right) \cdot \exp\left(-\frac{(E_1 - \mu_{\text{jet1}})^2}{2 \cdot \sigma_{\text{jet1}}^2}\right) \cdot \exp\left(-\frac{(E_2 - \mu_{\text{jet2}})^2}{2 \cdot \sigma_{\text{jet2}}^2}\right). \tag{6}$$

The original jet energies (mean energies) of jet 1 and jet 2 are represented by μ_{jet1} and μ_{jet2} respectively. The standard deviations of the jet energies, σ_{jet1} and σ_{jet2}, are taken as $\sqrt{E_1}$ and $\sqrt{E_2}$ in the algorithm. M_{lep} is the invariant mass of the dilepton system, σ_{lep} is fixed to 5 GeV as discussed in Section 3 considering the jet energy scale and resolution measurements with their associated uncertainties in ATLAS [17].

Since likelihood L^2 is maximised in principle, the negative logarithm of the likelihood will then be minimised as shown in Eq. 7 as :

$$-\ln L(E_1, E_2) = \frac{(M_{\text{combined}} - M_{\text{lep}})^2}{2 \cdot \sigma_{\text{lep}}^2} + \frac{(E_1 - \mu_{\text{jet1}})^2}{2 \cdot \sigma_{\text{jet1}}^2} + \frac{(E_2 - \mu_{\text{jet2}})^2}{2 \cdot \sigma_{\text{jet2}}^2}. \tag{7}$$

Given the approximations described above, the standard deviations for jet energies are approximated by $\sigma_{\text{jet}} \approx \sqrt{E}$, and $\sigma_{\text{lep}} = 5$ GeV. The final form for the minimised equation using a variable metric gradient method is:

$$-\ln L(E_1, E_2) = \frac{(M_{\text{combined}} - M_{\text{lep}})^2}{2 \cdot 5^2} + \frac{(E_1 - \mu_{\text{jet1}})^2}{2 \cdot E_1} + \frac{(E_2 - \mu_{\text{jet2}})^2}{2 \cdot E_2}. \tag{8}$$

5 Results

The distribution of the reconstructed scalar mass m_S is studied. The simulated $2\ell 2j$ signal together with the simulated main background Z+jets are investigated at the same time in order to monitor their relative contributions to the shape of the m_S distribution when varying the selections on the negative log-likelihood.

As the likelihood function is used in the search to separate $2\ell 2j$ events from those eventually considered for the $2\ell 2\nu$ channel, a range of numerical values is tested to optimise the final selected value of the negative log-likelihood function ($-\ln\ L$). After a certain selection value ($-\ln\ L \approx 16$), the number of $2\ell 2j$ signal events of this case is not much smaller than the ones in the cases where the selection is not implemented. This is the threshold final selection value. For $-\ln\ L$ less than the threshold selection value of 16, the events belong to the $2\ell 2j$ channel, and for $-\ln\ L$ otherwise, the events are made available for our $2\ell 2\nu$ channel as shown in Figure 3.

For further clarity of the likelihood method results for the orthogonality study, the $2\ell 2j$ signal selection efficiencies for the six mass points used in the analysis are calculated. The fractional percent displays the proportion of the $2\ell 2j$ signal events that satisfy the upper bound selection values on $-\ln\ L$ as shown in Figure 4.

Beyond a specific value selected, the percentage of remaining signal events saturates in the form of a plateau. This higher percentage is quite obvious in higher mass points. Using the threshold selection value of 16, the efficiencies of the mass points $[m_S, m_{Z_d}]$: [70, 20], [70, 35], [84, 31], [110, 30], [110, 55] and [183, 50] GeV used in the orthogonality study are : $40\%, 56\%, 55\%, 64\%, 77\%$ and 82 % respectively. This entails that with the obtained threshold selection value, as the mass points becomes higher, more events are selected for the $2l2j$ analysis channel with less events selected for the $2l2\nu$ analysis channel. Thus it is relatively easier to separate events between the two channels as the mass points are higher.

6 Conclusion

We have developed a likelihood-based method to classify the events as those belonging to the $2\ell 2j$ and $2\ell 2\nu$ analyses channels. The aim is to select events for $2\ell 2j$ that have a negative log-likelihood below 16 ($-\ln\ L < 16$). The $2\ell 2j$ events that are removed away in this selection are not signal-like. That means the reconstructed mass for m_S from the di-lepton and di-jet mass of these events is not commensurate.

[2]Likelihood function L which is a maximisation function, when expressed in the form of the negative logarithmic function $-\ln L$, it is a minimisation function whose numerical values are easier to work with.

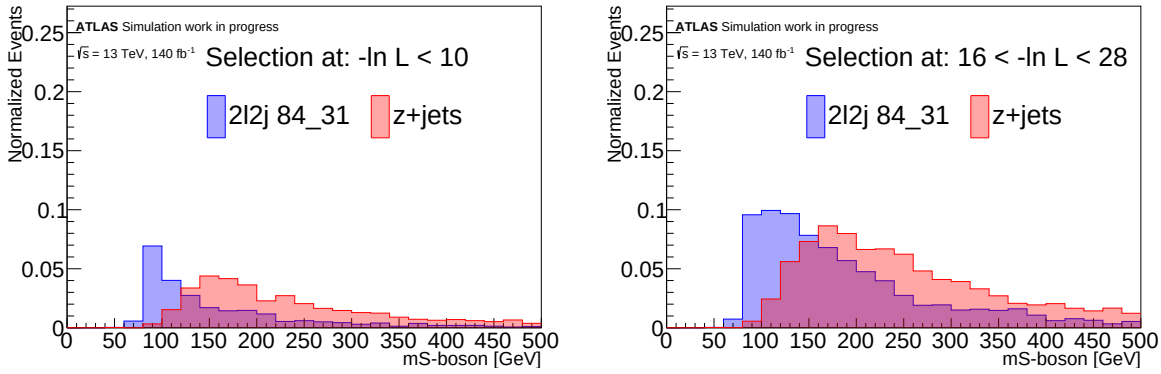

Figure 3: (*left*) The distribution of the scalar boson reconstructed mass when selecting the negative log-likelihood function $-\ln L < 10$, since 10 is less than the threshold selection value of 16, the events are selected for the $2\ell 2j$ channel. (*right*) Similar distribution but for $16 < -\ln\ L < 28$, the events are selected for the $2\ell 2\nu$ channel.

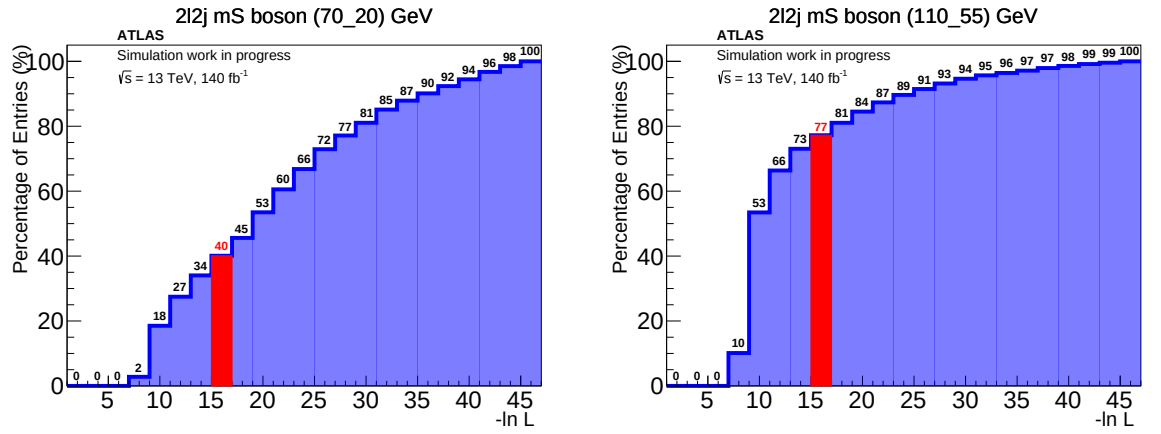

Figure 4: (*left*) For mass point [70, 20] GeV the percentage of $2\ell 2j$ events tends to plateau after a certain $-\ln\ L$ value. (*right*) For mass point [70, 20] GeV a higher $2\ell 2j$ yield percentage is more prominent after the same $-\ln\ L$ value.

References

[1] D. Curtin, R. Essig, S. Gori, and J. Shelton, "Illuminating dark photons with high-energy colliders," *JHEP*, vol. 02, p. 157, 2015.

[2] ATLAS Collaboration, "Search for a new scalar resonance decaying into Z bosons in four-lepton final states with the ATLAS detector at the LHC," *Journal of High Energy Physics*, vol. 2022, no. 7, p. 67, 2022.

[3] ATLAS Collaboration, "Search for dark photons produced in 13 TeV pp collisions with the ATLAS detector," *Physical Review D*, vol. 104, no. 11, p. 112006, 2021.

[4] ATLAS Collaboration, "Search for exotic Higgs boson decays to light resonances with the ATLAS detector," 2020, aTL-PHYS-PUB-2020-012. [Online]. Available: https://cds.cern.ch/record/2725735

[5] ATLAS Collaboration, "Search for invisible decays of a higgs boson produced via vector boson fusion in pp collisions at sqrt(s) = 13 tev with the atlas detector," *Physical Review D*, vol. 100, no. 1, p. 012006, 2019.

[6] ATLAS Collaboration, "Search for Higgs bosons decaying into new spin-0 or spin-1 particles in four-lepton final states with the ATLAS detector with 139 fb^{-1} of pp collision data at $\sqrt{s} = 13$ TeV," *JHEP*, vol. 03, p. 041, 2022.

[7] ATLAS Collaboration, "Search for Higgs boson decays to beyond-the-Standard-Model light bosons in four-lepton events with the ATLAS detector at $\sqrt{s} = 13$ TeV," *JHEP*, vol. 06, p. 166, 2018.

[8] ATLAS Collaboration, "Search for new light gauge bosons in Higgs boson decays to four-lepton final states in pp collisions at $\sqrt{s} = 8$ TeV with the ATLAS detector at the LHC," *Phys. Rev. D*, vol. 92, p. 092001, 2015.

[9] ATLAS Collaboration, "Search for a new scalar decaying into new spin-1 bosons in four-lepton final states with the atlas detector," arXiv:2410.16781 [hep-ex], URL: https://arxiv.org/abs/2410.16781, 2024, cERN-EP-2024-248.

[10] ATLAS Collaboration, "The ATLAS Experiment at the CERN Large Hadron Collider," *JINST*, vol. 3, p. S08003, 2008.

[11] ATLAS Collaboration, "Electron and photon performance measurements with the ATLAS detector using the 2015–2017 LHC proton–proton collision data," *JINST*, vol. 14, p. P12006, 2019.

[12] ATLAS Collaboration, "Muon reconstruction and identification efficiency in ATLAS using the full Run 2 pp collision data set at $\sqrt{s} = 13$ TeV," *Eur. Phys. J. C*, vol. 81, p. 578, 2021.

[13] M. Aaboud *et al.*, "Performance of missing transverse momentum reconstruction with the ATLAS detector using proton-proton collisions at $\sqrt{s}$ = 13 TeV," *Eur. Phys. J. C*, vol. 78, no. 11, p. 903, 2018.

[14] R. H. Dalitz and G. R. Goldstein, "The decay and polarization properties of the top quark," *Phys. Rev. D*, vol. 45, pp. 1531–1543, 1992.

[15] CMS Collaboration, "Measurement of the $t\bar{t}$ cross section using kinematic reconstruction," *JHEP*, vol. 12, p. 035, 2012.

[16] K. Kondo, "Dynamical likelihood method for reconstruction of events with missing momentum," *J. Phys. Soc. Jap.*, vol. 57, pp. 4126–4140, 1988.

[17] G. Aad *et al.*, "Jet energy scale and resolution measured in proton–proton collisions at $\sqrt{s} = 13$ TeV with the ATLAS detector," *Eur. Phys. J. C*, vol. 81, no. 8, p. 689, 2021.

[18] CMS Collaboration, "Measurement of the top-quark mass in the dilepton channel using the matrix element method," *Eur. Phys. J. C*, vol. 72, p. 2202, 2012, uses Gaussian constraints on invariant masses in per-event likelihood fits.

Simulation of X-ray and gamma radiation shielding properties of lithium-antimony-Lead-germanate glasses modified with chromium oxide using Phy-X/PSD software

L. Mdletshe[1], S. S. Ntshangase[1] , B. V. Kheswa[2] , S. N. T. Majola[2] , L. Makhathini[3] , S. P. Noncolela[1] , L. P. Masiteng[2] , B. Bhengu[1], N. Msabala[1], M. J. Mvelase[1,2], S. Mthalane[1], and M. N. Zuma[1]

[1]Department of Physics, University of Zululand, KwaDlangezwa 3886, South Africa
[2]Department of Physics, University of Johannesburg, Doornfontein 2028, South Africa
[3]Department of Physics, University of the Western Cape, Bellville 7535, South Africa

E-mail: linda.mdletshe@gmail.com

Abstract. The Phy-X/PSD software has been used to explore the effect of chromium oxide (Cr_2O_3) on the radiation shielding properties of glass systems with the chemical composition $10Li_2O+(30\text{-}x)Sb_2O_3+20PbO+40GeO_2+xCr_2O_3$, where x = 0.1, 0.2, 0.3, 0.4, 0.5 mol%. The key properties examined include the mass attenuation coefficient (MAC) and tenth value layer (TVL). These parameters were examined over an energy range of 20 to 300 keV. The results indicate that increasing the Cr_2O_3 content enhances the shielding properties of the glass systems examined. The analysis reveals that the sample with the highest Cr_2O_3 content demonstrates the highest MAC, along with the lowest TVL. This suggests that it offers better radiation shielding capabilities compared to the other samples.

1 Introduction

The increasing utilisation of nuclear technology in research, medical facilities, nuclear reactors, and various industries offers significant benefits but also poses potential risks due to ionising radiation [1, 2]. Careful oversight is necessary to mitigate these risks. One crucial safety measure is the application of radiation shielding materials. Different types of radiation require different shielding materials and techniques. For instance, highly penetrating gamma rays require materials with high density, such as lead or concrete, for effective shielding. However, these conventional materials have drawbacks, including a lack of transparent structure, which restricts their applications. Researchers have sought alternative materials that minimise these disadvantages. Glasses, ceramics, alloys, and polymers have been proposed as alternatives, each offering distinct advantages. Notably, glasses possess unique properties, such as transparency and high chemical resilience, making them viable options for radiation protection [3]. Effective radiation shielding materials must attenuate photons, which are highly penetrative. This can be achieved by utilising materials with high atomic numbers and densities. Researchers evaluate the potential of materials by assessing their physical properties such as linear attenuation coefficients, mass attenuation coefficients, mean free path, half-value layer, tenth-value layer, and effective atomic number [4].

Many studies have analysed the radiation shielding parameters of various glass systems, including germinate [5], borosilicate [6], boro-tellurite [7], and heavy metal oxide [8] glasses, at low, medium, and high energy levels. By analysing these parameters, researchers can identify which types of glass offer the most effective radiation shielding.
A recent study conducted by Sayyed et al. [9] examined the effect of chromium ions on the radiation-shielding properties of germanate glasses using the Phy-X/PSD software. The study focused on energies ranging from 0.284 to 1.33 MeV, revealing that the incorporation of chromium ions enhances the shielding performance of these glasses. However, their behavior at lower energies remains unexplored. Thus, the present study seeks to investigate the influence of adding chromium oxide to lithium-antimony-lead-germanate glasses within the 20 - 300 keV energy range, utilising the Phy-X/PSD simulation software. The study explores the potential of these glasses for X-ray and gamma-ray shielding. The targeted energy range is particularly relevant because of its application in low-energy photon-based technologies, including medical imaging methods such as computed tomography (CT), dental radiography, and airport security screening systems.

2 Simulation Methods

The Phy-X/PSD software has been used in the present work to investigate the radiation-shielding parameters of the five glass samples (S1-S5). The Phy-X/PSD program has been used to simulate the mass attenuation coefficient (MAC) and tenth-value layer (TVL) radiation-shielding properties of the S1-S5 samples. Phy-X/PSD is a user-friendly online photon shielding and dosimetry (PSD) software that was developed for calculating radiation shielding parameters in the 1 keV - 100 GeV energy region [4, 10]. The Phy-X/PSD simulation tool, which uses data from well-established photon interaction databases (NIST XCOM), has been widely employed in the literature for estimating radiation shielding parameters such as the mass attenuation coefficient (MAC) and the tenth-value layer (TVL). To run the program, the chemical composition of the glass sample as well as its density are required. The chemical compositions and density of each of the investigated samples used for running the program are listed in Table 1. The densities reported in this table were experimentally measured and obtained from a previously published study on the same glass systems [9].

Glass code	Glass composition	Density (gm/cm^3)
S1	$10Li_2O$-$29.9Sb_2O_3$-20PbO-$40GeO_2$-$0.1Cr_2O_3$	3.07
S2	$10Li_2O$-$29.8Sb_2O_3$-20PbO-$40GeO_2$-$0.2Cr_2O_3$	3.15
S3	$10Li_2O$-$29.7Sb_2O_3$-20PbO-$40GeO_2$-$0.3Cr_2O_3$	3.16
S4	$10Li_2O$-$29.6Sb_2O_3$-20PbO-$40GeO_2$-$0.4Cr_2O_3$	3.18
S5	$10Li_2O$-$29.5Sb_2O_3$-20PbO-$40GeO_2$-$0.5Cr_2O_3$	3.20

Table 1: The chemical composition of the investigated glass samples and their densities.

The radiation shielding properties of Li_2O+Sb_2O_3+PbO+GeO_2+Cr_2O_3 glass samples were investigated using their mass attenuation coefficients and tenth-value layers. These parameters are mathematically related to the photon linear attenuation coefficient (μ), given by equation 1,

$$I = I_0 e^{-\mu t}, \tag{1}$$

where I is the intensity of the attenuated photons after passing through the absorber with thickness, t, and I_o is the intensity of the initial photons. The attenuation of photons in an absorber occurs through photoelectric absorption, Compton scattering, and pair production. The mass attenuation coefficient parameter is related to μ through the following equation,

$$MAC = \frac{\mu}{\rho}, \tag{2}$$

where ρ is the density of the shielding material. The MAC represents the attenuation of a photon per unit mass of a material.

The TVL parameter characterises the thickness of a material at which the intensity of photons transmitted through it is reduced to 10% of the initial intensity. This parameter is mathematically related to μ, according to,

$$TVL = \frac{\ln 10}{\mu}. \tag{3}$$

3 Results and Discussion

This section presents and discusses the results obtained from the Phy-X/PSD simulation software. The software's accuracy was assessed by comparing its output with values reported in the literature, including experimental data and results from other theoretical tools such as XCOM [11] and Geant4 [12]. In particular, the experimental mass attenuation coefficient (MAC) values reported by Önder et al. [13] were compared with those generated by Phy-X/PSD. The comparison demonstrated good agreement between the experimental and simulated results.

The obtained results for the five investigated glass samples are discussed in terms of mass attenuation coefficients and tenth value layer within the 20 - 300 keV. Figure 1 shows the mass attenuation coefficient (MAC) for the investigated samples, plotted as a function of energy. The figure shows that the MAC values at low energies are high for all glass samples (S1-S5). These high values of MAC range from 36.692 - 36.731 cm^2/g at 20 keV, as clearly illustrated in the inset. These MAC values decrease with the increase of energy, reaching the lowest values at 300 keV. The slight increase in MAC values at energies around 30 keV and 90 keV is attributed to the binding energies for the electrons related to K-shell absorption of Sb ($\sim$ 32.9) and Pb ($\sim$ 88 keV) elements, respectively. The ability of the investigated glass materials to attenuate radiation is minimal at 300 keV. The radiation, at this energy, is less attenuated by the material compared to lower energies because, as the energy of radiation increases, the probability of interaction with the atomic electrons of the materials decreases. Instead, the radiation interacts more with the atomic nucleus, which generally leads to lower attenuation. Similar behavior was observed in the study conducted by Kheswa [14].

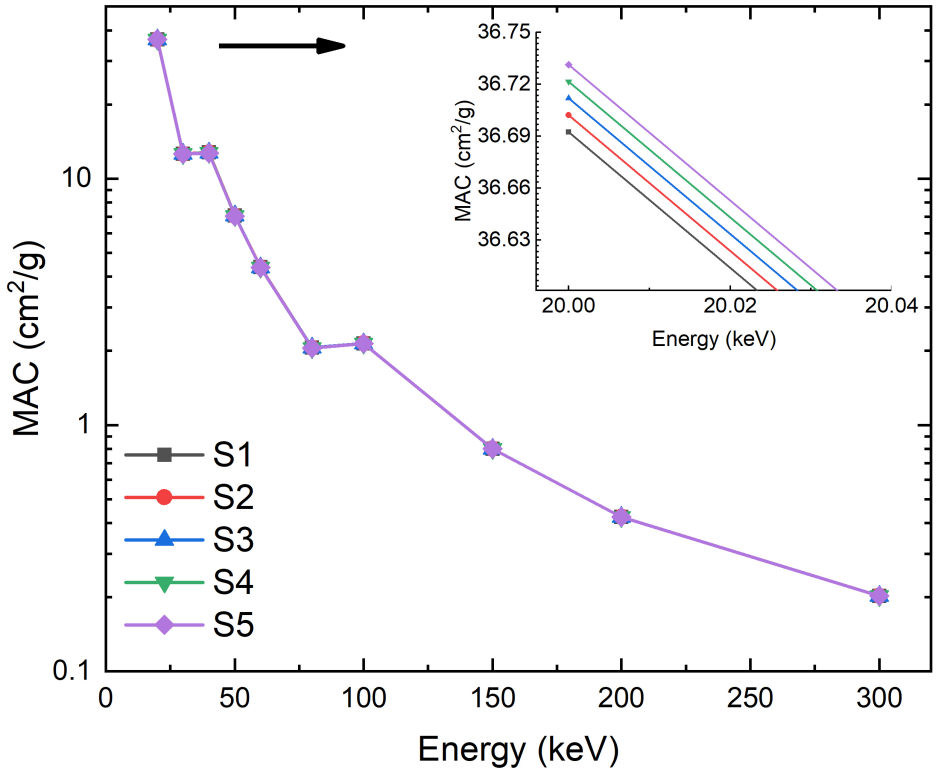

Figure 1: Mass attenuation coefficients for the S1-S5 glass samples. The inset shows a magnified view of the region near 20 keV.

In Figure 1, it should be noted that sample S1, containing a low concentration of chromium oxide (0.1 mol%), exhibits the lowest MAC values. The sample (S5) with the highest chromium oxide content (0.5 mol%) shows

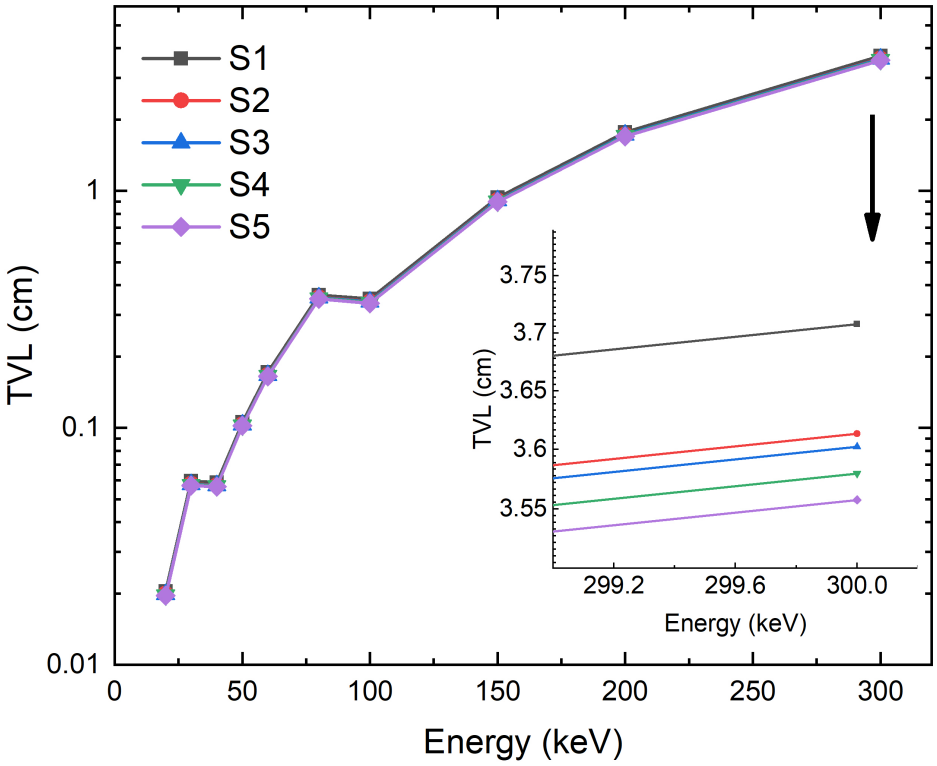

Figure 2: Tenth value layer for the S1-S5 glass samples. The inset shows a magnified view of the region near 300 keV.

the highest MAC values (see the inset). Since higher MAC values indicate better radiation shielding performance, these results suggest that increasing chromium oxide content enhances the shielding effectiveness of the germanate glasses.

Figure 2 illustrates the tenth-value layers for all investigated samples within the 20 - 300 keV. The lowest TVL values for all samples are observed at 20 keV. The TVL values increase with the increase in energy. The highest values of TVL for the S1-S5 samples, ranging from 3.708 to 3.558 cm, are observed at 300 keV. From the TVL shown in Figure 2, it can be seen that a small thickness of glass material is needed to absorb 90% of the initial intensity of radiation with low energies. As the energy of incoming radiation increases, the thickness of the glass material needed to absorb 90% of the incoming photons' intensity increases. In the figure, it is observed that the material thickness needed to absorb 90% of the initial photons is about 0.02 cm at 20 keV. The thickness of the material has to be increased to approximately 3.708 cm to be able to stop 90% of the incoming radiation with an energy of 300 keV, as clearly illustrated in the inset.
It is worth noting that the sample (S1) with the lowest content of Cr_2O_3 (0.1 mol%) has the highest values of TVL, and the sample (S5) with the highest Cr_2O_3 content (0.5 mol%) has the lowest values of TVL. Lower values of TVL suggest better radiation shielding capabilities. These results demonstrate that the glass sample (S5) has better shielding performance than the other investigated samples. This is consistent with the results obtained from the MAC parameter.

4 Conclusions

The impact of chromium oxide on the radiation-shielding properties of germanate glasses has been investigated using the Phy-X/PSD simulation software. The properties have been studied within the 20 - 300 keV energy range.

The results indicate that increasing the Cr_2O_3 content enhances the shielding properties of the glass systems examined. The analysis reveals that the sample with the highest Cr_2O_3 content demonstrates the highest MAC, along with the lowest TVL. This suggests that it offers better radiation shielding capabilities compared to the other samples. The observed performance enhancements of the glass system could be meaningful in specialised applications where material weight, transparency, or composition constraints are critical. Further research, including experimental validation and cost-effectiveness studies, would be necessary to assess the practical viability of these modified glass systems for commercial or clinical use.

References

[1] V. Venugopal, "Societal applications of nuclear technology in health care, industry and water resource management in india," *Energy Procedia*, vol. 7, pp. 553–559, June 2011.

[2] F. A. Mettler, "Medical effects and risks of exposure to ionising radiation," *Journal of Radiological Protection*, vol. 32, no. 1, p. N9, March 2012.

[3] M. Kurudirek, "Radiation shielding and effective atomic number studies in different types of shielding concretes, lead base and non-lead base glass systems for total electron interaction: A comparative study," *Nuclear Engineering and Design*, vol. 280, pp. 440–448, September 2014.

[4] E. Şakar, F. Özpolat, B. Alım, M. I. Sayyed, and M. Kurudirek, "Phy-x/psd: development of a user friendly online software for calculation of parameters relevant to radiation shielding and dosimetry," *Radiation Physics and Chemistry*, vol. 166, p. 108496, September 2020.

[5] M. I. Sayyed, K. M. Kaky, E. Şakar, U. Akbaba, M. M. Taki, and O. Agar, "Gamma radiation shielding investigations for selected germanate glasses," *Journal of Non-Crystalline Solids*, vol. 512, pp. 33–40, May 2019.

[6] D. Ş. Baykal, H. O. Tekin, and R. B. Ç. Mutlu, "An investigation on radiation shielding properties of borosilicate glass systems," *International Journal of Computational and Experimental Science and Engineering*, vol. 7, no. 2, pp. 99–108, July 2021.

[7] M. Halimah, A. Azuraida, M. Ishak, and L. Hasnimulyati, "Influence of bismuth oxide on gamma radiation shielding properties of boro-tellurite glass," *Journal of non-crystalline solids*, vol. 512, pp. 140–147, March 2019.

[8] P. Kaur, D. Singh, and T. Singh, "Heavy metal oxide glasses as gamma rays shielding material," *Nuclear Engineering and design*, vol. 307, pp. 364–376, August 2016.

[9] M. I. Sayyed, K. M. Kaky, and R. A. Anaee, "Chromium ions effects on Sb2O3-PbO-GeO2 glass properties for radiation protection," *Journal of Theoretical and Applied Physics*, vol. 17, p. 182413, January 2024.

[10] https://phy-x.net/PSD.

[11] L. Gerward, N. Guilbert, K. B. Jensen, and H. Levring, "Winxcom—a program for calculating x-ray attenuation coefficients," *Radiation physics and chemistry*, vol. 71, no. 3-4, pp. 653–654, October 2004.

[12] S. Agostinelli, J. Allison, K. a. Amako, J. Apostolakis, H. Araujo, P. Arce, M. Asai, D. Axen, S. Banerjee, G. Barrand *et al.*, "Geant4—a simulation toolkit," *Nuclear instruments and methods in physics research section A: Accelerators, Spectrometers, Detectors and Associated Equipment*, vol. 506, no. 3, pp. 250–303, March 2003.

[13] P. Önder, A. Turşucu, D. Demir, and A. Gürol, "Studies on mass attenuation coefficient, effective atomic number and electron density of some thermoluminescent dosimetric compounds," *Nuclear Instruments and Methods in Physics Research Section B: Beam Interactions with Materials and Atoms*, vol. 292, pp. 1–10, October 2012.

[14] B. V. Kheswa, "X-ray shielding properties of bismuth-borate glass doped with rare earth ions," *Open Chemistry*, vol. 21, no. 1, p. 20220345, June 2023.

This page intentionally left blank.

Radiation contamination in gold mine tailings soil samples using HPGe spectrometry

M.J. Mvelase[1,2], S.S. Ntshangase[1], P.L. Masiteng[2], S.N.T. Majola[2], B.V. Kheswa[2] and P.P. Maleka[3,4]

[1] Department of Physics, University of Zululand, KwaDlangezwa, South Africa
[2] Department of Physics, University of Johannesburg, Doornfontein, South Africa
[3] Department of Physics, University of the Western Cape, Bellville, South Africa
[4] Environmental Radioactivity Laboratory, iThemba LABS, Somerset West, South Africa

E-mail: emjay.mvelase@gmial.com

Abstract. An assessment of the radiation concentration in abandoned mines located near informal settlements in the west of Johannesburg was carried out. In this study, gamma spectrometry was used to measure the activity concentrations in the soil samples. The results show the activity concentrations for ^{226}Ra, ^{232}Th, and ^{40}K were 338.44$\pm$3.48, 10.06$\pm$0.68, and 126.15$\pm$10.90 Bq/kg, respectively. The radiological indices calculated from the activity concentration were above the acceptable global limits prescribed by the regulatory bodies. The mean radiological indices in descending order are AGDE $>$ Ra_{Eq} $>$ ADR $>$ ELCR $>$ AEDE $>$ I_a with values of 1129.54 $\pm$ 46.63 μSv/y $>$ 363.20 $\pm$ 7.81 Bq/kq $>$ 500.56 $\pm$ 15.90 nGy/h $>$ 5.62 $\pm$ 0.20$\times 10^{-3}$ $>$ 1.57$\pm$0.06 mSv/y $>$ 1.45$\pm$0.30. The concentration of uranium in the tailings, particularly around Soweto, exceeded the recommended levels, posing a significant health risk to the local population. The study suggests prohibiting the use of this soil for construction purposes.

1 Introduction

South Africa's wealth of natural resources, particularly metals and coal, has led to heavy pollution in once robust exploration areas [1]. Gold has been mined in the west of Johannesburg since the late 1800s [2]. Gold mining began in 1886 [3], leaving behind an area of approximately 400 km^2 of mine waste called tailings. The 270 dams and 380 mine tailings are reported to contain between 430,000 and 600,000 metric tonnes of low-grade U_3O_8 [4, 5]. The tailings in the Witwatersrand Basin have uranium concentrations up to 100 mg/kg, and this amount is comparable to or even exceeds that from certain uranium mines in Namibia or Germany [5] of up to 1752.1$\pm$17.5 Bq/kg for ^{238}U in Namibia [6].

Mining has profoundly shaped South Africa's economy, but this progress has come at a serious cost to public health, particularly for communities living near gold tailings [7]. During windy seasons, residents face a dangerous reality: dust clouds carrying uranium, thorium, and potassium particles [6] drift into their neighbourhoods, forcing them to breathe in harmful radioactive material. These mine tailings pose a double threat, containing not just radioactive elements but also toxic heavy metals like arsenic, chromium, and nickel [2]. When these particles lodge in people's lungs, they work together to cause devastating health problems. The list of potential illnesses is sobering: silicosis, tuberculosis, chronic lung diseases, asthma, emphysema, various cancers, and blood disorders [7]. Radiation affects people both from the outside, through gamma radiation, and from the inside when they breathe in radon gas. While our bodies can naturally recover from some radiation exposure, the damage to DNA can sometimes lead to lasting chromosomal changes [8]. The radiation comes from multiple sources - both natural background radiation that's always present in our environment and human-made sources like medical procedures, nuclear testing, and power plant accidents [9, 10, 11].

This health crisis is particularly evident in Soweto, where residents regularly voice concerns about dust pollution from nearby gold tailings, especially during dry, windy weather [12, 13]. Our research focuses on analyzing these tailings to measure both radioactive contamination and heavy metal pollution, with special attention to calculating the associated radiation hazard levels. This report presents our findings on radioactivity levels and their potential risks to human health.

2 Materials and Methods

2.1 Sample collection and preparation

Sixty three (63) soil samples were collected from the gold mines tailings in Crown Mines (CMO - 26°14'21"S 27°58'01"E), Consolidated Main Reef Gold (CMRG - 26°12'33"S 27°55'32"E), Roodepoort (RDP - 26°10'46"S 27°52'03"E), and Kloof (KLF - 26°07'51"S 27°49'22"E) in the west of Johannesburg, stored in plastic zipper bags, labeled with sample IDs, and then dried in an oven at 105 ^{o}C, crushed, homogenized, and pulverized into powder. Attention was paid closely to every sample to avoid cross-contamination. The samples were then taken to iThemba LABS for analysis. Empty Marinelli beakers were weighed, and the differences in masses were used to determine the masses of the soil samples. The samples were stored in sealed Marinelli beakers for 42 days to establish secular equilibrium among some daughters of ^{238}U and ^{232}Th series before γ-spectrometry analysis. This was done as naturally occurring radioactive materials (NORMs) contain radon gas that can escape from the samples, thus introducing disequilibrium. The background radiation was negligible as the detector was encased in a 10 cm thick lead layer.

2.2 The analysis of soil samples

We measured radioactive elements in soil samples with a high-purity germanium detector (HPGe), which allowed us to analyze gamma-ray emissions with excellent precision. The resolution of the detector was sharp - about 1.9 keV at the 1332 keV gamma ray line of cobalt-60. To obtain accurate readings, we waited until the samples had reached secular equilibrium before performing radiometric analysis. We then tracked specific gamma ray signals to measure each element: U-238 showed up at 186.20 keV (from Ra-226), 351.9 keV (from Pb-214), 609.3, 1120.4, and 1765 keV (from Bi-214). For thorium-232, we analyzed the 583.1 keV line of thallium-208 and the 911.20 keV line of Ac-228. Potassium-40 was easy to recognize with its characteristic emission line of 1460.80 keV.

3 Numerical Calculations

3.1 The efficiency of the detector and energy calibration curves

The gamma detector used in this analysis is the Lower Energy Germanium (LEGe) detector. The LEGe is a high-resolution germanium (HPGe) detector design optimized for detecting gamma rays at low energies. For efficiency calculation, the energy sources 45.539 keV for ^{210}Pb, 59.5 keV for ^{241}Am, 88 keV for ^{109}Cd, 122.1 keV for ^{57}Co, 165.9 keV for ^{139}Ce, 279.2 keV for ^{203}Hg, 391.7 keV for ^{113}Sn, 514 keV for ^{85}Sr, 661.65 keV for ^{137}Cs, 898 keV for ^{88}Y, 1173.2 keV for ^{60}Co, 1332.4 keV for ^{60}Co, and 1836.1 keV for ^{88}Y were used. The emission probabilities of different radionuclides were taken from various sources in the literature [13]. Figure 1 shows the efficiency and energy calibration curves, respectively.

3.2 The activity concentration in soil samples

Each sample was counted for 25200 seconds to reduce statistical uncertainty. The activity concentrations in the measured samples were computed using Equation (1) [14, 15]:

$$A(Bq/kg) = \frac{C_s - C_b}{I_\gamma \varepsilon m}, \tag{1}$$

where C_s is the count rate of the sample, and C_b is the background count rate, ϵ is the detector efficiency of the specific γ - radiation, ε is the absolute detector efficiency of the specific γ-ray, and m is the mass of the sample in kilograms. I_γ is the emission probability of a specific energy photopeak.

3.3 Evaluation of radiation indices

Following the calculation of the concentration of specific activity in the samples, the radiological indices of the samples were estimated from the following relations. The radium equivalent activity (Ra_{Eq}) was calculated using Equation (2) [8, 14]:

$$Ra_{Eq}(Bq/kg) = C_{Ra} + 1.43s + C_{Th} + 0.077C_K. \tag{2}$$

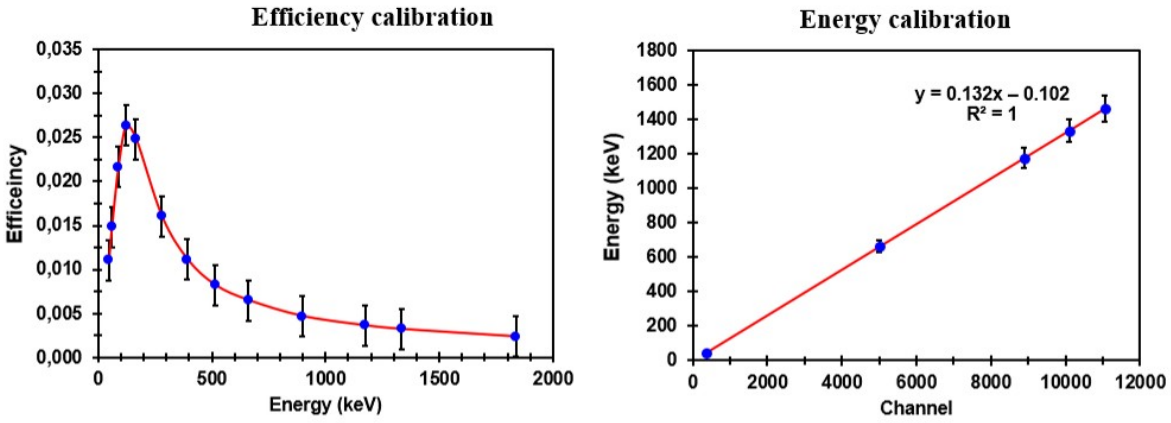

Figure 1: The efficiency of the detector (left) and energy calibration for specific γ-ray energies (right).

This index was calculated assuming that 1 Bq/kg of ^{226}Ra, 0.7 Bq/kg of ^{232}Th, and 13 Bq/kg of ^{40}K produce the same gamma dose rate. The indoor and outdoor absorbed dose rate (ADR) due to naturally occurring radioactive materials in air 1 metre above the ground is calculated using Equations (3) and (4) [8, 16]:

$$D_{Ind}(nGy/h) = 0.920C_{Ra} + 1.100C_{Th} + 0.0810C_K, \tag{3}$$

$$D_{Out}(nGy/h) = 0.462C_{Ra} + 0.604C_{Th} + 0.0417C_K, \tag{4}$$

where the coefficients of C_{Ra}, C_{Th}, and C_K are dose conversion factors in nGy/h per Bq/kg. The annual effective dose equivalent (AEDE) indoors and outdoors was estimated with Equations (5) and (6) as follows [8]:

$$AEDE_{In}(mSv/y) = D_{Ind}\times T\times 0.8\times F, \tag{5}$$

$$AEDE_{Out}(mSv/y) = D_{Out}\times T\times 0.2\times F, \tag{6}$$

where T is the number of hours in a year (365×24h = 8760 hours). F is a conversion factor from nGy/h to mSv/y with a value of 0.7×10^{-6}. The excess lifetime cancer risk (ELCR) in the indoor and outdoor environment was estimated using Equations (7) and (8) [8, 16, 17, 18]:

$$ELCR_{Ind} = AEDE_{Ind}\times DL\times RF, \tag{7}$$

$$ELCR_{Out} = AEDE_{Out}\times DL\times RF, \tag{8}$$

where DL is the life expectancy, which is about 70 years, and RF is the risk factor, which is given as 0.05 Sv^{-1}. The annual gonadal dose equivalent (AGDE) due to the specific activities of ^{226}Ra, ^{232}Th, and ^{40}K was calculated using Equation (9) [19]:

$$AGDE(\mu\text{Sv/y}) = 3.09C_{Ra} + 4.18C_{Th} + 0.314C_K. \tag{9}$$

The numbers 3.09, 4.18, and 0.314 are the respective conversion factors from the activity concentrations into total dose received by the organs of interest. The alpha index (I_α), which is used to estimate α-radiation from building materials is estimated using Equation (10) [20]:

$$I_\alpha = \frac{C_{Ra}}{200}. \tag{10}$$

In the above equations, C_{Ra}, C_{Th}, and C_K represent the radionuclide concentrations of ^{226}Ra, ^{232}Th, and ^{40}K.

4 Results and discussion

Sixty-three samples from four different tailings were analyzed at iThemba LABS using the HPGe detector, and the concentrations are dominated by ^{226}Ra and partly followed by ^{40}K Table 1. Figure 2 shows a typical γ-spectrum for NORM samples using a γ-detector.

In the samples, the ^{226}Ra ranged from 149.62±4.72 to 452.28±8.02 Bq/kg, with a mean of 338.44±3.48 Bq/kg, which is above the permissible limit of 35 Bq/kg [8]. The activity of ^{40}K ranged from 113.34±20.80 Bq/kg to 145.79±22.51 Bq/kg with a mean of 126.15±10.90 Bq/kg, which is below the permissible limit of 400 Bq/kg, and ^{232}Th ranged from 8.25±1.31 to 11.20±1.03 Bq/kg with a mean of 10.06±0.68 Bq/kg. The mean concentration of ^{226}Ra is 32 times that of ^{232}Th and about 3 times that of ^{40}K. In decreasing order: ^{226}Ra>^{40}K>^{232}Th.

Gold Tailings	Sample Identity	Specific Activity concentration (Bq/kg)		
		^{226}Ra	^{232}Th	^{40}K
Johannesburg, western areas	Kloof (KLF)	149.62±4.72	10.31±1.48	145.79±22.51
	Crown Mines (CMO)	303.02±6.60	8.25±1.31	113.34±20.80
	Consolidated Main Reef (CMRG)	448.86±8.00	10.46±1.56	117.92±21.97
	Roodepoort (RDP)	452.28±8.02	11.20±1.03	127.54±21.85
Statistics	Mean	338.44±3.48	10.06±0.68	126.15±10.90
	Min	149.62±4.72	8.25±1.31	113.34±20.80
	Max	452.28±8.02	11.20±1.03	145.79±22.51

Table 1: The average concentrations of specific activity in the different gold tailings soil samples.

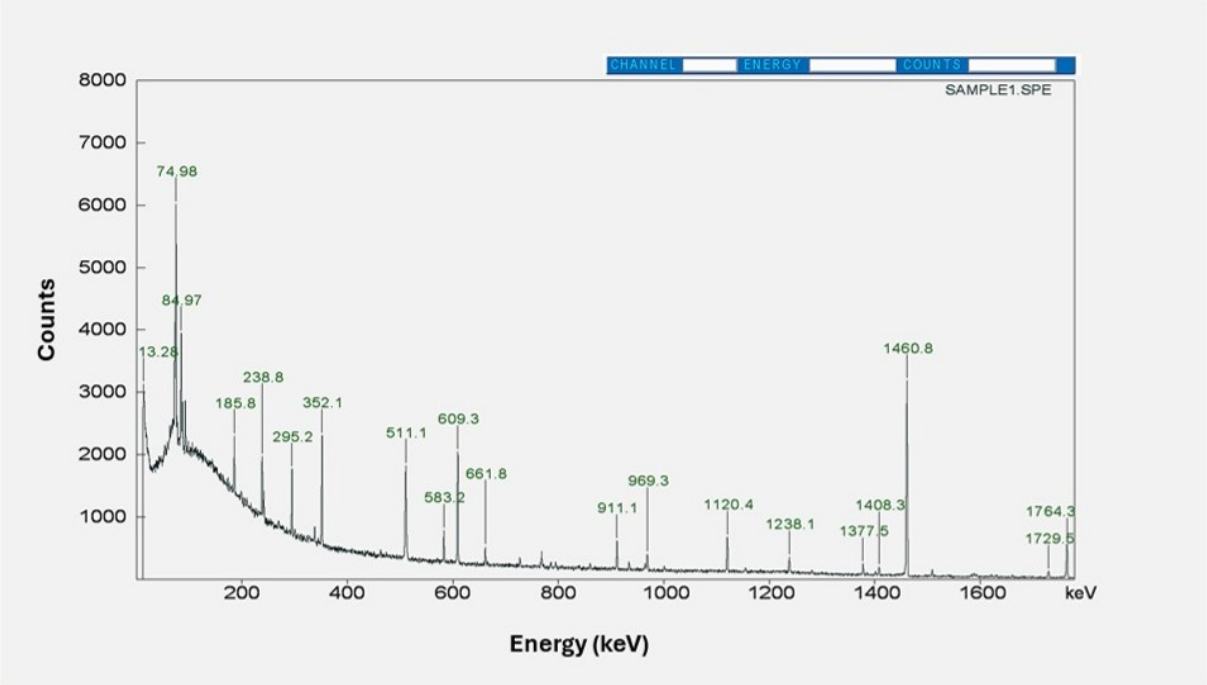

Figure 2: Typical HPGe gamma - ray spectrum due to the γ-emitting NORM in gold tailings soil samples [21].

The estimated radiological indices are presented in Table 2. The CMO and KLF samples had permissible Ra_{Eq} below 370 Bq/kg [8]. CMRG and RDP samples had Ra_{Eq} values of 475.61±1.91 and 478.10±1.76 Bq/kg, respectively. In all samples, indoor and outdoor ADR were above permissible limits of 84 and 59 nGy/h, respectively. The total AEDE was higher than the sum of 0.48 mSv/y and even higher than the global average of 1 mSv/y. The indoor and outdoor ELCR were high. The AGDE was high, with a maximum mean value of 1484.42±26.10 μSv/y in RDP and the minimum of 551.22±17.39 μSv/y in KLF samples. The mean I_α index in KLF samples was below a unity at 0.75±0.02, and it was above a unity in the rest.

Tailings	Radiological Hazards	Min	Max	Median	Mean	STDev	RV
	Ra_{Eq}(Bq/kg)	245.14±6.12	440.06±8.98	316.78±6.42	323.50±7.04	43.90	370
	ADR_{In} (nGy/h)	222.65±5.65	399.97±8.16	287.37±5.81	293.98±5.94	39.98	84
	ADR_{Out}(nGy/h)	113.52±2.84	203.65±4.16	146.42±2.97	149.73±3.27	20.31	59
CMO	$AEDE_{Tot}$(mSv/y)	1.23±0.01	2.21±0.14	1.59±0.10	1.63±0.02	0.22	0.48
	$ELCR_{Ind}(\times 10^{-3})$	3.83±0.10	6.87±0.14	4.94±0.04	5.05±0.11	0.69	1.16
	$ELCR_{Out}(\times 10^{-3})$	0.49±0.01	0.87±0.02	0.63±0.01	0.64±0.01	0.09	0.29
	AGDE (μSv/y)	764.13±19.27	1368.26±28.13	983.76±20.06	1006.34±22.10	136.10	300
	I_α	1.12±0.03	2.07±0.04	1.48±0.03	1.51±0.03	0.22	≤1
	Ra_{Eq}(Bq/kg)	236.77±6.25	702.52±10.23	476.93±6.08	475.61±1.91	114.36	370
	ADR_{In} (nGy/h)	217.37±5.68	644.74±3.91	437.11±5.48	436.52±1.73	104.94	84
	ADR_{Out}(nGy/h)	109.56±2.90	324.465±4.73	220.36±2.81	219.91±0.88	52.81	59
CMRG	$AEDE_{Tot}$(mSv/y)	0.67±0.05	1.99±0.12	1.35±0.06	1.35±0.02	0.32	0.48
	$ELCR_{Ind}(\times 10^{-3})$	1.88±0.07	5.57±0.19	3.78±0.09	3.78±0.03	0.91	1.16
	$ELCR_{Out}(\times 10^{-3})$	0.47±0.14	1.39±0.38	0.95±0.19	0.94±0.02	0.23	0.29
	AGDE (μSv/y)	736.11±19.61	2174.44±31.80	1479.65±18.95	1476±26.51	353.87	300
	I_α	1.11±0.03	3.40±0.05	2.24±0.03	2.26±0.03	0.55	≤1
	Ra_{Eq}(Bq/kg)	142.74±4.78	1406.45±14.16	458.66±8.11	478.10±1.76	266.97	370
	ADR_{In} (nGy/h)	130.86±4.42	1292.61±13.04	420.91±7.47	438.75±7.86	245.46	84
	ADR_{Out}(nGy/h)	66.07±2.23	650.43±6.56	212.08±3.76	221.08±3.87	123.46	59
RDP	$AEDE_{Tot}$(mSv/y)	0.72±0.02	7.14±0.06	2.23±0.04	2.42±0.04	1.36	0.48
	$ELCR_{Ind}(\times 10^{-3})$	2.25±0.08	22.19±0.22	7.23±0.13	7.53±0.13	4.21	1.16
	$ELCR_{Out}(\times 10^{-3})$	0.28±0.01	2.79±0.03	0.91±0.02	0.95±0.02	0.539	0.29
	AGDE (μSv/y)	444.81±15.16	4361.69±44.12	1423.89±25.37	1484.42±26.10	827.58	300
	I_α	0.65±0.02	6.80±0.07	2.17±0.04	2.26±0.04	1.30	≤1
	Ra_{Eq}(Bq/kg)	80.03±3.68	301.23±7.50	86.94±4.00	175.57±2.18	113.66	370
	ADR_{In} (nGy/h)	73.17±3.34	276.11±6.79	79.42±3.63	160.80±4.95	104.42	84
	ADR_{Out}(nGy/h)	27.20±7.72	138.49±11.89	40.39±8.12	81.48±9.69	52.71	59
KLF	$AEDE_{Tot}$(mSv/y)	0.40±0.02	1.53±0.04	0.44±0.04	0.89±0.03	0.58	0.48
	$ELCR_{Ind}(\times 10^{-3})$	1.26±0.06	4.74±0.02	1.36±0.06	2.76±0.09	1.79	1.16
	$ELCR_{Out}(\times 10^{-3})$	0.16±0.06	0.60±0.12	0.17±0.07	0.35±0.09	0.539	0.29
	AGDE (μSv/y)	252.791±11.85	943.72±23.70	274.39±25.37	551.22±17.39	355.07	300
	I_α	0.32±0.02	1.32±0.03	0.34±0.02	0.75±0.02	0.52	≤1

Table 2: Comparison of the gold tailings radiological indices with the recommended limit (RV).

5 Conclusion

Soil samples from gold tailings in the west of Johannesburg were collected and measured using a high-resolution HPGe γ-ray spectroscopy to assess radioactivity and associated health risk indices.

The analysis revealed only geogenic radionuclides and no anthropogenic radionuclides in the samples. The concentrations of ^{226}Ra, ^{232}Th, and ^{40}K were 338.44±3.48, 10.06±0.68, and 126.15±10.90 Bq/kg, respectively. The results indicated ^{222}Ra was higher than the global recommended average at all sites investigated. The different radiological indices exceeded the recommended values (RV) and in descending order the averages are AGDE > Ra_{Eq} > ADR > ELCR > AEDE > I_a with values 1129.54 ± 46.63 μSv/y > 363.20 ± 7.81 Bq/kq > 500.56 ± 15.90 nGy/h > 5.62 ± 0.20×10^{-3} > 1.57±0.06 mSv/y > 1.45±0.30.

Our findings indicate worrying levels of natural radioactivity at the investigated sites, with ^{238}U products above global averages, and there is a need to take both immediate and strategic long-term measures. Immediate measures include restricting access to the affected areas, erecting warning signs, and raising public awareness through print and social media. For strategic long-term measures, the contaminated soil should be covered with clean soil, and phytoremediation techniques should be applied to restore the area. Our results emphasize the need for continuous monitoring of radioactive pollution in the area to ensure public safety and the health of the environment.

Acknowledgments

The Department of Physics at the Faculty of Science and Agriculture, University of Zululand, supported this study. The author would like to extend special thanks to Mr A. Kwelilanga, an applied nuclear/radiation physicist at iThemba LABS, for his outstanding expertise in gamma spectrometric analysis.

References

[1] B. Kengni and H. Mostert, "Regulation and remediation of the impacts of mine wastes on land and water in south africa," *Journal of Energy & Natural Resources Law*, vol. 40, no. 3, pp. 337–360, 2022.

[2] C. Kamunda, M. Mathuthu, and M. Madhuku, "An assessment of radiological hazards from gold mine tailings in the province of gauteng in south africa," *International Journal of environmental research and public health*, vol. 13, no. 1, p. 138, 2016.

[3] M. C. Laker, "Environmental impacts of gold mining—with special reference to south africa," *Mining*, vol. 3, no. 2, pp. 205–220, 2023.

[4] E. Burford, M. Fomina, and G. Gadd, "Fungal involvement in bioweathering and biotransformation of rocks and minerals," *Mineralogical Magazine*, vol. 67, no. 6, pp. 1127–1155, 2003.

[5] F. Winde, "Uranium pollution of the wonderfonteinspruit, 1997-2008 part 1: Uranium toxicity, regional background and mining-related sources of uranium pollution," *Water Sa*, vol. 36, no. 3, pp. 239–256, 2010.

[6] M. Zivuku, N. A. Kgabi, and V. M. Tshivhase, "Assessment of radioactivity in particulate matter and soil from selected mining towns of erongo region, namibia," *Scientific African*, vol. 20, p. e01722, 2023.

[7] P. Chanda-Kapata, "Public health and mining in east and southern africa: A desk review of the evidence," *Zambia Ministry of Health with Training and Research Support Centre in the Regional Network for Equity in Health in East and Southern Africa (EQUINET)*, 2020.

[8] S. Unscear, "effects of ionizing radiation," *United Nations, New York*, pp. 453–487, 2000.

[9] M. Nassef and A. Kinsara, "Occupational radiation dose for medical workers at a university hospital," *Journal of Taibah University for Science*, vol. 11, no. 6, pp. 1259–1266, 2017.

[10] Y. Tomkiv, T. Perko, D. H. Oughton, I. Prezelj, M. C. Cantone, and E. Gallego, "How did media present the radiation risks after the fukushima accident: a content analysis of newspapers in europe," *Journal of Radiological Protection*, vol. 36, no. 2, p. S64, 2016.

[11] N. Yamaguchi, I. Taniyama, T. Kimura, K. Yoshioka, and M. Saito, "Contamination of agricultural products and soils with radiocesium derived from the accident at tepco fukushima daiichi nuclear power station: monitoring, case studies and countermeasures," *Soil science and plant nutrition*, vol. 62, no. 3, pp. 303–314, 2016.

[12] M. Mpanza, E. Adam, and R. Moolla, "Perceptions of external costs of dust fallout from gold mine tailings: West wits basin," *Clean Air Journal*, vol. 30, no. 1, pp. 1–12, 2020.

[13] N. Makhubele, P. Rathebe, T. Mbonane, J. Manganyi, G. Mizan, and M. D. Masekameni, "Indoor/outdoor particulate matter (respirable dust) and respirable crystalline silica source tracking in households located proximal to gold mine tailings in johannesburg, south africa," *Journal of Air Pollution and Health*, 2024.

[14] M. U. Khandaker, P. J. Jojo, and H. A. Kassim, "Determination of primordial radionuclides in natural samples using hpge gamma-ray spectrometry," *APCBEE Procedia*, vol. 1, pp. 187–192, 2012.

[15] M. Tzortzis, H. Tsertos, S. Christofides, and G. Christodoulides, "Gamma-ray measurements of naturally occurring radioactive samples from cyprus characteristic geological rocks," *Radiation Measurements*, vol. 37, no. 3, pp. 221–229, 2003.

[16] M. Akpanowo, I. Umaru, S. Iyakwari, E. O. Joshua, S. Yusuf, and G. B. Ekong, "Determination of natural radioactivity levels and radiological hazards in environmental samples from artisanal mining sites of anka, north-west nigeria," *Scientific African*, vol. 10, p. e00561, 2020.

[17] W. O. Aguko, R. Kinyua, J. G. Githiri *et al.*, "Natural radioactivity and excess lifetime cancer risk associated with soil in kargi area, marsabit-kenya," *Journal of Geoscience and Environment Protection*, vol. 8, no. 12, p. 127, 2020.

[18] H. Taskin, M. Karavus, P. Ay, A. Topuzoglu, S. Hidiroglu, and G. Karahan, "Radionuclide concentrations in soil and lifetime cancer risk due to gamma radioactivity in kirklareli, turkey," *Journal of environmental radioactivity*, vol. 100, no. 1, pp. 49–53, 2009.

[19] M. Tufail, "Radium equivalent activity in the light of unscear report," *Environmental monitoring and assessment*, vol. 184, no. 9, pp. 5663–5667, 2012.

[20] M. Al-Hwaiti, O. Al-Khashman, L. Al-Khateeb, and F. Freig, "Radiological hazard assessment for building materials incorporating phosphogypsum made using eshidiya mine rock in jordan," *Environmental Earth Sciences*, vol. 71, no. 5, pp. 2257–2266, 2014.

[21] C. Kalfas, M. Axiotis, and C. Tsabaris, "Spectrw: A software package for nuclear and atomic spectroscopy," *Nuclear Instruments and Methods in Physics Research Section A: Accelerators, Spectrometers, Detectors and Associated Equipment*, vol. 830, pp. 265–274, 2016.

This page intentionally left blank.

Exciting the Hoyle state in ^{12}C selectively populated using the ^{10}B(^{6}Li,^{4}He)^{12}C reaction

J. Carter[1], M. B. Ajani[1], S. O. O. John[1,2], F. Moosa[1] and I. T. Usman[1]

[1]School of Physics, University of the Witwatersrand, Johannesburg, 2050, South Africa
[2]Department of Physics, Nasarawa State University, Keffi, Nigeria

E-mail: john.carter@wits.ac.za

Abstract. An excited state in ^{12}C close to the 3α-breakup was predicted by Fred Hoyle in 1954 and was later identified by Cook *et al*. in 1957 as the 0^+ state lying at an excitation energy of 7.65 MeV. It was the key to understanding the production of ^{12}C and heavier elements in the core of young stars. Fusion of two α particles leads to the production of excited ^{8}Be* and then the capture of another α particle (α + ^{8}Be) produces excited ^{12}C* close to the Hoyle state. Subsequently, as opposed to the 3α-breakup of ^{12}C*, γ decay from the Hoyle state to the 2^+ (4.43 MeV) state and down to the ^{12}C ground-state 0^+ (0.0 MeV) results in the production of stable ^{12}C. However, the observed enhanced ^{12}C production rate in older hotter stars was speculated to proceed through excited states of the Hoyle state. Existence of the broad excited Hoyle states ^{12}C(2^+, 9.6 MeV) and ^{12}C(4^+, 13.3 MeV) has been reported only relatively recently, having previously not been identified because of other nearby strongly-excited states in ^{12}C. The ^{10}B(^{6}Li,α)^{12}C* reaction selectively excites 2^+ states in ^{12}C and because of the high Q-value = + 23.713 MeV, the high-energy α particles are easily identified with good energy resolution. Measurements were taken at the EN Tandem Van de Graaff accelerator of NRF-iThemba LABS (Gauteng) using ^{6}Li beams at and close to E_{Lab} = 20 MeV incident on a thin ^{10}B target. The observed high-energy α particles correspond to states excited in ^{12}C up to and above the second excited Hoyle state.

1 Introduction

Production of ^{12}C by nucleosynthesis in the core of younger stars was postulated by Fred Hoyle in the early 1950s. The abundance of ^{12}C is due to the triple-α process by which it is created. The triple-α process is a set of nuclear fusion reactions by which three ^{4}He nuclei are transformed into ^{12}C. At normal stellar temperatures, the energies of the nuclei are too low to overcome the Coulomb barrier and therefore to initiate fusion reactions. However, because of quantum mechanical tunneling through the Coulomb barrier, there is a possibility that the fusion reaction will occur. In the first reaction of the triple-α process, two α-particles fuse to form ^{8}Be. The Q-value for this reaction is − 93.7 keV. Since ^{8}Be nuclei are unstable, they rapidly decay back into two α-particles within a timescale of the order 10^{-16} s. However, at sufficiently high temperatures and densities there will always be a small but non-negligible fraction of ^{8}Be present. There is, therefore, a finite probability for a third α particle to tunnel in and form ^{12}C. The reaction rate for charged particles is determined by the Maxwell-Boltzmann velocity distribution and the probability of tunneling through the Coulomb barrier. Multiplication of the Maxwell-Boltzmann velocity distribution by the tunneling probability results in the so-called Gamow window [1]. Given the two-stage nature of the triple-α process, Hoyle pointed out that the reaction rate would be very slow at normal stellar temperatures and densities being unable to account for the observed abundance of ^{12}C. To overcome this, Hoyle suggested that ^{12}C must have an excited

state [2] with an energy slightly above the α + ^{8}Be ground-state energy (E_x = 7.37 MeV in ^{12}C) very nearly equal to the most effective energy for tunneling at normal stellar temperatures (10^8 K) [3]. This excited state of ^{12}C with an energy of 7.65 MeV and total angular momentum and parity $J^{\pi} = 0^+$ was discovered experimentally in 1957 by Cook *et al*. [4] and is known as the Hoyle state. If the Hoyle state did not exist or if its energy were slightly different, the abundance of ^{12}C would be reduced and so would the possibility of organic life. It should be noted that the Hoyle state lies slightly above the 3α-decay threshold in ^{12}C at E_x = 7.28 MeV.

Although numerous investigations have been made of the excited states in ^{12}C, the study of the structure of the Hoyle state and its possible excited states is still a subject of great interest. The Hoyle state was originally conjectured to be a linear chain of 3 α-particles (non-spherical) by Haruhiko Morinaga in 1956 [5], and as a result the $J^{\pi} = 0^+$ Hoyle state should be accompanied by excited states forming a $J^{\pi} = 0^+, 2^+, 4^+\ldots$ rotational band. It should be noted that in hotter stars for the observed ^{12}C production rate, solar models included an assumed excited 2^+ Hoyle state at E_x = 10 MeV in ^{12}C in the Nuclear Astrophysics Compilation of Reaction Rates (NACRE) in the 1980s. Only relatively recently has experimental evidence been presented for the 2^+ excitation of the Hoyle state (E_x = 9.6 MeV in ^{12}C) in 2009 by Freer *et al*. [6] using ^{12}C(*p*,*p*′) at E_p = 66 MeV, and in 2011 by Itoh *et al*. [7] using ^{12}C(α,α′) at E_α = 386 MeV, while for the 4^+ excitation of the Hoyle state (E_x = 13.3 MeV in ^{12}C) in 2011 by Freer *et al*. [8] using ^{12}C(α,3α)α at E_α = 22 MeV.

The aim of this work is to identify excited states in ^{12}C with particular reference to the Hoyle state and its excited states using the ^{10}B(^{6}Li,α)^{12}C reaction with a *Q*-value = + 23.713 MeV. Here, the relatively high positive *Q*-value allows states in ^{12}C to be excited up to and above the second excited Hoyle state using ^{6}Li beams provided by a relatively small accelerator.

2 Experimental Details

The experimental work was undertaken at NRF-iThemba LABS (Gauteng), Johannesburg, South Africa. Beams of ^{6}Li were provided by the EN Tandem Van de Graaff accelerator at energies close to E_{Lab} = 20 MeV, some three times the Coulomb barrier for the ^{6}Li + ^{10}B system. The ^{6}Li beam was incident on a thin self-supporting ^{10}B target of areal density 60 μg/cm^2 inside a small scattering chamber. A high-resolution Δ*E*-*E* Gas Ionisation Detector (GID) was attached to the rotatable offset-lid of the scattering chamber and could be positioned at scattering angles from θ_{Lab} = 0° to 130°. After going through a thin parylene entrance window, the scattered particles' Δ*E* energy-loss signals were obtained by passing through the iso-butane gas volume of the GID to be stopped by a silicon surface-barrier detector providing E_{stop}. The Δ*E* and E_{stop} signals (providing $E_{total} = E_{stop} + \Delta E$) were processed by a CAMAC-based multi-parameter data acquisition system. Figure 1 shows a typical Δ*E* *versus* E_{total} 2-dimensional plot, providing clear separation of the various *Z* products.

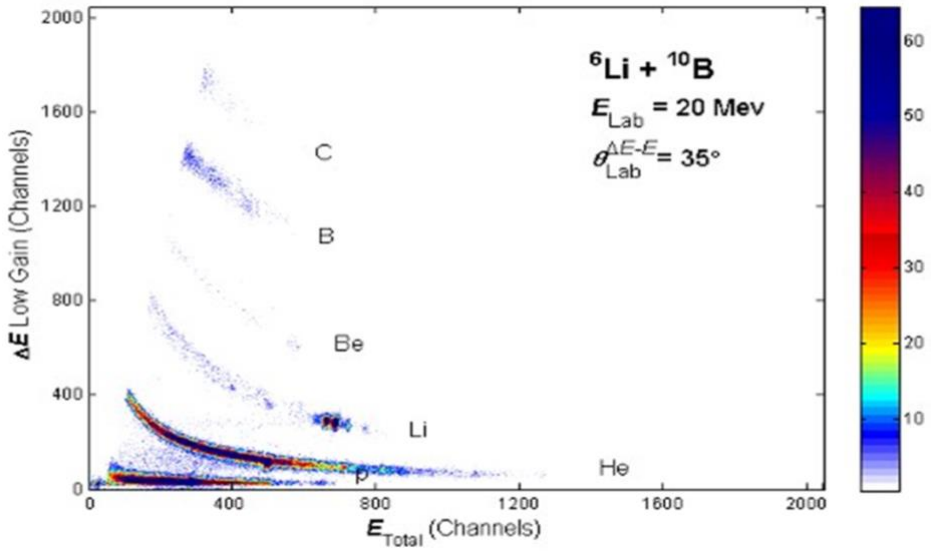

Figure 1: Typical 2-dimensional plot of the ^{6}Li + ^{10}B reaction products showing clear separation in *Z*.

After conversion from channels to measured energy in MeV, Figure 2 shows the resulting spectrum for the $Z = 2$ locus displayed in Figure 1, noting that both ^{3}He and ^{4}He products can be present. The upper part of the spectrum has been multiplied up by a factor of x15 and is shown in red. As can be seen, the first excited state ^{12}C(2^{+}, 4.43 MeV) and the fourth excited state ^{12}C (3^{-}, 9.64 MeV) are quite prominent with the ground state and Hoyle state, both 0^{+}, being quite weak. This apparent selectivity of the first 2^{+} state excited in ^{12}C was confirmed in an angular distribution from $\theta_{\mathrm{Lab}} = 15°$ to 130°.

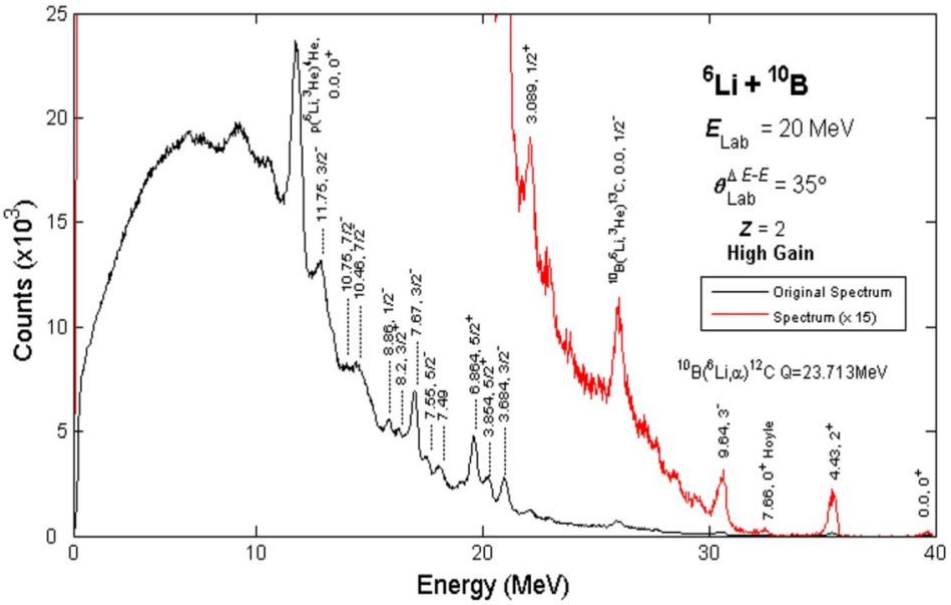

Figure 2: The $Z = 2$ locus of Figure 1 projected down onto the energy axis in MeV. The red spectrum is the original spectrum multiplied by a factor of 15 for the higher-energy peaks to be more easily seen.

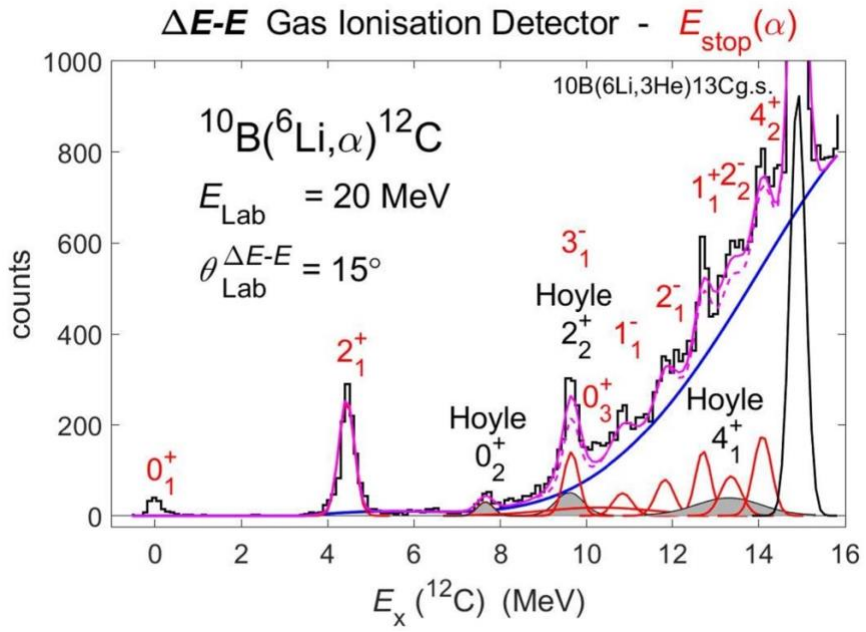

Figure 3: Excitation-energy spectrum for ^{12}C obtained using a kinematic conversion from the measured α-channel for the reaction ^{10}B(^{6}Li,α)^{12}C.

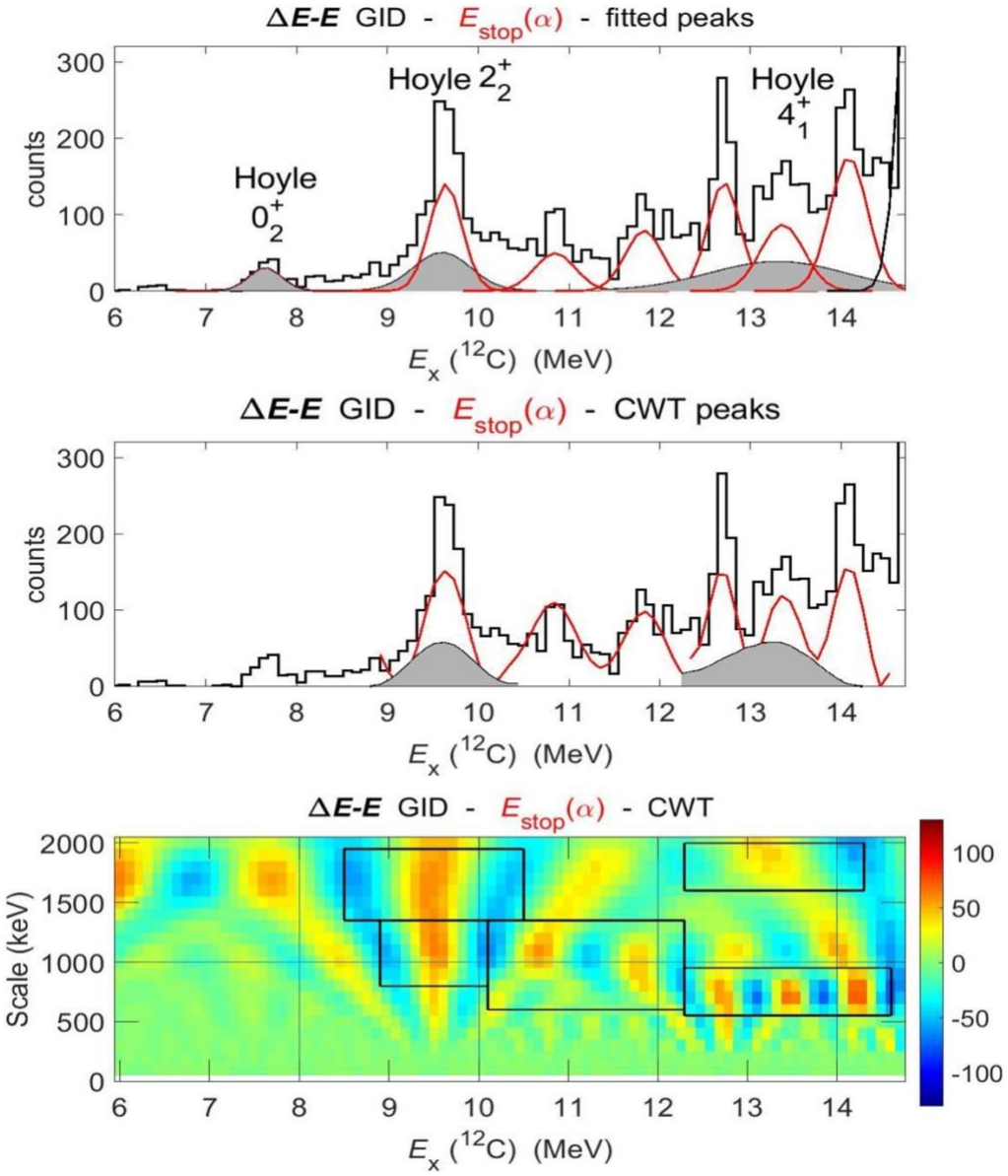

Figure 4. Top panel: resulting ^{12}C excitation-energy spectrum at θ_{Lab} = 15° after subtraction of the evaporation α-background from the measured α-channel data as shown in Figure 3. Fitted known states in ^{12}C are shown in red together with fitted known Hoyle states shown grey shaded as in Figure 3. Middle panel: measured ^{12}C excitation-energy spectrum as in top panel. Narrow peaks shown in red are from summed coefficients in the three lower rectangles while the excited Hoyle state peaks grey shaded are from summed coefficients in the upper two rectangles as indicated in the CWT coefficient plot of the lower panel. Adjacent relatively weak features (mainly yellow) are not considered. Lower panel: Wavelet Analysis CWT coefficient plot for the measured ^{12}C excitation-energy spectrum (histogram shown in upper and middle panels).

3 Results and Analysis

An energy spectrum of the states excited in ^{12}C via the ^{10}B(^{6}Li,α)^{12}C reaction was obtained using a kinematic conversion of the measured alpha energy spectrum and is shown in Figure 3 by the black histogram for a scattering angle of θ_{Lab} = 15° (best energy resolution and good count rate). Here, known states excited in ^{12}C are identified in red with the known Hoyle and Hoyle excited states shown grey shaded. The smooth continuous blue line underneath the measured histogram is a sixth-order polynomial sufficiently flexible to represent a background of evaporation α-particles from the ^{6}Li + ^{10}B scattering reaction. The continuous

purple line represents a fit to the histogram with all of the components while the dashed purple line excludes the Hoyle excited states. As can be seen, there is a reasonably good fit to the measured histogram using all of the components identified below, which deteriorates with the exclusion Hoyle excited states. However, such a fitting procedure is not entirely satisfactory and is subjective since some positions and widths of excited states may not have been determined from previous investigations. In addition, the exact formulation of the evaporation α-background is uncertain, which could lead to ambiguities in the final fit to the data. A more conventional representation of the measured ^{12}C excitation-energy spectrum is shown in the top panel of Figure 4 resulting from the subtraction of the evaporation α-particle background from the measured spectrum. Here, the well-known excited states in ^{12}C are shown by the red peaks and the previously identified excited Hoyle state peaks are shown grey shaded.

The use of Wavelet Analysis (details can be found in Ref. [9]), however, overcomes the problems of a multi-parameter fit to measured excitation-energy spectra. The positions and widths of states excited can be extracted directly from the two-dimensional plot of Wavelet coefficients. A Mother wavelet is chosen that best represents the features of the measured spectrum which, in the present case, can be fitted with Gaussian peaks. As such, a Complex Morlet (cosine folded with a Gaussian function) was used. Starting with a narrow Mother wavelet it is moved along the measured excitation-energy spectrum and the overlap with the data is determined as a function of excitation energy. The process is repeated by stretching the Mother wavelet to increase its width until a coefficient plot is obtained of scale *versus* excitation energy, as shown in the lower panel of Figure 4.

It should be noted that subtraction of the smooth continuous α-background from the measured ^{12}C excitation-energy spectrum does not influence the fine structure (peak positions and widths) extracted. Regions identified by the three lower rectangles in the lower panel of Figure 4 indicate the presence of clear maxima and minima in the coefficient plot which, after summing along the scale axis, represent the known ^{12}C excited states (red peaks shown in the middle panel of Figure 4). The two upper rectangles in the lower panel of Figure 4 indicate broader peaks and the presence of the underlying first and second excited Hoyle states (grey shaded peaks also shown in the middle panel of Figure 4). It can be seen that there is an excellent correspondence between the fitted peaks in the top panel of Figure 4 and the extracted peaks from Wavelet Analysis in the middle panel of Figure 4.

4 Summary and Outlook

The ^{10}B(^{6}Li,α)^{12}C reaction at Tandem energies allows access to excited states in ^{12}C up to about 20 MeV due to the very large positive *Q*-value of + 23.713 MeV. States with $J^{\pi} = 0^{+}$ are weakly populated, notably ^{12}C(0^{+}, ground state) and the Hoyle state ^{12}C(0^{+}, 7.6 MeV), while states with $J^{\pi} = 2^{+}$ and above are strongly populated, notably the first excited state ^{12}C(2^{+}, 4.43 MeV). As a result, the first excited Hoyle state ^{12}C(2^{+}, 9.6 MeV) and the second excited Hoyle state ^{12}C(4^{+}, 13.3 MeV) are prominently indicated in the Wavelet Analysis procedure. The novel use of Wavelet Analysis was able to identify the specific excited states in the measured ^{12}C excitation-energy spectrum. As such, it was possible to extract and confirm the existence of the first and second excited Hoyle states in ^{12}C. This was as opposed to a multi-parameter fitting procedure to measured excitation- energy spectra, which relies on a previous knowledge of states excited or an inference of possible states for an improved fit. The width of the first excited Hoyle state was found to be consistent with the width determined previously but the width of the second excited Hoyle state was found to be somewhat smaller, by about 15%, than the previous determination. A ^{10}B(^{6}Li,α)^{12}C coincidence measurement for α and ^{12}C to identify excited Hoyle states is ongoing.

References

[1] Gabor Gyula Kiss, "Proton induced reactions and the astrophysical *p*-process," PhD Thesis (University of Debrecen, 2008).

[2] F. Hoyle, *Astrophys. J. suppl.,* ser. 1, p. 121, 1954.

[3] Frank H. Hsu, "The Physical Universe: An Introduction to Astronomy," (University Science Books, 1982).

[4] C. W. Cook *et al*., *Phys. Rev.*, vol. 107, p. 508, 1957.

[5] H. Morinaga, *Phys. Rev.*, vol. 101, p. 254, 1956.

[6] M. Freer *et al*., *Phys. Rev. C*, vol. 80, 041303(R), 2009.

[7] M. Itoh *et al*., *Phys. Rev. C*, vol. 84, 054308, 2011.

[8] M. Freer *et al*., *Phys. Rev. C*, vol. 83, 034314, 2011.

[9] C. Torrence and G. P. Compo, *Bull. of the Am. Meteorological Soc*., vol. 69, no. 1, p. 61, 1998.

This page intentionally left blank.

DIVISION

C

PHOTONICS

Comparative Theoretical Analysis of Entangled Quantum States for Enhanced Sensing Applications

Kelvin Mpofu[1] **and Patience Mthunzi-Kufa**[2]

[1]Biophotonics, Photonic Centre, Manufacturing, Council of Scientific and Industrial Research (CSIR), Pretoria, South Africa

[2]School of Interdisciplinary Research and Graduate Studies (UNESCO), College of Graduate Studies, University of South Africa, Preller Street, Muckleneuk Ridge, Pretoria, South Africa

E-mail: kmpofu@csir.co.za

Abstract. Quantum metrology offers a route to enhance precision measurements by exploiting non-classical states of light. In this paper, we present a comparative theoretical analysis of phase sensitivity across several entangled quantum states, NOON, M&M, Twisted NOON, GHZ, Entangled Coherent States (ECS), and BAT states, under ideal conditions. Our findings reveal that Twisted NOON states achieve the highest enhancement in precision, exhibiting enhanced scaling beyond the conventional Heisenberg limit when orbital angular momentum is treated as an additional resource. The results highlight the value of tailoring quantum states to specific metrological tasks and provide a foundation for future experimental realizations in quantum sensing.

1 Introduction

In an era where precision underpins progress, metrology, the science of measurement, plays a foundational role across scientific and technological domains [1]. From calibrating atomic clocks to aligning satellite systems and enhancing diagnostic imaging, precise measurement systems are indispensable [2, 3]. Classical metrology, particularly optical interferometry, has long served as the gold standard in achieving high-precision measurements [4]. However, its capabilities are ultimately bounded by the Standard Quantum Limit (SQL), a fundamental sensitivity ceiling imposed by quantum noise associated with independent particles or photons [5]. Quantum metrology [6] seeks to transcend this boundary by harnessing non-classical resources, most notably quantum entanglement and squeezing. These uniquely quantum phenomena enable phase sensitivities that scale more favorably with resource number, often reaching or surpassing the Heisenberg Limit (HL), where phase uncertainty scales as $\Delta\varphi \sim 1/N$ as opposed to the SQL which scales as $\Delta\varphi \sim 1/\sqrt{N}$ [7]. The realization of this quantum advantage has profound implications for next-generation sensing, imaging, and navigation systems [7]. Numerous experimental efforts have demonstrated the feasibility of preparing the quantum states analyzed in this work. Coherent states, the cornerstone of classical optics, are readily produced using stable laser sources and are foundational in all quantum optics laboratories. NOON states have been experimentally realized in photonic platforms, with successful demonstrations up to five-photon NOON states using spontaneous parametric down-conversion and beam splitters, as reported by Afek et al. [8]. The experimental preparation of M&M states was demostrated for M=3 by Smith [9]. GHZ states, another maximally entangled resource, have been extensively realized across diverse platforms including photons, trapped ions, and superconducting qubits [10, 11]. Twisted NOON states, which embed orbital angular momentum (OAM) into entangled photons, have been generated using spatial light modulators and tailored optical elements, with experiments by Yang et al. [12]. Entangled Coherent States (ECS) have been synthesized in cavity-QED (quantum electrodynamics) and trapped-ion platforms using techniques [13]. Lastly, BAT states, which resemble symmetric ECS but are phase-insensitive, have not always been labeled explicitly in experimental work but have

analogues in delocalized single-photon interference experiments. Together, these experimental demonstrations provide strong support for the physical realizability of the quantum resources assessed in this comparative study. Among the most promising candidates for quantum-enhanced metrology are entangled states of light. These include NOON states [7], GHZ states [14], ECS [15], and more recent variants such as Twisted NOON [12] and M&M states. Each of these states offers different trade-offs between sensitivity, robustness, and experimental feasibility. Yet, a unified theoretical comparison of their phase precision performance under ideal conditions remains essential for guiding experimental design and deployment in real-world sensing platforms. This paper presents a comparative theoretical analysis of key entangled quantum states in the context of phase estimation, arguably the most fundamental task in optical quantum metrology. Other works do not put all the quatum states in one place for comparison.This work provides an extensive and more universal comparison of entangled states for sensing. Using analytical and numerical tools, we evaluate their performance based on Fisher Information and the Cramér-Rao bound. By doing so, we identify the quantum states best suited for achieving precision beyond the SQL and highlight the physical principles that enable their superior performance. The results serve as a roadmap for the rational design of entangled-state-based quantum sensors and provide insight into the fundamental limits of measurement precision.

2 Quantum states

This study investigates the theoretical phase sensitivity of various entangled quantum states in idealized interferometric metrology scenarios. The analysis is based on well-established tools in quantum estimation theory, namely the quantum Fisher information (QFI) and the Cramér-Rao bound, which provide lower limits on the precision of parameter estimation. In this study, we analyzed a variety of quantum states commonly proposed for enhanced phase estimation in optical interferometry. Each state represents a different quantum resource configuration with distinct precision scaling properties. The states are defined as follows:

- **NOON State:**

$$|\psi_{\text{NOON}}\rangle = \frac{1}{\sqrt{2}}\left(|N\rangle_a|0\rangle_b + |0\rangle_a|N\rangle_b\right). \tag{1}$$

  Where $|N\rangle$: Fock state with N photons (or particles) in a given mode. a, b are optical modes or interferometer arms (e.g., input/output ports of a Mach-Zehnder interferometer). This maximally path-entangled state achieves Heisenberg-limited phase sensitivity but is highly susceptible to photon loss.

- **M&M State:**

$$|\psi_{\text{M\&M}}\rangle = \frac{1}{\sqrt{2}}\left(|M\rangle_a|m\rangle_b + |m\rangle_a|M\rangle_b\right), \quad \text{with } M - m = N \tag{2}$$

  The M&M state is a generalization of the NOON state with unequal photon numbers in the two modes. Here M-m=N is the difference in photon number. A generalization of the NOON state with tunable imbalance, offering improved robustness at the cost of reduced entanglement.

- **Twisted NOON State:**

$$|\psi_{\text{Twisted}}\rangle = \frac{1}{\sqrt{2}}\left(|N, +\ell\rangle_a|0\rangle_b + |0\rangle_a|N, -\ell\rangle_b\right) \tag{3}$$

  This state incorporates orbital angular momentum ℓ, which improves sensitivity to angular displacement and offers enhanced phase precision scaling as $\Delta\varphi \sim 1/(\ell N)$.

- **GHZ State:**

$$|\psi_{\text{GHZ}}\rangle = \frac{1}{\sqrt{2}}\left(|0\rangle^{\otimes N} + |1\rangle^{\otimes N}\right) \tag{4}$$

  The Greenberger–Horne–Zeilinger (GHZ) state is a maximally entangled multi-particle. It is a multipartite entangled state analogous to the NOON state for qubits, achieving Heisenberg scaling in spin-based or atomic systems.

- **Entangled Coherent State (ECS):**

$$|\psi_{\text{ECS}}\rangle = \mathcal{N}_\alpha\left(|\alpha\rangle_a|0\rangle_b + |0\rangle_a|\alpha\rangle_b\right) \tag{5}$$

  where $\mathcal{N}_\alpha = \left[2(1 + e^{-|\alpha|^2})\right]^{-1/2}$ is the normalization constant. ECSs are optical analogs of cat states and offer sub-Heisenberg scaling under ideal conditions.

- **BAT State (Balanced Amplified Two-mode state):**

$$|\psi_{\text{BAT}}\rangle = \frac{1}{\sqrt{2}}\left(|\alpha\rangle_a|0\rangle_b + |0\rangle_a|\alpha\rangle_b\right) \tag{6}$$

The BAT state (Balanced Amplified Two-mode) describes a coherent superposition of single-mode excitations distributed across two optical modes. A simplified state with moderate entanglement and practical stability, suitable for experimental implementations with limited resources BAT states exhibit moderate entanglement and are experimentally accessible in interferometric setups using optical amplifiers.

- **Coherent State (Classical Benchmark):**

$$|\psi_{\text{coh}}\rangle = |\alpha\rangle_a|\beta\rangle_b \tag{7}$$

Here, $|\alpha\rangle$ and $|\beta\rangle$ are coherent states in modes a and b, respectively. These states follow classical statistics and are limited by the standard quantum limit $\Delta\varphi \sim 1/\sqrt{N}$.

Photon Number Dependence in ECS and BAT States
For coherent and coherent-derived states such as ECS and BAT, the resource N corresponds to the mean photon number $\langle\hat{n}\rangle = |\alpha|^2$. Consequently, their phase sensitivities follow

$$\Delta\phi_{\text{ECS}}, \Delta\phi_{\text{BAT}} \propto \frac{1}{\sqrt{\langle\hat{n}\rangle}}, \tag{8}$$

indicating sub-Heisenberg scaling but offering practical robustness and experimental feasibility.

Phase Estimation Framework
The phase estimation process is modeled within the configuration shown in Figure 1. Each quantum state is subjected to a unitary phase shift $U(\varphi) = \exp(i\varphi\hat{n})$ on one arm of the interferometer, where $\hat{n}$ is the photon number operator. For each quantum state, we compute the quantum Fisher information $\mathcal{F}_Q$, which quantifies the sensitivity of the state to small changes in the phase φ. The ultimate phase precision limit is then given by the quantum Cramér-Rao bound:

$$\Delta\varphi \geq \frac{1}{\sqrt{\mathcal{F}_Q}}. \tag{9}$$

This provides a lower bound on the standard deviation of any unbiased phase estimator.

3 Quantum sensing model

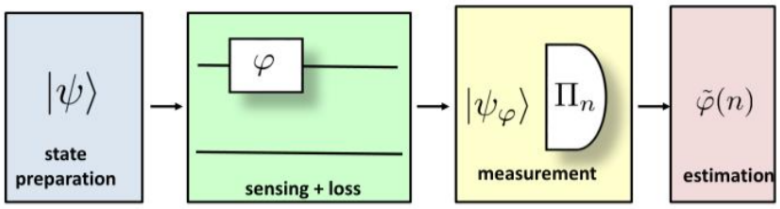

Figure 1: Schematic representation of a quantum metrology protocol. The process consists of four main stages: state preparation, sensing with loss, measurement, and estimation [16].

Description of the Protocol shown in Figure 1:

- **State Preparation $|\psi\rangle$:** A quantum state is prepared with the goal of enhancing sensitivity to an unknown parameter φ. Commonly used probe states include NOON, GHZ, M&M, ECS, and BAT states. These states typically exhibit quantum correlations or entanglement that are leveraged for sub-classical precision.
- **Sensing + Loss (φ):** The quantum state undergoes evolution under the parameter of interest, typically a phase shift φ. This is modeled as a unitary transformation $U(\varphi) = e^{i\varphi\hat{G}}$, where $\hat{G}$ is the generator (often the photon number operator). Simultaneously, photon loss is introduced via noise channels such as amplitude damping or beam-splitter models, impacting the fidelity and precision of the state.

- **Measurement** $(|\psi_\varphi\rangle, \Pi_n)$**:** After evolution, the state $|\psi_\varphi\rangle$ is measured using a suitable set of positive operator-valued measures (POVMs) $\{\Pi_n\}$. This results in a distribution of outcomes n that are dependent on φ. Measurement strategies (e.g., parity, photon counting, homodyne) influence the achievable sensitivity.
- **Estimation** $(\tilde{\varphi}(n))$**:** An estimator $\tilde{\varphi}(n)$ is applied to infer the parameter φ from the outcomes. The estimation performance is bounded by the quantum Cramér-Rao inequality:

$$\Delta\varphi \geq \frac{1}{\sqrt{F_Q[\rho_\varphi]}} \tag{10}$$

where $F_Q[\rho_\varphi]$ is the quantum Fisher information of the evolved (and possibly mixed) state. Different probe states offer different precision scalings, from the SQL to the Heisenberg limit, depending on their quantum resources and robustness to loss.

4 Quantum Cramér-Rao Bound and Fisher Information

Quantum Cramér-Rao Inequality

$$\Delta^2\tilde{\varphi} \geq \frac{1}{F_Q[\rho_\varphi]} \tag{11}$$

Quantum Fisher Information Definitions
For a general quantum state ρ_φ, the QFI is given by:

$$F_Q[\rho_\varphi] = \mathrm{Tr}(\rho_\varphi A_\varphi^2) \tag{12}$$

where A_φ is the symmetric logarithmic derivative (SLD) defined via:

$$\frac{d\rho_\varphi}{d\varphi} = \frac{1}{2}(\rho_\varphi A_\varphi + A_\varphi \rho_\varphi) \tag{13}$$

For Pure States
If $\rho_\varphi = |\psi_\varphi\rangle\langle\psi_\varphi|$, then the QFI simplifies to:

$$F_Q[|\psi_\varphi\rangle] = 4\left(\left\langle\dot{\psi}_\varphi\middle|\dot{\psi}_\varphi\right\rangle - \left|\left\langle\psi_\varphi\middle|\dot{\psi}_\varphi\right\rangle\right|^2\right) \tag{14}$$

where:

$$\left|\dot{\psi}_\varphi\right\rangle = \frac{d}{d\varphi}|\psi_\varphi\rangle \tag{15}$$

For Mixed States
The QFI for a mixed state ρ_φ can be calculated by minimizing the QFI over all purifications $|\Psi_\varphi\rangle$ such that:

$$\rho_\varphi = \mathrm{Tr}_E\left(|\Psi_\varphi\rangle\langle\Psi_\varphi|\right) \tag{16}$$

$$F_Q[\rho_\varphi] = \min_{|\Psi_\varphi\rangle} F[|\Psi_\varphi\rangle] \tag{17}$$

5 Results

Figures 2 and 3 illustrate the theoretical phase precision performance of the various entangled states under both ideal and lossy interferometric conditions. The performance metric used is the QFI, which directly determines the minimum achievable phase uncertainty via the quantum Cramér-Rao bound. This work only considered the ideal cases, with the lossy case being considered for future work. As shown in Figure 2, the NOON, GHZ, and M&M (with $M - m = N$) states achieve Heisenberg-limited scaling, with QFI scaling quadratically with photon number ($F_Q \propto N^2$). Among these, the Twisted NOON state outperforms all others, benefiting from an additional factor of orbital angular momentum ℓ, yielding a scaling of $\Delta\varphi \sim 1/(\ell N)$. Both ECS and BAT states display sub-Heisenberg scaling under ideal conditions. However, their QFI curves remain smooth and stable, suggesting ease of generation and favorable error tolerance in practical setups. The coherent state benchmark, following the SQL ($\Delta\varphi \sim 1/\sqrt{N}$), is clearly outperformed by all quantum-enhanced states in the ideal case.

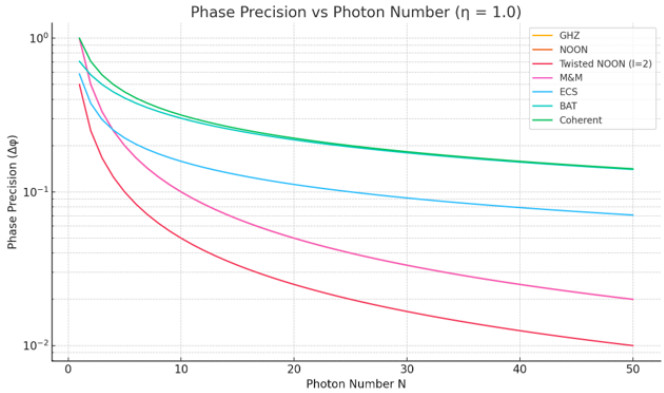

Figure 2: Phase estimation precision $\Delta\varphi$ as a function of photon number N under ideal lossless conditions ($\eta = 1.0$), comparing several quantum states including NOON, M&M (with $M - m = N$), Twisted NOON ($\ell = 2$), entangled coherent states (ECS), BAT states, and coherent states. The M&M configuration used here satisfies the condition $M - m = N$, aligning its scaling with the Heisenberg limit.

Influence of Increasing Topological Charge
The topological charge ℓ in the Twisted NOON state determines the OAM carried by each photon and directly influences the phase sensitivity. As ℓ increases, the effective scaling follows

$$\Delta\phi \propto \frac{1}{\ell N},$$

indicating that larger ℓ values enhance theoretical precision by providing a greater angular phase gradient. However, practical implementations face increasing challenges for higher ℓ due to mode broadening, reduced spatial overlap, and susceptibility to misalignment losses. Thus, while increasing ℓ improves sensitivity in principle, the achievable gain must be balanced against experimental stability and detection efficiency constraints.

Quantum-to-Coherent Precision Ratio Analysis
Figure 3 presents the quantum-to-coherent phase precision ratio (which can be interpreted as an enhancment factor in the precision of the quantum state over the coherent), defined as $\Delta\varphi_{\text{quantum}}/\Delta\varphi_{\text{coherent}}$, plotted as a function of photon number N under ideal (lossless) conditions ($\eta = 1.0$). This ratio quantifies the enhancement in phase estimation achievable by various quantum states compared to classical coherent states. A value less than 1 indicates a quantum advantage. As expected, the NOON and GHZ states (orange and gold curves) exhibit the most substantial improvement, adhering closely to Heisenberg-limited scaling. The twisted NOON states with orbital angular momentum $\ell = 2$ (red) further outperform standard NOON states due to their increased phase sensitivity from the additional angular degree of freedom. M&M states (pink), configured such that $M - m = N$, demonstrate a steady improvement with photon number, eventually exceeding the classical limit. In contrast, ECS (cyan) and BAT states (teal) yield precision ratios slightly below 1 across the entire range of N, indicating modest yet consistent quantum enhancements. These results collectively underscore the importance of state structure in optimizing quantum sensing protocols, especially when balancing sensitivity and scalability.

Clarification on Resource Definition
In quantum metrology, the resource typically refers to the number of photons or particles N used in the estimation process, which bounds the achievable sensitivity through the Heisenberg limit $\Delta\varphi \geq 1/N$. In this work, the Twisted NOON state introduces an additional degree of freedom associated with OAM ℓ. When OAM is considered as a separate resource, the effective phase sensitivity scales as $\Delta\varphi \sim 1/(\ell N)$. Therefore, the term "super-Heisenberg" used herein refers to an enhanced scaling relative to the standard photon-number resource, but does not violate the fundamental Heisenberg limit when both N and ℓ are treated as joint resources.

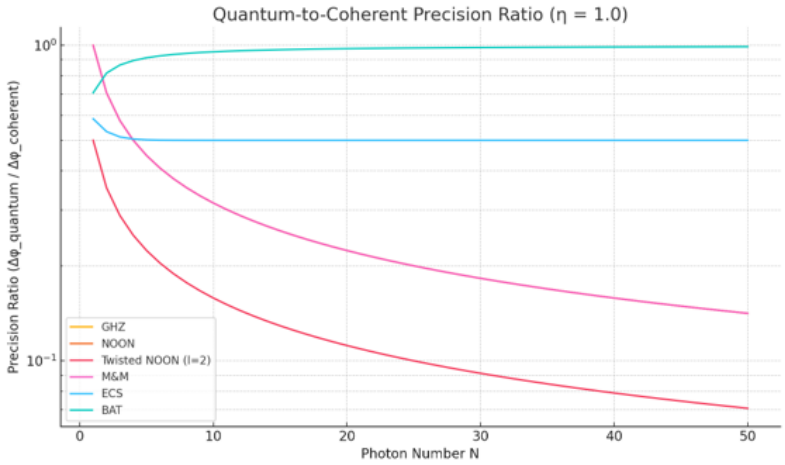

Figure 3: Quantum-to-coherent phase precision ratio as a function of photon number N in the ideal lossless case ($\eta = 1.0$). The plot shows $\Delta\varphi_{\text{quantum}}/\Delta\varphi_{\text{coherent}}$ for several quantum states including GHZ, NOON, Twisted NOON ($\ell = 2$), M&M, ECS, and BAT states. Values below 1 indicate improved precision over classical coherent states. Twisted NOON and NOON states display the greatest enhancement in precision with increasing N, while ECS and BAT provide modest yet consistent improvements. The GHZ is overlapping withe NOON so it is not missing in the plot.

Photon Number Dependence in ECS and BAT States
For coherent and coherent-derived states such as ECS and BAT, the resource count N corresponds to the mean photon number $\langle\hat{n}\rangle = |\alpha|^2$. The phase sensitivity for these states thus scales as

$$\Delta\varphi_{\text{ECS}} \sim \frac{1}{\sqrt{\langle\hat{n}\rangle}}, \quad \Delta\varphi_{\text{BAT}} \sim \frac{1}{\sqrt{\langle\hat{n}\rangle}}.$$

Although these states do not achieve Heisenberg scaling with photon number, their entanglement structure enables a modest enhancement over the standard quantum limit under ideal conditions.

6 Conclusion

In this study, we conducted a comprehensive theoretical comparison of phase sensitivity across several entangled quantum states relevant to quantum metrology. Specifically, we analyzed NOON, GHZ, M&M, Twisted NOON, ECS, and BAT states under ideal ($\eta = 1$) conditions using the QFI framework and the QCRB formalism. Our results confirm that NOON, GHZ, and M&M states (with $M - m = N$) achieve Heisenberg-limited scaling, with phase precision following $\Delta\varphi \sim 1/N$, highlighting their theoretical optimality under lossless conditions. Among these, the Twisted NOON states exhibited the highest precision, scaling as $\Delta\varphi \sim 1/(\ell N)$, due to their incorporation of orbital angular momentum ℓ, which introduces an additional degree of phase sensitivity. By contrast, while ECS and BAT states do not achieve Heisenberg scaling, they offer enhanced robustness and practicality. Their performance remains competitive in the presence of imperfections or anticipated loss, making them favorable candidates for real-world implementations where decoherence and photon loss are non-negligible. Coherent states, used as a classical benchmark, followed the SQL $\Delta\phi \sim 1/\sqrt{N}$, serving as a baseline to quantify the quantum enhancement achieved. To contextualize these findings, we also introduced a Quantum-to-Coherent Precision Ratio metric, which emphasizes the relative gain over classical strategies. Twisted NOON and M&M states exhibited the most significant quantum enhancement over the full photon-number range. The insights presented here provide a roadmap for tailoring quantum resources to specific sensing regimes. Future work will involve extending this analysis to lossy interferometric scenarios ($\eta < 1$), where the relative robustness of each state can be fully evaluated. Additionally, experimental efforts can focus on hybrid entangled states, integrating benefits of both path-entanglement and coherent superpositions, possibly achieving both robustness and enhanced precision. With increasing access to photonic quantum hardware, this theoretical foundation contributes to the ongoing translation of quantum-enhanced sensing concepts into practical technologies.

References

[1] S. Yadav, S. Rab, and M. Wan, "Metrology and sustainability in industry 6.0: Navigating a new paradigm," in *Handbook of quality system, accreditation and conformity assessment*. Springer, 2024, pp. 855–885.

[2] D. K. Aswal, S. Yadav, T. Takatsuji, P. Rachakonda, and H. Kumar, *Handbook of Metrology and Applications*. Springer Nature, 2023.

[3] K. Kassem, "Interferometric intensity correlation: from sensing to imaging," Ph.D. dissertation, University of Glasgow, 2024.

[4] G. Huang, C. Cui, X. Lei, Q. Li, S. Yan, X. Li, and G. Wang, "A review of optical interferometry for high-precision length measurement," *Micromachines*, vol. 16, no. 1, p. 6, 2024.

[5] V. Giovannetti, S. Lloyd, and L. Maccone, "Quantum-enhanced measurements: beating the standard quantum limit," *Science*, vol. 306, no. 5700, pp. 1330–1336, 2004.

[6] M. A. Taylor and W. P. Bowen, "Quantum metrology and its application in biology," *Physics Reports*, vol. 615, pp. 1–59, 2016.

[7] J. P. Dowling, "Quantum optical metrology–the lowdown on high-n00n states," *Contemporary physics*, vol. 49, no. 2, pp. 125–143, 2008.

[8] I. Afek, O. Ambar, and Y. Silberberg, "High-noon states by mixing quantum and classical light," *Science*, vol. 328, no. 5980, pp. 879–881, 2010.

[9] J. F. Smith III, "Generation and detection of quantum entangled states for quantum imaging," in *Quantum Information and Computation IX*, vol. 8057. SPIE, 2011, pp. 71–84.

[10] W.-B. Xing, X.-M. Hu, Y. Guo, B.-H. Liu, C.-F. Li, and G.-C. Guo, "Preparation of multiphoton high-dimensional ghz states," *Optics Express*, vol. 31, no. 15, pp. 24 887–24 896, 2023.

[11] H.-Q. Liang, J.-M. Liu, S.-S. Feng, and J.-G. Chen, "Remote state preparation via a ghz-class state in noisy environments," *Journal of Physics B: Atomic, Molecular and Optical Physics*, vol. 44, no. 11, p. 115506, 2011.

[12] Y. Ming, J. Tang, Z.-x. Chen, F. Xu, L.-j. Zhang, and Y.-q. Lu, "Generation of n00n state with orbital angular momentum in a twisted nonlinear photonic crystal," *IEEE Journal of Selected Topics in Quantum Electronics*, vol. 21, no. 3, pp. 225–230, 2014.

[13] Y. Li, H. Jing, and M.-S. Zhan, "Optical generation of a hybrid entangled state via an entangling single-photon-added coherent state," *Journal of Physics B: Atomic, Molecular and Optical Physics*, vol. 39, no. 9, p. 2107, 2006.

[14] C. F. Roos, M. Riebe, H. Haffner, W. Hansel, J. Benhelm, G. P. Lancaster, C. Becher, F. Schmidt-Kaler, and R. Blatt, "Control and measurement of three-qubit entangled states," *science*, vol. 304, no. 5676, pp. 1478–1480, 2004.

[15] J. Joo, W. J. Munro, and T. P. Spiller, "Quantum metrology with entangled coherent states," *Physical review letters*, vol. 107, no. 8, p. 083601, 2011.

[16] R. Demkowicz-Dobrzański, U. Dorner, B. Smith, J. Lundeen, W. Wasilewski, K. Banaszek, and I. Walmsley, "Quantum phase estimation with lossy interferometers," *Physical Review A*, vol. 80, no. 1, p. 013825, 2009.

This page intentionally left blank.

Nanoformulation of Pheophorbide-a for Photodynamic Therapy in a Human Lung Cancer Spheroid Model

K Moloudi[1], H Abrahamse[1], B P George[1*]

[1]Laser Research Centre (LRC) Department of Health Science, Doornfontein Campus, 2028, University of Johannesburg, Johannesburg, South Africa

*Correspondence: blassang@uj.ac.za; Tel.: +27-11-599-6926

Abstract. Pheophorbide a (PPBa) is a natural compound derived from chlorophyll, and its photophysical and photochemical properties make it useful as a photosensitizer for photodynamic therapy (PDT). However, stability of PPBa in biological environments and its bioavailability are crucial for effective therapy. Nanoparticle (NP) formulation of PPBa can improve its solubility and stability. The aim of this study is to make use of liposomal nanocomplex of PPBa as photosensitizer in PDT (660 nm at 15 J/cm^2 fluency) on A549 spheroid cells. Thin-film hydration method was used for synthesis of NPs. Characterization of Lipo@PPBa were carried out using UV-Vis spectroscopy, TEM, SEM, FTIR and DLS. Moreover, cytotoxicity of NPs was evaluated at various concentrations via MTT assay. The IC50 dose was determined to assess the phototoxic effects induced by 660 nm laser irradiation at an energy density of 15 J/cm². UV-Vis spectroscopy showed a specific peak at 220 nm for lipids and two peaks for PPBa at 400 nm and 670 nm, respectively. TEM and SEM images illustrated the 45 nm size and wavy crest shape of NPs respectively. DLS data showed that the NPs have positive surface charge with zeta potential of +6.13 ± 4.7 mV. MTT assay indicated that IC_{50} of Lipo@PPBa nanocomplex in dark and PDT and dark was 10 µg/mL and 7.5 µg/mL, respectively. In conclusion, Lipo@PPBa showed significant phototoxic effects on A549 spheroid cells. However, more investigations on targeted therapy using Lipo@PPBa is recommended.

1. Introduction

Lung cancer remains a significant global health challenge, with projections indicating a substantial increase in cases and deaths by 2050. Sharma et al estimate 3.8 million new cases and 3.2 million deaths globally by 2050 [1], while Guo et al. (2024) predict approximately 2.13 million cases and 1.61 million deaths in China and the United States [2]. Common treatment modalities include surgery, chemotherapy, radiotherapy, targeted therapy, and immunotherapy [3]. However, lung cancer is still a significant public health issue despite significant advancements in clinical diagnosis and treatment in recent decades.

Photodynamic therapy (PDT) is a promising treatment for lung cancer, involving photosensitizing agents activated by light to generate toxic oxygen radicals [4]. PDT for lung cancer faces several challenges despite its potential as a targeted treatment. These include limited light penetration in deep tissues, reliance on oxygen in hypoxic tumors, and the need for precise treatment planning [5]. Clinical studies have shown that PDT can prolong survival in inoperable lung cancer patients and improve quality of life. However, PDT remains underutilized in

lung cancer treatment due to insufficient clinical research evaluating its effectiveness and side effects [6]. Future developments in photosensitizer (PS) design potentially aided by nanotechnology, may help address these challenges and expand PDT's clinical application in lung cancer therapy [7].

Liposomal formulations of PSs such as pyropheophorbide-a and its derivatives have shown promise for enhancing PDT in cancer treatment. These formulations improve drug delivery, by increasing intracellular uptake up to 5-fold compared to free PSs [8]. Liposomal encapsulation also addresses the poor water solubility of porphyrins, enhancing their bioavailability and prolonging blood circulation [9]. Studies have demonstrated that liposomal porphyrins are more effective than free forms in inducing apoptosis in cancer cell lines [10].

In this study, a liposomal nanoformulation of pheophorbide-a (Lipo@PPBa) was employed in PDT using a 660 nm laser to treat A549 spheroid cells *in vitro.*

2. Materials and methods

2.1. Materials

The following reagents and materials were procured from Thermo Fisher in Johannesburg, South Africa: pheophorbide-a (16072, powder, >95% purity), MTT (11465007001), cholesterol (C8667), DSPC (P1138-1G), Dulbecco's Modified Eagle Medium (DMEM, D5796), chloroform (C2432), Fetal Bovine Serum (FBS), TrypLE (12604013), dimethyl sulfoxide (DMSO), phosphate-buffered saline (PBS), 96-well ultra-low attachment plates (174929), crystal violet (C0775, powder, >90% purity), and DAPI (D3571).

2.2. Synthesis and characterization of Lipo@PPBa complex

Lipo@PPBa were synthesized by the thin-film hydration method [11]. Briefly, DSPC (80 mg) and cholesterol (30 mg) were dissolved in chloroform, followed by solvent evaporation using a rotary evaporator for 70 min (at 75 °C and 65 rpm). The resulting samples of NPs were then stored at 8 °C for further characterization. To analyze and characterization of the Lipo@PPBa complex, various techniques were employed, including UV-Vis spectrophotometry, FTIR, dynamic light scattering (DLS), Transmission Electron Microscopy (TEM) and Scanning Electron Microscopy (SEM).

2.3. Spheroid cell culture and treatment

A549 lung cancer cell line (ATCC CCL-185), after the third passage, was harvested and counted using an automated cell counter. A total of 1,000 cells per well were then seeded into ultra-low attachment 96-well plates using DMEM) supplemented with 10% FBS and 1% penicillin-streptomycin (Sigma, USA). Plates were centrifuged at 1,000 rpm for 5 min to facilitate cell aggregation at the bottom. The cells were incubated at 37 °C in a humidified incubator with 5% CO_2 and 95% of O_2, and medium refreshed every other day. Once the spheroids reached an average diameter of approximately 400 µm after 3 days, they were exposed to varying concentrations (0–12 µg/mL) of Lipo@PPBa, with or without PDT (660 nm laser, 15 J/cm²). After 24 h, the spheroids were washed three times with PBS (1X), dissociated, and subjected to cytotoxicity, colony formation, and nuclear fragmentation assays. To assess the PDT potential of Lipo@PPBa, its IC_{50} dose (10 µg/mL) was applied in combination with 660 nm laser at a total fluence of 15 J/cm². The exposure time (in min) was determined using the specified equations:

$$\text{Intensity (W/cm}^2\text{)} = \text{Energy/Area} = 100\ \text{mW} / 3.14\text{x}1.72\ \text{cm} = 0.011\ \text{W/cm}^2 \quad (1)$$

$$\text{Area} = \pi r^2 = 3.14\text{x}1.72 = 9.074\ \text{cm}^2 \quad (2)$$

$$\text{Exposure time (min)} = \text{Dose (J/cm}^2\text{)/Intensity (W/cm}^2\text{)} = 15 / 0.011 = 1363.64 \simeq 22.72\ \text{min} \quad (3)$$

2.3.1. MTT assay and IC_{50} of Lipo@PPBa complex

The cytotoxic effects of Lipo@PPBa at varying concentrations (0, 2, 4, 6, 8, 10, and 12 µg/mL) on A549 spheroids, both without and with PDT (660 nm laser, 15 J/cm²), were evaluated using the MTT assay and ELISA (Perkin-Elmer, Midrand, South Africa. Briefly, the culture medium was removed, spheroids were rinsed with 1× PBS, and dissociated into single cells using 200 µL of TrypLE (1×) for 5 min. The cell suspension was washed with PBS and seeded into 96-well plates at a concentration of 2×10^4 cells/mL. Cells were incubated overnight at 37 °C in a humidified atmosphere containing 5% CO_2. After removing the medium, 20 µL of MTT solution (Sigma, USA) was added to each well and the plate was incubated for an additional 4 h. Cell viability was then quantified based on absorbance using equation (4):

$$\%\ \text{survival} = (\text{OD of experimental sample}) / (\text{OD of control sample}) \times 100. \quad (4)$$

2.3.2. Colony formation assay

The colony formation assay was employed to evaluate the clonogenic potential of individual A549 cells following treatment. Spheroids were exposed to the IC_{50} concentration (10 µg/mL) of Lipo@PPBa followed by irradiation (660 nm laser, 15 J/cm²), then dissociated using 200 µL of TrypLE to obtain single cells. A total of 1,000 cells were seeded into each well of a 6-well plate (M8562) containing DMEM and incubated for 14 days to allow colony formation. After the incubation, colonies were fixed using 5% formaldehyde and stained with 0.5% crystal violet for visualization. Colonies were imaged and quantified using an Inverted microscope and ImageJ software (version 1.48v). A colony was defined as a cluster containing at least 50 cells.

2.3.3. Nuclear fragmentation assay

The nuclear fragmentation assay was used to identify apoptotic features such as chromatin condensation and nuclear breakage for A549 spheroids treated with the IC_{50} dose (10 µg/mL) of Lipo@PPBa alone and following PDT. Next, the spheroids were washed three times with 1× PBS and dissociated using 200 µL of TrypLE. Approximately 1×10^5 cells were then seeded onto glass coverslips and fixed using 5% formaldehyde. The fixed cells were washed three times with PBS and permeabilized with 100 µL of 0.5% Triton X-100 in PBS for 15 min at room temperature. Subsequently, after additional PBS washes, cells were stained with 100 µL of DAPI solution (1 µg/mL in PBS) and incubated for 15 min in the dark at room temperature. Excess dye was removed with three PBS washes, and nuclear morphology was visualized using a fluorescence microscope (Wirsam Olympus CKX41) equipped with a DAPI filter (excitation ~358 nm, emission ~461 nm).

3. Statistical Analysis

Statistical analysis was conducted using one-way ANOVA followed by Tukey's post-hoc test in SPSS software (version 22). All experiments were performed in triplicate (n=3) and data are expressed as mean values ± SD (standard deviation). The value of $p^* < 0.05$, $p^{**} < 0.01$ was considered to be statistically significant.

4. Results and Discussion

4.1. Characterization of Lipo@PPBa

UV-vis spectroscopy revealed that the Lipo@PPBa complex exhibited an absorption peak ~220 nm, along with two distinct peaks corresponding to PPBa at approximately 400 nm and 670 nm (Figure 1A), as previously reported [12]. FTIR analysis further supported the successful encapsulation of PPBa. showing four notable peaks at 1351, 1600, 2736, and 2907 cm^{-1} for the liposomes, while free PPBa displayed five absorption bands at 670, 900, 1395, 1680, and 2922 cm^{-1}. Moreover, the Lipo@PPBa complex exhibited similar FTIR peaks at 1351, 1600, 2736, and 2907 cm^{-1} (Figure 1B). Similar spectral behavior was reported by Rani et al., where overlapping FTIR peaks confirmed the integration of therapeutic agents into lipid-based nanocarriers without significant chemical modification [13]. TEM analysis showed that the Lipo@PPBa complex had an average size of approximately 45.7 nm (Figure 1C). The SEM image and backscattered electron (BSE) image also illustrated a wavy morphology of the Lipo@PPBa complex (Figure 1D and E) and confirmed its successful loading onto the liposomes. Moreover, DLS analysis revealed that incorporating PPBa into liposomes led to an increase in particle size from 100.5 ± 3 nm to 251.8 ± 12 nm and a reduction in zeta potential from +17.01 ± 7 mV to +6.13 ± 4.7 mV. However, morphological analysis using TEM revealed an average particle size of ~45.7 nm, which is smaller than the hydrodynamic diameter measured by DLS (251.8 ± 12 nm). This discrepancy is commonly observed and attributed to the hydration shell measured by DLS, as also reported previously [14]. TEM-based sizes typically reflect the dry-state diameter, while DLS accounts for solvation and potential particle aggregation in solution.

Finally, DLS analysis showed an increase in particle size and a notable decrease in zeta potential after PPBa encapsulation, indicating positive changes in surface charge. The observed zeta potential of +6.13 ± 4.7 mV in Lipo@PPBa suggests moderate stability, suitable for short-term systemic delivery.

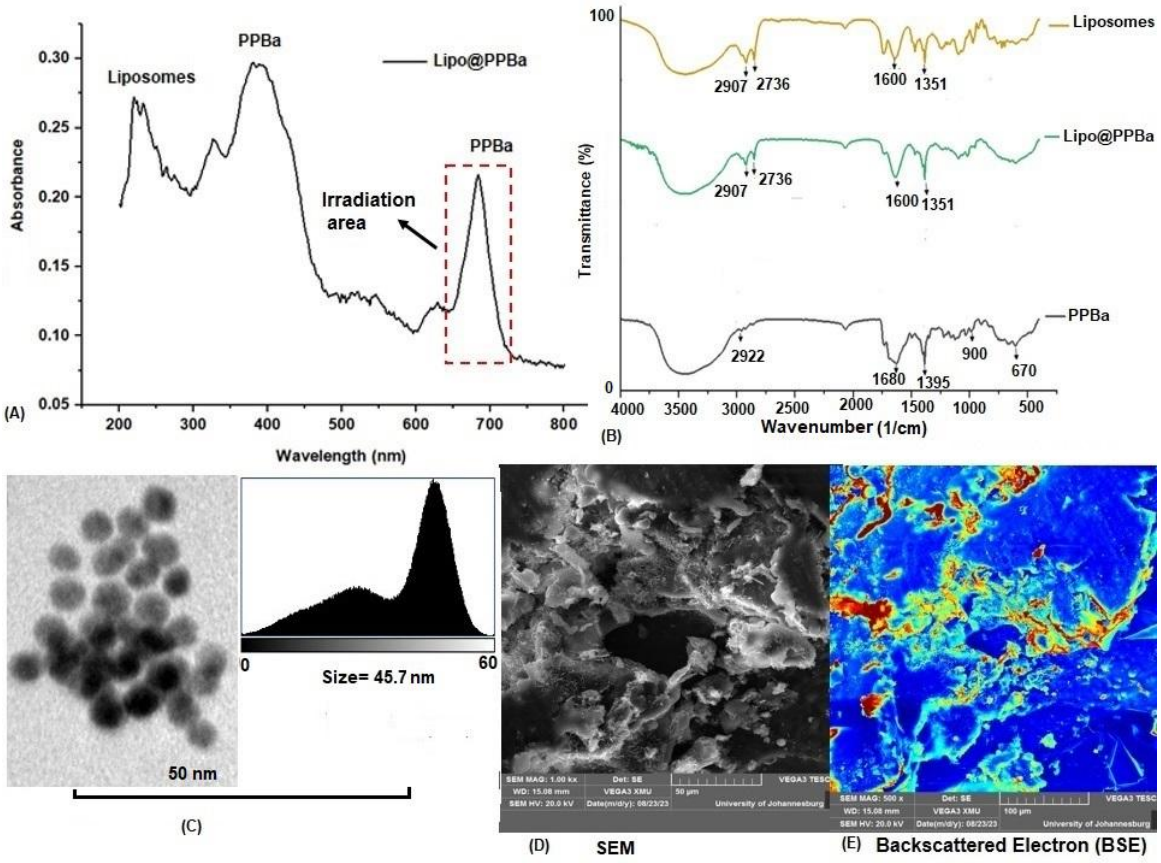

Figure .1. Various characterization tests for Lipo@PPBa nanocomplex: (A) UV-spectroscopy, (B) FTIR, (C) TEM (C), (D) SEM image and (E) backscattered electron (BSE).

4.2. Cyto and phototoxicity of Lipo@PPBa

As can be seen in Figure 2A and B, cell viability for Lipo@PPBa at the concentrations more than 4 µg/mL had significant toxicity compared with control group ($p<0.05$). Additionally, viability percentage for laser alone and Lipo@PPBa at various concentrations of 2, 4, 6, 8, 10, 12, 14 µg/mL post-PDT (15 J/cm^2) was 91%, 84%, 71%, 56%, 45%, 35%, 28% and 19%, respectively, (Figure 2C). The calculated IC_{50} of Lipo@PPBa post-PDT was 7.5 µg/mL compared to 10 µg/mL in dark. Notably, the data showed that the IC_{50} value post-PDT was 7.5 µg/mL, which is significantly lower than the IC_{50} under dark conditions (10 µg/mL), confirming that photodynamic activation enhances therapeutic efficacy. Additionally, the threshold dose (Td) of Lipo@PPBa was identified as 4 µg/mL (Figure 2D). These results collectively highlight that Lipo@PPBa exerts greater cytotoxic effects when activated by light and suggest its potential as an effective agent for PDT-based cancer therapy.

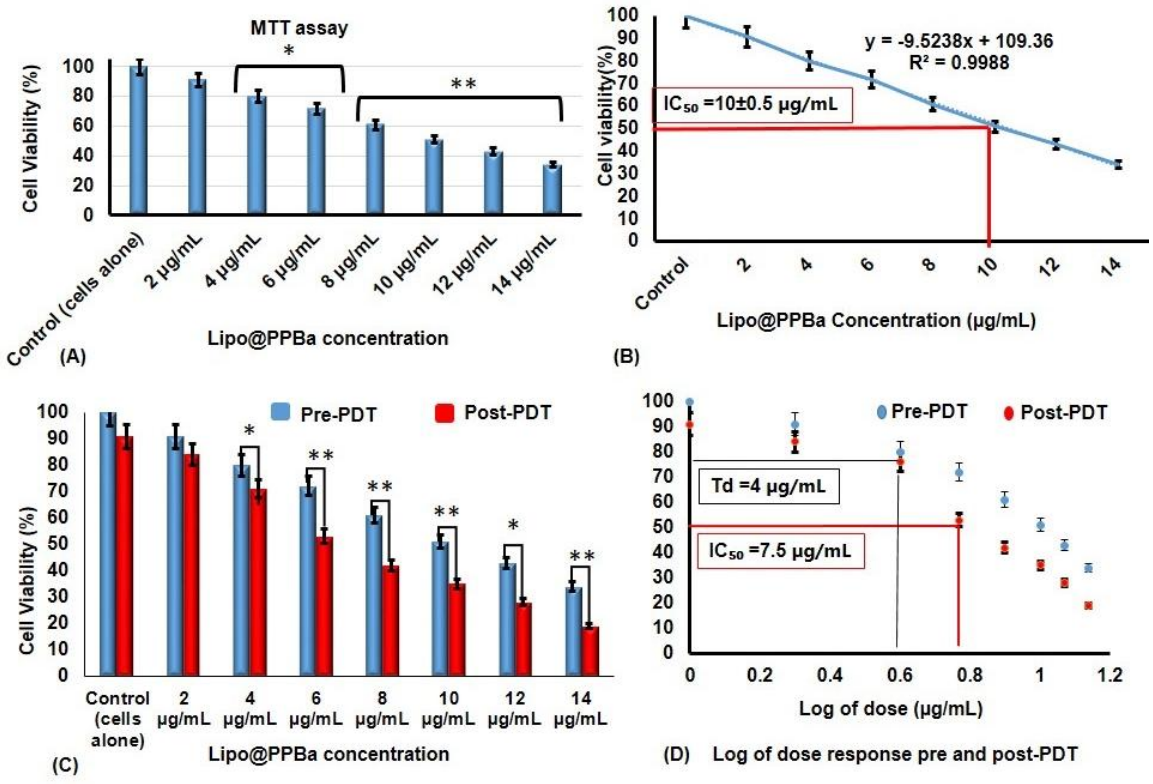

Figure .2. (A, B), MTT assay (cytotoxicity) and regression model of Lipo@PPBa, after 24 h. (C), cytotoxicity of Lipo@PPBa post-PDT, (D), Sigmoid model for Lipo@PPBa with and without PDT on A549 cancer cells.

4.3. Morphology, colony formation assay and nuclear fragmentations

Morphology (Figure 3A) and live/dead assay (Figure 3B) of spheroids illustrated that IC_{50} of Lipo@PPBa nanocomplex post-PDT caused shrinkage, dissociation and suppression of spheroids in comparison to other groups such as control, laser (alone) and IC_{50} of Lipo@PPBa nanocomplex in dark. Furthermore, cells treated with the IC_{50} concentration of Lipo@PPBa under PDT exhibited prominent nuclear fragmentation (Figure 3C). This effect was clearly visible under microscopic observation and indicated advanced stages of cell death. The extent of nuclear fragmentation in this group was significantly higher compared to the other groups. Finally, colony formation results demonstrated that the IC_{50} concentration of Lipo@PPBa reduced cell survival to 38±4 %, while for other groups such as control, laser and Lipo@PPBa was 100%, 88% and 51%, respectively, (Figure 3D and E). These findings highlight the enhanced cytotoxic effect of photoactivated Lipo@PPBa compared to non-irradiated and untreated conditions.

This outcome aligns with previous studies highlighting the effectiveness of PS-loaded nanocarriers in enhancing PDT outcomes. Zeng et al. (2021) demonstrated that Ce6-loaded lipid nanoparticles achieved about 35% survival in A549 cells under similar laser exposure conditions, indicating comparable efficacy in terms of colony inhibition [15]. However, the results validate the effectiveness of Lipo@PPBa as a promising nanocarrier capable of significantly impairing cancer cell proliferation when appropriately activated.

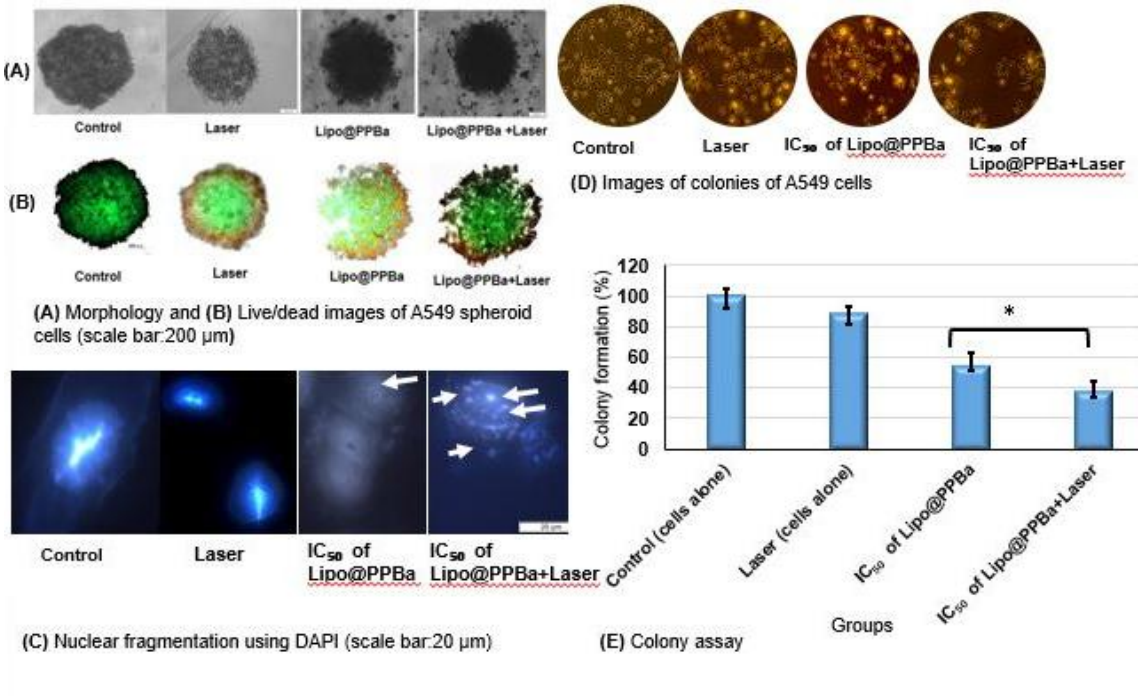

Figure 3. Various assessments of spheroid response to treatment: (A) shows the morphology of spheroids under a light microscope, (B) presents live/dead fluorescence images where green indicates live cells and red indicates dead cells, (C) displays nuclear fragmentation visualized using DAPI staining, (D) shows representative images of colony formation, and (E) quantifies the percentage of colony formation, ($p^* < 0.05$).

5. Conclusion

The nanoformulation of PPBa into liposomal carriers (Lipo@PPBa) demonstrates significant potential as a targeted and effective PS for PDT in a 3D human lung cancer spheroid model. Physicochemical characterization confirmed successful encapsulation of PPBa, favorable particle size, and stability, while optical analyses verified the retention of Lipo@PPBa's photodynamic properties. Compared to the non-irradiated formulations, light-activated Lipo@PPBa exhibited markedly enhanced cytotoxic effects, and a more pronounced inhibition of colony formation *via* nuclear fragmentation. These findings illustarte the importance of nanoparticle-based delivery systems in overcoming the limitations of conventional PDT and highlight Lipo@PPBa as a promising candidate for further preclinical development in lung cancer therapy. However, further investigations involving additional cell death markers, along with the inclusion of PPBa and unloaded liposomes as control groups, are necessary to strengthen the current findings. These limitations highlight the preliminary nature of our data. Future studies will aim to address these aspects to provide a more comprehensive understanding of the observed effects.

6. Acknowledgements

This work is based on the research funded by the South African Research Chairs initiative of the Department of science and technology and National Research Foundation (NRF) of South Africa (Grant No. 98337), South African Medical Research Council (Grant No. SAMRC EIP007/2021), as well as grants received from the NRF Research Development Grants for Y-Rated Researchers (Grant No: 137788), University Research Committee (URC), African Laser Centre (ALC), CSIR African Laser Centre research grant (HLHA26X Task ALC-R001), University of Johannesburg, and the Council for Scientific Industrial Research (CSIR)-National Laser Centre (NLC)

References

[1] Sharma R. 2022 Mapping of global, regional and national incidence, mortality and mortality-to-incidence ratio of lung cancer in 2020 and 2050. *International Journal of Clinical Oncology*.**27**:665-75.doi: 10.1007/s10147-021-02108-2

[2] Guo L, Zhu C, Cai L, Zhang X, Fang Y, Chen H, et al. 2024 Global burden of lung cancer in 2022 and projected burden in 2050. *Chinese Medical Journal*.**137**:2577-82.doi: 10.1097/CM9.0000000000003268

[3] Salmani-Javan E, Jadid MFS, Zarghami N. 2024 Recent advances in molecular targeted therapy of lung cancer: Possible application in translation medicine. *Iranian Journal of Basic Medical Sciences*.**27**:122.doi: 10.22038/IJBMS.2023.72407.15749

[4] Moloudi K, Abrahamse H, George BP. 2024 Co-delivery of berberine and gold nanoparticles on liposomes for photodynamic therapy against 3D lung cancer cells. *Materials Advances*.**5**:6185-95. doi.org/10.1039/d4ma00286e

[5] Jankun J. 2019 A thousand words about the challenges of photodynamic therapy: Challenges of photodynamic therapy. *Journal of Medical Science*.**88**:195-9.doi: 10.20883/medical.391

[6] Wang K, Yu B, Pathak JL. 2021 An update in clinical utilization of photodynamic therapy for lung cancer. *Journal of Cancer*.**12**:1154.doi: 10.7150/jca.51537

[7] Moloudi K, Abrahamse H, George BP. 2024 Application of liposomal nanoparticles of berberine in photodynamic therapy of A549 lung cancer spheroids. *Biochemistry and biophysics reports*.**40**:101877.doi: 10.1016/j.bbrep.2024.101877

[8] Guelluy P-H, Fontaine-Aupart M-P, Grammenos A, Lécart S, Piette J, Hoebeke M. 2010 Optimizing photodynamic therapy by liposomal formulation of the photosensitizer pyropheophorbide-a methyl ester: in vitro and ex vivo comparative biophysical investigations in a colon carcinoma cell line. *Photochemical and Photobiological Sciences*.**9**:1252-60.doi: 10.1039/c0pp00100g

[9] Zhou H, Xia L, Zhong J, Xiong S, Yi X, Chen L, et al. 2019 Plant-derived chlorophyll derivative loaded liposomes for tri-model imaging guided photodynamic therapy. *Nanoscale*.**11**:19823-31.doi: 10.1039/c9nr06941k

[10] Temizel E, Sagir T, Ayan E, Isik S, Ozturk R. 2014 Delivery of lipophilic porphyrin by liposome vehicles: Preparation and photodynamic therapy activity against cancer cell lines. *Photodiagnosis and photodynamic therapy*.**11**:537-45.doi: 10.1016/j.pdpdt.2014.07.006

[11] Xiang B, Cao D-Y. 2021 Preparation of drug liposomes by thin-film hydration and homogenization. *Liposome-based drug delivery systems (pp.1-11)*:25-35.doi: 10.1007/978-3-662-49320-5_2

[12] Moloudi K, Abrahamse H, George BP. 2025 Liposomes-based co-delivery of pheophorbide a and gold nanoparticles for thermo-photodynamic therapy purpose on lung cancer spheroids. *Results in Chemistry*.**15**:102234.doi.org/10.1016/j.rechem.2025.102234

[13] Rani A, Kaur R, Aldahish A, Vasudevan R, Balaji P, Dora CP, et al. 2025 Nanostructured Lipid Carriers (NLC)-Based Topical Formulation of Hesperidin for Effective Treatment of Psoriasis. *Pharmaceutics*.**17**:478. doi: 10.3390/pharmaceutics17040478

[14] Li R-T, Chen M, Yang Z-C, Chen Y-J, Huang N-H, Chen W-H, et al. 2022 AIE-based gold nanostar-berberine dimer nanocomposites for PDT and PTT combination therapy toward breast cancer. *Nanoscale*.**14**:9818-31.doi: 10.1039/d2nr03408e

[15] Zeng Q, Ma X, Song Y, Chen Q, Jiao Q, Zhou L. 2022 Targeting regulated cell death in tumor nanomedicines.*Theranostics*.**12**:817. doi: 10.7150/thno.67932

This page intentionally left blank.

Photonic-biosensing towards drug-resistant Tuberculosis diagnosis

Sipho Chauke[1,2], Mabotse Tjale[1], Charles Maphanga[1], Felix Dube[2], Saturnin Ombinda-Lemboumba[1,3], and Patience Mthunzi-Kufa[4]

[1]Manufacturing, Council for Scientific and Industrial Research (CSIR), Pretoria, South Africa
[2]Department of Molecular and Cell Biology, University of Cape Town, Cape Town, South Africa
[3]Départemente de Physique, Université des Sciences et Techniques de Masuku, Franceville, Gabon
[4]Engineering and Technology, University of South Africa (UNISA), Johannesburg, South Africa

E-mail: schauke@csir.co.za

Abstract. Early detection and treatment of tuberculosis (TB) remain key strategies to reduce transmission and disease progression. However, this is hampered by time-consuming, insensitive diagnostic methods, particularly for the detection of drug-resistant forms and in patients with human immunodeficiency virus infection (HIV). Several genes, such as *the RpoB* and *InhA* genes, contain mutations that are responsible for drug resistance. This study aimed to use an SPR-based biosensor platform to detect *RpoB* and *InhA* genes. DNA probes, specific to *RpoB* and *InhA*, were used as biorecognition elements to capture the corresponding target DNA sequences. The *RpoB* and *InhA* gene-specific thiolated DNA probes were immobilized on a gold-coated glass substrate before the target DNA was introduced for detection. As a negative control, a non-specific target to both genes was used to confirm the binding of the specific target. The shifts in the resonance angles indicated the binding properties associated with DNA hybridization between the specific target and the capture probe. The results obtained from this study demonstrated the use of a simple SPR setup and its potential for identifying genes associated with drug-resistant TB.

1 Introduction

Tuberculosis (TB) is a curable disease treated with first-line drugs such as rifampicin, isoniazid, pyrazinamide, and ethambutol [1]. This treatment regimen can last between six and nine months [1]. Due to the prolonged treatment periods, infected individuals will often stop adhering to the treatment regimen, thus increasing their chances of developing drug-resistant TB [1,2].

Multi-drug-resistant TB, on the other hand, is resistant to the two primary first-line TB drugs, rifampicin and isoniazid [2]. These first-line drugs target the *RNA polymerase β subunit* (*RpoB*) (rifampicin gene target) and *enoyl reductase* (*InhA*) (isoniazid gene target) within the TB bacteria [3]. Current diagnostic tests and assays that target the detection of these drug-resistant genes include the XpertUltra test and line probe assays [4,5]. Although effective, these diagnostic tests often require well-equipped facilities and can be quite laborious [4,6]. Some solutions include effectively diagnosing and monitoring the treatment using inexpensive and simple-to-use

diagnostic tests. Hence, easy-to-use, accurate, and sensitive methods can be developed as alternative diagnostic and/or detection tools [7].

Optical-based techniques can be used as alternatives since they have been applied to detect a wide range of pathogens, including *Mycobacterium tuberculosis* [7–9]. One such optical technique is surface plasmon resonance (SPR). SPR is an optical phenomenon that occurs when light interacts with the collective oscillations of free electrons, known as surface plasmons, at the interface between a metal and a dielectric material. When the frequency of the incident light matches the natural oscillation frequency of these electrons, resonance is achieved. In thin metal films, these surface plasmons can propagate along the metal-dielectric interface [10–12]. According to the solutions derived from Maxwell's equations, the oscillation of these surface plasmons can be described by the surface plasmon propagation wave constant, which can be mathematically derived from the dispersion relation [11,13]. The surface plasmon propagation wave constant (k_{spp}) is a key element for describing the continuous wave of the surface plasmons in the metal-dielectric material interface. Furthermore, the k_{spp} depends on several parameters, including the frequency of the incident light (ω), the speed of light (c), and the permittivity of both the metal ($\mathcal{E}_m$) and the dielectric ($\mathcal{E}_d$) [11,13]. Equation 1 below describes how light interacts with the metal surface by exciting the free electrons in the metal-dielectric interface.

$$k_{spp} = \frac{\omega}{c}\sqrt{\frac{\varepsilon_m \varepsilon_d}{\varepsilon_m + \varepsilon_d}} \qquad (1)$$

These interactions of the surface plasmons on the thin metal film are sensitive to changes in the refractive index on the metal surface [10,11,13]. This sensitivity characteristic is an advantage for various biosensing applications. Additional advantages of SPR include its label-free nature and requirement of small sample sizes for effective detection [14–16]. In addition, SPR-based biosensors have been used to detect the affinity binding of molecules in real-time due to their sensitivity [7]. The present study evaluates the use of SPR to detect two drug-resistant TB genes using single-stranded deoxyribonucleic acid (ssDNA) probes as biorecognition elements and the effects of changes in target concentration on the SPR angle.

2 Experimental

2.1 The optical setup

The optical setup used in this study has been described in our previous publication [17]. Briefly, the light source consisted of a Helium-Neon (HeNe) laser with a wavelength of 632.8 nm and an output power of 10 mW, and a beam size of 1 mm. The laser light was directed to a polarizing beam splitter, which split the laser light into the *p*- and *s*-polarized light. The *p*-polarized light beam was attenuated to 2 mW. The attenuated laser beam was directed to the sample through a BK7 prism coupled to a gold-coated sensor chip in the Kretschmann configuration. The reflected beam was subsequently directed to a photodiode detector/amplifier system for data acquisition.

2.2 Sensor chip fabrication and functionalization

Glass slides (5 x 5 cm) were cleaned with 100% ethanol and distilled water by sonicating for 10 minutes each. The glass slides were dried under N_2 gas. The slides were coated with titanium (5 nm) and then gold (50 nm) using a physical vapor deposition system (PVD) (Korvus Technology, United Kingdom). The coated slides (sensor chip) were then rinsed with 100% ethanol and distilled water and dried under N_2 gas. Once dry, silicone wells (9 x 9 mm) were placed on the sensor chip to create wells on the surface of the sensor chip. The first well on each sensor chip was used as the reference well (Au only). On each sensor chip, 30 µL of thiolated probes (10 µm) (*RpoB* probe: **5' HS-***CGTACCGTCGTTTACCGGGC* **3'**; *InhA* probe: **5' HS-***GATATAGCTCCCGTCCTCGG* **3'**) were immobilized in all the wells except for well 1. The sensor chip with the immobilized probes was incubated overnight in the 4ºC fridge. The unattached probes were washed off with 1X PBS, and the sensor chips were allowed to dry. Thereafter, specific targets (*RpoB* target: **5'** *GCCCGGTAAACGACGGTACG* **3'**; *InhA* target: **5'** *CCGAGGACGGGAGCTATATC* **3'**) were added in wells 3 of each sensor chip, while the non-specific target (**5'** *CATGGCAGCAAATGGCCCGC* **3')** was added in wells 4 of each sensor chip. The sensor chips were then incubated for 30 minutes in the 4ºC fridge. The sensor chips were washed with 1X PBS, allowed to dry, and then analyzed using the SPR optical setup.

2.3 Reflectivity analysis of the sensor chip surface and data processing

All the data were recorded at a constant temperature (~20°C). The signal of the changes in the reflected intensities was transduced by a photodiode amplifier/detector, from which the data were then processed and analyzed using OriginPro 8. The repeatability of the SPR angle shift experiments was calculated using equation 2:

$$Repeatability = \frac{\text{Resonance angle shift mean}}{\text{Resonance angle shift mean + Standard Error}} \times 100 \quad (2)$$

3 Results

3.1 Surface plasmon resonance

According to Zheng et al. [18], the sensing responses observed when using SPR are often influenced by the refractive index detected on the surface of the sensor chip. In this study, an SPR optical setup was used to detect two drug-resistant genes (*InhA* and *RpoB*). Single-stranded DNA (ssDNA) probes were used to capture biorecognition elements for target-specific DNA. Furthermore, the experimental data were obtained by monitoring changes in the shifts of the resonance angle of incident light and the reflected intensities of the sensor chips before and after the immobilization of the probes and target DNA (Figures 1 and 2).

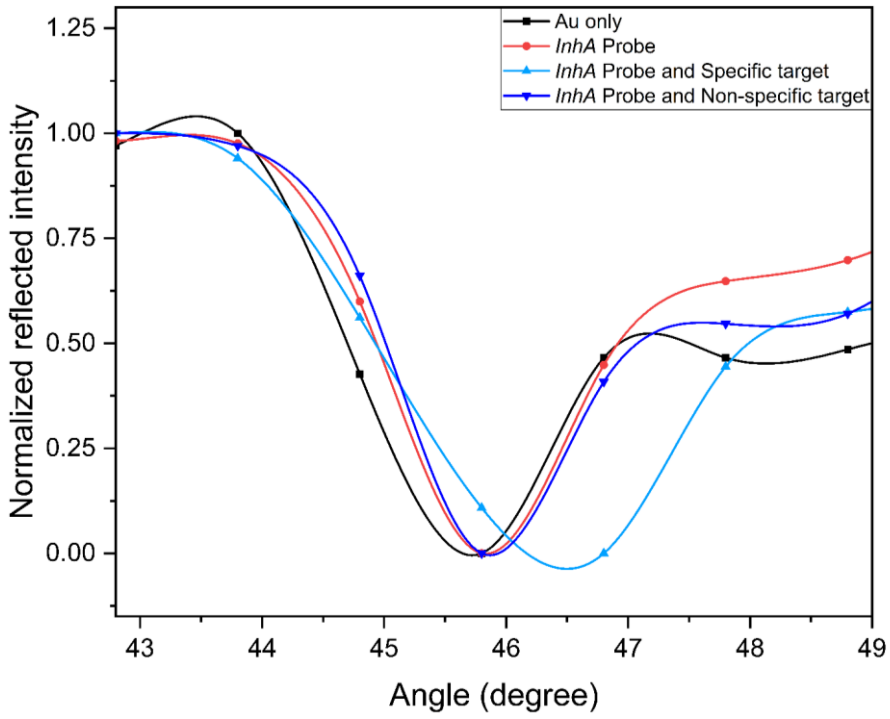

Figure 1: The normalized reflected intensities and resonance angle obtained for the *InhA* gene during the analysis of the hybridization kinetics between the gene's probe, its specific target, and the non-specific target.

In Figure 1, the resonance angle of incidence observed for the reference (Au only) was 45.80 degrees, while the resonance angles for the *InhA* probe, the probe with the specific target, and the probe with the non-specific target were 45.95, 46.74, and 46.03 degrees, respectively. The addition of the probe and the specific and non-specific target resulted in a shift towards the right when compared to the reference sample. According to Zheng et al. [18], the angle shifts that result from molecules binding to each other result in changes in the SPR angle of incidence due to changes in the refractive index and an increase in the mass detected on the sensor surface. The repeatability of three independent experiments evaluating the sensor chip surface and detecting the immobilized *InhA* probe

with the addition of the specific and non-specific targets, at constant concentrations of 10 µM, was calculated to be 99.4, 99.3, 99.5, and 99.0%, respectively.

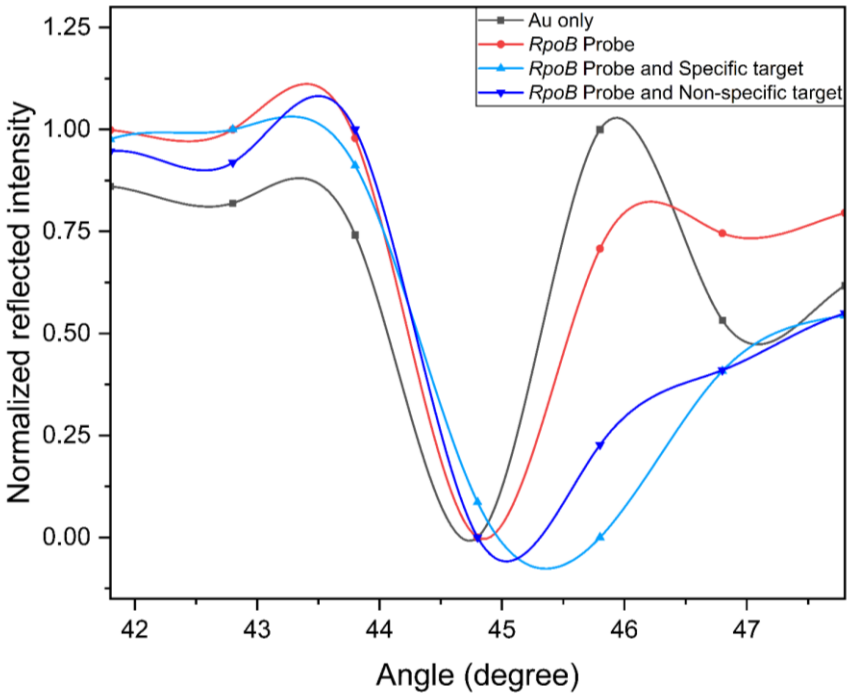

Figure 2: The normalized reflected intensities and resonance angles obtained for the *RpoB* gene during the analysis of the hybridization kinetics between the gene's probe, its specific target, and the non-specific target.

Similarly, Figure 2 shows the resonance angle peak of the incidence beam obtained for the *RpoB* probe with the specific target and the non-specific target. The resonance angle of incidence beam for the reference (Au only) was 44.70 degrees. In contrast, the immobilized *RpoB* probe and the *RpoB* probe with the non-specific target resulted in minor resonance incident angle shifts of 44.76 and 44.78 degrees, respectively, when compared to the reference (Au only). In addition, the *RpoB* probe with a specific target resulted in a resonance incident angle shift of 45.78 degrees. This observation is similar to what was noted in a study by Soares et al. [16], which investigated the hybridization of ssDNA targets and probes on a sensor chip. The repeatability of three independent experiments evaluating the sensor chip surface and detecting the immobilized *RpoB* probe with the addition of the specific and non-specific targets, at constant concentrations of 10 µM, was calculated to be 98.8%, 99.2%, 99.05%, and 98.9%, respectively.

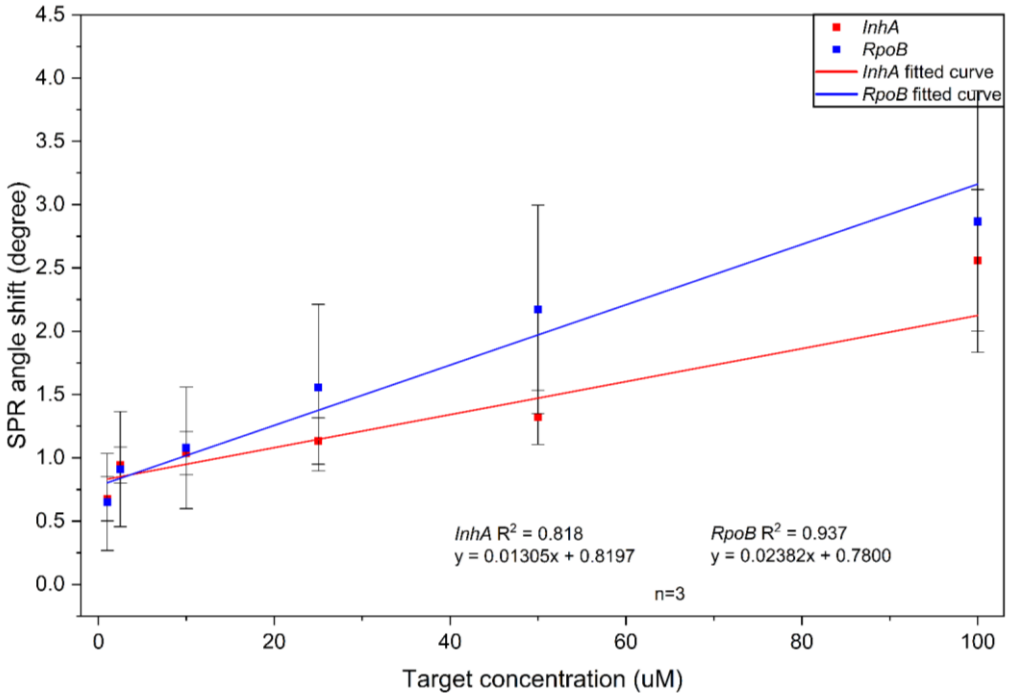

Figure 3: Linear fitted curves of the effects of changing the target concentration (in µM) bound to the probe on the SPR angle of incidence. Each curve represents the SPR angles obtained for each gene, indicating R^2 values of 0.818 and 0.937 for genes *InhA* and *RpoB*, respectively.

Figure 3 illustrates the variation of the SPR resonance angle shifts as a function of changing the target concentration. For *InhA*, target concentrations of 1, 2.5, 5, 10, 25, 50, and 100 µM resulted in resonance angle shifts of 0.677, 0.942, 1.037, 1.133, 1.32, and 2.56 degrees, respectively. Similarly, for *RpoB*, target concentrations of 1, 2.5, 5, 10, 25, 50, and 100 µM resulted in resonance angle shifts of 0.651, 0.911, 1.08, 1.554, 2.174, and 2.867 degrees, respectively. These results indicate that with increasing target concentration, there is an increase in the SPR resonance angle. This observation coincides with what was reported in studies that attribute SPR angle shifts to the increase in the mass detected on the sensor chip surface [18–21].

4 Conclusion

In this study, the sensitivity of the SPR platform was demonstrated by its ability to distinguish between the presence of the probe alone and its interaction with both specific and non-specific targets on the sensor chip surface. The SPR setup successfully detected target concentrations as low as 1 µM, with molecular interactions reflected as shifts in the SPR resonance angle. These findings highlight the effectiveness of single-stranded DNA (ssDNA) probes as biorecognition elements in SPR-based optical biosensing. Future studies may look at the use of different biorecognition elements for the detection of drug-resistant TB on an SPR-based sensor chip and SPR setup.

References

[1] World Health Organization 2024 *2024 Global tuberculosis report* (Geneva)
[2] Naidoo K, Perumal R, Ngema S L, Shunmugam L and Somboro A M 2024 Rapid Diagnosis of Drug-Resistant Tuberculosis–Opportunities and Challenges *Pathogens* **13**
[3] Liu Q, Yang D, Qiu B, Martinez L, Ji Y, Song H, Li Z and Wang J 2021 Drug resistance gene mutations and treatment outcomes in mdr-tb: A prospective study in Eastern China *PLoS Negl Trop Dis* **15** 1–15

[4] World Health Organization 2021 *Use of Xpert MTB/RIF and Xpert MTB/RIF Ultra on GeneXpert 10-colour instruments: WHO POLICY STATEMENT*
[5] Rahman A, Sahrin M, Afrin S, Earley K, Ahmed S, Rahman S M M and Banu S 2016 Comparison of Xpert MTB/RIF assay and genotype MTBDRplus DNA probes for detection of mutations associated with rifampicin resistance in mycobacterium tuberculosis *PLoS One* **11**
[6] Ocheretina O, Byrt E, Mabou M M, Royal-Mardi G, Merveille Y M, Rouzier V, Fitzgerald D W and Pape J W 2016 False-positive rifampin resistant results with Xpert MTB/RIF version 4 assay in clinical samples with a low bacterial load *Diagn Microbiol Infect Dis* **85** 53–5
[7] Srivastava S K, Van Rijn C J M and Jongsma M A 2016 Biosensor-based detection of tuberculosis *RSC Adv* **6** 17759–71
[8] Joshi H, Kandari D, Maitra S S and Bhatnagar R 2022 Biosensors for the detection of Mycobacterium tuberculosis: a comprehensive overview *Crit Rev Microbiol* **48** 784–812
[9] Apollonov V 2021 *Laser Therapy for Treating Tuberculosis*
[10] Butt M A 2025 Surface Plasmon Resonance-Based Biodetection Systems: Principles, Progress and Applications—A Comprehensive Review *Biosensors (Basel)* **15**
[11] Mendes J P, dos Santos P S S, Dias B, Núñez-Sánchez S, Pastoriza-Santos I, Pérez-Juste J, Pereira C M, Jorge P A S, de Almeida J M M M and Coelho L C C 2024 Exciting Surface Plasmon Resonances on Gold Thin Film-Coated Optical Fibers Through Nanoparticle Light Scattering *Adv Opt Mater* **12**
[12] Hong Y, Huh Y M, Yoon D S and Yang J 2012 Nanobiosensors based on localized surface plasmon resonance for biomarker detection *J Nanomater* **2012**
[13] Treebupachatsakul T, Boosamalee A, Chaithatwanitch K and Pechprasarn S 2022 Generalized figure of merit for plasmonic dip measurement-based surface plasmon resonance sensors *Biomed Opt Express* **13** 1784
[14] Singh P 2016 SPR Biosensors: Historical Perspectives and Current Challenges *Sens Actuators B Chem* **229** 110–30
[15] Trzaskowski M, Napiórkowska A, Augustynowicz-Kopeć E and Ciach T 2018 Detection of tuberculosis in patients with the use of portable SPR device *Sens Actuators B Chem* **260** 786–92
[16] Soares L, Csáki A, Jatschka J, Fritzsche W, Flores O, Franco R and Pereira E 2014 Localized surface plasmon resonance (LSPR) biosensing using gold nanotriangles: Detection of DNA hybridization events at room temperature *Analyst* **139** 4964–73
[17] Chauke S H, Ombinda-Lemboumba S, Dube F and Mthunzi-Kufa P 2024 Biosensing multidrug-resistant TB genes using SPR (SPIE-Intl Soc Optical Eng) p 39
[18] Zheng F, Chen Z, Li J, Wu R, Zhang B, Nie G, Xie Z and Zhang H 2022 A Highly Sensitive CRISPR-Empowered Surface Plasmon Resonance Sensor for Diagnosis of Inherited Diseases with Femtomolar-Level Real-Time Quantification *Advanced Science* **9**
[19] Beusink J B, Lokate A M C, Besselink G A J, Pruijn G J M and Schasfoort R B M 2008 Angle-scanning SPR imaging for detection of biomolecular interactions on microarrays *Biosens Bioelectron* **23** 839–44
[20] He L, Musick M D, Nicewarner S R, Salinas F G, Benkovic S J, Natan M J and Keating C D 2000 Colloidal Au-enhanced surface plasmon resonance for ultrasensitive detection of DNA hybridization *J Am Chem Soc* **122** 9071–7
[21] Ekgasit S, Tangcharoenbumrungsuk A, Yu F, Baba A and Knoll W 2005 Resonance shifts in SPR curves of nonabsorbing, weakly absorbing, and strongly absorbing dielectrics *Sens Actuators B Chem* **105** 532–41

A comparison of two biosensing recognition elements using SPR for the detection of drug-resistant genes

Sipho Chauke[1,2], Mabotse Tjale[1], Charles Maphanga[1], Felix Dube[2], Saturnin Ombinda-Lemboumba[1,3] and Patience Mthunzi-Kufa[4]

[1]Manufacturing, Council for Scientific and Industrial Research (CSIR), Pretoria, South Africa
[2]Department of Molecular and Cell Biology, University of Cape Town, Cape Town, South Africa
[3]Départemente de Physique, Université des Sciences et Techniques de Masuku, Franceville, Gabon
[4]Engineering and Technology, University of South Africa (UNISA), Johannesburg, South Africa

E-mail: schauke@csir.co.za

Abstract. The burden of tuberculosis (TB) infections is disproportionately high in low-income and resource-limited settings. This disparity exacerbates the emergence of multidrug-resistant (MDR) and extensively drug-resistant (XDR) *Mycobacterium tuberculosis* (Mtb), the bacterium that causes TB. Early detection and treatment of TB remain key strategies to reduce the spread and disease progression, particularly for the detection of drug-resistant forms. Therefore, optical-based diagnostic devices could solve this problem. Surface plasmon resonance (SPR) biosensors offer various advantages, including rapid analysis, high specificity, and sensitivity, as well as requiring small amounts of samples for analysis. For this study, two multidrug-resistant genes, namely, *catalase-peroxidase* (*KatG*) and *enoyl reductase* (*InhA*), were detected using a custom-built surface plasmon resonance (SPR) setup. Biotinylated and thiolated deoxyribonucleic acid (DNA) probes, specific to the two genes (*KatG* and *InhA*), were used as biorecognition elements to capture *KatG* and *InhA* target DNA. The SPR setup was used for the analysis of the binding interactions occurring on the gold-coated slides. The SPR biosensor setup indicated binding interactions through the changes in reflected intensities. The reflected intensities indicated the differences in the resonance angle between each experimental test. This is the initial step to identifying the best characterization of DNA as biorecognition elements for detecting drug-resistant mutations using an SPR-based setup.

1 Introduction

Tuberculosis (TB) is one of the most widespread diseases caused by a single bacterial infection [1]. The causal agent of TB is *Mycobacterium tuberculosis*. Globally, 10 million infections and 1.2 million deaths are attributed to TB infections [1]. This is because the bacteria, if not detected early and the correct treatment administered, can gain resistance to first-line drug regimens and develop into drug-resistant TB [2]. Other factors that contribute to drug resistance include poor adherence to the medication, poor drug quality, and late disease detection [3].

The most common drug resistance is to first-line drugs, Isoniazid and Rifampicin [4,5]. The targets of these two primary drugs are specific proteins in the TB bacteria: *RpoB* for rifampicin, and two targets for isoniazid - *enoyl-reductase* (*InhA*) and *catalase-peroxidase* (*KatG*). The pill/antibiotic/medication burden of TB treatment often leads to disadvantages of poor enzyme level elevation, adverse drug side effects, and poor bioavailability. As such, this can lead to the conversion of TB to drug-resistant strains such as multi-drug-resistant TB (MDR-TB) and extremely drug-resistant TB (XDR-TB) [1].

One of the main strategies to mitigate the conversion and spread of MDR-TB is early disease detection. Currently, this is done using molecular-based assays such as the line-probe assay, drug susceptibility testing (Gold standard), and Polymerase chain reaction (PCR)-based assays [6]. Some of these diagnostic assays/tools/methods, such as the GeneXpert and the UltraMDRplus, require facilities and equipment that are associated with expensive regular maintenance costs [7,8]. Thus, other methods, such as optical-based methods, have attracted attention as novel, effective, and rapid alternatives. One specific optical-based technique that has been studied is surface plasmon resonance (SPR).

SPR is characterized by its label-free, sensitive, and rapid detection capabilities, with the ability to detect small changes in complex analytes [9]. SPR is based on the principle of monitoring changes in optical parameters such as resonance angle, refractive index, and reflected intensity, which are interpreted by a signal transducer [10,11]. In the form of a biosensing technique, SPR can offer real-time detection of samples/molecules in complex analytes [12]. Detecting these molecules in complex analytes can be assisted by biorecognition elements, which aid in capturing the target molecules. The biorecognition elements can be in the form of antibodies, deoxyribonucleic acids (DNA) in the form of ssDNA probes, and/or enzymes [9,13].

Therefore, given that various biorecognition elements can be used in biosensing devices, this study aimed to determine which biorecognition element, between biotinylated probes and thiolated probes, would produce better detection results in the detection of MDR-TB, using a SPR-based platform.

2 Experimental

2.1 Custom-built SPR setup

A custom SPR setup was used in this study. The SPR setup consisted of a Helium-Neon (HeNe) (632.8 nm wavelength) laser with a 10-mW maximum power output. The laser beam was passed through a polarizing beam splitter to select the p-polarization. As shown in Figure 1, a sensor chip consisting of a glass slide coated with gold and mounted on a BK7 prism was immobilized on a rotating stage. The reflected p-polarization laser beam from the prism was directed to a photodiode detector connected to a computer for signal transduction.

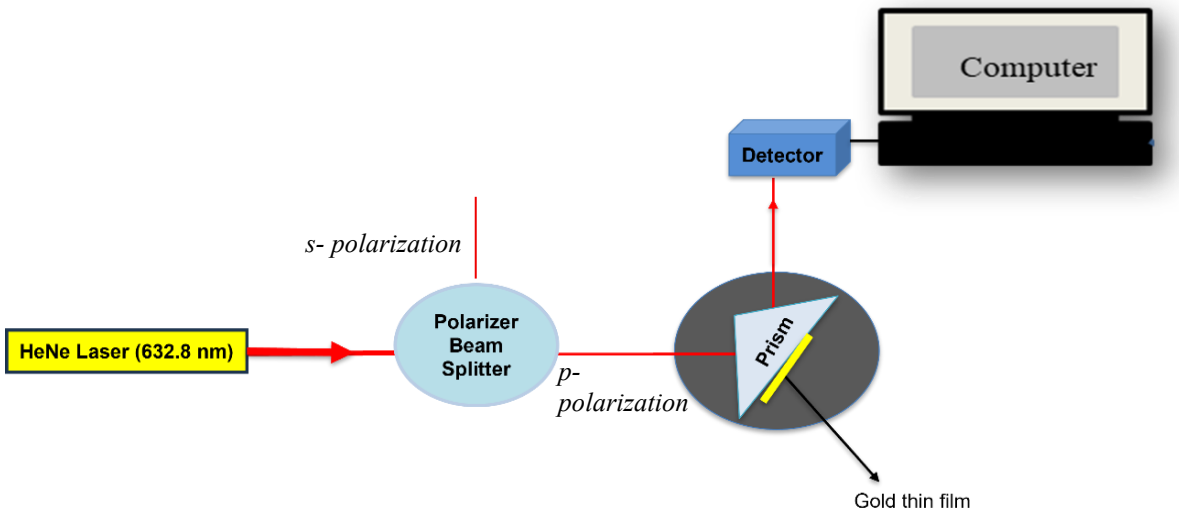

Figure 1: A schematic diagram of the custom-built SPR setup used in this study [14].

2.2 Biosensor chip surface functionalization

The sensor chips (gold-coated slides, 50 nm gold thickness) used in this study were initially cleaned with 100% ethanol and distilled water before use [14]. The sensor chips were dried under Nitrogen gas (N_2).

2.2.1 Thiolated probes immobilization

The thiolated probes (10 µM) (Figure 2) (*KatG* probe: 5' SH-GTCGAACCCGGTGAGGCCCA 3'; *InhA* probe: 5' SH-GATATAGCTCCCGTCCTCGG 3') were immobilized on the sensor chip surface by pipetting 30 µL of the thiolated probe solution. The sensor chip with the probes was then incubated overnight at 4 ºC (in the fridge). Afterward, the sensor chip surface was rinsed with distilled water and dried in the fume hood. Once dry, the sensor chips were analyzed using the custom-built SPR setup.

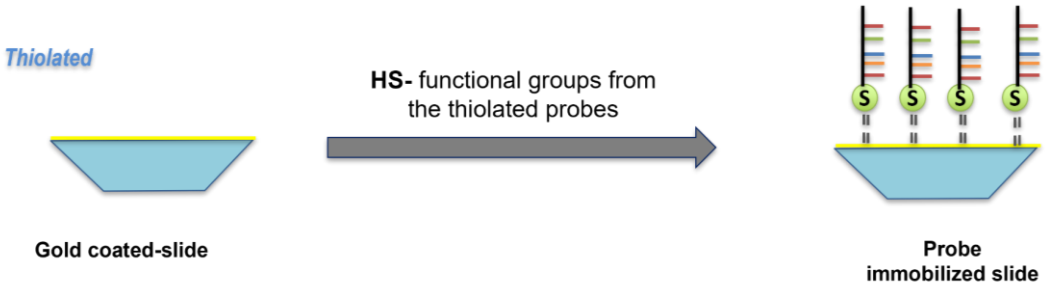

Figure 2: A simplified diagram of the immobilized thiolated DNA probes on the sensor chip surface.

2.2.2 Biotinylated probes immobilization

The sensor chip surface for the immobilization of the biotinylated probes (Figure 3) was treated with 1 mM 11-Mercaptoundecanoic acid (MuA) (Sigma-Aldrich, South Africa) at room temperature for 2 hours in the dark [14]. Afterward, the surface of the sensor chip was rinsed with 1X Phosphate-buffered saline (PBS, pH 7.4) to remove any residual silane/chemicals. The sensor chip was dried and then functionalized with NH functional groups using 30 µL of 1mM solutions of N-ethyl-N-(3-dimethylaminopropyl) carbodiimide hydrochloride (EDC) and 1mM N-hydroxysuccinimide (NHS) (Sigma-Aldrich, South Africa) dissolved in distilled water. The sensor chips were incubated for 10 minutes at room temperature and in the dark. The sensor chip surface was rinsed twice with 1X PBS (100 µL) and allowed to dry. Once dry, Neutravidin was added to the sensor chip's surface and incubated for 1 hour at room temperature. Following the incubation period, the sensor chip surface was rinsed with 1X PBS (100 µL) and allowed to dry. Six microliters (6 µL) (10 µM) of the biotinylated probes (KatG probe: 5' Biotin-GTCGAACCCGGTGAGGCCCA 3'; *InhA* probe: 5' Biotin-GATATAGCTCCCGTCCTCGG 3') were immobilized on the sensor chip surface overnight, in the dark at 4 ºC [14]. Afterward, the sensor chip was rinsed twice with 1X PBS and allowed to dry. Once dry, the sensor chips were analyzed using the custom-built SPR setup.

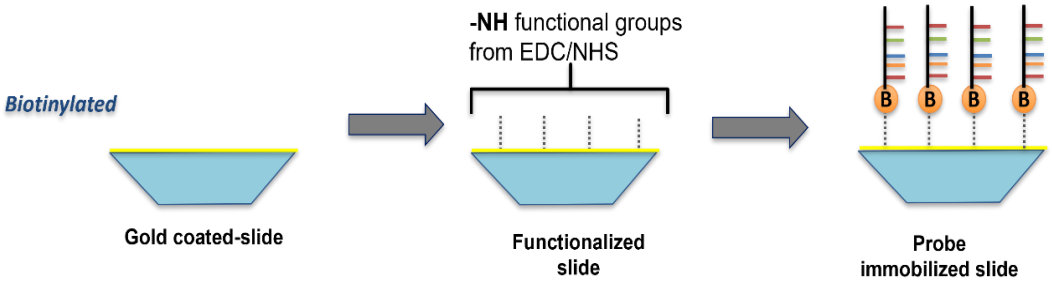

Figure 3: A simplified diagram of the immobilized biotinylated DNA probes on the sensor chip surface.

2.2.3 Sensor chip analysis and data processing (reflectance)

The signals detected by the photodiode amplifier system were recorded as changes in reflected intensities as a function of changes in the incident angle. Measurements were conducted for the sensor chip containing only the gold-coated slide, and the gold-coated slide functionalized with each probe. The reflected intensity data were collected at one-degree increments in the incident angle. The acquired data were subsequently processed and analyzed using OriginPro 8.

3 Results

The ssDNA probes (thiolated and biotinylated) were immobilized on the sensor chip surface due to their strong adsorption properties on the gold-coated surface [15]. Zhang et al. [15] reported an increase in DNA concentration on the gold-sensor chip leads to a broader and more pronounced SPR angle shift and dip. Simplified diagrams (figures 2 and 3) illustrate the immobilization process of DNA probes onto the sensor surface before analysis using the SPR system. The sensing surface of the gold-coated chip was excited by a HeNe laser source at a wavelength of 632 nm. The reflected light was continuously monitored in real-time using an optical analyzer (photodiode amplification system).

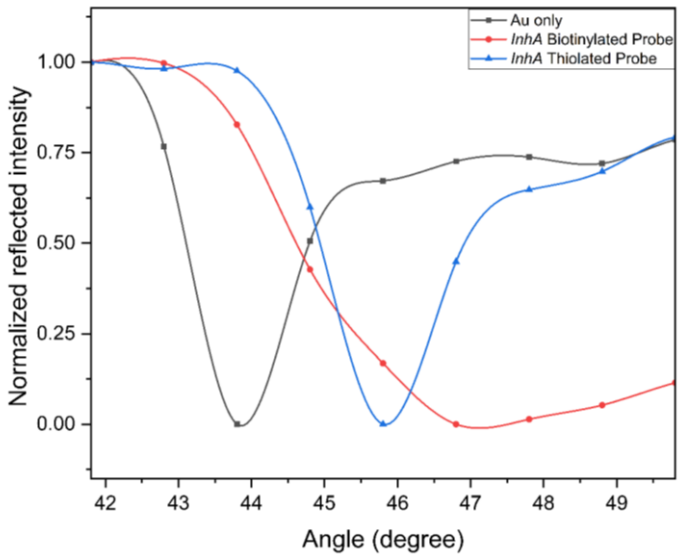

Figure 4: The normalized reflected intensity spectra as a function of angle variation showing the resonance angle shifts obtained for the biotinylated and thiolated *InhA* probe, relative to the sensor ship surface alone.

The data obtained for the *InhA* gene (Figure 4) showed notable changes in the resonance angle compared to the unmodified gold-coated sensor chip and those functionalized with biotinylated and thiolated *InhA* probes. The resonance angle of the bare gold-coated sensor chip was 43.8 degrees, whereas the functionalized chips with biotinylated and thiolated InhA probes exhibited a right shift to 46.8 and 45.8 degrees, respectively. Interestingly, the biotinylated *InhA* probe displayed a 1-degree greater resonance angle shift than the thiolated probe. The immobilization of biotinylated probes on the gold sensor chip surface introduced varying diluents and chemical properties, influencing DNA probe adsorption. According to Peterson et al. [16], thiolated probes enable covalent bonding between the gold and thiol group, facilitating self-assembly monolayer formation and probe attachment kinetics. In contrast, Avidin molecules (streptavidin and neutravidin) have been shown to enhance the signal and adsorption properties of DNA on gold sensor surfaces [16–18]. This may explain the greater resonance angle shift observed for the biotinylated *InhA* probe compared to the thiolated probe.

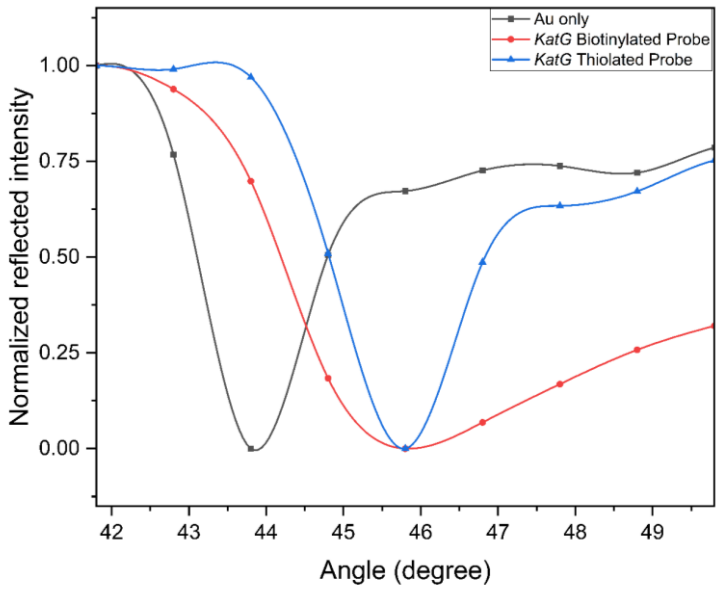

Figure 5: The normalized reflected intensity spectra as a function of angle variation showing the resonance angle shifts obtained for the biotinylated and thiolated *KatG* probe, relative to the sensor ship surface alone.

The *KatG* gene data, obtained using biotinylated and thiolated probes (Figure5), revealed changes in the resonance angle compared to the bare gold-coated sensor. Specifically, the resonance angle shifted from43.8 degrees for the gold-coated chip to 45.8 degrees for both the biotinylated and thiolated *KatG* probes. The observed red shift in resonance angles indicates changes in the molecular composition on the sensor chip surface, suggesting successful immobilization of the probes. This shift can be attributed to the formation of covalent and non-covalent bonds between the probes and the sensor surface. According to Soares [19] a red shift in the resonance angle is primarily due to the increased mass of newly bound molecules on the sensor surface [19].

The immobilization methods for biotinylated and thiolated probes differ significantly in terms of underlying chemistry and surface attachment mechanisms. Biotinylated probes require a multi-step process, where the sensor surface is first functionalized with amide groups using EDC/NHS, enhancing the binding affinity between neutravidin, NHS groups, and biotin on the probes. In contrast, thiolated probes can be immobilized directly onto the sensor chip surface without additional surface modifications. Notably, the multiple adhesion layers required for biotinylated probe immobilization can impact the SPR incident angle dips, influencing the observed signal. This highlights a key difference between the two immobilization approaches, with implications for probe performance and signal quality [20].

Depending on the implementation and optimization of the SPR-based methods, the specificity and sensitivity of an SPR-based method can vary. Furthermore, SPR-based platforms offer a complementary approach to the current diagnostic tools by providing real-time kinetic information and label-free detection [5,8,11]. While some of the current diagnostic tools for MDR-TB may excel in sensitivity and specificity, SPR-based platforms offer advantages in multiplexing and kinetic analysis [11].

4 Conclusion

Both types of probes (biotinylated and thiolated) for each gene displayed a red resonance angle shift. Several factors, such as the binding of the probes to the sensor chip surface, through covalent and non-covalent strategies, can be attributed to some of the findings obtained in this study. Therefore, the use of thiolated probes is a more cost-effective method compared to biotinylated probes, making it a preferred choice for low-cost applications. In addition, the data obtained affirms that an optical-based technique such as SPR can effectively detect changes on

the sensor chip's surface, such as the binding of single-stranded DNA probes. This shows that different DNA-based biorecognition elements can be used in optical-based detection.

References

[1] World Health Organization 2024 *2024 Global tuberculosis report* (Geneva)

[2] Khawbung J L, Nath D and Chakraborty S 2021 Drug resistant Tuberculosis: A review *Comp Immunol Microbiol Infect Dis* **74**

[3] Murray J F, Schraufnagel D E and Hopewell P C 2015 Treatment of tuberculosis: A historical perspective *Ann Am Thorac Soc* **12** 1749–59

[4] Günther G, Ruswa N and Keller P M 2022 Drug-resistant tuberculosis: advances in diagnosis and management *Curr Opin Pulm Med* **28** 211–7

[5] Koch A, Cox H and Mizrahi V 2018 Drug-resistant tuberculosis: challenges and opportunities for diagnosis and treatment *Curr Opin Pharmacol* **42** 7–15

[6] Bereda G 2021 Medication resistant tuberculosis: multi drugresistant and extensively drug resistant *J Lung Pulm Respir Res* **8** 155–8

[7] Vashist S K, Luppa P B, Yeo L Y, Ozcan A and Luong J H T 2015 Emerging Technologies for Next-Generation Point-of-Care Testing *Trends Biotechnol* **33** 692–705

[8] Pongpeeradech N, Kasetchareo Y, Chuchottaworn C, Lawpoolsri S, Silachamroon U and Kaewkungwal J 2022 Evaluation of the use of GeneXpert MTB/RIF in a zone with high burden of tuberculosis in Thailand *PLoS One* **17**

[9] Singh P 2016 SPR Biosensors: Historical Perspectives and Current Challenges *Sens Actuators B Chem* **229** 110–30

[10] Hammond J L, Bhalla N, Rafiee S D and Estrela P 2014 Localized surface plasmon resonance as a biosensing platform for developing countries *Biosensors (Basel)* **4** 172–88

[11] Prabhakar N, Arora K, Arya S K, Solanki P R, Iwamoto M, Singh H and Malhotra B D 2008 Nucleic acid sensor for M. tuberculosis detection based on surface plasmon resonance *Analyst* **133** 1587–92

[12] Shynkarenko O V. and Kravchenko S A 2015 Surface Plasmon Resonance Sensors: Methods of Surface Functionalization and Sensitivity Enhancement *Theoretical and Experimental Chemistry* **51** 273–92

[13] Wang R, Tombelli S, Minunni M, Spiriti M M and Mascini M 2004 Immobilisation of DNA probes for the development of SPR-based sensing *Biosens Bioelectron* **20** 967–74

[14] Chauke S H, Ombinda-Lemboumba S, Dube F and Mthunzi-Kufa P 2024 Biosensing multidrug-resistant TB genes using SPR (SPIE-Intl Soc Optical Eng) p 39

[15] Zhang Q, Zou X N and Chu L Q 2018 Surface Plasmon Resonance Studies of the Hybridization Behavior of DNA-Modified Gold Nanoparticles with Surface-Attached DNA Probes *Plasmonics* **13** 903–13

[16] Peterson A W, Heaton R J and Georgiadis R M 2001 *The effect of surface probe density on DNA hybridization* vol 29

[17] Guo Z, Guilfoyle R A, Thiel A J, Wang R, Smith L M, Maskos U, Southern E M, Gray D E, Case-Green S C, Fell T S, Dobson P J, Langmuir ; Piscevic D, Lawall R, Vieth M, Liley M, Okahata Y and Knoll W 1991 *Surface Plasmon Resonance Imaging Measurements of DNA Hybridization Adsorption and Streptavidin/DNA Multilayer Formation at Chemically Modified Gold Surfaces A C R e s e a r c h* vol 19

[18] Jordan C E, Frutos A G, Thiel A J and Corn R M 1997 Surface Plasmon Resonance Imaging Measurements of DNA Hybridization Adsorption and Streptavidin/DNA Multilayer Formation at Chemically Modified Gold Surfaces *Anal Chem* **69** 4939–47

[19] Soares L, Csáki A, Jatschka J, Fritzsche W, Flores O, Franco R and Pereira E 2014 Localized surface plasmon resonance (LSPR) biosensing using gold nanotriangles: Detection of DNA hybridization events at room temperature *Analyst* **139** 4964–73

[20] Hasler R, Cattozzo Mor D, Aktug G, Fossati S, Vu V T, Tamayo A, Giordani E, Ricciardi E, Giacomini P, Perutka J, Onder K, Kleber C, Samorì P, Huang C J and Dostalek J 2024 Surface plasmon resonance biosensor with anti-crossing modulation readout *Sens Actuators B Chem* **417**

Enhancing the Efficacy of Photodynamic Therapy: The Role of Hypocrellin B, Quercetin, and their combinations in a Human Breast Cancer Cell Line

Sheeja S. Rajan[1*] and Heidi Abrahamse[1]

[1]Laser Research Centre, Faculty of Health Sciences, University of Johannesburg, Johannesburg, South Africa

E-mail: srajan@uj.ac.za

Abstract. Photodynamic therapy (PDT) is an emerging treatment modality that utilizes photosensitizers and light to induce cytotoxic effects in cancer cells. This study investigates the combined therapeutic potential of hypocrellin B (HB) and quercetin (Quer) in PDT against human breast cancer cell lines. The primary objective was to evaluate the effects of PDT with HB, Quer, and their combination on cell viability, oxidative stress, mitochondrial integrity, and apoptosis in vitro. We utilized the MTT assay to assess cell viability post-PDT treatment, while reactive oxygen species (ROS) production was measured using a ROS assay to assess oxidative stress. Mitochondrial membrane potential was monitored to determine the effects on mitochondrial health. The results revealed that combination therapy with HB and Quer significantly enhanced cytotoxicity compared to individual treatments, as evidenced by a marked decrease in cell viability, elevated ROS production, and loss of mitochondrial membrane potential. Furthermore, our result suggests a synergistic effect between HB and Quer in enhancing PDT efficacy. These findings highlight the potential of HB and Quer as effective PDT agents for breast cancer therapy, supporting further exploration of their combination in clinical applications.

1 Introduction

In 2020, the estimated number of breast cancer cases in Africa was around 187,000, with projections indicating it could rise to 347,000 by 2040. At the same time, an estimate was made of the mortality rate to be 85,800 in 2020, with projections indicating an increase to 162,000 by 2040 [1]. The increase in both the rates of occurrence and death from breast cancer might be linked with range of risk factor, including alcohol intake, age progression, hormonal effects, genetic vulnerabilities, and harmful lifestyle choices [2]. Conventional cancer treatment modalities include surgery, radiation, chemotherapy, immunotherapy, endocrine therapy, and targeted therapy [3]. Unfortunately, these treatments come with significant disadvantages, such as harmful side effects and toxicities, which limit the administration of dosages [4]. PDT has recently attracted interest as an alternative to standard cancer treatments. PDT effectively destroys cancer cells by using targeted photochemical and/or photothermal mechanisms [5].

Photosensitizers obtained from entirely natural sources have garnered significant interest in the medical field due to their distinctive biological effects, diverse molecular compositions, and minimal toxicity risk [6]. HB is a naturally occurring pigment derived from perylquinone compounds found in the traditional Chinese herb *Hypocrella bambuase* [7]. HB-mediated PDT is a sanctioned and efficacious therapy for cancers such as

esophageal, nasopharyngeal, breast, lung, and ovarian. It enhances the sensitivity of human cells to chemicals and radiation due to hypocrellin's role in cell phototoxicity [8]. Quer is a bioflavonoid that is pharmacologically active and safe, found in abundance in onions, apples, broccoli, tomatoes, and citrus fruits [9]. Quer exhibits various therapeutic effects, including antioxidants, anti-inflammatory, antimicrobial, and anticancer properties. Quer is found in nature as either a glycoside or an aglycone, and both forms are biologically active [10]. However, because of its poor solubility and bioavailability, its therapeutic application is limited [10]. This study aimed to explore the potential of HB, Quer, their combination, and PDT-mediated treatment to induce apoptosis in MCF7 cells.

2 Materials and methods

2.1 Materials

Fetal bovine serum (FBS), Dulbecco's Modified Eagle Medium (DMEM) medium, Quer, 2–7' dichlorodihydrofluorescein diacetate (H_2-DCFDA), rhodamine 123 (Rh 123), 3-(4,5-dimethylthiazol-2-yl)-2,5-diphenyl tetrazolium bromide (MTT), and penicillin-streptomycin were sourced from Merck Chemicals Co. Lethabong, South Africa. HB was obtained from Cayman Chemicals (Biocom Africa, Johannesburg, South Africa).'

2.2 Cell lines and culturing

The research made use of the MCF7 'breast cancer cell line obtained from the American Type Culture Collection (ATCC; HTB22), located in Manassas, VA, USA.' This was authorized by the Research Ethical Committee (REC-2223-2023) at the University of Johannesburg. The cells were cultured as monolayers in DMEM media, enriched 'with 10% FBS, 100 U/mL penicillin and 100 µg/mL streptomycin, and maintained at 37°C in a 5% CO_2 incubator.' Three biological replicates were used with a seeding concentration of 1 × 10^4 cells/well between passage numbers 5 and 10. Before treatment, the cells were cultured for 24 hours to achieve 70–80% confluency.

2.3 Drug treatment and dosage determination study

MCF7 cells were treated with varying concentrations of HB (10, 20, 40, 80, and 100 ng/ml) and Quer (25, 50, 100, 250, and 500 µM), and DMSO was used as vehicle control. Initial experiments involving laser irradiation were conducted to determine the non-toxic dose of HB, Quer, combinations, and their-PDT for evaluating its effects. The cells were then cultured for 24 hours in a 5% CO_2 environment. Cell viability was estimated by using MTT assay, with measurements obtained using a PerkinElmer VICTOR NivoTM plate reader. Subsequently, IC_{50} values were determined, and the most effective doses were selected for subsequent investigations.

2.4 Irradiation by laser light

Cells treated with HB-PDT were rinsed and subjected to a 470 nm laser (97 mW) for 62 seconds at 5 J/cm² following incubation, while cells treated with Quer-PDT were rinsed and exposed to a 405 nm laser (97 mW) for 93 seconds at 5 J/cm². For more treatment, DMEM was used in place of the original medium.

2.5 Intracellular ROS Level Assessment

Intracellular ROS levels in MCF7 cells post-treatment were assessed. DCFH-DA dye, which is deacetylated to DCFH upon uptake and then oxidized to the fluorescent substance dichlorofluorescein, was briefly used to incubate cells [11]. Cells were treated with HB (40 ng/mL), Quer (50 µM), the combination (HB 20 ng/mL + Quer 25 µM), their-PDT for 4 hours, with separate groups serving as controls. Following treatment, DCFH-DA (5 µM final concentration) was added, and after 40 minutes of incubation in darkness, fluorochrome were measured at 485 and 535 nm for the excitation and emission wavelengths by using a PerkinElmer VICTOR NivoTM plate reader.

2.6 Mitochondrial Membrane Potential

Studying mitochondria and alterations in mitochondrial membrane potential has emerged as a key area of focus in the analysis of apoptosis. Following the incubation of the cells with HB (40 ng/mL), Quer (50 µM), the combination (HB 20 ng/mL + Quer 25 µM), and their-PDT, fluorescent dye Rh-123 (5 µM final concentration) was added to the cells. The cells were then kept in the incubator for 30 minutes. The cells were subsequently washed with PBS and examined under a fluorescent microscope with a blue filter. The fluorescence intensity was recorded at the excitation and emission wavelengths of 510 and 535 nm by using a PerkinElmer VICTOR NivoTM plate reader.

2.7 Statistical Analysis

The studies were carried out in biological triplicate (n = 3) on three independent experiments. 'Data analysis was performed using the GraphPad Prism 5 program (GraphPad program Inc., San Diego, CA, USA), which included a one-way analysis of variance (ANOVA) with Tukey's post hoc test and a two-tailed Student's t-test. Results are presented as mean ± standard deviation (SD), with significance defined as $p \leq 0.05$ for comparisons among experimental groups.'

3 Result and Discussion

MCF7 cells were treated with different concentrations of HB or Quer for 24 hours to evaluate the effectiveness of HB-PDT and Quer-PDT. Following this treatment, HB-treated cells were irradiated with a 470 nm laser, while Quer-treated cells were irradiated with a 405 nm laser. The cytotoxic effect, illustrated in Figure 1, was assessed 24 hours after HB, Quer, and their-PDT post-laser irradiation. This assessment reveals a reduction in % cell viability in comparison to the DMSO control. The light-dose response curve demonstrated that the cytotoxicity of HB, Quer, and their-PDT in MCF7 cells was dose-dependent. Our study demonstrated cell viability of 50% at HB (40 ng/mL) and 50% cell viability was achieved at 50 µM, and higher concentrations did not further reduce the cell viability. For our study we chose 50 µM, which indicates higher potency and reduces the risk of toxicity or adverse effects [3]. Cells were treated with HB (1.25 µM) for 5 hours, after which they were exposed to LED light at a wavelength of 470 nm and different energy densities, according to another study [12]. The study evaluated the viability of keloid fibroblasts using the MTT assay across several treatment groups: control, HB alone, LED alone, and HB-LED treatment. All treatments resulted in reduced cell viability, but the effect was most marked for HB-LED PDT. It is worth mentioning that the greatest decline in cell viability was observed 12 hours after treatment. At this point, the MTT assay showed that LED treatment alone caused a 16.57% reduction in cell viability, while HB treatment alone resulted in a 25.77% reduction. In contrast, HB-LED PDT resulted in a significant decrease in cell activity of 50.23% compared to the control group [13]. According to another study, the MTT assay revealed a significant reduction in the survival rate of HO-8910 cells after PDT treatment. Neither treatment with HB alone nor light irradiation alone showed a significant impact on cell survival [14]. A further study showed that Quer at concentrations of 50 and 100 µM significantly hindered cell proliferation [15]. A research team characterized the photosensitizing effect of Quer on the PDT of Hep-2 cancer cells in 2014. Quer's absorption wavelength is 557 nm. At a concentration of 50 µM, Quer improved the therapeutic effects of aluminium phthalocyanine tetrasulfonate (10 M), mediated PDT-induced cytotoxicity, and caused changes in the mitochondrial membrane potential (MMP) and apoptosis in cancer cells [16].

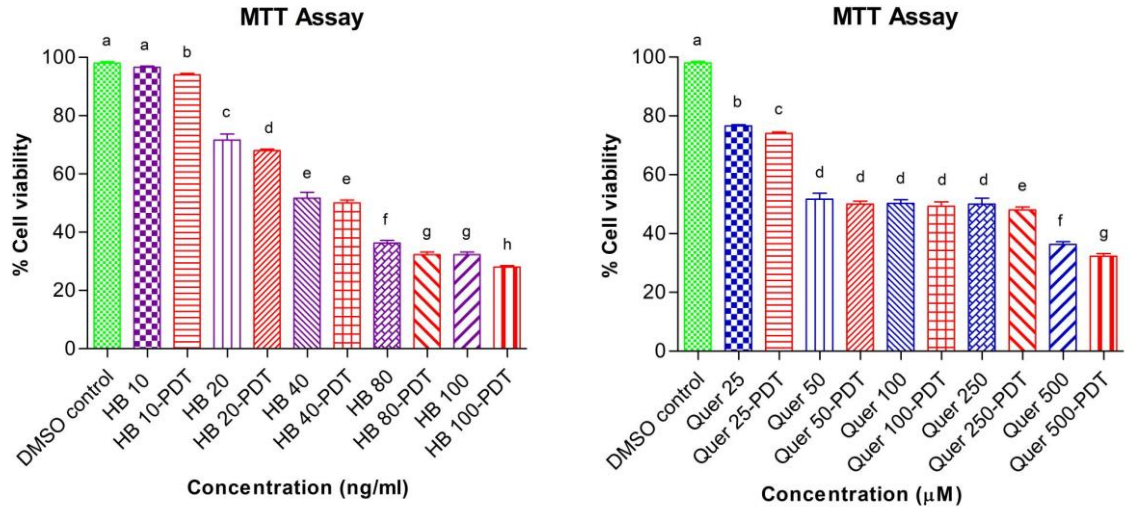

Figure 1: Cell viability of breast cancer cells (*MCF7*) after 24 h of HB, Quer, and their PDT treatment. The experimental results represent the mean ± standard deviation of three separate experiments conducted in triplicate. Statistical analysis was carried out using one-way analysis of variance (ANOVA) with Tukey's pairwise comparison. The letters represent statistical differentiation, while if means are indicated by the same letter, they are not significantly different at a significance level of $p \leq 0.05$.

Recent evidence suggests increasingly that ROS may be crucial in cancer treatment, especially in inducing apoptosis [17]. The impact of HB, Quer, combination, and their-PDT on reducing intracellular ROS levels in MCF7 cells was examined using different concentrations of these substances (illustrated in Figure 2). The application of HB, Quer, combination, and their-PDT treatments in MCF7 cells led to a statistically significant increase ($p \leq 0.05$) and a two-fold rise in overall ROS levels compared to the control group, particularly when compared to PDT alone. The research showed that combining HA with red light exposure significantly induces ROS-mediated cell death, resulting in inhibited cell proliferation, increased apoptosis, and autophagy induction in A431 cells [18].

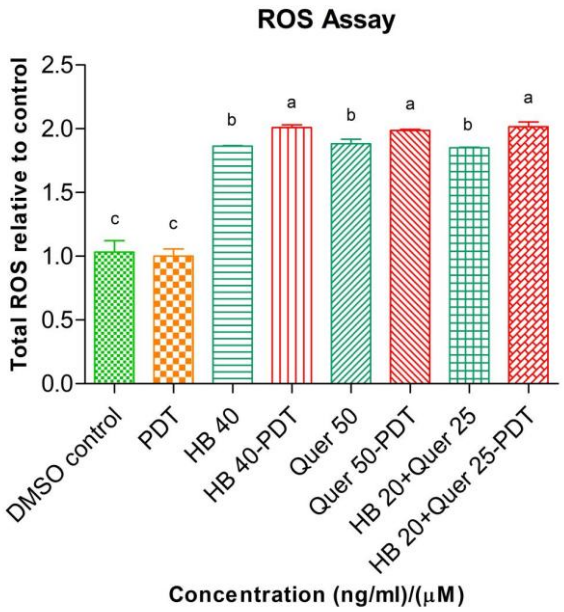

Figure 2: ROS generation of breast cancer cells (*MCF7*) of HB (ng/mL), Quer (μM), combination, and their PDT treatment. The experimental results represent the mean ± standard deviation of three separate experiments conducted in triplicate. Statistical analysis was carried out using one-way analysis of variance (ANOVA) with Tukey's pairwise comparison. The letters represent statistical differences at a significance level of $p \leq 0.05$.

The MMP changes in HB, Quer, combination, and their-PDT treated cells were illustrated in Figure 3. Compared to the DMSO control and PDT treatment alone, MMP was significantly reduced in cells treated with HB, Quer, the combination, and their-PDT. Another study used Rh123 staining to measure the MMP of MDA-MB-231 cells and discovered that HB treatment raised the proportion of cells with MMP collapse [19]. Another study demonstrated that the MMP in MCF7 cells are treated with 10 μM of quercetin rose by a factor of 1.43 [20]. Another study indicated that Quer combined with PDT led to a reduction in MMP and features of late apoptosis and/or the beginning stages of necrosis [16]. At different doses, MCF7 cell viability is reduced in a dose-dependent manner by both HB and Quer. Cytotoxicity approaches a plateau at higher levels (40 ng/mL for HB and 50 μM for Quer), suggesting that their photodynamic impact is saturated. As half of the effective individual concentrations (HB 40 ng/mL and Quer 50 μM), the final combination dose (HB 20 ng/mL + Quer 25 μM) was selected to determine whether lower doses may maximize cytotoxicity through synergy while limiting toxicity. The photodynamic effect of the combined HB and Quer treatment was maximized by irradiating the combination treatment at 470 nm since this wavelength showed more potency than 405 nm. The combined therapies have a larger cytotoxic effect than they would alone, with a more pronounced loss of mitochondrial membrane potential and a higher rise in ROS levels, suggesting a synergistic interaction that exacerbates mitochondrial dysfunction and oxidative stress. In this study, the final combination dose (HB 20 ng/mL + Quer 25 μM) was selected as half of the individually determined effective concentrations (HB 40 ng/mL and Quer 50 μM) that achieved

approximately 50% cell viability, with the rationale of evaluating whether a reduced dose of each agent in combination could enhance therapeutic efficacy through synergistic effects while minimizing potential toxicity.

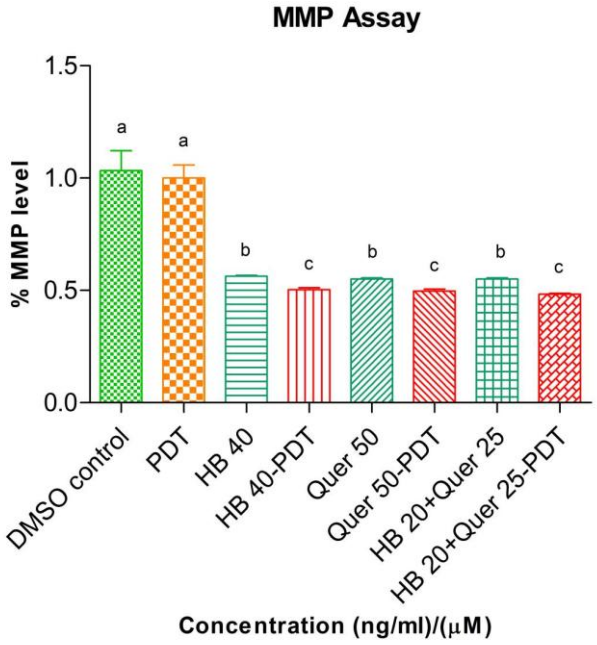

Figure 3: MMP levels of breast cancer cells (*MCF7*) of HB (ng/mL), Quer (μM), combination, and their PDT treatment. The experimental results represent the mean ± standard deviation of three separate experiments conducted in triplicate. Statistical analysis was carried out using one-way analysis of variance (ANOVA) with Tukey's pairwise comparison. The letters represent statistical differences at a significance level of $p \leq 0.05$.

4 Conclusion

To conclude, our research highlights the promise of HB and Quer as a powerful enhancer of PDT for treating human breast cancer. A series of biochemical assays, including MTT, intracellular ROS measurements, and MMP, demonstrate that the synergistic effect of HB, Quer, combination, and their-PDT significantly enhances cytotoxicity against breast cancer cells. This synergism seems to be driven by the induction of intracellular ROS accumulation, which enhances anticancer activity. These findings underscore the therapeutic potential of HB-PDT combinations and advocate for additional *in vivo* studies to investigate their clinical applicability and safety profiles in breast cancer management.

Acknowledgements

The authors extend their gratitude to 'the University of Johannesburg and the Laser Research Centre for their valuable contributions to this review. They also acknowledge the support received from the South African Research Chairs Initiative of the Department of Science and Technology and the National Research Foundation of South Africa (SARChI/NRF-DST) under Grant No. 98337.'

References

[1] J. P. J. Merlin, A. Crous, and H. Abrahamse, "Nano-phototherapy: Favorable prospects for cancer treatment," *WIREs Nanomedicine and Nanobiotechnology,* vol. 16, no. e1930, 2024, doi: https://doi.org/10.1002/wnan.1930

[2] Y-S. Sun, Z. Zhao, Z-N. Yang, F. Xu, H-J. Lu, Z-Y. Zhu, W. Shi, J. Jiang. P-P. Yao, and H-P. Zhu, "Risk Factors and Preventions of Breast Cancer," *International Journal of Biological Science,* vol. 13, pp. 1387–1397, 2017, doi: https://doi.org/10.7150/ijbs.21635

[3] J. P. J. Merlin, S. Mathavarajah, G. Dellaire, K. P. J. Murphy, and H. P. V. Rupasinghe, "A Dietary Antioxidant Formulation Ameliorates DNA Damage Caused by γ-Irradiation in Normal Human Bronchial

Epithelial Cells In Vitro," *Antioxidants*, vol. 11, no. 1407, 2022, doi: https://doi.org/10.3390/antiox11071407.

[4] T. L. Suraweera, J. P. J. Merlin, G. Dellaire, Z. Xu, and H. P. V. Rupasinghe, "Genistein and Procyanidin B2 Reduce Carcinogen-Induced Reactive Oxygen Species and DNA Damage through the Activation of Nrf2/ARE Cell Signaling in Bronchial Epithelial Cells In Vitro," *International Journal of Molecular Science,* vol. 24, no. 3676, 2023, doi: https://doi.org/10.3390/ijms24043676

[5] S. S. Rajan, R. Chandran, and H. Abrahamse, "Overcoming challenges in cancer treatment: Nano-enabled photodynamic therapy as a viable solution," *WIREs Nanomedicine and Nanobiotechnology,* vol. 16, no. e1942, 2024, doi: https://doi.org/10.1002/wnan.1942

[6] N. Zhao, X. Lin, S-S. Qi, Z. M. Luo, and S-L. Chen, "Yan De Novo Transcriptome Assembly in Shiraia bambusicola to Investigate Putative Genes Involved in the Biosynthesis of Hypocrellin A," *International Journal of Molecular Science,* vol. 17, no. 311, 2016, doi: https://doi.org/10.3390/ijms17030311.

[7] S. Law, C. Lo, J. Han, A. W. Leung, and C. Xu, "Antimicrobial photodynamic therapy with hypocrellin B against SARS-CoV-2 infection?," *Photodiagnosis and Photodynamic Therapy,* vol. 34, no. 102297, 2021, doi: https://doi.org/10.1016/j.pdpdt.2021.102297

[8] S. S. Rajan, R. Chandran, and H. Abrahamse, "Advancing photodynamic therapy with nano-conjugated Hypocrellin: Mechanisms and clinical applications," *International Journal of Nanomedicine,* vol. 196, pp. 11023-11038, 2024, doi: https://doi.org/10.2147/IJN.S486014

[9] R. A. Rather and M. Bhagat, "Quercetin as an innovative therapeutic tool for cancer chemoprevention: Molecular mechanisms and implications in human health," *Cancer Medicine,* vol. 9, no. 24, pp. 9181–9192, 2020, doi: https://doi.org/10..1002/cam4.1411

[10] G. D'Andrea, "Quercetin: A flavonol with multifaceted therapeutic applications?," *Fitoterapia*, vol. 106, pp. 256–271, 2015, doi: https://doi.org/10.1016/j.fitote.2015.09.018

[11] S. S. Rajan, R. Chandran, and H. Abrahamse, "Enhancing Photodynamic Therapy Efficiency in Human Lung Cancer Cells using Hypocrellin B" in *Proceeding of South African Institute of Physics*, Grahamstown, P. Neethling, Ed., 2024: SAIP

[12] Y. Jiang, X. Xia, A. W. Leung, J. Xiang, and C. Xu, "Apoptosis of breast cancer cells induced by hypocrellin B under light-emitting diode irradiation," *Photodiagnosis and Photodynamic Therapy,* vol. 9, pp. 337–343, 2012, doi: https://doi.org/10.1016/j.pdpdt.2012.03.009

[13] Y. Hu, C. Zhang, S. Li, Y. Jiao, T. Qi, G. Wei, and G. Han, "Effects of Photodynamic Therapy Using Yellow LED-light with Concomitant Hypocrellin B on Apoptotic Signaling in Keloid Fibroblasts," *International Journal of Biological Science,* vol. 13, pp. 319–326, 2017, doi: https://doi.org/10.7150/ijbs.17920

[14] Y. Jiang, A. W. Leung, J. Xiang, and C. Xu, "LED Light-Activated Hypocrellin B Induces Mitochondrial Damage of Ovarian Cancer Cells," *International Journal of Photoenergy,* vol. 2012, pp. 1–5, 2012, doi: https://doi.org/10.1155/2012/186752

[15] R. Wang, L. Yang, S. Li, D. Ye, L. Yang, Q. Liu, Z. Zhao, Q. Cai, J. Tan, and X. Li, "Quercetin inhibits breast cancer stem cells via downregulation of aldehyde dehydrogenase 1A1 (ALDH1A1), chemokine receptor type 4 (CXCR4), mucin 1 (MUC1), and epithelial cell adhesion molecule (EpCAM)," *Medical Science Monitor,* vol. 24, pp. 421-420, 2018, doi: https://doi.org/10.12659/MSM.908022

[16] R. D. P. Rodrigues, I. R. P. Tini, C. P. Soares, and N. S. da Silva, "Effect of photodynamic therapy supplemented with quercetin in Hep-2 cells," *Cell Biology International,* vol. 38, no. 6, pp. 716-722, 2014, doi: https://doi.org/10.1002/cbin.10251

[17] J. P. J. Merlin, G. Dellaire, K. Murphy, and H. P. V. Rupasinghe, "Vitamin-containing antioxidant formulation reduces carcinogen-induced dna damage through atr/chk1 signaling in bronchial epithelial cells in vitro," *Biomedicines,* vol. 9, no. 1665, 2021, doi: https://doi.org/10.3390/biomedicines9111665

[18] T. Niu, Y. Tian, G. Wang, G. Guo, Y. Tong, and Y. Shi, "Inhibition of ROS-NF-κB-dependent autophagy enhances Hypocrellin A united LED red light-induced apoptosis in squamous carcinoma A431 cells," *Cell Signaling,* vol. 69, no. 109550, 2020, doi: https://doi.org/10.1016/j.cellsig.2020.109550

[19] Y. Jia, X. Wang, Q. Liu, A. W. Leung , P. Wang, and C. Xu, "Sono *Ultrasonics,*dynamic action of hypocrellin B triggers cell apoptoisis of breast cancer cells involving caspase pathway," *Ultrasonics,* vol. 73, pp. 154-161, 2017, doi: http://dx.doi.org/10.1016/j.ultras.2016.09.013

[20] P. S. Ramos, C. Ferreira, C. L. A. Passos, J. L. Silva, and E. Fialho, "Effect of quercetin and chrysin and its association on viability and cell cycle progression in MDA-MB-231 and MCF-7 human breast cancer cells," *Biomedicine & Pharmacotherapy,* vol. 179, no. 117276, 2024, doi: https://doi.org/10.1016/j.biopha.2024.117276

Evaluation of Pheophorbide *a* Phototoxicity on Melanoma Cells Grown as Three-Dimensional Multicellular Tumour Spheroids

Nkune W Nkune[1] and Heidi Abrahamse[1]

[1]Laser Research Centre, Faculty of Health Sciences, University of Johannesburg, P.O. Box: 17011, Johannesburg 2028, South Africa.

E-mail: habrahamse@uj.ac.za

Abstract. Melanoma is the deadliest form of skin cancer, with a rapidly increasing incidence and a poor prognosis for patients diagnosed at advanced stages. Despite several available treatments, including surgical excision, chemotherapy, radiation therapy, and immunotherapy, resistance to these therapies remains a significant challenge, particularly when the tumour has metastasised. Photodynamic therapy (PDT) is a promising modality for the treatment of cancer because it is non-invasive and selectively damages the cancerous tissue, minimizing damage to adjacent healthy tissues. Currently, most PDT experiments are still conducted on two-dimensional (2D) monocultures, which fail to mimic the native three-dimensional (3D) tissue architecture accurately. Therefore, 3-D cell cultures serve as excellent models to resemble tumour tissue in terms of structural and functional properties. Commercially purchased A375 melanoma cells used in this study were cultured as 3-D tumour spheroid and treated with pheophorbide-a at varying doses (5-40 μM) and irradiated at a fluence of 10 J/cm^2 with a 660 nm diode laser. Post-irradiation cellular changes were observed using microscopy, adenosine 5′-triphosphate (ATP), and lactate dehydrogenase (LDH) assays. Photoactivated pheophorbide-a led to a significant dose-dependent response to PDT, demonstrating notable morphological changes, increased cytotoxicity, and reduced cell viability. The study indicated that PDT with pheophorbide-a is an effective treatment method for eradicating melanoma cancer cells *in vitro*.

1 Introduction

Melanoma is the deadliest skin cancer that develops from melanocytes, and its incidence has risen rapidly over for several decades worldwide [1]. Although it is a rare skin malignancy, it accounts for more than 70% of skin cancer-related deaths [2]. Melanoma does not present any symptoms in the early stages and is normally diagnosed in its advanced stages when metastasis has occurred, which makes it unresponsive to cancer treatments[3]. Current traditional therapies such as surgery, radiation, chemotherapy, immunotherapy, and biological therapy seldom yield a satisfactory prognosis in patients and cause unwanted side effects [4]. Therefore, it remains imperative to investigate therapeutic modalities with increased potency and minimal side effects to improve the quality and overall survival rate of patients diagnosed with metastatic melanoma. Photodynamic therapy (PDT), a phototherapeutic technique, has great potential to selectively damage tumour cells while sparing adjacent healthy cells. This light-based technique relies on a photoactive molecule, known as a photosensitizer, light of a specific wavelength, and molecular oxygen in tumour cells [5]. The excitation of PSs during the PDT process

triggers photochemical reactions that result in the generation of cytotoxic reactive oxygen species (ROS), which in turn damage cancer cells [2]. Pheophorbide *a* (PPB*a*) has been extensively investigated in cancer research due to its antioxidant, anti-inflammatory, and phototoxic properties. It is a naturally occurring anionic dye and a catabolic product of chlorophyll[6]. PPBa exhibits better phototoxic effects than PSs widely used in clinical trials, such as Photofrin, a mixture of hematoporphyrines that has poor absorption above 600 nm [7]. Studies have reported that PDT resistance to pigmented melanomas is attributed to the presence of melanin, as it serves as a photoprotectant that blocks any in-depth light penetration, reducing light aimed at targeted tumours, as well as absorbing and causing therapeutic light to scatter [5]. Melanin typically absorbs light between 500-600 nm, suggesting that effective treatment of melanotic melanomas may be achieved above this range due to unobstructed light transmittance [8]. PPB*a* exhibits a strong absorption peak between 650 and 700 nm, which falls within the tissue-penetrating wavelength range, making it one of the best candidates for PSs in melanoma treatment [8]. Most *in vitro* studies in PDT are still conducted on conventional two-dimensional (2-D) cell culture models, which fail to resemble *in vivo* tumours in terms of cell-cell interactions, complex tumour microenvironment, oxygen and nutrients, drug responses, and signaling mechanisms. As a result, significant discrepancies have been reported when transferring results from 2-D cell culture models to *in vivo* models. These misleading results have led to many anticancer agents failing clinical trials, which calls for the development of more reliable cell culture models, such as the three-dimensional (3-D) multicellular tumour spheroids (MCTS). 3-D cell culture models mimic many aspects of *in vivo* tumours, more importantly, drug resistance patterns observed in patients [9]. The current study evaluated the efficacy of PPB*a* in both *in vitro* 3-D cell culture models of the human melanoma A375 cell line to bridge the gap between preclinical and clinical studies.

2 Methodology

2.1 Cell culture

The study utilised commercially available human malignant melanoma A375 cells (Cellonex, 0012300), which were cultured in Dulbecco's Modified Eagle's medium (DMEM) supplemented with 10% Foetal Bovine Serum (FBS), 0.1% Amphotericin-B and Penicillin-Streptomycin. The cells were cultured in T175 culture flasks and maintained at 37 °C, 5% CO_2 and 85% humidity. Once the cells reached approximately 80-90% confluence, exhibited normal morphology, and were confirmed to be contamination-free, 4000 cells were seeded per well in low-attachment 96-well plates (Corning) in 200 µL of complete media to produce multicellular tumour spheroids (MCTS). Spheroid aggregation and growth were monitored daily under an inverted microscope to ensure uniform spheroid formation. Based on preliminary optimisation and established protocols [10], a seeding density of 4000 cells per well was determined to produce compact, viable spheroids with a diameter of approximately 450 µm after 96 hours. This time point was selected to maintain consistent spheroid morphology and optimal light penetration before PDT experiments.

2.2 UV-Visible Spectroscopy

UV-visible spectrophotometer (Genova 7315, Life Science Spectrophotometer, JENWAY) was used to validate characteristic absorption peaks of Pheophorbide *a* in Dimethyl sulfoxide (DMSO) at the resolution of 1 nm within 200-800 nm spectral region.

2.3 Photoactivation of Pheophorbide a photosensitizer

PPB*a* was initially dissolved in 100% DMSO to prepare a 1 mM stock solution and stored at -20 °C in the dark. Working concentrations (5-40 µM) were made fresh in complete DMEM media, ensuring that the final concentration in all wells did not exceed 0.05% (v/v). The photoactivation of PPBa was achieved by exposing melanoma cells to a continuous diode 660 nm laser at a fluence of 10 J/cm^2. The cells were then subjected to morphological screening and biochemical assays 24 h post-irradiation incubation. Parameters (wavelength 660 nm: spot size 9.1 cm^2: power output: 137 mW and irradiation time 11 min:06 sec)

2.4 Morphological Examination

Morphological changes of A375 MCTS were examined under a Wirsan Olympus CKX 41 inverted light microscope coupled with a digital camera (Olympus C5060-ADUS) after 24 hours of post-irradiation incubation

2.5 Cell Membrane Integrity Assay

The degree of cytotoxicity was determined by measuring the amount of lactate dehydrogenase (LDH) enzyme released from compromised cellular membranes of A375 MCTS. Briefly, 50 µL of media from all the samples were transferred to a flat-bottom 96-well microplate and mixed with 50 µL of reconstituted LDH substrate (Promega, G179A). The contents were mixed thoroughly, incubated in the dark for 30 minutes, and then analysed at 490 nm using a PerkinElmer VICTOR Nivo™.

2.6 Adenosine Triphosphate (ATP) Proliferation Assay

CellTiter-Glo® 3D luminescence (Promega, G968A) kit assessed cell proliferation in A375 MCTS by measuring ATP levels in metabolically active cells. Briefly, 100 µL of ATP substrate was added all the samples and agitated for 25 min, then an equal volume of media was added. The ATP luminescence was measured in Relative Light Units (RLU) using PerkinElmer, VICTOR Nivo™.

2.7 Live/Dead.

A375 spheroids treated with varying doses of PPBa with and without laser irradiation were stained with 1 µg/mL of ethidium bromide (EtBr) and acridine orange (AO) for 5 min in phosphate-buffered saline (PBS). Thereafter, the cells were rinsed three times with PBS, and fluorescent images were captured using fluor 488 nm and EtBr 603 nm channels under a Carl Zeiss Axio Z1 fluorescence microscope.

2.8 Statistical Analysis

Biochemical assays were carried out in triplicates for three separate experiments. Statistical analysis was performed using one-way analysis of variance (ANOVA)in Sigma Plot version 14. The Dunnett test was used to determine the statistically significant difference between the untreated control and experimental groups. The results were presented as mean values, standard error, and statistical significance ($p<0.05$*, $p < 0.01$**, and $p < 0.001$***).

3 Results

3.1.1 Absorption Spectra

As demonstrated in Figure 1, the UV-Vis absorption spectrum of pheophorbide-*a* exhibited a prominent Q band peak at 666 nm. This suggests that this PS is suitable for PDT applications, as its absorption is within the therapeutic window (600-800 nm).

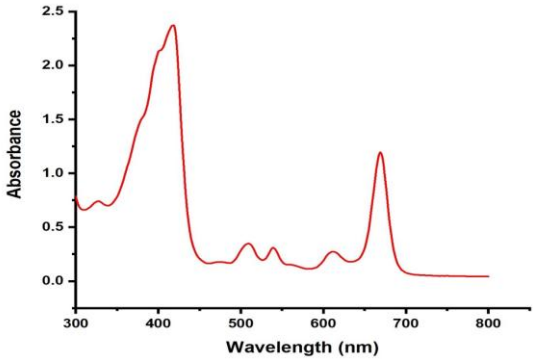

Figure 1 UV-Vis absorption spectrum of PPBa in DMSO

3.1.2 Morphology

In relation to Figure 2, MCTS treated with laser irradiation and increasing concentrations of PPBa exhibited no significant phenotypic changes when compared untreated MCTS, maintaining their original appearance. However, spheroids subjected to both PPBa and laser irradiation displayed a disrupted outer membrane, with the highest concentrations (20 & 40 µM) leading to complete rupture of the spheroids.

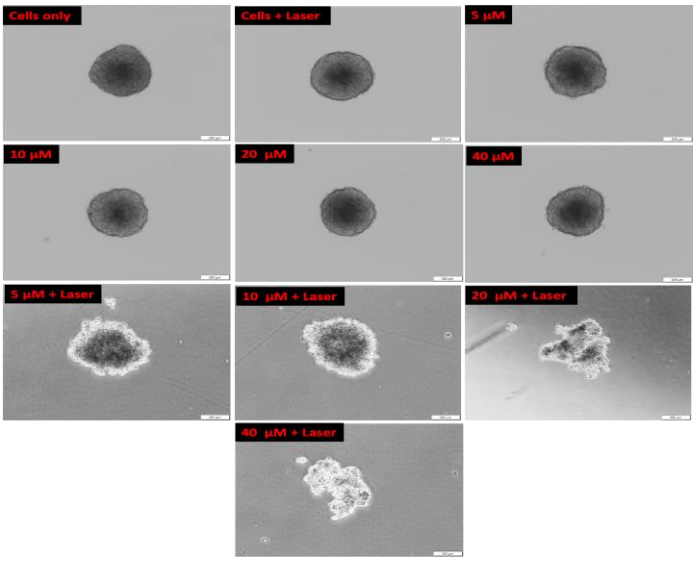

Figure 2 Control and experimental MCTSs treated with increasing doses of PPBa with and without laser irradiation at a fluency of 10 J/cm^2 (Scale bar 200 µm, 50X magnification).

3.1.3 Photodynamic therapy-induced phototoxicity

As shown in Figure 3A, there was no significant LDH detected in spheroids treated with laser irradiation alone or increasing doses of PPBa alone, when compared to untreated spheroids. In contrast, spheroids subjected to both laser irradiation and PPBa exhibited a significant, dose-dependent increase in LDH release compared to untreated cells (P<0.001***). IC_{50} concentration of PPBa was found to be 9.3 µM using a sigmoid curve (Figure 3B). In Figure 3 C, PDT-treated spheroids showed a significant dose-dependent decrease in cellular proliferation when compared to untreated cells (P<0.01** and P<0.001***).

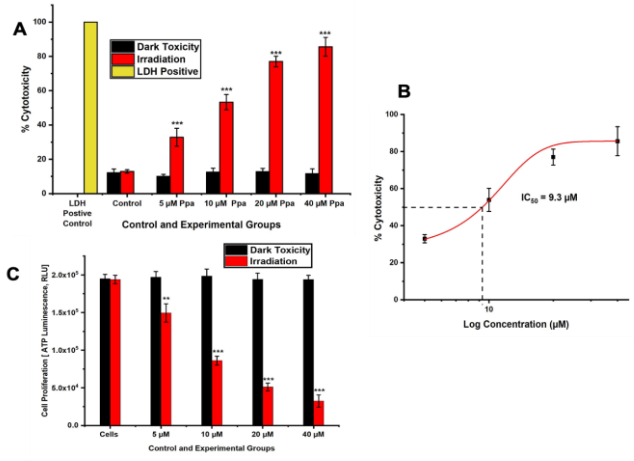

Figure 3 (A) Cellular membrane integrity determination using LDH assay **(B)** IC_{50} estimation using as a sigmoid curve **(C)** ATP quantification to determine cellular proliferation post PDT.

3.1.4 Live/Dead

Spheroids were stained with AO/EtBr to differentiate between live and dead cells based on membrane integrity. AO stains all nucleated cells and emits green fluorescent signals, while EtBr penetrates compromised cells and emits red fluorescent signals. In Figure 4, fluorescent images showed that control spheroids did not take up the EtBr staining (red), suggesting a negative cytotoxicity. While PDT-treated spheroids absorbed the EtBr stain due

to their compromised cytoplasmic membranes, a noticeable cellular shrinkage and rupturing were observed, indicating photodamage.

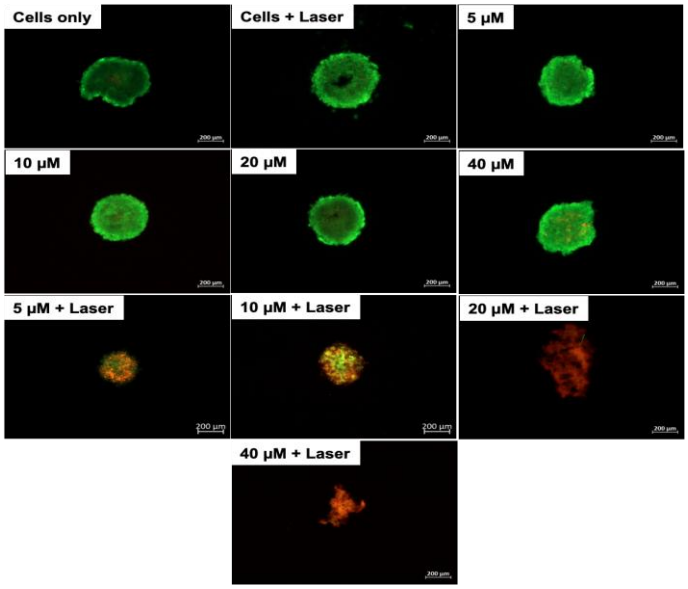

Figure 4: Fluorescent images of spheroids after dual staining with AO and EtBr to distinguish live and dead cells. (Scale bar 200 µm, 50X magnification).

4 Discussion and Conclusion

Our study revealed that PPB*a*-mediated PDT significantly inhibited A375 melanoma spheroids' viability in a dose-dependent manner. We observed significant morphological disruption, elevated LDH levels (suggesting compromised membrane integrity), and decreased ATP levels (reflecting decreased metabolic activity) in PDT-treated groups, which coincided with Haung et al.'s findings on the susceptibility of melanoma to PDT using longer wavelength [8]. The undetectable cytotoxicity in spheroids treated with PPBa without light exposure confirms its minimal toxicity in darkness, aligning with reports by Saide and colleagues [7]. More importantly, the PPB*a*'s Q-band absorption at 666 nm circumvents melanin-induced PDT resistance [5,8], as melanin absorbs light within 500-600 nm; therefore, there is negligible interference at this wavelength. Several lines of evidence have highlighted that 2-D cell culture models are more susceptible to PDT when compared to 3-D cell culture, since they poorly resemble in *vivo* tumours and drug-resistant patterns found in patients. We noted an IC_{50} concentration of PPB*a* of 9.3 µM at a fluence of 10 J/cm², while recent studies by Fakudze et al. reported an IC_{50} of 0.5 µM at a fluence of 1 J/cm² in 2-D cultured cancer cells[11]. These findings suggest that 2-D cell cultures produce unreliable and deceptive data that do not reflect or predict *in vivo* outcomes, leading to anticancer agents failing clinical trials [5].

The 3-D models closely mimic solid tumours, which enhances clinical translation ability. Therefore, the reported dose-dependent inhibitory effect in spheroids predicts in vivo tumour outcomes more accurately than monolayers, bridging the gap between *in vitro* and *in vivo* studies. However, future studies should investigate PPB*a*-mediated PDT in *in vivo* models of melanoma. While the current research focuses on the dose-dependent phototoxicity of PPBa a in 3-D melanoma spheroids, it remains essential to recognise certain limitations. The minimal cytotoxicity observed in the dark controls pertains only to A375 melanoma spheroids and should not be regarded as a definitive safety profile. This warrants further studies using non-cancerous epithelial or melanocyte cell lines to confirm PPB*a*'s tumour selectivity.

Furthermore, although ATP and LDH assays provided valuable data on cellular viability and membrane integrity, the mechanisms underlying the induction of cell death pathways were not examined. Future studies will include the quantification of apoptosis and necrosis biomarkers, such as Annexin V/PI, caspase activation, and the quantification of oxidative stress, as well as *in vivo* validation to substantiate these results. These considerations emphasise the provisional aspect of our findings and outline future steps for translational application. These considerations underscore the preliminary nature of our findings and outline the next steps toward translational relevance. Lastly, the spheroids were irradiated from above at 660 nm. Although the light potentially penetrates

the entire spheroid, its intensity is likely to decrease slightly with depth, just as in real tumours. In future studies, we will address this limitation by using fractionated dosing while rotating the plates or employing side illumination between doses to ensure even light exposure.

5 Acknowledgements

This work was supported by the South African Research Chairs Initiative of the Department of Science and Technology and National Research Foundation of South Africa (Grant No 98337), as well as grants received from the African Laser Centre (ALC).

6 Reference

[1] Y. Liu *et al.*, 'A tyrosinase-activated Pt(II) complex for melanoma photodynamic therapy and fluorescence imaging', *Sensors and Actuators B: Chemical*, vol. 374, p. 132836, Jan. 2023, doi: 10.1016/j.snb.2022.132836.

[2] X.-Y. Li *et al.*, 'Susceptibility and Resistance Mechanisms During Photodynamic Therapy of Melanoma', *Front Oncol*, vol. 10, p. 597, May 2020, doi: 10.3389/fonc.2020.00597.

[3] N. M. Helvind *et al.*, 'Routine PET-CT scans provide early and accurate recurrence detection in asymptomatic stage IIB-III melanoma patients', *European Journal of Surgical Oncology*, vol. 47, no. 12, pp. 3020–3027, Dec. 2021, doi: 10.1016/j.ejso.2021.06.011.

[4] J. B. Heistein, U. Acharya, and S. K. R. Mukkamalla, 'Malignant Melanoma', in *StatPearls*, Treasure Island (FL): StatPearls Publishing, 2025. Accessed: Jul. 20, 2025. [Online]. Available: http://www.ncbi.nlm.nih.gov/books/NBK470409/

[5] N. Nkune and H. Abrahamse, 'Nanoparticle-Based Drug Delivery Systems for Photodynamic Therapy of Metastatic Melanoma: A Review', *International Journal of Molecular Sciences*, vol. 22, p. 12549, Nov. 2021, doi: 10.3390/ijms222212549.

[6] N. Fakudze, H. Abrahamse, and B. George, 'Nanoparticles improved pheophorbide-a mediated photodynamic therapy for cancer', *Lasers Med Sci*, vol. 40, no. 1, p. 78, 2025, doi: 10.1007/s10103-025-04320-2.

[7] A. Saide, C. Lauritano, and A. Ianora, 'Pheophorbide a: State of the Art', *Marine Drugs*, vol. 18, no. 5, p. 257, May 2020, doi: 10.3390/md18050257.

[8] Y.-Y. Huang, D. Vecchio, P. Avci, R. Yin, M. Garcia-Diaz, and M. R. Hamblin, 'Melanoma resistance to photodynamic therapy: new insights', *Biol Chem*, vol. 394, no. 2, pp. 239–250, Feb. 2013, doi: 10.1515/hsz-2012-0228.

[9] S. Khanna, A. Chauhan, A. N. Bhatt, and B. S. R. Dwarakanath, 'Chapter 13 - Multicellular tumor spheroids as in vitro models for studying tumor responses to anticancer therapies', in *Animal Biotechnology (Second Edition)*, A. S. Verma and A. Singh, Eds., Boston: Academic Press, 2020, pp. 251–268. doi: 10.1016/B978-0-12-811710-1.00011-2.

[10] S. Rossi *et al.*, 'TNF-alpha and metalloproteases as key players in melanoma cells aggressiveness', *Journal of Experimental & Clinical Cancer Research*, vol. 37, no. 1, p. 326, Dec. 2018, doi: 10.1186/s13046-018-0982-1.

[11] N. T. Fakudze, P. Sarbadhikary, H. Abrahamse, and B. P. George, 'Dose response cytotoxicity studies with naturally derived photosensitizers against cancer cells', *J. Phys.: Conf. Ser.*, vol. 2970, no. 1, p. 012013, Mar. 2025, doi: 10.1088/1742-6596/2970/1/012013.

Evaluation of the Phototoxic effect of Chemically Synthesized Silver Nanoparticles on Breast Cancer Cells

Isaac Baidoo, Paromita Sarbadhikary and Blassan P George*

Laser Research Centre, Faculty of Health Sciences, University of Johannesburg, P.O. Box 17011, Doornfontein 2028, South Africa

E-mail: blassang@uj.ac.za

Abstract. Silver nanoparticles (AgNPs) are gaining attention in cancer treatment for their diverse cytotoxic actions, such as inducing reactive oxygen species (ROS), disrupting cancer cell metabolism, and potentially bypassing mechanisms of drug resistance. Beyond their intrinsic cytotoxicity, AgNPs also exhibit utility in drug delivery and cancer diagnostics. Notably, their ability to convert absorbed light into heat enables targeted photothermal therapy. This research investigates both the chemotoxic and phototoxic properties of silver nanoparticles (AgNPs) synthesized through a chemical reduction approach and applied to MCF-7 breast cancer cells. The synthesized AgNPs were characterized using ultraviolet-visible (UV–Vis) spectroscopy, dynamic light scattering (DLS), and Zetasizer analysis. Characterization revealed a surface plasmon resonance peak (SPR) at 401 nm, an average particle size of 119.3 nm, a zeta potential of −30.8 mV, and a polydispersity index (PDI) of 0.269, all of which indicate stable colloidal behavior suitable for biological applications. MTT assays showed dose-dependent cytotoxicity, with 64.4% cell viability at 5 μg/mL under dark conditions, which further decreased to 50.1% upon 405 nm laser irradiation (5 J/cm²). Photothermal assessment revealed a ~3 °C temperature increase in AgNP suspensions compared to a negligible rise (~1 °C) in control, confirming their photothermal conversion efficiency. Morphological changes observed via bright-field microscopy further supported AgNP-induced cell damage. These findings suggest that enhanced cytotoxicity results from a combination of localized hyperthermia and ROS production, highlighting the synergistic photothermal and photodynamic properties of AgNPs. Overall, this study demonstrates citrate-borohydride synthesized AgNPs exhibit enhanced photo-responsive cytotoxicity against breast cancer cells, warranting further investigation to evaluate their selectivity and potential translational applications.

1 Introduction

Breast cancer remains one of the most widespread malignancies affecting women globally and continues to account for a significant proportion of cancer-related deaths [1]. In the African region, it constitutes around 17% of all female cancers and contributes to roughly 20% of cancer mortality in women. In South Africa specifically, it is the leading cancer among women, with over 9,200 new cases diagnosed annually and an incidence rate of 50.8 per 100,000 [2, 3]. While conventional treatment strategies such as chemotherapy and radiotherapy have led to improvements in patient prognosis, they are still hindered by several limitations. These include systemic toxicity, lack of selectivity, and the eventual emergence of therapeutic resistance [4, 5]. Considering these challenges, nanotechnology has emerged as a powerful platform in cancer research, offering materials that can interact selectively with cellular targets. Among the various nanomaterials developed, AgNPs have attracted

substantial interest due to their distinct physicochemical characteristics and inherent cytotoxic capabilities toward cancer cells [6]. Nanoparticles build up more readily in tumour tissue due to the Enhanced Permeability and Retention (EPR) effect. This allows AgNPs to accumulate more effectively at the tumour site [7]. The cytotoxic potential of AgNPs is mainly linked to their ability to induce ROS, impair mitochondrial dynamics, and disrupt essential cellular signalling cascades [8]. Additionally, AgNPs serve as versatile carriers for anticancer drugs, helping to improve solubility, enhance bioavailability, and facilitate targeted delivery [9].

In addition to their inherent cytotoxic properties, AgNPs exhibit photo-responsive properties. Their strong SPR allows absorption of specific light wavelengths, converting them into localized heat, a plasmonic photothermal effect [10]. Light activation also enhances ROS generation, eliciting a photodynamic effect that intensifies oxidative stress in cancer cells [11]. These dual mechanisms make AgNPs promising anti-cancer agents for minimally invasive cancer therapies. Their efficacy, however, is influenced by factors such as particle size, surface charge, and colloidal stability, which are largely dictated by synthesis methods. Chemical reduction using sodium borohydride remains a widely adopted approach for generating stable, well-defined AgNPs [12]. As nanotechnology converges with phototherapy, the development of light-activated AgNP systems represents a growing frontier in nanomedicine, warranting further investigation into their physicochemical-biological interactions and therapeutic optimization. This work aims to evaluate the chemotoxic and phototoxic effects of chemically synthesized AgNPs on MCF-7 breast cancer cells, with a focus on their photothermal and photodynamic contributions under 405 nm laser irradiation.

2 Materials and Methods

2.1 Synthesis of AgNPs

AgNPs were synthesized via chemical reduction method [13]. Briefly, a 10 mL solution of 1 mM silver nitrate ($AgNO_3$) was prepared and heated to 45–50 °C under stirring (500 rpm), followed by the addition of 1 mL of 1 mM sodium citrate ($Na_3C_6H_5O_7$) as a reducing agent. Subsequently, 2–3 drops of 0.1 M sodium borohydride ($NaBH_4$) were added dropwise as a coalescence. The reaction was stirred vigorously for 5 minutes, with a yellowish-brown colour change confirming AgNP formation. The newly synthesised AgNPs were centrifuged to ascertain them in pellets, dried and weighed. After knowing the quantity, AgNPs were dissolved in distilled water and stored in 4 ºC for further analysis.

2.2 Characterization of AgNPs

The synthesized AgNPs were characterized to verify formation and evaluate physicochemical properties. UV–Vis absorption spectra were recorded between 300–600 nm using a VICTOR Nivo™ multimode plate reader (PerkinElmer) to confirm surface plasmon resonance. Particle size, PDI, and zeta potential were measured using a Zetasizer (v7.10, Malvern Instruments, UK) at a fixed scattering angle and controlled temperature.

2.3 Photothermal Effect Measurement

Photothermal activity was examined by dissolving 10 mg of freeze-dried AgNPs in 2 mL of Milli-Q water to yield a 5 mg/mL suspension. This solution was placed in a sterile 35 mm petri dish, while a control containing only 2 mL of Milli-Q water was prepared in parallel. Both samples were irradiated with 405 nm blue diode laser at an energy fluence of 5 J/cm². Surface temperature was monitored using an infrared thermal imaging camera at the start of irradiation and after 5 minutes of continuous laser exposure.

2.4 Cell Line and Culture Conditions

The human breast cancer cell line MCF-7 (ATCC® HTB-22™), obtained from the American Type Culture Collection (ATCC), was maintained in Dulbecco's Modified Eagle Medium (DMEM) supplemented with 10% fetal bovine serum (FBS) and 1% penicillin-streptomycin (Pen-Strep). Cells were maintained at 37 °C in a humidified incubator under 5% CO_2 atmosphere and sub-cultured upon reaching 70–80% confluency.

2.5 Treatment

To evaluate the chemo and phototoxic effects of AgNPs, MCF-7 cells were seeded in 96-well plates and treated with AgNP concentrations of 1.25, 2.5, 5, 10 and 20 µg/mL for 24 h. Phototoxicity was evaluated by treating cells with the same AgNP concentrations for 24 h, followed by irradiation using a 405 nm blue light diode laser at a light dose of 5 J/cm², with intensity maintained between 22 and 23 mW/cm². Control groups included an untreated group (without AgNPs treatment and irradiation) and a light control group (without AgNPs treatment).

2.6 MTT Cell Viability Assay

Cell viability was evaluated using the MTT (3-(4,5-dimethylthiazol-2-yl)-2,5-diphenyltetrazolium bromide) assay (Cell Proliferation Kit I, No. 11465007001, Invitrogen™), which is a yellow tetrazolium salt and is reduced into insoluble purple formazan crystals. In viable cells. Post treatment and incubation period, 10 µL of the MTT labelling reagent was added to each well and cells were incubated at 37 °C for 3 h. Formazan crystals were dissolved using 100 µL of Solubilization solution into each well, plates were made to stand overnight in the incubator, and the optical density at 540 nm was recorded using a VICTOR Nivo™ (PerkinElmer) multimode plate reader. Viability was calculated relative to untreated controls.

2.7 Morphological Analysis

Morphological changes were assessed using bright-field microscopy. MCF-7 cells treated with IC_{50} (half maximal Inhibitory Concentration) concentrations of AgNPs with and without irradiation were imaged alongside untreated groups using a Olympus CKX 41 inverted microscope with an Olympus C5060-ADUS camera equipped with CellSens software (v2.3).

2.8 Statistical analysis

All experiments were conducted in triplicate and repeated independently on three separate occasions. Statistical analysis was performed using one-way ANOVA to assess differences among AgNPs concentrations under dark and photo-irradiated (405 nm) conditions, followed by Tukey's post-hoc test for pairwise comparisons. A confidence level of 95% was applied, with $p < 0.05$ (*), $p < 0.01$ (**), and $p < 0.001$ (***) considered statistically significant. Analyses were performed using Origin2018.

3 Results

3.1 Characterisation of AgNPs

Fig. 1a shows that the formation of AgNPs through UV–Visible absorption spectroscopy with a distinct SPR peak at 401 nm. As shown in Fig 1b and Fig 1c, Dynamic light scattering also shows an average hydrodynamic diameter of approximately 119.3 nm, a zeta potential of −30.8 mV, and a polydispersity index of 0.269 at pH 7.4. These values indicate good colloidal stability and uniform particle distribution under physiological conditions.

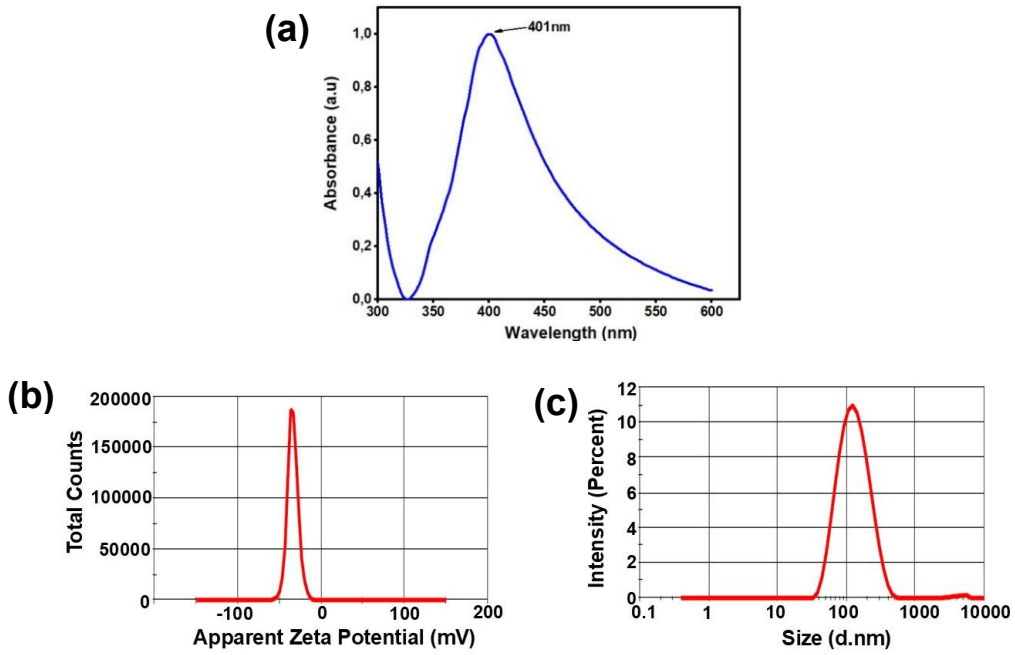

Figure 1. (a) UV–Visible absorption spectrum for AgNPs, (b) zeta potential, and (c) particle size.

3.2 Photothermal Activity of AgNPs

Fig. 2 shows the thermal response of AgNP suspensions and water (control) after 5 min of 405 nm laser irradiation at 5 J/cm². The AgNP-treated sample exhibited a temperature increase of approximately 2.8 °C, while the water control showed a minimal rise of ~0.9 °C. This indicates the moderate photothermal conversion ability of AgNPs under light exposure.

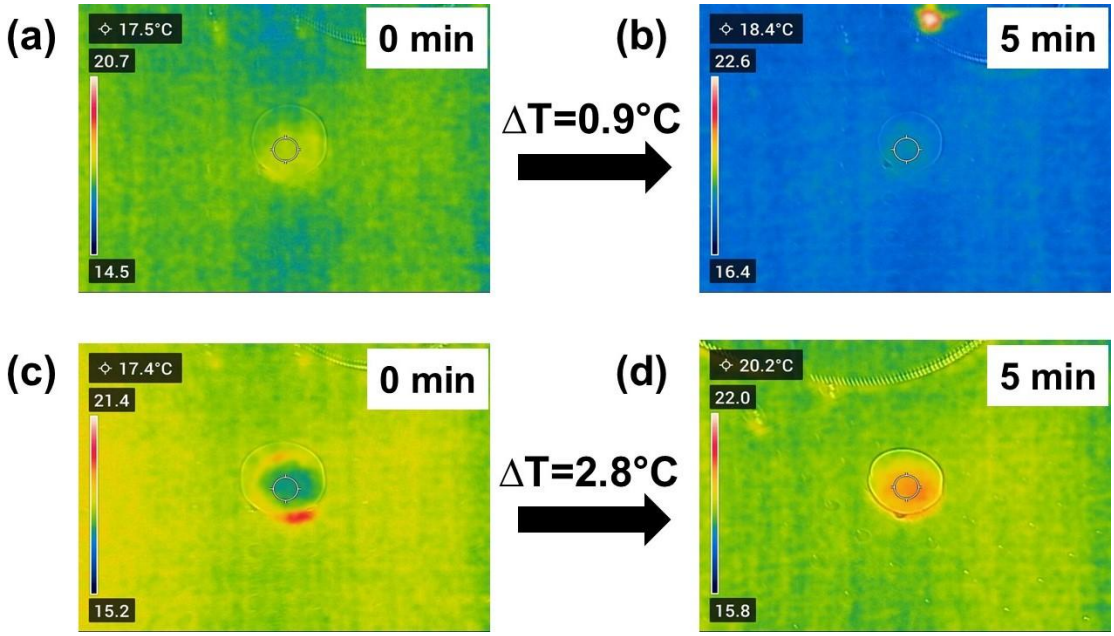

Figure 2: Thermal images showing temperature variation in (a, b) water and (c, d) chemically synthesized AgNPs at 0 min and after 5 min of 405 nm irradiation, respectively.

3.3 Chemotoxic and Phototoxic Effects on MCF-7 Cells

MCF-7 cells treated with AgNPs exhibited a concentration-dependent decrease in cell viability in both unirradiated and irradiated groups (Fig. 3a). The IC_{50} for AgNPs in the absence of irradiation (chemotoxicity) was determined to be 8.65±0.27 µg/mL. Upon irradiation, the IC_{50} dropped to 6.13±0.28 µg/mL, indicating a significant enhancement in cytotoxicity when combined with phototherapy (Fig. 3b). Significant differences ($p < 0.001$) in cell viability were observed between the control and all AgNP-treated concentrations under both dark and PDT (405 nm) conditions. The reduction in viability was concentration-dependent, with the PDT group showing enhanced cytotoxicity compared to the dark group.

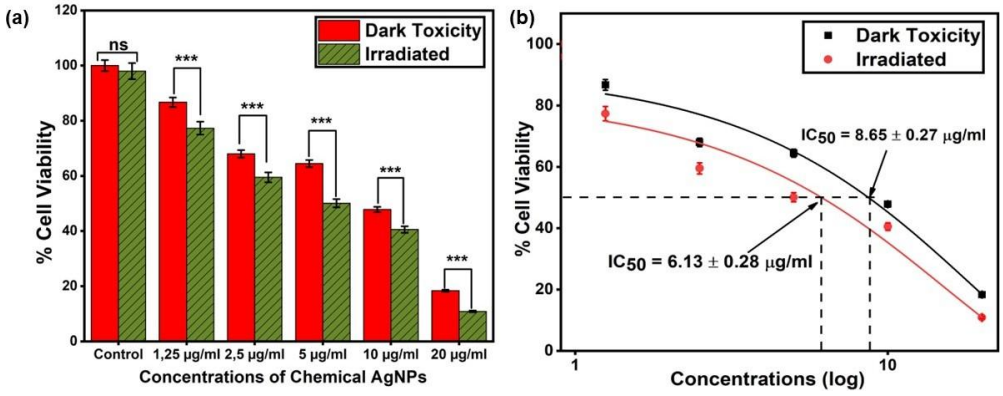

Figure 3. (a) Percentage cell viability of MCF-7 cells treated with AgNPs with and without light irradiation determined by MTT assay post 24 h, (b) sigmoidal concentration-response curve of both treatment groups. IC_{50} values are indicated for both treatment groups. Data points in the graphs are represented as mean ± SD from experiments repeated in triplicates. ***($p < 0.005$) indicate significant difference.

3.4 Treatment-induced morphological changes

Fig. 4 shows morphological changes in MCF-7 cells treated at IC_{50} concentrations. AgNP treatment combined with irradiation (Fig. 4c) induced pronounced morphological changes, including cell rounding, detachment from the culture surface, and membrane damage, compared to the untreated and unirradiated group.

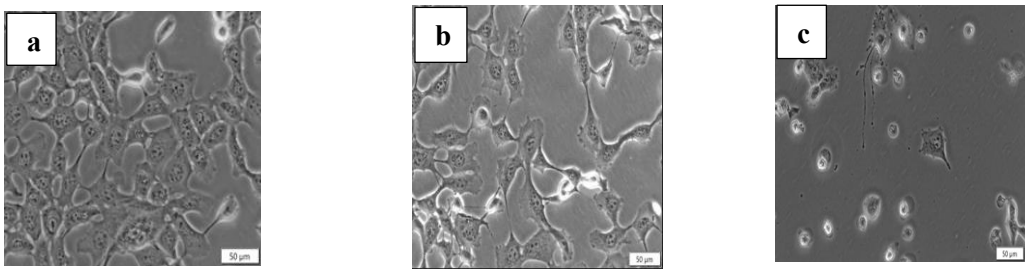

Figure 4. Phase contrast images of MCF-7 cells, (a) untreated control, (b) AgNPs-treated (dark), (c) AgNPs-treated (irradiated) at IC_{50} concentrations under a magnification of 50µm.

4 Discussion

The present study explored the chemotoxic and phototoxic potential of chemically synthesized AgNPs against the MCF-7 human breast cancer cell line. UV-Vis spectroscopy and DLS characterization (Fig. 1) confirmed the formation of stable, monodisperse nanoparticles with a characteristic SPR peak at 401 nm and a hydrodynamic size of 119.3 nm, appropriate for cellular interaction and uptake. These physicochemical properties are consistent with literature reports indicating that AgNPs with sizes around 100–120 nm exhibit efficient cellular internalization and interaction relevant to cytotoxic studies [14]. Cell viability analysis demonstrated a dose-dependent cytotoxic response under both dark and irradiated conditions. Notably, the IC_{50} value decreased from 8.65 µg/mL (dark) to 6.13 µg/mL upon 405 nm laser exposure, indicating enhanced cell killing due to phototoxic activation. This enhanced effect is likely driven by the combined influence of ROS generation and localized heat production via the plasmonic properties of AgNPs. These findings align with previous studies demonstrating the synergistic potential of nanoparticle-assisted phototherapy in cancer treatment. El-Hussein and Hamblin similarly observed that light-activated AgNPs induced DNA damage and apoptosis through ROS-mediated stress and disruption of mitochondrial membrane potential in lung cancer cells (A549), indicating that such phototoxic mechanisms may be effective across various cancer cell types [15].

The photothermal analysis confirmed a measurable temperature increase (2.8 °C) in AgNP under 405 nm laser irradiation, compared to a negligible rise (0.9 °C) in the control. While this increase may appear modest, it reflects localized intracellular heating, which, combined with oxidative stress may initiate apoptosis or necrosis in cancer cells [9]. This is further supported by the observed structural collapse and membrane disruption in treated cells, aligning with reports by Shipunova et al. (2022) where HER2-targeted AgNPs induced potent photothermal apoptosis in cancer models [16]. Morphological observations further supported the cytotoxic effect of AgNPs combined with phototherapy. Cells treated with AgNPs alone exhibited insignificant morphological alterations, compared to the significant structural damage, including membrane disruption and cell collapse in combined treatment group. Our preliminary results demonstrate that chemically synthesized AgNPs can act as photo-responsive materials that enhance cytotoxicity under blue-light exposure; however, further studies on normal cells and mechanistic pathways are required before any therapeutic relevance can be established.

These findings indicate that citrate-borohydride synthesized AgNPs can induce significant light-enhanced cytotoxicity, likely through synergistic ROS generation and local photothermal effects, consistent with previous reports in nanoparticle-assisted phototherapy systems [9, 15]. Further studies comparing responses in normal and cancerous cell models will be required to assess their potential selectivity and suitability for therapeutic development.

5 Conclusion

This study demonstrated that chemically synthesized AgNPs exhibit enhanced cytotoxic effects against MCF-7 breast cancer cells when irradiated at 405 nm. The ability of AgNPs to generate localized heat and the potential to generate ROS upon irradiation makes them photo-enhanced cancer agents. This suggests a promising direction for photo-activated nanoparticle research. Further mechanistic and comparative studies using both cancerous and normal cells are necessary to assess potential selectivity and in-vivo relevance.

Funding and Acknowledgements

The authors sincerely thank the South African Research Chairs initiative of the Department of Science and Technology and the National Research Foundation (NRF) of South Africa (Grant No 98337), South African Medical Research Council (Grant No. SAMRC EIP007/2021) as well as grants received from the NRF Research Development Grants for Y-Rated Researchers (Grant No. 137788), Council for Scientific Industrial Research (CSIR)-National Laser Centre (NLC), African Laser Centre (ALC) (Grant No. HLHA26X Task ALC-R001), and University Research Committee (URC) and Laser Research Centre (LRC), University of Johannesburg.

References

[1] F. Bray *et al.*, "Global cancer statistics 2022: GLOBOCAN estimates of incidence and mortality worldwide for 36 cancers in 185 countries," *CA: a cancer journal for clinicians,* vol. 74, no. 3, pp. 229-263, 2024.

[2] Y. Hamdi *et al.*, "Cancer in Africa: The Untold Story," (in English), *Frontiers in Oncology,* Original Research vol. Volume 11 - 2021, 2021-April-15 2021, doi: 10.3389/fonc.2021.650117.

[3] N. I. M. SOMDYALA, "Reducing the Burden of Cervix Cancer in a Rural Setting of South Africa."

[4] U. Anand *et al.*, "Cancer chemotherapy and beyond: Current status, drug candidates, associated risks and progress in targeted therapeutics," (in eng), *Genes Dis,* vol. 10, no. 4, pp. 1367-1401, Jul 2023, doi: 10.1016/j.gendis.2022.02.007.

[5] A. Zafar, S. Khatoon, M. Khan, J. Abu, and A. Naeem, "Advancements and limitations in traditional anti-cancer therapies: a comprehensive review of surgery, chemotherapy, radiation therapy, and hormonal therapy," *Discover oncology,* vol. 16, p. 607, 04/24 2025, doi: 10.1007/s12672-025-02198-8.

[6] M. M. Ammar *et al.*, "Nanotechnology in oncology: advances in biosynthesis, drug delivery, and theranostics," (in eng), *Discov Oncol,* vol. 16, no. 1, p. 1172, Jun 21 2025, doi: 10.1007/s12672-025-02664-3.

[7] P. Takáč *et al.*, "Do We Know Enough About the Safety Profile of Silver Nanoparticles in Oncology? A Focus on Novel Methods and Approaches," *International Journal of Molecular Sciences,* vol. 26, no. 11, p. 5344, 2025. [Online]. Available: https://www.mdpi.com/1422-0067/26/11/5344.

[8] X. An, W. Yu, J. Liu, D. Tang, L. Yang, and X. Chen, "Oxidative cell death in cancer: mechanisms and therapeutic opportunities," *Cell Death & Disease,* vol. 15, no. 8, p. 556, 2024/08/01 2024, doi: 10.1038/s41419-024-06939-5.

[9] S. Liu, S. Phillips, S. Northrup, and N. Levi, "The Impact of Silver Nanoparticle-Induced Photothermal Therapy and Its Augmentation of Hyperthermia on Breast Cancer Cells Harboring Intracellular Bacteria," (in eng), *Pharmaceutics,* vol. 15, no. 10, Oct 14 2023, doi: 10.3390/pharmaceutics15102466.

[10] R. M. Melo, G. M. Albuquerque, J. P. Monte, G. A. L. Pereira, and G. Pereira, "Recent Advances in the Application of Silver Nanoparticles for Enhancing Phototherapy Outcomes," *Pharmaceuticals,* vol. 18, no. 7, p. 970, 2025. [Online]. Available: https://www.mdpi.com/1424-8247/18/7/970.

[11] N. Alvarez and A. Sevilla, "Current Advances in Photodynamic Therapy (PDT) and the Future Potential of PDT-Combinatorial Cancer Therapies," (in eng), *Int J Mol Sci,* vol. 25, no. 2, Jan 13 2024, doi: 10.3390/ijms25021023.

[12] R. Khursheed *et al.*, "Biomedical applications of metallic nanoparticles in cancer: Current status and future perspectives," *Biomedicine & Pharmacotherapy,* vol. 150, p. 112951, 2022/06/01/ 2022, doi: https://doi.org/10.1016/j.biopha.2022.112951.

[13] U. T. Khatoon, K. V. Rao, J. V. R. Rao, and Y. Aparna, "Synthesis and characterization of silver nanoparticles by chemical reduction method," in *International Conference on Nanoscience, Engineering and Technology (ICONSET 2011)*, 28-30 Nov. 2011 2011, pp. 97-99, doi: 10.1109/ICONSET.2011.6167920.

[14] M. Akter *et al.*, "A systematic review on silver nanoparticles-induced cytotoxicity: Physicochemical properties and perspectives," (in eng), *J Adv Res,* vol. 9, pp. 1-16, Jan 2018, doi: 10.1016/j.jare.2017.10.008.

[15] A. El-Hussein and M. R. Hamblin, "ROS generation and DNA damage with photo-inactivation mediated by silver nanoparticles in lung cancer cell line," (in eng), *IET Nanobiotechnol,* vol. 11, no. 2, pp. 173-178, Mar 2017, doi: 10.1049/iet-nbt.2015.0083.

[16] V. O. Shipunova *et al.*, "Photothermal Therapy with HER2-Targeted Silver Nanoparticles Leading to Cancer Remission," *Pharmaceutics,* vol. 14, no. 5, p. 1013, 2022. [Online]. Available: https://www.mdpi.com/1999-4923/14/5/1013.

Rate equations for the control of Yb-171 ions

A. E. Iyer[1], **C. M. Steenkamp**[1,2] **and N. E. Payne**[1]

[1]Stellenbosch Photonics Institute, Physics Department, Stellenbosch University, Stellenbosch, 7600, South Africa
[2]National Institute for Theoretical and Computation Sciences, South Africa

E-mail: 23171480@sun.ac.za

Abstract. Rate equations are used to calculate the hyperfine state population dynamics of an ensemble of ytterbium-171 ions interacting with lasers. The application is to optimise the efficiency and timescales of quantum control processes that we plan to use in the laboratory. The effect of laser powers, polarisations and side-band carrier ratios for Doppler cooling and state preparation are investigated.

1 Introduction

Trapped ions are a leading physical implementation of qubits which can be used in quantum computers, offering long coherence times, scalability and the ability to be precisely controlled using lasers [1]. This study is part of a quantum control project with the long-term aim to realise unsharp measurements between two weakly entangled ytterbium ion isotopes, $^{171}Yb^{+}$ and $^{174}Yb^{+}$, in a linear Paul trap [2].

The basic control processes that must be achieved in the laboratory are Doppler cooling, state preparation, state detection and electron shelving. Doppler cooling reduces the temperature of the ions by cycles of absorption of red-detuned laser photons and spontaneous emission. During state preparation the ion is optically pumped into the qubit ground state. Electron shelving is achieved by populating and depopulating a long-lived metastable state. State detection is achieved by pumping a closed-loop transition that produces measurable fluorescence. Additional repump lasers are required to recover ions that have spontaneously decayed into dark states during the control processes.

The Einstein rate equations are a set of coupled first-order differential equations describing the time-dependent evolution of the ion's hyperfine state populations. Rate equations are suitable to describe atom-laser interactions, where the decay of the coherence between quantum levels is faster than the timescales on which we manipulate them, as is the case in our system [3]. We use a rate equation model to calculate the hyperfine state populations of $^{171}Yb^{+}$ during the quantum control processes that would be used in the experiment, to gain insights on how to increase the efficiency and estimate timescales. The numerical model includes up to 60 atomic states and 11 experimental parameters. The model is used to inform parameter choices in the laboratory and understand the timescales observed in the experiments.

2 Einstein rate equations

The interaction between an atom with states $|i\rangle$ and $|j\rangle$ and light that is close to resonance with the energy spacing between these states is described using the Einstein coefficients A and B. Specifically, the coefficient A_{ij} (s^{-1}) describes the spontaneous emission rate from a non-degenerate hyperfine state $|i\rangle$ to another single non-degenerate hyperfine state $|j\rangle$. The coefficient B_{ji} describes stimulated emission and B_{ij} stimulated absorption rates ($J^{-1} \cdot m^3 \cdot s^{-2}$).

Using the Wigner-Eckhart theorem [3, 4], A_{ij} can be written as

$$A_{ij} = A_{J'J}(2J'+1)(2F'+1)\begin{Bmatrix} J & J' & k \\ F' & F & I \end{Bmatrix}^2 \left\langle Fm_F \middle| F'm'_{F'}kq \right\rangle^2, \tag{1}$$

where primed quantum numbers are those of state $|i\rangle$ and the unprimed quantum numbers are those of state $|j\rangle$. The value k is the rank of the tensor operator involved. The rank of the electric dipole operator is one and the rank of the electric quadrupole operator is two. The quantum numbers in the expression are F for the total angular momentum, m_F for the magnetic quantum number, J for the total electronic angular momentum, I for the nuclear spin, and q can be interpreted as the projection of the photon angular momentum onto the quantisation axis. $A_{J'J}$ is the total spontaneous decay rate from the excited term to the ground term. This expression includes the Wigner-6j symbol and Clebsch-Gordon coefficient to calculate the transition rates for each pair of hyperfine states for different light polarisations.

The Einstein coefficient B_{ij} is calculated using the relation between the Einstein coefficients, $A_{ij} = \frac{\hbar\omega_{ij}^3}{\pi^2 c^3} B_{ij}$. We treat each atomic state individually, so that the degeneracy is one for all states, hence $B_{ij} = B_{ji}$.
The general expression for the rate equation is

$$\frac{dn_i}{dt} = \sum_{j=1, j\neq i}^{j=N} (n_j B_{ji} P_{ij} + n_j A_{ji} - n_i B_{ij} P_{ij} - n_i A_{ij}), \tag{2}$$

where N is the number of states in the model, n_i represents the probability of finding the system in state $|i\rangle$. The factor P_{ij} is the total energy density $P_{ij} = \int_0^\infty \rho_{ij}(\omega) s_{ij}(\omega) d\omega$ in J $\cdot$ m^{-3} $\cdot$ s. The atomic line-shape is described using a gaussian function $s_{ij}(\omega)$, centered around the atomic resonance frequency [3]. The laser spectral distribution $\rho_{ij}(\omega)$ is also modeled as a gaussian function of angular frequency ω and of laser properties such as laser intensity, bandwidth and detuning.
We express the set of rate equations in equation 2 in matrix form $\frac{d}{dt}\vec{n} = (M^{\text{spont}} + M^{\text{stim}})\vec{n}$ and solve them numerically in MATLAB using the ClebschGordan.m [5], Wigner6j.m [6] and Wigner3j.m [7] functions.

3 Results and discussion

The relevant 20 atomic states of ^{171}Yb$^+$ are shown in Figure 1. The ground and excited qubit states in the $^2S_{1/2}$ manifold are labeled $|0\rangle$ and $|1\rangle$. The laser-driven transitions included in the model are numbered, with the wavelength and sideband frequency indicated in the legend. The results of the rate equation model for a given set of laser parameters is the population evolution of the 60 hyperfine states for a specified time.

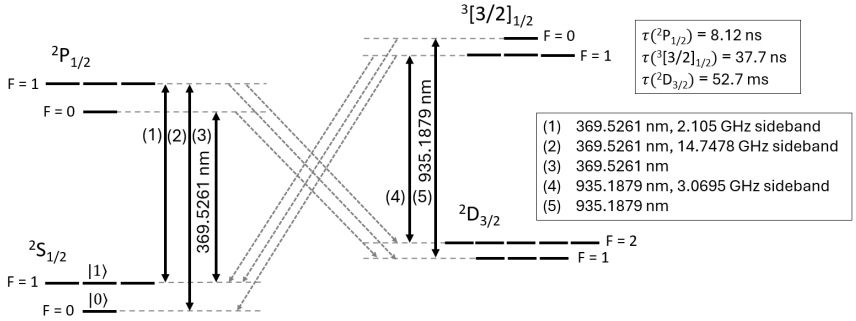

Figure 1: ^{171}Yb$^+$ level scheme with laser-pumped transitions (solid) and relevant decays (dashed). The wavelengths and sideband frequencies are indicated in the bottom right legend. The lifetimes for each level are captured in the top right legend.

To achieve Doppler cooling, transitions (2) and (3) are pumped by the 369 nm laser with a 14.7 GHz first order upper sideband to the $^2P_{1/2}$ states (lifetime 8.12 ns) [8]. In the experiment the 369 nm laser is red detuned by approximately 200 MHz so that it interacts most strongly (resonantly) with ions moving anti-parallel to the direction of propagation of the laser. In the simulation, on-resonance 369 nm light is used during Doppler cooling to simulate these moving atoms interacting with resonant light due to the Doppler shift. Cooling takes place

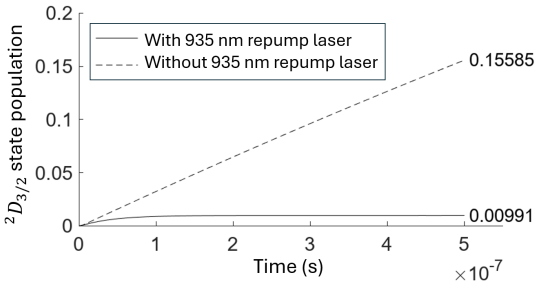

Figure 2: Accumulation of population in the $^2D_{3/2}$ states during Doppler cooling with and without 935 nm repumping. The 369 nm cooling laser power was implemented using sideband and carrier power percentages at 5% and 88.6%, respectively, of the total unmodulated carrier power, 48.4 μW. The sideband percentage corresponds to the 14.7 GHz sideband used during Doppler cooling. The 935 nm laser used sideband and carrier power percentages at 5.6% and 83.28%, respectively, of the total unmodulated carrier power, 0.49 mW. Both lasers use equal vertical and horizontal components.

when the ion undergoes sequential $^2S_{1/2}-^2P_{1/2}$ absorption-spontaneous emission cycles, which reduce the ion's momentum parallel to the laser beam. During cooling, a branching ratio of 0.5% from $^2P_{1/2}$ to the long-lived $^2D_{3/2}$ states (lifetime of 52.7 ms) removes ions from the cooling cycle. Figure 2 shows the the importance of the repump laser during Doppler cooling. In the absence of the repump laser, population accumulates in the $^2D_{3/2}$ states to a fraction of approximately 0.16 within 5 ps, whereas repumping maintains the $^2D_{3/2}$ below a fraction of 0.01. This is important as ions in the $^2D_{3/2}$ states do not participate in cooling, making the cooling inefficient.

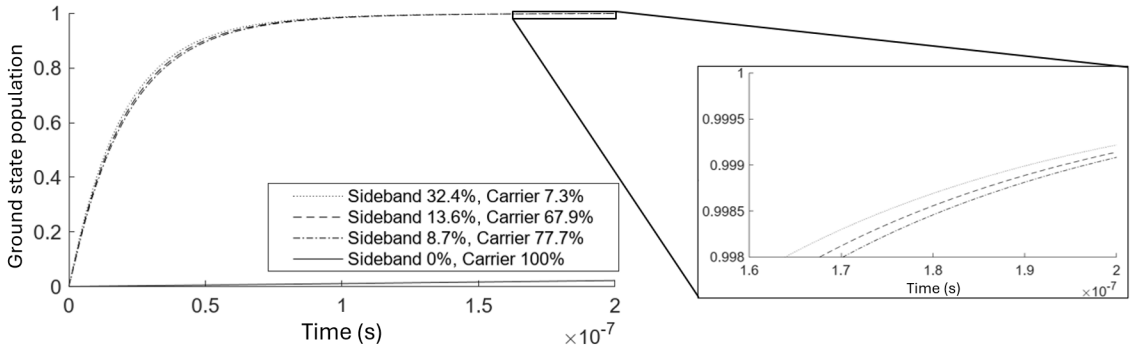

Figure 3: (Left) Increase in the $|0\rangle$ state population during state preparation for different 369 nm laser sideband-carrier ratios as measured in the laboratory and expressed as percentages of the total unmodulated carrier power, 48.4 μW. The initial state used for all runs is the final state after Doppler cooling ions from a pure excited state $|1\rangle$ for 50 ns. The 935 nm laser conditions were kept constant using both vertical and horizontal polarisation; and sideband and carrier power percentages at 5.6% and 83.28%, respectively, of the total unmodulated carrier power, 0.49 mW. (Right) Enlarged section of graph.

Qubits are initialised by pumping into the $|0\rangle$ state using the 369 nm laser and a 2.1 GHz first order upper sideband driving transitions (3) and (1) respectively, as in Figure 1. Figures 3 and 4 show the population in the $|0\rangle$ state as measure of the efficiency of state preparation under different laser parameters. Figure 3 shows that the 2.1 GHz sideband is essential to enable optical pumping into the $|0\rangle$ state. As sideband modulation increases, second order sidebands increase in size — decreasing the power distributed between the first order sideband used for our processes and the carrier beam. Figure 4 shows that the efficiency of state preparation depends on the laser polarisation, with mixed polarisation (equal vertical and horizontal polarisation) giving the highest population after 0.2 μs. These results give an indication of the time needed for state preparation under ideal conditions that inform the planning of experimental measurements. The model was also used to confirm that the populations of the relevant states do not change during state detection by driving transition (3) only.

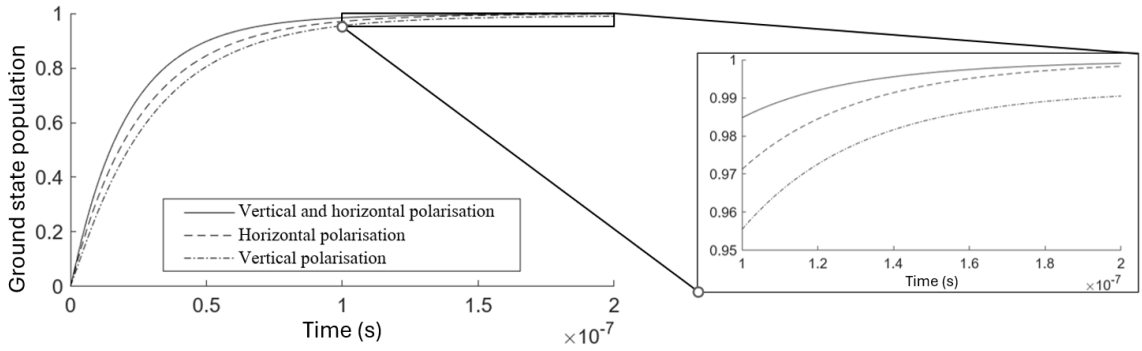

Figure 4: (Left) Increase in the $|0\rangle$ state population during state preparation for different 369 nm and 935 nm laser polarisations. The sideband-carrier percentages of the total power for the 369 nm laser were 13.6% and 67.9% respectively and the laser power at 48.4 μW. The sideband percentage corresponds to the 2.1 GHz sideband used during state preparation. The sideband-carrier percentages of the total power for the 935 nm laser were 5.6% and 83.28% respectively and the laser power at 0.49 mW. (Right) Enlarged section of graph.

4 Conclusions

The rate equation model makes it possible to understand the dynamics and time scales in relation to the experimental parameters, such as laser powers and side band powers. The results are useful to inform decisions on experimental parameters in our laboratory. Contrary to what we expect, the differences between the results in figures 3 and 4 appear negligible. This is because our energy density is high in all cases and partially saturates the transition. When reduced, changes in sideband power appear more noticeable. However, overall the results have shown the importance of efficient 935 nm repumping, and that state preparation efficiency is positively affected by the 2.1 GHz modulation and is marginally faster with a combination of both vertical and horizontal polarisation. We are also able to gauge how long state preparation takes under ideal circumstances. A current limitation of the model is that Zeeman shifts due to the external magnetic field have not been implemented yet. Future work includes modeling of a 411 nm transition from $^2S_{1/2}$ to $^2D_{5/2}$, which is a quadrupole transition into a metastable state, using the Optical Bloch Equations [9].

References

[1] H. Häffner, C. Roos, and R. Blatt, "Quantum computing with trapped ions," *Physics reports*, vol. 469, no. 4, pp. 155–203, 2008.

[2] S. Choudhary, T. Konrad, and H. Uys, "Implementation schemes for unsharp measurements with trapped ions," *Phys. Rev. A*, vol. 87, no. 1, p. 012131, 2013.

[3] D. A. Steck, "Quantum and atom optics," 2006, available online at http://steck.us/teaching.

[4] G. K. Woodgate, *ELEMENTARY ATOMIC STRUCTURE.* 1970, 01 1970. [Online]. Available: https://www.osti.gov/biblio/4055778

[5] D. Terr, "Clebschgordan.m," 2025, MATLAB Central File Exchange. Retrieved May 22, 2024. [Online]. Available: https://www.mathworks.com/matlabcentral/fileexchange/5276-clebschgordan-m

[6] A. B. Deb, "Wigner6j.m," 2025, MATLAB Central File Exchange. Retrieved May 22, 2024. [Online]. Available: https://www.mathworks.com/matlabcentral/fileexchange/16187-wigner6j-m

[7] D. Terr, "Wigner3j.m," 2025, MATLAB Central File Exchange. Retrieved May 22, 2024. [Online]. Available: https://www.mathworks.com/matlabcentral/fileexchange/5275-wigner3j-m

[8] J. Eschner, G. Morigi, F. Schmidt-Kaler, and R. Blatt, "Laser cooling of trapped ions," *Journal of the Optical Society of America B*, vol. 20, no. 5, pp. 1003–1015, 2003.

[9] S. Bester and C. Steenkamp, "Optical bloch modeling of magnetic dipole transitions in a four-state system and its application in ion trapping: tutorial," *Journal of the Optical Society of America B*, vol. 40, no. 4, pp. 830–848, 2023.

In vitro effects of blue laser light as an antimicrobial agent on microbial-infected fibroblast cells

F O Brenya[1] and N N Houreld[1]

[1]Laser Research Centre, University of Johannesburg, Johannesburg, South Africa

E-mail: nhoureld@uj.ac.za

Abstract. *Pseudomonas aeruginosa*, *Staphylococcus aureus*, and *Streptococcus pyogenes* are key pathogens that delay healing and pose challenges due to their antibiotic resistance. Antimicrobial photobiomodulation (aPBM) using blue light (400-470 nm) has been demonstrated to possess antibacterial properties; however, its effects on mammalian cells remain poorly understood. We investigated the effect of blue laser light (470 nm, 752 mW, 82.64 mW/cm², 10 J/cm², 121 s, 9.1 cm^2) on bacteria-infected human skin fibroblast cells. Human skin fibroblast cells (6×10^5 cells/mL) were co-cultured for 24 h with each of the three bacterial strains (1.50×10^3 CFU/mL) and then exposed to blue light. Human skin fibroblast cell viability and bacterial colony counts were assessed 24 h post-aPBM. Control cells infected with *S. aureus* (0 J/cm^2) exhibited 95.27% fibroblast cell viability and increased bacterial counts of 1.90×10^5 CFU/mL. Control cells infected with *S. pyogenes* (0 J/cm^2) showed 89.65% fibroblast cell viability, with bacterial colony counts increasing to 2.80×10^5 CFU/mL. Control cells infected with *P. aeruginosa* showed a percentage cell viability of 89.40% with bacterial colony counts increasing to 2.30×10^5 CFU/mL. In irradiated (10 J/cm^2) *S. aureus*-infected cells, *P. aeruginosa*-infected cells, and *S. pyogenes*-infected cells, fibroblast cell viability was 89.41%, 94.67%, and 77.68%, respectively, while bacterial colony counts decreased to 1.40×10^5 CFU/mL for both *S. aureus* and *P. aeruginosa*, and 1.30×10^5 CFU/mL for *S. pyogenes*. Blue light (470 nm, 82.64 mW/cm^2, 10 J/cm^2, 121 s) induced bacterial death while preserving fibroblast cell viability after a single exposure. aPBM has the potential to address the medical challenges associated with infected wounds and open new avenues for future research.

1 Introduction

Chronic wound infections pose a significant challenge in clinical settings, particularly when caused by antibiotic-resistant pathogens such as *Pseudomonas aeruginosa* (*P. aeruginosa*), *Staphylococcus aureus* (*S. aureus*), and *Streptococcus pyogenes* (*S. pyogenes*). These bacteria pose a significant threat due to their virulence, biofilm formation, and resistance to multiple antibiotics, collectively impeding effective treatment and delaying wound healing [1]. *P. aeruginosa*, a gram-negative opportunistic pathogen, has been implicated in hospital-acquired infections due to its intrinsic resistance mechanisms, including efflux pumps, enzymatic degradation of antibiotics, and biofilm formation [2]. Similarly, methicillin-resistant *S. aureus* (MRSA) and *S. pyogenes* are major contributors to skin and soft tissue infections, often exacerbating wound severity and prolonging recovery [3].

Given the limitations of conventional antibiotics, alternative antimicrobial strategies are being explored. One such approach is antimicrobial photobiomodulation (aPBM), which involves the use of blue light. Blue light

(400-470 nm) has demonstrated bactericidal effects via several mechanisms, including the generation of reactive oxygen species (ROS), disruption of bacterial membranes, and inhibition of biofilm formation [4, 5]. Despite promising antibacterial outcomes, the effects of blue light on mammalian cells, especially in microbial-infected tissue environments, remain underexplored [6-8].

This study investigated the *in vitro* effects of blue laser light (470 nm) on uninfected human fibroblasts and human fibroblasts infected with *P. aeruginosa*, *S. aureus*, or *S. pyogenes*. The goal was to assess whether blue light (470 nm and 10 J/cm^2) can reduce bacterial load while preserving host cell viability, thereby supporting its potential as a non-antibiotic therapeutic strategy for managing infected wounds.

2 Materials and Methods

BJ-5ta human fibroblasts (ATCC®, CRL-4001™) were seeded at a density of 6×10^5 cells/mL in Minimum Essential Medium (MEM) supplemented with 10% foetal bovine serum (FBS), 0.1 mM non-essential amino acids (NEAA), 2 mM L-glutamine, and 1 mM sodium pyruvate. Cultures were incubated at 37°C, 5% CO_2, and 85% humidity for 24 h to establish a stable monolayer. Uninfected fibroblasts, which served as controls, and fibroblast cultures infected with 1.5×10^3 CFU/mL of *S. aureus* (ATCC® 33592), *P. aeruginosa* (ATCC® 27853), or *S. pyogenes* (ATCC® 12384), were incubated on a shaker (at 100 rpm) for 24 h to ensure uniform bacterial distribution and enhance contact with the fibroblast monolayer. After incubation, cultures were exposed to aPBM using a blue laser (class IV diode, MDL-III-470-800 milliwatts, Changchun New Industries Optoelectronics Technology Company Limited, China; 470 nm, 752 mW, 82.64 mW/cm², 10 J/cm², 121 s, 9.1 cm^2). Non-irradiated samples (0 J/cm²) served as controls. These parameters were selected based on prior studies demonstrating effective biological responses without cytotoxicity [9-17].

Fibroblast viability and bacterial survival were assessed 24 h post-aPBM to allow sufficient time for cellular recovery and microbial response, ensuring accurate attribution of effects to the light treatment. Viability was measured using the Trypan Blue exclusion assay, where a 1:1 mixture of 0.4% Trypan Blue (Sigma-Aldrich, T8154) and cell suspension was loaded onto a counting slide and analysed with the Invitrogen Countess II FL automated cell counter. Viable cells excluded the dye, while non-viable cells appeared blue. Viability was calculated as the percentage of unstained cells relative to the total cell count. For bacterial quantification, culture media were collected and centrifuged. Bacterial suspensions were serially diluted (1.5×10^3) in sterile phosphate-buffered saline (PBS), and 100 µL aliquots were plated onto nutrient agar. Plates were incubated at 37°C for 24 h. Digital images were captured from a fixed height of 10 cm, and colonies were counted using the Revsci IncuCount™ Colony Counter. CFU/mL was calculated based on dilution factors and plated volume, with a detection limit of 10 CFU/mL [18-20].

Experiments were performed in triplicate (n = 3). Data is expressed as the mean ± standard error (SE) and analysed using one-way ANOVA with Tukey's post hoc test, with statistical significance set at $p < 0.05$. Ethical approval was granted by the University of Johannesburg Research Ethics Committee under clearance number REC-2758-2024.

3 Results

aPBM at 470 nm with 10 J/cm² significantly affected both fibroblast viability and bacterial survival (Table 1). In uninfected fibroblasts, viability significantly ($p < 0.05$) increased from 87.89% (0 J/cm²) to 96.41% (10 J/cm²). Among infected groups, *P. aeruginosa*-infected fibroblasts showed significantly ($p < 0.05$) improved viability post-aPBM (94.67%) compared to the non-irradiated control (89.40%). *S. aureus*-infected and *S. pyogenes*-infected fibroblasts exhibited a significant ($p < 0.05$) decrease in viability (89.41% and 77.68%, respectively) relative to their controls (95.27% and 89.65%, respectively).

Bacterial colony counts (CFU/mL) decreased significantly across all irradiated groups post-aPBM (Table 1). These reductions were statistically significant ($p < 0.05$), indicating broad-spectrum antimicrobial efficacy of 470 nm with 10 J/cm².

4 Discussion

aPBM (470 nm, 10 J/cm²) significantly modulates both fibroblast viability and bacterial survival. In uninfected fibroblast cultures, viability increased, confirming the non-cytotoxic and photobiomodulatory nature of the

treatment [21]. Among infected groups, *P. aeruginosa*-infected and *S. aureus*-infected fibroblasts showed a significant improvement in viability post-aPBM, suggesting a protective effect of light exposure. In contrast, *S. pyogenes*-infected cells exhibited a significant decline in viability, indicating a strain-specific stress response likely influenced by virulence factors and infection but not the aPBM [22]. These results suggest that aPBM enhanced fibroblast survival in certain infection contexts and maintained overall cell viability above 70% (Table 1), consistent with therapeutic safety thresholds [23].

Group	Bacterial Infection	Fibroblast Cell Viability (%) ± SE	Bacterial Colony Count (CFU/mL) ± SE
Fibroblast Cells (0 J/cm²)	None	87.89 ± 1.01	-
Fibroblast Cells (10 J/cm²)	None	96.41 ± 1.11	-
Control (0 J/cm²)	*S. aureus*-infected	95.27 ± 0.24	$1.90 \times 10^5 \pm 2.89 \times 10^3$
Control (0 J/cm²)	*P. aeruginosa*-infected	89.40 ± 0.25	$2.30 \times 10^5 \pm 2.89 \times 10^3$
Control (0 J/cm²)	*S. pyogenes*-infected	89.65 ± 0.25	$2.80 \times 10^5 \pm 2.89 \times 10^3$
Irradiated (10 J/cm²)	*S. aureus*-infected	89.41 ± 0.22*	$1.40 \times 10^5 \pm 2.89 \times 10^3$*
Irradiated (10 J/cm²)	*P. aeruginosa*-infected	94.67 ± 0.25*	$1.40 \times 10^5 \pm 2.89 \times 10^3$*
Irradiated (10 J/cm²)	*S. pyogenes*-infected	77.68 ± 0.59*	$1.30 \times 10^5 \pm 2.89 \times 10^3$*

Table 1. Effect of blue light (470 nm) on fibroblast cell viability and bacterial colony count. Significant differences compared to control (0 J/cm²) bacterial-infected cells are shown as *p<0.05.

Bacterial colony counts were significantly ($p < 0.05$) reduced across all irradiated groups, with CFUs decreasing by approximately 26% for *S. aureus*, 39% for *P. aeruginosa*, and 54% for *S. pyogenes*. These reductions support the broad-spectrum antimicrobial efficacy of blue light aPBM, consistent with previous reports targeting diverse pathogens [24].

These results highlight the potential of blue laser light (470 nm, 10 J/cm²) in reducing bacterial populations in human fibroblast cells infected with *P. aeruginosa*, *S. aureus*, and *S. pyogenes*. This antimicrobial effect was achieved without substantially compromising fibroblast cell viability. These findings support the potential of aPBM as a viable, non-antibiotic therapeutic approach for treating infected wounds. aPBM shows promise as a dual-action strategy for enhancing host cell viability while reducing bacterial load, with modeling studies [25] supporting its safety and efficacy. They also highlight the importance of tailoring light-based protocols to specific bacterial profiles to optimise therapeutic outcomes [26-29]. Further validation using assays like 3-(4,5-dimethylthiazol-2-yl)-2,5-diphenyltetrazolium bromide (MTT) assay or flow cytometry is recommended to confirm these effects and explore underlying mechanisms.

5 Conclusion

Irradiation with 470 nm at 10 J/cm² significantly improved fibroblast viability in non-infected cultures and reduced bacterial colony counts across all tested strains.

6 Acknowledgments

This research was supported by the South African Research Chairs Initiative (Grant No. 98337), funded by the Department of Science and Technology and the National Research Foundation (NRF) of South Africa. Additional funding was provided by the University of Johannesburg Research Committee (URC), the African Laser Centre (ALC), and the CSIR–National Laser Centre (NLC), which also supplied and set up all laser equipment.

References

[1] A. Elfadadny, "Antimicrobial activity of curcumin against multidrug-resistant pathogens: A mechanistic and therapeutic review," *Front. Microbiol.*, vol. 15, p. 137446, 2024, doi: 10.3389/fmicb.2024.137446.

[2] F. Giovagnorio, A. De Vito, G. Madeddu, S. G. Parisi, and N. Geremia, "Resistance in

Pseudomonas aeruginosa: A narrative review of antibiogram interpretation and emerging treatments," *Antibiotics*, vol. 12, no. 11, p. 1621, 2023, doi: 10.3390/antibiotics12111621.

[3] N. Asús, A. Cicchitti, C. Bertona, J. Gonzalez, G. Minuchin, E. Trinajstic, P. Minuchín, W. Rosales, and M. Rodriguez, "Phytotherapeutic strategies in diabetic wound healing: Insights from Latin American clinical practice," *Diabetes Obes. Int. J.*, vol. 7, no. S1, pp. 2572–7770, 2022, doi: 10.23880/doij-16000263.

[4] Y. Mu, Y. Shen, N. Gretz, M. Bouschbacher, T. Miethke, and M. Keese, "*Azadirachta indica*-derived compounds in wound infection control: A translational study," *Biomedicines*, vol. 13, no. 4, p. 868, 2025, doi: 10.3390/biomedicines13040868.

[5] T. P. Prado, A. C. Moraes, M. F. X. B. Cavalcanti, R. A. Cabette, and M. D. A. Trubiani, "Antibacterial properties of *Allium sativum* in diabetic wound models," *Life*, vol. 13, no. 2, p. 575, 2023, doi: 10.3390/life13020575.

[6] C. Dompe, "*Calendula officinalis* in wound granulation and epithelial repair: A clinical overview," *J. Clin. Med.*, vol. 9, no. 6, p. 1724, 2020, doi: 10.3390/jcm9061724.

[7] C. Dos Anjos, "*Camellia sinensis catechins* as antimicrobial agents: Mechanisms and clinical relevance," *Microbiol. Spectr.*, vol. 11, no. 2, pp. 2833–2855, 2023, doi: 10.1128/spectrum.02123-22.

[8] S. Föller, N. Regett, L. Lataster, G. Radziwill, and R. Takors, "Biotechnological enhancement of antimicrobial phytochemicals for wound care," *Appl. Microbiol. Biotechnol.*, vol. 108, no. 1, p. 13363, 2024, doi: 10.1007/s00253-023-13363-4.

[9] R. A. Alghamdi, M. Exposito-Rodriguez, P. M. Mullineaux, G. Brooke, and P. P. Laissue, "Cellular responses to herbal compounds in wound models," *Front. Cell Dev. Biol.*, vol. 9, p. 738786, 2021, doi: 10.3389/fcell.2021.738786.

[10] P. Mcmullan, A. B. White, O. Coker, S. Opal, S. Mcgee, and G. Rogers, "Photobiomodulation in chronic wound healing: A randomised clinical trial," *Photomed. Laser Surg.*, vol. 40, no. 9, p. 16, 2022, doi: 10.1089/pho.2022.0045.

[11] M. A. Nilforoushzadeh, M. Amirkhani, S. Zare, A. Mahmoudi, M. Heidari, and M. R. Hamblin, "Laser-assisted delivery of herbal antimicrobials for chronic wound healing," *J. Lasers Med. Sci.*, vol. 10, no. 5, pp. 7–S12, 2019, doi: 10.15171/jlms.2019.01.

[12] A. Cios, M. Gornowicz-Porowska, K. Bowszyc-Dmochowska, and M. Zaba, "Molecular mechanisms of herbal wound modulators: A systems biology approach," *Int. J. Mol. Sci.*, vol. 22, no. 5, p. 2437, 2021, doi: 10.3390/ijms22052437.

[13] B. Houchmandzadeh and P. Ballet, "Standardised antimicrobial testing of herbal extracts using microfluidic platforms," *J. Microbiol. Methods*, vol. 206, p. 106693, 2023, doi: 10.1016/j.mimet.2023.106693.

[14] M. Monteiro, "Laser-enhanced herbal therapy in wound care: A clinical pilot study," *Lasers Med. Sci.*, vol. 6, pp. 523–530, 2022, doi: 10.1007/s10103-022-03456-9.

[15] J. Krassovka, A. Borgschulze, B. Sahlender, T. Lögters, J. Windolf, and V. Grotheer, "*Calendula* and wound granulation: Histological and clinical correlations," *PLoS ONE*, vol. 14, no. 1, p. 209833, 2019, doi: 10.1371/journal.pone.0209833.

[16] F. Rossi, "Curcumin-mediated antimicrobial modulation in diabetic wound models," *Biomedicines*, vol. 9, no. 1, p. 41, 2021, doi: 10.3390/biomedicines9010041.

[17] V. Bumah, M.-M. D. S. Cashin, S. E. Enwemeka, C. Whelan, and H. T. Whelan, "Laser-enhanced eugenol delivery for biofilm disruption," *Lasers Med. Sci.*, vol. 36, no. 5, pp. 1035–1044, 2021, doi: 10.1007/s10103-021-03245-7.

[18] M. Maclean, S. J. Macgregor, J. Anderson, and G. Woolsey, "Photodynamic antimicrobial therapy using herbal photosensitizers," *Appl. Environ. Microbiol.*, vol. 75, no. 7, pp. 1932–1937, 2009, doi: 10.1128/AEM.01875-08.

[19] Y. Choi, O. E. Waldman, O. Sajda, T. Beck, C. Oh, and I. Kim, "Orthopaedic wound infection control using herbal adjuncts," *Foot Ankle Orthop.*, vol. 6, no. 3, pp. 2473011–42110269, 2023, doi: 10.1177/247301142110269.

[20] O. T. Harorli, M. Hatipoglu, and E. N. Yildiz, "Photobiomodulation and herbal synergy in wound care," *Photomed. Laser Surg.*, vol. 37, no. 8, pp. 457–464, 2019, doi: 10.1089/pho.2019.0045.
[21] P. Akuwudike, A. Eze, M. Okeke, and C. Nwankwo, "Public health implications of herbal wound care," *Front. Public Health*, vol. 11, p. 1297942, 2023, doi: 10.3389/fpubh.2023.1297942.
[22] A. Fietz, J. Hurst, and S. Schnichels, "Molecular profiling of herbal wound agents," *Int. J. Mol. Sci.*, vol. 23, no. 23, p. 14540, 2022, doi: 10.3390/ijms232314540.
[23] X. Liu, "Herbal wound care in public health systems," *Front. Public Health*, vol. 11, p. 1566179, 2025, doi: 10.3389/fpubh.2025.1566179.
[24] M. F. X. B. Cavalcanti, R. A. Cabette, A. C. Moraes, F. Diomede, O. Trubiani, and M. D. A. Trubiani, "Photobiomodulation and herbal synergy in diabetic wound healing: A preclinical evaluation," *Photomed. Laser Surg.*, vol. 42, no. 2, pp. 140–147, 2024, doi: 10.1089/pho.2023.0071.
[25] F. S. Ferreira, F. C. Cadoná, A. R. Aurélio, T. Martins, and H. M. F. Pivetta, "*Calendula* and laser-assisted wound healing: Histological and molecular insights," *Lasers Med. Sci.*, vol. 37, pp. 523–530, 2022, doi: 10.1007/s10103-021-03345-4.
[26] C. Supino, C. Pacheco-Soares, and N. Da Silva, "Photobiomodulation in herbal wound care: Cellular responses and clinical relevance," *Photomed. Laser Surg.*, vol. 10, no. 8, pp. 2525–3409, 2021, doi: 10.1089/pho.2021.0089.
[27] M. Furujo, Y. Tanaka, and S. Nakamura, "Photodynamic therapy with herbal agents: A novel approach to infected wound management," *Photodiagn. Photodyn. Ther.*, vol. 45, p. 103456, 2024, doi: 10.1016/j.pdpdt.2023.103456.
[28] P. L. Lam, "Herb–drug interactions and safety profiling: Implications for clinical practice," *Chem. Biol. Interact.*, vol. 320, p. 109023, 2020, doi: 10.1016/j.cbi.2020.109023.
[29] T. Dai, A. Gupta, C. K. Murray, M. S. Vrahas, G. Tegos, and M. R. Hamblin, "Blue light for infectious diseases: *Propionibacterium acnes*, *Helicobacter pylori*, and beyond," *Drug Resist. Updat.*, vol. 15, no. 4, pp. 223–236, 2012, doi: 10.1016/j.drup.2012.03.004.

This page intentionally left blank.

Photothermal Effects of Green-Synthesized Gold Nanoparticles using *Kniphofia porphyrantha* on MCF-7 Human Breast Cancer Cells

Mpho Mohlongo[1], Blassan George[1], and Heidi Abrahamse[1]

[1]Laser Research Centre, Faculty of Health Sciences, University of Johannesburg, P.O. Box 17011, Doornfontein 2028, South Africa

E-mail: habrahamse@uj.ac.za

Abstract. Breast cancer continues to be one of the main causes of cancer-related deaths among women worldwide, highlighting the need for targeted and less harmful treatment options. Gold nanoparticles have been identified as potential tools in nanomedicine because of their compatibility with biological systems, customizable surface chemistry, and distinctive optical characteristics. Nevertheless, traditional synthesis methods often utilize toxic reducing agents, which limit their use in medicine. This study investigates an environmentally friendly method for synthesizing gold nanoparticles using an extract from the *Kniphofia porphyrantha* plant and assesses their effectiveness in treating breast cancer. The gold nanoparticles were synthesized by utilizing extracts of the plant that function as both reducing agents and stabilizing agents. Spectrophotometric analysis was performed to confirm the optical properties of gold nanoparticles, while photothermal effects of synthesized gold nanoparticles on MCF-7 breast cancer cells were evaluated by assessing morphological changes, cellular viability, and cytotoxicity rates 24 h post-irradiation using a 525 nm laser with a fluence of 10 J/cm^2. Results showed a dose-dependent response to the treatment, demonstrated by significant morphological changes, increased cytotoxicity, and decreased cell viability compared to untreated cells, indicating the anticancer properties of green-synthesized gold nanoparticles. This highlights the dual advantages of plant-based gold nanoparticles: sustainable production and potential use in cancer therapy. These results encourage further exploration of the optical properties and biological activity of plant-based gold nanoparticles as promising candidates for cancer nanomedicine.

1 Introduction

Breast cancer remains a leading cause of cancer-related mortality among women worldwide. It was the second most commonly diagnosed cancer in 2022, with an estimated 2.3 million cases and approximately 660 000 deaths, accounting for 11.6% of all cancer cases and 6.9% of all cancer-related deaths [1, 2]. Current therapeutic strategies, such as chemotherapy, radiation therapy, and hormone therapy face significant limitations, including systemic toxicity, drug resistance, and non-specific targeting of healthy tissues. These challenges necessitate the development of innovative treatment modalities with enhanced specificity and reduced off-target effects [3, 4]. Photothermal therapy (PTT) has emerged as a promising non-invasive approach for selective tumour damage. This technique exploits the principle that cancer cells exhibit heightened sensitivity to hyperthermic conditions (41-48 °C) compared to healthy tissues, making PTT an attractive strategy for targeted therapy. When exposed

to visible or near-infrared (NIR) light, photothermal agents generate localized heat that induces protein denaturation, membrane disruption, and ultimately selective tumor cell necrosis [3, 5].

Gold nanoparticles (AuNPs) have gained substantial attention as ideal PTT agents due to their exceptional localized surface plasmon resonance (LSPR) properties. Key advantages include tuneable optical properties, enhanced thermal conversion, and passive tumour targeting. Conventional synthesis methods, however, frequently employ cytotoxic reduction agents (such as sodium borohydride) that compromise biocompatibility and necessitate extensive purification. Plant-mediated synthesis offers a sustainable alternative by utilizing phytochemicals as both reducing and stabilizing agents [3]. For example, extracts from the *Dunaliella salina* [6], *Azadirachta indica [*7], and other plant species have been successfully employed for AuNP synthesis, displaying significant cytotoxicity against breast cancer cells. A recent comprehensive review by Dheyab et al. highlights the growing interest in eco-friendly AuNP synthesis and its potential in cancer nanomedicine, reinforcing the relevance of this approach [8]. In this context, *Kniphofia porphyrantha*, a South African indigenous plant, contains abundant flavonoids and phenolic acids [9] that facilitate nanoparticle formation while potentially enhancing therapeutic efficacy [3, 10]. This study establishes a green synthesis protocol for AuNPs using *K. porphyrantha* extract and evaluates their optical properties relevant to PTT applications, photothermal cytotoxicity against MCF-7 breast cancer cells, and dose-dependent cytotoxic response under laser activation.

2 Methodology

2.1 Preparation of plant extract and synthesis of gold nanoparticles

Leaves of *K. porphyrantha* were sun-dried and finely powdered. Approximately 10 g of the powdered plant materials were mixed with 100 mL of methanol and boiled for 48 h at 55 °C and 100 rpm. After cooling to room temperature, the mixture was filtered using a 0.22 µm syringe filter to obtain the extract used for nanoparticle synthesis. Following this, 10 mL of plant extract was added to 50 mL of 0.1 mM aqueous chloroauric acid ($HAuCl_4$) solution. The reaction mixture was placed on a magnetic hot plate stirrer for 20 min at 90 °C and 100 rpm, followed by centrifugation at 18 000 rpm for 15 min. The resulting pellet was washed with deionized water and stored for further characterization and biological evaluation.

2.2 Characterization of gold nanoparticles

The green synthesized AuNPs were characterized using various analytical techniques:

2.2.1 UV-vis spectrometry to determine optical properties. Absorbance spectra were recorded between 300 and 800 nm to confirm the formation of AuNPs through surface plasmon resonance (SPR), typically peaking around 520 nm.

2.2.2 Size distribution and Zeta potential. Dynamic light scattering (DLS) and Zeta potential (ZP) were performed using the Malvern Zeta Sizer Nano series. DLS was used to measure the hydrodynamic diameter and particle size distribution to assess colloidal uniformity. ZP was used to evaluate the surface charge and predict colloidal stability.

2.2.3 Fourier Transform Infrared (FTIR) spectroscopy. FTIR spectroscopy was performed to identify functional groups involved in the reduction and stabilization of the synthesised AuNPs.

2.2.4 Transmission Electron Microscopy (TEM). The morphology and size distribution of the synthesised AuNPs was determined using TEM analysis.

2.3 Cell culture and treatment of experimental groups

The human breast adenocarcinoma MCF-7 (ATCC® HTB-22) cell line was maintained as monolayers in T75 flasks using Dulbecco's Modified Eagle Medium (DMEM) supplemented with 10% fetal bovine serum (FBS), 1% amphotericin B, and 1% penicillin-streptomycin. Cells were incubated at 37 °C in a humidified atmosphere of 95% air and 5% CO_2. For experiments, cells were seeded at 200 x 10^5 per plate in 3.5 cm diameter cell culture dishes and 1 x 10^6 cells per well in 96-well cell culture plates and allowed to adhere for 24 h prior to treatment. Cells were treated with varying concentrations (10, 25, 50, 100, & 200 µg/mL) of AuNPs and incubated for 24 h. After 24 h, treated cells were exposed to visible light diode laser (525 nm) at fluence of 10 J/cm^2 for 5 min.

2.4 Morphological analysis

Cellular morphological changes in MCF-7 cells were evaluated 24 h post treatment using inverted brightfield microscope (Olympus CKX41, Wirsam Scientific). Each treatment group, including cells exposed to AuNPs,

laser activation, AuNPs + laser activation, and untreated controls, was observed to assess alterations in cell structure, integrity, and density. Morphological features such as cell shrinkage, rounding, detachment and membrane blebbing were recorded as indicators of photothermal-induced cytotoxicity.

2.5 Cytotoxicity and cell proliferation analysis

Cytotoxicity was evaluated using the MTT assay (Roche Cell Proliferation Kit). 10 µL of MTT reagent was added to each well containing 90 µL cell culture medium, and the plate was incubated for 3 h at 37 °C. After incubation, 100 µL of solubilization buffer was added, and the plate was left overnight to ensure complete formazan dissolution. Absorbance was recorded at 570 nm using the VICTOR Nivo multimode microplate reader. Cellular proliferation was assessed using the CellTiter-Glo Luminescent Cell Viability Assay, which quantifies intracellular ATP as an indicator of metabolically active cells. Following treatment, the reagent was added to each well in accordance with the manufacturer's protocol. Luminescence was measured using the same multimode microplate reader.

2.6 Statistical analysis

All experiments were conducted in triplicate and independently repeated three times. Results were expressed as mean and standard error of the mean, comparisons between untreated and treated groups were performed using Dunnett test. Statistical significance was evaluated at a 95% confidence interval. Data analysis was conducted using SigmaPlot software. Significance levels were indicated as $p < 0.05$ (*), $p < 0.01$ (**) or $p < 0.001$ (***).

3 Results

3.1 Characterization of gold nanoparticles

3.1.1 UV-vis spectrometry

UV-vis spectrometry was used to confirm successful green synthesis of AuNPs and the interaction between *K. porphyrantha* and gold ions. As shown in Figure 1 below, UV-vis spectra of the plant extract displayed a strong absorbance peak at around 260 nm, which is typical for phytochemicals in plant materials. The presence of the additional SPR peak at 520 nm, is typical of AuNPs, indicating the successful formation of the AuNPs.

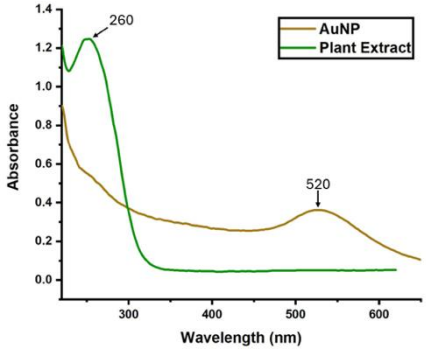

Figure 1: UV-vis absorption spectra of *Kniphofia porphyrantha* plant extract (260 nm) and green synthesized gold nanoparticles (520 nm).

3.1.2 Size distribution and ZP

The size and surface characteristics of the green-synthesized AuNPs were assessed using DLS and ZP analysis. As shown in Table 1, the Z-average diameter was determined to be 62.17 nm with a polydispersity index (PDI) of 0.348, suggesting intermediate polydispersity. ZP measurements indicated a mean surface charge of -15.9 mV, suggesting moderate colloidal stability, essential for preventing aggregation in aqueous media.

Table 1: Size distribution and charge of synthesized AuNPs.

Z-average diameter (d.m)	**PDI**	**Zeta potential (mV)**
62.17 nm	0.3488	-15.9

3.1.3 FTIR analysis

FTIR spectra (Figure 2) recorded between 4 000-400 cm^{-1} displayed characteristic peaks at ~2 870 (O-H stretching), ~1 630 cm^{-1} (C=O stretching), and ~1 500 cm^{-1} (aromatic C=C vibrations). These functional groups correspond to flavonoids and phenolic acids in *K. porphyrantha* extract, confirming their role as reducing and capping agents during AuNP synthesis.

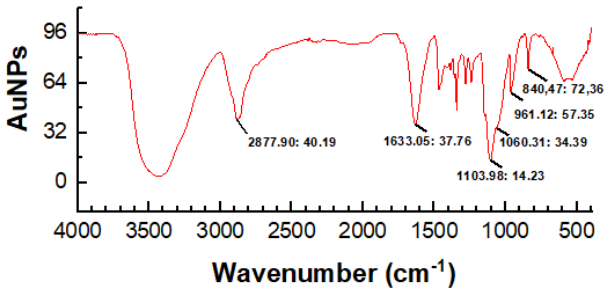

Figure 2: FTIR spectra displaying functional groups in AuNPs synthesized using *Kniphofia porphyrantha* extract.

3.1.4 TEM analysis

The TEM image (Figure 3) shows a cluster of AuNPs synthesised using *K. porphyrantha* extract. The AuNPs appear to be predominantly spherical, with slight variations in shape. Based on the scale bar (50 nm), individual nanoparticles range between 10-30 nm in diameter, while the entire cluster is approximately 150-200 nm.

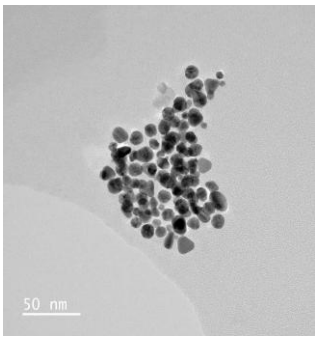

Figure 3: TEM morphology of AuNPs synthesized using *Kniphofia porphyrantha* extract.

3.2 Morphological analysis

The observed morphological changes in MCF-7 cells following treatment with green-synthesized AuNPs and PTT (Figure 4) included cell shrinkage, rounding of cells, detachment from the culture plate, and vesicle formation when compared to the untreated group.

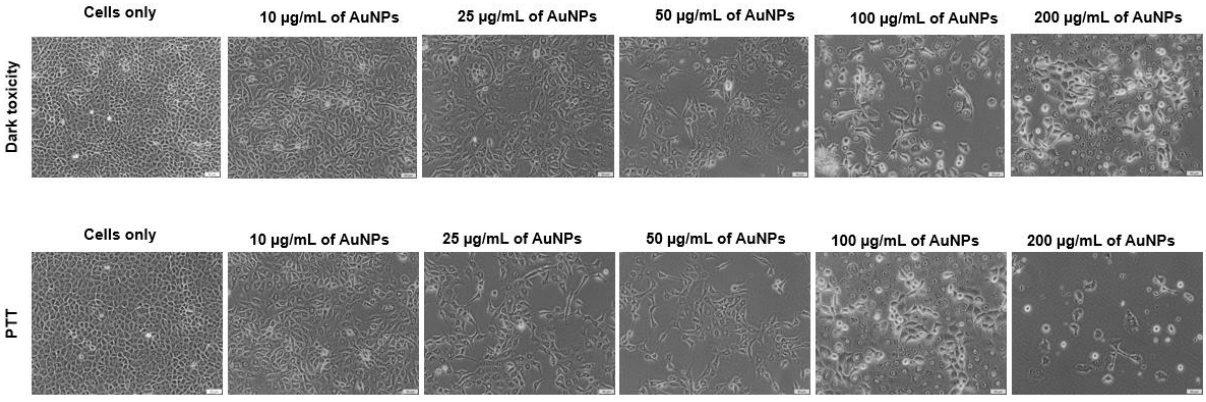

Figure 4: Inverted microscopy images showing the photothermal effects of green-synthesized AuNPs on MCF-7 cells under dark conditions (top row) and following PTT (bottom row). Cells were treated with increasing

concentrations of AuNPs (10, 25, 50, 100, & 200 µg/mL). In both conditions, dose-dependent morphological changes were observed, including cell shrinkage, rounding of cells, detachment from the culture plate, and vesicle formation.

3.3 Cytotoxicity and cell proliferation analysis

3.3.1 MTT cell viability analysis

MTT analysis (Figure 5) demonstrated a significant photothermal effect of green-synthesized AuNPs. Cells exposed to laser activation alone showed no noticeable decrease in cell viability compared to untreated cells only, indicating minimal toxicity. However, a significant dose-dependent decrease in cell viability was observed in cells treated with varying concentrations of AuNPs. On further analysis, following laser activation of these groups, cell viability significantly declined in a dose-dependent manner, with the most significant decrease in cell viability at 200 µg/mL.

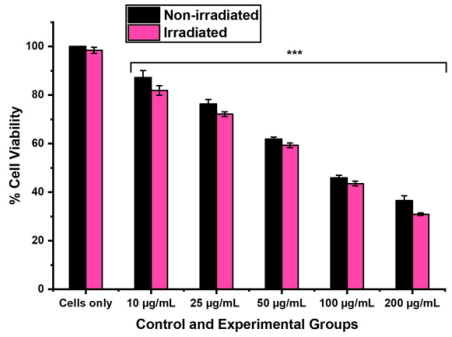

Figure 5: Quantitative MTT assay showing percentage cell viability of MCF-7 breast cancer cells treated with increasing concentrations (10, 25, 50, 100, 200 µg/mL) of green-synthesized AuNPs under dark (black) and PTT (pink) conditions. A significant dose-dependent reduction in cell viability was observed in both conditions, with increased cytotoxicity in PTT groups, confirming photothermal enhancement. *($p < 0.05$ (*), $p < 0.01$ (**) or $p < 0.001$ (***)).*

3.3.2 ATP cell proliferation analysis

ATP analysis (Figure 6) further confirmed the photothermal-induced inhibition of cell viability and proliferation. In non-irradiated cells, a steady decline of ATP levels was recorded across all concentrations, suggesting mitochondrial stress even without light activation. However, irradiated groups showed a greater decrease in ATP-derived luminescence, with the strongest inhibitory effect observed at 200 µg/mL.

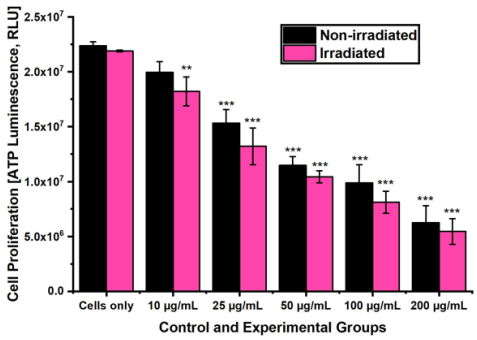

Figure 6: Quantitative ATP assay showing percentage cell proliferation of MCF-7 breast cancer cells treated with increasing concentrations (10, 25, 50, 100, 200 µg/mL) of green-synthesized AuNPs under dark (black) and PTT (pink) conditions. A significant decrease in cell proliferation was observed in a dose-dependent manner in both conditions, with a higher decline in PTT groups, confirming photothermal enhancement. *($p < 0.05$ (*), $p < 0.01$ (**) or $p < 0.001$ (***)).*

4 Discussion

Green-synthesized AuNPs have shown promising anticancer effects in several studies [11], including against breast cancer cell lines [6]. In this study, AuNPs synthesized using *K. porphyrantha* extract displayed a SPR peak at ~520 nm (Figure 1), confirming their suitability for laser-induced PTT. DLS analysis (Table 1) revealed an average size of 62.17 nm and a ZP of -15.9 mV, indicating moderate colloidal stability, sufficient to prevent aggregation, although higher absolute values (-30) are generally preferred for long-term dispersion. The PDI of 0.348 indicates intermediate polydispersity, suggesting that while the AuNPs are relatively uniform, some variations in size exist, which may influence cellular uptake and biodistribution. FTIR analysis (Figure 2) confirmed the involvement of phytochemicals in AuNP synthesis, with peaks corresponding to flavonoids and phenolic acids present in the plant extract. These findings are consistent with previous reports where phenolic compounds and flavonoids act as electron donors to reduce Au^{3+} ions to Au^{0}, while stabilizing the AuNPs. FTIR peaks for hydroxyl and carbonyl groups have been widely documented as indicators of phytochemical involvement in green synthesis. Previous reports on *Kniphofia* species confirm the presence of these compounds and their role in redox reactions. TEM images (Figure 3) confirmed spherical morphology, with an average diameter of 11 nm, consistent with optimal thermal conversion properties. The demonstrated moderate cytotoxicity at concentrations above 50 µg/mL in non-irradiated MCF-7 cells, with increased effects observed under photothermal conditions at 25 µg/mL, suggests that AuNPs are cytotoxic on their own. Morphological analysis (Figure 4) confirmed apoptotic features, such as membrane blebbing, rounding of cells, and cell detachment. Following laser activation, cell viability decreased significantly, with 60-70% cell death observed at 100-200 µg/mL (Figure 4). Increased levels of ATP depletion (Figure 6) suggest mitochondrial damage and metabolic shutdown. These results are consistent with cell death pathways such as apoptosis and necrosis [12]. Laser activation likely intensifies cellular stress through localized heating, disruption of protein function and cellular repair mechanisms, mitochondrial impairment, and cell membrane destabilization. In particular, thermal stress compromises membrane integrity, increasing permeability, and facilitating deeper nanoparticle uptake and intracellular damage [3]. Green-synthesised AuNPs from *K. porphyrantha* exhibited significant cytotoxicity at higher concentrations (≥ 10 µg/mL), with maximal effect at 200 µg/mL. This threshold is higher than reports from other plant-based AuNPs studies, where cytotoxicity was observed at concentrations as low as 2 µg/mL [13]. AuNPs exhibit strong LSPR, enabling them to absorb light at specific wavelengths and convert it into heat through non-radiative relaxation processes. When irradiated at the SPR wavelength (525 nm), AuNPs rapidly generate localized heat within the tumour microenvironment. This thermal energy induces protein denaturation, disrupts cellular membranes, and compromises mitochondrial function, leading to apoptosis or necrosis of cancer cells. The photothermal effect is highly selective because cancer cells are more sensitive to hyperthermic stress than normal cells, allowing targeted destruction with minimal damage to surrounding tissue. While previous studies have shown that *Kniphofia* extracts exhibit significant cytotoxicity against cancer cell lines [14], no other studies have reported on the use of *K. porphyrantha* extract for the green synthesis of AuNPs, highlighting its novelty and potential in cancer nanomedicine.

5 Conclusion

Green synthesized AuNPs from *K. porphyrantha* showed strong photothermal effects against MCF-7 breast cancer cells. Laser activation enhanced their cytotoxicity, reducing cell viability and ATP levels in a dose-dependent manner. This eco-friendly approach shows promise as selective and minimally invasive cancer therapy, supporting its potential for future clinical applications. This study did not include normal cell viability assays (e.g. lymphocytes), which are critical for assessing selectivity. Additionally, *in vivo* studies are necessary to validate therapeutic efficacy and biodistribution. Optimization of synthesis parameters to improve PDI and ZP to enhance uniformity and surface charge could improve their efficacy and stability. Furthermore, synthesizing AuNPs suitable for NIR activation is recommended for deeper tissue penetration and clinical relevance.

Acknowledgements

The authors thank the South African Research Chairs initiative of the Department of Science and Technology, the National Research Foundation (NRF) of South Africa, University Research Committee (URC), and the South African Medical Research Council (SAMRC). The research reported in this original article was supported by the South African Medical Research Council (SAMRC) through its Division of Research Capacity Development under the Research Capacity Development Initiative from funding received from the South African National Treasury. The content and findings reported/illustrated are the sole deduction, view, and responsibility of the researchers and do not reflect the official position and sentiments of the SAMRC.

References

[1] F. Bray *et al.*, "Global cancer statistics 2022: GLOBOCAN estimates of incidence and mortality worldwide for 36 cancers in 185 countries," (in eng), *CA Cancer J Clin,* vol. 74, no. 3, pp. 229-263, May-Jun 2024, doi: 10.3322/caac.21834.

[2] J. Ferlay *et al.* "Global Cancer Observatory: Cancer Today." International Agency for Research on Cancer. https://gco.iarc.who.int/today (accessed 11 December 2024, 2024).

[3] A. H. Faid, S. A. Shouman, N. A. Thabet, Y. A. Badr, and M. A. Sliem, "Laser Enhanced Combinatorial Chemo-photothermal Therapy of Green Synthesis Gold Nanoparticles Loaded with 6Mercaptopurine on Breast Cancer Model," *Journal of Pharmaceutical Innovation,* vol. 18, no. 1, pp. 144-148, 2023/03/01 2023, doi: 10.1007/s12247-022-09626-0.

[4] R. Chaudhari, V. Patel, and A. Kumar, "Cutting-edge approaches for targeted drug delivery in breast cancer: beyond conventional therapies," *Nanoscale Advances,* 10.1039/D4NA00086B vol. 6, no. 9, pp. 2270-2286, 2024, doi: 10.1039/D4NA00086B.

[5] M. Broadbent, S. J. Chadwick, M. Brust, and M. Volk, "Gold Nanoparticles for Photothermal and Photodynamic Therapy," *ACS Omega,* vol. 9, no. 44, pp. 44846-44859, 2024/11/05 2024, doi: 10.1021/acsomega.4c08797.

[6] A. K. Singh *et al.*, "Green synthesis of gold nanoparticles from Dunaliella salina, its characterization and in vitro anticancer activity on breast cancer cell line," *Journal of Drug Delivery Science and Technology,* vol. 51, pp. 164-176, 2019/06/01/ 2019, doi: https://doi.org/10.1016/j.jddst.2019.02.023.

[7] A. Mohammed Siddiq, R. Thangam, B. Madhan, and M. S. Alam, "Green (gemini) surfactant mediated gold nanoparticles green synthesis: Effect on triple negative breast cancer cells," *Nano-Structures & Nano-Objects,* vol. 19, p. 100373, 2019/07/01/ 2019, doi: https://doi.org/10.1016/j.nanoso.2019.100373.

[8] M. A. Dheyab *et al.*, "Green synthesis of gold nanoparticles and their emerging applications in cancer imaging and therapy: a review," *Reviews in Inorganic Chemistry,* vol. 45, no. 4, pp. 663-685, 2025, doi: doi:10.1515/revic-2024-0048.

[9] G. Nigussie, M. Tegegn, D. Abeje, and H. Melak, "A comprehensive review of the ethnomedicine, phytochemistry, pharmacological activities of the genus Kniphofia," (in eng), *Pharm Biol,* vol. 60, no. 1, pp. 1177-1189, Dec 2022, doi: 10.1080/13880209.2022.2085753.

[10] A. Ullah *et al.*, "Important Flavonoids and Their Role as a Therapeutic Agent," (in eng), *Molecules,* vol. 25, no. 22, Nov 11 2020, doi: 10.3390/molecules25225243.

[11] S. Sargazi *et al.*, "Application of Green Gold Nanoparticles in Cancer Therapy and Diagnosis," *Nanomaterials,* vol. 12, no. 7, p. 1102, 2022. [Online]. Available: https://www.mdpi.com/2079-4991/12/7/1102.

[12] S. L. Fink and B. T. Cookson, "Apoptosis, pyroptosis, and necrosis: mechanistic description of dead and dying eukaryotic cells," (in eng), *Infect Immun,* vol. 73, no. 4, pp. 1907-16, Apr 2005, doi: 10.1128/iai.73.4.1907-1916.2005.

[13] S. R. Alizadeh, P. Biparva, H. R. Goli, B. A. Khan, and M. A. Ebrahimzadeh, "Green Synthesis of AuNPs by Crocus caspius—Investigation of Catalytic Degradation of Organic Pollutants, Their Cytotoxicity, and Antimicrobial Activity," *Catalysts,* vol. 13, no. 1, p. 63, 2023. [Online]. Available: https://www.mdpi.com/2073-4344/13/1/63.

[14] S. Habtemariam, "Knipholone anthrone from Kniphofia foliosa induces a rapid onset of necrotic cell death in cancer cells," *Fitoterapia,* vol. 81, no. 8, pp. 1013-1019, 2010/12/01/ 2010, doi: https://doi.org/10.1016/j.fitote.2010.06.021.

This page intentionally left blank.

Riboflavin-mediated Photodynamic Therapy Induces Cytotoxic Effects in A549 Lung Cancer Cells

Malefo Tshepiso Mofokeng[1], Heidi Abrahamse[1]

[1]Laser Research Centre, University of Johannesburg, Johannesburg, South Africa

E-mail: habrahamse@uj.ac.za

Abstract. Lung cancer, a prevalent and deadly malignancy, arises from the uncontrolled growth of cells within the lungs, and it poses significant challenges in diagnosis and treatment. Photodynamic therapy (PDT) has promising therapeutic effects while causing minimal harm to healthy cells and tissues. This study explores the therapeutic potential and impact of riboflavin, a natural photosensitizer, and PDT against A549 lung cancer cells. The cells were treated with riboflavin at variable concentrations and irradiated using a laser of wavelength 470 nm at fluencies of 5 J/cm^2 and 15 J/cm^2. Following a period of 24 hours post-irradiation, the A549 cells were analyzed using biochemical assays, namely adenosine triphosphate and lactate dehydrogenase assays. In addition, morphological analysis post-irradiation, reactive oxygen species detection, and mitochondrion localization studies were performed. Changes in cell viability and morphology were observed post-treatment, indicating the cytotoxic effects of riboflavin-mediated PDT on A549 lung cancer cells. These findings suggest that riboflavin-mediated PDT might have potential as an anticancer treatment against lung cancer.

1 Introduction

Cancer is a fatal disease that continues to claim the lives of its victims on a global scale. For the past two decades, it has consistently ranked among the top five leading causes of death. Cancer affects both men and women, and individuals of almost any age. As of the current statistics, cancer is estimated to account for 20 million new cases and 10 million death-related cases in 2023, globally. This number is estimated to reach 35 million by 2050 [1]. According to the American Cancer Society, 618,120 cancer deaths and 2,041,910 new cancer cases are expected to occur in 2025 in the US [2]. South Africa faces a similar disease burden with over 80,000 cancer cases in 2019, which are expected to rise to 150,000 by 2030 [3]. Globally, lung cancer is rated number one, with high mortality and incidence rates [1]. The most common causes of lung cancer include tobacco smoking, excessive alcohol consumption, unhealthy diet choices, and environmental pollutants [4]. While there are conventional treatments and other advanced therapy modalities, cancer continues to remain fatal and life-threatening. Most of the known treatments are associated with serious side effects, and some are not as effective in eradicating the disease in its entirety. Photodynamic therapy (PDT) has gained traction as a minimally invasive treatment option that uses photosensitizing agents, known as photosensitizers, and laser therapy. Photosensitizers are molecules that can accumulate in cells and, upon light exposure at a specific wavelength, can become excited to generate reactive oxygen species, leading to apoptosis or other cell death pathways [5]. Riboflavin, also known as vitamin B2, is the photosensitizer of choice for this study due to its biocompatibility as a naturally-derived vitamin and its ability to generate reactive oxygen species upon light activation in the blue region of the visible spectrum [6]. Moreover,

there are very limited research studies of its use in lung cancer. Therefore, this study focuses on elucidating the potential cytotoxic effects of riboflavin with PDT on A549 lung cancer cells.

2 Methodology

2.1 Cell Culture and Maintenance of A549 Lung Cancer Cells

The A549 lung cancer cell line obtained from the American Type Culture Collection (A549, ATCC® CCL-185) was cultured in Rosewell Park Memorial Institute 1640 (RPMI) culture medium. The medium was supplemented with 1% amphotericin B, 1% penicillin/streptomycin antibiotics, and 10% fetal bovine serum (FBS). The cells were kept in a 37 ˚C incubator with 85% humidity and 5% CO_2 to promote an environment that supports optimal cell growth. Cell growth was observed every 24 hours, with media change being made every second day. The A549 passage numbers used for this study were kept between 26 and 29.

2.2 Riboflavin Absorbance Spectrum Analysis

The absorption spectrum of riboflavin was obtained by measuring the aqueous solution of the photosensitizer using a microplate reader (PerkinElmer, VICTOR Nivo™, South Africa).

2.3 Cell Treatment and Morphological Analysis

Following the optimal growth of A549 lung cancer cells in a T75 plate, they were then seeded into a 3.5 cm culture dish, using a seeding density of 3 x 10^5 cells/ml. The cells were allowed to attach, and after 24 hours, they were subjected to treatment using various concentrations of riboflavin (20, 40, 80, 110, 160, 320 µM) in the absence of laser. Subsequently, cells were also treated with the same varying concentrations of riboflavin and a 470 nm laser therapy with varying fluencies of 5 J/cm^2 and 15 J/cm^2. After 24 hours, the cell morphology was analyzed using an inverted light microscope (Wirsam, Olympus CKX41, Tokyo, Japan) to evaluate the cytotoxic effects of the treatment.

2.4 Cell Cytotoxicity Evaluation using Lactate Dehydrogenase (LDH) Assay

The cells were seeded into a 96-well cell culture-treated plate using a seeding density of 10 000 cells/well/100 µL and subjected to the treatment conditions as mentioned in section 2.3. After 24 hours of treatment, cell cytotoxicity was evaluated using the LDH Non-radioactive CytoTox 96 assay kit (Promega, G179A, USA). The experiment was performed by transferring 55 µL of the reconstituted LDH reagent into each well of the 96-well plate containing an equivalent volume (55 µL) of cell culture media. The solution was gently mixed for 5 minutes on a shaker and incubated for 30 minutes at room temperature, in the absence of light. The analysis was made by reading the absorbance at 490 nm using a microplate reader (PerkinElmer, VICTOR Nivo™, South Africa).

2.5 Cell Viability Assessment using Adenosine Triphosphate (ATP) Assay

The cells were seeded into a 96-well cell culture-treated plate using a seeding density of 10 000 cells/well/100 µL and subjected to the treatment conditions as mentioned in section 2.3 to determine the half maximal inhibitory concentration (IC_{50}). After 24 hours of treatment, cell viability was assessed using the ATP CellTiter-Glo® 3D reagent (Promega, G968A, USA). The experiment was performed by adding an 80 µL volume of the ATP reagent equal to the volume of the cell culture medium (80 µL) present in each well. The solution was vigorously mixed for 5 minutes to induce cell lysis. This was followed by an additional incubation step of 25 minutes at room temperature, in the absence of light. The cells were then transferred to an opaque white, flat-bottom 96-well plate, and the ATP luminescence was read using a microplate reader (PerkinElmer, VICTOR Nivo™, South Africa).

2.6 Determination of Reactive Oxygen Species Produced by A549 Cells

The amount of reactive oxygen species produced by A549 lung cancer cells before and after treatment were quantified using the 2',7'-dichlorofluorescin diacetate (DCFDA) cellular ROS assay kit (Abcam, ab113851, UK). The cells were seeded into a black, high binding, flat-bottom, 96-well microplate using a seeding density of 15 000 cells/well/100 µL and incubated for 24 hours to allow for adhesion of the cells to the plate. After incubation, the cell suspension was discarded, and the cells were washed twice using 1X phosphate-buffered saline (PBS). This was followed by staining with 20 µM DCFDA solution for 45 minutes at 37 ˚C, in the absence of light. Thereafter, the cells were washed once with 1X PBS and treated with the riboflavin IC_{50} concentration

of 114 μM for 4 hours, followed by 15 J/cm^2 laser irradiation treatment at 470 nm, including appropriate controls. The fluorescence was read at Ex485/Em535 nm using a microplate reader (PerkinElmer, VICTOR Nivo^{TM}, South Africa).

2.7 Mitochondrial Localization of Riboflavin Photosensitizer in A549 Cells

The A549 lung cancer cells were seeded into a 3.5 cm cell suspension dish with sterile coverslips using a seeding density of 2.5 x 10^5 cells/ml and incubated at 37 ˚C with 85% humidity and 5% CO_2. The cells were allowed to attach, and after 24 hours, the cells were subjected to treatment at a concentration of 114 μM for 4 hours. After treatment, the cells were washed thrice with ice-cold 1X PBS to remove unabsorbed riboflavin photosensitizer. The cells were then fixed using 1 mL of 4% paraformaldehyde at room temperature and incubated for 15 min. Post-incubation, the cells were washed thrice with PBS and permeabilized for 15 min using 0.5 % Triton X-100 in 1X PBS. The solution was discarded, and the cells were washed thrice with 1X PBS. A pre-warmed probe containing 100 nM mitochondrial tracker Mito Red CM x ROS (Invitrogen, M7512, US) was added to the petri dish and incubated with the cells for 30 min at 4 ˚C. After incubation, a thorough wash using PBS was performed, and the cells were counter-stained for 5 min at 37 ˚C using 300 nM of 4′,6-diamidino-2-phenylindole (DAPI) and rinsed thrice using 1X PBS. The treated coverslip was removed from the petri dish and mounted onto a microscope glass slide using fluoromount aqueous mounting medium. The slides were sealed with a clear nail polish and examined using widefield/confocal fluorescence microscope (Leica Mica Microscope, Johannesburg, South Africa).

2.8 Statistical Analysis of Experimental Data

All experiments in this study were conducted 3 times (n = 3). GraphPad Prism 5 software was employed as a tool for the analysis of the data acquired from each experiment. One-way analysis of variance (ANOVA) was carried out to determine the statistical significance of the mean values acquired from the treated groups, and these were compared to the mean values of the untreated A549 lung cancer cells (control group). Dunnett's test was conducted at a confidence interval of 95% and the mean values from each experimental group were plotted as mean ± standard error of the mean (SEM). The statistical significance was defined using p-values where $p < 0.05$*, $p < 0.01$**, and $p < 0.001$***.

3 Results and Discussion

3.1 Morphological Analysis

The A549 lung cancer cells were exposed to variable concentrations of riboflavin to study the dark-toxicity effects after 24 hours (Figure 1A). Alongside, the cells were exposed to the same variable concentrations and irradiated at fluences of 5 J/cm^2 and 15 J/cm^2 using a 470 nm laser to study the synergistic effects of the photosensitizer and laser (Figure 1). At 0 μM concentrations, there are no visible changes in the morphology when the cells were treated with the 470 nm laser at fluencies of 5 J/cm^2 and 15 J/cm^2, suggesting that PDT alone, with no photosensitizer, does not elicit any cytotoxic effects on the A549 cells. It is seen that increasing the concentration of riboflavin resulted in morphological changes, especially from 80 μM to 320 μM, in the presence and absence of laser. In addition, using a higher light dose of 15 J/cm^2 enhanced the cytotoxic effects against A549 lung cancer cells, as compared to when the cells were treated with riboflavin alone, or with a laser of 5 J/cm^2 (Figure 1). Moreover, the effects of the treatment are marked by a reduction in cell number and loss of cell shape and integrity, suggesting that cell death is occurring at this stage of treatment.

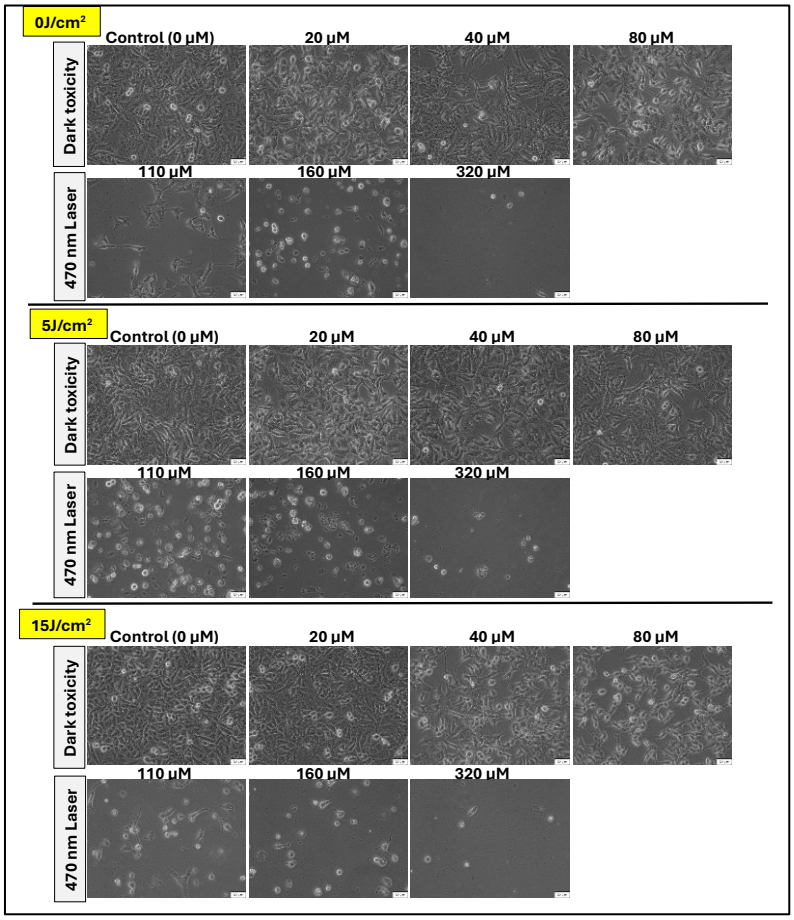

Figure 1: Morphological analysis of A549 lung cancer cells following a 24-hour treatment captured using a 20x objective lens. Riboflavin (0 – 320 µM) was tested at 0 J/cm^2 (dark toxicity), 5 J/cm^2, and 15 J/cm^2 light doses using a 470 nm laser.

3.2 Riboflavin Absorbance Spectrum Analysis

The absorption spectrum of riboflavin shows two distinct peaks at 372 nm and 445 nm. The strong absorbance peak at 445 nm influenced the choice of a 470 nm laser, as it is the closest available wavelength, and it can efficiently excite riboflavin.

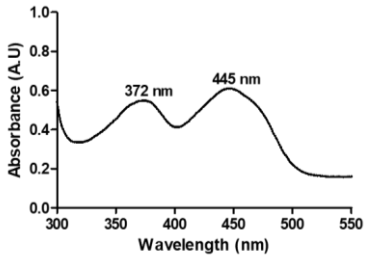

Figure 2: UV-Vis Absorption spectrum of riboflavin. Two maxima peaks are observed at 372 nm and 445 nm.

3.3 LDH Analysis

Lactate dehydrogenase, abbreviated as LDH, is one of the key enzymes found in all tissues and most cells. This enzyme plays a role in DNA metabolism and gluconeogenesis [7]. When A549 cells are subjected to treatment, their membrane integrity becomes compromised, leading to a release of LDH into the extracellular space [8].

Sensitive assays, such as the LDH cytotoxicity assay, can detect levels of LDH from the culture medium due to treatment. The control groups in Figure 3A are seen at a 0 µM concentration of riboflavin, with the LDH positive control included. The levels of LDH in the three control groups exclusive of riboflavin are lower than the LDH levels in the treated groups. Moreover, LDH levels in cells treated with a combination of riboflavin and higher light exposure (15 J/cm^2) significantly enhanced the cytotoxic effects against A549 lung cancer cells, compared to a lower light dose (5 J/cm^2), thus resulting in a greater increasing trend of LDH release, suggesting its enhanced tumor killing effect.

3.4 ATP Analysis

Adenosine triphosphate, also known as ATP, is an energy molecule that is found in all living cells, and it drives essential cellular processes [9]. Increasing levels of ATP from the cells are directly proportional to cell viability. Likewise, when cells experience cell death (due to treatment), the levels of ATP also drop. The ATP CellTiter-Glo® 3D reagent was used to quantify ATP levels in A549 lung cancer cells after treatment with riboflavin and laser. The half maximal inhibitory concentration (IC_{50}) was also determined using this assay and was found to be 114 µM using a 15 J/cm^2 fluence (Figure 3B). The ATP levels in control groups (0 µM) in the absence and presence of laser therapy remained higher, compared to treated cells (Figure 2B). Also, there is no statistical significance in the riboflavin concentrations at 20 µM and 40 µM in laser-treated groups, compared to the controls, indicating that most cells are still viable in these treatment conditions. ATP levels begin to drop significantly at 80 µM in both treatment groups, with a complete shutdown in cell viability seen at 320 µM. Both cells treated with riboflavin alone and those treated with riboflavin combined with laser therapy show significant changes in ATP levels as the concentration of the photosensitizer increases. However, an enhanced effect is observed at a higher light dose of 15 J/cm^2, suggesting that a higher light dose in this study enhanced the therapeutic efficacy of riboflavin.

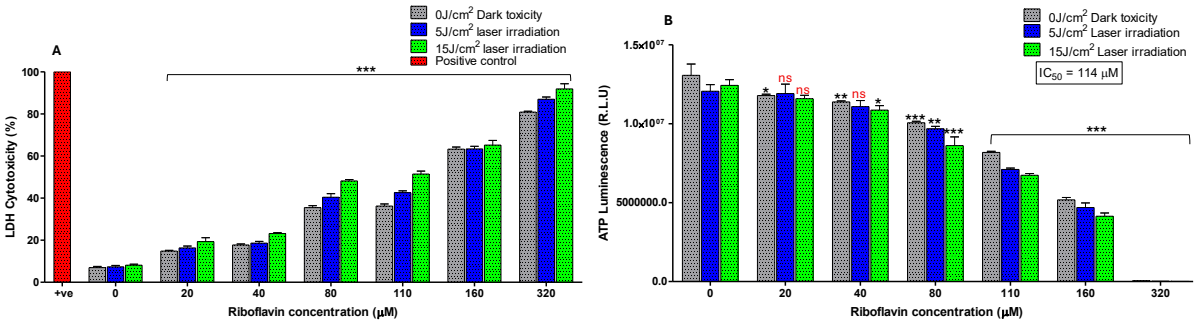

Figure 3: Biochemical assays indicating dark-toxicity and riboflavin-laser-treated groups in A549 lung cancer cells. (A) LDH cell cytotoxicity assessment 24 hours after treatment, (B) Dose-dependent cell viability ATP assay. The data is represented as mean ± standard error of the mean for each group with n = 3. Statistical significance assessed using one-way ANOVA is defined as $p < 0.05$*, $p < 0.01$**, and $p < 0.001$***, while ns is an indication of a non-significant group compared to the control sample.

3.5 Reactive Oxygen Species Analysis

The DCFDA assay is used to quantify the amount of reactive oxygen species produced by A549 lung cancer cells before and after treatment. DCFDA is a non-fluorescent dye that would enter the cells and, upon its oxidation by reactive oxygen species, will result in the formation of a fluorescent detectable compound DCF (2',7'-dichlorofluorescein) [10]. The resulting fluorescence is proportional to the levels of reactive oxygen species present. In the assay, a dimethyl sulfoxide (DMSO) control was included as it was the solvent utilized for dissolving riboflavin. The cells treated with both riboflavin and laser therapy resulted in a significant increase in reactive oxygen species production compared to non-treated cells (Figure 4). Also, there was no significant increase in reactive oxygen species production when cells were treated with riboflavin alone. Therefore, 15J/cm^2 laser treatment with the photosensitizer increased the amount of reactive oxygen species, thus contributing to oxidative stress within the cell.

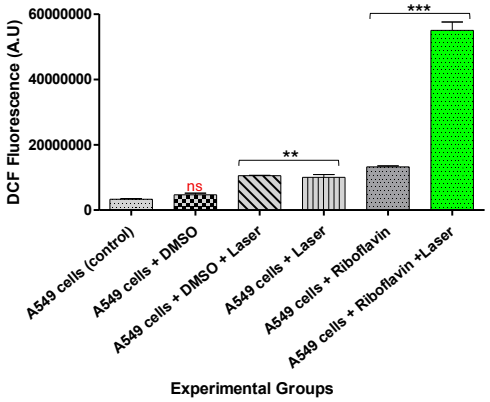

Figure 4: Cellular reactive oxygen species detection using DCFDA assay. The data is represented as mean ± standard error of the mean for each group at $n = 3$. Statistical significance assessed using one-way ANOVA is depicted as $p < 0.01$** and *** $p < 0.001$.

3.6 Drug Co-localization

Drug co-localization study using Mito-tracker resulted in the generation of fluorescent images in Figure 5 that show the DAPI (a nucleus marker), mitochondrial marker, riboflavin, and the merged images. The visible fluorescent signal in the merged image confirms the co-localization of riboflavin in the mitochondria. Mitochondria are known as an organelle that generates most of the cell's ATP. Since riboflavin co-localizes in the Mitochondrion, this correlates with the observed decrease in ATP levels following treatment, suggesting that riboflavin may directly impair mitochondrial function and thereby reduce cellular ATP production and cell survival.

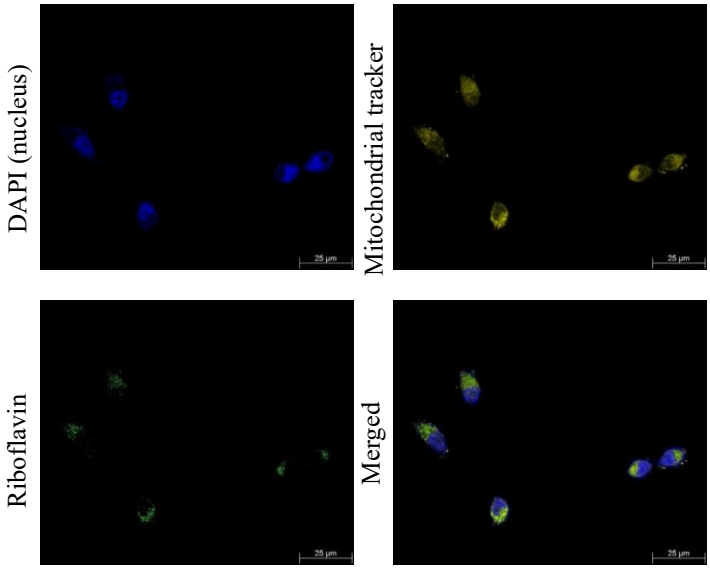

Figure 5: Intracellular (mitochondrial) localization of riboflavin in A549 lung cancer cells. The merged image shows the successful uptake of the photosensitizer (riboflavin) by the mitochondria.

4 Conclusion

Riboflavin is a naturally occurring vitamin that has gained attention in biomedical research as a photosensitizer for use in PDT [11]. In this study, the cytotoxic effects of riboflavin in the presence and absence of 470 nm laser therapy at 5 J/cm^2 and 15 J/cm^2 against A549 lung cancer cells were demonstrated. In the control groups, no cell damage occurred. When cells were subjected to treatment using PDT and riboflavin at high concentrations, enhanced cytotoxic effects were observed on A549 lung cancer cells, as compared to treatment with riboflavin

alone. In addition, using a higher light dose of 15 J/cm^2 enhanced the cytotoxic effects against A549 lung cancer cells, as compared to when the cells were treated with riboflavin alone, or with a laser of 5 J/cm^2. The changes were exhibited by cells losing their shape, loss of structural integrity, and changes in morphology. Biochemical assay results correlated with the morphological analysis, and these were marked by an increase in LDH levels, a drop in ATP levels as cells lost their viability, and a substantial increase in reactive oxygen species levels was observed. In addition, riboflavin localizes in the mitochondrion, indicating this organelle as one of the targets of PDT-induced cytotoxicity. These findings suggest that riboflavin-mediated PDT might have potential as an anticancer treatment against lung cancer. While this study demonstrates potential, further research is required to enhance the efficacy of riboflavin at lower concentrations to minimize the need for the high doses used.

Acknowledgements

The authors extend their gratitude to the Laser Research Center, the University of Johannesburg, the South African Research Chairs Initiative of the Department of Science and Technology, the National Research Foundation of South Africa, and the University of Johannesburg Global Excellence and Stature, Fourth Industrial Revolution (GES 4.0) Doctoral Scholarship. We also acknowledge Promolab Pty Ltd T/A Separations for their partnership with the Laser Research Centre, providing the Leica Mica Microhub in support of the microscopy images featured in this article.

Funding statement
This research is supported and funded by the South African Research Chairs Initiative of the Department of Science and Technology, the National Research Foundation of South Africa (SARChI/NRF-DST; grant number 98337), and the University of Johannesburg Global Excellence and Stature, Fourth Industrial Revolution (GES 4.0) Doctoral Scholarship.

References

[1] F. Bray *et al.*, "Global cancer statistics 2022: GLOBOCAN estimates of incidence and mortality worldwide for 36 cancers in 185 countries," *CA: A Cancer Journal for Clinicians*, vol. 74, no. 3, pp. 229–263, 2024, doi: 10.3322/caac.21834.

[2] R. L. Siegel, T. B. Kratzer, A. N. Giaquinto, H. Sung, and A. Jemal, "Cancer statistics, 2025," *CA: A Cancer Journal for Clinicians*, vol. 75, no. 1, pp. 10–45, 2025, doi: 10.3322/caac.21871.

[3] S. S. Africa, "Key Findings | Statistics South Africa." Accessed: Sep. 28, 2025. [Online]. Available: https://www.statssa.gov.za/?page_id=1856

[4] K. Zou *et al.*, "Etiology of lung cancer: Evidence from epidemiologic studies," *Journal of the National Cancer Center*, vol. 2, no. 4, pp. 216–225, Dec. 2022, doi: 10.1016/j.jncc.2022.09.004.

[5] Y. Cai *et al.*, "Phototherapy in cancer treatment: strategies and challenges," *Sig Transduct Target Ther*, vol. 10, no. 1, p. 115, Apr. 2025, doi: 10.1038/s41392-025-02140-y.

[6] A. Etemadi, M. Hamidain, S. Parker, and N. Chiniforush, "Blue Light Photodynamic Therapy With Curcumin and Riboflavin in the Management of Periodontitis: A Systematic Review," *Journal of Lasers in Medical Sciences*, vol. 12, p. e15, Apr. 2021, doi: 10.34172/jlms.2021.15.

[7] A. Farhana and S. L. Lappin, "Biochemistry, Lactate Dehydrogenase," in *StatPearls*, Treasure Island (FL): StatPearls Publishing, 2025. Accessed: Jul. 28, 2025. [Online]. Available: http://www.ncbi.nlm.nih.gov/books/NBK557536/

[8] Y. Feng, Y. Xiong, T. Qiao, X. Li, L. Jia, and Y. Han, "Lactate dehydrogenase A: A key player in carcinogenesis and potential target in cancer therapy," *Cancer Med*, vol. 7, no. 12, pp. 6124–6136, Nov. 2018, doi: 10.1002/cam4.1820.

[9] L. Huang, L. Otrokocsi, and B. Sperlágh, "Role of P2 receptors in normal brain development and in neurodevelopmental psychiatric disorders," *Brain Research Bulletin*, vol. 151, pp. 55–64, Sep. 2019, doi: 10.1016/j.brainresbull.2019.01.030.

[10] T. A. Kato, "DCFDA Assay for Oxidative Stress Measurement in Fluorometer," *Methods Mol Biol*, vol. 2933, pp. 87–91, 2025, doi: 10.1007/978-1-0716-4574-1_12.

[11] M. Insińska-Rak, M. Sikorski, and A. Wolnicka-Glubisz, "Riboflavin and Its Derivates as Potential Photosensitizers in the Photodynamic Treatment of Skin Cancers," *Cells*, vol. 12, no. 18, Art. no. 18, Jan. 2023, doi: 10.3390/cells12182304.

This page intentionally left blank.

Numerical Modeling and Simulation of a Fabry–Perot Sensor for Refractive Index Measurement

Sandisiwe Bangani[1], **James Jena**[2] **and David Waswa**[3]

[1,2,3],Department of Physics, Centre for Broadband Communication, Nelson Mandela University, Port Elizabeth, South Africa

E-mail: s215121457@mandela.ac.za

Abstract. The precise monitoring of chemical concentrations in liquids is critical for environmental, industrial, and biomedical applications. Optical fiber sensors, particularly those based on Fabry-Perot interferometry (FPI), offer high sensitivity, tolerance to harsh environments, and multi-sensing capabilities, making them ideal for detecting refractive index changes in various solutions. This study presents the modeling and simulation of an FPI sensor for real-time monitoring of refractive index changes in sugary aqueous solutions. The reflected spectra were studied using two signal processing techniques: fringe visibility and fast Fourier transform. The obtained sensitivities in refractive index units (RIU) varied between 2.093 a.u./RIU and 0.582 a.u./RIU for the latter method and 0.933 dB/RIU when analyzing the fringe visibility, giving a sensor resolution of 0.00107 RIU. The sensor's size and its all-in-fiber design enable remote and real-time monitoring, making it ideal for use in environmental monitoring, chemical sensing, and biomedical diagnostics.

1 Introduction

The refractive index (RI) is a crucial metric for describing an analyte and is commonly used in biomolecule detection, clinical diagnostics, drug analysis, pollution management, and monitoring [1, 2, 3]. The precise and dependable measurement of the refractive index of gases and liquids enables real-time detection of changes in concentration, contamination, or chemical reactions. While methods like Abbe refractometry [4] and prism-based [5] techniques are precise, traditional RI sensing approaches come with drawbacks: they are expensive, bulky, sensitive to environmental noise, and lack remote sensing capabilities. Optical fiber-based sensors have received significant attention in biological and environmental sensing due to their unique features, including corrosion resistance, immunity to electromagnetic interference, high precision, and compactness [6, 7].

Among different optical fiber sensing setups, fiber-based Fabry-Perot (FP) sensors have attracted considerable attention for refractive index measurements. The working principle of these sensors is based on the interference of multiple reflections in a cavity created by partially reflective surfaces. Modulation of the reflected interference signal occurs due to alterations in the optical path length or reflectivity at the cavity boundaries, resulting from variations in the external refractive index. The surrounding medium's refractive index can be determined through an accurate analysis of such modulation.

Conventional FP interferometric sensors can provide low-cost absolute RI measurements with low thermal sensitivity by modulating the phase of an FP fiber interferometer in response to a change in a physical parameter. FP RI sensors can measure RI with great sensitivity and resolution due to their resonant wavelength response. However, these sensors have some drawbacks, including temperature cross-sensitivity and complicated architectures. Also, according to the Fresnel law, the reflected light from the surface is extremely weak when the RI of the

measuring medium is near that of the optical fiber [8]. Therefore, these sensors can only measure materials with a lower RI than the RI of the core of the fiber, and this limits their practical applications.

In this study, we model and simulate a simple in-line F-P fiber sensor that measures the RI of a sugary solution without requiring the filling of any microscopic fiber cavities. The sensor is created by forming a short air cavity near the tip of a single-mode Germanium-doped fiber through etching and fusion splicing with an unetched fiber. Following splicing, the fiber is cleaved to create the second and third cavities. The reflected light from the fiber tip interferes with the light reflected from the air cavity. The RI of a liquid can be reliably determined by measuring the fringe contrast of its interference pattern in the reflected spectrum. The sensor measures refractive indices greater than air with exceptional linearity and precision, accounting for temperature fluctuations.

2 Methodology: Simulation Study

2.1 Sensor Model

A virtual air-cavity Fabry-Perot interferometer (FPI) sensor was modeled based on the physical sensor fabricated in the laboratory.

2.1.1 Chemical Etching: A single-mode photosensitive Germanium-doped core fiber is used. The fiber cladding and core are etched with hydrofluoric acid (HF, 50% by weight) for 8 minutes. Acid solutions with appropriate ratios can be used to taper or hollow the fiber tip due to varying etching rates between the core and cladding.
The chemical reaction between HF, germanium, and silica is:

$$SiO_2 + 6HF \rightarrow 2H_3O^3 + SiF_6^{2-}$$

$$GeO_2 + 6HF \rightarrow 2H_3O^3 + GeF_6^{2-}$$

The lower bond dissociation energy of Ge-O bonds (660 KJ/mol) compared to Si-O bonds (799 KJ/mol) [9] allows for faster etching of germanium-doped cores than fused silica cladding.

2.1.2 Fusion Splicing: The next step is to fuse the etched fiber with an unetched fiber. An air gap is generated in the splice, which can be used as a reflector. The size and shape of the air gap, as well as its reflectance and transmittance, are determined by three splicer parameters: fiber overlap, arc power, and arc duration. The last step includes cleaving the tip of the fiber to form the second cavity.

2.2 Sensor Operation Principle: Mathematical Model of the Sensor

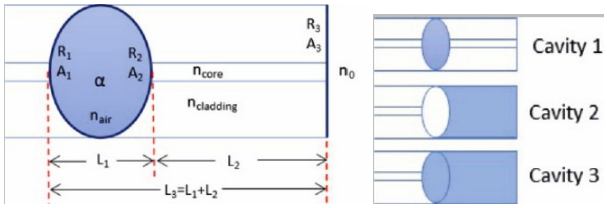

Figure 1: The schematic of the sensor sensor head (*left*), the three cavities (*right*) Ref. [10].

Figure 1 shows the sensing head that is composed of an air bubble enclosed within the fiber, which functions as an in-line FP interferometer. The first and second reflecting surfaces are the bubble's interfaces, forming the initial resonant cavity. Their reflection coefficients are R_1 and R_2, while their transmission coefficients are A_1 and A_2 (primarily related to surface imperfections). The second cavity is generated between the second and third reflective surfaces, with the latter representing the cleaved end of the fiber. Finally, we consider a third resonant cavity produced between the first and third reflective surfaces, with R_3 and A_3 being the reflection and transmission coefficients of the third mirror. The cavity loss factor is denoted as α, where n_{core} and $n_{cladding}$ are the refractive indices of the Ge-doped fiber core and silica cladding, respectively, and n_0 is the refractive index of the surrounding medium. L_1 and L_2 denote the lengths of cavities 1 and 2. The functioning principle of the sensor is based on the interference of light reflections across the three interfaces. The reflected spectrum's intensity of the three-beam interferometer can be represented as the sum of the intensities of each surface, plus a phase term, as illustrated below. A more detailed expression is given in [11].

$$R_{reflected} = R_1 + R_2 + R_3 + 2\sqrt{R_1R_2}cos(\phi_1) + 2\sqrt{R_2R_3}cos(\phi_2) + \sqrt{R_1R_3}cos(\phi_3) \quad (1)$$

where,

$$\phi_1 = \frac{4\pi n_{air} L_1}{\lambda}$$

$$\phi_2 = \frac{4\pi n_{Ge} L_2}{\lambda}$$

$$\phi_3 = \frac{4\pi (n_{air} L_1 + n_{Ge} L_2)}{\lambda}$$

The FP interferometer's response to changes in the refractive index of the surrounding medium is determined by the reflected intensity, therefore, fringe visibility is proportional to the reflectance of Mirror 3 (R_3) in the fiber's tip.

$$R_3 = (\frac{n_{Ge} - n_{sol}}{n_{Ge} + n_{sol}})^2 \tag{2}$$

where n_{Ge} and n_{sol} are the refractive indices of the Germanium-doped core fiber and those of the sugar solution. When the reflectance in mirror 3 increases, the reflected intensity drops (for $n_{Ge} > n_{sol}$), resulting in the drop in optical power and a decrease in fringe contrast/visibility, given below:

$$V = \frac{I_{max} - I_{min}}{I_{max} + I_{min}} \tag{3}$$

where I_{max} and I_{min} are the maximum and minimum intensities in the reflected spectra.

2.3 Virtual Experimental Setup

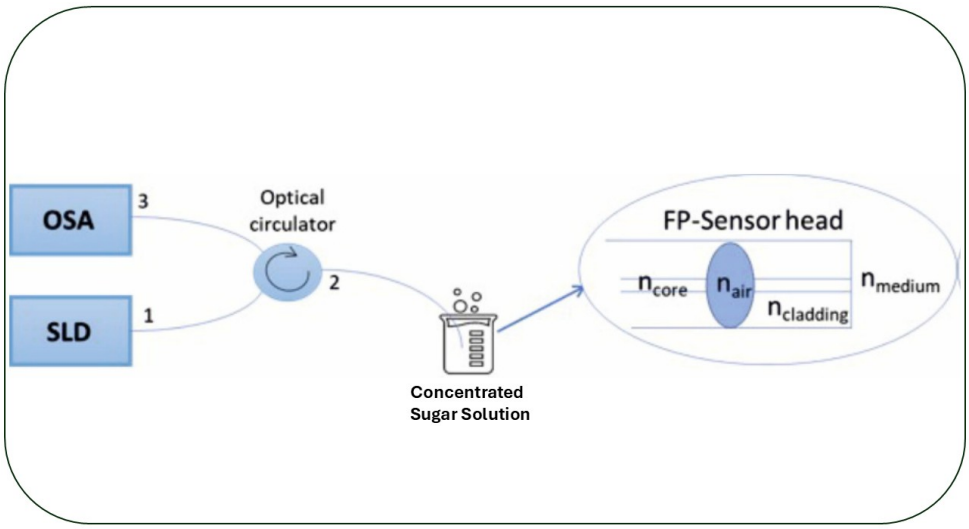

Figure 2: Experimental setup. OSA - Optical Spectrum Analyzer, SLD - superluminescent laser diode. n - refractive index Ref. [10].

Sucrose solutions were simulated by adding a range of 0 to 50 grams of sugar into a 100 mL distilled water container, increasing by steps of 5.55 grams.
Figure 2 shows the virtual setup used for the simulation; a superluminescent laser diode (SLD) is simulated to emit light within a wavelength range of 1500 to 1600 nm. The laser is connected to the FP interferometric sensor dipped in a sugar solution through port 2 of the optical circulator, which also directs the reflected signal from the sensor to the optical spectrum analyzer (OSA) through port 3, where the signal data are obtained. A wavelength range of 1520 to 1555 nm was chosen, and in this region, the signal's fringe contrast or visibility and reflected intensity were used to calculate the solution's refractive index. A Fast Fourier Transform (FFT) of the reflected spectra was performed, and the amplitudes of the frequency domain signals were correlated with the solution's refractive index.

Parameter	Value
n_{Ge}	1.47
n_{air}	1.00
L_1	150 μm
L_2	2000 μm
L_3	$L_1 + L_2$
α_1, α_2, α_3	0.02, 0.02, 0.05
r_1, r_2, r_3	0.36, 0.36, 0.05 $\rightarrow$ 0.01

Table 1: Values of parameters used in the calculation of the reflected spectrum for the sensor.

3 Results and Discussion

Figure 3 shows the simulated results of the reflected spectra at different sugar concentrations in water, and Table 1 contains the values of the parameters that were used in the calculation of the reflected spectra. An intensity shift can be observed in the signal as a result of an increase in the sugar concentration in the liquid. When sugar concentration increases, the light transmitted from the sensor to the solution interacts with the sugar particles, and some of it is absorbed or scattered; hence, the reflected signal loses intensity.

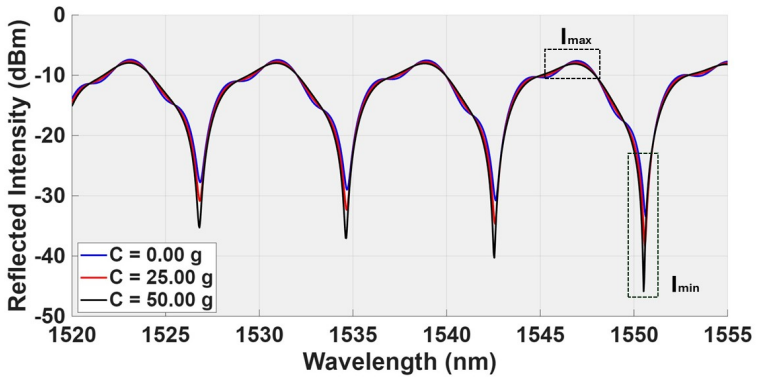

Figure 3: Reflected spectra at different sugar concentrations in the water.

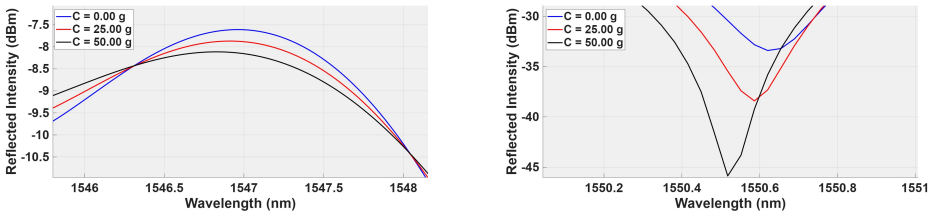

Figure 4: A zoom-in of the peaks (*left*), troughs (*right*) used as I_{max} and I_{min} in calculating the fringe contrast at different sugar concentrations.

The fringe contrast, sometimes referred to as visibility or modulation depth, is a measurement of the amplitude difference between the interference peaks and minima in the reflected spectrum in a Fabry-Perot (FP) interferometer fibre optic sensor, especially those with an open or exposed tip. The reflectivity of the cavity interfaces (reflectors) is essentially what controls this contrast. For an extrinsic FP sensor where one interface (reflector 3, in this case) is exposed to the surrounding environment (refractive index of n_{sol}), the reflectivity at that interface is given by

the Fresnel equation, that is, Equation 2 given above. As n_{sol} increases (from 1.333 to ≈ 1.410 in a 50 g sugar solution), the refractive index mismatch decreases, leading to a reduction in R_3. This reduces the overall fringe contrast and the cavity's finesse, which is an indicator of how sharp the fringes are.

Also, higher refractive indices, in particular, reduce the intensity of the reflected signal, which reduces the contrast between bright and dark fringes; this is shown in Figure 5. The achieved change in the fringe contrast (dB) per unit refractive index, that is, sensitivity, was 0.933 dB/RIU. A typical optical spectrum analyser has a resolution of 0.001 dB, therefore, we can find the resolution of this sensor to be $\frac{0.001dB}{0.933dB/RIU} = 1.07 \times 10^{-3}$RIU.

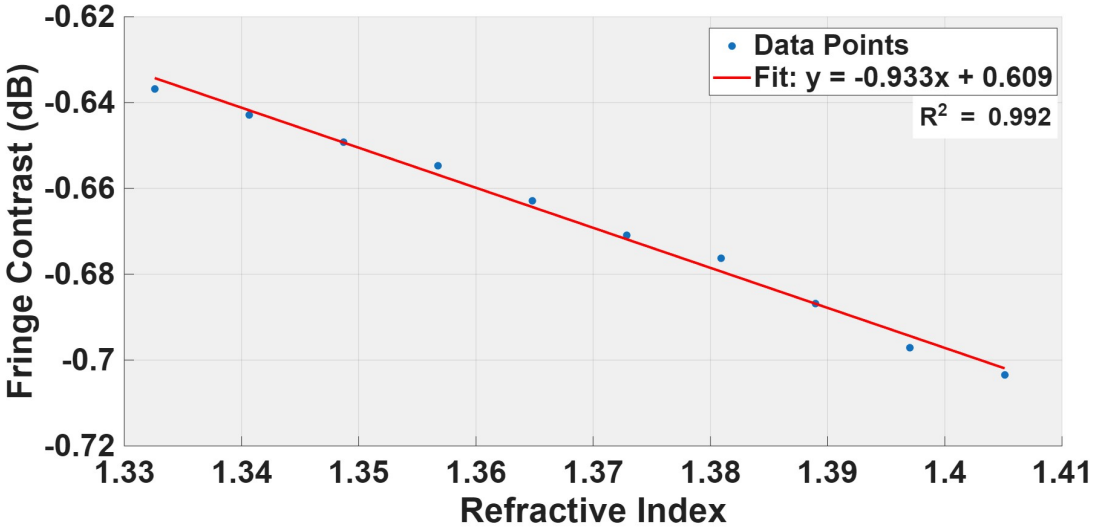

Figure 5: The fringe contrast vs refractive index in the wavelength range of 1520 to 1555 nm.

Figure 6 shows the Fast Fourier Transform (FFT) analysis of the simulated reflected spectra. FFT transforms the FP interference spectrum from the wavelength domain to the spatial frequency domain, revealing distinct peaks corresponding to individual cavity contributions. There are three regions of interest in the signals: Peaks 1, 2, and 3.

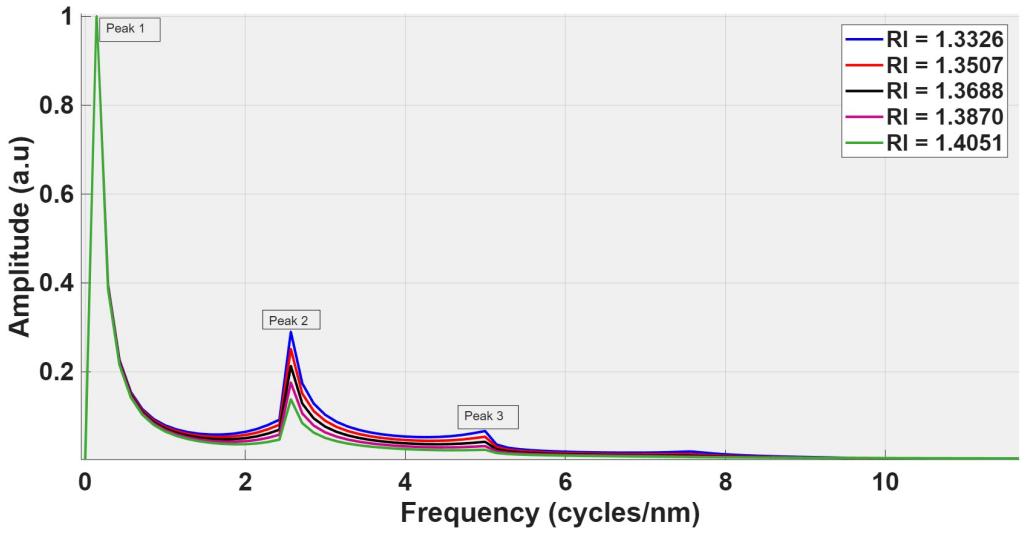

Figure 6: The Fast Fourier Transform of the reflected spectra.

Peak 1 corresponds to contributions from cavity 1 (air bubble) that lies entirely within the fiber, where both the optical path length (2nL) and refractive index (n_{air} = 1) remain constant while n_{sol} increases. The reflectivity at the two reflectors 1 and 2 also remains unchanged, and no part of this cavity is exposed to the solution. Its spatial frequency remains constant across all sucrose concentrations, serving as an internal reference that validates the stability of the sensor's core interference mechanism.

One of the reflectors in cavity 2 is at the fiber-solution interface, that is, reflector 3. Therefore, due to changes in the refractive index of the solution, the reflectivity at this interface also changes, according to equation 2. A lower reflectivity means weaker interference fringes, resulting in a lower FFT amplitude, hence the negative slope of the graph shown in Figure 7 (*top*). The achieved sensitivity in cycles per refractive index units in this cavity was 2.093 a.u./RIU.

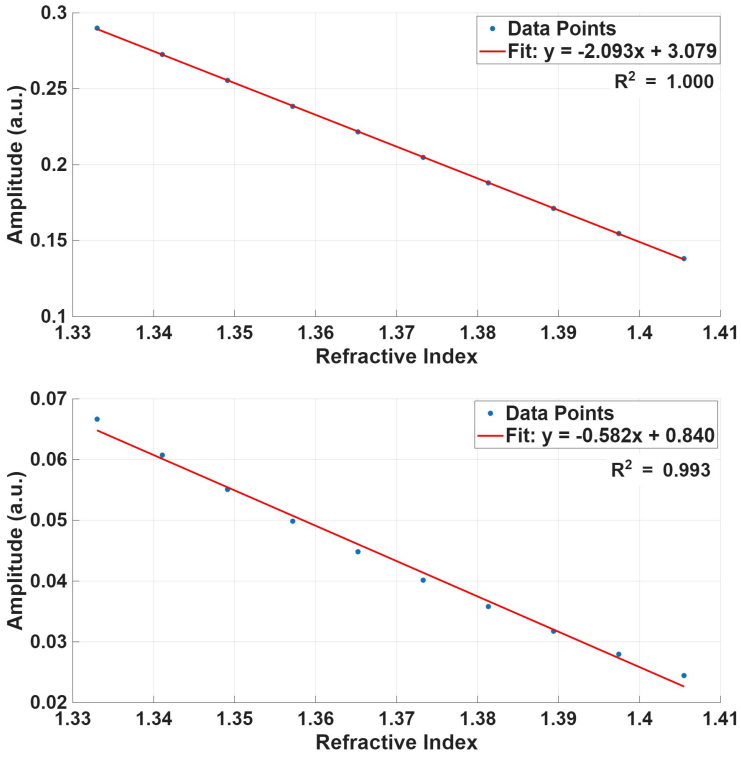

Figure 7: Calibration curves using spectral analysis from Peak 2 (*top*) , and Peak 3 (*bottom*) from Figure 6.

Cavity 3 includes the full length from the reflecting surfaces 1 to 3, so its reflectivity and interference strength are influenced by both internal and external interfaces. The overall contrast of decreases as the solution's refractive index increases, due to reduced reflectivity at reflector 3, and increased optical losses at the fiber-solution interface. Consequently, the amplitude of peak 3 in the FFT also decreases with increasing refractive index as shown in Figure 7 (*bottom*). The obtained sensitivity in this cavity is 0.582 a.u./RIU.

The intensity decay of Peaks 2 and 3 as a function of refractive index was used to create a calibration curve of FFT peak intensity versus RI, shown in 7. FFT effectively isolates overlapping interference contributions in complex FP structures, allowing for selective investigation of RI-sensitive components while isolating the environmentally stable reference (Peak 1). This is especially useful in hybrid or inline FP sensors, where several cavities coexist, such as in [10]. The amplitude reduction in Peaks 2 and 3 directly represents the Fresnel reflection loss at the fiber-medium interface, resulting in a physically interpretable RI response that does not rely on wavelength tracking fringe counting.
Thus, FFT analysis not only confirms the simulated sensor architecture by confirming the air cavity's presence and isolation (Peak 1), but it also provides a sensitive, stable, and interpretable metric for refractive index monitoring based on the intensity decay of external-medium-dependent peaks.

Figure 8 shows the changes in refractive index of the solution with increasing sugar concentration, with a sensitivity in refractive index per concentration of 0.0014 RIU/C. A solution's refractive index normally increases as its concentration increases because the presence of more solute particles in the solution influences how light passes through it. Specifically, a higher concentration increases the density of the medium, resulting in a higher refractive index, and light interferes with the solute particles, causing it to slow down.

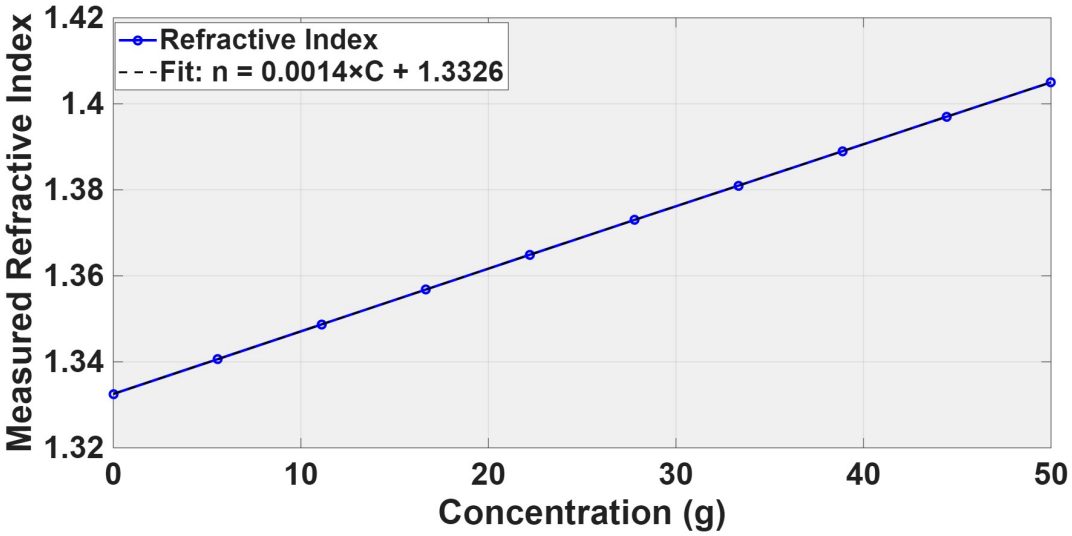

Figure 8: Calibration curve between concentration in the liquid in relation to its corresponding refractive index.

The simulation illustrates the relationship between the sensor's optical properties and the refractive index of the external medium, which is caused by evanescent field interaction at the sensor's tip. The air bubble cavity (modeled with fixed reflection coefficients r_1 = r_2 = 0.36) remains stable, resulting in a constant FFT Peak 1 serving as an internal reference. Because the low thermo-optic coefficient of air (-9.3 $\times$ 10^{-7} $^oC^{-1}$ [12]) reduces cross-sensitivity, this isolation is critical for adjusting for source variations or thermal effects.
Peaks 2 and 3 have decreasing intensities due to a change in reflection at the fibre-solution interface (r_3 dropping from $\approx$ 0.05 to 0.01 as RI approaches the fibre's 1.47). This reduces the effective finesse of the secondary cavities, resulting in decreased FFT amplitude. Physically, when the concentration of sugar increases, less light is reflected to the fibre due to $\alpha_3 \approx 0.05$.

4 Conclusion

In this study, we present a modeled and simulated approach for constructing in-line fiber Fabry-Pérot cavities, which involves etching a single-mode Germanium-doped silica core and splicing it to an unetched fiber to create a micrometer-sized air bubble within the fiber. After splicing, the fiber tip was cleaved, generating the sensor's cavities 2 and 3. The performance of the resulting FP interferometric sensor was examined for refractive index sensing of a sugar solution with varying concentration, and a sensitivity of 0.0014 RIU/C was achieved through simulation. The reflected spectra were analyzed using two signal processing techniques: fringe contrast/visibility and a fast Fourier transform. The obtained sensitivities ranged between 2.093 a.u./RIU and 0.582 a.u./RIU for the latter approach, and around 0.933 dB/RIU for evaluating fringe visibility.
The sensor is sensitive to variations in the refractive index, giving a resolution of 0.00107 RIU. The tiny, all-fiber structure allows both remote and real-time operation, making it ideal for chemical sensing, biological diagnostics, and environmental monitoring. The findings confirm that Fabry-Perot interferometric sensors provide a reliable and precise method for measuring refractive index in a variety of liquid media.

Acknowledgements
The author would like to acknowledge the guidance from the supervisors, Dr. David Waswa and Dr. James Jena. The author would also like to acknowledge Telkom's Centre of Excellence and CSIR for the financial support.

References

[1] V. S.-Y. Lin, K. Motesharei, K.-P. S. Dancil, M. J. Sailor, and M. R. Ghadiri, "A porous silicon-based optical interferometric biosensor," *Science*, vol. 278, no. 5339, pp. 840–843, 1997.

[2] F. Vollmer and S. Arnold, "Whispering-gallery-mode biosensing: label-free detection down to single molecules," *Nature methods*, vol. 5, no. 7, pp. 591–596, 2008.

[3] S. G. Patching, "Surface plasmon resonance spectroscopy for characterisation of membrane protein–ligand interactions and its potential for drug discovery," *Biochimica et Biophysica Acta (BBA)-Biomembranes*, vol. 1838, no. 1, pp. 43–55, 2014.

[4] J. Rheims, J. Köser, and T. Wriedt, "Refractive-index measurements in the near-ir using an abbe refractometer," *Measurement Science and Technology*, vol. 8, no. 6, p. 601, 1997.

[5] C.-C. Cheng, "Refractive index measurement by prism autocollimation," *American Journal of Physics*, vol. 82, no. 3, pp. 214–216, 2014.

[6] B. H. Lee, Y. H. Kim, K. S. Park, J. B. Eom, M. J. Kim, B. S. Rho, and H. Y. Choi, "Interferometric fiber optic sensors," *sensors*, vol. 12, no. 3, pp. 2467–2486, 2012.

[7] M. Hirsch, D. Majchrowicz, P. Wierzba, M. Weber, M. Bechelany, and M. Jędrzejewska-Szczerska, "Low-coherence interferometric fiber-optic sensors with potential applications as biosensors," *Sensors*, vol. 17, no. 2, p. 261, 2017.

[8] G. Z. Xiao, A. Adnet, Z. Zhang, F. G. Sun, and C. P. Grover, "Monitoring changes in the refractive index of gases by means of a fiber optic fabry-perot interferometer sensor," *Sensors and Actuators A: Physical*, vol. 118, no. 2, pp. 177–182, 2005.

[9] D. R. Lide, "Crc handbook of chemistry and physics, ; lide, dr, ed," 2006.

[10] M. Nespereira, J. M. Coelho, and J. M. Rebordão, "A refractive index sensor based on a fabry–pérot interferometer manufactured by nir laser microdrilling and electric arc fusion," in *Photonics*, vol. 6, no. 4. MDPI, 2019, p. 109.

[11] Z. L. Ran, Y. J. Rao, W. J. Liu, X. Liao, and K. S. Chiang, "Laser-micromachined fabry-perot optical fiber tip sensor for high-resolution temperature-independent measurement of refractive index," *Optics express*, vol. 16, no. 3, pp. 2252–2263, 2008.

[12] F. S. Meidanshahi, K. Madanipour, and B. Shokri, "Experimental study of the heat transfer process of air around atmospheric arc plasma," in *Optical Measurement Systems for Industrial Inspection VII*, vol. 8082. SPIE, 2011, pp. 1176–1183.

Voltage-Based Wavelength Tuning of a DFB Laser using a Frequency-to-Voltage Converter for OPLL Applications

Lilian Mutia[1], James Jena[1] and David Waswa[1]

[1]Centre for Broadband Communication, Department of Physics, Nelson Mandela University, Gqeberha, South Africa

E-mail: s230110703@mandela.acza

Abstract. We demonstrate voltage-based control of a Distributed Feedback (DFB) laser, forming a foundational step toward the implementation of an Optical Phase Locked Loop (OPLL). The voltage control mechanism was realized using the LM331N Frequency-to-Voltage Converter (FVC), which converts an offset frequency into a corresponding DC voltage signal. The voltage was directly fed into the DFB laser, effectively tuning its emission wavelength. A key challenge addressed in this work is the inherent 100 kHz upper limit of the LM331N-based FVC. By carefully modifying the circuit design, the conversion range is extended to accommodate frequencies of up to 3 MHz. The experimental results show a clear voltage response starting from 25 kHz, reaching approximately 4.6 V at 3 MHz. The results show a consistent frequency-voltage response, enabling effective wavelength tuning from 1551.725 nm to 1551.79 nm. This proof of concept shows a cost-effective and practical way of enabling coarse frequency locking in OPLLs which can be implemented at higher frequencies, essential for high-speed optical communication, coherent detection schemes, and Radio-over-Fibre (RoF) systems.

1 Introduction

The emergence of new technologies and broadband-intensive applications such as augmented and virtual reality (AR/VR), high-definition video streaming, autonomous vehicles, and Internet of Things (IoT) has led to an increase in the demand of high-speed, broadband, low-latency, reliable connectivity [1]. The all-electrical generation and processing of these high-frequency signals has proved challenging due to the bandwidth limitation of electrical components, electromagnetic interference, as well as the increasing cost and complexity of these components [2]. Although prevalent in millimeter waves (mmWave), the challenges also significantly affect the sub-6 GHz range, particularly when scalability and long-distance transmission are required. These challenges can be solved by Radio-over-Fiber (RoF) systems.

Radio-over-Fibre refers to the transmission of radio frequencies over optical fibres as opposed to free space. Optical fibres are advantageous as they have low attenuation, high bandwidth, and are immune to electromagnetic interference. The radio frequencies are generated through microwave photonics (MWP). These frequencies experience phase shifts which lead to instantaneous changes in frequency. To enable coherent detection, it is important to correct for these phase changes.

Phase stabilization can be achieved through different locking mechanisms such as optical injection locking (OIL), optical phase locked loop (OPLL) and optical injection phase-lock loop (OIPLL) [3]. OIL has been used to suppress unwanted sidebands [1] and to generate high frequencies in the orders of hundreds of gigahertz by injection locking to spectral lines from an optical comb [4], [5]. Though easier to implement compared to OPLL, it has a narrow locking range (few hundred MHz) and is extremely sensitive to changes in current and temperature. OIPLL is a solution to the milli-Kelvin precision challenge required to control the laser temperature [6], [7]. OILPLL combines two phase stabilization techniques; optical injection locking and phase locked loops. OIL is responsible for the reduction of wideband phase noise while the phase-locked loop controls the laser frequency drift and close-to-carrier phase noise [8]. OIPLLs have a wider locking range compared to OILs. However, their implementation is quite complex and are quite sensitive to environmental disturbances. Applications include coherent receivers [9], satellite-to-ground communication [3], and high-frequency signal synthesis [8].

Optical phase locked loops offer simpler implementation [3] than OIPLL. A heterodyne OPLL uses a master laser and a slave laser. The wavelength difference between the two lasers determines the value of the generated frequency. The two lasers are coupled and beat at a photodiode, generating a beat frequency. This frequency is compared to a frequency of the same value from a stable source using a mixer, which generates the sum and difference of the two frequencies. The high frequency components are filtered using a low pass filter. The offset frequency (difference) is converted to a proportional voltage which is fed back to the slave laser for tuning purposes. This feedback loop ensures that the slave laser always tracks the master laser, generating a stable frequency [1]. An OPLL attempts to maintain a constant phase relationship between the two lasers, even if the master laser drifts over time [3]. Due to their low phase noise and stable frequency output, they are widely used in quantum precision measurements [1], optical clock recovery in digital communication systems [10], dense wavelength-division multiplexed (DWDM) systems [11], LIDAR systems [12], sensing, spectroscopy [3], coherent terahertz photonics [13], and coherent optical communication systems [14]. Despite their numerous applications, OPLLs are difficult to realize in practice due to limitations in loop bandwidth and the short phase error propagation time within the loop, which is a function of laser linewidth [3]. To properly track and correct for phase fluctuations, the loop bandwidth of the OPLL should significantly exceed the linewidth of the laser to be controlled. Realizing such a bandwidth is difficult especially when working with broad linewidth lasers [15].

Most literature reports on using a mixer and loop filter to generate the phase error and control voltage respectively. However, in this research we focus on using a frequency-to-voltage converter (FVC) for coarse locking (frequency locking), before using a loop filter for phase locking. This approach is necessary when the frequency drift is too fast, too slow or too large as the loop filter has a limited capture range. Frequency locking is necessary in various research and commercial applications where a clear relationship between the slave laser and the reference signal is needed [15]. These applications include coherent optical communication systems [16], spectroscopic measurements [15], and frequency stabilization of high-power lasers [17]. An FVC operating at 5 GHz speeds in 0.18 m CMOS technology in the electrical domain was designed [18]. Frequency locking was achieved by using an FVC circuit that reduces frequency drifts to less than 400 Hz for time scales longer than 0.1 seconds. The authors reported that this system remained locked for a couple of hours. The value of the beat frequency is not indicated [15].

This work demonstrates a voltage-based wavelength tuning of a laser using an FVC with an extended range. The FVC used is built around the LM331N, which is commercially available and cost-effective. It has a frequency response of up to 100 kHz. In this work, we extend the frequency cut-off of the FVC by trading off the linearity. We demonstrate the ability of the voltage signal from the FVC to control laser wavelength and hence the frequency, and the tuning behavior of a standard distributed feedback (DFB) laser.

2 Experimental Methods

2.1 Characterization of the FVC

The set up for the characterization of the FVC included a low frequency signal generator (Beckman Industrial Function Generator), a power supply, a mixed signal oscilloscope (Tektronix MSO54), a digital multimeter, and the FVC circuit. The setup was as shown in Figure 1. The frequency generator was connected to the FVC via a BNC cable. The input frequency was monitored via the MSO while the output voltage was monitored via the digital multimeter. The frequency generator was tuned into the hundred kHz range and changes were observed in the output voltage. Figure 1 shows the FVC circuit.

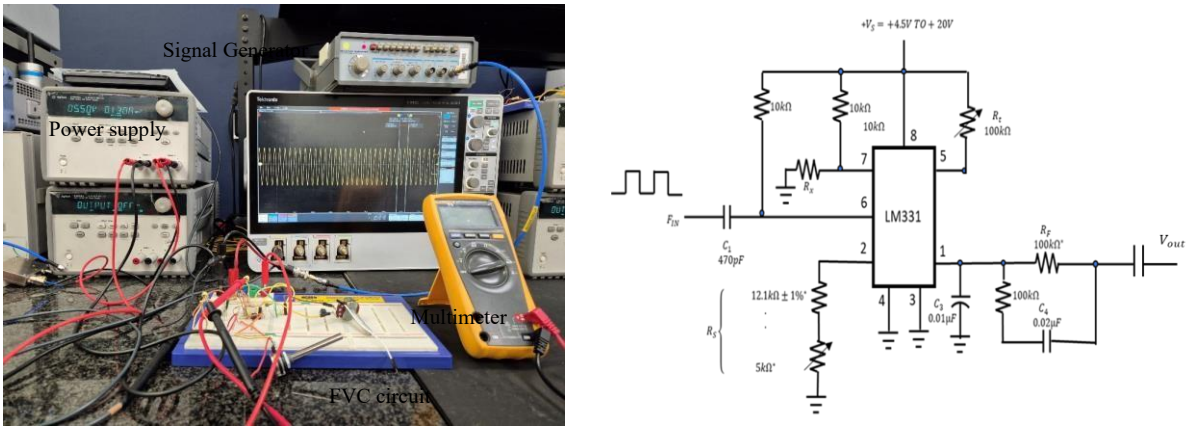

Figure 1: *(left)* Experimental set up for the characterization of the FVC, *(right)* the FVC circuit.

The experiment was repeated using an offset frequency as a result of mixing two electrical sources; a crystal oscillator as a reference signal and the Rohde & Schwarz SMB 100A signal generator producing RF signals as shown in Figure 2. The FVC requires quite a high gain, so an amplifier was used to increase the input voltage to the FVC.

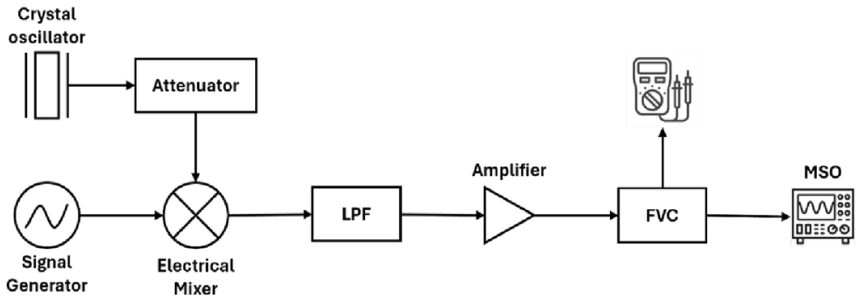

Figure 2: Experimental set up for the generation of the offset frequency and conversion to the control voltage.

2.2 Wavelength tuning of the DFB

Figure 3 shows the experimental setup for tuning the wavelength of the DFB. The beat frequency was generated using two NKT Koheras BASIK highly coherent laser modules at different but close wavelengths. The wavelengths of the master and slave lasers were 1550.1267 nm and 1550.1351 nm respectively, with a linewidth of less than 0.1 kHz. The relationship between the wavelength difference and the resultant frequency is given by Equation 1. However, characterization of the NKT lasers showed that to generate a frequency of 850 MHz, a wavelength difference of 0.0084 nm was required. The reference signal was generated using the Rubidium clock stabilized Rohde & Schwarz SMB 100A signal generator with its frequency set to match the beat frequency. The offset frequency was then passed through a low pass filter (DC – 22 MHz) with a 50 Ω impedance. The output voltage from the FVC was fed into the DFB laser and the wavelength shift as a result of changes in the offset frequency was viewed on the Anritsu MS9740B optical spectrum analyzer (OSA).

$$\Delta f = \frac{c}{\lambda^2}\Delta\lambda \tag{1}$$

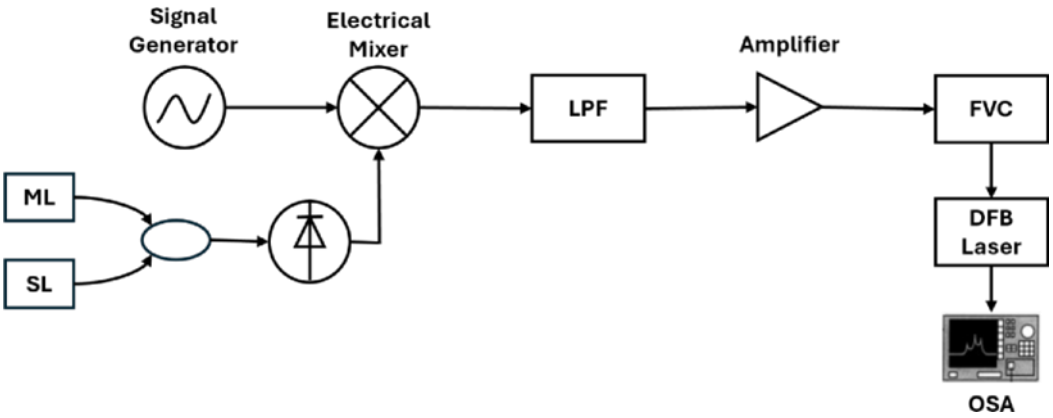

Figure 3: Experimental setup to demonstrate the tuning of the slave laser.

3 Results & Discussion

Figure 4 shows the results from the characterization of the FVC. There are two linear regions that can be used for correction of the laser; 20-40 kHz, and 45-330 kHz. At 0 MHz, the two signals are perfectly frequency matched, so the FVC output voltage is 0 V, and it remains in this state up to 25 kHz, as the FVC senses no frequency difference. At 25 kHz, the FVC outputs a voltage of 4.12 V, which would then be used for correction in an OPLL. The voltage increases linearly in both the 25–40 kHz and 45–330 kHz regions, with a steeper slope observed in the 25–40 kHz range. The change in slope at 40 kHz is due to the internal operation of the LM331N. At lower frequencies, the timing capacitor and internal current source produce higher sensitivity, resulting in a steeper slope. As frequency increases, switching delays and parasitic capacitances reduce the effective gain, producing a gentler slope. The original FVC circuit has an upper frequency limit of 100 kHz. With minor modifications, the upper limit was extended to 330 kHz, with a trade-off in linearity. This might slightly increase the latency of the feedback loop, which is negligible.

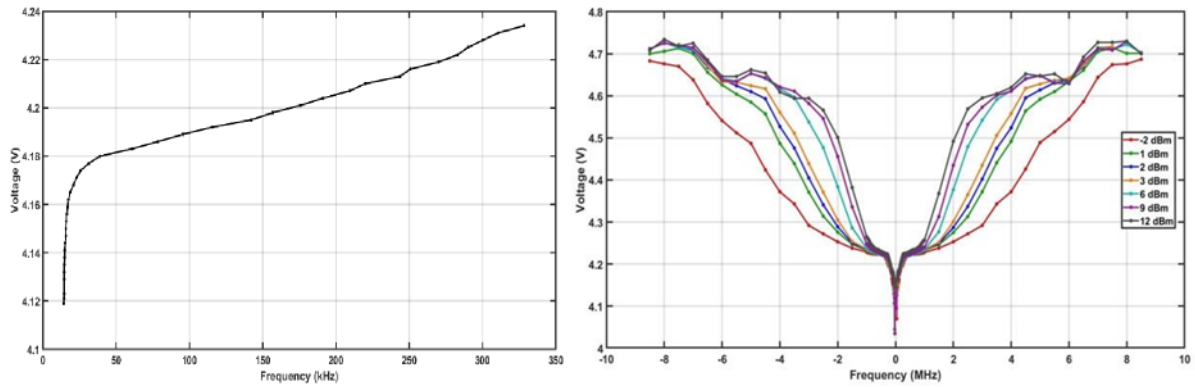

Figure 4: *(left)* Characterization of the FVC, *(right)* the frequency-voltage relationship for different signal generator powers.

This upper limit was further pushed using the setup shown in Figure 2. The results are shown in Figure 4. The voltage response was different for different signal generators. FVCs rely on amplitude-based detection. Therefore, the higher the input power, the stronger the signal, the more detectable the frequency information. The lower the input power, the weaker the signal, the more noisy or ambiguous the signal detection is. It can also be noted that FVC exhibits mirror symmetry about 0 MHz. This is because the FVC is only sensitive to the magnitude of the offset frequency, not its sign.

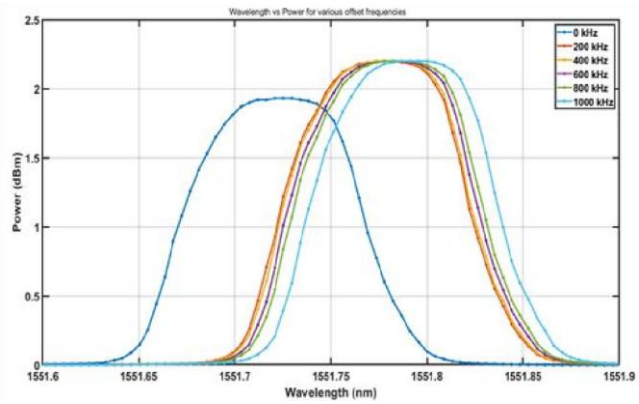

Figure 5: Wavelength tuning of the DFB laser.

The voltage from the FVC was used to drive the DFB laser, effectively tuning its wavelength. The results are shown in Figure 5. The DFB laser was initially at a wavelength of 1551.725 nm, which corresponded to a frequency offset of 0 kHz. The wavelength change was recorded after every 100 kHz. There was a significant power increase between the wavelength corresponding to a frequency offset of 0 kHz and the wavelength corresponding to an offset frequency of 100 kHz. This is because at 0 kHz, the output voltage is 0 V. However, at around 100 kHz, there was a significant increase in the output voltage, which was added to the DFB laser driver hence the increase in power. The output voltage increased gradually, leading to a gradual power increase. The DFB laser was tuned up to 1 MHz which corresponds to the maximum drift experienced by the beat frequency over a period of 1 hour.

4 Conclusion

In this experiment, the use of the LM331N FVC in frequency locking was demonstrated. The frequency limit of the FVC was extended from the standard 100 kHz to greater than 3 MHz, depending on the power of the input signal, with a trade-off in the linearity. This proof of concept demonstrates that the output voltage from the FVC can be used to tune the wavelength of the slave laser for stabilization. Such signals can be implemented in an OPLL when used to drive a slave laser to control its frequency relative to another coherent laser. An optical phase locked loop is used to lock the phase and frequency of a slave laser to master laser to ensure a stable frequency, which is necessary in coherent communication systems. When working with highly unstable frequencies, it is necessary to frequency lock before phase locking, hence the need for a frequency-to-voltage converter.

5 Acknowlegement

The authors gratefully acknowledge the African Laser Centre (ALC) for their financial support, as well as Telkom, the Centre for Broadband Communication, and Nelson Mandela University for providing laboratory resources and technical assistance.

References

[1] R. Xu *et al.*, “An optimized optical phase-locked loop with high bandwidth and stability for Raman laser generation,” *Phys. Scr.*, vol. 100, no. 6, p. 065014, June 2025, doi: 10.1088/1402-4896/add65f.

[2] K. Zeb *et al.*, “Broadband Optical Heterodyne Millimeter-Wave-over-Fibre Wireless Links Based on a Quantum Dash Dual-Wavelength DFB Laser,” *J. Light. Technol.*, vol. 40, no. 12, pp. 3698–3708, June 2022, doi: 10.1109/jlt.2022.3154652.

[3] K. Balakier, L. Ponnampalam, M. J. Fice, C. C. Renaud, and A. J. Seeds, “Integrated Semiconductor Laser Optical Phase Lock Loops,” *IEEE J. Sel. Top. Quantum Electron.*, vol. 24, no. 1, pp. 1–12, Jan. 2018, doi: 10.1109/JSTQE.2017.2711581.

[4] K. Zeb *et al.*, “A Quantum-Dash Dual-Wavelength DFB Laser for Optical Millimeter-Wave Radio-overFibre Systems,” in *Optical Fibre Communication Conference (OFC) 2021 (2021), paper W1J.5*, Optica Publishing Group, June 2021, p. W1J.5. doi: 10.1364/OFC.2021.W1J.5.

[5] H.-Y. Wang, C.-H. Cheng, B. Su, and G.-R. Lin, “QAM-GFDM of Dual-Mode VCSEL Mixed 28-GHz MMW Carrier for Fibre-Wireless Link,” *J. Light. Technol.*, vol. 39, no. 19, pp. 6076–6084, Oct. 2021.

[6] K. Balakier *et al.*, "Optical injection locking of monolithically integrated photonic source for generation of high purity signals above 100 GHz," *Opt. Express*, vol. 22, no. 24, p. 29404, Dec. 2014, doi: 10.1364/OE.22.029404.
[7] S. Fukushima, C. F. C. Silva, Y. Muramoto, and A. J. Seeds, "Optoelectronic millimeter-wave synthesis using an optical frequency comb Generator, optically injection locked lasers, and a unitraveling-carrier photodiode," *J. Light. Technol.*, vol. 21, no. 12, pp. 3043–3051, Dec. 2003, doi: 10.1109/JLT.2003.822250.
[8] G. J. Schneider, J. A. Murakowski, C. A. Schuetz, S. Shi, and D. W. Prather, "Radiofrequency signalgeneration system with over seven octaves of continuous tuning.," *Nat. Photonics*, vol. 7, no. 2, pp. 118– 122, Feb. 2013, doi: 10.1038/nphoton.2012.339.
[9] M. J. Fice, A. Chiuchiarelli, E. Ciaramella, and A. J. Seeds, "Homodyne Coherent Optical Receiver Using an Optical Injection Phase-Lock Loop," *J. Light. Technol.*, vol. 29, no. 8, pp. 1152–1164, Apr. 2011, doi: 10.1109/JLT.2011.2115993.
[10] T. Von Lerber, S. Honkanen, A. Tervonen, H. Ludvigsen, and F. Küppers, "Optical clock recovery methods: Review (Invited)," *Opt. Fibre Technol.*, vol. 15, no. 4, pp. 363–372, Aug. 2009, doi: 10.1016/j.yofte.2009.03.006.
[11] P. G. Goetz, H. Eisele, K.-C. Syao, and P. Bhattacharya, "1.55-um optical phase-locked loop operation with large loop delays and monolithically integrated p-i-n/HBT photoreceivers," in *Optoelectronic Integrated Circuits*, SPIE, Jan. 1997, pp. 243–249. doi: 10.1117/12.264223.
[12] N. Satyan, W. Liang, A. Kewitsch, G. Rakuljic, and A. Yariv, "Coherent Power Combination of Semiconductor Lasers Using Optical Phase-Lock Loops," *IEEE J. Sel. Top. Quantum Electron.*, vol. 15, no. 2, pp. 240–247, Mar. 2009, doi: 10.1109/JSTQE.2008.2011490.
[13] A. J. Seeds *et al.*, "Coherent terahertz photonics," *Opt. Express*, vol. 21, no. 19, p. 22988, Sept. 2013, doi: 10.1364/OE.21.022988.
[14] K. Kikuchi, T. Okoshi, M. Nagamatsu, and N. Henmi, "Degradation of bit-error rate in coherent optical communications due to spectral spread of the transmitter and the local oscillator," *J. Light. Technol.*, vol. 2, no. 6, pp. 1024–1033, Dec. 1984, doi: 10.1109/JLT.1984.1073700.
[15] T. Stace, A. N. Luiten, and R. P. Kovacich, "Laser offset-frequency locking using a frequency-to-voltage converter," *Meas. Sci. Technol.*, vol. 9, no. 9, pp. 1635–1637, Sept. 1998, doi: 10.1088/0957-0233/9/9/038.
[16] J. Harrison and A. Mooradian, "Linewidth and offset frequency locking of external cavity GaAlAs lasers," *IEEE J. Quantum Electron.*, vol. 25, no. 6, pp. 1152–1155, June 1989, doi: 10.1109/3.29240.
[17] M. Zhu and J. L. Hall, "Stabilization of optical phase/frequency of a laser system: application to a commercial dye laser with an external stabilizer," *JOSA B*, vol. 10, no. 5, pp. 802–816, May 1993, doi: 10.1364/JOSAB.10.000802.
[18] Hung Tien Bui and Y. Savaria, "Design of a High-Speed Differential Frequency-to-Voltage Converter and Its Application in a 5-GHz Frequency-Locked Loop," *IEEE Trans. Circuits Syst. Regul. Pap.*, vol. 55, no. 3, pp. 766–774, Apr. 2008, doi: 10.1109/TCSI.2008.916397.

Synthesis and characterization of Cerium III ion doped zinc selenide thin films

D. D. Hile[1,2,*], H. C. Swart[3], L. F. Koao[4], S. V. Motloung[5], R. E. Kroon[3], P. Mkwae[1], A. Reyes-Rojas[6], C. L. Ndlangamandla[1]

[1] Department of Physics, University of Zululand, KwaDlangezwa 3886, South Africa
[2] Department of Industrial Physics, Joseph Sarwuan Tarka University, Makurdi, Nigeria
[3] Department of Physics, University of the Free State, ZA9300, Bloemfontein, South Africa
[4] Department of Physics, University of the Free State, 9866, Phuthaditjhaba, South Africa
[5] Directorate: Postgraduate Studies, Central University of Technology, Private Bag X 20539, Bloemfontein, 9300, South Africa
[6] Materials Science Department. Centro de Investigacion' en Materiales Avanzados, S.C., Miguel de Cervantes 120, Complejo Industrial Chihuahua, 31109, Chihuahua, CHIH, Mexico

E-mail: HileD@unizulu.ac.za

Abstract. Ce^{3+} doped ZnSe thin films were synthesized on non-conducting glass slides via chemical bath deposition and annealed at various durations (0–2.0 h) to investigate their structural, morphological, optical, and luminescence properties. X-ray diffraction confirmed the formation of hexagonal ZnSe with improved crystallinity upon annealing. SEM and AFM analyses revealed morphology evolution and reduced surface roughness with increasing annealing time, peaking at 1.5 h. UV-Vis spectroscopy showed dual absorption edges attributed to ZnSe and Ce^{3+} transitions, with a corresponding band gap increase from 3.60 to 3.92 eV. Photoluminescence studies exhibited enhanced blue-green emissions due to Ce^{3+} 5d → 4f transitions, with maximum intensity at 1.5 h. CIE analysis confirmed emission in the blue region with high color purity (69 –76%). This work demonstrates, for the first time, the tunability of structural and luminescence properties of Ce^{3+}-doped ZnSe thin films synthesized by chemical bath deposition through controlled annealing duration, enabling optimized blue–green emissions with high color purity for optoelectronic applications.

1. Introduction

Zinc selenide (ZnSe) is a prominent II–VI semiconductor material known for its direct wide band gap (~2.7 eV at room temperature), high transparency in the visible range, and strong photoluminescent response, making it a suitable candidate for optoelectronic and luminescence-based applications [1]. Its unique properties enable a wide range of uses in blue-green light-emitting diodes (LEDs), flat panel displays, laser diodes, and optical sensors. However, its luminescence performance can be further enhanced through suitable doping strategies [2]. Among the various dopants, rare-earth ions such as trivalent cerium (Ce^{3+}) have gained attention due to their characteristic 4f–5d electronic transitions, which can significantly enhance emission in the blue to green region of the spectrum [3]. Ce^{3+} doping in semiconductor hosts can improve photoluminescence efficiency and introduce additional radiative recombination centers, thus broadening the potential of ZnSe thin films in display and lighting technologies. Despite

extensive work on ZnSe thin films, little attention has been given to Ce^{3+} doping via chemical bath deposition (CBD) and the role of annealing duration on structural and luminescent properties.

In this study, Ce^{3+}-doped ZnSe (ZnSe:Ce^{3+}) thin films were synthesized using the CBD technique, a low-cost and scalable method suitable for producing uniform and adherent films on glass substrates [4]. CBD offers good control over film thickness, composition, and surface morphology through optimization of deposition parameters such as bath composition, pH, temperature, and deposition time. Moreover, it provides a flexible route for ion incorporation into semiconductor matrices at relatively low processing temperatures.

To further influence the structural and optical characteristics, the deposited films were subjected to post-deposition annealing at various durations ranging from 0 to 2.0 hours. Annealing is known to improve crystallinity, reduce defect states, and enhance dopant activation, all of which can contribute to improved luminescence behavior. This study focuses on the effect of Ce^{3+} doping and annealing duration on the structural, morphological, optical, and photoluminescence properties of ZnSe thin films, with the goal of optimizing their performance for potential use in luminescent devices.

2. Methodology

Before the thin films deposition commenced, sodium selenosulphate Na_2SeSO_3 was prepared from selenium black powder (>99%), sodium sulfite (99.9%) and deionized water using a mixture ratio of 1:5:50, respectively. The mixture was refluxed at 80℃ for 4 h and a clear solution was obtained and used in this work. The ZnSe:Ce^{3+} thin films were deposited using a fixed volume of 0.1 M of zinc acetate (99.9%), 0.8 molar percentage of cerium (III) nitrate hexahydrate (99%) ions relative to the Zn^{2+} precursor concentration, hydrazine monohydrate (80%) and 0.6 M of the [Na_2SeSO_3]. After all precursors were thoroughly mixed in a 100 mL beaker, a clean glass slide was vertically inserted in the solution and reaction was allowed at 80 ℃ with gently stirring via hot plate. The deposition process lasted for 2 h after which the coated slide was removed, rinsed in deionized water to remove the loosely attached particles after which it was dried. The same process was repeated for four more times making a total of five samples after which one was retained as deposited (sample 0 h) while the other four were annealed at 0.5, 1.0, 1.5 and 2 h before taken for characterization. The annealing was done in an open air furnace and all the samples were allowed to cool down naturally.

3. Results and Discussion

3.1 X-ray diffraction (XRD)

The XRD used in this work is a Grazing incidence X-ray diffraction using an Empyrean diffractometer with CuK (λ = 1.54056 Å) at a grazing incidence angle of 0.3º. The samples as presented in Figure 1 were scanned from 2θ angles of 20 - 70º and all of them displayed hexagonal structure patterns with peaks at 25.88, 27.33, 29.38, 38.18, 45.48, 47.38, 49.38 and 53.82º corresponding to the (100), (002), (101), (102), (110), (103), (112) and (202) planes, respectively according to the JCPDS card number 15-0105, space group P63mc. No secondary peaks were found except for the 0 h sample, which show unreacted peaks of Se ions. The absence of either Ce-based peaks or any foreign impurity shows successful incorporation of the Ce^{3+} into the ZnSe lattice. The peak intensity of the (002) diffraction increases with annealing time which can be ascribed to improved crystallinity due to removal of residual defects incurred during the thin films deposition. The crystallize size *D* (nm) and the strain were estimated from the most intense peaks using Debye-Scherer formula [5]. The estimated result as presented in Table 1 shows increase in *D* (nm) with annealing time up to 1.5 h and then decreased slightly when compare to the 0 h sample. The strain values are small suggesting that the films are free of severe stress.

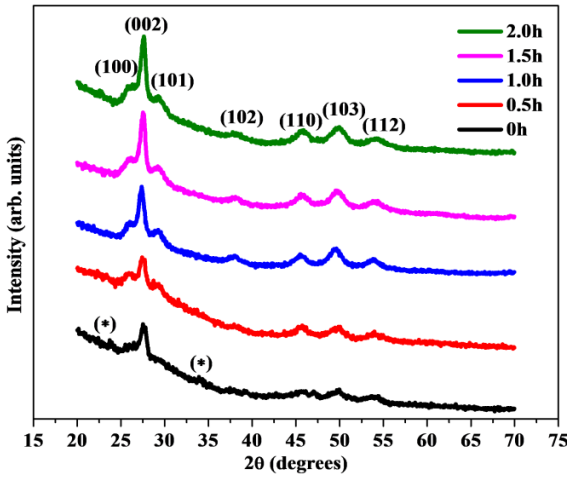

Figure 1. XRD diffraction patterns of the deposited ZnSe:Ce^{3+} films with different annealing time

Table 1. Structural parameters of the deposited ZnSe:Ce^{3+} thin films with different annealing time

Sample ID (h)	2θ (º)	FWHM	Intensity (arb. unit)	D(nm)	ε(x10^{-3})	Bandgap (eV)
0	27.52	0.80	1284	9	1.64	3.60
0.5	27.42	0.95	1260	9	1.7	3.72
1.0	27.37	0.80	2001	11	1.43	3.92
1.5	27.52	0.80	2495	11	1.43	3.92
2.0	27.62	0.85	2686	10	1.51	3.87

3.2 Scanning electron microscopy/ Surface Topography Analysis (AFM)

The surface morphology of the ZnSe:Ce^{3+}thin films annealed at different time intervals was examined using a JEOL JSM-7800F field emission scanning electron microscope, as shown in Figure 2 (a). The samples showed some variation in morphology, which arises solely due to differences in annealing time. At 0 h, the surface is characterized by randomly oriented nanosheets with sharp edges and high density, indicating a disordered nucleation process. Upon annealing at 0.5 h and 1.0 h, the sheets become more distinct and slightly more aligned, suggesting the onset of crystallite reorganization. At 1.5 h and 2.0 h, the nanosheets evolve into larger, more well-defined triangular structures with smoother surfaces and increased inter-particle spacing. This morphological evolution indicates enhanced crystallinity and grain coalescence due to thermal energy input during annealing. These changes are consistent with grain growth and surface energy minimization mechanisms, where prolonged thermal treatment facilitates the diffusion and reorientation of atoms, promoting better-defined and less defective crystalline structures as observed in the XRD results. This improved morphology is expected to enhance optical properties such as photoluminescence, as surface defects and grain boundaries generally act as non-radiative recombination centers.

Atomic force microscopy (AFM) was employed to examine the surface topography and roughness evolution of ZnSe:Ce^{3+} thin films annealed at different time intervals (0–2.0 h), as presented in Figure 2 (b). The analysis was performed over a scan area of 5 µm × 5 µm. The 2D AFM images clearly show a gradual smoothing of the surface with increasing annealing time from 0 h to 1.5 h, followed by a slight increase in roughness at 2.0 h. Initially, the 0 h sample displays a highly corrugated surface with large surface features and pronounced height variations (Ra = 77.92 nm, Rz = 674.53 nm). As annealing progresses to 1.5 h, the surface becomes more compact and uniform, with the average roughness (Ra) decreasing to 32.41 nm and maximum peak-to-valley height (Rz) to 304.47 nm. This suggests improved atomic diffusion and reorganization on the film surface due to the annealing, leading to

densification and smoothing of the film. However, at 2.0 h, a slight increase in surface roughness is observed (Ra = 43.26 nm, Rz = 423.35 nm), which may be attributed to localized grain growth or surface recrystallization processes. The root mean square roughness (Rq), maximum profile peak height (Rp), and maximum profile valley depth (Rv) follow a similar trend, further confirming the morphological transition. These observations highlight the critical role of annealing time in optimizing surface quality, which is crucial for enhancing optical and electronic performance, as smoother surfaces reduce scattering centers and trap states.

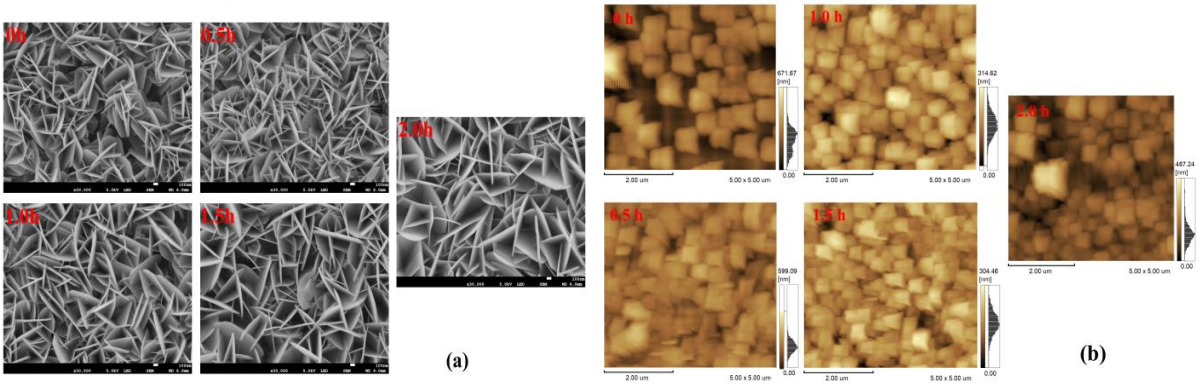

Figure 2. (a) SEM micrographs of ZnSe:Ce^{3+} thin films (b) 2D AFM images of ZnSe:Ce^{3+} thin films annealed at 0-2.0 h, showing surface evolution and roughness variation.

3.3 UV-Visible Absorption/Photoluminescence (PL)

The UV-Vis absorption spectra of the ZnSe:Ce^{3+} thin films annealed for different durations reveal two distinct absorption edges: a sharp edge at approximately 350 nm and a broader, less steep edge near 460 nm (circled with doted lines), as shown in Figure 3 (a). The absorption edge around 460 nm is attributed to the intrinsic band-to-band transition of the ZnSe host matrix, which is consistent with the known band gap of bulk ZnSe (~2.7 eV). This edge corresponds to the fundamental absorption of the semiconductor and reflects the transition of electrons from the valence band to the conduction band. The second absorption feature, observed around 350 nm (~3.5 eV), is likely associated with Ce^{3+}-related optical transitions, particularly the $4f^1 \rightarrow 5d^1$ allowed transition or may arise from Ce-induced defect or impurity states, which act as intermediate absorption levels between the valence and conduction bands. The presence of this additional absorption band suggests successful incorporation of Ce^{3+} ions into the ZnSe lattice and the creation of localized energy levels within the band gap. As annealing time increases, a slight blue shift (shift toward shorter wavelengths) in the absorption edge is observed from 0 h to 1.5 h, followed by a minor red shift at 2.0 h. This trend suggests increases in the optical band gap. The optical band gaps were evaluated from the graph of the square of absorbance (A^2) against the photon energy [6] as shown in Figure 3(b). The evaluated band gap values are between 3.60 – 3.92 eV with increased annealing time as presented in Table 1. The band gap increase due to annealing-induced modifications in the film microstructure. The band gap widening in this range is consistent with SEM and AFM observations of grain refinement and surface smoothening.

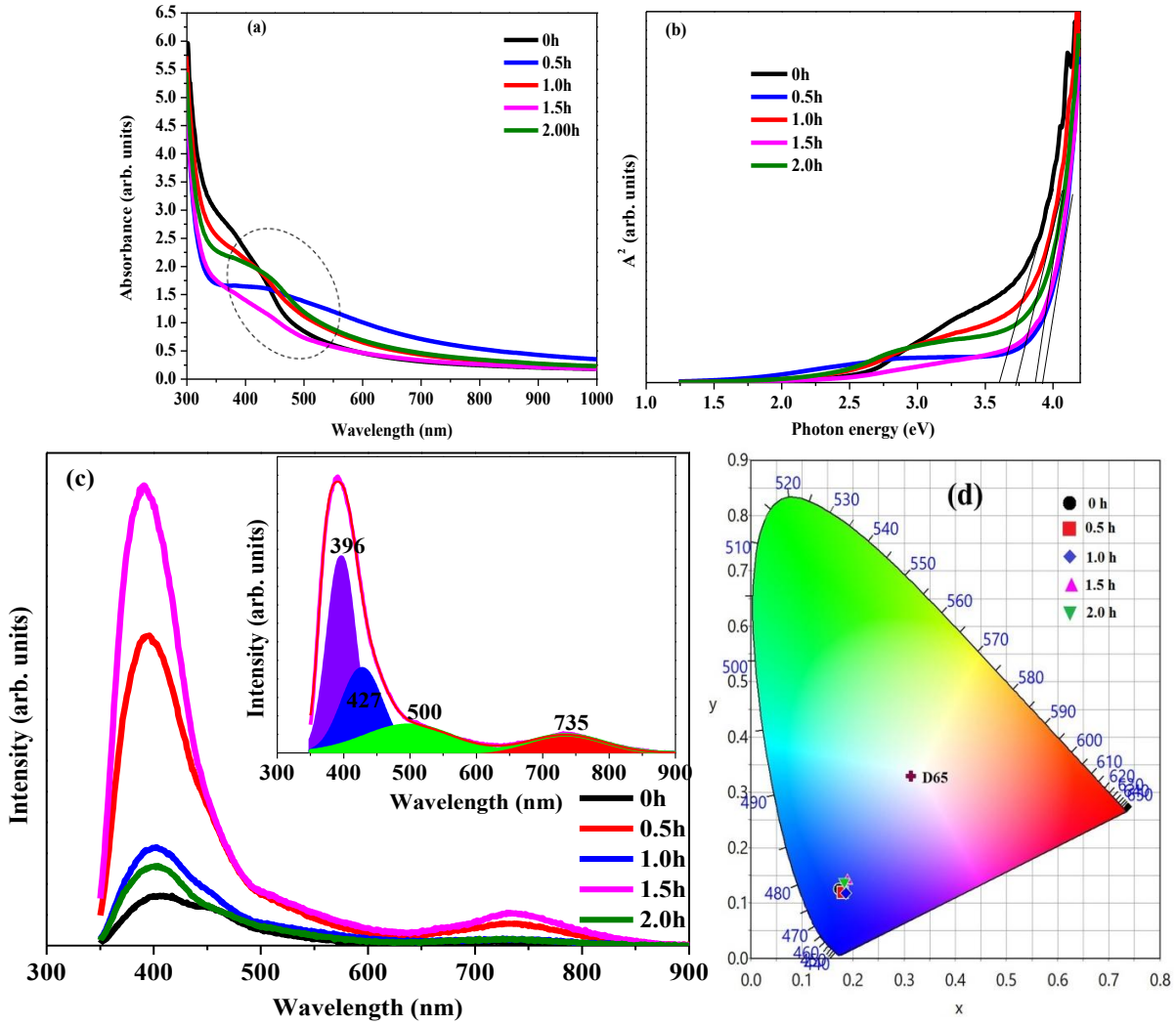

Figure 3 (a): UV-Vis absorbance spectra (b) Optical band gap (c) PL spectra of ZnSe:Ce^{3+} thin films (Inset: Gaussian deconvolution of the 1.5 h sample (d) the color chromaticity diagram of ZnSe:Ce^{3+} thin films.

The room-temperature PL of ZnSe:Ce^{3+} thin films annealed for various time intervals (0–2.0 h) was measured using a Kimmon IK Series 325 nm He-Cd laser, Horiba iHR320 spectrometer and Peltier cooled Hamamatsu R943-02 photomultiplier tube connected to a SR830 lock-in amplifier (Stanford Research Systems) and the spectra are shown in Figure 3(c). The PL spectra exhibit prominent emission bands in the UV and red regions as well as a broad shoulder in the visible spectral region. The emission intensity varies significantly with annealing time, reflecting the influence of thermal treatment on dopant activation, defect passivation, and crystallinity. The 0 h sample shows relatively weak PL intensity, indicating the presence of numerous non-radiative recombination centers such as surface defects and poor crystallinity. As annealing progresses, the PL intensity increases and reaches a maximum at 1.5 h, suggesting optimal thermal activation of the Ce^{3+} dopant and reduction of quenching centers. Beyond this point (2.0 h), a slight decrease in PL intensity is observed, likely due to dopant clustering or recrystallization effects that introduce new non-radiative pathways. To gain more insight into the emission characteristics, the spectrum of the 1.5 h annealed sample was deconvoluted (inset of Figure 3(c) middle), revealing two major peaks centered around ~470 nm (blue) and ~520 nm (green) in addition to the 394 nm (UV) and 735 nm (red). The UV and red peaks are due to non-stoichiometric point defect in ZnSe [7] while the blue and green emissions correspond to the Ce^{3+} 5d → 4f

transitions split by the crystal field and spin-orbit coupling effects within the ZnSe host matrix [3]. The observed enhancement and spectral purity of the PL emissions confirm that the ZnSe:Ce^{3+} thin films synthesized by CBD and thermally optimized at 1.5 h possess excellent potential for blue-green optoelectronic or phosphor applications.

The Commission Internationale de L'Eclairage (CIE) chromaticity study of the ZnSe:Ce^{3+} thin films samples is shown in Figure 3 (d). All the plotted coordinates fall in the blue region of the CIE diagram irrespective of the annealing period. The color purity was estimated using equation (1) **[8]**

$$Color\ purity = \sqrt{\frac{(x_s - x_i)^2 + (y_s - y_i)^2}{(x_d - x_i)^2 + (y_d - y_i)^2}}\ X\ 100\% \quad (1)$$

where x_s and y_s are the CIE source coordinates, x_i = 0.313 and y_i = 0.329 are the standard illuminant (D65) coordinates, and x_d and y_d are the coordinates of the dominants wavelengths. The estimated color purity of the thin films samples is between 69 – 76%.

Color purity shows the level of closeness of the emitted color to the D65. Higher color purity shows more color saturation thereby reflecting the more spectrally pure color at the dominants wavelengths while lesser color purity however shows that the spectral color is unsaturated and so it is closer to the D65 (white point) [8].

4. Conclusion

Ce^{3+}-doped ZnSe thin films were successfully synthesized by chemical bath deposition and optimized through post-deposition annealing. The films exhibited enhanced crystallinity, smoother morphology, and reduced surface roughness with increasing annealing time, reaching optimal properties at 1.5 h. Optical studies revealed dual absorption edges, band gap widening (3.60–3.92 eV), and strong blue-green photoluminescence attributed to Ce^{3+} 5d → 4f transitions. CIE analysis confirmed emission in the blue region with high color purity (69–76%). These results demonstrate the tunability of ZnSe:Ce^{3+} thin films via thermal processing, highlighting their potential for blue-green optoelectronic devices and phosphor-based lighting applications.

Acknowledgments

The authors affiliated with UNIZULU wish to acknowledge the research office, the National Research Foundation, UID: 99224, the University of the Free State, the South African Research Chairs Initiative of the Department of Science and Technology, the National Research Fund (NRF) (Grant 84415) and NRF incentive funding for rated researchers (Grant No: 126914) for the research support.

References

[1] S. Sheokand, D.S. Ahlawat, A. Singh, "Nickel doped zinc selenide nanoparticles for spin based dilute magnetic semiconductor applications", *Micro and Nanostructructures* , vol. 185, p. 207711, 2024. doi: https://doi.org/10.1016/j.micrna.2023.207711.

[2] C. Emir, A. Tataroglu, U. Gökmen, S.B. Ocak, "Analysis of the structural and optical characteristics of ZnSe thin films as interface layer", *Journal of Materials Science: Materials in Electronics,* vol. 36, p.168, 2025, doi:https://doi.org/10.1007/s10854-025-14221-3.

[3] N.I. Razip, M. Novita, K. Ogasawara, "Two-step model for predicting 4f→ 5d transition energies of Ce^{3+} in garnet-type oxides based on first-principles calculations and machine learning", *Optical Materials*, vol.159 p.116653, 2025, doi: https://doi.org/10.1016/j.optmat.2025.116653.

[4] A.Z. Arsad, A.W.M. Zuhdi, S.F.Abdullah, C.F. Chau, A. Ghazali, I. Ahmad, W.S.W. Abdullah, "Effect of Chemical Bath Deposition Variables on the Properties of Zinc Sulfide Thin Films:A Review", *Molecules* vol. 28, p.2780, 2023, doi: https://doi.org/10.3390/molecules28062780.

[5] V. Mehta, D. Shikha, J. Sharma, R.P. Chauhan, "Temperature effect on properties of chemical induced nanocrystalline ZnSe thin films", *Journal of Materials Science: Materials in Electronics,* vol. 29, pp. 8801–8808, 2018, doi:10.1007/s10854-018-8897-3.

[6] O.K., Echendu, F.B., Dejene, I.M., Dharmadasa, F.C., Eze, "Characteristics of Nanocrystallite-CdS Produced by Low-Cost Electrochemical Technique for Thin Film Photovoltaic Application: The Influence of Deposition Voltage", *International Journal of Photoenergy,* vol. 3989432, pp. 1–13(2017), doi: https://doi.org/10.1155/2017/3989432.

[7] D.D. Hile, L.F. Koao, H.C. Swart, S.V. Motloung, I. Ahemen, C.L. Ndlangamandla, "The effect of selenium ion concentration on zinc selenide thin films prepared by a photo-assisted chemical bath deposition method", *Semiconductor Science and Technology,* vol.39, p. 125001, 2024, doi: https://doi.org/10.1088/1361-6641/ad8813.

[8] D.D. Hile, H.C. Swart, S.V. Motloung, V.B. Pawade, R.E. Kroon, K.O. Egbo, L.F. Koao, Phase transformation on zinc selenide thin films deposited by photo-assisted chemical bath method: The effect of annealing temperature, *Materials Science in Semiconductor Processing,* vol.115, p. 105118, 2020, doi: https://doi.org/10.1016/j.mssp.2020.105118.

This page intentionally left blank.

Label-free optical biosensing as an alternative for HIV-1 drug-resistant mutation detection

MP Mcoyi[1], MY Lugongolo[1], K Mpofu[1] and P Mthunzi-Kufa[2]

[1]Council for Scientific and Industrial Research (CSIR), Photonics Centre, Pretoria, South Africa
[2]College of Science, Engineering, and Technology, University of South Africa, Gauteng, South Africa

E-mail: MMcoyi@csir.co.za

Abstract. Collectively, conventional assays for HIV-1 drug-resistant mutation detection have established the basis for understanding the mechanisms involved in drug-resistant mutations and have thus led to the development of antiretroviral therapy (ART) regimen that targets and suppress drug-resistant variants. Assays like Sanger sequencing, Next Generation Sequencing (NGS), and Polymerase Chain Reaction (PCR) are considered gold standards for HIV-1 drug-resistant mutation detection and have since been used to inform global guidelines, particularly the World Health Organization (WHO) resistance monitoring protocols. However, their significant impact has been hindered by high costs, turnaround time, speed, accessibility, complexity, and multiplexing. Hence, this study uses optical biosensors based on localized surface plasmon resonance spectroscopy as an alternative drug-resistant detection technique to counter some of the conventional assay shortfalls. Optical biosensors offer cost effectiveness, simple and potential for point-of-care development, which is vital particularly in resource-limited settings. In this study, localized surface plasmon resonance was successfully optimized for HIV-1 drug-resistant mutation detection.

1. Introduction

It has been more than four decades since the identification of human immunodeficiency virus (HIV-1), a causative agent of the acquired immunodeficiency syndrome (AIDS) and the first case was reported back in the year 1981 [1]. According to a report by UNAIDS/WHO, about 38.4 million individuals worldwide have HIV/AIDS (Ghosh, 2023). Also, about 40.1 million people have died because of HIV/AIDS since it started [2]. In the year 1991, the World Health Organization (WHO) predicted that 40 million people would be infected globally by year 2000 [3]. Since the 1980s, the fight against HIV has seen major progress with early efforts focused on community involvement through pleading for support, which resulted in making treatment affordable [4]. The introduction of highly active antiretroviral therapy (HAART) in the mid-90s revolutionized treatment by combining drugs to target the virus at multiple stages [5]. New drug classes emerged, and antiretroviral therapy (ART) proved highly effective in suppressing the virus [2]. By 2020, an estimated 87% of HIV-positive individuals aware of their status were receiving ART, with 90% of those on treatment achieving viral suppression [1]. However, challenges like limited access, stigma, and drug resistance remain counterproductive in the detection and subsequent mitigation of the spread of the virus. The emergence of drug-resistant mutations poses a significant and ongoing challenge to the efficacy of antiretroviral therapy (ART) [5]. Drug resistance occurs when the virus mutates, rendering antiretroviral drugs less effective in suppressing HIV replication. This can lead to virologic failure, where the virus remains detectable despite

treatment, increasing the risk of HIV-related illness, transmission, and the need for regimen adjustments [6]. Strategies such as regular monitoring of viral load and resistance testing are crucial for early detection and management of virologic failure. Combination therapies targeting multiple stages of the viral life cycle are being explored to prevent drug resistance and optimize treatment outcomes [6, 7]. Currently, drug-resistance mutations are detected through phenotypic assays and genotypic assays, including Sanger, next-generation sequencing, and Polymerase Chain Reaction (PCR), among other molecular assays. However, their significant impact has been hindered by high costs, turnaround time, speed, accessibility, complexity, and multiplexing.

This study proposes the use of label-free optical biosensors as an alternative for HIV-1 drug-resistant mutation detection. Optical biosensors are tools used to detect biological molecules. With advantages such as sensitivity, real-time monitoring, specificity, multiplexing capabilities, and not requiring biological labels for signal production. Optical biosensors can detect subtle concentrations of analytes, monitor interactions in real-time, provide specific detection of target molecules, and simultaneously detect multiple analytes in a single sample. Two key types of optical biosensors are Surface Plasmon Resonance (SPR) and Localized Surface Plasmon Resonance (LSPR). SPR occurs when light interacts with a metal surface, leading to shifts in resonance due to changes in the refractive index of the local dielectric environment. LSPR involves the excitation of localized surface plasmons in metallic nanoparticles, providing enhanced sensitivity for detecting subtle biomolecular interactions [8]. This study employs LSPR for HIV-1 drug-resistant mutation detection and was optimized for this application.

2. Methods and Materials

2.1 Materials

The citrate stabilized spherical gold nanoparticles (AuNPs) used in this study were purchased at Cytodiagnostics (Burlington, Canada). Phosphate buffered saline (PBS), nuclease-free water (H_2O), Biotin, Neutravidin, and Acetone were all purchased at Inqaba, South Africa. The (3-Aminopropyl) triethoxysilane (APTES), Polyethylene glycol (PEG), 1-Ethyl-3-diaminopropyl carbodiimide (EDC), N-hydroxysuccinimide (NHS) were purchased at Thermo-Fisher Scientific, South Africa. Isopropanol and absolute ethanol were used in this experimental approach.

2.2 Cleaning the slides and APTES incubation

The glass slides were cleaned via sonication in a glass Coplin staining jar of acetone, isopropanol, ethanol, and water for 5 minutes, respectively. The glass slides were dried with nitrogen (N2) gas, then they were dry baked on a hot plate (80 °C) for 10 minutes. To increase the surface energy and adhesion strength, the slides were exposed to O_2 plasma treatment. The slides were then incubated in a glass Coplin staining jar with APTES for 3 hours before washing them in glass Coplin staining jars containing toluene, methanol, ethanol, and water for 5 minutes, respectively. The glass slides were dried with N_2 gas and were ready to use immediately.

2.3 Conjugation of Gold Nanoparticles with PEG

To functionalize gold nanoparticles (AuNPs) with polyethylene glycol (PEG), prevent non-specific binding, and improve stability, 700 µl of AuNPs (60 nm) were centrifuged at 0.5 g for 30 minutes. After 30 minutes, the supernatant was decanted, and the absorbance of the AuNPs was screened through the UV-Vis spectrometer before diluting them with nuclease-free H_2O. Diluted AuNPs (5:10 in nuclease-free water) were conjugated with 0.2 mM of PEG to form a covalent (-SH-Au) bond and incubated for 3 hours. The unbound materials were centrifuged at 0.5 g for 15 minutes to separate the PEGylated AuNPs. Then the supernatant was removed and AuNPs were resuspended in fresh PBS. To activate the PEGylated AuNPs with NHS and EDC for covalent immobilization, an NHS/EDC solution was prepared by dissolving EDC and NHS with concentrations of 5 mg/ml in dH_2O water. Thereafter, the NHS/EDC mixture was mixed well with PEGylated AuNPs at room temperature for 1 hour in an orbital shaker. Following 1 hour incubation, the solution was centrifuged at 0.5 g for 15 minutes to pellet AuNPs and the supernatant decanted, and the AuNPs were resuspended in fresh PBS.

2.4 Neutravidin Immobilization

To immobilize Neutravidin onto NHS/EDC-activated AuNPs, Neutravidin solution was added to the NHS/EDC-activated AuNPs. The solution was incubated at room temperature on an orbital shaker for 2 hours. The solution was centrifuged for 15 minutes to remove unbound Neutravidin, and the pellet was resuspended in fresh PBS. To conjugate the biotin-labelled probe to neutravidin-functionalized AuNPs, the biotinylated probe was diluted to 5 µg/mL in PBS. Then, the biotinylated capture probe solution was added to the Neutravidin-functionalized AuNPs in a 1:10 ratio. The mixture was incubated at room temperature on an orbital shaker for 2 hours. Post 2 hours of incubation, the mixture was centrifuged at 0.5 g for 15 minutes, and the pellet was resuspended in PBS and ready

for hybridization experiments.

2.5 Data processing

The spectra were processed through OriginPro software (2025b) to present clarity and analysis. Raw data were baseline corrected to account for the setup offset and minor background noise. The overall trend and the plasmonic peak were fitted with a Hill-Langmuir model using nonlinear least-squares regression algorithm with increased regression coefficients (R^2). Smoothing was applied using Savitzky-Golay at polynomial order of 2 and frame size of 5 to minimize artifacts while preserving the peak position and shape. Microsoft Excel was used to also used forAbsorbance spectra were computed as $A = -\log_{10}(I/I_o)$ where I is the transmitted intensity and I_0 is the reference from a blank solution.

3. Results and Discussion

Gold nanoparticles (AuNPs) of three different sizes, 50 nm, 60 nm, and 90 nm were characterized for their absorption peak wavelengths. The screening of the peak wavelengths for each size helped in selecting the most suitable size for this study. The chosen geometry would enable us to evaluate the LSPR peak wavelength shift sensitivity with the highest absorbance intensity for downstream experimental procedures. As shown in Figure 1, the UV-Vis spectra indicates that 60 nm AuNPs have the highest absorption, and the selection is further supported by Mayer & Hafner (2011) [9], who noted that 60 nm AuNPs are considered ideal for balancing peak sharpness, as also shown in Figure 1. The 90 nm exhibits 0.372, the lowest absorbance intensity and a wavelength peak at 640 nm, 60 nm exhibits 0.659, the highest absorbance intensity at 580 nm, and finally the 50 nm exhibits 0.478 absorbance intensity at 577 nm. The data below represents preliminary characterization data for different sized spherical gold nanoparticles to guide the selection of the gold nanoparticles size for the optimization of the experimental approach.

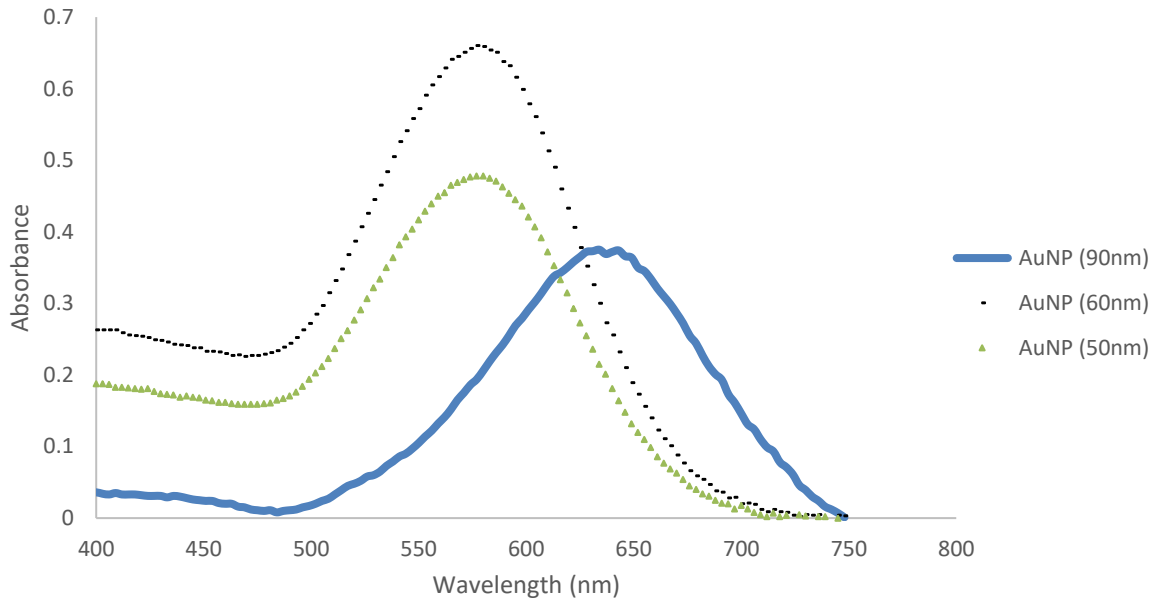

Figure 1: The UV-Vis spectra of gold nanoparticles of 50 nm, 60 nm, and 90 nm sizes screened on a UV-Vis Nanodrop 2000 spectrophotometer. This data served as characterization for the selection of experimental gold nanoparticle size.

The above Figure 1 indicates a well-documented behavior of gold nanoparticles, as the AuNPs size increases, the LSPR wavelength peak shifts to longer wavelengths, described as a red shift [10].The red shift increase is due to the oscillation electron damping and the plasmon modes multipolarity in larger AuNPs [11]. The 60 nm AuNPs exhibit a distinct absorbance peak and thus were chosen for the downstream hybridization experiments

for stable LSPR sensitivity. For hybridization experiments, 60 nm AuNPs were thus used and functionalized followed by immobilization of capture DNA probe and target DNA sequences. The capture DNA probe is made up of 24 bp and targets DNA in this study were a synthetic oligonucleotide of 90 bps. To mimic the clinical DNA, three oligonucleotides were designed which include sequences that do not possess the mutation of concern. In this study, the mutation of concern was M184V (-ATG to – GTG), and thus were looking at a single nucleotide polymorphism. A DNA capture probe included a CAT codon to directly hybridize with the wild-type codon, which acts as a positive control. The same capture probe would hybridize with the mutation oligonucleotide to form a partial duplex with a single mismatch. This allowed us to assess the sensitivity of our LSPR system in detecting small interactions and their alterations. The non-complementary DNA oligonucleotide included random codons (-TTT) which were acting as our negative control. The LSPR system has been previously optimized for the limit of detection, which was 0.003125 mg/ml of neutravidin and biotin capture probe binding [12].

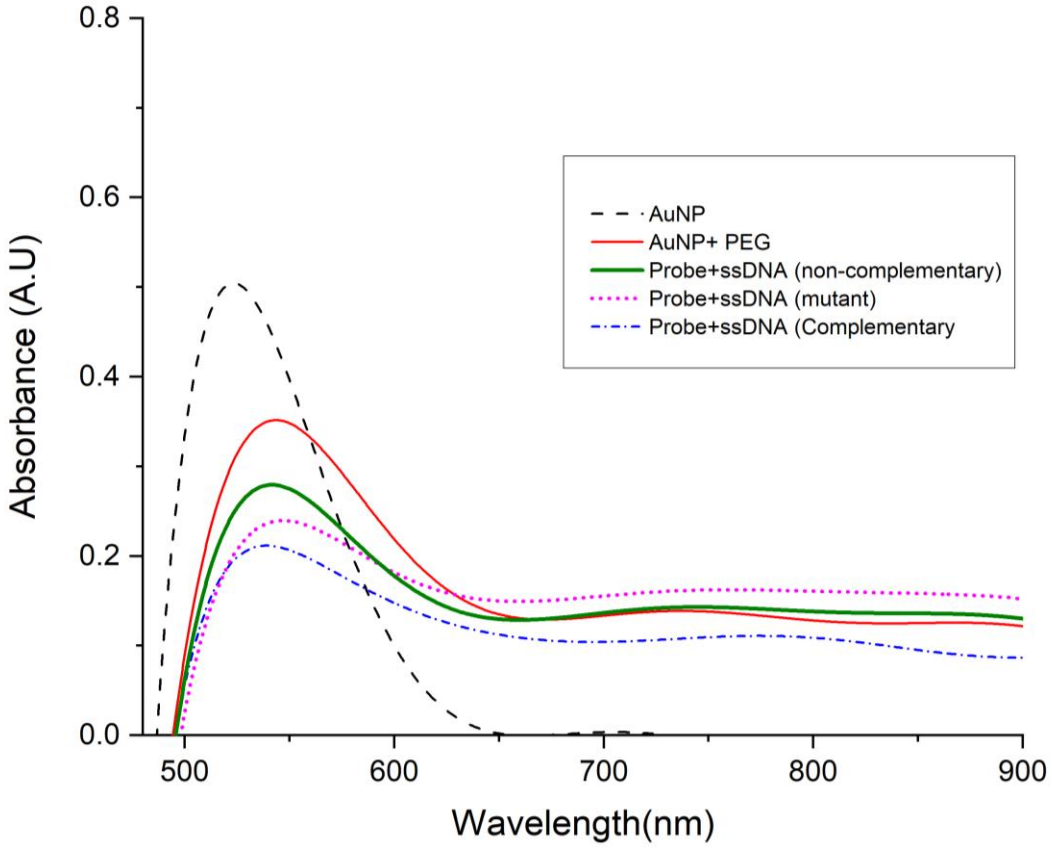

Figure 2: The normalized absorbance intensities of gold nanoparticles (AuNP) only, gold nanoparticles stabilized in PEG (AuNP+PEG), capture probe hybridized to a non-complementary single-stranded DNA (Probe+ssDNA) as a negative control, capture probe hybridized to a partial complementary ssDNA (mutant), and capture probe hybridized to a complementary ssDNA as a positive control.

Partial hybridization includes a single base change in the DNA sequence to mimic a mutation. The absorbance intensities decreased from those of AuNP alone, which has the highest absorbance, to the hybridization of the capture probe and complementary DNA, which has the lowest absorbance intensity. LSPR peak wavelength shifts, from AuNP alone and red shifts induced by refractive index changes through the hybridization of the capture probe and target analytes on the nanoparticle surface are observed in Figure 2.

The introduction of PEG sterically stabilizes gold nanoparticles, preventing aggregation and causing a slight decrease in absorbance intensity, as observed in Figure 2 above. This decrease can also be attributed to reduced

particle-to-particle interactions as a result of the PEG molecule (5000 Da). DNA hybridization typically results in minimal refractive index changes, generally around 1.4 [13], which is slightly higher than water and close to glycerol [14]. Hybridization forms double-stranded DNA from two single strands, leading to a modest local refractive index change. The shifts in LSPR wavelength tend to follow, though not perfectly, a linear trend with the refractive index change of the local medium [8]. Therefore, an increase in the local refractive index on the nanoparticle surface will induce a corresponding increase in LSPR wavelength shifts. In Figure 2 above, the wavelength shifts are not distinctively defined. And thus, we further analyzed (MS Excel) our data to indicate that indeed the DNA hybridization events are causing an LSPR wavelength shift. These are presented in Figure 3 below.

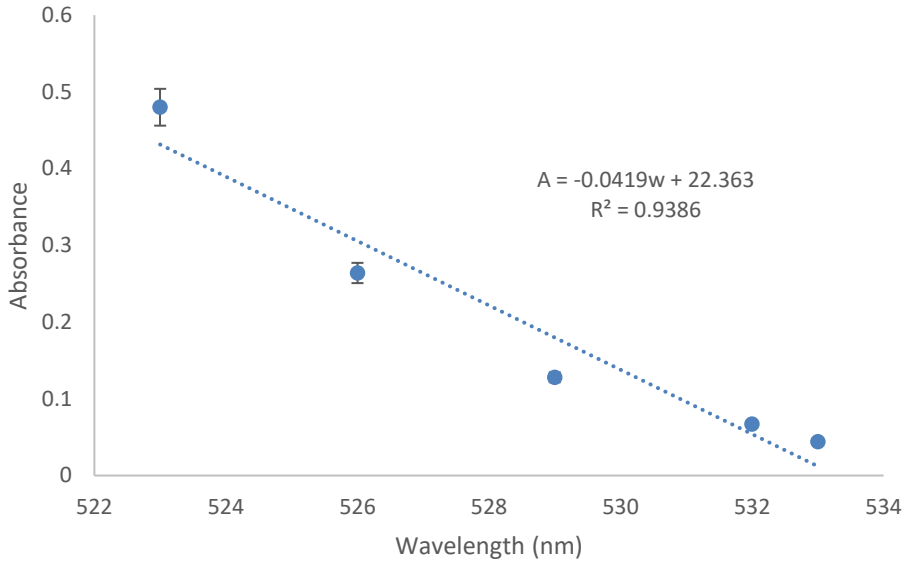

Figure 3: A curve quantifying the LSPR wavelength shifts and their absorbance intensity. The point with the highest absorbance intensity represents AuNP alone, and the point with the lowest absorbance intensity represents the hybridization between a capture probe and a complementary DNA. The linear model equation represents with an R^2 of 0.93 represents a good relationship between absorbance and wavelength.

This curve allows us to quantify LSPR wavelength shifts, which are sometimes subtle due to small refractive index changes on the nanoparticle surface. The trend suggests that PEG stabilization induces a larger LSPR wavelength peak shift than the hybridization of DNA sequences. Differences in hybridization of different DNA sequences, though small, are detected with this LSPR approach.

4. Conclusion

Early HIV-1 drug-resistant mutations detection can assist clinicians to advise on effective ART regimens, personalized therapy for targeted strains, and help in controlling the transmission and progression of the virus in communities. The detection turnaround time is thus critical to achieve these milestones, but this is not possible with the available laboratory-benchtop molecular techniques. LSPR can be developed into a point-of-care diagnostic assay for drug-resistant mutation detection, it is convenient and cost-effective. The custom built LSPR involved in this study was assessed for sensitivity with a limit of detection for intensity changes due to absorbance changes was 1442.81 nm and is presented as supplementary data. Our LSPR system was successful in detecting partial hybridization, which represents a single-nucleotide polymorphism pair mutation on our ssDNA target. With a distinctive peak wavelength shift of 3 (RIU) from uncomplimentary hybridization, our LSPR setup represents a sensitivity above the lower end (<1 nm) [15], thus indicating a successful mutation detection

technique. This study thus forms the basis for further optimization and development into a point-of-care drug-resistant mutation detection assay.

5. Acknowledgments

This study was supported by the national research foundation (NRF), Council for Scientific and Industrial Research (CSIR), Department of Science, Technology, and Innovation (DSTI), and the South African Medical Research Council (SAMRC).

References

[1] Joint United Nations Programme on HIV/AIDS., '"2008 Report on the global AIDS epidemic,", 2008.
[2] World Health Organization, '"HIV drug resistance: brief report 2024,", 2024.
[3] U.G. Assembly, '"Political declaration on HIV and AIDS: ending inequalities and getting on track to end AIDS by 2030,", vol. 8.
[4] [4] S. Luo and N. Wang, '"Human Immunodeficiency Virus/Acquired Immunodeficiency Syndrome Prevention and Control in China: Statistics, Challenges, and the Road Ahead," *Infectious Diseases & Immunity*, vol. 4, no. 04, pp. 149–151.
[5] G. Nikolopoulos, S. Bonovas, A. Tsantes and N.M. Sitaras, '"HIV/AIDS: recent advances in antiretroviral agents," *Mini Reviews in Medicinal Chemistry*, vol. 9, no. 8, pp. 900–910.
[6] S. SeyedAlinaghi, A.M. Afsahi, A. Moradi, Z. Parmoon, P. Habibi, P. Mirzapour, M. Dashti, A. Ghasemzadeh, E. Karimi and F. Sanaati, '"Current ART, determinants for virologic failure and implications for HIV drug resistance: an umbrella review," *AIDS research and therapy*, vol. 20, no. 1, pp. 74.
[7] F.E.T. Foka and H.T. Mufhandu, '"Current ARTs, virologic failure, and implications for AIDS management: a systematic review," *Viruses*, vol. 15, no. 8, pp. 1732.
[8] M.P. Mcoyi, K.T. Mpofu, M. Sekhwama and P. Mthunzi-Kufa, '"Developments in localized surface plasmon resonance," *Plasmonics*, pp. 1–40.
[9] K.M. Mayer and J.H. Hafner, '"Localized surface plasmon resonance sensors," *Chem.Rev.*, vol. 111, no. 6, pp. 3828–3857.
[10] W. Haiss, N.T. Thanh, J. Aveyard and D.G. Fernig, '"Determination of size and concentration of gold nanoparticles from UV− Vis spectra," *Anal.Chem.*, vol. 79, no. 11, pp. 4215–4221.
[11] A. Derkachova and K. Kolwas, '"Size dependence of multipolar plasmon resonance frequencies and damping rates in simple metal spherical nanoparticles," *The European Physical Journal Special Topics*, vol. 144, no. 1, pp. 93–99.
[12] M.P. Mcoyi, M. Lugongolo, C. Williamson, K. Mpofu, S. Ombinda-Lemboumba, S. Ndlovu and P. Mthunzi-Kufa, '"Evaluation of the limit of detection of the localized surface plasmon resonance label-free biosensor,", vol. 12840, pp. 104–110.
[13] A. Bonyar, '"Label-free nucleic acid biosensing using nanomaterial-based localized surface plasmon resonance imaging: a review," *ACS Applied Nano Materials*, vol. 3, no. 9, pp. 8506–8521.
[14] H. Chen, X. Kou, Z. Yang, W. Ni and J. Wang, '"Shape-and size-dependent refractive index sensitivity of gold nanoparticles," *Langmuir*, vol. 24, no. 10, pp. 5233–5237.
[15] M. Singh and A. Datta, '"LSPR excitation on Au nanorings from integrated hybrid plasmonic aperture waveguide and its application in methanol detection in the IR-band," *IEEE Sensors Journal*, vol. 19, no. 15, pp. 6119–6125.

This page intentionally left blank.

DIVISION

D

ASTROPHYSICS AND SPACE SCIENCE

Developing a Sky-End Fibre Aperture for the AMASE Fibre Bundle

Goratamang Gaedie [1,2], **Sabyasachi Chattophadyay**[1,2], **and Nidhi Mehandirrata**[2,3]

[1]Centre for Space Research, North-West University, Potchefstroom 2520, South Africa
[2]South African Astronomical Observatory, Observatory 7925, Cape Town, South Africa
[3]Department of Astronomy, University of Cape Town, 7700, South Africa

E-mail: ggaedie@gmail.com

Abstract. The Affordable Multiple-Aperture Spectroscopy Explorer (AMASE) project aims to enable high-resolution spectroscopy of ionised gas in galaxies. However, fabricating ultra-dense fibre bundles with micrometre-level precision presents significant challenges. We detail a fabrication process that combines precision machining, stress-reducing handling, and iterative polishing. Although the final prototype did not meet the optical performance targets, our methods reduced manual labour, improved reproducibility, and identified critical failure modes, providing essential information for future astrophotonic instrument designs.

1 Introduction

Over the past decade, there has been a growing emphasis on understanding the physical processes governing the interstellar medium (ISM) and star formation in the Milky Way and nearby galaxies [1; 2]. Integral Field Spectroscopy (IFS) has revolutionised this effort, enabling the study of spatially resolved kinematics, ionisation states, and chemical abundances across diverse galactic environments. Studies like MaNGA (Mapping Nearby Galaxies at Apache Point Observatory, which is part of SDSS-IV and conducts integral-field spectroscopy on approximately 10,000 nearby galaxies) [3] and SAMI (Sydney-AAO Multi-object Integral-field spectrograph, observing thousands of galaxies in various environments using multi-object IFU spectroscopy) [4; 5] have offered vital information on kiloparsec scales. However, these surveys lack spatial and spectral resolution to probe the fine structure and turbulence within individual HII regions at sub-parsec levels, which is critical to understanding star formation feedback [6; 7].

The Affordable Multiple Aperture Spectroscopy Explorer (AMASE) project addresses this gap through a novel, cost-effective design that combines an array of multifibre spectrographs with telephoto lenses [8]. AMASE targets a spectral resolution of $R \sim 15{,}000$ and a spatial resolution ($\sigma \sim 8.5$ kms^{-1}) capable of dissecting ionised gas structures from 0.1 to 100 parsecs in the Local Group galaxies. Key science goals of AMASE include: (1) characterising feedback-driven outflows in star-forming regions [9; 6]; (2) disentangling ionisation sources in diffuse ionised gas [6]; (3) calibrating strong-line metallicity diagnostics; and (4) improving photoionisation models with spatially resolved emission line data [7]. Achieving these goals requires precise control over the optical alignment and integrity of the fibre bundles that couple the spectrographs to the sky.

We present the design, fabrication, and metrological validation of the sky-end fibre instrument cable, a key component of AMASE. This system enables high-resolution, integral-field spectroscopy of ionised gas structures in the Milky Way and Local Group galaxies. A high density configuration of 547 fibres within a 1.858 mm regular hexagonal aperture achieves a core area-to-hexagon area ratio of approximately 50%, maximising photon throughput. We report on the design, metrology, and analysis of the quality of the fibre bundle.

2 Fabrication Methodology

The AMASE instrument uses 547 fibres with a core diameter of $50\,\mu\mathrm{m}$, each providing a spatial resolution of approximately 25.24 arcseconds on-sky. These fibres cover a hexagonal on-sky footprint with a long-axis span of 19.3 arcminutes, equivalent to a total field of view of roughly 79 arcmin^2 per spectrograph. The fibres are arranged in a hexagonal close-packed (HCP) geometry to maximise the fill factor and minimise interstitial space. Figure 5 is an illustration of the design of the hexagonal apertures used for AMASE.

The fibre holding aperture has a nominal diagonal dimension of $1.894\,\mathrm{mm}$. In Figure 1, this corresponds to the diagonal distance measured between the corner at circle one and the opposite corner at circle four. However, practical assembly constraints necessitated additional clearance to account for fibre-dimensional variability. The clearance was defined as follows:

$$\text{Clearance} = \Delta d \times \sqrt{N} \tag{1}$$

where Δd is the tolerance for the diameter of the fibre and N is the number of fibres along the dimension. Given (from the fibre supplier) a typical fibre diameter tolerance of $\pm 1\,\mu\mathrm{m}$, the required clearance becomes:

$$\text{Clearance} = 1\,\mu\mathrm{m} \times \sqrt{27} \approx 5.20\,\mu\mathrm{m} \tag{2}$$

The aperture diameters were then evaluated as offsets above the nominal value in multiples of the clearance. Extensive empirical testing identified that aperture dimensions should be in the range:

$$\text{Aperture} = 1.894\,\mathrm{mm} + \ \mathrm{m}\ \times \text{Clearance} \tag{3}$$

where m is a multiple of our clearance factor. A total of 12 apertures were produced, with three apertures made for each clearance size of 1.894 mm, 1.905 mm, 1.917 mm and 1.928 mm. These apertures exhibited a size variation of $\pm\ 0.1\,\mathrm{mm}$, aligned with the permissible error limit, alongside the standard aperture size. All apertures were machined with entry and exit chamfers to minimise surface-edge interference and aid fibre guidance.

Figure 1 shows the measurement of the smallest circles that fit within the aperture corners, used for quality assessment. These inspections were critical for verifying the dimensional conformity and suitability of the fabricated apertures.

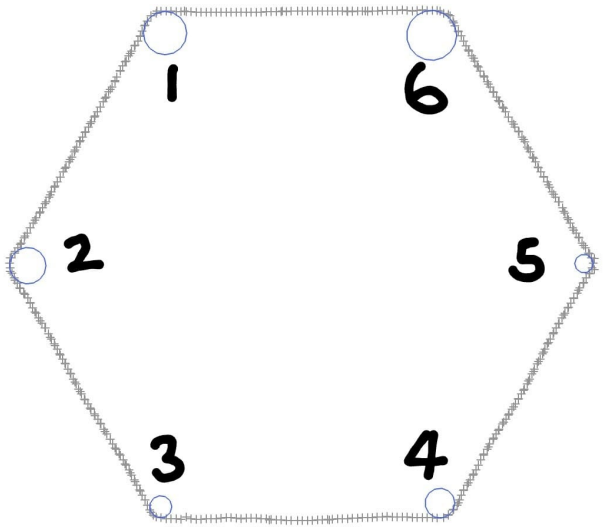

Figure 1: Microscopic (shadowgraph) inspection of the aperture quality and dimensional conformity. At each corner of the hexagonal aperture, the smallest possible circle has been fitted. The radii of these circles are: (1) 0.081 mm, (2) 0.068 mm, (3) 0.042 mm, (4) 0.056 mm, (5) 0.035 mm, and (6) 0.094 mm.

In Figure 1, the radii of the corner-fit circles are larger than the fibre radius ($39.5\,\mu\mathrm{m}$). Our goal is to arrange the fibres in a hexagonally close-packed lattice. In an ideal lattice, circles fit neatly across the width of the aperture. However, the flat walls of the hexagon meet at angles, leaving small triangular voids that do not perfectly

accommodate circular packing.

If the effective corner radius is larger than the diameter of the fibre, the extra space allows the fibres to shift, disrupting uniform packing. Conversely, if the corner radius is smaller than the diameter of the fibre, the fibres cannot intrude into the voids, ensuring that the lattice remains tight and all fibres are constrained by the aperture boundaries. This prevents wasted space where fibres could rattle or be misplaced, which is important for maximising fill factor and uniformity in optical fibre bundles.

The aperture sizes that were cleared for use were the 1.894 mm, 1.931 mm, 1.908 mm, and 1.901 mm; all the other apertures had large discrepancies, either the smoothness of the inside wall of the hexagons being too rough and could potentially bend and break the fibres during the insertion or the corners of the hexagons of the apertures were too large meaning the apertures were not tight enough.

2.1 Fibre Handling and Insertion

In each instance of attempting to insert fibres into an aperture, precisely 547 fibres of uniform length are cut. According to [10; 11], applying stress to the fibres can result in focal ratio degradation (FRD). Hence, the utilization of a cleaver for fibre cutting is essential, as it mitigates stress or possible damage to the fibres and decreases the roughness of the terminated surface.

A packing jig was employed to insert the fibers into the aperture, in addition to attempting manual insertion. Large fibres with strong core diameters (such as SMI 200 ($200\,\mu\mathrm{m}$ core diameter [12]) can be inserted by collectively pushing the bundle through a precision machined aperture, an approach that fails for weaker fibres ($50\,\mu\mathrm{m}$ core) that tend to buckle.

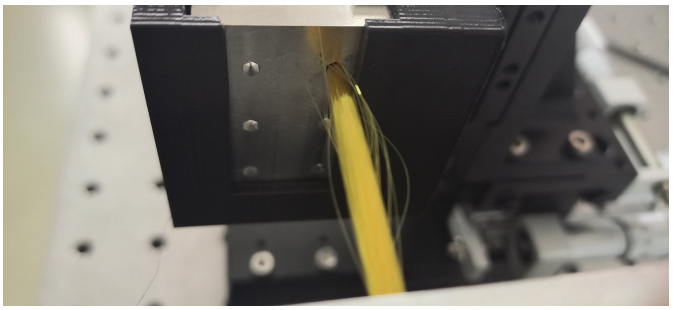

Figure 2: Packing jig and aperture holder used for staged fibre insertion.

Initially, the objective was to insert the fibres into the designated aperture with a nominal diameter of 1.894 mm post-removal of the fibre buffer. A solution consisting of 98% sulfuric acid was employed and heated to a temperature of 180 °C. The fibres were agitated to enhance the rate of the chemical reaction. Following the stripping process, the fibres were immersed in deionized water to neutralize the chemical reaction. The buffer-stripped fibres were subsequently consolidated using a heat shrink tube. An attempt was made to insert the stripped section of the fibres through the aperture, followed by the unstripped section. However, the stripped section was prone to breakage, and the aperture was insufficiently sized to accommodate the insertion of the unstripped fibre bundle.

Ultimately, isopropyl alcohol (IPA) was utilized to maintain the cohesion of the fibres, thus preventing their dispersion. The fibres were immersed in an IPA solution and placed within an ultrasonic cleaner. The insertion process was facilitated by thermally expanding the aperture slightly. Immersing the fibres in IPA and elevating the temperatures of both the room and aperture allowed for seamless insertion through the 1.931 mm aperture. The aperture size of 1.931 mm was determined to be the minimum feasible configuration for this procedure.

2.2 Adhesive Application and Curing

To ensure that the fibres remain intact and placed within, we use a transparent two-part epoxy adhesive 301 2.5GM BI-PAK 80168250001 from Epoxy Technology, Inc (EPO-TEK); the epoxy components are mixed within their original packaging prior to opening. After mixing, the two-part epoxy glue is poured into a resealable plastic cup. We carefully used a gauge 18 needle syringe to draw the glue from the cup, minimising the introduction of air bubbles. The glue is applied in phases to the fibre bundle; initially, it is added to the fibres on the aperture's

exit side, allowing it to penetrate by gently separating the fibres. The bundle is then slightly retracted through the aperture to facilitate glue flow. The bundle is left undisturbed at room temperature for 48 hours to fully cure. The result is depicted in Figure 3.

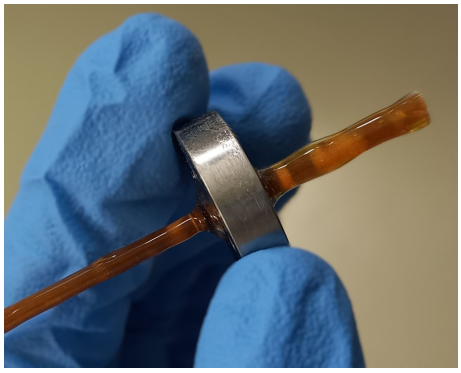

Figure 3: Fibre bundle after epoxy curing.

2.3 Polishing and Surface Preparation

The fibre bundle was subjected to a thorough multistep polishing process using various micron-scale polishing disks, as described by [13]. The procedure began with a coarse polishing stage, followed by successive steps using disks with grit sizes of 30, 15, 5, 3, and 1 µm. Each stage lasted 2 hours at respective rotational speeds of 5, 4.5, 4, 3.5, and 1 revolution per second, following the polishing protocol described in [13]. Adjustments in vertical load, speed, and polishing angle were introduced throughout the process to correct surface imperfections, including scratches and uneven patches. These irregularities were traced to the polishing setup rather than the fibre bundle itself. Iterative application of these refinements resulted in a smooth and uniform surface finish. The effectiveness of the final polishing step can be observed in Figure 4a, while the overall condition of the fully polished fibre bundle is shown in Figure 4b.

The quality of the polished ends of the fibres plays a crucial role in determining the amount of light that passes through a bundle of fibres and its scattering characteristics. Figure 4a shows how a small chip on one fibre and faint scratches larger than 1 µm illustrates the amplification of edge scattering and the reduction in performance due to the remaining surface flaws. On the scale of the entire bundle (Figure 4b), inconsistencies in brightness - including some dim fibres and about three fibres showing minimal or no light transmission - highlight the effects of polishing and packing imperfections. Small gaps and local misalignments between fibres decrease the effective packing density, allowing light to scatter into empty spaces rather than being transmitted efficiently. These structural factors add to the inherent attenuation processes such as absorption, contamination, or microbending, resulting in dimmer fibres within the bundle. Although visual examination can identify qualitative defects such as chips, scratches, voids, and variations in brightness, a quantitative evaluation of optical efficiency still necessitates direct throughput measurements. Apparent brightness alone cannot confirm efficiency, although it provides an early indication of polishing quality and bundle integrity.

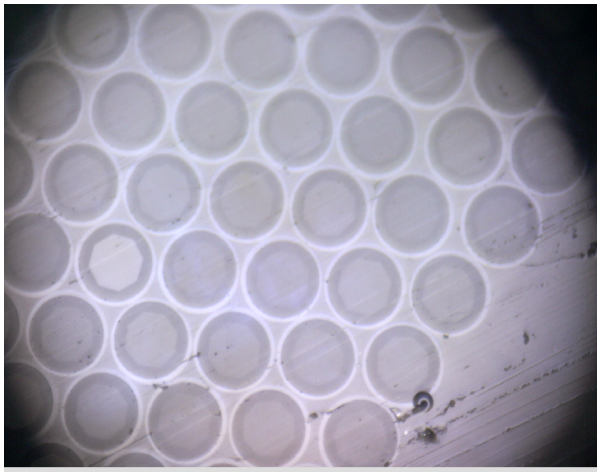

(a) Polished fibre bundle end face after the final 1 µm polishing step. The surface is generally smooth, though a small chip is visible on one fibre end, and faint scratches greater than 1 µm in length remain. These features indicate that while the polishing process largely removed irregularities from earlier stages, some minor defects persist.

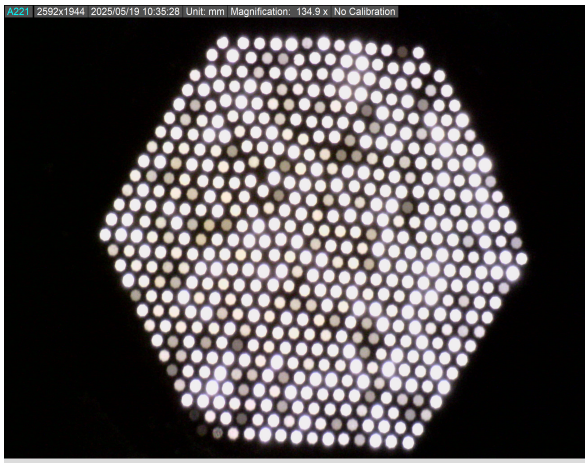

(b) Overall view of the completed fibre bundle after the full multistep polishing procedure. Most fibres appear bright, but several are noticeably dimmer, with approximately three fibres showing little or no transmission. Small gaps between fibres and slight positional shifts are also evident, indicating non-ideal packing uniformity.

Figure 4: Results of the fibre bundle polishing process. (a) Microscopic view of the end face after the final 1 µm polish, showing an overall smooth surface but with minor scratches and a small chip at one fibre end. (b) Macroscopic inspection of the fully polished bundle, where non-uniform brightness, dark fibres, inter-fibre gaps, and slight fibre misalignments are visible. These features highlight the influence of polishing quality and packing efficiency on optical performance.

3 Results

Measurement and analysis in error of the accuracy of the positioning of the fibres along the x and y axes, respectively, were performed as detailed by Gaedie et al. [14]. Fibre centroids were extracted from high-resolution microscope images using a custom Python-based image processing pipeline that applied thresholding, morphological filtering, and ellipse fitting. These detected positions were compared with an ideal hexagonal grid or an adaptively generated irregular grid, allowing for precise quantification of fibre placement deviations.

For the AMASE-SAAO fibre bundle, positional error analysis yielded standard deviations of $\sigma_{\mathrm{X}} = 14.79\,\mu\mathrm{m}$ and $\sigma_{\mathrm{Y}} = 11.10\,\mu\mathrm{m}$, with a radial error of $\sigma_{\mathrm{r}} = 9.50\,\mu\mathrm{m}$. These deviations reflect the practical limitations of packing core fibres $50\,\mu\mathrm{m}$ with low bending stiffness into a confined geometry, highlighting the importance of precise aperture machining and insertion techniques to minimise misalignment of the fibres.

4 Discussion

This project aimed to produce and evaluate a high-density fibre bundle for the AMASE spectrograph. Despite numerous efforts and extensive design revisions, the project did not meet its anticipated performance criteria, largely due to difficulties with accurately inserting fibres into apertures with precise tolerances. One key issue was inserting fibres into apertures that were either too tight or inadequately fitted. The required extremely fine tolerances further complicated the process. Redesigns involved enlarging aperture hole sizes, experimenting with different fibre types such as serum optical polymicro fibres, and trying varied insertion techniques, including chemical stripping and ultrasonic cleaning. However, achieving successful insertion with sufficient positional accuracy remained elusive. Even when fibres were successfully inserted, as in a 1.931 mm aperture, inconsistencies in the packing, ranging from 20 to $25\,\mu\mathrm{m}$, greatly exceeded the precision $\pm$ 3 $3\,\mu\mathrm{m}$ required for astronomical use. The uneven internal walls of the apertures further complicated the insertion process, and although polishing somewhat improved the situation, issues such as poor fill factors and uneven bundle faces persisted. A significant finding was related to the handling of fibres with varying diameters. For example, sturdier fibres, such as those in the SMI-200 bundle ($240\,\mu\mathrm{m}$ in diameter with buffer), were easier to insert without bending due to their rigidity. Their structural strength and easier creation of smooth inner walls for larger holes facilitated a straightforward

assembly process. In contrast, the smaller diameter fibres used in the AMASE bundles (79 µm) posed considerable challenges during fabrication and assembly, being more susceptible to bending and damage during insertion.

5 Conclusion

The development of a fibre instrumentation cable for AMASE was ultimately unsuccessful, despite improving our understanding of the physical and mechanical limits of the fibre bundle assembly; the project did not meet the required optical and positional criteria. The key conclusions are as follows.

- Injection of fibres into tight apertures with micrometre-level tolerance proved ineffective because of their mechanical fragility and size inconsistencies.
- The packing precision did not meet the standard $\pm$ 3 µm, with deviations often exceeding 20 µm.
- The polishing and termination processes added variability, which affected the uniformity of the fibre face.

These results reveal that conventional manual fabrication methods are not adequate for producing ultradense, small-core fibre bundles with high precision. Future work should investigate the following,

- Employ laser micro-machining or precision machining techniques for aperture fabrication.
- Adopt alternative designs such as individually machined fibre holes to prevent collective misalignment.
- Using alignment jigs and automated insertion tools to improve repeatability.
- Enhancing adhesive application techniques to ensure consistent distribution and reduce stress.

Although the project did not deliver the intended instrument, it has provided essential insight into the current limitations of fibre bundle fabrication methods. These findings will inform the next development phase for AMASE or similar astrophotonic instrumentation projects.

References

[1] R. C. Kennicutt and N. J. Evans, "Star Formation in the Milky Way and Nearby Galaxies," *ARA&A*, vol. 50, pp. 531–608, Sep. 2012.

[2] K. M. Ferrière, "The interstellar environment of our galaxy," *Reviews of Modern Physics*, vol. 73, no. 4, pp. 1031–1066, Oct. 2001.

[3] K. Bundy, M. A. Bershady, D. R. Law, R. Yan, N. Drory, N. MacDonald, D. A. Wake, B. Cherinka, J. R. Sánchez-Gallego, A.-M. Weijmans, D. Thomas, C. Tremonti, K. Masters, L. Coccato, A. M. Diamond-Stanic, A. Aragón-Salamanca, V. Avila-Reese, C. Badenes, J. Falcón-Barroso, F. Belfiore, D. Bizyaev, G. A. Blanc, J. Bland-Hawthorn, M. R. Blanton, J. R. Brownstein, N. Byler, M. Cappellari, C. Conroy, A. A. Dutton, E. Emsellem, J. Etherington, P. M. Frinchaboy, H. Fu, J. E. Gunn, P. Harding, E. J. Johnston, G. Kauffmann, K. Kinemuchi, M. A. Klaene, J. H. Knapen, A. Leauthaud, C. Li, L. Lin, R. Maiolino, V. Malanushenko, E. Malanushenko, S. Mao, C. Maraston, R. M. McDermid, M. R. Merrifield, R. C. Nichol, D. Oravetz, K. Pan, J. K. Parejko, S. F. Sanchez, D. Schlegel, A. Simmons, O. Steele, M. Steinmetz, K. Thanjavur, B. A. Thompson, J. L. Tinker, R. C. E. van den Bosch, K. B. Westfall, D. Wilkinson, S. Wright, T. Xiao, and K. Zhang, "Overview of the SDSS-IV MaNGA Survey: Mapping nearby Galaxies at Apache Point Observatory," *ApJ*, vol. 798, no. 1, p. 7, Jan. 2015.

[4] S. M. Croom, J. S. Lawrence, J. Bland-Hawthorn, J. J. Bryant, L. Fogarty, S. Richards, M. Goodwin, T. Farrell, S. Miziarski, R. Heald, D. H. Jones, S. Lee, M. Colless, S. Brough, A. M. Hopkins, A. E. Bauer, M. N. Birchall, S. Ellis, A. Horton, S. Leon-Saval, G. Lewis, Á. R. López-Sánchez, S.-S. Min, C. Trinh, and H. Trowland, "The Sydney-AAO Multi-object Integral field spectrograph," *MNRAS*, vol. 421, no. 1, pp. 872–893, Mar. 2012.

[5] J. J. Bryant, M. S. Owers, A. S. G. Robotham, S. M. Croom, S. P. Driver, M. J. Drinkwater, N. P. F. Lorente, L. Cortese, N. Scott, M. Colless, A. Schaefer, E. N. Taylor, I. S. Konstantopoulos, J. T. Allen, I. Baldry, L. Barnes, A. E. Bauer, J. Bland-Hawthorn, J. V. Bloom, A. M. Brooks, S. Brough, G. Cecil, W. Couch, D. Croton, R. Davies, S. Ellis, L. M. R. Fogarty, C. Foster, K. Glazebrook, M. Goodwin, A. Green, M. L. Gunawardhana, E. Hampton, I. T. Ho, A. M. Hopkins, L. Kewley, J. S. Lawrence, S. G. Leon-Saval, S. Leslie, R. McElroy, G. Lewis, J. Liske, Á. R. López-Sánchez, S. Mahajan, A. M. Medling, N. Metcalfe, M. Meyer, J. Mould, D. Obreschkow, S. O'Toole, M. Pracy, S. N. Richards, T. Shanks, R. Sharp, S. M. Sweet, A. D. Thomas, C. Tonini, and C. J. Walcher, "The SAMI Galaxy Survey: instrument specification and target selection," *MNRAS*, vol. 447, no. 3, pp. 2857–2879, Mar. 2015.

[6] L. Zhou, C. Federrath, T. Yuan, F. Bian, A. M. Medling, Y. Shi, J. Bland-Hawthorn, J. J. Bryant, S. Brough, B. Catinella, S. M. Croom, M. Goodwin, G. Goldstein, A. W. Green, I. S. Konstantopoulos, J. S. Lawrence, M. S. Owers, S. N. Richards, and S. F. Sanchez, "The SAMI Galaxy Survey: energy sources of the turbulent velocity dispersion in spatially resolved local star-forming galaxies," *MNRAS*, vol. 470, no. 4, pp. 4573–4582, Oct. 2017.

[7] S. Oh, M. Colless, F. D'Eugenio, S. M. Croom, L. Cortese, B. Groves, L. J. Kewley, J. van de Sande, H. Zovaro, M. R. Varidel, S. Barsanti, J. Bland-Hawthorn, S. Brough, J. J. Bryant, S. Casura, J. S. Lawrence, N. P. F. Lorente, A. M. Medling, M. S. Owers, and S. K. Yi, "The SAMI Galaxy Survey: the difference between ionized gas and stellar velocity dispersions," *MNRAS*, vol. 512, no. 2, pp. 1765–1780, May 2022.

[8] R. Yan, M. A. Bershady, M. P. Smith, N. MacDonald, D. Bizyaev, K. Bundy, S. Chattopadhyay, J. E. Gunn, K. B. Westfall, and M. J. Wolf, "The prototype telescope and spectrograph system for the AMASE project," in *Ground-based and Airborne Instrumentation for Astronomy VIII*, ser. Society of Photo-Optical Instrumentation Engineers (SPIE) Conference Series, C. J. Evans, J. J. Bryant, and K. Motohara, Eds., vol. 11447, Dec. 2020, p. 114478Y.

[9] D. R. Law, F. Belfiore, M. A. Bershady, M. Cappellari, N. Drory, K. L. Masters, K. B. Westfall, D. Bizyaev, K. Bundy, K. Pan, and R. Yan, "Sdss-iv manga: Understanding ionized gas turbulence using integral field spectroscopy of 4500 star-forming disk galaxies," *The Astrophysical Journal*, vol. 928, no. 1, p. 58, mar 2022. [Online]. Available: https://dx.doi.org/10.3847/1538-4357/ac5620

[10] J. Allington-Smith, C. Dunlop, U. Lemke, and G. Murray, "End effects in optical fibres," *Monthly Notices of the Royal Astronomical Society*, vol. 436, no. 4, pp. 3492–3499, 10 2013. [Online]. Available: https://doi.org/10.1093/mnras/stt1842

[11] A. D. Eigenbrot, M. A. Bershady, and C. M. Wood, "The impact of surface-polish on the angular and wavelength dependence of fiber focal ratio degradation," in *Ground-based and Airborne Instrumentation for Astronomy IV*, vol. 8446. SPIE, 2012, pp. 1822–1831. [Online]. Available: https://scholar.google.com/scholar?q=Eigenbrot+A.+D.%2C+Bershady+M.+A.+and+Wood+C.+M.+2012+Proc.+SPIE+8446+84465W

[12] S. Chattopadhyay and M. A. Bershady, "Early commissioning results of slit mask integral field units on the Southern African Large Telescope," in *Ground-based and Airborne Instrumentation for Astronomy X*, J. J. Bryant, K. Motohara, and J. R. D. Vernet, Eds., vol. 13096, International Society for Optics and Photonics. SPIE, 2024, p. 130962R. [Online]. Available: https://doi.org/10.1117/12.3017822

[13] M. P. Smith, S. Chattopadhyay, A. Hauser, J. E. Oppor, M. A. Bershady, and M. J. Wolf, "Development and characterization of a precisely adjustable fiber polishing arm," in *Advances in Optical and Mechanical Technologies for Telescopes and Instrumentation IV*, R. Navarro and R. Geyl, Eds., vol. 11451, International Society for Optics and Photonics. SPIE, 2020, p. 114516W. [Online]. Available: https://doi.org/10.1117/12.2563201

[14] G. A. Gaedie, S. Chattopadhyay, N. Mehandiratta, R. Yan, S. C. H. Hui, Z. Lin, Y. Qiao, I. S. W. Ho, A. Y. Zhu, D. Y. H. Cheung, M. Y. L. Lee, J. Zhang, R. Zhou, Y.-C. Lam, Y. Wang, and Q. Chen, "Development and calibration of sky end of the fibre cable for the affordable multiple aperture spectroscopy explorer (AMASE)," in *Astronomical Optics: Design, Manufacture, and Test of Space and Ground Systems V*, T. B. Hull, D. Kim, and P. Hallibert, Eds., vol. 13624, International Society for Optics and Photonics. SPIE, 2025, p. 136240G. [Online]. Available: https://doi.org/10.1117/12.3063918

APPENDIX A

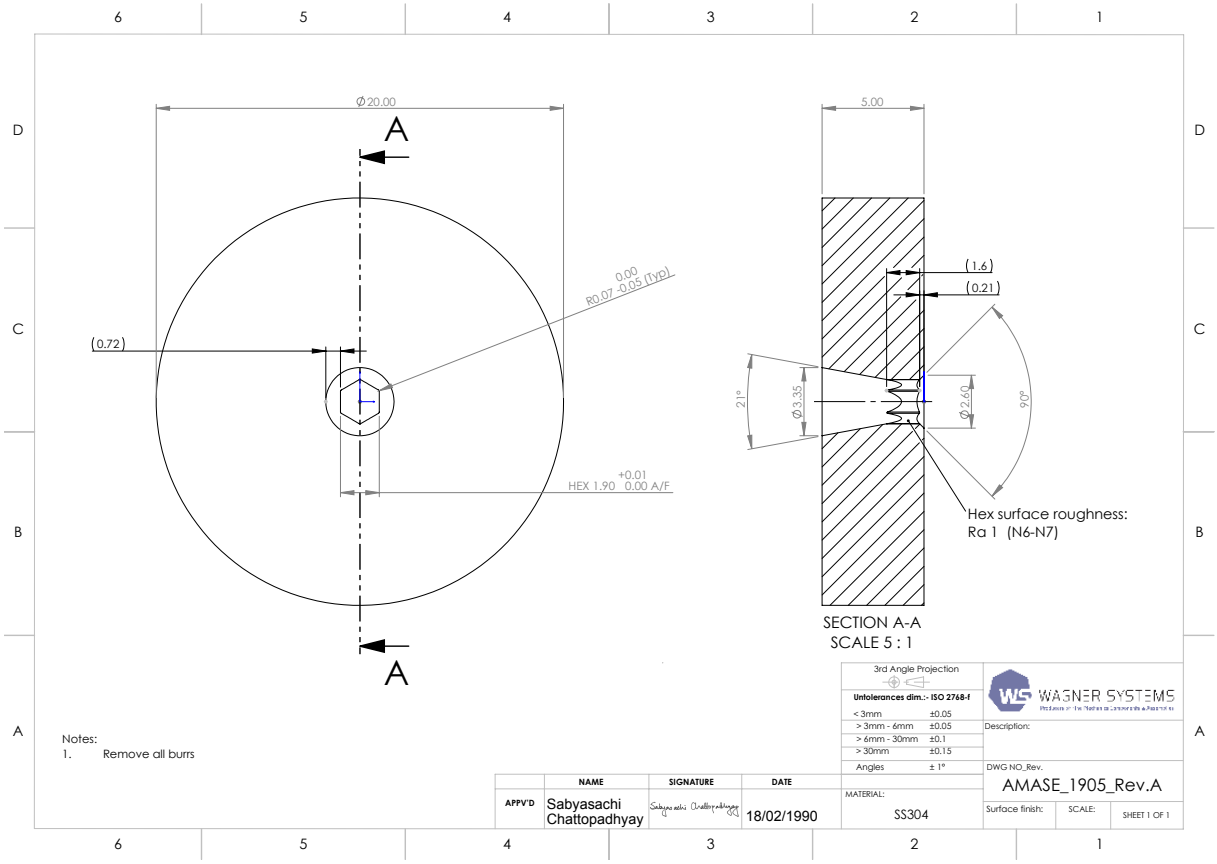

Figure 5: This CAD illustration showcases the 1.931 mm aperture, emphasizing the design of our stainless steel hexagonal fibre-holding apertures. These apertures are round, with a diameter of 20 mm and a thickness of 5 mm. On the flat circular surface displayed above, a chamfer is seen at the exit of the hexagon hole on the aperture. This chamfer is intentionally crafted to assist the fibres in exiting smoothly when passed through the aperture's opening. To the right, a sectional view (Section A-A) of the aperture shows a significant chamfer on the entrance side (3.35 mm wide), which simplifies the insertion into the aperture hole. In the central section (1.6 mm height), the hexagon is exactly 1.931 mm to hold the fibre securely in place, reducing the likelihood of fibre movement. This section is then followed by an exit side chamfer (0.21 mm height) that is visible on the left side's flat circular surface.

Characterisation and Calibration of the Kepler KL4040 sCMOS camera for Optical Observations at the UFS/Boyden Observatory

Hendrik J. van Heerden[1], **B. van Soelen**[1] **and W. Smit**[1]

[1]Department of Physics, University of the Free State, Bloemfontein, South Africa

E-mail: vanheerdenhj@ufs.ac.za

Abstract. The Kepler KL4040 sCMOS camera by Finger Lakes Instruments was evaluated for its suitability as an affordable alternative to older CCD sensors for optical photometry at the Boyden Observatory. Due to the sensor architecture where each pixel has its own electron to voltage converter, a thorough characterisation and calibration study was conducted to identify key performance factors and necessary considerations for operational implementation. The KL4040 achieves a high dynamic range by merging two 12-bit images into a single 16-bit image, with binning performed via software. Laboratory tests examined bias stability, dark current, and photo-response characteristics. Bias frames exhibited a 7.5% increase in mean counts as temperature rose from -15°C to 10°C, with dark current showing a linear temperature dependence. A small offset between the merged images for the 12-bit to 16-bit conversion was identified but was correctable through adjustments to the gain transition parameter that determines the offset value between high and low gain. Photo-response curves for the B, V, R, and I bands confirmed linearity across all bands. Fixed pattern noise, a known issue in sCMOS sensors, was effectively mitigated through bias and dark corrections. An on-sky test of the SA 107 star field, achieved photometric correction magnitudes on average within 2% of reported values. Additionally, we demonstrate photometry of the pulsating white dwarf binary system AR Sco which was performed on a 6 s cadence over a full orbit and show that the 118.2 s beat period could be easily recovered. These results confirm the KL4040 as a viable, cost-effective alternative to CCDs for photometry at the Boyden Observatory.

1 Introduction

Scientific-grade charge-coupled device (CCD) cameras have long been the standard for optical astronomical observations due to their low readout noise and well-understood behaviour. However, recent advances in scientific Complementary Metal Oxide (sCMOS) camera technology offer an appealing alternative, particularly in cost-sensitive environments.

The Kepler KL4040 sCMOS camera by Finger Lakes Instruments was acquired for deployment at the Boyden Observatory[1] as a potential upgrade path for ageing CCD systems. This camera features a large-format 4096 × 4096 pixel array, 9 × 9 µm pixel pitch, and a 52.1 mm sensor diagonal. Key specifications are provided in Table 1. Its architecture merges two 12-bit images (low and high gain) into a 16-bit output, enabling high dynamic range imaging, albeit with unique calibration challenges.

This paper presents the results of a laboratory and on-sky characterisation of the KL4040, focusing on dark current, bias stability, linearity, and photo-response[2]. We also demonstrate its scientific performance by recovering the known beat period of the white dwarf binary AR Sco from short-cadence photometry.

[1]The Boyden Observatory is located approximately 20 km North-East of Bloemfontein, South Africa and is operated by the University of the Free State.

[2]For general discussions on CCD or sCMOS device theory and characterisation refer to [1, 2]

Table 1: KL4040 Camera Specifications

Specification	**Value**
Peak Quantum Efficiency (QE)	74%
Effective Pixels	4096 × 4096
Pixel Size	9 µm
Sensor Diagonal	52.1 mm
Full Well Capacity	70,000 electrons
Typical Readout Noise	3.7 electrons
Dynamic Range	85.2 dB
Frame Rate	8 FPS via USB3 (23 FPS via QSFP V2)
Temperature Stability	0.1 °C
Dark Current at −10 °C	0.4 electrons/sec
Image Bit Depth	16-bit (merged from 2 × 12-bit)

2 Laboratory tests

For control of the operating environment (temperature, humidity and ambient light) during characterisation of the KL4040 a laboratory setup inspired by [3] and [4] was used. The setup consisted of a *dark box* to which the camera was mounted. Inside the box was an integrating sphere, which was illuminated by a VeraSol-2 AAA LED solar simulator from Newport[3]. This created a uniform light source and provided a simulated blackbody spectrum[4]. A variety of Johnson and Cousins photometric filters, as well as neutral density filters[5], were positioned between the solar simulator and the inlet to the dark box to control the colour spectrum as well as the intensity of the light reaching the sCMOS sensor. Tests done in the environment-controlled laboratory included bias response, dark current characterisation and dark signal non-uniformity and stability [5], as well as the photo-response linearity, colour dependence, and non-uniformity [4, 5].

2.1 Bias and Dark response

The characterisation of the bias and dark response of the camera found that the bias level has a strong linear dependence on temperature with a linear regression fit of $R^2 = 0.999$, as can be seen in Figure 1. An interesting result that was found was that there is an interplay between the bias level and the dark current for short dark exposure times, where the average dark current is less than the average bias current. Following the standard procedure of performing bias subtraction on the dark frames, can result in a subset of frames that have negative values (refer to Figure 2). Possible causes may be either a buildup of charge in the imaging sensor pixels and registrars, or could be due to incorrect black level calibration values as discussed in a post by Thiam-Guan Tan[6] and an online article by Qiu[7].

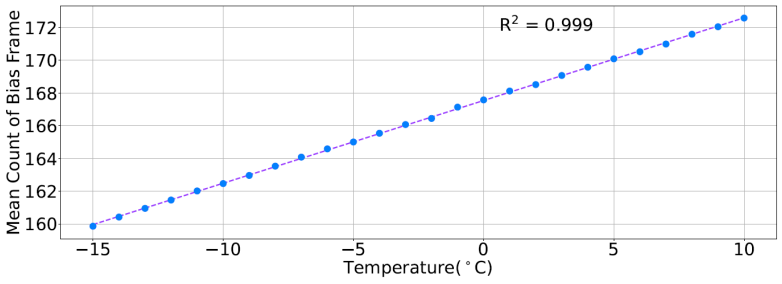

Figure 1: The mean count value of the bias frames as a function of the set sCMOS temperature.

[3]https://www.newport.com/p/VeraSol-2

[4]https://www.newport.com/n/solar-simulator-standards-definitions-and-comparisons

[5]https://www.edmundoptics.com/knowledge-center/application-notes/optics/ understanding-neutral-density-filters/

[6]http://pestobservatory.com/cmos-for-photometry/

[7]https://www.gamaelectronics.com.au/files/Dr.Qiu's Talking about Astronomical Photography.pdf

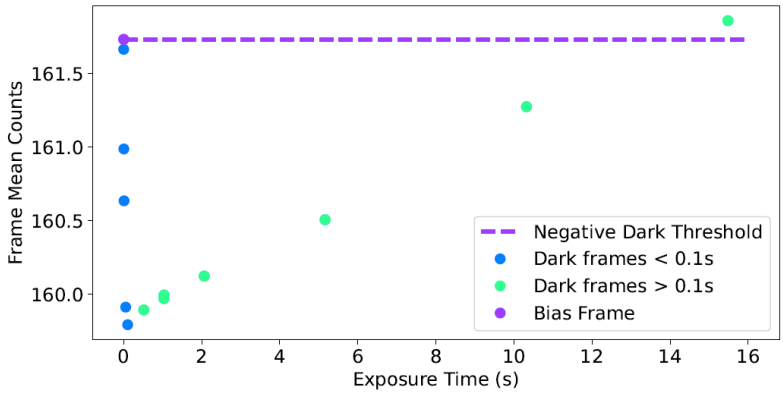

Figure 2: The mean count value of the bias (purple dashed lines) and dark frame (blue and green circles) as a function of exposure time.

The dark response is shown for exposure time and sensor temperature in Figure 3. There is a clear and strong increase in dark counts towards higher sensor temperatures and, to a lesser degree, longer exposure times. However, due to the higher dark signal non-uniformity (DSNU; a consequence of the physical architecture of the sensor) it is not advisable to use the mean dark level read from such a dark response curve. It was found that the best operational procedure is to use a dark frame - obtained at the same exposure time and temperature as the light (flat and data) frames - that has not been bias-corrected, in order to subtract both the bias and dark current simultaneously.

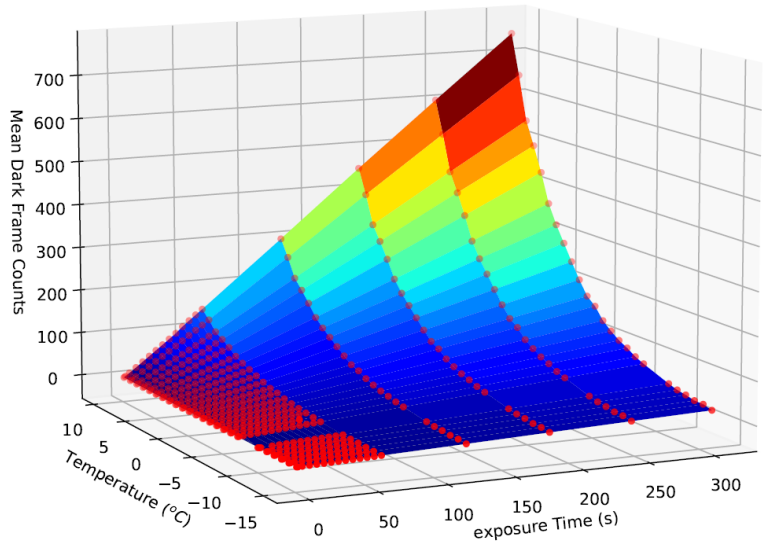

Figure 3: The dark response curve indicating counts relative to temperature and exposure times.

2.2 Photo-response and flat-fielding

During photo response tests using exposures through B, V, R_C, I_C filters, it was found that the sensor output over the generated 16-bit full well depth is linear up to 65000, as can be seen in Figure 4. This 16-bit image is generated by combining two 12-bit images, one read out at low gain and one read out at high gain, with the gain cross-over value set around 3800 counts. The cross-over gain region can be offset by setting the value in the camera software. This can be used to improve data quality that falls within this region, which is shown as the "V-Offset" in the figure.

When examining the logarithmic plots of pixel count distributions for a raw flat field versus a bias and dark corrected flat field (see Figure 5), distinct sensor characteristics become evident. A noticeable difference in photon

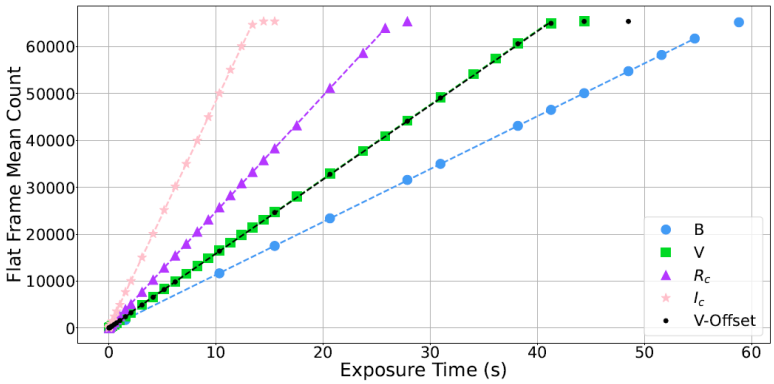

Figure 4: Photo response curve and test for linearity for B, V, R_C, I_C and V-offset.

response is observed between the top and bottom sections of the sensor. This variation arises from the architecture of the GSENSE4040 sensor chip, which is composed of four individual sub-chips arranged in a square configuration. The top two and bottom two sub-chips each have their own readout registers[8,9].

Additionally, the raw flat field image pixel count distribution (left) exhibits a prominent side lobe at higher counts, which is indicative of bias and dark noise. After applying the bias and dark corrections, these side lobes are effectively removed, as seen in the corrected flat field image pixel count distribution (right).

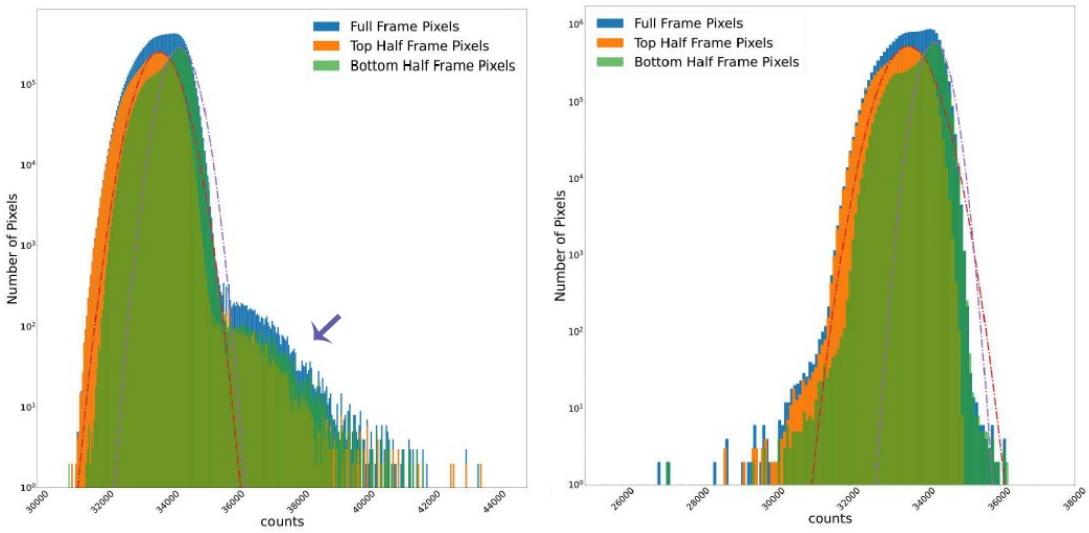

Figure 5: (*Left*) The raw flat field pixel counts distribution. A clear difference can be seen between the photo-response for the top and bottom chip sections, as well as bias and dark noise to the side as indicated by the arrow. (*Right*) The bias and dark corrected flat field clearly indicating a more even pixel distribution along with clearing of the side lobe due to bias and dark correction.

3 On-Sky tests

The most important tests were to see what quality of on-sky or science data the camera delivers. To make the tests independent of the telescope used, on-sky tests were performed using both a Celestron 14-inch as well as the large 60-inch Boyden Reflector. Using the Celestron 14-inch, photometric calibration observations of standard

[8] https://www.gpixel.com/en/pro_details_1199.html

[9] https://note.youdao.com/ynoteshare/index.html?id=ae2fabb24d1742f207ba75613648e7c4\&type=note\&_time=1647458420460

stars of different magnitudes and colours using UBVR$_C$I$_C$ filters were performed. This was done using stars in the SA 107 standard star field. After calibration the measured instrumental magnitudes and colour indices were calculated to within 2% of the reported catalogue values. There are some interesting features to note in Figure 6. First, the raw uncorrected stellar image (left) shows significant fixed pattern noise (FPN), a well known issue of CMOS sensors, which is due to the sensor architecture [6]. This pattern is also clearly visible in the column profile below the image. Second, is the clear break between the top and bottom sections of the sensor visible in the row profile on the right side of the image. Both of these features are corrected for by using a master dark (which also acted as a bias corrector) compiled from an equivalent temperature and exposure length dark signal frame set, and performing flat-fielding using the appropriate filter.

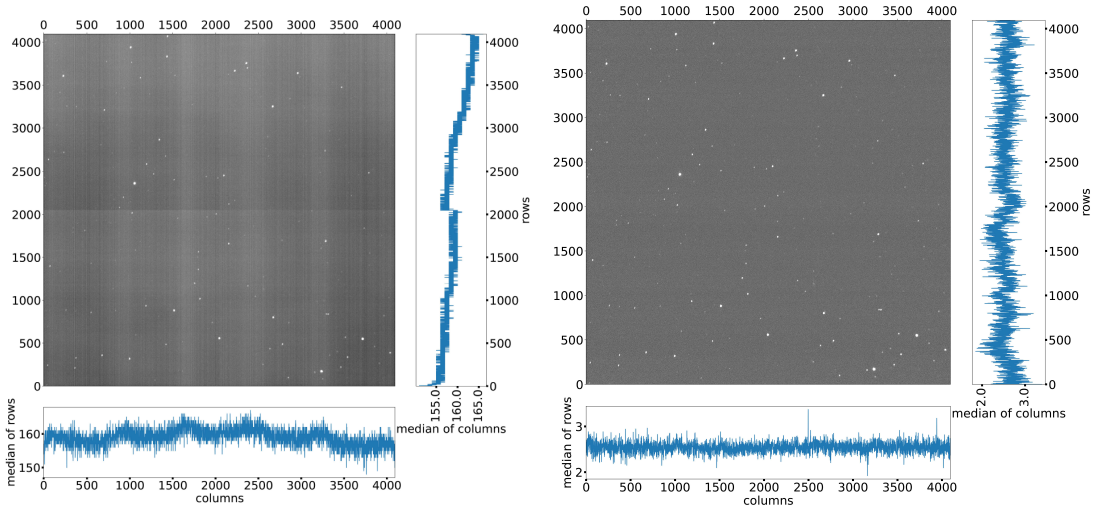

Figure 6: (*Left*) Raw star image from the SA 107 standard star field. (*Right*) Corrected star field. The median count value along the rows and columns are also shown.

A second test was performed using the 60-inch Boyden Reflector to investigate for how long, and how consistently the camera could operate in a continuous imaging mode. To this end a sequence of operations were conducted on AR Scorpii. AR Scorpii (AR Sco) is a unique white dwarf–red dwarf binary system that emits powerful pulsations across the electromagnetic spectrum, driven by the spin-down energy of a rapidly rotating magnetic white dwarf. It behaves like a pulsar, making it the first known white dwarf system to show such non-thermal, magnetospheric emission [7]. Observations were performed for several hours at a 6 second cadence, and analysis resulted in the expected phase diagram (Figure 7) with the well known beat period value of 118.2 seconds extracted from the data sets.

4 Conclusion

The characterisation of the KL4040 sCMOS camera highlights its viability as a modern, cost-effective alternative to traditional CCDs for optical photometry. Our laboratory tests confirm the sensor's sensitivity to thermal variation, which requires stable temperature control to ensure bias stability. A strong temperature dependence in dark current was observed, underscoring the importance of accurate calibration for low-light observations.

The dual-gain image merging introduces a small but correctable offset, manageable via proper gain crossover tuning. While FPN is an inherent feature of sCMOS architectures, it was effectively mitigated through bias and dark frame correction.

On-sky testing with the SA 107 standard star field demonstrated photometric consistency within 2% of catalogue values. Further validation through fast-cadence photometry of AR Sco confirmed the system's ability to recover known periodic signals, including the 118.2 s beat period.

While some software packages may produce artifacts during software binning, these can be avoided through careful pipeline selection or custom routines. With appropriate calibration workflows and attention to gain behaviour, the KL4040 is well suited for time-series photometry and other scientific imaging tasks at Boyden Observatory.

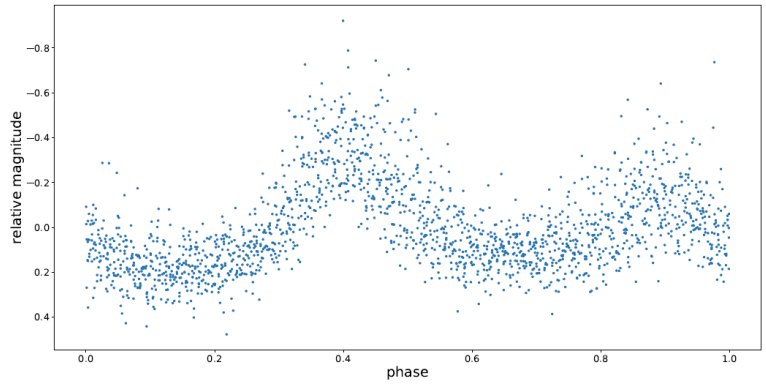

Figure 7: Phase diagram for AR Sco based on light curve data acquired using the KL4040 sCMOS.

Acknowledgment
This work is based on the research supported by the National Research Foundation of South Africa (Grant Numbers: 116300).

References

[1] S. B. Howell, *Handbook of CCD Astronomy*, 2nd ed., ser. Cambridge Observing Handbooks for Research Astronomers. Cambridge, UK: Cambridge University Press, 2006, vol. 5.

[2] D. S. Birney, G. Gonzalez, and D. Oesper, *Observational Astronomy*, 2nd ed. Cambridge, UK; New York, USA: Cambridge University Press, 2006.

[3] S. Karpov, A. Christov, A. Bajat, R. Cunniffe, and M. Prouza, "Characterization of modern ccd and cmos sensors for sky surveys," in *Revista Mexicana de Astronomía y Astrofísica Conference Series*, vol. 53, 2021, pp. 190–197.

[4] Z. Zhang, Y. Wang, R. Piestun, and Z. L. Huang, "Characterizing and correcting camera noise in back-illuminated scmos cameras," *Optics Express*, vol. 29, no. 5, pp. 6668–6690, 2021.

[5] U. Jain, A. Theuwissen, and D. Uwaerts, "Characterization of cmos image sensor," Master's thesis, Delft University of Technology, Mekelweg 5, 2628 CD Delft, Netherlands, 2016.

[6] T. Zhang, X. Li, J. Li, and Z. Xu, "Cmos fixed pattern noise removal based on low rank sparse variational method," *Applied Sciences*, vol. 10, p. 3694, 2020.

[7] T. R. Marsh, B. T. Gänsicke, S. Hümmerich, F.-J. Hambsch, K. Bernhard, C. Lloyd, E. Breedt, E. R. Stanway, D. T. Steeghs, S. G. Parsons, O. Toloza, M. R. Schreiber, P. G. Jonker, J. van Roestel, T. Kupfer, A. F. Pala, V. S. Dhillon, L. K. Hardy, S. P. Littlefair, A. Aungwerojwit, S. Arjyotha, D. Koester, J. J. Bochinski, C. A. Haswell, P. Frank, and P. J. Wheatley, "A radio-pulsing white dwarf binary star," *Nature*, vol. 537, no. 7620, pp. 374–377, 2016.

Multiwavelength observations of Active Galactic Nuclei in the Fornax Cluster.

Dejene Zewdie[1], **and S Ilani Loubser**[1]

[1]Centre for Space Research, North-West University, Potchefstroom 2520, South Africa

E-mail: dzewdie12@gmail.com.

Abstract. We present a multiwavelength study of active galactic nuclei (AGNs) in the Fornax cluster using X-ray data from eROSITA, optical spectroscopic observations from MUSE, and infrared imaging from WISE. We found three galaxies; FCC121 and FCC179 were recently reported in an X-ray study, but even though FCC184 meets the detection threshold, it was not reported. All three galaxies are studied using multi-wavelength data here. We also classified these three galaxies based on their optical emission lines to understand the photoionisation mechanisms. We found that FCC121, FCC179 and FCC184 are classified as composite galaxy, star-forming galaxy, and FCC184 is classified as a low ionisation nuclear emission line region (LINER), respectively. From X-ray observations, we find that FCC184 has a luminosity in the 0.2–2.3 keV range of $\log \mathrm{L_X} = 40.39\ \mathrm{ergs}^{-1}$, but its infrared colour is not characteristic of typical AGN. With MeerKAT observations, neutral atomic hydrogen (HI) is detected in all three galaxies. The HI morphology of FCC121 has an extended structure, while FCC179 may even be shaped by AGN feedback. The HI morphology of FCC184 was not resolved. Together, these multiwavelength observations reveal different types of AGN that may play an important role in the cluster environment.

1 Introduction

Active galactic nuclei (AGN) are energetic objects powered by gas accretion onto the supermassive black hole (SMBH) in the central region of the galaxy. These objects can generate a significant amount of radiative energy across the electromagnetic spectrum. Based on the unified model [1] and their physical properties, AGNs are broadly classified according to the line of sight of the observers to the accretion disk. This central region is surrounded by a toroidal structure of dust and gas, which can lead to vastly different appearances when observed from different viewing angles. Depending on how much dust is found along the line of sight and orientation angle, AGNs can be classified into two main types: Type 1 AGN and Type 2 AGN. Type 1 AGNs (unobscured) are those where we have a direct line of sight towards the central engine, while Type 2 AGNs (obscured) are those where dusty clouds block our view of the accretion disk and the broad-line region.

Massive galaxies are believed to have a SMBH with a mass in excess of $\geq 10^6\ \mathrm{M}_\odot$ at the centre; however, in most cases the SMBH is inactive [2]. SMBHs accrete most of their mass through AGN activity [3] and mergers. AGN activity in merging galaxies is obscured, both by dust in the optical and UV wavelengths, and by atomic gas in the X-ray regime. Numerical models [4] suggest that AGN activity significantly contributes to the quenching of star formation in massive galaxies through a process known as AGN feedback, in which the energy released from AGN (either radiatively or mechanically through jets) heats up and removes cold gas reservoirs. However, major mergers trigger intense episodes of star formation and obscure AGN activity [4]. With the complex nature of AGN, multiwavelength observations are crucial to gain a better understanding of the physics of the structure, formation, and evolution of AGN and their role in the host galaxy.

The Fornax cluster, one of the closest clusters in the Southern Hemisphere, is actively assembling mass, and galaxies are subject to a variety of physical processes [5]. Several multiwavelength observing campaigns were conducted to better understand the cluster environment and the mechanisms driving galaxy transformation. These include deep-optical imaging from the Fornax Deep Survey (FDS) [6, 7], which aimed to explore the structure and evolution of low-surface brightness features of dwarf galaxies. The MeerKAT Fornax survey which focusses on tracing the cold gas content, with the aim of studying the environmental effects on galaxy evolution within the cluster. [8, 9]. The Fornax3D survey [10], uses deep integral field spectroscopic observations for 33 bright galaxies within the virial radius of the Fornax cluster and provides detailed internal kinematics, dynamical structures, and evolutionary histories within the cluster. These multiwavelength observations provide a comprehensive view of physical processes, galaxy populations, the distribution of gas, and galaxy evolution.

Recently, Hou et al. [11] studied the eROSITA observations of the Virgo and Fornax clusters, showing that the detected X-ray sources are 50 and 10, respectively, and the X-ray AGN occupation rate is 3% in both clusters, which is less than in the field. In the Fornax cluster, 10 galaxies are detected in soft X-ray, and only one of them, FCC121, is detected in hard X-ray with a 2.3-5 keV luminosity of $6.6 \times 10^{41} \mathrm{ergs}^{-1}$ [11].

In this paper, we study a subset of the 10 confirmed AGN in the Fornax cluster, to better understand the role of AGN in the cluster environment. This article is arranged as follows. In Section 2, we describe the available multiwavelength observations. In Section 3, we describe the results and discussion of multiwavelength observations and AGN classifications. In Section 4, we summarise the main findings of this work. Throughout this paper, we assume a standard ΛCDM cosmology with $\mathrm{H}_0 = 70\ \mathrm{km\ s^{-1}\ pc^{-1}}$, $\Omega_\Lambda = 0.7$, and $\Omega_M = 0.3$, and all magnitudes present in the AB system and the wide-field infrared survey Explorer (WISE) Vega system.

2 Multiwavelength observations

In this study, we used publicly available data from the Spectrum-Roentgen-Gamma/eROSITA all-sky survey, optical spectroscopic data from Multi-Unit Spectroscopic Explorer (MUSE), and infrared data from Wide-field Infrared Survey Explorer (WISE) imaging to study three galaxies FCC121, FCC179, and FCC184. These three galaxies have been detected in HI by MeerKAT [9], and their ionised gas properties are being analysed in detail by Zewdie et al. (in preparation).

2.1 X-ray data

We used a publicly available X-ray detected source catalogue [12] from the eROSITA all-sky survey [13]. The survey includes a soft band (0.2 to 2.3 keV) and a hard band (2.3 to 5 keV). Recently, Hou et al. [11] studied the X-ray detected AGNs in the nearest two clusters, namely Virgo and Fornax. They used a $10''$ radius to cross-match the sky coordinates of galactic nuclei for both clusters, the Extended Virgo Cluster Catalog (EVCC) and Fornax Cluster Catalog (FCC) catalogues, which correspond to the physical scale of 0.8 kpc and 1.0 kpc, respectively. We repeated their experiment and found FCC184 with a $9.56''$ (0.86 kpc) separation distance. We estimated the X-ray luminosity of FC184 and find that at 0.2 to 2.3 keV it is $\log(\mathrm{L_X}/[\mathrm{erg/s}]) = 40.39$ and the X-ray luminosity of FCC121 and FCC179 is $\log(\mathrm{L_X}/[\mathrm{erg/s}]) = 41.31$ and $\log(\mathrm{L_X}/[\mathrm{erg/s}]) = 40.23$, respectively [11].

2.2 Optical spectroscopic data

The VLT/MUSE offers a field of view (FoV) of 1×1 arcmin^2, with a spatial sampling of 0.2×0.2 arcsec^2 per pixel. It covers a wavelength range of 4560 to 9300 Å, with a spectral sampling of 1.25 Å per pixel and a spectral resolution of $\sim$ 2.5 Å. A total of 33 bright galaxies ($\mu_\mathrm{B} = 15\ \mathrm{mag}$) were observed with MUSE as part of the Fornax3D survey [10] and other archival MUSE observations [14, 15]. We extracted nuclear spectra from the centre using 2 arcsec apertures and fitted Gaussian profiles for the four optical emission lines: Hα, [NII], [OIII], and Hβ. These emission lines were then used to classify galaxies according to their photo-ionisation mechanism using the Baldwin, Phillips & Terlevich (BPT) diagram [16]. With this BPT classification, we can classify galaxies as star-forming, AGN (Seyfert or LINER), or composite regions of both star-forming and AGNs.

2.3 Mid-infrared data

The WISE mission observed the full sky in four mid-IR photometric bands, centred at 3.4, 4.6, 12, and 22 μm (named W1, W2, W3, and W4), respectively. We used WISE colours to study IR-obscured AGNs by applying $\mathrm{W1} - \mathrm{W2} = 0.7$ mag cut [17], to investigate the existence of IR-obscured AGN activity in the Fornax cluster.

3 Results and discussion

3.1 Multiwavelength observations of AGNs in the Fornax cluster

We emphasise that each wavelength probed gives a better understanding of different types of AGN populations. We are interested in X-ray detected sources. We have 35 galaxies HI detected, 18 of which have optical spectroscopy

(Zewdie et al., in preparation), and three are X-ray detected. Two of these are also reported by [11], and all three galaxies were also HI detected by MeerKAT. Figure 1 shows the distribution of X-ray luminosity as a function of stellar mass [18]. In the figure, galaxies detected in X-rays, and studied in this study, are shown with red stars, while magenta circles are shown from a previous study [11]. Notably, our targets exhibit greater X-ray luminosity at stellar masses comparable to all the sources in Hou et al. [11]. All soft X-ray luminosities are $\log(\mathrm{L_X}/[\mathrm{erg/s}]) \geq 39$, indicating the dominance of a genuine X-ray AGN.

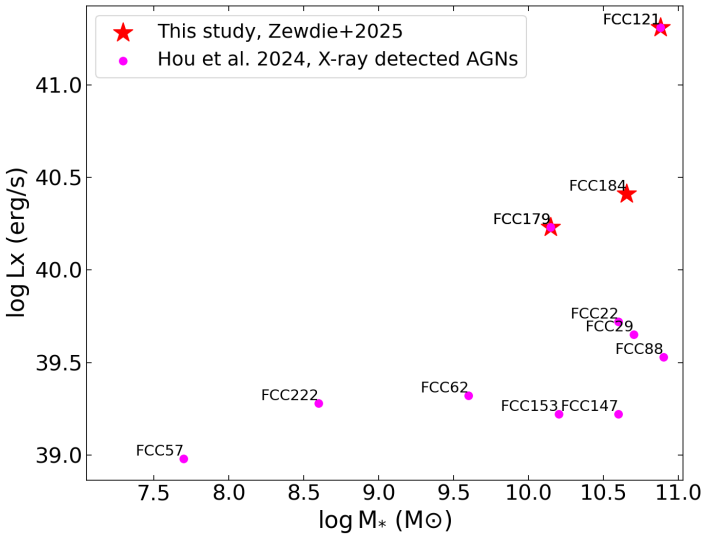

Figure 1: All soft X-ray detected galaxies in the Fornax cluster. The magenta dots are X-ray detected galaxies reported by Hou et al. [11], except FCC184 which we indicate with a red star. The only hard X-ray detected galaxy is FCC121.

We classified these three galaxies using four optical emission line ratios to differentiate their ionising mechanisms. We found that the three galaxies have different properties; FCC179 is classified as a star-forming galaxy, FCC121 is classified as a composite galaxy, and FCC184 is classified as LINER, as shown in Figure 2. We also used mid-infrared (MIR) colour diagnostics to separate AGN from non-AGN, using a $\mathrm{W1} - \mathrm{W2} = 0.7$ colour cut [17]. We found that FCC121 and FCC179 were in the AGN regime. This classification agrees with the BPT classification for FCC121. Our results suggest that FCC179 is an obscured AGN, as that is not evident in the optical BPT diagram but is confirmed by its X-ray detection. In contrast, FCC184 shows a WISE colour of almost zero, indicating that there is no significant excess of MIR from hot dust. This suggests either the absence of nuclear activity or the presence of a very low luminosity AGN, consistent with the LINER and soft X-ray detection.

Figure 3 shows the map of the ionised gas (from the MUSE observations) with the morphology of the HI (cold gas reservoir) from the MeerKAT observations. In both optical and MIR, FCC121 is classified as an AGN and its $\mathrm{H}\alpha$ emission is consistent with ongoing star formation and possible nuclear ionisation. The HI morphology of FCC121 has an extended structure and hosts a rich gas reservoir. In contrast, FCC179 shows that the strong $\mathrm{H}\alpha$ emission in the centre probably comes from the AGN. The morphology of the HI gas in FCC179 appears to be pushed away by the AGN feedback. We used HI gas contour levels of $5 \times 10^{19} \times 2^{\mathrm{n}}\ \mathrm{cm}^{-2}$. Similarly, the $\mathrm{H}\alpha$ emission lines of FCC184 dominated the centre of the galaxy, but the morphology of the HI was unresolved (angular resolution and sensitivity are not sufficient to map the spatial column density distribution). Iodice et al. [24] studied FCC179 and FCC184 by mapping their ionised gas, distinguishing HII regions, highly ionised or AGN regions, LINER-like emission regions, and areas powered by a mixture of massive star radiation and other ionisation sources. Their map indicates that FCC179 is dominated by star formation, with only localised AGN/LINER features, while FCC184 shows AGN-like gas motions, suggesting that weak AGN activity dominates its central region.

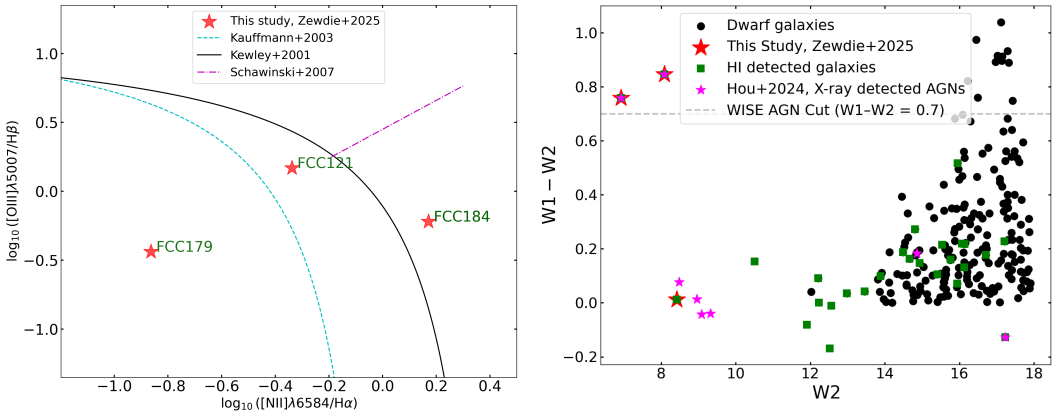

Figure 2: (*left*) The BPT diagram for the three galaxies (red stars) studied here. The BPT diagram shows that FCC121, FCC179, and FCC184 are classified as composite star-forming galaxies and a LINER, respectively. The dashed line shows the separation between pure star-forming and composite galaxies (mix of starburst and AGNs) [19]. The solid line represents the Kewley et al. [20] division between composite galaxies and AGN dominant and the dashed-dotted line shows the separation between Seyfert 2 and LINER sources [21]. (*right*) W1–W2 color versus W2 magnitude for galaxies in the Fornax cluster, to distinguish between AGNs and non AGNs based on their infrared properties. The horizontal dashed line is the WISE AGN cut, $\mathrm{W1} - \mathrm{W2} = 0.7$ [17]. The green squares are HI detected galaxies with MeerKAT [22], the magenta stars are X-ray detected AGN candidates [11], the black dots are Fornax member galaxies from FDS [23].

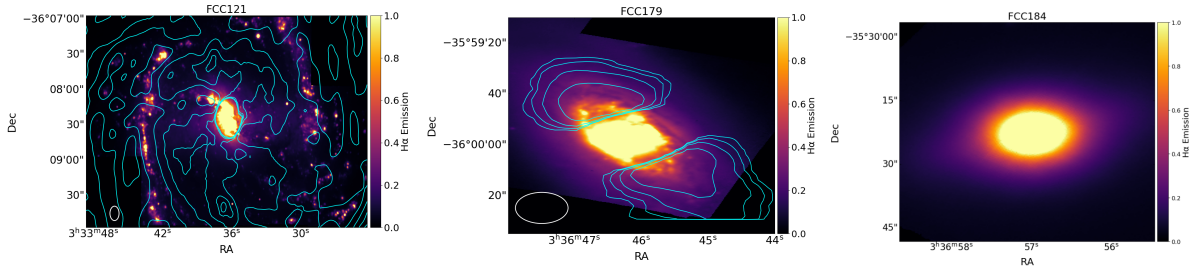

Figure 3: The Hα emission maps for the three galaxies from MUSE observations. The three galaxies are HI detected with MeerKAT, however, the HI in FCC184 was unresolved. In the left (FCC121) and middle (FCC179) panels, the HI column density is overlaid with cyan contours at level of $5 \times 10^{19} \times 2^{\mathrm{n}}$ cm^{-2} (for n = 0, 1, 2 ...). For both FCC179 and FCC212, the white ellipse in the lower-left corner shows the HI angular resolution of $12.23'' \times 9.56''$ which corresponds to physical sizes of 1.32×1.03 kpc for FCC121, and 0.70×0.55 kpc for FCC179.

4 Conclusions

We used a recently released X-ray source catalogue from eROSITA to identify galaxies detected in X-rays in the Fornax cluster for which we also have optical spectroscopic observations. We used WISE MIR colours to identify and study obscured AGN activity and dust emission. Among these three galaxies, FCC121 is the only one classified as an AGN with all the selection criteria. FCC179 is classified as a WISE AGN; however, the BPT diagram classifies it as a star-forming galaxy. This suggests that the galaxy could be heavily obscured by dust. Interestingly, the HI gas morphology of FCC179 suggests that AGN feedback is pushing the cold gas away. FCC184 is detected in X-rays, and the BPT diagram classifies it as a LINER, consistent with low-ionisation emission that may originate from weak AGN, shocks, or evolving stellar populations. The almost zero WISE colour indicates that there are no significant MIR excesses from hot dust, suggesting that if an AGN is present, it is faint, which agrees with the BPT classification. This study shows that sources are classified differently by the various classification schemes in different wavelengths and highlights the need to study sources with multiwavelength data.

5 Aknowledgements
This work is based on research supported in part by the National Research Foundation (NRF) of South Africa (NRF Grant Number: CPRR240414214079). Any opinion, finding, and conclusion or recommendation expressed in this material is that of the author(s), and the NRF does not accept any liability in this regard.

References

[1] R. Antonucci, "Unified models for active galactic nuclei and quasars." *ARA&A*, vol. 31, pp. 473–521, Jan. 1993.

[2] P. Padovani, D. M. Alexander, R. J. Assef, B. De Marco, P. Giommi, R. C. Hickox, G. T. Richards, V. Smolcic, E. Hatziminaoglou, V. Mainieri, and M. Salvato, "Active galactic nuclei: what's in a name?" *A&A Rev.*, vol. 25, no. 1, p. 2, Aug. 2017.

[3] A. Soltan, "Masses of quasars." *MNRAS*, vol. 200, pp. 115–122, Jul. 1982.

[4] P. F. Hopkins, L. Hernquist, T. J. Cox, and D. Kereš, "A Cosmological Framework for the Co-Evolution of Quasars, Supermassive Black Holes, and Elliptical Galaxies. I. Galaxy Mergers and Quasar Activity," *ApJS*, vol. 175, no. 2, pp. 356–389, Apr. 2008.

[5] M. J. Drinkwater, M. D. Gregg, and M. Colless, "Substructure and Dynamics of the Fornax Cluster," *ApJ*, vol. 548, no. 2, pp. L139–L142, Feb. 2001.

[6] E. Iodice, M. Capaccioli, A. Grado, L. Limatola, M. Spavone, N. R. Napolitano, M. Paolillo, R. F. Peletier, M. Cantiello, T. Lisker, C. Wittmann, A. Venhola, M. Hilker, R. D'Abrusco, V. Pota, and P. Schipani, "The Fornax Deep Survey with VST. I. The Extended and Diffuse Stellar Halo of NGC 1399 out to 192 kpc," *ApJ*, vol. 820, no. 1, p. 42, Mar. 2016.

[7] A. Venhola, R. Peletier, E. Laurikainen, H. Salo, E. Iodice, S. Mieske, M. Hilker, C. Wittmann, T. Lisker, M. Paolillo, M. Cantiello, J. Janz, M. Spavone, R. D'Abrusco, G. van de Ven, N. Napolitano, G. Verdoes Kleijn, N. Maddox, M. Capaccioli, A. Grado, E. Valentijn, J. Falcón-Barroso, and L. Limatola, "The Fornax Deep Survey with the VST. IV. A size and magnitude limited catalog of dwarf galaxies in the area of the Fornax cluster," *A&A*, vol. 620, p. A165, Dec. 2018.

[8] P. Serra, W. J. G. de Blok, G. L. Bryan, S. Colafrancesco, R. J. Dettmar, B. S. Frank, F. Govoni, G. I. G. Jozsa, R. C. Kraan-Korteweg, F. M. Maccagni, S. I. Loubser, M. Murgia, T. A. Oosterloo, R. F. Peletier, R. Pizzo, L. Richter, M. Ramatsoku, M. W. L. Smith, S. C. Trager, J. H. van Gorkom, and M. A. W. Verheijen, "The MeerKAT Fornax Survey," in *MeerKAT Science: On the Pathway to the SKA*, Jan. 2016, p. 8.

[9] D. Kleiner, P. Serra, F. M. Maccagni, M. A. Raj, W. J. G. de Blok, G. I. G. Józsa, P. Kamphuis, R. Kraan-Korteweg, F. Loi, A. Loni, S. I. Loubser, D. C. Molnár, T. A. Oosterloo, R. Peletier, and D. J. Pisano, "The MeerKAT Fornax Survey. II. The rapid removal of H I from dwarf galaxies in the Fornax cluster," *A&A*, vol. 675, p. A108, Jul. 2023.

[10] M. Sarzi, E. Iodice, L. Coccato, E. M. Corsini, P. T. de Zeeuw, J. Falcón-Barroso, D. A. Gadotti, M. Lyubenova, R. M. McDermid, G. van de Ven, K. Fahrion, A. Pizzella, and L. Zhu, "Fornax3D project: Overall goals, galaxy sample, MUSE data analysis, and initial results," *A&A*, vol. 616, p. A121, Aug. 2018.

[11] M. Hou, Z. Hu, and Z. Li, "An X-Ray Census of Active Galactic Nuclei in the Virgo and Fornax Clusters of Galaxies with SRG/eROSITA," *ApJ*, vol. 965, no. 2, p. L24, Apr. 2024.

[12] A. Merloni, G. Lamer, T. Liu, M. E. Ramos-Ceja, H. Brunner, E. Bulbul, K. Dennerl, V. Doroshenko, M. J. Freyberg, S. Friedrich, E. Gatuzz, A. Georgakakis, F. Haberl, Z. Igo, I. Kreykenbohm, A. Liu, C. Maitra, A. Malyali, M. G. F. Mayer, K. Nandra, P. Predehl, J. Robrade, M. Salvato, J. S. Sanders, I. Stewart, D. Tubín-Arenas, P. Weber, J. Wilms, R. Arcodia, E. Artis, J. Aschersleben, A. Avakyan, C. Aydar, Y. E. Bahar, F. Balzer, W. Becker, K. Berger, T. Boller, W. Bornemann, M. Brüggen, M. Brusa, J. Buchner, V. Burwitz, F. Camilloni, N. Clerc, J. Comparat, D. Coutinho, S. Czesla, S. M. Dannhauer, L. Dauner, T. Dauser, J. Dietl, K. Dolag, T. Dwelly, K. Egg, E. Ehl, S. Freund, P. Friedrich, R. Gaida, C. Garrel, V. Ghirardini, A. Gokus, G. Grünwald, S. Grandis, I. Grotova, D. Gruen, A. Gueguen, S. Hämmerich, N. Hamaus, G. Hasinger, K. Haubner, D. Homan, J. Ider Chitham, W. M. Joseph, A. Joyce, O. König, D. M. Kaltenbrunner, A. Khokhriakova, W. Kink, C. Kirsch, M. Kluge, J. Knies, S. Krippendorf, M. Krumpe, J. Kurpas, P. Li, Z. Liu, N. Locatelli, M. Lorenz, S. Müller, E. Magaudda, C. Mannes, H. McCall, N. Meidinger, M. Michailidis, K. Migkas, D. Muñoz-Giraldo, B. Musiimenta, N. T. Nguyen-Dang, Q. Ni, A. Olechowska, N. Ota,

F. Pacaud, T. Pasini, E. Perinati, A. M. Pires, C. Pommranz, G. Ponti, K. Poppenhaeger, G. Pühlhofer, A. Rau, M. Reh, T. H. Reiprich, W. Roster, S. Saeedi, A. Santangelo, M. Sasaki, J. Schmitt, P. C. Schneider, T. Schrabback, N. Schuster, A. Schwope, R. Seppi, M. M. Serim, S. Shreeram, E. Sokolova-Lapa, H. Starck, B. Stelzer, J. Stierhof, V. Suleimanov, C. Tenzer, I. Traulsen, J. Trümper, K. Tsuge, T. Urrutia, A. Veronica, S. G. H. Waddell, R. Willer, J. Wolf, M. C. H. Yeung, A. Zainab, F. Zangrandi, X. Zhang, Y. Zhang, and X. Zheng, "The SRG/eROSITA all-sky survey. First X-ray catalogues and data release of the western Galactic hemisphere," *A&A*, vol. 682, p. A34, Feb. 2024.

[13] R. Sunyaev, V. Arefiev, V. Babyshkin, A. Bogomolov, K. Borisov, M. Buntov, H. Brunner, R. Burenin, E. Churazov, D. Coutinho, J. Eder, N. Eismont, M. Freyberg, M. Gilfanov, P. Gureyev, G. Hasinger, I. Khabibullin, V. Kolmykov, S. Komovkin, R. Krivonos, I. Lapshov, V. Levin, I. Lomakin, A. Lutovinov, P. Medvedev, A. Merloni, T. Mernik, E. Mikhailov, V. Molodtsov, P. Mzhelsky, S. Müller, K. Nandra, V. Nazarov, M. Pavlinsky, A. Poghodin, P. Predehl, J. Robrade, S. Sazonov, H. Scheuerle, A. Shirshakov, A. Tkachenko, and V. Voron, "SRG X-ray orbital observatory. Its telescopes and first scientific results," *A&A*, vol. 656, p. A132, Dec. 2021.

[14] D. A. Gadotti, P. Sánchez-Blázquez, J. Falcón-Barroso, B. Husemann, M. Seidel, R. Leaman, G. Leung, G. van de Ven, M. Querejeta, F. Fragkoudi, A. d. de Lorenzo-Cáceres, J. Méndez-Abreu, I. Pérez, T. Kim, I. Martinez-Valpuesta, P. Coelho, C. Donohoe-Keyes, M. Martig, and J. Neumann, "Investigating the Formation and Evolution of Massive Disc Galaxies with the MUSE TIMER Project," *The Messenger*, vol. 173, pp. 28–32, Sep. 2018.

[15] N. Zabel, A. Loni, M. Sarzi, P. Serra, A. Chawla, T. A. Davis, D. Kleiner, S. I. Loubser, and R. Peletier, "A resolved, multiwavelength study of gas-rich dwarf galaxies in the Fornax cluster using MUSE, MeerKAT, and ALMA," *MNRAS*, vol. 535, no. 3, pp. 2538–2561, Dec. 2024.

[16] J. A. Baldwin, M. M. Phillips, and R. Terlevich, "Classification parameters for the emission-line spectra of extragalactic objects." *PASP*, vol. 93, pp. 5–19, Feb. 1981.

[17] R. J. Assef, D. Stern, C. S. Kochanek, A. W. Blain, M. Brodwin, M. J. I. Brown, E. Donoso, P. R. M. Eisenhardt, B. T. Jannuzi, T. H. Jarrett, S. A. Stanford, C. W. Tsai, J. Wu, and L. Yan, "Mid-infrared Selection of Active Galactic Nuclei with the Wide-field Infrared Survey Explorer. II. Properties of WISE-selected Active Galactic Nuclei in the NDWFS Boötes Field," *ApJ*, vol. 772, no. 1, p. 26, Jul. 2013.

[18] A. H. Su, H. Salo, J. Janz, E. Laurikainen, A. Venhola, R. F. Peletier, E. Iodice, M. Hilker, M. Cantiello, N. Napolitano, M. Spavone, M. A. Raj, G. van de Ven, S. Mieske, M. Paolillo, M. Capaccioli, E. A. Valentijn, and A. E. Watkins, "The Fornax Deep Survey (FDS) with the VST. XI. The search for signs of preprocessing between the Fornax main cluster and Fornax A group," *A&A*, vol. 647, p. A100, Mar. 2021.

[19] G. Kauffmann, T. M. Heckman, C. Tremonti, J. Brinchmann, S. Charlot, S. D. M. White, S. E. Ridgway, J. Brinkmann, M. Fukugita, P. B. Hall, Ž. Ivezić, G. T. Richards, and D. P. Schneider, "The host galaxies of active galactic nuclei," *MNRAS*, vol. 346, no. 4, pp. 1055–1077, Dec. 2003.

[20] L. J. Kewley, B. Groves, G. Kauffmann, and T. Heckman, "The host galaxies and classification of active galactic nuclei," *MNRAS*, vol. 372, no. 3, pp. 961–976, Nov. 2006.

[21] K. Schawinski, D. Thomas, M. Sarzi, C. Maraston, S. Kaviraj, S.-J. Joo, S. K. Yi, and J. Silk, "Observational evidence for AGN feedback in early-type galaxies," *MNRAS*, vol. 382, no. 4, pp. 1415–1431, Dec. 2007.

[22] D. Kleiner, P. Serra, F. M. Maccagni, A. Venhola, K. Morokuma-Matsui, R. Peletier, E. Iodice, M. A. Raj, W. J. G. de Blok, A. Comrie, G. I. G. Józsa, P. Kamphuis, A. Loni, S. I. Loubser, D. C. Molnár, S. S. Passmoor, M. Ramatsoku, A. Sivitilli, O. Smirnov, K. Thorat, and F. Vitello, "A MeerKAT view of preprocessing in the Fornax A group," *A&A*, vol. 648, p. A32, Apr. 2021.

[23] A. H. Su, H. Salo, J. Janz, A. Venhola, and R. F. Peletier, "Photometric properties of nuclear star clusters and their host galaxies in the Fornax cluster," *A&A*, vol. 664, p. A167, Aug. 2022.

[24] E. Iodice, M. Sarzi, A. Bittner, L. Coccato, L. Costantin, E. M. Corsini, G. van de Ven, P. T. de Zeeuw, J. Falcón-Barroso, D. A. Gadotti, M. Lyubenova, I. Martín-Navarro, R. M. McDermid, B. Nedelchev, F. Pinna, A. Pizzella, M. Spavone, and S. Viaene, "The Fornax3D project: Tracing the assembly history of the cluster from the kinematic and line-strength maps," *A&A*, vol. 627, p. A136, Jul. 2019.

Modelling Crab-like and Vela-like Pulsars and their Nebulae

T M Nyambe[1], C Venter[1,2], B W Stappers[3], and AK Harding [4]

[1] Centre for Space Research, North-West University, Private Bag X6001, Potchefstroom 2520, South Africa
[2] National Institute for Theoretical and Computational Sciences (NITheCS), Potchefstroom, 2520, South Africa
[3] Jodrell Bank Centre for Astrophysics, University of Manchester, Manchester M13 9PL, UK
[4] Theoretical Division, Los Alamos National Laboratory, Los Alamos, NM 58545, USA

E-mail: 31038018@mynwu.ac.za

Abstract. Crab-like and Vela-like pulsars are young, rapidly rotating neutron stars with strong magnetic fields. Their rotational energy powers pulsed radio and gamma-ray emissions, as well as the surrounding pulsar wind nebulae (PWNe). Crab-like pulsars power compact, high-luminosity nebulae and exhibit characteristic features such as phase-aligned radio and gamma-ray light curves, while Vela-like pulsars power more diffuse PWNe and exhibit phase lags between their radio and gamma-ray pulses. We identify a few bright pulsars and recover their geometric parameters, such as the magnetic inclination and viewing angle, by fitting radio polarisation data with the Rotating Vector Model (RVM). Then, we reproduce their joint radio and gamma-ray light curves using the radio Cone, Two-Pole Caustic, and Outer Gap models. This unified radio and gamma-ray modelling approach constrains the pulsar's geometry and helps us to identify the likely regions of particle acceleration within the magnetosphere, laying the foundation for the combined spectral and spatial modelling of their nebulae. Our results demonstrate a reasonable agreement between the models and observations, underscoring the significance of viewing geometry in pulsar emission.

1 Introduction

Pulsars, first discovered in 1967 by Jocelyn Bell and Antony Hewish [1], are rapidly rotating, highly magnetised neutron stars formed from the core collapse of massive stars with mass $> 8M_{\odot}$. Their combined rapid rotation and strong B-field generate a strong electric field, which extracts charged particles from the star's surface and accelerates them to relativistic energies, emitting radiation over most of the electromagnetic spectrum, from radio to gamma rays. Pulsars offer some of the most extreme environments in the universe, making them a valuable tool for studying physics under extreme conditions. A multi-wavelength study of pulsars is crucial because each emission mechanism (e.g., coherent radio emission, synchrotron radiation, or inverse Compton scattering) plausibly occurs in different regions within their magnetosphere and surrounding environment. The diversity in the observed shapes and structures of the pulse light curves across wavebands hints at where and how the radiation is generated within the complex geometric structure of the magnetosphere.

To unravel the dissipation processes implied by the light curves, there exist emission and geometric models that explain the complex magnetospheric structures and emission mechanisms of pulsars. Each model assumes a different emission location and B-field structure. The Rotating Vector Model (RVM) provides information about the basic geometric structure of the pulsar B-field relative to our line of sight [2]. The model assumes that the radio emission originates in a narrow region above the polar cap in a static, dipolar, vacuum field. The radio conal

model [3], the Two-Pole Caustic (TPC) model [4, 5], and the Outer Gap (OG) model [6, 7], place the radio and high-energy emission regions at specific locations within the magnetosphere, using either a vacuum retarded or force-free magnetic field. In the high-energy models, acceleration zones form due to the absence of the required charge density (i.e., relatively charge-depleted zones with a charge density lower than the Goldreich-Julian charge density, [8]). The rotational energy lost by the pulsar is converted into pulsed emission, but predominantly into a wind of relativistic particles that powers and shapes the surrounding pulsar wind nebula (PWN).

While research on pulsars has often focused on single-wavelength analysis, our work presents a holistic approach. We aim to build a unified pulsar-PWN framework by integrating the RVM, joint radio and gamma-ray light curve fitting, and PWN modelling. This approach allows us to cross-validate the geometric parameters across the different wavebands. Our objective is to constrain the geometric parameters of our selected Crab-like and Vela-like pulsars using the RVM. Next, we will simulate the radio and gamma-ray light curves based on the radio conal and high-energy (OG, TPC) models and then fit them to the observed data, comparing our results with those found by using the RVM. We will then use the geometric parameters constrained by the radio and gamma-ray models (the magnetic inclination angle α, and the viewing angle ζ) to guide our PWN modelling. We will additionally perform spectral and spatial modelling using a PWN model [9], as well as comparing our geometric constraints with those obtained by independent torus-jet fitting in the literature (e.g., [10]). Our approach in connecting the central pulsar to its extended energetic surrounding environment will follow the method of Maitra et al. [11], who demonstrated the importance of geometric parameter constraints for realistic PWN modelling, also incorporating independent results from jet-torus fitting. In this paper, we present our methodology and first results towards a unified understanding of the pulsar-PWN system.

2 Pulsar Sample And Data

The pulsars used for our study are selected based on specific criteria. They must be young ($\tau_{\rm c} < 150$ kyr) and located in the southern hemisphere, a geographical requirement due to the location of the MeerKAT radio telescope. Furthermore, our selection criteria required that our pulsars must have high-quality radio data, characterised by their high signal-to-noise ratio (SNR) and a well-shaped, S-shaped polarisation position angle (PA) curve, in combination with statistically significant gamma-ray pulsed emission, with a well-defined pulse profile. From our selection criteria, we were able to select 10 pulsars that demonstrate clear Crab-like and Vela-like characteristics. Table 1 shows the two examples of pulsars used in this paper. PSR B0301+19 is not included in our main sample due to its older age, but is used separately as a calibration source for our RVM fitting procedure [12]. We selected these types of pulsars because they represent different evolutionary stages and magnetospheric configurations, which offer an opportunity to test our integrated approach. We used high-quality gamma-ray data from the Third *Fermi* Pulsar Catalogue (3PC)[1], which contains data from 14 years of on-orbit observations from the *Fermi*-LAT [13]. The radio data used here are obtained exclusively from public archives such as the Australia Telescope National Facility (ATNF)[2] and the European Pulsar Network (EPN)[3] Data Archive and are well calibrated with established timing solutions.

PSR Name	P (s)	$\tau_{\rm c}$ (kyr)	Distance (kpc)	$B_{\rm s}$ (10^{12} G)	$\dot{E}_{\rm rot}$ (ergs/s)
B0301+19 (calibration source)	1.4	17000	0.749	1.36	1.9×10^{31}
J1048−5832 (Vela-like)	0.12	20.4	2.9	3.49	2.0×10^{36}

Table 1: The parameters for two representative pulsars: period P, characteristic age $\tau_{\rm c} = P/(2\dot{P})$, distance, surface dipole field $B_{\rm s} = 3.2 \times 10^{19}\sqrt{P\dot{P}}$ G, and spin-down power $\dot{E}_{\rm rot}$.

3 Method

3.1 Radio Emission Geometry: RVM

To understand pulsar emission, one must first understand the geometry of its B-field. The RVM [2] describes the observed radio PA swing as a function of spin phase Φ by assuming the magnetic dipole is rotating, while

[1] https://fermi.gsfc.nasa.gov/ssc/data/access/lat/3rd_PSR_catalog/

[2] https://www.atnf.csiro.au/research/pulsar/psrcat/

[3] https://psrweb.jb.man.ac.uk/epndb/

approximating the field structure as that of a static, non-retarded dipole in vacuum:

$$\Psi = \Psi_0 + \arctan\left(\frac{\sin\alpha\sin(\Phi-\Phi_0)}{\sin(\alpha+\beta)\cos\alpha - \cos(\alpha+\beta)\sin\alpha\cos(\Phi-\Phi_0)}\right),$$

where $\Psi(\Phi)$ is the observed PA, Ψ_0 is the reference position angle at the fiducial plane (phase Φ_0), α is the magnetic inclination angle, and β is the smallest angle (impact angle) between the magnetic axis and the observer's line of sight ζ.

Our RVM fitting process involved several steps we implemented in Python. We first extracted the Stokes parameters (I, Q, U, V) from our data and then debiased the linear polarisation (L) using the method explained in Everett et al. [12]. In cases where our PA was discontinuous, we inserted a 90° angle to account for different emission modes, as the classic RVM does not account for such cases. With our PA continuous, we performed a χ^2 minimisation to fit the RVM to the PA curve of our pulsar, using Python's Scipy curve fit function[4].

The parameters α and β are covariant, and if there are not enough data points, the solution may converge to a local minimum. To avoid this, we implemented a two-step fit strategy. First, we performed a χ^2 grid search and obtained robust initial guesses for our parameters α and β. Then, we used our optimised initial guess with the curve fit function, employing the Levenberg-Marquardt algorithm for our final fit [14].

3.2 Radio and Gamma-ray Light Curve Simulations

For our simulations, we used a geometric modelling code that uses various magnetospheric gap geometries, and assumed constant emissivity in the corotating frame [15, 3, 5]. Our simulation focused on the conal radio model, as well as the TPC and OG gamma-ray models. Each model predicts a different region of emission within the magnetosphere. Charged particles are extracted from the surface and accelerated to relativistic energies by the unscreened electric field. These charged particles emit gamma-ray photons via curvature radiation and interact with the intense B-field above the polar caps, producing electron-positron pairs that initiate a cascade. Gaps or charge-depleted regions act as accelerators of particles within the magnetosphere. The radio conal model places the radio emission at a low altitude above the stellar surface.

The TPC places the acceleration region along the last open B-field lines and stretches from the stellar surface to nearly up to the light cylinder. The accelerated charged particles produce caustics when the emission from different altitudes overlaps in phase, resulting in double-peaked light curves with bridge emission. The OG model places the acceleration gap above the null charge surface, where the Goldreich-Julian charge density changes sign, and extends outwards towards the light cylinder. We generate simulations of radio and gamma-ray light curves across a range of α and ζ values. These model light curves are then fit to observed ones by minimising the χ^2 statistic, following the method described by Seyffert et al. [16] to constrain the parameters α and ζ. By jointly fitting radio and gamma-ray light curves, one may potentially obtain stronger constraints.

4 Results

4.1 Radio RVM Fit Results: PSR B0301+19

Investigator	$\alpha\,[^\circ]$	$\beta\,[^\circ]$	$\Psi_0\,[^\circ]$	$\Phi_0\,[^\circ]$	χ^2	ν	χ^2_ν
This work	68.56 ± 18.39	2.86 ± 0.41	120.16 ± 0.65	-3.49 ± 0.06	84.01	52	1.62
Everett & Weisberg (2001) [12]	162.0 ± 11.8	0.96 ± 0.63	–	-3.71 ± 0.006	–	–	15.6
Blaskiewicz et al. (1991) [17]	69 ± 16	2.9 ± 0.3	–	–	–	–	1.42

Table 2: Comparison of RVM fit parameters for PSR B0301+19: our results, those of Everett and Weisberg [12], and the relativistic RVM of Blaskiewicz et al. [17]. The dashes indicates that the original paper did not report those parameters.

Our RVM fitting produced well-constrained geometric parameters (α, β, Ψ_0, and Φ_0) for PSR B0301+19. The results of our best-fit parameters are presented in Table 2 along with the associated uncertainties and the goodness-of-fit value χ^2_ν. Our results in Table 2 are compared with the results of other investigators on the same pulsar.

[4] `https://docs.scipy.org/doc/scipy/reference/generated/scipy.optimize.curve_fit.html`

Figure 1 shows the radio pulse profile observed for PSR B0301+19. The top panel displays the averaged pulse profile, and the bottom panel shows the polarisation PA (blue) with the best-fit RVM curve (red), indicating a reasonable fit. The derived values of α, β, and Ψ_0 show some consistency with previous studies of the same pulsar. Although the values of α and Φ_0 are close and our χ^2_ν is reasonably close to 1, the α of Everett and Weisberg seems very different. Even $180^\circ - \alpha = 18^\circ$ is different from 69°. This may be due to data quality issues that they encountered. In addition, differences in the fitting method, such as the fraction of the pulse phase they used, may also play a role.

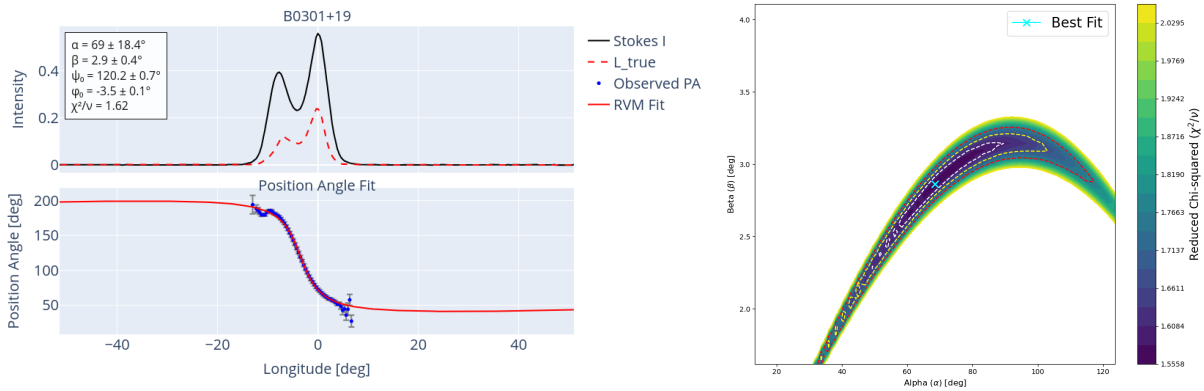

Figure 1: Plot of the RVM fitting for PSR B0301+19. The left panel displays the pulsar profile in Stokes parameters, intensity (black) and linear polarisation (red dashed). The PA is in blue, and the best-fit RVM is in red in the bottom left panel. The right panel displays the α-β plane. The image is a χ^2 contour plot, with the blue cross representing the best fit for B0301+19. The contours represent the 1σ, 2σ, and 3σ confidence regions for the fitted parameters (α and ζ), based on standard $\Delta\chi^2$ values of 2.30, 6.18, and 11.83, respectively, for a two-parameter fit [18].

4.2 Initial Radio And Gamma-ray Light Curve Simulations: PSR J1048-5832

Figure 2 shows the radio and gamma-ray light curves generated by our simulation for the radio cone, the TPC, and the OG models. Our simulations are illustrative examples, not fits to the actual data. The fitting of our simulated light curves to the observed data will be presented in a future work.

5 Conclusion

In this paper, we presented the methodology and initial results of a novel, multi-wavelength study of pulsar emission, integrating the radio RVM with joint radio and gamma-ray light curve simulations. Our application of the RVM to PSR B0301+19 has yielded geometric parameters of α and β that are consistent with the RVM modelling of other investigators. The difference in our results is due to the differing data quality and fitting method used by us and by them. We will next deploy our code to our sample of selected pulsars. We have also successfully produced the radio and gamma-ray light curves using the set of magnetospheric models (conal radio, TPC, and OG), and we have begun the process of jointly fitting these simulations to observed radio and *Fermi*-LAT data, thereby constraining the high-energy emission geometry. Our unified approach promises a direct comparison of the geometric parameters derived from the different wavebands and geometric models, which will offer us better insights into the complex magnetospheric structure and emission mechanisms of the pulsar-PWN system.

6 Future Work

In the future, we will focus on completing the fitting of our RVM and the simulated radio and gamma-ray light curves to the full observed dataset of our entire pulsar sample. Following this, we will apply a PWN model [9, 19] to model spectral and spatial data. We will also use published fitting results from the jet-torus PWN model to further constrain our model parameters. While our gamma-ray models are slightly dated, we use them to demonstrate our methodology, since they are computationally inexpensive and they produce skymaps (intensity vs. observer angle and phase) that are similar to those of the more expensive current sheet models. In future, we will implement a geometric current sheet model (e.g., [20]) and compare the resulting gamma-ray light curve predictions with

our current results. Our approach will be applied comparatively to Crab-like and Vela-like pulsars, which will contribute to our understanding of the complete pulsar-PWN system, bridging the gap between the energy supplier and its extended nebula.

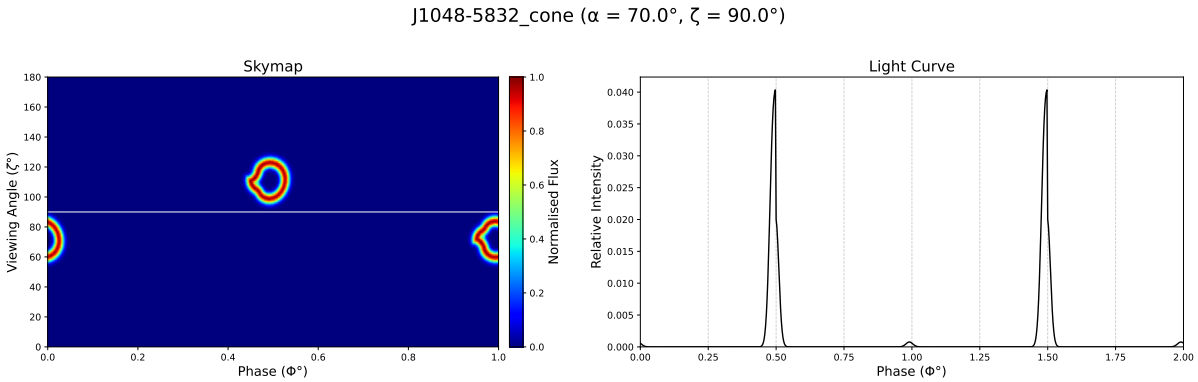

(a) Illustrative radio conal model of PSR J1048-5832 at $\alpha = 70^\circ$, $\zeta = 90^\circ$.

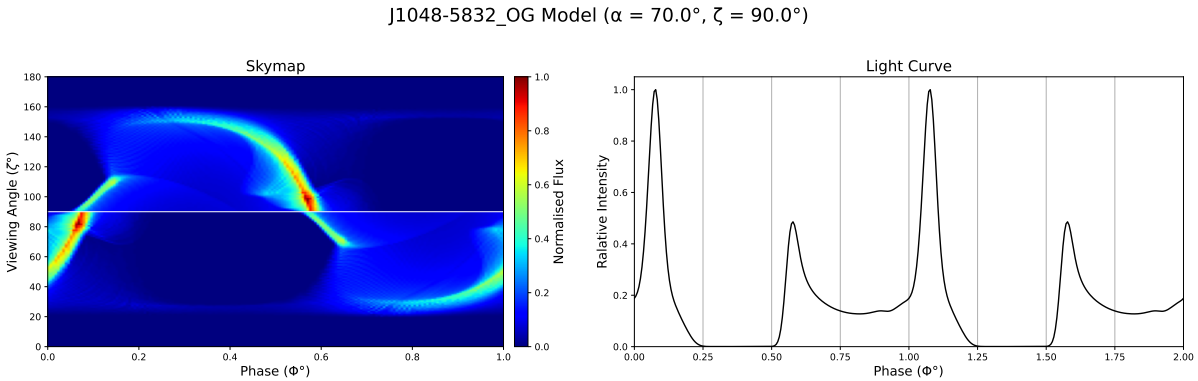

(b) OG model of PSR J1048-5832 with same geometry as Fig. 2a.

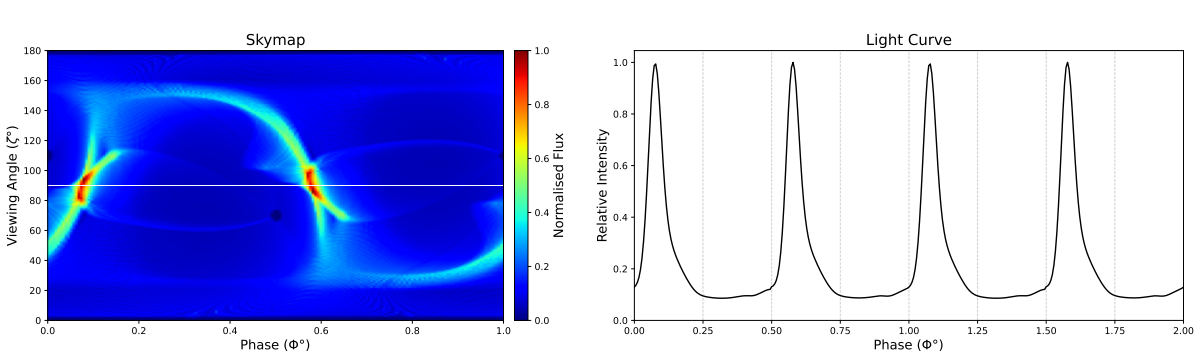

(c) TPC model of PSR J1048-5832 with same geometry as Fig. 2a.

Figure 2: Simulated phaseplots (left) and light curves (right) for PSR J1048-5832 under one radio and two gamma-ray models: (a) radio conal, (b) OG, and (c) TPC, all at $\alpha = 70^\circ$, $\zeta = 90^\circ$. The light curves are simulated to show two full rotations for clarity.

References

[1] A. Hewish, S. J. Bell, J. D. H. Pilkington, P. F. Scott, and R. A. Collins, "Observation of a Rapidly Pulsating Radio Source," *Nature*, vol. 217, no. 5130, pp. 709–713, Feb. 1968.

[2] V. Radhakrishnan and D. J. Cooke, "Magnetic Poles and the Polarization Structure of Pulsar Radiation," *Astrophys. Lett.*, vol. 3, p. 225, Jan. 1969.

[3] S. A. Story, P. L. Gonthier, and A. K. Harding, "Population Synthesis of Radio and γ-Ray Millisecond Pulsars from the Galactic Disk," *ApJ*, vol. 671, no. 1, pp. 713–726, Dec. 2007.

[4] J. Dyks and B. Rudak, "Two-Pole Caustic Model for High-Energy Light Curves of Pulsars," *ApJ*, vol. 598, no. 2, pp. 1201–1206, Dec. 2003.

[5] C. Venter, A. K. Harding, and L. Guillemot, "Probing Millisecond Pulsar Emission Geometry Using Light Curves from the *Fermi*/Large Area Telescope," *ApJ*, vol. 707, no. 1, pp. 800–822, Dec. 2009.

[6] K. S. Cheng, C. Ho, and M. Ruderman, "Energetic Radiation from Rapidly Spinning Pulsars. I. Outer Magnetosphere Gaps," *ApJ*, vol. 300, p. 500, Jan. 1986.

[7] R. W. Romani, "Gamma-Ray Pulsars: Radiation Processes in the Outer Magnetosphere," *ApJ*, vol. 470, p. 469, Oct. 1996.

[8] P. Goldreich and W. H. Julian, "Pulsar Electrodynamics," *ApJ*, vol. 157, p. 869, Aug. 1969.

[9] C. van Rensburg, C. Venter, A. S. Seyffert, and A. K. Harding, "Exploiting morphological data from Pulsar Wind Nebulae via a spatio-temporal leptonic transport code," *MNRAS*, vol. 492, no. 3, pp. 3091–3102, Mar. 2020.

[10] C. Y. Ng and R. W. Romani, "Fitting Pulsar Wind Tori," *ApJ*, vol. 601, no. 1, pp. 479–484, Jan. 2004.

[11] C. Maitra, F. Acero, and C. Venter, "Constraining the geometry of PSR J0855-4644: A nearby pulsar wind nebula with double torus/jet morphology," *A&A*, vol. 597, p. A75, Jan. 2017.

[12] J. E. Everett and J. M. Weisberg, "Emission Beam Geometry of Selected Pulsars Derived from Average Pulse Polarization Data," *ApJ*, vol. 553, no. 1, pp. 341–357, May 2001.

[13] D. A. Smith et al. , "The Third Fermi Large Area Telescope Catalog of Gamma-Ray Pulsars," *ApJ*, vol. 958, no. 2, p. 191, Dec. 2023.

[14] J. J. Moré, "The Levenberg-Marquardt algorithm: Implementation and theory," in *Lecture Notes in Mathematics, Berlin Springer Verlag*, 1978, vol. 630, pp. 105–116.

[15] J. Dyks, A. K. Harding, and B. Rudak, "Relativistic Effects and Polarization in Three High-Energy Pulsar Models," *ApJ*, vol. 606, no. 2, pp. 1125–1142, May 2004.

[16] A. S. Seyffert, C. Venter, A. K. Harding, J. Allison, and W. D. Schutte, "Implementation of a goodness-of-fit test for finding optimal concurrent radio and gamma-ray pulsar light curves," *arXiv e-prints*, p. arXiv:1611.01076, Nov. 2016.

[17] M. Blaskiewicz, J. M. Cordes, and I. Wasserman, "A Relativistic Model of Pulsar Polarization," *ApJ*, vol. 370, p. 643, Apr. 1991.

[18] P. R. Bevington and D. K. Robinson, *Data Reduction and Error Analysis for the Physical Sciences*. Boston: McGraw-Hill, 2003.

[19] A. Kundu, J. C. Joshi, C. Venter, N. E. Engelbrecht, W. Zhang, D. F. Torres, I. Sushch, and S. J. Tanaka, "Spatio-spectral-temporal modelling of two young pulsar wind nebulae," *MNRAS*, vol. 535, no. 3, pp. 2415–2435, Dec. 2024.

[20] J. Pétri, "Multi-wavelength pulse profiles from the force-free neutron star magnetosphere," *A&A*, vol. 687, p. A169, Jul. 2024.

Search for persistent radio emission towards selected localised Fast Radio Burst positions using the MeerKAT Telescope

Thulo Letsele[1], Lebogang Mfulwane[1], Christo Venter[1,2], James O. Chibueze [3,4], and Mechiel Christiaan Bezuidenhout[5,1]

[1]Centre for Space Research, North-West University, Private Bag X6001, Potchefstroom 2520, South Africa
[2]National Institute for Theoretical and Computational Sciences (NITheCS), Potchefstroom, 2520, South Africa
[3]Department of Mathematical Sciences, University of South Africa, Cnr Christian de Wet Rd and Pioneer Avenue, Florida Park, 1709, Roodepoort, South Africa
[4]Department of Physics and Astronomy, Faculty of Physical Sciences, University of Nigeria, Carver Building, 1 University Road, Nsukka 410001, Nigeria
[5]SKA Observatory, 2 Fir Street, Observatory 7925, Cape Town, South Africa

E-mail: thuloletsele1999@gmail.com

Abstract. Fast Radio Bursts (FRBs) are millisecond-duration radio pulses originating from cosmological distances, as indicated by their large dispersion measures. While numerous FRBs have now been localised to their host galaxies, a distinct class of compact electromagnetic counterpart, a Persistent Radio Source (PRS), has also been identified in some cases. Currently, only three, and possible a fourth repeating FRBs (FRB20121102A, FRB20190417A, FRB20190520B, and FRB20240114A) have confirmed associations with a PRS. Insight into progenitors, local environments, and the evolution of FRBs can be clarified by characterising these PRSs. In this work, we present 2 detected candidate PRSs using MeerKAT radio telescope data and one non-detection (as part of a larger study involving 25 FRB positions). Both FRB20221106 and FRB20181112 were found to have a host galaxy, and whether the detected radio continuum emission comes from the host galaxy or PRS is still an open question. High-resolution observations from a telescope such as e-MERLIN are required to resolve this question. If a compact PRS is detected, this telescope will provide the size, and investigate the flux variability and spectral shape of this compact PRS. Lastly, in the case of FRB220190102, which was observed over two epochs, no radio continuum was detected. However, a flux upper limit is provided for both epochs.

1 Introduction

Radio transients with signals lasting in the range of micro to milliseconds, and characterised by luminosities that make them visible over extragalactic distances [1, 2], are known as Fast Radio Bursts (FRBs). They were first discovered in 2007 when Duncan Lorimer and his student were analysing archival data of Manchester et al. [3], searching for a sub-population of pulsars known as rotating radio transients. FRBs were believed to be one-off events until the discovery of the first repeating FRB [4], which was localised with the Karl G. Jansky Very Large Array (VLA) to a dwarf star-forming galaxy of redshift of $z = 0.19$ following its discovery [5, 6]. The mechanism behind the radiation and the origin of FRBs remains a mystery.

Many researchers have proposed different possible progenitors for FRBs. These include the merging of a white dwarf and a black hole [7], the merger of binary white dwarf stars [8], the collision of two neutron stars [9], and the interaction of neutron stars with active galactic nuclei [10][1]. The magnetar model became an interesting model because [11] suggested that magnetar flares can produce FRBs. In addition, the association of the Galactic magnetar SGR J1935+2154 with FRB20200428 provided strong support for the magnetar model [12, 13].

The environment in which FRBs occur is also a subject of interest to researchers. A Persistent Radio Source (PRS) observed in the vicinity of the FRB environment may provide important constraints on this environment. Currently, there are three, and possible a fourth actively repeating FRBs associated with PRSs [14, 15, 5, 16]. Most of these PRSs show high Faraday rotation measures (RMs), which suggests that the environment contains a compact nebula that is highly magnetised. Bruni et al. [17] suggested that low RMs cannot be detected, and this can explain the low number of FRBs with PRSs. The nature of the PRS also remains a mystery, and scenarios proposed to explain this include a connection between supernova remnants and FRBs [18] and binary systems [19].

Three FRBs, namely FRB20181112, FRB20190102, and FRB20221106, form part of this work. FRB20181112 and FRB20190102 show dispersion measures (DMs) of 589.27 pc cm^{-3} and 363.6 pc cm^{-3}, with corresponding redshifts of $z = 0.4755$ and $z = 0.291$, respectively [20]. Both FRB20181112 and FRB20190102 are non-repeating FRBs that have significantly contributed to the Macquart relation and cosmological constraints [21]. Lastly, we include FRB20221106, which remains one of the least studied FRBs; not much information about this FRB is available.

The goal of this work is to expand this list of FRBs with identified PRSs. This will be done by searching for persistent radio emissions at FRB positions that have been well localised by the Australian Square Kilometre Array Pathfinder (ASKAP) telescope. If a radio source is detected, multiwavelength follow-up observations have to be conducted to confirm the existence of a PRS. However, if a radio source is not detected, this work will provide the upper flux limit. This work is part of a larger project involving follow-up of 25 well-localised FRB positions [22, 23, 24].
The paper is divided as follows: in Section 2, we present MeerKAT data reduction and describe how the images are produced. In Section 3, we provide our results, a subset of those presented elsewhere [24]. We conclude in Section 4.

2 Observations and Imaging

The observational campaigns were conducted with the MeerKAT radio telescope for open time proposals in 2021, 2022, and 2023 (SCI-20210212-CV-01, SCI-20220822-CV-01, SCI-20230907-CV-01, respectively). The observations were done using the L-band (856-1712 MHz) receiver, and the FRB positions were observed for 120 minutes on source for each epoch, with a phase calibrator observed for 2 minutes, every 15 minutes. Tables 1 and 2 contain important observation details, including observation date, Right Ascension (RA), Declination (Dec), and synthesised beam of the observed FRBs.

2.1 Calibration and Imaging

MeerKAT data were obtained in visibility format, and were converted into a Measurement Set (MS) format using the KAT Data Access Library[2]. The OXKAT3[25] analysis pipeline flags the low-gain bandpass edges on all baselines. In addition, radio frequency interferences are also flagged, and in cases where they might affect data, the `CASA` task such as `RFLAG` is used. The `TRICOLOR` and `TFCROP` packages are used for the target field and

[1] Authors provide one possible interaction scenario, which involves a neutron star or magnetar in the vicinity of a low-luminosity AGN. The relativistic electron–position beams from the AGN can impact the surrounding plasma cloud, which includes those associated with a neutron star environment (that is how they interact). This interaction can trigger shocks and bring about instabilities that generate coherent radio emission, which can provide a possible explanation for repeating FRBs in AGN environments.

[2] `www.github.com/ska-sa/katdal`

calibrators, respectively [26].

The OXKAT3 pipeline uses tasks from `CASA` to obtain the flux scale and corrections for residual delay calibrators, time-varying gain, and bandpass in the case of cross-calibration [26]. The corrections obtained are applied to the target field, and calibrated visibilities of the target field are extracted to obtain the science target. `WSClean` imager is then used to deconvolve and image the target data. In addition, deconvolution is applied to each subband image(obtained by dividing full bandwidth into 10 subbands with a bandwidth of 82 MHz each).

A Multi-Frequency Synthesis (MFS) map was generated with `WSClean` [27]. This map consists of the full bandwidth, which has a central frequency of 1283 MHz in joined deconvolution mode. Auto-masking from `WSClean` deconvolves each of the 10 subbands with an initial mask of $20\sigma_{\rm rms}$, i.e., 20 times the level of the root-mean-square (RMS) of the image. An artefact-free model of the target is created after the deconvolution process, and it is used for the self-calibration process. For this self-calibration process, tasks from `Cubical software` are used [28]. Lastly, the final image has a reduced $3\sigma_{\rm rms}$ threshold. At the end, CASA task `IMFIT` was used to fit a 2D Gaussian to the emission region in the convolved synthesis map, from which the deconvolved major and minor axes were obtained. The fitting region was defined by visual inspection of the intensity distribution rather than a strict signal-to-noise (S/N) threshold.

3 Results

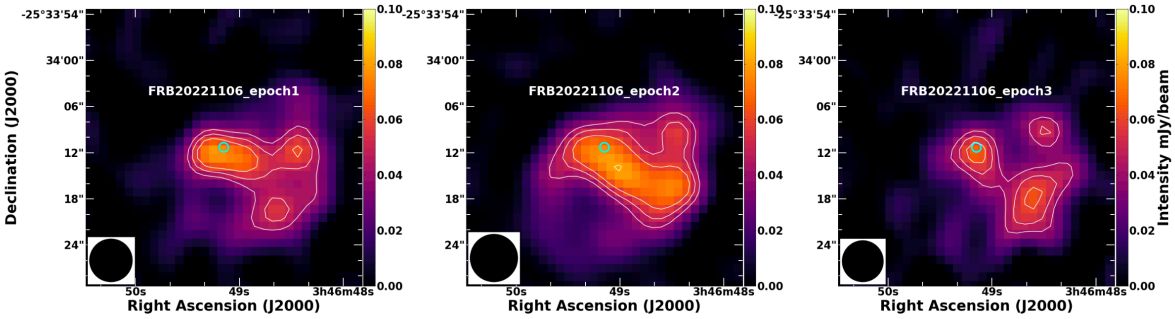

Figure 1: MeerKAT image of the FRB20221106 position with a $\sim 1''$ localisation uncertainty [29] as indicated by the green circle, observed during three different epochs. The black eclipse in the bottom left corner represents the beam size of MeerKAT, and the positional uncertainty of the detected radio source is $\sim 0.3''$, which is smaller than the beam size. The white contours indicate continuum radio emission that coincides with the FRB position, represented at 3, 9, and 12 times the image's RMS.

The position of FRB20221106 was observed over three epochs. During these observations, there is consistent detection of radio emissions, and Figure 1 reveals that FRB20221106 showed three different morphologies, and it also showed three different peak fluxes as indicated in Table 1. The small change in peak flux is in the range of $2-3\sigma$, which is not statistically significant. In addition, the change in integrated flux suggests that the source is not static, and shows a possible slow or variable evolution, which can be explained by an afterflow-like scenario. The source also expands as observed in the Maj$\times$Min axis, suggesting structural development. The consistent coincidence of the source with the FRB position, along with the observed flux evolution, suggests that the radio source is associated with the FRB.
This was not the first time flux variability was observed; a similar occurrence was seen in the case of FRB20190520B: A multi-wavelength study of FRB20190520B showed a $\approx 20\%$ decrease in flux at 3 GHz over 2 years [30]. It was concluded that the variability of FRB20190520B is unlikely due to scintillation, but rather suggests an evolving PRS on yearly timescales.

Another interesting position is that of FRB20181112, which was observed over two epochs (see Figure 2). While previous studies did not reveal any PRS associated with this FRB [31], our observations revealed radio emission in the direction of this FRB. This may indicate that there was low-level persistent emission or maybe afterglow-like activity, which was not detected previously due to sensitivity limits. The measured flux of this FRB appears to decline between the two epochs as shown in Table 1, but the change is within 2σ, which means it is not

Table 1: Detected persistent continuum emission from FRB20221106 and FRB20181112.

Source name	Observation date	R.A.(J2000)	Dec.(J2000)	Synthesised beam	RMS (mJy beam^{-1})	Peak Flux (mJy beam^{-1})	Maj×Min axis	Pos. Angle	Int. Flux (mJy)
FRB20221106	21-Nov-2023	03:46:49.15	-25:34:11.3	5".649×5".649	0.0048	0.0656± 0.0055	20".35×16".38	69°	0.5032
FRB20221106	05-Dec-2023	03:46:49.15	-25:34:11.3	6".264×6".264	0.0054	0.0807±0.0046	34".84×17".61	76°	0.5391
FRB20221106	20-Jan-2024	03:46:49.15	-25:34:11.3	5".452×5".452	0.0053	0.0579±0.0051	38".82×35".64	76°	0.4768
FRB20181112	19-Apr-2021	21:49:23.63	-52:58:15.4	7".304×7".304	0.0047	0.0484±0.0055	10".17×7".18	44°	0.0663
FRB20181112	03-Sep-2021	21:49:23.63	-52:58:15.4	5".940×5".940	0.0054	0.0291±0.0069	7".58×3".81	38°	0.0238

Table 2: Observational information of FRB20190102.

Source name	Observation date	R.A.(J2000)	Dec.(J2000)	Synthesised beam	rms mJy beam^{-1}	Upper limit mJy beam^{-1}
FRB20190102	10-Apr-2021	21:29:39.76	-79:28:32.5	5".709× 5".709	0.0054	< 0.0162
FRB20190102	05-Sep-2021	21:29:39.76	-79:28:32.5	6".723× 6".723	0.0055	< 0.0164

statistically significant. Additionally and importantly, a massive halo of gas surrounds the host galaxy of this FRB [31]. This host galaxy is situated in the southern part of the source, whereby the foreground is in the northern part. It was found that the contributions of this galaxy to DM and scattering are minimal, suggesting weakly magnetised halo gas. If the persistent radio emission is detected during follow-up observations by the e-MERLIN telescope, it is unlikely to be associated with the halo itself and may instead come from the host galaxy or the PRS.

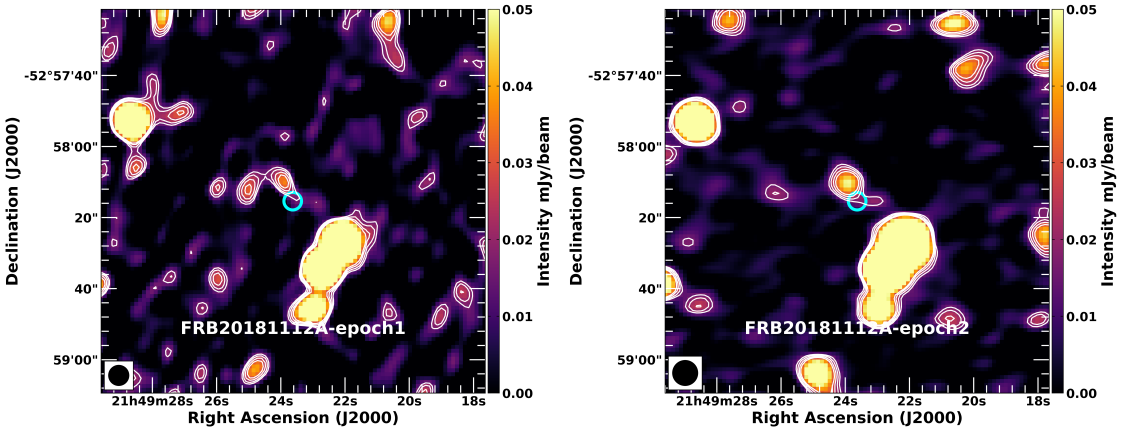

Figure 2: Same as in Figure 1, but for FRB20181112, observed during two different epochs with $\sim$0.5″ uncertainty of the FRB position [31]. The positional uncertainty of the detected radio source is $\sim$0.5″, again smaller than the beam. Although the emission is faint and extended, the FRB position lies well within the detected source extent.

The localisation of FRB20221106 by ASKAP has an uncertainty of $\sim$1″ [29], on the other hand, FRB20181112 was localised to within $\sim$0.5″ [31]. Our MeerKAT images have synthesised beams of $\sim$5–7″, which makes both FRBs better localised than the beam sizes. The positional uncertainties of the detected radio sources were estimated as $\sigma_{\rm pos} \approx {\rm FWHM}/(2 \times {\rm SNR})$ [32], which gives $\sim$0.2–0.3″ for FRB20221106 and $\sim$0.4–0.5″ for FRB20181112. One can see that these uncertainties are significantly smaller than the apparent source sizes (20–38″). This confirms that the FRB positions coincide with the detected emission. The absolute extent of the sources depend on a rather uncertain source distance, and thus the extended radio emission may either be due to the host galaxy structure, or the blending of multiple components.
Lastly, we did not detect any radio emission from FRB20190102 over two epochs as shown in Figure 3. Table 2 shows our derived flux upper limits.

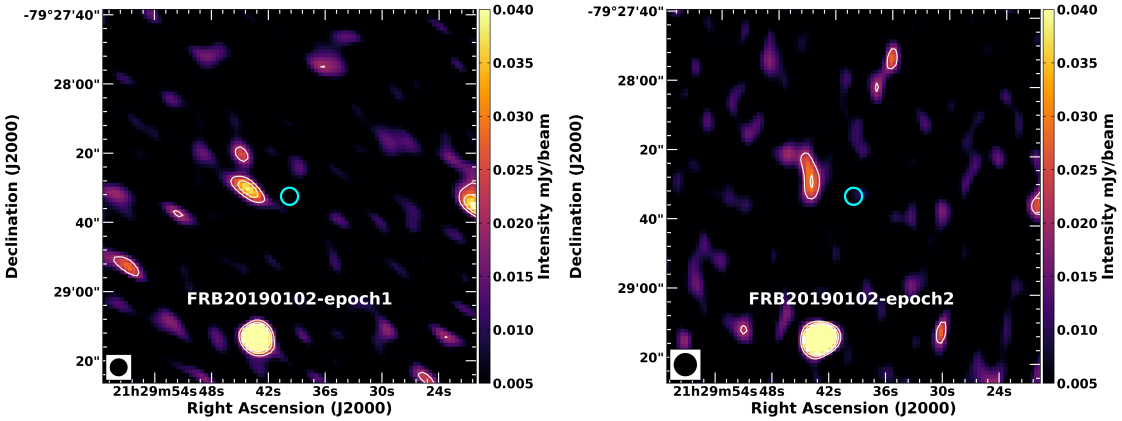

Figure 3: Same as Figure 2, but for FRB20190102.

4 Conclusion

As part of an ongoing study targeting 25 FRB positions, we presented results for 3 of them here. Out of the three FRB positions, we have two detections and one non-detection. For FRB20221106, we have positive detections for observations during three epochs. The position of the FRB20221106 coincides with a galaxy; whether the detected radio source originates from the PRS or the galaxy will remain to be seen. To answer this question, a telescope with high angular resolution, such as e-MERLIN, is required. Such a telescope will help us to identify compact PRSs from the observed radio sources. In addition, it will provide the size of the compact PRS if detected, and constrain its spectral shape and variability. In the case of FRB20181112, a telescope with high angular resolution is also needed to elucidate whether the host galaxy is the one providing the radio emissions, or if the emissions come from the PRS. Lastly, for FRB20190102, a flux upper limit was provided. To resolve the detected radio sources, a proposal for a telescope with high angular resolution will be written, which will help to determine if we have detected PRSs with MeerKAT.

Acknowledgements

This paper utilises MeerKAT L-band observational data from 2021, 2022, and 2023 open-time proposals (SCI-20210212-CV-01, SCI-20220822-CV-01, SCI-20230907-CV-01, respectively). The South African Radio Astronomy Observatory, a facility of the National Research Foundation, operates the MeerKAT telescope. The Inter-University Institute for Data Intensive Astronomy (IDIA) visualization lab https://idia.ac.za/citing-idia-ilifu-in-publications/ is used to for this work. IDIA is a partnership of the University of Cape Town, the University of Pretoria, the University of the Western Cape and the South African Radio astronomy Observatory. Thulo Letsele is grateful for financial support from the National Astrophysics and Space Science Programme (NASSP), which is a multi-institutional initiative, funded by DSI-NRF to train South African students in Astrophysics and Space Science.

References

[1] E. Petroff, J. W. T. Hessels, and D. R. Lorimer, "Fast radio bursts," *The Astronomy and Astrophysics Review*, vol. 27, no. 1, p. 4, May 2019.

[2] D. R. Lorimer, M. Bailes, M. A. McLaughlin, D. J. Narkevic *et al.*, "A Bright Millisecond Radio Burst of Extragalactic Origin," *Science*, vol. 318, no. 5851, p. 777, Nov. 2007.

[3] R. N. Manchester, G. Fan, A. G. Lyne, Kaspi *et al.*, "Discovery of 14 Radio Pulsars in a Survey of the Magellanic Clouds," *Astrophysical Journal*, vol. 649, no. 1, pp. 235–242, Sep. 2006.

[4] L. G. Spitler, P. Scholz, J. W. T. Hessels, S. Bogdanov *et al.*, "A repeating fast radio burst," *Nature*, vol. 531, no. 7593, pp. 202–205, Mar. 2016.

[5] S. Chatterjee, C. J. Law, R. S. Wharton, S. Burke-Spolaor *et al.*, "A direct localization of a fast radio burst and its host," *Nature*, vol. 541, no. 7635, pp. 58–61, Jan. 2017.

[6] S. P. Tendulkar, C. G. Bassa, J. M. Cordes, G. C. Bower *et al.*, "The Host Galaxy and Redshift of the Repeating Fast Radio Burst FRB 121102," *Astrophysical Journal Letters*, vol. 834, no. 2, p. L7, Jan. 2017.

[7] C. M. F. Mingarelli, J. Levin, and T. J. W. Lazio, "Fast Radio Bursts and Radio Transients from Black Hole Batteries," *Astrophysical Journal Letters*, vol. 814, no. 2, p. L20, Dec. 2015.

[8] K. Kashiyama, K. Ioka, and P. Mészáros, "Cosmological Fast Radio Bursts from Binary White Dwarf Mergers," *ApJ*, vol. 776, no. 2, p. L39, Oct. 2013.

[9] T. Totani, "Cosmological Fast Radio Bursts from Binary Neutron Star Mergers," *PASJ*, vol. 65, no. 5, p. L12, Oct. 2013.

[10] F. L. Vieyro, G. E. Romero, V. Bosch-Ramon, B. Marcote *et al.*, "A model for the repeating FRB 121102 in the AGN scenario," *Astronomy & Astrophysics*, vol. 602, p. A64, Jun. 2017.

[11] S. B. Popov and K. A. Postnov, "Hyperflares of SGRs as an engine for millisecond extragalactic radio bursts," in *Evolution of Cosmic Objects through their Physical Activity*, H. A. Harutyunian, A. M. Mickaelian, and Y. Terzian, Eds., Nov. 2010, pp. 129–132.

[12] C. D. Bochenek, V. Ravi, K. V. Belov *et al.*, "A fast radio burst associated with a Galactic magnetar," *Nature*, vol. 587, no. 7832, pp. 59–62, Nov. 2020.

[13] CHIME/FRB Collaboration, B. C. Andersen, K. M. Bandura, M. Bhardwaj, A. Bij *et al.*, "A bright millisecond-duration radio burst from a Galactic magnetar," *Nature*, vol. 587, no. 7832, pp. 54–58, Nov. 2020.

[14] A. M. Moroianu, S. Bhandari, M. R. Drout, J. W. T. Hessels *et al.*, "A milliarcsecond localization associates frb 20190417a with a compact, luminous persistent radio source and an extreme magneto-ionic environment," 2025. [Online]. Available: https://arxiv.org/abs/2509.05174

[15] C. H. Niu, K. Aggarwal, D. Li *et al.*, "A repeating fast radio burst associated with a persistent radio source," *Nature*, vol. 606, no. 7916, pp. 873–877, Jun. 2022.

[16] G. Bruni, L. Piro, Y. P. Yang, E. Palazzi *et al.*, "Discovery of a persistent radio source associated with FRB 20240114A," *Astronomy & Astrophysics*, vol. 695, p. L12, Mar. 2025.

[17] G. Bruni, L. Piro, Y.-P. Yang, S. Quai *et al.*, "A nebular origin for the persistent radio emission of fast radio bursts," 2024. [Online]. Available: https://arxiv.org/abs/2312.15296

[18] L. Connor, J. Sievers, and U.-L. Pen, "Non-cosmological FRBs from young supernova remnant pulsars," *Monthly Notices of the Royal Astronomical Society*, vol. 458, no. 1, pp. L19–L23, May 2016.

[19] B. Zhang, "A 'Cosmic Comb' Model of Fast Radio Bursts," *ApJ*, vol. 836, no. 2, p. L32, Feb. 2017.

[20] K. E. Heintz, J. X. Prochaska, S. Simha, E. Platts *et al.*, "Host Galaxy Properties and Offset Distributions of Fast Radio Bursts: Implications for Their Progenitors," *ApJ*, vol. 903, no. 2, p. 152, Nov. 2020.

[21] J. P. Macquart, J. X. Prochaska, M. McQuinn, K. W. Bannister *et al.*, "A census of baryons in the Universe from localized fast radio bursts," *Nature*, vol. 581, no. 7809, pp. 391–395, May 2020.

[22] J. O. Chibueze, M. Caleb, L. Spitler, H. Ashkar *et al.*, "A MeerKAT, e-MERLIN, H.E.S.S., and Swift search for persistent and transient emission associated with three localized FRBs," *MNRAS*, vol. 515, no. 1, pp. 1365–1379, Sep. 2022.

[23] F. Aharonian, A. Archaryya, J. Aschersleben, H. Ashkar, *et al.*, "H.E.S.S. programme searching for VHE gamma rays associated with FRBs," *arXiv e-prints*, p. arXiv:2507.02143, Jul. 2025.

[24] L. Mfulwane, J. Chibueze, T. Letsele, T. Nyambe *et al.*, "A MeerKAT search for persistent radio source candidates towards twenty-five localised Fast Radio Bursts." 2025, submitted to MNRAS.

[25] I. Heywood, "oxkat: Semi-automated imaging of MeerKAT observations," Astrophysics Source Code Library, record ascl:2009.003, Sep. 2020.

[26] J. P. McMullin, B. Waters, D. Schiebel, W. Young, and K. Golap, "CASA Architecture and Applications," in *Astronomical Data Analysis Software and Systems XVI*, ser. Astronomical Society of the Pacific Conference Series, R. A. Shaw, F. Hill, and D. J. Bell, Eds., vol. 376, Oct. 2007, p. 127.

[27] A. R. Offringa, B. McKinley, N. Hurley-Walker, F. H. Briggs *et al.*, "WSCLEAN: an implementation of a fast, generic wide-field imager for radio astronomy," *MNRAS*, vol. 444, no. 1, pp. 606–619, Oct. 2014.

[28] J. S. Kenyon, O. M. Smirnov, T. L. Grobler, and S. J. Perkins, "CUBICAL - fast radio interferometric calibration suite exploiting complex optimization," *MNRAS*, vol. 478, no. 2, pp. 2399–2415, Aug. 2018.

[29] R. M. Shannon, K. W. Bannister, A. Bera, S. Bhandari, and others., "The commensal real-time ASKAP fast transient incoherent-sum survey," *PASA*, vol. 42, p. e036, Jan. 2025.

[30] X. Zhang, W. Yu, C. Law *et al.*, "Temporal and Spectral Properties of the Persistent Radio Source Associated with FRB 20190520B with the VLA," *ApJ*, vol. 959, no. 2, p. 89, Dec. 2023.

[31] J. X. Prochaska, J.-P. Macquart, M. McQuinn *et al.*, "The low density and magnetization of a massive galaxy halo exposed by a fast radio burst," *Science*, vol. 366, no. 6462, pp. 231–234, Oct. 2019.

[32] J. J. Condon, "Errors in elliptical gaussian fits," *Publications of the Astronomical Society of the Pacific*, vol. 109, no. 732, p. 166, feb 1997. [Online]. Available: https://dx.doi.org/10.1086/133871

This page intentionally left blank.

Solar wind temperature anisotropy during Ulysses' first fast latitude scan

Ephrem Tesfaye Desta [1,2], **R. D. Strauss** [1,3] **and N. E. Engelbrecht**[1,3]

[1]Center for Space Research, North-West University, Potchefstroom, 2522, South Africa.
[2] Department of Physics, Addis Ababa University, Addis Ababa, 1176, Ethiopia
[3] National Institute for Theoretical and Computational Sciences (NITheCS), South Africa.

E-mail: 50156888@mynwu.ac.za

Abstract. Anisotropy is a property of turbulence in solar wind plasma in which velocity and magnetic fields fluctuate along and perpendicular to the ambient magnetic field. In situ measurements confirmed that the solar wind in the inner heliosphere exhibits a temperature anisotropy. The presence of this anisotropy results in magnetohydrodynamic (MHD) waves and instabilities. In this work, we analyze proton temperature anisotropy using Ulysses spacecraft data and investigate the radial variation of the temperature anisotropy for firehose and mirror instabilities. From Ulysses observations, we find that the firehose instability is dominant in the range between 3 au to 4.5 au.

1 Introduction

Study of solar wind plasma provides crucial insight into the dynamic interactions between solar particle emissions and the interplanetary medium. As the solar wind expands into a collisionless regime, particle motion is strongly influenced by the interplanetary magnetic field, producing temperature anisotropies and shaping plasma behavior [1]. Observations show that these anisotropies are constrained by kinetic instabilities [2], develop anisotropically with respect to the local magnetic field [3]. Observations from *Helios* have revealed that at 0.3 astronomical units (au) from the Sun, there are distinct anisotropic and isotropic populations of solar wind plasmas that become indistinguishable at 1 au [4]. This transitional region is known as the polytropic zone, where both isotropic and anisotropic plasmas coexist. The anisotropic cascade in this region is crucial as it facilitates significant energy transfer, especially in magnetized plasmas where large perpendicular wavenumbers ($k_\perp$) are dominant. The particle distribution functions in these plasmas often exhibit anisotropy, particularly in proton temperature, which can drive various instabilities.

Solar wind plasmas are frequently in a turbulent state characterized by a broad spectrum of fluctuations across various wave vectors. This turbulence promotes an ongoing cascade of energy between different wave vectors, leading to an anisotropic cascade in the presence of a background magnetic field (B_0). Theoretical models, simulations and observational data consistently show that energy is preferentially transferred to large values of $k_\perp$, where $k_\perp$ is the wave number perpendicular to B_0. This results in a cascade dominated by perpendicular fluctuations [5, 6].

In low-collisionality plasmas such as the solar wind, the particle distribution function can also display anisotropy relative to the magnetic field. Ulysses observations reveal that solar wind protons exhibit temperature anisotropies varying with distance [7]. Analysis of Ulysses data from 1993–1996 showed that both the south and north polar coronal holes have proton temperature anisotropies of $T_{\perp p}/T_{\|p}$ = 0.8 [8], while a polytropic index study of three consecutive Ulysses orbits (first, second, and third) during solar maximum and minimum periods [9] reported the corresponding temperature anisotropy ratios, $T_{\perp p}/T_{\|p}$, of 0.78, 0.75, and 0.79, respectively. These anisotropies can trigger kinetic instabilities such as firehose, mirror, and ion-cyclotron that act to constrain extreme departures

from isotropy [10, 2]. When $T_{\perp}p/T_{\parallel}p > 1$, the plasma may become unstable to parallel-propagating Alfvén/ion-cyclotron (A/IC) waves or non-propagating mirror modes [11, 12]. Conversely, when $T_{\perp p}/T_{\parallel p} < 1$, the plasma can excite fast-magnetosonic/whistler (FM/W) waves or oblique firehose modes [13, 14]. These instabilities help constrain the temperature anisotropy, driving the plasma toward a marginally stable state [10, 2].

The firehose instability, occurring when $T_{\parallel p} > T_{\perp p}$ is vital in regulating temperature anisotropy in high-β plasmas, where $\beta = 2\mu_0 n k_B T/B^2$ represents the ratio of plasma pressure to magnetic pressure. This instability has been extensively studied, revealing both parallel and oblique firehose modes as mechanisms that can relax anisotropy and prevent the plasma from becoming excessively elongated along the magnetic field [15, 14]. Observational studies, such as those by [16], have identified thresholds for these instabilities in the solar wind, underscoring their role in shaping proton distribution functions.

Similarly, the mirror instability, triggered when $T_{\perp p} > T_{\parallel p}$, imposes constraints on the perpendicular temperature in the solar wind. This instability is particularly relevant in high-β regions, where it leads to the formation of non-propagating structures that contribute to energy redistribution within the plasma [17, 2]. Additionally, the ion-cyclotron instability, which emerges under similar conditions, has been linked to the generation of Alfvén waves propagating along the magnetic field, further contributing to the turbulent cascade [18].

Understanding the interplay between these instabilities and the turbulent cascade is essential for comprehending the dynamics of the solar wind and other astrophysical plasmas. As the solar wind expands away from the Sun, these processes collectively influence the evolution of temperature anisotropies, resulting in a complex distribution of proton temperatures that reflects the balance between turbulent energy transfer and kinetic instabilities [19].

This paper investigates which instability is dominant while the solar wind plasma expands as function of heliocentric distance, by analyzing Ulysses data. This can gain deeper insights into the mechanisms regulating plasma behavior on a kinetic scale, enhancing our understanding of space weather and heliospheric conditions. The paper is organized as follows: section 2 presents dataset, method and results, while section 3 provides the discussion and conclusions.

2 Dataset, Methods and Results

We utilize the proton moments data from the Solar Wind Observations Over the Poles of the Sun [20] electrostatic instrument and we use magnetic field measurements from the magnetic field investigation instrument the Vector Helium, and other Flux Gate Magnetometer [21] experiment. The list of the data is available from NASA's SPDF-Coordinated Data Analysis Web [1] spanning from 1992 January 1 to 1998 December 31 [22]. Figure 1 shows the Ulysses spacecraft trajectory in the plane of radial distance and latitude and solar wind plasma parameters that we analyze in this study. During the first polar pass in 1994, Ulysses detected solar wind streams emerging from polar coronal holes, which are the source of more than two thirds of the heliosphere near solar minimum [23]. Such high-latitude outflows are widely regarded as the fundamental form of the solar wind, contributing roughly 50% of the total throughout a solar cycle and an even greater fraction during solar minimum [24]. Ulysses explores the region from 1.25 to 5.4 au and encountered mainly fast solar wind, especially at high latitudes, while some slow wind was measured closer to the ecliptic, below 1.5 au and beyond 4.5 au. More dense plasma with slow solar wind was measured around 1.5 au and in the range of 3 au to 4.5 au. This region has a more dense distribution and slow solar wind speed. The slow solar wind is measured in the range beyond 4.5 radial distance and latitude in the range $[60°, -20°]$ as shown in Figure 1.

This timing of the mission has enabled Ulysses to make direct measurements of the high-latitude solar wind coming from the Sun's polar coronal holes, and thus characterise the global structure of the heliosphere during solar minimum conditions when the corona is in its simplest configuration.

The Chew-Goldberger-Low model (CGL) fluid theory gives the two adiabatic equations of states, neglecting the heat flux vector, which are given by [25] as

$$\frac{d}{dt}\left(\frac{P_{\perp}}{nB}\right) = 0, \quad \text{and} \quad \frac{d}{dt}\left(\frac{P_{\parallel}B^2}{n^3}\right) = 0, \tag{1}$$

These would lead to an evolution for the parallel and perpendicular (with respect to $\mathbf{B}$) particle temperatures, $T_{\parallel}$ and $T_{\perp}$ as:

$$T_{\perp} \propto B \text{ and } T_{\parallel} \propto n^2/B^2, \tag{2}$$

where B is the magnitude of the ambient magnetic field and n is the plasma density. In the case of CGL double-adiabatic expansion, with a constant flow velocity and in a radial magnetic field, these parameters would change with the radial distance R as $B \propto n \propto R^{-2}$; consequently, the relations in (2) predict the development of strong

[1] `https://cdaweb.gsfc.nasa.gov/index.html`

temperature anisotropy

$$\frac{T_\perp}{T_\parallel} \propto R^{-2} \text{ and } \beta_\parallel \propto R^2, \tag{3}$$

A useful technique for studying solar wind temperature anisotropy is examining how $T_{\perp p}/T_{\parallel p}$ varies as a function of plasma-β

$$\frac{T_{\perp p}}{T_{\parallel p}} = 1 + \frac{a}{\left(\beta_\parallel - c\right)^b}. \tag{4}$$

Following [10], for our instability analysis we choose the fitting parameters where (a,b,c) are given by (0.43,0.42,-0.0004) for proton cyclotron instability (PCI), (0.77,0.76,-0.016) for mirror instability (MI), and (-0.47,0.53,0.59) for parallel firehose instability (PFH), and $\beta_\parallel = 2\mu_0 n_p k_B T_{\parallel p}/B_0^2$.

The radial profile and plasma properties of the spacecraft that we examine in this work are displayed in Figure 1.

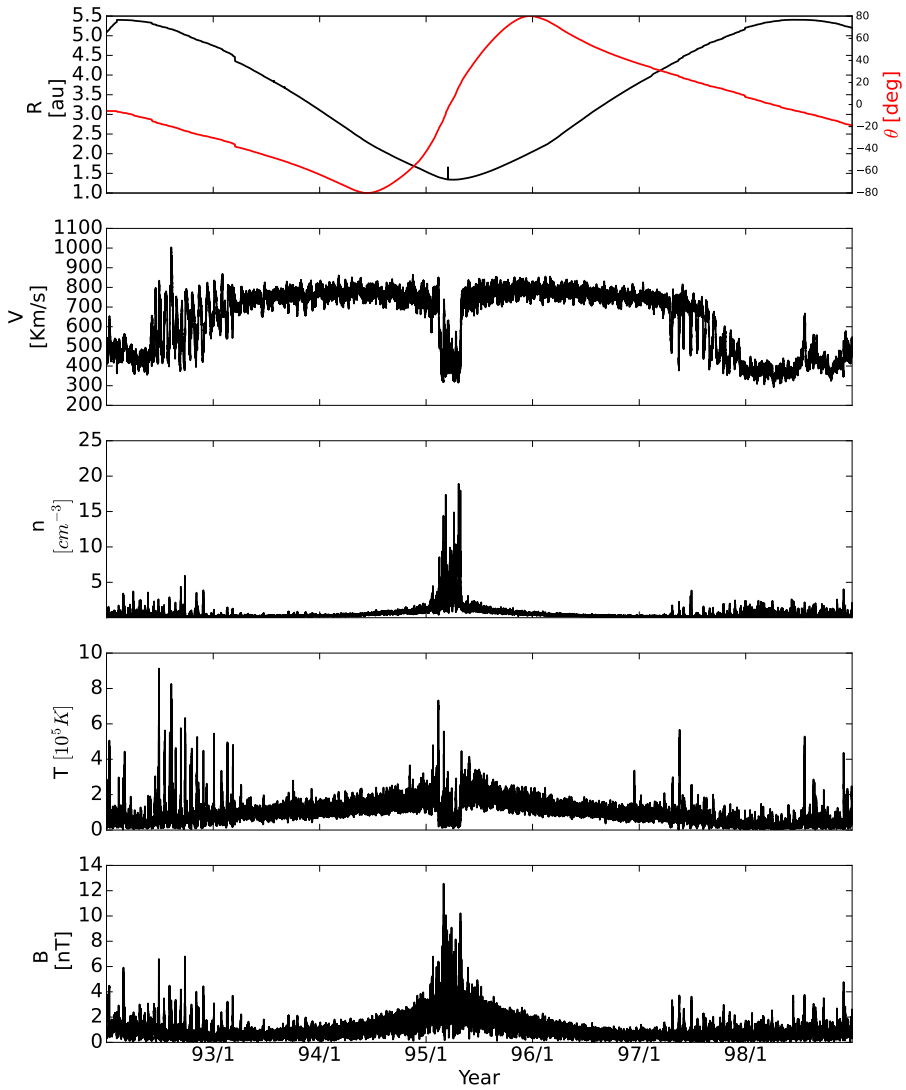

Figure 1: An overview of key parameters measured by Ulysses for this study: (top panel) heliocentric range (black) and heliolatitude (red) trajectory; (second panel) Solar wind speed; (third panel) plasma number density; (Fourth panel) temperature; (bottom panel) magnetic field of Ulysses.

3 Discussion and Conclusion

Figures 2a-i show the radial evolution of temperature anisotropy and the instability region that approaches the firehose threshold with increasing heliocentric distance from 1.25 to 5.75 au. Ulysses observations between 3 au and 4.5 au show that, on average, the temperature anisotropy ratio in the range $0.6 < T_{\perp p}/T_{\|p} < 0.9$ is in the mean stream component of the solar wind. In this range, we find an average value of $T_{\perp p}/T_{\|p} \approx 0.82$, which has similar results to studies by [8, 9].

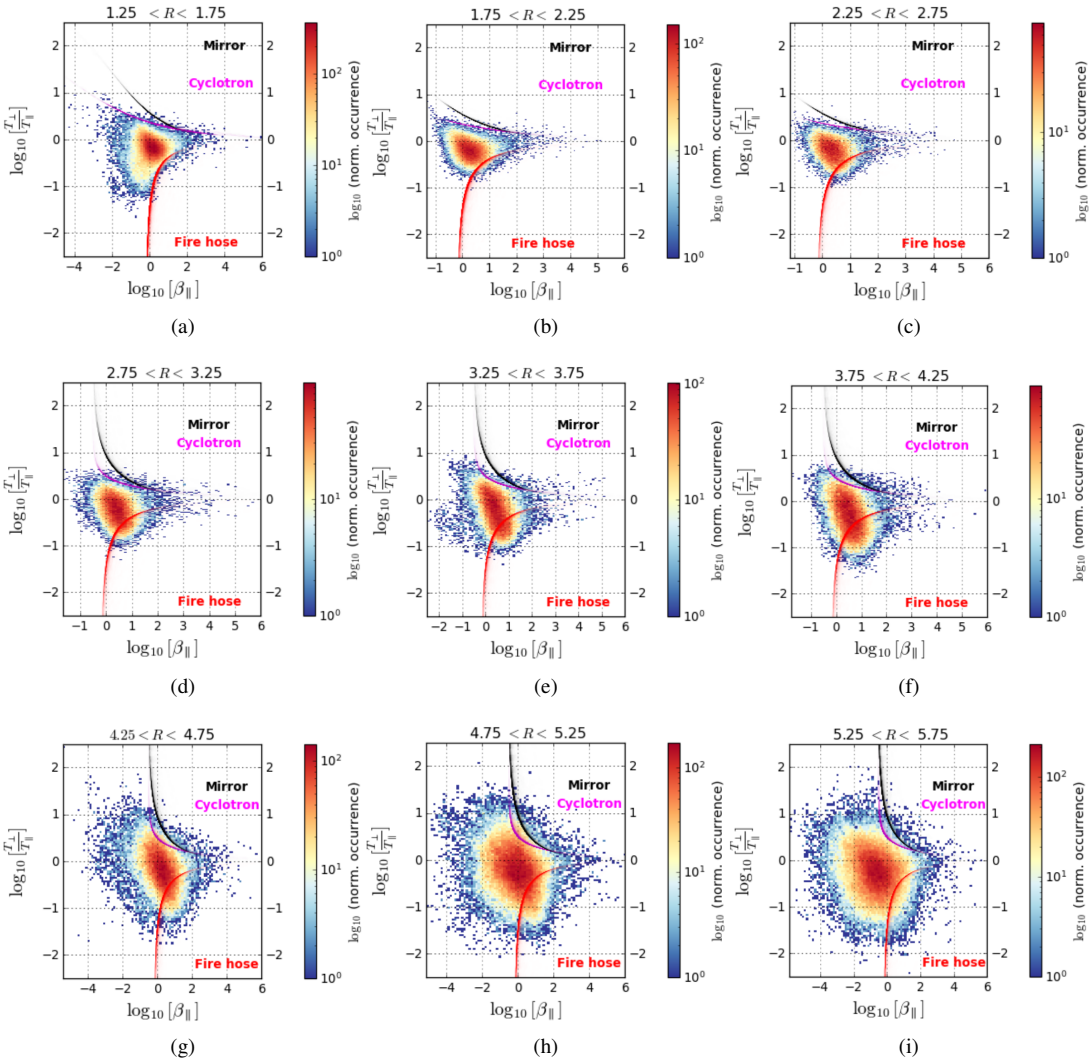

Figure 2: Logarithmic values of proton temperature anisotropy versus $\beta_{\|}$ at different heliocentric distances. Curves indicate the firehose (red), mirror (black), and cyclotron (magenta) instabilities

.

Based on Helios and Ulysses observation in the range of proton temperature anisotropy evolution from 0.3 to 2.5 au [26] indicated that both the slow and fast wind are found to approach the firehose instability regions with increasing distance. Similarly, based on the report by [7], the firehose instability plays a major role in constraining the proton anisotropy during solar wind expansion, and with increasing distance, the wind approaches the firehose instability region. Based on Ulysses' observations and empirical correlations of plasma parameters [7] indicated that a large portion of proton distribution in the solar wind has firehose instability.

This study highlights the significance of anisotropic cascades and temperature anisotropies driven by the background magnetic field and varying wave vectors in turbulent plasma. The Ulysses spacecraft data, covering heliocentric distances from 1.25 to 5.4 au, show how instabilities like the firehose and mirror modes affect the redistribution of energy within the solar wind, driven by temperature anisotropies relative to the magnetic field. The study

finds that firehose instability plays a dominant role in the regulation of proton anisotropy between 3 au and 4.5 au, where the solar wind approaches a marginally stable state. Our results show that in this region the temperature anisotropy ratio lies within the range $0.6 < T_{\perp p}/T_{\parallel p} < 0.9$, which is typical of the mean stream component of the solar wind. The average anisotropy $T_{\perp p}/T_{\parallel p}$ in this range is 0.82, which is close to previous studies [8, 9]. The presence of these instabilities facilitates an understanding of space weather and heliospheric conditions. This study provides crucial insights to understand energy transfer, wave-particle interactions, and space weather impacts, as its temperature and velocity anisotropies drive key instabilities and turbulence in space plasmas.

References

[1] E. Marsch, "Kinetic Physics of the Solar Corona and Solar Wind," *Living Reviews in Solar Physics*, vol. 3, no. 1, p. 1, Dec. 2006.

[2] S. D. Bale, J. C. Kasper, G. G. Howes, E. Quataert, C. Salem, and D. Sundkvist, "Magnetic Fluctuation Power Near Proton Temperature Anisotropy Instability Thresholds in the Solar Wind," *Phys. Rev. Lett.*, vol. 103, no. 21, p. 211101, Nov. 2009.

[3] T. S. Horbury, R. T. Wicks, and C. H. K. Chen, "Anisotropy in Space Plasma Turbulence: Solar Wind Observations," *Space Sci. Rev.*, vol. 172, no. 1-4, pp. 325–342, Nov. 2012.

[4] D. Stansby, D. Perrone, L. Matteini, T. S. Horbury, and C. S. Salem, "Alpha particle thermodynamics in the inner heliosphere fast solar wind," *A&A*, vol. 623, p. L2, Mar. 2019.

[5] P. Goldreich and S. Sridhar, "Toward a Theory of Interstellar Turbulence. II. Strong Alfvenic Turbulence," *ApJ*, vol. 438, p. 763, Jan. 1995.

[6] C. H. K. Chen, S. D. Bale, C. Salem, and F. S. Mozer, "Frame Dependence of the Electric Field Spectrum of Solar Wind Turbulence," *ApJ*, vol. 737, no. 2, p. L41, Aug. 2011.

[7] L. Matteini, P. Hellinger, B. E. Goldstein, S. Landi, M. Velli, and M. Neugebauer, "Signatures of kinetic instabilities in the solar wind," *Journal of Geophysical Research (Space Physics)*, vol. 118, no. 6, pp. 2771–2782, Jun. 2013.

[8] R. von Steiger and T. H. Zurbuchen, "Temperature Anisotropies of Heavy Solar Wind Ions from Ulysses-SWICS," in *Solar Wind Ten*, ser. American Institute of Physics Conference Series, M. Velli, R. Bruno, F. Malara, and B. Bucci, Eds., vol. 679. AIP, Sep. 2003, pp. 526–529.

[9] E. T. Desta, R. D. Strauss, and N. E. Engelbrecht, "Modeling of the Polytropic Index and Temperature Anisotropy in the Solar Wind," *ApJ*, vol. 966, no. 1, p. 142, May 2024.

[10] P. Hellinger, P. Trávníček, J. C. Kasper, and A. J. Lazarus, "Solar wind proton temperature anisotropy: Linear theory and WIND/SWE observations," *Geophys. Res. Lett.*, vol. 33, no. 9, p. L09101, May 2006.

[11] S. P. Gary and M. A. Lee, "The ion cyclotron anisotropy instability and the inverse correlation between proton anisotropy and proton beta," *J. Geophys. Res.*, vol. 99, no. A6, pp. 11 297–11 302, Jun. 1994.

[12] M. W. Kunz, A. A. Schekochihin, and J. M. Stone, "Firehose and Mirror Instabilities in a Collisionless Shearing Plasma," *Phys. Rev. Lett.*, vol. 112, no. 20, p. 205003, May 2014.

[13] K. B. Quest and V. D. Shapiro, "Evolution of the fire-hose instability: Linear theory and wave-wave coupling," *J. Geophys. Res.*, vol. 101, no. A11, pp. 24 457–24 470, Nov. 1996.

[14] P. Hellinger and H. Matsumoto, "New kinetic instability: Oblique Alfvén fire hose," *J. Geophys. Res.*, vol. 105, no. A5, pp. 10 519–10 526, May 2000.

[15] S. P. Gary, H. Li, S. O'Rourke, and D. Winske, "Proton resonant firehose instability: Temperature anisotropy and fluctuating field constraints," *J. Geophys. Res.*, vol. 103, no. A7, pp. 14 567–14 574, Jul. 1998.

[16] J. C. Kasper, A. J. Lazarus, and S. P. Gary, "Wind/SWE observations of firehose constraint on solar wind proton temperature anisotropy," *Geophys. Res. Lett.*, vol. 29, no. 17, p. 1839, Sep. 2002.

[17] O. A. Pokhotelov, R. Z. Sagdeev, M. A. Balikhin, and R. A. Treumann, "Mirror instability at finite ion-Larmor radius wavelengths," *Journal of Geophysical Research (Space Physics)*, vol. 109, no. A9, p. A09213, Sep. 2004.

[18] S. P. Gary, R. M. Skoug, J. T. Steinberg, and C. W. Smith, "Proton temperature anisotropy constraint in the solar wind: ACE observations," *Geophys. Res. Lett.*, vol. 28, no. 14, pp. 2759–2762, Jul. 2001.

[19] E. Marsch, "Waves and Turbulence in the Solar Corona," in *The Sun and the Heliosphere as an Integrated System*, ser. Astrophysics and Space Science Library, G. Poletto and S. T. Suess, Eds., vol. 317, Nov. 2004, p. 283.

[20] S. J. Bame, D. J. McComas, B. L. Barraclough, J. L. Phillips, K. J. Sofaly, J. C. Chavez, B. E. Goldstein, and R. K. Sakurai, "The ULYSSES solar wind plasma experiment," *A&AS*, vol. 92, no. 2, pp. 237–265, Jan. 1992.

[21] A. Balogh, T. J. Beek, R. J. Forsyth, P. C. Hedgecock, R. J. Marquedant, E. J. Smith, D. J. Southwood, and B. T. Tsurutani, "The magnetic field investigation on the ULYSSES mission - Instrumentation and preliminary scientific results," *A&AS*, vol. 92, no. 2, pp. 221–236, Jan. 1992.

[22] D. J. McComas, H. O. Funsten, J. T. Gosling, and W. R. Pryor, "Ulysses measurements of variations in the solar wind-interstellar hydrogen charge exchange rate," *Geophys. Res. Lett.*, vol. 26, no. 17, pp. 2701–2704, Sep. 1999.

[23] R. von Steiger, "Solar wind composition and charge states," in *Proceedings of the eigth International solar wind Conference: Solar wind eight*, ser. American Institute of Physics Conference Series, D. Winterhalter, J. T. Gosling, S. R. Habbal, W. S. Kurth, and M. Neugebauer, Eds., vol. 382, Jul. 1996, pp. 193–198.

[24] R. von Steiger and T. H. Zurbuchen, "Polar coronal holes during the past solar cycle: Ulysses observations," *Journal of Geophysical Research (Space Physics)*, vol. 116, no. A1, p. A01105, Jan. 2011.

[25] G. F. Chew, M. L. Goldberger, and F. E. Low, "The Boltzmann Equation and the One-Fluid Hydromagnetic Equations in the Absence of Particle Collisions," *Proceedings of the Royal Society of London Series A*, vol. 236, no. 1204, p. 117, Jul. 1956.

[26] L. Matteini, S. Landi, P. Hellinger, F. Pantellini, M. Maksimovic, M. Velli, B. E. Goldstein, and E. Marsch, "Evolution of the solar wind proton temperature anisotropy from 0.3 to 2.5 AU," *Geophys. Res. Lett.*, vol. 34, no. 20, p. L20105, Oct. 2007.

Understanding Interacting Dark Energy from a Dynamical Systems Analysis Approach

Marcel van der Westhuizen[1], **Amare Abebe**[1,2]

[1]Centre for Space Research, North-West University, Potchefstroom, South Africa
[2]National Institute for Theoretical and Computational Sciences (NITheCS), South Africa

E-mail: marcelvdw007@gmail.com

Abstract. Cosmological models in which dark matter and dark energy interact in a non-gravitational manner are known as Interacting Dark Energy (IDE) models and have been proposed to address many long-standing shortcomings and tensions in standard cosmology. Furthermore, recent results from the DESI Collaboration have suggested hints of dynamical dark energy, for which IDE models could provide a viable explanation. The relevance of IDE models underscores the need to understand their parameter space and potential limitations. Unfortunately, obtaining analytical solutions for the evolution of dark matter and dark energy densities is often not possible. To this end, we apply dynamical system analysis techniques to a well-known IDE model $Q = 3H\delta\rho_{\rm de}$, establishing an alternative method to find constraints on the parameter space that avoid the common pitfalls of these models, such as negative energy densities and future singularities, without the need for analytical solutions. We also show that our method can provide insight into the requirement for radiation, matter and dark energy dominated eras, accelerated future expansion, and how these models may address the coincidence problem. Using the techniques established here, researchers may investigate other IDE models that have escaped analysis to date.

1 Introduction

In standard cosmology, the expansion of the universe is described by the ΛCDM model, where the universe is dominated by two mysterious dark components, cold dark matter (CDM) and dark energy Λ, estimated to make up approximately 95% of the energy of the universe. Dark matter (DM) is usually modelled as a particle beyond the Standard Model introduced to explain galaxy rotation curves and many other astronomical and cosmological observations. Dark energy (DE) is usually assumed to be a cosmological constant Λ, which was introduced to account for the observed accelerated expansion of the universe. The ΛCDM model has been incredibly successful in describing cosmological data, as illustrated by measurements of the power spectrum of the Cosmic Microwave Background [1]. Although successful, the ΛCDM models face many challenges, which motivate research beyond the standard cosmological model. We will briefly mention five of these shortcomings, two of theoretical origin, and three that relate to recent increases in precision of cosmological data.

1. **The cosmological constant problem:** The predicted energy density of a cosmological constant is measured to be approximately 120 orders of magnitude smaller than the predicted value [2].
2. **The coincidence problem:** The DM and DE densities coincidentally have the same order of magnitude at the present moment when we measure it, while their energy densities are predicted to differ with many orders of magnitude in both the past and predicted future [3].
3. **The Hubble tension:** The $4\sigma - 6\sigma$ discrepancy of the estimation of the present expansion rate H_0 from early time probes such as CMB, and late time probes such as Type Ia Supernova [4].

4. **The $S8$ discrepancy:** The $2\sigma - 5\sigma$ discrepancy between late-time and early-time measurements of the parameter S_8, which is related to how matter clumps on cosmological scales [4].

5. **Hints of dynamical dark energy**: Recent measurements of baryonic acoustic oscillations (BAO) from the DESI collaboration provide a $2.8\sigma - 4.2\sigma$ preference for dynamical DE over the ΛCDM model [5].

In order to address the above-mentioned problems, a plethora of extensions to standard cosmology have been suggested, but we will focus on a group of models called interacting dark energy (IDE). IDE models are characterised by an hypothesised non-gravitational energy exchange between DM and DE. This has the consequence that the energies of neither DM nor DE are separately conserved, but instead the energy of the total dark sector is conserved, which leads to a modification of the standard conservation equation:

$$\begin{aligned} \dot{\rho}_{\rm dm} + 3H\rho_{\rm dm} = Q \quad ; \quad \dot{\rho}_{\rm de} + 3H(1+\omega)\rho_{\rm de} = -Q \\ \omega^{\rm eff}_{\rm dm} = -\frac{Q}{3H\rho_{\rm dm}} \quad ; \quad \omega^{\rm eff}_{\rm de} = \omega_{\rm de} + \frac{Q}{3H\rho_{\rm de}}. \end{aligned} \tag{1}$$

In (1), $\rho_{\rm dm}$ and $\rho_{\rm de}$ are the energy densities of DM and DE, respectively, $\dot{\rho}$ denotes differentiation with respect to cosmic time, $H = \frac{\dot{a}}{a}$ is the Hubble parameter, a the scale factor and ω is the DE equation of state. Most important is Q, the interaction function whose sign determines the direction of energy transfer, such that energy flows from DE to DM if $Q > 0$ (iDEDM regime), while energy flows from DM to DE if $Q < 0$ (iDMDE regime). The effect of the interaction can also be encapsulated using effective equations of state $\omega^{\rm eff}_{\rm dm/de}$, which provide equivalent fluid descriptions without an interaction, but instead with dynamical equations of state. IDE models were initially introduced to address the coincidence problem, as the interaction can allow DM and DE to dilute with expansion at the same rate [3], such that the problem is solved for either the past or future if $\omega^{\rm eff}_{\rm dm} = \omega^{\rm eff}_{\rm de}$. In recent years, it has been shown that IDE models can also help alleviate H_0 and S_8 tensions [4], increasing their popularity. Lastly, IDE models provide a natural mechanism to account for the recent hints of dynamical dark energy, while also allowing for phantom crossings [5]. Although IDE models have become popular, we would like to highlight the shortcomings of IDE models, such as negative energy densities and future singularities, and to provide find conditions to avoid them, if possible.

One of the problems is that the function Q is not agreed upon, and is usually decided phenomenologically. This leads to a plethora of interaction kernels Q, very few of which (1) can be analytically solved. Without analytical solutions for the evolution of $\rho_{\rm dm}$ and $\rho_{\rm de}$, the background dynamics of these models can be hard to predict, especially with regards to the possible presence of both negative energy densities and big rip future singularities. To this end, we apply techniques from dynamical systems analysis to find conditions that ensure radiation, matter and DE dominated eras, positive energy densities, future accelerated expansion, avoid a future singularity and to address the coincidence problem, all without the need for analytical solutions. We have chosen the most popular interaction kernel $Q = 3H\delta\rho_{\rm de}$ to show that our method finds convergent results with those obtained from analytical solutions given in [6]. The methods established here can be used to obtain similar conditions for any interaction kernel Q.

2 Background equations

To address the coincidence problem, we require that DM and DE redshift and dilute at the same rate in either the distant past or future. The ratio of DM to DE is given by:

$$r = \frac{\rho_{\rm dm}}{\rho_{\rm de}} = \frac{\Omega_{\rm dm}}{\Omega_{\rm de}} = \frac{\rho_{\rm dm,0}a^{-3(1+\omega^{\rm eff}_{\rm dm})}}{\rho_{\rm de,0}a^{-3(1+\omega^{\rm eff}_{\rm de})}} = r_0 a^{-3(\omega^{\rm eff}_{\rm dm}-\omega^{\rm eff}_{\rm de})} \quad ; \quad \zeta = 3(\omega^{\rm eff}_{\rm dm} - \omega^{\rm eff}_{\rm de}). \tag{2}$$

The magnitude of the deviation from $\zeta = 0$ indicates the degree of the coincidence problem, as $\zeta = 0$ corresponds to $\omega^{\rm eff}_{\rm dm} = \omega^{\rm eff}_{\rm de}$, where DM and DE redshifts at the same rate, fixing their ratio $r = \text{constant}$. In the ΛCDM model we have $\zeta = 3$, so if $\zeta < 3$ the coincidence problem is alleviated, which happens in the iDEDM regime, while $\zeta > 3$ worsens the problem, which happens in the iDMDE regime [3, 6]. Besides DM and DE, the universe also contains radiation (r) and baryonic matter (bm), whose density evolves with expansion of the universe as $\rho_{\rm r} = \rho_{\rm (r,0)}a^{-4}$ and $\rho_{\rm bm} = \rho_{\rm (bm,0)}a^{-3}$, respectively. The entire model may also be approximated as a single fluid, which has a total effective equation of state $\omega^{\rm eff}_{\rm tot}$ given by:

$$\omega^{\rm eff}_{\rm tot} = \frac{P_{\rm tot}}{\rho_{\rm tot}} = \frac{1}{3}\Omega_{\rm r} + \omega\Omega_{\rm de}, \tag{3}$$

where the last equality is obtained by assuming a flat universe, such that the density parameters $\Omega_i = \frac{8\pi G}{3H^2}\rho_i$ add up to satisfy $\Omega_{\rm r} + \Omega_{\rm bm} + \Omega_{\rm dm} + \Omega_{\rm de} = 1$. What makes $\omega^{\rm eff}_{\rm tot}$ useful is that it determines the fate of the universe,

such that $\omega_{\rm tot}^{\rm eff} \leq -\frac{1}{3}$ corresponds to accelerated expansion, while $\omega_{\rm tot}^{\rm eff} < -1$ corresponds to a big rip future singularity. A big rip singularity is characterised by both the DE density and the scale factor becoming infinite ($\rho_{\rm de} \to \infty \ ; \ a \to \infty$) within a finite time interval. This behaviour can be considered non-physical by researchers, and models that avoid this are preferred.

3 Dynamical systems analysis

Dynamical systems analysis is a well-established tool to study the stability of a system of equations. Solutions to the system of equations are known as critical points, where many of the trajectories corresponding to functions with different initial conditions may either diverge or converge. If the system is perturbed around a critical point, the system may diverge away from the point, called an unstable node, source or past attractor. Conversely, if the trajectories instead converge at the critical point, the point is classified as a stable node, sink or future attractor. Lastly, if some trajectories converge, while others diverge, the critical point is known as a saddle point. Mathematically, these points are classified according to sign of the eigenvalues obtained from the Jacobian matrix of the system of equations at that point. Specifically, if all eigenvalues are positive, the point is an unstable node; if some eigenvalues are positive while others are negative, we have a saddle point; and if all eigenvalues are negative we have a stable node. Additionally, zero eigenvalues correspond to a manifold of solutions. See [7] for a similar applications of these techniques to IDE models. The behaviour of the system at the future attractor is especially useful in determining the fate of the universe, no matter the initial conditions.

We will now consider the dynamical behaviour of an IDE model with the interaction kernel $Q = 3\delta H \rho_{\rm de}$. The system of equations was derived in [6], but we have added the flatness assumption to reduce the number of equations ($\Omega_{\rm r} = 1 - \Omega_{\rm bm} - \Omega_{\rm dm} - \Omega_{\rm de}$), as well as taken the derivative to the Hubble parameter $\Omega_{\rm i}' = \frac{d}{d\zeta}\Omega_{\rm i}$, which leads to the dynamical system:

$$\begin{aligned}
\Omega_{\rm de}' &= \Omega_{\rm de}\left[1 - \Omega_{\rm bm} - \Omega_{\rm dm} - \Omega_{\rm de}\left(1 - 3\omega\right) - 3\omega\right] - 3\delta\Omega_{\rm de} \\
\Omega_{\rm dm}' &= \Omega_{\rm dm}\left[1 - \Omega_{\rm bm} - \Omega_{\rm dm} - \Omega_{\rm de}\left(1 - 3\omega\right)\right] + 3\delta\Omega_{\rm de}, \\
\Omega_{\rm bm}' &= \Omega_{\rm bm}\left[1 - \Omega_{\rm bm} - \Omega_{\rm dm} - \Omega_{\rm de}\left(1 - 3\omega\right)\right],
\end{aligned} \tag{4}$$

where we also used the relation that $\frac{8\pi G}{3H^2}\rho_i = \Omega_i$. From the dynamical system in (4), we obtained three solutions corresponding to three critical points, alongside the eigenvalues λ of the Jacobian matrix at those points, whose stability we analyse one at a time. For this study, we have two assumptions regarding the parameter space: 1. $\omega < 0$ (DE has negative pressure) ; 2. $\delta < |\omega|$ (the interaction strength is not too strong)

Critical Point $P_{\rm r}$: radiation-dominated phase.

$$\Omega_{\rm bm} = 0, \quad \Omega_{\rm dm} = 0, \quad \Omega_{\rm de} = 0, \quad \to \quad \Omega_{\rm r} = 1 \quad ; \quad \lambda = \begin{bmatrix} 1 - 3(\delta + \omega) \\ 1 \\ 1 \end{bmatrix}. \tag{5}$$

Since we have the assumed condition that $(\delta+\omega) < 0$, this implies that the first eigenvalue is positive $1-3(\delta+\omega) > 0$. Since all eigenvalues are positive, this radiation-dominated phase is an unstable node (source).

$$\text{Conditions for : Radiation-dominated unstable node (source) } \left\{(\delta + \omega) < \tfrac{1}{3} \quad . \right. \tag{6}$$

Critical Point $P_{\rm m}$: matter-dominated phase.

$$\Omega_{\rm bm} = -\Omega_{\rm dm} + 1, \quad \Omega_{\rm dm} = \Omega_{\rm dm}, \quad \Omega_{\rm de} = 0, \quad \to \quad \Omega_{\rm r} = 0 \quad ; \quad \lambda = \begin{bmatrix} 0 \\ -1 \\ -3(\delta + \omega) \end{bmatrix}. \tag{7}$$

The coordinates in (7) correspond to a combination of baryonic and DM domination, alternatively, a *matter-dominated phase*, as shown by $\Omega_{\rm m} = \Omega_{\rm bm} + \Omega_{\rm dm} = -\Omega_{\rm dm} + 1 + \Omega_{\rm dm} = 1$. This critical point is also not a single point, but a line on the axis where the combination of the two densities equal to one, as seen in Figure 1 below. This behaviour is illustrated by the first eigenvalue being zero, indicating a line or manifold that consists of a continuous set of equilibria where the sum of baryonic and DM is equal to one. Furthermore, the second eigenvalue is negative, while the third eigenvalue is positive, which implies that this manifold also acts as a saddle point.

$$\text{Conditions for : Matter-dominated manifold of saddle points } \left\{\delta < -\omega \quad . \right. \tag{8}$$

Critical Point $P_{\mathrm{dm+de}}$: dark energy hybrid dominated phase.

$$\Omega_{\mathrm{bm}} = 0, \quad \Omega_{\mathrm{dm}} = -\frac{\delta}{\omega}, \quad \Omega_{\mathrm{de}} = 1 + \frac{\delta}{\omega}, \quad \rightarrow \quad \Omega_{\mathrm{r}} = 0 \quad ; \quad \lambda = \begin{bmatrix} 3(\delta+\omega) - 1 \\ 3(\delta+\omega) \\ 3(\delta+\omega) \end{bmatrix}. \tag{9}$$

From the coordinates in (9) we see that $\Omega_{\mathrm{dm}} + \Omega_{\mathrm{de}} = 1$ at this critical point, which corresponds to DM-DE hybrid dominated phase. We may note that DE will dominate DM at this critical point if $\delta < -\omega/2$, as this will cause $\Omega_{\mathrm{de}} > \Omega_{\mathrm{dm}}$. Immediately from the matter coordinate of the critical point, alongside the assumption that $\omega < 0$, we note that DM will be negative if:

$$\text{Conditions for } \Omega_{\mathrm{dm}} > 0: \quad \omega < 0 \text{ and } \delta > 0 \text{ (iDEDM regime)} \tag{10}$$

For the DE to remain positive $\Omega_{\mathrm{de}} = 1 + \frac{\delta}{\omega} > 0$ we need $\delta < -\omega$, which justifies our initial assumption about the magnitude of the interaction strength. From the assumption that $(\delta + \omega) < 0$, this implies $3(\delta + \omega) < 0$ and $3(\delta + \omega) - 1 < 0$, which means both eigenvalues are negative and the critical point is a stable node (sink).

$$\text{Conditions for}: \text{ Positive dark matter-dark energy hybrid dominated stable node } \begin{cases} \omega < 0 \\ 0 < \delta < -\omega \end{cases}. \tag{11}$$

The critical points and the behaviour of trajectories around these points can be seen by plotting phase portraits of the dynamical system in (4). In Figure 1, we see that this model has a past radiation-dominated attractor P_{r}, but does not show a single baryonic matter or DM-dominated saddle point. Instead, a manifold that consists of a continuous set of equilibria points can be seen located on the line where $\Omega_{\mathrm{bm}} = \Omega_{\mathrm{bm}} + \Omega_{\mathrm{dm}} = 1$. This manifold acts as a continuous set of matter-dominated saddle points P_{m}. To more clearly see the effects of the interaction term on the dark components, we also consider the 2D projection in the $(\Omega_{\mathrm{dm}}, \Omega_{\mathrm{de}})$ plane in the bottom panels of Figure 1, where we set $\Omega_{\mathrm{bm}} = 0$, as baryonic matter does not interact and will not influence if DM or DE crosses into negative densities. We see that the interaction most noticeably changes the stable node which acts as a future attractor from complete DE dominance in ΛCDM to a DM-DE hybrid dominance. Importantly, the sign of the interaction constant δ, which determines the direction of energy flow, will determine whether this future attractor point has negative energies. *For a small interaction in the iDEDM regime ($\delta > 0$), all energies will remain positive, while in the iDMDE regime ($\delta < 0$), DM will always become negative in the future ($\Omega_{\mathrm{dm}} < 0$).*

We now need to consider where the trajectories become negative by doing a boundary analysis. For the DE density to remain positive we need the DE flow lines $\Omega'_{\mathrm{de}} \geq 0$ at the boundary $\Omega_{\mathrm{de}} = 0$, so that the flow cannot cross into negative Ω_{de}. When we substitute the condition $\Omega_{\mathrm{de}} = 0$ into Ω'_{de} found in the dynamical system (4), we obtain $\Omega'_{\mathrm{de}}(\Omega_{\mathrm{de}} = 0) = 0$. Thus, we see that Ω'_{de} vanishes here and the flow is tangent to the line, which implies that the trajectories cannot cross into negative Ω_{de}, ensuring positive DE densities for any choice of parameters in the physically viable area. This is a direct consequence of the fact that as $\rho_{\mathrm{de}} \to 0$, then $Q = 3H\rho_{\mathrm{de}} \to 0$ and the energy flow stops before negative DE can be reached.

For DM to remain positive, we need the trajectories to remain within region bounded by three invariant sub-manifolds, illustrated by the green triangle in bottom left panel of Figure 1, connecting the critical points P_{r}, P_{m} and $P_{\mathrm{dm+de}}$. No trajectories will cross the line connecting P_{r} and P_{m}, as it is an invariant sub-manifold, while trajectories will also remain within the line connecting P_{m} and $P_{\mathrm{dm+de}}$, which is guaranteed from the flatness assumption $\Omega_{(\mathrm{dm},0)} + \Omega_{(\mathrm{de},0)} \leq 1$. Finally the line connecting P_{r} $(\Omega_{\mathrm{dm}}, \Omega_{\mathrm{de}}) = (0, 0)$ and $P_{\mathrm{dm+de}}$ $(\Omega_{\mathrm{dm}}, \Omega_{\mathrm{de}}) = (-\frac{\delta}{\omega}, 1 + \frac{\delta}{\omega})$ has the gradient $m = \frac{\Delta\Omega_{\mathrm{de}}}{\Delta\Omega_{\mathrm{dm}}} = \frac{1+\frac{\delta}{\omega}-0}{-\frac{\delta}{\omega}-0} = -\frac{\delta+\omega}{\delta}$. It should be noted that the slope will be positive $m > 0$, from the assumption $\delta + \omega < 0$ and $\delta > 0$ from previously derived constraint in (11). The positive slope ensures the slope is in the positive DM domain ($\Omega_{\mathrm{dm}} > 0$). We can find additional constraints on the initial coordinates $(\Omega_{(\mathrm{dm},0)}, \Omega_{(\mathrm{de},0)})$ to ensure positive energy, by requiring that these coordinates are below the invariant line connecting P_{r} and $P_{\mathrm{dm+de}}$:

$$\Omega_{(\mathrm{de},0)} \leq -\frac{\delta+\omega}{\delta}\Omega_{(\mathrm{dm},0)} \quad \rightarrow \quad \delta \leq -\frac{\omega}{\left(1 + \frac{1}{r_0}\right)}, \tag{12}$$

where $r_0 = \frac{\Omega_{(\mathrm{dm},0)}}{\Omega_{(\mathrm{de},0)}}$ and $\delta > 0$. Condition (12) can be combined with the constraint for positive critical points in (11) to obtain (1), which ensures positive energies at all points in the cosmological evolution. This is the same condition previously obtained using analytical solutions for the ratio r [7], or ρ_{dm} and ρ_{de} [6]. The asymptotic past and future behaviour of the model is given by substituting the critical points into (2) and (3), yielding Table 1.

$$\boxed{\text{Conditions for } \Omega_{\mathrm{dm/de}} \geq 0 \text{ throughout cosmological evolution: iDEDM with } 0 \leq \delta \leq -\frac{\omega}{\left(1 + \frac{1}{r_0}\right)}}. \tag{13}$$

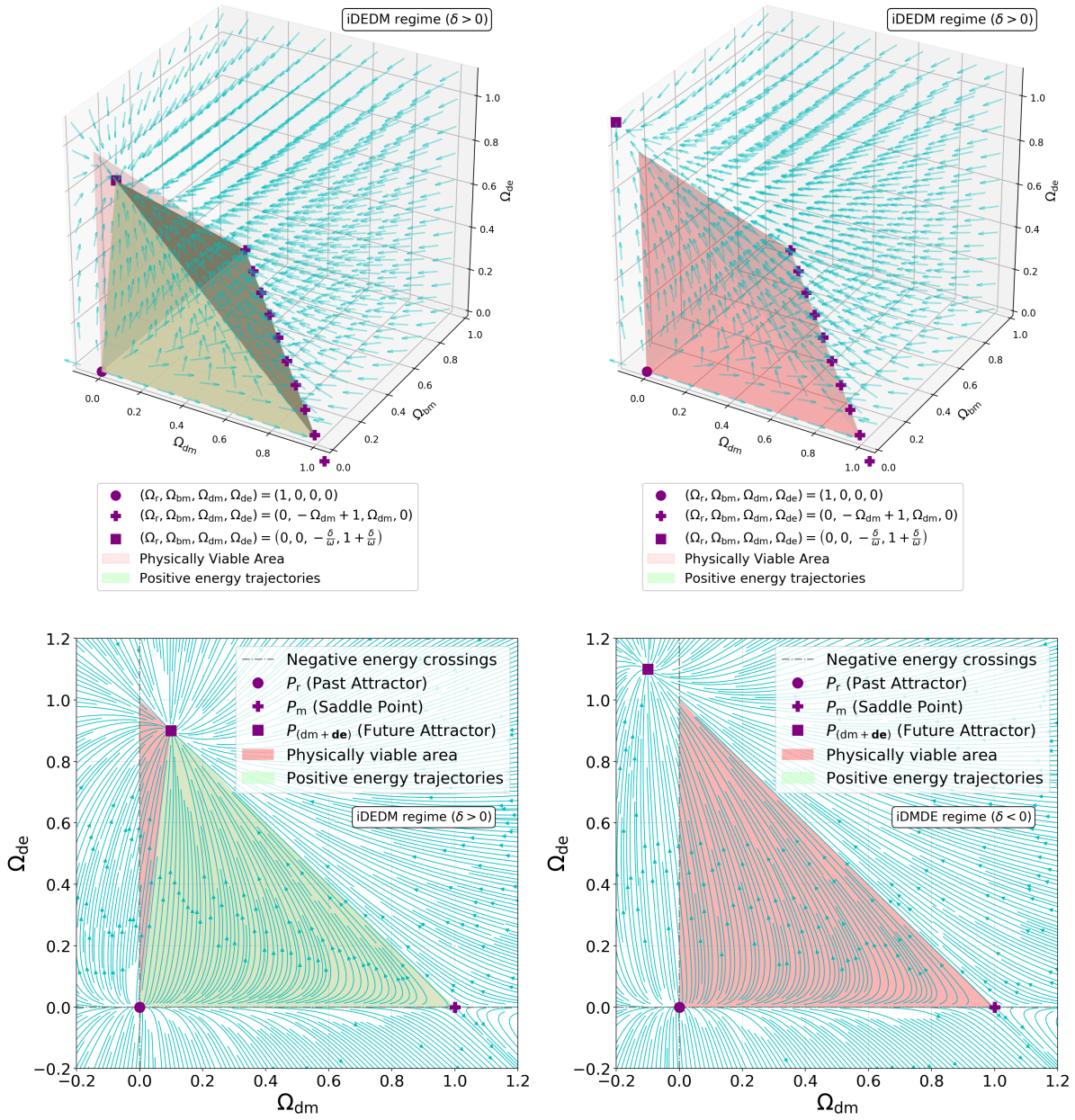

Figure 1: Phase portraits showing the evolution density parameters for the IDE model with interaction kernel $Q = 3H\delta\rho_{de}$. The top panels show 3D phase portraits with positive energy trajectories only found in the iDEDM regime $\delta = +0.1$ (left panels) and only negative energy trajectories in the iDMDE regime $\delta = -0.1$ (right panels). All trajectories share a radiation-dominated past attractor P_r, a matter-dominated saddle point P_m and a DM-DE hybrid dominated future attractor P_{dm+de}, where DM becomes negative in the iDMDE regime, indicated by trajectories leaving the red physically viable area. A 2D projection of the phase portraits in the $(\Omega_{dm}, \Omega_{de})$ plane (bottom panels) is obtained by setting $\Omega_{bm} = 0$. The bounded region connecting the three critical points, indicated by the green triangle, is used to derive the positive energy conditions found in (13).

	$P_{\rm r}$	$P_{\rm m}$	$P_{\rm dm+de}$
Class	Unstable node (source)	Saddle Point	Stable node (sink)
$\Omega_{\rm r}$	1	0	0
$\Omega_{\rm bm}$	0	$-\Omega_{\rm dm}+1$	0
$\Omega_{\rm dm}$	0	$\Omega_{\rm dm}$	$-\frac{\delta}{\omega}$
$\Omega_{\rm de}$	0	0	$1+\frac{\delta}{\omega}$
r	∞	∞	$-\frac{\delta}{\delta+\omega}$
$\omega_{\rm dm}^{\rm eff}$	0	0	$\omega+\delta$
$\omega_{\rm de}^{\rm eff}$	$\omega+\delta$	$\omega+\delta$	$\omega+\delta$
ζ	$-3(\omega+\delta)$	$-3(\omega+\delta)$	0
$\omega_{\rm tot}^{\rm eff}$	$\frac{1}{3}$	0	$\omega+\delta$

Table 1: Behaviour of IDE model $Q=3H\delta\rho_{\rm de}$ at critical points.

4 Conclusions

In this study, we performed a dynamical systems analysis of the IDE model $Q=3H\delta\rho_{\rm de}$, resulting in the positive energy conditions (13), which implies that *DM can only remain positive if there is a small interaction in the iDEDM regime*, in agreement with the analysis done in [7, 6]. This analysis also resulted in Table 1, where we see that our model is guaranteed to have past eras dominated by radiation $P_{\rm r}$ and matter $P_{\rm m}$, during which the severity of the coincidence problem is given by $\zeta=-3(\delta+\omega)$. Since $\omega<0$ and in the iDEDM regime $\delta>0$, we have $\zeta<3$, thus *alleviating* the coincidence problem in the past, while for the iDMDE regime where $\delta<0$, *worsening* the coincidence problem.

At the future attractor $P_{\rm dm+de}$, there is a hybrid DM-DE dominant phase , during which the DE and DM redshifts at the same rate $\omega_{\rm dm}^{\rm eff}=\omega_{\rm de}^{\rm eff}=\omega+\delta$, implying a fixed ratio of $r=-\frac{\delta}{\delta+\omega}$ and $\zeta=0$, *solving the coincidence problem in the future*. At this final attractor point, the model will show late-time accelerated expansion as long as $\omega_{\rm tot}^{\rm eff}=\omega+\delta\leq-\frac{1}{3}$, which will hold as long as $\delta\leq-\omega-\frac{1}{3}$. Lastly, DE can be in the phantom regime $\omega<-1$, but avoid a big rip singularity in the iDEDM regime ($\delta>0$), as long as the interaction strength is sufficiently positive such that $\omega_{\rm tot}^{\rm eff}=\omega+\delta\geq-1$. This is obtained when $\delta\geq-(\omega+1)$. All results obtained in this study agree with those in [7, 6], establishing these dynamical systems analysis techniques as an alternative method to understand the parameter space of IDE models, even without analytical expressions for the evolution of the density of DM and DE. We recommend that other researchers apply similar analysis to IDE models, so that we may better understand the implications of models that are candidates to address cosmological tensions.

References

[1] N. Aghanim *et al.*, "Planck 2018 results. VI. Cosmological parameters," *Astron. Astrophys.*, vol. 641, p. A6, 2020, [Erratum: Astron.Astrophys. 652, C4 (2021)].

[2] S. Weinberg, "The Cosmological Constant Problem," *Rev. Mod. Phys.*, vol. 61, pp. 1–23, 1989.

[3] L. P. Chimento, A. S. Jakubi, D. Pavon, and W. Zimdahl, "Interacting quintessence solution to the coincidence problem," *Phys. Rev. D*, vol. 67, p. 083513, 2003.

[4] E. Di Valentino *et al.*, "The CosmoVerse White Paper: Addressing observational tensions in cosmology with systematics and fundamental physics," *Phys. Dark Univ.*, vol. 49, p. 101965, 2025.

[5] K. Lodha *et al.*, "Extended Dark Energy analysis using DESI DR2 BAO measurements," 3 2025.

[6] M. A. van der Westhuizen and A. Abebe, "Interacting dark energy: clarifying the cosmological implications and viability conditions," *JCAP*, vol. 01, p. 048, 2024.

[7] G. Caldera-Cabral, R. Maartens, and L. A. Urena-Lopez, "Dynamics of interacting dark energy," *Phys. Rev. D*, vol. 79, p. 063518, 2009.

Implementing $F(T)$ Gravity in Boltzmann Codes: A Framework for Power Spectrum Computation

Robert Rugg[1], **Shambel Akalu**[1,2] **and Amare Abebe**[1,3]

[1]Centre for Space Research, North-West University, Potchefstroom 2531, South Africa
[2]Department of Physics, Wolkite University, Wolkite, Ethiopia
[3]National Institute for Theoretical and Computational Sciences (NITheCS), Potchefstroom 2520, South Africa

E-mail: 31770312@mynwu.ac.za

Abstract. This work investigates the non-linearity of the power-law model of $F(T)$ gravity, highlighting the Boltzmann solver CLASS's inability to handle nonlinear models. A second-order Taylor expansion is applied to the nonlinear field equations as a workaround, under the assumption that the extra degree of freedom (n), which quantifies deviations from the currently favored cosmological model (ΛCDM), remains small enough to preserve the key properties of the ΛCDM model. The Taylor expansion is supported by supernova data that indicate $n \leq 0.05$, allowing the power spectrum to be accurately computed within CLASS with a negligible truncation error for these values of n.

1 Introduction

High-redshift observations, notably those of the High-Z supernova search team, have revealed that the universe is undergoing accelerated expansion [1]. This behaviour is attributed to a negative pressure component commonly referred to as dark energy. The currently favoured cosmological model, ΛCDM, attributes this acceleration to a cosmological constant [2]. However, it faces challenges such as the Hubble tension [3] and the fine-tuning problem [4].

Alternative explanations for dark energy include models involving scalar fields, such as phantom fields with negative kinetic energy, canonical quintessence models, and interacting dark energy fluids [5]. A more direct approach involves modifying gravity itself by generalizing the gravitational action to include arbitrary functions of geometric scalars, such as $f(Q)$ [6], $f(R)$, and $f(T)$ [7].

In this work, we focus on the torsion-based formulation of gravity, where the Weitzenböck connection replaces curvature with torsion. This framework utilises the tetrad formalism [7] and constructs the Lagrangian density from the torsion scalar T, preserving local Lorentz and coordinate invariance [8]. Of particular interest is the generalised form $f(T)$, where the action becomes a function of T rather than T itself [9]. This generalisation, referred to as $f(T)$ gravity, extends the Teleparallel Equivalent of General Relativity (TEGR), and introduces second-order field equations with richer gravitational dynamics.

This study examines the power-law model of $f(T)$ gravity proposed in [9], which has proven advantageous for data fitting. We adapt the CLASS Boltzmann solver [10] to incorporate this model and analyse its implications for the cosmic microwave background (CMB) power spectrum. The structure of this paper is as follows. Section 2 introduces the background cosmology of $f(T)$ gravity and outlines the numerical methods used to adapt CLASS. Section 3 covers scalar perturbations and presents the resulting power spectrum. Section 4 concludes the study.

2 Background cosmology of f(T) gravity

For this work, Greek indices $\mu, \nu, ...$ are associated with spacetime coordinates (0,1,2,3) while capital Latin indices A,B,.. are associated with tangent spacetime coordinates. Lower case Greek and Latin indices are then associated with spatial and tangent spatial coordinates (1,2,3), respectively. In Teleparallel gravity, the underlying geometry used to describe spacetime is known as the tetrad-spin connection and describes the Lorentzian metric $g_{\mu\nu} = \eta_{AB} e^A_\mu e^B_\nu$, defining the Minkowski metric as $\eta_{AB} = \text{diag}(1, -1, -1, -1)$ [11]. To assume the non-degenerate characteristic, the inverse tetrad (E^μ_A) must satisfy $E^\mu_A e^A_\mu = \delta^\mu_\nu$. The affine connection as in the torsion scenario is then described as the Weitzenböck connection:

$$\hat{\Gamma}^\rho_{\mu\nu} = E^\rho_A(\partial_\nu e^A_\mu + \hat{w}^A_{B\nu} e^B_\nu), \tag{1}$$

where $\hat{w}^A_{B\nu}$ is defined as the spin connection, which in most background [11] and perturbative [12] cases, the inclusion of the spin connection amounts to the same equations of the pure tetrad formalism [13] and only restores Lorentz invariance. In general relativity, curvature was associated with the Levi-Civita connection; however, in Teleparallel gravity, the curvatureless property would result in a zero Riemann tensor. It is possible to relate the two theories through a general affine connection where the difference between the Weitzenböck and Levi-Civita connections is highlighted in the contorsion tensor ($\hat{K}^\rho_{\mu\nu}$) such that:

$$\begin{aligned} \hat{K}^\rho_{\mu\nu} &= \frac{1}{2}(\hat{T}^\mu_{\nu\,\rho} + \hat{T}^\mu_{\rho\,\nu} - \hat{T}^\mu_{\rho\nu}) \\ S^{\mu\nu}_\rho &= \frac{1}{2}(K^{\mu\nu}_\rho + \delta^\mu_\rho T^{\alpha\nu}_\alpha - \delta^\nu_\rho T^{\alpha\mu}_\alpha), \end{aligned} \tag{2}$$

where the torsion scalar $T = S^{\mu\nu}_\rho T^\rho_{\mu\nu}$ is the product of the torsion tensor and the super potential $S^{\mu\nu}_\rho$. This is similar to the General Relativity (GR) case where the Riemann tensor can be related to the Ricci scalar.

In the TEGR case, the action is calculated by the Lagrangian density T; however, in the case of generalised Teleparallel gravity, the torsion scalar in the Lagrangian is replaced by an arbitrary function $f(T) = -T + F(T)$. It is clear that the case of ΛCDM is recoverable in $F_T(T) = F_{TT}(T) = 0$ (first- and second-order derivatives of the function $F(T)$ with respect to the torsion scalar) implying a constant value $F(T)$ as in the constant case of ΛCDM. The generalised function then reduces to the TEGR case, which is equivalent to the GR case [14]. The action for the generalised case then reads:

$$\mathcal{S} = \int d^4x|e| \left[\frac{f(T)}{16\pi G} + L^m\right], \tag{3}$$

such that $|e| = det(e^A_\mu) = \sqrt{-g}$ and L^m is the matter Lagrangian. Assuming a spatially flat Friedmann-Robertson-Walker (FRW) metric such that the vierbein takes the form $e^A_\mu = \text{diag}(1, a, a, a)$ with a perfect matter fluid, the modified Friedmann equations can be written in the form:

$$\begin{aligned} H^2 &= -\kappa^2\rho + \frac{1}{6}F(T) - \frac{1}{3}TF_T(T), \\ \dot{H} &= -\frac{3}{2}H^2 - \frac{1}{2}\kappa^2 P + \frac{1}{2}(6H^2F_T + 2\dot{H}F_T + 24H^2\dot{H}F_{TT} + \frac{1}{2}F(T)), \end{aligned} \tag{4}$$

where ρ and P refer to the energy density and pressure associated with matter and radiation, with $T = 6H^2$. An effective dark energy density and pressure:

$$\begin{aligned} \rho_{\text{eff}} &= \frac{1}{\kappa^2}(\frac{1}{2}F(T) - TF_T(T)), \\ P_{\text{eff}} &= \frac{1}{\kappa}(6H^2F_T + 2\dot{H}F_T + 24H^2\dot{H}F_{TT} + \frac{1}{2}F(T)), \end{aligned} \tag{5}$$

can be deduced from the above equations, where an effective equation of state naturally arises as $w_{\text{eff}} = \frac{P_{\text{eff}}}{\rho_{\text{eff}}}$. This differs from the ΛCDM case where $w_{\text{eff}} = -1$, assuming a constant "dark energy", while this modified version of the TEGR case clearly indicates a dynamical dark energy.

3 The power-law model

This paper follows works in [15], where the $f(T)$ -ansatz (power law) $F(T) = \alpha(-T)^n$ [16] is assumed. If one assumes the perfect fluid, then it is possible to solve for ρ_{eff}, such that $\dot{\rho}_{\text{eff}} + 3H(1 + w_{\text{eff}}) = 0$, where $w_{\text{eff}} = P_{\text{eff}}/\rho_{\text{eff}}$, resulting in a more convenient dynamical dark energy written in dimensionless parameters equivalent to $\alpha(-T)^n$:

$$\rho_{\text{eff}} = \rho_{eff,0} E^n(z), \tag{6}$$

where the subscript $_{eff,0}$ refers to the density at redshift $z = 0$ and $E(z) = \frac{H(z)}{H_0}$. It is clear from this term that the dynamical dark energy returns to its non-dynamical form as a constant in the case $n = 0$. This nonlinear form arising from the power law model can be solved numerically. It is of great interest to find the power spectrum of the model, that will be generated using the CLASS Boltzman equation [10]. CLASS, is, however, ill equipped to handle non-linear forms such as the power law, and hence a less rigorous numerical approach of a second-order Taylor expansion as in [15], is taken around $n = 0$ with 6, such that:

$$\begin{aligned} E^2(z,n) &= E^2_\Lambda(z,0) + \left.\frac{dE^2(z,n)}{dn}\right|_{n=0} + \left.\frac{d^2E^2(z,n)}{dn^2}\right|_{n=0} + \ ..., \\ E^2(z,n) &= E^2_\Lambda(z) + \Omega_{\text{eff}} \ln E^2_\Lambda n + \left(\Omega_{\text{eff}} \ln^2 E^2_\Lambda + \frac{2\Omega_{\text{eff}} \ln E^2_\Lambda}{E^2_\Lambda}\right) \frac{n^2}{2} \ ..., \end{aligned} \tag{7}$$

where $E_\Lambda = \sqrt{\Omega_{m,0}(z+1)^3 + \Omega_{r,0}(z+1)^4 + \Omega_\Lambda}$ refers to the ΛCDM Friedmann equation with the subscripts m,r and Λ being matter, radiation, and dark energy, respectively. Ω is introduced as a dimensionless density corresponding to their respective components, denoted by i such that $\Omega_i = \frac{8\pi G}{3H^2(t)}\rho_i$. In addition, $n \ll 1$, as there is no expectation of differing significantly from ΛCDM, which would result in inadequate data fitting as seen in the figure below. In addition, the assumption $n \ll 1$ is supported by supernova results for f(T) [17], who reported a small constrained value of 0.044. For this small value, the truncation error from the second-order Taylor expansion is estimated to be negligible.

The second approximation technique was computed with `scipy`'s `fsolve` [18] in Python where no assumptions were made about the value of n. The curves labeled "fsolve" in Fig. 1 correspond to this full numerical solution, while the curves labeled "Taylor expansion" show the second-order Taylor expansion. It is clear from Fig. 1, that as the value of n increases, the percentage difference between the two methods increases significantly. This will clearly bias the results towards a small value of n, when the Taylor expansion is incorporated into the CLASS Boltzman solver for CMB data.

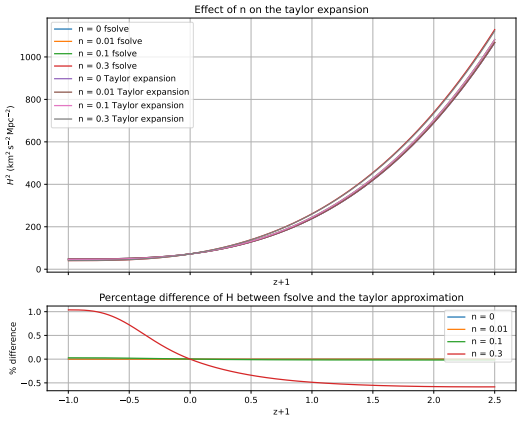

Figure 1: (Top) The Hubble parameter plotted for various values of n using both the second-order Taylor expansion method and `scipy`'s `fsolve` as a function of z. (Bottom) Percentage difference between the second order Taylor expansion method and `scipy`'s `fsolve` at specific values of n as a function of z for H^2.

3.1 Newtonian-gauge perturbations in F(T) gravity

Following the adjustments made in the CLASS Boltzman solver for the background cosmology, perturbations play an essential role in theoretical anisotropies. The following derivation is followed from [19] in which the metric formalism is reconstructed using a Newtonian gauge such that scalar modes ϕ and ψ are introduced as functions of spacetime coordinates where:

$$ds^2 = (1+2\psi)dt^2 - a^2(1-2\phi)\delta_{ij}dx^i dx^j. \tag{8}$$

Since the Boltzmann solver CLASS is set up in the more convenient Fourier space and conformal time ($\mathcal{H} = H/(1+z)$), the perturbed equations were converted accordingly using the mode expansion where k is introduced as the co-moving wave number related to the co-moving wavelength ($k = \frac{2\pi}{\lambda}$), such that:

$$\begin{aligned} \phi(t, \boldsymbol{X}) &= \frac{1}{(2\pi)^{\frac{3}{2}}} \int dk^3 \tilde{\phi}_k(t) e^{i\boldsymbol{k}\cdot\boldsymbol{x}}, \\ \psi(t, \boldsymbol{X}) &= \frac{1}{(2\pi)^{\frac{3}{2}}} \int dk^3 \tilde{\psi}_k(t) e^{i\boldsymbol{k}\cdot\boldsymbol{x}}, \end{aligned} \tag{9}$$

where ϕ and ψ are the scalar metric perturbations in the Newtonian gauge such that $T_1 = 12H(H\psi + \dot{\phi})$. The momentum constraint equation and the shear equation are sufficient to overlay the effects of perturbations on observables such as the CMB [20] with σ and u_k the shear and velocity perturbation of the matter fluid, respectively, such that:

$$\begin{aligned} \dot{\tilde{\phi}}_k &= -\mathcal{H}\tilde{\psi}_k + \frac{4\pi(\rho_m + p_m)\tilde{u}_k}{(12(\frac{\mathcal{H}}{a})^2 F_0'' - (1+F_0'))} \\ \tilde{\psi}_k &= \tilde{\phi}_k - \frac{4\pi G a^2 k^2}{1+F_0'}\sigma. \end{aligned}$$

The equations listed in 4, contain all relevant background evolutions for power-spectrum analysis. The Taylor expansion in Equation 7 are used to overcome CLASS's inability to handle non-linear Friedmann equations. The negative pressure associated with the cosmological constant in the ΛCDM model was turned off and simulated with the modified Friedmann Equation 4. This paper will mainly focus on temperature mapping with CMB_{TT} data and Figure 2 below is a representation of the modified Friedmann equations using the $F(T)$ power-law model.

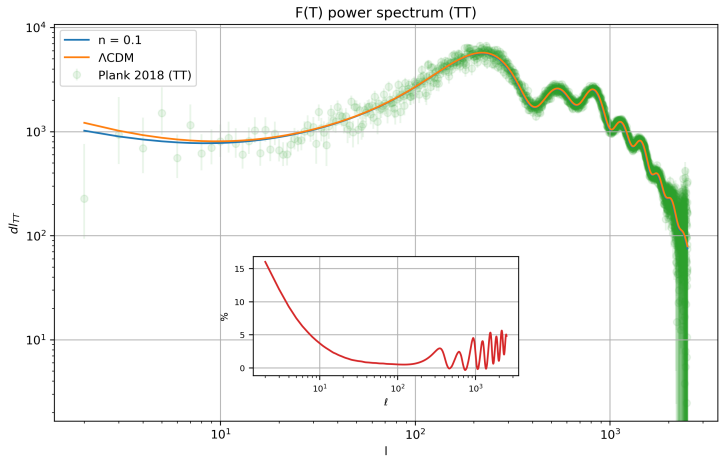

Figure 2: (Top) The power spectrum for the ΛCDM and $F(T)$ power law case plotted against temperature mapping data form the Planck mission for different multipole moments l. (Bottom) The percentage difference between the ΛCDM and the $F(T)$ power-law model over different multipole moments l.

It is clear from Figure 2 a large initial difference comes from the dynamical dark energy in the power-law case that has direct implications on gravitational potentials before recombination. Thus, the dynamical dark energy has a direct impact on the frozen photon-baryon fluid. In addition, the shape and peaks of each acoustic waves are directly affected, and most of the implications are associated with the slightly higher percentage difference prevalent

in the tail, indicating that $F(T)$ has direct consequences on the baryon density or matter density at recombination. The percentage difference also points towards stronger peak distortion than shape distortion, again indicating that $F(T)$ has an impact on the baryon-photon interactions.

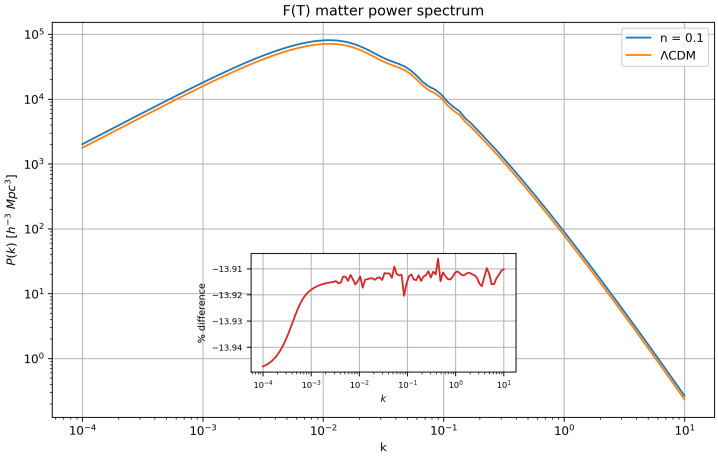

Figure 3: The matter power spectrum for the ΛCDM and the $F(T)$ power-law case plotted for different wavenumbers (k). The percentage difference between the ΛCDM and the $F(T)$ power-law model with $n = 0.1$ is indicated in the subplot within.

Figure 3 shows that $F(T)$ follows a very similar trend to ΛCDM. However, at $n = 0.1$, $F(T)$ gravity explores higher amplitudes, indicating a larger clustering of matter. It should also be noted that n is chosen as $n = 0.1$, but realistically expected to be lower. This would indicate a much lower difference, which is crucial as galaxy surveys are extremely sensitive regarding the matter power spectrum.

4 Conclusions

The second-order Taylor expansion serves as a viable approach to solve the non-linearity issues faced in CLASS. The difference between `scipy`'s `fsolve` shows a difference compared to the Taylor expansion approach of 1% at $n = 0.1$. It is well-reported that a small value of n is preferred as data surveys are extremely sensitive to the power spectrum. CLASS effectively generates the matter power spectrum and temperature fluctuations, which will perfectly allow for constraining of the power-law model. There is a sense of bias to this result, as n is assumed to be small in nature, but any large value of n would result in large likelihoods due to its large difference from the ΛCDM model which fits the data extremely well.

Using the second-order Taylor expansion effectively highlights the effect that a dynamical effective equation of state has on the power spectrum, producing a large difference at low multipoles. The effects of $F(T)$ gravity are largely observed in the shape and peaks of each acoustic wave, where the shape of the acoustic wave was slightly altered. Moreover, there appear to be larger effects on the damping tail, indicating the effect on matter densities at recombination. Finally, the matter power spectrum indicates a trend similar to ΛCDM at lower values of n, but indicates slightly more matter clustering.

References

[1] A. G. Riess *et al.*, "Observational Evidence from Supernovae for an Accelerating Universe and a Cosmological Constant," *The Astronomical Journal*, vol. 116, no. 3, pp. 1009–1038, Sep. 1998.

[2] P. J. E. Peebles and B. Ratra, "The Cosmological Constant and Dark Energy," *Reviews of Modern Physics*, vol. 75, no. 2, pp. 559–606, Apr. 2003.

[3] G. Simpson, K. Bolejko, and S. Walters, "Beyond LambdaCDM: How the Hubble tension challenges early universe physics," *Classical and Quantum Gravity*, vol. 42, no. 14, p. 143001, Jul. 2025.

[4] W. Hu and S. Dodelson, "Cosmic Microwave Background Anisotropies," *Annual Review of Astronomy and Astrophysics*, vol. 40, no. 1, pp. 171–216, Sep. 2002.

[5] E. D. Valentino *et al.*, "The CosmoVerse White Paper: Addressing observational tensions in cosmology with systematics and fundamental physics," May 2025.

[6] S. Sahlu, R. T. Hough, A. Abebe, and Á. De La Cruz-Dombriz, "Constraining viscous-fluid models in f(Q) gravity with data," *The European Physical Journal C*, vol. 85, no. 7, Jul. 2025.

[7] Y.-F. Cai, S. Capozziello, M. De Laurentis, and E. N. Saridakis, "$F(T)$ teleparallel gravity and cosmology," *Reports on Progress in Physics*, vol. 79, no. 10, p. 106901, Oct. 2016.

[8] K. Hayashi and T. Shirafuji, "New general relativity," *Physical Review D*, vol. 19, no. 12, pp. 3524–3553, Jun. 1979.

[9] E. V. Linder, "Einstein's Other Gravity and the Acceleration of the Universe," *Physical Review D*, vol. 81, no. 12, Jun. 2010.

[10] Diego Blas, Julien Lesgourgues, and Thomas Tram, "The Cosmic Linear Anisotropy Solving System (CLASS). Part II: Approximation schemes," *Journal of Cosmology and Astroparticle Physics*, vol. 2011, no. 07, pp. 034–034, Jul. 2011.

[11] S. Bahamonde, K. F. Dialektopoulos, C. Escamilla-Rivera, G. Farrugia, V. Gakis, M. Hendry, M. Hohmann, J. L. Said, J. Mifsud, and E. Di Valentino, "Teleparallel Gravity: From Theory to Cosmology," *Reports on Progress in Physics*, vol. 86, no. 2, p. 026901, Feb. 2023.

[12] A. Golovnev, "Perturbations in f(T) cosmology and the spin connection," *Journal of Cosmology and Astroparticle Physics*, vol. 2020, no. 04, pp. 014–014, Apr. 2020.

[13] M. Krššák and E. N. Saridakis, "The covariant formulation of f(T) gravity," *Classical and Quantum Gravity*, vol. 33, no. 11, p. 115009, Jun. 2016.

[14] S. Weinberg, *Cosmology*. Oxford ; New York: Oxford University Press, 2008.

[15] S. Nesseris, S. Basilakos, E. N. Saridakis, and L. Perivolaropoulos, "Viable f(T) models are practically indistinguishable from LCDM," *Physical Review D*, vol. 88, no. 10, p. 103010, Nov. 2013.

[16] G. Bengochea and R. Ferraro, "Dark torsion as the cosmic speed-up," *Physical Review D*, vol. 79, no. 12, Jun. 2009.

[17] S. Kumar, R. C. Nunes, and P. Yadav, "New cosmological constraints on $f(T)$ gravity in light of full Planck-CMB and type Ia supernovae data," *Physical Review D*, vol. 107, no. 6, p. 063529, Mar. 2023.

[18] P. Virtanen *et al.*, "SciPy 1.0: Fundamental algorithms for scientific computing in Python," *Nature Methods*, vol. 17, no. 3, pp. 261–272, Mar. 2020.

[19] S.-H. Chen, J. B. Dent, S. Dutta, and E. N. Saridakis, "Cosmological perturbations in f(T) gravity," *Physical Review D*, vol. 83, no. 2, p. 023508, Jan. 2011.

[20] E. D. Dio, F. Montanari, J. Lesgourgues, and R. Durrer, "The CLASSgal code for Relativistic Cosmological Large Scale Structure," *Journal of Cosmology and Astroparticle Physics*, vol. 2013, no. 11, pp. 044–044, Nov. 2013.

Cosmic-Ray Neutron Detectors for Soil Moisture Monitoring

A.M. Dumont[1], K.D. Moloto[1], and H. Havenga[2]

[1]Centre for Space Research, North-West University, Potchefstroom 2531, South Africa
[2]Unit for Environmental Sciences and Management, North-West University, Potchefstroom 2531, South Africa

E-mail: dumont.aimee@gmail.com

Abstract. Primary cosmic-rays are high-energy particles that enter the atmosphere of Earth via the heliosphere, generating cascades of secondary cosmic-ray particles when interacting with atmospheric atoms. These secondary cosmic-rays interact inversely with hydrogen atoms in soil moisture; when this interaction is measured, it provides a non-invasive method for monitoring moisture levels. Continuous neutron flux observations in soil can help to establish predictive models for evaporation, droughts, and floods which significantly impact the water resources of South Africa. This study employs a cosmic-ray neutron sensor (CRNS) probe equipped with a Boron triflouride (BF_3) detector positioned 1-2 m above ground. This sensor is capable of measuring soil moisture across a footprint of approximately 20 hectares in width and up to 0.3 m depth. This paper details the calibration process that relates the measured neutron intensity to gravimetric soil sampling, as well as determines a correlation between these gravimetric soil samples and rainfall. This approach can assist in precision water resource management, especially in a drought-prone country such as South Africa.

1 Introduction

Agriculture plays a vital role in South-Africa's economy: not only does it add $\sim 3\%$ to our GDP in 2024, it also provides the country with food security. Furthermore, from primary to secondary production, it is a source of job creation for ~ 1.1 million [1, 2]. As South Africa has periodic dry spells that affect the agricultural industry, early assessment of soil moisture reserves and constant monitoring could assist with water efficiency and effective crop yield [3, 4, 5, 6].

Primary cosmic-rays collide with atmospheric nuclei, creating cascades of secondary cosmic-ray particles that penetrate the soil, producing fast (epithermal) neutrons [7]. The hydrogen in the soil slows down the epithermal neutrons, creating thermal neutrons [5]. Compared to dry soil, saturated soil will contain an abundance of neutrons. This knowledge is known as Cosmic ray neutron sensing (CRNS) and provides an accurate and non-invasive method of detecting soil moisture in large areas [8, 9]. This method has been successfully applied in extreme environments to bridge the gap between point sensor data and large scale remote sensing (e.g. satellite) techniques [10, 11]. The sensor measures the background neutron flux, which has an inverse correlation to soil moisture content [12]. This study represents a pilot investigation into the CRNS model in soil moisture, and future work will extend the scope of this investigation as well as have the potential to add to the South African CRNS network and the potential to increase the global CRNS network later. This paper describes the BF_3 neutron monitor design and characteristics of the study site, with preliminary insights into the relation between neutron count and hydrogen [13].

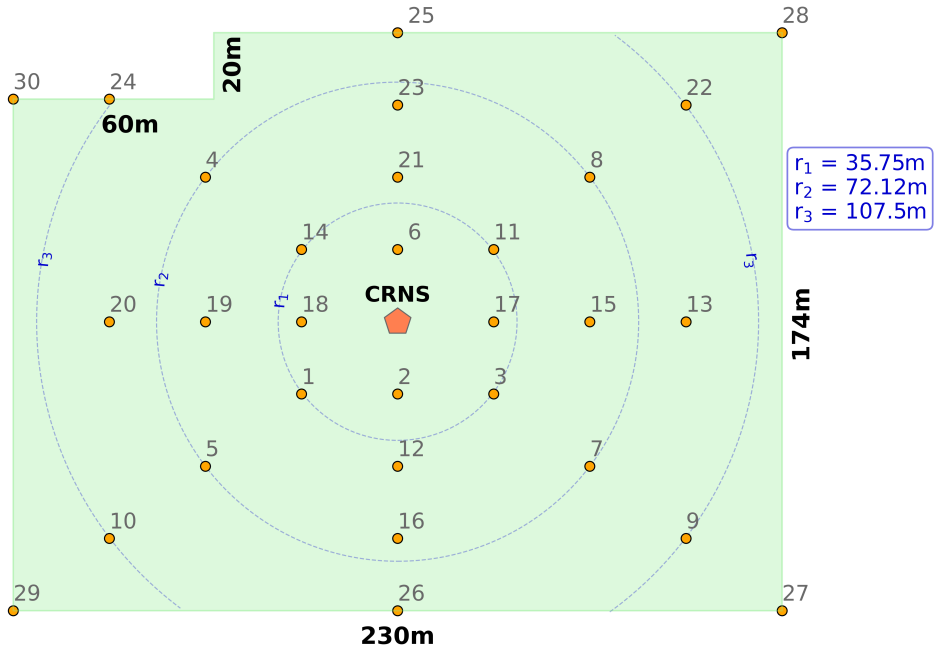

Figure 1: The layout of the site with the locations of instruments. The cosmic-ray neutron sensor (CRNS) is located in the centre of the field, with the soil moisture sensors (represented by orange points) positioned at different radii away from the CRNS. Two weather stations are positioned next to the field, as well as lead and lead-free neutron monitors (NM) are located in the shed for calibrating the CRNS.

2 Site description

Pienaarskamp farm is part of the North-West University (NWU) Center for Sustainable Agriculture and is located ~ 5 km from the Potchefstroom campus in North-West, South Africa (S26°38′59.99″, E27°5′23.99″). This study focuses on a field at the Pienaarskamp farm that covers an area of ~ 3.88 hectares , and was conducted between the 27 March 2025 – 24 June 2025. The soil is classified as a Magudu soil formation, contains between 10 – 20% of clay and appears to be reddish in colour on the structured horizon and a yellow-brown colour on the apedal horizon [14]. The site is located on slightly heterogeneous terrain; the soil drains water freely, and is used mainly for agricultural purposes. It is also fenced off to keep cattle out. During various stages of this project, sunflowers were planted and harvested in the selected field.

The CRNS (which is a lead-free neutron monitor) is located at the centre of the field, as seen in Figure 1, and is surrounded by 30 soil moisture sensors. The shed is located ~ 100 m away from the field, and harbours the lead neutron monitor as well as the lead-free neutron monitor.

3 Neutron monitor design

Three neutron monitors (as seen in Figure 2) were installed at the NWU Pienaarskamp. Two of the neutron monitors are located in a shed, on a solid concrete platform (shown in Figure 2 (a) and Figure 2 (b)), and one neutron monitor is located in the centre of the field described earlier (shown in Figure 3 (c)). The following subsections discuss the physical aspects and detection processes of the neutron monitors, which are detailed below.

3.1 Physical design

One of the neutron monitors in the shed is the lead neutron monitor (shown in Figure 2 (a)) that consists of a gas-filled detector surrounded by a thin inner polyethylene cylinder; this is placed inside the seven lead rings which are then encased in a thick outer polyethylene cylinder (as shown in Figure 2 (c)). The other neutron monitor (Figure 2(b)) is the lead-free neutron monitor (also referred to as the "bare" neutron monitor) that consists of a gas-filled detector encased in a polyethylene moderator cylinder, which is the same as the inner polyethylene cylinder in the lead neutron monitor. The neutron monitor positioned in the field (Figure 3(c)) is a lead-free neutron monitor, and it is placed vertically, unlike the other neutron monitors, which are placed horizontally. Below, the gas-filled detectors, shielding, and the lead around the detector are discussed in detail.

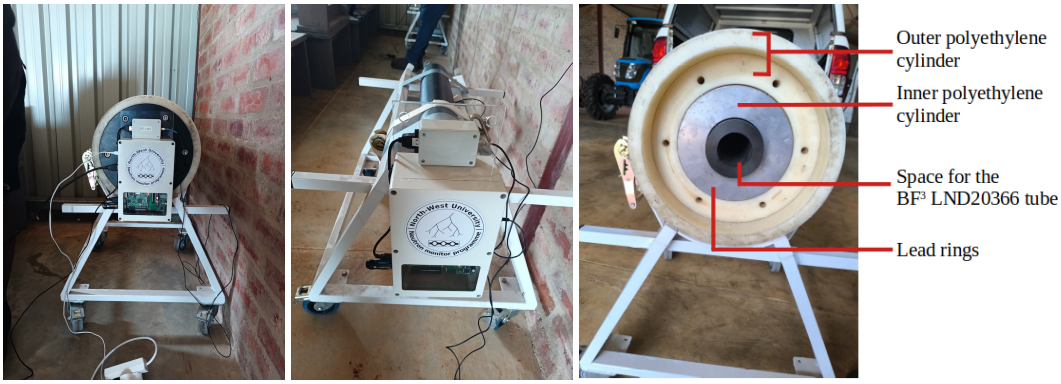

Figure 2: (a) Lead neutron monitor (b) Lead-free neutron monitor (c) Detailed front view of the lead neutron monitor

Type	Efficiency	Cost	Long term
BF_3	Less efficient	Inexpensive	Stable over long periods, can decrease from deposition on the anode wire
^3He	More efficient	Expensive	Helium leakage occurs, which causes drift parameters to appear after a period

Table 1: Comparison between the BF_3 and ^3He gas in neutron monitors [15].

3.1.1 Gas-filled thermal-neutron detectors

Gas-filled detectors are used to detect thermal neutrons (neutrons with ~ 0.025 eV) as atmospheric neutron particles react with the gas [16, 12]. There are two main gas-filled thermal neutron detectors, Helium-3 (^3He) and Boron Triflouride (BF_3), where both produce exothermic reactions and have strong neutron absorption cross-section [17, 18]. ^3He is not commonly used even though it performs similar to BF_3 in standard neutron monitors; there are a few differences between the gases; these are summarised in Table 1 [16, 15]. The gas-filled thermal neutron detectors used in this study are BF_3 LND20366[1] tubes, which are stable over long periods. These neutron detectors are stainless steel tubes with diameters of 51 mm and lengths of 652 mm. When high voltage is transmitted through the BF_3 molecules and ionises the gas, it creates a (n, α) reaction that splits the BF_3 molecules into alpha particles and lithium nuclei. This creates absorption of atmospheric neutron particles through the walls of the LND20366 tube.[17, 19, 20]. Having a gas-filled tube creates leakage of thermal neutrons and is susceptible to background radiation; therefore, the thin polyethylene cylinder decreases the number of thermal neutrons and the background sensitivity by 30%, while increasing the efficiency of neutron flux detected [20].

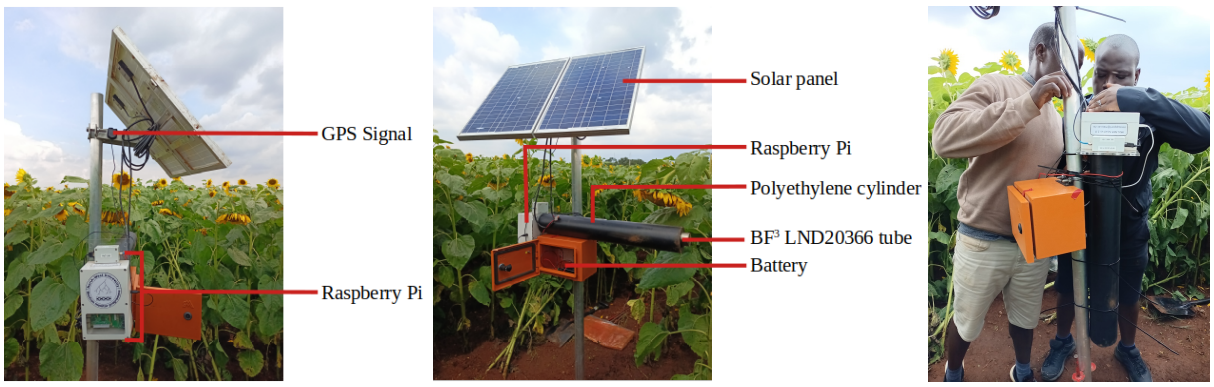

Figure 3: Components of the field NM. (a) Detailed front view of the field NM. (b) Detailed side view of the field nm. (c) Final position of the field NM, to decrease background neutron sensitivity.

[1] gas-filled tubes are manufactured by LND Inc., USA, and are available through `https://www.lndinc.com/`.

3.1.2 Lead and Shielding around the detector

There are seven lead rings inside the external polyethylene cylinder (as shown in Figure 2 (c)); each lead ring weighs $\sim$ 25 kg. The lead has a higher atomic mass, which creates secondary neutron particles (neutrons that are produced through the interaction with the BF_3 gas) through non-elastic interactions in which the lead nuclei become excited [21, 22]. This increases the detection of epithermal neutrons (neutrons that have an energy $\geq$ 0.5 eV) as the lead can produce multiple neutrons from a single atmospheric cosmic ray [12, 23]. The thick outer polyethylene cylinder of the lead neutron monitors shields the neutron monitor from detecting background radiation, while containing the neutrons that were produced from the lead rings [24].

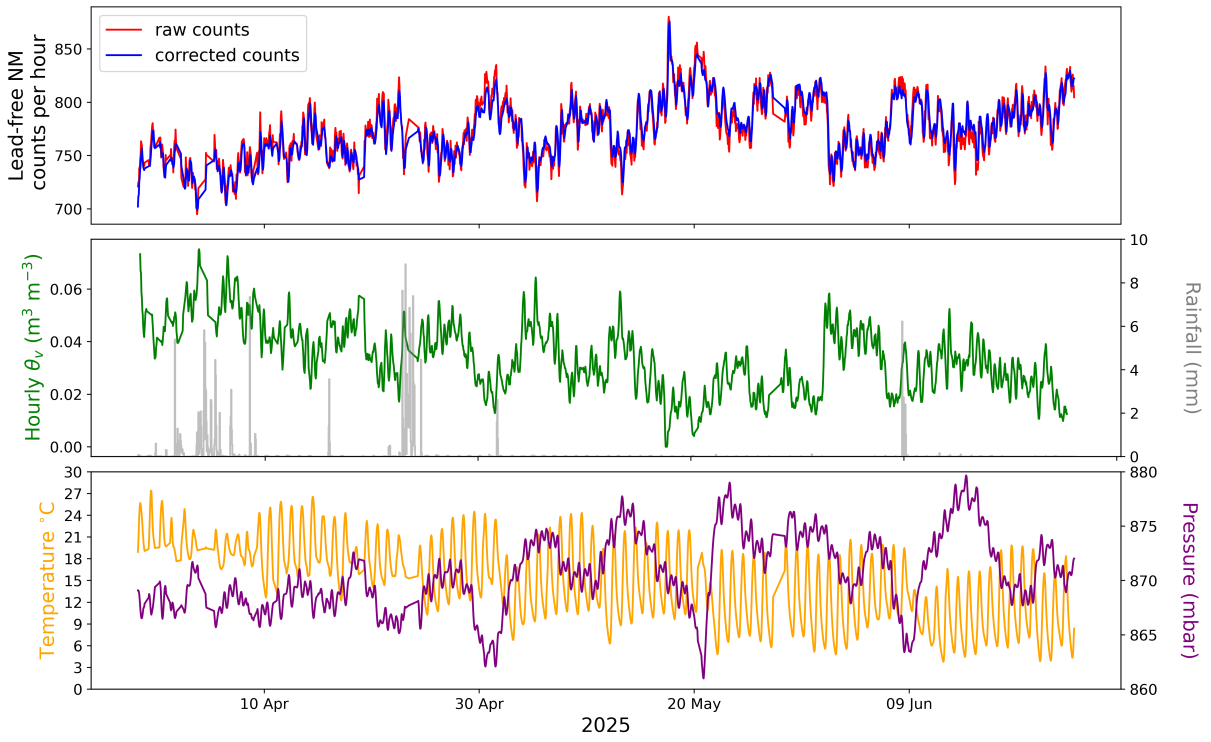

Figure 4: The first panel shows the raw count rates and the corrected count rates of the lead-free neutron monitor, which were obtained hourly between 27 March 2025 – 24th June 2025. The second panel shows the percentage of volumetric water content from the neutron flux alongside the rainfall over the same time period. The third panel shows the temperature and pressure.

3.2 Electronic components

Figure 3 shows all the electronics in the neutron monitors as detailed by Strauss et al. [15], where the head of the LND20366 tube is connected to the Raspberry Pi data logger, which was manufactured at the NWU. The solar panel is the power supply for the field neutron monitor, which transmits high voltage through the LND20366 tube and the data logger; the neutron monitors in the shed use a standard 230 V plug outlet. The GPS signal is used to ensure that the Raspberry Pi has the location and time to catalogue data. The system uses a 5V output solar-powered battery. The data logger contains Python 3 scripts to catalogue the raw count rate data, temperature, pressure, and the high voltage transmitted through the gas. The raw data are then binned in minute intervals when the scripts are processed in the Raspberry Pi.

4 Neutron count rate processing

Desilets et al. [25] determined that the conversion of count rates to volumetric water content ($\Theta(N)$) equation is given by,

$$\theta(N) = \left[\frac{a_0}{\left(\frac{N}{N_0}\right) - a_1} - a_2 + \theta_{lw} \right] \cdot \rho_{bulk} \; ; \tag{1}$$

where,

$$a_0 = 0.0808, \quad a_1 = 0.372, \quad a_2 = 0.0115\ . \tag{2}$$

Here a_0, a_1, and a_2 are empirical parameters of near-surface neutron intensity of a generic silica soil matrix, N is the corrected neutron count rate, N_0 is the neutron count rate over dry soil, θ_{lw} is the lattice water content, and ρ_{bulk} is the bulk density of the soil [25, 26]. The pressure correction (N),

$$N = N_{raw}\exp\left(\beta\Delta P\right) \tag{3}$$

was applied to the raw neutron count rate (N_{raw}), where β is the barometric coefficient of the tube, and ΔP is the change in pressure [15].

5 Preliminary results

During deployment, it was realised that the battery used was not sufficient to supply the system during initial startup, which led to invalid data on the field sensor. The design setup of the field and lead-free neutron monitors is the same, therefore the measurements from the lead-free neutron monitor can be used as true estimates of what is expected in the field neutron monitor measurements. The first panel in Figure 4 represents the hourly neutron count rate for the lead-free neutron monitor. This neutron monitor was installed at Pienaarskamp farm on the 27th March 2025, and was placed horizontally over a solid concrete platform. The second panel in Figure 4 converts the neutron count rates of the lead-free monitor to volumetric water content using Equation 1, where N are the lead-free count rates and N_0 are the lead count rates. The second panel also contains the rainfall over this period. There is a visible correlation between the volumetric water content and the rainfall. Although the second panel does not show much of an increase in volumetric water content, these readings can still be used to identify rainfall. An inverse correlation between the volumetric water and the count rate can be observed between the first two panels. The last panel shows the temperature and pressure from the lead-free neutron monitor, where an inverse correlation between the two can be observed. The temperature can be seen to decrease over time; this is due to seasonal changes from summer to winter.

6 Conclusion

This paper presents the calibration process of a CRNS setup. Even though the field neutron monitor data were unattainable, the process was conducted via the lead-free neutron monitor in the shed. The results showed that the neutron monitor could sense excess hydrogen atoms in the atmosphere. Furthermore, the volumetric water content was modelled to the rainfall in the area which determined that this is an accurate and efficient method for determining the amount of moisture in the soil.

In addition to future calibrations of the CRNS, the voltage of the field neutron monitor would have to be increased to obtain viable data; this highlights some limitations of calibration during field deployments such as attempted here. In addition, the volumetric water content should be compared to the data obtained from the soil sensors. Furthermore, the volumetric water content from the field neutron sensor should be modelled to the rainfall in the area. Nevertheless, the potential to use this technology in operational settings for water management remains promising and further investigations are being conducted. Attempts will be made to improve the instrument design, calibrate soil moisture to neutron flux using point sensors, and apply it to more real-world scenarios.

References

[1] Mar 2025. [Online]. Available: https://www.gov.za/blog/agriculture-vital-part-our-growth-story

[2] Mar 2025. [Online]. Available: https://nda.gov.za/images/Branches/EconomicaDevelopmentTradeandMarketing/StatistcandÂăEconomicAnalysis/statistical-information/economic-review-of-the-south-african-agriculture-2024.pdf

[3] A. Bennie and M. Hensley, "Advances in soil physics and soil water management research in south africa, 1979–2003," *South African Journal of Plant and Soil*, vol. 21, no. 5, pp. 268–277, 2004.

[4] H. McNairn, A. Merzouki, A. Pacheco, and J. Fitzmaurice, "Monitoring soil moisture to support risk reduction for the agriculture sector using radarsat-2," *IEEE Journal of Selected Topics in Applied Earth Observations and Remote Sensing*, vol. 5, no. 3, pp. 824–834, 2012.

[5] E. van Amelrooij, N. van de Giesen, J. Plomp, M. Thijs, and T. Fico, "Blosm: Boron-based large-scale observation of soil moisture: First laboratory results of a cost-efficient neutron detector," *HardwareX*, vol. 12, p. e00342, 2022.

[6] K. Furtak and A. Wolińska, "The impact of extreme weather events as a consequence of climate change on the soil moisture and on the quality of the soil environment and agriculture–a review," *Catena*, vol. 231, p. 107378, 2023.

[7] M. Zreda, D. Desilets, T. Ferré, and R. L. Scott, "Measuring soil moisture content non-invasively at intermediate spatial scale using cosmic-ray neutrons," *Geophysical research letters*, vol. 35, no. 21, 2008.

[8] A. Hawdon, D. McJannet, and J. Wallace, "Calibration and correction procedures for cosmic-ray neutron soil moisture probes located across australia," *Water Resources Research*, vol. 50, no. 6, pp. 5029–5043, 2014.

[9] J. Jakobi, J. A. Huisman, H. Fuchs, H. Vereecken, and H. Bogena, "Potential of thermal neutrons to correct cosmic-ray neutron soil moisture content measurements for dynamic biomass effects," *Water resources research*, vol. 58, no. 8, p. e2022WR031972, 2022.

[10] L. M. Scheiffele, G. Baroni, T. E. Franz, J. Jakobi, and S. E. Oswald, "A profile shape correction to reduce the vertical sensitivity of cosmic-ray neutron sensing of soil moisture," *Vadose Zone Journal*, vol. 19, no. 1, p. e20083, 2020.

[11] L. Myeni, M. E. Moeletsi, and A. D. Clulow, "Development and analysis of a long-term soil moisture data set in three different agroclimatic zones of south africa," *South African Journal of Science*, vol. 117, no. 5-6, 2021.

[12] M. Zreda, W. Shuttleworth, X. Zeng, C. Zweck, D. Desilets, T. Franz, and R. Rosolem, "Cosmos: The cosmic-ray soil moisture observing system," *Hydrology and Earth System Sciences*, vol. 16, no. 11, pp. 4079–4099, 2012.

[13] M. Köhli, J. Weimar, M. Schrön, R. Baatz, and U. Schmidt, "Soil moisture and air humidity dependence of the above-ground cosmic-ray neutron intensity," *Frontiers in Water*, vol. 2, p. 544847, 2021.

[14] S. C. W. Group, *Soil classification: a taxonomic system for South Africa*. Department of Agricultural Development, 1991, vol. 15.

[15] D. T. Strauss, S. Poluianov, C. Van Der Merwe, H. Krüger, C. Diedericks, H. Krüger, I. Usoskin, B. Heber, R. Nndanganeni, J. Blanco-Ávalos *et al.*, "The mini-neutron monitor: a new approach in neutron monitor design," *Journal of space weather and space climate*, vol. 10, p. 39, 2020.

[16] P. H. Stoker, L. I. Dorman, and J. M. Clem, "Neutron monitor design improvements," *Space Science Reviews*, vol. 93, no. 1, pp. 361–380, 2000.

[17] T. Crane and M. Baker, "Neutron detectors," *Passive Nondestructive Assay of Nuclear Materials*, vol. 13, pp. 1–28, 1991.

[18] P. Chatzispyroglou, J. L. Keddie, and P. J. Sellin, "Boron-loaded polymeric sensor for the direct detection of thermal neutrons," *ACS Applied Materials & Interfaces*, vol. 12, no. 29, pp. 33 050–33 057, 2020.

[19] W. Abson, P. Salmon, and S. Pyrah, "Neutron counters," *Journal of the Institution of Electrical Engineers*, vol. 4, no. 41, pp. 252–255, 1958.

[20] G. Grosshoeg, "Neutron ionization chambers," *Nuclear instruments and Methods*, vol. 162, no. 1-3, pp. 125–160, 1979.

[21] Y. V. Balabin, B. Gvozdevsk, E. Maurchev, E. Vashenyuk, and D. Dzhappuev, "Fine structure of neutron multiplicity on neutron monitors," *Astrophysics and Space Sciences Transactions (ASTRA)*, vol. 7, no. 3, p. 283, 2011.

[22] R. Bütikofer, "Ground-based measurements of energetic particles by neutron monitors," *Solar particle radiation storms forecasting and analysis*, vol. 444, pp. 95–112, 2018.

[23] N. Aiemsa-ad, D. Ruffolo, A. Sáiz, P.-S. Mangeard, T. Nutaro, W. Nuntiyakul, N. Kamyan, T. Khumlumlert, H. Krüger, H. Moraal *et al.*, "Measurement and simulation of neutron monitor count rate dependence on surrounding structure," *Journal of Geophysical Research: Space Physics*, vol. 120, no. 7, pp. 5253–5265, 2015.

[24] W. Nuntiyakul, A. Sáiz, D. Ruffolo, P.-S. Mangeard, P. Evenson, J. Bieber, J. Clem, R. Pyle, M. Duldig, and J. Humble, "Bare neutron counter and neutron monitor response to cosmic rays during a 1995 latitude survey," *Journal of Geophysical Research: Space Physics*, vol. 123, no. 9, pp. 7181–7195, 2018.

[25] D. Desilets, M. Zreda, and T. P. Ferré, "Nature's neutron probe: Land surface hydrology at an elusive scale with cosmic rays," *Water Resources Research*, vol. 46, no. 11, 2010.

[26] L. Stevanato, G. Baroni, Y. Cohen, C. L. Fontana, S. Gatto, M. Lunardon, F. Marinello, S. Moretto, and L. Morselli, "A novel cosmic-ray neutron sensor for soil moisture estimation over large areas," *Agriculture*, vol. 9, no. 9, p. 202, 2019.

This page intentionally left blank.

Identification of Cosmic Filaments using the Simba-C simulation and DisPerSE Filament Finder

Jaydon K. Durow[1], **Renier T. Hough**[1,2], **Amare Abebe**[1,2], **Yin-Zhe Ma**[3]

[1]Centre for Space Research, North-West University, Potchefstroom 2520, South Africa
[2]National Institute for Theoretical and Computational Sciences (NITheCS), Potchefstroom 2520, South Africa
[3]University of Stellenbosch, Stellenbosch 7602, South Africa

E-mail: jaydondurow@gmail.com

Abstract. We used the DisPerSE software to identify high-density regions of dark matter and gas, collectively called filaments, in a $0.8\,\mathrm{Mpc/h}$ thick slice of a Simba-C cosmological simulation at the $z = 0$ redshift. The identified filaments correlated well with the higher-density gas regions. We tested a wide range of different persistence thresholds, but saw no clear difference. Using the identified filaments, we examined the spatial distribution and physical properties of nearby gas particles. We also examined filament radii of $0.25\,\mathrm{Mpc/h}$, $0.5\,\mathrm{Mpc/h}$, and $0.75\,\mathrm{Mpc/h}$ to see their effect on the physical properties of gas particles. We determined, based on the temperature, metallicity, and star formation rate ranges typically seen in the higher density regions that the best filament radius was $0.5\,\mathrm{Mpc/h}$.

1 Introduction

The Universe at the largest scales is isotropic and homogeneous. It evolves according to the Friedmann equations, derived from general relativity [1]. But at smaller scales, which are observed to be inhomogeneous, we use gravitational perturbation theory to describe how these small deviations from homogeneity result in large changes to the structures in the Universe [1].

These complex structures at the largest scales of the Universe have been observed through observational catalogues of galaxies and simulations of the Universe [2]. These structures originated from small anisotropic matter distributions caused by weak ripples and quantum fluctuations in the otherwise uniform and rapidly expanding early universe [3]. These ripples have expanded and evolved due to gravitational forces into the Large-Scale Structure (LSS) or "Cosmic-Web" that we observe today [3].

The LSS consists of filaments of high concentrations of galaxies and gas clusters that are surrounded by large voids with extremely low dark and baryonic matter density [2]. These filaments were first seen in simulations, particularly the Millennium simulation [4], of the Universe [3]. The tidal field serves as the principal mechanism driving the formation of the LSS [5]. It characterizes the spatial variations of the gravitational potential, encapsulating how a fluid is compressed and stretched [6]. [6] demonstrated how the tidal shear field deforms the dark matter fluid element. Any initial anisotropies are magnified by the subsequent gravitational collapse of the dark matter, which gives rise to asymmetrical structure resembling walls and filaments [5]. The tidal field also influences the velocity shear field, which describes how the velocity of matter moves perpendicular to the rate of expansion [6]. This links gravitational dynamics to the motion of matter. Once light and baryonic matter decouple, the baryonic matter falls into these dark matter structures [5]. The over density in these structures lead to the clusters exceeding Jeans density and, along with a balance between the mass and temperature of the gas allows for star formation

[3]. These stars group together to form clusters of stars that then merge with each other to create galaxies and the galaxies come together to form galaxy clusters, called hierarchical assembly [3]. Since the Universe began in a nearly homogeneous state at these scales and evolved to the complex structure we see in the local Universe today, observations should find that the Universe becomes more homogeneous the further they observe from the local Universe. The furthest you can observe is the cosmic microwave background radiation (CMB).

Observations of the small inhomogeneities in the CMB, corresponding to small anisotropic matter distributions in the early Universe, has given a clear set of initial conditions for the evolution of the LSS [3]. Other observations of galaxies like the 2-degree Field Galaxy Redshift Survey, or 2dFGRS[1], and the Sloan Digital Sky Survey, or SDSS2[2], were the first galaxies surveys to have mapped the distribution of the local Universe [3]. They achieved this by obtaining spectra for over a million galaxies with the wide-field, ground-based telescope at Apache Point Observatory in New Mexico, and for approximately 250,000 galaxies with the Anglo-Australian Telescope. The link between the early near-uniform Universe and the complex structure seen today have been demonstrated through numerical simulation, observations and theory [3]. The DESI survey is the latest galaxy survey and has mapped millions of galaxies from $z = 0$ to $z \approx 4$ [7]. It will shed light on the LSS of the Universe like never before by giving us a more detailed and more complete look at our sky.

Whether or not the LSS plays a role in the evolution of galaxies and groups is still an open question [8]. In the conventional model the halo environment, where the galaxies form, plays the largest role in galaxy formation [8]. However, where galaxies form in relation to larger scale-structures have also been seen to affect not only clusters but galaxy and group properties as well [9]. [8] found that "the Cosmic-Web filaments play an important role in the evolution of groups and their central galaxies", where central galaxies are those with the highest luminosity in their respective groups. A major struggle in investigating the LSS is the need for an objective and quantitative method for identifying clusters, filaments, sheets and voids [10]. This is important to address a wide array of cosmological issues [10]. The LSS captures details about the physics of structure formation and global cosmology [10]. The nature of dark matter and dark energy, as well as the initial density fluctuations, have left their imprint on the LSS, and on its geometry and topology [10].

In this study we identify robustly the filaments in a `Simba-C` simulation and use the filaments to study physical properties of gas particles. In section 2, we discuss the role of cosmological simulations in the field of Cosmology as well as the details of the `Simba-C` simulation. In section 3, we explain how the `DisPerSE` program works and how we used it to extract the filaments from our `Simba-C` simulation. In section 4, we show our results, and in section 5, we give our conclusions.

2 Cosmological Simulations

Cosmological simulations are given a set of initial conditions, usually the CMB, to make the simulations as similar and realistic to our Universe as possible, but other Gaussian random fields are also used for statistical accuracy. These simulations then use gravity solvers and other physical theories, like AGN feedback mechanisms, to simulate cosmic events and objects. There are four types of cosmological simulations, as outlined by [11]:

- Zoom simulations with dark matter or N-body simulations (eg. `Aquarius, COZMIC I`).
- Zoom simulations with dark matter and baryonic matter or hydrodynamical simulations (eg. `FIRE-2, Auriga`).
- Large volume simulations with dark matter (eg. `Millennium`).
- Large volume simulations with dark matter and baryonic matter (eg. `Simba, Eagle, IllustrisTNG, Romulus, Astrid`).

Zoom simulations are primarily used to simulate smaller volumes with more detail, like simulating a galaxy [11]. Because of the greater level of detail, the computational requirements increase, restricting the size of the zoom simulations. Large-volume simulations, in contrast, cover much larger regions of the Universe and are used to study large-scale structures [11]. Therefore, we would primarily study LSS filaments in large volume simulations. Dark matter only simulations are N-body simulations which are easier to simulate, thus we can make larger simulations with the same computational cost, which allows us to have a larger sample size, and thus better statistics [11].

[1] http://www.2dfgrs.net/

[2] https://www.sdss.org/

Dark matter and baryonic matter simulations include the hydrodynamical equations that describe the baryonic matter and are thus more complicated to simulate compared to the N-body simulations [11]. Because of the added computational cost of the hydrodynamical simulation we can only run smaller box volume simulations compared to large-scale N-body simulations. Therefore, we use a large volume hydrodynamical simulation in order to see the effect baryons have on the LSS.

2.1 The `Simba-C` Simulation

The `Simba-C` simulation is based on the `Simba` large-scale cosmological simulation framework. `Simba` from [12] uses `GIZMO`, a hydrodynamics and gravity solver, to make simulation that includes both dark matter and baryonic matter. `Simba-C` includes the `Chem5` chemical enrichment model from [13, 14], that introduces more elements to the `Simba` framework, while also improving the stellar feedback model. The `Simba` simulation also includes black hole, star formation, and a Active Galactic Nuclei feedback model [15]. However, the `Simba` simulation wasn't explicitly tuned to z = 0 stellar masses and one discrepancy is the low-mass end of the galaxy stellar mass function [12].

Other large volume dark and baryonic matter simulations we could have used, are the `EAGLE`[3] simulation [16] or the `IllustrisTNG`[4] simulations [17]. `EAGLE` aimed to create a faithful population of galaxies by calibrating feedback to match key observations [16]. Balanced calibration means many observables come out right, but some fine-tuning means it's not an entirely independent "prediction" of galaxy formation, but rather a model constrained by present-day data [16]. `IllustrisTNG` is the next-generation of `Illustris` simulations with large volumes, including improved galaxy formation physics. Some strengths are its broad range of scales (from dwarf galaxies to clusters) and it is ideal for statistical studies of galaxy evolution [17]. Some limitations include the moderate resolution of the largest volume simulation (TNG300), which prevents full resolution of dwarf galaxies and their internal structures, and leads to less reliable satellite galaxy properties such as sizes and quenched fractions of the smallest systems [17].

We chose to use the `Simba-C` simulation from [15], because it offers a good balance between size and resolution, so that the filaments we are studying can be resolved and we can have a good sample size. We used a $25\,\mathrm{Mpc/h}$ box size with 256^3 gas particles and 256^3 dark matter particles. The gas particles had a mass of $1.8 \times 10^7\,\mathrm{M}_\odot$ and the dark matter particles had a mass of $9.6 \times 10^7\,\mathrm{M}_\odot$ [12]. The starting redshift was z = 127 and the ending redshift was z = 0. The gravitational softening length was $0.125\,\mathrm{kpc/h}$, and we used ΛCDM cosmology. The 2D infinitesimal[5] slice of the dark matter particles of the specific simulation we used can be seen in Figure 3. We used this 2D slice to identify the filaments and then identified gas particles in a $0.8\,\mathrm{Mpc/h}$ thick extract around the spline. We chose to use the dark matter particles because they mostly determine the shape of the filaments, and the gas particles fall into the filaments created by the dark matter.

3 `DisPerSE`

`DisPerSE` uses Morse and Persistence theory to identify astrophysical structures. Morse theory is a mathematical theory that describes how points in an arbitrary space can be grouped together depending on which maxima or minima they go to [18]. This can be seen in Figure 1. The set of all these groups of points is called a Morse complex and can be used to describe the space [18]. Persistence theory uses the differences between different critical values to determine which structures are more or less significant [18]. This difference is referred to as the persistence, and the value below which any persistence is disregarded is known as the persistence threshold. `DisPerSE` breaks up any given space into different sections and uses the sample of data as a density function and assigns a density to each section as shown in Figure 2 [18]. The difference between the values of the sections indicate the gradient of the space [18]. Using these gradients to group sections that go to the same maxima or minima, you make a Morse complex [18], as shown Figure 1 (bottom right). Different types of complexes represent filaments, walls and voids.

The algorithm applies these theories by going over all the given data points and identifying maxima and minima, as well as the points that go towards or away from those critical points, by comparing the data points values [18]. All the points that go away from or towards a critical point are grouped together [18]. All the groups of points are then grouped together depending on the type of critical point and are called manifolds [18]. These manifolds describe the topology of the space, and are thus identified as filaments [18].

[3] https://icc.dur.ac.uk/Eagle/index.php

[4] https://www.tng-project.org/

[5] In `YT`, a slice at $z = 0$ samples data values on that exact plane without integrating over any depth, therefore the slice has effectively zero thickness.

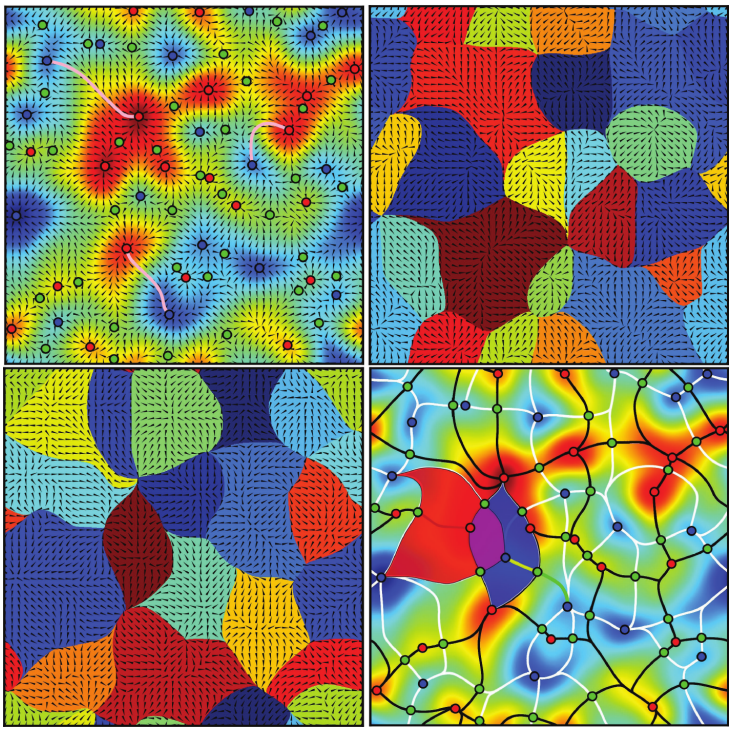

Figure 1: Top left: Gradient field with maxima (blue), minima (red) and saddle (green) critical points. Top right: Collection of sets of points which gradients point away from a particular maximum point. Bottom left: Collection of sets of points which gradients point towards a particular minimum. Bottom right: Set of manifolds of the different types of critical points called a Morse-Smale complex. Figure was taken from [18] with permission from T. Sousbie.

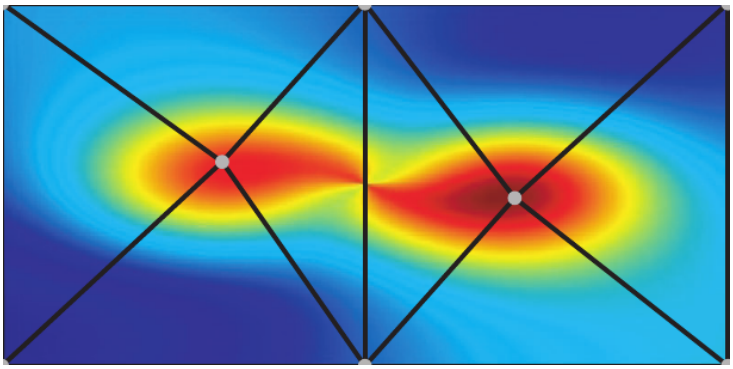

Figure 2: Illustrates a field of values; this can be a smooth function or a set of measured data, e.g. a piece of the sky. This field is broken up into triangles, the simplest 2D shape. Each point, line and area is then assigned the value underneath them or the average of values underneath them. Figure was taken from [18] with permission from T. Sousbie.

We converted the simulation file to a FITS file and applied a mask. With the mse command we used the up-Skl flag to identify the filaments and the cut flag to cut include a persistence threshold cut off. We used a wide range of persistence values and saw no notable difference. We then used the breakdown and smooth flags with the skelconv command to combine filaments that overlap and to obtain a smoother profile of the identified filaments

respectively. We used the toFITS flag with the skelconv command to get a FITS file of the identified filaments[6]. We then used the identified filaments to locate gas particles that were $0.25\,\mathrm{Mpc/h}$, $0.5\,\mathrm{Mpc/h}$ and $0.75\,\mathrm{Mpc/h}$ away from the filaments. We took the gas coordinates of a $0.8\,\mathrm{Mpc/h}$ extract from the simulation and identified which gas particles where within $0.25\,\mathrm{Mpc/h}$,$0.5\,\mathrm{Mpc/h}$ and $0.75\,\mathrm{Mpc/h}$ radii of tubes drawn in 3D. The extract from the simulation was kept at $0.8\,\mathrm{Mpc/h}$ so that we worked with a consistent number of particles.

4 Results

In Figure 3 (left panel), we see the identified filaments in red which we obtained from `DisPerSE` overlaid with the slice from the `Simba-C` simulation. We note that `DisPerSE` identified the filaments well except for the filaments identified in the void in the center of the left panel as well as the small offshoots from the main identified filaments. This could be because of the persistence threshold value we chose for the noise. In the right panel we used the identified filaments to map which gas particles in the simulation were within a 3D tubes with a radii of $0.25\,\mathrm{Mpc/h}$, $0.5\,\mathrm{Mpc/h}$, and $0.75\,\mathrm{Mpc/h}$ around the filament spline.

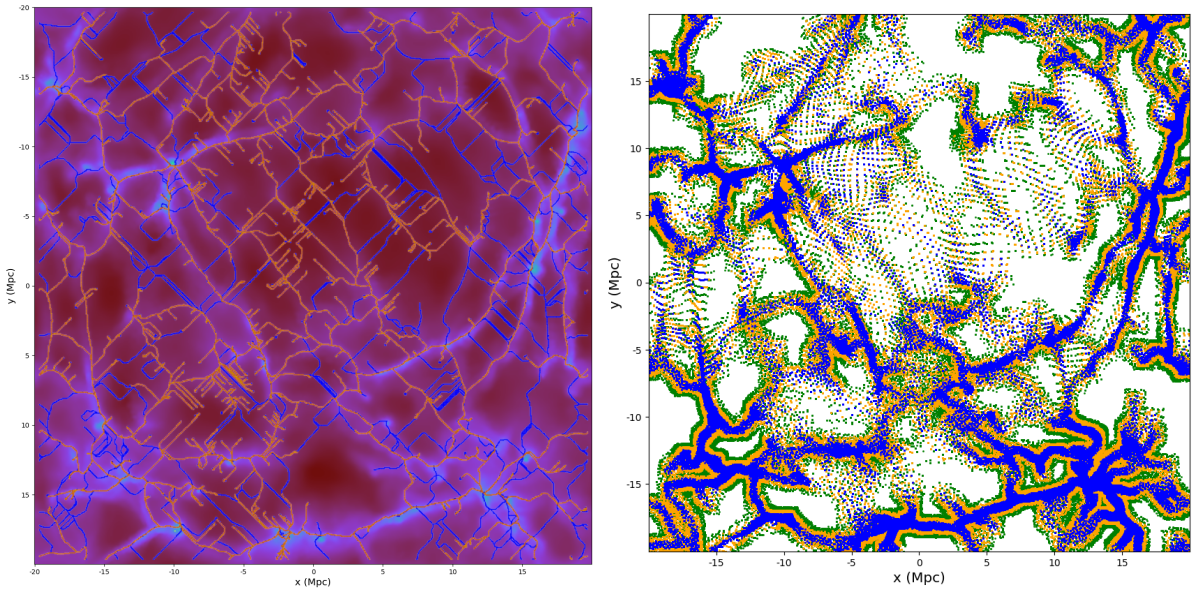

Figure 3: (Left) Filaments with the persistence threshold cut-off (red), filaments without the persistence threshold cut off (blue) overlayed with the 2D infinitesimal slice from the `Simba-C` simulation that we used. The `Simba-C` simulation slice is at the z=0 coordinate at redshift 0. Higher-density regions of gas are light blue indicating a density of about $10^{-29}\,\mathrm{g/cm^3}$ which we can see forms filamentary structures. (Right) Gas particles from a $0.8\,\mathrm{Mpc/h}$ extract from the `Simba-C` simulation within a 3D tube with a radius of $0.25\,\mathrm{Mpc/h}$ (blue), $0.5\,\mathrm{Mpc/h}$ (orange), $0.75\,\mathrm{Mpc/h}$ (green) around the identified filament spline.

In Figure 4 we plot 4 bar graphs showing the fraction of total gas particles at a range of density contrasts $(1+\delta)$, defined as $\rho/\bar{\rho}$, where ρ is the density of each gas particle and $\bar{\rho}$ is the average gas density in the simulation (top left), the temperatures (top right), the metallicities (bottom left) and the star formation rates (SFRs; bottom left). Each bar is divided between the particles inside and outside the filaments with radii of $0.25\,\mathrm{Mpc/h}$, $0.5\,\mathrm{Mpc/h}$, and $0.75\,\mathrm{Mpc/h}$, respectively. In Figure 4 (top left), we see that about 60 % of the gas density contrast is between $10^{-6.4} - 10^{-4.2}$ and less than 5 % of the gas density is between $10^{-1.9}$ and $10^{2.7}$. There is a sharp decrease in the number of gas particle with densities above $10^{-1.9}$. This means that most of our gas particles overall are under-dense which aligns with results from [19]. We also see that for higher densities there is no difference between the filaments with radii of $0.5\,\mathrm{Mpc/h}$ and $0.25\,\mathrm{Mpc/h}$, with the filament with a radius of $0.75\,\mathrm{Mpc/h}$ identifying all the particles. Only at lower densities can we observe a difference of around 10 % between the filaments with radii of $0.5\,\mathrm{Mpc/h}$ and $0.75\,\mathrm{Mpc/h}$ and the filaments with radii of $0.25\,\mathrm{Mpc/h}$ and $0.5\,\mathrm{Mpc/h}$ differ with around 25 %. We can see that the filaments with radii of $0.25\,\mathrm{Mpc/h}$, $0.5\,\mathrm{Mpc/h}$, and $0.75\,\mathrm{Mpc/h}$ includes about 24 %, 56 %,

[6]For a detailed guide, follow the tutorial at `https://www2.iap.fr/users/sousbie/web/html/indexd41d.html?`.

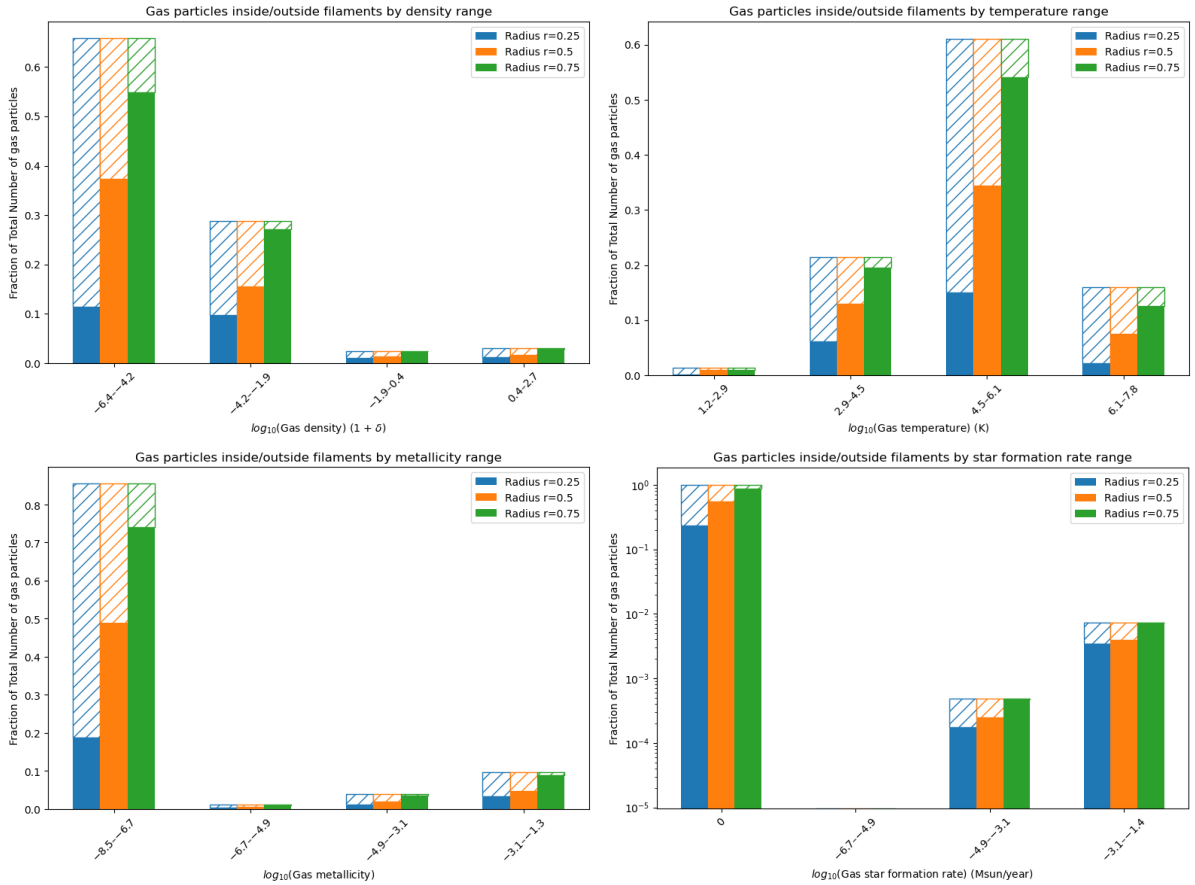

Figure 4: (Top Left) Bar plot of the fraction of the total number of the number of gas particles at different densities contrasts $(1+\delta)$, divided up between inside (solid) and outside (hatched) filaments of different radii, $0.25\,\mathrm{Mpc/h}$, $0.5\,\mathrm{Mpc/h}$, and $0.75\,\mathrm{Mpc/h}$, respectively. Similar bar plots for temperature (Top Right), metallicity (Bottom Left) and star formation rate (Bottom Right).

and 87 % of particles of any density, respectively. In Figure 4 (top right) we note that 60 % of the gas particles fall between $10^{4.5} - 10^{6.1}\,\mathrm{K}$. The intergalactic medium (IGM) is gradually heated to temperatures in the range $T \approx 10^5 - 10^7\,\mathrm{K}$, by gravitational accretion shocks emerging from collapsing regions, during the formation of the LSS [20]. This is called the warm hot intergalactic medium (WHIM), and contain about 50 % of the baryons at $z \approx 0$. We also see again that the difference between the filaments with radii of $0.25\,\mathrm{Mpc/h}$, $0.5\,\mathrm{Mpc/h}$ and $0.75\,\mathrm{Mpc/h}$ show about a 20 % difference between each of them for this temperature range. The wider filaments contain most of the gas particles at any temperature.

In Figure 4 (bottom left) we note that 85 % of the metallicity has a fraction between $10^{-8.5} - 10^{-6.7}$ with only 15 % having a fraction higher than that. This is because there are pristine gas clouds with zero metallicity, but the numerical method can not handle log(0) values, so they add a small amount of metallicity to these clouds so that the numerical method has no issues. Once again there is a 20 % difference between the filaments with radii of $0.5\,\mathrm{Mpc/h}$ and $0.75\,\mathrm{Mpc/h}$ and the filament with a radius of $0.25\,\mathrm{Mpc/h}$ contains much fewer gas particles at the lowest metallicities. Most of the gas particles in Figure 4 (bottom right) have a star formation rate of zero, with a very tiny fraction of them having star formation rates between $10^{-6.7} - 10^{-1.4}\,\mathrm{M_\odot/yr}$. Again we see that the $0.75\,\mathrm{Mpc/h}$ filament contains all the gas particles at the higher star formation rates. From this note that the $0.25\,\mathrm{Mpc/h}$ under identifies most of the particles, while $0.75\,\mathrm{Mpc/h}$ seems to over identify the particles and just returns all of the particles that $0.5\,\mathrm{Mpc/h}$ already classified as part of the filament.

If we compare our results in Figure 4 (top left) to that of [21] Figure 13 and [19] Figure 4 we see that our density contrast is shifted to much lower orders of magnitude, e.g $10^{-6.4} - 10^{2.7}$, compared to their range of $10^{-2} - 10^{2}$.

The smoothing scale determines the density values, but qualitative conclusions should be scale-independent [21]. Our shape agrees with the overall shape of their graph, thus our distribution seems to be correct; it is just shifted to lower densities. Our graph also spans more degrees of magnitude, the tail at the higher end of our graph is especially long. This could be because we only analysed a 2D case with no walls, thus we have extra weight at the nodes, as seen in Figure 13 of [21], could pull the tail of our graph to higher densities. If we compare our graph to Figure 4 from [19], particularly the `DisPerSE` graphs, their shape is also skewed to the lower densities. There are significant overlaps in the densities of different components of the LSS [21], making comparing which filament tube size yielded the most realistic morphology based on density difficult.

From numerical simulations we find up to 50 % of the Intergalactic Medium (IGM) has been heated to temperatures between $10^5 - 10^7\,\mathrm{K}$ at $z < 1$. From Figure 4 (top right) we note that between that range we have about 60 % of our gas particles, thus `Simba-C` over-predicts what we find in other numerical simulations by about 10 %, this could be because our simulation is at $z = 0$ thus the simulation has had more time to heat the gas through feedback. This temperature range also corresponds to the temperature range of filaments [20]. Thus a good radius for our filaments should identify mostly gas particle in this range. Both the $0.5\,\mathrm{Mpc/h}$ and $0.75\,\mathrm{Mpc/h}$ radii tubes is in agreement with this, while the $0.25\,\mathrm{Mpc/h}$ does not match this criterion. In Figure 4 (bottom left) we see that most gas particles have very low metallicity followed by a slight increase as the metallicity increases. This indicates as seen in Figure 4 of [22], how metallicity exhibits clustered behaviour, in this case clustered between $10^{-3.1} - 10^{-1.3}$. By far the most gas particles in Figure 4 (bottom right) have zero SFR with a slight increase of SFR from $10^{-4.9}\,\mathrm{M_\odot/yr}$. The specific SFR (sSFR) is defined as $sSFR = \frac{SFR}{M_*}$, where M_* is the stellar mass of the galaxy. In the `Simba-C` simulation the sSFR has a sharp peak at lower values and slowly increase from there [23]. All galaxies with a sSFR lower than -2.5 are binned together, thus because there is a cut-off we see very few gas particles with SFR between $10^{-6.7} - 10^{-4.9}$ [23]. This is supported by Figure 3 in [23], where we see that most of the sSFR is at -2.5 and then slowly increases to about -0.5. As shown by [22], higher-density environments exhibit higher metallicities and lower star formation rates (SFRs), whereas lower-density environments have lower metallicities and higher SFRs. This occurs because, in very dense and hot regions, star formation ceases, and the accumulation of older stars in these environments drives up the metallicity. Therefore, we want our higher density environments to reflect this, but when we lower the filament radius to include less lower metallicities we also decrease the higher metallicities. Similarly, if we increase our radius to include more low SFR we also increase our number of gas particles with a higher SFR. The $0.25\,\mathrm{Mpc/h}$ and $0.5\,\mathrm{Mpc/h}$ filament under identifies the higher metallicities by 50 % while the other filament tubes identify most of the higher metallicities. The $0.75\,\mathrm{Mpc/h}$ over identifies lower metallicities. Similarly the $0.25\,\mathrm{Mpc/h}$ filament contains too few low SFR gas particles. Because of the hierarchical nature of the filaments the choice of radius is arbitrary [10]. [10] used a filament radius of $0.5\,\mathrm{Mpc/h}$. They used this because of the influence of this size on filament to galactic evolution [10].

5 Conclusions

At the largest scales in our Universe we observe higher and lower dense regions called clusters, filaments, walls and voids. The identification of these filaments is important if we want to study how galaxies change as we move from voids to clusters. These structures are also found in cosmological simulations like, `Simba-C`. `Simba-C` is a large volume hydrodynamical simulation. Our analysis demonstrates that the `DisPerSE` cosmological filament finder can be used to help identify filaments in the `Simba-C` Simulation. This software uses mathematical theories to order and describe the data given to it, and outputs the identified structure. We can now identify the filaments in any slice of a `Simba-C` simulation, as well as identify where the gas particles are in relation to the identified filaments, seen in Figure 3. The filaments in the simulation that were identified correlated well with the higher density regions of gas particles in the slice. Some lower density regions where identified; this could be because of noise in the simulation. We tested a wide range of persistence threshold values and saw no notable difference. Important criteria for consideration when evaluating the effectiveness of the filament radius are: the filament radius needs to include most of the gas particles between $10^5 - 10^7\,\mathrm{K}$ at $z < 1$, as well as identify most of the higher metallicity and lower star formation rate gas particles. Based on these criteria we see that the $0.25\,\mathrm{Mpc/h}$ filament under identifies all of these. The $0.75\,\mathrm{Mpc/h}$ filament over identified particularly the higher star formation rates as well as the lower metallicities. The $0.5\,\mathrm{Mpc/h}$ filament identifies gas particles the well based in these criteria; it may still under-identify the higher metallicities and under-identify the temperature range between $10^5 - 10^7\,\mathrm{K}$.

In the future we could also expand this to the 3D case, as well as identify filaments at different times. Using the identified filaments we could look at the effect the proximity of galaxies to the filaments has on their H1 mass, accretion and growth, through studying their radial profiles. As well as see the effect on halo mass function, σ_8 value and matter power spectrum at late times. We can change some physical process, like modified gravity and changes to the initial power spectrum, in the simulation to see the effect it has on the filaments. Lastly, we can compare this method for identifying filaments to other methods, like friend-of-friend (fof) finder. There are also

different methods for identifying the thickness of filament that can be explored in the future, e.g. defining the filament thickness by their density or the gravitational potential.

References

[1] M. P. Hobson, G. P. Efstathiou, and A. N. Lasenby, *General relativity: an introduction for physicists*. Cambridge University Press, 2006. [Online]. Available: https://doi.org/10.1017/cbo9780511790904

[2] A. L. Coil, *The Large-Scale Structure of the Universe*. Dordrecht: Springer Netherlands, 2013, pp. 387–421. [Online]. Available: https://doi.org/10.1007/978-94-007-5609-0_8

[3] V. Springel, C. S. Frenk, and S. D. White, "The large-scale structure of the universe," *nature*, vol. 440, no. 7088, pp. 1137–1144, 2006. [Online]. Available: https://doi.org/10.1038/nature04805

[4] V. Springel, S. D. White, A. Jenkins, C. S. Frenk, N. Yoshida, L. Gao, J. Navarro, R. Thacker, D. Croton, J. Helly *et al.*, "Simulations of the formation, evolution and clustering of galaxies and quasars," *nature*, vol. 435, no. 7042, pp. 629–636, 2005. [Online]. Available: https://doi.org/10.1038/nature03597

[5] M. Cautun, R. Van De Weygaert, B. J. Jones, and C. S. Frenk, "Evolution of the cosmic web," *Monthly Notices of the Royal Astronomical Society*, vol. 441, no. 4, pp. 2923–2973, 2014. [Online]. Available: https://doi.org/10.1093/mnras/stu768

[6] Y. B. Zel'dovich, "Gravitational instability: An approximate theory for large density perturbations." *A&A*, vol. 5, pp. 84–89, Mar. 1970. [Online]. Available: https://ui.adsabs.harvard.edu/abs/1970A&A.....5...84Z

[7] A. Adame, J. Aguilar, S. Ahlen, S. Alam, D. Alexander, M. Alvarez, O. Alves, A. Anand, U. Andrade, E. Armengaud *et al.*, "Desi 2024 vi: cosmological constraints from the measurements of baryon acoustic oscillations," *Journal of Cosmology and Astroparticle Physics*, vol. 2025, no. 02, p. 021, 2025. [Online]. Available: https://doi.org/10.1088/1475-7516/2025/02/021

[8] A. Poudel, P. Heinämäki, E. Tempel, M. Einasto, H. Lietzen, and P. Nurmi, "The effect of cosmic web filaments on the properties of groups and their central galaxies," *Astronomy & Astrophysics*, vol. 597, p. A86, 2017. [Online]. Available: https://doi.org/10.1051/0004-6361/201629639

[9] H. Lietzen, E. Tempel, P. Heinämäki, P. Nurmi, M. Einasto, and E. Saar, "Environments of galaxies in groups within the supercluster-void network," *Astronomy & Astrophysics*, vol. 545, p. A104, 2012. [Online]. Available: https://doi.org/10.1051/0004-6361/201219353

[10] E. Tempel, R. Stoica, V. J. Martinez, L. Liivamägi, G. Castellan, and E. Saar, "Detecting filamentary pattern in the cosmic web: a catalogue of filaments for the sdss," *Monthly Notices of the Royal Astronomical Society*, vol. 438, no. 4, pp. 3465–3482, 2014. [Online]. Available: https://doi.org/10.1093/mnras/stt2454

[11] M. Vogelsberger, F. Marinacci, P. Torrey, and E. Puchwein, "Cosmological simulations of galaxy formation," *Nature Reviews Physics*, vol. 2, no. 1, pp. 42–66, 2020. [Online]. Available: https://doi.org/10.1038/s42254-019-0127-2

[12] R. Davé, D. Anglés-Alcázar, D. Narayanan, Q. Li, M. H. Rafieferantsoa, and S. Appleby, "Simba: Cosmological simulations with black hole growth and feedback," *Monthly Notices of the Royal Astronomical Society*, vol. 486, no. 2, pp. 2827–2849, 2019. [Online]. Available: https://doi.org/10.1093/mnras/stz937

[13] C. Kobayashi, A. I. Karakas, and M. Lugaro, "The origin of elements from carbon to uranium," *The Astrophysical Journal*, vol. 900, no. 2, p. 179, 2020. [Online]. Available: https://doi.org/10.3847/1538-4357/abae65

[14] C. Kobayashi, S.-C. Leung, and K. Nomoto, "New type ia supernova yields and the manganese and nickel problems in the milky way and dwarf spheroidal galaxies," *The Astrophysical Journal*, vol. 895, no. 2, p. 138, 2020. [Online]. Available: https://doi.org/10.3847/1538-4357/ab8e44

[15] R. T. Hough, D. Rennehan, C. Kobayashi, S. I. Loubser, R. Davé, A. Babul, and W. Cui, "Simba-C: an updated chemical enrichment model for galactic chemical evolution in the simba simulation," *Monthly Notices of the Royal Astronomical Society*, vol. 525, no. 1, pp. 1061–1076, 2023. [Online]. Available: https://doi.org/10.1093/mnras/stad2394

[16] J. Schaye, R. A. Crain, R. G. Bower, M. Furlong, M. Schaller, T. Theuns, C. Dalla Vecchia, C. S. Frenk, I. McCarthy, J. C. Helly *et al.*, "The eagle project: simulating the evolution and assembly of galaxies and their environments," *Monthly Notices of the Royal Astronomical Society*, vol. 446, no. 1, pp. 521–554, 2015. [Online]. Available: https://doi.org/10.1093/mnras/stu2058

[17] A. Pillepich, D. Nelson, L. Hernquist, V. Springel, R. Pakmor, P. Torrey, R. Weinberger, S. Genel, J. P. Naiman, F. Marinacci *et al.*, "First results from the illustristng simulations: the stellar mass content of groups and clusters of galaxies," *Monthly Notices of the Royal Astronomical Society*, vol. 475, no. 1, pp. 648–675, 2018. [Online]. Available: https://doi.org/10.1093/mnras/stx3112

[18] T. Sousbie, "The persistent cosmic web and its filamentary structure–i. theory and implementation," *Monthly Notices of the Royal Astronomical Society*, vol. 414, no. 1, pp. 350–383, 2011. [Online]. Available: https://doi.org/10.1111/j.1365-2966.2011.18394.x

[19] N. I. Libeskind, R. Van De Weygaert, M. Cautun, B. Falck, E. Tempel, T. Abel, M. Alpaslan, M. A. Aragón-Calvo, J. E. Forero-Romero, R. Gonzalez *et al.*, "Tracing the cosmic web," *Monthly Notices of the Royal Astronomical Society*, vol. 473, no. 1, pp. 1195–1217, 2018. [Online]. Available: https://doi.org/10.1093/mnras/stx1976

[20] S. Bertone, J. Schaye, and K. Dolag, "Numerical simulations of the warm-hot intergalactic medium," *Space Science Reviews*, vol. 134, no. 1, pp. 295–310, 2008. [Online]. Available: https://doi.org/10.1007/s11214-008-9318-3

[21] M. Cautun, R. van de Weygaert, B. J. T. Jones, and C. S. Frenk, "Evolution of the cosmic web," *Monthly Notices of the Royal Astronomical Society*, vol. 441, no. 4, pp. 2923–2973, 05 2014. [Online]. Available: https://doi.org/10.1093/mnras/stu768

[22] J. Molina-Calzada, M. Lara-López, J. Gallego, A. Hopkins, B. W. Holwerda, and A. López-Sánchez, "Galaxy and mass assembly (gama): From filaments to voids, how extreme environment affects gas metallicity and sfr in galaxies," *Astronomy & Astrophysics*, vol. 700, p. A267, 2025. [Online]. Available: https://doi.org/10.1051/0004-6361/202555871

[23] R. T. Hough, "Simulating the enrichment of cosmological gas," Ph.D. dissertation, North-West University, 2024.

This page intentionally left blank.

Investigating the latitudinal-dependent solar differential rotation rate using SDO/HMI Dopplergrams

Thembalethu Zulu[1] **and Ruhann Steyn**[1]

[1]Centre for Space Research, North-West University, Potchefstroom, South Africa

E-mail: zuluthembalethu318@gmail.com

Abstract. The solar photospheric differential rotation rate has novel implications for the structure of the heliospheric magnetic field. The rotation period at the solar poles is ∼35 days and ∼25 days at the equator. In this study, the Doppler shift of 116 Dopplergrams from the Helioseismic and Magnetic Imager instrument on board the Solar Dynamics Observatory are investigated to experimentally determine the photospheric differential rotation rate at different solar latitudes. A model is developed to describe the variation of surface speed with solar latitude. The results align with trends and behaviours reported in historical models from the literature, demonstrating consistency across studies. The findings confirm the latitudinal differential rotation of the Sun. The developed model of this study shows a deviation of 8. 45% slower compared to the Newton and Nunn model, 8. 38% slower compared to the Snodgrass model and 4. 33% slower compared to the Howard and Harvey model. This result is worth noting considering the difference in time scales, with the models in the literature using data spanning more than a decade, compared to the model developed in this study using 1.5 hours of collected data. The study not only confirms the theoretical expectations regarding solar rotation but also demonstrates the effectiveness of time-saving Doppler spectroscopic analysis and space-based solar observations in studying solar dynamics. The results contribute to a broader understanding of solar behaviour. These rapid, Doppler-based rotation estimates are directly usable as inputs or cross-checks for surface-flux transport and coronal/heliospheric models (e.g., PFSS and ballistic mapping), where the latitudinal shear sets the evolution of the open magnetic flux and the large-scale heliospheric current sheet geometry relevant to space-weather conditions.

1 Introduction

The rotation of the Sun has long been known to reflect some of the defining features of its nature and overall internal dynamics. Although many studies have attempted to explain solar rotation, it remains one of the least understood phenomena in solar physics [1]. Depending on the observer's frame of reference, the rate at which the Sun rotates can be distinguished by the synodic and sidereal rotation rates. The synodic rotation rate describes how fast the Sun appears to rotate relative to an observer on Earth. In contrast, the sidereal rotation rate refers to the rotation of the Sun relative to the fixed distant stars [2]. The photospheric rotation rate of the Sun is dependent on solar latitude [3],[4],[5],[6]. Over the past few decades, scientists have investigated the photospheric differential rotation rate of the Sun and different ways in which it shapes the basic understanding of the heliospheric magnetic field (HMF) [2],[7],[8].

Different models have been developed to characterise the photospheric solar differential rotation rate. Among these models, Newton and Nunn [4], Howard and Harvey [5], and Snodgrass [6] are of particular interest, as they provide

reliable and detailed results for this study, offering a strong benchmark for comparison with modern studies. It is worth noting that each of these models mentioned uses different techniques to determine the photospheric rotation rate. The Newton and Nunn model [4] traced sunspots across the solar disk for 11 years. In contrast, the Howard and Harvey model [5] was developed using Doppler shifts from spectral lines over a 2-year observational period, and the Snodgrass model [6] used both sunspot data and Doppler shift analysis over a 20-year observational period.

The photospheric differential rotation profile, typically written as

$$\omega(\theta) = A + B\sin^2(\theta) + C\sin^4(\theta), \tag{1}$$

is a key boundary condition for (i) surface-flux transport models that advect and shear radial field, (ii) coronal field extrapolations (e.g., PFSS) that depend on the evolving photospheric map, and (iii) heliospheric models and ballistic mappings that set the large-scale Parker-spiral and current-sheet morphology. Small changes in the equatorial rate A and shear terms B,C [9] alter the longitudinal evolution of open flux and, therefore, the connectivity and solar-wind conditions experienced near Earth. Providing a fast, SDO/HMI-based measurement of $\omega(\theta)$ therefore has practical value: it can be recomputed frequently, cross-validated against traditional feature-tracking values, and assimilated into operational or research pipelines to reduce systematic biases from using a single, fixed rotation law.

Newton and Nunn [4], Howard and Harvey [5], and Snodgrass [6] reported the mathematical relation between the differential rotation rate and latitude as follows:

$$\omega(\theta) = 2.904 - 0.492\sin^2(\theta)\ \mu\text{rad/s}, \tag{2}$$

$$\omega(\theta) = 2.779 - 0.351\sin^2(\theta) - 0.442\sin^4(\theta)\ \mu\text{rad/s}, \tag{3}$$

and

$$\omega(\theta) = 2.902 - 0.464\sin^2(\theta) - 0.328\sin^4(\theta)\ \mu\text{rad/s}. \tag{4}$$

Equations (2), (3), and (4) represent the Newton and Nunn model [4], the Howard and Harvey model [5], and the Snodgrass model [6], respectively. The graphical representation that relates these models mentioned above is shown in Figure 1. This study aims to use recent satellite data from the Solar Dynamics Observatory to better understand the latitudinal dependence of the solar photospheric rotation rate.

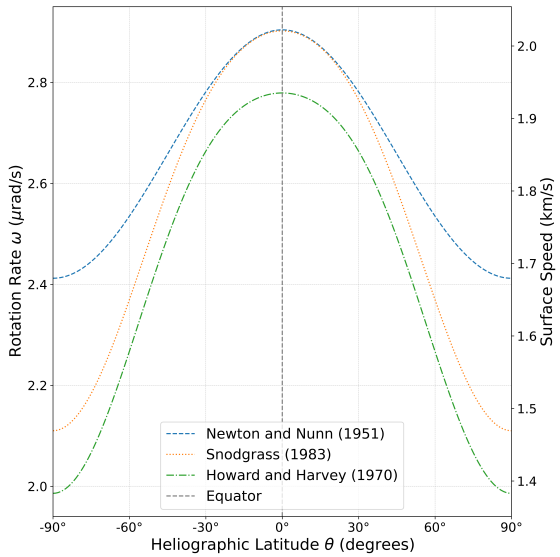

Figure 1: Solar differential rotation profiles of Newton and Nunn[4], Snodgrass [6], and Howard and Harvey[5]. The left y-axis indicates the rotation rate in μrad/s, while the right y-axis indicates the rotation rate in km/s. To guide the eye, the equator is shown by a vertical dashed line at 0°.

2 Data

The Dopplergrams are acquired from the Virtual Solar Observatory (VSO)[1]. The VSO is connected to the Joint Science Operations Centre (JSOC)[2], which, in turn, is linked to the Solar Dynamics Observatory (SDO)[3]. Data from the Helioseismic and Magnetic Imager (HMI)[4] instrument are accessed from the SDO, from which the Dopplergrams are obtained. These Dopplergrams are in Flexible Image Transport System (FITS) file format. The observation date is 1 July 2012, and the observational window spans 1.5 hours from 15:00 to 16:30 UTC. The date used in this study was chosen arbitrarily, specifically because there was an example of a quiet Sun, implying that there were not many active regions to interfere with the observations. This data set includes 116 Dopplergrams with 45-seconds cadence. The open source software package, Sunpy, is used for the analyses [10].

3 Results

A Doppler approach avoids feature-tracking biases (e.g., sunspot anchoring depth and evolutionary effects) and, with HMI's cadence, enables rapid estimation of $\omega(\theta)$ from short time observational windows. While our 1.5-hour observational window increases statistical uncertainty relative to multi-year studies, it demonstrates that near-real-time rotation curves can be produced directly from space-based Dopplergrams and compared to canonical laws. Figures 2-6 show examples of the Dopplergram intensity from a single SDO Dopplergram, focusing on different solar latitudes.

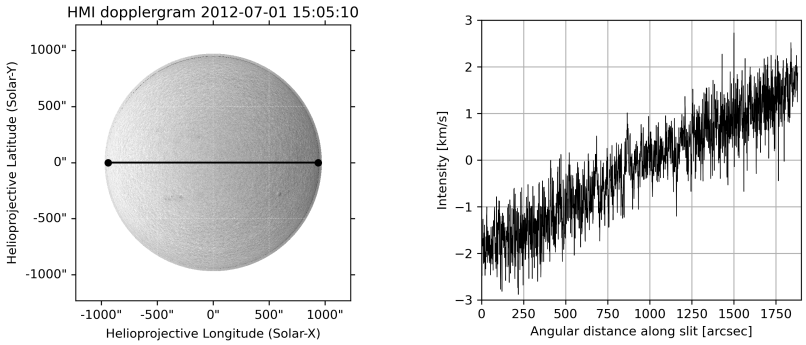

(a) (b)

Figure 2: (*a*) HMI Dopplergram observed at 15:05:10 on 1 July 2012. The solid indicates the equator ($0°$). (*b*) HMI Dopplergram intensity along the equator (from left to right).

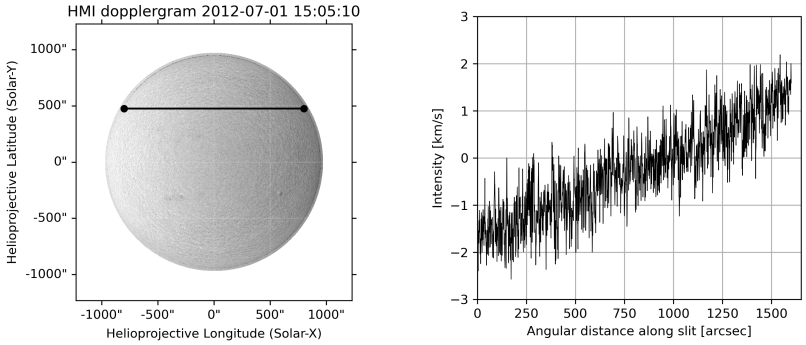

(a) (b)

Figure 3: (*a*) HMI Dopplergram observed at 15:05:10 on 1 July 2012. The solid line refers to the $45°$ latitude. (*b*) HMI Dopplergram intensity along the $45°$ solar latitude line (from left to right).

[1]VSO: `https://sdac.virtualsolar.org/cgi/search`

[2]JSOC: `http://jsoc.stanford.edu/`

[3]SDO: `https://sdo.gsfc.nasa.gov/data/`

[4]HMI: `http://hmi.stanford.edu/`

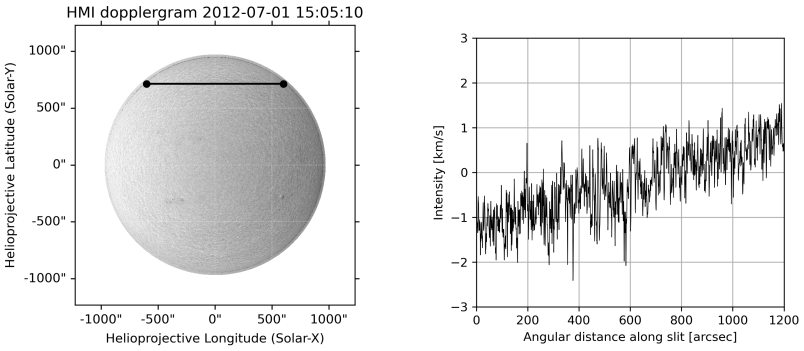

(a) (b)

Figure 4: (*a*) HMI Dopplergram observed at 15:05:10 on 1 July 2012. The solid line now indicates the 72° latitude. (*b*) HMI Dopplergram intensity along the 72° solar latitude line (from left to right).

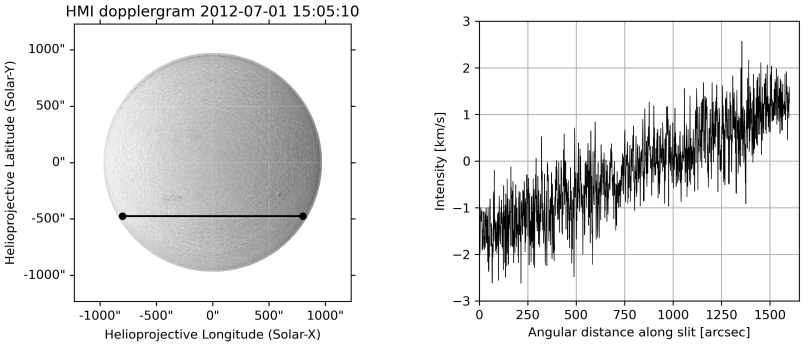

(a) (b)

Figure 5: (*a*) HMI Dopplergram observed at 15:05:10 on 1 July 2012. The solid line now indicates the $-45°$ latitude. (*b*) HMI Dopplergram intensity along the $-45°$ solar latitude line (from left to right).

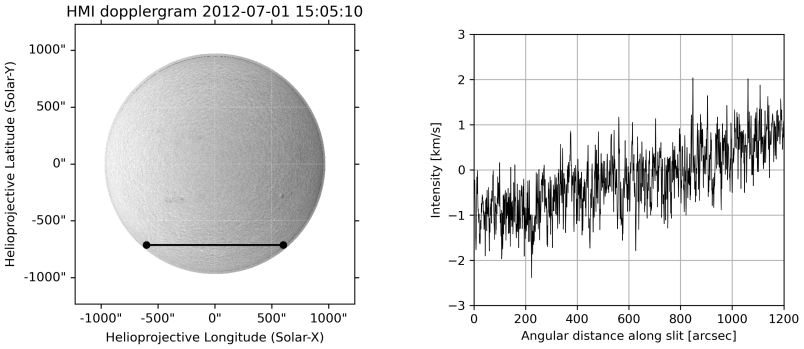

(a) (b)

Figure 6: (*a*) HMI Dopplergram observed at 15:05:10 on 1 July 2012. The solid line now indicates the $-72°$ latitude. (*b*) HMI Dopplergram intensity along the $-72°$ solar latitude line (from left to right).

Figure 2a and 2b shows the full-disk Dopplergram and Dopplergram intensity profile, respectively, along the solar equator (0 degrees). The Dopplergram intensity profile is notably noisy, as a result of omitting any smoothing

or averaging techniques during processing; instead, only a single Dopplergram was considered. The differential rotation rate at the equator ranges between -1.9 km/s and 1.9 km/s. The negative sign signifies that the east limb approaches the observer, whereas the positive sign shows that the west limb recedes from the observer. Note that, at the central meridian region of the Dopplergram, the line-of-site (LOS) differential rotation rate is zero relative to the observer. Figures 3-6 explain the same as Figure 2 with the differential rotation rates ranging between -1.5 km/s and 1.5 km/s in Figure 3b, -1.1 km/s and 1.1 km/s in Figure 4b, -1.5 km/s and 1.5 km/s in Figure 5b, and -1.1 km/s and 1.1 km/s in Figure 6b. A comparison across different latitudes of the Sun reveals a decrease in solar rotation further away from the equator. Moreover, the results also show a rotation rate symmetry across the solar equator.

Figure 7 shows the plot of the resulting model developed using SDO data compared to the three models in the literature. The SDO data is indicated by red dots, with accompanying error bars. A trend is fitted to the SDO data, shown as a solid blue line. Note that, for the construction of the SDO model, the SDO data was converted from a synodic period to a sidereal period [11].

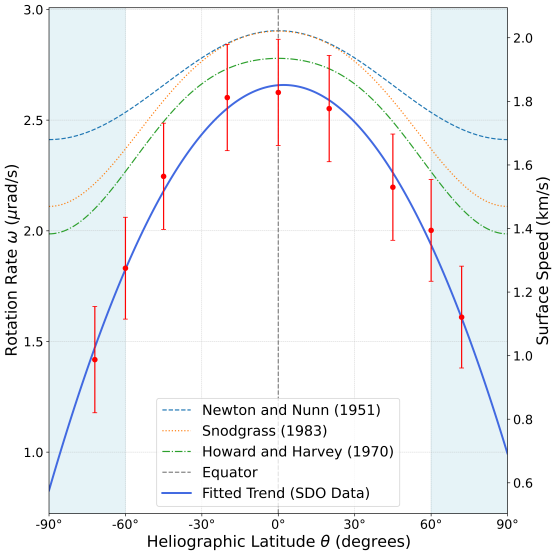

Figure 7: Comparison between the Newton and Nunn [4] model, the Snodgrass [6] model, the Howard and Harvey [5] model, and the model derived from SDO data in this study.

The model fitted using SDO data demonstrates the solar rotation profile. The model shows that the Sun's rotation rate is latitude dependent and is fastest at the equator with a surface speed of 1.83 km/s. In particular, the solar photospheric rotation rate decreases farther away from the equator. To determine the error bars, the expression $\sigma_\mu = \frac{\sigma}{\sqrt{N}}$ [12] is used, where σ_μ represents the standard error, σ represents the standard deviation, and N represents the number of data points used. These error bars indicate the uncertainty in the SDO data. Note that the data within the shaded region of Figure 7, i.e., between -90° & -60° (southern hemisphere), and 90° & 60° (northern hemisphere), are not reliable due to projection challenges close to the solar limb.

4 Conclusion

The SDO results presented in this study indicate an underestimated differential rotation rate, likely due to the relatively short observational window of 1.5 hours. By contrast, the models by Newton and Nunn, Howard and Harvey, and Snodgrass are based on 11 years, 2 years, and 20 years, respectively, of data collection, enabling more robust characterization. The error bars in Figure 7 suggest an uncertainty of approximately 0.24 radians/s in the SDO measurements. Despite this, the study confirms the photospheric latitudinal differential rotation rate using SDO Dopplergrams. The Dopplergrams, however, exhibit considerable noise, potentially due to the lack of averaging across the full set of 116 observations. Future work will aim to extend the observational window to one year to improve measurement accuracy and reliability. Beyond confirming the canonical latitude dependence, the main contribution is methodological: SDO/HMI Dopplergrams enable fast, reproducible estimates of $\omega(\theta)$ that can be refreshed and assimilated into solar-surface and heliospheric modeling workflows to probe sensitivity to the rotation law itself.

References

[1] J. G. Beck, "A comparison of differential rotation measurements–(invited review)," *Solar physics*, vol. 191, no. 1, pp. 47–70, 2000.

[2] C. Scott, R. Harrison, M. Owens, M. Lockwood, and L. Barnard, "Evidence for solar wind modulation of lightning," *Environmental Research Letters*, vol. 9, no. 5, p. 055004, 2014.

[3] H. B. Snodgrass and R. K. Ulrich, "Rotation of doppler features in the solar photosphere," *Astrophysical Journal, Part 1 (ISSN 0004-637X), vol. 351, March 1, 1990, p. 309-316.*, vol. 351, pp. 309–316, 1990.

[4] H. Newton and M. Nunn, "The sun's rotation derived from sunspots 1934–1944 and additional results," *Monthly Notices of the Royal Astronomical Society*, vol. 111, no. 4, pp. 413–421, 1951.

[5] R. Howard and J. Harvey, "Spectroscopic determinations of solar rotation," *Solar Physics*, vol. 12, no. 1, pp. 23–51, 1970.

[6] H. B. Snodgrass, "Magnetic rotation of the solar photosphere," *Astrophysical Journal, Part 1 (ISSN 0004-637X), vol. 270, July 1, 1983, p. 288-299.*, vol. 270, pp. 288–299, 1983.

[7] M. Owens, N. Crooker, and M. Lockwood, "Solar origin of heliospheric magnetic field inversions: Evidence for coronal loop opening within pseudostreamers," *Journal of Geophysical Research: Space Physics*, vol. 118, no. 5, pp. 1868–1879, 2013.

[8] M. J. Owens and R. J. Forsyth, "The heliospheric magnetic field," *Living Reviews in Solar Physics*, vol. 10, no. 1, p. 5, 2013.

[9] J. G. Beck, "A comparison of differential rotation measurements–(invited review)," *Solar physics*, vol. 191, no. 1, pp. 47–70, 2000.

[10] The SunPy Community, W. T. Barnes, M. G. Bobra, S. D. Christe, N. Freij, L. A. Hayes, J. Ireland, S. Mumford, D. Perez-Suarez, D. F. Ryan, A. Y. Shih, P. Chanda, K. Glogowski, R. Hewett, V. K. Hughitt, A. Hill, K. Hiware, A. Inglis, M. S. F. Kirk, S. Konge, J. P. Mason, S. A. Maloney, S. A. Murray, A. Panda, J. Park, T. M. D. Pereira, K. Reardon, S. Savage, B. M. Sipőcz, D. Stansby, Y. Jain, G. Taylor, T. Yadav, Rajul, and T. K. Dang, "The sunpy project: Open source development and status of the version 1.0 core package," *The Astrophysical Journal*, vol. 890, pp. 68–, 2020. [Online]. Available: https://iopscience.iop.org/article/10.3847/1538-4357/ab4f7a

[11] I. Skokić, R. Brajša, D. Roša, D. Hržina, and H. Wöhl, "Validity of the relations between the synodic and sidereal rotation velocities of the sun," *Solar physics*, vol. 289, pp. 1471–1476, 2014.

[12] P. R. Bevington and D. K. Robinson, "Data reduction and error analysis," *McGraw–Hill, New York*, 2003.

Exploring selection biases in radio spectral indices for superMIGHTEE radio-emitting galaxies

Sthabile Kolwa[1], Russ Taylor[2,3], Sushant Dutta[2], Dharam V. Lal[4], Lennart Heino[2] and Mattia Vaccari[2,3]

[1]Department of Mathematical Sciences, University of South Africa, Cnr Christian de Wet Rd and Pioneer Avenue, Florida Park, 1709, Roodepoort, South Africa
[2]Inter-University Institute for Data Intensive Astronomy, Department of Astronomy, University of Cape Town, Private Bag X3, Rondebosch, 7701, Cape Town, South Africa
[3]Inter-University Institute for Data Intensive Astronomy, Department of Physics and Astronomy, University of the Western Cape, Robert Sobukwe Road, Bellville, 7535, Cape Town, South Africa
[4]National Centre for Radio Astrophysics - Tata Institute of Fundamental Research Post Box 3, Ganeshkhind P.O., Pune 411007, India

E-mail: kolwasn@unisa.ac.za

Abstract. Radio spectral energy distributions allow us to infer the radiative origin of emission in galaxies. With the recent availability of catalogues of radio sources detected with interferometers such as MeerKAT (Meer Karoo Array Telescope) and the upgraded Giant Metrewave Radio Telescope (uGMRT), we have sufficient observational sensitivity to detect the faintest radio emission in galaxies. For this, we make use of the superMIGHTEE survey which combines data from the MIGHTEE (MeerKAT International GigaHertz Extragalactic Exploration) survey and the uGMRT. At this faint flux end, it is generally unclear which specific mechanisms produce radio emission. In this foundational study, we begin to tackle this quandary by obtaining constraints on spectral curvature using four-band radio detections spanning observed frequencies of 100 MHz - 2 GHz for radio-loud active galactic nuclei (AGN). We examine selection bias in the survey by comparing observations to simple Monte Carlo simulations. From these, we find that the faint source population (< 0.3 mJy) is dominated by steep spectrum sources due to flux-limit variation between the observed frequency bands. In the bright source population (> 10 mJy), an increased number of steep spectrum sources occur as a result of the Malmquist bias which selects the most radio-loud AGN and therefore sources with steep observed radio spectra.

1 Introduction

Wide-field extragalactic radio continuum surveys are an essential tool for studying galaxy evolution. With these surveys, it is possible to probe both nuclear activity and star-formation in galaxies through cosmic time [1]. Supernova remnants in star-forming galaxies produce synchrotron radiation due to the relativistic acceleration of electrons [3]. Free-free emission originates from HII regions [2]. At the nuclei of active galaxies, jets produced through accretion of gas onto the black-hole also accelerate relativistic electrons forming non-thermal synchrotron emission contributing to the radio continuum observed [4, 5]. With sufficient detection sensitivity, radio continuum surveys can obtain statistically significant samples of star-forming galaxies, radio-quiet quasars and low-luminosity radio galaxies [6]. An additional benefit is a constraint of star-formation rates and histories that do not require dust attenuation corrections due to the centimetre wavelengths of radio radiation [7].

With sensitive radio survey detections of nuclear activity and star-formation in galaxies, two distinct populations of sources emerge: AGN and star-forming galaxies (SFGs), where radio emission originates from the nucleus and star-forming regions, respectively [8]. The faint radio source population, in particular emerges at 1.4 GHz radio flux densities of approximately ≤ 1.0 mJy. The jet- and radiative-mode populations of radio galaxies also known as radio-loud active galactic nuclei are the most powerful radio sources and dominate at flux densities of > 1 mJy. Within the sub-mJy population, however, star-forming galaxies and young or restarted AGN host galaxies are the dominant groups of sources [9, 10, 11]. The radio-loud AGN population has been well studied in terms of both the AGN and host galaxy properties up to $z \sim 1.0$ [12]. The emerging faint source population at low redshifts, however, provide a new frontier for investigating the mechanisms powering radio emission in radio-quiet/faint AGN and star-forming galaxies on a statistical scale.

We can make use of radio spectral energy distributions (SEDs) to trace the origin of radio emission in galaxies [13]. When sufficient multi-frequency observations are available, we can fit emission models for thermal and non-thermal processes to the radio spectra and sufficiently to infer the underlying physics producing the observed radiation. Emission models are based on well-studied radio spectra of the Galactic Centre and objects in the nearby Universe [15, 16, 17, 18]. It is known, for instance, that at rest-frame frequencies of $1.0 \leq \nu_0 \leq 10$ GHz, spectral steepening is attributed to energy losses in cosmic ray electrons due to Inverse-Compton scattering as well as synchrotron radiation in optically thin plasma regions [14]. At lower rest-frame frequencies of $\nu_0 \leq 1$ GHz, steepening of radio spectra result from synchrotron self-Compton scattering in the optically thick plasma and also free-free absorption along the line-of-sight.

In situations where a sample of sources has incomplete data, however, and only a few radio frequency bands have significant ($> 5\sigma$) detections, we are limited from fitting complex models to the SED due to insufficient photometry. Rather, we will need to rely on the spectral index, α from the power law relation $S_\nu \propto \nu^\alpha$ to measure the gradient of a radio SED on a logarithmic scale.

Focussing on the poorly understood faint radio source population, we aim to determine how selection biases affect radio spectral index measures. With recent observations from the MIGHTEE (MeerKAT International GigaHertz Tiered Extragalactic Exploration) Survey [1] and surveys conducted with the upgraded Giant Metrewave Radio Telescope (uGMRT), we can detect the faint radio source population down to an rms (root mean square) noise threshold of approximately 2 μJy in flux. The comparable flux limits between MIGHTEE and uGMRT make the samples complete meaning we are able to properly constrain radio spectral indices across three bands for thousands of sources. With this sample, it is possible infer the radiative processes responsible for the radio emission for the non-jetted AGN and SFGs observed which leave for future work.

2 The superMIGHTEE Survey of XMM-LSS

superMIGHTEE refers to combination of survey data from the MIGHTEE project and uGMRT observations to produce deep radio continuum images at μJy sensitivity over a frequency range of 200 MHz to 2.5 GHz. The surveys are resolution-matched at $\sim 5''$. In this work, we make use of the MIGHTEE DR1 survey of the *XMM-Newton* Large Scale Structure Survey (XMM-LSS) field [19]. The XMM-LSS image mosaic comprises 45 MeerKAT pointings with a total integration time of 297.9 h. The image is taken in the L-band at a central frequency of 1.28 GHz. During calibration and imaging, a robust weighting parameter (rp) of $\mathrm{rp} = -1.2$ is applied to produce an image with a restoring beam of size $5'' \times 5''$ and a thermal noise level of 3.4 μJy/beam. The uGMRT DR1 Survey of XMM-LSS consists of two observing frequencies: band-3 centred at 390 MHz and band-4 at 650 MHz [20]. The survey coverage of superMIGHTEE are shown against that of LOFAR 144 MHz in Figure 1 (left).

2.1 Ancillary Data and Redshifts

Additional multiwavelength information on the radio sources in XMM-LSS are available from legacy surveys. We use an optical/near-infrared (NIR) catalogue comprising $YJHK_s$ photometry from the VISTA telescope's VIDEO (VISTA Deep Extragalactic Observations) Survey [21]. Additionally, we have optical photometry from the $GRIZy$ filters of the HyperSuprimeCam (HSC) *Subaru* Strategic Program (SSP) [22]. The observed photometric data are fit to emission templates using `LePHARE` [23]. Additionally, photometric estimations are obtained using the `GPz` machine learning procedure [24]. A consensus redshift is determined from both methods using a hierarchical Bayesian method described in [25].

2.2 Radio and optical/NIR cross-matching

We obtain radio catalogues of sources from the images by running the Python Blob and Detection Source Finder (`PyBDSF`) [26]. With these, we cross-match the `PyBDSF` source list with the optical/NIR catalogue for the field to obtain optical counterparts to the radio sources. In this, we find the nearest optical/NIR source in projection to a radio source within $1.2''$. This cross-match radius represents the angular scale beyond which true optical/NIR

counterparts to the radio sources are less likely to be found. The method of deriving this optimal cross-match radius is described in Section 6 of the superMIGHTEE DR1 release paper [20].

The number of radio sources in uGMRT band-3, band-4, and MIGHTEE L-band are 10,931, 16,284 and 72,187, respectively. After performing the radio-optical cross-matching we find 7,849, 14,129, and 31,763 radio sources with optical counterparts giving a 72%, 87%, and 44% completeness, respectively. The combined radio and optical/NIR catalogue provide redshifts for sources with optical counterparts. With this information, we can calculate radio luminosity at a reference frequency of ν_0 using the relation,

$$L_{\nu,0} = 4\pi(\nu_0/\nu)^{\alpha} d_L^2 (1+z)^{-\gamma} S_\nu, \tag{1}$$

where ν is the observing frequency, d_L is the luminosity distance, and $\gamma = \alpha + 1$. We adopt a canonical spectral index of $\alpha = -0.7$.

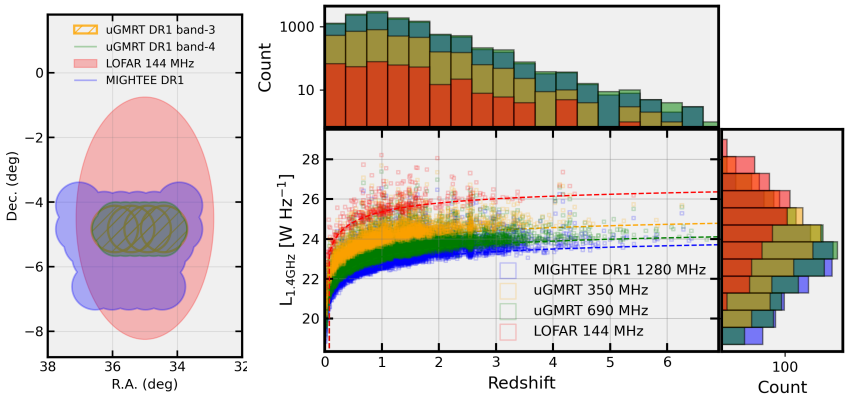

Figure 1: (*Left:*) The survey coverage of the uGMRT band-3 and -4, MIGHTEE DR1, and LOFAR 144 MHz surveys. The area covered is 6.9, 9.9, 14.4 and 27.0 deg^2 respectively. (*Right:*) The 1.4 GHz radio luminosity of the radio continuum surveys mentioned as a function of redshift is provided.

3 Data Analysis

3.1 Spectral Index and Curvature

The spectral index is defined as,

$$\alpha = \frac{d\log S_\nu}{d\log \nu} \tag{2}$$

where S_ν is the flux density and ν is the observed frequency. We calculate spectral indices over four frequency bands: uGMRT band-3 (390 MHz) and band-4 (650 MHz) as well as MIGHTEE L-band (1.28 GHz). This yields the spectral indices, α_{650}^{1280}, and α_{390}^{650}. We plot both these spectral indices against one another, forming a radio-colour plot that defines spectral shapes in each of its quadrants shown in Figure 2. Statistically the distribution of spectral shapes across of the plane indicates $\sim 2\%$ inverted, 78% steep, $\sim 5\%$ concave and 15% peaked radio sources. Additionally, a trend with radio flux density shows an increase peaked and inverted shapes with source brightness as seen in Figure 2. This trend is observed with radio luminosity as well. The thermal noise levels vary between the observed frequency bands with values of 32.0, 8.3, and 3.4 μ Jy/beam for uGMRT band-3, band-4 and MIGHTEE respectively. Hence, incompleteness between bands is likely to be affecting our distribution of observed radio spectral shapes.

3.2 Simulating Unbiased Spectral Shapes

A completeness-correction requires us to predict the distribution and number of radio spectral shapes (or types) that would occur without the flux incompleteness between bands. We make use of a Monte Carlo simulation to determine the unbiased radio spectral index distributions. We begin by generating a mock distribution of uGMRT band-4 (B4) flux densities which forms our seed distribution.

We convert B4 flux densities to band-3 (B3) and MIGHTEE mock flux densities by setting up a Gaussian distribution of spectral indices with a fixed mean of $\mu = -0.65$ and the standard deviation to $\sigma_{\rm rms} = 0.5$ for the 390-650 MHz distribution and $\mu = -0.45$ and $\sigma = 0.5$ for the 650-1280 MHz distribution based on the observed

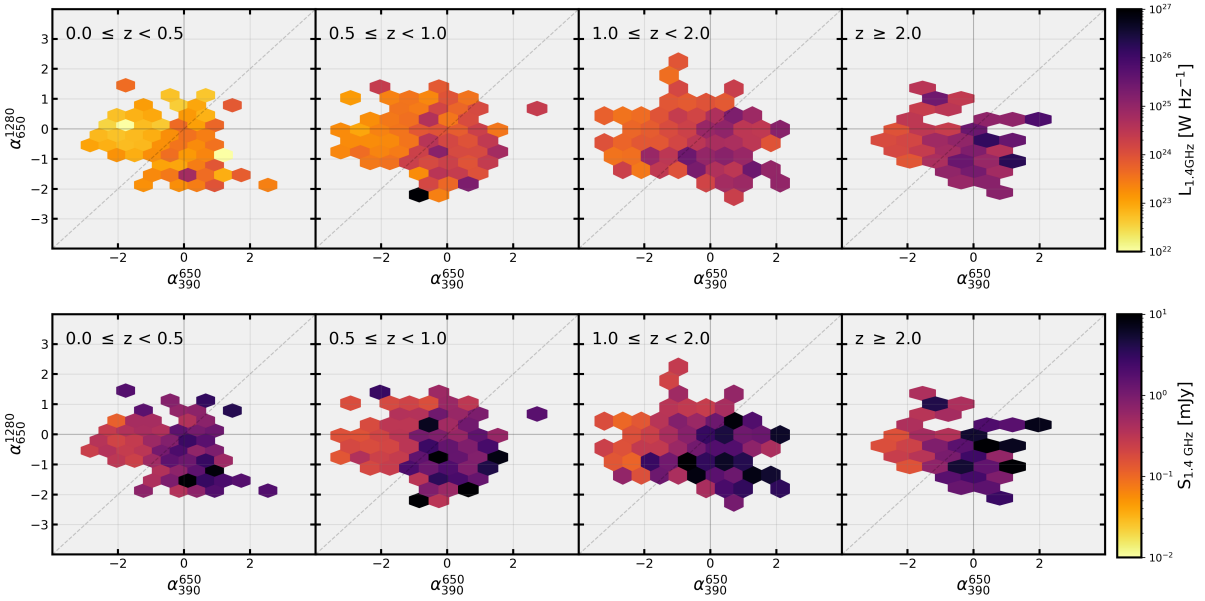

Figure 2: The radio colour-colour plot for superMIGHTEE detected sources across all three frequency bands. The colourbar represents 1.4 GHz flux density and luminosity at the top and bottom, respectively.

spectral index distributions. To convert B4 mock fluxes to B3 and MIGHTEE fluxes, we perform random draws of spectral indices from the observed spectral index distributions. With this method, we generate the underlying flux density distribution for B3 and MIGHTEE DR1. This ensures that the flux densities are not decoupled but rather dependent on one another. We then inject Gaussian noise to the underlying flux measures such that,

$$f_i = s_i + \delta_i \tag{3}$$

where f_i is the total flux, s_i is the underlying flux and δ_i represents the thermal noise inferred randomly from a distribution centred at $\mu = 0$ with a standard deviation equivalent to the $\sigma_{\rm rms}$ (flux limit) at a given frequency band. We then perform a $\rm S/N = 5$ cut on the mock flux density distributions. We use these mock flux densities to simulate spectral indices in the realistic case where thermal noise values are equivalent to those in the real surveys (for the *Monte Carlo: observed simulation*). We also simulate spectral indices in the ideal case where the thermal noise is identical across all observed frequency bands (for *Monte Carlo: underlying*).

4 Results

We compare the observed spectral indices to the Monte-Carlo simulated ones in Figure 3. The Monte Carlo simulation predicts a higher proportion of flat spectrum sources at flux densities of 300μJy/beam at the low frequency range of 390-650 MHz. For the higher frequency range, a higher proportion of flat spectrum is expected across 650-1280 MHz. Both of these discrepancies between observation and simulation are a result of flux-limit biases in the observations. At low observed frequencies, the faint sources which have flat spectra are missed due to the high uncertainty in thermal noise at lower frequencies (Eddington bias). At higher frequencies, flat spectrum sources are not observed as they are significantly faint in comparison to radio-loud AGN which dominate the population at the redshift limit of the survey (Malmquist bias).

5 Conclusion

Exploiting the heightened sensitivity of the uGMRT and MeerKAT arrays, we have assembled a radio continuum survey dataset for the superMIGHTEE survey covering the XMM-LSS field. We have used four frequency bands, uGMRT band-3, band-4, MIGHTEE DR1. Our observed spectral shapes are dominated by steep spectrum sources which we find to be an artefact of incompleteness between the observed radio frequency bands. Using Monte Carlo simulations, we predict both the underlying distribution of spectral indices for a complete sample. We find a discrepancy between simulation and observation such that faint flat spectrum are missed at low frequencies due to the Eddington bias. Bright flat spectrum sources are missed due to the Malmquist bias which results in a dominance of more powerful radio-loud AGN at the highest redshifts probed by the optical/NIR surveys.

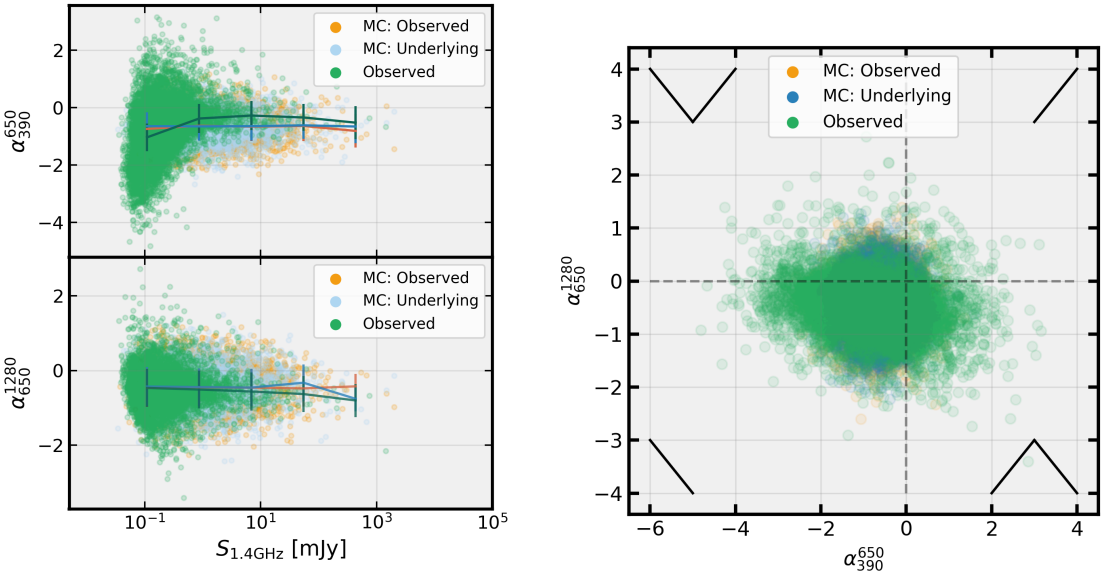

Figure 3: (*Left:*) The observed spectral index as a function of 1.4 GHz flux density shown against Monte Carlo simulated observed (*MC: Observed*) and underlying (*MC: Underlying*) distributions over frequency ranges, 390-650 MHz (*top*) and 650-1280 MHz (*bottom*). We provide a line joining the flux binned medians where the uncertainties are denoted by standard deviations within each flux bin. The lines for observed, *MC: Observed* and *MC: Underlying* are provided in green, red, and blue respectively. (*Right:*) The observed spectral curvature distribution shown against Monte Carlo simulated observed (*MC: Observed*) and underlying (*MC: Underlying*) distributions over frequency ranges, 390-650 MHz and 650-1280 MHz. Starting from the top right quadrant and moving clockwise, the spectral shapes represented are: inverted, concave, steep, and peaked.

References

[1] M. Jarvis, R. Taylor, I. Agudo, J. R. Allison, R. P. Deane, B. Frank, N. Gupta, I. Heywood, N. Maddox, K. McAlpine, M. Santos, A. M. M. Scaife, M. Vaccari, J. T. L. Zwart, E. Adams, D. J. Bacon, A. J. Baker, B. A. Bassett, P. N. Best, R. Beswick, S. Blyth, M. L. Brown, M. Bruggen, M. Cluver, S. Colafrancesco, G. Cotter, C. Cress, R. Davé, C. Ferrari, M. J. Hardcastle, C. L. Hale, I. Harrison, P. W. Hatfield, H. R. Klockner, S. Kolwa, E. Malefahlo, T. Marubini, T. Mauch, K. Moodley, R. Morganti, R. P. Norris, J. A. Peters, I. Prandoni, M. Prescott, S. Oliver, N. Oozeer, H. J. A. Rottgering, N. Seymour, C. Simpson, O. Smirnov, and D. J. B. Smith, "The MeerKAT International GHz Tiered Extragalactic Exploration (MIGHTEE) Survey," in *MeerKAT Science: On the Pathway to the SKA*, Jan. 2016, p. 6.

[2] Y. Terzian, "Radio Emission from H II Regions." *ApJ*, vol. 142, p. 135, Jul. 1965.

[3] J. J. Condon, "Radio emission from normal galaxies." *ARA&A*, vol. 30, pp. 575–611, Jan. 1992.

[4] G. de Zotti, M. Massardi, M. Negrello, and J. Wall, "Radio and millimeter continuum surveys and their astrophysical implications," *A&A Rev.*, vol. 18, no. 1-2, pp. 1–65, Feb. 2010.

[5] M. J. Hardcastle and J. H. Croston, "Radio galaxies and feedback from AGN jets," *New A Rev.*, vol. 88, p. 101539, Jun. 2020.

[6] P. N. Best, R. Kondapally, W. L. Williams, R. K. Cochrane, K. J. Duncan, C. L. Hale, P. Haskell, K. Małek, I. McCheyne, D. J. B. Smith, L. Wang, A. Botteon, M. Bonato, M. Bondi, G. Calistro Rivera, F. Gao, G. Gürkan, M. J. Hardcastle, M. J. Jarvis, B. Mingo, H. Miraghaei, L. K. Morabito, D. Nisbet, I. Prandoni, H. J. A. Röttgering, J. Sabater, T. Shimwell, C. Tasse, and R. van Weeren, "The LOFAR Two-metre Sky Survey: Deep Fields data release 1. V. Survey description, source classifications, and host galaxy properties," *MNRAS*, vol. 523, no. 2, pp. 1729–1755, Aug. 2023.

[7] J. S. Dunlop, R. J. McLure, A. D. Biggs, J. E. Geach, M. J. Michałowski, R. J. Ivison, W. Rujopakarn, E. van Kampen, A. Kirkpatrick, A. Pope, D. Scott, A. M. Swinbank, T. A. Targett, I. Aretxaga, J. E. Austermann, P. N. Best, V. A. Bruce, E. L. Chapin, S. Charlot, M. Cirasuolo, K. Coppin, R. S. Ellis, S. L. Finkelstein, C. C. Hayward, D. H. Hughes, E. Ibar, P. Jagannathan, S. Khochfar, M. P. Koprowski, D. Narayanan, K. Nyland, C. Papovich, J. A. Peacock, G. H. Rieke, B. Robertson, T. Vernstrom, P. P. v. d. Werf, G. W. Wilson, and M. Yun, "A deep ALMA image of the Hubble Ultra Deep Field," *MNRAS*, vol. 466, no. 1, pp. 861–883, Apr. 2017.

[8] P. Padovani, "The faint radio sky: radio astronomy becomes mainstream," *A&A Rev.*, vol. 24, no. 1, p. 13, Sep. 2016.

[9] C. Gruppioni, M. Mignoli, and G. Zamorani, "Optical identifications and spectroscopy of a faint radio source sample: the nature of the sub-mJy population," *MNRAS*, vol. 304, no. 1, pp. 199–217, Mar. 1999.

[10] M. Magliocchetti, S. J. Maddox, J. V. Wall, C. R. Benn, and G. Cotter, "The redshift distribution of FIRST radio sources at 1mJy," *MNRAS*, vol. 318, no. 4, pp. 1047–1067, Nov. 2000.

[11] I. Prandoni, L. Gregorini, P. Parma, H. R. de Ruiter, G. Vettolani, A. Zanichelli, M. H. Wieringa, and R. D. Ekers, "The ATESP radio survey. IV. Optical identifications and spectroscopy in the EIS-A region," *A&A*, vol. 369, pp. 787–796, Apr. 2001.

[12] T. M. Heckman and P. N. Best, "The Coevolution of Galaxies and Supermassive Black Holes: Insights from Surveys of the Contemporary Universe," *ARA&A*, vol. 52, pp. 589–660, Aug. 2014.

[13] P. A. G. Scheuer and P. J. S. Williams, "Radio Spectra," *ARA&A*, vol. 6, p. 321, Jan. 1968.

[14] C. L. Carilli, R. A. Perley, J. W. Dreher, and J. P. Leahy, "Multifrequency Radio Observations of Cygnus A: Spectral Aging in Powerful Radio Galaxies," *ApJ*, vol. 383, p. 554, Dec. 1991.

[15] K. A. Wills, A. Pedlar, T. W. B. Muxlow, and P. N. Wilkinson, "Low-frequency observations of supernova remnants in M82," *MNRAS*, vol. 291, no. 3, pp. 517–526, Nov. 1997.

[16] A. R. McDonald, T. W. B. Muxlow, K. A. Wills, A. Pedlar, and R. J. Beswick, "A parsec-scale study of the 5/15-GHz spectral indices of the compact radio sources in M82," *MNRAS*, vol. 334, no. 4, pp. 912–924, Aug. 2002.

[17] S. Roy, "Density of Warm Ionized Gas near the Galactic Center: Low Radio Frequency Observations," *ApJ*, vol. 773, no. 1, p. 67, Aug. 2013.

[18] E. Varenius, J. E. Conway, I. Martí-Vidal, R. Beswick, A. T. Deller, O. Wucknitz, N. Jackson, B. Adebahr, M. A. Pérez-Torres, K. T. Chyży, T. D. Carozzi, J. Moldón, S. Aalto, R. Beck, P. Best, R. J. Dettmar, W. van Driel, G. Brunetti, M. Brüggen, M. Haverkorn, G. Heald, C. Horellou, M. J. Jarvis, L. K. Morabito, G. K. Miley, H. J. A. Röttgering, M. C. Toribio, and G. J. White, "Subarcsecond international LOFAR radio images of the M82 nucleus at 118 MHz and 154 MHz," *A&A*, vol. 574, p. A114, Feb. 2015.

[19] C. L. Hale, I. Heywood, M. J. Jarvis, I. H. Whittam, P. N. Best, F. An, R. A. A. Bowler, I. Harrison, A. Matthews, D. J. B. Smith, A. R. Taylor, and M. Vaccari, "MIGHTEE: the continuum survey Data Release 1," *MNRAS*, vol. 536, no. 3, pp. 2187–2211, Jan. 2025.

[20] D. V. Lal, R. Taylor, S. Sekhar, C. Ishwara-Chandra, S. Dutta, and S. Kolwa, "The superMIGHTEE Project: MeerKAT and GMRT Together to Unveil the Deep Radio Sky," *ApJ*, vol. 991, no. 1, p. 9, Sep. 2025.

[21] M. J. Jarvis, D. G. Bonfield, V. A. Bruce, J. E. Geach, K. McAlpine, R. J. McLure, E. González-Solares, M. Irwin, J. Lewis, A. K. Yoldas, S. Andreon, N. J. G. Cross, J. P. Emerson, G. Dalton, J. S. Dunlop, S. T. Hodgkin, F. O. Le, M. Karouzos, K. Meisenheimer, S. Oliver, S. Rawlings, C. Simpson, I. Smail, D. J. B. Smith, M. Sullivan, W. Sutherland, S. V. White, and J. T. L. Zwart, "The VISTA Deep Extragalactic Observations (VIDEO) survey," *MNRAS*, vol. 428, no. 2, pp. 1281–1295, Jan. 2013.

[22] H. Aihara, R. Armstrong, S. Bickerton, J. Bosch, J. Coupon, H. Furusawa, Y. Hayashi, H. Ikeda, Y. Kamata, H. Karoji, S. Kawanomoto, M. Koike, Y. Komiyama, D. Lang, R. H. Lupton, S. Mineo, H. Miyatake, S. Miyazaki, T. Morokuma, Y. Obuchi, Y. Oishi, Y. Okura, P. A. Price, T. Takata, M. M. Tanaka, M. Tanaka, Y. Tanaka, T. Uchida, F. Uraguchi, Y. Utsumi, S.-Y. Wang, Y. Yamada, H. Yamanoi, N. Yasuda, N. Arimoto, M. Chiba, F. Finet, H. Fujimori, S. Fujimoto, J. Furusawa, T. Goto, A. Goulding, J. E. Gunn, Y. Harikane, T. Hattori, M. Hayashi, K. G. Hełminiak, R. Higuchi, C. Hikage, P. T. P. Ho, B.-C. Hsieh,

K. Huang, S. Huang, M. Imanishi, I. Iwata, A. T. Jaelani, H.-Y. Jian, N. Kashikawa, N. Katayama, T. Kojima, A. Konno, S. Koshida, H. Kusakabe, A. Leauthaud, C.-H. Lee, L. Lin, Y.-T. Lin, R. Mandelbaum, Y. Matsuoka, E. Medezinski, S. Miyama, R. Momose, A. More, S. More, S. Mukae, R. Murata, H. Murayama, T. Nagao, F. Nakata, M. Niida, H. Niikura, A. J. Nishizawa, M. Oguri, N. Okabe, Y. Ono, M. Onodera, M. Onoue, M. Ouchi, T.-S. Pyo, T. Shibuya, K. Shimasaku, M. Simet, J. Speagle, D. N. Spergel, M. A. Strauss, Y. Sugahara, N. Sugiyama, Y. Suto, N. Suzuki, P. J. Tait, M. Takada, T. Terai, Y. Toba, E. L. Turner, H. Uchiyama, K. Umetsu, Y. Urata, T. Usuda, S. Yeh, and S. Yuma, "First data release of the Hyper Suprime-Cam Subaru Strategic Program," *PASJ*, vol. 70, p. S8, Jan. 2018.

[23] S. Arnouts and O. Ilbert, "LePHARE: Photometric Analysis for Redshift Estimate," Astrophysics Source Code Library, record ascl:1108.009, Aug. 2011.

[24] P. W. Hatfield, M. J. Jarvis, N. Adams, R. A. A. Bowler, B. Häußler, and K. J. Duncan, "Hybrid photometric redshifts for sources in the COSMOS and XMM-LSS fields," *MNRAS*, vol. 513, no. 3, pp. 3719–3733, Jul. 2022.

[25] K. J. Duncan, M. J. Jarvis, M. J. I. Brown, and H. J. A. Röttgering, "Photometric redshifts for the next generation of deep radio continuum surveys - II. Gaussian processes and hybrid estimates," *MNRAS*, vol. 477, no. 4, pp. 5177–5190, Jul. 2018.

[26] N. Mohan and D. Rafferty, "PyBDSF: Python Blob Detection and Source Finder," p. ascl:1502.007, Feb. 2015.

This page intentionally left blank.

Wits Astronomical Plate Archive – preservation of a century of Southern Hemisphere astronomy at the Johannesburg Observatory

A. Jamieson[1], S. Colafrancesco[2], J. Carter[2], A. L. Carter[2], A. Chen[2], M. Hanibal[1], A. Joubert[3], N. Komin[2], D. Pheiffer[1], H. Veale[2], C. Volschenk[1,2], V. Carruthers[4] and J. Carruthers[5]

[1]Astronomical Society of Southern Africa (ASSA), Johannesburg Centre, South Africa
[2]School of Physics, University of the Witwatersrand, Johannesburg 2050, South Africa
[3]Council for Scientific and Industrial Research (CSIR), Pretoria 0184, South Africa
[4]Magaliesburg Association for Culture and Heritage (MACH)
[5]Department of History, University of South Africa (UNISA), Pretoria, South Africa

E-mail: alec.jamieson@telkomsa.net

Abstract. In the present digital age, there is a growing awareness to preserve the heritage of photographic astronomical observations by digitising the glass plate images, especially necessary since photographic emulsions deteriorate over time. The original exposure of a glass plate was often for a specific astronomical object. However, now using a modern digital camera, computer and Internet technology and the large number of standard stars on record, it has been possible to calibrate in the region of 60,000 stars, on average, on a single plate. Digitisation of the Franklin-Adams plates originating from the Johannesburg Observatory, going back a hundred years and online access to the data from those plates for later comparisons, could reveal new long-term astronomical variability.

1 Introduction

Astronomical photographic plates from the Franklin-Adams Star Camera representing a century of Southern Hemisphere astronomy at the Johannesburg Observatory were being held in the Council for Scientific and Industrial Research (CSIR) Archive in Pretoria, without having been accessed for about 30 years, after the Johannesburg Observatory closed in the late 1970s. In 2009 an astronomer at the South African Astronomical Observatory (SAAO) in Cape Town, Dr Ian Glass, on a visit to the CSIR Archive, was informed of the situation and that the space occupied was needed for other purposes. Doctor Glass circulated a notice to this effect to the Astronomical Society of Southern Africa (ASSA). At that time, the Librarian (A. Jamieson) of ASSA Johannesburg Centre (ASSA Jhb), was aware of some printed, Southern Hemisphere star charts in the Library. However, prior to this, ASSA Jhb had recorded the idea of locating the glass-plate originals, digitising them and posting them on the Internet if they could be found. Some sampling and estimating in the CSIR Plate Archive soon showed that the Archive contained approximately 10,000 plates, many more than the set of 556 glossy-paper prints of the glass-plate originals that had been made to cover the southern sky from -19° to -90° of declination [1]. The lack of access to the plates was not an indication that they were worthless, but an indication of how impractical it was to travel to far-off archives and manually search for the required plates decades after the plates were exposed and stored. The updated photographic record of the southern sky from

South Africa had taken nearly 20 years to complete and in the pre-digital era, dispatch by post of photographic prints of the glass plates to other observatories was the most practical method of distribution. These prints served as useful finder charts amongst the few Southern Hemisphere astronomical observatories in the early years of the 20th century.

The modified Franklin-Adams Star Camera was re-located in 1909 from England to Johannesburg by John Franklin-Adams after completing a Northern Hemisphere sky survey with the aim of observing Halley's Comet in 1910. Subsequently, John Franklin-Adams donated the Star Camera to the Transvaal Colonial Government on condition of repeating a sky survey for the Southern Hemisphere [2]. However, there were no plate registers in the CSIR Archive. Despite this setback, as recorded below, it was possible to proceed with the establishment of an Astronomical Plate Archive for a century of Southern Hemisphere astronomy at the Johannesburg Observatory.

2 First steps towards a new archive for the Franklin-Adams Star Camera Plates

Alternative accommodation for the Franklin-Adams Photographic Plates was deemed more urgent than digitising and Internet posting and at least six months storage was secured at the premises of a company in Johannesburg, with the plates being moved from the CSIR in October 2010. At the same time, quite by chance, Dr Keith Snedegar, Professor of History, Utah Valley University, USA was doing research at the CSIR Archive on the lives of early South African astronomers. He was well acquainted with astronomical plate preservation in the USA and later sent information on the Digital Access to a Sky Century at Harvard (DASCH) Project [3]. The DASCH project was an early development in the history of glass plate digitisation, based on highly specialised equipment, and the software developed for the calibration of the digitised plates was not published. In the early stages of the DASCH project, around 2005, numerous assessments of high-end (and high-cost) scanners were published by others. The DASCH project team decided to modify a micro-densitometer to digitise whole plates pixel by pixel at a pitch of approximately 10 microns (2500 dpi) [4]. The Harvard College Observatory (HCO) plate collection consists of about half a million plates and the HCO team soon decided to build a mark 2 precision plate scanner that could scan 4 pixels at a time relying on the precise position control of the micro-densitometer, at a budget cost of $50,000 US [5]. Such costs would be prohibitively expensive for the proposed Franklin-Adams Plate Archive scanner.

A major concern was then alleviated when the CSIR archivist traced 4 of the 5 Franklin-Adams plate registers, in 1980s correspondence, to the SAAO Library in Cape Town. However, the plates remained in temporary storage until 2014 when the School of Physics, University of the Witwatersrand, became aware of the difficulty that ASSA Jhb was having with finding permanent storage for the plates.

3 The University of the Witwatersrand (Wits) Astronomical Plates

Professor Sergio Colafrancesco, DST-NRF Research Chair in Radio Astronomy (Wits School of Physics) together with Prof John Carter, Head of School, promptly arranged to inspect the Franklin-Adams astronomical plates being held in temporary storage at the site of the former Johannesburg Observatory, and expressed support for the concept of safe storage and digitisation of the plates. The plates, some a century old, were moved to safe storage at the Wits School of Physics in April 2015 (see Figure 1) and there was an Inaugural Function later that year in November 2015 (see Figure 2).

The jacketed plates, about half of them, were returned to their compartmentalised wooden cabinets with the remainder still packed in plate number order with tissue paper separators in the same cardboard boxes used to hold them at the CSIR Archive. The only identification of the boxed plates was a plate serial number inscribed by hand on the emulsion side of each plate. The plate registers were not laid out in plate number order but in ranges of declination angles, typically 5° to 20° wide. For the boxed plates, it was very difficult to find the plate register information relating to a particular plate number. This would remain an unsolved problem while sampling and digitising the jacketed plates because all plate data were written on the outside of the plate jackets.

4 Progress in digitisation of Astronomical Photographic Plates

Shortly after the inauguration of the Wits Plate Archive, the 2nd AstroPlate International Workshop took place in March 2016 in Prague [6] noting that *"There are more than 7 million astronomical photographic plates and/or negatives around the globe, containing huge amounts of unique scientific data. The wide use of various*

digitization methods, together with development of dedicated software tools, allows effective and complete evaluation of these data for the first time."



Figure 1: Wits Astronomical Plate Archive showing jacketed plates in glass-fronted wooden cabinets against the wall at the back and on the left.

The AstroPlateII Proceedings [6] covered a workshop that presented a wide range of over 22 glass-plate preservation topics, including:

- presentations on the use of Digital Single Lens Reflex (DSLR) cameras instead of flat-bed scanners for digitising astronomical photographic plates and
- the Archives of Photographic Plates for Astronomical USE (APPLAUSE) Collaboration.

The APPLAUSE Collaboration [7] is a group of German astronomical observatories that have digitised about 85,000 photographic plates using high-resolution flat-bed scanners. Of further interest, the APPLAUSE Collaboration has also calibrated and stored online the digital files produced from the 85,000 glass plates using the open-source Python package called Pyplate.

5 Wits Plate Archive - Digitisation of the Jacketed Plate Sample

Professor Colafrancesco recommended the use of a DSLR camera and light table instead of a flat-bed scanner for digitising astronomical plates. This approach avoided the precision drive required for the moving parts of a flat-bed scanner and captured many megabits of information in a fraction of a second. Work then commenced on digitising a 1/40th sample of jacketed plates to give some idea of plate content, and for mastering the digitising method before digitising the whole plate collection. To facilitate space-craft navigation and support digital astronomy, there are now so many reference stars on record that there are enough on any plate for calibrating the brightness of all other stars on the plate. This greatly simplifies the calibration process for varying plate exposure conditions and varying lighting conditions for plate data capture. Digitising the jacketed plate sample commenced using a 34-megapixel Canon 5D Mark IV DSLR camera with suitable zoom lens, mounted on a tripod above a light table. The camera was connected to a Wi-Fi shutter release to keep the

camera steady and, with the reflex mirror permanently up, a tablet computer for convenient display of the camera plate image.



Figure 2: Wits Plate Archive Inaugural Function November 2015. (*top left and right*) Halley's Comet 1910. (*middle left*) Mrs. Hillary Veale, a Wits Alumna whose generous donation made the Plate Archive possible. (*middle right*) The Moon. (*bottom left*) Original packaging for unexposed photographic plates. (*bottom right*) Viewing plate examples on light table.

5.1 Importance of Astronomical Plate Registers

After the Franklin-Adams Plate Registers Volumes I to IV were formally transferred from the SAAO Library to the Wits School of Physics, inspection revealed that there were some loose pages and some of the pages were becoming brittle and easily torn. To protect against loss of the four irreplaceable registers, a photographic record of all written pages was made (using the DSLR camera as in Sec. 5 but with reflected light) to provide

working copies and avoid wear and tear of the originals. An unexpected advantage of computer on-screen register pages was that indistinct handwriting could be quickly resolved in most cases by zooming in on the text as necessary.

By way of example, computer access to Plate Register copies helped to confirm a disputed comet from 1971, observed in New Zealand. An American author of a book in preparation on disputed comets asked if a confirming plate existed in the Union Observatory (now Johannesburg Observatory) plate collection. A plate that matched the search criteria was found and a digitised copy was sent. Later, Telegram No. 5239 from the Central Bureau for Astronomical Telegrams confirmed recognition of Comet c/1971M1 (EDWARDS).

5.2 Accessing the Plate Register Data for the Boxed Plates

This was a long-term concern knowing that the plate registers were arranged in divisions of declination angle, typically 5° to 20°. Before computers could quickly sort lists of thousands of items, the register layout in declination order made sense for astronomers, and less so for archivists. An astronomer would have a better idea of relevant celestial co-ordinates and would have a better idea than an archivist of how to narrow down the search in the plate register.

The only way to connect over 10,000 plate numbers ranging from 1,000 to the mid 20-thousands listed in order of ranges of astronomical declination angle, is to work through the plate registers volume by volume and page by page noting plate, volume and page numbers. This handwritten information would then be recorded in a 10,000 line spreadsheet so that it could be sorted into plate number order. This would create the index connecting plate number to plate register entry and the official plate meta-data recorded in the plate registers. However, creating a 10,000 line spreadsheet sounds onerous, but some simplifications became apparent:

- Only plate and page numbers are required on every line.
- The page number requires a manual change about once every 30 plate numbers (capacity per page).
- The thousand digit in the plate number requires a manual increment about once in every 900 plate numbers.
- Only the 3 least significant digits of each plate number must be entered manually.
- In a plate number, the thousand digit repeats from the previous line and only needs to be increased manually when the last three digits reach 000.
- The spreadsheet multiplies the digits signifying thousands in the plate number by 1000, then adds the last 3 digits, streamlining data entry and reducing errors.

6 Summary and Outlook

The recent developments in cameras together with those in computers and the internet have had an enormous positive impact on the preservation and world-wide accessibility of the last century and a half of photographic astronomical observations which would have otherwise been lost. It is now possible to extract detailed information on many thousands of astronomical sources from a single plate, previously unthinkable at the time of exposure. The Wits Plate Archive is taking the first steps to preserve more of the limited Southern Hemisphere historical astronomical data accessible to present day astronomers. In a recent development, the new Wits Digitisation Centre (WDC), associated with the with the Wits Library, is poised to continue digitisation, using a high-end 150 MPixel digital camera, of the Wits Plate Archive of over 10,000 astronomical plates from the Franklin-Adams Star Camera reaching back by a century into the history of Southern Hemisphere astronomy at the Johannesburg Observatory.

It was through the foresight of Prof Sergio Colafrancesco that the heritage of the Wits Plate Archive was preserved for future use but it is very sad to note that Sergio passed away a few years after the Inaugural Function of the Wits Plate Archive. He is sorely missed.

References

[1] R.T.A. Innes, "Annual Report of the Union Observatory", Union Observatory Circulars, 1926.

[2] D. J. Vermeulen, "John Franklin-Adams" pp 22-25, "Appendix 6, The main telescopes at the Union/Republic Observatory" pp 117-118, in *Living Amongst the Stars at the Johannesburg Observatory*, Chris van Rensburg Publications (Pty) Limited, 2006.

[3] K. Snedegar 2009, DASCH home page http://hea-www.harvard.edu/DASCH

[4] S. Laycock *et al.*, undated ca. 2005, updated 2008 and 2018, "Digital access to a sky century at Harvard: initial photometry and astrometry", https://arxiv.org/pdf/0811.2005

[5] R. J. Simcoe *et al.,* undated circa 2005. "An ultra high-speed digitizer for the Harvard College Observatory astronomical plates", https://arxiv.org/ftp/astro-ph/papers/0610/0610351.pdf

[6] https://www.astroplate.cz

[7] https://www.plate-archive.org

Trends of Thermal Structure in the MLT Region Using SABER Observations Over Sutherland, South Africa

Blessing Mvana Nhlozi[1], Sifiso Ntshangase[1], Nkanyiso Mbatha[2], Makhosonke Dubazane[3]

[1]Department of Physics, University of Zululand, KwaDlangezwa 3886, South Africa
[2]Holistic Climate Change, CSIR, Pretoria 0001, South Africa
[3]Discipline of Physics, University of KwaZulu-Natal, Westville 3630, South Africa

E-mail: mvanablessing@gmail.com

Abstract. The Mesosphere and Lower Thermosphere (MLT) region, located between the stratosphere and ionosphere, plays a critical role in atmospheric dynamics and space weather. Using long-term temperature data from the Sounding of the Atmosphere using Broadband Emission Radiometry (SABER) instrument, this study investigates trends in the thermal structure of the MLT over Sutherland, South Africa. The aim is to characterize regional variability, and results reveal altitude-dependent cooling trends, with statistically significant long-term cooling observed in the 56–80 km and 100–107 km ranges, while the 90–100 km layer remains dynamically unstable with no clear trend. Seasonal cycles are prominent, with cold-point shifts and temperature anomalies linked to transient dynamical processes. A Physics-Informed LSTM model successfully captures seasonal variability and underlying trends, offering a physically consistent forecast of near-future temperature evolution.

1 Introduction

The Mesosphere and Lower Thermosphere (MLT) region, situated between the stratosphere and the ionosphere, is a crucial atmospheric layer that plays a vital role in energy exchange, atmospheric dynamics, and space weather interactions. One of the key observational tools for studying the MLT region is the Sounding of the Atmosphere using Broadband Emission Radiometry (SABER) instrument, which provides long-term temperature measurements to investigate trends and variations in atmospheric parameters [1].

Research shows that the MLT region is experiencing long-term temperature changes due to solar cycle effects, greenhouse gas cooling, and atmospheric wave propagation [2]. However, more localized studies are needed to better characterize regional differences in MLT region temperature trends, particularly in the Southern Hemisphere [3]. Despite advancements in lidar and satellite-based diagnostics, simultaneous storm-time observations of temperature and winds in the MLT region remain sparse. This limitation highlights the need for localized studies, such as those conducted over Sutherland, South Africa, to bridge gaps in understanding neutral dynamics during geomagnetic disturbances[4]. Sutherland, South Africa, is a strategic location for studying MLT region temperature trends due to its unique atmospheric and geographic characteristics.

To investigate these dynamics, this study uses SABER data to assess MLT region temperature trends over Sutherland. It applies both classical statistical techniques (e.g., Mann–Kendall, Sen's slope) and modern deep learning (DL) approaches, including Physics-Informed Neural Networks (PINNs). The goal is to identify altitude-dependent trends, quantify long-term variability, and test the feasibility of DL models. Ultimately, this work aims to address two key challenges: closing the data gap in Southern Hemisphere MLT studies and exploring whether advanced DL techniques can meaningfully enhance trend detection and forecasting in the upper atmosphere.

2 Methodology

The SABER instrument onboard National Aeronautics and Space Administration's Thermosphere, Ionosphere, Mesosphere, Energetics and Dynamics (TIMED) satellite has been routinely measuring temperature since 2002. We used the level-2 temperature data, downloaded from the SABER data portal. The dataset was spatially filtered using a $10^\circ \times 10^\circ$ latitude–longitude centered on Sutherland (32.4°S, 20.8°E). This corresponds to a spatial range of 27.4°S to 37.4°S in latitude and 15.8°E to 25.8°E in longitude, defined as $\pm 5^\circ$ around the central coordinates. The data were then processed through a custom data pipeline, which included several cleaning steps to ensure the quality and consistency of the SABER profiles. The preprocessing procedure involved addressing missing values, outliers, and low-quality measurements: (i) removing temperature profiles flagged by SABER with low quality indicators (QI < 2), (ii) discarding profiles with missing or non-physical temperature values, (iii) filtering out outliers using a $\pm 3\sigma$ threshold within each altitude bin, and (iv) interpolating profiles onto a uniform altitude grid. After cleaning, the data were aggregated into daily, monthly, and seasonal databases, which were subsequently used for the statistical analyses and deep learning experiments.

2.1 Statistical Trend Detection

The MK test is used to determine the presence of monotonic trends, and the Sequential Mann–Kendall (S-MK) test to identify the onset point of such trends. These non-parametric methods are ideal for climate data where distributional assumptions may not hold. A backward sequence was computed.

2.2 Deep Learning

Deep learning (DL) was employed to capture nonlinear interactions in the SABER temperature time series and enhance physical interpretability. We implemented a Physics-Informed Neural Network (PINN) framework following the approach of Yao et al. [5]. The network architecture consisted of:

- Input layer: sequences of temperature profiles across the altitude grid, concatenated with temporal features (day-of-year, time index).
- Hidden layers: a stack of two LSTM layers with 64 and 32 units, respectively, to capture temporal dependencies. Dropout layers (rate = 0.2) were included to prevent overfitting.
- Output layer: predicted temperature values at each altitude on the uniform grid.

Training procedure:

- Optimizer: Adam with a learning rate of 0.001.
- Loss function: A composite loss consisting of:
  1. Mean Squared Error (MSE) between predicted and observed temperatures.
  2. Physics-based loss enforcing the second-order nonhomogeneous ODE behavior observed in the time series. The ODE term incorporated the Sen slope computed from the statistical trend analysis to guide the network towards physically consistent solutions.
- Training/validation split: 80% of the data was used for training and 20% for validation. Early stopping with patience = 50 epochs was applied to avoid overfitting.
- Batch size: 32 sequences per batch.
- Epochs: The network was trained for a maximum of 500 epochs. An early stopping criterion with a patience of 50 epochs was applied, ensuring that training halted automatically when no further improvement in the validation loss was observed.

3 Results and Discussion

The MLT region is well stratified, as seen in Figure 1, with the cold layer (mesopause) between 95 and 100 km denoted by a noticeable thermal inversion. As is typical of a well-defined inversion layer, this layer, which is the coldest region of the atmosphere, is bounded by rising temperatures both below (mesosphere) and above (lower thermosphere). The absence of prominent horizontal anomalies suggests, on average, there has been a minimal planetary wave influence over the past 22 years, indicating relatively stable atmospheric conditions. However, temporal analysis in Figure 2 suggests otherwise, revealing multiple periods of abrupt thermal shifts indicative of

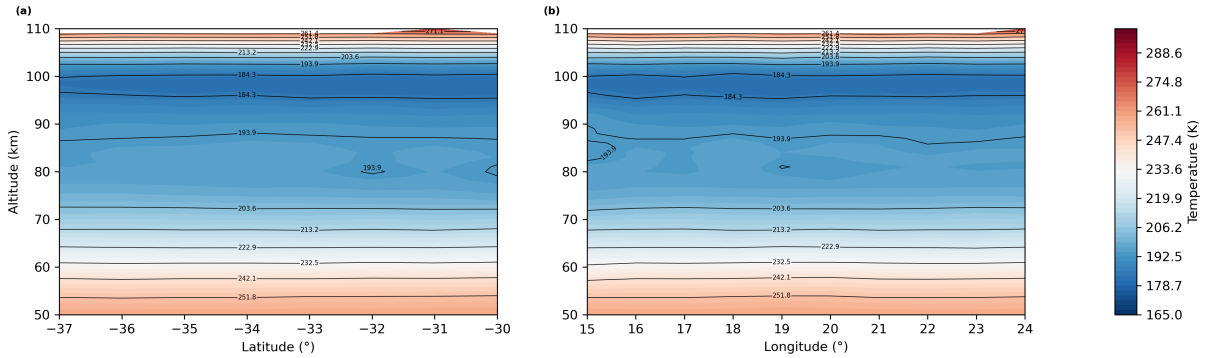

Figure 1: *Altitude versus Coordinates showing SABER temperature observations. (a) Zonal cross-section showing temperature variation with altitude and latitude. (b) Meridional cross-section showing temperature variation with altitude and longitude. Contour lines overlaid on colour-filled contours highlight temperature gradients in the mesosphere and lower thermosphere. Data from SABER observations. The colour bar shows temperature in Kelvin.*

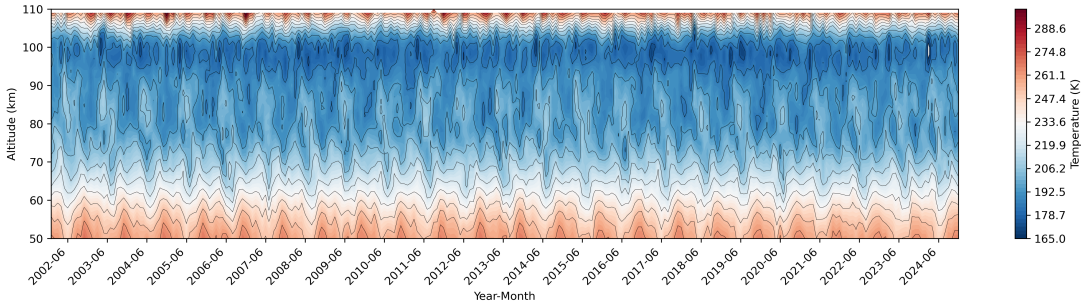

Figure 2: *Time–Altitude cross-section of monthly mean temperature (2002–2025). Colour-filled contours show temperature in Kelvin (K), with overlaid black contour lines for structure. X-axis represents time (June months from 2002 to 2024), and Y-axis shows altitude levels (50–109 km). This plot reveals temporal and vertical variability in the MLT region.*

transient dynamical influences.

Gravity wave breaking, which promotes upward momentum deposition and long-wave radiative cooling, is probably what keeps the cooling at the mesopause going. The temperature increase above 102 km can be the result of increased Joule dissipation or tidal heating, especially during times of intense geomagnetic activity. The stratified thermal structure observed over Sutherland is consistent with solstice-driven mesospheric circulation and may be enhanced by the site's high elevation (1.8 km), which favors gravity wave propagation into the MLT.

Figure 2 provides a time–altitude visualization that shows the consistent cold point while its downward shifts occur in isolated months, these are episodic rather than part of a persistent trend. A well-defined seasonal cycle is evident, with the cold point intensifying and shifting to lower altitudes during the winter (June–July) and warming in summer (December–January) reflect strong seasonal modulation. Increased upwelling and adiabatic cooling, which are traits of winter mesospheric dynamics in the Southern Hemisphere, are consistent with this behavior.

The cold point exhibits significant vertical and temporal change between 75 and 103 km, changing in depth, altitude, and intensity, underscoring the mesopause's dynamic character. In contrast, temperature structures near the lower and upper bounds of the profile are more thermally stable. However, several episodes break this seasonal regularity. For example, notable anomalies in 2007, 2013, and 2016, when the cold point weakens is followed by abrupt cooling in early 2018, may be linked to external drivers such as the Quasi-Biennial Oscillation (QBO), solar variability, or sudden stratospheric warmings.

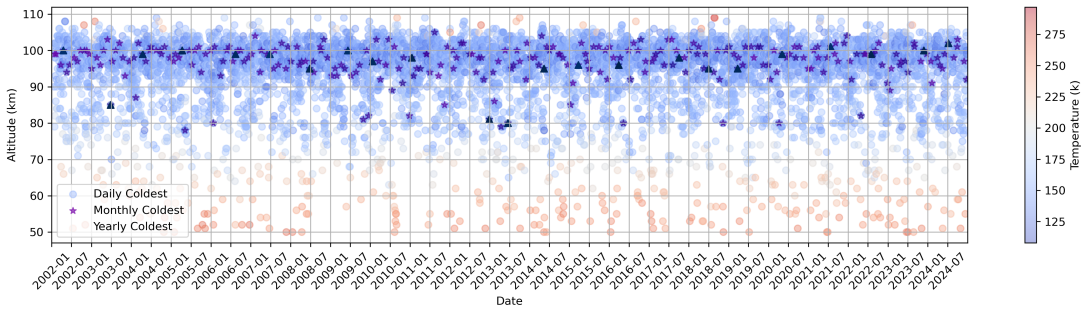

Figure 3: *Temporal distribution of coldest temperature points between 2002 and 2024. Daily cold points (circles), monthly averages (stars), and yearly minima (triangles). The vertical position represents the altitude bin where the minimum temperature was found, and the colour intensity corresponds to the coldest temperature recorded in each temporal group.*

A clear clustering is shown in Figure 3, where monthly minima (stars) are concentrated in the 95–105 km range, while the majority of cold points are located between 90 and 105 km. Periodic monthly cold spots below 90 km are probably caused by dynamic anomalies or temporary mesospheric inversions. In December 2004, July 2005, May–June 2009, June 2010, and a few months in 2012–2019, there are rapid decreases to 80 kilometers. These occurrences could be mesospheric disruptions or localized cold air invasions. The importance of seasonal extremes is further supported by the fact that yearly cold points (triangles) are more common during the warmer months of December through February. Anomalies below 85 km, including those in December 2012 and January 2003, point to anomalous cooling or exceptional mesopause descent. The absence of yearly minima during most of 2007 and 2013 may reflect data gaps, quality filtering, or unusually stable mesospheric conditions during those years.

Table 1: *Altitude-Resolved Temperature Trends from the Sequential Mann-Kendall (SMK) Test. The table summarizes trends across five altitude bands, based on the terminal UF values and their statistical significance.*

Altitude Range (km)	**Trend**	**UF End Value**	**Significance**
50-55	None	-1.42 to -1.87	Not significant
56-75	Cooling	-1.97 to -3.18	Strong
76-80	Cooling	-1.90 to -2.70	Moderate
81-99	None	-0.60 to -1.70	Not significant
100-109	Cooling	-1.60 to -1.88	Mild to Moderate

For lags 1–5, residual ACF is: [0.329 0.170 -0.029 0.094 -0.018]

With warm peaks regularly appearing in December or January and chilly minima in June or July, the graph in Figure 4 clearly illustrates an annual seasonal cycle that closely resembles the seasonal behavior depicted in Figures 1–3. Longer-term temperature undulations seem to be influenced by a secondary solar-related fluctuation in addition to this fundamental seasonal modulation.
A weak long-term cooling trend is apparent over the two-decade period, though it is partially obscured by short-term fluctuations and interannual variability. For instance, a warming event from July to November 2017 is abruptly followed by a sharp temperature drop in January 2018, suggesting transient forcings such as planetary wave intrusions or mesospheric disturbances. The MLT's susceptibility to transient dynamics is further highlighted by repeated irregular fluctuations from February to May, which may indicate increased short-term variability or transitional atmospheric states. Extreme temperatures typically cluster in the summer and winter months (January and July, respectively), which is consistent with other data.

To quantify the background tendency, a linear trend line was derived using Sen's slope estimator from the MK trend test. This trend is also used as a physics-informed constraint within the loss function of a Physics-Informed

LSTM (PI-LSTM) model, aiming to stabilize training on nonhomogeneous ordinary differential equations. The red line in Figure 4 shows the PI-LSTM forecast extending from January 2025 to December 2026. The model takes into account the learned trend and seasonal structure and extrapolates it forward, offering a physically consistent forecast rather than a purely data-driven one.

While the PI-LSTM model demonstrates some predictive capability, the overall performance should be interpreted cautiously. Several accuracy metrics (MAE, MSE, and RMSE) are relatively low, suggesting that the model reproduces the general magnitude of monthly temperatures. However, other metrics such as MAPE, MASE, and especially the negative NSE indicate that the model struggles with rapidly varying events, sharp temperature transitions, and the high intrinsic variability of the MLT region. The positive skill score and very high Forecast Skill Score (FSS) relative to a naïve persistence model indicate that the PI-LSTM captures the dominant seasonal structure and low-frequency variability better than a baseline, but its absolute accuracy remains modest. Thus, any claims of "strong performance" should be moderated: the physics-informed constraint improves physical interpretability and stability, but does not fully resolve the model's difficulty in predicting short-lived dynamical disruptions. These results highlight the value of the PI-LSTM framework more for qualitative trend-following and seasonal structure prediction than for precise numerical forecasting.

Despite its poor raw accuracy metrics, the model's strong seasonal monitoring and forecasting structure make it a great tool for qualitative insights and anomaly detection across multi-month periods. NSE and MASE, however, indicate that it may not adequately capture the seasonal structure or long-term trend because of the intrinsic variability in MLT dynamics and its limited feature set.

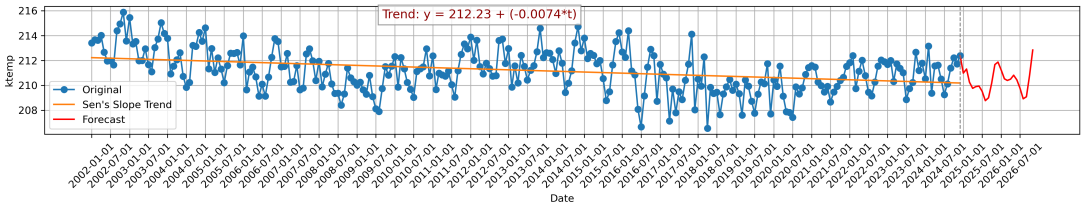

Figure 4: *Time series of observed temperature, overlaid with Sen's slope trend estimate and a 24-month forecast generated using a Physics-Informed Long Short-Term Memory (PI-LSTM) model. The vertical dashed line marks the transition from observed data to forecasted values. The linear trend equation, derived from Sen's slope, is displayed on the plot. This visualization highlights past temperature variability, estimated monotonic trend, and the model's prediction of near-future temperature evolution.*

Table 2: *Model performance metrics comparing the PI-LSTM model to a naïve baseline (last value persistence).*

Metric	**Value**	**Interpretation**
Mean Absolute Error	0.1176	Average monthly error is 0.12 units, indicating low deviation.
Mean Squared Error	0.0203	This low MSE supports the MAE result.
Root Mean Squared Error	0.1423	Similar to MAE but more sensitive to large errors.
Mean Absolute Percentage Error	29.44%	Model errors are 29% of actual values, typical for noisy data.
Symmetric MAPE	31.50%	Moderate performance, common for noisy geophysical data.
Mean Absolute Scaled Error	1.1192	Ideally, MASE should be <1.
Nash-Sutcliffe Efficiency	-0.1540	The model performs worse than the mean prediction.
Skill Score (vs. baseline)	0.4846	Model is 48.5% better than the naïve forecast.
Forecast Skill Score (FSS vs. naïve)	0.9797	Excellent skill compared to naïve forecast. Nearly perfect.
Quantile Loss (q=0.9)	0.3150	Model is reasonably good at predicting upper-bound temperatures
Pinball Loss (q=0.9)	0.09069	Measures accuracy of quantile forecast; lower is better.
Dynamic Time Warping (DTW)	0.5052	Thier is high similarity between predicted and actual sequences.

4 Conclusion

4.1 Summary

Using SABER satellite observations from 2002 to 2024, the present investigation examined seasonal patterns and long-term temperature trends in the MLT region above South Africa. Five altitude bands between 50 and 109 km were examined for statistically significant trends in mesospheric temperature using the SMK test. With peak magnitudes falling between 56 and 75 km, the results show a steady and noteworthy cooling trend in the 56–80 km range. While lower altitude (50–55 km and 81–99 km) do not display any statistically significant long-term trends, upper altitudes (100–109 km) show lesser but noticeable cooling.

Seasonal and interannual variations were prominent, especially during the months of July and January, which typically coincide with extrema in temperature anomalies. A notable anomaly occurred between July and November 2017, where temperatures surged sharply before dropping again in early 2018.

Using a Physics-Informed Long Short-Term Memory (PI-LSTM) model, the forecasting potential of deep learning techniques was investigated. Strong predictive performance was shown by the model, which was able to accurately capture seasonal cycles and the declining temperature trend over time. The stability and interpretability of the model were further enhanced by adding physical restrictions to the loss function.

4.2 Future Work

Several directions are proposed for future research. First, incorporating additional physical drivers such as solar flux indices, QBO, and geomagnetic activity may improve the model's ability to distinguish natural variability from climate trends. The Trend-Run model developed by Bencherif et al. [6] is considered to simulate MLT temperature trends as a function of major climate drivers. Thus, the Multiple Linear Regression (MLR) Model. Second, extending the spatial domain beyond South Africa to include other midlatitude and tropical sites could help generalize the model and reveal regional differences in mesospheric climate response. Taking into account supplementary studies such piecewise regression for multiple trend phases, wavelet transform for non-stationary cycles, and Empirical Mode Decomposition (EMD) in the event that nonlinear trends are suspected.

From a modeling standpoint, the depiction of temporal dependencies may be enhanced by additional PI-LSTM design optimization using methods like attention mechanisms or encoder-decoder schemes. Last but not least, merging observational data with ground-based or reanalysis datasets may enhance vertical resolution and lower observational uncertainty, opening the door for integrated frameworks for climate forecasting in the upper atmosphere.

References

[1] T.-Y. Huang and M. Vanyo, "Trends in the Airglow Temperatures in the MLT Region—Part 2: SABER Observations and Comparisons to Model Simulations," *Atmosphere*, vol. 12, p. 167, 2021.

[2] T. T. Ojo, Z. T. Katamzi-Joseph, K. T. Chu, M. A. Grawe, and J. J. Makela, "A climatology of the nighttime thermospheric winds over Sutherland, South Africa," *Advances in Space Research*, vol. 69, no. 1, pp. 209–219, 2022.

[3] X. R. Zhao, Z. Sheng, H. Q. Shi, L. B. Weng, and Q. X. Liao, "Long-term trends and solar responses of the mesopause temperatures observed by SABER during the 2002–2019 period," *Journal of Geophysical Research: Atmospheres*, vol. 125, no. 11, 2020.

[4] T. Yuan, P. D. Pautet, and M. J. Taylor, "Midlatitude mesosphere and lower thermosphere variations during the extreme gannon geomagnetic storm in May 2024," *Frontiers in Astronomy and Space Sciences*, vol. 11, p. 1516222, 2025.

[5] Y. Yao, X. Zhong, Y. Zheng, and Z. Wang, "A physics-incorporated deep learning framework for parameterization of atmospheric radiative transfer," *Journal of Advances in Modeling Earth Systems*, vol. 15, no. 5, p. e2022MS003445, 2023.

[6] H. Bencherif, V. Sivakumar, and R. Jimmy, "TREND-RUN model for performing the trend calculation on SAWS (South Africa Weather Service) atmospheric data," in *28th Annual Conference of South African Society of Atmospheric Sciences*, Sep. 2012, pp. 90–91.

This page intentionally left blank.

DIVISION

E

PHYSICS FOR DEVELOPMENT, EDUCATION, AND OUTREACH

Integrating modern technology into a selection of first-year physics experiments

Hendrik J. van Heerden[1], J.J. Terblans[1], R.A. Harris[1] and S. Cronje[1]

[1]Department of Physics, University of the Free State, Bloemfontein, South Africa

E-mail: vanheerdenhj@ufs.ac.za

Abstract. Hands-on laboratory work is essential in first-year physics education, yet traditional setups can lack precision, reliability, and long-term sustainability. In this study, we present upgrades to key first-year experiments (air-track, simple pendulum, and optics-based experiments), aimed at improving accuracy, repeatability, and operational longevity while retaining relevance to foundational teaching. For the air-track and pendulum experiments, we developed a custom Windows-based C# software interfaced with Arduino micro-controllers to streamline control and data acquisition. This upgrade improves measurement capabilities and enables experimental progression beyond basic measurements, while still allowing space for traditional "hands-on" approaches when desired. In optics, we replaced filament-based light sources with LED's, providing more stable and energy-efficient illumination. These enhancements offer flexible pathways for laboratory instruction: traditional methods can be maintained for conceptual engagement, while digital systems provide repeatability and opportunities for deeper exploration or advanced investigations. Importantly, the upgrades were implemented using cost-effective, in-house technical expertise, ensuring scalability and long-term sustainability.

1 Introduction

Laboratory work forms a cornerstone of first-year physics education, offering students their first opportunity to engage directly with physical phenomena and experimental methodology. Foundational experiments, such as those involving linear motion, pendulums, and basic optics, not only reinforce theoretical concepts but also shape students' attitudes toward physics as a discipline. However, many traditional laboratory setups remain unchanged for decades, relying on analog components and manual procedures that can limit accuracy, engagement, and relevance [1].

To enhance both the educational value, capabilities and longevity of these experiments, there is a need to continually modernize laboratory infrastructure. Integrating digital technologies into classical experiments helps bridge the gap between foundational teaching and the tools students could encounter in contemporary research or industry [2]. Modernized systems offer students more accurate and immediate feedback, enabling them to focus on underlying physical principles rather than the limitations of manual measurements. Upgrades such as digital control, automated data acquisition, and LED-based illumination not only improve measurement precision and reliability but also simplify maintenance and reduce long-term operational costs. Many older components—such as filament lamps, analog meters, and LPT-based PC interfaces—are increasingly obsolete and difficult to replace. In contrast, modern micro-controllers and PC interfaces offer long-term compatibility with current operating systems (e.g., Windows 10/11) and greater adaptability across a range of experiments.

Beyond technological improvements, such upgrades also enhance student experience. Exposure to modern tools builds confidence in handling scientific instrumentation and cultivates technical skills transferable to future

academic or professional settings [3]. Moreover, developing many of these upgrades in-house allowed us to tailor solutions to our instructional needs while avoiding the constraints and costs of commercial educational lab equipment [4].

In this paper, we present a set of practical upgrades implemented in several cornerstone first-year experiments: the air-track, the simple pendulum, basic optics (light-box and optical bench) and wavelength of light. We detail the design, implementation, and educational motivations behind each upgrade, and discuss the impact on teaching, learning, and long-term laboratory management.

2 Optical Experiments

2.1 Optics with a light box and optical bench

We present two experiments where we exchanged the light sources from incandescent filament lamps to LED sources. The first consideration is to make sure that the replaced light source fulfill the basic requirements in terms of spectrum and intensity required by the experiment. To this aim the spectra and intensities were measured for both the original incandescent as well as the new LED light sources. All optical spectra were measured and confirmed using the PASCO Spectrometry App (Version 2.5.1) and a Bluetooth connected PASCO Spectrometer PS-2600 in "Analyze Light" mode. As can be seen in Figure 1, the new LED source offered both a higher intensity and more balanced white light.

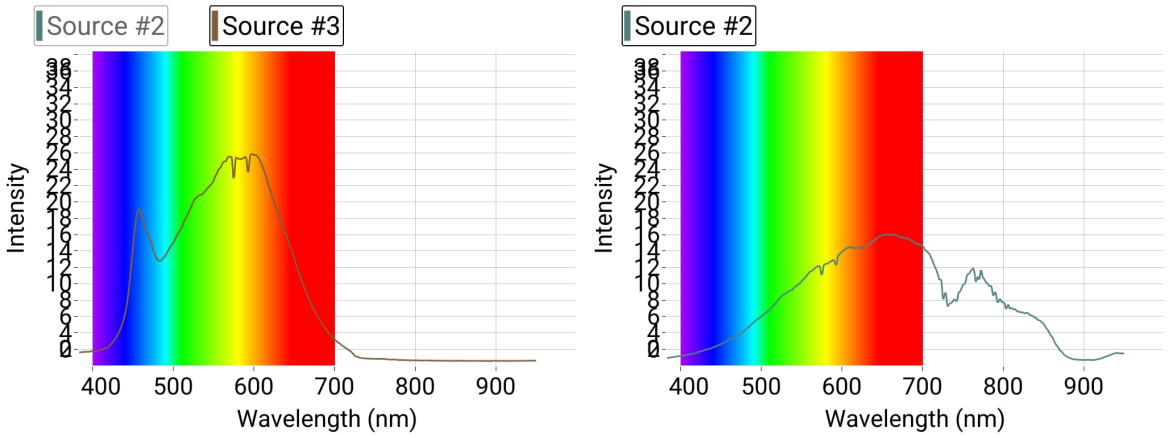

Figure 1: Spectral comparison between light sources: (*left*) new LED source (Source #3); (*right*) original incandescent light source used during optics experiments (Source #2).

The in-house design and build of the new LED sources also allowed us the opportunity to design an effective light housing to screen and direct the light as needed (Refer to Figure 2). This reduced experimental and laboratory environmental disturbances due to bright light sources visually impairing students relative to the experiments and their surroundings.

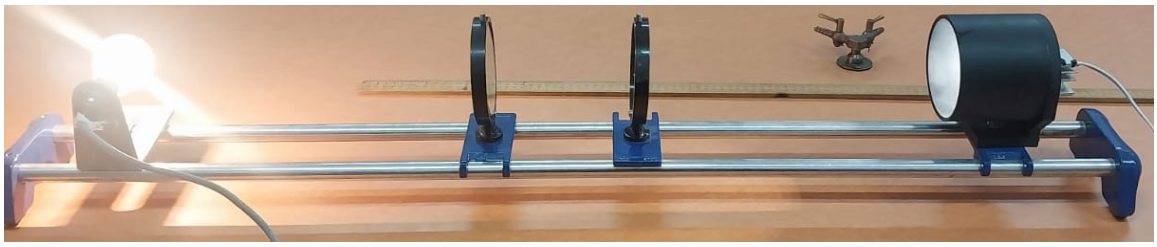

Figure 2: Visual comparison between older incandescent light technology and the new LED based light source as implemented on the optical bench experiment.

The greater intensity improves visibility of light ray's for tracing as well as optical effects such as magnification and reflection. The more balanced white light spectrum also results in an improved visual rainbow produced during diffraction through a prism setup (See Figure 3).

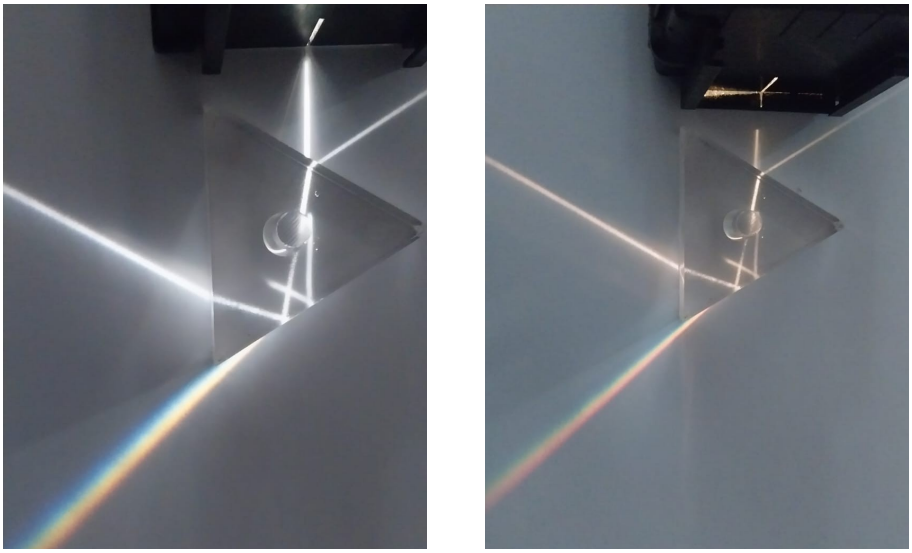

Figure 3: Visual comparison between light source color, luminosity and prism diffracted rainbow: (*left*) the new LED source; (*right*) original incandescent light source used in the optics with a light-box experiment.

2.2 Wavelength of light

The wavelength of light experiment was for many years done using an incandescent light-bulb with a continuous spectrum and an in-house made double slit using an aquadag coated glass plate onto which double-slits were made using a pair of razor blades. The basic setup resulted in interference patterns which were inconsistent between experiments and difficult to measure. A simpler and more repeatable approach was sought, in conjunction to a narrower spectral peak and better light source control per wavelength region. The experimental setup with the new narrow band LED's (Red, Green, Blue) and using a diffraction grating (refer to Figure 4), allows for the measurement of the required values as needed by the equation and geometry in Figure 5. This setup allows for determination of either the wavelength of the diffracted light λ, or conversely given the wavelength, the diffraction grating constant d.

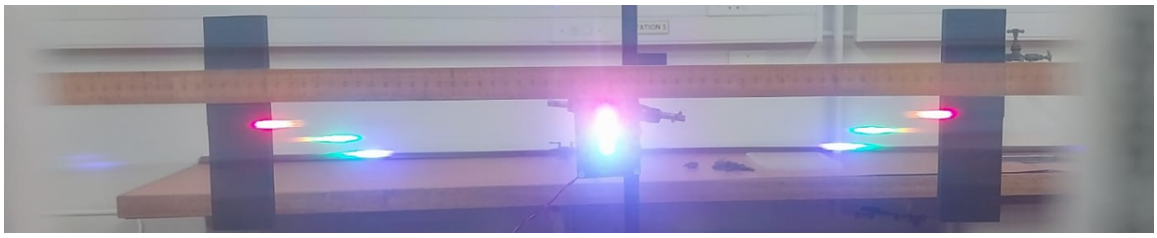

Figure 4: The diffraction images of the three LED's as seen through the diffraction grating, i.e. the student's perspective.

As an exercise to prove the experimental concept and consistency, the following measurements and analyses were conducted. Refer to Table 1 for all measurements and results. Using the determined maximum intensity wavelength peak for the red LED ($\lambda = 651$ nm) with the PASCO Spectrometer, the diffraction grating constant d was determined experimentally. This experimentally determined diffraction grating constant d_{exp} was then used to experimentally determine the wavelength values for green ($\lambda = 522$ nm) and blue ($\lambda = 461$ nm) light within an experimentally acceptable error range of $2 - 3$ % from expected values based on the peak positions for the green and blue LEDs. Wavelength uncertainties were estimated by propagating the errors in the calibrated grating constant d_{exp} and in the measured diffraction positions, ensuring that the experimentally determined values reflect setup-specific factors rather than relying solely on the manufacturer-specified grating constant d_{expected}.

$$\lambda = \frac{d}{m} \sin\left(\tan^{-1}\frac{y}{D}\right)$$

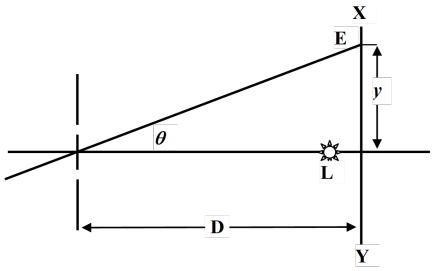

Figure 5: Equation used in the wavelength of light experiment (*left*), alongside the geometry of the setup (*right*).

Table 1: Calculation of d and λ using experimental data

Section	y_{avg} (mm)	D (mm)	$\sin(\tan^{-1}(y/D))$	d or λ (m)	Expected / Error
Red (651 nm)	254.5	750	0.32134	d_{exp}: 2.03×10^{-6} d_{expected}: 1.667×10^{-6} Error:	lines/mm: 493.61 lines/mm: 600 18%
Green (λ)	207	750	0.26605	λ: 5.39×10^{-7} Error:	Expected: 5.22×10^{-7} 3%
Blue (λ)	178.5	750	0.23153	λ: 4.69×10^{-7} Error:	Expected: 4.61×10^{-7} 2%

3 Mechanical Experiments

3.1 Universal interface and control software

A modern day trend in laboratory products is to makes use of an universal interface between experimental equipment and the computer. This approach simplifies experimental setups as it reduces the amount of unique equipment required to run multiple experiments. To this end a new in-house universal interface between the experimental equipment and the control computer was developed. This interface utilizes an Arduino to manage and control the different components based on connected equipment and user input, where-after it provides feedback to the user. The new interface makes use of an USB connection to the computer which acts like a virtual COM port. The older interface hardware that was unique to each specific experiment utilized either LPT or RS232 COM ports. Refer to Figure 6 for a visual comparison between the older and the new interface controller design. The interface and control software is structured as follows: The Arduino controls (set / get) all the physically connected devices, e.g. photo-gates, relays, electro-magnets as well as internal timers for timing measurements. The control software for the Arduino is a C# windows forms application that links the user to the Arduino via various input and control objects that can send commands and receive feedback and display that feedback for use in plotting and calculating values.

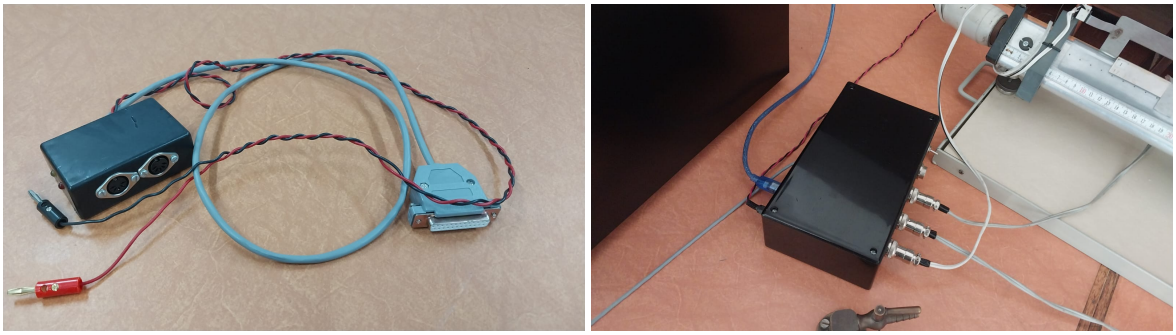

Figure 6: (*left*) Example of what the original air-track controller looks like. (*right*) New universal controller that interfaces with either the air-track equipment or the simple pendulum equipment.

The user software to the interface controller (refer to Figure 7) has a variety of functions and capabilities, including the ability to run diagnostics on specific components, i.e. testing photo gates, switching relays and electromagnets. It also provides the ability for configuring the specific experiment that is to be done, i.e. air-track or pendulum. Once configured the experimental sequence can be started, where-after measured values can be retrieved and used to complete a table and plot the values. The data retrieval process is interactive, in that the students needs to approve the values before they are read into the table. This allows the student the opportunity to identify and learn about data quality. This tabulated data can then be utilized in further educational activities such as trend identification, comparative analysis and etc.

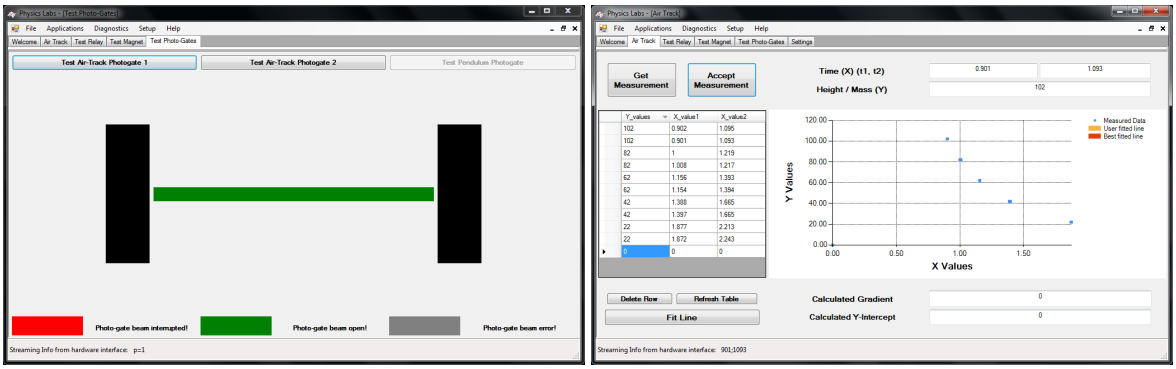

Figure 7: (*left*) Uni-controller interface software with the tab for the photo-gate diagnostics open. (*right*) Uni-controller interface software with the tab for the air-track experiment open with some measurements displayed.

3.2 The simple pendulum and the air track

To test the consistency and accuracy of the new Arduino-driven experimental control and measurement processes, a series of experimental runs were completed for the air-track and simple pendulum experiments. The experiments were set up and completed similarly to how undergraduate students will perform them. For the air-track, the following experimental setups were run: determining the relationship between the acceleration of a body and the force causing the acceleration (Force versus Acceleration), and determining the relationship between the mass and acceleration when a constant force is acting (Acceleration versus inverse of the mass). As the whole experiment revolves around Newton's Law, $\sum F = ma$, the expected outcomes should be a clear linear relationship in each case. The acceleration values are calculated from times measured between set displacements, with the timing triggered when the glider is released and measured when it breaks the photo-gates. Because there are two photo-gates available along the travel path, two time values can be measured per setup. To ensure stability the blower is started and allowed to stabilize for 5 seconds before each run of the glider.

For the simple pendulum, the experimental setups focused on the relationships between the length of the pendulum, the amplitude (starting angle), and the period of oscillation, i.e. $T = kl^z$. The first setup is used to calculate the gravitational constant g from the relationship $\log(T) = \log(k) + z\log(l)$, where T is the measured period and l is the measured length. From $k = \frac{2\pi}{\sqrt{g}}$, the value for g can be determined from a linear regression fit to the experimental data. The second setup is used to test the simple pendulum's small-angle approximation and observe deviations at larger angles for the relationship $T = kl^z$. The measured period values are obtained by counting photo-gate beam breaks and timing the intervals between them. As with the air-track, two measurements are made per setup, i.e., the period is measured twice. To ensure stability of the pendulum and minimize start/release effects 10 beam breaks are counted before the periods are measured.

For consistency checks we present in Figure 8 the results pertaining to the force vs. acceleration data for the air-track (left) and the period vs. length data for the simple pendulum (right). To check consistency and accuracy, i.e. repeatability of the experiment, the expectation is that for no change between measured setups the variation between measured values should be within acceptable experimental errors. Therefore, if we set the air-track to a specific configuration in terms of mass and force, then the measured acceleration values calculated from times measured to break photo-gate beams for $\Delta\ x = constant$ and $starting\ velocity = 0\ m.s^{-1}$, should have a very small variation. A simple test is to calculate the experimental mean of the standard deviations between measured values for similar setups, e.g. measured travel times for similar heights. The determined mean for the distribution of standard deviations for measured times for the force vs acceleration setup is $\sigma = 0.004243\ seconds$. Similarly

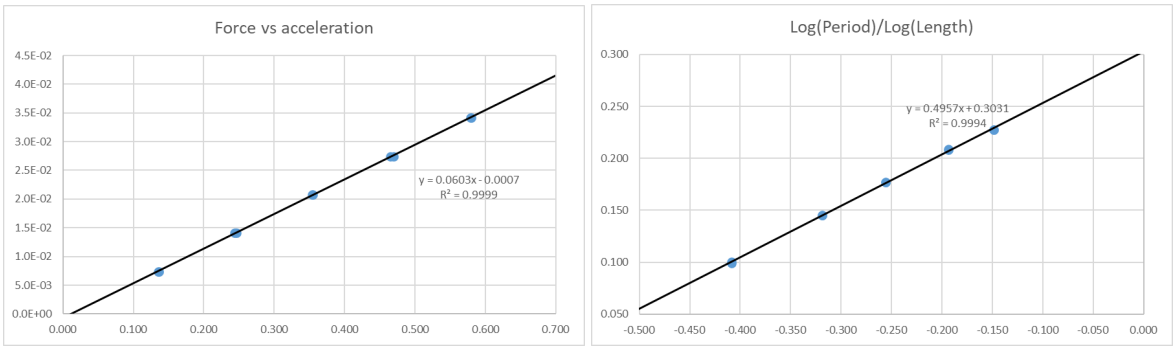

Figure 8: (*left*) Graph of the air-track experimental results based on experimental measurements of force vs acceleration. (*right*) Graph of simple pendulum experiment results based on experimental measurements of variation of the period versus the length.

for the simple pendulum the consistency can be checked by the deviation of the measured periods per configuration. This was measured at $\sigma = 0.000636\ seconds$.

While the new Arduino-driven interface demonstrably improves accuracy and repeatability, it is also important to reflect on the student learning experience. Manual methods, such as using a stopwatch to time pendulum oscillations, expose students to natural variability in their measurements and provide valuable practice in dealing with experimental uncertainty. By contrast, the automated interface reduces this variability to a negligible level, which is useful for advanced explorations (e.g., testing small-angle approximations), but may lessen the student's engagement with the practical challenges of real-world measurement. To balance these perspectives, the upgraded system can be implemented in a flexible manner: students may first perform measurements manually to confront the role of uncertainty via the use of a stopwatch for example, and subsequently repeat the experiment with the digital system to appreciate the advantages and limitations of modern instrumentation. This dual approach preserves the conceptual learning benefits of traditional methods, while still leveraging the precision and scalability offered by the new technology.

4 Conclusion

The modernization of first-year physics experiments through the integration of digital technologies has yielded measurable improvements in precision, repeatability, and ease of use, while simultaneously extending the longevity of laboratory infrastructure. Replacing outdated analog components with Arduino-driven control systems and adopting LED-based light sources has reduced timing variation, better-defined optical spectra and improved visibility of light-based effects, and simplified maintenance across multiple experiments.

At the same time, it is important to recognize that automation should complement, rather than replace, traditional hands-on learning. Manual methods such as stopwatch timing or direct measurement still hold significant pedagogical value, particularly for introducing students to the concepts of experimental error and uncertainty. The upgraded systems therefore provide a dual pathway: students can begin with foundational manual measurements to engage directly with experimental variability, and subsequently use modernized tools to explore advanced or extended investigations with improved accuracy.

A further outcome of this work is the demonstration of the critical role of in-house technical expertise in developing sustainable and affordable upgrades. By tailoring solutions to local teaching needs and available resources, institutions can modernize practical instruction at scale without dependence on costly proprietary systems.

Together, these developments illustrate how targeted, cost-effective technological enhancements can revitalize classical physics experiments—balancing foundational hands-on skills with exposure to contemporary instrumentation, and providing a progressive learning trajectory for undergraduate physics students.

References

[1] C. Wieman and N. G. Holmes, "Measuring the impact of an instructional laboratory on the learning of introductory physics," *American Journal of Physics*, vol. 83, no. 11, pp. 972–978, 2015.

[2] S. Z. Lahme, P. Klein, A. Lehtinen, A. Müller, P. Pirinen, L. Rončević, and A. Sušac, "Physics lab courses under digital transformation: A trinational survey among university lab instructors about the role of new digital technologies and learning objectives," *Phys. Rev. Phys. Educ. Res.*, vol. 19, p. 020159, Nov 2023.

[3] I. P. Sari and A. Suhandi, "Enhancing students' critical thinking skills in physics: Exploring problem-based learning and mobile technology integration in rotational dynamics education," *Journal of Physics: Conference Series*, vol. 2831, no. 1, p. 012002, 2025.

[4] J. M. Pearce, *Open-Source Lab: How to Build Your Own Hardware and Reduce Research Costs*. Elsevier, 2013.

This page intentionally left blank.

Transforming Physical Sciences teaching through targeted professional development

Mark Herbert and Bako Nyikun Audu

Department of Physics and Astronomy, University of the Western Cape, Cape Town, South Africa

E-mail: msherbert@uwc.ac.za

Abstract. Physical Sciences teachers in disadvantaged communities and under-resourced South African schools often face systemic barriers, including limited access to subject-specific professional development, inadequate teaching resources, and insufficient pedagogical support. These constraints contribute to persistent teacher-centred practices that limit learners' conceptual and procedural understanding. This paper reports on a targeted professional development initiative led by the Department of Physics and Astronomy at the University of the Western Cape, designed to strengthen both content knowledge and pedagogical practice among Physical Sciences teachers. The professional development employed a combination of short courses, interactive workshops, collaborative lesson planning, and the promotion of learner-centred strategies such as Modeling Instruction. This study assesses the impact of a short mechanics course on teachers' content knowledge, teaching practices, and confidence in delivering topics in mechanics within the Further Education and Training (FET) Physical Sciences curriculum. Data collected through pre- and post-tests and teachers' perception survey demonstrate significant improvements in teachers' content knowledge, confidence, and classroom practice. The findings highlight the transformative potential of practice-based and contextually responsive professional development in advancing the quality of Physical Sciences education in South African schools.

1 Introduction

Access to quality education is a fundamental right, yet many schools in disadvantaged communities, particularly those that are under-resourced, still struggle to deliver high-quality Science, Technology, Engineering, and Mathematics (STEM) education. These challenges stem from limited infrastructure, scarce resources, and a shortage of qualified and confident teachers, especially in the physical sciences. Research shows that traditional, teacher-centred pedagogies still dominate many science classrooms [1]. In this model, knowledge is transmitted by the teacher while learners passively listen, with an emphasis on rote learning and examination preparation rather than conceptual understanding, problem-solving, and scientific inquiry. This often leads to low engagement, poor understanding of how scientific knowledge is constructed, and negative attitudes toward STEM, particularly physical sciences, resulting in poor academic performance.

The problem is compounded by limited content knowledge and pedagogical confidence among many physical sciences teachers [2]. Without adequate training and support, teachers may avoid challenging topics, lack enthusiasm, and struggle to create engaging learning experiences for learners. These gaps directly affect learner retention outcomes, throughput and weaken the country's capacity to prepare youth for participation in the Fourth Industrial Revolution. To address these issues, the University of the Western Cape (UWC) has committed itself

to transformative education through its Institutional Operational Plan (IOP), which recognises the university's role in uplifting communities through human capital development. Within this framework, the UWC-STEAME (Science, Technology, Engineering, Arts, Mathematics, and Entrepreneurship) programme was developed as a multi-faculty initiative to support learners and teachers in mathematics and physical sciences.

Central to this initiative is the Department of Physics and Astronomy's Teacher Training and Development Programme, which aims to transform the teaching of physical sciences by strengthening teachers' content knowledge and pedagogical skills. Through structured short courses, workshops, mentoring, and classroom-based support, teachers are empowered to teach with greater confidence, creativity, and competence. The programme ultimately seeks to improve teaching quality, boost learner interest and success in sciences, and prepare learners for STEM careers. This study assesses the impact of a short mechanics course on teachers' content knowledge, teaching practices, and confidence in delivering mechanics within the Further Education and Training (FET) Physical Sciences curriculum.

2 Background and Literature Review

South Africa continues to face significant challenges in the teaching and learning of mathematics and physical sciences, particularly in under-resourced schools. These issues are rooted in historical inequalities, systemic infrastructure deficits, and a shortage of well-trained teachers. If left unaddressed, they will hinder the country's ability to produce STEM-capable graduates for the global economy and the Fourth Industrial Revolution [3]. The quality of teaching is a major determinant of learner achievement in physical sciences [4]. Teacher-centred teaching characterised by rote learning and minimal learner engagement remains widespread [1, 5]. The implication of this is that learners often become passive recipients of knowledge, with limited opportunities to develop critical thinking and problem-solving skills. A key factor in this underperformance is the inadequate content knowledge and pedagogical competence of many teachers [6]. Studies reveal that some teachers lack confidence in core physics topics, sometimes avoiding them entirely [2].

Assessment results reflect these challenges: the 2013 World Economic Forum 'Education rating' ranked South Africa second last globally for mathematics and science education, while Trends in International Mathematics and Science Study (TIMSS) data from 1995 to 2003 categorised South African learners as scientifically illiterate [7]. Also, the 2004 Department of Education survey found that over half of Intermediate Phase learners failed to meet expected outcomes in Natural Sciences, with the lowest average score in Earth and Beyond (31%) [8]. Costello et al [9] emphasised that scientifically literate teachers are essential for achieving meaningful learner scientific literacy [10]. There is broad consensus that sustained, subject-specific professional development is essential to address these gaps. Scholars such as Mlachila et al and "Mitchell ea al." [11, 12] identified poor teacher preparation, contextual inequality, and a lack of ongoing support structures—such as professional learning communities—as key contributors to underachievement in science. Effective professional development builds teacher capacity, confidence, and pedagogical skill, particularly when it is contextually relevant [13, 6].

The UWC-STEAME programme was launched to provide holistic support to teachers and learners in mathematics and physical sciences. Within this initiative, the Department of Physics and Astronomy's Teacher Training and Development Programme focuses on enhancing teachers' content knowledge and pedagogy using research-based strategies such as Modeling Instruction (MI). The Modeling Instruction approach is an inquiry-based approach widely used in the United States of America. Modeling Instruction is a pedagogical approach that emphasizes learning through the development and application of scientific models. Grounded in Modeling Theory (by Hestenes), it shifts the focus from rote procedures to the construction of conceptual understanding. The approach involves organizing curriculum around core scientific models, treating them as coherent structures of knowledge rather than isolated facts. Learners actively engage in scientific practices by collaboratively building, testing, and refining models to explain and predict physical phenomena [17]. The Modeling Instruction approach promotes active learning and scientific reasoning among learners by strengthening teacher pedagogical expertise and transforming classroom practice. In the context of this paper, the teachers' professional development programme aims to help teachers to improve learner performance and interest in mathematics and physical sciences which aligns with the Department of Basic Education's target of 450,000 science-based degree candidates by 2030 and the goals of the National Strategy for Mathematics, Science, and Technology published in 2018 [18].

3 Methodology

To address the research questions below, this study employed a quantitative approach to collect data to assess the impact of a short mechanics course on teachers' content knowledge, teaching practices, and confidence. The study involved ten Physical Sciences teachers from under-resourced secondary schools in disadvantaged communities in the Cape Flats who participated in the Department of Physics and Astronomy Teacher Development Programme. The mechanics course was delivered over a single school term (approximately three months), with six hours of contact time per week. The programme introduced Modeling Instruction, which was collaboratively adapted to align with CAPS requirements. Teachers were encouraged to engage in classroom discussions, think critically, and apply physics concepts using multiple representations to deepen conceptual understanding. During the workshops, the participants played the role of learners in engaging with the MI activities of guided inquiry and co-operative learning, and the facilitator played the role of the teacher. Also, when dealing with problem-solving activities, they were guided to select appropriate tools, such as pictorial representations, vector diagrams, free-body diagrams, and mathematical equations, tailored to specific problems like Newton's laws of motion. In the course of the workshop, teachers were actively supported in designing learner-centred lesson plans incorporating Modeling Instruction strategies, which include multiple representations and evidence-based problem-solving approaches from current Physics Education research.

Research Questions:

1) How did the mechanics course affect teachers' understanding of key mechanics concepts (content knowledge)?
2) In what ways did the course influence their teaching practices and confidence in teaching mechanics?

Instruments: Pre- and Post-Intervention Diagnostic Tests. The diagnostic tests, adapted from past matric question papers and covering key concepts in mechanics, were administered at the start and near the end of the course to assess changes in teachers' content knowledge [19]. Additionally, a final competency test was conducted on the last day to evaluate teachers' overall understanding and application of mechanics concepts after the intervention. A Teacher Perception Survey, comprising closed-ended Likert-scale questions was administered during the final week of the course. The survey explored teachers' perceptions of the course, their confidence in teaching mechanics, and the perceived influence of the programme on their classroom practices.

Data Analysis: Descriptive statistics (mean scores, percentage improvements, and standard deviations) were used to measure changes in content knowledge from the pre- to post-test and final test. Comparative analyses, such as paired sample t-tests, were employed (if sample size permits) to determine the statistical significance of changes in performance. Survey responses were analysed by calculating frequencies, percentages, and mean response values for each item to identify general trends in teacher perceptions and confidence levels. Pre-test solutions were not discussed with participants; however, targeted feedback was provided during the course to address common misconceptions and errors identified in pre-test responses to similar questions.

4 Results

4.1 Pre-and Post-test results

To evaluate teachers' mastery of the Mechanics course content, a diagnostic test was administered at the start (pre-test) and end (post-test) of the programme. The test covered key mechanics topics, including vectors in two dimensions, Newton's laws of motion, momentum, and energy. It comprised five multiple-choice questions and five structured (long) questions, each assessing conceptual understanding and application of these topics. Table 1 below compares the average marks scored by teachers in the pre-test and post-test across four topics: Vectors in Two Dimensions, Newton's Laws, Momentum, and Energy.

Topics	Average mark scored in Pre-Test	Average mark scored in Post-Test
Vectors in 2-dimensions	71%	87%
Newton's laws	44%	79%
Momentum	49%	94%
Energy	58%	92%

Table 1: Comparison of the average marks scored by teachers in pre-test and post-test across four topics

Identity	Pre-test	Post -test
Teacher 1	80%	83%
Teacher 3	78%	97%
Teacher 4	73%	97%
Teacher 5	70%	80%
Teacher 6	70%	78%
Teacher 7	33%	85%
Teacher 8	33%	78%
Teacher 9	33%	61%
Teacher 10	31%	83%

Table 2: Comparison of the average marks scored by teachers in pre-test and post-test

Overall, there is a significant improvement in average marks across all topics, with Momentum showing the largest gain (45%) and Vectors in 2-dimensions the smallest (16%). This suggests effective learning or teaching interventions between the tests.

Overall, all teachers showed improvement in performance from pre-test to post-test. The largest gains were observed with Teacher 8 and Teacher 9 (52% each), starting from the lowest pre-test scores (31% and 33%). Teacher 10 had the smallest improvement (3%), starting from a high pre-test score of 80%. Teachers with lower initial scores (e.g., Teacher 3, 6, 8, 9) generally showed more significant percentage increases, suggesting effective teaching interventions.

4.2 Perception survey results

Teacher Perception	*Responses*
1. On a scale of 1–5, how confident are you in your content knowledge after they mechanics course	*90% of teachers felt very confident*
2. To what extent do you feel that mechanics course deepened your understanding of the subject matter you teach?	*100% of the teachers felt that the course has deepened their understanding.*
3. How would you rate your ability to explain complex concepts to students after the mechanics' course?	*90% of teachers felt very confident*
4. After the mechanics course, how often do you incorporate learner-centred activities?	*80% of the teachers said they do now include always learner-centred activities in their teaching*
5. On a scale of 1–5, how effective do you find MI as a teaching approach for engaging learners in learning?	*90% said that it is very effective to engage learners in their learning.*

Table 3: Teachers' perception survey responses

Table 3 above presents the results from the perception survey suggest that the course had impact on participating teachers. Firstly, it enhanced teacher confidence (see Q1 and Q3) and deepened their conceptual understanding (see Q2), thereby fulfilling its objectives of strengthening both content mastery and pedagogical competence. These findings are corroborated by teachers' improved performance in the post-test assessment. Secondly, at the end of the course, 80% of teachers reported consistently employed learner-centred teaching strategies, indicating a notable shift toward more interactive and learner-focused practices. However, some teachers noted that

constraints such as limited resources and teaching time usually hinder the full implementation of Modeling Instruction in their classrooms. Thirdly, an overwhelming majority (90%) rated Modeling Instruction as highly effective in promoting learner engagement, highlighting the value of MI-based professional development for fostering active participation, conceptual understanding and the practices of how scientists think, talk and do science. Overall, the survey indicates that the course contributed meaningfully to the enhancement of teachers' confidence, pedagogical approaches, and commitment to more engaging modes of learner-centred teaching.

4.2 Limitations and Future Research

This study has notable limitations such as the small sample size restricts the generalizability of the findings. Although teachers reported increased confidence and improved conceptual understanding, only 80% consistently applied learner-centred strategies in their classrooms. This suggests persistent implementation challenges, potentially due to classroom constraints e.g., time limitations, large class sizes, limited resources, or the need for additional support. Despite these limitations, the study highlights promising directions for future research such as expanding the study to include a larger and more diverse teacher cohort, which could yield deeper insights into the long-term impact of professional development on teaching practices. Such research would be particularly valuable for understanding how targeted interventions can transform Physical Sciences education in South African classrooms.

4.3 Ethical Considerations

Ethical clearance was granted by the University of the Western Cape's Research Ethics Committee. All participating teachers provided informed consent. Anonymity and confidentiality were maintained throughout the data collection and reporting process

5 Conclusion

The study found that the cohort of teachers showed increased confidence, a deeper conceptual understanding, and an improved ability to explain complex concepts. This finding is in agreement with those of Ventista and Brown [15]. Additionally, most teachers reported consistently using learner-centred strategies, with a significant majority (90%) finding Modeling Instruction (MI) highly effective in engaging learners in the classroom [16]. These outcomes reflect both enhanced subject mastery and meaningful shifts toward modern pedagogical practices, aligning with research on effective professional development [15]. In summary, the course effectively strengthened Physical Sciences teachers' content and pedagogical knowledge. The results highlight the potential of targeted, practice-based professional development, such as Modeling Instruction to transform teaching and learning in South African classrooms.

References

[1] M. Mourshed, C. Chijioke & M. Barber. "How the world's most improved school systems keep getting better". McKinsey Report. McKinsey and Company. 2010. Canada https://www.afn.ca/uploads/files/education2/how_the_world_most_improved_school_systems_mckinsey,_2010.pdf

[2] L. Chisholm. "The challenge of South African schooling: dimensions, targets and initiatives. The Transformation Audit Review: from Inequality to inclusive Growth." 2012. www.academia.edu/4421143/The_Challenge_of_South_African_Schooling_Dimensions_Targets_and_Initiatives.

[3] SAIP. "The strategic plan on the enhancement of Physics training in South Africa". 2016. South Africa Institute of Physics. Pretoria

[4] NPC (2011). Improving Education Quality in South Africa. Report for the National Planning Commission. Education Reform following from a broader Research Report. Pretoria, South Africa.

[5] A.T. Barlow, M.T. Frick, H.L. Barker, and A.J. Phelps. "Modeling Instruction: The Impact of Professional Development on Instructional Practices" 2014. Science Educator. Vol. 23, No.1

[6] C. Kearney. "Efforts to Increase Students' Interest in Pursuing Mathematics, Science and Technology Studies and Careers". National Measures taken by 30 Countries – 2015 Report, European Schoolnet. 2016. Brussels.

[7] NPC TIMSS (2015). Highlights of Mathematics and Science Achievement of Grade 9 South African Learners authored by Vijay Reddy, Mariette Visser, Lolita Winnaar, Fabian Arends, Andrea Juan and Cas Prinsloo. Mail & Guardian December 2 to 8 2016.

[8] A.T. Barlow, M.T. Frick, H.L. Barker, and A.J. Phelps. "Modeling Instruction: The Impact of Professional Development on Instructional Practices" 2014. Science Educator. Vol. 23, No.1

[9] N. Pandor, News24. 2006. "Pandor addressed concerns about school dropout" rateshttps://www.google.com/search?q=+Pandor%2C+2006&sca_esv=827ca067cae54b45&sxsrf=AE3TifMTdp7fyG4lK4qBVGUyPx7RwOCJAg%3A1755081756205&source

[10] C. Costin. "Meaningful Education in Times of Uncertainty Collection of Essays: What is the Role of Teachers in Preparing Future Generations? Skills for a Changing World". 2017. The Brookings Institution. www.brookings.edu/research/meaningful-education-in-times-of-uncertainty.

[11] M. Mlachila and T. Moeletsi. "Struggling to Make the Grade: A Review of the Causes and Consequences of the Weak Outcomes of South Africa's Education System". IMF Working Paper. African Department. 2019. International Monetary Fund (IMF).

[12] R. Mitchell, R.A. Ayinselya, A.M Barrett, A.A. Cortez Ochoa, O. David, D. Imaniriho, Z.A. Nwako, N.W. Reda, and M. Singh. Teacher professional development in Africa: A critical synthesis of research evidence. CIRE, Bristol. 2024. https://doi.org/10.5281/zenodo.10944685

[13] D. Hestenes, C. Megowan-Romanowicz, S.E. Osborn Popp, J. Jackson, J. Robert, and R.J. Culbertson. "A graduate program for high school physics and physical science teachers". American Association of Physics Teachers. Am. J. Phys. 79 (9). 2011. http://aapt.org/ajp

[14] DBE. "National Strategy for Mathematics, Science & Technology (MST) Education 2019 – 2030" (Draft). Basic Education; Department of Basic Education. 2018. Pretoria, South Africa.

[15] O.M. Ventista and C. Brown "Teachers' professional learning and its impact on students' learning outcomes: Findings from a systematic review". Social Sciences & Humanities Open 8, 2023. 100565

[16] S. Verlinda, Sutopo and E. Latifah. "The Effectiveness of Modeling Instruction Learning on Students' Conceptual Understanding of Rotational Dynamic". Jurnal Penelitian Fisika dan Aplikasinya (JPFA) Volume 10, Issue 02, December 2020.

[17] Jane Jackson, Larry Dukerich, David Hestenes. "Modeling Instruction: An Effective Model for Science Education" SPRING 2008 VOL. 17, NO. 1

[18] Department of Basic Education (DBE) "National Strategy for Mathematics, Science and Technology MST Education in GET & FET (2019-2030)." (2018).

[19] Department of Basic Education. Matric Exam Revision, Past Papers (2016 to 2020). https://www.education.gov.za/Curriculum/NationalSeniorCertificate(NSC)Examinations/NSCPastExaminationpapers.aspx

Reimagining Curriculum Renewal: A case study of Physics and Astronomy

Bako Audu[1], Mark Herbert[1], Honjiswa Conana[2], Delia Marshall[1], Siyabulela Sabata[3], David Holgate[2], Admire Dube[2], Trevor Volkwyn[1] and Mfundo Zwane[3]

[1]Department of Physics and Astronomy, University of the Western Cape, Cape Town, South Africa
[2]Faculty of Natural Sciences, University of the Western Cape, Cape Town, South Africa
[3]Academic Planning Unit, University of the Western Cape, Cape Town, South Africa

E-mail: baudu@uwc.ac.za

Abstract. This paper aims to describe how UWC's Faculty of Natural Sciences is navigating national and institutional frameworks to renew its BSc curriculum in alignment with transformation, inclusivity, and academic excellence. Key drivers of this curriculum renewal are a move away from a more prescriptive 'programmatisation' approach to the BSc degree towards a more general, 'double major' BSc degree structure, as well as a push to develop graduates equipped with a wider set of graduate attributes, including technological skills, critical citizenship and social and environmental awareness. Drawing upon the overall conceptualisation of curriculum renewal at the Faculty of Natural Sciences of the University of the Western Cape, this study explores a non-linear, bottom-up approach to curriculum renewal. Implications for the physics and astronomy curriculum are discussed.

1 Introduction

The preparation of physics and astronomy graduates for a rapidly evolving global and local landscape has become a critical concern in higher education, particularly in contexts marked by scientific advancement and socio-economic transformation [14]. In South Africa, the South African Institute of Physics (SAIP) Benchmark Statement emerged to address concerns about graduate quality by promoting standardized content knowledge and skills across institutions [15]. However, its flexible implementation has raised questions about its effectiveness, especially as universities like the University of the Western Cape (UWC) navigate tensions between national standards and local priorities [1]. UWC, a historically disadvantaged institution with a strong physics and astronomy department, is deeply connected to transformative research initiatives like the Square Kilometre Array (SKA) and committed to educational redress. This paper examines how UWC is engaging in curriculum renewal through a faculty-wide "Curriculum Renewal Project", while addressing institutional limitations. Traditional curriculum models are linear and hierarchical [17], and often fail to meet the holistic needs of contemporary education, prompting a shift toward dynamic, non-linear models that emphasize stakeholder collaboration and contextual responsiveness [2,16].

Curriculum can be conceptualized as the structure and content of a programme of study that integrates various components aligned with disciplinary knowledge and learning goals. Ratcliff views it as the coherent core of a discipline [12], while Fraser and Bosanquet emphasize the importance of programme structure, content, and sequencing [7]. As Cornbleth argues, "How we conceive of curriculum and curriculum making is important

because our conceptions... shape how we see, think and talk about, study and act on the education made available to our students" [5]. Linear models like those of Taba prioritize content over adaptability [17], which does not align with the fast-evolving nature of science and technology [9]. Non-linear, outcome-driven models such as Barnett and Coate's "spaces of engagement" [2] and Wiggins and McTighe's backward design [19] offer more flexible alternatives. This paper builds on these frameworks and Audu and Marshall's emphasis on graduate attribute mapping [1] to propose a tailored renewal strategy.

2 Curriculum transformation in the UWC BSc degree

At the University of the Western Cape, there are several drivers of faculty-wide curriculum renewal. The first is an institutional shift away from the current BSc programme structure towards a more general 'double major' degree structure. The BSc programmes at the University of the Western Cape (UWC) were introduced in the early 2000s, following a national 'programmatisation' directive at the time, which entailed the restructuring of undergraduate degrees into well-defined programmes that were more closely aligned with meeting the needs of a growing economy, and producing work-ready graduates [6]. Some universities shifted wholesale to programme-based BSc curricula, but most university science faculties at the time maintained their pre-existing, flexible BSc degree structures. UWC was one of the universities that introduced a programme-based BSc structure, and currently offers nine rigid degree programmes (for example BSc (Physical Sciences) or BSc (Chemical Sciences). These programmes, designed to provide focused qualifications, have become restrictive, limiting students' ability to explore diverse module choices and adapt to new academic pathways. This rigidity restricts student mobility between disciplines, often leading to extended study durations or blocked pathways due to lack of choice and prerequisites. The Senate Academic Planning (SAP) committee identified rigidity in the current BSc programme structure as a barrier to interdisciplinary exploration, and the UWC Curriculum Transformation and Renewal Policy calls for more flexible curriculum structure [26].

The second driver of curriculum renewal is a strategic push to produce graduates responsive to the Fourth Industrial Revolution (4IR) with adaptable skills suited for a rapidly evolving technological landscape. Students also need to be equipped to participate in scientific endeavours directed at global challenges such as climate change, environment destruction and various dimensions of inequality. This policy emphasizes fostering adaptability, critical citizenship, and technological fluency. In this way, curricula are aligned with the UWC Graduate Attributes Charter, as well as with guidelines and benchmark statements of discipline organisations, such as the SAIP. The impetus for curriculum transformation also takes place within the national higher education context, with a recent Council on Higher Education (CHE) report [22] noting that this takes various forms in SA universities, including foregrounding employability and technological responsiveness, social justice, decoloniality and Africanisation. While the push for curriculum transformation in South African has been present since 1994, Lange argues there was more of a focus on the 'exoskeleton' of the curriculum (the structure of curriculum, NQF levels, access etc) and less on the 'what' of the curriculum. She notes that the student protests of 2015 & 2016 foregrounded the need for curriculum transformation [21].

To spearhead the faculty-wide curriculum renewal process, a working group was set up. The CHE report notes the importance of deep engagement with curriculum transformation at an institutional level, through engaging both senior management as well as academics and students on the ground [22]. For this reason, the working group comprised academics from academic planning and quality assurance, as well as academic representatives from departments, many with a particular interest in undergraduate education and foundational provision (such as academic literacy, computer literacy, quantitative literacy etc). The working group was headed by the Faculty Teaching and Learning Specialist, with strong involvement by the Faculty management team. The working group facilitated a series of meetings and workshops to get broad engagement from academic staff on the sort of science graduates UWC aspired to develop, in line with the UWC graduate attributes, and how these related to curriculum renewal. This paper describes how UWC's Faculty of Natural Sciences is currently navigating national and institutional frameworks to renew its BSc curriculum in alignment with transformation, inclusivity, and academic excellence. The paper explores implications for producing interdisciplinary, inclusive, and future-ready graduates in physics and astronomy.

2 Literature review and theoretical framework

Following the Faculty workshops which broadly discussed the sort of science graduates that UWC aspired to develop, a theoretical framework guiding the curriculum renewal was developed. This integrates Barnett and Coate's Curriculum Engagement Framework [2], Slattery's Postmodern Curriculum Theory [16], and Le Grange's Decolonizing Curriculum Framework [8] in the context of the transformation agenda of the university. The adopted integration features in the context of the theoretical framework are:

Barnett and Coate's Curriculum Engagement Framework [2]: In *Engaging the Curriculum in Higher Education*, the authors propose a triadic curriculum model emphasizing three domains: knowing, acting, and being. This framework prioritizes: *Knowing*: Disciplinary depth (e.g., quantum mechanics); *Acting*: Practical applications (e.g., being able to perform experiments); *Being*: Developing scientific identity. This relates to a deep disciplinary knowledge (e.g., physics and astronomy), practical application of knowledge through skills and practices and the development of students' identities as critical, reflective learners capable of navigating uncertainty and complexity in their disciplines. This framework ensures that curriculum renewal goes beyond content delivery to foster professional identity.

Slattery's Postmodern Curriculum Theory [16]: In *Curriculum Development in the Postmodern Era*, Patrick Slattery advocates for a postmodern approach that views curriculum as a dynamic, contextual, and interpretive process. Key principles include: Holistic and interdisciplinary learning; critical and contextual reflection, and also, socially responsive curriculum. Slattery's theory supports incorporating interdisciplinary connections (e.g., linking physics to philosophy, modern scientific knowledge and applications) and encouraging students to critically reflect on the cultural and historical development of scientific knowledge.

Le Grange's Decolonizing Framework [8]: In *Decolonising the University Curriculum*, Lesley Le Grange calls for curricula that challenge Eurocentrism, incorporate diverse epistemologies, and promotes social justice, equity and inclusion. This framework encourages integrating indigenous and environmental knowledge and local scientific contributions to make the curriculum more inclusive and contextually relevant.

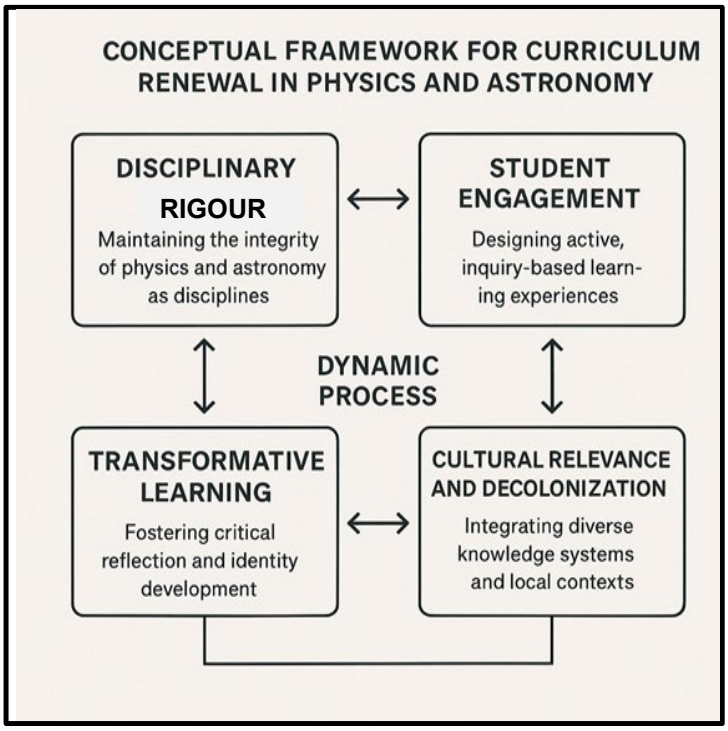

Figure 1: Conceptual framework for the integration of Barnett and Coate's Triad (Knowing, Acting, Being) with Slattery's Postmodern perspective, and Le Grange's Decolonising lens for curriculum renewal.

We developed the conceptual framework in Figure 1 to reflect the sort of science graduate the curriculum would aim to develop, focussing on disciplinary knowledge, desired skills and attributes, as well as addressing identity development of graduates as socially conscious and critical citizens. Figures 1 above and 2 below illustrate the frameworks and how these are integrated within UWC's Curriculum Renewal Project to support iterative, responsive, and inclusive curriculum design.

3.1 The curriculum process

Authors such as Priestley and Philippou [11] conceptualize curriculum making as a social practice, emphasizing the complex, multi-layered interactions between teachers, materials, and contexts in enacting curricula. In the

context of physics and astronomy curriculum renewal, this model offers a powerful framework for moving beyond top-down, prescriptive approaches to curriculum reform, which often prioritize standardized content delivery over contextual relevance and expertise.

Some scholars have identified a linear and hierarchical approach to curriculum process (see section 1). In this paper we present a non-linear approach to curriculum process. Figure 2 illustrates the curriculum transformation framework which guides the university-wide UWC Curriculum Renewal Project, and which informs the Science Faculty's curriculum renewal process. Here, the intended and enacted curricula interact dynamically, with feedback loops (shown by the arrows) between the two processes. The UWC Curriculum Renewal Project acts as the central hub, facilitating a continuous, iterative exchange where insights from both inquiry/development and inclusivity shape and refine the curriculum. This allows for ongoing adaptation and alignment with both academic standards and social justice goals, rather than a one-directional progression.

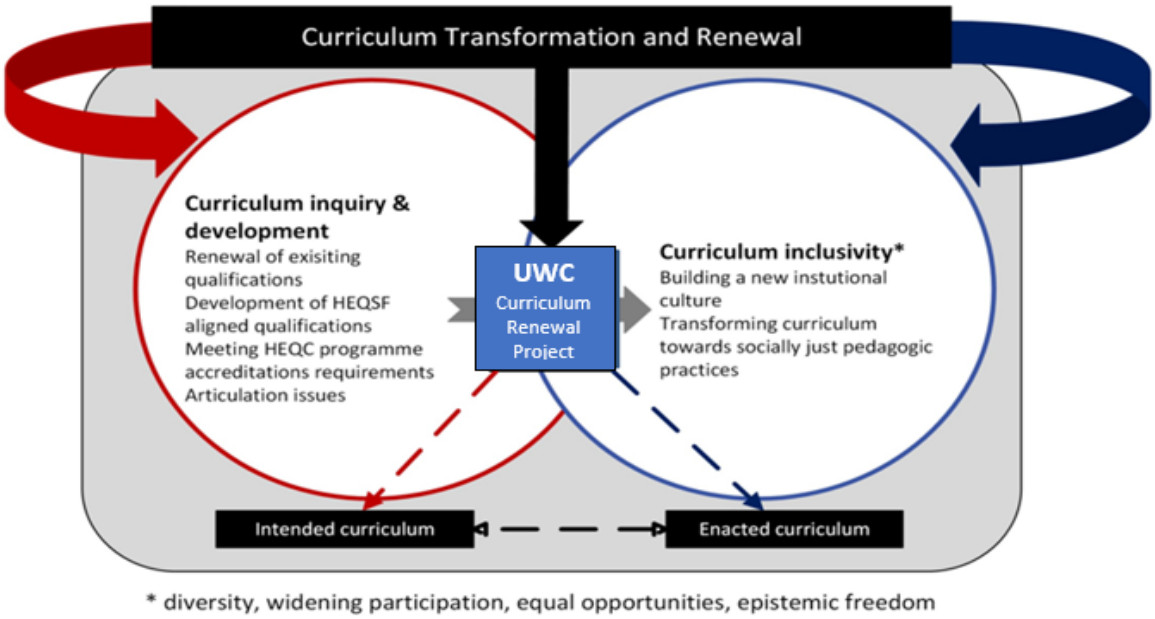

Figure 2: Curriculum transformative framework for UWC (developed by the UWC Curriculum Renewal Project).

4 Institutional factors shaping Faculty curriculum renewal

A collaborative, bottom-up approach: The Science Faculty's academic leadership has fostered a collaborative, bottom-up approach. The working group and the Department of Physics and Astronomy conceptualize curriculum making as a social practice, with multi-layered interactions between all stakeholders, materials, and contexts in enacting curricula. As noted earlier, this sustained engagement with Faculty staff was facilitated through a series of workshops with all departments over a sustained period. This bottom-up, social practice model provides a robust context for reimagining curriculum renewal in the Faculty, and in physics and astronomy in particular. The bottom-up approach enabled leadership to provide the stakeholders with agency to work towards curriculum that is inter-disciplinary and discipline grounded, adapted to diverse student needs, and that reflects the dynamic nature of the scientist of the 21st century. Academic leadership in this context also involves guiding faculty toward a forward-thinking vision that prepares students for the complexities of 21st-century scientist while addressing local and global challenges. This model underscores the importance of leadership in facilitating social practices that enable departments to develop, interpret and enact curricula in contextually relevant ways. Values, such as adaptability, inclusivity, and innovation, are critical in physics and astronomy, where rapid advancements (e.g., nanoscience) and interdisciplinary connections (e.g., with data science or environmental science) demand curricula that are dynamic and responsive [20]. The curriculum renewal process ensures that the undergraduate curriculum, including physics and astronomy, reinforce UWC's graduate attributes which include critical thinking, social responsibility, global citizenship, and adaptability, as well as disciplinary attributes specific to physics and astronomy, such as problem-solving, mathematical proficiency, and scientific inquiry [1].

Entrenching a change-supportive culture: Studies show that academics are often resistant to curriculum change [23]. 'Reimagining Curriculum Renewal' means developing and sustaining a change-supportive culture that is critical for the long-term success of curriculum renewal in physics and astronomy. This effort will set the path and prepare UWC physics and Astronomy graduates to excel while contributing to South Africa's scientific, economic and social development.

5 Reimagined Faculty curriculum renewal – implication for Physics & Astronomy

The reimagination of the BSc curriculum at the University of the Western Cape exemplifies a visionary and inclusive approach to curriculum renewal, ensuring relevance and societal impact. For physics and astronomy students, there will be particular benefits:

- Interdisciplinary collaboration: The introduction of a general BSc 'double major' degree structure will address the existing rigidity in the academic pathways and subject choices. The curriculum will empower students to customize their learning paths: Physics majors will no longer be restricted to a very narrow pool of 3rd year subjects to choose from (currently, maths, chemistry, computer science) but will now to able to pursue a range of subjects, including life sciences, biochemistry, statistics, geology. This promotes interdisciplinarity, long-term innovation and breaks down disciplinary silos.

- Graduate attribute alignment in the undergraduate curriculum: This entails more explicit embedding of the physics graduate attributes as set out in the SAIP benchmark statement, as well as the UWC graduate attributes, particularly those identified in a previous study with UWC students and alumni as needing more focus and development [24]. These include communication skills, computational skills, practical skills, and social and environmental awareness.

- Design a flagship module, "Science-In-Focus": An additional module to support scientific skill development across the entire degree, integrating academic literacy, computer literacy, quantitative literacy, information literacy and psychosocial support for students (including mental health and wellness, time management, collaboration and teamwork). It will also include financial skills, career advice, and 21st century skills such as AI literacy, and computational skills, scaffolded from year one to year 3 of study (building from basic computer literacy, introduction to coding using Python, and then advancing to skills required by specific disciplines (e.g. using Numpy, or R for life sciences students). Through the academic literacy component of this module, students will engage with texts that explore the social, ethical and environmental aspects of scientific knowledge and practices. Issues of social justice and sustainability will also be explored, as well as how decolonisation perspectives could inform science studies.

- Curriculum innovation: At the heart of curriculum renewal is the incorporation of innovative discipline content, practices, and engagements, such as flexible electives, to keep the curriculum relevant to contemporary scientific advancements. Authors such as Priestley and Drew [10] argue that innovative curriculum design involves creating opportunities for students to engage with cutting-edge content and practices that reflect the evolving nature of the discipline. In physics and astronomy, this could mean introducing electives on emerging fields like quantum computing, machine learning or nanotechnology, which allow students to explore specialized topics while developing transferable skills [20] and to engage with authentic scientific processes [13] such as experimental work or quantum computing. Prioritizing innovation ensure that the curriculum remains forward-looking and aligned with the demands of the global scientific landscape.

5.1 Lessons and challenges

As noted earlier, curriculum renewal has entailed an extensive process of engagement with departments through meetings and workshops, as well as extensive consultation with colleagues from the academic planning unit, quality assurance, the Registrar's office, institutional planning and DVC (Teaching & Learning). The reports and minutes from these meetings and workshops were analysed using a process of document analysis [25]. This

analysis showed that the curriculum renewal process has brought to the fore valuable lessons and challenges for the working group, as follows:

- Contact time: the introduction of the additional 'Science in Focus' module, and well as the more explicit focus on developing graduate attributes, may require more contact time.
- Time-tabling: the wider choice of subjects available to students will lead to timetabling challenges and difficulties in planning ahead the student numbers in individual courses.
- Student advising: with more choice of academic pathways, dedicated student advising will be crucial.
- Staff resistance: new interdisciplinary approaches challenge traditional practices and entrenched siloed identities. Developing and sustaining a change-supportive culture in the Science Faculty will be important.
- Lack of change-ready environment: there may be challenges with venues, laboratories and technology resources (including current university systems that support student registration and timetabling etc.).
- Re-looking the methods of assessment: a move towards more authentic assessment methods (e.g. portfolios, problem-based learning) will enable fuller assessment of graduate attributes.

6 Conclusion

This paper has described how UWC's Faculty of Natural Sciences is navigating national and institutional frameworks to renew its BSc curriculum, shifting from a rigid programme structure to a more flexible BSc degree structure, and the development of students equipped with 21st century skills and attributes, including technological skills, critical citizenship and social and environmental awareness. A non-linear, inclusive, bottom-up approach to curriculum renewal is being adopted that engages stakeholders at all levels and aligns with both disciplinary imperatives and institutional transformation goals. For the physics and astronomy curriculum, the curriculum renewal will lead to greater interdisciplinary collaboration, and more explicit graduate attribute alignment in the curriculum, based on the SAIP Benchmark Statement, and the UWC Charter of Graduate Attributes. The introduction of Science-In-Focus module and flexible module combination rules in the implementation of the reimagined curriculum will empower student choices that allows students to tailor their academic paths to diverse interests, interdisciplinary focus and career goals. This curriculum renewal process intends to equip graduates with disciplinary and interdisciplinary problem-solving, and adaptability skills essential for future-ready professionals in a rapidly evolving global landscape; by promoting inclusivity and coherence while leveraging existing resources to ensure sustainability. These efforts will ensure UWC produces scientifically proficient, socially conscious, and globally competitive science graduates going forward.

References

[1] B. N. Audu and D. Marshall, "The South African Institute of Physics (SAIP) benchmark statement and physics graduate preparedness: A case study of the University of the Western Cape," SAIP 2021 Proceedings, pp. 484–489, 2021.

[2] R. Barnett and K. Coate, *Engaging the Curriculum in Higher Education*. Maidenhead, UK: McGraw-Hill Education, 2005.

[3] L. Bencze and D. Hodson, "Towards a socially responsible science education," in *Science and Technology Education Promoting Wellbeing,* L. Bencze, Ed. Cham, Switzerland: Springer, 2017, pp. 11–30.

[4] Council on Higher Education and South African Institute of Physics, Review of Undergraduate Physics Education in Public Higher Education Institutions. Pretoria: CHE, 2013.

[5] C. Cornbleth, *Curriculum in Context*. London: Falmer Press, 1990.

[6] P. Ensor, "Contesting discourses in higher education curriculum restructuring in South Africa," *High. Educ*., vol. 48, no. 3, pp. 339–354, 2004.

[7] S. P. Fraser and A. M. Bosanquet, "The curriculum? That's just a unit outline, isn't it?" *Stud. High. Educ*., vol. 32, no. 1, pp. 89–104, 2007.

[8] L. Le Grange, "Decolonising the university curriculum," *S. Afr. J. High. Educ*., vol. 30, no. 2, pp. 1–12, 2016.

[9] J. Osborne and J. Dillon, *Science Education in Europe: Critical Reflections*. London: Nuffield Foundation, 2008.

[10] M. Priestley and V. Drew, "Professional enquiry: An ecological approach," in *SAGE Handbook of Curriculum, Pedagogy and Assessment*, D. Wyse, L. Hayward, and J. Pandya, Eds. London: SAGE, 2016, pp. 96–112.

[11] M. Priestley and S. Philippou, "Curriculum making as social practice," in *Curriculum Making in Europe: Policy and Practice within and across Diverse Contexts*, M. Priestley, D. Alvunger, S. Philippou, and T. Soini, Eds. Bingley: Emerald, 2018, pp. 151–169.

[12] J. L. Ratcliff, "What is curriculum and why do we need one?" in *Handbook of the Undergraduate Curriculum*, J. G. Gaff, J. L. Ratcliff, and Associates, Eds. San Francisco, CA: Jossey-Bass, 1997, pp. 5–29.

[13] T. D. Sadler, J. A. Foulk, and P. J. Friedrichsen, "Evolution of a model for socioscientific issue teaching," *Int. J. Educ. Math. Sci. Technol*., vol. 4, no. 2, pp. 75–87, 2016.

[14] South African Institute of Physics, Strategic Plan for the Transformation of Physics Education in South Africa. Pretoria: SAIP, 2004.

[15] South African Institute of Physics, Benchmark Statement for Undergraduate Physics Programmes. Pretoria: SAIP, 2015.

[16] P. Slattery, *Curriculum Development in the Postmodern Era*, 2nd ed. New York: Routledge, 2006.

[17] H. Taba, *Curriculum Development: Theory and Practice*. New York: Harcourt, Brace & World, 1962.

[18] C. Wieman, K. Perkins, and S. Gilbert, "Transforming science education," *Change*, vol. 40, no. 6, pp. 30–35, 2008.

[19] G. Wiggins and J. McTighe, *Understanding by Design*, 2nd ed. Alexandria, VA: ASCD, 2005.

[20] R. Duit, H. Gropengießer, U. Kattmann, M. Komorek, and I. Parchmann, "The model of educational reconstruction," in *Making Learning Visible*, D. Leach and D. Scott, Eds. Cham, Switzerland: Springer, 2010, pp. 13–37.

[21] L. Lange, "20 years of higher education curriculum policy in South Africa," *J. Educ*., vol. 67, pp. 1–26, 2017.

[22] Council on Higher Education, Reflecting, renewing, and realigning: A baseline study of conceptions of curriculum transformation in South African universities. Pretoria: CHE, 2025.

[23] S. Barrie, "A research-based approach to generic graduate attributes policy," *High. Educ. Res. Dev*., vol. 31, no. 1, pp. 79–92, 2012.

[24] B. N. Audu, D. Marshall, and C. Conana, "'It's not only the physics you know that matters': A case study of advancing graduate attributes," *S. Afr. J. High. Educ*., forthcoming.

[25] G. A. Bowen, "Document analysis as a qualitative research method," *Qual. Res*. J., vol. 9, no. 2, pp. 27–40, 2009.

[26] University of the Western Cape Curriculum Transformation Framework. Cape Town. UWC, 2021.

This page intentionally left blank.

Physics Students' Epistemological Beliefs about Science

P. Molefe[1], M. Khwanda[1] and B. Sondezi[1]

[1]Physics Department, University of Johannesburg, Auckland Park, Johannesburg, South Africa

E-mail: pmolefe@uj.ac.za

Abstract. Epistemological beliefs individuals hold about the nature of knowledge and learning play a crucial role in understanding and engaging in the physical sciences. These beliefs influence how students, educators, and researchers perceive scientific concepts, theories, and methodologies. A total of 89 first- and second-year students participated in this study, comprising 44 first-year students and 45 second-year student teachers. First-year students comprised 45.5% males and 54.5% females, while second-year student teachers consisted of 55.6% males and 44.4% females. All participants are South African high school graduates who are enrolling in the same introductory physics course. The investigation sought to determine whether inquiry-based learning improves the epistemological beliefs of students studying physics. The research employs a quantitative methodology. The questionnaire was administered in class four weeks after the commencement of the first semester via a Google Form. The selection of the Google Form was based on its capacity for efficient retrieval and analysis of student responses. The performance of the two groups was compared, given they have the same high school educational background, and both registered for Bachelor of Education with a physical science concentration at different levels. The results demonstrate that both student groups exhibit a broad distribution of epistemological beliefs, comparable within experimental margins of uncertainty; the major uncertainty arises from the inherent differences between the two groups of students.

1 Introduction

Science is an important subject in many parts of students' daily lives and real-life applicability. Physics, as a science topic, can help students enhance their logical and creative thinking skills. An understanding of physics is required as society faces tremendous challenges and opportunities around the world. Enhancing learning outcomes is a significant challenge facing physics education globally. The transition from rote learning to conceptual comprehension has exacerbated issues in university teaching and learning.

Considering this significant transformation in educational platforms, it is essential to evaluate if students' attitudes towards learning physics have shifted after intervention. An attitude assessment known as the Epistemological Beliefs about Physical Sciences (EBAPS) was employed for this purpose. This study presents preliminary findings from the EBAPS questionnaire administered to first- and second-year student teachers at the university.

Epistemological beliefs (EB) refer to convictions regarding the essence of knowledge and understanding [1]. Students' epistemological views influence their attitudes towards learning [2]. Each student possesses a distinct

array of attitudes, beliefs, and assumptions about their learning, the requisite abilities, and the expectations imposed upon them in the educational environment [3]. Understanding epistemic views is beneficial for both students and instructors. Education is changing, and old teaching methods are being replaced by more participatory and engaging approaches. Inquiry-based learning is one strategy that emphasizes student curiosity, critical thinking, and active study of issues. But what are the advantages of inquiry-based learning? This teaching technique promotes deeper knowledge, enhances problem-solving abilities, and enables students to take control of their learning path. Inquiry-based learning promotes active engagement by shifting from teacher-led instruction to a student-centered learning environment. Instead of memorizing information, students ask questions, investigate solutions, and build knowledge via hands-on experiences. Schools, universities, and corporate training programs frequently employ this strategy, demonstrating its effectiveness in a variety of learning settings.

This inquiry-based approach is presumed to help students develop more sophisticated epistemological beliefs. Numerous instructional approaches exist, including the conventional teacher-centered method, as well as the talk and chalk techniques, among others. The CAPS document advocates the inquiry-based method as the most effective way to foster a learner-centered approach [4].

Thus, epistemological ideas vary from rudimentary to very advanced stages. The complexity of epistemological beliefs based on EBAPS was further linked to Perry's framework of cognitive growth. Perry delineated four stages: *dualism*, *multiplicity*, *relativism*, and *commitment to content relativism* [5]. Dualism posits that knowledge is absolute, with the teacher's function being to convey it. Multiplism denotes the recognition of several perspectives while positing the existence of a specific yet uncovered truth. Relativism acknowledges that certain perspectives are superior to others. The most advanced beliefs and commitments in relativism entail forming and assessing adaptable commitments to ideas that incorporate personal values [6]. Perry's model and epistemological ideas can elucidate university students' experiences and alleviate challenging circumstances. It provides instructors with an understanding of the reasons behind students' difficulties and the most effective ways to assist them [5]. Epistemological beliefs affect learning, and the integration of these beliefs with Perry's model facilitated the categorisation of students' epistemological views towards science, based on their sophistication. University students enrolled in introductory physics and chemistry courses that align with algebra-based curricula are the target group for Physics EBAPS. Algebra serves as the foundation for both first- and second-year physics modules.

The research question that guided this study is: Does inquiry-based learning enhance the epistemological beliefs of physics students?

2 Methodology

A total of 89 first- and second-year students participated in this study, comprising 44 first-year students and 45 second-year student teachers. First-year students comprised 45.5% males and 54.5% females, while second-year student teachers consisted of 55.6% males and 44.4% females. All participants are South African high school graduates who are enrolling in the same introductory physics course, all the participants are enrolled in a university to pursue a Bachelor of Education with a physical science concentration. The first-year students have foundational mathematical skills for physics, and it was presumed that they had acquired these through an inquiry-based approach during their high school education, as advocated by CAPS [4]. The second-year students further developed their inquiry-based skills throughout their first-year at the university level. During the four-week teaching period, the lecturers employed a student-centered instructional method that encourages students to ask questions about class assignments, investigate real-world situations, and engage in hands-on activities. Rather than passively absorbing information, students take an active role in their learning process, which nurtures curiosity and promotes critical analysis of science.

The research employs a quantitative methodology. The questionnaire was administered in class four weeks after the commencement of the first semester via a Google Form. The selection of the Google Form was based on its capacity for efficient retrieval and analysis of student responses. The questionnaire was designed to be completed in 45 minutes, and all students finished within this timeframe. The students understood the objectives of questionnaire management and their voluntary involvement in all activities before the explanation of Google Forms management.

This study complied with rigorous ethical standards during its implementation. Participation in the surveys was completely voluntary, and all responses were gathered anonymously to safeguard participants' privacy. Electronic informed permission was acquired from all participants before data collection commenced. The study's

monitoring and evaluation protocols obtained formal ethical approval from the Faculty Research Ethics Committee, adhering to institutional regulations concerning research with human participants. Considering that this work is investigating students and their responses, ethical clearance was received from the institution before the beginning of this investigation, and the Ethics Reference Number associated with this work is 2024-09-02/Sondezi.

2.1 How do the two groups differ in terms of how they were taught?

Both groups received instruction through inquiry-based teaching during the initial four weeks of their university courses. The first-year students continued their engagement with inquiry-based learning initiated in high school, as endorsed by CAPS [4], whereas the second-year students experienced a greater emphasis on inquiry-based methodologies at the university level. Moreover, the tertiary level prioritized conceptual comprehension by implementing inquiry-based methodologies [7].

2.2 Data collection and analysis

The EBAPS instrument is a forced-choice tool intended to assess students' epistemologies, specifically their perspectives on the nature of knowledge and learning in science. Physics EBAPS targets students enrolled in introductory physics and chemistry and were optimised for algebraic courses. The instrument comprises 30 questions and was initially created and validated by [8]. The primary analytical focus was on ascertaining the mean difference between the two groups to assess their level of sophistication relative to unsophisticated beliefs, as indicated by EBAPS. A box and whisker plot were employed to summarize the acquired data. A box and whisker plot, or box plot, illustrates the five-number summary of a dataset sorted in ascending order [9]. The plot displays the minimum value, first quartile, median, third quartile, maximum value, and occasionally outliers. In a box plot, a box is delineated from the first to the third quartile. A vertical line intersects with the box at the median. EBAPS examines students' views along five non-orthogonal dimensions, called axes, which are defined in Table 1.

Variable	**EBAPS Dimensions**	**Extremely sophisticated (Scientific Beliefs)**	**Unsophisticated (Naïve beliefs)**
Axis 1	Structure of Knowledge	Single coherent system	Collections of isolated pieces
Axis 2	Nature of knowing and learning	Self-constructed	Propagated from authority (e.g., teachers)
Axis 3	Real-life applicability	Applicable to real life	Not applicable to real-life contexts
Axis 4	Evolving knowledge	Knowledge changes with time	Knowledge does not change with time
Axis 5	Source of the ability to learn	Acquired through time	Innate

Table 1: The table summarizes the EBAPS axes.

Knowledge View adapted from Perry's model	**Dualism**		**Multiplism**	**Relativism**	**Commitment to relativism**
	Unsophisticated (Naïve beliefs)	Developing Sophistication	Moderately sophisticated	Highly Sophisticated	Extremely Sophisticated
EBAPS Scale	Less than 1.5	1.6-2.3	2.4-2.9	3 - 3.4	Greater than 3.5
% EBAPS	0-39%	40-58%	60-74%	75%-85%	> 87.5 %

Table 2: Based on the table above, students' epistemological beliefs were categorized on a 0 to 4 scale (also adapted [10] and Perry's model of cognitive development).

Each item in Table 2, on the instrument, is evaluated on a scale from 0 to 4, where 0 signifies the least complex beliefs and 4 denotes the most advanced, expert-like beliefs. The scoring of EBAPS is non-linear and permits changes between questions. The subscale score is calculated as the mean of the values for each item within that subscale. The tool comprises three distinct item types: Likert scale items (strongly agree/strongly disagree), multiple-choice items, and discussion items. From the total of 30 questions from the EBAPS tool, a sample of two questions (24 and 29) is shown. It is important to note that the results obtained are analysed from the summative responses of all 30 questions that were administered to students.

Question 24: **Brandon:** A good science textbook should show how the material in one chapter relates to the material in other chapters. It shouldn't treat each topic as a separate "unit," because they're not really separate. **Jamal:** But most of the time, each chapter is about a different topic, and those different topics don't always have much to do with each other. The textbook should keep everything separate, instead of blending it all together. With whom do you agree? Read all the choices before circling one.

(a) I agree almost entirely with **Brandon**.; (b) Although I agree more with Brandon, I think Jamal makes some good points.; (c) I agree (or disagree) equally with Jamal and Brandon.; (d) Although I agree more with Jamal, I think Brandon makes some good points.; (e) I agree almost entirely with Jamal.

Question 29: Jose: In my opinion, science is a little like fashion; something that's "in" one year can be "out" the next. Scientists regularly change their theories back and forth. **Miguel**: I have a different opinion. Once experiments have been done and a theory has been made to explain those experiments, the matter is pretty much settled. There's little room for arguments.

(a) I agree almost entirely with Jose.; (b) Although I agree more with Jose, I think Miguel makes some good points.; (c) I agree (or disagree) equally with Miguel and Jose.; (d) Although I agree more with Miguel, I think Jose makes some good points.; (e) I agree almost entirely with Miguel.

3 Results

Figure 1 presents the summary of results obtained from first- and second-year students' responses using a box and whisker plot. The summary results of each axis are presented in the following subsections. The horizontal line and a cross in a box represent the median and mean, respectively. If the horizontal line is above the cross, it means the median is greater than the mean and vice versa. If the horizontal line intersects with the cross at its center, it means the median and the mean are equal. When reporting, the median will be in brackets after the mean.

3.1 Axis 1: Nature of knowing and learning (Questions: 1, 7, 11, 12, 13, 18, 26, 30)

Sample Question: To understand chemistry and physics, the formulas (equations) are really the main thing; the other material is mostly to help you decide which equations to use in which situations.

According to figure 1, the means for first- and second year are respectively 2.1(2.1) and 2.2(2.2). The first-year scores spread between 1.2 and 3.1 while the second year spread between 1.5 and 3.1. Based on Table 2**,** both first- and second-year students are categorized as developing sophistications in terms of their understanding of the structure of scientific knowledge. In other words, they are in the process of transformation in terms of their belief system towards the multiplism stage.

3.2 Axis 2: Nature of knowing and learning (Questions: 1, 7, 11, 12, 13, 18, 26, 30)

Sample Question: Tamara just read something in her science textbook that seems to disagree with her own experiences. But to learn science well, Tamara shouldn't think about her own experiences; she should just focus on what the book says.

The means for first- and second-year students are 2.4 (2.4) and 2.5 (2.7), respectively. According to table 2, their comprehension of the essence of knowledge and learning is at the multiplism stage, which is categorized as moderately sophisticated. Fifty percent of second-year students achieved scores over 2.7, indicating superior performance. Given that the minimum for both is 1.5 and the maximum exceeds 2.9, it can be inferred that there are few individuals remaining in the dualism stage and only a few in the relativism stage.

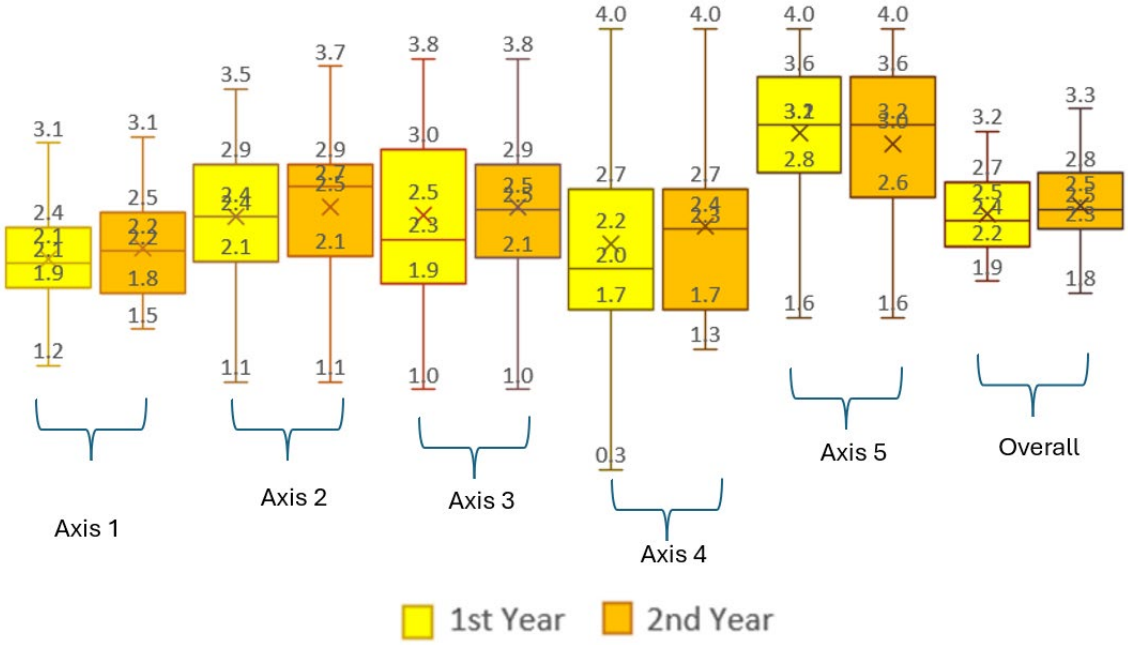

Figure 1: 1st and 2nd year students' EBAPS results

3.3 Axis 3: Real-life applicability (Questions: 3, 14, 19, 27)

Sample Question: Julia: I like the way science explains things I see in the real world. **Carla**: I know that's what we're "supposed" to think, and it's true for many things. But let's face it, the science that explains things we do in the lab at school can't really explain earthquakes, for instance. Scientific laws work well in some situations but not in most situations. **Julia**: I still think science applies to almost all real-world experiences. If we can't figure out how, it's because the stuff is very complicated, or because we don't know enough science yet.

The means for students in the first and second years are 2.5 (2.3) and 2.5 (2.5), respectively. According to Table 2, students' comprehension of the practical relevance of their learning is characterized by multiplism; nevertheless, only a limited number of students have attained the commitment to the relativism stage, as evidenced by the maximum score of 3.8 in Figure 1.

3.4 Axis 4: Evolving knowledge (Questions: 6, 28, 29)

Sample Question: Leticia: Some scientists think the dinosaurs died out because of volcanic eruptions, and others think they died out because an asteroid hit the Earth. Why can't the scientists agree? **Nisha**: Maybe the evidence supports both theories. There's often more than one way to interpret the facts. So we have to figure out what the facts mean. **Leticia**: I'm not so sure. In stuff like personal relationships or poetry, things can be ambiguous. But in science, the facts speak for themselves.

The means for students in the first and second years are 2.2 (2.0) and 2.4 (2.3), respectively. According to Table 2, both groups exhibit a dualistic stage in their comprehension of the evolution of knowledge; however, second-year students are advancing in sophistication, whereas first-year students maintain naïve notions.

Figure 1 indicates that 50% of both cohorts are evenly distributed throughout the developing, sophisticated, and moderately sophisticated categories for all axes 1-4, with students in the lowest and top quartiles extending beyond this distribution. Both groups demonstrate that they are in the developmental phase, and inquiry-based learning does not alter the epistemological beliefs of students.

3.5 Axis 5: Source of the ability to learn (Questions: 5, 9, 16, 22, 25)

Sample Question: Anna: I just read about Kay Kinoshita, the physicist. She sounds naturally brilliant.**Emily**: Maybe she is. But when it comes to being good at science, hard work is more important than "natural ability." I bet Dr. Kinoshita

does well because she has worked really hard. **Anna**: Well, maybe she did. But let's face it, some people are just smarter at science than other people. Without natural ability, hard work won't get you anywhere in science!

The mean scores for first- and second-year students are 3.1 (3.2) and 3.0 (3.2), respectively. Table 2 indicates that their understanding of the genesis of learning skills is highly sophisticated, as they are in the relativism stage; yet there are few students in the commitment to relativism stage.

4 Discussion of results

According to Figure 1, the epistemological views regarding physical sciences among second-year students on axes 1, 2, and 4 are marginally superior to those of first-year students, as indicated by the means and medians of these axes, and they can be classified as being at a developing stage of sophistication. In axis 3, both means are identical at 2.5; however, the median for first-year students is (2.3), which is lower than the median of (2.5) for second-year students. This information indicates that 50% of first-year students achieve scores exceeding (2.3), and 50% of second-year students attain scores beyond (2.5). In axis 5, a lower interquartile range in the first-year indicates that data are concentrated around the median, suggesting that a greater number of first-year students are at the relativism stage compared to second-year students, who exhibit a wider interquartile range and believe that the capacity to learn is developed over time. The first-year students may have outperformed the second-year students due to acquiring mathematical abilities in the initial four weeks, which acted as a review for them.

The findings reveal that the mean for both the first- and second-years is identical, yet their medians differ; the median for the first-year stands at (2.4), whereas the second-year has a median of (2.5). Consequently, second-year students exhibited a marginally superior performance, as 50% of them achieved scores exceeding (2.5). It may be suggested that prolonged engagement with inquiry-based approaches among second-year students could have contributed to this outcome. It has been observed that epistemological beliefs present a moderate level of difficulty in terms of change, necessitating extended durations of intervention efforts [11]. The epistemological beliefs regarding sciences for both students can be classified as moderately sophisticated, specifically within the multiplism stage. The expectation was that second-year students would demonstrate a more advanced level of understanding compared to first-year students due to their increased exposure to inquiry-based approaches [11]; however, the findings indicated a different outcome [12]. The results of this study indicated no significant difference between first- and second-year physics students concerning their advanced and basic concepts related to science. The results highlight the importance of utilizing inquiry-based learning to boost students' understanding and involvement in science, which is crucial for advancing educational results in the field. Figure 1 presents a box and whisker plot to encapsulate the findings [9].

5 Conclusion

The minor discrepancy may be attributed to the existence of two distinct groups of students. This study concludes that inquiry-based instruction conducted from week four of the first-year to week four of the second-year does not significantly influence students' epistemological beliefs (slight evidence in terms of overall medians). Inquiry-based teaching alone may be inadequate to effectuate those changes. The negligible difference in epistemological beliefs between the two groups supports the claim that examining epistemological beliefs is acknowledged as the initial step in instigating modifications in teacher education programs and fostering new perspectives on the teaching profession [13]. The results indicate that both groups of students have a wide spread of epistemological beliefs, comparable within experimental uncertainty; the major uncertainty lies with the fact that the two groups are different students.

5.1 *Overall students' mean and median responses: First year: 2.5 (2.4) and Second year: 2.5 (2.5)*

Classification: The overarching epistemological viewpoints of students can be categorized as a developing sophistication in their beliefs concerning knowledge and the process of knowing. Both student groups are classified as being in the multiplism stage of comprehension. Students have a moderate level of sophistication in their epistemological belief and the process of acquiring it.

Pedagogical implications: Activities designed should enhance their beliefs from dualism to commitment to relativism.

5.1 Limitations and Future Research

Since the study conducted in only one institution and only to first- and second-year physics students, the findings may not be representative of the epistemological beliefs of physics students in other institutions. Future research should explore the extent to which the no significant difference of epistemological beliefs may be substantiated

by a qualitative study that examines student teachers' perspectives and elucidates the inquiry-based teaching and learning approaches employed.

Acknowledgements
Thanks to the university for financial support. All participants are acknowledged.

References

[1] F. Berding, K. Rolf-Wittlake and J. Buschenlange, "Impact of different levels of epistemmic beliefs on learning processes and outcomes in vocational education and training," *World Journal of Education,* vol. 7(3), pp. 103- 114, 2017.

[2] Y. Park and H. Lim, "Meaning of Epistemological Belief Through Online Communication: Exploratory Study," 2012.

[3] E. Redish, J. Saul and R. Steinberg, "Student expectations in introductory physics," *American Journal of Physics,* vol. 66, no. 3, pp. 212-224, 1998.

[4] DBE, Curriculum and Assessment Policy Statement (CAPS): Physical Sciences Grades 10–12, Pretoria: Department of Basic Education, 2011.

[5] D. Barker, "The value of higher education does not lie only in acquired knowledge but rather in developing thinking abilities," *Perspective,* pp. 1-4, 2011.

[6] H. Green and M. Hood, "Significance of epistemological beliefs for teaching and learning in Psychology: a Review.," *Psychology Learning and Teaching,* vol. 12(2), pp. 168-178, 2013.

[7] U. Ramnarain, "Teachers' perceptions of inquiry-based learning in urban, suburban, township and rural high schools: The context-specificity of science curriculum implementation in South Africa," *Teaching and teacher education,* vol. 38, pp. 65-75, 2014.

[8] A. Elby, J. Frederiksen, C. Schwarz and B. White, "“The Epistemological Beliefs Assessment for Physical Science”," 2001. [Online]. Available: www.flagguide.org..

[9] J. W. Tukey, "Box-and-Whisker Plots. . Reading, MA: Addison-Wesley, pp. 39-43, 1977.," in *Exploratory Data Analysis*, MA: Addison-Wesley, 1977, pp. 39-43.

[10] Mirana, V.P., "Lesson Exemplars in Electricity and Students' Epistemological Beliefs," *SSRN Electronic Journal,* 2018.

[11] J. Brownlee, N. Purdie and G. Boulton-Lewis, "Changing epistemological beliefs in pre-service teacher education students," *Teacher in Higher Education,* vol. 6, no. 2, pp. 247-268, 2001.

[12] A. Elby, "Helping physics students learn how to learn," *American Journal of Physics,* vol. 69, 2001.

[13] S. Lee and D. Schallert, "Becoming a teacher: Coordinating past, present, and future selves with perspectival understandings about teaching," *Teaching and Teacher Education,* vol. 56, pp. 72-83, 2016.

This page intentionally left blank.

Pre-service student teachers' misconceptions about a simple electric circuit

Mphiriseni Khwanda[1], Paul Molefe[1] and Buyi Sondezi[1]

[1]Department of Physics, University of Johannesburg, Auckland Park, South Africa

E-mail: mkhwanda@uj.ac.za

Abstract. Despite all the efforts made by Physics Education Researchers in terms of strategies to enhance students' conceptual understanding of electric circuit phenomena, students still have conceptual difficulties related to solving problems related to electric circuits. The difficulty is worsened by the presence of misconceptions about electric circuit phenomena. In terms of constructivism, the preparation for teaching should start with identifying what students know prior to instruction. In line with this pedagogy, the research reports how a three-tier concept test was used to identify misconceptions the pre-service students have. Although the current study found significant correlation between students' level of confidence and conceptual understanding, it did find that most misconceptions are identifiable through explanations where students feel confident about their incorrect choices in the first tier.

1 Introduction and background

Teaching is a multifaceted endeavour that aims to facilitate students' comprehension of concepts applicable to real-life problem-solving. The same principle applies to the teaching of electricity, upon which we all rely to enhance our lives. Literature revealed that the teaching of electricity comes with a challenge because students interpret the relationship of potential difference, current and resistance using the ohm's law equation. Previously it was found that Introducing Ohm's law mathematically before qualitatively grasping its underlying theory poses a challenge, resulting in students applying the formulae without comprehending its significance [1]. In South Africa, the 2024 physical sciences diagnostic report indicated that most learners have challenges in applying mathematical principles [2]. Based on [2], electric circuit is still a challenge because only 44 % of learners passed the section in 2024 examination. [3] also highlighted that most students graduating from secondary school have a very basic understanding of basic circuits concepts like voltage, resistance, and current. Research conducted all over the world has revealed that students frequently hold misconceptions about the nature of electricity and how it behaves in basic circuits, and that these beliefs are resistant to modification even after several years of secondary school and post-school training [4].One of the factors that can assist in identifying misconceptions is the students' confidence in answering questions. The confidence students have is an indication of how certain they are in terms of understanding the concept [5]. According to [5] , students who are correctly confident can build more understanding of core concepts which is advantageous for applying and handling of sophisticated ideas. On the other hand, those who are incorrectly confident are likely to have misconceptions. The present study presented how misconceptions were revealed and was guided by the following research questions:

(1) How do students understand the impact of an electric field on the movement of charges in a circuit?
(2) How do students understand the difference between the conductor and a resistor in the context of basic electric circuit?

(3) How do students understand the global impact in a circuit of changing circuit element or the value of the circuit element?
(4) How do students compare the speed of charges in a conductor and a resistor?

2 Research Design and Procedures

The participants were forty-three first year Bachelor of Education (B. Ed) preservice student teachers (later to be referred to as students (52.4 % males and 47.6 % females) who were purposely chosen considering that they had learnt the subject in high school. The main intention was to diagnose misconceptions they have about basic electric circuit before instruction. The researchers developed a three-tier test for that reason. The use of a three-tier test to assess or diagnose misconceptions is common. For example, [6] developed a three-tier test to assess students' misconceptions about basic electric circuits and [7] did the same in assessing misconceptions in algebra to mention just a few. The current study structured the three-tier test as follows: the first part of the tier was a multiple choice, the second part was the reasons to be given by students for selecting the option in the first tier, and the third tier was their confidence level. When students explain the reasons behind their choice there will be the possibility of identifying new unreported conceptions and misconceptions. Data was collected using the google form for easy retrieval and analysis. The responses from the multiple choices and level of confidence were numerically counted and sorted according to similarities of the responses, and the explanation were phenomenographically [8] categorized based on the grouping of similar ideas on responses. Phenomenography was selected because of its power to guide effective instructional design and to enhance -based factors to enhance learning outcomes [9]. Figure 1 shows items on the designed three-tier test.

Instructions: Use figure 2 for answering all questions. In each question, first select your correct answer, then explain the reason(s) for your choice and lastly, rate your level of confidence in your choice of answer and the explanation you gave on the scale from level 1 to level 5. Level 1 represents not confident at all, while level 5 represents the fact that you are very confident.

Question 1*: When switch S is put on, which bulb will shine/glow first?*
A: All B: Bulb X C: Bulb Z
Explanation_____ Confidence level___

Question 2*: When switch S is put on, what will happen to the brightness of bulbs X and Z if the resistance of bulb Y is increased,*
A: bulbs X and Z will be brighter B: bulbs X and Z will be dimmer C: Bulb X same, bulb Z dimmer D: Bulb X brighter, Bulb Z same
Explanation_____ Confidence level___

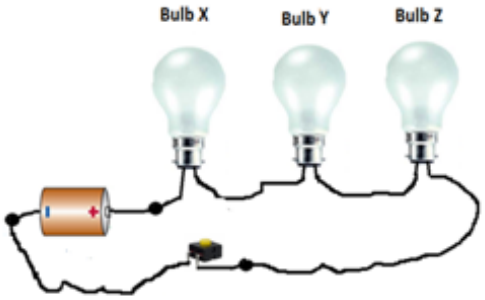

Question 3*: When switch S is on, it was found that bulbs X and Z are glowing , but bulb Z did not glow at all. The reason for bulb Z not glowing is because:*

A: Bulb Z has a very high resistance B: Bulb Z has a very low resistance C: Current will be too weak by the time it reaches z
Explanation_____ Confidence level___

Question 4: *When switch S is on, do you think the speed of charges through the whole circuit will be the same?*

A: Yes B : No C: Not sure
Explanation_____ Confidence level___

Figure 1: Three-tier concept test

3 Results and Discussion

In this section, the question will be presented, then its intention and later the results per question will be presented as subsections of the options selected by participants. The correct options are colored red together with their level of confidence.

3.1 Question 1 results: Which bulb will glow first?

The question probed students' understanding of how electric field causes charges to move simultaneously when the switch is turned on. Table 1 (left) represents percentage options and level of confidence selected by students. According to table 1, 40 % of students opted the correct choice which is "ALL", and another 40 % chose bulb X while the remaining chose bulb Z. It should be noted that all percentages were converted to the nearest whole number.

Confidence Level	ALL	Bulb X	Bulb Z
Level 1	7	5	0
Level 2	5	9	2
Level 3	9	9	0
Level 4	5	7	7
Level 5	14	9	9
Total	40	40	19

Table 1: Percent students' responses to question1

Confidence Level	Bulbs X &Z will be brighter	Bulbs X &Z will be dimmer	Bulb X same, and Z dimmer	Bulb X dimmer & Z brighter
Level 1	7	2	0	9
Level 2	2	9	5	0
Level 3	14	7	2	2
Level 4	0	7	5	0
Level 5	5	23	0	0
Total	28	49	12	12

Table 2: Percent students' responses to question 2

3.1.1 The ALL option Only one student (2 %) with a level 5 confidence rating gave the correct explanation. It was expected that all students with a level of confidence above 3, which is 20% of the correct choices will give the correct explanation, but their explanations were opposite. For example, one of the notable explanations given by a student with level 4 confidence rating was: "*In a series circuit, all the bulbs (X, Y, and Z) will light up at the same time when the switch is turned on. This is because in a series circuit, the current flows through each bulb one after the other, so the same amount of current reaches all bulbs at the same time*." The statement revealed two misconceptions: "*current flow in a sequence*" and "*same time related to same current in the series circuit*." The explanation shows that the students opted for the correct answer with the incorrect reasoning even if the level of confidence was high.

Another notable explanation given by a student with level 1 rating was "*Before the lights go on the current and voltage given by a battery will start by moving from positive to negative terminal without lighting the bulbs, by that it will be observing whether the bulbs are connected is series or parallel then the second move after checking it will turn on the light at the same time*." The explanation shows students' lack of understanding of what a voltage is and misconception at the same time. The idea that voltage first observes if the circuit is in series or parallel before turning the light is new misconception. Forty percent chose bulb X. One of the notable explanations given by student with level 1 is: "*Current flows from positive to negative terminal of the battery and bulb X is connected to the positive terminal of the battery, which means it will receive the current first to light*." This is what was called "the conventional direction of current challenge". It shows that conventional direction of current was not explained qualitatively [10].

3.1.2 The Bulb Z option One of the notable explanations given by a student was about the position of the switch in a circuit. *"As current flow from positive to negative, current will not pass switch S to reach Bulb Z."* That shows misunderstanding because current is the same in a series circuit.

3.2 Question 2 results: The impact of changing the resistance of bulb Z.

The question probed students' understanding of the global impact of changing and circuit element. The correct choice is: the brightness of bulbs X and Z will decrease because increasing the resistance of bulb Y will automatically increase the total resistance of the circuit, reducing the current at the same time. In series circuits the brightness of the bulb depends on current. Table 2 shows that 49 % of students opted for the correct choice and about 30 % of the 49 % have the level of confidence of above level 3, which means that they are confident about their choices and explanations they gave.

3.2.1 Bulbs X and Z will be brighter Table 1 (right) shows that this option was chosen by 28 % of the participants, and most of them were not that confident. However, one of the explanations by a student with confidence level 5 was: "Since *resistance is inversely proportional to the current bulb X and Z will receive a great current which will make them to increase in bright since their resistance is lowered."* Another notable

explanation was: "*The current flow to the bulb Y will be decreased allowing more current flow to the other two bulbs thus increasing their brightness*."

3.2.2 Bulbs X and Z will be dimmer Table 2 shows that the correct option was chosen by almost 50 % of students and only 14 % gave the correct explanations, the others revealed lack of understanding as revealed by the following statement: "*the answer i'm looking for i can't see...i would say the brightness of both X and Z would remain the same ...they are not affected by bulb Y's change...unless if the switch plays a part.*"

3.3 Question 3 results: Why is bulb Z not glowing?

This question was aimed at checking students' understanding of the difference between the conductor and the resistor.

Confidence level	Very high resistance	Very high low resistance	Current too weak by the time it reaches Z
Level 1	14	2	2
Level 2	14	2	0
Level 3	21	0	7
Level 4	12	2	5
Level 5	14	0	5
Total	74	7	19

Table 3: Percent of students' responses to question 3

Confidence Level	Yes	No	Not sure
Level 1	12	12	0
Level 2	2	2	5
Level 3	14	9	2
Level 4	5	16	2
Level 5	7	12	0
Total	**40**	**51**	**9**

Table 4: Percent of students' responses to question 4

In a basic series electric circuit with bulbs, when the switch is put on, energy transformation which causes the bulb to glow will happen in a resistor due to the speed of charges through the resistor. The series circuit was chosen because it has been noted that students already memorized that current is the same in series circuit. The results of this question were consistent with the one reported previously. The following sub-sections discuss the options and explanations preservice students gave.

3.3.1 A very high resistance option Based in table 3, this option was chosen by 74 % of preservice students and 26 % of their level of confidence was above level 3, which shows that they were confident about the choice of option and their explanations. However, their explanation revealed the misconception they have. They indicated that bulb Z has a very high resistance, that's why it is not glowing. Their reasoning was based on their lack of knowledge of the difference between a conductor and a resistor. The difference between a resistor and a conductor is key when teaching basic electric circuit using the field model *[4]*.

3.3.2 A very low resistance option This was the correct option scientifically. Bulb Z is not glowing because it is acting as the conductor with low resistance which doesn't get burnt when charges are moving through it. Only 7 % of the students opted for this one. Based on their explanations, it can be concluded that they guessed the answer. One of the explanations with level 4 confidence level was "The *more resistance a bulb has, the brighter it will be.*" This is only applicable when resistors are connected in series.

3.3.3 Current too weak by the time it reaches Z This option was a misconception also reported previously. Based in table 3, only 19 % selected this option, however their explanations revealed additional misconceptions as evident on the following notable explanations: **"***Current moves from positive to negative, so current was able to move from battery to X and Y then it is situated after them and it was opened leading to less current delivered to bulb Z because of the open switch."* Another interesting explanation by students with level confidence of 5 was as follows: *"Charges take a longer distance to reach Bulb Z which by then it will receive a shorter current."* This is the distance misconception and again can be solved by introducing the field model to teach basic DC circuit *[4]*. Again, another student indicated that: "*In a series circuit, the current flows through each component in sequence. As the current flows through each component, some of the energy is lost, reducing the current, by the time the current reaches bulb Z, it may be too weak to light it up*." This misconception was also reported in literature *[10]*.

3.4 Question 4 results: The speed of charges in basic electric circuit

This question was a continuation of question 3. The speed of charges in an electric circuit determines how energy can be converted. Scientifically charges move faster in a resistor than in a conductor even in a series circuit. The most appropriate answer is "yes". 40 % of students opted for the correct answer and their level of confidence is shown in table 2 (right).

Some of the misconception revealed by those who are confident but opted for incorrect choices are the following: Student 1 (confident level 5): "*The speed of the charges remains the same throughout the circuit*". This is a misconception that arises from the fact that current is the same in series circuit. To address this misconception, it is advisable to define current as "the number of charges that passes through a cross-section in one second. Student 2 indicated that: "*The flow of charges is referred to as current, and it must be noted that resistors in series divide voltage and share current, hence since the current is the same throughout, the speed of charges will be the same throughout as well*." Lastly, student 3 (confident level 4) indicated that: "*In a series circuit, the current flows through each component in sequence, resulting in a constant current that is the same throughout the circuit. As a result, the speed of charges is also the same throughout the circuit, as it is determined by the electric field."* Nothing significant about the last option "not sure option"

4 Conclusion

The misconception that "*current flows in sequence*" [10] in a circuit and the one that says "*the bulb nearest the positive terminal of the battery will shine first when the switch is put on*" can be handled well using the field model [4] using the fact that electric field is established throughout the whole circuit when the switch is put on. The misconception that "*Before the lights go on the current and voltage given by a battery will start by moving from positive to negative terminal without lighting the bulbs, by that it will be observing whether the bulbs are connected is series or parallel then the second move after checking it will turn on the light at the same time*" can be claimed to be new misconceptions and can also be dealt with using the field model [4]. It is worrying because teachers are not using the field model while teaching the basic electric circuit. The study recommends that textbooks or guides be written on how to teach basic electric circuits using the field model so that teachers can be professionally capacitated to teach using the model. The study concurs with [11] who recommended that "teacher education programs should involve misconceptions and also facilitate the development of conceptual perceptions about teaching" and [12] about further continuous research on the identifications and handling of misconceptions. Below is the summary of additional findings.

4.1 The difference between a conductor and a resistor.

Based on the analysis of preservice students' responses, it can be claimed that the students who participated in the study do not understand the difference between the conductor and resistor and in addition they also don't understand the fact that charges can move at different speed in a series circuit while maintaining the same current. According to *[4],* these challenges can be addressed by introducing the field model and qualitative emphasizing the role of the physical components of basic electric circuit before dealing with the conceptual quantities, like resistance, current and potential difference *[13]*.

4.2 Ohm's law challenge

The study presented two conceptual challenges related to Ohm's law and the conventional direction of electric current. *Ohm's law challenge* was described students' misinterpretation of Ohm's law as follows: While the current in the circuit depends on the resistance of the resistors, resistance do not depend on current but at the same time, during calculations related to Ohm's law equation V=IR, both current and potential difference can be used to estimate the resistance of the resistor. This challenge, if not handled qualitatively, can lead to misconceptions about the dependence of resistance on current and potential difference. This is what was called Ohm's law challenge in this study.

4.3 The current convention challenge

In this study, the current convention challenge was described as first year pre-service students' inability to understand that the current convention deals with direction of a positive test charge in an electric field region which is taken as the direction of current, not that current flow sequentially from one point to another. This challenge can also be resolved using the field model [4] where the rapid establishment of the field through the whole circuit almost at the speed of light explains the movement of all charges at the same time. If this challenge is not resolved, students can have misconceptions related to sequential reasoning [10] as revealed by some of the students who confidently answered question 1 as follows: *Bulb X will shine first because it is nearer to the*

positive terminal of the battery. Based on experiences of researchers, the majority of first year students have this misconception that is the reason it was called “the current convention challenge”. Preservice teachers’ lecturers are advised to design activities to deal with the challenge

4.4 Confidence “level and conceptual understanding

Although the current study found no correlation between students' confidence and conceptual understanding, it did find that most misconceptions are identifiable through explanations where students feel confident about their incorrect choices. Further research should be conducted to more institutions to determine if is always the case that students ‘confidence is unrelated to students’ conceptual understanding.

4.5 Limitation of the study

Based on the qualitative nature of the study limited to only first year preservice teachers at one university in South Africa, it cannot be generalized to other different contexts, however teachers and preservice lecturers can use the knowledge of identifying misconceptions when doing their preparations before intervention.

References

[1] R. Cohen, B. Eylon and U. Ganiel, "Potential difference and current in simple electric circuits: A study of students’concepts.," *American Journal of Physics,* vol. 51, no. 407, p. 407–412, 1983.

[2] Department of Basic Education, 2024 NATIONAL SENIOR CERTIFICATE (NSC) DIAGNOSTIC REPORT BOOK 1, Pretoria: Department of Basic Education, 2025.

[3] L. C. McDermott and P. Shaffer, " Research as a guide for curriculum development: an example from introductory electricity part I: Investigation of student understanding.," *American Journal of Physics,* vol. 60, no. 11, pp. 994-1003, 1992.

[4] S. Stocklmayer, "Teaching Direct Current Theory Using a Field Model.," *International Journal of Science Education,* vol. 32, no. 13, pp. 1801-1828, 2010.

[5] R. Sheldrake, "Confidence as motivational expressions of interest, utility, and other influences: Exploring under-confidence and over-confidence in science students at secondary school," *International Journal of Educational Research,* vol. 76, p. 50–65, 2016.

[6] H. Peşman and A. Eryilmaz, "Development of a Three-Tier Test to Assess Misconceptions About Simple Electric Circuits," *The Journal of Educational Research,,* vol. 103, p. 208–222, 2010.

[7] D. Nurwati, P. Suradi and N. Arsyad, "Development and Application of a Three-tier Test Diagnostic Instrument to Assess Junior High School Students’ Misconceptions in Algebra," in *Proceedings of the 1st International Conference on Advanced Multidisciplinary Research (ICAMR 2018)*, 2019.

[8] J. Jonathan Bayuo, L. Aziato, K. Wong, J. A.-O. H. Su and F. Wong, "Phenomenography: An emerging qualitative research design for nursing," *J Adv Nurs. ,* vol. 80, p. 821–834, 2024.

[9] F. Han and R. Ellis, "Using Phenomenography to Tackle Key Challenges in Science Education," *Frontiers in Psychology,* vol. 10, 2019.

[10] H. KÜÇÜKÖZER and S. KOCAKÜLAH, "Secondary School Students’ Misconceptions about Simple Electric Circuits," *Journal of TURKISH SCIENCE EDUCATION,* vol. 4, no. 1, pp. 101-115, 2007 .

[11] K. Moodley and E. Gaigher, "Teaching Electric Circuits: Teachers’ Perceptions and Learners’ Misconceptions," *Res Sci Educ,* 2017.

[12] I. Prastyaningrum and H. Pratama, "Student conception of Ohm’s law," in *J. Phys.: Conf. Ser.1321 022028*, 2019.

[13] M. Khwanda, P. Molefe and B. Sondezi, "Students’ understanding of physical components of electrical circuits".

Quantum computing education availability in South Africa

Coral Featherstone and Laing Lourens

NextGen Enterprises and Institutions Cluster, Council for Scientific and Industrial Research (CSIR), Pretoria, South Africa

E-mail: cfeatherstone@csir.co.za

Abstract. Quantum computing (QC) education in South Africa is gaining momentum through formal initiatives within universities, and research institutions. This study explores the availability of QC courses for South African students, assessing their target levels, prerequisites, and structure. By analysing prospectus documents, course content, and university websites across all 26 public universities, the study finds that only three institutions — WITS, UKZN, and SUN — explicitly provide QC modules. Many universities offer quantum physics as part of their physics curricula but do not extend this into standalone QC courses. These findings highlight gaps in course visibility, challenges with cross-departmental coordination, and missed opportunities to make QC education easier to find and a ccess. The results aim to support prospective students, educators, and policy-makers in strengthening national QC capability.

1 Introduction

QC is gaining prominence in education globally as quantum hardware matures. A document prepared for the Department of Science and Innovation (DSI) in 2021 by the South African Quantum Technology Initiative (SA QuTI) [1] highlighted education programmes as a key priorities. The document, prepared in 2021, served as the basis for investigating the current state of QC education content available to South African students.

SA QuTI identified three main centres for QC, University of KwaZulu-Natal (UKZN), University of the Witwatersrand (WITS), and Stellenbosch University (SUN) [1], also mentioning University of Pretoria (UP), University of Johannesburg (UJ), University of Cape Town (UCT), and identified several other universities (Cape Peninsula University of Technology (CPUT) and University of Zululand (UNIZULU)) as emerging centres. The document also mentioned that 10 local universities had staff and/or Postgraduate students interested in QC and quantum technology. This study aimed to identify universities offering programs specific to QC and to determine whether any additional institutions had introduced QC programs since 2021.

2 Research Objectives

In order to understand the current state of QC education available to South African students, the following research questions were considered:

1. Which South African universities offer QC education?
2. How is QC integrated into the curriculum at these universities?
   (a) Is it part of a general physics course, a module within a broader course, or a standalone course?
   (b) At what academic level (e.g., undergraduate, postgraduate) are these courses or modules offered?
3. What specific topics or content are covered in the QC courses or modules, if available?

3 Methodology

This study follows a qualitative research design using document analysis. This alignment allows for the systematic examination of institutional artefacts (university prospectuses) while acknowledging that interpretation is inherent in qualitative classification.

After identifying the 26 South African Universities, the enquiry proceeded in the following stages:

1. An online search was done in order to identify the prospectus documents (guide books) for each university. These documents were analysed for course content in order to identify modules that included quantum mechanics, and more specifically, QC components. These were analysed separately for undergraduate (UG) and postgraduate (PG).
2. For the universities where QC courses were identified, a search was performed in order to inspect the curricula of these courses. In cases where the curricula were not easily available, emails were sent to the identified universities requesting further information.
3. To supplement these findings, a targeted search using the "site:ac.za" domain and the phrase "quantum computing" was performed on the Google search engine from January 2024 to October 2025 to find additional references to quantum computing within institutional websites. Results were screened for relevance and cross-verified against the prospectus documents for consistency.

A simple web search did not return all the prospectus documents required, so each university's website was visited. The prospectus documents are cited alongside the university names in Table 1. A reflection on the prospectus documents is provided in Section 5.

4 Results and Discussion

4.1 Prospectus-Based Survey of Quantum Education in South Africa

This section analyses the presence of QC and quantum physics (QP) content in officially published prospectus documents, accessed via university websites. The analysis covers listings for the 2025 or 2026 academic years, depending on availability.

Table 1 provides a high-level summary of whether UG, and PG level quantum physics and QC content was explicitly mentioned. It is important to note that the presence of general physics subjects (e.g., "Physics II") without detailed descriptions often made it unclear whether QP or QC was included. In such cases, entries were marked as indeterminate. The table also lists counts of results (for the 26 official universities) for a general web search for the phrase "quantum computing" and restricted to the domain ".ac.za" for the date range January 2024 to October 2025.

Table 2 lists the few universities whose prospectus documents explicitly mention QC modules or topics. Overall, prospectus content suggests that QC is mentioned explicitly in only a small number of universities, and full module descriptions remain limited or absent. Further clarification from the universities was sought directly and is presented in Section 4.2.

UCT's UG prospectus mentions QC in a summary under physics [17], but doesn't expand on particular course detail. An analysis of UCT's physics curriculum does not reveal any QC content [18].

While not found in any prospectus, UJ's Mathematics and Applied Mathematics department website indicates that they occasionally offer a QC module [44].

WITS offers two structured electives within their Faculty of Engineering and the Built Environment. Although not indicated by any prospectus QC is listed as a research interest within the WITS Structured Light Laboratory [34], indicating that QC at PG level is a probability.

UKZN has a UG and PG prospectus [22] indicating a physics department/s on two campuses, but neither contains details of the specific modules on offer. As with SUN, they are one of the known QC nodes, and as their quantum website indicates, do in fact teach QC and offer QC PG research.

VUT only mentions quantum physics once in the description of a module called "Physical Chemistry IV" [40].

For the universities where QC courses were identified, a search was performed in order to inspect the curricula of these courses. In cases where the curricula were not easily available, emails were sent to the identified universities requesting further information This examination suggests that while many South African universities include

QP in their curricula, only two institutions explicitly mention QC in their prospectus documentation: WITS, and

University	QP UG	QP PG	QC UG	QC PG	Result count
Cape Peninsula University of Technology (CPUT) [2]	×	×	×	×	0
Central University of Technology (CUT) [3]	×	×	×	×	0
Durban University of Technology (DUT) [4]	×	×	×	×	0
Mangosuthu University of Technology (MUT) [5, 6]	×	×	×	×	0
Nelson Mandela University (NMU) [7]	✓	?	×	×	3
North-West University (NWU) [8, 9]	×	×	×	×	0
Rhodes University (RU) [10]	?	?	×	×	0
Sefako Makgatho Health Sciences University (SMU) [11]	?	?	×	×	1
Sol Plaatje University (SPU) [12]	?	×	×	×	0
Stellenbosch University (SUN) [13, 14, 15]	✓	✓	?	✓	31
Tshwane University of Technology (TUT) [16]	✓	✓	×	×	0
University of Cape Town (UCT) [17, 18]	✓	✓	×	×	8
University of Fort Hare (UFH) [19]	✓	✓	×	×	2
University of the Free State (UFS) [20]	×	×	×	×	2
University of Johannesburg (UJ) [21]	?	?	×	×	14
University of KwaZulu-Natal (UKZN) [22]	?	?	?	?	9
University of Limpopo (UL) [23]	×	×	×	×	0
University of Mpumalanga (UMP) [24, 25, 26, 27]	×	×	×	×	0
University of Pretoria (UP) [28]	×	×	×	×	8
University of South Africa (UNISA) [29]	✓	?	×	×	4
University of the Free State (UFS) [20]	×	×	×	×	2
University of the Western Cape (UWC) [30, 31]	✓	✓	?	?	0
University of the Witwatersrand (WITS) [32, 33, 34]	✓	✓	✓	?	17
University of Venda (UNIVEN) [35]	×	×	×	×	0
University of Zululand (UNIZULU) [36, 37, 38, 39]	?	?	×	×	1
Vaal University of Technology (VUT) [40, 41]	?	?	×	×	0
Walter Sisulu University (WSU) [42, 43]	✓	✓	×	×	1

Table 1: Map of Quantum Physics (QP) and Quantum Computing (QC) in South African university prospectuses by undergraduate (UG) and postgraduate (PG) alongside counts of results for a general search for the phrase "quantum computing" and restricted to the domain ".ac.za" for the date range January 2024 to October 2025

✓ means Yes; × means No; ? means not specified, inferred, or unclear from available sources.

University	Department	Level	Module Details
SUN	Computer Science	PG	65048-746 Adv. Topics II - Quantum Computing [15]
UCT	Department of Physics	UG	QC is mentioned in the physics summary of the main prospectus [17]; however, no courses mentioned in the physics prospectus specify any QC content [18]
UKZN	School of Chemistry and Physics	UG/PG	QC in summary and module list; PHYS714: Quantum Computation
WITS	School of Electrical and Information Engineering	UG/PG	ELEN4022A: Full Stack Quantum Computing (2025)

Table 2: Universities listing explicit quantum computing modules or research in their prospectus documents.

SUN, preferring instead to host quantum specific websites [1,2,3]. Among these – and again strictly according to the available prospectuses – WITS provides a standalone module dedicated to full-stack quantum computing, UKZN lists QC in both UG and PG materials, and SUN, provides a PG module on advanged QC topics.

Several universities offer courses such as quantum mechanics or quantum theory at advanced UG levels, with some (such as UNISA and UP) also including course codes and module descriptions. However, these are typically embedded within broader physics or applied sciences degrees.

4.2 Curriculum Overview for Universities that offer QC Courses

This section aims to analyse the different topics and content available in QC courses. This section starts with Table 3 which summarises the specific QC courses on offer at South African Universities before discussing curricula for these courses, as well as other information provided by relevant departments upon request.

University	Course code	Level
SUN	65048-746 - Adv. Topics II - Quantum Computing	Honours
UKZN	One courses is given under two course codes. Detail is given in Section 4.2.2. The university has PG QC opportunities.	
	COMP718 Contemporary Topics in Computer Science B	Honours
	PHYS737 Advanced Topics in Quantum Physics	Honours
WITS	ELEN4022A - Full Stack Quantum Computing [33, 32]. Emphasis on real hardware, quantum algorithms, and applied engineering techniques. Assumes programming skills and basic knowledge of quantum mechanics and linear algebra.	Honours elective
	ELEN7069A - Applied Quantum Computing [33]. Course description for ELEN7069A was not publicly available or provided at the time of writing.	Masters

Table 3: Summary of responses from individuals within universities known to provide QC content

4.2.1 SUN From the available information on the SUN Faculty of Science website, there is an honours module offered to Computer Science students [15]. The curriculum is not described on this page, although it is mentioned that "this course on quantum computing is specifically designed for computer science honours students, so Physics as undergraduate is not a prerequisite".

4.2.2 UKZN UKZN indicated that they provide one QC course with two course codes targeted at computer science and physics students. The course is divided into two parts, "Basic principles of quantum computing and quantum algorithms", and "Quantum algorithms for machine learning". Part 1 of the course covers: postulates of quantum computing, qubits, quantum gates, quantum circuits, universal gate sets and advanced techniques for quantum circuits, Deustch-Jozsa algorithm, quantum simulation algorithm, quantum search algorithm, quantum Fourier transform, and Shor's Algorithm. Part 2 of the course covers: data encoding, quantum kernel methods, variational quantum classifiers, Harrow-Hassidim-Lloyd algorithm (HHL) and matrix inversion, and quantum advantage in machine learning.

4.2.3 WITS WITS University offers two official QC courses within its Faculty of Engineering and the Built Environment. According to the provided course outline, ELEN4022A introduces QC with a focus on near-term applications and implementation on real quantum hardware. It builds on students' prior knowledge of quantum mechanics and programming and covers topics such as quantum algorithm design, quantum information processing, hardware constraints, and applied quantum engineering techniques. The course also includes exposure to industry-recognised toolchains and emphasises practical approaches to solving constrained real-world problems. Members of the unit were kind enough to provide us with attendance information. In the first year 22 students took the course, which was considered high for an elective. Subsequent years saw the attendance move to 21, then 7, and 9. It appears as though students are becoming more intimidated by the course. This is in agreement with international

[1] https://www.wits.ac.za/witsq/research/computing/

[2] https://quantum.sun.ac.za/

[3] https://quantum.ukzn.ac.za/

literature which is making a concerted effort to make QC more accessible to students [45, 46, 47, 48, 49, 50]. They also thought that Covid19 may have played a role in the drop in attendance. There is also some indication that PG QC activity takes place within the Structured light Laboratory within WITS' School of Physics. The lab conducts QC research primarily focused on photonic quantum systems.

4.2.4 African Institute for Mathematical Sciences (AIMS) Since AIMS follows a "visiting lecturer" model, the courses on offer differ from year to year. The 2024/2025 curriculum included masters level courses on "Quantum Computing", "Quantum Information", "Lie Algebras and Representation Theory" and "Hilbert Space Theory", as well as more general skills courses on problem solving in mathematics and physics [51].

4.3 Targeted Web Search for "Quantum Computing"
A targeted search restricted to South Africa's academic web domain (site:ac.za) and the phrase "quantum computing" was performed on the Google search engine. The search from January 2024 to October 2025, which overlaps with the years of the prospectuses that were identified ending at the time of writing. Table 1 shows the result count. Table 4 shows the result counts for organisations with the academic web domain, that were not one of the 26 official public universities.

The results were mostly consistent with the prospectus documents, although UKZN had a lower search count than would be expected. The National Institute for Theoretical and Computational Sciences has strong ties to UKZN and SUN; which may account for the low UKZN article count. The search results also showed that the African Institute for Mathematical Sciences occasionally has QC courses and a private university called Richfield Graduate Institute of Technology presents some IBM-based QC courses. Most of the low-count results were general articles mentioning that QC was important and highlighting known individuals in the field. The Centre for High Performance Computing (CHPC) has recently acquired access for South African universities and academics to QC hardware, which accounts for their presence in the results.

University	**Result count**
African Institute for Mathematical Sciences (AIMS)	3
Centre for High Performance Computing (CHPC)	4
The National Institute for Theoretical and Computational Sciences (NITheCS)	19
Richfield Graduate Institute of Technology (Pty) Ltd	3

Table 4: Counts of results for a general search for the phrase "quantum computing" and restricted to the domain ".ac.za" for the date range January 2024 to October 2025 for academic domain results outside of the 26 official universities.

5 Reflections and Recommendations

Prospectuses were often difficult to locate and varied in structure, with some hosted per faculty and others as individual module listings. Improving public access through consolidated or indexed pages would benefit prospective students, as demonstrated by Durban University of Technology [4], and Nelson Mandela University [7].

A complication with finding QC courses is that it is difficult to determine which department provides the courses. This study found that QC could be offered under physics, mathematics, or computing and in engineering as was the case with WITS University. Sanusi and Deriba claim that South Africa lacks studies on STEM educational experiences [52]. The authors did not find literature on QC education experiences in South Africa. The mapping of prospectus content (see Tables 1 and 2), indicates an opportunity for strategic curriculum development to ensure alignment with emerging quantum technologies and national capacity-building efforts for South Africa.

6 Conclusion

The teaching of QC remains limited to a small number of institutions — specifically, SUN, UKZN, and WITS. While QC is most often situated within physics departments, WITS is also offering it in the Engineering department. Some South African universities are offering modules from one department under different codes for computer science students, demonstrating a more interdisciplinary approach.

In many cases, locating course information through prospectuses or public sources proved difficult, suggesting that some relevant material may not be readily visible to prospective students. This may contribute to an under-representation of interested students who might otherwise pursue the subject. Only two universities provided full module descriptions or descriptors in the prospectus documents, out of the 26 universities in South Africa; making it difficult to assess the consistency or depth of QC instruction nationally.

Future research could include student satisfaction surveys in order to better understand which aspects of QC courses present challenges, especially for those from non-physics backgrounds.There is limited insight into how QC is being taught at the high school or non-graduate levels. Further studies could explore this gap and support curriculum design efforts in improving QC accessibility in South African universities.

References

[1] National Working Group for Quantum Technology, "Framework for quantum technology driven research and innovation in South Africa," Department of Science and Innovation (DSI), Tech. Rep., 2021, available at: https://saquti.org/wp-content/uploads/2025/02/framework-for-quantum-technology-driven-research-and-innovation-in-south-africa-003.pdf.

[2] Cape Peninsula University of Technology. (2026) Undergraduate prospectus 2026. Accessed June 30, 2025. [Online]. Available: https://www.cput.ac.za/study/apply

[3] Central University of Technology, Free State. (2025) Undergraduate and postgraduate programmes offered. Accessed June 30, 2025. [Online]. Available: https://www.cut.ac.za/programmes-offered

[4] Durban University of Technology. (2025) 2025 faculty handbooks. Accessed June 30, 2025. [Online]. Available: https://www.dut.ac.za/student_services/handbooks

[5] Mangosuthu University of Technology. (2025) Undergraduate prospectus 2025. Accessed June 30, 2025. [Online]. Available: https://www.mut.ac.za/wp-content/uploads/2023/09/Undergraduate-Prospectus.pdf

[6] ——. (2025) Faculty of Engineering prospectus 2025. Accessed June 30, 2025. [Online]. Available: https://www.mut.ac.za/wp-content/uploads/2024/11/2025-Engineering-Propectus.pdf

[7] Nelson Mandela University. (2026) Undergraduate prospectus 2025/2026. Accessed June 30, 2025. [Online]. Available: https://www.mandela.ac.za/Study-at-Mandela/Discovery/Quick-guides

[8] North-West University. (2025) Undergraduate prospectus 2025. Accessed July 31, 2025. [Online]. Available: https://studies.nwu.ac.za/sites/studies.nwu.ac.za/files/files/undergrad/2025/2025Grade-12-Prospectus.pdf

[9] ——. (2026) Physics prospectus 2026. Accessed July 31, 2025. [Online]. Available: https://studies.nwu.ac.za/sites/studies.nwu.ac.za/files/files/yearbooks/2025/17_FENG-PG-2025_BM.pdf

[10] Rhodes University. (2025) Curriculum selection – admission gateway. Accessed June 30, 2025. [Online]. Available: https://www.ru.ac.za/admissiongateway/application/curriculumselection

[11] Sefako Makgatho Health Sciences University. (2026) Prospectus 2026. Accessed July 31, 2025. [Online]. Available: https://www.smu.ac.za/wp-content/uploads/2025/04/SMu-Prospectus-2025_2026.pdf, https://www.smu.ac.za/3d-flip-book/smu-prospectus-2025_2026

[12] Sol Plaatje University. (2026) Undergraduate prospectus 2026. Accessed June 30, 2025. [Online]. Available: https://www.spu.ac.za/wp-content/uploads/2025/04/2026-Undergraduate-Prospectus.pdf

[13] Stellenbosch University. (2025) Undergraduate prospectus 2025. Accessed June 30, 2025. [Online]. Available: https://www.sun.ac.za/english/Documents/Yearbooks/Current/Science-2025.pdf

[14] ——. (2025) Data Science and Computational Thinking. Accessed July 30, 2025. [Online]. Available: https://www.sun.ac.za/english/pgstudies/Pages/Data%20Science/School-for-Data-Science-PG-programmes.aspx

[15] Department of Computer Science, Stellenbosch University. (2025) Postgraduate modules. Last updated July 21, 2025. [Online]. Available: https://www.cs.sun.ac.za/teaching/PG/

[16] Tshwane University of Technology. (2025) Faculty of Science prospectus 2025. Accessed June 30, 2025. [Online]. Available: https://tut.ac.za/images/prospectus/Part8_Science_2025.pdf

[17] University of Cape Town. (2026) Undergraduate prospectus 2026. Accessed June 30, 2025. [Online]. Available: https://uct.ac.za/sites/default/files/media/documents/ug-prospectus-2026-april.pdf

[18] ——. (2026) Physics prospectus 2026. Accessed June 30, 2025. [Online]. Available: https://science.uct.ac.za/sites/default/files/content_migration/science_uct_ac_za/2535/files/UCT_Physics_handbook_2020.pdf

[19] University of Fort Hare. (2025) 2025 undergraduate prospectus — Science. Accessed June 30, 2025. [Online]. Available: https://www.ufh.ac.za/wp-content/uploads/2025/01/2025-SA-Prospectus-Online-Version.pdf

[20] University of the Free State. (2025) Undergraduate prospectus 2025. Accessed June 30, 2025. [Online]. Available: https://www.ufs.ac.za/docs/librariesprovider44/study-at-the-ufs/ufs-undergrad-prospectus-2025---future-focused.pdf

[21] University of Johannesburg. (2025) Undergraduate prospectus 2025. Accessed June 30, 2025. [Online]. Available: https://www.uj.ac.za/wp-content/uploads/2024/03/uj-undergraduate-prospectus-2025.pdf

[22] University of KwaZulu-Natal. (2025) Undergraduate prospectus 2025. Accessed June 30, 2025. [Online]. Available: https://ww1.applications.ukzn.ac.za/prospectus

[23] University of Limpopo. (2025) Prospectus 2025. Accessed June 30, 2025. [Online]. Available: https://www.ul.ac.za/wp-content/uploads/2024/12/Student-Prospectus-2025.pdf

[24] University of Mpumalanga. (2025) Bachelor of Information and Communication Technology. Accessed October 15, 2025. [Online]. Available: https://www.ump.ac.za/Study-with-us/Faculties-and-Schools/Faculty-of-Agriculture-and-Natural-Sciences/School-of-Computing-and-Mathematical-Sciences/Bachelor-of-Information-and-Communication-Technolo.aspx

[25] ——. (2025) Bachelor of Science Degree. Accessed October 15, 2025. [Online]. Available: https://www.ump.ac.za/Study-with-us/Faculties-and-Schools/Faculty-of-Agriculture-and-Natural-Sciences/School-of-Biology-and-Environmental-Sciences/Bachelor-of-Science-Degree.aspx

[26] ——. (2025) Master of Computing. Accessed October 15, 2025. [Online]. Available: https://www.ump.ac.za/Study-with-us/Faculties-and-Schools/Faculty-of-Agriculture-and-Natural-Sciences/School-of-Computing-and-Mathematical-Sciences/Master-of-Computing.aspx

[27] ——. (2025) Master of Science. Accessed October 15, 2025. [Online]. Available: https://www.ump.ac.za/Study-with-us/Faculties-and-Schools/Faculty-of-Agriculture-and-Natural-Sciences/School-of-Biology-and-Environmental-Sciences/Master-of-Science.aspx

[28] University of Pretoria. (2025) Undergraduate prospectus 2025. Accessed June 30, 2025. [Online]. Available: https://www.up.ac.za/media/shared/368/Faculty%20Brochures/2025/up_ug-prospectus-2025_nsc-ieb_devv5_web.zp246017.pdf

[29] University of South Africa. (2025) Prospectus 2025. Accessed June 30, 2025. [Online]. Available: https://www.unisa.ac.za/static/corporate_web/Content/Colleges/CSET/documents/2025%20CSET%20Prospectus.pdf,https://www.unisa.ac.za/sites/corporate/default/Register-to-study-through-Unisa/Subjects-&-modules/All-modules/Quantum-Physics-%E2%80%93-PHY3702

[30] University of the Western Cape. (2025) Physics 314 - quantum physics and applications. Accessed October 15, 2025. [Online]. Available: https://ap.uwc.ac.za/download.aspx?file=http://172.16.202.219/sasilive/MODUL_2025PHY314_12b041f1070f54fb.pdf

[31] ——. (2025) Physics 722 - quantum and statistical physics. Accessed October 15, 2025. [Online]. Available: https://ap.uwc.ac.za/download.aspx?file=http://172.16.202.219/sasilive/MODUL_2025PHY722_0ae883c84e1110be.pdf

[32] University of the Witwatersrand, *ELEN4022A Full Stack Quantum Computing – 2025*, 2025, module document provided by user.

[33] University of the Witwatersrand, Johannesburg, *2025 Rules and Syllabuses - Faculty of Engineering and the Built Environment*, Johannesburg, South Africa, Apr. 2025. [Online]. Available: https://www.wits.ac.za/media/wits-university/students/academic-matters/documents/2025%20EBE%20Rules%20and%20Syllabuses.pdf

[34] University of the Witwatersrand, *Wits Structured Light Laboratory*, 2025, module document provided by user.

[35] University of Venda. (2026) 2026 undergraduate student information brochure. Accessed June 30, 2025. [Online]. Available: https://www.univen.ac.za/wp-content/uploads/2025/04/2026-UNIVEN-Undergraduate-Student-Information-Brochure.pdf

[36] University of Zululand. (2025) 2026 Undergraduate Brochure. Accessed June 30, 2025. [Online]. Available: https://www.unizulu.ac.za/wp-content/uploads/2025/02/2026-Brochure-for-undergraduate.pdf

[37] ——. (2025) 2025 FSAE undergraduate handbook. Accessed June 30, 2025. [Online]. Available: https://www.science.unizulu.ac.za/wp-content/uploads/2025/01/2025-FSAE-Undergraduate-Handbook-1.pdf

[38] ——. (2025) 2025 Department of Engineering handbook. Accessed June 30, 2025. [Online]. Available: https://www.science.unizulu.ac.za/wp-content/uploads/2025/01/2025-Department-of-Engineering-Handbook.pdf

[39] ——. (2025) 2020 Postgraduate handbook. Accessed June 30, 2025. [Online]. Available: https://www.science.unizulu.ac.za/wp-content/uploads/2020/01/2020-FSA-Postgraduate-Handbook.pdf;https://www.science.unizulu.ac.za/physics/postgraduate

[40] Vaal University of Technology. (2025) 2025 Applied Sciences prospectus. Accessed June 30, 2025. [Online]. Available: https://vut.ac.za/wp-content/uploads/2025/06/Prospectus-Applied-Sciences-2025-UPDATED-2024-29-October-2024.pdf

[41] ——. (2025) 2025 fet prospectus. Accessed June 30, 2025. [Online]. Available: https://vut.ac.za/wp-content/uploads/2025/06/Prospectus-2025-FET-FINAL_18-Oct-24.pdf

[42] Walter Sisulu University. (2025) Faculty of Natural Sciences. Accessed June 30, 2025. [Online]. Available: https://www.wsu.ac.za/index.php/en/faculties-wsu/natural-sciences

[43] ——. (2025) Faculty of Engineering, Built Environment and IT. Accessed June 30, 2025. [Online]. Available: https://www.wsu.ac.za/index.php/en/faculties-wsu/engineering-built-env-and-it

[44] University of Johannesburg. (2025) Mathematics and Applied Mathematics postgraduate studies. Accessed July 30, 2025. [Online]. Available: https://www.uj.ac.za/faculties/science/departments-2/mathematics-and-applied-mathematics/postgraduate-studies

[45] P. P. Angara, U. Stege, and A. MacLean, "Quantum computing for high-school students an experience report," in *2020 IEEE International Conference on Quantum Computing and Engineering (QCE)*. IEEE, 2020, pp. 323–329.

[46] P. P. Angara, U. Stege, A. MacLean, H. A. Muller, and T. Markham, "Teaching quantum computing to high-school-aged youth: A hands-on approach," *IEEE Transactions on Quantum Engineering*, vol. 3, 2022.

[47] G. Carrascal, A. A. Del Barrio, and G. Botella, "First experiences of teaching quantum computing," *The Journal of Supercomputing*, vol. 77, no. 3, pp. 2770–2799, 2021.

[48] D. Franklin, J. Palmer, W. Jang, E. M. Lehman, J. Marckwordt, R. H. Landsberg, A. Muller, and D. Harlow, "Exploring quantum reversibility with young learners," in *ICER 2020 - Proceedings of the 2020 ACM Conference on International Computing Education Research*, 2020.

[49] C. C. Tappert, R. I. Frank, I. Barabasi, A. M. Leider, D. Evans, and L. Westfall, "Experience teaching quantum computing," *ASCUE Proceedings*, vol. 46, 2019.

[50] O. Salehi, Z. Seskir, and I. Tepe, "A computer science-oriented approach to introduce quantum computing to a new audience," *IEEE Transactions on Education*, vol. 65, no. 1, 2022.

[51] African Institute for Mathematical Sciences. (2024) Course overview and abstracts - 2024/2025 - Structured Master's stream. Accessed October 15, 2025. [Online]. Available: https://docs.google.com/document/d/1K7tYarC4P9xS-Mq-b_UjRnJrxegXZjaIw1RGyiXgy2Y/edit?tab=t.0

[52] I. T. Sanusi and F. G. Deriba, "What do we know about computing education in Africa? A systematic review of computing education research literature," *arXiv preprint arXiv:2406.11849*, 2024.

An Introduction to Quantum Computing - Teaching the Basics

Taariq GH Surtee[1], Ken Nixon[2] and Isaac Nape[3]

[1]Research Office, The University of the Witwatersrand, Johannesburg, South Africa
[2]School of Electrical and Information Engineering, The University of the Witwatersrand, Johannesburg, South Africa
[3]School of Physics, The University of the Witwatersrand, Johannesburg, South Africa

E-mail: Taariq.surtee@wits.ac.za

Abstract. Quantum computing has rapidly evolved since its emergence around 2016, leveraging principles of quantum mechanics to perform computations in ways classical computers cannot. We outline a tested approach to teaching quantum computing in a relatable manner, utilising concepts already familiar to students from various disciplines. By comparing classical and quantum logic gates and circuits, attendees will build a foundational understanding of the topic. Thereafter, the paper delves into set theory and probability as essential steps toward comprehending quantum states and the Bloch sphere. It will conclude with an exploration of quantum circuits and simple algorithms, incorporating hands-on examples to demystify the technology and illustrate its core principles and potential applications. All teaching slides are available at: https://doi.org/10.71796/wits-figshare.30646676.v1

1 Introduction

As quantum computing begins to reshape academic research and industry applications—particularly in fields that demand high-performance computation—it is essential to integrate quantum computing into educational and training programs. Ensuring a workforce equipped with the knowledge and skills to utilise this technology is crucial, especially as many companies are already strategising to leverage quantum computing's potential once it matures and becomes commercially viable. By introducing quantum computing concepts early across various domains, we can foster a generation of experts poised to lead advancements in this transformative technology.

While Quantum computing is an emerging and rapidly advancing field at the intersection of physics, mathematics, and engineering [1, 2]. There is a common misconception that quantum computing is reserved exclusively for physicists or experts in quantum science. Many of its fundamental components, such as quantum circuits and quantum gates, have clear parallels to classical computing, providing a basis for introducing quantum computing. For example, operations like addition and multiplication can be taught using quantum circuits in a manner conceptually aligned with Boolean logic, making them highly accessible to electronics students [3]. This overlap offers a powerful opportunity: by leveraging pre-existing knowledge, quantum computing can be taught more intuitively. Similar analogies can be drawn in other fields.

Furthermore, quantum phenomena such as superposition and state collapse, often viewed as abstract or esoteric, can be made more accessible through the use of visual aids, probability theory, and practical examples.

These are concepts well established in engineering, statistical sciences, and financial modelling curricula [4, 5]. By drawing these connections, educators can present quantum computing in a relatable and structured manner, thereby demystifying the subject for non-physics students across various disciplines.

Current hardware has experienced significant growth over the last few decades, including an increase in the number of qubits, cloud-based access, and the proliferation of quantum hardware approaches (e.g., ion-based, superconducting qubits, and photonics); however, most current systems remain noisy. Nonetheless, certain classes of computations can already be implemented through near-term intermediate-scale quantum (NISQ) computing [6]. Significant advancements are also being made to overcome the limitations caused by noise, aiming toward fault-tolerant (i.e., error-free) quantum computing architectures that fulfil all the requirements [7].

In this paper, we outline a tested approach to teaching quantum computing in a relatable manner, utilising concepts already familiar to students from various disciplines. We describe how this method has been implemented with students at different levels, detailing the strategies and tools used to bridge classical knowledge with quantum principles. We encourage course coordinators and lecturers to draw from this work and adapt it to suit their environment and teaching style. The slide stack is here: https://doi.org/10.71796/wits-figshare.30646676.v1

2 Methodology

This paper undertakes a comprehensive exploration of foundational concepts in quantum computing, including the Bloch sphere, superposition, qubits, quantum gates, circuits, measurement, and quantum states. The objective is to develop an introductory curriculum tailored for novice learners in the field. Each concept is systematically introduced within specific lectures, accompanied by clearly defined learning goals and engaging activities. Lecturers are encouraged to customise this introductory course and use it as a non-examinable introduction, or develop it further into a full stack quantum computing course.

The role of lecturers is paramount in facilitating this introductory course, as they prepare students for further academic pursuits in quantum computing. Educators must leverage their strengths and employ pedagogical methodologies that build upon students' existing knowledge, gradually incorporating novel concepts. A diverse array of teaching strategies will be utilised, encompassing visualisations, simulations, interactive tools, hands-on experiments, and the reinforcement of previously acquired knowledge, as advocated by [8-10].

A thorough understanding of quantum computing necessitates an interdisciplinary approach, integrating principles from classical computing—such as electric circuits and algorithms—with quantum-specific elements, including quantum gates and circuits. Moreover, supplemental topics in quantum physics— noise and fault tolerance—will serve to enrich students' comprehension of the subject matter. Essential mathematical constructs, particularly those related to different number bases, linear algebra, and probability, will also be examined.

To optimise pedagogical methodologies, it is crucial to provide access to a plethora of resources [10-12], including online resources, cutting-edge technologies, scholarly publications, and interactive workshops. Given the emergent nature of quantum computing, a wealth of online resources is readily available. Noteworthy texts in the field include "Introduction to Classical and Quantum Computing," [13] "IBM Qiskit," [14] and "Learn Quantum Computation Using Qiskit," [15] among others.

In summary, this paper outlines a methodical approach to introducing quantum computing by integrating interdisciplinary knowledge and promoting collaborative efforts among educators across various fields, including physics, engineering, mathematics and computer science. The subsequent section will offer a detailed breakdown of the course curriculum as structured by lecture.

3 Detailed outline of the course

This section outlines key concepts that will guide students through their exploration of quantum computing. The course begins with an examination of quantum computer hardware, distinguishing it from classical computers. Subsequently, it transitions to the fundamental principles of quantum computing, emphasising the distinctions between these two computing domains and when each is needed. Through this approach, students will gain an enhanced understanding of the evolving landscape of computational theory and practice.

3.1 Lecture 1 - What do quantum computers look like

The primary goal of this lecture is to provide an in-depth exploration of the historical development of quantum computing technologies and outline a strategic roadmap for future advancements in this dynamic field. The lecture should commence with a foundational overview of how classical computing is based on bits (0s and 1s) as the fundamental units for decision-making processes [16]. In contrast, the discussion should introduce the principles of quantum computing, which leverages qubits to represent a superposition of states, thereby enabling the simultaneous exploration of infinite possibilities [17]. This distinction will be emphasised as paramount, with the assurance that clarity will emerge as the course progresses.

A significant portion of the lecture should focus on quantum computing hardware. The lecturer should present a variety of up-to-date images illustrating quantum chips and the refrigeration systems used to house the colloquially named "chandeliers." Key concepts to be examined include superconductors and advanced refrigeration techniques to mitigate noise. To explain noise, the lecturer may employ analogies, such as the deterioration of old radio signal quality as the distance to the transmitter increases, or the pixelation of video quality due to rendering constraints. Such comparisons can reveal that reading quantum output in noisy quantum computers has implications for the reliability of obtaining answers. This should be coupled to the reason why fridges operate at the extraordinarily low temperature of -273.15 °C to optimise noise reduction.

The lecture should conclude with an introduction to the software ecosystem that supports quantum computing. Lectures should base the discussion on the particular quantum access they have available. In this case, IBM Qiskit [14], is utilised. An overview of the IBM quantum computer roadmap provides students with insight into industry trends and trajectories, sparking ideas about where they may want to take their research.

Ultimately, the objective of this lecture is to provide students with a comprehensive understanding of the current landscape of quantum computing hardware, while highlighting pertinent research in materials science and noise reduction techniques. By the end of the session, students will have a clear understanding of the distinction between bits and qubits, as well as the inherent physical limitations of quantum hardware.

3.2 Lecture 2 and 3 - Background mathematics and statistics

The goal of this lecture is to establish the foundational mathematics and statistics pertinent to both classical and quantum computing. The full adder electronic circuit serves as an effective example for illustrating the parallels between classical and quantum algorithms.

The lecturer starts the lecture with a full explanation of the concepts of decimal (Base 10) and binary (Base 2) number systems, using references like [16]. The lecturer should teach students how to convert decimal numbers to their binary equivalents and provide some addition examples to familiarise them with the binary number system. This groundwork lays the foundation for the full adder circuit.

Simulated random number generation on classical computers versus quantum random number generation should be emphasised again. This cements set theory and probability for grasping quantum output. In this segment of the lecture, the rules and symbols associated with set theory are presented, followed by an introduction to probability distributions and bell curves. Once students have an understanding of set theory, the concept of a single qubit, along with the probabilities associated with qubits' output, should be discussed. This discussion can subsequently expand to encompass multiple qubits and how probability theory could explain output.

By the end of this lecture, students are expected to possess a solid understanding of basic mathematics in base two and set theory. Students may express curiosity regarding other numeric bases, such as base 8 or base 16, and the lecturer should be prepared to demonstrate these as well. More advanced mathematical concepts, including complex numbers, linear algebra, and unitary matrices, can be introduced at this stage; however, lecturers should exercise caution, recognising that these topics constitute a course in their own right. Depending on the students' backgrounds, the lecturer may choose to explore these subjects in one or two lectures, or, as the authors did, include them in the Full Stack Quantum Computing course.

3.3 Lecture 4 and 5 - Binary decision making, electronic circuits, logic gates and quantum circuits.

The primary goal of this section is to introduce binary decision making and develop the theory of how binary circuits work to implement binary decision making on computers. An exploration of quantum circuits follows this.

Lecturers should start by posing yes/no questions, using easy to follow binary decision tree examples, and explain that final decisions are a comprehensive set of single binary decisions. Subsequently, to show this in computer architecture, a straightforward electrical switch comprising a single on/off switch and a light bulb is introduced. This analogy facilitates an understanding of how computers use electric power as voltage differences to represent binary data (ones and zeros).

Expanding on the simple switch, the discussion can progress to circuits featuring switches arranged in series and parallel, which represent AND and OR gates, respectively. Once students grasp the functions of AND and OR gates, they should be introduced to the complete set of classical logic gates. A chalkboard exercise could then be employed, prompting students to evaluate the outputs of all classical logic gates, thereby reinforcing their understanding of the material.

Lecturers should follow with a simple (half) adder that disregards carry-over, illustrating the inputs and outputs associated with each gate. Thereafter, the classical full adder should be introduced. It can then be clarified that central processing units (CPUs) consist of billions of circuits, wherein transistors function like switches, establishing the logic circuits essential for computation. While students might find it challenging to interpret a quantum full adder at this stage, lecturers can present an overview of what a quantum full adder circuit looks like, noting that this will be revisited in subsequent lectures.

By methodically progressing from binary decision trees to electric circuits, through logic gates, and culminating in full adder circuits, students gain insight into how abstract decision-making theory and mathematics are transposed into hardware that constitutes both classical and quantum computing architectures. Although they may not yet have the capability to process data through a quantum full adder, students will be able to discern the similarities and differences that characterise the two computational frameworks.

3.4 Lecture 6 and 7 – Superposition, Block spheres, quantum gates, and quantum circuits

The goal of this section is to introduce quantum computing through the development of quantum circuits. The lectures commence with the essential quantum concept of superposition. Superposition is typically explained through the Schrödinger's cat thought experiment. While this example is useful, a plasma ball serves as a more engaging and interactive visual tool to represent the Bloch Sphere.

Lecturers must review Cartesian and complex coordinate systems, if necessary, before the introduction of the Hadamard gate as a representation of superposition. The nature of qubit state collapse upon measurement should be thoroughly discussed. Lecturers can utilise the visual representation of the plasma ball to illustrate superposition by demonstrating how the numerous plasma lines converge into a singular line upon touch, explaining that this is analogous to collapse and measurement.

The discussion should shift to quantum gates using the plasma ball and explore the parallels between quantum gates and classical gates. Lecturers must exercise caution, as the Pauli-X, Y, and Z gates (analogous to classical NOT gates but in 3-dimensional space), the quantum Controlled NOT (CNOT) gate, and the Toffoli gate (a reversible controlled NOT gate) have corresponding classical counterparts. Despite this correlation, students often struggle to understand how the operations of quantum gates on qubits translate into practical data manipulation in real-world applications. Clarification can be achieved through illustrative examples, such as the dice analogy presented in this lecture and Grover's algorithm in subsequent lectures. Students should be assured that as they progress through additional algorithms, the concepts are likely to become more comprehensible.

Lecturers should now work through the first quantum circuit, the five-qubit dice circuit. The choice of five sides is strategic for several reasons. 5-qubit quantum computers are openly available at the time of writing this paper. Additionally, the five-qubit algorithm can be interpreted in two ways: either as a five-sided die or as a 32-sided die. This flexibility allows for algorithms to either count the qubits that yield an output of 1 or to apply binary-to-decimal conversion to compute the total output for a 32-sided die. This algorithm serves to introduce hybrid computational techniques, wherein a classical computer performs the final tally.

Lecturers should select five students to personify qubits, instructing them to randomly denote binary values of either 0 or 1 by raising or lowering their fingers. This interactive component facilitates counting students (qubits) who display a raised finger (indicating a value of 1) for the 5-sided dice.

Furthermore, the analogy of dice serves to illustrate the concepts of simulated random number generation on classical computers versus quantum random number generation. Lecturers should note that visualising a five-sided die can be challenging for students. Lastly, discussions on how the characteristics of a ten-sided die differ from those of two five-sided dice should be prompted to test the understanding of probability theory. This example robustly integrates mathematical concepts, probability theory, and notions of randomness, thereby reinforcing the principles taught in prior lectures.

3.5 Lecture 8 - First complex Algorithm – Grovers

The goal of this lecture is to show how quantum gates manipulate input data to produce user outputs. Grover's algorithm serves as an excellent introductory complex algorithm for students, effectively illustrating the concept of data search speed through relatable analogies.

As an interactive example, the comparison to a physical book highlights how classical algorithms sequentially assess each page and word until locating the desired result. In stark contrast, Grover's algorithm employs a quantum approach that allows for simultaneous examination of all pages, thereby exponentially enhancing search efficiency. The circuit design associated with Grover's algorithm establishes a robust framework for demonstrating key concepts, such as oracles, qubit flipping, and phase alterations, which are integral to data manipulation within quantum computing. Despite the significant differences between classical circuits and their quantum counterparts, Grover's algorithm provides visual and mathematical insights that show the potential of quantum computing.

The presented slides detail the procedural steps and underlying mathematics inherent in Grover's algorithm, effectively pinpointing the probable locations of the sought data. This instructional framework demonstrates the distinctions between classical and quantum gates, emphasising phase flipping techniques on tangible data in real-world contexts. Additional slides touch on quantum advantage and current areas of research interest.

This lecture concludes an introduction to Quantum Computing. By now, students should have a fairly good understanding of the differences between classical and quantum computing, as well as the distinctions between quantum algorithms and their classical counterparts. They should differentiate between classical and quantum data search methodologies, articulate the mathematical foundations of Grover's algorithm, and comprehend the practical significance of quantum gates and phase flipping in data processing. Lecturers can encourage students to study the Deutsch-Jozsa algorithm next and discuss options for further study with them.

4 Recommendations

Throughout the previous section, insights from student questions and reactions shaped the lecture series. It should not be interpreted as one size fits all. Depending on the student cohort, lecturers can choose to dedicate time to topics that are more relevant to the students in that cohort. For example, mathematics and applied mathematics students may appreciate how mathematics explains the quantum gates, while economists will be interested in optimisation algorithms. The authors have intentionally refrained from formalising the material into a structured introduction or an examinable course, as it remains a pilot program. As the course is delivered to increasingly diverse cohorts, it undergoes continual refinement. Therefore, lecturers are encouraged to customise these suggestions to meet their individual objectives.

This iterative process enables lecturers to refine their presentations based on feedback, thereby addressing student needs more effectively. Recommendations to enhance the introductory lesson include developing interactive and descriptive tools, such as videos that demonstrate full adders, various circuits, block diagrams, and the mathematics underlying algorithm execution, providing a comprehensive understanding of circuits.

Structures courses, such as the Full Stack Quantum Computing course, delve into linear algebra, Python programming, and noise management to demonstrate how the gates manipulate data and further embed the principles. Artificial intelligence should also be considered due to its code generation capabilities. Lecturers can utilise resources such as Qiskit [18], MATLAB [19], Python [18], and AI to generate quantum circuits and algorithms.

5 Challenges and Future Directions

Quantum computing encompasses some complex concepts that are challenging for non-physicists to grasp. However, it is an emerging technology that has a global impact. Many institutions cannot afford to house quantum

computers; hence, fundamental teaching like this and cloud access are essential. Lecturers should take on the challenge of using this article as a platform to design courses that suit their environments. AI offers tools that simplify the creation of videos to demonstrate additional concepts, such as block spheres, bra-ket linear algebra, and circuit gates. Lecturers can adapt the teaching methodologies mentioned here with AI tools to design more in depth courses on quantum computing.

6 Conclusion

The introductory quantum computing course has been designed to complement the Full Stack Quantum Computing course at the University of the Witwatersrand. The primary objectives of this course are to introduce foundational concepts in quantum thinking, clarify the distinctions between classical and quantum computing, and engage students through visual aids, active participation, and exploration of common quantum circuits. This course serves as a framework for lecturers, encouraging them to customise their teaching programs to align with their pedagogical styles and the diverse backgrounds of their students. From experience, some attendees may require more in-depth coverage of topics like binary mathematics, while others may require optimisation. Lecturers need to ensure they have a comprehensive understanding of all subjects within this curriculum to accommodate the requirements of their students. This approach will facilitate a richer learning experience and prepare students for further academic pursuits in quantum computing.

References

[1] S. S. Gill *et al.*, "Quantum computing: A taxonomy, systematic review and future directions," *Software: Practice and Experience,* vol. 52, no. 1, pp. 66-114, 2022.

[2] T. D. Ladd, F. Jelezko, R. Laflamme, Y. Nakamura, C. Monroe, and J. L. O'Brien, "Quantum computers," *nature,* vol. 464, no. 7285, pp. 45-53, 2010.

[3] M. A. Sohel, N. Zia, M. A. Ali, and N. Zia, "Quantum computing based implementation of full adder," in *2020 IEEE International conference for innovation in technology (INOCON)*, 2020: IEEE, pp. 1-4.

[4] O. Choustova, "Toward quantum-like modeling of financial processes," in *Journal of Physics: Conference Series*, 2007, vol. 70, no. 1: IOP Publishing, p. 012006.

[5] R. Orús, S. Mugel, and E. Lizaso, "Quantum computing for finance: Overview and prospects," *Reviews in Physics,* vol. 4, p. 100028, 2019.

[6] J. Preskill, "Quantum computing in the NISQ era and beyond," *Quantum,* vol. 2, p. 79, 2018.

[7] A. Katabarwa, K. Gratsea, A. Caesura, and P. D. Johnson, "Early fault-tolerant quantum computing," *PRX quantum,* vol. 5, no. 2, p. 020101, 2024.

[8] K. A. Connor, B. H. Ferri, and K. Meehan, "Models of mobile hands-on STEM education," in *2013 ASEE Annual Conference & Exposition*, 2013, pp. 23.910. 1-23.910. 17.

[9] A. Katal and V. K. Singh, "Curriculum design and development: a case for higher education in India," 2022.

[10] C. K. Larive, "A picture is worth a thousand words: animations and simulations in the teaching of analytical science," *Analytical and Bioanalytical Chemistry,* vol. 390, no. 1, pp. 71-75, 2008.

[11] B. Fahad Mon, A. Wasfi, M. Hayajneh, A. Slim, and N. Abu Ali, "Reinforcement learning in education: A literature review," in *Informatics*, 2023, vol. 10, no. 3: MDPI, p. 74.

[12] V. Kumar and D. S. Kumar, *Innovative Pedagogy and Quality Concerns in Teacher Education*. Academic Guru Publishing House, 2024.

[13] T. G. Wong, *Introduction to classical and quantum computing*. Rooted Grove Omaha, NE, USA, 2022.

[14] IBM Quantum. "Qiskit." IBM. https://www.ibm.com/quantum/qiskit (accessed July 29, 2025).

[15] A. Abbas *et al.*, "Learn quantum computation using qiskit.(2020)," *www.learn.qiskit.org/course/quantum-hardwarepulses/calibrating-qubits-using-qiskitpulse#frequencysweep,* 2022.

[16] Y. Feaster, F. Ali, and J. O. Hallstrom, "Serious toys: teaching the binary number system," in *Proceedings of the 17th ACM annual conference on Innovation and technology in computer science education*, 2012, pp. 262-267.

[17] R. Sutor, *Dancing with qubits* (no. 2). Packt Publishing Birmingham, UK, 2019.

[18] R. Loredo, *Learn quantum computing with Python and IBM quantum experience*. Packt Publishing, 2020.

[19] MathWorks. "Quantum Computing with MATLAB." MathWorks. https://www.mathworks.com/products/quantum-computing.html (accessed July 30, 2025).

Some roles of physics in climate science with examples in Southern Africa

Irvy M.A. Gledhill[1]

[1]School of Mechanical, Industrial, and Aeronautical Engineering, University of the Witwatersrand, Johannesburg, South Africa

E-mail: igle.gledhill@wits.ac.za

Abstract. Physics is well embedded in climate science, and its contributions are expanding. This work aims to illustrate a few of the surprising or growing roles of physics, providing very short outlines of case studies of relevance to Southern Africa. Two disasters highlight attribution science, the scarcity of data in southern Africa, and the need for functioning Early Warning systems. Longer-term forecast of El Niño-linked drought is needed, and the non-linear nature of system models of the El Niño Southern Oscillation is cited. This introduces some contributions of theoretical physics to the theory of climate and a challenge in computational physics in models for Africa. The use of quantum physics in countering the spread of malaria is mentioned. Finally, since the Southern Ocean climate system affects both Southern Africa and global circulation profoundly, an example of physics applied to understanding ice mechanics is provided. A systematic way of finding research gaps by linking physics to climate science is proposed, and engagement of the physics community with the crisis is suggested.

1 Introduction

The change in the Earth's climate is a threat to all its inhabitants, and the evidence for this statement is accumulating steadily [1-5]. The monthly global average surface temperature remained over 1.5 °C higher than preindustrial values for 12 consecutive months up to June 2024 [6]. We are at a watershed where the decisions made in the next five years will determine the future of humanity. While recognizing that physics is deeply embedded in many current initiatives, the purposes of this paper are to describe some examples of physics contributions to climate science that are relevant to Southern Africa; to lay the groundwork for a systematic approach to finding new research gaps for pure and applied physics (especially theoretical and computational physics) in climate science; and thereby to promote the engagement of the physics community in Southern Africa with the problems of climate change.

This paper is not intended to cover the widely spread existing research in, or about, the Southern African region. IUPAP[1] created Working Group 21 (WG21) to promote the unique roles that physics can, and should, play in these sciences, as physicists respond to the climate crisis and the threats to the future of the planet. The initiative is relevant to Sustainable Development Goal 13, Climate action[2], and the International Decade of Sciences for Sustainable Development[3]. It is not the intention of WG21 to perform research, since many

[1]International Union of Pure and Applied Physics IUPAP WG21, Physics for climate change action and sustainable development
[2] United Nations Resolution A/RES/70/1/E adopted on 25 September 2015, https://www.un.org/en/development/desa/population/migration/generalassembly/docs/globalcompact/A_RES_70_1_E.pdf
[3] United Nations Resolution A/RES/77/326 adopted on 25 August 2023, https://docs.un.org/en/A/RES/77/326

international bodies exist to do this. WG21 can, however, promote action among members, and the present work is aimed at developing initiatives within the physics community of Southern Africa. Institutes, departments, scientists and companies are respectfully acknowledged but very few can be mentioned in this small set of illustrations, including, for example contributors to IPCC[4] Reports [1].

1.1 Structuring the interaction between two extensive fields

In understanding the current roles of physics in this context, it may be useful to find links between physics sub-disciplines and the components of climate science, treated as a driver and an area of application. As a first exercise, for selected cases, links have been made between developments in physics or related to physics, and at least one application area in the climate context. For test purposes a single publication has been used in selected cases. Data-backed analysis of literature is becoming considerably more widely used, and validation of the results of automated studies is improving. It may be possible to stimulate new and original physics by enabling visualisation that makes gaps in knowledge more easily identifiable. Some simple diagrams have been used to demonstrate how such a study might be structured. For initial demonstration purposes, the fields of physics are taken as those for which IUPAP has designated commissions, affiliated commissions or working groups, and the fields of climate science are adopted from the structure of IPCC reports.

It is noted that much of climate, sustainability and regenerative development research lies outside the academic journal base and is usually published in the form of peer-reviewed reports. Reports that are fundamental in assisting physicists to navigate the field might be cited [1 – 5]. For future purposes it would be useful to provide a similar scheme for the sustainability space, which is deeply dependent on physics.

2 Case study examples

2.1 Attribution of extreme events to anthropogenic forcing and the Kwa-Zulu Natal floods of April 2022

On 11-12 April 2022, the eThekwini region of Kwa-Zulu Natal (KZN), South Africa, experienced nearly 300 mm of rainfall in 24 hours, extreme flooding, over 430 fatalities, and serious damage to infrastructure and housing [7]. The South African Weather Service (SAWS) and the eThekwini municipality issued warnings, but with limited effect: the warnings were not received by all, many people did not know what to do, and there was a disproportionate effect on marginalised communities [7, 8]. The case is a good illustration of the use of the relatively new science of attribution and is one in which Southern African authors are active [7, 8]. Detection and attribution are defined by the IPCC as follows[5]: *Climate varies continually on all time scales. Detection of climate change is the process of demonstrating that climate has changed in some defined statistical sense, without providing a reason for that change. Attribution of causes of climate change is the process of establishing the most likely causes for the detected change with some defined level of confidence.* The likelihood of occurrence of extreme events can be derived as a function of intensity for the natural (pre-industrial) climate from, for example, the ERA5 observational data[6]. The actual, or present, climate and probable future climate can also be modelled. The World Weather Attribution Protocol [9] defines the methods acceptable in the chain of reasoning that leads from observation, through model analysis, model evaluation, and eventually to communication statements. The probabilities of an event with intensity above a certain threshold can be compared between the natural climate and the actual climate (Figure 1)[10]. The conclusions of the study included an assessment that the return time of the event is about 20 years in the present climate but would have been about 40 years in a climate 1.2 °C cooler.

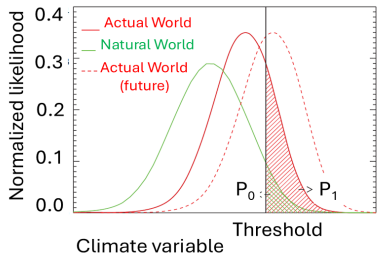

Figure 1: An illustration of the Probability Density Functions of a climatic variable. The probabilities of exceeding a prespecified threshold (P1 and P0) are represented by the hatched areas [10] (Image: CC-BY-4.0).

[4] Intergovernmental Panel on Climate Change
[5] IPCC Fourth Assessment Report, 2007, Glossary https://archive.ipcc.ch/publications_and_data/ar4/wg1/en/annexessglossary-a-d.html
[6] European Centre for Medium-Range Weather Forecasts (ECMWF), ERA5 dataset, https://www.ecmwf.int/

Contributions from fields of physics are mapped the left side of Figure 2. Physicists may be able to identify potentially productive gaps among these areas of study. Physicists also make impact in the direct applications of instrumentation, earth observation, ground station data, disaster risk assessment and reduction, and the effectiveness of Early Warning Systems (EWS) [9]. There is scope for physics in the determination of what constitutes an extreme event ([1], Glossary) and in defining thresholds. Extending the thinking in terms of the full function of EWS, socio-ecological systems are the most critical factor in the success of EWS: "an extreme event should not mean that there has to be a disaster"[7]. Physics community initiatives could consider combining localized disaster warning with indigenous knowledge systems, and applying theory of change in terms of the real needs of a community and the long-term goals and conditions needed for survival and success.

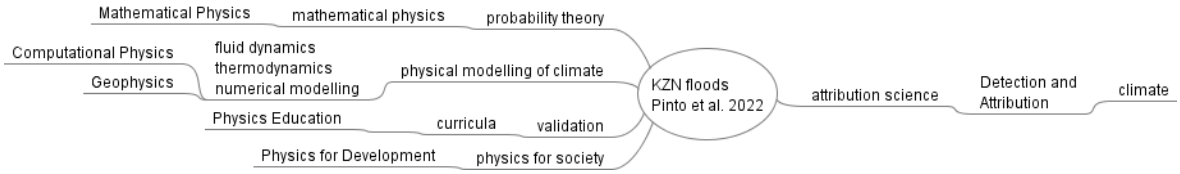

Figure 2: Contributions from fields of physics through Pinto *et al.* (2022)[7] to climate science.

2.2 Data scarcity

The example of the KZN floods illustrates the scarcity of reliable data in South Africa [7]. Time-dependent temperature and precipitation data is a critical input to provide reasonable predictions and analyses. The KZN analysis [7] indicates that daily rainfall data available for South Africa was not sufficiently gap-free and did not cover enough decades (1950-2022); only 70 stations of the 194 SAWS stations in the study were able to provide data of the quality required for attribution. The availability and quality of high-quality persistent data is low and has been declining in Africa and Southern Africa (see [11] Figure 7.1). SAEON, the South African Environmental Observation Network, is now active increasing observation sites and EWS effectiveness through collaborations with communities [12]. Disaster Risk Reduction requires action throughout Southern African nations for realistic national science policy and implementation in an all-of-government model, and scientific organisations have a distinct role to play.

2.3 Modelling and non-linear systems: the Southern African drought of 2024 and ENSO

In February, 2024, less than 20% of the expected rainfall was experienced, and a prolonged drought took place in Zimbabwe, Zambia, Malawi, Angola, Mozambique and Botswana [13]. Crops failed among rain-fed subsistence farms and food insecurity affected an estimated 71 million people by November 2024 [14]. Climate attribution studies of this event indicated multiple drivers, notably concluding that the El Niño event was a key driver, and that the prolonged drought was twice as likely during El Niño years [13]. Understanding the teleconnections between El Niño events and Southern Africa in a warmer world requires global and mesoscale modelling [15] and shows correlation of El Niño events with low southern African rainfall (except in south-eastern regions). Prediction of an El Niño event can be made at present with reasonable confidence from observations between 6 and 12 months before July, and impacts are observed between November and March. The need for warning at longer lead-times is clear. In terms of a physical understanding, the proposal that the El Niño Southern Oscillation (ENSO) can be conceptually modelled as a non-linear system was first made in 1986 by Vallis [16], seeking a physics-based model for the qualitative aspects of the system. A set of three equations similar to the Lorentz equations, based on three variables (east and west ocean temperatures and a wind-driven current velocity), was able to produce ENSO-like behaviour. Vallis models continue to provide a basis for research.

General Circulation Models (GCMs) have potential to make predictions at time scales greater than 9 months, possibly up two years, the time scale being limited by computational costs [17]. A knowledge of the underlying non-linear physics describing ENSO makes it clear that initial conditions are critical, and therefore that pooling multiple models in an ensemble may obscure the development of El Niño events [17].

2.4 The theory of climate: complex systems and stochastic dynamics

The Nobel Prizes in Physics awarded in 2021 illustrated the fact that pure physics has made fundamental contributions in unexpected ways. Parisi, receiving the award "for the discovery of the interplay of disorder and fluctuations in physical systems from atomic to planetary scales", had been investigating Ising networks and spin

[7] M.M. Bopape (SAEON), 21 July 2025, https://www.youtube.com/watch?v=vxWBjW1X6Mg

glasses, of which P.W. Anderson said “the history of spin glass may be the best example I know of the dictum that a real scientific mystery is worth pursuing to the ends of the Earth for its own sake, independently of any obvious practical important or intellectual glamour” [18]. Parisi developed the calculation of macroscopic thermodynamic properties using replicated partition functions and a new long-range order parameter, eventually demonstrating the role of random fluctuations in controlling Earth's climate states over long epochs [19], and redefining the link between weather and climate (Figure 3). Hasselmann addressed a stochastic model relating short-time scale perturbations of weather to long time scale drift, or climate [20] (Figure 2), and was awarded the Nobel Prize for “the physical modelling of Earth’s climate, quantifying variability and reliably predicting global warming” together with Manabe [21], who developed the fundamental models for an atmosphere in thermal equilibrium with convection.

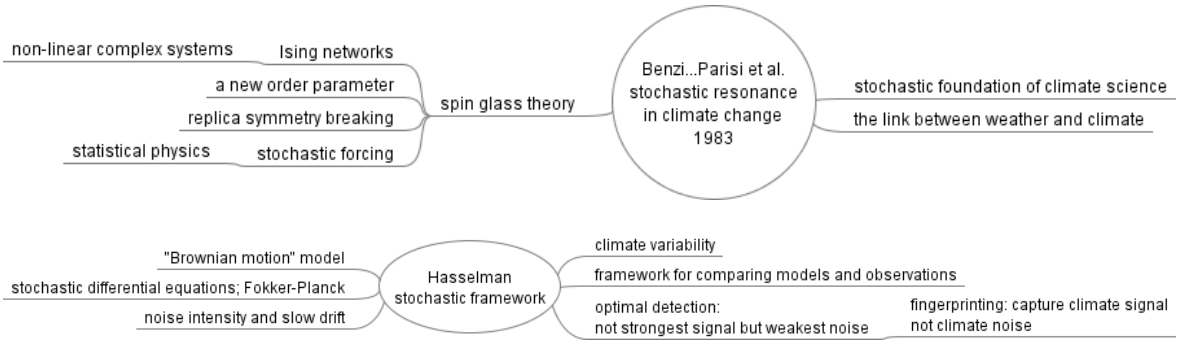

Figure 3: (*top*) Complex systems [19] and (*bottom*) stochastic differential equations [20] in climate science.

2.5 GCMs and Earth System Models: fluid dynamics, thermodynamics and computational physics

The fundamental formulation of Manabe [21] underpins the GCMs and Earth System Models (ESMs) which now pose challenges for physicists and engineers in, for example, atmospheric turbulence, multiscale modelling, and cryosphere-ocean-atmosphere interaction. GCM and ESM predictions concerning Southern Africa made in 2021 include more frequent and intense multi-year droughts (as experienced in 2024), more frequent and intense heat waves with impact on human health and mortality (as quantified by the Lancet Countdown 2025 [22]), and more intense tropical cyclones (now seen as more frequent landfalls over Mozambique [4]).

The development of an African ESM is an essential tool for quantifying climate tipping points for the continent [3, 23]. A gap of interest lies in modelling African thunderstorms. Considerable progress has been made in the northern hemisphere in modelling specific thunderstorm instances where reflectivity observations from Doppler Ku-band radar are available. Turbulent Large Eddy Simulations at this scale provide remarkably good models in comparison, showing the existence of a hydraulic jump above supercell thunderstorms at the tropopause [24]. These simulations are computationally expensive, but may lead to reasonable sub-grid models.

2.6 Infectious and vector-borne diseases: quantum physics

There is abundant evidence of the profound influence of pollution and climate change on health [22], including, for example, the spreading of the areas affected by malaria [25]. X-ray diffraction and synchrotron studies provide target protein structures and the Protein Data Bank[8] provides open access to this data. Among the tools of rational drug design is Density Functional Theory (DFT). Quantum mechanics now plays a routine role not only in condensed matter physics but in seeking treatments and vaccines for infectious diseases, and DFT methodology is widely used in Africa; training in electronic structure modelling has taken place through many initiatives across Africa over more than two decades[9]. An example in the use of DFT for ligand-protein interaction energy calculation is the search for malaria treatments or vaccines [26]. In these initiatives, computational physicists find themselves well-prepared to join teams which stretch through the spectrum of physicists and biochemists to clinicians.

2.7 Polar science and the cryosphere: ice mechanics, computational physics and remote observation

The Southern Ocean can be considered to control climate in the southern one-third of the world [27]. Southern Africa’s marine economies are profoundly influenced by the Southern Ocean climate system and the Southern

[8] Protein Data Bank, https://www.rcsb.org/

[9] Including African School on Electronic Structure Methods and Applications https://www.asesma.org/

Annular Mode (SAM), an oscillation on the scale of decades in the natural climate. At present, we are in a positive phase of the SAM ([27] and [28], Ch. 4, Fig. 4.27), the Westerly winds have strengthened, and both the Westerlies and the Antarctic Circumpolar Current have contracted towards the pole. Model projections indicate that increased atmospheric CO_2 is likely to prolong this phase, increasing CO_2 degassing from the major carbon sink in the Southern Ocean, increasing upwelling of warm Circumpolar Deep Water, increasing ice shelf recession and influencing the latitude of the Intertropical Convergence Zone [27]. Antarctic research is therefore of significant importance to Southern Africa. South African research entities[10] carry out exploration of the Southern Ocean and of Antarctic conditions and climate. Most ice properties are measured in Arctic conditions, offering Southern Africa geographic advantage and scope in determining material properties, structure and texture, historic climatic conditions and sea ice dynamics in the field and through computational models [29]. Ice drift studies reveal drivers of Southern Ocean dynamics [30].

3 A systematic approach

It is beyond the scope of the present author and paper to give more than a speculative outline of the way in which a publication-based survey might be carried out. A tree structure can be selected to represent a discipline, such as "physics" (e.g. IUPAP as above) or "climate science" (e.g. IPCC) with a systematic representation of subdiscipline keywords at a selected level of granulation. The task is to produce visual relational maps that can be explored by a critical human to investigate promising research directions. Some AI, Machine Learning and Large Language Model tools directed at conducting literature searches are able to map related publications in network diagrams. A chord diagram that can provide hierarchical edge bundling may prove useful as a preliminary visualisation. Humans are essential throughout the design cycle for such a process, in critical reading of the material, and in responsible use of AI.

4 Conclusions and Recommendations

An aim of this study was to show some of the expanding roles of physics, highlighting some less frequently mentioned aspects and successes, and seeking research areas in which physicists may make effective contributions. The examples cited offer opportunities for research in computational and theoretical physics, applied physics and quantum physics. Specific gaps related to physics in attribution science, Early Warning Systems, data scarcity and health science have been identified.

In seeking ways to find productive research and application gaps by linking physics to impact in the present crisis, a simple mapping of relations between physics and climate science has been shown. It is recommended that this method should be considered for an automated analysis of literature in both climate and sustainability science as a systematic way of approaching research gaps for physics in climate science.

It has been shown that changes in floods, droughts, large-scale oceanic and cryosphere processes, and disease ranges have profound effects on Southern Africa. In response, it is recommended that the South African Institute of Physics, with its partners, should consider initiatives to promote existing and new roles of physics in the present climate crisis, including those in sustainability science. In some of the examples above, community engagement, entrenching evidence-based science communication, curriculum development, raising of awareness within the physics community, and engagement in science diplomacy are possible. In terms of policy, it is important to note that these cases illustrate valuable contributions of physics both as a fundamental basic science in its own right, and as a partner in transdisciplinary work. These recommendations overlap with the mission of IUPAP WG21 and it is recommended that joint opportunities should be taken to foster regional capabilities and to make global impact in climate physics.

References

[1] IPCC Sixth Assessment Reports, [Online]. Available: https://www.ipcc.ch/assessment-report/ar6/

[2] World Meteorological Organization (WMO), The state of the climate 2024, Geneva, WMO-No. 1347, 2024.

[3] R. Scholes et al., "A Climate Science Future for South Africa," Global Change Institute, U. Witwatersrand, 2020, https://www.safsc.org.za/wp-content/uploads/2020/06/Climate-Science-Doc_June-2020.pdf

[4] IPCC AR6 Chapter 9, 2022. [Online]. Available: https://www.ipcc.ch/report/ar6/wg2/chapter/chapter-9/

[10] SAEON, SANAP South African National Antarctic Programme, and MARiS Marine and Antarctic Research Centre for Innovation and Sustainability, University of Cape Town are some examples.

[5] Sendai Framework for Disaster Risk Reduction 2015-2030, 2015. [Online]. Available: https://www.undrr.org/publication/sendai-framework-disaster-risk-reduction-2015-2030

[6] Copernicus Climate Change Service, "Global Climate Highlights 2024," [Online]. Available: https://climate.copernicus.eu/global-climate-highlights-2024

[7] I. Pinto *et al.*, "Climate change exacerbated rainfall causing devastating flooding in Eastern South Africa," World Weather Attribution (WWA) Report, 2022.

[8] M. M. Bopape et al., "Weather Related Disasters in South Africa from 1980 to 2023," *Environ. Dev.*, 101254, 2025.

[9] S. Philip et al., *Adv. Stat. Climatol. Meteorol. Oceanogr.*, vol. 6, pp. 177–203, 2020.

[10] P. A. Stott et al., *WIREs Clim. Change,* vol. 7, pp. 23–41, 2016. doi: 10.1002/wcc.380.

[11] T. Dinku, "Chapter 7 - Challenges with availability and quality of climate data in Africa," in *Extreme Hydrology and Climate Variability*, A, M. Melesseet al., Eds, Elsevier, pp. 71-80, 2019.

[12] South African Environmental Observation Network, "SAEON Strategy 2030", 2020. [Online]. Available: https://www.saeon.ac.za/

[13] J. Kimutai et al., "El Niño key driver of drought in highly vulnerable Southern African countries," WWA Report, 2024. doi: 0.25561/110770

[14] reliefweb, SADC Regional Humanitarian Appeal: Addendum on El Niño-Induced Drought (November 2024), 2024. https://reliefweb.int/report/zimbabwe/sadc-regional-humanitarian-appeal-addendum-el-nino-induced-drought-november-2024

[15] J. Steinkopf and F. Engelbrecht, "The El Niño–Southern Oscillation teleconnection to southern Africa in a changing climate," *Environ. Res. Lett.,* vol. 20, 084001, 2025.

[16] G. K. Vallis, *Science*, vol. 232 pp. 243-5, 1986. doi: 10.1126/science.232.4747.243.

[17] N. Lenssen et al., "Strong El Niño events lead to robust multi-year ENSO predictability," *Geophys. Res. Lett.*, vol. 51, e2023, GL106988, 2023. doi: https://doi.org/10.1029/ 2023GL106988

[18] P. W. Anderson, "Spin Glass 1: A Scaling Law Rescued," *Physics Today*, January 1988, 1988.

[19] R. Benzi, G. Parisi et al., "A Theory of Stochastic Resonance in Climatic Change," *SIAM J. on Appl. Math.*, vol. 43, pp. 565-578, 1983. doi: 10.1137/0143037

[20] K. Hasselmann, *tellus*, vol. 28, pp. 473-485, 1976. doi: https://doi.org/10.3402/tellusa.v28i6.11316

[21] S. Manabe, and R. F. Strickler, *J. Atmos. Sci.,* vol. 21, pp. 361–385, 1964.

[22] M. Romanello et al., "The 2024 report of the Lancet Countdown," *The Lancet*, vol. 404, pp. 1847 – 1896, 2025. doi: 10.1016/S0140-6736(24)01822-1

[23] T. R. Maisha et al., Water Research Commission WRC report no. 3181/1/24, 2025. [Online]. Available: https://www.wrc.org.za/wp-content/uploads/mdocs/3181%20final.pdf

[24] M. O'Neill et al., *Science,* vol. 373, pp. 1248-1251, 2021.

[25] Malaria Atlas Project, "Climate Impacts on Malaria in Africa," November 2024, 2024. [Online]. Available: https://malariaatlas.org/project-resources/climate-change/

[26] P. M. A. Mekoung et al., *Curr. Med. Chem.*, vol. 32, pp. 8466 – 8478, 2025.

[27] B. Davies, "Southern Annular Mode", Royal Holloway University of London, 2023. [Online]. Available: https://www.antarcticglaciers.org/glaciers-and-climate/southern-annular-mode/

[28] IPCC AR6 Chapter 4, 2022. [Online]. Available: https://www.ipcc.ch/report/ar6/wg1/chapter/chapter-4/

[29] F. Paul et al., "Sea ice mechanics," *Comput. Methods Mater. Sci.*, vol. 23, pp. 5–54, 2023.

[30] A. Womack et al., *The Cryosphere*, vol. 18, pp. 205–229, 2024. doi: https://doi.org/10.5194/tc-18-205-2024

This page intentionally left blank.

DIVISION

F

APPLIED PHYSICS

Energy Balance Closure Analysis Based on Eddy Covariance Flux Tower Observations

Lufuno Takalani[1], Sophie Mulaudzi[2], Tshifhiwa Ranwaha[2] and Eric Maluta[3]

[1]Vuwani Science Resource Centre, University of Venda, Thohoyandou, South Africa
[2]Department of Physics, University of Venda, Thohoyandou, South Africa
[3]Green Technology Confucius Institute, University of Venda, Thohoyandou, South Africa

E-mail: lufuno.takalani@univen.ac.za

Abstract. Energy balance closure is a fundamental principle in micrometeorology, ensuring that all energy fluxes within an ecosystem are properly accounted for. The eddy covariance (EC) method, widely used for measuring land – atmosphere exchanges of energy and mass, often exhibits energy closure discrepancies, particularly across different timescales. This study investigates ecological year energy closure using flux tower data collected over multiple years at Skukuza, Kruger National Park. Energy closure was assessed using the fundamental balance equation $R_n - G = H + LE$, where net radiation (R_n), soil heat flux (G), sensible heat flux (H), and latent heat flux (LE) were analysed across different timescales. Radiation shields and soil heat flux sensors were employed to capture variations in energy fluxes. Statistical analysis of multiple ecological years revealed that energy closure varies significantly with seasons, with wetter years exhibiting lower energy imbalances compared to drier years. The findings indicate that energy closure improves with increased turbulence (frictional velocity) but remains incomplete due to measurement uncertainties, sensor sampling scales, and ecosystem heterogeneities. Results highlight a persistent energy closure gap, with an average closure of approximately 80%, consistent with other EC studies globally. The study underscores the challenges in achieving full energy balance closure and emphasizes the need for improved sensor calibration, turbulence parameterization, and data correction techniques. These insights are crucial for refining EC methodologies and enhancing the accuracy of land-atmosphere energy exchange assessment in semi-arid ecosystems.

1 Introduction

The energy balance closure problem occurs when measured turbulent fluxes of sensible and latent heat (H + LE) do not fully account for the available net radiation minus ground heat flux (Rn – G), causing systematic underestimation of ecosystem energy fluxes. Globally and in South Africa, this is common in heterogeneous landscapes like savannas due to surface variability, measurement errors, and unaccounted storage terms. This gap affects sustainability and climate change studies because accurate energy flux estimates are essential for modeling water cycles, predicting carbon sequestration, and assessing ecosystem responses to climate variability. Measurements of Eddy Covariance (EC) flux are essential for estimating the flow of energy, water, and carbon between ecosystems and the atmosphere. They support the validation of climate models and the evaluation of ecosystem responses to climate change. EC data enhance estimates of the global carbon budget and facilitate remote sensing applications.

The significance of study provides critical insights into the factors causing energy balance non-closure in Skukuza, helping improve the accuracy of turbulent flux measurements in savanna ecosystems. Its findings are significant for South Africa's climate and sustainability studies, as they enhance modeling of carbon and water cycles under changing environmental conditions. Evapotranspiration (ET) includes evaporation and transpiration, which is the process by which water moves from the soil to the atmosphere through plants, evaporation from the capillary fringe of the groundwater table, and water evaporation from the soil surface and water bodies into the atmosphere. Because ET connects the energy, carbon, and water cycles, it has a major impact on the interactions between the atmosphere and the terrestrial surface. Particularly in arid and semiarid habitats, where it may be responsible for almost the whole surface water budget, ET controls the energy and water balance of the Earth's hydrosphere, atmosphere, and biosphere (Fisher et al., 2017; Oki and Kanae, 2006; Morillas et al., 2013).

Because warmer air carries more water vapour that is transpired by plants and evaporates from the soil surface, warming of the land and atmosphere fundamentally alters ET. This causes changes in the seasonality and patterns of precipitation and soil moisture, which alter the equilibrium of the water cycle's constituent elements and could lead to severe weather conditions like floods. Determining agricultural and ecosystem water use, detecting drought, quantifying land-atmosphere feedback, evaluating the impact of human activity on the water cycle and surface energy budget, and validating and refining the parameterization of land surface models all depend on accurate ET estimation (Purdy et al., 2018). Generally, the water balance or energy balance is used to estimate ET.

2 Methodology

2.1 The study Area- The Skukuza Eddy Covariance flux tower, Kruger National Park

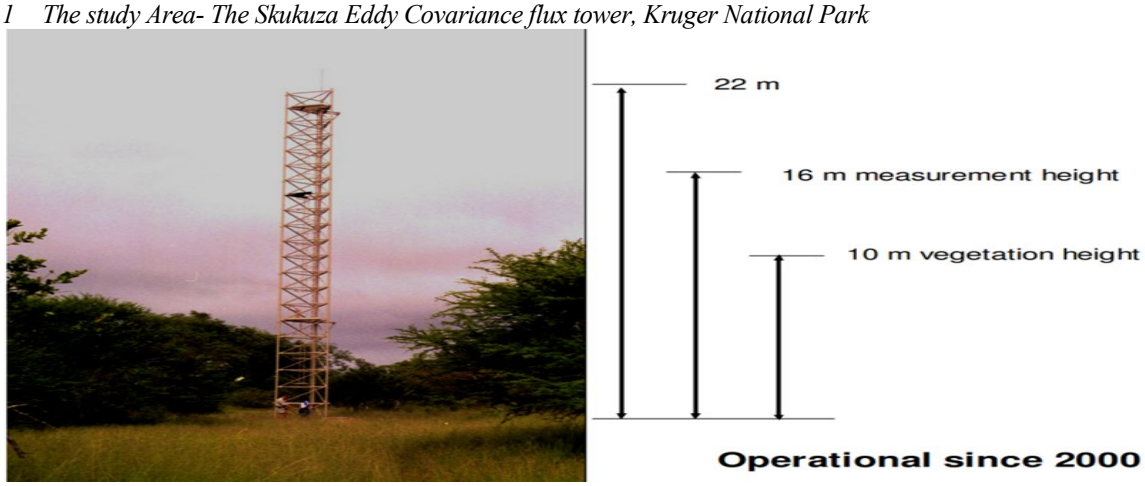

Figure 1. The Skukuza FLUXNET tower. Located in the Kruger National Park, within the semi-arid savanna biome. Vegetation: Combretum and Acacia trees. Climate: Distinct wet and dry seasons. Continuous EC measurements since 2000.

Measurement Type	Instrument(s)
Gas fluxes	LI-7500 infrared gas analyzer
Wind & heat fluxes	Gill Wind Master Pro & Campbell CSAT3 ultrasonic anemometers
Radiation	Kipp & Zonen albedometers and pyrgeometer
Micrometeors	Air temperature, humidity, rain gauge
Soil moisture	CS615L TDR probes at multiple depths
Data handling	Data loggers, tower-top computers, periodic on-site visits

Table 1: The Skukuza covariance flux tower parameters and instrumentation.

2.2 Energy Balance Closure

Energy Balance Closure (EBC) refers to how well the measured incoming and outgoing energy components at the Earth's surface balance out, according to the law of conservation of energy. Energy balance closure is a fundamental principle in micrometeorology, ensuring that all energy fluxes within an ecosystem are properly accounted for.

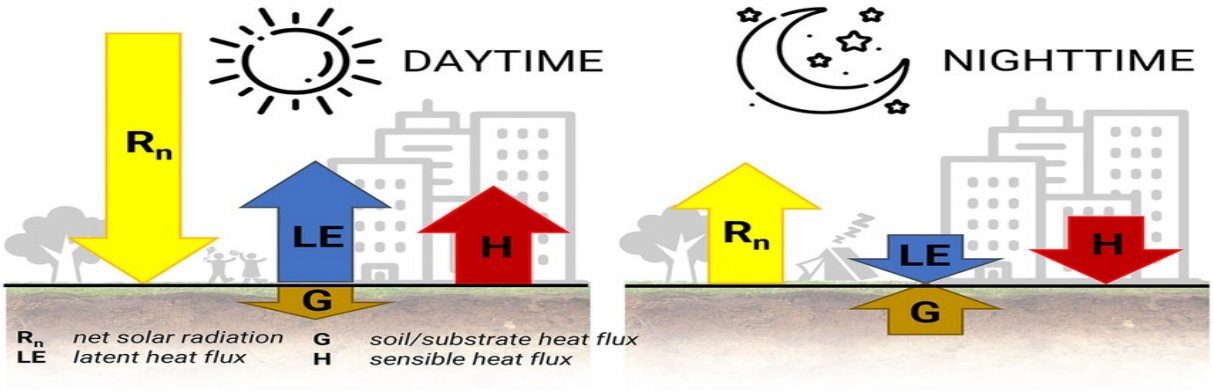

Figure 2: Illustration of a typical surface energy balance with key flux components based on the daytime and nighttime fluxes.

The figure 2 illustration shows how net radiation (Rn) is partitioned into latent heat flux (LE), sensible heat flux (H), and ground heat flux (G). During the day, incoming solar energy drives upward LE and H, while at night reduced Rn leads to energy release from the surface back to the atmosphere and soil.

Energy closure was assessed using the fundamental balance equation:

$$R_n - G = H + LE \quad (1)$$

Where net radiation (R_n), soil heat flux (G), sensible heat flux (H), and latent heat flux (LE).

Lack of energy balance closure undermines the reliability of micrometeorological measurements, especially in flux networks like FLUXNET, and makes it harder to use the data confidently for research, agriculture, and climate Modeling. The problem of not having Energy Balance Closure (EBC) arises when the measured energy inputs and outputs at the land surface do not balance, meaning:

$Rn-G \neq H+LE$ - no closure (2)

$Rn-G = H+LE$ - energy closure (3)

This form is often used to assess the partitioning of net radiation into turbulent heat fluxes only.

$Rn-G = H+LE + G$ - Surface energy closure (4)

$Rn= H+LE$ - simplified form of the surface energy balance equation. When the time scale is long enough (daily or longer), so G ≈0

3 Results and discussion

Energy balance closure is a quality check for eddy covariance data used in climate, hydrology, and ecosystem studies. Poor closure could indicate incomplete or biased measurements, reducing confidence in results like evapotranspiration rates or carbon fluxes. While the results focus on energy balance closure metrics (R^2 and slope), all these parameters like gas concentrations, turbulence, radiation, micrometeorology, soil moisture, and data handling form the backbone of the study. They help explain the physical processes behind the observed fluxes and the residual non-closure of energy, making the interpretations scientifically robust.

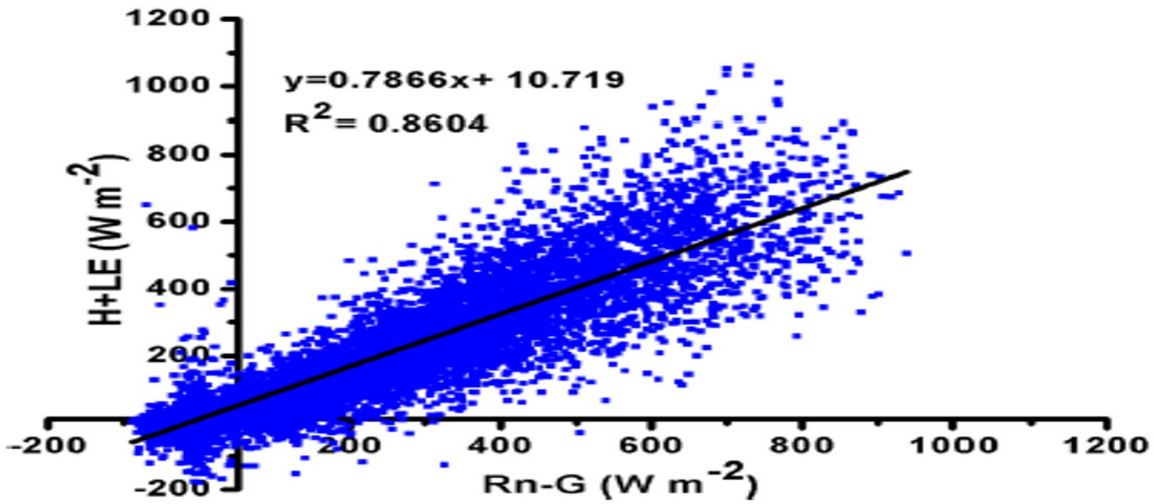

Figure 3: Energy balance closure for the entire study period, considering half-hourly averaged data.

The figure 3, shows a strong linear relationship ($R^2 = 0.86$) between available energy (Rn−G) and turbulent fluxes (H+LE), indicating good energy balance closure at the flux tower. The slope (0.79) suggests that ~79% of available energy is accounted for by turbulent fluxes, with some underestimation likely due to measurement errors or storage terms. The results confirm reliable flux measurements but highlight the common energy imbalance issue in eddy covariance studies. In another a study conducted in the semi-evergreen primary forest of Kaziranga National Park, Assam, India (Feb 2016–Jan 2017), energy balance closure reached up to 83% under neutral conditions. Latent heat flux dominated, showing strong evapotranspiration and reliable surface energy flux measurements.

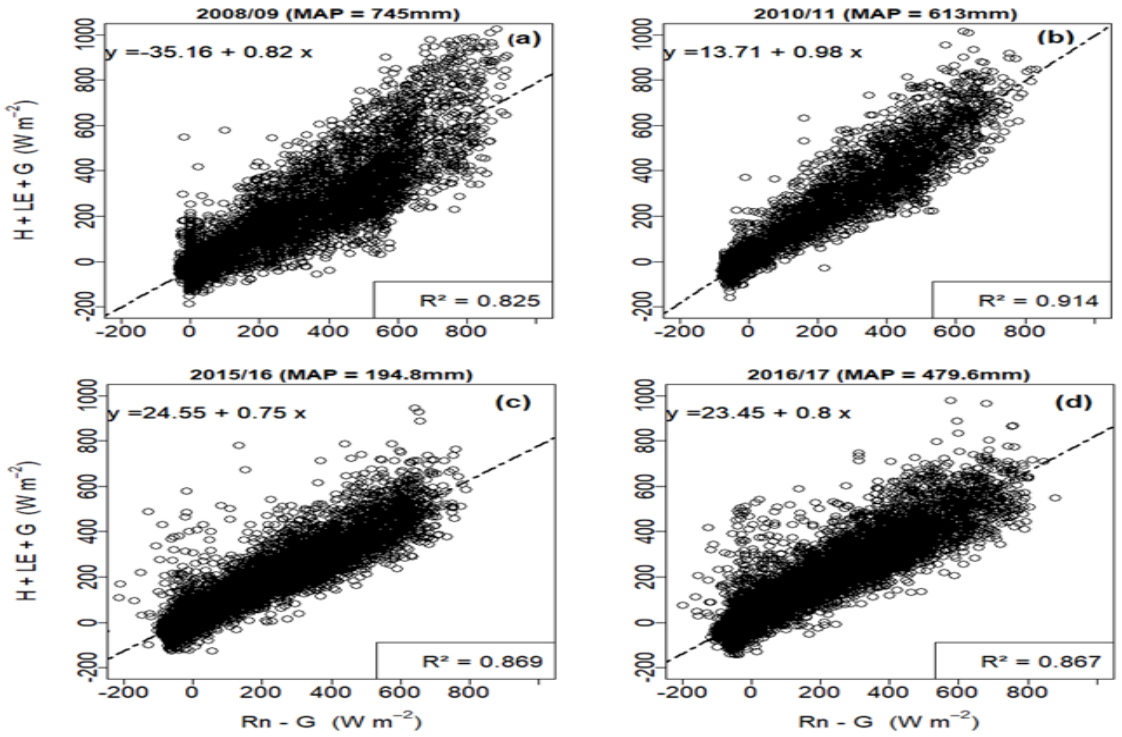

Figure 4: Combined plot of Monthly Energy Balance Closure (EBC) for Skukuza, Kruger National Park, across four years.

In Figure 4(a), 2008/09 Mean Annual Precipitation (MAP) = 745 mm, $R^2 = 0.825$; Moderate correlation with a slope of 0.75 shows ~74% of net radiation is converted into turbulent fluxes, but energy imbalance stays. Figure 4(b) 2010/11 (MAP = 613 mm), $R^2 = 0.914$; Very strong correlation with near-unity slope (0.96) suggests best energy balance closure and accurate turbulent energy partitioning. figure 4(c) 2015/16 (MAP = 194.8 mm), $R^2 = 0.8404$; Strong correlation with a slope of 0.869 under dry conditions shows good energy relationship despite reduced rainfall and lower energy closure. Figure 4(d) 2016/17 (MAP = 479.6 mm), $R^2 = 0.867$. High correlation with a slope of 0.78 reflects improved energy balance under moderate rainfall but still underestimates full closure.

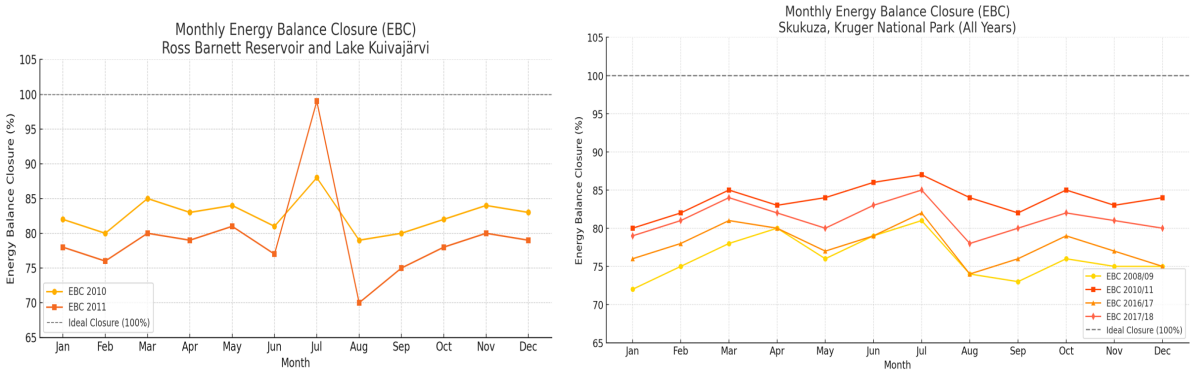

Figure 5: Comparison of the Combined plot of Monthly Energy Balance Closure (EBC) for Skukuza, Kruger National Park across four years and Monthly Energy Balance Closure (EBC) for 2010 and 2011 at Ross Barnett Reservoir and Lake Kuivajärvi.

Observations in figure 5, shows seasonal variation, with July–October often having higher EBCs. 2010/11 and 2017/18 had the highest closure values (up to ~87%). All values are below the ideal 100% closure, which is typical due to surface heterogeneity, instrument limitations, and energy storage terms. In another similar review of studies at Ross Barnett Reservoir and Lake Kuivajärvi showed monthly energy balance closure ranged from 70% to 99%, with annual averages of 83% (2010) and 79% (2011). The effective transfer coefficients for heat are aligned with previous lake studies, validating the use of bulk transfer models (Nordbo et al., 2011; Xiao et al., 2013).

Year	R^2	Slope	Interpretation	Reason for Energy Non-Closure
2008/09	0.739	0.75	Moderate EBC; ~74% of Rn partitioned to H+LE	Surface heterogeneity, storage terms (G, biomass), instrument error
2010/11	0.874	0.96	Best EBC; strong coupling of Rn to H+LE	Minimal imbalance; underestimation of minor energy sinks
2015/16	0.840	0.73	Good EBC despite drought; weak moisture fluxes	Sparse vegetation, reduced LE, soil moisture limitations
2016/17	0.836	0.78	High EBC; ~78% closure	Residual storage (G), unmeasured advection, canopy effects

Table 2: Summary of Skukuza findings of results

The table 2 above, shows varying energy balance closure (EBC) across years, with 2010/11 achieving the best closure (R2=0.874R^2=0.874R2=0.874, slope 0.96), indicating strong flux reliability. Lower slopes in 2008/09 and 2015/16 reflect missing energy sinks due to heterogeneity, drought, or soil moisture stress. Overall, results confirm good flux performance but highlight persistent non-closure from storage, advection, and canopy effects.

Causes of unclosed energy balance:

- Inaccurate Flux Estimates Eddy covariance (EC) systems may underestimate latent and/or sensible heat fluxes, especially under complex terrain or atmospheric conditions.
- Uncertainty in Evapotranspiration (ET)Latent heat flux (LE) is used to estimate ET. If the energy balance does not close, ET estimates may be wrong, affecting water resource management and climate modelling.
- Model Calibration Errors: Land surface and climate models rely on correct flux data. An unclosed energy balance can lead to biased model parameters or incorrect conclusions about surface processes.
- Misinterpretation of Ecosystem Function Energy imbalance may give false impressions of ecosystem productivity, stress, or water-use efficiency.
- Difficulty in Comparing Sites or Years Without closure, comparing flux data across sites or seasons becomes problematic because you cannot distinguish between true variation and instrumental or methodological errors.
- Data Correction Challenges Researchers often apply post-processing corrections (e.g., Bowen ratio energy balance closure, residual methods), which introduce assumptions and potential biases.

4 Conclusion

Study at Skukuza (Kruger National Park), shows energy balance closure ranged around 80% across years, with better closure during wet seasons. For example, 2010/11 showed improved closure compared to 2008/09, indicating seasonal and interannual variability in energy partitioning. Challenges were due to turbulence, sensor placement, and terrain. The suggestion is to integrate EC with remote sensing, upscaling and modelling. This study is highly relevant for improving the accuracy of climate models and understanding ecosystem responses to climate variability. It supports better water resource management, especially in arid and semi-arid regions facing increased climate stress. Enhancing energy balance measurements informs sustainable land-use planning and agricultural practices. Future studies can build on this data to advance remote sensing integration and climate adaptation strategies.

References

[1] Fisher, J.B., et al. (2017). The future of evapotranspiration: Global requirements for ecosystem functioning, carbon and climate feedback, agricultural management, and water resources. Water Resources Research, 53(4), 2618–2626. https://doi.org/10.1002/2016WR020175

[2] Oki, T., & Kanae, S. (2006). Global hydrological cycles and world water resources. Science, 313(5790), 1068–1072. https://doi.org/10.1126/science.1128845.

[3] Morillas, L., Villagarcía, L., Domingo, F., et al. (2013). Environmental factors affecting a simple model for predicting evapotranspiration in semiarid mountainous areas. Journal of Hydrology, 505, 167–179. https://doi.org/10.1016/j.jhydrol.2013.09.041.

[4] Purdy, A.J., Kahle, A.B., & Fisher, J.B. (2018). Radiometric correction of airborne thermal infrared imagery using a simulation-based method. Remote Sensing of Environment, 210, 1–9. https://doi.org/10.1016/j.rse.2018.03.003

[5] Nordbo, A., Launiainen, S., Mammarella, I., Leppä, J., & Vesala, T. (2011). Long-term energy balance of a boreal lake determined from eddy covariance and lake temperature profile measurements. Tellus B: Chemical and Physical Meteorology, 63(5), 950–963. https://doi.org/10.1111/j.1600-0889.2011.00541.x

[6] Xiao, W., Liu, C., & Wang, K. (2013). Energy balance closure at a subtropical coniferous plantation in China. Advances in Atmospheric Sciences, 30, 145–158. https://doi.org/10.1007/s00376-012-2018-7.

What are the most suitable basic irradiance models for Southern Africa?

Sindiswa M. Figlan[1], Hartmut Winkler[1]

[1]Department of Physics, University of Johannesburg, Johannesburg, South Africa

E-mail: sindiswafiglan@gmail.com

Abstract. Solar irradiance modelling is critical for determining local solar energy potential. Several past studies have analysed the more easily attainable Global Horizontal Irradiance (GHI) within Southern Africa. However, less research has been carried out on the physically more useful Direct Normal Irradiance (DNI) and Diffuse Horizontal Irradiance (DHI). This study aims to alleviate this by investigating for these local sites simple clear sky models which are solely dependent on the solar zenith angle and identifying the appropriate scaling parameters for DNI and DHI. The accuracy of the Meinel model for DNI and a Logarithmic model for DHI are evaluated and compared to the Power Law model more commonly used in solar irradiance modelling. The model evaluations were conducted using 1-minute resolution data taken from 5 stations within the SAURAN network: Vanrhynsdorp, Richtersveld, Graaff-Reinet (all located in South Africa), Gaborone (Botswana) and Windhoek (Namibia) over the period 2014-2021, with a minimum of 13 clear sky days selected per station covering all seasons.

1 Introduction

Southern Africa is a region of high solar irradiance potential, making it a prime location for solar energy generation [1]. To effectively quantify this potential, solar irradiance modelling is crucial. Thus, accurate and reliable evaluations of simple solar irradiance in clear sky conditions (days which contain minimum cloud coverage) in Southern Africa are essential.

Irradiance is defined as the photon power per unit area incident on a collecting surface and hence depends on the alignment and potential shading of this surface. Three measures of irradiance are commonly studied (see e.g. [2] for a full description):

- Global Horizontal Irradiance (GHI) constitutes the irradiance determined by an upward-facing horizontal collector. Recorded photons include those from the solar beam as well as scattered solar photons that reach the collector from other directions (i.e. the sky background).
- Direct Normal Irradiance (DNI) is the irradiance measurement of the solar beam (excluding photons incident from other directions) obtained by a collecting surface directly facing the Sun.
- Diffuse Horizontal Irradiance (DHI) is, as with GHI, recorded on a horizontal upward facing collector, but with the Sun shaded, i.e. it measures the irradiance from the sky only.

GHI measurements are the easiest and most cost effective, given that they do not require supplementary solar tracking equipment. Possibly because of this, much of the research on solar evaluation in Southern Africa has

focused on GHI [3, 4, 5]. However, DNI and DHI are more significant to gain a physical understanding of the solar energy potential of concentrating solar power [6] as well as tilted and solar tracking dependent photovoltaic systems. Thus, the evaluation of DNI and DHI models is important.

Highly complex irradiance models depend on multiple variables (e.g. [7]). These models are not always practical as the measurements of most of the additional variables are often not available for the required location. Furthermore, model variables such as water vapour concentrations can be highly variable even at intra-day levels, meaning that the extra levels of complexity and potential intra-day corrections in advanced models are of little consequence when investigating long-term averages. Hence old models employing minimal variables and equation parameters characterise clear-sky days surprisingly well [4, 5], and perform even better when one adjusts model parameters. The improved performance is understandable given that the original parameters were determined at sites at different altitudes above sea level (implying greater or smaller transmissivity) or in areas when urban smog and pollution levels were considerably higher.

2 Theory

We will represent GHI, DNI and DHI through the symbols G, B and D respectively. Using geometric arguments, one can immediately show that these quantities are interrelated by the equation

$$G = B\cos\zeta + D \tag{1}$$

where ζ is the solar zenith angle. Another important parameter directly linked to the solar zenith angle is the ratio of the direct solar beam path through the Earth's atmosphere relative to the corresponding path should the Sun be positioned directly overhead. This ratio is referred to as the relative airmass and is here designated with the symbol m. The exact relationship between ζ and m is highly complex due to Earth curvature and refraction effects. However, as long as the Sun is not too close to the horizon, the approximation

$$m \sim 1/\cos\zeta \tag{2}$$

is adequate, with a discrepancy between the true and approximate relative airmasses of just 3% at $\zeta = 80°$.

Another key quantity in solar irradiance study is the top-of-the-atmosphere DNI, B_0, i.e. the value of B just before the solar beam encounters attenuation through atmospheric particles. B_0 has a small and accurately calculable seasonal dependence due to the elliptical nature of the Earth's orbit around the Sun.

The models discussed in this paper will be based on two quantities readily determinable from the measured values of B and D, namely the transmittance ψ and the sky brightness δ. These are defined as follows:

$$\psi = B/B_0 \ , \ \delta = Dm/B_0 \tag{3}$$

In particular, in this paper we only test models that describe ψ and δ as functions of one variable only, that being the solar zenith distance quantified through the airmass. In other words, $\psi = \psi(m)$ and $\delta = \delta(m)$. Furthermore, all models investigated had model equations that only contained two parameters. We chose to express the first of these parameters as the model value of the functions ψ and δ at relative airmass $m = 2$, i.e. $\psi(2)$ and $\delta(2)$. This is a particularly appropriate choice given that $m = 2$, corresponding to a solar elevation angle of 30° above the horizon, occurs twice a day throughout the year at all of our stations. The mathematically more natural $m = 1$ on the other hand is only achieved in the tropics, and then only twice a year.

3 Methodology

3.1 Irradiance data

In this study, the performance of ten basic two-parameter clear sky solar irradiance models, each only dependent on the solar zenith angle, were evaluated through the evaluation of DNI and DHI data from five stations across Southern Africa that form part of the South African Radiometric Network (SAURAN) [8]. These stations, details of which have been compiled in Table 1, all had pyranometers and pyrheliometers operating on site for several years (see [7] for full instrumentation and operational details). The model performance was assessed using high resolution (1-minute) radiometric data, with 13-21 clear sky days evaluated for each station.

Name of station	Country	Altitude (m)	Latitude (degrees S)	Longitude (degrees E)
Vanrhynsdorp	South Africa	130	16.7615	28.5608
Richtersveld	South Africa	141	18.7383	31.6175
Graaff Reinet	South Africa	660	24.5858	32.4855
Gaborone	Botswana	1014	25.9340	24.6610
Windhoek	Namibia	1683	17.0750	22.5650

Table 1: Selected SAURAN stations with their location coordinates and altitude above sea level.

Days were classified as clear if the irradiance curves showed minimal fluctuations (i.e. the curves were free of sudden irradiance changes greater than ~1% typically associated with the passage of a cloud). Additionally, clear days were categorised based on atmospheric aerosol concentrations using criteria explained in [8]. Figure 1 illustrates and contrasts partly cloudy, high-aerosol and low-aerosol clear sky conditions.

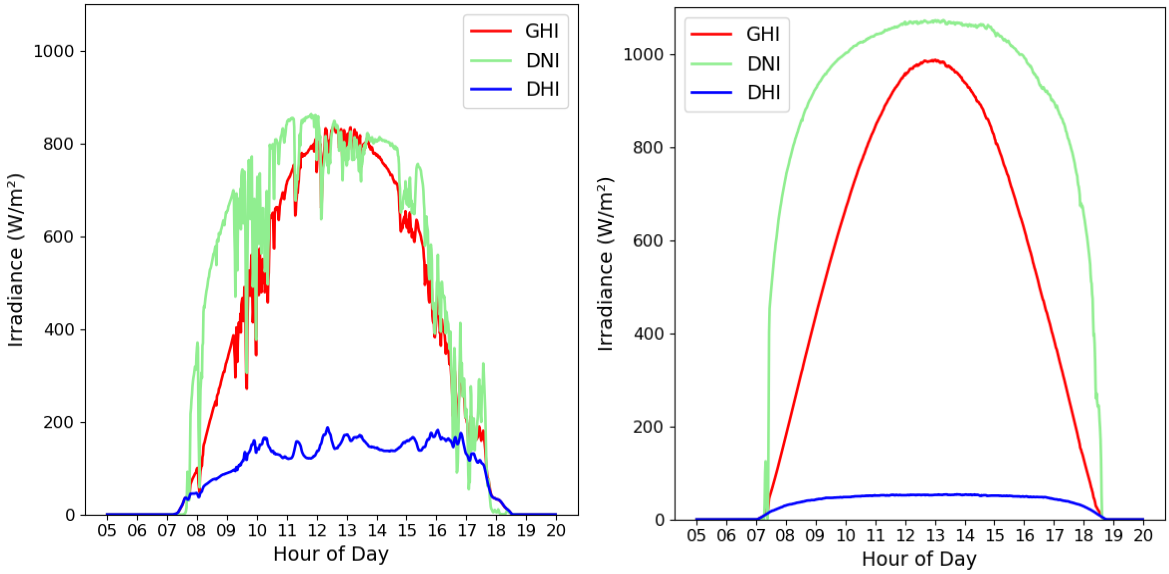

Figure 1: Sample plots of GHI, DNI and DHI recorded at the Windhoek station. (*left*) Partly cloudy sky with high aerosol loading on 12-08-2018. (*right*) Clear sky with minimal aerosol loading on 27-08-2018.

3.2 Model linearisation

For each irradiance component, DNI and DHI, 5 models were evaluated respectively. Each model was expressed in terms of the relative airmass m (see Eq. 2) which quantifies the amount of atmosphere the solar beam passes through in its path to the ground, measured as a ratio relative to the vertical path and is related to the solar zenith angle. For the accuracy of model evaluation, the solar zenith angle was restricted to $\zeta < 80°$. This decision was based on findings that suggest the models lose their reliability when the sun is positioned at higher angles.

The linearization of the model involved several steps: first, the original model from the literature was examined to determine the nature of its proportionality. Next, the parameters from the original model were generalized, and the proportionality constant C was evaluated by assuming a suitable value for m. The model was parametrized with $m = 2$, and from this, the expression for the first scaling parameter was derived at $m = 2$. Following this, the equation was linearized, allowing for the revised model parameters to be determined from the slope and y-intercept of the resulting plot. The choice of airmass of $m = 2$ is significant because this value is reached daily regardless of the year or season. The first scaling parameter $\psi(2)$ for DNI and $\delta(2)$ for DHI, determines the height of the graph while the second scaling parameter q dictates the spread of the curve. The procedure employed is detailed in equations 3 to 8 using the Power Law DNI model as an example. The Power Law model has been widely utilized in some of the earliest irradiance studies, and continues to be a common choice today:

- Biga and Rosa [9] gave their DNI power law model as an expression that is mathematically equivalent to $B = (926\ \mathrm{W/m^2})\times(\cos\zeta)^{0.29}$.
- Applying Equations 2 and 3, the mathematical form of this expression is thus $\psi = Cm^q$ where C is a constant (in this case equal to $(926\ \mathrm{W/m^2})/B_0$) while q (in this case equal to –0.29) is the first of the two model parameters.
- In this case the mathematical form is readily linearised by applying natural logarithms to both sides of the equation and algebraic manipulation: $\ln\psi = q\ \ln m + \ln C$. If the model is correct, it would then yield a linear graph when plotting $\ln\psi$ vs. $\ln m$, with a slope of q and a y-intercept of $\ln C$.
- We are left evaluating $\ln C$ in terms of q and $\psi(2)$. Substituting $m = 2$ into the mathematical form we get $\psi(2) = C\times 2^q$, i.e. $C = 2^{-q}\psi(2)$, and hence $\ln C = -q\ln 2 + \ln\psi(2)$. This results in the linear relation given in Table 2.

Table 2 also gives the names, mathematical forms and linearized forms for the remaining 9 models explored in this study. The derivations of the linearized forms are fully detailed in [2].

	Model name	Form	Y	=	slope	×	X	+	y-intercept
DNI	Archer [10]	$\psi = C\exp(-qm)$	$\ln\psi$	=	$-q$	×	m	+	$\ln\psi(2)+2q$
	Sharma [11]	$\psi^{-1} = C(qm+1)$	ψ^{-1}	=	$q/(\psi(2)(2q+1))$	×	m	+	$(\psi(2)(2q+1))^{-1}$
	Meinel [12]	$\ln\psi = Cm^q$	$\ln(-\ln\psi)$	=	q	×	$\ln m$	+	$\ln(-\ln\psi(2))-q\ln 2$
	Power Law [9]	$\psi = Cm^q$	$\ln\psi$	=	q	×	$\ln m$	+	$\ln\psi(2)-q\ln 2$
	Logarithmic [13]	$\psi = C-q\ln m$	ψ	=	$-q$	×	$\ln m$	+	$\psi(2)+q\ln 2$
DHI	ASHRAE [14]	$\delta = Cm\exp(-qm)$	$\ln(\delta/m)$	=	$-q$	×	m	+	$\ln\delta(2)+2q-\ln 2$
	Power Law [9]	$\delta = Cm^q$	$\ln\delta$	=	q	×	$\ln m$	+	$\ln\delta(2)-q\ln 2$
	Adapt. Fritz [15]	$\delta = C(1-\exp(-qm))$	δ/m	≈	$-q\delta(2)/(4-4q)$	×	m	+	$\delta(2)/(2-2q)$
	Daneshyar [16]	$\delta = C-q\zeta$	δ	=	$-\delta(1)q$	×	ζ	+	$\delta(1)$
	Logarithmic [8]	$\delta = C-q\ln m$	δ	=	$-q$	×	$\ln m$	+	$\delta(2)+q\ln 2$

Table 2: The investigated DNI and DHI irradiance models, with their general mathematical form and their linearized expressions. Note: for the Daneshyar model $\delta(2) = 2\delta(1)(1-q\cos^{-1}(0.5))$ and ζ is in radians.

3.3 Goodness of fit comparisons

The data obtained for a specific day are then plotted in the graph appropriate to each model and linearly fitted. To rigorously assess the model's performance in relation to the experimental data, three statistical indicators are determined to quantify the goodness of the model fits to the data (see in [5] for their mathematical definitions): the root mean square error (RMSE) and mean absolute error (MAE), both of which provides insights of the overall deviation between the experimental and model predicted data, and R^2, the standard coefficient of determination, whose value may range between 0 (meaning no correlation) to 1 (perfect correlation).

4 Results

The scaling parameters for each investigated day and model were calculated from the slope and y-intercept expressions listed in Table 2. The determined average scaling parameters and goodness of fit measures are summarised in Table 3. Examples of plots for specific models at specific stations on individual days are displayed in Figure 2.

We observed several notable trends within the data. As anticipated, we find that with increasing altitude the value of $\psi(2)$ tends to increase (see Figure 3) due to the shorter atmospheric traverse there, and correspondingly $\delta(2)$ then tends to decrease due to less scattering events. Most models exhibit altitude dependence for the q-parameter, with the exception of the Meinel model. As expected, higher aerosol levels lead to decreases in $\psi(2)$ and increases in $\delta(2)$. In evaluation of the goodness of model fit across the models, we find that the best performing models (RMSE and MAE small, R^2 approaching 1) are the Meinel model for DNI and the Logarithmic model for model for DHI. Conversely, the popular Power Law model performs worst for DNI, which is evident from the curvature of the plot in Figure 2. The Adapted Fritz and Daneshyar models are clearly inferior to the other DHI models tested.

	Model name	$\psi(2)$ or $\delta(2)$	q	R^2	RMSE	MAE
DNI	Archer	0.6540 ± 0.0303	0.1269 ± 0.0186	0.9885	0.770	0.623
	Sharma	0.6508 ± 0.0324	0.1994 ± 0.0454	0.9928	0.696	0.589
	Meinel	0.6487 ± 0.0298	0.6447 ± 0.0547	0.9943	0.523	0.417
	Power Law	0.6377 ± 0.0300	–0.3151 ± 0.0432	0.9777	1.103	0.910
	Logarithmic	0.6431 ± 0.0162	0.1874 ± 0.0162	0.9904	0.720	0.572
DHI	ASHRAE	0.0873 ± 0.0141	0.1689 ± 0.0182	0.9371	0.402	0.297
	Power Law	0.0800 ± 0.0131	0.5734 ± 0.0655	0.9651	0.400	0.295
	Adapt. Fritz	0.1015 ± 0.0174	0.1148 ± 0.0145	0.9091	1.016	0.649
	Daneshyar	0.0828 ± 0.0128	0.0067 ± 0.0015	0.8514	2.217	1.469
	Logarithmic	0.0870 ± 0.0137	–0.0518 ± 0.0079	0.9679	0.349	0.271

Table 3: Determined average scaling parameters with uncertainties and average R^2, RMSE and MAE for each model. These averages were calculated using the entire analysed data set, i.e. all stations and aerosol levels.

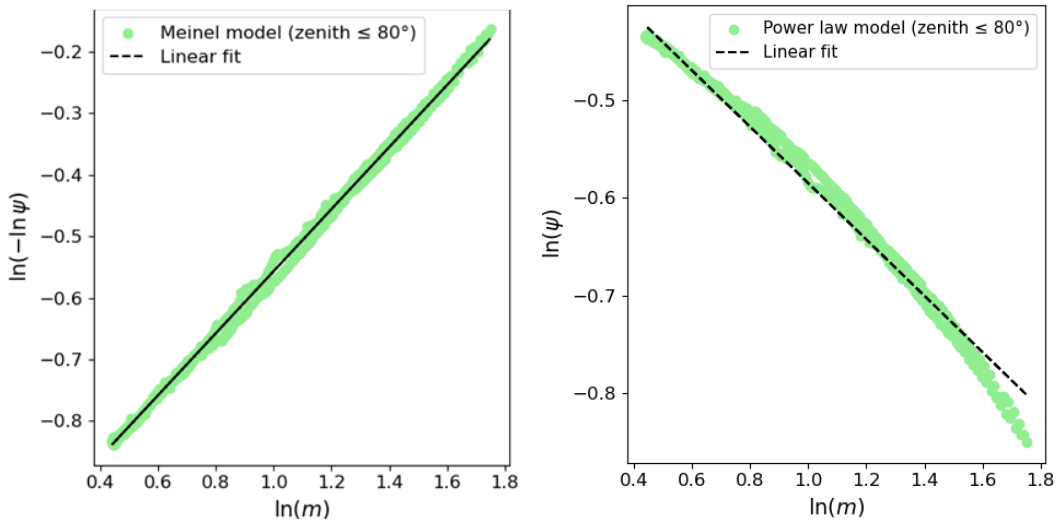

Figure 2: Linearised DNI model plots for Vanrhynsdorp, 13 May 2017. (*left*) Meinel model. (*right*) Power Law model.

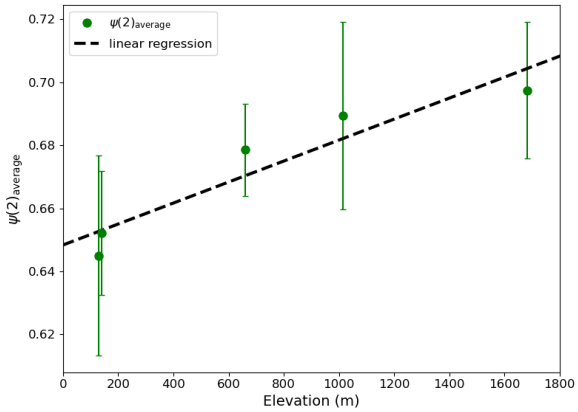

Figure 3: Illustration of the dependence of the $\psi(2)$ scaling parameter with site altitude.

5 Discussion and Conclusion

The The Meinel model outperformed all other models for DNI across all stations in this study and its q-parameter appears independent of site altitude, indicating its suitability for Southern African conditions. The higher $\psi(2)$ values obtained for all DNI models compared to their original formulation indicates that the atmosphere over Southern Africa is more transparent, with the parameters determined here more suitable for local irradiance modelling. The theoretical exploration of the constant q-value in the Meinel model should be pursued. The Power law model demonstrated inferior performance compared to other models under clear sky low aerosol conditions, particularly when modelling at solar zenith angles near 80° limit point.

For the DHI models, the Logarithmic model demonstrated the best performance. However, the model needs to be tested on a larger dataset to validate these findings. Contrarily, the Daneshyar model performed worst, suggesting that the fit and parameters derived from the original study in the aerosol-rich atmosphere of Tehran, Iran, is not suited for DHI characterisation in the typically clearer atmosphere over Southern Africa.

References

[1] T. P. Fluri, "The potential of concentrating solar power in South Africa," *Energy Policy*, vol. 37, pp. 5075-5080, 2009.

[2] S. M. Figlan, "Investigating the accuracy of basic single-variable irradiance models under clear sky conditions in Southern Africa," MSc thesis, University of Johannesburg, 2024. [Online]. Available: https://hdl.handle.net/10210/513539

[3] A. J. Drummond and E. Vowinckel, (1957). "The distribution of solar radiation throughout Southern Africa," *Journal of Meteorology*, vol. 14, no. 4, pp. 343-353, 1957.

[4] B. Mabasa B., M. D. Lysko, H. Tazvinga, N. Zwane, and S. J. Moloi, "The performance assessment of six global horizontal irradiance clear sky models in six climatological regions in South Africa," *Energies*, vol. 14, no. 9, 2583, 2021, doi:10.3390/en14092583.

[5] L. Javu, "Validating clear sky irradiance models in different parts of South Africa," MSc thesis, University of Johannesburg, 2021. [Online]. Available: https://hdl.handle.net/10210/498256.

[6] S. A. Kalogirou, "Solar thermal collectors and applications," *Progress in Energy and Combustion Science,* vol. 30, pp. 231-295, 2004.

[7] C. Gueymard, "Prediction and performance assessment of mean hourly global radiation," *Solar Energy,* vol. 68, pp. 285-303, 2000.

[8] M. J. Brooks *et al*., "SAURAN: A new resource for solar radiometric data in Southern Africa," *Journal of Energy in Southern Africa*, vol. 26, no. 1, pp. 2-10, 2015.

[9] A. J. Biga and R. Rosa, "Contribution to the study of the solar radiation climate of Lisbon," *Solar Energy*, vol. 23, no. 1, pp. 61-67, 1979.

[10] R. E. Schultze, "A physically based method of estimating solar radiation from sun cards," *Agricultural Meteorology*, vol. 16, pp. 85-101, 1976.

[11] M. R. Sharma and R. S. Pal, "Interrelationships between total, direct, and diffuse solar radiation in the tropics," *Solar Energy*, vol. 9, no. 4, pp. 183-192, 1965.

[12] A. B. Meinel and M. P. Meinel, *Applied Solar Energy: An Introduction*. Addison-Wesley Publishing Company, 1976.

[13] J. G. Williams, "Change in transmissivity parameter with atmospheric path length," *Journal of Applied Meteorology*, vol. 15, pp. 1321-1323, 1976.

[14] ASHRAE, *Handbook of Fundamentals*. American Society of Heating, Refrigerating and Air-Conditioning Engineers, 1972.

[15] L. D. Williams, R. G. Barry, and J. T. Andrews, "Application of computed global radiation for areas of high relief," *Journal of Applied Meteorology*, vol. 11, pp. 526-530, 1972.

[16] M. Daneshyar, "Solar radiation statistics for Iran," *Solar Energy*, vol. 21, no. 4, pp. 345-349, 1978.

Monitoring of the performance of a small-scale PV system based on Power Law (PLM) approach

AD Kapim Kenfack[1*], NM Thantsha[1], T Nkwashu[1] and M Msimanga[1,2]

[1]PV Nanocomposite R&D Platform, Department of Physics, Tshwane University of Technology, Private BagX680, Pretoria, South Africa
[2]NRF-iThemba LABS, PBag WITS 2050, Johannesburg, South Africa

E-mail: kapimkenfackad@tut.ac.za

Abstract. This paper proposes a mathematical approach to monitor the performance of a small-scale rooftop photovoltaic (PV) system based on the power law model (PLM). This model is commonly used to predict the I-V curves of solar cells under standard test conditions (STC). The shape parameters of the PLM, named as m and μ in this study, were determined using experimental data collected under normal weather conditions (irradiation and temperature) based on the Newton-Raphson algorithm iterative method. The calculations performed on MATLAB revealed that the shape parameters are not significantly affected by both temperature and irradiation, as shown by their low correlation coefficients of 29.6 % and -11.0%, respectively with μ followed by -20.1% and -18.8% respectively, with m. However, it turns out that the shape parameters are strongly correlated to the electrical parameters: μ is strongly correlated to the fill factor, with a correlation factor of 95.8% while m strongly depends on voltage with a correlation factor of 78.4%. Additionally, this approach predicts the output electrical parameters of the PV system with high accuracy, with the mean values of R^2, RMSE, and correlation r of about 99%, 3.07 %, and 99%, respectively. Furthermore, the parameter μ is seen to vary between 0.8 and 1 during winter and from 0.5 to 0.8 in summertime, while m fluctuates between 10 and 20 during winter and from 10 to 25 in summertime. This approach offers high accuracy because the shape parameters consider the dynamical behavior of the losses (internal and external), which vary under different weather conditions. The limitation of the model lies in the fact that there is insufficient information to link the shape parameters to other electrical parameters, such as the ideal factor, saturation current, shunt and series resistance, to perform the qualitative investigations based on these parameters.

1 Introduction

Renewable energy has the potential to be a sustainable solution capable of tackling both the energy crisis and climate issues [1-3]. Among renewable energy sources, photovoltaic (PV) energy appears to be a promising candidate that can satisfy the energy demand due to its long lifetime of about 20 years, environmental friendliness, and cost-effectiveness. However, the main challenge with PV energy is that it depends totally on weather conditions (irradiation, temperature, humidity, wind, etc.), which vary randomly and make the prediction of power production difficult [4-6]. Energy produced by PV modules has been estimated in the past decade through the mathematical modelling of PV modules with the single-diode model (SDM) [7-9], and double-diode model (DDM) [10]. Their approaches are based on extracting the electrical parameters (short circuit current, saturation current, ideality factor, shunt, and series resistance) under standard test condition (STC). However, this approach

offers high accuracy only for STC as defined by the manufacturer because the parameters extracted are fixed, but it offers poor prediction outdoors in real-time monitoring. Hao et al. [11] recently proposed a mathematical model of the losses (shunt and series resistance), saturation current, and ideality factor, which vary with the weather conditions to predict characteristic I-V curves, albeit with low accuracy. Karmalkar et al., proposed the Power Low Model (PLM) based on shape parameters to improve the prediction of I-V curves of solar cells under STC [12]. Zhang et al., combined PLM and SDM to predict the I-V curve of a solar cell also under STC [13]. From the works mentioned above, we remark that the extraction of the shape parameters was carried out (only for STC) by proposing different mathematical models to predict the I-V curve of a solar cell. Thus, this work aims to extract the shape parameters for real-time conditions and not just for a solar cell but rather for a small-scale PV system by using real-time weather conditions collected to predict in real-time the performance (current, voltage, maximum power) of a typical small-scale PV system (~ 2 kW). The content of the work is organized as follows: Section 2 lays out the mathematical background , describing the various parameters involved in PLM. The various mathematical models, such as short circuit current and open circuit voltage, are established, leading to the extraction of shape parameters based on the Newton-Raphson method. Sections 3 and 4 are dedicated to the methodology and presentation of the variation in shape and electrical parameters over time respectively, closed by a conclusion and limitations.

2 Mathematical modelling procedure

The power law model (PLM) is made of four parameters, including the short-circuit current, open circuit voltage, and the two shape parameters μ and m . The choice of model is justified by its non-linear behaviour, but also by the fact it has only two parameters capable of describing the non-linear dynamics of a solar cell. The normalized *i-v* characteristics curves of PLM its expressed as [12]

$$i = 1 - \left[1 - \mu\left(G,T\right)\right] v - \mu\left(G,T\right) v^{m(G,T)} \tag{1}$$

wherein $i = I/I_{sc}$ and $v = V/V_{oc}$ are normalized current and voltage, I and V are current and voltage output of the device while $\mu\left(G,T\right)$ and $m\left(G,T\right)$ are the shape parameters. From Eq.(1), the short-circuit current I_{sc} and open circuit voltage V_{oc} are expressed as follows [14]

$$I_{sc} = \frac{G}{G_{ref}}\left[I_{scref} + K_i\left(T - T_{ref}\right)\right] \tag{2}$$

$$V_{oc} = V_{ocref} - K_V\left(T - T_{ref}\right) \tag{3}$$

Wherein I_{scref} and V_{ocref} are the short circuit current and open circuit voltage of the PV system under standard test condition (STC) at the reference temperature T_{ref} and G_{ref} is the reference irradiation normalized by 1000 W/m^2. G and T represent the irradiation and the solar panel temperature obtained from the experiment within the day, K_i and K_V represent the temperature constant of photocurrent and voltage, respectively. Knowing that the normalized power is expressed as $p = i \cdot v$, at the maximum power we have

$$\frac{\partial p}{\partial v} = v_p \left.\frac{\partial i}{\partial v}\right|_{i=i_p, v=v_p} + i_p = 0 \tag{4}$$

After rearrangement, Eq. (4) can be rewritten as

$$\left.\frac{\partial i}{\partial v}\right|_{i=i_p, v=v_p} = -\frac{i_p}{v_p} \tag{5}$$

Differentiating Eq. (1) and substituting it into Eq. (4), we have

$$\mu = \left(-\frac{i_p}{v_p} + 1\right)\left(\frac{1}{1 - m \cdot v_p^{m-1}}\right) \tag{6}$$

wherein i_p and v_p and define the dimensionless current and voltage at the maximum power. Equations (1) and (6) form a system of nonlinear equations that can be solved using the Newton-Raphson iteration method in order to extract the shape parameters for various weather conditions, which is expressed as follows

$$m_{k+1} = m_k - \frac{f\left(m_k\right)}{f_p\left(m_k\right)} \tag{7}$$

wherein the objective function $f\left(m^k\right)$ It's expressed as follows

$$f\left(m_k\right) = -i_p + 1 - \left[1 - \mu\left(G,T,m_k\right)\right]v_p - \mu\left(G,T,m_k\right)v_p^{m_k} \tag{8}$$

The derivative function of f denoted f_p it's expressed as

$$f_p = \frac{\partial \mu}{\partial m_k} v_p - \frac{\partial \mu}{\partial m_k} v_p^{m_k} - \mu \cdot \log\left(v_p\right) \cdot v_p^{m_k} \tag{9}$$

Then the final formula implemented in the Newton-Raphson algorithm is expressed as

$$m_{k+1} = m_k - \frac{-i_p + 1 - \left[1 - \mu\left(G,T,m_k\right)\right]v_p - \mu\left(G,T,m_k\right)v_p^{m_k}}{\frac{\partial \mu}{\partial m_k} v_p - \frac{\partial \mu}{\partial m_k} v_p^{m_k} - \mu \cdot \log\left(v_p\right) \cdot v_p^{m_k}} \tag{10}$$

wherein $\frac{\partial \mu}{\partial m_k} = \left[-\frac{i_p}{v_p} + 1\right]\left(\frac{v_p^{m_k - 1} + m_k \cdot \log\left(v_p\right) \cdot v_p^{m_k - 1}}{\left(1 - m_k \cdot v_p^{m_k - 1}\right)^2}\right)$ and k represents the iteration order.

The resolution of Eq. (10) allows for the determination of the shape parameters and so the prediction of the PV system's real-time performance.

3 Methodology

The small 2 kW PV system installed on the rooftop of the Arcadia campus of the Tshwane University of Technology in Pretoria, South Africa, was used as a test bed in this study. The irradiation and the temperature were measured as weather parameters to monitor the PV system dynamics in real time using the PLM approaches. The PV system is made of two strings of PV modules of monocrystalline silicon half-cut cells, each containing 12 identical PV modules connected in series.

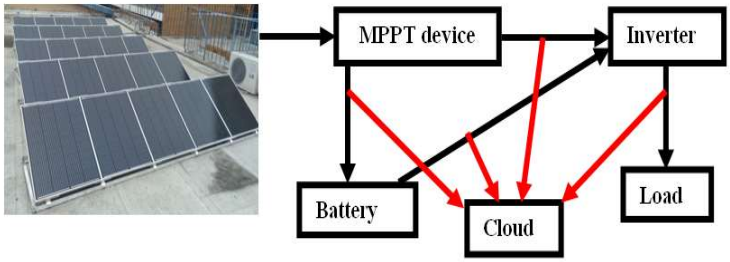

Figure 1: Overview image of the small-scale PV system.

The data collection was conducted over 17 days, from 11 a.m. to 2 p.m., to avoid shading created by an adjacent building on the panels from 8 a.m. to 11 a.m. and 2 p.m. to 6 p.m. The step collection of the data was set to 15 minutes and saved in the cloud, as shown in Figure 1. This work presents variations in shape parameters and compares experimental and predicted data from PLM. The experiment was done during the winter and summer periods to check the behavior of this system under different weather conditions. The output electrical parameters, such as power, fill factor, current, and voltage, obtained through the experiment at the maximum power, were compared with the same parameters obtained using PLM.

4 Results and discussion

4.1 Variation of the shape parameters

This subsection focuses on the variation of shape parameters extracted using the experimental data as shown in Figure 1. The graphs present two zones, first pink for the winter period while green for summertime.

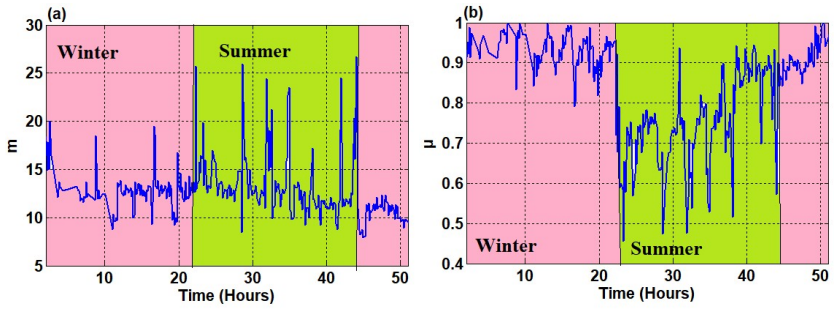

Figure 2: variation of the shape parameters versus time.

The graphs show that the two parameters tend to be vary in opposite directions. In fact, during wintertime, m and μ vary between 10 to 15 and 0.8 to 1, respectively while during summertime they vary between 10 to 25 and 0.5 to 0.8. This shows that during winter, the slope around the short circuit situation is conserved and the shape of the I-V curve is preserved, wherein μ is around 1 and m is closer to 10 [13]. In contrast, during summertime, the slope is steeply downward at the short circuit position because of the low value of μ, leading to the loss of the I-V curve shape. In this situation, the quality of the device is altered due to the recombination that occurs due to the high temperature of the PV module. Thus, m and μ can be used both to check the quality and to predict the performance of the PV cell, module and system in real-time, as shown in the correlation on Table 1.

	I_p	V_p	FF	P_p	G	T	μ	m
I_p	1							
V_p	-0.567	1						
FF	-0.023	-0.024	1					
P_p	-0.439	-0.439	0.490	1				
G	0.814	-0.506	-0.130	0.794	1			
T	0.746	-0.631	0.296	0.695	0.628	1		
μ	0.478	-0.236	0.958	0.485	-0.110	0.296	1	
m	-0.427	0.784	-0.282	-0.334	-0.188	-0.201	-0.511	1

Table 1: Correlation table between the data.

4.2 Variation of the output electrical parameters

This part focuses on the variation of the output electrical parameters, known as current, voltage, fill factor, and power at the maximum operating point obtained through PLM and experiment. The number of peaks shown in Figures 3(a) and (d) define the number of days of the experiment. They reflect the maximum incident irradiation received by the PV system. The graphs are divided into two periods: winter and summer. We noticed a good fit of the PLM approaches with the experiment compared to ref [14] due to the performance metrics displayed in Table 2.

	Fill factor	Current (A)	Voltage (V)	Power (W)	Mean value
R^2	99%	99%	99%	99%	99%
RMSE	0.005%	0.2%	0.07%	12%	3.07%
r	99%	99%	99%	99%	99%

Table 2: Performance metrics.

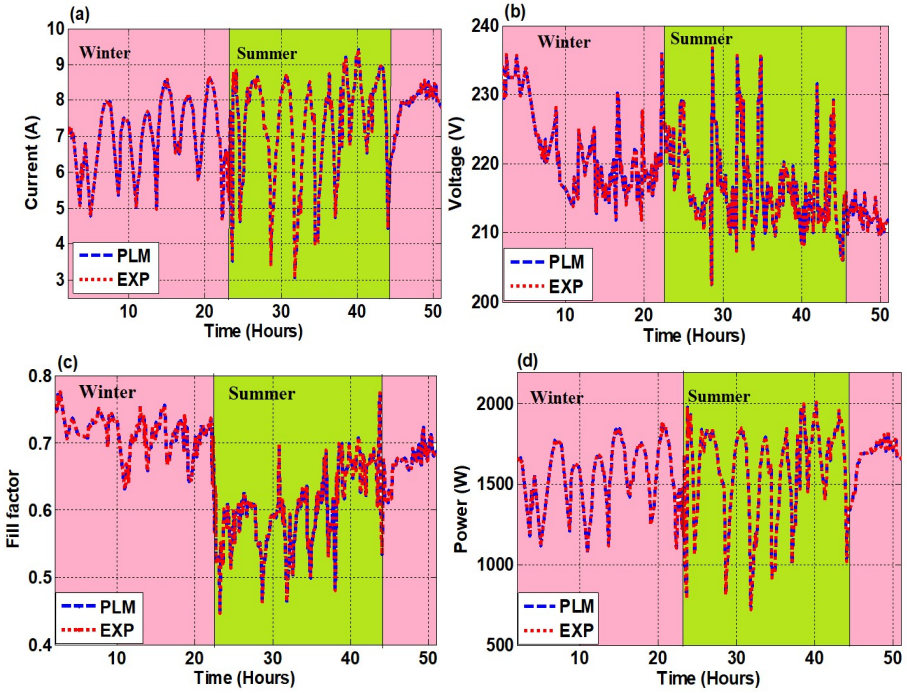

Figure 3: Variation of the electrical parameters versus time (a) current, (b) voltage (c) fill factor (d) power.

During winter (pink band), the fill factor variations inform us that the I-V curve shape is preserved, due to the high value oscillating around 0.7, but the output current and power are relatively low, while the voltage is high. In fact, during wintertime, small-scale PV systems are subjected to a relatively low irradiation level, leading to a low environmental temperature. Thus, the thermal agitation of the carriers in each PV module is minimized because of natural cooling. Then, the low incident irradiation during winter will excite many carriers, but few are extracted. Thus, the carriers stand at the PN junction to increase the voltage as depicted in Figure 3(b). During summertime, we have high power and current due to high irradiance levels, but the fill factor and the voltage are relatively low. This behaviour shows that the losses become non-negligible at high irradiance (high temperature) due to the decrease of the fill factor and voltage. Thus, these losses altered the quality of the PV system by reducing the fill factor, leading to the presence of the recombination effect in the system. Additionally, we notice from Table 1 that μ and m are strongly correlated to the fill factor and voltage. This means that the quality of the system can be checked through μ while the variation of the voltage can be investigated using m.

5 Conclusion

This paper aimed to propose a mathematical model to predict the performance of a small-scale PV system using the power law model (PLM) commonly used to predict the I-V characteristics of solar cells in standard test conditions (STC). The shape parameters (m, μ), involved in the modeling of PLM are extracted using experimental data (irradiation, module temperature, power, current, and voltage) collected in outdoor conditions for 17 days. The results reveal that the shape parameters depend more on output electrical parameters than on weather conditions (irradiation and temperature). We also found that this model offers a good fit because of R^2, correlation (r), and RMSE of about 99%, 3.07 %, and 99%, respectively. Additionally, this model (PLM) offers high performance because it considers the dynamic behavior of the losses (resistance, recombination effect) in the system, which varies under weather conditions. The limitations of this model are such that the shape parameters can only be known once the experimental data are collected. Additionally, this model does not give much information about the behaviour of the electrical parameters in real-time, such as ideality factor, saturation current, shunt and series resistance, to monitor internally the behaviour of the PV system.

Acknowledgments

The authors gratefully acknowledge financial and material support from the Tshwane University of Technology PV Nanocomposites R&D Platform and iThemba LABS of the National Research Foundation of South Africa (Grant number: CPRR23031582676).

References

[1] A.D Kapim Kenfack, M Msimanga, "Effect of low-cost hole transport layers (HTLs) on the performance parameters of lead-free homojunction CsGeI2Br-based perovskite solar cells," *Next Material*, vol. 6, p. 100482, 2025.

[2] A. D. Kapim Kenfack, M. Msimanga, "Machine Learning Approaches to Optimize the Performance of the Novel Stable Lead-free Heterojunction CsGeI3/CsSn($I_{1-x}Br_x$)3-based Perovskite Solar Cell", *J. Electron Mater.* vol.54, pp. 1278-1292, 2025, doi: https://doi.org/10.1007/s11664-024-11630-8.

[3] A.D. Kapim, C.A. Nangmetio, and N.J. Kuatche, "Computational improvement of the performance of thermoelectric element (Generator and Cooler) using an external magnetic field". *J. Electron. Mater*. vol.52, pp. 951-959, 2023, doi: https://doi.org/10.1007/s11664-022-10072-4.

[4] H.Y Zhang, H. Lu, T. Gu, M. Yang, 2022. "A novel method for performance estimation of the photovoltaic module without setting reference conditions". *Int. J. Electr. Power Energy Syst*. vol.134, pp. 107439, 2022.

[5] R.S Pal, V. Mukherjee, "A novel population-based maximum point tracking algorithm to overcome partial shading issues in solar photovoltaic technology". *Energy Convers. Manage*. vol. 244, pp. 114470, 2021.

[6] F.B. Pelap, E.K. Tagne, and A.D.K. Kenfack, "Numerical Optimization of a Tandem Solar Cell based on InxGa1-xN". *J. Ren. En*. Vol. 24, pp. 25-39, 2021 doi:https://doi.org/10.54966/jreen.v24i1.971.

[7] E. Cuce, P.M Cuce, H.I. Karakas, T. Bali, 2017. "An accurate model for photovoltaic (PV) modules to determine electrical characteristics and thermodynamic performance parameters". *Energy Convers. Manage*. vol. 146, pp. 205-216, 2017, doi:https://doi.org/10.1016/j.enconman.2017.05.022.

[8] P. Hao, Y. Zhang, H. Lu, Z. Lang, "A novel method for parameter identification and performance estimation of PV module under varying operating conditions". *Energy Convers. Manage*.vol. 247, 114689, 2021.

[9] P. Hao, Y. Zhang, "An improved method for parameter identification and performance estimation of PV modules from manufacturer datasheet based on temperature-dependent single-diode model". *IEEE J. Photovolt.* Vol.11, pp. 1446-1457, 2021,doi: https://doi.org/10.1109/JPHOTOV.2021.3114592.

[10] V.J. Chin, Z. Salam, K. Ishaque, "An accurate modelling of the two-diode model of PV module using a hybrid solution based on differential evolution". *Energy Convers. Manage*. vol.124, pp. 42-50, 2016, doi:https://doi.org/10.1016/j.enconman.2016.06.076.

[11] Lu. Hao, Z. Yunpeng, P. Hao, J. Ma, Z. Li, T. Gu, M. Yang, "Evolution of the shape parameters of photovoltaic module as a function of temperature and irradiance :New method of performance prediction without setting reference conditions", *Energy Reports*, vol.8, pp. 13859-13875, 2022.

[12] S. Karmalkar, H. Saleem, "The power law J-V model of an illuminated solar cell", *Solar Energy Materials & Solar Cells,* vol. 95, pp.1076-1084, 2011, doi:https://doi.org/10.1016/j.solmat.2010.12.005.

[13] C. Zhang, Y. Zhang, J. Su, T. Gu, M. Yang ".Modeling and prediction of PV module performance under different operating conditions based on power-law I–V model". *IEEE J. Photovolt*. Vol. 10, no 6, pp. 1816-1827, 2020, doi:https://doi.org/10.1109/JPHOTOV.2020.3016607.

[14] T. Nkwashu, N.M Thantsha, A.D Kapim Kenfack, M Msimanga, "An Analytical Model of the 2kW Photovoltaic System Performance at Tshwane University of Technology", *Proceeding of SAIP2024, 68th Annual conference of the South Africa Institute of Physics*, pp 569-575, ISBN:978-1-0370-2645-4.

First-Principles Investigation of The Structural, Mechanical, and Optical Properties of $CsPbI_3$ Perovskite for Solar Cell Applications

X Mkhatshwa[1], T.S Ranwaha [1], E.K Rugut [1], L Phuthu[1] and N.E Maluta[2,3]

[1]Department of Physics, University of Venda, P/Bag X 5050, Thohoyandou, 0950

[2]Green Technology Confucius Institute, University of Venda, P/Bag X 5050, Thohoyandou, 0950

[3]The National Institute for Theoretical and Computational Sciences (NITheCS), Gauteng 2000, South Africa

E-mail: scelo3079@gmail.com

Abstract. The growing global energy crisis necessitates the search for sustainable and environmentally friendly alternatives to fossil fuels. In this study, the first-principles, density functional theory (DFT) calculations were employed to investigate the structural, electronic, optical, and mechanical properties of the all-inorganic halide perovskite compound $CsPbI_3$, a promising material for clean energy applications. Using the generalised gradient approximation (GGA-PBE functional) within the Materials Studio Software, the crystal structure was optimized, and the electronic band structure, density of states (DOS), and optical properties were calculated and analyzed. The results revealed that the inorganic halide perovskite $CsPbI_3$ exhibits a suitable bandgap and strong optical absorption, making it a potential candidate for efficient solar cell applications. Mechanical property calculations, including elastic constants, bulk modulus, shear modulus, Young's modulus, and Poisson's ratio, confirmed the material's mechanical stability, satisfying the stability criteria for cubic systems. The material resisted shear deformation and ductile behaviour, as indicated by a bulk-to-shear modulus ratio (B/G) of 2.01 and supportive Pugh's and Poisson's ratios. Furthermore, low reflectance and high optical conductivity suggest excellent optoelectronic performance, while thermodynamic analysis confirmed its stability under operating conditions. Overall, the study provides valuable theoretical insights into the suitability of $CsPbI_3$ perovskite for solar energy harvesting and other energy-related applications, contributing to the advancement of clean and sustainable energy technologies.

1 Introduction

Recently, the rising energy demand has driven experts to investigate alternatives to fossil fuels. Solar energy emerges as a crucial alternative to conventional fossil fuels, providing a clean and nearly limitless energy source [1]. As a result, significant efforts are being made to build economical and environmentally friendly technologies that harness the energy spectrum for solar cells and thermoelectric generators [1,2]. The photovoltaic process, along with the Seebeck and Peltier thermal electric conversion processes, is essential and deserves deeper investigation [3]. The primary challenge at present is identifying appropriate materials, with extensive research being conducted to assess their energy conversion efficiency [3,4]. Halide perovskites, defined by the general

formula ABX_3, are under consideration as advanced materials for the efficient capture of solar and thermal energy [3,4]. Because of their long carrier diffusion lengths, simple construction procedure, and customisable band gaps, inorganic metal halide perovskites have enormous potential for solar cell applications. Furthermore, these materials demonstrate exceptional light absorption capabilities and show enhanced chemical and thermal stability relative to other organometallic perovskites, positioning them as promising options for solar cell applications. Improving the photovoltaic and optical characteristics of inorganic solar cells by utilizing tunable perovskite compounds through modifications of A-site or X-site ions and implementing mixed-ion strategies can yield beneficial outcomes [4]. A number of studies have investigated the structural and electronic properties of inorganic halide perovskites through DFT, yet thorough analyses that combine mechanical and optical evaluations are still scarce. This study utilized first-principles density functional theory (DFT) to thoroughly investigate the structural, mechanical, optical, and elastic properties of inorganic halide perovskites, highlighting their potential for energy conversion and promoting additional exploration in this area.

2 Computational Method

The density functional theory (DFT) calculations were performed using the generalised gradient approximation (GGA) classified by Perdew-Burke-Ernzerhof (PBE) to describe the exchange-correlation functional [5,6]. All calculations were conducted using Cambridge Serial Total Energy Package (CASTEP) simulation codes on Material Studio of BIOVIA [5,6]. Geometric optimization of the atomic structures was conducted using the Broyden Fletcher Goldfarb Shanno (BFGS) algorithm, which iteratively minimizes the total energy by moving the atoms to achieve the most stable configuration with the lowest ground-state energy. The states of the orbitals Cs(d), I (p), and Pb (p) were studied. A cutoff energy of 500 eV was used for the plane-wave basis, and an 8×8×8 Monkhorst-Pack mesh was employed for integration over the irreducible Brillouin zone. The fixed basis set and ultra-soft pseudopotential were used throughout the study. The total energy tolerance was 1×10^{-5} eV per atom, and the maximum force threshold was 0.01 eV/Å, which implied that the atomic locations and lattice parameters were relaxed.

3 Results and Discussion

3.1 Structural properties

The structural properties, including lattice constants, bond angles, and unit cell volume, are essential in defining the stability, symmetry, and electronic behaviour of perovskite materials such as $CsPbI_3$, which in turn directly affects their photovoltaic and optoelectronic performance. The optimized structural parameters of $CsPbI_3$, derived from density functional theory (DFT), are detailed in Table 1. These parameters are crucial for comprehending its phase stability and informing both theoretical and device-level design.

Parameters	$CsPbI_3$	Literature[7]
a (Å)	10.65	10.46
b (Å)	4.85	4.80
c (Å)	18.03	17.78
α (°)	90	90
β(°)	90	90
γ (°)	90	90
Volume($Å^3$)	931.29	893.10

Table 1: Structural properties of inorganic halide perovskite $CsPbI_3$

The calculated structural parameters of $CsPbI_3$ are presented in Table 1. The optimized lattice constants are determined to be a = 4.847 Å, b = 10.65 Å, and c = 18.03 Å, with $\alpha = \beta = \gamma = 90°$, signifying an orthorhombic crystal symmetry. The unit cell volume measured is 930.80 $Å^3$. The observed values align with the established structural properties of $CsPbI_3$ in its orthorhombic phase. The substantial b and c parameters indicate the stratified organization of ions in the crystal lattice. The presence of 90° angles indicates that there is no distortion or tilting present in the perovskite framework. The considerable unit cell volume suggests a roomy lattice, which may enhance ionic mobility and support optoelectronic applications. Our calculated lattice parameters are very close and comparable with the previously reported literature [7].

3.2 Mechanical Properties

The elastic characteristics are essential for elucidating the structural stability and stiffness of materials. Mechanical stability is a vital criterion for evaluating a material's appropriateness for many applications. The mechanical properties of solid materials are primarily determined by the elastic constants, which govern the crystal's response to external forces that induce strain or stress on its atoms.

Parameters	$CsPbI_3$	Stability
C_{11}	22.13	$C_{11} - C_{12} > 0$
C_{12}	10.45	$C_{11} + 2C_{12} > 0$
C_{44}	9.08	$C_{44} > 0$
B(GPa)	12.411	
E(GPa)	15.522	
G_v	6.009	
Y	0.29	
A	1.55	
$C_{11} - C_{12}$	11.68	
$C_{11} + 2C_{12}$	43.03	
B/G	2.065	

Table 2: Calculated Elastic constants and values of bulk, Young's, Shear modulus, Anisotropy, and Poisson's ratio.

The mechanical properties of solid materials are fundamentally influenced by the elastic constants, which dictate how a crystal reacts to external forces that impose strain or stress on its atoms [8]. A trio of elastic constants (C_{11}, C_{12}, and C_{46}) is adequate for analyzing the mechanical behavior of any cubic system. The numerical values of the three independent elastic coefficients, along with the bulk and shear moduli, Pugh ratio, Young's modulus, and Poisson's ratio for cubic, are presented in Table 2. The independent elastic coefficients C_{ij}, bulk modulus (B), shear modulus (G), and Young's modulus (E) are provided in GPa, with the anticipated numerical values for B, G, E, and v computed through Hill's averaging scheme. The data indicate that the material exhibits stiffness and resistance to compression, as shown by a bulk modulus value of 12.411 GPa. Additionally, a Young's modulus of 15.522 GPa suggests that the material is also resistant to shear deformation. The Poisson's ratio is measured at 0.29, suggesting that the longitudinal strain exceeds the transverse strain in this ternary mixture. The calculated values of the independent elastic coefficients listed in Table 2 meet the Born mechanical stability criteria for cubic systems [6] when applied to Equation (1), confirming that cubic is a mechanically stable material.

$$C_{11} - C_{12} > 0\ ,\ C_{11} + 2C_{12} > 0;\ C_{446} > 0 \quad (1)$$

Table 1 provides an evaluation of the material's ductility and brittleness, which are essential criteria in cell manufacture. Pugh's criterion posits that a material is deemed brittle when the bulk-to-shear modulus (B/G) ratio is below the critical threshold of 1.75, but it is categorized as ductile if the ratio is beyond this value [9]. The calculated B/G ratio in Table 1 is 2.065, surpassing 1.75, indicating that it is a ductile material based on its metallic properties.

3.3 Optical Properties

The optical characteristics of $CsPbI_3$ were examined by DFT to assess its suitability for optoelectronic and photovoltaic applications. Figure 1 illustrates the calculated real and imaginary components of the dielectric functions of $CsPbI_3$.

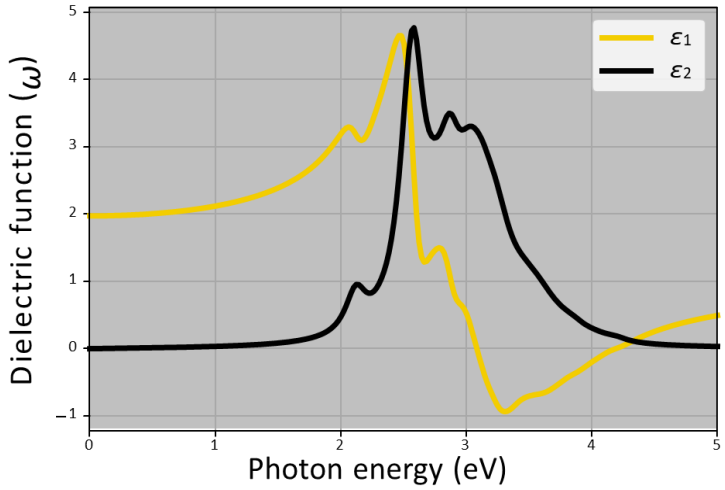

Figure 1: The optical Dielectric function of inorganic halide perovskite $CsPbI_3$

In this context, the yellow line represents the real part, and the black line represents the imaginary part. At zero photon energy, the calculated dielectric function shows that $CsPbI_3$ has a dielectric constant of approximately 2. At higher photon energy, however, the imaginary part peaks at 2.5 eV, indicating enhanced absorption or energy loss as the imaginary part is analogous to the optical absorption [7].

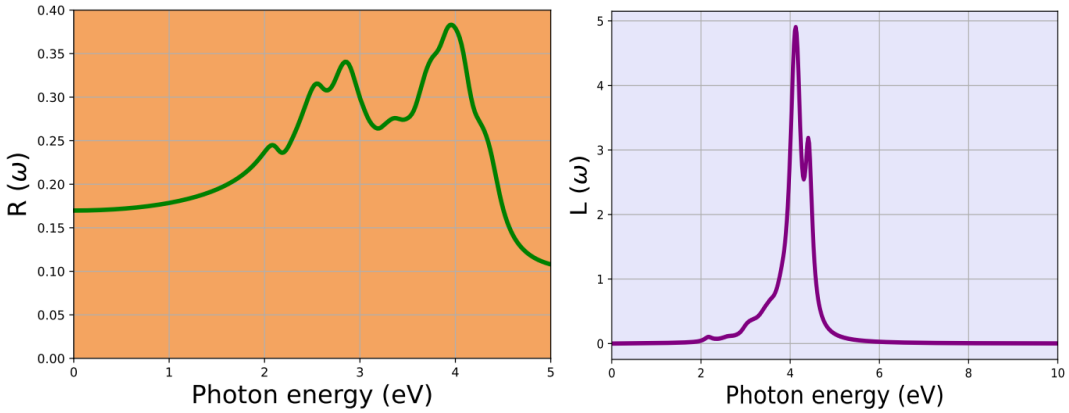

Figure 2: Reflectivity(a) and, Loss function(b), of inorganic halide perovskite $CsPbI_3$

Figure 2 illustrates that at a photon energy of 0 eV, the material begins to reflect 17% of the incoming solar radiation from the sun. At the peak, the material reflects 37% of the incoming solar radiation, indicating its efficiency, suggesting a high charge transfer or real conductivity at this photon energy. The reflectivity spectra shows the highest peak observed at 3.8 eV, indicating that perovskites has the potential to function as an outstanding coating material. Furthermore, the peak reflectivity value was observed when the real part of the dielectric function was negative, indicating that the material behaves as metallic within this energy range. The energy loss function characterizes the energy dissipation experienced by a high-velocity electron as it traverses a material. The peaks observed in Figure 2(b) of the loss function spectra indicate the characteristics linked to plasma resonance. The observed resonant energy loss occurs at 4.1 eV.

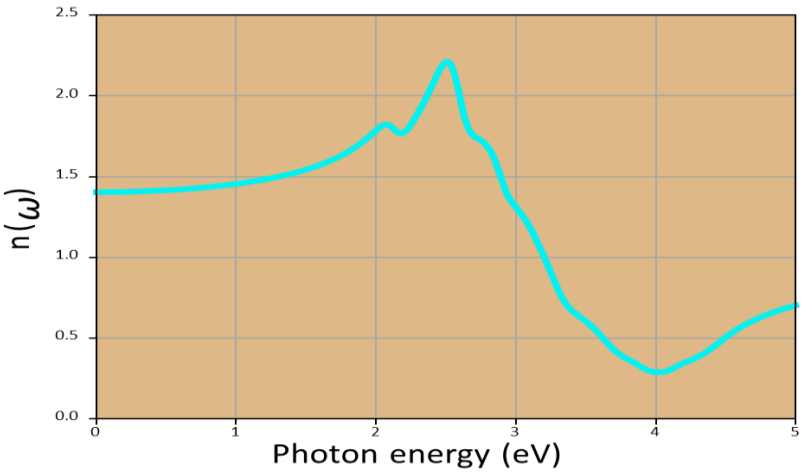

Figure 3: Calculated Optical Refractive index of inorganic halide perovskite $CsPbI_3$

The refractive indices are illustrated in Figure 3 as a function of photon energy. From this data, we established that the static refractive index attained a peak value of 2.3 at 2.5 eV, while at zero photon energy, the static refractive index was approximately 1.40. In this scenario, the refractive index of all the computed compounds exceeds one, as photons experience a delay upon entering a material due to their interactions with electrons.

3.4. Thermal properties

The thermodynamic properties of $CsPbI_3$ were calculated using first-principles density functional theory, emphasizing the changes in free energy, entropy, and heat capacity (C_v) as functions of temperature [9]. The evaluation of these properties is essential for assessing the thermal stability and energy conversion efficiency of perovskite-based materials in optoelectronic applications.

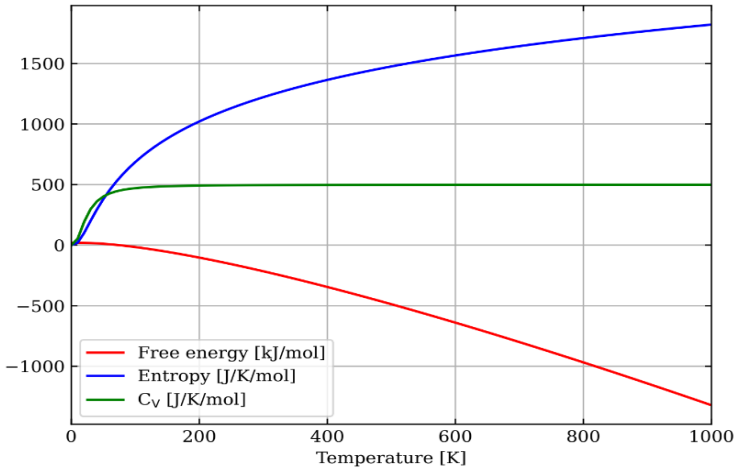

Figure 4: Thermal properties of inorganic halide perovskite $CsPbI_3$

The graph illustrates the changes in free energy, entropy, and heat capacity (C_v) of $CsPbI_3$ as a function of temperature, derived from the DFT calculations. As the temperature rises from 0 K to 1000 K, there is a notable decrease in the free energy of $CsPbI_3$, which exemplifies the characteristics of thermodynamically stable materials. This decline suggests that the system attains greater energetic favorability as temperatures increase. The material's entropy shows a consistent increase throughout the temperature range, indicating a rise in disorder within the crystal structure as atomic vibrations become more pronounced. This gradual increase is consistent with core thermodynamic principles, as entropy is anticipated to rise alongside temperature. Furthermore, the heat capacity (C_v) of $CsPbI_3$ demonstrates a trend of increase with temperature, initially escalating quickly and subsequently nearing a saturation point at approximately 600 K. This behavior indicates that the material attains a threshold in its capacity to absorb further thermal energy for each degree of temperature rise, aligning with the Dulong–Petit law noted in solid-state materials.

4 Conclusion

First-principles calculations were utilized to explore the structural, optical, and mechanical properties of inorganic halide perovskites $CsPbI_3$. The optical characteristics of this material exhibit low reflectance, indicating potential applications in enhancing the overall efficiency of solar cells and various optoelectronic energy devices. The mechanical stability of $CsPbI_3$ indicates that the material is capable of preserving its structure when subjected to mechanical stress. The material exhibited ductility, evidenced by a bulk to shear quotient (B/G) of 2.065, surpassing the critical threshold of 1.75. This inherent ductility was further corroborated by the calculated values of Pugh's ratio and Poisson's ratio. The thermodynamic analysis of $CsPbI_3$ demonstrates its thermal stability and consistent behavior as temperature rises, supported by the observed trends in free energy, entropy, and heat capacity. The characteristics confirm its appropriateness for applications in high-temperature optoelectronics and photovoltaics.

Acknowledgements

The authors confidently acknowledge the Centre for High-Performance Computing (CHPC) for generously providing computing resources, and express gratitude to the Department of Science and Innovation (DSI) for their invaluable financial support.

References

[1] Q. Mahmood, M. H. Alhossainy, M. S. Rashid, T. H. Flemban, H. Althib, T. Alshahrani, … and A. Laref, "First-principles study of lead-free double perovskites Rb_2TeX_6 (X = Cl, Br, and I) for solar cells and renewable energy," *Materials Science and Engineering: B*, vol. 266, p. 115064, 2021, doi: https://doi.org/10.1016/j.mseb.2021.115064.

[2] H. Albalawi, G. Nazir, M. Younas, S. Al-Qaisi, M. G. B. Ashiq, J. Alzahrani, … and T. Ghrib, "Study of lead-free vacancy ordered double perovskites Cs_2TeX_6 (X = Cl, Br, I) for solar cells, and renewable energy," *Physica Scripta*, vol. 97, no. 9, p. 095801, 2022, doi: https://doi.org/10.1088/1402-4896/ac83b2.

[3] P. M. Maleka, R. S. Dima, O. M. Ntwaeaborwa, and R. R. Maphanga, "Study of inorganic lead halide perovskites properties using first-principles density functional theory for photovoltaic and optoelectronic devices," *Materials Today: Proceedings*, vol. 62, pp. S12–S22, 2022, doi: https://doi.org/10.1016/j.matpr.2022.02.177.

[4] P. M. Maleka, R. S. Dima, O. M. Ntwaeaborwa, and R. R. Maphanga, "Density functional theory study of Br doped $CsPbI_3$ perovskite for photovoltaic and optoelectronic applications," *Physica Scripta*, vol. 98, no. 4, p. 045505, 2023, doi: https://doi.org/10.1088/1402-4896/acb8ac.

[6] T. S. Ranwaha, N. E. Maluta, and R. R. Maphanga, "DFT Study of selected croconate dye molecules for application in dye sensitized solar cells

[7] Zhang, B. B., Song, H., Wang, Y., Zhao, Y., Xia, J., & Dong, B. (2018). The preparation and characterization of quasi-one dimensional $CsPbI_3$ perovskites. *Journal of Crystal Growth, 498*, 1-6. https://doi.org/10.1016/j.jcrysgro.2018.12.001

[8] T. Ranwaha, I. Elegbeleye, N. Maluta, and R. Maphanga, "Optical and electronic properties of croconates dye molecules adsorbed on TiO_2 brookite nanocluster for dye sensitized solar cells application,"*Materials Express*, vol. 10, no. 11, pp. 1917–1924, 2020, doi: https://doi.org/10.1166/mex.2020.1863.

[9] E. K. Rugut, N. E. Maluta, R. R. Maphanga, R. E. Mapasha, and J. K. Kirui, "A Density Functional Theory insight into structural, mechanical, and optical properties of Rb_2LiTlF_6 double perovskite," *Advanced Engineering Materials*, vol. 26, no. 5, p. 2300995, 2024, doi: https://doi.org/10.1002/adem.202300995.

Listening with Light: Acoustic sensing over live fibre networks using Coherent Optical Transceivers

Max Brenner, Alice V Drozdov and Mitchell A Cox*

School of Electrical and Information Engineering, University of the Witwatersrand, Johannesburg, South Africa

E-mail: Mitchell.Cox@wits.ac.za

Abstract. Environmental vibrations change the state of polarisation and phase of light in optical fibres. Modern coherent transceivers actively track and compensate these distortions using digital signal processing, presenting an opportunity to repurpose this tracked data for environmental sensing purposes. Although polarisation and phase data have enabled sub-Hz geophysical monitoring, their use for audible-frequency acoustic sensing remains unexplored. This paper presents preliminary laboratory results in which airborne sounds interacting with a fibre segment yield clear signatures in both the state of polarisation and carrier-phase data extracted from an optical coherent transceiver, allowing the reconstruction of single tones, frequency sweeps and complex audio. These findings demonstrate proof of concept for acoustic sensing over live fibre links. Future work will quantify the system's sensitivity, bandwidth and noise floor, and investigate sensor-fusion strategies to enhance detection performance.

1 Introduction

Optical fibre infrastructure forms the backbone of modern telecommunications networks [1]. These fibres are sensitive to environmental disturbances like changes in temperature, pressure and vibration, all of which alter the fibre's physical properties and, in turn, modulate the properties of the light within [1]. This inherent sensitivity has been exploited in applications such as earthquake and tsunami sensing [2]. In the field of fibre acoustic sensing, techniques such as Distributed Acoustic Sensing (DAS) are well established but typically require specialist hardware and dedicated dark fibres, precluding deployment on active data-carrying links [3]. Similarly, interferometric methods demand additional costly hardware [3]. An alternative approach makes use of the digital signal processing (DSP) capabilities of modern coherent optical transceivers, which continually estimate channel state information such as the light's state of polarisation (SOP) and carrier phase, to compensate for impairments and recover transmitted data [4]. By analysing this readily available information, recent work has successfully demonstrated the sensing of very low-frequency geophysical phenomena, such as earthquakes and ocean swells, over live transoceanic links [2]. However, the extension of this technique to detect and characterise signals within the human audible acoustic spectrum (20 Hz to 20 kHz [5]) remains largely unexplored. This gap presents an opportunity to repurpose existing live optical fibres for acoustic sensing without incurring the cost of new deployments and while maintaining simultaneous data transmission. This paper presents a preliminary experimental demonstration of audible-range acoustic sensing over a coherent optical link. Single-frequency tones, frequency sweeps and complex broadband audio signals are recovered from both SOP and phase channels extracted from a commercial coherent transceiver. These results demonstrate proof of concept for this method of audible-range acoustic sensing and lay the groundwork for future work, which will focus on comprehensive system characterisation, comparative analysis of SOP and phase sensing channels, as well as sensor fusion techniques to improve signal detection.

2 Sensing Principle and Data Extraction

2.1 Acoustic Modulation of Optical Signals

The principle behind this sensing technique lies in the physical interaction between acoustic waves and the optical fibre. An acoustic wave impinging on a fibre induces time-varying mechanical strain and pressure. These perturbations modulate the properties of the light propagating within, with two properties that are actively tracked by the DSP of the optical coherent transceiver being the phase and the SOP [3]:

Phase Modulation: The acoustic strain alters both the fibre's physical length (L) and its refractive index (n) via the elasto-optic effect [6]. This directly modulates the accumulated phase (ϕ) of the light, as given by:

$$\Delta\phi = \frac{2\pi}{\lambda_0}\Delta(nL) \tag{1}$$

where λ_0 is the vacuum wavelength [6]. This phase modulation is the primary information carrier in many interferometric sensors.

Polarisation Modulation: Mechanical stress also induces local, time-varying birefringence (B) in the fibre [7], where B is given by:

$$B = |n_x - n_y| \tag{2}$$

where n_x and n_y are the x and y axis refractive indices [7]. This causes the two orthogonal polarisation modes to travel at different velocities, accumulating a differential phase shift (retardance) that changes the light's overall SOP [8]. The change in SOP is therefore an indicator of the acoustic perturbation.

2.2 Data Extraction from a Coherent Transceiver

Polarisation tracking is performed by the transceiver's adaptive 2×2 Multiple-Input Multiple-Output (MIMO) equaliser. The equaliser's filter tap coefficients, updated via the Constant Modulus Algorithm (CMA), are contained in four vectors, $\mathbf{w}_{ab}$, where the subscripts $a, b \in \{H, V\}$ denote the polarisation components. These filter taps converge to represent the inverse of the fibre's Jones matrix [9]. The equalised fields, y_H and y_V, are recovered from the received fields, x_H and x_V, through the convolution operation described by:

$$\begin{bmatrix} y_H(n) \\ y_V(n) \end{bmatrix} = \begin{bmatrix} \mathbf{w}_{HH}^T & \mathbf{w}_{VH}^T \\ \mathbf{w}_{HV}^T & \mathbf{w}_{VV}^T \end{bmatrix} \begin{bmatrix} \mathbf{x}_H(n) \\ \mathbf{x}_V(n) \end{bmatrix} \tag{3}$$

where n is the discrete time index, and $\mathbf{x}_H(n)$ and $\mathbf{x}_V(n)$ are vectors containing the present and past samples of the input signals.

To analyse the slowly-varying polarisation effects, we consider the frequency response of these filters, given by the Discrete-Time Fourier Transform, $W_{ab}(\omega)$. The DC component of this response, $W_{ab}(0)$, is used to determine the SOP. The coefficients used for this calculation, $W_{HH}(0)$ and $W_{VH}(0)$, correspond to the top row of the inverse Jones matrix. They describe the SOP of the signal component at the receiver that was originally launched in the horizontal polarisation. The normalised Stokes parameters (s_1, s_2, s_3) are calculated as follows [3]:

$$s_1 = \frac{|W_{HH}(0)|^2 - |W_{VH}(0)|^2}{S_0} \tag{4}$$

$$s_2 = \frac{2|W_{HH}(0)||W_{VH}(0)|\cos(\Delta\phi)}{S_0} \tag{5}$$

$$s_3 = \frac{2|W_{HH}(0)||W_{VH}(0)|\sin(\Delta\phi)}{S_0} \tag{6}$$

where the total power is given by:

$$S_0 = |W_{HH}(0)|^2 + |W_{VH}(0)|^2 \tag{7}$$

and the relative phase is given by [10]:

$$\Delta\phi = \arg(W_{HH}(0)W_{VH}^*(0)) \tag{8}$$

Tracking these parameters allows one to observe SOP variation caused by acoustic waves.

Carrier Phase: Following polarisation equalisation, a principal component analysis-based carrier phase estimation block compensates for phase drifts [2]. The output of this stage provides a direct measurement of the carrier phase variations, including those induced by acoustic signals.

By logging these two data streams, the coherent transceiver, designed for communication, is effectively repurposed as a dual-channel acoustic sensor.

3 Experimental Setup and Methodology

The experimental setup, shown schematically in Figure 1, is designed to measure the response of a coherent optical link to airborne acoustic signals in a controlled environment. The system's core is a coherent optical transceiver platform, which allows for real-time extraction of SOP and carrier phase data from its DSP pipeline.

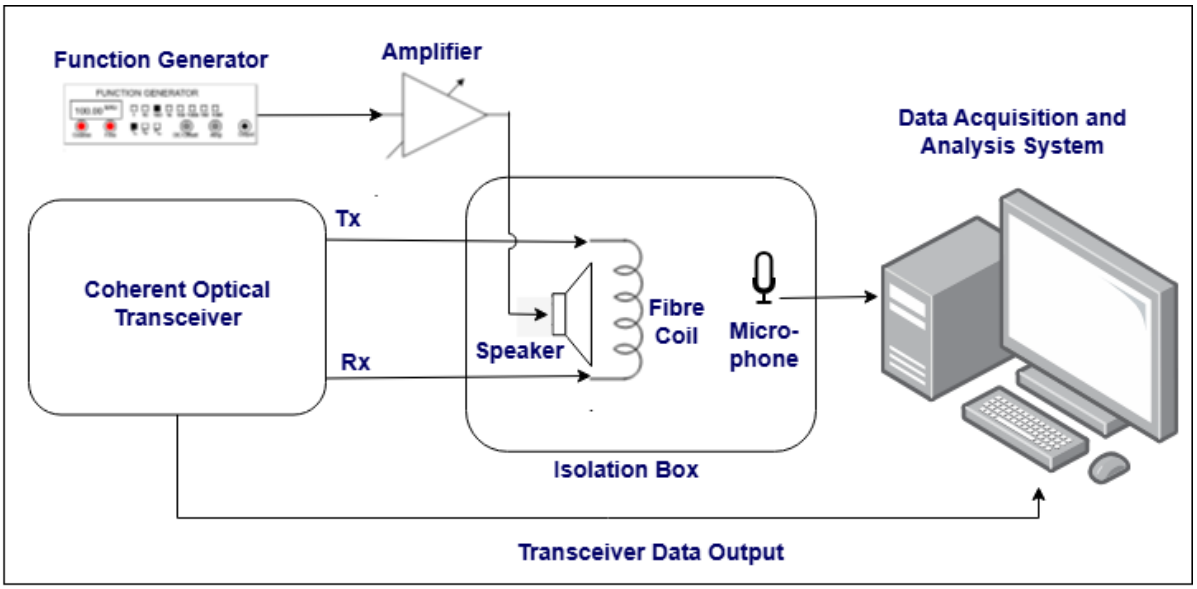

Figure 1: Diagram of the Experimental Setup

The FPGA-based transceiver employs a 15 kHz-linewidth laser operating at 1550 nm and manages the modulation and signal reception at 2 GS/s. Within the DSP, the two key data sources for sensing are SOP information, derived from the coefficients of a 17-tap per-branch 2x2 MIMO adaptive equaliser updated via the CMA algorithm, and phase information, extracted from a principal component-based carrier phase estimation block using 64-symbol block averaging. The update rates and processing parameters (e.g., CMA step-size, block averaging) of these DSP stages fundamentally define the achievable sensing bandwidth. For the experiments presented, the final logged data rate for both SOP and phase parameters was limited to 15.2 kS/s due to data streaming and storage constraints. Recorded data was analysed in Python (v3.10.12), using NumPy (v2.2.6) for numerical computation, SciPy (v1.15.3) for spectral analysis, and Matplotlib (v3.10.3) for visualisation. Spectrograms and Power Spectral Density (PSD) plots were used to observe the temporal evolution and relative power of the detected frequency components for each signal type. These analyses enabled qualitative evaluation of the system's ability to detect and resolve the applied acoustic stimuli.

The sensing medium is a 1-metre segment of standard OS2 single-mode fibre, housed within a custom-built, acoustically isolated enclosure lined with dense foam to minimise external noise. The majority of the fibre is taped to the enclosure's base, leaving a 10 cm segment untaped and free to interact with the sound field. An external function generator and amplifier drive a speaker positioned 5 cm away from this untaped fibre segment. To precisely quantify the acoustic stimulus, a microphone is placed adjacent to the fibre, also 5 cm from the speaker, ensuring that the Sound Pressure Level (SPL) it records accurately represents the acoustic pressure at the fibre. The resulting SOP and phase data streams are sent to a logging computer via an ethernet cable.

To evaluate the system's acoustic sensing performance, three types of acoustic signals were generated, played through the speaker and directed at the untaped fibre segment: First, a pure 3 kHz sine wave was played, producing an SPL of approximately 112 dB at the fibre. This served as a baseline test to confirm that the system could reliably detect a continuous tone in both SOP and phase data streams. To characterise the system's response across a wider frequency range, both linear and sinusoidal sweeps were performed, covering 20 Hz to 4 kHz. This experiment aimed to observe the frequency-dependent sensitivity and to identify any resonant peaks or nulls in the system's response. The input SPL varied with frequency due to the speaker's inherent frequency response. Finally, a segment of broadband audio (music) was played to qualitatively assess the system's ability to resolve a complex, non-stationary signal with multiple, simultaneous, and time-varying frequency components.

4 Results

The results from the three experiments demonstrate the system's ability to detect and resolve various acoustic signals via SOP and carrier phase measurements. This section presents representative spectrograms and PSD plots for each experiment, highlighting key observations.

4.1 Experiment 1: Single-Frequency Tone

Figure 2 shows the spectrograms of the SOP and carrier phase data streams when subjected to a 3 kHz continuous tone at the fibre. Both channels exhibit a distinct spectral line at 3 kHz, confirming successful detection. The carrier phase data additionally reveals harmonics at 6 kHz, which are absent in the SOP data, indicating different channel characteristics. Furthermore, the phase data shows a lower noise floor, evident from the stronger contrast between signal and background. The slight decay in signal amplitude over the measurement period, visible in both spectrograms, is attributed to minor experimental drift in the acoustic coupling.

Figure 3 presents the corresponding PSDs for SOP and carrier phase, reinforcing these findings by showing a clear peak at 3 kHz in both cases, with a significant secondary peak at 6 Khz showing in the phase data. To quantify the difference in noise between the two channels, the Signal-to-Noise Ratio (SNR) was estimated from the PSD by comparing the integrated power within the signal's frequency band to the power within an adjacent, equivalent-width noise band. The SNR for the S3 parameter (which exhibited the highest SNR of the three Stokes parameters) was 4.65dB, in contrast to the carrier phase SNR of 18.17dB. This difference in SNR is primarily due to the fibre's higher longitudinal compliance, which results in a stronger phase modulation compared to the SOP modulation from transverse compression. A secondary factor is the higher sensitivity of the carrier phase recovery algorithm to rapid fluctuations compared to the equaliser from which the SOP is determined.

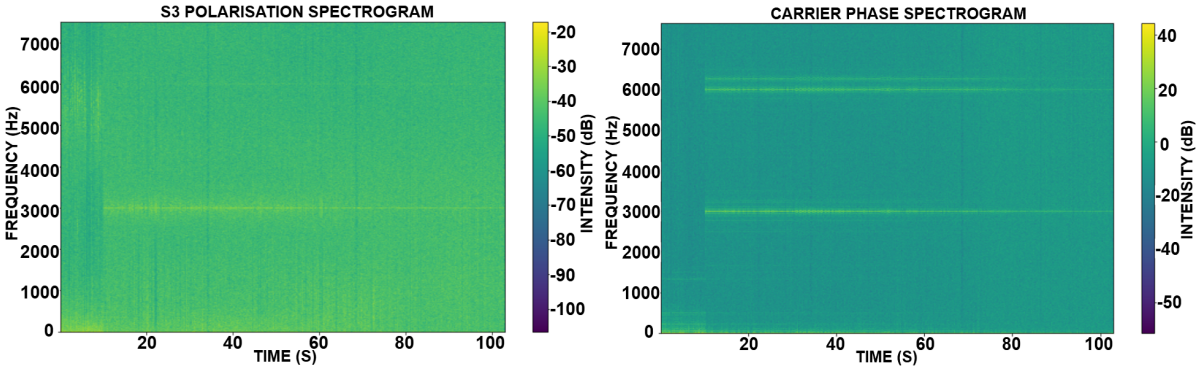

Figure 2: Spectrograms of (*left*) SOP and (*right*) carrier phase data streams during 3 kHz tone excitation. Both show clear detection of the fundamental frequency, while the phase data additionally exhibits harmonics.

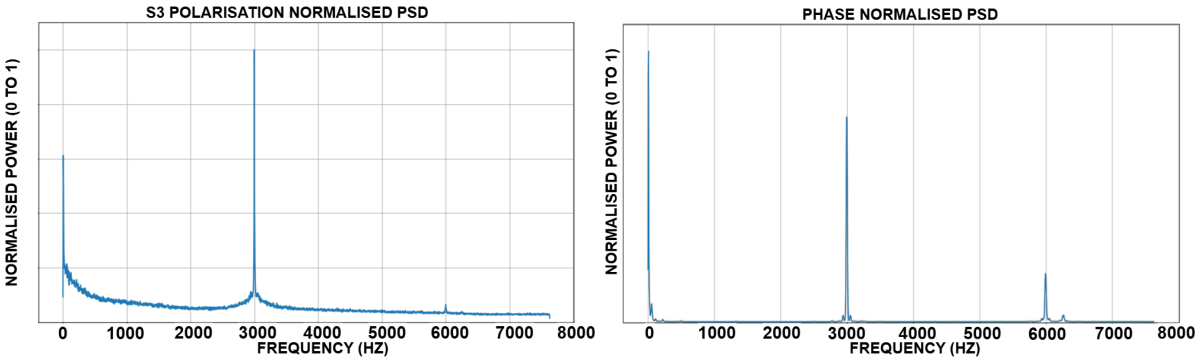

Figure 3: PSD plots of (*left*) SOP and (*right*) carrier phase data during 3 kHz tone excitation, showing strong peaks at the excitation frequency.

4.2 Experiment 2: Frequency Sweeps

Figure 4 shows spectrograms of SOP and phase data for both linear and sinusoidal acoustic frequency sweeps. In all cases, the detected signal closely follows the applied sweep, demonstrating consistent system response over the full frequency range. Harmonics are observed in both polarisation and phase channels.

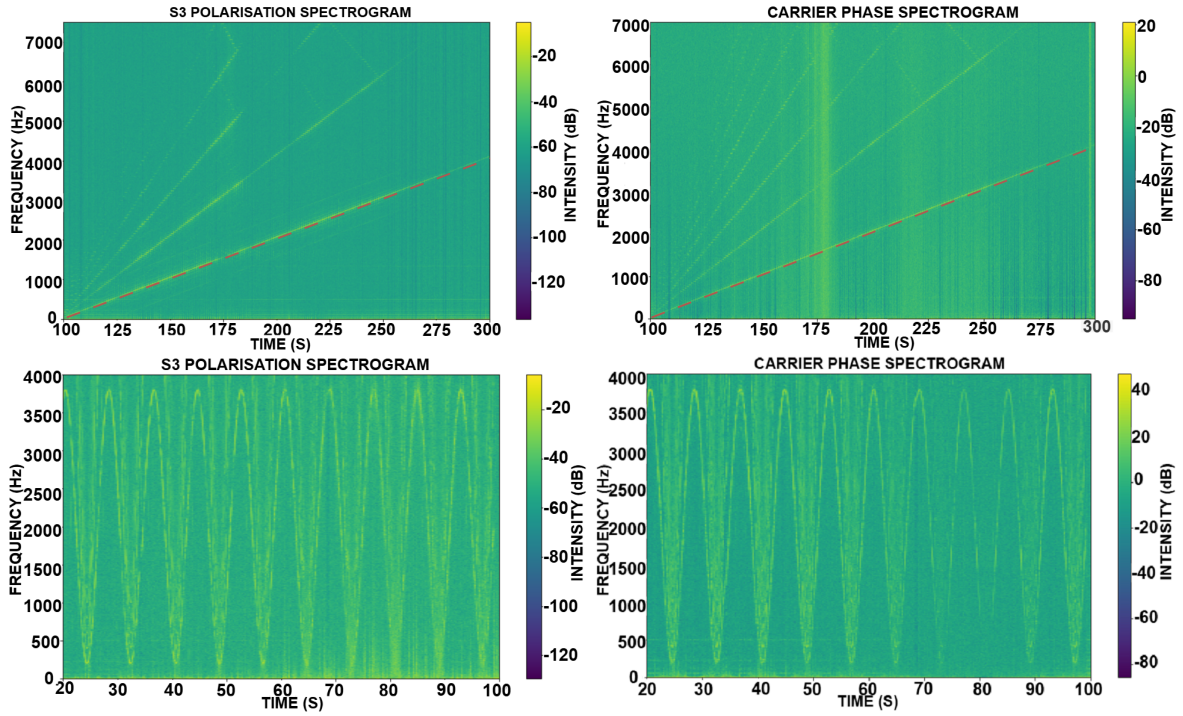

Figure 4: Spectrograms of SOP (*left*) and carrier phase (*right*) data during (*top row*) linear and (*bottom row*) sinusoidal frequency sweeps. Both channels follow the sweep (*red line*) consistently and exhibit additional harmonics.

4.3 Experiment 3: Broadband Audio Signal

For the broadband audio test, the signal was reconstructed from the SOP and phase channels, both of which exhibited strong similarity to the original audio. Only the SOP spectrogram is shown in Figure 5 for brevity. The detected SOP spectrogram closely matches the original, demonstrating the system's ability to resolve complex signals with multiple simultaneous frequency components.

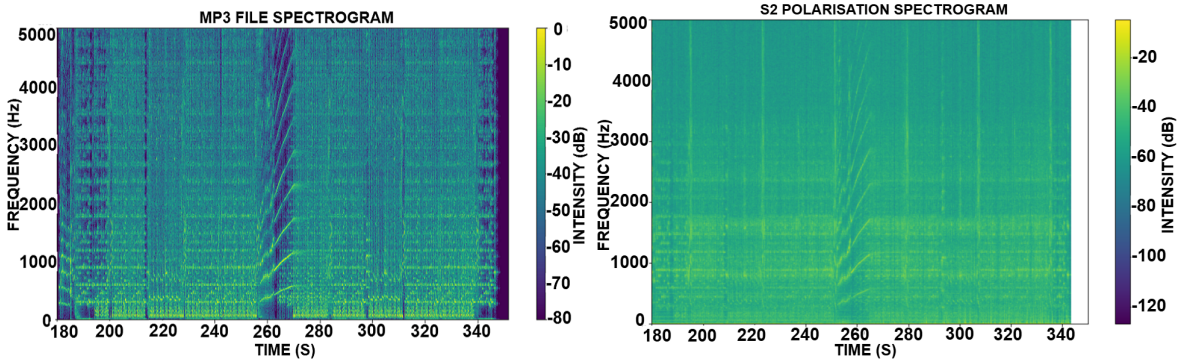

Figure 5: Spectrograms of (*left*) original broadband audio signal and (*right*) SOP data reconstructed signal. The strong correspondence demonstrates the system's ability to resolve complex acoustic signals.

5 Discussion

These preliminary results demonstrate that both the SOP and phase data extracted from a coherent transceiver are capable of detecting and reconstructing complex, broadband acoustic signals, thereby validating the core concept of this sensing approach. In addition, the distinct characteristics exhibited by the polarisation and phase channels highlight the potential for advanced sensor-fusion techniques. While these findings establish proof of concept, a comprehensive characterisation of the system's minimum detectable SPL, bandwidth, noise floor, measurement repeatability, and long-term stability remains outstanding. This systematic evaluation will constitute the primary focus of future work, which will also include a quantitative comparison of polarisation and phase channels across different deployment scenarios such as overhead lines, underground conduits and subsea cables. Additionally, future work will explore sensor-fusion strategies that combine polarisation and phase information, possibly augmented by machine-learning algorithms, to enhance signal-to-noise ratio and detection accuracy. Ultimately, this research aims to lay the groundwork for transforming existing global telecommunication networks into a dual-purpose network for both communication and acoustic sensing.

6 Conclusion

This work demonstrates the use of SOP and phase data from coherent transceivers for acoustic sensing. Future work will quantify system performance, compare SOP and phase sensing channels, evaluate deployment scenarios, and examine sensor fusion techniques to improve detection capability.

References

[1] E. Ip, F. Ravet, H. Martins, M.-F. Huang, T. Okamoto, S. Han, C. Narisetty, J. Fang, Y.-K. Huang, M. Salemi, E. Rochat, F. Briffod, A. Goy, M. del Rosario Fernández-Ruiz, and M. G. Herráez, "Using Global Existing Fiber Networks for Environmental Sensing," *Proceedings of the IEEE*, vol. 110, no. 11, pp. 1853–1888, Nov. 2022, conference Name: Proceedings of the IEEE. [Online]. Available: https://ieeexplore.ieee.org/document/9881563

[2] M. Mazur, J. C. Castellanos, R. Ryf, E. Börjeson, T. Chodkiewicz, V. Kamalov, S. Yin, N. K. Fontaine, H. Chen, L. Dallachiesa, S. Corteselli, P. Copping, J. Gripp, A. Mortelette, B. Kowalski, R. Dellinger, D. T. Neilson, and P. Larsson-Edefors, "Transoceanic Phase and Polarization Fiber Sensing using Real-Time Coherent Transceiver," in *2022 Optical Fiber Communications Conference and Exhibition (OFC)*, 2022, pp. 1–3.

[3] Z. Zhan, M. Cantono, V. Kamalov, A. Mecozzi, R. Müller, S. Yin, and J. C. Castellanos, "Optical polarization–based seismic and water wave sensing on transoceanic cables," *Science*, vol. 371, no. 6532, pp. 931–936, 2021, _eprint: https://www.science.org/doi/pdf/10.1126/science.abe6648. [Online]. Available: https://www.science.org/doi/abs/10.1126/science.abe6648

[4] M. Mazur, L. Dallachiesa, R. Ryf, D. Wallberg, E. Börjesson, M. Bergroth, B. Josefsson, N. K. Fontaine, H. Chen, D. T. Neilson, J. Schröder, P. Larsson-Edefors, and M. Karlsson, "Real-Time Monitoring of Cable Break in a Live Fiber Network using a Coherent Transceiver Prototype," 2023, _eprint: 2307.01291. [Online]. Available: https://arxiv.org/abs/2307.01291

[5] I. Abu-Mahfouz, "Vibration and Sound Measurements," in *Instrumentation:Theory and Practice Part II: Sensors and Transducers*, I. Abu-Mahfouz, Ed. Cham: Springer International Publishing, 2022, pp. 51–76. [Online]. Available: https://doi.org/10.1007/978-3-031-79211-3_4

[6] L. Kruger and H. J. Theron, "Optical fibre Mach-Zehnder Microphone," in *2007 SBMO/IEEE MTT-S International Microwave and Optoelectronics Conference*, Oct. 2007, pp. 389–391. [Online]. Available: https://ieeexplore.ieee.org/abstract/document/4404287

[7] A. K. Ghatak and K. Thyagarajan, *An Introduction to Fiber Optics*. Cambridge University Press, Jun. 1998.

[8] J. S. Baba, B. D. Cameron, and G. L. Cote, "Effect of temperature, pH, and corneal birefringence on polarimetric glucose monitoring in the eye," *Journal of Biomedical Optics*, vol. 7, no. 3, pp. 321–328, Jul. 2002, publisher: SPIE. [Online]. Available: https://www.spiedigitallibrary.org/journals/journal-of-biomedical-optics/volume-7/issue-3/0000/Effect-of-temperature-pH-and-corneal-birefringence-on-polarimetric-glucose/10.1117/1.1484163.full

[9] M. S. Faruk and S. J. Savory, "Digital Signal Processing for Coherent Transceivers Employing Multilevel Formats," *Journal of Lightwave Technology*, vol. 35, no. 5, pp. 1125–1141, 2017.

[10] E. Collett, *Field guide to polarization*. SPIE press Bellingham, 2005, vol. 15.

First-principles study of various sodium-oxide molecules on nitrogen-doped graphene for high-performance sodium-oxygen battery

C Fwalo[1,2] and R E Mapasha[1,3]

[1]Department of Physics, University of Pretoria, Pretoria, South Africa
[2]Department of Physics, Copperbelt University, Kitwe, Zambia
[3]National Institute for Theoretical and Computational Sciences, Matieland, South Africa

E-mail: fwalochewe99@gmail.com

Abstract. To discover a material that can help mitigate issues surrounding the practical implementation of the sodium-oxygen battery (SOB), various materials, including 2D materials such as nitrogen-doped graphene (NGr), have been investigated due to their exceptional properties, like large surface area and excellent ion transport. However, there has been limited reporting on its use as a cathode additive in SOB. In this study, we investigated the adsorption mechanisms of various sodium oxides (Na_xO_2, where x = 1, 2, 3, and 4) on nitrogen-doped NGr, employing density functional theory (DFT). The results indicated that the discharge products are strongly anchored with binding energies ranging between -1.98 and -2.91 eV. These values suggest that NGr can effectively prevent the discharge products from easily dissociating into the electrolyte during electrochemical processes. Moreover, examining the complex charge density distributions supports the strong interactions between the molecules and the substrate. Notably, we observed that the metallic properties of the material were enhanced and preserved after adsorption, which is crucial for ion transport during battery operation. Overall, the findings suggest that NGr is a promising candidate for the next-generation SOB.

1 Introduction

Due to the increase in technological advancements, there has been a growing energy demand, leading to a higher reliance on fossil fuels, which significantly contributes to the effects of climate change. In light of this, scientists and engineers are making concerted efforts to develop energy-storing systems that can surpass the energy density of fossil fuels. While lithium-ion battery (LIB) possesses high energy and power densities, it also face several limitations [1, 2]. Consequently, alternative systems such as metal-air batteries, including sodium-oxygen battery (SOB) [1], is being considered for its exceptional properties, such as high theoretical capacity and low operational costs. However, SOB encounter challenges like weak adsorption of discharge products and poor conduction in the cathode during the discharging process, which hinder its practical implementation.

Given that the cathode is the component most affected by these issues, numerous materials have been investigated as potential cathode additives. Among these, graphene and nitrogen-doped graphene (NGr) are at the forefront of this investigation due to their remarkable properties, including large surface area, lightweight nature, excellent ion transport, and mechanical strength [2, 3, 4]. Because of these properties, adsorption and

diffusion mechanisms of sodium on NGr have been investigated and determined it to be a potential electrode material for next-generation sodium-ion battery [5]. Despite extensive studies on NGr as a potential cathode for metal-air batteries [4], there remains a knowledge gap regarding the mechanisms of various sodium oxides (Na_xO_2) on NGr, which can leverage its excellent properties to revolutionize SOB technology. In this study, we employed density functional theory (DFT) to investigate the adsorption and diffusion mechanisms of various Na_xO_2 on NGr, aiming to determine their influence on the effectiveness of NGr as a cathode additive for the efficient sodium-oxygen battery (SOB). We systematically optimized the configurations, calculated the adsorption energies, and assessed their corresponding charge density distributions. Additionally, we calculated the bands structures to evaluate the stability of electronic conductivity post-adsorption.

2 Computational Methods

All the density functional theory (DFT) calculations were performed using Quantum ESPRESSO [6]. The generalized gradient approximation (GGA) [7] within the Perdew-Burke-Ernzerhof (PBE) functional [8] was employed to treat the exchange and correlation energies. To model the core electrons in the systems, we utilized the projector augmented wave (PAW) potential [9] as a pseudopotential. A kinetic energy cut-off of 544 eV was applied, using a plane-wave basis set to obtain the ground state energy. The Monkhorst-Pack scheme [10] was implemented with a K-points mesh of 6 x 6 x 1 within the Brillouin zone [11]. A nitrogen-doped graphene (NGr) supercell of size 4 × 4 × 1 (containing 31 carbon atoms and 1 nitrogen atom) was modelled and subsequently optimized. The optimization involved fully relaxing the structure until all atomic positions converged within an energy difference of 10 - 5 eV, with a Hellman-Feynman force convergence criterion set to 10 - 6 eV/Å. The Methfessel-Paxton (MP) occupational function [12] was adopted for electron smearing. To minimize the influence of periodic images, a vacuum of 15 Å along the C-axis was included in the model. The adsorption energies (E_{ads}) of various Na_xO_2 were determined using the following expression:

$$E_{ads} = \frac{E_{(complex)} - E_{(NGr)} - n * E_{(adsorbate)}}{n} \tag{1}$$

Where $E_{(complex)}$ the total energy of the substrate is adsorbed with the adsorbate, $E_{(NGr)}$ is the total energy of the pristine NGr, and $E_{(adsorbate)}$ is the total energy of the free-adsorbate. For the charge density distribution between the adsorbate and graphene, we adopted the following equation:

$$\rho = \rho_{(adsorbate+NGr)} - \rho_{(NGr)} - \rho_{(adsorbate)} \tag{2}$$

Here, $\rho_{(adsorbate+NGr)}$ is the charge density of the substrate with the adsorbate, $\rho_{(NGr)}$ is the charge density of the substrate detached from the complex, and $\rho_{(adsorbate)}$ is the charge density of the adsorbate detached from the complex.

3 Results and Discussions

3.1 Optimized configurations and Charge density distributions of NaO_2 and Na_4O_2 on NGr

The operation of a battery follows a processes of discharge and charging, where during the discharging process the oxidized anode produces the Na ion which diffuse via the electrolyte towards the cathode and reacts with the oxygen which diffuses the system through the porous cathode to form various Na_xO_2 along the process as shown in equation 3. And during the reverse, which is the charging process, the formed Na_xO_2 breaks down, with Na-ions diffusing back to the anode and O_2 diffusing outside the ambient environment. Notably, from the discharge products, NaO_2 and Na_4O_2 are considered to be the most stable and least stable, respectively. Hence, they are being intensively investigated for a comprehensive understanding of the battery operations. The following mechanisms depicts what takes place during the electrochemical processes in the battery:

$$\begin{aligned} &NGr + Na^+ + e^- + O_2 \rightarrow NaO_2@NGr \\ &NaO_2@NGr + Na^+ + e^- \rightarrow NaO_2@NGr \\ &Na_2O_2@NGr + Na^+ + e^- \rightarrow Na_3O_2@NGr \\ &Na_3O_2@NGr + Na^+ + e^- \rightarrow Na_4O_2@NGr. \end{aligned} \tag{3}$$

The adsorption energy of the electrode material is very important to ascertain its ability to enhance the performance of the battery. To accurately calculate this significant property, the molecule and isolated NGr substrate were fully optimized separately as shown in Figure 1. Consequently, the configurations of the molecules on NGr were fully optimized as shown in Figure 2b, followed by the calculation of their corresponding adsorption energies. Therefore, we calculated the adsorption energies of all species taking part in the overall electrochemical processes, and the results are presented in Table 1.

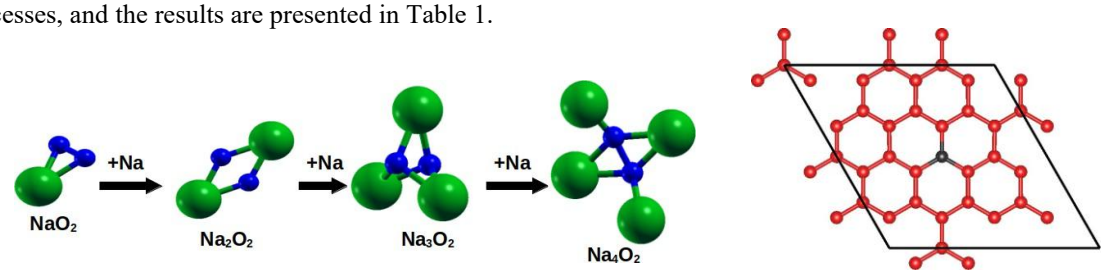

(a) (b)

Figure 1: Optimized molecules of various Na_xO_2, and NGr supercell of size 4 × 4 × 1, consisting of 31 carbon atoms and 1 nitrogen atom. The green, black, red and blue balls denote sodium (Na), nitrogen (N), carbon (red) and oxygen (O) atoms, respectively.

The results revealed that all the discharge products are strongly anchored with values ranging from -0.36 to -0.89 eV, strong enough to prevent them from dissociation into the electrolyte during the discharging process. This is significant as it helps to enhance the cycle life of the battery.

System	Eads (eV)	Charge density |e|
NaO_2	-1.98	0.04
Na_2O_2	-2.13	0.45
Na_3O_2	-2.3	0.95
Na_4O_2	-2.91	1.00

Table 1: Calculated E_{ads} (eV), and charge density (|e|) of various Na_xO_2 on NGr.

As the adsorption takes place on the surface of the NGr, the species or adsorbates are observed to have been strongly attached and near the doped nitrogen, attributed to its high affinity for electrons. This shows the strong interaction between the NGr and the adsorbates. Therefore, to check the extent of the interaction, the microscopic mechanisms of the electron being shared in the system are very significant to be known. To accomplish this, we calculated the charge density distribution in the systems of NaO_2 and Na_4O_2 as illustrated in Figures 2a and 2b, respectively. Additionally, the quantity of the charge densities was calculated as detailed in Table 1, and it was found that the charge was transferred from Na_xO_2 and NGr, with accumulation (yellow) from the Na ions towards the surface of NGr for all the systems investigated (Figure 2). Notably, charge depletion was observed between the oxygen atoms, suggesting its high affinity for electrons.

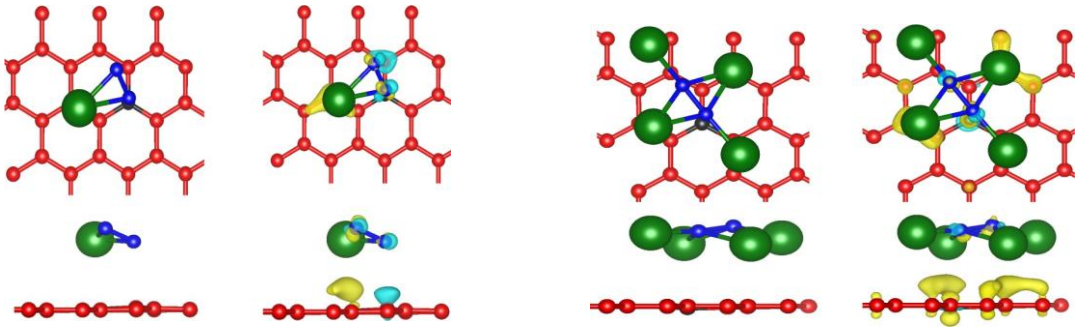

(a) (b)

Figure 2: Optimized Configurations and Charge density distributions of NaO_2 and Na_4O_2 on the NGr: (a) NaO_2, (b) Na_4O_2. Where charge accumulation and depletion are denoted by the colours yellow and cyan, respectively.

Ultimately, the charge density distributions and quantities being transferred provide strong evidence of electronic interaction between adsorbates and the NGr. This strong interaction arises from the nitrogen atom doped into the graphene, which is very important for achieving efficient and optimal battery operation.

3.2 Metallic characteristics of NGr adsorbed with various Na_xO_2

The electronic conductivity of any material as an electrode is very significant the enhanced battery operation. Therefore, before being used as an electrode, the metallic properties are investigated.

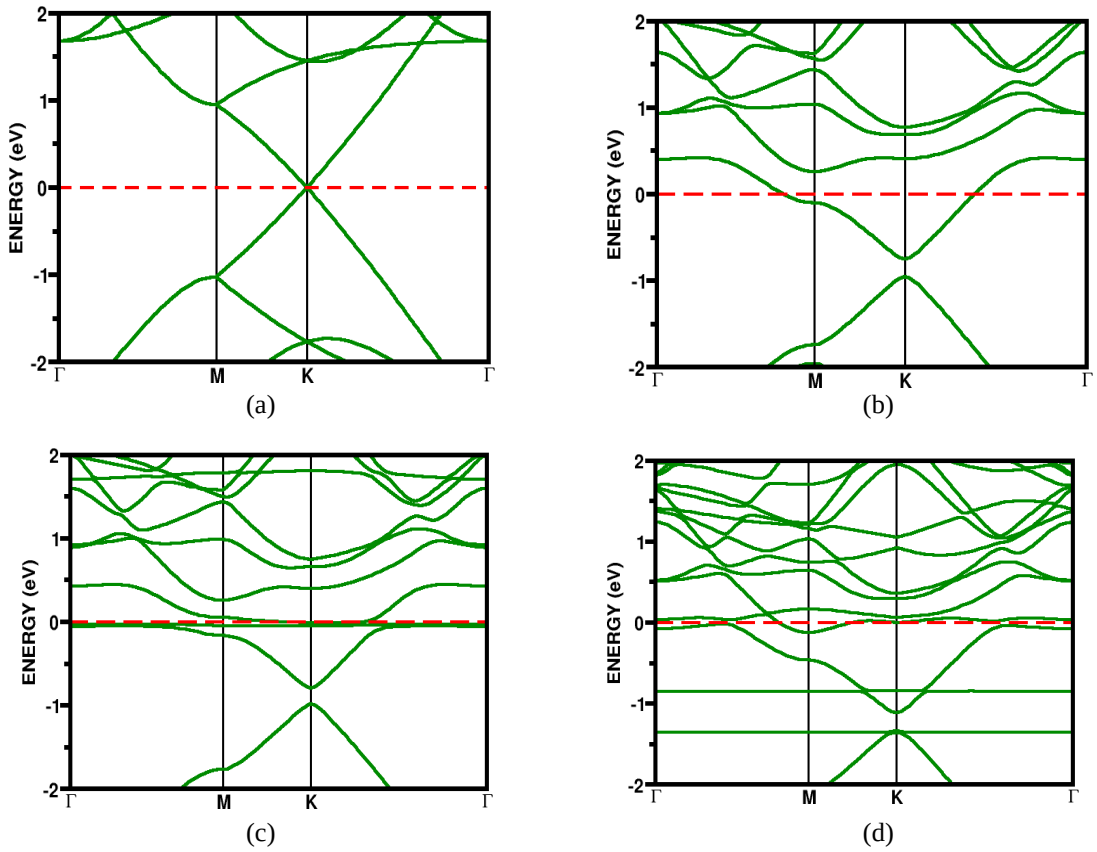

Figure 3: Bands structure of NGr adsorbed with Na_xO_2: (a) pristine G, (b) pristine NG, (c), NaO_2, and (d) Na_4O_2. The dashed red line denotes the Fermi level.

In this work, we investigated the pristine graphene (Gr), NGr, and post-adsorption of the NaO_2 and Na_4O_2. The results showed that Gr is semi-metallic with cone Dirac along the Fermi level as shown in Figure 3a. The obtained results are similar to the previous reported study [4]. For the NGr, it was found that the metallic properties are enhanced as shown in Figure 3b, this is very significant for battery operations, as it shows the capability of the material to be able to charge and discharge the ions during the operation. Hence, improving the cycle life of the system. After the adsorption of NaO_2 (Figure 3c), the Fermi level was observed to have shifted upwards as the bands moved towards, showing the enhanced electronic conduction in the system. This trend was similarly observed for the system of Na_4O_2 (Figure 3d), where the Fermi level moved upwards and bands downwards. Suggesting that not only were the metallic properties preserved, but also enhanced. Overall, the adsorption of the non-conductive various Na_xO_2 on NGr improves its electronic conductivity, which is very important for the optimal operation of the battery.

4 Conclusion

In summary, DFT was to explore the adsorption and diffusion mechanisms of Na_xO_2 on NGr and assess their impact on its electronic properties. The findings indicated that Na_xO_2 species are strongly adsorbed on NGr with values ranging between -1.98 and -2.91 eV, highlighting its essential role in preventing dissociation into the electrolyte during the discharging process. Moreover, the calculated charge density distributions revealed significant electronic interactions between the discharge products and NGr, with charge sharing evident from the

iso-surfaces. Notably, the metallic characteristics of NGr were preserved despite the adsorption of non-conductive Na_xO_2, suggesting that NGr effectively mitigates poor conductivity and premature dissociation issues. This supports the potential for developing a practically implemented SOB.

Conflicts of interests
The authors declare no conflict of interest.

Acknowledgements
The University of Pretoria, through the Department of Innovation and Research, is acknowledged for supporting this project financially. Additionally, the Centre for High-Performance Computing (CHPC) in Cape Town, South Africa, is acknowledged for providing us with computational resources (Project name: MATS1429). R.E.M. recognises the National Institute for Theoretical and Computational Sciences (NITheCS) for the financial support.

References

[1] J. W. Choi, D. Aurbach, "Promise and reality of post-lithium-ion batteries with high energy densities," *Nature Reviews Materials*, vol. 1, no. 4, p. 1–16, 2016.

[2] S. K. Das, S. Lau, L. A. Archer, "Sodium–oxygen batteries: a new class of metal–air batteries," *Journal of Materials Chemistry A*, vol. 2, no. 32, p. 12623–12629, 2014.

[3] P. Avouris, C. Dimitrakopoulos,"Graphene: synthesis and applications", *Materials Today*, vol. 15, p. 86–97, 2012.

[4] J. H. Lee, S. G. Kang, I. T. Kim, S. Kwon, I. Lee, S. G. Lee, "Adsorption mechanisms of lithium oxides (LixO2) on N-doped graphene: a density functional theory study with implications for lithium–air batteries", *Theoretical Chemistry Accounts*, vol. 135, no. 3, p. 50, 2016.

[5] H. W. Lee, et al, "Mechanism of sodium adsorption on N-doped graphene nanoribbons for sodium ion battery applications: A density functional theory approach", *Carbon*, vol. 119, p. 492-501, 2017.

[6] P. Giannozzi, O. Andreussi, T. Brumme, O. Bunau, M. B. Nardelli, M. Calandra, R. Car, C. Cavazzoni, D. Ceresoli, M. Cococcioni, et al., "Advanced capabilities for materials modelling with quantum espresso", *Journal of Physics: Condensed Matter*, vol. 29, no. 46, p. 465901, 2017.

[7] S. Grimme, "Semiempirical GGA-type density functional constructed with a long-range dispersion correction", *Journal of Computational Chemistry*, vol. 27, no. 15, p. 1787–1799, 2006.

[8] J. P. Perdew, K. Burke, M. Ernzerhof, Perdew, "PBE functional", *Physical Review Letters*, vol. 80, no. 4, p. 891, 1998.

[9] P. E. Blöchl, "Projector augmented-wave method", *Physical review B*, vol. 50, no. 24, p. 17953, 1994.

[10] H. J. Monkhorst, J. D. Pack, "Special points for brillouin-zone integrations", *Physical Review B*, vol. 13, no. 12, p. 5188, 1976.

[11] D. J. Chadi, "Special points for brillouin-zone integrations", *Physical Review B*, vol. 16, no. 4, p. 1746, 1977.

[12] M. Methfessel, A. Paxton, "High-precision sampling for brillouin-zone integration in metals. *Physical Review B*, vol. 40, no. 6, p. 3616, 1989.

This page intentionally left blank.

A novel approach to quantifying electron densities of HiP-CT imaging

Preveshin Maduray[1], Timothy Brooks[2], Simon Connell[2], Charis Harley[1], Neil Martinson[3], Threnesan Naidoo[4], Adrie Steyn[4] and Gordon Wells[4]

[1]Electrical and Electronic Engineering Science, University of Johannesburg, Johannesburg, South Africa
[2]Mechanical Engineering Science, University of Johannesburg, Johannesburg, South Africa
[3]Perinatal and HIV Research Unit, University of Witwatersrand, Johannesburg, South Africa
[4]Africa Health Research Unit, University of Kwa-Zulu-Natal, Durban, South Africa

E-mail: preveshinm@uj.ac.za

Abstract. Artificial Intelligence (AI) classification as a methodology and approach to identify Tuberculosis (TB) in patients has become a topic of increasing interest in the past few decades. This is in large part due to the increasing demand for faster methods of detecting TB to reduce spread. However, such methodologies require large datasets so that algorithms can learn the manifestations of TB in the lung. Some of these datasets are private due to patient confidentiality, and the publicly available ones are limited in number. The AI industry has exhausted publicly available chest X-ray (CXR) scans and now look for alternate methods to further develop research in the field. The study focuses on developing methods to translate 3D information on effective electron density using Hierarchical Phase Contrast tomography (HiP-CT) on a human lung to 3D segmented images based on differentiated effective atomic number and mass density. The purpose of this methodology is to create a digital phantom as a synthetic model of a human lung where pathologies of the various stages of TB can be inserted. Monte Carlo modeling of X-ray radiography can then be performed on sets of such digital phantoms to produce a library of 2D conventional X-ray radiographs labeled with details of the occurrence of TB pathologies. This synthetic data set can be used to train an AI classifier. The study will leverage HiP-CT scans produced by the European Synchrotron Research Facility (ESRF) beamline BM05. These are high-resolution 3D scans of complete human organs. To create a synthetic dataset, the Geant4 toolkit will be used to simulate labeled 2D X-ray radiographs starting from the properties and physiological conditions of a lung. This information is gathered from the HiP-CT images; to understand the material properties of the HiP-CT images, the phase shift (δ) and the effective mass densities (ρ_{eff}) of the organic materials within the lung must be known. Thus, this research builds on the derivation of equations and the calculation of these parameters as inputs for simulation and describes our workflow towards the synthetic images.

1 Introduction

Tuberculosis (TB) is a significant global health crisis facing many countries and one of the leading causes of death from a single infectious disease [1]. Through early detection, the disease can be cured and the spread contained. A chest radiograph allows experienced physicians to identify the early presence of TB. However, the process requires a keen eye and an experienced professional in the field of radiography, where some cases may lead to inconsistent diagnostics due to poor imaging contrast.

To reduce/mitigate false diagnosis, AI tools are leveraged to assist in TB detection. These solutions are based on machine learning (ML) algorithms that assist in identifying the different ways TB manifests from Chest X-Rays (CXR) of diagnosed patients. For an ML algorithm to detect TB from a CXR, a repository of CXR data (preferably labeled) is required for the algorithm to learn how TB presents in the lung. The size of the dataset required in order to ensure that the algorithm is trained properly is often found to be quite large, which can hinder progress in the field.

The comparative study covered in [2] investigates different ML techniques used for TB detection. The study, in addition, outlines the different datasets used to train and test the accuracy of the algorithms. An important aspect of the study covered in [2] which forms the foundation for the research covered in this study, is the overuse of publicly available CXR datasets. Due to privacy constraints, the only available CXR datasets are those made available to the public; researchers have exhausted the use of these datasets to the point of testing algorithms on the same data on which they were trained. This process is repeated for each "improved" technique used for detection, inevitably increasing the accuracy in detection.

The purpose of the conducted study is to create a computationally simulated 3D healthly lung model that can be modified in a stochastic way to demonstrate the different manifestations of TB at different locations, following the natural physiological conditions of a diseased human lung. The aim is to create a labeled dataset of CXR images of healthy and TB infected lungs that can be used to train ML algorithms for TB detection. This process introduces new CXR data to the public and allows the manipulation of the model to suit different pathologies according to the different stages TB manifests in the lung. This introduces a dataset that has never been explored nor published in existing literature.

For this part of the study we leverage a 3D scanned digital human lung dataset from the ESRF, scanned from beamline 05 (BM05) using Hierarchical Phase-Contrast Tomography (HiP-CT). With this dataset, the aim is to translate the 3D information of the effective electron density ρ_{eff} from the dataset of the HiP-CT scanned organ into 3D segmented images based on the differentiated effective atomic number Z_{eff} and mass density ρ_{mass}.

The main purpose of this study will focus on the translation of information from the HiP-CT dataset to a material composition format as an additional data preparation step before including it into the Geant4 toolkit. Geant4 will then be used to model the X-ray particle transport through the lung to the detector forming the usual 2D X-ray absorption contrast radiographs. This software leverages Monte Carlo modeling of random particle interactions with matter to create a 2D conventional X-ray radiograph image with labeled TB pathologies.

2 Particle Interaction in X-ray Diagnostics

In x-ray diagnostics, the linear attenuation of a material at a specified energy E is separable into two parts; the contributions from the photoelectric cross-section σ_{PE} and the scattering cross-section σ_{SC} [3]. The relationship of the attenuation coefficient and the two components at the beam energy E, can be expressed as,

$$\mu = \rho_{mass} \frac{N_A}{A_{mass}} (\sigma_{PE}(E) + \sigma_{SC}(E)) \tag{1}$$

where ρ_{mass} is the mass density of the material, N_A is Avogadro's constant (N_A = $6.022 \times 10^{23}\text{mol}^{-1}$) and A_{mass} represents the atomic mass of a material.

According to [3], the cross-sections σ_{PE} and σ_{SC} can be given by the following formulas, where σ_{SC} can be described as a combination of Compton scattering and coherent scattering cross-sections,

$$\sigma_{PE}(E) \sim K \frac{Z^m}{E^3} \qquad \sigma_{SC}(E) = Z[\phi_{\text{KN}}(E) + \phi_{\text{coh}}(Z, E)] \tag{2}$$

where K is a constant and Z^m is the effective atomic number of a material raised to a constant [3]. $\phi_{\text{KN}}(E)$ represents the Klein-Nishina cross-section and $\phi_{\text{coh}}(Z, E)$ represents the coherent scattering cross-section. However, the contribution of the coherent scattering cross-section of the X-ray is negligible and thus, using the expression of the electron density expressed as a function of the linear attenuation μ [3],

$$\mu = \rho_e \left[\frac{\phi_{PE}(E)}{Z} + \phi_{\text{KN}}(E) \right] = \rho_e [K \frac{Z^{m-1}}{E^3} + \phi_{\text{KN}}(E)] \tag{3}$$

Recall that the Compton scattering cross-section was derived from the Klein-Nishina formula equation (3). Here, Compton scattering is divided into two parts; the Compton scattered (σ_{scatt}) and Compton absorption (σ_{absp}).

$$\sigma_c = 2\pi {r^2}_e \{ \frac{1+\gamma}{\gamma^2} [\frac{2(1+\gamma)}{1+2\gamma} - \frac{1}{\gamma} ln(1+2\gamma)] + \frac{1}{2\gamma} ln(1+2\gamma) - \frac{1+3\gamma}{(1+2\gamma)^2} \} \tag{4}$$

At X-ray energies, the low energy limit, the Compton absorption becomes small, and the Compton cross-section becomes,

$$\sigma_c = 2\pi {r^2}_e [1] \equiv \phi_{\text{KN}}(E) \tag{5}$$

The dependence of the photo-electric cross section on the atomic number of the material is Z^5. However the dependence of the Compton scattering cross section is Z^1, as equation (5) is on a per electron basis. If both processes occur together in a compound or mixture, then it will lead to an effective Z as discussed in the next section.

3 Methodology

3.1 Mass Density Derivation

X-ray computed tomography (CT) is an imaging technique based on principles discussed above. The normal implementation uses absorption contrast radiography to produce the 2D X-ray images that are tomographically combined into a 3D image [3]. It is also possible to base the tomography on X ray phase contrast imaging, as in the HiP-CT technique described above. The refractive index of a material can be defined by the equation $n = 1-\delta+i\beta$ where δ represents the real part of the refractive index and β its imaginary part. The real part, δ is responsible for the phase contrast and the imaginary part, β is responsible for the absorption contrast. The attenuation of the transmitted X-ray is proportional to $\mu = 4\pi\lambda^{-1}\beta$ [3]. The real part δ is related to the imaginary part via the Kramers-Kronig relations. At X-ray energies, the real part is typically three to four orders of magnitude larger than the imaginary part. Therefore for X-ray tomography, phase contrast imaging will typically display much higher sensitivity to small variations in material composition and density, and have a much higher dynamical range. Phase contrast imaging has become the preferred technique at synchrotron light sources.

The phase contrast retrieval in HiP-CT uses the Paganin approximation where one assumes a constant ratio of the decrement of the real part of the refractive index (δ) and the imaginary part of the refractive index (β) [4, 5, 6]. The 3D image scales proportionally to both the electron density and the X-ray attenuation coefficient. As the imaginary part is larger, it will dominate, so we are using this in image conversion algorithm [4, 5, 6]. HiP-CT uses high energies and this makes the approximation more valid (the duality phase/attenuation applies exactly in the high energy limit).

The phase shift δ demonstrates a proportional relationship with the electron density ρ_e of a material and an inverse relationship with the incident beam energy E [3],

$$\delta = \frac{\rho_e r_e \hbar^2 c^2}{2\pi E^2} \tag{6}$$

where r_e represents the classical radius of an electron r_0=2.82 x 10^{-15} m, $\hbar$ is the reduced Planck's constant and c is the speed of light. In reference [3], an equation representing the effective atomic number Z_{eff} for a mixture of several elements each with a different Z is derived,

$$Z_{eff} = \sqrt[k]{\sum_i f_i (Z_i)^k} \tag{7}$$

where f_i represents the total number of electrons associated with each element in a compound and Z_i is the atomic number of the elements. In reference [7], k is defined by the parametrization of the Z-dependence at high photon energies, and is defined by $k = B(E)lnZ + C(E)$ [7]. However, in reference [8], k is defined as 2.94 for biological specimens. One notes that this is intermediate between the Z^5 and Z^1 atomic number dependence of the photo-electric effect and the Compton effect respectively.

According to [3], the effective electron density can be defined as follows and can be written as a function of the effective atomic number (Z_{eff}) ,

$$\rho_{eff} = \frac{\rho_{mass} N_A Z_{eff}}{A_{mass}} = \frac{\rho_{mass} N_A \sqrt[k]{\sum_i f_i (Z_i)^k}}{A_{mass}} \tag{8}$$

To calculate the phase shift for a material, substitute equation (8) in (6), the following is derived;

$$\delta = \frac{[\rho_{mass} N_A \sqrt[k]{\sum_i f_i(Z_i)^k}] r_e \hbar^2 c^2}{2\pi E^2 A_{mass}} \tag{9}$$

Equation (9), describes the proportionality between the phase shift (δ) and the effective electron density (ρ_{eff}) of a material expressed as a product of the effective atomic number (Z_{eff}) and the mass density (ρ_{mass}).

The term "effective" associated with the atomic number and electron density is derived from the average of the Z-dependence with different exponents and two or more elements in a compound. Thus, in this case an assumption is made where the value of k is a substitute for biological materials. A key point from equation (9) is that a 3D HiP-CT digital image is quantitative in the effective electron density δ.

This section forms the foundation of the study, as equations (8) and (9) will be used to quantify the electron densities as well as understanding the phase shift of different materials present in a HiP-CT dataset.

4 Results and Discussion

The left figure of 1 below is a healthy lung sample scanned at the ESRF using HiP-CT at a resolution of $100\,\mu\text{m}$. The scans were captured on beamline 05 (BM05) [9, 10]. Identifying the different organic materials and the different segments of the organ present in the data set is a challenge, this would require an experienced radiologist to assist with compartmentalizing the different subsections of the lung.

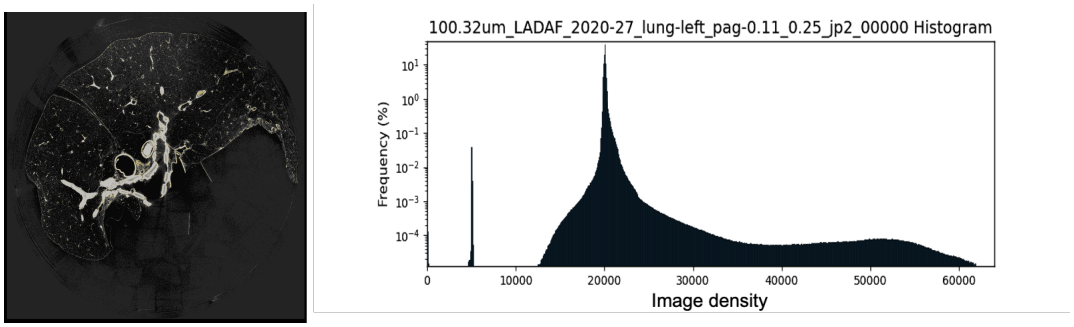

Figure 1: (*left*)Healthy lung lobe scanned at the ESRF using HiP-CT. The grey scale is proportional to the effective electron density ρ using the equation from equation (9) and the known compositions of these materials [9, 10] (*right*) Image Threshold for Agar Segmentation. The x-axis is currently a 2 byte integer. It is proportional to the effective electron density ρ. [9, 10]

The right figure of Figure 1 above, represents the image histogram, this identifies a number proportional to the effective electron density per voxel. The image density provides information on the number of different organic materials present in left figure of figure 1. Areas of the lung such as voids are filled with a percentage of ethanol, depending on the preparation protocol, including blocks of agar, can be used to calibrate the effective electron density, as the elemental composition of these materials is known.

An agar segmentation performed on the dataset aids in understanding the organic material present and assists with differentiating between the organ material and the supporting structures. Understanding the effective electron densities of all materials in the dataset allows the segmentation of the lung structure into specific materials. These can then be mapped into the lung structure in terms of a material composition and a density, such that the correct effective density is achieved. This is then the final 3D model including a description of geometry and materials that is used for building a simulation of the lung model in Geant4.

The image on the left of figure 2, represents a segmentation of the agar blocks used to maintain the upright structure of the organ for scanning. The organ is contained in a jar filled with fluid that is a percentage of formalin and ethanol with the addition of the agar blocks.

The image on the right of figure 2 is an illustration of the simulation setup in the Geant4 environment. The simulation was conducted using a CT dataset from [11], this was done to test the proof of concept using the Geant4 toolkit. The purpose of using the Geant4 toolkit over other forward projection software, was due to superior simulation fidelity of Monte Carlo (Geant4) methods over the deterministic methods. Simple forward projection or any other deterministic models are unable to provide the detail and accuracy of a full event-by-event simulation such as Geant4. For the purpose of ML, we would want to prevent the algorithm from learning artifacts produced from

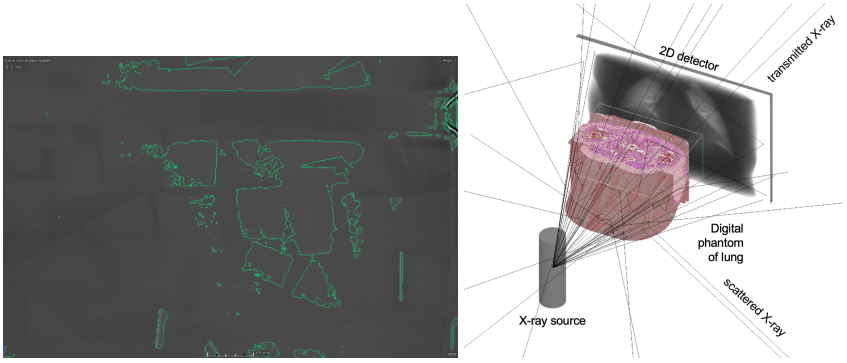

Figure 2: (*left*) Agar Segmentation [9, 10]. (*right*) and Geant4 Simulation Construction [11]

a poor projection. The emphasis on scattered photons in this study is essential to understanding and forecasting how much noise will be introduced to the simulation.

By understanding the effective properties of materials, the interaction between photons and the materials will produce the scattered and transmitted X-rays, where the transmitted X-rays would be reconstructed into a simulated CXR with TB manifestations according to the digital phantom.

Using equations (8) and (9) will assist in calculating the effective properties of organic compounds from the HiP-CT dataset and their phase shifts. For a given A_{mass}, k and ρ_{mass}, the following table represents the calculated Z_{eff}, ρ_{eff} and δ for different materials that can be found within the dataset.

Material	A_{mass} (g/mol)	k	ρ_{mass} (g/cm^3)	Z_{eff}	ρ_{eff} (e/cm^3)	δ
water	18	2.94	1	5.50	1.84x10^{23}	3.57x10^{-9}
formalin	20	2.94	1.09	6.99	2.29x10^{23}	4.45x10^{-9}
ethanol	24	2.94	0.789	6.62	1.31x10^{23}	2.54x10^{-9}
protein	22	2.94	1.35	6.63	2.45x10^{23}	4.75x10^{-9}
fat	26	2.94	0.92	6.59	1.40x10^{23}	2.72x10^{-9}
carbohydrate	24	2.94	1.5	7.25	2.73x10^{23}	5.30x10^{-9}
bone	20	2.94	1.85	13.39	7.40x10^{23}	1.44x10^{-8}
agar	13.35	2.94	1.032	7.16	3.33x10^{23}	6.47x10^{-9}

Table 1: Table representing Atomic Mass Number (A_{mass}), Parametrization Dependence (k), Mass Density (ρ_{mass}), Effective Atomic Number (Z_{eff}), Effective Electron Density (ρ_{eff}) and Phase Shift (δ) of several materials [12, 13, 14]

The range of A_{mass} and ρ_{mass} for protein, fat, carbohydrates and bone is specific to a general composition of compounds found in lung tissue and the chest cavity. For water, formalin, ethanol and agar, this is specific to the procedure for scanning in a HiP-CT application.

Table 1 represents a quantitative value for different materials that can be present in a HiP-CT dataset. Water was selected due to the possibility of trace compounds present in the lung or on the surface; formalin and ethanol were selected as the organ is submerged into formalin which is responsible for preserving the organ and ethanol used for inflating the specimen. Proteins, fat, and carbohydrates were selected as these compounds are the main constituents of organ tissue in varying percentages according to tissue type and function. Bone was selected however, no bone material is present in the dataset but understanding the effective electron density is important since a 2D CXR would include the entirety of the chest cavity, including bone material. Agar was selected as it is the material used to maintain the upright structure of the organ during scanning and is quite distinguishable in the left image of figure 2. The importance of quantifying ethanol and agar is essential for the following steps of segmentation, since majority of the sample is submerged or supported by these compounds, by removing materials of these effective electron densities, the final segmentation may only include areas of densities of the dataset that we are most interested in and require for building a simulation.

5 Conclusion

The research proposes a novel technique for quantifying the ρ_{eff} and δ of a HiP-CT dataset which aligns with the objective of creating a labeled synthetic data set of CXR absorption radiographs that can be used in many

different applications. The objective of the study aims to leverage high-resolution HiP-CT 3D imaging to create 2D radiographs. This requires an understanding of how to extract material quantities based on effective electron density as appropriate for a phase contrast high-resolution HiP-CT dataset and then how to use this information to create a low-resolution 2D absorption contrast radiographic image. This technique creates uniformity between the calculated variables and how the HiP-CT datasets are quantified, serve as a calibration for a translation between the sources. The HiP-CT dataset contains the effective electron density information, and by performing a threshold-based segmentation one can separate the different materials present in the dataset to identify the structure of the organ and separate the tissue compounds. The segmentation technique identifies the material present in the image on a per voxel basis. Given an A_{mass} and ρ_{mass} for a biological constant k, using equation (8) and equation (9), the ρ_{eff} and δ for a specific compound can be calculated. This aligns a quantitative value to a material compound.

The quantitative information is captured in Geant4. The pathologies can be inserted in healthy tissue in a deterministic manner so that a synthetic model made of known materials and associated densities can be simulated. In this manner, TB pathologies can be introduced into the model to create a labeled digital phantom and 2D radiographs can be captured. This method introduces a workflow for generating a synthetic dataset of labeled pathologies and introduces the prospect of creating images that can demonstrate more than one pathology. In this manner, we aim to build an AI classification tool that has been trained on a multitude of ways the disease can present itself.

References

[1] N. Pattamapaspong *et al.*, "Imaging of thoracic tuberculosis: pulmonary and extrapulmonary," *BJR|Open*, vol. 6, no. 1, p. 31, 09 2024.

[2] R. S. Prasad *et al.*, "A comparative study of detection of tuberculosis using machine learning & deep learning," in *2023 10th International Conference on Computing for Sustainable Global Development (INDIACom)*, 2023, pp. 1217–1221.

[3] Z. Qi *et al.*, "Quantitative imaging of electron density and effective atomic number using phase contrast CT," *Physics in medicine and biology*, vol. 55, pp. 2669–77, 05 2010.

[4] P. Cloetens *et al.*, "Holotomography: Quantitative phase tomography with micrometer resolution using hard synchrotron radiation x rays," *Applied Physics Letters*, vol. 75, no. 19, pp. 2912–2914, 11 1999.

[5] D. M. Paganin and D. Pelliccia, "Chapter two - x-ray phase-contrast imaging: a broad overview of some fundamentals," in *Advances in Imaging and Electron Physics*, ser. Advances in Imaging and Electron Physics, M. Hÿtch and P. W. Hawkes, Eds. Elsevier, 2021, vol. 218, pp. 63–158. [Online]. Available: https://www.sciencedirect.com/science/article/pii/S1076567021000501

[6] Y. Sekiguchi *et al.*, "Classification and assessment of retrieved electron density maps in coherent x-ray diffraction imaging using multivariate analysis," *J Synchrotron Radiat.*, 2016.

[7] W. Langeveld, "Effective atomic number, mass attenuation coefficient parameterization, and implications for high-energy x-ray cargo inspection systems," *Physics Procedia*, vol. 90, pp. 291–304, 12 2017.

[8] R. C. Murty, "Effective Atomic Numbers of Heterogeneous Materials," *Nature*, vol. 207, no. 4995, pp. 398–399, Jul. 1965.

[9] P. Tafforeau *et al.*, "Two zooms at 2.51um in the upper apical lobe of the left lung from the body donor ladaf-2020-27," 2021. [Online]. Available: https://doi.esrf.fr/10.15151/ESRF-DC-572216900

[10] R. P. Xian *et al.*, "A multiscale x-ray phase-contrast tomography dataset of a whole human left lung," 2022. [Online]. Available: https://doi.org/10.1038/s41597-022-01353-y

[11] S. M. Mostafavi, "COVID19-CT-Dataset: An Open-Access Chest CT Image Repository of 1000+ Patients with Confirmed COVID-19 Diagnosis," 2021. [Online]. Available: https://doi.org/10.7910/DVN/6ACUZJ

[12] M. Kurudirek, "Effective atomic numbers and electron densities of some human tissues and dosimetric materials for mean energies of various radiation sources relevant to radiotherapy and medical applications," *Radiation Physics and Chemistry*, vol. 102, p. 139–146, 01 2014.

[13] R. Manohara *et al.*, "The effective atomic numbers of some biomolecules calculated by two methods: A comparative study," *Medical physics*, vol. 36, pp. 137–41, 02 2009.

[14] W. Woodard and D. R. White, "The composition of body tissues," *British Journal of Radiology*, vol. 59, no. 708, pp. 1209–1218, 1986.

TGF-β Pathway Modulation: A Key Mechanism of Photobiomodulation Induced Tenogenesis

Amarachi Albert[1], Heidi Abrahamse[1] and Anine Crous[1]

[1]Laser Research Centre, University of Johannesburg, Johannesburg, South Africa

E-mail: acrous@uj.ac.za

Abstract. Adipose-derived mesenchymal stem cells (ADMSCs) have remarkable regenerative capabilities when activated by tenogenic stimuli, including Connective Tissue Growth Factor (CTGF). This study investigates whether photobiomodulation (PBM) enhances CTGF-induced tenogenesis by modulating the TGF-β signalling pathway. ADMSCs were cultivated on two-dimensional culture plates and subjected to PBM at 525 nm (green light), 825 nm (near-infrared), and consecutive irradiation using both wavelengths at a fluence of 10 J/cm² each. Cells were cultured for 10 days in CTGF- and ascorbic acid-enriched induction medium. The control group consisted of cells treated just with induction media without PBM, whereas the standard group was sustained in full growth medium. Cell proliferation were evaluated by adenosine triphosphate (ATP) and lactate dehydrogenase (LDH) tests for metabolic activity and membrane integrity, Sirius Red staining for collagen deposition, and qPCR for tenogenic gene expression utilising Collagen type I alpha 1 (COL1A1). PBM influenced the experimental groups by diminishing ATP synthesis, decreasing LDH release in experimental samples relative to the standard, and enhancing collagen deposition as evidenced by microscopic examination and quantification, when using 825 nm and consecutive irradiation compared to the control sample. Gene expression analysis validated the overexpression of the tenogenic marker COL1A1. Enhanced collagen production is intricately associated with the modification of the TGF-β pathway, which is pivotal in facilitating the differentiation of ADMSCs into tenocytes through the activation of SMAD signalling and the upregulation of downstream effectors such scleraxis (Scx). The findings indicate that PBM promotes tenogenesis via metabolic and molecular pathways, including TGF-β-mediated collagen production, positioning PBM as a potentially beneficial adjunct to tendon regeneration methods.

1 Introduction

Stem cell-driven approaches to tendon regeneration are rapidly advancing in musculoskeletal research, with adipose-derived mesenchymal stem cells (ADMSCs) emerging as a preferred source due to their accessibility, robust proliferative capacity, and tenogenic differentiation potential under appropriate inductive cues. [1-3]. Among these, the Transforming Growth Factor-beta (TGF-β) signalling pathway—particularly via downstream mediators such as Connective Tissue Growth Factor (CTGF)—plays a central role in driving ADMSCs toward the tenocyte lineage by activating key transcriptional regulators like scleraxis and promoting the synthesis of tendon-specific extracellular matrix proteins, including collagens type I and III [4, 5]. Ascorbic acid synergistically supports this process by enhancing collagen maturation and stabilizing the extracellular matrix [6, 7]. Photobiomodulation (PBM), the application of low-intensity light at specific wavelengths, has gained recognition for its ability to enhance stem cell behaviour by stimulating mitochondrial activity, increasing adenosine triphosphate (ATP) production, and modulating intracellular signalling cascades such as the TGF-β/Smad axis [8, 9]. Emerging evidence suggests that PBM may further potentiate tenogenesis by augmenting

TGF-β-induced collagen expression, thereby improving extracellular matrix organization and functional tendon regeneration [10].

2 Data Analysis

2.1 Cell culture

Immortalized adipose-derived mesenchymal stem cells (ASC52telo; hTERT-immortalized, SCRC-4000, ATCC, Manassas, VA, USA) were cultured in Corning® cell culture flasks (CLS431080, Sigma-Aldrich) using Dulbecco's Modified Eagle Medium (DMEM; D5796, Sigma-Aldrich, Johannesburg, South Africa) supplemented with 10% foetal bovine serum (FBS; S0615, (Biochrom), Whitehead Scientific, Cape Town, South Africa), 0.5% Penicillin-Streptomycin (P4333, Sigma-Aldrich), and 0.5% Amphotericin B (A2942, Sigma-Aldrich). Cells were maintained at 37 °C in a humidified environment with 5% CO_2 and 85% relative humidity using a Heracell™ 150i CO_2 incubator (51026280, Thermo Fisher Scientific, Johannesburg, South Africa), until 80%-90% confluenecy, the cells were seeded in a complete media at 600 densities per well in Nunclon Delta 96-well plates (Thermo Fisher Scientific, 167008), and they were left to adhere for 24 hours. The treatment groups were further changed into the induction media (Combination of; CTGF-20 µl, Ascorbic Acid -125 µl, FBS-2500 µl, Penicillin-Streptomycin-250 µl, Amphotericin B-250 µl) and later exposed to PBM while the standard remained in the complete media without PBM. During the experiment, media changes were performed every two days. The cells were monitored for changes in morphology, proliferation, and gene expression related to the transforming growth factor-beta (TGF-β) pathway. Various assays, including ATP Assay – Cell Proliferation, lactate dehydrogenase (LDH) Assay – cytotoxicity, Sirius Red- Collagen Quantification, Giemsa Stain- cell morphology and Quantitative PCR, were employed to assess the cellular responses to PBM.

2.2 Laser Treatment (Irradiation)

Laser treatment was performed once off 24 hours after cell seeding using a green 525 nm diode laser (National Laser Centre, EN 60825-1:2007) with a 100–240 VAC, 47–63 Hz 5A laser source (OptoElectronics Tech. Co., Ltd., Changchun, China), a near-infrared 825 nm diode laser (National Laser Centre, Pretoria, South Africa) driven by a 1000 mA source (Model 4210, Arroyo Instruments, CA, USA), and a consecutive wavelength mode (525 nm + 825 nm). Each laser group received a fluence of 10J/cm². The laser output po wer (in mW) was quantified using a Field Mate Laser Power Meter (1098297, Coherent, Johannesburg, South Africa), and irradiation times were calculated to match the target fluence. Laser beams were adjusted to uniformly cover the adherent cell monolayer without affecting neighbouring wells. Three experimental groups were defined based on treatment conditions. Group 1 comprised cells cultured in induction medium and exposed to PBM at 525 nm with a fluence of 10 J/cm². Group 2 included cells receiving induction medium and irradiated with PBM at 825 nm, also at a fluence of 10 J/cm². Group 3 involved cells treated with induction medium and exposed to a consecutive PBM protocol using both 525 nm and 825 nm wavelengths consecutively at 10 J/cm² each, by first exposing the cells to 525 nm and followed by 825 nm. Furthermore, there was a standard group in which cells were cultured in complete medium without induction or PBM treatment and a control group, where cells received the induction medium without PBM exposure. The green and near-infrared lasers used in this study were both diode lasers operating in continuous wave mode. The green laser had a wavelength of 525 nm with a power output of 565 mW, corresponding to a power density of 62.20 mW/cm², delivered over a spot size of 9.62 cm². To achieve a fluence of 10 J/cm², the irradiation time was set to 2 minutes and 40 seconds. In comparison, the near-infrared laser operated at a wavelength of 825 nm with a lower power output of 121 mW, resulting in a power density of 13.32 mW/cm² over the same spot size of 9.62 cm². For this laser, a fluence of 10 J/cm² was reached with an irradiation time of 11 minutes and 44 seconds. The formula below was employed to derive the exposure time corresponding to each laser wavelength. Where, mW/cm2= power density, W/cm2=intensity, and s=exposure duration.

$$\mathrm{mW/cm^2} = \frac{\mathrm{mW}}{\pi \times (r^2)}$$

$$\mathrm{W/cm^2} = \frac{\mathrm{mW/cm^2}}{1000}$$

$$\mathrm{Time\ (s)} = \frac{\mathrm{J/cm^2}}{\mathrm{W/cm^2}}$$

2.3 Proliferation assay

The ATP - proliferation assay was conducted to measure cellular energy levels. The culture media in each well was removed and replaced with 1x PBS (50 µl) and CellTiter-Glo 3D reagent (Promega, G9681) (50 µl). The plate was covered with foil and placed on the shaker for 5 minutes and then incubated for 30 minutes at room

temperature. After incubation the supernatant was transferred to a Corning 96-well opaque-walled plate (Sigma-Aldrich, CLS3912) and luminescence was measured using the VICTOR Nivo Plate Reader (Perkin Elmer, HH3522019094).

2.4 Lactate Dehydrogenase (LDH assay)

The LDH assay was used to assess cell membrane integrity. After treatment, (50 µl) culture supernatants were collected from each well and added in a flat-bottomed Corning 96-well clear plate (Sigma-Aldrich, CLS3370), (50 µl) ofCytoTox96 reagent (Promega, G1780) was also added. The plate was covered with foil and incubated in the dark, at room temperature, for 30 minutes. The absorbance was read at 490 nm using the VICTOR Nivo Plate Reader (Perkin Elmer, HH3522019094), indicating the extent of cell damage or cytotoxicity based on LDH enzyme release. An LDH positive control was analysed by lysing untreated cells using 10 µl of lysis buffer and incubated at 37°C for 45minutes, 50 µl of the lysed cell solution was added to the clear 96 well plate (Sigma-Aldrich, CLS3370), and 50 µl of LDH reagent (Promega, G1780), it was further incubated for 30minutes in the dark. The absorbance was read at 490 nm using the VICTOR Nivo Plate Reader (Perkin Elmer, HH3522019094), indicating the effectiveness of the LDH reagent.

2.5 May-Grünwald / Giemsa Staining

Giemsa staining was used to evaluate the morphology and differentiation of ADMSCs, focusing on size, shape, and nuclear-cytoplasmic features. Cells were fixed in absolute methanol (50 µl), for 5 minutes, washed with (50 µl) 1x PBS, stained with (50 µl) May-Grünwald for 4 minutes and (50 µl) Giemsa Stain for 6 minutes, washed with (50 µl) 1x PBS until clear. It was observed under an inverted light microscope, and images were taken at different objective lens.

2.6 Collagen Quantification

Collagen quantification was performed using Sirius Red assay (Sigma-Aldrich, 365548). Fixed cells were stained with Sirius Red, which binds specifically to collagen. After washing off the excess stain, each well was replaced with 50 µl of a 1:1 mixture of 0.1% NaOH and absolute methanol for 30 minutes. The absorbance was measured at 540 nm using the VICTOR Nivo Plate Reader (Perkin Elmer, HH3522019094). The intensity of absorbance correlated with the amount of collagen present in the sample.

2.7 Sirius Red Staining

Sirius Red staining was performed to assess collagen deposition. The supernatant was removed and washed with (200 µl) of pre-warmed PBS. The Cells were fixed with 70% ethanol for 30 minutes and washed with (200 µl) of pre-warmed PBS, the cells were further stained with 0.1% Sirius red (Sigma-Aldrich, 365548) prepared in a 1.3% saturated picric acid solution for 1 hour at room temperature. After incubation, excess stain was removed through PBS washes. Collagen presence was visualized under an inverted light microscope based on red coloration intensity and images were taken at different objective lens.

2.8 Gene Expression

Collagen type I alpha 1 (COL1A1), Collagen Type III Alpha 1 Chain (COL3A1), Tenascin-C (TNC), Biglycan (BGN) expression was quantified using real-time PCR. Total RNA was extracted, where an average of 17,2 µg/ml RNA was reverse transcribed to cDNA, and amplified with the specific primers. Gene expression levels were normalized to a housekeeping gene, Glyceraldehyde-3-phosphate dehydrogenase (GAPDH). COL1 and COL3 encode the major structural collagens of tendons, TNC is a glycoprotein linked to tendon development and remodelling, and BGN is a proteoglycan necessary for collagen fibrillogenic and tendon matrix organization, and relative quantification was calculated using $2-\Delta\Delta ct$ method to assess the tenogenic differentiation of ADSCs.

2.9 Statistical analysis

Statistical analysis was done, using one-way ANOVA on Sigma plot version 14. Experimental groups, controls and standards were performed in quadruplicate (n=4) for all quantitative assays. All data was expressed as mean values, standard deviation and graphically represented. A p value of <0.05 (*), <0.01 (**) and <0.001 (***) was considered statistically significant. Morphology served as qualitative analysis where n=1.

3 Results and Discussion

3.1 Assessment of Cell Proliferation, Cytotoxicity, and Morphological Integrity

Adenosine triphosphate is a crucial marker of metabolically active and viable cells, with luminescence-based ATP assays providing a sensitive measure of cellular energy levels and mitochondrial function [11].

Metabolically active, viable cells with higher ATP levels are more likely to proliferate than cells with low ATP content. This study evaluated cell proliferation measuring ATP levels 10 days after PBM treatment. Figure 1A illustrates that the control group demonstrated significantly elevated ATP luminescence relative to all PBM-treated groups ($p < 0.001$), signifying enhanced metabolic activity. Treatment with 525 nm, 825 nm, or a combination of both wavelengths led to diminished ATP levels. Decreased cellular ATP can indicate that cells are redirecting energy toward differentiation rather than proliferation, reflecting the well-established inverse relationship between these two processes [12]. Lactate dehydrogenase, a cytoplasmic enzyme released due to membrane integrity loss, is a recognised indicator of cytotoxicity [13]. The LDH assay revealed that irradiated cells showed a significant reduction in LDH release compared to the standard ($p < 0.05$). A greater reduction was observed when the control was compared to the standard ($p < 0.01$), whereas only a slight increase in LDH release was noted when comparing irradiated samples to the control. Morphological evaluation using Giemsa staining further supported these findings. Ten days post PBM treatment, cells in the light-treated groups exhibited morphological features consistent with early tenocyte-like differentiation, including elongated spindle- shaped profiles and aligned growth patterns (Figure 1C).

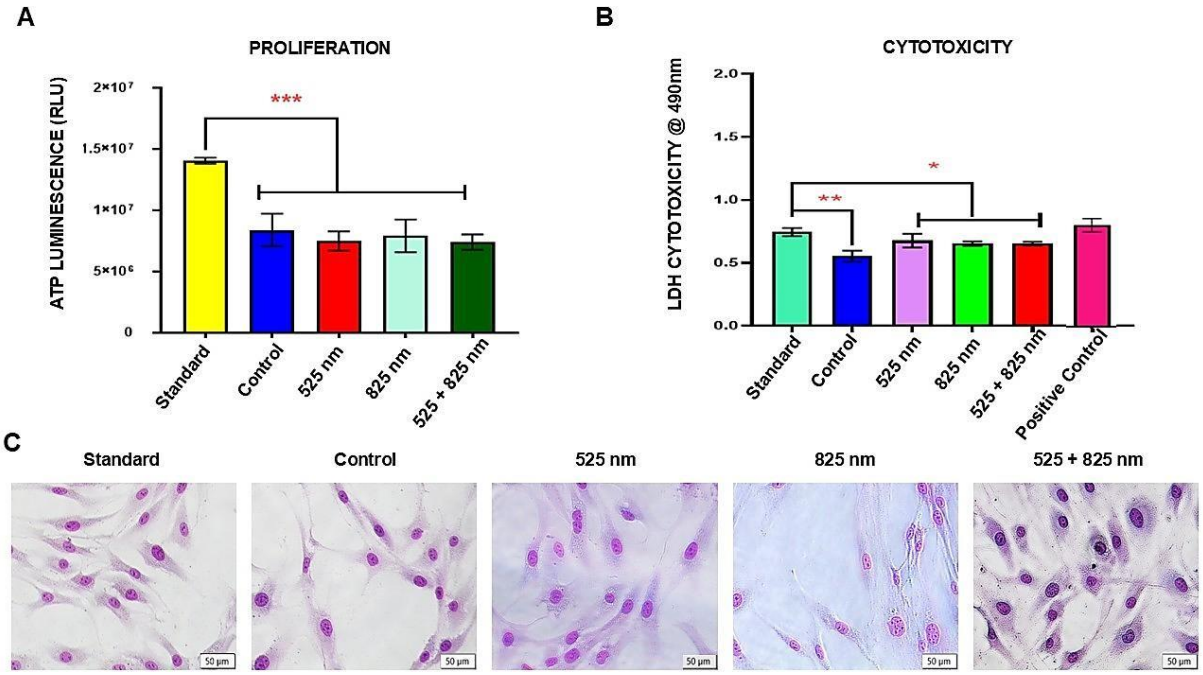

Figure 1: Evaluation of Cell Health and Morphology 10 days post PBM treatment. A) ATP luminescence was highest in standard cells and reduced in PBM-treated groups. B) LDH release was significantly lower in 525 nm and 525+825 nm-treated groups, indicating reduced cytotoxicity. C) May-Grünwald/Giemsa staining revealed morphological features suggestive of tenocyte-like differentiation following PBM.

3.2 Collagen production and genetic expression

To assess extracellular matrix (ECM) remodelling, collagen synthesis was assessed by Sirius Red staining, which identifies collagen-specific hydroxyproline levels. Figure 2A illustrates a small increase in absorbance at 540nm in the 825 nm and 525+825 nm groups relative to the 525 nm and control groups. Despite the lack of statistical significance, these alterations may suggest wavelength-dependent control of collagen synthesis. Morphological staining with Sirius Red (Figure 2C) clearly validated increased collagen deposition in the 825 nm and combination groups. This pattern may indicate PBM-induced activation of the TGF-β signalling cascade, which is recognised for facilitating fibroblast-to-tenocyte transition and promoting COL1A1 transcription during tendon matrix remodelling. In each PBM groups, COL1A1, a crucial indicator of tenogenic commitment, was uniformly downregulated, suggesting limited transcriptional activity under the given circumstances. COL3A1 remained constant at 825 nm or the 525 nm+825 nm group, although it exhibited a slight rise with 525 nm PBM. Strong upregulation of TNC, especially at 525 nm PBM, demonstrated its function in fostering tenogenic differentiation. 525 nm increased BGN expression, 825 nm significantly decreased it, and the dual wavelength brought it back to near baseline. The expression values are displayed as the $\log_2$ fold-change in comparison to the control.

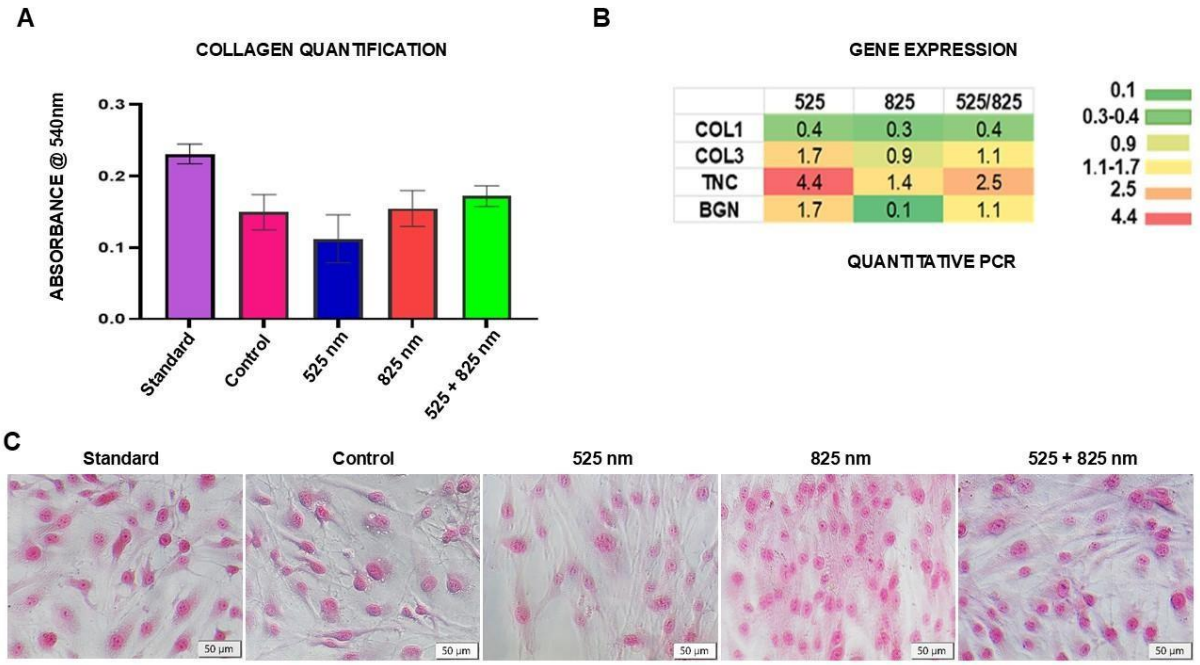

Figure 2: Collagen quantification, gene expression, and morphological analysis. A) 825 nm and 525 nm + 825 nm groups showed minimal collagen increase (Sirius Red absorbance). B) Heat map of tenogenic gene expression in ADSCs (Day 10 post-PBM). COL1 downregulated in all groups; 525 nm moderately increased COL3 and BGN, strongly upregulated TNC; 525 nm + 825 nm restored BGN and slightly elevated TNC; 825 nm inhibited most genes. Expression values shown as fold-change (log_2) relative to control. C) ECM deposition patterns confirmed by Sirius Red staining.

Our data show no statistically significant enhancement in collagen deposition, ATP levels, or overall morphological differentiation at 10 J/cm² across different wavelengths when assessed 10 days post-PBM. However, gene-level trends—particularly TNC upregulation at 525 nm and BGN suppression at 825 nm—suggest wavelength-specific modulation rather than strong tenogenic commitment. These findings are consistent with the known parameter sensitivity of PBM, where wavelength, fluence, and exposure schedule critically influence cellular outcomes. [14]. In tendon healing models, many studies indicate that PBM enhances collagen I/III content and improves tendon organisation at red/ near infra-red settings (about 630–880/830 nm) and dose regimens that differ from those employed in this study, suggesting a favourable therapeutic window outside the parameters utilised here [15, 16]. In contrast, research on ADMSCs and other MSCs indicates that some wavelength-fluence combinations result in negligible alterations in viability/ATP or lineage commitment, further emphasising dose-dependence and cell-context effects [17]. Concerning biochemical co-stimulation, CTGF is an established tenogenic signal that can induce COL1A1 and other tenogenic markers in a dose- and time-dependent manner through FAK/ERK and TGF-β-related pathways; however, our PBM settings did not enhance COL1A1 levels beyond control in the presence of CTGF, indicating a lack of additive synergy at 10 J/cm² [18]. The disparity between our minor gene-level alterations (e.g., TNC↑ at 525 nm) and the absence of functional or biochemical improvements corresponds with findings indicating the bioeffects of PBM can be dissociated across measurements when dosage is suboptimal [14].

4 Conclusion

Among the tested parameters (525 nm, 825 nm, or consecutive; 10 J/cm²; Day 10), PBM did not significantly improve collagen deposition, ATP levels, or morphological differentiation of ADMSCs subjected to CTGF-based tenogenic induction. However, 525 nm increased TNC and had a modest effect on COL3A1, while 825 nm inhibited BGN. In comparison to publications on PBM-enhanced collagen production and tendon healing at different wavelengths and fluences, our findings indicate that parameter optimisation is crucial and that PBM alone may be

inadequate without biochemical or mechanical co-stimulation. Future research should delineate the wavelength-fluence-timing range (including pulsing), assess the synergistic effects of CTGF, ascorbate, and mechanical stress, and investigate earlier temporal intervals to capture transitory metabolic responses.

References

[1] P. A. Zuk *et al.*, "Human adipose tissue is a source of multipotent stem cells," *Molecular biology of the cell,* vol. 13, no. 12, pp. 4279-4295, 2002.

[2] B. Wei and J. Lu, "Characterization of tendon-derived stem cells and rescue tendon injury," *Stem cell reviews and reports,* vol. 17, no. 5, pp. 1534-1551, 2021.

[3] H.-S. Chen, Y.-L. Chen, H.-J. Harn, J.-S. Lin, and S.-Z. Lin, "Stem cell therapy for tendon injury," *Cell Transplantation,* vol. 22, no. 4, pp. 677-684, 2013.

[4] Y.-J. Kahm, R.-K. Kim, U. Jung, and I.-G. Kim, "Epithelial membrane protein 3 regulates lung cancer stem cells via the TGF-β signaling pathway," *International Journal of Oncology,* vol. 59, no. 4, pp. 1-9, 2021.

[5] Y. Ramazani *et al.*, "Connective tissue growth factor (CTGF) from basics to clinics," *Matrix Biology,* vol. 68, pp. 44-66, 2018.

[6] F. Sommer *et al.*, "Ascorbic acid modulates proliferation and extracellular matrix accumulation of hyalocytes," *Tissue engineering,* vol. 13, no. 6, pp. 1281-1289, 2007.

[7] T. Abe, Y. Abe, Y. Aida, Y. Hara, and K. Maeda, "Extracellular matrix regulates induction of alkaline phosphatase expression by ascorbic acid in human fibroblasts," *Journal of cellular Physiology,* vol. 189, no. 2, pp. 144-151, 2001.

[8] M. R. Hamblin and T. N. Demidova, "Mechanisms of low level light therapy," *Mechanisms for low-light therapy,* vol. 6140, p. 614001, 2006.

[9] D. Mokoena, S. S. D. Kumar, N. N. Houreld, and H. Abrahamse, "Role of photobiomodulation on the activation of the Smad pathway via TGF-β in wound healing," *Journal of Photochemistry and Photobiology B: Biology,* vol. 189, pp. 138-144, 2018.

[10] H. Li *et al.*, "The mechanisms and functions of TGF-β1 in tendon healing," *Injury,* vol. 54, no. 11, p. 111052, 2023.

[11] E. Ulukaya, F. Ozdikicioglu, A. Y. Oral, and M. Demirci, "The MTT assay yields a relatively lower result of growth inhibition than the ATP assay depending on the chemotherapeutic drugs tested," *Toxicology in vitro,* vol. 22, no. 1, pp. 232-239, 2008.

[12] S. Ruijtenberg and S. van den Heuvel, "Coordinating cell proliferation and differentiation: Antagonism between cell cycle regulators and cell type-specific gene expression," *Cell Cycle,* vol. 15, no. 2, pp. 196-212, 2016/01/17 2016, doi: 10.1080/15384101.2015.1120925.

[13] G. Fotakis and J. A. Timbrell, "In vitro cytotoxicity assays: comparison of LDH, neutral red, MTT and protein assay in hepatoma cell lines following exposure to cadmium chloride," *Toxicology letters,* vol. 160, no. 2, pp. 171-177, 2006.

[14] D. D. Silva, A. Crous, and H. Abrahamse, "Photobiomodulation Dose–Response on Adipose-Derived Stem Cell Osteogenesis in 3D Cultures," *International Journal of Molecular Sciences,* vol. 25, no. 17, p. 9176, 2024. [Online]. Available: https://www.mdpi.com/1422-0067/25/17/9176.

[15] J. K. Lim, J. H. Kim, G. T. Park, S. H. Woo, M. Cho, and S. W. Kang, "Efficacy of Light-Emitting Diode-Mediated Photobiomodulation in Tendon Healing in a Murine Model," *International Journal of Molecular Sciences,* vol. 26, no. 5, p. 2286, 2025.

[16] A. C. d. F. Marques *et al.*, "Photobiomodulation therapy on collagen type I and III, vascular endothelial growth factor, and metalloproteinase in experimentally induced tendinopathy in aged rats," *Lasers in medical science,* vol. 31, no. 9, pp. 1915-1923, 2016.

[17] A. Crous, M. J. Rensburg, and H. Abrahamse, "Photobiomodulation Effects of Single Near-Infrared (825 nm), Green (525 nm) and Combination of Wavelengths on Adipose-Derived Mesenchymal Stem Cell Physiology," 2021.

[18] X. Li, S. Pongkitwitoon, H. Lu, C. Lee, R. Gelberman, and S. Thomopoulos, "CTGF induces tenogenic differentiation and proliferation of adipose-derived stromal cells," *Journal of Orthopaedic Research®,* vol. 37, no. 3, pp. 574-582, 2019.

First-Principle Study of $NaMnNbPO_4$ as a Cathode Material for Sodium-Ion Battery

M.V Mudimeli[1], T.S Ranwaha[1], S Patel[1], R.R Randela[1], R.S Dima[3] and N.E Maluata[2,3]

[1]Department of Physics, University of Venda, P/ Bag X 5050, Thohoyandou, 0950
[2]Green Technology Confucius Institute, University of Venda, P/ Bag X 5050, Thohoyandou, 0950
[3]National Institute for Theoretical and Computational Sciences (NITheCs), Gauteng, South Africa

E-mail: Tshifhiwa.Ranwaha@univen.ac.za

Abstract. Sodium-ion batteries (SIBs) are emerging as a sustainable and cost-effective alternative to lithium-ion batteries due to the natural abundance and low cost of sodium. This study employs first-principles density functional theory (DFT) to explore the structural, electronic, mechanical, and thermal properties of $NaMnPO_4$ and its niobium-doped variant, $NaMnNbPO_4$, as cathode materials for SIBs. The results show that Nb doping results in a slight stretching of lattice parameters and expansion of volume, indicating minimal structural distortion. Electronic density of states (DOS) analysis revealed that $NaMnPO_4$ is a semiconductor, while Nb doping induces a transition toward half-metallic behaviour. The doped compound also exhibits enhanced mechanical rigidity and improved thermal stability, evidenced by higher elastic moduli, sound velocities, and Debye temperature. These improvements suggest that Nb-doped $NaMnPO_4$ is a promising high-performance cathode material for next-generation sodium-ion batteries.

1 Introduction

The rising demand for sustainable energy solutions such as solar, wind, and tidal power has prompted the development of electrochemical energy storage (EES) systems. EES is an eco-friendly technology that transforms electrical and chemical energy into energy storage and subsequently releases it via chemical processes [1]. Among the various EES technologies, rechargeable batteries play a vital role in producing clean energy storage since they are cost-effective, require low maintenance, and have a long cycle life. Lithium-ion batteries (LiBs) are widely used as an energy storage system in portable devices (e.g., laptops, tablets and phones), particularly due to their high energy density and extended lifespan. However, the limited amount of lithium on Earth has led to high manufacturing costs, causing a hindrance to its application in large-scale energy storage systems. Thus, there is an urgent need for an alternative to lithium-based batteries. Sodium and lithium both share similar physical and chemical characteristics, as they are members of the same group in the periodic table, the alkali metals [2]. Sodium is the sixth most abundant element in the Earth's crust and is widely available in the form of sodium chloride (common salt) [3], which further reduces production costs. Hence, sodium-ion batteries have gained significant attention as a promising alternative to LIBs.

Despite sharing similar intrinsic properties to those of LIBs, the larger ionic radius and high atomic weight of sodium lead to sluggish ionic movement between the electrodes and increase the stress on the host material during cycling, which can result in lower energy density and shorter cycle lifetime [4-6]. Consequently, there is a need to identify and enhance electrode materials with better electrochemical performance, including high energy density and longer lifespan. Recent studies have focused on enhancing cathode materials, as these materials significantly influence cycle performance and contribute to the overall energy density achievable. Transition metal phosphates, specifically NaMP04 (M = Ni, Co, and Mn), are recognized as effective cathode materials for sodium-ion batteries. This is attributed to their high thermal stability and elevated cut-off voltages [7-9], in comparison to other cathode materials such as transition metal oxides, polyanionic compounds, Prussian blue, and various organic compounds [2]. A study conducted by Dima et al. [10] investigated the stability and voltage window of NaMnP04 using first-principles calculations based on density functional theory (DFT). The lattice parameter and cell volume changes were found to be less than 7 %, indicating that the structure remained intact during the discharging process [10]. The voltage value was found between 4.655 V and 5.132 V, which implied that the voltage window is suitable to be applied as SIBs cathodes, and NaMnP04 could be treated as a potential SIB cathode material. In this study, DFT was used to investigate the electrochemical performance of $NaMnPO_4$, focusing on its structural, electronic, and thermal properties. To enhance its electrochemical performance and electronic conductivity, Nb substitution was introduced to form $NaNbMnPO_4$, with the aim of developing a high-voltage cathode material suitable for next-generation sodium-ion batteries (SIBs).

2 Computational Method

Density Functional Theory (DFT) calculations were performed using the Vienna Ab Initio Simulation Package (VASP) code, based on the projector augmented wave (PAW) method. A spin-polarized generalized gradient approximation (GGA) was employed to solve the Kohn–Sham equations using the Perdew–Burke–Ernzerhof (PBE) exchange–correlation functional and plane-wave pseudopotentials. The valence states considered were Na (3s), Mn (3d, 4s), O (2s, 2p), and P (3p). To account for strong on-site Coulomb repulsion in Mn 3d electrons, the Hubbard correction term (GGA+U) with an effective U value of 5.0 eV was applied, consistent with previous studies and validated by test calculations. All results were obtained in the ferromagnetic configuration since the ground-state energies of other spin states were nearly degenerate. Geometry optimisation of $NaMnPO_4$ was performed using a plane-wave cutoff energy of 560 eV, with Brillouin zone sampling carried out using the Monkhorst–Pack scheme and a 5 × 5 × 7 k-point mesh. Full structural relaxation was achieved when the residual force on all atoms was less than 0.01 eV/Å. Doping was introduced by applying the random substitution technique to replace Mn with Nb, yielding $NaMnNbPO_4$ structures. The structural, mechanical, electronic, and thermodynamic properties of both pristine and doped systems were computed. Elastic constants were obtained from a Taylor expansion of the total energy using a finite strain of 0.005, and the electronic density of states (DOS) was calculated using Gaussian smearing with a width of 0.05 eV for both spin-up and spin-down orientations.

3 Results and Discussion

3.1 Structural properties

The structural properties of $NaMnPO_4$ and $NaMnNbPO_4$ have been calculated and are presented in Table 1. The structural properties for $NaMnPO_4$ have been calculated and are compared with previous DFT and experimental literature values. The computed values for $NaMnPO_4$ align closely with those obtained from experimental results and other prior DFT studies [10]. The substitution of Mn with Nb results in a slight increase in the lattice parameter and unit cell volume, suggesting that Nb doping leads to minimal structural distortion. The lattice parameter a exhibited a decrease, whereas b and c showed a slight increase.

	Literature		$NaMnPO_4$	Deviations		$NaMnNbPO_4$
	Experimental [10]	DFT [10]	This work	Experimental	DFT	This work
a(Å)	10.528	10.421	9.093	9.093	1,435	4.923
b(Å)	6.321	6.132	6.864	6.864	0.188	6.449
c(Å)	4.985	4.864	5.091	5.091	0.106	10.195
Volume($Å^3$)	331.740	310.579	322.101	322.101	9.639	323.149
Band gap (eV)		3.161	3.161	3.370		0.185

Table 1: Structural Properties of NaMnPO4 and NaMnNbPO4.

The unit cell volume of $NaMnPO_4$ increased from 322.101 Å³ to 323.149 Å³ for the doped structure $NaMnNbPO_4$, suggesting successful incorporation of the Nb atom without compromising the structural stability of the host material [4]. These changes are attributed to the larger atomic radius of Nb compared to Mn, which results in a small lattice expansion. Despite this expansion, the overall orthorhombic crystal structure remains intact, demonstrating that $NaMnPO_4$ can accommodate Nb substitution without significant degradation [4].

3.2 Electronic Properties

The electronic properties of $NaMnPO_4$ and $NaMnNbPO_4$ were examined through an analysis of their spin-polarised density of states (DOS). This enhanced the comprehension of the material's electron behaviour and its capacity to conduct electricity.

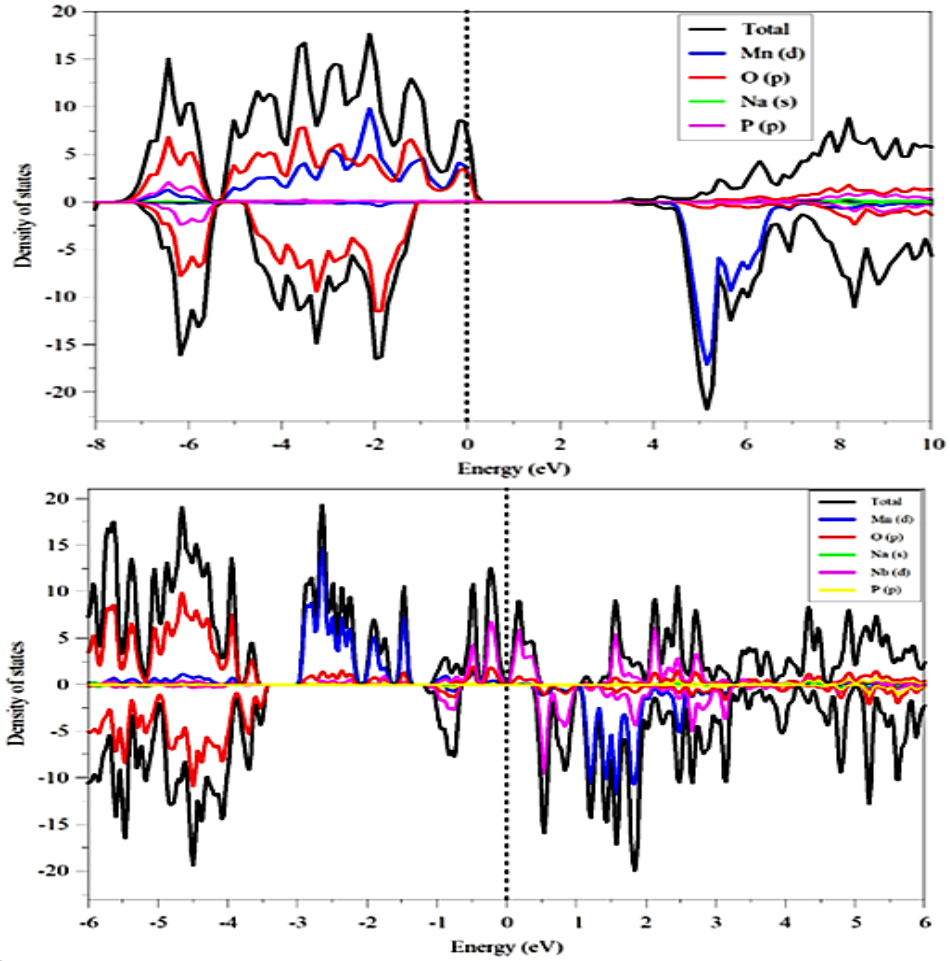

Figure 1: Spin Polarized DOS of(top) $NaMnPO_4$ and (bottom)$NaNbMnPO_4$.

The density of states for $NaMnPO_4$ indicates a distinct energy gap separating the valence band from the conduction band. This indicates that it functions similarly to a semiconductor, requiring a certain amount of energy to facilitate electron movement and enable current flow. This property is advantageous for battery materials, as it regulates electron movement during charging and discharging [4]. After doping with niobium (Nb), the DOS of $NaMnNbPO_4$ changed. The energy gap became smaller in one of the spin channels, and part of the gap disappears. This suggests that the material exhibits partial metallic behaviour in one spin direction, while retaining its semiconducting properties in the opposite direction. This behaviour is characterized as half-metallic, which can be beneficial in batteries by improving electrical conductivity while regulating electron flow. The enhanced conductivity in $NaMnNbPO_4$ may enhance the efficiency of sodium-ion batteries by facilitating electron mobility within the material during operation.

3.3 Mechanical properties

The mechanical properties of $NaMnPO_4$ and $NaMnNbPO_4$ were studied using their elastic constants. These values allow us to determine how strong and stable the materials are under pressure or stress.

$$(C_{11} + C_{12}),\ (C_{11} + C_{33} + 2C_{13}) > 0$$

$$(2C_{11} + C_{33} + 2C_{12} + 4C_{13}) > 0$$

$$C_{11} > 0,\ C_{33} > 0,\ C_{44} > 0 \textit{ and } C_{44} > 0$$

	$NaMnPO_4$	$NaMnNbPO_4$
C_{11}	124.46	172.12
C_{12}	61.43	52.22
C_{13}	58.55	79.79
C_{22}	125.29	200.71
C_{23}	51.49	60.73
C_{33}	148.46	148.49
C_{44}	42.28	59.36
C_{55}	49.01	58.47
C_{66}	46.71	58.41

Table 2: Elastic constants (C_{ij}) for $NaMnPO_4$ and $NaMnNbPO_4$.

The results indicate that all elastic constants are positive and satisfy the mechanical stability criteria for orthorhombic crystals. This indicates that both materials exhibit mechanical stability, a crucial factor for materials used in battery applications. An analysis of the two materials indicates that $NaMnNbPO_4$ exhibits superior values for the majority of elastic constants. This indicates that the addition of Nb enhances the strength and stiffness of the material.

	B_H	G_H	E_H	B/G	ν
$NaMnPO_4$	81.48	42.36	108.30	1.924	0.275
$NaMnNbPO_4$	99.42	55.36	141.15	1.780	0.263

Table 3: Bulk, shear and Young's moduli, Poisson's and Pugh's ratio.

After doping $NaMnPO_4$ with Nb, a notable enhancement in mechanical strength was recorded. The bulk modulus (B), which reflects the resistance to volume change under pressure, increased from 81.48 in the undoped compound to 99.42 in the doped structure. Similarly, the shear modulus (G), which pertains to the resistance against shape deformation, increased from 42.36 to 55.86. The Young's modulus (E), a measure of overall stiffness, increased from 108.30 to 141.15. The observed increases indicate that Nb doping enhances the material's strength and improves its resistance to mechanical deformation.

The analysis focused on Pugh's ratio (B/G) and Poisson's ratio (ν) to assess the ductility of the materials. A Pugh's ratio exceeding 1.75 typically signifies ductile behaviour. The values for $NaMnPO_4$ and $NaMnNbPO_4$ were found to be 1.924 and 1.780, respectively, indicating that both materials exhibit ductility. The values of Poisson's ratio were determined to be 0.275 for $NaMnPO_4$ and 0.263 for $NaMnNbPO_4$. The value exceeds 0.25, indicating that the material exhibits ductility [6].

The results indicate that Nb doping preserves the structural integrity of $NaMnPO_4$ while simultaneously improving its mechanical strength and flexibility. Consequently, $NaMnNbPO_4$ demonstrates enhanced durability and dependability as a cathode material in sodium-ion batteries [2].

3.4 Thermodynamic properties

The Debye temperature (θ_D) was calculated from the average sound velocity (v_m) using the equation [1]:

$$\theta_D = \frac{h}{k_B}\left(\frac{3}{4\pi}\right)^{\frac{1}{3}} v_m \quad (1)$$

where h and k_B are Planck's and Boltzmann's constants, respectively, the average sound velocity in polycrystalline systems, v_m, is evaluated by the expression:

$$v_m = \left[\frac{1}{3}\left(\frac{2}{v_t^3} + \frac{1}{v_l^3}\right)\right]^{-\frac{1}{3}} \quad (2)$$

where v_t and v_l are the mean longitudinal and transverse sound velocities, which can be related by the shear and bulk moduli from Navier's equations:

$$v_t = \left(\frac{3B+4G}{3\rho}\right)^{\frac{1}{2}} \quad (3)$$

$$v_{l=} \left(\frac{G}{\rho}\right)^{\frac{1}{2}} \quad (4)$$

	ρ	V_t	V_l	V_m	θ_D
$NaMnPO_4$	3309	3576	6634	3984	512.7
$NaMnNbPO_4$	3944	3760	6454	4181	551.1

Table 4: Calculated volumetric density, sound velocities, and Debye temperature.

With the introduction of the Nb dopant, there was an observed increase in both the average sound velocity and the Debye temperature. The Debye temperature increased from 512.7 K for $NaMnPO_4$ to 551.1 K for $NaMnNbPO_4$. This increase suggests that Nb-doped $NaMnPO_4$ exhibits enhanced bonding and improved thermal stability. The observed enhancements indicate that the doped material exhibits superior capabilities in managing heat and mechanical vibrations, making it more suitable for prolonged use in sodium-ion batteries.

3.5 Conclusion

Density functional theory was employed to investigate the effects of Nb doping on the structural, electronic, mechanical, and thermal properties of $NaMnPO_4$. The findings indicate that the doped material maintains structural stability with negligible distortion. Nb substitution resulted in alterations to the electronic structure, indicating a decrease in the band gap and evidence of half-metallic behavior, which could enhance electrical conductivity. Furthermore, the doped compound demonstrated improved mechanical strength and thermal stability, as evidenced by elevated elastic moduli and Debye temperature. The integration of these enhancements positions $NaMnNbPO_4$ as a highly promising candidate for sodium-ion battery cathodes with superior performance.

4 Acknowledgements

I would like to thank the Department of Physics and the Green Technology Confucius Institute at the University of Venda for their support and access to computational resources. I also acknowledge the National Institute for Theoretical and Computational Sciences (NITheCS). Special thanks to the South African Institute of Physics (SAIP) for providing a platform to present this research.

References

[1] H. Yang, S. Zhang, B. Chen, S. Xiang, Y. Xu, B. Yin, and E. Ackom, "The battery storage management and its control strategies for power system with photovoltaic generation," *in Emerging Trends in Energy Storage Systems and Industrial Applications*, Academic Press, 2023, pp. 441–484.

[2] M. He, S. Liu, J. Wu, and J. Zhu, "Review of cathode materials for sodium-ion batteries," *Progress in Solid State Chemistry*, vol. 74, p. 100452, 2024, doi: 10.1016/j.progsolidstchem.2024.100452.

[3] P. Phogat, S. Dey, and M. Wan, "Comprehensive review of sodium-ion batteries: Principles, materials, performance, challenges, and future perspectives," *Materials Science and Engineering: B*, vol. 312, p. 117870, 2025, doi: 10.1016/j.mseb.2024.117870.

[4] G. Li, X. Lou, C. Peng, C. Liu, and W. Chen, "Interface chemistry for sodium metal anodes/batteries: A review," *Chemical Synthesis*, vol. 2, no. 3, 2022, doi: 10.20517/cs.2022.19.

[5] A. Rudola, K. Saravanan, S. Devaraj, H. Gong, and P. Balaya, "$Na_2Ti_6O_{13}$: A potential anode for grid-storage sodium-ion batteries," *Chemical Communications*, vol. 49, no. 67, pp. 7451–7453, 2013, doi: 10.1039/C3CC44381G.

[6] H. W. Kim, H. J. Kim, H. Byeon, J. Kim, J. W. Yang, Y. Kim, and J. K. Kim, "Binder-free organic cathode based on nitroxide radical polymer-functionalized carbon nanotubes and gel polymer electrolyte for high-performance sodium organic polymer batteries," *Journal of Materials Chemistry A*, vol. 8, no. 35, pp. 17980–17986, 2020, doi: 10.1039/D0TA04526H.

[7] M. Minakshi, D. Mitchell, R. Jones, F. Alenazey, T. Watcharatharapong, S. Chakraborty, and R. Ahuja, "Synthesis, structural and electrochemical properties of sodium nickel phosphate for energy storage devices," *Nanoscale*, vol. 8, no. 22, pp. 11291–11305, 2016, doi: 10.1039/C6NR01179A.

[8] M. Minakshi and D. Meyrick, "Reversible sodiation in maricite $NaMn_{1/3}Co_{1/3}Ni_{1/3}PO_4$ for renewable energy storage," *Journal of Alloys and Compounds*, vol. 555, pp. 10–15, 2013, doi: 10.1016/j.jallcom.2012.11.203.

[9] K. T. Lee, T. N. Ramesh, F. Nan, G. Botton, and L. F. Nazar, "Topochemical synthesis of sodium metal phosphate olivines for sodium-ion batteries," *Chemistry of Materials*, vol. 23, no. 16, pp. 3593–3600, 2011, doi: 10.1021/cm200450y.

[10] R. S. Dima, P. M. Maleka, E. N. Maluta, and R. R. Maphanga, "First-principles study on sodium de-intercalation from $NaMnPO_4$," *Materials Today: Proceedings*, vol. 62, pp. S7–S11, 2022, doi: 10.1016/j.matpr.2022.02.076.

TileCoM Firmware Developments for ATLAS Tile Calorimeter Phase-II Upgrades

Brenton Tapfumanei Munhungewarwa[1] and Mpho Gift Doctor Gololo[1]

[1]Department of Electrical and Electronics Engineering Sciences, University of Johannesburg, Johannesburg Auckland Park, South Africa

E-mail: brenton.tapfumanei.munhungewarwa@cern.ch

Abstract. The High-Luminosity Large Hadron Collider (HL-LHC) necessitates a comprehensive electronics upgrade of the ATLAS Tile Calorimeter (TileCal) to ensure robust operation under increased radiation and data-rate conditions. To address this, the ATLAS TileCal has introduced the Phase-II upgrade, which involves a complete replacement of the existing electronic system. As part of the Phase-II upgrade, the Tile Computer-on-Module (TileCoM) has been developed to enable real-time monitoring and control of the TileCal Preprocessor (TilePPr) sub-modules. TileCoM provides a critical interface between the Detector Control System (DCS) and TilePPr modules, including the Compact Processing Module (CPM), Advanced Telecommunications Computing Architecture (ATCA) carrier, and Trigger Data Acquisition Interface (TDAQi). TileCoM's firmware integrates the IPbus protocol for register access, I2C for low-level sensor control, and Gigabit Ethernet for high-throughput data transfer, together with a custom Open Platform Communications Unified Architecture (OPC UA) server. Initial validation tests at CERN, conducted using the Avnet Ultra96-V2 development board, successfully demonstrated reliable TileCoM-CPM communication and firmware functionality, marking a key milestone toward current developments.

1 Introduction

The Large Hadron Collider (LHC) is the biggest particle accelerator ever built. It is located at the European Organization for Nuclear Research (CERN) along the Swiss-French boarder [1]. CERN is currently upgrading the LHC into a more powerful version called the High-Luminosity Large Hadron Collider (HL-LHC). The HL-LHC is poised to revolutionize high-energy physics by enabling luminosity levels 5-7 times greater than those of the current LHC [2].

ATLAS is one of the two general-purpose detectors at the LHC at CERN, designed to explore fundamental questions about the nature of matter and the universe. It plays a pivotal role in advancing particle physics, with its most notable contribution being the discovery of the Higgs boson in 2012 [3]. The ATLAS detector uses a hadronic calorimeter to capture and process energy coming from particle collisions from within the LHC. The calorimeter is called the Tile Calorimeter (TileCal) [4].

With the forthcoming HL-LHC upgrades expected to increase the collider's luminosity, the TileCal must undergo significant improvements to handle elevated levels of radiation and data throughput. These changes

necessitate a comprehensive upgrade of its readout electronics, including the introduction of the TileCal Preprocessor (TilePPr) boards [5].

2 ATLAS Tile Calorimeter Phase-II Upgrades

The ATLAS TileCal is a hadronic calorimeter system within the ATLAS experiment at the LHC. It plays a vital role in measuring the energy of hadrons, jets and the identification of missing transverse energy in collision events [6]. As the LHC transitions into the HL-LHC, the need for a major upgrade to the TileCal electronics readout system has become essential.

Figure 1 illustrates the existing electronic readout architecture employed during the standard LHC operations. In this system, signals from the photomultiplier tubes (PMTs) are digitized by the front-end electronics and then passed through a pipeline to the Read-Out Driver (ROD) modules via optical links. While this architecture has been robust, its limitations become apparent under the extreme data rates and radiation environments anticipated in the HL-LHC.

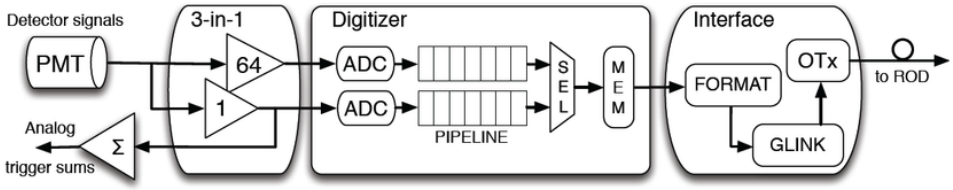

Figure 1: TileCal Electronic Readout Chain for the LHC [7]

To meet the demands of the HL-LHC, a significant redesign of the entire readout chain is being implemented. Figure 2 presents the ATLAS TileCal Phase 2 Upgrade, which introduces a modular and highly parallelized structure.

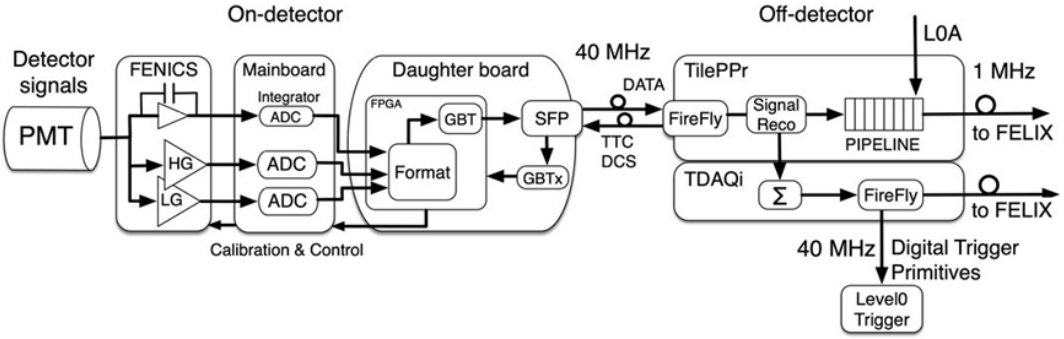

Figure 2: TileCal Electronic Readout Chain for the HL-LHC [8]

The existing LHC TileCal readout system includes 32 ROD boards housed in Versa Module Europa (VME) crates, supporting 256 uplinks. The Phase-II HL-LHC upgrade transforms this infrastructure, introducing 32 TilePPr boards housed in Advanced Telecommunications Computing Architecture (ATCA) crates, supporting 4096 uplinks with a total Data Acquisition (DAQ) bandwidth of 40 Gbps as shown in Table 1. Each TilePPr includes multiple PCBs with FPGAs, Firefly optical transceivers, and power management ICs.

Feature	TileCal (LHC)	TileCal (Phase II Upgrade)
Number of Uplinks	256	4096 (with redundancy)
Uplink Bandwidth	800 Mbps	9.6 Gbps
Number of Downlinks	256	2048
Off-Detector Boards	32 ROD	32 TilePPr
Off-Detector Crates	4 VME	4 ATCA
Bandwidth to DAQ	3.2 Gbps (ROS)	40 Gbps (FELIX)

Table 1: Evolving Demands on the Electronic Readout Chain — LHC Compared to HL-LHC [9]

3 The Tile-Preprocessor

The TilePPr is a critical component of the upgraded TileCal readout system for the ATLAS detector at the HL-LHC. It forms the off-detector electronics of the TileCal for Phase 2 upgrades. The TilePPr processes data signals coming from physical measurements captured by PMTs and interfaces with the Trigger Data Acquisition Interface (TDAQi) to aggregate acceptable events before transferring them to the Front-End LInk eXchange (FELIX) system [10].

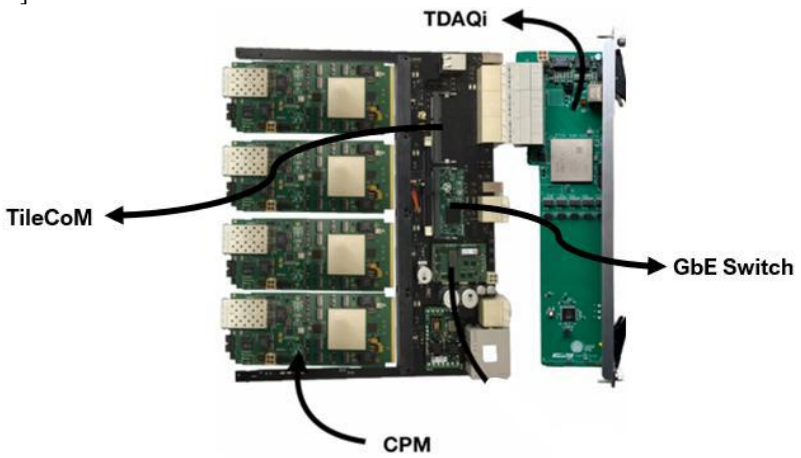

Figure 3: Tile Calorimeter Pre-Processor Module

Figure 3 illustrates the integration of the TilePPr PCBs, developed as part of the ATLAS TileCal Phase-II upgrade. Digitized signals coming from the on-detector electronics are transmitted to the Compact Processing Modules (CPM). Each CPM hosts a Kintex UltraScale Plus (KU+) FPGA. These FPGAs are responsible for the initial stages of data acquisition, formatting, and processing. The input is received via high-speed Firefly optical transceivers. At the centre of the architecture is the Tile Computer on Module (TileCoM), a Zynq-based Multi-processor System on Chip (MPSoC) that serves as the core monitoring and configuration unit. TileCoM interfaces with the ATCA infrastructure, CPMs, and TDAQi through an onboard Gigabit Ethernet (GbE) switch [11]. It also has access to distributed sensors across the system, allowing it to monitor operational parameters such as temperatures, voltages, and currents. The TDAQi board acts as a bridge between the TilePPr and the ATLAS Data Acquisition system. It receives pre-processed data from the CPMs via the ATCA backplane and transmits it to the FELIX using high-speed optical links. It also generates trigger primitives that allow the processing of only useful events from the ATLAS detector.

4 Tile-Preprocessor Monitoring Framework

4.1 Software

The software framework supporting TilePPr monitoring is built on the AlmaLinux operating system, running on the Zynq UltraScale+ MPSoC-based TileCoM module. Currently, the TileCoM evaluation board operates using CentOS however, there is an ongoing migration to AlmaLinux.

A key component of the software system is the Open Platform Communications Unified Architecture (OPC UA) server. This server is hosted directly on TileCoM and is responsible for exposing sensor data to the DCS. It is implemented using the Quasar C++ framework, which greatly simplifies OPC UA development by allowing server structures to be defined through XML schema files. Quasar also provides templates and utility modules that make it easier to embed custom data acquisition logic into the OPC UA node tree.

For the testing implementation conducted at CERN, the OPC UA server streamed data to an InfluxDB time-series database through a Telegraf data collector as shown in Figure 4. This intermediate step provided seamless routing of sensor data into a visual analysis environment. Grafana was used as the dashboarding tool to create interactive and real-time plots for various sensor categories.

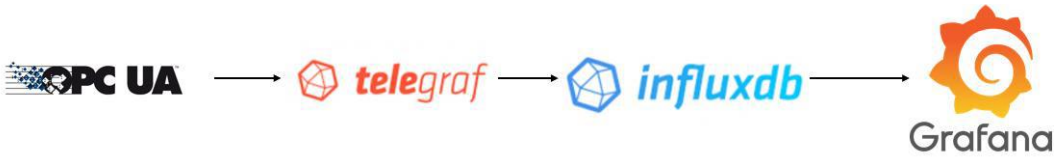

Figure 4: OPC UA Server Integration with Grafana

4.2 Hardware

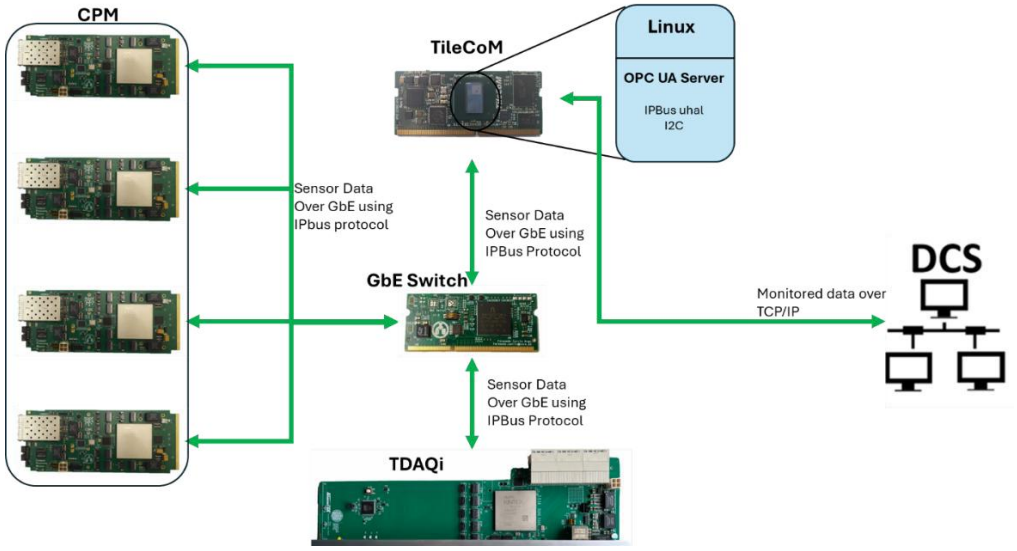

Figure 5: Tile-PPr Monitoring Framework

The hardware monitoring framework of the TilePPr is designed to support high-throughput sensor data acquisition in the demanding environment of the HL-LHC. Each TilePPr unit houses over 1,000 analog and digital sensors distributed across its sub-modules, including the CPM, ATCA board, and the TDAQi. Figure 5 shows how the different TilePPr PCBs are connected together for monitoring through TileCoM

Sensor data acquisition from the TilePPr subsystems is handled through IPbus, a low-level protocol designed at CERN for FPGA register access. IPbus enables TileCoM to poll voltages, currents, and temperatures from distributed TilePPr PCBs such as the CPMs. All sensor data is routed through a Gigabit Ethernet (GbE) switch integrated within the ATCA crate. This switch interconnects the TilePPr PCBs with TileCoM, which serves as the centralized processing node.

Aside from monitoring the off-detector electronics, TileCoM is also used for remotely configuring and programming the FPGAs on the TilePPr PCBs. It also routes clocking signals to some of the TilePPr Modules.

5 Results From Testing at CERN

To validate the functionality and performance of the developed monitoring system, experimental tests were conducted at CERN using the TileCoM evaluation board interfaced with a CPM. The primary objective was to verify end-to-end data acquisition from onboard sensors using the OPC UA server deployed on TileCoM, with real-time sensor data relayed over GbE via the IPbus protocol. The TileCoM firmware was first installed on the Avnet Ultra96-V2 development board. This board served as a functional prototype for evaluating TileCoM's monitoring capabilities. It was connected to a live CPM unit from the TilePPr assembly.

Figure 6 shows the monitoring data acquired from the CPM through TileCoM. This data was visualized using Grafana. A total of 45 sensor points were actively monitored:

- 10 sensors originated from the TileCoM board itself (MPSoC core voltages and onboard temperature sensors),
- 35 sensors were accessed from the CPM unit, primarily power rails and temperature sensors.

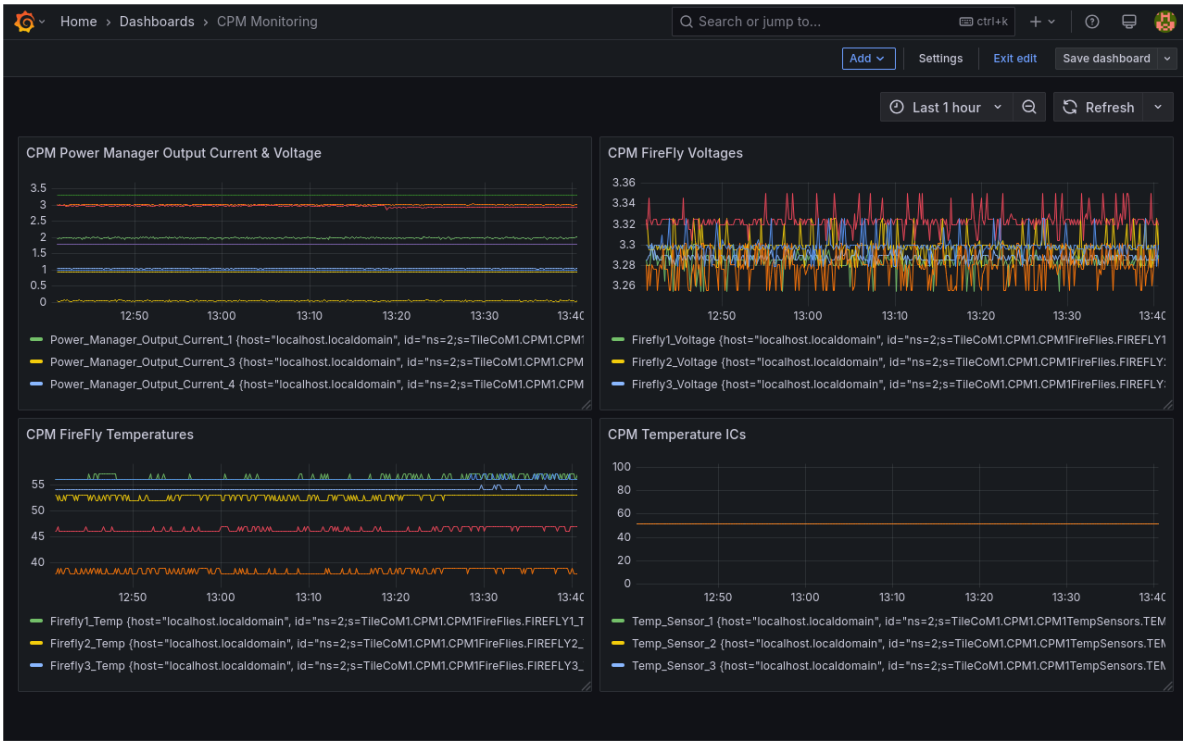

Figure 6: CPM Sensor Data Monitoring and Display over Grafana

5.1 Sensor Data Quality Validation

Following successful data acquisition, a quality analysis was conducted to compare sensor readings against known datasheet specifications. The focus was placed on the CPM's Power Management Unit, which incorporates LTM4644 DC-DC converters. According to the manufacturer's datasheet, these regulators guarantee a voltage regulation accuracy within ±1.5% under nominal conditions. A color-coded validity heatmap (Figure 7) was generated to visualize the percentage of readings that remained within the tolerance band for each sensor over time. Green indicates full compliance (valid data), while red highlights out-of-range or invalid readings. The majority of sensors showed consistent behaviour and remained within the tolerance limits as shown in Figure 7. The temperature IC readings were flagged faulty this is due to an addressing error in the I2C library used. This is currently being corrected.

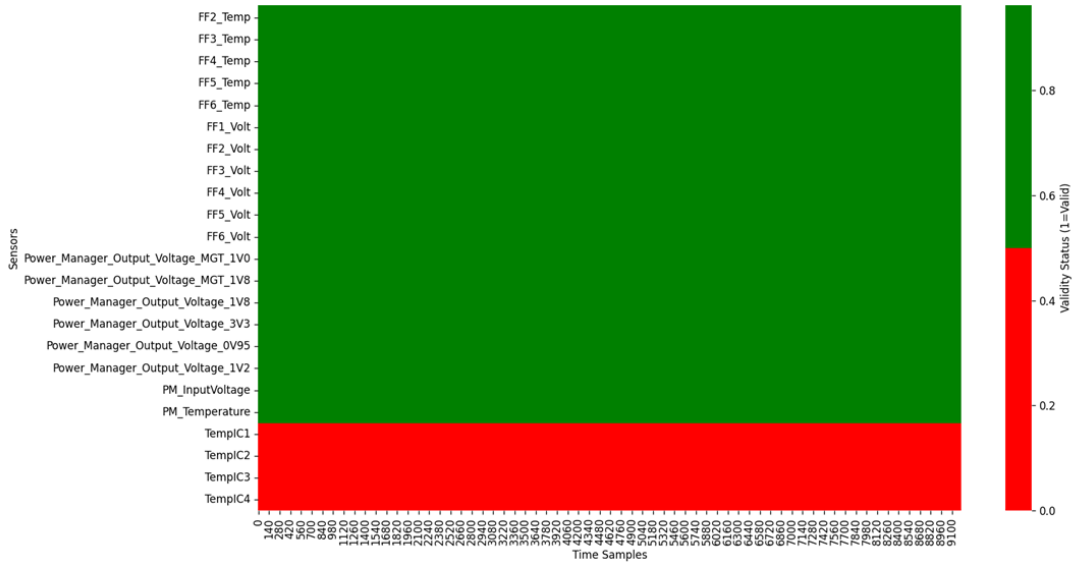

Figure 7: Sensor Data Quality Check on the CPM Power Manager with a ±1.5% Tolerance

6 Conclusion

This research work addresses a critical challenge in ensuring the functionality and reliability of the upgraded TileCal system within the ATLAS detector at the HL-LHC. The study aims to support the operational demands of the HL-LHC, characterized by higher radiation levels and increased data throughput by designing and implementing a monitoring system for the TilePPr module. The research is expected to provide significant insights into the design and validation of advanced monitoring technologies offering practical benefits to high-energy physics experiments. Additionally, it will establish a framework for future upgrades, ensuring the long-term reliability of the ATLAS detector.

References

[1] L. Evans and P. Bryant, "LHC Machine," *JINST*, vol. 3, S08001, 2008.

[2] G. Apollinari, O. Brüning, T. Nakamoto, and L. Rossi, "High Luminosity Large Hadron Collider (HL-LHC)," *CERN Yellow Rep*. 2015-005, 2015, arXiv:1705.08830.

[3] G. Aad et al. (ATLAS Collaboration), "Observation of a new particle in the search for the Standard Model Higgs boson with the ATLAS detector at the LHC," *Phys. Lett. B*, vol. 716, pp. 1–29, 2012.

[4] G. Aad et al. (ATLAS Collaboration), "Readiness of the ATLAS Tile Calorimeter for LHC collisions," *Eur. Phys. J. C*, vol. 70, pp. 1193–1236, 2010.

[5] F. Carrió Argos and A. Valero, "The PreProcessor Module for the ATLAS Tile Calorimeter at the HL-LHC," *Nucl. Instrum. Meth. A*, vol. 958, p. 162487, 2020.

[6] ATLAS Collaboration, "Operation and performance of the ATLAS Tile Calorimeter in Run 1," *Eur. Phys. J. C*, vol. 78, no. 12, p. 987, 2018.

[7] F. Carrió and A. Valero, "Clock Distribution and Readout Architecture for the ATLAS Tile Calorimeter at the HL-LHC," in *Proc. IEEE Real Time Conference*, Williamsburg, VA, USA, Oct. 2018.

[8] ATLAS Collaboration, "Technical Design Report for the Phase-II Upgrade of the ATLAS Tile Calorimeter," *CERN-LHCC-2017-019*, CERN, 2017.

[9] F. Carrió, P. Moreno, and A. Valero, "Performance of the Tile PreProcessor Demonstrator for the ATLAS Tile Calorimeter Phase II Upgrade," *JINST*, vol. 11, no. 03, C03047, 2016.

[10] J. Valls et al., "The Readout Architecture of the TileCal Demonstrator Project for the ATLAS Upgrade," *IEEE Transactions on Nuclear Science*, vol. 67, no. 1, pp. 89–96, Jan. 2020. doi: 10.1109/TNS.2019.2951542

[11] M. G. D. Gololo, Development of TileCoM Firmware and Software for the Off-Detector Electronics of the ATLAS Tile Calorimeter at the HL-LHC, Ph.D. dissertation, Inst. for Collider Particle Physics, Dept. of Physics, Univ. of the Witwatersrand, Johannesburg, South Africa, Aug. 2023.

DFT Study of the TiO_2 Anatase (100) Surface Doped with Be for Application in DSSCs

T S Ranwaha[1], R R Randela[1], N E Maluta[2,3] and R R Maphanga[3]

[1]Department of Physics, University of Venda, P/ Bag X 5050, Thohoyandou, 0950
[2]Green Technology Confucius Institute, University of Venda, P/ Bag X 5050, Thohoyandou, 0950
[3]National Institute for Theoretical and Computational Sciences, Gauteng, South Africa

E-mail: tshifhiwa.ranwaha@univen.ac.za

Abstract. Dye-sensitized solar cells (DSSCs) are an innovative photovoltaic technology, characterized by their cost-effectiveness, impressive efficiency, and adaptable structure. Titanium dioxide (TiO_2), especially in its anatase phase, is extensively utilized as a photoanode material because of its advantageous electronic and chemical characteristics. Nonetheless, the broad bandgap of pure TiO_2 restricts its ability to absorb light in the visible spectrum, consequently diminishing its photovoltaic efficiency. This study utilized density functional theory (DFT) to explore the electronic and optical characteristics of the Be-doped (100) anatase TiO_2 surface. The generalized gradient approximation (GGA) employing the Perdew–Burke–Ernzerhof (PBE) functional was applied to characterize the exchange-correlation effects, as executed in the Materials Studio package. The findings demonstrate that the introduction of beryllium into anatase TiO_2 effectively reduces the bandgap, leading to improved absorption in the visible light spectrum. Furthermore, the doped surface demonstrates decreased reflectivity, which is beneficial for enhancing light harvesting in DSSCs. This study illustrates that the incorporation of Be significantly alters the optical and electronic properties of anatase TiO_2, enhancing its potential as a more effective option for dye-sensitized solar cell applications.

Keywords: Anatase TiO_2, (100) surface, beryllium, doping, dye-sensitized solar cells, bandgap, density functional theory.

1 Introduction

Solar energy presents a practical approach to addressing the environmental pollution issues caused by excessive fossil fuel consumption and the increasing energy needs resulting from population growth. The utilization of solar cells produces energy in the form of directly usable electricity and eliminates the need for fuel, positioning them as an optimal solution for effectively harnessing this abundant solar energy [1,2]. At present, Silicon solar cells are being utilized and installed on building rooftops to improve energy efficiency, in conjunction with the development of large-scale solar power plants to replace thermal energy sources. While it offers advantages like high photoconversion efficiency (PCE) and a lifespan of over 20 years, it encounters obstacles including limited stability under extended UV exposure, a relatively low open-circuit voltage, and the reliance on expensive or volatile liquid electrolytes, which impede its large-scale commercial implementation. [1].

Dye-sensitized solar cells (DSSCs) present advantages including low manufacturing costs, a variety of dye choices, transparency, versatility, and impressive power conversion efficiency in low-intensity conditions [3-5]. The photocatalyst itself serves as a vital element in photocatalytic systems. Titanium dioxide (TiO_2) serves as a widely used photocatalyst; nonetheless, its application frequently faces limitations due to its broad band gap energy, which restricts its efficacy to the ultraviolet region of the electromagnetic spectrum. An effective strategy

to overcome this limitation involves the sensitization of TiO_2 using dyes that can absorb light within the visible spectrum [6,7]. This research examines the structural, electronic, and optical characteristics of TiO_2 anatase (100) that has been doped with Beryllium.

2 Computational Method

The density functional theory (DFT) calculations were performed using the CASTEP simulation package with the use of generalized gradient approximation (GGA). A kinetic cut-off energy of 650 eV was utilized for the set of plane-wave basis. A 7 × 7 × 3 Monkhorst–Pack mesh was carried out for the integrations over the irreducible Brillouin zone. The convergence of the total energy within 1.0×10^{-6} eV/atom is used to guarantee the accuracy of the calculations. The anatase TiO_2 structure was optimized, from which a (1 0 0) Miller index was cleaved to form a (100) anatase TiO_2 surface. The appropriate vacuum slab was built, with vacuum and crystal thicknesses used for the slabs are 15.0 Å and 19.05 Å, respectively. The substitution of doping was performed on (100) anatase TiO_2, whereby one titanium atom at the top layer was replaced by a beryllium atom. The electronic partial density of state and optical properties of the beryllium-doped system was calculated.

3 Results and Discussion

3.1 Structural properties

This anatase belongs to the family of TiO_2 polymorphs, which includes rutile and brookite. This investigation involved the optimization of the bulk structure of anatase TiO_2 to confirm the accuracy of the model. The calculations employed k-points and energy cut-off values established through convergence tests, as previously outlined. Geometry optimizations were conducted in a single step using an unconstrained volume to ascertain equilibrium bulk parameters and reference energies. The ground state energy configuration for pure anatase TiO_2 was established by computing the lattice parameters along with their associated minimum energy values.

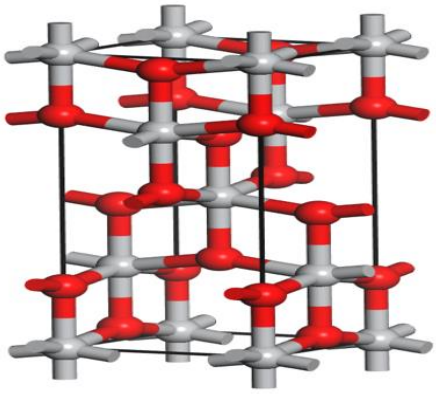

Figure 1: TiO_2 anatase bulk structure.

The calculated lattice parameters a, b, and c are presented in Table 1, alongside reported experimental values and earlier theoretical findings for comparison. The calculated results align well with both the experimental findings and the existing literature. The lattice parameters derived in this study align closely with the experimental data, exhibiting deviations of 0.0088% for the a-axis, 0.0088% for the b-axis, and 0.0264% for the c-axis. The observed percentage deviations fall within the range of reasonable and acceptable values for DFT calculations.

The refined structural characteristics of the TiO_2 anatase are presented in Table 1. The parameters presented demonstrate that the computational results achieved align well with both experimental data and other theoretically reported values. The computed discrepancies from the experimental findings align more closely with those documented by Gao *et al* [8].

	EXPERIMENTAL [8]	THIS WORK		LITERATURE [9]	
		Results	Deviation (%)	Results	Deviation (%)
a(Å)	3.7848	3.7760	0.0088	3.7431	0.0417
b(Å)	3.7848	3.7760	0.0088	3.7431	0.0417
c(Å)	9.5124	9.4860	0.0264	9.4812	0.0312

Table 1: Optimized structural parameters for bulk anatase TiO_2 compared with experimental and previous theoretical results.

The energy of the anatase TiO_2 bulk structure after optimization was -9913.570370450 eV, for pure anatase TiO_2 (100) surface was -9911.685047841 eV, and for Be-doped anatase TiO_2 was -8704.77733852 eV. The lattice parameters of the surfaces differ from those of the bulk structure; for the bulk structure, a = 3.7760, b = 3.7760, and c = 9.4860, while for the surface, they change to a = 3.7760, b = 9.4860, and c = 11.8880.

3.2 Electronic Properties

The calculated band gap of pure anatase TiO_2 is around 2.092 eV, which is lower than the experimental value of 3.2 eV, attributed to the underestimation by the GGA functional. This is due to the limitation of the DFT method. The limitation is caused by the fact that the discontinuity in the exchange correlation potential, which is not considered within the framework of DFT. However, the discussions on the energy gap will not be affected because only the relative energy changes are of concern. The calculated band gap of the cleaved surface TiO_2 anatase (100) is 3.077 eV, which is about 0.985 eV greater than the calculated band gap of pure anatase TiO_2, but it is 0.123 eV smaller than the experimental value (3.2 eV) due to the cleaving of the TiO_2 anatase structure. The determined band gap of Be-doped TiO_2 anatase (100) is 2.340 eV, which is roughly 0.737 eV less than that of undoped TiO_2 anatase (100). The Be dopant effectively narrows the band gap while avoiding the formation of isolated states, a feature considered to enhance photocatalytic activity. The findings suggest that the incorporation of Be atoms into the TiO_2 surface leads to a reduction in the band gap of TiO_2, consequently shifting its absorption into the visible light spectrum.

Our results regarding beryllium doping align with computational results reported by Ma *et al.* [10], who investigated the doping mechanisms, dopant formation energies, electronic structures, and optical properties for Be, Mg, Ca, Sr, and Ba doped anatase TiO_2. Their results suggested that alkaline earth metal (AEM) dopants shift the valence bands (VBs) to higher energy. Specifically, the dopant-state energies for Ca, Sr, and Ba are quite higher than the Fermi levels, while Be and Mg dopants lead to spin-polarized gap states near the top of the VBs, which is consistent with our findings.

The density of states (DOS) quantifies the number of accessible states per unit energy at each energy level that electrons can occupy. A substantial density of states at a specific energy level indicates a multitude of accessible states for electron occupancy, whereas a density of states of zero signifies the absence of available states. Figures 2 and 3 present the electronic energy density of states for the bulk structure of TiO_2 anatase, the TiO_2 anatase (100) surface, and the Be-TiO_2 anatase (100) surface, respectively.

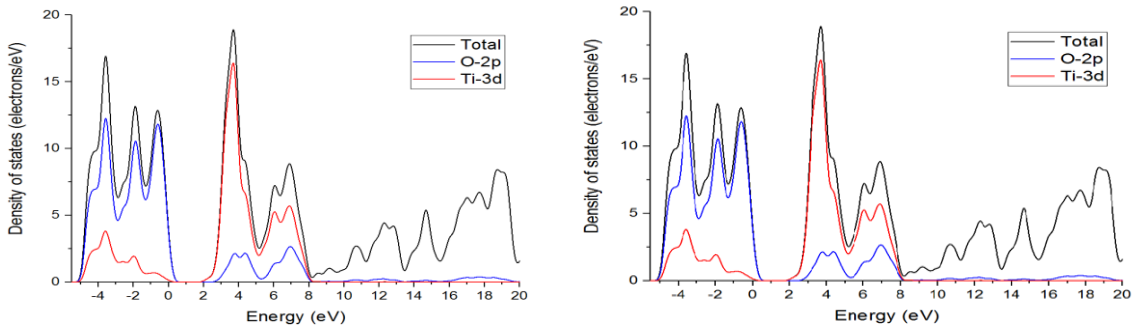

Figure 2: Partial density of states of (left)TiO_2 anatase bulk structure and (right) pure TiO_2 anatase (100).

Figures 4 illustrate that the Be-doped anatase TiO_2 (100) surface enhances the availability of states for electron occupation, attributed to the introduction of Be impurity states within the band gap. The introduction of

an impurity state in the Be-doped TiO_2 anatase (100) surface results in the formation of a "hole" within the particle, which contributes to the narrowing of the TiO_2 anatase band gap. In the un-doped scenario, the valence band of TiO_2 anatase is mainly formed from O-2p orbitals, while the conduction band is predominantly made up of Ti-3d orbitals.

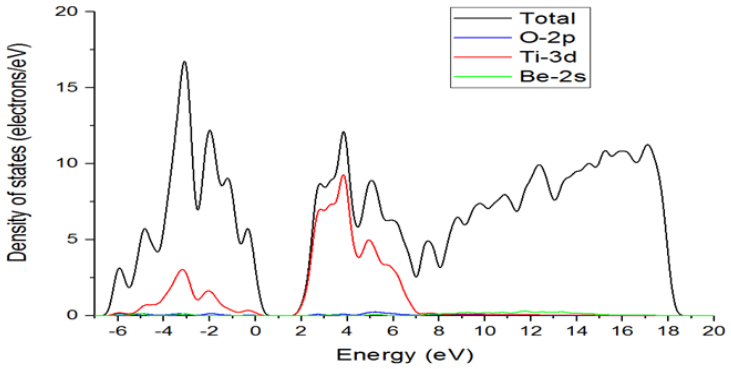

Figure 3: Density of states of Be-doped TiO_2 anatase (100).

For the doped system, the s orbital of the alkaline earth metal (Be) hybridizes with the p orbital, generating coordination fields that interact with the nearest oxygen atoms. The orbital resonance between oxygen and beryllium suggests the formation of a Be-O bond. The valence band of the doped system contains the hybridized orbitals of Be, and the conduction band includes the s-p orbital of Be. These findings are supported by Ma *et al.* [10], who reported that in doped cases, the s orbitals of AEMs hybridize with p (for Be and Mg) or p-d orbitals (for Ca, Sr, Ba) through the promotion of s electrons to p and d orbitals, creating coordination fields that interact with the nearest oxygen atoms. They also reported that the band shifts in Be and Mg-doped cases are very small, while Ca, Sr, and Ba dopants induce an elevation of VBs and generate dopant states in the gap for Ca and Ba-doped cases.

3.3 Optical properties

Figure 4 displays the reflectivity spectra of bulk anatase TiO_2, pure anatase TiO_2 (100) surface, and Be-doped anatase TiO_2 (100) surface across a wavelength range of approximately 0 – 2000 nm. The Be-doped surface exhibits significantly reduced reflectivity in both the ultraviolet (UV) and infrared (IR) regions compared to the undoped systems. However, in the visible region, the Be-doped surface shows higher reflectivity than the pure surface. This enhancement may be attributed to the presence of Be impurity states, which alter the surface's electronic structure and optical response.

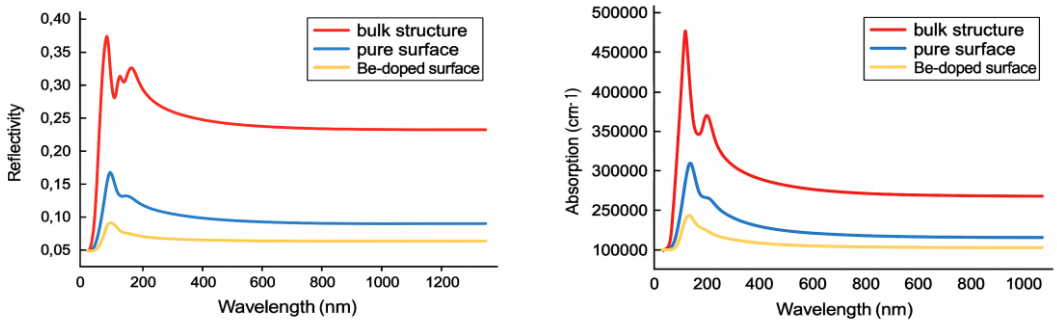

Figure 4: (Left)Reflectivity and (Right)Absorption for bulk TiO_2 bulk structure, pure anatase TiO_2 (100) surface and Be- doped anatase TiO_2 (100) surface.

The absorption spectrum, presented in Figure 4, provides insights into the light-harvesting capabilities of the materials. The absorption onset is used to estimate the optical band gap. Notably, the Be-doped anatase TiO_2 exhibits enhanced absorption in the visible and near-infrared regions. This can be attributed to the dopant-induced states within the band gap, which facilitate sub-bandgap optical transitions. It is important to note that the

electronic band gap differs from the optical band gap, which considers excitonic and many-body interactions. The presence of Be dopants effectively narrows the optical band gap, enabling better absorption of solar radiation.

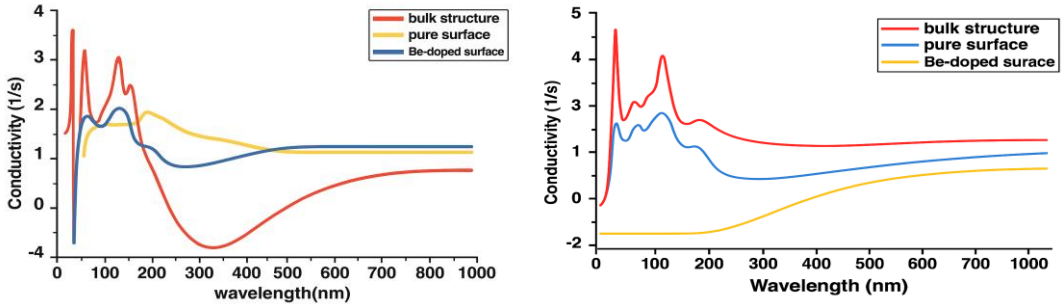

Figure 5: Conductivity (Left) Imaginary part and (Right) Real part for bulk TiO_2 bulk structure, pure 100 anatase TiO_2 surface and Be-doped 100 anatase TiO_2 surface.

Figure 5 shows the imaginary part of the optical conductivity and the real part. Optical conductivity relates to how the material responds to time-varying electric fields, linking current density to the applied electric field across different frequencies. These results indicate that the Be-doped anatase TiO_2 surface can conduct under optical excitation across a broader wavelength range, supporting its potential for improved photo-induced charge transport.

4 Conclusion

Beryllium-doped anatase TiO_2 (100) surfaces have been successfully studied using first-principles density functional theory. The structural, electronic, and optical properties of the anatase TiO_2 bulk structure, pure (100) anatase TiO_2 surface, and doped surface were calculated. The calculated results demonstrate that Be-doping can improve the photocatalytic performance of the anatase TiO_2 (100) surface. Specifically, the Be dopant narrows the band gap of anatase TiO_2 (100), shifting the absorption spectrum to the visible range, which enables the solar cell to absorb more photons. The Be-doped anatase TiO_2 (100) shifts the absorption to longer wavelengths, improves optical absorbance, limits reflectance in the visible light and near-infrared (IR) regions, and reduces the band gap of anatase TiO_2, leading to an improvement in dye-sensitized solar cells.

References

[1] P. Roy, A. K. Vats, L. Tang, Y. Kurokawa, and S. S. Pandey, "Controlling adsorption of two dyes on TiO_2 surface to improve the efficiency of see-through dye-sensitized solar cells," *Solar Energy*, vol. 269, p. 112339, 2024.

[2] C. Battaglia, A. Cuevas, and S. De Wolf, "High-efficiency crystalline silicon solar cells: status and perspectives," *Energy & Environmental Science*, vol. 9, pp. 1552–1576, 2016.

[3] M. Freitag, J. Teuscher, Y. Saygili, X. Zhang, F. Giordano, P. Liska, J. Hua, S. M. Zakeeruddin, J. E. Moser, M. Grätzel, and A. Hagfeldt, "Dye-sensitized solar cells for efficient power generation under ambient lighting," *Nature Photonics*, vol. 11, no. 6, pp. 372–378, 2017.

[4] C. C. P. Chiang, C. Y. Hung, S. W. Chou, J. J. Shyue, K. Y. Cheng, P. J. Chang, Y. Y. Yang, C. Y. Lin, T. K. Chang, Y. Chi, H. L. Chou, and P. T. Chou, "PtCoFe nanowire cathodes boost short-circuit currents of Ru(II)-based dye-sensitized solar cells to a power conversion efficiency of 12.29%," *Advanced Functional Materials*, vol. 28, no. 3, 2018.

[5] H. Michaels, M. Rinderle, R. Freitag, I. Benesperi, T. Edvinsson, R. Socher, A. Gagliardi, and M. Freitag, "Dye-sensitized solar cells under ambient light powering machine learning: towards autonomous smart sensors for the Internet of Things," *Chemical Science*, vol. 11, no. 11, pp. 2895–2906, 2020.

[6] R. Li, T. Li, and Q. Zhou, "Impact of titanium dioxide (TiO_2) modification on its application to pollution treatment—A review," *Catalysts*, vol. 10, p. 804, 2020.

[7] Z. Zhang, Y. Ma, X. Bu, Q. Wu, Z. Hang, Z. Dong, and X. Wu, "Facile one-step synthesis of TiO_2/Ag/SnO_2 ternary heterostructures with enhanced visible-light photocatalytic activity," *Scientific Reports*, vol. 8, p. 10532, 2018.

[8] P. Gao, W. Jing, Q. Liu, and W. Zhou, "First-principles study on anatase TiO_2 codoped with nitrogen and praseodymium," *Journal of Physics B: Atomic, Molecular and Optical Physics*, vol. 19, no. 8, 2010.

[9] J. K. Burdett, T. Hughbanks, G. J. Miller, J. W. Richardson, and J. V. Smith, "First-principles studies of the effect of nitrogen impurities on the energy gap of rutile $TiO_{2-x}N_x$ by pseudopotential approaches," *Journal of the Chemical Society*, vol. 109, pp. 3639–3645, 1987.

[10] J. Ma, C. Zhang, J. Gong, Y. Wu, S. Kou, Y. Hua, Y. Chen, J. L. Zi, and H. Chen, "The electronic structure and optical properties of alkaline-earth metals doped anatase TiO_2: A comparative study of screened hybrid function and generalized gradient approximation," *Materials*, vol. 8, no. 8, pp. 5508–5525, 2015.

Deep Learning for High Throughput Decision Making on Diamond Content of PET Activated Kimberlite Rocks

Nicholas Connell[1], Timothy Brooks[2], Tiego Mpai[2], Thendo Nemakhavhani[3], Simon Connell[2] and Charis Harley[1]

[1]Department of Electrical and Electronic Engineering Science, Faculty of Engineering and the Built Environment, University of Johannesburg, Johannesburg, South Africa
[2]Department of Mechanical Engineering Science, Faculty of Engineering and the Built Environment, University of Johannesburg, Johannesburg, South Africa
[3]Physics Department, University of Johannesburg, P.O.Box 524. Auckland Park 2006, Johannesburg, South Africa.

E-mail: nickpconnell@gmail.com

Abstract. A preliminary study was conducted on the feasibility of training a convolutional neural network classifier on cubic samples taken from synthesized positron emission tomography images. The images were synthesized through simulation. The best performing model achieved a recall of 0.98 on diamonds $5\,\mathrm{mm}$ (1.14 ct) in size and larger. It achieved a false positive rate lower than 1 in 1000.

1 Introduction

Every diamond mining company faces the same problem. How can they ensure they recover all the diamonds from the rocks they dig out of the ground. Currently crushing is employed to break the rocks and reveal the diamonds. This method carries the risk of breaking large diamonds into smaller, less profitable pieces. Considering that deposits contain on average only a few carats of diamond per $10\,000\,\mathrm{kg}$ of rock, this method is also highly energy intensive and costly. The MinPET technique is a novel application of positron emission tomography (PET) to mineral sorting [1–3]. The technique reduces the amount of crushing required because it can image the inside of rocks as large as $100\,\mathrm{mm}$. Thus the technique lowers the likelihood of diamonds breaking and could lower the energy consumption of a mine.

Figure 1a shows a concept design for the MinPET system. The system is fed pre-crushed rock with a maximum size of $100\,\mathrm{mm}$. The crushed rock is irradiated with a $40\,\mathrm{MeV}$ gamma ray beam to activate PET isotopes via the giant dipole resonance. Then the activated rock is sent to a hold hopper where it waits for approximately $23\,\mathrm{min}$ for all the shorter lived species to decay away thus reducing the background signal. The rocks pass through a planar detector array where they are imaged by the PET process. The 3D images are processed to identify any diamonds (cf. Figure 1b). This information is sent to the ejector system which extracts any rocks that were identified as diamond bearing.

The goal of this study was to investigate the feasibility of automating the diamond identification step, i.e., to automate searching scanned PET images of kimberlite rocks for diamonds. Convolutional neural networks (CNNs) show great promise in this area as they have already been used to detect signs of Alzheimer's disease in PET images of the brain [4, 5], as well as classifying ovarian cancer in whole body PET images [6]. Unfortunately, there are no databases of PET images of diamond-containing and barren kimberlite rocks large enough to train a CNN. Thus, a method of simulation to produce the required quantities of synthetic labelled data is presented.

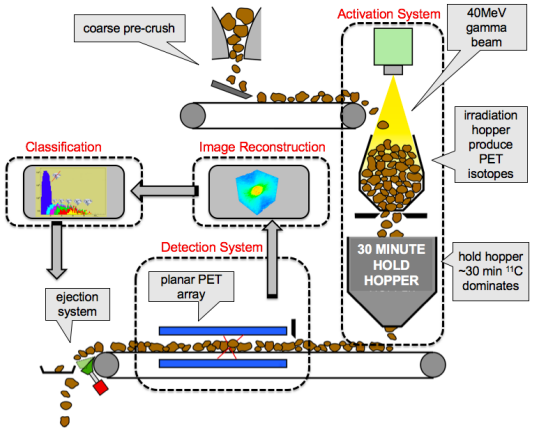

(a) System plant flow: activation, holding, detection, reconstruction, classification, and ejection.

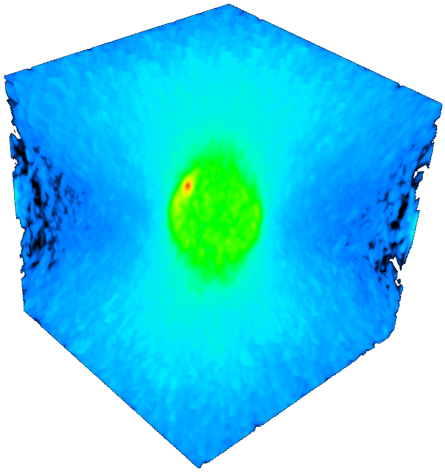

(b) Reconstructed image of a 10 mm diameter diamond (red) in a 100 mm diameter kimberlite rock (green).

Figure 1: (a) MinPET process schematic and (b) PET image reconstruction.

2 Methodology

The study consisted of four stages. First, synthetic data was generated through simulations built with the Geant4 software [7]. Second, 3D PET images were reconstructed from the synthetic data using maximum likelihood expectation maximisation (MLEM) written in Python using the ASTRA Toolbox [8]. Third, training data was extracted from the images. Fourth, 3D CNNs written in Python using Tensorflow [9] and Keras [10] were trained on the synthesized data to classify rock samples as diamond bearing or barren.

2.1 Simulation

This section describes the inputs and the outputs as well as what does and does not change between simulations. The simulation code had many contributors and is described here [3]. It uses the Geant4 software framework a C++ toolkit developed for simulating the passage of particles through matter. It has been applied in accelerator design, space engineering, and medical, nuclear, and particle physics [7].

A simulation requires the following inputs: sizes, shapes, positions, and material compositions of any kimberlite rocks, diamonds, and detector pixels; the production cross-sections, half-lives, and reaction details of the necessary PET isotopes; the time spent in the hold hopper; the distribution of electron flux during irradiation; and two seeds for the random number generators. The velocity of the conveyor belt is specified along with a "distance per run" variable to overcome the the fact that Geant4 does not support dynamic movement. Which is achieved by running a sequence of sub-simulations where the rocks incrementally change their position. The simulation tracks each photon pair individually and produces a list of all the pairs where both photons hit the detectors. The list includes the following information: the coordinates of the hits, the timestamp, and the final energies of the photons. N.B. the real detectors consider two hits to be coincident only when they come from different detector planes, their hit times are at most 2 ns apart, and there no other hits that could plausibly be coincident with either of the two hits being considered.

The kimberlite rock was a sphere 100 mm in diameter, the average material composition of kimberlite is listed in Table 1. The diamond was a sphere, its diameter and location within the rock was randomised for each simulation. There were two rectangular detector arrays separated by 300 mm. The detector pixels were 2.84 mm wide cuboid Bismuth Germanate crystals. They were arranged into a 16×16 grid coupled to a silicon photomultiplier (SiPM) with a 0.2 mm inter-crystal gap. The SiPMs were arranged into 4x4 grids called MinPET units (MPU) with 2 mm gaps, and a detector was an 8x6 array of MPUs with 5 mm gaps.

To take advantage of digital oversampling to improve the image quality, the detectors were rotated in tandem by one degree about the axis vertical to the virtual conveyor belt and again by one degree around the axis perpendicular to said belt. The belt speed was $1\,\mathrm{m\,s^{-1}}$. The initial distribution of flux was assumed to be uniform at $2.8 \times 10^{13}\,\mathrm{cm^{-2}}$, as this achieved the required activity yielding about 1 million coincidence lines per rock. Details of the PET isotopes and their reactions are recorded in Table 2. The hold hopper time was set to 23 min, this time was chosen to ensure maximum sensitivity for the carbon-11 signal considering the background isotope signals.

The distance per run was set to $0.2\,\mathrm{mm}$. The seeds were randomised for each simulation. The Geant4 simulations were validated in detail by benchmarking to experimental data [11].

Compound	Si_4O_2	MgO	CaO	CO_2	H_2O	Fe_2O_3	FeO
Mass Fraction (%)	42.6	28.6	5.3	5	5	4.7	3.3
Compound	Al_2O_3	TiO_2	K_2O	P_2O_5	MnO	Na_2O	
Mass Fraction (%)	2.5	1.8	0.7	0.2	0.2	0.1	

Table 1: Average mass-fractions of compounds found in Southern African kimberlite [12].

Reaction	$^{12}C(\gamma,n)^{11}C$	$^{16}O\ (\gamma,n\alpha)\ ^{11}C$	$^{16}O\ (\gamma,n)\ ^{15}O$	$^{40}Ca\ (\gamma,np)\ ^{38}K$	$^{54}Fe\ (\gamma,n)\ ^{53}Fe$	$^{46}Ti\ (\gamma,n)\ ^{45}Ti$
$\langle\sigma\rangle$ (mb)	0.188	0.001	0.180	0.112	1.42	1.61
$\tau_{1/2}$ (s)	1220	1220	122	458	510	11088

Table 2: PET-isotopes and their parent atoms with the effective reaction cross-section for photons from a $40\,\mathrm{MeV}$ electron beam and the resultant isotope half life, $\tau_{1/2}$. The effective cross section, $\langle\sigma\rangle$, combines the bremsstrahlung production probability with the cross section.

2.2 PET Image Reconstruction

This section describes how the 3D PET images were reconstructed. For the purposes of reconstruction the z-axis is defined as piercing the centres of both detectors, the x-axis is parallel to the conveyor belt, and the origin is at the centre of the space between the two detectors. The output of a simulation is a set of pairs of coincident photons. For each pair the line connecting the two hits is computed. A 4D sinogram is created by binning the lines according to their polar and azimuthal angles and the x and y coordinates of their intersection with the plane at $z = 0$ (the mid-plane). A MLEM algorithm computes the image from the 4D sinogram.

The first step after the simulation is to compensate for the motion of the rock. This entails identifying the time at which the rock was at the origin, t_{origin}, and shifting the coordinates (x, y, z) of each hit in the pair forward or backwards along the direction of travel according to the time when they were recorded, t_{hit}. The velocity of the rock, v_{belt}, a constant $1\,\mathrm{m\,s^{-1}}$, is decomposed into its x, y, and z components and the following equation, $x' = x + v_{belt}(t_{origin} - t_{hit})$, is used to compute the new (x', y', z') coordinates.

The second step is to create a 4D sinogram by binning the coincident pairs. First, for each coincident pair the line joining the two hits is computed so that the polar angle θ, azimuthal angle ϕ, and coordinates of intersection with the mid-plane, (x, y), can be derived. The equations for computing these values are elementary and not included here. Note that the positive z-axis was chosen to be $\theta = 0$ and the positive x-axis to be $\phi = 0$. Second, lines with a polar angle $\theta > \pi/4$ are discarded to emulate the trigger design in the real detector which does not reliably accept coincidence events where $\theta > \pi/4$. Third, the lines are binned according to their mid-plane intercepts. The bin width in the x and y axes was $2\,\mathrm{mm}$. Fourth, the lines are binned according to their polar angle θ. The bin width was $\pi/90\,\mathrm{rad}$. The polar bins were numbered from 0 to 44, with the 0th bin touching the z-axis. Fifth, the lines are binned according to their azimuthal angle ϕ. The bin width is dependant on the corresponding polar angle bin. This special binning divides a hemisphere into approximately equal chunks, not unlike an igloo's snow bricks. The number of azimuthal bins N_ϕ is computed using, round $\left(180 \cdot \sin\left(\frac{n_\theta}{45} \cdot \frac{\pi}{2}\right)\right)$, where n_θ is the polar bin, unless $n_\theta = 0$ in which case $N_\phi = 1$.

The third step is computing the PET image from the sinogram. For this purpose a basic MLEM algorithm was implemented in Python using the Astra Toolbox library [8] to make use of GPU accelerated matrix computation. The reconstruction volume was defined to be cube centred on the origin with side lengths of $300\,\mathrm{mm}$ (150 voxels). The image was initialised to have uniform PET activity and a uniform material density. The algorithm iterates on these to reconstruct the activity and material density from the data. Figure 1b shows an example of a PET image reconstructed using this process.

2.3 Data preparation

The global minimum and maximum values from all the PET images were extracted so that they could be rescaled to the interval $[0, 1]$ to improve numerical stability during training. 40 cubes with side lengths of $42\,\mathrm{mm}$ (21 voxels)

were sampled randomly from each image. It was ensured that 20 of the cubes contained the image's diamond and 20 contained kimberlite but never diamond. This was performed to increase the size of the data set and balance the dataset.

We ran 3000 simulations where the diameter of the diamond in mm was sampled uniformly from the half open interval $(0, 15]$. This provided $60\,000$ diamond containing cubes and $60\,000$ barren cubes. These cubes were used to train the models and validate the hyperparameters.

Ten sets of 301 simulations were run, within a given set the diamond diameter was constant. There was one set for each of the ten integer diameters from $1\,\mathrm{mm}$ to $10\,\mathrm{mm}$. Thus, in each set there were $12\,040$ cubes; half were diamond bearing, while half were barren kimberlite. This was done so that the performance metrics of the final model could be accurately measured for different sizes of diamond.

2.4 CNN Architecture and Hyperparameter Tuning

The CNN models were implemented in Python and used the Tensorflow and Keras APIs for GPU accelerated training. The activation function for every layer was the rectified linear unit (ReLU), except for the last layer which used the sigmoid activation function. The Adadelta stochastic gradient descent optimizer was used with learning rate initialised to 0.001 and decay rate set to 0.95. Binary cross-entropy was chosen as the loss function. The train/validation split was set to 2:1. The basic model, shown in Table 3, had an average pooling layer that downsampled the input layer to increase the speed of training at the cost of some accuracy. This was followed by two copies of the following: a convolution layer and a max pooling layer with valid padding to shrink the size of the dimensions. The fourth layer had two convolution layers in sequence followed by a max pooling layer like the second and third layers. The final three layers flattened the output then applied two fully connected layers with 64 and 1 nodes respectively.

Grid search was employed to find the best combination of hyperparameters. The grid was composed from the following selections of hyperparameters: adding up to 6 copies of the fourth layer; setting the number convolution kernels per layer: 64, 128, 256; changing the number of training epochs: 10, 15, and 20; changing the batch size: 10 and 15; applying gaussian smoothing to denoise the images or not; and excluding images that contained diamonds smaller than 5 mm in diameter or not.

Layer	Type	Window Size	Stride	Padding	Activation	Output shape	Kernels
0	Input					21x21x21	
1	Average pool	2x2x2	2x2x2	same		11x11x11	
2 a	Convolution	3x3x3	1x1x1	same	ReLU	11x11x11	256
2 b	Max pool	2x2x2	1x1x1	valid		10x10x10	
3 a	Convolution	3x3x3	1x1x1	same	ReLU	10x10x10	256
3 b	Max pool	2x2x2	1x1x1	valid		9x9x9	
4 a,b	2x Convolutions	3x3x3	1x1x1	same	ReLU	9x9x9	256
4 c	Max pool	2x2x2	1x1x1	valid		8x8x8	
5	Flatten					256	
6	Fully Connected				ReLU	64	
7	Fully Connected				Sigmoid	1	

Table 3: Structure of the basic CNN classifier.

3 Results and Discussion

The grid search hyperparameter tuning scheme devised in the preceding section succeeded in finding a model that achieved an accuracy on the validation set of 0.9989. This model had 6 extra copies of the fourth layer and 256 kernels in each convolution layer. The model was trained for 20 epochs on data that had not been denoised with gaussian smoothing on a batch size of 15. Lastly, the training data did not include cubes that contained diamonds with diameters smaller than 5 mm. This model's performance metrics on the ten test datasets is recorded in Figure 2. The model's recall scores suggest that it can find 98% of all diamonds that are $5\,\mathrm{mm}$ or larger in diameter. However, there is a precipitous drop in the recall score when it is tested on diamonds smaller than $5\,\mathrm{mm}$ in diameter. Only 3 false positives were recorded across all ten test datasets, which is very promising and implies that the model's threshold for labelling a cube as diamond containing was high and favoured correctly rejecting barren cubes rather than correctly accepting small diamonds. The low ROC AUC scores for diamonds smaller than $5\,\mathrm{mm}$ in diameter reinforce this point. The accuracy curve combines the results of the recall and false positives

rates and reinforces them. The final results of this study show that the model was able to learn to distinguish between diamond bearing and barren cube samples.

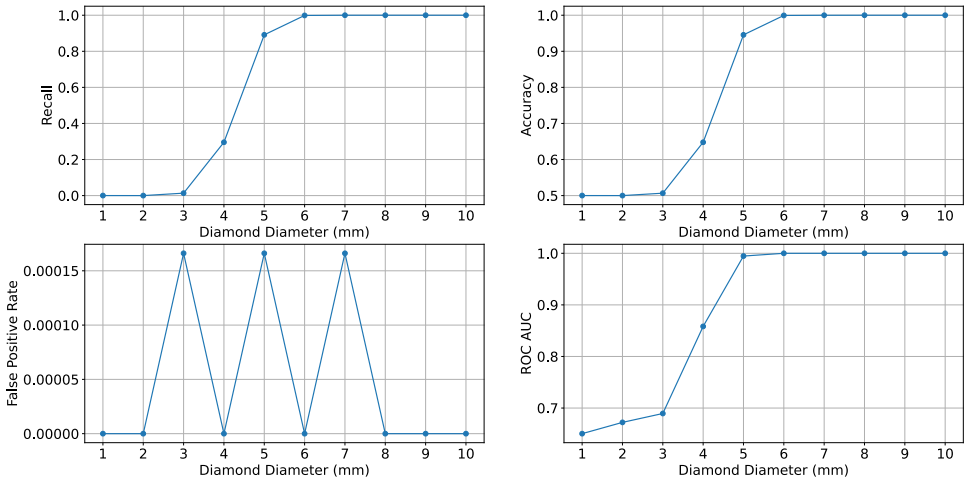

Figure 2: Plots showing test data performance of best performing CNN model: Recall (upper left), Accuracy (upper right), FPR (lower left), and ROC AUC (lower right).

While the results of this study are promising there are still limitations that affect how reliable the results are. The training data consisted of small cubic samples of the PET images and not the whole image, thus the model is not production ready. More realistic simulations would contain naturally shaped rocks and diamonds instead of perfect spheres. Lastly, such simulations would also have many more rocks and the spatial distribution of the PET isotopes within them would not be uniform. This increase in realism would require models to adapt to new image artefacts, such as gaps between rocks, that are not present in the simplistic simulations.

The AI training methodology and hyperparameter tuning scheme have their own limitations. The default learning rate in Keras was used for the Adadelta optimiser, and tuning this could significantly improve the model's performance and affect convergence speed. Cross-validation was not performed during hyperparameter tuning, which would provide a better assessment of general model performance. The number of kernels was the same for all the convolution layers, and so in future work we would choose to optimise each layer individually as this may increase convergence speed. There are better tools and algorithms for conducting the hyperparameter tuning that would allow a more efficient exploration of the hyperparameter space and in so doing lead to better tuned models.

Another limitation speaks to the current model architecture, which could be investigated more thoroughly. Including a dropout layer would introduce a source of regularisation, while removing the average pooling may improve model performance. We lack insight into whether the model is basing its score on diamond voxels or nearby artefacts, investigating this could be done with class activation mapping techniques like Gradient-weighted Class Activation Mapping (Grad-Cam) [13].

Furthermore, the basic CNN in this study was inspired by a model used for classifying lung nodules [14], however there are other more sophisticated models for computer vision such as Residual Networks (RES-Net [15], Visual Geometry Group networks (VGG) [16], and YOLO [17]. Applying transfer learning to them or borrowing elements of their design into our architecture could lead to significant improvements in model performance.

4 Conclusion

This study has provided ample evidence that a CNN classifier can be trained to distinguish between diamond bearing and barren samples of kimberlite. The process of synthesizing the data and training the model is valid. The best performing model achieved a recall of 0.98 on diamonds $5\,\mathrm{mm}$ (1.14 ct) in size and larger. It achieved a false positive rate much lower than 1 in 1000. These results are promising and suggests that similar or better performance may be expected for models trained on more realistic data. The next steps are increasing the realism of the simulations as discussed in section 3, changing the training data from small cubic samples to full PET images, and investigating more sophisticated model architectures.

References

[1] E. Chinaka, Z., Zibi, J. V. Rooyen, S. Connell, and M. Cook, "Radiation Shielding Analysis and Optimisation for the MinPET Kimberlite Sorting Facility Using the Monte Carlo Calculation Code, MCNPX," in *The Proceedings of SAIP2016*, 2016, pp. 386–391.

[2] M. Cook, M. Tchonang, E. Chinaka, M. Bhamjee, F. Bornman, and S. Connell, "Overview of the Mineral-PET Run-of-Mine Diamond Bearing Rock Sorter," in *The Proceedings of SAIP2016*, 2016, pp. 479–484.

[3] M. Cook, "Remote Detection of Light Elements Using Positron Emission Tomography," PhD thesis, University of Johannesburg, 2014.

[4] A. B. Tufail, Y.-K. Ma, M. K. A. Kaabar *et al.*, "Classification of Initial Stages of Alzheimer's Disease through Pet Neuroimaging Modality and Deep Learning: Quantifying the Impact of Image Filtering Approaches," *MATHEMATICS*, vol. 9, no. 23, DEC 2021.

[5] G. Castellano, A. Esposito, E. Lella, G. Montanaro, and G. Vessio, "Automated detection of Alzheimer's disease: a multi-modal approach with 3D MRI and amyloid PET," *SCIENTIFIC REPORTS*, vol. 14, no. 1, MAR 3 2024.

[6] M. H. Sadeghi, S. Sina, M. Alavi, and F. Giammarile, "The OCDA-Net: a 3D convolutional neural network-based system for classification and staging of ovarian cancer patients using [18F]FDG PET/CT examinations," *ANNALS OF NUCLEAR MEDICINE*, vol. 37, no. 12, pp. 645–654, DEC 2023.

[7] S. Agostinelli et al. (GEANT4 Collaboration), "GEANT4: A Simulation Toolkit," *Nuclear Instruments and Methods in Physics Research*, vol. A 506, pp. 250–303, 2003.

[8] W. V. Aarle, W. Palenstijn, J. Cant, E. Janssens, F. Bleichrodt, A. Dabravolski, J. D. Beenhouwer, K. Batenburg, and J. Sijbers, "Fast and Flexible X-ray Tomography Using the ASTRA Toolbox," *Optics Express*, vol. 24, pp. 25 129–25 147, 2016.

[9] M. Abadi, A. Agarwal, P. Barham *et al.*, " TensorFlow: Large-Scale Machine Learning on Heterogeneous Systems," 2015, software available from tensorflow.org. [Online]. Available: https://www.tensorflow.org/

[10] F. Chollet *et al.*, "Keras," https://keras.io, 2015.

[11] T. Nemakhavhani, D. Unwuchola, R. Andrew, M. Cook, S. Connell, S. Ballestrero, U. Uggerhøj, S. Møller, P. Aggerholm, N. Hertel, and J. Swartz, "The MinPET Diamond Discovery Technique," *Submitted to the Proceedings of the SAIP2017, the 62nd Annual Conference of the South African Institute of Physics,(Stellenbosch/2017)*, 2018. [Online]. Available: http://events.saip.org.za

[12] M. Tchonang, M. C. F. Bornman, S. Connell, and S. Ballestrero, "Elemental Analysis of Kimberlite and Associated Country Rock," *Proceedings of SAIP2013: the 58th Annual Conference of the South African Institute of Physics, edited by Roelf Botha and Thulani Jili, ISBN: 978-0-620-62819-8.*, pp. 502–506, 2014. [Online]. Available: http://events.saip.org.za

[13] R. R. Selvaraju, M. Cogswell, A. Das *et al.*, "Grad-CAM: Visual Explanations from Deep Networks via Gradient-Based Localization," *International Journal of Computer Vision*, vol. 128, no. 2, p. 336–359, Oct. 2019. [Online]. Available: http://dx.doi.org/10.1007/s11263-019-01228-7

[14] J. Dewit, "2nd Place Solution for the 2017 National Datascience Bowl," https://juliandewit.github.io/kaggle-ndsb2017/, 2017, accessed: 2024-07-29.

[15] K. He, X. Zhang, S. Ren, and J. Sun, "Deep Residual Learning for Image Recognition," 2015. [Online]. Available: https://arxiv.org/abs/1512.03385

[16] K. Simonyan and A. Zisserman, "Very Deep Convolutional Networks for Large-Scale Image Recognition," 2015. [Online]. Available: https://arxiv.org/abs/1409.1556

[17] J. Redmon, S. Divvala, R. Girshick *et al.*, "You Only Look Once: Unified, Real-Time Object Detection," 2016. [Online]. Available: https://arxiv.org/abs/1506.02640

IoT-Based Environmental Conditions Monitoring of a Sawtooth Greenhouse: A Foundation for Anomaly Detection and Computational Fluid Dynamics

Abdool Sattar Cassim[1], Emmanuel Igumbor[1], Simon Henry Connell[1], Michael Rudolph[2], Rethabile Kgolobe[3], Charis Harley[3], Muaaz Bhamjee[4], and Tim Brooks[1]

[1]Department of Mechanical Engineering Science, University of Johannesburg, Johannesburg, South Africa
[2]Centre for Ecological Intelligence, University of Johannesburg, Johannesburg, South Africa
[3]Department of Electrical and Electronic Engineering Science, University of Johannesburg, Johannesburg, South Africa
[4]Clean Energy Research Group, Department of Mechanical and Aeronautical Engineering, University of Pretoria, Pretoria, South Africa

E-mail: abdoolsattarcassim@gmail.com

Abstract. There is a shortage of food production in the world, and the United Nations has predicted that if there is no conscious mitigation plan, the world may face food limitations in the future. One of the strategies adopted to mitigate the shortage of food production is the greenhouse intervention. However, it is necessary to understand the environmental conditions required to ensure optimal crop production in a typical greenhouse. A fourth industrial revolution technology, namely the Internet of Things was used to measure the internal environmental conditions (temperature and relative humidity), of a greenhouse. This was combined with climate data. The work was performed at a sawtooth-shaped greenhouse at the Centre for Ecological Intelligence at the University of Johannesburg. The high temperatures of $40\,^{\circ}\mathrm{C}$ and the low relative humidity of 20% found during the day in some locations make the environment suitable only for crop varieties grown in dry climates. Tomatoes in hotter and drier locations were observed to have poorer health than in other locations. The measured data inside the greenhouse have larger temperature and humidity ranges than the ERA5-Land data for the local environment. Spectrum analysis was also performed. The results indicate the need for a control system to manage the irrigation schedule, fertiliser treatment, and vent openings. The study is designed to progress onward to decision support by AI, informed by computational fluid dynamics modelling. Ultimately there would be an optimisation of the various strategies for controlling the growth conditions.

1 Introduction

Due to the increase in population and severe climate change, Africa and the rest of the world face a persistent food shortage, and many citizens live in food insecurity [1]. Unpredictable weather patterns from the consequences of climate change, among others, further exacerbate the food production crisis [2]. Until now, farmers in Africa have relied mainly on traditional farming methods. The industrialisation of farming has resulted in significant mechanization, which results in higher fossil fuel usage and non-tailored agricultural practices to specific crops [3]. This also results in over-fertilising and watering based on uniform crop needs, which may sometimes lead to food

waste, poor crop quality, and water waste [4], as well as run-off pollution to water sources [5]. As such, traditional farming methods are losing traction in the realm of smart agriculture [6].

Smart agriculture involves collecting data to generate insight into environmental conditions and their impact on the production of agricultural produce. Internet of Things (IoT) technologies such as microcontrollers and sensors can be used to collect data as they are capable of providing real-time monitoring of plant health, soil moisture, temperature, relative humidity (RH), and CO_2, which dictate crop growth quality [7]. This ensures improved crop health by incorporating data into a larger intelligent control ecosystem. In addition, it facilitates a significant reduction of water waste, efficient control of fertilizer resources, and an increase in crop growth yield and quality [8]. However, the installation of IoT is challenging to implement in large area farms, where there is no closed area or controlled climate. As such, greenhouses are gaining interest as a technology that is used to improve controlled farming systems by providing a controlled environment that is otherwise difficult to achieve in the outdoors. This level of control can provide suitable climate conditions for crop production. Controlling environmental conditions could be efficient if a well-assisted natural circulation is implemented through an effective vent design. Important factors in greenhouse design include the shape of the roof opening, which influences aerodynamics and consequently natural cooling, as well as the greenhouse cover material for solar absorption. These can be optimised through computational fluid dynamics (CFD).

CFD is a numerical computer-aided method that provides numerical approximate solutions to the Navier-Stokes equations, including coupled physics such as heat and mass transfer [9]. CFD has been implemented to simulate various weather patterns in greenhouses, providing the efficient design of greenhouse environmental conditions and performance [10]. A CFD model of a greenhouse can be developed using temperature, RH, and airflow measurements as boundary and validation inputs, alongside detailed information on the greenhouse geometry, ensuring that simulations accurately represent the measured environmental conditions and can be validated against real data. IoT, CFD, and novel Machine Learning (ML) techniques can be combined into a digital twin of a greenhouse fed on real-time data. The digital twin can predict changing weather patterns, help farmers increase crop yield, and reduce resource wastage. Recently, an environmental monitoring sensor which utilises electronic and fiber optic sensors has been deployed at CERN to monitor RH and temperature distribution in ATLAS Inner Tracker [11]. This same analytical method and technology were deployed to a typical greenhouse to monitor its environmental conditions. While IoT implementation has been covered extensively in [12, 13, 14, 15], most researchers do not apply the technology to large-scale greenhouses, especially those having natural ventilation, such as sawtooth greenhouses. Additionally, data collection timeframes are often very short in most literature, with little detailed data analysis provided to explain how the collected data is refined. Data pre-processing is a crucial step for CFD and ML applications for increased accuracy and validity. Lastly, no papers use Fast-Fourier Transform (FFT) analysis to assess greenhouse data especially for double-roofed sawtooth greenhouses and validated with climate data.

In this study, an in-house sensor was used to investigate the temperature and RH profile of a novel sawtooth greenhouse. IoT techniques and data analysis were employed to determine the best placement for specific plant selection based on the measured internal greenhouse temperature, RH, and pressure conditions. An in-depth error analysis and processing methodology using Savitzky-Golay smoothing was developed. The results obtained form a starting point for CFD modelling, further incorporated into a digital twin of the greenhouse.

2 Methodology

A greenhouse located at the Centre for Ecological Intelligence (CEI) at the University of Johannesburg Bunting Road Campus (Latitude -26.18955, Longitude 28.01157) was used for this study. It is 23 metres long and 18.65 metres wide, with a height of 6.3 metres. Various crops, including tomatoes, basil, eggplant, and radish, are cultivated in the greenhouse. As shown in Figure 1, the greenhouse is a double-roofed, sawtooth-type greenhouse where the roofs have a half-Rankine aerodynamic shape. The expectation is that when the wind flows over the roof, it creates vortices (shown as swirls on the vents) that refresh the internal air by bringing cool air into the interior (blue arrows) and sucking hot air out of the interior (red arrows). Figure 1 presents a preliminary CFD result of the greenhouse using the final dataset from this study, serving as a proof-of-concept for the integration of IoT data with the methodology presented in this paper.

Wio terminals are part of the SEEED Wio family [16]. It generally refers to a series of IoT development boards. The Wio terminal acts as a module that is designed for quick prototyping and easy integration into various IoT applications. These boards are particularly known for their wireless communication capabilities, compact design, and ease of use. The Wio terminals use an ATSAMD51 microcontroller and support an I2C connection. These Wio terminals, with their peripherals, were used as data logging devices with digital output BME280 dual temperature and RH sensors. The terminals were connected via a WiFi network to a cloud that logs data remotely from the sensors to a ThingSpeak [17] dashboard that can be downloaded for analysis. The temperature and RH readings were generated.

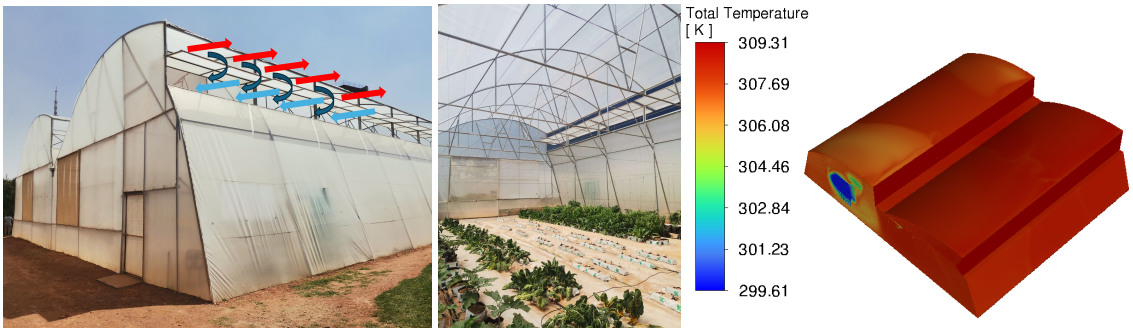

Figure 1: (*left*) CEI Agrihub Sawtooth greenhouse at University of Johannesburg. Note the vents which form part of the aerodynamic roof shape. The swirls represent vortices that bring cool air into the greenhouse and flush out hot air, which is represented by red arrows, to the outside. (*middle*) Internal structure of the greenhouse with various crops within the greenhouse. (*right*) Preliminary CFD result conducted on the greenhouse using afternoon conditions as boundary conditions.

The sensors were used to log data over fifty days to obtain meaningful results of temperature and RH fluctuations in the greenhouse in three primary locations over the length of a tomato crop along the greenhouse. The data collected was then passed through a series of data analysis steps to refine data quality and determine the temperature and RH profiles. Once the data for a single location is downloaded, it is segmented into separate days, where each day's data is binned into minutes. The average temperature and RH are then calculated for each bin to produce an average $24\,\mathrm{h}$ temperature and RH profile of the greenhouse. Thereafter, the average profiles were calculated by taking the average of all three locations to produce a single profile for temperature and RH. The data is filtered for outliers and smoothed using a Savitzky-Golay filter. The smoothed data is then treated as the null hypothesis in a likelihood fit (Chi-squared) of the data. The error bars are determined by linear scaling (with an offset) to achieve a reduced chi-squared value of unity where the smoothed curve forms the null hypothesis (pre-accepted by inspection). The results can be seen in Figure 2. The plot is compared to data from ERA5-Land [18] 2m near-surface air temperature (T_{2m}) and RH data for trend verification. This comparison is also shown in Figure 2. A Fast Fourier Transform (FFT) is used to search for daily and any possible other frequency components.

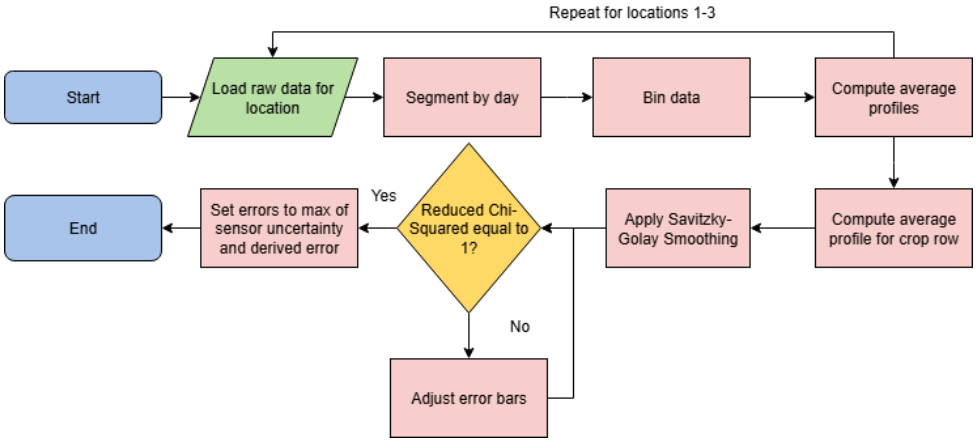

Figure 2: Data analysis process used in study to produce average temperature and RH profiles.

3 Results and Discussions

The results of this study are divided into two components: temperature and RH results obtained, and the FFT plots for analyzing the cyclical variations present in the greenhouse climate. The RH for ERA5-Land was calculated

from the dewpoint and the temperature using the Magnus formula [19]:

$$\gamma(T, RH) = \ln\left(\frac{R_H}{100}\right) + \frac{bT}{c+T}, \quad T_{d_p} = \frac{c\,\gamma(T, RH)}{b - \gamma(T, RH)} \tag{1}$$

where the constants are $b = 17.625$ and c =243.04 °C. The ERA5-Land T_{2m} and the 2m dewpoint temperature represent the temperature (T) and the dewpoint temperature (T_{dp}), respectively, as input in equation 1 for $\gamma(T, RH)$ and T_{d_p} to solve for the RH.

3.1 Temperature and RH distribution in the greenhouse

Figure 3 shows the average temperature and RH profiles in the greenhouse. Furthermore, the plot of ERA5-Land for temperature and RH was included. The sensor reading in the greenhouse suggests an increase in temperature during sunrise. However, during dawn, there was a drop in temperature. Similar behaviour was noticed for the ERA5-Land temperature distribution. However, the greenhouse retains a higher temperature than the outside around 00:00 hours. This is due to the greenhouse obtaining high solar gains in the daytime and retaining the heat. Additionally, the temperature increase is more pronounced than the outside, showing the efficacy of solar retention within the greenhouse. This is also noted from the longer heat retention shown from daytime to later, from 18:00 to 22:00 hours. The maximum temperature of 40 °C is relatively high. This suggests that careful selection of plants that may not be adversely affected by high temperatures should be introduced into the greenhouse. For example, well-known crops that can tolerate high temperature 35 °C-45 °C such as okra (Abelmoschus esculentus) [20], eggplant (Brinjal/Solanum melongena) [21], sweet potato (Ipomoea batatas) [22], hot peppers/Chili (Capsicum spp.) [23], tomato and maize [24] should be candidates to thrive in the studied greenhouse. A drop in temperature was also noticed during the midday peak. Several factors are speculated to have contributed to this. For instance, the sensors may have suffered a drift due to overheating or improper solar shielding, leading to a dip in the temperature. Similarly, sensor placement within the greenhouse may have influenced this drop as the developed microclimate in one part of the greenhouse may differ from the other areas. Furthermore, during midday, there was an irrigation schedule, and due to the hot temperature, the water began to evaporate, which caused a fogging effect in the greenhouse. This is consistent with observations from Kumar *et al.* [25]. In addition, the roof shape and vent could also play a role in the dip in temperature because the roof provides a shading impact at this time. However, more sensors and longer data collection period would be needed to rule out any causes of the dip. Additionally, CFD can provide more insight into the temperature dip. These limitations will be addressed in future studies and their implications on the crops.

The sensor's RH profile, obtained as shown in Figure 3, is consistent with ERA5-Land RH measurements. This suggests that the obtained data are accurate. There was a relatively high RH at night. The effect of the high temperatures can be seen on the moisture and RH conditions. The RH distribution is as low as 10% during midday. Additionally, the rise in RH at midday, complementary to the drop in temperature, can be seen, which supports the idea of evaporation creating the dip at these times. However, the vents do not appear to provide enough cooling in these locations, possibly due to the wind patterns during the data collection period.

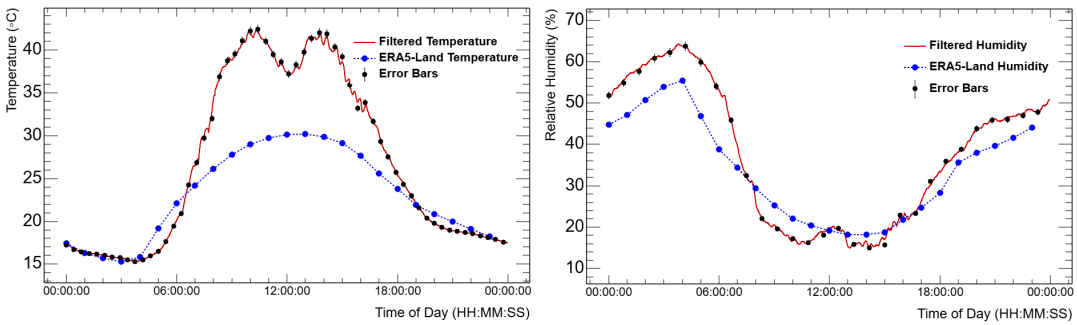

Figure 3: The plots of the average (*left*) temperature, and (*right*) RH profiles for a single row in the greenhouse.

3.2 FFT Analysis

Figure 4 shows the plots of the FFT of the ERA5-Land and sensor data collected from the greenhouse with amplitude in degrees Celsius. The ERA5-Land spectrum shows a strong peak at one cycle/day, which is the diurnal temperature variation expected from day/night variation. The higher order harmonics are resulting from harmonic distortion caused by a non-sinusoidal shape. The sensor's greenhouse FFT spectrum shows a strong peak at one cycle/day, which is coherent with the ERA5-Land data and expected from diurnal changes. Additionally, there

is an indication of a 2-cycle/day peak, from the double peak resulting from the midday dip seen in the average temperature profile. The one cycle/day peak from the measured data is much higher than the ERA5-Land, showing the increased solar gain in the greenhouse as compared to the outside.

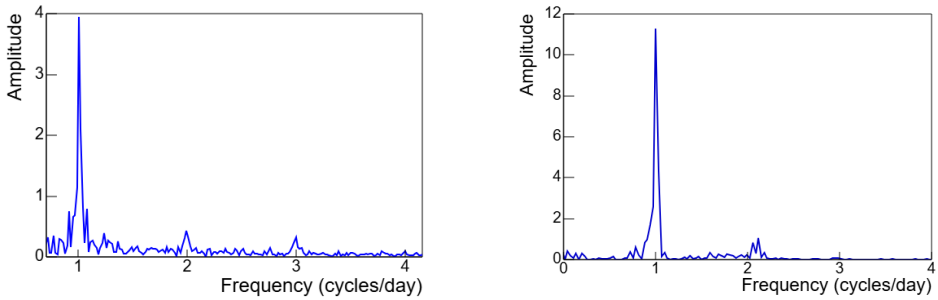

Figure 4: The FFT plots of (*left*) ERA5-Land data, and (*right*) data from the sensor in the greenhouse. The amplitude is in degrees Celsius

Overall, the greenhouse retains high temperatures in the day and high RH at night. There is no evidence of the expected cooling effect from the vents. The results of this study are important as they will serve as the basis for future studies by applying CFD, which can then further support the strategic design of the greenhouse. Furthermore, IoT sensor technology has been used to monitor the temperature and RH distribution in a greenhouse, and the likelihood of selected crops being cultivated in the greenhouse was proposed.

4 Conclusion

IoT sensors were used to quantify the temperature and RH profiles. The temperature and RH environmental conditions of the greenhouse were collected for fifty days. The obtained results show that during the day at midday, the temperature could rise to $45\,^{\circ}\mathrm{C}$, which is higher than the ERA5-Land maximum of $30\,^{\circ}\mathrm{C}$. This was reflected in the measured data FFT spectrum having a higher power magnitude than ERA5-Land. However, during the night the temperature was as low as $15\,^{\circ}\mathrm{C}$. The high temperature could be beneficial to the cultivation of heat-tolerant crops. The RH levels in the position of the row of tomato crops were not consistent in higher temperature ranges, leaving the plants suitable for this area of the greenhouse limited to high-temperature-resilient crops. The framework presented in this study provides a more robust statistical mechanism for analysing greenhouse data which in principle should lead to better quality data that can be used as input and validation data for CFD and ML workflows. Future studies will build on this data and include companion CFD studies that will determine the optimal vent positions in the greenhouse for air circulation and cooling. Data collected using the IoT system can validate the CFD results so that it reflects real-time behaviour as demonstrated in the preliminary CFD for the afternoon conditions. An ML model that can predict internal weather patterns using weather station data and the current real-time data being collected will be deployed. This will lead to real-time decision-making tools for water schedules, to provide optimal water usage, and prevent crop wastage. Together with the CFD, this will form a digital twin of the greenhouse fed by real-time data, whilst using high-performance computing capabilities to infer plant health from environmental monitoring tools. This can provide the necessary information to help improve crop production.

5 Acknowledgment

The authors acknowledge the support of the Centre for Ecological Intelligence (CEI) and the University of Johannesburg in this study. Opinions expressed and conclusions arrived at are those of the authors and are not necessarily to be attributed to the CEI, the University of Johannesburg, or the University of Pretoria.

References

[1] E. Abbade and H. Dewes, "Food insecurity worldwide derived from food supply patterns," *Food Security*, vol. 7, pp. 109–120, 2015.

[2] J. Verschuur, S. Li, and P. Wolski, "Climate change as a driver of food insecurity in the 2007 lesotho-south africa drought," *Scientific Reports*, vol. 11, p. 3852, 2021.

[3] R. Singh and G. Singh, "Traditional agriculture: a climate-smart approach for sustainable food production," *Energy, Ecology and Environment*, vol. 2, pp. 296–316, 2017.

[4] M. Girma and A. Jemal, "Irrigation system in israel: A review," *International Journal of Water Resources and Environmental Engineering*, vol. 7, pp. 29–37, 2015.

[5] I. Zahoor and A. Mushtaq, "Water pollution from agricultural activities: A critical global review," *International Journal of Chemical and Biochemical Sciences*, vol. 23, pp. 164–176, 2023.

[6] D. Avgoustaki and G. Xydis, "How energy innovation in indoor vertical farming can improve food security, sustainability, and food safety?" *Advances in Food Security and Sustainability*, vol. 5, pp. 1–51, 2020.

[7] C. Maraveas and T. Bartzanas, "Application of internet of things (iot) for optimized greenhouse environments," *AgriEngineering*, vol. 3, pp. 954–970, 2021.

[8] A. Ikram, W. Aslam, and R. Aziz, "Crop yield maximization using an iot-based smart decision," *Journal of Sensors*, vol. 2022, p. 2022923, 2022.

[9] E. Khalil, "Cfd history and applications," *CFD Letters*, vol. 4, p. 1, 2021.

[10] G. Martin and D. Monfet, "High-density controlled environment agriculture (cea-hd) air distribution optimization using computational fluid dynamics (cfd)," *Engineering Applications of Computational Fluid Mechanics*, vol. 18, p. 2297027, 2024.

[11] L. Scherino, E. Schioppa, A. Arapova, and G. Berruti, "Fiber optic sensors in the atlas inner detector," *Nuclear Instruments and Methods in Physics Research Section A*, vol. 1029, p. 166470, 2022.

[12] S. Asane, S. Salve, S. Birajdar, S. Borkar, and P. Gawali, "Iot-driven smart greenhouse system for real-time environmental monitoring," *European Journal of Science, Research and Review*, 2025. [Online]. Available: https://www.wisdomgale.com/ejsrr/?mno=302657922

[13] S. Mondal and M. Patil, "Iot-enabled smart greenhouses: Real-time environmental monitoring and climate control," in *SHS Web of Conferences*, vol. 216, 2025, p. 01067.

[14] M. Moreno, O. Suarez, and A. Garcia, "Iot-based automated greenhouse for deep water culture hydroponic system," in *2021 2nd Sustainable Cities Latin America Conference (SCLA)*, 2021, pp. 1–6.

[15] M. Thillai Rani, S. Rahul, S. Govardhan, S. Velmurugan, J. Rejina Parvin, P. Rohini, and R. Rajkumar, "Iot based smart and economic greenhouse monitoring and auto-tuned control system for rural farming," *Journal of Theoretical and Applied Information Technology*, vol. 102, 2024.

[16] Seeed Studio. (2023) Wio terminal introduction. [Online]. Available: https://wiki.seeedstudio.com/Wio_Terminal_Intro/

[17] MathWorks. (2023) Thingspeak iot analytics platform. [Online]. Available: https://thingspeak.mathworks.com/

[18] J. Muñoz Sabater, "Era5-land hourly data from 1950 to present," 2019.

[19] M. Lawrence, "The relationship between relative humidity and the dewpoint temperature in moist air: A simple conversion and applications," *Bulletin of the American Meteorological Society*, vol. 86, pp. 225–234, 2005.

[20] S. Benchasri, "Okra (abelmoschus esculentus (l.) moench) as a valuable vegetable of the world," *Ratarstvo i povrtarstvo*, vol. 49, pp. 105–112, 2012.

[21] F. Shimira and H. Taskin, "Current progress on the responses of eggplant to ultra-low temperatures during production," *Horticultural Studies*, vol. 39, pp. 1–7, 2022.

[22] G. Sun, Y. Gou, and L. Zhang, "Effects of different temperatures on the physiological characteristics of sweet potato (ipomoea batatas l. lam) storage roots and growth of seedlings during the sprouting and seedling period," *Plants*, vol. 14, p. 868, 2025.

[23] R. Rosmaina and Z. Zulfahmi, "Temperature critical threshold for yield in chili pepper (capsicum annuum l.)," *SABRAO Journal of Breeding and Genetics*, vol. 54, pp. 627–637, 2022.

[24] T. Zhu, C. Fonseca De Lima, and I. De Smet, "The heat is on: how crop growth, development, and yield respond to high temperature," *Journal of Experimental Botany*, vol. 72, pp. 7359–7373, 2021.

[25] K. Srinivas Kumar, M. Jha, K. Tiwari, and A. Singh, "Modeling and evaluation of greenhouse for floriculture in subtropics," *Energy and Buildings*, vol. 42, pp. 1075–1083, 2010.

Extraction of Natural Dye from Bidens pilosa: Solvent Effects and Dye Adsorption on TiO_2 Nanoparticles for Dye-sensitized Solar Cell Applications

R.R Randela[1], T.S Ranwaha[1] L.M Mathomu[2], R.R Maphanga[3,4] and N.E Maluta[1,3]

[1]Physics Department, University of Venda, Thohoyandou, 0950, South Africa
[2]Department of Biochemistry and Microbiology, University of Venda, Thohoyandou, 0950, South Africa
[3]National Institute for Theoretical and Computational Sciences (NITheCS), Gauteng, 2000, South Africa
[4]Next Generation Enterprises and Institutions Cluster, Council for Scientific and Industrial Research, Pretoria 0001, South Africa

E-mail: ronelronella.randela@univen.ac.za

Abstract. Organic plant-based dye for dye-sensitized solar cells (DSSCs) has gained great interest due to their low cost of manufacturing and environmental friendliness. Most plants in nature contain pigments such as chlorophyll, anthocyanin and betalain that can be used in DSSCs. In this study, the solvents used to extract dye from *B. pilosa* leaves as a sensitizer for DSSC were MeOH and water. The dye extracted from *B. pilosa* contained chlorophyll. MeOH was more efficient than water according to the noted absorbance at 665 nm. The molecules responsible for exhibiting a broader range of absorbance is known to be pheophytin found within the chlorophyll extracted from the *B. pilosa* plant. Furthermore, the optical properties using density functional theory (DFT) were computed to optimize the properties of pheophytin. The UV-Vis optimization indicated the absorbance at 450 – 700 nm while the energy gap was observed at 2.06 eV. The experimental and the theoretical UV-Vis analysis outcomes agree, and the study shows that the dye molecule from *B. pilosa* is an efficient sensitizer for DSSCs.

1 Introduction

The utilization of titanium dioxide (TiO_2) as a fundamental semiconductor for the dye-sensitized solar cells has been an included advantage because it can be synthesized utilizing either natural or inorganic strategies. As of now, investigations are towards the green synthesis of TiO_2 to moderate climate change since green synthesis processes are eco-friendly and non-toxic [1]. The interest in the field of green nanomaterials has significantly increased in recent years [2-4]. A strong motivation for this interest is that nanoparticles regularly have physical and chemical properties different from those made by large-scale materials, which generates a variety of unused potential applications in different areas of innovation [3,4]. The improvement of techniques for nanosized powders has become increasingly important due to their characteristics, which include a high surface area, enhanced homogeneity, and uniform chemical composition.

Dye Sensitized Solar Cells (DSSCs) are mostly sensitized by chemical synthetic dyes since their photoelectric transformation effectiveness can reach 11 – 12% [5]. However, these kinds of synthetic dyes have high production costs and can effortlessly cause natural contamination; in comparison, natural products and vegetables are irreplaceable. Besides, they are natural, easily reachable, and cheap. Hence, natural products can decrease the cost of DSSCs and accomplish more economical and natural protection effects.

In this study, the synthesis and characterization of the TiO_2 nanoparticle from *B. pilosa* plant extract was performed. The presence of chlorophyll pigment in the extract was identified with the help of UV-VIS spectroscopy and Fourier Transform Infrared Spectroscopy (FTIR). The characterization studies of TiO_2 nanoparticles were also carried out.

2 Methodology

2.1 Experimental method

2.1.1 Preparation of B. pilosa plant extracts The plant was collected at the University of Venda at the site of an agricultural field. The plant was washed using deionized water (DI) several times and was left to dry in the laboratory at room temperature until all the moisture contents of the roots were removed. The dried leaves were ground into fine powder using a pestle, a mortar, a household blender and a small sieve. The extraction process was performed by mixing 10% (w/v) of powder of leaves with MeOH in a 50 mL conical tube; similarly, it was done for DI. After 24 hours on a rotating platform, the centrifugation process was performed to separate the liquids from the solid-liquid mixture at a speed of 5000 rpm for 15 minutes. Finally, the solid residues were filtered using a 0.22 μm syringe filter to acquire a purely natural dye solution. The extracts were characterized using a UV-Vis spectrophotometer.

2.1.2 Preparation of TiO_2 nanoparticles The TiO2 NPs were prepared by dissolving 5 g of titanium (iv) oxide into 225 mL of DI under magnetic stirring for 4 hours. Then, 25 ml of the extract was slowly added and placed in a shaking incubator machine for 24 hours at room temperature. The colour of the resulting solutions changed from milky white to green after adding the extracts, and then from green to brown after 24 hours. The color change is mainly due to the reduction of the metal ions (Ti4+), which indicates the formation of TiO_2 NPs [6]. The watch glasses were used to dry the solutions in an Ecotherm oven at a temperature of 180 °C. The synthesized nanoparticles were characterized using a spectrophotometer, and the dried samples were characterized using a scanning electron microscope (SEM), Fourier Transform Infrared Spectroscopy (FTIR) and X-ray diffraction (XRD).

2.2 Computational method

The structure of the dye molecule was built using Material Studio on a 3D atomistic window. Material Studio software was used for the simulation of the absorption bands and optical absorption, respectively. The optical properties of the dye molecule were performed using first-principles calculations based on density functional theory (DFT), which uses a plane-wave pseudopotential method. We used generalized gradient approximation (GGA) in the scheme of Perdew-Burke-Ernzerhof (PBE) to describe the exchange-correlation function using the coarse quality and all band/EDFT as an electronic minimizer [7]. The calculations of HOMO-LUMO and UV-Vis of dye molecules were performed using Valence Approximate Molecular Orbital Package (VAMP) Module.

3 Results and Discussion

3.1 Absorption Spectrum of dye molecules

The absorption spectra of extracted dye from *B. pilosa* using different solvents were compared as shown in Figure 1(A and B) and Figure 2. Chlorophyll extracted from *B. pilosa* indicates the wide absorption which ranges from 350 nm to 700 nm. The absorbance of the dye shows a broad range of wavelength frequency between 395 nm to 665 nm, which is located within the visible range, and with three main peaks located at 420, 530 and 665 nm.

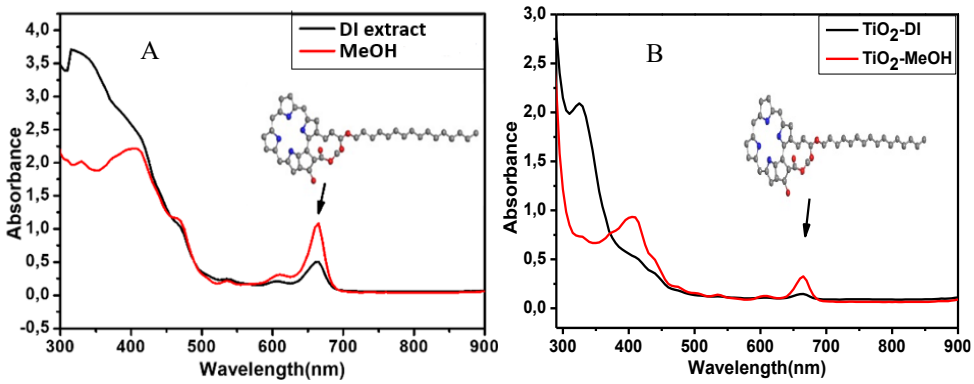

Figure 1: (A) UV-VIS absorption spectra B.pilosa extracts and (B) UV-VIS absorption spectra of synthesized TiO2 using *B. pilosa* extracts

Figure 1(A and B) illustrates the UV-VIS absorption spectra of *B. pilosa* and the UV-VIS absorption spectra of synthesized TiO2 using *B. pilosa* in the visible light spectrum (400 – 665 nm) extracted using DI and MeOH respectively. A similar absorption peak of the extracts extracted using DI and MeOH was observed at a wavelength of 665 nm. The absorption peaks of the dye in this study are similar to the absorption spectrum of chlorophyll reported previously by [2]. The absorption peak for MeOH and DI indicates the presence of chlorophyll pigment. *B. pilosa* is identified to be rich in chlorophyll, and chlorophyll is efficient in photosynthesis [8].

The high absorption peak ranges from 600 - 700 nm and a maximum peak absorbance at 665 nm shown it has been known that chlorophyll extracted with DI has the broader region of the visible light spectrum in the range of 400 nm to 665 nm [8] compared to chlorophyll extracted with MeOH and is in good agreement with the work reported previous [8,9] since the broader absorption peak of DI is at 665 nm. However, in the presence of titanium oxide, the absorbance values of chlorophyll decrease without a change in the peak position, as shown in Figure 1.

The decrease in the absorption value of chlorophyll upon the addition of titanium dioxide nanoparticles indicates the electronic level interaction of the nanoparticles with the surface of the dye molecules [10,11]. The decrease in the absorbance value also raises the possibility of the adsorption of chlorophyll on the surface of nanoparticles and the formation of a ground-state complex of the chlorophyll-titanium oxide. It has been previously reported that TiO_2 also showed absorption only in the UV region with the absorption edge at around 410 nm [12]. The absorption bands of sensitized TiO_2 revealed a redshift; this was mainly caused by the existence of chlorophyll [9].

3.2 The FTIR analysis of synthesized TiO_2 nanoparticles using B. pilosa.

FTIR analysis was performed to examine and identify the possible functional groups found in green extraction and green-synthesized TiO_2 nanoparticles using the *B. pilosa* plant.

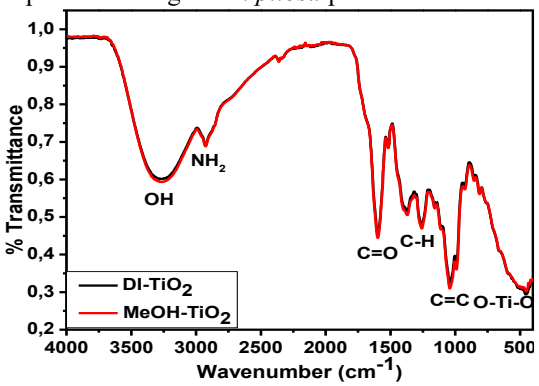

Figure 2. The FTIR analysis of synthesized TiO2 nanoparticles using *B. pilosa*.

The recorded FTIR spectra of TiO_2 with natural dye extracted from *B. pilosa* indicate most of the characteristic peaks of chlorophyll derivatives such as pheophytin, porphyrin, and chlorins. Chlorophylls and their derivatives have characteristic infrared bands corresponding to C=O, C=C, C-H, and N-H groups. The characteristic C=O band corresponding to the ketone in the cyclopentanone ring of pheophytin is observed at 1735 cm^{-1} for both extracts and synthesized extracts using TiO_2-NPs. Similarly, the C=C vibrations of pheophytin are observed around 1610 cm^{-1} and 1600 cm^{-1} for extracts and synthesized extracts, respectively, which is in good agreement with previous work [11].

Vibrational bands positioned at 2850 cm^{-1} to 2927 cm^{-1} have contributed to the N-H stretching of amide II [11]. The region of 1310 cm^{-1} and 1376 cm^{-1} are contributed to the amide III vibration and the H-C-H [11,13] the wavenumber at 1225 cm^{-1} is assigned to the stretching vibrations of the C-O for the ester groups [6,13]. The FTIR spectral analysis also confirms the presence of pheophytin in *B. pilosa* extracts, which is well-matched with the UV–VIS obtained in Figure 1.

3.3 SEM, TEM and EDS Analysis

The morphological features of the prepared nanoparticles were performed using TEM and SEM, Figure 4 below indicates the TEM and SEM images of synthesized nanoparticles using *B. pilosa* leaf extracts. The TEM and SEM images of synthesized nanoparticles indicate the particles being distributed in a spherical shape, even though some aggregation and agglomeration were observed.

The tendency of the particles to agglomerate was directly related to the crystal size obtained, EDS analysis indicates the presence of the elements such as Ti and O, which confirms the presence of TiO_2 NPs and other elements were found on EDS elements such as potassium (K), aluminum (Al) and silicon (Si) were observed for both DI and MeOH; magnesium (Mg), Plutonium (Pu), Si, K and Al were observed. These are elements that can possibly be found in a *B. pilosa* plant. The results of this study are consistent with other studies that have reported the detection of elemental Ti at 5 keV [14].

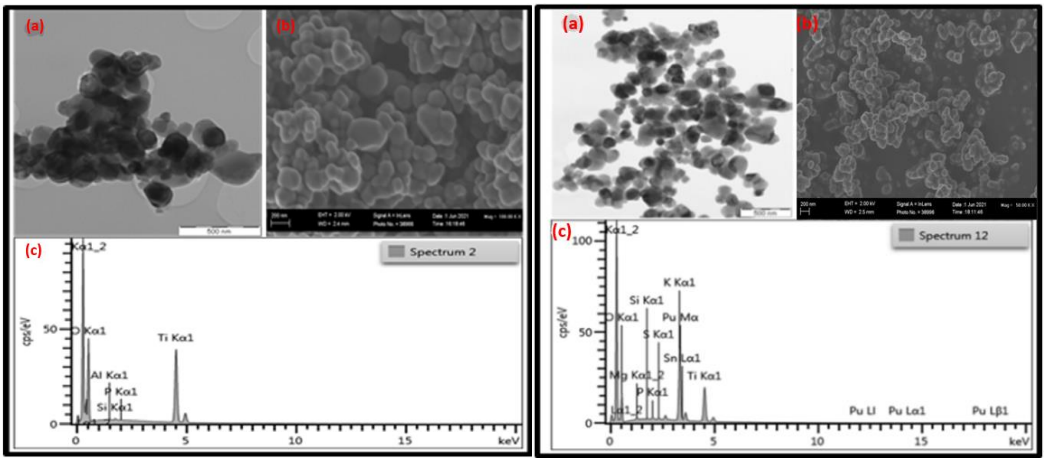

Figure 4: DI: (a) TEM, (b)SEM, (c) EDS MeOH: (a) TEM, (b)SEM, (c) EDS

3.4 XRD analysis of synthesized TiO_2 NPs

XRD patterns of TiO_2 nanocrystalline are shown in Figure 5. A relatively short 2θ range (22 – 30°) and small scan rate were chosen. For each pattern, there was a peak at about 25.4°, which is marked as anatase (1 0 1). No peaks could be found with respect to the other two phases of TiO_2, that is, rutile and brookite. The result corresponds to that obtained in SEM studies in Figure 4 (A and B), which is in excellent agreement with previous studies [8]. Several peaks were observed (1 0 1), (0 0 4), (2 0 0), and (2 0 4), demonstrating the anatase phase of TiO_2 for all the cases [10].

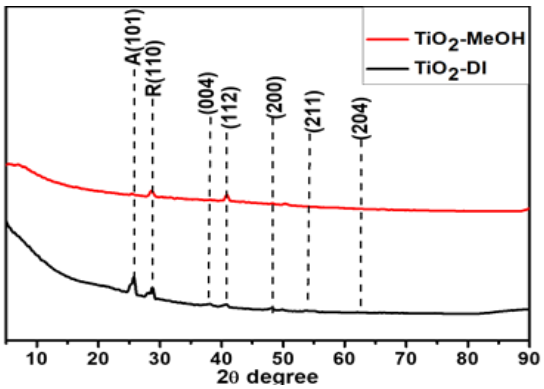

Figure 5. XRD analysis of synthesized TiO2 NPs using *B. pilosa*.

3.5 Energy level and isodensity of the Pheophytin dye

In Figure 6, pheophytin shows a lower absorbance of sunlight in both the visible region and near-infrared region with a lower oscillator strength, resulting in lower efficiency. However, with the addition of the effect of solvents introduced on the pheophytin dye molecule, it is observed that the MeOH solvent absorbs more sunlight at a higher oscillating strength, resulting in obtaining higher efficiency in the visible region. MeOH has a higher absorbance in the visible region at 405 and 407 nm, and water at 494 nm. This is in good agreement with the previous work [15]. Computational and experimental absorbances are comparable with each other since the pheophytin molecule absorbs in both visible and near-infrared regions and can be observed in Figure 1(A) and Figure 6 for both absorbance spectra.

The HOMO-LUMO energy gap of a pheophytin molecule was calculated using the following equation

$$E_{gap} = \text{HOMO} - \text{LUMO} \quad (1)$$

Where E_{gap} is the energy gap

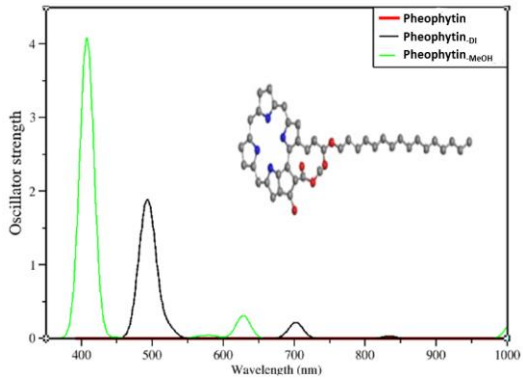

Figure 6. The UV-VIS absorption spectra of a pheophytin molecule

	HOMO	LUMO	E_{gap} (eV)
Pheophytin	-7.656	-5.596	2.06
Pheophytin-$_{DI}$	-8.391	-5.596	2.7
Pheophytin-$_{MeOH}$	-8.568	-5.02	3.5

Table: 1 HOMO-LUMO energy levels of dye molecules

Table 1 displays the HOMO and LUMO energies of pheophytin and pheophytin affected by solvents. The HOMO–LUMO energy gap values for pheophytin are 2.06 eV, while for pheophytin with the effect of solvents (MeOH, water), they are 3.5 eV and 2.7 eV, respectively, which agrees well with the HOMO and LUMO values reported [16] on a photoactive layer of DSSCs based on natural dyes. The lower HOMO-LUMO energy gap of the sensitizer enhances absorption at higher wavelengths and the photocurrent response of DSSCs. The lower energy gap between the HOMO and LUMO of the sensitizer enhances the absorption of photons in higher spectral

regions of the solar spectrum. The pheophytin dye molecule has a relatively low HOMO-LUMO energy gap of 2.06 eV, which will facilitate electron excitation.

A high HOMO energy indicates that high compounds/molecules facilitate electron transfer, so that chemical bonds will be easily formed. High LUMO energy for dye molecules will facilitate the injection of electrons from the semiconductor so that the recombination of dye to the ground level will be faster. In dye molecules with relatively low HOMO-LUMO energy, pheophytin and pheophytin-MeOH show the basis for determining the ability of a molecule to become a sensitizer in DSSCs and are comparable to the literature [15,16].

4 Conclusion

Computational first-principle calculations were based on the density functional theory to investigate the electronic and optical properties of pheophytin dye molecules extracted from the *B. pilosa* plant leaves. In both experimental and computational contexts, MeOH exhibited a higher absorbance compared to DI. Therefore, MeOH is the most effective solvent for extracting and absorbing dyes, as it can absorb a broader spectrum of dye molecules than DI, owing to its superior ability to interact with and dissolve various compounds.

The DFT calculation shows that the extracted dye has a smaller HOMO-LUMO gap compared to the e band gap of TiO_2 semiconductor polymorphs; they also show that the UV-VIS absorption spectrum shows absorption peaks in the visible to near-infrared, which presents evidence for photo absorption in those. Hence, it is concluded that the use of dye extract from *B. pilosa* can enhance the performance of DSSCs.

5 Acknowledgement

This work was supported through the NRF Thuthuka and National Institute for Theoretical Physics (NITheCS). We would like to thank the University of Venda for the support to carry out this research and the Center for High Performance Computing (CHPC) for access to their computing facility.

References

[1] S. Sharma, R. Uttam, and K. N. Uttam, "Interaction of chlorophyll with titanium dioxide and iron oxide nanoparticles: A temperature-dependent fluorescence quenching study," *Anal. Lett.*, vol. 53, no. 12, pp. 1851–1870, 2020.

[2] S. Krishnan and A. Shriwastav, "Application of TiO_2 nanoparticles sensitized with natural chlorophyll pigments as catalyst for visible light photocatalytic degradation of methylene blue," *J. Environ. Chem. Eng.*, vol. 9, no. 1, p. 104699, 2021.

[3] A. Gour and N. K. Jain, "Advances in green synthesis of nanoparticles," *Artif. Cells Nanomed. Biotechnol.*, vol. 47, no. 1, pp. 844–851, 2019, doi: 10.1080/21691401.2019.1577878.

[4] J. V. M. Zoccal, F. O. Arouca, and J. A. S. Gonçalves, "Synthesis and characterization of TiO_2 nanoparticles by the method Pechini," *Mater. Sci. Forum*, vol. 660, pp. 385–390, 2010.

[5] Y. Chiba, A. Islam, Y. Watanabe, R. Komiya, N. Koide, and L. Han, "Dye-sensitized solar cells with conversion efficiency of 11.1%," *Jpn. J. Appl. Phys.*, vol. 45, no. 7L, pp. L638–L640, 2006.

[6] W. Ahmad, K. K. Jaiswal, and S. Soni, "Green synthesis of titanium dioxide (TiO_2) nanoparticles by using Mentha arvensis leaves extract and its antimicrobial properties," *Inorg. Nano-Met. Chem.*, vol. 50, no. 10, pp. 1032–1038, 2020.

[7] S. Jana and P. Samal, "Assessment and benchmarking of proposed exchange-correlation approximations in density functional theory," Ph.D. dissertation, School of Physical Sciences, NISER, Bhubaneswar, India, 2021.

[8] S. Mahmoud, B. S. Mohamed, and H. Killa, "Synthesis of different sizes TiO_2 and photovoltaic performance in dye sensitized solar cell," *Front. Mater.*, vol. 8, p. 385, 2021.

[9] A. Torchani, S. Saadaoui, R. Gharbi, and M. Fathallah, "Sensitized solar cells based on natural dyes," *Curr. Appl. Phys.*, vol. 15, no. 3, pp. 307–312, 2015.

[10] R. Syafinar, N. Gomesh, M. Irwanto, M. Fareq, and Y. M. Irwan, "Chlorophyll pigments as nature-based dye for dye-sensitized solar cell (DSSC)," *Energy Procedia*, vol. 79, pp. 896–902, 2015.

[11] R. Ramanarayanan, P. Nijisha, C. V. Niveditha, and S. Sindhu, "Natural dyes from red amaranth leaves as light-harvesting pigments for dye-sensitized solar cells," *Mater. Res. Bull.*, vol. 90, pp. 156–161, 2017.

[12] J. Dharma, A. Pisal, and C. T. Shelton, "Simple method of measuring the band gap energy value of TiO2 in the powder form using a UV/Vis/NIR spectrometer," *Application Note*, Shelton, CT: PerkinElmer, pp. 1–4, 2009.

[13] V. Shanmugam, S. Manoharan, A. Sharafali, S. Anandan, and R. Murugan, "Green grasses as light harvesters in dye sensitized solar cells," *Spectrochim. Acta A Mol. Biomol. Spectrosc.*, vol. 135, pp. 947–952, 2015.

[14] S. Wuryanti, "The performance of solar cells using chlorophyll dye from Syzygium paniculatum," *Clean Energy*, vol. 5, no. 3, pp. 433–440, Sep. 2021.

[15] Z. Rahmatika, "Theoretical modification of pheophytin using Cu, Ni, and Zn atoms as a sensitizer for dye-sensitized solar cell (DSSC)," *J. Phys. Conf. Ser.*, vol. 1788, no. 1, p. 012006, 2021.

[16] J. Hasegawa, Y. Ozeki, K. Ohkawa, M. Hada, and H. Nakatsuji, "Theoretical study of the excited states of chlorin, bacteriochlorin, pheophytin a, and chlorophyll a by the SAC/SAC−CI method," *J. Phys. Chem. B*, vol. 102, no. 7, pp. 1320–1326, 1998.

This page intentionally left blank.

The South African contribution based on the TileCoM and Tile GbE Switch to the Tile Pre-Processor Modules for the ATLAS Tile Calorimeter: Progress and Current Status

Mpho Gift Doctor Gololo[1]

[1]Department of Electrical and Electronics Engineering Sciences, University of Johannesburg, Johannesburg, Auckland Park, South Africa

E-mail: mphog@uj.ac.za

Abstract. University of Johannesburg contributes 24% and Instituto de Fisica Corpuscular contributes 76% to the final design of the Tile Pre-Processor (TilePPr) Modules for the ATLAS Tile Calorimeter at the High-Luminosity Large Hadron Collider (HL-LHC). The contributions are quantified in terms of software and firmware developments, together with the production of Printed Circuit Boards (PCBs). This work focuses on the status of the Tile Computer-on-Module (TileCoM) and the Tile Gigabit Ethernet Switch (Tile GbE) in terms of firmware, software, and hardware integration. The procurement of 62 Xilinx Field Programmable Gate Arrays (FPGA) for the Compact Processing Module (CPM) and 60 Zynq FPGAs for the TileCoM is complete and ready to be installed on the PCB. Additionally, a dedicated test station at the University of Johannesburg has been established to integrate the TileCoM, Tile GbE, and CPM for validation in terms of sensor data acquisition and performance testing. Significant progress has also been made on the TileCoM's Open Platform Communications Unified Architecture (OPC UA) server, a key component for remote control and monitoring. This contribution provides an update on these developments, highlighting South Africa's vital contributions to the ATLAS Tile Calorimeter Phase-II upgrade.

1 Introduction

The Large Hadron Collider (LHC) at CERN is the world's most powerful particle accelerator, enabling discoveries in fundamental physics. In preparation for its next evolution, the High Luminosity LHC (HL-LHC) aims to increase the instantaneous luminosity by a factor of 5 to 7 beyond the original design of the LHC [1]. With data-taking expected to begin in 2030, the HL-LHC will enhance the physics reach of experiments like ATLAS, providing a tenfold increase in the accumulated dataset.

The ATLAS detector is a general-purpose experiment designed to study Higgs physics, possible physics beyond the Standard Model, and electroweak symmetry breaking. The Tile Calorimeter (TileCal), a sampling hadronic calorimeter made of steel absorbers and scintillating plastic tiles, is the central component of ATLAS's calorimetric system. It is separated into two extended barrels and a central barrel. Photomultiplier tubes (PMTs) read out barrel sections that are divided into modules [2].

A front-end system installed on the detector and a back-end system situated in the counting room make up the current TileCal readout chain. Analog data is sent to the Digitizer Boards for digitization and data transfer through the Read-Out Drivers (RODs) after the front-end boards amplify and shape PMT signals [3].

This paper presents the South African (SA) contribution from the University of Johannesburg (UJ) to the

ATLAS Tile Calorimeter off-detector electronics. UJ contributes 24% and Instituto de Fisica Corpuscular (IFIC) contributes 76% towards the final design of the off-detector electronics for the ATLAS Tile Calorimeter Phase-II upgrades. Figure 1 presents the ATLAS Tile Calorimeter current electronic readout system. This electronic readout system is not able to accommodate the HL-LHC requirements.

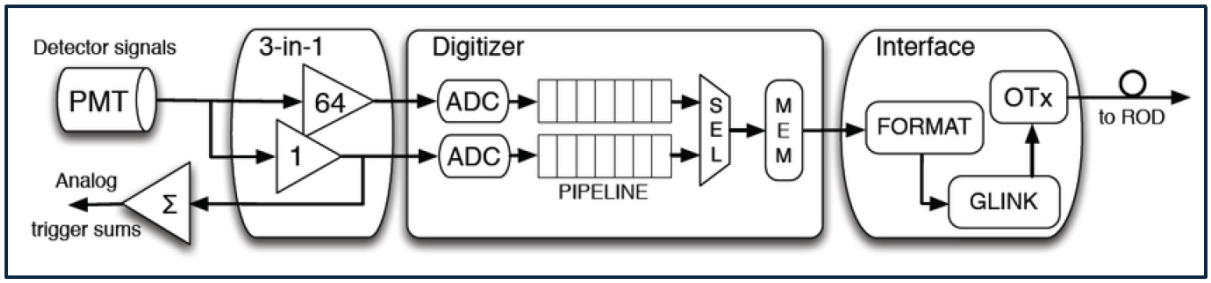

Figure 1: The ATLAS Tile Calorimeter current electronic readout system [3]

2 ATLAS TileCal Phase-II

An important component of the larger ATLAS Phase-II endeavor is the TileCal Phase-II Upgrade. A fully digital and redundant system will replace the entire readout chain as part of the update [4]. Redesigned Front-End Boards (FEBs), Main Boards (MBs), Daughter Boards (DBs), and a potent off-detector module known as the Tile PreProcessor (TilePPr) are all part of the new architecture as presented in Figure 2 [5].

The back-end system's primary component is the TilePPr [6]. It interfaces with the ATLAS Trigger and Data Acquisition (TDAQ) system, processes data in real-time, and receives high-speed optical data from all FEBs. It has a bespoke Ethernet switch, data buffering, timing modules, and Field-Programmable Gate Arrays (FPGAs) [7]. The current LHC TileCal readout system consists of 32 ROD boards installed in VME crates, providing 256 uplinks. With the Phase-II HL-LHC upgrade, this architecture is replaced by 32 TilePPr boards hosted in ATCA crates, delivering 4096 uplinks and a total DAQ bandwidth of 40 Gbps. Each TilePPr integrates multiple PCBs equipped with FPGAs, FireFly optical transceivers, and dedicated power management ICs.

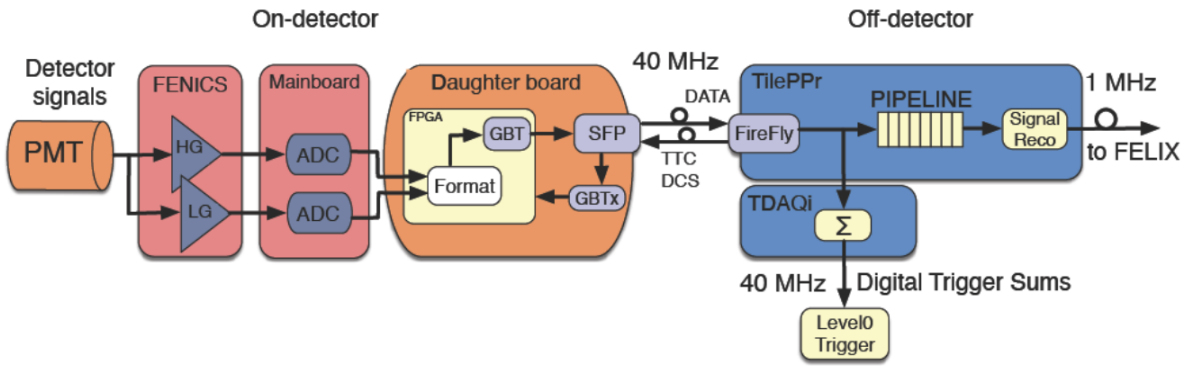

Figure 2: The ATLAS Tile Calorimeter Phase-II upgrade electronic readout system [5]

Redundancy and radiation-hardness were key considerations in the design of the entire system, which allows for smooth functioning even in the severe circumstances anticipated in the HL-LHC period [8].

2.1 Tile Computer On-Module (TileCoM)

For slow control and system monitoring, the TilePPr has a small embedded control module called the Tile Computer On-Module (TileCoM), shown in Figure 3. It functions as a Linux-based Zynq UltraScale FPGA plat-

form that supports several I/O protocols (I2C, SPI, UART, and GPIO) and has Ethernet connectivity. The interconnection of all these subsystems is shown on the left of Figure 3. Voltage, temperature, and current sensors are among the TilePPr components whose configuration and health monitoring are controlled by the TileCoM. Additionally, it offers a web interface for firmware management and remote diagnostics. During HL-LHC operation, the TileCoM, which was partially developed by the UJ, is essential for guaranteeing real-time diagnostics of the off-detector electronics[9, 10].

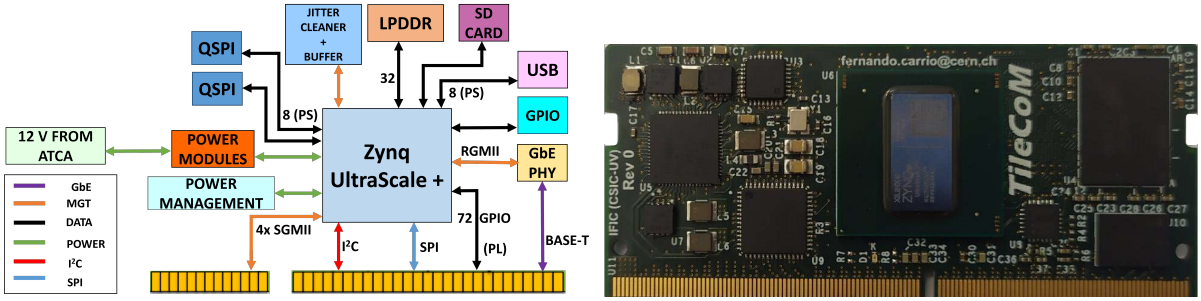

Figure 3: (*left*) The Tile Computer-On-Module block diagram. (*right*) The Tile Computer-On-Module PCB.

2.2 Tile GbE Switch

In order to provide internal data routing between its different TilePPr modules, including communication with the TileCoM, Control Processing Module (CPM), and TDAQi, the Tile GbE Switch (Figure 4) is a specially created Ethernet switching module integrated within the TilePPr. The switch is designed for redundancy and low-latency communication, and it supports several Gigabit Ethernet channels. The block diagram shown on the left of Figure 4 shows the relation and connection of the components for the full functionality of the Ethernet switch. It makes it possible for the TilePPr's control, monitoring, and data streaming features to be seamlessly integrated. The UJ has conducted extensive testing and signal integrity validation, and South African industry partners Trax Interconnect and Jemstech have been in charge of PCB production and assembly of the boards. Its effective implementation improves the TileCal data collecting system's overall flexibility and maintainability.

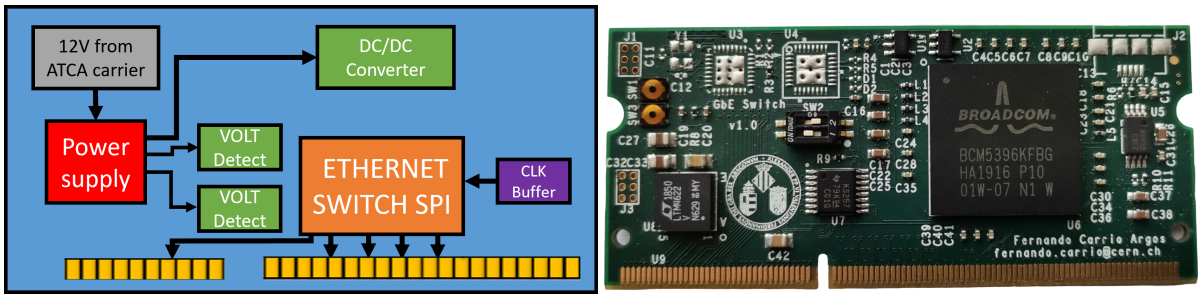

Figure 4: (*left*) TileGbE GbE Switch Block Diagram. (*right*) The Tile GbE Switch PCB.

3 UJ ATLAS TileCal Phase-II Projects

As mentioned above, UJ is contributing 24% towards the final TilePPr design. This is in terms of both the hardware and firmware developments. At UJ, three main initiatives have been led:

3.1 Control and Monitoring via TileCoM

The TilePPr is slowly controlled, monitored, and configured by the TileCoM, an embedded system. It delivers Ethernet-based diagnostics, handles firmware updates via network protocols, and reads out sensor data (temperature, voltage, and current). UJ created unique firmware in VHDL and C++ to support SPI, UART, and I2C protocols. Figure 5 shows the control and monitoring results via TileCoM.

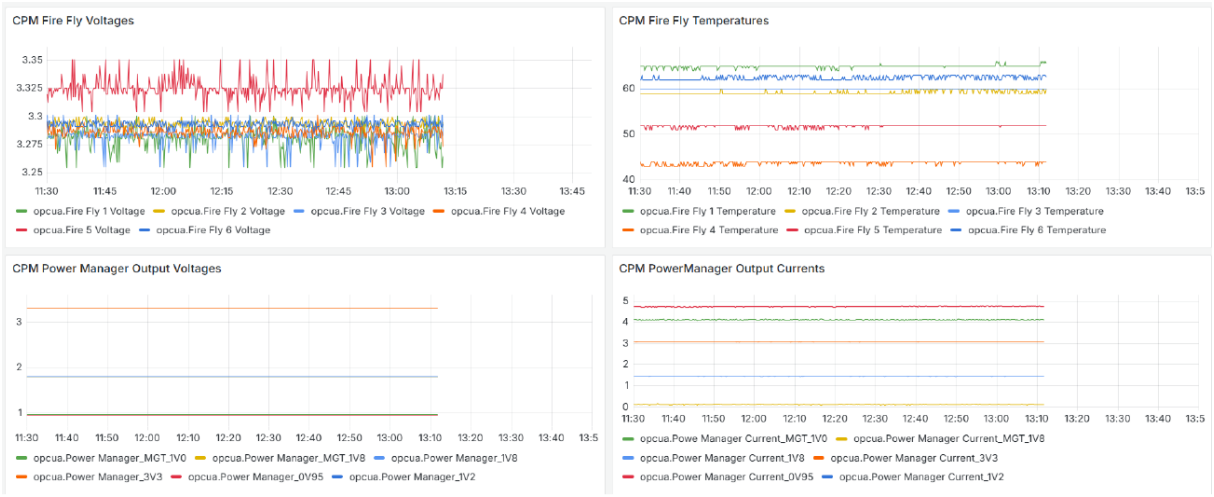

Figure 5: Control and Monitoring results via TileCoM

3.2 Testing of the Tile GbE Switch PCB

Another addition from UJ is the Tile GbE Switch, which makes it easier for internal subsystems to communicate via Ethernet. The carrier board and TileCoM have been successfully integrated with the switch. Figure 6 shows the simulation results from a software called Allegro Cadence (OrCAD) [11] for the differential plot for SDD22 and SDD11 parameters on the left. The effective analog bandwidth required to preserve digital edges is set by the driver 10–90% rise time, t_{rise}, via the rule of thumb BW$\approx$0.35/t_{rise}. The realistic simulation would cover the conservative driver rise time of 100 ps for the targeted Gigabit-Ethernet application; therefore, the primary spectral content would be below $\approx$5 GHz. However, the S-parameter plots are presented over the full 0–30 GHz range to provide a complete view of the channel behavior and to ensure compatibility with both present and potential future high-speed applications.

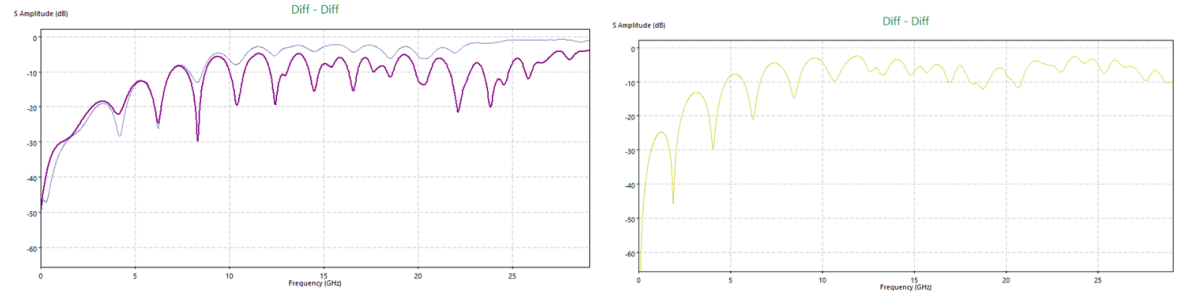

Figure 6: (*left*) The differential plot for SDD22 and SDD11 parameter. (*right*) The difference in error between adapters SDD22 and SDD11 shows that there is no error between the two adapters for SDD22 and SDD11.

3.3 Predictive ML for Anomaly Detection

UJ is using machine learning (ML) technologies to examine sensor data from the TileCoM in order to guarantee long-term operational integrity. A Machine Learning Naive Bayes model was implemented to analyze and predict sensor readings on a dataset that contains 320,710 rows and 31 columns of sensor measurements. The ML model is applied to test prediction accuracy across multiple sensor readings and evaluate the model's ability to capture patterns in the measured data. A real-time web dashboard called Grafana is used to visualize the data in this work, which makes use of the PyTorch and Scikit-learn frameworks [12, 13]. Figure 7 shows the ML model flowchart procedure followed for anomaly detection in the data on the left and the results using the predicted and the test data on the right of Figure 7. The model learns patterns across all the sensors, and once the model learns a behavior pattern from one Firefly temperature column, it can generalize this knowledge to the other Firefly sensors.

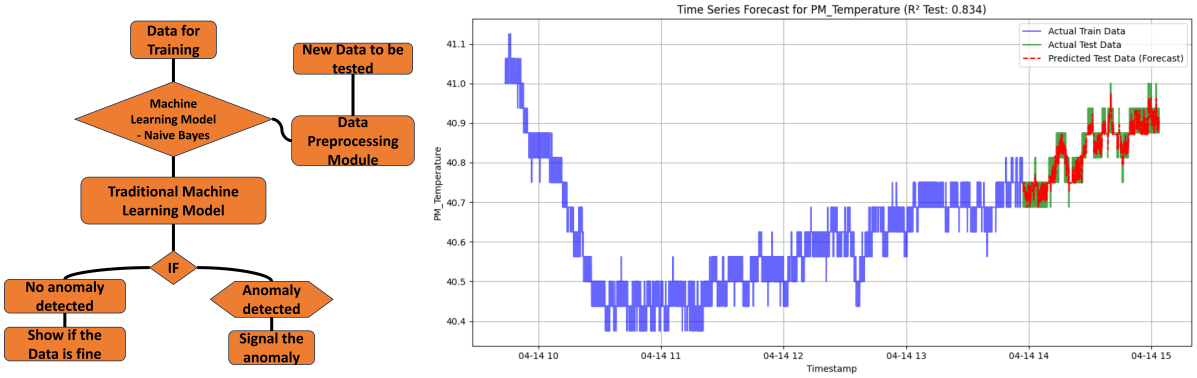

Figure 7: (*left*) The machine learning model flowchart . (*right*) The machine learning model predicted results (red dashed line) are consistent with the test data shown in green.

4 TilePPr Pre-production status and test bench

At UJ, a specific test bench was set up for the purpose of functionally validating each TilePPr subsystem. TileCoM, a GbE switch, FPGA commercial boards, oscilloscopes for validating analog signals, and a 12V DC power supply with programmable current limitations are all included in the bench. To verify communication stability, power integrity, and inter-module compatibility, integration tests have been conducted. Pre-production testing is in line with the TileCal Phase-II commissioning schedule as of July 2025.

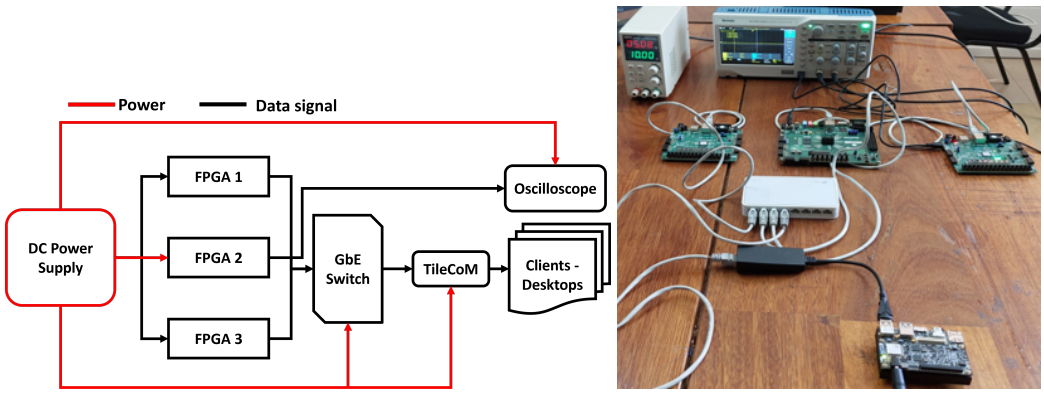

Figure 8: (*left*) Block diagram of the test be. (*right*) UJ-TilePPr test bench.

Figure 8 shows the UJ-TilePPr test bench with a block diagram of the modules connected and the PCBs used to test before they can be shipped to CERN for insertion in the Tile Calorimeter electronic system. It can be seen that all the modules are powered from the same DC power supply, which is one of the requirements of the electronic system. Electrical and communication tests were performed during the tests. For electrical tests, 12V was supplied to the three (3) FPGAs, the GbE Switch, and the TileCoM to measure and validate power across the voltage regulators. The communication tests involved sending packets of data among all the connected modules and visualizing this communication on the desktop through the TileCoM operating system. There are ongoing minor firmware improvements, especially in TileCoM's monitoring and exception-handling capabilities. In Q4 2025, full pre-production deployment is anticipated.

5 Conclusion

The HL-LHC's unparalleled radiation environment and data volume present urgent requirements that the ATLAS TileCal Phase-II upgrade attempts to meet. The UJ is a prime example of South Africa's increasing dominance in detector electronics, embedded firmware, and machine learning applications for instrumentation, thanks to its substantial contributions to the TilePPr system.

The integration of the last pre-production components at CERN and getting ready for the full system commissioning in 2027–2028 will be the main goals of future development. The cooperation between UJ, CERN, IFIC,

Heidelberg University (HU), and regional businesses serves as a strong example of long-term, international scientific collaborations.

6 Acknowledgement
The National Research Foundation (NRF), iThemba LABS, and SA-CERN are all acknowledged by the authors for their financial and infrastructural assistance in making this study feasible. South Africa's involvement in the ATLAS Tile Calorimeter Phase-II Upgrade at the HL-LHC has advanced thanks in large part to their contributions of financial support, technical cooperation, and access to research resources.

References

[1] CERN, "The High Luminosity LHC Project," https://home.cern/science/accelerators/high-luminosity-lhc, 2025, accessed: July 2025.

[2] G. Aad and A. Collaboration, "Readiness of the ATLAS Tile Calorimeter for LHC collisions," *Eur. Phys. J. C*, vol. 70, p. 1193–1236, 2010.

[3] A. Collaboration, "Operation and performance of the ATLAS Tile Calorimeter in Run 1," *Eur. Phys. J. C*, vol. 78, p. 987, 2018.

[4] G. Drake, "The new front-end electronics for the atlas tile calorimeter phase 2 upgrade," in *2015 IEEE Nuclear Science Symposium and Medical Imaging Conference (NSS/MIC)*. IEEE, 2015, pp. 1–6.

[5] ATLAS Collaboration, "Technical Design Report for the Phase-II Upgrade of the ATLAS Tile Calorimeter," CERN, Tech. Rep. CERN-LHCC-2017-019, ATLAS-TDR-028, 2020.

[6] F. Carrió and A. Valero, "Clock Distribution and Readout Architecture for the ATLAS Tile Calorimeter at the HL-LHC," in *Proceedings of the IEEE Real Time Conference*, Williamsburg, VA, USA, Oct. 2018.

[7] F. Carrió, D. Álvarez, V. Castillo, L. Cerdá, A. Ferrer, L. Fiorini, Y. Hernández, E. Higón, P. Moreno, and C. Solans, "The preprocessors for the atlas tile calorimeter phase ii upgrade," in *2015 IEEE Nuclear Science Symposium and Medical Imaging Conference (NSS/MIC)*. IEEE, 2015, pp. 1–3.

[8] T. Mkrtchyan, "A radiation tolerant readout link and control board for the phase-ii upgrade of the atlas hadronic tile calorimeter," in *2018 IEEE Nuclear Science Symposium and Medical Imaging Conference Proceedings (NSS/MIC)*. IEEE, 2018, pp. 1–3.

[9] M. G. D. Gololo, F. C. Argos, F. Martins, and B. Garcia, "Firmware developments on the tilecom for the phase-ii upgrade of the atlas tile calorimeter," in *Journal of Physics: Conference Series*, vol. 1690, no. 1. IOP Publishing, 2020, p. 012054.

[10] M. G. D. Gololo, F. C. Argos, and B. Mellado, "Tile computer-on-module for the atlas tile calorimeter phase-ii upgrades," *Journal of Instrumentation*, vol. 17, no. 06, p. P06020, 2022.

[11] A. C. (OrCAD). (2025) Allegro x design platform. [Online]. Available: https://www.cadence.com/en_US/home/tools/pcb-design-and-analysis/allegro-x-design-platform.html

[12] A. Chatterjee and B. S. Ahmed, "Iot anomaly detection methods and applications: A survey," *Internet of Things*, vol. 19, p. 100568, 2022.

[13] S. Raschka, Y. H. Liu, and V. Mirjalili, *Machine Learning with PyTorch and Scikit-Learn: Develop machine learning and deep learning models with Python*. Packt Publishing Ltd, 2022.

Simulation and Image Reconstruction for a Low-CostPET Detector Concept

Jemma Bagg[1], James Keaveney[2] and Ryan Justin Atkin[1,2]

[1]Physics, University of Cape Town, Cape Town, South Africa
[2]Physics, African Institute for Mathematical Sciences (AIMS), Cape Town, South Africa

E-mail: bggjem001@myuct.ac.za

Abstract. This project aims to develop a digital workbench through simulation to evaluate variouslow-cost PET detector designs. This workbench provides a fast and efficient way to reach a decision as to whether the low-cost system can produce clinically relevant images as well as determine how these designs can be optimised. The first preliminary low-cost detector design has a smaller geometry and simplified modules when compared to the commercial Philips Vereos system. Both detector models were simulated using GATE (Geant4 Application for Tomographic Emission). Data generated from the simulation is then reconstructed using a custom Maximum Likelihood Expectation Maximisation (MLEM) algorithm. The two images produced by the detectors are then compared using the Mean Squared Error (MSE) and the Structural Similarity Index Measure (SSIM), which are metrics that are able to quantify how similar the two images are. Working through this digital workbench allows for systemic evaluation of the clinical relevance of different low-cost PET designs. Future work will explore the integration of machine learning techniques to improve the image quality of the images produced by the low-cost detector design.

1 Introduction

Positron Emission Tomography (PET) is one of the most sensitive imaging techniques that is currently available in the medical world. It allows physicians to monitor metabolic activity, localise tumours and assess treatment efficiency. This is achieved by injecting patients with a radiotracer, which is absorbed by metabolically active or diseased cells, making them visible to the scanner.

It is because PET scans are so useful that the World Health Organisation (WHO) has recommended a PET scanner ratio of two scanners per million people to meet population needs [1]. In South Africa, there are currently 21 PET scanners [2], meaning nearly six times this number would be needed to align with WHO's suggested ratio, given a population of approximately 60 million people. Access to this small number of scanners is also extremely uneven. More than half of South Africa's PET scanners are located in the private healthcare sector, which serves only 18% of the population, leaving the remaining 82% with extremely limited access to this advanced imaging technology [2].

Developing a low-cost PET scanner would be a critical step towards addressing these disparities and bridging the gap in access, making advanced medical imaging more widely accessible. Beyond direct cost savings, low-cost PET systems can also reduce downstream healthcare costs, such as unnecessary tests, procedures, and prolonged treatments by enabling accurate and early diagnosis [3]. Having PET scanners more widely accessible

would also help alleviate many logistical obstacles, such as reducing the travel costs that many South Africans cannot afford when seeking the healthcare they need.

This project aims to create a digital workbench in order to evaluate the performance of low-cost PET detector designs. At the end of this workbench, an informed decision can be made as to whether the low-cost design is producing clinically relevant images. However, due to the smaller geometry and simplified modules of the low-cost design, it will almost always produce lower-quality images using conventional image reconstruction techniques when compared to the standard PET systems that already exist. This is why this project also explores the idea of enhancing the image reconstruction algorithm with machine learning (ML) in order to improve the image quality.

2 PET Imaging and Detection Principles

2.1 Physics Background

In PET imaging, patients are injected with a radiotracer that contains a positron-emitting isotope. Positron-emitting isotopes are radioactive and unstable, and so to become more stable, a proton in the nucleus transforms into a neutron through a process called beta plus (β+) decay. This results in the emission of a positron (e+) and an electron neutrino (ν_e), as shown in Equation 1, where Z is the proton number and A is the mass number.

$$\mathrm{M}(Z,A) \rightarrow \mathrm{M}(Z-1,A) + e^{+} + \nu_e \tag{1}$$

Over time, this tracer accumulates in specific tissues in the body, depending on its biological properties. For example, the tracer will accumulate in the brain and in tumours, where glucose metabolism is high [4]. Once inside the body, the isotope decays and emits a positron, and when this positron encounters an electron in nearby tissue, they undergo an annihilation reaction. This is a fundamental process in which a particle and its antiparticle collide and their combined mass is converted into energy. The result of the annihilation reaction is the emission of two photons, each with an energy of 511 keV (the rest mass energy of the electron or positron), emitted in nearly opposite directions (approximately 180 degrees apart). These photons are detected by a ring of scintillation detectors that surround the patient.

2.2 Scintillation Detectors

When the photons produced by the positron annihilation interact with the scintillation detector, they deposit energy into the detector material. This energy causes excitation of the atoms and molecules within the scintillator. As these excited states decay back to their original state, they release the excess energy in the form of visible light photons ([5], [6]).

The amount of scintillation light produced is proportional to the energy deposited by the incident photon, making it a reliable measure of the energy of the incident photon. To convert this light into an electrical signal, PET detectors use photomultiplier tubes (PMTs) or, in modern systems, silicon photomultipliers (SiPMs) [7].

Each scintillator captures the 3D position of the interaction on the scintillator, the detection time and the energy deposited by the photon. By applying energy discrimination (keeping only events near 511 keV) and using coincidence timing, photon pairs can be identified. A straight line, known as a line of response (LOR), is drawn between the two detection points. While the LOR defines the path between two coincident detections, it only constrains the annihilation event to lie somewhere along the line; it does not indicate the exact location of the event. There are methods that can be used to reduce this positional uncertainty, such as adding time-of-flight information, however the uncertainty will always be there which is why further image reconstruction algorithms are needed to reconstruct the original radiotracer distribution in the body.

2.3 Image Reconstruction

The primary task of an image reconstruction algorithm for a PET detector is to take the incomplete spatial data and transform it into an accurate image. In PET imaging, the data is mainly collected in list-mode format, which is then binned into a sinogram. A sinogram is a convenient way to represent the measured coincidence data. It is plotted using two parameters derived from each LOR: the perpendicular distance of the LOR from the centre of the scanner (the radial distance) and the angle at which the LOR intersects the imaging plane. Each point in the sinogram thus corresponds to a specific LOR created by two coincident photon detections. The sinogram is then used as the input for many image reconstruction algorithms, which can take it and reconstruct the original distribution of radio tracer activity within the patient.

3 The DigitalWorkbench

3.1 3.1 Simulation Framework

The simulations in this project were performed using GATE [8], an open-source platform developed by the OpenGate collaboration. GATE builds on the Geant4 Monte Carlo toolkit [9] and provides a dedicated interface for medical imaging simulations.

The first preliminary design is a compact PET system with simplified modules and smaller geometry, as these are both the first steps to take when trying to reduce the cost of the PET system. A module refers to an array of scintillators. This compact design is compared with a commercial Philips Vereos Digital PET system. The key differences between these two detector designs are highlighted in Table 1.

	Philips Vereos Detector	Low-Cost Detector
Radius	500 mm	160 mm
Module Dimensions	19 mm × 131.4 mm × 164 mm	15 mm × 24 mm × 24 mm
Pixels per module	1280	64

Table 1: Table showing the key differences between the low-cost, compact PET system and a commercial Philips Vereos system.

The Philips Vereos System acts as a ground truth reference for the low-cost PET system. The Philips system is known to produce images that are of a clinical standard [10], and so if the low-cost design is able to produce images of the same quality, then it has a high chance of being clinically usable. Figure 1 shows the visualisation of the two detector designs using GATE, the left image shows the low-cost PET system and the image on the right shows the commercial Philips Vereos system.

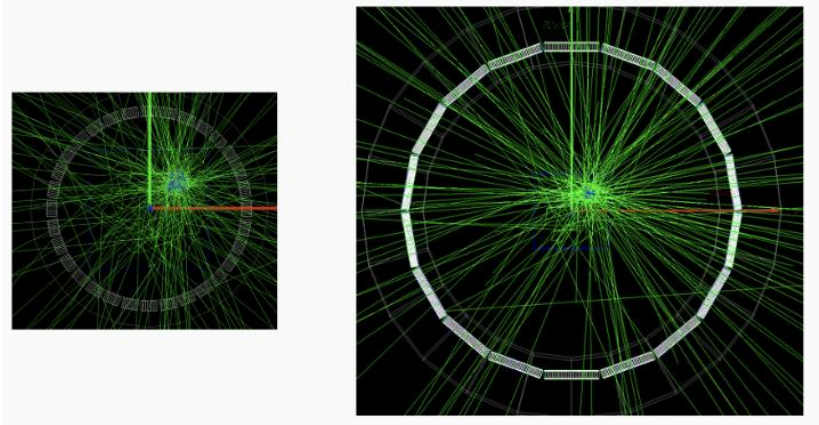

Figure 1: Visualisations of the two PET detector designs using GATE. The left image shows the low-cost system and the right image shows the commercial Philips Vereos system. The green lines represent simulated photon paths. The two images are shown on the same scale.

3.1.1 Phantoms In PET simulations, phantoms are objects that are used to mimic human tissue to validate detector performance and image reconstruction accuracy. GATE offers the flexibility to define a range of phantoms with controlled activity distributions. To simulate a realistic PET scan, a realistic brain phantom is being developed. The brain was selected as the primary focus due to the compact geometry of the low-cost detector system, which is better suited to imaging smaller regions.

The brain phantom is created by voxelising publicly available CT scan datasets into anatomically accurate regions. Voxelistion refers to the process of converting a 3D object into a grid of small volumetric units called voxels, the 3D counterpart of pixels. This is achieved by stacking the 2D slices from the CT scan to construct a 3D volume, where each voxel encodes local information, such as tissue density. Once the volume has been fully voxelised, it serves as the digital phantom input for the GATE simulation. A schematic representation of this process is shown in Figure 2.



Figure 2: Process of voxelising a CT brain scan to create a digital phantom for PET simulation. From left to right: (1) a 2D CT slice of the brain, (2) stacking of multiple 2D slices to form a 3D volume, (3) conversion of the volume into a voxel grid and (4) voxelised phantom placed inside a simulated PET scanner geometry

3.2 The Maximum Likelihood Expectation Maximisation Algorithm

The Maximum Likelihood Expectation Maximisation (MLEM) algorithm is an iterative reconstruction method widely used in PET imaging. Its objective is to estimate the spatial distribution of radiotracer activity that most likely accounts for the detected data, which is assumed to follow Poisson statistics due to the random nature of radioactive decay ([11], [12]).

The algorithm starts with an initial estimate of the radiotracer distribution (the image), which is forwardprojected to generate an estimated sinogram. This simulated sinogram represents the projection data that would be observed if the current image estimate were correct.

Rather than computing a simple difference between the measured and estimated sinograms, MLEM evaluates the likelihood that the measured data D would occur given the forward projection of the image estimate $P(I)$, denoted as $L(D \mid P(I))$. A correction term is derived based on this likelihood, and it is then backprojected, updating only those voxels that contributed to each LOR.

This iterative cycle is repeated until the reconstructed image sufficiently explains the measured data. Figure 3 shows an example of reconstructed images of spherical sources using a custom implementation of the MLEM algorithm. The images in Figure 3 were produced using simulated data, and no normalisation correction for geometric effects was applied. These reconstructions are deliberately shown in their under-converged state as preliminary outputs from the custom MLEM algorithm.

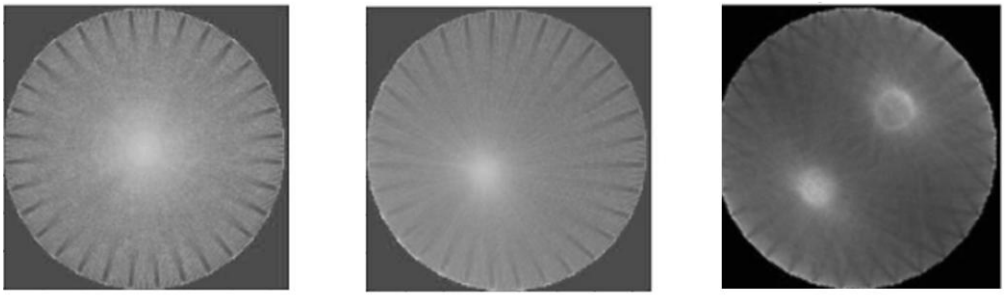

Figure 3: Reconstructed PET images using a custom MLEM algorithm. No normalisation correction for geometric effects was applied.

3.3 Image Comparison Metrics

Once the reconstructed images have been produced by both detector designs, a suitable metric is needed to quantify how similar the two images are. If the low-cost detector produces images that are highly similar to those generated by the commercial Philips Vereos detector, this would provide strong evidence that it may be viable for clinical use.

One of the most widely used image comparison metrics is the mean squared error (MSE), which calculates the average squared difference between corresponding pixels of two images. However, despite its simplicity, MSE is known to perform poorly in capturing perceived visual quality, particularly when structural distortions are present [13]. Studies have shown that MSE can report nearly identical values for images that appear very different to the human eye and that a large MSE doesn't necessarily mean important structural information is lost [14]. This is a key limitation when comparing medical images, where structural information is critical.

To address this, the Structural Similarity Index Measure (SSIM) was developed as an alternative to MSE. The core idea behind the SSIM is that the human visual system is highly sensitive to structural changes, and therefore, image quality should be assessed based on the preservation of structural information ([13], [14]). SSIM evaluates the similarity between two images based on three components at each pixel: luminance (brightness), contrast and structure. In this project, SSIM is used as the main comparison metric between the low-cost and Vereos PET reconstructions. The SSIM values were computed using the structural similarity function from the scikit-image library [15]. The SSIM score ranges from -1 to 1, where a value of 1 indicates perfect structural similarity.

Figure 4 presents a comparison between the reconstructed images produced by the Philips system (left) and the low-cost PET system (right). The reconstructions in Figure 4 were generated using simulated data with 10 iterations and 1 subset, without scatter corrections. No post-filtering was applied. The activity visible outside the sphere reflects both under-convergence and the lack of scatter correction. The low-cost system yielded a MSE of 0.00493 and a SSIM of 0.6504. The relatively low SSIM score reflects the visual degradation observed, where the reconstruction from the low-cost system appears significantly noisier and contains more artefacts compared to the Philips reference.

The hot sphere in Figure 4 had a radius of $r = 2$ cm and contained a source activity of 370 MBq of ^{18}F. This corresponds to a mean activity concentration of 11.0 MBq/mL at $t = 0$.

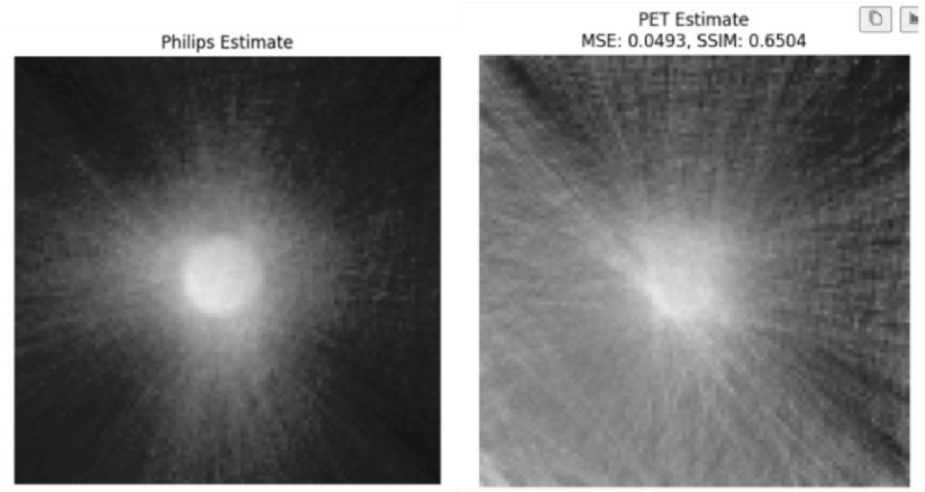

Figure 4: Comparison of reconstructed PET images from the commercial Philips Vereos system (left) and the low-cost PET system (right). Both reconstructions were obtained using 10 iterations of the MLEM algorithm with no subsets or scatter corrections. The low-cost design achieved a SSIM of 0.6504 and an MSE of 0.00493.

4 Outlook

This project is still in its early stages, and one of the main challenges currently faced is the limitation in computational resources. On a standard laptop, the simulation is capable of running for only 0.1 seconds of scan time, whereas a full clinical PET scan typically lasts around 20 minutes. Scaling up to these realistic scan conditions will therefore require significant optimisation of the workflow. This becomes even more important as the anthropomorphic brain phantom is introduced, which significantly increases the complexity and volume of the data.

Figure 4 shows that the simplified modules and reduced geometry of the low-cost system lead to an inherently noisier and lower-quality image, quantified by the calculated SSIM of 0.6504. To address this, future work will focus on incorporating machine learning (ML) techniques for de-noising and reconstruction enhancement. These methods have already shown successful results in similar studies [16], and this project will make use of these results to improve the images produced by the low-cost PET system. Specifically, these studies have shown that ML can effectively restore image quality from limited or noisy data [16], addressing one of the primary challenges faced by the low-cost system. Once integrated, these ML-enhanced image reconstruction algorithms are expected to enable the low-cost system to achieve image quality comparable to that of standard PET scanners.

5 Conclusions

A fast and efficient evaluation pipeline is essential when developing low-cost PET detector systems. The ability to simulate and assess different designs allows researchers to address two key questions: Does the design produce clinically relevant images? And is the performance sufficient to serve as a viable alternative to high-cost commercial systems?

References

[1] M. Sathekge, J. M. Warwick, A. Doruyter, and M. Vorster, "Appropriate indications for positron emission tomography/computed tomography: College of nuclear physicians of the colleges of medicine of south africa," *South African Medical Journal*, 2015. [Online]. Available: https: //doi.org/10.7196/SAMJ.2015.v105i11.10180

[2] A. G. Doruyter, J. Parkes, J. Carr, and J. M. Warwick, "Pet-ct in brain disorders: The south african context," *SA Journal of Radiology*, 2021. [Online]. Available: https://doi.org/10.4102/sajr.v25i1.2201

[3] A. Ellmann, "Pet/ct in south africa: a lost cause?" *SA Journal of Radiology*, 2008. [Online]. Available: https://journals.co.za/doi/10.10520/EJC100837

[4] National Research Council (US), Committee on the Mathematics and Physics of Emerging Dynamic Biomedical Imaging, *Mathematics and Physics of Emerging Biomedical Imaging*. Washington, D.C.: National Academies Press, 1996. [Online]. Available: https://www.ncbi.nlm.nih.gov/books/NBK232475/

[5] S. R. Cherry, J. A. Sorenson, and M. E. Phelps, *Physics in Nuclear Medicine*, 4th ed. Philadelphia: Elsevier Saunders, 2012.

[6] E. Moser, X. Zhang, M. Judenhofer, and S. Cherry, "Overview of pet detector technology and performance as part of the explorer total-body pet scanner project," *Physics in Medicine & Biology*, 2018.

[7] G. F. Knoll, *Radiation Detection and Measurement*, 4th ed. John Wiley & Sons, 2010.

[8] OpenGATE Collaboration, "The opengate collaboration – monte carlo simulations for medical imaging and radiotherapy," http://www.opengatecollaboration.org/.

[9] S. Agostinelli, J. Allison, K. Amako, J. Apostolakis, H. Araujo, P. Arce, M. Asai, D. Axen, S. Banerjee, G. Barrand et al., "Geant4—a simulation toolkit," *Nuclear Instruments and Methods in Physics Research Section A: Accelerators, Spectrometers, Detectors and Associated Equipment*, 2003.

[10] J. van Sluis, J. R. de Jong, J. A. Schaar, R. A. Dierckx, R. J. Borra, and R. Boellaard, "Performance characteristics of the digital philips vereos pet/ct system," 2020.

[11] L. A. Shepp and Y. Vardi, "Maximum likelihood reconstruction for emission tomography," *IEEE Transactions on Medical Imaging*, 1982.

[12] K. Lange and R. Carson, "Em reconstruction algorithms for emission and transmission tomography," *Journal of Computer Assisted Tomography*, 1984.

[13] Z. Wang, A. C. Bovik, H. R. Sheikh, and E. P. Simoncelli, "Image quality assessment: From error visibility to structural similarity," *IEEE Transactions on Image Processing*, 2004. [Online]. Available: https://ieeexplore.ieee.org/document/1284395

[14] Z. Wang and A. C. Bovik, "Mean squared error: Love it or leave it? a new look at signal fidelity measures," *IEEE Signal Processing Magazine*, 2009. [Online]. Available: https://ieeexplore.ieee.org/document/4775883

[15] scikit-image developers, "Image similarity: Structural similarity index (ssim)," https://scikit-image.org/docs/ 0.25.x/auto_examples/transform/plot_ssim.html, 2024.

[16] F. Hashimoto, Y. Onishi, K. Ote, H. Tashima, A. J. Reader, and T. Yamaya, "Deep learning-based pet image denoising and reconstruction: a review," *Radiological Physics and Technology*, 2024. [Online]. Available: https://doi.org/10.1007/s12194-024-00780-3

Thermal analysis of Ampreg-21 Epoxy and Bi composite material using the Cone Calorimeter

Hlongwane Moses[1], Mokoana Vincent[1] and Asante Joseph[1]

[1]Department of Physics, Tshwane University of Technology, Pretoria, South Africa

E-mail: Asantejko@tut.ac.za

Abstract. Organic polymers with inorganic reinforced composites are in daily use both domestically and industrially in coating, adhesives, primers, aeronautic utilities, electro-optical devices and sensors, among others. These polymer-based materials are competing with metallic alloys in terms of cost and functionality such as durability, strength, and other physical and chemical properties. However, the effect of heat on some of these polymer-based composites, brings some undesirable changes that affect product functionality. In addition, inorganic additives to organic epoxy resin have shown promising flame-retardant effects and increasing electrical conductivity. One particular epoxy polymer, Ampreg 21™, impregnated with Bi inorganic fillers of different weight percentages (0; 0.46; 0.90; and 1.38 wt%) was the focus of this study. The Dual Cone Calorimeter was set to irradiate the samples with 35 kW/m^2 and 50 kW/m^2 external heat fluxes, yielding the thermal performances of the binary composites in terms of the heat release rate (HRR), fire spread index (FIGRA), smoke release rate (SPR), smoke spread index (SMOGRA), time-to-ignition (TTI), and the maximum rate of heat emission (MARHE) of the composite samples. The results show that increasing Bi content in the epoxy decrease the parametric values linked to the fire performance of the samples. Thus, the Bi powder additives, being good heat conductor, assist in spreading heat in the matrix and as a result also serve as fire retardant in the composite. For the 35 kW/m^2 irradiation, TTI decrease from 89 s (neat sample) to 70 s (1.39 wt% Bi); Peak HRR decrease from 818.95 kW/m^2 (neat) to 698.9 kW/m^2 (1.39 wt% Bi); FIGRA decreases from 2.48 W/s (neat) to 1.49 W/s (1.39 wt% Bi); SMOGRA decrease from 5.08 m^2/s^2 to 3.83 m^2/s^2; and MARHE decreases from 416.6 kW/m^2 to 393.7 kW/m^2. For the 50 kW/m^2 irradiation, TTI decreases from 38 s (neat sample) to 31 s (1.39 wt% Bi); Peak HRR decreases from 1361.73 kW/m^2 (neat) to 675.03 kW/m^2 (1.39 wt% Bi); FIGRA decreases from 4.78 W/s (neat) to 2.25 W/s (1.39 wt% Bi); SMOGRA decreases from 9.39 m^2/s^2 to 6.27 m^2/s^2; and MARHE decreases from 632.3 kW/m^2 to 425.7 kW/m^2. Clearly, increasing Bi additives in the range used, decrease TTI, pHRR, FIGRA, SMOGRA, and MARHE values. Thus, good thermal performance of the composites were achieved with increasing concentration of the Bi additives.

1 Introduction

Organic polymers with inorganic reinforced composites are in daily use both domestically and industrially and are competing with metallic alloys in terms of cost and functionality [1,2]. However, the effect of heat on some of these polymer-based composites, brings some undesirable changes that affect product functionality. Inorganic additives to organic epoxy resin have shown promising flame-retardant effects and increasing electrical conductivity. Flame-retardant effects are measured in terms of decreasing HRR, FIGRA, MARHE, SPR and SMOGRA which parameters can be obtained from Cone Calorimeter measurements.

2 Materials and methods

2.1 Sample

Liquid epoxy resin (Ampreg 21TM) and its slow hardener were purchased from Advanced Materials Technology (Pty) Ltd, in South Africa. Different low weight percentages of Bi inorganic nanoparticle fillers were added to the Ampreg 21 in its liquid state. The composites were then poured into steel mould (wet with easy removal fluid) and mixed vigorously using magnetic stirrer till homogeneous mixture was obtained and left to cure for 24 hours. Altogether eight samples were fabricated: 2x neat (epoxy only), 2x epoxy with 0.46 wt% Bi; 2x epoxy with 0.90 wt% Bi; and 2x epoxy with 1.38 wt% Bi. The samples were cut to: 10 x 10 x 0.3 cm^3 for Cone Calorimeter measurements. Samples were irradiated with two external heat fluxes: 35 and 50 kW/m^2.

2.2 Cone Calorimeter

The Cone Calorimeter is considered as the most significant bench scale instrument in fire testing due to the small sample sizes used for the test [3]. Cone Calorimetric testing serves as an elegant way to conduct research into the fire performance (in the development stage). From each of the set external heat fluxes mentioned above, the Fire Test Technology (FTT) Dual Cone Calorimeter, conformed to ISO 5660 standard, was used to measure the following parameters: heat release rate (HRR); smoke production rate (SPR); mass loss rate (MLR); time to ignition (TTI); sustained flaming time; maximum average rate of heat emission (MARHE) and other derived parameters such as: fire spread index (FIGRA) and smoke spread index (SMOGRA). FIGRA is an index used for indicating how fast combustion of a material develops [4]. FIGRA provides estimation on the rate of fire spread or development and expressed as the ratio of peak HRR (pHRR) and the time at which the pHRR occurs. Similarly, SMOGRA, is closely related to SPR and it indicates the smoke spread measure of a sample [5]. SMOGRA is expressed as the ratio of peak SPR (pSPR) and the time at which the pSPR occurs. Figure 1 shows the Cone Calorimeter with a burning sample on a load cell.

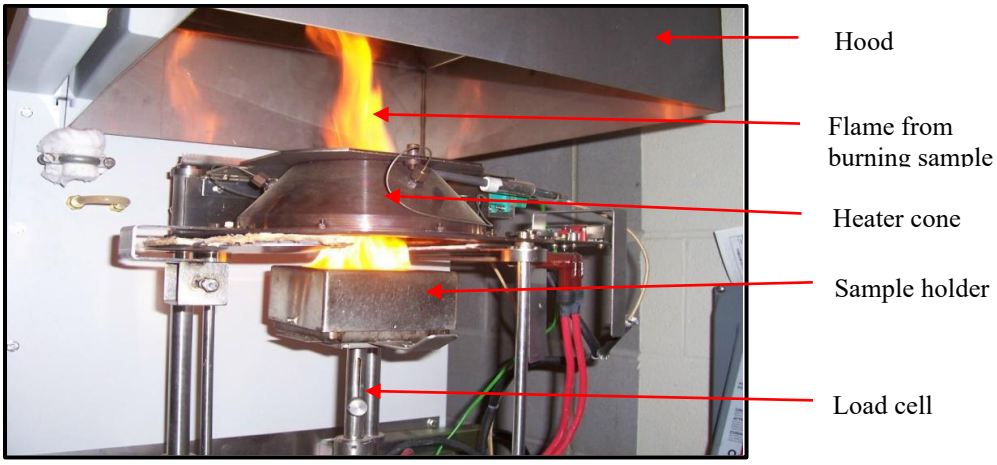

Figure 1: Section of the Cone Calorimeter showing a burning sample

3 Results

The heat release and the smoke production rates of the samples irradiated with external heat flux of 35 kW/m^2 are shown in Figure 2 (a) and (b), respectively. The effect of the two external heat fluxes, 35 and 50 kW/m^2, on a sample is shown in Figure 3 (a) the Neat Ampreg21 and (b) Ampreg-0.46 wt% Bi binary composite samples. Other samples were measured in similar way. The overall results of the thermal performance of the samples are displayed in Tables 1 and 2, for external heat flux irradiations of 35 and 50 kW/m^2, respectively.

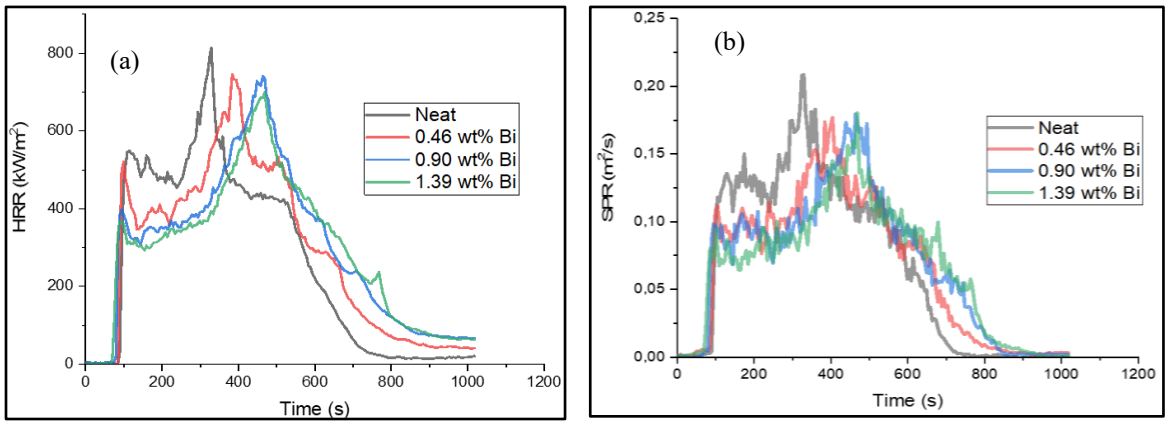

Figure 2: (a) HRR and (b) SPR profiles of samples irradiated at 35 kW/m^2

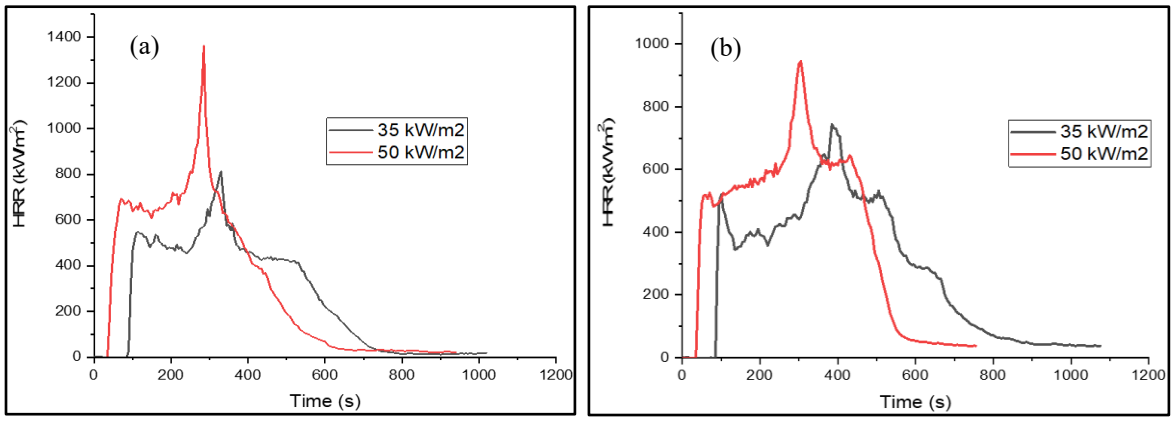

Figure 3: (a)Ampreg21neat and (b) Ampreg-0.46 wt% Bi binary composite samples irradiated at 35 and 50 kW/m^2

Sample 35 (kW/m^2)	TTI (s)	Peak HRR (kw/m^2)	FIGRA (W/s)	Peak SPR (m^2/s)	SMOGRA (m^2/s^2)	MARHE (kW/m^2)
Neat	89	819.0	2.48	0.183	5.08	416.6
0.46% Bi	89	745.1	1.94	0.177	4.37	408.2
0.90% Bi	81	740.2	1.59	0.173	3.93	393.7
1.39% Bi	70	698.9	1.49	1.180	3.83	374.0

Table 1: Thermal performance results from 35 kW/m^2 external flux irradiation

Sample 50 (kW/m^2)	TTI (s)	Peak HRR (kw/m^2)	FIGRA (W/s)	Peak SPR (m^2/s)	SMOGRA (m^2/s^2)	MARHE (kW/m^2)
Neat	38	1361.7	4.78	0.268	9.39	632.3
0.46% Bi	38	937.4	3.12	0.213	7.09	496.8
0.90% Bi	37	1012.3	2.74	0.236	6.22	540.5
1.39% Bi	31	675.0	2.25	0.238	6.27	425.7

Table 2: Thermal performance results from 50 kW/m^2 external flux irradiation

4 Discussions

The heat release rate (HRR), Maximum Average Rate of Heat Emission (MARHE), Fire Spread Index (FIGRA) and Smoke Spread Index (SMOGRA) values determine heat safety hazard of a material [5]. The lower the values the better the fire safety hazard. Ignition controls the flame spread and fire growth, whereas the pHRR controls the flame spread [6].

In Figure 2 (a) and (b), the peaks of HRR and SPR decrease with increasing time for increasing Bi content in the composite. Also, the two peaks shift to the right for increasing Bi content. These are attributed to the better thermal conductivity of Bi in the matrix which allows received heat to spread inside the composite. Besides, Bi imparts stronger char-forming ability to the matrix [7]. In addition, time to ignition, seems to decrease with increasing Bi content which further suggest the synergy of Bi in promoting aromatization structures in the condensed phase of the epoxy. Furthermore, the area under each HRR vs time profile indicates the total heat release (THR). In Figure 2(a), the neat Ampreg21 epoxy sample have the highest THR. Just like peak HRR, THR values decrease with increasing Bi additives.

Figure 3 (a) -Ampreg21 neat and (b) – Ampreg21-0.46 wt% Bi binary composite, show the role of external heat fluxes on the burning behaviour of the samples. The HRR profiles shift to the left for higher external heat flux with the corresponding shorter TTI. The higher external flux results in faster decomposition of the sample and hence, the shorter TTI. Also, the peak HRR decrease for smaller external heat flux. Thus, for the epoxy neat sample, Figure 3(a), irradiated by 50 kW/m^2, time to ignition is 38 s as compared to 89 s from the 35 kW/m^2 irradiation. Just like THR, the increasing presence of Bi additives in the composites, decrease MARHE and FIGRA values of the samples [7]. See Tables 1 and 2. Smoke production rate (SPR) is one of the fire safety parameters in thermal investigations of a material. SPR is related to Smoke Growth Rate Index (SMOGRA) and the Total Smoke Release (TSR) of a burning sample. In the case of toxicity, for all samples irradiated by either 35 or 50 kW/m^2 external heat fluxes, the smoke spread, SMOGRA values decrease with increasing Bi content. One such example is shown in Figure 2(b). Tables 1 and 2 show all the summary of the thermal performance parametric properties of the Ampreg21 neat and with Bi additives binary samples that were subjected to the two external heat fluxes of 35 and 50 kW/m^2. All parametric values decrease with increasing Bi content. Similar study by Xu et al. [7] confrims the flame retardant behaviour of Bi in epoxy matrix.

5 Conclusion

The fire performance of the Ampreg21 epoxy-Bi composite samples have been investigated. All the fire performance parameters, namely, peak HRR, peak SPR, MARHE, FIGRA and SMOGRA, obtained from the Cone Calorimeter measurements, decrease with increasing addition of Bi nano-powder in the epoxy (from 0.46, 0.9 and 1.38 wt%). The reason being the peculiar nature of Bi: better thermal conductivity in dispersion heat received and its ability in imparting stronger char formation in the composite; thereby, serving as flame retardant in the organic Ampreg21 epoxy.

References

[1] K. Korniejenko, B. Tyliszczak, M. Łach, J. Mikuła, M. Hebdowska-Krupa and D. Mierzwiński, “Organic Polymers Reinforced Inorganic Polymers - An Overview,” *IOP Conf. Ser.: Mater. Sci. Eng*. doi:10.1088/1757-899X/416/1/012090, 2018.

[2] L. Guo, W. Yuan, Z. Lu and C.M. Li, “Polymer/nanosilver composite coatings for antibacterial applications,” *Collision & Surface Analysis: Physicochem. Eng, Aspects*, vol. 439, pp. 69-83, 2013.

[3] B. Schartel and T.R. Hull, "Development of fire-retarded materials—Interpretation of cone calorimeter data," *Fire and Materials,* vol. 31, pp. 327-354, 2007.

[4] Q.T. Nguyen, P. Tran, T.D. Ngo and P. Mendis, "Experimental and computational investigations on fire resistance of GFRP composite for building façade," *Science Direct, Composite Part B: Engineering*, vol. 62, pp. 218-229, 2014.

[5] L.M. Kekana, J.K.O. Asante and B Mwakikunga, “The effect of repeated washings on thermal protective performances of one most used structural firefighting turnout gear in the Gauteng Province in South Africa,” *Journal of Fire Sciences*, vol. 43, no. 1, pp. 1-8, https://doi.org/10.1177/07349041241249635, 2024.

[6] T.R. Hull, "Challenges in fire testing: reaction to fire tests and assessment of fire toxicity." In: Horrocks AR and Price D (eds) *Advances in Fire Retardant Materials*. Woodhead Publishing, pp. 255-290, 2008.

[7] Z.S. Xu, H.Y. Jia and L. Yan, "Synergistic effect of bismuth oxide and mono-component intumescent flame retardant on the flammability and smoke suppression properties of epoxy resins," *Polym Adv Technol* vol. 31, pp. 25–35, https://doi.org/10.1002/pat.4744. 2020.

This page intentionally left blank.

Integration of Grid-Scale Battery Energy Storage in Solar Microgrids for Rural Communities in Limpopo Province

Pfesesani Netshilonwe[1], Fhulufhelo Nemangwele[1] and Mukovhe Ratshitanga[2]

[1]Department of Physics, University of Venda, Thohoyandou, South Africa
[2]Department of Electrical, Electronic and Computer Engineering, Cape Peninsula University of Technology, Bellville, South Africa

E-mail: pfesesani.netshilonwe@univen.ac.za

Abstract. The persistent challenge of community blackouts resulting from load reduction and shedding necessitates immediate and effective solutions. These power interruptions not only disrupt daily activities but also create imbalances in supply and demand. At the core of this issue lies the inflated cost of electricity and the continual annual tariff hikes. Consequently, some consumers are driven to engage in illegal connections, theft, and meter tampering as a means to mitigate their expenses, which exacerbates the problem of load reduction. This study explores the potential for integrating grid-scale battery energy storage with solar photovoltaic systems to enhance energy access for rural communities in Limpopo. Employing the Herman-beta method, we estimated the electricity demand based on the 2022 census data from Statistics South Africa. The technical and economic performance of the communities, specifically Ka-Dzingidzingi, Duthuni, and Mookgopong non-urban areas, was evaluated using Homer software, focusing on the integration of these communities with grid-scale solar photovoltaic systems. We compared the economic metrics of solar photovoltaic module capacities of 250W, 375W, and 500W, alongside the selection of a 48V, 14.4kWh lithium-ion battery for the grid-scale implementation. Our findings indicate that the system utilising a 500W solar module yields the most favourable outcomes, with the lowest Net Present Cost and Levelized Cost of Energy across the assessed communities. Specifically, the Net Present Cost values were R77.30 million, R137.54 million, and R199 million for Ka-Dzingidzingi, Duthuni, and Mookgopong non-urban areas, respectively, while the corresponding Levelized Cost of Energy figures were 1.83R/kWh, 1.58R/kWh, and 0.71R/kWh. The metrics for return on investment, internal rate of return, and simple payback period suggest that the success of this initiative hinges on securing investments from both private and public sectors. A collaborative approach in financing will facilitate improved electricity delivery to these communities in Limpopo, thereby significantly enhancing their overall quality of life.

1 Introduction

The issue of power blackouts in Limpopo province, caused by load reduction and shedding, and sometimes due to minor natural weather disruptions, demands urgent solutions. These interruptions disrupt both social life and economic operations in the communities [1]. Communities need access to affordable and reliable electricity provision as it is vital for social development, especially in rural areas. However, challenges continue to persist, including unreliable supply of electricity and unbearably expensive electricity costs. As the cost of purchasing

electricity increases annually and the government seem not to care, several consumers resort to illegal connections and meter tampering to save on costs, and that further strains the power grid, resulting in load reduction and shedding [2]. That is why it is essential to lay out a comprehensive strategy to ensure stable, reliable and affordable electricity access in rural areas, and in this case, it is rural communities of Limpopo province. This paper investigates integrating grid-scale battery energy storage systems with solar photovoltaic (PV) microgrids as a backup solution for rural communities' energy challenges. The aim of the study is to assess the technical and economic feasibility of this integration. For technical and economic simulations, Homer Pro software has been employed as it is at the forefront of microgrid optimisation simulations [3], and for load estimations, the Herman-beta method has been employed as it is the probabilistic approach to designing residential electrical distribution systems [4]. The findings will determine the viability of investing in this solution to enhance energy resilience in Limpopo's rural areas by observing the system's net present cost (NPC), levelized cost of energy (LCOE), return on investment (ROI), internal rate of returns (IRR) and simple payback years (SPB).

To the author's knowledge, there is a need to continue researching solar microgrids integrated with battery storage for rural communities because battery storage solar microgrids have emerged as a vital solution to address energy access challenges in rural areas, particularly in regions where the national grid experiences technical difficulties. These systems possess the capacity to deliver reliable, decentralised, and sustainable electricity. Authors in [5] highlight that rural electrification through centralised grids frequently encounters elevated transmission costs and significant delays, rendering decentralised solutions a more pragmatic alternative. Solar microgrids integrated with battery storage systems effectively address the challenge of solar intermittency, thus providing a reliable power supply essential for fulfilling the energy requirements of lighting, healthcare, education, and small-scale enterprises in off-grid communities [6]. This combination enhances the resilience of local energy systems, enabling sustained operations and contributing to developmental goals in these areas. Authors in [7] highlight that the incorporation of battery energy storage systems enhances power reliability and grid stability. This integration not only mitigates intermittency issues associated with renewable energy sources but also facilitates energy availability during non-generating hours, thereby supporting socio-economic development initiatives. The environmental and economic advantages of solar microgrids with energy storage systems further highlight their critical importance. Conventional rural electrification methods that depend on diesel generators not only exacerbate greenhouse gas emissions but also incur significant operational expenses related to fuel logistics and equipment maintenance [8]. Battery-backed solar systems enhance the reduction of reliance on fossil fuels while providing substantial long-term economic benefits. Research indicates their scalability and flexibility to meet localised energy requirements, facilitating progressive implementation in alignment with the evolving demands of the community [9]. Battery storage solar microgrids significantly bolster community resilience, particularly in regions susceptible to climate-induced disruptions, by providing a stable and renewable energy supply. These systems serve as more than just a technical solution; they function as transformative mechanisms that advance energy justice, promote economic inclusion, and foster environmental sustainability in underserved rural areas. Their integration facilitates decentralised energy access, reduces reliance on fossil fuels, and enhances grid stability, ultimately contributing to a more equitable energy landscape [10].

2 Experiment

2.1 Description of the selected site

The three selected sites for analysis are located in Limpopo Province, South Africa. The locations are: Ka-Dzingidzingi, which is the village located in Greater Giyani municipality, Duthuni village, located in Thulamela municipality, and the last location selected, Mookgopong Non-Urban (NU), which is the area found in Mookgopong municipality. The average solar global horizontal irradiance at these locations is recorded at about 6.46 kWh/m²/day average. The mean monthly temperature averages sit at about 25.62 °C [11].

2.2 Population statistics of selected locations

Table 1 below shows the population statistics of the selected location extracted from the Statistics South Africa database, based on the census that was conducted in 2022. The table shows the locations, municipalities, population size, and number of consumers (N), which in some sources it is referred to as the number of houses in the selected location. The table shows that Ka-Dzingidzingi is the location with the least population, Duthuni is in the middle, and Mookgopong NU has the highest population of the selected population. This population metric is essential for load modelling using the Herman-Beta method from the NRS-034 of 2012.

Locations	Municipalities	Population size	Number of consumers (N)
Ka-Dzingidzingi	Greater Giyani	4 749	1 153
Duthuni	Thulamela	8 431	2 200
Mookgopong NU	Mookgopong	12 411	4 200

Table 1: Population data of the selected locations

3 The Herman-Beta method

3.1 Load modelling using probabilistic distribution function (PDF)

The Herman-Beta method employs a probabilistic distribution function to evaluate various loads, consumer connections, and types of network topology. This distribution function is characterised by three key design parameters: alpha (a), beta (b), and the circuit break parameter (c). To derive the estimated maximum demand for residential loads, expressed in kVA or kW, we utilise the following formula (Equation 1), contingent upon knowing the specific values of a, b, and c. Standardised values for these parameters can be referenced in the 2007 publication titled "Electricity Distribution – Guidelines for the Provision of Electricity Distribution Network in Residential Areas", found in NRS-034 [12].

$$L = 0.23 * N * \frac{C}{a+b} * \left[a + 1.28\sqrt{\frac{a*b}{N(a+b+1)}}\right] \quad (1)$$

where L represent the maximum load in kVA or kW, N denote the total number of consumers, and a and b are parameters related to the load current model. The parameter c functions as the scaling factor, which corresponds to the size of the circuit breaker. When the load is accessible, we can derive estimates for the load parameters for any value of c by applying the standard deviation (σ) and mean (μ) derived from equations 2 and 3, as well as the probability density function (PDF) mean from equation 4 [12].

$$\mathrm{a} = \frac{\mu(c\mu - \mu^2 - \sigma^2)}{c\sigma^2} \quad (2)$$

$$\mathrm{b} = \frac{(c - \mu)(c\mu - \mu^2 - \sigma^2)}{c\sigma^2} \quad (3)$$

$$c = \frac{a}{a+b} \quad (4)$$

3.2 Consumer classifications and design load current parameters

Table 2 delineates the classification of consumers based on design load parameters pertinent to rural settlements and villages, as well as the associated design parameters. The classification comprises eight distinct consumer categories, spanning from rural settlements to urban multi-story estates. For the purposes of this investigation, we will focus exclusively on two categories: rural settlements and rural villages.

Consumer classes	a	b	c	μ (A)	σ (A)
Rural settlement	0.35	2.88	20	2.17	3.03
Rural village	0.48	2.13	20	3.65	4.07

Table 2: Consumer class and design parameters [12]

4 Microgrid design for all locations

4.1 Microgrid design schematics

A microgrid is a small-scale energy system comprising distributed energy resources and loads [13]. The system can be configured for either grid-connected or off-grid operation, providing a viable alternative for delivering reliable and cost-effective energy solutions to consumers. This sub-section outlines the models of the various components that form the microgrid system developed for this study. The architecture of the microgrid includes a 500W solar photovoltaic system, a 14.4 kWh battery bank operating at 48 V, 500 kW electrolysers, and integration with the utility grid. The design, illustrated in Homer Pro software, is detailed in Figure 2, which

includes schematic diagrams that depict both the peak load in kW and the average daily energy consumption in kWh/day for each selected site.

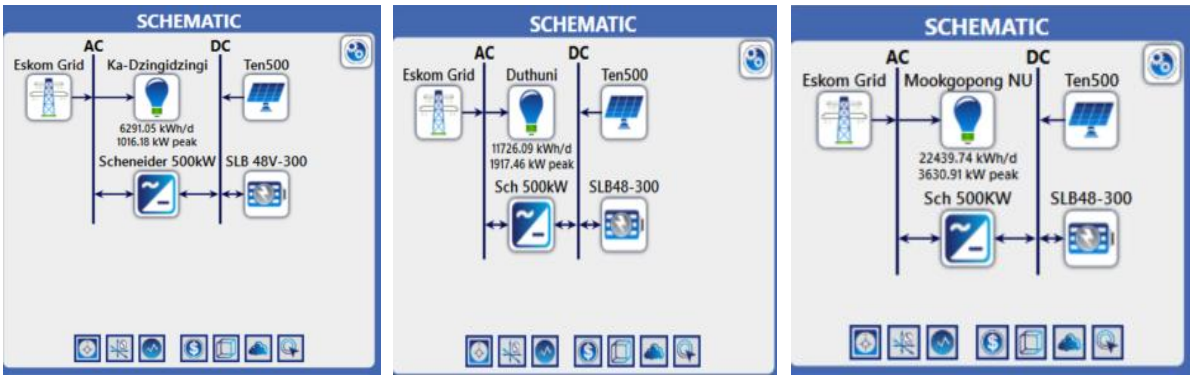

Figure 1. Schematic diagrams for selected locations in Homer software

4.2 Estimated electric load for selected locations and component sizing

As shown in Figure 1 above, the estimated load for Ka-Dzingidzingi is 1016.18kW_{peak}, followed by the one for Duthuni, which is about 1917.46kW_{peak}, and lastly is Mookgopong, sitting at 3630.91kW_{peak}

Locations	Estimated peak load (kW)	Number of solar panels	Number of inverters
Ka-Dzingidzingi	1 016.18	1 848	2 x 500 kW
Duthuni	1 917.46	3 486	3 x 500 kW
Mookgopong NU	3 630.91	6 602	4 x 500 kW

Table 3: Estimated peak load with component sizing

5 Results

5.1 Technical Findings

The technical analysis of this investigation focuses on several key factors related to microgrid performance, including energy production, consumption, excess energy, and the renewable energy fraction, which is defined as the fraction of energy delivered to the load that originated from renewable power sources across various locations. The presence of excess energy indicates that the energy generated is sufficient to meet the demands of the system; notably, in all examined locations, energy consumption remains below energy production, allowing for surplus energy to be utilised for battery charging. A significant contributor to the high levels of energy production in the Limpopo province is the region's elevated solar irradiance, coupled with the robust backup capabilities provided by the integrated battery systems. Furthermore, the investigation reveals a high renewable energy fraction, which can be attributed to a combination of favourable environmental conditions, the availability of effective energy storage solutions, and a substantial installed capacity of renewable energy technologies. This synergy of factors supports the overall efficiency and sustainability of the proposed microgrids in the study.

Locations	Energy produced (kWh/year)	Energy consumed (kWh/year)	Excess energy (kWh/year)	Renewable fraction (%)
Ka-Dzingidzingi	2 382 102	2 344 021	7 385	27.7
Duthuni	4 957 321	4 831 899	23 162	44.8
Mookgopong NU	20 775 999	19 922 495	116 869	78.4

Table 4: Technical results for proposed microgrid optimisation

5.2 Economic findings

The economic findings of this investigation, as shown in Table 5, look at the capital expenditure, LCOE, NPC, ROI, IRR and SPB. Capital expenditure refers to the total financial resources allocated primarily for investment in the acquisition, maintenance, or enhancement of assets, including but not limited to buildings, machinery, and infrastructure [14]. Larger projects typically necessitate greater capital expenditure. An analysis presented in Table 5 reveals that the proposed microgrid system for Ka-Dzingidzingi has the lowest anticipated capital costs among the selected locations, ranking next to Duthuni, while Mookgopong follows with the highest costs. This discrepancy is attributed to the size of the microgrid systems, with Ka-Dzingidzingi microgrid operating at approximately 1016.18 kW, compared to Duthuni 1917.46 kW and Mookgopong NU's substantial 3630.91 kW capacity. In the economic analysis of energy projects, two critical metrics are the NPC and the LCOE. NPC represents the total cost of a project over its lifetime, while LCOE reflects the average cost per unit of electricity, expressed in rand per kilowatt-hour (R/kWh) in South Africa [15]. When the NPC and LCOE of a project are significantly higher than those of comparable completed projects, it may indicate that pursuing the project is unwise, as the lengthy payback period could result in a financial loss. In this investigation, the Ka-Dzingidzingi location has the lowest NPC at 77.30 million rand, attributed to minimal capital investment. Duthuni follows with an NPC of 137.54 million, while Mookgopong NU has a substantially higher NPC of approximately 252.67 million. Conversely, the analysis reveals that Mookgopong, despite having the highest NPC, achieves the lowest LCOE of 0.71 R/kWh. This can be attributed to its larger microgrid size, which results in high energy production, coupled with a long operational lifetime of about 25 years, no fuel costs, and a high degree of renewable energy integration. Duthuni presents a moderate LCOE of 1.58 R/kWh, and Ka-Dzingidzingi, which has the smallest proposed microgrid, experiences a relatively high LCOE of around 1.83 R/kWh due to its limited energy production capacity. In analysing historical data, it becomes evident that recovering investment in energy systems can often take a decade or more. This protracted payback period is primarily attributed to the high initial investment costs compared to the relatively lower LCOE associated with these systems. Consequently, the success and viability of such investments are likely to be enhanced through collaborative efforts between private enterprises and public entities, fostering a synergy that maximises both financial and operational efficiencies.

Locations	Capital (R)	LCOE (R/kWh)	NPC (R)	ROI (%)	IRR (%)	SPB (yr)
Ka-Dzingidzingi	5.88 M	1.83	77.30 M	4.1	6.3	11.85
Duthuni	17.5 M	1.58	137.54 M	5.5	8.2	10.11
Mookgopong NU	117 M	0.71	252.67 M	3.1	5.0	13.30

Table 5: Economic results for proposed microgrid optimisation

6 Conclusion

This paper explores the integration of grid-scale battery energy storage systems with solar PV microgrids as a sustainable backup solution to address the energy challenges of power failures, load reduction, and load shedding in rural communities of Limpopo province. The study meticulously evaluates the technical and economic feasibility of this integrated system. Utilising the Herman-beta method for load modelling, alongside Homer Pro software for system configuration and economic simulations, the analysis focused on three rural communities with varied characteristics specifically differing population densities, ambient temperatures, and global horizontal irradiance levels. A critical component in the simulation setup was consumer classification, which significantly informed the calculation of peak electric loads via the Herman-beta method. The findings indicate a direct correlation between population density and peak load demands; for instance, Ka-Dzingidzingi, with a lower population density, exhibited lower peak loads, while Mookgopong NU, characterised by a higher population density, demonstrated elevated peak load demands. The modelling results show that the proposed system can generate sufficient electricity, yielding surplus energy across all studied locations. This surplus not only contributes to battery charging but is also available to support these communities during power outages and peak usage periods in the morning and evening. From an economic perspective, the adoption of this integrated system appears vital for the enhancement of energy supply in these rural areas. However, the financial viability presents a mixed picture; while the system offers half benefits, half losses, the recovery of investment for stakeholders could take over a decade due to the substantial capital costs associated with battery storage installation. A key economic metric, the LCOE is below 2.00R/kWh, indicating potential acceptance by local communities. For successful deployment, collaborative investment between the public energy sector and private investors is essential. A structured partnership could facilitate the realisation of this project, ensuring a viable energy solution for the targeted rural populations.

References

[1] C. Hachem-Vermette and S. Yadav, "Impact of power interruption on buildings and neighbourhoods and potential technical and design adaptation methods," *Sustainability,* vol. 15, no. 21, p. 15299, 2023. https://doi.org/10.3390/su152115299

[2] S. S. S. R. Depuru, L. Wang and V. Devabhaktuni, "Electricity theft: Overview, issues, prevention and a smart meter-based approach to control theft," *Energy Policy,* vol. 39, no. 2, pp. 1007-1015, 2011. https://doi.org/10.1016/j.enpol.2010.11.037

[3] A. F. Ahamed, R. R. Vibahar, S. Purusothaman, M. Gurudevan and P. Ravivarma, "Optimisation of hybrid microgrid of renewable energy efficiency using Homer software," *Revista Geintec-Gestao Inovacao E Tecnologias,* vol. 11, no. 4, pp. 3427-3441, 2021.

[4] M. J. Chihota, "Applying the Herman-Beta probabilistic method to MV feeders," 2015. http://hdl.handle.net/11427/24292

[5] E. Baldwin, J. N. Brass, S. Carley and L. M. MacLean, "Electrification and rural development: issues of scale in distributed generation," *Wiley Interdisciplinary Reviews: Energy and Environment,* vol. 4, no. 2, pp. 196-211, 2015. https://doi.org/10.1002/wene.129

[6] A. K. Patwary, M. A. Sayem, M. A. Hossain and M. A. Halim, "A review of energy storage systems (ESS) for integrating renewable energies in microgrids," *Control Systems and Optimisation Letters,* vol. 2, no. 1, pp. 103-112, 2024. DOI: https://doi.org/10.59247/csol.v2i1.68

[7] M. M. Y. T. Islam, G. Giannoccaro, Y. Mi, M. La Scala, M. N. Rajabi and J. Wang, "Improving reliability and stability of the power systems: A comprehensive review on the role of energy storage systems to enhance flexibility," *IEEE Access,* 2024. 10.1109/ACCESS.2024.3476959

[8] S. Olówósejéjé, P. Leahy and A. P. Morrison, "A practical approach for increased electrification, lower emissions and lower energy costs in Africa," *Sustainable Futures,* vol. 2, p. 100022, 2020. https://doi.org/10.1016/j.sftr.2020.100022

[9] A. F. Güven, Ş. Türkmen, E. Aşıklı and G. Örnek, " Investigating the effects of different types of battery impacts in energy storage systems on standalone hybrid renewable energy systems," *Karadeniz Fen Bilimleri Dergisi,* vol. 13, no. 3, pp. 943-964, 2023. https://doi.org/10.31466/kfbd.1275823

[10] J. Nyangon, "Climate-proofing critical energy infrastructure: Smart grids, artificial intelligence, and machine learning for power system resilience against extreme weather events," *Journal of Infrastructure Systems,* vol. 30, no. 1, p. 03124001, 2024. https://doi.org/10.1061/JITSE4.ISENG-2375

[11] P. Netshilonwe, F. Nemangwele and M. Ratshitanga, "An Economic Performance Overview of Microgrids for Limpopo Province Rural Areas," *IEEE PES/IAS PowerAfrica,* pp. 1-7, 2024. 10.1109/PowerAfrica61624.2024.10759448

[12] R. Takalani and B. Bekker, "Load and load growth models for rural microgrids, and how to future-proof designs," *In 2020 International SAUPEC/RobMech/PRASA Conference,* pp. 1-6, 2020. 10.1109/SAUPEC/RobMech/PRASA48453.2020.9041001

[13] A. Muhtadi, D. Pandit, N. Nguyen and J. Mitra, "Distributed energy resources based microgrid: Review of architecture, control, and reliability," *IEEE Transactions on Industry Applications,* vol. 57, no. 3, pp. 2223-2235, 2021. 10.1109/TIA.2021.3065329

[14] R. R. Danda, "Financial Services in the Capital Goods Sector: Analysing Financing Solutions for Equipment Acquisition," *Library Progress International,* vol. 44, no. 3, pp. 25066-25075, 2024.

[15] Y. Z. Alharthi, M. K. Siddiki and G. M. Chaudhry, "Techno-economic analysis of hybrid PV/wind system connected to utility grid," *In 2019 IEEE Texas Power and Energy Conference (TPEC),* pp. 1-6, 2019. 10.1109/TPEC.2019.8662156

Preliminary Investigation of the Mechanical Properties of Tissue Biopsies

Kayode Dada[1] and Risimati Mavunda[1]

[1]Department of Mechanical Engineering Science, University of Johannesburg, Johannesburg, South Africa

E-mail: kdada@uj.ac.za

Abstract. Cancer induction and progression have been significant challenges faced by humanity. Several procedures and methods have been used to detect the different stages within the clinical setting. However, many of these clinical tests are geared towards biochemical cues. We investigated the resected tissues from three patients (one colorectal and two breast tissues) retrieved from a biobank. A slice from each sample was cut out, attached to a disc, and placed inside a Cypher VRS atomic force microscope. The cut-out tissue was then hydrated with phosphate buffer saline. The indentation curves of the samples were then acquired and fit into the Derjaguin-Muller-Toporov model to extract the mechanical properties needed. The mean Young's modulus obtained for the colorectal normal biopsy was 3.31±5.32 MPa, while the corresponding value for the cancer cut-out was 2.94±2.87 kPa. However, the mean values for the two breast tissues were 180.25±113.32 and 469.28±480.31 kPa. The corresponding average values of the Young's moduli distribution of the cancer section of the breast tissues were 48.61±87.06 and 32.22±12.01 kPa, respectively. This preliminary investigation reveals differences in indentation measurements between cancer and non-cancer tissue sections, and these differences also vary across different indentation spots within the tissues.

1 Introduction

Cancer is generally defined as a disease that results from the uncontrolled growth of cells [1]. This arises when there is a significant deficiency in or damage to the cells' deoxyribonucleic acid (DNA). The abnormal cells can either continue to grow at the primary site, invade neighbouring sites or spread to distant sites in the body [2]. Cancer is usually characterised based on the primary affected tissue or organ (such as the brain, breast, colon, cervix, skin, etc.) [2]. The induction and progression in the body have been significant challenges facing humanity over the decades. The different cancer cases have resulted in many fatalities, and the incidences around the world are still very high. The World Health Organisation global observatory report estimates that mortalities and incidences of cancer will continue to rise [3]. Other reports say at least one in every four or five people will develop cancer in a lifetime [4]. However, several procedures and methods are being used to detect the stages of cancer presented within a clinical setting. These include physical examination, biochemical assays, conventional X-rays, computed tomography, magnetic resonance imaging and diagnostic nuclear imaging [4, 5, 6]. Although these methods provide clinical notes on the nature of the tumour or cancer, the inherent information on the metastatic potential of the cells of the tissue is minimal. This presents a challenge for physicians who focus solely on eradicating the solid tumour and clearing any remaining microscopic cells after surgery. Thus, seeking techniques that can augment the current diagnostic techniques used in a clinical environment is essential.

Biomechanics is an important technique proven to assist in understanding other diseases [8]. This has been applied to biological species at the cellular, tissue and organ levels [7, 8]. At the cellular level, different tools and techniques have been used to retrieve the vital information on the mechanical properties of the cells. These techniques include optical tweezing, micro-pipetting, laser tweezing, micro-particle tracking, force indentation, magnetic twisting and substrate stretching. The mechanical properties of the cells acquired include elasticity, adhesion, viscoelasticity, mechanosensing, and mechanotransduction [10]. Other reports that investigate cancer cells show that the mechanics of the cells are relevant in describing the development, progression, and metastatic nature of cancer [10, 11]. However, basic biomechanical information about the biopsy of cancer tissues is minimal.

In this study, we investigated the distribution of the mechanical properties of tissue biopsies in their native state. The biopsies were studied using an indentation tool in a liquid medium without conventional tissue processing (such as staining and embedding). To achieve this, we used an atomic force microscope (AFM), indicated in Figure 1 (right), operated in a contact mode.

2 Materials and Methods

2.1 Materials

The tissues, shown in Figure 1 (left), used in this study were obtained from the biobank at the Obafemi Awolowo University Teaching Hospital, Nigeria. An approval to access the biopsies was granted by the ethics and research committee of the institution under the protocol number ERC/2022/01/03. In this presentation, samples from three patients (two breast and one colorectal biopsies) were analysed. It should be noted that each biopsy sample was separated into normal and cancer sections based on the pathologist's clinical judgement before being stored in the tissue bank. An Asylum Cypher High Resolution AFM and a cantilever with a spherical probe make up the setup of the indentation tool. Phosphate buffer saline (PBS) was used to create a liquid medium during indentation measurements, and formaldehyde was used to preserve the tissue after retrieval from the tissue bank until the measurement day.

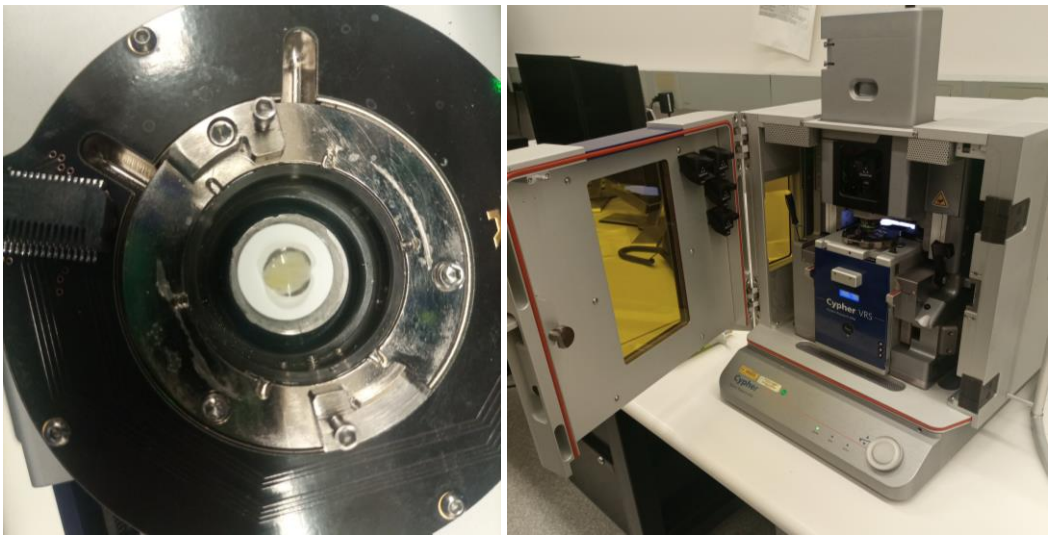

Figure 1: (*left*) A hydrophobic barrier was created around the tissues. (*right*) An Asylum Cypher AFM

2.2 Methods

The summarised workflow for the acquisition of indentation curves is subsequently shown here. The cantilever, with a spring constant ranging from 0.1 to 2 N/m, of the AFM was calibrated before measurement using the thermal noise method. This was achieved by aligning the laser spot on the cantilever, followed by a frequency sweep to find the appropriate resonance peak. After this, the setpoint was optimised to achieve a reproducible and stable tracking of the tissues. It was also optimised to prevent the breaking of the AFM probe during indentation. This procedure was repeated daily before the indentation of the samples. The tissues obtained from the bank have already been sectioned into normal

and cancer biopsies by the physicians before retrieval from the tissue bank. Approximately 1 mm of each resected tissue was cut out and glued to the AFM metal disc. After this, about 50 µl of PBS was added to the tissue and placed on the AFM stage. The cantilever was carefully fitted into its holder, and then 20 µl of PBS was added to the AFM cantilever tip, which has a spherical shape and a radius of 500 nm. The holder was then placed in the AFM stage, above the initially fitted sample. After positioning the sample and the cantilever, the cantilever holder was gently lowered to create a water column with the liquid on the tissue sample. The set parameters for the measurement include scan size between 5 – 20 µm, scan rate of 1 – 2.44 Hz and a setpoint of 1V. Due to the nature of the samples, each indentation curve was assessed before processing. Deflection-distance curves that do not indicate any possible sample indentation were excluded from further processing. The rejected cases sometimes result when the cantilever picks up some tissue samples during withdrawal. The indentation curves were obtained as deflection-distance curves. The curves were then processed, with AtomicJ [13], using the Derjaguin-Muller-Toporov (DMT) model [13], defined as

$$P = \frac{4E\sqrt{R}}{3(1-\nu^2)}\delta^{3/2} - 2\pi\gamma R \quad (1)$$

Where P is the applied load, E is the Young's modulus of the sample, R is the radius of the cantilever probe, ν is the Poisson ratio, taken generally as 0.5 because of the incompressible nature of biological materials, δ is the indentation depth, and γ is the surface energy. The last term $2\pi\gamma R$, represents the adhesion force.

3 Results and Discussion

This study examined the preliminary mechanical characteristics of three tissues resected from cancer patients. The tissues were stored in a biobank after clinical separation of the normal and cancer sections. The complete distributions of the Young's modulus (blue colour), adhesion work (green colour) and the deformation (yellow colour) are presented in Figures 2-4.

The Young's modulus was assessed to understand the stiffness of the tissues using a nano-indentation tool. These preliminary results indicate that cancer biopsies exhibit lower stiffness than normal tissues. This is in tandem with previous results reported for single-cell analysis [14]. However, the distributions in Figures 2A, 3A, and 4A show that some indented spots in the normal tissues still have values that fall within the range of the distribution noted from the cancer tissues (Figures 2D, 3D and 4D). This trend is also supported by Chen *et al*. [15], who reported lower Young's moduli using the Hertz–Sneddon model compared to the DMT model employed in this study. These findings suggest that the stiffness at the nano-scale level for tissues obtained from cancer patients can be heterogeneous, and further analysis should be carried out to understand the extent of these overlaps. This can also mean that the mechanical signature affected by point-to-point measurement is cell-dependent rather than the whole tissue.

Another property examined is the extent of deformation of the samples under indentation stress. This deformation can affect cell-to-cell interaction or when a cell tries to manoeuvre through channels (e.g. vessels) with a narrower dimension. A comparison in Figure 2 (B and E) shows that the extent of deformation is more evenly distributed in the breast cancer tissue compared to the normal tissue. Also, the mean deformation value was higher in the cancer tissues. This finding was also suggested by Ezenwafor *et al*. [16], who analysed the extent of deformation in the different grades of triple-negative breast cancer tissues. They opined that these differences may be due to the roles of the remodelling of the actin filaments in the tissues. However, the measurements by Ezenwafor *et al.* were carried out in air as opposed to the liquid measurement employed in this study. A similar trend was observed in the colorectal tissues, as shown in Figure 4 (B and E). This may be due to the ability of the constituent cells that make up the tissue to deform under stress. This can allow the cells to disintegrate and migrate to a new site, as also suggested by West et al. [17]. This process is usually the hallmark of metastasis. An exception was noted with the breast biopsy measurements in Figures 3 (B and E). A previous report indicated that this may result from the alteration in the cytoskeletal architecture of the cells that form the tissue under study [14, 15]. Thus, further details of the roles of the cytoskeleton in cells extracted from such tissues are imperative.

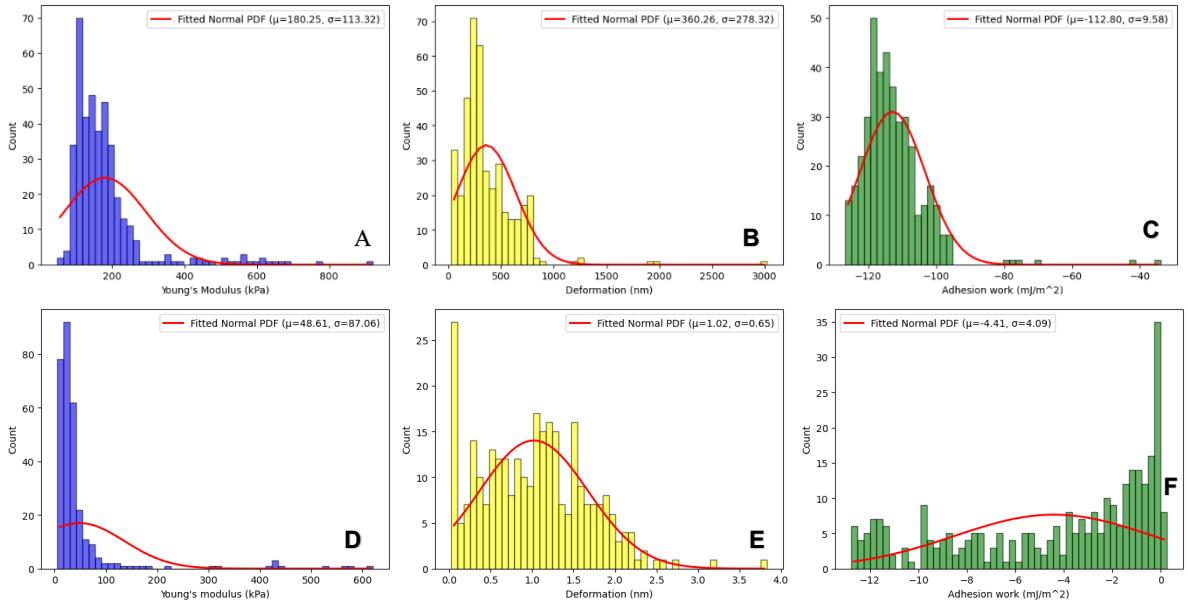

Figure 2: Distribution of the mechanical properties of breast biopsy (BP1) from a patient. (*top*) Histograms represent a normal tissue biopsy. (*bottom*): Cancer tissue biopsy

In Figures indicated with C and F, we presented the mechanical properties that show the adhesive capacity of the tissue samples. It represents the energy per unit area required to separate two adhering surfaces. Comparing the biopsy measurements, it was observed that the values of the work of adhesion of cancer samples are higher than those of normal tissues. The expression of cell adhesion molecules (CAMs) has been implicated in causing these differences, as previously reported by Kai et al. [20]. This implies that the cellular components of the cancer tissues are likely to be more adhesive than their normal counterparts. Although there are some overlaps at some indented points, as shown in Figures 3 (C, F) and 4 (C, F). These overlaps also suggest that the mechanical properties of tissues are inherently heterogeneous.

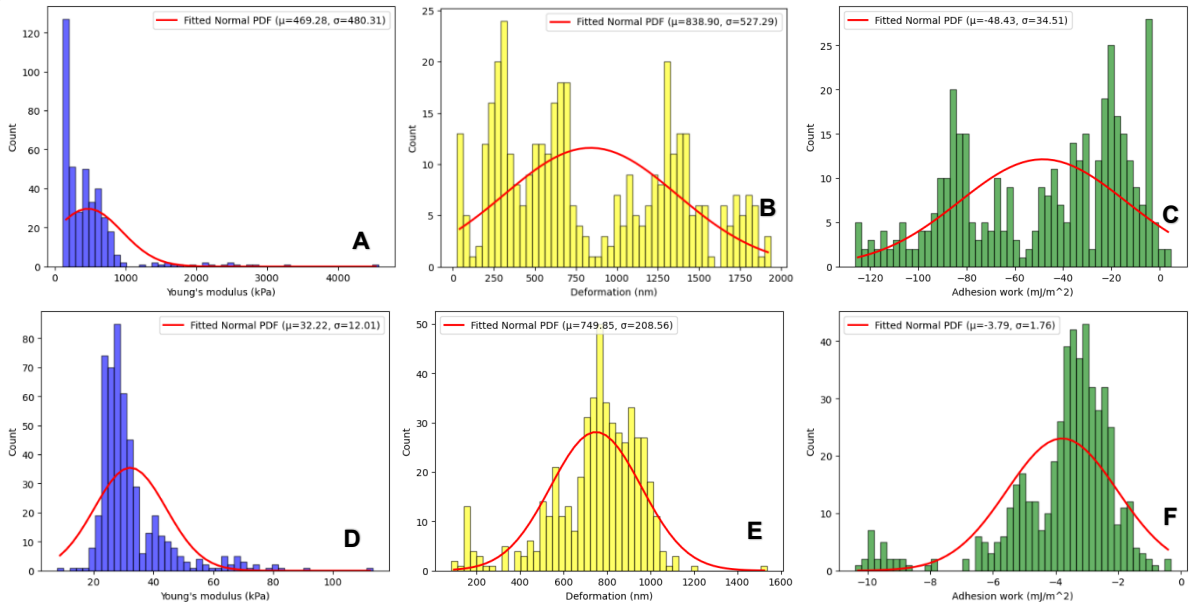

Figure 3: Distribution of the mechanical properties from breast tissue biopsy (BP2) resected from another patient. (*top)* Indicates the distribution for the normal biopsy. (*bottom*) Figures represent the cancer biopsy

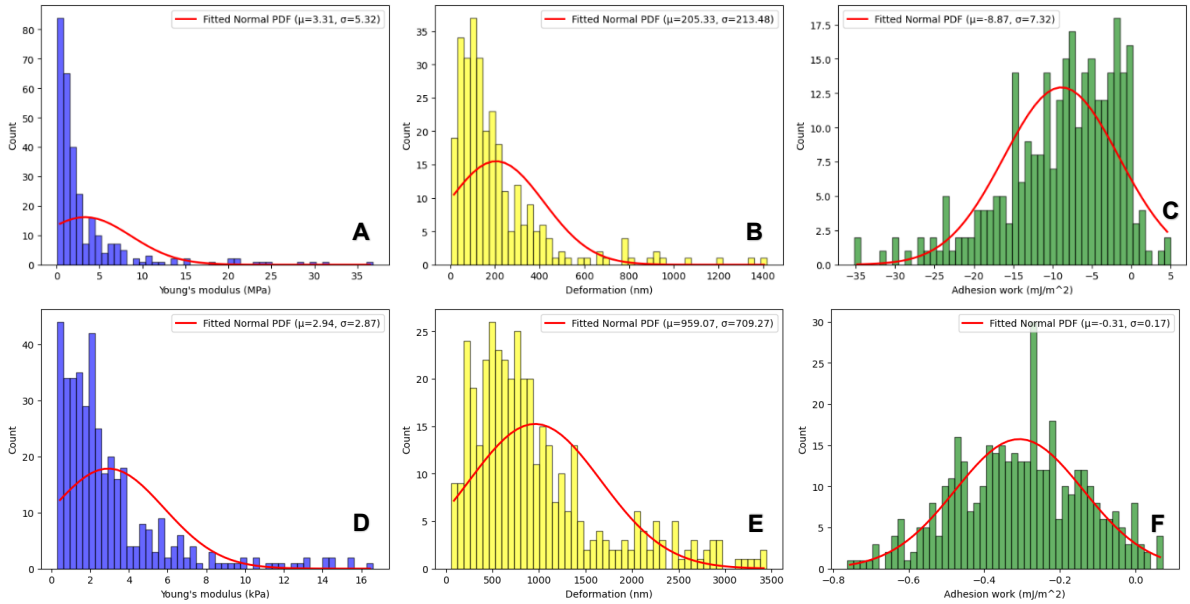

Figure 4: Distribution of the mechanical properties from a biopsy from the colorectal tissue (CRT) bank. (*top*) Figures represent normal tissue. *(bottom*) Figures are distributions for cancer sections

4 Conclusion

In this paper, we demonstrate that the distribution of the measured mechanical parameters of tissue biopsies is crucial for enhancing the understanding of the average values typically reported of these parameters. Additionally, the obtained parameters depend on the type of tissue being investigated. Thus, it is crucial to understand these distributions for improved classification of cut-outs from resected tissues in clinical diagnosis.

5 Limitations

In this study, we were unable to measure the topography of the samples in their native state. This limitation was experienced as the cantilever continuously gets stuck during imaging. Also, a few tissues were measured.

6 Acknowledgement

The authors would like to appreciate the following institutions and organisations for their contributions to the success of this study: Obafemi Awolowo University Teaching Hospital, Ile-Ife, Nigeria; Sentech SOC Ltd; University of Johannesburg; Nuclear Medicine, University of the Witwatersrand; and Centre for Functional Nanomaterials, Brookhaven National Laboratory, United States of America.

References

[1] M.-A. Majérus, “The cause of cancer: The unifying theory,” *Advances in Cancer Biology - Metastasis*, vol. 4, p. 100034, Jul. 2022, doi: 10.1016/j.adcanc.2022.100034.

[2] S. Gerstberger, Q. Jiang, and K. Ganesh, “Metastasis,” *Cell*, vol. 186, no. 8, pp. 1564–1579, Apr. 2023, doi: 10.1016/j.cell.2023.03.003.

[3] IARC, “Estimated numbers from 2022 to 2050, Males and Females, age [0-85+],” Available: https://gco.iarc.fr/tomorrow/en/dataviz/trends?multiple_populations=1.

[4] R. Zheng *et al.*, “Global, regional, and national lifetime probabilities of developing cancer in 2020,” *Sci Bull (Beijing)*, vol. 68, no. 21, pp. 2620–2628, Nov. 2023, doi: 10.1016/j.scib.2023.09.041.

[5] P. Gromek *et al.*, “Revisiting the standards of cancer detection and therapy alongside their comparison to modern methods,” *World J Methodol*, vol. 14, no. 2, Jun. 2024, doi: 10.5662/wjm.v14.i2.92982.

[6] B. K. Prasanth, S. Alkhowaiter, G. Sawarkar, B. D. Dharshini, and A. R. Baskaran, “Unlocking Early Cancer Detection: Exploring Biomarkers, Circulating DNA, and Innovative Technological Approaches,” *Cureus*, Dec. 2023, doi: 10.7759/cureus.51090.

[7] T. Penzkofer and C. M. Tempany-Afdhal, "Prostate cancer detection and diagnosis: the role of MR and its comparison with other diagnostic modalities – a radiologist's perspective," *NMR Biomed*, vol. 27, no. 1, pp. 3–15, Jan. 2014, doi: 10.1002/nbm.3002.
[8] Y. Nematbakhsh and C. T. Lim, "Cell biomechanics and its applications in human disease diagnosis," *Acta Mechanica Sinica*, vol. 31, no. 2, pp. 268–273, Apr. 2015, doi: 10.1007/s10409-015-0412-y.
[9] T. Lu and C. Chang, "Biomechanics of human movement and its clinical applications," *Kaohsiung J Med Sci*, vol. 28, no. 2S, Feb. 2012, doi: 10.1016/j.kjms.2011.08.004.
[10] T. P. Lele *et al.*, "Tools to Study Cell Mechanics and Mechanotransduction," 2007, pp. 441–472. doi: 10.1016/S0091-679X(07)83019-6.
[11] W. Yu *et al.*, "Cancer cell mechanobiology: a new frontier for cancer research," *Journal of the National Cancer Center*, vol. 2, no. 1, pp. 10–17, Mar. 2022, doi: 10.1016/j.jncc.2021.11.007.
[12] S. C. Schwager, P. V. Taufalele, and C. A. Reinhart-King, "Cell–Cell Mechanical Communication in Cancer," *Cell Mol Bioeng*, vol. 12, no. 1, pp. 1–14, Feb. 2019, doi: 10.1007/s12195-018-00564-x.
[13] P. Hermanowicz, M. Sarna, K. Burda, and H. Gabryś, "AtomicJ: An open source software for analysis of force curves," *Review of Scientific Instruments*, vol. 85, no. 6, Jun. 2014, doi: 10.1063/1.4881683.
[14] S. Kwon, W. Yang, D. Moon, and K. S. Kim, "Comparison of Cancer Cell Elasticity by Cell Type," *J Cancer*, vol. 11, no. 18, pp. 5403–5412, 2020, doi: 10.7150/jca.45897.
[15] X. Chen *et al.*, "Atomic force microscopy reveals the mechanical properties of breast cancer bone metastases," *Nanoscale*, vol. 13, no. 43, pp. 18237–18246, 2021, doi: 10.1039/D1NR03900H.
[16] T. Ezenwafor *et al.*, "Nanoindentation study of the viscoelastic properties of human triple negative breast cancer tissues: Implications for mechanical biomarkers," *Acta Biomater*, vol. 158, pp. 374–392, Mar. 2023, doi: 10.1016/j.actbio.2023.01.011.
[17] A.-K. V. West *et al.*, "Dynamics of cancerous tissue correlates with invasiveness," *Sci Rep*, vol. 7, no. 1, p. 43800, Mar. 2017, doi: 10.1038/srep43800.
[18] E. Gasser *et al.*, "Deformation under flow and morphological recovery of cancer cells," *Lab Chip*, vol. 24, no. 16, pp. 3930–3944, 2024, doi: 10.1039/D4LC00246F.
[19] T.-H. Kim *et al.*, "Cancer cells become less deformable and more invasive with activation of β-adrenergic signaling," *J Cell Sci*, vol. 129, no. 24, pp. 4563–4575, Dec. 2016, doi: 10.1242/jcs.194803.
[20] F. Kai, A. P. Drain, and V. M. Weaver, "The Extracellular Matrix Modulates the Metastatic Journey," *Dev Cell*, vol. 49, no. 3, pp. 332–346, May 2019, doi: 10.1016/j.devcel.2019.03.026.

Synthesis and characterization of biomass-based graphitic carbon for sustainable energy storage.

Thokozane Mlotshwa[1,2], Lordwell Jhamba[2], Eric Maluta[2] and Joseph Kirui[2]

[1]Department of Physics, University of Limpopo, Private Bag X 1106, Sovenga, 0727, South Africa
[2]Department of Physics, University of Venda, Private Bag X 5050, Thohoyandou, 0950, South Africa

E-mail: thokozane.mlotshwa@ul.ac.za

Abstract. Biomass waste conversion into useful materials is one of the contributing factors towards green energy techniques and achieving the set out sustainable development goals. The current work focuses on converting biomass waste as tea extracts into carbonaceous materials and analyse it for carbon rich material and potential application in LIBs as anode material. Pyrolysis method and KOH activation were used to carbonise tea waste extracts into desired carbon-based material. The colour and textural properties of the synthesized tea based carbonaceous material suggests a notably significant degree of graphitization and a high carbon content, which is ideal for candidacy in sustainable energy storage enhancements. Liquid suspension indicates insoluble behaviour normally observed for most carbonaceous materials. SEM analysis indicates a layered and flaky structure that is primarily expected for graphite anode structure. EDX indicates a favourable amount of carbon denoting a biomass-based carbonaceous material that could be used as an anode material in LIBs for possible energy storage enhancements. XRD findings indicates a likely peak at $2\theta = 26.5°$ corresponding to the phase (002) primarily dominant for graphite. Mass comparisons reveal that a substantial quantity of biomass is necessary to produce adequate amounts of activated carbon.

1 Introduction

The synthesis and application of biomass-based materials have drawn more attention from researchers due to the host of biomass feedstocks available for conversion into useful materials, sustainability, and cost-effectiveness. Graphite, a non-renewable resource, is the most popular material used in lithium-ion batteries (LIB) as an anode material for lithium-ion intercalation. Current LIB requires critical raw materials, efficient manufacturing, recycling processes and end of life management. To mitigate the aforementioned factors, the utilization of biodegradable resources, such as biomass, to produce valuable products is noteworthy.

Carbonaceous materials are utilized in several applications, including energy storage and conversion, filtration systems, fuel cells, supercapacitors, bioimaging, and tissue engineering. Conventional and sustainable methods for acquiring carbon-based materials are necessary due to their remarkable properties, including high electrical conductivity, thermal stability, mechanical strength, and extensive surface area, rendering them versatile for various applications. Nature offers a vast array of easily disposable, environmentally friendly, and varied resources that can be converted into superior carbonaceous materials with the right qualities for certain uses. Plant and animal

wastes are converted into carbonaceous materials, which are then heated to high temperatures in a low-oxygen environment. The result is a black powder with high carbon content, high surface area, and low nutrient content [1].

Carbon-based materials formed from biomass products offer an alternative for managing waste and byproducts and the naturally occurring raw materials are cost-effective for materials engineering making them an appealing option for consideration. Among its many applications, biomass-based carbon is being investigated as a potential means of improving the viability of smart materials, supercapacitor electrodes and expanded use in electrochemical energy storage, solar light photocatalytic, hydrogen generation and as premium anode material in lithium-ion batteries (LIBs) [2]. Numerous biomass feedstocks such as sawdust, cornstalk, coconut shell, wood and bamboo were used to manufacture superior graphitic carbon for a wider variety of uses [3]. Green tea waste was tried for a supercapacitor electrode by Sankar *et al.*, they obtained nanoflakes with large pore volume and higher surface area leading to potentially higher performance electrode material [4]. The latter prompted the inquiry of tea waste applicability in other types of storage devices such as batteries.

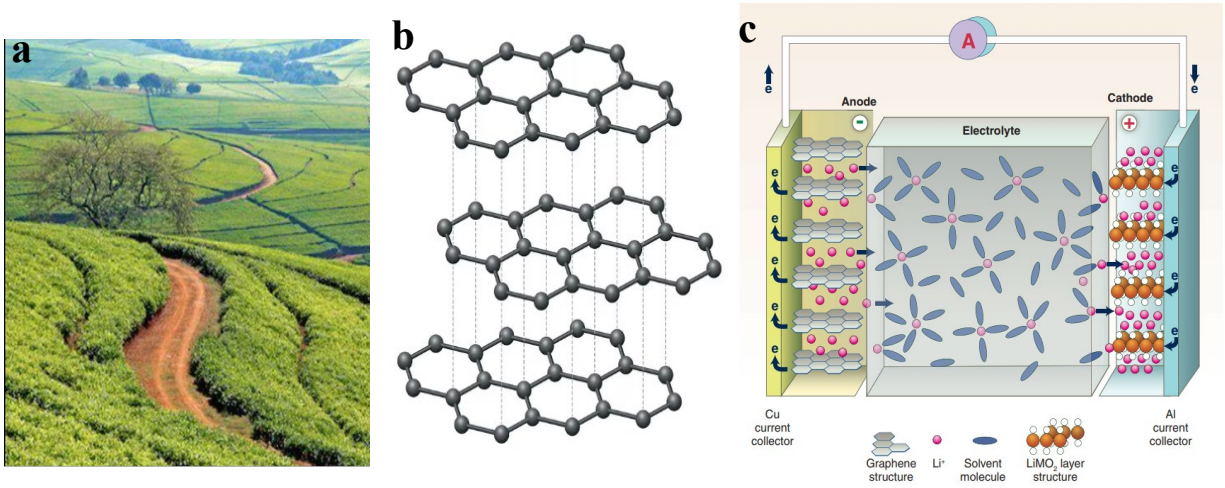

Figure 1: *(a)* Tea plantation, *(b)* graphite structure and *(c)* its application is storage device [5].

Figure 1 (a) shows a large area of tea plantation indicating the large quantity of tea waste that can be produced. Graphite is made up of layers of carbon atoms that are covalently bonded to form hexagonal rings as shown in figure 1 (b). It is used as an anode material in LIB. Lithium ions flow form the cathode through the semipermeable electrolyte and build up on the anode while electrons flow from the external circuit during charging and vice versa during discharging as depicted in figure 1 (c). Graphite is dimensionally stable, allowing lithium-ion intercalation without significant damage from swelling, which makes it the dominant anode material in LIBs. In the present work, tea extracts were used as eco-friendly, cost-effective, and commercially viable alternative for the synthesis of activated carbon, due to its carbonaceous similarities to natural graphite. Due to the level of carbonization, a chemical process involving potassium hydroxide (KOH) as an activating agent has been adopted to synthesize the activated carbon as it is recommended for carbonization enhancement during biomass activation. These results are analyzed in line with the known results for synthetic graphite (SG) as our guiding base material.

2 Methodology

2.1 Materials

Tea extracts from a local plantation were purchased from a local supermarket for convenience. KOH was obtained from Sigma-Aldrich. A muffle furnace through a pyrolysis method was used for carbonization. Deionized water was used to prepare aqueous solutions used during the experiment. The activated tea waste graphitic material (TWGM) sample was characterized by examining the presence of functional groups using a Bruker FTIR spectrometer. Scanning electron microscope (SEM) and energy dispersive X-ray spectroscopy (EDX) analysis were obtained through Zeiss Gemini Sigma 500 VP.

2.2 Synthesis of Activated-TWGM

Figure 2 shows the experimental setup for the synthesis of TWGM using tea extracts, through electrical furnace-assisted carbonization at very low oxygen levels as described by Sankar *et al.* [4]. Tea wastes products were sorted, washed dried and grinded to obtain fine tea waste. Briefly, A sample of 19 g of fine tea waste (TW) was transferred into a crucible for thermal treatment. The heating rate of $10℃/min$ was used to increase the temperature of the muffle furnace and maintained at 500℃ for 60 minutes to achieve total carbonization of our biomass sample. The carbonized materials were then allowed to cool to ambient temperature and KOH was added at a molar ratio of 1/4 (TW/KOH) for carbon activation. The muffle furnace was further used to thermally treat the mixture at 600 ℃, which was also maintained for 120 minutes using the same heating rate to activate the TW carbon product. Thereafter, the KOH-activated TWGM product was ground with a pestle in a mortar. Using a magnetic stirrer at speed of 200 r/min without heating, the fine activated-TWGM powder was mixed with deionized water for 6 hours. The water treatment process was done with an intention of enhancing the quality and purity of the graphitized activated TW. Schematic illustration with images of the synthesis procedure from TW to TWGM is summarized in figure 2.



Figure 2: Schematic illustration of the synthesis method.

3 Results and discussion

3.1 Physical observations

Figure 3 (a) shows a pictorial view of commercially available synthetic graphite (SG) while (b) depicts current TWGM, (c) and (d) shows TWGM dissolved in deionised water for 0 and 24 hours respectively. SG is in dissolvable in certain fluids such as ethanol and deionised water, our TWGM displays the same characteristics as shown in figure 3 (d).

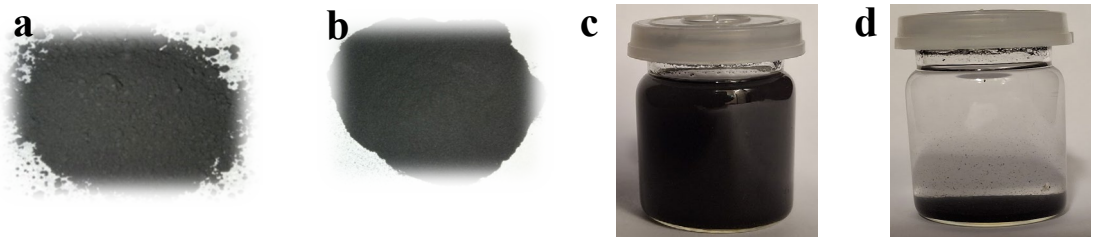

Figure 3: *(a)* SG powder *(b)* produced TWGM *(c)* and *(d)* TWGM liquid suspension.

Characterisation techniques such as SEM, FTIR and XRD analysis were used to verify similar morphologies and microstructural characteristics suggested by the black colour, smooth texture and insoluble of SG and current TWGM. Both the SG and TWGM's textural qualities were observed to be quite similar, they felt delicate and soft

against the hand. The SG tended to form clusters as evident in figure 3 (a) with the appearance of solid granule-like formations. The compact appearance of TWGM powder in figure 3 (b) mainly attributes to the grinding process done posterior to KOH activation and water treatment, resulting in a greater degree of refinement. In contrast to these findings, the goal of this work is to show that biomass products, such as tea waste, may possess the optimal qualities required to improve a variety of technological developments such as sustainable energy storage.

3.2 SEM and EDX analysis

Our TWGM displays the stacking of layers giving layered structure normally observed for most carbon materials as shown in figure 4 (a). The corresponding EDX spectra shows a significant presence of carbon which is 24.95 % which is also desirable for graphite-based materials indicated by figure 4 (b). Strong presence of oxygen and carbon elements are observed from the EDX spectra denoting constituents consistent for graphitic structures. Large amounts of K and O elements results from KOH activation.

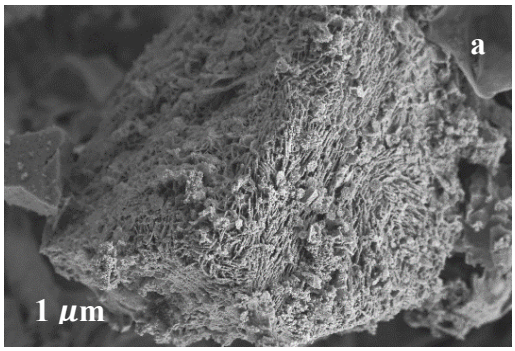

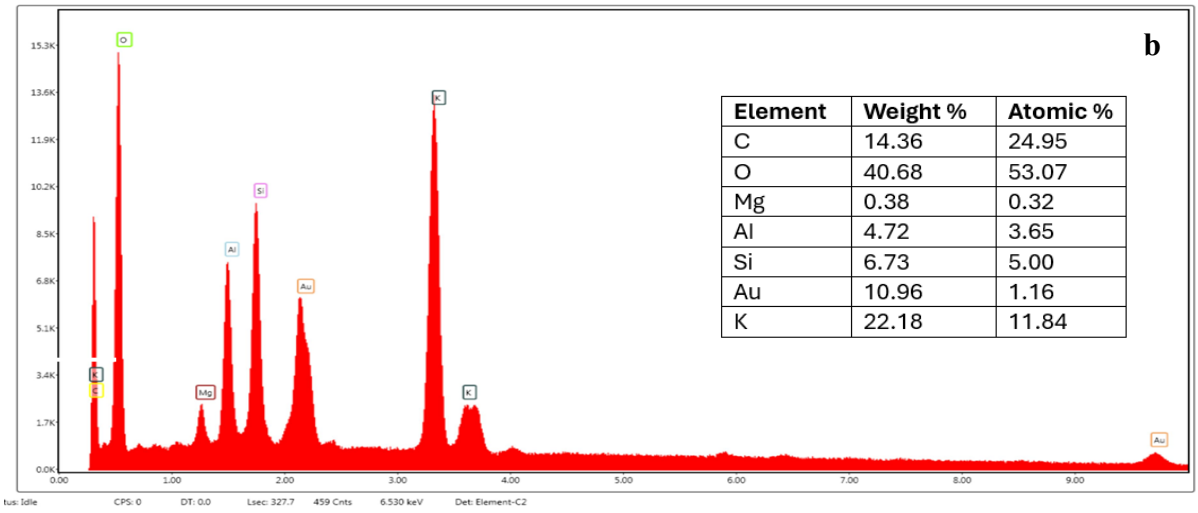

Element	Weight %	Atomic %
C	14.36	24.95
O	40.68	53.07
Mg	0.38	0.32
Al	4.72	3.65
Si	6.73	5.00
Au	10.96	1.16
K	22.18	11.84

Figure 4. (a) SEM and (b) EDX spectra for TWGM

3.3 FTIR analyses

The surface chemical properties of TWGM as analyzed by FTIR are shown in figure 5. The O – H stretching vibration of the hydroxy functional group is responsible for the weak development of an absorption band at about 3500 cm^{-1}. The band at about 2500 cm^{-1} is attributed to the $O-H$ of the carboxylic acids. The band at about 2300 cm^{-1} indicates that $C=C$ stretching may be present. The potential presence of the nitro ($R\text{-}NO_2$) group is represented by the peak at about 1400 cm^{-1} however the literature suggests that the C – N amine group is more likely to be present [5]. The band at 975.13 cm^{-1} corresponds to a $C-H$ Alkene (Out-of-plane band). The C – H aromatic band is located at about 800 cm^{-1}. The average peak intensities indicate that the volatile chemicals were

successfully eliminated during heat treatment because they show very slight traces of functional groups containing nitrogen and oxygen.

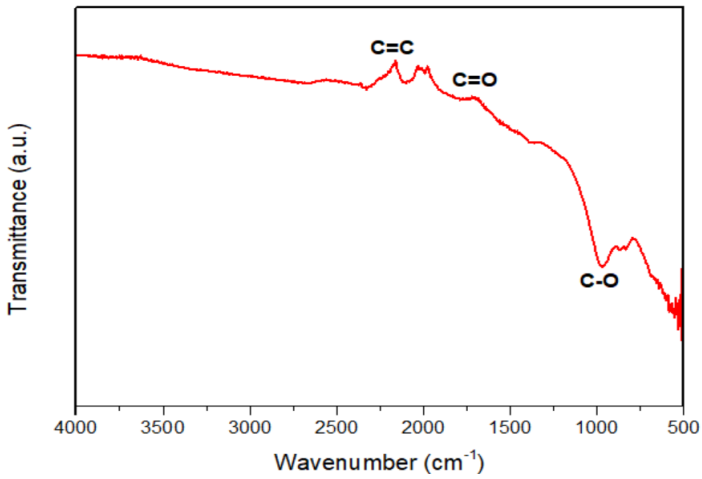

Figure 5: FTIR spectra for TWGM

3.4 XRD analyses

As shown in figure 6, a strong XRD peak was observed by Ain *et al.* at $2\theta = 26.5°$ with a light peak at $2\theta = 54.5°$ attributed to the (002) and (004) planes with d-spacing of 3.5 Å and 1.9 Å respectively [6]. The enlarged peak of figure 6 shows a potentially smaller peak at the region corresponding to the (002) plane. A dominant peak is observed at $2\theta = 34.0°$ which is desirable to be located at $2\theta = 26.5°$ corresponding to the (002) plane primarily observed for graphite. The inset of figure 6 shows the desired dominant peak corresponding to the (002) plane generally observed for graphite; our findings indicate that possible enhancement to our methodology could result in a similar dominant peak at the same position.

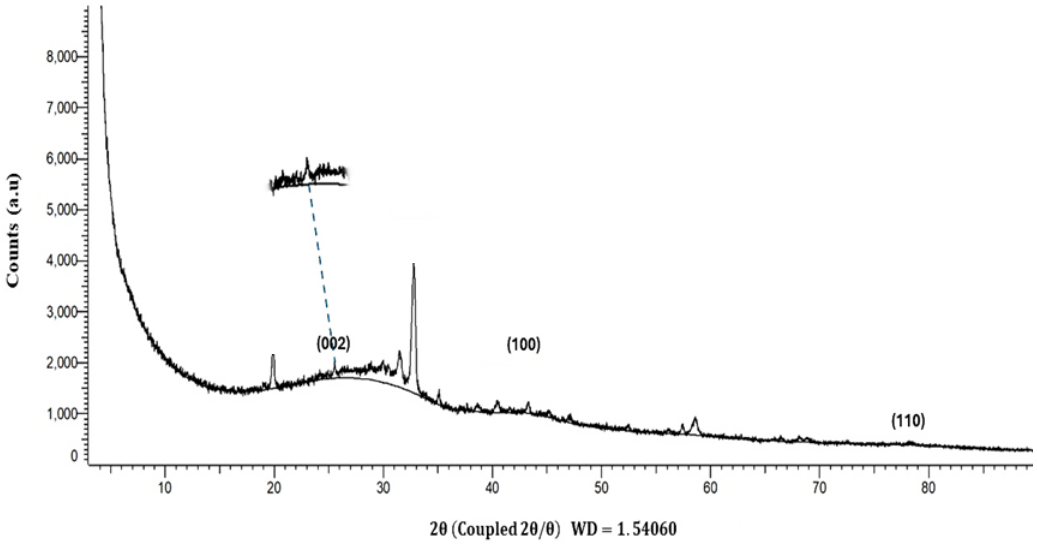

Figure 6: XRD spectrum for tea waste graphitic carbon.

Table 1 compares the feedstock mass to obtained carbonaceous product; this indicates that more biomass feedstock is required to obtain sufficient product. The mass loss percentage was calculated by equation 1 below.

$$x = \frac{M_0 - M_t}{M_0 - M_f} \times 100\ \% \tag{1}$$

where M_0 is the initial mass, M_f is the final mass and M_t is the mass over time [7].

Biomass	Pre-carbonisation mass (g)	Mass over time (g)	Post-carbonisation mass (g)	Mass Percentage loss (%)
Tea extract	19.00	8.83	5.10	73.16

Table 1: Biomass feedstock to product mass comparisons.

73.16 % of initial mass is lost during the carbonisation process. Calcination at very high temperatures usually removes liquids and other impurities in the samples resulting in reduced mass. The mass measurements and weight comparison of the TWGM throughout the experiment, from pre-carbonization until the final product was obtained, revealed that the TWGM was 26.84 % of the original mass without the use of a catalyst, which implied 73.16 % elimination of volatile traces.

4 Conclusion

TWGM was successfully synthesized using tea waste as a high carbon content biomass resource. The colour and textural properties of TWGM with reference to known SG suggests a notably significant degree of graphitization. Our sample indicates insoluble property similar to SG. The quantitative results showed that tea waste has a high carbon content, which is ideal for candidacy in sustainable energy storage enhancements. The average peak intensities indicate that the volatile chemicals were successfully eliminated during heat treatment as indicated by the FTIR results. XRD reveals a potential peak corresponding to the (002) plane primarily dominant for SG. Mass loss percentage shows that a very large amount of biomass is required to obtain enough product, in a way reducing land pollution. These findings suggest that tea waste extracts can further be investigated to confirm their applicability in energy storage devices as an anode candidate primarily in LIBs. More analysis through BET, Raman and electrochemical testing can be done to further the scope of this work.

5 Acknowledgements

We would like to acknowledge the University of Venda and the University of Limpopo for financial assistance. Dr T Malwela and Mr S Nemakanga for SEM and FTIR analysis respectively.

References

[1] X. Ma, B Zhou, A Budai, A Jeng, X Hao, D Wei, Y Zhang and D Rasse., “Study of Biochar Properties by Scanning Electron Microscope – Energy Dispersive X-Ray Spectroscopy (SEM-EDX),” 2016.

[2] C. L. Williams, T. L. Westover, R. M. Emerson, J. S. Tumuluru, and C. Li, “Sources of Biomass Feedstock Variability and the Potential Impact on Biofuels Production,” 2016.

[3] A. S. Kamal, R. Othman, and N. H. Jabarullah, “Preparation and synthesis of synthetic graphite from biomass waste: A review,” 2020.

[4] S. Sankar, A Ahmad, A Inamdar, H Im, Y Lee, D Kim and S Lee, “Biomass-derived ultrathin mesoporous graphitic carbon nanoflakes as stable electrode material for high-performance supercapacitors,” 2019.

[5] B. Dunn, H. Kamath, and J.-M. Tarascon, “Electrical Energy Storage for the Grid: A Battery of Choices System power ratings, module size,” 2011.

[6] Q. T. Ain, S. H. Haq, A. Alshammari, M. A. Al-Mutlaq, and M. N. Anjum, “The systemic effect of PEG-nGO-induced oxidative stress in vivo in a rodent model,” 2019.

[7] J. S. Teh, Y. H. Teoh, H. G. How, and F. Sher, “Thermal analysis technologies for biomass feedstocks: A state-of-the-art review,” 2021.

The detection of HIV using plasmonically active colloidal gold nanoparticles

Masixole Lugongolo[1], Phumulani Mcoyi[2], Luleka Mngwengwe and Saturnin Ombinda-Lemboumba[1,2]

[1]Photonics Centre, Council for Scientific and Industrial Research, Pretoria, South Africa
[2]Departement de Physique, Université des Sciences et Techniques de Masuku, B.P 943, Franceville Gabon

E-mail: mlugongolo@csir.co.za

Abstract. Localized surface plasmon resonance (LSPR) phenomenon occurs when incident light of specific wavelength excites the free electrons on the gold nanoparticles surface, which then leads to the enhancement of the nanoparticle surface electromagnetic field. The enhanced electromagnetic field has a short decay length and is localized in LSPR as opposed to the surface plasmon resonance (SPR) where the activated surface plasmons propagate. The short electromagnetic field decay length in LSPR means that it is highly sensitive to the refractive index changes near the gold nanoparticles surface rather than the bulk refractive index in SPR. This makes this technique efficient particularly to changes induced by subtle interactions. In this work, LSPR was used to differentiate between samples with HIV and the ones with no HIV. A glass slide was treated with 1% APTES solution in ethanol before depositing a layer of gold nanoparticles. An anti-HIV-gp120 antibody was added as a biorecognition element prior to the addition of the HIV pseudovirus as the analyte. Thereafter the slide was analyzed on an LSPR system using a green LED light. The results showed that when using 50 nm gold nanoparticles, there was a clear distinction between a sample with the HIV pseudovirus and the one without it as shown by the varying light transmission intensities between the negative sample and the sample with the virus. This denotes that LSPR is sensitive enough as a label free detection method for virus detection. This can be used for the development of simple and cost-effective ways of detecting various diseases in developing countries.

1 Introduction

By the end of 2023, globally, there was an estimated 40 million individuals living with Human immunodeficiency virus (HIV), which demonstrates that this infection remains a public health challenge [1] There remains no cure for the HIV infection and according to the World Health Organization (WHO) recommendations all people should get tested and the infected ones are to start treatment as early as they are aware of their HIV status regardless of their CD4 count [2] This therefore has created a need to increase testing platforms, thus reaching as many people as possible irrespective of geographical location and socioeconomic factors. The investigation of photonics-based technologies for HIV diagnostics seeks to provide a sensitive, accurate and simple to use device that can be used at point of care particularly in resource limited settings. Localized surface plasmon resonance (LSPR) is one of the promising photonics-based technologies that can be used for the detection of HIV. The LSPR describes a phenomenon that occurs when the incident light of a specific wavelength excites free electrons on the surface of nanoparticles, which results in the enhancement of the nanoparticle surface

electromagnetic field. The enhanced electromagnetic field has a short, localized decay length, thus making the LSPR highly sensitive to the refractive index changes near the nanoparticles surface [3]. In the LSPR system when the refractive index increases, the wavelength peak of the incident light shifts towards the longer wavelengths (red shift) whereas the decrease of the refractive index causes a blue shift. This shift facilitates the detection of various analytes due to changes in the refractive index [4]. Thereby making this technique efficient particularly to changes induced by subtle interactions.

LSPR biosensing is performed without the use of dyes, thus simplifying the process and reducing costs. Owing to the strong electromagnetic field enhancements, LSPR allows the detection of analytes at low concentration. This type of biosensor can be integrated into microfluidic devices and multiplexed and enabling the simultaneous detection of multiple analytes in portable diagnostic systems. In this work LSPR was used for the detection of Human immunodeficiency virus (HIV) with the aim of developing a laser driven real-time microfluidic, multiplexed device that can be used in resource limited settings. Furthermore, this work aims to contribute towards the UNAIDS 95-95-95 fast track strategy of eradicating HIV/AIDS by 2030. This strategy states that by 2030 95% of people living with HIV (PLHIV) should know their infection status, 95% of those living with the virus should be receiving antiretroviral treatment, and 95% of all those on treatment be virally suppressed [5]The detection of HIV was performed by coating glass slides with gold nanoparticles and functionalizing the slide using anti-HIV-gp120 antibody before the addition of the virus and analyzing on the LSPR system.

2 Methodology

2.1 Localized surface plasmon resonance system

The work presented here was performed using an LSPR system as described in Mcoyi et al 2024 [6] The system consisted of a 520 nm light emitting diode (LED) as a light source (Thorlabs, PL201, Pout < 1mW). The light was directed to the XYZ stage, where a glass sample slide was placed for detection. A focusing lens was used to couple the light into the optical fiber, which guided the light to the spectrometer connected to the computer for spectra acquisition.

2.2 Preparation of a sample slide and samples

Glass slides were washed by sonication in acetone, absolute ethanol, and ultrapure water. After drying with nitrogen gas, the slides were then treated with oxygen plasma (hydroxylation). Glass slides were then silane treated by incubation in 1% APTES (3-Aminopropyltriethoxysilane) (Sigma-Aldrich) for 24hr at room temperature. After incubation, the slides were washed with water and dried. Multiple wells were created on the glass slide for different samples (which are gold nanoparticles (AuNPs), gold nanoparticles conjugated to the anti-HIV gp120 antibody (Abcam, ab21179) (AuNPs-Ab) and the conjugate with the virus (AuNPs-Ab-virus). In the first well, 250µl of 60 nm (Cytodiagnostics, Canada) nanoparticles were added, in wells 2 and 3, 250 µl of the AuNPs-Ab conjugate was added (conjugation process outlined in section 2.3) and allowed stabilize by letting them stand for one hour at room temperature. In the third well, 100µl of the HIV pseudovirus was added and incubated for 1 hour at 4ºC. Pseudovirus production is summarized in section 2.4.

2.3 Conjugation of the antibody to the nanoparticles

Similar ratios of N-hydroxysuccinimide (NHS) (Sigma-Aldrich, 56480), 1-Ethyl-3-(3-dimethylaminopropyl)-carbodiimide (EDC) (Sigma-Aldrich, E7750) and polyethylene glycol (SH-PEG-COOH) (Sigma-Aldrich, 757845) were mixed in ultrapure water and shaken for an hour. Thereafter, the anti-HIV-1 gp120 antibody (Ab) was added to the solution and further mixed for 2 hours on an orbital shaker before filtering and washing twice with 1X phosphate-buffered saline (PBS) in a 50 kDA filter. Fifteen microlitres of the activated antibody were eluted by inverting the filter and spinning it down. Subsequently, 12µL of the activated antibody was mixed with 200µL of 1:2 diluted 50 nm gold nanoparticles and incubated for an hour to form a AuNPs-Ab bioconjugate. This was then characterized by UV-Vis absorption spectroscopy.

2.4 Production of the HIV pseudovirus

The HIV pseudovirus was produced by transfecting 293T/17 cells using a transfection reagent as described by Lugongolo et al [7]. Briefly, cells were seeded in a T75 flask with 4µg of HIV-1 Plasmid and 8µg of env HIV-1 plasmid backbone. The supernatant containing the pseudovirus was harvested after 48 hours and filtered with a 0.45µm filtration system and stored in cryovials at 80ºC.

3 Results

To optimize and characterize the LSPR system, a simulation approach was used to analyze the impact of gold nanoparticle size on the LSPR peak shift. It is documented that the optical response of gold nanoparticles differs from small to large nanoparticles. In small nanoparticles, the response is mainly dominated by absorption, while in larger nanoparticles, the optical outcome is dominated by scattering [8]. Theoretical modeling of gold nanoparticles is possible with Mie theory, which is adapted in Maxwell's equation for spherical particles accommodate optical outcomes and has been successfully used to model optical extinction. Figure 1A shows the simulated effect of nanoparticle size with corresponding LSPR peak shifts and how peaks shift with varying nanoparticle sizes. The LSPR peak shifts increase as nanoparticle size increases.

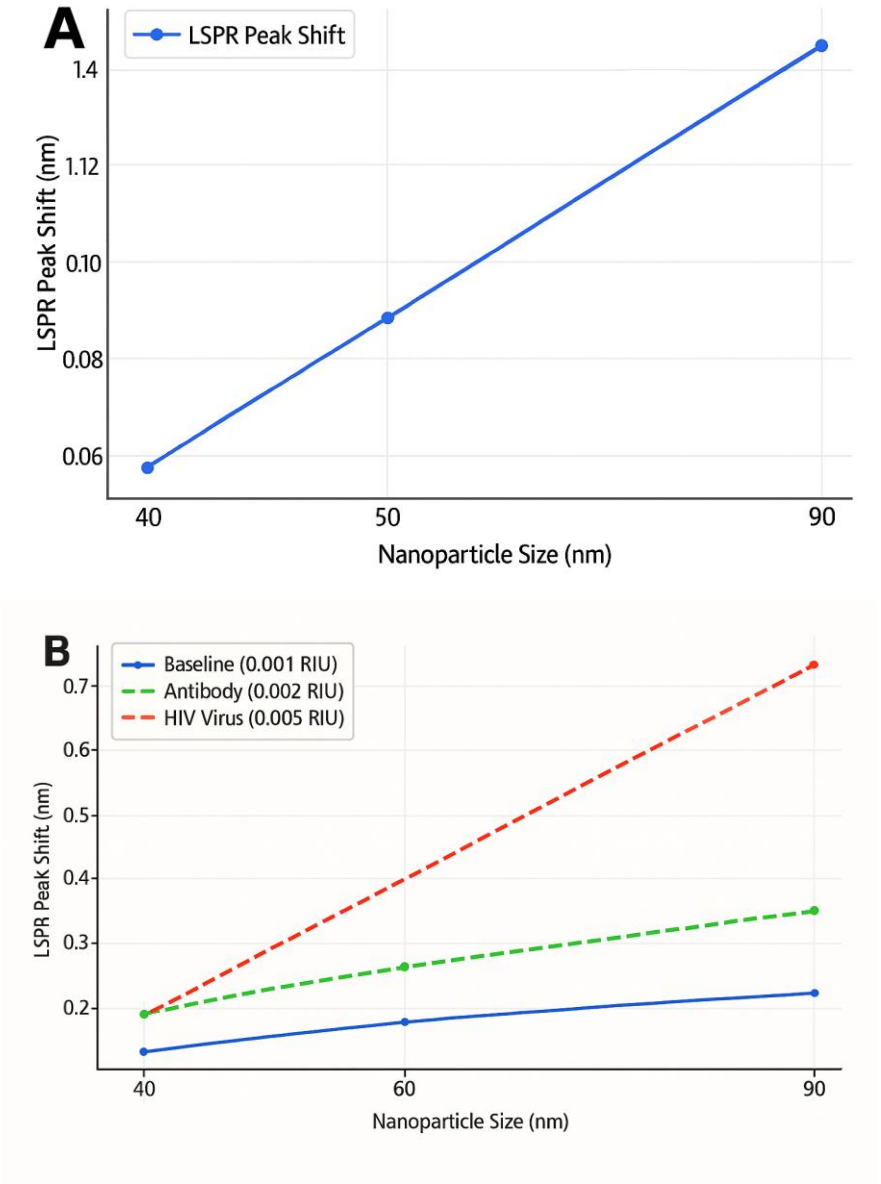

Figure 1: Simulated effect of nanoparticles showing (A) different nanoparticle sizes and their LSPR peak shifts. (B) Simulated effect of nanoparticles with varying sizes (blue line), nanoparticles conjugated to antibody (green line) and nanoparticles conjugated to the antibody and the virus (red line) and their LSPR peak shifts.

The shifts are distinctively visible for all sizes of gold nanoparticles, with 40 nm exhibiting the smallest peak shifts, and 90 nm exhibiting the highest peak shifts. An increase in nanoparticle sizes correlates with higher LSPR wavelength peaks as larger nanoparticles absorb at higher wavelengths. The LSPR wavelength shift can be further induced by refractive index changes around the nanoparticle surface as shown in figure 1B. In this instance, the impact of refractive index as small as 0.001 was observed for antibody binding to the gold nanoparticles, and 0.003 following the addition of the virus to the nanoparticles-antibody conjugate. This analysis suggests that the bigger sized gold nanoparticles are more sensitive to subtle refractive index changes. The results exhibit a true relationship between LSPR peak wavelength shifts and changes in refractive indices, which tends to follow a linear trend [3, 9]. The simulation data was used to guide the selection of the gold nanoparticles sizes for the experimental work. The data suggests that 90 nm gold nanoparticles are ideal for analyzing and detecting HIV through refractive-index sensing. However, the LSPR extinction in bigger sized nanoparticles is predominantly due to scattering rather than absorption exhibited by small sized nanoparticles. The transition between absorption to scattering occurs around a diameter of 70 nm. The experiment focused on absorption, and after fixing the peak absorption wavelength for transmitted intensity to analyze the binding of HIV to specific antibody, the experimental work was performed using 50 nm sized gold nanoparticles. The 50 nm nanoparticles used in the study were first diluted from 1:1 to 1:5 dilution to determine the best dilution that would be used for the experiments. At higher concentrations, nanoparticles can form aggregates, which tend to alter LSPR properties thus leading to a broader LSPR peak which reduces sensitivity. As such it is recommended to dilute the nanoparticles to achieve minimal intraparticle interaction [10]. Figure 2 shows UV-Vis spectra of 50 nm gold nanoparticles at different dilutions. The absorption peak of the 50 nm gold nanoparticles is at 525 ± 5 nm. The dilution of the gold nanoparticles in distilled water resulted in a 1 nm wavelength peak shift, which aligns with literature [11]. The proceeding dilutions did not result in a further refractive index change, which suggests that the gold nanoparticles were stable and that low concentrations did not induce refractive index changes.

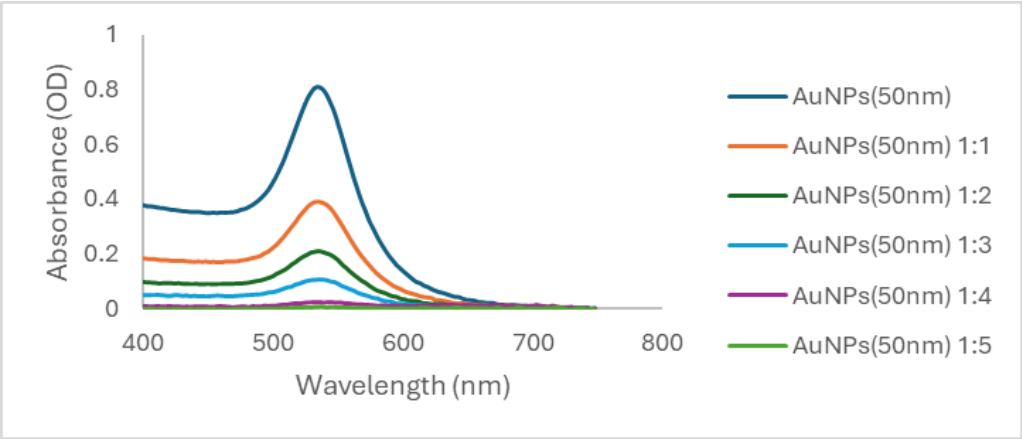

Figure 2: The UV-Vis spectra of gold nanoparticles (50nm) at different dilutions.

The nanoparticles at 1:2 dilution were used in this work, and they were conjugated with the antibody and the virus was also added to the conjugate. The UV-Vis results in figure 3 exhibit a small peak near 280 nm, typical of protein presence in the antibody sample and sample with virus. The sample with the virus had a notable peak at 280 nm due to high protein levels from the antibody and the virus. AuNPs display a strong plasmon resonance peak around 535 nm, which slightly shifts and decreases in intensity when conjugated with antibody and virus to 538 nm, indicating successful binding events. These spectral changes confirm that the LSPR of AuNPs is sensitive to surface modifications, making this technique effective for detecting biomolecular interactions. The wavelength shift and reduction in the peak intensity after the addition of the antibody the virus is typical of nanoparticles when molecules bind to their surface or when their local environment changes [12].

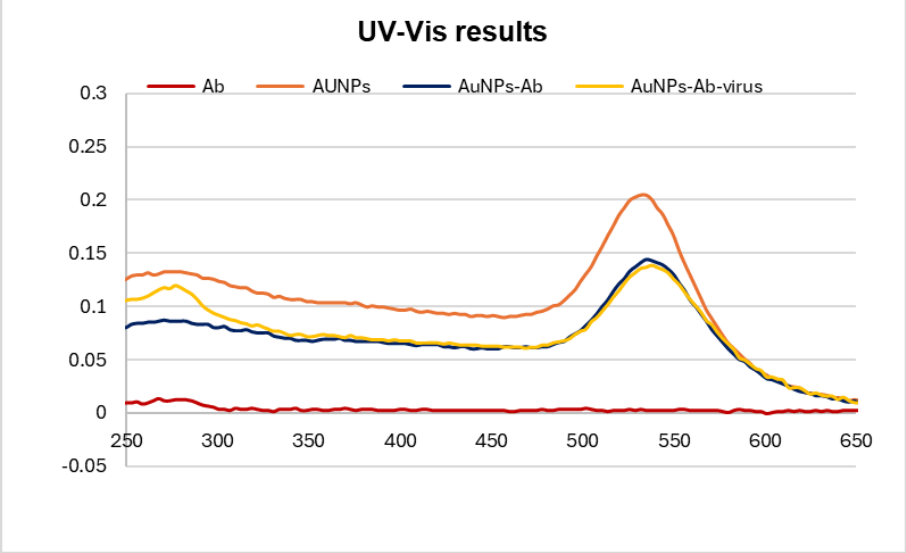

Figure 3: The UV-Vis spectra of gold nanoparticles (535 nm), antibody conjugated with the antibody (538 nm), and the virus bound to the conjugate (538 nm).

Herein, LSPR analysis was performed using a 520 nm LED light. To distinguish between samples with HIV and the ones without HIV, transmittance intensity was measured. As shown in figure 4, AuNPs exhibit the highest transmittance intensity of 36000, followed by the AuNPs+Ab conjugate at 32000, while the sample containing the virus showed a transmittance intensity of 27000.

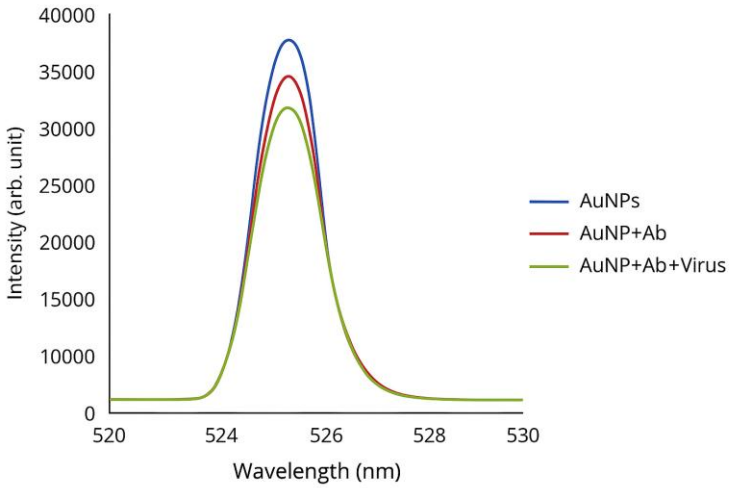

Figure 4: The transmittance intensity of gold nanoparticles, gold nanoparticle-antibody conjugate as well as the sample in which the virus was bound to the conjugate.

The results demonstrated that as different substances bind to the surface of the slide, the amount of transmitted light decreases. The variation in transmitted light levels across different samples is attributed to changes in refractive index. This further confirms that the virus was successfully bound to the antibody, which is specific to the virus used in this study. The notable differences in the transmitted intensity levels among the three samples

confirm the sensitivity of the LSPR to refractive index changes, as also demonstrated in figure 1B. The control sample containing nanoparticles only is expected to have a lower refractive index compared to the other two samples, while the sample, with the virus would exhibit the lowest transmittance intensity.

4 Conclusion

These preliminary findings confirmed the sensitivity of LSPR for refractive index changes as demonstrated by the notable differences in transmittance intensity levels of the different samples. Further work is still required to investigate how variations in nanoparticles geometry affect plasmonic behaviour and determine the refractive index sensitivity observed here. In addition, the specificity, the limit of detection of the LSPR technique in detecting HIV needs to be investigated.

5 Acknowledgements

This work was supported by the Council of Scientific and Industrial Research, National Research Foundation, and Department of Science, Innovation and Technology and the South African Medical Research Council.

References

[1] UNAIDS, "2024 global AIDS report — The Urgency of Now: AIDS at a Crossroads." [Online]. Available: http://www.wipo.int/

[2] World Health Organization, "Consolidated guidelines on HIV prevention, testing, treatment, service delivery and monitoring: recommendations for a public health approach*."* [Online]. Available: https://www.who.int/publications/i/item/9789240031593

[3] K. M. Mayer and J. H. Hafner, "Localized surface plasmon resonance sensors," *Chem Rev*, vol. 111, no. 6, pp. 3828–3857, Jun. 2011, doi: 10.1021/CR100313V.

[4] S. Kastner *et al.*, "LSPR-Based Biosensing Enables the Detection of Antimicrobial Resistance Genes," *Small*, vol. 19, no. 33, Aug. 2023, doi: 10.1002/SMLL.202207953.

[5] UNAIDS,"Understanding Fast-Track: accelerating action to end the AIDS epidemic by 2030." [Online]. Available: https://www.unaids.org/sites/default/files/media_asset/201506_JC2743_Understanding_FastTrack_en.pdf

[6] M. Mcoyi, K. Mpofu, M. Lugongolo, C. Williamson, S. Ombinda-Lemboumba, and P. Mthunzi-Kufa, "Evaluation of nanoparticle fabrication for improved localized surface plasmon resonance response," *MATEC Web of Conferences*, vol. 406, p. 10002, Dec. 2024, doi: 10.1051/matecconf/202440610002.

[7] M. Y. Lugongolo, S. L. Manoto, S. Ombinda-Lemboumba, M. Maaza, and P. Mthunzi-Kufa, "The effects of low-level laser therapy on both HIV-1 infected and uninfected TZM-bl cells," *J Biophotonics*, vol. 10, no. 10, pp. 1335–1344, Oct. 2017, doi: 10.1002/jbio.201600217.

[8] J. Olson, S. Dominguez-Medina, A. Hoggard, L. Y. Wang, W. S. Chang, and S. Link, "Optical characterization of single plasmonic nanoparticles," Jan. 07, 2015, *Royal Society of Chemistry*. doi: 10.1039/c4cs00131a.

[9] M. P. Mcoyi, K. T. Mpofu, M. Sekhwama, and P. Mthunzi-Kufa, "Developments in Localized Surface Plasmon Resonance," 2024, *Springer*. doi: 10.1007/s11468-024-02620-x.

[10] S. Biswas, J. Duan, D. Nepal, K. Park, R. Pachter, and R. A. Vaia, "Plasmon-induced transparency in the visible region via self-assembled gold nanorod heterodimers," *Nano Lett*, vol. 13, no. 12, pp. 6287–6291, Dec. 2013, doi: 10.1021/nl403911z.

[11] M. Gul, M. Kashif, S. Muhammad, S. Azizi, and H. Sun, "Various Methods of Synthesis and Applications of Gold-Based Nanomaterials: A Detailed Review," Apr. 02, 2025, *American Chemical Society*. doi: 10.1021/acs.cgd.4c01687.

[12] Y. Q. He, S. P. Liu, L. Kong, and Z. F. Liu, "A study on the sizes and concentrations of gold nanoparticles by spectra of absorption, resonance Rayleigh scattering and resonance non-linear scattering," *Spectrochim Acta A Mol Biomol Spectrosc*, vol. 61, no. 13–14, pp. 2861–2866, Oct. 2005, doi: 10.1016/j.saa.2004.10.035.

Wind Potential in Local Areas

Muriel Matumba[1], Lufuno Takalani[1,2], Sophie Mulaudzi[1] , Tshifhiwa Ranwaha[1]and Eric Maluta[3]

[1]Department of Physics, University of Venda, Thohoyandou, South Africa
[2]Vuwani Science Resource Centre, University of Venda, Thohoyandou, South Africa
[3]Green Technology Confucius Institute, University of Venda, Thohoyandou, South Africa

E-mail : rotondwamuriel@gmail.com

Abstract. Rural regions are largely reliant on non-renewable energy sources and frequently experience energy shortages. To lessen dependency on fossil fuels and advance sustainability in these areas, alternative renewable energy sources like wind energy must be investigated. By examining wind speed, direction, and flux data gathered using a weather station and eddy covariance flux tower, this study evaluates the wind energy potential in nearby locations. Determining the viability of small-scale wind energy plants is the aim. The demand for renewable energy sources increases and has intensified global interest in wind energy as an effective alternative to fossil fuels. Wind energy is also environmentally beneficial, which makes it a very important component in the shift to sustainable energy systems. Wind energy has become an intense alternative to non-renewable energy systems. If wind energy is effectively used, it can supply a substantial amount of the world's electrical needs because it is abundant, renewable and not polluting. The analysis shows that small-scale projects are possible and whether the local wind conditions are appropriate for wind energy generation. It might also draw attention to the seasons or environmental factors with the greatest potential for wind generation. The study recommends small-scale wind energy systems in appropriate locations, considering the findings. The best sites and wind turbine parameters should be investigated in further detail. To promote sustainable growth, policymakers must incorporate wind energy into regional energy planning. The need to minimize greenhouse gas emissions, the finite nature of fossil fuel resources, and growing concerns about environmental sustainability have all contributed to a change in the global energy landscape. Even though wind energy is becoming more popular, there are still few region-specific evaluations that consider both technical and meteorological considerations.

1 Introduction

Energy produced by naturally occurring sources is commonly referred to as renewable energy. Since it can be made use of without polluting or significantly affecting the environment, such energy sources are sustainable, which offers a clean energy source. Recently, wind energy has been a growing energy source in the world, and wind power is one of the most widely used alternative sources of energy. Wind energy has been used for centuries for navigation and agriculture. Today, the use and technology of wind energy have been developing very fast. Limited reserves of fossil fuels and their negative impacts on the environment lead institutions, organizations and governments to find out more efficient technologies and new and renewable energy resources to produce energy in the natural environment [1].

There is still a demand for sustainable, dependable electricity in many South African rural areas. Even though most cities are linked to the national grid, some isolated places still heavily rely on non-renewable resources like firewood and diesel generators, have limited access to clean energy, and experience frequent blackouts. In addition to posing environmental problems, this dependence restricts the area's capacity for economic growth, healthcare, and education. In South Africa's transition to a more sustainable and equitable energy future, renewable energy, especially solar and wind, is more crucial than ever.

Wind energy is frequently marketed as a cheap and environmentally friendly way to produce power, particularly in places where it might not be feasible to construct grid infrastructure. It's not as easy as just setting up wind turbines wherever the wind blows; there must be enough steady wind at a given location to produce electricity effectively for wind energy to be feasible. The absence of long-term data or access to sophisticated measurement equipment is the primary reason why the wind energy potential of many rural areas, including Vuwani, has not been fully evaluated.

2 Methodology

This study analyses publicly available wind data from the Southern African Universities Radiometric Network (SAURAN) to close that gap. The long-term, high-quality meteorological data provided by SAURAN is gathered from a network of stations located throughout Southern Africa [2]. With this information, we evaluated Vuwani's wind conditions to see if wind power, either alone or in combination with solar power, could be a viable option for the locals. We analyzed the daily and weekly wind patterns using simple statistical methods such as histograms and time series. We also computed Wind Power Density (WPD) to assess the energy present in the wind and used the Weibull distribution, a popular technique for modelling wind speed probabilities. We concluded by comparing our results with typical wind turbine performance curves to determine how well typical turbines would function under these circumstances.



Figure 1. SAURAN station at University of Venda

The meteorological data used in this study came from the SAURAN open source, a public platform that provides high-resolution weather and solar data from a network of stations throughout Southern Africa. A weather station in the vicinity of Vuwani, Limpopo, was chosen for this case study. Data on a range of meteorological factors, such as wind direction and speed, are sent by the station every half hour. Acquiring wind data in CSV format over several weeks was the first step in the process to guarantee temporal representativeness. To fix outliers, missing values, and formatting errors, the dataset underwent preprocessing. For uniformity, all wind speed readings were standardized to meters per second (m/s), and timestamps were translated to a datetime format. To make sure the wind direction data matched the accurate timestamps and speed observations, they were also verified [3].

An exploratory analysis of the data was done to give a preliminary picture of the wind patterns in the area. Plots of time series were created to show how wind speed changed over the chosen time frame. The distribution of wind speeds was examined using histograms, and the predominant wind directions were identified using directional plots. We then fitted the wind speed data to the Weibull distribution. Wind energy studies frequently employ the Weibull distribution because it accurately captures the probabilistic behaviour of wind speeds. To estimate the scale parameter (λ) and shape parameter (k), the maximum likelihood estimation method was employed. The frequency and consistency of various wind speeds can be inferred from these factors. Based on the air density and wind speed data, the WPD was computed using the following formula [4]:

$$WPD = \frac{1}{2}.\rho.V^3 \quad (1)$$

where V is the wind speed and ρ is the air density, which is taken to be 1.225 kg/m³. WPD is a crucial factor in assessing the feasibility of installing wind turbines since it gives an indication of the amount of wind energy that is available per unit area. Lastly, the calculated WPD values were contrasted with standardized wind turbine power curves, including those of larger commercial-scale 1.5 MW turbines and smaller 1–5 kW turbines. The anticipated energy yield and efficiency under local wind conditions could be evaluated due to this comparison [5].

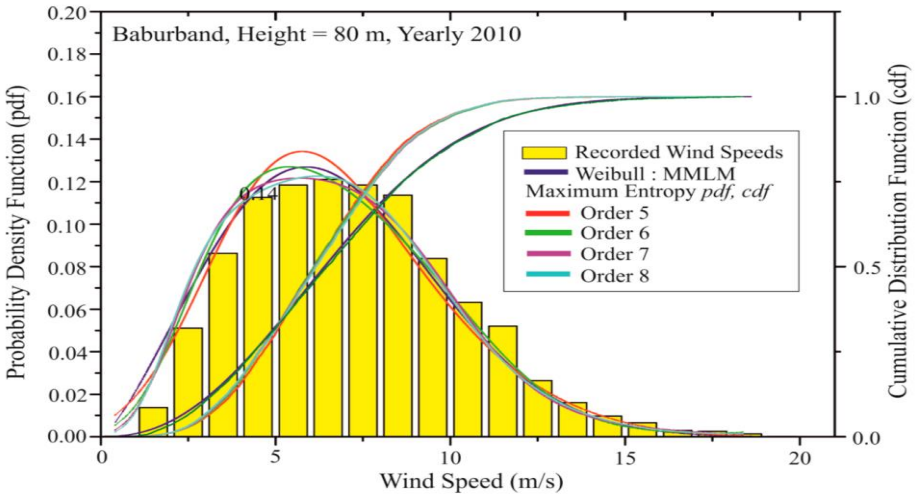

Figure 2. Comparison of wind energy using maximum entropy [6].

Figure 2 shows the wind speed distribution at Baburband, located in Pakistan (height = 80 m) for the year 2010. The yellow bars represent recorded wind speed data, while various lines compare the fit of Weibull (MMLM) and Maximum Entropy models of different orders (5 to 8) to this data. The left y-axis shows the probability density function (PDF) and the right y-axis the cumulative distribution function (CDF).

3 Results and Discussion

According to Figure 3, the time series plot, Vuwani's wind speeds changed greatly from day to day. The speeds varied from 0.2 m/s to 3.2 m/s at their lowest points. There were a few days with comparatively strong wind activity, most notably January 19 and 20. Wind speeds during most of the period, however, were less than 2 m/s, showing a lack of kinetic energy for conversion. These results show the region's wind resources' temporal fluctuation.

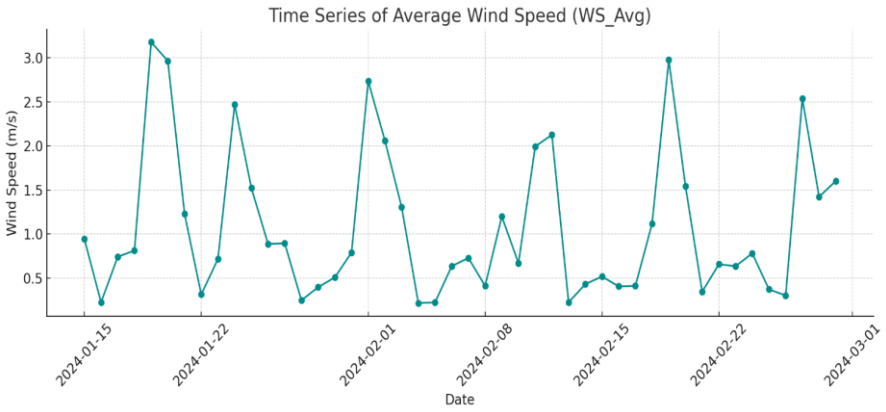

Figure 3. Time Series Plot (WS_Avg)

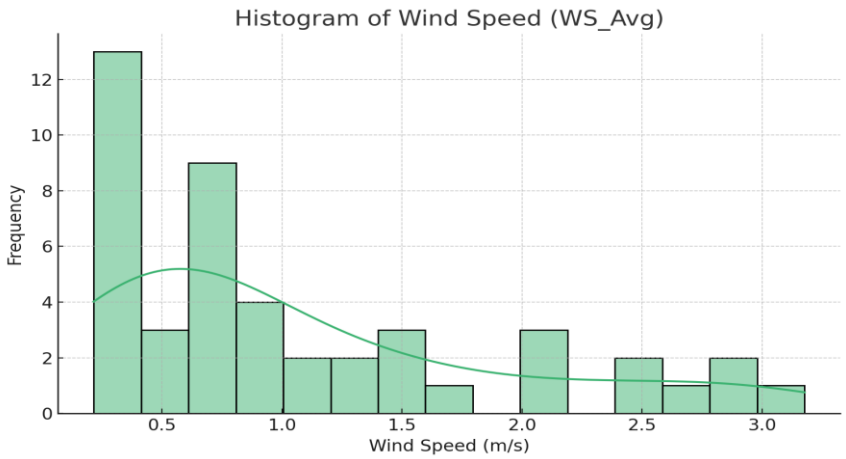

Figure 4. Histogram of Wind Speeds distribution

The wind speed histogram, Figure 4, showed a distribution that was skewed to the right, with many observations concentrated at lower speeds. Very few wind speeds were higher than 3 m/s, and the majority were below 1.5 m/s. Inland rural regions where vegetation, height, and terrain may impede airflow are likely to show this distribution pattern.

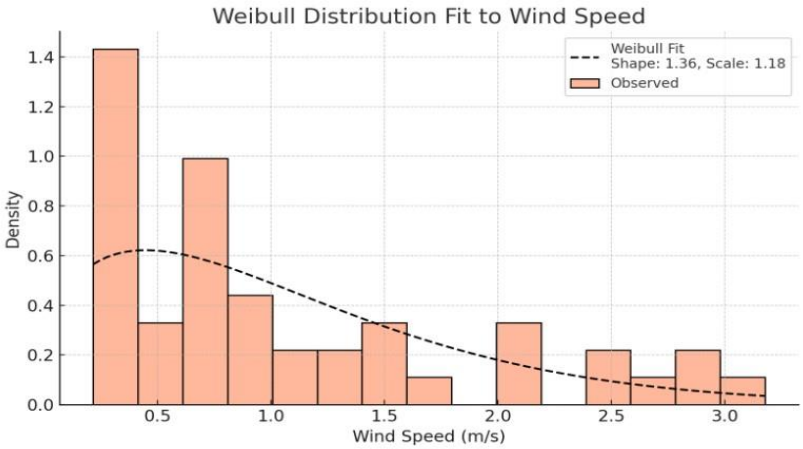

Figure 5. Weibull Distribution Fit

According to Figure 5, the fitted Weibull parameters, the wind regime is extremely variable and unpredictable, with a shape parameter (k) less than 2. Confirming the overall weakness of wind speeds in the area, the scale parameter (λ) was likewise rather low. According to these results, Vuwani does not have regular, strong winds needed for the best wind turbine performance.

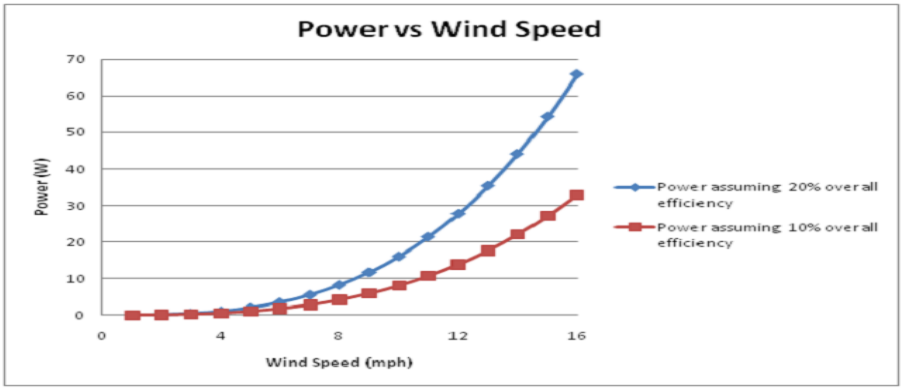

Figure 6. Wind cycle- Wind power density

Vuwani's energy potential is categorized as poor by international standards based on the computed WPD and measured wind speeds. The smallest criterion (~200 W/m²) suggested for utility-scale wind turbines was far higher than the average WPD. Under these circumstances, conventional commercial turbines would function inefficiently, if at all. The study revealed limited but potential use for very low-power (<1 kW) systems meant for off-grid homes when compared to small-scale turbine power curves. In hybrid energy systems, these might work well in conjunction with solar panels to boost total system output and dependability [7].

For the planning of renewable energy in Vuwani and other rural locations, the study's findings carry several implications. First off, this area is not a good place for large wind turbines due to the low wind speeds and poor WPD. Investing in such infrastructure would probably lead to economic inefficiencies and poor performance. This does not, however, completely rule out Vuwani using wind energy. Small wind turbines can supply extra energy for electronic device charging, water pumping, and lighting when combined with solar photovoltaic (PV) systems in hybrid configurations. These systems are particularly important for outlying residences, educational institutions, or medical facilities that are not wired into the national grid.

Furthermore, the research's methodology, which makes use of publicly accessible SAURAN data and basic statistical tools, shows a scalable strategy that may be duplicated in other rural regions. Before investing in more costly feasibility studies or installations, policymakers, engineers, and community planners can utilize this approach to conduct initial assessments. The significance of incorporating regional weather information into national energy plans is further emphasized by this study. Localized opportunities or limits may be overlooked by centralized planning that is exclusively focused on generic datasets or regional averages. More specialized and efficient energy solutions can be created by integrating site-specific data.

4 Conclusion

Using SAURAN weather data and statistical modelling methods, this study aimed to assess the wind energy potential of Vuwani, a rural location in South Africa. According to the research, the area's wind speeds are low, erratic, and insufficient for producing wind energy on a large scale. Estimates of wind power density confirm that only tiny turbines may be practical, and even these would benefit from solar energy system integration. However, the research offers important new information about South Africa's rural renewable energy environment. It shows how useful open-access data and simple statistical techniques are for performing first-site evaluations. Underserved areas may benefit greatly from hybrid renewable systems if proper planning and technology selection are made.

References

[1] J. A. Carta, P. Ramirez, and S. Velazquez, "A review of wind speed probability distributions used in wind energy analysis," *Renewable and Sustainable Energy Reviews*, vol. 13, no. 5, pp. 933–955, 2009, doi: 10.1016/j.rser.2008.05.005.

[2] S. Mathew, *Wind Energy: Fundamentals, Resource Analysis and Economics*. Berlin, Germany: Springer, 2006.

[3] SAURAN, "Southern African Universities Radiometric Network," 2023. [Online]. Available: https://www.sauran.net

[4] J. F. Manwell, J. G. McGowan, and A. L. Rogers, *Wind Energy Explained: Theory, Design and Application*, 2nd ed. Hoboken, NJ, USA: John Wiley & Sons, 2009.

[5] W. Weibull, "A statistical distribution function of wide applicability," *Journal of Applied Mechanics*, vol. 18, no. 3, pp. 293–297, 1951.

[6] MDPI, "Energies Journal," *Energies*, vol. 9, no. 10, p. 842, 2016. [Online]. Available: https://www.mdpi.com/1996-1073/9/10/842

[7] R. Saidur, N. A. Rahim, M. R. Islam, and K. H. Solangi, "Environmental impact of wind energy," *Renewable and Sustainable Energy Reviews*, vol. 15, no. 5, pp. 2423–2430, 2011, doi: 10.1016/j.rser.2011.02.024.

A Python-Flask Application for Modelling Surface Plasmon Resonance in Biosensors for Educational and Research use

Kelvin Mpofu[1] **and Patience Mthunzi-Kufa**[2]

[1]Biophotonics, Photonic Centre, Manufacturing, Council of Scientific and Industrial Research (CSIR), Pretoria, South Africa

[2]School of Interdisciplinary Research and Graduate Studies (UNESCO), College of Graduate Studies, University of South Africa, Preller Street, Muckleneuk Ridge, Pretoria, South Africa

E-mail: kmpofu@csir.co.za

Abstract. We present an open-source, browser-based simulation tool for modelling Surface Plasmon Resonance (SPR) in biosensing applications, developed using Python and the Flask web framework. This application, termed the Surface Plasmon Resonance App (SPRA), enables users to visualize reflectance curves in real time, based on configurable parameters including incident wavelength, metal film thickness, and refractive indices of media such as gold, glass, plasma, and whole blood. The tool incorporates Drude-based optical models for metals and experimentally validated refractive index equations for biological materials. Designed with accessibility and scalability in mind, the SPRA is lightweight, installation-free, and suitable for low-resource settings, making it particularly valuable for undergraduate optics education, remote learning environments, and early-stage prototyping of SPR-based biosensors. Reflectance profiles can be exported for further analysis, and the app includes embedded demonstrations aligned with recent literature. By bridging theoretical modelling with an intuitive web interface, this platform addresses key barriers to SPR engagement in under-resourced contexts, while promoting a deeper conceptual understanding of plasmonic phenomena.

1 Introduction

Surface Plasmon Resonance (SPR) is a powerful optical sensing technique that enables real-time, label-free detection of molecular interactions at the nanoscale [1]. It is extensively used in pharmaceutical development, biomedical diagnostics, food safety, and environmental monitoring [2, 3, 4]. In its most common implementation, the Kretschmann configuration (Fig. 1), SPR occurs when TM-polarized light passes through a high-index prism and reflects off a thin metallic film, typically gold. At a specific incident angle, resonance between the incoming photons and surface plasmons is established, leading to a sharp dip in reflected light intensity. This resonance angle is exquisitely sensitive to changes in the refractive index of the medium adjacent to the metal surface, making SPR ideal for biosensing applications. However, despite its widespread use and scientific importance, access to SPR technology remains limited in many developing countries and educational institutions [5, 6, 7]. Commercial SPR instruments are expensive, involve complex optical alignments, and require specialized training. These barriers hinder student engagement, early-stage prototyping, and open-ended experimentation in optics and biosensor development.

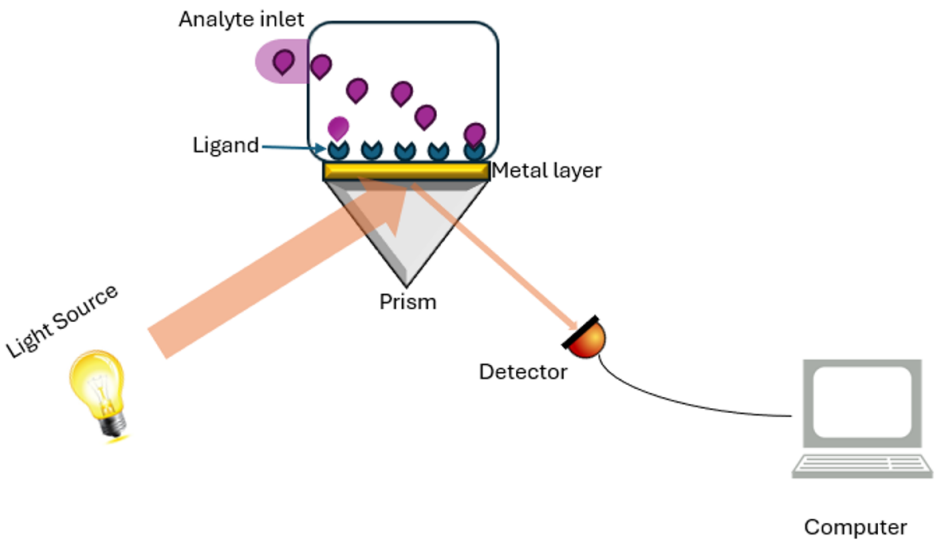

Figure 1: Schematic illustration of a SPR sensing setup in the Kretschmann configuration. TM-polarized light from a source passes through a prism and reflects off a thin metal film (typically gold), exciting surface plasmons at the metal–dielectric interface. Binding events between analytes and ligands at the sensor surface cause a refractive index change, shifting the SPR angle. The reflected light intensity is detected and processed in real time by a connected computer.

Numerous simulation tools have been developed to bridge this gap. Examples include MATLAB-based Fresnel simulators, Mathematica notebooks for multilayer stack analysis, and proprietary platforms like COMSOL Multiphysics or LabVIEW-controlled interfaces. While powerful, these tools are often encumbered by license fees, large installation footprints, or steep learning curves. This has created a noticeable gap for open, lightweight, and educational SPR modelling tools, especially in resource-constrained environments where browser-based tools are more viable than desktop applications. They tend to also be very convoluted and difficult to use.

To address this challenge, we developed a lightweight, browser-based Surface Plasmon Resonance simulator, named the Surface Plasmon Resonance App (SPRA), built using Python and Flask (Fig's. 2 and 3). The app allows users to model reflectance profiles of SPR systems in the Kretschmann configuration, with inputs for wavelength, metal layer thickness, and refractive indices of various media including BK7 glass, gold, water, and biological fluids. It computes angle-dependent reflectance using electromagnetic theory and visualizes the characteristic SPR dip interactively. Importantly, users can export simulation data for further analysis in Excel or CSV format. The SPRA is designed for accessibility: it runs on low-resource devices, requires no installation, and can be deployed on local or online servers. Its modular structure supports future upgrades including quantum light integration and multilayer stack modelling.

A live demonstration video of the SPRA is available at: SPRAvideo, showcasing its interactive features and educational potential. In this paper, we detail the theoretical foundation, implementation, and utility of SPRA as a practical and pedagogical platform. To the best of our knowledge, this is the first Flask-based open-source SPR simulator tailored for biosensing education and prototyping within under-resourced contexts. By integrating fundamental SPR theory with modern web technologies, this tool bridges the gap between theoretical understanding and practical experimentation. It serves as both an educational aid and a prototyping platform for researchers, students, and engineers engaged in plasmonic sensor development. Validation was done with comparable Mathematica code.

2 Methodology

This section describes the design architecture, optical computation framework, and input parameter handling of the SPRA. The tool was engineered to balance computational precision with front-end responsiveness, ensuring real-time interactivity for educational and research users. Code for this work can be found at SPRA.

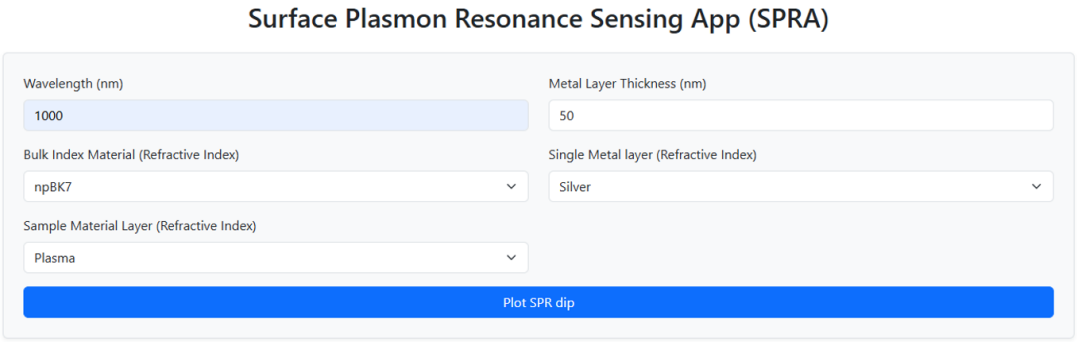

Figure 2: User interface of the Surface Plasmon Resonance Sensing App (SPRA), enabling users to simulate reflectance curves based on configurable inputs such as incident wavelength, metal layer thickness, and refractive indices of the prism, metal, and sample layers. The dropdown menus support common materials like BK7 glass and plasma, making the tool suitable for both educational use and biosensing prototyping.

2.1 System Architecture

SPRA was developed using the Python Flask microframework, interfacing with front-end technologies such as HTML5 and JavaScript (Plotly.js) for dynamic user interaction. Numerical back-end calculations leverage NumPy and SciPy for matrix operations, complex refractive index calculations, and electromagnetic modelling. The application is fully browser-based and deployable on local servers or cloud platforms without installation requirements.

2.2 Optical Model and Reflectance Calculation

Reflectance $R(\theta)$ as a function of incidence angle θ is calculated using Fresnel's equations for a three-layer system (glass-metal-analyte). A discrete angular sweep (40° to 80°, 0.1° resolution) is performed to capture the characteristic SPR dip with high fidelity. The equation used is:

$$R(\theta) = \left| \frac{r_{01} + r_{12} e^{2ik_{z1}d}}{1 + r_{01} r_{12} e^{2ik_{z1}d}} \right|^2,$$

where r_{ij} are the complex Fresnel reflection coefficients, k_{z1} is the z-component of the wavevector in the metal, and d is the metal thickness.

2.3 Material Models

The optical response of gold is modelled using the Drude dispersion relation:

$$\varepsilon(\omega) = \varepsilon_\infty - \frac{\omega_p^2}{\omega^2 + i\gamma\omega}.$$

Refractive indices for analyte layers (e.g., water, blood, plasma) are derived either from user input or from literature-sourced empirical equations. BK7 glass and standard biological fluids are pre-loaded for convenience.

2.4 User Interface and Data Handling

The user interface allows dynamic entry of system parameters and generates interactive plots using Plotly.js. Simulated data can be exported in CSV or Excel format for further analysis or incorporation into experimental design. The modular design permits future upgrades, including quantum light modelling or multilayer stack extensions.

3 Results and Use Case

3.1 Simulated Reflectance Curve

An example simulation for a gold film on BK7 glass with blood as the analyte layer is shown in Figure 3. The sharp dip indicates the resonance angle, which shifts with refractive index changes due to binding events. In this simulation, the Surface Plasmon Resonance Sensing App (SPRA) was configured with an incident light wavelength of 1000nm, a silver metal layer of 50nm thickness, a BK7 glass prism (denoted as npBK7) as the bulk index material, and plasma as the sample analyte medium.

3.2 *Educational and Research Value*

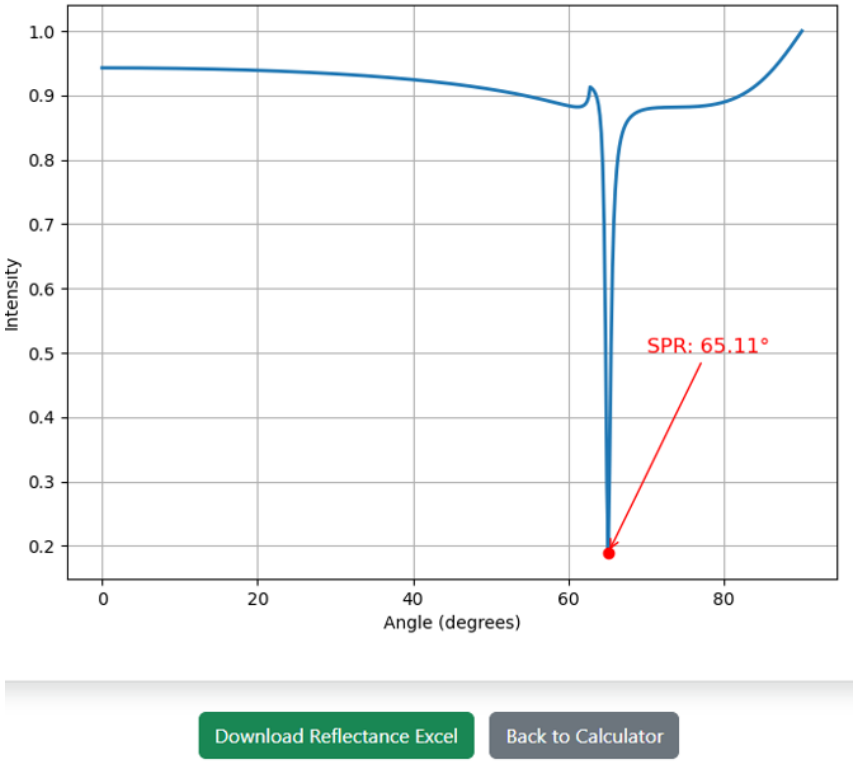

Figure 3: Simulated reflectance curve displaying the characteristic dip associated with surface plasmon resonance (SPR). This dip occurs at a specific angle of incidence where resonance conditions are met, indicating strong coupling between incident photons and surface plasmons at the metal–dielectric interface.

To further demonstrate the versatility of the SPRA, a second case study was performed using aluminium as the metallic layer and plasma as the analyte medium. In this configuration, the prism substrate was defined as BK7 glass (npBK7), with a metal thickness of 50 nm and an incident wavelength of 1000 nm (see Fig. 4). Compared with the gold-based simulation presented earlier, aluminium introduces different plasmonic dispersion characteristics, resulting in a shifted resonance dip.

As shown in Fig. 4, the reflectance curve displays a distinct resonance dip at approximately 62°. The depth and angular position of this dip differ from the gold-based case, underscoring how both the choice of metal and the analyte refractive index influence resonance behaviour. For learners in remote or resource-constrained settings, such comparative examples illustrate the sensitivity of SPR to design parameters and provide hands-on opportunities to explore material trade-offs without requiring laboratory hardware.

The SPRA application has the potential to be valuable in both educational and research contexts, particularly within undergraduate optics curricula and in the early-stage development of SPR-based biosensing systems. By simulating reflectance behavior and visualizing the angular SPR dip (Figure 3), the tool enables users to intuitively explore the impact of various system parameters, such as wavelength, metal thickness, and refractive index, on resonance behavior. Key advantages of the application include:

- **Real-time parameter adjustment:** Users receive immediate visual feedback when modifying system parameters, facilitating rapid experimentation and conceptual understanding.
- **Data export capability:** Simulated reflectance curves can be exported in a standardized format for further analysis in external software, supporting deeper investigation and integration into experimental workflows.
- **Platform independence:** As a browser-based application, it requires no local installation or specialized hardware, making it highly accessible for remote learning, classroom demonstrations, and field prototyping.

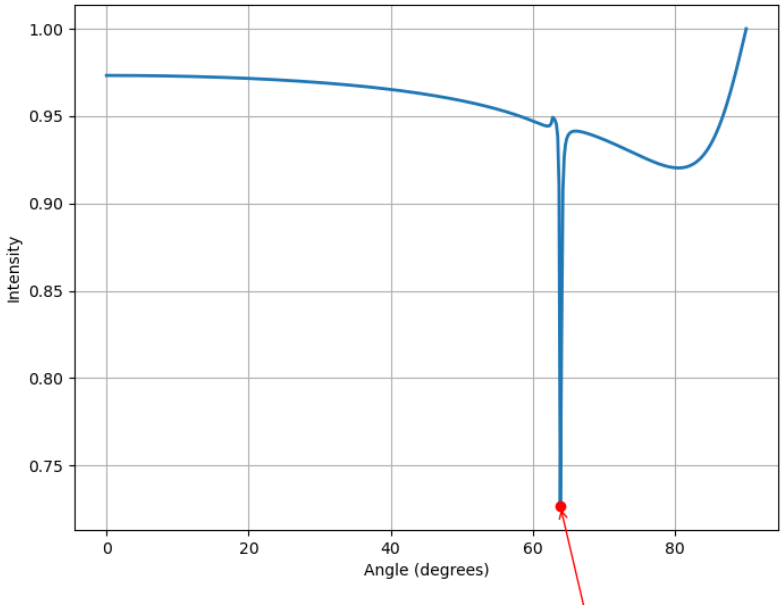

Figure 4: Simulated reflectance profile for an aluminium (50 nm) film on BK7 glass with plasma as the analyte layer, at a wavelength of 1000 nm. The sharp dip around 62° indicates the surface plasmon resonance angle.

3.3 Limitations and Usage Guidance

While the SPRA provides a practical and lightweight platform for simulating reflectance curves, it is important to acknowledge its current limitations. First, the tool implements Fresnel-based calculations for a simplified three-layer system (prism–metal–analyte). Complex multilayer architectures, surface roughness, and inhomogeneous analyte distributions are not yet supported. Second, the Drude model for metals captures general optical behaviour but may deviate from experimental data at certain wavelengths where interband transitions dominate. Third, the refractive index values for biological fluids are based on literature models or user inputs, which may not fully capture sample variability. Finally, the app does not replace experimental calibration: its outputs should be interpreted as a guide for understanding parameter trends, not as absolute predictions. Users who apply SPRA in their research are encouraged to acknowledge it as an educational and prototyping tool. Appropriate citation of this work will ensure transparency and provide context for how simulations were performed. Where possible, simulation results should be complemented by laboratory validation or comparison with more rigorous modelling platforms.

4 Conclusion

The Surface Plasmon Resonance App (SPRA) offers a powerful, accessible platform for simulating SPR-based biosensing phenomena, with direct relevance to both education and early-stage research. By integrating core optical theory with interactive visualization and a flexible Python-Flask backend, the tool allows users to explore how key system parameters, such as wavelength, film thickness, and analyte refractive index, modulate reflectance and shift the SPR angle. The application's lightweight, browser-based architecture removes traditional barriers of cost, installation, and hardware dependency, enabling broader participation in photonics and biosensing fields. Beyond simulation, its export functionality facilitates data-driven analysis and integration into broader workflows. As a next step, future iterations will incorporate multilayer stack models, support for broadband illumination and wavelength scanning, and quantum-enhanced source modelling. Taken together, the SPRA represents a significant step toward democratizing access to SPR education and prototyping tools, fostering skills development in optics, photonics, and biomedical engineering across diverse learning environments.

References

[1] R. B. Schasfoort, *Handbook of surface plasmon resonance*. Royal Society of Chemistry, 2017.

[2] P. Englebienne, A. V. Hoonacker, and M. Verhas, "Surface plasmon resonance: principles, methods and applications in biomedical sciences," *Journal of Spectroscopy*, vol. 17, no. 2-3, pp. 255–273, 2003.

[3] K. Mpofu, S. Ombinda-Lemboumba, and P. Mthunzi-Kufa, "Classical and quantum surface plasmon resonance biosensing," *International Journal of Optics*, vol. 2023, no. 1, p. 5538161, 2023.

[4] D. Capelli, V. Scognamiglio, and R. Montanari, "Surface plasmon resonance technology: Recent advances, applications and experimental cases," *TrAC Trends in Analytical Chemistry*, vol. 163, p. 117079, 2023.

[5] S. Gulati, "Technology-enhanced learning in developing nations: A review," *International review of research in open and distributed learning*, vol. 9, no. 1, pp. 1–16, 2008.

[6] O. Tokel, F. Inci, and U. Demirci, "Advances in plasmonic technologies for point of care applications," *Chemical reviews*, vol. 114, no. 11, pp. 5728–5752, 2014.

[7] R. Schasfoort, "Introduction to surface plasmon resonance," 2017.

Development and Qualification of a Fibre Optic Sensor Package for ITk Environmental Monitoring

Doomnull Unwuchola[1], Lerothodi Leeuw[1], Loan Truong[2], Simon Connell[2], Xola Mapekula[2], Matthew Connell[2], Abdool Cassim[2] and Bongani Maqabuka[2]

[1]Department of Physics and Astronomy, University of the Western Cape, Cape-Town, South Africa
[2]Department of Mechanical Engineering Sciences, University of Johannesburg, Johannesburg, South Africa

E-mail: doomnull@gmail.com

Abstract. The High-Luminosity Large Hadron Collider requires precise environmental monitoring in the ATLAS Inner Tracker to prevent water condensation that could damage detector electronics. This study focuses on the development and the performance of Fibre Optic Sensor packages. Each package is made up of a Long Period Grating sensor and two Fibre Bragg Grating sensors for accurate temperature, dose and relative humidity measurements in a harsh radiation environment. Extraction of the relative humidity (and Dew point) involves the decoupling of the effects of the measured temperature and radiation dose which requires compensation to be accurate. The temperature and relative humidity measurements may depend on location in the 2D (temperature, relative humidity) plane, as indicated by some measurements. This could be an effect of the packaging or a systematic physics effect of the FOS sensors. Calibration studies were performed to assess any possible dependency of temperature calibration on relative humidity in order to determine whether it arises from real sensor sensitivity or external factors such as packaging constraints. Calibration protocols were extended, and compensation algorithms refined to improve measurement accuracy. This work presents a compensation methodology for the Fibre Optic Sensor package to ensure accurate measurements of humidity in the ATLAS Inner Tracker during the High-Luminosity Large Hadron Collider era.

1 Introduction

The High-Luminosity Large Hadron Collider (HL-LHC) represents the next major upgrade of the LHC at CERN which is aiming to increase the instantaneous luminosity by a higher factor [1]. This larger collision rate will give better chances for precision measurements and the discovery of rare processes. However, it comes with significant challenges for the stability and longevity of the ATLAS detector systems.

A major requirement for the ATLAS Inner Tracker (ITk) is its environmental monitoring to prevent conditions that could lead to water condensation inside the detector volume. Condensation poses a serious risk to sensitive electronics and could result in permanent damage or degraded detector performance [1, 2]. Maintaining stable operating conditions therefore requires accurate and real-time measurements of temperature, relative humidity, and accumulated radiation dose within a complex and harsh radiation environment.

Conventional electronic sensors face limitations in the high-radiation regions of the ITk due to radiation-induced damage and signal degradation [1, 2, 3]. Fibre Optic Sensors (FOS) have emerged as a promising alternative, offering inherent advantages such as immunity to electromagnetic interference, compactness, and radiation resistance[3]. In particular, Long Period Grating (LPG) and Fibre Bragg Grating (FBG) sensors have demonstrated the potential to measure key environmental parameters with high accuracy [3, 4, 5, 6, 7].

However, to assess the dew point by the accurate monitoring and extraction of temperature (T) and relative humidity (RH) from FOS data is a non-trivial issue. The measured RH is strongly coupled to both the local T and the radiation dose (D). This demands careful calibration and compensation algorithms to disentangle the above mentioned effects. Additionally, preliminary studies indicate that the response of the sensors may vary with location in the two-dimensional (T, RH) parameter space, either due to genuine sensor physics or packaging-related constraints. Understanding and mitigating these dependencies is essential to ensure reliable environmental monitoring.

Presented in this work is the quality assurance and checks (QA/QC) performed on one of the dedicated Fibre Optic Sensor (FOS) packages for the ATLAS ITk, performed at 25 °C, the expected maximum operating temperature of the ITk when all cooling elements are switched off [8]. Each FOS package comprises of three grating-based point sensors (one LPG sensor and two FBG sensors per package). This work describes the pre-irradiation, irradiation and post-irradiation calibration procedures performed including its extension to assess the possible dependence of temperature calibration on relative humidity. The performance of these sensor packages is evaluated under laboratory conditions representative of the ATLAS ITk as outlined in Table 1.

Table 1: The FOS requirements for RH monitoring.

Parameter	**Value**
Accuracy	$\Delta_{\text{RH}} < 3.5\%$ (between 0 and 10% RH)
	$\Delta_{\text{RH}} < 10\%$ (above 10% RH)
Precision	$\sigma_{\text{RH}} < 1.7\%$ (between 0 and 10% RH)
	$\sigma_{\text{RH}} < 5\ \%$ (above 10% RH)
Typical operating temperature	-20 °C
Maximum operating temperature	25 °C

2 Fibre Optic Sensor Packages and Measurement Method

To ensure accurate environmental monitoring in the ATLAS Inner Tracker (ITk) during the High-Luminosity Large Hadron Collider era, dedicated Fibre Optic Sensor (FOS) packages were developed and tested under controlled conditions. Each sensor package is designed to provide simultaneous measurements of temperature, relative humidity, and radiation dose in a harsh radiation environment where conventional electronic sensors would be susceptible to damage and signal degradation. The sensor package integrates three grating-based point sensing elements: two Fibre Bragg Grating (FBG) sensors and one Long Period Grating (LPG) sensor.

2.1 FBG working principle

The sensing characteristics of FBGs are based on the periodic modulation in the fiber core of the refractive index [1, 3]. The typical grating period of an FBG is less than 1 μm. An FBG is created where there is a permanent photo-induction of the refractive index of the single mode optical fibre core. This periodic modulation of the refractive index causes reflection of light in a narrow band of less than 1 nm [7]. The resonant wavelength of this band is called the Bragg wavelength (λ_{B}) and is dependent on the fibre effective refractive index n_{eff} and the pitch of the grating Λ (grating period), according to the Bragg condition: $\lambda_{\text{B}} = 2\, n_{\text{eff}}\, \Lambda$.

The FBG is sensitive to changes in strain and temperature, since these can affect the refractive index and grating pitch. Strain along the axis of the fiber can change the grating period through elastic behaviour and the effective refractive index can be changed through the elasto-optic effect [3]. On similar grounds, temperature changes can affect the grating pitch through thermal expansion/ contraction and can affect the refractive index through the thermo-optic effect. These changes induce a Bragg wavelength shift ($\Delta\lambda_{\text{B}}$) due to the change in strain ($\Delta\epsilon$) and thermal effects (ΔT) can be expressed as follows [3]:

$$\frac{\Delta\lambda_B}{\lambda_B} = (1 - P_e)\epsilon + \big[(1 - P_e)\alpha + \zeta\big]\Delta T \tag{1}$$

where P_e is the photo-elastic constant, ϵ is the strain induced on the fibre, α and ζ are the thermal-expansion and thermo-optic coefficients of the fibre, respectively. The FBG responds to both temperature variations and strain which demands the application of proper methods to decouple the effect of temperature and strain from its readings (compensation) [9]. The sensors are encased in a neoceram frame designed to maintain a constant strain on the FBG throughout its lifetime, ensuring it is sensitive only to temperature.

2.2 LPG operation principle

The LPG sensor, which is similar to the FBGs, is a grating-based point sensor. This photonic device is created by inducing a periodic index modulation of the core of a single mode optical fibre along a few centimeters of its length [3]. The period of the perturbation is longer than the FBG counterpart: it goes typically from 0.1 to 0.5 mm and the length of the grating is usually around 20 or 30 mm. In the present study, the length of the LPG is 30 mm while each FBG has a length of 8 mm. The grating perturbation leads to coupling of the core and cladding modes of the transmitted light. Coupling occurs for a discrete number of cladding modes, each defined by a resonant wavelength where the phase-matching condition is met [5, 3, 1]:

$$\lambda_{\text{res,i}} = (n_{\text{eff,co}} - n^{i}_{\text{eff,cl}})\Lambda \tag{2}$$

where Λ is the grating period and $n_{\text{eff,co}}$ and $n^{i}_{\text{eff,cl}}$ are the effective refractive indexes of the core and of the ith cladding mode respectively. In case of relative humidity sensors based on LPG technology, an appropriate hygrosensitive material (micro-polycrystalline TiO_2) has to be selected such that the water absorption/desorption of water by the coating itself modifies its refractive index and/or volume, without affecting the adhesion of the coating on the fiber [10, 3]. Both volume and refractive index changes shift the resonant wavelength of the LPG attenuation band. In the the present experiments, a pre-strain of around 0.3 N is applied to the LPG by attaching a 30 g weight to the fibre during assembly. Once the fibre is secured in the package, the pre-strain is maintained by clamping in the neoceram frame, ensuring that the LPG remains under a constant strain.

2.3 FOS package

Neoceram was chosen as the material for the package frame because has a negligible change of dimensions within the operating temperature range of the sensors. The FOS are calibrated to temperature and RH through two separate laboratory tests: a temperature scan, where temperature is varied while RH is kept constant, and a RH scan where RH is varied and temperature is kept constant. Each sensor in the package is sensitive to temperature, the radiation hard FBG is insensitive to dose (while the radiation soft FBG and the LPG are sensitive to dose) and the LPG is additionally sensitive to RH. Once the radiation hard FBG has been calibrated using the conventional Pt10k temperature sensor, its signal can be used to track temperature, and these measurements can be combined with the temperature calibration functions determined in the lab to temperature-compensate the radiation soft FBG and LPG. Similarly, the results of the irradiation campaign can be used to calibrate the radiation soft FBG and the LPG to the dose recieved (0 - 2.0 MGray). The readings of the radiation soft FBG can then be used to measure dose, and allow for dose compensation of the LPG. Using the combination of the three sensors, a single calibrated FOS package could measure temperature, dose and RH without the need for any reference sensors. The next section covers the campaign to characterise the FOS response to radiation by irradiating the package with a 24 GeV/c momentum proton beam in the IRRAD facility at CERN [11].

3 Discussion and Results

The calibration and characterisation of the FOS package were done using data recorded in three stages: pre-irradiation, during irradiation, and post-irradiation.

3.1 Pre-irradiation campaign

The pre-irradiation commences by using sensors in the FOS package and commercially available sensors (Pt10k and Honeywell HIH-4000) to measure temperature and relative humidity changes in a custom-built climatic chamber [1]. The data collected were then used for the T and RH calibration. The standard conventional sensor, Pt10k, responds to T while the HIH-4000 sensor responds to RH. These sensors are used to calibrate the FOS in several steps. First, the FOS response to temperature is characterised by conducting a temperature test, where the peak wavelength shift, $\Delta\lambda$, of each sensor is recorded at different temperatures, while RH is kept constant. Along with the temperature readings from the Pt10k, the resulting ($\Delta\lambda$, T) points can be fit with a line to determine a linear temperature calibration function for each fibre optic sensor. An example of this fit is shown for the LPG in Figure 1 (left). The LPG response to humidity is then characterised in a similar fashion through a humidity test, where $\Delta\lambda$ is recorded at multiple RH values, while temperature is kept constant. Figure 1 (right) shows the resulting RH calibration curve for the LPG from the ($\Delta\lambda$, RH) points, using the RH measurements from the HIH sensor (the FBGs are not sensitive to RH, so no RH calibration function is developed for them). This method of combining the T and (RH) measurements of the Pt10k (HIH) over time with the response of the FOS can be summarised in the following equation:

$$(t, \lambda_{\text{T}})_{\text{FOS}} \;\&\; (t, \text{T})_{\text{pt10k}} \rightarrow (\text{T}_{\text{FOS}}, \lambda_{\text{FOS}}) \;:\; (t, \lambda_{\text{RH}})_{\text{FOS}} \;\&\; (t, \text{RH})_{\text{HIH}} \rightarrow (\text{RH}_{\text{FOS}}, \lambda_{\text{FOS}}) \tag{3}$$

The set-up was used to regulate the T and RH in order to determine their thermo-hygrometric response. For T characterisation: RH was constant at 0% while T was varied. Conversely, for RH characterisation, T was constant at 25 °C while RH was varied. Using equation (3), the T and RH calibration curves for the LPG is obtained as shown in Figure 1(*right*).

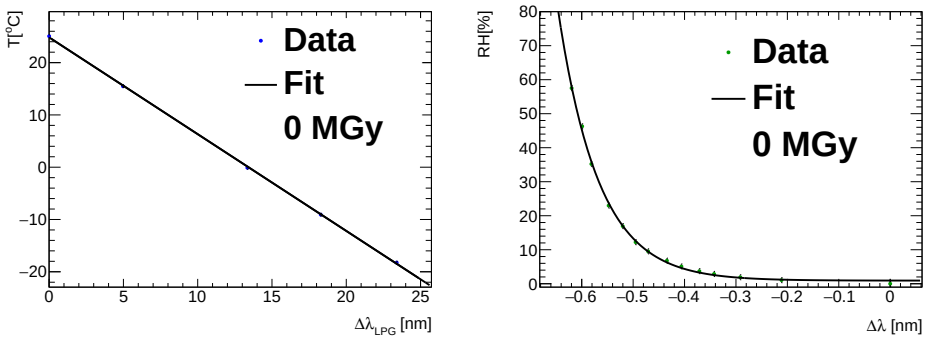

Figure 1: (*left*) Evaluated T calibration curve for the LPG for pre-irradiation campaign (*right*) Evaluated RH calibration curve for the LPG for pre-irradiation campaign. The 0 MGy on the plot indicate that the package is not irradiated (pre-irradiation campaign).

From Figure 2 (*left*) it can be seen that the LPG closely tracks the reference HIH sensor. Figure 2 (*right*) demonstrates that the FOS measurements are well within the accuracy requirements specified in Table 1.

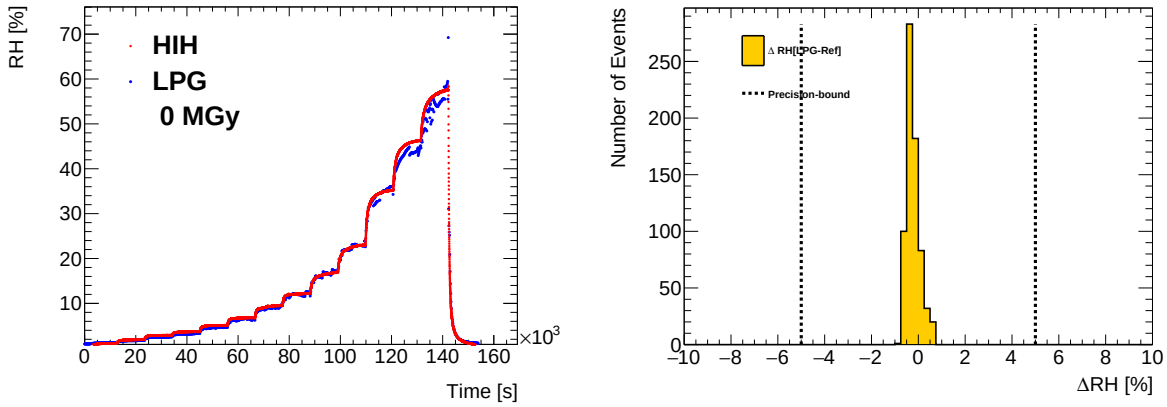

Figure 2: (*left*) Measurements of RH over time during the pre-irradiation test for the HIH (red) and the LPG (blue). (*right*) Accuracy of the LPG shown as a histogram of the difference between LPG and HIH measurements of RH, for RH<10% - the dotted lines show the bounds specified by Table 1.

3.2 FOS Functionality during irradiation campaign

The Irradiation campaign took place at CERN IRRAD facility. The FOS was exposed to a 24 GeV/c proton beam which applied a cumulative fluence of 7.56×10^{15} protons per cm^2 over 1 week. As seen in Figure 3 (*left*), the sensor spectrum is redshifted such that the resonant wavelength of the final spectrum is 57 nm larger than that of the first spectrum. The shift in the resonant wavelength of the LPG over time is shown in Figure 3 (right).

3.3 Post-irradiation campaign

The calibration for the post-irradiation campaign is similar to that of pre-irradiation using equation (3) to acquire the T and RH calibration curves. From the post-irradiation plots in Figure 4 (*left*), the FOS still almost exactly matches the conventional sensor and the FOS readout minus HIH readout shows that the FOS meets the specification. Figure 4(*right*) demonstrates that the LPG measurements of RH are well within the specifications laid out in Table 1.

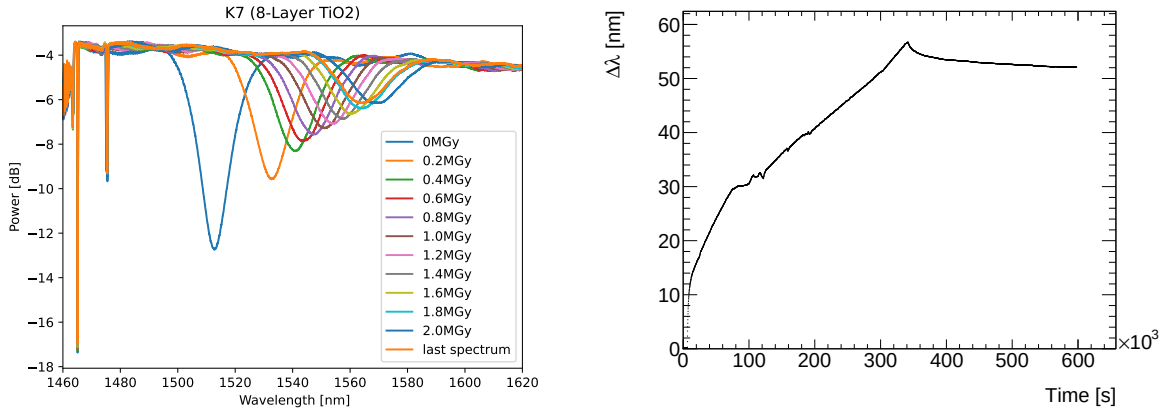

Figure 3: (*left*) FOS power spectra measured at different radiation doses (K7 is the serial number of the LPG).(*right*) Wavelength shift with increasing radiation dose.

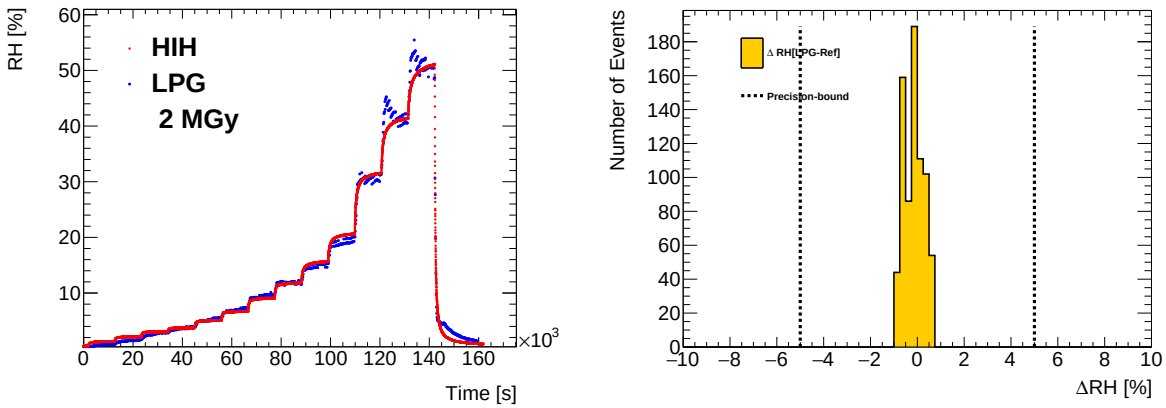

Figure 4: (*left*) Measurements of RH over time during the post-irradiation test for the HIH (red) and the LPG (blue). (*right*) Accuracy of the LPG shown as a histogram of the difference between LPG and HIH measurements of RH for RH<10% - the dotted lines show the bounds specified by Table 1.

3.4 RH Calibration curves at different radiation dose and sensitivity

When the FOS packages are finally installed around the ATLAS detector, they will not be physically accessible for a long period of time. This demands further characteristation studies in a varying radiation environment from 0 - 2 MGray. Our approach for this is to use the data-driven RH calibration curves of the pre-irradiation (0 MGy) and post-irradiation (2 MGy) campaign to acquire interpolation functions for different radiation doses as shown in Figure 5 (*right*). By differentiating the fit function of the RH calibration curves, the sensitivity of the respective sensor shown in Figure 5 (*left*) is acquired. Despite the reduction of the sensitivity of the sensor due to exposure to high radiation doses, a response to changes in RH can still be obtained in the low RH range of RH < 10%.

4 Conclusion and future work

QA/QC have been carried out on a typical FOS package to be deployed for environmental monitoring of the conditions in the ATLAS Inner Tracker. In the work presented, tests were performed at the maximum operating temperature of 25 °C. For the pre-irradiation and post-irradiation campaign, comparing the FOS RH readout to that of the conventional RH sensor readout indicates that RH variance is within the allowed specification. This implies that the FOS package achieved the specifications. The cross-sensitivity of the LPG to RH and T is overcome by performing a temperature-compensation using the temperature reading from the radiation hard FBG and the temperature calibration fit for the LPG. The work presented here is being continued by performing QA/QC on the FOS packages at −20 °C, the normal operating temperature of the ATLAS ITk.

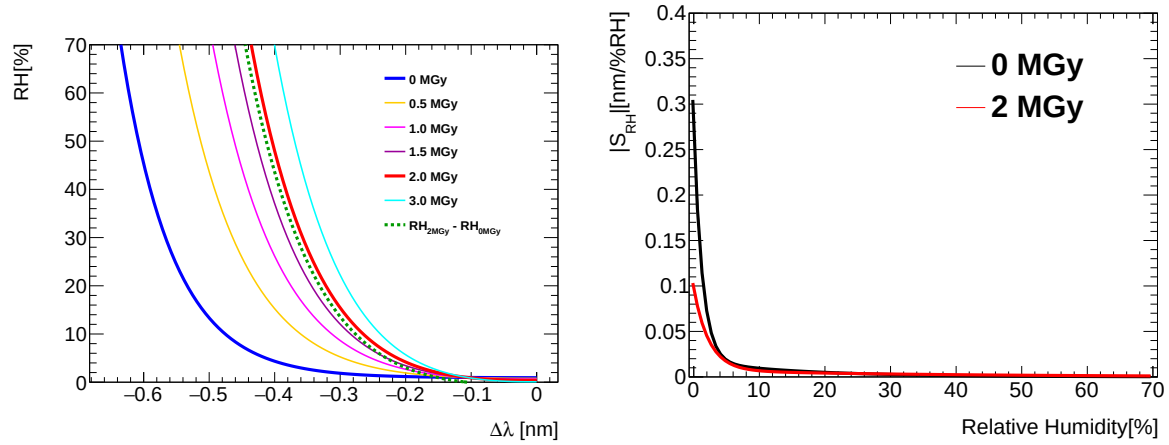

Figure 5: (*left*) RH-dose calibration functions interpolated/extrapolated to seven different dose exposures. (*right*) LPG sensitivity to RH at two different dose exposures.

References

[1] L. Scherino, E. Schioppa, A. Arapova, G. Berruti, W. Bock, A. Boniello, A. Borriello, S. Campopiano, M. Consales, A. Cusano, F. Esposito, A. Iadicicco, S. Kachiguine, P. Mikulic, K. Nagai, T. Neves, P. Petagna, G. Quero, D. Robinson, A. Srivastava, P. Vaiano, N. Venturi, M. Zarrelli, A. Zotti, and S. Zuppolini, "Fiber optic sensors in the atlas inner detector," *Nuclear Instruments and Methods in Physics Research Section A: Accelerators, Spectrometers, Detectors and Associated Equipment*, vol. 1029, p. 166470, 2022. [Online]. Available: https://www.sciencedirect.com/science/article/pii/S0168900222000997

[2] The ATLAS Collaboration, "Atlas pixel ibl: Stave quality assurance," 2014.

[3] G. Berruti, "Radiation tolerant fiber optic humidity sensors for high energy physics applications," Ph.D. thesis, CERN, 2015.

[4] L. Madhavan and M. Chattopadhyay, "Temperature and strain sensitivity of long period grating fiber sensor," *International Journal of Research in Engineering and Technology*, vol. 4, no. 2, pp. 776–782, 2015.

[5] A. M. Vengsarkar, P. J. Lemaire, J. B. Judkins, V. Bhatia, T. Erdogan, and J. E. Sipe, "Long-period fiber gratings as band-rejection filters," *Journal of Lightwave Technology*, vol. 14, no. 1, pp. 58–65, 1996.

[6] A. Cusano, A. Cutolo, and J. Albert, *Fiber Bragg Grating Sensors: Recent Advancements, Industrial Applications and Market Exploitation*. Bentham Science Publishers, 2011.

[7] K. O. Hill and G. Meltz, "Fiber Bragg grating technology fundamentals and overview," *Journal of Lightwave Technology*, vol. 15, no. 8, pp. 1263–1276, 1997.

[8] ATLAS Collaboration, "ATLAS Inner Tracker Strip Detector: Technical Design Report," 2017. [Online]. Available: https://cds.cern.ch/record/2257755

[9] Y.-J. Rao, "In-fibre grating sensors," *Measurement Science and Technology*, vol. 8, no. 4, p. 355, apr 1997. [Online]. Available: https://doi.org/10.1088/0957-0233/8/4/002

[10] M. Consales, G. Berruti, A. Borriello, M. Giordano, S. Buontempo, G. Breglio, A. Makovec, P. Petagna, and A. Cusano, "Nanoscale TiO_2-coated LPGs as radiation-tolerant humidity sensors for high-energy physics applications," *Optics Letters*, vol. 39, pp. 4128–4131, 2014.

[11] P. Pelissou *et al.*, "IRRAD/CHARM, a CERN Irradiation Facility for Accelerator & Experiments Radiation Hardness Qualification," in *Proceedings of the 2024 IEEE Radiation Effects Data Workshop (REDW) in conjunction with 2024 NSREC*, Ottawa, ON, Canada, 2024, pp. 1–6. [Online]. Available: https://doi.org/10.1109/REDW61286.2024.10759157

The development of the atmospheric monitoring system for a balloon-borne system

Kwanele Mazibuko[1], Marco Mariola[2] and Michael Kosch[3]

[1] School of Chemistry and Physics, University of KwaZulu-Natal, Durban, 4000, South Africa
[2]School of Mechanical Engineering, University of KwaZulu-Natal, Durban, 4041, South Africa
[3]SANSA, P.O. Box 32, Hermanus, 7200, South Africa

E-mail: 223036470@stu.ukzn.ac.za

Abstract. In this work, the atmospheric monitoring device for a balloon-borne system is proposed, aiming to overcome the limitations of ground-based monitoring platforms (Automatic Weather Stations). The manuscript proposed a system that can be adapted, produced in-house, and easily modified to meet the needs of the research for atmospheric data collection at different altitudes. The system is based on an ATmega328P microcontroller, which integrates a Global Positioning System module for precise positioning and a LoRa module for long-range communication. The hardware consists of a main control board and a separate sensor board. The manuscript details the system architecture, component selection, and the software development process. The ground station software was tested by sending simulated data via the serial port. Future work includes completing and testing the system.

1 Introduction

Atmospheric monitoring systems are essential for monitoring weather conditions and assessing air quality, which is critical for public health as well as climate research. While ground-based devices offer localised data, there remains a gap in measurements at higher altitudes of the atmosphere. The use of balloon enables us to monitor atmospheric parameters at high altitudes in real-time, which is essential for understanding global climate patterns, air quality, and enhancing our understanding of upper atmospheric phenomena. The information collected from the balloon can also be used in other scenario, as for example the atmospheric phenomena close to an airport, or to predict the trajectory of a scientific rocket, or more in general an unmanned vehicle. The development of balloon-borne systems began long ago as airborne transportation evolved from kites to unmanned balloons and weather balloons for weather monitoring [1]. One of the earliest valuable uses of balloons for scientific purposes was demonstrated in the early 20th century, when the tropopause was discovered. Over time, balloon-borne systems have found applications in academia and civilian sectors to support aviation. When developing such systems, it is important to consider the environment in which they operate in. Since some sensors, like those for humidity and temperature, need to be directly exposed to the environment, finding suitable sensors that can be operational at the high altitude becomes essential, since temperatures in the troposphere can drop to about -55 °C depending on the region and season [2].

The design of this balloon-borne system utilizes devices already available on the market and that are open-source. It features an NTC (Negative temperature coefficient) 10 KΩ thermistor for temperature sensing. The NTC thermistors are thermally sensitive resistors that change their resistance as the temperature varies [3]. Their large change in resistance with only a small temperature change provides greater resolution. This enables the system to detect and measure small temperature differences more accurately.

2 System Boards

The developed balloon-borne system consists of two boards, with the first being the main board, which serves as the system's core. This board includes the MCU (Microcontroller Unit) ATmega328P, known for its use in Arduino boards. The MCU controls the entire system. The main board also features the GPS (Global Positioning System) Neo-6m, providing positioning information such as time, latitude, longitude, and altitude. The board is provided with an onboard transmitter to send the collected data to the ground station. Data is transmitted in binary format for efficiency. Although it is possible to transmit data as a string of characters, binary transmission is advantageous because it reduces transmission time and energy consumption. The MCU used has limited Random Access Memory (RAM) storage, necessitating working around this limitation. Additionally, the board includes a power monitor to track battery life. Monitoring the power helps take measures before the system completely shuts down. The electronic schematic of the main board is shown on the right of Figure 1.

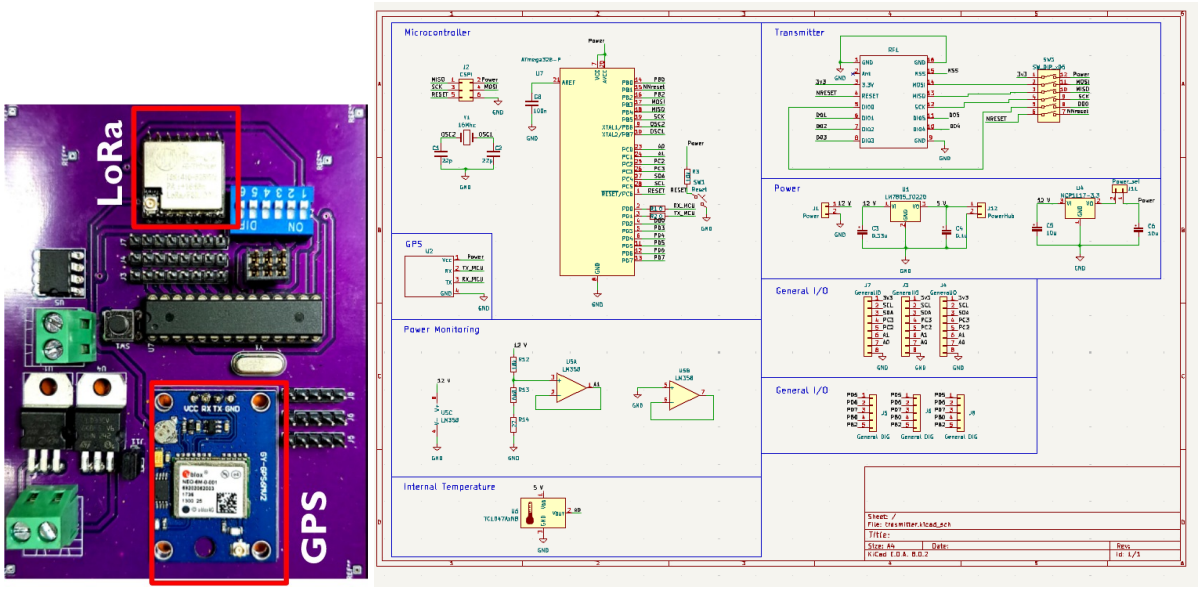

Figure 1: (*left*)Main board. (*right*) The schematic of the main board.

The second board, which is physically separated by the main boards, includes the conditioning circuit of the sensors used.The circuit of the sensor board is represented in Figure 2.

The sensors were chosen according to the following requirements:

- Weight[1].
- Operation temperature range.
- Efficiency.
- Flexibility.

The Printed Circuit Board (PCB) of the sensor board was produced in-house, and the main board was then sent for fabrication. To make the PCB, we used the toner transfer method. The first step was to print the PCB design on the blue press and peel sheet, and melt it on top of the copper-clad board using a hot iron. After transferring the PCB design to the copper board, rectification was done through a permanent marker. The PCB was placed in ferric chloride for etching. Using available digital/analog pins of the MCU on the main board, the sensor board can be connected. Since the payload must be within the regulated weight, one of the most critical parts that characterizes the weight and the period of the mission is the power subsystem. The main board includes several parts. The power subsystem is made of two voltage regulators that reduce the 12V power supply to work as two independent power sources. One power source is used to power the MCU on the main board and any other service that runs at 5V. The second power source is dedicated to the transmitter and sensors, which operate with 3.3V.

[1]Actual safety regulations imposes a payload mass, less than 2kg

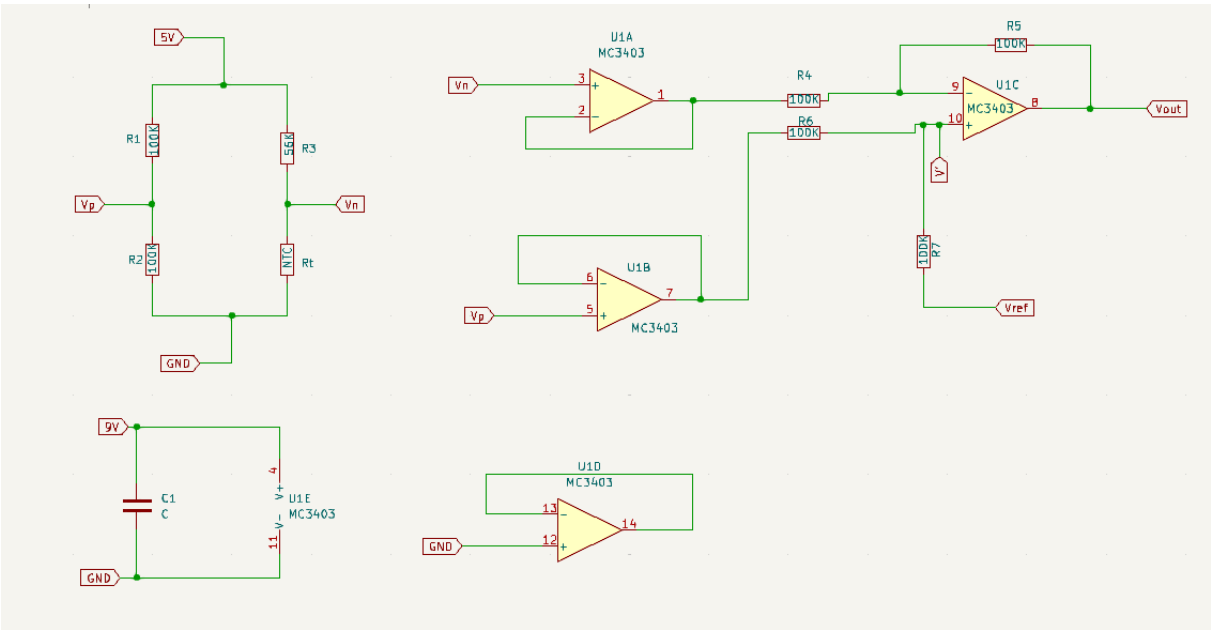

Figure 2: The schematic of the sensor board.

3 System Operation

The system architecture, illustrated in Figure 1, consists of a GPS module that communicates with the microcontroller unit via a USART interface, enabling serial data transmission. A LoRa transmitter is connected to the MCU, utilizing the SPI protocol. The main board's design is flexible, with MCU ports and pins arranged in a parallel setup that makes it easier to add extra sensors without requiring a new design. Considering a battery of 12V, power monitoring is achieved through a voltage divider that shifts the voltage level from 0V to 5V. Additionally, an onboard temperature sensor provides real-time internal BUS temperature readings, thereby enabling continuous monitoring of the system.

3.1 LoRa Transmitter

LoRa is a wireless radio frequency (RF) communication technology developed by Semtech, offering a significantly greater communication range and lower power consumption compared to traditional technologies like Wi-Fi and Bluetooth. While LoRa supports bidirectional communication, it operates in half-duplex mode, allowing for either transmission or reception, but not simultaneously [4]. LoRa transmitters operate by converting digital data into chirped RF waveforms using chirp pulses, through a specialized modulation scheme called Chirp Spread Spectrum (CSS) [5], which was initially developed for radar use in the 1940s [6]. Since our system is not yet tested and fully developed for data transmission, the distance it will depend on the power used by the transmitter, and the receiver system on the ground station, for example the antenna used.

4 System Software and Testing

In this paragraph, to avoid any ambiguity, it is necessary to state that the real transmission is not yet tested, but what was tested was the ground station software, where simulated data was transmitted via USB from an Arduino board and a computer. The same data format will be transmitted from the balloon once the embedded board is completed and properly tested. At the ground station, we have developed a software that receives the atmospheric parameters, as well as the geographical coordinates, as a series of 23 bytes, which are read byte by byte and reconstructed into usable information. Once the 23 bytes are correctly received, the software at the ground station can calculate the 3D velocity of the balloon and monitor the internal status of the payload and the service systems. The balloon-borne system that is developed does not do calculations; calculations are done on the ground station. The system only transmits the data; this works around the computational limitations of the MCU.

The ground station software test was conducted utilizing a Neo-6M GPS module, extracting time, latitude, longitude, and altitude data. Atmospheric parameters were simulated using International Telecommunication Union (ITU) models, and the system battery of 12V was reduced to mimic real-world balloon system data collection

conditions. The data format chosen for the application was successfully interpreted by the ground station shown in Figure 3. For this test, a Mega2560 microcontroller unit was used because it has four UARTs, which simplify the transmission from the MCU to the computer, and between the module GPS and the MCU. The main board has an ATmega328p which has only one UART. In the case of the main board, the GPS module uses the UART of the ATmega328p, while the transmission from the LoRa and the MCU is performed through SPI. This approach allowed for thorough validation of the software functionality before assembling the transmitter and the receiver. Notably, the GPS module required at least 4 minutes to determine its precise location during a cold start.

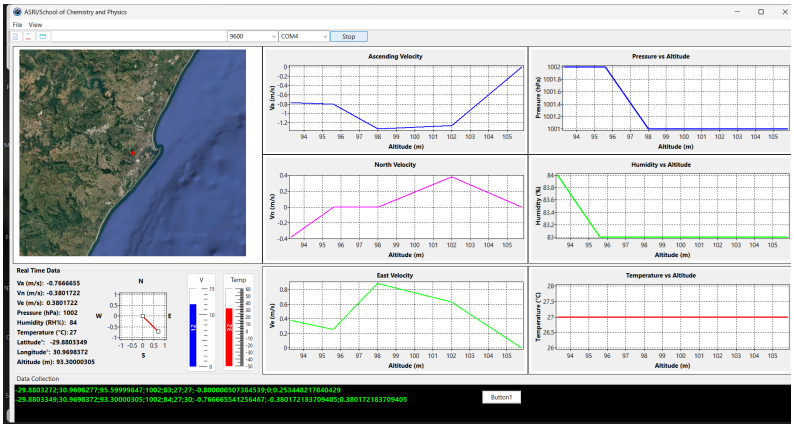

Figure 3: The software showing simulated data.

5 Temperature conditioning circuit, and Experimental Results

We measure using Arduino, so the analog voltage level from the analog sensors cannot be greater than 5 V (since the voltage reference of the Analog Digital Converter cannot be greater than the supply voltage of the MCU). With the NTC that we have, we can measure between -40 °C to 30 °C. The middle value that we have is -5 °C, but we take -10 °C as the average value because using an ice cube with salt we can measure -10 °C. From the datasheet at -10 °C the NTC resistance is R = 55.5KΩ [7], since there is no commercial value of R = 55.5 KΩ that is why R_3 from the circuit shown in Figure 2 is 56 KΩ. With this circuit design, we built at -10 °C we obtain V_p as 2.447 V, which is approximated to 2.5 V. We did not want the Wheatstone bridge circuit to be directly connected to the microcontroller, so we added the operational amplifier. With the operational amplifier we have the separation of the circuit, so we do not have any loss of voltage.

5.1 Circuit Operation

The circuit shown in Figure 2 has V_{ref} (reference voltage) which is used for exploiting all range of Arduino. The circuit makes a difference of (V_p - V_n) because Arduino reads only values from 0 V to 5 V.
If V_n is greater than V_p, then V_d (voltage difference) will be negative, but in our case it becomes 0 V because Arduino cannot read negative voltage.

By using the superposition: if V_p = 0 V and V_{ref} = 0 V this is equivalent to the inverting operational amplifier [8], then

$$V_{out} = -\left(\frac{R_5}{R_4}\right) V_n$$

$$R_5 = R_4 \Rightarrow V_{\text{out}} = -V_n$$

By using Miller Theorem: If $V_n = 0$, and $V_p \neq 0$, and $V_{\text{ref}} \neq 0$

$$V' = \frac{\left(\frac{V_p}{R_6} + \frac{V_{\text{ref}}}{R_7}\right)}{\left(\frac{1}{R_6} + \frac{1}{R_7}\right)}$$

Considering

$$R_7 = R_6 \Rightarrow V' = \frac{V_p + V_{\text{ref}}}{2}$$

This is equivalent to the non-inverting operational amplifier [8].

$$V_{\text{out}} = \left(1 + \frac{R_7}{R_6}\right) V' \quad \text{and if } R_6 = R_7, \text{ then}$$

$$V_{\text{out}} = 2V' = V_p + V_{\text{ref}}$$

Thanks to this, we can make this translation. The final solution for V_{out} (output voltage) is:

$$V_{\text{out}} = V_{\text{out (superposition)}} + V_{\text{out (Miller)}}$$

$$V_{\text{out}} = -V_n + V_p + V_{\text{ref}} = (V_p - V_n) + V_{\text{ref}} = V_d + V_{\text{ref}}$$

5.2 Experiment

V_p is fixed to 2.5 V, from the datasheet at -40 °C the resistance R_t = 341KΩ using the voltage divider from the Wheatstone bridge

$$V_n = 5 \cdot \frac{R_t}{R_3 + R_t} = 5 \cdot \frac{341{,}000}{56{,}000 + 341{,}000} = 5 \cdot \frac{341{,}000}{397{,}000} \approx 4.29\,\text{V}$$

At the output we expect V_{out} to be:

$$V_{\text{out}} = -V_n + V_p + V_{\text{ref}} = -4.29 + 2.5 + 2.5 = 0.71\,\text{V}$$

At 30 °C the resistance R_t = 8KΩ

$$V_n = 5 \cdot \frac{R_t}{R_3 + R_t} = 5 \cdot \frac{8{,}000}{56{,}000 + 8{,}000} = 5 \cdot \frac{8{,}000}{64{,}000} \approx 0.63\,\text{V}$$

At the output we expect V_{out} to be:

$$V_{\text{out}} = -V_n + V_p + V_{\text{ref}} = -0.63 + 2.5 + 2.5 = 4.37\,\text{V}$$

Experimentally by comparison with an existing thermocouple and comparing our result at -10 °C, we obtain an output voltage of approximately 2.5 V at -12 °C using an ice cube with salt, which is close to the expected value.

From Vd, we can derive what is the actual value of R_t

$$V_p - V_n = \left(\frac{5}{R_1 + R_2}\right) R_2 - \left(\frac{5}{R_3 + R_t}\right) R_t = V_d$$

$$R_t = \frac{R_3\big(R_2(5 - V_d) - V_d R_1\big)}{V_d R_2 + R_1(5 + V_d)}$$

With R_t now we can find the temperature using the Steinhart–Hart equation :

$$\frac{1}{T(K)} = -2.0345 \times 10^{-3} + 7.1544 \times 10^{-4}\big[\ln(R_t)\big] - 1.5150 \times 10^{-6}\big[\ln(R_t)\big]^3$$

An HS4103 can replace an NTC thermistor since it can accurately measure both relative humidity and temperature. It uses a Micro Electro Mechanical Systems (MEMS) sensor to detect changes in humidity and temperature in its environment [9]. The sensor is factory-calibrated, so no user calibration is required.

6 Conclusions

From a steady location, and with simulated parameters, the software receiver seemed to be working correctly. The NTC sensing is characterised by a sensor that can operate to a minimum temperature of -40 °C. The system can be easily change by recalculating the wheatstone bridge for an NTC rated for low temperatures. The sensor board can be reconfigured to the researcher's needs, as it can be produced separately from the main board. Future work will consist of programming the microcontroller unit to transmit the data through the LoRa transmitter, placing the power subsystem, and launching the balloon system.

7 Acknowledgement
This work is supported by the National Astrophysics and Space Science Programme (NASSP).

References

[1] National Weather Service (NOAA), "Out of thin air: The history and evolution of upper-air observations," https://vlab.noaa.gov/web/nws-heritage/-/out-of-thin-air-the-history-and-evolution-of-upper-air-observations, 2019, nOAA Virtual Lab, Accessed: 2025-07-25.

[2] MeteoSwiss, "Troposphere and tropopause," https://www.meteoswiss.admin.ch/weather/weather-and-climate-from-a-to-z/troposphere-and-tropopause.html, 2025, accessed: 2025-07-25.

[3] TDK Electronics AG, "General technical information for thermistor sensors," https://www.tdk-electronics.tdk.com/download/531116/19643b7ea798d7c4670141a88cd993f9/pdf-general-technical-information.pdf, 2018, accessed: 2025-10-20.

[4] Shenzhen Ai-Thinker Technology Co., Ltd., "Ra-02 lora product specification v1.1," https://docs.ai-thinker.com/_media/lora/docs/c048ps01a1_ra-02_product_specification_v1.1.pdf, 2017, accessed: 2025-07-25.

[5] The Things Network, "What are lora and lorawan?" https://www.thethingsnetwork.org/docs/lorawan/what-is-lorawan/, Mar. 2024, accessed: 2025-07-25.

[6] N. Dziengel, "The history, evolution, and utility of chirp spread spectrum," https://www.inpixon.com/blog/history-evolution-utility-chirp-spread-spectrum, Nov. 2023, accessed: 2025-07-25.

[7] M. E. Components, "P-ntc-10k (181021) ntc technical data," https://www.mantech.co.za/datasheets/products/p-ntc-10k-181021_sgt.pdf, Mantech Electronic Components, 2015, datasheet.

[8] T. L. Floyd, *Electronic Devices (Conventional Current Version)*, 9th ed. Upper Saddle River, NJ, USA: Pearson Prentice Hall, 2011.

[9] Renesas Electronics, "Hs4103 datasheet," https://www.renesas.com/en/document/dst/hs41xx-datasheet?r=1575156, 2025, accessed: 2025-07-25.

Automated photovoltaic module imaging for high throughput data capture and analysis

MT Sivewright [1], EE Van Dyk[2] and FJ Vorster[2]

Department of Physics, Nelson Mandela University, Port Elizabeth, South Africa

E-mail: s223099996@mandela.ac.za

Abstract. Photovoltaic (PV) module imaging has become a critical tool for assessing the performance, reliability, and degradation of PV modules. Automated imaging systems that use advanced hardware and image processing software tools allow for efficient high-throughput data capture across large-scale solar installations. These systems use different imaging techniques such as visible light (RGB) imaging, Thermal Infrared (TIR) imaging, ultraviolet fluorescence (UVF) imaging, electroluminescence (EL) imaging, and line sensor scanning. These imaging techniques allow for the detection of faults or anomalies in PV modules. We report on a project focusing on the development of a system for high-throughput visual and UV-F imaging of PV modules deployed in utility-scale PV plants. The work follows a two-step approach whereby two systems will be built. The first step consists of a laboratory-based imaging system to test the proof of concept. This system utilizes an Arduino MEGA 328P microcontroller for position control and a Raspberry Pi 5 8 GB for sensor control, image capturing and storage. The images are then processed later through stitching and basic visual classification. The second step will use techniques determined to be effective from the initial system to build an onsite imaging and sensing system that allows for rapid, large-scale image capture for further image processing and classification. This allows for more data and images to be captured and thus processed as opposed to manual methods. At the same time, this method has a much greater resolution as opposed to drone imaging. This paper presents the design, manufacture, optimization and preliminary results from the laboratory-based system.

1Introduction

Crystalline silicon (c-Si) PV modules consist of multiple bonded materials - glass, encapsulant, cells, interconnections, and backsheet - forming several interfaces. These interfaces can act as pathways for contaminants, causing degradation and reducing performance [1]. Effective encapsulation is essential for ensuring module reliability and extending operational life. Field inspections have shown that degradation related to poor encapsulation is a common cause of PV system failure. Proper encapsulation protects against moisture, UV radiation, and mechanical stress, helping the module retain stable performance over time [1]. A fault in a PV module occurs when its power output is lower than expected due to either temporary factors (e.g., shading, dirt) or permanent issues (e.g., cracks, encapsulant degradation, disconnections) [2]. Fault detection techniques help identify these issues and, although some may overlap, they enable comprehensive module characterization [2]. These techniques are typically categorized into DC and AC side methods, with the DC side further divided into electrical and imaging-based approaches [2]. The main imaging techniques are visual inspection, thermal infrared (TIR), and electroluminescence (EL) [2], [3]. For effective detection, a technique

should: (A) detect faults without disrupting power, (B) localize the fault, (C) be cost-effective and adaptable, (D) have a simple structure, and (E) apply to various PV systems [4].

Existing visual inspection methods often rely on manual image capture for each PV module [5]. While this approach provides high-resolution imagery and is suitable for small-scale systems, it becomes impractical and costly for large-scale PV plants due to the time and labour involved [5]. Unmanned Aerial Vehicles (UAVs) offer a faster alternative but are limited by lower image quality and susceptibility to weather conditions [5]. Moreover, regulatory constraints such as South Africa's restriction on drone flights within 10 km of airstrips and during nighttime pose additional challenges. A solution is needed that combines high-resolution imaging with scalability to meet the demands of large PV installations.

2 Theory

Crystalline silicon (c-Si) PV modules typically consist of a glass front cover, a polymeric encapsulant layer, followed by mono- or polycrystalline silicon cells, another polymeric encapsulant layer, and a polymeric back sheet or glass in the case of a bifacial PV module [6]. A standard photovoltaic (PV) module production process typically includes the following steps: glass washing and drying; tabbing of cell ribbons and soldering of the cell matrix; module lay-up with cross-connection soldering; embedding of the module layers; edge sealing and framing; junction box attachment; and final power measurement [6]. Embedding in terms of PV modules is the process in which the cell matrix is placed into a PV module. There are several types of embedding, but all experience challenges to achieve uniform and sufficient curing or cross-linking levels to ensure strong adhesion and stable laminates.

The decrease in efficiency and lifespan of a module is attributed mostly to optical degradation and electrical mismatch [7]. Optical faults are the result of poor quality of the encapsulant layer, prolonged exposure to high temperatures and humidity, and ingress of oxygen into the module, accelerating corrosion [1], [7]. Figure 1 shows the process of water or oxygen ingress into the PV module through the backsheet and into the encapsulant layer, resulting in a change in the composition of the encapsulant known as quenching [1]. This change in composition of the encapsulant has an effect on the fluorescence of the material and thus will fluoresce at a different wavelength, allowing for identification of microcracks in a PV cell that are not seen with visual imaging [1]. This highlights the need for multiple image techniques to fully understand the performance of a PV module.

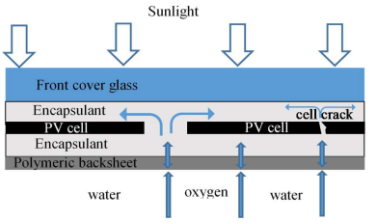

Figure 1. Ingress of water and oxygen into a PV module [8]

Multiple types of imaging techniques are used to fully characterise a PV module. For example, detection techniques employed to identify optical failures are different from those employed for the detection of electrical failures. Optical failures may be seen by the naked eye, such as visual imaging or UVF, whereas electrical losses resulting from defects such as cracked cells or a disconnected string require electroluminescence imaging [4]. Visual imaging can be performed by the naked eye at an illumination level of 1000 lux and requires basic imagery equipment [4]. Due to this effect, EL imaging is one of the most common imaging techniques used.

Traditional methods of imaging are comprised of two fields, laboratory- and field-based [8]. Laboratory-based testing is optimum for testing such as EL, as lighting and external interference can be minimised [8]. However, with the development of large-scale PV plants a field-based testing is needed [8]. Field testing relies on labour extensively, requiring additional time and resources, leading to a limit to the number of modules that can be tested within a reasonable amount of time [8]. A team at Sandia National Laboratories proposed a solution to this problem by developing a robot PV monitoring system that reduced human intervention, allowing for adaptably to different-sized PV systems and imaging techniques [9]. This work is similar in that automated image capture and basic processing as an expected outcome that has a direct application in the PV industry.

3 Methodology

To develop an on-site imaging system, a lab-based prototype was first required to test the camera hardware, control systems, and image processing software. The implementation of this prototype, referred to as the "Gantry," followed a structured process. First, the problem was defined, and a design solution proposed. Next, both electrical and mechanical components were modelled in SolidWorks. The Gantry was then constructed based on the CAD model, and a software control system was developed. Finally, a Python script was implemented to stitch the captured images into a single high-definition composite.

3.1 Definition of Problem and Proposed Solution.

The problem definition established the need to capture high-definition images using various imaging techniques to identify faults within PV modules. The system must be semi-autonomous, requiring only relative information about the module and the selected imaging technique. It should feature a user interface for operator interaction and store captured images for later access. Additionally, the system must support multiple cameras and accommodate additional sensors for testing purposes. It should be adaptable to different module sizes and designed to serve as the foundation for a fully on-site imaging system.

A proposed solution was developed in which the system is controlled by a Raspberry Pi for high-level operations and user interface, while an Arduino Mega handles low-level control tasks. The mechanical design follows a two-axis, dual-drive configuration utilizing three stepper motors to ensure precise movement. The system accommodates PV modules up to 2.4 × 1.3 meters, covering the size range of most modern modules. A Python script facilitates communication between the Raspberry Pi, camera, sensors, microcontroller, and operator, providing comprehensive system control and support for all integrated features.

3.2 Design and Construction of the Gantry.

The CAD model of the gantry is shown in Figure 2. The structure of the gantry is built from 45 x 45 mm Bosch Rexroth extrusion to allow for the ease of assembly and any modification needed. The design uses a dual-drive motor setup whereby the Y axis is controlled by two NEMA 32 stepper motors to reduce racking caused by the large design. The X axis is controlled by another NEMA 32 motor mounted to the axis or 'rack'. Additionally, the rack is built from a 20 x 40 mm V slot extrusion with a V-Plate as the end effector, which allows for the mounting of a Raspberry Pi 5 8gb with a Pi-Camera 3 NOIR 12MP and a Sony IMX477 12 MP camera. Each axis is driven with V belt and pulley with a minimum resolution of 0.1 mm/step on the X axis and 0.18 mm /step on the Y axis.

The design incorporates 3D printed components for rapid prototyping of custom parts, as shown in the figure 3, where a bracket securely holds the Raspberry Pi, cameras, and additional sensors mounted to the V-Plate. The Raspberry Pi manages the high-level system control and provides a user interface via a Python script. It communicates with an Arduino Mega 2560 microcontroller over USB using serial communication to manage low-level tasks such as controlling the stepper motors, reading sensor inputs, handling user interfaces, and monitoring an emergency stop button. The Arduino, along with the motor drivers, power supplies, and physical interface components, is housed in a ventilated control box, shown in Figure 4. Manual control of the system can be performed using onboard buttons and a joystick, without requiring communication with the Raspberry Pi.

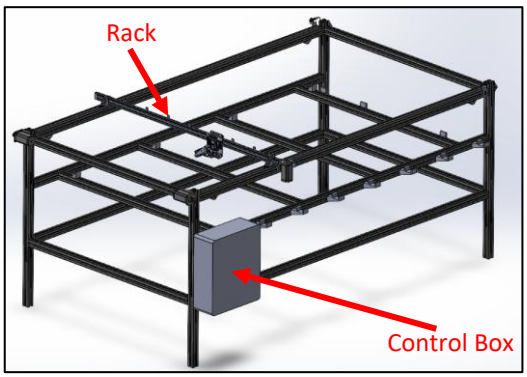

Figure 2. CAD design of Gantry

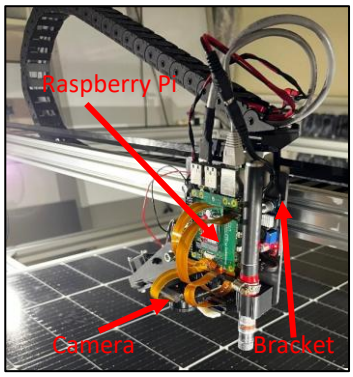

Figure 3. Raspberry Pi and Sensors



Figure 4. Control Box

3.3 Image capture, stitching, and processing.

The image capture sequence begins by entering the setup through a Python command prompt. During setup, the user inputs the dimensions of the PV module, selects the desired camera, and chooses between UV or visual imaging. Once configured, a 3D array of positional coordinates is generated to define all target locations. The Raspberry Pi then sequentially sends each position to the Arduino. When the Arduino confirms it has reached the specified position, the Pi captures an image using the selected camera. Each captured image is stored on a 500GB SSD HAT and tagged with an identifying position for traceability. The ID tag in each photo is identified as CXRYCZ where X refers to the position in the X-axis range starting from 0, and right to left of the module when viewed from the front in portrait orientation. Y is similar to X but defines the row number from top to bottom of the PV module. The determination of positions of positions in the array of coordinates is determined by the camera selected, the size of the module, and the overlap of images for stitching.

4 Results and Discussion

Two fault detection techniques were used, viz. visual imaging and ultra-violet fluorescence (UVF) imaging. To increase the lighting and reduce glare from laboratory lighting, four 10 W cool white (6000 K) lights were used to illuminate the module. Each module was cleaned thoroughly before testing, as the main scope was to detect permanent damage/faults within the module.

4.1 Challenges with image capture and stitching.

Capturing and stitching images to create a cohesive, single image is a complex task that requires both advanced computational processing and precise mechanical design. One of the challenges encountered is image overexposure caused by reflections from the extrusion frame under LED illumination. This issue can be mitigated by applying a non-reflective film over the extrusion frame to reduce glare. Another challenge includes stitching difficulties, particularly at the image edges, where alignment may fall within a cell rather than between them. Although machine vision software such as OpenCV, which relies on pattern recognition, has been employed, the repetitive and featureless nature of PV modules limits its effectiveness. As a result, a more reliable approach involves precise mechanical indexing of the module and implementing edge detection to identify full cell boundaries. This ensures stitching is performed at consistent locations outside the edges of each cell, improving alignment and overall image quality.

4.2 Image processing and correction.

To improve the quality of the final stitched image, each image must first be rotated and corrected for distortion before stitching can occur. The rotation process is illustrated in the Figure 5, beginning with the initial image capture (A). A greyscale mask is then applied to enhance edge visibility (B), followed by a binary threshold to reduce noise and isolate key features (C). OpenCV's edge detection is subsequently used to identify points of interest in the image (D). Based on these detected edges, OpenCV generates lines and computes their equations (E), typically identifying either the cell fingers or the cell's outer edge if the fingers are not visible. Lines with angles greater than 5 degrees from horizontal are discarded, and the image is rotated using the median angle of the remaining lines (F). Since rotation introduces void regions along the image edges, the final step is to crop the image to remove these empty borders (G).

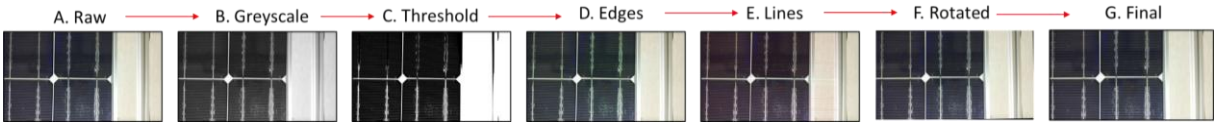

Figure 5. Process of image correction for a single image before stitching

Figure 6 shows a stitched 540 W module with dimensions of 1130 x 2260 mm, this being one of the largest modules able to be tested by the gantry. Images were captured using Raspberry Pi Camera 3 NOIR with 12 MP resolution. Each image size is roughly 1.9 MB, with a total of 56 images captured, resulting in a 223.6 MB image when stitched together. Basic image stitching and blending are performed after the images are captured.

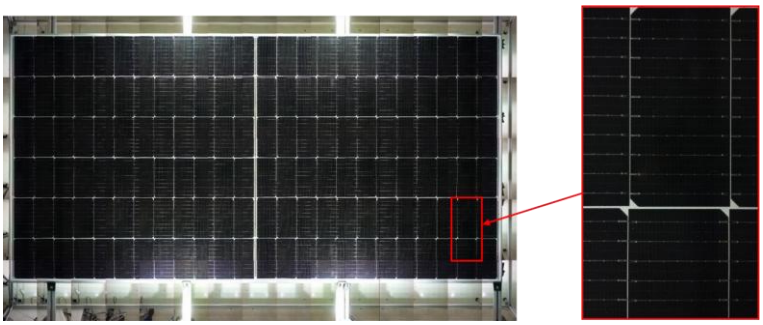

Figure 6. Stitched visual image of large PV module with reference to a single image.

4.3 Faults and Defects: Visual Imaging

Several modules were tested using the visual imaging system developed. Figure 7 highlights both manufacturing defects in PV modules and permanent damage caused by prolonged environmental exposure after installation. Manufacturing faults such as trace misalignment, irregular cell patterns, and finger defects can introduce minor mismatches within the module, leading to reduced power output. Edge chips, often caused during the doping process of the silicon cell, can act as stress concentrators and result in cracks due to mechanical impact or thermal cycling. These cracks may propagate, leading to microcracks, cell disconnects, and further degradation of both the module's performance and lifespan. Additional defects shown in the figure include cell delamination and flux oxidation, which reduce module efficiency by generating localized heat and applying thermal stress to affected cells. The scratch seen in Figure 7 was caused by contact with the frame of another module, depositing aluminium onto the glass surface; this scratch is considered non-permanent and does not affect performance significantly.

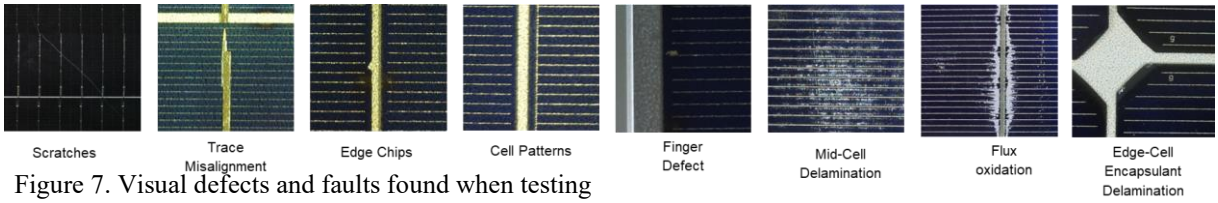

Figure 7. Visual defects and faults found when testing

4.4 Faults and Defects found using UVF Imaging.

Several modules were tested using UVF imaging, and the following results were obtained from the module shown in Figure 8. The figure illustrates a module whose backsheet fluoresces when exposed to ultraviolet light. A low-pass filter (LEE Filter 101 Yellow) was used to reduce glare and saturation in images captured by the Raspberry Pi 3 NOIR camera. Figure 9 reveals evidence of fluorescence quenching, a phenomenon where the module's encapsulant is exposed to moisture or oxygen through the backsheet. This exposure alters the molecular structure of the polymer, thereby changing its fluorescence behaviour under UV light. Additionally, figure 10 shows a localized area within one cell exhibits unexpected fluorescence, which may be due to a small hole in the cell or a deposit of fluorescent material from the backsheet onto the cell's front surface. This hole is also visible in the standard visible spectrum, suggesting a physical defect within the cell. If present, such a defect can lead to cracking of the cell, ultimately decreasing the power output and shortening the lifespan of the module.

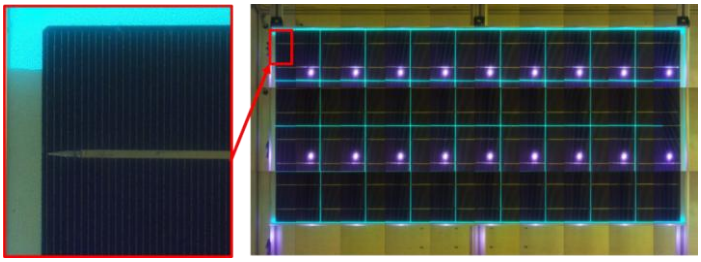

Figure 8. Stitched UVF image with indication of fluorescent material

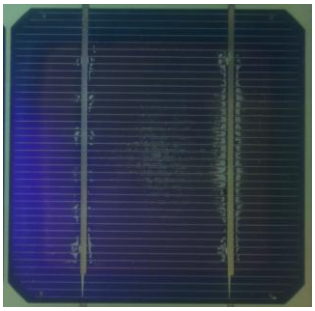

Figure 9. UVF: Quenching pattern

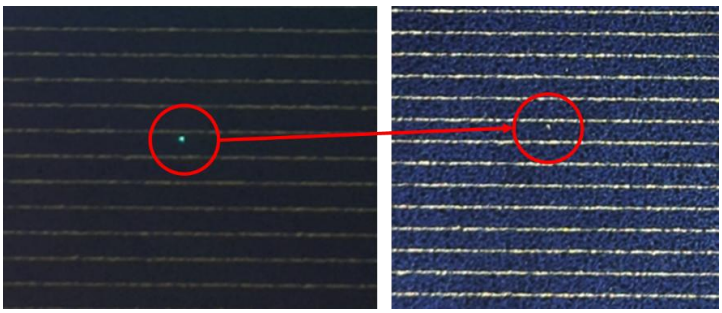

Figure 10. Hole in cell

5 Conclusion

The development and testing of a laboratory-based imaging gantry for automated visual and UVF inspection of PV modules demonstrates a promising approach for high-throughput, high-resolution fault detection. The system integrates precise mechanical motion control, modular hardware, and advanced image processing to provide detailed insights into both manufacturing defects and long-term degradation of PV modules. Key features include a robust mechanical design, adaptable imaging modes, automated image capture, and custom stitching algorithms capable of producing large composite images suitable for diagnostic analysis.

Preliminary results confirm the system's effectiveness in detecting common visual and UVF-related faults, such as edge chipping, cell delamination, and quenching caused by encapsulant degradation. Although challenges remain—particularly in image alignment and illumination conditions—preprocessing techniques such as edge detection, rotation correction, and cropping have led to significant improvements in overall image quality and stitching accuracy. However, further refinement is still required.

This proof-of-concept system establishes a solid foundation for future on-site deployment, where the methodology can be scaled to accommodate utility-scale PV installations. Future work will focus on enhancing image processing and stitching algorithms, incorporating additional testing techniques such as electroluminescence (EL), and increasing automation to enable real-time, large-scale PV inspection with minimal human intervention.

6 Acknowledgements

The authors wish to acknowledge assistance from colleagues and financial support from Nelson Mandela University and the Department of Science Technology and Innovation of South Africa.

References

[1] F. Vorster and E. Van Dyk, Proceedings of the 6th Southern African Solar Energy Conference (SASEC), 2019, East London, ISBN 978-0-7972-1825-3
[2] S. R. Madeti and S. N. Singh, 2017, Sol. Engy., **158**, 161–185
[3] I. Polymeropoulos, S. Bezyrgiannidis, E. Vrochidou, and G. A. Papakostas, 2024, MDPI Tech., **12**
[4] H. Al Mahdi, P. G. Leahy, M. Alghoul, and A. P. Morrison, 2024, MDPI Tech. **4** 43–82
[5] V. Carletti, A. Greco, A. Saggese, and M. Vento, 2020, J Amb. Int. Hum. Comp. **11** 2027–40
[6] C. W. Hilti, I. Haedrich, and K.-A. Weiss, 2013, Photo. Int. 85–92
[7] D. Wu, J. Zhu, T. R. Betts, and R. Gottschalg, 2014, Prog. Photovolt.: Res. Appl. **22** 796–809
[8] R. del Prado Santamaría, M. Dhimish, G. A. dos Reis Benatto, T. Kari, P. B. Poulsen, and S. V. Spataru, MDPI Tech., 2025, **16**
[9] M. Y. Vazquez Nieves, A. M. Colón González, and J. L. Braid, 2023, Inst. of Ele. and Electr. Eng. Inc.

DFT studies of the photocatalytic properties of $BaTiO_3$ doped with V and W for hydrogen production

Phuthu Lutendo[1], Baloyi Magezi[1], Ranwaha Tshifhiwa[1], Dima Ratshilumela[2] and Maluta Eric[3,4]

[1]Department of Physics, University of Venda, Thohoyandou, South Africa
[2]Next Generation Enterprises and Institutions, CSIR, Pretoria, South Africa
[3]National Institute for Theoretical and Computational Sciences, Gauteng, South Africa
[4]Green Technology Confucius Institute, University of Venda, P/ Bag X 5050, Thohoyandou, 0950

E-mail: lutendo.phuthu@univen.ac.za

Abstract. The perovskite $BaTiO_3$ has been widely used as a catalyst for the synthesis of hydrogen through water splitting. However, the reaction cannot be initiated by visible light due to the large energy band gap of $BaTiO_3$. This work investigates the prospect of using the most powerful portion of solar energy, visible light, to drive the water splitting reaction. This is achieved by investigating the impact of Mono-doping and Co-doping on the electronic and optical properties of $BaTiO_3$ using first-principles density functional theory calculations. The doping elements used are Vanadium (V) and Tungsten (W). The computations were performed using the Generalized Gradient Approximation (GGA) and Local Density Approximation (LDA). The results show a reduced band gap and an increase in the optical response.

1 Introduction

The utilisation of solar radiation to perform water-splitting and make hydrogen is widely regarded as a highly advantageous method for generating clean chemical fuels, establishing renewable energy sources, and mitigating the impact of global warming and environmental concerns [1, 2]. Despite significant efforts to create sophisticated materials, the primary obstacle that persists is the reduced efficiency and selectivity for hydrogen (H_2) production using solar energy. Within these methods, semiconductor-based photocatalytic hydrogen production is regarded as one of the most viable pathways for sustainable green energy generation [3]. In recent years, researchers have discovered multiple productive methods to enhance the effectiveness of photocatalysis for water splitting. Commonly, precious metals such as platinum (Pt), ruthenium (Ru), rhodium (Rh), copper (Cu), silver (Ag), and gold (Au) are typically incorporated onto metal oxide surfaces to suppress electron-hole recombination [4]. Using the composition of semiconductors is an additional approach designed to extend light absorption into the visible range for hydrogen production through water splitting. When a semiconductor is connected to another that has a lower conduction band level, electrons transfer from the higher to the lower conduction band, resulting in effective separation of electrons and holes [5]. In addition, the process of cation and anion doping is highly effective in enhancing hydrogen production when exposed to visible light. This is due to its ability to shift the photo-response of a semiconductor with a broad energy band gap into the visible light spectrum. Experimental evidence has proven that pure $BaTiO_3$ can operate as a photocatalyst for hydrogen generation through water splitting [6, 7]. Nevertheless, $BaTiO_3$ possesses a relatively wide band gap of 3.2 eV, restricting its absorption to the ultraviolet region of the solar spectrum and rendering it inactive under visible

light irradiation [8]. One effective approach to reduce the band gap energy of $BaTiO_3$ and extend its optical response in the visible light region is by doping $BaTiO_3$ with a foreign element. This study uses such an approach to tailor the band gap of $BaTiO_3$ and enhance the optical response capability in the visible light region by examining the effects of mono-doping on its electronic and optical properties through first-principles density functional theory calculations.

2 Computational Details

The geometry optimization has been performed using density functional theory within the generalized gradient approximation (GGA) employing the Perdew-Burke-Ernzerhof (PBE) functional along with norm-conserving pseudopotentials, as implemented in the Cambridge Serial Total Energy Package (CASTEP) code on BIOVIA Material Studio [9, 10]. GGA was chosen over local density approximation (LDA) because it provides more accurate lattice parameters and structural features, which are crucial for forecasting the electrical and optical behaviour of $BaTiO_3$. While both underestimate band gaps, GGA more accurately reflects doping-induced trends in band gap decrease and visible light absorption. The plane-wave basis set was truncated at a cutoff energy of 380 eV, and Brillouin zone sampling was performed using a 6×6×6 Monkhorst-Pack scheme k-point grid.

3 Results

3.1 Structural Properties

A 2×2×2 supercell of $BaTiO_3$ was constructed from a unit cell. Figure 1 (a) shows the structure of a pure $BaTiO_3$ 2×2×2 supercell. Figure 1 (b) shows the structure of a doped $BaTiO_3$ 2×2×2 supercell system. The doping was done by substituting the Ti atom with either V or W. The lattice parameters of the optimized pure $BaTiO_3$ structure were calculated. The lattice parameters derived from the calculations are summarized in Table 1. The obtained results show good agreement with the experimental measurements within a percentage error of 4.279% as well as the theoretically calculated lattice parameter values [11, 12]. The calculated Ti-O bond length was 2.084 Å and is in good agreement with the experimental value of 2.008 Å.

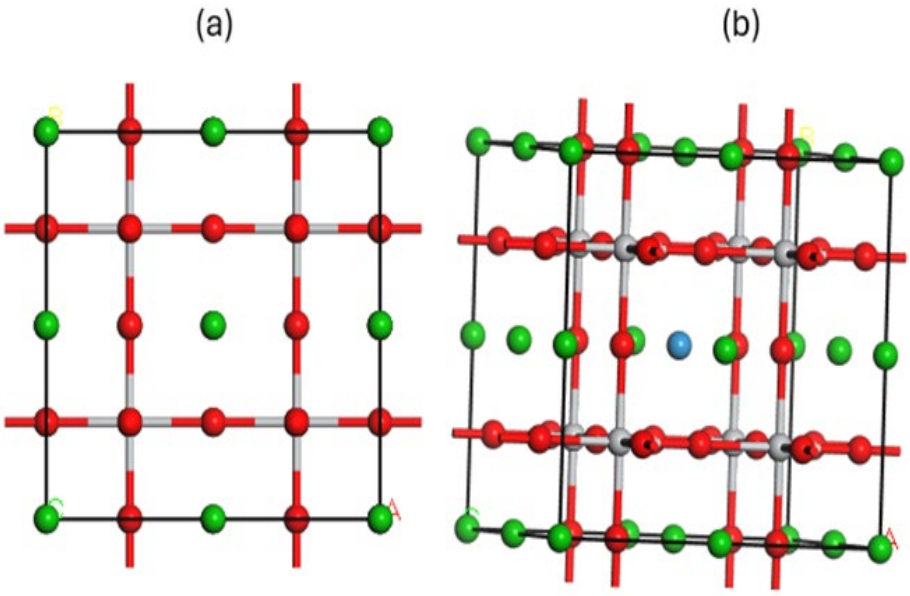

Figure 1: (a) $BaTiO_3$ 2 × 2 × 2 Supercell structure and (b) Doped $BaTiO_3$ 2 × 2 × 2 Supercell structure

Parameters	This work	Experimental [11]	Theoretical [12]
a (Å)	4.167	3.996	4.030
b (Å)	4.167	3.996	4.030
c (Å)	4.167	3.996	4.030

Table 1: Lattice parameter of pure $BaTiO_3$

3.2 Electronic Properties

To understand the electronic properties of the $BaTiO_3$ structure, the band structure calculations were obtained in order to understand the energy levels that the electrons can occupy. Figure 2 (a) shows the band structure calculations of an undoped $BaTiO_3$ $2 \times 2 \times 2$ supercell structure. The dotted black lines at the zero energy represent the Fermi level. The calculations reveal a band gap of 2.219 eV, defined by the difference between the maximum valence band (MVB) and the minimum conduction band (MCB). The band gap is less compared to the experimental reported value of 3.2 eV [8]. The inconsistency in this work and the reported experimental band gap is due to the fact that the GGA calculations underestimate the band gap. However, the underestimation does not affect the reliability of the remaining calculations. Figure 2 (b) and (c) illustrate the band structures of the V-doped $BaTiO_3$ $2 \times 2 \times 2$ supercell structure and W-doped $BaTiO_3$ 2x2x2 supercell structure, respectively. The calculations show that when $BaTiO_3$ $2 \times 2 \times 2$ supercell structure is doped with V and W, the band gap reduces to 1.345 and 0.232 eV, respectively.

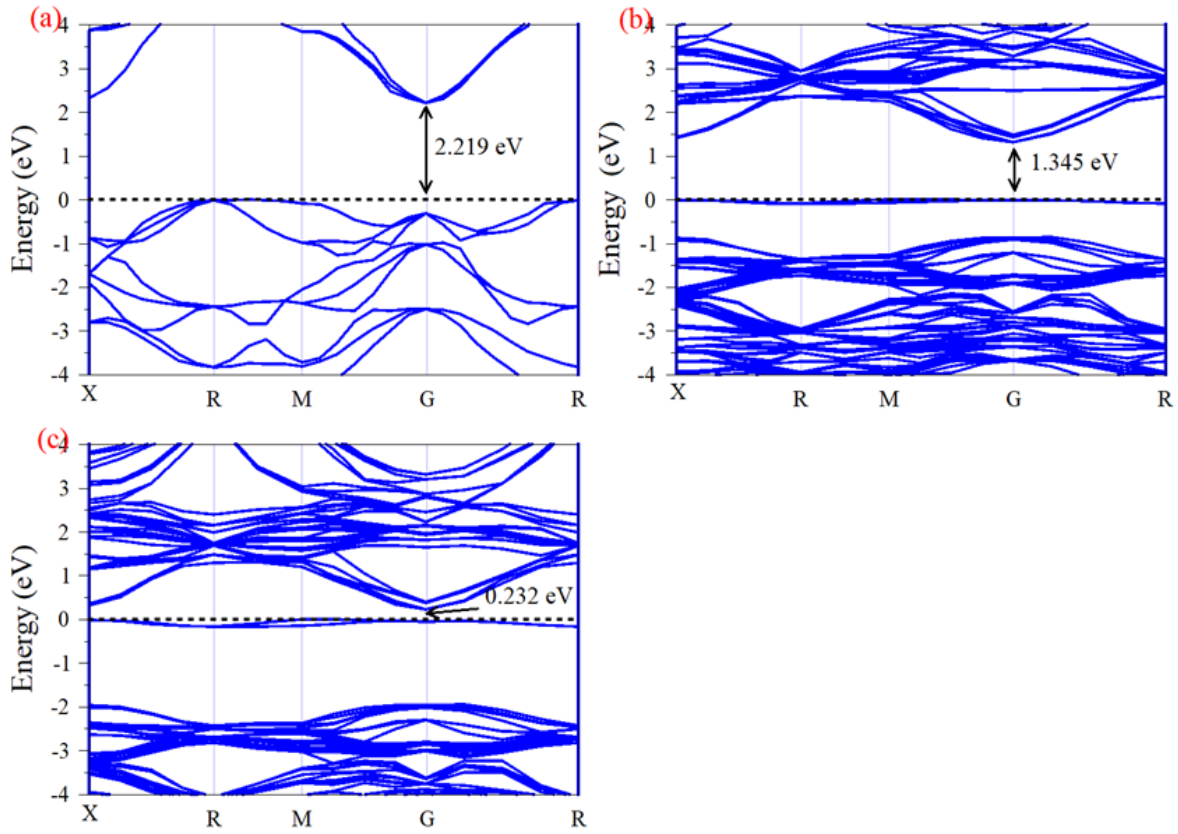

Figure 2: Calculated band structure of (a) $BaTiO_3$ $2 \times 2 \times 2$ supercell, (b) V- $BaTiO_3$ $2 \times 2 \times 2$ Supercell, and (c) W-$BaTiO_3$ $2 \times 2 \times 2$ Supercell.

To study the number of electronic states available within a specific energy range and the contribution of particular orbitals, both the total density of states (TDOS) and partial density of states (PDOS) were calculated. Figure 3 (a) depicts the calculated TDOS and PDOS of the $BaTiO_3$ 2×2×2 supercell structure. The electron distribution in $BaTiO_3$ is from the contribution of the 6s states of Ba, 3d states of Ti, and 2p states of O atomic shells. It is observed that the Ti 3d states dominate the conduction band (CB), while the O 2p states are the major contributors to the valence band (VB). The 6s states of Ba have less contribution in the TDOS of $BaTiO_3$ 2×2×2 supercell structure. The band gap is observed within the energy range of 0.5-2 eV. Figure 3 (b) and (c) depict the calculated TDOS and PDOS of the doped $BaTiO_3$ 2×2×2 supercell structure. Upon doping with V and W, as shown in Figures 3 (b) and (c), impurity states emerge at the Fermi level, resulting in a reduction of the band gap.

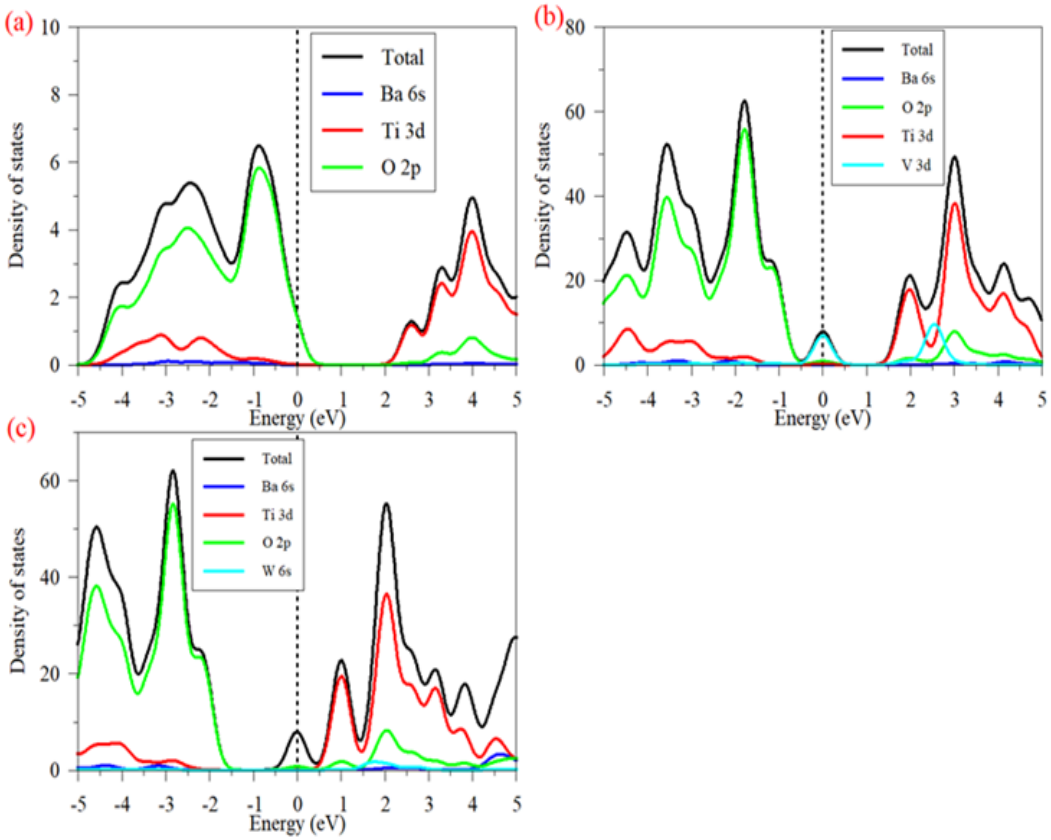

Figure 3: Calculated TDOS and PDOS of (a) $BaTiO_3$ 2 × 2 × 2 supercell, (b) V- $BaTiO_3$ 2 × 2 × 2 supercell, and (c) W-$BaTiO_3$ 2 × 2 × 2 supercell.

3.3 Optical Properties

To investigate how the $BaTiO_3$ 2×2×2 supercell structure and doped structures respond to electromagnetic radiation, particularly visible, and the optical absorptions were calculated. The calculated optical absorptions are shown in Figure 4. Represented by the black curve line, the absorption curve of pure $BaTiO_3$ 2×2×2 supercell structure pronounces strong absorption in the ultraviolet region, while the absorption in the visible region is comparatively weak. It is observed that at a wavelength of more than 600 nm of wavelength, pure $BaTiO_3$ 2×2×2 supercell structure absorption depletes. In comparison, the incorporation of V and W at the Ti sites causes a redshift, indicating enhanced absorption at longer wavelengths.

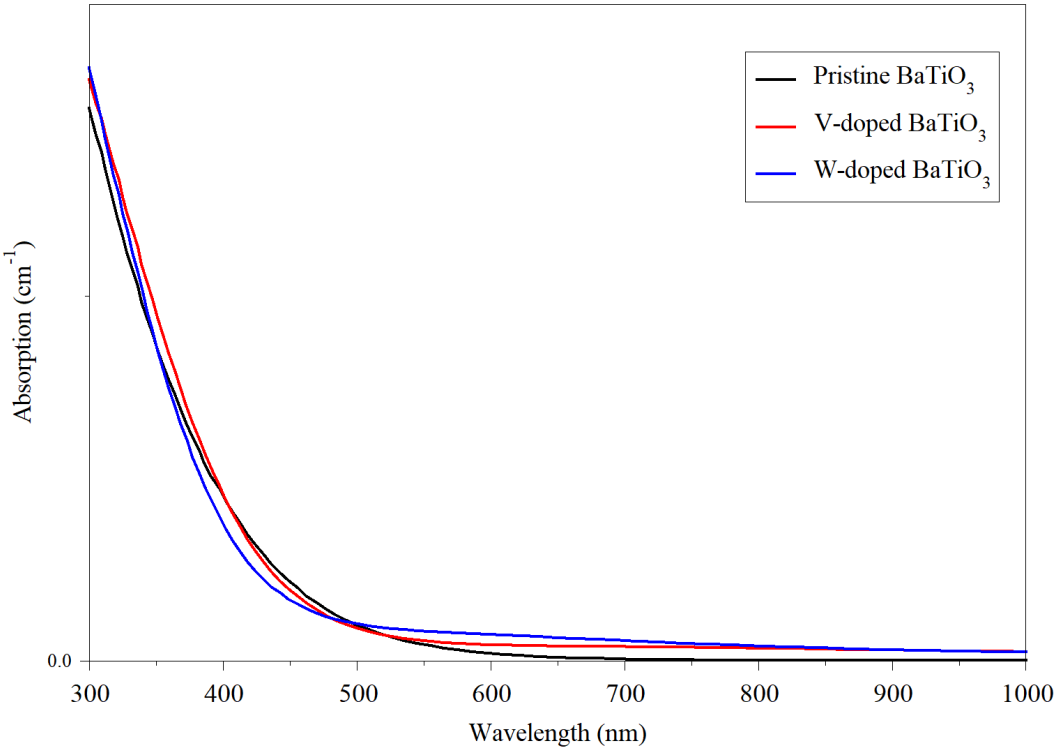

Figure 4: Optical absorption of pure and doped $BaTiO_3$ 2x2x2 supercell.

4 Conclusion

Using the first principle approach based on density functional theory, the electronic and optical properties of $BaTiO_3$ were successfully obtained. The calculated lattice parameters were compared with the literature and are in good agreement with previously reported experimental and theoretical values. While GGA underestimated the band gap energy, it did not affect the comparison of the pure structure with the doped structure. The results show that the band gap energy of $BaTiO_3$ is reduced when $BaTiO_3$ is doped with V and W. The reduced band gap energy allows electrons to move from VB to CB with less probability of charge recombination. The density of states analysis shows that the reduced band gap energy resulted from the impurities that were induced in the Fermi energy. From the optical absorption, the dopants allow $BaTiO_3$ to have an absorption increase in the visible region. This result enables $BaTiO_3$ to be effective for water splitting.

References

[1] A. Boretti, "Which thermochemical water-splitting cycle is more suitable for high-temperature concentrated solar energy?," *International Journal of Hydrogen Energy*, vol. 47, no. 47, pp. 20462–20474, Jun. 2022, doi: https://doi.org/10.1016/j.ijhydene.2022.04.159.

[2] M. Aravindan and P. Kumar, "Hydrogen towards sustainable transition: A review of production, economic, environmental impact and scaling factors," *Results in Engineering*, vol. 20, p. 101456, Dec. 2023, doi: https://doi.org/10.1016/j.rineng.2023.101456.

[3] C.-H. Liao, C.-W. Huang, and J. C. S. Wu, "Hydrogen Production from Semiconductor-based Photocatalysis via Water Splitting," *Catalysts*, vol. 2, no. 4, pp. 490–516, Dec. 2012, doi: https://doi.org/10.3390/catal2040490.

[4] P. Ebrahimi, A. Kumar, and M. Khraisheh, "A review of recent advances in water-gas shift catalysis for hydrogen production," *Emergent Materials*, vol. 3, no. 6, pp. 881–917, Aug. 2020, doi: https://doi.org/10.1007/s42247-020-00116-y.

[5] Y. Mohammed, Hafeez Yusuf Hafeez, J. Mohammed, Abdussalam Balarabe Suleiman, Chifu Ebenezer Ndikilar, and Miftahu Gambo Idris, "Hydrogen production via photocatalytic water splitting using spinel ferrite-based photocatalysts: Recent and future perspectives," *Next energy*, vol. 4, pp. 100145–100145, Jul. 2024, doi: https://doi.org/10.1016/j.nxener.2024.100145.

[6] H.-C. Huang, C.-L. Yang, M.-S. Wang, and X.-G. Ma, "Chalcogens doped $BaTiO_3$ for visible light photocatalytic hydrogen production from water splitting," *Spectrochimica acta. Part A, Molecular and biomolecular spectroscopy*, vol. 208, pp. 65–72, May 2019, doi: https://doi.org/10.1016/j.saa.2018.09.048.

[7] K. Xue *et al.*, "Composition-driven morphological evolution of $BaTiO_3$ nanowires for efficient piezocatalytic hydrogen production," *Chemosphere*, vol. 338, pp. 139337–139337, Jul. 2023, doi: https://doi.org/10.1016/j.chemosphere.2023.139337.

[8] T. Chen *et al.*, "Room temperature synthesized $BaTiO_3$ for photocatalytic hydrogen evolution," *Journal of alloys and compounds*, vol. 754, pp. 184–189, Jul. 2018, doi: https://doi.org/10.1016/j.jallcom.2018.04.300.

[9] G. Kresse and J. Furthmüller, "Efficiency of ab-initio total energy calculations for metals and semiconductors using a plane-wave basis set," *Comput. Mater. Sci.*, vol. 6, no. 1, pp. 15–50, Jul. 1996, doi: https://doi.org/10.1016/0927-0256(96)00008-0.

[10] G. Kresse and J. Furthmüller, "Efficient iterative schemes forab initiototal-energy calculations using a plane-wave basis set," *Physical Review B*, vol. 54, no. 16, pp. 11169–11186, Oct. 1996, doi: https://doi.org/10.1103/physrevb.54.11169.

[11] H. Gao, J. Cao, L. Liu, and Y. Yang, "Theoretical investigation on the structure and electronic properties of barium titanate," *Journal of Molecular Structure*, vol. 1003, no. 1, pp. 75–81, Sep. 2011, doi: https://doi.org/10.1016/j.molstruc.2011.07.024.

[12] M. Hasan and A. K. M. Akther Hossain, "Structural, electronic and optical properties of strontium and nickel co-doped $BaTiO_3$: A DFT based study," *Computational Condensed Matter*, vol. 28, p. e00578, Sep. 2021, doi: https://doi.org/10.1016/j.cocom.2021.e00578.

Reconfigurable Payload Power Management System for Rockets

Marco Mariola[1] **and Tyrone A. Swanepoel**[1]

[1]Aerospace Systems Research Institute, University of KwaZuluNatal, Durban, South Africa
E-mail: mariolam@ukzn.ac.za

Abstract. In modern aerospace systems, the integration of payload electronics with the rocket's primary power infrastructure introduces constraints related to power compatibility, isolation, activation timing, and inertia distribution. This paper presents a reconfigurable payload power management system designed to provide galvanic isolation and touch-less activation for payloads with independent power supplies. The proposed system enables activation of payloads post-integration via a contact-less transformer interface, eliminating the need for umbilical connections, thus mitigating issues such as battery discharge during launch delays and minimising disassembly requirements. A thyristor-based power-on circuit ensures reliable one-way activation of the controller, while custom-designed optical isolated switching modules provide safe, low-resistance connections between payloads and their power sources. The design minimise the event of possible ground loops, allows for modularity, and provides robustness in plasma environments. A modular and symmetrical hardware layout enables seamless integration into spin-stabilised rockets. Preliminary testing confirms the system's robustness and suitability for deployment in dynamic aerospace environments.

1 Introduction

The power system for an aerospace vehicle is organically designed according to the needs and characteristics of the service systems and payloads. If a payload needs to be activated or powered by the rocket's energy source, the payload designers are constrained to follow the specification dictated by the rocket's power system requirements. The standard described is advisable and safe, but in the proposed design, we are considering a power management system that can be relatively flexible, for customers who want to use a battery within its payload. If a payload has its own battery, it can be activated before being enclosed in the rocket. However, in the event of a possible launch delay, the battery may discharge, necessitating the disassembly of the rocket to recharge the power sources. The proposed system permits the integration of the payload into the rocket without being activated. Once the nose cone is closed, just before the launch, the electronics can be activated without any umbilical using the touchless transformers. The system permits control of a payload, ensuring the galvanic isolation between the payload and the rest of the rocket's electronic systems. The isolation prevents the ground loop and propagation of failures.

2 High level system description

The power management system is configured to command the switching of internally-powered payloads. To better understand how the payloads are connected, it is useful to observe the high level diagrams of Figure 1. In the block diagram, with S_{wn}, is indicated the n switch belonging to payload n, while Sw_g is the general switch that activates the controller board. In a similar system, the physical switching can be a transistor BJT or a MOSFET high or low side connected. In both of these scenarios, the ground is shared between the payload and the controller board. In the device the switches and the controller block are galvanically isolated. The isolation is required to avoid ground loops. The switch Sw_g is used to activate the controller. The SW_g is not a mechanical switch, but represents a thyristor activated by a touch-less transformer positioned externally to the rocket's nose cone. The only flaw in the design is that once the control board is active, it is not possible to shut down the system.

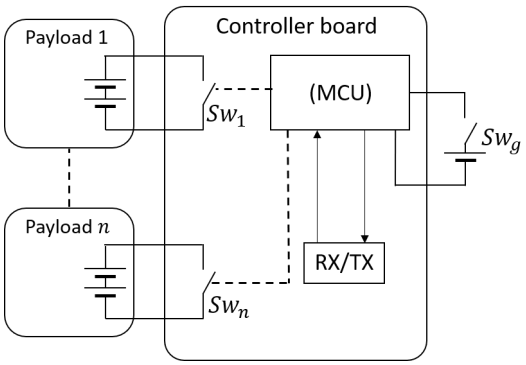

Figure 1: High level block diagram, of the power management system.

3 Boot-up of the controller board

The nose cone's geometric design enables optimal payload integration, achieving a balanced mass distribution around its central axis. A schematic representation of the cone and the position of the touch-less transformer is represented on the left of Figure 2. In the system, the power controller board is positioned at the bottom, and just above the battery pack[1].

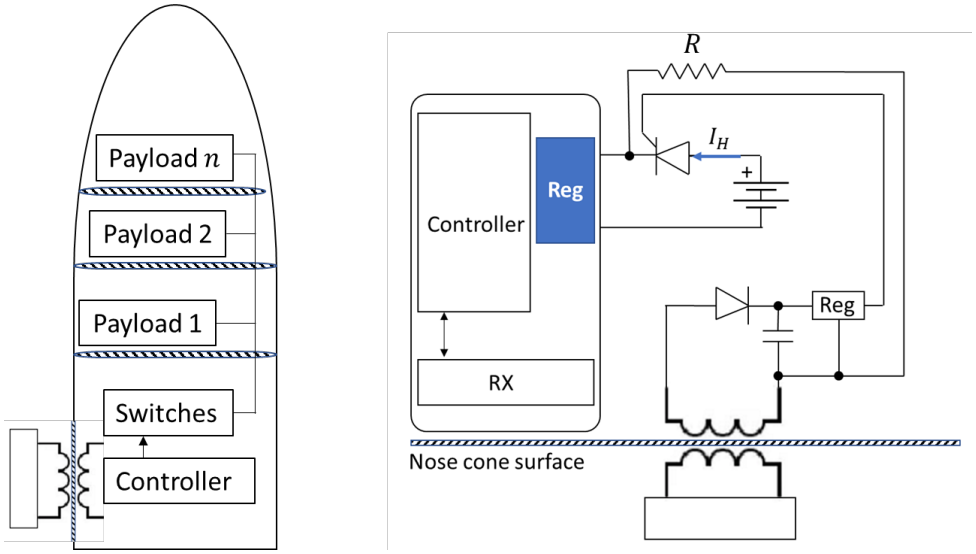

Figure 2: (*left*) Possible payload distribution, and position of the touch-less transformer. (*right*) Activation system of the controller board.

Once the rocket is positioned on the gantry, the primary coil of the transformer is close to the secondary coil, as depicted on the right of Figure 2. Just before the launch, from the Mission Control Room the primary is activated and from the secondary, the alternating voltage is rectified by a simple filter. The rectified signal is processed by a linear regulator, generating a controlled output voltage that supplies the necessary gate current to sustain thyristor conduction. In this scenario the thyristor is used, since in direct current, if the load draws a current equal to or greater than the holding current I_H, the thyristor stays in a conduction state. The resistance R is used just for polarization purposes. Unfortunately, once the controller board is activated, it is not possible to deactivate. The circuit proposed was tested with the micro-controller with all the pins at logic level zero, and it was observed that the current drawn is sufficient to keep the thyristor in a conduction state.

[1]This is not a constraint, and it depends on the specific needs of the system

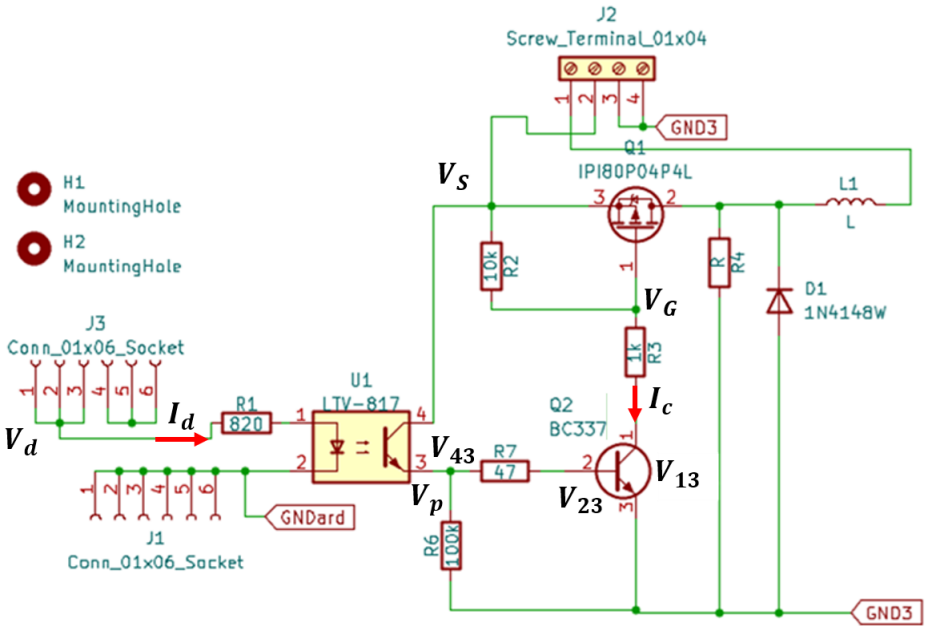

Figure 3: Single switch schematic. The printed circuit board is designed in a way that allows the stacking of two switches, to exploit the vertical geometrical distribution.

4 The switches

Electronically controlled switching systems can be implemented using various methods, including mechanical relays or photo-coupled solid-state relays, which offer galvanic isolation and are resistant to vibration. Given the need for protection circuitry due to the presence of plasma, a custom-designed circuit solution is required.

4.1 Circuit qualitative analysis

The switch is controlled by a Micro-controller Unit (MCU), through the connector J3. The connector J1 shares the MCU ground. Considering a high logic level of $5V$, and at the low logic level, the voltage is approximately 0V. The battery of the payload is connected at pin 2 of the connector J2, with a voltage V_S. When the MCU pin is at the low logic level, the current I_d is zero, and there is no photon emitted by the LED of the optocoupler. The absence of the light results in the transistor working within the cut-off region, and the voltage V_p is approximately 0V[1]. For these values of V_p, the transistor Q2 is also cut-off, and the voltage on the gate node is $V_G = V_S$. Since $V_G - V_S = 0$V, the P-channel MOSFET Q1 results as an open circuit. The power absorbed in this working point is approximately 0V.

If the control pin of the MCU changes to V_p, the current I_d flows into the LED of the optocoupler, and if it is properly designed, the voltage V_{43} decreases to a value between 0.1V and 0.2V. At the node V_p the voltage is now close to V_S, and a base current I_B flows to the transistor Q2. The base current saturates the transistor Q2, and the voltage V_{13} decreases between 0.7V and 0.8V. Since $V_{GS} = V_G - V_S < 0$V the resistance between the drain and source is approximately 0V, and now the current can flow from the positive of the battery to the payload, with a minimal drop of voltage[2].

Ideally, the circuit proposed can work in its current state, but for an aerospace vehicle, it is necessary to include some protection against plasma bubbles. If the vehicle, encounters plasma, there is a possibility of spikes being present at the drain of the MOSFET, which destroy the device. By placing an inductor L1 the MOSFET is protected. If the current flows into the inductor, at the same instant the MOSFET becomes an open circuit, the highest voltage will be present at the source. By placing the diode, when the MOSFET is in an off-state, the voltage across the inductor forward biases the diode, and the energy will be discharged into the inductor.

4.2 Design of the switching and the controller board

The circuit is designed to work with TTL logic; this means that the logic level 1 corresponds to 5V, and the logic level 0 corresponds to 0V. When the logic level 0 is present, the voltage V_d is equal to 0V, and the MOSFET can be simply seen as an open circuit. In the following calculations, the values of the tested circuit are left out, since

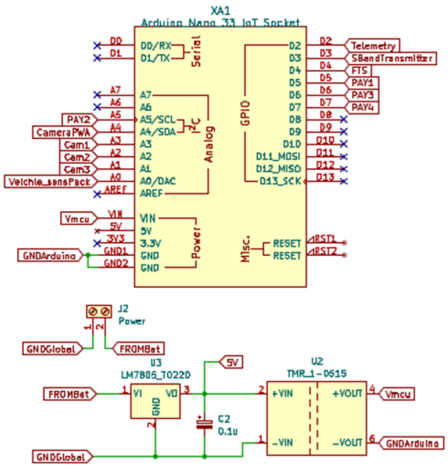

Figure 4: Schematic of the controller board.

the reader can replicate the design, by using other components[2]. In the design it is also necessary consider the maximum deliverable current of the digital pin of the MCU. When $V_d = 5\text{V}$, the current that flows into the LED is:

$$I_d = \frac{V_d - 1.2}{R1}. \tag{1}$$

The current I_d needs to be able to saturate the transistor, in order to achieve a voltage V_{43} of at least 0.2V. In this specific case the current I_d is 5mA. After the current I_d is determined, the voltage across the transistor of the optocoupler V_{43} is known, and the voltage V_p is:

$$V_p = V_S - V_{43}. \tag{2}$$

The base current I_{R7} can be determined by the generalised Ohm's Law, as shown in Equation (3).

$$I_{R7} = \frac{V_p - V_{BE}}{R7}. \tag{3}$$

The voltage $V_{BE} = V_{23}$ can be considered constant. In this design, for the BC337, the voltage Base-emitter can be considered at 0.7V. The base current calculated reduces the voltage V_{13} to 0.2V. The current I_C only depends on the resistance $R2$ and $R3$. The collector current is determined by Equation (4).

$$I_c = \frac{V_s - 0.2}{R2 + R3}. \tag{4}$$

The voltage at the gate V_G is:

$$V_G = I_c \times R3 + V_{13}. \tag{5}$$

The voltage between the gate and the source $V_{GS} = V_G - V_S$, is negative, and the MOSFET results in a small resistance between the source and the drain. In general this circuit can be used with any P-channel MOSFET, but because the system works at low voltage levels, a digital MOSFET is required to obtain a minimal resistance[3]. As was stated in the previous sections, the switches are controlled via the controller board. The controller board implements the MCU. The MCU is powered by using a DC-DC converter with a separate ground[3]. In this way the MCU is also galvanically isolated. The schematic of the main board is shown in Figure 4. The power for the controller board is connected to a voltage regulator [4], whose output is connected to a DC-DC converter. The adopted DC-DC converter has the input and output ground separated. The design wants to avoid any sources of noise that can potentially exist in the overall system.

[2]In some specific case, for example, it is necessary to use a space-grade optocoupler, which may have different electrical characteristics. The circuit can also change according to the MCU use, since some MCUs do not run at 5V, but at 3.3V

[3]To use a standard MOSFET will increase the complexity of the circuit in order to generate a negative polarisation voltage at the gate.

5 The hardware design

The hardware proposed needs to be implemented into a small rocket that is spin-stabilized. The inertia distribution requires particular attention, and the device was designed to be symmetric with respect to the centre of rotation. The controller board is designed to allocate the switching boards as stackable devices. The geometry of the final prototype is represented in Figure 5 . The actual design considers an Arduino Nano, and in this project RX of

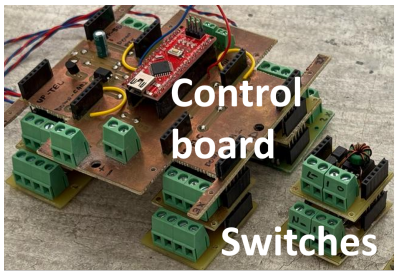

Figure 5: Picture of the tested board.

the controller board is represented by the serial communication between the MCU and the computer in the control room. It is possible to replace the Arduino Nano used in this system with an Arduino Nano ESP32, which has the same pinout configuration as the Arduino Nano, but the WiFi is embedded in the board[5].

6 Validation and scalability

The system proposed was ground tested validated, but further analysis are planned. The electrical validation was conducted by replicating a current load between 1A and 2A. According to the designed track width of the printed circuit board, and the MOSFET used, the system can technically hold grater values of current, but since the system can be potentially enclosed into a rocket, high temperature environment should be mitigated.
The intention of the manuscript is to give a possible solution to control several payloads in a safe manner with the payloads having their own power requirements, and internal power source. In the case of this design, the system is stackable as represented in Figure 5. According to the specific geometrical requirements, it is possible to change the topology of the whole circuit. The assembly proposed is drawn in a way that the switching board occupies as minimal space as possible. Can be potentially applied in a multitude of applications, by always considering its inertial distribution for a specific aerospace application.

7 Future work

As was mentioned in the paper,in the switching system, is included the touchless activation system able to power the payloads, and services the rocket. Currently when the system is activated, it is not possible to switch the payloads off. It is necessary to improve the design by considering a deactivation system. The deactivation of the thyristor results in the deactivation of the power system, which can be achieved by placing the anode and cathode of the thyristor at the same potential using a relay. The proposed solution is not unique, but others will be investigated.

8 Conclusion

The proposed power management system offers a practical and adaptable solution for integrating independently powered payloads into launch vehicles. By employing galvanically isolated switching mechanisms and a touchless transformer-based activation circuit, the system addresses critical challenges such as pre-launch battery depletion, ground loop interference, and electromagnetic susceptibility. The modular architecture, based on stackable boards and compact controller design, facilitates integration in geometrically constrained and dynamically sensitive rocket environments. Future iterations may incorporate bidirectional communication and deactivation capabilities, particularly through the adoption of microcontrollers with wireless interfaces such as the Arduino Nano ESP32[5]. The proposed system contributes meaningfully to the development of robust and adaptable aerospace subsystems, especially in the context of reconfigurable payload deployment and autonomous flight readiness.

Acknowledgement
This work is supported by the Department of Science, Technology and Innovation .

References

[1] T. L. Floyd, *Electronic devices*. Pearson, 2012.

[2] Infineon, "IPB80P04P4L-06," https://docs.rs-online.com/bba9/A700000009480860.pdf, Infineon Technologies AG, 81726 Munich, Germany, 2019, Accessed: 2025-07-30.

[3] Mornsun, "DC/DC Converter B_S-1WR3 Series," https://www.mantech.co.za/datasheets/products/b_s-1wr3-190403a.pdf, 2018, Accessed: 2025-07-30.

[4] Texas Instruments, "A7800 SERIES POSITIVE-VOLTAGE REGULATORS," https://cdn.sparkfun.com/assets/1/7/7/3/2/LM7805.pdf, "2003", Accessed: 2025-07-30.

[5] Arduino, "Arduino Nano ESP32," https://docs.arduino.cc/resources/datasheets/ABX00083-datasheet.pdf, 2025, Accessed: 2025-07-30.

Design of a slotted Invelox-based wind delivery system for domestic low wind speed operation.

Anesu Chitura[1], Ngwarai Shambira[1] and Patrick Mukumba[1]

[1]Department of Computational Sciences, Faculty of Science & Agriculture, University of Fort Hare, Alice 5700, South Africa

E-mail: 201714884@ufh.ac.za

Abstract. Features such as the omni directional intake, the nozzle-diffuser section as well as the diffuser section of the Increased velocity (Invelox) wind delivery system augment incident air to a cut in wind speed of most small-scale wind turbines systems. Despite these properties, the Invelox delivery system suffers from immediate pressure difference leading to flow separation within the throat section. This significantly reduces the suction capacity of the intake thus diminishing aerodynamic performance of the system. Amid other scholars that have researched to improve it, this study modified the original Invelox setup by employing a slotted diffuser section. Such a structure utilizes available wind thus making energy more accessible and sustainable. The aim is to improve the expansion area and subsequently avoid flow separation on the diffuser wall. The geometry was developed and simulated in an OPEN FOAM environment where the effect to the performance of the Invelox system as well as the augmented velocity is then observed. The results show an improved pressure gradient leading to an improved flow profile within the diffuser. The introduction of a slot was shown to improve the speed up ratio of the throat thus emphasising the potential of the improvement. The 9% improvement in velocity augmentation proved potential and pointed to more optimisation to realise even better augmentation.

1 Introduction

Residential wind energy conversion is increasingly vital for generating distributed power and reducing reliance on fossil fuels. In the context of global efforts to lower carbon emissions and combat climate change, wind power offers a clean alternative. However, wind applications in residential areas face key challenges, including low wind speeds and high turbulence due to surrounding buildings. At Fort Hare University, the area under study, average wind speeds are typically below 3 m/s as investigated by [1]. Under such low wind conditions, even turbines designed for low-speed performance, such as the Savonius type, fail to start, as the available wind energy is insufficient to overcome their cut-in speed threshold. The wind resource is too weak for off-the-shelf small-scale wind turbines to operate effectively on their own. To address this limitation, an augmentation or interfacing device is necessary to improve the velocity and quality of the incoming wind. A wind delivery system serves this purpose by increasing wind velocity and quality, enabling the turbine housed within to operate more smoothly and reliably.

1.1 Literature review

The concept of using augmentation devices to bridge the gap between slow-moving wind and turbines with higher cut-in speeds has gained attention in residential wind applications. Diffuser-based wind turbine shrouds have been widely studied for this purpose [2]. For example, [2] used the simplex algorithm to optimize the shape of a diffuser, achieving a 1.76-fold increase in incident wind speed. Key geometric parameters such as flange height and angle were identified as critical to performance, with [3] using Design of Experiments and one-factor-at-a-time methods to narrow down the most influential design variables to three, highlighting the importance of

interactional effects. In addition to diffusers, concentrators (or nozzles) have been explored as augmentation devices [4,5], and combinations of concentrator-diffuser systems have been examined by [6]. Such systems address the interaction between geometric elements, with [6] analyzing the relationship between augmented throat velocity and six parameters in a concentrator-diffuser configuration, resulting in an increase in wind speed by a factor of 1.953. Efforts have also been made to integrate wind turbines directly into building structures, using the building itself as a shroud to augment wind speeds [7]. Among such systems, the Invelox wind delivery system is considered one of the most promising. It features a raised omnidirectional intake that removes the need for yaw mechanisms, channels wind through a funnel, bends toward a nozzle and throat (where the turbine is placed), and exhausts the used wind through a gradually expanding diffuser [8]. Although effective, the system faces challenges such as escaping air, recirculation, and flow separation [9]. This study however, uses the basic Invelox setup combined with the use of a slot in the diffuser section to improve the airflow and hence augmentation.

The study aims to enhance wind augmentation in the throat region by modifying the Invelox system with a multi-slot diffuser. By incorporating a multi-slot diffuser into the conical section, this design addresses these issues by directing energetic air streams to control the boundary layer along the diffuser walls, thereby delaying or preventing flow separation. The aerodynamic performance is analysed using an empty wind delivery system, without a turbine, to isolate the effect of the diffuser modification.

Mathematical framework

As a fluid, free-stream moving air possesses kinetic energy. This total energy (e) is represented by Equation 1.

$$e = \frac{p}{\rho} + \frac{|v|^2}{2} = \frac{P_0}{\rho} \tag{1}$$

Where p indicates the pressure, and P_0 denotes the power extracted from the rotor. V is the velocity vector and ρ is the density. After air is collected by the omnidirectional intake of the INVELOX system, it is directed toward the nozzle-diffuser section. In the throat section, work is done by the air on the turbine blades, converting its energy into mechanical energy. Before reaching the turbine blades, the airflow experiences shear losses, which can be neglected for simplicity. Thus, the power in the wind passing through the INVELOX system can be expressed as in Equation 2.

$$Power = \eta \dot{m}[P_{atm} - P_{out}] + \rho \frac{V_{in}^2}{2} - \rho \frac{V_{out}^2}{2} \tag{2}$$

Where, $\dot{m}$ is the mass flow rate, and η is the efficiency. Equation 2 above highlights the two main mechanisms through which the INVELOX system extracts power from incident wind. These are: (1) the increase in kinetic energy, represented by the term $\rho \frac{V_{in}^2}{2} - \rho \frac{V_{out}^2}{2}$, and (2) the change in potential energy as the wind flows from the inlet to the outlet. These two effects enable INVELOX turbines to harness more power than conventional bare wind turbines.

2 Materials and Methods

The geometry of the Increased Velocity (INVELOX) wind delivery system was developed using *Shaper* within the *Salome* platform. This original geometry served as the basis for constructing a modified version of the system, incorporating structural enhancements to improve wind augmentation. To validate the simulation

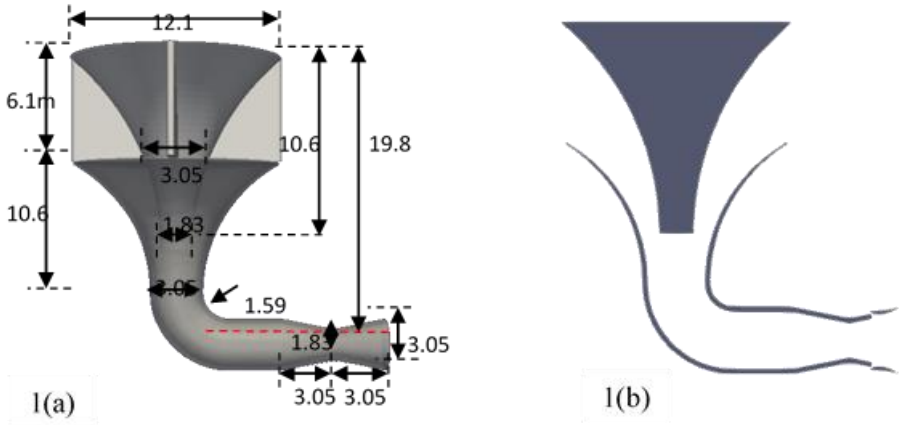

Figure 1. Dimensions and design of the original Invelox system as adapted from [8]

approach and software configuration, a replica of the original INVELOX design was created, meshed, and used to conduct a grid independence study following standard practices [10].

The improved version features a slot at the throat section of the INVELOX system, as shown in Figure 1(b), along with an E432 airfoil-shaped diffuser. This configuration helps avoid a sudden pressure change at the throat section and subsequently prevents choking of the delivery system. This modification is expected to enhance flow within the system, thereby improving the augmentation of incident wind.

2.1 Mesh Development, grid independence check, and validation

The goal of the mesh independence study was to establish a mesh that meets all quality requirements while eliminating mesh sensitivity and minimizing computational cost in terms of time and resources. The mesh size was varied from 670294 to 1848672 cells, up to the point where less than 1% change was observed in the results. A mesh consisting of 1542645 cells was selected, with a non-orthogonality of 63 and a skewness of 3.04, values considered very good for high-quality meshing in Openfoam. A length scale of 1 m was adopted for the geometrical setup, and an upstream wind speed of 6.7 m/s was used, in line with values reported in the literature [11]. Prism layers were applied along wall boundaries to maintain an operational y^+ value of 35, which falls within the logarithmic region of the boundary layer. The k–ε turbulence model was chosen for the simulations due to its suitability for high Reynolds number flows. Figure 2 presents the mesh independence results for the 12 cases studied, with the selected mesh indicated by a star marker. The figure also compares the current results with those from previous research by other scholars.

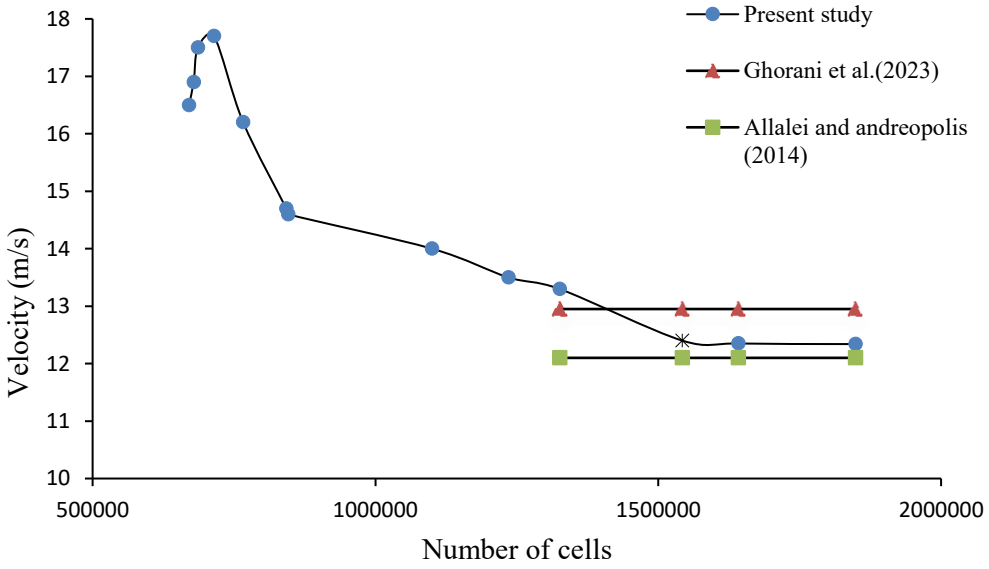

Figure 2. Mesh independence testing.

2.2 CFD simulation set up

Computational Fluid Dynamics (CFD) was used to analyse the influence of geometric parameters on wind speed augmentation at the INVELOX throat section. This method utilises statistical decomposition, wherein the local value of a flow variable is expressed as the sum of a mean and its fluctuating component. Applying this decomposition to the Navier–Stokes equations leads to the Reynolds-Averaged Navier–Stokes (RANS) formulation:

Continuity Equation:

$$\nabla.\overline{\mathrm{U}} = 0 \tag{3}$$

Momentum Equation:

$$\frac{\partial \overline{U}}{\partial t} + \nabla.\left(\overline{U\overline{U}}\right) = g - \nabla\overline{p} + \nabla.\left(\nu\nabla\overline{U}\right) + \overline{\mathrm{U}'\mathrm{U}'}. \tag{4}$$

Where, ν is the kinematic viscosity, U represents velocity and p is the kinematic pressure. The term $\overline{\mathrm{U}'\mathrm{U}'}$ represents the Reynolds stress tensor, which accounts for turbulent fluctuations. This term is as a result of averaging the Navier-stokes equations and is solved by applying turbulence models. Numerical simulations were performed using the SimpleFoam solver in Openfoam under steady-state conditions. The flow medium was limited

to air, with a velocity inlet of 6.7 m/s, a pressure outlet of zero-gauge pressure, and no-slip wall conditions applied to all solid surfaces. A realisable k–ε turbulence model was used to better accurately simulate recirculating and separated flows. The SIMPLE algorithm was applied for pressure–velocity coupling along with moderate under-relaxation factors to ensure stability and convergence. For numerical discretisation, the Least Squares Cell-Based method was used for gradient calculations, while second-order discretisation schemes were employed for pressure, momentum, and turbulence equations to enhance solution fidelity. A bounded Gauss linear upwind scheme was used for divergence terms, Gauss linear for gradient terms, and Gauss linear corrected for Laplacian terms to account for mesh non-orthogonality and improve numerical accuracy.

3 Results and Discussion

The chosen mesh as outlined in the previous section was simulated and part of the results are shown in Figure 3 below. In Figure 3 (a), streamlines present how air escapes the intake and only a fraction of the air is drawn into the system. Some of the air steams that do enter the omnidirectional intake gets misdirected and develop recirculation areas as shown in figure 3 (b). The vector plots in Figure 3 (b) highlight the density of streamlines as well as the direction in which the travel as they move through the INVELOX setup. Dense vectors can be seen around the shoulders of the bottom funnel as well as in the diffuser sections which is consistent with what other scholars observe.

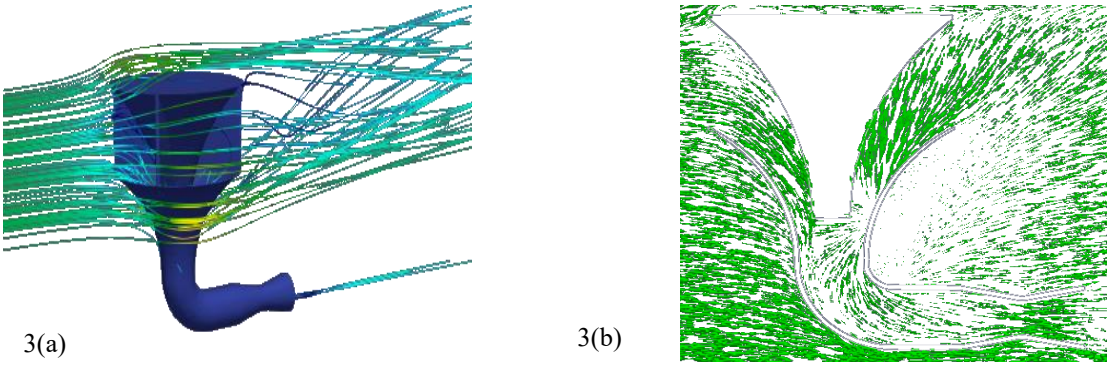

3(a) 3(b)

Figure 3. Simulation of the chosen solution.

The chosen solution was simulated using the same settings as the original setup, with the only modification being reducing the upstream wind speed to 3 m/s to mimic flow rates found in residential areas, which better suited our study area. Figures 4 (a) – 4 (d) compare the throat section of the original configuration with the modified one. The pressure plots (Figures 4 (a) and 4 (b) show a greater reduction in pressure as the flow constricts at the throat, indicating an improvement in flow velocity in accordance with Bernoulli's principle. The lighter colour scheme in the modified version illustrates the extended region of pressure reduction compared to the original. Similarly, the velocity profiles (Figures 4 (c) and 4 (d) display a more pronounced darker colour, suggesting a slight increase in velocity at the throat section due to the addition of a slot in the nozzle-diffuser section of the INVELOX system. To validate this observation, a horizontal line was drawn across the pressure field and a 100-point plot over this line is presented in Figure 5. Likewise, a vertical line was drawn at the throat section of both the original and improved setups. Figure 5 compares the pressure and velocity distributions along a horizontal line through the centre of the venturi section. The slotted version shows an increase in peak velocity from 3.19 m/s to 3.48 m/s and a deeper pressure drop from −4.86 Pa to −5.56 Pa. Notably, the slotted version exhibits improved pressure recovery, returning to values similar to the original INVELOX setup despite the greater initial drop. This suggests the potential for using a shorter diffuser, which would be advantageous in spatially constrained installations [12].

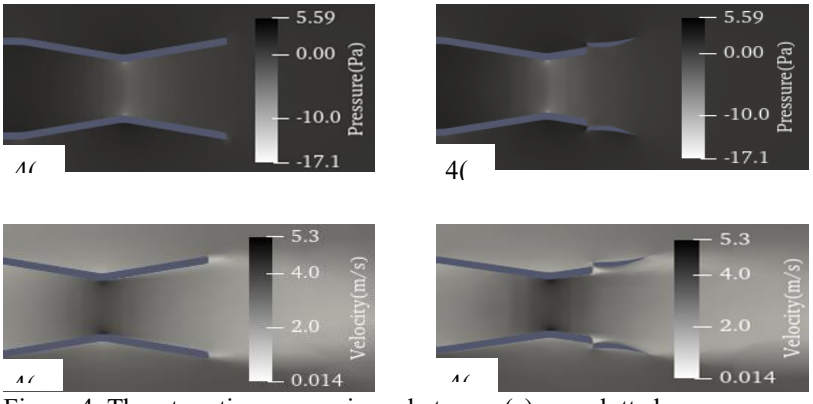

Figure 4. Throat section comparisons between (a) non-slotted pressure simulation, (b) slotted pressure simulation, (c) non-slotted velocity

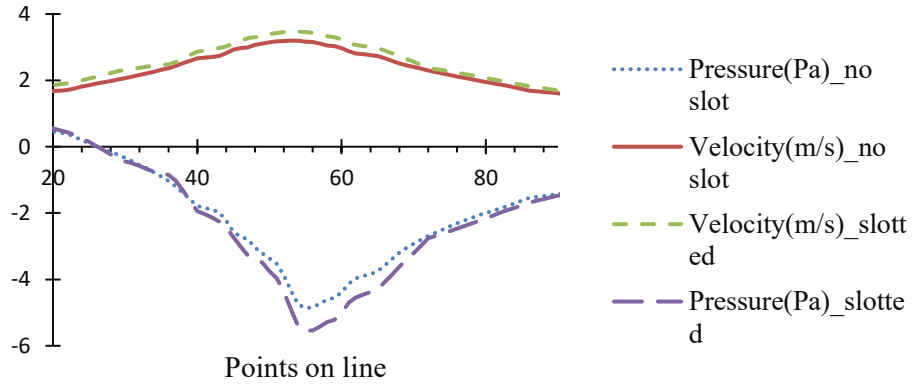

Figure 5: Pressure-Velocity for slotted and non-slotted INVELOX.

Figure 6 displays the velocity along a vertical line that runs through the throat section of Invelox. The graph is not horizontal showing that the velocity peaks towards the walls of the throat and reduced towards the central part of the throat. This is not desirable for the application of a wind turbine since it reduces the blade tip speed of the operating turbine [13]. Such diminished uniformity of the flow profile increases blade vibration leading to a noisy setup. This setup however would perform slightly different should a turbine be installed. Loading effects would exhibit more hindering easy flow of wind within the nozzle-diffuser section.

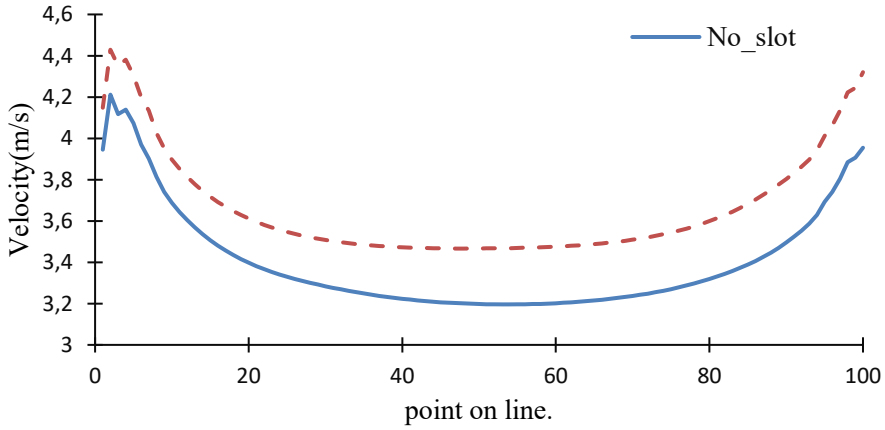

Figure 6: Velocity for slotted and non-slotted INVELOX along vertical throat line.

4 Conclusions and Recommendations

The slotted INVELOX setup demonstrated consistent improvements over the original configuration across all points along the centreline. The original setup peaked at 3.9 m/s with an average velocity of 3.3 m/s, while the slotted configuration achieved a higher peak of 4.3 m/s and averaged 3.6 m/s. In terms of the speed ratio, the original recorded 1.1, whereas the slotted version reached 1.2 an approximate 9% improvement. Although seemingly modest, this gain is encouraging, especially considering that no geometric optimization has yet been applied. The next phase of the study will focus on optimizing the geometric parameters to achieve the most effective configuration of the slotted INVELOX design. The current results show that the slotted version has potential for application in low-speed, turbulent wind conditions that are typically underutilized. This analysis is useful for influencing policy to effect the use of residential area wind leading to energy accessibility. Post-optimization, further validation using alternative optimization techniques will be conducted to ensure robustness. The anticipated outcomes include improved speed ratios, more uniform flow through the throat section, and enhanced augmentation levels, all of which strengthen the case for deploying such technology in residential areas

across South Africa. Development of a prototype and subsequent field testing under varied flow conditions will follow to confirm practical feasibility and performance.

References

1. Shambira, N.; Mukumba, P.; Makaka, G. Assessing the Wind Energy Potential : A Case Study in Fort Hare , South Africa , Using Six Statistical Distribution Models. *Applied Sciences* **2025**, *15*, 2778.
2. Elsayed, A.M. Design Optimization of Diffuser Augmented Wind Turbine. *CFD Letters* **2021**, *13*, 45–59.
3. Gujar, S.; Auti, A.; Kale, S. Advancements in Wind Energy: Exploring the Potential of Diffuser Augmented Wind Turbines (DAWTs). *SSRG International Journal of Mechanical Engineering* **2025**, *12*, 12–23, doi:10.14445/23488360/IJME-V12I1P102.
4. Shonhiwa, C.; Makaka, G.; Mukumba, P.; Shambira, N. Determination of Optimal Geometry for an Empty Concentrator Augmented Wind Turbine. *Physical Science International Journal* **2023**, *27*, 75–90, doi:10.9734/psij/2023/v27i6815.
5. Shambira, N.; Makaka, G.; Mukumba, P. Analytical Models for Concentrator and Diffuser Augmented Wind Turbines: A Review. *International Journal of Smart Grid and Clean Energy* **2021**, *10*, 123–132.
6. Shambira, N.; Makaka, G.; Mukumba, P. Velocity Augmentation Model for an Empty Concentrator-Diffuser-Augmented Wind Turbine and Optimisation of Geometrical Parameters Using Surface Response Methodology. *Sustainability (Switzerland)* **2024**, *16*, doi:10.3390/su16041707.
7. Bošnjaković, M.; Veljić, N.; Hradovi, I. Perspectives of Building-Integrated Wind Turbines (BIWTs). *Smart Cities* **2025**, *8*, 1–27, doi:10.3390/smartcities8020055.
8. Allaei, D.; Tarnowski, D.; Andreopoulos, Y. INVELOX with Multiple Wind Turbine Generator Systems. *Energy* **2015**, *93*, 1030–1040, doi:10.1016/j.energy.2015.09.076.
9. Ghorani, M.M.; Karimi, B.; Mirghavami, S.M.; Saboohi, Z. A Numerical Study on the Feasibility of Electricity Production Using an Optimized Wind Delivery System (Invelox) Integrated with a Horizontal Axis Wind Turbine (HAWT). *Energy* **2023**, *268*, 126643, doi:10.1016/j.energy.2023.126643.
10. Hosseini, S.R.; Ganji, D.D. A Novel Design of Nozzle-Diffuser to Enhance Performance of INVELOX Wind Turbine. *Energy* **2020**, *198*, 117082, doi:10.1016/j.energy.2020.117082.
11. García Auyanet, A.; Verdin, P.G. Numerical Study of the Effect of Flap Geometry in a Multi-Slot Ducted Wind Turbine. *Sustainability* **2022**, *14*, 12032, doi:10.3390/su141912032.
12. Dighe, V.; Suri, D.; Avallone, F.; Van Bussel, G. Ducted Wind Turbines in Yawed Flow: A Numerical Study. *Wind Energ. Sci.* **2021**, *6*, 1263–1275, doi:10.5194/wes-6-1263-2021.

Acknowledgments:

Special acknowledgement to the Postgraduate Studies and Postdoctoral Fellowships Unit, National Research Foundation (NRF), the Department of Research, Partnership and Innovation (DRPI) at the University of Fort Hare, Research Niche Area (RNA), Renewable Energy—Wind, for their financial support.

Optimising the Geometry of an Empty Concentrator-Diffuser Augmented Wind Turbine Using Genetic Algorithm.

Ngwarai Shambira[1], Patrick Mukumba[1] and Golden Makaka[1]

[1]Department of Computational Sciences, Faculty of Science & Agriculture, University of Fort Hare, Alice 5700, South Africa

E-mail: nshambira@ufh.ac.za

Abstract. The growing demand for electricity in off-grid regions and rising global energy needs driven by population growth underscore the urgent need to explore renewable energy alternatives to fossil fuels, key contributors to carbon emissions and climate change. Wind energy offers a sustainable option, but is challenged by its variability and low-speed performance in certain regions. This study investigates a performance enhancement strategy using an empty concentrator-diffuser augmented wind turbine (CDaugWT) to boost wind speed at the rotor, enabling continuous operation in areas with average wind speeds below 4 m/s. A velocity augmentation model served as the objective function, correlating the augmentation ratio with six geometric parameters. A genetic algorithm (GA), an evolutionary optimisation method, was used to determine the optimal design. Results showed that wind speed at the throat could increase up to 1.981 times. These findings closely aligned with results from response surface methodology (RSM), with only a 1.4 % deviation, validating the accuracy of the GA approach. The optimised geometric values included a diffuser angle of 10.1°, a concentrator angle of 20.0°, a concentrator length of 396.3 mm ($0.66R_{th}$), a diffuser length of 994.8 mm ($1.65R_{th}$), a throat length of 74.5 mm ($0.12R_{th}$), and a flange height of 104.4 mm ($0.17R_{th}$), where R_{th} is the throat radius. Computational fluid dynamics (CFD) simulations further validated these results, showing only a 0.58% difference. The study confirms that integrating optimisation algorithms such as GA into the design process of CDaugWT systems can significantly enhance wind turbine performance, making wind energy more viable for low-wind-speed regions.

1 Introduction

Increased global energy consumption, particularly in rural and off-grid areas, has prompted researchers to explore sustainable alternatives to fossil fuels. Wind energy, being abundant and renewable, presents a promising solution. However, its efficiency is often constrained by variability and low wind speeds in many regions. To address this, researchers have explored augmented wind turbine technologies that enhance performance under suboptimal wind conditions. One of the most promising innovations in this field is the concentrator-diffuser augmented wind turbine, also known as the wind lens turbine [1]. This technology enhances wind capture by incorporating concentrator and diffuser elements, sometimes with a flange, to reduce back pressure and increase wind speed through the rotor plane [2], [3]. Several studies have demonstrated the effectiveness of this approach. For instance, [4] reported a velocity augmentation ratio of 1.32 using converging-diverging ducts, although the design exhibited issues related to backflow. The study in [5] developed a compact wind turbine with an adjustable

diffuser, achieving a 39.75% average velocity augmentation. These studies highlight the suitability of CDaugWT systems for improving wind energy capture in low-resource environments.

To further enhance performance, single-objective evolutionary metaheuristic optimisation algorithms, such as GA, have been employed to optimise the geometrical configuration of CDaugWT. For example, [6] used a multi-objective GA to maximise power output and minimise drag and thrust force simultaneously. Similarly, [7] applied a GA in conjunction with the RSM to optimise seven geometric parameters of a ducted turbine system, resulting in a velocity augmentation ratio of 2.18 at the throat. These optimisation algorithms typically rely on surrogate models to serve as objective functions. For example, [8] employed CFD and the RSM to develop quadratic surrogate models, achieving a velocity augmentation ratio of up to 2.16 at the throat with high accuracy (R^2 = 0.9937). Likewise, [9] constructed a high-accuracy response surface-based velocity augmentation model (R^2 = 0.9581). Importantly, this model accounts for interaction effects among all geometrical parameters, a feature often neglected in earlier studies, thus providing more precise optimisation outcomes.

This study uses the model developed in [9] as the objective function for a GA aimed at optimising the geometry of an empty CDaugWT under low wind speed conditions ($\leq$ 2 m/s).

2 Materials and Methods

This study employed a structured approach to optimise the geometry of a CDaugWT. A quadratic surrogate model based on RSM was used as the objective function, with the velocity augmentation ratio as the target metric. The optimisation was performed using GA, and results were validated through computational fluid dynamics simulations in ANSYS Fluent 2022R1 software. MATLAB codes for the GA optimisation were developed and executed successfully in MATLAB R2021a. Detailed steps are outlined in Sections 2.1 to 2.4.

2.1 Geometry and Parameters

The concentrator-diffuser system geometry was defined using six key parameters recognised through literature studies: diffuser angle (θ_d), concentrator angle (θ_c), concentrator length (L_c), diffuser length (L_d), throat length (L_{th}), flange height (H_f) [10], [11]. All dimensions were normalised with respect to the throat radius (R_{th}) to allow generalisation of the results. Figure 1 illustrates the geometry of the CDaugWT design.

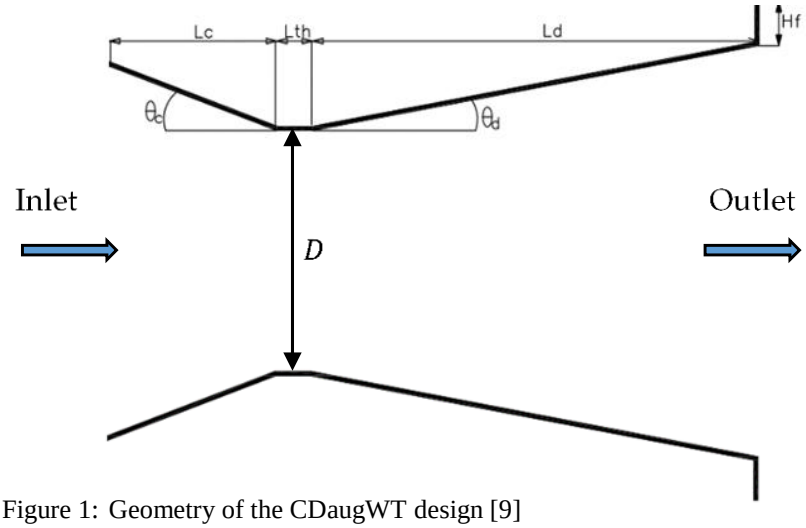

Figure 1: Geometry of the CDaugWT design [9]

2.2 Objective Function $\left(\frac{V_{th}}{V_\infty}\right)$

A velocity augmentation model was used as the objective function. The goal was to maximise the velocity augmentation ratio, $A_v = \frac{V_{th}}{V_\infty}$, where V_{th} is the velocity at the throat, and V_∞ is the free-stream velocity. This model, developed in [9], is a quadratic regression metamodel based on six geometric design parameters. It serves as the fitness function in GA and is used to optimise the empty CDaugWT geometry for maximum wind speed augmentation. The velocity augmentation model is given as shown in Equation 1.

$$\frac{V_{th}}{V_\infty} = -0.752974 + 0.355948\ A + 0.280702\ B - 0.00431128\ C - 0.00217402\ D - 0.0133117\ E + 0.000363692\ F + 0.000214108\ (A{\cdot}C) + 4.976{\times}10^{-6}\ (C{\cdot}D) + 1.447{\times}10^{-5}\ (D{\cdot}E) - 0.0218753\ A^2 - 0.00701959\ B^2 - 3.20027{\times}10^{-6}\ C^2. \quad (1)$$

This function estimates throat wind speed, guiding the GA to maximise velocity augmentation by optimising turbine geometry. The six design parameters (A–F) used in optimisation are continuous variables, each constrained within specific ranges. These include the diffuser angle (θ_d), ranging from 9.0° to 10.5° (A), and the concentrator angle (θ_c), ranging from 19.0° to 20.5° (B). The concentrator length (L_c) varies between 327.10 mm and 397.90 mm (C), while the diffuser length (L_d) ranges from 927.10 mm to 997.90 mm (D). The throat length (L_{th}) spans 60.40 mm to 74.60 mm (E), and the flange height (H_f) is bounded between 90.40 mm and 104.60 mm (F). These ranges define the design space for the genetic algorithm used in optimising the CDaugWT Design geometry.

2.3 Optimisation algorithm

The genetic algorithm, introduced by Holland (1975), is a nature-inspired optimisation technique based on natural selection and the principle of "survival of the fittest." GA is a semi-stochastic and semi-deterministic search method that evolves a population of candidate solutions across generations to find optimal or near-optimal results [6]. This study applied GA to optimise six geometric parameters of the CDaugWT design. The algorithm was implemented in MATLAB and structured around the following iterative steps [7]:

- Initialise the population with randomly generated individuals (design solutions).
- Evaluate each individual using a defined objective function derived from the velocity augmentation model.
- Select parents based on fitness scores.
- Crossover parent pairs to generate new offspring.
- Mutate offspring to introduce diversity.
- Repeat evaluation, selection, crossover, and mutation for multiple generations.
- Select the best solution based on the highest augmentation performance.

The algorithm was implemented in MATLAB with a population size of 100, a crossover rate of 0.8, a mutation rate of 0.05, and 200 generations. The fitness function used a negated objective to enable maximisation within GA's minimisation framework. A schematic of the GA process is shown in the figure below.

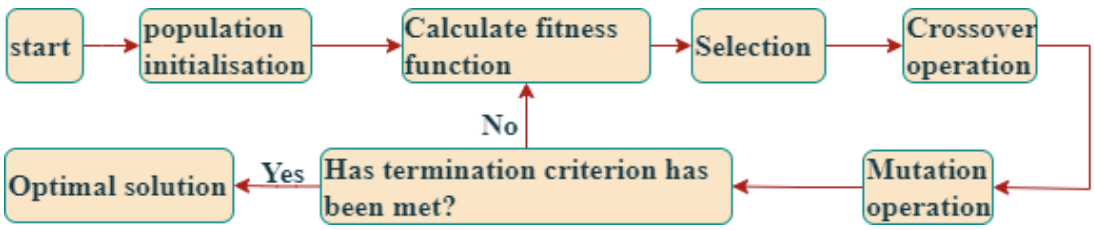

Figure 2: Flow chart of genetic algorithm

2.4 Validation

The response surface methodology results from [12] were used to validate and compare the GA optimisation results. Additionally, computational fluid dynamics was employed to simulate airflow through the CDaugWT system, as detailed in [9]. The simulations were conducted using ANSYS Fluent software, solving the steady, incompressible Reynolds-Averaged Navier–Stokes (RANS) equations with the SST k-ω turbulence model, a hybrid of the k-ε and k-ω models selected for its balance between accuracy and computational efficiency [13]. Second-order upwind schemes were utilised for the convection-diffusion terms, and a convergence criterion of $1{\times}10^{-6}$ was applied. This CFD analysis provided a detailed understanding of wind acceleration effects and was instrumental in verifying the GA optimisation results. The whole numerical procedure is available in [9].

3 Results and Discussion

3.1 Optimisation Results

The optimisation results presented in Table 1 show that the GA identified an optimal design with the following parameters: θ_d (Diffuser angle): 10.1˚, θ_c (Concentrator angle): 20.0˚, L_c: 396.3 mm (0.66R_{th}), L_d: 994.8 mm (1.65R_{th}), L_t: 74.5 mm (0.12R_{th}), H_f: 104.4 mm (0.17R_{th}). The RSM yielded slightly different optimal values, as shown in Table 1. The GA-predicted throat velocity was slightly higher than that of RSM, with a slight deviation of 0.58% when compared to CFD results, while the difference between GA and RSM predictions was 1.4%. These small discrepancies confirm the reliability and accuracy of the GA optimisation method. Moreover, the GA configuration achieved a maximum augmentation ratio of 1.981, indicating a near doubling of wind speed at the turbine's throat and demonstrating superior performance in enhancing flow velocity through geometric optimisation. Figure 3 depicts the 3D CDaugWT design generated in ANSYS Fluent, based on the optimal geometric parameters obtained from the GA optimisation.

Table 1: Optimised throat wind speed values validation with CFD results.

Method	θ_d	θ_c	$L_c(mm)$	L_d(mm)	L_{th}(mm)	H_f(mm)	V_{th} (m/s)	CFDV_{th} (m/s)	% difference
RSM	10.0°	20.0°	375	975	70	100	3.906	3.8980	0.02
GA	10.1˚	20.0°	396.3	994.8	74.5	104.4	3.961	3.9382	0.58

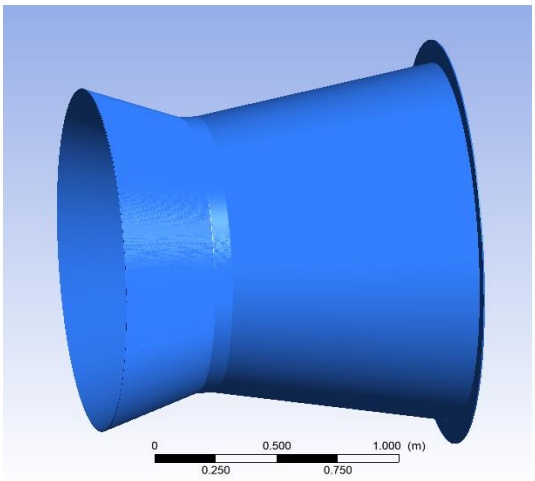

Figure 3. The CDaugWT design.

3.2 CFD Analysis

The CFD velocity streamlines confirmed significant flow acceleration through the throat region of the CDaugWT. The diffuser geometry facilitated controlled expansion and effective pressure recovery, while the concentrator section focused the incoming airflow, resulting in increased velocity at the throat. Figure 4 presents the velocity and pressure contour distributions and the corresponding axial velocity and pressure profiles for the CDaugWT configuration optimised using the GA.

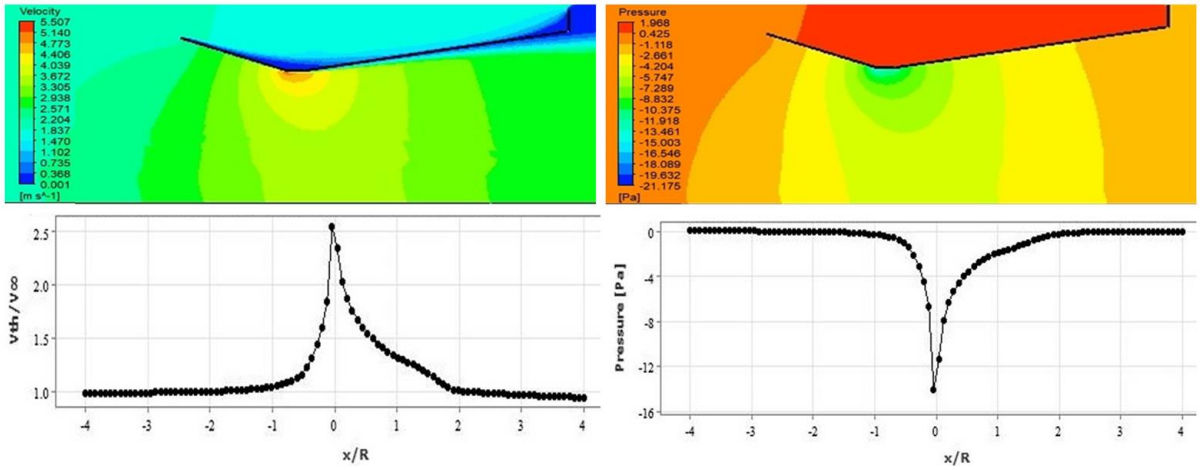

Figure 4: Velocity, pressure contour distributions, and axial profiles for the CDaugWT design using the GA.

4 Conclusions and Recommendations

This study demonstrates that the application of a genetic algorithm to optimise the geometry of a concentrator-diffuser augmented wind turbine design can substantially enhance turbine performance in low wind-speed regions. The optimised configuration achieved nearly a twofold increase in throat velocity, with results showing strong agreement with both response surface methodology and computational fluid dynamics validations. These findings suggest that well-designed CDaugWT systems have the potential to extend the operational capabilities of small-scale wind turbines, making them viable in areas previously considered unsuitable due to low wind speeds. Field testing of the optimised CDaugWT design geometry is recommended to validate the simulation results under real-world conditions. Future research could incorporate multi-objective optimisation approaches that consider structural integrity, cost, and material weight to enhance practical deployment. Additionally, exploring other artificial intelligence-based optimisation methods, such as particle swarm optimisation, whale optimisation algorithm, and grey wolf optimisation, may offer improvements in convergence speed and robustness, potentially leading to even more efficient design outcomes.

References

[1] M. A. Rahmatian, P. Hashemi Tari, M. Mojaddam, and S. Majidi, “Numerical and experimental study of the ducted diffuser effect on improving the aerodynamic performance of a micro horizontal axis wind turbine,” *Energy*, vol. 245, p. 123267, 2022.

[2] Y. Ohya, T. Karasudani, T. Nagai, and K. Watanabe, “Wind lens technology and its application to wind and water turbine and beyond,” *Renew. Energy Environ. Sustain.*, vol. 2, no. 2, pp. 1–6, 2017.

[3] N. Shambira, G. Makaka, and P. Mukumba, “Analytical models for concentrator and diffuser augmented wind turbines: A review,” *Int. J. Smart Grid Clean Energy*, vol. 10, no. 2, pp. 123–132, 2021.

[4] J. Ye *et al.*, “Effects of divergent angle on the flow behaviors in low speed wind accelerating ducts,” *Renew. Energy*, vol. 152, pp. 1292–1301, 2020.

[5] N. K. Siavash, G.Najafi, T. T. Hashjin, B. Ghobadian, and E. Mahmoodi, “An innovative variable shroud for micro wind turbines,” *Renew. Energy*, vol. 145, pp. 1061–1072, 2020.

[6] T. A. Khamlaj and M. P. Rumpfkeil, “Analysis and optimisation of ducted wind turbines,” *Energy*, vol. 162, pp. 1234–1252, 2018, doi: 10.1016/j.energy.2018.08.106.

[7] M. A. Rahmatian, A. N. Shahrbabaki, and S. P. Moeini, “Single-objective optimisation design of convergent-divergent ducts of ducted wind turbine using RSM and GA, to increase power coefficient of a small-scale horizontal axis wind turbine,” *Energy*, vol. 269, p. 126822, 2023.

[8] J. Taghinezhad, S. Abdoli, V. Silva, S. Sheidaei, R. Alimardani, and E. Mahmoodi, “Computational fluid dynamic and response surface methodology coupling: A new method for optimisation of the duct to be used in ducted wind turbines,” *Heliyon*, vol. 9, p. e17057, 2023.

[9] N. Shambira, G. Makaka, and P. Mukumba, “Velocity Augmentation Model for an Empty Concentrator-Diffuser-Augmented Wind Turbine and Optimisation of Geometrical Parameters Using Surface Response Methodology,” *Sustainability*, vol. 16, p. 1707, 2024.

[10] M. Aldhufairi, M. K. H. Muda, F. Mustapha, K. A. Ahmad, and N. Yidris, "Design of Wind Nozzle for Nozzle Augmented Wind Turbine," *J. Adv. Res. Fluid Mech. Therm. Sci.*, vol. 95, no. 1, pp. 36–43, 2022.
[11] L. Ramayee, K. Supradeepan, P. R. Reddy, and V. Karthik, "Design of shorter duct for wind turbines to enhance power generation: a numerical study," *J. Brazilian Soc. Mech. Sci. Eng.*, vol. 44, no. 4, pp. 1–16, 2022.
[12] N. Shambira, G. Makaka, and P. Mukumba, "Velocity Augmentation Model for an Empty Concentrator-Diffuser-Augmented Wind Turbine and Optimisation of Geometrical Parameters Using Surface Response Methodology," *Sustain.*, vol. 16, no. 4, 2024, doi: 10.3390/su16041707.
[13] O. O. Ajayi, L. Unser, and J. O. Ojo, "Implicit rule for the application of the 2-parameters RANS turbulence models to solve flow problems around wind turbine rotor profiles," *Clean. Eng. Technol.*, vol. 13, p. 100609, 2023.

Acknowledgements: Special acknowledgement to the National Research Foundation (NRF), the Department of Research, Partnership and Innovation (DRPI) at the University of Fort Hare, Research Niche Area (RNA), Renewable Energy—Wind, for their financial support.

Enhancing Rural Electrification: An In-depth Analysis and Optimisation of PV/Hydrogen Fuel Cell/Battery-Powered Microgrids.

S Muronga, D Tinarwo, TS Mulaudzi, JK Kirui, I Mnandi, K Madzivhandila, A Ramalata

Department of Physics, University of Venda: University Rd, Thohoyandou,0950

E-mail: murongashandukani8@gmail.com

Abstract. Access to reliable and affordable electricity remains a critical barrier to development in rural South Africa, where communities are plagued by a complete lack of grid connection or grid instability due to an ageing infrastructure and ongoing load-shedding. As extending the centralised grid is often economically prohibitive, this study investigates the viability of a decentralised hybrid microgrid as a sustainable alternative. The hybrid energy system was modelled and optimised using HOMER software, integrating photovoltaic (PV) generation, battery storage, and hydrogen fuel cells across various capacity combinations to minimise cost while guaranteeing reliability. The analysis confirms that coupling batteries for short-term load balancing with fuel cells for long-term energy storage creates a synergistically resilient system. An optimal configuration comprising a 148 kW PV array, 64 kWh battery storage, and a 40 kW fuel cell was identified, achieving a minimal Net Present Cost of R5.22 million and a competitive Levelized Cost of Energy of R2.62/kWh. These results unequivocally demonstrate that hybrid PV/H_2/Battery systems are a technically and economically sustainable solution for advancing rural electrification and energy security in South Africa.

1 Introduction

Access to reliable and affordable electricity is a pressing challenge in deep rural South Africa, where numerous communities are either off-grid or experience frequent interruptions due to load-shedding and outdated infrastructure [1]. Although national electrification initiatives have made strides, extending the central grid to these remote areas is often economically impractical and environmentally detrimental [2]. In light of this, decentralised energy systems driven by renewable resources are emerging as compelling alternatives for rural electrification. South Africa has high solar irradiance, with daily solar radiation levels between 4.5 and 6.5 kWh/m², positioning photovoltaic (PV) technology as a highly viable and abundant energy solution [3]. The intermittent nature of solar energy introduces reliability issues, particularly in the absence of sufficient energy storage and backup systems. To mitigate these challenges, hybrid microgrids combining PV with battery storage for short-term load management and hydrogen fuel cells for long-duration energy storage are being recognised as promising solutions [4].

Hydrogen fuel cells offer a remarkable capability to convert surplus solar energy into hydrogen through electrolysis during peak generation times, subsequently reconverting it into electricity during low sunlight, providing a clean, zero-emission energy storage option [5]. Such systems enhance immediate energy response

and long-term reliability when integrated with batteries. However, optimising these components' sizing, cost, and performance necessitates a comprehensive techno-economic and environmental modelling approach tailored to the unique local context. Mbali and Dzobo (2021) developed a hybrid PV/Diesel/Battery system for the Upper BlinkWater community, utilising HOMER and Reticmaster software. Their study confirmed the system's technical feasibility, showing an average electricity cost of R1.1093/kWh and an annual diesel consumption of 16,685 L [6]. Unlike previous rural electrification studies, this work uniquely integrates a comparative simulation of PV/H_2/Battery microgrids under rural South African socio-technical constraints.

This study aims to optimise PV/Hydrogen Fuel Cell/Battery hybrid microgrids for rural South African applications, ensuring a reliable energy supply while minimising life-cycle costs. Additionally, this research supports the overarching goals of national decarbonisation and energy equity. The insights gained are intended to inform policy, planning, and implementation strategies that enhance energy access, promote local economic development, and build community resilience.

2 Methodology

This study uses PV panels, a fuel cell, batteries, and a DC to AC Inverter, modelled in HOMER, to simulate an off-grid hybrid system. PV panels are the primary power source, batteries supply energy during low solar periods, and the fuel cell activates when both cannot meet demand. Excess PV energy powers electrolysis to produce hydrogen and recharge batteries, ensuring a reliable off-grid supply.

2.1 Study Area and System Architecture

The Masia Community Development Centre in Masia Tshikarani (23.1836° S, 30.3098° E), Collins Chabane Local Municipality, Limpopo, South Africa, currently lacks a functional grid connection and depends on a limited 19.8 kW PV system that meets only part of its energy needs. This study explores a resilient, scalable off-grid hybrid microgrid combining PV panels, hydrogen fuel cells, and battery storage to meet the Centre's full energy demand. A detailed walk-through energy audit established the facility's daily energy demand, inventorying all electrical appliances and recording their nameplate power ratings to form a baseline consumption estimate. It was used to create a daily demand profile. Using HOMER for simulation and optimisation, the design excludes grid integration, reflecting the current disconnection and aiming for energy independence. Modelling inputs include load demand, solar resource data, and component specifications. Figure 1 presents the ideal system alongside seasonal and daily load profiles, showing an average daily demand of 425.6 kWh and a peak of 64.78 kW, while the graph highlights consumption trends.

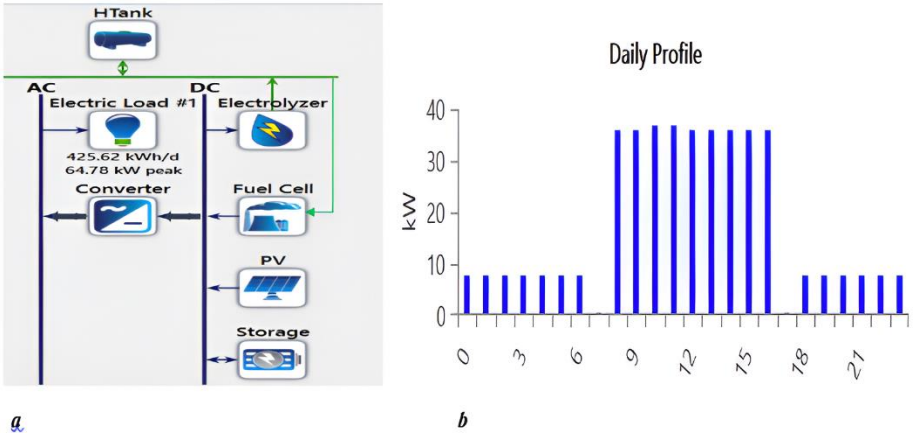

Figure 1: (a)Hybrid energy system architecture.(b) Daily load profile

2.2 Renewable source assessment

Monthly solar irradiation data were obtained from the National Renewable Energy Laboratory (NREL), temperature data were obtained from the NASA (National Aeronautics and Space Administration) Surface Meteorology and Solar Energy (SSE) database embedded within HOMER Pro and the Masia Community Development Centre's coordinates were input into HOMER software [7]. Figure 2 below shows an average daily

solar irradiation of 5.85 kWh/m² in 2023. Solar irradiance ranges from 3.93 to 6.5 kWh/m² per day, with peaks in January, November, and December, and the lowest in June. The clearness index varies from 0.501 in February to 0.650 in July. Figure 3 shows the temperature variation at the Masia Community Development Centre over the year, with a recorded daily average low of 15.58°C in July and a high of 25.54°C in January. This fluctuation reflects the seasonal trends of the Southern Hemisphere, showcasing warmer in summers and cooler winters, which is crucial for evaluating microgrid performance.



Figure 3: Monthly average temperature



Figure 2 Solar irradiation and clearness of the Masia community development centre

2.3 System components

This study employs photovoltaic (PV) panels, a fuel cell, batteries, and a DC to AC Inverter modelled in HOMER software to simulate and analyse an off-grid hybrid energy system. The PV system serves as the primary power source, while the batteries provide energy during periods of low solar input. If the PV panels and batteries cannot meet the energy demand, the fuel cell activates to supply additional power. Any excess energy generated by the PV panels is utilised for electrolysis, which produces hydrogen and recharges the batteries, thereby ensuring a reliable off-grid energy supply. [8].

a. PV generator model: The power generated by the solar photovoltaic (PV) panels is given by [8, 9]

$$P_{PV} = P_{R-PV}\left[\frac{G}{G_{ref}}\right]\left[1 + K_T(T_c - T_{ref})\right] \qquad 2.3.1$$

Where: P_{PV} is the power generated by the solar photovoltaic (PV) panels, P_{R-PV} is the rated power at the reference condition, G is the solar radiation in $^{W}/_{m^2}$, G_{ref} is the solar radiation at a reference condition and is given by $G_{ref} = 1000\,^{W}/_{m^2}$, T_{ref} is the total cell temperature at reference conditions ($T_{ref} = 25℃$), K_T is the temperature coefficient of the PV panels, T_c The cell temperature.

b. Battery model: The battery capacity, C(t) at a point in time t, is calculated by HOMER with the equation [10]:

$$C(t) = C(t-1) - \eta_{batt}\left(\frac{P_B(t)}{V_{Bus}}\right)\Delta t \quad 2.3.2$$

where: $C(t-1)$ Battery capacity at the previous increment; $P_B(t)$ Battery input /output power given by: $P_B(t) = E_g(t) - E_i(t)$

c. Fuel cell model: The output power of a fuel cell(FC) was determined by the following [11].

$$P_{FC} = (P_{tank-FC})(\eta_{FC}) \quad 2.3.3$$

Where: P_{FC} is the output power of the fuel cell (in kilowatts, kW), $P_{tank-FC}$ is the input power supplied from the hydrogen tank to the fuel cell, and η_{FC} is the efficiency of the fuel cell.

- The equation estimates the power transferred from the electrolyser to the hydrogen storage tank.

$$P_{elec-tank} = (P_{ren-elec})(\eta_{elec}) \quad 2.3.4$$

Where: η_{elec} is the electrolyser efficiency assumed to be constant.

- The output energy stored by the hydrogen tank is estimated using the equation below [12].

$$E_{H_2\,.tank} = E_{H_2.tank}(t-1) + \left[P_{elec.tank}(t) - \frac{P_{tank.FC}}{\eta_{Storage}}\right]\Big/\Delta t \quad 2.3.5$$

d. Financial metrics: The Net Present Cost(NPC), which is the **t**otal cost of installing and operating the system over its entire lifetime, and Levelized Cost of Energy (LCEO), which is the: HOMER calculates NPC by the formula [10, 13, 14]:

$$NPC = \frac{C_{ann.tot}}{CRF(i \times proj)} \quad 2.3.6$$

Where: $C_{ann.tot}$ is the total annualised cost of the system, CRF is the capital recovery factor, i is the interest rate in %, and $proj$ is the project lifetime.

The capital recovery factor (CRF) is determined by [10, 13, 14] :

$$CRF(i,N) = \frac{i(1+i)^N}{(1+i)^N - 1} \quad 2.3.7$$

Where: i is the real interest rate, and N is the period/number of years.

HOMER uses the following equation to calculate the Levelized Cost of Energy [10, 13]:

$$LCOE = \frac{C_{ann.tot}}{E_{prim} + E_{def}} \quad 2.3.8$$

Where: $C_{ann.tot}$ is the total annualised cost, E_{prim} is the total amount of primary load that the system serves per year, E_{def} is the total amount of deferrable load the system serves per year.

3 Results and Discussion

This study conducted a comprehensive simulation of the PV/Battery/Fuel Cell configuration using a range of capacity combinations. The objective was to identify the most cost-effective and reliable system setup to meet energy demands while ensuring optimal performance and minimising losses. Table 1 below shows the optimisation results for hybrid energy system configurations featuring photovoltaic (PV) panels, battery storage, fuel cells, hydrogen tanks, DC to AC Inverters, and electrolysers, based on their Net Present Cost (NPC), Levelized Cost of Energy (LCOE), and Operation & Maintenance (O&M) costs. Configuration 1 emerges as the most economically viable option with the lowest NPC of R5.22 million, LCOE of R2.62, and O&M costs of R167,733.00 utilising a 148 kW PV system and 40 kW fuel cell. In contrast, Configuration 2 increased

electrolyser size results in higher costs, while Configurations 3 and 4 show diminished returns on investment despite larger hydrogen tank capacities. Configuration 5, although having a slightly lower LCOE, also reflects significant costs. Overall, Configuration 1 is identified as the most cost-effective solution for rural electrification with a hybrid PV/H_2 fuel cell/battery microgrid.

Table 1: Optimisation results of the PV-Fuel cell-battery hybrid power system

Configuration	PV (kW)	Batt kW	FC (kW)	H_2 Tank (kg)	INV (kW)	EL (kW)	NPC (R)	LCOE (R/kWh)	O&M (R/year)
1	148	64	40	1000	72.9	30	5.22M	2.62	167 733.00
2	150	64	40	1000	30	1200	5.80M	2.92	188 671.00
3	150	64	40	1400	200	70	8.74M	4.40	272 040.00
4	150	64	50	2000	133	50	9.05M	5.55	309 342.00
5	125	64	60	3000	167	30	9.61M	4.83	390 771.00

3.1 Energy production

Figure 4 shows monthly electricity generation from solar PV and the fuel cell, with PV as the primary source (>20 MWh/month) and the fuel cell as backup (<3 MWh/month). Peak PV output occurs in March and April due to higher solar irradiance. Grid contributions are minimal, indicating firm solar reliance. The hybrid system produces 273,314 kWh annually, 242,516 kWh (88.7%) from PV and 30,779 kWh (11.3%) from the fuel cell, with a 100% renewable fraction and just 0.0877% capacity shortage, demonstrating high reliability.

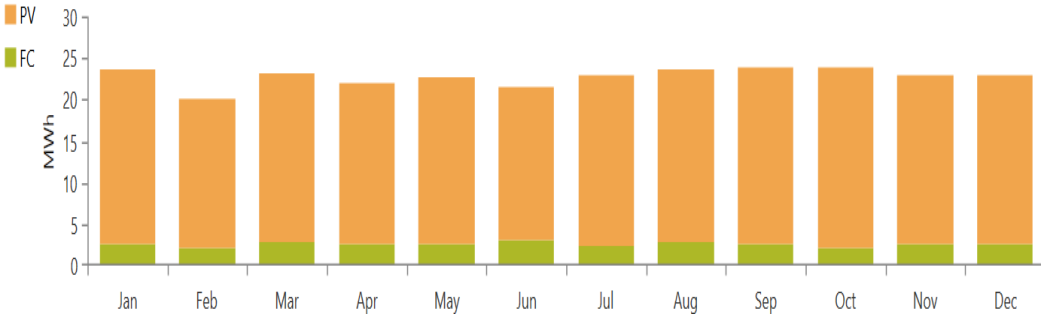

Figure 4: Monthly energy production from PV and FC

Figure 5 demonstrates annual photovoltaic (PV) power generation variability under different conditions, highlighting a significant winter output reduction due to shorter daylight hours. The system consistently meets daily energy demands, producing surplus energy stored in batteries or converted into hydrogen fuel, enhancing its reliability. Despite less favourable weather during the winter months, the PV array's capacity to provide a steady energy supply further contributes to its dependability. A seasonal trend emerges, resembling a bell curve, with energy production peaking from spring to early autumn. During this peak period, output remains consistently high between 8 AM and 4 PM, reaching its maximum midday.

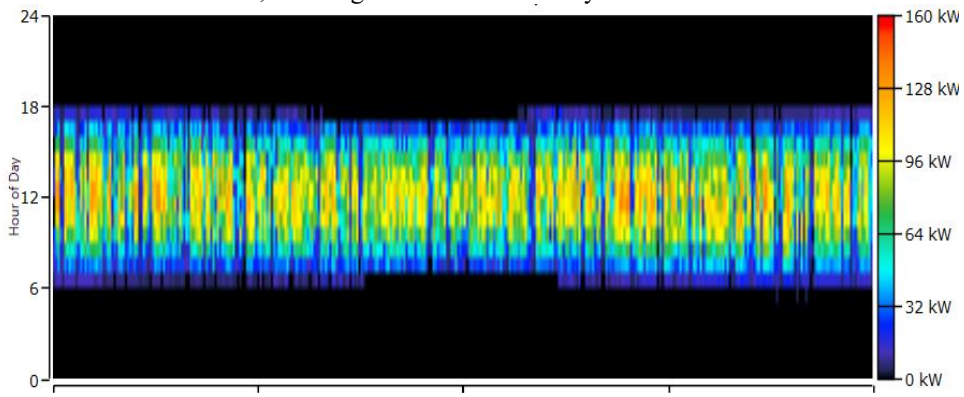

Figure 5: The power output from the PV array

Figure 6 illustrates the activity of the fuel cell throughout an entire year. It shows that the fuel cell is primarily active during daylight hours, especially between 06:00 and 18:00, with peak activity around midday. This pattern indicates that the fuel cell is mainly used as backup support during periods of high demand or when solar energy is insufficient. During nighttime, activity is minimal or non-existent, represented by predominantly black and dark blue regions on the figure. The fuel cell is utilised more frequently in winter due to reduced solar irradiance and shorter daylight hours. It operates non-continuous, demand-driven manner, supplementing the hybrid system only when needed. This suggests that, under normal conditions, there is a primary reliance on solar photovoltaic (PV) energy and battery storage.

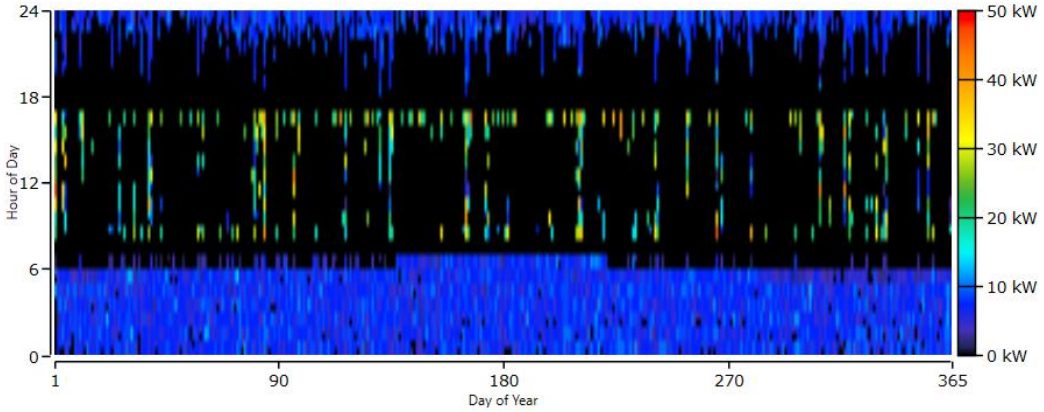

Figure 6: The power output from the Fuel cell

4 Conclusion

The simulation of a hybrid microgrid that combines photovoltaic (PV) systems, hydrogen fuel cells, and batteries presents a viable and cost-effective solution for rural electrification in South Africa. The analysis demonstrates that integrating hydrogen fuel cells for long-term storage alongside batteries for short-term use significantly enhances system resilience in off-grid applications for remote areas. The study affirms that an optimally sized hybrid microgrid comprising photovoltaic generation, battery storage, and a hydrogen fuel cell system presents a robust and economically superior solution for off-grid rural electrification. Configuration 1 (148 kW PV, 64 kWh battery, 40 kW fuel cell) emerged as the most economical, boasting a Net Present Cost of R5.22 million and a Levelized Cost of Energy of R2.62/kWh. The key innovation lies in the synergistic use of technologies: batteries manage daily variability, while the fuel cell guarantees long-term energy security. This model effectively balances cost-efficiency with unwavering reliability, positioning hybrid PV-hydrogen systems as a critical, sustainable technology for addressing energy poverty in remote South African regions.

References

[1] G. Viljoen and F. Dube, "Realising the Right to Electricity Through Off-Grid Power Solutions in South Africa," *Potchefstroom Electronic Law Journal*, vol. 26(1), pp. 1-5, 2023.

[2] V. Motjoadi, P. Bokoro and M. Onibonoje, "A review of microgrid-based approach to rural electrification in South Africa: Architecture and policy framework," *Energies*, vol. 13, no. 9, pp. 1-22, 2020.

[3] F. Ismail, "Use of solar energy to control the environment for aquaponics in low income communities (Doctoral dissertation, Cape Peninsula University of Technology," 2020. [Online]. Available: https://www.researchgate.net/publication/366006900.

[4] D. Adebayo, J. Ajiboye, U. Okwor, A. Muhammad, C. Ugwuijem, E. Agbo and V. Stephen, "Optimising energy storage for electric grids: Advances in hybrid technologies," *Management*, vol. 10, pp. 1-11, 2025.

[5] IRENA, Green hydrogen-A guide to policy making, Abu Dhabi: International Renewable Energy Agency (IRENA), 2020.

[6] L. Mbali and O. Dzobo, "Design of an Off-grid Hybrid PV/Diesel Energy System with Battery Storage for Electrification of a Remote Region: A Case Study of Upper Blink Water Community, South Africa," in *Proceedings of 2021 IEEE AFRICON*, Arusha, Tanzania, 2021:IEEE.

[7] H. Al-Najjar, H. El-Khozondar, C. Pfeifer and R. Al Afif, "Hybrid grid-tie electrification analysis of bio-shared renewable energy systems for domestic application.," *Sustainable Cities and Society,* vol. 77, pp. 1-17, 2022.

[8] B. Adebanji, O. Atoki, T. Fasina, O. Adetan and A. Abe, "Comparative study of off-grid and grid-connected hybrid power system: issues, future prospects, and policy framework," *Indonesian Journal of Electrical Engineering and Computer Science,* vol. 22(2), pp. 752-759, 2021.

[9] K. Okedu, R. Uhunmwangho and N. Bassey, "Comparative Study of on and off Grid Tied Integrated Diesel Solar PV Generation System," *International Journal of Engineering Technologies,* vol. 1, no. 1, pp. 19-25, 2015.

[10] T. Lambert, P. Gilman and P. Lilienthal, "Micropower system modeling with HOMER," *Integration of Alternative Sources of Energy,* vol. 1(1), pp. 379-385, 2006.

[11] A. Alturki, "Optimal design for a hybrid microgrid-hydrogen storage facility in Saudi Arabia," *Energy, Sustainability and Society,* vol. 12(1), pp. 1-17, 2022.

[12] F. Thanaa, M. Eskander and M. T. El-Hagry, "Energy flow and management of a hybrid wind/PV/fuel cell generation system," *Energy Conversion and Management,* Vols. 47(9-10), pp. 1264-1280, 2006.

[13] R. Dash, L. Behera, B. Mohanty and P. Kumar, "Cost and sensitivity analysis of a microgrid using HOMER-Pro software in both grid connected and standalone mode," in *2018 International Conference on Recent Innovations in Electrical, Electronics & Communication Engineering (ICRIEECE)*, Bhubaneswar, India, 2018:IEEE.

[14] S. Asamoah, S. Gyamfi, F. Uba and G. Mensah, "Comparative assessment of a stand-alone and a grid-connected hybrid system for a community water supply system: A case study of Nankese community in the eastern region of Ghana," *Scientific African,* vol. 17, p. e01331, 2022.

DIVISION

G

THEORETICAL AND COMPUTATIONAL PHYSICS

Computational Fluid Dynamics Study of Turbulence Effects in Heat Pipe Heat Exchangers for Power-Cell Micro-Reactors

Katlego Pule[1], Emmanuel Igumbor[1], Mbolahasina Ralijaona[1], Simon Connell[1], and Johan Slabber[2]

[1]Department of Mechanical Engineering Science, University of Johannesburg, Johannesburg, South Africa

[2]Mechanical Engineering, University of Pretoria, Lynnwood Road, Hatfield, 0028, Pretoria, South Africa

E-mail: katlegopule59@gmail.com

Abstract. The increasing demand for efficient thermal management systems in micro-reactors has underscored the importance of heat pipe heat exchangers (HPHEs). Heat, when extracted from the reactor, is conveyed to the working fluid, which, if not isolated, can lead to the distribution of contaminants in the secondary cycle. These contaminant can lead to environmental degradation through oxidation, carburization, or decarburization of alloys. Specifically, the HPHE could be used to eliminate tritium contamination from entering the secondary cycle through heat transfer management. In this study, a simulation model was developed to investigate the effect of different turbulence models on a newly designed HPHE, using computational fluid dynamics. Two turbulence models, k-epsilon (k-ϵ) and the Large Eddy Simulation (LES), were evaluated. Helium and air were used as hot and cold fluids, respectively, while Lead-Bismuth Eutectic was used as an intermediate fluid within the heat pipes. The LES result showed a reduction in helium temperature from $1023\,\mathrm{K}$ to $500\,\mathrm{K}$ and a corresponding increase in that of the air from $403\,\mathrm{K}$ to $722\,\mathrm{K}$. The k-ϵ model, on the other hand, showed a significant heat reduction acting on helium from $1023\,\mathrm{K}$ to $723\,\mathrm{K}$. The air temperature has increased from $403\,\mathrm{K}$ to $722\,\mathrm{K}$. In contrast to the k-ϵ, the LES turbulence model provided better heat control performance of the HPHE. Overall, this study demonstrates that the designed HPHE can be effectively used to control temperature and mitigate the formation of contaminants in a micro-reactor.

1 Introduction

Heat pipe heat exchanger (HPHE) technology is used to dissipate excess heat generated by refrigerators, air conditioners, and greenhouses [1], among others. This is common in industrial applications, data centers, and power plants, where efficient cooling and heat control are needed to prevent overheating [1]. In a nuclear micro-reactor, the HPHE plays a crucial role, contributing to the safe and efficient cooling of its operational systems [1]. Furthermore, HPHE systems are used to facilitate the transfer of heat from the primary coolant loop to the secondary cooling loop in a micro-reactor. The primary coolant loop circulates the coolant through the reactor core and absorbs the thermal energy from the nuclear fission process [2]. The secondary cooling loop accepts heat via the primary cooling loop through the intermediate working fluid. Finally the heat is used to produce steam to drive turbines and generate electricity [2]. The efficiency of a micro-reactor is closely linked to the performance of the HPHE systems [2]. The heat exchange process directly influences the thermal efficiency of the micro-reactor. The HPHE

is used to manage and dissipate heat during abnormal or emergency conditions, such as a cooling loss accident or a shutdown of the reactor [3]. Therefore, maximizing the thermal efficiency of the micro-reactor, results in increased electricity generation [3]. Depending on the temperature range and application, HPHEs use a variety of working fluids; however, in the event of a leak or system failure, some of these fluids may present contamination risks [4]. When selecting fluids, thermodynamic efficiency and environmental effects must be considered [5]. Ammonia has been widely used for heating and cooling, especially when high thermal power is required [5]. However, when released into the atmosphere, ammonia poses serious health and environmental hazards due to its extreme toxicity and corrosiveness [5]. Ethanol and methanol are frequently utilized in low-temperature applications; nonetheless, they are both poisonous and combustible, with methanol posing significant hazards when inhaled or applied to the skin [6]. Helium is also used in a micro-reactor. In a micro-reactor, the impurities generated in the helium fluid can lead to environmental degradation of high-temperature alloys used in reactor internals [7]. These impurities, which may include water vapor and carbon compounds, can cause oxidation, carburization, or decarburization of the alloys [7]. Therefore, there is a need to control the heat in a micro-reactor using an intermediate heat exchanger. The heat exchanger can be deployed to eliminate the tritium contamination from entering the secondary cycle [8].

Computational Fluid Dynamics (CFD) is an engineering tool used for modeling complex systems across a range of disciplines [9]. Numerous studies have utilized CFD to investigate fluid flow behavior, thermal management, velocity profiles, relative humidity, and heat transfer in various engineering applications [9]. More recently, CFD has been employed to analyze thermal performance and flow behavior in heat exchangers [10]. Also, a CFD study on microchannel heat sinks for electronic cooling, focusing on different hydraulic diameters, surface area, and channel count using water under steady-state conditions with a constant heat flux and mass flow rate has been reported [11]. Increasing the number of channels and hydraulic diameter significantly reduced surface temperatures [11]. To enhance heat transfer in a concentric tube heat exchanger when equipped with trapezoidal vortex generators (VGs), a CFD study was deployed [12]. The study revealed that all configurations with VGs showed elevated thermal performance compared to the baseline [12]. For instance, placing VGs inside the tube produce the highest improvements in heat transfer ratios and thermal enhancement factors [12].

South Africa has been experiencing shortage of power supply and drastic effort must be taken to address this problem. Recently, a new micro-reactor design has been called for in South Africa to enhance power generation. However, before the micro-reactor can function efficiently, it is essential to control its heat performance. Therefore, a new HPHE must be designed to ensure efficient heat management. To facilitate this design, CFD simulation must be conducted to provide valuable insights into the performance of the newly designed HPHE. However, no studies have yet been carried out on this newly designed HPHE. Therefore, it becomes necessary to deploy the CFD simulation method to investigate the thermal behavior of HPHE. Various turbulence models, such as the k-epsilon, k-omega, Reynolds Stress Model, and Large Eddy Simulation (LES), are implemented in CFD. We intend to trial some selected turbulence models to determine which is most suitable for efficient heat management in the newly designed HPHE. In this study, helium was used as a hot fluid, and air as a cold fluid. A lead bismuth eutectic (LBE) was used as an intermediate working fluid.

2 Methodology

CFD was used to model a simplified geometry of the HPHE. The HPHE consists of two sets of pipes conjoined at their own plenums and immersed in a working fluid, LBE, similar to reference [13]. LBE has melting and boiling points of $396\,\mathrm{K}$ and $1943\,\mathrm{K}$ [14], respectively. Since the LBE alloy has substantially higher boiling points, operating a reactor with LBE coolant at much higher temperatures is not a risk [13]. It also serves as an excellent radiation shield, absorbing gamma radiation, and does not readily react with water, air, or helium to form contaminants that can cause harm to the performance of a typical micro-reactor [14]. In this study, while the inlet temperature of the helium fluid was set to $1023\,\mathrm{K}$, that of the air was set to $403\,\mathrm{K}$.

The HPHE involves two primary physical phenomena: fluid flow and heat transfer. Helium flows from one end of the pipes, transferring heat to the surrounding LBE. The LBE, on the other hand, flows around the helium and air pipes and within an enclosure box while transferring heat from the helium to the air pipe. Finally, the air flows inside its designated pipe from one end and receives the transferred heat. This interplay of fluid flow and heat transfer in an HPHE is essential for thermal management of a micro-reactor. In this study, we used commercially available software (Ansys Fluent 2024 R2 version) [15] for all CFD simulations.

The CFD solves the Navier-Stokes equations of momentum, continuity, and energy (see Table 1). In this study, we focused on only two turbulence models (the $k-\epsilon$ model and LES). Furthermore, we also consider the effect of buoyancy in the turbulent flow by applying the Boussinesq approximation. In the governing equations, the $\vec{u}$ represents the velocity vector, p is the static pressure, and ρ is the fluid density. The μ is the dynamic viscosity, while μ_t is the turbulent (eddy) viscosity. T is the temperature and c_p is the specific heat capacity at constant pressure. The turbulent kinetic energy is given by k, and its dissipation rate by ϵ. The thermal conductivity is denoted as λ. The term P_k refers to the production of turbulent kinetic energy. Buoyancy effects are included via the buoyancy force vector $\vec{F_b} = \rho\vec{g}\beta(T - T_{\text{ref}})$, where $\vec{g}$ is gravitational acceleration, β is the thermal expansion

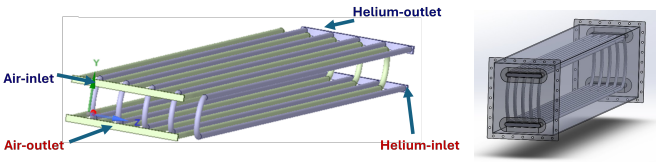

Figure 1: (*left*) The geometry structures of the HPHE. The air inlet is located at the top, and the helium inlet is located at the bottom. Air plenums and pipes are green, and helium plenums and pipes are blue. The air inlet plenum is located at the top as air flows into the chambers and then exits from the outlet, which is located at the bottom of the HPHE. Helium inlet is seen on the other side of the HPHE at the bottom, and it flows from the bottom up through the chambers of the helium pipes. (*right*) The LBE enclosure box. LBE is injected into the enclosure box.

coefficient, and T_{ref} is a reference temperature. The Φ represents viscous dissipation in the energy equation. In the LES turbulence, quantities with a bar represent filtered values of the quantities; $\overline{u_i u_j}$ is a filtered product of velocity components u_i, u_j, and τ_{ij} is the sub-grid scale (SGS) stress tensor. The SGS turbulent viscosity ν_t is modeled using the Smagorinsky model $\nu_t = (C_s\Delta)^2|\bar{S}|$, where C_s is the Smagorinsky constant, Δ is the filter width, and $\bar{S}$ is the strain rate magnitude.

Table 1: The continuity, Navier-Stokes equations of momentum, energy, and the turbulence equations.

Continuity	$\nabla \cdot \vec{u} = 0$
Momentum	$\rho\left(\frac{\partial \vec{u}}{\partial t} + \vec{u}\cdot\nabla\vec{u}\right) = -\nabla p + \mu\nabla^2\vec{u} + \vec{F_b} + \vec{F_t}$
Energy	$\rho c_p\left(\frac{\partial T}{\partial t} + (\vec{u}\cdot\nabla)T\right) = \nabla\cdot(\lambda\nabla T)$
Boussinesq approximation	$\vec{F_b} = \rho\vec{g}\beta(T - T_{\text{ref}})$
k Equation	$\frac{\partial(\rho k)}{\partial t} + \nabla\cdot(\rho k\vec{u}) = \nabla\cdot\left(\left(\mu + \frac{\mu_t}{\sigma_k}\right)\nabla k\right) + P_k - \rho\epsilon$
ϵ Equation	$\frac{\partial(\rho\epsilon)}{\partial t} + \nabla\cdot(\rho\epsilon\vec{u}) = \nabla\cdot\left(\left(\mu + \frac{\mu_t}{\sigma_\epsilon}\right)\nabla\epsilon\right) + C_{1\epsilon}\frac{\epsilon}{k}P_k - C_{2\epsilon}\rho\frac{\epsilon^2}{k}$
Turbulent Viscosity	$\mu_t = C_\mu\frac{\rho k^2}{\epsilon}$
LES Momentum	$\frac{\partial\bar{u}_i}{\partial t} + \bar{u}_j\frac{\partial\bar{u}_i}{\partial x_j} = -\frac{1}{\rho}\frac{\partial\bar{p}}{\partial x_i} + \nu\frac{\partial^2\bar{u}_i}{\partial x_j^2} - \frac{\partial\tau_{ij}}{\partial x_j}$
SGS Stress (LES)	$\tau_{ij} = \overline{u_i u_j} - \bar{u}_i\bar{u}_j, \quad \nu_t = (C_s\Delta)^2\lvert\bar{S}\rvert$

Table 2: Boundary conditions applied to helium-air HPHE for flow and thermal analysis.

Boundary	**Flow conditions**	**Thermal**
Helium inlet	Mass flow of 0.035 kg/s	1023 K
Helium outlet	Atmospheric pressure	Backflow 1023 K
Air inlet	Mass flow of 0.14 kg/s	403 K
Air outlet	Atmospheric pressure	Backflow 1023 K
Helium pipe	No slip condition	Convection ($h = 1790$ W/(m$^2\cdot$K))
Air pipe	No slip condition	Convection ($h = 264$ W/(m$^2\cdot$K))
HPHE box	No slip condition	Zero heat flux

The boundary conditions (BC) supplemented by auxiliary conditions are used to specify how the fluid behaves against solid walls, inlets, and interfaces, as well as provide control over the simulations. The simulation determines the outlet temperatures. The BC parameters are listed in Table 2. The inlets were taken as mass flow inlets, while the outlets were set as pressure outlets at atmospheric pressure levels. The "no-slip" condition was applied to the walls of air, helium, and LBE to capture heat transfer and realistic turbulence within the walls. Convection

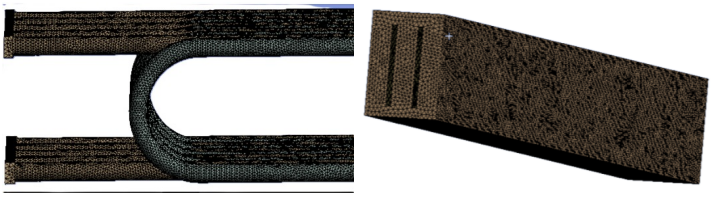

Figure 2: (*left*) Side view of the mesh for the air and helium pipes. (*right*) The meshed LBE enclosure box.

is imposed at the pipe boundaries to correctly capture heat transfer between the helium and air pipe, through the working fluid. The heat transfer coefficients (h) for helium and air are listed in Table 2 as 1790 W/m^{2}K and 264.00 W/m^{2}K, respectively.

The HPHE geometry was carefully meshed, leading to a total of 25 million cells. The mesh was finer around the pipes to accurately capture the heat transfer occurring in those regions. Figure 2 displays the mesh around the pipes. To obtain a more robust implementation of steady-state flow, we used the coupled pressure-velocity coupling scheme [16]. The coupled pressure-velocity coupling scheme combines the continuity and momentum equations to calculate the pressure in a pressure-based solver. Simulations were done using the finite volume method with under-relaxation of variables and second-order spatial and temporal discretization. Gradients were discretized using a cell-based least-squares method [15].

3 Results and Discussion

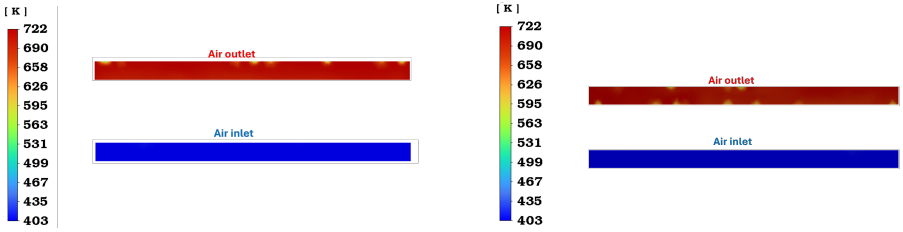

Figure 3: The temperature profiles of the air flow in the HPHE; (*left*) k-ϵ model and (*right*) LES model.

Several studies in CFD focus on heat transfer in heavy liquid metals, where the CFD simulation techniques have been validated [17, 18]. In one such study, Trevor validated mercury experiment results have demonstrated that CFD simulations can reliably predict temperatures under normal operating conditions [17], which serves as the basis for the validation of this present CFD study.

Figure 3 displays the image of the temperature profile of cool air in the HPHE. Using the k-ϵ model, we observed that the outlet temperature of air reaches 722 K. In the air pipe, there was a smooth, layered profile, which suggests a relatively uniform heat transfer from the hot region. However, the bulk convection primarily governs the flow, with minimal impact from turbulent mixing. Also for the LES model as shown in Figure 3 (right), we observed an outlet temperature increase to 722 K, exhibiting greater temperature variation and noticeable fluctuations in the contours across the plenum. This shows the existence of eddies and turbulent structures captured by the LES model, resulting in improved mixing and a more accurate prediction of heat transfer. The k-ϵ and LES models yielded a comparable outlet temperature. However, the LES offers a more comprehensive understanding of flow instabilities and spatial temperature gradients.

Figure 4 displays the image of the temperature profile of hot fluid in the HPHE. The k-ϵ model shows that the outlet temperature decreases from 1023 K to approximately 723 K, reflecting a cooling effect of 300 K. The LES model showed a significantly greater cooling effect, with the helium outlet temperature decreasing to as low as 500 K. The outlet contours exhibit increased turbulence-induced irregularities, facilitating localized mixing that improves heat transfer. In contrast to LES, the k-ϵ model tends to overestimate turbulent dissipation, which suppresses mixing in the flow. This reduces mixing directly, which leads to an under prediction of heat transfer [19].

Figure 5 illustrates the thermal energy distribution in the LBE box, comparing LES and k-ϵ models. The k-ϵ model displays a stratified temperature profile in the LBE, with high-temperature regions (ranging from 465 K to over 1023 K) concentrated in the core, indicating limited mixing. In contrast, LES yields a chaotic, spatially varied distribution with swirling structures and eddies, demonstrating enhanced mixing and heat transport. This improved

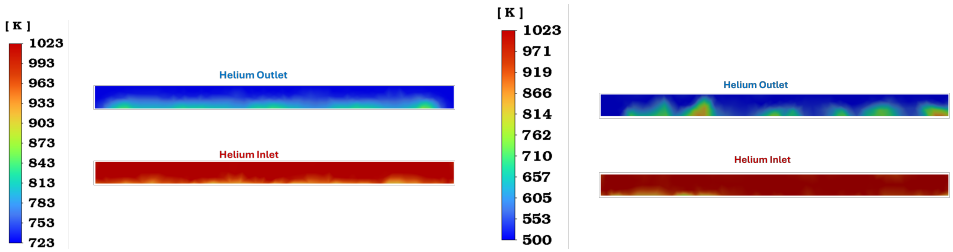

Figure 4: The hot fluid (helium) temperature profile of the HPHE. (*left*) k-ϵ model, and (*right*) LES model.

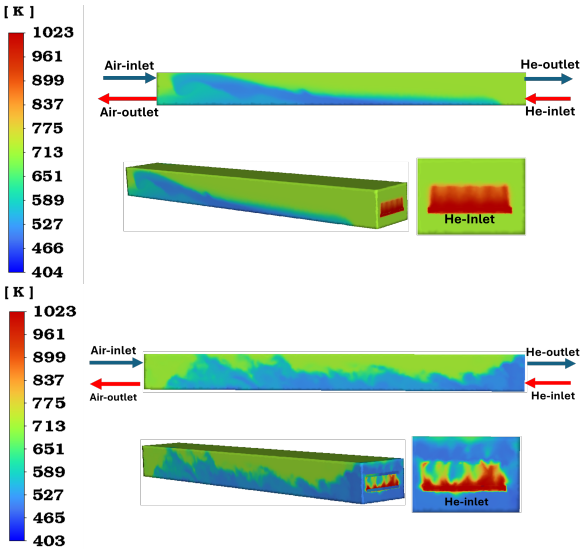

Figure 5: (*left*) k-ϵ model and (*right*) LES model of the temperature distribution within the LBE enclosure box.

mixing helps identify potential thermal hotspots and advances understanding of heat transfer in the micro-reactor environment. LES thus captures complex convective behavior crucial for micro-reactor safety and thermal control when using HPHE. These results provide theoretical insight into HPHE application for heat management in micro-reactors intended for power generation..

4 Conclusion

A CFD simulation of the LES and k-ϵ turbulent model on the thermal control of a HPHE intended for use in micro-reactors was studied. While the two models could be used to facilitate thermal control in an HPHE, the LES model shows greater heat transfer than the k-ϵ model. By using the LES, the fine-scale eddies and transitional flow effects in the fluid flow of the HPHE was captured. In contrast to the k-ϵ model, which predicted cooling performance at only $723\,\mathrm{K}$, the LES model indicated a drop in helium temperature from $1023\,\mathrm{K}$ to $500\,\mathrm{K}$. However, the LES model air outlet temperature was observed to be $722\,\mathrm{K}$ whereas k-ϵ predicted the same air outlet temperature. The choice of turbulence models directly affects the thermal control and performance of a typical HPHE. LES provides a greater heat reduction in helium temperature. The k-ϵ model, on the other hand, tends to overestimate turbulent dissipation. To validate these results, a thermal test will be conducted at NECSA in the future. In addition, future work will focus on studying other turbulence models, particularly RANS-based approaches such as the k-ω model, as well as hybrid turbulence models like Detached Eddy Simulation.

Acknowledgments

The authors are grateful to the University of Johannesburg for the provision of the computer servers. This work is supported by the research grant from Lesedi Nuclear Services. Prof Johan Slabber acknowledges the University of Pretoria and PCMR (pty) Ltd. The Center for High Performance Computing (CHPC) is acknowledged for the use of its computing facilities.

References

[1] Y. S. Jeong, K. M. Kim, I. G. Kim, and I. C. Bang, "Hybrid heat pipe based passive in-core cooling system for advanced nuclear power plant," *Applied Thermal Engineering*, vol. 90, pp. 609–618, 2015.

[2] R. Laubscher and R. T. Dobson, "Theoretical and experimental modelling of a heat pipe heat exchanger for high temperature nuclear reactor technology," *Applied Thermal Engineering*, vol. 61, no. 2, pp. 259–267, 2013.

[3] T. Hamidouche and E.-K. Si-Ahmed, "Analysis of loss of coolant accident in MTR pool type research reactor," *Progress in nuclear energy*, vol. 53, no. 3, pp. 285–289, 2011.

[4] J. S. Yoo, S. Qin, S. A. Balderrama Prieto, and E. Hisahara, "A comparative evaluation and selection of high-temperature heat exchangers for application to integrated energy systems," Idaho National Laboratory (INL), Idaho Falls, ID (United States), Tech. Rep., 2023.

[5] A. Zini, L. Socci, G. Vaccaro, A. Rocchetti, and L. Talluri, "Working fluid selection for high-temperature heat pumps: A comprehensive evaluation," *Energies*, vol. 17, no. 7, p. 1556, 2024.

[6] T. Log and A. L. Moi, "Ethanol and methanol burn risks in the home environment," *International journal of environmental research and public health*, vol. 15, no. 11, p. 2379, 2018.

[7] P. L. Suryawanshi, S. P. Gumfekar, B. A. Bhanvase, S. H. Sonawane, and M. S. Pimplapure, "A review on microreactors: Reactor fabrication, design, and cutting-edge applications," *Chemical Engineering Science*, vol. 189, pp. 431–448, 2018.

[8] S. R. Sherman and T. M. Adams, "Tritium barrier materials and separation systems for the NGNP," *Savannah River National Laboratory Report WSRC-STI-2008-00358, Rev. 0*, 2008.

[9] T. Norton, B. Tiwari, and D.-W. Sun, "Computational fluid dynamics in the design and analysis of thermal processes: a review of recent advances," *Critical reviews in food science and nutrition*, vol. 53, no. 3, pp. 251–275, 2013.

[10] S. Almahmoud and H. Jouhara, "Experimental and theoretical investigation on a radiative flat heat pipe heat exchanger," *Energy*, vol. 174, pp. 972–984, 2019.

[11] G. Anjaneya, S. Sunil, S. Kakkeri, M. M. Math, M. Vaibhav, C. Solaimuthu, C. Durga Prasad, and H. Vasudev, "Numerical simulation of microchannel heat exchanger using CFD," *International Journal on Interactive Design and Manufacturing (IJIDeM)*, vol. 18, no. 8, pp. 5847–5863, 2024.

[12] R. Aridi, S. Ali, T. Lemenand, J. Faraj, and M. Khaled, "CFD analysis on the spatial effect of vortex generators in concentric tube heat exchangers–a comparative study," *International Journal of Thermofluids*, vol. 16, p. 100247, 2022.

[13] B. Gromov, Y. S. Belomitcev, E. Yefimov, M. Leonchuk, P. Martinov, Y. I. Orlov, D. Pankratov, Y. G. Pashkin, G. Toshinsky, V. Chekunov *et al.*, "Use of lead-bismuth coolant in nuclear reactors and accelerator-driven systems," *Nuclear Engineering and Design*, vol. 173, no. 1-3, pp. 207–217, 1997.

[14] G. Toshinsky, A. Dedul, O. Komlev, A. Kondaurov, V. Petrochenko *et al.*, "Lead-bismuth and lead as coolants for fast reactors," *World Journal of Nuclear Science and Technology*, vol. 10, no. 02, p. 65, 2020.

[15] A. Fluent, "Ansys fluent theory guide 2021 r2," *ANSYS, Canonsburg, PA*, vol. 33, 2021.

[16] H.-H. Lee, *Finite element simulations with ANSYS workbench 2023: Theory, applications, case studies*. SDC publications, 2023.

[17] T. V. Dury, "Heat transfer to a heavy liquid metal in curved geometry: Code validation and cfd simulation for the megapie lower target," *Nuclear Instruments and Methods in Physics Research Section A: Accelerators, Spectrometers, Detectors and Associated Equipment*, vol. 562, no. 2, pp. 859–862, 2006.

[18] A. Papukchiev and S. Buchholz, "Validation of ANSYS CFX for gas and liquid metal flows with conjugate heat transfer within the european project THINS," *Nuclear Engineering and Design*, vol. 312, pp. 338–350, 2017.

[19] A. Guardo, M. Coussirat, M. Larrayoz, F. Recasens, and E. Egusquiza, "Influence of the turbulence model in CFD modeling of wall-to-fluid heat transfer in packed beds," *Chemical Engineering Science*, vol. 60, no. 6, pp. 1733–1742, 2005.

Adiabatic elimination approach to the completely positive master equation for open quantum Brownian motion

Ayanda Zungu[1], Ilya Sinayskiy[2,3], and Francesco Petruccione[3,4]

[1]Centre for Space Research, North-West University, Mahikeng 2745, South Africa
[2]Discipline of Physics, School of Agriculture and Science, University of KwaZulu-Natal, Durban 4001, South Africa
[3]National Institute for Theoretical and Computational Sciences (NITheCS), South Africa
[4]School of Data Science and Computational Thinking and Department of Physics, Stellenbosch University, Stellenbosch 7604, South Africa

E-mail: arzngu@gmail.com

Abstract. Open quantum Brownian motion (OQBM) was introduced as a scaling limit of discrete-time open quantum walks, providing a new class of quantum Brownian motion. In this case, the dynamics of the Brownian particle are governed by dissipative interactions with a thermal bath and depend on the quantum internal state of the Brownian particle. In this proceeding, we outline the derivation of a completely positive master equation for OQBM using the adiabatic elimination of fast variables method for a weakly driven open Brownian particle confined within a harmonic potential and dissipatively coupled to a thermal bath. We illustrate the derivation using examples of initial Gaussian and non-Gaussian distributions. For both examples, the OQBM dynamics converge to Gaussian distributions for various system-bath parameters. From the resulting dynamics, we also derive equations for the first, second, and third cumulants of the position distribution of the OQBM walker. Interestingly, we find that the third cumulant is non-zero, which reveals that the intrinsic generator of the evolution is non-Gaussian.

1 Introduction

Recently, Attal *et al.* [1] introduced the formalism of discrete-time open quantum walks (OQWs) as a new type of quantum walks (QWs) to incorporate the dissipative dynamics of open quantum systems [2]. OQWs rely entirely on the non-unitary evolutions induced by the interaction between the walker and its environment, and rest upon the implementation of appropriate completely positive trace-preserving (CPTP) maps [2, 3]. Unlike the traditional unitary QWs [4, 5], where quantum interference over the nodes of a graph determines the probability of finding the walker, in OQWs, the probability of finding the quantum walker on a particular node depends on both the structure of the underlying graph and the walker's quantum internal state. Ref. [6] demonstrated that OQWs can perform dissipative quantum computation and generate complex quantum states. Interested readers can find recent developments on this subject in [7].

Shortly after the introduction of OQWs, Bauer *et al.* [8] introduced *open quantum Brownian motion* (OQBM) as a scaling limit of discrete-time OQWs, providing a new class of quantum Brownian motion. In this case, the dynamics of the quantum Brownian particle depends not only on the dissipative interactions with a thermal bath but also on the state of the internal degree of freedom of the quantum Brownian particle. Recently, a microscopic derivation of OQBM for a free Brownian particle subject to decoherent interaction with a thermal bath was proposed [9, 10]. In our recent work [11], we extended this framework by deriving OQBM in a generic dissipative

scenario using the adiabatic elimination of fast variables technique [12, 13, 14]. However, this approach led to a master equation that is not completely positive, consistent with the limitations of the standard Caldeira-Leggett model [15]. To resolve the issue of positivity, we now apply the rotating wave approximation (RWA) [16] to the system-bath interaction Hamiltonian. This leads to a completely positive master equation for OQBM in the case of a weakly driven open Brownian particle confined within a harmonic potential and dissipatively coupled to a thermal bath.

This proceeding has the following structure: In Section 2, we introduce the microscopic Hamiltonian for this model and derive a completely positive Born-Markov master equation for the reduced dynamics. In Section 3, we write the resulting master equation in coordinate representation, and briefly outline the adiabatic elimination of fast variables method and derive a completely positive master equation for OQBM. Section 4 presents the numerical illustrations of the OQBM dynamics for various system-bath parameters and the equations for the cumulants of the OQBM walker. The detailed derivation and the terms and parameters omitted here will be provided in [17]. Lastly, in Section 5, we conclude.

2 Completely positive Born-Markov master equation

The total Hamiltonian of the system and bath can be written as

$$\hat{H} = \hat{H}_S + \hat{H}_B + \hat{H}_{SB}, \tag{1}$$

where $\hat{H}_S$, $\hat{H}_B$, and $\hat{H}_{SB}$ denote the Hamiltonians of the system, the bath, and the system-bath interaction, respectively, which reads

$$\hat{H}_S = \frac{\hat{p}^2}{2m} + \frac{m\omega^2\hat{x}^2}{2} + \frac{\hbar\omega_0}{2}\hat{\sigma}_z + \hbar\Omega\hat{\sigma}_x, \tag{2}$$

$$\hat{H}_B = \sum_n \hbar\omega_n \hat{a}_n^\dagger \hat{a}_n, \tag{3}$$

$$\hat{H}_{SB} = \hbar\big(\hat{x} + \alpha\hat{\sigma}_x\big)\sum_n g_n\big(\hat{a}_n + \hat{a}_n^\dagger\big). \tag{4}$$

Here, $\hat{x}$ and $\hat{p}$ denote the position and the momentum operators of the Brownian particle, m is the mass of the Brownian particle, and $\frac{m\omega^2\hat{x}^2}{2}$ represents the harmonic potential trapping the particle with frequency ω. The Hamiltonian for the two-level system (2LS) representing internal degree of freedom, is denoted by $\frac{\hbar\omega_0}{2}\hat{\sigma}_z$, with ω_0 being the transition frequency, and $\hbar\Omega\hat{\sigma}_x$ describes a weak classical driving of the inner degree of freedom ($\Omega \ll \omega_0$) [18, 19]. The operators $\hat{\sigma}_{i=x,y,z}$ are the standard Pauli matrices and the bath is described by the annihilation and creation operators, $\hat{a}_n$ and $\hat{a}_n^\dagger$, respectively, satisfying the standard bosonic commutation relations $[\hat{a}_n, \hat{a}_m^\dagger] = \delta_{n,m}$, and ω_n are frequencies of the corresponding oscillators. The system-bath coupling strength is denoted by g_n, and a constant α is a relative coupling strength.

To derive the reduced density matrix $\hat{\rho}_S(t)$, we assume that the system is weakly coupled to the thermal bath, allowing us to trace out the bath variables and obtain the Born–Markov master equation [2, 19]. The generic Born-Markov master equation [2, 19], when applied to our system, becomes

$$\frac{d}{dt}\hat{\rho}_S(t) = -\frac{i}{\hbar}\big[\hat{H}_S, \hat{\rho}_S\big] - \frac{1}{\hbar^2}\int_0^\infty d\tau \mathrm{tr}_B\Big[\hat{H}_{SB}(0), \big[\hat{H}_{SB}(-\tau), \hat{\rho}_S(t)\otimes\hat{\rho}_B\big]\Big]. \tag{5}$$

Above, $\hat{H}_{SB}(-\tau)$ denotes the system-bath interaction Hamiltonian in the interaction picture. We define the bath's density matrix at thermal equilibrium as $\hat{\rho}_B = \mathcal{Z}^{-1}\exp(-\beta\hat{H}_B)$, where the temperature is $T = (k_B\beta)^{-1}$, k_B is the Boltzmann constant and the partition function is $\mathcal{Z} = \mathrm{tr}_B[\exp(-\beta\hat{H}_B)]$. In principle, Eqn. (5) does not guarantee that the resulting dynamical equation will take the Gorini–Kossakowski–Sudarshan–Lindblad (GKSL) form [2, 20, 21]. To derive the master equation in GKSL form, one must apply the rotating-wave approximation (RWA) [16] (which corresponds to neglecting the rapidly oscillating terms) to the system-bath interaction Hamiltonian (4), which yields: $\hat{H}_{SB} = \hbar x_0\sum_n g_n(\hat{a}^\dagger\hat{a}_n + \hat{a}\hat{a}_n^\dagger) + \hbar\alpha\sum_n g_n\big(\hat{a}_n\hat{\sigma}_+ + \hat{a}_n^\dagger\hat{\sigma}_-\big)$, where, $x_0 = \sqrt{\hbar/2m\omega}$ and $\hat{\sigma}_\pm$ are the Pauli raising and lowering operators of the 2LS, satisfying $[\hat{\sigma}_+, \hat{\sigma}_-] = \hat{\sigma}_z$. In the interaction picture, we assume that the classical driving term in the system Hamiltonian (2) is very weak, i.e., $\Omega \ll \omega_0$. By doing this, we get

$$\hat{H}_{SB}(-\tau) = x_0\sum_n g_n\hat{a}^\dagger\hat{a}_n e^{i(\omega_n-\omega)\tau} + \mathrm{h.c.} + \alpha\sum_n g_n\hat{a}_n\hat{\sigma}_+ e^{i(\omega_n-\omega_0)\tau} + \mathrm{h.c.} \tag{6}$$

Using the above expression (6), and choosing the spectral density of the form $\sum_n |g_n|^2 \to \int d\tilde{\omega} J(\tilde{\omega})$, we derive the following completely positive Born-Markov master equation for the reduced dynamics:

$$\frac{d}{dt}\hat{\rho}_S(t) = \mathcal{L}_{\rm QHO}\hat{\rho}_S + \mathcal{L}_{\rm 2LS}\hat{\rho}_S + \mathcal{L}_{\rm cross}\hat{\rho}_S, \tag{7}$$

where $\mathcal{L}_{\rm QHO}\hat{\rho}_S$ describes the dissipator of the quantum harmonic oscillator, which reads

$$\mathcal{L}_{\rm QHO}\hat{\rho}_S(t) = -\frac{i}{\hbar}\big[\hat{H}_{\rm QHO}, \hat{\rho}_S\big] - \bar{\alpha}_1\big[\hat{x}, [\hat{x}, \hat{\rho}_S]\big] - \bar{\alpha}_2\big[\hat{p}, [\hat{p}, \hat{\rho}_S]\big] + i\bar{\alpha}_3\Big(\big[\hat{p}, \{\hat{x}, \hat{\rho}_S\}\big] - \big[\hat{x}, \{\hat{p}, \hat{\rho}_S\}\big]\Big). \tag{8}$$

Equation (8) represents a Caldeira-Leggett [15] type of master equation with an extra term $[\hat{p}, [\hat{p}, \hat{\rho}_S]]$, which allows us to write Eqn. (8) in GKSL form [20, 21]. The second term in Eqn. (7), $\mathcal{L}_{\rm 2LS}\hat{\rho}_S$, has the form of the well-known quantum optical master equation for the 2LS [18, 19] and describe a dissipation of a weakly driven internal degree of freedom. The last term in Eqn. (7), $\mathcal{L}_{\rm cross}\hat{\rho}_S$, denotes a "cross-term" dissipator that captures dissipative coupling between external and internal degrees of freedom.

3 Adiabatic elimination and the OQBM master equation

In order to demonstrate that Eqn. (7) can be written as OQBM, we need to show that it could be represented as a diagonal representation in position, and this can be done by starting from a generic non-diagonal representation, defined as $\hat{\rho}_S(t) = \int_{-\infty}^{+\infty} dxdy\rho(x,y) \otimes |x\rangle\langle y|$. Subsequently, we make a coordinate transformation to canonical form via $u = (x+y)/2$ and $v = x - y$. In the rotated coordinate, we obtain

$$\frac{\partial}{\partial t}\rho(u,v) = \mathcal{L}_{\rm QHO}\rho + \mathcal{L}_{\rm 2LS}\rho + \mathcal{L}_{\rm cross}\rho, \tag{9}$$

where

$$\mathcal{L}_{\rm QHO}\rho(u,v) = \left[\frac{i\hbar}{m}\frac{\partial^2}{\partial v \partial u} - \frac{im\omega^2}{\hbar}uv - \bar{\alpha}_1 v^2 + \bar{\alpha}_2\hbar^2\frac{\partial^2}{\partial u^2} + 2\hbar\bar{\alpha}_3\left(1 + u\frac{\partial}{\partial u}\right) - 2\hbar\bar{\alpha}_3 v\frac{\partial}{\partial v}\right]\rho, \tag{10}$$

$$\mathcal{L}_{\rm 2LS}\rho(u,v) = -i\Big[\Big(\frac{\omega_0}{2} - \beta_3\Big)\hat{\sigma}_z + \Omega\hat{\sigma}_x, \hat{\rho}_S\Big] + \beta_1\mathcal{L}[\hat{\sigma}_-, \hat{\sigma}_+]\rho + \beta_2\mathcal{L}[\hat{\sigma}_+, \hat{\sigma}_-]\rho, \tag{11}$$

$$\mathcal{L}_{\rm cross}\rho(u,v) = \left(\frac{\partial}{\partial u}\hat{m}_1 + \frac{\partial}{\partial v}\hat{m}_2 + u\hat{m}_3 + v\hat{m}_4\right)\rho. \tag{12}$$

Here, $\mathcal{L}[\hat{A}, \hat{A}^\dagger]\hat{\rho} := \hat{A}\hat{\rho}\hat{A}^\dagger - (1/2)(\hat{A}^\dagger\hat{A}\hat{\rho} + \hat{\rho}\hat{A}^\dagger\hat{A})$, is the standard GKSL dissipator and $\hat{m}_1$, $\hat{m}_2$, $\hat{m}_3$, and $\hat{m}_4$ are the super-operators acting on the internal degree of freedom. The above system $\rho(u,v)$ involves two variables, u and v, where u denotes the slow variable and v denotes the fast variable, with the latter being the one we eliminate. Assuming $(m\omega)^2 \sim k_B T$ and that $\bar{\alpha}_1$ is larger than all the system parameters, we use the adiabatic elimination of fast variables [12, 13, 14] to derive the position distribution function $\bar{\rho}(u)$: $\bar{\rho}(u) = \int_{-\infty}^{+\infty} dv\rho(u,v)$. After performing the adiabatic elimination, we obtained that $v = 0$, which implies that $u = x$, and derive a completely positive master equation for the diagonal elements, which defines OQBM [8, 9, 10, 11]:

$$\frac{\partial}{\partial t}\bar{\rho}(x,t) \approx -\lambda_1 x\frac{\partial}{\partial x}\bar{\rho} - \lambda_2 x^2\bar{\rho} + \hat{m}_1\frac{\partial}{\partial x}\bar{\rho} + x\hat{m}_3\bar{\rho} + \lambda_3\frac{\partial^2}{\partial x^2}\bar{\rho} + \lambda_4\frac{\partial}{\partial x}(x\bar{\rho}) + \mathcal{L}_{\rm 2LS}\bar{\rho}. \tag{13}$$

The diffusive term ($-\lambda_1 x\frac{\partial}{\partial x}\bar{\rho} - \lambda_2 x^2\bar{\rho} + \lambda_3\frac{\partial^2}{\partial x^2}\bar{\rho} + \lambda_4\frac{\partial}{\partial x}(x\bar{\rho})$) describes the propagation of the Brownian particle. The Lindblad term ($\mathcal{L}_{\rm 2LS}\bar{\rho}$) describes the dissipative dynamics of the internal state of the Brownian particle. The remaining term ($\hat{m}_1\frac{\partial}{\partial x}\bar{\rho} + x\hat{m}_3\bar{\rho}$) is a 'decision-making' term, describing the interaction between the external and internal degrees of freedom of the Brownian particle.

4 Numerical results and discussion

The reduced density matrix $\bar{\rho}(x,t)$ of the open quantum Brownian particle can be expressed as

$$\bar{\rho}(x,t) = \begin{pmatrix} \rho_{1,1}(x,t) & \rho_{1,2}(x,t) \\ \rho_{2,1}(x,t) & \rho_{2,2}(x,t) \end{pmatrix}, \tag{14}$$

where the diagonal elements $\rho_{1,1}(x,t)$ and $\rho_{2,2}(x,t)$ represent the probability of the system being in the first or the second quantum state, respectively, and the off-diagonal elements $\rho_{1,2}(x,t) = (\rho_{2,1}(x,t))^*$ represent quantum coherences. Using the above expression (14), the master equation (13) can be rewritten as

$$\begin{aligned}
\frac{\partial}{\partial t}\rho_+ &= \left\{\lambda_3\frac{\partial^2}{\partial x^2} + \Delta_1 x\frac{\partial}{\partial x} + \lambda_4 - \lambda_2 x^2\right\}\rho_+ - 2\delta_1\frac{\partial}{\partial x}C_I + 2\tilde{a}_2\frac{\partial}{\partial x}C_R,\\
\frac{\partial}{\partial t}\rho_- &= \left\{\lambda_3\frac{\partial^2}{\partial x^2} + \Delta_1 x\frac{\partial}{\partial x} + \Delta_2 - \lambda_2 x^2\right\}\rho_- - \bar{\beta}\rho_+ + \left\{4\tilde{a}_7 x - 4\Omega + 4\delta_2\frac{\partial}{\partial x}\right\}C_I\\
&\quad - \left\{4\tilde{a}_8 x + 4\delta_3\frac{\partial}{\partial x}\right\}C_R,\\
\frac{\partial}{\partial t}C_R &= \left\{\lambda_3\frac{\partial^2}{\partial x^2} + \Delta_1 x\frac{\partial}{\partial x} + \Delta_3 - \lambda_2 x^2\right\}C_R + \left\{\tilde{a}_8 x + \delta_3\frac{\partial}{\partial x}\right\}\rho_- + \frac{1}{2}\tilde{a}_2\frac{\partial}{\partial x}\rho_+,\\
\frac{\partial}{\partial t}C_I &= \left\{\lambda_3\frac{\partial^2}{\partial x^2} + \Delta_1 x\frac{\partial}{\partial x} + \Delta_4 - \lambda_2 x^2\right\}C_I + \left\{\Omega - \tilde{a}_7 x - \delta_2\frac{\partial}{\partial x}\right\}\rho_- - \frac{1}{2}\delta_1\frac{\partial}{\partial x}\rho_+,
\end{aligned} \tag{15}$$

where $\rho_\pm = \rho_{1,1}(x,t) \pm \rho_{2,2}(x,t)$, $C_R = \mathrm{Re}(\rho_{1,2}(x,t))$, $C_I = \mathrm{Im}(\rho_{1,2}(x,t))$. To explore the behavior of OQBM, we integrate the system of partial differential equations (15) numerically. We consider Gaussian and non-Gaussian initial distributions for the open Brownian particle and assume that the internal degree of freedom is initially a pure state described by

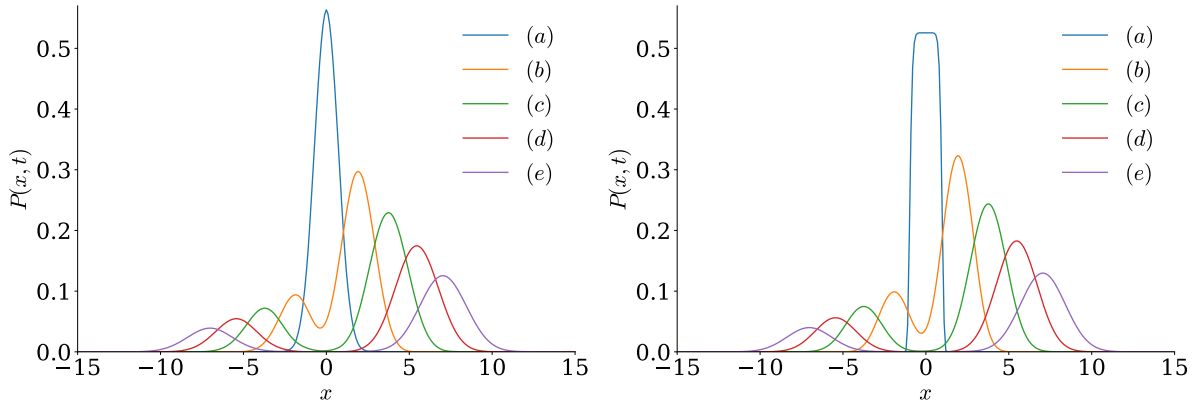

Figure 1: The position probability distribution $P(x,t)$ of the open quantum Brownian particle for different moments of time. The initial distribution is given by Eqn. (16), with $\theta = \pi/6$, $\phi = \pi/4$. The *left panel* and the *right panel* correspond to $j = 2$ and $j = 10$, respectively. Curves (a) to (e) correspond to times 0, 50, 100, 150, and 200, respectively. Other parameters are set to $\Omega = 0.3$, $\beta = \Delta_1 = \Delta_2 = \tilde{a}_7 = 10^{-3}$, $\Delta_3 = \lambda_2 = \lambda_4 = \delta_1 = \tilde{a}_8 = 10^{-4}$, $\Delta_4 = 8\times10^{-3}$, $\lambda_3 = 5\times10^{-3}$, $\delta_2 = 3\times10^{-2}$, $\delta_3 = 10^{-2}$, and $\tilde{a}_2 = -4\times10^{-2}$. For times $t \geq 50$, the profile splits into two Gaussians.

$$\bar{\rho}_j(x,0) = \frac{1}{2I_j}e^{-x^j} \otimes \begin{pmatrix} 2\cos^2\theta & \sin 2\theta e^{-i\phi} \\ \sin 2\theta e^{i\phi} & 2\sin^2\theta \end{pmatrix}, \tag{16}$$

where $I_j = \int_{-\infty}^{+\infty} dx e^{-x^j}$, $\theta \in [0,\pi)$, $\phi \in [0,2\pi)$, and $j > 0$. Figure 1, shows the position probability distribution $P(x,t) = \mathrm{tr}\big(\rho_+(x,t)\big)$ of finding the open Brownian particle at position x at time t. The *left panel* of Fig. 1 demonstrates that for the initial Gaussian distribution (for $j = 2$) and a chosen set of parameters, the OQBM walker probability distributions split into two Gaussian distributions at time $t \geq 50$. In the *right panel* of Fig. 1, one can see clearly that even with a non-Gaussian initial distribution (for $j = 10$), the position probability distribution of the open Brownian particle converges into a mixture of Gaussian distributions at times $t \geq 50$, for various parameters.

To derive the equations for the cumulants of the position distribution of the OQBM walker, we take the logarithm of the generating function of the characteristic function of the scaled reduced density matrix $\tilde{\rho}(\xi,t)$ as

$\ln\bar{\rho}(k,t) = \ln\langle e^{-ik\xi}\rangle = \ln\int_{-\infty}^{+\infty} d\xi\tilde{\rho}(\xi,t)e^{-ik\xi} = \sum_{n=1}^{\infty}\frac{(-ik)^n}{n!}\langle\xi^n\rangle_c$. Assuming a Gaussian initial state of the form (16) for $j=2$, and assuming $\langle x^4\rangle_c = 0$. For the zeroth order $(-ik)^0$, we derive

$$0 = \bar{\lambda}_2\langle x\rangle_c^2 + \bar{\lambda}_2\langle x^2\rangle_c + \Delta_1 - \lambda_4. \tag{17}$$

The above expression (17) can be written as $\langle x\rangle_c^2 + \langle x^2\rangle_c = \langle x^2\rangle = \frac{\hbar}{2m\omega\tilde{x}_0^2}\big(2n(\omega)+1\big)$, which shows that the second moment $\langle x^2\rangle$ of the position is related to the quantum mechanical zero-point energy and the thermal occupation $n(\omega)$.

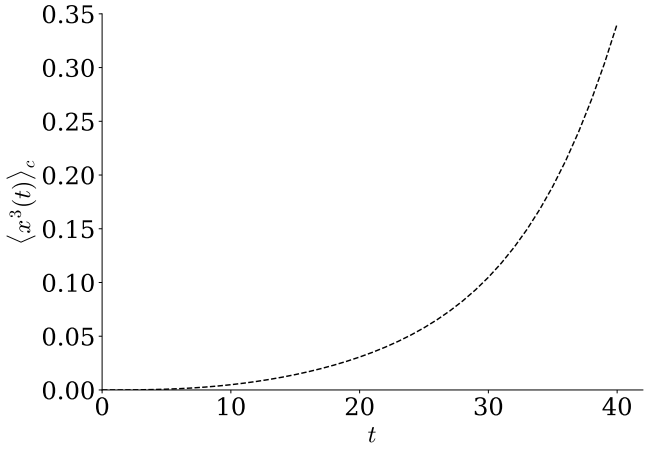

Figure 2: The evolution of the third-order cumulant $\langle x^3\rangle_c$ as functions of time. The initial distribution is given by Eqn. (16) with $\theta = \pi/8$ and $\phi = \pi/4$. Other parameters are set to $\Omega = \bar{a}_7 = 10^{-2}, \beta = 5\times10^{-3}, \chi = 0.25, \bar{\lambda}_2 = 10^{-3}, \Delta_1 = 4\times10^{-2}, \bar{\lambda}_3 = 3\times10^{-2}, \Delta_3 = \bar{\delta}_3 = \bar{a}_2 = 3\times10^{-3}, \Delta_4 = 9\times10^{-2}, \bar{a}_8 = 6\times10^{-3}, \bar{\delta}_1 = 9\times10^{-3}$, and $\bar{\delta}_2 = 2\times10^{-2}$.

5 Conclusion

In this contribution, we outlined the microscopic derivation of a completely positive master equation for OQBM using the adiabatic elimination of fast variables method for a weakly driven open Brownian particle confined in a harmonic potential and dissipatively coupled to a thermal bath. We numerically solve the derived master equation for a reduced density matrix of the OQBM for Gaussian and non-Gaussian initial conditions. Both examples show how the OQBM dynamics converge to Gaussian distributions even for the non-Gaussian initial distribution. We found that the third-order cumulant $\langle x^3\rangle_c$ does not vanish, indicating deviations from Gaussianity. The OQBM master equation describes an example of quantum-classical master equations, which now seem to be finding application in various fields, including gravity theories [22, 23, 24]. Future studies along this line of research will explore the generalization of OQBM to gravity-related theories.

References

[1] S. Attal, F. Petruccione, C. Sabot, and I. Sinayskiy, *Phys. Lett. A* **376**, 1545 (2012); *J. Stat. Phys.* **147**, 832 (2012).

[2] H.-P. Breuer and F. Petruccione, *The Theory of Open Quantum Systems* (Oxford University Press, Oxford, 2002).

[3] K. Kraus, *States, Effects and Operations: Fundamental Notions of Quantum Theory* (Springer-Verlag, Berlin, 1983).

[4] Y. Aharonov, L. Davidovich, and N. Zagury, *Phys. Rev. A* **48**, 1687 (1993).

[5] J. Kempe, *Contemp. Phys.* **44**, 307 (2003).

[6] I. Sinayskiy and F. Petruccione, *Phys. Scr.* **T 151**, 014077 (2012).

[7] I. Sinayskiy and F. Petruccione, *Eur. Phys. J. Spec. Top.* **227**, 1869 (2019).

[8] M. Bauer, D. Bernard, and A. Tilloy, *Phys. Rev. A* **88**, 062340 (2013); *J. Stat. Mech.* **2014**, P09001 (2014).

[9] I. Sinayskiy and F. Petruccione, *Phys. Scr.* **2015**, 014017 (2015).

[10] I. Sinayskiy and F. Petruccione, *Fortschr. Phys.* **65**, 1600063 (2017).

[11] A. Zungu, I. Sinayskiy and F. Petruccione, *arXiv:2503.10379* (2025).

[12] H. A. Kramers, *Physica* **7**, 284 (1940).

[13] N.G. Van Kampen, *Phys. Rep.* **124**, 69 (1985).

[14] C. Gardiner, *Handbook of stochastic methods* (Springer, Berlin, 1985).

[15] A. Caldeira and A. Leggett, *Phys. A* **121**, 587 (1983); *Ann. Phys. (NY)* **149**, 374 (1983).

[16] B. Thimmel, P. Nalbach, and O. Terzidis, *Eur. Phys. J. B* **9**, 207 (1999).

[17] A. Zungu, I. Sinayskiy and F. Petruccione, *Microscopic derivation of completely positive master equation for the description of open quantum Brownian motion of a particle in a potential*, in preparation.

[18] M. O. Scully and M. S. Zubairy, *Quantum Optics* (Cambridge University Press, Cambridge, 1997).

[19] H. J. Carmichael, *Statistical Methods in Quantum Optics 1: Master Equations and Fokker-Planck Equations* (Springer, Berlin, 2002).

[20] V. Gorini, A. Kossakowski, and E. C. G. Sudarshan, *J. Math. Phys.* **17**, 821 (1976).

[21] G. Lindblad, *Commun. Math. Phys.* **48**, 119 (1976).

[22] L. Diósi, *J. Phys. Conf. Ser.* **306**, 012006 (2011).

[23] I. Layton, J. Oppenheim, and Z. Weller-Davies, *Quantum* **8**, 1565 (2024); I. Layton and J. Oppenheim, *PRX Quantum* **2**, 020331 (2024).

[24] A. Tilloy, *SciPost Physics* **17**, 083 (2024).

Fluorinated Graphdiyne under Strain: A First-Principles Study of Electronic and Optical Properties

N Saghir[1], G J Rampho[1] and M Khenfouch[2]

[1]Department of Physics, University of South Africa (UNISA), 28 Pioneer Avenue, Florida Park, Roodepoort, Johannesburg, South Africa.
[2]Materials, Electrical Systems, Energy and Environment Laboratory (LMS3E), Materials and Energy Engineering Group, Faculty of Applied Sciences, Department of Applied Physics, Ait Melloul, Ibn Zohr University, 86153 Agadir, Morocco.

E-mail: 58564160@mylife.unisa.ac.za

Abstract. Fluorine-doped graphdiyne, a modified two-dimensional carbon allotrope, offers promising tunability of electronic properties for flexible electronics and optoelectronic applications. Using first-principles calculations based on density functional theory, this study systematically investigates the influence of tensile strain on the electronic and optical properties of fluorine-doped graphdiyne. The results reveal that the fluorine-doped graphdiyne exhibits a direct band gap that shows a strong dependence on mechanical strain, increasing from 0.76 eV to 1.98 eV at 12% biaxial strain, demonstrating pronounced strain sensitivity. Under biaxial tensile strain, the band gap increases progressively with increasing strain, indicating effective modification. Additionally, tensile strain enhances the thermodynamic stability of the 4% and 8% biaxial strain framework. Furthermore, the optical absorption of the strained fluorine-doped graphdiyne. is enhanced under strain, particularly in the visible range, making it a promising candidate for flexible optoelectronic and photovoltaic applications.

1 Introduction

Graphdiyne (GDY), a novel two-dimensional (2D) carbon allotrope composed of sp and sp^2-hybridized carbon atoms, has garnered significant attention for its unique electronic structure, natural band gap, and high carrier mobility [1,2]. Unlike graphene, GDY possesses a direct band gap (~1.22 eV) [3], making it inherently suitable for electronic and optoelectronic applications where the ideal range is comparable to that of silicon (≈1.1 eV). Due to its porous structure and chemical versatility, GDY has shown potential in a wide range of fields, including energy storage [4], catalysis [5], energy conversion [6], and nano electronics [7].

Heteroatom doping is an effective strategy to tailor the electronic, chemical, and structural properties of two-dimensional materials. Among various dopants such as nitrogen, boron, and chlorine, fluorine is particularly attractive because of its highest electronegativity, strong electron-withdrawing ability, and small atomic radius, which allow it to significantly alter local charge distribution and bonding without severely distorting the carbon lattice. Previous studies have demonstrated that fluorine incorporation can effectively modulate band structure, improve chemical stability, and enhance adsorption properties of GDY-based systems [8, 9, 10-12]. These modifications can enhance chemical reactivity and enable precise control over GDY's semiconducting behaviour.

Additionally, strain engineering is a widely used technique to tune the band structure of 2D materials without altering their chemical composition [13, 14]. Applied tensile or compressive strain can significantly impact charge transport, band dispersion, and stability. While pristine and doped GDY have been studied under strain

[15], the combined effect of fluorine doping and mechanical deformation remains unexplored. This work investigates the electronic and optical properties of fluorine-doped GDY (C_16 F_2) (FGDY) under biaxial strain using density functional theory (DFT). By systematically analyzing strain-induced changes in the band structure, density of states (DOS), and absorption, we demonstrate how doping and strain synergistically tune the optoelectronic characteristics of GDY, providing valuable insights for its use in flexible electronics, strain sensors, and adaptive optoelectronic devices.

2 Computational details

First-principles calculations were conducted using the CASTEP module within the Materials Studio framework [16], based on density functional theory (DFT). The generalized gradient approximation (GGA) using the Perdew–Burke–Ernzerhof (PBE) functional was employed for geometry optimization, while the screened hybrid functional HSE06 was applied for single-point electronic structure calculations to overcome the well-known underestimation of band gaps inherent in GGA [17]. Spin effects were neglected in all simulations. A plane-wave cutoff energy of 450 eV and a 6×6×1 Monkhorst–Pack k-point grid were used for Brillouin zone sampling. To simulate isolated monolayers, a 15 Å vacuum was introduced along the z-axis normal to the GDY plane.

The system was fully relaxed with convergence criteria of 2.0×10^{-6} eV/atom for total energy and 0.05 eV/nm for atomic forces. All electronic property analyses were based on these relaxed structures [18]. A 2×2×1 supercell of fluorine-doped GDY (FGDY) was constructed, and biaxial tensile strain was applied by varying the in-plane lattice parameters symmetrically. During strain application, the cell vectors were modified according to the desired strain percentage, while the internal atomic positions were allowed to relax ensuring that the imposed strain was maintained without artificially constraining atomic displacements. This approach allowed the structure to reach its equilibrium configuration under each strain condition. The formation energy was computed using the conventional total-energy difference between the doped and pristine structures with elemental reference chemical potentials. The optimized atomic configuration of the fluorine-doped graphdiyne monolayer and the directions of the applied biaxial tensile strain are illustrated in Figure 1.

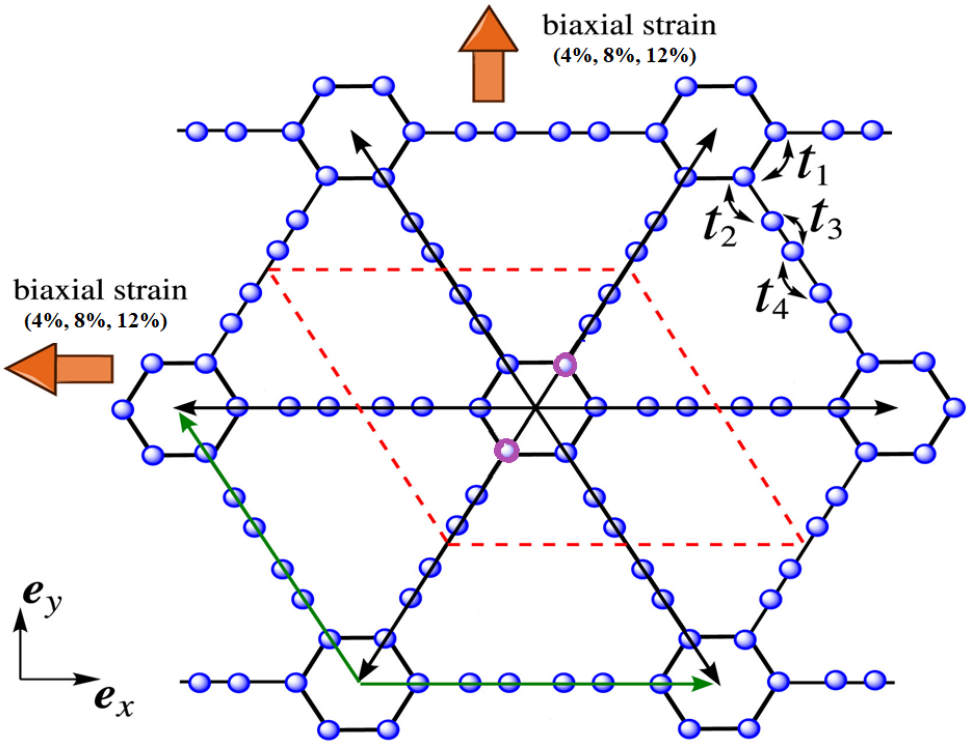

Figure 1: Optimized atomic structure of fluorine-doped graphdiyne (FGDY) showing the directions of applied symmetrical biaxial tensile strain. Grey spheres represent carbon atoms, and light-green spheres denote fluorine atoms. The bond types t_1, t_2, t_3, and t_4 correspond to distinct C–C linkages within the hexagonal and acetylenic units of the GDY lattice. Arrows indicate the in-plane biaxial tensile strain applied along both the x and y directions.

3 Results and discussions

3.1 Geometrical Structures

To determine the structure's stability, we calculated the formation energies of the strained structure. The computed results are displayed in Table 1.

Strain type	Lattice constant (Å)	Band gap (eV)	Formation energy (eV)
Unstrained	18.762	0.760	-2.93
Biaxial 4%	19.512	0.831	-3.05
Biaxial 8%	20.263	1.120	-3.13
Biaxial 12%	21.013	1.981	-2.72

Table 1: Calculated lattice constants, electronic band gaps, and formation energies of fluorine-doped graphdiyne (FGDY) under varying biaxial tensile strain (0 %, 4 %, 8 %, and 12 %). The increasing band gap and variation in formation energy reflect the influence of strain on the electronic and thermodynamic stability of the structure.

As seen in Table 1, the formation energy becomes more negative from 0 % to 8 % strain (−2.93 → −3.13 eV), indicating increased thermodynamic stability up to 8 %. At 12 %, it increases (becomes less negative) to −2.72 eV, implying reduced thermodynamic favorability at higher strain. The overall negative formation energies for all cases confirm that the strained FGDY systems are energetically favorable. The optimized lattice constant of unstrained FGDY (18.762 Å) is in close agreement with previously reported values for pristine GDY (18.70 Å [9]) and fluorinated GDY (18.75 Å [18]), confirming the reliability of the computational setup and optimization parameters. The average C–C bond length increases from 1.41 Å (unstrained) to 1.45 Å and 1.48 Å at 4 % and 8 % strain, respectively, while the C–F bond length expands slightly from 1.38 Å to 1.40 Å at 12 % strain. These gradual elongations confirm that tensile strain weakens orbital overlap between C and F atoms, which explains the observed widening of the band gap.

3.2 Electronic Properties

The combined effect of fluorine doping, along with applied strain, alters the lattice parameters and atomic configuration of graphdiyne, thereby significantly influencing its electronic properties.

3.2.1 Band Structures and Density of States Figure 2 illustrates the electronic band structures of pristine and biaxial strained graphdiyne (FGDY) under 4%, 8%, and 12% strain, and computed using the hybrid HSE06 functional, which is known for yielding more accurate band gap predictions [18]. A dense k-point grid of 40×40×1 was employed to ensure convergence of the electronic properties. As shown in Fig. 2(a), the unstrained GDY exhibits a direct band gap of 0.760 eV. Upon applying 4% biaxial strain, Fig. 2(b) reveals a slight increase in the band gap to 0.831 eV, maintaining its direct nature. At 8% strain, as illustrated in Fig. 2(c), both the conduction band minimum (CBM) and valence band maximum (VBM) remain located at the high symmetry point K of the Brillouin zone, confirming a direct band gap of 1.120 eV. Further increasing the strain to 12% significantly widens the band gap to 1.981 eV, as seen in Fig. 2(d). Among all configurations, 12% strained FGDY shows the largest band gap, followed by 8% and 4%, with the unstrained structure having the smallest band gap.

The total and partial density of states (DOS) of FGDY under different strain levels provide further insight into the orbital origins of the band-structure evolution. In the unstrained system, the valence-band maximum (VBM) is mainly contributed by C-2p orbitals with minor hybridization from F-2p states, while the conduction-band minimum (CBM) originates predominantly from C-2p antibonding orbitals. As biaxial strain increases to 4 % and 8 %, these C-2p and F-2p peaks shift toward higher energy, widening the band gap in agreement with the band-structure results. At 12 % strain, the DOS shows a clear separation between valence and conduction states, corresponding to a gap of approximately 1.98 eV, consistent with the direct gap predicted from the HSE06 band structures. The progressive shift of the DOS peaks and reduction in their overlap demonstrate that tensile strain weakens C–C and C–F orbital interactions, thereby tuning the electronic dispersion and enhancing semiconducting behaviour.

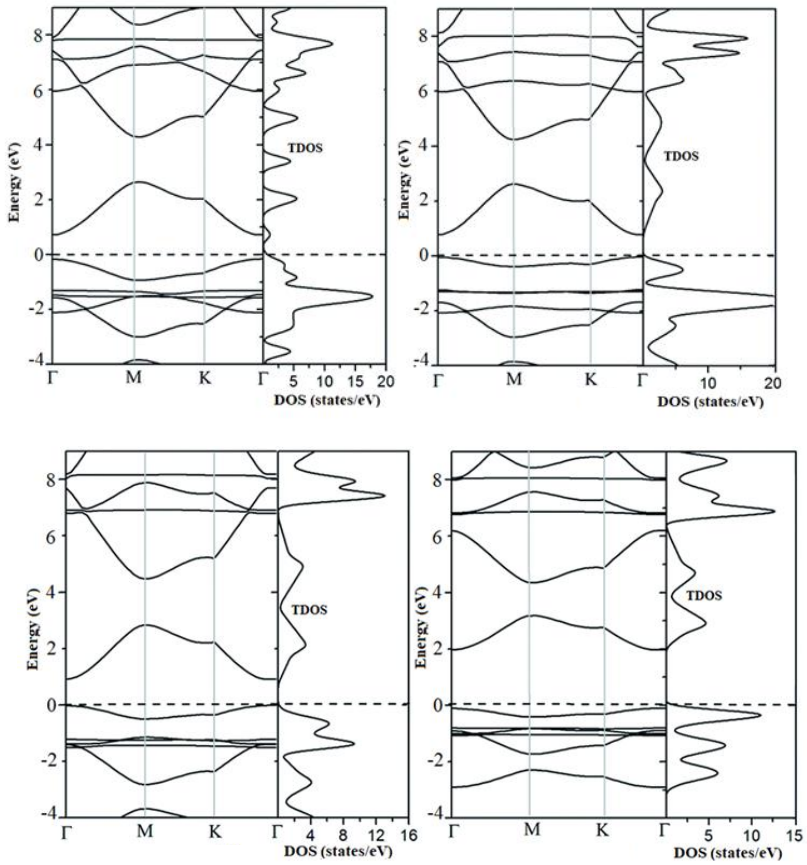

Figure 2: Total density of states and band gap structures for: (*top left*) Unstrained GDY. (*top right*) 4% Biaxially-strained GDY (*bottom left*) 8% Biaxially-strained GDY. (*bottom right*) 12% Biaxially-strained GDY.

3.3 Optical Properties

3.3.1 Absorbance and Dielectric function The optical response of fluorine-doped graphdiyne was analyzed in terms of the complex dielectric function, $\varepsilon(\omega) = \mathrm{Re}\,\varepsilon(\omega) + \mathrm{Im}\,\varepsilon(\omega)$, where Re ε(ω) and Im ε(ω) represent the real and imaginary components, respectively. The symbols E∥x and E∥y denote light polarized parallel to the in-plane *x* and *y* directions. A real as well as imaginary component of the dielectric function for both the unstrained and strained (with a strain of 4%, 8% and 12%) C12F2 monolayers was computed for light polarized in-plane along the *x*- and *y*-directions. These results are presented in Figure 4. It is evident that the optical spectra of the 8% and 12% biaxially strained monolayers exhibit isotropy with respect to light polarized along the *x*- and *y*-axes, whereas unstrained and 4% biaxial strain induces anisotropy. Furthermore, for all structures, the optical response demonstrates significant anisotropy within the in-plane directions. For the biaxial 8% monolayer, the first peak in the imaginary part of the dielectric function, Imε_αβ (ω), occurs at 1.15 eV for light polarized within the plane. Noticeably, applying biaxial strain 4%, 8% and 12% causes a slight blue shift (shift to higher energy) of the absorption edge in Imε for E∥x at low frequencies. Conversely, the absorption edge of Imε for E∥y shifts toward lower energies under 4% biaxial strain. Along the E∥x direction, the $C_{16}F_2$ monolayer exhibits a static dielectric constant (Reε_0) of 3.71. Under 12% biaxial strain, Reε_0 decreases in all polarization directions. Under 12% biaxial strain, the static dielectric constant rises in the E∥x direction but drops in the E∥y direction. Figure 5 displays an absorption coefficient, α_{ij} (ω), for each polarization direction. Under in plane polarization, both the unstrained and strained C16F2 monolayers exhibit their first absorption band between 1.08 eV and 1.48 eV, falling in the infrared to near infrared region. This initial peak originates at the Γ point and arises from electron transitions between 1C dominated valence states and F dominated conduction states. A second absorption band appears near 1.78 eV for both x and y directions for every structure examined, placing it within the visible range—an energy window well suited to optoelectronic applications. The most intense absorption feature for in plane polarization is broad, extending over approximately 3.41 eV to 5.19 eV.

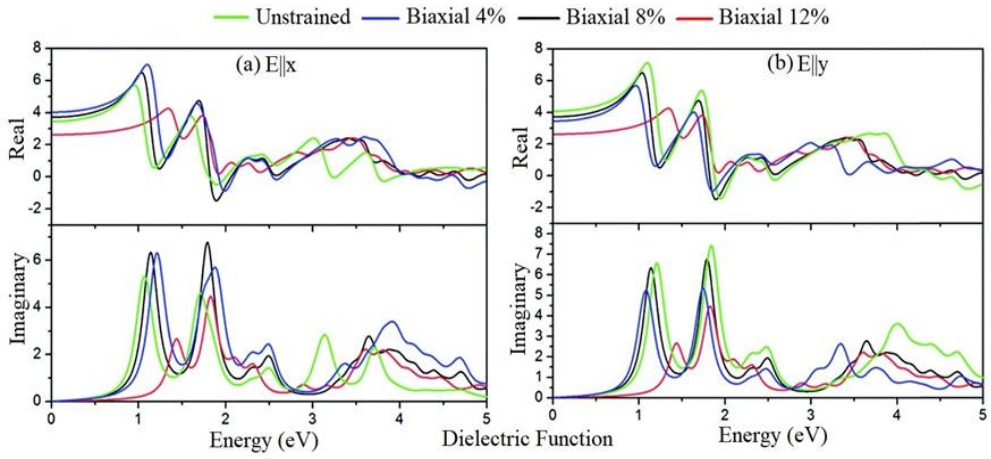

Figure 3: Graphs of Dielectric function for monolayer FGDY unstrained and with biaxial strain (4%, 8%, and 12%) for light polarized within the plane along the x and y directions.

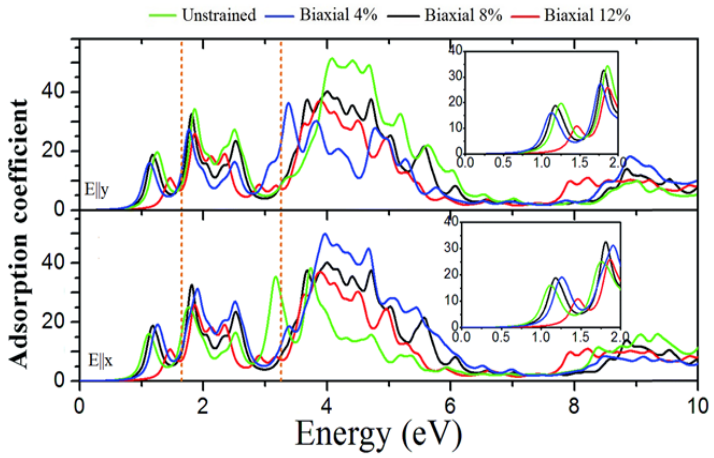

Figure 4: Graph of absorption coefficient for monolayer FGDY unstrained and with biaxial strain (4%, 8%, and 12%) for the in-plane (E||x and E||y) light polarizations.

4 Conclusion

The present study investigates how fluorine doping under biaxial strain influences the electronic and optical behavior of graphdiyne (FGDY) using first-principles DFT calculations. The results demonstrate that FGDY possesses a tunable direct band gap, which increases systematically with the application of strain—from 0.76 eV (unstrained) to 1.98 eV at 12% biaxial strain—highlighting its strong strain-dependent electronic characteristics. This band gap modulation is attributed to the strain-induced elongation of C–C bonds and modified orbital interactions that reduce overlap between the valence and conduction bands.

The structural stability of FGDY improves under moderate strain, as evidenced by the increasingly negative formation energies at 4% and 8% strain. However, beyond 8%, a decrease in formation energy suggests a threshold beyond which stability begins to diminish. Optical analysis further reveals that strain not only enhances light absorption but also causes notable shifts in the dielectric function and absorption spectra. In particular, biaxial strain induces a blue shift in the absorption edge for E||x polarization, while the dielectric response becomes increasingly isotropic at higher strain levels. The strong and broad absorption in the visible range (1.80–5.19 eV) under strain underscores the potential of FGDY for optoelectronic applications.

Overall, the synergistic effects of fluorine doping and mechanical strain offer an effective approach for engineering the band structure and optical response of graphdiyne, making FGDY a promising candidate for flexible electronics, strain sensors, and next-generation optoelectronic devices.

References

[1] D. Malko, C. Neiss, F. Viñes, and A. Görling, "Competition for graphene: Graphynes with direction-dependent Dirac cones," *Phys. Rev. Lett.*, 108, 086804 (2012).

[2] G. Li, Y. Li, H. Liu, Y. Guo, Y. Li, and D. Zhu, "Architecture of graphdiyne nanoscale films," *Chem. Commun.*, 46, 3256–3258 (2010).

[3] X. Zhang, Y. Li, H. Zhou, and Z. Liu, "Electronic and optical properties of graphdiyne and its derivatives: A first-principles insight," *Mater. Today Commun.*, 109622 (2024).

[4] S. Zhang, M. Xie, F. Li, Z. Yan, H. Zhang, J. Wang, and Y. Liu, "Semiconducting group 15 monolayers: A broad range of band gaps and high carrier mobilities," *ACS Appl. Mater. Interfaces*, 8(13), 8467–8473 (2016).

[5] X. Gao, H. Liu, D. Wang, and Y. Li, "Graphdiyne: A promising carbon allotrope for versatile applications," *Nat. Commun.*, 3, 884 (2012).

[6] X. Zhang, Y. Li, H. Zhou, and Z. Liu, "Graphdiyne: The Emerging Energy Conversion Material," *Adv. Funct. Mater.*, 35, 24691 (2025).

[7] Y. Xu, X. Zhu, C. Li, and Y. Liu, "Ultrathin graphdiyne membranes for efficient hydrogen separation," *Nat. Nanotechnol.*, **13**, 766–772 (2018).

[8] R. Li, T. Chen, P. Zhao, and X. Zhang, "Doped-graphdiyne: Synthesis, Theoretical Prediction and Applications," *Nanoscale Horiz.*, 10, 201 (2025).

[9] M. Han, J. Zhao, and C. Liu, "Nitrogen and Fluoride Co-Doped Graphdiyne with Metal Interfaces for Enhanced Catalytic Activity," *Carbon*, 211, 2337 (2023).

[10] Y. Guo, L. Zhang, Q. Liu, and Y. Li, "Electronic properties and stability of fluorine-doped graphdiyne: A first-principles study," *Carbon*, 195, 135–144 (2022).

[11] R. Zhao, T. Wang, H. Jiang, and X. Zhou, "Surface and electronic modulation of fluorinated graphdiyne under external perturbations," *Appl. Surf. Sci.*, 610, 155416 (2024).

[12] C. Peng, J. Chen, M. Li, and S. Yu, "Optoelectronic response and charge redistribution in fluorinated graphdiyne monolayers," *J. Phys. Chem. C*, 126, 21384–21392 (2022).

[13] L. Chen, X. Zhou, and P. Ye, "Strain-Modulated Defect Engineering of Two-Dimensional Materials," *npj 2D Mater. Appl.*, 8, 472 (2024).

[14] Y. Wang, C. Cong, and T. Yu, "Raman spectroscopy study of mechanically strained monolayer graphene," *Nano Res.*, 7, 441–449 (2014).

[15] J. Liu, Y. Wang, W. Li, Z. Wang, and J. Wang, "Strain-dependent electronic and optical properties of monolayer black phosphorus," *J. Appl. Phys.*, 121, 185701 (2017).

[16] B. Tang, Q. Luo, Q. Zhang, Z. Wu, and Z. L. Ran, "First-principles study of strained graphyne structures," *J. Synth. Cryst.*, 43, 1269–1274 (2014).

[17] J. P. Perdew, K. Burke, and M. Ernzerhof, "Generalized gradient approximation made simple," *Phys. Rev. Lett.*, 77, 3865–3868 (1996).

[18] G. L. Liu, S. Zhou, and D. Z. Fan, "Electronic structure of strained graphdiyne," *J. Shenyang Univ. Technol.*, 39, 622–626 (2017).

Laplacian eigenmodes in twisted periodic topologies for new physics models

Anele Ncube[1,2], Aldo Deandrea[2,1], Alan S. Cornell[1] and Rhameez S. Herbst[3]

[1] Department of Physics, University of Johannesburg, PO Box 524, Auckland Park 2006, South Africa.
[2] Université Claude Bernard Lyon 1, CNRS/IN2P3, IP2I UMR 5822, 4 Rue Enrico Fermi, F-69100 Villeurbanne, France.
[3] Department of Mathematics and Applied Mathematics, University of Johannesburg, PO Box 524, Auckland Park 2006, South Africa.

E-mail: ancube@uj.ac.za

Abstract. Laplacian eigenmodes in non-trivial topologies (e.g. having twisted periodicity) are important in constructing a complete picture of the physics at play within models that incorporate compact extradimensional spaces. Determining these eigenmodes analytically is generally unwieldy, and the existing standard numerical methods have limited ability as spatial dimensions increase and when computing higher-index eigenmodes is required. To determine the feasibility of using physics-informed neural networks to compute Laplacian eigenmodes, we apply them to three primitive test cases: the Möbius strip, the real projective plane ($\mathbb{R}P_2$) and the 3-torus ($\mathbb{T}_3$) in Cartesian coordinates. The potential performance of the neural networks approach beyond solving the simpler cases is estimated in terms of the approximation errors obtained by comparing them with known analytical solutions.

1 Introduction

The reduction of extra dimensions (i.e. compactification) is a crucial route for achieving the phenomenology of new physics in extra dimensions [1]. Compactification has its roots in seminal works, such as Ref. [2], where masses were generated in 4D space-time induced by higher-dimensional supergravity [3]. Subsequently, further realisations of compactification have considered, to a greater extent, extradimensional spaces with flat metrics, and, to a lesser extent, those with curved metrics, though phenomenologically the latter provide more interesting properties. For example, curved spaces give rise to a potential for specific 4D scalar fields, which gives them masses not arising otherwise [1]. Among negatively curved spaces, a special case is the nilmanifold, a manifold that has found use as a compactification scheme for Type II string theories and M theory, e.g. see Refs. [4, 5].

An n-nilmanifold (here n denotes the number of spatial dimensions) is a smooth manifold $\mathcal{M}_n$ obtained by quotienting a nilpotent Lie group A by a discrete subgroup Γ, i.e. $\mathcal{M}_n = A/\Gamma$. In general, Lie groups can be viewed as n-dimensional manifolds [6]. For the 3-nilmanifold, the Lie group of concern is the Weyl group, which is the only solvable Lie group in 3D [3]. Given that the associated Lie algebra is the Heisenberg algebra, $\mathcal{M}_3$ is otherwise known as the Heisenberg nilmanifold. For the Heisenberg algebra

$$[V_1, V_2] = -\mathtt{f} V_3, \quad [V_1, V_3] = [V_2, V_3] = 0, \tag{1}$$

where $\mathtt{f}$ is a structure constant, the terms $V_{a=1,2,3}$ are contravariant vectors from which Maurer-Cartan one-forms $e^{a=1,2,3}$ (i.e. covariant vectors) can be determined [3]. The V_a and e^a terms form the basis of the (co)-tangent space of $\mathcal{M}_3$ whose metric in terms of the one-forms is [6]

$$ds^2 = (e^1 + ae^3)^2 + (e^2 + be^3) + c^2(e^3)^2; a, b \in \mathbb{R}, \tag{2}$$

where c is not a true parameter and can be set to unity without loss of generality.

$\mathcal{M}_3$ is parameterised by dimensionless angular coordinates $x^{m=1,2,3} \in [0, 1]$ related to the Maurer-Cartan one-forms according to [1, 6]

$$e^1 = r^1 dx^1; \quad e^2 = r^2 dx^2; \quad e^3 = r^3(dx^3 + Nx^1 dx^2); \quad N = \frac{r^1 r^2}{r^3}\mathtt{f} \in \mathbb{Z}^*, \tag{3}$$

with $r^{m=1,2,3}$ being radii (they have units of length same as $e^{m=1,2,3}$). The topology of $\mathcal{M}_3$ is represented by discrete (or "twist") identifications describing how a unit cube, with $x^{m=1,2,3}$ as coordinates, is deformed via the joining of points on opposite faces to construct this space. They are the following

$$(x^1, x^2, x^3) \sim (x^1, x^2 + 1, x^3) \sim (x^1, x^2, x^3 + 1) \sim (x^1 + 1, x^2, x^3 - Nx^2). \tag{4}$$

These identifications lead to the interpretation of $\mathcal{M}_3$ as a twisted fibration over a circle (in other words, a 2-torus in the x^2 and x^3 directions with changing geometry along the base circle parameterised by x^3, the fibre coordinate) [3, 6]. As such, $\mathcal{M}_3$ may be thought of as a twisted torus, a concept that can be applied in more general terms to nilmanifolds with spatial dimensions higher than $n = 3$.

The Laplacian on $\mathcal{M}_3$ has been used as a tractable example to construct the phenomenology of fields for toy models (e.g. scalars [6], gauge bosons [1] and spinors [7]) in extra dimensions. Mathematically, we have at hand a Sturm-Liouville problem that can be solved analytically, giving closed-form expressions for the associated eigenvalue spectrum. Concerning the physical significance of the solutions, the eigenvalues of the Laplacian correspond to masses, and the eigenfunctions provide a natural expansion basis for fields in extra dimensions. For more detailed models of negatively curved spaces, numerical analysis becomes necessary; however, common approaches (as found in most textbooks) are limited by the non-trivial and convoluted nature of the spaces involved.

This work focuses on testing physics-informed neural networks (PINNs) as a new numerical approach to the Laplacian on non-trivial topologies, beginning with calculable cases in $n = 2$ and 3 dimensional spaces with flat metrics. Ultimately, the aim is to test PINNs on the Laplacian on $\mathcal{M}_3$. As such, Section 2 will review the Laplacian on various spaces, starting with the relatively simple (i.e. the Möbius strip and real projective plane both in 2D space, and the 3-torus in 3D) and building up to the not so simple case of $\mathcal{M}_3$. Results of numerical analysis (using PINNs) of the Laplacian on each of these spaces are given in Section 3, where the performance of the PINN approach is reported in terms of relative mean square errors. Finally, discussions on the advantages of PINNs and their potential applicability in more challenging, less tractable extradimensional cases are discussed in the last section (Section 4).

2 Theory

To explore the Laplacian on $\mathcal{M}_3$ using numerical analysis, it is natural to first consider related spaces that represent simple building blocks by which $\mathcal{M}_3$ is constructed. These simpler spaces shall be described in this section, followed by the expressions of their eigenvalue spectra. Thereafter, the eigenvalues expected from $\mathcal{M}_3$ are given. Note that, in general, the Laplacian of a scalar field is

$$\nabla^2\Phi = \frac{1}{\sqrt{g}}\partial_m(\sqrt{g}g^{mn}\partial_n\Phi), \tag{5}$$

where g_{mn} is the metric for our flat-space Möbius strip, $\mathbb{R}P_2$ and $\mathbb{T}_3$, with $m, n = 1, 2, 3$. Therefore, the Laplacian is simply

$$\nabla^2\Phi = (\partial_1^2 + \partial_2^2 + \partial_3^2)\Phi. \tag{6}$$

Setting $a = b = 0, c = 1$; $r^1 = r^2 = r^3 = 1$ and $\mathtt{f} = 1$, the metric of $\mathcal{M}_3$ (i.e. Equation 2) has components [6]

$$g_{11} = 1; \quad g_{22} = 1; \quad g_{23} = g_{32} = 1; \quad g_{33} = 1 + x^2, \tag{7}$$

where $g = 1$ and the Laplacian is given as

$$\nabla^2\Phi = (\partial_1^2 + (\partial_2 - x^1\partial_3)^2 + \partial_3^2)\Phi. \tag{8}$$

Imposing the relevant topology-based boundary conditions (i.e. discrete identifications), Equations (6) and (8) can be solved analytically using the method of separation of variables for the former and the Hermite differential

equation for the latter. While Equation (4) dictates the twisted periodic boundary conditions for $\mathcal{M}_3$, the relevant identifications for the simpler spaces are for the

$$\text{Möbius strip:} \quad (x^1, x^2) \sim (x^1 + 1, -x^2), \quad x^{m=1,2} \in [-0.5, 0.5]^2; \tag{9}$$

$$\mathbb{R}P_2: \quad (x^1, x^2) \sim (x^1 + 1, -x^2) \sim (-x^1, x^2 + 1), \quad x^{m=1,2} \in [-0.5, 0.5]^2; \tag{10}$$

$$\mathbb{T}_3: \quad (x^1, x^2, x^3) \sim (x^1, x^2 + 1, x^3) \sim (x^1 + 1, x^2, x^3) \sim (x^1, x^2, x^3 + 1), \quad x^{m=1,2,3} \in [0, 1]^3. \tag{11}$$

For the Möbius strip, apart from the periodic boundary condition, there is a Dirichlet boundary condition; namely: $\Phi(x^1, 0.5) = \Phi(x^1, -0.5) = 0$. The corresponding eigenvalue spectra (λ) are [6, 8, 9]

$$\text{Möbius strip:} \quad \lambda^2_{n_1,n_2} \supset \left\{\pi^2 \left(n_1^2 + n_2^2\right)\right\}_{\substack{n_1 \in \mathbb{Z}; n_2 \in \mathbb{N}\setminus\{0\} \\ n_1+n_2 \text{ odd}}}, \tag{12}$$

$$\mathbb{R}P_2: \quad \lambda^2_{n_1,n_2} \supset \left\{\pi^2 \left(n_1^2 + n_2^2\right)\right\}_{n_1,n_2 \in \mathbb{Z},} \tag{13}$$

$$\mathbb{T}_3: \quad \lambda^2_{n_1,n_2,n_3} \supset \left\{4\pi^2 \left(n_1^2 + n_2^2 + n_3^2\right)\right\}_{n_1,n_2,n_3 \in \mathbb{Z}}. \tag{14}$$

Note the two-fold and three-fold degeneracies in the 2D and 3D cases, respectively. The corresponding eigenfunctions can be found in Refs. [6, 9]. For $\mathcal{M}_3$ there are two families of eigenstates; namely, $\mathbb{T}_2$ modes satisfying the x^3 independent form of Equation (8) and fibre modes satisfying the x^3 dependent Laplacian. In this case, we have

$$\mathbb{T}_2: \quad \mu^2_{p,q} \supset \left\{4\pi^2 \left(p^2 + q^2\right)\right\}_{p,q \in \mathbb{Z}}, \tag{15}$$

$$\mathcal{M}_3: \quad M^2_{n,k,\ell} \supset \left\{(2\pi k)^2 \left(1 + \frac{2n+1}{2\pi|k|}\right)\right\}_{k \in \mathbb{Z}\setminus\{0\}, n \in \mathbb{N}}, \tag{16}$$

where the ℓ index, not appearing in Equation (16), but appearing in the associated eigenfunctions implies degeneracy of level $|k|$, since $0 \leq \ell \leq |k| - 1$. Importantly, note that the associated eigenfunctions on $\mathcal{M}_3$ are non-separable in the coordinates $x^{m=1,2,3}$, unlike the associated eigenfunctions on the other simpler spaces. Both Equations (15) and (16) form complete sets of eigenvalues whose corresponding eigenmodes can naturally serve as expansion bases for fields in higher-dimensional spaces. Note also that the eigenvalues scale with the sizes of the spaces and the specific forms given are relevent for the specified radii and lengths for the sides of the deformed unit squares and unit cubes.

3 Numerical analysis

Knowing the exact solutions of the Laplacian on some example 2D and 3D spaces, numerical methods like PINNs can be tested, allowing us to infer their potential performance in problems that are non-trivial, not easily calculable (due to the negative spatial curvature). Some of the calculable cases also provide physically interesting properties, which make them, in their own right, worth studying.

3.1 Principle of the analysis

Using PINNs, we begin with an ansatz consisting of many tunable parameters to be updated based on the evaluation of the Laplacian and the relevant boundary conditions at selected points (i.e. the unlabelled training points). Since no approximation is required to numerically evaluate the derivatives like mesh-based methods (e.g. using the Cornish & Turok approach [10]), the contribution of truncation errors to numerical errors is alleviated. Given below is the algorithm followed by the PINN approach, where note that the terms w^ℓ_{jk} and b^ℓ_j denote the tunable weights of the neural network (NN) ansatz $f(x_i)$ serving as the approximate solution to the differential equation. To facilitate the solving of a differential equation, the same is embedded in the loss function $\mathcal{L}$ that includes the physical constraints and extra terms that penalise $f(x_i) = 0$ and enforce the scanning of $\hat{E}$ in the positive direction. With the latter loss term, training over a set number of epochs encourages the learning of several $\hat{E}$ (note: an epoch consists of a single run through the entire training data). The total loss is given generically as

$$\mathcal{L} = \mathcal{L}_{PDE} + \mathcal{L}_{BC} + \mathcal{L}_{\text{extra}}. \tag{17}$$

The loss terms $\mathcal{L}_{PDE}, \mathcal{L}_{BC}$ are mean square errors of the PDE (residual) and the boundary conditions; $\mathcal{L}_{\text{extra}}$ dynamically constrains $f(x_i, \theta)$ and $\hat{E}$. Specifically, $\mathcal{L}_{\text{extra}}$ is given as [11]

$$\mathcal{L}_{\text{extra}} = \frac{1}{\|\hat{f}\|^2} + \frac{1}{\|\hat{E}\|^2} + \|e^{-\hat{E}_{\text{init}} + \hat{E}_{\text{step}}}]\|^2, \tag{18}$$

where the first two terms penalise the $f(x_i) = 0$ and $E = 0$ as solutions to the PDE. The third term enforces the learning of eigenvalues in ascending order as the NN runs through its training loop. To clarify, the algorithm for optimizing ansatz $f(x_i, \theta)$ (by minimising $\mathcal{L}(\theta)$) is

- Initialise $\hat{E} = 1$ and NN ansatz parameters $\theta = \left\{ w_{jk}^{\ell}, b_j^{\ell} \right\}_{1 \leq \ell \leq L}$ randomly from e.g. $U(-\sigma, \sigma)$.
- **For each** epoch **in** training epochs:
  1. **Input** x_i (training points) + **Evaluate** $f(x_i, \theta)$ and $\mathcal{L}(\theta)$.
  2. **Backpropagate:** compute $\dfrac{\partial \mathcal{L}}{\partial \theta} = \left\{ \dfrac{\partial \mathcal{L}}{\partial w_{jk}^{\ell}}, \dfrac{\partial \mathcal{L}}{\partial b_j^{\ell}} \right\}_{1 \leq \ell \leq L}$ with automatic differentiation.
  3. **Update** θ**:** according to your chosen gradient-based (hence the previous step) optimisation algorithm (e.g. ADAM is a standard optimiser) [12].
  4. **Increment** $\hat{E}$ after specified epochs (enforces search for eigenvalue near the new $\hat{E}$).

Möbius strip	$\mathbb{R}P_2$	$\mathbb{T}_3$	$\mathcal{M}_3$
	E_n		$\mu_{p,q}^2$
E_1/2: 4.95	E_2/2: 9.82	E_1/2: 9.87	$\mu_{0,1}^2$/2: 19.74
(0.2928%)	(0.0225%)	(0.0426%)	(0.0265%)
E_2/2: 24.67	E_3/2: 19.74	E_2/2: 19.74	$\mu_{1,1}^2$/2: 39.54
(-0.004%)	(0.0094%)	(-0.0101%)	(0.1450%)
E_4/2: 64.15	E_4/2: 24.81	E_3/2: 29.62	$\mu_{0,2}^2$/2: 78.87
(-0.0087%)	(0.5597%)	(0.0320%)	(-0.1145%)
E_5/2: 83.87	E_5/2: 39.48	E_4/2: 39.46	$\mu_{2,1}^2$/2: 99.33
(-0.0233%)	(0.0018%)	(-0.0351%)	(0.6387%)
E_7/2: 143.11	E_8/2: 64.15	E_5/2: 49.34	$\mu_{2,2}^2$/2: 158.04
(-0.0028%)	(0.0008%)	(-0.0189%)	(0.0769%)

Table 1: First five PINN approximated eigenvalues and their percentage errors.

3.2 Details of the implementation

We used the PyTorch library in Python to implement PINNs using a fully-connected neural network as the architecture, incorporating the PDE of interest in the loss function, and using the ADAM optimiser as our NN update algorithm. For the relatively simple 2D and 3D spaces, solved analytically by trigonometric functions, it was sufficient to use a single hidden-layer NN with input and output nodes dictated by the variables of the PDE. In general, training was carried out for at most $\sim 10^6$ epochs, with a learning rate of $\sim 10^{-1}$ and the number of training points set to 4^n for $n = 2$ or 3 dimensions of space. These are intentionally rough specifications because they are parameters that are not directly determined by the physics at hand. They are instead related to the optimisation algorithm and its optimal configuration in relation to the setup of other parts of the PINN, such as the architecture.

3.3 Results

Table 1 and Figure 1 give the low-lying eigenvalues of the Laplacian on the 2D and 3D spaces of interest. Figure 1 is an example plot of the typical losses and approximations of the eigenvalues generated as training progresses. The tunable parameter representing the eigenvalue (initially set to one) converges on discrete points in eigenvalue space where the PINN loss is minimised. The losses are subsequently pushed out of the minima to scan for higher eigenstates. The duration, in epochs, of convergence to a particular eigenvalue (seen as plateaus in the plot of the PINN approximate eigenvalues) is indirectly controlled by the $\hat{E}_{\text{step}}$ in the last loss term of Equation (18).

As can be inferred from Table 1, the Laplacian on twisted periodic manifolds is well approximated by our mainly standard PINN algorithm with the topology enforced as boundary conditions in the loss function as in

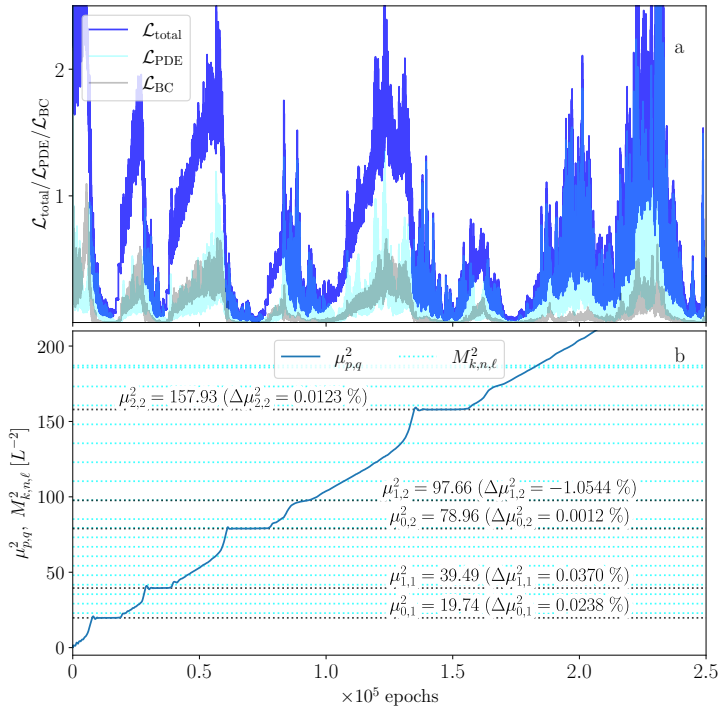

Figure 1: The PINN total loss and it components given in the top panel, and approximations of $\mu^2_{p,q}$ in the bottom panel, as given exactly by Equation 15.

Equation (17). For many of the identified eigenmodes, the accuracy of the approximations relative to the exact values is high (i.e. <1% relative mean square error). However, some eigenvalues (e.g. the $\mu^2_{1,2}$ approximation seen in Figure 1) have larger errors compared to others due to the algorithm spending less time minimising the loss (i.e. learning the eigenvalue) at those values. Partial control of the convergence duration can be achieved by tweaking the $\hat{E}_{\text{step}}$ (reducing it increases the duration, at the cost of reduced speed of adjustment of the eigenvalue parameter).

Given so far are the $\mathbb{T}_2$ modes of the Laplacian in $\mathcal{M}_3$. As can be seen in Figure 1, the $\mu^2_{p,q}$ eigenvalues are learned while the $M^2_{k,n,\ell}$ eigenvalues are not identified. There is, therefore, a limitation to the standard implementation of PINNs in the multivariable contexts where separation of variables occurs by default, making non-separable functions (such as the fibre modes) difficult to learn. What our results show is that twisted periodic topology is not, per se, a challenge for PINNs (nor is dimensionality). This point is borne out by our PINN's favorable performance considering the twisted periodic topology of the Möbius strip and $\mathbb{R}P_2$, and the high-dimensional case of $\mathbb{T}_3$. As such, there is a good chance to numerically determine $M^2_{k,n,\ell}$ for $\mathcal{M}_3$ given an effective modification to the PINN algorithm, currently under investigation.

4 Discussions and Conclusions

This work sought to test a recently developed numerical method based on artificial neural networks [13] in the context of particle physics phenomenology on compactified extradimensional spaces. The task at hand was to solve the Laplacian on the 3-nilmanifold, a space whose topology can be thought of as consisting of several compounding aspects; namely, three spatial dimensions, non-trivial topology, and negatively curved geometry. Since the Möbius strip, $\mathbb{R}P_2$, and $\mathbb{T}_3$ capture these aspects separately, they were naturally the first test cases considered. The accuracy remained comparable across different numbers of dimensions and boundary conditions considered, implying PINNs adapt well in various scenarios. We can attribute this to the use of automatic differentiation in lieu of numerical differentiation, an approach that facilitates exact evaluation of gradients and, as such, avoids the truncation errors of commonly used numerical methods.

Our standard PINN approach runs into challenges when applied to $\mathcal{M}_3$ because the optimisation algorithm favours removing x^3 dependence, such that the problem being solved is the Laplacian on $\mathbb{T}_2$ with eigenvalues $\mu^2_{p,q}$. This is a simpler problem to solve, not only because of the reduced dimensionality and relatively more trivial

periodic boundary conditions, but also because the solution functions are separable (the fibre modes are not). Alleviating this challenge requires enforcing the learning of non-separable functions in problems simultaneously satisfied by two or more families of linearly independent solutions (like we see with the Laplacian on $\mathcal{M}_3$).

Future work will continue to look at twisted periodic topologies, but with more focus on curved geometry, such as the curved Möbius strip that has been studied extensively within the literature using traditional numerical techniques [8, 9]. A more rigorous comparison between PINNs and other established techniques, such as Cornish & Turok [10], would be worth conducting to determine the advantages of the approach more fully. In terms of physically significant problems, the PINN approach could be applied in not analytically tractable cases, such as those involving gauge fields and fermions (no localised fields), the direction followed by Ref. [6].

Acknowledgements
ASC is supported in part by the National Research Foundation (NRF) of South Africa; AMN is supported by iThemba LABS and Campus France.

References

[1] D. Andriot and D. Tsimpis, "Laplacian spectrum on a nilmanifold, truncations and effective theories," *J. High Energy Phys.*, vol. 2018, p. 96, 2018.

[2] J. Scherk and J. H. Schwarz, "How to get masses from extra dimensions," *Nucl. Phys. B*, vol. 153, pp. 61–88, 1979. [Online]. Available: https://www.sciencedirect.com/science/article/pii/0550321379905923

[3] A. Chatzistavrakidis and L. Jonke, "Matrix theory compactifications on twisted tori," *Phys. Rev. D*, vol. 85, p. 106013, May 2012. [Online]. Available: https://link.aps.org/doi/10.1103/PhysRevD.85.106013

[4] S. Kachru, M. B. Schulz, P. K. Tripathy, and S. P. Trivedi, "New supersymmetric string compactifications," *J. High Energy Phys.*, vol. 2003, no. 03, p. 061, apr 2003. [Online]. Available: https://dx.doi.org/10.1088/1126-6708/2003/03/061

[5] C. Hull and R. Reid-Edwards, "Flux compactifications of string theory on twisted tori," *Fortschr. Phys.*, vol. 57, no. 9, pp. 862–894, 2009. [Online]. Available: https://onlinelibrary.wiley.com/doi/abs/10.1002/prop.200900076

[6] D. Andriot, G. Cacciapaglia, A. Deandrea, N. Deutschmann, and D. Tsimpis, "Towards kaluza-klein dark matter on nilmanifolds," *J. High Energy Phys.*, vol. 2016, no. 6, p. 169, 6 2016. [Online]. Available: https://doi.org/10.1007/JHEP06(2016)169

[7] A. Deandrea, F. Dogliotti, and D. Tsimpis, "Dirac operator spectrum on a nilmanifold," *Nucl. Phys. B*, vol. 982, p. 115895, 2022.

[8] T. Kalvoda, D. Krejčiřík, and K. Zahradová, "Effective quantum dynamics on the möbius strip," *J. Phys. A: Math. Theor.*, vol. 53, no. 37, p. 375201, aug 2020. [Online]. Available: https://dx.doi.org/10.1088/1751-8121/ab8b3a

[9] Z. Li and L. R. Ram-Mohan, "Quantum mechanics on a möbius ring: Energy levels, symmetry, optical transitions, and level splitting in a magnetic field," *Phys. Rev. B*, vol. 85, p. 195438, May 2012. [Online]. Available: https://link.aps.org/doi/10.1103/PhysRevB.85.195438

[10] N. J. Cornish and N. G. Turok, "Ringing the eigenmodes from compact manifolds," *Class. Quantum Grav.*, vol. 15, no. 9, p. 2699, sep 1998. [Online]. Available: https://dx.doi.org/10.1088/0264-9381/15/9/016

[11] H. Jin, M. Mattheakis, and P. Protopapas, "Unsupervised neural networks for quantum eigenvalue problems," 2020. [Online]. Available: https://arxiv.org/abs/2010.05075

[12] D. P. Kingma and J. Ba, "Adam: A method for stochastic optimization," 2017. [Online]. Available: https://arxiv.org/abs/1412.6980

[13] M. Raissi, P. Perdikaris, and G. Karniadakis, "Physics-informed neural networks: A deep learning framework for solving forward and inverse problems involving nonlinear partial differential equations," *J. Comput. Phys.*, vol. 378, pp. 686–707, 2019. [Online]. Available: https://www.sciencedirect.com/science/article/pii/S0021999118307125

Electronic and elastic properties of hexagonal molybdenum disulphide

Magopa Kekana[1*, 2], Mokete Mahladisa[1], Malili Matshaba[1], Lucky Sikhwivhilu[2, 3], Bulelwa Ntsendwana[2] and Thuto Mosuang[1]

[1]Department of Physics, University of Limpopo, Polokwane, South Africa
[2]Advanced Materials Division, Mintek, Randburg, South Africa
[2]Department of Chemistry, University of Venda, Thohoyandou, South Africa

E-mail: tshephomcdonald@gmail.com

Abstract. Electronic and elastic properties of hexagonal molybdenum disulphide (MoS_2) are investigated using the full potential all electrons linearised augmented plane waves method. GGA_PBE_sol generalized gradient approximation energy functional was chosen when calculating the electronic structure and elastic properties. Electronic band structure and density of states suggest a semiconductor material with an indirect narrow energy band gap of 1.45 eV pinned at the Fermi level. The GGA_PBE_sol approach was used to compute elastic constants C_{11}, C_{12}, C_{13}, C_{33}, and C_{44}, bulk modulus (B_o), shear modulus (G), Young's modulus (Y), and B_o/G ratio. Deviation of some parameters from related literature results has been addressed.

1 Introduction

Two-dimensional (2D) molybdenum disulphide (MoS_2), a family of transition metal dichalcogenides (TMDs), has attracted tremendous interest in materials technology due to its unique, fascinating physical and chemical properties [1], [2]. Such interest lies in its capability to fulfil future demands in the nano-electronic industry on flexibility, adaptability, and multi-device functionality [2]. As an analogue of graphene, MoS_2 is part of a family of more than forty (40) kinds of TMD materials with an MX_2 formula where M stands for transition metals (Mo, W) and X for chalcogens (S, Se) [2]. It is a layered, structured sandwich material, where each layer consists of covalently bound S-M-S slabs, held together by weak van der Waals (vdW) forces. Shin et al. [1] and Larentis et al. [3] highlight 2D MoS_2 through electronic, optical, and mechanical properties as one of the most studied TMDs with potential interest in various modern technological applications. Expanding on this material of interest, MoS_2 has excellent semiconducting (n-type) properties, with tunable energy band gaps, where bulk MoS_2 exhibits an indirect band gap of 1.29 eV [3], while turning from bulk to single layer portrays a direct band gap of 1.8 eV [4]. Furthermore, prospective applications of MoS_2, which include field effect transistors (FETs) with a large on-off ratio, applications of strong photoluminescence, and controllable valley and spin polarisation [5], all of which have been studied both theoretically and experimentally. As a member of transition metal disulphides, MoS_2 has emerged as an excellent candidate for the study of fundamental physics in 2D materials [4], [6], [7]. Various studies have been conducted on the modification of electronic and mechanical properties of MoS_2 and the related group VI TMDs [8], [9], [10]. Lu et al. [11] investigated the strain-dependent electronic and magnetic properties of 2D monolayer and bilayer MoS_2 by using first-principles calculations. Zhou et al. [10] investigated the MoS_2-based nanostructures, including atomic defects, nanoholes, nanodots, and antidots with spin-polarized density functional theory. Additionally, Muratore et al. [12] reported on the thermal transport properties of MoS_2 thin

films. Recently, Yuan et al. [13] investigated the phonon vibrations and thermal properties of MoS_2. The study revealed that no imaginary phonon frequency is observed in the whole Brillouin zone (BZ), indicating that the bulk MoS_2 is dynamically stable. Furthermore, the geometric and electronic structures of graphene adsorption on MoS_2 monolayer have also been studied by density functional theory [9]. However, many properties of bulk MoS_2, such as electronic and elastic properties, still lack in-depth investigation. With the increasing interest in the advanced applications of 2D-related materials, such as MoS_2, especially at the nanoscale, the electronic and mechanical properties of these materials become an important part in the overall evaluation of the quality and suitability of a particular application. Various 2D-related materials exhibit different microstructural dynamics and defects, which make it quite challenging to examine both their electronic and elastic properties. As a result of increased complexity, novel multicomponent materials and difficulty in obtaining pure crystals of sufficient size, experimental determination of electronic and mechanical properties is quite a challenge [14]. Lately, with increased computational power and much improved methodologies, density functional theory (DFT) calculations on electronic and mechanical properties of MoS_2 reached an accuracy level such that calculated quantities are more or less comparable with measured values [15], [16]. Within all these investigations, the calculation of elastic constants is of utmost importance because many other parameters in relation to the mechanical properties can be extracted from them. They are fundamental parameters in understanding interatomic interactions, mechanical stability, phase transitions, materials strength, and the internal structure of materials, and much more [1], [2]. It is expected that this study will assist with an in-depth analysis of this material with a possible guide to its applications. Furthermore, the consistent implementation of DFT calculations on 2D MoS_2, which can also be extended to other 2D TMDs, will assist the experimentalists in better assessing the reliability of their data where there are no experimental data or conflicting data available. Furthermore, it must be stated that the preferred DFT full-potential linearized augmented planewave (FP-LAPW) method makes use of different variants to calculate the electronic structure of crystals or molecules [17]. In the local orbitals variant, the method uses a very accurate numerical design to solve the DFT Kohn-Sham equations. Such a numerical design can reach accuracy at the micro-Hartree energy range. The numerical design also has an option for semi-local exchange-correlation as well as hybrid functionals. Supercell or density functional perturbation theory (DFPT) can also be considered when calculating lattice dynamics [17]. Excited states effects are calculated using the time-dependent DFT (TDDFT) variant, in the linear-response scheme, having a variety of exchange-correlation kernels [17].

2 Computational details

Electronic and elastic properties calculations of hexagonal MoS_2 are based on density functional theory (DFT) employing the full potential all-electrons linearized augmented plane waves method as implemented in the exciting code [18]. The generalized gradient approximation of the Perdew-Burke-Ernzerhof for solids (GGA_PBE_sol) version [16] was used to describe the exchange correlation functional. A convincing k-points mesh of $4 \times 4 \times 3$, having expanded the periodic basis wave-functions in the Brillouin zone, produced a ground state total energy of -2.63×10^5 eV for GGA. A hexagonal space group P63/mmc (no: 194) symmetry crystal lattice, with the Wyckoff atomic positions occupation: Mo^{4+} occupying $2d^-$ (0.667 0.333 0.250); S^{2-} occupying $4f^-$ (0.667 0.333 0.633) so that a unit cell consisting of two molybdenum and four sulphur ions in 4^+ and 2^- oxidation states was generated as shown in figure 1.

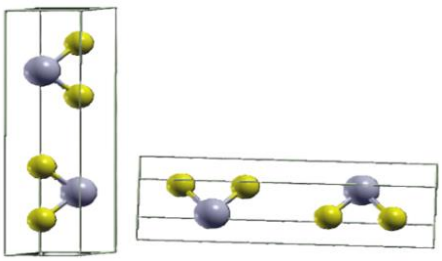

Figure 1: Visualisation of the hexagonal MoS_2 unit cell, where grey balls represent (Mo), and yellow balls represent (S). (*left*) Vertical alignment. (*right*) Horizontal alignment.

All electron linearized plane waves calculations were performed with reference to the following individual atomic electronic states: Mo ($4s^2$ $4p^6$ $4d^5$ $5s^1$) and S ($3s^2$ $3p^4$). The confirmed geometries were all optimised. Good convergence was achieved with the total energy and the number of k-points used for the methods considered. For

each intended calculation, the atomistic positions were fully relaxed according to the Hellmann–Feynman forces until the maximum atomic force was less than 0.03 eV/Å and the total energy difference was less than 1×10^{-3} eV/atom.

3 Results and discussion

3.1 Crystal structure

The structural properties of the hexagonal MoS_2 crystal model were calculated based on the symmetry outlined in the methodology section. Table 1 presents the calculated equilibrium lattice constants, minimum energy (E_o), and bulk modulus (B_o). The calculated lattice parameters, as depicted in table 1, together with available theoretical and experimental data for comparison, clearly show excellent agreement on hexagonal MoS_2 with the experimental [19] and theoretical [20] disclosed data, together with the studies disclosed by Shehu et al. [21]. Yet according to table 1, a c_0/a_0 ratio deviation of about 1.98% from the Ataca *et al*. [20] calculations and about 2.36% from the experiments [19] has been noted. Again, variation of the minimum energy (E_0) of about 1.89% also demonstrates comparable change. Such minor deviations suggest effects due to intra-layer ionic and interlayer van der Waals forces in metal dichalcogenide systems. Different computational approaches may also handle such metal-insulator compounds differently in their core and valence states fusion. Such structural parameters are generally noted in various coating, sensing, energy conversion materials strength [1], [2].

	a_o [Å]	b_o [Å]	c_o [Å]	c_o/a_o	E_o [eV]	B_o [GPa]
Present calculations	3.141	3.141	12.52	3.984	-2.640×10^5	82.28
Other calculations [20]	3.199	3.199	12.50	3.905	-4.990×10^3	63.36
Experiments [19]	3.160	3.160	12.30	3.890	-	-

Table 1: Equilibrium parameters of the hexagonal MoS_2. *a, b,* and *c* are lattice parameters. E_0 and B_0 are the minimum energy and bulk modulus, respectively.

3.2 Electronic properties

The band structure and density of states (DOSs) play an important role when analysing electronic properties of materials. When investigating the electronic properties, the first notion to consider is the band structure as depicted in figure 2. An energy gap of about 1.450 eV exists between the valence and conduction bands at the Fermi level, indicating that MoS2 has a narrow band gap. The results were found to be slightly higher than the reported experimental value of 1.290 eV disclosed by Peelaers and Van de Walle [3]. However, that is lower than the gap reported by Xiaofeng F et al. [22] of 1.650 eV, calculated using GGA and experimentally measured energy gap (1.800 eV) [4].

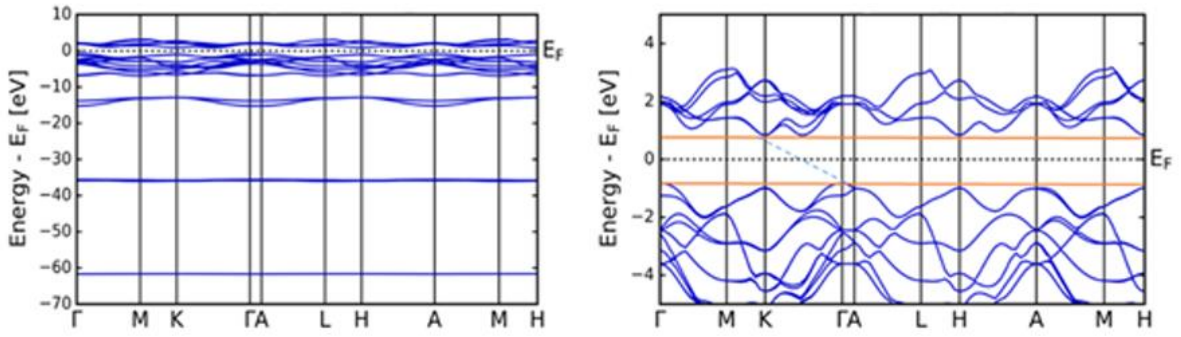

Figure 2: (*left*) Full GGA electronic band structure of hexagonal MoS_2 at 0 GPa. (*right*) Electronic band structure of hexagonal MoS_2 zoomed to within ±4.8 eV of the Fermi level.

In fact, the underestimation of the band gap is a well-known drawback of GGA calculations [23]. From this figure, it can be observed that the bottom of the conduction band and the top of the valence band are not at the same k-point. Such an electronic structure is invoked by the eminent intraband relaxation of electrons or holes in a semiconductor, which is influenced by the increase in the number of layers from mono-, bi-, multi- to bulk-layers [4]. Thus, it results in the alterations or change in the band order between the upper and the lower band, which leads to the weakness or non-observation of the luminescence in association with the excitation states; hence, the material portrays the indirect band gap semiconducting properties [4]. The DOS is an important tool for understanding the bonding properties and their contribution to the electronic properties of the material. Therefore, the total DOS of hexagonal MoS_2 was also calculated as shown in figure 3. From figure 3, the TDOS of hexagonal` MoS_2 can be divided into three sections. In the valence band, there are two regions: a large band located at -5.5 to -2.1 eV and a very tiny band, -1.8 to -1.2 eV. In the conduction band, the bands occupy the region 0.9 to 2.9 eV. As evident from the TDOS of hexagonal MoS_2, it can be concluded that a high flux of electrons density is located in the valence band, with core electrons occupying the lowest large band: -5.5 to -2.1 eV. Some of the valence electron densities occupy the tiny valence band region: -1.8 to -1.2 eV, whilst others can be obtained at the conduction band region: 0.9 to 2.9 eV. The DOS of hexagonal MoS_2 was disclosed by Wei, et al. [24] where in their study, they reported on five (5) regions of DOS of hexagonal MoS_2 while it is disclosed only on three (3) regions of DOS of hexagonal MoS_2. Consequently, in the present study, it was found to compare well with their study only on the three (3) regions (C, D, and E) of their study, which shows a great concurrence and good predictions in examining the bonding properties of hexagonal MoS_2.

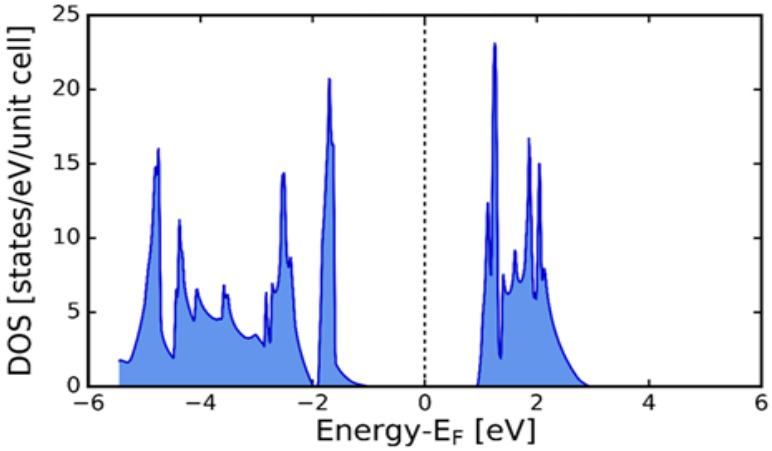

Figure 3: The total density of states (TDOS) of hexagonal MoS_2.

3.3 Elastic properties

The elastic constants (C_{ij}) are an important tool for examining the mechanical properties of various materials, especially for 2D hexagonal MoS_2 in relation to its special application conditions, such as internal strain and thermo-elastic stress. The elastic stiffness tensor is related to the stress tensor and strain tensor by Hooke's law. The elastic constants C_{ijkl} with respect to the finite strain variables are defined [25] as:

$$C_{ijkl} = \left(\frac{\partial \sigma_{ij}(x)}{\partial e_{kl}}\right)_X \quad (1)$$

where σ_{ij} and e_{kl} are the applied stress and Eulerian strain tensors, and X and x are the coordinates before and after the deformation, respectively. Elastic tensor C_{ijkl} is known to have 21 independent components. But, considering the crystal symmetry of a material, this number can be reduced. Currently, for the 2D hexagonal structured MoS_2, those independent components are reduced to five components, i.e., C_{11}, C_{12}, C_{13}, C_{33}, and C_{44}. The mechanical stability criteria for hexagonal structured systems are defined by:

$$C_{44} > 0, \;\; C_{11} > |C_{12}|, \;\; C_{33}(C_{11} + C_{12}) > 2C_{13}^2 \quad (2)$$

The obtained results of the C_{ij} in the current study were all calculated at 0 GPa as depicted in table 2, together with experimental and theoretical disclosed data [24], [26]. As observed, the calculated elastic constants are

positive as demonstrated in table 2, indicating that the system is stable, and that the material satisfies the Born mechanical stability limitations as outlined by equation (2). In addition, it can be seen that C_{11}, C_{12} and C_{33} values are slightly higher than other calculated [21, 31, 32] and measured [26] values, but the conditions $C_{11} > |C_{12}|$ and $C_{33}(C_{11} + C_{12}) > 2C_{13}^2$ are satisfied. It can also be noted that the vdW-DF [21] correction functional values are closer to the experimental [26] values than other calculated values. The issue of higher acquired values in comparison with measured results could be attributed to the initial chosen structural parameters and procedures followed when performing convergence tests, as well as optimizations. Moreover, to examine the physical properties of the material, the elastic moduli of hexagonal MoS_2 were computed from the five elastic constants highlighted. Physical quantities that are known to affect the elastic properties of the material are bulk modulus (B_0), Young's modulus (Y), and shear modulus (G). B_0 is known to be closely related to the cohesive energy, which is used to define the average atomic bond strength of the system [27]. The Y is used to measure the stiffness of a solid as a function of atomic bond strength [28], while the G is assigned when describing the planar stiffness or rigidity of a material [29]. Such quantities are used when describing the materials' machinability index. Secondary components can be obtained, such as the ratio of the bulk modulus B_0 to the constant C_{44}. It should be noted that usually, the higher the value of the ratio (B_0/C_{44}), the better the machinability index. Such a ratio, in the current study, was found to be 15.15, which therefore validates that the material portrays a profound machinability index. The Y value is found to be positive, which reveals the nature of linear tensile or compressive stiffness towards atomic bonding strength. The quantity assists in understanding how atoms of the system are arranged linearly, which also complements the machinability of the material. Moreover, Pugh et al. [30] proposed the ratio B_0/G to describe the ductility and brittleness of a material, as a result of the assumption made of B_0 to constitute the resistance to fracture deformation, while G outlines the resistance to plastic deformation. Based on this criterion, the value that separates ductile and brittle materials is about 1.75. So, if $B_0/G > 1.750$, the material is ductile, while if B_0/G <1.750, the material is brittle. In the current work, as outlined in table 2, the ratio B_0/G (1.440) is less than 1.750. This indicates that hexagonal MoS_2 is brittle at 0 GPa. This was also found to be in good agreement with the results disclosed by Yuan et al. [31].

	Present	GGA [32]	LDA [31]	VdW-DF2 [21]	Experimental [26]
C_{11}	257.9	211.2	240.7	207.4	238.0
C_{12}	63.50	49.38	53.64	60.75	-54.00
C_{13}	2.465	3.078	8.500	20.49	23.00
C_{33}	87.88	36.735	56.110	68.87	52.00
C_{44}	5.47	30.043	26.100	28.17	19.00
B_o	82.28	63.36	50.86	65.56	47.65 ± 0.3
Y	139.5	199.5	107.4	111.5	-
G	57.31	55.11	46.76	45.84	-
B_0/G	1.440	1.140	1.090	1.430	-

Table 2: The calculated (in GPa) elastic constants C_{ij} together with elastic bulk modulus (B_0), Young's modulus (Y), shear modulus (G), and B_0/G of hexagonal MoS_2 at 0 GPa, respectively.

4 Conclusion

The study investigated the structural, electronic, and elastic properties of hexagonal MoS_2 using first-principles calculations within the GGA_PBE_sol exchange-correlation functional. The calculated lattice parameters were found to be in good agreement with both theoretical and experimental data. The calculated band gap energy of hexagonal MoS_2 was obtained to be 1.450 eV, portraying an indirect n-type semiconductor. However, the applied energy functional overestimated the band gap in relation to other theoretical and experimental findings. The analysis of the DOS indicates that there is a flux of electron density within the valence band. That is a great property for the enhancement of the material's atelicity. Lastly, mechanical properties demonstrated that the system's strength is mechanically stable and conveys the ductility characteristics, which were all found to be in good accord with reported experiments and theory. The analysis of these properties, along with agreement across various studies, underscores the growing interest in atomically thin transition-metal dichalcogenides and their potential advantages and challenges, particularly for electronics, sensing, and energy applications. This understanding helps scientists collaborate with high-tech industries to tune the materials' physical properties.

Acknowledgements
The authors wish to acknowledge the University of Limpopo (UL) and Mintek for financial support. The Centre for High Performance Computing (CHPC) is recognised for the research facilities used in this work.

References

[1] S. Shin, B., Zhu, Y., Bojarczuk, N.A., Jay Chey, S. and Guha, "Control of an interfacial MoSe2 layer in Cu2ZnSnSe4 thin film solar cells: 8.9% power conversion efficiency with a TiN diffusion barrier," Appl. Phys. Lett., vol. 5, no. 101, (2012).

[2] A. . Wilson, J.A. and Yoffe, "The transition metal dichalcogenides discussion and interpretation of the observed optical, electrical and structural properties," Adv. Phys., vol. 73, no. 18, pp. 193–335, (1969).

[3] H. Peelaers and C. G. Van De Walle, "Effects of strain on band structure and effective masses in MoS2," Phys. Rev. B - Condens. Matter Mater. Phys., vol. 86, no. 24, p. 241401, (2012).

[4] K. F. Mak, C. Lee, J. Hone, J. Shan, and T. F. Heinz, "Atomically thin MoS2: A new direct-gap semiconductor," Phys. Rev. Lett., vol. 105, no. 13, p. 136805, (2010).

[5] D. Xiao, G. Bin Liu, W. Feng, X. Xu, and W. Yao, "Coupled spin and valley physics in monolayers of MoS2 and other group-VI dichalcogenides," Phys. Rev. Lett., vol. 108, no. 19, p. 196802, (2012).

[6] W. Zheng, X. Liu, J. Xie, G. Lu, and J. Zhang, "Emerging van der Waals junctions based on TMDs materials for advanced gas sensors," Coordination Chemistry Reviews, vol. 447. p. 214151, (2021).

[7] Y. Ravi Kumar, K. Deshmukh, T. Kovářík, and S. K. Khadheer Pasha, "A systematic review on 2D materials for volatile organic compound sensing," Coord. Chem. Rev., vol. 461, (2022).

[8] H. Zeng, G. Bin Liu, J. Dai, Y. Yan, B. Zhu, R. He, L. Xie, S. Xu, X. Chen, W. Yao, et al., "Optical signature of symmetry variations and spin-valley coupling in atomically thin tungsten dichalcogenides," Sci. Rep., vol. 3, no. 1, p. 1608, (2013).

[9] Y. Ma, Y. Dai, M. Guo, C. Niu, and B. Huang, "Graphene adhesion on MoS2 monolayer: An ab initio study," Nanoscale, vol. 3, no. 9, pp. 3883–3887, (2011).

[10] Y. Zhou, P. Yang, H. Zu, F. Gao, and X. Zu, "Electronic structures and magnetic properties of MoS2 nanostructures: Atomic defects, nanoholes, nanodots and antidots," Phys. Chem. Chem. Phys., vol. 15, no. 25, pp. 10385–10394, (2013).

[11] P. Lu, X. Wu, W. Guo, and X. C. Zeng, "Strain-dependent electronic and magnetic properties of MoS2 monolayer, bilayer, nanoribbons and nanotubes," Phys. Chem. Chem. Phys., vol. 14, no. 37, pp. 13035–13040, (2012).

[12] C. Muratore, V. Varshney, J. J. Gengler, J. Hu, J. E. Bultman, A. K. Roy, B. L. Farmer, and A. A. Voevodin, "Thermal anisotropy in nano-crystalline MoS2 thin films," Phys. Chem. Chem. Phys., vol. 16, no. 3, pp. 1008–1014, (2014).

[13] J. Yuan, Z. Lv, Q. Lu, Y. Cheng, X. Chen, and L. Cai, "First-principles study of the phonon vibrational spectra and thermal properties of hexagonal MoS2," Solid State Sci., vol. 40, pp. 1–6, (2015).

[14] Y. Kawazoe, "Can ab initio simulation really predict properties of materials prior to experimental," Bull. Mater. Sci., vol. 22, no. 5, pp. 901–904, (1999).

[15] A. D. Becke, "Density-functional exchange-energy approximation with correct asymptotic behavior," Phys. Rev. A, vol. 38, no. 6, pp. 3098–3100, (1988).

[16] J. P. Perdew, K. Burke, and M. Ernzerhof, "Generalized gradient approximation made simple," Phys.

Rev. Lett., vol. 77, no. 18, pp. 3865–3868, (1996).

[17] A. Gulans, S. Kontur, C. Meisenbichler, D. Nabok, P. Pavone, S. Rigamonti, S. Sagmeister, U. Werner, and C. Draxl, "Exciting: A full-potential all-electron package implementing density-functional theory and many-body perturbation theory," J. Phys. Condens. Matter, vol. 26, no. 36, p. 363202, (2014).

[18] C. Vorwerk, B. Aurich, C. Cocchi, and C. Draxl, "Bethe-Salpeter equation for absorption and scattering spectroscopy: Implementation in the exciting code," Electron. Struct., vol. 1, no. 3, p. 037001, (2019).

[19] J. P. Perdew, A. Ruzsinszky, G. I. Csonka, O. A. Vydrov, G. E. Scuseria, L. A. Constantin, X. Zhou, and K. Burke, "Restoring the density-gradient expansion for exchange in solids and surfaces," Phys. Rev. Lett., vol. 100, no. 13, p. 136406, (2008).

[20] C. Ataca, H. Şahin, E. Aktuörk, and S. Ciraci, "Mechanical and electronic properties of MoS2 nanoribbons and their defects," J. Phys. Chem. C, vol. 115, no. 10, pp. 3934–3941, (2011).

[21] S. A. Yamusa, A. Shaari, N. A. M. Alsaif, I. M. Alsalamah, I. Isah, and N. Rekik, "Elucidating the Structural, Electronic, Elastic, and Optical Properties of Bulk and Monolayer MoS2 Transition-Metal Dichalcogenides: A DFT Approach," ACS Omega, vol. 7, no. 49, pp. 45719–45731, (2022).

[22] X. Fan, C. H. Chang, W. T. Zheng, J. L. Kuo, and D. J. Singh, "The electronic properties of single-layer and multilayer MoS2 under high pressure," J. Phys. Chem. C, vol. 119, no. 19, pp. 10189–10196, (2015).

[23] M. Orio, D. A. Pantazis, and F. Neese, "Density functional theory," Springer, vol. 102, no. 2, pp. 443–453, (2009).

[24] W. Wei, L., Jun-fang, C., Qinyu, H. and Teng, "Electronic and elastic properties of MoS2," Phys. B Condens. Matter, vol. 405, no. 10, pp. 2498–2502, (2010).

[25] D. C. Wallace and H. Callen, "Thermodynamics of Crystals," Am. J. Phys., vol. 40, no. 11, pp. 1718–1719, (1972).

[26] J. L. Feldman, "Elastic constants of 2H-MoS2 and 2H-NbSe2 extracted from measured dispersion curves and linear compressibilities," J. Phys. Chem. Solids, vol. 37, no. 12, pp. 1141–1144, (1976).

[27] K. A. Gschneidner, "Physical Properties and Interrelationships of Metallic and Semimetallic Elements," Solid State Phys. - Adv. Res. Appl., vol. 16, no. C, pp. 275–426, (1964).

[28] A. Q. Morrison, E. D. Case, F. Ren, A. J. Baumann, D. C. Kleinow, J. E. Ni, T. P. Hogan, J. D'Angelo, N. A. Matchanov, T. J. Hendricks, et al., "Elastic modulus, biaxial fracture strength, electrical and thermal transport properties of thermally fatigued hot pressed LAST and LASTT thermoelectric materials," Mater. Chem. Phys., vol. 134, no. 2–3, pp. 973–987, (2012).

[29] D. M. Teter, "Computational alchemy: the search for new superhard materials," MRS Bull., vol. 23, no. 1, pp. 22–27, (1998).

[30] S. F. Pugh, "XCII. Relations between the elastic moduli and the plastic properties of polycrystalline pure metals," London, Edinburgh, Dublin Philos. Mag. J. Sci., vol. 45, no. 367, pp. 823–843, (1954).

[31] J. N. Yuan, Y. Cheng, X. Q. Zhang, X. R. Chen, and L. C. Cai, "First-principles study of electronic and elastic properties of hexagonal layered crystal MoS2 under pressure," Zeitschrift fur Naturforsch. - Sect. A J. Phys. Sci., vol. 70, no. 7, pp. 529–538, (2015).

[32] L. Wei, C. Jun-fang, H. Qinyu, and W. Teng, "Electronic and elastic properties of MoS2," Physica B: Condensed Matter vol. 405, no.10 pp. 2498-2502, (2010).

This page intentionally left blank.

Eigenvalue determination for a Toy and Woods-Saxon potentials using an unsupervised PINN

J T Tshipi[1] **and A S Cornell**[2]

[1]Department of Physical and Earth Sciences, Sol Plaatje University, Kimberley, South Africa
[2]University of Johannesburg, Department of Physics, PO Box 524, Auckland Park, Johannesburg, 2006, Gauteng, South Africa

E-mail: tshegofatso.tshipi@spu.ac.za

Abstract. Traditional numerical methods are widely used to determine eigenvalues in quantum few-body systems. However, comparatively fewer studies have explored modern machine learning approaches such as Physics-Informed Neural Networks (PINNs) for this purpose. In this work, we apply PINNs to solve the two-body radial Schrödinger equation and compute the low-lying S-wave bound states for a toy molecular potential and the Woods-Saxon potential. The PINN was observed to initially converge to the ground state before transitioning to higher excited states, regardless of the starting point, which is consistent with theory. For the molecular potential, the predicted first and second bound-state energies achieved relative errors of $1.482\times10^{-2}\%$ and $6.37\times10^{-3}\%$, respectively. In a preliminary study, the Woods-Saxon potential achieved the relative errors for the first three bound states of $2.99\times10^{-1}\%$, $2.38\times10^{-1}\%$ and 14.85%. These results are promising and demonstrate that PINNs have the potential to offer a viable alternative to traditional numerical methods for solving bound-state quantum eigenvalue problems. Especially with further optimisation of the neural network architecture.

1 Introduction

Bound states play an important role in our understanding as well as predicting the stable of matter from nucleons to atoms. These states occur when particle(s) are confined to a fixed region of space by an attractive force, resulting in negative energies and localized wave functions; that is, they are non-zero inside the potential and zero elsewhere. In quantum few-body problems, bound states are determined by solving the Schrödinger equation to obtain eigenvalues, corresponding to bound state energies, and eigenfunctions which describe the wave function. Determining these bound states, numerically, typically involves search algorithms, such as bisection [1] or Newton-Raphson [2] methods, to find energies alongside ordinary differential equation (ODE) solvers (like Runge–Kutta [3] or the Numerov method [4]) to find the corresponding wave functions.

In this proceeding we shall explore the application of the Physics-Informed Neural Network (PINN) framework to calculate low-lying S-wave bound states. This approach was successfully used in [5] to determine bound state eigenpairs for simple textbook potentials, i.e. the (in)finite square well and harmonic oscillator. Here we shall we investigate its efficiency by solving for bound state eigenpairs using a toy molecular potential [6, 7] and the Woods-Saxon potential [8]. These two potentials offer a more realistic representation of the nuclear potential since they are short-ranged, have finite width and finally their shapes at the edge changes smoothly [9].

2 Theory of Bound states

We shall consider two spinless neutral particles that interact via a short-range central potential $V(r)$. The radial Schrödinger equation describing the relative motion of the particles with reduced mass μ, is

$$\left[-\frac{\hbar^2}{2\mu}\frac{d^2}{dr^2}+\frac{\ell\left(\ell+1\right)}{r^2}+V(r)\right]\psi_\ell(r)=E\psi_\ell(r). \tag{1}$$

Here ℓ represents the orbital angular momentum while E and $\psi_\ell(r)$ denote the bound state energy and radial wave function, respectively. As we are only interested in determining the S-wave bound-states, i.e. $\ell=0$, the centrifugal barrier term will become zero, thus increasing the probability of forming a bound state. The Schrödinger equation (1) becomes

$$\left[-\frac{\hbar^2}{2\mu}\frac{d^2}{dx^2}+V(r)\right]\psi(r)=E\psi(r). \tag{2}$$

To obtain the physical solutions of (2) we will impose boundary conditions at $r=0$ and $r\to\infty$ making this a Dirichlet problem. These kinds of problems can only have solutions at certain discrete energies, since it is not always possible to satisfy the physical boundary condition [10]. At the origin, we have $\psi(0)=0$ this is true for all types of solutions e.g bound, resonance and scattering states. For bound states, the particle μ is trapped and thus confined to a particular region in space by an attractive force. Therefore the probability of finding the particle beyond the walls of the potential decays to zero. As such the boundary conditions we require are

$$\psi(0)=0 \qquad \text{and} \qquad \psi(r)\xrightarrow[r\to\infty]{}0. \tag{3}$$

We will now use the unsupervised neural network approach proposed in [5] to determine the bound state energies and the corresponding wave functions, where this approach is capable of solving (2) when both E and $\psi(r)$ are unknowns.

3 Potentials

3.1 Toy potential

The first potential we will consider is the toy molecular potential shown in Figure 1. The potential [6, 7]

$$V(r)=5.0\exp\left[-0.25\left(r-3.5\right)^2\right]-8\exp\left(r-0.2r^2\right), \tag{4}$$

is primarily used as a testbed for assessing the performance of new theoretical models as it generates both bound and resonance states. We solve (2) using atomic units [11] i.e., the energies are measured in MeV, distance in femtometre(fm) and $\hbar^2/(2\mu)=1/2\text{MeV}\cdot\text{fm}^{-2}$. To determine the bound state eigenvalues and the wave functions for this potential, we use the boundary conditions $\psi_0(0)=\psi_0(5)=0$.

3.2 Woods-Saxon potential

The Woods-Saxon potential, see Figure 1, is used to model the mean field potential that the nucleons feel inside the nucleus [9]. The standard form of the Wood-Saxon potential [8] is given by

$$V(r)=-\frac{V_0}{1+\exp\left(\frac{r-R}{d}\right)}. \tag{5}$$

Here we will use the parameters found in [12], $R=r_0A^{\frac{1}{3}}$ with $r_0=1.1$fm and $d=0.6$fm. The value of the strength $V_0=31.20$ MeV. The boundary conditions $\psi_0(0)=\psi_0(13)=0$ will be used to determine bound states eigenpairs from equation (2).

4 Computing bound states with PINN

In setting up our neural network to solve to solve for the eigenvalues of the S-wave Schrödinger equation (2) for the potentials (4) and (5), we shall follow the approach detailed in [5], which the reader may consult for more details. In this approach the trial wave function of (2) is given by

$$\psi(r)=f_b+g(r)N(r,E;\theta). \tag{6}$$

The network $N(r,E;\theta)$ is a single-output neural network (NN) with two hidden layers and two inputs: r and E. The total trainable parameters of the network are represented by θ. Figure 2 illustrates how both the eigenvalue

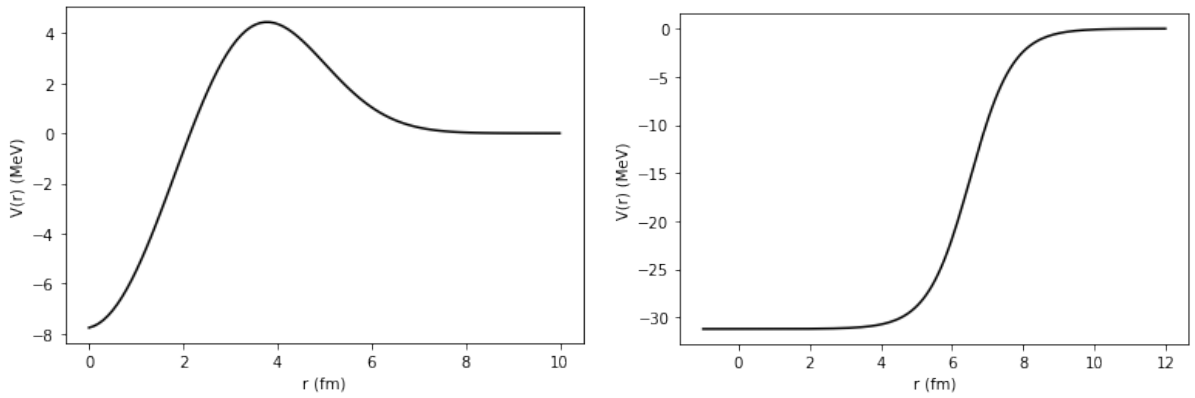

Figure 1: (*left*) The toy molecular potential and (*right*) the Woods-Saxon potential used as inputs for solving the Schrödinger equation and determining the system's energy levels and wavefunctions.

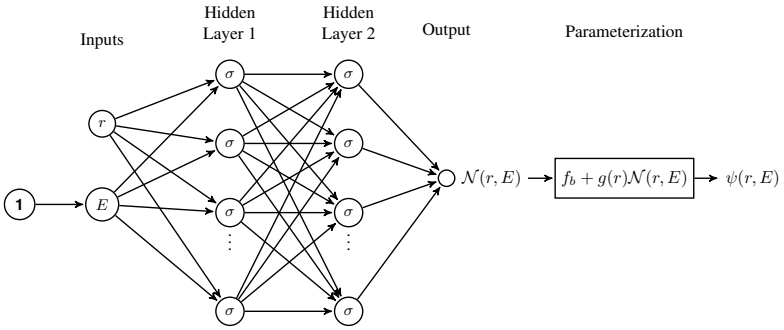

Figure 2: The network architecture of the unsupervised NN. σ represents non-linear activation function.

E and the trial solution $\psi(r)$ are determined; the eigenvalue E is obtained by passing a constant vector of ones (having the same number of points as r) through a single linear neuron, whose weights are subsequently updated via optimisation. Thereafter, both r and E are fed into a feed-forward NN to produce the output $N(r, E; \theta)$. Finally, the parametric trick in (6) is applied to estimate the wave function. The parametric function $g(r)$ plays an important role in the performance of the NN. As recommended in [13], it should be smooth and bounded; therefore, we adopt the form given in [5],

$$g(r) = \left(1 - e^{-(r-r_{min})}\right)\left(1 - e^{-(r-r_{max})}\right). \tag{7}$$

Here, r is the domain, and r_{min} and r_{max} are the end points of the domain. It can be easily verified that the trial solution (6) satisfies the boundary conditions (3). The bound state energies and the corresponding wave functions are determined by minimising the following composite loss function

$$\mathcal{L}(\theta) = \nu_{DE}\mathcal{L}_{DE} + \nu_f\mathcal{L}_f + \nu_\lambda\mathcal{L}_\lambda + \nu_{drive}\mathcal{L}_{drive}, \tag{8}$$

where

$$\mathcal{L}_{DE} = \left\langle \left(\left[-\frac{\hbar^2}{2\mu}\frac{d^2}{dr^2} + V(r) \right] \psi(r) - E\psi(r) \right)^2 \right\rangle_r \tag{9}$$

$$\mathcal{L}_f = \frac{1}{\langle f(r,E)^2 \rangle_r}, \quad \mathcal{L}_E = \frac{1}{\langle E^2 \rangle} \quad \text{and} \quad \mathcal{L}_{drive} = \left\langle e^{-E+c} \right\rangle. \tag{10}$$

$\langle\cdot\rangle_r$ represents taking an average over the variable r and $\langle\cdot\rangle$ represents the simple sample mean. The $\mathcal{L}_{DE}$ loss ensures that the estimated eigen-pairs satisfy the Schrödinger equation while $\mathcal{L}_f$ and $\mathcal{L}_E$ encourage the NN to learn non-trivial solutions of the wave-function solution $\psi(r)$ and the energy E. Finally, $\mathcal{L}_{drive}$ drives the NN to scan for larger eigenvalues. The derivatives with respect to the inputs and training weights are determined using

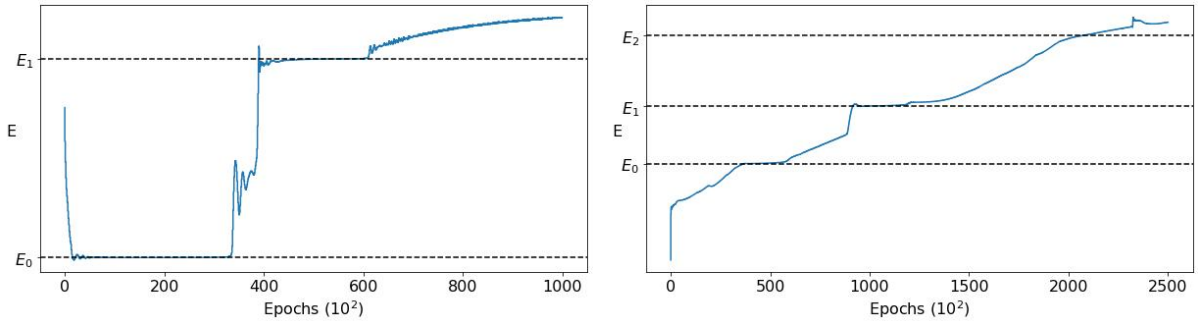

Figure 3: Eigenvalue search history during training for: (*left*) the toy molecular potential and (*right*) the Woods-Saxon potential. The dashed lines indicate the exact eigenvalues of both potentials.

automatic differentiation [14]. In the training stage, the $\mathcal{L}_{drive}$ loss term is gradually increased by incrementing the value of c in regular intervals. As mentioned earlier, this will encourage the NN to search for higher eigenpairs. At every epoch a batch of r points in the interval $[r_{min}, r_{max}]$ is perturbed by adding a Gaussian noise. This is done to prevent the NN from learning the solutions only at fixed intervals.

In determining the bound states eigen-pairs for the molecular potential (4), we used a NN with 50 nodes per hidden layer and the sin activation function [5]. The domain was divided into 100 equally spaced collocation points, and 10^5 training epochs were used. We found, empirically, that setting $\nu_{DE} = \nu_f = \nu_\lambda = \nu_{drive} = 1$ in equation (8) produced optimal results. The hyperparameters used for the Woods-Saxon potential (5) were the following: 380 collocation points, 300 units per hidden layer, 250×10^3 training epochs. Here we set $\nu_{DE} = 10^{-7}, \nu_f = 10^{12}, \nu_\lambda = 10^4$ and $\nu_{drive} = 1$, this will ensure that all the individual loss terms (9 - 10) contribute equally to the total loss. For both potentials, we added a Gaussian noise of $\mathcal{N}\left(\mu = 0, \sigma^2 = 0.06 r_{max}\right)$ to the batch input data for every epoch and the loss function was minimized using the Adam optimizer [15] with the learning rate of 8×10^3.

5 Results

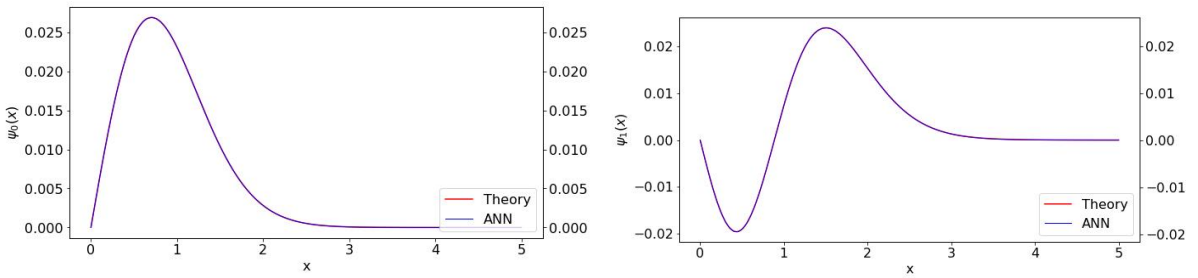

Figure 4: S-wave functions for the toy potential in Equation (4). (*left*) Ground state wave functions: true (red) and predicted (blue). (*right*) First excited state wave functions: true (red) and predicted (blue).

n	E (MeV)	Relative error(%)	Ref
0	-4.571182814	-	[7]
	-4.570504665	1.482×10^{-2}	This work
1	-0.884280776	-	[7]
	-0.884224414	6.37×10^{-3}	This work

Table 1: The eigenvalues for the S-wave bound states for the toy potential (4).

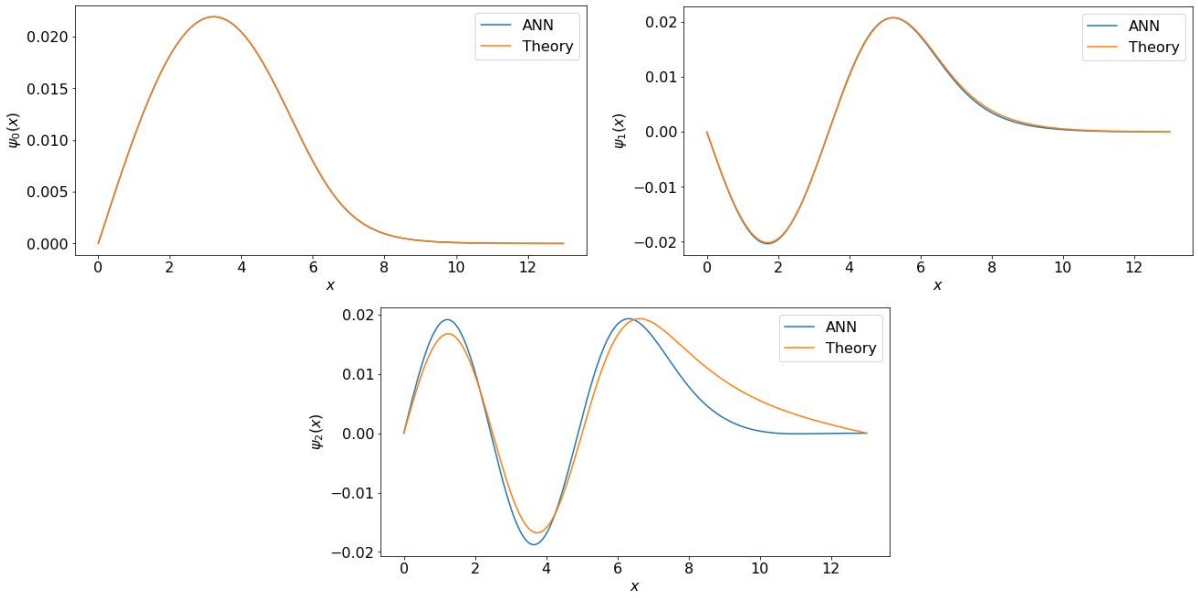

Figure 5: S-wave functions for the Woods-Saxon potential (Equation 5): (*top left*) ground state, (*top right*) first excited state, and (*bottom*) second excited state. The red curves are the true eigenfunctions and the blue curves are the predicted wave functions.

n	E (MeV)	Relative error(%)	Ref
0	-27.00085	-	[12]
	-26.920	2.99×10^{-1}	This work
1	-16.42311	-	[12]
	-16.384	2.38×10^{-1}	This work
2	-3.40020	-	[12]
	-2.895	14.85	This work

Table 2: The eigenvalues for the S-wave bound states for the potential (5).

As shown in Figure 3, the NN initially converges to the lowest energy level (the ground state) before moving on to excited states. This behaviour occurs regardless of the starting point. It aligns with a well-known property of NNs and PINNs: they tend to learn low-frequency components of a solution before capturing higher-frequency ones [16]. Tables 1–2 list the predicted eigenvalues and their corresponding absolute relative errors. Figures 4–5 compare the predicted and theoretical wavefunctions for the two potentials. Based on the width of the E_0 plateau in the *left* panel of Figure 3, we expect E_0 to have the smallest relative error. However, the results show that the network finds it easier to 'learn' the first excited state. One possible explanation is that the driving term $\mathcal{L}_{drive}$ pushed the network toward higher energy levels before the ground state eigenvalue was 'fully learned'.

6 Conclusion

In this work, we applied the unsupervised PINN approach to solve for the eigenpairs of the two-body radial Schrödinger equation. The results indicate that PINNs have the potential, if properly tuned, to serve as a viable alternative to traditional numerical methods for solving bound-state quantum eigenvalue problems. The loss term weights and hyperparameters were adjusted manually. In our work, we plan to implement adaptive loss weighting using the method proposed in [17], and to employ the Hyperopt package [18] for automated hyperparameter optimisation. Furthermore, since the Hamiltonian for bound states is Hermitian this implies that the wave functions are orthonormal and normalisable, we will add these properties into the loss function to make it more robust. By incorporating these approaches into the training process, it has the potential to reduce the occurrence of spurious bound-state solutions and improve prediction accuracy across different potential models.

Acknowledgments
JTT gratefully acknowledges funding from the Absa Research Grant (Sol Plaatje University) for providing the equipment essential to this research. ASC is partially supported by the National Research Foundation of South Africa.

References

[1] G. E. Collins and A. G. Akritas, "Polynomial real root isolation using descarte's rule of signs," in *Proceedings of the Third ACM Symposium on Symbolic and Algebraic Computation*, ser. SYMSAC '76. New York, NY, USA: Association for Computing Machinery, 1976, p. 272–275.

[2] R. Landau, M. Paez, and C. Bordeianu, *Computational Physics. Problem Solving with Computers, 2nd*, 1 2007.

[3] C. Runge, "Über die numerische auflösung von differentialgleichungen," *Mathematische Annalen*, vol. 46, no. 2, pp. 167–178, 1895.

[4] B. Noumerov, "A method of extrapolation of perturbations," *Monthly Notices of the Royal Astronomical Society, Vol. 84, p. 592-592*, vol. 84, pp. 592–592, 1924.

[5] H. Jin, M. Mattheakis, and P. Protopapas, "Physics-informed neural networks for quantum eigenvalue problems," 07 2022, pp. 1–8.

[6] S. Rakityansky, S. Sofianos, and K. Amos, "A method for calculating the jost function for analytic potentials," *Il Nuovo Cimento B (1971-1996)*, vol. 111, no. 3, pp. 363–378, 1996.

[7] S. Sofianos and S. Rakityansky, "Exact method for locating potential resonances and regge trajectories," *Journal of Physics A: Mathematical and General*, vol. 30, no. 10, p. 3725, 1997.

[8] R. D. Woods and D. S. Saxon, "Diffuse surface optical model for nucleon-nuclei scattering," *Physical Review*, vol. 95, no. 2, p. 577, 1954.

[9] K. S. Krane, *Introductory nuclear physics*. John Wiley & Sons, 1991.

[10] S. A. Rakityansky, *Jost functions in quantum mechanics*. Springer, 2022, no. PUBDB-2023-02231.

[11] L. Landau and E. Lifshitz, "M 1965 quantum mechanics," *London: Pergamon Press) p*, vol. 72, p. 73, 1981.

[12] S. Rakityansky and I. Gopane, "Effective-range parameters and vertex constants for λ-nuclear systems," *International Journal of Modern Physics E*, vol. 26, no. 04, p. 1750014, 2017.

[13] M. Mattheakis, D. Sondak, A. S. Dogra, and P. Protopapas, "Hamiltonian neural networks for solving equations of motion," *Physical Review E*, vol. 105, no. 6, p. 065305, 2022.

[14] A. Griewank and A. Walther, *Evaluating derivatives: principles and techniques of algorithmic differentiation*. SIAM, 2008.

[15] D. P. Kingma and J. Ba, "Adam: A method for stochastic optimization," *arXiv preprint arXiv:1412.6980*, 2014.

[16] S. Wang, S. Sankaran, H. Wang, and P. Perdikaris, "An expert's guide to training physics-informed neural networks," *arXiv preprint arXiv:2308.08468*, 2023.

[17] L. D. McClenny and U. M. Braga-Neto, "Self-adaptive physics-informed neural networks," *Journal of Computational Physics*, vol. 474, p. 111722, 2023.

[18] J. Bergstra, D. Yamins, and D. Cox, "Making a science of model search: Hyperparameter optimization in hundreds of dimensions for vision architectures," in *International conference on machine learning*. PMLR, 2013, pp. 115–123.

Coherent State Path Integrals and Vacuum Structure in Thermal ϕ^4 Theory on a Finite Volume

Rens Roosenstein[1,2,3], **W. A. Horowitz**[1,4]

[1]Department of Physics, University of Cape Town, Cape Town, South Africa
[2]Institute for Theoretical Physics, University of Amsterdam, Amsterdam, The Netherlands
[3]Theory Group, Nikhef, Amsterdam, The Netherlands
[4]Department of Physics, New Mexico State University, Las Cruces, New Mexico, 88003, USA

E-mail: rens.roosenstein@gmail.com

Abstract. We present a derivation of the thermal partition function in scalar thermal field theories with an emphasis on finite-size effects. By carefully transitioning from the Hamiltonian operator formalism to the path integral using coherent states, we obtain corrections to the partition function that expose vacuum structures. These corrections are rarely discussed in previous literature.

1 Introduction

Understanding the behavior of matter under extreme conditions — such as those present in the early universe or recreated in heavy-ion collisions — is a central goal of high-energy physics. In particular, the study of the Quark-Gluon Plasma (QGP) provides deep insights into the early universe and the dynamics of strongly interacting matter. A powerful framework for investigating such systems is *Thermal Field Theory* (TFT), which extends Quantum Field Theory (QFT) to finite temperature and density. TFT is widely used in high-energy physics, nuclear physics, and cosmology, and plays a crucial role in describing phenomena such as cosmological phase transitions, thermal particle production, and QGP formation in heavy-ion collisions at RHIC (Brookhaven National Lab) and the LHC (CERN). It is also an essential tool in lattice QCD studies of the QCD equation of state and in modeling dense astrophysical systems such as neutron stars and their mergers. Recent applications of TFT include finite-size effects and Casimir physics at finite temperature [1, 2, 3, 4]. For comprehensive reviews of TFT, see e.g. [5, 6, 7, 8, 9].

A key quantity in TFT is the thermal partition function, which encodes the equilibrium statistical properties of quantum fields. Here, we focus on the path integral formulation of the partition function in a scalar field theory and present recent results obtained from a careful construction of the path integral using coherent states [10]. The standard treatments in TFT derive the path integral representation of the partition function by inserting decompositions of unity $\mathbb{1} \equiv \int d\phi\, |\phi\rangle\langle\phi|$ and $\mathbb{1} \equiv \int d\pi\, |\pi\rangle\langle\pi|$ using eigenstates of the field operator and its canonically conjugate momentum, $\hat{\phi}\,|\phi\rangle = \phi\,|\phi\rangle$, $\hat{\pi}\,|\pi\rangle = \pi\,|\pi\rangle$. While the use of these unities makes the derivation of the path integral straightforward, it is unclear how these eigenkets and, especially, the integrals over them, are defined. In our derivation, we rather use well-defined coherent states.

Of special mention in our derivation is the connection between coherent states in the field basis with coherent states in the ladder basis; deferring the details for now,

$$\begin{aligned} |\boldsymbol{\alpha}(\tau,t)\rangle &\sim e^{i\int d^n x\, \phi(\tau,\mathbf{x})\hat{\pi}(t,\mathbf{x}) - \pi(\tau,\mathbf{x})\hat{\phi}(t,\mathbf{x})}\,|0\rangle \\ &\sim e^{\int \frac{d^n p}{(2\pi)^n 2E_{\mathbf{p}}}\left(\alpha(\tau,\mathbf{p})\hat{a}^\dagger(t,\mathbf{p}) - \alpha^*(\tau,\mathbf{p})\hat{a}(t,\mathbf{p})\right)}\,|0\rangle\,, \end{aligned} \tag{1}$$

where

$$\hat{a}(t,\mathbf{p})\,|\boldsymbol{\alpha}(\tau,t)\rangle = \alpha(\tau,\mathbf{p})\,|\boldsymbol{\alpha}(\tau,t)\rangle\,. \tag{2}$$

Through this derivation, we show that the vacuum energy contribution to the action arises naturally in the path integral of the free theory when the Hamiltonian is expressed in terms of ladder operators. We then extend the use of coherent states in the field-operator basis to the interacting theory. For the interacting case, we find, alongside the vacuum energy, a novel contribution to the action: a vacuum bubble that acts as a mass correction.

2 Motivation

The final goal that motivated this research was to analytically compute next-to-leading order (NLO) finite-size corrections to the QCD equation of state. Understanding these corrections is of growing importance across a wide range of physical systems, as discussed in the introduction 1, where the thermodynamic limit is applicable.

The reason we are interested in the influence of finite system size on the thermodynamic and statistical properties of the QGP is mainly because this is a largely unexplored area of research. The Casimir effect, predicted by Dutch physicist Hendrik Casimir for electromagnetic systems in 1948 [11], provides a striking example of how confinement in finite volumes can induce measurable modifications to physical observables. Figure 1 shows experimental measurements from [12], illustrating that Casimir forces are detectable at length scales on the order of $200\,\mathrm{nm}$. While the effect is relatively small at such distances, its magnitude increases significantly as the system size decreases, becoming comparable to atmospheric pressures around $10\,\mathrm{nm}$.

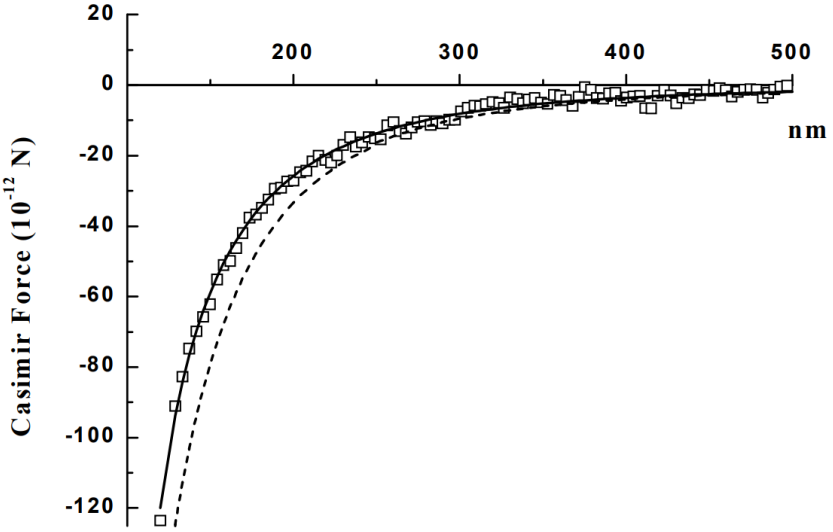

Figure 1: Casimir Force plot. Figure adapted from [12].

Given that the QGP formed in heavy-ion collisions occupies volumes on the scale of a nucleus, these finite-size corrections to thermodynamic quantities such as pressure and energy density may be significant. For example, [2] shows that even in a simple, non-interacting massless scalar field theory, finite volume effects induce substantial deviations in thermodynamic observables. Such corrections could alter the QGP equation of state and, consequently, affect key transport properties like η/s. Importantly, the sign and magnitude of these finite volume effects remain largely unexplored, raising the possibility that the QGP might exhibit different fluidity characteristics at finite system size than those inferred from infinite volume approximations. This motivates a systematic study of finite size effects on the thermodynamics and hydrodynamics of the QGP.

The path toward this ambitious goal involves several intermediate steps. As a first step, we have computed the partition function of an interacting ϕ^4 theory in a finite volume at finite temperature. Subsequent steps include computing the equation of state and the trace anomaly for a range of interacting quantum field theories in finite volumes. Starting with scalar theories such as ϕ^4, we will gradually advance to more complex systems, including fermionic theories, spin systems relevant to condensed matter physics, and ultimately, QCD. Each step serves both as a validation of our methods and as a bridge toward applications in realistic settings.

The relevance of these results extends to numerical simulations as well. In particular, the analytical finite-size corrections computed here can serve as benchmarks and guiding insights for Lattice QCD simulations, where volume effects must be carefully controlled and interpreted. More broadly, this line of research aims to enhance our theoretical understanding of quantum fields in confined geometries, offering deeper analytical control over models that underpin many frontier topics in high-energy and condensed matter physics.

3 Results

All derivations in this section are performed in discretized spacetime. However, for readability, we present the results directly in their continuum-limit form. A number of technical subtleties are omitted for brevity. For a more detailed and rigorous treatment, we refer the reader to Ref. [10].

3.1 Free Theory Partition Function

For the sake of simplicity, we start to examine a free massive single component scalar field theory in $n+1$ dimensions. The weak $\lambda\phi^4$ interactions for this classical real scalar theory will follow later on. Due to the thermal system, the discretization even in equilibrium is non-trivial. The Lagrangian for the considered theory[1] is

$$\begin{aligned} \mathcal{L} &= \frac{1}{2}\partial_\mu\phi\partial^\mu\phi - \frac{1}{2}m^2\phi^2, \\ \phi^*(t,\mathbf{x}) &= \phi(t,\mathbf{x}). \end{aligned} \tag{3}$$

In our scalar field theory, we assume that the vacuum expectation value of the scalar field is zero, $\langle\phi(t,\mathbf{x})\rangle_0 = 0$, as is typical for scalar theories in thermal equilibrium without spontaneous symmetry breaking. Furthermore, no specific spatial boundary conditions are imposed on the fields, as we will not explicitly evaluate the partition function.

The Hamiltonian is obtained via a Legendre transform,

$$\begin{aligned} \mathcal{H} &\equiv \pi\dot{\phi} - \mathcal{L}, \quad \pi \equiv \frac{\partial\mathcal{L}}{\partial\dot{\phi}} = \dot{\phi} \\ \therefore \mathcal{H} &= \frac{1}{2}\left(\pi^2 + (\nabla\phi)^2 + m^2\phi^2\right). \end{aligned}$$

In order to construct the path integral formulation function of the partition function in a controlled way, we start with the trace over the thermal density matrix,

$$Z = \mathrm{Tr}\{e^{-\beta H}\}, \tag{4}$$

where $\beta = \frac{1}{T}$.

Applying trotterization [13], we divide the partition function in eq. 4 into $N \to \infty$ segments and insert complete sets of coherent states in between each segment to find the thermal trace trotter formula (for further details, see Ref. [10])

$$Z = \prod_{i=0}^{N} N_i \int d\alpha_i(\mathbf{p}) d\alpha_i^*(\mathbf{p}) \left\langle \boldsymbol{\alpha}_N \right| e^{-\frac{\beta}{N}\hat{H}} \left| \boldsymbol{\alpha}_{N-1} \right\rangle \left\langle \boldsymbol{\alpha}_{N-1} \right| e^{-\frac{\beta}{N}\hat{H}} \left| \boldsymbol{\alpha}_{N-2} \right\rangle \cdots \left\langle \boldsymbol{\alpha}_1 \right| e^{-\frac{\beta}{N}\hat{H}} \left| \boldsymbol{\alpha}_0 \right\rangle. \tag{5}$$

We emphasize that the trace has been discretized into segments of length $\frac{\beta}{N}$ and is periodic at the boundaries, such that $|\boldsymbol{\alpha}_N\rangle \equiv |\boldsymbol{\alpha}_0\rangle$.

By evaluating the matrix elements in Eq. 5, and performing a well-motivated change of variables followed by a Fourier transformation, we obtain a path integral over field configurations weighted by the exponentiated Euclidean action. A careful treatment of this procedure reveals that the vacuum energy contribution emerges naturally as part of the path integral. Although the full derivation involves several subtleties, the resulting path integral expression for the thermal partition function in the free theory takes the form

$$\begin{aligned} Z &= \mathrm{Tr}\left[e^{-\beta\hat{H}}\right] \\ &= \int D\phi\, e^{-S^E + \langle\hat{H}\rangle_0}, \end{aligned} \tag{6}$$

[1] We work with the mostly-minus metric in $D = n+1$ Minkowskian spacetime; $\eta^M_{\mu\nu} = \mathrm{diag}(+1,-1,\cdots,-1)$, use natural units throughout this work, $\hbar = c = k_B = 1$, and denote $\mathrm{i} \equiv \sqrt{-1}$.

where

$$S^E = \int_0^\beta d\tau \int d^n\mathbf{x} \frac{1}{2}\left[\dot{\phi}^2 + (\nabla\phi)^2 + m^2\phi^2\right]. \tag{7}$$

3.2 Interacting ϕ^4 Theory Partition Function

When interactions are included, we will show that some vacuum expectation values (VEV) arise that couple to the other terms in the Lagrangian and modify the structure of the counterterms. We start with the bare scalar ϕ^4 Lagrangian in $D = n + 1$ dimensions and with the coupling constant λ_0,

$$\mathcal{L}_0 \equiv \frac{1}{2}\partial_\mu\phi_0\,\partial^\mu\phi_0 - \frac{1}{2}m_0^2\phi_0^2 - \frac{\lambda_0}{4!}\phi_0^4, \tag{8}$$

and renormalize using multiplicative renormalization. We define

$$\begin{aligned} \phi_0 &\equiv \sqrt{Z_\phi}\phi_r, \quad Z_\phi \equiv 1 + \delta_\phi, \\ m_0 &\equiv \frac{\sqrt{Z_m}}{\sqrt{Z_\phi}} m_r, \quad Z_m \equiv 1 + \frac{\delta_m}{m_r}, \\ \lambda_0 &\equiv \frac{Z_\lambda}{Z_\phi^2}\lambda_r, \quad Z_\lambda \equiv 1 + \frac{\delta_\lambda}{\lambda_r}. \end{aligned} \tag{9}$$

Inserting the renormalized parameters from eq. 9 into the bare Lagrangian, eq. 8 yields

$$\begin{aligned} \mathcal{L}_r &= \mathcal{L}_{\text{free}} + \mathcal{L}_{\text{int}}, \\ \mathcal{L}_{\text{free}} &= \frac{1}{2}\partial_\mu\phi_r\,\partial^\mu\phi_r - \frac{1}{2}m_r^2\phi_r^2, \\ \mathcal{L}_{\text{int}} &= -\frac{\lambda_r}{4!}\phi_r^4 + \frac{1}{2}\delta_\phi\partial_\mu\phi_r\,\partial^\mu\phi_r - \frac{1}{2}\delta_m\phi_r^2 - \frac{\delta_\lambda}{4!}\phi_r^4. \end{aligned} \tag{10}$$

Performing a Legendre transform then gives the renormalized Hamiltonian,

$$\begin{aligned} \mathcal{H}_r =& \mathcal{H}_{\text{free}} + \mathcal{H}_{\text{int}}, \\ \mathcal{H}_{\text{free}} =& \frac{1}{2}\pi_r^2 + \frac{1}{2}(\nabla\phi_r)^2 + \frac{1}{2}m_r^2\phi_r^2, \\ \mathcal{H}_{\text{int}} =& \frac{\lambda_r}{4!}\phi_r^4 + \frac{1}{2}\delta_\phi\left(\pi_r^2 + \frac{1}{2}(\nabla\phi_r)^2\right) + \frac{1}{2}\delta_m\phi_r^2 \\ &+ \frac{\delta_\lambda}{4!}\phi_r^4. \end{aligned} \tag{11}$$

Going through the same procedure as for the free theory, we start off with the trace over the thermal density matrix of the renormalized ϕ^4 theory, trotterize, insert complete sets of coherent states and compute the matrix elements. This process reveils the following form of the path integral partition function of the renormalized interacting ϕ^4 theory:

$$\begin{aligned} Z &= \text{Tr}\left[e^{-\beta\hat{H}_r}\right] \\ &= \int D\phi\, e^{-S_r^E + \frac{\lambda_r+\delta_\lambda}{4}\langle\hat{\phi_r}^2\rangle_0\phi_r^2 + \langle\hat{H}_r\rangle_0}, \end{aligned} \tag{12}$$

where

$$S_r^E = \int_0^\beta d\tau \int d^n\mathbf{x}\left[\frac{1}{2}\dot{\phi}_r^2 + \frac{1}{2}(\nabla\phi_r)^2 + \frac{1}{2}m^2\phi_r^2 + \frac{\lambda}{4!}\phi_r^4 + \frac{1}{2}\delta_m\phi_r^2 + \frac{\delta_\lambda}{4!}\phi_r^4\right]. \tag{13}$$

In the path integral of eq. 12, we have found the usual Euclidean action, the VEV of the Hamiltonian, but notable exception from the literature arises from the coupling between the VEV $\langle 0|\,\hat{\phi}^2\,|0\rangle$ and the classical field configurations ϕ^2. This coupling introduces a nontrivial correction to the mass counterterm and marks a key distinction from the standard path integral formulations in the literature where such couplings between operator VEVs and classical fields are absent.

4 Conclusions and Outlook

In this work, we systematically derived the path integral formulation of the thermal partition function for a scalar quantum field theory from first principles. We began by constructing the partition function for a free scalar field theory using well-defined field-theoretic coherent states. In contrast to the ill-defined resolutions of unity used in the standard literature, based on eigenstates of field operators, we employed rigorously defined coherent states to formulate the path integral.

We provided an explicit connection between coherent states in the ladder operator basis and those in the field operator basis. This mapping is crucial for deriving the path integral formulation of the interacting theory partition function and, to our knowledge, has not been presented elsewhere. In both the ladder operator basis, and the field operator basis, the vacuum energy emerges explicitly through the matrix element of the Hamiltonian with coherent states. In both approaches, we obtained an identical, well-defined path integral representation of the partition function as a finite product of integrals over real numbers. This includes the familiar Euclidean action as well as an explicit vacuum expectation value (VEV) of the Hamiltonian, absent from traditional treatments.

We then extended our formalism to the interacting ϕ^4 theory using the field-basis coherent states. In this case, we found two novel contributions in the exponent of the partition function: (i) the VEV of the full Hamiltonian and (ii) a second VEV coupling the vacuum bubble $\langle 0|\hat{\phi}^2|0\rangle$ to the mass term ϕ^2. These terms are not present in any standard derivation and emerge before integration over conjugate momenta, pointing to their structural origin in the path integral formulation.

Given that traditional treatments miss these VEVs, we are led to question the validity of assuming a resolution of the identity via $\mathbb{1} = \int d\phi\, |\phi\rangle\langle\phi|$ and $\mathbb{1} = \int d\pi\, |\pi\rangle\langle\pi|$. In particular, we have found no rigorous construction in the literature for defining the identity operator in terms of field eigenstates. We suspect this assumption is the root cause of the discrepancy.

Whether these additional VEVs have physical consequences remains an open and intriguing question. Consider first the VEV of the Hamiltonian. While often regarded as physically irrelevant, this term plays a central role in the Casimir effect, where energy differences between confined and infinite-volume vacua manifest as measurable forces. Additionally, in gravitational theories, this VEV could contribute to an effective cosmological constant.

The second VEV, which couples to the mass term, implies that the effective mass depends on the system's finite size. This could have significant consequences for physical observables, especially in systems with spontaneous symmetry breaking (SSB). In such scenarios, even more vacuum diagrams could couple to the theory: the tadpole, for example, might couple to a ϕ^3 term, and the three-point (Mercedes) diagram to a ϕ term. Furthermore, the sign of the vacuum correction is not guaranteed, if negative and sufficiently large, it could induce SSB even if the bare mass is positive. Such a shift would impact phase structure, thermodynamic quantities like pressure, energy and entropy density, the speed of sound, and the trace anomaly.

Looking forward, our approach provides a concrete foundation for computing higher-order corrections to thermodynamic observables in both infinite and finite volumes. This enables systematic investigations of how finite-size effects modify the equation of state and trace anomaly in scalar field theories [3, 4]. These studies offer an ideal testbed for later extensions to fermions and gauge fields. In particular, carrying out an analogous construction in Quantum Electrodynamics (QED), and ultimately in Quantum Chromodynamics (QCD), would allow for nonperturbative evaluation of finite-volume corrections to the QCD equation of state. Such corrections could have significant implications for lattice QCD simulations [14, 15, 16] and for the interpretation of signals of quark-gluon plasma formation in small systems. They may also impact observables sensitive to conformal symmetry breaking [17, 18], such as flow in small heavy-ion collisions [19] or energy-energy correlators [20, 21, 22, 23], which are increasingly being explored as precision probes of the QGP.

Acknowledgements

The author wishes to thank Giordano Cintia, Charles Gale, Sangyong Jeon, Isobel Kolbé, Sam van Leuven, Mikko Laine, Rob Pisarski, Jean Du Plessis, Alexander Rothkopf, Matt Sievert, and Michael Zantedeschi for insightful discussions. Additionally, the author gratefully acknowledge support from the South African National Research Foundation (NRF), the SA-CERN Collaboration, and the Institute for Theoretical Physics Amsterdam (ITFA).

References

[1] I. Ghisoiu, "Finite size effects in quantum field theory," Master's thesis, Bielefeld U., 2010.

[2] S. Mogliacci, I. Kolbé, and W. A. Horowitz, "Geometrically confined thermal field theory: Finite size corrections and phase transitions," *Phys. Rev. D*, vol. 102, no. 11, p. 116017, 2020.

[3] W. Horowitz and A. Rothkopf, "The QCD Equation of State in Small Systems," *SciPost Phys. Proc.*, vol. 10, p. 025, 2022.

[4] W. A. Horowitz and J. F. D. Plessis, "Finite system size correction to NLO scattering in ϕ^4 theory," *Phys. Rev. D*, vol. 105, no. 9, p. L091901, 2022.

[5] N. P. Landsman and C. G. van Weert, "Real and Imaginary Time Field Theory at Finite Temperature and Density," *Phys. Rept.*, vol. 145, p. 141, 1987.

[6] J. I. Kapusta and C. Gale, *Finite-temperature field theory: Principles and applications*, ser. Cambridge Monographs on Mathematical Physics. Cambridge University Press, 2011.

[7] M. Laine and A. Vuorinen, *Basics of Thermal Field Theory: A Modern Primer*, ser. Lecture Notes in Physics. Cham, Switzerland: Springer, 2016, vol. 925.

[8] M. Strickland, *Relativistic Quantum Field Theory, Volume 3*. IOP, 11 2019.

[9] M. G. Mustafa, "An introduction to thermal field theory and some of its applications," 2022, arXiv preprint: 2207.00534. [Online]. Available: https://arxiv.org/abs/2207.00534

[10] R. Roosenstein, M. Attems, and W. A. Horowitz, "Coherent State Path Integral Reveals Unexpected Vacuum Structure in Thermal Field Theory," 7 2025. [Online]. Available: https://arxiv.org/abs/2507.11608

[11] H. B. G. Casimir, "On the attraction between two perfectly conducting plates," *Proc. K. Ned. Akad. Wet.*, vol. 51, pp. 793–795, 1948.

[12] G. L. Klimchitskaya and V. M. Mostepanenko, "Experiment and theory in the Casimir effect," *Contemp. Phys.*, vol. 47, pp. 131–144, 2006.

[13] H. F. Trotter, "On the product of semi-groups of operators," *Proceedings of the American Mathematical Society*, vol. 10, no. 4, pp. 545–551, 1959.

[14] T. Umeda, S. Ejiri, S. Aoki, T. Hatsuda, K. Kanaya, Y. Maezawa, and H. Ohno, "Fixed scale approach to equation of state in lattice QCD," *Phys. Rev. D*, vol. 79, p. 051501, 2009.

[15] A. Bazavov, T. Bhattacharya, M. Cheng, and P. Petreczky, "Equation of state and QCD transition at finite temperature," *Phys. Rev. D*, vol. 80, p. 014504, 2009.

[16] P. Huovinen and P. Petreczky, "QCD equation of state and hadron resonance gas," *Nucl. Phys. A*, vol. 837, p. 26, 2010.

[17] A. V. Belitsky, "QCD evolution equations," in *The Phenomenology of Large N(c) QCD*, 4 2002, pp. 128–142.

[18] M. Attems, J. Casalderrey-Solana, D. Mateos, I. Papadimitriou, D. Santos-Oliván, C. F. Sopuerta, M. Triana, and M. Zilhão, "Thermodynamics, transport and relaxation in non-conformal theories," *JHEP*, vol. 10, p. 155, 2016.

[19] L. Yan, "A flow paradigm in heavy-ion collisions," *Int. J. Mod. Phys. A*, vol. 32, no. 14, p. 1730005, 2017.

[20] D. M. Hofman and J. Maldacena, "Conformal collider physics: Energy and charge correlations," *JHEP*, vol. 05, p. 012, 2008.

[21] H. Chen, I. Moult, X. Zhang, and H. X. Zhu, "Rethinking jets with energy correlators: Tracks, resummation, and analytic continuation," *Phys. Rev. D*, vol. 102, no. 5, p. 054012, 2020.

[22] C. Andres, F. Dominguez, R. Kunnawalkam Elayavalli, J. Holguin, C. Marquet, and I. Moult, "Resolving the Scales of the Quark-Gluon Plasma with Energy Correlators," *Phys. Rev. Lett.*, vol. 130, no. 26, p. 262301, 2023.

[23] A. Budhraja, H. Chen, and W. J. Waalewijn, "ν-point energy correletors with FastEEC: Small-x physics from LHC jets," *Phys. Lett. B*, vol. 861, p. 139239, 2025.

Numeric exploration of Non-trivial emergent phenomena in Quark-Gluon Plasma

Nia O'Callaghan[1] **and WA Horowitz**[1,2]

[1] Department of Physics, University of Cape Town, Rondebosch 7701, South Africa
[2] Department of Physics, New Mexico State University, Las Cruces, New Mexico, 88003, USA

E-mail: OCLJON001@myuct.ac.za

Abstract. We present here an analysis of probe quark behavior in a thermal Quark-Gluon Plasma via the AdS/CFT correspondence, modeling them as string endpoints with specific boundary conditions. We study both heavy (on-mass-shell) and light (off-mass-shell) quarks initially at rest, exploring analytic solutions where possible and using Wolfram's *Mathematica* for numerical solutions elsewhere. This enables comparison and verification. Due to difficulties in obtaining these numeric string solutions, we also examine numerical solutions for a point particle in the same spacetime geometries as a simpler test case. Although not all objectives were achieved, we present our findings, discuss limitations, and outline future research directions.

1 Introduction

The study of Quark-Gluon Plasma (QGP) advances our understanding of the quantum universe, especially the strong force and particle dynamics. Found in heavy ion collisions at RHIC and LHC, QGP is a complex, deconfined state of matter that challenges previous assumptions of a gas-like behavior, as evidenced by anisotropic momentum distribution [1, 2] (known as *elliptic flow*, [1, 2]). Both weak and strong coupling regimes are supported: perturbative QCD effectively predicts high transverse momentum observables [3] assuming weak coupling, while near-ideal hydrodynamics describes low transverse momentum observables [4, 5] assuming strong coupling.

Our investigation focuses on probe quarks interacting with QGP, modeled via AdS/CFT as strings in a String Theory. We aim to solve the string equations of motions allowing us to analyze the displacements of string endpoints, reflecting probe quark motion and allowing extraction of QGP transport coefficients. Due to absent analytic solutions, we develop numerical solutions in Wolfram's *Mathematica* to model these strings in the general case, validating with simpler known cases. Additionally, we examine point particles in the same spacetime geometries as a simplified approach to inform our methods and address challenges in the full string analysis.

2 The String Case

2.1 Theory

As established in Section 1, we are ultimately interested in solving the equations of motion for a string in Anti-de Sitter or *AdS* spacetime for the purposes of connecting this motion to that of a probe quark via the AdS/CFT correspondence [6, 7]. More specifically, we want to solve the equations of motion arising from the Polyakov [8, 9, 10, 7] action,

$$S_P = -\frac{T}{2}\int_{\mathcal{M}} d^2\sigma\,\sqrt{-h}h^{ab}G_{\mu\nu}\partial_a X^\mu \partial_b X^\nu = -\frac{T}{2}\int_{\mathcal{M}} d^2\sigma\,\sqrt{-h}h^{ab}\gamma_{ab}\,, \tag{1}$$

where T is the string tension, $\mathcal{M}$ is the worldsheet of the string with coordinates $\sigma^a = (\tau, \sigma)^a$ and volume element $d^2\sigma = d\tau d\sigma$ (indexed with Latin indices to distinguish them from target spacetime objects, which are indexed with

Greek indices), $X^\mu = X^\mu(\tau, \sigma)$ are the coordinates of the string (to be understood as mapping functions from the string worldsheet to the target spacetime), $\gamma_{ab} := G_{\mu\nu}\partial_a X^\mu \partial_b X^\nu$ is the metric induced on the worldsheet by the pullback of the target spacetime metric $G_{\mu\nu}$ along the mapping functions X^μ, h_{ab} is the metric on the worldsheet itself (with inverse h^{ab} and determinant h), and natural units are used unless otherwise stated. The equations of motion resulting from the extremization of (1) are

$$\nabla_a \Pi^a_\mu - \Gamma^\alpha_{\mu\nu}\Pi^a_\alpha \partial_a X^\nu = 0 \tag{2}$$

where $\Pi^a_\mu = -Th^{ab}G_{\mu\nu}\partial_b X^\nu$ are the canonical momentum densities obtained from the action (1) via the usual procedure, $\Gamma^\alpha_{\mu\nu}$ are the usual Christoffel symbols of the target spacetime metric $G_{\mu\nu}$, and ∇_a is the covariant derivative on the string worldsheet from the Levi-Civita connection associated with the worldsheet metric h_{ab}. The worldsheet itself is taken to be a square given by $\mathcal{M} = [0, \sigma_f] \times [0, \sigma_f]$.

We analyze the equations of motion for two string cases: both endpoints fixed representing a heavy, on-mass-shell quark; and one fixed and one free endpoint representing a light, off-mass-shell quark [7, 11]. For the heavy case, we apply Dirichlet boundary conditions at both ends: $\frac{\partial X^1}{\partial \tau}(\tau, 0) = \frac{\partial X^1}{\partial \tau}(\tau, \sigma_f) = 0$. For the light case, we apply a Dirichlet condition at one end ($\frac{\partial X^1}{\partial \tau}(\tau, 0) = 0$) and a Von Neumann condition at the other ($\Pi^1_1(\tau, \sigma_f) = 0$).

Our focus is on $AdS_5 \times S^5$ spacetime, dual to $\mathcal{N} = 4$ Super Yang-Mills CFT[1]. Since no analytic solutions exist there[2] , we use the simpler AdS_3-Schwarzschild geometry, where solutions are known (as derived in [7, 11]), allowing validation of our numeric results before tackling the full $AdS_5 \times S^5$ spacetime.

These solutions employ static ($X^0(\tau, \sigma) = t = \tau$) and conformal gauges[3] ($h_{ab} = \eta_{ab} = \mathrm{diag}(-1, 1)$). We adopt the notation $X^1(\tau, \sigma) = r(t, \sigma)$ to make our use of the static gauge explicit and refer to this coordinate as the "radial" direction for consistency, regardless of its geometric interpretation.

This AdS_3-Schwarzschild spacetime geometry is equivalently described by the metrics

$$ds^2_{\mathrm{AdS}} = -f_{\mathrm{Ads}}(r)dt^2 + \frac{dr^2}{f_{\mathrm{Ads}}(r)} + \frac{r^2}{l^2}; \quad ds^2_{\mathrm{Tort}} = f_{\mathrm{Tort}}(r)(-dt^2 + dr^2_*) + \frac{r_H^2}{l^2}\coth\left(\frac{r_H r_*}{l^2}\right)dx^2\,, \tag{3}$$

in the usual (t, r, x) radial coordinates (which we will refer to as "AdS coordinates") and in the (t, r_*, x) tortoise coordinates, respectively. In equations (3), x is the single transverse direction, l is the curvature radius of the spacetime, r_H is the radial position of the black hole horizon, and we have defined the metric factors

$$f_{\mathrm{AdS}}(r) := \frac{r^2}{l^2}h_3(r) = \frac{r^2 - r_H^2}{l^2}\,; \quad f_{\mathrm{Tort}}(r_*) := \frac{r_H^2}{l^2}\,\mathrm{csch}\left(\frac{r_H r_*}{l^2}\right)^2\,, \tag{4}$$

with the use of the usual AdS_d-Schwarzschild *blackening factor*, defined for a general number of spacetime dimensions d as $h_d(r) := 1 - \left(\frac{r_H}{r}\right)^{d-1}$.

Along with the equations of motion (2) for the string itself, we also have the worldsheet constraint equation arising from the extremization of (1) with respect to the worldsheet metric h_{ab}, $h_{ab} = 2\gamma_{ab}(h^{cd}\gamma_{cd})^{-1} \iff \frac{\gamma_{ab}}{\sqrt{-\gamma}} = \frac{h_{ab}}{\sqrt{-h}}$, where γ is the determinant of the induced metric γ_{ab}. For our uses, we make note of this constraint equation only for completeness since it is not used by the numeric solver, as our choice of the conformal gauge eliminates any dynamics from the worldsheet metric which would need to make use of the constraint equation.

2.2 Numeric Results

Making use of the *NDSolve* function built into Wolfram's *Mathematica* to numerically solve equation (2) in the above established spacetime geometry, we are able to obtain numeric solutions in both the heavy and light cases. Figure 1 shows parametric plots of the radial component $X^1(\tau, \sigma) = r(t, \sigma)$ of these solutions in the static gauge, along with plots of the corresponding analytic solutions. These solutions were computed via the *Finite Element Method* algorithm within *NDSolve*, with default settings for control parameters, and in the AdS coordinate system using the initial condition of a statically stretched string so as to agree with the analytic solutions, $r(0, \sigma) = r_s + \frac{\sigma}{\sigma_f}l_s$, where l_s is the spacial extent of the string and $r_s := (1 + \varepsilon)r_H$ is the *stretched horizon* introduced to regulate an IR divergence at the black hole horizon [7, 11], with $0 < \varepsilon \ll 1$.

[1] In the appropriate limiting cases, this field theory provides a good approximation for QCD [6, 12].

[2] While certain special case analytic solutions for the motion of the string in AdS_5-Schwarzschild and $AdS_5 \times S^5$ are known [13, 14, 15], they are unsuitable for use in our case. This is primarily due either to the analytic solutions being approximate perturbative results, as in [13], or else considering a different physical configuration (primarily in the form of the initial and boundary conditions applied) than the one we are interested in, as in [14, 15] as well as in [13].

[3] To be technically correct, this is not the gauge that the term "conformal gauge" usually refers to, but rather a closely related gauge choice that is more restrictive and commonly used [8], which has the added benefit of eliminating the remaining gauge freedom after making use of the static gauge

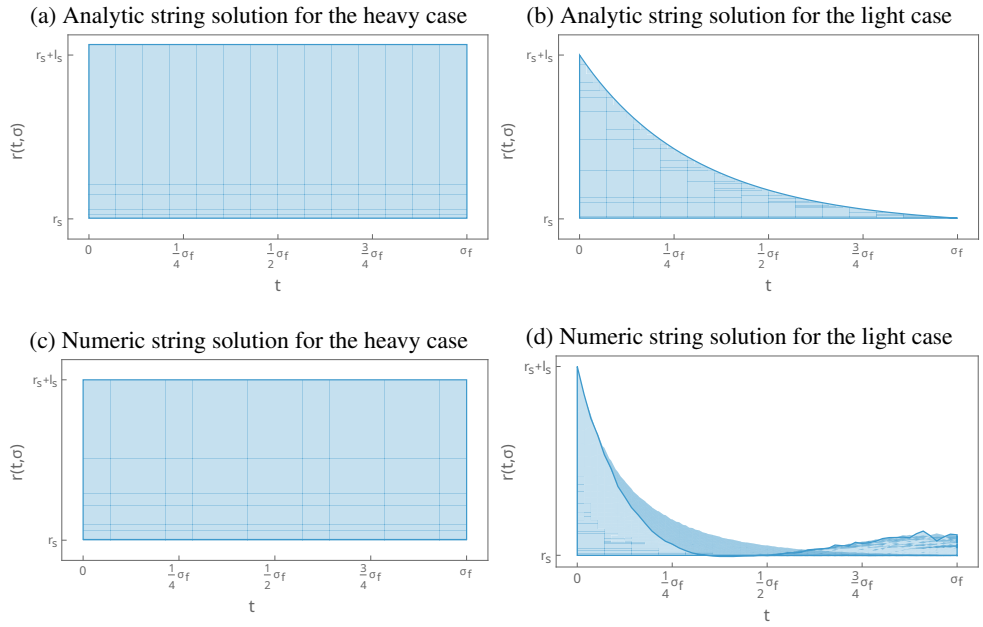

Figure 1: Parametric plots in AdS coordinates of the analytic (*top*) and numeric (*bottom*) string solutions in both the heavy (*left*) and light (*right*) cases. These plots show the full spacial extent of the string on the vertical axis, plotted over time on the horizontal.

Figure 1 shows good agreement for the heavy case but significant deviation for the light case. In the heavy case, the string remains nearly static, consistent with analytic solutions [7], though not perfectly mirroring it numerically[4]. The light case exhibits non-physical behavior: the endpoint folds over itself (as indicated by the shaded region in plot 1d), falling inward faster than the speed of light motion of the analytic endpoint, implying superluminal speeds of the numeric endpoint. Deviations are about one-tenth of the string length—much larger than numerical errors alone could account for. The initial, rough agreement between the numeric endpoint and the analytic solution (indicated by the rough alignment of the shaded region in plot 1d and the trajectory in plot 1b) suggests the main error lies at the endpoint, owing to issues with the boundary conditions. The cause of these boundary issues remain unclear, as they are provided as an input to the numeric solver and should therefore be enforced internally.

Due to persistent difficulties in aligning the numeric string solution with the analytic results, particularly for the light case, we will instead analyze a point particle in the same spacetime geometries. This simplifies the problem, helps understand the geometric issues, and may guide future corrections. Once the string boundary issues are resolved, we aim to extend our approach to AdS_5-Schwarzschild spacetime, expecting agreement with existing special case solutions [13, 14, 15] in these special cases.

3 The Point Particle Case

3.1 Theory

The trajectory of a point particle is known as a geodesic of the spacetime it exists within. These geodesics can be understood as generalisations of the notation of a straight line [16, 17]; they are the paths that extremize the invariant spacetime interval between two events, analogous to how straight lines extremize the Euclidean distance between two points. This logic leads to a standard textbook derivation such as given is [16, 17, 10, 18] of the geodesic equation for a trajectory $x^\mu(\lambda)$ parameterised by an arbitrary (affine) parameter λ,

$$\frac{d^2x^\mu}{d\lambda^2} + \Gamma^\mu_{\nu\rho}\frac{dx^\nu}{d\lambda}\frac{dx^\rho}{d\lambda} = 0\,. \tag{5}$$

[4]More careful comparison of the numeric and analytic solutions in the heavy case reveal a slight discrepancy: despite appearing the same in figure 1, the numeric solution has the string gradually fall below the position predicted by the analytic solution (*i.e.*, for a position of the string at a given σ value, the corresponding radial position of the string in the numeric solution, $r(t,\sigma)$, gradually falls below the radial position for the same value of σ predicted by the analytic solution as t increases). A full quantitative examination of this and other errors with the numeric solutions produced here are omitted for brevity, though they are expanded upon in the upcoming thesis on this topic.

The motion of a point particle in a curved spacetime can also be determined from the extremization of one of the following three actions, which we would expect to all give equivalent trajectories [16, 17, 8, 10, 18],

$$S_m := -m \int d\lambda \sqrt{-\dot{x}^2}; \qquad S_2 := m^2 \int d\lambda \, \dot{x}^2; \qquad S_e := \frac{1}{2} \int d\lambda \left(\frac{\dot{x}^2}{e} - em^2 \right), \tag{6}$$

where $\dot{x}^2 = G_{\mu\nu} \frac{dx^\mu}{d\lambda} \frac{dx^\nu}{d\lambda}$, m is the mass of the particle, and $e = e(\lambda)$ is an additional degree of freedom (known as the "einbein") introduced. The S_m action is the usual reparameterisation invariant action for a massive point particle, S_2 is the "square" of this action preferred for its simplicity and direct connection to equation (5) despite the loss of reparameterisation invariance [16], and S_e is an additional action that avoids the complicating factor of the square root present in the S_m action without the loss of reparameterisation invariance by introducing the additional einbein object [8], which has the added benefit of remaining valid for massless particles (for which the S_m and S_2 actions are invalid). For the massless case, we do have one additional method to solve for the trajectory of the particle, and this is to make use of the fact that massless particles must travel on lightlike (null) trajectories. These trajectories satisfy $\dot{x}^2 = 0$ which, by making use of the static gauge $x^0(\lambda) = t(\lambda) = \lambda$, gives us a first order differential equation that can be solved to find $x^1(\lambda) = r(\lambda)$.

The equations of motion arising from the three actions, S_m, S_2, S_e in equation (6), can be written as the parallel transport of the canonical momentum arising from the relevant action via the usual procedure, as given in equation (7). In the case of the einbein action, we additionally need to consider the equations of motion for the einbein itself, which come out to be the constraint equation (8) [8].

$$\frac{D}{d\lambda} \pi^{(i)}_\mu = \dot{x}^\nu \nabla_\nu \pi^{(i)}_\mu = 0 \tag{7}$$

$$0 = \frac{\dot{x}^2}{e^2} + m^2, \tag{8}$$

where $\dot{x}_\mu = G_{\mu\nu} \frac{dx^\nu}{d\lambda}$, $i \in \{m, e, 2\}$ is the same label as the subscript on the associated action, $\pi^{(i)}_\mu$ is the canonical momentum obtained from the corresponding action, and $\frac{D}{d\lambda} = \dot{x}^\nu \nabla_\nu$ is the parallel transport operator [16]. All the difference arising from the specifics of the different actions are contained within the different canonical momenta.

In all cases, we will use the initial conditions $x^\mu(0) = (t(0), r(0))^\mu = (0, 1)^\mu$ and $\dot{t}(0) = 1$. In the massive case, we will then use $\dot{r}(0) = 0$ and solve equation (8) to obtain possible values for $e(0)$, while for the massless case we will obtain $\dot{r}(0)$ from the other initial conditions to place the particle on a null trajectory at $\lambda = 0$. We will then attempt to numerically solve all versions of equation (7) from the different actions, as well as variations on these equations and the free initial conditions[5]. This leads to a huge number of different potential configurations for the numeric solutions which will be run via *NDSolve* and, once non-physical solutions have been ruled out[6], these solutions will be compared. Table 1 shows the final counts of the number of solution configurations, the number of non-physical solutions, the number of solutions that were not able to be solved[7], and the final count of remaining numeric solutions both in Minkowski spacetime and in the two coordinate systems for AdS_3-Schwarzschild spacetime established in Section 2.1. In all cases, we will take the metric to have the form $ds^2 = -f(r)dt^2 + g(r)dr^2$, which allows us to recover all three cases by the forms of $f(r), g(r)$[8].

3.2 Numeric Results

Numeric point particle trajectories are computed using *NDSolve*'s default parameters and methods. Due to the numerous variations, we focus on comparing individual solutions against a designated "reference solution": analytic null trajectories[9] in the massless case and numeric solutions to the geodesic equation (5) in the massive case ,

[5]To be specific, the equations (7) and (8) (and/or the derivative of (8)) are reformed either programmatically or manually into equivalent equations through usual manipulation and simplification procedures. While all variations of these equations are obvious mathematically (and therefore physically) equivalent, the different forms lead to different numeric performance. Additionally, certain cases for the einbein action have unfixed initial conditions for the einbein itself (or its derivative); we will explore the options of $-1, 0,$ or 1 for $\dot{e}(0)$ in either case and $e(0)$ in the massless case.

[6]Solutions are deemed non-physical and ruled out if they either do not satisfy at least one of the initial conditions laid out above, or else if the solution for the time coordinate has $\dot{t}(\lambda) < 0$, as time must be an increasing function. As in the string case discussed in Section 2.2, it is unclear as to why certain numeric solutions do not satisfy the relevant initial conditions, as they are supplied to the *NDSolve* function and so should be enforced in the numeric solver itself.

[7]Meaning that *NDSolve* returned a fatal error in trying to find numeric solutions that was unable to be resolved.

[8]Minkowski spacetime corresponds to $f(r) = g(r) = 1$, AdS_3-Schwarzschild spacetime in AdS coordinates by $f(r) = \frac{1}{g(r)} = f_{\text{AdS}}(r)$ and in tortoise coordinates with $f(r) = g(r) = f_{\text{Tort}}(r)$; where $f_{\text{AdS}}(r)$ and $f_{\text{Tort}}(r)$ are as in equations (4).

[9]These analytic solutions to the null trajectory condition $\dot{x}^2 = 0$ were computed via the *DSolve* function within *Mathematica* and confirmed by hand, though the solutions themselves are ommited for brevity.

	Minkowski		AdS		Tortoise		Final Count		
	M	Ml	M	Ml	M	Ml	M	Ml	Total
Initially	12	18	180	244	180	244	372	506	878
Failed to run	0	2	128	125	115	238	243	365	608
Non-physical	0	0	34	39	40	3	74	42	116
Finally	12	16	18	80	25	3	55	99	154

Table 1: Counts of the number of solutions available, computed, and ruled out, in Minkowski spacetime and in AdS and tortoise coordinates for AdS_3-Schwarzschildspacetime. The column labels "M" and "Ml" refer to the massive and massless particle cases respectively.

since analytic solutions for (5) are unavailable[10] for AdS_3-Schwarzschild. Deviations from the reference solutions are measured by maximum and RMS differences, with solutions ranked by RMS deviation. Each solution's label indicates its specific variations and parameters. Table 2 displays the top three solutions for both cases. In the massive case, solutions based on the simplified geodesic equation outperform those using the einbein action; for the massless case, einbein solutions perform equally well, comparable to massive geodesics. Deviations are much smaller than the characteristic scales[11], indicating suitably accurate numeric solutions.

Massive		Massless	
	3.7007×10^{-17}		3.7007×10^{-17}
GeoMSimpAds	1.1102×10^{-16}	Ec0d2e0ep1MlAds	1.1102×10^{-16}
	1.6239×10^{-14}		3.7007×10^{-17}
GeoMSimpTort	9.2370×10^{-14}	Ec0d2e0ep1MlSimpAds	1.1102×10^{-16}
	6.8894×10^{-8}		3.7007×10^{-17}
Ec0d1e1ep0MSimpTort	7.0336×10^{-8}	Ec0d2e1ep0MlAds	1.1102×10^{-16}

Table 2: Table of the RMS (top) and maximum (bottom) deviations from the reference solution for the top three solutions in each mass case, ordered by RMS deviation. Each solution label encodes information about the solution configuration. Labels begin with the equation used (either "Geo" or "E" for use of the geodesic equation (5) or the einbein action S_e in equation (6), respectively) and end with the coordinate system computed in (either "AdS" or "Tort" for AdS or tortoise coordinates, respectively). Labels contain the term "Simp" if they were simplified using the *FullSimplify* function built into *Mathematica*.

4 Conclusions and Outlook

Section 3.2 indicates no action consistently yields the best equations of motion. The geodesic equation (5) from the S_2 action performs well across a large number of cases, though not best in any. The standard S_m action produces equations that are not numerically solvable, while the einbein action S_e is solvable in *most* cases but often sensitive to initial conditions, constraints, and coordinate choices. Future work should investigate why certain actions or configuration choices fail or depend so sensitively on these factors and whether adjusting solver settings are able to remedy the issues encountered. Given the geodesic equation's robustness, comparing solutions primarily to it and seeking an analytic solution for detailed analysis is advisable.

For the string case, insights from the point particle suggest adding non-physical degrees of freedom (such as a non-trivial worldsheet metric, in analogy to the point particle einbein) to improve stability. Exploring equations from the Nambu-Goto action is also an option, although it may face similar issues as S_m and S_2 unless those failures are understood. Additionally, point particle geodesic solutions can serve as seeds for string solutions to enhance stability. Note that we avoided any interpretation of the results found in the context of QGP physics, and in particular we have not related the behaviour of string endpoints to that of the probe quarks. The reason for this, aside from the obvious issues encountered in our string solutions, is due to the change made from the full $AdS_5 \times S^5$

[10] It should be noted that analytic solutions for a null geodesic exist is AdS_3-Schwarzschild and AdS_5-Schwarzschild [15], though not for general non-null geodesics.

[11] Such as initial position, $r(0) = 1$, of the particle or black hole horizon radius, $r_H = 0.3$.

spacetime required by the AdS/CFT correspondence to our simpler case of AdS_3-Schwarzschild spacetime, where this correspondence no longer holds.

Aside from these modifications to the string system, there are multiple other routes for improvements in future work. It is worthwhile investigating the use of different numeric solvers[12] for generating numeric solutions. More careful consideration of the appropriateness of boundary and initial conditions applied is also warranted, particularly as mentioned in [14].

Acknowledgements
NO and WAH thank the National Research Foundation (NRF), the National Institute for Theoretical and Computational Physics (NITheCS), and the SA-CERN collaboration for their generous financial support during the course of this work.

References

[1] M. Gyulassy, "The qgp discovered at rhic," in *NATO Advanced Study Institute: Structure and Dynamics of Elementary Matter*, Mar. 2004, pp. 159–182.

[2] U. W. Heinz and P. F. Kolb, "Early thermalization at rhic," *Nucl. Phys. A*, vol. 702, pp. 269–280, 2002.

[3] A. Majumder and M. Van Leeuwen, "The theory and phenomenology of perturbative qcd based jet quenching," *Prog. Part. Nucl. Phys.*, vol. 66, pp. 41–92, 2011.

[4] U. Heinz and R. Snellings, "Collective flow and viscosity in relativistic heavy-ion collisions," *Ann. Rev. Nucl. Part. Sci.*, vol. 63, pp. 123–151, 2013.

[5] C. Gale, S. Jeon, and B. Schenke, "Hydrodynamic modeling of heavy-ion collisions," *Int. J. Mod. Phys. A*, vol. 28, p. 1340011, 2013.

[6] J. M. Maldacena, "The large n limit of superconformal field theories and supergravity," *Adv. Theor. Math. Phys.*, vol. 2, pp. 231–252, 1998.

[7] A. K. Mes, R. W. Moerman, J. P. Shock, and W. A. Horowitz, "Strongly coupled heavy and light quark thermal motion from ads/cft," *Annals Phys.*, vol. 436, p. 168675, 2022.

[8] D. Tong, "String theory," Jan. 2009.

[9] A. M. Polyakov, "Quantum geometry of bosonic strings," *Phys. Lett. B*, vol. 103, pp. 207–210, 1981.

[10] B. Zwiebach, *A first course in string theory*. Cambridge University Press, Jul. 2006.

[11] R. W. Moerman and W. A. Horowitz, "A semi-classical recipe for wobbly limp noodles in partonic soup," May 2016.

[12] G. 't Hooft, "A planar diagram theory for strong interactions," *Nucl. Phys. B*, vol. 72, p. 461, 1974.

[13] S. S. Gubser, "Drag force in ads/cft," *Phys. Rev. D*, vol. 74, p. 126005, 2006.

[14] C. P. Herzog, A. Karch, P. Kovtun, C. Kozcaz, and L. G. Yaffe, "Energy loss of a heavy quark moving through n=4 supersymmetric yang-mills plasma," *JHEP*, vol. 07, p. 013, 2006.

[15] P. M. Chesler, K. Jensen, and A. Karch, "Jets in strongly-coupled n = 4 super yang-mills theory," *Phys. Rev. D*, vol. 79, p. 025021, 2009.

[16] S. M. Carroll, *Spacetime and Geometry: An Introduction to General Relativity*. Cambridge University Press, Jul. 2019.

[17] D. Tong, "Lectures on general relativity," https://www.damtp.cam.ac.uk/user/tong/gr.html, 2022, lecture notes, University of Cambridge.

[18] R. d'Inverno, *Introducing Einstein's relativity*. Clarendon Press, 1992.

[12] Such as the *GNU scientific library* in C, differential equation libraries in Python, or making use of other program suites (such as *MATLAB*) and their associated solvers in place of *Mathematica*'s *NDSolve*.

Parameterizing the Geometry of the QGP on an Event-by-Event Basis

Ben Bert[1], **Coleridge Faraday**[1] **and W.A. Horowitz**[1,2]

[1]Department of Physics, University of Cape Town, 7701 Rondebosch, South Africa
[2]Department of Physics, New Mexico State University, Las Cruces, New Mexico, 88003, USA

E-mail: ben.bert.1303@gmail.com

Abstract. Ultra-relativistic heavy-ion collisions create a nuclear fireball that serves as a powerful laboratory for probing the frontiers of Quantum Chromodynamics (QCD). In recent years, there has been growing interest in the study of small collision systems—such as proton-proton (pp) and proton-nucleus (pA)—at facilities like RHIC and the LHC. Many of the assumptions underlying the energy loss formalism developed in the Djordjevic-Gyulassy-Levai-Vitev (DGLV) model, break down in these small systems. In this work, we present an extension of the energy loss model developed by Faraday and Horowitz (FH) which itself is an extension of the DGLV formalism that specifically accounts for the unique features of small system dynamics. This is achieved by relaxing the large formation time approximation and introducing an additional correction term that accounts for short path lengths in the medium. By relaxing these assumptions, one encounters a more intricate analytic structure for the energy loss, and thus increased computational demands; we address this challenge by developing a novel numerical scheme. Our approach accurately parametrizes the geometry of the quark-gluon plasma (QGP), resulting in a dramatic computational speedup—improving efficiency by up to seven orders of magnitude.

1 Introduction

The nuclear modification factor (R_{AA}) is a key observable for studying the energy loss of high transverse momentum (p_T) particles traversing the Quark-Gluon Plasma (QGP). Rooted in Bjorken's jet quenching framework, the R_{AA} quantifies the suppression of particle yields in heavy-ion collisions relative to proton-proton systems [1]. Experiments at RHIC observed a suppression in light hadron spectra by a factor of five, signaling strong partonic energy loss in the QGP [2].

More recently, signatures of QGP formation—including quarkonium suppression, strangeness enhancement, and collective flow—have also been identified in small collision systems—such as pp and pA—at RHIC and the LHC [3]. However, small systems pose unique challenges, such as centrality bias, which arises from correlations between soft and hard particles [4].

Azimuthal anisotropies in detected spectra, as quantified by the v_n flow coefficients, offer further insights into the properties of the QGP, including transport properties and the path-length-dependent energy loss of partons [5, 6].

The azimuthal anisotropies can be characterized through a Fourier decomposition of the observed spectra, the Fourier decompositions are given in terms of the v_n Fourier coefficients and the event plane angle ψ_n. Due to detector acceptance effects and finite particle multiplicity, the measured event plane angles fluctuate event-by-event around the true event plane angles. To account for these fluctuations, *resolution factors* are introduced to correct the measured v_n coefficients; the resolution factors however, induce an ambiguity into the measured v_n coefficients [7]. The *scalar product* method of measuring the v_n coefficients, couples soft and hard hadrons in a

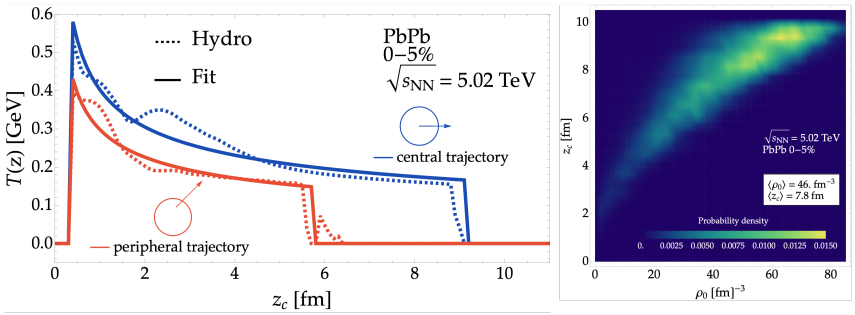

Figure 1: (Left): Comparison of temperature distributions obtained from hydrodynamic simulations (dotted curves) and the corresponding fitted temperature distribution (solid curves) for two paths through the medium. The red curves have initial positions of $\mathbf{x}_0 = (1.5, 4.5)$ fm and angles $\phi = \pi/4$, and are representative of characteristic *peripheral* trajectories; the blue curves have initial positions of $\mathbf{x}_0 = (0, 0)$ fm and angles $\phi = 0$, and are representative of characteristic *central* trajectories. The hydrodynamic temperature distribution comes from a PbPb 0–5% collision system at $\sqrt{s_{NN}} = 5.02$ TeV. For the peripheral trajectory, $z_c = 5.7$ fm and $\rho_0 = 30.5$ fm^{-3}; for the central trajectory, $z_c = 9.1$ fm and $\rho_0 = 74.9$ fm^{-3}. (Right): Correlation between ρ_0 and z_c parameters for 0–5% PbPb collision system at $\sqrt{s_{NN}} = 5.02$ TeV. The first moments for the $P_{geo}(\rho_0, z_c)$ distribution (with the angular dependency integrated out) are found for this collision system to be $\langle\rho_0\rangle = 46.0$ fm^{-3} and $\langle z_c\rangle = 7.8$ fm.

given centrality while avoiding the ambiguities induced by the resolution factors and is thus considered to be a more robust measurement of the v_n coefficients [8, 9].

It has proven to be a challenge on theoretical grounds to simultaneously predict the R_{AA} and the v_n coefficients—a tension known as the $R_{AA} \otimes v_n$ puzzle. One of the contributions known to effect the tension is attributed to the omission of soft-sector fluctuations and event-by-event fluctuations of the initial state [5].

In this work we use the energy loss model developed by Faraday and Horowitz (FH) which has extended the DGLV radiative energy loss formalism by including short path-length corrections and collisional energy loss using Hard Thermal Loop (HTL) kinematics [10]. Their model adopts a static, brick-like medium and parameterizes the scattering center using an effective path length [10, 11, 12, 13, 14].

The primary focus of this manuscript will to be to develop a framework that describes the nuclear modification factor while simultaneously describing the anisotropic flow harmonics. We extend upon the work of FH by including event-by-event fluctuations of the bulk geometry and relaxing the brick-like and static simplification of the bulk's geometry.

2 Parametrization of Trajectories

The energy loss of a parton in the QGP depends on its path and the medium's geometry. As calculating energy loss for all possible trajectories can be computationally expensive (see section 2.2 for a more in depth discussion), we follow the previous work of [10, 11] by mapping each trajectory to two parameters—which the energy loss can be made to be dependent on—the energy loss can then be averaged over these parameters to capture the global effects of the collision system.

We model the energy loss in terms of a scattering center density $\bar{\rho}$, which is related to the medium density ρ *via* $\rho = (N_s/A_\perp)\bar{\rho}$, where N_s is the number of scatterings, $A_\perp$ the transverse area of the medium. The medium density ρ can be expressed in terms of the medium's temperature through elementary thermodynamic relations as $\rho = 4\zeta(3)(4 + n_f)T^3/(\pi^2)$. To model ρ along each trajectory, we fit the medium density with power-law profile as $\rho_{fit}(z) = \rho_0 \left(\tau_0/z\right)^{1.2} \theta(z_c - z)\theta(z - \tau_0)$, with the formation time of the medium $\tau_0 = 0.4$ fm. The choice of τ_0 is made as this is the turn-on time for the hydrodynamics simulations we use [15]. The corresponding fitted temperature profile is then $T_{fit}(z) = \left(\pi^2\rho_{fit}(z)/4\zeta(3)(4 + n_f)\right)^{1/3}$. For each path, the cutoff z_c is determined by the distance at which the hydrodynamic temperature distribution drops below the thermalization temperature, and ρ_0 is fixed by ensuring that the area under the temperature curve is the same for both the hydrodynamic temperature profile (obtained from the IP-Glasma model [15]) and the fitted temperature profile. In fig. 1 (Left) we show a comparison of the hydrodynamic temperature distribution and the fitted temperature distribution for two characteristic paths through the medium.

To generalize to an entire event ensemble, we define a probability distribution over (ρ_0, z_c) for a fixed angle ϕ through the medium by assuming that the initial parton production scales with n_{coll}, the number of binary

collisions density. In fig. 1 (Right) we show the correlation between the ρ_0 and z_c parameters for a PbPb 0–5% collision system at $\sqrt{s_{NN}} = 5.02$ TeV.

2.1 Energy Loss

In this work, we model the energy loss of a parton moving through the QGP by taking into account radiative and elastic contributions. Following FH [10, 12, 13, 14] we use the WHDG [11] formalism along with its short path length correction [16] to model the radiative sector of the energy loss, and we model the elastic energy loss by using an effective field theory called Hard Thermal Loops (HTL). Our implementation of the energy loss relaxes the static brick assumption used by FH; the formalism we make use of allows the Debye mass μ and gluon mass m_g to depend on the temperature of the medium at each point of the parton's trajectory through the medium.

2.2 Numerical challenges of the energy loss

Conceptually, the most simple method of calculating the energy loss on a path-by-path basis would be to compute the energy loss using the true hydrodynamic temperature profile and then using the expression for ρ to find the associated medium density. To capture the global effects, one would then simply average over all the different paths through the medium. However, the total number of paths one would need to consider to resolve the QGP would typically involve ~ 20 angles and a grid of size $\sim 15 \times 15(\text{fm})^2$ with intervals of $\sim 0.05(\text{fm})$. To capture the event-by-event fluctuations, one would need to calculate the energy loss another $\sim 10^3$ times, one for each event. Note that the parameters specified here are estimates of the typical resolution used in model, but the specific values will vary depending on the collision system.

This computational expensiveness is why we introduce the ρ_0 and z_c parameters, as these parameters allow us to calculate the energy loss as a function of the two parameters and then use a distribution of the ρ_0 and z_c parameters (see the right panel of fig. 1) to capture the global effects. The entire phase space of possible paths requires a grid of ρ_0 and z_c parameters such that $\rho_0 \in [1, 100]$ fm^{-3} and $z_c \in [0.4, 11]$ fm with intervals of 10 fm^{-3} and 1 fm respectively. Thus, calculating the energy loss by using the fitted parameter method proves to be seven orders of magnitude faster than more direct method described in the preceding paragraph. Note that the evaluating the energy loss in terms of the fitted parameters closely resembles the energy loss calculation done if we were to use the true hydrodynamic temperature profile; this good agreement between the two methods validates the use of the fitted parameter method.

3 Observables

3.1 Nuclear Modification Factor

The nuclear modification factor of a parton q in an $A + A$ collision system is defined as

$$R^q_{AA}(p_T, \phi) \equiv \frac{d^2N^q_{AA,f}/dp_T d\phi}{N_{coll}\, d^2N^q_{pp,f}/dp_T d\phi} = \int \frac{dx}{1-x} P_{tot}\,(x|\phi)\, \frac{f^q_{AA}\left(\frac{p_T}{1-x}, \phi\right)}{f^q_{pp}(p_T, \phi)} \tag{1}$$

where $d^2N^q_{AA,f}/dp_T d\phi$ and $d^2N^q_{pp,f}/dp_T d\phi$ are the parton spectra in $A+A$ and $p+p$ collisions after interactions with the medium respectively; N_{coll} is the average number of binary collisions, typically calculated using the Glauber model [17]. The second equality in eq. (1) grants us access to the R_{AA} on theoretical grounds, and is true if one assumes the following: (1) The partonic spectrum of the initial state in a $p + p$ collision, scales like the partonic spectrum of the initial state in an $A+A$ collision, weighted by $1/N_{coll}$. (2) All modifications to the $A+A$ differential spectrum arises from the energy loss through interactions with the medium. (3) The proton-proton spectrum is unmodified by the medium. Note that we have defined the notational device $f^q_{pp/AA}(p_T, \phi)$ as:

$$f^q_{pp}(p_T, \phi) \equiv \frac{d^2N^q_{pp,i}}{dp_T d\phi} \qquad \& \qquad f^q_{AA}(p_T, \phi) \equiv \frac{1}{N_{coll}} \frac{d^2N^q_{AA,i}}{dp_T d\phi} \tag{2}$$

where in eq. (2), the i subscript is used to denote the spectrum of the initial state.

3.2 Azimuthal Anisotropies

The observed azimuthal anisotropy in high-p_T hadrons allows for the study of the energy loss and the path length dependence of hard partons moving though the QGP [5]. In this work, an analogue to the $v_n\{SP\}$ coefficients measured experimentally is developed from a theoretical point of view (see section 3.4). This is done so that the theory predictions made in our study are more comparable to what is being observed experimentally. As part of the framework developed here, we incorporate event-by-event fluctuations of the initial state into the calculation of the v_n and $v_n\{SP\}$ coefficients. In fig. 2 we demonstrate that accounting for these fluctuations is crucial for addressing the $R_{AA} \otimes v_2$ puzzle.

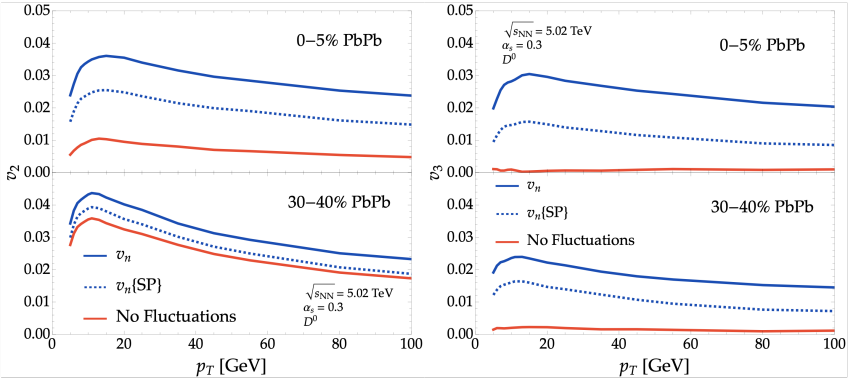

Figure 2: (Left): Comparison of Fourier, Scalar Product v_2 and the Fourier v_2 without fluctuations as a function of p_T for D^0 mesons. The event-by-event fluctuations are turned off by evaluating eq. (5) with R_{AA} averaged over all events instead of event-by-event R_{AA}. All curves are calculated with the strong coupling fixed at $\alpha_s = 0.3$. The top (bottom) panel shows the results where the geometric average is calculated over a PbPb 0-5% (30-40%) centrality collision system. (Right): The same as (Left) but for v_3 instead of v_2.

3.3 Azimuthal Anisotropies from Fourier Expansions

The azimuthal anisotropy in the distributions of the observed final state hadrons can be characterized by a Fourier expansion [7]

$$\frac{2\pi}{N^{h,k}_{AA,f}}\frac{dN^{h,k}_{AA,f}}{d\phi} = \frac{R^{h,k}_{AA}(p_T,\phi)}{R^{h,k}_{AA}(p_T)} = 1 + 2\sum_{n=1}^{\infty} v_n^k \cos\left(n\left[\phi - \psi_n^k\right]\right) \tag{3}$$

where the v_n^k coefficients are the uniquely determined Fourier coefficients, ψ_n^k are the event plane angles, and the k index specifies a particular event.

3.4 Scalar Product v_n

The scalar product (SP) method of determining the reaction plane experimentally is achieved through the use of $\vec{Q}_n$ flow vectors. The $\vec{Q}_n$ vectors provide an approximation to the reaction plane and are determined from the final state particles *via* [7]

$$\mathcal{Q}_n \equiv Q_n e^{in\Psi_n} = \sum_j e^{in\phi_j}, \tag{4}$$

One may then take the real and imaginary parts of $\mathcal{Q}_n$ to be the x and y component of the $\vec{Q}_n$ vector respectively. To access the $\vec{Q}_n$ in our energy loss formalism, we make use of the IP-Glasma model which is then evolved with the MUSIC viscous relativistic $(2+1)$ D hydrodynamics code, followed by UrQMD microscopic hadronic transport [15]. The j index in eq. (4) is summed over final state particles from all oversampled UrQMD simulations and the azimuthal angle is $\phi_j = \arctan 2\left(p_j^y, p_j^x\right)$. The $v_n\{SP\}$ coefficients are defined here as

$$v_n\{SP\} \equiv \frac{\left\langle \vec{u}_n \cdot \vec{Q}_n \right\rangle}{\sqrt{\langle Q_n^2 \rangle}} = \sum_{k=1}^{N_e} \frac{\int_0^{2\pi} d\phi\; R^{h,k}_{AA}(p_T,\phi)\vec{Q}_n^k \cdot \vec{u}_n^k(\phi)}{2\pi\sqrt{\langle Q_n^2\rangle} N_e R^{h,k}_{AA}(p_T)} \tag{5}$$

in line with what is commonly done experimentally [8, 9]. In eq. (5) the vector $\vec{u}_n$ is defined as $\vec{u}_n \equiv (\cos n\phi, \sin n\phi)$, where ϕ is the azimuthal direction of the hadronic candidate. The quantity $\langle \vec{u}_n \cdot \vec{Q}_n \rangle$ in eq. (5), is an average over all events and over different $\vec{u}_n$ vectors associated with the observed hadrons; $\langle Q_n^2 \rangle$ is only averaged over the events. The second equality in eq. (5) provides us access to the $v_n\{SP\}$ coefficient on theoretical grounds, and follows from the first equality in eq. (5) if one assumes that the distribution of initial hard jet production is proportional to the number of binary collision density $n^k_{coll}(\vec{x})$.

4 Results

In this section we present our model's predictions for the R_{AA} and v_2 coefficients. All comparisons to data are made with the strong coupling α_s varied between 0.25 and 0.3. Note that we only present results for large system data (PbPb) as calculations for small systems are yet to be complete.

In fig. 3 we show the prediction of the model for charged particles in PbPb collisions at 0-5% and 30-40% centrality for both the R_{AA} and the v_2. The R_{AA} data is from the CMS [18] and ATLAS [19] experiments respectively; the v_2 data comes from the same collaborations [8, 9].

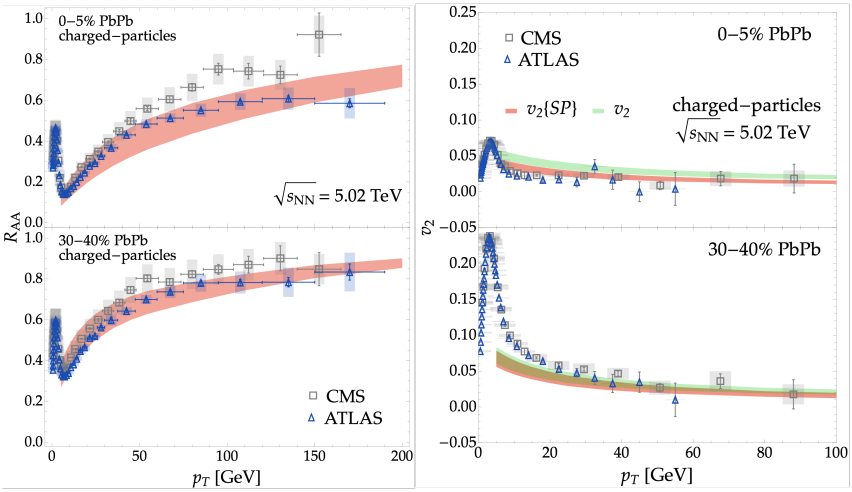

Figure 3: (Left): Comparison of R_{AA} predictions to CMS [18] and ATLAS [19] data for charged particles in 0-5% (top) and 30-40% (bottom) PbPb. (Right): v_2 predictions for charged particles vs CMS/ATLAS in 0-5% (top) and 30-40% (bottom) PbPb [8, 9].

5 Conclusions and Outlook

In this manuscript, we presented a modification to the formalism developed by FH [10, 12, 13, 14], in which the static brick assumption has been relaxed. The model we present here takes into account the temperature profile of the medium as a function of the parton's path through said medium; the dynamic nature of the temperature on a path-by-path basis is captured by parametrizing a power law dependency (through ρ_{fit}) of the medium density through two fitted parameters. The energy loss of a parton moving through the medium can be calculated in terms of these two fitted parameters, this leads to a dramatic numerical speed up—which is vitally important for statistically robust modeling of event-by-event fluctuations.

For high-p_T charged particles, the model is in good agreement with v_2 data for PbPb collisions systems and shows the correct qualitative centrality dependence as the model's predictions for the v_2 increase as the collisions become more peripheral. The same conclusions can be drawn for the models predictive capabilities when comparing to the R_{AA} of high-p_T charged particles in PbPb collision systems.

Future work will focus on completing the model's predictions for small collision systems by performing a χ^2 minimization to find the optimal value of α_s which best describes both the R_{AA} and v_2 data in large systems, and then using this extracted value of α_s to make predictions for small systems, as done in [14]. As the initial state effects are thought to be more pronounced in small systems, another route of future work will be to perform an analysis of the effects of the initial temperature dependence (*i.e.* before the formation time τ_0) on the energy loss and the associated observables. Furthermore, the effects of our choice of parameterization of the medium density is to be compared to the results obtained when using the true hydrodynamic temperature profile on a path-by-path basis is planned for future work.

Acknowledgements

The authors would like to thank the South African National Research Foundation (NRF), the National Institute for Theoretical and Computational Sciences (NITheCS), and the SA-CERN collaboration.

References

[1] J. D. Bjorken, "Energy loss of energetic partons in quark-gluon plasma: Possible extinction of high p_t jets in hadron-hadron collisions," Fermilab, Tech. Rep. FERMILAB-PUB-82-059-THY, 1982, unpublished.

[2] K. Adcox *et al.*, "Suppression of hadrons with large transverse momentum in central Au+Au collisions at $\sqrt{s_{NN}}$ = 130-GeV," *Phys. Rev. Lett.*, vol. 88, p. 022301, 2002.

[3] J. F. Grosse-Oetringhaus and U. A. Wiedemann, "A Decade of Collectivity in Small Systems," Jul. 2024, arXiv:2407.07484 [hep-ex].

[4] J. Adam *et al.*, "Centrality dependence of particle production in p-Pb collisions at $\sqrt{s_{\rm NN}}$= 5.02 TeV," *Phys. Rev. C*, vol. 91, no. 6, p. 064905, 2015.

[5] J. Noronha-Hostler, B. Betz, J. Noronha, and M. Gyulassy, "Event-by-event hydrodynamics + jet energy loss: A solution to the $R_{AA} \otimes v_2$ puzzle," *Phys. Rev. Lett.*, vol. 116, no. 25, p. 252301, 2016.

[6] M. Aaboud *et al.*, "Measurement of the suppression and azimuthal anisotropy of muons from heavy-flavor decays in Pb+Pb collisions at $\sqrt{s_{\rm NN}} = 2.76$ TeV with the ATLAS detector," *Phys. Rev. C*, vol. 98, no. 4, p. 044905, 2018.

[7] M. Luzum and J.-Y. Ollitrault, "Eliminating experimental bias in anisotropic-flow measurements of high-energy nuclear collisions," *Phys. Rev. C*, vol. 87, no. 4, p. 044907, 2013.

[8] M. Aaboud *et al.*, "Measurement of the azimuthal anisotropy of charged particles produced in $\sqrt{s_{\rm NN}}$ = 5.02 TeV Pb+Pb collisions with the ATLAS detector," *Eur. Phys. J. C*, vol. 78, no. 12, p. 997, 2018.

[9] A. M. Sirunyan *et al.*, "Azimuthal anisotropy of charged particles with transverse momentum up to 100 GeV/c in PbPb collisions at $\sqrt{s}_{NN}$=5.02 TeV," *Phys. Lett. B*, vol. 776, pp. 195–216, 2018.

[10] C. Faraday, A. Grindrod, and W. A. Horowitz, "Inconsistencies in, and short pathlength correction to, $R_{AA}(p_T)$ in A + A and p + A collisions," *Eur. Phys. J. C*, vol. 83, no. 11, p. 1060, 2023.

[11] S. Wicks, W. Horowitz, M. Djordjevic, and M. Gyulassy, "Elastic, inelastic, and path length fluctuations in jet tomography," *Nucl. Phys. A*, vol. 784, pp. 426–442, 2007.

[12] C. Faraday and W. A. Horowitz, "Collisional and radiative energy loss in small systems," *Phys. Rev. C*, vol. 111, no. 5, p. 054911, 2025.

[13] ——, "A unified description of small, peripheral, and large system suppression data from pQCD," *Phys. Lett. B*, vol. 864, p. 139437, 2025.

[14] ——, "Statistical analysis of pQCD energy loss across system size, flavor, $\sqrt{s_{NN}}$, and p_T," May 2025, arXiv:2505.14568 [hep-ph].

[15] B. Schenke, C. Shen, and P. Tribedy, "Running the gamut of high energy nuclear collisions," *Phys. Rev. C*, vol. 102, no. 4, p. 044905, 2020.

[16] I. Kolbe and W. A. Horowitz, "Short path length corrections to Djordjevic-Gyulassy-Levai-Vitev energy loss," *Phys. Rev. C*, vol. 100, no. 2, p. 024913, 2019.

[17] M. L. Miller, K. Reygers, S. J. Sanders, and P. Steinberg, "Glauber modeling in high energy nuclear collisions," *Ann. Rev. Nucl. Part. Sci.*, vol. 57, pp. 205–243, 2007.

[18] V. Khachatryan *et al.*, "Charged-particle nuclear modification factors in PbPb and pPb collisions at $\sqrt{s_{\rm N\,N}} =$ 5.02 TeV," *JHEP*, vol. 04, p. 039, 2017.

[19] G. Aad *et al.*, "Charged-hadron production in pp, p+Pb, Pb+Pb, and Xe+Xe collisions at $\sqrt{s_{\rm NN}} = 5$ TeV with the ATLAS detector at the LHC," *JHEP*, vol. 07, p. 074, 2023.

Classical and Quantum Mechanics of Non-holonomic Constraints

W. A. Horowitz[1,2] **and Alexander Rothkopf**[3]

[1]Department of Physics, University of Cape Town, Private Bag X3, Rondebosch 7701, South Africa
[2]Department of Physics, New Mexico State University, Las Cruces, New Mexico, 88003, USA
[3]Department of Physics, Korea University, Seoul 02841, Republic of Korea

E-mail: wa.horowitz@uct.ac.za

Abstract. Modern classical and quantum physics is based on Hamilton's variational action principle. Holonomic constraints, constraints that depend on coordinates alone, can be incorporated into a modified Hamilton's variational action principle through the use of Lagrange multipliers. Non-holonomic constraints, those that depend on coordinates and velocity, such as rolling without slipping, have for 180 years eluded a variational action formulation. We present first results on incorporating non-holonomic constraints into a variational action principle and discuss the implications for classical and quantum mechanics.

1 Introduction

It is not an overstatement to write that modern physics is based on Hamilton's Principle of Extremized Action [1]. The biggest advantage of the action formulation is the natural encoding of symmetries at the start of the treatment, which has been of fundamental importance in the formulation of quantum field theories [2]. Within classical mechanics, one of the major advantages of the action formulation is its ability to handle systems with constraints, e.g. a mass on the end of a rigid rod or a bead on a rotating hoop[1] [1]. Constraints are generally classified as either holonomic (depending only on the coordinates) or non-holonomic (depending on the coordinates and the velocities) [1]. As will be described in some detail below, the treatment of holonomic constraints is "easy." On the other hand, for reasons that will be expanded upon below, the treatment of non-holonomic constraints is "hard." In particular, holonomic constraints may be straightforwardly incorporated into a variational action principle treatment seen by undergraduate students of physics. However, non-holonomic constraints, in fact, *cannot* be incorporated into a variational action principle in the usual way [4, 5]. What we will present here is a novel incorporation of non-holonomic constraints into a variational action principle [6] inspired by the Schwinger-Keldysh technique in quantum mechanics [7, 8].

[1]The action principle's facility with constraints is even valuable in the field theoretic context as gauge fixing can be thought of as a constraint on a field [3].

2 Unconstrained Motion

Recall the usual derivation of the Euler-Lagrange equations in point particle classical mechanics [1]. One defines the action S in terms of the Lagrangian L as

$$S \equiv \int_{t_i}^{t_f} dt\, L(q^i, \dot{q}^i, t), \tag{1}$$

where the q^i are generalized coordinates and $\dot{q}^i \equiv (d/dt)q^i$. One may then derive the usual Euler-Lagrange equations by varying the action

$$\begin{aligned} \delta S &= \int_{t_i}^{t_f} dt\, \frac{\partial L}{\partial q^i}\delta q^i + \frac{\partial L}{\partial \dot{q}^i}\delta \dot{q}^i \\ &= \int_{t_i}^{t_f} dt\, \frac{\partial L}{\partial q^i}\delta q^i + \frac{\partial L}{\partial \dot{q}^i}\frac{d}{dt}(\delta q^i) \\ &= \frac{\partial L}{\partial \dot{q}^i}\delta q^i\Big|_{t_i}^{t_f} + \int_{t_i}^{t_f} dt \left[\frac{\partial L}{\partial q^i}\delta q^i - \frac{d}{dt}\frac{\partial L}{\partial \dot{q}^i}\right]\delta q^i. \end{aligned} \tag{2}$$

Under the assumption that the start and end points of the motion (at the fixed start and end times t_i and t_f, respectively) are fixed, then $\delta q^i(t_i) = \delta q^i(t_f) = 0$; the boundary term in Eq. 2 vanishes. Since the variations δq^i are all independent and arbitrary, the Fundamental Theorem of the Calculus of Variations tells us that

$$\frac{\partial L}{\partial q^i}\delta q^i - \frac{d}{dt}\frac{\partial L}{\partial \dot{q}^i} = 0. \tag{3}$$

Notice our crucial reliance on the so-called transposition rule

$$\delta \dot{q}^i(t) = \frac{d}{dt}\left[\delta q^i(t)\right] \tag{4}$$

in our derivation of Eq. 3.

3 Holonomic Constraints

Suppose now that we restrict the motion of our system such that

$$f(q^i, t) = 0. \tag{5}$$

Since the constraint depends only on the coordinates q^i, this constraint is holonomic. (If the function f depends explicitly on time, then the constraint is rheonomic; if f does not depend explicitly on time, then the constraint is scleronomic.)

There are now several ways of solving the problem, all of which yield physically correct trajectories for the system. The first method of solving the problem involves reducing the degrees of freedom: one solves for one of the q^i in terms of the other q^i through the use of $f = 0$. One may then apply Hamilton's Principle to the remaining degrees of freedom in exactly the same way as in the unconstrained case. In the second method, one retains all the original degrees of freedom, but then one applies the Lagrange-d'Alembert Principle, which is a generalization of Hamilton's Principle. The Lagrange-d'Alembert Principle states that the action of a constrained system is extremized to variations in the paths, where the variations in the paths themselves must be consistent with the constraints; i.e.

$$\begin{aligned} \delta S &= \int_{t_i}^{t_f} dt \left[\frac{\partial L}{\partial q^i}\delta q^i + \frac{\partial L}{\partial \dot{q}^i}\delta \dot{q}^i\right]_{f(q^i+\delta q^i,t)=0} \\ &= \int_{t_i}^{t_f} dt \left[\frac{\partial L}{\partial q^i}\delta q^i - \frac{d}{dt}\frac{\partial L}{\partial \dot{q}^i}\right]\delta q^i\Big|_{f(q^i+\delta q^i,t)=0}. \end{aligned} \tag{6}$$

in deriving the second line, we used the fact (which one can show) that the transposition rule Eq. 4 holds for holonomic constraints [4, 3]. The difficulty with Eq. 6 is that because the variations are constrained, some of the variations depend on the others; i.e. the variations δq^i are *not* all independent and arbitrary. As a result, we cannot utilize the Fundamental Theorem of the Calculus of Variations, and thus we cannot make further analytical

progress[2]. The third method by which we may approach holonomic constraints is through undetermined multipliers. Since $f(q^i + \delta q^i, t) = 0$ we must have that

$$\frac{\partial f}{\partial q^i}\delta q^i = 0 \qquad \Rightarrow \qquad \lambda(t)\left[\frac{\partial f}{\partial q^i}(q^j, t)\right]\delta q^i(t) = 0. \tag{7}$$

Since $\lambda(t)\left[\frac{\partial f}{\partial q^i}(q^j, t)\right]\delta q^i(t) = 0$ we may safely add it to Eq. 6:

$$\delta S = \int_{t_i}^{t_f} dt\, \left[\frac{\partial L}{\partial q^i}\delta q^i - \frac{d}{dt}\frac{\partial L}{\partial \dot{q}^i} + \lambda\frac{\partial f}{\partial q^i}\right]\delta q^i\Big|_{f(q^i+\delta q^i,t)=0}. \tag{8}$$

Now, consider one of the q^α as dependent on the other q^i through the constraint f, i.e. $q^\alpha\big(q^i(t), t\big)$. Let us now choose, or determine, $\lambda(t)$ such that

$$\frac{\partial L}{\partial q^\alpha} - \frac{d}{dt}\frac{\partial L}{\partial \dot{q}^\alpha} + \lambda\frac{\partial f}{\partial q^\alpha} = 0. \tag{9}$$

We now have that

$$\delta S = \int_{t_i}^{t_f} dt\, \left[\frac{\partial L}{\partial q^i}\delta q^i - \frac{d}{dt}\frac{\partial L}{\partial \dot{q}^i} + \lambda\frac{\partial f}{\partial q^i}\right]\delta q^i, \tag{10}$$

where now the equation holds true for *all* i, where for $i = \alpha$ the equation is true through the choice of λ and for $i \neq \alpha$ the variations are all independent and arbitrary. We may thus apply our Fundamental Theorem of the Calculus of Variations for the $i \neq \alpha$ coordinates and, further, rely on our choice of λ for the $i = \alpha$ coordinate, and determine that

$$\frac{\partial L}{\partial q^i}\delta q^i - \frac{d}{dt}\frac{\partial L}{\partial \dot{q}^i} + \lambda\frac{\partial f}{\partial q^i} = 0 \tag{11}$$

for all i. As a final means of computing the trajectory for the motion of our classical system, we may "adjoin" to our original Lagrangian the term

$$\lambda(t) f(q^i, t) \tag{12}$$

and extremize the action in the same way as Hamilton's Principle, treating the q^i and λ as all independent and arbitrary coordinates. One may see by varying the adjoined action in this way that one reproduces exactly the same equations of motion Eq. 11, along with the original constraint equation $f = 0$.

4 Non-holonomic Constraints

Non-holonomic constraints $g(q^i, \dot{q}^i, t) = 0$ are much more difficult to handle than holonomic constraints. Shockingly, the correct equations of motion for non-holonomic constraints were only derived in 2011 [4],

$$\frac{\partial L}{\partial q^\alpha} - \frac{d}{dt}\frac{\partial L}{\partial \dot{q}^\alpha} + \lambda\frac{\partial g}{\partial \dot{q}^\alpha} = 0. \tag{13}$$

One would like to understand how to derive the equations of motion for non-holonomically constrained systems, Eq. 13, from a variational action principle. Such a variational principle would allow one to use all the techniques and utilize all the power of a variational action principle used for unconstrained and holonomically constrained motion in the non-holonomic setting. Further, one would presumably be able to consider the quantum mechanics of a non-holonomically constrained system by performing the path integral with such an action formulation of the problem.

Unfortunately, there are several obstructions to finding a variational action principle formulation of non-holonomic constraints in classical mechanics. First, the transposition rule does not generally hold: one cannot

[2]In principle, one could put Eq. 6 on a computer and (potentially, depending on technical details) numerically find an extremum subject to the constrained variations.

assume that $\delta\dot{q}^i = (d/dt)\delta q^i$ for non-holonomic systems as there are non-trivial correlations between the coordinates and their velocities induced by any non-holonomic constraints. Second, adjoining the Lagrangian with the constraint leads to spurious forces:

$$\begin{aligned} L \quad &\Rightarrow \quad L + \lambda g \\ \Rightarrow \quad \frac{\partial L}{\partial q^\alpha} - \frac{d}{dt}\frac{\partial L}{\partial \dot{q}^\alpha} + \lambda\frac{\partial g}{\partial \dot{q}^\alpha} - \lambda\frac{d}{dt}\frac{\partial g}{\partial \dot{q}^i} + \dot{\lambda}\frac{\partial g}{\partial \dot{q}^i} &= 0 \end{aligned} \tag{14}$$

The physics described by Eq. 14 is known as "vakonomic mechanics"[3]. It is even claimed (and seeminly well-justified) that it is, in fact, *impossible* to find a variational action principle that reproduces, upon extremization, the correct equations of motion Eq. 13 [4].

The means by which one *can* generate an action whose variation yields the correct equations of motion for a non-holonomically constrained system Eq. 13 is to *double* the degrees of freedom. Such a doubling of the degrees of freedom is entirely natural within the Schwinger-Keldysh framework of quantum mechanics [7, 8] in which one considers the expectation value of an operator:

$$\begin{aligned} \langle\hat{\mathcal{O}}\langle(t_f) &= \langle\psi(t_f)|\hat{\mathcal{O}}(t_f)|\psi(t_f)\rangle \\ &= \langle\psi(t_i)|\hat{U}^\dagger_{\hat{H}}(t_f,t_i)\hat{\mathcal{O}}(t_f)U^\dagger_{\hat{H}}(t_f,t_i)|\psi(t_i)\rangle. \end{aligned} \tag{15}$$

One may think of Eq. 15 as the evolution of the system from t_i to t_f, followed by the evolution of the system back to t_i from t_f; the path 1 from t_i to t_f is then *connected* at t_f to the path 2 back to t_i from t_f. One then has that the action for the full evolution from t_i to t_f and then back to t_i from t_f is given by

$$S[q^i_1, q^i_2] = \int_{t_i}^{t_f} dt \left[L\big(q^i_1(t), \dot{q}^i_1(t), t\big) - L\big(q^i_2(t), \dot{q}^i_2(t), t\big)\right]. \tag{16}$$

It's often very useful to define the $\pm$ coordinates in terms of the above $1, 2$ coordinates as follows:

$$q_+ \equiv \frac{1}{2}(q_1 + q_2) \tag{17}$$

$$q_- \equiv q_1 - q_2. \tag{18}$$

In the $\hbar \to 0$ limit, the q_+ becomes the classical path while q_- describes the quantum fluctuations around that classical path. Using these new $\pm$ coordinates, we may define an action adjoined with *two* Lagrange multipliers,

$$S[q^i_+, q^i_-] = \int_{t_i}^{t_f} dt \left[L\big(q^i_1(t), \dot{q}^i_1(t), t\big) - L\big(q^i_2(t), \dot{q}^i_2(t), t\big)\right] + \lambda_- g(q^i_+, \dot{q}^i_+, t) - \lambda_+ q^i_- \left.\frac{\partial g}{\partial \dot{q}^i}\right|_{q=q_+}, \tag{19}$$

whose variation, treating all coordinates and multipliers as independent and arbitrary, yields the correct non-holonomic equations of motion, Eq. 13[4].

One would like to confirm whether or not the extremization of the action Eq. 19 yields the correct trajectory for a non-holonomically constrained classical system. The canonical non-holonomically constrained system is rolling without slipping. This system is extremely useful as there are several methods by which one can find the correct motion; we show in Fig. 1 (top left) that all methods, including our novel extremization of the action, yield identical trajectories. In particular, we show that the trajectories from the known correct equations of motion, Eq. 13, and those from extremizing our novel action Eq. 19 are identical. In producing the trajectory from the novel action, we discretize the action, relying on fourth-order, summation-by-parts finite difference operators on a discrete time grid and minimize using the `FindMinimum` routine of `Mathematica` [6].

What is amazing is that our action formulation can also handle hard-wall constraints, see Fig. 1 (top right), and dissipative systems, see Fig. 1 (bottom).

5 Conclusions

We have shown here the first variational action principle that captures the physics of non-holonomic constraints in classical mechanics. The key insight is to utilize classically the doubled degrees of freedom of the quantum Schwinger-Keldysh approach and introduce *two* undetermined multipliers for each non-holonomic constraint [6].

[3] While Eq. 14 do not describe the motion of a physical system, they do describe the motion when is system is controlled [9].

[4] Note that the $L's$ in terms of the $q'_i s$ in the action Eq. 19 should be thought of as $L's$ of $q_i(q_\pm)$.

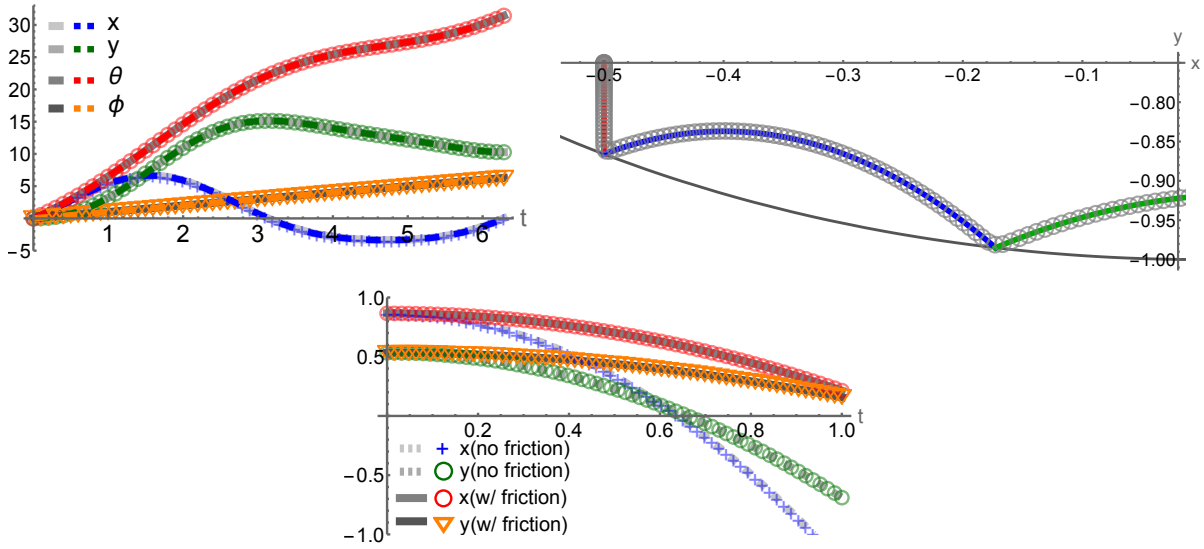

Figure 1: (Top Left) Plots of $x(t)$, $y(t)$, $\theta(t)$, $\phi(t)$ for a 1 kg disc under the force of gravity with $g = 9.8$ m/s^2, of radius 1 m, with $I_S = 1/2$ kg m^2, and $I_D = 1/4$ kg m^2 rolling and spinning down an incline of angle $\alpha = \pi/6$ with initial values $x_i = 0$ m, $\dot{x}_i = 5$ m/s, $y_i = 0$ m, $\dot{y}_i = 0$ m/s, $\theta_i = 0$, $\dot{\theta}_i = 5$ 1/s, $\phi_i = 0$, and $\dot{\phi}_i = 1$ 1/s from the semi-holonomic equations of motion (solid gray), non-holonomic equations of motion (dashed color), and the extremum of Eq. 19 (color symbols). (Top Right) Plots of $x(t)$ and $y(t)$ for a point mass initially at rest falling within a barrel with perfectly elastic collisions with the wall from Newton's Second Law (solid colors) and from the extremum of Eq. 19 (gray circles). (Bottom) Plots of the distance travelled by an object on an inclined plane with angle $\alpha = \pi/6$ from Newton's Second Law (gray) and from the extremization of our action Eq. 19 (colored symbols) in the absence of friction and with friction, with coefficient of kinetic friction $\mu = 0.4$.

The result is Eq. 19. We find that the extrema of Eq. 19 reproduce the correct classical equations of motion for non-holonomically constrained systems [4]. We find, further, that this action can handle systems with general inequality constraints and dissipative forces, neither of which can be handled with the usual single degree of freedom Hamilton's Principle or Lagrange-d'Alembert Principle.

Future work includes 1) considering the path integral version of Eq. 19 to examine the quantum mechanics of systems with non-holonomic constraints, 2) attempting to derive Eq. 19 from first principles, and 3) applying the techniques shown here to the conformal gauge in string theory in order to extend work on exact symmetry preservation in the numerical solution of partial differential equations [10]. Some recent progress has been made on 2) by computing the $\hbar \to 0$ limit of the unconstrained Schwinger-Keldysh action and showing that the results reproduce the correct initial value Euler-Lagrange equations.

Acknowledgements
WAH thanks the South African National Research Foundation (NRF) and the SA-CERN Collaboration for financial support. AR thanks Korea University for support through project K2503291 Ab-initio simulation of the real-time dynamics of non-relativistic fermions as well as project K2511131.

References

[1] H. Goldstein, C. P. Poole, and J. L. Safko, *Classical Mechanics*, 3rd ed. Addison-Wesley, 2002.

[2] S. Weinberg, *The Quantum theory of fields. Vol. 1: Foundations*. Cambridge University Press, 6 2005.

[3] B. Bert and W. A. Horowitz, "Integrable Non-Holonomic Constraints and Gauge Fixing in Classical Field Theory." [Online]. Available: https://arxiv.org/abs/2505.20684

[4] M. R. Flannery, "d'Alembert–Lagrange analytical dynamics for nonholonomic systems," *Journal of Mathematical Physics*, vol. 52, no. 3, p. 032705, 2011.

[5] W. A. Horowitz and A. Rothkopf, "Even More Generalized Hamiltonian Dynamics." [Online]. Available: https://arxiv.org/abs/2408.14420

[6] A. Rothkopf and W. A. Horowitz, "A unifying action principle for classical mechanical systems," 2024. [Online]. Available: https://arxiv.org/abs/2409.11063

[7] J. S. Schwinger, "Brownian motion of a quantum oscillator," *J. Math. Phys.*, vol. 2, pp. 407–432, 1961.

[8] L. V. Keldysh, "Diagram Technique for Nonequilibrium Processes," *Sov. Phys. JETP*, vol. 20, pp. 1018–1026, 1965.

[9] A. M. Bloch, *Nonholonomic Mechanics and Control*, 2nd ed., ser. Interdisciplinary Applied Mathematics, P. S. Krishnaprasad and R. M. Murray, Eds. New York, NY: Springer New York, 2015, vol. 24.

[10] A. Rothkopf, W. A. Horowitz, and J. Nordström, "Exact symmetry conservation and automatic mesh refinement in discrete initial boundary value problems," *J. Comput. Phys.*, vol. 524, p. 113686, 2025.

Energy Loss as a Probe of Quark-Gluon Plasma Formation Across Collision System Size

Coleridge Faraday[1], **W. A. Horowitz**[1,2]

[1]Department of Physics, University of Cape Town, Private Bag X3, Rondebosch 7701, South Africa
[2]Department of Physics, New Mexico State University, Las Cruces, New Mexico, 88003, USA

E-mail: frdcol002@myuct.ac.za

Abstract. The quark-gluon plasma (QGP) forms when protons and neutrons melt at temperatures over 100,000 times hotter than the Sun's core—conditions achieved in high-energy heavy-ion collisions, such as those involving lead or gold nuclei at the Large Hadron Collider (LHC) and the Relativistic Heavy Ion Collider (RHIC). More recent observations suggest that small droplets of QGP may also form in rare, high-multiplicity proton-proton and proton-lead collisions. One way to probe the QGP is by measuring the suppression of high-momentum particles, which lose energy to the medium as they traverse it. If QGP forms in these small systems, non-negligible suppression is expected; however, no conclusive evidence of energy loss in such systems has been measured. Oxygen-oxygen collisions conducted at the LHC in July 2025 offer a new opportunity to test QGP formation in smaller systems. In this work, we use a statistically driven analysis of R_{AA} data from large collision systems to constrain an energy loss model that incorporates small-system-size corrections. We then make novel predictions for small systems including $p/d + A$ and $\mathrm{O} + \mathrm{O}$ collisions. Our results show that high-momentum particle suppression in central $p/d + A$ collisions agrees with central photon-normalized $d + \mathrm{Au}$ data from RHIC but deviates significantly from central Glauber-normalized LHC $p + \mathrm{Pb}$ results. We argue that this discrepancy likely arises from event selection biases. Upcoming minimum bias $\mathrm{O} + \mathrm{O}$ measurements will provide key insights into the system size dependence of energy loss and QGP formation in an environment free from selection biases.

1 Introduction

The quark-gluon plasma (QGP) is a state of deconfined quarks and gluons formed at extreme temperatures in the ultra-relativistic collision of heavy ions [1]. While there is overwhelming evidence for QGP formation in large systems like $\mathrm{Au} + \mathrm{Au}$ and $\mathrm{Pb} + \mathrm{Pb}$ collisions, a key question in the field is whether QGP can form in smaller systems such as $p/d/^3\mathrm{He} + \mathrm{Au}$. Surprisingly, signatures of collective behaviour, such as multi-particle correlations, appear to turn on smoothly as a function of particle multiplicity, irrespective of system size, suggesting the formation of tiny QGP droplets even in high-multiplicity $p + \mathrm{Pb}$ and $p + p$ collisions [2]. However, another key QGP signature, the suppression of high-transverse-momentum (p_{T}) particles due to partonic energy loss [3], presents a puzzle. While this suppression is unambiguously observed in central A+A collisions [4, 5], measurements in small systems are contradictory: RHIC has observed suppression in central d+Au collisions [6], whereas LHC measurements in $p + \mathrm{Pb}$ collisions show an enhancement [7, 8]. This tension motivates a quantitative theoretical investigation.

This work aims to better understand the theoretical expectation for energy loss in small systems based on matching experimental data in large systems. We employ a perturbative quantum chromodynamics (pQCD) based energy loss model that includes both collisional [9, 10] and radiative [11] energy loss channels, and importantly,

incorporates small-system-size corrections to both the collisional [10, 12] and radiative energy loss [13, 14]. To make robust predictions, we first constrain our model's single free parameter, the effective strong coupling $\alpha_s^{\text{eff.}}$, through a rigorous χ^2 statistical analysis against a wide array of high-p_{T} hadron suppression data from central heavy-ion collisions at RHIC and the LHC. This procedure allows us to establish a well-calibrated baseline from which to make zero-parameter extrapolations to smaller systems.

Our extrapolations to small systems show good agreement with the photon-normalized $R_{d\text{Au}}$ data from PHENIX [6], which minimizes sensitivity to event selection biases. In contrast, our predictions disagree with Glauber-model-normalized $R_{p\text{Pb}}$ data from the LHC [7, 8], which are known to be more sensitive to such biases [8]. We argue that this discrepancy likely reflects experimental biases rather than a failure of the energy loss paradigm. A promising way to clarify this issue is to study oxygen-oxygen collisions, where the no-energy-loss baseline is under better theoretical control and the system is large enough to expect suppression even in minimum bias events [15]. In July 2025, O + O collisions at $\sqrt{s_{NN}} = 5.36$ TeV were conducted at the LHC; however, experiments have not yet reported data. In this work, we present novel predictions for minimum bias O + O collisions using our model constrained entirely by large-system data.

2 Theoretical Framework

Our theoretical framework is described in detail in our previous works [12, 14, 16] and is based on the Wicks-Horowitz-Djordjevic-Gyulassy (WHDG) model [17]. The model computes energy loss via two primary mechanisms: gluon radiation (radiative energy loss) and elastic scattering (collisional energy loss). To make realistic predictions, we utilize fluctuating, initial conditions provided by IP-Glasma [18] to determine the distribution of event-by-event path lengths and temperatures. Realistic parton production and fragmentation is also included in the model, and energy loss is calculated on a path-by-path basis.

The radiative energy loss is calculated using the DGLV opacity expansion formalism [11] to first order in opacity. A key feature of our model is the inclusion of a short path length correction (SPLC), which allows for the more rigorous extrapolation of the large-system results to small systems, where the standard assumption of a large, static medium breaks down [13]. We previously showed [14] that the naive inclusion of the SPLC violates the large formation time (LFT) approximation [13] that is made in the DGLV formalism. To remedy this, we introduced a novel kinematic cutoff on the radiated gluon's transverse momentum, which enforces the self-consistency of the calculation across all system sizes [16]. The exact value of this cutoff, along with the transition between hard thermal loop (HTL) and vacuum propagators in the collisional energy loss calculation [9, 10], constitutes the main theoretical uncertainties in our model. We quantify these uncertainties by performing our analysis with the cutoff varied up and down by factors of two, and for two different collisional energy loss models: Braaten and Thoma (BT) [9] and HTL-only [10].

The central observable of interest in this work is the *leading hadron nuclear modification factor* defined as

$$R_{AB}^{h}(p_T) \equiv \frac{\mathrm{d}N^{AB\to h+X}/\mathrm{d}p_T}{\langle N_{\text{coll}}\rangle \mathrm{d}N^{pp\to h+X}/\mathrm{d}p_T}, \tag{1}$$

for the collision $A + B$ and final state hadron h, where $dN^{AB(pp)\to h+X}$ is the differential number of measured hadrons h in the collision $A+B$ ($p+p$) and N_{coll} is the number of binary nucleon-nucleon collisions. The quantity R_{AB} is normalized such that suppression of the final state in $A+B$ collision leads to $R_{AB} < 1$ and no modification of the final state spectrum leads to $R_{AB} = 1$.

3 Statistical Analysis

To make zero-parameter predictions for small systems, we first constrain our model's sole free parameter: the effective strong coupling $\alpha_s^{\text{eff.}}$. The χ^2 is defined as:

$$\chi^2(\alpha_{\text{s}}^{\text{eff}}) = \sum_{i,j}[y_i - \mu_i(\alpha_{\text{s}}^{\text{eff}})](C^{-1})_{ij}[y_j - \mu_j(\alpha_{\text{s}}^{\text{eff}})], \tag{2}$$

where $\vec{y}$ is the vector of experimental data points, $\vec{\mu}(\alpha_{\text{s}}^{\text{eff}})$ is the vector of corresponding theory predictions, and C is the covariance matrix that accounts for statistical, systematic, and normalization uncertainties and their correlations. As a function of p_T, statistical uncertainties are uncorrelated, normalization uncertainties are fully correlated, and systematic uncertainties are modelled as "length-correlated", which allows points closer together in p_T to be correlated while points further apart are uncorrelated [19]. To extract $\alpha_s^{\text{eff.}}$, we minimize the χ^2 against all available R_{AB} data for charged hadrons, π^0 mesons, D mesons, and B mesons at $\sqrt{s_{NN}} = 5.02$ TeV and $\sqrt{s_{NN}} = 200$ GeV with 8 GeV $\leq p_T \leq$ 50 GeV and a centrality of 0–50%. These requirements resulted in 197 data points from LHC and 98 data points from RHIC being included in our analysis.

4 Results and Discussion

Figure 1 shows a representative sample of the experimental data (markers) that was used in our extraction of $\alpha_s^{\text{eff.}}$ and the equivalent post-extraction model result (red bands). The global fit to central and semi-central heavy-ion data yields a good description of all available measurements, with best-fit values of $\alpha_{\text{s}}^{\text{eff}} = 0.41^{+0.14}_{-0.10}$ at RHIC and $\alpha_{\text{s}}^{\text{eff}} = 0.37^{+0.11}_{-0.08}$ at the LHC. The uncertainties are dominated by the theoretical model variations and **not** statistical uncertainties associated with the extraction. The ability for our model to reproduce experimental data across a wide range of centralities and flavours gives us confidence to extrapolate our results to small systems.

With the model constrained, we make predictions for small systems with no additional tuning. Figure 2 compares our predictions to central $d+\text{Au}$ data at RHIC and central $p+\text{Pb}$ data at the LHC. The $d+\text{Au}$ data measured by PHENIX uses direct-photons to provide a model-independent normalization for the R_{AB} while the $p+\text{Pb}$ data are measured by ALICE and ATLAS and uses the Glauber model to calculate the normalization. We observe that a non-negligible suppression of $R_{AB} \sim 0.75$ is measured in $d+\text{Au}$ collisions, in good agreement with our model predictions. In contrast, the LHC data shows enhancement of $R_{AB} \simeq 0.9$–1.2 in stark disagreement with our model predictions.

We argue that the striking discrepancy at the LHC is not a failure of the energy loss paradigm but is instead due to significant event selection biases (*centrality bias*) in the experimental analyses [8]. Centrality bias refers to a non-trivial correlation between the production of high-p_T particles and the total multiplicity, which is used to determine the centrality. There is evidence [8] that such biases, and additionally model dependencies related to the assumptions made in various Glauber-style models [26], may significantly affect the normalization of the centrality-cut R_{AB}.

An interesting proposal is to avoid centrality bias by considering only minimum bias collisions [15]. In particular, $\text{O}+\text{O}$ is an ideal system: small enough to probe the onset of QGP, yet large enough to expect measurable suppression even without centrality selection [15]. In anticipation of the experimental measurements of R_{AB} from

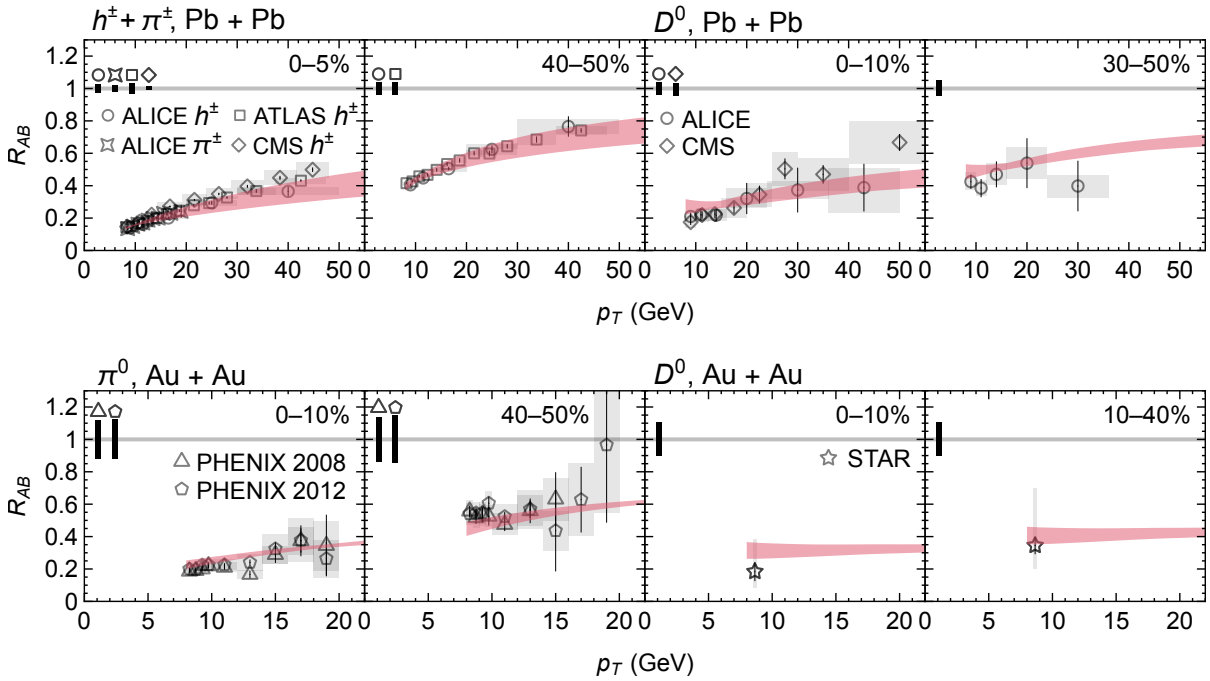

Figure 1: R_{AB} as a function of p_T for a representative sample of the experimental data that is used in our global extraction of $\alpha_s^{\text{eff.}}$. Experimental data is shown with open markers and our constrained model results are shown as a red band. Panels from left-to-right and top-to-bottom results show $h^{\pm}$ and $\pi^{\pm}$ mesons produced in 0–5% and 40–50% centrality $\sqrt{s_{NN}} = 5.02$ TeV $\text{Pb}+\text{Pb}$ collisions [5, 7, 20, 21], D^0 mesons produced in 0–10% and 30–50% centrality $\sqrt{s_{NN}} = 5.02$ TeV $\text{Pb}+\text{Pb}$ collisions [22, 23], π^0 mesons produced in 0–10% and 40–50% centrality $\sqrt{s_{NN}} = 0.2$ TeV $\text{Au}+\text{Au}$ collisions [4, 24], and D^0 mesons produced in 0–10% and 10–40% centrality $\sqrt{s_{NN}} = 0.2$ TeV $\text{Au}+\text{Au}$ collisions [25]. Statistical experimental uncertainties are represented by error bars, systematic uncertainties by shaded boxes, and global normalization uncertainties by bars at unity. The width of the model bands corresponds to the theoretical model uncertainty.

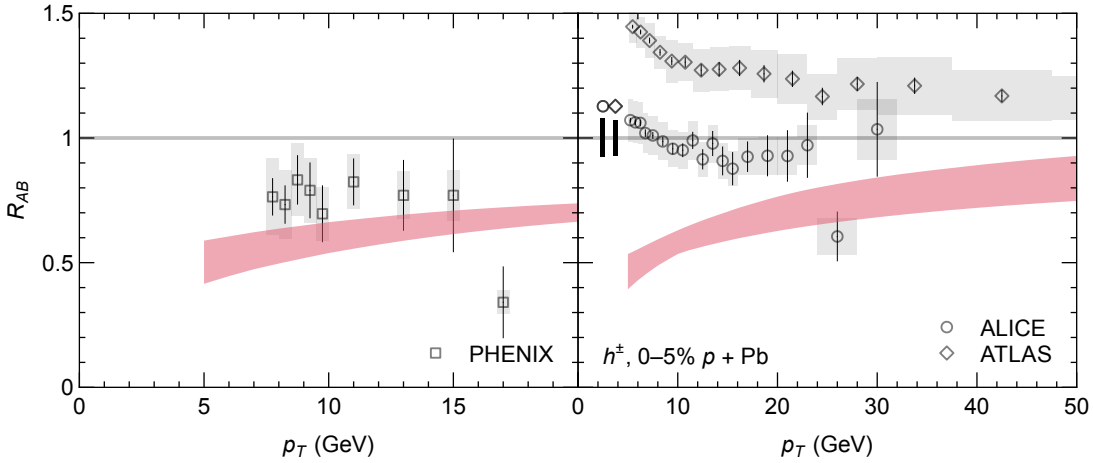

Figure 2: Predicted and measured R_{AA} for central small systems. Left: π^0 suppression in 0–5% $\sqrt{s_{NN}} = 200$ GeV $d+\mathrm{Au}$ collisions at RHIC, with photon-normalized data from PHENIX [6]. Right: $h^{\pm}$ suppression in 0–5% $\sqrt{s_{NN}} = 5.02$ TeV $p+\mathrm{Pb}$ collisions at the LHC. Band width indicates the theoretical uncertainty.

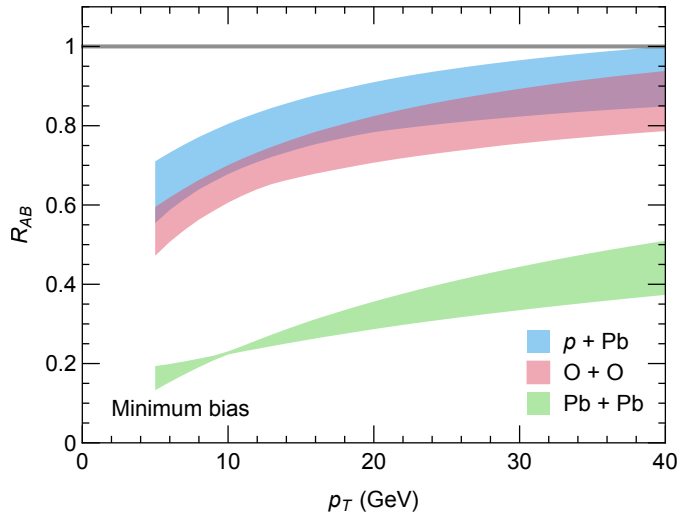

Figure 3: Model predictions for π^0 production in minimum bias $\sqrt{s_{NN}} = 5.02$ TeV $p+\mathrm{Pb}$ (blue), $\sqrt{s_{NN}} = 5.36$ TeV $\mathrm{O}+\mathrm{O}$ (red), and $\sqrt{s_{NN}} = 5.02$ TeV $\mathrm{Pb}+\mathrm{Pb}$ (green) collisions, ordered least to most suppressed. The band width indicates the theoretical uncertainty.

the short run of oxygen-oxygen collisions at $\sqrt{s_{NN}} = 5.36$ TeV that was conducted at the LHC in July of 2025, we now present novel predictions from our model for $\mathrm{O}+\mathrm{O}$ collisions. Figure 3 plots the minimum bias (0–100% centrality) predictions from our model for $p+\mathrm{Pb}$ collisions (blue), $\mathrm{O}+\mathrm{O}$ collisions (red), and $\mathrm{Pb}+\mathrm{Pb}$ collisions (green). We observe that for the p_T range of 5–30 GeV there is R_{AB} of 0.6–0.8 predicted by our model for $\mathrm{O}+\mathrm{O}$ collisions. This fairly significant suppression suggests that the upcoming $\mathrm{O}+\mathrm{O}$ data may reveal measurable QGP-induced energy loss, offering a clean test that could help reconcile the tension between low- and high-p_T observables in small systems.

5 Conclusions and outlook

We have performed a comprehensive statistical analysis of high-p_{T} hadron suppression using a pQCD-based energy loss model that includes small-system-size corrections. Our energy loss model include event-by-event fluctuations in the initial state, distributions of path lengths, realistic hadronization and production spectra, and a quantitative estimate of various important theoretical uncertainties. By constraining the model's single parameter,

$\alpha_s^{\text{eff.}}$, on a wide array of data from heavy-ion collisions, we generated zero-parameter predictions for small systems. After constraining our model, we found good agreement with R_{AB} measured in $\mathrm{Pb}+\mathrm{Pb}$ and $\mathrm{Au}+\mathrm{Au}$ collisions across a wide range of final state hadrons, centralities, and p_T.

We then applied our large-system-constrained model to small collision systems. Our predictions agree well with the central d+Au R_{AB} measured data by PHENIX [6], which does not rely on the Glauber model to normalize the R_{AB}. However, we find strong tension with p+Pb results from the LHC, which show slight enhancement rather than suppression. We argue that this discrepancy is likely due to event selection biases and model dependencies, which are known to be important in small systems [8, 26]. The consistency between our model and the RHIC data, combined with the expected theoretical biases in LHC measurements, supports the interpretation that QGP-induced energy loss in high-multiplicity small systems remains a strong possibility. Interestingly, simple energy loss models also predict similar suppression in peripheral large systems and central small systems [27], suggesting that in order to accurately describe peripheral large system data one *requires* non-negligible suppression in small systems.

To further clarify the system size dependence of partonic energy loss, we presented new model predictions for O+O collisions at $\sqrt{s_{\mathrm{NN}}} = 5.36$ TeV. We predict a clear suppression signal in minimum bias events, with $R_{\mathrm{AA}} \sim 0.6$–0.8 for $5 \leq p_T \leq 30$ GeV. Since centrality selection is not expected to be necessary in O + O to observe suppression [15], forthcoming measurements will hopefully provide a cleaner and less ambiguous test of energy loss and QGP formation in small systems. Such data will be crucial for understanding how QGP formation and energy loss depends on system size. Looking forward, progress in understanding energy loss in small systems will require theoretical control over correlations between jet production and soft multiplicity, improved computation of early-time energy loss [28, 29], and the derivation of small system size corrections to the equation of state [30, 31] and subsequent hydrodynamic evolution.

Acknowledgements
We thank Raymond Ehlers, Joseph Bahder, Jan Fiete Grosse-Oetringhaus, Peter Jacobs, and Yen-Jie Lee for productive discussions. Computations were performed using facilities provided by the University of Cape Town's ICTS High Performance Computing team: `http://hpc.uct.ac.za`. CF and WAH thank the National Research Foundation, the National Institute for Theoretical and Computational Sciences, and the SA-CERN collaboration for their generous financial support during the course of this work.

References

[1] W. Busza, K. Rajagopal, and W. van der Schee, "Heavy Ion Collisions: The Big Picture, and the Big Questions," *Ann. Rev. Nucl. Part. Sci.*, vol. 68, pp. 339–376, 2018.

[2] J. F. Grosse-Oetringhaus and U. A. Wiedemann, "A Decade of Collectivity in Small Systems," 7 2024.

[3] M. Gyulassy and L. McLerran, "New forms of QCD matter discovered at RHIC," *Nucl. Phys. A*, vol. 750, pp. 30–63, 2005.

[4] A. Adare *et al.*, "Suppression pattern of neutral pions at high transverse momentum in Au+Au collisions at $\sqrt{s_{NN}} = 200$ GeV and constraints on medium transport coefficients," *Phys. Rev. Lett.*, vol. 101, p. 232301, 2008.

[5] S. Acharya *et al.*, "Transverse momentum spectra and nuclear modification factors of charged particles in pp, p-Pb and Pb-Pb collisions at the LHC," *JHEP*, vol. 11, p. 013, 2018.

[6] N. J. Abdulameer *et al.*, "Disentangling Centrality Bias and Final-State Effects in the Production of High-pT Neutral Pions Using Direct Photon in d+Au Collisions at sNN=200 GeV," *Phys. Rev. Lett.*, vol. 134, no. 2, p. 022302, 2025.

[7] G. Aad *et al.*, "Charged-hadron production in pp, p+Pb, Pb+Pb, and Xe+Xe collisions at $\sqrt{s_{\mathrm{NN}}} = 5$ TeV with the ATLAS detector at the LHC," *JHEP*, vol. 07, p. 074, 2023.

[8] J. Adam *et al.*, "Centrality dependence of particle production in p-Pb collisions at $\sqrt{s_{\mathrm{NN}}}$= 5.02 TeV," *Phys. Rev. C*, vol. 91, no. 6, p. 064905, 2015.

[9] E. Braaten and M. H. Thoma, "Energy loss of a heavy quark in the quark - gluon plasma," *Phys. Rev. D*, vol. 44, no. 9, p. R2625, 1991.

[10] S. Wicks, "Fluctuations with small numbers: Developing the perturbative paradigm for jet physics in the QGP at RHIC and LHC," Other thesis, 2008.

[11] M. Djordjevic and M. Gyulassy, "Heavy quark radiative energy loss in QCD matter," *Nucl. Phys. A*, vol. 733, pp. 265–298, 2004.

[12] C. Faraday and W. A. Horowitz, "Collisional and radiative energy loss in small systems," *Phys. Rev. C*, vol. 111, no. 5, p. 054911, 2025.

[13] I. Kolbe and W. A. Horowitz, "Short path length corrections to Djordjevic-Gyulassy-Levai-Vitev energy loss," *Phys. Rev. C*, vol. 100, no. 2, p. 024913, 2019.

[14] C. Faraday, A. Grindrod, and W. A. Horowitz, "Inconsistencies in, and short pathlength correction to, $R_{AA}(p_T)$ in A + A and p + A collisions," *Eur. Phys. J. C*, vol. 83, no. 11, p. 1060, 2023.

[15] A. Huss, A. Kurkela, A. Mazeliauskas, R. Paatelainen, W. van der Schee, and U. A. Wiedemann, "Predicting parton energy loss in small collision systems," *Phys. Rev. C*, vol. 103, no. 5, p. 054903, 2021.

[16] C. Faraday and W. A. Horowitz, "Statistical analysis of pQCD energy loss across system size, flavor, $\sqrt{s_{NN}}$, and p_T," 5 2025.

[17] S. Wicks, W. Horowitz, M. Djordjevic, and M. Gyulassy, "Elastic, inelastic, and path length fluctuations in jet tomography," *Nucl. Phys. A*, vol. 784, pp. 426–442, 2007.

[18] B. Schenke, C. Shen, and P. Tribedy, "Running the gamut of high energy nuclear collisions," *Phys. Rev. C*, vol. 102, no. 4, p. 044905, 2020.

[19] S. Cao *et al.*, "Determining the jet transport coefficient $\hat{q}$ from inclusive hadron suppression measurements using Bayesian parameter estimation," *Phys. Rev. C*, vol. 104, no. 2, p. 024905, 2021.

[20] S. Acharya *et al.*, "Production of charged pions, kaons, and (anti-)protons in Pb-Pb and inelastic pp collisions at $\sqrt{s_{NN}}$ = 5.02 TeV," *Phys. Rev. C*, vol. 101, no. 4, p. 044907, 2020.

[21] V. Khachatryan *et al.*, "Charged-particle nuclear modification factors in PbPb and pPb collisions at $\sqrt{s_{\mathrm{N\,N}}} = 5.02$ TeV," *JHEP*, vol. 04, p. 039, 2017.

[22] S. Acharya *et al.*, "Measurement of D^0, D^+, D^{*+} and D_s^+ production in Pb-Pb collisions at $\sqrt{s_{\mathrm{NN}}} = 5.02$ TeV," *JHEP*, vol. 10, p. 174, 2018.

[23] A. M. Sirunyan *et al.*, "Nuclear modification factor of D^0 mesons in PbPb collisions at $\sqrt{s_{\mathrm{NN}}} = 5.02$ TeV," *Phys. Lett. B*, vol. 782, pp. 474–496, 2018.

[24] A. Adare *et al.*, "Neutral pion production with respect to centrality and reaction plane in Au+Au collisions at $\sqrt{s_{NN}}$=200 GeV," *Phys. Rev. C*, vol. 87, no. 3, p. 034911, 2013.

[25] J. Adam *et al.*, "Centrality and transverse momentum dependence of D^0-meson production at mid-rapidity in Au+Au collisions at $\sqrt{s_{\mathrm{NN}}} = 200\,\mathrm{GeV}$," *Phys. Rev. C*, vol. 99, no. 3, p. 034908, 2019.

[26] G. Aad *et al.*, "Transverse momentum, rapidity, and centrality dependence of inclusive charged-particle production in $\sqrt{s_{NN}} = 5.02$ TeV p + Pb collisions measured by the ATLAS experiment," *Phys. Lett. B*, vol. 763, pp. 313–336, 2016.

[27] C. Faraday and W. A. Horowitz, "A unified description of small, peripheral, and large system suppression data from pQCD," *Phys. Lett. B*, vol. 864, p. 139437, 2025.

[28] D. Avramescu, V. Băran, V. Greco, A. Ipp, D. I. Müller, and M. Ruggieri, "Simulating jets and heavy quarks in the glasma using the colored particle-in-cell method," *Phys. Rev. D*, vol. 107, no. 11, p. 114021, 2023.

[29] J. Barata, S. Hauksson, X. Mayo López, and A. V. Sadofyev, "Jet quenching in the glasma phase: Medium-induced radiation," *Phys. Rev. D*, vol. 110, no. 9, p. 094055, 2024.

[30] W. Horowitz and A. Rothkopf, "The QCD Equation of State in Small Systems," *SciPost Phys. Proc.*, vol. 10, p. 025, 2022.

[31] R. Roosenstein, M. Attems, and W. A. Horowitz, "Coherent State Path Integral Reveals Unexpected Vacuum Structure in Thermal Field Theory," 7 2025.

Solving the One-dimensional Schrödinger equation using a set of Daubechies wavelet scaling functions

Obiageli Ezenwachukwu[1], **Moritz Braun**[1]

[1]Department of Physics, University of South Africa, P O Box 392, 0003, UNISA, South Africa

E-mail: 46124586@mylife.unisa.ac.za

Abstract. In this contribution basis sets derived from Daubechies wavelets scaling functions are used to solve the one-dimensional Schrödinger equation on the interval $[-x_{\max} : x_{\max}]$. We present the results for the harmonic oscillator as function of the number N of intervals. Double logarithmic fits of the energy error against N are also shown. Fast convergence is found.
Finally, we discuss applications to the three-dimensional Schrödinger equation, particularly in the context of density functional calculations.

1 Introduction

In solving the Kohn-Sham equations for the orbitals, the choice of a basis set decides strongly the accuracy of a code [1]. Daubechies wavelet scaling functions have most of the properties desired for a basis set used to simulate isolated or inhomogeneous systems, such as molecules and materials [2, 3]. They are compactly supported, meaning they are non-zero only within a finite interval [3, 4]. This property makes them well-suited for approximating data with sharp discontinuities. Their orthogonality ensures that the basis set is well-behaved and stable [4], leading to accurate results in density functional theory (DFT) calculations. They can accurately represent polynomial functions, and their regularity and smoothness make them a powerful and efficient basis set for DFT calculations [1], enabling accurate yet computationally feasible simulations of electronic structures.

1.1 Definition of Daubechies wavelet scaling functions

The provision of a systematic and localized basis set by wavelet scaling functions makes it crucial for achieving both high accuracy [4] and computational efficiency [1, 3], reducing computational cost. When the best wavelet scaling function adapted to data is chosen, the data is sparsely represented. This sparse coding makes wavelet scaling functions an excellent tool for data compression [5]. Wavelet scaling could be used in other applied fields of science such as in astronomy, acoustics, nuclear engineering, sub-band coding, signal and image processing, neurophysiology, magnetic resonance imaging [3, 5], speech discrimination, and optics. They can also be used in fractals, turbulence, earthquake-prediction, radar, human vision [6], and pure mathematics applications such as solving partial differential equations [1]. Scientists sought more suitable functions than the sines and cosines that form the basis of Fourier analysis to approximate fluctuating, intermittent signals and sharp spikes [5]. However, because functions like sines and cosines are non-local and extend infinitely, they are poorly suited for approximating data with sharp discontinuities [7]. For the compression of sparsely represented data, an excellent tool is needed, and wavelet scaling is adapted for this purpose.

The maximally symmetric Daubechies wavelet scaling function ϕ of order 8 (shown in the figure below) is used. One always uses scaling functions for the purpose of expanding wave functions. This function vanishes outside the interval [-7,8]. These Daubechies wavelet scaling functions exist for any arbitrary positive integer order.

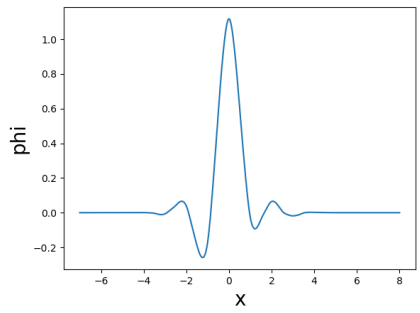

Figure 1: Daubechies wavelet scaling function of order 8.

They have to be evaluated on a grid, using the pyWavelets library.

The Daubechies scaling basis functions are defined as [1, 4]:

$$f_i^h(x) = \frac{1}{\sqrt{h}}\phi\left(\frac{x}{h} + \frac{x_{max}}{h} - i\right). \tag{1}$$

In the equation 1 above, h is the distance between the scaling functions.
Calculations were done using Python, Numpy and PyWavelets. For us to use such functions on a finite interval we need to modify some of the basis functions, such that they become periodic on $-x_{max}$ to x_{max}.
The overlap matrix

$$u_{ij} = \int_{-x_{max}}^{x_{max}} g_i(x) g_j(x) dx \tag{2}$$

is mostly sparse. To evaluate u_{ij} we use the trapezoidal rule with $n_i = 15000$ intervals for each interval h after using cubic spline interpolation on the Daubechies scaling functions. The n_i is the number of integration intervals. Here $g_i(x)$ are the modified scaling basis functions that satisfy periodic boundary conditions on the interval.
The potential energy matrix

$$v_{ij} = \int_{-x_{max}}^{x_{max}} g_i(x) x^2 g_j(x) dx \tag{3}$$

is evaluated in a similar way.
The kinetic energy matrix

$$k_{ij} = \int_{-x_{max}}^{x_{max}} g\prime_i(x) g\prime_j(x) dx \tag{4}$$

is evaluated by first calculating the derivative of the respective basis functions. Thus, we obtain the Hamiltonian matrix as

$$h_{ij} = k_{ij} + v_{ij}. \tag{5}$$

1.2 Harmonic Oscillator

The Schrödinger equation of the one-dimensional harmonic oscillator is given by:

$$-\frac{d^2\psi_n(x)}{dx^2} + x^2\psi_n(x) = E\psi_n(x)\,. \tag{6}$$

Energy eigenvalues of the quantum harmonic oscillator are

$$E_v = 2v + 1\,. \tag{7}$$

We are interested in the ground state energy which is 1. Here we use the $x_{max} = 6$.

N	δE
6	0.00415612
12	$6.54564790 \times 10^{-6}$
18	$4.90738339 \times 10^{-8}$
24	$1.15641696 \times 10^{-9}$
30	$6.16224849 \times 10^{-11}$
36	$9.40092448 \times 10^{-12}$

Table 1: Errors in the ground state energy of the harmonic oscillator.

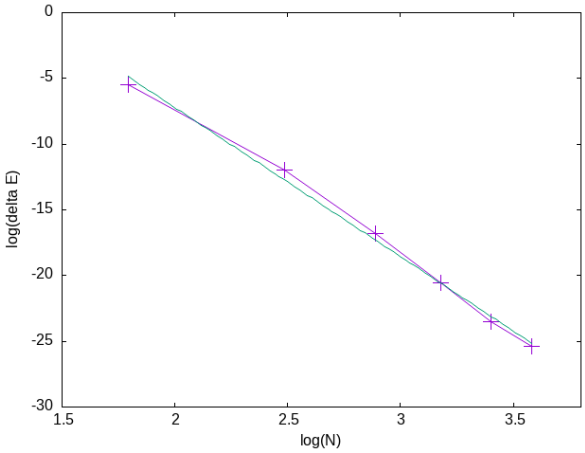

Figure 2: Least square fit of $\delta E = a + b \log N$.

2 Results of calculations for the harmonic oscillator

The ground state energy errors for the harmonic oscillator are given in table 1. N stands for the number of intervals between 0 and x_{max}, we have a total $2N$ intervals. δE simply stands for the error of the ground state energy $E = 1$. The full calculation takes place on $[-x_{max}, x_{max}]$.

2.1 Discussion and conclusion

We can see that as the number of intervals increased, δE decreased, converging towards 0. This shows that a calculation using Daubechies wavelet scaling basis functions converges quickly based on the plot. We see δE decreasing consistently with increasing N. In figure 2 above, log δE is plotted versus log N. The straight line is the least square fit.

We intend to study small molecules with the number of atoms, $n_A \leq 10$. The nuclear coordinates will be derived from molecular information in XYZ files. Three-dimensional Schrödinger-like equations will be employed to solve the density functional approach. The code is under development.

Acknowledgements

Obiageli Ezenwachukwu acknowledges support from UNISA (University of South Africa).

References

[1] T. Deutsch and L. Genovese, "Wavelets for electronic structure calculations," *EDP Sciences,*, p. 33–76, 2011.

[2] B. Natarajan, M. E. Casida, L. Genovese, and T. Deutsch, "Wavelets for density-functional theory and post-density-functional-theory calculations," *Nova Science Publishers, Inc.*, 2011.

[3] L. Genovese, A. Neelov, S. Goedecker, T. Deutsch, S. A. Ghasemi, A. Willand, D. Caliste, O. Zilberberg, M. Rayson, A. Bergman *et al.*, "Daubechies wavelets as a basis set for density functional pseudopotential calculations," *The Journal of Chemical Physics*, vol. 129, no. 1, 2008.

[4] A. I. Neelov and S. Goedecker, "An efficient numerical quadrature for the calculation ofthe potential energy of wavefunctions expressed in thedaubechies wavelet basis," *Journal of Computational Physics*, vol. 217, pp. 312–339, 2006.

[5] A. Graps, "An introduction to wavelets," *IEEE Computational Science and Engineering, Summer 1995*, vol. 2, no. 2, 1995.

[6] L. Andersson, N. Hall, B. Jawerth, and G. Peters, "Wavelets on closed subsets of the real line," *Recent Advances in Wavelet Analysis*, vol. 3, pp. 1–61, 1994.

[7] V. Finěk, "Daubechies wavelets on intervals with application to BVPs," *Applications of Mathematics*, vol. 49, no. 5, pp. 465–481, 2004.

Discriminating Multiprong Jet Substructure with right handed charged gauge boson and heavy right handed neutrino

Hannah van der Schyf[1]

[1]School of Physics, University of the Witwatersrand, Johannesburg, South Africa

E-mail: havnders@cern.ch

Abstract. A wide array of jet substructure based techniques have been used to discriminate large-radius jets coming from the hadronic decay of top quarks against those from light quarks or gluons. However, discriminating jets with more than three-prongs have been much less explored. Many new novel searches have been considered with jets having more than 3 prongs and thus discriminating jets with such as these would be greatly beneficial. In this work, a new physics signal of a boosted right handed heavy neutrino decaying to a top and bottom quark along with a charged lepton is investigated. The aim is to see which jet substructure observables can be sensitive to identify this signal over the top quark pair production background processes. From early investigation we find that τ_N substructures variables may be good candidates in discriminating these multiprong jets.

1 Introduction

1.1 Jet Basics

In collider physics, Jets are experimental signatures of quarks and gluons in high energy collisions, such as the proton-proton collisions at the LHC (Large hadron Collider) [1]. That makes these jet observables extremely important and useful for countless analyses in high energy physics.

The strong interactions of quarks and gluons is inherently different from what is seen in weak interactions. Particles carrying colour charge cannot exist freely as observed by those carrying electroweak charge, this is due to colour confinement in QCD (Quantum Chromodynamics). This ensemble of quarks and gluons are commonly referred to as partons, this results in a collection of partons in a colourless bound state called hadrons. Quarks can radiate gluons, in the same manner as how electrically charged particles can radiate photons, these gluons can then split to quark anti-quark pairs, as how photons can split to a lepton pair. This means a single parton may create a shower of partons, this shower interacts with the detector, resulting in energy deposits in a number of calorimeter cells in a "cone-like" shape [2]. This collimated collection of bunches of hadrons is what creates our jet, where ideally each bunch would form from a single parton. It is important to note, that jets are not fundamental objects, but a construction of hadrons originating from a single parton [1].

A generic jet forming algorithm is used to construct these jets [1], which can be described as a set of inputs with four momenta, p_N^h mapped to a set of jets with four momenta, p_M^j. Where these inputs may be hadrons or other detector objects. Thus in the general algorithm we have $p^j = \sum_{i \in j} p_i^h$ where $N > M$. There are more explicit jet algorithms used which in turn decide which objects are inputs for the jet construction, such as energy deposits in calorimeter or tracks. The most commonly used algorithm, and the algorithm used in this study, is the anti-k_T algorithm [3]. It begins with the highest p_T (transverse momentum, momentum along the beam line) object as the initial input and then absorbs all other softer objects (objects having lower p_T) around to construct the jet with radius R (at the LHC the most commonly used radius definitions are $R = 0.4$ for standard jets and $R = 1.0$ for large radius jets). Jets can also be b-tagged and top-tagged, this means the jet has been found to originate from a bottom quark or top quark respectively.

1.2 Jet substructure

"Jets can exhibit internal substructure ('prongs'), reflecting the number of hard partons produced in their origin. These prongs are distinct substructure or "branches" inside a jet, usually tracks or subjets [1]. N-subjettiness refers to the categorisation of how many dominant flows of energy are inside a large radius jet [4, 5]. For a top quark, this would be reconstructed as a large radius top-tagged jet. The top quark decays to a W and a bottom quark ($t \rightarrow Wb$) the W then decays to a lepton and neutrino pair or up-type quark and a down-type quark. Thus the final state of the top quark decay is a b-tagged jet and quark or lepton pair. This would result in the large radius jet having substructure with three distinctive energy flow directions of tracks, 2 subjets coming from the individual leptons or quarks a subjet coming from the b-tagged jet. The radiation patterns and substructure of jets can be unique and distinct for different scenarios, thus jet substructure tools were developed to exploit this information. The τ_N substructure variable can be used to exploit the number of prongs or subjets inside a jet given by [1],

$$\tau_N = \frac{1}{d_0} \sum_{k=0}^{k=N} p_{T,k} \times \Delta R_{min,k} \tag{1}$$

where k is the subjet constituent and $\Delta R_{min,k}$ is the minimum distance of constituent k and the nearest subjet. The normalisation factor d_0 is the p_T sum of all constituents multiplied by jet radius to ensure $0 < \tau_N < 1$. Using this definition τ_N describes how well a jet can be defined as having N or fewer jets, by assessing how well the constituents are aligned to the axis of the subjets. Taking the ratios of different τ_N values can allow us to identify multiprong jets over another. τ_{32} allows us to identify three prong over two prong decay, and in same fashion τ_{21} allows us to identify two prong over one prong decay.

Using jet substructure for jets with more than 3 prongs is scarcely ventured territory. However, in many cases substructure variables are extremely valuable for signal to background discrimination. The aim of this study is to determine whether τ_N variables can be used to discriminate 4 prong structure from 3 prong structure. This would be extremely useful for future analysis considering new topologies and analysis which may not have currently useful discriminating variables.

2 The Model

2.1 Left-Right symmetric models

This study uses simulated Monte Carlo sample events from MadGraph5 [6] showered with Pythia8 [7], the model used is from the Left-Right symmetric models (LRSMs) [8, 9, 10, 11]. These models predict a particle spectrum with several extra states such as new charged and neutral gauge bosons, extra (pseudo)scalars and three generations of right-handed neutrinos. These models also provide naturally small neutrino masses through the seesaw mechanism [12]. The specific model for this study is the production of a right handed charged gauge boson (W_R) and a right handed heavy neutrino (N_R) [13], as it provides a 4 prong jet, which can be seen below.

2.2 The signal

The W_R decays to a N_R and a lepton, the N_R then decays to a top quark, a bottom quark and an additional lepton. The Feynman diagram in Figure 1 shows the decays and final states of W_R. In most cases the top quark is highly boosted, this would result in high p_T distribution and therefore, the top quark's transverse momentum distribution is shifted to high values. Events are only selected if containing two muons, this is due to the fact that muons are a cleaner signature at detector level for a proposed search [14, 15]. Jets can often be misidentified as electrons and vice versa [16, 17]. Thus using muons results in a more efficient final state which allows for a better discrimination of the jet prongs, as well, at least one top-tagged jet is required in the final state. The top-tagged jet will be a large radius jet consisting of a b-tagged jet and the W boson decay structure, thus at least one b-tagged jet is selected. This presents us with a final state consisting of two muons, a b-tagged jet and a top-tagged large radius jet. In the sample generated and used in this study, the W_R has a mass of 5.1 TeV and the N_R has a mass of 2.25 TeV [13].

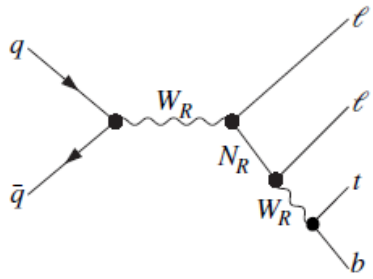

Figure 1: Feynman diagram showing the right-handed charged boson decay, and the heavy right handed neutrino decay [13].

3 Results

To ensure the correct final state objects are being used to reconstruct the W_R, kinematic variables are plotted. The leading (muon with highest P_T) and subleading (muon with 2nd highest P_T) muon p_T is shown in Figure 2. The top-jet is expected to be the leading large radius jet. In Figure 3, it is clear the leading large radius has the mass of the top jet. Thus, we can select the leading large radius jet as our top jet [18]. The bottom jet is chosen by selecting the leading jet that is b-tagged. The p_T of the top jet and b-tagged jet are shown in Figure 4.

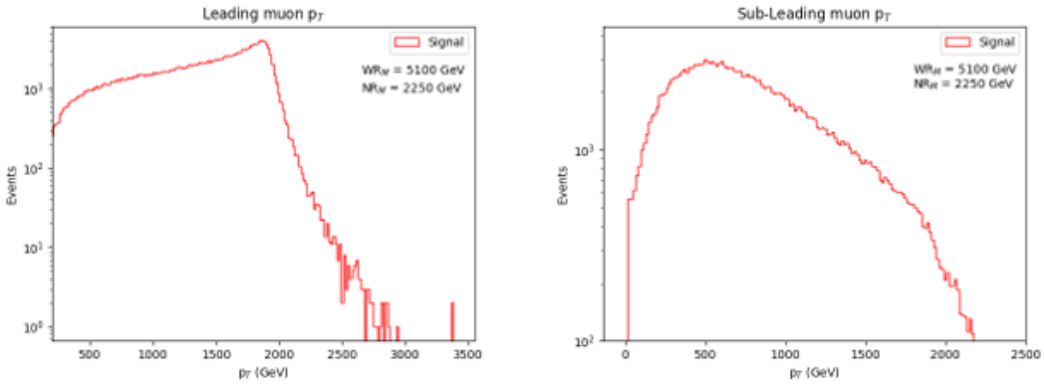

Figure 2: (*left*) Leading muon p_T. (*right*) Subleading muon p_T.

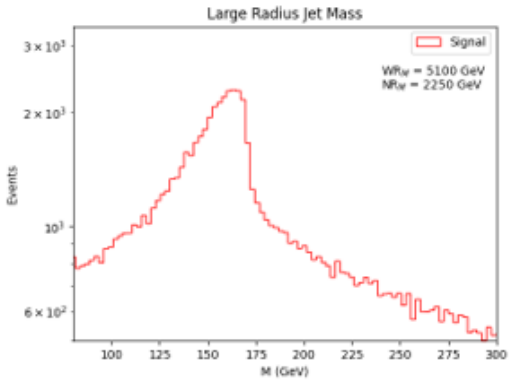

Figure 3: Large radius jet mass.

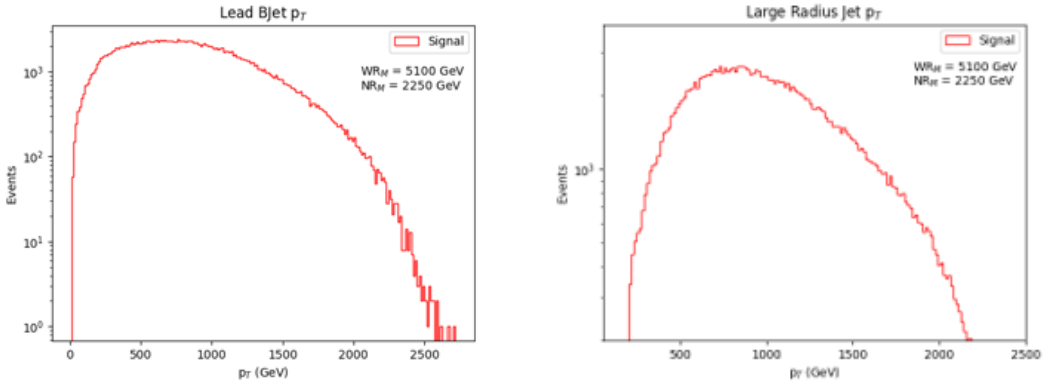

Figure 4: (*left*) b-tagged jet mass. (*right*) Top jet p_T.

The W_R is then reconstructed by taking the invariant mass of the final state objects. We vector sum the four momenta of the leading and sub-leading muons, the leading b-tagged jet as well as the chosen leading large radius jet for the top jet. The invariant mass of the final state objects is shown in Figure 5, from this figure we can see than the invariant mass peaks around the mass of the 5.1 TeV so we are able to reconstruct the W_R.

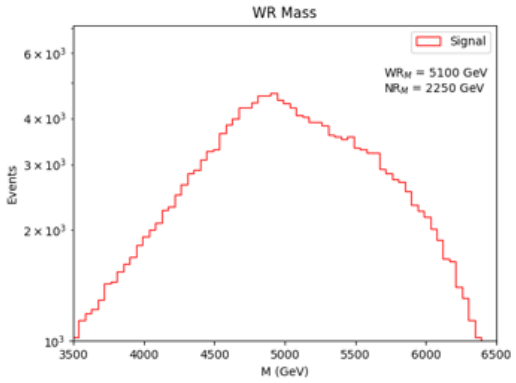

Figure 5: Invariant mass of the leading and subleading muons, the b-tagged jet and the chosen top jet.

4 Discriminating jet prong substructure

In order to compare a 3-prong jet to a 4-prong jet a SM (Standard Model) semi-leptonic $t\bar{t}$ sample was generated using Pythia8, version 8.3. Various τ_N variables were calculated and the ratios taken for both samples. Figures 6 to 7 show these variables plotted comparing the W_R signal to the SM semi-leptonic $t\bar{t}$ sample. Although the shapes are similar, there are clear differences between the signal and the SM top sample. This shows promise in using substructure variables to discriminate multiprong jets with more than 3 prongs.

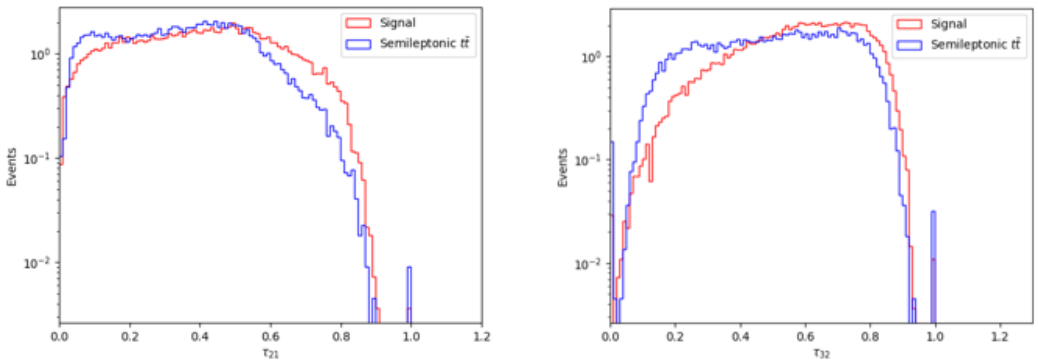

Figure 6: (*left*) τ_{21} comparing 4-prong signal and 3-prong $t\bar{t}$. (*right*) τ_{32} comparing 4-prong signal and 3-prong $t\bar{t}$.

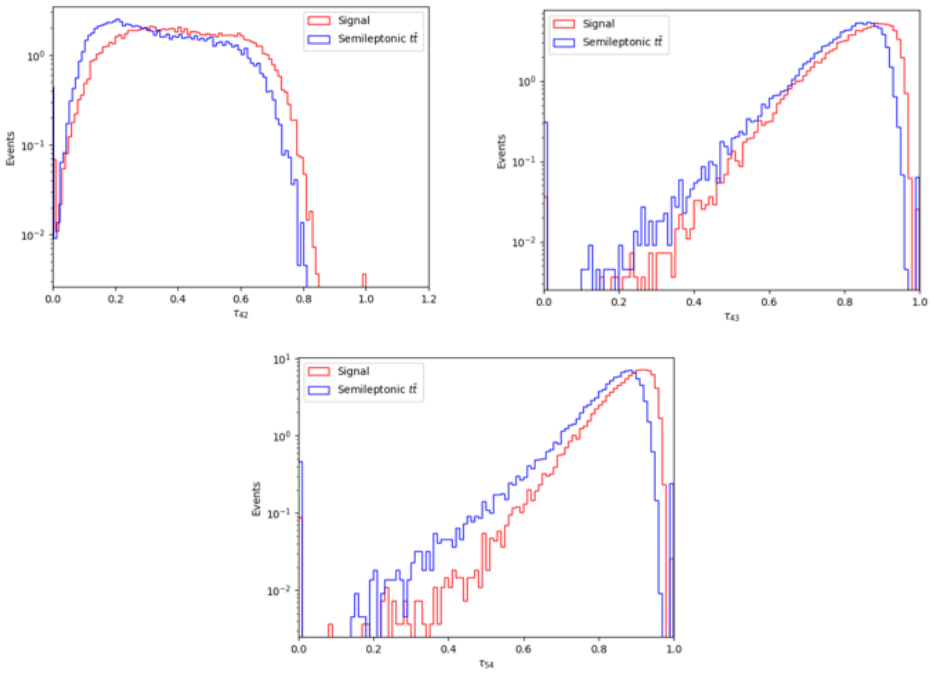

Figure 7: (*top left*) τ_{42} comparing 4-prong signal and 3-prong $t\bar{t}$. (*top right*) τ_{43} comparing 4-prong signal and 3-prong $t\bar{t}$. (*bottom*) τ_{54} comparing 4-prong signal and 3-prong $t\bar{t}$.

5 Conclusion

This study shows promise for future discrimination of multiprong jet substructure. Using a sample where we are able to reconstruct the charged gauge boson which has a 4-prong substructure. We compare this to a SM semi-leptonic $t\bar{t}$ sample which has a 3-prong jet substructure. Although the discrepancies are not substantial, this still shows that 3-prong substructure can be discriminated from a 4-prong substructure. Future studies would involve calculating τ_N with different jet reconstruction algorithms, as well as investigating and comparing other substructure variables.

Acknowledgments

I would like to extend thanks to the IThemba LABS SA-CERN programme excellence scholarship, providing me with funding during my PhD studies. This study is part of an ongoing project involving Benjamin Fuks and Adil Jueid with a larger scope. We thanks Adil Jueid for preparing the signal sample used in this study. I also thank my supervisor, Prof. Deepak Kar, for his guidance and assistance with this study.

References

[1] D. Kar, *Experimental Particle Physics*. IOP Publishing Limited, 2019.

[2] ATLAS Collaboration, "A measurement of the calorimeter response to single hadrons and determination of the jet energy scale uncertainty using lhc run-1 pp-collision data with the atlas detector," *Eur. Phys. J. C*, vol. 77, p. 26, 2017.

[3] M. Cacciari, G. P. Salam, and G. Soyez, "The anti-kt jet clustering algorithm," *Journal of High Energy Physics*, vol. 2008, no. 04, p. 063, 2008.

[4] J. Thaler and K. Van Tilburg, "Identifying boosted objects with n-subjettiness," *Journal of High Energy Physics*, vol. 2011, no. 3, pp. 1–28, 2011.

[5] R. Kogler, B. Nachman, A. Schmidt, L. Asquith, E. Winkels, M. Campanelli, C. Delitzsch, P. Harris, A. Hinzmann, D. Kar *et al.*, "Jet substructure at the large hadron collider," *Reviews of Modern Physics*, vol. 91, no. 4, p. 045003, 2019.

[6] J. Alwall, R. Frederix, S. Frixione, V. Hirschi, F. Maltoni, O. Mattelaer, H.-S. Shao, T. Stelzer, P. Torrielli, and M. Zaro, "The automated computation of tree-level and next-to-leading order differential cross sections, and their matching to parton shower simulations," *Journal of High Energy Physics*, vol. 2014, no. 7, pp. 1–157, 2014.

[7] T. Sjöstrand, S. Ask, J. R. Christiansen, R. Corke, N. Desai, P. Ilten, S. Mrenna, S. Prestel, C. O. Rasmussen, and P. Z. Skands, "An introduction to pythia 8.2," *Computer physics communications*, vol. 191, pp. 159–177, 2015.

[8] R. N. Mohapatra and J. C. Pati, "Left-right gauge symmetry and an "isoconjugate" model of cp violation," *Physical Review D*, vol. 11, no. 3, p. 566, 1975.

[9] J. C. Pati and A. Salam, "Lepton number as the fourth "color"," *Physical Review D*, vol. 10, no. 1, p. 275, 1974.

[10] G. Senjanovic and R. N. Mohapatra, "Exact left-right symmetry and spontaneous violation of parity," *Physical Review D*, vol. 12, no. 5, p. 1502, 1975.

[11] G. Senjanović, "Spontaneous breakdown of parity in a class of gauge theories," *Nuclear Physics B*, vol. 153, pp. 334–364, 1979.

[12] R. N. Mohapatra and A. Y. Smirnov, "Neutrino mass and new physics," *Annual Review of Nuclear and Particle Science*, vol. 56, pp. 569–628, 2006.

[13] M. Frank, B. Fuks, A. Jueid, S. Moretti, and Ö. Özdal, "A novel search strategy for right-handed charged gauge bosons at the large hadron collider," *Journal of High Energy Physics*, vol. 2024, no. 2, pp. 1–34, 2024.

[14] CMS Collaboration, "Performance of cms muon reconstruction from proton–proton to heavy-ion collisions," *J. Instrum.*, vol. 19, no. 9, p. P09012, 2024.

[15] ATLAS Collaboration, "Muon reconstruction efficiency and momentum resolution of the atlas experiment in proton–proton collisions at $\sqrt{s} = 7$ TeV in 2010," *Eur. Phys. J. C*, vol. 74, no. 9, p. 3034, 2014.

[16] ——, "Performance of electron identification and jet→electron fake rate studies in the atlas detector," ATLAS internal note / public note (DS106020, DS105802) "e-ID Performance using Release v13/ v14 MC Samples", 2010.

[17] CMS Collaboration, "Performance of τ_h reconstruction and identification in cms with 2015 data," *J. Instrum.*, vol. 11, no. 01, p. P01019, 2016.

[18] ATLAS Collaboration, "Measurement of the top quark mass with the atlas detector using $t\bar{t}$ events with a high transverse momentum top quark," *Physics Letters B*, vol. 867, p. 139608, 2025.

Probing the Dead Cone using the Lund Jet Plane

Ofentse Matlhakola [1,2], Isobel Kolbé [1,2,3] and Deepak Kar [1]

[1] School of Physics, University of the Witwatersrand, Johannesburg, South Africa
[2] Mandelstam Institute for Theoretical Physics (MITP), University of the Witwatersrand, Johannesburg, South Africa
[3] National Institute for Theoretical and Computational Sciences (NITheCS), Stellenbosch University, Cape Town, South Africa

E-mail: ofentsematlhakola1@students.wits.ac.za

Abstract. The Lund Jet Plane (LJP), mapping the momentum and angular orientation of radiation from a parton, aids in studying jet substructure. Here, we use the LJP to investigate the Dead Cone effect, where gluon radiation around a massive quark is suppressed in heavy-flavour jets. We develop a method to observe this phenomenon using simulated collider events. Although the emission density within the resulting LJP for bottom-tagged jets shows a hint of a suppression, further refinement to the analysis is required for a more conclusive observation.

1 Introduction

In high-energy colliders, we study the fundamental constituents of matter, which include quarks and gluons (collectively known as partons). The goal is to better understand and validate predictions made by Quantum Chromodynamics (QCD), the theory that describes the strong force or the interaction of quarks by the exchange of gluons. At such high energies, new quark pairs can be created. As a quark/antiquark moves away from the collision point, it loses energy by emitting soft gluons in a cascading process called a parton shower [1]. Eventually, the low-energy quark combines with other quarks to form particles called hadrons. When many hadrons are produced in the same direction, they form a spray of particles collected in a constructed object called a jet, which can be detected in experiments.

The probability of soft-gluon radiation from a quark depends on the quark mass. It was predicted [2] that below a critical angle, soft-gluon radiation is suppressed around the forward axis of a radiating massive quark, an effect known as the Dead Cone. The Dead Cone is more pronounced in parton showers of heavy quarks compared to light quarks, as it follows the relation [2]:

$$\theta_{DC} \sim \frac{m_Q}{E_Q}\,, \tag{1}$$

where θ_{DC} is the size of the suppressed region, m_Q is the mass of the quark, and E_Q is the energy of the quark. According to this relation, gluon radiation is suppressed at angular scales smaller than m_Q/E_Q, making the effect more significant for heavier quarks at lower energies. There are challenges to observing the Dead Cone experimentally. The direction of the quark changes as it radiates (see fig. 1), making it difficult to precisely define the quark direction in analysis. Additionally, the Dead Cone region can be contaminated by contributions from other processes in the collision, such as pile-up and underlying event (UE). Figure 1 presents an illustration of a jet initiated by a charm quark, it shows the formation of the Dead Cone while neglecting subsequent processes such as hadronization.

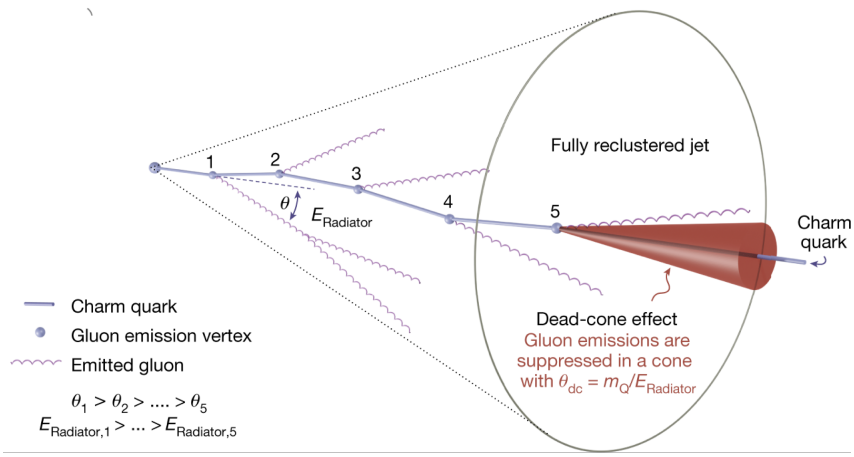

Figure 1: Schematic detailing branchings inside a jet[3]. At each splitting node, the quark mass remains constant, while its energy decreases. Gluon emissions are suppressed within an angular region proportional to the ratio of the quark's mass to its energy; this is the dead cone. The red cone represents the dead cone region for the final splitting, which can be revealed by declustering the jet step by step, following the numbered sequence.

In this study, the Lund Jet Plane (LJP) is used to investigate the Dead Cone effect in the parton shower of a bottom quark (mass $\sim$ 4.2 GeV). The LJP is a two-dimensional plot which provides a theoretical representation of the phase space within jets [4]. It typically plots the momentum fraction of an emission against its angle relative to the emitting core, though other splittings properties can also be visualized. This representation allows us to probe different physical processes occurring at various energy scales within a jet [4].

2 Analysis

The Monte Carlo based event generator called PYTHIA8 [5] was used to simulate 13 TeV high-energy proton-proton collisions. PYTHIA8 simulates the parton shower, incorporating the Dead Cone effect for heavy quark showers. It then performs the hadronization and outputs a list of final-state particles produced in the event. The aim is to develop an experimental analysis that observes the Dead Cone effect. For this, the RIVET analysis toolkit [6] was used to analyze the events. Because individual quarks cannot be directly detected, we rely on jets to study their behaviour. The most commonly used jet clustering algorithm is the anti-k_T [7], mainly because it aligns with particle detection through their energy deposits in calorimeters at the LHC. The anti-k_T algorithm clusters particles in momentum space, starting from the one with the highest momentum and sequentially adding nearby particles within a defined radius that sets the jet size.

In the analysis, a tagging procedure that identifies jets containing B-hadrons (particles that contain a bottom quark) is applied, then such jets are isolated as heavy-flavour jets. After tagging, the jet with the highest transverse momentum (p_T) is selected in each event. To reconstruct the internal cascade, the jets are reclustered using the Cambridge/Aachen (C/A) algorithm. The C/A algorithm mimics the angular-ordered structure of a QCD parton shower. As its inputs, charged particle tracks in the central part of a detector are used because they offer better resolution than calorimeter deposits in the detector. Unlike anti-k_T, the C/A algorithm clusters particles in angular space, starting with the closest pair [8]. Once the jet is reclustered, the branching history can be retrieved by undoing the C/A clustering procedure. Each declustering step returns a splitting into two prongs, and the soft prong is taken to represent the emission , which is then recorded as a point on the LJP.

Figure 2 presents the full and primary lund planes. The full lund plane is constructed by recording all emissions within the jet, from following both prongs at each step. However, the interest is in the primary lund plane, which captures only the emissions from the jet-initiating quark. It is constructed by following the harder prong. Each emission is then plotted on the plane, with the angular separation from the quark on the x-axis, and the quark's energy at the time of emission on the y-axis. To reduce contamination from hadron decays which add low-momentum splittings, a selection on the relative transverse momentum of each emission (k_T) is necessary. Specifically, we require $k_T > 0.2$ GeV, in line with the hadronization scale, $\Lambda_{QCD} \sim 200$ MeV.

The above choice of coordinates allows an investigation of the Dead Cone effect, with the suppression expected to occur in the soft-collinear region of the LJP (bottom right region). This follows from eq. (1); the effect becomes

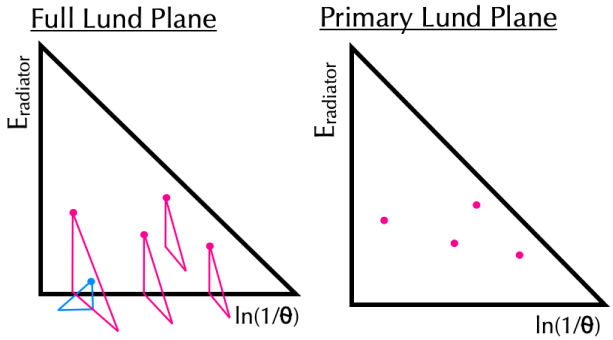

Figure 2: (*left*) Schematic of a full lund plane, illustrating all splittings within a jet. $E_{radiator}$ denotes the energy of the core particle, while θ represents the angle between the core and the emitted particle. The pink triangles indicate the phase space for primary emissions (pink points), whereas the blue triangle corresponds to the phase space for secondary emissions (blue points). (*right*) Schematic of a primary Lund plane, showing only primary splittings inside a jet.

more significant for heavier quarks at lower energies. To identify the suppression, we compare the radiation pattern of b-jets to that of light-quark jets, where the Dead Cone is not expected. The same analysis is repeated in light-quark events for reference.

3 Results and Discussions

Figure 3 shows the LJP for jets containing a B-Hadron. The red curve serves as a visual guide to indicate the expected region of the suppression for different quark energies (below and to the right of the red curve). Figure 4, shows horizontal slices through the LJP in different energy bins. They show the jet emission density, Q, spanning the entire angular scale. This density is obtained by tracing the primary branch throughout the jet's splitting sequence.

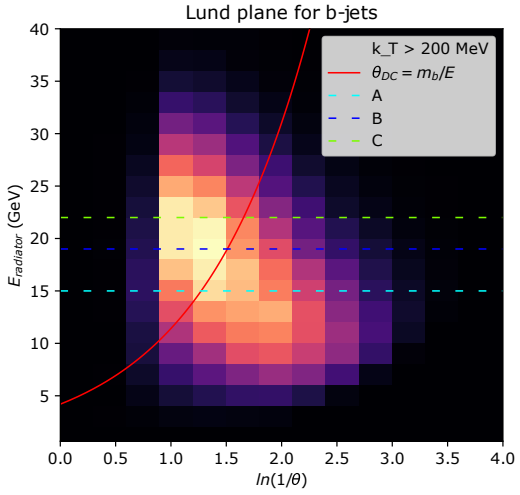

Figure 3: The average emission density, for R = 0.4 and 30 GeV < p_T < 40 GeV b-tagged jets. The red curve corresponds to the onset of the dead cone region for different radiator energies, beyond which soft-gluon radiation is suppressed. Lines A, B, and C represent horizontal slices at different radiator energies.

For a direct comparison, each slice is overlaid with the corresponding slice from light-quark jets at the same energy bins. The overlaid plots are labeled A and C, matching the reference keys in fig. 3. The Ratio plot on the

bottom panel of both plots shows inclusive-jets/inclusive-jets for the red curve and b-jets/inclusive-jets for the blue curve. In plot A, there is hardly any difference in the emission pattern for b-jets and light-jets, this means there is no suppression. In plot C, there is a hint of a suppression, which may suggest the presence of the Dead Cone. However, we cannot conclusively attribute this suppression to the Dead Cone effect, as its location does not align with the expected onset indicated by the red curve in fig. 3. It is possible that a Dead Cone signature is present, but residual contamination from hadron decays may still be affecting the result, despite our efforts to mitigate this in the analysis.

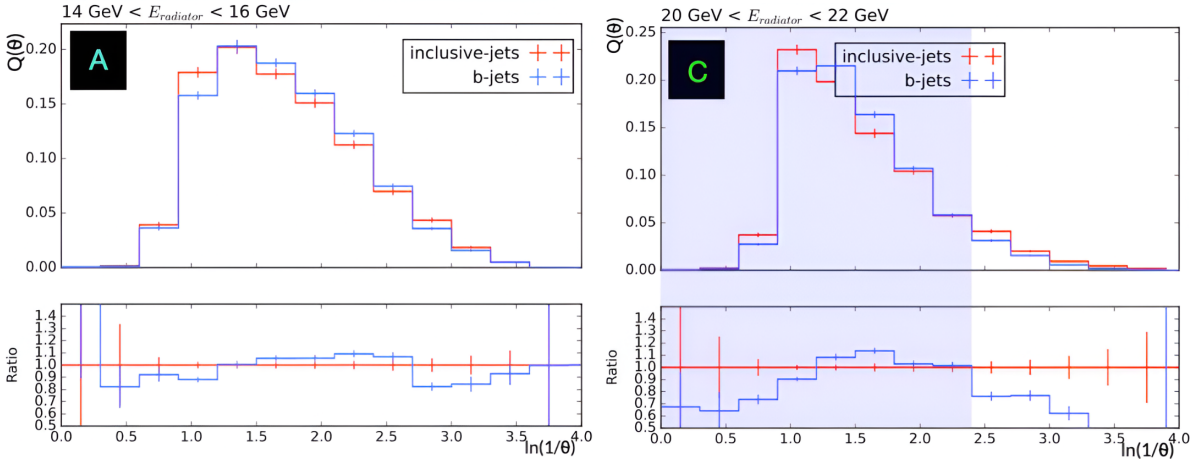

Figure 4: Example slices of the LPJ in different energy bins. Ratio is inclusive-jets/inclusive-jets for the red curve and b-jets/inclusive-jets for the blue curve. (a) shows no statistically significant suppression. (b) shows some suppression for small angle emissions, indicated by the unshaded area. For this energy bin, according to the red curve in fig. 3, the suppression is expected to begin at $\ln(1/\theta) \sim 1.56$.

4 Conclusions

We used the Lund Jet Plane to study the Dead Cone effect in b-tagged jets. Signs of a suppression were observed, but contamination from hadron decays may still be present. We believe that imposing a stronger k_T threshold on emissions may further reduce contamination from these decays and better isolate the effect. Additionally, applying a jet grooming technique known as Soft Drop [9] may suppress contributions from pile-up and UE.

Acknowledgments

The financial support provided by the SA-CERN collaboration through iThemba LABS is hereby acknowledged.

References

[1] M. Bengtsson and T. Sjöstrand, "A comparative study of coherent and non-coherent parton shower evolution," *Nuclear Physics B*, vol. 289, pp. 810–846, 1987.

[2] Y. L. Dokshitzer, V. A. Khoze, and S. Troyan, "On specific qcd properties of heavy quark fragmentation ('dead cone')," *Journal of Physics G: Nuclear and Particle Physics*, vol. 17, no. 10, p. 1602, 1991.

[3] ALICE Collaboration, "Direct observation of the dead-cone effect in quantum chromodynamics," *Nature*, vol. 605, no. 7910, pp. 440–446, 2022.

[4] F. A. Dreyer, G. P. Salam, and G. Soyez, "The lund jet plane," *Journal of High Energy Physics*, vol. 2018, no. 12, pp. 1–42, 2018.

[5] C. Bierlich, S. Chakraborty, N. Desai, L. Gellersen, I. Helenius, P. Ilten, L. Lönnblad, S. Mrenna, S. Prestel, C. T. Preuss *et al.*, "A comprehensive guide to the physics and usage of pythia 8.3," *SciPost Physics Codebases*, p. 008, 2022.

[6] C. Bierlich and A. Buckley, "Robust Independent Validation of Experiment and Theory: Rivet version 3," *SciPost Phys.*, vol. 8, p. 026, 2020. [Online]. Available: https://scipost.org/10.21468/SciPostPhys.8.2.026

[7] M. Cacciari, G. P. Salam, and G. Soyez, "The anti-kt jet clustering algorithm," *Journal of High Energy Physics*, vol. 2008, no. 04, p. 063, 2008.

[8] S. Bentvelsen and I. Meyer, "The cambridge jet algorithm: Features and applications," *The European Physical Journal C-Particles and Fields*, vol. 4, no. 4, pp. 623–629, 1998.

[9] A. J. Larkoski, S. Marzani, G. Soyez, and J. Thaler, "Soft drop," *Journal of High Energy Physics*, vol. 2014, no. 5, pp. 1–46, 2014.

This page intentionally left blank.

Piston-Driven Shock Wave Test Problem for Validating Magnetohydrodynamic Models in Astrophysics

Magdeline M. Seabi [1], **Azwinndini Muronga**[2]

[1]Department of Physics, Nelson Mandela University, South Campus, University Way, Summerstrand, Gqeberha, South Africa, 6001
[2]Nelson Mandela University, South Campus, University Way, Summerstrand, Gqeberha, South Africa, 6001

E-mail: s226052184@mandela.ac.za,magdeline.seabi@nithecs.ac.za

Abstract. Understanding matter under extreme conditions is critical for both astrophysical and high-energy physics applications. This study presents a hydrodynamic piston-driven shock model, developed to generate analytical benchmark solutions for shock propagation in core-collapse supernovae environments. The model captures key features of compressible flow, including forward shock formation based on the Rankine–Hugoniot jump conditions. In parallel, the Brio–Wu relativistic magnetohydrodynamics (MHD) shock tube is simulated using the PLUTO code to validate its ability to resolve complex wave structures in magnetised plasmas. Together, these two models provide complementary tools for verifying numerical shock solvers and establishing a foundation for future extensions involving relativistic magnetohydrodynamics (RMHD).

1 Introduction

Matter under extreme temperature, density, and magnetic fields occurs in both astrophysical environments and relativistic heavy-ion collisions (HIC). In HIC, nuclei collide near light speed, forming a quark-gluon plasma (QGP) with energy densities above 10 GeV/fm^3 and flow velocities exceeding $0.6c$ [1]. Here, c is the speed of light. Non-central collisions generate transient magnetic fields up to $\sim 10^{18}$ G, inducing MHD effects such as transverse flow anisotropy and the chiral magnetic effect. Similarly, in core-collapse supernovae (CCSNe), the iron core reaches nuclear density ($\sim 2.7 \times 10^{14}$ g/cm^3), producing a bounce shock that accelerates matter to $0.3c$–$0.4c$ [2]. Pre-collapse fields of $\sim 10^4$ G can be amplified to 10^{15}–10^{16} G via flux freezing, differential rotation, and magnetorotational instabilities, influencing shock collimation and aiding the explosion [3]. Understanding matter under these conditions is essential for interpreting supernovae, neutron star mergers, and experimental results from RHIC and the LHC.

Magnetic fields strongly affect shock propagation in both contexts. In HIC, transverse nuclear motion produces extreme, short-lived fields ($\sim 10^{-23}$ s), while in CCSNe, amplified fields interact with shocks and infalling matter, introducing anisotropic stresses and modifying wave behaviour. RMHD provides the framework to study such systems, capturing fast and slow magnetosonic waves, Alfvén waves, and relativistic effects where fluid velocities approach the speed of light [4, 5, 6, 7].

To validate RMHD codes, test problems with known or expected solutions are employed. The piston-driven shock tube problem is particularly useful: a piston drives a shock into a medium, generating sharp gradients and wave structures while allowing study of magnetic field amplification through compression.

In the present study, a one-dimensional piston-driven shock tube problem in both hydrodynamic and MHD contexts is developed and analysed using Python. As part of the validation strategy, the well-known Brio–Wu shock tube problem [8] is simulated, which serves as a classical MHD test case involving multiple wave structures and

discontinuities. The model is implemented using the PLUTO code [9], an open-source and widely-used computational fluid dynamics tool tailored for astrophysical flows. The objective is to evaluate the ability of the PLUTO code to handle RMHD shock structures and provide a basis for more complex, multidimensional simulations in astrophysics. By establishing the fidelity of numerical results against analytical expectations and known physical behaviours, the aim is to contribute to the development of effective computational frameworks for high-energy astrophysical modelling.

2 Theoretical and Computational Framework

This study aims to construct a robust piston-driven shock model capable of describing magnetised astrophysical plasmas in extreme conditions, such as those encountered in CCSNe. While classical test problems such as the Brio–Wu shock tube are invaluable not only for describing the HIC model but also for verifying numerical solvers, they do not reflect the physical mechanisms governing shock generation in realistic supernova environments.

To address this limitation, a piston-driven shock model is designed specifically tailored for RMHD conditions. However, given the inability to locate publicly available RMHD piston-driven shock models in open-source frameworks through online search, this work takes a stepwise approach: starting from classical hydrodynamics, analytical model is built and validated for piston-driven shocks, extend these to MHD (in theory and Python), and ultimately aim to develop a fully relativistic RMHD version compatible with the PLUTO code. This framework section lays out the theoretical foundation, starting from general conservation laws, then narrows down to the formulation required for numerical implementation, and finally explains the structure of our validation pipeline.

Conservation Laws in Relativistic Magnetohydrodynamics

The evolution of a magnetised relativistic fluid is governed by conservation of baryon number and energy-momentum [4, 10]:

$$\partial_\mu N^\mu = 0 \qquad \text{(Mass Conservation)} \tag{1}$$

$$\partial_\mu T^{\mu\nu} = 0 \qquad \text{(Energy-Momentum Conservation)} \tag{2}$$

Here, $N^\mu = \rho u^\mu$ is the rest-mass current, where ρ is the proper rest-mass density and u^μ the fluid four-velocity. The total stress-energy tensor includes both matter and electromagnetic contributions:

$$T^{\mu\nu} = (\rho h + p)u^\mu u^\nu + p g^{\mu\nu} - b^\mu b^\nu + \frac{1}{2} b^2 g^{\mu\nu}$$

where $h = 1 + \epsilon + p/\rho$ is the specific enthalpy, p is the thermal pressure, b^μ is the magnetic field four-vector in the fluid rest frame, and $g^{\mu\nu}$ is the spacetime metric. These equations reduce to their hydrodynamic or non-relativistic forms by neglecting appropriate terms. The inclusion of b^μ introduces anisotropic stresses and additional wave modes (e.g., Alfvén, fast/slow magnetosonic), making RMHD essential for modelling shock propagation in magnetised CCSNe scenarios.

Numerical Formulation

For computational applications, Eqs. (1)–(2) are written in conservative form [4]:

$$\partial_t \mathbf{U} + \partial_x \mathbf{F}(\mathbf{U}) = 0 \tag{3}$$

with:

$$\mathbf{U} = \begin{pmatrix} D \\ S^x \\ \tau \\ B^y \\ B^z \end{pmatrix}, \quad \mathbf{F} = \begin{pmatrix} D v^x \\ S^x v^x + p^* - (b^x)^2 \\ S^x - D v^x + p^* v^x - b^0 b^x \\ B^y v^x - B^x v^y \\ B^z v^x - B^x v^z \end{pmatrix}$$

Here:

$$D = \rho\gamma, \quad S^x = \rho h \gamma^2 v^x + b^2 v^x - b^0 b^x, \quad \tau = \rho h \gamma^2 - p + \frac{1}{2} b^2 - (b^0)^2 \tag{4}$$

D is the conserved rest-mass density, S^x is x-component of the total momentum density, τ is the total energy density minus rest-mass energy, $\gamma = (1 - v^2)^{-1/2}$ is the Lorentz factor, $\vec{v}$ is the fluid velocity, and $p^* = p + \frac{1}{2} b^2$ is the total pressure. These expressions define the conserved quantities $\mathbf{U}$ and their fluxes $\mathbf{F}$ as functions of the primitive variables [6].

In this study, the Newtonian version of the mathematical framework outlined above, and the above framework are applied in complementary computational settings. First, a stand-alone Python implementation of the 1D piston-driven shock problem is developed based on the conservation laws and shock conditions, allowing for the generation of controlled benchmark profiles under hydrodynamic and magnetohydrodynamic (MHD) conditions. Second,

The PLUTO code is used to numerically solve the same equations using high-resolution shock-capturing schemes, including Riemann solvers. This dual-framework approach enables both analytical insight and robust numerical verification of MHD shock dynamics, serving as a foundation for future relativistic RMHD extensions.

Rankine–Hugoniot Jump Conditions for Shock Analysis

To compute analytical post-shock states for benchmark validation, the Rankine–Hugoniot jump conditions for relativistic magnetohydrodynamics (RMHD) are applied across the shock front [4].

$$[\![\rho\gamma\vec{v}]\!] = 0 \quad \text{(Mass Flux Continuity)} \tag{5a}$$

$$[\![(\rho h + b^2)\gamma^2 v^2 + p + \frac{1}{2}b^2 - (b^x)^2]\!] = 0 \quad \text{(Momentum Flux)} \tag{5b}$$

$$[\![(\rho h + b^2)\gamma^2\vec{v} - b^0 b^x]\!] = 0 \quad \text{(Energy Flux)} \tag{5c}$$

These conditions enforce conservation of mass, momentum, and energy in the presence of both relativistic velocities and magnetic fields. The symbol $[\![\cdot]\!]$ denotes the jump in a quantity across the discontinuity (i.e., the difference between post-shock and pre-shock values). The fluid velocity $\vec{v}$ entering the flux terms is defined relative to the shock front. In practical implementation, the shock speed $\vec{v}_s$ is specified or iteratively adjusted in the laboratory frame, and the fluid velocities on either side of the shock are transformed into the shock rest frame via $\vec{v} = \vec{v}_{\text{fluid}} - \vec{v}_s$. The full RMHD jump conditions include contributions from the fluid pressure, specific enthalpy, and electromagnetic stresses via the magnetic field four-vector b^μ. Together with a closure relation such as the relativistic ideal gas equation of state, $p = (\Gamma - 1)\rho\epsilon$, the jump conditions form a non-linear algebraic system that can be solved numerically. The resulting post-shock profiles for pressure, density, velocity, and magnetic field serve as reference solutions against which RMHD code outputs can be validated.

3 Test Case Rationale and Model Setup

Two benchmark problems are considered in this study as highlighted above, to evaluate the accuracy of numerical shock solvers and validate the numerical and to build the analytical framework: the Brio–Wu shock tube and a hydrodynamic (HD) piston-driven shock model. Both are implemented in one spatial dimension (1D). While the Brio–Wu shock tube is a classical and well-established RMHD test, it does not physically model how shocks are launched in core-collapse supernovae (CCSNe). Nevertheless, it is retained here to verify that the PLUTO code correctly resolves known RMHD wave structures, such as fast and slow shocks, contacts, and rotational discontinuities. The core of this study is the piston-driven shock model, developed incrementally to provide a physically motivated setup relevant to CCSNe.

Brio–Wu Shock Tube Model

The Brio–Wu shock tube [8] is a classical MHD test problem. It consists of a one-dimensional domain initially divided by a diaphragm separating two distinct fluid states. In this study, the Brio–Wu model is used to validate the PLUTO RMHD solver, ensuring it reproduces the expected wave structures under known initial conditions. This provides a canonical benchmark for code verification prior to the implementation of more physically motivated setups.

Hydrodynamic Piston-Driven Shock Model

The piston-driven shock model represents a physically motivated test for simulating shock formation via mechanical compression. A piston initially located at x_0 begins moving into a stationary, unmagnetised fluid, imposing a discontinuity that generates a rightward-propagating shock [11]. This configuration emulates conditions relevant to CCSNe, where a bounce shock propagates into infalling stellar material. The model is governed by conservation of mass, momentum, and energy in a HD context and admits analytical solutions through the Rankine–Hugoniot jump conditions.

The development of the piston-driven model follows this process: starting with the classical HD case, a full numerical and analytical solutions are constructed; the model will then be extended to include magnetic fields, forming an MHD variant; finally, the framework will be adapted for RMHD within PLUTO. At the current stage, the PLUTO CFD HD, MHD, and RMHD piston-driven shock models are under development, so results are not included here. This staged approach ensures robust validation at each complexity level and supports future applications in simulating bounce-induced shocks in magnetised CCSNe environments.

Together, the Brio–Wu and piston-driven shock models provide complementary benchmarks: the former confirms the code's ability to resolve multiple RMHD wave modes, while the latter offers a controlled, physically motivated scenario for shock propagation, forming a foundation for future multidimensional CCSNe simulations.

4. Results and Discussion

Brio–Wu Shock Tube Model

The Brio–Wu problem [8] is the MHD analogue of the classical Sod shock tube and is widely used to validate numerical schemes for MHD [12, 9]. It extends the hydrodynamic Sod problem by including transverse magnetic fields, thereby exciting the full set of MHD waves. The initial setup consists of a discontinuity separating two magnetised plasmas of differing density, pressure, and transverse magnetic field, as illustrated in the left panel of Figure 1 with the following initial and boundary conditions were implemented shown in Table 1 below:

Table 1: Initial conditions and X1-boundary conditions for the Brio–Wu RMHD shock tube.

Region / Side	ρ	p	v_x	v_y	v_z	B_x	B_y	**X1-Boundary**
Left	1.0	1.0	0.0	0.0	0.0	0.5	1.0	outflow
Right	0.125	0.1	0.0	0.0	0.0	0.5	-1.0	outflow

The simulation results for the Brio-Wu shock tube are presented in code units. The characteristic units for the normalization are based on the right state's initial conditions.

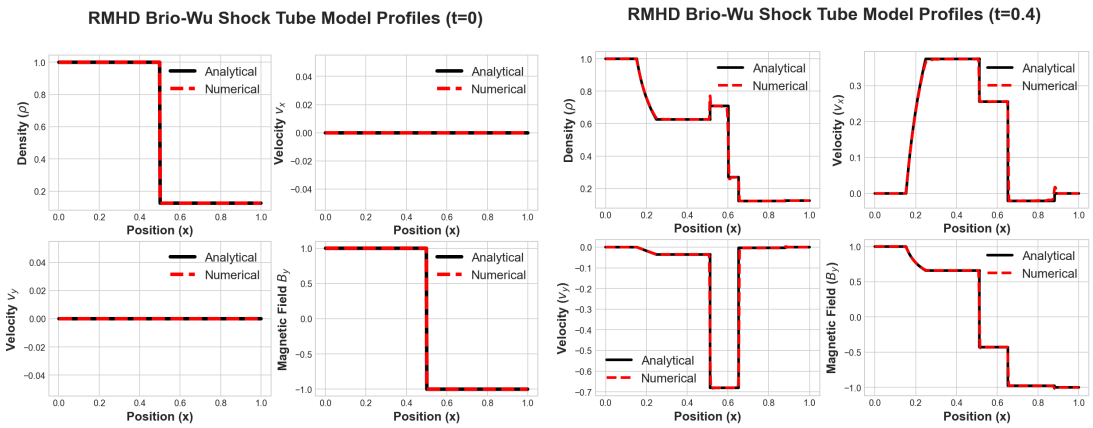

Figure 1: (*Left*) Initial conditions for the Brio–Wu RMHD shock tube at $t = 0.0$. (*Right*) Numerical profiles at $t > 0$ showing the characteristic MHD wave structure

The left panel shows the initial discontinuity at $t = 0$, which initiates a complex wave interaction across the domain. The initial time-step in the simulation is set as `first_dt` $= 1 \times 10^{-6}$, which is smaller than the CFL-limited value. The solver will start with this small value and quickly adjust to the CFL-limited time-step of approximately $\Delta t \approx 3.1 \times 10^{-4}$ as the simulation progresses. By $t = 0.4$ (right panel), the simulation reproduces the full RMHD wave fan. The resulting wave structure includes a fast rarefaction wave expanding into the high-pressure, high-density left state ($x \approx 0.15$-0.30). A slow compound wave develops behind a contact discontinuity, which transports the density step downstream ($x \approx 0.45$). A slow shock propagates ahead of the contact into the right state ($x \approx 0.55 - 0.65$), followed by a second fast rarefaction wave expanding into the low-pressure, low-density right state ($x \approx 0.85$–1.0). These features, including the flip in the transverse magnetic field B_y and stepwise changes in velocity and density, demonstrate the solver's ability to accurately capture anisotropic MHD wave propagation.

Small, localised overshoots are observed near the contact discontinuity and adjacent shocks. These features are common in Godunov-type shock-capturing schemes, arising from the interplay between numerical dissipation and dispersion inherent to the chosen reconstruction method (e.g., MUSCL, PPM, WENO), approximate Riemann solver (HLL-family, Roe-type, HLLD), and finite spatial resolution. Contacts and tangential magnetic field reversals are particularly challenging to capture without either added dissipation, which smears sharp features, or very high-order, non-oscillatory reconstruction, which can produce small Gibbs-like overshoots.

Importantly, these overshoots are minor, and do not affect the global wave ordering or conservation properties: the principal shocks, rarefactions, and discontinuities remain at expected positions and amplitudes when compared to reference solutions [9, 12]. Remedies to mitigate these artifacts include (i) grid refinement, (ii) using more dissipative or hybrid Riemann solvers, (iii) slope limiting or monotonicity-preserving reconstructions, and (iv) divergence-control methods or constrained transport for the magnetic field [9]. Convergence studies demonstrating reduction of overshoots with increasing resolution can further confirm their numerical, rather than physical, origin.

Overall, the Brio–Wu shock tube test confirms that the implemented solver accurately reproduces the full RMHD wave family. While this test remains a benchmark for assessing RMHD schemes, it has limited direct correspondence to realistic astrophysical systems. Therefore, a piston-driven setup is introduced in subsequent sections to provide a more physically motivated analogue for validating MHD shocks in supernova environments.

Hydrodynamic Piston-Driven Shock Model

The piston-driven shock problem models a piston located at $x = 0.01$ moving into a stationary gas at $t = 0.0$; Figure 2 (*Left*), analogous to the classical treatment of Landau & Lifshitz [11]. This motion generates a rightward-propagating shock wave. Ahead of the shock, the gas remains at its initial pressure and at rest, while the gas in the compressed region moves with the same velocity as the piston. The following initial and boundary conditions indicated in Table 2 were implemented:

Table 2: Initial conditions and X1-boundary conditions for the analytical piston-driven hydrodynamic shock model.

Region / Side	ρ	p	v_x	**X1-Boundary**
Pre-shock (Region 1)	0.125	1.0	0.0	outflow
Post-shock (Region 2)	ρ_2	p_2	0.5	moving piston

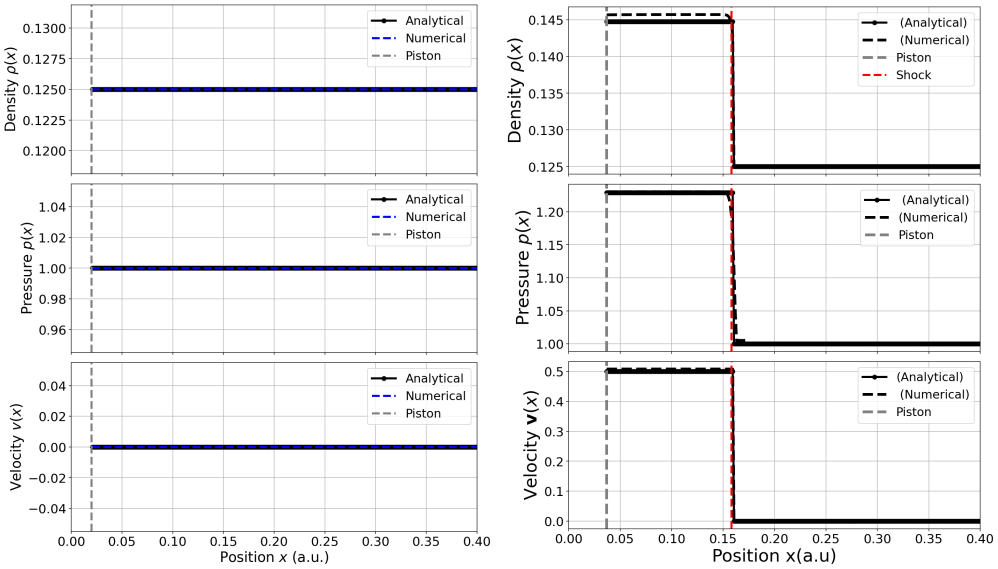

Figure 2: (*Left*) Initial conditions for the HD piston-driven shock model at $t = 0.00$. (*Right*) Comparison of analytical and numerical solutions for the hydrodynamic piston-driven shock at $t = 0.08$.

The numerical setup in `PLUTO` used a uniform one-dimensional grid of 800 zones in x, adaptive mesh refinement up to four levels, and a CFL number of 0.3, with an initial time-step `first_dt` $= 10^{-6}$. Figure 2 compares the numerical profiles with the analytical post-shock values at $t = 0.08$. Density and pressure exhibit the expected plateau structure behind the shock, with the piston located at $x_p \simeq 0.04$ and the shock at $x_s \simeq 0.16$ [11]. Agreement with analytical predictions is within $< 1.2\%$ for density, pressure, and velocity, demonstrating that the solver accurately captures the compression ratio and post-shock velocity. This validates the piston-driven HD model as a controlled benchmark for systematically testing numerical solvers against analytical approximations.

The results of the convergence are not presented here explicitly; however, the robustness of the results was verified by performing resolution test runs with 200, 400, and 800 zones, which confirmed that the shock structure and post-shock values remain stable once the resolution exceeds 400 zones. Thus, the adopted 800-zone resolution provides a numerically converged solution. The piston-driven setup, therefore, offers a reliable hydrodynamic framework for future extensions to MHD and RMHD, where magnetic field amplification, anisotropic stresses, and relativistic effects will further modify shock propagation in CCSNe.

Therefore, in summary, this piston-driven setup captures the essential hydrodynamics: the compression ratio and post-shock velocity align with theoretical predictions, the post-shock region expands appropriately in front of the shock. It provides a controlled framework for systematically testing numerical solvers and validating analytical approximations. The framework also allows for direct extension to MHD and RMHD, where magnetic field amplification, anisotropic pressure, and relativistic effects modify post-shock properties and propagation dynamics,

relevant to core-collapse supernovae. By establishing a physically consistent benchmark at the hydrodynamic level, this piston-driven setup forms a foundation for future multi-dimensional simulations in PLUTO.

5 Conclusions

This study developed and validated a one-dimensional piston-driven shock model as a benchmark for astrophysical shock propagation. In addition to the Brio–Wu shock tube, which confirmed that the PLUTO code reproduces the full RMHD wave family, the piston-driven model was shown to yield analytical and numerical solutions consistent with the Rankine–Hugoniot jump conditions. The excellent agreement between analytical predictions and simulation results demonstrates the reliability of this framework as a controlled test problem.

The novelty of this work lies in establishing the piston-driven shock model theoretically as a physically motivated validation tool for astrophysical applications, particularly the bounce-induced shocks in core-collapse supernovae and building the model in PLUTO. Unlike classical shock-tube setups that idealize shock formation, the piston model directly represents mechanical shock generation through compression, providing a more realistic analogue of supernova dynamics. By confirming the consistency of the model with analytical solutions and verifying its numerical convergence, this study lays the foundation for systematic extensions to magnetohydrodynamic (MHD) and relativistic MHD (RMHD) regimes.

Future work will focus on extending this validated piston-driven framework to include magnetic field amplification, anisotropic stresses, and relativistic effects, enabling more realistic simulations of shock evolution in CCSNe. Such developments will provide a robust pathway toward multi-dimensional, physically consistent modelling of extreme astrophysical environments.

Acknowledgements

The authors would like to thank the Centre for Broadband Communication team, Dr Isobel Kolbe at the University of Witwatersrand, Mr Paul Wekesa, Dr Zelalem Urgessa at Nelson Mandela University, the Postgraduate Research Office at Nelson Mandela University, the National Research Foundation (NRF), and the National Institute for Theoretical and Computational Sciences (NITheCS) for support.

References

[1] J.-P. Blaizot1, "Ultrarelativistic heavy ion collisions theoretical overview," *Journal of Physics: Conference Series*, vol. 50, no. 1, p. 1, nov 2006. [Online]. Available: https://dx.doi.org/10.1088/1742-6596/50/1/001

[2] A. Burrows, "Colloquium: Perspectives on core-collapse supernova theory," *Reviews of Modern Physics*, vol. 85, no. 1, p. 245, 2013.

[3] H.-T. Janka, "Explosion mechanisms of core-collapse supernovae," *Annual Review of Nuclear and Particle Science*, vol. 62, pp. 407–451, 2012, Downloaded from www.annualreviews.org.

[4] J. P. Goedbloed and S. Poedts, *Principles of Magnetohydrodynamics*. Cambridge University Press, 2004.

[5] B. Giacomazzo and L. Rezzolla, "The whisky code: a new numerical code for general relativistic magnetohydrodynamics," *Classical and Quantum Gravity*, vol. 24, no. 12, pp. S235–S258, 2007.

[6] L. Rezzolla and O. Zanotti, *Relativistic Hydrodynamics*. Oxford University Press, 9 2013.

[7] J. M. Martí and E. Müller, "Numerical hydrodynamics in special relativity," *Living Rev.*, vol. 6, no. 7, p. 3, 2003. [Online]. Available: https://doi.org/10.12942/lrr-2003-7

[8] M. Brio and C. Wu, "An upwind differencing scheme for the equations of ideal magnetohydrodynamics," *Journal of Computational Physics*, vol. 75, no. 2, pp. 400–422, 1988. [Online]. Available: https://www.sciencedirect.com/science/article/pii/0021999188901209

[9] A. Mignone, G. Bodo, S. Massaglia, T. Matsakos, O. Tesileanu, C. Zanni, and A. Ferrari, "Pluto: A numerical code for computational astrophysics," *The Astrophysical Journal Supplement Series*, vol. 170, no. 1, p. 228–242, May 2007. [Online]. Available: http://dx.doi.org/10.1086/513316

[10] A. Anile, *Relativistic Fluids and Magneto-Fluids: With Applications in Astrophysics and Plasma Physics*. Cambridge University Press, 1989.

[11] L. D. Landau and E. M. Lifshitz, *Fluid Mechanics*, 2nd ed., ser. Course of Theoretical Physics. Oxford: Pergamon Press, 1987, vol. 6.

[12] B. Giacomazzo and L. Rezzolla, "The exact solution of the riemann problem in relativistic magnetohydrodynamics," *Journal of Fluid Mechanics*, vol. 562, pp. 223–259, 2006.

Reservoir Computing for Predicting Chaotic Dynamical Systems

Taheer Jooma Abbajee[1], **Keegan Anderson**[1,4], **Muaaz Bhamjee**[2,5], **Maria Vivien Visaya**[1,3,4]

[1]Department of Mathematics and Applied Mathematics, University of Johannesburg, Johannesburg, South Africa
[2]Clean Energy Research Group, Department of Mechanical and Aeronautical Engineering, University of Pretoria, Pretoria, South Africa
[3]DSTI-NRF Centre of Excellence in Mathematical and Statistical Sciences, University of the Witwatersrand, Johannesburg, South Africa
[4]National Institute for Theoretical and Computational Sciences, Stellenbosch University, Stellenbosch, South Africa
[5]Department of Mechanical Engineering Science, University of Johannesburg, Johannesburg, South Africa

E-mail: taheerjooma@gmail.com

Abstract.

Time-series prediction involves forecasting future values by analysing historical data to detect patterns, trends, and variations; chaotic systems are particularly challenging to predict due to their sensitivity on initial conditions. Two primary prediction approaches exist: data-driven and model-based methods. Reservoir computing (RC) is a data-driven model derived from recurrent neural networks (RNNs), in which the hidden layer is replaced by a fixed, high-dimensional dynamical system known as the "reservoir". In this framework, only a single readout layer is trained using linear regression, while all other connections remain fixed. This model reduces certain complexity (compared to RNNs) while maintaining performance, and excels in predicting time-series from unknown systems. We demonstrate this using the logistic, sine and Hénon maps. The model provided successful short- and medium-term prediction, but remains limited in long-term forecasting. It also inferred key dynamical properties (e.g., fixed points, correlation maps, Lyapunov exponents) not explicitly present in the training data. Our results confirm that RC as an effective alternative to RNNs and highlights its potential for applications in complex systems modelling.

1 Introduction

Chaotic dynamical systems are deterministic but are often difficult to predict due to sensitive dependence on initial conditions. It is often the case that one might only have access to the observed chaotic time series generated by an unknown dynamical system [1]. Reservoir computing is a machine learning algorithm that emerged in the early 2000s as a simplified alternative to RNNs that can be trained on a sample of known time series data and can then be used to predict and analyse the dynamics of the underlying system [1]. In this study, we apply established RC methodologies to well-known chaotic systems including the logistic, sine, and Hénon maps to evaluate predictive performance and relate reservoir behaviour to key dynamical features such as fixed points, correlation maps, and Lyapunov exponents. This work aims to demonstrate a rigorous and pedagogical application of RC for understanding and predicting chaotic dynamics.

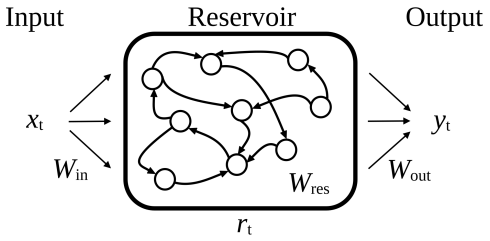

Figure 1: Schematic of a reservoir computer architecture.

2 Reservoir Computing Model

our RC model, adapted from [2, 3], consists of three layers: an input layer, a reservoir, and an output layer (as shown in Figure 1). Consider a RC comprising of d_r reservoir nodes with an input–output space of dimension d_x. At each time-step $t \in \mathbb{N}_0$, let $x_t \in \mathbb{R}^{d_x}$ be the input to the RC, $r_t \in \mathbb{R}^{d_r}$ the hidden reservoir state and $y_t \in \mathbb{R}^{d_x}$ the output of the RC. Note that d_r is often chosen such that $d_r > d_x$, this is to ensure a higher dimensional mapping of input time-series to the reservoir space. The input layer consists of a matrix $W_{\text{in}} \in \mathbb{R}^{d_r \times d_x}$ which maps the input vector x_t to the reservoir space. The elements of W_{in} are randomly chosen from a uniform distribution between $[-\sigma, \sigma]$, where σ is chosen such that the elements of $W_{\text{in}}x_t$ lie between $(-1, 1)$. The reservoir is the most important layer and is responsible for computing the next reservoir state. The evolution of the reservoir states is given by

$$r_{t+1} = \tanh(W_{\text{in}}x_t + W_{\text{res}}r_t + b), \tag{1}$$

where $W_{\text{in}}x_t$ is the output of the input layer, $W_{\text{res}} \in \mathbb{R}^{d_r \times d_r}$ is the reservoir weight matrix, and $b \in \mathbb{R}^{d_r}$ is a constant bias term of the form $\beta\mathbf{1}$, where $\beta \in (-1, 1)$ and $\mathbf{1} \in \mathbb{R}^{d_r}$. The reservoir weight matrix can be thought of as an adjacency matrix that represents the connections of the nodes in the reservoir. The matrix W_{res} is chosen randomly to have a set sparsity (τ) and spectral radius (ρ). The output layer consists of a matrix $W_{\text{out}} \in \mathbb{R}^{d_x \times d_r}$ that maps the reservoir states back to the target dimension $\mathbb{R}^{d_x}$. The matrix W_{out} is the only parameter learned during training and is subsequently used to generate the prediction y_{t+1} given by

$$y_{t+1} = W_{\text{out}}r_t. \tag{2}$$

3 General Set-up of our RC model

In order to set-up our RC model we follow a procedure similar to the one described by Hara and Kokubu [3]. Assume we have observed time-series data $\{x_t\}_{t\in\mathbb{N}_0}$, then choose $T_0, T_1, T_2 \in \mathbb{N}$ such that $T_0 < T_1 < T_2$ and we can partition the time-series data into three subsets: $\{x_t\}_{t=0}^{T_0}$, $\{x_t\}_{t=T_0+1}^{T_1}$, and $\{x_t\}_{t=T_1+1}^{T_2}$. Lastly, we choose r_0, W_{in}, W_{res} and b as described in Section 2.

During the warm-up phase $(0 \le t \le T_0)$ the reservoir states are updated according to equation (1). This phase is used to eliminate transient behaviour caused by the choice of initial conditions x_0 and r_0. During the training phase $(T_0 + 1 \le t \le T_1)$ we continue to update the reservoir states according to equation (1) and collect all the reservoir states and input vectors into the respective matrices $R = [r_{T_0+1} \quad r_{T_0+2} \quad r_{T_0+3} \quad \cdots \quad r_{T_1}]$ and $X = [x_{T_0+1} \quad x_{T_0+2} \quad x_{T_0+3} \quad \cdots \quad x_{T_1}]$. We can then find W_{out} by solving the minimisation problem $\arg\min_{W_{\text{out}}\in\mathbb{R}^{d_x\times d_r}} \|W_{\text{out}}R - X\|^2$ which has the least squares solution $W_{\text{out}} = XR^T(RR^T)^{-1}$.

A one-step prediction $(T_1 + 1 \le t \le T_2)$ can now be completed using equations (1) and (2). The output time series $\{y_t\}_{t=T_1+1}^{T_2}$ is expected to be nearly identical to the target time series $\{x_t\}_{t=T_1+1}^{T_2}$. Since $y_t = W_{\text{out}}r_t$ is expected to be approximately equal to x_t, we can substitute equation (2) for x_t in equation (1) to obtain

$$r_{t+1} = \tanh(W_{\text{in}}W_{\text{out}}r_t + W_{\text{res}}r_t + b). \tag{3}$$

Equation (3) is known as the autonomous reservoir system. After training, the reservoir evolves on its own and can be thought of as a dynamical system of the form $r_t : \mathbb{R}^{d_r} \to \mathbb{R}^{d_r}$. In order to find the optimal hyper-parameters for our RC model, we employ a two-step procedure: first, we explore the hyper-parameter space and find promising regions using random searches; thereafter, Bayesian optimisation is used to refine and extract the optimal hyper-parameters. Table 1 contains all optimum hyper-parameters used in our study.

4 Generalised Synchronisation

Generalized synchronisation (GS) is a type of synchronisation that occurs when the state of one system is completely dependent on the state of another system. The independent system is often called the drive system while the dependent system is referred to as the response system [4].

Hyper-parameters				
Dynamical system	ρ	τ	σ	β
Logistic map	0.866350431222052	0.94	1.2667028204891229	$8.680828069765185 \times 10^{-5}$
Sine map	0.8353366916477455	0.96	1.5641523755434774	$7.422063288375644 \times 10^{-6}$
Hénon map	0.6074166603943667	0.95	0.35371283527605013	-0.5996761514948162

Table 1: Hyper-parameters used for all simulations.

Definition 4.1 (Drive and response systems) *Suppose a drive system is given by a dynamical system (M, ϕ), then a response system $F : \mathbb{R}^N \times M \to \mathbb{R}^N$ is given by $r_{t+1} = F(r_t, x_t)$, where $x_t = \phi^t(x_0) \in M$, $x_0 \in M$, $r_t \in \mathbb{R}^N$, and $t \in \mathbb{N}_0$.*

A reservoir computer is essentially a drive-response system where the discrete dynamical system (M, ϕ) is the drive system, and the evolution of the reservoir states is the response system [5].

Definition 4.2 (Generalised Synchronisation [4]) *Let $V \subseteq \mathbb{R}^N$. A GS between a drive and a response system is a map $g : M \to \mathbb{R}^N$ such that for any $r_0 \in V$ and for any $x_0 \in M$, the following holds $g(x_{t+1}) = F(r_t, x_t) = r_{t+1}, \quad$ for all $t \in \mathbb{N}_0$. If $V \subset \mathbb{R}^N$, then g is called a local GS, and if $V = \mathbb{R}^N$ then g is called a global GS.*

In our RC model, the readout mapping W_{out} approximates the inverse of the GS mapping: $g(x_{t+1}) = F(r_t, x_t) = r_{t+1} \Rightarrow x_{t+1} = g^{-1}(r_{t+1}) \approx W_{\text{out}} r_{t+1} = y_{t+1}$. The existence of g^{-1} is generally not global and depends on the behaviour of the inputs x_t and the differentiability of g [6]. This link enables the RC model to reconstruct system dynamics and make predictions. Closely related to GS is the Echo State Property (ESP).

Definition 4.3 (Echo State Property [7]) *Let $r_0, r'_0 \in \mathbb{R}^{d_r}$ be initial reservoir states. Let $\{x_t\}_{t \in \mathbb{N}_0}$, $x_t \in \mathbb{R}^{d_x}$, be a given input time-series. A reservoir map $F : \mathbb{R}^{d_r} \times \mathbb{R}^{d_x} \to \mathbb{R}^{d_r}$ has the ESP if the sequences $r_{t+1} = F(r_t, x_t) \quad$ and $\quad r'_{t+1} = F(r'_t, x_t)$ satisfy $\|r_{t+1} - r'_{t+1}\| \to 0$ as $t \to \infty$.*

The ESP ensures stability in our model as past inputs gradually lose their influence over time, just as the intensity of an echo fades with time. When a reservoir satisfies the ESP, its internal states are uniquely determined by the input, forming a functional relationship with the driving system. Thus, the ESP can be viewed as a sufficient condition for GS, allowing the reservoir to reproduce the underlying system dynamics [7, 8, 9]. In order to better understand the ESP we will look at contracting reservoir maps.

Definition 4.4 (Contraction of reservoir maps [2]) *A reservoir map $F : \mathbb{R}^{d_r} \times \mathbb{R}^{d_x} \to \mathbb{R}^{d_r}$ is called globally state contracting if there exists a constant $c \in (0, 1)$ such that for any $r, r' \in \mathbb{R}^{d_r}$ and $x \in \mathbb{R}^{d_x}$ it follows that $\|F(r, x) - F(r', x)\| \leq c\|r - r'\|$.*

Theorem 4.1 ([2]) *A reservoir map $F : \mathbb{R}^{d_r} \times \mathbb{R}^{d_x} \to \mathbb{R}^{d_r}$ that is globally contracting has the global ESP.*

For RC model in section 2, the system is contracting and satisfies the ESP if the largest singular value of the reservoir weight matrix is less than one [10]; alternatively, a sufficient condition is that its spectral radius is less than one [10]. To set a reservoir matrix with a specific spectral radius, a random sparse matrix W is generated, its spectral radius $\rho(W)$ is computed, and the matrix is normalized by dividing by $\rho(W)$ to obtain a matrix with unit spectral radius, which is then scaled to the desired value during tuning. Traditional RCs use the hyperbolic tangent $(\tanh)$ activation to produce smooth, bounded, nonlinear dynamics conducive to the ESP, while conditions for non-standard activations are discussed in [2].

5 Simulations and Predictions

The RC model is configured using the hyper-parameters listed in Table 1. All reservoirs satisfy the condition $\rho(W_{\text{res}}) < 1$, ensuring that the ESP holds. To evaluate the performance of our RC model, we set $d_r = 10$, $T_0 = 50$, $T_1 = 100$, and $T_2 = 150$, and apply the model to the following dynamical systems:

- The logistic map with parameter 3.91, $x_{t+1} = 3.91 x_t(1 - x_t)$, with $x_0 = 0.63$;
- The sine map with parameter 0.955, $x_{t+1} = 0.955 \sin(\pi x_t)$, with $x_0 = 0.71$;
- The reduced 1-D Hénon map with classical parameters $a = 1.4$ and $b = 0.3$, $x_{t+1} = 1 - 1.4x_t^2 + 0.3x_{t-1}$, with $x_0, x_1 = 0$.

Furthermore, we note that a warm-up time of $T_0 = 50$ time-steps mitigates the effects of initial conditions. The code used to simulate and analyse the above dynamical systems is available on GitHub[1].

[1] `[https://github.com/TaheerJooma/SAIP_rcs`

5.1 One-step and reservoir prediction

Inspecting Figure 2 and Table 2, it can be observed that the one-step predictions are remarkably similar to the actual time series, however analysing the reservoir prediction we see that our predictions have deteriorated slightly but are still similar to the actual time series. This is due to fact that the reservoir prediction has no access to the observed time-series and instead uses its own past predictions to calculate future predictions.

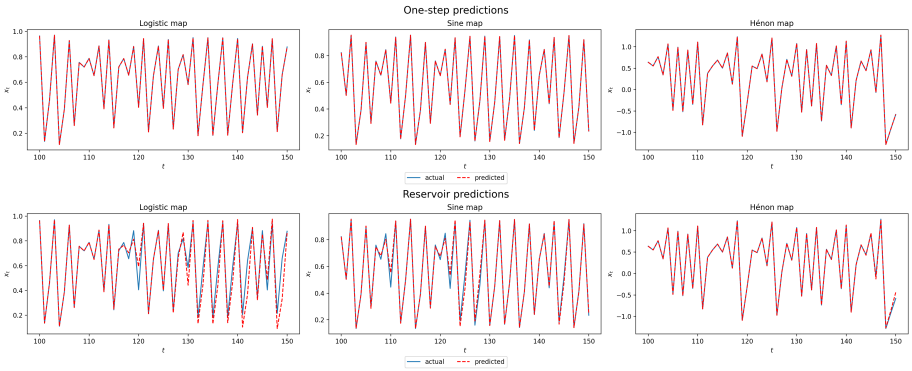

Figure 2: Actual vs predicted trajectories for the one-step and reservoir predictions.

one-step and reservoir prediction errors						
Dynamical system	MAE		MSE		RMSE	
	one-step	reservoir	one-step	reservoir	one-step	reservoir
Logistic map	0.00158448	0.04413210	0.00000310	0.00676420	0.00176089	0.08224477
Sine map	0.00081580	0.01575847	0.00000082	0.00097293	0.00090569	0.03119181
Hénon map	0.00070524	0.00716956	0.00000085	0.00053447	0.00092096	0.02311868

Table 2: Error analysis for the one-step and reservoir predictions.

5.2 Valid prediction time

The valid prediction time (VPT) [6] provides an indication of how many future reservoir predictions our RC model can perform within a given threshold $\epsilon > 0$, and is defined as

$$VPT = \min_{t\in\mathbb{N}} RMSE(n) = \min_{t\in\mathbb{N}} \sqrt{\frac{1}{n}\sum_{t=1}^{n}(x_t - y_t)^2} > \epsilon, \tag{4}$$

where n is the number of data points, $\epsilon = std(\{x_t\}_{t=T_0+1}^{T_1})$, x_t is the actual value at time-step t, and y_t is the predicted value at time-step t. In order to gain an idea of the number of reservoir predictions our model can perform within a given threshold, we calculate the VPT as defined in equation 4 for a hundred different initial conditions of our target system and analyse the data in a boxplot illustrated in Figure 3.

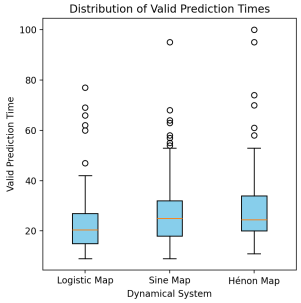

Figure 3: Distribution of VPTs.

Mean of VPT over 100 samples	
Dynamical system	Mean VPT
Logistic map	23.06
Sine map	28.19
Hénon map	29.44

Table 3: Mean VPT for 100 samples.

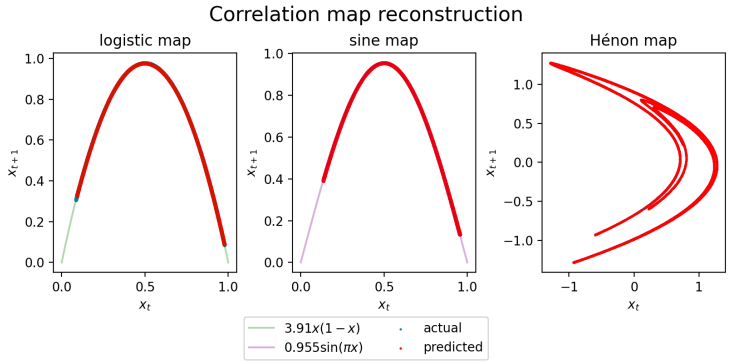

Figure 4: Actual vs predicted correlation maps.

Comparison of fixed points				
Dynamical system	Actual	Predicted		MAE
		Spurious	Non spurious	
Logistic map	0, $\frac{291}{391}$	1.5297709	-0.00994626, 0.74397722	0.00994626, 0.00026830
Sine map	0, 0.72540262	± 2.06426943, -0.7252752	-0.00000396, 0.72505301	0.00000396, 0.00034961
Hénon map	$\frac{-7\pm\sqrt{609}}{28}$	None	0.63147419, -1.13309976	0.00011971, 0.00174529

Table 4: Comparison of actual and predicted fixed points.

Notice that the data in Figure 3 contains numerous outliers. This can be explained by considering the overall stability of the initial condition used. If the initial condition lies in or around a stable region of the target dynamical system then the VPT will be fairly large as the time series is more predictable. Conversely, if the initial condition lies in or around an unstable region of the target dynamical system then the VPT will be smaller as the time series is more unstable, hence less predictable. From Table 3, we see that our model on average can reliably predict between 23-29 steps into the future, depending on which map is being forecasted.

5.3 Correlation map reconstruction

A correlation map between y_t and y_{t+1} describes and visualises how y_t is related to y_{t+1}. In order to visualise the predicted correlation map we plot y_t vs y_{t+1} for 10 000 points. From Figure 4 it can be seen that the predicted correlation maps are almost identical to the actual correlation maps in both shape and structure.

5.4 Prediction of fixed points

In order to find predicted fixed points we will first solve for r^* in the equation $r^* = \tanh((W_{\text{in}}W_{\text{out}} + W_{\text{res}})r^* + b)$. The predicted fixed points of the target system is then given by $y^* = W_{\text{out}}r^*$. It is important to note that since y^* is a projection of r^* to a lower dimensional space $\mathbb{R}^{d_x}$, both y^* and r^* share the same stability. The stability is determined by analysing the eigenvalues of the Jacobian matrix $J(r) = \text{diag}\big[1 - \tanh^2((W_{\text{in}}W_{\text{out}} + W_{\text{res}})r^* + b)\big](W_{\text{in}}W_{\text{out}} + W_{\text{res}})$. Table 4 lists and compares the actual and computed fixed points, and reveals numerous spurious fixed points. The spurious fixed points can easily be identified and eliminated as they are outliers when compared to the training data. Examining the errors in Table 4 it can be observed that our RC model is capable of predicting actual fixed points up to at least two decimal places. Lastly, all the actual and predicted fixed points were found to be unstable.

5.5 Prediction of Lyapunov exponents

Lyapunov exponents quantify the divergence rate of nearby trajectories, with positive values indicating sensitivity to initial conditions and potential chaos. For a discrete system $x_{n+1} = f(x_n)$, they are defined as $\lambda = \lim_{N\to\infty} \frac{1}{N}\sum_{n=0}^{N-1} \ln \frac{||v_{n+1}||}{||v_n||}$, where $v_{n+1} = Df(x_n)v_n$. We approximated the Lyapunov exponents of the autonomous reservoir system using QR decomposition [11]. Table 5 shows the model predicts Lyapunov exponents accurately to at least two decimal places. The maximal exponent inversely correlates with predictive performance, consistent with previous reports that higher maximal exponents yield shorter VPTs and larger errors [6, 12].

Comparison of Lyapunov exponents			
Dynamical system	Actual	Predicted	MAE
Logistic map	0.49123091	0.50002128	0.00879036
Sine map	0.45938807	0.46568606	0.00629799
Hénon map	0.42081703, -1.62478983	0.41453935, -1.61709175	0.00627768, 0.00769809

Table 5: Comparison of actual and predicted Lyapunov exponents.

6 Conclusions

This study looked at a RC approach for predicting and analysing chaotic dynamical systems based solely on observed time-series. The reservoir achieved short- to medium-term predictions and captured key dynamical properties not explicitly present in the training data, though long-term forecasting remains limited by the target system's maximal Lyapunov exponent. While spurious fixed points are present and common in higher-dimensional embeddings, stability analysis shows all fixed points are repelling and trajectories remain within the target system's natural bounds, consistent with correlation map reconstructions, resulting in minimal impact on predictive accuracy. Future work could explore reservoir space embeddings and tests on higher-dimensional systems.

Acknowledgements

MVV acknowledges funding from the DSI-NRF Centre of Excellence in Mathematical and Statistical Sciences (CoE-MaSS). The authors also thank the Faculty of Science at the University of Johannesburg, for scholarship support, and the Centre for High Performance Computing (CHPC), South Africa, for providing computational resources. The opinions and conclusions expressed are those of the authors and do not necessarily reflect the views of CoE-MaSS, NITheCS, CHPC, or the Universities of Johannesburg and Pretoria.

References

[1] A. Aussem, "Dynamical recurrent neural networks towards prediction and modeling of dynamical systems," *Neurocomputing*, vol. 28, no. 1-3, pp. 207–232, 1999.

[2] P. Singh, L. Sankaranarayanan, and B. Raman, "Contraction, criticality, and capacity: A dynamical-systems perspective on echo-state networks," *arXiv preprint arXiv:2507.18467*, 2025.

[3] M. Hara and H. Kokubu, "Learning Dynamics by Reservoir Computing (In Memory of Prof. Pavol Brunovský)," *Journal of Dynamics and Differential Equations*, vol. 36, no. S1, pp. 515–540, Feb. 2024.

[4] N. F. Rulkov, M. M. Sushchik, L. S. Tsimring, and H. D. Abarbanel, "Generalized synchronization of chaos in directionally coupled chaotic systems," *Physical Review E*, vol. 51, no. 2, p. 980, 1995.

[5] A. Nazerian, C. Nathe, J. D. Hart, and F. Sorrentino, "Synchronizing chaos using reservoir computing," *Chaos: An Interdisciplinary Journal of Nonlinear Science*, vol. 33, no. 10, pp. 103–121, 2023.

[6] J. A. Platt, S. G. Penny, T. A. Smith, T.-C. Chen, and H. D. Abarbanel, "A systematic exploration of reservoir computing for forecasting complex spatiotemporal dynamics," *Neural Networks*, vol. 153, pp. 530–552, 2022.

[7] A. Ohkubo and M. Inubushi, "Reservoir computing with generalized readout based on generalized synchronization," *Scientific reports*, vol. 14, no. 1, p. 30918, 2024.

[8] L. Grigoryeva, A. Hart, and J.-P. Ortega, "Chaos on compact manifolds: Differentiable synchronizations beyond the Takens theorem," *Physical Review E*, vol. 103, no. 6, p. 062204, 2021.

[9] T. Lymburn, D. M. Walker, M. Small, and T. Jüngling, "The reservoir's perspective on generalized synchronization," *Chaos: An Interdisciplinary Journal of Nonlinear Science*, vol. 29, no. 9, 2019.

[10] H. Jaeger, "The 'echo state' approach to analysing and training recurrent neural networks—with an erratum note," *Bonn, Germany: German national research center for information technology gmd technical report*, vol. 148, no. 34, p. 13, 2001.

[11] M. Sandri, "Numerical calculation of lyapunov exponents," *Mathematica Journal*, vol. 6, no. 3, pp. 78–84, 1996.

[12] C. Zhang, J. Jiang, S.-X. Qu, and Y.-C. Lai, "Predicting phase and sensing phase coherence in chaotic systems with machine learning," *Chaos: An Interdisciplinary Journal of Nonlinear Science*, vol. 30, no. 8, 2020.

Testing $f(Q)$ gravity as a solution for the H_0 and S_8 tensions

Dumiso Mithi[1], **Shambel Sahlu**[1,2,3] **and Amare Abebe**[1,2]

[1]Centre for Space Research, North-West University, Potchefstroom 2520, South Africa
[2]National Institute for Theoretical and Computational Sciences (NITheCS), South Africa
[3]Department of Physics, Wolkite University, Wolkite, Ethiopia

E-mail: 28145410@mynwu.ac.za

Abstract. In this work, we investigate a modified gravity framework based on the $f(Q)$ gravity model, where Q is the non-metricity scalar, specifically focussing on the parameterisation $f(Q) = \alpha + \beta Q^n$ as a possible solution to the Hubble constant (H_0) and matter fluctuation amplitude (S_8) tensions. Using recent observational data sets, including baryon acoustic oscillations (BAO) from the Dark Energy Spectroscopic Instrument (DESI), cosmic chronometers (CC), type Ia supernovae from the Pantheon+ and SH0ES compilations, growth rate data (f), and redshift-space distortion measurements (f_{σ_8}), we constrain the free parameters of the ΛCDM and $f(Q)$ models via the Markov Chain Monte Carlo (MCMC) method. Our analysis shows that the $f(Q)$ model can alleviate the tensions H_0 and S_8 and demonstrates strong observational support in all combinations of data sets considered in this study based on the ΔBIC criterion. However, this result is accompanied by relatively large uncertainties in MCMC-derived H_0 values, suggesting possible parameter degeneracies when assuming the present condition $f_Q \equiv \partial f/\partial Q = 1$. We compare our findings with previous studies that relax certain assumptions of the model and find improved parameter constraints. Finally, we outline plans for future work to perform a comprehensive statistical evaluation of the capability of the $f(Q)$ model to resolve the H_0 and S_8 tensions by combining early- and late-time cosmological measurements without restrictive assumptions.

1 Introduction

In modern physics, the indispensable and foundational theory of space, time, and gravitation, where gravity is understood as the curvature of spacetime is *General Relativity* (GR), formulated by Einstein in 1915 [1, 2]. GR has proven remarkably successful, accurately predicting a wide range of phenomena, including planetary motion, light deflection, gravitational time delay, and black hole dynamics. It has been rigorously tested across a wide range of scales, from submillimeter laboratory experiments to solar system distances ($\sim 10^{14}\ m$), including strongly gravitating binary pulsar systems. A major milestone came with the first direct detection of gravitational waves by the Laser Interferometer Gravitational-Wave Observatory, coinciding with the 100th anniversary of GR [2]. However, several large-scale observations such as the accelerated expansion of the universe from type Ia supernovae (SNe Ia) observations [3], and galactic rotation curve velocity measurements [4, 5] pose significant challenges for GR.

To address these discrepancies within the standard cosmological framework, the Lambda Cold Dark Matter (ΛCDM) model was introduced, which incorporates a cosmological constant (Λ) and cold dark matter as essential components [6]. Although the ΛCDM model resolves some of the shortcomings of GR such as the observed accelerated expansion of the universe, it also introduces its own challenges. One such issue is the fine-tuning problem, where the theoretical value of the dark energy density derived from quantum field theory is $\gtrsim 10^{121}$ times the observed value. Another is the coincidence problem, where the dark energy and dark matter densities are of the same order of magnitude today, despite evolving differently over time. Furthermore, observational tensions exists

between early- and late-time measurements of key cosmological parameters, namely the measured values of the Hubble constant (H_0) and the matter fluctuation amplitude parameter (S_8).

Early-universe measurements suggest $H_0 = 67.4 \pm 0.5$ km/s/Mpc and $S_8 = 0.831 \pm 0.013$, while late-time observations yield $H_0 = 73.04 \pm 1.04$ km/s/Mpc and $S_8 = 0.766^{+0.020}_{-0.014}$. These discrepancies correspond to tensions of approximately 5σ for H_0 and 3.1σ for S_8, respectively [6]. Various approaches have been proposed to overcome the shortcomings of the standard ΛCDM model, including dynamical dark energy, interactions between dark matter and dark energy, and radiation-based models. A compelling alternative is to modify gravity itself. Rather than introducing new matter fields or exotic energy components such as inflation or dark energy, modified gravity theories aim to explain both early- and late-time cosmic acceleration and structure formation through changes to the underlying laws of gravity. In recent decades, numerous such models have been developed to account for observations of galaxy and cluster dynamics, large-scale structure (LSS), Cosmic Microwave Background (CMB) anisotropies, and the present accelerated expansion, without invoking dark matter or dark energy [6, 7].

The idea of modifying gravity dates back to Einstein's later work, in which he attempted to unify GR and electromagnetism using affine connections, a concept introduced by mathematicians like Weyl. Although unification was not achieved, Einstein's approach gave rise to a formulation where gravity is mediated by torsion rather than curvature, which forms the foundation of metric teleparallel gravity. Later advancements showed that gravity could also emerge from non-metricity in flat, torsionless geometries. This led to the concept of the geometric trinity of gravity, which recognises three physically equivalent but geometrically distinct formulations of GR: curvature-based, torsion-based, and non-metricity-based, all rooted in metric-affine geometry. This trinity has attracted growing interest for its ability to provide new insights into the foundations of GR and address long-standing issues such as gravitational energy-momentum and black hole entropy [7]. In this study, we focus on a modified gravity model based on nonmetricity named $f(Q)$-gravity to explore its potential to resolve tensions H_0 and S_8.

2 $f(Q)$ Cosmology

In $f(Q)$-gravity, the mathematical description between the geometry of spacetime and the distribution of matter can be obtained from the modified Einstein-Hilbert action [7]:

$$S_Q = \frac{1}{2\kappa}\int \sqrt{-g}\,[f(Q) + \mathcal{L}_m]\,d^4x, \tag{1}$$

where $\kappa = \frac{8\pi G}{c^4}$ with G being the Newtonian constant, g is the determinant of the metric $g_{\mu\nu}$, $\mathcal{L}_m$ is the matter lagrangian density, and $f(Q)$ is an arbitrary function of non-mentricity scalar Q defined as $Q = -Q_{\alpha\mu\nu}P^{\alpha\mu\nu}$. Furthermore, $Q_{\alpha\mu\nu} \equiv \nabla_\gamma g_{\mu\nu}$ and $P^\alpha{}_{\mu\nu} \equiv \frac{1}{4}\left(-Q^\alpha{}_{\mu\nu} + 2Q_{(\mu}{}^\alpha{}_{\nu)} - Q^\alpha g_{\mu\nu} - \tilde{Q}^\alpha g_{\mu\nu} - \delta^\alpha_{(\mu}Q_{\nu)}\right)$ are the non-metric tensor with two independent traces ($Q_\alpha = Q_\alpha{}^\mu{}_\mu$ and $\tilde{Q} = Q^\mu_{\alpha\mu}$) and the superpotential term, respectively [7, 8]. Furthermore, the Action (1) in a flat spacetime is equivalent to GR for $f(Q) = Q$. Now, setting $8\pi G = c^4 = 1$ to vary the action (1) with respect to the metric tensor and setting it to zero yields the following field equations:

$$\frac{2}{\sqrt{-g}}\nabla_\alpha(\sqrt{-g}f_Q P^\alpha_{\mu\nu}) + \frac{1}{2}f g_{\mu\nu} + f_Q(P_{\mu\alpha\beta}Q_\nu^{\alpha\beta} - 2Q_{\alpha\beta\mu}P_\mu^{\alpha\beta}) = T_{\mu\nu}, \tag{2}$$

where $T_{\mu\nu} = -\frac{2}{\sqrt{-g}}\frac{\delta\sqrt{-g}\mathcal{L}_m}{\delta g^{\mu\nu}}$ is the energy-momentum tensor, f is $f(Q)$, and $f_Q \equiv \frac{\partial f}{\partial Q}$. For cosmological application, we consider the line element $ds^2 = -dt^2 + a(t)^2\delta_{ij}dx^i dx^j$ which corresponds to the spatially flat Friedman-Lemaitre-Robertson-Walker (FLRW) metric, in which δ_{ij} is the Kronecker delta and $a(t)$ is the cosmic scale factor used to define the Hubble expansion rate $H \equiv \frac{\dot{a}}{a}$ with a dot representing the derivative with respect to cosmic time. As a result, one assumes that the Universe is composed of a perfect fluid [9]:

$$T_{\mu\nu} = (\rho + P)u_\mu u_\nu + P q_{\mu\nu}, \tag{3}$$

such that the total energy density and total pressure, respectively, become

$$\rho_{tot} = 6H^2 f_Q - \frac{1}{2}f, \tag{4}$$

$$P_{tot} = \frac{1}{2}f - 2f_Q(\dot{H} + 3H^2 + 12H^2\dot{H}\frac{f_{QQ}}{f_Q}), \tag{5}$$

where $f_{QQ} \equiv \frac{\partial^2 f}{\partial Q^2}$ and the non-metric tensor becomes $Q = 6H^2$ then the modified Friedmann and Raychaudhuri equations are

$$3H^2 = \frac{1}{2f_Q}(\rho_{tot} + \frac{f}{2}), \tag{6}$$

$$\dot{H} + 3H^2 = -\frac{1}{2f_Q}(24H^2\dot{H}f_{QQ} + P_{tot} - \frac{f}{2}). \tag{7}$$

In this work, to solve the modified Friedmann and Raychaudhuri equation, we use the $f(Q)$-gravity model reconstructed using observation data without any prior ansatz on the underlying cosmological background by means of the Markov Chain Monte Carlo (MCMC) integration technique applied to the combined likelihood of the SNIa Pantheon sample and observational Hubble data from S. Capozziello and R. D'Agostino [10] as

$$f(Q) = \alpha + \beta Q^n, \tag{8}$$

where α, β, n are constant parameters that match the observational data after numerical reconstruction based on rational Pade approximations. The model matches GR when $\alpha = 0$ and $\beta = n = 1$, while it matches the ΛCDM model when $\alpha = -2\Lambda$ and $\beta = n = 1$. As a result, the partial derivative of the model with respect to Q is

$$f_Q = \beta n Q^{n-1}, \tag{9}$$

and using the fact that when the model in use was constructed, it was concluded that G_{eff} coincided with G at the present epoch translated to $f_Q = 1$ we get the following relation:

$$\beta = \frac{6H_0^2}{n(6H_0^2)^n}. \tag{10}$$

Assuming a non-relativistic matter and substituting Equations (7), (8), and (9) into the modified Friedmann Equation (6), the normalised Hubble parameter ($h(z) = \frac{H(z)}{H_0}$) after some mathematical manipulations becomes

$$h(z) = \sqrt{\left(\frac{\Omega_{m,0}(1+z)^3 + \frac{\Omega_\alpha}{2}}{2 - \frac{1}{n}}\right)^{\frac{1}{n}}}, \tag{11}$$

where $\Omega_{m,0}$ is the dimensionless matter density parameter of the present value, and $\Omega_\alpha = \frac{\alpha}{3H_0^2}$ is a dimensionless parameter introduced in this study to ensure that $h(z)$ remains dimensionless. From Equation (11) we may deduce that $n \neq 0$ and $n > \frac{1}{2}$. As a result, in the next subsection we will use recent cosmological data to constrain Equation (11) and the flat ΛCDM model given as

$$h(z) = \sqrt{\Omega_{m.0}(1+z)^3 + (1 - \Omega_{m,0})}. \tag{12}$$

2.1 Cosmological observation

The datasets used are baryon acoustic oscillation (BAO) measurements from the Dark Energy Spectroscopic Instrument (DESI) [11], cosmic chronometers (CC) from Hubble parameter measurements [12], Type Ia supernova (SNIa) distance moduli from the Pantheon+ and SH0ES compilations (PantheonP+SH0ES) [13], growth-of-structure data (f) from L. Perenon et al. [14], and redshift-space distortion data ($f\sigma_8$) from F. Skara and L. Perivolaropoulos [15].

Furthermore, using the updated MCMC simulation package *Kosmulator* [16], we constrain the model parameters $\Omega_{m,0}$, σ_8, γ, Ω_α, n, H_0, r_d, and M_{abs}, following the methodology of S. Sahlu et al. [17] for applying these datasets. Since σ_8 and $\Omega_{m,0}$ are constrained, the structure growth parameter S_8 is indirectly determined via

$$S_8 = \sigma_8\sqrt{\frac{\Omega_{m,0}}{0.3}}. \tag{13}$$

Here, σ_8 is the amplitude of matter clustering on $8\,h^{-1}$ Mpc scales, γ is the growth index, r_d is the sound horizon at the drag epoch (in Mpc), and M_{abs} is the calibrated absolute magnitude of SNIa. Although r_d and H_0 carry physical units, we omit them in the reported values for brevity and clarity; it should be understood that these are not dimensionless quantities.

The free parameters and their uniform prior ranges are:

$$0 \leq \Omega_{m,0} \leq 1, \quad 0 \leq \sigma_8 \leq 1, \quad 0 \leq \gamma \leq 1, \quad 0 \leq \Omega_\alpha \leq 2,$$
$$0.5 < n \leq 2, \quad 0 \leq H_0 \leq 100, \quad 100 \leq r_d \leq 200, \quad -22 \leq M_{\text{abs}} \leq -15.$$

The fixed parameters with their fiducial values are $\Omega_{m,0} = 0.315$, $\sigma_8 = 0.8120$, $H_0 = 67.4$, and $r_d = 147.05$ from Planck 2018 [18]; $\gamma = 0.55$ from E. V. Linder and R. N. Cahn [19]; and $M_{\text{abs}} = -19.25$ from A. Mhamdi et al. [20].

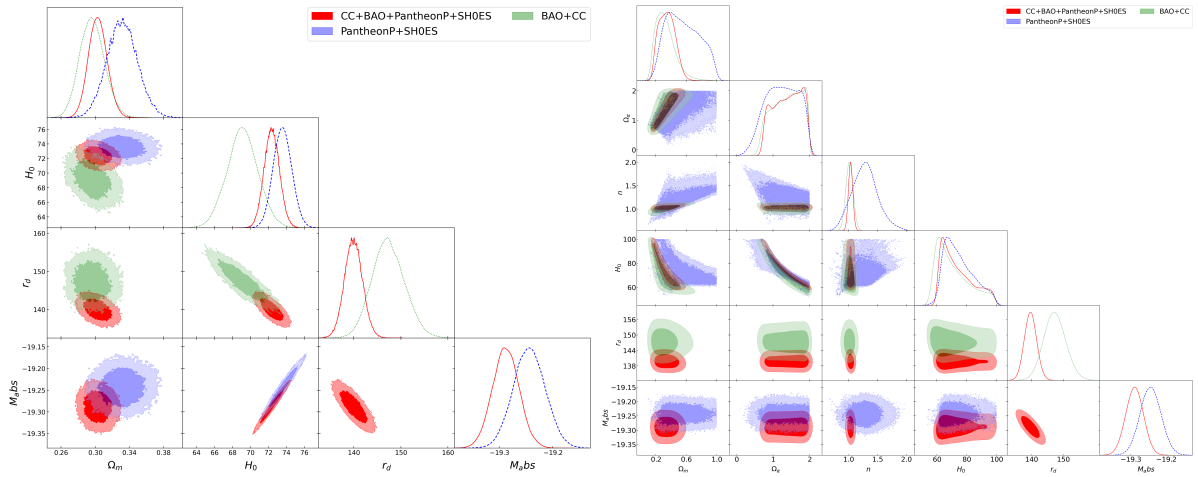

Figure 1: (*left*) Figure shows the contour plots and Gaussian graphs of the parameter distributions for the best-fit parameters of the ΛCDM mode, whereas (*right*) Figure presents the same for the $f(Q)$ model, using different combinations of CC, BAO, and SNIa (Pantheon+ SH0ES) datasets to refine the best-fitting values of the free parameters. Here, on this graphs Ω_m represent the value of $\Omega_{m,0}$, and the corresponding parameter values are all listed in Table 1.

3 Discussion and Conclusion

According to the latest measurements from DESI BAO by A.G. Adame et al. [11] and the 2000 SNIa sample compilation from the Union Through UNITY project by D. Rubin et al. [21], the best-fit values for the matter density parameter are $\Omega_{m,0} = 0.295^{+0.015}_{-0.015}$ and $\Omega_{m,0} = 0.356^{+0.028}_{-0.028}$, respectively. A recent late-time constraint from the combined Pantheon+SH0ES datasets by D. Brout et al. [13] yields $\Omega_{m,0} = 0.334^{+0.018}_{-0.018}$, while the combination of BAO and cosmic chronometers (CC) of S. Sahlu et al. [17] gives $\Omega_{m,0} = 0.296^{+0.015}_{-0.014}$ within the flat ΛCDM model. A direct combination of Pantheon+SH0ES and early-time probes such as BAO must be approached with caution due to degeneracies, particularly in the absolute magnitude calibration of SNIa. As noted in the literature, such combinations are often avoided unless a model explicitly accounts for the overlapping information. These degeneracies can be mitigated by incorporating complementary measurements sensitive to both early- and late-time expansion histories, such as Planck's CMB data. This approach has been demonstrated in joint analyses by A.G. Adame et al. [11] and D. Brout et al. [13], which combined BAO, CMB and Pantheon + data to obtain model-consistent cosmological parameters.

In this work, we break the degeneracy between BAO and Pantheon+SH0ES by including CC data. This is evidenced by the nearly circular 2D contour plots, reduced uncertainties, and approximately Gaussian posterior distributions for the ΛCDM model, as shown in the left panel of Figure 1. Furthermore, considering the DESI BAO and Union Through UNITY datasets, the values of Ω_m with their uncertainties under the flat ΛCDM model show that, when taking the lower bound of DESI BAO ($\Omega_m - \sigma_-$) and the upper bound of Union Through UNITY ($\Omega_m + \sigma_+$), all best fit values Ω_m in Table 1 lie within the combined acceptable range $0.28 \lesssim \Omega_m \lesssim 0.384$, indicating consistency between these constraints. A similar agreement is found for the $f(Q)$ model, except for the combinations BAO+CC+PantheonP+SH0ES, BAO+CC+$f\sigma_8$+f, and $f\sigma_8$+f, where the best-fit values Ω_m fall outside this range, suggesting possible tension or inconsistency. For the f_{σ_8} combination, $\Omega_{m,0}$ lies slightly below the lower bound, but its upper bound remains within the acceptable range.

Early-universe measurements suggest $H_0 = 67.4 \pm 0.5$, while late-time observations yield $H_0 = 73.04 \pm 1.04$ within the ΛCDM framework. This well-known tension is also evident in Table 1. However, as shown in Table 1, the best-fit values of the Hubble constant H_0 for the $f(Q)$ model in various combination datasets range approximately between 68 and 73 km/s/Mpc, with uncertainties spanning roughly 8–16 km/s/Mpc. This indicates that the different combinations of data sets are internally consistent, as their ranges 1σ overlap significantly and there is no tension among them. Moreover, compared to the late-time measurement $H_0 = 73.04 \pm 1.04$ km/s/Mpc, the best-fit values $f(Q)$ remain fully compatible, showing that this model can simultaneously accommodate both the combined cosmological datasets used here and the local late-time measurement without any significant discrepancy.

As mentioned, early-time measurements based on the ΛCDM model for a flat universe yield $S_8 = 0.834^{+0.016}_{-0.016}$. In particular, a persistent tension is observed in all combinations of datasets, which consistently produce lower S_8 values compared to this estimate of the early time. The only exception occurs for the combined dataset f_{σ_8} +

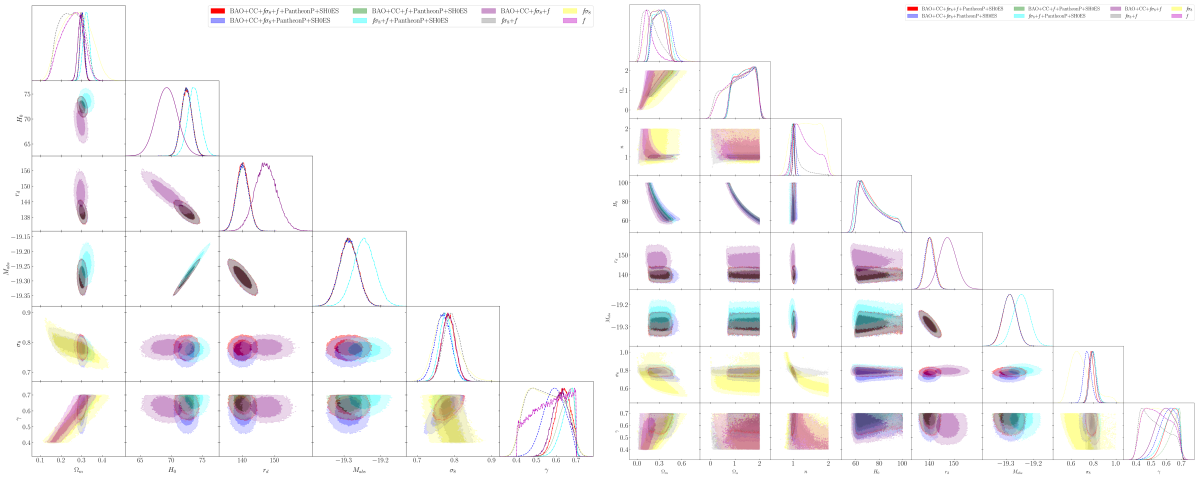

Figure 2: (*left*) Figure shows the contour plots and Gaussian graphs of the parameter distributions for the best-fit parameters of the ΛCDM mode, whereas (*right*) Figure presents the same for the $f(Q)$ model, using different combinations of CC, BAO, f_{σ_8}, f,and SNIa (Pantheon+ SH0ES) datasets to refine the best-fitting values of the free parameters. Here, on this graphs Ω_m represent the value of $\Omega_{m,0}$, and the corresponding parameter values are all listed in Table 1 too.

f+PantheonP+SH0ES, whose best-fit value and associated uncertainty fall within the 1σ range of the early-time measurement. However, tension S_8 remains present even in this case, indicating that the discrepancy has not been fully resolved within this model. Furthermore, examining the constraints S_8 within the $f(Q)$ framework reveals two internal clusters among the combinations of data sets. The first group, which includes the BAO+CC+PantheonP+SH0ES combinations, shows a generally consistent clustering amplitude with S_8 values ranging between 0.78 and 0.82, indicating that there is no significant internal tension. The second group, comprising combinations $f\sigma_8$ and $f\sigma_8 + f$, produces considerably smaller S_8 values (~ 0.59–0.65), introducing internal tension within the model. Compared with the estimate of early time ΛCDM, $S_8 = 0.834^{+0.016}_{-0.016}$, only the $f\sigma_8 + f$+PantheonP+SH0ES combination remains fully consistent within the range 1σ, while the other combinations fall slightly below, reflecting mild to moderate tension. In general, the $f(Q)$ model demonstrates a reduction in the S_8 tension relative to ΛCDM, although some internal discrepancies persist depending on the combination of the data set.

Hence, before we perform a statistical analysis to investigate whether there is observational support for the $f(Q)$ model, to quantify the degree to which the model fits the data and then summarise the results in Table (2), following the methodology of D. Mithi [6]. We first numerically differentiate equations (11) and (12) with respect to redshift. Following the methodology of [6, 22], we then derive the deceleration parameter (q), effective equation of state (w_{eff}), the statefinder parameters (r, s), and the Om diagnostic (Om). Their behaviours are shown in Figures (3 and 4) as paired plots, in the same order, to identify the type of dark energy responsible for cosmic acceleration at the background level.

The results presented in Table 2, when examining Δ AIC and applying the AIC interpretation, indicate that the $f(Q)$ model has somewhat considerably less observational support for the dataset combinations BAO+CC+$f\sigma_8$+f+PantheonP+SH0ES, BAO+CC+f+PantheonP+SH0ES, $f\sigma_8$+f+PantheonP+SH0ES, BAO+CC+$f\sigma_8$+f, $f\sigma_8$+f, and f. For the remaining combination of data sets, there is no observational support. However, when examining ΔBIC and using the BIC interpretation, the $f(Q)$ model shows very strong observational support. In the $f(Q)$ model, the inferred values of H_0 and S_8 appear to be elevated when using these datasets. Although this elevation is consistent with strong observational support according to ΔBIC, it appears to originate from large uncertainties and degeneracies associated mainly with Ω_m and H_0, rather than from a genuine physical resolution of tensions. The presence of large error bars and slanted non-Gaussian confidence contours (see the right panels of Figures 1 and 2) further supports this interpretation. The uncertainty in Ω_m is particularly large in the Pantheon+SH0ES dataset but smaller for BAO+CC+PantheonP+SH0ES, BAO+CC+$f\sigma_8$+f, and $f\sigma_8$+f (see Table 1), pointing to possible parameter degeneracies in the current model $f(Q)$. Consequently, assuming $f_Q = 1$ leads to degeneracies within the current framework.

Interestingly, this same model has been studied without assuming $f_Q = 1$ by S. A. Narawade and B. Mishra [23] and by D. Mhamdi et al. [24]. Narawade and Mishra, using Hubble parameter and PantheonP+SH0ES data, reported best-fit values of $H_0 = 69.5^{+2.3}_{-1.9}$ and $H_0 = 70.7^{+2.7}_{-2.7}$, respectively, while Mhamdi et al., combining

Model	Observation	$\Omega_{m,0}$	Ω_{α}	n	H_0	r_d	$M_{\rm abs}$	γ	σ_8	S_8
ΛCDM	BAO+CC+PantheonP+SH0ES	$0.303^{+0.011}_{-0.010}$	—	—	$72.389^{+0.852}_{-0.844}$	$139.918^{+1.911}_{-1.868}$	$-19.288^{+0.025}_{-0.025}$	—	—	—
	PantheonP+SH0ES	$0.332^{+0.018}_{-0.018}$	—	—	$73.584^{+1.039}_{-1.000}$	—	$-19.244^{+0.030}_{-0.029}$	—	—	—
	BAO+CC	$0.296^{+0.015}_{-0.014}$	—	—	$69.131^{+1.716}_{-1.697}$	$147.246^{+3.631}_{-3.311}$	—	—	—	—
	BAO+CC+$f\sigma_8$+f+PantheonP+SH0ES	$0.302^{+0.010}_{-0.010}$	—	—	$72.412^{+0.875}_{-0.857}$	$139.985^{+1.916}_{-1.885}$	$-19.288^{+0.026}_{-0.025}$	$0.633^{+0.037}_{-0.040}$	$0.783^{+0.018}_{-0.018}$	$0.785^{+0.020}_{-0.020}$
	BAO+CC+$f\sigma_8$+PantheonP+SH0ES	$0.303^{+0.011}_{-0.011}$	—	—	$72.394^{+0.854}_{-0.856}$	$139.963^{+1.900}_{-1.872}$	$-19.288^{+0.025}_{-0.025}$	$0.590^{+0.056}_{-0.057}$	$0.769^{+0.021}_{-0.022}$	$0.771^{+0.023}_{-0.024}$
	BAO+CC+f+PantheonP+SH0ES	$0.301^{+0.010}_{-0.010}$	—	—	$72.439^{+0.863}_{-0.845}$	$140.024^{+1.867}_{-1.853}$	$-19.287^{+0.025}_{-0.025}$	$0.651^{+0.033}_{-0.045}$	—	—
	$f\sigma_8$+f+PantheonP+SH0ES	$0.322^{+0.015}_{-0.015}$	—	—	$73.644^{+1.015}_{-0.981}$	—	$-19.245^{+0.030}_{-0.029}$	$0.661^{+0.027}_{-0.039}$	$0.776^{+0.017}_{-0.017}$	$0.802^{+0.021}_{-0.021}$
	BAO+CC+$f\sigma_8$+f	$0.295^{+0.014}_{-0.014}$	—	—	$69.237^{+1.693}_{-1.681}$	$147.210^{+3.489}_{-3.316}$	—	$0.622^{+0.041}_{-0.043}$	$0.784^{+0.018}_{-0.018}$	$0.770^{+0.020}_{-0.019}$
	$f\sigma_8$+f	$0.249^{+0.058}_{-0.058}$	—	—	—	—	—	$0.541^{+0.101}_{-0.091}$	$0.792^{+0.023}_{-0.021}$	$0.717^{+0.035}_{-0.034}$
	$f\sigma_8$	$0.271^{+0.072}_{-0.073}$	—	—	—	—	—	$0.542^{+0.106}_{-0.096}$	$0.776^{+0.034}_{-0.029}$	$0.742^{+0.038}_{-0.037}$
$f(Q)$	BAO+CC+PantheonP+SH0ES	$0.342^{+0.111}_{-0.113}$	$1.419^{+0.404}_{-0.471}$	$1.037^{+0.038}_{-0.037}$	$71.383^{+15.326}_{-8.071}$	$139.715^{+1.922}_{-1.908}$	$-19.289^{+0.025}_{-0.025}$	—	—	—
	PantheonP+SH0ES	$0.543^{+0.267}_{-0.213}$	$1.263^{+0.489}_{-0.486}$	$1.284^{+0.215}_{-0.217}$	$73.283^{+12.813}_{-8.148}$	—	$-19.244^{+0.030}_{-0.029}$	—	—	—
	BAO+CC	$0.309^{+0.139}_{-0.108}$	$1.412^{+0.406}_{-0.483}$	$1.017^{+0.063}_{-0.063}$	$68.109^{+15.572}_{-8.064}$	$147.281^{+3.505}_{-3.345}$	—	—	—	—
	BAO+CC+$f\sigma_8$+f+PantheonP+SH0ES	$0.303^{+0.087}_{-0.094}$	$1.403^{+0.397}_{-0.444}$	$1.004^{+0.024}_{-0.025}$	$72.246^{+14.997}_{-8.465}$	$140.037^{+1.891}_{-1.836}$	$-19.288^{+0.025}_{-0.025}$	$0.636^{+0.041}_{-0.053}$	$0.779^{+0.024}_{-0.023}$	$0.782^{+0.027}_{-0.026}$
	BAO+CC+$f\sigma_8$+PantheonP+SH0ES	$0.337^{+0.104}_{-0.108}$	$1.426^{+0.394}_{-0.461}$	$1.031^{+0.034}_{-0.035}$	$71.362^{+14.956}_{-7.985}$	$139.738^{+1.890}_{-1.838}$	$-19.288^{+0.025}_{-0.025}$	$0.614^{+0.053}_{-0.063}$	$0.744^{+0.034}_{-0.031}$	$0.791^{+0.039}_{-0.037}$
	BAO+CC+fPantheonP+SH0ES	$0.310^{+0.087}_{-0.094}$	$1.428^{+0.399}_{-0.446}$	$1.006^{+0.022}_{-0.023}$	$71.693^{+14.641}_{-8.302}$	$140.112^{+1.906}_{-1.857}$	$-19.287^{+0.025}_{-0.025}$	$0.655^{+0.032}_{-0.053}$	—	—
	$f\sigma_8$+f+PantheonP+SH0ES	$0.315^{+0.099}_{-0.102}$	$1.402^{+0.413}_{-0.452}$	$0.965^{+0.037}_{-0.040}$	$71.428^{+15.940}_{-8.949}$	—	$-19.245^{+0.029}_{-0.030}$	$0.632^{+0.045}_{-0.060}$	$0.796^{+0.031}_{-0.028}$	$0.817^{+0.036}_{-0.033}$
	BAO+CC+$f\sigma_8$+f	$0.270^{+0.090}_{-0.088}$	$1.400^{+0.415}_{-0.460}$	$0.984^{+0.030}_{-0.035}$	$69.757^{+15.693}_{-8.638}$	$147.297^{+3.512}_{-3.368}$	—	$0.593^{+0.064}_{-0.068}$	$0.792^{+0.026}_{-0.025}$	$0.753^{+0.029}_{-0.028}$
	$f\sigma_8$+f	$0.168^{+0.134}_{-0.093}$	$1.220^{+0.554}_{-0.735}$	$1.028^{+0.235}_{-0.087}$	—	—	—	$0.514^{+0.113}_{-0.082}$	$0.790^{+0.031}_{-0.028}$	$0.587^{+0.047}_{-0.044}$
	$f\sigma_8$	$0.270^{+0.155}_{-0.121}$	$1.247^{+0.531}_{-0.678}$	$1.393^{+0.408}_{-0.409}$	—	—	—	$0.544^{+0.100}_{-0.095}$	$0.677^{+0.115}_{-0.076}$	$0.646^{+0.074}_{-0.066}$

Table 1: Best-fit cosmological parameters for the ΛCDM and $f(Q)$ models across various dataset combinations. The derived parameter $S_8 = \sigma_8\sqrt{\frac{\Omega_m}{0.3}}$, including propagated 1σ uncertainties, is also presented to test structure growth consistency. The discussion and statistical analysis of these results are explained in the Discussion and Conclusion section.

Model	Observation	$\log(\mathcal{L})$	χ^2	$\chi^2_{\rm red}$	AIC	BIC	ΔAIC/ΔBIC
ΛCDM	BAO+CC+PantheonP+SH0ES	−764.852	1489.704	0.878	1497.704	1519.457	0.000/0.000
	PantheonP+SH0ES	−726.328	1452.656	0.878	1458.656	1474.894	0.000/0.000
	BAO+CC	−13.730	27.459	0.687	33.459	38.743	0.000/0.000
	BAO+CC+$f\sigma_8$+f+PantheonP+SH0ES	−764.437	1528.875	0.862	1540.875	1573.781	0.000/0.000
	BAO+CC+$f\sigma_8$+PantheonP+SH0ES	−760.905	1521.809	0.865	1533.809	1566.668	0.000/0.000
	BAO+CC+f+PantheonP+SH0ES	−747.918	1495.836	0.875	1505.836	1533.069	0.000/0.000
	$f\sigma_8$+f+PantheonP+SH0ES	−746.177	1492.354	0.862	1502.354	1529.653	0.000/0.000
	BAO+CC+$f\sigma_8$+f	−33.266	66.532	0.564	76.532	90.593	0.000/0.000
	$f\sigma_8$+f	−19.364	38.728	0.503	44.728	51.874	0.000/0.000
	$f\sigma_8$	−15.992	31.984	0.508	37.984	44.553	0.000/0.000
$f(Q)$	BAO+CC+PantheonP+SH0ES	−749.559	1499.119	0.885	1511.119	1543.749	13.415/24.292
	PantheonP+SH0ES	−777.163	1554.326	0.941	1564.326	1591.390	105.675/116.501
	BAO+CC	−20.199	40.398	1.063	50.398	59.204	16.939/20.461
	BAO+CC+$f\sigma_8$+f+PantheonP+SH0ES	−765.513	1531.026	0.864	1547.026	1590.900	6.151/17.119
	BAO+CC+$f\sigma_8$+PantheonP+SH0ES	−763.960	1527.920	0.869	1543.920	1587.731	10.111/21.064
	BAO+CC+f+PantheonP+SH0ES	−748.403	1496.806	0.877	1510.806	1548.932	4.970/15.863
	$f\sigma_8$+f+PantheonP+SH0ES	−747.611	1495.223	0.864	1509.223	1547.442	6.869/17.789
	BAO+CC+$f\sigma_8$+f	−34.089	68.178	0.588	82.178	101.864	5.647/11.271
	$f\sigma_8$+f	−19.761	39.523	0.527	49.523	61.433	4.795/9.559
	$f\sigma_8$	−16.563	33.127	0.543	43.127	54.075	5.143/9.522

Table 2: Statistical results for the ΛCDM and $f(Q)$ models using various dataset combinations, following the observation order of Table 1. Here, χ^2 denotes the chi-squared statistic, $\chi^2_{\rm red}$ the reduced chi-squared, AIC and BIC are Alkaine and Bayesian Information Criterion respectfully are model selection statistics used to determine how well does the model fit the data. Whereas, ΔAIC and ΔBIC are differences relative to the ΛCDM baseline and are used as a decision-making valuable tool to judge the observation support a model has. The judgment to the model is given in the text.

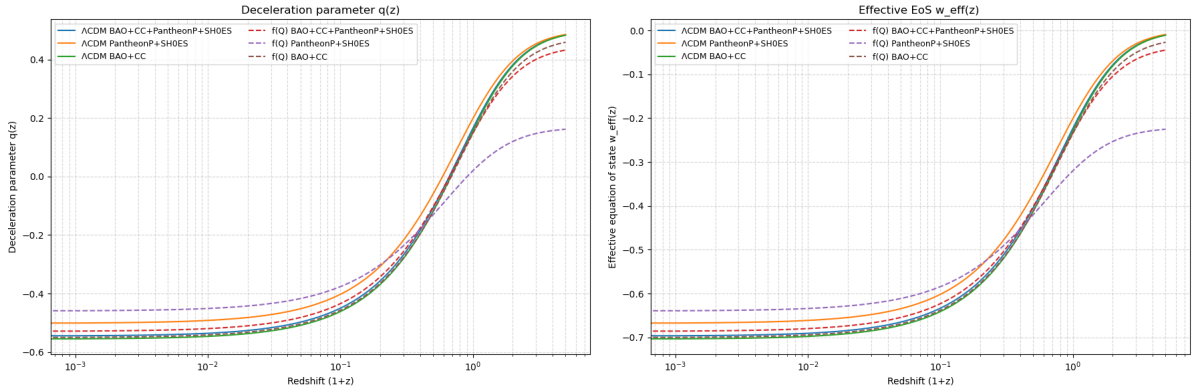

Figure 3: (*Left*) The deceleration parameter $q(z)$ as a function of redshift, and (*right*) the effective equation-of-state parameter $w_{\text{eff}}(z)$ as a function of redshift, are shown for both the ΛCDM and $f(Q)$ models. The curves are obtained using the best-fit parameters listed in Table 1, illustrating the physical behaviour of the two models across dataset combinations including BAO, CC, and PantheonP+SH0ES only. The $q(z)$ for $f(Q)$ model exhibits the almost the same trend as ΛCDM when considering the results for the combinations of BAO+CC +PantheonP+SH0ES and BAO+CC where as when the +PantheonP+SH0ES observation suggests weakly deceleration and weakly acceleration during matter and dark energy domination respectively which contradict the observed observation of the universe. Furthermore, when examining the ω_{eff} graph the $f(Q)$ model still exits the same trend as the ΛCDM model for the same data sets combinations BAO+CC +PantheonP+SH0ES and $BAO + CC$ where as when the +PantheonP+SH0ES observation it suggest that the universe during a supposed matter domination era felt the effect of dark energy at high redshift and whereas at low redshift dark energy component behaves dynamically rather than as a cosmological constant and the universe is accelerating, but less strongly than in ΛCDM.

PantheonP+SH0ES, CC, and redshift-space distortion measurements, obtained $H_0 = 71.65^{+0.84}_{-0.84}$. In all cases, the model was well constrained, with smaller uncertainties and no evidence of parameter degeneracy. However, these studies did not explicitly investigate whether the model can resolve the tensions H_0 and S_8.

In conclusion, although the $f(Q)$ model used in this study currently shows elevated values of H_0 and S_8 and strong observational support under ΔBIC, a rigorous re-evaluation is still required to determine whether this support holds in a more complete analysis. In future work, we will re-examine the model without assuming $f_Q = 1$, incorporating both early- and late-time cosmological measurements. This approach is expected to reduce the large uncertainties and parameter degeneracies observed here and to provide a definitive test of whether the $f(Q) = \alpha + \beta Q^n$ model can simultaneously address the tensions H_0 and S_8. Furthermore, it is important to note that another valuable area of research is needed to verify the non-degeneracy that exists between BAO and Pantheon+ SH0ES data when combined with complementary measurements sensitive to early and late expansion histories.

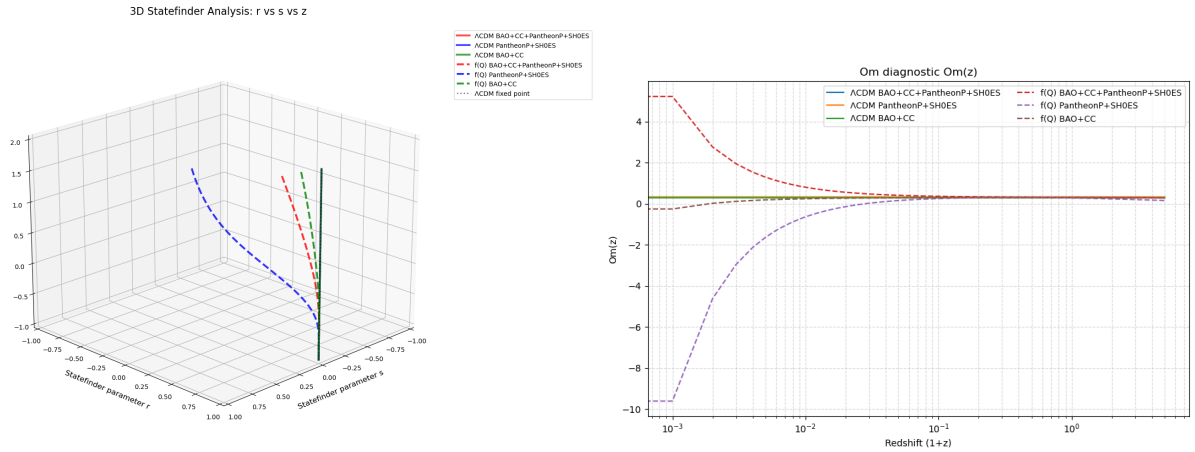

Figure 4: (*Left*) The statefinder parameter $r(z)$ as a function of redshift, against statefinder parameter $s(z)$ as a function of redshift and (*right*) the Om diagnostic $\mathrm{Om}(z)$ as a function of redshift, are shown for both the ΛCDM and $f(Q)$ models. The curves are obtained using the best-fit parameters listed in Table 1, illustrating the physical behaviour of the two models across dataset combinations including BAO, CC, and PantheonP+SH0ES only. The physical interpretation of $r(z)\ vs\ s(z)\ vs\ z$ for all redshift has the statefinders $r < 1$ and $s > 0$ indicates that dark energy behaves more phantom-like. However, as much as it does so for all data set dark enrgy is Nearly cosmological constant, but slightly phantom-like for the data sets combinations BAO+CC+PantheonP+SH0ES and BAO+CC. Furthermore, looking at the $Om(z)$ the ΛCDM curves remains constant with redshift, as expected for a cosmological constant, In contrast, the $f(Q)$ model's curves for all data sets combinations used here show a redshift-dependence evolution, particularity at low z indicating deviation from ΛCDM and suggesting an effective dynamical dark energy behaviour. Furthermore, at very high redshifts, only the PantheonP+SH0ES data combination for the $f(Q)$ model appears to deviate from the ΛCDM prediction, implying that the expansion rate differs from that expected in the early universe. This deviation could suggest the presence of an early dark energy component or stem from an inaccurate calibration of the matter density. However, this can be fully assessed by incorporating early-time measurements and examining the matter power spectrum.

References

[1] S. M. Carroll, *Spacetime and Geometry: An Introduction to General Relativity*. Cambridge University Press, 2019.

[2] A. A. Coley and D. L. Wiltshire, ''What is general relativity?'' *Physica Scripta*, vol. 92, no. 5, p. 053001, May 2017.

[3] A. G. Riess *et al.*, ''Observational evidence from supernovae for an accelerating universe and a cosmological constant,'' *The Astronomical Journal*, vol. 116, no. 3, pp. 1009–1038, 1998.

[4] V. C. Rubin, W. K. F. Jr., and N. Thonnard, ''Rotational properties of 21 sc galaxies with a large range of luminosities and radii, from ngc 4605 (R = 4kpc) to ugc 2885 (R = 122kpc),'' *The Astrophysical Journal*, vol. 238, pp. 471–487, 1980.

[5] P. J. E. Peebles, ''Large-scale background temperature and mass fluctuations due to scale-invariant primeval perturbations,'' *The Astrophysical Journal Letters*, vol. 263, pp. L1–L5, 1982.

[6] D. Mithi, ''Dynamical systems analysis in cosmology,'' Masters dissertation, North-West University (South Africa), 2024.

[7] L. Heisenberg, ''Review on f(Q) gravity,'' *Physics Reports*, vol. 1066, pp. 1–78, May 2024.

[8] S. Sahlu, Á. de la Cruz-Dombriz, and A. Abebe, ''Structure growth in f (Q) cosmology,'' *Monthly Notices of the Royal Astronomical Society*, vol. 539, no. 2, pp. 690–703, May 2025.

[9] J. A. Nájera, C. Aráoz Alvarado, and C. Escamilla-Rivera, ''Constraints on $f(Q)$ logarithmic model using gravitational wave standard sirens,'' *Monthly Notices of the Royal Astronomical Society*, vol. 524, no. 4, pp. 5280–5290, Oct. 2023.

[10] S. Capozziello and R. D'Agostino, ''Model-independent reconstruction of f(Q) non-metric gravity,'' *Physics Letters B*, vol. 832, p. 137229, Sep. 2022.

[11] A. G. Adame *et al.*, ''DESI 2024 VI: cosmological constraints from the measurements of baryon acoustic oscillations,'' *Journal of Cosmology and Astroparticle Physics*, vol. 2025, no. 2, p. 021, Feb. 2025.

[12] M. Moresco, R. Jimenez, L. Verde, A. Cimatti, and L. Pozzetti, ''Setting the Stage for Cosmic Chronometers. II. Impact of Stellar Population Synthesis Models Systematics and Full Covariance Matrix,'' *The Astrophysical Journal*, vol. 898, no. 1, p. 82, Jul. 2020.

[13] D. Brout *et al.*, ''The Pantheon+ Analysis: Cosmological Constraints,'' *The Astrophysical Journal*, vol. 938, no. 2, p. 110, Oct. 2022.

[14] L. Perenon, J. Bel, R. Maartens, and A. de la Cruz-Dombriz, ''Optimising growth of structure constraints on modified gravity,'' *J. Cosmology Astropart. Phys.*, vol. 2019, no. 6, p. 020, Jun. 2019.

[15] F. Skara and L. Perivolaropoulos, ''Tension of the E_G statistic and redshift space distortion data with the Planck-Λ CDM model and implications for weakening gravity,'' *Phys. Rev. D*, vol. 101, no. 6, p. 063521, Mar. 2020.

[16] R. T. Hough, A. Abebe, and S. E. S. Ferreira, ''Viability tests of f(R)-gravity models with Supernovae Type 1A data,'' *European Physical Journal C*, vol. 80, no. 8, p. 787, Aug. 2020.

[17] S. Sahlu, R. T. Hough, A. Abebe, and Á. de la Cruz-Dombriz, ''Constraining viscous fluid models in $f(Q)$ gravity with data,'' *arXiv e-prints*, p. arXiv:2408.02775, Aug. 2024.

[18] P. Collaboration, ''Planck 2018 results. vi. cosmological parameters,'' *Astronomy & Astrophysics*, vol. 641, p. A6, 2020.

[19] E. V. Linder and R. N. Cahn, ''Parameterized beyond-Einstein growth,'' *Astroparticle Physics*, vol. 28, no. 4-5, pp. 481–488, Dec. 2007.

[20] D. Richardson, R. L. Jenkins, III, J. Wright, and L. Maddox, ''Absolute-magnitude Distributions of Supernovae,'' *The Astronomical Journal*, vol. 147, no. 5, p. 118, May 2014.

[21] D. Rubin, G. Aldering, M. Betoule, A. Fruchter, X. Huang, A. G. Kim, C. Lidman, E. Linder, S. Perlmutter, P. Ruiz-Lapuente, and N. Suzuki, ''Union through UNITY: Cosmology with 2000 SNe Using a Unified Bayesian Framework,'' *The Astrophysical Journal*, vol. 986, no. 2, p. 231, Jun. 2025.

[22] M. L. Tong and Y. Zhang, ''Cosmic age, statefinder, and Om diagnostics in the decaying vacuum cosmology,'' *Phys. Rev. D*, vol. 80, no. 2, p. 023503, Jul. 2009.

[23] S. A. Narawade and B. Mishra, ''Phantom Cosmological Model with Observational Constraints in f(Q) Gravity,'' *Annalen der Physik*, vol. 535, no. 5, p. 2200626, May 2023.

[24] D. Mhamdi, A. Bouali, S. Dahmani, A. Errahmani, and T. Ouali, ''Cosmological constraints on f (Q) gravity with redshift space distortion data,'' *European Physical Journal C*, vol. 84, no. 3, p. 310, Mar. 2024.